Yucca Mountain Site Description

Volume I: Sections 1 – 5

Yucca Mountain Project
Yucca Mountain Site Description
TDR-CRW-GS-000001 REV 02 ICN 01
April 2004

Originator:
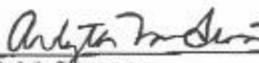
Ardyth M. Simmons
Lead Author

4/16/04
Date

ICN Manager:

Roger J. Henning

4/16/2004
Date

Checker:

Bart J. Vandenplas

4/16/2004
Date

Quality Engineering Representative:

Kenneth O. Gilkerson
QER

04/16 2004
Date

Responsible Manager:
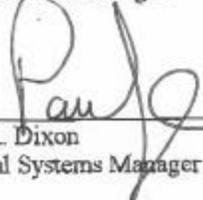
Paul R. Dixon
Natural Systems Manager

4-16-04
Date

ACKNOWLEDGEMENTS

INTENTIONALLY LEFT BLANK

CHANGE HISTORY

Revision Number	Interim Change No.	Date of Revision	Description of Change
0	0	September 1998	Initial Issue (under Document Identifier B00000000-01717-5700-00019)
1	0	July 14, 2000	Revision to reorganize the presentation of material, update sections with new information, and meet requirements of new procedures.

Reorganization included:

- Added an Introduction

- Split the section on Hydrologic System into sections on Surface Water Hydrology, Unsaturated Zone Hydrology, and Saturated Zone Hydrology

- Split the section on Geochemistry into sections on Geochemical Framework and Factors Affecting Radionuclide Transport

- Created a separate section on Tectonic Hazards

- Added a section on Natural Analogues.

The document was updated to include information available through the end of fiscal year 1999. In some areas, it was possible to include more recent results.

1	1	September 20, 2000	Document changed to address acceptance conditions identified in accordance with AP-7.5Q (Submittal, Review, and Acceptance of Deliverables). In addition, changes were also made to correct minor errors and for editorial purposes. Change bars in the margin mark text and tables that have been changed, with the following exceptions: in Sections 8, 9, and others where PTn was designated as "Paintbrush Tuff nonwelded unit", this has been changed to "Paintbrush nonwelded unit";

CHANGE HISTORY (Continued)

Revision Number	Interim Change No.	Date of Revision	Description of Change
1	1	September 20, 2000	in addition, the term C-Holes Complex was standardized in those sections. Table 6.3-1 was deleted, and the following table renumbered. Figures 11.2-3 to 11.2-5 were deleted, and the following four figures were renumbered. Changes were also made to the following figures: 1.1-1, 2.2-1, 4.2-18, 4.3-10, 4.3-12, 4.5-30, 4.5-31, 4.8-5, 4.8-6, 4.8-13, 4.8-26 to 4.8-29, 4.8-50 to 4.8-52, 4.8-57, 4.9-4, 5.2-9, 5.2-10, 5.2-12, 5.2-14, 5.2-15, 5.3-32, 5.3-34 to 5.3-36, 6.4-12, 8.1-4, 8.2-1, 8.2-7, 8.2-12, 8.2-24, 8.2-25, 8.2-27 to 8.2-41, 8.3-4, 8.3-14, 8.5-11, 8.5-13, 9.2-1, 9.3-2, 9.3-30, 11.4-1, 11.4-2, 12.2-2, 12.3-6, 12.3-12, 12.3-31 to 12.3-48, 12.3-57, 13.3-1, 13.4-6, 13.4-7, 13.4-24, and 13.4-27

2	0	January 16, 2004	**General Changes:**
			
			• Reorganized Table of Contents:
			
			  – Deleted Section 2 (Geographic Setting and Demography) and incorporated geographic setting into new Section 2 (Regional Geologic Setting),
			
			  – Deleted Section 3 (Nearby Industrial, Transportation, and Military Facilities),
			
			  – Split Section 4 (Geologic Framework) into new Section 2 (Regional Geologic Setting), new Section 3 (Geology of the Yucca Mountain Site Area), and new Section 4 (Tectonics and Tectonic Hazards) Chlorine-36 discussion (Section 4.6.6.6) moved to new Section 7 (Unsaturated Zone Hydrology). Divided Section 4.8 (Integrated Site Model) between new Sections 3 (Geology of the Site Area) and 5 (Geochemistry), as applicable.
			
			  – Removed discussion of meteorology

Revision Number	Interim Change No.	Date of Revision	Description of Change
			from Section 6 (Climatology and Meteorology)

- Deleted Section 7 (Surface Water Hydrology) and incorporated condensed material into new Section 3 (Geology of the Yucca Mountain Site Area) and new Section 7 (Unsaturated Zone Hydrology)

- Renumbered Section 8 (Unsaturated Zone Hydrology) to new Section 7

- Renumbered Section 9 (Saturated Zone Hydrology) to new Section 8. Condensed Section 9.5 (Water Resources for the Site) material into new Sections 3 and 6

• Merged Section 10 (Factors Affecting Radionuclide Transport), and Section 11 (Integrated Natural System Response to Thermal Loading) material into new Section 5 (Geochemical Conditions and Factors Affecting Radionuclide Transport).

- Merged Section 12 (Tectonic Hazards) into new Section 4 (Tectonics and Tectonic Hazards)

- Deleted Section 13 (Natural Analog).

Eliminated discussion of numerical modeling and analysis for postclosure in sections related to process models (except discussion of modeling results that link to data collection and conceptual models).

Condensed material in all sections.

Added new information collected and published since 1999, including results from the Death Valley Regional Flow System project.

Added references, as appropriate, to studies

Revision Number	Interim Change No.	Date of Revision	Description of Change

conducted by investigators outside YMP.

Specific Changes to Individual Sections

Section 2 (Regional Geologic Setting): Added new material on erosion rates, the Highway 95 fault, surficial mapping of Quaternary deposits; and provided an updated interpretation of regional geology, based on compilation of drilling information, Nye County drilling lithology logs, and recent mapping in support of the regional groundwater flow model.

Section 3 (Geology of the Yucca Mountain Site Area): Standardized stratigraphic discussion; added isopach maps from the Geologic Framework Model (previously in Section 4.8); added flooding and erosion discussions previously found in Sections 7.3 and 7.4, respectively; added information on Quaternary structures to Site Structure discussion previously in Section 4.5; updated geologic discussions to incorporate recent information obtained from the Exploratory Studies Facility and the Enhanced Characterization of the Repository Block , mapping of southern extension of repository footprint, geotechnical studies in Midway Valley, and the analysis of maximum flood potential in the vicinity of the ESF North Portal; studies of the Quaternary stratigraphy and recency of faulting in Midway Valley; compilations of recent regional geologic maps and structure sections; and a description of flooding in Fortymile Wash. Added Section 3.7.7 on dynamic soil and rock properties for use in evaluating ground motions and developing recommendations for foundations for a Waste Handling Building.

Section 4 (Tectonics and Tectonic Hazards): Removed igneous consequence analyses and seismic hazard analyses; added alternate tectonic models and studies by others.

CHANGE HISTORY (Continued)

Revision Number	Interim Change No.	Date of Revision	Description of Change
			Section 5 (Geochemical Conditions and Processes Affecting Radionuclide Transport): Added new information on sorption properties in alluvium, updated isotopic studies of groundwater and fracture-filling materials, updated Section 5.4 (previously Section 11) with more recent results of thermal tests.
			Section 6 (Climate: Past, Present, and Future): Added new climate data.
			Section 7 (Unsaturated Zone Hydrology): added new information from in situ testing in the Exploratory Studies Facility and Enhanced Characterization of the Repository Block Cross-Drift.
			Section 8 (Saturated Zone Hydrology): included new geochemistry data and interpretations for both the region and the site; included new data from testing at C-Wells and the Alluvial Testing Complex. Reorganized old Sections 9.2 (Regional Flow System) and 9.3 (Saturated Zone Flow within the Yucca Mountain Subsystem).
2	1	April 2004	Document changed to address acceptance conditions identified in accordance with AP-7.5Q (Submittal, Review, and Acceptance of Deliverables). In addition, changes were also made to correct minor errors, bring forward selected sentences or paragraphs from Rev01 ICN01 where detail in Rev02 was insufficient for the License Application needs, and for editorial purposes (to make consistent with LA style guide). Change bars in the margin mark text and tables that have been changed.

INTENTIONALLY LEFT BLANK

CONTENTS

CONTENTS (Continued)

CONTENTS (Continued)

CONTENTS (Continued)

CONTENTS (Continued)

CONTENTS (Continued)

CONTENTS (Continued)

INTENIONALLY LEFT BLANK

FIGURES

FIGURES (Continued)

FIGURES (Continued)

TABLES

INTENTIONALLY LEFT BLANK

ACRONYMS AND ABBREVIATIONS

φ	diameter
ε$_r$	dielectric permittivity
°C	degrees Centigrade
°F	degrees Fahrenheit
~	approximately
μm	micron
‰	parts per mil
acre-ft	acre-feet
agl	above ground level
alk/Ca	ratio of total alkalinity to dissolved calcium
AR	activity ratios
BSC	Bechtel SAIC Company, LLC
b.y.	billions of years
cal	calories
cm	centimeters
CRWMS	Civilian Radioactive Waste Management System
d	days
DECOVALEX	Development of coupled models and their validation against experiments in nuclear waste isolation
DFBA	pentafluorobenzoic acid
DOE	U.S. Department of Energy
DOPA	dihydroxyphenylalinine
DST	Drift Scale Test
ECRB	Enhanced Characterization of the Repository Block
ENSO	El Niño Southern Oscillation
ESF	Exploratory Studies Facility
FBA	fluorinated benzoic acid
ft	feet
g	grams
g	acceleration of gravity
GHG	greenhouse gasses
GP	poorly graded gravel
GPa	gigapascals
GP-GM	poorly graded gravel w/silt
GROA	Geologic Repository Operations Area
GW-GM	well-graded gravel w/silt
HLW	high-level radioactive waste
HPZ	high-permeability zone

ACRONYMS AND ABBREVIATIONS (Continued)

I	initiation of transition to glacial climate
in.	inches
INFIL	numerical distributed-parameter net-filtration model
J_a	joint-alteration number
J_n	joint-set number
J_r	joint-roughness number
J_w	joint water-reduction number
K	hydraulic conductivity
ka	one thousand years (refers to age)
kb	kilobars
K_d	distribution coefficient
kg	kilograms
km	kilometers
KTI	Key Technical Issue
k.y.	thousand years (refers to a time interval)
L	liters
L_i	lateral flow
LANL	Los Alamos National Laboratory
LCA	lower carbonate aquifer
LPZ	low-permeability zone
μg	micrograms
m	meters
M	magnitude (unspecified scale)
M&O	Management and Operating Contractor
Ma	one million years (refers to age)
MAP	mean annual precipitation
MAT	mean annual temperature
mGal	milligals
mi	miles
MIS	marine isotope stages
MJ	megajoules
M_L	Richter local magnitude
M_o	seismic moment
mm	millimeters
M_{max}	maximum magnitude
MPa	megapascals
M_w	moment magnitude
m.y.	million year (refers to a time interval)

ACRONYMS AND ABBREVIATIONS (Continued)

NAFA   Nordic aquatic fulvic acid
NC-EWDP   Nye County Early Warning Drilling Program
nm   nanometers
NOAA   National Oceanic and Atmospheric Administration
NRC   U.S. Nuclear Regulatory Commission
NRG   north ramp geologic
nT   nanoTeslas
NWPA   Nuclear Waste Policy Act of 1982

OIS   oxygen isotope stage

Pa   pascal
PDF   probability density function
PDO   Pacific Oscillation Decadal
PFBA   difluorobenzoic acid
PM   particulate matter
PM_{10} particulate matter up to 10 micrometers in size
PMF   probable maximum flood
Pmol   picomoles
ppm   parts per million
ppmv   parts per million by volume
PSHA   Probabilistic Seismic Hazard Analysis
PVHA   Probabilistic Volcanic Hazard Analysis

Q   rock-mass quality
Q seismic quality factor

RCTS   resonant column and torsional shear
RMEI   reasonably maximally exposed individual
RMR   rock-mass rating
RQD   rock quality designation

s   seconds
SASW   spectral analysis of surface waves
SHT   Single Heater Test
SLPM   standard liters per minute
SMOW   standard mean ocean water
SNL   Sandia National Laboratories
SPT   standard penetration test
SRF   stress-reduction factor

T   initiation of transition to interglacial climate
TDS   total dissolved solids
TH   thermal-hydrologic
THC   thermal-hydrologic-chemical

ACRONYMS AND ABBREVIATIONS (Continued)

THM	thermal-hydrologic-mechanical
TM	thermal-mechanical
TSPA	total system performance assessment
TU	Tritium Units
USGS	U.S. Geological Survey
W	watts
YMP	Yucca Mountain Project
YMSD	Yucca Mountain Site Description
yr	years

CHEMICAL ELEMENTS

Ag	silver
Al	aluminum
Am	americium
Ar	argon
B	boron
Ba	barium
Bi	bismuth
Br	bromine
C	carbon
Ca	calcium
Ce	cerium
Cl	chlorine
Co	cobalt
Cm	curium
Cr	chromium
Cs	cesium
Cu	copper
Eu	europium
F	fluorine
Fe	iron
H	hydrogen
He	helium
Hg	mercury
I	iodine

K   potassium
Kr   krypton

La   lanthanum
Li   lithium

Mg   magnesium
Mn   manganese

N   nitrogen
Na   sodium
Nb   niobium
Nd   neodymium
Ni   nickel
Np   neptunium

O   oxygen

Pa   protactinium
Pb   lead
Po   polonium
Pt   platinum
Pu   plutonium

Ra   radium
Rb   rubidium
Rn   radon

Sb   antimony
Sc   scandium
Se   selenium
Si   silicon
Sm   samarium
Sr   strontium

Tc   technetium
Te   tellurium
Th   thorium
Ti   titanium

U   uranium

Xe   xenon

ACRONYMS AND ABBREVIATIONS (Continued)

Y   yttrium

Zr   zirconium

LITHOSTRATIGRAPHIC, HYDROGEOLOGIC, OR THERMAL-MECHANICAL UNITS

CHv   Calico Hills vitric hydrogeological unit
CHz   Calico Hills zeolitic hydrogeological unit
CFu   Crater Flat undifferentiated hydrogeological unit
CHn   Calico Hills nonwelded hydrogeological unit

Mvs   Sedimentary and metavolcanic rocks of Mesozoic age

P1   Clastic rocks of Paleozoic-Precambrian age
P2   Carbonate rocks of Paleozoic age
pCgm   igneous and metamorphic rocks of Precambrian age
PP   Prow Pass Tuff
PTn   Paintbrush Tuff nonwelded hydrogeological unit

Qp   Playa deposits of Quarternary age
QTv   Volcanic rocks of Quarternary-Tertiary age
QTvf   Valley fill of Quarternary-Tertiary age

Tac   Calico Hills Formation
Tacbs   Calico Hills Formation basal sandstone
Tacbt   Calico Hills Formation bedded tuff
Tcbuv   Bullfrog Tuff upper vitric nonwelded zone
Tcp   Prow Pass Tuff
Tcpbt   pre-Prow Pass Tuff bedded tuff
Tcplc   Prow Pass Tuff lower crystalline nonwelded zone
Tcplv   Prow Pass Tuff lower vitric nonwelded zone
Tcpmd   Prow Pass Tuff moderately-densely welded zone
Tcpuc   Prow Pass Tuff upper crystalline nonwelded zone
Tcpuv   Prow Pass Tuff upper vitric nonwelded zone
TJg   Granitic rocks of Tertiary-Late Jurassic age
TCw   Tiva Canyon welded hydrogeological unit
Tmbt1   pre-Rainier Mesa Tuff bedded tuff
Tpbt1   pre-Topopah Spring Tuff bedded tuff
Tpbt2   pre-Pah Canyon bedded tuff
Tpbt3   pre-Yucca Mountain bedded tuff
Tpbt4   pre-Tiva Canyon bedded tuff
Tpcpll   Tiva Canyon Tuff crystal-poor lower lithophysal zone
Tpcpln   Tiva Canyon Tuff crystal-poor lower nonlithophysal zone
Tpcplnc   Tiva Canyon Tuff crystal-poor lower nonlithophysal columnar subzone

Tpcpmn	Tiva Canyon Tuff crystal-poor middle nonlithophysal zone
Tpcpul	Tiva Canyon Tuff crystal-poor upper lithophysal zone
Tpcpv	Tiva Canyon Tuff crystal-poor vitric zone
Tpcpvl	Tiva Canyon Tuff crystal-poor vitric nonwelded subzone
Tpcpv2	Tiva Canyon Tuff crystal-poor vitric moderately welded subzone
Tpcpv3	Tiva Canyon Tuff crystal-poor vitric Densely welded subzone
Tpp	Pah Canyon Tuff
Tpt	Topopah Spring Tuff
Tptpll	Topopah Spring Tuff crystal-poor lower lithophysal zone
Tptpln	Topopah Spring Tuff crystal-poor lower nonlithophysal zone
Tptplnc	Topopah Spring Tuff crystal-poor lower nonlithophysal columnar subzone
Tptpmn	Topopah Spring Tuff middle nonlithophysal zone
Tptpul	Topopah Spring Tuff crystal-poor upper lithophysal zone
Tptpv	Topopah Spring Tuff crystal-poor vitric zone
Tptpv1	Topopah Spring Tuff crystal-poor vitric nonwelded subzone
Tptpv2	Topopah Spring Tuff crystal-poor vitric zone-moderately welded subzone
Tptpv3	Topopah Spring Tuff vitric zone-densely welded subzone
Tptrl	Topopah Spring Tuff crystal-rich lithophysal zone
Tptrn	Topopah Spring Tuff crystal-rich nonlithophysal zone
Tptrv	Topopah Spring Tuff crystal-rich vitric zone
Tptrv1	Topopah Spring Tuff crystal-rich vitric zone-densely welded subzone
Tptrv2	Topopah Spring Tuff crystal-rich vitric zone-nonwelded to moderately welded subzone
Tptrv3	Topopah Spring Tuff crystal-rich vitric zone nonwelded subzone
Tptrl	Topopah Spring Tuff crystal-rich lithophysal zone
Tpy	Yucca Mountain Tuff
TSw	Topopah Spring welded hydrogeological unit
TSw1	Topopah Spring welded, lithophysal-rich thermal-mechanical unit
TSw2	Topopah Spring welded, lithophysal-poor thermal-mechanical unit
TSw3	Topopah Spring welded, vitrophyre thermal-mechanical unit
Tv	Volcanic rocks of Tertiary age
Tvs	Volcanic and volcaniclastic rocks Tertiary age

INTENTIONALLY LEFT BLANK

EXECUTIVE SUMMARY

The *Yucca Mountain Site Description* summarizes, in a single document, the current state of knowledge and understanding of the natural system at Yucca Mountain. It describes the geology; geochemistry; past, present, and projected future climate; regional hydrologic system; and flow and transport within the unsaturated and saturated zones at the site. In addition, it discusses factors affecting radionuclide transport, the effect of thermal loading on the natural system, and tectonic hazards.

The *Yucca Mountain Site Description* is broad in nature. It summarizes investigations carried out as part of the Yucca Mountain Project since 1988, but it also includes work done at the site in earlier years, as well as studies performed by others. The document has been prepared under the Office of Civilian Radioactive Waste Management quality assurance program for the Yucca Mountain Project.

Yucca Mountain is located in Nye County in southern Nevada. The site lies in the north-central part of the Basin and Range physiographic province, within the northernmost subprovince commonly referred to as the Great Basin. The basin and range physiography reflects the extensional tectonic regime that has affected the region during the middle and late Cenozoic Era. Yucca Mountain was initially selected for characterization, in part, because of its thick unsaturated zone, its arid to semiarid climate, and the existence of a rock type that would support excavation of stable openings. In 1987, the United States Congress directed that Yucca Mountain be the only site characterized to evaluate its suitability for development of a geologic repository for high-level radioactive waste and spent nuclear fuel.

Regional Geologic Setting–The Great Basin consists of fault-bounded basins and mountain ranges, complicated by volcanic activity that has occurred within the past 15 million years. The mountain ranges of the Great Basin, mostly tilted fault-bounded blocks, may extend for more than 80 km (50 mi), are 8 to 24 km (5 to 15 mi) wide, rise 300 to 1,500 m (1,000 to 5,000 ft) above the floors of the intervening basins, and occupy approximately 40 to 50 percent of the total land area. The deep structural depressions forming the basins contain sedimentary fill of late Tertiary and Quaternary ages, ranging in thickness from a few hundred meters (hundreds of feet) to more than 3 km (2 mi). The floors of closed basins are nearly level to gently sloping and are often covered, in part, by playas. Open basins are, in general, moderately to deeply dissected with axial drainage ways.

Typically, faults in this setting include normal and strike-slip faults that reflect the extensional deformation caused by plate tectonic interactions at the western margin of the North American continent during the middle and late Cenozoic Era. The Great Basin is segmented into tectonic domains, structurally bounded blocks of the Earth's crust characterized by deformations that distinguish them from adjacent domains. Three regional tectonic domains characterize Yucca Mountain and its surrounding environs: the Walker Lane domain, which includes the site; the Basin and Range domain, to the northeast; and the Inyo-Mono domain, to the southwest.

Pre-Cenozoic rocks in the Yucca Mountain region are comprised of upper Precambrian (Proterozoic) through Paleozoic marine strata. Mesozoic rocks are preserved only in small volumes in the region. The pre-Cenozoic rocks have undergone successive generations of

faulting, fracturing, and broad-to-local folding and are important because they include the main regional aquifers and aquitards.

Cenozoic rocks of the Yucca Mountain geologic setting fall into three general groups: sedimentary (including volcaniclastic) rocks of pre-middle Miocene age that predate creation of the southwestern Nevada volcanic field; a volcanic suite of middle to late Miocene age that constitutes the southwestern Nevada volcanic field; and Plio-Pleistocene basalts and basin sediments. Quaternary deposits (deposited in the last 1.8 m.y.) in the Great Basin consist of alluvial, colluvial, and eolian sediments and minor volcanic deposits. In the vicinity of Yucca Mountain, the volcanic rocks are basaltic in composition.

Site Geology–Past and modern geomorphic processes have been investigated at Yucca Mountain in order to assess their hazard to the high-level radioactive waste repository. Yucca Mountain is composed of volcanic rocks that resulted from eruptions within the southwestern Nevada volcanic field between about 14 and 11 million years ago, in Miocene time. The rocks are primarily pyroclastic flows and tephra fallout deposits. One of these flow deposits, the Topopah Spring Tuff, contains the horizon currently designated for waste emplacement. The Tiva Canyon Tuff overlies the Topopah Spring Tuff, and the Calico Hills Formation underlies it. Studies have identified the properties and characteristics of these formations as they relate to the movement of gas and water through the rocks and the ability of the rocks to slow the transport of radionuclides.

On a broad scale, the volcanic rocks can be grouped into welded and nonwelded units with differing hydrogeologic and thermal-mechanical properties. Lithophysae (cavities formed by vapor concentration as the deposits cool) characterize some portions of the welded units and can affect rock properties. Glassy (vitric) zones are also characteristic of the volcanic rocks in some horizons. The matrix mineralogy of the tuffs at Yucca Mountain consists of silica polymorph minerals (cristobalite, tridymite, and quartz) and potassium feldspar. Zeolite minerals are abundant in the Calico Hills Formation in the northern portion of the site. Fracture-filling minerals consist of silica polymorphs, calcite, clays, zeolites, iron oxides, and manganese oxides.

The structural geology of Yucca Mountain and vicinity is dominated by a series of north-striking normal faults along which the Tertiary volcanic rocks were tilted eastward and displaced hundreds of meters down to the west. This faulting occurred during a period of extensional deformation in middle to late Miocene time. These through-going faults divided the site area into several blocks, each of which is further deformed by minor faults. Displacement along some of these faults has continued into Quaternary time and has been evaluated as part of the seismic hazard assessment for Yucca Mountain. The nature and distribution of Quaternary deposits have been used to assess the extent, ages, and magnitude of Quaternary faulting events for the seismic hazard analysis and to evaluate climatic changes during Quaternary time.

Tectonic Models and Tectonic Hazards–The geologic record provides clear evidence that both volcanic eruptions and earthquakes have occurred in the vicinity of Yucca Mountain during the Quaternary period. The youngest nearby volcano (the Lathrop Wells Cone) erupted approximately 80,000 years ago. Faults bounding Yucca Mountain have also been active in Quaternary time. The interval between successive earthquakes on active faults ranges from

thousands to tens of thousands of years, with smaller recurrence intervals for faults in Death Valley, more than 50 km (30 mi) west of Yucca Mountain.

Volcanic and seismic hazards have been analyzed probabilistically and are taken into account in preclosure design (seismic) and postclosure performance assessment (volcanic and seismic). The volcanic hazard analysis indicates that the mean annual frequency of intersection of the repository footprint by an igneous dike is on the order of 1.6×10^{-8}. Studies have also evaluated the probable characteristics of any future volcanic eruption that might disrupt a repository at Yucca Mountain. The most commonly cited magma ascent scenario is related to tectonic extension of a pull-apart basin controlled by local, deep-seated normal faults. Strike-slip faulting related to the Walker Lane domain is a possible contributing factor.

Studies to evaluate seismic hazards at Yucca Mountain focused on characterizing the contemporary seismic environment, the history of faults active during the Quaternary Period, and the attenuation of ground motion from local and regional earthquakes. Both ground motion and fault displacement hazards were examined. The earthquake scenario with the greatest likelihood of occurrence is the planar fault (i.e., rift-graben) model in combination with a component of dextral shear (a pull-apart basin model).

Factors Affecting Radionuclide Transport–The geochemical characteristics of both surficial deposits and of the volcanic units play roles in defining groundwater compositions at Yucca Mountain. The volcanic units at Yucca Mountain consist principally of rhyolites and high-silica rhyolites, with lesser volumes of quartz latite rocks above the repository horizon. The surficial deposits are derived from these bedrock units and, thus, exhibit similar geochemical characteristics. The volcanic rocks are locally represented by glassy units that, at elevations of up to 100 m (330 ft) above the present water table, have been altered to zeolites. The zeolitic horizons provide cation-exchange barriers for some waste elements and function as units of low permeability. Geochemical studies provide evidence for the effective barrier characteristics, not only of major zeolitic horizons, but also of minor amounts of fracture-coating minerals, such as manganese oxides.

The geochemical composition of unsaturated zone waters and groundwater is a factor that affects radionuclide transport. In general, unsaturated zone pore waters have higher total dissolved solid concentrations than perched or saturated zone waters, reflecting the low surface infiltration rates. Most major chemical characteristics of the pore waters appear to be established by soil-zone processes, such that waters entering the bedrock are usually saturated with respect to calcite and amorphous silica. Pore waters show the effects of cation exchange reactions with zeolites, with increasing sodium and decreasing divalent cation concentrations occurring at depth. In addition, strontium and uranium series isotopic data indicate considerable pore water equilibration with the matrix rocks in the unsaturated zone.

Geochemical and isotopic data in waters from the unsaturated zone and saturated zone at Yucca Mountain are consistent with a flow model in which all unsaturated zone waters, including perched waters, originate at the surface of the mountain. Although flow paths appear to be predominantly vertical, there is evidence for lateral flow in some units. This water presumably flowed along pathways that included fractures, faults or both. Recharge to perched and saturated

zone waters is likely along fracture pathways, not by pore water flow through the unsaturated rock matrix.

Radionuclide Transport–A number of factors affect the transport of radionuclides within the unsaturated and saturated zones. These factors include radionuclide solubility and speciation, sorption, the effects of organics on sorption, matrix diffusion, and the effects of colloids. Radionuclides of concern for Yucca Mountain are neptunium, plutonium, americium, technetium, iodine, and uranium. Sorption coefficients for radionuclides of interest were determined using water and rock samples from the site. Batch experiments were performed at several pH levels to evaluate the impact of pH variations on the sorption coefficient. The potential effects of organics on actinide sorption were evaluated in batch experiments with model organic compounds in water and rock samples from the site. Models were developed to explain the sorption coefficient data and to allow prediction of coefficient values under anticipated conditions. Dynamic transport studies include crushed-tuff column experiments under flowing conditions, solid-rock column experiments, and experiments with alluvium. In addition, the transport of radionuclides through fractures was examined to assess the retardation that can be provided by radionuclide diffusion into the matrix and sorption onto the minerals coating Yucca Mountain fractures. Colloid-facilitated transport of radionuclides has been studied in the laboratory using waters collected from Yucca Mountain or synthesized to reflect Yucca Mountain waters.

In addition to laboratory studies of factors affecting radionuclide transport, field studies have also been carried out. A transport test at Busted Butte was designed to validate and improve the site-scale model of flow and transport in the unsaturated zone. To test conceptual saturated zone transport models, two major cross-hole, forced-gradient tracer tests at the C-holes complex were carried out. Observed responses of nonsorbing tracers were consistent with matrix diffusion behavior. This result supports the use of a dual-porosity conceptual model to describe radionuclide transport through the saturated, fractured volcanic rocks near Yucca Mountain. Results also suggest that the use of laboratory-derived radionuclide sorption parameters in field-scale transport predictions is defensible. Three single-borehole injection-withdrawal tracer tests were conducted in saturated alluvium at the Alluvial Testing Complex. In contrast to the tuffs, the alluvium exhibited behavior more like that of a porous continuum model (i.e., less diffusion into stagnant fluids). This result may be scale dependent, such that over longer transport times, diffusion becomes more important.

Thermal Loading Effects–The radioactive wastes emplaced at Yucca Mountain will generate a large amount of heat from the radioactive decay. This heat will influence hydrologic, mechanical, and chemical conditions in both the near-field (drift scale) and far-field (mountain scale). Consequently, there are several sets of coupled processes that must be taken into account to determine the overall performance of the repository in the unsaturated zone. These coupled processes include thermal-hydrologic, thermal-mechanical, and thermal-chemical processes, and combinations of these. Both laboratory and field studies (Large Block Test, Single Heater Test, Drift Scale Test) were carried out to address these issues. Thermal-hydrologic behavior of a repository was examined for conditions that included boiling in the host rock, coalescence of boiling zones around individual drifts, heterogeneity of heating along drifts, use of backfill, and use of a drip shield.

Two key quantities affect thermal-hydrologic conditions within emplacement drifts: temperatures at the drift wall and the temperature gradient between the waste package and the drift wall. The likelihood of water seeping into the drift is strongly affected by whether temperatures at the drift wall are above the boiling point. Keeping the drift wall above the boiling point will limit the tendency for seepage.

Thermal-mechanical-hydrologic investigations included study of thermal-mechanical effects on fracture flow; mechanical loading of waste packages through creep, block failures, or seismic loading; and thermal-mechanical effects on hydrology. Efforts to characterize the in situ geomechanical environment at Yucca Mountain have included hydraulic fracturing measurements of in situ stress and estimates of rock-mass strength based on empirical criteria. Thermal properties of the volcanic rock have been measured on a large number of laboratory specimens and also estimated from field data obtained in the Single Heater Test. Thermal-mechanical effects on fluid flow through fractures have been inferred from field observations and a laboratory experiment on a 0.5-m (1.6-ft) scale tuff block. The laboratory tests have also included an effort to assess the possible effect of radiation on elastic modulus and compressive strength.

The heat produced by the repository waste will affect geochemical processes in several ways. For example, the equilibrium states of reactions are generally temperature dependent. Mineral solubilities, aqueous speciation, equilibrium-phase assemblages, mineral hydration states, and solid-state phase transformations all depend on temperature as well. At elevated temperatures, water vapor, liquid water, and CO_2 gas will interact with the existing tuff mineralogy (and introduced materials) to dissolve and precipitate phases and modify the water chemistry. Mineral stability and phase equilibria are temperature-dependent. At higher temperatures, the conversion of unstable cristobalite to more stable chalcedony or the stable quartz form is accelerated (though this may be significant only in the presence of liquid water). Changes in permeability and porosity, in turn, may accompany phase transformations and mineral dissolution-precipitation reactions, and flow paths may be altered for additional impact. Studies examined mineral dissolution and precipitation, mineral stability, the evolution of in-drift water chemistry, and fluid-rock interactions.

The field thermal tests have produced data that improve the understanding of the conceptual thermal-hydrologic, thermal-mechanical, and thermal-hydrologic-chemical processes. They have also enhanced the confidence of the models of those processes. All field thermal tests confirm the concept that heat drives moisture away in vapor form. The vapor will flow mostly along fractures away from the heat source that will create a dryout region surrounding the heat source. The vapor will condense into water when it reaches the cooler region. Most of the condensate will flow in fractures. Some of the condensate will be imbibed into the matrix, but the amount may be much smaller than that which flows in the fractures. The orientation of the fractures and gravity will control the flow direction of the condensate. When the condensate flows back to the heat source, it will be evaporated and condensed, and condensate refluxing along fractures will occur. This condensate refluxing will provide a better chance for rock-water interaction. Without assistance from extrinsic factors, such as infiltration, rewetting of the dryout region will be slower than the drying process. The field thermal tests so far have not observed re-wetting.

Climate–Climate in the vicinity of Yucca Mountain affects the amount of water that can infiltrate into the mountain and the level of the water table. Climates wetter than today have been dominant over the past several hundred thousand years in the Yucca Mountain vicinity. Interglacial climates, such as the present climate, persisted only about 20 percent of the time. During much of the next 10,000 years, it is expected that the climate at Yucca Mountain will be wetter and cooler than it is today.

Regional and local evidence indicates that the Yucca Mountain site has experienced, over the past several hundred thousand years, many different climate states, ranging from glacial to interglacial conditions. Glacial and intermediate climate periods sustained greater effective moisture with greater infiltration and recharge than the present interglacial period. Long-term past climate proxy data were simplified into four climate states (interglacial, monsoon, intermediate, glacial), each with different levels of effective moisture. Climate states typical of the past 500,000 years are thought likely to reoccur in the next 500,000 years. However, changes to the water table elevation are not expected to exceed those already inferred from the zeolite alteration evidence discussed above.

Unsaturated Zone Hydrology–The repository is located in the unsaturated zone, which extends below the repository to the water table (top of the saturated zone). The amount of water contacting waste packages ultimately affects all aspects of repository performance, from waste package lifetime to radionuclide movement. The amount of water contacting the waste packages is limited by the seepage into the repository, which depends on the nature of percolation through the repository host rock in the unsaturated zone. Once radionuclides are released from a waste package, the unsaturated zone system beneath the repository, together with the engineered barrier system, delays radionuclide movement and reduces the concentration of radionuclides during transport to aquifers beneath the repository.

Boreholes drilled, sampled, tested, and monitored at the site defined the vertical and lateral distribution of hydrogeologic units, hydrologic properties of the rocks, thermal and other geophysical conditions and properties, chemistry of the contained fluids, pneumatic pressure, and water content and potential. Additional data for some of these parameters have been obtained from the excavation of the Exploratory Studies Facility and the Enhanced Characterization of the Repository Block Cross Drift, and from boreholes drilled from the drifts or alcoves of these tunnels.

Studies of unsaturated zone hydrology addressed net infiltration, percolation, fracture-matrix interaction, accumulation of perched water, lateral flow, and deep percolation to the water table. These processes determine the amount of water that may seep into repository drifts, possibly come in contact with waste packages, and eventually reach the water table.

Geochemical and isotopic data for waters from the unsaturated zone are consistent with a flow model in which all unsaturated zone waters, including perched waters, originate at the surface of the mountain. Although flow paths appear to be predominantly vertical, there is evidence that suggests lateral flow in some units. Some isotopic data suggest that water may have flowed rapidly to at least the depth of the Exploratory Studies Facility. This water presumably flowed along pathways that included fractures and faults. Radiocarbon dating of unsaturated zone gas samples provides uncorrected radiocarbon ages ranging from modern to 16,000 years. Stable

isotope values provide confirmatory evidence that pore water in the Topopah Spring Tuff is glacial in origin, whereas porewater in the underlying nonwelded units of the Calico Hills Formation is post-glacial in origin. Other isotopic dating methods, such as chlorine-36 and uranium series, suggest that some of the pore water may be much older.

Deposits of calcite and opal in fractures and cavities also mark pathways of past percolation of water through the unsaturated zone. The localized deposition of secondary minerals along fractures indicates precipitation under unsaturated conditions. Geochronologic studies of these minerals indicate that the unsaturated conditions, at least at the level of the Exploratory Studies Facility, have persisted for several million years.

The conceptual model of fluid flow in the unsaturated zone at Yucca Mountain, developed from monitoring and test results, consists of several important flow processes and issues. Infiltration is spatially and temporally variable because of the nature of the storm events that supply precipitation, and variation in soil cover and topography. As a result of the relatively high density of interconnected fractures and low matrix permeabilities in the Tiva Canyon Tuff, infiltration pulses move rapidly through the fracture system with little attenuation relative to travel times in the matrix. Because of relatively high matrix permeability and porosity and low fracture densities of the underlying Paintbrush nonwelded lithostratigraphic units, predominantly fracture flow in the Tiva Canyon Tuff becomes dominantly matrix flow in the nonwelded units. There is evidence of lateral flow of liquid water within the Paintbrush nonwelded unit. Unsaturated flow of liquid water in the Topopah Spring Tuff, below the Paintbrush nonwelded units, is primarily through fractures.

The occurrence of perched water near the contact between the Topopah Spring Tuff and the underlying nonwelded Calico Hills Formation indicates that the Topopah Spring Tuff basal vitrophyre (glassy tuff) and the nonwelded character of the Calico Hills Formation serve as barriers to vertical flow and cause lateral flow. Below the repository horizon, both the Calico Hills Formation and the underlying units of the Crater Flat Group have vitric and zeolitic components that differ by the degree of hydrothermal alteration. Because the zeolitic rocks of the Calico Hills Formation and the Crater Flat Group have low matrix permeability and some fracture permeability, a relatively small amount of water may flow through the zeolitic units. Conversely, but similar to the Paintbrush nonwelded units, the vitric rocks of the Calico Hills Formation and the Crater Flat Group have relatively high matrix porosity and permeability and, therefore, mostly porous-medium flow predominates in these rocks.

Saturated Zone Hydrology–The saturated zone underlying Yucca Mountain and the surrounding region represents an additional component of the path along which radionuclides could be transported from the repository at Yucca Mountain. The Alkali Flat-Furnace Creek groundwater basin underlies the repository and is a part of the central Death Valley subregion of the Death Valley regional groundwater flow system. Potentiometric data from widely spaced boreholes indicate that groundwater flows southward from upland recharge areas in the volcanic terrain of Pahute and Rainier mesas, beneath Timber Mountain, and southward toward the Yucca Mountain area. The groundwater flows through aquifers of the Tertiary volcanic and volcaniclastic sequence beneath Crater Flat, Yucca Mountain, and Jackass Flats, eventually ascending into the valley-fill sedimentary deposits of the Amargosa Desert. A regional aquifer in the Paleozoic carbonate rocks underlies the Tertiary volcanic rocks in the Yucca Mountain

vicinity. Comparison of major-ion and isotopic content data from waters of the lower carbonate aquifer with those from the volcanic units implies that there has been little mixing of water from the lower carbonate aquifer with that of the overlying Tertiary volcanic aquifers beneath Yucca Mountain. Flow paths inferred based on chemical and isotopic data are in general agreement with those based on potentiometric gradients.

In the immediate vicinity of Yucca Mountain, hydrogeologic data indicate that groundwater flows towards the repository area from the north and from the west, and away from the repository initially in a southeasterly direction toward Fortymile Wash and Jackass Flats, then south-southwestwardly toward the Amargosa Desert. Beneath the crest of Yucca Mountain, flow is entirely in the lower volcanic aquifers and deeper units. However, at Fortymile Wash, the upper volcanic aquifer dips beneath the water table and dominates the flow system. Limited data on the vertical hydraulic gradient indicate that an upward gradient exists between the carbonate aquifer and the volcanic aquifers at a location southeast of the repository and could extend to the area underlying the repository as well.

Movement of groundwater in the saturated zone within the Death Valley regional groundwater flow system has been conceptualized as a series of relatively shallow and localized flow paths that are superimposed on deeper regional flow paths. Hydrochemical and isotopic data from analysis of water samples derived from the Death Valley regional groundwater flow system, and from smaller flow systems within it, provide complementary, indirect data for interpreting hydrogeologic relationships and help to reduce uncertainties regarding regional groundwater flow patterns and rates of flow. Data derived from temperature profiles measured within several boreholes drilled at and near Yucca Mountain and the Nevada Test Site also have been used to estimate vertical thermal gradients and infer conductive heat-flow patterns within the saturated zone underlying Yucca Mountain and the surrounding area. These estimated and inferred parameters have, in turn, been used to interpret such phenomena as fault-controlled flow and vertical mixing that occur within the groundwater flow system, and to determine possible relationships of local flow systems to deeper underlying regional flow systems.

Hydrochemical data indicate that water in the volcanic aquifer beneath Yucca Mountain and Crater Flat was probably recharged during past wetter climate conditions, originating largely from local infiltration, some via perched water zones during late Pleistocene to early Holocene time. Carbon-14 dating of groundwater beneath Yucca Mountain provides uncorrected ages of predominantly 7,000 to 11,000 years; the estimated true age of the saturated zone groundwater is about 2,000 years younger.

Numerous faults that exist within the local saturated zone subsystem influence the movement of groundwater by variously serving as either preferential pathways or barriers to flow. The Solitario Canyon fault, on the west side of Yucca Mountain, acts as a barrier to west-to-east groundwater flow. However, the Solitario Canyon fault may also provide a conduit for upward flow to the volcanic aquifers from the underlying carbonate aquifer. Other north-trending faults at Yucca Mountain may also provide conduits for upward flow, as evidenced by linear anomalies in water temperature.

The long-term stability of the elevation of the groundwater table in the vicinity of Yucca Mountain has been evaluated by studies of natural existing spring features and paleodischarge

sites, packrat midden sites, groundwater samples, and mineralogical and isotopic indicators. Results of these studies indicate that, during the past two pluvial periods, if water-table gradients were similar to modern-day gradients, as is suggested by alternate-climate modeling simulations, the groundwater table could have been situated a maximum of about 115 to 120 m (380 to 396 ft) higher than the current water table level beneath Yucca Mountain. This corresponds to the extent of zeolitized rock above the water table, as observed in boreholes penetrating the water table.

Although there is mineralogic evidence for a water table rise beneath Yucca Mountain of as much as 115 to 120 m, the age of such a rise is poorly constrained and may represent conditions from 10 million years ago. Other reported large rises at paleodischarge sites assumed greater depth to water than is now known to exist, and in some cases involved deposits of unknown age. The most reliably dated paleo-spring deposits (where depth to water is known) suggest groundwater table rises of only 10 to 30 m (33 to 98 ft) in the last 15,000 years.

INTENTIONALLY LEFT BLANK

1. INTRODUCTION

Investigations of the Yucca Mountain site (Figure 1-1) began in 1978 to determine whether it is suitable for development as the nation's first geologic repository for permanent geologic disposal of high-level (radioactive) waste (HLW) and spent nuclear fuel. In response to the Nuclear Waste Policy Act of 1982 (NWPA) [DIRS 101681], the U.S. Department of Energy (DOE) developed a Site Characterization Plan that was approved in 1988. Formal site characterization began in 1989 following the amendment to the NWPA in 1987. NWPA Amendments Act of 1987 [DIRS 100016] directed the DOE to characterize only Yucca Mountain and to report to Congress if the Secretary of Energy determined the site to be unsuitable for development as a repository.

This Revision 2 of the *Yucca Mountain Site Description* (YMSD) presents the current understanding of the features, events, and processes composing the natural system at and near the Yucca Mountain site. Characterization of the natural system is necessary to assess the ability of a geologic repository to isolate radioactive waste. The natural system is the framework within which compatible engineered components of a repository must be designed. To meet NRC requirements, the Yucca Mountain Project (YMP) must demonstrate, with reasonable expectation, that the total system performance is such that the allowable 10 CFR Part 63 [DIRS 156605] annual dose of 15 millirem to the reasonably maximally exposed individual (RMEI) is not exceeded.

The Yucca Mountain site is located in Nye County in southern Nevada, approximately 160 km (100 mi) northwest of Las Vegas (Figure 1-1). Some of the characteristics of Yucca Mountain that led to its consideration as the site for a geologic repository include its arid to semiarid climate, depth to the water table, and its location remote from population centers. For waste emplaced in the unsaturated zone, low precipitation, slow movement of water through rock, and a thick zone of unsaturated rock would limit the amount of water available to contact waste packages. This would contribute to a long lifetime for the waste packages, accompanied by slow degradation of the waste form within the packages. For any radionuclides that escape the waste packages, the natural system would provide chemical and physical barriers that would retard their transport away from the repository, thereby limiting possible exposure to the public.

Adequate knowledge of the natural system was essential to making an informed decision in 2002 about the suitability of a repository at Yucca Mountain for the nation's civilian HLW and spent nuclear fuel. The current level of understanding of the natural system at Yucca Mountain indicates that the multiple barriers of combined natural and engineered systems will provide the needed long-term safety of a geologic repository at the site. This understanding is a basis for the License Application the DOE is preparing. Among the factors that will be relied upon for waste isolation are features of the natural system that provide:

- Limited seepage of water into the emplacement drifts
- Solubility limits of dissolved radionuclides in Yucca Mountain waters
- Retardation of radionuclide migration in the unsaturated and saturated zones
- Dilution of radionuclide concentrations during migration.

The License Application will also address those features, events, and processes of the natural system that might disrupt the repository, such as climate change, igneous events, and seismic activity (vibratory ground motion and fault displacement). In addition, the License Application will provide added confidence through multiple lines of evidence that include insights from natural analogs (other sites having features and processes that have a bearing on the long-term performance of the Yucca Mountain site).

Investigations of the natural system at Yucca Mountain provide an important part of the technical basis for demonstrating the long-term safety of a geologic repository at the site. They also provide information needed to substantiate safety during the operational period of a repository before it is permanently closed. Thus, the information on the natural system presented here supports the development of a safety case for a geologic repository at Yucca Mountain.

1.1   OBJECTIVE AND SCOPE

The YMSD summarizes existing information on the natural system at Yucca Mountain and is based mainly on YMP reports. Analyses and models are not discussed in the YMSD, except for references to conceptual models and numerical models that guide the collection of site data. The YMSD also incorporates relevant information from publications produced by other investigators outside the YMP, including consideration of certain interpretations and hypotheses that differ from those developed by YMP investigators.

Topics covered by the YMSD are:

- Regional geographic and geologic settings (Section 2)

- Geology of the site (Section 3)

- Tectonic models and tectonic hazards (Section 4)

- Factors affecting radionuclide transport under ambient and thermally perturbed conditions (Section 5)

- Past, present, and future climates (Section 6)

- Surface water and unsaturated zone flow and transport (Section 7)

- Saturated zone flow and transport (Section 8).

The description of the Yucca Mountain site and surrounding region contained in this document represents the state of knowledge at a particular point in time. Results described are generally those available based on data collected through December 2002. The discussion of natural analogs is retained in the *Natural Analogue Synthesis Report* (BSC 2002 [DIRS 160405]), and is not discussed in each chapter, as may be applicable, as was stated in the technical work plan (BSC 2003 [DIRS 166243], Section 1).

1.2 QUALITY ASSURANCE

The activity of preparing the YMSD was determined to be quality affecting (BSC 2003 [DIRS 166243], Section 8). However, the data and information contained herein are presented as reference only and include both qualified and unqualified information (BSC 2003 [DIRS 166243], Section 1). This report is not intended as a stand-alone source used to address safety or waste-isolation issues. Rather, information for those purposes should be obtained from original source documents cited herein. Revision 2 of the YMSD was prepared in accordance with AP-3.11Q, *Technical Reports*.

The Technical Data Management System of the Yucca Mountain Project should be consulted regarding the quality status of any data identified by Data Tracking Number and discussed in this report. For this reason, quality status of data is not documented in the YMSD. Similarly, the quality status of any software mentioned in this report can be obtained from the baseline of qualified software.

1.3 YUCCA MOUNTAIN PROJECT BACKGROUND

The Nuclear Waste Policy Act of 1982 [DIRS 101681], which established the HLW disposal program for the United States, requires, in Section 113, that a general plan be prepared for characterizing a candidate repository site. In 1988, the DOE produced the *Site Characterization Plan Yucca Mountain Site, Nevada Research and Development Area, Nevada* (DOE 1988 [DIRS 100282]). This plan described a comprehensive program to provide the information and data needed to evaluate the suitability of the Yucca Mountain site and to satisfy U.S. Nuclear Regulatory Commission requirements for licensing. Implementation of this plan was intended to provide the information needed to design a repository that would work in harmony with the natural system and to evaluate the expected performance of the repository and site as a total system. The previous revision of this YMSD (REV 01) (CRWMS M&O 2000 [DIRS 151945]) was one of several documents developed to provide site characterization information supporting the site suitability evaluation. In 2002, the site was recommended by the President of the United States for development as a repository. In that same year, the U.S. Congress passed a joint resolution signed into law by the President that designated the site for development as a repository.

Information described in this version of the YMSD includes general characteristics partially supporting the requirements defined in 10 CFR Part 63 [DIRS 156605].

The site characterization project, as it has evolved since 1988, has included surface-based testing and investigations, underground testing, and laboratory studies and modeling activities for the evaluation of repository performance. Surface-based studies have included the following:

- Mapping geologic features, including lithologic units, faults, fractures, and volcanic features

- Drilling boreholes into the mountain to identify the geologic units present at depth, measure the depth of the water table and properties of the unsaturated and saturated hydrologic system, observe the rate at which water moves from the surface into the rock below, and determine air and water movement properties above the water table

- Using gravitational, magnetic, electrical, and seismic methods to infer the distribution and properties of geologic units and structures at depth

- Monitoring earthquake activity

- Heating a large block of rock to observe the subsequent effects of heat on its hydrologic, mechanical, and chemical properties.

Boreholes provide a key source of information for characterizing the Yucca Mountain site. In addition to providing data on the stratigraphy and structure of the site, they also provide access for in situ testing and samples for laboratory testing. Boreholes have been drilled for many different purposes at Yucca Mountain (Figure 1-2). The convention for naming boreholes provides information on their location and purpose (Dyer 1992 [DIRS 149070]).

The single largest characterization effort of the YMP involved construction of the Exploratory Studies Facility (ESF) to gain access to the subsurface for exploration and testing at the depth of the repository. The 7.9-km (4.9-mi) long, 7.6 m (25 ft) diameter underground tunnel (Figure 1-3) that constitutes the main part of the ESF was completed in 1997. A second tunnel constructed for studies of the western portion of the Enhanced Characterization of the Repository Block (ECRB) was completed in 1998. (This 2.7-km (1.7 mi) long, 5.0 m (16.4 ft) diameter second tunnel is referred to as the Cross-Drift.) Investigative work in the ESF and ECRB Cross-Drift focused primarily on thermal and hydrologic testing and confirmation of rock properties. The relationship of these underground facilities to the current proposed layout of the repository is shown in Figure 1-4. Underground studies have included:

- Geologic mapping of underground openings

- Investigations of rock geotechnical properties

- Characterization of hydrologic, geologic, and chemical properties of lithologic units, pore waters, and fault zones

- Air-injection and liquid-release tests to characterize fracture flow and seepage

- Isotopic studies of flow pathways above the repository horizon

- The Single Heater Test and the Drift Scale Test, which investigated the behavior of the natural system under thermal loads.

An additional field study facility was constructed at Busted Butte, 8 km (5 mi) to the southeast of the ESF (Figure 1-4), to evaluate flow and transport in the nonwelded tuff units that lie between the repository horizon and the water table. At Yucca Mountain, these rock units are located approximately 140 m (450 ft) below the level of the repository. At Busted Butte, these units are exposed at the surface. The studies listed above were also conducted at this facility, with the exception of thermal tests.

Laboratory testing has augmented the surface and underground tests carried out at the Yucca Mountain site. Laboratory studies allow properties and processes to be investigated under

controlled conditions. Laboratory tests include those to determine mechanical, chemical, and hydrologic properties of rock samples in support of repository design and development of process models. (Process models are used to identify and understand important processes and relationships among them. A similar term, abstraction models, refers to the abridged versions of process models that are typically implemented in the probabilistic risk assessment.) Tests also quantify properties of radionuclides that affect their transport, if released from a repository. Additional laboratory tests include those to examine the chemical properties of ambient water samples and the effects of heat on the behavior and chemical properties of water in the host rock.

The results of these site characterization investigations, as reported in the YMSD (REV 01) (CRWMS M&O 2000 [DIRS 151945]) and summarized in this revision to that report, are the primary basis for the DOE description of the Yucca Mountain site. These results are supplemented in this revision by relevant information from other studies that have been carried out, including some that offer alternative interpretations. Together, they document the current understanding of the natural system at Yucca Mountain.

1.4 REPORT ORGANIZATION

This revision of the YMSD is organized into eight sections, seven of which address different technical topics. Following this Introduction (Section 1), the regional geographic and geologic settings within which Yucca Mountain is situated are summarized (Section 2). Next, the stratigraphic and structural framework of the Yucca Mountain site is described, and site geoengineering properties are discussed (Section 3). Section 4 discusses the tectonic setting of Yucca Mountain, including potential volcanic and seismic hazards to a geologic repository. Section 5 discusses factors affecting radionuclide transport. These factors include the mineralogy and chemistry of the host rock and chemistry of vadose zone and groundwater at the site (Section 5.2). Section 5.3 reports experimental work in radionuclide transport and retardation involving site-specific parameters. Section 5.4 addresses radionuclide transport as it is affected by coupled thermal-hydrologic-mechanical-chemical processes.

Following these sections, the essential role of water, the most important element of the natural systems impacting repository performance, is addressed, from its start as precipitation through its movement in the unsaturated and saturated zones. The first topics to be discussed are the paleoclimate, present climatology and meteorology of the site, and future climate scenarios (Section 6). Then, the surface-water hydrology of the site and flow and transport processes in the unsaturated zone are presented in Section 7. Characteristics of regional groundwater flow and site-specific saturated zone flow and transport are presented in Section 8.

Units for values provided in this document are generally given in the system of units (metric or English) in which they were originally reported in source documents or originally collected. Conversion to units of the alternative measurement system is indicated in parentheses to aid readers who are not familiar with one or the other system. For some values, for which there is no standard alternative unit, no conversion is given.

1.5 REFERENCES

The following is a list of the references cited in this section. Column 1 represents the unique six-digit numerical identifier (the Document Input Reference System [DIRS] number), which is placed in the text following the reference callout (e.g., BSC 2002 [DIRS 160405]). The purpose of these numbers is to assist the reader in locating a specific reference. Within the reference list, multiple sources by the same author (e.g., BSC 2002) are sorted alphabetically by title.

1.5.1 Documents Cited

160405   BSC (Bechtel SAIC Company) 2002. *Natural Analogue Synthesis Report*. TDR-NBS-GS-000027 REV 00 ICN 02. Las Vegas, Nevada: Bechtel SAIC Company. ACC: MOL.20020520.0288.

166243   BSC 2003. *Technical Work Plan for: Yucca Mountain Site Description for LA*. TWP-WIS-MD-000005 REV 03. Las Vegas, Nevada: Bechtel SAIC Company. ACC: DOC.20031125.0004.

164519   BSC 2004. *D&E / PA/C IED Subsurface Facilities.* 800-IED-WIS0-00101-000-00A. Las Vegas, Nevada: Bechtel SAIC Company. ACC: ENG.20040309.0026.

151945   CRWMS M&O (Civilian Radioactive Waste Management System Management and Operating Contractor) 2000. *Yucca Mountain Site Description*. TDR-CRW-GS-000001 REV 01 ICN 01. Las Vegas, Nevada: CRWMS M&O. ACC: MOL.20001003.0111.

100282   DOE (U.S. Department of Energy) 1988. *Site Characterization Plan Yucca Mountain Site, Nevada Research and Development Area, Nevada*. DOE/RW-0199. Nine volumes. Washington, D.C.: U.S. Department of Energy, Office of Civilian Radioactive Waste Management. ACC: HQO.19881201.0002.

149070   Dyer, J.R. 1992. "Borehole Designations Used for Existing Boreholes." Letter from J.R. Dyer (DOE/YMSCO) to W.L. Clarke (LLNL), L.R. Hayes (USGS), J.A. Canepa (LANL), T.E. Blejwas (SNL), M.D. Voegele (SAIC), R.F. Pritchett (REECo), R.L. Bullock (RSN), and L.D. Foust (M&O, TRW), May 8, 1992. ACC: NNA.19920522.0070.

1.5.2 Codes, Standards, Regulations, and Procedures

156605   10 CFR 63. Energy: Disposal of High-Level Radioactive Wastes in a Geologic
                  Repository at Yucca Mountain, Nevada. Readily available.

                  AP-3.11Q, Rev. 4, ICN 0. *Technical Reports*. Washington, D.C.: U.S. Department
                  of Energy, Office of Civilian Radioactive Waste Management.
                  ACC: DOC.20030827.0015.

101681   Nuclear Waste Policy Act of 1982. 42 U.S.C. 10101 et seq. Readily available.

100016   Nuclear Waste Policy Amendments Act of 1987. Public Law No. 100-203, 101
                  Stat. 1330. Readily available.

INTENTIONALLY LEFT BLANK
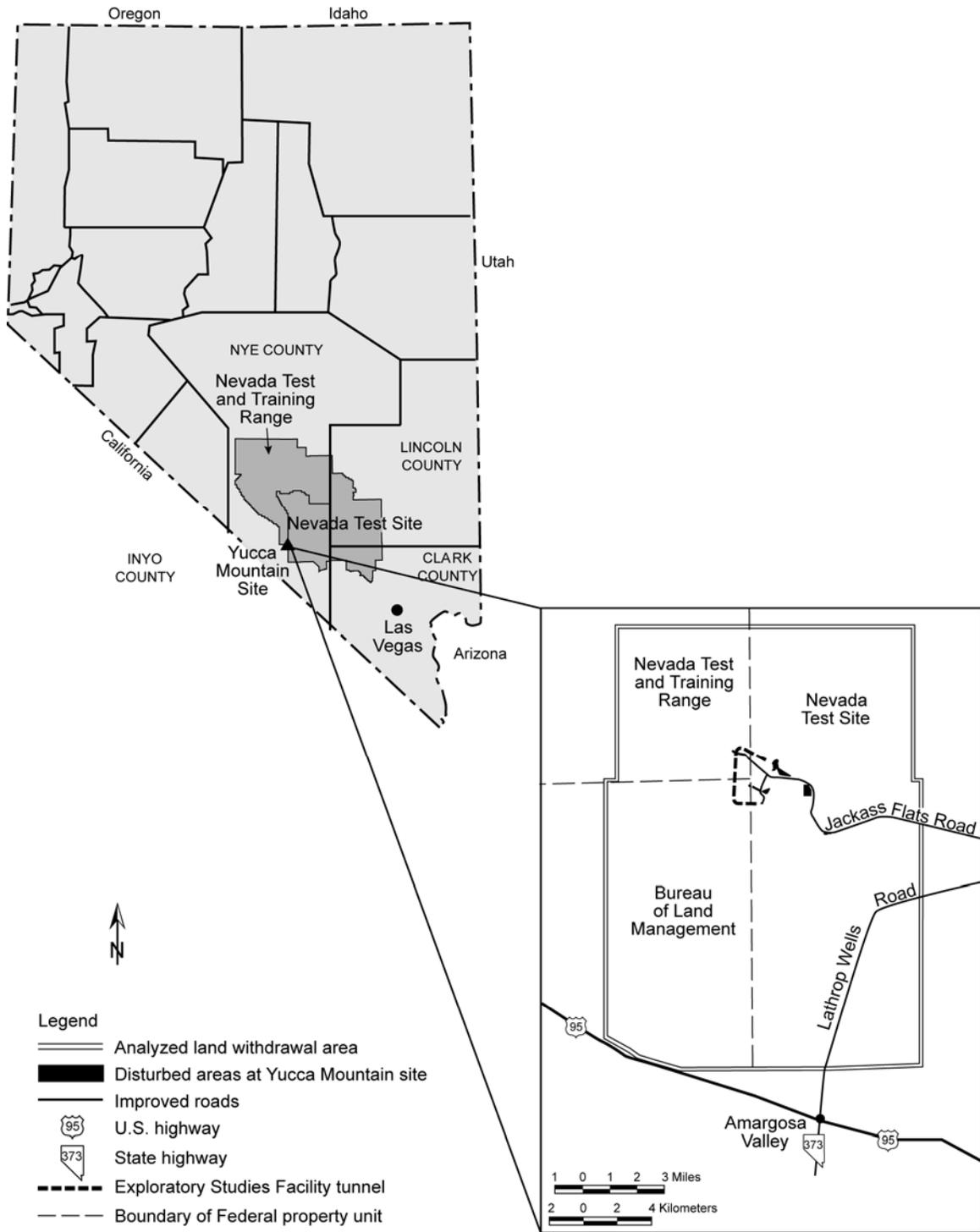
Source: Modified from CRWMS M&O 2000 [DIRS 151945], Figure 1.1-1

NOTE: Not to scale.

Figure 1-1. Location of Yucca Mountain, Nevada

Legend

⬠ Engineering Design Borehole
⬠ Geologic Borehole
▲ Geophysical Borehole
○ Groundwater Chemistry Borehole
▣ Heat Flow Borehole
⊙ Hydrologic Borehole
☐ Natural Infiltration Borehole
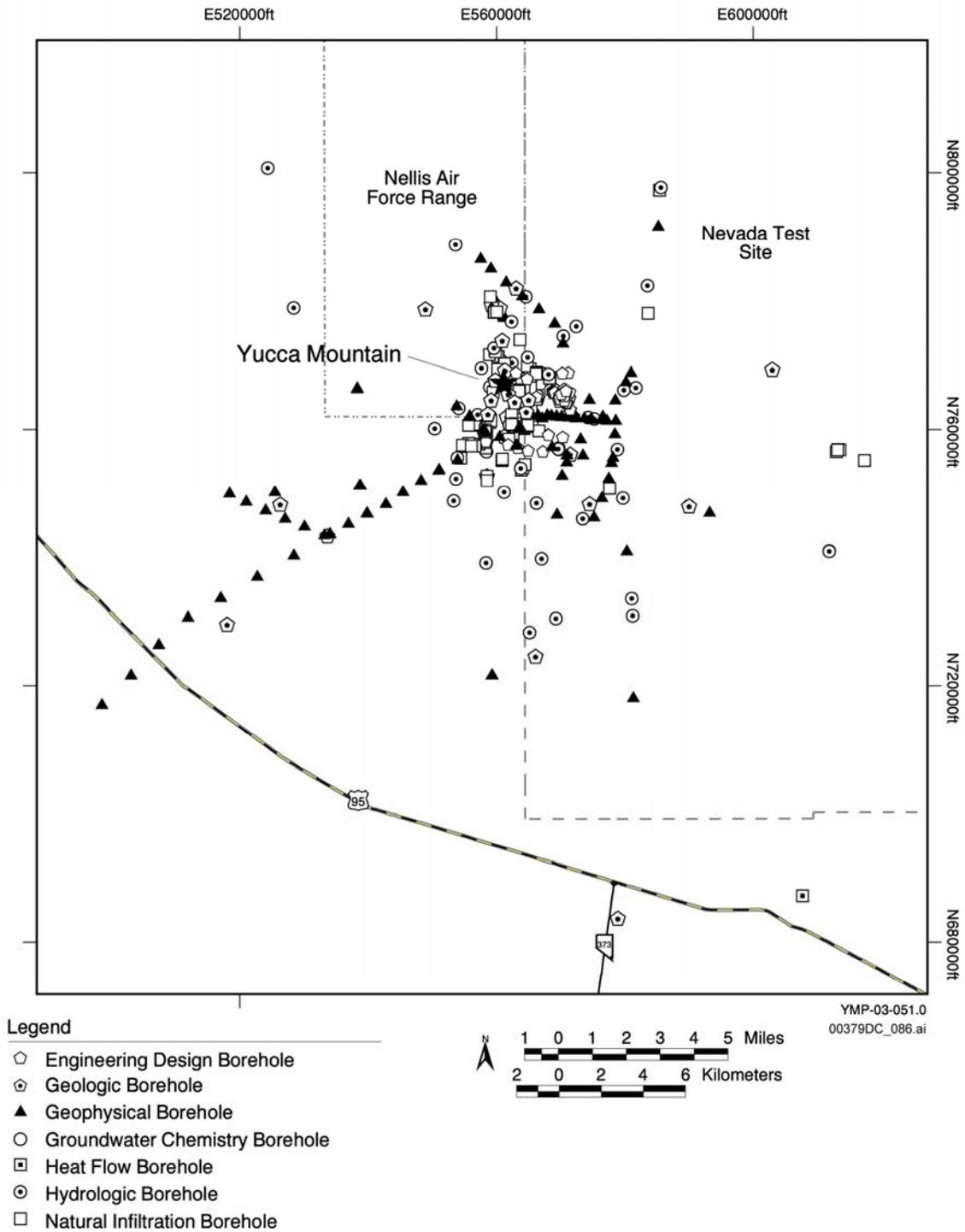
Source: Modified from CRWMS M&O 2000 [DIRS 151945], Figure 1.3-1

NOTE: Additional boreholes drilled by Nye County and more detail of the site area are shown in Figure 8-10.

Figure 1-2. Boreholes Drilled by the Yucca Mountain Project to Characterize the Yucca Mountain Vicinity through the Year 2000
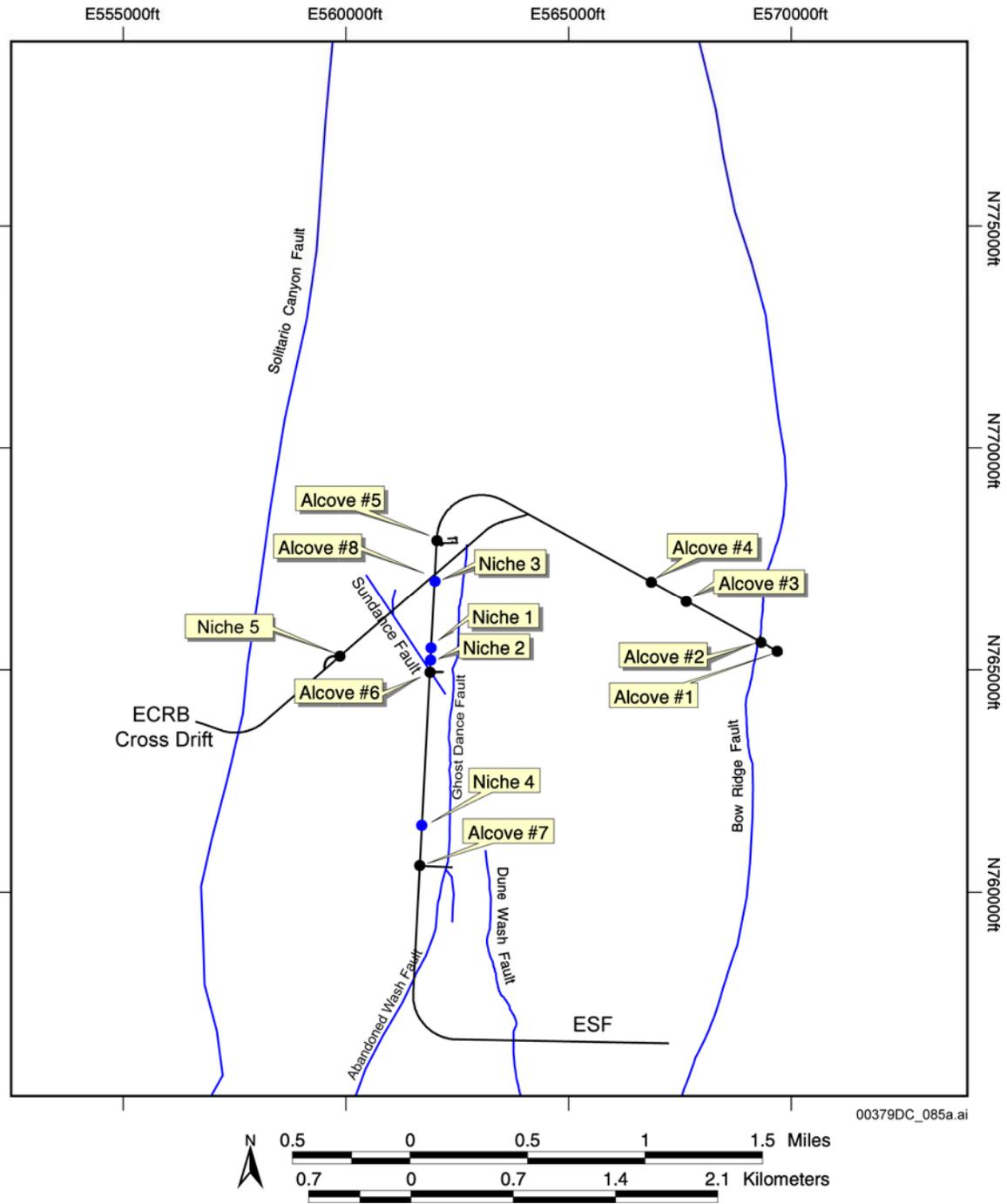
Source: Modified from CRWMS M&O 2000 [DIRS 151945], Figure 1.3-2

Figure 1-3.   Exploratory Studies Facility and Enhanced Characterization of the Repository Block Cross
                    Drift Showing Locations of Testing Alcoves and Niches
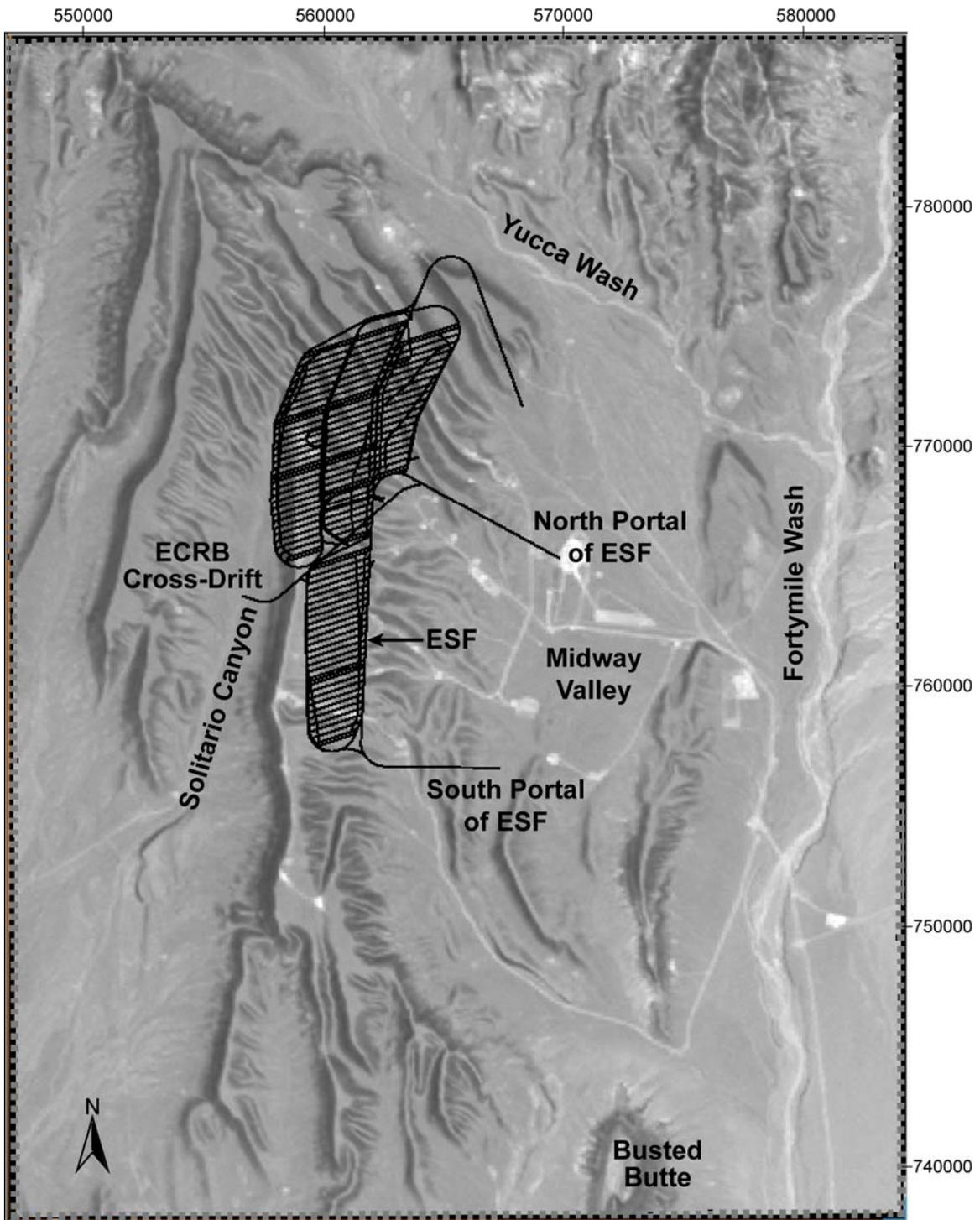
Source: BSC 2004 [DIRS 164519]

NOTE: Eastings and Northings given in feet.

Figure 1-4. An Example of the Layout of the Yucca Mountain Repository

2. REGIONAL SETTING

The regional geologic setting for Yucca Mountain consists of those physiographic, tectonic, stratigraphic, and structural elements that contribute to the evolution and current geologic condition of the site. The setting provides a context for understanding the active geologic processes at Yucca Mountain and evaluating its geology. Conclusions regarding the site geology need to be consistent with the regional framework. The regional geologic setting thus constrains the descriptive and process models that will be used to assess the ability of the natural system to contribute to the satisfactory performance of the site.

The information presented about this regional geologic setting is more general than the information focusing on the Yucca Mountain site provided in subsequent sections. Regional information is drawn mainly from existing geologic literature; that is, the published text books, papers, reports, and other referenced documents were not prepared specifically for the Yucca Mountain Project (YMP). Therefore, the data they contain were not collected and the analyses were not carried out under the YMP quality assurance program. The papers and reports did, however, undergo peer review for publication. Differences in interpretation among scientists are to be expected and are reflected in this discussion of regional geology. These differences are especially apparent in some of the maps in this section because a geologic map is both a summary of field observations and an interpretation of those observations.

Maps that summarize the surface distribution of rocks of different age groups are compiled from a number of sources. The maps that depict locations of thrust faults, folds, detachment faults, and shear zones are also drawn from existing publications to show specific features discussed in the text. The maps, therefore, differ in details, depending on the scope and scale of the investigation and subject being emphasized.

The main value of a review of regional studies is to provide a context within which geologic interpretations and tectonic models of the Yucca Mountain site can be judged or validated on the basis of investigations beyond the immediate area of Yucca Mountain.

This revision of the *Yucca Mountain Site Description* (YMSD) provides an updated interpretation of regional geology (for example, Fridrich 1998 [DIRS 101098]; 1999 [DIRS 118942]) and adds new information regarding the Highway 95 fault that was not available for Revision 1.

2.1 GEOGRAPHIC SETTING

2.1.1 Site Geography

The Yucca Mountain site is located in Nye County in southern Nevada, approximately 160 km (100 mi.) northwest of Las Vegas (see Figure 1-1), on land controlled by three federal agencies: the U.S. Air Force (Nevada Test and Training Range), the DOE Nevada Test Site, and the Bureau of Land Management (see Figure 1-1).

The Yucca Mountain site and surrounding areas are in the southern Great Basin, the northernmost subprovince of the Basin and Range physiographic province (Figure 2-1a). The topography of the Yucca Mountain site and surrounding region is typical of the Great Basin and

the larger Basin and Range Province, which are "generally characterized by more or less regularly spaced, generally north-south trending mountain ranges and intervening alluvial basins that were formed by faulting" (DOE 1996 [DIRS 102871], p. 4-74). The Yucca Mountain tectonic setting is discussed in greater detail in Section 4.

Elevation changes and variations in topographic relief are considerable within the area of the Yucca Mountain site. On the Nevada Test Site, elevation varies "from less than 1,000 m (3,280 ft) above sea level in Frenchman Flat and Jackass Flats to about 2,340 m (7,680 ft) on Rainier Mesa, and about 2,200 m (7,220 ft) on Pahute Mesa" (DOE 1996 [DIRS 102871], p. 4-74). Within 80 km (50 mi.) south of the Yucca Mountain site, Death Valley, California, presents the lowest point in the Western Hemisphere—86 m (282 ft) below sea level at Badwater (National Park Service 1998 [DIRS 101444]).

Yucca Mountain is an irregularly shaped volcanic upland that reaches an elevation ranging from about 1,500 to 1,930 m (4,900 to 6,330 ft) at the crest and has about 650 m (2,100 ft) of relief. The Yucca Mountain climate is arid, and the mountain receives less than 25 cm (10 in.) of rain per year (DOE 1988 [DIRS 102886], p. A-2). Section 6.2 presents the climatic conditions in the Yucca Mountain region.

There are no perennial streams in the general vicinity of the Yucca Mountain site. As discussed in Section 7, the streams are ephemeral, fed by runoff from snowmelt and from precipitation during storms that are most common in winter. Storms also occur occasionally in spring and fall, and localized thunderstorms occur infrequently during the summer (DOE 1996 [DIRS 102871], p. 4-107). Surface water runoff in the Yucca Mountain area is through Fortymile Canyon and south through Fortymile Wash. Jackass Flats, east of the Yucca Mountain site and one of the three primary valleys on the Nevada Test Site, is topographically open with drainage via the Fortymile Wash (Figure 1-4). The Fortymile drainage, in turn, intersects the Amargosa River in the Amargosa Desert about 32 km (20 mi.) southwest of the Nevada Test Site. The Amargosa River enters Death Valley at its southern end, turns to the northwest, and terminates near the center of the valley. The Great Basin subprovince is an internally draining basin (i.e., precipitation that falls over the basin has no outlet to the Pacific Ocean) (DOE 1996 [DIRS 102871], p. 4-107). Figure 7-4 shows the surface water features of the Yucca Mountain region.

2.1.2 Physiographic Setting

The Yucca Mountain region lies in the south-central part of the Basin and Range Physiographic Province, and is within the northernmost subprovince (commonly referred to as the Great Basin) that encompasses nearly all of Nevada, as well as adjacent parts of Utah, Idaho, Oregon, and California (Figure 2-1a). The southern margin of the Great Basin subprovince is considered to be the Garlock fault and its northeast projection (Figure 2-1b). South of this fault lies the northeastern part of the Mojave Desert that is characterized by relatively small, irregularly shaped basins and ranges.

The region surrounding Yucca Mountain can be further subdivided into several well-defined physiographic areas that reflect regional variations in their geologic characteristics. These areas include (Figure 2-1b):

- The large elongate north-northeast-trending basins and ranges of the central Great Basin.

- The somewhat smaller, more arcuate, and more closely spaced basins and ranges of the southeast Great Basin.

- The massive ranges and deep basins of the southwest Great Basin (Inyo-Mono subsection of Carr 1984 [DIRS 101037], pp. 9 and 26).

- The highly variable terrane of the Walker Lane belt, which trends northwest between the southeastern and southwestern segments of the Great Basin to the south, and between the central Great Basin and Sierra Nevada to the north (Figure 2-1b). The Yucca Mountain area is located within this physiographic area. The geologic relations indicate that many (perhaps most) of these landscape features in this subprovince took on their basic topographic form during the period 12.7 to 11.7 Ma (Fridrich 1998 [DIRS 101098], pp. 14 and 15; 1999 [DIRS 118942], p. 184, Figure 6).

The mountain ranges of the Great Basin, mostly tilted, fault-bounded blocks, may extend for more than 80 km (50 mi), are generally 8 to 24 km (5 to 15 mi) wide, rise 300 to 1,500 m (1,000 to 5,000 ft) above the floors of the intervening basins, and occupy approximately 40 to 50 percent of the total land area. The deep structural depressions forming the basins contain sedimentary-fill deposits of late Tertiary and Quaternary ages, ranging in thickness from a few hundred meters to more than 3 km (1.8 mi). The floors of closed basins are nearly level to gently sloping and parts are commonly covered by playas. Open basins are, generally, moderately to deeply dissected with axial drainage ways. Within this landscape, erosion and erosional processes are in the high, steep, and relatively wet uplands, whereas deposition and depositional processes are more dominant in the low, relatively arid lowlands.

Yucca Mountain lies near the center of the upper Amargosa River drainage basin, which originates in the Pahute Mesa/Timber Mountain area to the north and includes the main tributary systems of Beatty and Fortymile Washes (Figure 2-2). The basic drainage pattern of the area was established soon after the caldera collapse and resurgent dome formation that followed the Late Cenozoic eruptions in the southwestern Nevada volcanic field, and the gross pattern has changed little since then (Huber 1988 [DIRS 101248], p. 1).

Yucca Mountain and the surrounding area can be subdivided into eight clearly defined physiographic elements (Figure 2-2) that combine to produce a variable and diverse terrane typical of the Walker Lane. Six of these (Amargosa Desert, Bare Mountain, Crater Flat, Jackass Flats [including Fortymile Wash], Pinnacles Ridge, and Beatty Wash) are further discussed in the YMSD (REV 01) (CRWMS M&O 2000 [DIRS 151945], Section 4.2). The two features that pertain most to the repository are Yucca Mountain and Fortymile Wash, which are described in the Site Geology Section (Section 3).

2.2   TECTONIC SETTING

Tectonic setting refers to the geological architecture or structural configuration of the different rock masses in the area. The tectonic setting of the Great Basin is characterized in large part by fault-bounded basins and mountain ranges (including Yucca Mountain) complicated by volcanic activity that occurred within the past 15 m.y. Typically, faults in this setting include normal and strike-slip faults that reflect the extensional deformation caused by plate tectonic interactions at the western margin of the North American continent during the middle to late Cenozoic time era (e.g., Bohannon and Parsons 1995 [DIRS 101865]). The Great Basin is segmented into tectonic domains that are structurally bounded blocks of the Earth's crust characterized by deformations that distinguish them from adjacent domains. Tectonic domains exist at different scales. This section addresses domains at a regional scale. Three regional tectonic domains characterize Yucca Mountain and its surrounding environs: the Walker Lane domain, which includes the site; the Basin and Range domain to the northeast; and the Inyo-Mono domain to the southwest (Figure 2-3).

2.2.1   Walker Lane Domain

Yucca Mountain lies within the Walker Lane domain, an approximately 100-km-wide (60-mi-wide) structural belt along the west side of the Basin and Range domain (Figure 2-3). The domain, also referred to as the Walker Lane belt (Stewart 1988 [DIRS 100083]), or simply the Walker Lane, extends northwestward from the vicinity of Las Vegas, Nevada, subparallel to the Nevada-California border, into northern California.   The domain is characterized as an assemblage of crustal blocks separated by discontinuous northwest-striking right-lateral faults and northeast-striking left-lateral faults (Stewart 1988 [DIRS 100083], pp. 686 and 696; Carr 1990 [DIRS 104669], p. 284). Because of its structural heterogeneity, the Walker Lane is recognized as a tectonic terrane distinct from the Basin and Range only at a regional scale. The local northwest-striking faults give the domain its overall structural grain and deformation style, obscuring basin and range structure to varying degrees (Section 4.1.2.2). Although there is no definitive eastern structural boundary to the Walker Lane domain as a whole, the Las Vegas Valley shear zone (Figure 2-3) can be interpreted as an eastern bounding structure for the domain's southern segment.

The Walker Lane domain is subdivided into sections, each of which is characterized by a distinct structural pattern (Stewart 1988 [DIRS 100083], p. 686). With respect to the tectonic setting of Yucca Mountain, only three of these sections are of concern: (1) the Goldfield section, which includes the Yucca Mountain site and is characterized by irregular (in places arcuate) ranges, lack of major northwest-striking strike-slip faults, and a scarcity of major "basin-range" faults (Stewart 1988 [DIRS 100083], p. 694); (2) the Spotted Range-Mine Mountain section, which abuts the Goldfield section to the south and is dominated by northeast-striking left-lateral faults; and (3) the Spring Mountains section, which is dominated by Paleozoic and Precambrian rocks that largely preserve pre-Basin and Range structural patterns (Figure 2-3).

2.2.2   Basin and Range Domain

The Basin and Range domain (Figure 2-3) is also a physiographic province with the physiography being virtually a direct expression of the bedrock structure (Stewart 1980

[DIRS 103020], p. 110). Structurally, the province is characterized by generally north-south aligned ranges separated by basins filled with thick alluvium deposits derived from the adjacent ranges (Figures 2-1a and 2-1b). The ranges are separated by distances as much as 25 to 30 km (16 to 19 mi), but many ranges arc toward one another and merge along strike. The general small-scale spatial pattern was aptly likened by Gilbert (1875 [DIRS 105430]) to an "army of caterpillars marching north out of Mexico." This pattern is the result of a generally east-west directed extension that began in Tertiary time and continues at present (e.g., Stewart 1980 [DIRS 103020], p. 105f; Hamilton and Myers 1966 [DIRS 105920], p. 527). Rocks of all geologic ages, from Precambrian to Pleistocene, are deformed by this extension. Deformation is typically expressed as complex normal faulting that has facilitated the rotation of blocks to various dips around nearly horizontal axes. Thus, each range is fundamentally an assemblage of tilted fault blocks and is bounded by a major range-front fault. Seismic reflection profiles show that this style of deformation extends beneath the intervening basins where it is buried by alluvium (Catchings 1992 [DIRS 102496]).

2.2.3   Inyo-Mono Domain

The Inyo-Mono domain includes all of the extended terrane west of the Furnace Creek-Death Valley fault zone, east of the Sierra Nevada front, and north of the Garlock fault (Figure 2-3). Its northern end is defined by the termination of the Fish Lake Valley fault and a major right step in the population of active northwest-striking faults along a "northeast-striking structural zone" (Carr 1984 [DIRS 101037], p. 30, Figure 3). However, on the basis of gross structure and landform pattern, the domain could be projected northward to the northern terminus of the White Mountains (Stewart 1988 [DIRS 100083], p. 693) (Figure 2-3). It includes modern basins and ranges with great structural and topographic relief, including the Death Valley Basin and Panamint Range. Because of its ongoing tectonic activity and exposure of originally deep-seated crustal rocks, the Inyo-Mono domain is an important part of the regional geologic setting of Yucca Mountain and it contains some of the more tectonically active structures in the Yucca Mountain region.

The Inyo-Mono domain was identified by Carr (1984 [DIRS 101037], pp. 9 and 26) as a subsection of the southwestern Great Basin, distinct from the Walker Lane domain. Carr (1984 [DIRS 101037], p. 26) emphasized the pronounced northwest structural and physiographic trends, particularly the "long, linear valleys of north-northwest trend that are outlined by pronounced thoroughgoing structures with abundant evidence of Holocene and local historic faulting." He contrasted this tectonic pattern with the display of "adjacent transform-like offsets or large-scale oroflexing common to many elements of the Walker Lane belt" (Carr 1984 [DIRS 101037], p. 26). Stewart (1988 [DIRS 100083], p. 692), citing Carr (1984 [DIRS 101037]), also recognized the distinct tectonic character of the Inyo-Mono domain, but he included it as a section of the Walker Lane domain because of the major north-northwest striking right-lateral faults.

Figure 2-4 shows the general location of Precambrian and Paleozoic outcrops whereas Figure 2-5 shows the general location of stratified Mesozoic and Tertiary outcrops.

Extension in the Inyo-Mono domain is dominated by dextral strike-slip and oblique transtension resulting in elevated crustal blocks and intervening deep, high-relief basins (Blakely et al. 1999

[DIRS 149763], p. 5). Structural relief is very great, in part, because detachment faulting has unroofed some of the ranges, including the Funeral Range and Black Mountains (Figure 2-4). Distinctive as this domain is, it may be partly represented within the Walker Lane domain by less developed features, including Amargosa Valley and Sarcobatus Flat, and perhaps even the Amargosa Desert rift zone of Wright (1989 [DIRS 107335], p. 2). Further discussion with implications for Yucca Mountain is appropriate under the evaluation of tectonic models (Section 4.3).

2.3 REGIONAL STRATIGRAPHY AND LITHOLOGY

The stratigraphy and lithology of the regional geologic setting are relevant to the characterization of Yucca Mountain because these geological elements provide much of the history of deposition and deformation that has affected the site. They also constitute the framework for understanding other aspects of the Yucca Mountain site, including its structural geology and tectonics, geoengineering properties, mineral resource potential, hydrology, and geochemistry. Regional stratigraphy is not relevant to the tectonic domains described in the previous section because deposition and metamorphism reflect a series of evolving geologic environments that preceded formation of the domains and that no longer exist in the Great Basin. Section 4.2.2 of the YMSD (REV 01) (CRWMS M&O 2000 [DIRS 151945]), and literature referenced therein, present a more detailed description of rock stratigraphic units at a regional scale than is included here. Section 3 of this document contains detailed descriptions of stratigraphic units occurring in the immediate vicinity of Yucca Mountain.

2.3.1 Pre-Cenozoic Rocks

Pre-Cenozoic rocks in the Yucca Mountain region are chiefly represented by upper Precambrian (Proterozoic) through Paleozoic marine strata (Figure 2-6). Mesozoic rocks are of minor importance to Yucca Mountain, as they are preserved only in the western part of the Inyo-Mono domain (chiefly marine strata) and near the southern part of the Walker Lane domain (chiefly continental strata). Small Mesozoic igneous intrusions are found near Yucca Mountain. The Precambrian section is dominated by siliciclastic strata; the Paleozoic section is dominated by limestones and dolomites. These rocks have undergone successive generations of faulting, fracturing, and broad to local folding about both vertical and subhorizontal axes. In the area of the southwestern Nevada volcanic field and within the Goldfield section of the Walker Lane, the pre-Cenozoic rocks are not well exposed; hence, their pre-middle Miocene structural configuration is uncertain near Yucca Mountain. The pre-Cenozoic rocks are important, however, because they include the main regional aquifers and aquitards.

2.3.2 Precambrian Rocks

Exposures of Precambrian rocks are generally limited to areas south and west of Yucca Mountain (Figure 2-4 [Figure 2-5 depicts Mesozoic igneous and sedimentary rocks, and Tertiary sedimentary rocks]). These rocks compose two major assemblages: an older, metamorphosed basement assemblage (no basal contact is exposed), and a younger, metasedimentary assemblage, the uppermost unit of which is partly Cambrian. The older assemblage consists chiefly of quartzofeldspathic gneisses and quartz-feldspar-mica schists of metasedimentary or

metaigneous origin. The gneisses and schists are typically intruded by granitic veins or larger, deformed bodies of granite or pegmatite.

Regionally, the Upper Proterozoic units thicken and become increasingly calcareous from the southeast to northwest (Stewart 1970 [DIRS 106913], p. 7; Diehl 1976 [DIRS 102786], p. 58). They form the basal units of a miogeoclinal section and represent a marine depositional environment characterized by passive margin conditions and simple lithologies, chiefly siliciclastic rocks that grade upward into Paleozoic carbonate rocks. The exposed Precambrian section in the Yucca Mountain region ranges in thickness from 100 m (328 ft) to more than 6 km (3.7 mi), forming a sedimentary wedge that thickens to the northwest (Stewart 1970 [DIRS 106913], p. 7). The Proterozoic rocks, with their weakly to strongly metamorphosed fabrics, form a regional aquitard or barrier to groundwater flow (Winograd and Thordarson 1975 [DIRS 101167], p. C40).

2.3.3   Paleozoic Rocks

Paleozoic rocks form the dominant bedrock in an arcuate pattern from southwest of Yucca Mountain to the east side of the Nevada Test Site (Figure 2-4). In the Yucca Mountain region, they comprise three lithosomes: a lower, Cambrian through Devonian, dominantly carbonate lithosome; a middle, Mississippian, fine-grained siliciclastic lithosome; and an upper, Pennsylvanian to Mid-Permian, carbonate lithosome. The lower carbonate lithosome represents deposition in a deep to shallow marine passive continental margin (outer shelf to upper rise) setting (e.g., see Poole et al. 1992 [DIRS 105353], p. 46). By Late Devonian time these conditions were interrupted by the Antler orogeny, the main result of which in the Yucca Mountain region was an influx of clay, silt, and sand into the depositional record (Trexler et al. 1996 [DIRS 107005], p. 1739). A carbonate platform (continental shelf) depositional environment was reestablished in Pennsylvanian time across much of the region, except in the Inyo-Mono domain where a deeper trough or slope environment was formed (Stewart 1980 [DIRS 103020], p. 46; Dunne 1986 [DIRS 102861], p. 5).

Although the Cambrian carbonates are resistant to erosion, in many places they are characterized by brecciation that is confined to certain stratigraphic layers. At least two generations of breccia are present, the oldest of which may be of primary origin (submarine debris flows). One or more post-consolidation breccias, most likely of tectonic origin, are associated with interclastic voids in many parts of the calcareous section. This condition has enhanced cavernous dissolution, favoring the flow of groundwater. This feature, as well as the regional extent and uniformity, provides the conditions that make the lower carbonate lithosome a regional aquifer (the lower carbonate aquifer of Winograd and Thordarson (1975 [DIRS 101167], p. C14).

The character of the Cambro-Ordovician carbonate section differs markedly from that of the Upper Ordovician Eureka Quartzite. The upper part of the Eureka Quartzite is typically a dense, white, sucrose quartzite that forms a unit as much as 150 m (500 ft) thick that is closely fractured. The fractured sections are locally an aquifer. The Eureka Quartzite is succeeded by the shallow-water Ely Springs Dolomite, which marks a recurrence of the carbonate depositional regime. Ordovician strata grade up through the Ely Springs Formation, interrupted by minor erosional gaps, into dolomites that form the Siluro-Devonian section (Figure 2-6) (Stewart 1980 [DIRS 103020], pp. 25 and 28).

The Silurian system is thin and areally restricted relative to the rest of the Paleozoic section in southern Nevada (Stewart 1980 [DIRS 103020], p. 28). It is generally about 150 m (500 ft) thick in the Yucca Mountain region (Stewart 1980 [DIRS 103020], p. 30). At Yucca Mountain, rocks of this age were penetrated below 1,244 m (4,081 ft) in well UE-25 p#1 (Carr et al. 1986 [DIRS 102046], Plate 1).

The Devonian section is thick and extensive across southern Nevada (Figure 2-4). In the Yucca Mountain region, it consists of a succession of limestone and dolomite that typically includes intervals of thick-bedded, gray, crystalline dolomite; fossiliferous, thin- or slabby-bedded or cherty limestone; and silty-sandy or quartzitic beds. The lithologic and stratigraphic variability, fossil assemblage, and presence of numerous erosional breaks indicate deposition in shallow (shelf to upper slope) water, dominated at times by reef bank environments. Devonian strata tend to be siltier upsection and toward the northwest, a lithostratigraphic distinction that becomes more pronounced in the overlying Mississippian section (Stevens et al. 1991 [DIRS 150281], p. 884).

Mississippian strata in the Yucca Mountain region are represented by sharply contrasting, but locally intertonguing, lithologies. The strata are a detrital section that thickens to more than 3,000 m (10,000 ft) toward its westward source (Stewart 1980 [DIRS 103020], p. 41), and a comparatively thinner and more uniform carbonate section that extends southeastward from the vicinity of Mercury and the Spotted Range, where it is about 300 m (1,000 ft) thick (Barnes et al. 1982 [DIRS 124232]).

Barnes et al. (1982 [DIRS 124232]) mapped three Mississippian carbonate units at the Nevada Test Site. Along the west side of Yucca Flat, the Mississippian section is mostly the shaley, western facies, represented by the Eleana Formation (Figure 2-6). The upper part of the Eleana Formation is chiefly calcareous turbidities, which is represented farther east and south by the Chainman Shale (Figure 2-6), a monotonous siltstone or mudstone several hundred meters thick, interbedded with sparse quartz sandstone. The Chainman Shale (formerly Eleana Formation) crops out in the CP Hills and core of the Calico Hills (Cole and Cashman 1999 [DIRS 114714], p. 7; Cole et al. 1994 [DIRS 104709], pp. 68 and 71; Sawyer et al. 1995 [DIRS 104580], p. 29) (exposures too small to display in Figure 2-4). About 770 m (2,520 ft) of Chainman Shale were penetrated by Borehole UE-25 a #3 in the Calico Hills. The hole bottomed in Silurian or Devonian dolomite (Maldonado et al. 1979 [DIRS 106333], p. 1). The borehole revealed low-grade thermal metamorphism of the shale, which provides one possible explanation for a magnetic anomaly that encompasses the Calico Hills (Majer et al. 1996 [DIRS 104685], Plate 2). Alternatively, the anomaly could be explained by a depositionally thick section of Miocene tuff above the Paleozoic contact.

Rocks of Pennsylvanian to Permian age in the Yucca Mountain region are represented by the Tippipah Limestone (Figure 2-6), a thick- to thin-bedded, gray limestone, but locally silty and cherty (Frizzell and Shulters 1990 [DIRS 105454]). The Tippipah is exposed only at the east side of the Nevada Test Site, at the southern end of the Eleana Range (Syncline Ridge), and at the southern end of the CP Hills (Figure 2-4), where it is disconformable with the Chainman Shale (Cole et al. 1994 [DIRS 104709], p. 75).

The total thickness of the pre-Tertiary section at the Nevada Test Site is estimated at about 11,500 m (37,730 ft) (Frizzell and Shulters 1990 [DIRS 105454]). Miocene rocks west and south of Yucca Mountain, chiefly of igneous origin in the Inyo-Mono domain, are younger than about 16 Ma (Figure 2-7b).

2.3.4   Mesozoic Rocks

The nearest stratified Mesozoic rocks (Figure 2-7a) are in that part of California that lies inside a 100-km-radius of Yucca Mountain (Figure 2-5). Their closest occurrence in Nevada is to the northwest in the Grapevine Mountains along the California/Nevada border and south and east of Charleston Peak, in the Spring Mountains (Figure 2-5). There, at the latitude of Las Vegas, a thick, well-exposed section of Mesozoic rock (Figure 2-7a) forms Wilson Cliffs (Longwell et al. 1965 [DIRS 104621], Plate 1). Mesozoic strata are not a factor in the hydrologic or tectonic phenomena relevant to Yucca Mountain, but a discussion of this time period is presented in an earlier version of the YMSD (REV 01) (CRWMS M&O 2000 [DIRS 151945], Section 4.2.2.1.3). Mesozoic rocks younger than Early Jurassic in the Yucca Mountain setting are intrusive, consisting of widely scattered granitic stocks and mafic dikes. Miocene rocks west and south of Yucca Mountain, chiefly of igneous origin in the Inyo-Mono domain, are younger than about 16 Ma (Figure 2-7b).

2.3.5   Cenozoic Rocks

Cenozoic rocks of the Yucca Mountain geologic setting (Figure 2-8) fall into three general groups: pre-Middle Miocene sedimentary (including volcaniclastic) rocks that predate creation of the southwestern Nevada volcanic field, the middle to late Miocene volcanic suite that constitutes the southwestern Nevada volcanic field, and the Plio-Pleistocene basalts and basin sediments. These lithostratigraphic groups are not well defined in terms of system boundaries (e.g., Tertiary or Quaternary), so systemic distinctions will not be emphasized in the following sections.

At Yucca Mountain and in the surrounding area, Cenozoic rocks (Figure 2-8) overlie complexly deformed Paleozoic and Precambrian rocks along a profound erosional unconformity (Scott 1990 [DIRS 106751]) (Figures 2-4 and 2-5). The distribution, geometry, and attitudes of these older rocks, and the extent to which these factors influenced the distribution and structure of the Cenozoic units, is indeterminable, given the present paucity of subsurface data. The age of the regional unconformity is also unknown, but erosional downcutting, possibly associated with extension, most likely was under way in Late Cretaceous (post-Santonian) time. The various Cretaceous stocks and dikes are all post-kinematic or indicate the influence of an extensional stress field during emplacement. The age of the basal Cenozoic deposits is unknown. The oldest such deposits within a 100-km radius of Yucca Mountain are at least late Oligocene, but such deposits may include older basal colluvium or lag conglomerates.

2.3.5.1   Tertiary Rocks

Pre-middle Miocene sedimentary rocks are widely distributed in Nevada (Stewart 1980 [DIRS 103020], p. 87). Their distribution and heterogeneous continental character imply that they were deposited in restricted basins that may have been precursors to the present basins

(Stewart 1980 [DIRS 103020], p. 92). The deposits in the Yucca Mountain area typically consist of a basal conglomerate, lacustrine limestone, and tuffs (e.g., rocks of Pavit Springs and other local units, Figure 2-8). The conglomerate is comprised of locally derived clasts (Precambrian or Paleozoic provenance), commonly of cobble to boulder size, and is typically poorly sorted and set in an oxidized matrix. The textural characteristics range from those associated with colluvial deposits to those associated with fanglomerates and stream-channel gravels. The conglomerate typically intertongues with and is overlain by a characteristically pinkish-cream to buff or tan crystalline or clayey-silty lacustrine limestone. In outcrop, the limestone commonly shows soft-sediment deformation features, local slump folding, and algal mat structures. In upsection, the limestone is interbedded with and ultimately overlain by tuffaceous sandstone and distal air-fall tuffs of uncertain provenance. Strata of this age and lithologic assemblage are found in and near Rock Valley, east of Yucca Mountain (Figure 2-5) (see Section 2.4.3.4).

The presence of air-fall tuffs high in the Oligocene section heralds a period of catastrophic explosive volcanism that culminated in the creation of the southwestern Nevada volcanic field 15 to 7.5 Ma (Stewart et al. 1977 [DIRS 106928], p. 67; Carr et al. 1986 [DIRS 104670], p. 3; Sawyer et al. 1994 [DIRS 100075], p. 1304). The earliest of these great eruptions is represented by the Monotony Tuff, a unit dated at 27.3 Ma (Figure 2-8) and exposed mainly north of Yucca Mountain in the Belted Range and Rhyolite Hills (Sawyer et al. 1995 [DIRS 104580], p. 28). The Monotony Tuff has a maximum exposed thickness of about 200 m (660 ft). It was erupted from a caldera located in the area of the present Pancake Range and northern Reveille Range (Figure 2-7b) (Ekren et al. 1971 [DIRS 105242], p. 25; Sawyer et al. 1995 [DIRS 104580], p. 28). (The Pancake Range is north of the Reveille Range.) The sequence of upper Oligocene through middle Miocene tuffs and associated sediments forms an important part of the Tertiary section in the region north and east of Yucca Mountain. Ekren et al. (1971 [DIRS 105242], p. 24) report more than 6,000 m (20,685 ft) of such strata ranging in age from 27 to 7 Ma.

Deposition of the tuffs and establishment of the great caldera complexes interrupted and locally obliterated the established Tertiary depositional regime in the Yucca Mountain geologic setting. This regime continued elsewhere, however, with modifications imposed by tectonism, until nearly the end of the Miocene, when fundamental changes in climate and regionally active extensional faulting put an end to it throughout the southern Great Basin.

In the vicinity of Yucca Mountain, in Rock Valley (Figure 2-2), the Oligocene rocks of Winapi Wash are succeeded by a complex assemblage of bouldery and poorly sorted stream gravel, volcanic arkose, shale and siltstone, freshwater limestone and marl, and a variety of tuffs. This assemblage is informally designated as "rocks of Pavits Spring" and of Miocene age (Poole et al. 1965 [DIRS 106568]). The fluvial-lacustrine environment inherited from the Oligocene persisted in Rock Valley until the Ammonia Tanks Tuff was deposited at 11.4 Ma (Figure 2-8). Gravel (unit Tsd) (Carr et al. 1986 [DIRS 102046], Figure 12, pp. 28 and 30), possibly correlative with the rocks of Pavits Spring, was penetrated by well UE-25 p #1 at Yucca Mountain at a depth near the Paleozoic unconformity (Figure 3-7 and see Section 2.4.3.4).

The explosive volcanism that led up to and culminated in the formation of the southwestern Nevada volcanic field is the most significant depositional event of the Cenozoic Era with respect to Yucca Mountain. It resulted in the formation of at least six major calderas between approximately 15 and 7.5 Ma (Sawyer et al. 1994 [DIRS 100075], p. 1304), created Yucca

Mountain, and brought to a close the regional deposition that spans domains of the Yucca Mountain geologic setting. The record of regional tuff deposition begins within the rocks of Pavits Spring. Tuff deposition is also documented in the eastern part of the Nevada Test Site, where Redrock Valley Tuff (15.3 Ma) (Sawyer et al. 1995 [DIRS 104580], p. 26) and the tuff of Yucca Flat (15 Ma) (Sawyer et al. 1995 [DIRS 104580], p. 26, Table 1) are significant components. The succession of tuff and lava units that form Yucca Mountain are listed in Figure 2-8 and described in detail in Section 3. Several units that are widely distributed in the southwestern Nevada volcanic field include the Crater Flat Group (about 13.25 Ma), Calico Hills Formation (12.9 Ma), Paintbrush Group (12.8 to 12.7 Ma), and Timber Mountain Group (11.6 to 11.4 Ma) (Sawyer et al. 1994 [DIRS 100075], p. 1305). The lowest of the tuffs that forms the foundation of Yucca Mountain is the Lithic Ridge Tuff (14 Ma) (Sawyer et al. 1994 [DIRS 100075], p. 1305). Although pre-Lithic Ridge tuffs are in the rocks of Pavits Springs and beneath Yucca Mountain, little is known about their extent, age, and stratigraphic relation. In fact, caldera sources for all but the Tiva Canyon Tuff and the Timber Mountain Group tuffs are uncertain (Sawyer et al. 1994 [DIRS 100075], p. 1304).

Lipman et al. (1966 [DIRS 100773], p. F1) first noted that the Topopah Spring Tuff and Tiva Canyon Tuff of the Paintbrush Group might represent eruptions from a zoned magma chamber. They attributed the zoning to fractional crystallization such that the upper portion of the chamber evolved to a rhyolitic composition and was the first magma erupted from the base of each ash-flow sheet. Eruption from successively deeper portions of the magma chamber produced less siliceous ejecta with a higher proportion of crystals (which had settled into a deeper part of the magma chamber) such that the upper levels of the ash-flow sheets are crystal-rich quartz latites. Noble and Hedge (1969 [DIRS 105197], p. C137) noted that strontium was more radiogenic in the first (older) erupted parts of the ash flows and concluded that the upper part of the magma chamber had assimilated crustal rocks. Working in a similar volcanic sequence, Stuckless and O'Neil (1973 [DIRS 106945], p. 1995) used strontium and oxygen isotopes and bulk rock chemistry to show that fractional crystallization and wall-rock assimilation occurred simultaneously, resulting in early-formed crystals that were less radiogenic than their enclosing matrix. They proposed that the ash-flow complexes were generated by partial melting in the lower crust, but neodymium isotope studies of several ash-flow complexes, including those of the Timber Mountain area, indicate a large component of mantle-derived basalt (Perry et al. 1993 [DIRS 106492], p. 879).

In another interpretation, Broxton et al. (1989 [DIRS 100024], p. 5984) proposed that small volume eruptions at the caldera complex occurred in a series of cycles from individual shallow magma reservoirs. Broxton et al. (1989 [DIRS 100024], p. 5983) infer that the differentiation and emplacement process was repeated for each major eruption sequence or group. Peak volcanism in the southwestern Nevada volcanic field occurred during eruption of the Paintbrush and Timber Mountain Groups, when more than 4,500 km^3 (1,078 mi^3) of magma were erupted in two episodes separated by a span of approximately 1 m.y. (Sawyer et al. 1994 [DIRS 100075], pp. 1311 and 1312).

The Wahmonie Formation (Poole et al. 1965 [DIRS 106568]) forms a sequence of andesite and dacite lava flows erupted from a source north of Skull Mountain and south of Shoshone Mountain. The Wahmonie Formation forms a distinctive marker between the Crater Flat Group tuffs and the Calico Hills Formation east of Yucca Mountain. Rocks of the Wahmonie

Formation are characteristically dark, Fe-rich, massive or thick-bedded lava flows, autoclastic breccias, and agglomerates. The lower part of the Wahmonie Formation includes interbedded volcaniclastic sediments–debris flows, lahars, and mudslides–that indicate initial deposition in a relatively high-relief setting. The basal volcanic and volcaniclastic interval was formerly called the Salyer Formation (Poole et al. 1965 [DIRS 106568]; Frizzell and Shulters 1990 [DIRS 105454]), but is now reduced to member status (Sawyer et al. 1995 [DIRS 104580], p. 19).

The Calico Hills Formation is named for exposures in the northwestern part of the Calico Hills (Sawyer et al. 1994 [DIRS 100075], p. 1307). It consists of rhyolite lavas, bedded and locally zeolitized tuffs, and nonwelded ash-flow tuffs. In the Yucca Mountain area, it is 50-300 m (160 to 980 ft) thick (Sawyer et al. 1995 [DIRS 104580], p. 18; Sawyer et al. 1994 [DIRS 100075], p. 1307). In earlier maps and reports, the unit is referred to informally by various designations, such as rhyolite of Calico Hills (Lipman and McKay 1965 [DIRS 104158]), tuffs and lavas of Calico Hills (Carr et al. 1986 [DIRS 104670], p. 4, Figure 2), or rhyolite lavas and tuffaceous beds of Calico Hills (Frizzell and Shulters 1990 [DIRS 105454]).

The largest and most important of the tuff sequences of Yucca Mountain is the Paintbrush Group (Figure 2-8), which consists of a succession of well-stratified rhyolites and quartz latites totaling about 610 m (2,000 ft) thick. The group includes four formations: (from the bottom up) Topopah Spring Tuff (12.8 Ma), Pah Canyon Tuff, Yucca Mountain Tuff, and Tiva Canyon Tuff (12.7 Ma). The Topopah Spring Tuff directly overlies tuffs of the Calico Hills Formation at Yucca Mountain (Sawyer et al. 1994 [DIRS 100075], p. 1308). The Topopah Spring Tuff is subdivided into eleven mappable units (Day et al. 1998 [DIRS 101557]) based on crystallinity, degree of welding, and development of lithophysae. The Topopah Spring tuff is the host rock for the planned radioactive waste repository and is described in Section 3 of this document and in the earlier version of the YMSD (REV 01) (CRWMS M&O 2000 [DIRS 151945]).

The Paintbrush Group was faulted and eroded following deposition of the 12.7 Ma Tiva Canyon Tuff and, thus, is in unconformable contact with the overlying Timber Mountain Group (Fridrich 1999 [DIRS 118942], p. 184). The Timber Mountain Group, which consists of the Rainier Mesa and Ammonia Tanks Tuffs, forms a major eruptive volume of siliceous rhyolites and quartz latites. Only the Rainier Mesa Tuff is present at Yucca Mountain (chiefly at Plug Hill and Rainier Ridge [Day et al. 1998 [DIRS 101557]), but both formations are widely distributed within the western half of Crater Flat Basin and at the west end of the Crater Flat south-bounding cuesta, where outcrop thicknesses are as great as 240 m (790 ft) (Fridrich 1999 [DIRS 118942], p. 187). The unit is described in Section 3.3.4.8.

Other eruptive sequences and calderas associated with the southwestern Nevada volcanic field include the Black Mountain caldera (9.4 Ma) and Stonewall Mountain volcanic center (7.5 Ma) (Figure 2-5) (Sawyer et al. 1994 [DIRS 100075], pp. 1305 and 1306). The various tuffs and lavas erupted in the post-11-Ma period form important volumes of rock in the Pahute Mesa-Sarcobatus Flat-Bullfrog Hills area northwest of Yucca Mountain. They are not, however, directly relevant to the history or makeup of Yucca Mountain. The youngest tuff at Yucca Mountain is the Rainier Mesa Tuff of the Timber Mountain Group.

Physical properties of the tuff and lava units of the southwestern Nevada volcanic field contrast greatly across formational contacts, but tend to be uniform laterally over wide areas. This characteristic results from:

1. The conditions of deposition (large batches of homogenized material deposited rapidly over large areas)

2. Differences in initial composition of each eruptive batch

3. Postdepositional processes of welding, vapor-phase crystallization, autolytic and pneumatolytic alteration, and gas dispersion.

As a result, some tuff units are physically similar to ceramics or glass, whereas others are loose and porous, vesicular and closely fractured, or chemically altered. Understanding the spatial variation of these properties contributes to modeling the behavior of a repository under thermal loading and to the modeling of hydrologic processes. More detailed information on the properties of the tuffaceous rocks at Yucca Mountain is presented in Section 3.3.

Miocene rocks west and south of Yucca Mountain, chiefly of igneous origin in the Inyo-Mono domain, are younger than about 16 Ma. These include the central Death Valley volcanic field (Wright et al. 1981 [DIRS 107354], p. 7) and an irregular belt of volcanic rocks that extends from the Owlshead Mountains and southern Panamint Range eastward toward the Kingston Range, Greenwater Range, Black Mountains, and Furnace Creek basin (Figure 2-7b). In this region, tuffs of the Artists Drive Formation date from about 14 to 6 Ma (Wright et al. 1991 [DIRS 107350]). Above this lie the Furnace Creek and Funeral Formations, with a combined total thickness of about 3,600 m (11,800 ft) of pyroclastic sediments, basalt flows, and intertonguing conglomerates, sandstones, and mudstones. Basalts near the base of the Funeral Formation are dated at about 4 Ma (McAllister 1973 [DIRS 104764]). Wright et al. (1991 [DIRS 107350]) noted that this rock assemblage is most likely the direct result of Neogene local basin subsidence and extension.

The central Death Valley volcanic field is underlain by the Willow Spring Pluton, a diorite dated between 11.6 and 10 Ma, that is exposed along the west side of the Black Mountains (Figure 2-7b) (Asmerom et al. 1990 [DIRS 104431], pp. 224 and 225). The diorite is intruded by small granite bodies. Basalt extrusion in the Resting Springs Range of about the same age (11.7 Ma) was followed by extensive silicic to mafic volcanism during the 10.5 to 5 Ma period. Volcanism culminated in the 8.5- to 6.5-Ma period with eruption of the Shoshone volcanic suite, chiefly dacites and rhyodacite tuffs (with associated sediments) exposed in the eastern Black Mountains and southern part of the Greenwater Range (Figure 2-7b). Silicic volcanism ceased in this area about 5 to 6 Ma with deposition of rhyolites of the Greenwater volcanic suite (Noble 1941 [DIRS 105202], p. 956; Drewes 1963 [DIRS 144978], p. 42). Thereafter, diminishing basaltic volcanism continued into late Pleistocene time, as in the Goldfield section of the Walker Lane domain to the east.

The advent of basaltic volcanism at about 11 Ma signaled the end of crustal magmatism in the construction of Yucca Mountain. It indicates the generation of small, discrete batches of basaltic magma at upper mantle depths (60 km [40 mi]) capable of making their way quickly to the

surface in the Crater Flat basin (Figure 2-9) (Crowe et al. 1995 [DIRS 100110], pp. 5-16 and 5-17). The history, evolution, and character of Plio-Pleistocene basaltic volcanism proximal to Yucca Mountain (within 25 km [15 mi] of the repository) is treated by Crowe et al. (1995 [DIRS 100110]) and Vaniman et al. (1982 [DIRS 101031]).

The oldest basalts in Crater Flat are dated at about 11.3 Ma, indicating that episodes of basaltic volcanism began soon after eruption of the Ammonia Tanks Tuff (11.45 Ma). However, no further basaltic volcanism occurred in Crater Flat until 3.7 Ma, when a group of five northwest-aligned scoria cones and lava flows were emplaced in southeastern Crater Flat (Figure 2-9). This latter episode represents the largest volume basaltic emplacement in Crater Flat. The complex was formed largely from Hawaiian-type fissure eruptions and aa flows. Lava-filled fissures and feeder dikes are oriented north-south. The deposit was subsequently cut by faulting that produced dip-slip offsets of more than 1 m (3 ft), west side down (Crowe et al. 1995 [DIRS 100110], p. 2-20).

2.3.5.2 Quaternary Rocks and Sediments

Quaternary deposits in the Great Basin consist of alluvial, colluvial, and eolian sediments and minor volcanic deposits. In the vicinity of Yucca Mountain, the volcanic rocks are basaltic in composition. These eruptions represent a continuation of the activity during the late Tertiary. Following the episode at 3.7 Ma, a subsequent basaltic eruption episode occurred between 1.2 and 0.8 Ma. It consists of four cinder cones (Little Cones, Red Cone, Black Cone, and Makani Cone) aligned north-northeast along the axis of Crater Flat (Figure 2-9) and Sleeping Buttes northwest of Yucca Mountain. Most of the volume from this episode is associated with the Red and Black cones, and the area covered overlaps the area of the earliest basaltic eruption (11.3 Ma).

The most recent episode of basaltic volcanism created the Lathrop Wells Cone (Figure 2-9), a complex of fissure eruptions, spatter and scoria cones, and aa flows. Satellite spatter cones at the east base of the main cone have a northwest alignment. The Lathrop Wells Cone complex is dated at about 80 ka (Heizler et al. 1999 [DIRS 107255], pp. 767 and 768). Its complex emplacement history was discussed by Crowe et al. (1995 [DIRS 100110]) as well as Heizler et al. (1999 [DIRS 107255]).

Other basaltic groups in the Yucca Mountain vicinity include the 380-ka Sleeping Butte volcanic centers, located 45 km (30 mi) northwest of Yucca Mountain, and the Amargosa Valley basalt, located about 3 km (1.8 mi) south of the Amargosa Valley crossroads (Crowe et al. 1995 [DIRS 100110], p. 2-19). A basalt is buried, but was sampled by drilling; basalt samples gave $^{40}Ar/^{39}Ar$ isochron ages of 3.8 and 4.4 Ma (Crowe et al. 1995 [DIRS 100110], p. 2-19). The eruptive history of Quaternary basaltic volcanism in the Yucca Mountain region is discussed in more detail in Section 4.

Apart from sporadic and volumetrically minor basaltic volcanism, Quaternary deposition in the Yucca Mountain geologic setting is chiefly restricted to alluvial basin deposition. In many basins, alluvial deposition is a continuation of sediment infilling that was well under way in late Miocene time. For example, in Mid Valley east of Yucca Mountain (Figure 2-10), a continuous alluvial section 300 to 400 m (980 to 1,310 ft) thick includes a several-meter-thick interval of

7.5 Ma ash-fall Spearhead Tuff (McArthur and Burkhard 1986 [DIRS 104766], pp. 26, 27, and 41). The tuff, penetrated by two boreholes, is overlain by about 360 m (1,180 ft) of fine to coarse sand and sandy gravel derived from the basin flanks.

Closed basins in the area accumulated alluvial sediment hundreds of meters (about 1,000 ft) thick throughout the Plio-Pleistocene, in response to continued faulting, subsidence, and range flank erosion. Mid Valley and Frenchman Flat, Yucca Flat, and Crater Flat basins, and especially the basins of the Inyo-Mono terrane (Figure 2-10), contain sediment that includes coarse alluvial clastic facies (e.g., debris flow deposits, colluvium, fan-sheet gravel) and lakebed-playa deposits (e.g., siliceous clays, marls, evaporites). In some basins aggradation has reached levels sufficient to have formed spillways so that alluvial deposition is graded to an adjacent valley or basin (e.g., Crater Flat basin is graded into Amargosa Valley [Figure 2-10]).

Although present deposition and erosion generally occur at very low rates and sporadically because of the arid climate, the middle to late Pleistocene depositional record (locally dated by distal ash layers like the 760-ka Bishop Ash (Sarna-Wojcicki and Pringle 1992 [DIRS 104578]) indicates a highly variable and localized succession of sedimentary deposits, possibly analogous to the middle Miocene rocks of Pavits Spring, but without the tuffaceous volcanic component. Sediment input is dominated by highly local sources that control the lithologies of the coarse clastic components. Lake or marsh deposits are virtually the best datable records because they contain fine sediment and rare, but radiometrically datable, volcanic ash beds. In some places, large accumulations of eolian sands are banked up against range flanks or as dune accumulations, notably Big Dune (BD on Figure 4-10), south of Bare Mountain (Figure 2-10).

Surficial mapping of Quaternary deposits in the Yucca Mountain site area has been progressively refined over the years. Table 2-1 compares various units designated by different studies within the region. Early work in the Nevada Test Site region differentiated three major late Cenozoic stratigraphic units using correlation characteristics (e.g., Hoover et al. 1981 [DIRS 106177]; Hoover 1989 [DIRS 101247]), and was patterned after work done in the Vidal Junction area in the Mojave Desert (e.g., Bull 1991 [DIRS 102040], pp. 102 and 103). Taylor (1986 [DIRS 102864]) demonstrated the usefulness of soils for stratigraphic correlations and estimation of surficial unit ages within the Yucca Mountain area. Using this tool, six major allostratigraphic units were mapped by Peterson (1988 [DIRS 106512], Appendix B), Faulds et al. (1994 [DIRS 105126]), and Peterson et al. (1995 [DIRS 106519], pp. 380 to 385) in the Crater Flat area.

Wesling et al. (1992 [DIRS 107290]) mapped the surficial geology of Midway Valley at a scale of 1:6,000. This study delineates alluvial geomorphic surfaces, as defined by Bull and Ku (1975 [DIRS 102051], Appendix 2.5G) and Bull (1991 [DIRS 102040], pp. 51 and 52), that represent informal allostratigraphic units consisting of deposits separated by bounding unconformities, such as geomorphic surfaces. Eight alluvial geomorphic surfaces (QT0 through Qa7) ranging in age from Plio-Pleistocene to Holocene, as well as colluvium and eolian deposits, are identified on maps by Wesling et al. (1992 [DIRS 107290]) and are described in Section 3, Table 3-2.

2.4 REGIONAL STRUCTURE AND TECTONIC DEFORMATION

The geologic framework of Yucca Mountain is characterized by two distinctly different structural styles: an earlier compressional "mountain building" style of regional folding and overthrusting, and a later extensional "basin forming" style of regional normal and strike-slip faulting. The following sections discuss the structures resulting from these two styles of deformation.

2.4.1 Compressional Tectonics of the Yucca Mountain Region

The compressional style records orogenic events that occurred primarily during the Paleozoic, followed by a peak event in the Mesozoic that terminated an extensive period of marine deposition. Compressional deformation of Precambrian age is also recorded in Proterozoic and older rocks, but no orogenic pattern has been determined from the sparsely exposed rocks.

The earliest mountain-building event that affected Paleozoic rocks in the Yucca Mountain geologic setting was the Antler Orogeny (Figure 2-6) (Stewart 1980 [DIRS 103020], p. 36, Figure 22). Antler orogenic deformation is expressed chiefly by the Roberts Mountains overthrust belt, which is located well north of Yucca Mountain. The thrusting during late Devonian and early Mississippian time created a mountain range and marine foreland basin along its eastern margin into which the coarse sediment that eroded from the thrust belt was deposited. Ketner (1998 [DIRS 151766]) indicated that evidence for a strong compressional component during the Antler Orogeny is equivocal and that the orogeny may have been dominated by vertical tectonics.

The Antler Orogeny is important in the Yucca Mountain region for two reasons:

1. The fine-grained, terrigenous lithology of the Devonian/Mississippian Eleana (and especially the Mississipian Chainman Shale) lithosome forms a major Paleozoic aquitard north and east of Yucca Mountain, as well as a potential source rock for hydrocarbons.

2. The subsequent juxtaposition of three distinct but coeval facies (i.e., Antler-derived clastic debris, black Chainman Shale, and Mississippian and older carbonates) aids in recognizing the structural configurations that formed during the subsequent Sevier-Cordilleran Orogeny.

Mountain building in the near vicinity of Yucca Mountain began with an eastward-encroaching uplift in latest Permian to Triassic time and culminated during the Mesozoic with the cretaceous Sevier Orogeny (Stewart 1980 [DIRS 103020], p. 77; Fleck 1970 [DIRS 150625]; Armstrong 1968 [DIRS 101583], p. 429f). The Cretaceous Sevier Orogeny resulted in a broadly north- to northeast-trending fold-thrust system (Figure 2-11). The thrust sheets are typically complicated by overturned or dismembered folds and local reverse or overthrust faults. The major thrusts are continuous along the strike for distances of more than 100 km (60 mi) and exhibit stratigraphic juxtapositions that indicate translations of tens of kilometers. Nevertheless, the history of thrust faulting in the Yucca Mountain region, and the identity of each fault from place to place, is uncertain because of erosion, subsequent extension, and burial beneath Tertiary and Quaternary rocks and surficial deposits over wide areas. Therefore, only a general

treatment, with an emphasis on geometric relations relevant to issues concerning Yucca Mountain, is presented here.

Two major thrusts are recognized in the vicinity of Yucca Mountain: the Belted Range thrust (Figure 2-11) (Caskey and Schweickert 1992 [DIRS 102407], p. 1318; Cole and Cashman 1999 [DIRS 114714], p. 8) and CP thrust (Caskey and Schweickert 1992 [DIRS 102407], p. 1316; Barnes and Poole 1968 [DIRS 101612], p. 233; Carr 1984 [DIRS 101037], p. 52) (Figure 2-11). The Belted Range thrust (Figure 2-11) is the structurally lower and older thrust. It may be represented in an outcrop at Bare Mountain (referred to as the Meiklejohn Peak thrust), possibly in the core of the Calico Hills (see discussion of Calico Hills in the earlier version of the YMSD (REV 01) (CRWMS M&O 2000 [DIRS 151945]), and by exposures at the south end of the Belted Range west of Yucca Flat (Caskey and Schweickert 1992 [DIRS 102407], pp. 1318 and 1321; Cole and Cashman 1999 [DIRS 114714], p. 7). Displacement across the Belted Range thrust is estimated to range from a minimum of 7 km (4.3 mi) (Cole and Cashman 1999 [DIRS 114714], p. 8) to more than 25 km (15 mi) (Caskey and Schweickert 1992 [DIRS 102407], p. 1320) (Figures 2-4, 2-11). Cole and Cashman (1999 [DIRS 114714]) interpreted all of the abovementioned exposures to be of the same thrust, which led them to show it in a cross section beneath Yucca Mountain. However, the thrust, if present, at depth represents an older tectonic regime than the one that exists today and does not constitute an active seismic source.

Below the Belted Range thrust, a stack of imbricate slices or "plates" place Middle Devonian strata and the Eleana Formation over the Chainman Shale along a subhorizontal thrust exposed in the Eleana Range (Trexler et al. 1996 [DIRS 107005], p. 1756). Thrusts that form the base of this duplex zone cut upsection into Mississippian strata, then form a décollement within the weak Chainman Shale (Trexler et al. 1996 [DIRS 107005], p. 1757). The duplex stack extends about 7 km (4.3 mi) outboard (east) of the main Belted Range thrust; it includes structures at Calico Hills (Calico Hills plate), Mine Mountain (Mine Mountain plate), the Eleana Range (Castle plate, Dolomite Hill plate, and Grouse Canyon plate), and Quartzite Ridge at the northern border of the NTS (Figure 2-11) (Trexler et al. 1996 [DIRS 107005], p. 1739; Cole and Cashman 1999 [DIRS 114714], pp. 10 and 11). A component of the duplex stack in this northern area was identified as the Tippipah thrust by Robinson (1985 [DIRS 106674], p. 7). Westward projection of the Belted Range thrust implies that the magnetic gradient present beneath the volcanic deposits at the north end of Yucca Mountain represents the duplex stack thrust southward against the Silurian rocks penetrated by well UE-25 p #1 (Carr et al. 1986 [DIRS 102046], p. 16).

Many thrust systems in the Yucca Mountain region are associated with regional folds. Robinson (1985 [DIRS 106674], p. 5) inferred that the major structure encompassing Yucca Mountain is a synclinorial basin spanning the area between Bare Mountain and the Halfpint Range, a distance of more than 80 km (50 mi) (Figures 2-4 and 2-11). In his interpretation, the basin is asymmetric, having steep to overturned limbs on the Bare Mountain side and along Rock Valley. The basin is bounded on the southeast by the Rock Valley fault zone and northeast by a "major northeast-trending thrust system," the Tippipah thrust zone (Robinson 1985 [DIRS 106674], p. 5) (the Belted Range thrust of Caskey and Schweickert 1992 [DIRS 102407] and Trexler et al. 1996 [DIRS 107005]). The principal deformation within the basin consists of broad, concentric folds 8 to 24 km (5 to 15 mi) apart that strike within 30° of north and plunge northward. Robinson (1985 [DIRS 106674], pp. 5 and 19) based his interpretations of fold structure on exposed dips, data from well UE-25 p #1, and aeromagnetic data. As a corollary to

this tectonic interpretation, Robinson (1985 [DIRS 106674], p. 16) inferred that the Mine Mountain and CP thrusts are minor structures; he indicated they were local slides that occurred in response to regional folding. Whether Robinson's (1985 [DIRS 106674]) assessment of fold geometry, and the relative magnitudes of folding and thrusting, is correct, there is little doubt that large-amplitude regional folds have accompanied thrust faulting in the region.

It is unclear when overthrusting and regional folding generally ceased in the Yucca Mountain region. The presence of undeformed Upper Cretaceous intrusives indicates that deformation did not continue through Cretaceous time. The Belted Range thrust, as correlative to the Last Chance thrust, probably originated prior to latest middle Triassic time and ceased activity by about 93 Ma, the age of the Climax stock (Naeser and Maldonado 1981 [DIRS 105156], p. 46), a granodiorite intruded in complexly folded Ordovician strata north of Yucca Flat (Houser and Poole 1960 [DIRS 106183]). The age of the CP and Gass Peak thrusts, which cut the Belted Range thrust, would be younger. The Keystone thrust was probably moving by Early Jurassic time (Burchfiel et al. 1974 [DIRS 102080], p. 1021). By late Jurassic time, deformation was well underway in the Great Basin (Armstrong 1968 [DIRS 101583], p. 449). Thus, the Sevier Orogeny (Armstrong 1968 [DIRS 101583], p. 451; Fleck 1970 [DIRS 150625], p. 1718) was a short-lived compressional event in the Yucca Mountain region.

2.4.2 Extensional Tectonics of the Yucca Mountain Region

Snow and Wernicke (2000 [DIRS 159400]) have recently reviewed much of the information available on extensional tectonics in the central Basin and Range. They concluded (p. 659) that 250 to 300 km of extension was caused by west-northwest motion of the Sierra Nevada block away from the Colorado Plateau, at rates initially as great as 2 cm/yr and at 1.5 to 1 cm/yr during the last 5 m.y. (Figure 2-1b). Recent research indicates that most of the current extension, as indicated by strain measurements and seismicity, is concentrated along the eastern and western margins of the Basin and Range (Thatcher et al. 1999 [DIRS 119053], Figure 1; Martinez et al. 1998 [DIRS 159031], p. 569). The following summarizes earlier research on the extension in the Yucca Mountain region.

Extension in the Yucca Mountain region was shown by several workers to be active by late Oligocene time (Axen et al. 1993 [DIRS 101597], p. 64; Sawyer et al. 1994 [DIRS 100075], p. 1314; Hardyman and Oldow 1991 [DIRS 106084], p. 285; Ekren and Byers 1984 [DIRS 144980], p. 214; Dilles et al. 1993 [DIRS 104872], p. 425; Snow and Wernicke 2000 [DIRS 159400], p. 688). Other workers indicated that it was probably earlier (Eaton 1982 [DIRS 105228], p. 412; Hodges and Walker 1992 [DIRS 106153], p. 563; Axen et al. 1993 [DIRS 101597], p. 64; Applegate et al. 1992 [DIRS 144782], p. 519; Smith 1991 [DIRS 106819], p. 189). The first phase of extension, sometimes referred to as "pre-basin and range faulting" (Zoback et al. 1981 [DIRS 108663], p. 420), continued into middle Miocene time. Extension during this early phase is thought to have migrated from east-northeast to west-southwest and to have been unaffected by oblique shear (Seedorff 1991 [DIRS 106765], Figures 5 to 8). Although this phase of regional extension progressed under the influence of a generally uniform east-northeast oriented least principal stress (Zoback et al. 1981 [DIRS 108663], p. 422), northwest-directed oblique shear did influence the course of extension toward the west side of the widening province at an early date (Stewart 1992 [DIRS 106922], pp. 7 and 9). By early Miocene time (and likely by middle to late Oligocene), the characteristic

features of the Walker Lane had been established, namely discontinuous north-northwest-striking dextral faults and east-northeast-striking sinistral faults (Ekren and Byers 1984 [DIRS 144980], p. 203; Hardyman and Oldow 1991 [DIRS 106084], p. 289; Stewart 1988 [DIRS 100083], p. 686). Deep-seated detachment may also have been an important mechanism of Paleogene extension in this region. Geobarometry and fission-track dates indicate that subhorizontal mylonites, presumably indicative of predetachment shear (Hamilton 1987 [DIRS 150436], pp. 157 and 165; Hamilton 1988 [DIRS 100037], p. 80), were generated at depths of at least 15 km (9 mi) beneath the Funeral-Bare Mountains area during this phase of deformation (Hoisch and Simpson 1993 [DIRS 106162], pp. 6823 and 6824; Hoisch et al. 1997 [DIRS 111854], p. 2830).

The main extensional features within the tectonic setting of Yucca Mountain were established by about 15 Ma, namely a basin-and-range structural pattern defined chiefly by north-south-oriented basins or troughs and fault zones associated with Walker Lane, including the Rock Valley fault zone.

The late Oligocene interval was punctuated by deposition of ash-fall tuffs from eruptions east and north of Yucca Mountain (Axen et al. 1993 [DIRS 101597], p. 62). The advent of siliceous volcanism marked an important tectonic development in the early phase of extension. It signaled the culmination of regional crustal heating, the so-called "ignimbrite flare-up," during which large volumes of siliceous magma were emplaced in the middle to upper crust (Seedorff 1991 [DIRS 106765], p. 133).

Like the progress of early extension, magmatism proceeded from north to south through the Great Basin. In the south it seems to have generally lagged behind the extension. Thus, the southwestern Nevada volcanic field may have been generated in an area of crust weakened by deep extensional basins and, therefore, conducive to volcanic venting (Axen et al. 1993 [DIRS 101597], pp. 68 and 73). However, an alternative interpretation proposed by Sawyer et al. (1994 [DIRS 100075], pp. 1314 and 1316) postulates that the Oasis Valley-Timber Mountain caldera complex formed in an area of minor crustal extension and that significant extension proximal to Yucca Mountain occurred after formation of the caldera complex. A basin analysis by Blakely et al. (1999 [DIRS 149763]) indicated that the southwestern Nevada volcanic field (including Yucca Mountain) formed within an assemblage of deep extensional basins, which indicates that the present basin configuration was well established prior to the formation of Yucca Mountain. A clastic sedimentary deposit, the rocks of Pavits Spring (Hinrichs 1968 [DIRS 106140]), and the comparable Esmeralda Formation (Stewart and Diamond 1990 [DIRS 106927]) also imply that deepening and integration of basins in the Yucca Mountain region occurred prior to formation of the southwestern Nevada volcanic field.

The rocks of Pavits Spring record basin integration and increased structural and topographic relief by way of thick, torrential-stream boulder gravels and volcanic arkoses (Hinrichs 1968 [DIRS 106140]). Increasingly proximal volcanic activity is indicated by increasing contributions of tuffs upsection, including, ultimately, the major components of the southwestern Nevada volcanic field, beginning around 14 Ma with units of the Crater Flat Group.

The course and extent of basin evolution in the Yucca Mountain area are only generally perceived, but it seems clear that considerable extension and basin deepening preceded the volcanic activity that created Yucca Mountain.

The culminating tectonic event in the geologic evolution of the region and, coincidentally, the initiating event for the structural formation of Yucca Mountain was the creation of the southwestern Nevada volcanic field. This field was produced by a succession of at least five voluminous and numerous smaller eruptions that occurred over 7.5 m.y., from about 15 to 7.5 Ma. The greatest of these eruptions created the volcanic pile (the Miocene Paintbrush and Timber Mountain Groups) of which Yucca Mountain is a part. Posteruptive deflation likely created at least some of the present structural framework of Yucca Mountain, assuming that some post-Paintbrush Group subsidence of Crater Flat basin can be attributed to the withdrawal of the underlying magma chamber (Carr 1990 [DIRS 104669], p. 300). Local domainal extension, involving some strike-slip displacements, clockwise rotation of crustal blocks, basin subsidence, and range uplift, continued in the Walker Lane during the phase of siliceous volcanism (Sawyer et al. 1994 [DIRS 100075], p. 1314). Yucca Mountain was affected by this activity in the 12.7- to 9-Ma interval, as evidenced by continued subsidence and extension across the Crater Flat basin and the collapse of the Jackass Flats area and of volcanic terrane farther east.

The advent of basaltic volcanism at about 11 Ma signals the end of crustal-level magmatism in the vicinity of Yucca Mountain. It indicates the generation of small, discrete batches of basaltic magma at upper-mantle depths (45 to 60 km) capable of making their way quickly to the surface (Crowe et al. 1995 [DIRS 100110], p. 4-2).

From about 11 to 7 Ma, the style of tectonic deformation in the Yucca Mountain region became more clearly one of narrow basin subsidence, possibly accompanied by adjacent range uplift. Analysis of faults near Yucca Flat and in the Basin and Range province to the east indicate that the present stress regime originated around 9 Ma. Before that time, the least compressive stress was oriented in a more westerly or southwesterly direction (Zoback et al. 1981 [DIRS 108663], p. 430; Minor 1995 [DIRS 106373], p. 10,524). Minor (1995 [DIRS 106373], p. 10,525) concluded that the stress field in the Yucca Mountain region rotated clockwise as much as 65° in the 11.45- to 9-Ma interval. The clockwise stress rotation is recognized elsewhere in the region (Carr 1984 [DIRS 101037], p. 84; Zoback et al. 1981 [DIRS 108663], pp. 425 and 427; Michel-Noël et al. 1990 [DIRS 106359], pp. 155 and 169), but estimates of its timing vary (Wernicke et al. 1988 [DIRS 149959], p. 1756). Hardyman and Oldow (1991 [DIRS 106084], p. 295) envision a clockwise stress rotation of as much as 90° in the northern Walker Lane that began in the late Oligocene and attained its present state in the late Miocene. This style of tectonism continues at present, focused most conspicuously at Frenchman Flat and Yucca Flat east of Yucca Mountain and in Death Valley to the west (Figure 2-10). Some basins are quiescent or have not been active since the middle Pleistocene, including Mid Valley, Jackass Flats, and Amargosa Valley. Nevertheless, historic seismicity and occasional large earthquakes accompanied by subsidence–such as the Cedar Mountain, Fairview Peak, and Dixie Valley earthquakes–indicate that basin subsidence is sporadic. Presently, strike-slip faulting is active in the Inyo-Mono terrane to the west (Figure 2-12) and in Rock Valley (Figure 2-13) (Coe et al. 1996 [DIRS 101528], pp. 4.13-6 and 4.13-7).

2.4.3 Contemporary Deformation

Large earthquakes on range-front faults during the past 100 years indicate that Basin and Range extension is still under way. Epicenter distribution patterns and geodetic strain data indicate that strain is presently concentrated primarily north of Yucca Mountain, in a zone along latitude 37°N (the intermountain seismic belt), in the eastern California shear zone, and in the central Nevada seismic zone (Figure 2-3) (Bennett et al. 1999 [DIRS 127984], p. 373, Figure 1). High geodetic extension rates characterize these active areas (Bennett et al. 1998 [DIRS 150433], p. 566; Savage et al. 1995 [DIRS 104553], p. 20,266). Dixon et al. (1995 [DIRS 102793], p. 762) note that northwest motion of the Sierra Nevada block is accomplished by a combination of east-west extension on north-striking normal faults, and by dextral motion on northwest-striking strike-slip faults of the Walker Lane and eastern California shear zone (Figure 2-3). Geologic evidence indicates that the eastern California shear zone has been a zone of high strain since late Miocene time (10 to 6 Ma) (Dixon et al. 1995 [DIRS 102793], p. 760). Dixon et al. (1995 [DIRS 102793], p. 761) report 8.8 mm/yr (0.35 in./yr) at N9° ± 5°W. The integrated strain rate across the eastern California shear zone is 12.1 ± 1.2 mm/yr (0.48 ± 0.05 in./yr) at N38° ± 5°W (Dixon et al. 1995 [DIRS 102793], p. 767).

Strain surveys show that the direction of extension in the Great Basin is toward the northwest, comparable to the direction of σ_3, the least compressive stress (Minster and Jordan 1984 [DIRS 106377], p. 13; 1987 [DIRS 106379], p. 4802; Gordon et al. 1993 [DIRS 105433]; Dixon et al. 1995 [DIRS 102793]; Savage et al. 1995 [DIRS 104553]; Keefer et al. 1997 [DIRS 105123]). The northern Basin and Range appears to be moving at 4.9 ± 1.3 mm/yr (0.2 ± .05 in./yr) west-southwest with respect to the continental interior and southern Great Basin (Savage et al. 1995 [DIRS 104553], p. 20,265) by means of crustal extension.

The relatively high strain rate of the northern Basin and Range is at least partly accommodated by the central Nevada seismic zone (Figure 2-3). The motion of the Sierra Nevada block relative to Ely, Nevada, is 9.1 ± 1.5 mm/yr (0.36 ± 0.06 in./yr) at N16° ± 8°W (Savage et al. 1995 [DIRS 104553], p. 20,257). Trilateration data show that at least 2.7 mm/yr (0.11 in./yr) of this extension is taken up by the central Nevada seismic zone (Savage et al. 1995 [DIRS 104553], p. 20,265). In contrast, the southern Basin and Range has an extension rate of 3 mm/yr (0.12 in./yr) or less (Sauber 1989 [DIRS 104546], p. 123). The boundary between these two regions of differing extension, the intermountain seismic zone, is at about 37°N latitude (Harmsen and Rogers 1986 [DIRS 106092], p. 1561; Smith and Arabasz 1991 [DIRS 105406], p. 192, Figure 7), a boundary that may represent a regional shear zone (Savage et al. 1995 [DIRS 104553], p. 20,258) containing local and perhaps transient seismicity zones (Rogers et al. 1987 [DIRS 100176], p. 77). The intermountain seismic zone accommodates the differential extension between the northern and southern Basin and Range provinces; the slip rate in this zone is estimated at about 3.2 mm/yr (0.13 in./yr) (Savage et al. 1995 [DIRS 104553], p. 20,267). The high strain rate zones such as the central Nevada seismic zone, may represent concentrations of active deformation among relatively stable crust blocks (Savage et al. 1995 [DIRS 104553], p. 20,265).

The kinematic boundary condition for Basin and Range deformation (the relative motions of the Pacific and North American plates) has been nearly constant for at least the past 3.4 m.y. (Harbert and Cox 1989 [DIRS 106068], p. 3061), which is within the time span for activity of the

Inyo-Mono domain (Hodges et al. 1989 [DIRS 106156], p. 462). During this time, tectonic activity has gradually shifted westward, from the Death Valley-Furnace Creek fault to the Owens Valley fault (Dixon et al. 1995 [DIRS 102793], p. 765) (Figure 2-12). Dixon et al. (1995 [DIRS 102793], p. 765) indicate that the Walker Lane accommodates significant dextral shear. The central Nevada seismic zone trends obliquely across the older Walker Lane (Savage et al. 1995 [DIRS 104553], p. 20,267). Therefore, it would seem that the westward migration of tectonism in the Inyo-Mono domain and historical surface-rupturing earthquake activity along the central Nevada seismic zone represent a concentration of crustal strain of regional extent and significant longevity. This strain zone appears to be shifting westward and perhaps northward (Dixon et al. 1995 [DIRS 102793], p. 769), away from any involvement with Yucca Mountain.

The extensional tectonic evolution of the Yucca Mountain region produced significant structures that bear on interpretations of the history of deformation and on the development of tectonic models that include Yucca Mountain. Sections 4.2.3.2.1 to 4.2.3.2.6 of the earlier version of the YMSD (REV 01) (CRWMS M&O 2000 [DIRS 151945]) discuss these regional structures: the Funeral Mountains detachment, Bullfrog Hills detachment, Las Vegas Valley shear zone, Death Valley-Furnace Creek-Fish Lake Valley fault, and northeast-trending strike-slip fault zones located east of Yucca Mountain. Abbreviated discussions are included here for these faults and those with possible current activity which were not found to have recent offset.

2.4.3.1   Detachments

The Funeral Mountains detachment fault is a major feature that has denuded the core of the Funeral Mountains, revealing the broad, smooth lower plate surface (Figure 2-14). It seems clear that the lower plate (i.e., the subjacent crust) rose up during or shortly following detachment to give the range its present crest and perhaps much of its overall relief. Uplift occurred late during the phase of regional Miocene extension. Fission-track dates of apatite, sphene, and zircon from the lower plate rock indicate that cooling through the temperature interval of 285°C to 120°C (equivalent to about 10 to 5 km [6 to 3 mi] burial depth) took place between 10 and 9 Ma (Holm and Dokka 1991 [DIRS 106163], p. 1777), with surface exposure having occurred sometime after 6 Ma (Hoisch and Simpson 1993 [DIRS 106162], p. 6822).

The contact between the upper and lower plates along the east side of the Funeral Mountains shows evidence of pronounced shearing, but the amount of slip is unknown. The Titus Canyon Formation and a thick lower Miocene lava flow and associated tuff are much faulted, but can be seen on both remote-sensor imagery and mapping to be generally continuous along the Grapevine Mountains for at least 22 km (14 mi), thus precluding major deformation before eruption of the middle Miocene ash flows. Most of the Cenozoic extension postdates 9 Ma, but may predate 7.5 Ma. This accords with the late Miocene cooling ages, determined through fission-track studies by Hoisch and Simpson (1993 [DIRS 106162], p. 6805) and Holm and Dokka (1991 [DIRS 106163], p. 1775) that record the tectonic denudation of the northwest end of the lower plate of the Funeral Mountains. Tectonic denudation of these midcrustal rocks and the rotation and detachment faulting of the Miocene supracrustal rocks were thus of about the same age and must have been linked kinematically.

There is a second detachment exposed in the Bullfrog Hills (Figure 2-14). In this area, an assemblage of highly disrupted and structurally discordant, variably tilted tuff blocks of the southwestern Nevada volcanic field is spread out into Amargosa Valley from a source located between the northern flank of Bare Mountain and the west side of Oasis Valley. The assemblage is separated from Bare Mountain by the shallow, north-dipping, generally east-striking Fluorspar Canyon fault (Figure 2-14). This fault represents the near-headwall of the detachment, as well as the accommodation plane for westward translation. The headwall (or breakaway) fault of the Bullfrog Hills is exposed along a north-trending line that defines at least 1 km (0.6 mi) of stratigraphic offset that occurred between 12.7 and 11.6 Ma (Fridrich 1998 [DIRS 101098], p. 36; 1999 [DIRS 118942], p. 184, Figure 6). This line or zone connects with the Fluorspar Canyon fault. The more evident high-angle faults that segment the Bullfrog Hills farther west terminate against the trace of the low-angle Fluorspar Canyon fault (Figure 2-14). After 12.7 Ma, the breakaway zone occupied at least three successively more westward positions (Fridrich 1998 [DIRS 101098], p. 17; 1999 [DIRS 118942], p. 189).

Extension of the Bullfrog Hills began with northwest-side-down faulting during the 11.6- to 12.7-Ma interval (Hoisch et al. 1997 [DIRS 111854], p. 2818). The faulting produced translation and tilting that ranges from 45° at the head to at least 70° in the hills just east of Beatty (Figure 2-14) (Fridrich 1998 [DIRS 101098], p. 15; 1999 [DIRS 118942], p. 184). The translated and rotated blocks are separated by small wedge-shaped troughs filled with rockslide breccia and coarse alluvium (Fridrich 1998 [DIRS 101098], p. 15; 1999 [DIRS 118942], p. 186). This entire assemblage was then largely blanketed by the Timber Mountain Group tuff and rhyolite of Fleur-de-lis Ranch, which was subsequently faulted. The Ammonia Tanks Tuff is tilted 20° to 45° eastward. A cap of 10.7 Ma basalt is also faulted, but is much less tilted (Hoisch et al. 1997 [DIRS 111854], p. 2818). Severe brecciation and sliding occurred in the 11.4 Ma rhyolite and sediments in the northern Bullfrog Hills (Minor and Fleck 1994 [DIRS 150656], p. 75). The faulting appears to have become inactive and the Bullfrog Hills stabilized between about 9.8 Ma (Weiss et al. 1991 [DIRS 150661], p. A246) and 6.3 Ma (Weiss et al. 1988 [DIRS 150660], p. A399), following the opening of the western Amargosa Valley and Sarcobatus Flats basins (Figure 2-14) after 10 Ma (Weiss et al. 1993 [DIRS 107199]; Hoisch et al. 1997 [DIRS 111854], p. 2819). When the system became inactive at 7 or 8 Ma, the master fault dipped steeply beneath the Grapevine Mountains, which before 12 Ma lay close to the unmetamorphosed Paleozoic strata of Bare Mountain. The trace of the steep, active fault migrated about 35 km (22 mi) in 4 or 5 m.y. at a rate of about 7 to 9 mm/yr (0.3 to 0.4 in./yr). Hoisch et al. (1997 [DIRS 111854], p. 2830) calculated a rate of 12 mm/yr (0.5 in./yr) that continued to about 10.3 Ma.

2.4.3.2   The Las Vegas Valley Shear Zone

The Las Vegas Valley shear zone (Figure 2-15) represents the eastern boundary of the Walker Lane south of Rock Valley (Stewart 1988 [DIRS 100083], pp. 688 and 695). This feature is important to the Yucca Mountain geologic setting because it forms a major structural boundary (Figure 2-3) and plays a role in some tectonic models applicable to Yucca Mountain. However, little is known about geologic relations within the zone because it is buried by Pleistocene alluvium, exhibits little or no seismic activity, and cannot be well characterized using available geophysical data. The shear zone is generally thought to be a right-lateral strike-slip fault, chiefly on the evidence of displaced traces of Mesozoic thrust faults on either side

(Longwell 1974 [DIRS 104619], p. 985; Stewart 1988 [DIRS 100083], p. 695) and the clockwise curvature of the major ranges on the east side. The generally accepted displacement of more than 40 km (25 mi) along the central part of the shear zone (Burchfiel 1965 [DIRS 102052], p. 185) is thought to have occurred between 15 and 10 Ma (Bohannon 1984 [DIRS 104521], p. 59; Hudson et al. 1994 [DIRS 100986], p. 273).

The northern reach of the Las Vegas Valley shear zone is subject to differing interpretations (Hinrichs 1968 [DIRS 106140]; Fox and Carr 1989 [DIRS 105435], p. 42; Caskey and Schweickert 1992 [DIRS 102407], p. 1325, Figure 3; Burchfiel 1965 [DIRS 102052], p. 186). Burchfiel (1965 [DIRS 102052], p. 186) considered the northwestern projection of the zone to continue into the Specter Range thrust, as shown on Figure 2-15. Burchfiel's interpretation requires an episode of substantial south-southeast-directed compression in early Tertiary times to produce 1,830 m or more stratigraphic offset along the 50° to 60° northwest-dipping Specter Range thrust, as well as approximately 35 km of right-lateral offset along the Las Vegas Valley shear zone as projected into Mercury Valley.

The Las Vegas Valley shear zone also has been interpreted as an accommodation zone (Guth 1981 [DIRS 105817], p. 769; Carr 1984 [DIRS 101037], p. 13; Hamilton 1988 [DIRS 100037], p. 79) or a "transfer fault" (Duebendorfer and Black 1992 [DIRS 102827], p. 1109) that marks the lateral margin of a large tract of detachment faults thought to include the Spotted Range and ranges farther southeast (Guth 1981 [DIRS 105817], p. 770). This interpretation avoids structural problems at the northern end of the shear zone with the assumption that lateral displacement decreases to zero somewhere northwest of Indian Springs, a consequence of extension in this region (Guth 1981 [DIRS 105817], p. 769). The accommodation model of Duebendorfer and Black (1992 [DIRS 102827]) requires 10 to 20 km (6 to 12 mi) of slip to be absorbed by oroclinal bending in the Specter Range, but evidence for such compression during the 14- to 13-Ma interval has not been recognized in or near Rock Valley. Therefore, arcing the Las Vegas Valley shear zone to the west through Mercury Valley into alignment with the left-lateral Rock Valley fault zone is not a viable tectonic interpretation. However, an independent calculation by Caskey and Schweickert (1992 [DIRS 102407], p. 1328) implied that the amounts of extension between correlative structures found both north and south of the shear zone are not significantly different, which diminishes the importance of an accommodation or transfer mechanism.

The Las Vegas Valley shear zone is, thus, plausibly related to one of two opposed tectonic mechanisms: (1) lateral accommodation that attends detachment faulting or (2) north-south oriented lateral compression that has resulted in oroclinal bending and some right-lateral slip. The issue of oroclinal bending is of considerable tectonic interest because it implies a mechanism of lateral compression (or "constriction") (Wernicke et al. 1988 [DIRS 149959], p. 1754) in a tectonic regime apparently dominated by extension.

As much as 55 km (34 mi) of middle to late Miocene north-south crustal shortening is estimated in the northern Black Mountains along the Lake Mead fault zone (Anderson et al. 1994 [DIRS 101488], p. 1381), which is compatible with both right-lateral slip and domain-boundary compression along the Las Vegas Valley shear zone (Anderson et al. 1994 [DIRS 101488], p. 1403) (Figure 2-15). Paleomagnetic studies indicate that the vertical-axis, clockwise bending in ranges along the north side of the shear zone is not a consequence of simple fault drag

(Sonder et al. 1994 [DIRS 106881], p. 786), but represents a broad zone of combined crushing and local rotation of blocks on the order of a few kilometers (Nelson and Jones 1987 [DIRS 105171], p. 13; Sonder et al. 1994 [DIRS 106881], p. 782).

The sedimentological character of Tertiary strata and structural features near the south end of the Spotted Range (Figure 2-15) indicate that the apparent range-scale drag folding (oroflexing) associated with the Las Vegas Valley shear zone was formed in pre-late Oligocene time (Cole and Cashman 1999 [DIRS 114714], p. 35). Right-lateral transpression seems to have culminated in a late Miocene event that involved the crushing and bending of extended terrane north and east of the shear zone. Extension in the Sheep and Desert ranges evidently continued late, during deposition of strata tentatively correlated with the Miocene Horse Spring Formation (Guth 1981 [DIRS 105817], pp. 766 and 767) (Figure 2-11). In that case, right-lateral transpression that possibly had begun as early as 29 Ma likely peaked prior to about 14-13 Ma (Hudson et al. 1994 [DIRS 100986], p. 258).

2.4.3.3 Death Valley-Furnace Creek-Fish Lake Valley Fault

The combined Death Valley-Furnace Creek-Fish Lake Valley fault system forms the only major, thoroughgoing fault system in the Yucca Mountain region (Figure 2-12). The fault system is significant because it is a major domain boundary that separates a region of high strain rate and seismic activity (Inyo-Mono domain) from one of relatively low strain rate and highly diverse structure and seismic activity (Walker Lane). The fault system varies in structural style along strike, and links with associated lateral structures are uncertain. Therefore, its role in local fault development is open to interpretation. It may represent the eastern border of a series of transtensional pull-aparts (Burchfiel and Stewart 1966 [DIRS 102053], p. 439; Blakely et al. 1999 [DIRS 149763], p. 13), or it may represent range-front faults linked by strike-slip segments that are evolving into an increasingly coherent structure, propagated northward along a strike distance of about 350 km (220 mi).

The southern part of the fault system, the Death Valley fault segment, is primarily an oblique right-lateral range-front fault. It follows the salients and reentrants of the Black Mountains front, varying in strike from north-south to N40°W. For the most part, the Death Valley fault dips moderately to steeply west, but toward its southern end dips range from 35° to 65° to the east or northeast (Piety 1996 [DIRS 106540], pp. 141 and 318). Fault length is uncertain because of disagreement on definition of its poorly exposed end points. A minimum length of 51 km (32 mi) for the Death Valley fault is based on nearly continuously exposed west-facing scarps (Piety 1996 [DIRS 106540], p. 142); a minimum length for the Furnace Creek fault is 105 km (65 mi) (Piety 1996 [DIRS 106540], p. 190); and a minimum length for the Fish Lake Valley fault is 80 km (50 mi) (Figure 2-12) (Piety 1996 [DIRS 106540], p. 181).

The total offset of the Death Valley fault is unknown, but the dip-slip component, estimated from bedrock relief, is about 4,570 m (15,000 ft) (Wills 1989 [DIRS 150666], p. 197). Hooke (1972 [DIRS 106165], p. 2091) estimated a Holocene dip-slip displacement of about 63 m, based on elevation differences of coeval lakeshore features on the east and west sides of Death Valley. Fleck (1970 [DIRS 150223], p. 2811) considered that most of the vertical displacement on the Death Valley fault is ancient, probably having its inception before deposition of the Furnace Creek Formation (about 6 Ma). Estimates of total lateral offset toward the south end of the fault

range from 1.2 to 50 km (0.75 to 31 mi), depending on the age of offset rock units (Piety 1996 [DIRS 106540], p. 319). Estimates of late Tertiary and Quaternary offset range from 35 km (22 mi) (Butler et al. 1988 [DIRS 150435], p. 406) to about 20 km (12 mi) (Brady 1986 [DIRS 150434], p. 2). Estimates of Pleistocene offset toward the south end of the fault range from about 15 to 200 m (50 to 660 ft), with estimates of 1.2 to 3 m (4 to 10 ft) per event based on displaced drainage (Piety 1996 [DIRS 106540], pp. 321 and 322). Toward the south end of the Black Mountains, the Death Valley fault has mostly strike-slip displacement (Piety 1996 [DIRS 106540], p. 319). Holocene activity along the Death Valley fault is expressed by a 10.5 m (34 ft) scarp in an alluvial fan near Mormon Point. The average per event displacement is estimated to be 2.5 to 3.5 m (8 to 11 ft) (Klinger and Piety 1996 [DIRS 160351], p. 57).

The Furnace Creek fault is chiefly a right-lateral strike-slip fault that extends through alluvial fans along the central part of Death Valley. The continuous fault trace is well expressed in most remote-sensor images, probably because of the well-developed Pleistocene to Holocene scarp that ranges in cumulative relief from 0.3 to 23 m (1 to 75 ft) (Piety 1996 [DIRS 106540], p. 190). Estimates of total lateral offset, based on displaced Precambrian units, are uncertain. The estimates range from 97 km (60 mi) to less than 8 km (5 mi) (Wright and Troxel 1967 [DIRS 107337], p. 937; Piety 1996 [DIRS 106540], p. 190). Piety (1996 [DIRS 106540], p. 191) reported estimates of Pleistocene lateral offset of 21 m (69 ft) and 46 m (151 ft), and of single-event Holocene offsets of 1.5 to 2.7 m (5 to 9 ft) or less. Klinger and Piety (1996 [DIRS 160351], p. 57) reported an average lateral displacement per Holocene event of 4.5 m (15 ft).

A link between the Death Valley and Furnace Creek faults is not well established. The main trace of the Furnace Creek fault may veer southeastward along the southern end of the Funeral Mountains and into the Amargosa trough, and may even link up with structures along the east side of Amargosa Valley (Wright and Troxel 1967 [DIRS 107337], p. 947, Figure 2). The Death Valley fault may intersect or merge with the Furnace Creek fault across the alluvial-filled valley between the Funeral and Black mountains, a 19-km-long (12-mi-long) gap termed the "transition zone" by Klinger and Piety (1996 [DIRS 160351], p. 9). The structural nature of the inferred linkage is unclear, the fault traces and fold forms are relatively short, trend in various directions, and form a relatively wide zone (Klinger and Piety 1996 [DIRS 160351], p. 9).

Toward its northern end, between the Grapevine Mountains and Last Chance Range (Figure 2-12), the Furnace Creek fault is distributed into a number of fault planes forming a zone that extends into Fish Lake Valley. The Fish Lake Valley fault is thought to have propagated northward from the Furnace Creek fault sometime between 12 and 4 Ma (Reheis 1993 [DIRS 105367], p. 376). The fault dies out in a series of folds near the north end of Fish Lake Valley (Stewart 1967 [DIRS 106912], pp. 133 to 139). The northernmost 80 km (50 mi) or more of this zone of strike-slip and primarily dip-slip range-front faults is called the Fish Lake Valley fault. Estimates of maximum lateral displacement range from 25 km (15.5 mi) (Piety 1996 [DIRS 106540], p. 182) to 48 km (30 mi) (McKee 1968 [DIRS 105029], p. 512). Estimates of maximum vertical displacement range up to 750 m (2,460 ft) (Reheis and McKee 1991 [DIRS 145271], p. 40). The upper Pleistocene dip-slip component on the Fish Lake Valley is as much as 64 m (210 ft) (Brogan et al. 1991 [DIRS 104554], p. 1), and a Pleistocene lateral displacement as much as 122 m (400 ft) is recorded (Sawyer 1991 [DIRS 106729], p. 126). Pleistocene activity along the fault has been high; vertical displacement of as much as 540 m

(1,772 ft) may have accrued within the past 740 ka (Reheis and McKee 1991 [DIRS 145271], p. 38). However, modeling by Dixon et al. (1995 [DIRS 102793], p. 765), based on space geodesy, indicates that activity along the Death Valley-Furnace Creek-Fish Lake Valley fault system has slowed during the past few million years as slip is increasingly taken up to the west, mainly along the Owens Valley fault zone. This transference of right-lateral slip activity to the west is reflected by the historical seismicity along the eastern California shear zone (Figure 2-3) (Dixon et al. 1995 [DIRS 102793], p. 765) and its convergence northward with the Fish Lake Valley fault.

2.4.3.4 Northeast-Trending Strike-Slip Fault Zones and Spotted Range-Mine Mountain Structural Zone

The Spotted Range-Mine Mountain structural zone (Figure 2-3) (Carr 1984 [DIRS 101037], p. 30; Stewart 1988 [DIRS 100083], p. 694, referred to as "section") is distinguished by prominent east-northeast trending, left-lateral, strike-slip faults, and fault zones: Rock Valley fault zone, Mine Mountain fault, Wahmonie fault zone, and Cane Spring fault (Figure 2-13). The structural zone forms a discrete section of the Walker Lane domain (Stewart 1988 [DIRS 100083], pp. 694 and 695). It does not have a counterpart in the adjacent Basin and Range or Inyo-Mono domains.

The largest and most tectonically significant structural component of the Spotted Range-Mine Mountain structural zone is the Rock Valley fault zone (Coe et al. 1996 [DIRS 101528]), an unusually well-exposed domain section lying between the Spring Mountains and Goldfield sections of the Walker Lane (Figures 2-3, 2-13) (Stewart 1988 [DIRS 100083], p. 695). It is presently seismogenic and constitutes a potential seismic source relatively close to Yucca Mountain, exceeded in size only by the Furnace Creek fault, which is farther from Yucca Mountain.

The Rock Valley fault zone coincides with a band of broad aeromagnetic lows bounded by a parallel gradient (-300 to -400 nT) (Glen and Ponce 1991 [DIRS 105564]) along the south side of Little Skull Mountain and extending eastward to Frenchman Flat, a distance of about 40 km (25 mi). The geophysical data and local stratigraphy and structure indicate that the fault zone is part of a complex structural trough about 5 km wide. Three major fault sets compose the Rock Valley fault zone: (1) continuous, predominantly strike-slip faults that strike N65° to 80°E for distances of 15 km (9 mi) or more; (2) shorter normal, strike-slip, and/or reverse bridging faults that strike N25° to 50°E; and (3) minor normal and strike-slip faults that strike N10° to 15°W.

The zone is further complicated by N25°E-striking faults that project into Rock Valley from the north. These faults might be related tectonically (but not specifically) to the Cane Spring fault and Wahmonie fault zone, which strikes through the gap between Skull and Little Skull Mountains (Figure 2-13).

A seismic-reflection profile (Majer et al. 1996 [DIRS 104685], p. 23, Figure 46) was shot across the Rock Valley fault zone about midway along its length. The southern end of the profile (Figure 2-16) is located north of a complex bounding fault or within a zone of complex fault-controlled structure. This zone defines the southern margin of Rock Valley and inferred structural trough, the footwall of which is indicated by Paleozoic outcrop south of the profile's

end of line. One of three major Rock Valley fault strands, RV3, appears to be the southernmost plane of a zone of faulting perhaps 100 m (330 ft) wide. Disruption in interval A and a general down-to-the-north flexure of Tertiary strata mark the location of the zone in the profile (Figure 2-16). The data indicate that offset of the Tertiary-Paleozoic contact is about 122 m down to the north. This is possibly the major structural expression of the southern fault strand of the Rock Valley fault zone. Another mapped southern fault strand, RV4, is not expressed in the seismic profile. This is also the case for the mapped medial strand (RV1). The vertical-offset component for these two strands is probably less than acoustic resolution.

The largest displacement is on the step fault (Figure 2-16), located 300 m north from RV1. The step fault possibly bridges the northern and medial strands of the Rock Valley fault zone. The seismic profile shows that this deep fault forms the southern side of a depression about 500 m wide and 200 m deep filled with Pleistocene alluvium. The Tertiary-Paleozoic contact is downdropped about 190 m along the step fault.

The north side of the trough may mark the location of the northern fault strand (down to the south). However, there is no trace of a throughgoing fault at the surface or in the uppermost few hundred feet of the seismic profile. The trace of the northern fault strand is not expressed in the mapped geology or in aerial photographs within 2 to 3.5 km to either side of the seismic profile. In other words, the profile crosses a 5.5-km gap in the surface trace of the northern fault strand. The profile indicates a down-to-the-south fault at about CDP Station 320 that is buried by about 122 m of Pleistocene alluvium and/or Wahmonie dacite (Twt).

Offsets along the fault planes are rarely demonstrable because crosscutting features are uncommon. Estimates of total lateral offset of no more than 1.6 to 4 km are based on regional considerations (Barnes et al. 1982 [DIRS 124232]) and geophysical data (Kane and Bracken 1983 [DIRS 106275], p. 9). A few observed lateral offsets range from 30 to 40 m. However, these offsets appear to be pre-Pleistocene and may actually be the total of several series of smaller events spaced closely enough in time to have prevented erosional discrimination of smaller component slips.

Historically, earthquakes have occurred frequently toward the west end of Rock Valley, in the vicinity of Little Skull Mountain, Striped Hills, and Specter Range. Data summarized by Rogers et al. (1981 [DIRS 106700], pp. 9 and 15; 1987 [DIRS 100176], p. 37) indicate that the earthquakes were of mostly small magnitude events ($M \leq 4.0$) that occurred from near surface to depths of about a 10 km on north- to northeast-striking faults with left-lateral strike-slip and oblique-slip mechanisms (Rogers et al. 1987 [DIRS 100176], p. 31). Most of the strike-slip mechanisms were in the 4- to 9-km depth range. Fault-plane solutions for pre-1993 earthquakes are in accord with the sense of slip of the mapped faults, but no individual seismogenic faults have been identified (Rogers et al. 1987 [DIRS 100176], p. 37).

The Cane Spring fault is expressed as a conspicuous rectilinear fault-line scarp lineament (Reheis and Noller 1991 [DIRS 102891], Plate 3) that strikes N54°E along the north flank of Mount Salyer (Figure 2-13). The Cane Spring fault is mapped for a total length of about 8 km. It evidently controls the location of Cane Spring, a large perched spring that gives the fault its name. Mapping by Ekren and Sargent (1965 [DIRS 105241]) does not indicate a southwest projection of the fault into Rock Valley. Outcrops show the Cane Spring fault to be a nearly

vertical shear zone about 1.5 m wide. The fault plane controls a discontinuous scarp that locally attains a relief as much as 3 m across the beds of a few downslope gullies that cross the lineament west of Cane Spring. Local kinematic features imply left-lateral offset, but gross lithologic contacts indicate a dominantly normal, north-side-down movement. Poole et al. (1965 [DIRS 106568]) posit three generations of alternating dip slip in addition to strike slip, but the basis for this inference is unclear. The contrast in landforms across the fault is pronounced, indicating that the bulk of the offset has been dip-slip. The southeast side of the fault (upthrown block) shows numerous lineaments diverging south from the fault trace at angles of 30° to 45°. These probably represent splay faults or fractures indicative of the sinistral mechanism. Total offset along the Cane Spring fault is unknown; no indications of late Pleistocene activity were observed and aerial photos show that the oldest and deepest stream courses cross the fault without being offset. The most recent activity may have been 100 ka or older.

The Mine Mountain fault (Orkild 1968 [DIRS 106458]) extends along the south flank of Mine Mountain as two N35°E-striking subparallel faults that are separated by as much as 200 m (Figure 2-13). The faults interconnect and splay, and they apparently entrain slices that are tens of meters across. At Mine Mountain, the Tiva Canyon Tuff is offset for a distance of 1.2 km in a left-lateral sense across the fault zone. No exposures of the fault have been found, so the attitude of the fault plane(s) is unknown. Orkild (1968 [DIRS 106458]) interpreted the faults as oblique left-lateral, down to the south. The offset Tertiary units dip about 30°W, so given a steeply south-dipping fault (85° or more), purely normal displacement of about 500 to 600 m (1,640 to 1,970 ft) could produce the apparent left-lateral offset shown on the geologic map (Orkild 1968 [DIRS 106458]). Considering slip relations on other faults in the region, an oblique slip seems most likely.

Because no detailed Quaternary mapping has been done in the Mine Mountain quadrangle, the relation of faulting to Quaternary stratigraphy is unknown. The surficial map of the 7½-minute Skull Mountain quadrangle to the south (Swadley and Huckins 1990 [DIRS 106952]) (Figure 2-13) indicates that the fans overlying the projected Mine Mountain fault zone are constructed of middle to late Pleistocene alluvium (Swadley and Huckins 1990 [DIRS 106952]). Reconnaissance along and across the southern alluvial flank of Shoshone Mountain and examination of aerial photos of this area revealed evidence of complex faulting, but no evidence was observed of late Quaternary displacements, scarps in alluvium, or transcurrent fault traces in alluvium extending southwest of Mine Mountain. Weakly etched, short lineaments are found where the bedrock pediment is thinly covered. These features probably represent erosion focused by shattered bedrock. No thoroughgoing fault plane was observed among the variously tilted and sheared pediment blocks, but a strong northeast-oriented, shear-controlled fabric is evident in numerous bedrock exposures within fan gullies. The breccia is typically sliced by irregular, subplanar fractures that strike N20° to 45°E, and dip 85°S to 90°S, but have no slip indicators.

The total late Tertiary normal-fault displacement along the Shoshone Mountain range front is difficult to judge, both because faulting is distributed across a zone more than 1 km wide and because the volcanic units were deposited on a surface of high relief (as much as 100 m) eroded in faulted Paleozoic blocks and in the overlying Wahmonie Formation. Where observable, the style of displacement is one of obverse dip away from the slope rather than toward it, in the sense of a rotated slump block. This style, along with the sinistral shear component, indicates

that Shoshone Mountain probably pulled away obliquely west-southwest from a subsiding basin and that faulting was preceded by formation of a down-to-basin monocline.

No lineaments or other expressions of Quaternary faulting have been recognized to define a projection of the Mine Mountain fault in the fan deposits graded to Yucca Valley to the east. A smooth 32-mGal-gravity gradient that defines the structural west flank of Yucca Valley (Healey et al. 1987 [DIRS 106118]) indicates that the fault does not project into Yucca Valley. To the southwest, the situation is more problematic.

The northern strand of the Mine Mountain fault zone was projected by Orkild (1968 [DIRS 106458]) to trend southwest across Mid Valley along the southeast flank of Shoshone Mountain, where it is depicted as a down-to-the-south range-front fault. Seismic profiles illustrated and interpreted by McArthur and Burkhard (1986 [DIRS 104766], pp. 61, 63, 67, and 69) cross the projection of the Mine Mountain fault zone in Mid Valley. The profiles indicate disruption of reflections along the projection of the fault zone, but the nature of deformation is ambiguous. Simple large-scale block tilting is not in evidence and, therefore, the garbled reflections probably represent distributed shear rather than a few individual fault planes. Because reflections cannot be traced northward across the inferred fault-plane profiles, lateral offset rather than normal displacement is indicated.

Maldonado (1985 [DIRS 104160]) retained Orkild's range-front fault projection, but also projected the more southerly of the two Mine Mountain fault strands southwest across Mid Valley and out across Jackass Flats to a point due west of Little Skull Mountain (Figure 2-13). A range-front fault certainly exists where Orkild has mapped it, but YMP field work did not reveal any evidence for the left-lateral fault trace projection of Maldonado (1985 [DIRS 104160]). Nevertheless, there is good evidence for strike-slip faulting in bedrock exposures along the base of Shoshone Mountain and in a low bluff of Paintbrush Tuff (evidently an outlier of the Little Skull Mountain block) located just west of the old Field Operations Center (about 15 km south east of the Exploratory Studies Facility).

The 1:100,000 scale Bouguer gravity map of the Nevada Test Site (Healey et al. 1987 [DIRS 106118]) provides little indication of a significant crustal fault along the inferred projection of the Mine Mountain fault zone in northern Jackass Flats. Here, the fault projection passes across an area in Jackass Flats of virtually no gradients or conspicuous anomalies. In Mid Valley, the projection passes along the northwest flank of a large gravity minimum that represents the main depression of Mid Valley, and the fault could, thus, be considered a bounding structure to the depression (Figure 2-13).

The 1:100,000 scale aeromagnetic map of the Beatty quadrangle (Glen and Ponce 1991 [DIRS 105564]) shows strongly aligned gradients and separation of distinct anomaly patterns along the projection of the Mine Mountain fault zone into Jackass Flats. The aeromagnetic gradients indicate that the fault-zone projection is about 800 m wide along Shoshone Mountain, and that it widens to about 1.5 km as it crosses Jackass Flats south of Calico Hills. This zone of aligned steep gradients and linear and positive anomalies extends into a crudely annular anomaly pattern of short, steep highs rimmed with negative anomalies, about 8 km in diameter, centered west of the old Field Operations Center within area 25.

The westward extent and possible interaction of the convergent, westward extensions of the Rock Valley fault zone and Mine Mountain fault are unknown. Carr (1984 [DIRS 101037], p. 16) projected the Spotted Range-Mine Mountain structural zone of the Walker Lane belt, which is characterized by northeast-striking left-lateral faults, west into California to the Furnace Creek fault zone (Figure 2-17). However, no faults resembling the Rock Valley fault zone are known to transect the Funeral Mountains and, therefore, the fault zone probably extends no farther west than a line drawn from the west side of Little Skull Mountain south to the west end of the Skeleton Hills (Figure 2-13). Laterally sheared Paleozoic rocks and local Miocene volcanic rocks exposed along this line imply the existence of a N5° to 15° E-striking fault or shear zone. A fault along this trend is also indicated by gravity and aeromagnetic anomaly gradients, a hydraulic barrier (Winograd and Thordarson 1975 [DIRS 101167], p. C75), and seismic reflection data (Brocher et al. 1993 [DIRS 102002], p. 35), as well as sparse west-facing scarps in alluvial fans.

Attempts to find a segment of the Rock Valley fault zone west of the line described above (which is referred to as the Gravity fault, Figure 2-9) have been unsuccessful. Lineaments in the Amargosa Valley, however, indicate that a segment of the Rock Valley fault zone may exist beneath the Amargosa Valley. On the other hand, the main strands of the Rock Valley fault zone veer to the south into the Specter Range east of the Striped Hills (Figure 2-13). Thus, it is still unclear whether the zone even extends all the way to the western end of Rock Valley, let alone into Amargosa Valley.

2.4.3.5   Highway 95 Fault

Surface geologic mapping, geophysical evidence, and subsurface investigations indicate the presence of a large-offset, east-west striking concealed fault, referred to as the Highway 95 fault (Fridrich 1998 [DIRS 101098], p. 6). The fault occurs in the subsurface along the northeast margin of the Amargosa Desert, directly south of the southernmost extent of Yucca Mountain and Crater Flat (Figure 2-9). The Highway 95 structure possesses several unique characteristics. It appears to dip near-vertically, may have a length of about 15 km, terminates against the Bare Mountain fault on the west, and extends to the middle of Fortymile Wash on the east. Potter et al. (2002 [DIRS 159091]) show the fault just south of Highway 95, crossing U.S. Route 95 just southwest of the Lathrop Wells Cone (Figure 2-9). Its presence is based on a conspicuous alignment of low-lying hills just northeast of U.S. Route 95 and south of Crater Flat. These hills also mark the southwest edge of exposed volcanic rocks. However, the welding characteristics and thicknesses of the Paintbrush Group rocks exposed along this margin do not appear indicative of the extreme distal margin of pyroclastic deposition. Directly south of the low-lying hills that mark the southern extent of Yucca Mountain, moderate to steep aeromagnetic gradients also terminate abruptly. South of the inferred location of the Highway 95, within the northern Amargosa Valley, (1) conspicuous linear magnetic anomalies are absent, and (2) a broad gravity high occurs that has been interpreted as a Paleozoic basement high (Ackermann et al. 1988 [DIRS 103004], Figure 3.3, pp. 27 to 30). This is composed of Paleozoic carbonate rock that is covered by little or no volcanic rock, and is juxtaposed against a northern block. The northern block is composed of rocks of the Miocene Paintbrush and Crater Flat Groups (Potter et al. 2002 [DIRS 159091]).

The geophysical interpretations are, in part, supported by subsurface stratigraphic information. The absence or pronounced thinning of magnetized Miocene volcanic rock within the southern block is confirmed in several deep drill holes. Carr et al. (1995 [DIRS 104671]) reported that less than 40 m of tuff, suspected of being part of the Timber Mountain Group, overlies Paleozoic dolomite and limestone in drill hole Felderhoff Federal 25-1, less than 6 km south of the suspected location of the Highway 95 fault (Sweetkind et al. 2001 [DIRS 159092]). More recently, two drill holes, NC-EWDP-19D1 and NC-EWDP-2DB, which were drilled in close proximity to the Highway 95 structure, indicate an abrupt variation in the thickness and lithologic character of the buried Topopah Spring Tuff. Drill hole NC-EWDP-19D1, located directly south of the inferred trace of the Highway 95 fault in the area of one of the local moderate to steep aeromagnetic gradients, encountered about 130 m of nonwelded tuff that is suspected of being part of the lowermost Topopah Spring Tuff. Although uniformly nonwelded, Spengler and Dickerson (DTN: GS031108314211.005 [DIRS 168526]) indicated that much of the localized, anomalously thick tuff in NC-EWDP-19D1 may have been preserved on the downthrown side of the Highway 95 fault, thus producing the conspicuous aeromagnetic anomaly. In contrast, drill hole NC-EWDP-2DB, located 2 km to the southwest, within the southern block, encountered only 27 m of the Topopah Spring Tuff, having variations in welding consistent with characteristics of outcrops at the southern extent of Yucca Mountain (DTN: GS011008314211.001 [DIRS 158690]). To best accommodate abrupt differences in the thickness and lithologic character of the Topopah Spring Tuff between drill holes NC-EWDP-19D and NC-EWDP-2DB, the existence of a southeast trending splay to the Highway 95 fault has also been indicated (DTN: GS031108314211.005 [DIRS 168526]). Alternatively, the main trace of the Highway 95 fault may actually occur farther to the south, between NC-EWDP-19D and NC-EWDP-2DB, instead of the location indicated by Potter et al. (2002 [DIRS 159091]).

Based primarily on the dichotomous relative stratigraphic position of outcrops of Topopah Spring Tuff along different segments of the northern down-thrown block, the Highway 95 fault is suspected of having a component of lateral slip. The anomalous stratigraphic setting—wherein welding is present within the Topopah Spring Tuff in drill hole NC-EWDP-2DB, presumably closer to the distal edge of this pyroclastic flow deposit, but absent in drill hole NC-EWDP-19D, presumably closer to its source–provides supporting evidence. However, the amount of lateral slip is unclear, and the sense of lateral displacement remains incompletely understood. Fridrich (1998 [DIRS 101098]) notes the existence of a more extensive structure, called the Carrara fault, which not only coincides with trace of the Highway 95 fault, but would also extend northward along the southwestern flank of Bare Mountain. Slemmons indicated that the Carrara fault is a right-lateral strike-slip fault. Sweetkind et al. (2001 [DIRS 159092]) note that an outcrop of Miocene Ammonia Tanks Tuff appears displaced to the west on the south side of the inferred trace of the Highway 95 fault relative to where this formation crops out north of the fault (Swadley and Carr 1987 [DIRS 101300]). In contrast, it was indicated that a component of sinistral lateral movement along the Highway 95 fault is a structurally controlled pull-apart basin (DTN: GS031108314211.005 [DIRS 168526]). This may explain the development of a deep graben beneath Fortymile Wash (Ponce et al. 2001 [DIRS 158733]). Additional deep drilling in the area of southern Fortymile Wash and northern Amargosa Valley may help resolve this uncertainty.

2.4.3.6   Other Regionally Significant Faults

The earlier version of the YMSD (REV 01) (CRWMS M&O 2000 [DIRS 151945]) provides additional discussions of several other single, regionally important, faults. A complete list of known and suspected Quaternary faults that might produce ground motion at Yucca Mountain is presented in Section 4 of this document (Figure 4-23), and those pertinent to the site geology are also discussed in Section 3.5 of this document.

2.5   REFERENCES

The following is a list of the references cited in this document. Column 1 represents the unique six digit numerical identifier, which is placed in the text following the reference callout (e.g., CRWMS M&O 2000 [DIRS 144054]). The purpose of these numbers is to assist the reader in locating a specific reference. Within the reference list, multiple sources by the same author (e.g., CRWMS M&O 2000) are sorted alphabetically by title.

2.5.1   Documents Cited

103004   Ackermann, H.D.; Mooney, W.D.; Snyder, D.B.; and Sutton, V.D. 1988. "Preliminary Interpretation of Seismic-Refraction and Gravity Studies West of Yucca Mountain, Nevada and California." Chapter 3 of *Geologic and Hydrologic Investigations of a Potential Nuclear Waste Disposal Site at Yucca Mountain, Southern Nevada*. Carr, M.D. and Yount, J.C., eds. Bulletin 1790. Denver, Colorado: U.S. Geological Survey. TIC: 203085.

101488   Anderson, R.E.; Barnhard, T.P.; and Snee, L.W. 1994. "Roles of Plutonism, Midcrustal Flow, Tectonic Rafting, and Horizontal Collapse in Shaping the Miocene Strain Field of the Lake Mead Area, Nevada and Arizona." *Tectonics, 13*, (6), 1381-1410. Washington, D.C.: American Geophysical Union. TIC: 232896.

144782   Applegate, J.D.R.; Walker, J.D.; and Hodges, K.V. 1992. "Late Cretaceous Extensional Unroofing in the Funeral Mountains Metamorphic Core Complex, California." *Geology, 20*, (6), 519-522. Boulder, Colorado: Geological Society of America. TIC: 248258.

101583   Armstrong, R.L. 1968. "Sevier Orogenic Belt in Nevada and Utah." *Geological Society of America Bulletin, 79*, 429-458. Boulder, Colorado: Geological Society of America. TIC: 217561.

104431   Asmerom, Y.; Snow, J.K.; Holm, D.K.; Jacobsen, S.B.; Wernicke, B.P.; and Lux, D.R. 1990. "Rapid Uplift and Crustal Growth in Extensional Environments: An Isotopic Study from the Death Valley Region, California." *Geology, 18*, 223-226. Boulder, Colorado: Geological Society of America. TIC: 233164.

101597   Axen, G.J.; Taylor, W.J.; and Bartley, J.M. 1993. "Space-Time Patterns and Tectonic Controls of Tertiary Extension and Magmatism in the Great Basin of the Western United States." *Geological Society of America Bulletin, 105*, 56-76. Boulder, Colorado: Geological Society of America. TIC: 224970.

101612   Barnes, H. and Poole, F.G. 1968. "Regional Thrust-Fault System in Nevada Test Site and Vicinity." *Nevada Test Site*. Eckel, E.B., ed. Memoir 110. Boulder, Colorado: Geological Society of America. TIC: 221562.

124232   Barnes, H.; Ekren, E.B.; Rodgers, C.L.; and Hedlund, D.C. 1982. *Geologic and Tectonic Maps of the Mercury Quadrangle, Nye and Clark Counties, Nevada*. Miscellaneous Investigations Series Map I-1197. Denver, Colorado: U.S. Geological Survey. TIC: 227106.

150433   Bennett, R.A.; Wernicke, B.P.; and Davis, J.L. 1998. "Continuous GPS Measurements of Contemporary Deformation Across the Northern Basin and Range Province." *Geophysical Research Letters, 25*, (4), 563-566. Washington, D.C.: American Geophysical Union. TIC: 248140.

127984   Bennett, R.A.; Davis, J.L.; and Wernicke, B.P. 1999. "Present-Day Pattern of Cordilleran Deformation in the Western United States." *Geology, 27*, (4), 371-374. Boulder, Colorado: Geological Society of America. TIC: 246484.

149763   Blakely, R.J.; Jachens, R.C.; Calzia, J.P.; and Langenheim, V.E. 1999. "Cenozoic Basins of the Death Valley Extended Terrane as Reflected in Regional-Scale Gravity Anomalies." *Cenozoic Basins of the Death Valley Region*. Wright, L.A. and Troxel, B.W., eds. Special Paper 333. Pages 1-16. Boulder, Colorado: Geological Society of America. TIC: 248054.

104521   Bohannon, R.G. 1984. *Nonmarine Sedimentary Rocks of Tertiary Age in the Lake Mead Region, Southeastern Nevada and Northwestern Arizona*. Professional Paper 1259. Denver, Colorado: U.S. Geological Survey. TIC: 218213.

101865   Bohannon, R.G. and Parsons, T. 1995. "Tectonic Implications of Post-30 Ma Pacific and North American Relative Plate Motions." *Geological Society of America Bulletin, 107*, (8), 937-959. Boulder, Colorado: Geological Society of America. TIC: 233033.

150434   Brady, R.H., III 1986. "Stratigraphy and Tectonics of the Northern Avawatz Mountains at the Intersection of the Garlock and Death Valley Fault Zones, San Bernardino County, California -- A Field Guide." *Quaternary Tectonics of Southern Death Valley, California Field Trip Guide, 1986 Annual Meeting and Field Trip of the Friends of the Pleistocene, Pacific Cell, October 31-November 2, 1986*. Troxel, B.W., ed. Pages 1-12. Shoshone, California: Bennie W. Troxel. TIC: 248139.

102002   Brocher, T.M.; Carr, M.D.; Fox, K.F., Jr.; and Hart, P.E. 1993. "Seismic Reflection Profiling Across Tertiary Extensional Structures in the Eastern Amargosa Desert, Southern Nevada, Basin and Range Province." *Geological Society of America Bulletin, 105*, 30-46. Boulder, Colorado: Geological Society of America. TIC: 224981.

104554   Brogan, G.E.; Kellogg, K.S.; Slemmons, D.B.; and Terhune, C.L. 1991. *Late Quaternary Faulting Along the Death Valley-Furnace Creek Fault System, California and Nevada*. Bulletin 1991. Denver, Colorado: U.S. Geological Survey. TIC: 206275.

100024   Broxton, D.E.; Warren, R.G.; Byers, F.M.; and Scott, R.B. 1989. "Chemical and Mineralogic Trends Within the Timber Mountain–Oasis Valley Caldera Complex, Nevada: Evidence for Multiple Cycles of Chemical Evolution in a Long-Lived Silicic Magma System." *Journal of Geophysical Research, 94*, (B5), 5961-5985. Washington, D.C.: American Geophysical Union. TIC: 225928.

102051   Bull, W.B. and Ku, T.L. 1975. *Age Dating of the Late Cenozoic Deposits in the Vicinity of the Vidal Nuclear Generating Station Site*. Appendix 2.5G. Oakland, California: Woodward-Clyde Consultants. TIC: 217184.

102040   Bull, W.B. 1991. *Geomorphic Responses to Climate Change*. New York, New York: Oxford University Press. TIC: 223847.

102052   Burchfiel, B.C. 1965. "Structural Geology of the Specter Range Quadrangle, Nevada, and Its Regional Significance." *Geological Society of America Bulletin, 76*, 175-192. Boulder, Colorado: Geological Society of America. TIC: 217853.

102053   Burchfiel, B.C. and Stewart, J.H. 1966. "Pull-Apart Origin of the Central Segment of Death Valley, California." *Geological Society of America Bulletin, 77*, 439-441. Boulder, Colorado: Geological Society of America. TIC: 218356.

102080   Burchfiel, B.C.; Fleck, R.J.; Secor, D.T.; Vincelette, R.R.; and Davis, G.A. 1974. "Geology of the Spring Mountains, Nevada." *Abstracts with Programs - Geological Society of America, 85*, 1013-1022. Boulder, Colorado: Geological Society of America. TIC: 217346.

104628   Burchfiel, B.C. and Davis, G.A. 1988. "Mesozoic Thrust Faults and Cenozoic Low-Angle Normal Faults, Eastern Spring Mountains, Nevada, and Clark Mountains Thrust Complex, California." *This Extended Land, Geological Journeys in the Southern Basin and Range, Field Trip Guidebook, Geological Society of America, Cordilleran Section Meeting, Las Vegas, Nevada, 1988*. Weide, D.L. and Faber, M.L., eds. Pages 87-106. Boulder, Colorado: Geological Society of America. TIC: 234473.

150435   Butler, P.R.; Troxel, B.W.; and Verosub, K.L. 1988. "Late Cenozoic History and Styles of Deformation Along the Southern Death Valley Fault Zone, California." *Geological Society of America Bulletin, 100*, (3), 402-410. Boulder, Colorado: Geological Society of America. TIC: 248137.

102046   Carr, M.D.; Waddell, S.J.; Vick, G.S.; Stock, J.M.; Monsen, S.A.; Harris, A.G.; Cork, B.W.; and Byers, F.M., Jr. 1986. *Geology of Drill Hole UE25p#1: A Test Hole Into Pre-Tertiary Rocks Near Yucca Mountain, Southern Nevada*. Open-File Report 86-175. Menlo Park, California: U.S. Geological Survey. ACC: HQS.19880517.2633.

101037   Carr, W.J. 1984. *Regional Structural Setting of Yucca Mountain, Southwestern Nevada, and Late Cenozoic Rates of Tectonic Activity in Part of the Southwestern Great Basin, Nevada and California*. Open-File Report 84-854. Denver, Colorado: U.S. Geological Survey. ACC: NNA.19870325.0475.

104670   Carr, W.J.; Byers, F.M., Jr.; and Orkild, P.P. 1986. *Stratigraphic and Volcano-Tectonic Relations of Crater Flat Tuff and Some Older Volcanic Units, Nye County, Nevada*. Professional Paper 1323. Denver, Colorado: U.S. Geological Survey. TIC: 216598.

104669   Carr, W.J. 1990. "Styles of Extension in the Nevada Test Site Region, Southern Walker Lane Belt; An Integration of Volcano-Tectonic and Detachment Fault Models." Chapter 13 of *Basin and Range Extensional Tectonics Near the Latitude of Las Vegas, Nevada*. Wernicke, B.P., ed. Memoir 176. Boulder, Colorado: Geological Society of America. TIC: 222540.

104671   Carr, W.J.; Grow, J.A.; and Keller, S.M. 1995. *Lithologic and Geophysical Logs of Drill Holes Felderhoff Federal 5-1 and 25-1, Amargosa Desert, Nye County, Nevada*. Open-File Report 95-155. Denver, Colorado: U.S. Geological Survey. TIC: 218310.

102407   Caskey, S.J. and Schweickert, R.A. 1992. "Mesozoic Deformation in the Nevada Test Site and Vicinity: Implications for the Structural Framework of the Cordilleran Fold and Thrust Belt and Tertiary Extension North of Las Vegas Valley." *Tectonics, 11*, (6), 1314-1331. Washington, D.C.: American Geophysical Union. TIC: 232936.

102496   Catchings, R.D. 1992. "A Relation Among Geology, Tectonics, and Velocity Structure, Western to Central Nevada Basin and Range." *Geological Society of America Bulletin, 104*, 1178-1192. Boulder, Colorado: Geological Society of America. TIC: 234317.

102498   Cemen, I. and Wright, L.A. 1990. "Effect of Cenozoic Extension on Mesozoic Thrust Surfaces in the Central and Southern Funeral Mountains, Death Valley, California." Chapter 14 of *Basin and Range Extensional Tectonics Near the Latitude of Las Vegas, Nevada*. Memoir 176. Boulder, Colorado: Geological Society of America. TIC: 222540.

150229   Cemen, I.; Wright, L.A.; and Prave, A.R. 1999. "Stratigraphy and Tectonic Implications of the Latest Oligocene and Early Miocene Sedimentary Succession, Southernmost Funeral Mountains, Death Valley Region, California." *Cenozoic Basins of the Death Valley Region*. Wright, L.A. and Troxel, B.W., eds. Special Paper 333. Pages 65-86. Boulder, Colorado: Geological Society of America. TIC: 248054.

101528   Coe, J.A.; Yount, J.C.; and O'Leary, D.W. 1996. "Preliminary Results of Paleoseismic Investigations of the Rock Valley Fault System." Chapter 4.13 of *Seismotectonic Framework and Characterization of Faulting at Yucca Mountain, Nevada*. Whitney, J.W., ed. Milestone 3GSH100M. Denver, Colorado: U.S. Geological Survey. TIC: 237980. ACC: MOL.19970129.0041.

104709   Cole, J.C.; Trexler, J.H., Jr.; Cashman, P.H.; and Hudson, M.R. 1994. "Structural and Stratigraphic Relations of Mississippian Rocks at the Nevada Test Site." *Geological Investigations of an Active Margin, Geological Society of America Cordilleran Section Guidebook, 27th Annual Meeting, San Bernardino, California, March 21-23, 1994*. McGill, S.F. and Ross, T.M., eds. Pages 66-75. Redlands, California: San Bernardino County Museum Association. TIC: 237835.

114714   Cole, J.C. and Cashman, P.H. 1999. *Structural Relationship of Pre-Tertiary Rocks in the Nevada Test Site Region, Southern Nevada*. Professional Paper 1607. Denver, Colorado: U.S. Geological Survey. TIC: 245877.

140211   Corbett, K.; Wrucke, C.T.; and Nelson, C.A. 1988. "Structure and Tectonic History of the Last Chance Thrust System, Inyo Mountains and Last Chance Range, California." *This Extended Land, Geological Journeys in the Southern Basin and Range, Field Trip Guidebook, Geological Society of America, Cordilleran Section Meeting, Las Vegas, Nevada, 1988*. Weide, D.L. and Faber, M.L., eds. Special Publication No. 2. Pages 269-292. Las Vegas, Nevada: University of Nevada, Las Vegas, Department of Geoscience. TIC: 232933.

100110   Crowe, B.; Perry, F.; Geissman, J.; McFadden, L.; Wells, S.; Murrell, M.; Poths, J.; Valentine, G.A.; Bowker, L.; and Finnegan, K. 1995. *Status of Volcanism Studies for the Yucca Mountain Site Characterization Project*. LA-12908-MS. Los Alamos, New Mexico: Los Alamos National Laboratory. ACC: HQO.19951115.0017.

151945   CRWMS M&O (Civilian Radioactive Waste Management System Management and Operating Contractor) 2000. *Yucca Mountain Site Description*. TDR-CRW-GS-000001 REV 01 ICN 01. Las Vegas, Nevada: CRWMS M&O. ACC: MOL.20001003.0111.

101557   Day, W.C.; Potter, C.J.; Sweetkind, D.S.; Dickerson, R.P.; and San Juan, C.A. 1998. *Bedrock Geologic Map of the Central Block Area, Yucca Mountain, Nye County, Nevada*. Miscellaneous Investigations Series Map I-2601. Washington, D.C.: U.S. Geological Survey. ACC: MOL.19980611.0339.

102786   Diehl, P. 1976. "Stratigraphy and Sedimentology of the Wood Canyon Formation, Death Valley Area, California." *Geologic Features, Death Valley, California.* Troxel, B.W. and Wright, L.A., eds. California Division of Mines and Geology Special Report 106. Pages 51-62. Sacramento, California: California Division of Mines and Geology. TIC: 232853.

104872   Dilles, J.H.; John, D.A.; and Hardyman, R.F. 1993. "Evolution of Cenozoic Magmatism and Tectonism Along a Northeast-Southwest Transect Across the Northern Walker Lane, West-Central Nevada -- Part I." *Crustal Evolution of the Great Basin and the Sierra Nevada, Field Trip Guidebook for the 1993 Joint Meeting of the Cordilleran/Rocky Mountain Sections of the Geological Society of America, Reno, Nevada, May 19-21, 1993.* Lahren, M.M.; Trexler, J.H., Jr.; and Spinosa, C., eds. Pages 409-452. Reno, Nevada: University of Nevada, Reno, Mackay School of Mines. TIC: 241232.

102793   Dixon, T.H.; Robaudo, S.; Lee, J.; and Reheis, M.C. 1995. "Constraints on Present-Day Basin and Range Deformation from Space Geodesy." *Tectonics, 14,* (4), 755-772. Washington, D.C.: American Geophysical Union. TIC: 234271.

102886   DOE (U.S. Department of Energy) 1988. *Site Characterization Plan, Yucca Mountain Site, Nevada Research and Development Area, Nevada.* DOE/RW-0199. Volume I, Part A. Washington, D.C.: U.S. Department of Energy, Office of Civilian Radioactive Waste Management. ACC: HQO.19881201.0002.

102871   DOE 1996. *Final Environmental Impact Statement for the Nevada Test Site and Off-Site Locations in the State of Nevada.* DOE/EIS 0243. Volume 1. Las Vegas, Nevada: U.S. Department of Energy, Nevada Operations Office. TIC: 226875.

144978   Drewes, H. 1963. *Geology of the Funeral Peak Quadrangle, California, on the East Flank of Death Valley.* Professional Paper 413. Washington, D.C.: U.S. Geological Survey. TIC: 233111.

102827   Duebendorfer, E.M. and Black, R.A. 1992. "Kinematic Role of Transverse Structures in Continental Extension: An Example from the Las Vegas Valley Shear Zone, Nevada." *Geology, 20,* 1107-1110. Boulder, Colorado: Geological Society of America. TIC: 236844.

102861   Dunne, G.C. 1986. "Geologic Evolution of the Southern Inyo Range, Darwin Plateau, and Argus and Slate Ranges, East-Central California–An Overview." *Guidebook and Volume, Field Trip Number 2, Mesozoic Evolution of Southern Inyo, Argus and Slate Ranges, Geologic Evolution of Tucki Mountain, Central Panamint Range, Field Trip Number 14, Stratigraphy and Structure of Metamorphic Framework Rocks, Lake Isabella Area, Southern Sierra Nevada, Cordilleran Section of the Geological Society of America, Los Angeles, California, March 25-28, 1986.* Pages 3-21. Los Angeles, California: Geological Society of America, Cordilleran Section. TIC: 232850.

105228   Eaton, G.P. 1982. "The Basin and Range Province: Origin and Tectonic Significance." *Annual Review of Earth and Planetary Science, 10*, 409-440. Palo Alto, California: Annual Reviews. TIC: 225015.

105241   Ekren, E.B. and Sargent, K.A. 1965. *Geologic Map of the Skull Mountain Quadrangle, Nye County, Nevada*. Geologic Quadrangle Map GQ-387. Washington, D.C.: U.S. Geological Survey. TIC: 216989.

105242   Ekren, E.B.; Anderson, R.E.; Rogers, C.L.; and Noble, D.C. 1971. *Geology of the Northern Nellis Air Force Base Bombing and Gunnery Range, Nye County, Nevada*. Professional Paper 651. Washington, D.C.: U.S. Geological Survey. TIC: 201531.

144980   Ekren, E.B. and Byers, F.M., Jr. 1984. "The Gabbs Valley Range--A Well-Exposed Segment of the Walker Lane in West-Central Nevada." *Western Geological Excursions Volume 4*. Lintz, J., Jr., ed. Pages 203-215. Boulder, Colorado: Geological Society of America. TIC: 233077.

105126   Faulds, J.E.; Bell, J.W.; Feuerbach, D.L.; and Ramelli, A.R. 1994. *Geologic Map of the Crater Flat Area, Nevada*. Geophysical Investigations Map 101. Reno, Nevada: University of Nevada, Reno. TIC: 211484.

105335   Fleck, R.J. 1967. *The Magnitude, Sequence, and Style of Deformation in Southern Nevada and Eastern California*. Ph.D. dissertation. Berkeley, California: University of California, Berkeley. TIC: 241075.

150223   Fleck, R.J. 1970. "Age and Tectonic Significance of Volcanic Rocks, Death Valley Area, California." *Geological Society of America Bulletin, 81*, 2807-2815. Boulder, Colorado: Geological Society of America. TIC: 239588.

150625   Fleck, R.J. 1970. "Tectonic Style, Magnitude, and Age of Deformation in the Sevier Orogenic Belt in Southern Nevada and Eastern California." *Geological Society of America Bulletin, 81*, 1705-1720. Boulder, Colorado: Geological Society of America. TIC: 217008.

105435   Fox, K.F., Jr. and Carr, M.D. 1989. "Neotectonics and Volcanism at Yucca Mountain and Vicinity, Nevada." *Radioactive Waste Management and the Nuclear Fuel Cycle, 13*, 37-50. New York, New York: Harwood Academic Publishers. TIC: 200232.

101098   Fridrich, C.J. 1998. *Tectonic Evolution of the Crater Flat Basin, Yucca Mountain Region, Nevada*. Open-File Report 98-33. Denver, Colorado: U.S. Geological Survey. ACC: MOL.19981014.0298.

118942   Fridrich, C.J. 1999. "Tectonic Evolution of the Crater Flat Basin, Yucca Mountain Region, Nevada." Chapter 7 of *Cenozoic Basins of the Death Valley Region*. Wright, L.A. and Troxel, B.W., eds. Special Paper 333. Boulder, Colorado: Geological Society of America. TIC: 248054.

105454   Frizzell, V.A., Jr. and Shulters, J. 1990. *Geologic Map of the Nevada Test Site, Southern Nevada*. Miscellaneous Investigations Series Map I-2046. Denver, Colorado: U.S. Geological Survey. TIC: 200459.

105430   Gilbert, G.K. 1875. "Report on the Geology of Portions of Nevada, Utah, California, and Arizona Examined in the Years 1871-1872." *U.S. Geographical and Geological Surveys West of the 100th Meridian*. Volume 3, Part 1. Washington, D.C.: U.S. Geological Survey. Readily available.

105564   Glen, J.M. and Ponce, D.A. 1991. *Aeromagnetic Map of the Beatty Quadrangle, Nevada–California*. Open-File Report 91-105. Menlo Park, California: U.S. Geological Survey. TIC: 204237.

105433   Gordon, D.; Ma, C.; and Ryan, J.W. 1993. "Results from the CDP Mobile VLBI Program in the Western United States." *Contributions of Space Geodesy to Geodynamics: Crustal Dynamics*. Smith, D.E. and Turcotte, D.L., eds. Geodynamics Series Volume 23. Pages 131-138. Washington, D.C.: American Geophysical Union. TIC: 245668.

105817   Guth, P.L. 1981. "Tertiary Extension North of the Las Vegas Valley Shear Zone, Sheep and Desert Ranges, Clark County, Nevada." *Geological Society of America Bulletin, Part I, 92*, (10), 763-771. Boulder, Colorado: Geological Society of America. TIC: 217559.

105920   Hamilton, W. and Myers, W.B. 1966. "Cenozoic Tectonics of the Western United States." *Reviews of Geophysics, 4*, (4), 509-549. Washington, D.C.: American Geophysical Union. TIC: 201734.

150436   Hamilton, W. 1987. "Crustal Extension in the Basin and Range Province, Southwestern United States." *Continental Extensional Tectonics*. Coward, M.P.; Dewey, J.F.; and Hancock, P.L., eds. Geological Society Special Publication No. 28. Pages 155-176. Oxford, England: Geological Society. TIC: 248138.

100037   Hamilton, W.B. 1988. "Detachment Faulting in the Death Valley Region, California and Nevada." Chapter 5 of *Geologic and Hydrologic Investigations of a Potential Nuclear Waste Disposal Site at Yucca Mountain, Southern Nevada*. Carr, M.D. and Yount, J.C., eds. Bulletin 1790. Denver, Colorado: U.S. Geological Survey. TIC: 203085.

106068   Harbert, W. and Cox, A. 1989. "Late Neogene Motion of the Pacific Plate." *Journal of Geophysical Research, 94*, (B3), 3052-3064. Washington, D.C.: American Geophysical Union. TIC: 240848.

106084 Hardyman, R.F. and Oldow, J.S. 1991. "Tertiary Tectonic Framework and Cenozoic History of the Central Walker Lane, Nevada." *Geology and Ore Deposits of the Great Basin, Symposium Proceedings, Reno/Sparks, Nevada, April 1-5, 1990.* Raines, G.L.; Lisle, R.E.; Schafer, R.W.; and Wilkinson, W.H., eds. *1*, 279-301. Reno, Nevada: Geological Society of Nevada. TIC: 246285.

106092 Harmsen, S.C. and Rogers, A.M. 1986. "Inferences About the Local Stress Field from Focal Mechanisms: Applications to Earthquakes in the Southern Great Basin of Nevada." *Bulletin of the Seismological Society of America, 76*, (6), 1560-1572. El Cerrito, California: Seismological Society of America. TIC: 237978.

106118 Healey, D.L.; Harris, R.N.; Ponce, D.A.; and Oliver, H.W. 1987. *Complete Bouguer Gravity Map of the Nevada Test Site and Vicinity, Nevada.* Open-File Report 87-506. Menlo Park, California: U.S. Geological Survey. TIC: 203192.

107255 Heizler, M.T.; Perry, F.V.; Crowe, B.M.; Peters, L.; and Appelt, R. 1999. "The Age of Lathrop Wells Volcanic Center: An $^{40}Ar/^{39}Ar$ Dating Investigation." *Journal of Geophysical Research, 104*, (B1), 767-804. Washington, D.C.: American Geophysical Union. TIC: 243399.

106140 Hinrichs, E.N. 1968. "Geologic Structure of Yucca Flat Area, Nevada." *Nevada Test Site.* Eckel, E.B., ed. Memoir 110. Boulder, Colorado: Geological Society of America. TIC: 221562.

106156 Hodges, K.V.; McKenna, L.W.; Stock, J.; Knapp, J.; Page, L.; Stemlof, K.; Silverberg, D.; Wust, G.; and Walker, J.D. 1989. "Evolution of Extensional Basins and Basin and Range Topography West of Death Valley, California." *Tectonics, 8*, (3), 453-467. Washington, D.C.: American Geophysical Union. TIC: 240829.

106153 Hodges, K.V. and Walker, J.D. 1992. "Extension in the Cretaceous Sevier Orogen, North American Cordillera." *Geological Society of America Bulletin, 104*, 560-569. Boulder, Colorado: Geological Society of America. TIC: 233061.

106162 Hoisch, T.D. and Simpson, C. 1993. "Rise and Tilt of Metamorphic Rocks in the Lower Plate of a Detachment Fault in the Funeral Mountains, Death Valley, California." *Journal of Geophysical Research, 98*, (B4), 6805-6827. Washington, D.C.: American Geophysical Union. TIC: 232889.

106161 Hoisch, T.D. 1995. "Conditions of Metamorphism in Lower-Plate Rocks at Bare Mountain, Nevada - Implications for Extensional Faulting." Chapter 2 of *Characterization of Detachment Faults in the Yucca Mountain Region.* Denver, Colorado: U.S. Geological Survey. ACC: MOL.19960305.0440.

111854   Hoisch, T.D.; Heizler, M.T.; and Zartman, R.E. 1997. "Timing of Detachment Faulting in the Bullfrog Hills and Bare Mountain Area, Southwest Nevada: Inferences from ^{40}Ar/^{39}Ar, K-Ar, U-Pb, and Fission Track Thermochronology." *Journal of Geophysical Research, 102*, (B2), 2815-2833. Washington, D.C.: American Geophysical Union. TIC: 246062.

106163   Holm, D.K. and Dokka, R.K. 1991. "Major Late Miocene Cooling of the Middle Crust Associated with Extensional Orogenesis in the Funeral Mountains, California." *Geophysical Research Letters, 18*, (9), 1775-1778. Washington, D.C.: American Geophysical Union. TIC: 232885.

106165   Hooke, R.L. 1972. "Geomorphic Evidence for Late-Wisconsin and Holocene Tectonic Deformation, Death Valley, California." *Geological Society of America Bulletin, 83*, (7), 2073-2098. Boulder, Colorado: Geological Society of America. TIC: 217330.

106177   Hoover, D.L.; Swadley, W C; and Gordon, A.J. 1981. *Correlation Characteristics of Surficial Deposits with a Description of Surficial Stratigraphy in the Nevada Test Site Region*. Open-File Report 81-512. Denver, Colorado: U.S. Geological Survey. ACC: NNA.19870406.0033.

101247   Hoover, D.L. 1989. *Preliminary Description of Quaternary and Late Pliocene Surficial Deposits at Yucca Mountain and Vicinity, Nye County, Nevada*. Open-File Report 89-359. Denver, Colorado: U.S. Geological Survey. ACC: NNA.19900403.0406.

106183   Houser, F.N. and Poole, F.G. 1960. *Preliminary Geologic Map of the Climax Stock and Vicinity, Nye County, Nevada*. Miscellaneous Geologic Investigations Map I-328. Washington, D.C.: U.S. Geological Survey. TIC: 233020.

101248   Huber, N.K. 1988. *Late Cenozoic Evolution of the Upper Amargosa River Drainage System, Southwestern Great Basin, Nevada and California*. Open-File Report 87-617. Menlo Park, California: U.S. Geological Survey. ACC: NNA.19930216.0062.

100986   Hudson, M.R.; Sawyer, D.A.; and Warren, R.G. 1994. "Paleomagnetism and Rotation Constraints for the Middle Miocene Southwestern Nevada Volcanic Field." *Tectonics, 13*, (2), 258-277. Washington, D.C.: American Geophysical Union. TIC: 232935.

106201   Hunt, C.B. and Mabey, D.R. 1966. *Stratigraphy and Structure Death Valley, California, General Geology of Death Valley, California*. Professional Paper 494-A. Washington, D.C.: U.S. Geological Survey. TIC: 221399.

150225   Jennings, C.W. 1977. *Geologic Map of California*. California Geologic Data Map Series, Map No. 2. Sacramento, California: California Division of Mines and Geology. TIC: 217022.

106275   Kane, M.F. and Bracken, R.E. 1983. *Aeromagnetic Map of Yucca Mountain and Surrounding Regions, Southwest Nevada.* Open-File Report 83-616. Denver, Colorado: U.S. Geological Survey. TIC: 201297.

105123   Keefer, W.R.; Coe, J.A.; Pezzopane, S.K.; and Hunter, W.C. 1997. *Geodesy and Contemporary Strain in the Yucca Mountain Region, Nevada.* Open-File Report 97-383. Denver, Colorado: U.S. Geological Survey. ACC: MOL.19980219.0826.

151766   Ketner, K.B. 1998. *The Nature and Timing of Tectonism in the Western Facies Terrane of Nevada and California--An Outline of Evidence and Interpretations Derived from Geologic Maps of Key Areas.* Professional Paper 1592. Denver, Colorado: U.S. Geological Survey. TIC: 248753.

160351   Klinger, R.E. and Piety, L.A. 1996. *Evaluation and Characterization of Quaternary Faulting on the Death Valley and Furnace Creek Faults, Death Valley, California.* Seismotectonic Report 96-10. Denver, Colorado: Bureau of Reclamation, Technical Service Center, Seismotectonics and Geophysics Group. ACC: MOL.19970718.0394.

106303   Ku, T-L.; Bull, W.B.; Freeman, S.T.; and Krauss, K.G. 1979. "Th^{230}-U^{234} Dating of Pedogenic Carbonates in Gravelly Desert Soils of Vidal Valley, Southeastern California." *Geological Society of America Bulletin, 90,* (Part I), 1063-1073. Boulder, Colorado: Geological Society of America. TIC: 238165.

104158   Lipman, P.W. and McKay, E.J. 1965. *Geologic Map of the Topopah Spring SW Quadrangle, Nye County, Nevada.* Geologic Quadrangle Map GQ-439. Denver, Colorado: U.S. Geological Survey. TIC: 212352.

100773   Lipman, P.W.; Christiansen, R.L.; and O'Connor, J.T. 1966. *A Compositionally Zoned Ash-Flow Sheet in Southern Nevada.* Professional Paper 524-F. Washington, D.C.: U.S. Geological Survey. TIC: 219972.

104621   Longwell, C.R.; Pampeyan, E.H.; Bowyer, B.; and Roberts, R.J. 1965. *Geology and Mineral Deposits of Clark County, Nevada.* Bulletin 62. Reno, Nevada: Nevada Bureau of Mines and Geology. TIC: 217110.

104619   Longwell, C.R. 1974. "Measure and Date of Movement on Las Vegas Valley Shear Zone, Clark County, Nevada." *Geological Society of America Bulletin, 85,* 985-990. Boulder, Colorado: Geological Society of America. TIC: 232897.

104685   Majer, E.L.; Feighner, M.; Johnson, L.; Daley, T.; Karageorgi, E.; Lee, K.H.; Williams, K.; and McEvilly, T. 1996. *Surface Geophysics.* Volume I of *Synthesis of Borehole and Surface Geophysical Studies at Yucca Mountain, Nevada and Vicinity.* Milestone OB05M. Berkeley, California: Lawrence Berkeley National Laboratory. ACC: MOL.19970610.0150.

106333   Maldonado, F.; Muller, D.C.; and Morrison, J.N. 1979. *Preliminary Geologic and Geophysical Data of the UE25a-3 Exploratory Drill Hole, Nevada Test Site, Nevada.* USGS-1543-6. Denver, Colorado: U.S. Geological Survey. TIC: 203082.

104160   Maldonado, F. 1985. *Geologic Map of the Jackass Flats Area, Nye County, Nevada.* Miscellaneous Investigations Series Map I-1519. Reston, Virginia: U.S. Geological Survey. TIC: 203087.

159031   Martinez, L.J.; Meertens, C.M.; and Smith, R.B. 1998. "Rapid Deformation Rates Along the Wasatch Fault Zone, Utah, from First GPS Measurements with Implications for Earthquake Hazard." *Geophysical Research Letters, 25*, (4), 567-570. Washington, D.C.: American Geophysical Union. TIC: 246585.

104764   McAllister, J.F. 1973. *Geologic Map and Sections of the Amargosa Valley Borate Area-Southeast Continuation of the Furnace Creek Area-Inyo County, California.* Miscellaneous Geologic Investigations Map I-782. Washington, D.C.: U.S. Geological Survey. ACC: NNA.19901005.0029.

104766   McArthur, R.D. and Burkhard, N.R. 1986. *Geological and Geophysical Investigations of Mid Valley.* UCID-20740. Livermore, California: Lawrence Livermore National Laboratory. ACC: HQS.19880517.2757.

104772   McDonald, E. and McFadden, L.D. 1994. "Quaternary Stratigraphy of the Providence Mountains Piedmont and Preliminary Age Estimates and Regional Stratigraphic Correlations of Quaternary Deposits in the Eastern Mojave Desert, California." *Geological Investigations of an Active Margin, Geological Society of America Cordilleran Section Guidebook, 27th Annual Meeting, San Bernardino, California, March 21-23, 1994.* McGill, S.F. and Ross, T.M., eds. Pages 205-210. Redlands, California: San Bernardino County Museum Association. TIC: 237835.

105029   McKee, E.H. 1968. "Age and Rate of Movement of the Northern Part of the Death Valley-Furnace Creek Fault Zone, California." *Geological Society of America Bulletin, 79*, 509-512. Boulder, Colorado: Geological Society of America. TIC: 240329.

106359   Michel-Noel, G.; Anderson, R.E.; and Angelier, J. 1990. "Fault Kinematics and Estimates of Strain Partitioning of a Neogene Extensional Fault System in Southeastern Nevada." Chapter 7 of *Basin and Range Extensional Tectonics Near the Latitude of Las Vegas, Nevada.* Wernicke, B.P., ed. Memoir 176. Boulder, Colorado: Geological Society of America. TIC: 222540.

150656   Minor, S.A. and Fleck, R.J. 1994. "Miocene Landsliding and Extensional Faulting in the Upper Plate of the Bullfrog Hills Detachment Fault System, Northern Bullfrog Hills, Southern Nevada." *Abstracts with Programs - Geological Society of America, 26*, (2), 75. Boulder, Colorado: Geological Society of America. TIC: 248269.

106373   Minor, S.A. 1995. "Superposed Local and Regional Paleostresses: Fault-Slip Analysis of Neogene Extensional Faulting Near Coeval Caldera Complexes, Yucca Flat, Nevada." *Journal of Geophysical Research, 100*, (B6), 10,507-10,528. Washington, D.C.: American Geophysical Union. TIC: 236631.

106377   Minster, J.B. and Jordan, T.H. 1984. "Vector Constraints on Quaternary Deformation of the Western United States East and West of the San Andreas Fault." *Tectonics and Sedimentation Along the California Margin*. Crouch, J.K. and Bachman, S.B., eds. Volume 38. Pages 1-16. Los Angeles, California: Society of Economic Paleontologists and Mineralogists, Pacific Section. TIC: 234807.

106379   Minster, J.B. and Jordan, T.H. 1987. "Vector Constraints on Western U.S. Deformation from Space Geodesy, Neotectonics, and Plate Motions." *Journal of Geophysical Research, 92*, (B6), 4798-4804. Washington, D.C.: American Geophysical Union. TIC: 234809.

106382   Monsen, S.A.; Carr, M.D.; Reheis, M.C.; and Orkild, P.P. 1992. *Geologic Map of Bare Mountain, Nye County, Nevada*. Miscellaneous Investigations Series Map I-2201. Reston, Virginia: U.S. Geological Survey. TIC: 231183.

105156   Naeser, C.W. and Maldonado, F. 1981. "Fission-Track Dating of the Climax and Gold Meadows Stocks, Nye County, Nevada." *Shorter Contributions to Isotope Research in the Western United States*. Professional Paper 1199-E. Washington, D.C.: U.S. Geological Survey. TIC: 213600.

101444   National Park Service 1998. *Death Valley National Park.* Washington, D.C.: National Park Service. TIC: 239799.

105171   Nelson, M.R. and Jones, C.H. 1987. "Paleomagnetism and Crustal Rotations Along a Shear Zone, Las Vegas Range, Southern Nevada." *Tectonics, 6*, (1), 13-33. Washington, D.C.: American Geophysical Union. TIC: 232895.

105197   Noble, D.C. and Hedge, C.E. 1969. "[87]Sr/[86]Sr Variations Within Individual Ash-Flow Sheets." *Geological Survey Research 1969, Chapter C*. Professional Paper 650-C. Pages C133-C139. Washington, D.C.: U.S. Geological Survey. TIC: 232920.

105202   Noble, L.F. 1941. "Structural Features of the Virgin Spring Area, Death Valley, California." *Geological Society of America Bulletin, 52*, 941-999. Boulder, Colorado: Geological Society of America. TIC: 239855.

106458   Orkild, P.P. 1968. *Geologic Map of the Mine Mountain Quadrangle, Nye County, Nevada*. Geologic Quadrangle Map GQ-746. Washington, D.C.: U.S. Geological Survey. ACC: NNA.19930412.0012.

106492   Perry, F.V.; DePaolo, D.J.; and Baldridge, W.S. 1993. "Neodymium Isotopic Evidence for Decreasing Crustal Contributions to Cenozoic Ignimbrites of the Western United States: Implications for the Thermal Evolution of the Cordilleran Crust." *Geological Society of America Bulletin, 105*, 872-882. Boulder, Colorado: Geological Society of America. TIC: 225116.

106512   Peterson, F.F. 1988. "Consultant's Report: Soil-Geomorphology Studies in the Crater Flat, Nevada, Area." Appendix B of *Quaternary Geology and Active Faulting at and Near Yucca Mountain*. Reno, Nevada: Nevada Bureau of Mines and Geology. TIC: 222315.

106519   Peterson, F.F.; Bell, J.W.; Dorn, R.I.; Ramelli, A.R.; and Ku, T.L. 1995. "Late Quaternary Geomorphology and Soils in Crater Flat, Yucca Mountain Area, Southern Nevada." *Geological Society of America Bulletin, 107*, (4), 379-395. Boulder, Colorado: Geological Society of America. TIC: 235112.

106540   Piety, L.A. 1996. *Compilation of Known or Suspected Quaternary Faults Within 100 km of Yucca Mountain, Nevada and California*. Open-File Report 94-112. Denver, Colorado: U.S. Geological Survey. ACC: MOL.19971009.0003.

158733   Ponce, D.A.; Blakely, R.J.; Morin, R.L.; and Mankinen, E.A. 2001. *Isostatic Gravity Map of the Death Valley Ground-Water Model Area, Nevada and California*. Miscellaneous Field Studies MF-2381-C. Denver, Colorado: U.S. Geological Survey. TIC: 253069.

106568   Poole, F.G.; Elston, D.P.; and Carr, W.J. 1965. *Geologic Map of the Cane Spring Quadrangle, Nye County, Nevada*. Geologic Quadrangle Map GQ-455. Denver, Colorado: U.S. Geological Survey. ACC: NNA.19920219.0010.

105353   Poole, F.G.; Stewart, J.H.; Palmer, A.R.; Sandberg, C.A.; Madrid, R.J.; Ross, R.J., Jr.; Hintze, L.F.; Miller, M.M.; and Wrucke, C.T. 1992. "Latest Precambrian to Latest Devonian Time; Development of a Continental Margin." Chapter 2 of *The Cordilleran Orogen: Conterminous U.S.* Burchfiel, B.C.; Lipman, P.W.; and Zoback, M.L., eds. Volume G-3. Boulder, Colorado: Geological Society of America. TIC: 244017.

159091   Potter, C.J.; Sweetkind, D.S.; Dickerson, R.P.; and Killgore, M.L. 2002. *Hydrostructural Maps of the Death Valley Regional Flow System, Nevada and California*. Miscellaneous Field Studies Map MF-2372. Denver, Colorado: U.S. Geological Survey. TIC: 253072.

106659   Reheis, M.C.; Harden, J.W.; McFadden, L.D.; and Shroba, R.R. 1989. "Development Rates of Late Quaternary Soils, Silver Lake Playa, California." *Soil Science Society of America Journal, 53*, 1127-1140. Madison, Wisconsin: Soil Science Society of America. TIC: 224798.

145271   Reheis, M.C. and McKee, E.H. 1991. "Late Cenozoic History of Slip on the Fish Lake Valley Fault Zone, Nevada and California." *Late Cenozoic Stratigraphy and Tectonics of Fish Lake Valley, Nevada and California: Road Log and Contributions to the Field Trip Guidebook, 1991 Pacific Cell, Friends of the Pleistocene*. Open-File Report 91-290. Pages 26-45. Denver, Colorado: U.S. Geological Survey. TIC: 235375.

102891   Reheis, M.C. and Noller, J.S. 1991. *Aerial Photographic Interpretation of Lineaments and Faults in Late Cenozoic Deposits in the Eastern Part of the Benton Range 1:100,000 Quadrangle and the Goldfield, Last Chance Range, Beatty, and Death Valley Junction 1:100,000 Quadrangles, Nevada and California*. Open-File Report 90-41. Denver, Colorado: U.S. Geological Survey. ACC: NNA.19901031.0001.

106661   Reheis, M.C.; Sowers, J.M.; Taylor, E.M.; McFadden, L.D.; and Harden, J.W. 1992. "Morphology and Genesis of Carbonate Soils on the Kyle Canyon Fan, Nevada, U.S.A." *Geoderma, 52*, 303-342. Amsterdam, The Netherlands: Elsevier. TIC: 224418.

105367   Reheis, M.C. 1993. "Neogene Tectonism from the Southwestern Nevada Volcanic Field to the White Mountains, California: Part II. Late Cenozoic History of the Southern Fish Lake Valley Fault Zone, Nevada and California." *Crustal Evolution of the Great Basin and the Sierra Nevada, Field Trip Guidebook for the 1993 Joint Meeting of the Cordilleran/Rocky Mountain Sections of the Geological Society of America, Reno, Nevada, May 19-21, 1993*. Lahren, M.M.; Trexler, J.H., Jr.; and Spinosa, C., eds. Pages 370-382. Reno, Nevada: University of Nevada, Reno, Mackay School of Mines. TIC: 241556.

106656   Reheis, M.C. and Sawyer, T.L. 1997. "Late Cenozoic History and Slip Rates of the Fish Lake Valley, Emigrant Peak, and Deep Springs Fault Zones, Nevada and California." *Geological Society of America Bulletin, 109*, (3), 280-299. Boulder, Colorado: Geological Society of America. TIC: 234885.

106674   Robinson, G.D. 1985. *Structure of Pre-Cenozoic Rocks in the Vicinity of Yucca Mountain, Nye County, Nevada—A Potential Nuclear-Waste Disposal Site*. Bulletin 1647. Washington, D.C.: U.S. Geological Survey. TIC: 203083.

106700   Rogers, A.M.; Harmsen, S.C.; and Carr, W.J. 1981. *Southern Great Basin Seismological Data Report for 1980 and Preliminary Data Analysis*. Open-File Report 81-1086. Denver, Colorado: U.S. Geological Survey. ACC: NNA.19870518.0068.

100176   Rogers, A.M.; Harmsen, S.C.; and Meremonte, M.E. 1987. *Evaluation of the Seismicity of the Southern Great Basin and Its Relationship to the Tectonic Framework of the Region*. Open-File Report 87-408. Denver, Colorado: U.S. Geological Survey. ACC: HQX.19880315.0004.

104578   Sarna-Wojcicki, A.M. and Pringle, M.S., Jr. 1992. "Laser-Fusion ^{40}Ar/^{39}Ar Ages of the Tuff of Taylor Canyon and Bishop Tuff, E. California-W. Nevada." *Eos Transactions (Supplement), 73*, (43), 633. Washington, D.C.: American Geophysical Union. TIC: 210058.

104546   Sauber, J. 1989. *Geodetic Measurement of Deformation in California.* NASA Technical Memoir 100732. Washington, D.C.: National Aeronautics and Space Administration. TIC: 242343.

104553   Savage, J.C.; Lisowski, M.; Svarc, J.L.; and Gross, W.K. 1995. "Strain Accumulation Across the Central Nevada Seismic Zone, 1973-1994." *Journal of Geophysical Research, 100*, (B10), 20,257 to 20,269. Washington, D.C.: American Geophysical Union. TIC: 236811.

100075   Sawyer, D.A.; Fleck, R.J.; Lanphere, M.A.; Warren, R.G.; Broxton, D.E.; and Hudson, M.R. 1994. "Episodic Caldera Volcanism in the Miocene Southwestern Nevada Volcanic Field: Revised Stratigraphic Framework, ^{40}Ar/^{39}Ar Geochronology, and Implications for Magmatism and Extension." *Geological Society of America Bulletin, 106*, (10), 1304-1318. Boulder, Colorado: Geological Society of America. TIC: 222523.

104580   Sawyer, D.A.; Wahl, R.R.; Cole, J.C.; Minor, S.A.; Laczniak, R.J.; Warren, R.G.; Engle, C.M.; and Vega, R.G. 1995. *Preliminary Digital Geological Map Database of the Nevada Test Site Area, Nevada.* Open-File Report 95-0567. Denver, Colorado: U.S. Geological Survey. TIC: 232986.

106729   Sawyer, T.L. 1991. "Quaternary Faulting and Holocene Paleoseismicity of the Northern Fish Lake Valley Fault Zone, Nevada and California." *Pacific Cell, Friends of the Pleistocene, Guidebook for Field Trip to Fish Lake Valley, California-Nevada, May 31-June 2, 1991.* Pages 114-138. Boulder, Colorado: Friends of the Pleistocene. TIC: 241390.

106751   Scott, R.B. 1990. "Tectonic Setting of Yucca Mountain, Southwest Nevada." Chapter 12 of *Basin and Range Extensional Tectonics Near the Latitude of Las Vegas, Nevada.* Wernicke, B.P., ed. Memoir 176. Boulder, Colorado: Geological Society of America. TIC: 222540.

106765   Seedorff, E. 1991. "Magmatism, Extension, and Ore Deposits of Eocene to Holocene Age in the Great Basin – Mutual Effects and Preliminary Proposed Genetic Relationships." *Geology and Ore Deposits of the Great Basin, Symposium Proceedings, Reno/Sparks, Nevada, April 1-5, 1990.* Raines, G.L.; Lisle, R.E.; Schafer, R.W.; and Wilkinson, W.H., eds. *1*, 133-178. Reno, Nevada: Geological Society of Nevada. TIC: 246285.

130186   Slate, J.L. 1991. "Quaternary Stratigraphy, Geomorphology, and Geochronology of Alluvial Fans, Fish Lake Valley, Nevada and California." *Pacific Cell, Friends of the Pleistocene Guidebook for Field Trip to Fish Lake Valley, California-Nevada, May 31-June 2, 1991.* Pages 94-113. Boulder, Colorado: Friends of the Pleistocene. TIC: 247644.

150228   Slate, J.L.; Berry, M.E.; Rowley, P.D.; Fridrich, C.J.; Morgan, K.S.; Workman, J.B.; Young, O.D.; Dixon, G.L.; Williams, V.S.; McKee, E.H.; Ponce, D.A.; Hildenbrand, T.G.; Swadley, W C; Lundstrom, S.C.; Ekren, E.B.; Warren, R.G.; Cole, J.C.; Fleck, R.J.; Lanphere, M.A.; Sawyer, D.A.; Minor, S.A.; Grunwald, D.J.; Laczniak, R.J.; Menges, C.M.; Yount, J.C.; Jayko, A.S.; Mankinen, E.A.; Davidson, J.G.; Morin, R.L.; and Blakely, R.J. 2000. *Digital Geologic Map of the Nevada Test Site and Vicinity, Nye, Lincoln and Clark Counties, Nevada, and Inyo County, California, Revision 4; Digital Aeromagnetic Map of the Nevada Test Site and Vicinity, Nye, Lincoln, and Clark Counties, Nevada, and Inyo County, California; and Digital Isostatic Gravity Map of the Nevada Test Site and Vicinity, Nye, Lincoln, and Clark Counties, Nevada, and Inyo County, California.* Open-File Report 99-554—A, —B, and —C. Denver, Colorado: U.S. Geological Survey. TIC: 248049; 251985; 251981.

106819   Smith, D.L. 1991. "Large-Magnitude Oligocene Extension in Central Nevada." *Abstracts with Programs - Geological Society of America, 23,* (6), A188-A189. Boulder, Colorado: Geological Society of America. TIC: 233072.

105406   Smith, R.B. and Arabasz, W.J. 1991. "Seismicity of the Intermountain Seismic Belt." Chapter 11 of *Neotectonics of North America.* Slemmons, D.B.; Engdahl, E.R.; Zoback, M.D.; and Blackwell, D.D., eds. The Geology of North America Decade Map Volume I. Boulder, Colorado: Geological Society of America. TIC: 240998.

106868   Snow, J.K. 1992. "Large-Magnitude Permian Shortening and Continental-Margin Tectonics in the Southern Cordillera." *Geological Society of America Bulletin, 104,* 80-105. Boulder, Colorado: Geological Society of America. TIC: 232888.

159400   Snow, J.K. and Wernicke, B.P. 2000. "Cenozoic Tectonism in the Central Basin and Range: Magnitude, Rate, and Distribution of Upper Crustal Strain." *American Journal of Science, 300,* (9), 659-719. New Haven, Connecticut: Yale University, Kline Geology Laboratory. TIC: 253039.

106881   Sonder, L.J.; Jones, C.H.; Salyards, S.L.; and Murphy, K.M. 1994. "Vertical Axis Rotations in the Las Vegas Valley Shear Zone, Southern Nevada: Paleomagnetic Constraints on Kinematics and Dynamics of Block Rotations." *Tectonics, 13,* (4), 769-788. Washington, D.C.: American Geophysical Union. TIC: 232894.

150281   Stevens, C.H.; Stone, P.; and Belasky, P. 1991. "Paleogeographic and Structural Significance of an Upper Mississippian Facies Boundary in Southern Nevada and East-Central California." *Geological Society of America Bulletin, 103,* (7), 876-885. Boulder, Colorado: Geological Society of America. TIC: 223783.

106912   Stewart, J.H. 1967. "Possible Large Right-Lateral Displacement Along Fault and Shear Zones in the Death Valley-Las Vegas Area, California and Nevada." *Geological Society of America Bulletin, 78*, 131-142. Boulder, Colorado: Geological Society of America. TIC: 201778.

106913   Stewart, J.H. 1970. *Upper Precambrian and Lower Cambrian Strata in the Southern Great Basin California and Nevada*. Professional Paper 620. Washington, D.C.: U.S. Geological Survey. TIC: 232997.

106928   Stewart, J.H.; Moore, W.J.; and Zietz, I. 1977. "East-West Patterns of Cenozoic Igneous Rocks, Aeromagnetic Anomalies, and Mineral Deposits, Nevada and Utah." *Geological Society of America Bulletin, 88*, 67-77. Boulder, Colorado: Geological Society of America. TIC: 217235.

106926   Stewart, J.H. and Carlson, J.E. 1978. *Geologic Map of Nevada*. Denver, Colorado: U.S. Geological Survey. TIC: 233975.

103020   Stewart, J.H. 1980. *Geology of Nevada, A Discussion to Accompany the Geologic Map of Nevada*. Special Publication 4. Reno, Nevada: Nevada Bureau of Mines and Geology. TIC: 219557.

100083   Stewart, J.H. 1988. "Tectonics of the Walker Lane Belt, Western Great Basin: Mesozoic and Cenozoic Deformation in a Zone of Shear." *Metamorphism and Crustal Evolution of the Western United States*. Ernst, W.G., ed. Rubey Volume 7. Pages 683-713. Englewood Cliffs, New Jersey: Prentice-Hall. TIC: 218183.

106927   Stewart, J.H. and Diamond, D.S. 1990. "Changing Patterns of Extensional Tectonics; Overprinting of the Basin of the Middle and Upper Miocene Esmeralda Formation in Western Nevada by Younger Structural Basins." Chapter 22 of *Basin and Range Extensional Tectonics Near the Latitude of Las Vegas, Nevada*. Wernicke, B.P., ed. Memoir 176. Boulder, Colorado: Geological Society of America. TIC: 222540.

106922   Stewart, J.H. 1992. "Walker Lane Belt, Nevada and California--An Overview." *Structure, Tectonics and Mineralization of the Walker Lane: Geological Society of Nevada, Proceedings Volume, Walker Lane Symposium, April 24, 1992, Reno, Nevada*. Craig, S.D., ed. Pages 1-16. Reno, Nevada: Geological Society of Nevada. TIC: 235059.

106945   Stuckless, J.S. and O'Neil, J.R. 1973. "Petrogenesis of the Superstition-Superior Volcanic Area as Inferred from Strontium- and Oxygen-Isotope Studies." *Geological Society of America Bulletin, 84*, 1987-1998. Boulder, Colorado: Geological Society of America. TIC: 232884.

101300   Swadley, W C and Carr, W.J. 1987. *Geologic Map of the Quaternary and Tertiary Deposits of the Big Dune Quadrangle, Nye County, Nevada, and Inyo County, California*. Miscellaneous Investigations Series Map I-1767. Denver, Colorado: U.S. Geological Survey. TIC: 203089.

106952   Swadley, W C and Huckins, H.E. 1990. *Geologic Map of the Surficial Deposits of the Skull Mountain Quadrangle, Nye County, Nevada.* Miscellaneous Investigations Series Map I-1972. Denver, Colorado: U.S. Geological Survey. ACC: NNA.19910110.0002.

159092   Sweetkind, D.S.; Dickerson, R.P.; Blakely, R.J.; and Denning, P.D. 2001. *Interpretive Geologic Cross Sections for the Death Valley Regional Flow System and Surrounding Areas, Nevada and California. Miscellaneous Field Studies Map MF-2370.* Denver, Colorado: U.S. Geological Survey. TIC: 251903.

102864   Taylor, E.M. 1986. *Impact of Time and Climate on Quaternary Soils in the Yucca Mountain Area of the Nevada Test Site.* Master's thesis. Boulder, Colorado: University of Colorado. TIC: 218287.

105432   Taylor, W.J.; Bartley, J.M.; Fryxell, J.E.; Schmitt, J.G.; and Vandervoort, D.S. 1993. "Tectonic Style and Regional Relations of the Central Nevada Thrust Belt." *Crustal Evolution of the Great Basin and the Sierra Nevada, Field Trip Guidebook for the 1993 Joint Meeting of the Cordilleran/Rocky Mountain Sections of the Geological Society of America, Reno, Nevada, May 19-21, 1993.* Lahren, M.M.; Trexler, J.H., Jr.; and Spinosa, C., eds. Pages 57-96. Reno, Nevada: University of Nevada, Reno, Mackay School of Mines. TIC: 241238.

119053   Thatcher, W.; Foulger, G.R.; Julian, B.R.; Svarc, J.; Quilty, E.; and Bawden, G.W. 1999. "Present-Day Deformation Across the Basin and Range Province, Western United States." *Science, 283,* (5408), 1714-1718. Washington, D.C.: American Association for the Advancement of Science. TIC: 246227.

107005   Trexler, J.H., Jr.; Cole, J.C.; and Cashman, P.H. 1996. "Middle Devonian–Mississippian Stratigraphy On and Near the Nevada Test Site: Implications for Hydrocarbon Potential." *AAPG Bulletin, 80,* (11), 1736-1762. Tulsa, Oklahoma: American Association of Petroleum Geologists. TIC: 233004.

107009   Tschanz, C.M. and Pampeyan, E.H. 1970. *Geology and Mineral Deposits of Lincoln County, Nevada.* Nevada Bureau of Mines and Geology Bulletin 73. Reno, Nevada: University of Nevada, Reno, Mackay School of Mines. TIC: 232876.

107012   Turner, H.W. 1900. "The Esmeralda Formation." *The American Geologist, 25,* 168-170. Minneapolis, Minnesota: Geological Publishing Company. TIC: 232891.

107048   USGS (U.S. Geological Survey) 1976. *Field Trip to Nevada Test Site.* Open-File Report 76-313. Denver, Colorado: U.S. Geological Survey. ACC: NNA.19920814.0122.

101305   USGS 1984. *A Summary of Geologic Studies Through January 1, 1983, of a Potential High-Level Radioactive Waste Repository Site at Yucca Mountain, Southern Nye County, Nevada.* Open-File Report 84-792. Menlo Park, California: U.S. Geological Survey. ACC: NNA.19891009.0305.

101031   Vaniman, D.T.; Crowe, B.M.; and Gladney, E.S. 1982. "Petrology and Geochemistry of Hawaiite Lavas from Crater Flat, Nevada." *Contributions to Mineralogy and Petrology, 80*, 341-357. Berlin, Germany: Springer-Verlag. TIC: 201799.

107155   Wang, Y.; McDonald, E.; Amundson, R.; McFadden, L.; and Chadwick, O. 1996. "An Isotopic Study of Soils in Chronological Sequences of Alluvial Deposits, Providence Mountains, California." *Geological Society of America Bulletin, 108*, (4), 379-391. Boulder, Colorado: Geological Society of America. TIC: 234946.

150660   Weiss, S.I.; Noble, D.C.; and McKee, E.H. 1988. "Volcanic and Tectonic Significance of the Presence of Late Miocene Stonewall Flat Tuff in the Vicinity of Beatty, Nevada." *Abstracts with Programs - Geological Society of America, 20*, (7), A399. Boulder, Colorado: Geological Society of America. TIC: 248273.

150661   Weiss, S.I.; McKee, E.H.; Noble, D.C.; Connors, K.A.; and Jackson, M.R. 1991. "Multiple Episodes of Au-Ag Mineralization in the Bullfrog Hills, SW Nevada, and Their Relation to Coeval Extension and Volcanism." *Abstracts with Programs - Geological Society of America, 23*, (6), A246. Boulder, Colorado: Geological Society of America. TIC: 248274.

107199   Weiss, S.I.; Noble, D.C.; Worthington, J.E., IV; and McKee, E.H. 1993. "Neogene Tectonism from the Southwestern Nevada Volcanic Field to the White Mountains, California, Part I. Miocene Volcanic Stratigraphy, Paleotopography, Extensional Faulting and Uplift Between Northern Death Valley and Pahute Mesa." *Crustal Evolution of the Great Basin and the Sierra Nevada, Field Trip Guidebook for the 1993 Joint Meeting of the Cordilleran/Rocky Mountain Sections of the Geological Society of America, Reno, Nevada, May 19-21, 1993*. Lahren, M.M.; Trexler, J.H., Jr.; and Spinosa, C., eds. Pages 353-369. Reno, Nevada: University of Nevada, Reno, Mackay School of Mines. TIC: 232926.

107208   Wells, S.G.; McFadden, L.D.; Renault, C.E.; and Crowe, B.M. 1990. "Geomorphic Assessment of Late Quaternary Volcanism in the Yucca Mountain Area, Southern Nevada: Implications for the Proposed High-Level Radioactive Waste Repository." *Geology, 18*, 549-553. Boulder, Colorado: Geological Society of America. TIC: 218564.

149959   Wernicke, B.; Axen, G.J.; and Snow, J.K. 1988. "Basin and Range Extensional Tectonics at the Latitude of Las Vegas, Nevada." *Geological Society of America Bulletin, 100*, (11), 1738-1757. Boulder, Colorado: Geological Society of America. TIC: 233007.

105531   Wernicke, B.P.; Hodges, K.V.; and Walker, J.D. 1986. "Geological Setting of the Tucki Mountain Area, Death Valley National Monument, California." *Mesozoic and Cenozoic Structural Evolution of Selected Areas, East-Central California, Cordilleran Section, 82nd Annual Meeting, March 25-28, 1986, Los Angeles, California*. Guidebook and Volume, Trips 2 and 14. Pages 67-80. Boulder, Colorado: Geological Society of America. TIC: 241240.

107290   Wesling, J.R.; Bullard, T.F.; Swan, F.H.; Perman, R.C.; Angell, M.M.; and Gibson, J.D. 1992. *Preliminary Mapping of Surficial Geology of Midway Valley Yucca Mountain Project, Nye County, Nevada Interim Data Report*. SAND91-0607. Albuquerque, New Mexico: Sandia National Laboratories. ACC: NNA.19920410.0053.

107309   Whitney, J.W. and Taylor, E.M., eds. 1996. "Quaternary Paleoseismology and Stratigraphy of the Yucca Mountain Site Area." Chapter 4 of *Seismotectonic Framework and Characterization of Faulting at Yucca Mountain, Nevada*. Whitney, J.W., ed. Milestone 3GSH100M. Denver, Colorado: U.S. Geological Survey. TIC: 237980. ACC: MOL.19970129.0041.

150666   Wills, C.J. 1989. "A Neotectonic Tour of the Death Valley Fault Zone, Inyo County." *California Geology, 42*, (9), 195-200. Sacramento, California: California Division of Mines and Geology. TIC: 248276.

101167   Winograd, I.J. and Thordarson, W. 1975. *Hydrogeologic and Hydrochemical Framework, South-Central Great Basin, Nevada-California, with Special Reference to the Nevada Test Site*. Geological Survey Professional Paper 712-C. Washington, D.C.: United States Government Printing Office. ACC: NNA.19870406.0201.

107337   Wright, L.A. and Troxel, B.W. 1967. "Limitations on Right-Lateral, Strike-Slip Displacement, Death Valley and Furnace Creek Fault Zones, California." *Geological Society of America Bulletin, 78*, 933-950. Boulder, Colorado: Geological Society of America. TIC: 241025.

107354   Wright, L.A.; Troxel, B.W.; Burchfiel, B.C.; Chapman, R.H.; and Labotka, T.C. 1981. *Geologic Cross Section from the Sierra Nevada to the Las Vegas Valley, Eastern California to Southern Nevada*. Map and Chart Series MC-28M. Boulder, Colorado: Geological Society of America. TIC: 217716.

107335   Wright, L.A. 1989. "Overview of the Role of Strike-Slip and Normal Faulting in the Neogene History of the Region Northeast of Death Valley, California-Nevada." *Late Cenozoic Evolution of the Southern Great Basin, Selected Papers from the Workshop, University of Nevada-Reno, November 10-13, 1987*. Ellis, M.A., ed. Open-File Report 89-1. Pages 1-11. Reno, Nevada: Nevada Bureau of Mines and Geology. TIC: 225187.

107350   Wright, L.A.; Thompson, R.A.; Troxel, B.W.; Pavlis, T.L.; DeWitt, E.H.; Otton, J.K.; Ellis, M.A.; Miller, M.G.; and Serpa, L.F. 1991. "Cenozoic Magmatic and Tectonic Evolution of the East-Central Death Valley Region, California." *Geological Excursions in Southern California and Mexico, Guidebook, 1991 Annual Meeting, Geological Society of America, San Diego, California, October 21-24, 1991*. Walawender, M.J. and Hanan, B.B., eds. Pages 93-127. San Diego, California: San Diego State University. TIC: 236161.

150227   Wright, L.A.; Greene, R.C.; Cemen, I.; Johnson, F.C.; and Prave, A.R. 1999.
          "Tectonostratigraphic Development of the Miocene-Pliocene Furnace Creek Basin and
          Related Features, Death Valley Region, California." *Cenozoic Basins of the Death
          Valley Region*. Wright, L.A. and Troxel, B.W., eds. Special Paper 333.
          Pages 87-114. Boulder, Colorado: Geological Society of America. TIC: 248054.

108731   Yount, J.C.; Shroba, R.R.; McMasters, C.R.; Huckins, H.E.; and Rodriguez, E.A.
          1987. *Trench Logs from a Strand of the Rock Valley Fault System, Nevada Test Site,
          Nye County, Nevada*. Miscellaneous Field Studies Map MF-1824. Reston, Virginia:
          U.S. Geological Survey. TIC: 203093.

108663   Zoback, M.L.; Anderson, R.E.; and Thompson, G.A. 1981. "Cenozoic Evolution of
          the State of Stress and Style of Tectonism of the Basin and Range Province of the
          Western United States." *Philosophical Transactions of the Royal Society of London,
          Series A, (300)*, 407-434. London, United Kingdom: Royal Society of London.
          TIC: 218137.

2.5.2   Data Listed by Data Tracking Number

158690   GS011008314211.001. Interpretation of the Lithostratigraphy in Deep Boreholes
          NC-EWDP-19D1 and NC-EWDP-2DB Nye County Early Warning Drilling
          Program. Submittal date: 01/16/2001.

168526   GS031108314211.005. Subsurface Geologic Interpretations Along Cross Sections
          Nye-1, Nye-2, and Nye-3, Southern Nye County, Nevada -- 2002. Submittal date:
          11/21/2003.

150703   MO0004YMP00004.001. Fault Systems. Submittal date: 04/14/2000.

150697   MO0006YMP00063.000. Walker Lane Belt in Relation to Physiographic
          Subdivisions of the West-Central and Southern Great Basin. Submittal date:
          06/21/2000.

150638   MO0006YMP00067.000. Pleistocene Depositional Basins and Drainage Features.
          Submittal date: 06/26/2000.

150698   MO0006YMP98118.003. Physiographic Subdivisions of the Yucca Mountain Area.
          Submittal date: 06/19/2000.

166376   MO0312SEPSDCDU.000. Comparison of Depositional Units and Related Soils at Yucca Mountain with Local and Regional Surficial Stratigraphies. Submittal date: 03/13/2003.

166378   MO0312SEPSDSRP.000. Interpretation of Seismic Reflection Profile Across Rock Valley. Submittal date: 12/13/2003.

166377   MO0312SEPSDTQS.000. Tertiary and Quaternary Stratigraphic Units of Yucca Mountain. Submittal date: 12/13/2003.

INTENTIONALLY LEFT BLANK
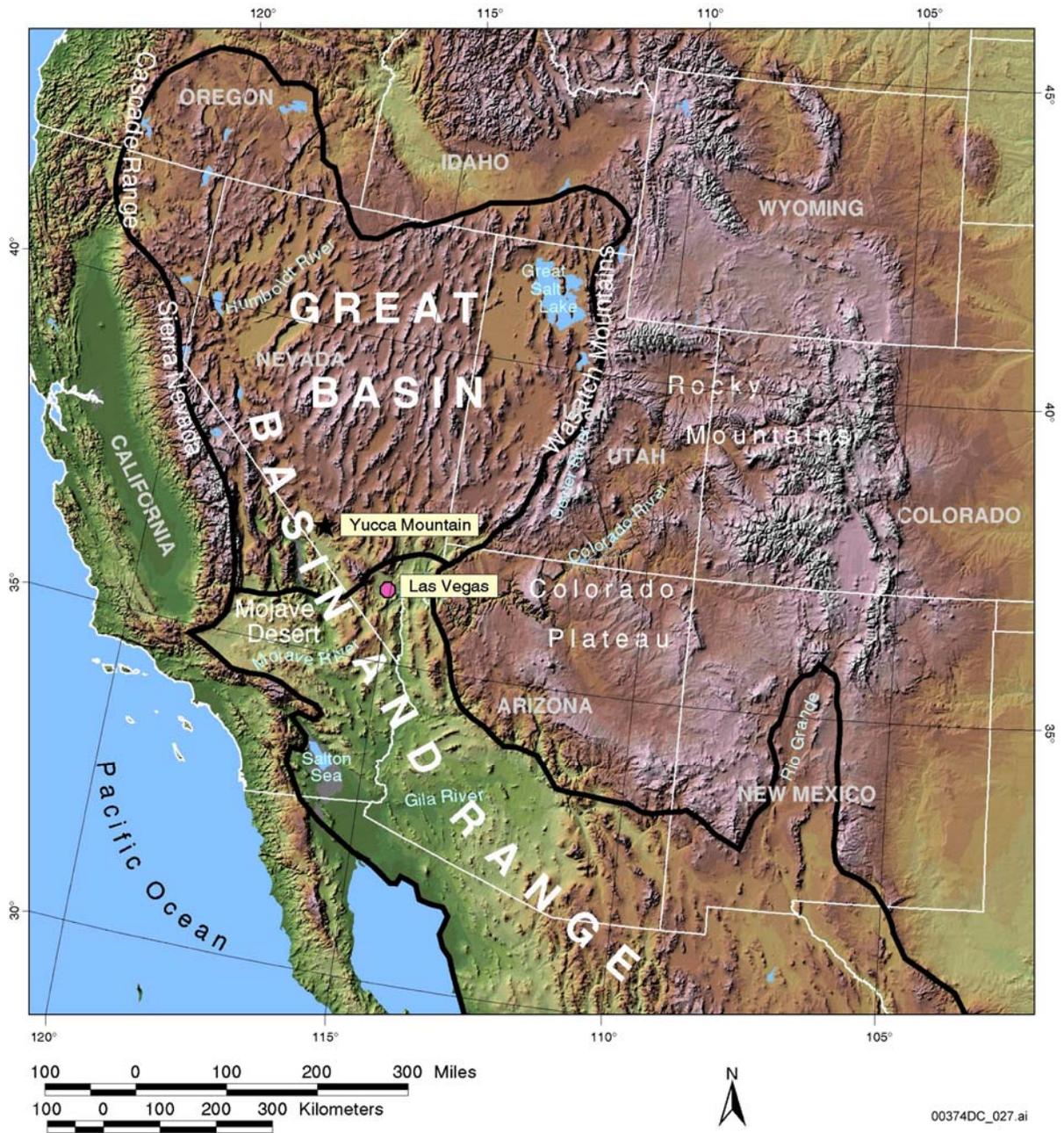
DTN: MO0006YMP00063.000 [DIRS 150697]

Source: Modified from CRWMS M&O 2000 [DIRS 151945], Figure 4.4-1

Figure 2-1a. Approximate Locations of the Physiographic Subdivisions Surrounding the Great Basin of the Basin and Range Physiographic Province

DTN: MO0006YMP00063.000 [DIRS 150697]
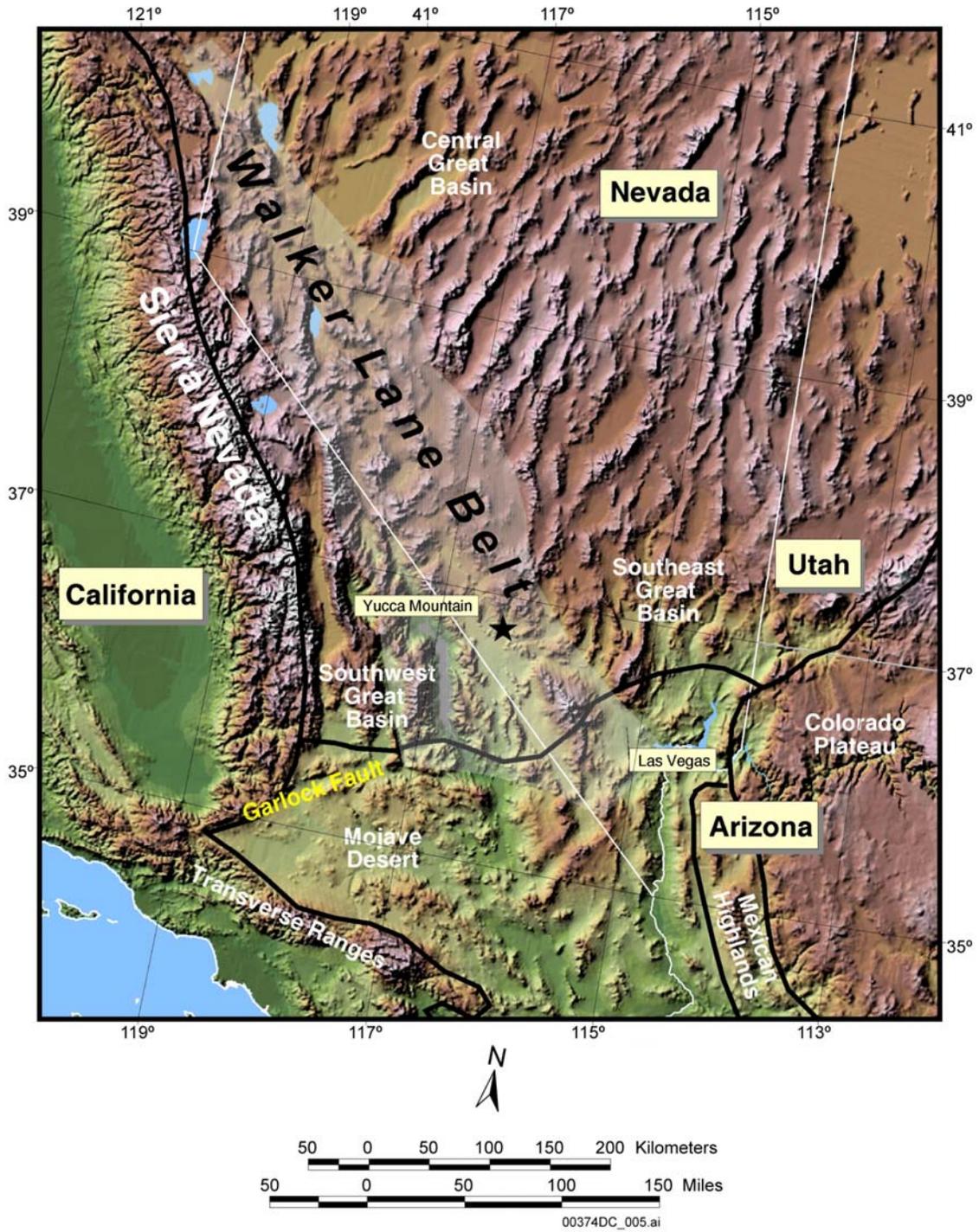
Source: Modified from CRWMS M&O 2000 [DIRS 151945], Figure 4.4-1

Figure 2-1b. Approximate Locations of the Physiographic Subdivisions of the West-Central and Southern Great Basin Showing the Walker Lane Belt
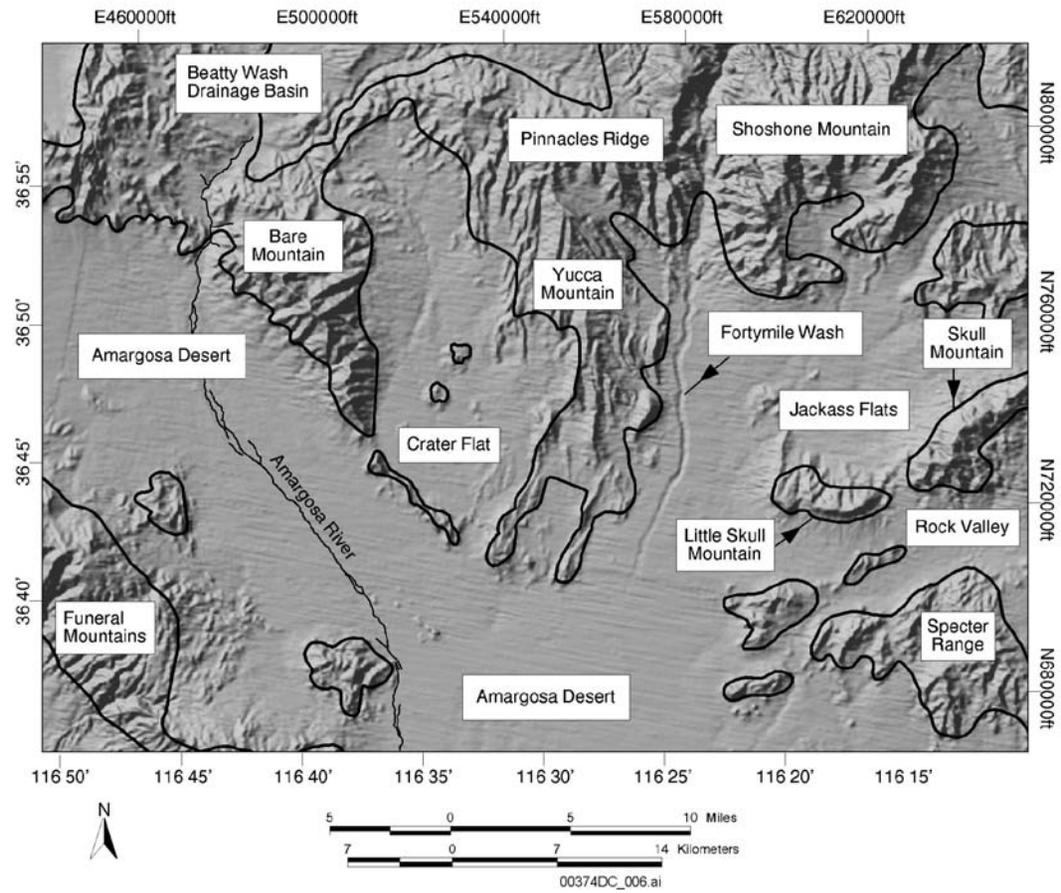
DTN: MO0006YMP98118.003 [DIRS 150698]

Source: CRWMS M&O 2000 [DIRS 151945], Figure 4.4-2

Figure 2-2.   Physiographic Features of the Yucca Mountain Region
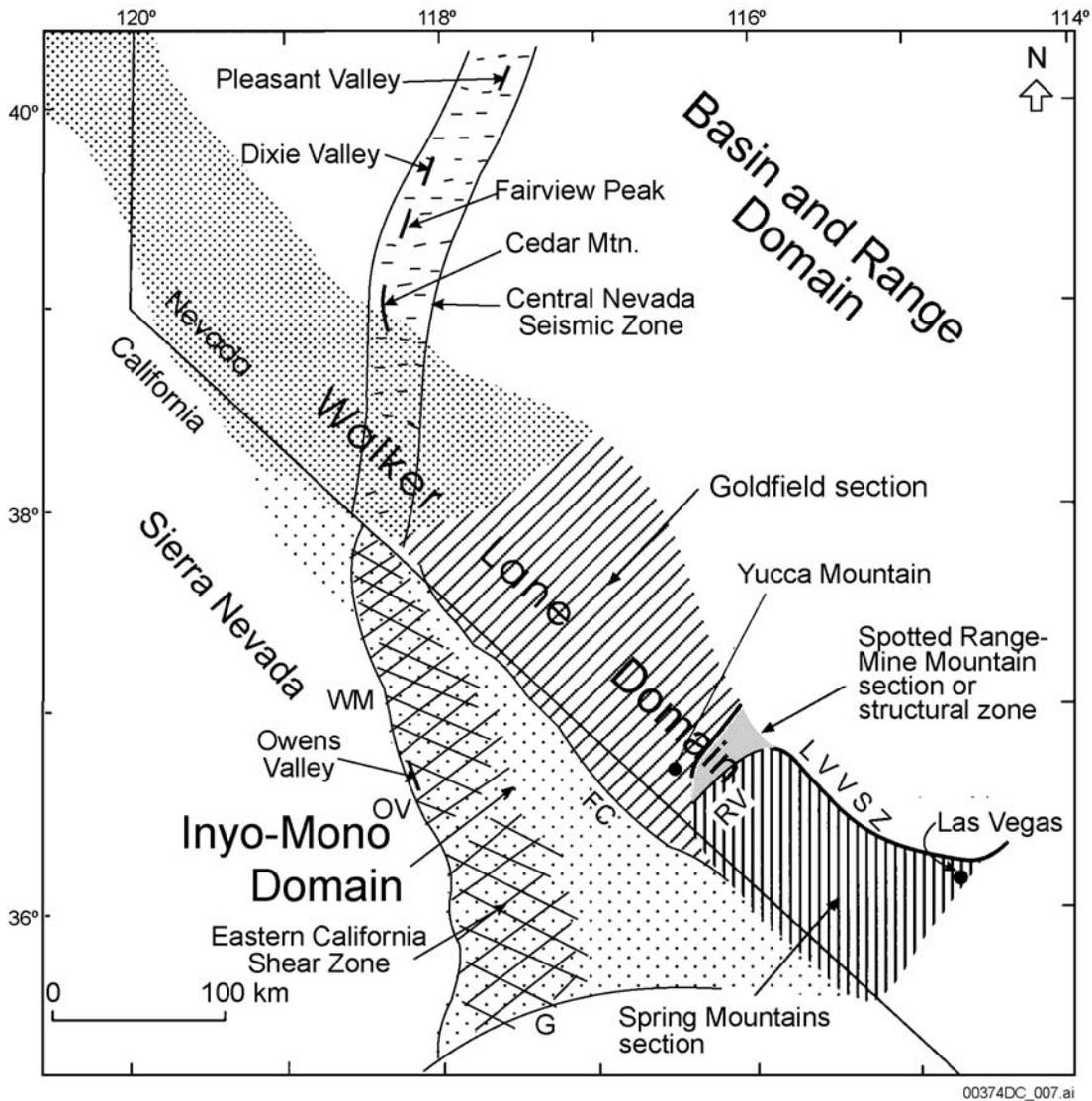
Source: Stewart 1988 [DIRS 100083], Figure 25-3

NOTES: FC = Furnace Creek fault, G = Garlock fault, LVVSZ = Las Vegas Valley Shear Zone, OV = Owens Valley fault, RV = Rock Valley fault, WM = White Mountain fault.

Figure 2-3. Regional Tectonic Domains for Yucca Mountain and Surrounding Environs, plus Sections of the Walker Lane and Zones of Historical Seismic Activity
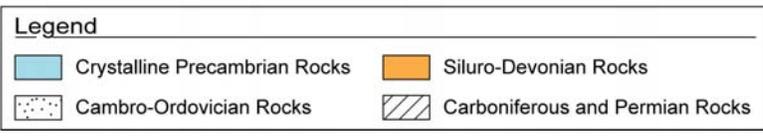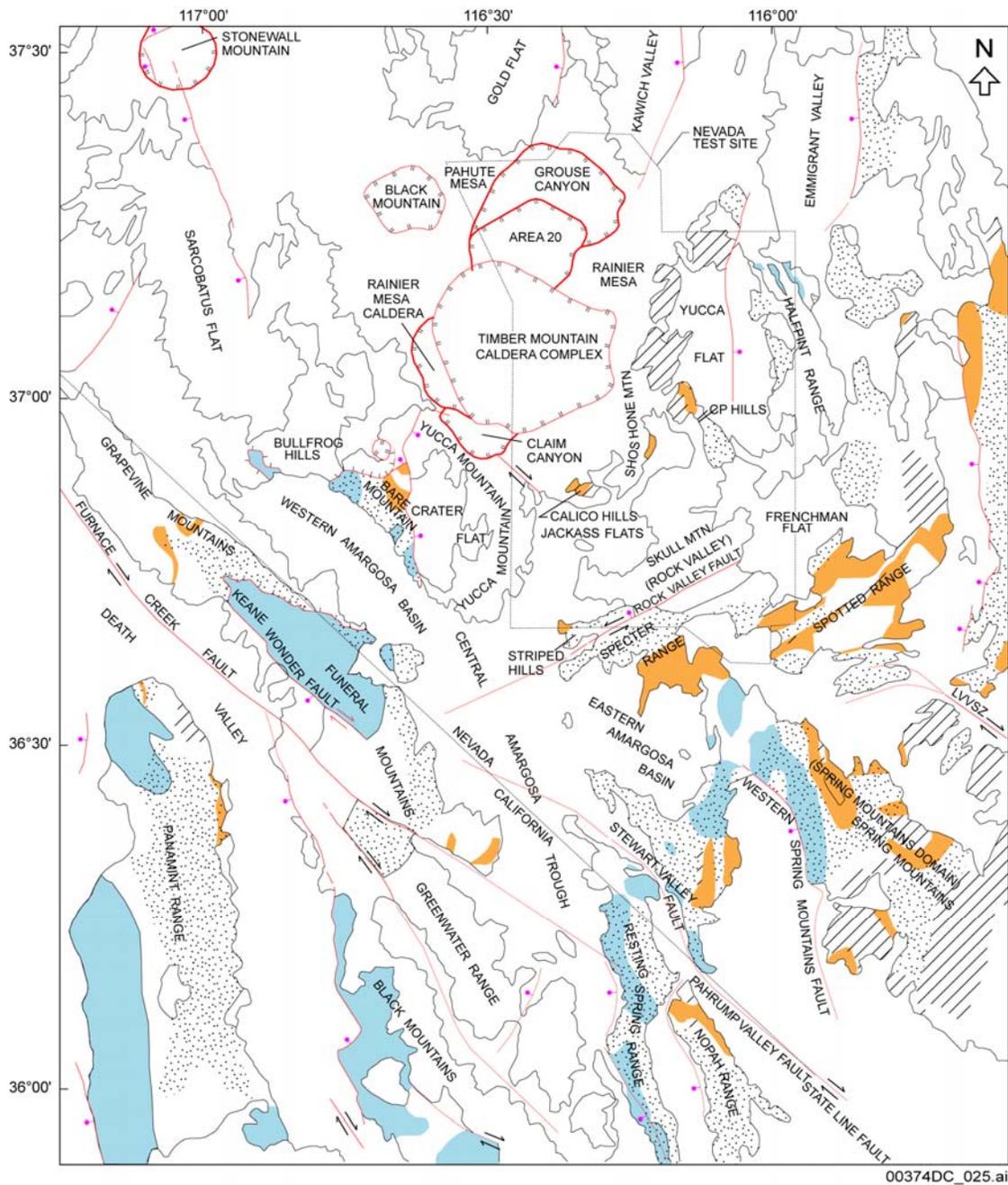
Legend

🟦 Crystalline Precambrian Rocks		🟧 Siluro-Devonian Rocks	
⣿ Cambro-Ordovician Rocks		▨ Carboniferous and Permian Rocks	

Sources: Frizzell and Shulters 1990 [DIRS 105454]; Stewart and Carlson 1978 [DIRS 106926]; Tschanz and Pampeyan 1970 [DIRS 107009], Plate 2; Jennings 1977 [DIRS 150225]

NOTES: All areas of outcrop are outlined. Precambrian exposures are shown by shading on this generalized map. All of the Wood Canyon Formation is shown as Precambrian, although part is Cambrian in age.

Figure 2-4. Generalized Precambrian/Paleozoic Outcrop Map of the Yucca Mountain Region
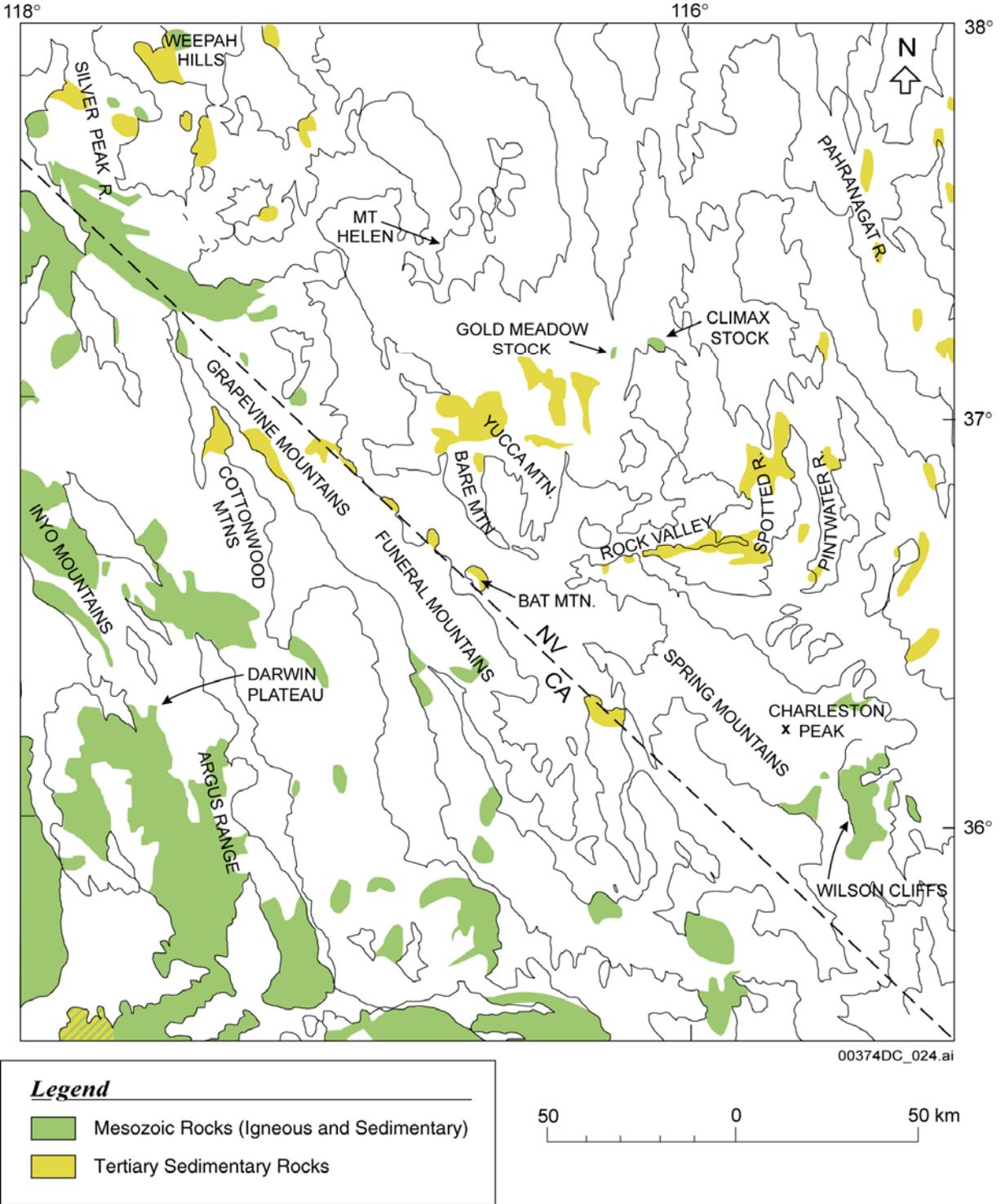
Legend

Mesozoic Rocks (Igneous and Sedimentary)

Tertiary Sedimentary Rocks

Sources: Frizzell and Shulters 1990 [DIRS 105454]; Stewart and Carlson 1978 [DIRS 106926]; Tschanz and Pampeyan 1970 [DIRS 107009], Plate 2; Jennings 1977 [DIRS 150225]

Figure 2-5.   Generalized Outcrop Location of Stratified Mesozoic and Tertiary Rocks within 100 km of Yucca Mountain

Death Valley-Funeral Mtns **Bare Mtn-Specter R.-N. Spring Mtns** **Yucca Flat-Spotted R.-Belted R.** **Depositional and Hydrologic Environment**

Age	NW	SE	NW	SE	NW	SE	West	East

Permian — Owens Valley Fm. — Bird Spring Fm. — Humboldt Orogeny: Regional Unconformity — Carbonate Platform Shelf - Paludal Deposition — Upper Carbonate Aquifer

Pennsylvanian — Keeler Canyon Formation — ? Bird Spring Formation — Tippipah Limestone

Mississippian — Rest Spring Shale / Perdido Fm. / Tin Mountain Ls. — Meiklejohn ? Fm. — Chainman Sh. / Eleana Fm. — Rogers Spring Ls. / Timpi Ls. / Mercury Ls. — Monte Cristo Limestone — Narrow Cyn Ls. — Antler Orogeny: Foreland Basin — Upper Clastic Aquitard

Devonian — Lost Burro Formation — ?—? Flourspar Cyn Fm. — Devils Gate Ls. / Sultan Fm. — Guilmette Fm. / Simonson Dol. — Passive Continental Margin — Shelf - Slope - Rise Deposition — Lower Carbonate Aquifer

Silurian — Hidden Valley Dolomite — Rks. of Tarantula Cyn. / Lone Mtn Dol. / Roberts Mtn Fm. — Laketown Fm. / Nevada Fm. — Nevada Fm. / Dolomite of Spotted R. — Sevy Dolomite

Ordovician — Ely Springs Dolomite / Eureka Quartzite / Pogonip Group — Antelope Valley Limestone / Nine-Mile Formation / Goodwin Limestone

Cambrian — Nopah Formation / Bonanza King Formation / Carrara Formation / Zabriski Quartzite

Precambrian — Wood Canyon Formation / Sterling Quartzite / Johnnie Formation — ? Base Not Exposed ? — Rifting and trough filling — Lower Clastic Aquitard

Pahrump Group: Noonday Dolomite / Kingston Peak Fm. / Beck Spring Dol. / Crystal Spring Fm.

World Beater Complex — Huronian Folding and Metamorphism

00374DC_017.ai

Sources: Hunt and Mabey 1966 [DIRS 106201]; Corbett et al. 1988 [DIRS 140211]; Dunne 1986 [DIRS 102861]; Cemen and Wright 1990 [DIRS 102498]; Burchfiel 1965 [DIRS 102052]; Fleck 1967 [DIRS 105335]; Burchfiel and Davis 1988 [DIRS 104628]; Monsen et al. 1992 [DIRS 106382]; USGS 1976 [DIRS 107048]; 1984 [DIRS 101305]

Figure 2-6. Precambrian and Paleozoic Stratigraphic Units of the Yucca Mountain Region
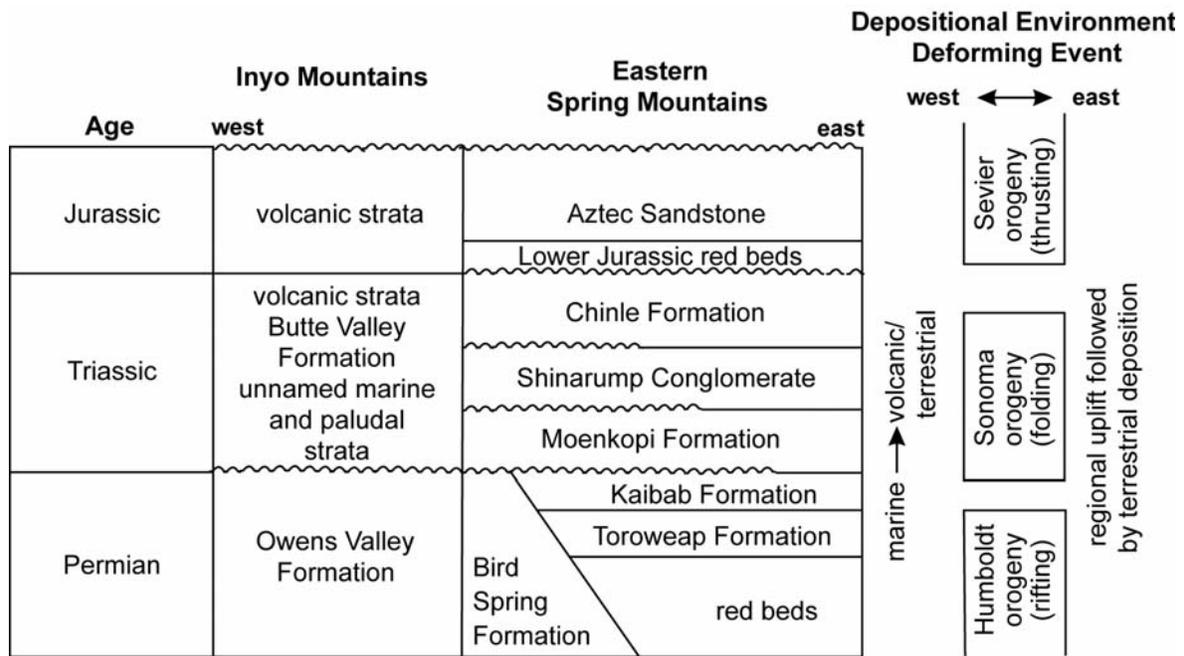
Sources: Hunt and Mabey 1966 [DIRS 106201]; Corbett et al. 1988 [DIRS 140211], p. 271; Burchfiel and Davis 1988 [DIRS 104628], p. 90

NOTE: The Kaibab, Toroweap Formations, and red beds are not lithologic equivalents of the Bird Spring Formation; they overlie the Bird Spring Formation, but they are partly age-equivalent.

Figure 2-7a. Permian and Mesozoic Stratigraphic Units of the Yucca Mountain Region
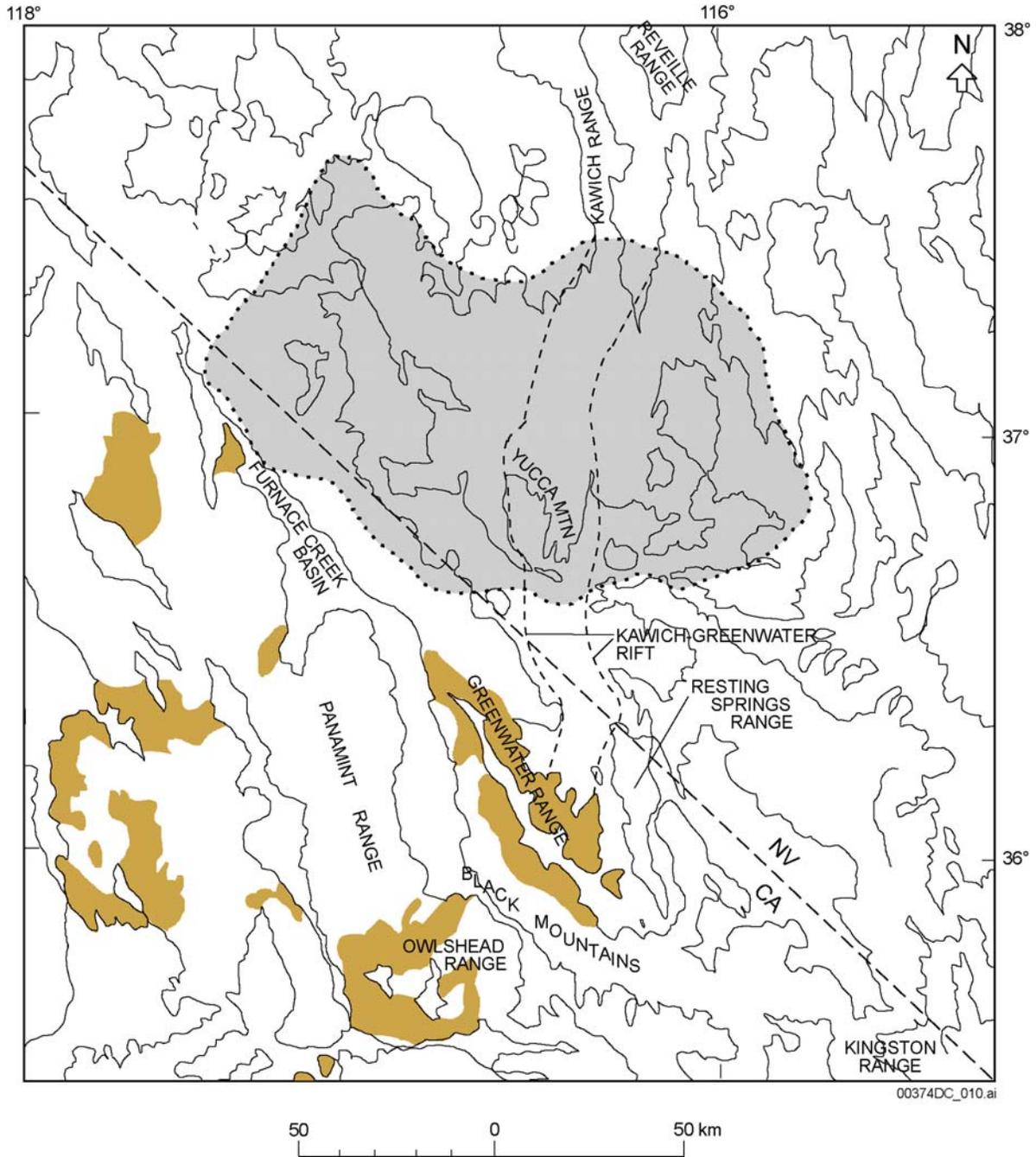
DTNs: MO0312SEPSDCDU.000 [DIRS 166376]; MO0312SEPSDTQS.000 [DIRS 166377]

Sources: Carr 1990 [DIRS 104669]; Jennings 1977 [DIRS 150225]

NOTES: Dashed lines indicate approximate borders of the Kawich-Greenwater rift of Carr (1990 [DIRS 104669]). The Kawich-Greenwater rift is also discussed in Section 4.3 of CRWMS M&O (2000 [DIRS 151945]). The dotted boundary indicates the general extent of the southwestern Nevada volcanic field; brown shading indicates coeval igneous rocks of the Inyo-Mono domain.

Figure 2-7b. Approximate Extent of the Southwestern Nevada Volcanic Field and Coeval Igneous Rocks of the Inyo-Mono Domain

Funeral and Grapevine Mountains,
Death Valley Region

Age		Rocks of the Southwestern Nevada Volcanic Field	AGE GROUPING UNIT	AGE (Ma)	Approximate Age			
Plio-Pleisto-cene			Pliocene and Quaternary Volcanics: (Interbedded with alluvium)		3 Ma	Funeral Formation	basalt	
			Lathrop Wells cone	0.074-0.084				
			Bishop Tuff ashfall	0.76			cgl.	
			Crater Flat cinder cones	0.77-1.17				
			Older Crater Flat flows	3.7	5 Ma			
Miocene	late		Latest Miocene Units:			Furnace Creek Fm (2000 m)	fluvio-lacustrine alluvium	Esmeralda Formation
			Late Miocene basin fill	(10-7)				
			(locally includes:)					
			Spearhead Tuff	7.5±0.03				
			Unnamed ashfall	8-8.5				
			Thirsty Canyon Tuff	9.4			local basalts	
			Rocks of Rainbow Mountain	10.47				
			Rock-avalanche breccia	(10.5)				
			Twisted Canyon basalt and tuff	10.7	6 Ma			
			Major Volcanic Period (11-14 Ma) Units:			Artist Drive Fm (~2500 m)	ss. cgl.	
			Rock-avalanche breccia	(11.5)				
			Timber Mountain Group:					
			Ammonia Tanks Tuff	11.45±0.03				
			Rainier Mesa Tuff	11.6±0.03				
			Rhyo. of Fluorspar Canyon	11.6-11.17			volcanics and basalts	
			Rock-avalanche breccia	12.6-11.8				
			Windy Wash lavas/tuffs	12.5	14 Ma			
			Paintbrush Group:			Bat Mtn. Fm	ss. fan-glomerate	
			Tiva Canyon Tuff	12.7±0.03				
	middle		Yucca Mountain Tuff	-				
			Pah Canyon Tuff	-				
			Topopah Spring Tuff	12.8±0.03				
			Calico Hills Fm. tuffs	12.9±0.04				
			Wahmonie/Salyer Fms.	13.0±0.10	16 Ma	Kelley's Wells Ls (100 m)		
			Crater Flat Group:	13.1				
			Prow Pass Tuff	13.25±0.04				
			Bullfrog Tuff	13.35			ls.	
			Rhyo. of Propector Pass	13.45				
			Tram Tuff	13.9				
			Lithic Ridge Tuff	Approximately 15.2-14				
	early		Older tuffs	15.1±0.06				
			(Tuff of Yucca Flat)				ls. tuff	Titus Canyon Formation
			Pre-Southwest Nevada Volcanic Field Units:		20 Ma	Amargosa Valley Fm (800 m)	red ss.	
			Rocks of Pavits Spring and rocks of Joshua Hollow	(14?-16)				
Oligo-cene			"Green Conglomerate"	(16?-20)			ls., tuff	
			Winapi Wash/Titus Canyon Fm.	(25?-30)				
			Slide Breccia	?			cgl.	
			Monotony Tuff	27.3	?25 Ma			

00374DC_020.ai

DTNs: MO0312SEPSDCDU.000 [DIRS 166376]; MO0312SEPSDTQS.000 [DIRS 166377]

Sources: Sawyer et al. 1994 [DIRS 100075]; Cemen et al. 1999 [DIRS 150229], p. 69; Wright et al. 1999 [DIRS 150227]; Slate et al. 2000 [DIRS 150228], pp. 23 and 33; Fridrich 1999 [DIRS 118942], p. 175; Turner 1900 [DIRS 107012]

NOTES: ls = limestone; ss = sandstone; cgl. = conglomerate; Rhyo. = Rhyolite

Figure 2-8. Tertiary and Quaternary Stratigraphic Units of the Yucca Mountain Region
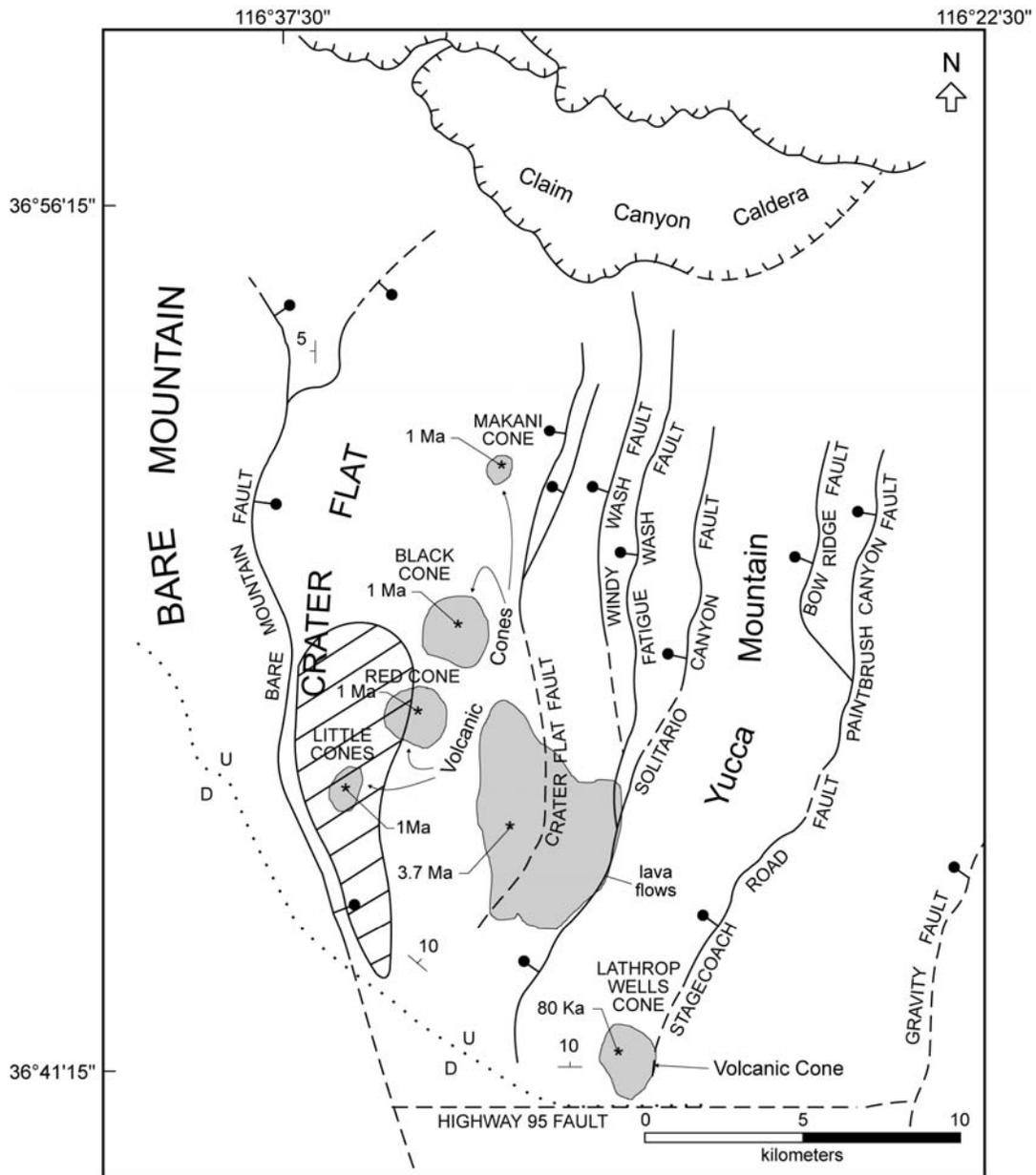
Source: Modified from Fridrich 1999 [DIRS 118942], Figures 11 and 12

NOTE: Faults, bar, and ball symbols are shown on downthrown side.

Figure 2-9. Late Neogene and Pleistocene Features at and near Yucca Mountain

Legend

Amargosa River
Fortymile Wash
Las Vegas Valley Watershed
County Boundaries
State Boundaries
Depositional Basins

N

5   0   5   10   15   Miles
10   0   10   20   Kilometers
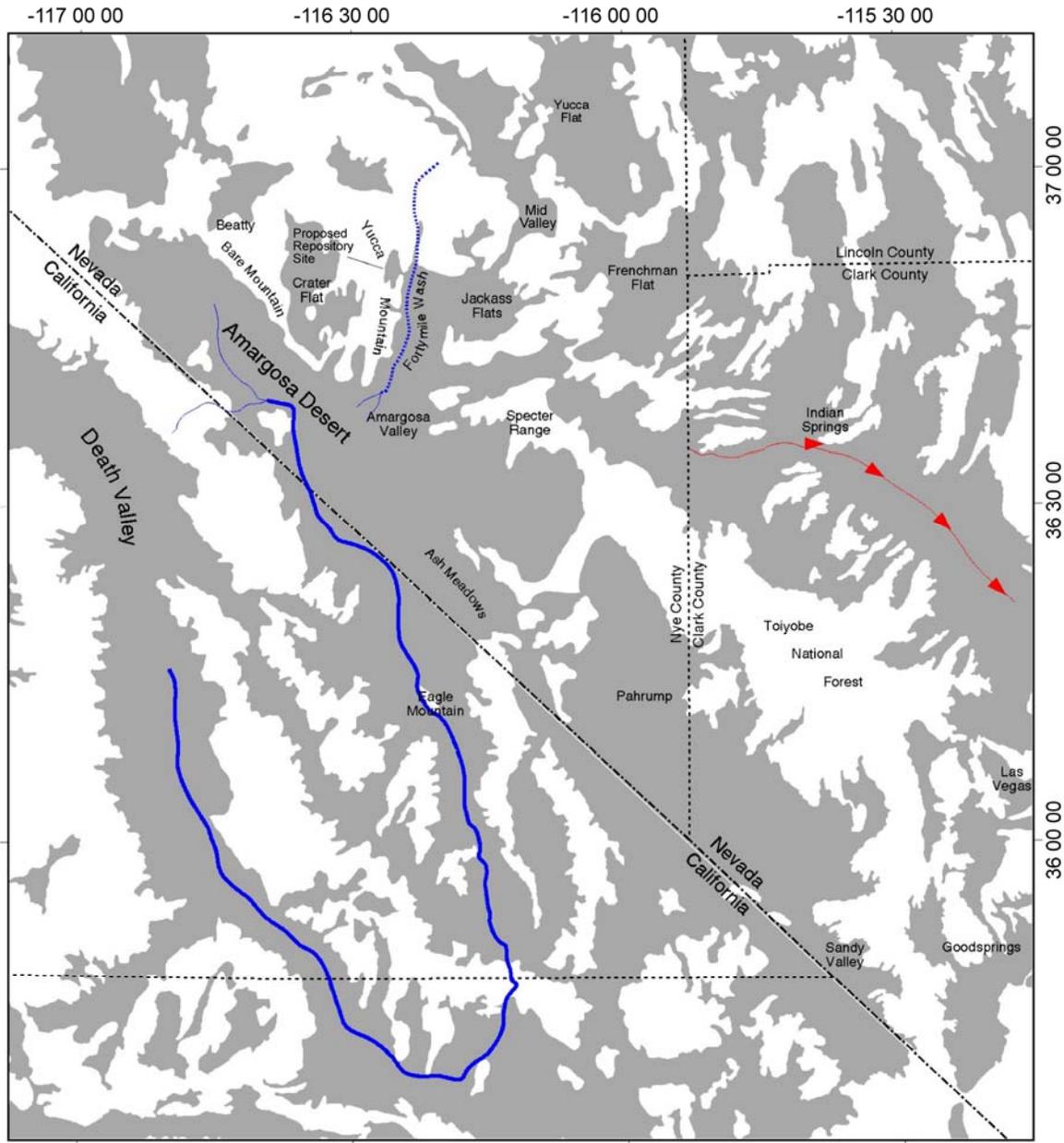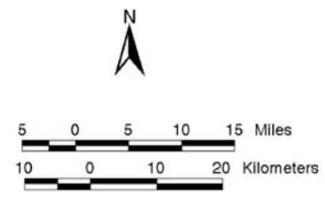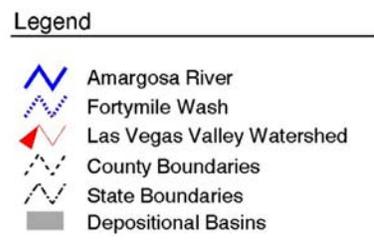
DTN: MO0006YMP00067.000 [DIRS 150638]

Source: CRWMS M&0 2000 [DIRS 151945], Figure 4.2-13

Figure 2-10.   Pleistocene Depositional Basins and Drainage Features
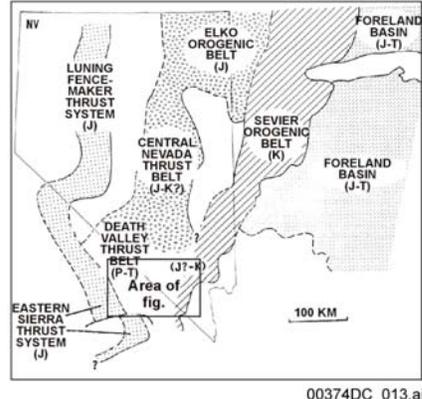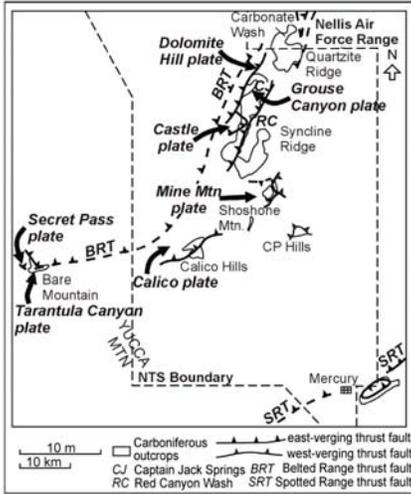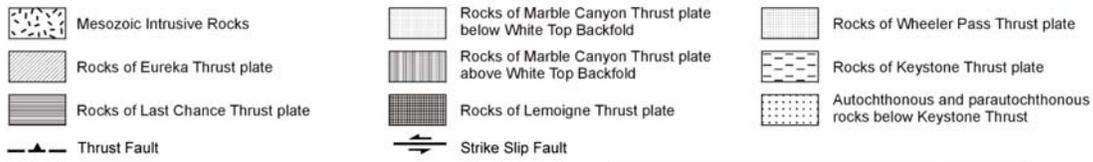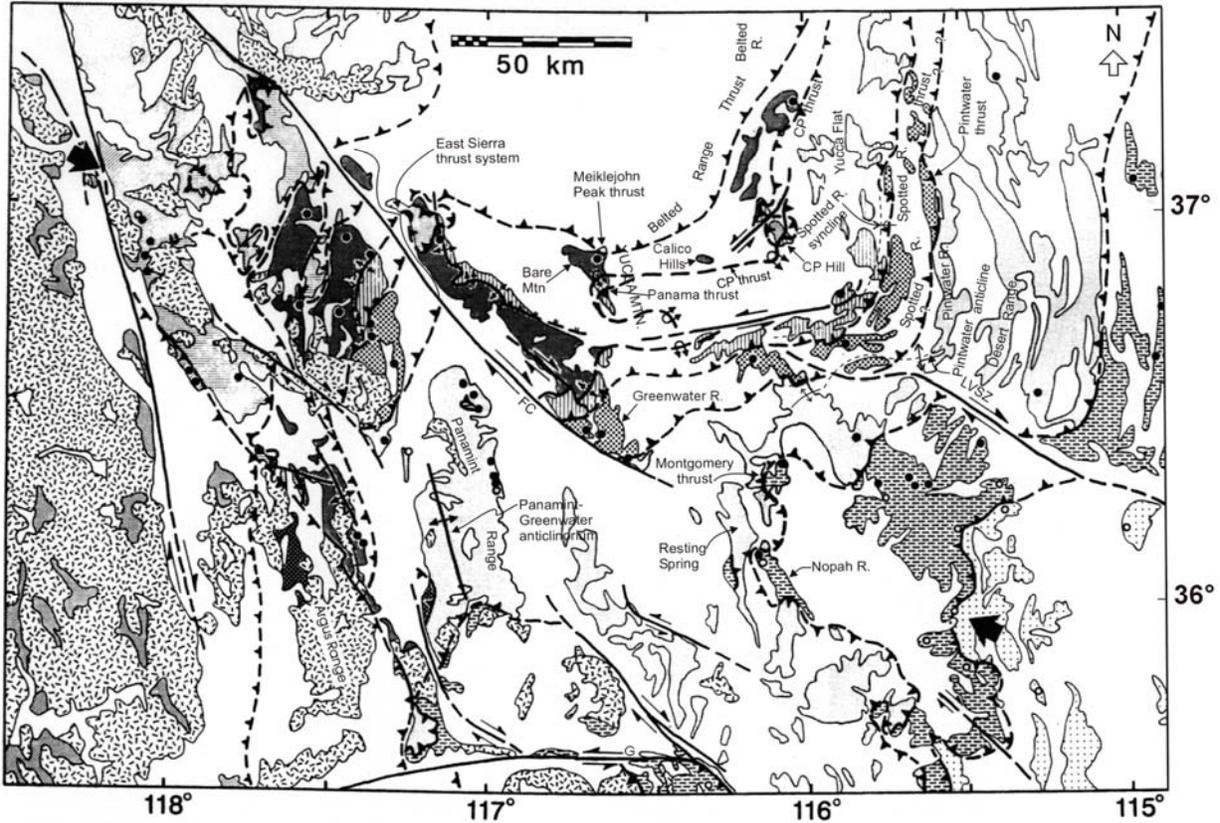
Sources: Snow 1992 [DIRS 106868]; Taylor et al. 1993 [DIRS 105432]; Trexler et al. 1996 [DIRS 107005]

NOTES: Fault traces are dashed where covered; teeth point to overthrust (upper) plate; double-arrowed "U" indicates overturned fold.

Figure 2-11. Generalized Compressional Features of the Yucca Mountain Region
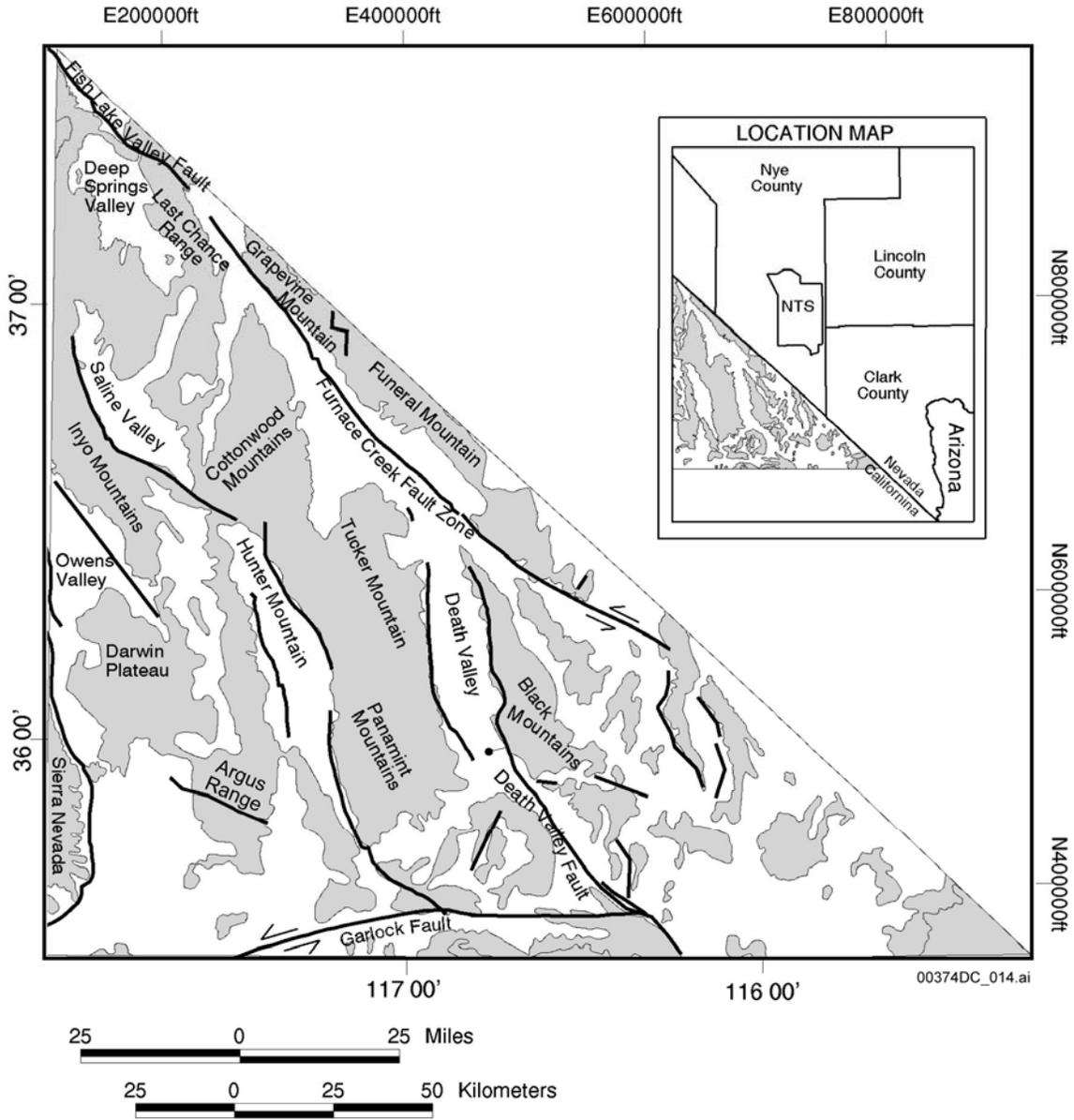
DTN: MO0004YMP00004.001 [DIRS 150703]

Sources: Wernicke et al. 1986 [DIRS 105531]; Piety 1996 [DIRS 106540]

Figure 2-12.   Major Faults of the Inyo-Mono Domain

Sources: Hinrichs 1968 [DIRS 106140]; Frizzell and Shulters 1990 [DIRS 105454]; Yount et al. 1987 [DIRS 108731]

Figure 2-13. General Geology of the Rock Valley Fault Zone
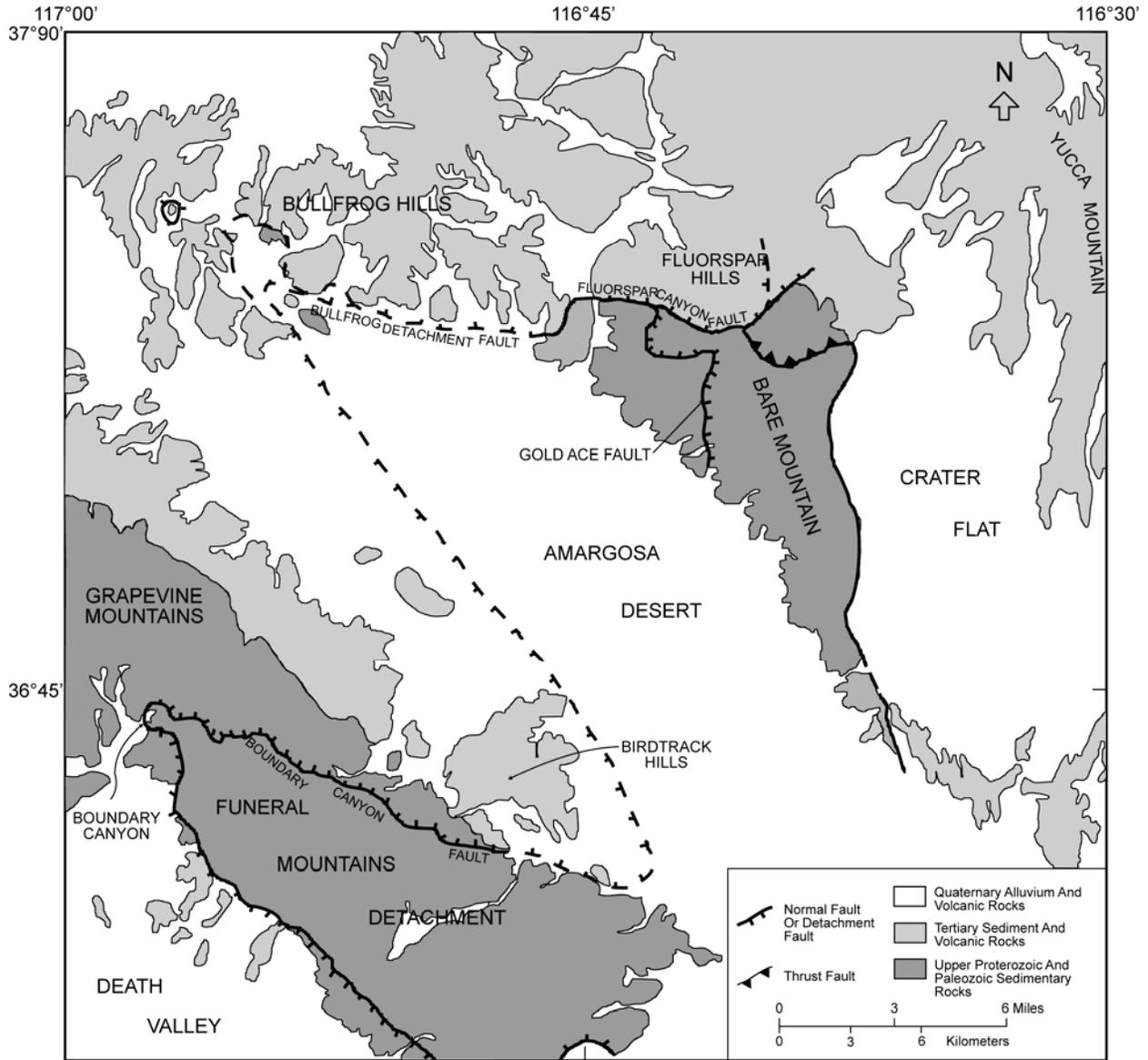
Source: Hoisch 1995 [DIRS 106161]

Figure 2-14. Funeral Mountains Detachment
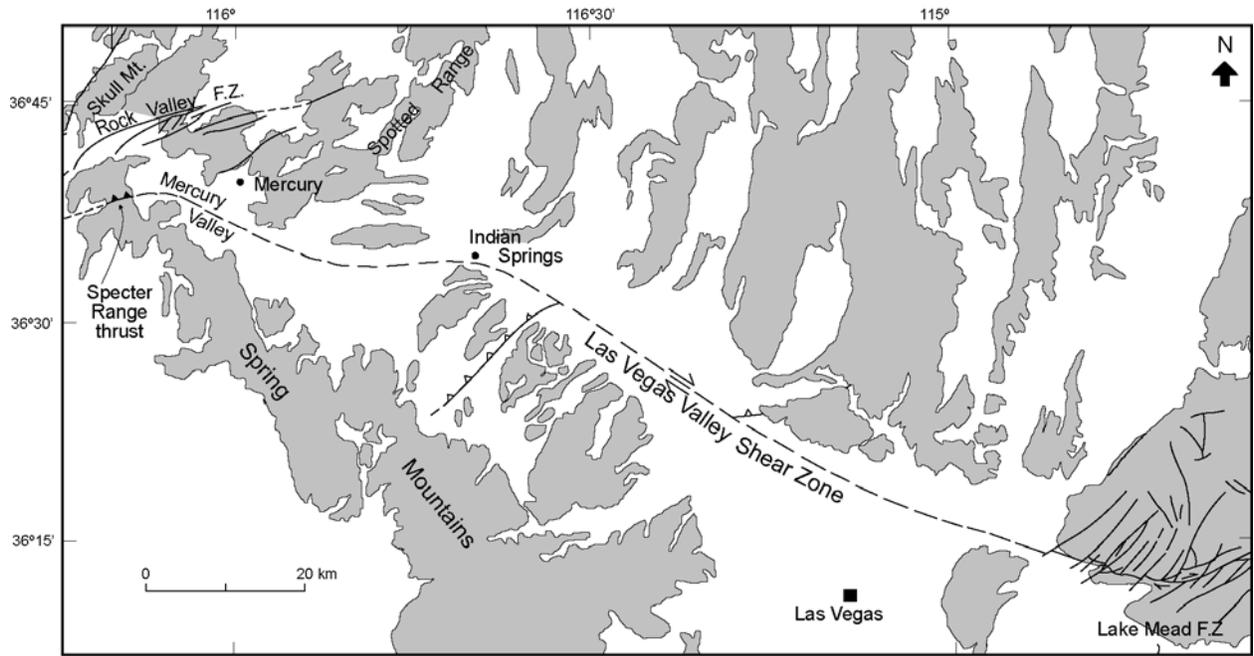
00374DC_003.ai

Source: Burchfiel 1965 [DIRS 102052]

Figure 2-15. Las Vegas Valley Shear Zone
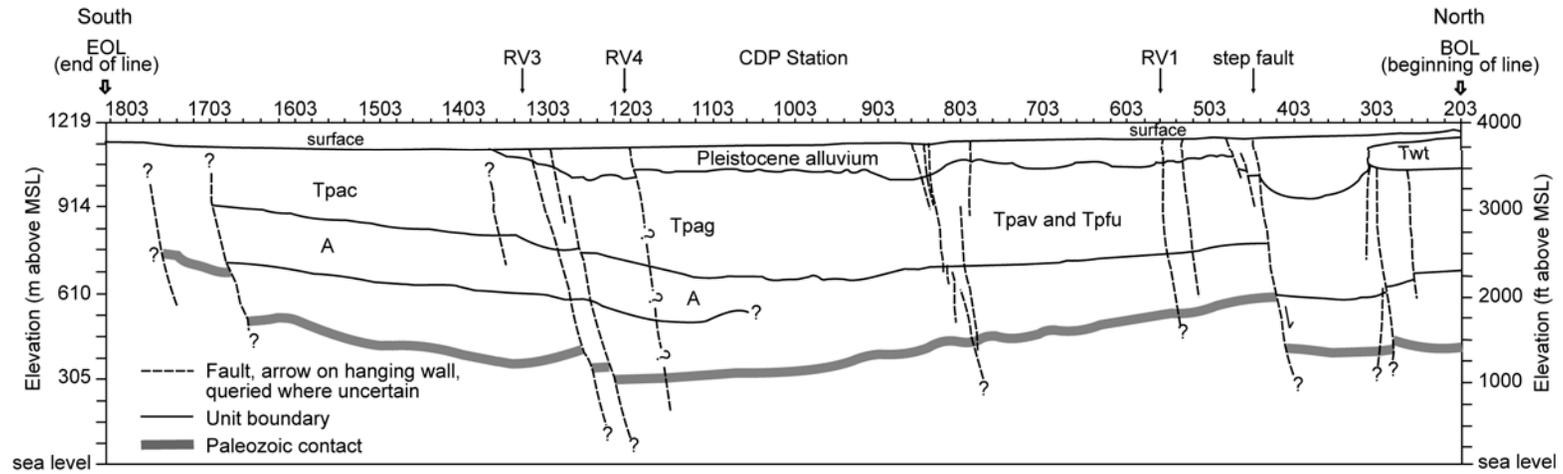
DTN: MO0312SEPSDSRP.000 [DIRS 166378]

Source: Coe et al. 1996 [DIRS 101528], Figure 4.13.2

NOTES: RV1, RV3, and RV4 indicate major fault strands of the Rock Valley fault zone. BOL indicates beginning of line (northern end). Tpac, Tpag, Tpav, and Tpfu are subunits of Pavits Spring. Twt is the Wahmonie Formation; A is the highly reflective part of Tpac below which there is no information.

Figure 2-16.   Interpretation of Seismic Reflection Profile across Rock Valley
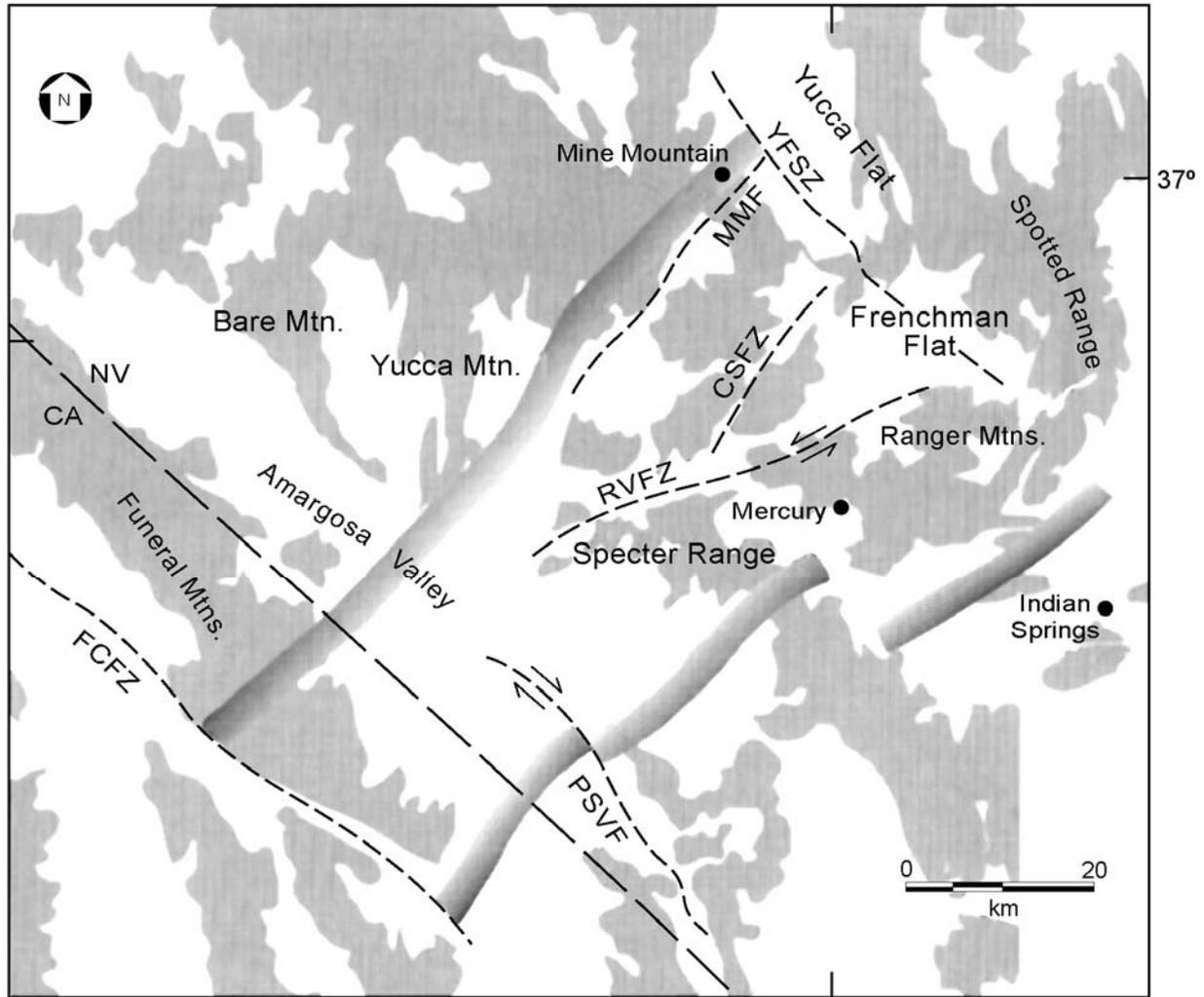
Source: Carr 1984 [DIRS 101037], Figure 7

NOTES: CSFZ = Cane Spring fault zone; FCFZ = Furnace Creek fault zone; MMF = Mine Mountain fault zone; PSVF = Pahrump-Stewart Valley fault zone; RVFZ = Rock Valley fault zone; YFSV = Yucca Frenchman shear zone

Figure 2-17. Spotted Range-Mine Mountain Structural Zone Depicted by Northeast-Trending Shaded Borders

INTENTIONALLY LEFT BLANK

Table 2-1. Comparison of Depositional Units and Related Soils at Yucca Mountain with Local and Regional Surficial Stratigraphies

Yucca Mountain Area, Nevada[a]	Lower Colorado River, California-Arizona[b]	Yucca Wash, Nevada[c]	Crater Flat, Nevada[d]	Silver Lake, California[e]	Kyle Canyon Fan, Nevada[f]	Fish Lake Valley Nevada-California[g]	Providence Mountains[h]
				Holocene			
Q7 (<0.2)	Q4b (0)	Q1a (0)	Modern (0)	Modern (0)	Q4 (0)	Late Marble Creek (0-0.75 yrs)	Qf8 (0-2.8, <0.1)
Q6 (<1)	Q4a (0.1-2) Q3c (2-4) Q3b (4-8)	Q1b (<0.2)	Crater Flat (0.4-1.5)	Q3b3 (0.5-2.5) Q3b2 (2.0-4.5)		Middle Marble Creek (1-1.6) Early Marble Creek (1.9-5.3)	Qf7 (0-4.2, ~1) Qf6 (3-8, 4)
Q5 (2-17)	Q3a (8-12)	Q1c (3-30, ~10)	Little Cones (7-11)	Q3b1 (6-11)	Q3-upper (4-80, 15)	Leidy Creek (6.4-10)	Qf5 (8-18, ~10)
Q4 (30-100)	Q2c (12-70)	Q2b (140-160)	Late Black Cone (>17-30)	Q3a (13-50)	Q3-lower (4-80, 50)	Indian Creek (50-130?)	Qf4 (17-75, ~50)
Q3 (100-250)	Q2b (70-200)	Q2c (270-300)	Early Black Cone (>159-200)	Q2b (110-130) Q2a (140-190)	Q2 (18-750, 130)		Qf3 (29-758, ~150)
Q2 (~400)	Q2a (400-758)		Yucca? (>343-375)	Q1b (>400->650)			
Q1 (500->758)	Q2a (400-758)	Qta (900-2000)	Solitario (>433-<758)	Q1b (>400->650)	Q1 (750-800, 800)	McAfee Creek (600?-758)	Qf2 (29-758, ~600)
Q0 (>758)	Q1 (>1200)	QT (900-2000)		Q1 (>650->800)		Perry Aiken Creek (>758)	Qf1 (758-4000, ~1500)

Sources: [a] Whitney and Taylor 1996 [DIRS 107309]

[b] Bull and Ku 1975 [DIRS 102051]; Ku et al. 1979 [DIRS 106303]; Bull 1991 [DIRS 102040]

[c] Hoover 1989 [DIRS 101247]; Taylor 1986 [DIRS 102864]

[d] Peterson 1988 [DIRS 106512]; Peterson et al. 1995 [DIRS 106519]

[e] Reheis et al. 1989 [DIRS 106659]; Wells et al. 1990 [DIRS 107208]

[f] Reheis et al. 1992 [DIRS 106661]

[g] Slate 1991 [DIRS 130186]; Reheis and Sawyer 1997 [DIRS 106656]

[h] McDonald and McFadden 1994 [DIRS 104772]; Wang et al. 1996 [DIRS 107155]

NOTES: Numbers in parentheses refer to age estimates in thousands of years; dates presented on this table are derived from a variety of sources and methods, and are intended for comparison purposes only; number after this range is the preferred age estimate. Preferred ages for "Yucca Mountain area, Nevada (this study)" were determined using scientific judgment and considered all available data, including their reliability and uncertainty.

INTENTIONALLY LEFT BLANK

3. GEOLOGY OF THE YUCCA MOUNTAIN SITE AREA

3.1 INTRODUCTION

Geologic and related investigations at Yucca Mountain center on a rectangular area of some 165 km^2 (65 mi^2) that covers the central part of the mountain (Figure 3-1) and is informally referred to as the "site area" with respect to the geologic repository for high-level radioactive wastes (HLWs). Geologic mapping at various scales and detailed stratigraphic and structural studies have been conducted there, as well as in adjacent areas, such as contiguous parts of the Nevada Test Site to the east, starting in the 1960s. These mapping activities and related studies were then pursued with increased effort starting in the late 1980s as an integral part of a broad, interdisciplinary characterization program designed to comprehensively evaluate the suitability of the site to host safe and permanent waste disposal (DOE 1988 [DIRS 100282]). Knowledge and understanding of the natural systems—nature of the rocks involved and their post-depositional and deformational histories—are essential for repository design, geologic hazard analysis, and performance assessment.

Results of the geologic studies conducted in the Yucca Mountain site area, many of which have been published, are summarized in this section. Much of the accumulated information being summarized was presented in greater detail in Sections 4, 7.3, and 7.4 of the *Yucca Mountain Site Description* (YMSD) REV 01 (CRWMS M&O 2000 [DIRS 151945]). Principal sources of data that have become available more recently, which are also incorporated into the present discussion, include: (1) studies of the Quaternary stratigraphy and recency of faulting in Midway Valley (Figure 3-2) by Swan et al. (2001 [DIRS 158784]); (2) compilations of regional geologic maps and structure sections by Potter et al. (2002 [DIRS 160060]); (2002 [DIRS 159091]), and Sweetkind et al. (2001 [DIRS 159092]); (3) results of a series of Quaternary fault studies reported by Keefer et al. (2003 [DIRS 159419]); and (4) a description of flooding in Fortymile Wash by Tanko and Glancy (2001 [DIRS 159895]).

3.2 PHYSIOGRAPHY AND GEOMORPHOLOGY

3.2.1 Physiographic Setting of Yucca Mountain and Vicinity

Yucca Mountain, in southwest Nevada (Figure 3-1), lies in the south-central part of the Great Basin that forms the northern subprovince of the Basin and Range physiographic province (Figure 2-1b). More specifically, Yucca Mountain occupies part of the Walker Lane belt, a major structural lineament considered to be a zone of transition between (1) the central and southeastern parts of the Great Basin, characterized by dip-slip normal faulting and typical basin and range topography; and (2) the southwestern Great Basin, typified by both dip-slip and strike-slip faulting and irregular topography (Carr 1984 [DIRS 101037]). Yucca Mountain itself is situated on the south flank of the southwestern Nevada volcanic field, which consists of a series of volcanic centers from which large volumes of pyroclastic flow and fallout tephra deposits were erupted from about 14.0 to 11.4 Ma (Byers et al. 1976 [DIRS 104639]; Sawyer et al. 1994 [DIRS 100075]. Accordingly, the mountain and many of the adjacent landforms carry the imprint of the area's extensive volcanic history, as well as its deformational history.

The area surrounding Yucca Mountain can be divided into eight clearly defined physiographic elements that combine to produce a variable and diverse terrane typical of the Walker Lane (Figure 2-2). Three of these—Yucca Mountain and the bordering features to the east and west, Fortymile Wash and Crater Flat, respectively (Figure 3-1)—are described below. The other five—Amargosa Desert, Bare Mountain, Pinnacles Ridge, Beatty Wash, and Jackass Flats—are discussed in Section 4 of the *Yucca Mountain Site Description* REV 01 (CRWMS M&O 2000 [DIRS 151945]).

3.2.1.1   Yucca Mountain

Yucca Mountain is an irregularly shaped upland, 3- to 8-km wide and about 35 km long, that stretches from near Beatty Wash at the northwest end to near the north edge of the Amargosa Desert at the south end (Figure 2-2). The crest of the mountain reaches elevations of 1,500 to 1,930 m, about 125 to 275 m higher than the floors of adjacent washes and lowlands. The dominantly north-trending pattern of structural blocks characterizing this prominent upland area is controlled by high-angle block-bounding faults (Scott and Bonk 1984 [DIRS 104181]; Day et al. 1998 [DIRS 100027]) with vertical displacements of several hundred meters in places. The fault blocks, composed of volcanic rocks of Miocene age, are tilted eastward, so that the fault-bounded west-facing slopes are generally high and steep, in contrast to the more gentle and commonly deeply dissected east-facing slopes. The valleys are generally narrow and V-shaped along their upper and middle reaches, but, locally, contain flat, alluviated floors in their lower reaches. Valley morphology ranges from shallow, straight, steeply sloping gullies and ravines to relatively deep, bifurcating, gently sloping valleys and canyons. The hillslopes between ridge crests and valley floors typically include at least three general forms: narrow upper convexities, extensive straight segments, and broad lower concavities. Drainage from the west flank of the mountain flows southward down narrow fault-controlled canyons and out into Crater Flat. Drainage from the east flank flows southeastward down Yucca, Drill Hole, and Dune washes into Fortymile Wash (Figure 3-2).

3.2.1.2   Crater Flat

Crater Flat, flanked by Bare Mountain on the west and Yucca Mountain on the east, is a structural basin approximately 24 km long and 6 to 11 km wide (Figure 2-2). The basin has the overall form of a graben (or, perhaps more appropriately, a half-graben), its west side having been downdropped several kilometers along the east-dipping Bare Mountain fault, and its east side downdropped a few hundred meters along a series of west-dipping normal faults that form the west slope of Yucca Mountain (Carr 1984 [DIRS 101037]; Simonds et al. 1995 [DIRS 101929]; Fridrich 1999 [DIRS 118942]). The axial part of the basin floor, covered by alluvial deposits that overlie a thick (as much as 3 km) sequence of late Cenozoic volcanic rocks, rises gradually from altitudes of about 840 m at the south end to as much as 1,280 m at the foot of Yucca Mountain to the north. Four basaltic vents and their associated lava flows form prominent cones that attain heights ranging from 27 to 140 m above the alluviated surface of the central basin area.

3.2.1.3 Fortymile Wash

Fortymile Wash drains an area of approximately 62 km^2 east and northeast of Yucca Mountain. From its northern headwaters, it flows southward through Fortymile Canyon, a steep-sided drainage course some 300 m deep in places, and continues down the south-sloping piedmont that forms the west end of Jackass Flats (Figure 3-1). Along this latter reach, the wash has cut a nearly linear trench, 150 to 600 m wide and as much as 25 m deep, into the Quaternary alluvial deposits of the piedmont. This entrenchment gradually decreases downslope until the wash merges with the general level of the piedmont near the northeast margin of the Amargosa Desert basin (Figure 2-2).

3.2.1.4 Other Topographic Features

In addition to the major landforms described above, three buttes or ridges (Busted Butte, Fran Ridge, and Alice Ridge) and an alluvial flat (Midway Valley) form prominent topographic features on the east side of Yucca Mountain, and two narrow, linear drainage courses (Solitario Canyon and Fatigue Wash) are to the west. Busted Butte, Fran Ridge, and Alice Ridge (Figure 3-2) are faulted bedrock areas rising 110 to 200 m above the surrounding terrain. Midway Valley, lying between these features and the east slope of Yucca Mountain to the west, is an alluviated lowland that slopes gently eastward from an elevation of about 1,220 m in its northwestern part to 1,070 m at a low point between Alice and Fran ridges. Tributaries to Fortymile Wash head in northwest-trending washes along the east slope of Yucca Mountain, the most prominent of which is Yucca Wash (Figure 3-2), and flow eastward across Midway Valley. A number of other washes are incised features toward the south end of Yucca Mountain, the largest being Dune Wash.

Drainages in Solitario Canyon and Fatigue Wash rise in upland areas in the northern part of Yucca Mountain at elevations of approximately 1,425 m and 1,675 m, respectively, and flow southward in narrow, linear valleys to enter northeastern Crater Flat at an elevation of about 1,200 m. The two valleys have been incised in bedrock some 175 to 275 m and are fault-controlled (Day et al. 1998 [DIRS 100027]). The north end of a third fault-controlled valley, Windy Wash, also extends into the northwestern part of the site area (Figure 3-2). The associated faults (with the same names) are discussed in Section 3.5.

3.2.2 Geomorphology

3.2.2.1 Influence of Tectonism and Quaternary Faulting

As described above, and as will be described in more detail in Section 3.5, Yucca Mountain is characterized by a series of fault blocks bounded by parallel north-striking, primarily dip-slip faults that transect a broad apron of Miocene volcanic rocks and give rise to linear valleys and ridges, such as the crest of Yucca Mountain and the adjoining Solitario Canyon (Figure 3-2). Fault scarps, commonly visible along these faults, are generally located between the bedrock footwall and Quaternary colluvium on the hanging wall. The scarps appear sharp, with fault dips of 55° to 75°, because the exposed volcanic rocks weather slowly (see Section 3.4). A pattern of enhanced erosion at the base of the scarps near channels and rills indicates that the scarps have been noticeably enhanced by hillslope erosion and, in essence, are fault-line scarps.

Several of the block-bounding faults show evidence of Quaternary displacements that (1) influenced depositional patterns of surficial materials on hillslopes and on adjacent valley or basin floors, and (2) in places, produced visible scarps in bedrock outcrops and surficial deposits along some fault traces. However, low rates of offset and long recurrence intervals between successive faulting events on faults in the site area during Quaternary time (slip rates: 0.002-0.05 mm/yr [0.00008 to 0.002 in./yr)]; recurrence intervals: 20 to 140 k.y. (see discussion in Section 4.3; also, Keefer et al. 2003 [DIRS 159419]) have resulted in subtle landforms and contributed to the preservation of early and middle Pleistocene deposits on Yucca Mountain hillslopes (Whitney and Harrington 1993 [DIRS 107303]).

A striking feature of Yucca Mountain hillslopes is the lack of well-defined, rounded alluvial fans at the base of the slopes. On the west side of Yucca Mountain, hillslopes are of nearly uniform gradients, decreasing gradually from 32° near ridge tops to about 15° near the base, because of the homogeneous nature of the underlying volcanic tuff at the ridge crest, and because the low rates of uplift have not caused over-steepened slopes or high relief. As a result, the lower slopes of Yucca Mountain appear more like pediments than alluvial fans, which is most evident where early and middle Pleistocene deposits are truncated and overlain by a thin veneer (less than one meter thick) of late Pleistocene-Holocene alluvium and eolian deposits.

Fault scarps are commonly visible along the block-bounding faults. The scarps are generally located between the bedrock footwall and colluvium on the hanging wall. The bedrock scarps appear sharp, with fault dips of 55° to 75° (Simonds et al. 1995 [DIRS 101929]) because the volcanic bedrock weathers very slowly (see bedrock weathering rates below). The exposed fault scarps along the Solitario Canyon and Northern Windy Wash faults were exposure-dated by cosmogenic ^{14}C to determine whether Holocene surface ruptures may have formed the scarps (Harrington et al. 1994 [DIRS 106100], p. A303). Analyses of the in situ cosmogenic radiocarbon from both scarps indicate that both scarps have been exposed for more than 20 k.y. A pattern of enhanced erosion at the base of the scarps near channels and rills indicates that the scarps have been significantly enhanced by hillslope erosion. The Stagecoach Road fault also exhibits a prominent scarp where eolian sand has washed away from a scarp formed in a well-cemented, reworked tuff. Thus, most prominent scarps at Yucca Mountain appear to be fault-line scarps, tectonic in origin but significantly enhanced by erosion.

3.2.2.2   Influence of Volcanism

Bedrock in the Yucca Mountain site area is entirely composed of volcanic outflow sheets whose caldera sources lay north of the site area. Much of the original morphology of this giant sheet of pyroclastic flows and fallout tephra that covered the area of Yucca Mountain and vicinity is no longer preserved, having been broken and segmented by subsequent faulting. A general southward decrease in elevation may, in part, reflect the regional depositional gradient away from the nearby volcanic centers to the north (Figure 3-1). As indicated above, the effects of subsequent faulting and tilting of fault blocks have obscured much of the initial landscape created by the volcanic activity.

With respect to the volcanic rock sequences now exposed in the site area, differing characteristics between units, particularly the degree of welding, impart varying resistances to erosion, locally creating subdued bench-like topography. However, the nonwelded, less resistant

units are commonly thin compared to the welded, more resistant units, so that the effect of differential erosion is of relatively minor geomorphic importance.

3.2.2.3   Influence of Climate

Climatic conditions exert a strong influence on geomorphic processes and, thus, are an important factor in controlling depositional and erosional patterns. The effects of climate on the evolution of landforms at Yucca Mountain are discussed in Section 3.4.5.

3.3   SITE STRATIGRAPHY

3.3.1   Introduction

Mid-Tertiary volcanic rocks, consisting mostly of pyroclastic-flow and fallout tephra deposits with minor lava flows, dominate the exposed bedrock formations in the Yucca Mountain site area (Figure 3-2). The stratigraphy of these rocks forms the basic framework for the modeling and analyses of rock properties, mineral distributions, faulting and fracturing, hydrologic flow, and radionuclide transport. As such, they have been a major focus of stratigraphic studies in the area, resulting in a number of published descriptive and interpretive reports (for example, Sawyer et al. 1994 [DIRS 100075]; Buesch et al. 1996 [DIRS 100106]) that have defined what is now generally recognized as the standard hierarchical sequence of named units and subunits composing the principal volcanic rock groups and formations. The detailed order (and descriptions) of both major and minor subdivisions is given in Tables 4.5-1 and 4.5-2 of the YMSD (REV 01) (CRWMS M&O 2000 [DIRS 151945]) and will not be repeated here. However, a summary table listing the succession, general lithologies, and thicknesses of major units is presented in Table 3-1. Detailed descriptions of the Tertiary volcanic rocks have also been compiled into the *Yucca Mountain Project Stratigraphic Compendium* (CRWMS M&O 1996 [DIRS 101535]).

The stratigraphic framework thus established has other site characterization investigations, including (1) geologic mapping ranging from standard scales for general-purpose mapping (1:24,000; 1:6,000) to more expanded scales (1:2,400 or larger) along fault zones and on cleared exposures for fracture studies and for peripheral wall mapping in the Exploratory Studies Facility (ESF); (2) defining and correlating hydrogeologic and thermal-mechanical units; and (3) three-dimensional modeling of rock properties.

Surficial deposits of Quaternary age are also widely distributed throughout the Yucca Mountain site area (Figures 3-1 to 3-3). These deposits, mostly alluvium and colluvium, commonly capped with a thin veneer of eolian silt and sand, have, likewise, been studied extensively, particularly in trenches excavated across faults, to determine the extent, ages, and magnitude of Quaternary faulting events for seismic hazard analysis (see Section 4.3.2). In addition, the nature and distribution of surficial materials provide a record of climatic changes during much of Quaternary time, which is an important aspect of site characterization. A generalized map of surficial deposits is shown in Figure 3-3.

The Integrated Site Model (ISM) merges the detailed project stratigraphy into model stratigraphic units that are most useful for constructing the primary subsequent models and the repository design. The ISM was developed to provide a consistent volumetric portrayal of the

rock layers, rock properties, and mineralogy of the Yucca Mountain site. The ISM consists of three components:

- Geologic Framework Model (GFM) (BSC 2002 [DIRS 159124])
- Rock Properties Model (RPM) (BSC 2002 [DIRS 159530])
- Mineralogic Model (MM) (BSC 2002 [DIRS 158730]).

The GFM, Version 2000 (BSC 2002 [DIRS 159124]) represents a three-dimensional interpretation of the geology surrounding the repository site at Yucca Mountain. The GFM encompasses and is limited to an area of 65 mi^2 (168 km^2) and a volume of 185 mi^3 (771 km^3). The boundaries of the GFM (shown in Figure 8-8) were chosen to encompass the exploratory boreholes and to provide a geologic framework for hydrologic flow and radionuclide transport modeling through the unsaturated zone over the area of interest. The depth of the model is constrained by the inferred depth of the Tertiary-Paleozoic unconformity. The GFM was constructed from geologic map and borehole data. Additional information from measured stratigraphic sections, gravity profiles, and seismic profiles was also considered.

The GFM provides a baseline representation of the locations and distributions of 50 rock layers and 44 faults in the subsurface of the Yucca Mountain area, for use in geoscientific modeling and repository design. The input data from geologic mapping and boreholes provide controls at the ground surface and down to the total depths of the boreholes; however, most of the modeled volume is unsampled and uncertainty is high. The GFM is an interpretative and predictive tool that provides a representation of reality within the estimated uncertainty.

The RPM (BSC 2002 [DIRS 159530]) provides exhaustive, three-dimensional, discretized, numerical representations of several important hydrologic and thermal rock properties (porosity, bulk density, matrix saturated hydraulic conductivity, and thermal conductivity) that are intended for further use in numerical design and performance assessment analyses. The four composite modeling units defined for this analysis encompass the majority of the rocks within the unsaturated zone throughout the immediate vicinity of the repository at Yucca Mountain.

The MM (BSC 2002 [DIRS 158730]) models the abundance and distribution of 10 minerals and mineral groups within 22 stratigraphic sequences in the Yucca Mountain area, for use in geoscientific modeling and repository design. The input data from the GFM provide stratigraphic controls, and quantitative analyses of mineral abundances by x-ray diffraction at 24 boreholes provide controls for mineralogy; however, most of the modeled volume is unsampled. The MM is, therefore, an interpretation and a prediction tool rather than an absolute representation of reality. The model possesses an inherent level of uncertainty that is a function of data distribution and geologic complexity, and predictions or alternative interpretations that fall within the range of uncertainty are considered acceptable. Uncertainty in the model is mitigated by the application of sound geologic principles.

3.3.2 General Features of the Volcanic Rocks

Much has been published describing and interpreting the origin and deposition of ash-flow tuffs and the post-depositional processes that influence their physical and chemical properties (e.g., see the fundamental studies of Smith 1960 [DIRS 150469]; Smith 1960 [DIRS 106836];

Ross and Smith 1961 [DIRS 106714]). With respect to the thick tuffaceous sequences at Yucca Mountain, these topics have also been discussed in detail in various reports (e.g. Buesch et al. 1996 [DIRS 100106]; CRWMS M&O 2000 [DIRS 151945]) and will not be included here, except to summarize the principal criteria used to differentiate units and subunits that form the basic stratigraphic framework and to present general lithologic and mineralogic descriptions.

Division of formations into lithostratigraphic units was initially proposed for rocks in the Yucca Mountain area by Warren et al. (1989 [DIRS 107175], p. 387). Buesch et al. (1996 [DIRS 100106], p. 3, Table 1) applied this terminology in greater detail following close examination and analysis of many samples collected from outcrops and from borehole cores within the planned site area.

In general, individual formations represent either volumetrically large eruptive units or a series of products interpreted to have formed from compositionally distinct magma bodies. The Tiva Canyon and Topopah Spring tuffs of the Paintbrush Group (Table 3-1), which are the most widespread bedrock units exposed at Yucca Mountain, are classic examples of a compositional zonation characterized by an upper crystal-rich (greater than 10 percent crystal fragments) member and a more voluminous, lower crystal-poor (less than 5 percent crystal fragments) member (Lipman et al. 1966 [DIRS 100773]). A transition zone in crystal abundance, typically 5 to 10 m thick, is included as a basal unit of the crystal-rich member (Buesch et al. 1996 [DIRS 100106], Table 2). Compositionally, the rocks include high-silica rhyolites (greater than 75 percent SiO_2) and subordinate quartz-latites (less than 75 percent SiO_2) (Figure 3-4). Many of the interstratified bedded tuffs and local lava flows that are distinct from overlying and underlying formations (Table 3-1) probably represent small-volume eruptions.

3.3.3 Criteria for Differentiating Volcanic Rock Units

In the Yucca Mountain area, separation of formations into subunits is based on macroscopic features (for example, degree of welding) of the rocks as they appear in exposures and borehole cores (Buesch et al. 1996 [DIRS 100106]). Their identification is augmented by quantitative mineralogy (Bish and Chipera 1986 [DIRS 100030]; Chipera et al. 1995 [DIRS 111081]), borehole geophysics (Bechtel SAIC Company, LLC [BSC] 2002 [DIRS 157829], Attachment I; Muller and Kibler 1984 [DIRS 105141]; Nelson et al. 1991 [DIRS 101272]; Nelson 1996 [DIRS 101270]; CRWMS M&O 1996 [DIRS 101535]; CRWMS M&O 1997 [DIRS 103564]), rock properties such as density and porosity (Moyer et al. 1996 [DIRS 100162], pp. 55 to 80; Flint 1998 [DIRS 100033]), and geochemical composition (Spengler and Peterman 1991 [DIRS 106896]; Peterman and Futa 1996 [DIRS 106494]).

Much of the following discussions will focus on the Tiva Canyon and Topopah Spring Tuffs, because each contains rock sequences exhibiting a range of properties that readily provides a basis for detailed stratigraphic subdivision. Geotechnical information for the site of the repository surface facilities is described in BSC (2002 [DIRS 157829], Section 6).

3.3.3.1 Lithologic and Rock-Property Criteria

Important lithologic and rock-property criteria for differentiating volcanic rock units include: (1) variations in grain size and sorting, (2) relative abundance of volcanic glass (vitric versus devitrified), (3) degree of welding, (4) types and degree of crystallization, (5) relative abundance of lithophysae, (6) amount and types of glass alteration, and (7) fracture characteristics. These rock properties, some of which are graphically portrayed in Figure 3-5 with respect to subdivisions of the Tiva Canyon and Topopah Spring tuffs, are the combined products of the primary processes of eruption and deposition, the secondary processes of cooling and crystallization of lava flows or of welding and crystallization of some pyroclastic flows, and post-eruptive processes, such as alteration by infiltrating aqueous solutions and by fracturing and faulting from tectonism.

The lithologic and rock-property criteria listed above, as well as their respective applications toward subdividing formations and members of formations at Yucca Mountain, have been discussed in detail by Buesch et al. (1996 [DIRS 100106]). Of these, two are mentioned briefly here as being especially important for distinguishing zones and subzones within the volcanic sequences. One is the presence or absence of lithophysae (spherical to oblate cavities), which is a condition that is used to define some of the principal zones, particularly within the Tiva Canyon and Topopah Spring tuffs (Figure 3-5), and are closely associated with variously welded units. The other criterion is the degree of welding, a property that distinguishes many subzones and also provides a principal means of separating hydrogeologic and thermal-mechanical units based on whether they are nonwelded, partially welded, moderately welded, or densely welded zones. Such zones are vertically distributed in a single cooling unit of ash-flow tuff, with nonwelded rocks at the top and bottom of the deposit and increasingly welded rocks toward the center (Smith 1960 [DIRS 150469], pp. 153 to 157; see Figure 3-5). Relatively thick deposits, such as the Tiva Canyon and Topopah Spring tuffs, may have the complete welding range (CRWMS M&O 2000 [DIRS 151945], Table 4.5-2), both laterally and vertically, but thin deposits may lack the more welded parts. In general, the degree of welding controls porosity, which ranges from 45 to 65 percent for nonwelded rocks, 25 to 45 percent for partially welded rocks, 10 to 25 percent for moderately welded rocks, and less than 10 percent for densely welded rocks (Buesch 2000 [DIRS 166307]). As such, the degree of welding is an important factor in the hydrogeologic and thermal-mechanical properties of the volcanic units in the site area (for example, see Flint 1998 [DIRS 100033]).

3.3.3.2 Mineralogic Criteria

Mineralogy plays an important role in differentiating lithostratigraphy units, as distinct crystallized and altered zones commonly form in ash-flow tuffs. (Note: Use of the term zone in this sense is not to be construed as having the same connotation as its use in defining principal subdivisions of the crystal-rich and crystal-poor members of the Tiva Canyon and Topopah Spring tuffs.) Four such zones recognized by Smith (1960 [DIRS 150469]) in his fundamental studies of ash-flow tuffs are summarized as follows:

1. Vitric zones–These are created where the original glassy components remained as glass after the period of high-temperature crystallization and final cooling of the deposit had ended.

2. High-temperature devitrification zones–The process of high-temperature devitrification forms rocks composed mostly of feldspar and silica minerals (quartz, cristobalite, tridymite) with minor amounts of other minerals, which texturally form the ground mass that has crystallized within the former glass particle sites.

3. Vapor-phase zone–This zone can be divided into (1) vapor-phase corrosion, whereby glass is corroded to form secondary porosity, and (2) vapor-phase mineralization, which occurs as the temperature cools and minerals, such as tridymite or cristobalite and sanidine, precipitate.

4. Alteration and crystallization zones–These are zones in which high porosity and permeability facilitate alteration of glass, producing sillar textures, and iron oxidizes in the glass to form variegated red and orange colors. Common, low-temperature alteration products include smectite and the zeolitic minerals, clinoptilolite and mordenite.

Based largely on the mineralogical characteristics listed above, Buesch et al. (1996 [DIRS 100106]) observed several crystallization and alteration zones in the Yucca Mountain Tuffs as shown for the Tiva Canyon and Topopah Spring tuffs in Figure 3-5. Vitric and vitric + vapor-phase mineral zones, for example, formed at the top and bottom of each of these formations. Devitrified rocks, which characterize most of the Tiva Canyon and Topopah Spring, are included in the crystallized and crystallized + vapor phase or moderate-temperature alteration mineral zones.

In most of the formations, contacts between vitric and devitrified boundaries (including zones of vapor-phase corrosion and mineralization) are commonly marked by intervals of several millimeters to several meters that contain clay and/or zeolite alteration minerals. In some of the deeper formations, vitric rocks near this vitric-devitrified contact are pervasively altered to zeolite, but typically there appear to be two alteration stages. The contact between the nonlithophysal zone (Tptpln) and the vitrophyre of the vitric densely welded subzone (Tptplv) in the crystal-poor member of the Topopah Spring Tuff (Table 3-5) represents a relatively abrupt contact between high-temperature devitrified rock and underlying glassy rock. However, commonly there is a thin transition interval consisting of well-developed argillic or zeolitic alteration (Levy 1984 [DIRS 101392], pp. 27 to 31; Levy 1984 [DIRS 104577]; Levy and O'Neil 1989 [DIRS 116960], p. 322; Chipera et al. 1995 [DIRS 111081], p. 17; Buesch and Spengler 1999 [DIRS 107236], p. 36). Reexamination of core, cuttings, borehole video, and borehole geophysical logs shows that this alteration interval occurs in most Yucca Mountain site area boreholes, and locally is as much as several meters thick. Levy and O'Neil (1989 [DIRS 116960], p. 325, Table 1) determined that the alteration to clays and zeolites near this contact occurred at a moderate temperature, approximately 40°C to 100°C (104°F to 212°F), and proposed that this alteration occurred during the cooling phase of the Topopah Spring Tuff. Recognizing that argillic and zeolitic alteration occurred near the crystallization front in many formations, this moderate temperature alteration might be a more common phenomenon than previously thought. The significance of this moderate temperature alteration has not been evaluated for hydrogeologic and thermal-mechanical modeling. Two possible additional locations of this type of alteration in Paintbrush Group rocks include the argillic alteration that is common near the vitric-devitrified contact in the crystal-poor Tiva Canyon Tuff, and the zeolitic

alteration that occurs near the vitric-devitrified contact in the crystal-rich Topopah Spring Tuff (quantitative mineralogic data in UZ#16 from Chipera et al. 1995 [DIRS 111081], p. 18]).

Analyses of samples from the Yucca Mountain unsaturated zone indicate that smectite, clinoptilolite, and mordenite are the dominant low-temperature alteration products (Bish and Chipera 1989 [DIRS 101195], pp. 12 to 13). The low-temperature alteration potential of any lithologic unit depends upon rock composition, rock texture, proximity to structure, and water-rock interaction (Buesch and Spengler 1999 [DIRS 107236], p. 36). Volcanic glass that crystallized at high temperatures generally is not susceptible to alteration, except under high-temperature hydrothermal conditions.

However, high porosity and permeability, whether inherited from the deposition process or induced by fracturing, typically promote alteration of glass because of the high surface area of the particles. As a result of zeolitization, glass shards can be partially or completely replaced, and porosity can be reduced by in-filling with zeolite. Moderately to densely welded glassy rocks, including the crystal-poor vitrophyre of the Topopah Spring Tuff and obsidian in lava flows, have relatively low porosity and permeability, and are not readily altered except along fractures, as observed in some boreholes.

Alteration to clays and zeolites occurs in three fundamentally different lithostratigraphic, structural, and hydrologic settings (Broxton et al. 1987 [DIRS 102004]): two in the unsaturated zone (faults and fractures, and perched water horizons) and one in the saturated zone. Alteration within the unsaturated zone is suspected to be associated with faults, throughgoing fracture systems, and perched water horizons or horizons of lateral flow. One example of the importance of alteration along fractures is illustrated in numerous boreholes where video shows that the crystal-poor, vitric, densely welded subzone of the Topopah Spring Tuff has been significantly altered along high-angle fractures (Levy 1984 [DIRS 104577], pp. 961 and 963). Other sources of clay minerals not described by Broxton et al. (1987 [DIRS 102004]) are several paleosols and beds of redeposited materials, where clays probably result from pedogenic processes. Rocks beneath ancient or present saturated zones can be pervasively altered (Broxton et al. 1987 [DIRS 102004], p. 104). The contact between vitric to pervasively zeolitized rock in nonwelded tuffaceous rocks occurs at or within a single bed in a few boreholes, but in others the transition can be as much as 30 m (98 ft) thick; the gradational alteration depends on grain size.

3.3.3.3 Geochemical Criteria

Volcanic rocks at Yucca Mountain show systematic variations in their chemical (Lipman et al. 1966 [DIRS 100773], pp. F2, F41) and isotopic compositions (Noble and Hedge 1969 [DIRS 105197]), resulting from differentiation and assimilations in the magma chamber that lead to zonation within the erupted ash flows. The most abundant chemical constituents of both vitric and devitrified tuffs are SiO_2 and Al_2O_3, and the abundances of these two constituents in various units are shown in Figure 3-4. In summary, the data show that (1) the Calico Hills Formation, Yucca Mountain Tuff, and crystal-poor members of the Tiva Canyon and Topopah Spring tuffs are predominantly high-silica rhyolites; (2) tuffs in the Crater Flat Group exhibit a compositional range that falls between high- and low-silica rhyolites; (3) the Lithic Ridge and Pah Canyon tuffs consist of low-silica rhyolites; and (4) the crystal-rich members of both the Tiva Canyon and Topopah Spring tuffs are largely quartz latites.

The distribution and concentration of rare earth and trace elements are likewise useful for stratigraphic correlation and for the identification of altered zones. The rare earth elements are diagnostic as geochemical tracers, as demonstrated in a series of diagrams showing chondrite-normalized lanthanide-element abundances in various stratigraphic units in the site area that were presented by the CRWMS M&O (2000 [DIRS 151945], Figures 4.5-14 to 4.5-19).

Analyses of rock samples collected from several different outcrop localities and boreholes show that trace-element concentrations vary systematically with stratigraphic position. Peterman et al. (1993 [DIRS 106498]), for example, prepared a graph (Figure 3-6a) showing concentrations of titanium and zirconium in the sequence of formations cored in borehole UE-25 a#1 (borehole locations shown in Figure 3-7). In this borehole, the break between the crystal-rich and crystal-poor members of the Topopah Spring Tuff is clearly evident at a depth of about 160 m (Figure 3-6a). Similar variations in trace-element concentrations from one borehole to another, as well as to outcrop sections, indicate a general lateral continuity of the volcanic-rock units. Quartz latites exhibit higher lanthanide content and little or no Eu anomaly compared to the rhyolites (Figure 3-6b).

Knowledge of the normal, igneous variations in the geochemistry allows identification of altered zones based on trace element abundance. Unlike Zr and Ti (Figure 3-6a), post-depositional fluid movements and transport of carbonate by infiltrating water more easily mobilize Sr. Even outcrop samples are susceptible to Sr and Ca additions because of the abundant soil carbonate at Yucca Mountain. Zeolitization and clay alteration are evident in the crystal-poor, vitric, densely welded rocks of the Topopah Spring Tuff in Borehole UE-25 a #1. Sr concentrations increase dramatically due to addition of Sr to the rock during alteration (Figure 3-6c). Peterman et al. (1991 [DIRS 106496], p. 692) calculate water/rock ratios of at least 100 during alteration, assuming that groundwater is the altering fluid.

3.3.3.4 Borehole Geophysical Log Criteria

Suites of geophysical logs, commonly including caliper, gamma ray, density, induction, resistivity, and neutron logs, were collected from several tens of boreholes across the Yucca Mountain site area. Reflecting changes in rock properties, these logs can be used to correlate lithostratigraphic features. For example:

1. Increased welding causes matrix density to increase and porosity to decrease.

2. Mineral alteration (from clays and zeolites) causes a decrease in resistivity and an increase in neutron absorption, resulting in a high apparent neutron porosity.

3. Differences in magnetic susceptibility and remanence depend on the chemistry of the rock and Earth's magnetic field at the time of eruption and deposition.

4. Devitrification forms highly magnetic minerals that typically increase the magnetic field of the rocks, whereas alteration typically reduces the intensity of many magnetic properties. Figure 3-8, showing combined geophysical log-and-core data obtained in Borehole UE-25 UZ #16, illustrates correlations that can be made between log responses and various lithologic and mineralogical features within some of the major stratigraphic units.

Core measurements and studies of geophysical logs from numerous boreholes have led to several general observations regarding the relations between lithologic features and gamma-ray, density, resistivity, and magnetic-log responses (Nelson et al. 1991 [DIRS 101272]; Nelson 1994 [DIRS 105177]; Nelson 1996 [DIRS 101270]; Buesch et al. 1996 [DIRS 104616]; Rautman and Engstrom 1996 [DIRS 101008], pp. 33 to 41; Rautman 1996 [DIRS 106635], pp. 33 to 38; Engstrom and Rautman 1996 [DIRS 100670]; CRWMS M&O 1996 [DIRS 101534]; CRWMS M&O 1997 [DIRS 103564];). These observations include the following:

1. The Tiva Canyon Tuff exhibits relatively uniform, high-density log responses, alternating with lower and more erratic density log responses; a uniform, high-intensity gamma-ray log; high resistivity; and a low-amplitude, reverse-remanent magnetic field.

2. The contacts of bedded tuffs interstratified between the Tiva Canyon and Topopah Spring tuffs (Table 3-1) typically show sharp, moderate-to-large changes in density, resistivity, neutron responses, and computed porosity that mimic the bedded characteristics of these units. The pre-Pah Canyon Tuff bedded-tuff unit characteristically has a broad, relatively smooth decrease in density and increase in resistivity and porosity.

3. In the northern part of the site area, the Yucca Mountain and Pah Canyon tuffs display characteristic welding profiles that are distinctive in relation to the associated bedded tuff units, but toward their southern extents, these two formations are almost indistinguishable on geophysical logs from the bedded-tuff units.

4. The Topopah Spring Tuff is characterized by relatively uniform, high-density log values alternating with lower, more highly variable density log values; a highly uniform, high-intensity gamma-ray log; high resistivity; and a low amplitude, normal-remanent magnetic field.

5. Tuffaceous rocks of the Calico Hills Formation produce low-amplitude gamma-ray log values, low-density and resistivity log values, and a nonperturbed magnetic field. Parts of the formation that are altered to clays and zeolites have a slightly higher density and lower resistivity compared to vitric rocks.

6. The upper part of the Prow Pass Tuff is characterized by high resistivity and enhanced gamma-ray activity. A normal-remanent magnetic field anomaly at the top serves as an excellent marker.

7. The Bullfrog Tuff appears as a zone of high-amplitude, gamma-ray log values and erratically higher density and resistivity, with a large-amplitude, normal-remanent magnetic field. A decrease in welding at the top and bottom of the formation helps to define it on the logs.

8. Tram Tuff has two different geophysical log signatures. The upper unit is easily recognized by its very high amplitude, reverse-remanent magnetic field log and by high values of gamma radiation, density, and resistivity. The lower unit, which is

typically lithic rich, shows only low-level magnetic field perturbations and moderate values for gamma radiation, density, and resistivity.

As indicated, geophysical logs have been invaluable in correlating lithostratigraphic features across the Yucca Mountain site area. The logs can also be used to calculate porosity and saturation curves (Nelson 1993 [DIRS 105176]; Nelson 1994 [DIRS 105177]; Nelson 1996 [DIRS 101270]; CRWMS M&O 1996 [DIRS 101534]) that serve as primary input for porosity and property models (Rautman 1996 [DIRS 106635]).

3.3.4 Descriptions of Rock Units

Formations and intervening bedded-tuff units that make up the Tertiary volcanic-rock sequence at Yucca Mountain are shown in Table 3-1, together with ranges in thicknesses and brief generalized lithologic descriptions. Subdivisions of each of the formations, and their detailed lithologic descriptions, are given in Tables 4.5-1 and 4.5-2 of the YMSD (REV 01) (CRWMS M&O 2000 [DIRS 151945]). Two stratigraphic Fence Diagrams, Figures 3-9 and 3-10, drawn with the top of the Topopah Spring Tuff serving as a datum, show the distribution and thicknesses of formations across portions of the Yucca Mountain site area. Bedded-tuff units, commonly too thin to plot separately at small scales, are included in the overlying formational units. Descriptions of the bedded-tuff units are also included with the overlying formations in the following discussions.

3.3.4.1 Pre-Cenozoic Rocks

Pre-Cenozoic rocks, believed to consist primarily of upper Precambrian and Paleozoic sedimentary strata, underlie the Tertiary volcanic rocks at Yucca Mountain. Relatively sparse information is available on their thickness and overall lithology. The only direct evidence of the presence of Paleozoic strata under Yucca Mountain is in Borehole UE-25 p #1, which penetrated Paleozoic carbonate rocks in the depth interval 1,244 to 1,805 m (4,081 to 5,923 ft) (Figure 3-9). These rocks, almost entirely dolomites, have been correlated with the Lone Mountain Dolomite and Roberts Mountains Formation on the basis of exposures at Bare Mountain to the west (Monsen et al. 1992 [DIRS 106382]), and on the presence of Silurian-age conodonts (Carr et al. 1986 [DIRS 102046], pp. 17 and 18). Descriptions of pre-Cenozoic rocks in the Yucca Mountain region are given in Section 2.3.1, and further details are compiled in the *Yucca Mountain Project Stratigraphic Compendium* (CRWMS M&O 1996 [DIRS 101535], pp. 4-1 to 4-25).

3.3.4.2 Pre-Lithic Ridge Volcanic Rocks

The oldest known volcanic rocks in the Yucca Mountain region were deposited approximately at 14 Ma and underlie the Lithic Ridge Tuff (Sawyer et al. 1994 [DIRS 100075], Table 1). Because these pre-Lithic Ridge Tuff rocks are not exposed at Yucca Mountain, information about their extent and stratigraphic relations is limited to where they have been penetrated in boreholes. In Boreholes USW G-1, USW G-2, and USW G-3 (Figure 3-10), the sequence consists of bedded-tuffaceous deposits, pyroclastic-flow deposits, and quartz-latitic to rhyolitic lavas and flow breccia (Broxton et al. 1989 [DIRS 104556], p. 7). Penetrated thicknesses vary from approximately 45 m (148 ft) in USW G-3 to approximately 350 m (1,148 ft) in USW G-2. In

Borehole UE-25 p #1 (Figure 3-9), 180 m (590 ft) of older, altered tuff occurs between the Lithic Ridge Tuff and Paleozoic strata (Muller and Kibler 1984 [DIRS 105141], Table 1). Initial compositions of these older tuffs are poorly known, because they are altered to clays, calcite, and chlorite (Spengler et al. 1981 [DIRS 101297], pp. 18 to 25, 37 to 39; Bish and Vaniman 1985 [DIRS 101196], Figure B-5). These data have been used to determine their alteration history (Bish and Aronson 1993 [DIRS 100006], pp. 154 and 155).

3.3.4.3 Lithic Ridge Tuff

The Lithic Ridge Tuff is a thick, massive pyroclastic flow deposit (Carr et al. 1986 [DIRS 104670], pp. 10 to 13). It ranges in thickness from 185 m (607 ft) at Borehole USW G-2 to 304 m (997 ft) in Boreholes USW G-3 and USW GU-3. The formation is nonwelded to moderately welded and has been extensively altered to clay and zeolite minerals. Many slight variations in the degree of welding, crystal-fragment ratios, and lithic-fragment content indicate that several eruptive surges are represented.

3.3.4.4 Dacitic Lava and Flow Breccia

Dacitic lava and flow breccia overlie the Lithic Ridge Tuff in deep drill holes in the northern and western parts of the Yucca Mountain site area (Figures 3-9 and 3-10) but are absent elsewhere. The thickness of the unit is 111 m (364 ft) in Borehole USW H-1 (Rush et al. 1984 [DIRS 101054], Table 1) and 249 m (817 ft) in Borehole USW H-6 (Figure 3-9; Craig et al. 1983 [DIRS 101207], Table 1). In Borehole USW G-1, most of the unit is flow breccia made up of angular to subangular dacite fragments, commonly from 2 to 10 cm (0.8 to 4 in.) long, which are intercalated with lava blocks ranging from 1 m to more than 17 m (3 ft to more than 56 ft) thick (Spengler et al. 1981 [DIRS 101297], p. 36). The breccia is autoclastic, indicating that its formation is largely because of fragmentation of semisolid and solid lava during relatively slow flow. About 8 m (26 ft) of reworked pyroclastic fallout and bedded-tuff deposits underlie the flow breccia in Borehole USW G-1 (Spengler et al. 1981 [DIRS 101297], p. 37).

3.3.4.5 Crater Flat Group

The Crater Flat Group consists of three formations of moderate- to large-volume pyroclastic flow deposits—Tram, Bullfrog, and Prow Pass tuffs (Table 3-1)—and interstratified bedded tuffs (Sawyer et al. 1994 [DIRS 100075], Table 1). The group ranges in composition from high-silica rhyolites of the majority of the Paintbrush Group and the distinctive lower-silica rhyolites of the Pah Canyon Tuff (Figure 3-4). The group is distinguished from other pyroclastic units in the vicinity of Yucca Mountain by the relative abundance of quartz and biotite crystal fragments. In addition, the Prow Pass Tuff and, to a lesser degree, some parts of the Bullfrog Tuff contain distinctive lithic clasts of reddish-brown mudstone. The Tram Tuff overlies dacitic lavas and flow breccias in the northern part of Yucca Mountain and the Lithic Ridge Tuff in the southern part (Broxton et al. 1989 [DIRS 104556], p. 38) (Figures 3-9 and 3-10).

3.3.4.5.1 Tram Tuff

Several depositional units have been distinguished within the Tram Tuff, based on the abundance and types of pumice and lithic clasts in pyroclastic flow deposits and rare, bedded-tuff interbeds. The most easily recognized stratigraphic divisions are the lower lithic-rich unit, which in itself

can be locally divided into a lower lithic-poor and an upper lithic-rich set of subunits, and an upper lithic-poor unit. Both lithic-rich and lithic-poor units have been identified and described in several Boreholes, including UE-25 p #1, USW G-1, UE-25 b #1, USW G-3, and USW H-1 (Spengler et al. 1981 [DIRS 101297], pp. 17 and 18; Maldonado and Koether 1983 [DIRS 101805], p. 29; Scott and Castellanos 1984 [DIRS 101291], p. 36).   In Borehole USW G-2, the upper lithic-poor unit is absent, and the lithic-rich unit is well developed (Maldonado and Koether 1983 [DIRS 101805], p. 29). Welding is variable throughout the Tram Tuff (Scott and Castellanos 1984 [DIRS 101291], pp. 36 and 37) and locally, the large concentration of lithic clasts (such as in Borehole USW G-2) apparently reduced the degree of welding. In general, the lithic-poor unit is more densely welded than the underlying lithic-rich unit. Phenocrysts include quartz, feldspar, abundant biotite (30 to 50 percent of phenocrysts in the upper part), and very rare hornblende.

Argillic and zeolitic alteration occurs in both units of the Tram Tuff. In the lithic-poor unit, the alteration appears to occur in two zones separated by the zone of maximum welding. Both the upper and lower parts of the formation are altered to clinoptilolite ± mordenite. In the vicinity of Borehole USW G-1, however, analcime appears in the lower part, and in Borehole USW G-2, analcime is the dominant zeolite in both the upper and lower parts.

The thickness of the Tram Tuff across the Yucca Mountain site area ranges from 0 to 370 m (0 to 1,200 ft) (Figure 3-11). A regional isopach map by Carr et al. (1986 [DIRS 104670], Figure 11) shows the thickness of the formation to be in excess of 400 m (1,310 ft) in the northern part of Crater Flat to the west.

The lower lithic-rich unit overlies a complex sequence of altered and weathered pyroclastic fallout deposits and minor pyroclastic flow deposits (e.g., see Diehl and Chornack 1990 [DIRS 100135], pp. 141 to 152). With respect to the seven boreholes plotted in Figures 3-9 and 3-10, these pre-Tram Tuff bedded tuffs (included in the Tram Tuff interval) range in thickness from 0 in Borehole UE-25 p #1 to 21 m (69 ft) in Borehole USW G-2.

3.3.4.5.2   Bullfrog Tuff

Descriptions of the Bullfrog Tuff, which is exposed only in limited outcrops in the northwest corner of the site area, are based primarily on studies of core from Boreholes USW G-1 and USW G-4 (Spengler et al. 1981 [DIRS 101297], pp. 16 and 17; Spengler and Chornack 1984 [DIRS 101357], pp. 73 to 76). The formation is composed of two pyroclastic-flow deposits, both of which are simple cooling units, separated by an interval of pumiceous fallout. Thicknesses range from 15 to 366 m (49 to 1,200 ft) (Figure 3-12).   Regionally, Carr et al. (1986 [DIRS 104670], Figure 14) show the formation to be as much as 400 m (1,310 ft) thick in an area of maximum deposition in the southern part of Crater Flat.

The upper pyroclastic-flow unit is variably welded and altered to zeolites or clay or both. The lower unit is moderately welded in its central portion, and the intervening pumiceous deposit is partly to moderately welded. Pumice clasts constitute as much as 20 to 25 percent of the rock. Crystal fragments include quartz, feldspar, biotite, and minor pyroxene.

The pre-Bullfrog Tuff bedded-tuff unit (included in the Bullfrog Tuff interval) consists largely of weathered pyroclastic-flow deposits interbedded with thin zones of fallout tephra. Diehl and Chornack (1990 [DIRS 100135], Figure 34, pp. 128 to 139) correlated five marker horizons through the sequence between Boreholes USW G-1, USW G-2, and USW G-4. Thicknesses of the unit in the seven boreholes in Figures 3-9 and 3-10 range from 6 to 22 m (20 to 72 ft). In addition to an intervening bedded tuff, the Bullfrog Tuff can be differentiated from the overlying Prow Pass Tuff on the basis of crystal assemblages and bulk chemistry (Moyer and Geslin 1995 [DIRS 101269], p. 40). In contrast to the abundant biotite and rare pyroxene in the Bullfrog Tuff, for example, the Prow Pass Tuff contains altered orthopyroxene and biotite in about equal amounts.

3.3.4.5.3   Prow Pass Tuff

The Prow Pass Tuff consists of four variably welded pyroclastic deposits formed by eruptions from an unidentified source between 13.0 and 13.25 Ma (Sawyer et al. 1994 [DIRS 100075], Table 1, p. 1307). The sequence is 0 to 194 m (0 to 636 ft) thick within the site area (Figure 3-13). Descriptions and unit thickness (except for the pre-Prow Pass Tuff bedded tuff) given below are summarized from Moyer and Geslin (1995 [DIRS 101269]), based in large part on studies of core samples from Boreholes USW G-1, USW G-2, USW GU-3, USW G-4, USW UZ-14, UE-25 a#1, UE-25 c#1 (and nearby UE-25 c#2 and UE-25 c#3), and UE-25 UZ #16, as well as from observations of exposures at Prow Pass (Figure 3-2).

The basal bedded-tuff unit (pre-Prow Pass Tuff bedded tuff), less than 1 m to about 3.5 m (3 to 11 ft) thick in the boreholes shown in Figures 3-9 and 3-10 (included in the Prow Pass Tuff interval), consists of welded and zeolitically altered tuffaceous deposits. The unit includes a laminated ash deposit overlying a highly variable sequence of pumiceous fallout and pyroclastic flow deposits. A thin (approximately 0.5 m [1.6 ft]) basal breccia, containing angular clasts of the underlying Bullfrog Tuff and, locally, other volcanic lithologies, is present in several places.

The lowermost pyroclastic flow deposit of the Prow Pass Tuff (designated unit 1 by Moyer and Geslin 1995 [DIRS 101269], p. 28), with an aggregate thickness of 25 to 70 m (82 to 230 ft), consists of three subunits separated on the basis of their lithic clast content. The subunits are generally similar, with zeolitically altered matrices. The next overlying unit (unit 2) is a sequence of pyroclastic flow deposits that have not been subdivided because they lack distinguishing characteristics. However, locally preserved ash horizons and abrupt changes in the amounts and sizes of pumice and lithic clasts, indicate at least three flow deposits in most boreholes studied. The aggregate thickness ranges from about 3 to 34 m (10 to 111 ft). Six subunits, defined by changes in the degree of welding or the intensity of vapor-phase alteration, characterize the third flow deposit (unit 3). Its thickness ranges from 40 m (131 ft) to nearly 80 m (262 ft). The top unit of the Prow Pass Tuff (unit 4), which ranges from 4 m (13 ft) to as much as 20.5 m (67 ft) thick in cored boreholes, can be divided into three irregularly distributed subunits differentiated by changes in the average diameter and percentage of pumice clasts that decrease stratigraphically upward.

Rocks in units 1, 2, and 4 are typically altered to zeolite (clinoptilolite or mordenite or both near the water table) and lesser amounts of clay throughout most of Yucca Mountain. Analcime occurs in the lower part of the Prow Pass Tuff to the north (in Borehole USW G-2), but is not

found in any part of the formation to the south. Units 2 and 4 are vitric in the southwestern part of the central block, with vitric rocks in unit 4 occurring as far north as Borehole USW H-5.

Among its characteristics, the Prow Pass Tuff is distinguished by the presence of altered orthopyroxene, in addition to biotite as crystal fragments, and by distinctive fine-grained, oxidized lithic inclusions of red mudstone. Both the orthopyroxene and the mudstone inclusions need to be considered in evaluating interactions with radionuclides. The Prow Pass Tuff and overlying Calico Hills Formation have different amounts of crystal fragments, proportions of quartz in the crystal assemblage, and chemical compositions. The basal bedded-tuff and sandstone units of the Calico Hills serve as consistent stratigraphic markers in several boreholes studied (Diehl and Chornack 1990 [DIRS 100135], p. 49, Figure 32).

3.3.4.6 Calico Hills Formation

The Calico Hills Formation and the underlying bedded tuffs potentially comprise one of the most significant barriers to the migration of exchangeable cations at Yucca Mountain. Despite its great heterogeneity, the formation has a consistently high matrix porosity (average 28 to 35 percent; e.g., see Moyer and Geslin 1995 [DIRS 101269], Figure 19), which indicates an important role for matrix flow of the groundwater. Other properties, particularly permeability, are extremely variable and strongly dependent on mineralogy. Permeability drops by about two orders of magnitude, and sorption by cation exchange rises as much as five orders of magnitude, in the transition from vitric to zeolitic character within the formation. Fine-scale variations in matrix properties occur within centimeters, and lateral continuity in properties is poor (Broxton et al. 1993 [DIRS 107386], Figures 4 and 14).

The Calico Hills Formation is a complex series of rhyolite tuffs and lavas that resulted from an episode of volcanism approximately 12.9 Ma (Sawyer et al. 1994 [DIRS 100075], Tables 1 and 3). Five pyroclastic units, overlying a bedded-tuff unit and a locally occurring basal sandstone unit, were distinguished in the Yucca Mountain area by Moyer and Geslin (1995 [DIRS 101269], pp. 5 to 8). The formation thins southward across the site area, from composite thicknesses of as much as 457 m (1,500 ft) to only about 15 m (50 ft) (Figure 3-14). The following descriptions are summarized from Moyer and Geslin (1995 [DIRS 101269], pp. 5 to 8), whose studies are based on examinations of cores and observations of outcrops in the same boreholes and surface locality as those listed above for the Prow Pass Tuff.

The basal volcaniclastic sandstone unit of the Calico Hills Formation (not included in Table 3-1) is interbedded with rare reworked pyroclastic flow deposits. Thicknesses of the unit range from 0 to 5.5 m (0 to 18 ft). The overlying bedded tuff (labeled pre-Calico Hills Formation bedded tuff in Table 3-1), 9 to 39 m (30 to 128 ft) thick, is composed primarily of pyroclastic fall deposits. Each of the five pyroclastic units forming the bulk of the formation consists of one or more pyroclastic flow deposits separated by locally preserved fall horizons. Ash-fall and ash-flow deposits beneath the repository block give way to lava flows to the north and east.

X-ray diffraction of drill-core samples by Caporuscio et al. (1982 [DIRS 101322], p. 32), Bish and Vaniman (1985 [DIRS 101196], Appendix A), and Bish and Chipera (1986 [DIRS 100030]) and of outcrop samples by Broxton et al. (1993 [DIRS 107386], pp. 18 to 35) show an abundance of authigenic zeolites in all Calico Hills Formation units. Zeolitized tuffs are primarily the

products of diagenetic alteration in which the original volcanic glass dissolved and zeolites precipitated at ambient temperatures in a water-rich environment. In the case of the Calico Hills Formation, the pyroclastic units have extremely high clinoptilolite and mordenite contents (40 to 80 percent; Caporuscio et al. 1982 [DIRS 101322]; Vaniman et al. 1984 [DIRS 101363]; Bish and Vaniman 1985 [DIRS 101196]; Bish and Chipera 1986 [DIRS 100030]) that contrast with the somewhat lower zeolite content of the bedded tuffs and basal sandstone (Moyer and Geslin 1995 [DIRS 101269], p. 10). Mapping of the distribution of zeolites shows that (1) they are more widely present in the bedded tuffs than in the pyroclastic units, and (2) zeolite mineralization is pervasive in the northern part of Yucca Mountain but absent in some southern locations. In the vicinities of Boreholes USW GU-3 and USW H-4 (Moyer and Geslin 1995 [DIRS 101269], Figure 8), for example, the entire formation is vitric, and in Borehole USW H-5, where the bedded tuff at the base is zeolitized but the remainder is not. Detailed information on the composition of zeolites is given in Section 5.2.1.1. The presence of zeolitized zones within the Calico Hills, as well as within other formations such as the Prow Pass Tuff, has important implications with respect to paleohydrologic interpretations and the potential development of natural barriers to contaminant (radionuclide) movement by groundwater.

The complex series of rhyolite tuffs and lavas in the Calico Hills grades laterally from completely zeolitized to unaltered vitric rock from east to west across the repository area. Crystal fragments are predominantly quartz, feldspar, and biotite, with trace magnetite and accessory clinopyroxene, ilmenite, allanite, and zircon. The formation is distinguished from the Topopah Spring Tuff by differences in mineralogy and chemical composition. Lithostratigraphic units of the former have crystal assemblages, with a higher proportion of quartz and higher calcium and barium contents than units of the latter.

3.3.4.7   Paintbrush Group

The Paintbrush Group consists of four formations, each composed primarily of pyroclastic flow deposits interstratified with small-volume pyroclastic flow and fallout tephra deposits, and, locally, lava flows and secondary volcaniclastic deposits from eolian and fluvial processes (Buesch et al. 1996 [DIRS 100106]). In ascending order, the formations include the Topopah Spring, Pah Canyon, Yucca Mountain, and Tiva Canyon tuffs. This group is one of the most widespread and voluminous caldera-related assemblages in the southwestern Nevada volcanic field (Sawyer et al. 1994 [DIRS 100075], p. 1307). The Topopah Spring Tuff forms the host rock for the repository, and, therefore, is one of the most intensely studied formations at Yucca Mountain. Locations of eruptive centers for the Topopah Spring and Pah Canyon tuffs are uncertain, but the Claim Canyon caldera (Figure 3-1) is the identified source of the Tiva Canyon Tuff and possibly the Yucca Mountain Tuff (Byers et al. 1976 [DIRS 104639], pp. 21 to 38; Sawyer et al. 1994 [DIRS 100075], Table 1, p. 1308).

The Paintbrush Group is dominated volumetrically by the Topopah Spring and Tiva Canyon tuffs. The Yucca Mountain and Pah Canyon tuffs are volumetrically minor units, but are of potential hydrologic importance because of their high-matrix porosity compared to the Tiva Canyon and Topopah Spring tuffs, which are largely densely welded with low-matrix porosity. The welded tuffs also have higher fracture abundance and connectivity, providing stratified contrasts in unsaturated zone hydrologic properties in the Paintbrush Group rocks above the repository.

Descriptions of the formations within the Paintbrush Group are generalized from detailed studies of outcrops and borehole cores by Buesch et al. (1996 [DIRS 100106]), supplemented by core descriptions obtained from Geslin et al. (1995 [DIRS 103330]); Geslin and Moyer (1995 [DIRS 101226]); and Moyer et al. (1995 [DIRS 103777]). Divisions of the Tiva Canyon and Topopah Spring tuffs into members, zones, subzones, and intervals (Buesch et al. 1996 [DIRS 100106], Table 2) indicate that both are simple cooling units within the site area (Lipman et al. 1966 [DIRS 100773]). The interplay among depositional, welding, crystallization, and fracturing processes produces unit contacts that range from sharp to gradational. Depositional contacts, such as the bases of pyroclastic flow, and fallout deposits and redeposited material, are examples of sharp contacts. Tops of these deposits are typically sharp but may be gradational where there is evidence of reworking or pedogenesis. The transition from nonwelded to densely welded tuff is typically gradational, such as near the base of the Topopah Spring Tuff in Boreholes USW GU-3 and USW WT-2. Contacts of several lithostratigraphic units correspond with hydrogeologic and thermal-mechanical unit boundaries throughout Yucca Mountain and have been used in the development of three-dimensional geologic and hydrogeologic models (Tables 3-5 and 7-1).

3.3.4.7.1   Topopah Spring Tuff

The Topopah Spring Tuff includes the host-rock units for the repository. As such, its characteristics are of direct importance to repository design, unsaturated zone hydrologic flow and radionuclide transport, and total system performance assessment (TSPA). A complete description of the Topopah Spring Tuff is presented in Buesch et al. (1996 [DIRS 100106], Appendix 2).

The Topopah Spring Tuff is 0 to 381 m (0 to 1,250 ft) thick in the Yucca Mountain site area (Figure 3-15). The formation is divided into a lower crystal-poor member and an upper crystal-rich member. Vitric rocks form zones at the top and bottom of the formation, and alternating lithophysal and nonlithophysal zones characterize the remaining parts of the two members. Further subdivision is based largely on the degree of welding, crystal content and assemblage, and size and abundance of pumice and lithic clasts.

The Topopah Spring Tuff is compositionally zoned, with an upward chemical change from high-silica rhyolite in the crystal-poor member to quartz latite (also referred to as quartz trachyte) in the crystal-rich member (Lipman et al. 1966 [DIRS 100773], p. F3; Sawyer et al. 1994 [DIRS 100075], p. 1313). The two members are also clearly distinguishable on the basis of mineralogy and trace-element concentrations (Figure 3-6a). The lower part of the formation, which is the repository horizon, is one of the most chemically homogeneous rock types in the region (note the close clustering of analyses in the high-silica rhyolite portion of Figure 3-4). The homogeneity of the major-element chemistry also extends to trace elements. Somewhat greater chemical variability is seen in the quartz latites of the crystal-rich members. The crystal-poor member, characterized by 3 percent or less of felsic crystal fragments, is divided into vitric rocks of the vitric zone near the base and (in ascending order) devitrified rocks of the lower nonlithophysal, lower lithophysal, middle nonlithophysal, and upper lithophysal zones (Figure 3-5; Buesch et al. 1996 [DIRS 100106], pp. 41 to 44). The latter four zones form the host rock for the repository. The vitric zone is divided primarily on the basis of degrees of welding, which range upward from a nonwelded to partially welded subzone at the base, through

a moderately welded subzone, to a densely welded subzone at the top. The vitric, densely welded subzone, commonly referred to as the vitrophyre, is identified as an important subunit within the Topopah Spring welded thermal-mechanical unit (Table 3-5).

Within the devitrified, rhyolitic portion of the Topopah Spring Tuff, crystal fragments are minor constituents (5 percent or less) of the rock, with the remainder consisting of fine-grained devitrification minerals. These devitrification products are principally feldspars plus a variable combination of the silica polymorphs tridymite, cristobalite, and quartz. Abundance of quartz is a useful stratigraphic marker within the devitrified, rhyolitic Topopah Spring Tuff, but quartz-crystal fragments are nevertheless much less abundant (less than 0.5 percent) than groundmass quartz (approximately 20 percent) throughout this interval. The silica polymorph distributions are particularly important because of their thermal stability, dissolution properties, and properties that create inhalation hazards.

A transitional zone, commonly referred to as the vitric-zeolitic transition that is composed of partly devitrified vitrophyre, extends downward from the base of the lower nonlithophysal zone into the crystal-poor vitric zone through a stratigraphic interval ranging from about 3 to 30 m (10 to 100 ft) in thickness. In many parts of Yucca Mountain, the moderately welded and nonwelded subzones at the base of the crystal-poor vitric zone are overprinted by zeolite alteration zones (Buesch et al. 1996 [DIRS 100106], p. 21). Accordingly, a vitric-zeolitic boundary can be drawn that varies within a narrow range of stratigraphic positions, but generally coincides closely with the contact between the moderately welded subzone and the overlying densely welded subzone (Buesch and Spengler 1999 [DIRS 107236], Figures 8, 9, and 10).

The vitric-zeolitic transition zone that separates vitric tuffs from underlying zeolitic tuffs is interpreted to have been an approximately planar surface, the configuration and position of which were originally related to the configuration and position of the static water table at the time of alteration (e.g., Levy 1991 [DIRS 100053], p. 481). This interpretation is based largely on recognition that zeolitization requires the presence of abundant water over a long period of time (e.g., Levy 1991 [DIRS 100053], p. 481), a condition that favors a laterally extensive water table rather than local perched-water tables. Observations regarding the present stratigraphic and structural relations of the vitric-zeolitic transition zone within the lower Topopah Spring Tuff, as well as similar zones in other formations, have a direct bearing on interpretations regarding alteration history.

The crystal-rich member of the Topopah Spring Tuff is characterized by greater than 10 percent crystal fragments, with a crystal-transition subzone at the base where crystal abundance increases upward from 3 to 10 percent. The member is divided into lithophysal, nonlithophysal, and vitric zones (Figure 3-5). Rocks in the lower two zones are devitrified, and the division is based on the presence or absence of lithophysae. The vitric zone at the top of the member is distinguished by preservation of the volcanic glass to form rocks with a vitreous luster that typically grade upward from densely welded to nonwelded. This zone is a particularly important geochemical subunit because it is relatively impermeable; impedance of downward flow and reaction of water with quartz-latitic glass provides an important geochemical marker in unsaturated zone waters (Vaniman and Chipera 1996 [DIRS 100089], p. 4,420).

A tuffaceous rock unit (pre-Topopah Spring Tuff bedded tuff) that lies between the Topopah Spring and the Calico Hills Formation is 0 to 17 m (0 to 56 ft) thick in the boreholes plotted in Figures 3-9 and 3-10; it is included in the Topopah Spring interval.

3.3.4.7.2 Pah Canyon Tuff

The Pah Canyon Tuff is a simple cooling unit (Christiansen 1979 [DIRS 102562], Table 1) composed of multiple-flow units that are poorer in silica content than the high-silica rhyolites of several of the other volcanic-rock units (Figure 3-4). The formation reaches its maximum thickness of about 79 m (260 ft) in the northern part of Yucca Mountain (Figure 3-16), and thins southward to zero in the vicinity of Borehole UE-25 UZ #16 (Moyer et al. 1996 [DIRS 100162], Figures 19 and 46). The formation varies from nonwelded to moderately welded and, throughout much of the area, vitric pumice clasts are preserved in a nondeformed matrix that was sintered or lithified by vapor-phase mineralization. Crystal fragments in the matrix and in large pumice clasts constitute 5 to 10 percent of the rock, with a greater proportion of feldspars relative to mafic minerals (biotite and clinopyroxene). Lithic clasts of devitrified rhyolite (as much as 5 percent of the rock) are common, and clasts of porphyritic obsidian are in some horizons. Shards are either poorly preserved clear glass or form devitrified material. The high water saturation of porous nonwelded units in the Pah Canyon Tuff, as well as in the overlying Yucca Mountain Tuff, leads to a relatively high degree of alteration where there is an underlying barrier to transmission. Because of the relatively impermeable upper vitrophyre of the underlying Topopah Spring Tuff, the alteration of the Pah Canyon Tuff (typically to smectite) is generally more extensive than that of the overlying Yucca Mountain Tuff. Therefore, despite its minor volume, the Pah Canyon Tuff has an important impact on reactions between unsaturated zone water and the host tuffs.

The pre-Pah Canyon Tuff bedded tuff, 3 to 10 m thick (10 to 33 ft) in the boreholes plotted in Figures 3-9 and 3-10 (included in the Pah Canyon Tuff interval), consists of moderately well-sorted pumiceous tephra with thin layers of lithic-rich fallout and very fine-grained ash at the base.

3.3.4.7.3 Rhyolites of Black Glass Canyon, Delirium Canyon, and Zig Zag Hill

Relatively small amounts of rhyolite lava flows and related tephra deposits crop out locally in the northern part of the Yucca Mountain site area (Day et al. 1998 [DIRS 100027]). The rhyolite of Zig Zag Hill is exposed in one small outcrop in the vicinity of the Prow in the northwest corner of the area (Figure 3-2), where it forms a thin unit (thickness 10 m or less) between the Pah Canyon Tuff and the pre-Yucca Mountain Tuff bedded tuff. The Delirium Canyon and Black Glass Canyon units occur in limited outcrops in the northeast and north-central parts of the area. Lava flows in the Delirium Canyon are as much as 250 m (820 ft) thick, and ash-flow tuffs are as much as 100 m (328 ft) thick. The combined unit is considered to be equivalent to parts of both the Rhyolite of Zig Zag Hill and the pre-Yucca Mountain Tuff bedded tuff (Day et al. 1998 [DIRS 100027]). The Rhyolite of Black Glass Canyon, 2 to 14 m (6 to 46 ft) thick, lies stratigraphically between the Yucca Mountain Tuff and the pre-Yucca Mountain Tuff bedded tuff (Day et al. 1998 [DIRS 100027]).

3.3.4.7.4   Yucca Mountain Tuff

The Yucca Mountain Tuff is a simple cooling unit that is nonwelded throughout much of the Yucca Mountain area, but is partially to densely welded where it thickens in the northern and western parts. The formation is thickest in the northern part of the site area, but thins to zero to the south (Figure 3-17). Although typically vitric in most locations in the central part, the tuff is increasingly devitrified where it is thick. The formation is nonlithophysal throughout Yucca Mountain, but contains lithophysae where densely welded in northern Crater Flat. The Yucca Mountain Tuff is chemically similar to the high-silica rhyolites of the Tiva Canyon and Topopah Spring tuffs (Figure 3-4). It contains both plagioclase and sanidine crystal-fragments, which is also characteristic of the rhyolitic parts of the Topopah Spring but not of the Tiva Canyon that contains only sanidine phenocrysts.

The pre-Yucca Mountain Tuff bedded tuff consists of pumiceous, vitric, nonwelded pyroclastic-flow deposits. In the boreholes shown in Figures 3-9 and 3-10, the unit, which is included in the Yucca Mountain Tuff interval, ranges from less than 1 m to as much as 46 m (less than 3 to 150 ft) in thickness.

3.3.4.7.5   Tiva Canyon Tuff

The Tiva Canyon Tuff is a large-volume, regionally extensive, compositionally zoned (from rhyolite to quartz latite) tuff sequence that forms most of the rocks exposed at the surface of Yucca Mountain site area (Day et al. 1998 [DIRS 100027]). Accordingly, most vertical recharge pathways that pass through the repository block encounter these rocks, and the minerals therein play a large part in determining unsaturated zone groundwater composition. Thicknesses of those portions of the formation penetrated in boreholes or observed in outcrops range from less than 50 m to as much as 175 m (165 to 575 ft). Separation of the formation into a lower crystal-poor member and an upper crystal-rich member, and into zones within each of these members, is based on criteria similar to those discussed above for the Topopah Spring Tuff.

The rhyolitic crystal-poor member is divided into five zones. In ascending order, these are the vitric, lower nonlithophysal, lower lithophysal, middle nonlithophysal, and upper lithophysal zones (Figure 3-5; Buesch et al. 1996 [DIRS 100106], pp. 35 to 39). Division into subzones is based on vitric versus devitrified rocks, degree of welding, differences in pumice clasts, presence or absence of lithophysae, and fracture morphology. The lowest part of the member consists of densely welded to nonwelded high-silica rhyolitic glass. The crystal-poor member and overlying crystal-rich member are separated by a thin transitional subzone, in which there is an upward increase in crystal content and an increase in the proportion of mafic relative to felsic crystal fragments.

The quartz-latitic crystal-rich member consists primarily of devitrified, nonlithophysal material, which locally contains lithophysae near the base. The unit is capped by a thin (less than 1 m) vitric zone that is only locally preserved and typically has been eroded from most of Yucca Mountain. The crystal-rich nonlithophysal zone is divided into four subzones based upon such depositional features as abundance of crystal fragments and pumice. Much of this zone has undergone corrosion and alteration, which has significantly increased its porosity compared to the overlying and underlying rocks.

The pre-Tiva Canyon bedded tuff is characterized by thin beds of fallout tephra deposits interbedded with thin oxidized, weathered zones (Diehl and Chornack 1990 [DIRS 100135], pp. 62 to 64). Thicknesses of the unit penetrated in the seven boreholes plotted in Figures 3-9 and 3-10 (shown as part of the Tiva Canyon Tuff interval) range from less than 1 m to 3 m (less than 3 to 10 ft).

3.3.4.7.6   Post-Tiva Canyon/Pre-Rainier Mesa Tuffs and Lava Flows

Several rhyolite lava flows and fallout tephra deposits are in the upper part of the Paintbrush Group in the vicinity of Yucca Mountain (Buesch et al. 1996 [DIRS 100106]; see Figure 3-2). These units, lying between the top of the Tiva Canyon Tuff and the base of the pre-Rainier Mesa bedded tuff, include (in ascending order) the post-Tiva Canyon Tuff bedded tuff, rhyolite of Vent Pass, tuff unit "X," and rhyolite of Comb Peak (Table 3-1). The rhyolitic lavas and ash-flow tuffs of the Vent Pass unit are exposed in the north-central part of the site area where thicknesses are as much as 150 m (492 ft) (Day et al. 1998 [DIRS 100027]). Lavas and tuffs of the rhyolite of Comb Peak form extensive outcrops in the large area of bedrock in the northeast part of the site area, north of Midway Valley and Yucca Wash. These rocks aggregate maximum thicknesses of nearly 130 m (427 ft) (Day et al. 1998 [DIRS 100027]).

A 6 to 23 m (20 to 75 ft) thick lithic-rich pyroclastic-flow deposit was penetrated in several boreholes on the west side of Midway Valley near Exile Hill (such as Borehole UE-25 RF #3, Figure 3-7) and is exposed in the excavation for the North Portal of the ESF (Swan et al. 2001 [DIRS 158784], Figure 14). This deposit was referred to informally as tuff unit "X" by Carr (1992 [DIRS 101520], pp. A-12 to A-23). The unit is a pumiceous, nonwelded, in-part zeolitic ash-flow that was tentatively correlated with the rhyolite of Comb Peak by Buesch et al. (1996 [DIRS 100106], Table 2). Additional descriptions based on core studies from boreholes on the west side of Exile Hill were given by Geslin et al. (1995 [DIRS 103330], pp. 28 and 29).

The post-Tiva Canyon Tuff bedded tuff is a tuffaceous-rock unit commonly consisting of numerous depositional sequences separated by possible paleosols (Buesch et al. 1996 [DIRS 100106], Table 2). Thicknesses in several boreholes near Exile Hill range from less than 2 to 4.5 m (less than 7 to 15 ft) (Carr 1992 [DIRS 101520], pp. A-13 and A-14, p. A-23; Geslin et al. 1995 [DIRS 103330], pp. 36 and 37).

3.3.4.8   Timber Mountain Group

The Timber Mountain Group includes all quartz-bearing, pyroclastic-flow, and fallout-tephra deposits erupted, about 11.5 Ma, from the Timber Mountain caldera complex, the south edge of which lies just north of the area shown in Figure 3-1, (Byers et al. 1976 [DIRS 104639], pp. 38 to 47; Sawyer et al. 1994 [DIRS 100075], p. 1308, Table 1). The complex consists of two overlapping, resurgent calderas: an older caldera, formed by the eruption of the Rainier Mesa Tuff and a younger, nested caldera, formed by the eruption of the Ammonia Tanks Tuff (Minor et al. 1993 [DIRS 106376], p. 14; Sawyer et al. 1994 [DIRS 100075], p. 1308).

3.3.4.8.1   Rainier Mesa Tuff

The Rainier Mesa Tuff is a compositionally zoned, compound cooling unit consisting of high-silica rhyolite tuff overlain by a considerably thinner quartz latite tuff that is restricted to

the vicinity of the Timber Mountain caldera (Byers et al. 1976 [DIRS 104639], p. 39). The formation does not occur across much of Yucca Mountain, but is locally exposed on the downthrown blocks of large faults in valleys toward the south end of the mountain (Day et al. 1998 [DIRS 100027]; see Figure 3-2). It is also exposed in the extreme northwest corner of the site area and was penetrated in a few boreholes on the east side. Based on examination of cores from Boreholes UE-25 NRG #2, UE-25 NRG #2b, UE-25 NRG #2c, and UE-25 NRG #2d (UE-25 NRG #2 is shown in Figure 3-7; the other boreholes are nearby), the Rainier Mesa Tuff consists of a nonlithified to lithified and partially welded pyroclastic flow deposit generally less than 30 m (98 ft) thick (Geslin and Moyer 1995 [DIRS 101226], pp. 11 and 12; Geslin et al. 1995 [DIRS 103330], pp. 27, 29). A maximum thickness of 240 m (787 ft) was observed in the southwestern part of Crater Flat (Fridrich 1999 [DIRS 118942], Figure 10).

The pre-Rainier Mesa Tuff bedded tuff consists of nonlithified fallout-tephra and pyroclastic-flow deposits (Geslin and Moyer 1995 [DIRS 101226], pp. 11 and 12; Geslin et al. 1995 [DIRS 103330], pp. 27 to 29). The sequence occupies intervals of about 17 m (55 ft) in Boreholes UE-25 NRG #2c and UE-25 NRG #2d (located near Borehole UE-25 NRG #2, Figure 3-7), and is characterized by moderately well-sorted white pumice lapilli and volcanic lithic clasts.

3.3.4.8.2 Ammonia Tanks Tuff

The Ammonia Tanks Tuff is not present across Yucca Mountain, but is exposed in the southern part of Crater Flat and was penetrated by one borehole in the Crater Flat area (Fridrich 1999 [DIRS 118942], Figure 10). The formation consists of welded to nonwelded rhyolite tuff, with highly variable thicknesses (maximum as much as 215 m [705 ft]).

3.3.4.9 Younger Basalt

The youngest volcanic rocks in the Yucca Mountain site area (not included in Table 3-1) are represented by thin basalt dikes that were intruded, along some minor faults, near the head of Solitario Canyon (Day et al. 1998 [DIRS 100027]). The dikes consist of fine-grained olivine-bearing basalt, locally combined with scoria and altered glass that were dated as 10 Ma (Crowe et al. 1995 [DIRS 100110], pp. 2 to 11). Basalt also forms scoria cones, thin lava flows, and flow breccias in Crater Flat basin to the west (Figure 3-1), where they have been studied by Crowe et al. (1995 [DIRS 100110]) and Heizler et al. (1999 [DIRS 107255], pp. 800 and 801). The Crater Flat basin basalts are discussed further in Section 4.2.

3.3.5 Rock Geochemistry of Yucca Mountain and Vicinity

Yucca Mountain is made primarily of pyroclastic deposits with rare lava flows, as well as colluvium, alluvium, and soils. The surface materials contain mixed constituents, including pedogenic calcite and opal. As such, they are significant sources of dissolved material introduced into recharge pathways but participate as transport pathways only at a distance from the site. Soils and colluvium are important in their effects on recharge hydrochemistry; since these materials and their effects are discussed in Sections 3.3.7.2 and 5.3.3.4, the emphasis in this section is on the pyroclastic units.

The existing chemical variability of the pyroclastic units at Yucca Mountain is the combined result of variable original magmatic compositions, syngenetic alteration (i.e., alteration that occurred during deposition of the pyroclastic units), regional hydrothermal alteration, diagenesis, and chemical exchange with groundwater. The role of surficial deposits and pyroclastic lithologies in determining groundwater compositions is covered in Section 5.2.2. This section provides the lithologic background for the principal rock units in which recharge, flow, and transport occur.

The initial magmatic compositions of the pyroclastic units are reflected in the glass fragments, lithic inclusions, and phenocrysts that constitute the original erupted materials. Superimposed on these initial compositions are variations in mineralogy and chemistry introduced by alteration. The chemical and mineralogic features of the rock matrix, fractures, and faults provide information on the record of hydrochemistry and transport at Yucca Mountain.

Evaluation of rock geochemistry provides information on past or ongoing transport of elements that can be related to the transport of radioactive waste. Determinations of mineral distributions at the site can be used with mineral-based sorption data to model site performance in three dimensions. Rock geochemistry affects groundwater compositions through mineral and glass dissolution and alteration to other minerals, principally in vitric units, and by cation exchange, principally in zeolitic horizons. However, even minor fracture minerals, such as manganese oxides, can operate as oxidation-reduction sites and have a strong effect on trace constituents in solution (Section 5.2.2.2). The mineral distributions at the site are also important in predicting mineral stability and dissolution-precipitation reactions under a repository-induced thermal load (Section 5.4).

3.3.5.1 Nature and Origin of Primary Geochemical Variability

In this section, the primary geochemical and mineralogic variability in the rock units present at Yucca Mountain is discussed with respect to its impact on the effects of alteration, the role that rock compositions play in affecting aqueous geochemistry, and the geochemical effects that impact radionuclide transport.

Compositionally, both the vitric and devitrified tuffs can be classified based on their silica (SiO_2) and alumina (Al_2O_3) content, as shown in Figure 3-4. Most of the tuffs at Yucca Mountain are rhyolites or high-silica rhyolites. The distinctive quartz-latitic units at Yucca Mountain are less common and are principally within the upper zones of the Tiva Canyon and Topopah Spring tuffs (Figure 3-4). The Rainier Mesa Tuff also contains an upper quartz-latitic portion.

Individual pyroclastic eruptive cycles at Yucca Mountain are variably zoned in composition. The best-studied example, the Topopah Spring Tuff, provides a record of progressive evacuation of a single magma chamber that was compositionally zoned downward from phenocryst-poor high-silica rhyolite to phenocryst-rich quartz latite (Lipman et al. 1966 [DIRS 100773]; Schuraytz et al. 1989 [DIRS 107248]). During the eruption, magma was drawn from progressively deeper parts of the magma chamber, resulting in a tuff that is zoned from high-silica rhyolite at the (early erupted) base, to quartz latite at the (late-erupted) top. The geochemical differences between quartz-latitic and rhyolitic tuffs provide stratigraphic markers,

particularly in lanthanide-element composition. Use of these markers is described in Section 3.3.5.2.

The temporal progression of crystallization and alteration in devitrified tuff, beginning with high-temperature events over 12 Ma and continuing today, is illustrated by the Topopah Spring Tuff. (A detailed discussion of these processes is provided in Sections 3.3.5.1.1 and 3.3.5.1.2.) Following eruption and emplacement of the Topopah Spring Tuff, the uppermost (quartz latitic) and lowermost (high-silica rhyolite) portions of this compound volcanic series cooled rapidly, preserving thin, nonwelded vitric margins. Glassy portions between the nonwelded vitric margins and the central devitrified mass retained enough heat to compact and weld, but not to crystallize, and formed densely welded vitrophyres (the quartz-latitic upper vitrophyre and the high-silica rhyolitic lower vitrophyre). The vast majority (about 90 percent) of the erupted material, between these two vitrophyres, retained enough heat to promote crystallization of all glass. This material is the devitrified core of the Topopah Spring Tuff. Water vapor released from crystallizing glasses in this devitrified core formed a hot fluid from which vapor-phase minerals crystallized along early-formed fractures and within pockets formed by gas expansion (lithophysal cavities). The vapor-phase minerals are dominantly feldspars and silica minerals (especially tridymite) but also include a variety of other minerals (e.g., amphibole, pseudobrookite, and manganese-garnet). Crystallization of some of these minerals may have continued as the possibly supercritical fluid cooled to water vapor and ultimately condensed as liquid water. Much of the tridymite along fractures is now pseudomorphed by quartz that may have formed during this transition. Minerals continued to precipitate in fractures and cavities in the repository host rock long after the end of the volcanic cooling cycle. Minerals that may still be forming today include zeolites, clays, opal, calcite, and possibly manganese oxides, although the manganese-oxides are commonly on fracture surfaces below the calcite-silica coatings. Ages of secondary minerals are discussed in Section 7.7.2.

Lithic inclusions and phenocrysts affect the bulk chemistry of a tuff in proportion to their abundance. The measured phenocryst content of Yucca Mountain tuffs varies from less than 1 volume percent to as much as approximately 25 volume percent, and lithic fragments average a few volume percent (Byers et al. 1976 [DIRS 104639], Figures 5 and 9; Broxton et al. 1993 [DIRS 107386], Appendix A). Quartz-latitic units have consistently high phenocryst abundances, but rhyolitic units have variable phenocryst abundances. Among the major rhyolitic units in the vicinity of Yucca Mountain, the bedded tuff at the base of the Calico Hills Formation has the highest phenocryst content (up to about 25 volume percent). The upper part of the Bullfrog Tuff also has phenocryst content as high as 25 volume percent.

The principal phenocrysts in the tuffs are sanidine, plagioclase, quartz, and biotite. There are many other phenocrysts, such as amphibole, clinopyroxene, orthopyroxene and accessory magnetite, ilmenite, monazite, zircon, apatite, allanite, and perrierite, but these are present in amounts much less than 1 volume percent (Broxton et al. 1993 [DIRS 107386], Appendix A). In general, the potassium content of sanidine phenocrysts increases with depth among the rocks at Yucca Mountain. Also, biotite provides a measure of iron/magnesium ratios among units; the biotites that occur from the rhyolite of the Topopah Spring Tuff down through the bottom of the Crater Flat Group are more iron-rich than those that occur above and below.

Although phenocryst compositions have little cumulative effect on aqueous transport, they can provide sites where sorptive alteration phases are concentrated (e.g., manganese oxides concentrated around altered iron-titanium-oxide phenocrysts; Section 5.3.1.2). Because phenocrysts reflect host magma chemistry, variations in phenocryst composition represent a subtle overprint on the generally bivariate compositions (rhyolite versus quartz latite) that characterize the major geochemical subdivisions at Yucca Mountain (Broxton et al. 1989 [DIRS 100024], pp. 5965 to 5978). A discussion of the major mineralogic and chemical features above, within, and below the Topopah Spring Tuff, the host rock at Yucca Mountain, is provided below.

Above the Host Rock–The Rainier Mesa Tuff of the Timber Mountain Group (Section 3.4) is the youngest extensive tuff unit exposed at Yucca Mountain, although it is only preserved at lower elevations along the flanks of Yucca Mountain. The occurrences at Yucca Mountain are vitric. As such, they are local sources for silica and trace minerals released by chemical weathering over the approximate 12-m.y. history of Yucca Mountain. The Rainier Mesa Tuff includes both high-silica rhyolite and quartz latite subunits.

The Paintbrush Group at Yucca Mountain is dominated by the Tiva Canyon and Topopah Spring tuffs. These tuffs provide most of the surface exposures of Yucca Mountain, and, except for their nonwelded tops and bases, are densely welded and of low matrix porosity. The Yucca Mountain and Pah Canyon tuffs are sandwiched between these two units, and though volumetrically minor, are of potential hydrologic importance because of their relatively high matrix porosity and low fracture abundance compared to the Tiva Canyon and Topopah Spring tuffs. Thus, unsaturated zone hydrologic properties above the repository horizon are strongly stratified (Sections 7.3 and 7.7).

The Tiva Canyon Tuff is compositionally zoned from a thin quartz-latitic, vitric-to-devitrified upper portion to a predominantly high-silica rhyolitic, devitrified lower sequence. The high-silica rhyolites of the Paintbrush Group have an exceptionally small compositional range (Figure 3-4). Across parts of Yucca Mountain, the quartz-latitic upper part of the Tiva Canyon Tuff is vitric or partially vitric. These glasses may be particularly reactive in interactions with recharge waters or with runoff. The lowest part of the Tiva Canyon Tuff consists of densely welded to nonwelded high-silica rhyolitic glass. This interval provides another horizon of potential water accumulation in the unsaturated zone, with associated dissolution and mineral alteration.

The Yucca Mountain Tuff is chemically very similar to the high-silica rhyolites of the Tiva Canyon and Topopah Spring tuffs (Figure 3-4). At Yucca Mountain, the Yucca Mountain Tuff is largely vitric, nonwelded, and porous, but may be locally devitrified to silica minerals and feldspar. Although this unit is rhyolitic, it contains both plagioclase and sanidine phenocrysts, whereas the only feldspar phenocrysts in the rhyolitic Tiva Canyon Tuff are of sanidine. This two-feldspar phenocryst composition is also characteristic of the rhyolitic portions of the Topopah Spring Tuff.

The Pah Canyon Tuff is a chemical anomaly within the Paintbrush Group. It is a two-feldspar tuff that has markedly sodium-rich plagioclase and is somewhat lower in silica content than the high-silica rhyolites (Figure 3-4). It has a rare-earth-element composition more similar to Yucca

Mountain quartz latites than to other rhyolites (Vaniman et al. 1996 [DIRS 105946], Volume 1, Section 5, pp. 5 and 6). The Pah Canyon Tuff is, like the Yucca Mountain Tuff, nonwelded, porous, and largely vitric (but locally devitrified). The high saturation of the porous nonwelded units, such as the Yucca Mountain and Pah Canyon units, is more effective in producing alteration where there is an underlying barrier to transmission. Thus, because of the relatively impermeable upper vitrophyre of the underlying Topopah Spring Tuff, the alteration of the immediately overlying Pah Canyon Tuff (principally to smectite) is often more extensive than that of the stratigraphically higher Yucca Mountain Tuff. Therefore, despite its minor volume, the Pah Canyon Tuff has a significant impact on the reactions between unsaturated zone waters and the host tuffs.

The Host Rock: The Topopah Spring Tuff–The transition from quartz latite to rhyolite in the Topopah Spring Tuff is marked by progressively decreasing abundances of phenocrysts (from about 17 to 2 percent) and, in particular, by the appearance of quartz phenocrysts and the loss of clinopyroxene phenocrysts. Lithic fragments average less than 1 percent. The lower two-thirds of the unit, including the repository horizon are rhyolitic and phenocryst-poor. The bulk of the rock consists of fine-grained devitrification minerals (Byers and Moore 1987 [DIRS 101321], Figures 2 to 5), principally feldspars, plus a variable combination of the silica polymorphs tridymite, cristobalite, and quartz; the relative proportions of silica polymorphs vary with depth and between lithophysal and nonlithophysal zones. Quartz phenocryst abundance is a useful stratigraphic marker within the devitrified rhyolitic Topopah Spring Tuff, but quartz phenocrysts are nevertheless rare (less than 0.5 percent) throughout this interval.

Peterman and Cloke (2002 [DIRS 162576]) and BSC 2003 [DIRS 166347] analyzed 20 core samples from four members of the rhyolite member of the Topopah Spring Tuff—the upper lithophysal, the middle nonlithophysal, lower lithophysal, and lower nonlithophysal zones (the repository would be in the last three)—and found that these units are chemically very similar. SiO_2 concentrations varied from 75.4 to 77.1 weight percent (mean, 76.29); Al_2O_3 from 12.4 to 12.9 weight percent (mean, 12.55); K_2O from 4.75 to 5.01 weight percent (mean, 4.83); Na_2O from 3.35 to 3.68 weight percent (mean, 3.52); and total iron as Fe_2O_3, about 1 percent. No other oxide component was more than 1 percent of the total BSC (2003 [DIRS 166347], Table 6.14.1-3). Trace element data are summarized in BSC (2003 [DIRS 166347], Table 6.14.2-2).

The devitrified rhyolitic Topopah Spring Tuff is generally devoid of zeolites, except for minor occurrences along some fractures. However, samples recovered from drill hole USW UZ-16 contain up to 14 percent of the zeolite mineral stellerite ($CaAl_2Si_7O_{18} \bullet 7H_2O$; Byers and Moore 1987 [DIRS 101321]). Higher stellerite abundances correlate with lower feldspar abundances. The stellerite has effectively accumulated calcium from groundwater. As a result, the stellerite-bearing Topopah Spring Tuff has higher CaO. Otherwise, it is compositionally similar to the unaltered high-silica rhyolite.

Below the Host Rock–The rhyolitic ash flows of the Calico Hills Formation beneath the Topopah Spring Tuff have exceptionally large variability in composition, with normalized anhydrous SiO_2 values ranging between 76 and 80 percent (Figure 3-4). These values are based on vitric samples showing no evidence of alteration (although the highest silica sample may have been somewhat silicified). Where zeolitization has occurred, the silica content is little changed.

The typical alteration phases are clinoptilolite [$(Ca, Na, K)_{2-3} Al_3(Al, Si)_2 Si_{13}O_{36} \bullet 12H_2O$] plus minor smectite. Mordenite [$(Ca, Na_2, K_2) Al_2Si_{10}O_{24} \bullet 7H_2O$] is also present and becomes as abundant, or more abundant, than clinoptilolite toward the north at Yucca Mountain. Chabazite ($Ca_2Al_4Si_8O_{24} \bullet 12H_2O$) is present in the south, although it is never as abundant as clinoptilolite. Below the Calico Hills Formation, nonwelded tuffs are pervasively zeolitized, and the primary geochemical variability is masked by this alteration, which can greatly alter the abundance of sodium, potassium, magnesium, calcium, and strontium. For these units, the primary geochemical variability discussed below is based upon the better-preserved welded, devitrified strata.

Below the Calico Hills Formation lie the rhyolitic ash flows and bedded tuffs of the Crater Flat Group (Prow Pass, Bullfrog, and Tram tuffs with increasing depth). There is a general similarity of quartz-sanidine-plagioclase-biotite phenocryst populations throughout the Crater Flat Group, although there is a general increase in the potassium content of sanidine and in the calcium content of plagioclase with depth, from the Prow Pass to the Tram tuffs. Pyroxene occurs in the upper two tuffs (Prow Pass and Bullfrog) and, despite its minor abundance, may play a role in radionuclide retardation in the Prow Pass Tuff (Section 5.3.3.1). All three of the Crater Flat tuffs have devitrified central portions, with abundant feldspar and quartz and, at least initially, had vitric margins, which were largely altered to zeolites in the early alteration history of Yucca Mountain. The zeolitization is dominated by clinoptilolite in the south and by clinoptilolite plus mordenite to the north. Analcime ($NaAlSi_2O_6 \bullet H_2O$) partially replaces these sorptive zeolites up into the lower parts of the Prow Pass Tuff in the northern part of Yucca Mountain, but from Drill Hole Wash southwards, analcime does not occur in significant amounts above the lower alteration zone in the Tram Tuff.

The older volcanic units at Yucca Mountain include the Lithic Ridge Tuff and unnamed older tuffs, designated A, B, and C, plus occurrences of dacitic lavas. These deeper units are far below the water table (about 1.5 to 2.5 km) and are, therefore, unlikely to be of significance with respect to transport from the repository horizon. In general, these tuffs and lavas are thoroughly altered to analcime and, with increasing depth, to albite, with associated smectite/illite, calcite, and lesser pyrite, barite, and other phases (Bish and Chipera 1989 [DIRS 101195], Appendices A and B).

3.3.5.1.1   Syngenetic Geochemical Processes

Thick pyroclastic deposits like the Topopah Spring and Tiva Canyon tuffs were erupted and emplaced at temperatures from more than 650°C to 985°C (Schuraytz et al. 1989 [DIRS 107248], p. 5933, Figure 9) and probably required about 100 to 1,000 yr to cool (Riehle 1973 [DIRS 107094]). Early in the cooling period, the interiors of such tuffs welded by viscous flow and compaction of the glass particles. The process of welding continued to temperatures as low as 475°C in the basal vitrophyre of the Topopah Spring Tuff (Rosenbaum 1986 [DIRS 107160], p. 12,833). After substantial welding had occurred, the tuff in the hottest parts of the interior devitrified, crystallizing to an assemblage of alkali feldspar, tridymite, cristobalite, and quartz, plus a variety of accessory minerals. The faster cooling upper and lower margins of the deposits did not weld and experienced little or no devitrification. Some of the moderately to densely welded portions toward the outer margins did not devitrify and have survived in a glassy state (vitrophyres).

In addition to the pervasive devitrification in the interiors of ash flows, localized syngenetic alteration occurred along fractures within and below devitrified tuff at the downward transition from devitrified to vitric tuff in both the Topopah Spring and Tiva Canyon tuffs. The alteration was caused by a combination of water entrained in the ash flow and infiltrating meteoric water that interacted with the rock and occurred during the very late stages of cooling, at near-ambient temperatures (e.g., 50ºC or lower) (Levy and O'Neil 1989 [DIRS 116960], p. 321). The tuffs were also subject to fracturing, faulting, and brecciation during cooling (Levy 1993 [DIRS 104579], p. 544).

The geochemical significance of devitrification and syngenetic alteration for site characterization is twofold. The original distribution of vitric and devitrified tuffs largely determined the locations of zeolitic and nonzeolitic rocks, respectively, in those parts of Yucca Mountain where the rocks have been subject to zeolitization. In addition, the field-scale distribution of hydrologic properties reflects the distribution of devitrified and vitric, as well as zeolitic and nonzeolitic, tuffs. Devitrified tuffs have low matrix porosity, so that many rock-water geochemical interactions occur more readily in the fractures than in the matrix.

Syngenetic alteration generally pertains to the interaction of still-hot rock with infiltrating meteoric water. Alteration of the syngenetic type can serve as a natural analog for hydrothermal alteration in a repository environment. Within the context of in situ thermal tests at Yucca Mountain (Section 5.4), characterization of syngenetic alteration allows researchers to identify alteration products of the tests with greater confidence because test products may be mineralogically similar to natural alteration products. This type of research has also been used to address postulated recent surface-discharging hydrothermal activity in the Yucca Mountain area and how it might be distinguished from syngenetic alteration that occurred more than 10 m.y. ago (Stuckless 1991 [DIRS 130503]; Stuckless et al. 1998 [DIRS 100086]).

Geochemical Variability Associated with Devitrification–The term devitrification, as applied to the pyroclastic deposits at Yucca Mountain, denotes high-temperature crystallization of volcanic glass to a largely anhydrous mineral assemblage. The major mineralogic components of the devitrified rocks are alkali feldspar and two or more silica phases. From the top of the Topopah Spring Tuff down through the top of the lower lithophysal zone, the typical silica phases in the groundmass are cristobalite and tridymite. In the remainder of the devitrified section, cristobalite and quartz are the characteristic silica phases.

Comparisons of the major-element compositions of brown cryptocrystalline devitrified groundmass and vitrophyre glass in the Topopah Spring Tuff indicate general similarities (Byers 1985 [DIRS 101573], pp. 15 to 18), suggesting that little or no bulk-chemical change occurred during devitrification. Devitrified groundmass from the lower Topopah Spring Tuff devitrified-vitric transition zone (the Tptplnc2-Tptpv3 interval of Buesch et al. 1996 [DIRS 100106], p. 8), with its higher potassium content, diverges in composition from vitrophyre glass and groundmass away from the transition zone.

Geochemical Variability Associated with Syngenetic Alteration–Most syngenetic alteration is located in and near devitrified-vitric transition zones, and the alteration itself represents a transition from devitrification to glass dissolution and secondary-mineral precipitation of mostly zeolites, clay, and silica phases. These transition zones were favored sites for alteration during

the late-stage cooling of thick tuff deposits because the reactive glass could be contacted by heated fluids coming from the warmer interior of the deposit. The volume of rock affected by syngenetic alteration is highly variable throughout Yucca Mountain, especially because much of the alteration is concentrated along and adjacent to fractures. In general, the cumulative thickness of syngenetically altered rock is on the order of tens of meters or less.

The basis for interpreting this alteration as syngenetic is its common textural association with devitrification (Levy 1984 [DIRS 104577], pp. 961 to 963). Data from a few geochronologic studies of silica from older portions of fracture and cavity coatings have yielded ages a few million years younger than the ages of the ash flows (Paces et al. 1999 [DIRS 129772], pp. S4 to S5; Cowan et al. 1993 [DIRS 150070], p. 1038). The potential causes of this discrepancy are discussed by Neymark et al. (2002 [DIRS 158673] pp. 724 to 726).

Alteration in the Topopah Spring Tuff, in the interval from the lower nonlithophysal zone to the top of the nonwelded base, is the most widespread and volumetrically abundant example of syngenetic alteration in the unsaturated zone at Yucca Mountain. Common mineral constituents of this alteration include alkali feldspar, smectite, heulandite, and silica minerals. Minor constituents, not present everywhere, include mordenite, calcite, iron and manganese oxides, and erionite.

Depending on the proportions of secondary minerals, this alteration can involve substantial bulk chemical change relative to the original vitric tuff (Levy 1984 [DIRS 101392], pp. 57, 65, 66, 74). Another effect of abundant smectite formation, in particular, has been a volume increase of alteration products compared to the volume of the original glass (Levy and Valentine 1993 [DIRS 106681], pp. 147 to 148). The excess product materials, some in colloidal form, migrated through the rock, filling primary and secondary pore spaces.

3.3.5.1.2   Diagenetic Geochemical Processes

The most extensive post-cooling mineralogic and geochemical change affecting the rocks at Yucca Mountain has been the diagenetic zeolitization of nonwelded glassy tuffs. Diagenetic alteration involved dissolution of glass pyroclasts by groundwater at ambient temperatures (e.g., 50°Cor lower) and precipitation of clinoptilolite with or without lesser amounts of mordenite, smectite, silica, iron-manganese oxides and hydroxides, and other minor phases. Chemical changes and introduction of chemical variability associated with this alteration are functions of the compositions of the secondary minerals and variability in their relative proportions caused by transport of dissolved or colloidal components into and out of the altered rock. Additional chemical variability has been superimposed on zeolitic rocks by cation exchange between clinoptilolite and percolating groundwater. Zeolitic rocks in the deeper parts of Yucca Mountain have been subjected to differing and additional alteration, with calcite formed in part by calcium released through sodium exchange for calcium in analcime or albite formation, and an increase in the illite-to-smectite ratio of clays.

The downward transition from vitric to zeolitized tuffs is a gross feature common to all Yucca Mountain drill holes and outcrops. The exact position of the vitric-zeolitic transition has not been precisely fixed throughout the mountain, but the persistence of this feature across the mountain makes it an important part of the evidence relating the timing of zeolitization to

pyroclastic depositional events and tectonism. Of particular importance for nuclear waste repository performance, the transition also marks changes in the hydraulic and sorption properties of nonwelded tuffs.

Researchers studying zeolitization in the Yucca Mountain region have made a variety of inferences about the hydrologic regimes in which zeolitization occurred. Although a few probable examples of perched water alteration have been recognized, alteration is generally believed to occur at or below a static water level (Vaniman et al. 1996 [DIRS 105946], Volume I, pp. 2, 25). The Yucca Mountain glass and zeolite distribution data provide no evidence that a widespread perched water table has ever existed. Known examples of probable perched water zeolitization have a much smaller vertical and lateral extent than the main mass of zeolitized tuffs. The working hypothesis is that most zeolitization occurred around or below the static water level present at the time of alteration, and that glass in nonwelded tuffs is preserved only where the rocks have not been subjected to prolonged saturation. This concept forms one basis for estimating the highest static water level ever reached at Yucca Mountain (Section 3.3.4.7.1).

3.3.6 Correlation of Lithostratigraphic, Hydrogeologic, and Thermal-Mechanical Units

Three primary stratigraphic systems have been developed to investigate the distribution of lithostratigraphic, hydrogeologic, and thermal-mechanical units at Yucca Mountain. Common to all these systems are the properties of bulk rock density, grain density, and porosity. Changes in these rock properties result in commensurate changes in many of the associated hydrogeologic and thermal-mechanical properties that define units whose boundaries coincide with a particular stratigraphic contact.

As shown in Table 7-1, lithostratigraphic units within the Tertiary volcanic-rock sequence are grouped into five major hydrogeologic units—in descending order, Tiva Canyon welded unit, Paintbrush Tuff nonwelded unit, Topopah Spring welded unit, Calico Hills nonwelded unit, and Crater Flat unit—that were defined principally on the basis of major variations in the degree of welding (Montazer and Wilson 1984 [DIRS 100161], pp. 14 to 19). Hydrogeologic properties of these units in the unsaturated zone at Yucca Mountain are presented in Section 7.2 and will not be discussed here, except to make specific mention of the Paintbrush nonwelded hydrogeologic unit (PTn), which is of special interest to stratigraphic and hydrologic studies in the site area. The distribution and characteristics of this unit are discussed in detail by Moyer et al. (1996 [DIRS 100162]) and Buesch and Spengler (1999 [DIRS 107236], pp. 31, 36).

The PTn occupies the stratigraphic interval between the top of the vitric zone in the upper part of the crystal-rich member of the Topopah Spring Tuff upward to the base of the densely welded rocks of the vitric zone in the lower part of the crystal-poor member of the Tiva Canyon Tuff (Table 3-1; see Buesch et al. 1996 [DIRS 100106], Table 4). In the boreholes shown in Figures 3-9 and 3-10, the base of the interval in the upper part of the Topopah Spring ranges from 75 to 113 m (246 to 370 ft) above the repository host rock in the crystal-poor member of that formation. As indicated by hydrologic studies, the PTn, which consists primarily of nonwelded to partially welded, in part highly porous (as much as 65 percent porosity; Moyer et al. 1996 [DIRS 100162], Table 3), pyroclastic-flow deposits and bedded tuffs, has the

capability of controlling the lateral flow of ground water (see Section 8.2) and is, therefore, of particular importance to the performance assessment of the repository.

Stratigraphic units with distinct thermal and mechanical properties within the volcanic-rock sequence at Yucca Mountain were identified by Ortiz et al. (1985 [DIRS 101280], Table 1). As with the hydrogeologic units, the boundaries of thermal-mechanical units with lithostratigraphic zones and subzones (Table 3-5) are based on changes in macroscopic features that define lithostratigraphic units and permit the preliminary correlation of laboratory measurements with specific lithostratigraphic units (Buesch et al. 1996 [DIRS 100106], Table 4). Analytical data indicate that most thermal-mechanical unit boundaries roughly correspond to (1) lithostratigraphic contacts that mark the transition from vitric, moderately welded rocks to densely welded subzones; or (2) the contact between the vitric, moderately welded rocks and devitrified rocks. Additional criteria are based on the percentage of lithophysae. Detailed discussions of the thermal and mechanical properties of the various thermal-mechanical units are given in Section 3.7.

Tuffs occurring within the unsaturated zone beneath Yucca Mountain are identified by lithostratigraphic name and by major and detailed hydrogeological unit nomenclatures in Table 7-1. The following discussion summarizes units of principal importance to flow and transport in the unsaturated zone at Yucca Mountain. The definition of major hydrogeological units comes from Montazer and Wilson (1984 [DIRS 100161], pp. 9 to 19). Their abbreviation of each of the five major hydrogeological units (i.e., TC, P, TS, CH, and CF) has been modified slightly from previous thermal-mechanical units. In order to be more descriptive, a lowercase letter has been added to these abbreviations indicating whether the unit is welded (w), nonwelded (n), or undifferentiated (u).

3.3.6.1 Tiva Canyon Welded (TCw) Hydrogeological Unit

The TCw is the most prevalent hydrogeological unit exposed at the land surface. The unit is composed of moderately to densely welded, highly fractured pyroclastic flow deposits of the Tiva Canyon Tuff. The deposits are of variable thickness resulting from erosion. Within the repository area, the maximum thickness of the TCw is about 150 m along Yucca Crest, whereas in alluvial washes east of Yucca Crest, the TCw may be completely eroded (Montazer and Wilson 1984 [DIRS 100161], p. 14; Rousseau et al. 1999 [DIRS 102097], p. 30). Vapor-phase corrosion of volcanic glass and pumice in the lower TCw imparts a secondary porosity beneath central and northern Yucca Mountain (Buesch et al. 1996 [DIRS 100106], pp. 35 to 36; Flint 1998 [DIRS 100033], p. 21). The lower boundary of the TCw has been defined as the contact between the densely welded, vitric subzone (Tpcpv3) and the moderately welded, vitric subzone (Tpcpv2) of the Tiva Canyon Tuff. Because Tpcpv3 is typically very thin and only observed beneath southeastern Yucca Mountain, the base of Tpcpv2 is selected as the lower TCw boundary for the purpose of defining layers within the mountainscale numerical grids.

TCw–PTn transition—Tuffs grade gently downward over a few tens of centimeters from densely welded (Tpcpv3, where present; otherwise, the lower nonlithophysal zone of the TCw or the upper portion of Tpcpv2) to nonwelded (Tpcpv1), accompanied by an increase in matrix porosity and a decrease in fracture frequency. Many fractures in the lower TCw terminate at the contact between TCw and PTn, or their apertures are greatly reduced across this boundary.

Alteration to clay minerals is common at the base of the TCw (Moyer et al. 1996 [DIRS 100162], pp. 1 to 2, 16 to 17, 88, and Table 3; Buesch et al. 1996 [DIRS 100106], pp. 35 to 36) and is correlated with observed increases in saturation (Flint 1998 [DIRS 100033], p. 8 and Figures 6 and 7). Changes in fracture characteristics and the occurrence of alteration minerals at the TCw-PTn contact may have important implications for downward flow of water at this interface.

3.3.6.2   Paintbrush Nonwelded (PTn) Hydrogeological Unit

The PTn consists of layers of predominantly nonwelded and bedded tuffs (particularly in the current repository footprint) with high matrix porosity and low fracture frequency (Moyer et al. 1996 [DIRS 100162]). The layers include the nonwelded vitric (i.e., glassy) subzone at the base of the Tiva Canyon Tuff (Tpcpv1), the bedded tuff Tpbt4, the Yucca Mountain Tuff (Tpy), the bedded tuff Tpbt3, the Pah Canyon Tuff (Tpp), the bedded tuff Tpbt2, and the nonwelded to moderately welded vitric tuffs at the top of the Topopah Spring Tuff (Tptrv3, Tptrv2). Thickness of the PTn hydrogeological unit ranges from about 110 to 20 m (north to south) across the repository area, and thickens to over 160 m beneath the northernmost part of Yucca Mountain. Lateral variation in welding associated with the substantial thickening of two PTn units (Tpy and Tpp), in addition to the variable distribution of altered (e.g., smectitic and zeolitic) intervals, make rock-hydrological properties within the PTn highly heterogeneous. Through-going fracture networks are rare and are typically associated with faults (Rousseau et al. 1999 [DIRS 102097], p. 54). The bottom of the PTn is defined as the contact between the moderately and densely welded, crystal-rich vitric subzones (Tptrv2 and Tptrv1, respectively). Given the overall large storage capacity of the highly porous rock matrix, the PTn unit may effectively dampen transient pulses of infiltration and distribute the downward flow of water more evenly.

PTn–TSw transition—A thin, but prevalent layer of argillic alteration is observed in the pre-Pah Canyon bedded tuff (Tpbt2), near the base of the PTn (Moyer et al. 1996 [DIRS 100162], pp. 53 and 80), and may behave as a capillary or permeability barrier to flow (Rousseau et al. 1999 [DIRS 102097], p. 25). Below this horizon, crystal-rich vitric tuffs grade sharply downward from nonwelded (Tptrv3) to densely welded (Tptrv1), accompanied by a sharp decrease in matrix porosity and an increase in fracture frequency. These changes in porosity and fracture characteristics may create saturated conditions above this contact that may reinitiate fracture flow into the TSw.

3.3.6.3   Topopah Spring Welded (TSw) Hydrogeological Unit

Sharing many characteristics of the TCw, the TSw is composed of moderately to densely welded, pyroclastic flow deposits with intense fracturing (Buesch et al. 1996 [DIRS 100106], pp. 19 to 21). A key difference between the TSw and the TCw is the existence of a well-developed, densely welded, crystal-poor vitrophyre (i.e., rock with a glassy groundmass) near the base of the TSw (Buesch et al. 1996 [DIRS 100106], p. 23; Rousseau et al. 1999 [DIRS 102097], p. 22). (The densely welded, basal vitrophyre of the TCw is very thin and occurs only beneath southeastern Yucca Mountain.) Thickness of the TSw ranges from about 280 to 350 m in the repository area. The base of the TSw is defined as the contact between the densely and moderately welded, crystal-poor vitric subzones (Tptpv3 and Tptpv2, respectively). In

descending lithostratigraphic order (using the nomenclature of Buesch et al. 1996 [DIRS 100106], Table 2), the key units within the TSw are:

- **Tptrv1 and/or uppermost Tptrn**—thin (~2 m thick), crystal-rich upper vitrophyre of the TSw, characterized by very low porosity and intense fracturing.

- **Tptrn**—crystal-rich nonlithophysal unit with well developed secondary porosity imparted by vapor-phase corrosion of volcanic glass and pumice clasts.

- **Tptrl & Tptpul**—crystal-rich and crystal-poor upper lithophysal units.

- **Tptpmn**—crystal-poor middle nonlithophysal unit (repository layer).

- **Tptpll**—crystal-poor lower lithophysal unit (repository layer).

- **Tptpln**—crystal-poor lower nonlithophysal unit; contains a highly fractured subzone and frequent clay alteration near base of unit (repository layer). Perched water is observed in several locations within the lower part of this unit.

- **Tptpv3**—crystal-poor basal vitrophyre, characterized by very low porosity and intense fracturing near unit top; alteration minerals (e.g., smectite, zeolite) commonly found at top of unit.

TSw–CHn transition—Tuffs grade downward from densely welded to nonwelded over several meters, accompanied by an increase in matrix porosity and a decrease in fracture frequency. Furthermore, much of the vitric material occurring above and below this boundary has been altered to clays or zeolites. Alteration occurs (although not ubiquitously) along fractures in the densely welded basal vitrophyre (Tptpv3) of the TSw, as well as within the high porosity, nonwelded matrix of the CHn (Broxton et al. 1987 [DIRS 102004], pp. 89 to 110; Bish and Chipera 1989 [DIRS 101195], Appendix A; CRWMS M&O 2000 [DIRS 138960], Section 6.3). Alteration near this contact has been linked to the occurrence of perched water and has important implications for transport and retardation of radionuclides.

3.3.6.4   Calico Hills Nonwelded (CHn) Hydrogeological Unit

Comprised of predominantly nonwelded pyroclastic flow and fall deposits, the CHn extends from the base of the crystal-poor, densely welded vitrophyre to the water table, except where units below the base of the upper vitric portion of the Bullfrog Tuff (Tcbuv) lie above the water table (which occurs in certain areas beneath Yucca Crest). The key units of the CHn include the moderately welded to nonwelded vitric subzones at the base of the Topopah Spring Tuff (Tptpv2 and Tptpv1, respectively), the bedded tuff Tpbt1, the Calico Hills Formation (Tac), the bedded tuff Tacbt, the entire Prow Pass Tuff (Tcpuv–upper vitric, Tcpuc–upper crystalline, Tcpmd–moderate/densely welded, Tcplc–lower crystalline, Tcplv–lower vitric, and Tcpbt–bedded tuff), and the upper vitric portion of the Bullfrog Tuff (Tcbuv). Within the current repository footprint, the thickness of the CHn ranges from about 180 to 320 m. Many different lithologies, distinguished by depositional history and degree of welding, by matrix color, and by the size, amount, and composition of pumice and lithic material, are contained within this interval. In a

hydrogeological context, however, the most significant features in the CHn are the abundance and distribution of zeolites. The distribution of abundance of clays and zeolites beneath the repository horizon is difficult to determine because mineral data from only a small number of boreholes are available and because the degree of alteration is highly variable.

3.3.6.5 Crater Flat Undifferentiated (CFu) Hydrogeological Unit

The CFu consists of any units that occur above the water table and below the base of the upper vitric portion of the Bullfrog Tuff (Tcbuv). This includes portions of welded and nonwelded units from the Bullfrog and Tram tuffs. Within the repository area, the thickness of the CFu ranges from 0 (in the northern and eastern portions) to about 140 m (along the southwestern edge of the repository). Because of the limited number of deep boreholes, sufficient data are not available to fully characterize these tuffs. Nevertheless, the volume of CFu material is small and restricted to the southwestern area of Yucca Mountain.

3.3.7 Quaternary Stratigraphy

3.3.7.1 Introduction

Surficial geologic mapping and chronographic studies of surface and near-surface deposits, soils, and geomorphic surfaces provide essential data for determining the history of deposition, erosion, and faulting during Quaternary time (Pleistocene and Holocene, 1.65 Ma to recent), which is of primary interest and importance to site characterization. To this end, such studies at Yucca Mountain have resulted in the recognition and differentiation of several principal surficial units, which are composed mostly of alluvium and colluvium, with minor amounts of eolian and debris-flow sediments that mantle hillslopes and cover the floors of valleys and washes. Figure 3-3 shows the general distribution of Quaternary sediments in and around the site area.

Early studies of Quaternary stratigraphy in the vicinity of Yucca Mountain, particularly in the area of the Nevada Test Site to the east, included those by Hoover and Morrison (1980 [DIRS 106173]); Hoover et al. (1981 [DIRS 106177]); Swadley et al. (1984 [DIRS 102917]); and Hoover (1989 [DIRS 101247]). These studies resulted in the general recognition of three major units ranging in age from Pliocene and early Pleistocene to late Pleistocene and Holocene. Swadley et al. (1984 [DIRS 102917]) mapped these units in Midway Valley, which adjoins Yucca Mountain to the east (Figure 3-2). However, no detailed mapping that further subdivided the surficial sequence had been published in that area until Taylor (1986 [DIRS 102864]) distinguished six different units in the fluvial terrace and alluvial fan deposits along Yucca and Fortymile Washes, as well as in a small area in the northernmost part of Midway Valley. Taylor's (1986 [DIRS 102864]) study strongly emphasized variations in surface characteristics and soil development.

Currently, separation of the Quaternary stratigraphic sequence in the Yucca Mountain site area into eight individual units (designated, in ascending order, as QT0, Qa1-Qa7) is based principally on the mapping by Wesling et al. (1992 [DIRS 107290]) of alluvial deposits and overlying geomorphic surfaces in Midway Valley. An alluvial geomorphic surface is analogous to an allostratigraphic unit, which is a mappable stratiform body that is defined and delineated on the basis of its bounding discontinuities (North American Commission on Stratigraphic

Nomenclature 1993 [DIRS 106417]). The principal criteria used for subdivision include: (1) relative stratigraphic and geomorphic position, (2) lithologic characteristics, (3) soil-profile development, (4) degree of desert pavement development, (5) amount and degree of desert-varnish accumulation, and (6) degree of preservation of original bar-and-swale topography.

Sedimentologic properties of the various alluvial units are similar. In general, fluvial deposits are predominantly sandy gravel with interbedded gravelly sand and sand. The fluvial facies include relatively coarse-grained channel bars and intervening finer-grained swales. The sediment texture in the bars and swales is dependent on their position within the landscape (proximal or distal-fan region) and the sediment source. In the proximal alluvial-fan regions, grain size is greater where larger material is available for transport and where streamflow is concentrated. In the distal reaches of the fans, sediment is finer grained, although coarser-grained facies are present locally. Gravel size ranges from pebble to boulder, and clasts generally are subangular to subrounded. Table 3-2 presents a summary of diagnostic surface and soil properties for the various surficial units. Descriptions given below are summarized from Section 4.4 of the YMSD (REV 01) (CRWMS M&O 2000 [DIRS 151945]), Swan et al. (2001 [DIRS 158784], pp. 8 to 21), and Whitney et al. (2003 [DIRS 159418]). A discussion of the regional stratigraphic relations of Quaternary surficial deposits is presented in Section 2.

Although the relative ages of the deposits, soils, and geomorphic surfaces around Yucca Mountain are well established, there is only limited direct numerical age control. Establishing a reliable temporal framework is difficult because of the inherent uncertainties involved in dating complex geomorphic and pedogenic systems in an arid environment. The difficulties are further compounded by the general lack of suitable materials for dating and by the fact that the ages of individual deposits vary not only from top to bottom but also laterally, owing to their time-transgressive nature. The two primary dating techniques used in the Quaternary studies are: (1) U-series disequilibrium dating of carbonate- and silica-rich materials in soils, and (2) thermoluminescence dating of the silt-size fraction of eolian and fluvial sediments. These methods have been widely applied in recent years and are considered to provide the most reliable ages for surficial deposits in the Yucca Mountain area.

The numerical dating of the various surficial units (QT0, Qal-Qa7) that compose the Quaternary sequence at Yucca Mountain is based primarily on samples collected from units Qa2-Qa5, as they were defined and mapped in the Midway Valley and Fortymile Wash areas (Wesling et al. 1992 [DIRS 107290]). The ages of these four units, as determined by thermoluminescence and U-series analyses, are plotted in Figure 3-18, which shows probability density functions (PDF) for the resulting data. Each PDF is constructed from the sum of normal distribution functions that represent the numerical ages combined with laboratory errors, normalized by the number of dates ("N," shown in Figure 3-18 above each PDF) from each stratigraphic unit (shown as Qa2-Qa5 beneath each PDF). The normal distribution function for each date is based on the mean and a 3-sigma range, which is spread about the mean out to plus and minus 3 times the 2-sigma (95 percent confidence) laboratory errors (see Whitney et al. 2003 [DIRS 159418]). The relative scale for each PDF is expressed in percent relative-probability per thousand years. The median age (number beside bar) and the plus and minus 2-sigma (numbers at limits of shaded area) age ranges for the units are derived from the cumulative distribution functions summed from each PDF, such that each shaded area represents the principal age

distribution based on a subset number ("n," in figure) of dates. The data show that, for units Qa2, Qa4, and Qa5, there is a distinct clustering of dates within relatively narrow segments of the age ranges (shaded areas on each of the PDFs, Figure 3-18), which are interpreted to best represent the main periods of deposition and soil development or both for those units. Dates not within these ranges (unshaded area) could be caused by miscorrelation of the sampled deposits, or they could, in fact, represent valid extensions of the age boundaries, thus indicating that it may not be possible to establish absolute temporal boundaries between successive units. In the case of unit Qa3, there is an indication that at least two depositional episodes may be included in the unit as a whole.

Based on the numerical age data discussed above, the preferred ages of the dated surficial deposits are: Qa2, middle Pleistocene; Qa3, middle(?) to late Pleistocene; Qa4, late Pleistocene; and Qa5, latest Pleistocene to early Holocene. With regard to unit Qa1, there is evidence indicating that it is associated with a period of deposition as old as the Bishop ash, which is dated as 760 ka (Sarna-Wojcicki et al. 1997 [DIRS 109161]) and therefore considered to be of middle to possibly early Pleistocene age. The age of underlying unit QT0 is assumed to be greater than 760 ka and is, perhaps, as old as Pliocene. Units Qa6 and Qa7 are presumed to be less than 7 ka, with Qa6 assigned a middle-to-late Holocene age and Qa7 being the deposit presently accumulating along the modern stream courses.

3.3.7.2   Descriptions of Quaternary Stratigraphic Units

3.3.7.2.1   Unit QT0

QT0 consists of a single terrace remnant at the north end of Alice Ridge (Figure 3-2). The surface forms a pronounced topographic bench (elevation 1,168 m) that is 25 m higher than unit Qa1 and 46 m above the active channel of Yucca Wash. Deposits associated with QT0 consist of lag gravel on a bedrock surface eroded into the Tiva Canyon Tuff; the clasts are exotic to Alice Ridge. Because of its limited areal extent and the extensive postdepositional erosion of the surface, no detailed soil data were collected from the QT0 surface. The thickness of the unit is unknown but is probably only a few meters. The early Quaternary to possibly Tertiary age of unit QT0 is based not only on its stratigraphic position relative to Qa1, but also on its highly dissected and eroded nature and its rounded landform morphology.

3.3.7.2.2   Unit Qa1

Qa1 is preserved at the surface on the Yucca Wash alluvial fan in northern Midway Valley. The fan surface has been dissected by younger drainages and is preserved as slightly rounded interfluves. Qa1 is also found on the west flank of Yucca Mountain and in northeastern Crater Flat. Locally, the desert pavement associated with the Qa1 surface is well developed, but in most areas, it has been extensively degraded. Freshly exposed rock surfaces on clasts, fragments of secondary carbonate and silica platelets, and surface or near-surface calcic horizons collectively impart a light tonal quality to the unit when viewed in the field or on aerial photographs. Although darkly varnished clasts are present in some areas, surface clasts typically are not darkly varnished; angular, unvarnished clasts are common on the surface. Many clasts are fractured and strongly weathered. No original depositional bar-and-swale morphology is preserved on the surface. A buried soil was observed beneath Qa1 at a depth of 2.5 m (8 ft) in

one soil pit, but no buried soils were encountered to depths of more than 3.3 m (11 ft) in other soil pits.

Strongly developed Qa1 soil is greater than 1.5 to 2.0 m (4.9 to 6.6 ft) thick and has a laminar petrocalcic horizon (Kqm) with stage IV carbonate morphology at or near the surface (Table 3-2; see footnotes at bottom of table for an explanation of soil horizons). The petrocalcic horizon locally is overlain by as much as 30 cm (12 in.) of fine-grained eolian sand and silt with Btk and Btkq soil horizons that appear to be much younger than the underlying petrocalcic horizon formed in alluvial sediments.

As stated earlier, the association of the Qa1 unit with the Bishop Ash, dated as 760 ka (Sarna-Wojcicki et al. 1997 [DIRS 109161]), is indicative of a middle, and possibly early, Pleistocene age. The slightly rounded, eroded morphology of Qa1 surfaces, as well as the strongly developed soils, are similar to deposits that have been assigned an early-to-middle Pleistocene age elsewhere in Nevada and California (for example, Wells et al. 1990 [DIRS 107207]; Harden et al. 1991 [DIRS 106072]; Harden et al. 1991 [DIRS 106077]; Slate 1991 [DIRS 130186]; Reheis et al. 1992 [DIRS 106661]; McDonald and McFadden 1994 [DIRS 104772]).

3.3.7.2.3   Unit Qa2

Qa2 is recognized at the surface primarily as thin elongated patches of alluvium in Midway Valley, where it is inset into unit Qa1. The unit has a well-developed desert pavement that contains darkly varnished clasts, some of which are split and fractured but still show varnish development on fractured surfaces. The original bar-and-swale morphology has been reduced to the height of the larger clasts above the surface. The upper part of the unit typically has a cap of eolian silt and fine sand ranging from 30 to 50 cm (12 to 20 in.) thick. Thicknesses of unit Qa2 observed in soil pits vary from 2.5 m (8 ft) to more than 3.5 m (11.5 ft).

The strongly developed Qa2 soil has a 40 to 70-cm (16 to 27.5 in.) thick argillic horizon (Btkq) and a zone of carbonate and silica accumulation typically exhibiting stage II to III+ (maximum IV) carbonate morphology (Table 3-2). Av and Bkq soil horizons occur in eolian sediments that accumulated on the surface.

3.3.7.2.4   Unit Qa3

Qa3 forms large remnant alluvial fan surfaces as well as fluvial terraces. It is one of the dominant map units in the Yucca Mountain area and underlies the main Fortymile Wash terrace. As indicated earlier, it may represent more than one depositional period within the Pleistocene. A well-developed desert pavement containing darkly varnished clasts characterizes the Qa3 surface, which has a dark brown or black tone on color aerial photographs (Table 3-2). Larger clasts, some more than 30 cm in diameter, are distributed on the surface in diffuse, poorly defined bars. The original depositional bar-and-swale morphology has been reduced to the height of individual clasts above the surface. The thickness of unit Qa3 averages approximately 2 to 2.5 m (6.6 to 8.2 ft) and locally exceeds 3.3 m (10.8 ft) as observed in soil pits and along the Fortymile Wash terraces.

The strongly developed Qa3 soil has a 20 to 75 cm thick (8 to 30 in.) argillic (Bt and Bkq) horizon overlying a 100 to 130-cm thick (39 to 51 in.) horizon of secondary carbonate and silica accumulation (Table 3-2). Clay films and strong blocky structure are characteristic of the argillic horizon that also commonly has accumulations of secondary carbonate and silica. A Bkq or weakly developed Kq horizon having Stage II-III carbonate morphology typically underlies the Btkq horizon.

3.3.7.2.5 Unit Qa4

Qa4 consists of small, inset fluvial-terrace and alluvial-fan remnants on the east side of Yucca Mountain. The desert pavement of the Qa4 surface ranges from loosely to tightly interlocking and is noticeably less well developed than pavements formed on the older fluvial surfaces. Indistinct depositional bars are preserved as diffuse accumulations of larger clasts. Bar-and-swale relief on Qa4 mostly has been reduced to clast height above the surface. The thickness of Qa4 averages about 1 m (3.3 ft) and does not exceed 2 m (6.6 ft) where observed in soil pits.

The strongly developed Qa4 soil is characterized by a reddened argillic horizon and accumulations of carbonate and silica. The upper part of the soil exhibits silica accumulation, stage I-II carbonate morphology, and a strongly developed Bkq horizon with a sandy or silty clay-loam texture. Continuous, thin-to-moderately thick clay films coat ped faces of the Bkq soil horizon, which is overlain by an Av soil horizon.

3.3.7.2.6 Unit Qa5

Qa5 occurs as inset terraces along drainages. The desert pavement is loosely packed and poorly formed, and surface clasts have minor accumulations of rock varnish (Table 3-2). Qa5 surfaces display well-developed, bar-and-swale morphology, the amount of relief being related to landscape position and sediment sources, with the coarsest-grained bars lying in the proximal-fan regions. Smaller, lower, partly buried bars lie on distal fans, where the intervening swales are partly filled by fine-grained eolian silts and sands. Surface clasts are relatively unweathered. In soil-pit and trench exposures, the average thickness of Qa5 is approximately 1 m (3.3 ft), and the maximum observed thickness is about 2.5 m (8.2 ft).

Weakly developed soils are formed on Qa5. Soil development is stronger in the swales, where a silt-rich zone occurs in the upper 30 to 40 cm (12 to 16 in.) of the unit; soils are more weakly developed on bars. The soil typically has a Bwk or incipient Btjk horizon, weak subangular blocky structure, and colloidal stains on grains. Carbonate is disseminated in the matrix, and below about 30 cm (12 in.) depth in the Bk horizon, the bottoms of clasts have powdery coats of carbonate (stage I carbonate morphology). Where Qa5 is sufficiently thick, the carbonate content decreases below the Bk horizon to form a transitional horizon (BC or CB) or a Ck. Where Qa5 is relatively thin and underlain by a buried soil, the Bk persists to the base of the unit.

3.3.7.2.7 Unit Qa6

Qa6 occurs along the active washes as low floodplains less than 1 m (3.3 ft) above the active channels and as vegetated bars. No desert pavement has developed, and surface clasts are

unvarnished and unweathered. Relief on the Qa6 surface is primarily the result of preservation of original bar-and-swale morphology. Locally, an eolian cap as much as 5 to 10 cm (2 to 4 in.) thick buries all but the largest surface clasts. Natural outcrops and man-made exposures indicate that the total thickness of the unit does not exceed 2 m (6.6 ft).

Qa6 soils lack the significant eolian cap common to the older surfaces (Av horizon), and soil development is limited to minimal oxidation of the deposit and sparse accumulation of carbonate (Table 3-2). Carbonate is more concentrated toward the upper 10 cm (4 in.) of the deposit, although the matrix typically contains widely disseminated carbonate. Clasts in the upper 30 cm (12 in.) have little visible carbonate, yet effervesce when hydrochloric acid is applied. Carbonate varies from isolated patches on the undersides of clasts to relatively continuous thin coatings. Evidence that many clasts within the deposit have been reworked from older deposits includes randomly oriented carbonate coatings on clasts and percussion marks where the coatings have been chipped from the clasts.

3.3.7.2.8   Unit Qa7

Qa7 consists of deposits along active channels and the adjacent floodplains. No desert pavement has formed on the surface, and no desert varnish occurs on clasts, except that which may be on clasts reworked from older surfaces. Clasts are unweathered, and the original depositional bar-and-swale relief is unaltered. The total exposed thickness of Qa7 does not exceed 2 m (6.6 ft).

No in situ pedogenic alterations were observed for Qa7 deposits, but the matrix contains reworked, disseminated carbonate. Reworking of older surficial materials is also indicated by numerous clasts with thick accumulations of carbonate. Such clasts appear to be distributed randomly throughout Qa7, and coatings, originally formed on clast bottoms, have no preferred orientation in the reworked deposits.

3.3.7.2.9   Colluvial Deposits

Colluvial deposits are undifferentiated as surficial map units because of their limited areal extent and the limited exposure of all but the youngest deposits. Descriptions given below are generalized from those of Swan et al. (2001 [DIRS 158784], pp. 17 and 18, Figure 7), which were based on sequences exposed in trenches and soil pits on the east side of Exile Hill (Figure 3-2).

Colluvial and debris-flow deposits generally consist of gravelly silty sands and silty fine-to-medium gravel, with pebble-to-small cobble clasts. The deposits are poorly sorted, nonbedded to crudely bedded, predominantly matrix-supported, and locally clast-supported, with as much as 90 percent gravel. The gravels are composed of subangular to angular pebbles with lesser amounts of cobbles as much as 20 cm (8 in.) in diameter and small boulders as much as 30 cm (12 in.) in diameter. The thickness of individual colluvial units is generally less than 2 to 3 m (6.6 to 9.8 ft) based on trench and soil-pit exposures.

Colluvial deposits, possibly equivalent to surficial unit Qa5, have thin, weakly developed soils with an AB horizon over a weakly developed Bwk horizon. Colluvial deposits of probable Qa4 age display well-developed Bkq textural B horizons 40 to 50 cm (16 to 20 in.) thick. Units

possibly equivalent to Qa3 and Qa2 have multiple superimposed soils consisting of Bkq and Btjkq horizons with stage II carbonate morphology. The oldest exposed colluvium deposits have strongly developed Kqm horizons. Some patches of darkly varnished colluvial-boulder deposits found on upper hillslopes are considered to be middle-to-late Quaternary in age (Whitney and Harrington 1993 [DIRS 107303]), but most of undifferentiated colluvium mapped on hillslopes have surface characteristics of units Qa5 and Qa6. Colluvium having surface characteristics similar to unit Qa4 surfaces commonly occurs near the toe of the hillslope. In view of these correlations, colluvial deposits appear to represent an age range comparable to that of alluvial deposits (middle Pleistocene to Holocene).

3.3.7.2.10 Eolian Deposits

Two types of eolian sediment were observed in the Yucca Mountain area: (1) reworked eolian deposits within sand ramps surrounding Busted Butte and along the southeastern margin of Midway Valley (Figure 3-2), and (2) thin accumulations of silt and fine sand in the A and B horizons of most surface soils and relict accumulations within some buried soils.

Sand ramps at Busted Butte and in southeastern Midway Valley are composed of a stacked sequence of eolian-colluvial units that have textures of pebbly, silty, fine- to medium-grained sand interbedded with sandy, pebble-to-cobble gravel. Minor alluvial sandy, pebble-gravel deposits are present locally. The deposits are poorly to moderately sorted, moderately bedded to massive, and predominantly matrix-supported, although the alluvial gravel and parts of some colluviums are locally clast-supported. Gravel clasts are angular to subangular and commonly less than 5 cm (2 in.) in diameter, but some clasts are as large as 50 cm (20 in.) in diameter. Maximum thickness of the sand-ramp deposits exceeds 15 m (49 ft).

A weakly to moderately interlocking desert-pavement covers most of the sand-ramp surfaces. Soil development in near-surface deposits consists of a well-developed Bkq horizon with a sandy, clay-loam texture that appears to be similar to the soil formed on surficial unit Qa4. Typically, one or more buried soils occur within the deposits.

The presence of Bishop tephra in lower sand-ramp deposits at Busted Butte (Whitney et al. 1985 [DIRS 107314]; Menges et al. 1994 [DIRS 106344], p. 2380) and at other localities near Yucca Mountain (Hoover 1989 [DIRS 101247]) indicates that those landforms began forming within the region prior to about 760 ka. At Busted Butte, some of the buried soils have been dated as middle to late Pleistocene (Menges et al. 1994 [DIRS 106344]). Multiple buried soils above the Bishop tephra indicate that accumulation of the sand ramps is episodic and punctuated by periods of surface stabilization and soil formation. Numerical ages of 73±9 ka and 38±6 ka from two successive units in the upper 3 m of the deposits, in a trench in southern Midway Valley, possibly indicate the ages of two of the more recent depositional episodes, and another date of 6±1 ka from the surface "A" horizon is indicative of continuing accumulation of eolian sediments during the Holocene (Menges et al. 2003 [DIRS 159412]).

A few to several tens-of-centimeters of eolian silt and fine sand have accumulated on most alluvial geomorphic surfaces and have been incorporated into soil profiles formed on those surfaces. These eolian accumulations are not mapped separately because of their broad areal distribution and relatively thin nature. Models of desert pavement and soil formation recognize

the importance of eolian accumulations as a source for the fine-earth fraction, carbonate, and soluble salts that occur in otherwise clean sandy-gravel deposits in arid regions (Birkeland 1984 [DIRS 101847], pp. 290 and 291; McFadden et al. 1987 [DIRS 105023]; McFadden and Weldon 1987 [DIRS 105022]; McDonald and McFadden 1994 [DIRS 104772]).

3.3.7.3 Trenching Activities

Information on the stratigraphic relations among surficial deposits was augmented considerably by the large-scale mapping and detailed descriptions of vertical sequences that were observed in natural exposures and in trenches excavated across those faults suspected of being active during Quaternary time. Within the site area, 52 exploratory trenches and natural exposures were cleaned and logged to determine the extent of Quaternary tectonic activity with respect to: (1) the number, amount of displacement, and age of individual surface-rupturing events causing earthquakes; (2) fault slip rates; and (3) recurrence intervals between successive events on a given fault. Results of the detailed Quaternary fault studies are given in Keefer et al. (2003 [DIRS 159419]) and brief summaries of the data for block-bounding faults are presented in Section 3.5.3. Interpretations of the paleoseismic data with respect to seismic-risk analysis is given in Section 4.3.2.

In many of the individual trench studies, exposed deposits were classified independently of the standard stratigraphic sequence of units mapped in surface exposures. However, numerical ages were also obtained for many of the trenched deposits, so that correlations with the established framework could be made and similarities noted between correlative units, which was especially true in terms of comparable degrees of soil development. The combined surface and subsurface data provide a valuable chronostratigraphic record for interpreting changes in climatic conditions influencing erosion and deposition (see Section 3.4) and for determining the history and magnitude of Quaternary deformation (see Sections 3.5 and 4).

3.3.7.4 Pedogenic Calcite and Opaline Silica Deposits

Pedogenic carbonate with subordinate opaline silica (calcrete) is present both as slope-parallel deposits and as remobilized fracture fillings. These deposits have generated a controversy as to the possible existence of an adverse condition. Szymanski (1987 [DIRS 100184]; 1989 [DIRS 106963]) postulated that these deposits were formed by groundwater rising to the surface and, therefore, through the repository horizon. Section 4.4.5 of the YMSD (REV 01) (CRWMS M&O 2000 [DIRS 151945]) summarized the work done to resolve this question and described the reasoning behind the conclusion that there are no paleogroundwater discharge deposits in the immediate vicinity of Yucca Mountain. In fact, the closest such deposit is approximately 15 km to the southwest (see Section 8).

The pedogenic deposits are generally poorly indurated and fine grained. The average calcite-weight fraction of the well-developed calcretes is only 53 percent, whereas spring deposits may be pure calcite. The rest of the calcretes consist of tuffaceous detritus, plus a small amount of exotic rock fragments. Ooids and pellets are locally abundant. The preserved fossils are of roots rather than aquatic animals. The mineralogic, chemical, and isotopic characteristics of the calcretes is summarized in Section 4.4.5 of the YMSD (REV 01) (CRWMS M&O 2000 [DIRS 151945]).

3.3.7.5   Distribution of Quaternary Deposits in the Yucca Mountain Area

The Quaternary landscape in the Yucca Mountain area has been affected by physical weathering. It also reflects colluvial, eolian, and alluvial processes that have responded to varying climates and climatic changes. The topography of the mountain and adjacent basins, which have been formed by extensional tectonic processes over the past 14 million years, is an additional factor influencing landscape development at Yucca Mountain. Patterns of Quaternary deposits reflect both the tectonic environment and the climatic history of the area.

One noteworthy map pattern at Yucca Mountain is the preservation of early and middle Quaternary colluvial deposits on many hillslopes (e.g., Whitney and Harrington 1993 [DIRS 107303], p. 1008). Techniques using cosmogenic isotopes, volcanic ashes, cation-ratio dating, and U-series dating have been used to determine the ages of these deposits. The preservation of older Quaternary deposits indicates that hillslope erosion processes have been ineffective in eroding colluvial deposits that were weathered from bedrock during the colder, pluvial climatic episodes (Whitney and Harrington 1993 [DIRS 107303], p. 1014, Table 1). The slow removal of hillslope colluvium is also reflected in the lack of either large or steep alluvial fans at the base of the slopes of Yucca Mountain. The lack of fans along the base of tilted fault blocks is a strong indication of very low rates of tectonic activity. Quaternary uplift rates are generally 0.01 mm/yr. (0.0004 in./yr) around Busted Butte, along part of Fran Ridge, and on the slopes of the unnamed flanks of southern Yucca Mountain. These sandy deposits are products of a very dry and windy climate that took place during some part of the interglacial component of the climatic cycle. Up to six buried soils have been found in some sand ramps, which demonstrate the cyclic nature of dry, arid conditions at Yucca Mountain (Menges and Whitney 1996 [DIRS 106343], p. 4.4-5). The presence of Bishop ash near the base of several sand ramps indicates that eolian sand deposition goes back at least 760 thousand years. The preservation of essentially unconsolidated sand on Yucca Mountain hillslopes underscores again the ineffective hillslope erosional processes during the last half of the Quaternary.

The distribution of Quaternary deposits of different ages in Crater Flat appears to reflect the ongoing opening, or extension, of the basin. Deposits of Q1 to Q3 age are concentrated on the eastern side of the basin near or adjacent to Yucca Mountain. Deposits of Q5 and Q6 age are concentrated along the basin's southwestern and southern margin, with the area of maximum subsidence defined on the regional seismic reflection line (Brocher et al. 1998 [DIRS 100022], Figure 6). A strong contrast in runoff patterns can be seen between the east-flowing alluvial fans from Bare Mountain and the southerly slope of the drainage of central Crater Flat. This drainage contrast probably reflects the presence of a buried fault in central Crater Flat, and possibly a buried splay of the Bare Mountain fault near the base of the Bare Mountain fans. The Bare Mountain fans are not rounded in typical fan shape, but terminate against a sharp, north-trending lineament defined only by a change in drainage patterns. Fault-controlled sedimentation has occurred along the Windy Wash and Fatigue Wash faults. Uplifted early to middle Quaternary alluvium is juxtaposed with late Quaternary alluvium and colluvium.

On the east side of Yucca Mountain, sedimentation patterns do not appear to reflect active tectonism, except where colluvial wedges have deposited locally against fault scarps. The northerly trend of Fortymile Wash, which is parallel to but not coincident with the Paintbrush Canyon fault, has raised questions about whether its origin is in part tectonically influenced.

Several geophysical studies, summarized in Oliver et al. (1995 [DIRS 106447], pp. 44 and 109 to 111), suggest that a very shallow graben may exist beneath the central alluvial portion of the wash (south of the canyon); however, the regional seismic reflection line does not show any significant offset of the Tertiary-Paleozoic contact beneath the wash. No evidence of Quaternary tectonic activity has been associated with the wash. The southerly depositional pattern of the wash is controlled by the base level of the Amargosa Valley.

Midway Valley is underlain largely by Q1 and Q2 deposits because of a stream capture of Yucca Wash that appears to have taken place during the middle Quaternary (Taylor 1986 [DIRS 102864], pp. 17 to 21). During Q1 time, Yucca Wash flowed southeastward into Fortymile Wash through the gap between Alice Ridge and Fran Ridge. After Q2 time, Yucca Wash flowed eastward into Fortymile Wash north of Alice Ridge. In general, colluvial deposits that are produced during pluvial climates dominate hillslopes. The erosion and redistribution of these deposits takes place during drier climates, when hillslopes are no longer stabilized by vegetation. Hence, most of the alluvial map units in the basins and valleys that dominate the landscape at Yucca Mountain were deposited during interpluvial episodes. Eolian deposits record exceptionally dry and windy conditions that occurred in the climatic cycle, whereas paleodischarge deposits from springs were deposited during the wetter and cooler conditions of the pluvial part of the cycle. (Section 8.4 contains a complete description of paleodischarge deposits and history.) Multiple dating and descriptions of soils, surfaces, and deposits support the existence of these deposition patterns at Yucca Mountain.

3.4 EROSION, DEPOSITION, AND FLOODING

3.4.1 Introduction

Past and modern geomorphic processes have been investigated at Yucca Mountain in order to assess the surficial characteristics at the HLW repository. The studies were especially designed to estimate the long-term average rates of erosion on the ridge crests and hillslopes of the mountain to determine the potential for erosional breaching of the underground storage facility. Information about patterns of erosion and deposition is used to characterize any potential surface redistribution of radioactive waste that may be deposited on the ground surface.

Flow characteristics of Fortymile Wash (Figure 3-2) are of particular importance because of concern over whether radioactive waste products could be entrained by flow within this drainage system, transported downstream, and subsequently become incorporated within the flow of the Amargosa River (Figure 2-2).

Much of the material in the following sections is summarized from detailed discussions presented in Sections 7.3 and 7.4 of the YMSD (REV 01) (CRWMS M&O 2000 [DIRS 151945]). In addition, data and interpretations resulting from studies by Coe et al. (1997 [DIRS 104691]); Glancy and Beck (1998 [DIRS 155679]); Forester et al. (1999 [DIRS 109425]); and Tanko and Glancy (2001 [DIRS 159895]) are incorporated. Flood characterization information in the vicinity of the North Portal is provided in BSC (2002 [DIRS 157928]). Because stream-gauge and related data are typically recorded in English units, such terms will be used for those kinds of measurements, as well as for some other measurements and recorded data

as appropriate. However, distances and certain other units will be stated in metric terms for consistency with other sections.

3.4.2 Erosion and Deposition in the Present Climate

The dry, semiarid climate in the northern Mojave Desert, characterized by low annual precipitation (mean of 125 mm/yr (5 in.) at 5,000 ft (1,524 m) elevation; see Section 6) and infrequent rainstorms, is responsible for the kinds and rates of modern surficial processes at Yucca Mountain. Runoff at Yucca Mountain and streamflow in Fortymile Wash are, therefore, infrequent and almost always follow intense, local thunderstorms. Such storms commonly produce flash floods, currently the major flood hazard at and near Yucca Mountain (Glancy 1994 [DIRS 101227]), during which the flow of water and rock debris typically causes hillslope erosion and the deposition of coarse debris on alluvial fans and in stream channels. Erosion and deposition of sediment within and along the channel systems also affect the hydraulic characteristics of future flood flows by changing the geometry of stream channels. Design storms (local precipitation events producing probable maximum flood-peak discharges in a small drainage basin; see Bullard 1986 [DIRS 100107], p. 8), probable maximum floods, and maps of flood-prone areas at Yucca Mountain are described in the YMSD (REV 01) (CRWMS M&O 2000 [DIRS 151945], Section 7.3).

Runoff in Fortymile Wash infiltrates the stream channel at high rates downstream past Yucca Mountain to distal reaches of its alluvial fan (Osterkamp et al. 1994 [DIRS 100602], pp. 503 and 504). As a result of progressive downstream channel losses and flow attenuation, channel capacity decreases along the approximately 24 km (15 mi) stretch that extends south and southwest from the northern, upstream reaches to U.S. Highway 95 at the northeast edge of Amargosa Valley (Figure 2-2). Along this section of Fortymile Wash, large-scale sediment deposition transforms the entrenched channel into a broadly braided alluvial fan. Farther downstream to the southwest, the weakly defined distributory channels continue for another 22 km (13.6 mi) or more to a diffuse junction with the wide and braided Amargosa River (Figure 2-2). Data regarding the general runoff characteristics of Fortymile Wash and the contributions of that tributary and the upper Amargosa River Basin to flows that reached the river-basin terminus in Death Valley during the latter part of the twentieth century (Glancy and Beck 1998 [DIRS 155679]) are summarized in Section 3.4.3.

In the present climate, eolian processes of sand movement and dust deposition are active around Yucca Mountain. Modern dust deposition of silt and clay in southern Nevada and nearby California ranges from 4.3 to 15.7 $g/m^2/yr$ (Reheis and Kihl 1995 [DIRS 106653], Table 7). Annual dust flux increases with mean annual temperature, but appears to more closely reflect changes in annual precipitation (relative drought conditions) rather than temperature. Playa and alluvial sources produce about the same amount of dust per unit area. However, the total volume of dust produced is much larger from alluvial sources. The mineralogic and major oxide composition of dust samples indicates that sand and some silt is locally derived and deposited, whereas clay and some silt can be derived from distant sources. Modern and Holocene dust has been accumulating below desert pavements and on hillslopes in the region.

Sand movement is active in the Amargosa Valley, just south of Yucca Mountain, where a large star dune, called Big Dune, has accumulated sand over 80 m (260 ft) high (Swadley and

Carr 1987 [DIRS 101300]). Flood sands from Fortymile Wash, and from Windy Wash, which drains Crater Flat, are two of the main sources of sand for Big Dune.

3.4.3   Flooding History and Potential

3.4.3.1   Introduction

The current major flood hazard at and near Yucca Mountain probably is flash flooding (Glancy 1994 [DIRS 101227], p. 1). Flash floods are the result of intense rainfall and runoff from localized convective storms or from high-intensity precipitation cells within regional storm systems. Flash floods and associated debris movement commonly result in degradation of mountainous terrain, development of alluvial fans, and evolution of drainage channel morphology. Flood flows range in character from water-dominated (Newtonian) fluids, which have widely varying concentrations of entrained sediments, to sediment-dominated debris flows (non-Newtonian or Bingham fluids), which contain interstitial water. A debris flow is the mass movement of loose, granular rock material mixed with water and air; its hydraulic characteristics are intermediary between those of landslides and water floods, and thus it has flow characteristics different from either of these processes.

Flood hazards are caused by the flow of water and rock debris. Flowing water is destructive because of its capacity to erode and inundate, and because of its momentum. The associated process of debris transport can cause wide-scale damage during erosion, movement, and deposition. In the semiarid southwest, the damage potential of debris transport commonly is greater than that of the water carrying the debris. Therefore, effective flood hazard mitigation at Yucca Mountain depends on understanding flowing water and debris, particularly knowledge of debris transport.

Transported debris generally causes damage by erosion of the stream channel along the flow path, impact with obstacles, abrasion of material swept into the flow, and burial of objects and groundwater surfaces. Resulting landscape modifications commonly are vivid. Erosion and deposition of sediment within (and along) the channel system also affect the hydraulic characteristics of future flood flows by changing the geometry of stream channels.

The following sections summarize studies on the history of drainage system patterns, ancient and historical surface water flow conditions, and historical flood occurrences and flood discharges in the Yucca Mountain region. Data derived from these studies advance the understanding of past climatic, geomorphic, and streamflow conditions and, in some cases, the understanding of future climatic and surface hydrologic conditions within the region.

3.4.3.2   Flooding History

Non-aboriginal settlement of southern Nevada dates back about 150 years; written records of floods are scarce. However, floods leave evidence of high stage levels in the form of sediments deposited in valleys, and even as high water marks that, in some circumstances, can be dated by ^{14}C techniques. Actual stream gauging records in the Yucca Mountain region date only from the early 1960s (Table 7-3).

Glancy (1994 [DIRS 101227], p. 29) discussed the geologic evidence found for prehistoric flooding in Coyote Wash on Yucca Mountain. Trenches excavated across and along the modern-day channel exhibited sediments indicative of multiple flood events, including debris-flow deposits. Glancy (1994 [DIRS 101227], p. 30) concluded that moderately indurated sediments overlying the bedrock and underlying the stream terraces adjacent to the channel were probably deposited during the late Pleistocene or early Holocene (mostly more than 10 thousand years ago), and that nonindurated sediments overlying the older sediments were probably of Holocene age (less than 10 thousand years ago). Using surficial boulders near the trenches, Glancy (1994 [DIRS 101227], p. 38) estimated the magnitude of the flood that deposited them during the Holocene. Assuming the flood was water dominated (Newtonian fluid) and all the boulders were emplaced by the same flood, a peak discharge of 68 m^3/s (2,400 ft^3/s) was estimated to have occurred in the North Fork of Coyote Wash. The combined flows of the north and south forks could result in a peak flow as large as 142 m^3/s (5,000 ft^3/s).

Ely (1997 [DIRS 108873], p. 177) synthesized flood records from 19 rivers in Arizona and southern Utah, including more than 150 radiocarbon dates and evidence of more than 250 flood deposits. Ely (1997 [DIRS 108873], p. 175) concluded that the largest floods over the past 5,000 years cluster into distinct time periods related to regional and global climatic fluctuations. High-magnitude floods were frequent during the periods from 5,000 to 3,600 years ago (^{14}C dating), from 1,100 to 900 years ago, and from 500 years ago onward. In contrast, the periods from 3,600 to 2,200 years before present, and from 800 to 600 years before the present were characterized by less frequent large floods. A strong connection was found (Ely 1997 [DIRS 108873], p. 175) between wet El Niño conditions and large floods associated with winter storms and tropical cyclones.

A flood that occurred on February 24, 1969, is believed to have been, overall, the most severe flood in the Amargosa River Basin during recent times. The peak flow on that date in Fortymile Wash, at a point just downstream from the Yucca Mountain road crossing (located 3.4 km (2.1 mi) north and 1.3 km (0.8 mi) east of the southeast corner of the site area), was estimated by Squires and Young (1984 [DIRS 102783], p. 12) at about 20,000 ft^3/s (566 m^3/s) on the basis of channel geometry and residual evidence discovered during a flood prediction study. This estimate was independently supported by the recollection of a Nevada Test Site security guard, who witnessed the flood from the high south-terrace about 5.5 km (3.4 mi) downstream from the road crossing and described the flow as wall-to-wall water, about 4 ft (1.2 m) deep, across the 800 to 900 ft (240 to 275 m) wide flood plain at the bottom of the incised channel. At an average depth of 4 ft (1.2 m), the cross-sectional flow area would be on the order of 3,200 to 3,600 ft^2 (297 to 334 m^2). Assuming a peak flow of 20,000 ft^3/s (566 m^3/s), the resultant average velocity would have been about 5.5 to 6.25 ft/s, (1.7 to 1.9 m/s), depending on cross-sectional area. For comparison, average runoff velocities recorded at a gauging station located near Borehole UE-25 J-13 (Figure 3-7), 0.8 km (0.5 mi) south of the Yucca Mountain road crossing, during March 1995 (peak flow of 3,000 ft^3/s (85 m^3/s); see Table 7-3) and February 1998 (peak flow of 200 ft^3/s [5.7 m^3/s]) were 7 to 8 ft/s (2.1 to 2.4 m/s) and 3 ft/s (0.9 m/s), respectively (Tanko and Glancy 2001 [DIRS 159895]).

Effects of the 1969 flood were noted by Hunt (1975 [DIRS 159900], p. 15) in his description of "Death Valley's Most Recent Lake." He estimated that 80 mi^2 (51,200 acres) (207 km^2) of the Badwater Basin salt pan in Death Valley were flooded to depths of as much as 3 ft (0.9 m), and

thereby calculated a resultant lake volume of about 50,000 acre-ft (62 million m^3). He further estimated peak discharge of the Amargosa River near its terminus, near the south end of the salt pan, at about 750 ft^3/s (21 m^3/s) (Hunt 1975 [DIRS 159900], Figure 12, p. 23).

Fortymile Wash flowed on March 3, 1983, as a result of a regional rainstorm that may have melted some snowpack at the higher basin altitudes (Pabst et al. 1993 [DIRS 100170] pp 22-23). Flow peaked at 570 ft^3/s (16 m^3/s), as recorded by the gauging station near Borehole UE-25 J-13 (Figure 3-7), and at about 400 ft^3/s (11 m^3/s) downstream at a gauging station near U.S. Highway 95. Fortymile Wash flowed three times in the summer of 1984 in response to convective rainstorms during a prolonged and unusually intensive monsoon storm season. Magnitudes of the three flows (July 21–22, July 22, and August 19, 1984) were recorded as follows: (1) at the station near Borehole UE-25 J-13 approximately 1,860, approximately 150, and approximately 850 ft^3/s, (53, approximately 4, and approximately 24 m^3/s) respectively; and (2) at the station near U.S. Highway 95 approximately 1,430, approximately 100, and approximately 380 ft^3/s (approximately 40, approximately 3, and approximately 11 m^3/s), respectively (Pabst et al. 1993 [DIRS 100170], pp. 11, 22, and 23).

Fortymile Wash did not flow again within the site area for almost 11 years following the 1984 summer storms (Glancy and Beck 1998 [DIRS 155679], p. 60). It next flowed for 10 to 12 hours on March 11, 1995, in upper-basin reaches as the result of a regional rainstorm, and was probably amplified by rainfall-induced snowmelt from highlands north of Yucca Mountain (Beck and Glancy 1995 [DIRS 104463]). Stretches of the Amargosa River also flowed for 10 to 12 hours on the same day. This runoff event is important because it is the first documented storm wherein Fortymile Wash and the Amargosa River flowed simultaneously throughout their mainstream-channel reaches to Death Valley. The peak flow of 3,000 ft^3/s (85 m^3/s) that was recorded at the gauging station near Borehole UE-25 J-13, decreased to 1,200 ft^3/s (34 m^3/s) near Amargosa Valley (Tanko and Glancy 2001 [DIRS 159895], Table 2). A similarly triggered runoff, but of lower magnitude and intensity, occurred on February 22 and 23, 1998 (Tanko and Glancy 2001 [DIRS 159895] Table 2). Again, Fortymile Wash, with a peak flow of 200 ft^3/s (6 m^3/s), and the Amargosa River flowed simultaneously throughout their main stem-channel reaches to Death Valley.

Streamflow data collected in February 1998 verify that moderate runoff from the Yucca Mountain area can flow to Death Valley (Glancy and Beck 1998 [DIRS 155679], pp. 60 and 61). The recorded data indicate that, although throughflows are relatively infrequent, they are not rare. Fortymile Wash flowed six times during 15 years from March 1983 through February 1998, and at least eight times during the 29 years from 1969 to 1998 (Tanko and Glancy 2001 [DIRS 159895], Table 2; and Glancy and Beck 1998 [DIRS 155679], p. 61). Streamflow data for Fortymile Wash and Amargosa River collected during runoffs of 1995 and 1998 indicate that most, and possibly all, of the six, pre-1995 flows probably continued downstream to Death Valley (Glancy and Beck 1998 [DIRS 155679], p. 61).

3.4.3.3   Flood Potential

Because of heavy damage and loss of life from flash flooding, much attention has been directed to assessing flood potential in southern Nevada. Several principal investigations were conducted that are applicable to the Yucca Mountain region.

Crippen and Bue (1977 [DIRS 108874], p. 1, Figures 1 to 19) analyzed floods at 883 sites throughout the United States with drainage areas of less than 10,000 mi.[2] (25,900 km^2), and developed regional envelope curves relating drainage area to peak discharge. These curves make it possible to estimate peak discharge of a basin from its area, which generally is known. The curve for Region 16, which includes most of Nevada (Crippen and Bue 1977 [DIRS 108874], Figure 18) was modified by Crippen (1982 [DIRS 108887], Figure 2). None of the local floods recorded approach the magnitude of the regional maximum discharges estimated by the Crippen and Bue (1977 [DIRS 108874]) or Crippen (1982 [DIRS 108887]) data.

Moosburner (1978 [DIRS 108876], p. 1) summarized peak discharges, gauge heights, and flood dates at continuous record stream gauges, and peak flow measurements at other stream sites throughout Nevada through the water year 1977. Moosburner (1978 [DIRS 108876], Figure 2) presented a graph relating peak discharge per unit area to drainage area for selected stations.

Several investigations have been carried out to determine the flooding potential of specific areas in the vicinity of Yucca Mountain. These include investigations of Topopah Wash in eastern Jackass Flats (east of Yucca Mountain, Figure 7-5b), Fortymile Wash and southwestern tributaries (east of Yucca Mountain), and Drill Hole Wash (on the eastern flank of Yucca Mountain).

Christensen and Spahr (1980 [DIRS 108879], p. 21) used records of 71 gauged basins in Nevada to estimate 100-year, 500-year, and maximum potential floods in the Topopah Wash area. Typical cross sections of peak stages and a map showing estimated areas of inundation for various recurrence frequencies were presented by Christensen and Spahr (1980 [DIRS 108879], Figure 7 and Plate 1).

Squires and Young (1984 [DIRS 102783], pp. 15 and 31) used records of 12 gauging stations adjacent to the Nevada Test Site to estimate 100-year and 500-year flood magnitudes of Fortymile Wash and its principal southwestern tributaries, Busted Butte (now Dune), Drill Hole, and Yucca washes. The Region 16 envelope curve of Crippen and Bue (1977 [DIRS 108874], p. 15) was used by Squires and Young to estimate the regional maximum floods. Squires and Young (1984 [DIRS 102783]) presented typical cross sections of peak stages (Figures 14 to 17) and a map (Plate 1) showing estimated areas of inundation for various recurrence frequencies.

Bullard (1986 [DIRS 100107], p. 2, Plates 2 and 3, and Table 10) developed probable maximum flood hydrographs for 15 sites within 11 small drainage basins on Yucca Mountain when vertical shafts were being planned to access the repository rock strata. Four additional probable maximum flood hydrographs were also developed for sites just downstream of the confluence of two upstream drainage basins by adding the results of the upstream probable maximum flood hydrographs (Bullard 1986 [DIRS 100107], pp. 2 and 8). Both local and general maximum precipitation events were used to compute probable maximum floods (PMFs) for the 11 small drainage basins, which ranged in area from 0.01 to 4.31 mi.[2] (0.03 to 11.2 km^2) (Bullard 1986 [DIRS 100107], p. 2 and Table 10).

Bullard's local probable maximum flood peak discharges ("Thunderstorm PMF") ranged from 245 to 43,300 ft^3/s (7 to 1,230 m^3/s), and volumes ranged from 7 to 3,096 acre-ft (8,600 to 3,819,000 m^3). The general probable maximum flood peak discharges ("General Storm PMF")

ranged from 16.8 to 6,419 ft^3/s (0.48 to 182 m^3/s), and volumes ranged from 4 to 2,169 acre-ft (4,900 to 2,674,000 m^3) (Bullard 1986 [DIRS 100107], Table 10). As local probable maximum floods always have larger peaks and volumes than general probable maximum floods, the former is preferable to the latter for design purposes (Bullard 1986 [DIRS 100107], p. 8). The probable maximum flood peak discharges of Bullard (1986 [DIRS 100107]) are larger than a regional maximum flood envelope curve and local gauge flood data.

Bullard (1992 [DIRS 108883], Table 1 and Figure 2) developed probable maximum flood hydrographs for an additional seven sites at Yucca Mountain when tunnels instead of shafts were being planned to access the repository rock strata. Only local precipitation events were used to compute probable maximum floods for the small drainage basins of interest, because Bullard's (1986 [DIRS 100107], p. 8) study showed this to be the preferred design storm. The probable maximum flood peak discharges ranged from 360 to 33,500 ft^3/s (10.2 to 949 m^3/s), and volumes ranged from 14 to 2,800 acre-ft (17,300 to 3,450, m^3) (Bullard 1992 [DIRS 108883], Figures 17 and 22). As can be seen in Figure 7.3-1 (see also Bullard 1992 [DIRS 108883], Figure 24), the probable maximum flood peak discharge (as computed by Bullard) is significantly higher than the regional maximum flood as estimated by the USGS envelope curve, especially for the smallest drainage areas.

Blanton (1992 [DIRS 100530], p. 2 and 3) computed new probable maximum floods for the Bullard (1992 [DIRS 108883]) sites using a bulking factor of two (proposed by the U.S. Bureau of Reclamation) to account for increased flow depths caused by the presence of entrained air, debris, and sediment load relative to clear water flow. Blanton (1992 [DIRS 100530], p. 3) applied this bulking factor to adjust the Bullard (1992 [DIRS 108883]) clear water probable maximum flood hydrographs. Blanton then routed the adjusted hydrographs through measured cross sections and plotted maximum flood inundation areas (Blanton 1992 [DIRS 100530], p. 7).

In 1999, additional hydrologic engineering studies were initiated in the area of the North Portal Pad. These studies reviewed the previous work of Blanton (1992 [DIRS 100530]) and Bullard (1986 [DIRS 100107]; 1992 [DIRS 108883]) in light of existing and planned surface modifications. The proposed modifications included a centralized interim storage facility and rail access via a railroad/highway bridge (trestle). When these studies are completed, the results will be reported in future Yucca Mountain Project documents.

Stream gauging data used in USGS national and regional reports (Crippen and Bue 1977 [DIRS 108874]; Moosburner 1978 [DIRS 108876]; Thomas et al. 1994 [DIRS 108885]) were collected under standard methodologies described in Section 7.1.4. The regional paleoflood data analyzed and interpreted by Ely (1997 [DIRS 108873]) were derived from many other investigations listed in Ely (1997 [DIRS 108873], Table 1).

The studies of flood potential of specific areas in the Yucca Mountain region used two principal data sources; USGS stream gauging records and National Weather Service Hydrometeorological Report 49, *Probable Maximum Precipitation Estimates, Colorado River and Great Basin Drainages* (Hansen et al. 1977 [DIRS 108888]).

3.4.4 Variability in Quaternary Processes

The kinds and rates of geomorphic processes on Yucca Mountain have varied considerably during the Quaternary in response to the many cycles of climate change that took place. At present, semiarid conditions prevail in the southern Great Basin. During much of Quaternary time, however, cooler and wetter conditions existed (Forester et al. 1999 [DIRS 109425]); thus most of the surficial deposits mapped on and around Yucca Mountain are the products of climatic conditions that were different from the present. Under the present climate, the landscape is dominated by warm temperatures and eolian processes, with infrequent storms producing localized runoff, whereas during cooler and wetter climates, there were changes in the type and density of vegetation, increases in runoff and streamflow, and the potential for longer periods of freezing. Because rates of erosion vary under different climates, a model of landscape response is described below to anticipate how geomorphic processes may change at Yucca Mountain in the future.

3.4.5 Model of Landscape Response to Quaternary Climate Change

The model of landscape response proposed for the Yucca Mountain region is an area-specific modification that builds upon the general semiarid landscape model of Bull (1991 [DIRS 102040], Chapters 3, 4). The landscape model is primarily driven by climate change and emphasizes different depositional and erosional processes that were active, especially on hillslopes, during different phases of the Quaternary climatic cycle. Several factors help to determine the texture and volume of sediments derived during a specific climatic phase, including: (1) amplitude and duration of climate change in terms of differences in both temperature and precipitation; (2) the type and distribution of both summer and winter precipitation; and (3) the sensitivity of the bedrock (Bull 1991 [DIRS 102040], p. 159, Table 3.5) to effects of these climatic changes. Rock types that have a high climatic sensitivity (e.g., coarse-grained granites) respond to wetter climate by weathering rapidly, a process that produces large quantities of relatively fine-grained material resulting in high volumes of hillslope sediment that is delivered to adjacent lowlands. Conversely, rock types that are more resistant to climate change (e.g., welded tuffs) respond slowly to wetter climate and may show little response to either a short-term or small-amplitude (or both) climate change. During long, wetter phases, such rock types, which dominate the bedrock at Yucca Mountain, may produce only small quantities of fairly coarse-grained sediments that result in thin, coarser-grained alluvial basin deposits.

In the landscape response model for the Yucca Mountain region, major geomorphic work (i.e., erosion and deposition) occurs primarily during climatic transitions, with times of more stable climate being times of relative landscape stability. The greater the magnitude in temperature and precipitation fluctuations during these transitions, the greater the landscape response. Thus, the times of climate transition are the times during which more rapid modification of the landscape occurs.

The landscape-response model to climate change in the Yucca Mountain region ideally has four phases, with the following primary characteristics:

1. Pluvial (full glacial) conditions are generally characterized by much wetter and colder conditions than now exist. Bedrock weathering occurs by both block extraction, caused by freeze-and-thaw processes (Whitney and Harrington 1993 [DIRS 107303], p. 1016), and by other physical weathering that results in reduction of initial block size. Chemical weathering processes are relatively ineffective and may produce only minor granular disintegration and small amounts of fine-grained material. The quantity of large blocks and smaller clasts that are produced depends upon the duration of the colder and wetter conditions. The dominant hillslope process that moves material downslope is rock-and-soil creep. Deposition of bouldery colluvium, produced during cold pluvial conditions, protects parts of the lower hillslope from subsequent debris-flow stripping (Whitney and Harrington 1993 [DIRS 107303], p. 1016). Colluvial aprons that cover the lower hillslope form during these climatic episodes and, if conditions persist long enough, grow headward up the hillslope until they reach the hillslope summit. Hillslope surface stability is enhanced by vegetation, which results in low-sediment yield into stream-valley drainage. Streams may incise through alluvium and form stream terraces. Wetter periods are times of accelerated soil formation as eolian-deposited carbonate is moved by water from near the surface to deeper within the soil, resulting in formation of carbonate horizons. During these wetter periods, fine-grained materials also accumulate in soil horizons. Pluvial conditions result in the chemical weathering of material in this soil zone to produce a fine-grained (silt-and-clay rich) reddish horizon.

2. The pluvial to interpluvial (interglacial) climatic transition is characterized by progressively warmer and typically drier conditions that result in lower vegetation density, especially on hillslopes, which become progressively destabilized. Sediment yield from the hillslopes increases primarily through debris-flow transport of previously weathered material to the basin floor. Physical erosion of bedrock on the hillslope is not an efficient process, as evidenced by a lack of incised bedrock channels on the hillslope. Instead, broad, shallow channels are only minimally cut into the hillslope bedrock. A change in precipitation regimes occurs from relatively equally distributed seasonal precipitation of the pluvial conditions to drier summers with infrequent thunderstorms. Debris-flow stripping of hillslopes occurs during infrequent, high-intensity, short-duration thunderstorms, resulting in alluvial fan building and valley aggradation. Eolian activity may increase.

3. Interpluvial (interglacial) conditions are characterized by much warmer and generally drier conditions. Low-intensity and infrequent high-intensity precipitation and runoff result in low-vegetation density, with little to no grassland. Infrequent hillslope stripping results in local aggradation and fan building. Main valleys aggrade slowly or remain essentially stable, whereas smaller washes aggrade more quickly. Deposition of eolian silt dominates surfaces and enhances carbonate buildup in near-surface soils, forming Av (vesicular) soil horizons beneath desert pavements. Eolian fine-grained material is also deposited on hillslopes within the matrices of boulder deposits (Whitney and Harrington 1993 [DIRS 107303], p. 1015). Sporadic, large-sediment

yield from hillslopes continues until most colluvium has been removed; then hillslopes begin to stabilize as a result of a lack of sediment that can be moved toward the basins.

4. The interpluvial to pluvial transition is characterized by progressively greater and more seasonally equal precipitation and cooler temperatures. Increasing precipitation results in increased vegetation density, greater hillslope stability, and lower hillslope sediment yields. Hillslope deposition begins as increased vegetation density retards removal of hillslope colluvium and enhances trapping of eolian material on the hillslopes. As more sediment is trapped on hillslope and runoff increases from greater precipitation, trunk streams change from aggradation to incision in valley segments above stable base levels.

3.4.6   Quaternary Erosion Rates at Yucca Mountain

Erosion rates were examined on hillslopes and bedrock outcrops on ridge crests in the Yucca Mountain site area. Initially, the surface exposure age of hillslope boulder deposits was calculated using the rock-varnish, cation-ratio dating method (Harrington and Whitney 1987 [DIRS 106095], pp. 967 to 970). Subsequently, cosmogenic beryllium-10 was also used to determine vertical erosion rates on bedrock outcrops on ridge crests of Yucca Mountain. Comparison of various dating methods had shown that the beryllium-10 method is the most reliable.

3.4.6.1   Erosion Rates on Bedrock Ridges at Yucca Mountain

On the ridge crests of Yucca Mountain, exposed bedrock outcrops are eroded by exfoliation (detachment of thin-rock sheets) and grusification (the grain-by-grain weathering of rock). The cosmogenic beryllium-10 method was chosen over other dating methods because of its usefulness in directly determining, for a sampled outcrop, the maximum possible rate of bedrock erosion (Faure 1986 [DIRS 105559], pp. 419 and 420), assuming that erosion proceeded at a gradual and constant rate over the exposure duration. The vertical bedrock erosion rate is calculated from the measurement of a single nuclide (beryllium-10) in multiple surface samples. The concentration of a cosmogenic nuclide is controlled by the production rate of that isotope and by the erosion of the surface. If the exposure time is considered infinite, the maximum erosion rate, based on a measurement of that concentration, can be calculated.

Analyses of beryllium-10 concentrations in quartz separates from tuffaceous bedrock exposed on Antler Ridge and the adjacent ridge to the south (Figure 3-2), on the east flank of Yucca Mountain, indicate a maximum possible erosion rate of bedrock to range from 0.04 to 0.27 cm/k.y. (0.016 to 0.106 in./k.y.) (CRWMS M&O 1998 [DIRS 103514], p. 3.4-40, Table 3.4-6). This low rate, which integrates all erosion that has taken place along these ridge crests during all, or at least a large part of, the Quaternary indicates a remarkable erosion stability for the Yucca Mountain landscape. Such a rate was confirmed by a study involving a 1-Ma basalt flow in Crater Flat about 4.5 km (2.8 mi) west of the site area (see Section 2.3.5.1), also based on cosmogenic beryllium-10 dating of exposed surfaces, shows a maximum erosion rate of the lava to be 0.02 cm/k.y. (0.008 in./k.y.) (20 cm [0.66 ft] since the flow cooled; see CRWMS M&O 2000 [DIRS 151945], Section 7.4.2.3).

3.4.6.2 Hillslope Erosion Rates from Dated Colluvial Boulder Deposits

Surface exposure ages of relict boulder deposits on Yucca Mountain and nearby hillslopes were dated to calculate the long-term rate of removal of unconsolidated material on the middle and lower hillslopes of Yucca Mountain. In addition, the depth of erosion in a 50 m (164 ft) zone on either side of the deposit, including channel incision, was measured (YMP 1993 [DIRS 100520], Table 5). The paleotopographic hillslope surface was assumed to be represented by the top of the boulder deposit on the hillslope. Because of the present low relief across the middle hillslope (2 m [6.6 ft] maximum), and inasmuch as stripping of hillslopes by debris flows is the dominant process presently moving material down these hillslopes, the modern relief on these hillslopes is probably a maximum for much of the late Quaternary.

Boulder deposits, with boulders 0.3 to 2 m (1 to 6.6 ft) in diameter, range from wide continuous mantles to isolated narrow bands that typically are bounded by gullies. Eleven such deposits were sampled (Whitney and Harrington 1993 [DIRS 107303], p. 1013) for cation-ratio dating (Table 3-3): six on the flanks of Yucca Mountain, three on the southwest hillslope of Skull Mountain (20 km [12.4 mi] to the east; Figure 2-2), one on the northeast slope of Little Skull Mountain (10 km [6.2 mi] to the southeast; Figure 2-2), and one on the east slope of Buckboard Mesa (25 km [15.5 mi] north-northeast of Yucca Wash). The erosion rate was calculated based on the amount of erosion that had occurred on the hillslope since the boulder deposit formed, divided by the surface-exposure age of the deposit. Both the rock varnish cation ratio and the in situ cosmogenic nuclide dating methods (Harrington and Whitney 1987 [DIRS 106095], Figure 1, p. 968; Whitney and Harrington 1993 [DIRS 107303], pp. 1013 and 1014; Gosse et al. 1996 [DIRS 105757], pp. 135 to 142) were applied. (See Section 7.4.2.2 of the YMSD (REV 01), CRWMS M&O 2000 [DIRS 151945], for a detailed discussion on rock varnish and cosmogenic dating of these deposits). The estimated varnish cation ratio ages of the analyzed samples range from 140 ka to 1,510 ka as shown in Table 3-3. Of the various dating methods used the beryllium-10 method is the most reliable. Ages of several of the sampled deposits by cosmogenic dating are given in Table 3-4. The long-term erosion rates from stripping of unconsolidated material from Yucca Mountain hillslopes were calculated to be less than 0.6 cm/k.y. (0.2 in./k.y.) (average of about 0.2 cm/k.y. [0.08 in./k.y.], based on a range of 0.02 to 0.6 cm/k.y. [0.008 to 0.24 in./k.y.]; YMP 1993 [DIRS 100520], Table 5).

3.4.6.3 Hillslope Erosion during the Latest Pleistocene-Holocene Interval

The climatic cycles recorded within the valley alluvium in Fortymile Wash and Midway Valley indicate a general landscape stability, punctuated by short pulses of either hillslope stripping or valley incision. The presence of relict boulder deposits that cover parts of most hillsides is evidence that hillslope stripping was incomplete, even through several climate cycles. The time interval during which surficial unit Qa5 (latest Pleistocene-Holocene, 18 to 2 ka; see Figure 3-18 and Section 3.3.7.2.6) was deposited in Midway Valley and Fortymile Wash can be used to estimate the amount of erosion taking place on Yucca Mountain hillslopes within the 18- to 2-ka period. This period covers the last pluvial to interpluvial transition, which was a time of climatic change to semiarid conditions that favored erosional stripping of hillslope sediment. Based on: (1) an average thickness of 1 m (3.3 ft) for unit Qa5 (Swan et al. 2001 [DIRS 158784], p. 17) covering a depositional area of approximately 5.2 km^2 (2 mi^2) in Midway Valley, and (2) a source area of exposed hillslopes contributing eroded material totaling about 19.5 km^2 (7.5 mi^2),

the estimated mean depth of unconsolidated material removed from hillslopes along the east side of Yucca Mountain to form the volume of sediments represented by unit Qa5 is 27 cm (0.9 ft). Assuming that this mean depth of erosion took place during the 16-k.y. period of Qa5 deposition, an erosional rate of 1.7 cm/k.y. (0.7 in./k.y.) is indicated, although it should be noted that this rate does not incorporate either the addition of eolian sediments to the hillslopes or the amount of detritus that moved through Midway Valley and into Fortymile Wash. If unit Qa5, on the other hand, was considered in terms of bedrock erosion (the density of the tuffaceous rocks is about one-third greater than the unconsolidated sediments), the amount of bedrock eroded was 18 cm (7 in.), which computes to a rate of 1.1 cm/k.y. (0.43 in./k.y.).

In the 10 k.y. prior to Qa5 deposition, the climate was wetter, hillslopes were more densely vegetated, and little material was being removed from the surrounding hillslopes. The erosion rate for the complete climatic cycle, from 28 to 2 ka for the Yucca Mountain hillslopes, was, therefore, 1.04 cm/k.y. (0.41 in./k.y.) for unconsolidated material and 0.7 cm/k.y. (0.27 in./k.y.) for hillslope bedrock.

3.4.6.4 Hillslope Erosion near Yucca Mountain during a 1984 El Niño Storm

During a two-day storm in July 1984, several debris flows were triggered on Jake Ridge, located in the northeast corner of the Yucca Mountain site area (Figure 3-2). Rainfall intensities ranged up to 73 mm/hr (2.9 in./hr) during this unusual El Niño storm that stalled over the south slope of Jake Ridge. Using digital elevation models from aerial photographs taken before and after the storm, a debris volume of 7,040 m^3 (249,000 ft^3) was redistributed during the two-day storm (Coe et al. 1997 [DIRS 104691]). The maximum and mean depths of erosion in the study area were about 1.8 m and 5 cm (6 and 1.6 ft), respectively. The mean depth of deposition on the lower hillslope was 16 cm (0.52 ft). It is difficult to assess the recurrence of such an extreme erosional event. However, Coe et al. (1997 [DIRS 104691]) suggested that the recurrence interval is significantly longer than 500 years.

3.4.6.5 Erosion on Volcanic Landforms in Crater Flat

Surface exposure dating and radiometric ages of basaltic flows and cones show that erosion of topographic highs in the vicinity of Yucca Mountain has proceeded very slowly. Erosional modification of flows was evaluated at the Black Cone center where the flows erupted approximately 1 Ma. Rock samples for cosmogenic ^{10}Be analysis were collected from an outcrop of degraded pressure ridge where a K-Ar age of 1.0 ± 0.1 m.y. was obtained (CRWMS M&O 1998 [DIRS 123196], Table 2.B, p. 2-13). Cosmogenic ^{10}Be surface exposure ages, adjusted for existing shielding conditions and assuming no recent erosion of the rock surface because of the presence of thick continuous coatings of rock varnish, are 1,000, 750, 550, and 440 k.y. The minimum exposure age of the lava is taken to be the approximately 1,000-k.y. date because all geologic factors affecting the exposure history of the flow surfaces (erosion, burial, uncompensated shielding) will result in exposure ages that are younger than the true age. The measured ^{10}Be in these samples could have originated only from cosmic ray bombardment of the lava surface after the flow cooled. This exposure age is similar to and consistent with a K-Ar age of 1.0 ± 0.1 m.y. (CRWMS M&O 1998 [DIRS 123196], Table 2.B, p. 2-13) for the time of flow deposition, and overlaps each of three other K-Ar ages reported by CRWMS M&O (1998 [DIRS 123196], Table 2.B, p. 2-13).

A maximum erosional lowering of the flow surface was calculated for the sample with the greatest exposure age in order to constrain the amount of erosion that has occurred on this bedrock outcrop since deposition of the flow. The maximum erosion rate at this site is 0.02 cm/k.y., assuming constant, gradual erosion. Using this erosion rate, the total eroded material from the flow surface at this site since the time of deposition is approximately 20 cm, and for the other sites with younger exposure ages is still less than 1 m. This low erosion rate on the crest of a pressure ridge on the Black Cone flows indicates that erosion of such volcanic features occurs very slowly in this area and that volcanic rocks are relatively insensitive to the range of climatic conditions that have existed in the Yucca Mountain area since the mid-Quaternary.

The low erosional rates for the Crater Flat basalts can be explained by a model that includes armoring by desert varnish. The evolution of stable surfaces on lava flows starts with minor erosional degradation of the primary surfaces of the flow soon after deposition. Rock varnish accumulation then begins on these semi-stable surfaces. The erosional stability of the rock surfaces would be enhanced by continuing deposition of rock varnish until the rock surface is completely covered by a fairly thick coating of varnish. Varnish accumulation ultimately results in the long-term stability of these rock surfaces. This hypothesis is supported by field evidence from boulder deposit clasts that commonly possess little to no weathering rind on the rocks beneath the rock varnish coating, indicating that formation of an impermeable rock varnish coating began soon after boulder deposition.

As noted earlier, both the approximately 1-Ma cinder cones and the younger (approximately 80 ka) cinder cone of Lathrop Wells have retained much of their original morphology. In the latter case, Wells et al. (1990 [DIRS 107208], p. 551) concluded that the cone slope is virtually unmodified by erosion, such that the morphology is similar to the 15- to 20-ka cones of the Cima volcanic field.

3.4.7 Erosional History of Fortymile Wash

Fortymile Wash (Figure 3-2), a principal tributary of the Amargosa River drainage basin lying within the site area, flows through the 25 km (15.5 mi)-long Fortymile Canyon, then continues southward for about another 20 km (12.4 mi) along the east side of Yucca Mountain before entering the eastern part of the Amargosa Desert (Figure 2-2; see Section 3.2.1.3). Between the mouth of the canyon and the Amargosa Desert, the stream channel is entrenched as much as 25 m (82 ft) in alluvial fill. The depth of incision decreases over a 6 km (3.7 mi) reach, where the channel becomes the head of a long fan that crosses the Amargosa Desert. Analysis of the Fortymile Canyon sedimentary provenance and altitude distribution of volcanic rocks (Lundstrom and Warren 1994 [DIRS 106326], p. 2121) indicates that the canyon was formed during the late Miocene or Pliocene, sometime before 3 Ma. A relict gravel deposit exposed in Fortymile Wash contains a different lithology than the Quaternary gravel fills, probably indicating that the present drainage captured a formerly northward-flowing drainage along the moat of the Timber Mountain caldera (Figure 2-4), north of the site area, sometime after 9 Ma and before 3 Ma.

The summary of the alluvial and incision history of Fortymile Wash that follows is based largely on detailed descriptions and interpretations presented in Section 7.4.2.5 of the YMSD (REV 01) (CRWMS M&O 2000 [DIRS 151945]).

The stratigraphy of the surficial deposits, within and flanking Fortymile Wash, records a complex history of aggradation and channel incision, as shown diagrammatically in two cross sections: (1) the northern one (Figure 3-19) located at a point between Alice Ridge west of the wash (Figure 3-2) and the western toe of what is termed the Calico Fan across the wash to the east at the east edge of the site area; and (2) the southern one (Figure 3-19) located near the Yucca Mountain road crossing, which is 4 km (2.5 mi) north and 1.3 km (0.8 mi) east of the southeast corner of the site area (locations shown in Figure 3-7). Evidence for multiple episodes of downcutting can be seen by comparing the different stratigraphic sequences on the east and west walls of the two cross sections. At the Yucca Mountain road crossing (Figure 3-19), there are four coarse, gravelly alluvial units on the west wall, each capped by a soil representative of pluvial conditions when vegetation was dense and the stream channel was not being aggraded. The buried soils on the west wall are missing from the east wall, indicating that the alluvial fill on the east side of the wash wall is older than the 50 to 100 ka soils at the top of the fill, but younger than the 300 to 500 ka buried soil exposed in the west wall. Farther north, at the Calico fan site, the 170 ka buried soil on the west side is missing on the east wall (Figure 3-19; note that these older ages are based on determinations by the U-series dating-method). Exposed in gullies in the east wall are late-Tertiary gravels and middle-Pleistocene eolian deposits that are overlain by Qa3 alluvium. These unconformities are evidence of at least two episodes of downcutting that predate the deposition of that unit. If the 170 ka age on the buried soil in the west wall is valid, then a major incision and erosion of the older alluvium took place during the climatic time of oxygen isotope stage (OIS) 6 of the global climate record (derived from marine cores; see Imbrie et al. 1984 [DIRS 100047]), the wettest climatic episode at the end of the middle Pleistocene. This is the same time that the largest and last deep (depth greater than 90 m [295 ft]) lake existed in Death Valley (Forester 1999 [DIRS 130125], p. 69; Lowenstein 1999 [DIRS 130132], p. 142), as noted in Section 3.4.8.

The alluvium of Qa3 (Figure 3-19) that underlies the main Fortymile Wash stream terrace was subsequently deposited during the interglacial OIS 5e-5a, and it has developed a soil that is primarily of OIS 4 age.

The most recent incision of Fortymile Wash (Lundstrom et al. 1996 [DIRS 136523], p. A-522) probably took place during the latter part of the pluvial episode, OIS 4 (Winograd et al. 1988 [DIRS 109186], p. 1277, Figure 4), from about 116 to 60 ka, and the early part of OIS 3 (about 55 to 40 ka). Within 2 m (6.5 ft) of the present channel of Fortymile Wash are remnants of a strath terrace with a thin alluvial deposit mapped as Qa4 at the Yucca Mountain road crossing (Figure 3-19). This terrace most likely represents a pause in the downcutting of Fortymile Wash during the relatively short interglacial climate represented by OIS 3. The last 2 to 4 m (6.5 to 13 ft) of incision probably occurred during the last pluvial climate at Yucca Mountain, 22 to 18 ka. Aggradation has taken place in the channel and on the lower Fortymile Wash fan, represented by Qa5 deposits, during the Pleistocene-Holocene transition and continuing through the Holocene to the present. Thus, the history of Fortymile Wash is consistent with the climatic-geomorphic, process-response model described in Section 3.4.6.

Based solely on thermoluminescence-dating of silt in sand-dominated horizons in soils capping the alluvial units in the west wall of Fortymile Wash, and the belief that the oldest dated deposit is less than 150 ka, Lundstrom et al. (1998 [DIRS 136539], pp. 69 to 74) advanced the interpretation that 13 m (43 ft) of aggradation occurred in the wash from 140 to 50 ka, followed by about 20 m (66 ft) of incision between 36 and 24 ka. This interpretation, however, does not account for the occurrence of buried soils in the west wall that are not present on the east wall (Figure 3-19). This is an important stratigraphic relation, indicating a much longer period (perhaps as much as 500 k.y.) of sediment accumulation along the wash.

In summary, a comprehensive interpretation of Fortymile Wash, using all buried soils and the U-series dates obtained from the central wash, reveals a complex history of four-to-five cut-and-fill cycles spanning the middle-to-late Quaternary. The incision in the wash occurred over a limited vertical range in elevation of not more than several tens of meters. Furthermore, the wash did not cut and fill the same channel each time, but, instead, migrated laterally across the Fortymile Wash fan. Thus, the channel during the middle and late Quaternary was incised during pluvial periods. Then, during the transition to interpluvial climates, when hillslopes were most actively stripped, the wash aggraded and migrated laterally prior to the next cutting cycle.

3.4.8 Regional Climatic Data Supporting Middle and Late Quaternary Incision in Fortymile Wash

The relative intensity and duration of the various cutting and filling cycles that are represented in Fortymile Wash need to be considered in a regional context (i.e., with respect especially to Death Valley) as to which climate cycle had greater water availability and for what time period. Two periods of extensive lake development, both with ascribed depths of 90 m (295 ft), have been described in Death Valley: (1) a freshwater lake, ranging in age from 216 to 150 ka as dated by the U-series method (Lowenstein 1997 [DIRS 109129]; Lowenstein 1999 [DIRS 130132], p. 142; U.S. Geological Survey [USGS] 2001 [DIRS 158378]); and (2) a saline lake, ranging in age from 35 to 10 ka (Li et al. 1997 [DIRS 148201], p. 1368). The presence of a large freshwater lake, which is considered to be the one that was 90 m (295 ft) deep, for more than 60 k.y. in Death Valley is interpreted to be a strong indication that there was far more available water on the landscape for a much longer period of time (correlative with OIS 6) than during the 25 k.y. duration of a saline lake (probably of much shallower depth) from 35 to 10 ka (generally correlative with OIS 2). It is, therefore, reasonable to conclude that more extensive incision occurred in Fortymile Wash during the 60 k.y. period of OIS 6 than during the 20 k.y. period of OIS 2.

3.4.9 Potential for Future Erosion and Deposition at Yucca Mountain

Most of the streams that drain eastward down the east slope of Yucca Mountain cross Midway Valley and flow into Fortymile Wash. Although the true base-level for these tributary valleys is Fortymile Wash, the effective base-level is the floor of Midway Valley, which is presently undergoing aggradation because of the existing interpluvial, warm and dry climate. Since at least the beginning of the Holocene, local storms have activated debris-flow stripping of the hillslopes around Midway Valley, resulting in a rising base-level as sediments accumulate on the valley floor. If a period of incision were to ensue as a result of a change in climate to one of greater effective moisture, the main drainage course in Midway Valley would ultimately start to

incise its valley floor, then erode headward, thereby initiating a period of downcutting in the tributary valleys and the removal of channel-fill deposits. If this climatic condition continued for a long enough period of time, potentially all of the alluvium in these valleys would be moved to the floor of the valley.

However, exposure of the fill in Coyote Wash, located immediately south of Dead Yucca Ridge (Figure 3-2), demonstrates that such a complete emptying of the alluvium in the tributary valleys did not occur during the last glacial cycle (Glancy 1994 [DIRS 101227]). Relict Pleistocene fill documents the incomplete stripping of the valley alluvium during the last two climatic cycles. The climate change to a regime favoring sediment removal that began approximately 28 ka did not last long enough to allow complete sediment removal from these tributary valleys. Since approximately 15 to 18 ka, when the climate began to become drier, these valleys have been in an aggradation mode. The incomplete removal of hillslope and valley alluvium in the tributary valleys during the 10,000 to 13,000 wet years of the last climate cycle indicates that more than 10 k.y. is needed to remove alluvium from these valleys, assuming that the climate for that time interval was favorable for erosion. Based on the Coyote Wash data regarding erosion in the valleys along the east slope of Yucca Mountain, it would require substantially more than 10 k.y. to effectively remove the alluvium and to begin actively eroding the bedrock floors of the washes. Because evidence shows that aggradation and degradation cycles respond to regional climatic changes, there is no indication, based on an analysis of future climates in the Yucca Mountain region by the USGS (2001 [DIRS 158378]), that another period of downcutting of more than a few meters will occur in Fortymile Wash and its tributaries within the next 10 k.y.

Another important factor to consider, relative to future incision of Fortymile Wash and its tributaries, is that the effective base-level for Fortymile Wash is the broad expanse of the surface of Amargosa Valley alluvium. No substantial incision within the present valley of Fortymile Wash is possible unless a major incision, or deep headcut, occurs far downstream in the present Amargosa River valley, migrates some 60 miles (100 km) or more upstream through the present fill of Amargosa Valley, and continues headward through the present alluvial fan of Fortymile Wash. Headcutting across the Amargosa Valley over the next 10 k.y. seems unlikely, not only because of the long distance involved, but also because no evidence of earlier Quaternary valley incision has been found along the Amargosa River.

3.5   SITE STRUCTURAL GEOLOGY

3.5.1   Introduction

The structural geology of Yucca Mountain and vicinity is dominated by a series of north-striking normal faults along which Tertiary volcanic rocks were tilted eastward and displaced hundreds of meters, predominantly down-to-the-west primarily during a period of extensional deformation in middle-to-late Miocene time (Figure 3-20). These through-going faults divided the site area into several structural blocks, each of which is further deformed by minor faults. The complex pattern of faulting is shown in detail on two bedrock geologic maps based on extensive field investigations that were conducted largely in 1996 and 1997 as an integral part of the Yucca Mountain site characterization program. The two maps are: (1) a 1:24,000 scale map by Day et al. (1998 [DIRS 100027]) covering the 165 km^2 (65 mi^2) of the site area (Figures 3-1 and 3-2), and (2) a 1:6,000 scale map by Day et al. (1998 [DIRS 101557]) covering 41 km^2 (15.7 mi^2) of

the central part of the site area that includes the repository block itself. At these scales, it was possible to map individually many of the stratigraphic subdivisions (zones, some subzones, and bedded-tuff units) within various volcanic formations (see Section 3.3.4) and to record faults, generally with displacements as little as 5 m (16 ft) at the 1:24,000 scale and as little as 1.5 m (5 ft) at the 1:6,000 scale. The map by Day et al. (1998 [DIRS 100027]) incorporated the work of Dickerson and Drake (1998 [DIRS 102929], map scale 1:6,000) in the northeastern part of the site area.

The studies by Day et al. (1998 [DIRS 100027]) and Day et al. (1998 [DIRS 101557]) benefited substantially from earlier mapping and structural interpretations of areas within and around the site area by Christiansen and Lipman (1965 [DIRS 100566]), Lipman and McKay (1965 [DIRS 104158]), and Scott and Bonk (1984 [DIRS 104181]). The latter map, at a scale of 1:12,000 and considered to be largely reconnaissance in nature, was particularly useful, in that numerous zones within the Tiva Canyon and Topopah Spring tuffs (the principal bedrock units at Yucca Mountain; see Section 3.3) were defined and mapped, resulting in the delineation of minor faults not previously recognized. Regional map compilations by Frizzell and Shulters (1990 [DIRS 105454]) and Potter et al. (2002 [DIRS 160060]) place the geology of Yucca Mountain in a regional context (see also, Section 2).

In addition to the maps mentioned above, Simonds et al. (1995 [DIRS 101929]) compiled a 1:24,000 scale fault-map that incorporated all known information on Quaternary to recent fault activity in the Yucca Mountain area. This map served as a guide for the trenching and detailed study of exposed surficial deposit sequences to determine the extent, magnitude, and ages of Quaternary deformational events. Studies of the structural relations exposed in the trench excavations are described in a series of published reports (Keefer et al. 2003 [DIRS 159419]).

Detailed maps and descriptions of faults and fracture systems encountered in the ESF and cross drift have been presented in several reports, including Mongano et al. (1999 [DIRS 149850]) and those identified by the data tracking numbers (DTNs: GS971108314224.020 [DIRS 105561], GS971108314224.027 [DIRS 160064], GS970208314224.005 [DIRS 109597], and GS971183117462.001 [DIRS 158751]). Discussions in this section (Section 3.5) of specific geologic structures use summary data from these reports where those structures are exposed in the ESF and cross drift.

The faults at Yucca Mountain display anastomosing geometries in plan view. Numerous bifurcations and splays are indicated by the merging and branching of individual fault strands. These patterns indicate that many of the faults or fault splays are structurally interconnected along strike. The overall pattern suggests that the faults on the east and west sides of Yucca Mountain represent two major subparallel interconnected fault systems. How these systems are kinematically related to one another is not obvious from the mapping or from geophysical data. However, a number of factors suggest that distributed faulting events (i.e., simultaneous rupture on more than one individual fault), have occurred on both the east and west sides of Yucca Mountain. Fault characteristics that support distributed faulting include the following:

- Close spacing between faults

- Interconnectedness of many faults

- Timing of paleoseismic events (summarized in Pezzopane et al. 1996 [DIRS 106528])

- Patterns of principal and distributed faulting observed from historical earthquake ruptures in the Great Basin (Pezzopane and Dawson 1996 [DIRS 103265]).

Accounting for the various geologic processes, evidence exists for recurrent middle to late Quaternary fault displacement activity on the block-bounding Quaternary faults in the Yucca Mountain site area. At least two, and as many as eight, individual displacement events are evident. These events are associated with discrete displacements related to either individual or scenario earthquakes. The events due to fracturing and fissuring with no detectable offset are nearly as common as displacement events. The fracturing events, if tectonic in origin, record relatively frequent, small- to moderate-magnitude earthquakes that do not produce measurable rupture at the surface. Alternatively, they are a record of distributed faulting and fracturing produced by rarer, larger-magnitude, surface-rupture earthquakes on one of several nearby faults, or large distant earthquakes.

3.5.2 Description of Geologic Structures

The most conspicuous structural characteristic of the Yucca Mountain site area is its division into discrete, east-dipping structural blocks, each separated and bounded by north-trending, down-to-the-west normal faults (Figures 3-20, 3-21). Accordingly, the following discussions focus on features of these major block-bounding faults and the intervening, internally deformed structural blocks, which combine to form the area's basic geologic framework. This approach departs from that presented in an earlier version of the *Yucca Mountain Site Description* REV 01 (CRWMS M&O 2000 [DIRS 151945]), in which the site area was divided into 11 structural domains based largely on a distinction of local structures. The domain boundaries were mostly drawn to either: (1) include only small parts of an individual structural block, or (2) incorporate portions of adjacent structural blocks, thereby cutting across block-bounding faults and the prevailing structural grain of the site area (CRWMS M&O 2000 [DIRS 151945]). As a consequence, use of the domainal concept as the most appropriate means of distinguishing the primary structural patterns of Yucca Mountain is not continued. However, the term domain is applied in a more regional and conventional sense in a later discussion of tectonic models, following the definition of a Crater Flat structural domain by Fridrich (1999 [DIRS 118942]) that encompasses all of the structural features in the site area.

Another important difference between the present discussion of site structure and that given in CRWMS M&O (2000 [DIRS 151945]) is that the latter included the Dune Wash, Midway Valley, and Busted Butte faults as block-bounding faults, whereas, based on their limited areal extent or small displacements, or both (see Figures 3-20, 3-21), they are clearly minor features in comparison and, therefore, are more appropriately treated as intrablock faults. Additional detail on some faults, both major and minor, is included, based on more recent data from the ESF, cross drift, and boreholes.

3.5.3 Block-Bounding Faults

Block-bounding faults are spaced 1 to 5 km (0.6 to 3 mi) apart and include, from east to west within the site area, the Paintbrush Canyon, Bow Ridge, Solitario Canyon, Fatigue Wash, and

Windy Wash faults (Figure 3-20). The Crater Flat faults, lying west of the site area, are also included in the discussion of block-bounding faults because they form the west boundary of the structural block that occupies the northwestern-most corner of the site area. Fault descriptions are summarized primarily from: (1) bedrock geologic maps of Day et al. (1998 [DIRS 100027]; [DIRS 101557]) and Dickerson and Drake (1998 [DIRS 102929]); (2) a compilation of fault data by Simonds et al. (1995 [DIRS 101929]); (3) a regional geologic map compiled by Potter et al. (2002 [DIRS 160060]); and (4) a series of reports describing the results of mapping of trenches to determine the history of Quaternary deformation along the major faults, in and adjacent to, the site area (Keefer et al. 2003 [DIRS 159419]).

Displacements along block-bounding faults are mainly dip-slip (down-to-the-west), with subordinate strike-slip or oblique-slip components of movement exhibited by some faults. Seismic reflection data are interpreted to indicate that the faults penetrate and offset the Tertiary-Paleozoic contact between Yucca Mountain (Brocher et al. 1998 [DIRS 100022], Figure 6). Strain is transferred between block-bounding faults along relay faults that intersect the block-bounding faults at oblique angles and provide an intrablock kinematic link between some of the bounding structures. Fault scraps visible along many fault traces dip from 50° to 80° to the west.

3.5.3.1   Paintbrush Canyon Fault

The Paintbrush Canyon fault is the major block-bounding fault between Midway Valley to the west and the line of small ridges (Busted Butte, Fran, and Alice ridges) to the east (Figures 3-20 and 3-21). The fault is exposed for a distance of approximately 5 km (3 mi) in bedrock forming highlands north of Yucca Wash (Figure 3-2), where it is shown as a west-dipping (56° to 76°) normal fault. In that area, Paintbrush Group rhyolite lava flows are downdropped against rocks of the Topopah Spring and Pah Canyon tuffs and the Calico Hills Formation (Dickerson and Drake 1998 [DIRS 102929], Plates 1 and 2), and the fault trace is marked by a discontinuous, west-dipping fault-scarp 0.3 to 4.0 m (1 to 13 ft) in height.

The Paintbrush Canyon fault extends to the south beneath the alluvium of Midway Valley for some 5 km (3.1 mi) before strands are exposed for about 1 km in bedrock along the west side of Fran Ridge (Day et al. 1998 [DIRS 100027], Figure 3). A major splay trends southwest from a point toward the north end of Fran Ridge, circles around the west side of San Juan Hill, and joins the main trace toward the south end of Fran Ridge. From there northward, the fault length is 11 km (6.8 mi). However, it may continue southward for another 8 km (5 mi) to a possible intersection with the Stagecoach Road fault beyond the south edge of the site area (Figure 3-20), in which case the total fault length may be as much as 19 km (11.8 mi) (Potter et al. 2002 [DIRS 160060]). The Stagecoach Road fault forms that part of the east boundary of the Bow Ridge-Solitario Canyon structural block that lies south of the site area (Figure 3-20).

Estimates of the amount of bedrock displacement on the Paintbrush Canyon fault range from 210 m (690 ft) in the northern segment (Dickerson and Drake 1998 [DIRS 102929], Plate 1) to as much as 500 m (1,640 ft) along other segments (Scott and Bonk 1984 [DIRS 104181], Sheet 2). The fault also shows evidence of multiple surface-rupturing events during the Quaternary, causing offsets of 5.5 to 8.0 m (18 to 26 ft) in surficial deposits as measured in trenches and at

natural exposures at locations near Alice Ridge, Busted Butte, and in the southern part of Midway Valley (Menges et al. 2003 [DIRS 159412]).

3.5.3.2 Bow Ridge Fault

The Bow Ridge fault is well exposed along a 200 m (656 ft)-long segment on the west side of Exile Hill (Figure 3-2), where the Rainier Mesa Tuff is faulted down against the crystal-rich and crystal-poor members of the Tiva Canyon Tuff along a low fault-line bedrock escarpment (Day et al. 1998 [DIRS 100027]). From there north, it extends beneath surficial deposits to the north side of Yucca Wash, a distance of about 4 km (2.5 mi), and then continues for another 1.5 km (0.9 mi) to the north edge of the site area, cutting bedrock composed mostly of rhyolite lavas and the Pah Canyon Tuff of the Paintbrush Group. South of Exile Hill, the Bow Ridge fault is shown by Day et al. (1998 [DIRS 100027]) to extend southward beneath surficial deposits for about 3.25 km (2 mi) to a point where it is exposed in bedrock (Tiva Canyon Tuff is displaced) for a short distance along the west side of Bow Ridge (Figure 3-2). From there, the fault trace is projected to the southeast beneath alluvium for another 2.5 km (1.5 mi) to a possible intersection with the Paintbrush Canyon fault (Figure 3-20) for a total length of about 11.5 km (7.1 mi).

Bedrock is displaced about 125 m (410 ft) down to the west along the Bow Ridge fault at the west side of Exile Hill (Scott and Bonk 1984 [DIRS 104181], Sheet 2). The fault dips 75° to 80° W (Simonds et al. 1995 [DIRS 101929]) and net displacement is left-oblique. It was intersected 200 m (656 ft) inside the north ramp of the ESF, where it was observed to strike north-south and dip 75° W, and to downdrop the pre-Rainier Mesa Tuff bedded tuff against units of the Tiva Canyon Tuff with approximately 128 m (420 ft) of down-to-the-west dip-slip stratigraphic separation along a 2.7 m (8.9 ft) wide brecciated fault zone (DTNs: GS971108314224.020 [DIRS 105561]; GS971108314224.027 [DIRS 160064]). A north-trending fault with down-to-the-east dip-slip offset of 7 m (23 ft) in a 5 m (16 ft) wide fractured and brecciated zone was intersected some 235 m (770 ft) farther west in the ESF and is believed to be antithetic to, and to terminate against, the Bow Ridge fault at depth. This feature appears to correlate with a strand mapped at the surface in the hanging-wall block (Figures 3-20 and 3-21; see Day et al. (1998 [DIRS 100027]). Exposures in trenches that were excavated across projections of the Bow Ridge fault beneath surficial deposits at the Exile Hill locality, notably trench 14D described by Menges et al. (2003 [DIRS 159412]), revealed small-displacement Pleistocene faulting events, with a total offset of 0.5 to 1.22 m (1.6 to 4 ft).

3.5.3.3 Solitario Canyon Fault

The longest, continuously exposed fault trace in the site area is associated with the Solitario Canyon fault, which forms the western boundary of the central part of Yucca Mountain that contains the repository block. The main trace extends from the south margin of Yucca Wash, at the north edge of the mountain, to the south edge of the site area, a distance of about 14 km (8.7 mi), and then continues for at least another 3 km (1.9 mi) to where it is shown to have a possible connection with the Southern Windy Wash fault system (Potter et al. 2002 [DIRS 160060]). There are numerous associated fault splays, particularly toward the south end (Day et al. 1998 [DIRS 100027]; 1998 [DIRS 101557]; Scott and Bonk 1984 [DIRS 104181]).

The Solitario Canyon fault is well expressed along the east side of Solitario Canyon where, for much of its length, it forms a prominent fault-line scarp as much as 5 m (16 ft) in height along the bedrock-alluvium contact at the base of a large topographic bedrock escarpment (Figure 3-2). Bedrock faults split off the main-fault trace near the mouth of Solitario Canyon, and one connects to the southeast with a prominent, west-facing, fault-line scarp as much as 15 m (49 ft) high at the base of a prominent bedrock escarpment. This splay, referred to as the Iron Ridge fault (named by Scott 1992 [DIRS 106755]), extends southeast and south for 8 km (26 ft) and appears to intersect the Stagecoach Road fault south of the site area (Figure 3-20; Potter et al. 2002 [DIRS 160060]).

Along the northernmost 3-km-section of the Solitario Canyon fault within the site area, the displacement of bedrock (Tiva Canyon Tuff) is about 50 m (164 ft) down to the east. Displacements farther south, however, are all down to the west, as discussed below, so the fault demonstrates a scissors movement.

Along the central section of the Solitario Canyon fault, where two main strands were mapped by Day et al. (1998 [DIRS 100027]; see Figure 3-20), units of the Tiva Canyon Tuff in the hanging wall of the eastern strand were downfaulted against rocks of the Topopah Spring Tuff that form all but the upper slopes of the steep, west flank of Yucca Mountain (Figure 3-2). The down-to-the-west displacement is shown to be 450 m (1,476 ft) along a fault zone dipping about 65° W by Day et al. (1998 [DIRS 100027], Cross Section B-B'). Some left-oblique slip is also indicated by slickensides displayed locally on fault scarps. The western fault-strand is covered by surficial deposits for most of its extent. Farther south, the faulting involves units of the Topopah Spring Tuff, and the down-to-the-west displacement is less owing to the transfer of strain to fault splays.

A cross drift, branching off near the west end of the north ramp of the ESF, extends in a southwest direction to intersect the central section of the Solitario Canyon fault (Figure 3-20). Only the eastern strand was reached in the boring, at which point the fault plane is defined by an 8 to 12 cm (3 to 5 in.) thick zone of fault gouge separating rocks in the upper part of the crystal-poor member of the Topopah Spring Tuff in the hanging wall (west side) from rocks in the lower part of that member in the footwall. The down-to-the-west displacement is about 260 m (853 ft) (DTNs: GS990908314224.010 [DIRS 152631]; GS991108314224.015 [DIRS 151042]). The 260 m fault plane (853 ft) strikes N18°W and dips 62°W; slickenside rakes average 40°. Wide zones (30 to 40 m [98 to 131 ft]) of brecciation and fracturing are in both the hanging wall and footwall blocks, being most intense in the latter.

The Iron Ridge fault is a major splay trending south-southeast off the main trace of the Solitario Canyon fault (Day et al. 1998 [DIRS 100027]). It has an average dip of 68°W where observed at the surface, with down-to-the-west offset along the northern trace of the Iron Ridge fault, rocks in the uppermost Tiva Canyon Tuff are downdropped against the middle part of the Topopah Spring Tuff, a down-to-the west displacement of approximately 100 m (328 ft). Farther south, the amount of displacement increases to about 300 m (984 ft) (Day et al. 1998 [DIRS 101557]).

The Solitario Canyon fault was trenched at eleven locations along the fault trace, with most being sited where the fault extends beneath surficial deposits. Mapping of several of the excavations recorded evidence of multiple middle-to-late Quaternary surface-rupturing events

(Ramelli et al. 2003 [DIRS 159413]), with the total amount of displacement ranging from 1.7 to 2.5 m (5.6 to 8.2 ft) at various sites. One trench was excavated across the Iron Ridge fault, and at least one Quaternary faulting event occurred there, with a possible displacement of about 2 m (6.6 ft).

3.5.3.4 Fatigue Wash Fault

The Fatigue Wash fault is mapped as a nearly continuous 9 km (5.6 mi) long, south-southwest-trending fault along Fatigue Wash (Day et al. 1998 [DIRS 100027]). Except locally, where it forms a fault-line scarp at the base of bedrock escarpments (mainly Yucca Mountain and Pah Canyon Tuffs, and basal units of the Tiva Canyon Tuff) on the east side of the wash, the fault is buried by surficial deposits (Figure 3-2). From the mouth of Fatigue Wash, the fault is shown by Potter et al. (2002 [DIRS 160060]) to continue south for a distance of another 8 km (5 mi) to a possible intersection with splays of the southern Windy Wash fault south of the site area (also, see Simonds et al. 1995 [DIRS 101929]).

The amount of down-to-the-west displacement of bedrock toward the north end of the Fatigue Wash fault zone is about 100 m (328 ft), but where it emerges from Fatigue Wash to the south, displacement is about 400 m (1,312 ft) (Day et al. 1998 [DIRS 100027], Cross Section B-B'; see Figure 3-21). Average dip of the fault plane is 73°W (Simonds et al. 1995 [DIRS 101929]), and slickenside lineations indicate a moderate amount of left-slip movement.

Studies of surficial deposits exposed in trench excavations across the south-central segment of the Fatigue Wash fault, and measurements of scarp profiles near the trenches, provide evidence that five or more paleoearthquakes occurred on the fault since middle Pleistocene time (Coe et al. 2003 [DIRS 159411]). The amount of displacement of the Quaternary units ranges from 1 to 3 m (3.3 to 9.8 ft).

3.5.3.5 Windy Wash Fault

The Windy Wash fault is expressed as a prominent fault-line scarp on the east side of Windy Wash. It is traceable nearly continuously from the south rim of the Claim Canyon caldera, one of the eruptive centers in the southwestern Nevada volcanic field (Christiansen and Lipman 1965 [DIRS 100566]), to the southeast edge of Crater Flat, a distance of about 25 km (15.5 mi). It is a complex fault system consisting of two main sections, referred to as the Northern Windy Wash and Southern Windy Wash faults (Figure 3-20), with down-to-the-west displacements, separated by a 4 to 5 km (2.5 to 3.1 mi) long discontinuous zone of east-facing scarps (Simonds et al. 1995 [DIRS 101929]). Only about a 5.5 km (3.4 mi) long segment of the northern section occurs in the northwest corner of the site area, where it is marked by a west-dipping fault-line scarp at the base of a bedrock escarpment formed largely by units of the Topopah Spring Tuff on the footwall and Yucca Mountain and Tiva Canyon Tuffs on the hanging wall (Figure 3-2; Day et al. 1998 [DIRS 100027]). The amount of down-to-the-west displacement of bedrock along this well-exposed segment, on a fault plane with an average west dip of about 63°, is more than 500 m (1,640 ft).

Trenches were excavated only across the north end of the Southern Windy Wash fault, the mapping of which provided evidence of as many as eight surface-rupturing events during middle

to late Quaternary time that resulted in a total net displacement of 3.7 m (12.1 ft) in the surficial deposits (Whitney et al. 2003 [DIRS 159416]). With regard to the 5.5 km (3.4 mi) long segment of the Northern Windy Wash fault in the northwest corner of the site area, Simonds et al. (1995 [DIRS 101929]) show a nearly continuous scarp along the bedrock-alluvium contact that is interpreted to be indicative of probable Quaternary movement.

3.5.3.6   Northern and Southern Crater Flat Faults

The Northern and Southern Crater Flat faults lie entirely to the west of the site area (Figure 3-20), but are included here because they form the west boundary of the Windy Wash-Crater Flat structural block to be discussed later. These two faults compose a complex fault system that can be traced discontinuously for a total length of as much as 20 km (12.4 mi) (Menges and Whitney 2003 [DIRS 160061]) along the east side of Crater Flat, although the relations between the main north and south sections are obscured by surficial deposits in intervening areas. Individual exposures of the fault traces are generally less than 1 km (0.6 mi) long, with some being as much as 2 km (1.2 mi) in length. The fault traces are marked in places by small, discontinuous bedrock-scarps, subtle scarps and lineaments in alluvium, and short bedrock-alluvium contacts. A 3.5 km (2.2 mi) long segment of the southern fault is marked by a linear contact between Pliocene basalt on the east and Quaternary alluvium on the west that locally produces a west-facing scarp (Simonds et al. 1995 [DIRS 101929]).   Trenches were excavated across both sections of the fault system, showing evidence of at least three Quaternary faulting events that displaced surficial deposits about 0.75 m (2.5 ft) on the Southern Crater Flat fault (Taylor 2003 [DIRS 159414]) and four to five Quaternary events that displaced surficial deposits 1.2 m (3.9 ft) on the Northern Crater Flat fault (Coe 2003 [DIRS 159410]). The amount of bedrock displacement could not be determined.

3.5.4   Structural Blocks and Intrablock Faults

The six structural blocks delineated by the block-bounding faults within the Yucca Mountain site area range in width from 1 to 6 km (0.6 to 3.7 mi) (Figure 3-20). Average dip of the tilted volcanic rock units within individual blocks is about 10°E (Figure 3-21), with increasing dips (to as much as 30°) near the east sides of the blocks in the hanging wall blocks. Each of the blocks is segmented by numerous faults with mostly north to northwest trends.   Like the block-bounding faults, displacements are mainly dip-slip, down-to-the-west, but there are some with down-to-the-east offsets that define shallow intervening graben structures.   Notable exceptions are the northwest-trending, largely strike-slip (right lateral) faults in Drill Hole, Pagany, and Sever washes in the north-central part of the site area (Figure 3-20).

Principal intrablock features within individual structural blocks are discussed briefly in the following sections.

3.5.4.1   Structural Block East of the Paintbrush Canyon Fault

Geologic relations across much of the eastern part of the site area, east of the Paintbrush Canyon fault, are poorly known because of the thick blanket of alluvium in Fortymile Wash and over the western part of Jackass Flats (Day et al. 1998 [DIRS 100027]; see Figure 3-1).   However, bedrock exposures on Busted Butte and Fran and Alice ridges, as well as in the highlands north

of Yucca Wash and on both sides of Fortymile Canyon, indicate that a discrete structural block occupies this portion of the area. As yet, there is insufficient evidence for defining an eastern-block boundary. The easternmost down-to-the-west normal fault mapped in the northeastern part of the site is inferred by Potter et al. (2002 [DIRS 160060]) to extend south following Fortymile Wash to a point near the north end of Busted Butte, based in part on differences in the attitude of rock units on opposite sides of Fortymile Canyon and, in part, on the projection of stratal dips in the Topopah Spring Tuff on Fran Ridge with respect to the top of that formation in Borehole UE-25 J-13, just east of the wash (see Figures 3-7 and 3-9). Such a fault is shown in Figure 3-20, but its existence has not been confirmed, nor can it be labeled a block-bounding fault, based on the available evidence.

Areas of exposed bedrock within the structural block are cut by minor faults. Those in the highlands in the northern part are down-to-the-west normal faults involving various units of the Paintbrush Group and the Calico Hills Formation. Those on Busted Butte and Fran Ridge are mostly splays off the Paintbrush Canyon fault, producing down-to-the-west displacements in rocks of the Paintbrush Group and locally forming north-trending zones 0.5 to 1 km (0.3 to 0.6 mi) wide. One such fault trends north-south through the center of Busted Butte (hence, the name), and another, termed the Busted Butte fault (Figure 3-20) cuts across the east side with about 170 m (558 ft) of down-to-the-east displacement (Day et al. 1998 [DIRS 100027]).

3.5.4.2   Bow Ridge-Paintbrush Canyon Block

The Bow Ridge-Paintbrush Canyon structural block is characterized by bedrock areas in both the northern and southern parts, separated by a large expanse of surficial deposits in Midway Valley. Several north- to northwest-trending normal faults, most with down-to-the-west displacements, were mapped in rhyolite lavas of the Paintbrush Group in the area that lies between the Bow Ridge and Paintbrush Canyon faults north of Yucca Wash (Dickerson and Drake 1998 [DIRS 102929]). At the south end of the block, south of Midway Valley, a few minor faults outlining some small graben structures were mapped in rocks of the Tiva Canyon Tuff exposed on Bow Ridge. One of these faults is the Midway Valley fault, which was shown by Day et al. (1998 [DIRS 100027]) to extend north from the Bow Ridge exposures as a concealed fault beneath alluvium for 8 km (5 mi) before reaching the faulted outcrops north of Midway Valley. Bedrock displacements (normal, down to the west) are shown by Scott and Bonk (1984 [DIRS 104181]) and Day et al. (1998 [DIRS 100027]) to be 100 m and 30 m (328 and 98 ft), respectively. Results of geophysical surveys further support the presence of the Midway Valley fault, as well as other north-trending faults beneath the alluvium of the valley floor (Swan et al. 2001 [DIRS 158784], p. 37; Ponce 1993 [DIRS 106552]; Ponce and Langenheim 1994 [DIRS 102333]) (see Section 3.5.7).

The Exile Hill fault (shown in Figure 3-21) is a minor, down-to-the-east normal fault along the east side of Exile Hill that trends north across the location of the surface facilities at the east end of the north ramp of the ESF (Swan et al. 2001 [DIRS 158784], pp. 37 to 39). The fault is shown by Day et al. (1998 [DIRS 100027]) to merge southward with the Midway Valley fault and northward with the eastern strand of the Bow Ridge fault. An exposure in the excavation at the North Portal of the ESF shows the bedrock unit referred to as tuff "X" to be downfaulted against the crystal-rich member of the Tiva Canyon Tuff (see Table 3-1); estimated displacement is 15 to 30 m (49 to 98 ft) (Swan et al. 2001 [DIRS 158784], p. 38). Two other minor faults cut bedrock

on Exile Hill: northwest-trending East and West Portal faults, with dip-slip to oblique-slip displacements of 10 m (33 ft) or less. These two faults are classed as relay structures by Day et al. (1998 [DIRS 100027], p. 10), linking the Bow Ridge and Exile Hill faults. The southeast-trending part of the Bow Ridge fault is also considered to be a relay structure between the main north-trending section of that fault and the Paintbrush Canyon fault to the southeast.

The results of a drilling program to continuously core several closely spaced boreholes within an area on the east side of Exile Hill (designated as the prospective surface facilities for waste-handling; Swan et al. 2001 [DIRS 158784], Figure 2) indicated the presence of several north-trending normal faults buried beneath surficial deposits within the 800-m-wide zone between the Exile Hill and Midway Valley faults (DTNs: GS030783114233.001 [DIRS 164561]; MO0008GSC00286.000 [DIRS 157306]). Most exhibit displacements (both down-to-the-east and down-to-the-west) ranging from a few meters to 45 m (148 ft), but one that traverses the central part of the surface facilities area and merges with the Exile Hill fault to the north, was observed to have as much as 90 m (295 ft) of down-to-the-east displacement of bedrock units within the Tiva Canyon Tuff.

None of the intrablock faults in the Bow Ridge-Paintbrush Canyon structural block shows evidence of Quaternary activity (Swan et al. 2001 [DIRS 158784], p. 45; DTNs: GS030783114233.001 [DIRS 164561]; MO0008GSC00286.000 [DIRS 157306]).

3.5.4.3 Solitario Canyon-Bow Ridge Structural Block

The structural block bounded on the west by the Solitario Canyon fault and on the east by the Bow Ridge fault (and in part by the Paintbrush Canyon fault) is really the largest block in the Yucca Mountain site area, ranging from about 2 km (1.2 mi) to 5 km (3.1 mi) in width (Figure 3-20). Because it also hosts the repository, structural features within the block are of special interest and importance to site characterization. Numerous faults with varying orientations and displacement directions have been mapped (Day et al. 1998 [DIRS 100027]). Among the more prominent of these is the Iron Ridge fault, a major splay of the Solitario Canyon fault that was described in the foregoing section on that fault. In essence, the Iron Ridge fault, with displacements of 180 to 245 m, bounds the east side of a subblock within the major block.

The Ghost Dance fault, another prominent intrablock fault, trends north-south some 150 to 200 m (492 to 656 ft) east of the main drift of the ESF (Figure 3-20). It was mapped in considerable detail by Day et al. (1998 [DIRS 101557]). The fault extends south from about 0.25 km (0.16 mi) south of Drill Hole Wash to Broken Limb Ridge, a distance of 2.5 km (1.6 mi) (Figure 3-2). Farther south, the fault bifurcates, striking to the southwest into the Abandoned Wash fault (Scott and Bonk 1984 [DIRS 104181]) and to the southeast toward (but not into) the Dune Wash fault (Figure 3-20). Down-to-the-west displacements along the Ghost Dance fault in surface exposures vary from a maximum of 27 m (89 ft) in the central part between Split Wash and Broken Limb Ridge, where the brecciated zone between splays is as much as 150 m (492 ft) wide, to a minimum of less than 3 m (9.8 ft) along segments to the south (Day et al. 1998 [DIRS 101557], pp. 9 and 10).

The Ghost Dance fault does not extend far enough north to be encountered in the north ramp of the ESF (Day et al. 1998 [DIRS 101557]). However, a shear with a thin (1 to 10 cm [0.4 to 4 in.] thick) gouge zone and less than 0.1 m (0.33 ft) offset was mapped along the projected north strike of the fault in the cross drift by Mongano et al. (1999 [DIRS 149850], pp. 51 and 52). The fault was also intersected toward the south end of the Main Drift, where it was observed to strike N25°E with a vertical dip, and to have only 1.2 m (4 ft) of down-to-the-west offset in rocks of the crystal-poor member of the Topopah Spring Tuff (DTN: GS970208314224.005 [DIRS 109597]). In exposures in alcoves excavated off the Main Drift, displacements range from 6 to about 25 m (20 to 82 ft) along fault damage zones 0.6 to 1.0 m (2 to 3.3 ft) wide (DTN: GS971183117462.001 [DIRS 158751]). The Ghost Dance fault was trenched at several locations, but studies of the excavations reported no evidence of Quaternary movements (Taylor et al. 2003 [DIRS 159415]).

The Sundance fault is mapped as a 750 m (2,461 ft) long, 70 m (230 ft) wide zone of small discontinuous faults trending northwest from Live Yucca Ridge to Dead Yucca Ridge (Potter et al. 1999 [DIRS 107259]). The fault, with down-to-the-east bedrock displacement, ranging from 6 to 11 m (20 to 36 ft), terminates west of the trace of the Ghost Dance fault (Day et al. 1998 [DIRS 101557]). It was intersected in both the main drift of the ESF and the cross drift. In the main drift, the fault appears to have several meters of down-to-the-west offset within a 20 cm (7.9 in.) thick gouge zone (Mongano et al. 1999 [DIRS 149850], pp. 52 and 54). This observed offset is opposite to that observed at the surface. In the cross drift, the Sundance fault likewise appears to have down-to-the-west-displacement of a few meters (DTNs: GS990908314224.010 [DIRS 152631]; GS991108314224.015 [DIRS 151042]). Like the Ghost Dance fault, there is no evidence to indicate that Quaternary activity took place along the Sundance fault (Taylor et al. 2003 [DIRS 159415]).

From where it branches off the Ghost Dance fault, the Abandoned Wash fault continues southwest and south for about 5 km (3.1 mi) (Figure 3-20). It is exposed in bedrock (Tiva Canyon Tuff) along its northern trace, then is buried by alluvium to the south. The fault displays as much as 24 m (79 ft) of down-to-the-west displacement, marked by a fault scarp dipping 81°W (Dickerson and Drake 2003 [DIRS 160062]). The southeast-trending Dune Wash fault, in contrast, is concealed beneath surficial deposits of Dune Wash for most of its indicated length of 5 km (3.1 mi), being exposed only at the north end where bedrock (Tiva Canyon Tuff) is displaced about 50 m (164 ft) down to the west. To the west, the East Ridge fault, with at least 120 m (394 ft) of down-to-the-east displacement, defines the west side of a feature referred to as the Dune Wash graben (Day et al. 1998 [DIRS 100027]). This prominent downfaulted feature may terminate south against the southern extension of the Paintbrush Canyon fault, but the relations are obscured by surficial deposits.

Sever, Pagany, and Drill Hole washes are prominent northwest-trending drainages in the northern part of the Solitario Canyon-Bow Ridge/Paintbrush Canyon structural block that appear to be controlled by northwest-striking faults (Figure 3-20). The faults were identified on the basis of geophysical investigations, bedrock mapping, and examination of drill cores from Drill Hole Wash (Scott et al. 1984 [DIRS 106763]). A similar fault also was inferred to project beneath the Quaternary alluvial deposits of Yucca Wash by Scott (1992 [DIRS 106755]), but more extensive geologic and geophysical investigations have not confirmed its existence (Langenheim and Ponce 1994 [DIRS 104492]; Dickerson and Drake 1998 [DIRS 102929];

Day et al. 1998 [DIRS 100027]). The Sever Wash and Pagany Wash faults are exposed in bedrock and locally have produced small bedrock scarps. The Drill Hole Wash fault is concealed by Quaternary alluvium, but two faults encountered in the north ramp of the ESF were correlated with the Drill Hole Wash fault zone (DTNs: GS971108314224.020 [DIRS 105561]; GS971108314224.027 [DIRS 160064]). Approximately 4 m (13 ft) of vertical separation were observed on these features, and horizontal slickensides also indicate strike-slip movement, but the total amount of displacement could not be determined. Quaternary alluvial terraces on the floors of the washes do not appear to be displaced by the northwest-trending faults. A trench excavated across the Pagany Wash fault exposed faulted bedrock on the trench floor, but the overlying bedrock regolith and colluvial units are not displaced (Taylor et al. 2003 [DIRS 159415]).

The northwest-trending faults are steeply dipping and thought to be strike-slip faults because fault plane surfaces locally contain slickenside lineations that are nearly horizontal, and vertical displacements generally are less than 5 to 10 m (16 to 33 ft) (Scott et al. 1984 [DIRS 106763], p. 18). The Sever Wash and Pagany Wash faults show slickenside orientations and Riedel shears that indicate right-lateral slip, with the amount of displacement estimated to be about 40 m (131 ft) on each fault (Scott et al. 1984 [DIRS 106763]). The two faults are each about 4 km (2.5 mi) long. Both appear to terminate against the Solitario Canyon fault to the west and, although concealed, are postulated to terminate against a down-to-the-east north-trending fault at the eastern toe of Bleach Bone Ridge (Figure 3-2) (Day et al. 1998 [DIRS 101557]). The Drill Hole Wash fault is also about 4 km (2.5 mi) long and may also terminate against the same north-trending fault.

A closely spaced series of normal faults form an asymmetric graben-like feature that trends north from Boundary Ridge across the toes of Antler and Live Yucca Ridges (Figure 3-2); some are shown in Figures 3-20 and 3-21. Cumulative offset ranges to as much as 30 m (98 ft). Such fault clusters were referred to as imbricate fault zones by Scott (1990 [DIRS 106751]) and were considered to be characteristic of the more intense deformation that took place along the east side of some structural blocks where stratal dips become steeper.

3.5.4.4   Fatigue Wash/Solitario Canyon Structural Block

The prominent feature in the Fatigue Wash/Solitario Canyon structural block is the east-dipping sequence of volcanic rocks that make up Jet Ridge (Figure 3-2). Several normal faults, mostly with small offsets in the Tiva Canyon, Yucca Mountain, and Pah Canyon tuffs, are in the northern part of the block (Figure 3-20). The most extensive is a northwest-trending feature about 2.5 km (1.6 mi) long with down-to-the-east displacement exhibited mainly in rocks of the Yucca Mountain Tuff. A number of faults also cut bedrock (Tiva Canyon Tuff) farther south along the east slope of Jet Ridge, including the 4.5 km (2.8 mi) long, north-northeast-trending intrablock Boomerang Point normal fault. North- to northwest-trending, down-to-the-west normal faults at the south ends of both Jet Ridge and Boomerang Point were considered by Day et al. (1998 [DIRS 100027], p. 10) to be relay faults linking the Fatigue Wash and Boomerang Point faults and the Boomerang Point and Solitario Canyon faults, respectively. Structural relations farther south in this structural block are obscured by surficial deposits.

3.5.4.5 Windy Wash/Fatigue Wash Structural Block

West Ridge and Fatigue Wash (to the east) occupy that portion of the Windy Wash-Fatigue Wash structural block lying within the western part of the Yucca Mountain site area (Figure 3-20). Intrablock structures are mainly small-displacement normal faults in the northern and central parts of West Ridge. A cluster of closely spaced, northwest-trending relay faults terminate against the Northern Windy Wash fault to the west and the Fatigue Wash fault to the east (Day et al. 1998 [DIRS 100027], p. 10). Displacements are both down to the southwest and down to the northeast, with a cumulative offset of about 60 m (197 ft) down to the southwest. The structural block terminates just south of the southwest corner of the site area, at the apparent junction between the two bounding faults (Figure 3-20).

3.5.4.6 Crater Flat/Windy Wash Structural Block

Only the northeastern part of the Crater Flat-Windy Wash structural block lies within the site area (Figure 3-20). A few north-trending normal faults in bedrock are present in that area, with one fault showing Yucca Mountain Tuff in the hanging wall downdropped (west side down) against ash-flow tuffs of the Calico Hills Formation in the footwall (Day et al. 1998 [DIRS 100027]). Much of the block elsewhere along the east margin of Crater Flat is covered by surficial deposits, so that little of the structure can be directly observed. Locations of faults shown on the 1:50,000-scale map compilation by Potter et al. (2002 [DIRS 160060]) are based largely on interpretation of geophysical surveys in the interior of Crater Flat proper.

3.5.5 Vertical Axis Rotation

An important characteristic of the existing fault patterns at and near Yucca Mountain is a noticeable change from the predominant northerly fault trends within the site area proper to more northeasterly trends in adjacent areas toward the south end of the mountain (Fridrich 1999 [DIRS 118942], Figure 8; Rosenbaum et al. 1991 [DIRS 106708]) (see Figure 3-20). This relation is attributed to a progressive north-to-south increase in post-12.7 Ma, vertical-axis rotation, clockwise from 0° (no rotation) in an area near the Prow (Figure 3-2) to about 30° in an area about 10 km (6.2 mi) south of the site area. This increase is interpreted to be the result of right-lateral deformation within the Walker Lane structural belt (Fridrich 1999 [DIRS 118942], Figure 8; Rosenbaum et al. 1991 [DIRS 106708]). Within the site area itself, vertical rotation varies from 0° at the Prow to 5° at the latitude of Busted Butte. Commensurate with the north-to-south increase in the clockwise vertical-axis rotation is a general southward increase in displacements along block-bounding faults. In intrablock areas, the transition from a less-extended terrane in the northern part of Yucca Mountain to a more-extended terrane farther south is generally expressed by the appearance of numerous, closely spaced minor normal-faults that coalesce and gain displacement to the south, as well as wider, fault-bounded half grabens.

3.5.6 Deformation within Fault Zones

Because faults represent potential hydrologic pathways and zones of poor rock quality, deformation along the faults bordering the repository area has been extensively studied. Map patterns demonstrate that tectonic mixing of various Paintbrush Group lithologies has occurred within the most intensely deformed parts of block-bounding fault systems. This is most apparent

in the Solitario Canyon fault system (Scott and Bonk 1984 [DIRS 104181]; Day et al. 1998 [DIRS 101557], p. 7). In this wide (as much as 400 m [1,312 ft]) system, lenses from stratigraphically diverse parts of the Tiva Canyon Tuff are juxtaposed. Slices of Topopah Spring Tuff are also mixed, and in some areas lenses from more than one Paintbrush Group formation are tectonically juxtaposed (Day et al. 1998 [DIRS 101557]). Tectonic mixing is also apparent along the Northern Windy Wash fault system west of the Prow, along the Bow Ridge fault system in the saddle between Bow Ridge and Boundary Ridge, and in the Paintbrush Canyon fault system along the west flank of Fran Ridge (Scott and Bonk 1984 [DIRS 104181]; Day et al. 1998 [DIRS 101557]). Individual fault strands within these tectonically mixed zones are brecciated. In some cases, the fault-bounded lenses are internally brecciated.

In addition to tectonic mixing, there are areas where coherent blocks of Tiva Canyon Tuff, as much as 250 m (820 ft) wide, dip to the west, opposite to the prevailing easterly dips of the major structural blocks (Scott and Bonk 1984 [DIRS 104181], Sheet 1). Locally, anticlines with axes subparallel to the fault zone are present within individual fault slices and in the immediate footwall of the Solitario Canyon fault. These folds are likely produced by local transpression that folded and rotated volcanic strata. Mapped fold hinges may actually be small-displacement, brittle, fault zones occurring at shallow-structural levels. Thrust faults are mapped within the Solitario Canyon fault system and in the hanging wall of the Bow Ridge fault near the South Portal of the ESF (Day et al. 1998 [DIRS 101557]). The anastomosing pattern of faults that characterizes these fault systems also produced individual fault splays that cut into both the hanging wall and footwall.

As indicated earlier, the eastern (main) strand of the Solitario Canyon fault was encountered in the west end of the cross drift (Figure 3-20), where about 260 m (853 ft) of down-to-the-west offset placed the lower nonlithophysal zone of the Topopah Spring Tuff in the footwall against the upper lithophysal zone of the Topopah Spring Tuff in the hanging wall. However, the tectonic mixing described above is also seen within the fault zone at depth in the cross drift, where there is a breccia composed of clasts of the overlying lower nonlithophysal zone of the Tiva Canyon Tuff. Footwall deformation (mostly brecciation) is fairly extensive in the area of the drift, extending approximately 50 m (164 ft) east of the main fault (DTN: GS991108314224.015 [DIRS 151042]).

3.5.7 Geophysical Surveys

Several geophysical methods, including seismic reflection, gravity, and magnetic surveys, were used in attempts to characterize the subsurface geologic structure within the Yucca Mountain site area (Figure 3-22). Such surveys, however, have met with varying degrees of success. Seismic reflection profiling, for example, which is a commonly preferred method for imaging subsurface structure and was conducted along most of the lines shown in Figure 3-22, is difficult because the propagation of seismic energy is greatly inhibited by the fracturing and lithologic heterogeneities that characterize much of the thick sequences of volcanic rocks. Gravity data were also obtained along most of the survey lines and were used primarily to interpret regional structure, as well as to assist in locating faults and determining their displacements in local areas. Ground magnetic surveys, as well as aeromagnetic data, were mainly used to infer fault locations and offsets, especially where the relatively magnetic Topopah Spring Tuff was involved in the faulting. Attempts were made to detect and characterize buried faults and geologic

heterogeneities using the magnetotelluric method, but this method was limited, unless supplemented by other geophysical techniques.

The results of geophysical surveys in the site area are reported in numerous publications, including Fitterman (1982 [DIRS 159312]); Senterfit et al. (1982 [DIRS 159314]); Smith and Ross (1982 [DIRS 159315]); Pankratz (1982 [DIRS 130172]); McGovern (1983 [DIRS 159316]); USGS (1984 [DIRS 101305]); Frischknecht and Raab (1984 [DIRS 159317]); Charles B. Reynolds & Associates (1985 [DIRS 159318]); Ponce (1993 [DIRS 106552]); Ponce and Langenheim (1994 [DIRS 102333]); Majer et al. (1996 [DIRS 104685]); Brocher et al. (1998 [DIRS 100022]); CRWMS M&O (2000 [DIRS 151945], Section 4.6); and Swan et al. (2001 [DIRS 158784]). Applicable findings from these sources are summarized below.

Data from the generally east-trending, 32 km (20 mi)-long seismic-reflection survey across Crater Flat, Yucca Mountain, Midway Valley, and Fortymile Wash (lines REG-2 and REG-3, Figure 3-22) were interpreted to reflect a series of west-dipping normal faults that project through the volcanic rocks and displace the Tertiary volcanic rock/pre-Tertiary sedimentary rock contact at depth (Brocher et al. 1998 [DIRS 100022], Figures 6, 13, and 14). A suggestion that this contact is formed by an active detachment fault beneath Yucca Mountain (e.g., Scott 1990 [DIRS 106751], pp. 269 and 270; Hamilton 1988 [DIRS 100037], p. 62) is therefore inconsistent with the seismic reflection data.

Ponce (1993 [DIRS 106552]) and Ponce and Langenheim (1994 [DIRS 102333]) conducted gravity and magnetic surveys (Figure 3-22) in Midway Valley, from which anomalies were identified that were interpreted to be faults concealed by the thick alluvial deposits covering the central part of the valley. One of the anomalies was presumed to be associated with the Midway Valley fault, with the data indicating a vertical displacement of several tens of meters in the underlying bedrock. Ponce and Langenheim (1994 [DIRS 102333], p. 8) also interpreted data from ground magnetic surveys to indicate that north-trending faults could be traced continuously across Yucca Wash, thus casting doubt on the existence of a northwest-trending fault along the floor of the wash that had been postulated by earlier investigators (e.g., Scott and Bonk 1984 [DIRS 104181]).

Because a primary question to be addressed in the site area is the amount, style, depth, and continuity of faulting in the repository block itself, various geophysical methods were compared to evaluate their effectiveness in imaging both a block-bounding fault (Bow Ridge fault) and a prominent intrablock fault (Ghost Dance fault). Results of these surveys, summarized below, are discussed in detail in CRWMS M&O (2000 [DIRS 151945], Section 4.6.5.3).

In the case of the Bow Ridge fault, only the ground-based gravity as well as the aeromagnetic surveys were found to yield reliable results. The gravity data show a distinct gravity low on the hanging wall of this block-bounding fault where bedrock is buried by less dense surficial deposits. The aeromagnetic data show a high on the footwall side and a low on the hanging wall side, a relation that is interpreted as a signature of displacement of the relatively magnetic Topopah Spring Tuff. Seismic-reflection surveys produced unreliable results.

Ground-based magnetic and magnetotelluric profiling worked well for detecting the Ghost Dance fault, whereas ground-based gravity and standard high-resolution, seismic-reflection

surveys (those with 6 to 12 m [20 to 39 ft] station spacings) did not record significant anomalies. The ground-based magnetic data indicate a characteristic magnetic low, typically about 100 m (328 ft) wide, on the footwall of the fault, and the magnetotelluric data show a clear change in resistivity for the fault. On very high-resolution, seismic-reflection lines (station spacing 1 to 2 m [3.3 to 6.6 ft]), displacement of reflections was apparent across the Ghost Dance fault, thus enabling individual splays to be mapped in places.

The general conclusion was that standard geophysical techniques employed at Yucca Mountain are best suited for detection of faults with at least tens of meters of offset (CRWMS M&O 2000 [DIRS 151945], Section 4.6.5.3).

3.5.8   Fractures

Combined three-dimensional studies of fractures in natural and cleared exposures, boreholes, and underground excavations (ESF and cross drift) have led to important conclusions regarding their distribution and characteristics in the Yucca Mountain site area. Attributes of fracture systems within the principal formations that are most closely associated with the repository—Tiva Canyon and Topopah Spring tuffs, Calico Hills Formation, and Prow Pass Tuff, as well as some of the major units within the PTn hydrogeologic unit—and the study methods employed, are described in considerable detail in CRWMS M&O (2000 [DIRS 151945], Section 4.6.6, Tables 4.6-1 to 4.6-4). The data presented in that report, based principally on detailed studies by Sweetkind and Williams-Stroud (1996 [DIRS 100182]) and Sweetkind et al. (1997 [DIRS 106960]), were used to characterize fracture systems in support of: (1) surface-infiltration model development (Flint and Flint 1994 [DIRS 103746]), (2) numerical simulations of discrete fracture networks (Anna and Wallman 1997 [DIRS 104329]), (3) calculations of bulk-rock permeability for use in equivalent-continuum models of the unsaturated zone (Schenker et al. 1995 [DIRS 101055]; Arnold et al. 1995 [DIRS 101423]), (4) studies bearing on the mechanical stability of the repository, and (5) investigations to determine the paleostress history of Yucca Mountain. A detailed description of fracture attributes and textures in the repository host horizon rocks is described in Mongano et al (1999 [DIRS 149850]; see also DTNs: GS990908314224.010 [DIRS 152631]; GS991108314224.015 [DIRS 151042]). This is a summary document of the geology and fracture characteristics encountered during the excavation of the Enhanced Characterization of the Repository Block (drift) (ECRB). Some of the general relations that were observed between fracture patterns and lithology and of fracturing in fault zones are briefly summarized below.

Fracture characteristics in the pyroclastic flows in the Yucca Mountain site area are primarily controlled by variations in the degree of welding and secondarily by lithophysal development, alteration, and pumice content. Such controls affected fracture spacing, fracture type, number of fracture sets, continuity of individual fractures within each lithostratigraphic unit, and the connectivity of fractures within the network as a whole. Fracture networks commonly act as important preexisting lines of weakness in the rock mass, having originated as cooling joints that formed as tensional openings in response to contraction during cooling of the volcanic rock mass. Subsequent extensional strain could then be accommodated through distributed slip along the preexisting joint sets. The presence of thin breccia zones along such joints, and observable slip lineations along their surfaces, are indicative of joint reactivation. Tectonic fractures are also common in the volcanic rocks, having been developed independently of the cooling-joint

sets in response to regional or local stresses, and are recognized as discontinuities across which simple opening (face separation) or less than 10 cm (3.9 in.) of displacement has occurred in contrast to reactivated joints.

Because fracturing in zones adjacent to fault planes exerts an important influence on hydrologic-flow pathways, many fracture studies focused on the frequency and characteristics of fractures near some of the faults close to the repository block, particularly of fracture sets exposed in the ESF and cross drift. Although the amount of fracturing associated with faults depends, in part, on the lithologic units involved, the width of a fracture zone in the immediate vicinity of a fault generally correlates with the amount of fault offset. Intrablock faults, with small amounts of displacement (1 to 5 m [3.3 to 16.4 ft]), exhibit fracture zones 1 to 2 m (3.3 to 6.6 ft) wide, whereas block-bounding faults with tens of meters of offset have zones ranging in widths as much as 6 to 10 m (20 to 33 ft).

Because the Ghost Dance fault transects the repository area (Figure 3-20), studies have concentrated on fracture patterns exposed in an excavation for the USW UZ-7a drillpad (Figure 3-7) and on a cleared pavement on the south flank of Antler Ridge (Figure 3-2). One generalization is that the amount of total rock damage and fracturing is greater in the hanging wall than in the footwall. At the USW UZ-7a locality, for example, the intervening rock between the west-dipping main fault and a secondary east-dipping fault 42 m (138 ft) to the west, in the hanging wall, is intensely broken and consists of a complex network of short-length fractures, whereas rocks (lower part of the lower-lithophysal zone of the Tiva Canyon Tuff) in the footwall east of the main fault trace are noticeably less fractured. At the Antler Ridge locality, there are 13 to 20 m (43 to 66 ft) of cumulative down-to-the-west displacement across several splays of the Ghost Dance fault distributed over a map width of 100 to 150 m (328 to 492 ft) (Day et al. 1998 [DIRS 101557]). The fracture network in various units of the Tiva Canyon Tuff within or proximal to the fault zone is dominated by closely spaced, steeply dipping fractures, many of which show minor amounts of offset, that may be the result of their proximity to the fault. Alternatively, they may be more closely related to an imbricate zone of faults mapped farther east toward the toe of Antler Ridge (Day et al. 1998 [DIRS 101557]). In the case of the Sundance fault, it occupies a well-defined single strand in places where cooling joints are poorly developed in the crystal-rich member of the Tiva Canyon, but where there is a greater abundance of cooling joints, the displacement is distributed across a broader zone (Potter et al. 1999 [DIRS 107259], pp. 13 and 14).

3.5.9   Stratigraphic Relations across Faults and Timing of Deformation

Stratigraphic relations across both block-bounding and intrablock faults in the Yucca Mountain site area show evidence of episodic movement throughout the depositional period (12.8 to 12.7 Ma) of the Paintbrush Group. Several examples of such evidence are discussed in detail in CRWMS M&O (2000 [DIRS 151945], Section 4.6.3.3), a few of which are summarized below.

1. Near the mouth of Solitario Canyon, the stratigraphic interval of the pre-Pah Canyon bedded tuffs and the Pah Canyon Tuff thins across a prominent splay of the Solitario Canyon fault, from a thickness of 7 m (23 ft) on the hanging wall to 2 m (6.6 ft) on the footwall. As observed by Day et al. (1998 [DIRS 100027], p. 17), the top of the

Topopah Spring Tuff is offset 13 m (43 ft), whereas the bases of the Yucca Mountain and Tiva Canyon Tuffs are offset only 3 m (9.8 ft).

2. At a locality near the Prow (Figure 3-2), pre-Yucca Mountain Tuff bedded tuffs thicken abruptly across the north end of the Fatigue Wash fault. Along a parallel fault 150 m (492 ft) to the west, a 45 m (148 ft) thick rhyolite flow between the Pah Canyon Tuff and the pre-Yucca Mountain Tuff bedded tuffs in the hanging wall is absent in the footwall, implying that at least 45 m (148 ft) of displacement occurred after deposition of the Pah Canyon.

3. Growth faulting along the Ghost Dance fault during deposition of the crystal-rich member of the Topopah Spring Tuff and overlying bedded tuffs at the base of the Tiva Canyon Tuff is indicated by a 30 m (98 ft) decrease in the thickness of the upper lithophysal zone of the Topopah Spring observed on a lithologic log of Borehole USW UZ-7a, which penetrates the fault. Combined with a 15 m (49 ft) offset of the Tiva Canyon Tuff observed during surface mapping, the relations are interpreted by Day et al. (1998 [DIRS 101557]) to indicate that: (a) about 15 m (49 ft) of post-Topopah Spring, pre-Tiva Canyon displacement took place, followed by an additional offset of 15 m (49 ft) after deposition of the Tiva Canyon, and (b) a small amount of fault-related topography existed prior to Tiva Canyon time.

4. Numerous minor faults (splays of the Busted Butte fault, Figure 3-20) on the west side of Fran Ridge and the north end of Busted Butte, displace the top of the Topopah Spring Tuff and the pre-Pah Canyon bedded tuffs 1 to 10 m (3.3 to 33 ft), but the pre-Tiva Canyon Tuff bedded tuff unit and the base of the Tiva Canyon are unfaulted (Day et al. 1998 [DIRS 101557]); further discussion is provided by CRWMS M&O (2000 [DIRS 151945], Section 4.6.3.3.1).

In addition to the episodic deformation during the deposition of various units within the Paintbrush Group, there was an episode of faulting and tilting of strata between deposition of the Tiva Canyon Tuff and that of the Timber Mountain Group rocks. Near the mouth of Solitario Canyon, for example, a complex of small faults splaying off the main trace of the Solitario Canyon fault and displacing Paintbrush Group tuffs, is overlapped by unfaulted Rainier Mesa Tuff (Day et al. 1998 [DIRS 100027]). Fridrich (1999 [DIRS 118942], Figures 2, 3, and 4) interpreted stratal dips in the site area to indicate that: (1) the Tiva Canyon Tuff was tilted 10° to 20° to the east and southeast prior to the deposition of the Rainier Mesa (11.6 Ma), (2) less than 5° of eastward tilting occurred during the period 11.6 to 10.5 Ma, and (3) less than 5° of eastward tilting took place after 10.5 Ma. Scott (1990 [DIRS 106751], p. 268), using compaction foliations, suggested that there is more than 10° of discordance between the Rainier Mesa and Tiva Canyon Tuffs west and northwest of Busted Butte. In much of the site area, however, mapping by Day et al. (1998 [DIRS 100027]) indicated the Rainier Mesa Tuff was displaced by faulting and tilted nearly the same amount as the Tiva Canyon Tuff.

As indicated in descriptions of the block-bounding faults (Section 3.5.3), deformation also continued through Quaternary time.

3.5.10 Geologic Structure of the Pre-Cenozoic Rocks

The local geology of the Paleozoic rocks that underlie Yucca Mountain is known from a single Borehole (UE-25 p #1, see Section 3.3.4.1 and Figure 3-9). Based on exposures in other areas, such as Bare Mountain 12 km (7.5 mi) to the west of Yucca Mountain (Monsen et al. 1992 [DIRS 106382]) and Calico Hills 3 km (1.9 mi) to the east (Potter et al. 2002 [DIRS 160060]), the pre-Cenozoic rocks of the region were highly deformed at some time prior to the deposition of the Tertiary volcanic rocks. Robinson (1985 [DIRS 106674], Plate 1) presented a geologic map of the Proterozoic and Paleozoic rocks of the Yucca Mountain region. The map shows the inferred distribution of Paleozoic strata (Silurian to Mississippian) that directly underlie the volcanic rocks and, for the most part, occupy a broad syncline. Recent compilations by Potter et al. (2002 [DIRS 159091]) and Sweetkind et al. (2001 [DIRS 159092]) show the deep subsurface structure of an extensive region in southwestern Nevada and adjacent parts of California, based largely on the projection of features from structures mapped in exposed areas and on interpretations of available geophysical and borehole information. One of the structures inferred to have involved the Paleozoic rocks beneath Yucca Mountain is an east-west trending, south-vergent thrust fault-block (CP thrust fault; Cole 1997 [DIRS 159090], p. 9) that was projected to extend from the CP Hills, some 25 km east of Yucca Mountain, westward to connect with a similarly oriented thrust fault (Panama Thrust) mapped in Lower Paleozoic rocks at Bare Mountain (Potter et al. 2002 [DIRS 159091]; Sweetkind et al. 2001 [DIRS 159092], Cross Section H-24). The existence of this feature is uncertain; however, it does not appear to have affected the structural patterns observed in Tertiary volcanic rocks, or produced any known seismic activity.

3.5.11 Tectonic Models

Various tectonic models have been proposed for the Yucca Mountain region, each reflecting a different concept of extension in the Basin and Range province. These are discussed in detail in Section 4.1.2. None of the proposed models has been advanced as a preferred model because the available data lead to nonunique interpretations. Deep or large-scale regional crustal conditions cannot be readily investigated and are inferred from geophysical data.

In development of alternate regional tectonic models that encompasses Yucca Mountain, several elements of the structural geology and tectonic history of the site area prove especially useful:

1. Regional extensional stresses controlled the location and development of the north-trending, block-bounding faults (CRWMS M&O 2000 [DIRS 151945], Section 4.6.7.4) primarily during the period 13 to 11 Ma (Minor 1995 [DIRS 106373], p. 10,524; Minor et al. 1996 [DIRS 106374]; Fridrich et al. 1999 [DIRS 107333], pp. 202 and 203).

2. Clockwise vertical-axis rotation created northeast-striking fault segments in the southern part of the site area and elsewhere in the region between 11.6 and 11.45 Ma (Rosenbaum et al. 1991 [DIRS 106708], pp. 1,971 to 1,977; Hudson et al. 1996 [DIRS 106194]).

3. Stresses imposed by caldera-scale volcanism affected the kinematics of large faults (Minor 1995 [DIRS 106373], pp. 10,525 and 10,527; Minor et al. 1996 [DIRS 106374]).

4. Major faults at Yucca Mountain are interpreted from seismic reflection data to penetrate downward through, and to offset, the Tertiary-Paleozoic contact (Brocher et al. 1998 [DIRS 100022], Figure 6).

5. Deformation continued from late Miocene into late Quaternary time. Quaternary surface-rupturing events occurred on some of the block-bounding faults, causing cumulative Pleistocene displacements as much as 8 m (26 ft).

In terms of structural style and deformational history, Yucca Mountain is closely linked to Crater Flat Basin to the west, as indicated in Section 4. In view of that relation, Fridrich (1999 [DIRS 118942], p. 170) proposed that the two tectonic features form a single, graben-like structural domain—the Crater Flat domain—that is distinct from adjacent domains. The domainal boundaries, with the exception of the west boundary, are either largely concealed or are poorly defined by exposed geologic features. As described by Fridrich (1999 [DIRS 118942], pp. 174 to 176, Figure 3), the boundaries of the Crater Flat structural domain are as follows:

1. The west boundary is formed by the Bare Mountain fault, a down-to-the-east, range-front normal fault that separates Crater Flat Basin from Bare Mountain to the west (see Section 2.0). The fault splits into three faults toward the north end of Bare Mountain. It is concealed south of Crater Flat, but produces a relatively strong gravity anomaly. A seismic reflection profile across the fault indicates that the fault plane dips about 64°E. About 3.5 km (2.2 mi) of bedrock (Precambrian and Paleozoic) displacement (Brocher et al. 1998 [DIRS 100022], p. 956) formed the basin.

2. The north boundary is drawn, in part, along the south margin of the Timber Mountain caldera complex (south boundary of the Claim Canyon caldera shown on Figure 3-1) and, in part, along the northwest-southeast trend of Yucca Wash. The linearity of this Yucca Wash trend was interpreted by some investigators (e.g., Scott and Bonk 1984 [DIRS 104181]) to be indicative of faulting but for which no confirming evidence was found by later geologic and geophysical studies (e.g., Day et al. 1998 [DIRS 100027]; Dickerson and Drake 1998 [DIRS 102929]).

3. The east boundary may be defined by the largely concealed down-to-the-west Gravity fault (Winograd and Thordarson 1975 [DIRS 101167], p. C75) as interpreted from geophysical data (see Section 2.0).

4. The south boundary is entirely concealed. It may be formed by a feature termed the Highway 95 fault that is inferred from geophysical and borehole data to extend east-southeast just south of the area included in Figure 3-1. The inferred subsurface trace is delineated on the geologic map compiled by Potter et al. (2002 [DIRS 160060]), who show the Yucca Mountain faults as terminating to the south at that fault line.

Because the geologic relations along much of the bounding limits of the Crater Flat structural domain are concealed, the extent to which the fault patterns may have been controlled by tectonic movements along those boundaries, or were influenced by forces external to the domainal area, could not be determined. Fridrich (1999 [DIRS 118942], p. 193) concluded, however, that the selection of a model that best explains the structural style and tectonic history of the domain requires a broader regional context, especially one that takes into account the strike-slip faulting of the Walker Lane belt. For further discussion of tectonic models, refer to Section 4.1.2.

3.6 NATURAL RESOURCES

Natural resources represent potential causes for inadvertent human intrusion, which is one of four disruptive events scenarios being considered for the TSPA License Application per 10 CFR 63.114(a) and 10 CFR 63.321 [DIRS 156605].

3.6.1 Introduction

Identification and evaluation of the natural resources in the Yucca Mountain area have been the subject of several reports prepared as part of the site characterization program. Included among these are: (1) Castor et al. (1999 [DIRS 104706]) and CRWMS M&O (2001 [DIRS 159125]) for metallic minerals; (2) Castor and Lock (1995 [DIRS 102411]) and CRWMS M&O (2001 [DIRS 159125]) for industrial rocks and minerals; (3) Barker (1994 [DIRS 104433]), Grow et al. (1994 [DIRS 100036]), Cashman and Trexler (1995 [DIRS 107423]), Trexler et al. (1996 [DIRS 107005]), Castor et al. (1999 [DIRS 104706]), French (2000 [DIRS 107425]), and CRWMS M&O (2001 [DIRS 159125]) for hydrocarbon and other energy resources; and (4) Flynn et al. (1996 [DIRS 112530]) and CRWMS M&O (2001 [DIRS 159125]) for geothermal resources. Summary discussions on the various resources, given below, are based largely on these reports.

3.6.2 Metallic Mineral Resources

Nevada is well known for production of several metallic resources, including gold, silver, copper, and mercury (Nevada Bureau of Mines and Geology 1997 [DIRS 105301], p. 3). Similarly, the region surrounding Yucca Mountain contains deposits or potentially economic amounts of these resources (Castor et al. 1999 [DIRS 104706], Plate 1). Although episodes of alteration and mineralization followed the deposition of the Paintbrush Group tuffaceous rocks in areas a few kilometers away, it appears that the hydrothermal activity resulting in mineral deposits elsewhere did not extend into the Yucca Mountain area. This conclusion is based on studies of the mineralogy, petrography, and alteration of numerous rock samples, geophysical data, geologic mapping, remote sensing imagery, and results of chemical analyses, which, combined, show no direct evidence for economic mineralization. Detailed descriptions and interpretations of the studies and tests that were conducted in the site area are presented by Castor et al. (1999 [DIRS 104706]), who found that the small, largely trace amounts of the minerals that were detected (for example, tin, gold, and uranium) were far below the concentrations or the volumes required for any consideration to be given to economic development.

3.6.3   Industrial Rocks and Minerals

The Yucca Mountain region contains many deposits of industrial rocks and minerals (Castor and Lock 1995 [DIRS 102411], p. 1; CRWMS M&O 2001 [DIRS 159125]). Barite, clay minerals, fluorite, and zeolite have been identified in samples from Yucca Mountain. Building stone, construction aggregate, limestone, pumice, silica, and vitrophyre/perlite are also present. Based on such factors as quality and quantity of the resource, accessibility, and competition from alternate, more readily available sources of supply elsewhere in the region, none of these commodities is considered to be of economic importance (CRWMS M&O 2000 [DIRS 151945], pp. 4.9-5 to 4.9-8).

3.6.4   Hydrocarbon and Other Energy Resources

There are few data for determining the extent to which the essential elements for the generation and accumulation of oil and gas—source rocks, favorable maturation history, reservoir rocks, and sealing and trapping conditions—are developed in the Yucca Mountain area. Only one Borehole (UE-25 p #1, Figures 3-7 and 3-9) was drilled deep enough to penetrate rocks below the Tertiary volcanic sequence. These pre-Tertiary rocks were identified as strata representing the Lone Mountain Dolomite and Roberts Mountains Formation of Silurian age (see Section 3.3.4.1). No oil shows or residue were reported from an examination of the borehole cores (Carr et al. 1986 [DIRS 104670]). To date, no significant volumes of oil or gas have been found in southern Nevada or adjacent California and Arizona.

French (2000 [DIRS 107425]), in an assessment of the hydrocarbon potential of the Yucca Mountain area, concluded that, although the basic elements of a viable petroleum system are present, comparisons with known producing fields in the region indicate that (1) the volume of potential source rock is limited, and (2) one of the important seals of the region (an unconformity at the base of valley-fill sediments in some producing areas) is not well developed. Based on these and other factors, French (2000 [DIRS 107425], p. 39) and Grow et al. (1994 [DIRS 100036], p. 1314) interpret the geologic conditions at Yucca Mountain to indicate a low potential for the generation and accumulation of oil and gas.

Other energy resources—tar sands, oil shale, and coal—are not known to exist in the rocks underlying Yucca Mountain, and have not been detected in any of the boreholes drilled in the area or recognized in outcrops in nearby areas. (See Castor et al. 1999 [DIRS 104706], pp. 172 to 175).

3.6.5   Geothermal Resources

A comprehensive treatment of heat flow and thermal gradients in the Yucca Mountain area is presented in Section 8.3.5. As pointed out in that discussion, Flynn et al. (1996 [DIRS 112530]), citing geological, geophysical, and geochemical findings, as well as chemical geothermometry and the very low measured thermal gradient, concluded that there is no potential for geothermal development in the area.

3.7 SITE GEOENGINEERING PROPERTIES

3.7.1 Introduction

This section describes the geoengineering properties of geologic materials that will be important in the construction, operation, and performance of the repository. These properties include the physical, mechanical, thermal, thermal-mechanical, and other relevant properties of the various units of geologic material constituting the site (see Section 3.3 and Table 3-5). In addition to studying the geoengineering properties of the rock units at, or near, the repository block, properties have been collected from other units for far-field effects and for the design of surface facilities. These properties will be used for short- and long-term stability modeling of the repository openings, and for the determination of the block sizes that could potentially fall and create an unsafe environment for repository workers or damage to the waste package or both.

3.7.1.1 Stratigraphic Framework

The general stratigraphy of the area is illustrated briefly in Table 3-5 and detailed in another section of this document (see Section 3.3).

Rocks important to repository design are mainly the ash-flow deposits within the Miocene Paintbrush Group. Principal criteria used in subdividing the four formations within the group—Tiva Canyon, Yucca Mountain, Pah Canyon, and Topopah Spring Tuffs—are discussed in Section 3.3.3. In Table 3-5, the main formational subdivisions (zones and subzones) are listed by name and by the abbreviated symbols used as a convenient means for identifying the individual lithostratigraphic units being studied, as well as correlative thermo-mechanical and hydrogeologic units. Such symbols, based largely on Buesch et al. (1996 [DIRS 100106]), are used for designating the units being sampled for various analytical purposes as shown in many of the ensuing tables. Of primary interest to the geoengineering-property studies were the four units of the Topopah Spring Tuff: upper lithophysal (Tptpul), middle nonlithophysal (Tptpmn), lower lithophysal (Tptpll), and lower nonlithophysal (Tptpln) zones, which constitute the projected host rocks for the repository (Table 3-5).

3.7.1.2 Geographic Distribution of Data

Most of the data presented in this section were collected to support the design and construction of the ESF, and the repository. The primary focus of the data collection program has been the four lithostratigraphic units, within the Topopah Spring Tuff, that compose the repository host rock.

3.7.2 Rock Characteristics

3.7.2.1 Rock Structural Data from Boreholes

The rock characteristics data presented here were developed primarily from Boreholes UE-25 NRG #1, UE-25 NRG #2, UE-25 NRG #2a, UE-25 NRG #3, UE-25 NRG #4, UE-25 NRG #5, USW NRG-6, and USW NRG-7a. The Tptpmn was also described by Boreholes USW SD-7, USW SD-9, USW SD-12, and USW UZ-14. Borehole locations are shown in Figure 3-23. A detailed description of the core logging process is presented in Brechtel et al. (1995

[DIRS 101493]). Data developed from the core included core recovery, locations of fractures, fracture characteristics, hardness, weathering, rock quality designation (RQD), and lithophysal and other voids.

3.7.2.1.1   Core Recovery

Core recovery can generally be used as an indicator of relative rock quality. Borehole studies (see CRWMS M&O 1997 [DIRS 103564]) indicate that rock quality calculated from core data was relatively low for all stratigraphic units. Substantial amounts of core in all lithostratigraphic units were either lost or recovered as rubble. Combining data from each of the boreholes, the amount of lost core for the Tptpmn lithostratigraphic unit was 15 percent of the total core length, as summarized in the recovery data presented in Table 3-6. Rubble zones accounted for 20 percent of the total length.

3.7.2.1.2   Rock Quality Designation

Core recovery is related to the quality of rock encountered in a boring and is influenced to some degree by the drilling technique and type and size of core barrel used. The RQD (Deere 1968 [DIRS 102775]) is a recovery ratio that provides an alternative estimate of in situ rock quality. This ratio is determined by considering only pieces of core that are at least 100 mm (3.9 in.) long. The ratio between the total length of such core recovered and the length of core drilled on a given run, expressed as a percentage, is the RQD, as follows (Deere 1968 [DIRS 102775]):

$$RQD(\%) = \frac{\sum \text{Piece lengths} \geq 100 \text{ mm } (3.9 \text{ in})}{\text{Interval length}} \times 100 \qquad \text{(Eq. 3-1)}$$

This index has been widely used as a general indicator of rock-mass quality (Q) and is an input for rock-mass classification systems, such as rock-mass rating (RMR), discussed in Section 3.7.4.1. RMR and Q are indices that consider characteristics of the rock mass, such as the degree of jointing, strength, and groundwater condition, to classify the rock mass according to rock quality. The RQD used for geotechnical design considered all breaks in the core, including those identified as drilling-induced.

Rock-mass properties are discussed in Section 3.7.4. Enhanced RQD, as assessed at the tunnel scale, was much higher than borehole RQD. This is believed to be an artifact of the borehole RQD calculations, and these calculations include mechanical- and drilling-induced fractures, along with natural fractures. In addition, there is an apparent tendency of the lithophysal zones to produce rubble zones at the core scale, due to dry drilling in brittle rocks, that do not significantly affect stability at the tunnel scale.

3.7.2.2   Potential Key Blocks in Underground Excavations

Key blocks are rock wedges, formed by the intersection of geologic discontinuities and an excavation surface, that are kinematically able to move into the excavation. Key-block analyses were performed to verify that ground support being installed in the ESF was adequate (Kicker et al. 1997 [DIRS 106288]). Analyses were done before completion of the ESF to compare the size of potential key blocks that might be present in the north ramp to the size of

blocks projected for the main drift alignment, assuming that the joint sets encountered in the north ramp also would be encountered in the main drift. In addition, analyses of a 100 m (328 ft) section of the north ramp were performed to assess the importance of the subhorizontal vapor-phase parting structure that occurs periodically in the welded units.

- A key-block-stability analysis software program was used to estimate maximum key-block sizes. The maximum potential key-block size is the volume of the largest key block that could potentially form, given a defined excavation configuration and a particular combination of joint-set orientations. Software used to carry out the analysis is discussed in Kicker et al. (1997 [DIRS 106288]). Specific individual joints cannot be positioned in specific locations. The analysis is nonprobabilistic, but determines the maximum potential block types and volumes based on the provided joint-set data. A statistical description of the probable block sizes formed by fractures around the emplacement drifts was developed for each of the lithologic units of the repository-host horizon. The change in drift profile resulting from progressive deterioration of the emplacement drifts was assessed both with and without backfill. Further details on drift degradation studies are reported in BSC (2003 [DIRS 162711]).

3.7.3 Laboratory Properties of Intact Rock

3.7.3.1 Physical Properties

Bulk and physical-property measurements were performed on specimens of tuff prepared from cores recovered from the surface-based north ramp geologic (NRG) boreholes and systematic drilling boreholes, and the Single Heater Test (SHT) and Drift Scale Test (DST) within the ESF.

3.7.3.1.1 Density and Porosity

Density can vary substantially within a tuff rock mass because of variations in mineralogy, porosity, and welding. Porosity can be calculated from the relationship of average grain density and dry bulk density, and also from the relationship of saturated bulk density and dry bulk density. Total porosity has a predominant effect on the elastic constants and rock strength, whereas the size, shape, and distribution of pores throughout the rock has a second-order effect.

Summaries of the dry bulk densities, saturated bulk densities, average grain densities, and porosities for specimens from the NRG boreholes are given in Tables 3-7 through 3-10, and are presented in detail in Martin et al. (1994 [DIRS 104760]; 1995 [DIRS 104761]) and Boyd et al. (1996 [DIRS 101491]; 1996 [DIRS 101492]). Not surprisingly, the average dry-bulk density of the nonwelded tuffs (about 1.28 g/cm^3) is substantially lower than those of the welded-tuff units (between 2.12 and 2.35 g/cm^3). For the nonwelded tuffs, the mean-average grain density is about 2.40 g/cm^3, with a range of 2.24 to 2.65 g/cm^3; for the welded tuffs, the mean is 2.55 g/cm^3 and the range 2.44 to 2.61 g/cm^3. In addition, the mean porosities are about 0.45 for the nonwelded tuffs and 0.09 to 0.16 for the welded, nonlithophysal tuffs. In the highly welded zones with lithophysal cavities (e.g., the upper and lower lithophysal zones within the Topopah Spring Tuff), the lithophysal porosities must be added to the porosities noted above, and they can vary from 0 to 0.30.

BSC (2002 [DIRS 157829]) presents statistical summaries of physical properties of rock determined from laboratory tests performed on samples from Boreholes UE-25 NRG #2, UE-25 NRG #2a, UE-25 NRG #2b, UE-25 NRG #3, and USW NRG #6, USW NRG #7a, USW SD-9, and USW SD-12. Statistical values of dry density, saturated density, particle density, and porosity determined from the laboratory tests, are summarized by lithostratigraphic unit in BSC (2002 [DIRS 157829], Table 34). Only pre-Tiva Canyon bedded tuff (Tpbt4) and younger units are included. Values of porosity, void ratio, and saturation-water content that were calculated from the mean values of specific gravity and dry density are also presented in BSC (2002 [DIRS 157829], Table 35). Comparisons of mean values of total density from the gamma-gamma surveys with those from resonant column and torsional shear (RCTS) tests and from previous laboratory measurements on NRG and SD borehole samples, are presented in BSC (2002 [DIRS 157829], Figure 235).

3.7.3.1.2 Mineralogy

The mineralogy and petrology of the volcanic rocks at Yucca Mountain have been described extensively in studies of both drill core and outcrop samples (see Sections 5.2.1 and 3.3 for a summary). Previous studies (e.g., Price 1983 [DIRS 102941]; Price et al. 1985 [DIRS 106602]; 1987 [DIRS 100173]) have shown that whereas porosity has a large effect, mineralogy and petrography have a relatively minor effect on geoengineering properties, although there are some minerals that could affect the rock's thermal-mechanical behavior at elevated temperatures. These minerals include cristobalite, which undergoes a phase transition and volume change at elevated temperatures, and smectite and zeolites, which dehydrate at elevated temperatures, with accompanying volume reduction. However, neither smectite nor zeolite minerals are of a sufficient enough volume to alter the mechanical properties of the repository horizon.

3.7.3.2 Thermal Properties

Several recent reports have documented results of thermal testing, analysis, and modeling, including BSC 2002 [DIRS 160319], BSC 2002 [DIRS 160771], BSC 2003 [DIRS 166242], BSC 2003 [DIRS 166358], and BSC 2003 [DIRS 164670].

The *Thermal Testing Measurements Report* (BSC 2002 [DIRS 160771]) documents the comprehensive set of measurements taken within the Yucca Mountain Project (YMP) Thermal Testing Program since its inception in 1996. Only brief discussions are provided for different data sets. These are intended to impart a clear sense of the applicability of data, so that they will be used properly within the context of measurement uncertainty.

The *Thermal Conductivity of the Potential Repository Horizon Model Report* (BSC 2002 [DIRS 160319]) assesses the spatial variability and uncertainty of thermal conductivity in the host horizon for the repository at Yucca Mountain. More specifically, the lithostratigraphic units studied are located within the Topopah Spring Tuff (Tpt) and consist of the upper lithophysal zone (Tptpul), the middle nonlithophysal zone (Tptpmn), the lower lithophysal zone (Tptpll), and the lower nonlithophysal zone (Tptpln). The Tptpul is the layer directly above the repository host layers, which consist of the Tptpmn, Tptpll, and the Tptpln.

The *Thermal Conductivity of the Non-Repository Lithostratigraphic* Layers (BSC 2003 [DIRS 166242]) develops values for thermal conductivity and its uncertainty for the non-repository layers of Yucca Mountain. The lithostratigraphic units studied are units of the Geologic Framework Model (GFM) MDL-NBS-GS-000002 REV 01 (BSC 2002 [DIRS 159124]) located within the Timber Mountain Group, the Tiva Canyon Tuff formation, the Yucca Mountain Tuff formation, the Pah Canyon Tuff formation, the Topopah Spring Tuff formation excluding the repository layers, the Calico Hills formation, the Prow Pass Tuff formation, the Bullfrog Tuff formation, and the Tram Tuff formation.

The *Laboratory Thermal Conductivity Testing for the Tptpll Lithostratigraphic Unit* (BSC 2003 [DIRS 166358]) summarizes thermal conductivity of the Tptpll (Topopah Spring Lower Lithophysal) lithostratigraphic unit, using a combination of laboratory and field techniques. Laboratory tests are useful in determining rock matrix properties and assessing the effects of moisture content and porosity under controlled conditions. The purpose of the laboratory testing described in this document has been to substantially supplement the Yucca Mountain Project (YMP) database for laboratory thermal conductivity measurements for the Tptpll unit. The lithologic description of this unit is given in several reports, e.g., the reports from Rautman and Engstrom on Boreholes USW SD-12 and USW SD-7 (1996 [DIRS 100642] and [DIRS 101008], respectively). The lithostratigraphic units of the repository horizon will experience the highest temperature excursions, therefore there is a need to focus on the thermal properties of these units.

The *Heat Capacity and Thermal Expansion Coefficients Analysis Report* (BSC 2003 [DIRS 164670]) developed heat capacity values for the host and surrounding rock layers for the waste repository at Yucca Mountain. The specific objective was to determine the rock grain and rock mass heat capacities for the geologic stratigraphy identified in the *Mineralogic Model (MM3.0) Analysis Model Report* (BSC 2002 [DIRS 158730]). The temperature range of interest in this analysis is 25°C to 325 °C. This interval is broken into three separate temperature intervals: 25°C to 94°C, 95°C to 325°C, which correspond to the pre-boiling, trans-boiling, and post-boiling regimes.

3.7.3.2.1   Thermal Conductivity

Thermal conductivity is a measure of a material's ability to transmit heat. Thus, it is an important parameter for numerically simulating the transient temperature field resulting from heat generated by emplaced radioactive waste.

Characterization of the thermal conductivities of Yucca Mountain tuffs has been ongoing since 1980 (Lappin 1980 [DIRS 102927]). Data (from Boreholes USW G-1, USW G-2, USW GU-3, and USW G-4) published through 1988 were reviewed by Nimick (1989 [DIRS 105180]), who summarized only data for which supporting documentation was available. The summarized reports include Lappin et al. (1982 [DIRS 104566]), Lappin and Nimick (1985 [DIRS 104565]), Nimick and Lappin (1985 [DIRS 105191]), and Nimick et al. (1988 [DIRS 102921]). Furthermore, Nimick (1990 [DIRS 105189]) presented analyses of data for not only the welded, devitrified portion of the Topopah Spring Tuff, but also the units overlying and immediately underlying the Topopah Spring unit. Additional measurements of thermal conductivity were performed on core specimens from Yucca Mountain by Sass et al. (1988 [DIRS 100644]), using

a needle-probe technique. However, the moisture content in these specimens was uncertain (see discussion in Nimick 1990 [DIRS 101396]).

Data presented here are for 95 specimens from Boreholes USW NRG-4, USW NRG-5, USW NRG-6, and USW NRG-7a (Brodsky et al. 1997 [DIRS 100653]; CRWMS M&O 1997 [DIRS 103564]). In addition, as part of the characterization for the SHT, four and twenty (respectively) samples of middle nonlithophysal Topopah Spring Tuff were tested for thermal conductivity (CRWMS M&O 1996 [DIRS 101428]). Moisture contents were either air-dried (as received), oven-dried, vacuum-saturated, or partially saturated (intermediate between air-dried and vacuum-saturated).

Variation in thermal conductivity with saturation is listed for temperatures less than 100°C in Table 3-11. Variations for higher temperatures are shown in Table 3-12. The data were compiled in this manner rather than for each 25°C interval because thermal conductivity is not strongly temperature dependent. In addition, samples from the SHT block were tested in the air-dried state and thermal conductivity data from the DST block specimens were collected on saturated samples. In both cases, the results are consistent with those from the NRG specimens.

Averaged thermal conductivities ranged from 1.2 to 1.9 W/(mK) (watts per meter Kelvin) for TCw, from 0.4 to 0.9 W/(mK) for PTn, from 1.0 to 1.7 W/(mK) for TSw1, and from 1.5 to 2.3 W/(mK) for TSw2. Thermal conductivities from the nonwelded tuffs were distinctly lower than the welded-tuff data.

Further evaluation of the mean values (e.g., Tables 3-11 and 3-12) indicates that thermal conductivity generally increases with increasing saturation and increasing temperature. However, the effect is much more pronounced for saturation. Above 100°C, thermal conductivity shows little temperature dependence. Decreases in conductivity with increasing temperature, observed in saturated specimens, are attributed to dehydration (Brodsky et al. 1997 [DIRS 100653]).

Brodsky et al. (1997 [DIRS 100653]) compared the data from NRG#4, NRG#5, NRG#6, and NRG#7, and previous data from USW G-1, USW G-2, USW G-3, and USW G-4 (Nimick 1989 [DIRS 105180]). These two data sets compared well for the welded Topopah Spring tuffs. In contrast, the values for nonwelded Paintbrush samples reported by Nimick (1989 [DIRS 105180]) are higher, by about a factor of two, than those reported in Brodsky et al. (1997 [DIRS 100653]) and CRWMS M&O (1997 [DIRS 103564]). However, Nimick's data were limited to only two tests on samples taken 3 km (1.9 mi) from the nearest NRG boreholes.

The effective thermal diffusivity (thermal conductivity divided by the volumetric heat capacitance) of crushed tuff was measured in two bench-scale tests (Ryder et al. 1996 [DIRS 100694]). In each test, a cylindrical volume of 1.58 m^3 was filled with crushed tuff particles to form an effective porosity of 0.48. Temperatures near the heater reached 700°C, with a large volume of material exceeding 100°C. Thermal diffusivity was estimated post-test, using three different analysis methods. The range of calculated thermal diffusivities was $5.0 \times 10^{-7} \text{ m}^2/\text{s}$ to $6.6 \times 10^{-7} \text{ m}^2/\text{s}$, which is on the same order of magnitude as the thermal diffusivity used for crushed backfill in the TSPA for 1993 (CRWMS M&O 1997 [DIRS 103564]).

Several studies (e.g., Rautman and McKenna 1997 [DIRS 100643]) have correlated thermal conductivity with an easily measured physical property, such as porosity. Lappin et al. (1982 [DIRS 104566]) documented thermal conductivities of the major silicate phases in tuff and discuss calculating the matrix conductivities from the conductivities of components and measured values of porosity and saturation, using the geometric mean approach of Woodside and Messmer (1961 [DIRS 107330]). A data compilation is presented in Nimick (1989 [DIRS 105180]). Nimick (1990 [DIRS 101396]) introduces the use of the Brailsford and Major (1964 [DIRS 101999]) equation for calculating matrix-thermal conductivity to replace the geometric mean equation, and uses the Brailsford and Major (1964 [DIRS 101999]) equation for calculation of matrix porosity. Nimick (1990 [DIRS 105189]) summarizes the data for 15 samples of Topopah Spring Tuff and estimates matrix conductivities and in situ thermal conductivities for these samples.

Supplemental thermal conductivity tests were performed using core samples obtained from various locations within the Tptpll (lower lithophysal unit) accessed from the ECRB Cross-Drift. The test core samples were extracted from the large-diameter boreholes drilled for rock mechanics testing. The average thermal conductivities obtained for dry and wet samples were, respectively, 1.7 and 2.1 W/(mK) (DTN: SN0209L01A1202.001 [DIRS 163601]). The testing included examination of sample-size effect in laboratory measurement of thermal conductivity for the Tptpll (lower lithophysal) tuff. Details of the test methods and results are presented by BSC (2003 [DIRS 166358]).

Recent reports develop geostatistical models that describe the variability of thermal conductivity in the host rock units (BSC 2002 [DIRS 160319]) and nonhost rock units (BSC 2003 [DIRS 166242]). Additional discussion of modeling thermal properties is provided in Section 7.10.

3.7.3.2.2 Thermal Expansion

Thermal expansion is the tendency of a material to undergo a change in volume as a result of a change in temperature. The coefficient of linear thermal expansion is defined as the change in length per degree Celsius, expressed as a fraction of the length at 0°C.

Thermal expansion measurements on tuffs are reported in Lappin (1980 [DIRS 102927]) for samples from UE-25 a#1, Well J13, and G-tunnel, and in Schwartz and Chocas (1992 [DIRS 106739]) for 109 specimens from UE-25 a#1, USW G-1, USW G-2, USW G-4, and USW GU-3. The results of these measurements generally compare well with those of the measurements discussed below. Seventy-eight of the 109 specimens reported by Schwartz and Chocas (1992 [DIRS 106739]) were tested unconfined, and 31 were tested at nominally 10 megapascal (MPa) confining pressure.

Thermal expansion tests were also performed on 120 specimens from NRG#4, NRG#5, NRG#7a, and SD-12. The unconfined tests are reported in Brodsky et al. (1997 [DIRS 100653]). Five SD-12 specimens were tested under confined conditions and reported in Martin et al. (1997 [DIRS 104758]). In addition, nine and seventeen thermal expansion tests, respectively, were performed for the SHT (CRWMS M&O 1996 [DIRS 101428]) and the DST (CRWMS M&O 1997 [DIRS 101539]). All specimens were from the Tptpmn (middle nonlithophysal) tuff

facies. Because previous work (Brodsky et al. 1997 [DIRS 100653]) had shown that, for welded tuff, moisture content has no appreciable effect on thermal expansion, all tests were conducted on initially air-dried samples.

Thermal expansion measurements were made using a push-rod dilatometer. Test specimens were right-circular cylinders, approximately 50.8 mm (2 in.) in length and 25.4 mm (1 in.) in diameter. Moisture contents were either air-dried, oven-dried, or vacuum-saturated. Tests were conducted over the temperature range of 30°C to more than 300°C.

Mean coefficients of thermal expansion from surface-based borehole specimens are presented in Table 3-13 for heating phases and in Table 3-14 for cooling phases. The mean thermal expansion coefficients do show some borehole-to-borehole variation. However, the complete data set is presented in Brodsky et al. (1997 [DIRS 100653]). The mean thermal expansion coefficient was highly temperature dependent and ranged from $6.6 \times 10^{-6}/°C$ to $50 \times 10^{-6}/°C$ for TCw; from negative values to $16 \times 10^{-6}/°C$ for PTn; from $6.3 \times 10^{-6}/°C$ to $44 \times 10^{-6}/°C$ for TSw1; and from $6.7 \times 10^{-6}/°C$ to $37 \times 10^{-6}/°C$ for TSw2. Data are also summarized in CRWMS M&O (1997 [DIRS 103564]) and in Brodsky et al. (1997 [DIRS 100653]).

Additional data were collected for middle nonlithophysal Topopah Spring samples from the SHT region and the DST block. The mean thermal expansion coefficients for the SHT samples ranged from 7.5×10^{-6} to $52 \times 10^{-6}/°C$ and were temperature dependent during the heating cycle. Complete data and analysis are presented in CRWMS M&O (1996 [DIRS 101428]).

Statistical summaries for mean coefficients of thermal expansion for specimens from the DST block are discussed in CRWMS M&O (1997 [DIRS 101539]). The values from SHT and DST samples are generally consistent. The mean DST values are consistently higher than those for the SHT. However, the mean values are typically within one standard deviation of each other.

These data (e.g., Tables 3-13 and 3-14) indicate that at a transition temperature of 150° to 200°C, the mean thermal-expansion coefficient increases more steeply for the welded tuffs than for the nonwelded tuffs. A transition is to be expected in the welded devitrified specimens, because of phase changes in tridymite and cristobalite, which occur, with or without quartz, as primary devitrification products in many samples of Yucca Mountain welded tuffs. Phase transitions involving large volume changes in synthetic tridymite take place at approximately 117°C and 163°C, and in synthetic cristobalite at approximately 272°C (Papike and Cameron 1976 [DIRS 105344]). However, phase-transition temperatures have been shown to vary significantly because of lattice variations found in these minerals naturally (Thompson and Wennemer 1979 [DIRS 111126]). Hysteresis is associated with the phase changes because the phases invert at higher temperature during heating than during cooling (Brodsky et al. 1997 [DIRS 100653]).

The sharp increase in mean coefficients of thermal expansion, beginning at approximately 200°C in welded tuffs, is not attributed to thermally induced fracturing or differential expansion, because these behaviors would not be significant during the second heating phase. Also, the DST data indicate sharp increases for both cycles (CRWMS M&O 1997 [DIRS 101539]). Three specimens from the DST suite of tests did not show the increase in mean coefficients of thermal expansion at elevated temperature. This difference in behavior is attributed to different concentrations of cristobalite and tridymite (see details in CRWMS M&O 1997 [DIRS 101539]).

Although thermal expansion was independent of saturation state for welded specimens, the data from the nonwelded specimens did depend on saturation state (Brodsky et al. 1997 [DIRS 100653]). Nonwelded specimens with high moisture contents contracted during testing near 100°C, causing a temporary sharp decrease in the mean thermal expansion coefficient. This is presumed to be the result of reducing the pore water and the dehydration of hydrated glass. The expansion characteristics of the welded specimens seemed to be independent of saturation state, and the curves for different saturation states show similar behavior (Brodsky et al. 1997 [DIRS 100653]). This is to be expected because there is so little water in the welded samples, even when saturated.

Martin et al. (1997 [DIRS 104758]) conducted a suite of confined thermal expansion tests to determine if strain hysteresis and transition temperature effects would be suppressed by elevated confining pressures. Because confining pressure effects for specimens tested between 1 and 30 MPa were small (Martin et al. 1997 [DIRS 104758]), data from these pressures were averaged together and compared with data from unconfined tests. At temperatures below approximately 150°C, the coefficient of thermal expansion is slightly lower for unconfined tests than for confined tests. However, at higher temperatures (150°C to 250°C), the mean values approach one another, and the scatter among the unconfined tests encompasses the results for the confined tests.

The effect of specimen size was investigated using samples from Busted Butte (location shown in Figure 3-2) and from Boreholes USW G-1, USW G-2, USW GU-3, and USW G-4 (CRWMS M&O 1997 [DIRS 103564]). The original test data included five sets of tests that illustrate size effects. For all depths except the Calico Hills unit sampled in USW G-2, mean thermal-expansion coefficients are higher for the smaller specimens. However, the statistical difference in mean values at different scales of measurements were relatively small. In situ testing (Section 3.7.4.2) provides another method for calculating rock mass thermal expansion.

Recently, additional thermal expansion experiments have been run on large (approximately 0.29 m in diameter) samples from the upper and lower lithophysal zones within the Topopah Spring Tuff. For the temperature range from 40°C to 200°C, the preliminary results are similar to results from nonlithophysal samples (DTNs: SN0208L01B8102.001 [DIRS 165211]; SN0211L01B8102.002 [DIRS 165218]).

Variability of matrix thermal expansivity is evaluated by BSC (2003 [DIRS 164670]).

3.7.3.2.3   Heat Capacity

Heat capacity is the amount of energy required to raise a unit mass through a unit temperature increase. The database for heat-capacity measurements consists of theoretical values calculated by Nimick and Connolly (1991 [DIRS 100690]) from chemical and mineralogical data, and from experimental values reported by Brodsky et al. (1997 [DIRS 100653]).

Bulk chemical analyses of 20 tuff samples from Yucca Mountain were used to calculate heat capacities of the solid components of the tuffs as a function of temperature. The data were combined with grain density, matrix porosity, lithophysal-cavity abundance, mineral abundance, in situ saturation, and the properties of water to estimate rock-mass heat capacitances.

Calculations were completed for the temperature range of 25°C to 275°C (CRWMS M&O 1997 [DIRS 103564]). Summary mineralogic and chemical data are reported in Connolly and Nimick (1990 [DIRS 101529]) and thermal-capacitance calculations and results are given in Nimick and Connolly (1991 [DIRS 100690]).

Heat capacity was measured for 10 air-dried specimens from UE-25 NRG #4 and UE-25 NRG #5 (Brodsky et al. 1997 [DIRS 100653]). Test specimens were air-dried, right-circular cylinders approximately 57.0 mm (2.24 in.) in length and 50.8 mm (2 in.) in diameter. Tests were conducted over the temperature range of 30° to 300°C, using an adiabatic pulse calorimeter.

Thermal-capacitance (heat capacity multiplied by specimen density) results are summarized in Table 3-15 and plotted on Figure 3-24, along with data from Nimick and Connolly (1991 [DIRS 100690]). A complete data presentation is included in Brodsky et al. (1997 [DIRS 100653]) and CRWMS M&O (1997 [DIRS 103564]). Mean thermal-capacitance ranges from 1.6 J/cm^3/Kelvin to 2.1 J/cm^3 /Kelvin for TSw1 and from 1.8 J/cm^3/ Kelvin to 2.5 J/cm^3/ Kelvin for TSw2 (Table 3-15).

Experimentally determined values of heat capacity increased with temperature, reaching a localized peak of 2.4 and 2.1 J/cm^3/ Kelvin at between 150° to 170°C for the TSw1 and TSw2 units, respectively. This peak may be related to a phase change, but the data presented here were insufficient to correlate peaks more specifically. The peaks in specific heat at these temperatures are at a temperature range associated with the phase change in tridymite (163°C). It is also evident that there were no substantial changes in measured specific heat for these air-dried specimens at 100°C, indicating that dehydration effects were minor (Brodsky et al. 1997 [DIRS 100653]).

The calculated (Nimick and Connolly 1991 [DIRS 100690]) and experimentally determined values of thermal capacitance are given in Figure 3-24. For both data sets, values for TSw2 are higher than for TSw1. The theoretical data show a decrease at 100°C caused by the heat of water vaporization. The air-dried test specimens showed no comparable decrease.

Heat capacity for lithostratigraphic units in the unsaturated zone is modeled by BSC (2003 [DIRS 164670]), based on measured mineral abundances.

3.7.3.3   Mechanical Properties

Elastic moduli and strength values have been collected in experiments on specimens from cores recovered from many boreholes at Yucca Mountain (Olsson and Jones 1980 [DIRS 102940]; Price 1983 [DIRS 102941]; Price et al. 1984 [DIRS 106604]; Nimick et al. 1985 [DIRS 105195]; Martin et al. 1993 [DIRS 160036]; 1994 [DIRS 104760]; 1995 [DIRS 104761]; 1997 [DIRS 101432]; Boyd et al. 1996 [DIRS 101491]; 1996 [DIRS 101492]), on specimens from outcrop blocks from Busted Butte (Price 1986 [DIRS 106589]; Price et al. 1985 [DIRS 106602]; 1987 [DIRS 100173]), on specimens from the SHT (CRWMS M&O 1996 [DIRS 101428]), and from the DST (CRWMS M&O 1997 [DIRS 101539]). One objective of the measurements was to establish a baseline set of properties to study the vertical and lateral variability of bulk and mechanical properties at Yucca Mountain. Therefore, the baseline tests were on ground,

right-circular cylindrical specimens of tuff, with a nominal 2:1 length-to-diameter ratio, that were water-saturated and tested to failure at a constant strain rate of $10^{-5}\,s^{-1}$ under ambient temperature and pressure conditions. In the early baseline studies (i.e., prior to 1986), nominal specimen size was 25.4 mm (1 in.) in diameter, whereas the later experiments were generally on samples with a nominal diameter of 50.8 mm (2 in.).

In addition to the compression experiments, many indirect-tension (i.e., Brazilian) tests have been performed to determine the tensile strength of the welded, nonlithophysal tuffs. Also, the baseline results were instrumental in providing the results needed to interpret experiments performed to determine the effects of other environmental factors (e.g., confining pressure, temperature, time dependence, anisotropy) and sample characteristics (e.g., sample size and lithophysal content).

Additional information on mechanical properties of the lithophysal Topopah Spring tuff is available from a testing program that involved large core samples from the ESF and from surface boulders. The study provided information on the effects of lateral variability, sample size, confining pressure, temperature, saturation, normal stress, and creep stress on the mechanical properties (BSC 2003 [DIRS 166355]; also BSC 2003 [DIRS 166660], Section 8.4).

3.7.3.3.1   Static and Dynamic Elastic Moduli

The static-elastic properties of Young's moduli and Poisson's ratios were computed from the stress-strain data obtained for the specimens tested in quasistatic, laboratory-compression experiments (summaries of these data are given in Tables 3-16 and 3-17). Compressional and shear-wave ultrasonic velocity measurements were measured, both parallel and normal, to the axis of the cylindrical-test specimen (a summary of the velocity measurements is given in Table 3-18) to compute the elastic anisotropy of the specimen. In addition, the compressional and shear-wave velocity, combined with specimen density, were used to compute the dynamic Young's modulus and Poisson's ratio.

In general, Young's modulus has been shown to be predominantly dependent on the porosity of the sample tested (Olsson and Jones 1980 [DIRS 102940]; Price 1983 [DIRS 102941]; Price and Bauer 1985 [DIRS 106590]; Price et al. 1994 [DIRS 160052]; 1994 [DIRS 161290]), whereas Poisson's ratio appears to be independent of porosity (Price 1983 [DIRS 102941]; Price et al. 1994 [DIRS 161290]). Based on the least-squares fits determined by Price et al. (1994 [DIRS 161290]), an average Young's modulus for samples with porosity-volume fractions of 0.1, 0.3, and 0.5 are 32.1, 7.7, and 1.9 gigapascals (GPa), respectively. The Poisson's ratios range from 0.01 to 0.40 and average slightly above 0.20 (Price et al. 1994 [DIRS 161290]).

Also, as with most rock types, the dynamic Young's moduli calculated from tuff velocity and density data have been found to be higher than the measured static values. The measured difference is on the order of 30 percent (Price et al. 1994 [DIRS 160052]).

In situ seismic methods were used to measure low-strain, shear-wave, and compression-wave velocities and laboratory-test methods were used to measure low-strain shear-modulus in both rock and surficial materials for use in evaluating ground motions. Results of these measurements are presented in BSC (2002 [DIRS 157829]) and are discussed in Section 3.7.7.

3.7.3.3.2 Unconfined Compressive Strength

The unconfined (or uniaxial) strength data for the Yucca Mountain stratigraphic units are summarized in Table 3-19. Similar to the trends in the Young's modulus data, the compressive-strength results vary primarily as a result of rock porosity (Olsson and Jones 1980 [DIRS 102940]; Price 1983 [DIRS 102941]; Price and Bauer 1985 [DIRS 106590]; Price et al. 1994 [DIRS 160052]; 1994 [DIRS 161290]).

The modes of fracture in most of the unconfined compression tests were similar. The fractures producing failure were, in general, axial in nature. In fact, many of these tensile-type fractures terminated through the ends of the specimens.

In most cases, little inelastic volumetric strain (dilatancy) is observed in tests on the welded tuffs (CRWMS M&O 1997 [DIRS 103564]), unlike many crystalline rocks that begin to dilate at stresses as low as 50 percent of the fracture strength. However, in the welded tuffs, little nonlinearity in the volumetric strain is observed until the specimens are close to failure, indicating little, if any, fracture interaction during the onset of failure (Brace et al. 1966 [DIRS 101990] and Scholz 1968 [DIRS 104568]).

3.7.3.3.3 Tensile Strength

Indirect tensile-strength tests, commonly referred to as Brazilian tests, were carried out on nonlithophysal specimens with nominal specimen size of 38.1 mm (1.5 in.) in length and 50.8 mm (2 in.) in diameter. The tensile strengths determined from these tests are summarized in Table 3-20 and range from 0.2 to 16 MPa. As expected, the resultant strength values are directly related to the degree of welding in the sample.

3.7.3.3.4 Property Variability

Boyd et al. (1995 [DIRS 120650]) stated that there was little lateral variability in the mechanical properties at a given stratigraphic level among the NRG boreholes along the axis of the north ramp. However, as has been noted above, there is significant vertical variability because of the large differences in total sample porosity. Following a large base of mechanical property experiments in the early 1980s, Price (1983 [DIRS 102941]) analyzed the data statistically and determined that porosity was the predominant factor affecting the Young's moduli and strengths. Later studies (e.g., Price et al. 1993 [DIRS 106601]) have qualitatively determined that smaller differences in these properties result from fabric and pore-structure characteristics.

While there is significant scatter in the elastic and strength data at a given porosity, porosity is still a good predictor of mechanical behavior (i.e., for both Young's modulus and strength values). This conclusion is the result of good fits to mechanical properties versus porosity data from two sample sizes (25.4 mm [1 in.] and 50.8 mm [2 in.] in nominal diameters). Other studies (e.g., Price et al. 1994 [DIRS 160052]) have shown that ultrasonic velocities, dynamic moduli, and tensile strength data also have distinct relationships with porosity.

3.7.3.3.5   Correlations and Parametric Effects of Mechanical Properties

With the inherent variability (i.e., variability even within a set of samples with presumably equivalent porosities) in the mechanical properties of the tuffs, it is imperative that a suite of samples designed for any parametric testing be collected from as small a volume of rock as possible.

Confining Pressure–The effects of confining pressure on elastic and strength properties have been investigated on a limited number of samples. The tests have been performed at pressures ranging from ambient (i.e., unconfined) to 10 MPa.

Results of confined compression tests indicate that the axial-stress difference at failure increases with increasing confining pressure, using a standard Mohr-Coulomb failure criterion to analyze the data. The six sets of early data (Price 1983 [DIRS 102941]) on smaller samples (25.4 mm [1 in.] in diameter) gave ranges of cohesion and angle of internal friction from 10 to 35 MPa and 4° to almost 70°, respectively. In addition, there were general indirect relationships between both properties and porosity, for a porosity range of 0.09 to 0.40. Later data on larger samples (50.8 mm [2 in.] in diameter) show a wider range in cohesion (3 to 51 MPa) and a narrower range in internal friction (50° to 65°) (Boyd et al. 1996 [DIRS 101491]; 1996 [DIRS 101492]; Martin et al. 1997 [DIRS 101432]).

Temperature–There have been few investigations on the effect of temperature on the mechanical properties of tuff. Price (1983 [DIRS 102941]) presented a few data from other sources that showed a decrease in strength with temperature increases to 200^oC. However, the results were so limited that no definitive conclusions could be drawn.

To examine the effects of temperature on welded TSw2, 17 confined-compression experiments were performed at a nominal temperature of 150°C on specimens recovered from Borehole USW SD-9 (CRWMS M&O 1997 [DIRS 103564]). Measurements were conducted at effective confining pressures of 1, 5, and 10 MPa, with pore pressure always 5 MPa. The experiments were performed at a nominal strain rate of 10^{-6} s^{-1}. The high-temperature, confined-compression-test data indicated a clear increase in strength between effective pressures of 1 and 5 MPa (CRWMS M&O 1997 [DIRS 103564]). However, there was no apparent increase in the mean strength of the tuff between 5 and 10 MPa confining pressure. Comparison of ambient and elevated temperature (150°C) tests indicated that the effect of temperature on the strength of welded tuff from thermal-mechanical unit TSw2 was small. Similarly, Young's moduli and Poisson's ratios, measured at the elevated temperature, were not much different from those measured at room temperature (CRWMS M&O 1997 [DIRS 103564]).

Time Dependence–A time dependence in the mechanical behavior of the Yucca Mountain welded tuffs was first observed in a series of experiments performed at all of the baseline conditions (see Section 3.7.3.3). Several experiments were run at each of four strain rates: 10^{-3}, 10^{-5}, 10^{-7}, and 10^{-9} s^{-1}. Average strength increased by about 10 percent for each order-of-magnitude increase in strain rate from 10^{-9} to 10^{-5} s^{-1}. However, the average strength data from the 10^{-3} s^{-1} experiments were about 25 percent lower than the 10^{-5} s^{-1} data. This reversal in the strength trend is believed to be the result of transient-pore pressures in the tests run under dynamic loading (i.e., 10^{-3} s^{-1}).

A series of creep experiments were performed to test the indications from the strain-rate experiments of moisture-assisted crack growth as the failure mechanism in the welded tuffs, (Martin et al. 1995 [DIRS 100159]; 1997 [DIRS 148875]). A total of 12 creep experiments were performed on 50.8 mm (2 in.) diameter samples of nonlithophysal, welded tuff at confining pressures from 5 to 10 MPa, pore pressures of 4.5 MPa, temperatures from ambient up to 225°C, and a variety of constant stresses. The conclusions from these experiments are as follows:

- Insignificant amounts of strain are measured during loading of less than about 90 percent of the unconfined compressive strength.

- The strains measured during tests with a high creep stress are small.

- When a sample failed under constant stress loading, the failures were relatively unstable and occurred after only a short transient-creep phase.

- The welded tuff appeared to be failing under a mechanism of static fatigue.

Additional creep experiments were begun to quantify the static-fatigue behavior for a given porosity level. Several nonlithophysal, welded tuff samples were tested at different stress levels, with the times to failure recorded. The data collected affirmed the static-fatigue behavior and indicated large changes in times-to-failure with only slight changes in the stress condition. However, the tests were terminated prior to the completion of the entire test series. A new series of constant stress tests is being planned to quantify static-fatigue behavior more completely.

Anisotropy–Tuffs are formed through flow, compaction, and welding, resulting in a rock that is physically anisotropic. The nonrandom orientation of voids and inclusions can result in the variation of mechanical (and other) properties with the direction of measurement (i.e., anisotropy), but the mechanical anisotropy calculated from ultrasonic velocity measurements on nonlithophysal welded tuffs from the TSw2 tuff unit was found to be generally less than 10 percent (e.g., Martin et al. 1992 [DIRS 160028] and Price et al. 1991 [DIRS 161289]). This variation is small relative to the natural scatter in the mechanical properties from samples with equivalent total porosities. Therefore, it is not considered to be an important factor in the modeling of the near- and far-field behavior of the repository rock.

Sample Size–The scaling of the laboratory mechanical-property data to the large-scale in situ conditions is important for repository modeling. The rock properties of large blocks between fractures represent an intermediate size between the small-scale intact (nonfractured) samples tested in the lab and the repository-scale-size zone that includes both intact rock and discontinuities (including fractures and bedding planes). To begin to address this issue, Price (1986 [DIRS 106589]) studied the effect of sample size on the unconfined compressive strength and elastic moduli of welded tuff using TSw2 specimens recovered from Busted Butte, adjacent to Yucca Mountain (Figure 3-2). The data indicate that Young's modulus and Poisson's ratio are independent of sample size. However, the compressive-strength data show a decrease of slightly more than a factor of two as the specimen diameter increases from 25.4 to 228.6 mm (1 in. to 9 in.). A power-law fit to the strength-versus-sample diameter data shows a strength of about 70 MPa for a theoretical TSw2 sample of infinite diameter. Further work by Price (1993 [DIRS 160023]) indicated an empirical model that related strength, sample diameter, and porosity (see discussion in the next section).

Lithophysal Porosity–The units within the Topopah Spring tuff contain varying amounts of lithophysae, from no lithophysal-volume fraction to as much as 0.20 to 0.25. Lithophysae are generally spherical, to sometimes slightly flattened, cavities, from a centimeter to as much as several tens of centimeters in diameter, commonly lined with a thin layer of feldspars, silica minerals, and other vapor-phase mineral deposits (Price et al. 1985 [DIRS 106602]).

An initial study of the effects of these features on the mechanical properties of welded tuffs was performed by Price et al. (1985 [DIRS 106602]) on outcrop samples of the upper lithophysal horizon within the Topopah Spring tuff, taken from Busted Butte. Ten samples, with nominal diameters of 267 mm (10.5 in.), were tested at the baseline conditions. The mean Young's modulus, Poisson's ratio, and strength were 15.5 GPa, 0.16, and 16.2 MPa, respectively. Price (1993 [DIRS 160023]) used these data to test his strength, size, and porosity model and found the predicted strength to be within 10 percent of the mean strength measured in the experiments.

3.7.3.3.6   Hardness

Schmidt hammer-rebound-hardness measurements were conducted on samples from the NRG boreholes to produce early strength estimates and to supplement the rock mechanics test data. Measurements were performed following the suggested methods of the International Society of Rock Mechanics (Bamford et al. 1981 [DIRS 149007]), and the analysis of the results incorporates suggested improvements to the International Society of Rock Mechanics methods by Goktan and Ayday (1993 [DIRS 105583]). Pieces of core were selected on nominal 3 m (9.8 ft) intervals downhole and clamped in a testing anvil weighing a minimum of 20 kg. A group of 20 rebound-hardness measurements was then conducted. The data are presented in detail in Brechtel et al. (1995 [DIRS 101493]), along with estimates of unconfined compressive strength based upon a correlation with Schmidt hammer data. These results gave estimates of unconfined compressive strength that were comparable to other methods (see Section 3.7.3.3.2) for the TCw and TSw2 thermal-mechanical units, but overestimated strength in the PTn and TSw1 units.

3.7.3.3.7   Mechanical Properties of Fractures

In any rock unit, there are discontinuities, such as bedding planes, faults, and fractures. It is important to study the mechanical properties of these features, such as normal stiffness, shear stiffness, cohesion, and coefficient of friction.

Natural fractures from Boreholes UE-25 NRG #4, USW NRG-6, USW NRG-7, USW SD-9, and USW SD-12 have been tested by Olsson and Brown (1994 [DIRS 100169]; 1997 [DIRS 106453]). For each test, Olsson and Brown reported the normal stress, shear and normal-stiffness functions, shear strength, residual shear strength, and dilation angle at peak-shear stress. Also, the friction angle, ϕ, and cohesion, C, were reported for each of four thermal-mechanical units. Data are summarized in Tables 3-21, 3-22, and 3-23.

The normal stiffness for Yucca Mountain fractures increases with increasing normal stress, as is typical for interfaces of any type (Olsson and Brown 1994 [DIRS 100169]; 1997

[DIRS 106453]). However, there is wide variability from fracture-to-fracture, which is indicated by the large standard deviations in the properties.

Additional data are presently being collected in direct-shear experiments on natural fractures in core taken from the ESF.

3.7.4 Rock-Mass Properties

Structural or compositional discontinuities in the rock mass can cause thermal-mechanical properties to differ from laboratory-measured tests of intact samples. Two major field tests, the SHT and the DST, together with the associated background investigations, have produced much of the information that supports current understanding of rock mass properties for the host rock. In addition, other large-scale tests of thermal and mechanical responses have been performed, as summarized below.

For the SHT, instruments were installed and used to measure rock responses to heating and cooling. Thermal measurements included temperature measurements using thermocouples, resistance temperature devices, and thermistors. Mechanical instrumentation included multiple-point borehole extensometers, tape extensometers, surface-mounted wire extensometers, load cells on rock-bolts, and a borehole jack. Additional instrumentation was installed to measure hydrologic and chemical responses (CRWMS M&O 1999 [DIRS 129261]).

The DST consisted of a nearly 50 m (164 ft) long, 5 m (16.4 ft) diameter heated drift, connecting drifts, a plate-loading niche opening, and a data-collection-system. Thermal, mechanical, hydrologic, and chemical responses were recorded using approximately 3,700 sensors, many located in boreholes. In the heating phase, more than $10,000 \text{ m}^3$ of rock were heated to above 100°C, and the temperature at the drift wall was maintained at 200°C for more than 2 years (CRWMS M&O 1997 [DIRS 101539]). Rock-mass deformation modulus was measured by means of a plate-loading test situated in a niche opening near the entrance to the heated drift (CRWMS M&O 1998 [DIRS 108306]).

3.7.4.1 Rock-Mass Classification

Rock mass quality data were collected in preconstruction exploration boreholes, in the ESF and in the ECRB. The Q system (Barton et al. 1974 [DIRS 101541]) and the RMR system (Bieniawski 1989 [DIRS 101715]) were employed in ESF construction activities as the basis for empirical design of excavation ground support and empirical correlation with rock-mass properties.

The calculation of RMR requires six parameters that consider the strength of the rock, the RQD, the joint spacing, the condition of joint surfaces, the groundwater environment, and a factor for the adjustment of joint orientation toward the excavation.

Table 3-24 correlates ranges of RMR with relative descriptions of rock quality. Parameter values are assigned based on classification guidelines presented by Bieniawski (1989 [DIRS 101715]). Adjustments for joint orientation can be made to the RMR to account for the effects of the direction-of-mining approach. When application of the RMR index is limited to an estimation of rock-mass mechanical properties in drift-design methodology, adjustment for joint

orientation is not applied. Borehole estimates of RMR do not include adjustment for joint orientation, because joint orientations cannot be determined from core. The scanline data does include the adjustment for joint orientation factor, because joint-orientations can, in fact, be evaluated with respect to the tunnel axis. Borehole RQD was calculated as described in Section 3.7.3, and rock-mass RQD was calculated from tunnel scanline data using two methods described in CRWMS M&O (1997 [DIRS 103564]). RMR values for boreholes and for ESF scanlines are presented in Brechtel et al. (1995 [DIRS 101493]), Kicker et al. (1997 [DIRS 106288]), Sandia National Laboratories ([SNL] 1995 [DIRS 106851]), and CRWMS M&O (1997 [DIRS 103564]; 1997 [DIRS 101539]). RMR values for the ECRB Cross-Drift are given in Mongano et al. (1999 [DIRS 149850]).

Q, as defined by Barton et al. (1974 [DIRS 101541]), is calculated from six parameters: RQD, a joint-set number (J_n), joint-roughness number (J_r), a joint-alteration number (J_a), a joint water-reduction number (J_w), and a stress-reduction factor. The first term in the expression (RQD/J_n) describes the block size, the second term (J_r/J_a) the interblock shear strength, and the third term (J_w/stress-reduction factor) the effect of the active stress. Relative classes of rock quality based on the overall value of Q have been assigned by Barton et al. (1974 [DIRS 101541]). Data and methodology used to estimate Q and RMR from the core data are described in Brechtel et al. (1995 [DIRS 101493]), Kicker et al. (1997 [DIRS 106288]), and CRWMS M&O (1997 [DIRS 103564]).

Q data were also generated for 5 m (16.4 ft) intervals of the ESF, based on scanline observations made on the excavation surface. Scanline refers to the determination of parameters along linear traces within the interval, as opposed to a detailed mapping of the features in the interval. The methodology used for the scanline Q determinations is described in CRWMS M&O (1997 [DIRS 103564]). In addition, Q values were also determined from full-peripheral field mapping of the ESF. Complete data and detailed analyses are presented in CRWMS M&O (1997 [DIRS 103564]; 1997 [DIRS 101539]) and Mongano et al. (1999 [DIRS 149850]).

An empirical method for assessing the Q-system parameter, called the stress-reduction factor (Kirsten 1988 [DIRS 120631]), has been applied to some data sets, resulting in the determination of a modified Q value. The method and analysis are described in detail in CRWMS M&O (1997 [DIRS 100930]). The Q values calculated by the Kirsten approach, defined as $Q_{modified}$, are typically higher for both data sets and are generally in closer agreement to the RMR values.

Table 3-25 presents a concise statistical description of Q in the ESF, including the cumulative frequency of occurrence at 5, 20, 40, 70, and 90 percent. These frequencies correspond to the five Q categories, as defined by Hardy and Bauer (1991 [DIRS 102920]), and serve as the basis for evaluating the potential range of rock-mass conditions. Table 3-25 also includes the original borehole values used in the ESF ground-support design analysis. As shown, these values resulted in conservative estimates of Q and a conservative ground-support system.

Q was higher in the upper parts of the Topopah Spring Tuff than in the corresponding portions of the Tiva Canyon Tuff (CRWMS M&O 1997 [DIRS 103564]). Poor Q, anticipated in the upper lithophysal zone of the Topopah Spring Tuff (Tptpul), was not observed, in part because the fracturing was not well developed and generally limited to one set of fracture orientation. The inhomogeneities in the Tptpul, caused by large lithophysae and relatively small fractures within

the rock, had little negative effect on the rock mass at the excavation scale. Where the middle nonlithophysal zone, Tptpmn, was exposed in excavations of the main drift, Q was relatively high.

The ESF ground support guidelines (CRWMS M&O 1996 [DIRS 101429]) specify ranges of Q for associated ground support (Classes I through V). Based on these guidelines and Q indices from early ESF scanline data, ground-support requirements were projected for each thermal-mechanical unit. Table 3-26 presents the recommended ground support with respect to the specified range of Q values.

Q data were determined in the ECRB Cross-Drift from detailed line surveys following the same procedures used in the ESF. RMR values were determined, including and excluding lithophysae. Lithophysae were found to have only a minimal effect on the determination of RMR (Mongano et al. 1999 [DIRS 149850]). Generally, there was good correlation with results for the same rock units in the ESF. A summary of the RMR and Q values in the cross drift is presented in Mongano et al. (1999 [DIRS 149850]).

Two ground-support classes were considered for the cross drift: systematic bolting and steel sets (Mongano et al. 1999 [DIRS 149850]). However, the high Q values that were determined indicated that little support was required in the stratigraphic units exposed in the cross drift.

Additional information on rock mass classification, and statistical development of summary information for use in design, is provided by BSC (2003 [DIRS 166660], Section 8).

3.7.4.2 Rock-Mass Thermal Properties

Correlations have been developed or proposed for thermal-mechanical properties at the rock-mass scale (Nimick and Connolly 1991 [DIRS 100690]). Thermal conductivity at the intact scale has been shown to be a function of porosity, saturation, and temperature. Thermal property differences at the rock-mass scale are related to additional fracture porosity not present in intact samples, and additional lithophysal porosity for lithophysal units. The effect of fracture porosity is considered to be small, but the effect of lithophysal porosity is more important.

Data collected through May 1997 from SHT in the Tptpmn unit (middle nonlithophysal) tuff indicate that the temperature distribution around the heater was radially symmetric (CRWMS M&O 1997 [DIRS 101540]). This indicated that thermal conduction was the primary mode of heat transfer (CRWMS M&O 1997 [DIRS 101540]). Some anomalous temperature readings indicated convective transport of heat in fractures. The available thermal data also indicate the formation of a dry-out zone, in which the 100°C isotherm extended approximately 1 meter radially from the heater (CRWMS M&O 1997 [DIRS 101540]).

The thermal expansion coefficient of the rock mass adjacent to the SHT was determined from selected multipurpose borehole extensometer displacements and temperatures. The calculated rock-mass thermal-expansion coefficient ranged between about 4×10^{-6}/°C and 6×10^{-6}/°C. Additional detail on the thermal expansion analysis and results is provided by SNL (1997 [DIRS 106867]), CRWMS M&O (1997 [DIRS 101540]), and CRWMS M&O (1999

[DIRS 129261]). Rock-mass thermal expansion coefficients calculated from the SHT are generally smaller than laboratory-determined values for the middle nonlithophysal unit.

Rautman (1995 [DIRS 100692]) developed a correlation between thermal conductivity and a two-dimensional geostatistical model of porosity at Yucca Mountain. The relationship of laboratory measurements of thermal conductivity to porosity, saturation, and temperature is summarized in Section 3.7.3.3. Results of geostatistical modeling of thermal conductivity are presented by Rautman (1995 [DIRS 100692]).

Additional field measurements of thermal conductivity in situ, include: 1) interpretation of the large-scale temperature field around the DST, 2) borehole measurements using the Rapid Estimation of Thermal Conductivity and Diffusivity method which were part of the DST, and 3) in situ borehole thermal conductivity tests in the Tptpll (lower lithophysal) tuff unit. The results obtained by the first two of these methods apply to the Tptpmn (middle nonlithophysal) tuff. Interpretation of the large-scale temperature field around the DST is reported by BSC (2001 [DIRS 157330], Section 6), concluding that the appropriate values of in situ dry thermal conductivity for modeling thermal test response in the middle nonlithophysal tuff unit are in the range 1.56 to 1.67 W/(mK), and that appropriate values for wet thermal conductivity range from 2.00 to 2.33 W/(mK) (BSC 2001 [DIRS 157330], Section 7). The Rapid Estimation of Thermal Conductivity and Diffusivity method and results are described by BSC 2002 [DIRS 160771]. The mean thermal conductivity value obtained from the Rapid Estimation of Thermal Conductivity and Diffusivity measurements, for the middle nonlithophysal tuff, was approximately 1.8 W/(mK).

A series of three in situ thermal conductivity tests were fielded in the ECRB Cross-Drift to investigate the in situ behavior of the Tptpll (lower lithophysal) tuff. Each of these tests consisted of one or more heater boreholes adjacent to one or more temperature-monitoring boreholes. The test configurations consisted of one 2-hole test, one 3-hole test, and one 6-hole test. Thermal conductivity was obtained by joint curve-fitting of the recorded temperature-time histories. The average in situ thermal conductivity values ranged from approximately 1.74 to 2.10 W/(mK) (DTNs: SN0206F3504502.012 [DIRS 159145]; SN0208F3504502.019 [DIRS 161883]; SN0206F3504502.013 [DIRS 159146]).

3.7.4.3 Rock-Mass Mechanical Properties

3.7.4.3.1 Rock-Mass Strength

Rock-mass mechanical properties have been estimated using the approach proposed by Hardy and Bauer (1991 [DIRS 102920]). This approach uses laboratory test data and the RMR values to estimate mechanical properties at the rock-mass scale for use in equivalent continuum analyses. The estimated properties are listed in Table 3-27. Ranges of the rock-mass properties are estimated, based on RMR from scanline data and the average of the appropriate, intact-rock property. Complete analysis is presented in CRWMS M&O (1997 [DIRS 103564]). Two sets of empirical rock-mass-strength criteria, Yudhbir et al. (1983 [DIRS 108730]) and Hoek and Brown (1988 [DIRS 106158]), were adopted for the drift design methodology, and an average of the two predicted strengths was used to develop a power-law relationship of rock-mass strength versus confining pressure. Design parameters for rock-mass elastic modulus (Serafim and

Pereira 1983 [DIRS 101711]), Poisson's ratio, and Mohr-Coulomb strength were developed for each thermal-mechanical unit.

Rock-mass strengths, based on the empirical strength criteria of Yudhbir et al. (1983 [DIRS 108730]) and Hoek and Brown (1988 [DIRS 106158]), have been developed for the thermal-mechanical units (CRWMS M&O 1997 [DIRS 103564]). Information required for obtaining rock-mass strength includes Q indices, intact-rock, uniaxial-compressive strengths, and the triaxial-compressive strength data. The rock-mass-strength criteria were generated for the five categories of Q, based on frequency of occurrence, of 5, 20, 40, 70, and 90 percent (presented in Section 3.7.4.1).

The equation proposed by Yudhbir et al. (1983 [DIRS 108730]) for calculation of rock-mass strength is:

$$\sigma_1 = A\sigma_c + B\sigma_c \left(\frac{\sigma_3}{\sigma_c}\right)^{\alpha}$$

(Eq. 3-2)

where

σ_1 = strength of the rock mass
A = a dimensionless parameter, dependent on the RMR
σ_c = intact-rock, uniaxial-compressive strength
α, B = rock material constants, dependent on rock type
σ_3 = confining stress

The value of "A" for the rock mass is obtained from the design rock-mass rating by the following equation from Yudhbir et al. (1983 [DIRS 108730]):

$$A = e^{0.0765(RMR_D) - 7.65}$$

(Eq. 3-3)

The material constants B and α are related to the rock type and are determined by a curve-fitting of the confined, compressive-strength test results.

Table 3-28 lists the values of B and α, as well as σ_c, for each unit. For the TCw thermal-mechanical unit, NRG core triaxial-test data were used to determine B and α, using the method outlined in Hardy and Bauer (1991 [DIRS 102920]) and Lin et al. (1993 [DIRS 104585]). These data were originally published in Brechtel et al. (1995 [DIRS 101493]). For the undifferentiated overburden and PTn thermal-mechanical units, NRG uniaxial compression and Brazilian tensile-strength tests were used to determine B and α, with modifications of the method suggested by Hardy and Bauer (1991 [DIRS 102920]) and Lin et al. (1993 [DIRS 104585]). These data were originally published in Brechtel et al. (1995 [DIRS 101493]). For the TSw1 and TSw2 thermal-mechanical units, triaxial-test data from samples from SD-9 and SD-12 were used to determine B and α, using the method outlined in Hardy and Bauer (1991 [DIRS 102920]) and Lin et al. (1993 [DIRS 104585]). Only five data points for each unit were available to evaluate these constants.

The Hoek and Brown (1988 [DIRS 106158]) rock-mass-strength criterion is shown in the following equation:

$$\sigma_1 = \sigma_3 + \sqrt{m\sigma_c\sigma_3 + s\sigma_c^2} \qquad \text{(Eq. 3-4)}$$

where

σ_1 = strength of the rock mass
σ_3 = confining stress
m = a constant that depends on the properties of the rock = $m_i e^{(RMR-100)/28}$
σ_c = intact-rock, uniaxial-compressive strength
s = a constant that depends on the extent to which the rock is fractured = $e^{(RMR-100)/9}$

The parameter m_i is the constant for intact rock and is determined by curve-fitting of the confined compressive-strength test data. Values for m_i are listed in Table 3-28. Data sources and derivations are given in CRWMS M&O (1997 [DIRS 103564]).

The design rock-mass strengths for each Q category were calculated by averaging the strengths determined from both Yudhbir et al. (1983 [DIRS 108730]) and Hoek and Brown (1988 [DIRS 106158]) criteria, following the procedure of Hardy and Bauer (1991 [DIRS 102920]).

A power-law relationship of the form:

$$\sigma_1 = A + B\sigma_3^C \qquad \text{(Eq. 3-5)}$$

was employed to describe the nonlinear, design, rock-mass strength. The parameters A, B, and C were determined by curve-fitting the strength envelopes using a least-squares method and are included in Table 3-27 for 40 percent cumulative frequency for each thermal-mechanical unit. The design rock-mass strength envelopes for the TSw2 unit, based on ESF scanline data, are presented in Figure 3-25. Complete design rock-mass-strength envelopes for other thermal-mechanical units and resulting power-law constants are given for all rock-mass classes in each thermal-mechanical unit in CRWMS M&O (1997 [DIRS 103564]).

The Mohr-Coulomb strength parameters, including cohesion and angle of internal friction and the dilation angle, are commonly used to describe rock-mass strength in numerical analysis. The strength parameters were developed from the least-squares, curve-fits of strength-data pairs (σ_1, σ_3) produced using the power-law criterion described above and summarized for 40 percent frequency in Table 3-27.

A Mohr-Coulomb failure criterion was employed relating the shear and normal stress on the plane of failure to cohesion and angle of internal friction as represented by the following equation:

$$\tau = C_0 + \sigma_n \tan\phi \qquad \text{(Eq. 3-6)}$$

where

C_0 = cohesion

ϕ = angle of internal friction

The least-squares best fit was performed over the range of confining pressures, from 0 to 3 MPa, which is representative of the projected range in minimum principal stresses near the boundary of the excavations. Table 3-27 includes the resulting Mohr-Coulomb strength parameters for 40 percent cumulative frequency of occurrence (see complete results in CRWMS M&O 1997 [DIRS 103564]).

The nonassociated flow rule, suggested by Michelis and Brown (1986 [DIRS 106360]), which uses a dilation angle equal to half the internal friction angle, was considered suitable for the tuff (Hardy and Bauer 1991 [DIRS 102920]). The resulting values for dilation angles are also listed in Table 3-27, with complete results presented in CRWMS M&O (1997 [DIRS 103564]).

Two additional empirical methods were used for assessing rock-mass strength properties: the Geological Strength Index (Hoek and Brown 1988 [DIRS 106158]) and the Rock Mass Index (Palmstrom 1996 [DIRS 106476]; 1996 [DIRS 105310]). Properties estimated included rock-mass elastic modulus, cohesion (intact and joint), friction angle, unconfined compressive strength, and tensile strength. Complete analyses and results are presented in CRWMS M&O (1997 [DIRS 100930]).

In addition, three slot tests were performed in the ESF and the ECRB Cross-Drift, in the Tptpll and Tptpul lithophysal units, to investigate in situ strength and deformability. The tests were designed to evaluate: in situ stress acting normal to the slots, rock-mass deformation moduli, cyclic loading/unloading behavior, and rock strength. Slot Test #2 was also heated to investigate rock-mass thermal-mechanical behavior. Each test is described as follows:

- Slot Test #1– Located in the highly fracture Tptpll (lower lithophysal) unit, in the ESF South Ramp. Two parallel, vertical slots were excavated in the wall, oriented perpendicular to the tunnel. The area of each slot was approximately 2.2 m^2 and the distance between them was 1.2 m. A large-diameter (30.5 cm) borehole was drilled halfway between the slots to observe deformation and failure behavior. The maximum pressure applied in the flatjacks (prior to indication of rock failure) was 6.07 MPa.

- Slot Test #2–Located in a relatively unfractured exposure of the Tptpul (upper lithophysal) unit, in the ESF main tunnel. The test configuration was the same as Test #1, with the addition of six heater boreholes around the test. After the ambient testing, the heaters were operated for two weeks to raise the temperature of the rock volume to approximately 90°C, and a series of mechanical measurements was repeated. The maximum pressure applied in the flatjacks (at indication of rock failure) was 10.7 MPa.

- Slot Test #3–Located in the ECRB Cross-Drift, where the Tptpll (lower lithophysal) tuff was selected to be representative. The test configuration was the same as the other slot tests, except that the location was moved to the floor of the drift to avoid the stress

concentration at the tunnel springline (halfway up the wall). Because of inelastic deformation in response to loading, the maximum flatjack pressure achieved in the test was 6.8 MPa.

Additional details of the slot test methods and results are presented by BSC (2003 [DIRS 166660], Section 8.7.4).

3.7.4.3.2 Rock-Mass Elastic Moduli

Serafim and Pereira (1983 [DIRS 101711]) developed a correlation between the RMR and the rock-mass elastic modulus (*E*) that was recommended for use by Hardy and Bauer (1991 [DIRS 102920]). The correlation is shown in the following equation:

$$E = 10^{\,(RMR\text{-}10)/40} \hspace{4cm} \text{(Eq. 3-7)}$$

where

     E is measured in GPa

Because the equation does not incorporate the intact-rock elastic modulus, the predicted rock-mass elastic modulus can exceed the intact-rock elastic modulus at high RMR values. An upper-bound limit of the rock-mass modulus was, therefore, set equal to the intact-rock modulus (Table 3-28). Calculated rock-mass moduli, based on design RMR values, are shown for 40 percent cumulative frequency of occurrence in Table 3-27. Complete results are presented in CRWMS M&O (1997 [DIRS 103564]).

Rock-mass moduli determined by using the Geological Strength Index and Rock Mass Index described in Section 3.7.4.3.1 resulted in modulus values that significantly exceeded the mean-intact value for the undifferentiated overburden, PTn, and TSw1 thermal-mechanical units, based on field-mapping data (CRWMS M&O 1997 [DIRS 100930]). The Rock Mass Index empirical methodology applied in this analysis resulted in a significantly smaller range of E values that is more consistent with the intact value for these units. The Rock Mass Index method may be a more appropriate empirical methodology for assessing the rock-mass modulus for the range of Q values in the ESF (CRWMS M&O 1997 [DIRS 100930]).

Rock-mass elastic moduli were also determined in situ as part of the SHT, using the NX borehole jack (Goodman jack). Results, procedures, and analysis are described in SNL (1997 [DIRS 106867]) and in CRWMS M&O (1997 [DIRS 101540]). In addition, borehole-jack tests were run before heater startup in August 1996 and again in October 1996, November 1996, and March 1997. Jacking tests were run along the SHT borehole at various depths.

Field rock-mass moduli from borehole jack testing in the SHT block ranged from about 3 to 23 GPa (CRWMS M&O 1997 [DIRS 101540]). The data show thermally induced stiffening of the rock mass in the region near the heater, with rock-mass moduli in this region increasing from 8 GPa in November 1996 to 23 GPa in March 1997. This modulus increase is caused by the closing of fractures by rock-matrix thermal expansion.

Ambient in situ rock-mass moduli, calculated from SHT borehole jacking, are lower than laboratory values determined for intact specimens. This is consistent with previous in situ experiments conducted in welded tuff in G-tunnel, which indicated that the modulus values for in situ tests were about half the intact laboratory-determined value (CRWMS M&O 1997 [DIRS 101540]).

Four plate-loading tests were conducted as part of the DST, two in 1998, one in October 2000, and one in April 2003, to measure the rock-mass deformation modulus at ambient and heated conditions. They were performed in a plate-loading niche opening located at the southeastern corner of the DST (CRWMS M&O 1998 [DIRS 108306]). The test loaded the rock mass horizontally, using large, square-shaped flatjacks that pressed against both walls of the opening. The design of the tests was based on test standards from the International Society of Rock Mechanics (ASTM 1985 [DIRS 149445]; ASTM 1985 [DIRS 160054]). The plate-loading test data suggest a rock-mass modulus ranging from approximately 20 to 60 GPa at this location (DTNs: SN0011F3912298.023 [DIRS 158399]; SN0310F3912298.054 [DIRS 168527]). In general the initial loading and reloading responses were linear (average applied load vs. displacements). The loading and unloading moduli generally increased with applied pressure, and the rock on the hotter side of the test opening (proximal to the DST) was approximately twice as stiff as on the cooler side. The cooler side also exhibited more loading/unloading hysteresis.

3.7.5 In Situ Stress Conditions

Design of the repository requires knowledge of the magnitude, direction, and variability of the preconstruction in situ state of stress for the analysis and design of stable underground openings, as well as for the prediction of short-term and long-term rock-mass deformation. Detailed results of in situ stress measurements in tuffs at Yucca Mountain are contained in Lee and Haimson (1999 [DIRS 129667]).

Table 3-29 presents a summary of the estimated in situ stress at the repository horizon. The direction of the maximum principal stress is vertical, because of the lithostatic load. At the repository level, the vertical stress, on the average, has been taken to be 7.0 MPa (Stock et al. 1984 [DIRS 103148]; CRWMS M&O 1995 [DIRS 101426]). Horizontal stresses are expected to be lower and to range from 3.5 to 4.2 MPa, although the range may be as wide as 2.1 to 7.0 MPa. These in situ stress values were generally confirmed by a stress profile calculated for the ESF test area (Stock and Healy 1988 [DIRS 101022]), which showed a vertical stress of 6.0 MPa at a depth of 300 m (984 ft). Horizontal stress for the same depth ranged from 2.1 to 4.2 MPa.

Hydraulic fracturing tests performed for ambient characterization of the DST block measured in situ stresses in the TSw2 unit (SNL 1997 [DIRS 106854]; CRWMS M&O 1997 [DIRS 101539]). Results were generally consistent, but revealed somewhat lower in situ stresses than previously estimated. Tests were conducted in Borehole ESF-AOD-HDFR#1, drilled from the ESF, at depths approximately 240 to 249 m (787 to 817 ft) below ground surface. The downhole testing equipment consisted of a hydraulic-fracturing, straddle-packer system, which was lowered to predetermined hydraulic-fracturing test intervals. An impression-packer orienting tool was used to obtain an oriented trace of the induced hydraulic fracture on the borehole wall, and test-interval pressure and flow rate were digitally monitored.

A series of five hydraulic-fracturing tests were conducted in the DST block, but only one test yielded what were considered reliable results. Based on this test result, the principal horizontal stresses around this borehole were estimated to be (SNL 1997 [DIRS 106854]): σ_h (least-horizontal principal stress) = 1.7 ($\pm$ 0.1) MPa acting in the N75°W ($\pm$ 14°) direction and σ_H (greatest-horizontal principal stress) = 2.9 ($\pm$ 0.4) MPa acting in the N15°E ($\pm$ 14°) direction. Because vertical stress was not measured, it was approximated as the weight of the overburden at the depth of the tests as follows (SNL 1997 [DIRS 106854]): σ_v (vertical stress) = 3.7 MPa.

Although the measured horizontal stresses differ, both are smaller than the vertical stress. This measured-stress regime, one of low horizontal magnitudes, is in accord with the predominant local normal faults. The north-northeastern, maximum-horizontal, stress direction is subparallel to the average strike of these faults and is supported by previous measurements in the Yucca Mountain area (Zoback and Healy 1984 [DIRS 108657]). Additional information is presented in SNL (1997 [DIRS 106854]) and CRWMS M&O (1997 [DIRS 101539]).

3.7.6   Excavation Characteristics of the Rock Mass

Geotechnical monitoring data were developed during excavation of the north ramp starter tunnel and upper Tiva Canyon Alcove to provide the basis for design verification. The north ramp starter tunnel was constructed to prepare for the construction of the ESF north ramp, main drift, and south ramp. The upper Tiva Canyon Alcove was excavated off the north ramp starter tunnel to provide access for site characterization testing. Design-verification studies are being performed to monitor and observe the long-term behavior of openings in the range of rock conditions to be encountered in the repository host rock, to observe and evaluate the construction of the ESF (with respect to implications for repository construction and performance), and to collect information for design of the ventilation systems in the repository (DOE 1988 [DIRS 100282]).

3.7.6.1   Excavation Methods Used at Yucca Mountain

Both SNL (1995 [DIRS 106851]) and CRWMS M&O (1997 [DIRS 101537]) addressed evaluations of mining methods and monitoring of ground-support systems and drift stability. Rock-mass-quality evaluations, an evaluation of as-built mapping data, and blast-vibration monitoring were performed as part of the mining-methods evaluation. An evaluation of rock-structure data from surface and underground mapping is presented in Section 3.7.2; an evaluation of Q data is presented in Section 3.7.4, and blast monitoring is discussed in this section and in CRWMS M&O (1997 [DIRS 103564]).

The north ramp starter tunnel was constructed to launch the 7.6 m (24.9 ft) diameter tunnel-boring machine to construct the ESF north ramp, main drift, and south ramp. The north ramp starter tunnel, upper Tiva Canyon Alcove, Alcove 2, and sections of the Alcove 5 thermal testing facility were excavated by drilling and blasting. In addition, the ECRB Cross-Drift was excavated by a tunnel-boring machine, with a starter tunnel excavated by drill and blast methods.

3.7.6.2 Potential Airborne Particulate Health Hazards during Excavation

Potential health hazards during excavation include the effects of minerals that become airborne during tunneling operations, which can produce respiratory ailments. Specific safety and health concerns related to rock-mass mineralogies at Yucca Mountain include respiratory effects of the zeolite, erionite, and the silica minerals, including quartz and cristobalite, encountered during daily underground activities. These minerals occur in varying proportions in the different lithologies at Yucca Mountain, as reported in Vaniman et al. (1996 [DIRS 105946]).

Health-related issues associated with airborne mineral particles released by excavation at Yucca Mountain were evaluated by combining quantitative x-ray diffraction analyses of mineral distributions with published information on mineral toxicity and carcinogenicity. The risk from the minerals that may be of potential concern as airborne particles during construction or operation can be minimized by safe, modern mining practices (e.g., by maintaining low dust levels and adequate ventilation). The crystalline silica minerals fall into this category.

Apart from vitric and vitrophyre zones at Yucca Mountain, the crystalline silica minerals are typically 3 to 40 percent by weight for all other tuff units, including the devitrified rhyolitic Topopah Spring Tuff (in which the ESF and the repository horizon are located). The silica minerals in these devitrified rocks are generally quartz and cristobalite, with more variable and generally lesser amounts of tridymite. However, the vitric tuffs are rocks with inherently low abundances of crystalline silica. Total crystalline-silica abundances in these vitric tuffs are all 7 percent or less. Typical abundances are about 4 percent by weight.

Some potentially hazardous minerals, such as palygorskite, sepiolite, and mordenite, are limited in location to fractures, so exposures to these minerals will likely be minimal, particularly if low dust levels are maintained. In addition, palygorskite is generally at depths shallower than the repository horizon, and mordenite is in the deeper zeolitized units below the repository horizon. Consequently, these minerals probably pose a minimal risk at Yucca Mountain.

Erionite, a fibrous zeolite, has been determined to have a carcinogenic potential and may pose a risk if encountered in sufficient quantity, even when standard, modern mining practices are followed. However, the presence of erionite at Yucca Mountain appears to be restricted to zones immediately below the repository horizon and in the lower Tiva Canyon Tuff.

Dust and wall-rock samples were analyzed from tunnel-boring machine water-use and surfactant-use test intervals, as well as from routine tunnel-boring machine operations in the ECRB at Yucca Mountain. Dust production was diminished by about half with water application at the cutter head, but adding surfactant to the applied water caused increased dust production comparable to the dust produced during dry excavation (Harrington 1998 [DIRS 124658]).

Constituent minerals of the unexcavated bulk rock are fractionated by tunnel boring machine fragmentation. Silica-mineral abundances within respirable size materials in the Tptpul horizon vary individually, but are cumulatively only 60 to 75 percent of their abundance in the unexcavated rock (Harrington 1998 [DIRS 124658]).

3.7.6.3   Ground Support

Ground support in the ESF includes rock bolts, lattice girders, steel-fiber reinforced shotcrete, and steel sets (CRWMS M&O 1997 [DIRS 103564]). Wire mesh and channel straps are used to control loose materials between rock bolts. Rock-bolt monitoring was accomplished using rock-bolt load cells and instrumented rock bolts. Convergence pins were attached to the lattice girders in the first 10 m (33 ft) of the ESF to monitor the displacement of these components of the ground-support system. Vibrating wire-strain gauges and convergence pins were attached to steel sets throughout the ESF to monitor the changes in rock loading. Convergence-pin arrays and borehole extensometers were installed in rock supported by Swellex bolts (CRWMS M&O 1997 [DIRS 103564]).

3.7.6.3.1   Measured Rock-Bolt Loads

Rock-bolt load cells were installed along the north ramp starter tunnel and on the highwall at the North Portal. All bolts had some load bleed-off and have settled into generally stable trends, in which bolt loads are relatively constant. No load increases that would indicate rock loosening were observed from the time of installation to June 1996. The bolt loads that were used range from 0.1 to 16.0 percent of the bolt-yield strength (CRWMS M&O 1997 [DIRS 103564]).

The results from instrumented rock bolts in the upper Tiva Canyon Alcove were similar to those observed in other areas, with bolt loads remaining well below the bolt-yield strength (SNL 1995 [DIRS 106851]).

Eight rock-bolt load cells were also installed as part of the SHT to evaluate the effects of elevated temperature on bolt performance. Complete data and analysis are presented in SNL (1997 [DIRS 106867]) and CRWMS M&O (1997 [DIRS 101540]). Four rock bolts were installed on the heated side of the thermal-mechanical alcove below the level of the heater, and four additional bolts were installed on the opposite, cool side of the alcove. The load measured in all the load cells has generally decreased, with an average decrease of 1.37 percent for rock bolts on the ambient (cool) side and 3.45 percent for rock-bolts on the heated side. The two largest decreases were measured in the rock-bolt load cells nearest the heater (CRWMS M&O 1997 [DIRS 101540]).

3.7.6.3.2   Portal Lattice Girder Deformation

Deformation of the portal lattice girders embedded in shotcrete was tracked using convergence data collected by a tape extensometer. The deformations have remained fairly constant after the initial settling (SNL 1995 [DIRS 106851]), and the monitoring data from June 1995 to June 1996 showed a continuing trend of no closure (CRWMS M&O 1997 [DIRS 101537]).

3.7.6.3.3   Steel Set Deformation

Vibrating wire-strain gauges were installed on 33 steel sets from January 1995 through June 1996. The strain gauges were attached to the steel sets both before and after installation in the tunnel. When the gauges were attached before installation, stress changes in the web of the steel sets caused by jacking loads were monitored during the steel-set installation process. Strain changes that occurred during jacking installation indicated a generally similar pattern of tensile

and compressive stress change in the steel. The measured strain changes during jacking indicated stress changes between 10 and 180 MPa (CRWMS M&O 1997 [DIRS 101537]).

Strains remained generally constant after installation, indicating an absence of rock-loading around the steel sets being monitored. Most of the steel sets were installed in the Tiva Canyon and in the undifferentiated overburden units. However, similar trends were observed for steel sets in the Paintbrush units (CRWMS M&O 1997 [DIRS 103564]).

3.7.6.3.4 Installed Ground Support versus Rock-Mass-Quality Projections

Installed ground support has been compared to ground support as projected, based on the Q determined for 5 m (16.4 ft) intervals for the ESF (CRWMS M&O 1997 [DIRS 103564]; 1997 [DIRS 100930]). Projected ground-support classes were defined as a function of the Q value that would provide the recommended ground support to cover the expected range of ground conditions. The installed ground-support classes are shown in Figure 3-25, together with the spatial distribution of $Q_{modified}$ values. The installed ground-support class was generally in agreement with, or more conservative than, the scanline-based $Q_{modified}$ value (CRWMS M&O 1997 [DIRS 100930]).

3.7.7 Dynamic Rock and Soil Properties

BSC (2002 [DIRS 157829]) presents a compilation and provides basic interpretation of data acquired during 2000 and 2001 for use in evaluating ground motions for the Yucca Mountain Site Characteristic Project, and also for use in developing recommendations for foundations for surface facilities at the North Portal. The data acquired in 2000 and 2001 included geologic data from borings and test pits, shear-wave and compression-wave arrival times from downhole seismic surveys, shear-wave and compression-wave travel times from suspension-seismic surveys in boreholes, caliper and gamma-gamma wireline surveys in boreholes, shear-wave velocity profiles from spectral analysis of surface waves (SASW) surveys, and laboratory RCTS tests. Data were acquired in the surface facilities area, along the north ramp and main drift of the ESF, near the crest of Yucca Mountain, and in the Fran Ridge Borrow Area.

3.7.7.1 Surface Facilities Area

Fifteen Boreholes (UE-25 RF #14 through UE-25 RF #29) and four test pits (TP-WHB-1 through -4) were completed in the surface facilities area. Locations of the borings and test pits are presented in BSC (2002 [DIRS 157829], Figure 2). Geologic data acquired in the boreholes included depth below ground surface of lithostratigraphic subunit contacts; depth below ground surface and dips of faults and other structural features; rock hardness, welding, and fracture density; percent-core recovery, and RQD. Detailed geologic borehole logs are presented in BSC (2002 [DIRS 157829], Attachment I). Each of the test pits was mapped and logged and results of the mapping are shown on test-pit logs and photomosaic test-pit maps presented in BSC (2002 [DIRS 157829], Attachments III and IV).

3.7.7.1.1 In-Situ Geoseismic Surveys

The collection, analyses, and estimates of shear-wave velocities and compression-wave velocities from downhole seismic-velocity surveys in 16 Boreholes (UE-25 RF #14 through

UE-25 RF #29) at the surface facilities site are described in BSC (2002 [DIRS 157829]).
Measurements were obtained in both rock and overlying surficial soil. Shear-wave and
compression-wave velocity profiles, along with generalized lithology taken from the borehole
logs, are presented in BSC (2002 [DIRS 157829], Figures 4 to 19). Values of shear-wave
velocity and compression-wave velocity measurements are summarized for all boreholes in BSC
(2002 [DIRS 157829], Figures 20 and 21). Overall, the shear-wave velocities increased with
depth in the top 30 m, and similar trends were observed in the compression-wave profiles
(BSC 2002 [DIRS 157829]). Calculated mean, median, and mean plus one standard-deviation
velocity profiles are also presented in BSC (2002 [DIRS 157829], Figures 22 and 23). Values of
Poisson's ratio were calculated from shear-wave and compression-wave velocities and, in
general, a range of values from 0.15 to 0.40, typical of geologic materials, is indicated for most
of the velocity layers (BSC 2002 [DIRS 157829]).

Suspension seismic P and S wave logging was also performed in Boreholes UE-25 RF #14
through UE-25 RF #29 at the surface facilities site and is described in detail in BSC (2002
[DIRS 157829]). The shear-wave interval-velocity data obtained in the borings were examined
statistically in two ways. The data acquired at 0.5 m (1.6 ft) intervals were divided into 1.5 m
(4.9 ft) sets and the mean, median, mean-plus-one standard deviation, and mean-minus-one
standard deviation were calculated for each set. These values are presented graphically in BSC
(2002   [DIRS 157829],   Figures 30   and 31])   for   both   receiver-to-receiver   and
source-to-near-receiver   travel-time   differences.   The   data   were   also   divided   into
lithostratigraphic units, and the same statistical parameters were calculated and are also
presented in BSC (2002 [DIRS 157829], Figures 32 and 33). The compression-wave,
interval-velocity data were examined statistically in the same way and the results presented in
BSC (2002 [DIRS 157829], Figures 34 and 35) for source-to-receiver data only. Poisson's ratio
was calculated from the shear-wave and compression-wave velocities and examined statistically
in the same manner as the shear-wave and compression-wave data. Plots of calculated Poisson's
ratio by depth interval and by lithostratigraphic unit are included in BSC (2002 [DIRS 157829],
Figures 36 and 37).

SASW surveys were performed during 2000 and 2001 to estimate the shear-wave velocity
structure to a depth of approximately 45 m at closely spaced intervals near the footprint of the
surface facilities area (BSC 2002 [DIRS 157829]). A total of 40 SASW surveys were performed
in the area of the surface facilities, and the locations of the survey lines are presented in BSC
(2002 [DIRS 157829], Figure 43). Five of the surveys were combined with other adjacent
surveys, and the results of the 35 shear-wave velocity profiles estimated from the SASW surveys
are presented in BSC (2002 [DIRS 157829], Figures 54 to 89). Most of the profiles are similar
to, and begin with, shear-wave velocities near the surface of less than 300 m/s and quickly
increase to velocities of 750 to 1,250 m/s at depth. Mean, median, and mean-plus and minus-one
standard-deviation profiles for all the profiles are also presented in BSC (2002 [DIRS 157829],
Figure 91).

Caliper and gamma-gamma wireline surveys were performed in Boreholes UE-25 RF #16,
UE-25 RF #18,   UE-25 RF #20,   UE-25 RF #21,   UE-25 RF #22,   UE-25 RF #24,   and
UE-25 RF #28. Results of the density measurements obtained from the gamma-gamma surveys
are presented in BSC (2002 [DIRS 157829], Table 12 and Figure 101). A trend of increasing

density with depth can be observed in the data from southeast of the Exile Hill fault splay, and another can be observed between density and lithostratigraphic unit (BSC 2002 [DIRS 157829]).

Comparisons of shear-wave velocities from downhole and suspension-survey methods were made by plotting the shear-wave velocity profiles on common graphs for visual comparison (BSC 2002 [DIRS 157829], Figures VII-1 to VII-16). Comparisons were also made based on interpreted velocity profiles and plots of accumulated travel time versus depth-and-average shear-wave velocity versus depth were compared (BSC 2002 [DIRS 157829], Figures VIII-1 to VIII-16 and VIII-17a to VIII-23a). Finally, quarter-wave amplification ratios were calculated and plots of amplification ratio versus depth for the deeper profiles were presented in BSC (2002 [DIRS 157829], Figures VIII-17b to VIII-23b). BSC (2002 [DIRS 157829]) presents detailed discussions of the comparisons in individual boreholes and indicates that the agreement between downhole and suspension results is sometimes very good and sometimes only fair. Additional details regarding the comparisons of shear-wave velocities from borehole seismic methods, including the methods used to calculate travel time, average shear-wave velocity, and quarter-wavelength amplification ratio, are presented in BSC (2002 [DIRS 157829]).

3.7.7.1.2   Laboratory Tests

Laboratory tests using RCTS equipment were performed to evaluate the dynamic properties of both rock (tuff) and surficial soil (alluvium) from the surface facilities area. The tuff and alluvium samples were from Boreholes UE-25 RF #14 to UE-25 RF #17. Eighteen samples of intact tuff specimens and one reconstituted alluvial specimen were tested. The values of shear-wave velocity (V_s), shear modulus (G_{max}), and material damping ratio (D_{min}) measured at small shearing strains (strains less than 0.00035) for the tuff and alluvial specimens, are summarized in BSC (2002 [DIRS 157829], Tables 19 to 22).

Variations in G_{max}, with normalized confining pressure for tuff samples measured by resonant column testing, are presented in BSC (2002 [DIRS 157829], Figures 115 to 117). In general, only small increases in G_{max} were exhibited, with ranges in confining pressures from ¼ to 4 times the in-situ mean total stresses ($\sigma_{in\text{-}situ}$). The variation in V_s, measured at ($\sigma_{in\text{-}situ}$), with dry-unit weight of tuff specimens is shown in BSC (2002 [DIRS 157829], Figure 118). There is a general trend of increasing V_s with increasing dry-unit weight and a similar trend between total-unit weight and V_s was observed. Variations in D_{min} with normalized confining pressure for tuff samples, are also shown in BSC (2002 [DIRS 157829], Figures 120 to 122). As for G_{max}, D_{min} shows little effects of confining pressure. The effects of time of confinement at a constant isotropoic stress state and excitation frequency on G_{max} and D_{min} for tuff samples were also investigated and found to be small. The nonlinear behavior of tuff specimens, including the influence of shearing strain on the shear modulus and damping ratio, were also investigated and presented in BSC (2002 [DIRS 157829], Figures 123 to 138).

The effects of confining pressure on G_{max} and D_{min} for the reconstituted alluvium sample were investigated, and the sample was observed to behave like a granular soil (BSC 2002 [DIRS 157829], Figures 139 and 140). The effects of excitation frequency on G_{max} and D_{min} for the alluvium sample were found to be small. The influence of shearing strain on the shear modulus and damping ratio are presented in BSC (2002 [DIRS 157829], Figures 141 to 143) and indicate the material is behaving like a granular soil. Additional information regarding the

testing procedures and the resulting small-strain and nonlinear behavior of the intact tuff specimens and the small- and large-strain behavior of the reconstituted alluvial specimen is presented in BSC (2002 [DIRS 157829]).

3.7.7.2 North Ramp and Main Drift of the Exploratory Studies Facility

SASW surveys were performed in the ESF main drift tunnel in 2001. A total of five surveys were performed along the north-south drift in the ESF at the locations indicated in BSC (2002 [DIRS 157829], Figure 144). The purpose of these measurements was to provide information on the shear-wave velocity structure between the emplacement area and the crest of Yucca Mountain. The sites were selected to represent a range in materials exposed along the main drift (BSC 2002 [DIRS 157829]). The dynamic properties of five tuff specimens from the North Portal area of the ESF were also evaluated in the laboratory using RCTS equipment.

The shear-wave velocity profiles obtained from the SASW surveys are presented in BSC (2002 [DIRS 157829], Figures 145 to 149). The SASW results in the tunnel demonstrate that the intact rock with few fractures exhibits shear-wave velocities in the range of 1,800 to 2,100 m/s. Where the tuff fractures near the tunnel walls, these values are in the range of 900 to 1,200 m/s (BSC 2002 [DIRS 157829]). These tests probably did not sample the most highly fractured or most unfractured exposures of tuff in the ESF.

Five intact tuff specimens obtained from large-diameter core samples from the North Portal area of the ESF were dynamically tested. The initial specimen properties and the test pressures and types of tests performed are presented in BSC (2002 [DIRS 157829], Tables 23 and 24). In general, the small-strain behavior of the tuff was found to be similar to that of the tuff obtained from the surface facilities area (BSC 2002 [DIRS 157829], Figures 152 and 153). The effects of excitation frequency on G_{max} and D_{min} were found to be small. The influence of shearing strain on the shear-modulus and damping ratio are presented in BSC (2002 [DIRS 157829], Figures 154 to 156). These specimens show more nonlinearity than those obtained from the surface facilities area and these differences were thought to be attributed to disturbances from the tunnel-boring process and the likelihood of micro-cracking in the specimens.

3.7.7.3 Crest of Yucca Mountain

A program of shallow, downhole-velocity measurements and SASW surveys along the Yucca Mountain crest and downslope (east) was performed in 2000 and 2001 (BSC 2002 [DIRS 157829]). Vertical seismic profiling surveys had previously been performed in six boreholes (Daley et al. 1994 [DIRS 149544]), but only one borehole was located within the surface projection of the emplacement area as defined in July 2001 (BSC 2002 [DIRS 157829], Figure 157).

3.7.7.3.1 Spectral Analysis of Surface Waves Surveys

A total of 33 SASW surveys were performed during 2000 and 2001 on top of Yucca Mountain, generally above the emplacement area at the locations indicated in BSC (2002 [DIRS 157829], Figure 157). All individual shear-wave velocity profiles are presented in BSC (2002 [DIRS 157829], Figures 161 to 191). A composite profile is presented in BSC (2002 [DIRS 157829],

Figure 192). The median, mean, and 16th and 84th percentile-profiles are also shown in BSC (2002 [DIRS 157829], Figure 193). Many of the profiles indicate low-velocity zones beneath the higher-velocity rock and are consistent with the limited downhole shear-wave velocity data (BSC 2002 [DIRS 157829]).

Of the 22 surveys performed along or near the crest, 13 surveys were orientated approximately parallel to the crest of Yucca Mountain, and nine were orientated approximately perpendicular to the crest, and generally downslope of the crest. A comparison of the mean shear-wave velocity profile from surveys orientated parallel to the crest, and the mean profile from surveys orientated perpendicular to the crest, indicates a difference of up to about 180 m/s in the top 45 m (148 ft) (BSC 2002 [DIRS 157829], Figure 196). It was speculated in BSC (2002 [DIRS 157829]) that this difference may be related to anisotropy because of fracturing in the near-surface volcanic units of Yucca Mountain.

Three SASW surveys were performed to measure the shear-wave velocity of the exposed, visually intact but weathered rock. Because of the rock outcrop size, only very close receiver spacings (0.15 m to 0.3 m [0.5 to 1 ft]) could be used. The shear-wave velocities ranged from about 975 to 1,430 m/s, and the three shear-wave velocity profiles are presented in BSC (2002 [DIRS 157829], Figure 191). The shear-wave velocities from the exposed rock are much higher than the velocities recorded for wavelengths ranging from approximately 1.5 to 6 m (4.9 to 19.7 ft) from the other surveys. These results illustrate the difference between local and global measurements of surface-wave velocity at a discontinuous rock or soil (or both) site with lateral variability (BSC 2002 [DIRS 157829]).

3.7.7.3.2   Downhole Seismic Surveys

Shear-wave and compression-wave velocities were measured in eight existing boreholes along, or near, the crest of Yucca Mountain in 2002. These downhole velocity surveys were performed in the few open boreholes, previously used for neutron-logging, above the emplacement area on Yucca Mountain. A list of the neutron-logging holes that were surveyed and their locations are presented in BSC (2002 [DIRS 157829], Table 25 and Figure 202).

Very little of the compression-wave data acquired in these surveys were usable. Final values of the shear-wave velocities are presented in BSC (2002 [DIRS 157829], Table 26 and Figures 203 to 210). A composite of all profiles is presented in BSC (2002 [DIRS 157829], Figure 211), illustrating the large variability in the shear-wave velocities in the top 15 m. This variability is also reflected in the mean, median, and plus-and-minus-one, standard-deviation profiles shown in BSC (2002 [DIRS 157829], Figure 212). The wide range in the values of shear-wave velocities and the apparent lack of stratigraphic correlation between holes, demonstrate the heterogeneous nature of the volcanic deposits that comprise the Yucca Mountain site (BSC 2002 [DIRS 157829]).

3.7.7.4   Fran Ridge Borrow Area

The dynamic properties of ten reconstituted specimens from the Fran Ridge Borrow area were evaluated using RCTS equipment. The specimens were compacted to dry densities that ranged from 90 to 97 percent of the maximum dry density determined during the laboratory

static-testing program. Four of the specimens were tested in two stages to evaluate the small- and large-strain properties at molding water contents during the first stage, and at increased water content during the second stage to investigate the impact on the dynamic properties of increasing the water content of the fill after placement. The test pressures and types of tests performed on the specimens are presented in BSC (2002 [DIRS 157829], Table 30).

The variation of G_{max} with confining pressure for the 10 specimens is presented in BSC (2002 [DIRS 157829], Figure 218). Results of the dynamic testing indicated that G_{max} generally increased with increasing dry-unit weight and, for the denser specimens, decreased with increasing water content. The variation of D_{min} with confining pressure for the 10 specimens is presented in BSC (2002 [DIRS 157829], Figure 219). The values of D_{min} decreased with increasing confining pressure, as expected. The influence of shearing strain on the shear modulus and damping ratio were found to be small. Complete details and results of the dynamic testing program are presented in BSC (2002 [DIRS 157829]).

3.7.8 Engineering Properties of Surficial Material

3.7.8.1 Surficial Sedimentary Deposits

The late Tertiary and Quaternary surficial sedimentary deposits of the Yucca Mountain area consist of colluvium, fan alluvium, eolian sand sheets, ramps and dunes, and spring discharge or marsh deposits (see Section 3.3). These range in age from Pliocene to Holocene. The deposits are grouped into eight major units, plus locally important eolian and marsh deposits (described in detail in Section 3.3.6).

Man-made fill overlies colluvial and alluvial material at the North Portal Pad, an area approximately 244 to 366 m (800 to 1,200 ft) by 183 to 213 m (600 to 700 ft) where the ESF tunnel portal was constructed. Muck piles along the eastern side of the North Portal Pad rise to about 5.2 to 9.1 m (17 to 30 ft) above the pad surface (CRWMS M&O 1999 [DIRS 109209]).

3.7.8.2 Surficial Soil Investigations

3.7.8.2.1 Investigations at the North Portal Area

A preliminary geotechnical investigation was conducted between October 1998 and March 1999 for the design of the surface facilities at the North Portal Pad. The results are presented in CRWMS M&O (1999 [DIRS 109209]). Additional data were acquired during 2000 and 2001 for use in developing foundation recommendations for the surface facilities at the North Portal. BSC (2002 [DIRS 157829]) documents the acquisition of geologic, geophysical, and geotechnical data to support engineering calculations for surface facilities as well as ground motion analyses for the repository. Geotechnical evaluations and recommendations for foundations for the surface facilities are presented in BSC (2002 [DIRS 159262]). The surface facilities include several structures planned for construction in the North Portal area.

Logs of 15 borings (UE-25 RF #14 through UE-25 RF #29) drilled in the surface facilities area between June 2000 and November 2002 are presented in BSC (2002 [DIRS 157829]). These borings ranged in depth from about 30 to 210 m below ground surface and were performed to supplement previous borings made in the site vicinity, including UE-25 RF #13 described in

CRWMS M&O (1999 [DIRS 109209]). BSC (2002 [DIRS 157829]) also presents the logs of four test pits (TP-WHB-1 through -4) excavated to study and analyze soil properties in the surface facilities area. Six 1.8 m (5.9 ft) ring-density tests and sixteen 0.5 m (1.6 ft) sand-cone density tests were performed within the test-pit excavations, and the results of the tests are summarized in BSC (2002 [DIRS 157829], Table 6). A plot of the total densities measurements in the alluvium obtained from the test pits, gamma-gamma surveys, and previous data is also presented in BSC (2002 [DIRS 157829], Figure 236).

Based on available information, including construction records, the North Portal Pad fill-material consists of coarse granular alluvium and colluvium, and tuffaceous rocks excavated from various sources. Some of the fill was placed to create a working platform for construction operations that supported scientific experiments conducted in the ESF, and tunnel muck was also discharged around the edge of the construction pad. The materials were placed in a manner that was not well documented (CRWMS M&O 1999 [DIRS 109209]), and so it is not considered an engineered fill (CRWMS M&O 1999 [DIRS 109209]). Nonengineered fill was encountered in 10 of the 16 boreholes that have been advanced in the North Portal area since construction of the fill pad began in 1992 (BSC 2002 [DIRS 157829]). The extent of nonengineered fill is described in BSC (2002 [DIRS 157829]).

Surficial deposits encountered at the surface or beneath existing fill in the North Portal Area include alluvium, colluvium, and minor windblown deposits, and are collectively referred to in this section as alluvium. Of the sixteen recent borings (UE-25 RF #13 through UE-25 RF #29) performed in the North Portal Area, all but RF#15 encountered alluvium at the ground surface or beneath 1.5 to 8.5 m (4.9 to 28 ft) of fill. The maximum thickness of alluvium reported in the boring logs was 36.6 m (120 ft) in boring RF #19 (BSC 2002 [DIRS 157829]). All four of the test pits TP-WHB-1 through -4 encountered alluvium over their full depth of approximately 6 m (19.7 ft) below ground surface (CRWMS M&O 1999 [DIRS 109209]).

The alluvium consists primarily of interbedded caliche-cemented and noncemented, poorly sorted, course-grained gravel, with sand and some fines, cobbles, and boulders (BSC 2002 [DIRS 159262]). The fines content of samples of alluvium from the test pits and boreholes are generally low, usually between 3 and 20 percent, but can be as high as 40 percent in the near-surface colluvium near Exile Hill (CRWMS M&O 1999 [DIRS 109209]). Based on visual logging (BSC 2002 [DIRS 157829]), the alluvium classifies in the Unified Soil Classification (ASTM D 2487-00 2000 [DIRS 159575]) system primarily as poorly-graded gravel (GP), poorly-graded gravel with silt (GP-GM), and well-graded gravel with silt (GW-GM).

The equivalent Standard Penetration Test (SPT) N_1 values (SPT test results corrected to overburden pressure of 0.1 MPa) are greater than 50 (CRWMS M&O 1999 [DIRS 109209]). The dense nature of the alluvial material is also indicated by the relative high values of shear-wave velocity measured in the downhole and suspension surveys at Boreholes UE-25 RF #13 through UE-25 RF #29 and by SASW surveys on, and adjacent to, the existing fill pad (BSC 2002 [DIRS 157829]).

Geotechnical laboratory tests were performed on samples of the alluvium obtained from test pits TP-WHB-1 through -4. These tests included particle-size distribution, water content, maximum and minimum index-unit weights, specific gravity, and liquid and plastic limits. The test results

are summarized in BSC (2002 [DIRS 157829], Table 13). Because of the granular nature of the alluvium and paucity of clay particles (as inferred from the results of liquid and plastic limits tests) the alluvium's expansion potential is insignificant (BSC 2002 [DIRS 159262]). Based on the relative density values measured by the in situ tests in test pits TP-WHB-1 through -4, the alluvium has a relative density greater than 50 percent and is generally medium dense to dense (BSC 2002 [DIRS 159262]).

Geotechnical design recommendations for the engineering properties of the alluvium at the surface facilities are presented in BSC (2002 [DIRS 159262], Table 3). Recommended design values for moist unit weight, shear strength, compressibility, and interface-friction coefficient are presented. Details regarding the development of the geotechnical parameters are presented in BSC (2002 [DIRS 159262]). The recommended design parameters were based on field-investigation and laboratory-test data summarized in BSC (2002 [DIRS 157829]).

3.7.8.2.2   Other Investigations in the North Portal and Midway Valley Areas

There have been numerous other investigations to determine the physical properties of soils in the site vicinity, primarily the North Portal and the Midway Valley areas. Between 1984 and 1985, three studies (Neal 1985 [DIRS 101618]; 1986 [DIRS 102331]; Ho et al. 1986 [DIRS 102324]) addressed surface facilities and soils. Neal (1985 [DIRS 101618]) presents the general boring logs for eight exploratory borings (UE-25 RF #1 through UE-25 RF #8) in the vicinity of Exile Hill. Neal (1986 [DIRS 102331]) incorporates three additional holes (UE-25 RF #9, UE-25 RF #10, and UE-25 RF #11) and extends the depth of one of the original holes (UE-25 RF #3). A study in 1986 (Ho et al. 1986 [DIRS 102324]) involved four test trenches in the western portion of Midway Valley and south of Exile Hill. The test pits, in general, corresponded to exploratory boring locations UE-25 RF #1, UE-25 RF #2, UE-25 RF #3, and UE-25 RF #5.

Another investigation (McKeown 1992 [DIRS 102330]) studied the surficial materials for the North Ramp Surface Facility of the ESF. The report is based on data from geologic mapping, pavement mapping, 73 test pits, laboratory test data on samples from seven test pits, and four Boreholes: UE-25 RF #1, UE-25 RF #10, and UE-25 RF #11, located in Midway Valley, and UE-25 NRG #1.

McKeown (1992 [DIRS 102330]) found that the soil is generally composed of silty sand and silty gravels, with fines ranging from 4 to 30 percent, with much smaller amounts of clayey sand and clayey gravel, with fines ranging from 29 to 40 percent. Physical property data and test-pit logs for seven portal-pad test pits and 39 road-alignment test pits are reported (McKeown 1992 [DIRS 102330]). These seven portal-pad test pits are representative of materials and foundation conditions for the ESF North Ramp Surface Facility.

All the soil in the North Ramp Surface Facility pad area is carbonate-cemented to some degree. The soil is caliche-cemented from just below the surface to several feet deep adjacent to the hill and decreasing away from the hill. However, the material appeared to be adequate for founding the relatively temporary, low-load structures contemplated. Calculations, estimated settlement, and references were also reported (McKeown 1992 [DIRS 102330]).

A recent study (Swan et al. 2001 [DIRS 158784]) presented the results of investigations to characterize the surficial deposits and quaternary faulting in Midway Valley. An integral part of the surficial geology studies was the siting and excavation (or reexcavation) of five trenches: MWV-T4, -T5, -T6, -T7, and A/BR-3. Locations of the trenches and detailed descriptions of the thick alluvial deposits in Midway Valley are presented in Swan et al. (2001 [DIRS 158784]).

3.7.8.2.3   Investigations for Potential Borrow Areas

Between 1988 and 1989, two studies were conducted of three potential borrow-pit areas for the ESF (Holmes & Narver 1989 [DIRS 105117]; Daffern and Thummala 1988 [DIRS 105116]). The locations of these pit areas are shown in Holmes & Narver (1989 [DIRS 105117] Exhibit 1). These reports present estimated quantities of aggregate and fill material. A gravel pit near the northeast side of Fran Ridge, southeast of Yucca Mountain, supplies select fill, road gravel, and backfill (McKeown 1992 [DIRS 102330]). Four samples of alluvial sand and gravel were obtained from this existing borrow area in 2001 to evaluate it as a potential source of the engineered fill for future North Portal surface facilities (BSC 2002 [DIRS 157829]).

The four samples obtained from widely spaced locations at the Fran Ridge Borrow Area were combined into a single sample and subsequently split so that various geotechnical laboratory static and dynamic tests could be performed. Static laboratory testing included particle-size distribution, maximum and minimum index-unit weights, specific gravity and absorption, liquid and plastic limits, compaction characteristics, and triaxial tests. Dynamic tests were performed on reconstituted samples using RCTS equipment.

The composite sample obtained from the Fran Ridge Borrow area was classified as poorly-graded sand (SP) according to the *Unified Soil Classification System* (ASTM D 2487-00 2000 [DIRS 159575]) but included 48.3 percent gravel-size particles and could be assigned a borderline classification of SP/GP. Liquid-and-plastic-limits tests indicated that the soil sample was nonplastic. A compaction test performed in accordance with ASTM D 1557-91 (1998 [DIRS 102391]) indicated a maximum dry-weight unit-weight of 1.82 g/cm^3 and an optimum water content of 11 percent (BSC 2002 [DIRS 157829] Figure 215). Triaxial tests were performed under isotropically consolidated, drained conditions at confining stresses ranging from 0.056 to 0.42 MPa. Two strength envelopes were fitted to the triaxial data, including a traditional straight line Mohr-Coulomb failure envelope and a curved-failure envelope that reflects the influence of confining pressure on shear strength. Details from the static laboratory testing program are presented in BSC (2002 [DIRS 157829]).

The dynamic properties of ten specimens of the proposed fill material for the surface facilities foundations were evaluated in the laboratory using RCTS equipment. Results of the dynamic tests are discussed in Section 3.7.7.4. Complete details of the dynamic testing program on the proposed fill materials from the Fran Ridge Borrow area are presented in BSC (2002 [DIRS 157829]).

Geotechnical design recommendations for engineered fill obtained from the Fran Ridge Borrow Area for use at the surface facilities are presented in BSC (2002 [DIRS 159262], Table 3). Recommended design values for moist-unit weight, shear strength, compressibility, and

interface-friction coefficient are presented. Details regarding the development of the geotechnical parameters are presented in BSC (2002 [DIRS 159262]. The recommended design parameters were based on field investigation and laboratory testing data summarized in BSC (2002 [DIRS 157829]).

3.7.9 Summary

Geoengineering properties data were developed in both the laboratory and the field. These properties have been described in the context of their relevance for design and construction of the repository and include rock structure, potential key blocks, rock-physical properties (porosity, density, and mineralogy), rock-thermal properties (thermal conductivity, thermal expansion, and heat capacity), rock-mechanical properties (elastic moduli, compressive strength, and fracture properties), rock-mass properties, in situ stress, excavation characteristics, dynamic soil and rock properties, and engineering properties of surficial material. These data are used in designing the repository, evaluating the behavior of the natural system under thermal loading (Section 5.3), evaluating design-ground motions, and assessing long-term performance. The early data concentrated on the middle nonlithophysal section of Topopah Spring Tuff (i.e., thermal-mechanical unit TSw2). However, with a design shift in the stratigraphic horizons for the repository, recent data-gathering activities have placed heavy emphasis on the lithophysal horizons within the Topopah Spring Tuff.

3.8 REFERENCES

The following is a list of the references cited in this document. Column 1 represents the unique six digit numerical identifier, which is placed in the text following the reference callout (e.g., CRWMS M&O 2000 [DIRS 144054]). The purpose of these numbers is to assist the reader in locating a specific reference. Within the reference list, multiple sources by the same author (e.g., CRWMS M&O 2000) are sorted first by date and then alphabetically by title.

3.8.1 Documents Cited

104329 Anna, L.O. and Wallman, P. 1997. "Characterizing the Fracture Network at Yucca Mountain, Nevada, Part 2. Numerical Simulation of Flow in a Three-Dimensional Discrete Fracture Network." *Fractured Reservoirs: Characterization and Modeling.* Hoak, T.E.; Klawitter, A.L.; and Blomquist, P.K., eds. Denver, Colorado: Rocky Mountain Association of Geologists. TIC: 245651.

101423 Arnold, B.W.; Altman, S.J.; Robey, T.H.; Barnard, R.W.; and Brown, T.J. 1995. *Unsaturated-Zone Fast-Path Flow Calculations for Yucca Mountain Groundwater Travel Time Analyses (GWTT-94).* SAND95-0857. Albuquerque, New Mexico: Sandia National Laboratories. ACC: MOL.19960327.0336.

149007 Bamford, W.E.; van Duyse, H.; Nieble, C.; Rummel, F.; Broch, E.; Franklin, J.A.; Atkinson, R.H.; Tarkoy, P.J.; and Deere, D.U. 1981. "Suggested Methods for Determining Hardness and Abrasiveness of Rocks." *Rock Characterization Testing & Monitoring, ISRM Suggested Methods.* Brown, E.T., ed. New York, New York: Pergamon Press. TIC: 209865.

104433   Barker, C.E. 1994. *Thermal and Petroleum Generation History of the Mississippian Eleana Formation and Tertiary Source Rocks, Yucca Mountain Area, Southern Nye County, Nevada.* Open-File Report 94-161. Denver, Colorado: U.S. Geological Survey. TIC: 234479.

101541   Barton, N.; Lien, R.; and Lunde, J. 1974. "Engineering Classification of Rock Masses for the Design of Tunnel Support." *Rock Mechanics, 6*, (4), 189-236. New York, New York: Springer-Verlag. TIC: 219995.

104463   Beck, D.A. and Glancy, P.A. 1995. *Overview of Runoff of March 11, 1995, in Fortymile Wash and Amargosa River, Southern Nevada.* Fact Sheet FS-0xx-95. Draft. Las Vegas, Nevada: U.S. Geological Survey. ACC: MOL.19960715.0133.

101715   Bieniawski, Z.T. 1989. *Engineering Rock Mass Classifications.* New York, New York: John Wiley & Sons. TIC: 226350.

101847   Birkeland, P.W. 1984. *Soils and Geomorphology.* New York, New York: Oxford University Press. TIC: 236909.

101196   Bish, D.L. and Vaniman, D.T. 1985. *Mineralogic Summary of Yucca Mountain, Nevada.* LA-10543-MS. Los Alamos, New Mexico: Los Alamos National Laboratory. ACC: MOL.19950412.0041.

100030   Bish, D.L. and Chipera, S.J. 1986. *Mineralogy of Drill Holes J-13, UE-25A#1, and USW G-1 at Yucca Mountain, Nevada.* LA-10764-MS. Los Alamos, New Mexico: Los Alamos National Laboratory. ACC: MOL.19950412.0044.

101195   Bish, D.L. and Chipera, S.J. 1989. *Revised Mineralogic Summary of Yucca Mountain, Nevada.* LA-11497-MS. Los Alamos, New Mexico: Los Alamos National Laboratory. ACC: NNA.19891019.0029.

100006   Bish, D.L. and Aronson, J.L. 1993. "Paleogeothermal and Paleohydrologic Conditions in Silicic Tuff from Yucca Mountain, Nevada." *Clays and Clay Minerals, 41*, (2), 148-161. Long Island City, New York: Pergamon Press. TIC: 224613.

100530   Blanton, J.O., III 1992. *Nevada Test Site Flood Inundation Study, Part of U.S. Geological Survey Flood Potential and Debris Hazard Study, Yucca Mountain Site for United States Department of Energy, Office of Civilian Radioactive Waste Management.* Denver, Colorado: U.S. Department of the Interior, Bureau of Reclamation. ACC: MOL.20010724.0302.

120650   Boyd, P.J.; Martin, R.J., III; and Price, R.H. 1995. "Variability of the Physical Properties of Tuff at Yucca Mountain, NV." *Rock Mechanics, Proceedings of the 35th U.S. Symposium, University of Nevada, Reno, 5-7 June 1995.* Daemen, J.J.K. and Schultz, R.A., eds. Pages 511-516. Brookfield, Vermont: A.A. Balkema. TIC: 225160.

101491   Boyd, P.J.; Price, R.H.; Martin, R.J.; and Noel, J.S. 1996. *Bulk and Mechanical Properties of the Paintbrush Tuff Recovered from Boreholes UE25 NRG-2, 2A, 2B, and 3: Data Report*. SAND94-1902. Albuquerque, New Mexico: Sandia National Laboratories. ACC: MOL.19970102.0002.

101492   Boyd, P.J.; Price, R.H.; Noel, J.S.; and Martin, R.J. 1996. *Bulk and Mechanical Properties of the Paintbrush Tuff Recovered from Boreholes UE25 NRG-4 and -5: Data Report*. SAND94-2138. Albuquerque, New Mexico: Sandia National Laboratories. ACC: MOL.19970102.0004.

101990   Brace, W.F.; Paulding, B.W., Jr.; and Scholz, C.H. 1966. "Dilatancy in the Fracture of Crystalline Rocks." *Journal of Geophysical Research, 71*, (16), 3939-3953. Washington, D.C.: American Geophysical Union. TIC: 226778.

101999   Brailsford, A.D. and Major, K.G. 1964. "The Thermal Conductivity of Aggregates of Several Phases, Including Porous Materials." *British Journal of Applied Physics, 15*, 313-319. London, England: Institute of Physics. TIC: 223876.

101493   Brechtel, C.E.; Lin, M.; Martin, E.; and Kessel, D.S. 1995. *Geotechnical Characterization of the North Ramp of the Exploratory Studies Facility*. SAND95-0488/1 and 2. Two volumes. Albuquerque, New Mexico: Sandia National Laboratories. ACC: MOL.19950502.0004; MOL.19950502.0005.

101495   Brocher, T.M.; Hart, P.E.; Hunter, W.C.; and Langenheim, V.E. 1996. *Hybrid-Source Seismic Reflection Profiling Across Yucca Mountain, Nevada: Regional Lines 2 and 3*. Open-File Report 96-28. Menlo Park, California: U.S. Geological Survey. ACC: MOL.19970310.0094; MOL.19970310.0107.

100022   Brocher, T.M.; Hunter, W.C.; and Langenheim, V.E. 1998. "Implications of Seismic Reflection and Potential Field Geophysical Data on the Structural Framework of the Yucca Mountain-Crater Flat Region, Nevada." *Geological Society of America Bulletin, 110*, (8), 947-971. Boulder, Colorado: Geological Society of America. TIC: 238643.

100653   Brodsky, N.S.; Riggins, M.; Connolly, J.; and Ricci, P. 1997. *Thermal Expansion, Thermal Conductivity, and Heat Capacity Measurements for Boreholes UE25 NRG-4, UE25 NRG-5, USW NRG-6, and USW NRG-7/7A*. SAND95-1955. Albuquerque, New Mexico: Sandia National Laboratories. ACC: MOL.19980311.0316.

102004   Broxton, D.E.; Bish, D.L.; and Warren, R.G. 1987. "Distribution and Chemistry of Diagenetic Minerals at Yucca Mountain, Nye County, Nevada." *Clays and Clay Minerals, 35*, (2), 89-110. Long Island City, New York: Pergamon Press. TIC: 203900.

104556   Broxton, D.E.; Byers, F.M., Jr.; and Warren, R.G. 1989. *Petrography and Phenocryst Chemistry of Volcanic Units at Yucca Mountain, Nevada: A Comparison of Outcrop and Drill Hole Samples*. LA-11503-MS. Los Alamos, New Mexico: Los Alamos National Laboratory. ACC: NNA.19890224.0089.

100024   Broxton, D.E.; Warren, R.G.; Byers, F.M.; and Scott, R.B. 1989. "Chemical and Mineralogic Trends Within the Timber Mountain–Oasis Valley Caldera Complex, Nevada: Evidence for Multiple Cycles of Chemical Evolution in a Long-Lived Silicic Magma System." *Journal of Geophysical Research, 94*, (B5), 5961-5985. Washington, D.C.: American Geophysical Union. TIC: 225928.

107386   Broxton, D.E.; Chipera, S.J.; Byers, F.M., Jr.; and Rautman, C.A. 1993. *Geologic Evaluation of Six Nonwelded Tuff Sites in the Vicinity of Yucca Mountain, Nevada for a Surface-Based Test Facility for the Yucca Mountain Project*. LA-12542-MS. Los Alamos, New Mexico: Los Alamos National Laboratory. ACC: NNA.19940224.0128.

157330   BSC (Bechtel SAIC Company) 2001. *Thermal Tests Thermal-Hydrological Analyses/Model Report*. ANL-NBS-TH-000001 REV 00 ICN 02. Las Vegas, Nevada: Bechtel SAIC Company. ACC: MOL.20011116.0025.

159124   BSC 2002. *Geologic Framework Model (GFM2000)*. MDL-NBS-GS-000002 REV 01. Las Vegas, Nevada: Bechtel SAIC Company. ACC: MOL.20020530.0078.

157829   BSC 2002. *Geotechnical Data for a Potential Waste Handling Building and for Ground Motion Analyses for the Yucca Mountain Site Characterization Project*. ANL-MGR-GE-000003 REV 00. Las Vegas, Nevada: Bechtel SAIC Company. ACC: MOL.20021004.0078.

158730   BSC 2002. *Mineralogic Model (MM3.0) Analysis Model Report*. MDL-NBS-GS-000003 REV 00 ICN 02. Las Vegas, Nevada: Bechtel SAIC Company. ACC: MOL.20020423.0151.

157928   BSC 2002. *Preliminary Hydrologic Engineering Studies for the North Portal Pad and Vicinity*. ANL-EBS-MD-000060 REV 00. Las Vegas, Nevada: Bechtel SAIC Company. ACC: MOL.20021028.0123.

159530   BSC 2002. *Rock Properties Model Analysis Model Report*. MDL-NBS-GS-000004 REV 00 ICN 03. Las Vegas, Nevada: Bechtel SAIC Company. ACC: MOL.20020429.0086.

159262   BSC 2002. *Soils Report for North Portal Area, Yucca Mountain Project*. 100-00C-WRP0-00100-000-000. Las Vegas, Nevada: Bechtel SAIC Company. ACC: MOL.20021015.0323.

160319   BSC 2002. *Thermal Conductivity of the Potential Repository Horizon Model Report.* MDL-NBS-GS-000005 REV 00. Las Vegas, Nevada: Bechtel SAIC Company. ACC: MOL.20020923.0167.

160771   BSC 2002. *Thermal Testing Measurements Report.* ANL-NBS-HS-000041 REV 00. Las Vegas, Nevada: Bechtel SAIC Company. ACC: MOL.20021004.0314.

162711   BSC 2003. *Drift Degradation Analysis.* ANL-EBS-MD-000027 REV 02. Las Vegas, Nevada: Bechtel SAIC Company. ACC: DOC.20030709.0003.

164670   BSC 2003. *Heat Capacity and Thermal Expansion Coefficients Analysis Report.* ANL-NBS-GS-000013 REV 00. Las Vegas, Nevada: Bechtel SAIC Company. ACC: DOC.20030820.0002.

166347   BSC 2003. *In Situ Field Testing of Processes.* ANL-NBS-HS-000005 REV 02. Las Vegas, Nevada: Bechtel SAIC Company. ACC: DOC.20031208.0001.

166358   BSC 2003. *Laboratory Thermal Conductivity Testing for the Tptpll Lithostratigraphic Unit.* ANL-EBS-MD-000064 REV 00. Las Vegas, Nevada: Bechtel SAIC Company. ACC: DOC.20031015.0002.

166660   BSC 2003. *Subsurface Geotechnical Parameters Report.* 800-K0C-WIS0-00400-000-00A. Las Vegas, Nevada: Bechtel SAIC Company. ACC: ENG.20040108.0001.

166355   BSC 2003. *The Mechanical Properties of Lithophysal Tuff: Laboratory Experiments.* TDR-EBS-MD-000027 REV 00C. Las Vegas, Nevada: Bechtel SAIC Company. ACC: MOL.20031209.0141. TBV-5656.

166242   BSC 2003. *Thermal Conductivity of Non-Repository Lithostratigraphic Layers.* MDL-NBS-GS-000006 REV 00. Las Vegas, Nevada: Bechtel SAIC Company. ACC: DOC.20030815.0001.

100106   Buesch, D.C.; Spengler, R.W.; Moyer, T.C.; and Geslin, J.K. 1996. *Proposed Stratigraphic Nomenclature and Macroscopic Identification of Lithostratigraphic Units of the Paintbrush Group Exposed at Yucca Mountain, Nevada.* Open-File Report 94-469. Denver, Colorado: U.S. Geological Survey. ACC: MOL.19970205.0061.

104616   Buesch, D.C.; Spengler, R.W.; Nelson, P.H.; and Flint, L.E. 1996. "Correlation of Lithologic Features, Hydrogeologic Properties, and Borehole Geophysical Logs at Yucca Mountain, Nevada." *Abstracts with Programs - Geological Society of America.* Page A-521. Boulder, Colorado: Geological Society of America. TIC: 234349.

107236   Buesch, D.C. and Spengler, R.W. 1999. "Stratigraphic Framework of the North Ramp Area of the Exploratory Studies Facility, Yucca Mountain." *Hydrogeology of the Unsaturated Zone, North Ramp Area of the Exploratory Studies Facility, Yucca Mountain, Nevada*. Rousseau, J.P.; Kwicklis, E.M.; and Gillies, D.C., eds. Water-Resources Investigations Report 98-4050. Denver, Colorado: U.S. Geological Survey. ACC: MOL.19990419.0335.

166307   Buesch, D.C. 2000. "Application of Theoretical Relations of Density, Porosity, and Composition in Volcanic Rocks, Yucca Mountain, Nevada." *Abstracts with Programs - Geological Society of America, 32*, (7), A-89. Boulder, Colorado: Geological Society of America. TIC: 249113.

102040   Bull, W.B. 1991. *Geomorphic Responses to Climate Change*. New York, New York: Oxford University Press. TIC: 223847.

100107   Bullard, K.L. 1986. *PMF (Probable Maximum Flood) Study for Nevada Nuclear Waste Storage Investigation Project*. Denver, Colorado: U.S. Department of the Interior, Bureau of Reclamation. ACC: NNA.19891019.0314.

108883   Bullard, K.L. 1992. *Nevada Test Site Probable Maximum Flood Study, Part of U.S. Geological Survey Flood Potential and Debris Hazard Study, Yucca Mountain Site for U.S. Department of Energy, Office of Civilian Radioactive Waste Management*. Denver, Colorado: U.S. Department of the Interior, Bureau of Reclamation. ACC: MOL.20010730.0396.

104639   Byers, F.M., Jr.; Carr, W.J.; Orkild, P.P.; Quinlivan, W.D.; and Sargent, K.A. 1976. *Volcanic Suites and Related Cauldrons of Timber Mountain-Oasis Valley Caldera Complex, Southern Nevada*. Professional Paper 919. Washington, D.C.: U.S. Geological Survey. TIC: 201146.

101573   Byers, F.M., Jr. 1985. *Petrochemical Variation of Topopah Spring Tuff Matrix with Depth (Stratigraphic Level), Drill Hole USW G-4, Yucca Mountain, Nevada*. LA-10561-MS. Los Alamos, New Mexico: Los Alamos National Laboratory. ACC: HQS.19880517.1103.

101321   Byers, F.M., Jr. and Moore, L.M. 1987. *Petrographic Variation of the Topopah Spring Tuff Matrix Within and Between Cored Drill Holes, Yucca Mountain, Nevada*. LA-10901-MS. Los Alamos, New Mexico: Los Alamos National Laboratory. ACC: NNA.19900510.0144.

101322   Caporuscio, F.; Vaniman, D.; Bish, D.; Broxton, D.; Arney, B.; Heiken, G.; Byers, F.; Gooley, R.; and Semarge, E. 1982. *Petrologic Studies of Drill Cores USW-G2 and UE25b-1H, Yucca Mountain, Nevada*. LA-9255-MS. Los Alamos, New Mexico: Los Alamos National Laboratory. ACC: NNA.19870519.0041.

102046   Carr, M.D.; Waddell, S.J.; Vick, G.S.; Stock, J.M.; Monsen, S.A.; Harris, A.G.; Cork, B.W.; and Byers, F.M., Jr. 1986. *Geology of Drill Hole UE25p#1: A Test Hole Into Pre-Tertiary Rocks Near Yucca Mountain, Southern Nevada.* Open-File Report 86-175. Menlo Park, California: U.S. Geological Survey. ACC: HQS.19880517.2633.

101037   Carr, W.J. 1984. *Regional Structural Setting of Yucca Mountain, Southwestern Nevada, and Late Cenozoic Rates of Tectonic Activity in Part of the Southwestern Great Basin, Nevada and California.* Open-File Report 84-854. Denver, Colorado: U.S. Geological Survey. ACC: NNA.19870325.0475.

104670   Carr, W.J.; Byers, F.M., Jr.; and Orkild, P.P. 1986. *Stratigraphic and Volcano-Tectonic Relations of Crater Flat Tuff and Some Older Volcanic Units, Nye County, Nevada.* Professional Paper 1323. Denver, Colorado: U.S. Geological Survey. TIC: 216598.

101520   Carr, W.J. 1992. "Structural Model for Western Midway Valley Based on RF Drillhole Data and Bedrock Outcrops." Appendix A of *Summary and Evaluation of Existing Geological and Geophysical Data Near Prospective Surface Facilities in Midway Valley, Yucca Mountain Project, Nye County, Nevada.* Gibson, J.; Swan; F.; Wesling, J.; Bullard, T.; Perman, R.; Angell, M.; and DiSilvestro, L. SAND90-2491. Albuquerque, New Mexico: Sandia National Laboratories. ACC: NNA.19910709.0001.

107423   Cashman, P.H. and Trexler, J.H., Jr. 1995. "Task 8: Evaluation of Hydrocarbon Potential." Section VI of *Evaluation of the Geologic Relations and Seismotectonic Stability of the Yucca Mountain Area, Nevada Nuclear Waste Site Investigation (NNWSI), Progress Report 30 September 1995.* DOE/NV/10461-T76. Reno, Nevada: University of Nevada, Reno, Mackay School of Mines. TIC: 224579.

102411   Castor, S.B. and Lock, D.E. 1995. *Assessment of Industrial Minerals and Rocks in the Controlled Area.* Reno, Nevada: Nevada Bureau of Mines and Geology. ACC: MOL.19980717.0139.

104706   Castor, S.B.; Garside, L.J.; Tingley, J.V.; La Pointe, D.D.; Desilets, M.O.; Hsu, L-C.; Goldstrand, P.M.; Lugaski, T.P.; and Ross, H.P. 1999. *Assessment of Metallic and Mined Energy Resources in the Yucca Mountain Conceptual Controlled Area, Nye County, Nevada.* Open-File Report 99-13. Reno, Nevada: Nevada Bureau of Mines and Geology. TIC: 245099.

159318   Charles B. Reynolds & Associates. 1985. *Final Report, 1985 Repository Surface Facility Seismic Survey, Yucca Mountain Area, NTS, Nye County, Nevada.* Albuquerque, New Mexico: Charles B. Reynolds & Associates. ACC: MOL.19970415.0158.

111081   Chipera, S.J.; Vaniman, D.T.; Carlos, B.A.; and Bish, D.L. 1995. *Mineralogic Variation in Drill Core UE-25 UZ#16, Yucca Mountain, Nevada.* LA-12810-MS. Los Alamos, New Mexico: Los Alamos National Laboratory. ACC: NNA.19940427.0099.

108879   Christensen, R.C. and Spahr, N.E. 1980. *Flood Potential of Topopah Wash and Tributaries, Eastern Part of Jackass Flats, Nevada Test Site, Southern Nevada.* Open-File Report 80-963. Lakewood, Colorado: U.S. Geological Survey. TIC: 203211.

100566   Christiansen, R.L. and Lipman, P.W. 1965. *Geologic Map of the Topopah Spring NW Quadrangle, Nye County, Nevada. Geologic Quadrangle Map GQ-444.* Washington, D.C.: U.S. Geological Survey. TIC: 212357.

102562   Christiansen, R.L. 1979. "Cooling Units and Composite Sheets in Relation to Caldera Structure." *Ash-Flow Tuffs.* Chapin, C.E. and Elston, W.E., eds. Special Paper 180. Pages 29-42. Boulder, Colorado: Geological Society of America. TIC: 239132.

104691   Coe, J.A.; Glancy, P.A.; and Whitney, J.W. 1997. "Volumetric Analysis and Hydrologic Characterization of a Modern Debris Flow Near Yucca Mountain, Nevada." *Geomorphology, 20*, (1-2), 11-28. Amsterdam, The Netherlands: Elsevier. TIC: 241945.

159410   Coe, J.A. 2003. "Quaternary Faulting on the Northern Crater Flat Fault." Chapter 11 of *Quaternary Paleoseismology and Stratigraphy of the Yucca Mountain Area, Nevada.* U.S. Geological Survey Digital Data Series. Keefer, W.R.; Whitney, J.W.; and Taylor, E.M., eds. Denver, Colorado: U.S. Geological Survey. ACC: MOL.20031208.0113. TBV-5659.

159411   Coe, J.A.; Oswald, J.; Vadurro, G.; and Lundstrom, S.C. 2003. "Quaternary Faulting on the Fatigue Wash Fault." Chapter 8 of *Quaternary Paleoseismology and Stratigraphy of the Yucca Mountain Area, Nevada.* U.S. Geological Survey Digital Data Series. Keefer, W.R.; Whitney, J.W.; and Taylor, E.M., eds. Denver, Colorado: U.S. Geological Survey. ACC: MOL.20031208.0113. TBV-5659.

159090   Cole, J.C. 1997. *Major Structural Controls on the Distribution of Pre-Tertiary Rocks, Nevada Test Site Vicinity, Southern Nevada.* Open-File Report 97-533. Denver, Colorado: U.S. Geological Survey. TIC: 245917.

101529   Connolly, J.R. and Nimick, F.B. 1990. *Mineralogic and Chemical Data Supporting Heat Capacity Determination for Tuffaceous Rocks.* SAND88-0882. Albuquerque, New Mexico: Sandia National Laboratories. ACC: NNA.19890928.0125.

150070   Cowan, D.L.; Priest, V.; and Levy, S.S. 1993. "ESR Dating of Quartz from Exile Hill, Nevada." *Applied Radiation and Isotopes, 44*, (7), 1035-1039. New York, New York: Pergamon Press. TIC: 224595.

101207   Craig, R.W.; Reed, R.L.; and Spengler, R.W. 1983. *Geohydrologic Data for Test Well USW H-6 Yucca Mountain Area, Nye County, Nevada*. Open-File Report 83-856. Denver, Colorado: U.S. Geological Survey. ACC: NNA.19870406.0058.

108874   Crippen, J.R. and Bue, C.D. 1977. *Maximum Floodflows in the Conterminous United States*. Water-Supply Paper 1887. Washington, D.C.: U.S. Geological Survey. TIC: 217532.

108887   Crippen, J.R. 1982. "Envelope Curves for Extreme Flood Events." *Journal of the Hydraulics Division, Proceedings of the American Society of Engineers, 108,* (HY10), 1208-1212. New York, New York: American Society of Civil Engineers. TIC: 235452.

100110   Crowe, B.; Perry, F.; Geissman, J.; McFadden, L.; Wells, S.; Murrell, M.; Poths, J.; Valentine, G.A.; Bowker, L.; and Finnegan, K. 1995. *Status of Volcanism Studies for the Yucca Mountain Site Characterization Project*. LA-12908-MS. Los Alamos, New Mexico: Los Alamos National Laboratory. ACC: HQO.19951115.0017.

101426   CRWMS M&O (Civilian Radioactive Waste Management System Management and Operating Contractor) 1995. *Controlled Design Assumptions Document*. B00000000-01717-4600-00032 REV 02. Las Vegas, Nevada: CRWMS M&O. ACC: MOL.19961010.0090.

101427   CRWMS M&O 1995. *ESF Ground Support Design Analysis*. BABEE0000-01717-0200-00002 REV 00. Las Vegas, Nevada: CRWMS M&O. ACC: MOL.19960409.0355.

101534   CRWMS M&O 1996. Borehole Geophysics. Volume II of *Synthesis of Borehole and Surface Geophysical Studies at Yucca Mountain, Nevada and Vicinity*. BAAA00000-01717-0200-00015 REV 00. Las Vegas, Nevada: CRWMS M&O. ACC: MOL.19970114.0138.

101428   CRWMS M&O 1996. *Characterization of the ESF Thermal Test Area*. B00000000-01717-5705-00047 REV 01. Las Vegas, Nevada: CRWMS M&O. ACC: MOL.19970116.0187.

101429   CRWMS M&O 1996. *Exploratory Studies Facility 7.62 m Tunnel Ground Support Master Sections*. BABEE0000-01717-2100-40151 REV 00. Las Vegas, Nevada: CRWMS M&O. ACC: MOL.19960930.0103.

101535   CRWMS M&O 1996. *Yucca Mountain Project Stratigraphic Compendium*. BA0000000-01717-5700-00004 REV 01. Las Vegas, Nevada: CRWMS M&O. ACC: MOL.19970113.0088.

101539   CRWMS M&O 1997. *Ambient Characterization of the Drift Scale Test Block*. BADD00000-01717-5705-00001 REV 01. Las Vegas, Nevada: CRWMS M&O. ACC: MOL.19980416.0689.

100930   CRWMS M&O 1997. *Confirmation of Empirical Design Methodologies*. BABEE0000-01717-5705-00002 REV 00. Las Vegas, Nevada: CRWMS M&O. ACC: MOL.19980219.0104.

100223   CRWMS M&O 1997. *Determination of Available Volume for Repository Siting*. BCA000000-01717-0200-00007 REV 00. Las Vegas, Nevada: CRWMS M&O. ACC: MOL.19971009.0699.

101537   CRWMS M&O 1997. *Evaluation of Geotechnical Monitoring Data from the Exploratory Studies Facility July 1995 to June 1996*. BAB000000-01717-5705-00003 REV 01. Las Vegas, Nevada: CRWMS M&O. ACC: MOL.19970813.0117.

101540   CRWMS M&O 1997. *Single Heater Test Status Report*. BAB000000-01717-5700-00002 REV 01. Las Vegas, Nevada: CRWMS M&O. ACC: MOL.19980416.0696.

103564   CRWMS M&O 1997. *Yucca Mountain Site Geotechnical Report*. B00000000-01717-5705-00043 REV 01. Two volumes. Las Vegas, Nevada: CRWMS M&O. ACC: MOL.19971017.0736; MOL.19971017.0737.

108306   CRWMS M&O 1998. *Drift Scale Test Progress Report No. 1*. BAB000000-01717-5700-00004 REV 01. Las Vegas, Nevada: CRWMS M&O. ACC: MOL.19990209.0240.

123196   CRWMS M&O 1998. "Geology and Geochronology of Basaltic Volcanism in the Yucca Mountain Region." Chapter 2 of *Synthesis of Volcanism Studies for the Yucca Mountain Site Characterization Project*. Deliverable 3781MR1. Las Vegas, Nevada: CRWMS M&O. ACC: MOL.19990511.0400.

103514   CRWMS M&O 1998. *Yucca Mountain Site Description*. B00000000-01717-5700-00019 REV 00. Las Vegas, Nevada: CRWMS M&O. ACC: MOL.19981202.0492.

109209   CRWMS M&O 1999. *Preliminary Geotechnical Investigation for Waste Handling Building, Yucca Mountain Site Characterization Project*. BCB000000-01717-5705-00016 REV 00. Las Vegas, Nevada: CRWMS M&O. ACC: MOL.19990625.0182.

129261   CRWMS M&O 1999. *Single Heater Test Final Report*. BAB000000-01717-5700-00005 REV 00 ICN 1. Las Vegas, Nevada: CRWMS M&O. ACC: MOL.20000103.0634.

138960   CRWMS M&O 2000. *Mineralogical Model (MM3.0)*. MDL-NBS-GS-000003 REV 00 ICN 01. Las Vegas, Nevada: CRWMS M&O. ACC: MOL.20000120.0477.

151945   CRWMS M&O 2000. *Yucca Mountain Site Description*. TDR-CRW-GS-000001 REV 01 ICN 01. Las Vegas, Nevada: CRWMS M&O. ACC: MOL.20001003.0111.

159125   CRWMS M&O 2001. *Natural Resources Assessment*. ANL-NBS-GS-000001 REV 00. Las Vegas, Nevada: CRWMS M&O. ACC: MOL.20010406.0010.

105116   Daffern, D.D. and Thummala, V. 1988. "Siting of Borrow Pits Locations - Area 25." Letter from D.D. Daffern and V. Thummala (Holmes & Narver) to L.C. Bruno (Holmes & Narver), December 21, 1988, NTS:TEC:MTL:89-24, with enclosures. ACC: NNA.19890414.0071.

149544   Daley, T.M.; Majer, E.L.; and Karageorgi, E. 1994. *Combined Analysis of Surface Reflection Imaging and Vertical Seismic Profiling at Yucca Mountain, Nevada.* LBL-36467. Berkeley, California: Lawrence Berkeley National Laboratory. TIC: 247870.

100027   Day, W.C.; Dickerson, R.P.; Potter, C.J.; Sweetkind, D.S.; San Juan, C.A.; Drake, R.M., II; and Fridrich, C.J. 1998. *Bedrock Geologic Map of the Yucca Mountain Area, Nye County, Nevada.* Geologic Investigations Series I-2627. Denver, Colorado: U.S. Geological Survey. ACC: MOL.19981014.0301.

101557   Day, W.C.; Potter, C.J.; Sweetkind, D.S.; Dickerson, R.P.; and San Juan, C.A. 1998. *Bedrock Geologic Map of the Central Block Area, Yucca Mountain, Nye County, Nevada.* Miscellaneous Investigations Series Map I-2601. Washington, D.C.: U.S. Geological Survey. ACC: MOL.19980611.0339.

102775   Deere, D.U. 1968. "Geological Considerations." Chapter 1 of *Rock Mechanics in Engineering Practice.* Pages 1-20. New York, New York: John Wiley & Sons. TIC: 234672.

102929   Dickerson, R.P. and Drake, R.M., II 1998. *Geologic Map of the Paintbrush Canyon Area, Yucca Mountain, Nevada.* Open-File Report 97-783. Denver, Colorado: U.S. Geological Survey. ACC: MOL.19981014.0302.

160062   Dickerson, R.P. and Drake, R.M., II 2003. *Geologic Map of South-Central Yucca Mountain, Nye County, Nevada.* Preliminary Working Draft. Denver, Colorado: U.S. Geological Survey. ACC: MOL.20031203.0380.

100135   Diehl, S.F. and Chornack, M.P. 1990. *Stratigraphic Correlation and Petrography of the Bedded Tuffs, Yucca Mountain, Nye County, Nevada.* Open-File Report 89-3. Denver, Colorado: U.S. Geological Survey. ACC: NNA.19901102.0006.

100282   DOE (U.S. Department of Energy) 1988. *Site Characterization Plan Yucca Mountain Site, Nevada Research and Development Area, Nevada.* DOE/RW-0199. Nine volumes. Washington, D.C.: U.S. Department of Energy, Office of Civilian Radioactive Waste Management. ACC: HQO.19881201.0002.

108873   Ely, L.L. 1997. "Response of Extreme Floods in the Southwestern United States to Climatic Variations in the Late Holocene." *Geomorphology, 19,* (1997), 175-201. Amsterdam, The Netherlands: Elsevier. TIC: 238833.

100670   Engstrom, D.A. and Rautman, C.A. 1996. *Geology of the USW SD-9 Drill Hole, Yucca Mountain, Nevada*. SAND96-2030. Albuquerque, New Mexico: Sandia National Laboratories. ACC: MOL.19970508.0288.

105559   Faure, G. 1986. *Principles of Isotope Geology*. 2nd Edition. New York, New York: John Wiley & Sons. TIC: 237212.

105417   Feighner, M.; Johnson, L.; Lee, K.; Daley, T.; Karageorgi, E.; Parker, P.; Smith, T.; Williams, K.; Romero, A.; and McEvilly, T. 1996. *Results and Interpretation of Multiple Geophysical Surveys at Yucca Mountain, Nevada*. LBL-38200. Berkeley, California: Lawrence Berkeley National Laboratory. TIC: 253163.

159312   Fitterman, D.V. 1982. *Magnetometric Resistivity Survey Near Fortymile Wash, Nevada Test Site, Nevada*. Open-File Report 82-401. Denver, Colorado: U.S. Geological Survey. ACC: HQS.19880517.2674.

103746   Flint, A.L. and Flint, L.E. 1994. "Spatial Distribution of Potential Near Surface Moisture Flux at Yucca Mountain." *High Level Radioactive Waste Management, Proceedings of the Fifth Annual International Conference, Las Vegas, Nevada, May 22-26, 1994. 4*, 2352-2358. La Grange Park, Illinois: American Nuclear Society. TIC: 210984.

100033   Flint, L.E. 1998. *Characterization of Hydrogeologic Units Using Matrix Properties, Yucca Mountain, Nevada*. Water-Resources Investigations Report 97-4243. Denver, Colorado: U.S. Geological Survey. ACC: MOL.19980429.0512.

112530   Flynn, T.; Buchanan, P.; Trexler, D.; Shevenell, L.; and Garside, L. 1996. *Geothermal Resource Assessment of the Yucca Mountain Area, Nye County, Nevada*. BA0000000-03255-5705-00002. Las Vegas, Nevada: University and Community College System of Nevada. ACC: MOL.19960903.0027.

130125   Forester, R. 1999. "Ostracodes as Indicators of Present and Past Hydrology in Death Valley." *Proceedings of Conference on Status of Geologic Research and Mapping in Death Valley National Park, Las Vegas, Nevada, April 9-11, 1999*. Slate, J.L., ed. Open-File Report 99-153. Pages 69-70. Denver, Colorado: U.S. Geological Survey. TIC: 245245.

109425   Forester, R.M.; Bradbury, J.P.; Carter, C.; Elvidge-Tuma, A.B.; Hemphill, M.L.; Lundstrom, S.C.; Mahan, S.A.; Marshall, B.D.; Neymark, L.A.; Paces, J.B.; Sharpe, S.E.; Whelan, J.F.; and Wigand, P.E. 1999. *The Climatic and Hydrologic History of Southern Nevada During the Late Quaternary*. Open-File Report 98-635. Denver, Colorado: U.S. Geological Survey. TIC: 245717.

107425   French, D.E. 2000. *Hydrocarbon Assessment of the Yucca Mountain Vicinity, Nye County, Nevada*. Open-File Report 2000-2. Reno, Nevada: Nevada Bureau of Mines and Geology. ACC: MOL.20000609.0298.

118942   Fridrich, C.J. 1999. "Tectonic Evolution of the Crater Flat Basin, Yucca Mountain Region, Nevada." Chapter 7 of *Cenozoic Basins of the Death Valley Region*. Wright, L.A. and Troxel, B.W., eds. Special Paper 333. Boulder, Colorado: Geological Society of America. TIC: 248054.

107333   Fridrich, C.J.; Whitney, J.W.; Hudson, M.R.; and Crowe, B.M. 1999. "Space-Time Patterns of Late Cenozoic Extension, Vertical Axis Rotation, and Volcanism in the Crater Flat Basin, Southwest Nevada." Chapter 8 of *Cenozoic Basins of the Death Valley Region*. Wright, L.A. and Troxel, B.W., eds. Special Paper 333. Boulder, Colorado: Geological Society of America. TIC: 248054.

159317   Frischknecht, F.C. and Raab, P.V. 1984. "Time-Domain Electromagnetic Soundings at the Nevada Test Site, Nevada." *Geophysics, 49*, (7), 981-992. Tulsa, Oklahoma: Society of Exploration Geophysicists. TIC: 237417.

105454   Frizzell, V.A., Jr. and Shulters, J. 1990. *Geologic Map of the Nevada Test Site, Southern Nevada*. Miscellaneous Investigations Series Map I-2046. Denver, Colorado: U.S. Geological Survey. TIC: 200459.

101226   Geslin, J.K. and Moyer, T.C. 1995. *Summary of Lithologic Logging of New and Existing Boreholes at Yucca Mountain, Nevada, March 1994 to June 1994*. Open-File Report 94-451. Denver, Colorado: U.S. Geological Survey. ACC: MOL.19941214.0057.

103330   Geslin, J.K.; Moyer, T.C.; and Buesch, D.C. 1995. *Summary of Lithologic Logging of New and Existing Boreholes at Yucca Mountain, Nevada, August 1993 to February 1994*. Open-File Report 94-342. Denver, Colorado: U.S. Geological Survey. ACC: MOL.19940810.0011.

105522   Gile, L.H.; Peterson, F.F.; and Grossman, R.B. 1966. "Morphological and Genetic Sequences of Carbonate Accumulation in Desert Soils." *Soil Science, 101*, (5), 347-360. Baltimore, Maryland: Williams & Wilkins. TIC: 225823.

101227   Glancy, P.A. 1994. *Evidence of Prehistoric Flooding and the Potential for Future Extreme Flooding at Coyote Wash, Yucca Mountain, Nye County, Nevada*. Open-File Report 92-458. Denver, Colorado: U.S. Geological Survey. ACC: NNA.19940606.0001.

155679   Glancy, P.A. and Beck, D.A. 1998. "Modern Flooding and Runoff of the Amargosa River, Nevada–California, Emphasizing Contributions of Fortymile Wash." *Quaternary Geology of the Yucca Mountain Area, Southern Nevada, Field Trip Guide, Prepared for the 1998 Annual Meeting of the Friends of the Pleistocene, Pacific Cell, October 9-11, 1998*. Taylor, E.M., ed. Pages 51-62. Boulder, Colorado: Friends of the Pleistocene. TIC: 244815.

105583   Goktan, R.M. and Ayday, C. 1993. "A Suggested Improvement to the Schmidt Rebound Hardness ISRM Suggested Method with Particular Reference to Rock Machineability." *International Journal of Rock Mechanics and Mining Science & Geomechanics Abstracts, 30*, (3), 321-322. New York, New York: Pergamon Press. TIC: 234422.

105757   Gosse, J.C.; Reedy, R.C.; Harrington, C.D.; and Poths, J. 1996. "Overview of the Workshop on Secular Variations in Production Rates of Cosmogenic Nuclides on Earth." *Radiocarbon, 38*, (1), 135-147. New Haven, Connecticut: Yale University, Kline Geology Laboratory. TIC: 234452.

100036   Grow, J.A.; Barker, C.E.; and Harris, A.G. 1994. "Oil and Gas Exploration Near Yucca Mountain, Southern Nevada." *High Level Radioactive Waste Management, Proceedings of the Fifth Annual International Conference, Las Vegas, Nevada, May 22-26, 1994. 3*, 1298-1315. La Grange Park, Illinois: American Nuclear Society. TIC: 210984.

100037   Hamilton, W.B. 1988. "Detachment Faulting in the Death Valley Region, California and Nevada." Chapter 5 of *Geologic and Hydrologic Investigations of a Potential Nuclear Waste Disposal Site at Yucca Mountain, Southern Nevada*. Carr, M.D. and Yount, J.C., eds. Bulletin 1790. Denver, Colorado: U.S. Geological Survey. TIC: 203085.

108888   Hansen, E.M.; Schwarz, F.K.; and Riedel, J.T. 1977. *Probable Maximum Precipitation Estimates, Colorado River and Great Basin Drainages*. Hydrometeorological Report No. 49. Silver Spring, Maryland: U.S. Department of Commerce, National Oceanic and Atmospheric Administration. TIC: 220224.

106072   Harden, J.W.; Slate, J.L.; Lamothe, P.; Chadwick, O.; Pendall, E.; and Gillespie, A. 1991. *Soil Formation on the Trail Canyon Alluvial Fan, Fish Lake Valley, Nevada*. Open-File Report 91-291. Denver, Colorado: U.S. Geological Survey. TIC: 234749.

106077   Harden, J.W.; Taylor, E.M.; Hill, C.; Mark, R.K.; McFadden, L.D.; Reheis, M.C.; Sowers, J.M.; and Wells, S.G. 1991. "Rates of Soil Development from Four Soil Chronosequences in the Southern Great Basin." *Quaternary Research, 35*, 383-399. New York, New York: Academic Press. TIC: 234438.

102920   Hardy, M.P. and Bauer, S.J. 1991. *Drift Design Methodology and Preliminary Application for the Yucca Mountain Site Characterization Project*. SAND89-0837. Albuquerque, New Mexico: Sandia National Laboratories. ACC: NNA.19910808.0105.

106095   Harrington, C.D. and Whitney, J.W. 1987. "Scanning Electron Microscope Method for Rock-Varnish Dating." *Geology, 15*, 967-970. Boulder, Colorado: Geological Society of America. TIC: 203298.

106100   Harrington, C.D.; Whitney, J.W.; Jull, A.J.T.; and Phillips, W. 1994. "Implications of Surface-Exposure Dating of Scarps Along the Solitario Canyon and Windy Wash Faults, Yucca Mountain, Nevada, by In Situ Produced Cosmogenic 14C." *Abstracts with Programs - Geological Society of America, 26,* (7), A-303. Boulder, Colorado: Geological Society of America. TIC: 234891.

124658   Harrington, C.D. 1998. "Request for Approval of Revised Milestone SP32P5M4, 'Dust and Wall-Rock Hazardous Mineral Distributions in the East-West Cross Drift, Yucca Mountain, Nevada' (Preliminary Report: Hazardous Mineral Distributions) by D. Vaniman et al." Letter from C.D. Harrington (LANL) to L. Hayes (CRWMS M&O), October 27, 1998, EES-13-10-98-226, with enclosure. ACC: MOL.20000110.0184.

150417   Harrington, C.D. 2000. "Descriptive and Calculated Data for Ages of Boulder Deposits Around Yucca Mountain." E-mail from C.D. Harrington (LANL) to R. Quittmeyer (CRWMS M&O), June 27, 2000, with attachment. ACC: MOL.20000629.0594.

107255   Heizler, M.T.; Perry, F.V.; Crowe, B.M.; Peters, L.; and Appelt, R. 1999. "The Age of Lathrop Wells Volcanic Center: An ^{40}Ar/^{39}Ar Dating Investigation." *Journal of Geophysical Research, 104,* (B1), 767-804. Washington, D.C.: American Geophysical Union. TIC: 243399.

102324   Ho, D.M.; Sayre, R.L.; and Wu, C.L. 1986. *Suitability of Natural Soils for Foundations for Surface Facilities at the Prospective Yucca Mountain Nuclear Waste Repository*. SAND85-7107. Albuquerque, New Mexico: Sandia National Laboratories. ACC: NNA.19890327.0053.

106158   Hoek, E. and Brown, E.T. 1988. "The Hoek-Brown Failure Criterion - A 1988 Update." *Proceedings of the 15th Canadian Rock Mechanics Symposium, Toronto, Canada, October 1988*. Pages 31-38. Toronto, Canada: University of Toronto Press. TIC: 240286.

105117   Holmes & Narver 1989. *Borrow Pit Material Evaluation ES Auxillary Pads, Area 25*. Mercury, Nevada: Holmes & Narver. ACC: NNA.19890920.0226.

106173   Hoover, D.L. and Morrison, J.N. 1980. *Geology of the Syncline Ridge Area Related to Nuclear Waste Disposal, Nevada Test Site, Nye County, Nevada*. Open-File Report 80-942. Denver, Colorado: U.S. Geological Survey. TIC: 203106.

106177   Hoover, D.L.; Swadley, W C; and Gordon, A.J. 1981. *Correlation Characteristics of Surficial Deposits with a Description of Surficial Stratigraphy in the Nevada Test Site Region*. Open-File Report 81-512. Denver, Colorado: U.S. Geological Survey. ACC: NNA.19870406.0033.

101247   Hoover, D.L. 1989. *Preliminary Description of Quaternary and Late Pliocene Surficial Deposits at Yucca Mountain and Vicinity, Nye County, Nevada.* Open-File Report 89-359. Denver, Colorado: U.S. Geological Survey. ACC: NNA.19900403.0406.

159322   Hopkins, D.M. 1975. "Time-Stratigraphic Nomenclature for the Holocene Epoch." *Geoderma, 14*, 2. New York, New York: Elsevier. TIC: 252967.

106194   Hudson, M.R.; Minor, S.A.; and Fridrich, C.J. 1996. "The Distribution, Timing, and Character of Steep-Axis Rotations in a Broad Zone of Dextral Shear in Southwestern Nevada." *Abstracts with Programs - Geological Society of America, 28*, (7), A-451. Boulder, Colorado: Geological Society of America. TIC: 234723.

159900   Hunt, C.B. 1975. *Death Valley, Geology, Ecology, Archaeology.* Berkeley, California: University of California Press. TIC: 246234.

100047   Imbrie, J.; Hays, J.D.; Martinson, D.G.; McIntrye, A.; Mix, A.C.; Morley, J.J.; Pisias, N.G.; Prell, W.L.; and Shackleton, N.J. 1984. "The Orbital Theory of Pleistocene Climate: Support from a Revised Chronology of the Marine δ^{18}O Record." *Milankovitch and Climate, Understanding the Response to Astronomical Forcing.* Berger, A.; Imbrie, J.; Hays, J.; Kukla, G.; and Saltzman, B., eds. Pages 269-305. Boston, Massachusetts: D. Reidel Publishing Company. TIC: 225740.

159419   Keefer, W.R.; Whitney, J.W.; and Taylor, E.M., eds. 2003. *Quaternary Paleoseismology and Stratigraphy of the Yucca Mountain Area, Nevada.* U.S. Geological Survey Digital Data Series. Denver, Colorado: U.S. Geological Survey. ACC: MOL.20031208.0113. TBV-5659.

106288   Kicker, D.C.; Martin, E.R.; Brechtel, C.E.; Stone, C.A.; and Kessel, D.S. 1997. *Geotechnical Characterization for the Main Drift of the Exploratory Studies Facility.* SAND95-2183. Albuquerque, New Mexico: Sandia National Laboratories. TIC: 227586.

120631   Kirsten, H.A.D. 1988. "Discussion on Q-System." *Rock Classification Systems for Engineering Purposes, Symposium held in Cincinnati, Ohio, June 25, 1987.* Kirkaldie, L., ed. Pages 85-88. Philadelphia, Pennsylvania: American Society for Testing and Materials. TIC: 221986.

104492   Langenheim, V.E. and Ponce, D.A. 1994. "Gravity and Magnetic Investigations of Yucca Wash, Southwest Nevada." *High Level Radioactive Waste Management, Proceedings of the Fifth Annual International Conference, Las Vegas, Nevada, May 22-26, 1994. 4*, 2272-2278. La Grange Park, Illinois: American Nuclear Society. TIC: 210984.

102927   Lappin, A.R. 1980. *Preliminary Thermal Expansion Screening Data for Tuffs.* SAND78-1147. Albuquerque, New Mexico: Sandia National Laboratories. ACC: NNA.19870406.0163.

104566   Lappin, A.R.; VanBuskirk, R.G.; Enniss, D.O.; Butters, S.W.; Prater, F.M.; Muller, C.B.; and Bergosh, J.L. 1982. *Thermal Conductivity, Bulk Properties, and Thermal Stratigraphy of Silicic Tuffs from the Upper Portion of Hole USW-G1, Yucca Mountain, Nye County, Nevada.* SAND81-1873. Albuquerque, New Mexico: Sandia National Laboratories. ACC: HQS.19880517.1669.

104565   Lappin, A.R. and Nimick, F.B. 1985. *Bulk and Thermal Properties of the Functional Tuffaceous Beds in Holes USW G-1, UE-25a#1, and USW G-2, Yucca Mountain, Nevada.* SAND82-1434. Albuquerque, New Mexico: Sandia National Laboratories. ACC: NNA.19890315.0020.

129667   Lee, M.Y. and Haimson, B.C. 1999. "Initial Stress Measurements in the Exploratory Studies Facility Yucca Mountain, Nevada." *Rock Mechanics for Industry, Proceedings of the 37th U.S. Rock Mechanics Symposium, Vail, Colorado, USA, 6-9 June 1999.* Amadei, B.; Kranz, R.L.; Scott, G.A.; and Smeallie, P.H., eds. *2*, 743-750. Brookfield, Vermont: A.A. Balkema. TIC: 245246.

106681   Levy, S. and Valentine, G. 1993. "Natural Alteration in the Cooling Topopah Spring Tuff, Yucca Mountain, Nevada, As an Analog to a Waste-Repository Hydrothermal Regime." *Proceedings of the Topical Meeting on Site Characterization and Model Validation, FOCUS '93, September 26-29, 1993, Las Vegas, Nevada.* Pages 145-149. La Grange Park, Illinois: American Nuclear Society. TIC: 102245.

101392   Levy, S.S. 1984. *Petrology of Samples from Drill Holes USW H-3, H-4, and H-5, Yucca Mountain, Nevada.* LA-9706-MS. Los Alamos, New Mexico: Los Alamos National Laboratory. ACC: MOL.19970729.0322.

104577   Levy, S.S. 1984. "Studies of Altered Vitrophyre for the Prediction of Nuclear Waste Repository-Induced Thermal Alteration at Yucca Mountain, Nevada." *Scientific Basis for Nuclear Waste Management VII, Symposium held November 14-17, 1983, Boston, Massachusetts.* McVay, G.L., ed. *26*, 959-966. New York, New York: Elsevier. TIC: 204393.

116960   Levy, S.S. and O'Neil, J.R. 1989. "Moderate-Temperature Zeolitic Alteration in a Cooling Pyroclastic Deposit." *Chemical Geology, 76,* (3/4), 321-326. Amsterdam, The Netherlands: Elsevier. TIC: 237819.

100053   Levy, S.S. 1991. "Mineralogic Alteration History and Paleohydrology at Yucca Mountain, Nevada." *High Level Radioactive Waste Management, Proceedings of the Second Annual International Conference, Las Vegas, Nevada, April 28-May 3, 1991.* *1*, 477-485. La Grange Park, Illinois: American Nuclear Society. TIC: 204272.

104579   Levy, S.S. 1993. "Surface-Discharging Hydrothermal Systems at Yucca Mountain - Examining the Evidence." *Scientific Basis for Nuclear Waste Management XVI, Symposium held November 30-December 4, 1992, Boston, Massachusetts.* Interrante, C.G. and Pabalan, R.T., eds. *294*, 543-548. Pittsburgh, Pennsylvania: Materials Research Society. TIC: 208880.

148201   Li, J.; Lowenstein, T.K.; and Blackburn, I.R. 1997. "Responses of Evaporite Mineralogy to Inflow Water Sources and Climate During the Past 100 k.y. in Death Valley, California." *Geological Society of America Bulletin, 109*, (10), 1361-1371. Boulder, Colorado: Geological Society of America. TIC: 247723.

104585   Lin, M.; Hardy, M.P.; and Bauer, S.J. 1993. *Rock Mass Mechanical Property Estimations for the Yucca Mountain Site Characterization Project.* SAND92-0450. Albuquerque, New Mexico: Sandia National Laboratories. ACC: NNA.19921204.0013.

104158   Lipman, P.W. and McKay, E.J. 1965. *Geologic Map of the Topopah Spring SW Quadrangle, Nye County, Nevada.* Geologic Quadrangle Map GQ-439. Denver, Colorado: U.S. Geological Survey. TIC: 212352.

100773   Lipman, P.W.; Christiansen, R.L.; and O'Connor, J.T. 1966. *A Compositionally Zoned Ash-Flow Sheet in Southern Nevada.* Professional Paper 524-F. Washington, D.C.: U.S. Geological Survey. TIC: 219972.

130132   Lowenstein, T. 1999. "200-K.Y. Paleoclimate Record from Core DV 93-1, Badwater Basin, Death Valley, California." *Proceedings of Conference on Status of Geologic Research and Mapping in Death Valley National Park, Las Vegas, Nevada, April 9-11, 1999.* Slate, J.L., ed. Open-File Report 99-153. Pages 142-144. Denver, Colorado: U.S. Geological Survey. TIC: 245245.

109129   Lowenstein, T.K. 1997. "Death Valley Salt Core: 200,000 Year Paleoclimate Record from Sedimentary Structures, Saline Mineralogy, Fluid Inclusions in Halite, and Ostracodes." *GBASH 97, Great Basin Aquatic System History, Fifty Years of Geologic, Biologic, and Hydroclimatic Progress in Lake Cenozoic Aquatic System History, September 17-20, 1997, Salt Lake City, Utah.* Salt Lake City, Utah: University of Utah. TIC: 247450.

106326   Lundstrom, S.C. and Warren, R.G. 1994. "Late Cenozoic Evolution of Fortymile Wash: Major Change in Drainage Pattern in the Yucca Mountain, Nevada Region During Late Miocene Volcanism." *High Level Radioactive Waste Management, Proceedings of the Fifth Annual International Conference, Las Vegas, Nevada, May 22-26, 1994. 4*, 2121-2130. La Grange Park, Illinois: American Nuclear Society. TIC: 210984.

136523   Lundstrom, S.C.; Paces, J.B.; and Mahan, S.M. 1996. "Late Quaternary History of Fortymile Wash, Southern Nevada: A Record of Geomorphic Response to Climate Change in the Yucca Mountain Region." *Abstracts with Programs - Geological Society of America, 28*, (7), A-552. Boulder, Colorado: Geological Society of America. TIC: 247474.

136539   Lundstrom, S.C.; Paces, J.B.; and Mahan, S.A. 1998. "Late Quaternary History of Fortymile Wash in the Area Near the H-Road Crossing." *Quaternary Geology of the Yucca Mountain Area, Southern Nevada, Field Trip Guide, Annual Meeting of the Friends of the Pleistocene, Pacific Cell, October 9-11, 1998*. Taylor, E.M., ed. Pages 63-76. Boulder, Colorado: Friends of the Pleistocene. TIC: 244815.

104685   Majer, E.L.; Feighner, M.; Johnson, L.; Daley, T.; Karageorgi, E.; Lee, K.H.; Williams, K.; and McEvilly, T. 1996. *Surface Geophysics*. Volume I of *Synthesis of Borehole and Surface Geophysical Studies at Yucca Mountain, Nevada and Vicinity*. Milestone OB05M. Berkeley, California: Lawrence Berkeley National Laboratory. ACC: MOL.19970610.0150.

101805   Maldonado, F. and Koether, S.L. 1983. *Stratigraphy, Structure, and Some Petrographic Features of Tertiary Volcanic Rocks at the USW G-2 Drill Hole, Yucca Mountain, Nye County, Nevada*. Open-File Report 83-732. Denver, Colorado: U.S. Geological Survey. ACC: NNA.19870506.0143.

104760   Martin, R.J.; Price, R.H.; Boyd, P.J.; and Noel, J.S. 1994. *Bulk and Mechanical Properties of the Paintbrush Tuff Recovered from Borehole USW NRG-6: Data Report*. SAND93-4020. Albuquerque, New Mexico: Sandia National Laboratories. ACC: MOL.19940811.0001.

104761   Martin, R.J.; Price, R.H.; Boyd, P.J.; and Noel, J.S. 1995. *Bulk and Mechanical Properties of the Paintbrush Tuff Recovered from Borehole USW NRG-7/7A: Data Report*. SAND94-1996. Albuquerque, New Mexico: Sandia National Laboratories. ACC: MOL.19950316.0087.

148875   Martin, R.J.; Noel, J.S.; Boyd, P.J.; and Price, R.H. 1997. *Creep Properties of the Paintbrush Tuff Recovered from Borehole USW NRG-7/7A: Data Report*. SAND95-1759. Albuquerque, New Mexico: Sandia National Laboratories. ACC: MOL.19971017.0661.

101432   Martin, R.J.; Noel, J.S.; Boyd, P.J.; and Price, R.H. 1997. *The Effects of Confining Pressure on the Strength and Elastic Properties of the Paintbrush Tuff Recovered from Boreholes USW NRG-6 and USW NRG-7/7A: Data Report*. SAND95-1887. Albuquerque, New Mexico: Sandia National Laboratories. ACC: MOL.19971017.0662.

104758   Martin, R.J.; Noel, J.S.; Boyd, P.J.; Riggins, M.; and Price, R.H. 1997. *Thermal Expansion of the Paintbrush Tuff Recovered from Borehole USW SD-12 at Pressures 30 MPa: Data Report*. SAND95-1904. Albuquerque, New Mexico: Sandia National Laboratories. ACC: MOL.19971017.0680.

160028   Martin, R.J., III; Price, R.H.; Boyd, P.J.; and Haupt, R.W. 1992. *Anisotropy of the Topopah Spring Member Tuff*. SAND91-0894. Albuquerque, New Mexico: Sandia National Laboratories. ACC: NNA.19920522.0041.

160036   Martin, R.J., III; Price, R.H.; Boyd, P.J.; and Noel, J.S. 1993. *Unconfined Compression Experiments on Topopah Spring Member Tuff at 22º C and a Strain Rate of 10 $^{-9}$ s $^{-1}$: Data Report*. SAND92-1810. Albuquerque, New Mexico: Sandia National Laboratories. ACC: NNA.19930728.0088.

100159   Martin, R.J., III; Price, R.H.; Boyd, P.J.; and Noel, J.S. 1995. *Creep in Topopah Spring Member Welded Tuff*. SAND94-2585. Albuquerque, New Mexico: Sandia National Laboratories. ACC: MOL.19950502.0006.

104772   McDonald, E. and McFadden, L.D. 1994. "Quaternary Stratigraphy of the Providence Mountains Piedmont and Preliminary Age Estimates and Regional Stratigraphic Correlations of Quaternary Deposits in the Eastern Mojave Desert, California." *Geological Investigations of an Active Margin, Geological Society of America Cordilleran Section Guidebook, 27th Annual Meeting, San Bernardino, California, March 21-23, 1994*. McGill, S.F. and Ross, T.M., eds. Pages 205-210. Redlands, California: San Bernardino County Museum Association. TIC: 237835.

105022   McFadden, L.D. and Weldon, R.J., II 1987. "Rates and Processes of Soil Development on Quaternary Terraces in Cajon Pass, California." *Geological Society of America Bulletin, 98*, (3), 280-293. Boulder, Colorado: Geological Society of America. TIC: 241011.

105023   McFadden, L.D.; Wells, S.G.; and Jercinovich, M.J. 1987. "Influences of Eolian and Pedogenic Processes on the Origin and Evolution of Desert Pavements." *Geology, 15*, (6), 504-508. Boulder, Colorado: Geological Society of America. TIC: 241037.

159316   McGovern, T.F. 1983. *An Evaluation of Seismic Reflection Studies in the Yucca Mountain Area, Nevada Test Site*. Open-File Report 83-912. Denver, Colorado: U.S. Geological Survey. ACC: NNA.19870518.0072.

102330   McKeown, M. 1992. *Soil and Rock Geotechnical Investigations Field and Laboratory Studies, North Ramp Surface Facility Exploratory Studies Facility, Yucca Mountain Project, Nevada*. Technical Memorandum 3610-92-35. Denver, Colorado: U.S. Department of Interior, Bureau of Reclamation. ACC: NNA.19930607.0020.

106344   Menges, C.M.; Wesling, J.R.; Whitney, J.W.; Swan, F.H.; Coe, J.A.; Thomas, A.P.; and Oswald, J.A. 1994. "Preliminary Results of Paleoseismic Investigations of Quaternary Faults on Eastern Yucca Mountain, Nye County, Nevada." *High Level Radioactive Waste Management, Proceedings of the Fifth Annual International Conference, Las Vegas, Nevada, May 22-26, 1994. 4*, 2373-2390. La Grange Park, Illinois: American Nuclear Society. TIC: 210984.

106343   Menges, C.M. and Whitney, J.W. 1996. "Summary of Quaternary Faulting on the Paintbrush Canyon, Stagecoach Road, and Bow Ridge Faults." Chapter 4.4 of *Seismotectonic Framework and Characterization of Faulting at Yucca Mountain, Nevada*. Whitney, J.W., ed. Milestone 3GSH100M. Denver, Colorado: U.S. Geological Survey. TIC: 237980. ACC: MOL.19970129.0041.

159412   Menges, C.M.; Taylor, E.M.; Wesling, J.R.; Swan, F.H.; Coe, J.A.; Ponti, D.J.; and Whitney, J.W. 2003. "Summary of Quaternary Faulting on the Paintbrush Canyon, Stagecoach Road, and Bow Ridge Faults." Chapter 5 of *Quaternary Paleoseismology and Stratigraphy of the Yucca Mountain Area, Nevada*. U.S. Geological Survey Digital Data Series. Keefer, W.R.; Whitney, J.W.; and Taylor, E.M., eds. Denver, Colorado: U.S. Geological Survey. ACC: MOL.20031208.0113. TBV-5659.

160061   Menges, C.M. and Whitney, J.W. 2003. "Distribution of Quaternary Faults at Yucca Mountain." Chapter 3 of *Quaternary Paleoseismology and Stratigraphy of the Yucca Mountain Area, Nevada*. U.S. Geological Survey Digital Data Series. Keefer, W.R.; Whitney, J.W.; and Taylor, E.M., eds. Denver, Colorado: U.S. Geological Survey. ACC: MOL.20031208.0113. TBV-5659.

106360   Michelis, P. and Brown, E.T. 1986. "A Yield Equation for Rock." *Canadian Geotechnical Journal, 23*, 9-17. Ottawa, Ontario, Canada: National Research Council of Canada. TIC: 237800.

106373   Minor, S.A. 1995. "Superposed Local and Regional Paleostresses: Fault-Slip Analysis of Neogene Extensional Faulting Near Coeval Caldera Complexes, Yucca Flat, Nevada." *Journal of Geophysical Research, 100*, (B6), 10,507-10,528. Washington, D.C.: American Geophysical Union. TIC: 236631.

106376   Minor, S.A.; Sawyer, D.A.; Wahl, R.R.; Frizzell, V.A., Jr.; Schilling, S.P.; Warren, R.G.; Orkild, P.P.; Coe, J.A.; Hudson, M.R.; Fleck, R.J.; Lanphere, M.A.; Swadley, W C; and Cole, J.C. 1993. *Preliminary Geologic Map of the Pahute Mesa 30' x 60' Quadrangle, Nevada*. Open-File Report 93-299. Denver, Colorado: U.S. Geological Survey. TIC: 225082.

106374   Minor, S.A.; Hudson, M.R.; and Fridrich, C.J. 1996. "Fault-Slip Data Bearing on the Miocene Tectonic Development of Northern Crater Flat Basin, Southern Nevada." *Abstracts with Programs - Geological Society of America, 28*, (7), A-192. Boulder, Colorado: Geological Society of America. TIC: 236626.

149850   Mongano, G.S.; Singleton, W.L.; Moyer, T.C.; Beason, S.C.; Eatman, G.L.W.; Albin, A.L.; and Lung, R.C. 1999. *Geology of the ECRB Cross Drift - Exploratory Studies Facility, Yucca Mountain Project, Yucca Mountain, Nevada*. Deliverable SPG42GM3. Denver, Colorado: U.S. Geological Survey. ACC: MOL.20000324.0614.

106382   Monsen, S.A.; Carr, M.D.; Reheis, M.C.; and Orkild, P.P. 1992. *Geologic Map of Bare Mountain, Nye County, Nevada*. Miscellaneous Investigations Series Map I-2201. Reston, Virginia: U.S. Geological Survey. TIC: 231183.

100161   Montazer, P. and Wilson, W.E. 1984. *Conceptual Hydrologic Model of Flow in the Unsaturated Zone, Yucca Mountain, Nevada.* Water-Resources Investigations Report 84-4345. Lakewood, Colorado: U.S. Geological Survey. ACC: NNA.19890327.0051.

108876   Moosburner, O. 1978. *Flood Investigations in Nevada Through 1977 Water Year.* Open-File Report 78-610. Carson City, Nevada: U.S. Geological Survey. TIC: 235972.

106397   Morrison, R.B. 1991. "Quaternary Stratigraphic, Hydrologic, and Climatic History of the Great Basin, with Emphasis on Lakes Lahontan, Bonneville, and Tecopa." Chapter 10 of *Quaternary Nonglacial Geology: Conterminous U.S.* The Geology of North America Volume K-2. Boulder, Colorado: Geological Society of America. TIC: 240796.

101269   Moyer, T.C. and Geslin, J.K. 1995. *Lithostratigraphy of the Calico Hills Formation and Prow Pass Tuff (Crater Flat Group) at Yucca Mountain, Nevada.* Open-File Report 94-460. Denver, Colorado: U.S. Geological Survey. ACC: MOL.19941208.0003.

103777   Moyer, T.C.; Geslin, J.K.; and Buesch, D.C. 1995. *Summary of Lithologic Logging of New and Existing Boreholes at Yucca Mountain, Nevada, July 1994 to November 1994.* Open-File Report 95-102. Denver, Colorado: U.S. Geological Survey. TIC: 224224.

100162   Moyer, T.C.; Geslin, J.K.; and Flint, L.E. 1996. *Stratigraphic Relations and Hydrologic Properties of the Paintbrush Tuff Nonwelded (PTn) Hydrologic Unit, Yucca Mountain, Nevada.* Open-File Report 95-397. Denver, Colorado: U.S. Geological Survey. ACC: MOL.19970204.0216.

105141   Muller, D.C. and Kibler, J.E. 1984. *Preliminary Analysis of Geophysical Logs from Drill Hole UE-25p#1, Yucca Mountain, Nye County, Nevada.* Open-File Report 84-649. Denver, Colorado: U.S. Geological Survey. ACC: HQS.19880517.1353.

106399   Munsell Color Company 1994. *Munsell Soil Color Charts.* 1994 Revised Edition. New Windsor, New York: GretagMacbeth. TIC: 238646.

105301   NBMG (Nevada Bureau of Mines and Geology) 1997. *The Nevada Mineral Industry 1996.* Meeuwig, D., ed. Special Publication MI-1996. Reno, Nevada: Nevada Bureau of Mines and Geology. TIC: 240403.

101618   Neal, J.T. 1985. *Location Recommendation for Surface Facilities for the Prospective Yucca Mountain Nuclear Waste Repository.* SAND84-2015. Albuquerque, New Mexico: Sandia National Laboratories. ACC: NNA.19870406.0061.

102331   Neal, J.T. 1986. *Preliminary Validation of Geology at Site for Repository Surface Facilities, Yucca Mountain, Nevada*. SAND85-0815. Albuquerque, New Mexico: Sandia National Laboratories. ACC: NNA.19870824.0060.

101272   Nelson, P.H.; Muller, D.C.; Schimschal, U.; and Kibler, J.E. 1991. *Geophysical Logs and Core Measurements from Forty Boreholes at Yucca Mountain, Nevada*. Geophysical Investigations Map GP-1001. Denver, Colorado: U.S. Geological Survey. ACC: NNA.19920211.0022.

105176   Nelson, P.H. 1993. "Estimation of Water-Filled and Air-Filled Porosity in the Unsaturated Zone, Yucca Mountain, Nevada." *High Level Radioactive Waste Management, Proceedings of the Fourth Annual International Conference, Las Vegas, Nevada, April 26-30, 1993. 1*, 949-954. La Grange Park, Illinois: American Nuclear Society. TIC: 208542.

105177   Nelson, P.H. 1994. "Saturation Levels and Trends in the Unsaturated Zone, Yucca Mountain, Nevada." *High Level Radioactive Waste Management, Proceedings of the Fifth Annual International Conference, Las Vegas, Nevada, May 22-26, 1994. 4*, 2774-2781. La Grange Park, Illinois: American Nuclear Society. TIC: 210984.

101270   Nelson, P.H. 1996. *Computation of Porosity and Water Content from Geophysical Logs, Yucca Mountain, Nevada*. Open-File Report 96-078. Denver, Colorado: U.S. Geological Survey. ACC: MOL.19980529.0444.

158673   Neymark, L.A.; Amelin, Y.; Paces, J.B.; and Peterman, Z.E. 2002. "U-Pb Ages of Secondary Silica at Yucca Mountain, Nevada: Implications for the Paleohydrology of the Unsaturated Zone." *Applied Geochemistry, 17*, (6), 709-734. New York, New York: Elsevier. TIC: 252598.

105191   Nimick, F.B. and Lappin, A.R. 1985. *Thermal Conductivity of Silicic Tuffs from Yucca Mountain and Rainier Mesa, Nye County, Nevada*. SAND83-1711/1J. Albuquerque, New Mexico: Sandia National Laboratories. TIC: 218836.

105195   Nimick, F.B.; Price, R.H.; Van Buskirk, R.G.; and Goodell, J.R. 1985. *Uniaxial and Triaxial Compression Test Series on Topopah Spring Tuff from USW G-4, Yucca Mountain, Nevada*. SAND84-1101. Albuquerque, New Mexico: Sandia National Laboratories. ACC: MOL.19980602.0332.

102921   Nimick, F.B.; Shephard, L.E.; and Blejwas, T.E. 1988. *Preliminary Evaluation of the Exploratory Shaft Representativeness for the Yucca Mountain Project*. SAND87-1685. Albuquerque, New Mexico: Sandia National Laboratories. ACC: NNA.19900510.0022.

105180   Nimick, F.B. 1989. *Thermal-Conductivity Data for Tuffs from the Unsaturated Zone at Yucca Mountain, Nevada*. SAND88-0624. Albuquerque, New Mexico: Sandia National Laboratories. ACC: NNA.19890515.0133.

105189   Nimick, F.B. 1990. *The Thermal Conductivity of Seven Thermal/Mechanical Units at Yucca Mountain, Nevada.* SAND88-1387. Albuquerque, New Mexico: Sandia National Laboratories. ACC: NNA.19891213.0201.

101396   Nimick, F.B. 1990. *The Thermal Conductivity of the Topopah Spring Member at Yucca Mountain, Nevada.* SAND86-0090. Albuquerque, New Mexico: Sandia National Laboratories. ACC: NNA.19890516.0183.

100690   Nimick, F.B. and Connolly, J.R. 1991. *Calculation of Heat Capacities for Tuffaceous Units from the Unsaturated Zone at Yucca Mountain, Nevada.* SAND88-3050. Albuquerque, New Mexico: Sandia National Laboratories. ACC: NNA.19910308.0017.

105197   Noble, D.C. and Hedge, C.E. 1969. "Sr^{87}/Sr^{86} Variations Within Individual Ash-Flow Sheets." *Geological Survey Research 1969, Chapter C.* Professional Paper 650-C. Pages C133-C139. Washington, D.C.: U.S. Geological Survey. TIC: 232920.

106417   North American Commission on Stratigraphic Nomenclature 1993. "North American Stratigraphic Code." *American Association of Petroleum Geologists Bulletin, 67,* (5), 841-875. Tulsa, Oklahoma: American Association of Petroleum Geologists. TIC: 247569.

106447   Oliver, H.W.; Ponce, D.A.; and Hunter, W.C., eds. 1995. *Major Results of Geophysical Investigations at Yucca Mountain and Vicinity, Southern Nevada.* Open-File Report 95-74. Menlo Park, California: U.S. Geological Survey. ACC: MOL.19980305.0122.

102940   Olsson, W.A. and Jones, A.K. 1980. *Rock Mechanics Properties of Volcanic Tuffs from the Nevada Test Site.* SAND80-1453. Albuquerque, New Mexico: Sandia National Laboratories. ACC: NNA.19870406.0497.

100169   Olsson, W.A. and Brown, S.R. 1994. *Mechanical Properties of Seven Fractures from Drillholes NRG-4 and NRG-6 at Yucca Mountain, Nevada.* SAND94-1995. Albuquerque, New Mexico: Sandia National Laboratories. ACC: MOL.19941007.0081.

106453   Olsson, W.A. and Brown, S.R. 1997. *Mechanical Properties of Fractures from Drillholes UE25-NRG-4, USW-NRG-6, USW-NRG-7, USW-SD-9 at Yucca Mountain, Nevada.* SAND95-1736. Albuquerque, New Mexico: Sandia National Laboratories. ACC: MOL.19970224.0064.

101280   Ortiz, T.S.; Williams, R.L.; Nimick, F.B.; Whittet, B.C.; and South, D.L. 1985. *A Three-Dimensional Model of Reference Thermal/Mechanical and Hydrological Stratigraphy at Yucca Mountain, Southern Nevada.* SAND84-1076. Albuquerque, New Mexico: Sandia National Laboratories. ACC: MOL.19980602.0331.

100602   Osterkamp, W.R.; Lane, L.J.; and Savard, C.S. 1994. "Recharge Estimates Using a Geomorphic/Distributed-Parameter Simulation Approach, Amargosa River Basin." *Water Resources Bulletin, 30*, (3), 493-506. Minneapolis, Minnesota: American Water Resources Association. TIC: 237428.

100170   Pabst, M.E.; Beck, D.A.; Glancy, P.A.; and Johnson, J.A. 1993. *Streamflow and Selected Precipitation Data for Yucca Mountain and Vicinity, Nye County, Nevada, Water Years 1983-85.* Open-File Report 93-438. Carson City, Nevada: U.S. Geological Survey. ACC: NNA.19931019.0043.

129772   Paces, J.B.; Neymark, L.A.; Whelan, J.F.; Peterman, Z.E.; Marshall, B.D.; and Amelin, Y.V. 1999. "Characteristics of Unsaturated-Zone Fracture Flow Interpreted from Calcite and Opal Deposits at Yucca Mountain, Nevada." *Eos, Transactions (Supplement), 80*, (17), S4. Washington, D.C.: American Geophysical Union. TIC: 246468.

106476   Palmstrom, A. 1996. "Characterizing Rock Masses by the RMi for Use in Practical Rock Engineering, Part 1: The Development of the Rock Mass Index (RMi)." *Tunnelling and Underground Space Technology, 11*, (2), 175-188. New York, New York: Pergamon Press. TIC: 240850.

105310   Palmstrom, A. 1996. "Characterizing Rock Masses by the RMi for Use in Practical Rock Engineering, Part 2: Some Practical Applications of the Rock Mass Index (RMi)." *Tunnelling and Underground Space Technology, 11*, (3), 287-303. New York, New York: Pergamon Press. TIC: 240849.

130172   Pankratz, L.W. 1982. *Reconnaissance Seismic Refraction Studies at Calico Hills, Wahmonie, and Yucca Mountain, Southwest Nevada Test Site, Nye County, Nevada.* Open-File Report 82-478. Denver, Colorado: U.S. Geological Survey. TIC: 203127.

105344   Papike, J.J. and Cameron, M. 1976. "Crystal Chemistry of Silicate Minerals of Geophysical Interest." *Reviews of Geophysics and Space Physics, 14*, (1), 37-80. Washington, D.C.: American Geophysical Union. TIC: 240938.

106496   Peterman, Z.E.; Spengler, R.W.; Futa, K.; Marshall, B.D.; and Mahan, S.A. 1991. "Assessing the Natural Performance of Felsic Tuffs Using the Rb-Sr and Sm-Nd Systems - A Study of the Altered Zone in the Topopah Spring Member, Paintbrush Tuff, Yucca Mountain, Nevada." *Scientific Basis for Nuclear Waste Management XIV, Symposium held November 26-29, 1990, Boston, Massachusetts.* Abrajano, T.A., Jr. and Johnson, L.H., eds. *212*, 687-694. Pittsburgh, Pennsylvania: Materials Research Society. TIC: 203656.

106498   Peterman, Z.E.; Spengler, R.W.; Singer, F.R.; and Dickerson, R.P. 1993. "Isotopic and Trace Element Variability in Altered and Unaltered Tuffs at Yucca Mountain, Nevada." *High Level Radioactive Waste Management, Proceedings of the Fourth Annual International Conference, Las Vegas, Nevada, April 26-30, 1993. 2,* 1940-1947. La Grange Park, Illinois: American Nuclear Society. TIC: 208542.

106494   Peterman, Z.E. and Futa, K. 1996. *Geochemistry of Core Samples of the Tiva Canyon Tuff from Drill Hole UE-25 NRG#3, Yucca Mountain, Nevada.* Open-File Report 95-325. Denver, Colorado: U.S. Geological Survey. ACC: MOL.19961118.0132.

162576   Peterman, Z.E. and Cloke, P.L. 2002. "Geochemistry of Rock Units at the Potential Repository Level, Yucca Mountain, Nevada (includes Erratum)." *Applied Geochemistry, 17,* (6, 7), 683-698, 955-958. New York, New York: Pergamon. TIC: 252516; 252517.

103265   Pezzopane, S.K. and Dawson, T.E. 1996. "Fault Displacement Hazard: A Summary of Issues and Information." Chapter 9 of *Seismotectonic Framework and Characterization of Faulting at Yucca Mountain, Nevada.* Whitney, J.W., ed. Milestone 3GSH100M. Denver, Colorado: U.S. Geological Survey. TIC: 237980. ACC: MOL.19970129.0041.

106528   Pezzopane, S.K.; Whitney, J.W.; and Dawson, T.E. 1996. "Models of Earthquake Recurrence and Preliminary Paleoearthquake Magnitudes at Yucca Mountain." Chapter 5 of *Seismotectonic Framework and Characterization of Faulting at Yucca Mountain, Nevada.* Whitney, J.W., ed. Milestone 3GSH100M. Denver, Colorado: U.S. Geological Survey. TIC: 237980. ACC: MOL.19970129.0041.

106552   Ponce, D.A. 1993. "Geophysical Investigations of Concealed Faults Near Yucca Mountain, Southwest Nevada." *High Level Radioactive Waste Management, Proceedings of the Fourth Annual International Conference, Las Vegas, Nevada, April 26-30, 1993. 1,* 168-174. La Grange Park, Illinois: American Nuclear Society. TIC: 208542.

102333   Ponce, D.A. and Langenheim, V.E. 1994. *Preliminary Gravity and Magnetic Models Across Midway Valley and Yucca Wash, Yucca Mountain, Nevada.* Open-File Report 94-572. Menlo Park, California: U.S. Geological Survey. ACC: MOL.19990406.0399.

107259   Potter, C.J.; Dickerson, R.P.; and Day, W.C. 1999. *Nature and Continuity of the Sundance Fault.* Open-File Report 98-266. Denver, Colorado: U.S. Geological Survey. TIC: 246609.

160060   Potter, C.J.; Dickerson, R.P.; Sweetkind, D.S.; Drake, R.M., II; Taylor, E.M.; Fridrich, C.J.; San Juan, C.A.; and Day, W.C. 2002. *Geologic Map of the Yucca Mountain Region, Nye County, Nevada.* Geologic Investigations Series I-2755. Denver, Colorado: U.S. Geological Survey. TIC: 253945.

159091   Potter, C.J.; Sweetkind, D.S.; Dickerson, R.P.; and Killgore, M.L. 2002. *Hydrostructural Maps of the Death Valley Regional Flow System, Nevada and California.* Miscellaneous Field Studies Map MF-2372. Denver, Colorado: U.S. Geological Survey. TIC: 253072.

102941   Price, R.H. 1983. *Analysis of the Rock Mechanics Properties of Volcanic Tuff Units from Yucca Mountain, Nevada Test Site.* SAND82-1315. Albuquerque, New Mexico: Sandia National Laboratories. ACC: NNA.19870406.0181.

106604   Price, R.H.; Spence, S.J.; and Jones, A.K. 1984. *Uniaxial Compression Test Series on Topopah Spring Tuff from USW GU-3, Yucca Mountain, Southern Nevada.* SAND83-1646. Albuquerque, New Mexico: Sandia National Laboratories. ACC: NNA.19870406.0252.

106590   Price, R.H. and Bauer, S.J. 1985. "Analysis of the Elastic and Strength Properties of Yucca Mountain Tuff, Nevada." *Research & Engineering Applications in Rock Masses, Proceedings of the 26th U.S. Symposium on Rock Mechanics, Rapid City, South Dakota, June 26-28, 1985.* Ashworth, E., ed. Pages 89-96. Boston, Massachusetts: A.A. Balkema. TIC: 218790.

106602   Price, R.H.; Nimick, F.B.; Connolly, J.R.; Keil, K.; Schwartz, B.M.; and Spence, S.J. 1985. *Preliminary Characterization of the Petrologic, Bulk, and Mechanical Properties of a Lithophysal Zone Within the Topopah Spring Member of the Paintbrush Tuff.* SAND84-0860. Albuquerque, New Mexico: Sandia National Laboratories. ACC: NNA.19870406.0156.

106589   Price, R.H. 1986. *Effects of Sample Size on the Mechanical Behavior of Topopah Spring Tuff.* SAND85-0709. Albuquerque, New Mexico: Sandia National Laboratories. ACC: NNA.19891106.0125.

100173   Price, R.H.; Connolly, J.R.; and Keil, K. 1987. *Petrologic and Mechanical Properties of Outcrop Samples of the Welded, Devitrified Topopah Spring Member of the Paintbrush Tuff.* SAND86-1131. Albuquerque, New Mexico: Sandia National Laboratories. ACC: NNA.19870601.0013.

161289   Price, R.H.; Boyd, P.J.; Martin, R.J.; Haupt, R.W.; and Noel, J.S. 1991. "Mechanical Anisotropy of the Yucca Mountain Tuffs." *High Level Radioactive Waste Management, Proceedings of the Second Annual International Conference, Las Vegas, Nevada, April 28-May 3, 1991. 1,* 268-271. La Grange Park, Illinois: American Nuclear Society. TIC: 204272.

160023   Price, R.H. 1993. "Strength-Size-Porosity Empirical Model for Yucca Mountain Tuff." *EOS, Transactions (Supplement), 74,* (43), 571. Washington, D.C.: American Geophysical Union. TIC: 210057.

106601   Price, R.H.; Martin, R.J., III; and Boyd, P.J. 1993. "Characterization of Porosity in Support of Mechanical Property Analysis." *High Level Radioactive Waste Management, Proceedings of the Fourth Annual International Conference, Las Vegas, Nevada, April 26-30, 1993. 2*, 1847-1853. La Grange Park, Illinois: American Nuclear Society. TIC: 208542.

160052   Price, R.H.; Boyd, P.J.; Noel, J.S.; and Martin, R.J., III 1994. "Relationship Between Static and Dynamic Rock Properties in Welded and Nonwelded Tuff." *Rock Mechanics Models and Measurements Challenges from Industry, Proceedings of the 1st North American Rock Mechanics Symposium, the University of Texas at Austin, 1-3 June 1994*. Nelson, P.P. and Laubach, S.E., eds. Pages 505-529. Brookfield, Vermont: A.A. Balkema. TIC: 254896.

161290   Price, R.H.; Martin, R.J., III; Boyd, P.J.; and Noel, J.S. 1994. "Mechanical and Bulk Properties in Support of ESF Design Issues." *High Level Radioactive Waste Management, Proceedings of the Fifth Annual International Conference, Las Vegas, Nevada, May 22-26, 1994. 4*, 1987-1992. La Grange Park, Illinois: American Nuclear Society. TIC: 210984.

159413   Ramelli, A.R.; Oswald, J.A.; Vadurro, G.; Menges, C.M.; and Paces, J.B. 2003. "Quaternary Faulting on the Solitario Canyon Fault." Chapter 7 of *Quaternary Paleoseismology and Stratigraphy of the Yucca Mountain Area, Nevada*. U.S. Geological Survey Digital Data Series. Keefer, W.R.; Whitney, J.W.; and Taylor, E.M., eds. Denver, Colorado: U.S. Geological Survey. ACC: MOL.20031208.0113. TBV-5659.

100692   Rautman, C.A. 1995. *Preliminary Geostatistical Modeling of Thermal Conductivity for a Cross Section of Yucca Mountain, Nevada*. SAND94-2283. Albuquerque, New Mexico: Sandia National Laboratories. ACC: MOL.19960320.0109.

106635   Rautman, C.A. 1996. "Integrated Rock Properties Models at Yucca Mountain, Nevada." Abst*racts with Programs - Geological Society of America, 28*, (7), A-521. Boulder, Colorado: Geological Society of America. TIC: 234937.

100642   Rautman, C.A. and Engstrom, D.A. 1996. *Geology of the USW SD-12 Drill Hole Yucca Mountain, Nevada*. SAND96-1368. Albuquerque, New Mexico: Sandia National Laboratories. ACC: MOL.19970613.0101.

101008   Rautman, C.A. and Engstrom, D.A. 1996. *Geology of the USW SD-7 Drill Hole Yucca Mountain, Nevada*. SAND96-1474. Albuquerque, New Mexico: Sandia National Laboratories. ACC: MOL.19971218.0442.

100643   Rautman, C.A. and McKenna, S.A. 1997. *Three-Dimensional Hydrological and Thermal Property Models of Yucca Mountain, Nevada*. SAND97-1730. Albuquerque, New Mexico: Sandia National Laboratories. ACC: MOL.19980311.0317.

106661   Reheis, M.C.; Sowers, J.M.; Taylor, E.M.; McFadden, L.D.; and Harden, J.W. 1992. "Morphology and Genesis of Carbonate Soils on the Kyle Canyon Fan, Nevada, U.S.A." *Geoderma, 52*, 303-342. Amsterdam, The Netherlands: Elsevier. TIC: 224418.

106653   Reheis, M.C. and Kihl, R. 1995. "Dust Deposition in Southern Nevada and California, 1984-1989: Relations to Climate, Source Area, and Source Lithology." *Journal of Geophysical Research, 100*, (D5), 8893-8918. Washington, D.C.: American Geophysical Union. TIC: 234886.

107094   Riehle, J.R. 1973. "Calculated Compaction Profiles of Rhyolitic Ash-Flow Tuffs." *Geological Society of America Bulletin, 84*, 2193-2216. Boulder, Colorado: Geological Society of America. TIC: 224792.

106674   Robinson, G.D. 1985. *Structure of Pre-Cenozoic Rocks in the Vicinity of Yucca Mountain, Nye County, Nevada—A Potential Nuclear-Waste Disposal Site*. Bulletin 1647. Washington, D.C.: U.S. Geological Survey. TIC: 203083.

107160   Rosenbaum, J.G. 1986. "Paleomagnetic Directional Dispersion Produced by Plastic Deformation in a Thick Miocene Welded Tuff, Southern Nevada: Implications for Welding Temperatures." *Journal of Geophysical Research, 91*, (B12), 12,817-12,834. Washington, D.C.: American Geophysical Union. TIC: 233555.

106708   Rosenbaum, J.G.; Hudson, M.R.; and Scott, R.B. 1991. "Paleomagnetic Constraints on the Geometry and Timing of Deformation at Yucca Mountain, Nevada." *Journal of Geophysical Research, 96*, (B2), 1963-1979. Washington, D.C.: American Geophysical Union. TIC: 225126.

106714   Ross, C.S. and Smith, R.L. 1961. *Ash-Flow Tuffs: Their Origin, Geologic Relations, and Identification*. Professional Paper 366. Reston, Virginia: U.S. Geological Survey. TIC: 216668.

102097   Rousseau, J.P.; Kwicklis, E.M.; and Gillies, D.C., eds. 1999. *Hydrogeology of the Unsaturated Zone, North Ramp Area of the Exploratory Studies Facility, Yucca Mountain, Nevada.* Water-Resources Investigations Report 98-4050. Denver, Colorado: U.S. Geological Survey. ACC: MOL.19990419.0335.

101054   Rush, F.E.; Thordarson, W.; and Pyles, D.G. 1984. *Geohydrology of Test Well USW H-1, Yucca Mountain, Nye County, Nevada*. Water-Resources Investigations Report 84-4032. Denver, Colorado: U.S. Geological Survey. ACC: NNA.19870518.0067.

100694   Ryder, E.E.; Finley, R.E.; George, J.T.; Ho, C.K.; Longenbaugh, R.S.; and Connolly, J.R. 1996. *Bench-Scale Experimental Determination of the Thermal Diffusivity of Crushed Tuff*. SAND94-2320. Albuquerque, New Mexico: Sandia National Laboratories. ACC: MOL.19961111.0011.

109161   Sarna-Wojcicki, A.M.; Meyer, C.M.; and Wan, E. 1997. "Age and Correlation of Tephra Layers, Position of the Matuyama-Brunhes Chron Boundary, and Effects of Bishop Ash Eruption on Owens Lake, as Determined from Drill Hole OL-92, Southeast California." Chapter 7 of *An 800,000-Year Paleoclimatic Record from Core OL-92, Owens Lake, Southeast California*. Smith, G.I. and Bischoff, J.L., eds. Special Paper 317. Boulder, Colorado: Geological Society of America. TIC: 236857.

100644   Sass, J.H.; Lachenbruch, A.H.; Dudley, W.W., Jr.; Priest, S.S.; and Munroe, R.J. 1988. *Temperature, Thermal Conductivity, and Heat Flow Near Yucca Mountain, Nevada: Some Tectonic and Hydrologic Implications*. Open-File Report 87-649. Denver, Colorado: U.S. Geological Survey. TIC: 203195.

100075   Sawyer, D.A.; Fleck, R.J.; Lanphere, M.A.; Warren, R.G.; Broxton, D.E.; and Hudson, M.R. 1994. "Episodic Caldera Volcanism in the Miocene Southwestern Nevada Volcanic Field: Revised Stratigraphic Framework, $^{40}Ar/^{39}Ar$ Geochronology, and Implications for Magmatism and Extension." *Geological Society of America Bulletin, 106*, (10), 1304-1318. Boulder, Colorado: Geological Society of America. TIC: 222523.

101055   Schenker, A.R.; Guerin, D.C.; Robey, T.H.; Rautman, C.A.; and Barnard, R.W. 1995. *Stochastic Hydrogeologic Units and Hydrogeologic Properties Development for Total-System Performance Assessments*. SAND94-0244. Albuquerque, New Mexico: Sandia National Laboratories. ACC: MOL.19960318.0528.

104568   Scholz, C.H. 1968. "Microfracturing and the Inelastic Deformation of Rock in Compression." *Journal of Geophysical Research, 73*, 1417-1432. Washington, D.C.: American Geophysical Union. TIC: 234866.

107248   Schuraytz, B.C.; Vogel, T.A.; and Younker, L.W. 1989. "Evidence for Dynamic Withdrawal from a Layered Magma Body: The Topopah Spring Tuff, Southwestern Nevada." *Journal of Geophysical Research, 94*, (B5), 5925-5942. Washington, D.C.: American Geophysical Union. TIC: 225936.

106739   Schwartz, B.M. and Chocas, C.S. 1992. *Linear Thermal Expansion Data for Tuffs from the Unsaturated Zone at Yucca Mountain, Nevada*. SAND88-1581. Albuquerque, New Mexico: Sandia National Laboratories. ACC: NNA.19920710.0122.

106763   Scott, R.B.; Bath, G.D.; Flanigan, V.J.; Hoover, D.B.; Rosenbaum, J.G.; and Spengler, R.W. 1984. *Geological and Geophysical Evidence of Structures in Northwest-Trending Washes, Yucca Mountain, Southern Nevada, and Their Possible Significance to a Nuclear Waste Repository in the Unsaturated Zone*. Open-File Report 84-567. Denver, Colorado: U.S. Geological Survey. ACC: HQS.19880517.1447.

104181 Scott, R.B. and Bonk, J. 1984. *Preliminary Geologic Map of Yucca Mountain, Nye County, Nevada, with Geologic Sections.* Open-File Report 84-494. Denver, Colorado: U.S. Geological Survey. ACC: HQS.19880517.1443.

101291 Scott, R.B. and Castellanos, M. 1984. *Stratigraphic and Structural Relations of Volcanic Rocks in Drill Holes USW GU-3 and USW G-3, Yucca Mountain, Nye County, Nevada.* Open-File Report 84-491. Denver, Colorado: U.S. Geological Survey. ACC: NNA.19870519.0095.

106751 Scott, R.B. 1990. "Tectonic Setting of Yucca Mountain, Southwest Nevada." Chapter 12 of *Basin and Range Extensional Tectonics Near the Latitude of Las Vegas, Nevada.* Wernicke, B.P., ed. Memoir 176. Boulder, Colorado: Geological Society of America. TIC: 222540.

106755 Scott, R.B. 1992. *Preliminary Geologic Map of Southern Yucca Mountain, Nye County, Nevada.* Open-File Report 92-266. Denver, Colorado: U.S. Geological Survey. ACC: MOL.19960416.0311.

159314 Senterfit, R.M.; Hoover, D.B.; and Chornack, M. 1982. *Resistivity Sounding Investigation by the Schlumberger Method in the Yucca Mountain and Jackass Flats Area, Nevada Test Site, Nevada.* Open-File Report 82-1043. Denver, Colorado: U.S. Geological Survey. ACC: HQS.19880517.2865.

101711 Serafim, J.L. and Pereira, J.P. 1983. "Considerations on the Geomechanical Classification of Bieniawski." *Proceedings of the International Symposium on Engineering Geology and Underground Construction, Lisbon, Portugal, 1983. 1,* II.33-II.44. Lisbon, Portugal: Sociedade Portuguesa de Geotecnia, Laboratório Nacional de Engenharia Civil. TIC: 226267.

101929 Simonds, F.W.; Whitney, J.W.; Fox, K.F.; Ramelli, A.R.; Yount, J.C.; Carr, M.D.; Menges, C.M.; Dickerson, R.P.; and Scott, R.B. 1995. *Map Showing Fault Activity in the Yucca Mountain Area, Nye County, Nevada.* Miscellaneous Investigations Series Map I-2520. Denver, Colorado: U.S. Geological Survey. TIC: 232483.

130186 Slate, J.L. 1991. "Quaternary Stratigraphy, Geomorphology, and Geochronology of Alluvial Fans, Fish Lake Valley, Nevada and California." *Pacific Cell, Friends of the Pleistocene Guidebook for Field Trip to Fish Lake Valley, California-Nevada, May 31-June 2, 1991.* Pages 94-113. Boulder, Colorado: Friends of the Pleistocene. TIC: 247644.

159315 Smith, C. and Ross, H.P. 1982. *Interpretation of Resistivity and Induced Polarization Profiles with Severe Topographic Effects, Yucca Mountain Area, Nevada Test Site, Nevada.* Open-File Report 82-182. Denver, Colorado: U.S. Geological Survey. ACC: NNA.19940208.0108.

106836 Smith, R.L. 1960. "Ash Flows." *Geological Society of America Bulletin, 71,* 795-842. Boulder, Colorado: Geological Society of America. TIC: 225926.

150469   Smith, R.L. 1960. "Zones and Zonal Variations in Welded Ash Flows." *Shorter Contributions to General Geology*. Professional Paper 354-F. Pages 149-159. Denver, Colorado: U.S. Geological Survey. ACC: NNA.19891107.0102.

106851   SNL (Sandia National Laboratories) 1995. *Evaluation of Geotechnical Monitoring Data from the ESF North Ramp Starter Tunnel April 1994 to June 1995*. SAND95-1675. Albuquerque, New Mexico: Sandia National Laboratories. ACC: MOL.19960508.0122.

106867   SNL 1997. *Evaluation and Comparative Analysis of Single Heater Test Thermal and Thermomechanical Data: Third Quarter Results (8/26/96 through 5/31/97)*. Albuquerque, New Mexico: Sandia National Laboratories. ACC: MOL.19980209.0374.

106854   SNL 1997. *Hydraulic Fracturing Stress Measurements in Test Hole ESF-AOD-HDFR#1, Thermal Test Facility, Exploratory Studies Facility at Yucca Mountain*. WA-0065. Albuquerque, New Mexico: Sandia National Laboratories. TIC: 237818.

101297   Spengler, R.W.; Byers, F.M., Jr.; and Warner, J.B. 1981. *Stratigraphy and Structure of Volcanic Rocks in Drill Hole USW-G1, Yucca Mountain, Nye County, Nevada*. Open-File Report 81-1349. Denver, Colorado: U.S. Geological Survey. ACC: NNA.19870406.0222.

101357   Spengler, R.W. and Chornack, M.P. 1984. *Stratigraphic and Structural Characteristics of Volcanic Rocks in Core Hole USW G-4, Yucca Mountain, Nye County, Nevada with a Section on Geophysical Logs by D.C. Muller and J.E. Kibler*. Open-File Report 84-789. Denver, Colorado: U.S. Geological Survey. ACC: NNA.19890804.0012.

106896   Spengler, R.W. and Peterman, Z.E. 1991. "Distribution of Rubidium, Strontium, and Zirconium in Tuff from Two Deep Coreholes at Yucca Mountain, Nevada." *High Level Radioactive Waste Management, Proceedings of the Second Annual International Conference, Las Vegas, Nevada, April 28-May 3, 1991*. *2*, 1416-1422. La Grange Park, Illinois: American Nuclear Society. TIC: 204272.

102783   Squires, R.R. and Young, R.L. 1984. *Flood Potential of Fortymile Wash and Its Principal Southwestern Tributaries, Nevada Test Site, Southern Nevada*. Water-Resources Investigations Report 83-4001. Carson City, Nevada: U.S. Geological Survey. ACC: HQS.19880517.1933.

103148   Stock, J.M.; Healy, J.H.; and Hickman, S.H. 1984. *Report on Televiewer Log and Stress Measurements in Core Hole USW G-2, Nevada Test Site October-November, 1982*. Open-File Report 84-172. Menlo Park, California: U.S. Geological Survey. ACC: NNA.19870406.0157.

101022   Stock, J.M. and Healy, J.H. 1988. "Stress Field at Yucca Mountain, Nevada." Chapter 6 of *Geologic and Hydrologic Investigations of a Potential Nuclear Waste Disposal Site at Yucca Mountain, Southern Nevada*. Carr, M.D. and Yount, J.C., eds. Bulletin 1790. Denver, Colorado: U.S. Geological Survey. TIC: 203085.

130503   Stuckless, J.S. 1991. "An Evaluation of Evidence Pertaining to the Origin of Vein Deposits Exposed in Trench 14, Nevada Test Site, Nevada." *High Level Radioactive Waste Management, Proceedings of the Second Annual International Conference, Las Vegas, Nevada, April 28-May 3, 1991*. *2*, 1429-1438. La Grange Park, Illinois: American Nuclear Society. TIC: 204272.

100086   Stuckless, J.S.; Marshall, B.D.; Vaniman, D.T.; Dudley, W.W.; Peterman, Z.E.; Paces, J.B.; Whelan, J.F.; Taylor, E.M.; Forester, R.M.; and O'Leary, D.W. 1998. "Comments on 'Overview of Calcite/Opal Deposits at or Near the Proposed High-Level Nuclear Waste Site, Yucca Mountain, Nevada, USA: Pedogenic, Hypogene, or Both' by C.A. Hill, Y.V. Dublyansky, R.S. Harmon, and C.M. Schluter." *Environmental Geology, 34*, (1), 70-78. New York, New York: Springer-Verlag. TIC: 238097.

102917   Swadley, W C; Hoover, D.L.; and Rosholt, J.N. 1984. *Preliminary Report on Late Cenozoic Faulting and Stratigraphy in the Vicinity of Yucca Mountain, Nye County, Nevada*. Open-File Report 84-788. Denver, Colorado: U.S. Geological Survey. ACC: NNA.19870519.0104.

101300   Swadley, W C and Carr, W.J. 1987. *Geologic Map of the Quaternary and Tertiary Deposits of the Big Dune Quadrangle, Nye County, Nevada, and Inyo County, California*. Miscellaneous Investigations Series Map I-1767. Denver, Colorado: U.S. Geological Survey. TIC: 203089.

158784   Swan, F.H.; Wesling, J.R.; Angell, M.M.; Thomas, A.P.; Whitney, J.W.; and Gibson, J.D. 2001. *Evaluation of the Location and Recency of Faulting Near Prospective Surface Facilities in Midway Valley, Nye County, Nevada*. Open-File Report 01-55. Denver, Colorado: U.S. Geological Survey. TIC: 251592.

100182   Sweetkind, D.S. and Williams-Stroud, S.C. 1996. *Characteristics of Fractures at Yucca Mountain, Nevada: Synthesis Report*. Administrative Report. Denver, Colorado: U.S. Geological Survey. ACC: MOL.19961213.0181.

106960   Sweetkind, D.S.; Anna, L.O.; Williams-Stroud, S.C.; and Coe, J.A. 1997. "Characterizing the Fracture Network at Yucca Mountain, Nevada, Part 1. Integration of Field Data for Numerical Simulations." *Fractured Reservoirs: Characterization and Modeling*. Hoak, T.E.; Klawitter, A.L.; and Blomquist, P.K., eds. Denver, Colorado: Rocky Mountain Association of Geologists. TIC: 245651.

159092   Sweetkind, D.S.; Dickerson, R.P.; Blakely, R.J.; and Denning, P.D. 2001. *Interpretive Geologic Cross Sections for the Death Valley Regional Flow System and Surrounding Areas, Nevada and California.* Miscellaneous Field Studies Map MF-2370. Denver, Colorado: U.S. Geological Survey. TIC: 251903.

100184   Szymanski, J.S. 1987. *Conceptual Considerations of the Death Valley Groundwater System with Special Emphasis on the Adequacy of this System to Accomodate [Accommodate] the High-Level Nuclear Waste Repository.* Draft. Las Vegas, Nevada: U.S. Department of Energy, Nevada Operations Office. ACC: NN1.19881122.0086.

106963   Szymanski, J.S. 1989. *Conceptual Considerations of the Yucca Mountain Groundwater System with Special Emphasis on the Adequacy of This System to Accommodate a High-Level Nuclear Waste Repository.* Three volumes. Las Vegas, Nevada: U.S. Department of Energy, Nevada Operations Office. ACC: NNA.19890831.0152.

159895   Tanko, D.J. and Glancy, P.A. 2001. *Flooding in the Amargosa River Drainage Basin, February 23-24, 1998, Southern Nevada and Eastern California, Including the Nevada Test Site.* Fact Sheet 036-01. Carson City, Nevada: U.S. Geological Survey. ACC: MOL.20010924.0092.

102864   Taylor, E.M. 1986. *Impact of Time and Climate on Quaternary Soils in the Yucca Mountain Area of the Nevada Test Site.* Master's thesis. Boulder, Colorado: University of Colorado. TIC: 218287.

159414   Taylor, E.M. 2003. "Quaternary Faulting on the Southern Crater Flat Fault." Chapter 10 of *Quaternary Paleoseismology and Stratigraphy of the Yucca Mountain Area, Nevada.* U.S. Geological Survey Digital Data Series. Keefer, W.R.; Whitney, J.W.; and Taylor, E.M., eds. Denver, Colorado: U.S. Geological Survey. ACC: MOL.20031208.0113. TBV-5659.

159415   Taylor, E.M.; Menges, C.M.; and Buesch, D.C. 2003. "Results of Paleoseismic Investigations on the Ghost Dance Fault." Chapter 6 of *Quaternary Paleoseismology and Stratigraphy of the Yucca Mountain Area, Nevada.* U.S. Geological Survey Digital Data Series. Keefer, W.R.; Whitney, J.W.; and Taylor, E.M., eds. Denver, Colorado: U.S. Geological Survey. ACC: MOL.20031208.0113. TBV-5659.

108885   Thomas, B.E.; Hjalmarson, H.W.; and Waltemeyer, S.D. 1994. *Methods for Estimating Magnitude and Frequency of Floods in the Southwestern United States.* Open-File Report 93-419. Tucson, Arizona: U.S. Geological Survey. TIC: 243258.

111126   Thompson, A.B. and Wennemer, M. 1979. "Heat Capacities and Inversions in Tridymite, Cristobalite, and Tridymite-Cristobalite Mixed Phases." *American Mineralogist, 64*, 1018-1026. Washington, D.C.: Mineralogical Society of America. TIC: 239133.

107005   Trexler, J.H., Jr.; Cole, J.C.; and Cashman, P.H. 1996. "Middle Devonian–Mississippian Stratigraphy On and Near the Nevada Test Site: Implications for Hydrocarbon Potential." *AAPG Bulletin, 80,* (11), 1736-1762. Tulsa, Oklahoma: American Association of Petroleum Geologists. TIC: 233004.

101305   USGS (U.S. Geological Survey) 1984. *A Summary of Geologic Studies Through January 1, 1983, of a Potential High-Level Radioactive Waste Repository Site at Yucca Mountain, Southern Nye County, Nevada.* Open-File Report 84-792. Menlo Park, California: U.S. Geological Survey. ACC: NNA.19891009.0305.

158378   USGS 2001. *Future Climate Analysis.* ANL-NBS-GS-000008 REV 00 ICN 01. Denver, Colorado: U.S. Geological Survey. ACC: MOL.20011107.0004.

101363   Vaniman, D.; Bish, D.; Broxton, D.; Byers, F.; Heiken, G.; Carlos, B.; Semarge, E.; Caporuscio, F.; and Gooley, R. 1984. *Variations in Authigenic Mineralogy and Sorptive Zeolite Abundance at Yucca Mountain, Nevada, Based on Studies of Drill Cores USW GU-3 and G-3.* LA-9707-MS. Los Alamos, New Mexico: Los Alamos National Laboratory. ACC: NNA.19870519.0043.

105946   Vaniman, D.T.; Bish, D.L.; Chipera, S.J.; Carlos, B.A.; and Guthrie, G.D., Jr. 1996. *Chemistry and Mineralogy of the Transport Environment at Yucca Mountain.* Volume I of *Summary and Synthesis Report on Mineralogy and Petrology Studies for the Yucca Mountain Site Characterization Project.* Milestone 3665. Los Alamos, New Mexico: Los Alamos National Laboratory. ACC: MOL.19961230.0037.

100089   Vaniman, D.T. and Chipera, S.J. 1996. "Paleotransport of Lanthanides and Strontium Recorded in Calcite Compositions from Tuffs at Yucca Mountain, Nevada, USA." *Geochimica et Cosmochimica Acta, 60,* (22), 4417-4433. New York, New York: Pergamon Press. TIC: 231351.

107175   Warren, R.G.; Sawyer, D.A.; and Covington, H.R. 1989. "Revised Volcanic Stratigraphy of the Southwestern Nevada Volcanic Field." *Proceedings of the Fifth Symposium on Containment of Underground Nuclear Explosions, Santa Barbara, California, September 19-21, 1989.* Olsen, C.W. and Carter, J.A., eds. CONF-8909163. *2,* 387. Santa Barbara, California: Mission Research Corporation. TIC: 227166.

107207   Wells, S.G.; McFadden, L.D.; and Harden, J. 1990. "Preliminary Results of Age Estimations and Regional Correlations of Quaternary Alluvial Fans Within the Mojave Desert of Southern California." *At the End of the Mojave: Quaternary Studies in the Eastern Mojave Desert.* Reynolds, J., ed. Pages 45-53. Redlands, California: San Bernardino County Museum Association. TIC: 246793.

107208 Wells, S.G.; McFadden, L.D.; Renault, C.E.; and Crowe, B.M. 1990. "Geomorphic Assessment of Late Quaternary Volcanism in the Yucca Mountain Area, Southern Nevada: Implications for the Proposed High-Level Radioactive Waste Repository." *Geology, 18*, 549-553. Boulder, Colorado: Geological Society of America. TIC: 218564.

107290 Wesling, J.R.; Bullard, T.F.; Swan, F.H.; Perman, R.C.; Angell, M.M.; and Gibson, J.D. 1992. *Preliminary Mapping of Surficial Geology of Midway Valley Yucca Mountain Project, Nye County, Nevada Interim Data Report.* SAND91-0607. Albuquerque, New Mexico: Sandia National Laboratories. ACC: NNA.19920410.0053.

107314 Whitney, J.W.; Swadley, W C; and Shroba, R.R. 1985. "Middle Quaternary Sand Ramps in the Southern Great Basin, California and Nevada." *Abstracts with Programs - Geological Society of America, 17*, (7), 750. Boulder, Colorado: Geological Society of America. TIC: 209960.

107303 Whitney, J.W. and Harrington, C.D. 1993. "Relict Colluvial Boulder Deposits as Paleoclimatic Indicators in the Yucca Mountain Region, Southern Nevada." *Geological Society of America Bulletin, 105*, 1008-1018. Boulder, Colorado: Geological Society of America. TIC: 208099.

159416 Whitney, J.W.; Simonds, F.W.; Shroba, R.R.; and Murray, M. 2003. "Quaternary Faulting on the Windy Wash Fault." Chapter 9 of *Quaternary Paleoseismology and Stratigraphy of the Yucca Mountain Area, Nevada.* U.S. Geological Survey Digital Data Series. Keefer, W.R.; Whitney, J.W.; and Taylor, E.M., eds. Denver, Colorado: U.S. Geological Survey. ACC: MOL.20031208.0113. TBV-5659.

159418 Whitney, J.W.; Taylor, E.M.; and Wesling, J.R. 2003. "Quaternary Stratigraphy and Mapping in the Yucca Mountain Area." Chapter 2 of *Quaternary Paleoseismology and Stratigraphy of the Yucca Mountain Area, Nevada.* U.S. Geological Survey Digital Data Series. Keefer, W.R.; Whitney, J.W.; and Taylor, E.M., eds. Denver, Colorado: U.S. Geological Survey. ACC: MOL.20031208.0113. TBV-5659.

101167 Winograd, I.J. and Thordarson, W. 1975. *Hydrogeologic and Hydrochemical Framework, South-Central Great Basin, Nevada-California, with Special Reference to the Nevada Test Site.* Geological Survey Professional Paper 712-C. Washington, D.C.: United States Government Printing Office. ACC: NNA.19870406.0201.

109186 Winograd, I.J.; Szabo, B.J.; Coplen, T.B.; and Riggs, A.C. 1988. "A 250,000-Year Climate Record from Great Basin Vein Calcite: Implications for Milankovitch Theory." *Science, 242*, 1275-1280. Washington, D.C.: American Association for the Advancement of Science. TIC: 222215.

107330 Woodside, W. and Messmer, J.H. 1961. "Thermal Conductivity of Porous Media, I. Unconsolidated Sands." *Journal of Applied Physics, 32*, (9), 1688-1699. New York, New York: American Institute of Physics. TIC: 217510.

100520 YMP (Yucca Mountain Site Characterization Project) 1993. *Evaluation of the Potentially Adverse Condition "Evidence of Extreme Erosion During the Quaternary Period" at Yucca Mountain, Nevada.* Topical Report YMP/92-41-TPR. Las Vegas, Nevada: Yucca Mountain Site Characterization Office. ACC: NNA.19930316.0208.

108730 Yudhbir; Lemanza, W.; and Prinzl, F. 1983. "An Empirical Failure Criterion for Rock Masses." *Proceedings of the Fifth International Congress on Rock Mechanics, Melbourne, Australia, 1983. 1*, B1-B8. Rotterdam, The Netherlands: A.A. Balkema. TIC: 226278.

108657 Zoback, M.D. and Healy, J.H. 1984. "Friction, Faulting, and In Situ Stress." *Annales Geophysicae, 2*, (6), 689-698. Paris, France: European Geophysical Society, Gauthier-Villars. TIC: 234995.

3.8.2 Codes, Standards, Regulations, and Procedures

156605 10 CFR 63. Energy: Disposal of High-Level Radioactive Wastes in a Geologic Repository at Yucca Mountain, Nevada.

102391 ASTM D 1557-91. 1998. *Standard Test Method for Laboratory Compaction Characteristics of Soil Using Modified Effort (56,000 ft-lbf/ft3 (2,700 kN-m/m3)).* West Conshohocken, Pennsylvania: American Society for Testing and Materials. TIC: 242992.

159575 ASTM D 2487-00. 2000. *Standard Practice for Classification of Soils for Engineering Purposes (Unified Soil Classification System).* West Conshohocken, Pennsylvania: American Society for Testing and Materials. TIC: 253080.

149445 ASTM D 4394-84. 1985. *Standard Test Method for Determining the In Situ Modulus of Deformation of Rock Mass Using the Rigid Plate Loading Method.* Philadelphia, Pennsylvania: American Society for Testing and Materials. TIC: 231530.

160054 ASTM D 4395-84. 1985. *Standard Test Method for Determining the In Situ Modulus of Deformation of Rock Mass Using the Flexible Plate Loading Method.* Philadelphia, Pennsylvania: American Society for Testing and Materials. TIC: 231530.

3.8.3 Data Listed by Data Tracking Number

164561 GS030783114233.001. Geotechnical Borehole Logs for the Waste Handling Building, Yucca Mountain Project, Nevada Test Site, Nevada, Version 7/16/03. Submittal date: 07/23/2003.

166432 GS930108314221.003. Isotopic and Trace Element Variability in Altered and Unaltered Tuffs at Yucca Mountain, Nevada. Submittal date: 01/20/1993.

109597   GS970208314224.005. Geology of the Main Drift - Station 28+00 to 55+00, Exploratory Studies Facility, Yucca Mountain Project, Yucca Mountain, Nevada. Submittal date: 02/21/1997.

105561   GS971108314224.020. Revision 1 of Detailed Line Survey Data, Station 0+60 to Station 4+00, North Ramp Starter Tunnel, Exploratory Studies Facility. Submittal date: 12/03/1997.

160064   GS971108314224.027. Revision 1 of Detailed Line Survey Data, Alcove 2 (BRFA), Exploratory Studies Facility. Submittal date: 12/03/1997.

158751   GS971183117462.001. Characteristics of the Ghost Dance Fault at Yucca Mountain. Submittal date: 11/10/1997.

152631   GS990908314224.010. Geology of the ECRB Cross Drift: Graphical Data. Submittal date: 09/14/1999.

151042   GS991108314224.015. Geology of the ECRB Cross Drift: Tabular Data. Submittal date: 11/05/1999.

166510   LA000000000026.002. Rock-Varnish Cation Ratio Data and Rock-Varnish Dating Curve Calibration Sites Data. Submittal date: 01/15/1993.

152554   MO0004QGFMPICK.000. Lithostratigraphic Contacts from MO9811MWDGFM03.000 to be Qualified Under the Data Qualification Plan, TDP-NBS-GS-000001. Submittal date: 04/04/2000.

150699   MO0006YMP99059.001. Potential Repository Site Investigation Area. Submittal date: 06/20/2000.

157306   MO0008GSC00286.000. Exploratory Studies Facility (ESF) North Portal Pad, Waste Handling Building (WHB) Profile Sections #3, #4, #5, #6, #7, and #8. Submittal date: 08/17/2000.

153777   MO0012MWDGFM02.002. Geologic Framework Model (GFM2000). Submittal date: 12/18/2000.

166513   MO0312SEPSD10B.000. Descriptive and Calculated Data for the Cosmogenic 10-BE Sample. Submittal date: 12/19/2003.

166403   MO0312SEPSDBCT.000. Average Fracture Normal Stiffness and Average Shear Strength for Fractures for Thermal-Mechanical Units. Submittal date: 12/14/2003.

166404   MO0312SEPSDCSW.000. Compressional and Shear Wave Velocities on Dry Specimens. Submittal date: 12/14/2003.

166396   MO0312SEPSDCTE.000. Mean Coefficient of Thermal Expansion. Submittal

date: 12/14/2003.

166491   MO0312SEPSDDGS.000. Summary of Diagnostic Surface and Soil Properties of Map Units at Yucca Mountain. Submittal date: 12/16/2003.

166402   MO0312SEPSDDNP.000. Dry Bulk Density, Saturated Bulk Density, Average Grain Density, and Porosity Summarized by Thermal-Mechanical Unit. Submittal date: 12/14/2003.

166477   MO0312SEPSDDRM.000. Design Rock-Mass Strength Envelopes for TSw2 Thermal-Mechanical Unit, Exploratory Studies Facility Scanline Data. Submittal date: 12/16/2003.

166560   MO0312SEPSDGCS.000. Generalized Cross Sections of the Evolution of Fortymile Wash, Showing Quaternary Ages of Units. Submittal date: 12/19/2003.

166401   MO0312SEPSDIRC.000. Intact Rock Constants for Rock-Mass Strength Criteria for Thermal-Mechanical Units. Submittal date: 12/14/2003.

166476   MO0312SEPSDLPC.000. Lithostratigraphy, Porosity from Core and Geophysical Logs, and Quantitative Mineralogy in Borehole UE-25 UZ#16. Submittal date: 12/16/2003.

166493   MO0312SEPSDNTM.000. Calculated Values of Thermal Capacitance of the Rock Mass at Selected Temperatures for Nine Thermal/Mechanical Units. Submittal date: 12/16/2003.

166397   MO0312SEPSDPRA.000. Peak Shear Stress, Residual Shear Stress, and Applied Normal Stress for Fractures. Submittal date: 12/14/2003.

166394   MO0312SEPSDPYM.000. Intact Young's Modulus and Intact Rock Poisson's Ratio for Thermal-Mechanical and Lithostratigraphic Units. Submittal date: 12/14/2003.

166399   MO0312SEPSDRMP.000. Estimated Rock-Mass Mechanical Properties for Rock-Mass Rating at 40 Percent Cumulative Frequency of Occurrence for Each Thermal-Mechanical Unit. Submittal date: 12/14/2003.

166400   MO0312SEPSDRRQ.000. Rock-Mass Rating (RMR) and Rock Mass Quality (Q) Values for Thermal-Mechanical Units. Submittal date: 12/14/2003.

166393   MO0312SEPSDRTC.000. Rock Thermal Conductivities. Submittal date: 12/14/2003.

166395   MO0312SEPSDTCP.000. Thermal Capacitance for TSw1 and TSw2 Thermal Mechanical Units. Submittal date: 12/14/2003.

166484   MO0312SEPSDTFF.000. The Tuffs of Yucca Mountain, Classified by Silica/Alumina Composition. Submittal date: 12/16/2003.

166398   MO0312SEPSDUAT.000. Uniaxial Compressive Strength and Brazilian Tensile Strength for Thermal-Mechanical and Lithostratigraphic Units. Submittal date: 12/14/2003.

109059   MO9906GPS98410.000. Yucca Mountain Project (YMP) Borehole Locations. Submittal date: 06/23/1999.

158399   SN0011F3912298.023. Plate-Loading Rock Mass Modulus Data (with Results from 0/16/2000 through 10/17/2000). Submittal date: 11/30/2000.

159145   SN0206F3504502.012. Revised Thermal Conductivity, Volumetric Heat Capacity and Thermal Diffusivity Data for ECRB Thermal K Test 1 (Two-Hole Test). Submittal date: 06/07/2002.

159146   SN0206F3504502.013. Revised Thermal Conductivity, Volumetric Heat Capacity and Thermal Diffusivity Data for ECRB Thermal K Test 3 (Three-Hole Test, with Results from 1/22/2002 through 4/9/2002). Submittal date: 06/07/2002.

161883   SN0208F3504502.019. Thermal Conductivity, Volumetric Heat Capacity and Thermal Diffusivity Data for ECRB Thermal K Test 2 (Six-Hole Test). Submittal date: 08/30/2002.

165211   SN0208L01B8102.001. Thermal Expansion Properties of Lithophysal Tuff, Batch #1 (Test Dates: August 3, 2002 through August 16, 2002). Submittal date: 08/28/2002.

163601   SN0209L01A1202.001. Thermal Conductivity Laboratory Data (Including Densities and Porosities) Generated in FY02 on the Topopah Springs Lower Lithophysal (Tptpll) Lithostratigraphic Unit. Submittal date: 09/23/2002.

165218   SN0211L01B8102.002. Thermal Expansion Properties of Lithophysal Tuff, Batch #2 (Test Dates: October 20, 2002 through October 25, 2002). Submittal date: 11/13/2002.

166458   SN0308F3710195.003. Hydraulic Fracturing Stress Measurements in Test Holes: ESF-GDJACK #1, and ESF-GDJACK #5, Exploratory Studies Facility at Yucca Mountain, Nevada. Submittal date: 08/29/2003.

168527   SN0310F3912298.054. Updated Plate-Loading Rock Mass Modulus Data for 2003. Submittal date: 10/27/2003.

166436   SNF29041993002.041. Yucca Mountain Site Characterization Project Geology and Rock Structure Log for Drillhole USW NRG-6, Rev. 1. Submittal date: 02/06/1995.

166437   SNF29041993002.042. Yucca Mountain Site Characterization Project Geology and Rock Structure Log for Drillhole USW NRG-7/7A, Rev. 1. Submittal date: 02/06/1995.

166435   SNF29041993002.054. Geology and Rock Structure Log for Drillhole USW SD-12, 650-800 ft, Rev. 0. Submittal date: 03/23/1995.

166433   SNF29041993002.075. Geology and Rock Structure Log for Hole USW SD-7, 0-950ft, Rev1. Submittal date: 09/11/1995.

166434   SNF29041993002.076. Geology and Rock Structure Log for Hole USW SD-9, 0-1350 ft., Rev 1. Submittal date: 09/11/1995.

166438   SNF29041993002.079. Geology and Rock Structure Log for Hole USW UZ-14, 700-850 ft, Rev. 0. Submittal date: 08/17/1995.

131356   SNF37100195002.001. Hydraulic Fracturing Stress Measurements in Test Hole: ESF-AOD-HDFR1, Thermal Test Facility, Exploratory Studies Facility at Yucca Mountain. Submittal date: 12/18/1996.

148289   SNL01C12159302.002. Laboratory Measurements of Heat Capacity/Thermal Capacitance, for Boreholes UE25 NRG-4 and NRG-5. Submittal date: 02/07/1996.
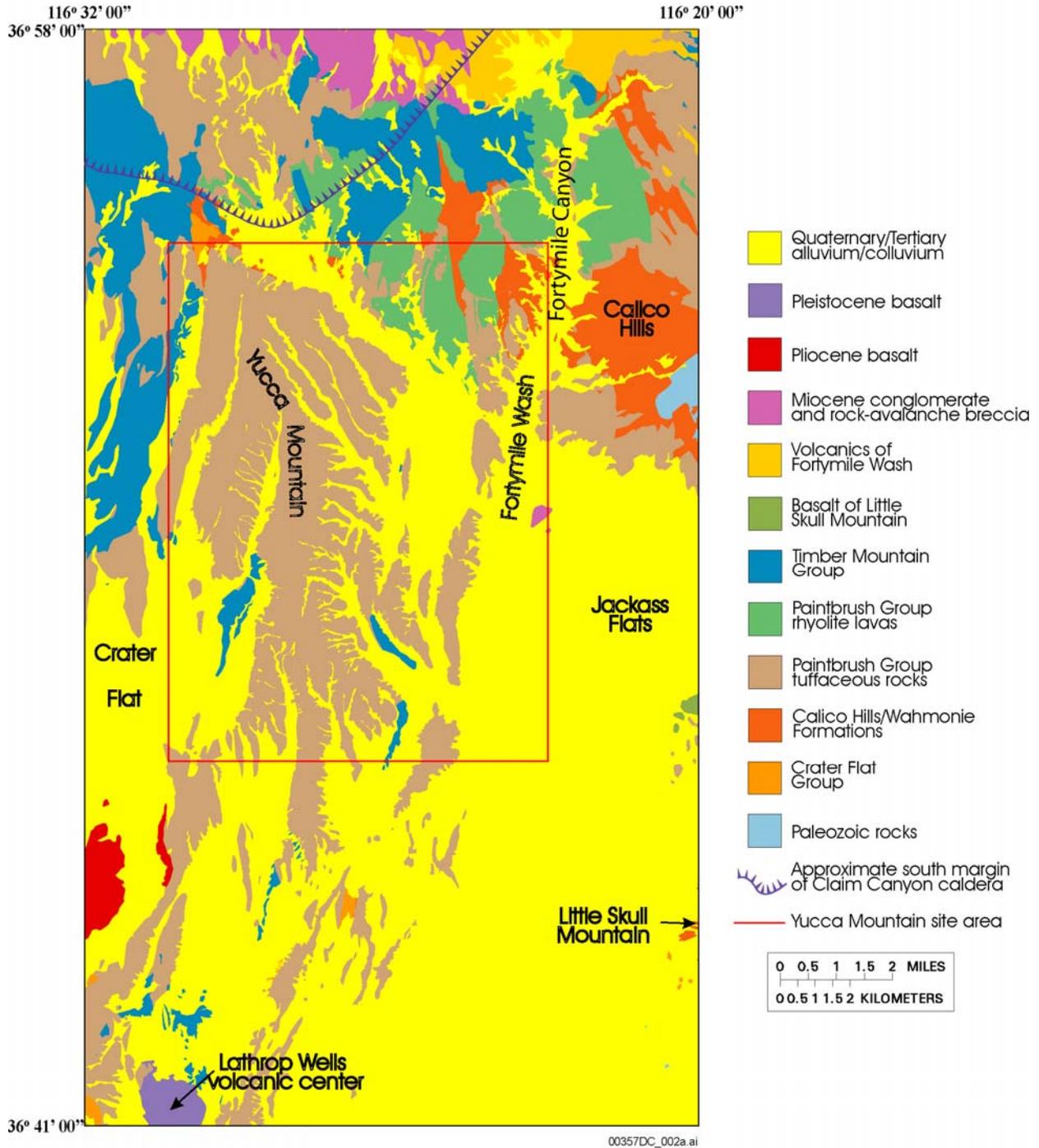
Source: Modified from Potter et al. 2002 [DIRS 160060]

Figure 3-1. Simplified Geologic Map Showing Distribution of Major Lithostratigraphic Units in the Yucca Mountain Site Area and Vicinity
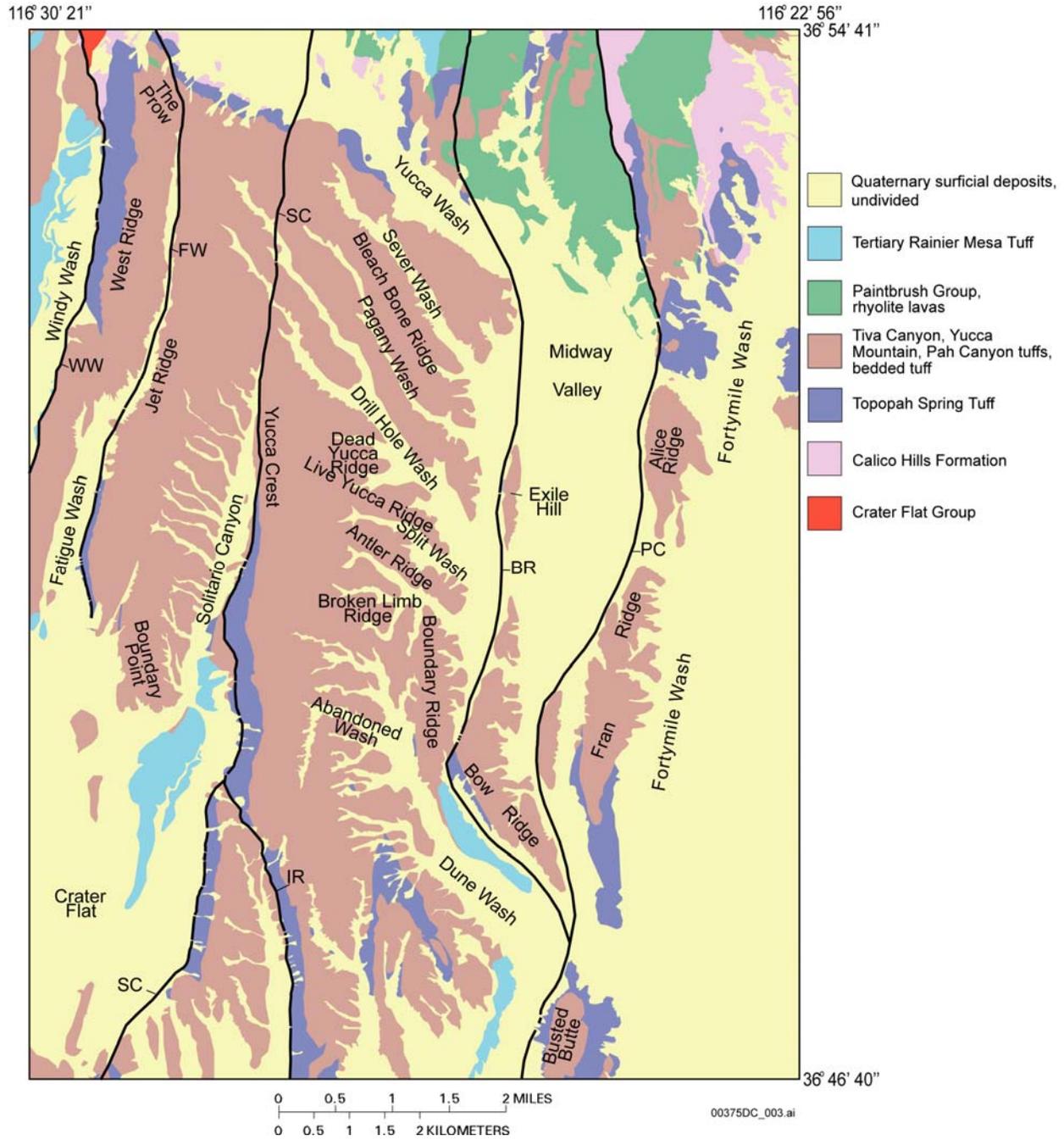
Source: Generalized from Potter et al. 2002 [DIRS 160060]

NOTE: Faults shown with solid lines, although large segments of some are concealed or inferred beneath Quaternary deposits. Labeled faults: BR = Bow Ridge; FW = Fatigue Wash; IR = Iron Ridge; PC = Paintbrush Canyon; SC = Solitario Canyon; WW = Windy Wash.

Figure 3-2. Map of Yucca Mountain Site Area Showing Distribution of Principal Stratigraphic Units, Block-Bounding Faults, and Locations of Geographic Features Named in Text

MAP UNITS

Holocene alluvium
(Units Qa5-Qa7)

Middle Pleistocene to
Holocene alluvium
(Units Qa2-Qa4)

Early to Middle
Pleistocene alluvium
(Units Qa0-Qa1)

Early Pleistocene to
Holocene eolian
deposits

Tertiary bedrock

00375DC_026a.ai
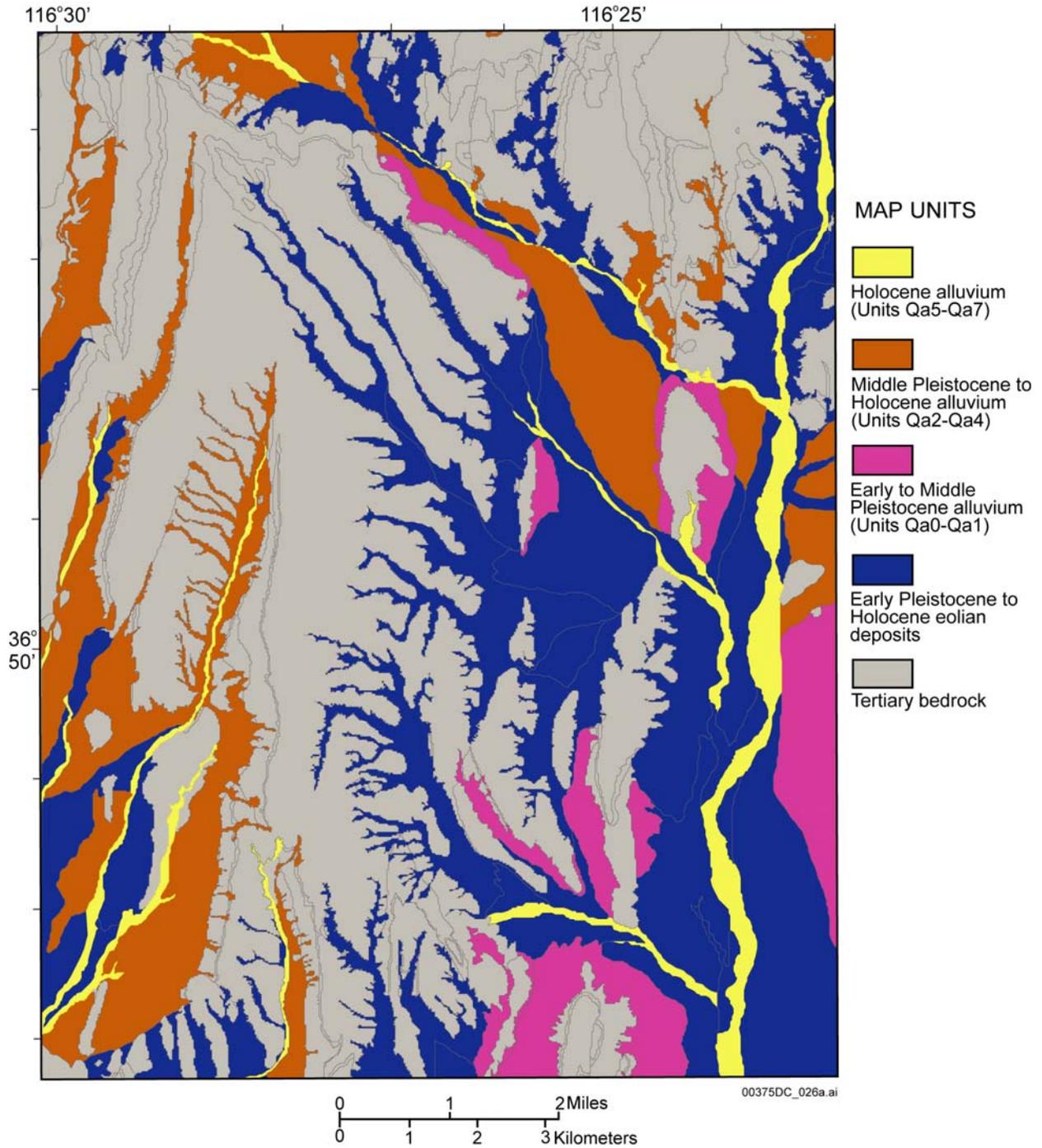
Source: Potter et al. 2002 [DIRS 160060]

Figure 3-3. Generalized Map of Surficial Deposits
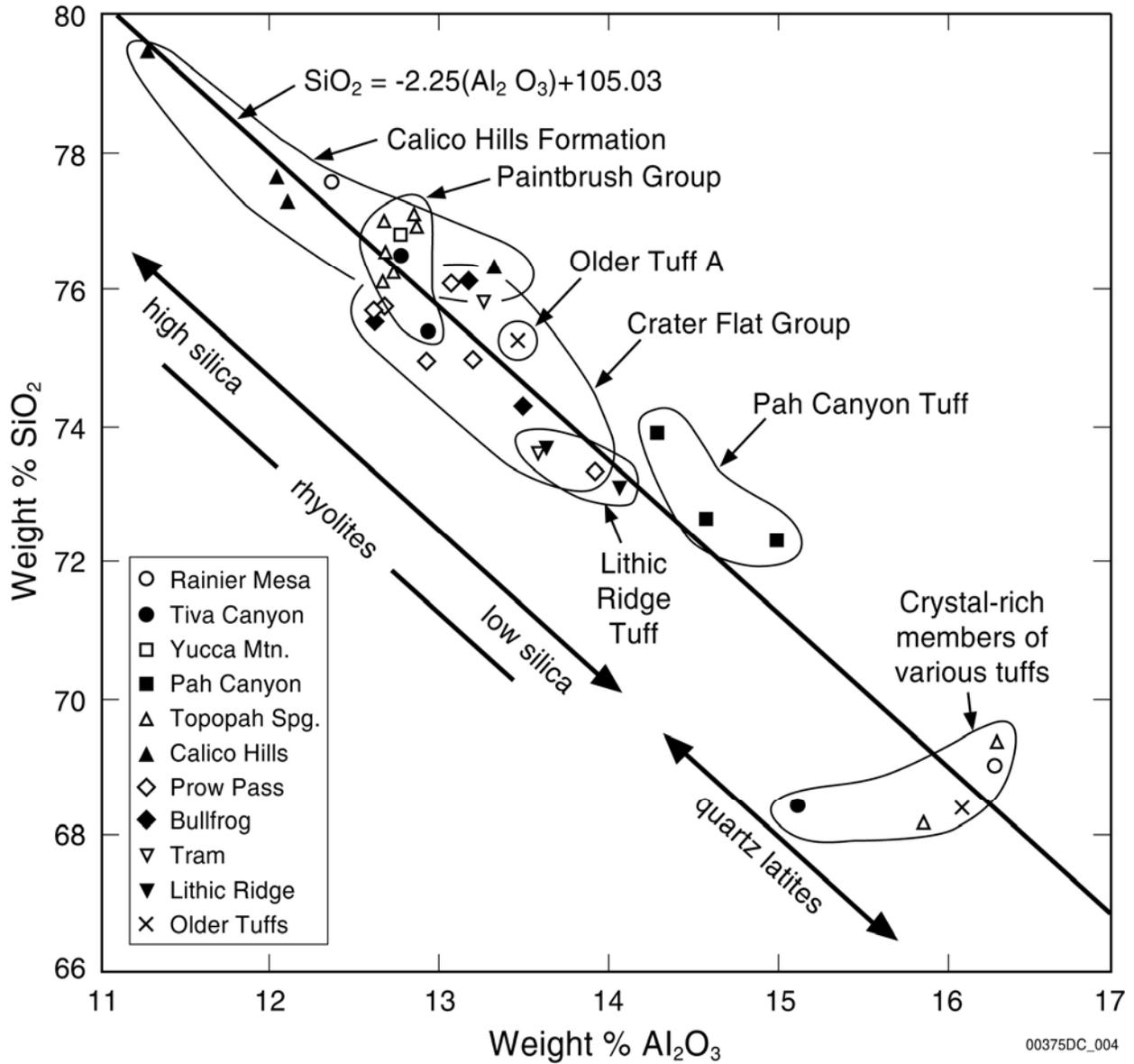
Source: Vaniman et al. 1996 [DIRS 105946], Figure 1-3

Figure 3-4. The Tuffs of Yucca Mountain, Classified by Silica/Alumina Composition

Tiva Canyon Tuff

Topopah Spring Tuff

W C CF

W C CF

Crystal-rich member
vitric zone

nonlithophysal zone

lithophysal zone

Crystal-poor member

upper lithophysal zone
mostly low-angle fractures with
rough surfaces

middle nonlithophysal zone
(lithophysae-bearing subzone occurs locally)
mostly high-angle fractures with
very smooth surfaces

lower lithophysal zone
mostly low-angle fractures with
rough surfaces

hackly fractured subzone - mostly low-angle
fractures with very rough surfaces

lower nonlithophysal zone

hackly subzone - mostly low-angle
fractures with very rough surfaces

subzones previously
not divided, locally
near the base three
subzones are
identified by types of
pumice clasts

columnar subzone - mostly high-
angle fractures with smooth
surfaces with three intervals based
on types of pumice clasts

vitric zone

Zones of welding (W)

- Densely ⇐ lithophysae)
- Moderately
- Partially
- Nonwelded

Zones of crystallization (C)

- Crystallized
- Crystallized + vapor-phase minerals
- Vitric / Vitric + vapor-phase or moderate temperature alteration minerals

Crystal fragments (CF)

- Greater than 10 percent
- 5 to 10 percent
- Less than 5 percent
- Unit locally absent

00375DC_005.ai

Source: Adapted from Buesch et al. 1996 [DIRS 100106], Figure 2

NOTE: Not to scale.

Figure 3-5. Graphical Columns of Zones in the Tiva Canyon and Topopah Spring Tuffs at Yucca Mountain
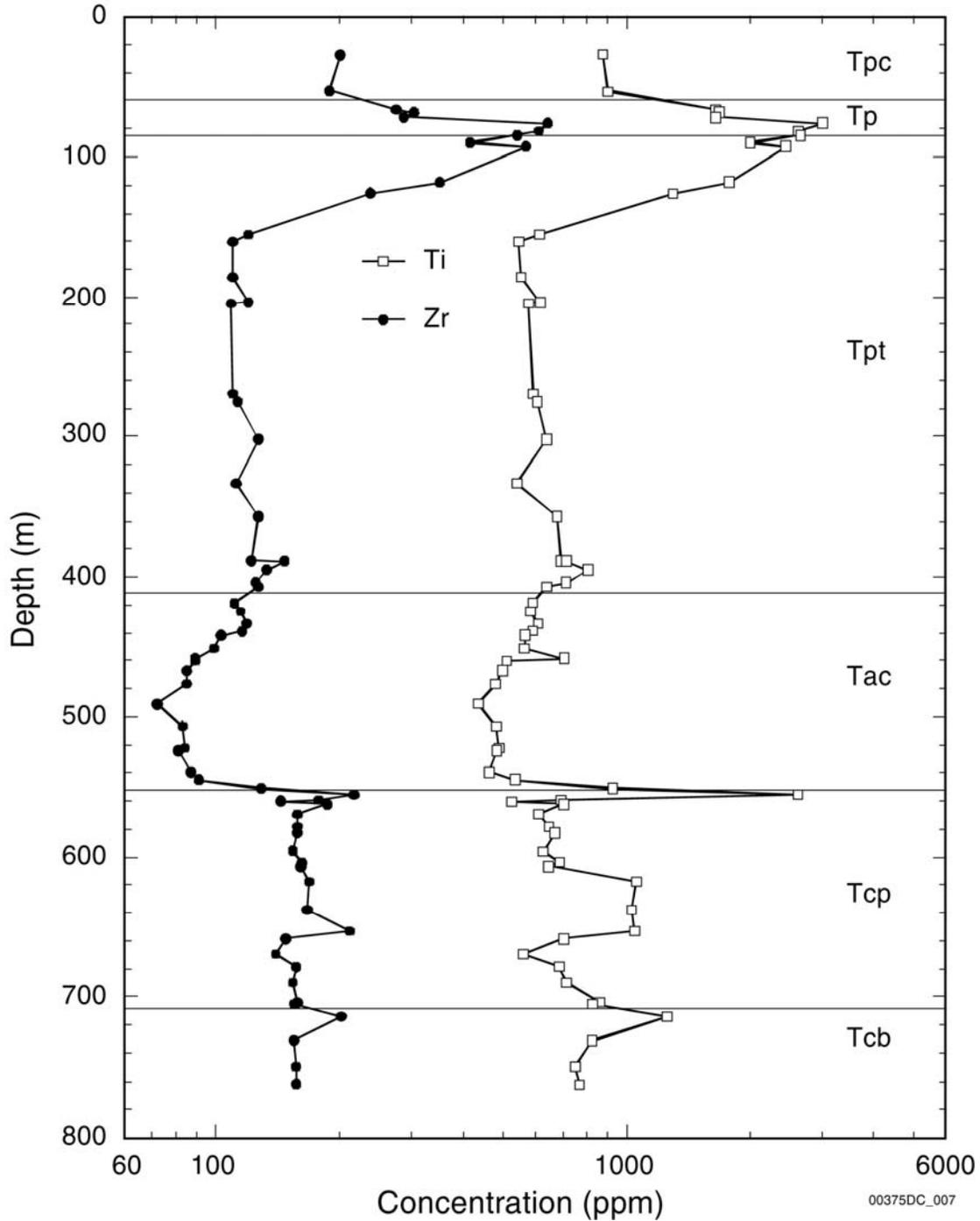
NOTE: Upper part of Topopah Spring Tuff (Tpt) shows the sharp increases in titanium and zirconium concentrations typical of the crystal-rich member. Tp = undivided units between Tiva Canyon (Tpc) and Topopah Spring Tuffs; Tac = Calico Hills Formation; Tcp = Prow Pass Tuff; Tcb = Bullfrog Tuff; m = meters; ppm = parts per million. Location of Borehole UE-25 a#1 is shown on Figure 3-7.

Figure 3-6a. Graph Showing Concentrations of Titanium (Ti) and Zirconium (Zr) as a Function of Depth for Core Samples from Borehole UE-25 a#1
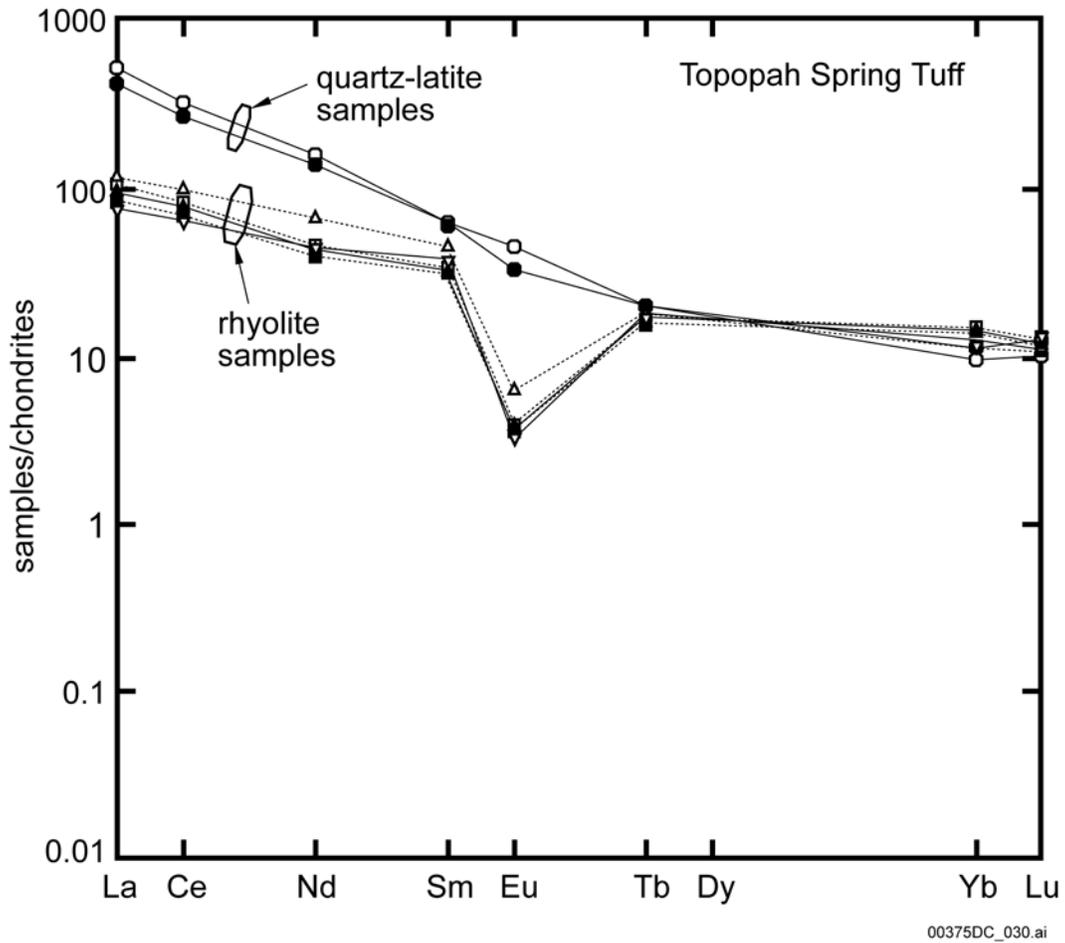
Source: Vaniman et al. 1996 [DIRS 105946], Figure 1.12

NOTE: Values represent whole-rock analyses.

Figure 3-6b. Chondrite-Normalized Lanthanide Abundances in the Topopah Spring Tuff
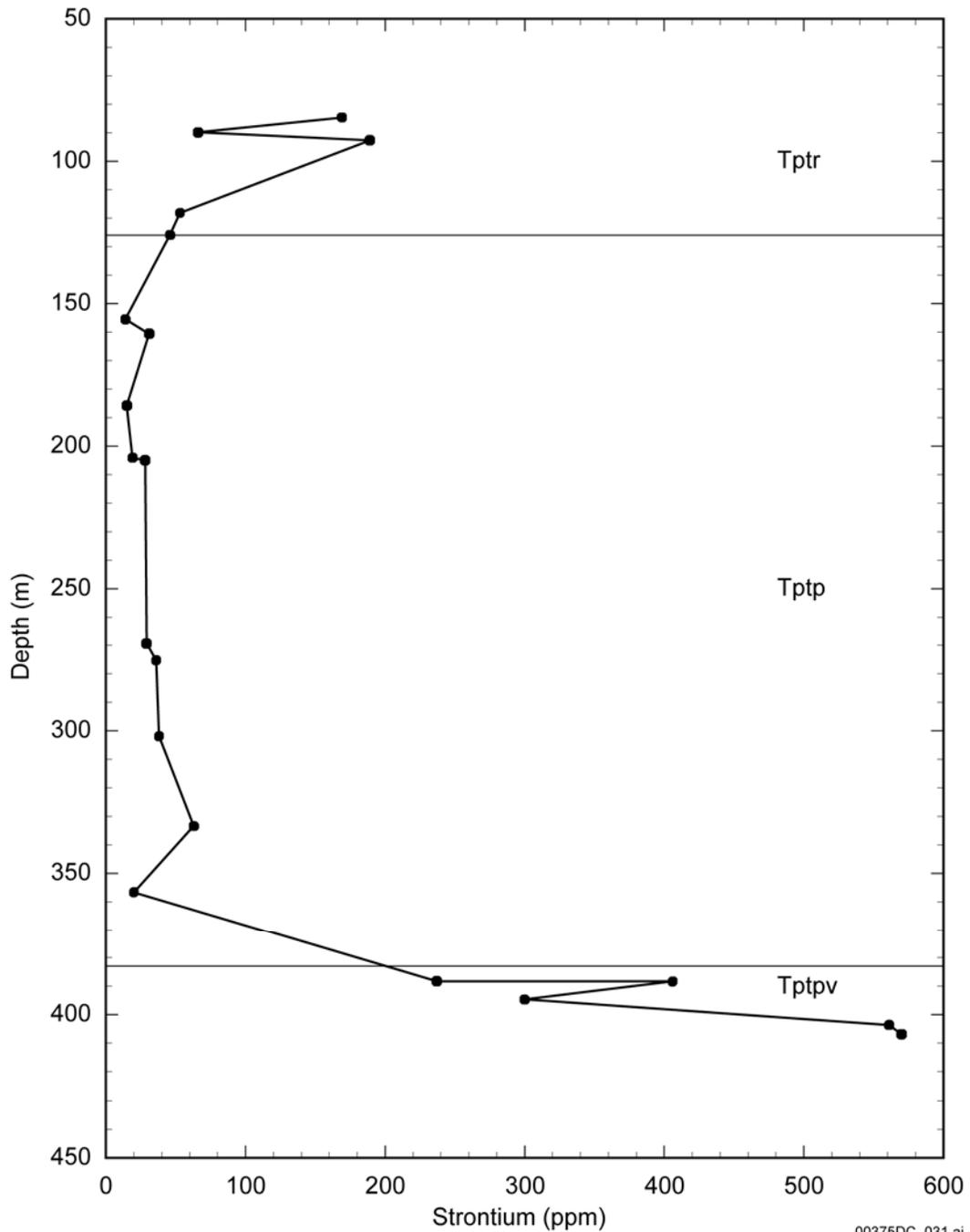
Source: Peterman et al. 1993 [DIRS 106498], Figure 4

NOTE: Unit abbreviations on this diagram are: Tptr - Topopah Spring Tuff Crystal-Rich Member, Tptp -
         Topopah Spring Tuff Crystal-Poor Member, Tptpv - Topopah Spring Tuff Crystal-Poor Vitric
         Zone. At this locality, the basal vitrophyre (Tptpv) is altered, which results in these unually high Sr
         concentrations.

Figure 3-6c.   Strontium Concentration as a Function of Depth for Core Samples of Topopah Spring Tuff
                from Borehole UE-25 a#1
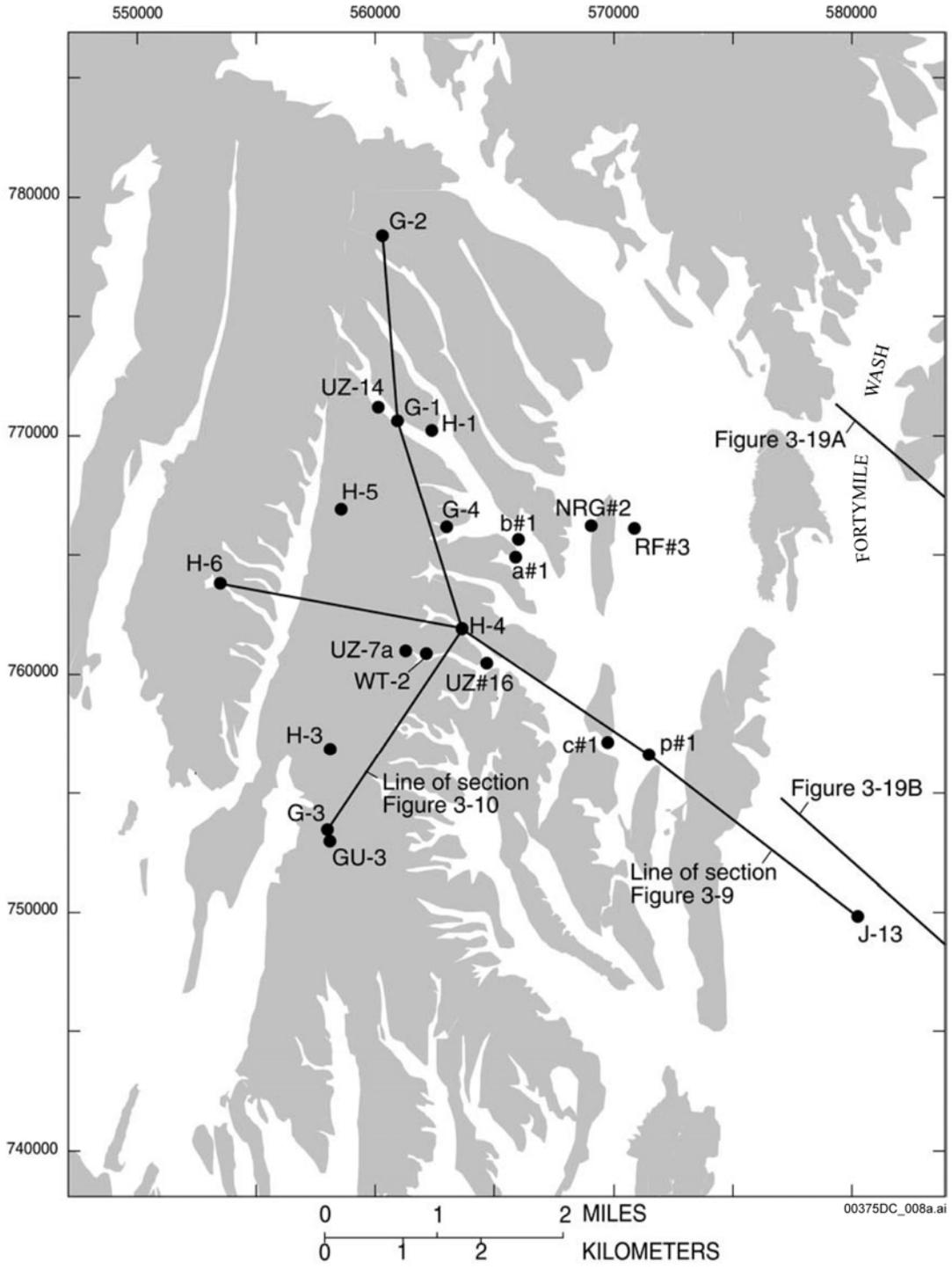
DTN: MO9906GPS98410.000 [DIRS 109059]

NOTE: Reference coordinates correspond to Nevada State Coordinate System (in feet). Borehole numbers are not shown with prefixes UE-25 or USW.

Figure 3-7. Index Map Showing Locations of Stratigraphic Cross Sections (see Figures 3-9 and 3-10) and Boreholes Mentioned in Text and Cross Sections across Fortymile Wash (see Figure 3-19)

UE-25 UZ#16

Legend:
- Porosity (P. Nelson)
- 105 Porosity
- RH Porosity
- ■ > 5% Differential Porosity
- ▲ Water Seep (video)
- ▲ Glass
- ◇ Quartz +Feldspar
- ◆ Tridymite
- ▼ Cristobalite
- Smectite+Mica
- Clinoptilolite +Mordenite
- ● Opal-CT
- Minor Minerals
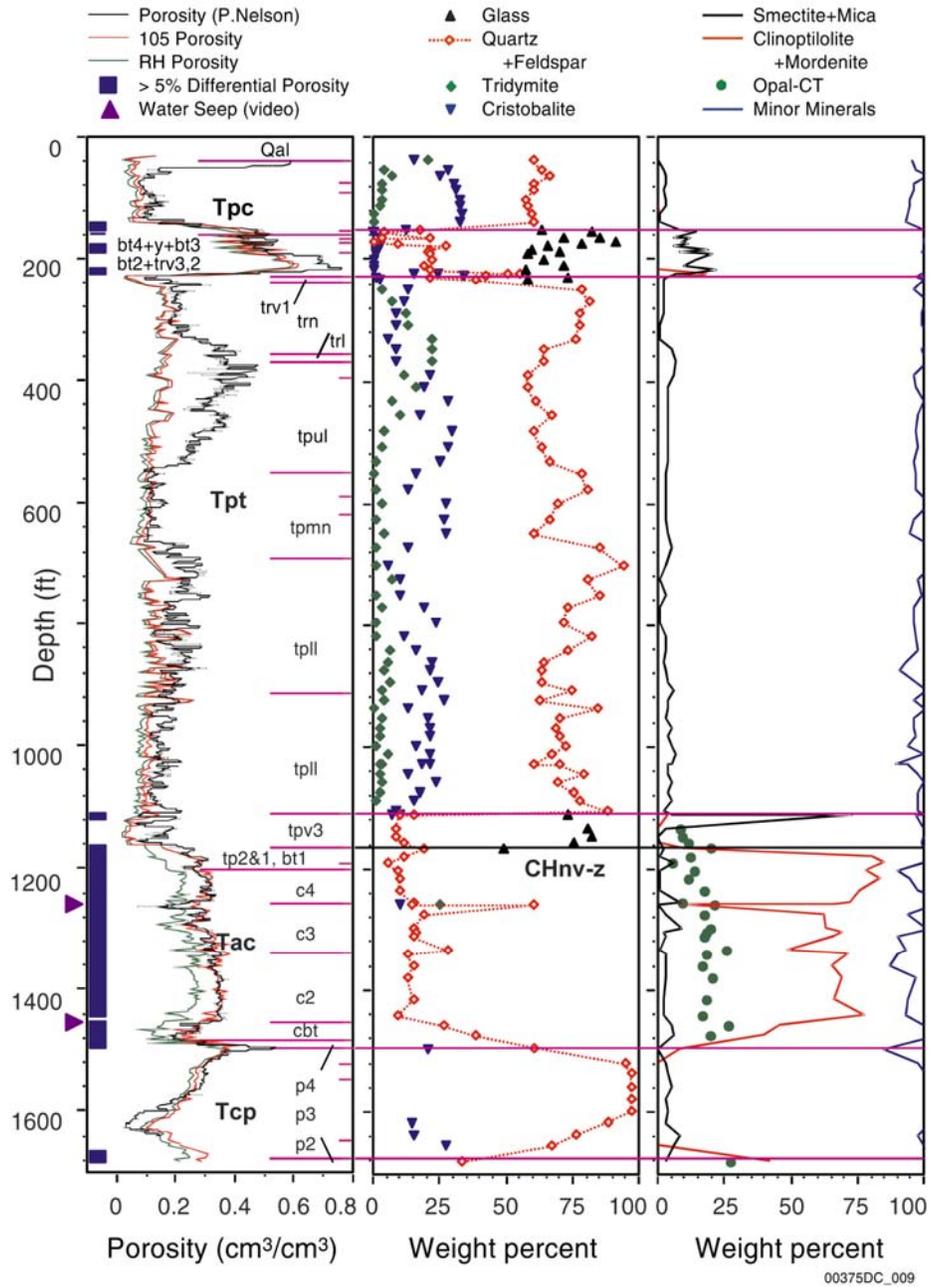
DTN: MO0312SEPSDLPC.000 [DIRS 166476]

Source: From CRWMS M&O 1996 [DIRS 101534], Plate 11

NOTE: Note that values for minor minerals in the right-hand column are given on a reverse scale (zero to right). Quantitative mineralogy is based on X-ray diffraction. Qal = Quaternary alluvium; Tpc = Tiva Canyon Tuff; Tp = bedded tuffs and upper part of vitric zone of Topopah Spring Tuff; Tpt = Topopah Spring Tuff; Tac = Calico Hills Formation; Tcp = Prow Pass Tuff; ft = feet; cm³ = cubic centimeter; 105 = sample oven-dried at 105°C; RH = relative humidity.

Figure 3-8. Lithostratigraphy, Porosity from Core and Geophysical Logs, and Quantitative Mineralogy in Borehole UE-25 UZ#16
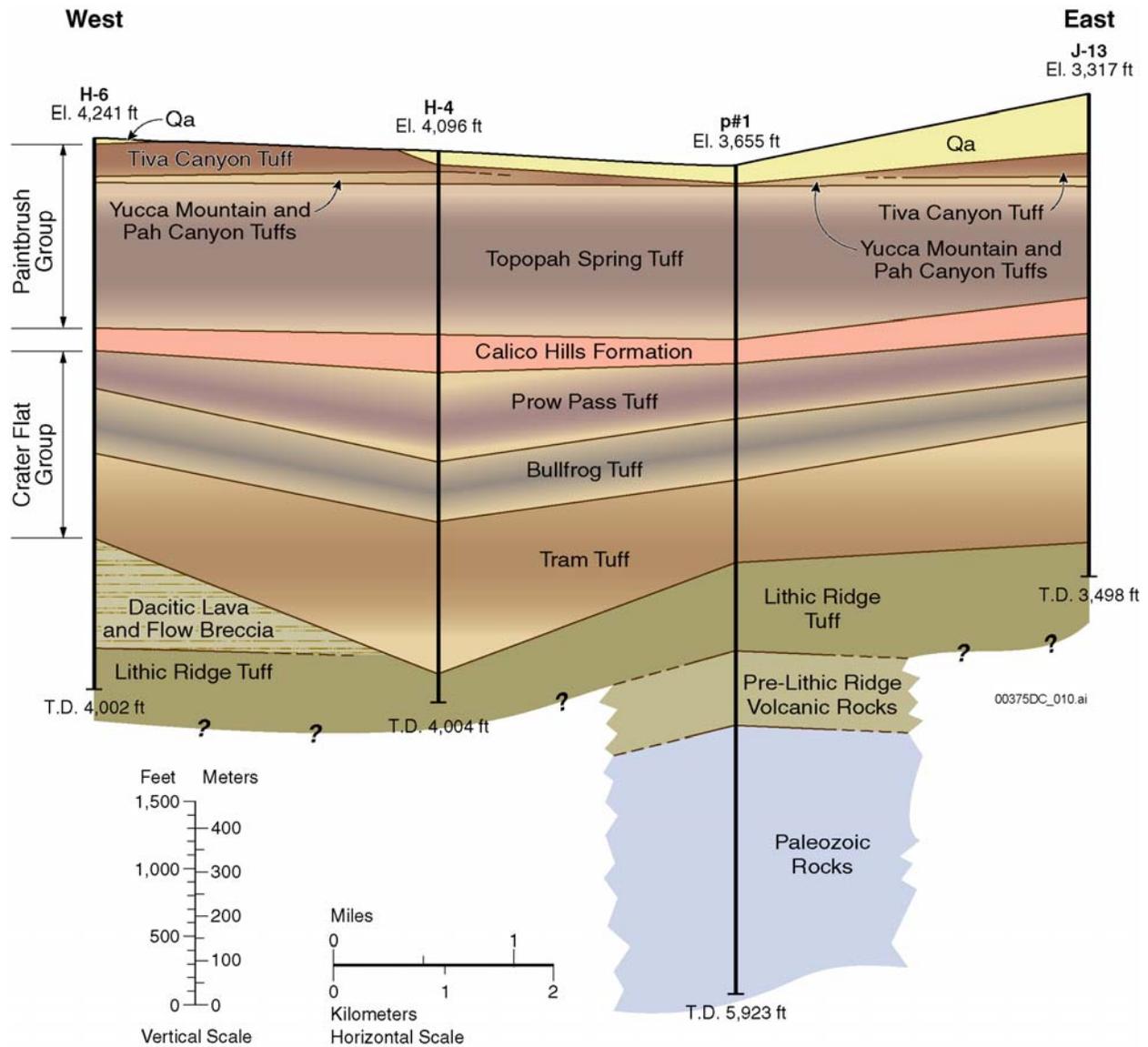
DTN: MO0004QGFMPICK.000 [DIRS 152554]. Location of section shown in Figure 3-7

NOTE: Datum is from the top of Topopah Spring Tuff. Well data are from a tabulation of lithostratigraphic contacts identified in the plotted boreholes. Bedded-tuff units are included at the base of the overlying formation. Qa = Quaternary deposits; El. = ground elevation; T.D. = total depth.

Figure 3-9. East-West Fence Diagram

South　　　　　　　　　　　　　　　　　　　　　　　　　　　North
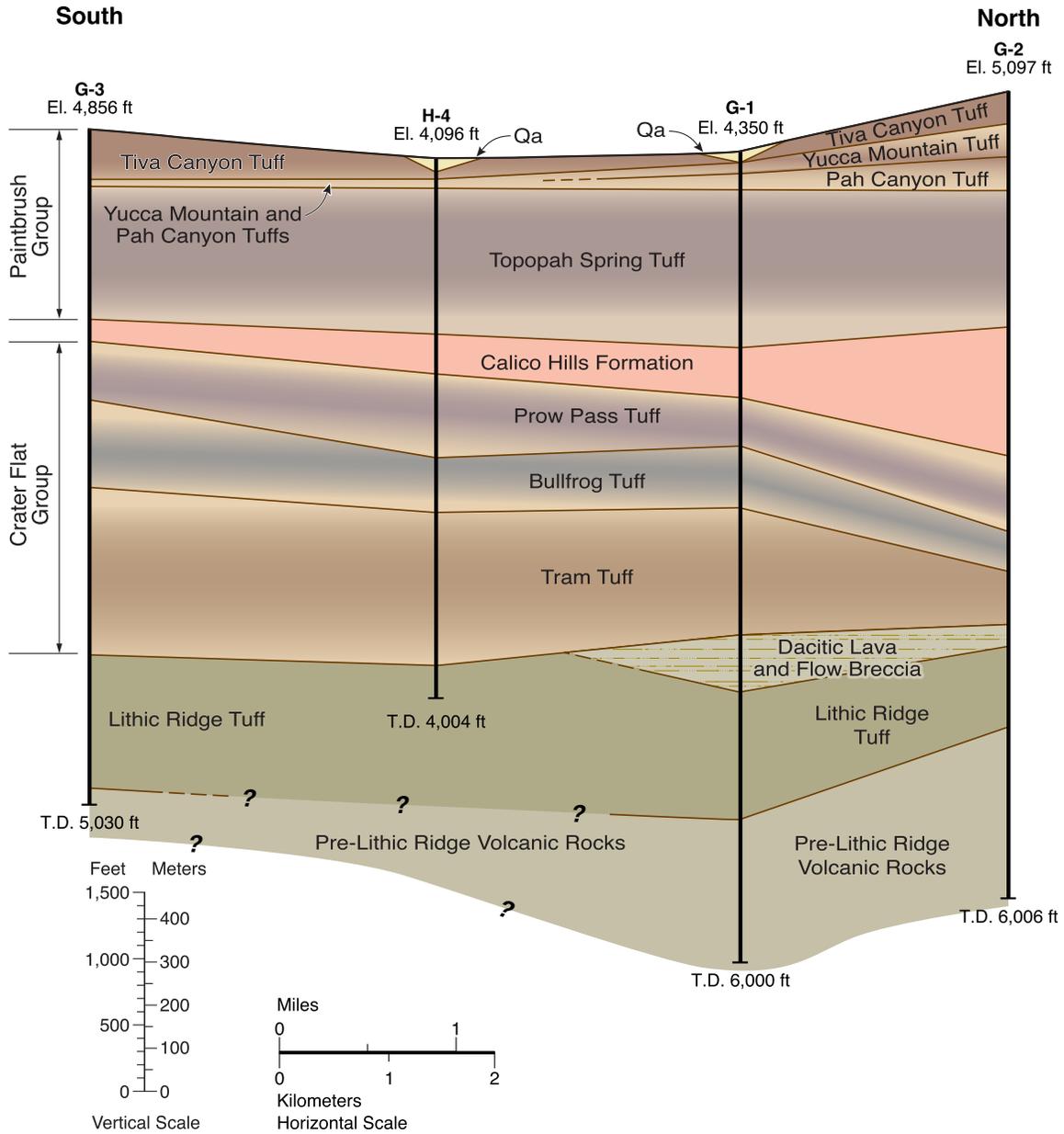
DTN: MO0004QGFMPICK.000 [DIRS 152554]. Location of section shown in Figure 3-7

NOTE: Datum is at the top of Topopah Spring Tuff. Well data are from a tabulation of lithostratigraphic contacts identified in the plotted boreholes. Bedded-tuff units are included at the base of the overlying formation. Qa = Quaternary deposits; El. = ground elevation; T.D. = total depth.

Figure 3-10. North-South Fence Diagram

DTN: MO0012MWDGFM02.002 [DIRS 153777]
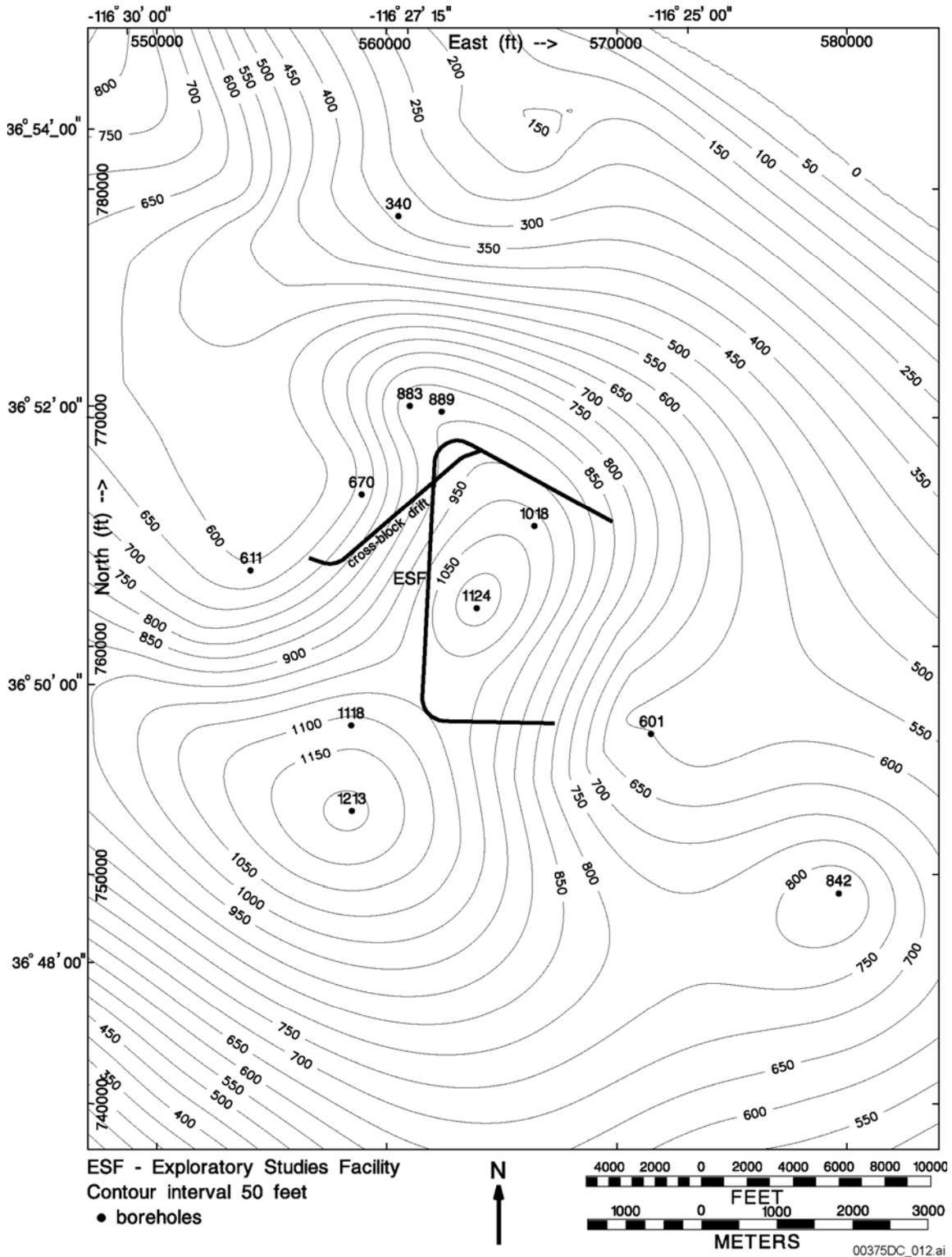
Source: BSC 2002 [DIRS 159124], Figure 25

Figure 3-11. Isochore Map of the Tram Tuff
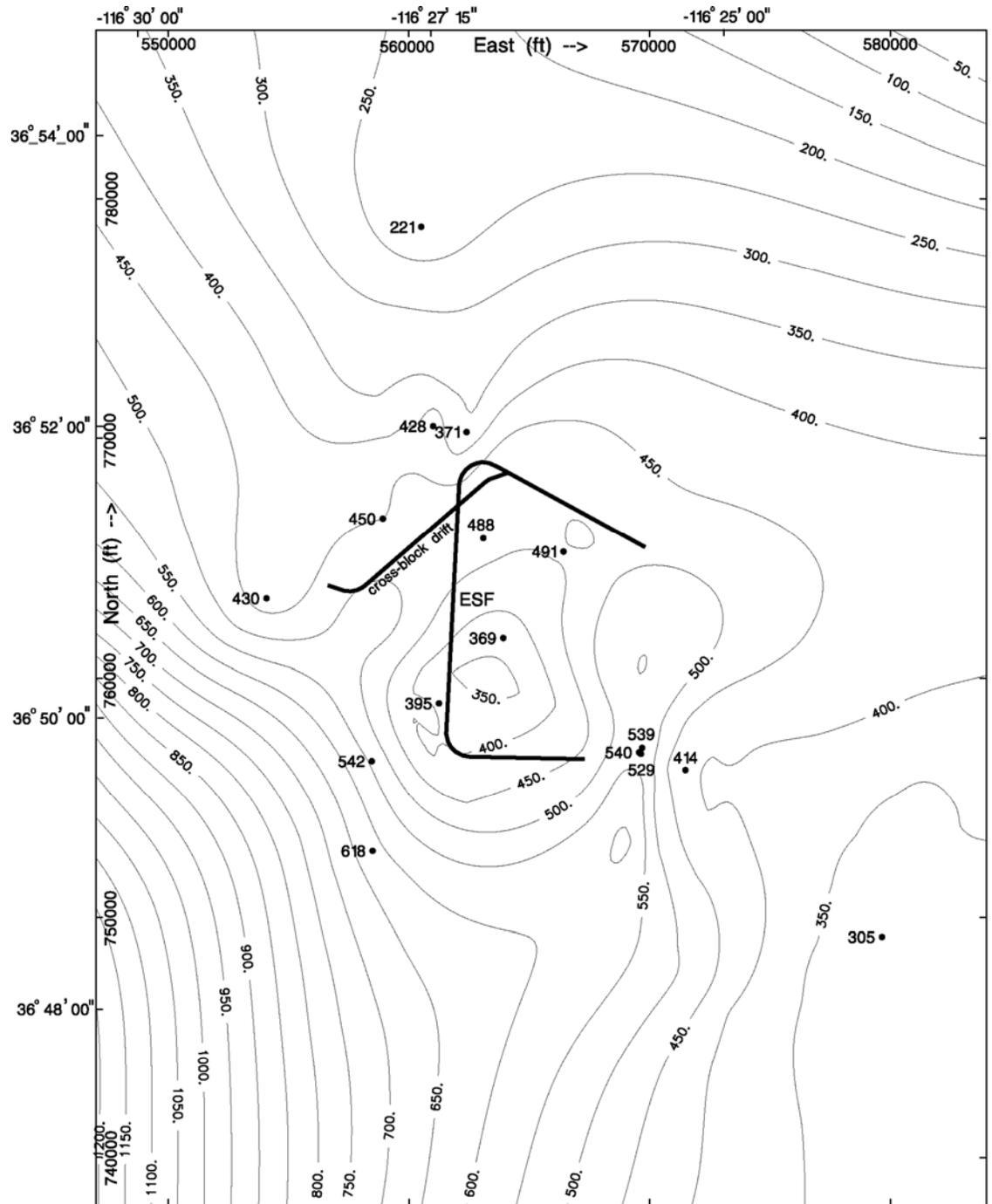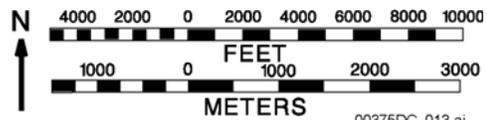
DTN: MO0012MWDGFM02.002 [DIRS 153777]

Source: BSC 2002 [DIRS 159124], Figure 24

Figure 3-12. Isochore Map of the Bullfrog Tuff
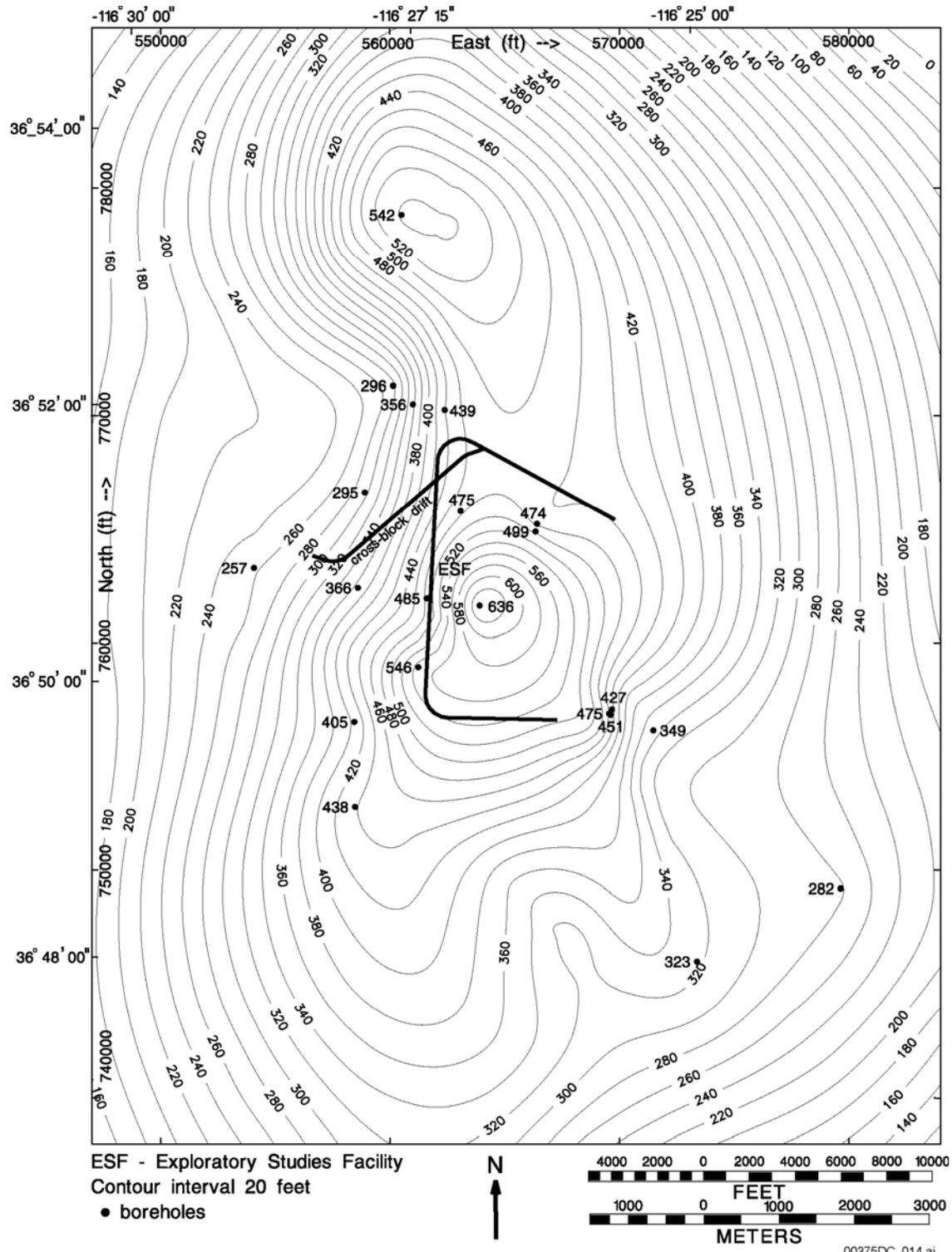
DTN: MO0012MWDGFM02.002 [DIRS 153777]

Source: BSC 2002 [DIRS 159124], Figure 23

Figure 3-13. Isochore Map of the Prow Pass Tuff
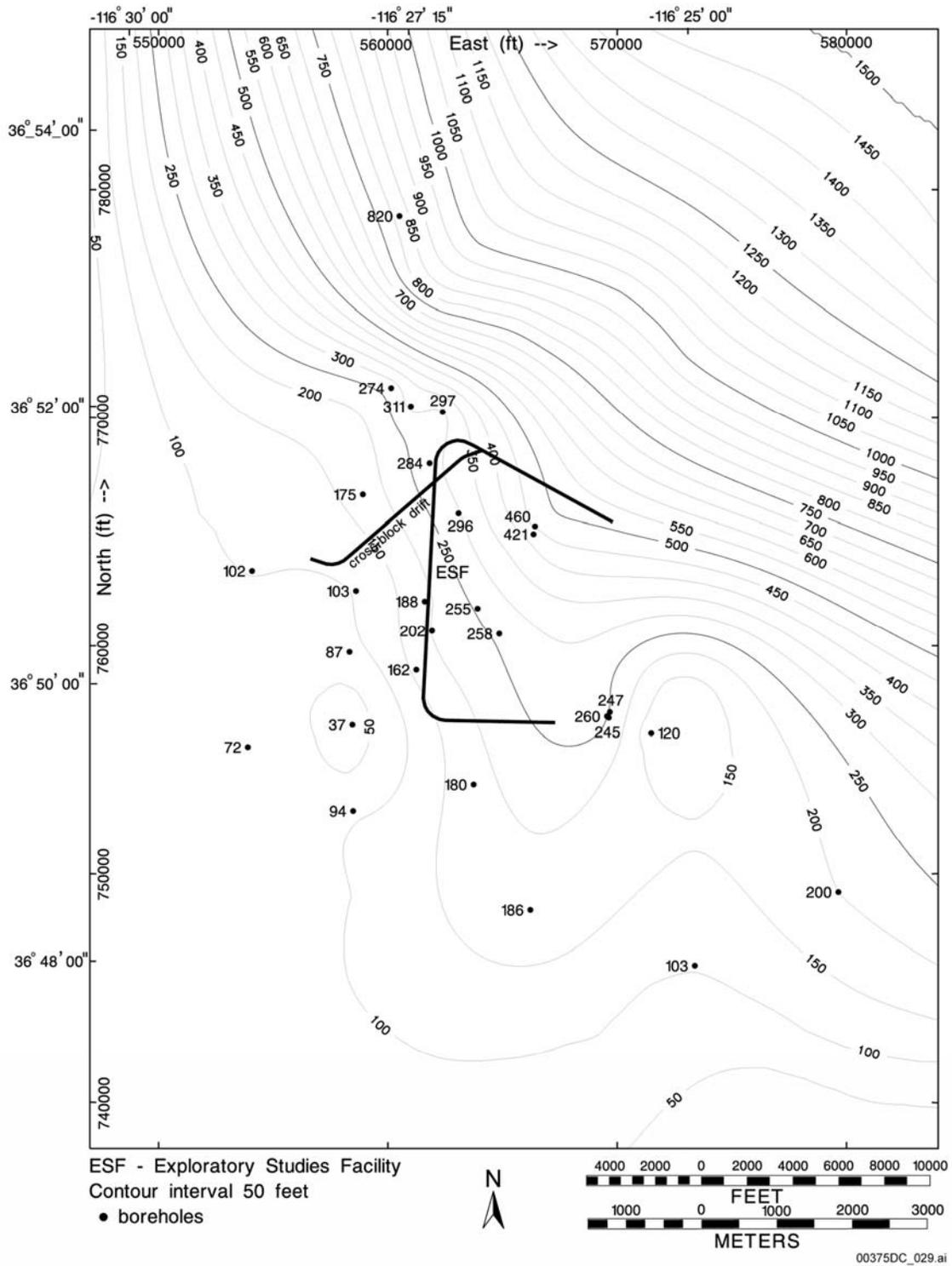
DTN: MO0012MWDGFM02.002 [DIRS 153777]

Source: BSC 2002 [DIRS 159124], Figure 22

Figure 3-14. Isochore Map of the Calico Hills Formation
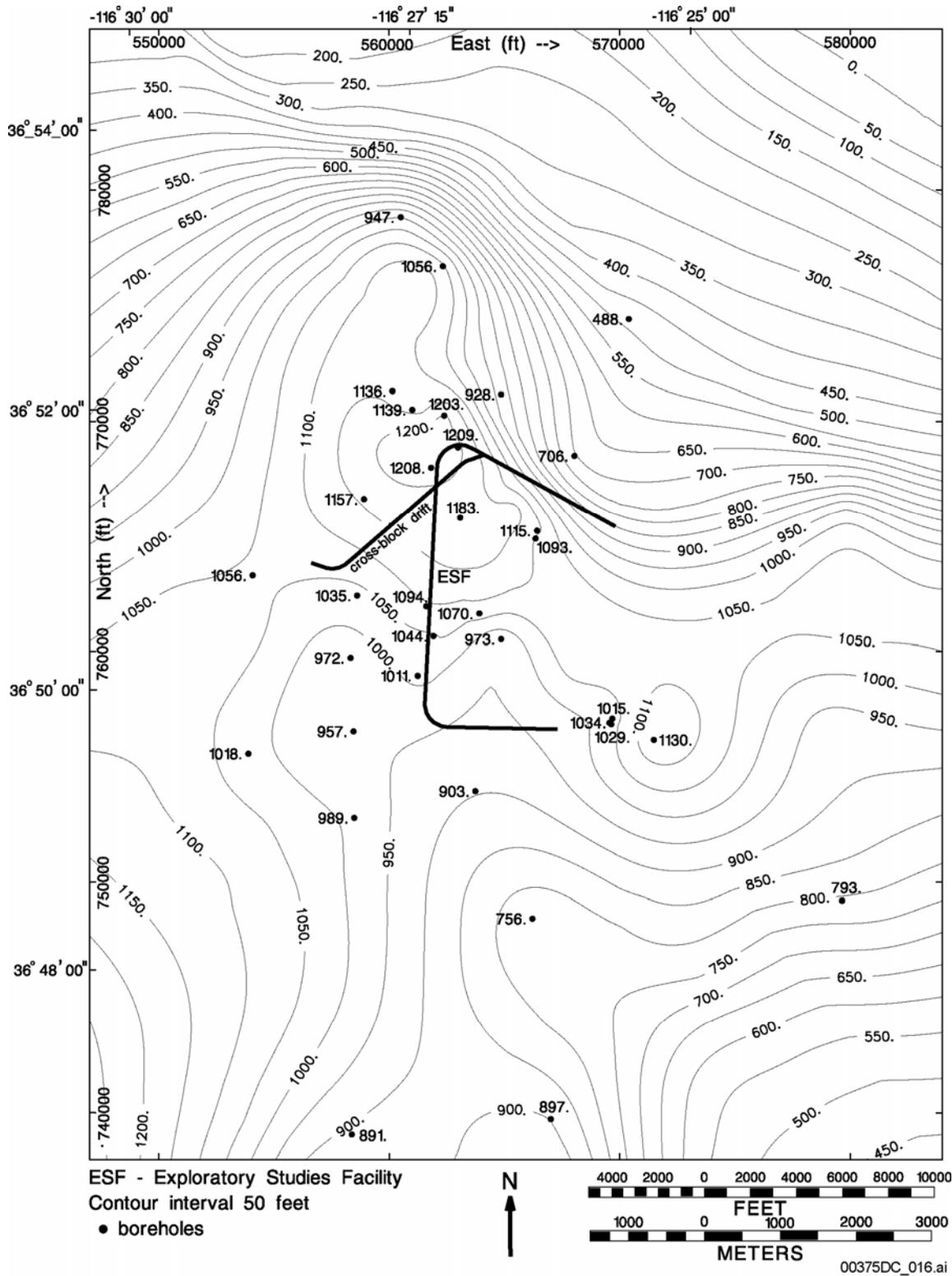
DTN: MO0012MWDGFM02.002 [DIRS 153777]

Source: BSC 2002 [DIRS 159124], Figure 18

Figure 3-15. Isochore Map of the Topopah Spring Tuff

DTN: MO0012MWDGFM02.002 [DIRS 153777]

Source: BSC 2002 [DIRS 159124], Figure 16

Figure 3-16. Isochore Map of the Pah Canyon Tuff
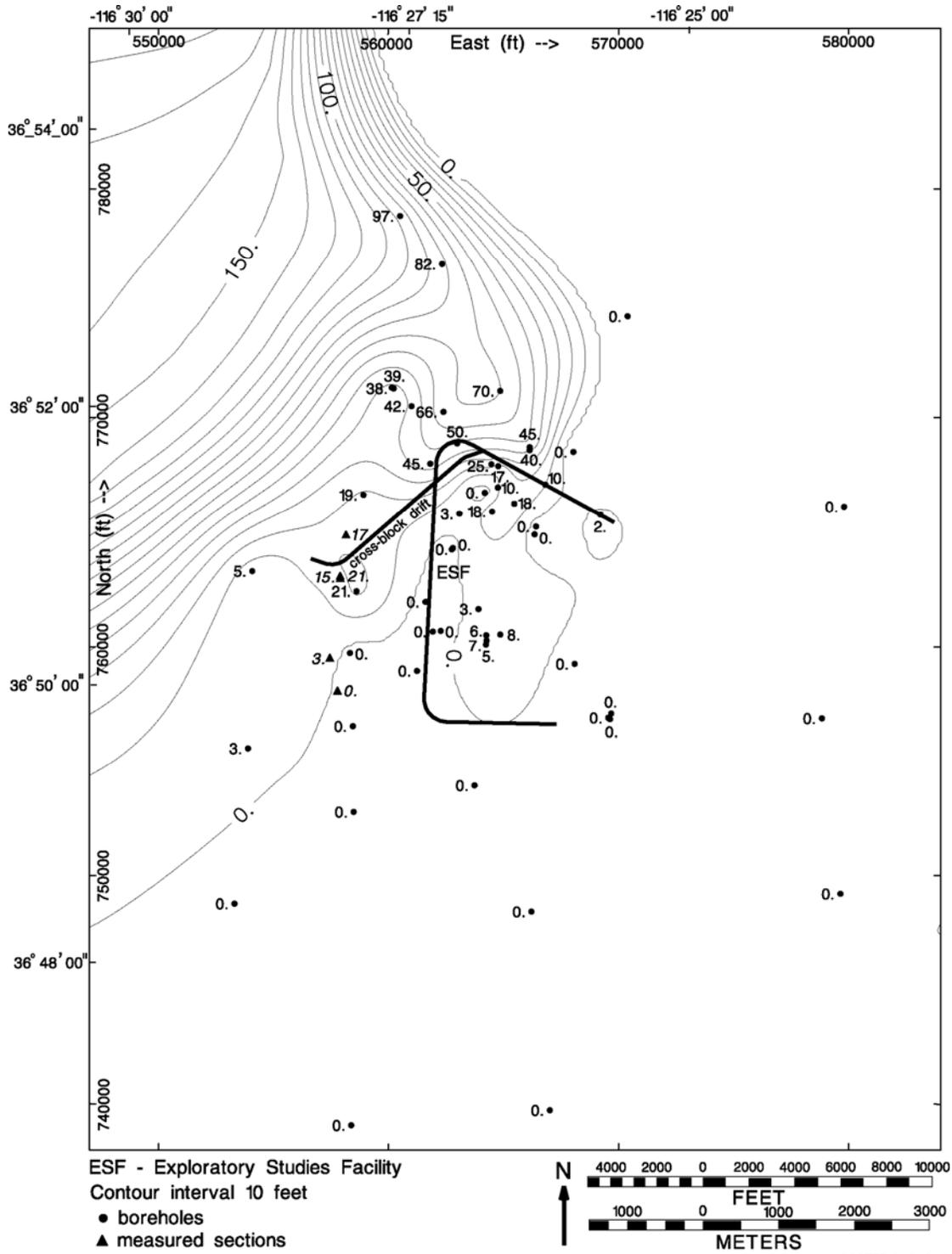
DTN: MO0012MWDGFM02.002 [DIRS 153777]

Source: BSC 2002 [DIRS 159124], Figure 15

Figure 3-17. Isochore Map of the Yucca Mountain Tuff
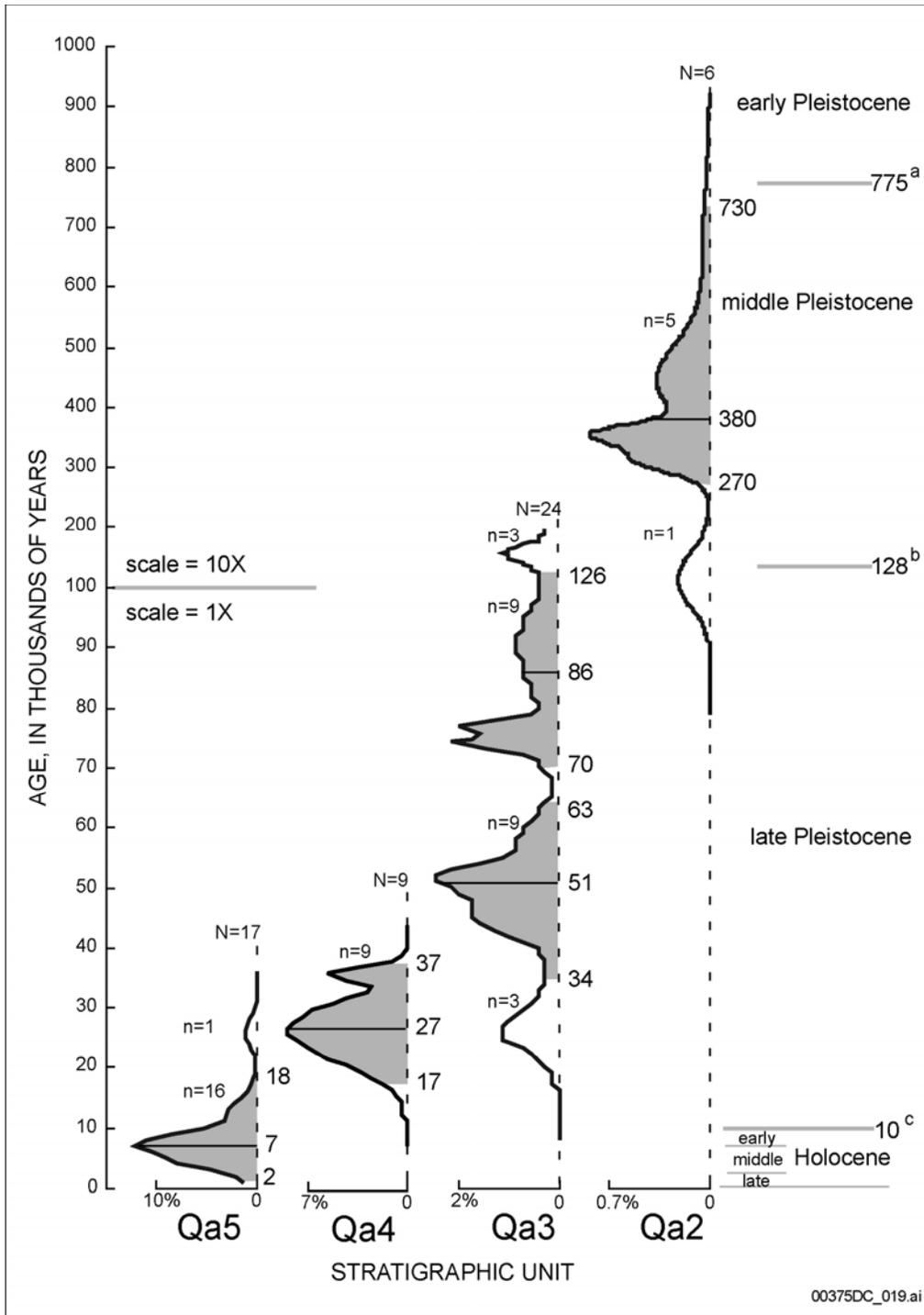
Source: Whitney et al. 2003 [DIRS 159418]

NOTE: Note the change in scale at 100,000 years: (a) Matuyama-Brunhes chronozone boundary (Morrison 1991 [DIRS 106397]); (b) astronomical age of marine oxygen-isotope substage 5e boundary (Imbrie et al. 1984 [DIRS 100047]); (c) arbitrary age suggested for Pleistocene-Holocene boundary (Hopkins 1975 [DIRS 159322]). Ages are given in thousands of years.

Figure 3-18. Plot Showing Age Distribution of Mapped Quaternary Units Qa2–Qa5 in the Midway Valley and Fortymile Wash Areas

Figure (a) Calico Fan Site — cross section from Northwest to Southeast showing Thin Veneer of Qa5 2-18 ka, Qa3 (22-40 ka), Qa3 (170 ka?), Fortymile Wash, Qa6-7, Qa5. Southeast side: Thin Veneer of Qa5 2-17 ka, 20-50 ka, 50-120 ka Qa3, >1 m.y. Ash, Miocene Cemented Gravel, Calico Fan, Qa5/Qa3, 220-280 ka, Eolian Sand.

Figure (b) Yucca Mountain Road Crossing — cross section from Northwest to Southeast showing Thin Veneer of Qa5 2-18 ka, 74±3 ka, Qa3, Sever Wash, Qa3?, Qa3, 50-60 ka, Qa2? (300-500 ka), Qa2?/Qa1? (>400 ka), Q?, 20-36 ka, Qa4, Qa6-7, Qa5, 27-31 ka, Qa4, Thin Veneer of Qa5 2-18 ka, 50-100? ka, Qa3, Fortymile Wash, Qa4 may be a strath terrace into Qa3 material.

Not to Scale

00357DC_021.psd

DTN: MO0312SEPSDGCS.000 [DIRS 166560]

Source: CRWMS M&O 2000 [DIRS 151945], Figure 7.4-4

NOTE: Dates are based on Whitney et al. 2003 [DIRS 159418], Table 4. Locations of cross sections are shown in Figure 3-7. See Section 3.3.6 for unit definitions.

Figure 3-19. Generalized Cross Sections of the Evolution of Fortymile Wash

Source: Potter et al. 2002 [DIRS 160060]

NOTE: All faults are shown with solid lines, although many segments are concealed or inferred. Symbols and abbreviations: bar and bell = downthrown side of fault; arrows = relative direction of strike-slip movement; ESF = Exploratory Studies Facility; CD = Cross-Drift. Cross Section refers to Figure 3-21. Not all faults shown on Figure 3-21 are shown on the figure. Additional information is available in BSC 2002 [DIRS 157829] and Potter et al. 2002 [DIRS 160060].

Figure 3-20. Distribution of Faults in the Yucca Mountain Site Area and Adjacent Areas to the South and West
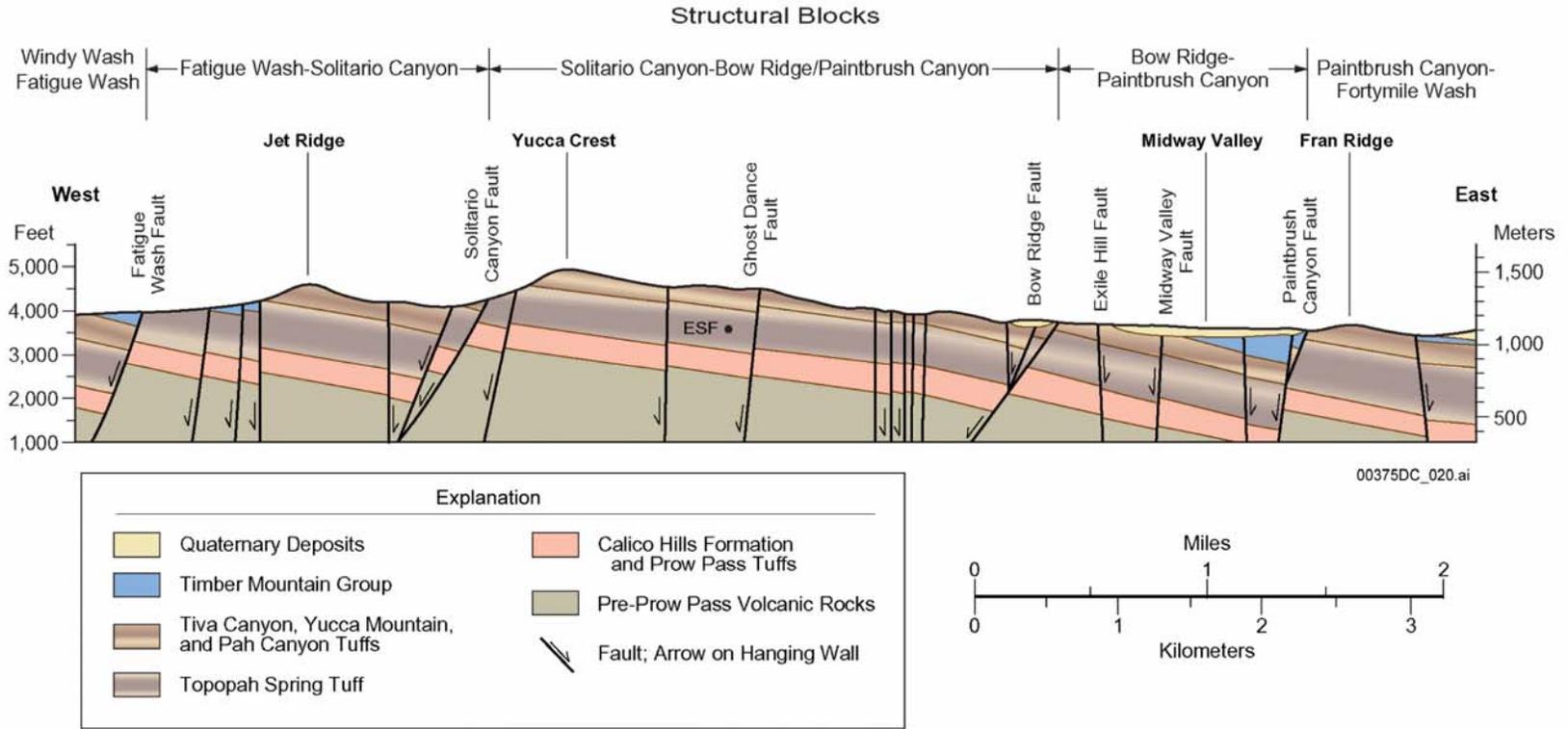
Source: Simplified from Day et al. 1998 [DIRS 100027], Cross Section B-B'

NOTE: Line of section shown in Figure 3-20; ESF = Exploratory Studies Facility (location of intersection along line of section). Not all faults shown are plotted in Figure 3-20.

Figure 3-21. East-West Structure Section across Yucca Mountain Site Area
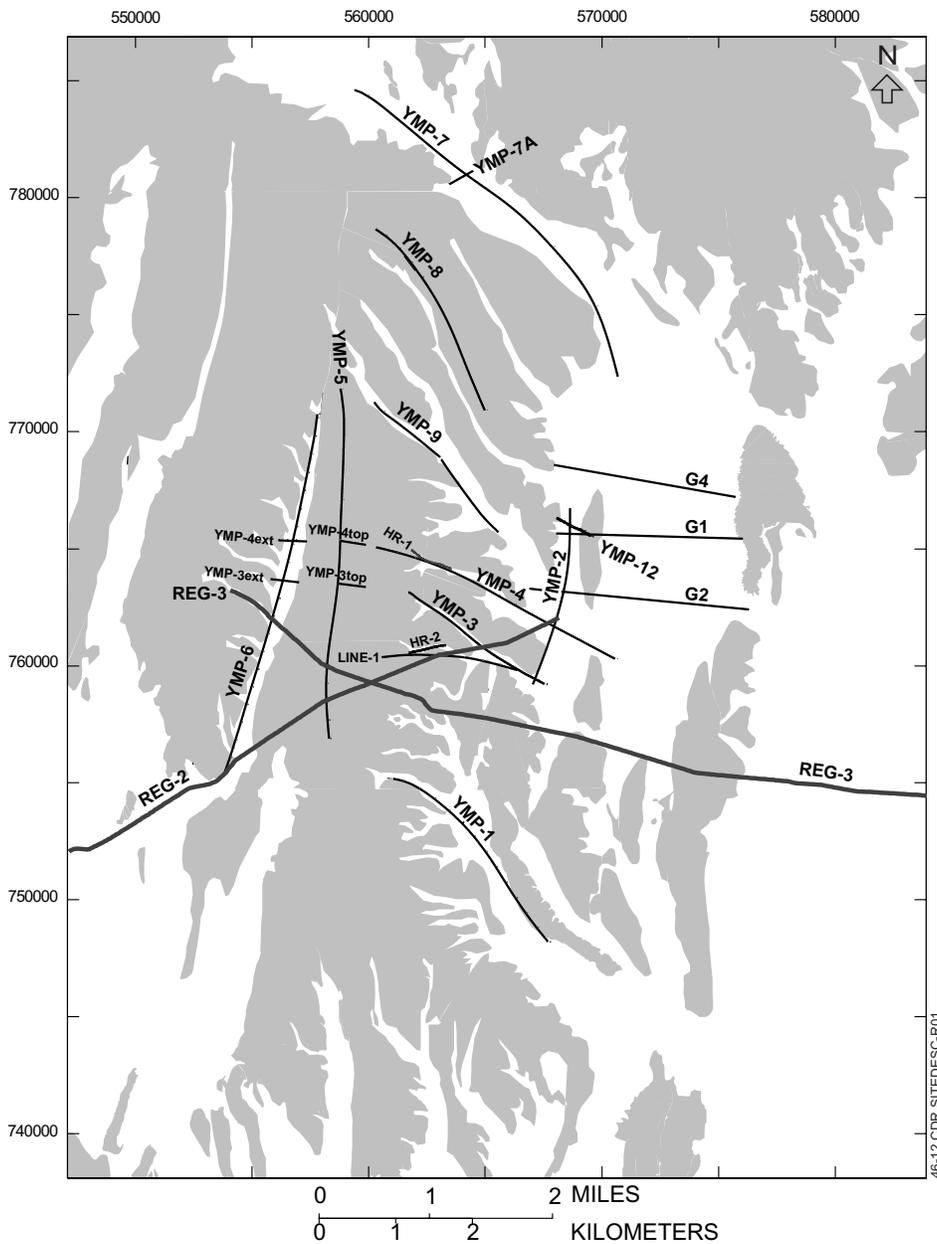
DTN: SNL01C12159302.002 [DIRS 148289]

Source: Modified from Majer et al. 1996 [DIRS 104685], Figure 1

NOTE: Shaded areas are exposed volcanic bedrock. Seismic reflection data were collected along all lines labeled "REG" and "YMP". Of these, REG-2 and REG-3 are regional seismic reflection lines (Brocher et al. 1996 [DIRS 101495]), and HR-1 and HR-2 are very–high–resolution seismic reflection lines (station spacings 1 to 2 m). All others are standard high-resolution seismic reflection lines (station spacing 6 to 12 m; Feighner et al. 1996 [DIRS 105417]. Ground-based gravity data were collected along all lines, except YMP-3top, YMP-4top, YMP-7, HR-1, HR-2, and Line-1. Ground magnetic data were collected along all lines, except YMP-3top, YMP-3 ext, YMP-4top, YMP-4 ext, HR-2, and Line-1. Magnetotelluric data were collected only along YMP-3. Lines G1, G2, and G4 are gravity and magnetic surveys of Ponce and Langenheim 1994 [DIRS 102333]. Reference coordinates correspond to the Nevada State Coordinate System (in feet).

Figure 3-22. Index Map Showing Location of Geophysical Surveys in the Yucca Mountain Site Area
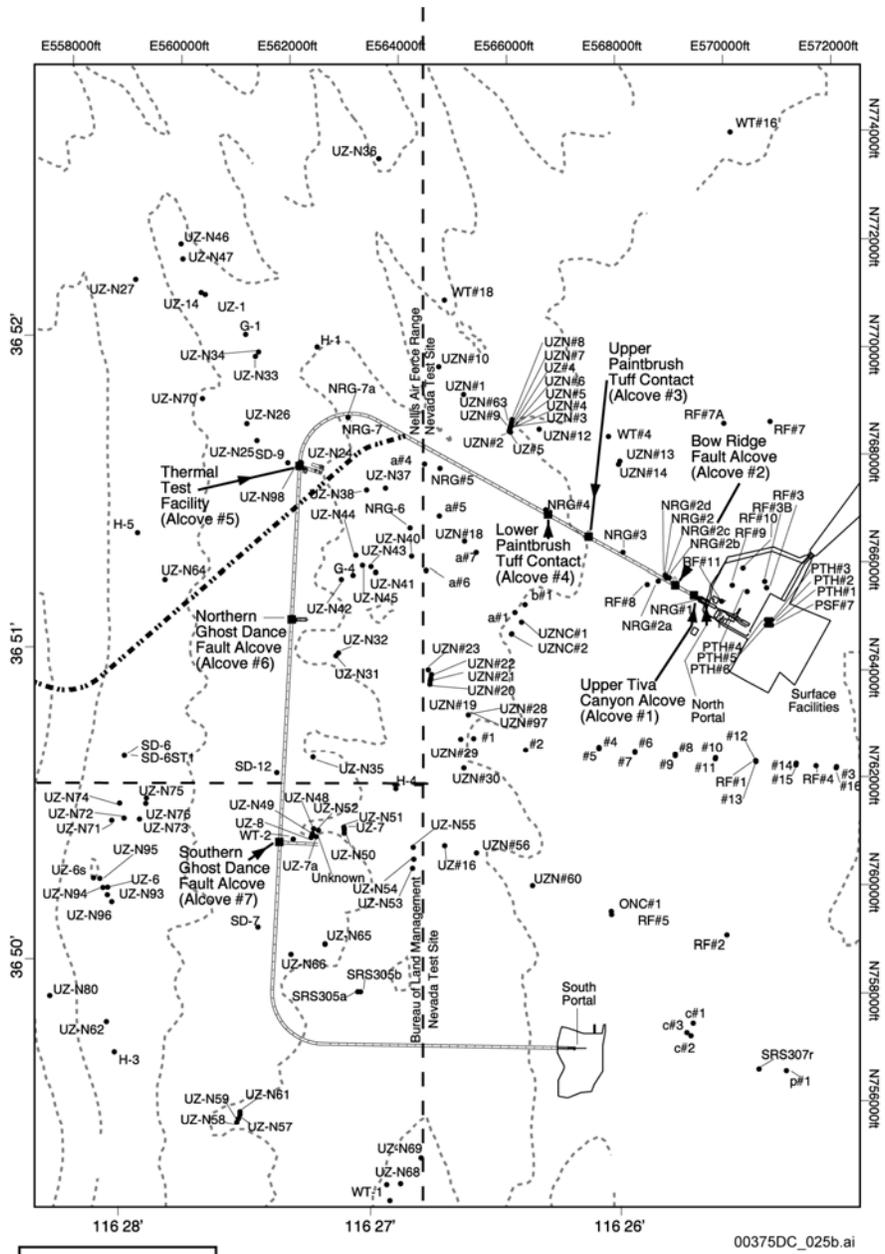
Modified from DTN: MO0006YMP99059.001 [DIRS 150699]

NOTE: Additional information is available in BSC 2002 [DIRS 157829].

Figure 3-23. Plan Map Showing up to 2000 the Exploratory Studies Facility and Yucca Mountain Site Characterization Project Boreholes
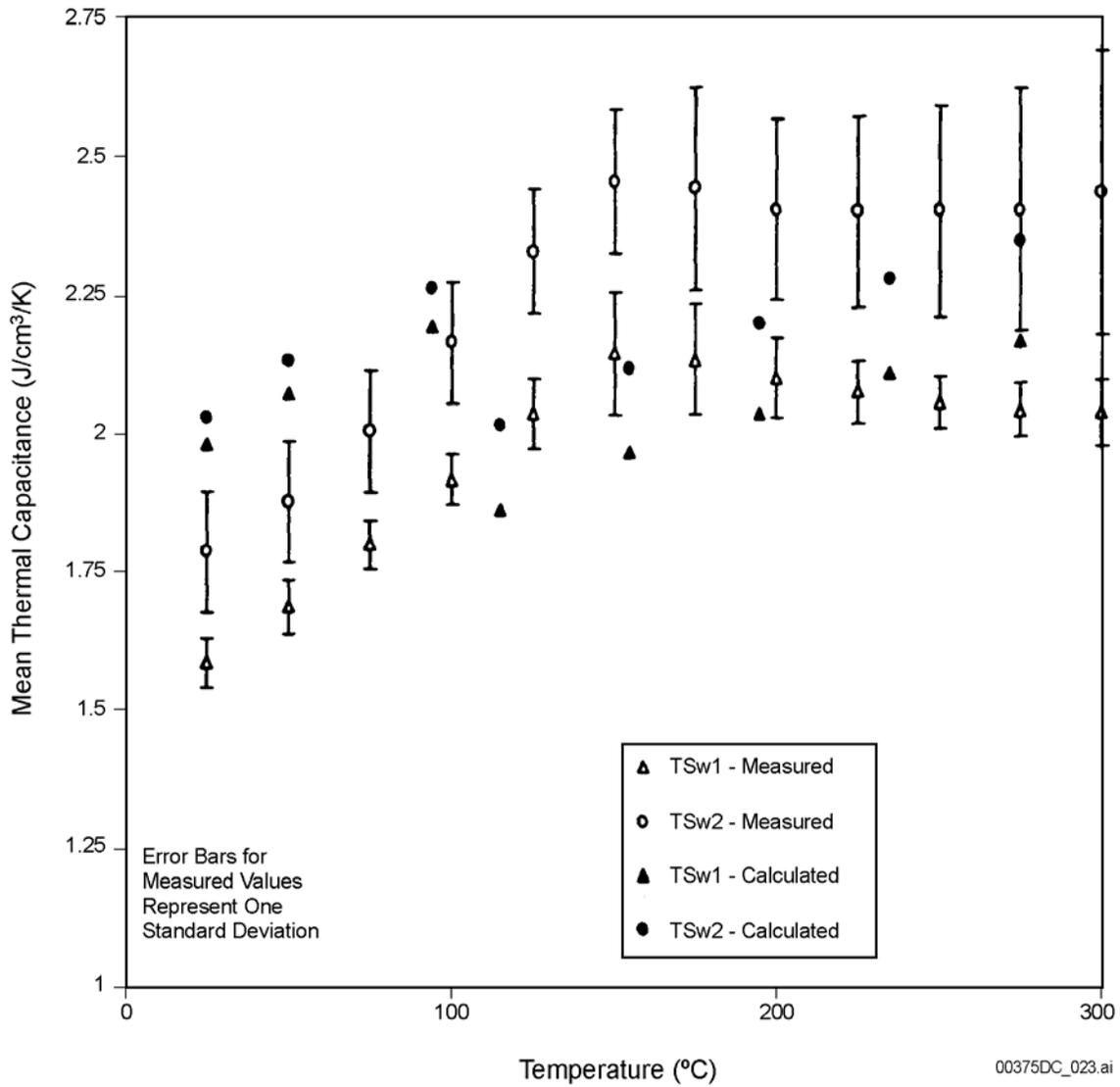
Figure 3-24. Measured and Calculated Values of Thermal Capacitance for TSw1 and TSw2 Thermal Mechanical Units
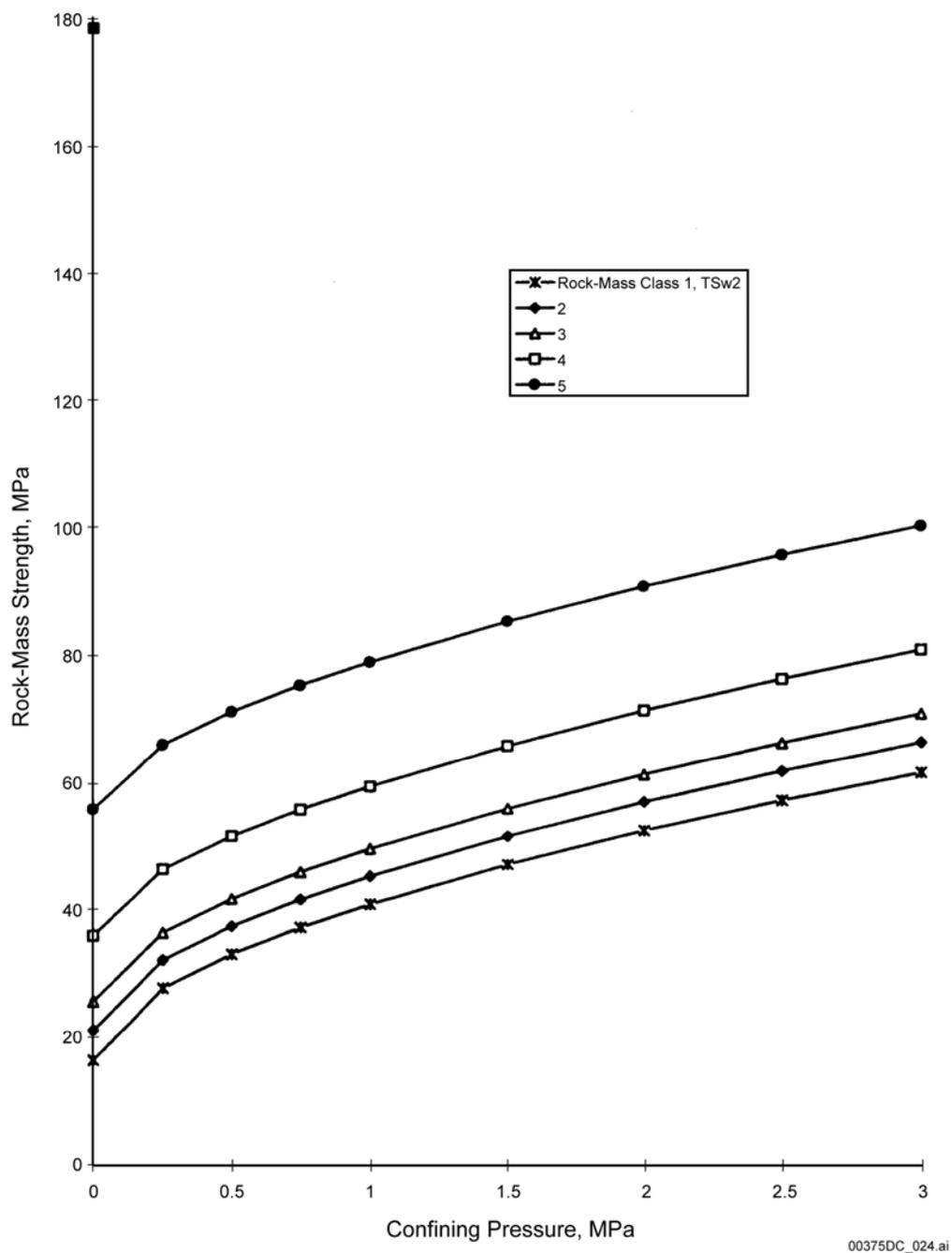
DTN: MO0312SEPSDDRM.000 [DIRS 166477]; MO0312SEPSDNTM.000 [DIRS 166493]

Source: CRWMS M&O 1997 [DIRS 103564], Figure 7-1, p. 7-11

Figure 3-25. Design Rock-Mass Strength Envelopes for TSw2 Thermal-Mechanical Unit, Exploratory Studies Facility

INTENTIONALLY LEFT BLANK

Table 3-1. Generalized Stratigraphic Column of Tertiary Volcanic Rocks in the Yucca Mountain Site Area

Group	Formation/Unit		Thickness in Site Area (meters)	General Lithology
Timber Mountain	Ammonia Tanks Tuff		Not present in area	Welded to nonwelded rhyolite tuff
	Rainier Mesa Tuff		Generally <30	High-silica rhyolite and quartz latite tuffs
	Pre-Rainier Mesa Tuff bedded tuff		17[a]	Nonlithified pyroclastic-flow deposits
Paint-brush	Rhyolite of Comb Peak		<130	Rhyolite lava flows and related tephra; pyroclastic-flow deposits
	Tuff Unit "X"		6–23[b]	
	Rhyolite of Vent Pass		0–150	
	Post-Tiva Canyon Tuff bedded tuff		<2–4.5	Pyroclastic-flow and fallout tephra deposits
	Tiva Canyon Tuff	Crystal-rich member	<50–175	Compositionally zoned (rhyolite to quartz latite) tuff sequence; each member divided into several zones and subzones[c]
		Crystal-poor member		
	Pre-Tiva Canyon Tuff bedded tuff		<1–3[d]	Pyroclastic fallout tephra deposits with thin weathered zones
	Yucca Mountain Tuff		0–55	Nonwelded to densely welded pyroclastic-flow deposit
	Rhyolite of Black Glass Canyon		2–14	Rhyolite lava flows and related tephra
	Rhyolite of Delirium Canyon		<250 (lava) <100 (ash flows)	
	Rhyolite of Zig Zag Hill		<10	
	Pre-Yucca Mountain Tuff bedded tuff		<1–46[d]	Nonwelded pyroclastic-flow deposits
	Pah Canyon Tuff		0–79	Pyroclastic-flow deposits; abundant large pumice clasts
	Pre-Pah Canyon Tuff bedded tuff		3–10[d]	Vitric to devritified and altered fallout tephra and ash-flow tuff
	Topopah Spring Tuff	Crystal-rich member	0–381	Compositionally zoned (rhyolite to quartz latite) tuff sequence; each member divided into several zones and subzones[c]. Repository host rock is within crystal-poor member[e]
		Crystal-poor member		
	Pre-Topopah Spring Tuff bedded tuff		0–17[d]	Bedded tuffaceous deposits
	Calico Hills Formation		15–457	Rhyolite tuffs and lavas; contains five pyroclastic units
	Pre-Calico Hills Formation bedded tuff		9–39[d]	Pyroclastic-flow and coarse-grained fallout deposits

Table 3-1. Generalized Stratigraphic Column of Tertiary Volcanic Rocks in the Yucca Mountain Site Area (Continued)

Group	Formation/Unit	Thickness in Site Area (meters)	General Lithology
Crater Flat	Prow Pass Tuff	15–194	Includes four variably welded pyroclastic-flow deposits
	Pre-Prow Pass Tuff bedded tuff	<1–3.5[d]	Pumiceous tuffs and pyroclastic-flow deposits
	Bullfrog Tuff	15–366	Includes two pyroclastic-flow deposits separated by a pumiceous fallout unit
	Pre-Bullfrog Tuff bedded tuff	6–11[d]	Pyroclastic-flow deposits with thin zones of fallout tephra
	Tram Tuff	0–370	Pyroclastic-flow deposits and bedded tuffs
	Pre-Tram Tuff bedded tuff	0–21[d]	Pyroclastic-flow and fallout deposits
	Dacitic lava and flow breccia	111–249[f]	Dacitic lavas and flow breccia; bedded tuff at base
	Lithic Ridge Tuff	185–304[g]	Pyroclastic-flow deposit
	Pre-Lithic Ridge Tuff volcanic rocks	45–350+[h]	Pyroclastic-flow deposits and bedded tuffs

NOTES: [a] Thickness in Boreholes UE-25 NRG-#2C and UE-25 NRG-2D.

[b] Thicknesses in boreholes near Exile Hill.

[c] Member subdivisions described in Table 4.5-2 of CRWMS M&O 2000 [DIRS 151945], based principally on Buesch et al. 1996 [DIRS 100106].

[d] Thicknesses in the seven boreholes shown in Figures 3-9 and 3-10.

[e] Repository host rock, includes upper lithophysal (lower part), middle nonlithophysal, lower lithophysal, and lower nonlithophysal zones of the crystal-poor member of the Topopah Spring Tuff.

[f] Thickness in Borehole USW H-6.

[g] Thickness in Borehole USW G-3.

[h] Thickness in Borehole USW G-2.

Table 3-2. Summary of Diagnostic Surface and Soil Properties of Map Units at Yucca Mountain

	Surface Characteristics[a]					Soil Characteristics			
Map Unit	Desert Pavement[b]	Desert Varnish[c]	Rubification[d]	Depositional Bar Relief[e]	Horizon Sequence[f]	Structure[g]	Clay Films[h]	Maximum Reddening[i]	Maximum Carbonate Stage[j]
Qa7	None	1±2 12	4	high, unaltered	Cu	sg	N.P.	10YR	N.P.
Qa6	None	0±0 0	0	high, unaltered	A-Ck	sg	N.P.	10YR	N.P.
Qa5	Weak to moderate	1±1 28	33	Moderately high, slightly altered	A-Bwk/Btjk-Bk-Ck	1 vf-f sbk	N.P.-1 n co	10YR	I
Qa4	Moderate to strong	62±27 97	87	Low	Av-Btkq-Bkq-Ck	2-3 f-m sbk	3 n-mk pf	7.5YR	I-II
Qa3	Strong	43±28 94	54	Low	Av-BA-Btkq-Kq-Bkq-Ck	3 m sbk	3 n-mk pf	7.5YR	II+-III
Qa2	Strong	80 est. 100 est.	100 est.	Low	Av-Btq-Btkq-Kq-Bkq-Ck	3 m sbk	3 mk pf	7.5-5YR	IV
Qa1	Locally strong	20±21 84	80	None	Av-BA-Btkq-Kqm-Bkq-Ck	m-3 m pl	2 n pf	10-7.5YR	IV
QT0	Degraded						Eroded		

Table 3-2. Summary of Diagnostic Surface and Soil Properties of Map Units at Yucca Mountain (Continued)

	Surface Characteristics[a]					Soil Characteristics				
Map Unit	Desert Pavement[b]	Desert Varnish[c]	Rubification[d]	Depositional Bar Relief[e]	Horizon Sequence[f]	Structure[g]	Clay Films[h]	Maximum Reddening[i]	Maximum Carbonate Stage[j]

DTN: MO0312SEPSDDGS.000 [DIRS 166491]

Source: Whitney et al. 2003 [DIRS 159418], Table 3

NOTES: [a] See Wesling et al. 1992 [DIRS 107290] for detailed definitions of surface parameters.

[b] Describes the relative degree of interlocking of surface clasts, based on qualitative estimate.

[c] The first number is the average varnish cover (percent ±1); the second number refers to the percent of varnished clasts. Wesling et al. 1992 [DIRS 107290].

[d] Gives the percent rubified clasts; from Wesling et al. 1992 [DIRS 107290].

[e] Gives the relative height of despositional bars from the top of the bar to the trough of the adjacent swale.

[f] Refers to the sequence of soil horizons that is representative of each map unit. Abbreviations for master horizons: A = surface horizon, characterized by accumulation of organic matter and typically as a zone of illuviation of clay, sesquioxides, silica, gypsum, carbonate, and/or salts; B = subsurface horizon, characterized by a redder color, stronger structure development, and/or accumulation of secondary illuvial materials (clay, sesquioxide, silica, gypsum, and salts); C = subsurface horizon that may appear similar or dissimilar to the parent material and includes unaltered material and material in various stages of weathering; K = subsurface horizon, engulfed with carbonate to the extent that its morphology is determined by the carbonate. Abbreviations for master horizon modifiers: j = used in conjunction with other modifiers to denote incipient development of that particular feature or property; k = accumulation of carbonates; m = strong cementation; q = accumulation of silica; t = accumulation of clay; u = soil properties undifferentiated; v = vesicular structure; w = color or structural B horizon.

[g] Abbreviations: sg = single grained; m = massive; 1 = weak; 2 = moderate; 3 = strong; vf = very fine; f = fine; m = medium; pl = platy; sbk = subangular blocky.

[h] Abbreviations: N.P. = not present; 1 = few; 2 = common; 3 = many; n = thin; mk = moderately thick; pf = ped face; co = colloidal stains.

[i] Hue is determined using the Munsell Soil Color Chart, Munsell Color Company 1994 [DIRS 106399].

[j] Terminology is from Gile et al. 1966 [DIRS 105522] and Birkeland 1984 [DIRS 101847].

Table 3-3. Varnish Cation Ratio Age Estimates from Boulder Deposits around Yucca Mountain

Sample	Age (Uncertainty) (ka)
YME-1	640 (*610-670*)
YME-2	170 (*140-180*)
YMW-1	465 (*400-515*)
YMW-2	645 (*630-660*)
YMW-3	710 (*680-740*)
YMN-1	760 (*710-820*)
LSM-1	960 (*930-990*)
SKM-1	800 (*760-830*)
SKM-2	830 (*800-880*)
SKM-3	1180 (*1110-1270*)
SKM-3A	990 (*960-1030*)
BM-1	1380 (*1260-1510*)

DTN: LA000000000026.002 [DIRS 166510]

Source: Modified from CRWMS M&O 1998 [DIRS 103514],
              Table 3.4-7

Table 3-4.   Ranges in Calculated Cation Ratio Dates (Revised Calibration) and Cosmogenic Nuclide Dates for the Four Boulder Deposits around Yucca Mountain

Boulder Deposit Location	Age Range	Minimum	Maximum
Buckboard Mesa	585±146	439	731
	640±160	480	800
Average (rounded)		460	765
Skull Mountain	845±211	634	1056
	420±105	315	525
	1210±303	907	1513
Average (rounded)		620	1030
Yucca Mountain (East)[a]	645±161	484	806
	280±70	210	350
	215±54	161	269
	295±74	221	369
	165±41	124	206
Yucca Mountain (West)[b]	1410±353	1057	1763
	7220±1818	5452	9088
	360±90	270	450

DTN: MO0312SEPSD10B.000 [DIRS 166513]

Source: Harrington 2000 [DIRS 150417]

NOTE: [a] Investigators chose the oldest range as most representative; rounded to 480 to 805.
            [b] Investigators deleted the oldest range and averaged the other two; rounded to 660 to 1,100.

Table 3-5. Comparison of Several Stratigraphic Subdivisions of Mid-Tertiary Volcanic Rocks at Yucca Mountain

Lithostratigraphic Units[a,d,e,f]		Thermal-Mechanical Units[a,b]
Timber Mountain Tuff (Tm)	Rainier Mesa member (Tmr)	Undifferentiated overburden (UO)
	Pre-Rainier Mesa bedded tuff (Tmbt1)	
PAINTBRUSH GROUP (Tp)		
	rhyolite of Comb Peak (Tpk); includes the pyroclastic flow deposit (Tpki) that is informally referred to as tuff unit "X" (Tpki)	
	post-Tiva Canyon bedded tuff (Tpbt5)	
Tiva Canyon Tuff (Tpc)	crystal-rich member (Tpcr) vitric zone (Tpcrv) -nonwelded subzone (Tpcrv3) -moderately welded subzone (Tpcrv2) -densely welded subzone (Tpcrv1) nonlithophysal zone (Tpcrn) lithophysal zone (Tpcrl)	Tiva Canyon welded (TCw)[d]
	crystal-poor member (Tpcp) upper lithophysal zone (Tpcpul) middle nonlithophysal zone (Tpcpmn) lower lithophysal zone (Tpcpll) lower nonlithophysal zone (Tpcpln) -hackly subzone (Tpcplnh) -columnar subzone (Tpcplnc) vitric zone (Tpcpv) -densely welded subzone (Tpcpv3)[c]	
	-moderately welded subzone (Tpcpv2) -nonwelded subzone (Tpcpv1)	Paintbrush nonwelded (PTn)
	pre-Tiva Canyon bedded tuff (Tpbt4)	
Yucca Mountain	Yucca Mountain Tuff (Tpy)	
Pah Canyon Tuff (Tpp)	Pah Canyon Tuff (Tpp)	
	pre-Pah Canyon bedded tuff (Tpbt2)	

Table 3-5. Comparison of Several Stratigraphic Subdivisions of Mid-Tertiary Volcanic Rocks at Yucca Mountain (Continued)

Lithostratigraphic Units[a,d,e,f]		Thermal-Mechanical Units[a,b]
Topopah Spring Tuff (Tpt)	crystal-rich member (Tptr) vitric zone (Tptrv) -nonwelded subzone (Tptrv3) -moderately welded subzone (Tptrv2)	Paintbrush nonwelded (PTn)
	-densely welded subzone (Tptrv1)	Topopah Spring welded, lithophysae-rich (TSw1)
	lithophysal zone (Tptrl)	
	crystal-poor member (Tptp) upper lithophysal zone (Tptpul) [upper part]	
Repository Host Horizon	upper lithophysal zone (Tptpul) [lower part]	
	middle nonlithophysal zone (Tptpmn)	Topopah Spring welded, lithophysae-poor (TSw2)
	lower lithophysal zone (Tptpll) lower nonlithophysal zone (Tptpln)	
	vitric zone (Tptpv)	Topopah Spring welded vitrophyre (TSw3)
	-densely welded subzone (Tptpv3) -moderately welded subzone (Tptpv2)	
	-nonwelded subzone (Tptpv1) pre-Topopah Spring bedded tuff (Tpbt1)	
Calico Hills (Tac)	Calico Hills Formation (Tac)	Calico Hills nonwelded (CHn)
	pre-Calico Hills bedded tuff (Tacbt)	

Source: CRWMS M&O 1997 [DIRS 103564], Table 2-1, p. 2-3, Table 3-1, p. 3-5

NOTES: [a] Buesch et al. 1996 [DIRS 100106].
          [b] Ortiz et al. 1985 [DIRS 101280].
          [c] Where preserved, the base of the crystal-poor densely welded subzone (Tpcpv3) forms the base of the TCw thermal-mechanical and hydrogeologic units (Buesch et al. 1996 [DIRS 100106]).
          [d] CRWMS M&O 1997 [DIRS 100223].
          [e] Moyer et al. 1995 [DIRS 103777].
          [f] Geslin et al. 1995 [DIRS 103330].

Table 3-6. Summary of Core Recovery Data for Topopah Spring Tuff Middle Nonlithophysal Zone

Boreholes	Core Logged (m)	Whole Core Recovered (m)	% of Total	Lost Core (m)	% of Total	Rubble Zones (m)	% of Total	Lost Core and Rubble (m)	% of Total
SD-7	36.6	21.2	57.9	3.9	10.7	11.5	31.4	15.4	42.1
SD-9	33.5	23.4	69.9	4.8	14.3	5.3	15.8	10.1	30.1
SD-12	39.6	27.4	69.2	3.5	8.8	8.7	22.0	12.2	30.8
NRG-6	30.5	21.8	71.5	2.7	8.9	6.0	19.7	8.7	28.5
NRG-7/7A	36.6	17.3	47.2	12.5	34.2	6.8	18.6	19.3	52.8
UZ-14	33.5	26.3	78.5	3.2	9.5	4.0	11.9	7.2	21.5
Total	210.3	137.4	65.3	30.6	14.5	42.3	20.1	72.9	34.7

SD-7 DTN: SNF29041993002.075 [DIRS 166433]; SD-9 DTN: SNF29041993002.076 [DIRS 166434]; SD-12
DTN: SNF29041993002.054 [DIRS 166435]; NRG#6 DTN: SNF29041993002.041 [DIRS 166436];
NRG#7a DTN: SNF29041993002.042 [DIRS 166437]; UZ-14 DTN: SNF29041993002.079 [DIRS 166438]

Source: CRWMS M&O 1997 [DIRS 103564], Table 2-2, p. 2-8

Table 3-7. Dry Bulk Density Summarized by Thermal-Mechanical Unit

Unit	Mean	Standard Deviation	Range	Number of Data
Undifferentiated Overburden	1.28	0.10	1.13 to 1.53	22
TCw	2.16	0.22	1.45 to 2.37	121
PTn	1.28	0.21	1.00 to 1.78	57
TSw1	2.16	0.08	1.94 to 2.40	176
TSw2	2.27	0.08	1.84 to 2.42	112
TSw3	2.35	0.00	2.34 to 2.35	4
CHn1	NA	NA	NA	NA

DTN: MO0312SEPSDDNP.000 [DIRS 166402]

Source: Modified from CRWMS M&O 1997 [DIRS 103564], Table 5-1, pp. 5-5 to 5-7

NOTES: All densities are given in grams per cubic centimeter (g/cm^3).
NA = Not Available.

Table 3-8. Saturated Bulk Density Summarized by Thermal-Mechanical Unit

Unit	Mean	Standard Deviation	Range	Number of Data
Undifferentiated Overburden	1.69	0.07	1.56 to 1.85	21
TCw	2.30	0.14	1.87 to 2.43	131
PTn	1.74	0.13	1.56 to 2.04	56
TSw1	2.30	0.05	2.12 to 2.46	176
TSw2	2.37	0.03	2.26 to 2.45	133
TSw3	2.36	0.01	2.35 to 2.37	6
CHn1	1.87	0.03	1.85 to 1.90	3

DTN: MO0312SEPSDDNP.000 [DIRS 166402]

Source: Modified from CRWMS M&O 1997 [DIRS 103564], Table 5-2, pp. 5-8 to 5-10

NOTE: All densities are given in grams per cubic centimeter (g/cm^3).

Table 3-9. Average Grain Density Summarized by Thermal-Mechanical Unit

Unit	Mean	Standard Deviation	Range	Number of Data
Undifferentiated Overburden	2.35	0.04	2.30 to 2.46	25
TCw	2.53	0.03	2.44 to 2.61	76
PTn	2.38	0.08	2.24 to 2.65	54
TSw1	2.55	0.02	2.50 to 2.60	124
TSw2	2.55	0.03	2.42 to 2.61	109
TSw3	2.37	0.01	2.37 to 2.38	3
CHn1	NA	NA	NA	NA

DTN: MO0312SEPSDDNP.000 [DIRS 166402]

Source: Modified from CRWMS M&O 1997 [DIRS 103564], Table 5-3, pp. 5-11 to 5-13

NOTES: All densities are given in grams per cubic centimeter (g/cm^3).
NA = Not Available.

Table 3-10. Porosity Summarized by Thermal-Mechanical Unit

Unit	Mean	Standard Deviation	Range	Number of Data
Undifferentiated. Overburden	45.2	3.7	35.2 to 51.0	25
TCw	14.2	9.5	4.8 to 44.5	121
PTn	46.7	8.4	27.9 to 59.4	64
TSw1	15.9	4.0	6.8 to 32.1	203
TSw2	11.3	3.0	3.8 to 27.7	143
TSw3	1.2	0.3	0.7 to 1.4	4
CHn1	NA	NA	NA	NA

DTN: MO0312SEPSDDNP.000 [DIRS 166402]

Source: Modified from CRWMS M&O 1997 [DIRS 103564], Table 5-4, pp. 5-14 to 5-16

NOTES: All porosities are given in percents (%).
NA = Not Available.

Table 3-11. Rock Thermal Conductivities at Temperatures below 100°C for Samples from Boreholes UE-25 NRG#4, UE-25 NRG#5, USW NRG-6, and USW NRG-7a

Thermal-Mechanical Unit	Thermal Conductivity (W/mK)											
	Saturated			Partially Saturated			Air Dry			Dry		
	Sample Mean	Sample Standard Deviation	Sample Count	Sample Mean	Sample Standard Deviation	Sample Count	Sample Mean	Sample Standard Deviation	Sample Count	Sample Mean	Sample Standard Deviation	Sample Count
TCw	1.89	0.12	18	1.39	0.56	18	1.58	0.16	9	1.17	0.35	18
PTn	0.92	0.13	42	0.57	0.12	33	0.35	0.13	12	0.38	0.10	49
TSw1	1.70	0.19	50	1.23	0.46	11	1.21	0.12	30	0.98	0.26	59
TSw2	2.29	0.42	51	ND	ND	ND	1.66	0.10	24	1.49	0.44	48

DTN: MO0312SEPSDRTC.000 [DIRS 166393]

Source: CRWMS M&O 1997 [DIRS 103564], Table 5-12, p. 5-49

NOTES: Sample refers to the number of test measurements, not the number of specimens tested. Measurements were made at multiple temperatures and during both heating and cooling for some specimens.
ND = No Data.

Table 3-12. Rock Thermal Conductivities at Temperatures above 100°C for Samples from Boreholes UE-25 NRG#4, UE-25 NRG#5, USW NRG-6, and USW NRG-7a

Thermal-Mechanical Unit	Thermal Conductivity (W/mK)		
	Dry		
	Sample Mean	Sample Standard Deviation	Sample Count
TCw	1.53	0.17	57
PTn	0.42	0.14	102
TSw1	1.15	0.15	173
TSw2	1.59	0.10	125

DTN: MO0312SEPSDRTC.000 [DIRS 166393]

Source: CRWMS M&O 1997 [DIRS 103564], Table 5-14, p. 5-50

NOTES: Sample refers to the number of test measurements, not the number of specimens tested. Measurements were made at multiple temperatures and during both heating and cooling for some specimens.

Table 3-13. Mean Coefficient of Thermal Expansion during Heat-Up for Samples from Boreholes UE-25 NRG#4, UE-25 NRG#5, USW NRG-7a, and USW SD-12

T/M Unit	Saturation State	Statistics	Mean Coefficient of Thermal Expansion on Heat-Up (10^{-6}/°C)										
			25-50°C	50-75°C	75-100°C	100-125°C	125-150°C	150-175°C	175-200°C	200-225°C	225-250°C	250-275°C	275-300°C
TCw	Saturated	Mean	7.09	7.62	8.08	10.34	13.17	15.20	16.99	18.99	21.38	27.42	42.99
		Std. Dev.	0.43	0.15	0.50	1.52	1.23	1.57	1.41	0.96	1.23	1.94	37.35
		Count	4	4	4	4	4	4	4	3	3	3	3
	Dry	Mean	6.60	8.29	9.62	10.53	12.69	14.90	17.03	20.68	29.64	36.49	49.15
		Std. Dev.	1.49	0.99	1.06	1.60	1.55	1.91	2.31	5.41	21.88	16.97	34.24
		Count	10	10	10	7	7	7	7	7	7	7	7
PTn			25-50°C	50-75°C	75-100°C	100-125°C	125-150°C	150-175°C	175-200°C	200-225°C	225-250°C	250-275°C	275-300°C
	Saturated	Mean	4.46	4.28	-1.45	-30.42	5.54	4.47	0.64	-4.65	-9.79	-13.46	-12.96
		Std. Dev.	0.38	1.61	3.63	21.47	0.41	0.79	1.03	4.05	7.85	11.12	12.90
		Count	4	4	4	4	3	3	3	2	2	2	2
	Dry	Mean	4.55	4.24	3.36	-4.78	6.46	5.69	3.61	0.56	-2.98	-5.81	-7.25
		Std. Dev.	0.74	1.46	2.40	11.12	0.98	1.41	2.58	5.81	9.12	11.36	10.80
		Count	12	12	12	10	10	10	10	10	10	10	10
TSw1			25-50°C	50-75°C	75-100°C	100-125°C	125-150°C	150-175°C	175-200°C	200-225°C	225-250°C	250-275°C	275-300°C
	Saturated	Mean	6.56	7.32	6.83	6.92	10.72	14.28	20.98	36.82	41.64	42.76	43.81
		Std. Dev.	1.16	0.60	1.60	3.28	1.74	3.26	7.01	20.49	17.35	13.19	13.65
		Count	10	10	10	10	10	9	9	8	8	8	8
	Dry	Mean	6.29	7.60	8.39	8.96	10.37	15.51	23.67	34.24	34.00	36.07	38.74
		Std. Dev.	1.22	1.02	0.89	1.20	1.38	4.53	11.07	20.30	13.70	13.23	13.78
		Count	33	33	33	28	28	27	26	25	25	25	25

Table 3-13. Mean Coefficient of Thermal Expansion during Heat-Up for Samples from Boreholes UE-25 NRG#4, UE-25 NRG#5, USW NRG-7a, and USW SD-12 (Continued)

T/M Unit	Saturation State	Statistics	Mean Coefficient of Thermal Expansion on Heat-Up (10^{-6}/°C)										
			25-50°C	50-75°C	75-100°C	100-125°C	125-150°C	150-175°C	175-200°C	200-225°C	225-250°C	250-275°C	275-300°C
TSw2	Saturated	Mean	7.14	7.47	7.46	9.07	9.98	11.74	13.09	15.47	19.03	25.28	37.19
		Std. Dev.	0.65	1.51	1.21	2.41	0.77	1.28	1.40	1.75	3.09	6.87	14.27
		Count	19	19	19	19	19	19	19	16	16	16	16
	Dry	Mean	6.67	8.31	8.87	9.37	10.10	10.96	12.22	14.52	20.79	25.13	35.13
		Std. Dev.	1.20	0.42	0.40	0.55	0.88	1.16	1.50	2.57	17.03	10.07	14.56
		Count	40	40	40	40	40	38	38	35	35	35	35

DTN: MO0312SEPSDCTE.000 [DIRS 166396]

Source: CRWMS M&O 1997 [DIRS 103564], Table 5-17, p. 5-58

NOTES: The negative coefficients of the thermal expansion are apparent and indicate that some samples were observed to contract in the temperature ranges containing the negative values. The contractions are interpreted as drying phenomena.

T/M = thermal-mechanical; Std. Dev. = standard deviation.

Table 3-14. Mean Coefficient of Thermal Expansion during Cool-Down for Samples from Boreholes UE-25 NRG#4, UE-25 NRG#5, USW NRG-7a, and USW SD-12

T/M Unit	Saturation State	Statistics	Mean Coefficient of Thermal Expansion on Cool-Down (10^{-6}/°C)										
			300-275°C	275-250°C	250-225°C	225-200°C	200-175°C	175-150°C	150-125°C	125-100°C	100-75°C	75-50°C	50-35°C
TCw	Saturated	Mean	14.72	21.97	33.53	37.01	23.81	18.48	15.72	13.51	12.09	10.78	10.85
		Std. Dev.	3.76	6.79	16.44	26.18	10.01	3.25	1.96	1.48	1.28	1.36	1.96
		Count	3	3	3	3	4	4	4	4	4	4	4
	Dry	Mean	17.46	26.34	36.95	33.72	22.86	17.58	13.89	11.77	10.21	9.35	6.59
		Std. Dev.	3.70	6.88	11.50	14.21	3.16	2.00	2.39	2.22	1.56	1.15	2.20
		Count	7	7	7	7	7	7	7	7	9	9	9
			300-275°C	275-250°C	250-225°C	225-200°C	200-175°C	175-150°C	150-125°C	125-100°C	100-75°C	75-50°C	50-35°C
PTn	Saturated	Mean	15.58	9.12	7.20	6.39	6.98	6.29	5.93	5.36	5.12	4.33	1.94
		Std. Dev.	1.04	0.84	0.29	0.17	1.51	0.78	0.47	0.36	0.34	0.84	2.93
		Count	2	2	2	2	3	3	3	4	4	4	4
	Dry	Mean	11.22	7.91	6.78	6.45	6.47	6.53	6.11	5.80	5.52	4.82	2.41
		Std. Dev	2.46	1.00	0.81	0.90	1.14	1.35	1.30	1.16	0.89	0.84	0.86
		Count	10	10	10	10	10	10	10	10	12	12	12
			300-275°C	275-250°C	250-225°C	225-200°C	200-175°C	175-150°C	150-125°C	125-100°C	100-75°C	75-50°C	50-35°C
TSw1	Saturated	Mean	15.07	19.87	24.05	26.15	27.57	26.66	28.19	19.89	11.46	9.92	9.35
		Std. Dev.	4.68	7.82	9.85	7.37	8.36	9.91	18.04	8.05	2.01	1.54	1.06
		Count	8	8	8	8	9	9	10	10	10	10	10
	Dry	Mean	16.68	20.71	24.16	23.26	26.74	25.34	25.55	17.78	10.53	9.22	6.95
		St. Dev.	4.13	7.78	10.61	7.29	9.32	9.35	14.94	8.53	2.15	1.51	2.49
		Count	25	25	25	25	26	27	28	28	33	33	33
			300-275°C	275-250°C	250-225°C	225-200°C	200-175°C	175-150°C	150-125°C	125-100°C	100-75°C	75-50°C	50-35°C
TSw2	Saturated	Mean	21.89	27.83	26.55	21.38	17.31	14.06	12.49	11.52	10.27	9.48	8.81
		Std. Dev	6.16	10.36	10.01	5.70	3.07	1.38	1.32	2.00	0.62	0.63	0.62
		Count	16	16	16	16	19	19	19	19	19	19	19
	Dry	Mean	20.57	24.31	24.20	21.16	18.45	14.34	11.74	10.51	9.54	8.87	7.48
		Std. Dev	4.88	7.55	8.08	6.24	9.36	4.23	3.03	2.26	1.79	1.56	1.99
		Count	35	35	35	35	38	38	40	40	40	40	40

DTN: MO0312SEPSDCTE.000 [DIRS 166396]

Source: CRWMS M&O 1997 [DIRS 103564], Table 5-18, p. 5-59

NOTE: T/M = thermal-mechanical; Std. Dev. = standard deviation.

Table 3-15. Thermal Capacitance for TSw1 and TSw2 Thermal-Mechanical Units

TSw1				TSw2			
Temperature (°C)	Mean : ρCp (J/cm^{3}K)	Standard Deviation (J/cm^{3}K)	No. Of Tests	Temperature (°C)	Mean ρCp (J/cm^{3}K)	Standard Deviation (J/cm^{3}K)	No. of Tests
25	1.58	0.05	3	25	1.79	0.11	7
50	1.68	0.05	3	50	1.88	0.11	7
75	1.80	0.05	3	75	1.97	0.11	7
100	1.91	0.05	3	100	2.16	0.11	7
125	2.03	0.06	3	125	2.32	0.11	7
150	2.14	0.11	3	150	2.45	0.13	7
175	2.13	0.10	3	175	2.43	0.18	7
200	2.09	0.07	3	200	2.40	0.16	7
225	2.07	0.06	3	225	2.39	0.17	7
250	2.05	0.05	3	250	2.39	0.19	7
275	2.03	0.05	3	275	2.39	0.22	7
300	2.03	0.06	3	300	2.43	0.26	7

DTN: MO0312SEPSDTCP.000 [DIRS 166395]

Source: CRWMS M&O 1997 [DIRS 103564], Table 5-21, p. 5-67

NOTE: ρCp = thermal capacitance.

Table 3-16. Mean and Standard Deviation of Intact Young's Modulus for Thermal-Mechanical Units and Lithostratigraphic Units

Thermal-Mechanical Unit	Lithostratigraphic Unit	Elastic (Young's) Modulus[a]	
		Mean (GPa)	Std. Dev. (GPa)
Undifferentiated		3.9	1.9
	Tmr	3.4	2.7
	Tpki	4.3	0.8
	Tpbt5	ND	ND
TCw		29.4	10.8
	Tpcrv	ND	ND
	Tpcrn	15.2	8.4
	Tpcpul	23.7	6.9
	Tpcpmn	35.0	7.4
	Tpcpll	34.3	5.2
	Tpcpln	34.3	7.7
PTn		2.5	4.0
	Tpcpv	7.2	7.6
	Tpbt4	1.8	1.1
	Tpy	5.2	3.1
	Tpbt3	0.3	0.1
	Tpp	1.1	0.6
	Tpbt2	0.8	0.6
	Tptrv	0.9	0.9
TSw1		20.4	6.8
	Tptrn	20.7	6.3
	Tptrl	10.5	3.3
	Tptpul	21.4	8.5
TSw2		33.0	5.9
	Tptpmn	32.9	5.5
	Tptpll	27.5	7.5
	Tptpln	35.5	5.5
TSw3		37.4	15.0
	Tptpv	37.4	15.0
CHn		5.6	1.6
	Tpbt1	3.9	ND
	Tac	6.5	0.6

DTN: MO0312SEPSDPYM.000 [DIRS 166394]

Source: CRWMS M&O 1997 [DIRS 103564], Table 2-7, p. 2-21

NOTES: [a] quasi-static.

Std. Dev. = standard deviation; ND = No Data.

Table 3-17. Mean and Standard Deviation of Intact Rock Poisson's Ratio for Thermal-Mechanical Units and Lithostratigraphic Units

Thermal-Mechanical Unit	Lithostratigraphic Unit	Poisson's Ratio[a]	
		Mean	Standard Deviation
Undifferentiated		0.09	0.07
	Tmr	0.03	0.03
	Tpki	0.14	0.05
	Tpbt5	ND	ND
TCw		0.21	0.11
	Tpcrv	ND	ND
	Tpcrn	0.20	0.03
	Tpcpul	0.19	0.02
	Tpcpmn	0.27	0.29
	Tpcpll	0.21	0.05
	Tpcpln	0.21	0.02
PTn		0.23	0.17
	Tpcpv	0.11	0.06
	Tpbt4	0.34	0.40
	Tpy	0.16	0.01
	Tpbt3	0.24	0.06
	Tpp	0.29	0.12
	Tpbt2	0.23	0.09
	Tptrv	0.21	0.08
TSw1		0.23	0.07
	Tptrn	0.23	0.06
	Tptrl	0.29	0.02
	Tptpul	0.25	0.13
TSw2		0.21	0.04
	Tptpmn	0.21	0.03
	Tptpll	0.21	0.06
	Tptpln	0.24	0.05
TSw3		0.24	0.13
	Tptpv	0.24	0.13
CHn		0.17	0.12
	Tpbt1	0.11	ND
	Tac	0.20	0.16

DTN: MO0312SEPSDPYM.000 [DIRS 166394]

Source: CRWMS M&O 1997 [DIRS 103564], Table 2-8, p. 2-22

NOTES: [a] quasi-static.
          ND = No Data.

Table 3-18. Comparison of the Mean and Standard Deviation of Compressional and Shear Wave Velocities on Dry Specimens (NRG and SD Boreholes)

Thermal-Mechanical Unit	TCw	TCw	PTn	PTn	TSw1	TSw1	TSw2	TSw2
Wave Type	P	S	P	S	P	S	P	S
Mean Velocity (km/s)	4.37	2.81	2.69	1.90	3.74	2.35	4.16	2.79
Standard Deviation	0.49	0.13	0.70	0.31	0.39	0.20	0.67	0.11
Range (Min.-Max.)	2.87-4.79	2.35-3.01	1.54-3.75	1.37-2.46	2.77-4.63	2.05-2.93	2.67-4.71	2.41-3.01
Number of Samples	66	42	11	11	57	38	50	47

DTN: MO0312SEPSDCSW.000 [DIRS 166404]

Source: CRWMS M&O 1997 [DIRS 103564], Table 5-29, p. 5-97

NOTE: P = compression; S = shear.

Table 3-19. Mean and Standard Deviation of Uniaxial Compressive Strength for Thermal-Mechanical and Lithostratigraphic Units

Thermal-Mechanical Unit	Lithostratigraphic Unit	Uniaxial Compressive Strength Mean (MPa)	Standard Deviation (MPa)
Undifferentiated Overburden		7.1	4.9
	Tmr	7.6	7.5
	Tpki	6.8	1.8
	Tpbt5	ND	ND
TCw		127.5	92.7
	Tpcrv	ND	ND
	Tpcrn	36.0	33.0
	Tpcpul	62.1	26.5
	Tpcpmn	167.2	64.1
	Tpcpll	230.9	105.3
	Tpcpln	172.3	58.1
PTn		6.4	7.0
	Tpcpv	16.6	19.8
	Tpbt4	3.5	1.74
	Tpy	19.3	7.0
	Tpbt3	1.3	0.7
	Tpp	3.4	2.3
	Tpbt2	3.1	2.1
	Tptrv	3.5	2.0
TSw1		58.2	30.7
	Tptrn	59.0	28. 3
	Tptrl	26.7	9.3
	Tptpul	65.2	44.4
TSw2		167.9	65.5
	Tptpmn	187.5	64.9
	Tptpll	103.8	60.7
	Tptpln	144.4	39.6
TSw3		16.4	ND
	Tptpv	16.4	ND
CHn		23.2	3.0
	Tpbt1	20.5	ND
	Tac	24.6	2.7

DTN: MO0312SEPSDUAT.000 [DIRS 166398]

Source: Modified from CRWMS M&O 1997 [DIRS 103564], Table 2-9, p. 2-23

NOTE: ND = No Data.

Table 3-20. Brazilian Tensile Strength for Thermal-Mechanical and Lithostratigraphic Units

Thermal-Mechanical Unit	Lithostratigraphic Unit	Brazilian Tensile Strength	
		Mean (MPa)	Standard Deviation (MPa)
Undifferentiated Overburden		0.88	0.72
	Tmr	1.23	1.27
	Tpki	0.70	0.24
	Tpbt5	ND	ND
TCw		8.88	3.66
	Tpcrv	ND	ND
	Tpcrn	5.23	2.80
	Tpcpul	9.63	0.73
	Tpcpmn	10.10	4.75
	Tpcpll	12.20	4.39
	Tpcpln	11.00	1.75
PTn		0.66	1.17
	Tpcpv	2.64	2.04
	Tpbt4	0.3	ND
	Tpy	3.00	ND
	Tpbt3	0.10	ND
	Tpp	0.19	0.19
	Tpbt2	0.35	0.31
	Tptrv	0.1	ND
TSw1		5.48	2.32
	Tptrn	5.49	2.09
	Tptrl	4.81	1.36
	Tptpul	5.69	3.06
TSw2		8.91	3.39
	Tptpmn	11.56	3.80
	Tptpll	8.29	2.99
	Tptpln	7.75	2.59
TSw3		3.97	0.32
	Tptpv	3.97	0.32
CHn		ND	ND
	Tpbt1	ND	ND
	Tac	ND	ND

DTN: MO0312SEPSDUAT.000 [DIRS 166398]

Source: CRWMS M&O 1997 [DIRS 103564], Table 2-11, p. 2-25

NOTE: ND = No Data.

Table 3-21. Average Fracture Normal Stiffness at 2.5-Megapascal Normal Stress for Each of the Four Thermal-Mechanical Units Sampled

Thermal-Mechanical Unit	Normal Stiffness at 2.5 MPa[a] (MPa/mm)	Number of Tests
TCw	37.3 ± 4.0	2
TSw1	50.1 ± 17.6	16
TSw2	73.5 ± 38.2	11
CHn1	47.7 ± 5.4	4

DTN: MO0312SEPSDBCT.000 [DIRS 166403]

Source: CRWMS M&O 1997 [DIRS 103564], Table 5-39, p. 5-143

NOTE: [a] Uncertainty is indicated as ± one standard deviation.

Table 3-22. Average Shear Strength Parameters for Fractures from Each of the Four Thermal-Mechanical Units Sampled

Thermal-Mechanical Unit	Cohesion (C)[a] (Mpa)	Coefficient of Friction[a] (tan ϕ)	Number of Tests
TCw	0.03 ± N/A	1.03 ± N/A	2
TSw1	1.63 ± 0.68	0.76 ± 0.08	16
TSw2	0.86 ± 0.81	0.87 ± 0.09	12
CHn1	1.69 ± 1.55	0.78 ± 0.25	4

DTN: MO0312SEPSDBCT.000 [DIRS 166403]

Source: CRWMS M&O 1997 [DIRS 103564], Table 5-40, p. 5-143

NOTE: [a] Uncertainty is indicated as ± one standard deviation.
N/A = not applicable.

Table 3-23. Peak Shear Stress, Residual Shear Stress, and Applied Normal Stress for Fractures

Thermal-Mechanical Unit	Lithologic Unit	Specimen ID Number	σ (MPa)	τp (MPa)	τr (MPa)
TCw	Tpcpll	NRG-6-27.6-28.1-SNL	5.0	5.16	4.93
	Tpcplnc	NRG-6-102.9-103.4-SNL	15.0	15.46	10.20
TSw1	Tptrl	NRG-4-670.5-671.1-SNL	2.5	3.49	2.59
	Tptrn	NRG-6-380.9-381.3-SNL	2.5	3.68	2.95
	Tptpmn	SD-12-688.2-688.6-SNL	2.5	3.62	3.31
	Tptrn	NRG-4-537.8-538.2-SNL	5.0	5.48	5.21
	Tptrn	NRG-4-608.7-609.2-SNL	5.0	4.44	4.17
	Tptrn	NRG-6-297.4-297.7-SNL	5.0	5.16	5.01
	Tptrn	NRG-6-424.0-424.5-SNL	5.0	5.28	3.98
	Tptrn	NRG-7-367.2-367.8-SNL	5.0	6.47	4.2
	Tptrn	NRG-7-408.8-409.6-SNL	5.0	4.18	3.71
	Tptrn	NRG-6-296.0-296.4-SNL	10.0	11.89	6.59
	Tptrn	NRG-6-401.5-401.9-SNL	10.0	11.10	7.84
	Tptpul2	NRG-6-485.9-486.3-SNL	10.0	10.19	7.82
	Tptrn	NRG-7-434.7-435.3-SNL	10.0	6.85	6.02
	Tptrn	NRG-7-447.2-448.1-SNL	10.0	9.45	5.41
	Tptrn	NRG-7-317.3-317.8-SNL	15.0	11.50	10.70
	Tptrn	NRG-7-430.2-430.9-SNL	15.0	13.26	9.09
TSw2	Tptpmn	NRG-6-782.3-782.6-SNL	2.5	1.92	1.80
	Tptpln	SD-9-1255.9-1256.3-SNL	2.5	2.37	2.29
	Tptpln	SD-12-1072.5-1073.0-SNL	2.5	3.31	2.67
	Tptpll	SD-9-1132.2-1132.9-SNL	5.0	5.45	4.53
	Tptpll	SD-9-1171.1-1171.8-SNL	5.0	5.48	4.81
	Tptpln	SD-12-1072.5-1073.0-SNL	5.0	6.62	5.23
	Tptpln	SD-9-1254.7-1255.2-SNL	10.0	7.68	7.10
	Tptpln	SD-9-1254.7-1255.2-SNL	10.0	8.97	8.34
	Tptpmn	SD-12-778.1-780.0-SNL	10.0	12.00	10.38
	Tptpll	NRG-6-935.0-935.3-SNL	15.0	11.89	8.56
	Tptpll	SD-9-1141.2-1141.5-SNL	15.0	14.00	14.0
	Tptpll	SD-9-1144.2-1145.1-SNL	15.0	15.50	10.2
CHn1	Tac	SD-9-1480.7-1481.8-SNL	2.5	3.52	2.89
	Tac	SD-9-1480.7-1481.8-SNL	5.0	4.35	3.66
	Tac	NRG-7-1511.3-1512.0-SNL	5.0	7.03	4.81
	Tac	SD-9-1480.7-1481.8-SNL	10.0	9.45	5.46

DTN: MO0312SEPSDPRA.000 [DIRS 166397]

Source: CRWMS M&O 1997 [DIRS 103564], Table 5-41, p. 5-144

NOTE: σ = normal stress; τp = peak shear stress; τr = residual shear stress.

Table 3-24. Geomechanical Classification of Rock Masses Based on Rock-Mass Rating

Rock-Mass Class	Relative Rating	Range in Rock-Mass Rating
I	very good	81 - 100
II	good	61 - 80
III	fair	41 - 60
IV	poor	21 - 40
V	very poor	<20

Source: CRWMS M&O 1997 [DIRS 103564], Table 6-1, p. 6-3

NOTE: Classification guidelines are from Bieniawski (1989 [DIRS 101715]).

Table 3-25. Summary of Rock-Mass Quality Values

Thermal-Mechanical Unit	Rock-Mass Quality Category	Cumulative Frequency	Rock-Mass Rating (RMR)			Rock-Mass Quality (Q)			$Q_{modified}$ (Kirsten Approach)	
			NRG Borehole[a]	Scanline	Full-Peripheral	ESF Design[b] (NRG Boreholes)	Scanline[c]	Full-Peripheral[c]	Scanline[c]	Full-Peripheral[c]
TCw	1	5%	51.00	47.00	43.00	0.38	0.21	0.33	0.99	0.46
	2	20%	56.00	53.80	54.00	0.68	0.44	0.81	2.35	2.27
	3	40%	59.00	58.80	60.00	2.08	1.01	1.80	4.96	4.39
	4	70%	67.00	66.60	66.00	5.66	5.22	4.15	18.12	9.60
	5	90%	72.00	74.10	74.00	9.14	38.44	14.50	67.78	22.24
UO	1	5%	50.40	48.90	51.00	ND	5.03	2.00	7.79	3.90
	2	20%	52.90	62.60	59.00	ND	18.67	16.00	8.62	7.19
	3	40%	55.88	66.70	64.00	ND	30.00	24.00	12.55	9.69
	4	70%	59.42	72.60	86.00	ND	38.00	33.00	15.84	14.58
	5	90%	60.00	87.00	86.00	ND	625.00	42.00	244.64	17.36
PTn	1	5%	45.00	53.70	56.00	0.15	1.54	1.28	0.52	0.32
	2	20%	52.00	61.20	61.00	0.28	5.56	4.20	1.11	0.70
	3	40%	55.00	71.10	70.00	0.66	7.80	9.00	2.30	0.98
	4	70%	65.00	74.00	77.00	1.62	13.11	13.00	10.59	1.43
	5	90%	70.00	87.00	80.00	3.74	616.88	25.00	41.97	3.50
TSw1	1	5%	49.00	48.10	41.00	0.24	0.38	0.48	1.35	0.77
	2	20%	53.00	55.10	48.00	0.87	2.07	1.60	5.78	2.59
	3	40%	57.00	61.40	54.00	1.73	5.13	3.70	13.55	4.79
	4	70%	62.00	74.10	63.00	5.09	31.90	10.00	67.00	9.66
	5	90%	70.00	92.00	70.00	12.00	231.50	22.00	372.90	18.34

Table 3-25. Summary of Rock-Mass Quality Values (Continued)

Thermal-Mechanical Unit	Rock-Mass Quality Category	Cumulative Frequency	Rock-Mass Rating (RMR)			Rock-Mass Quality (Q)				
			NRG Borehole[a]	Scanline	Full-Peripheral	ESF Design[b] (NRG Boreholes)	Scanline[c]	Full-Peripheral[c]	Q$_{modified}$ (Kirsten Approach)	
									Scanline[c]	Full-Peripheral[c]
TSw2	1	5%	51.00	53.00	44.00	0.30	0.55	0.47	3.26	0.82
	2	20%	56.00	58.10	52.00	0.65	1.18	1.03	6.22	1.90
	3	40%	58.00	62.10	56.00	1.91	2.78	1.70	11.46	3.43
	4	70%	63.00	66.10	62.00	3.75	6.18	4.10	25.47	6.99
	5	90%	67.00	72.10	68.00	8.44	16.28	9.30	56.14	15.07

DTN: MO0312SEPSDRRQ.000 [DIRS 166400]

Source: CRWMS M&O 1997 [DIRS 100930], Table 11, p. 72

NOTES: [a] From SNL 1995 [DIRS 106851].
[b] From CRWMS M&O 1995 [DIRS 101427].
[c] Values of Q are extracted from rank-ordered intervals whose cumulative frequency is closest to the corresponding Q category cumulative frequency.
ND = No Data.

Table 3-26. Exploratory Studies Facility Ground-Support Guidelines

Ground-Support Class	Range of Q for Ground-Support Class	Exploratory Studies Facility Ground-Support Recommendation
V	0.01-0.1	W8 steel sets, spaced 610 mm, with full lagging.
IV	0.1-0.4	W8 steel sets, spaced 610 to 1220 mm, with WWF and lagging as necessary.
III	0.4-4.0	Rock-bolts nominal 1,000 × 1,000 mm spacing with WWF. Spot bolt as necessary. Plus 100 to 150 mm shotcrete.[a] (Class III-A Alternative: W6 steel sets, spaced 1,220 mm, with WWF and partial lagging as needed).
II	4.0-10.0	Rock-bolts nominal 1,000 × 1,000 mm spacing, with WWF. Spot bolt as necessary. Pins and channel may be used to secure mesh as needed. (Class II-A Alternative: W6 steel sets, spaced 1,220 mm with WWF.)
I	>10.0	Rock-bolts nominal 1,500 × 1,500 mm spacing, with WWF. Spot bolt as necessary. Pins and channel may be used to secure mesh as needed. (Class I-A Alternative: W6 steel sets, spaced 1,220 to 1,800 mm with WWF.)

Source: CRWMS M&O 1997 [DIRS 103564], Table 6-18, p. 6-59

NOTES: [a] Although shotcrete was called for by design, shotcrete was not used, except in the starter tunnel. WWF = welded wire fabric or interlocking steel mesh.

Table 3-27. Estimated Rock-Mass Mechanical Properties for Rock-Mass Rating at 40 Percent Cumulative Frequency of Occurrence for Each Thermal-Mechanical Unit

Rock-Mass Mechanical Property	Thermal-Mechanical Unit				
	UO	TCw	PTn	TSw1	TSw2
Strength = $A+B\sigma_3^{\ c}$					
Uniaxial Compressive Strength:A (MPa)	0.88	14.4	1.51	6.4	25.4
B	12.018	14.337	9.585	9.271	23.687
C	0.729	0.709	0.719	0.712	0.571
Mohr-Coulomb Failure					
Cohesion (MPa)	1.1	5.5	1.3	3.3	8.9
Angle of Internal Friction (deg)	52	55	48	47	59
Dilation Angle (deg)	26	27	24	24	30
Deformation Modulus (GPa)	4.3	25.7	2.5	18.9	31.1
Poisson's Ratio	0.14	0.21	0.2	0.26	0.21

DTN: MO0312SEPSDRMP.000 [DIRS 166399]

Source: CRWMS M&O 1997 [DIRS 103564], Table 2-15, p. 2-31

Table 3-28. Intact Rock Constants for Rock-Mass Strength Criteria

Thermal-Mechanical Unit		Yudhbir Criterion		Hoek and Brown Criterion	Intact Rock Compressive (MPa)
		B	α	mi	σc
UO (Tuff "X")		8.10	1.00	125.64	6.8
TCw		2.50	0.64	18.50	125.1
PTn	Tiva Canyon, Yucca Mountain	4.56	1.00	17.64	8.0
	Bedded- Tuffs, Pah Canyon	6.10	1.00	150.97	
TSw1		2.62	0.663	10.60	56.9
TSw2		1.63	43	19.68	178.5

DTN: MO0312SEPSDIRC.000 [DIRS 166401]

Source: CRWMS M&O 1997 [DIRS 103564], Table 7-2, p. 7-4

Table 3-29. Summary of In Situ Stresses at the Repository Horizon

Hydraulic Fracturing Measurements				
	DTN: SN0308F3710195.003 [DIRS 166458]		DTN: SNF37100195002.001 [DIRS 131356]	
Parameter	Value		Value	
Vertical Stress	4.3 to 4.7 Mpa		NM	
Minimum Horizontal Stress	2.1 Mpa	+/- 0.1 Mpa	1.7 Mpa	+/- 0.1 Mpa
Maximum Horizontal Stress	3.5 Mpa	+/- 0.1 Mpa	2.9 Mpa	+/- 0.4 Mpa
Bearing of Minimum Horizontal Stress	N65°W	+/- 15°	N75°W	+/- 14°
bearing of Maximum Horizontal Stress	N25°E	+/- 15°	N15°E	+/- 14°
Historical Estimate of In Situ Stress Conditions [a]				
Parameter	Average Value	Range of Values		
Vertical Stress	7.0 Mpa	5.0 - 10.0 MPa		
Minimum Horizontal/Vertical Stress Ratio	0.5	0.3 - 0.8		
Maximum Horizontal/Vertical Stress Ratio	0.6	0.3 - 1.0		
Bearing of Minimum Horizontal Stress	N57°W	N50°W - N65°W		
Bearing of Maximum Horizontal Stress	N32°E	N25°E - N40°E		

DTNs: SN0308F3710195.003 [DIRS 166458]; SNF37100195002.001 [DIRS 131356]

Source: [a] CRWMS M&O 1997 [DIRS 103564], Table 3-2, p. 3-23

NOTE: NM = Not Measured.

4. TECTONICS AND TECTONIC HAZARDS

Tectonic deformation in the Yucca Mountain region has resulted in local disruptive events that include faulting and basaltic volcanism. Because the regional tectonic setting of Yucca Mountain (i.e., the Great Basin) presently is undergoing deformation, faulting is likely to occur and volcanism may occur near Yucca Mountain in the future. Section 4.1 discusses the utilization and evaluation of tectonic models for Yucca Mountain and its setting, Section 4.2 summarizes knowledge of volcanic events and volcanic hazards, and Section 4.3 covers seismicity and seismic hazards relevant to Yucca Mountain.

4.1 TECTONICS AND TECTONIC MODELS: INTRODUCTION

A tectonic model represents the geologic structure of a portion of the Earth's crust and illustrates how the structural assemblage has evolved through time. A tectonic model incorporates the geometry of and the spatial relations among structures such as faults, and the mechanisms by which structures interact and respond to regional stress. The model seeks to demonstrate the relations among processes of deformation that are driven by long-term crustal stresses (i.e., extension) and heat flow. Tectonic models for Yucca Mountain and its geologic setting attempt to explain observed geologic structure and geophysical data in light of the history of volcanism and fault movement, uplift and subsidence, and lateral extension. By integrating known properties and behavior of rocks under stress, a tectonic model can show, at least conceptually, how Yucca Mountain might continue to evolve within the current tectonic setting.

Tectonic models can be expressed in various ways (e.g., physical, mathematical). The following treatment presents conceptual models that are illustrated by maps and cross sections. A conceptual tectonic model reconstructs the evolution of deformation based on field and instrumental (e.g., geophysical, geochemical) observations rather than on quantified parameters. As such, conceptual models offer considerable flexibility and accessibility.

4.1.1 Model Elements

Model elements are aspects of the real world that are addressed by the model. These may also be considered as model constraints. An adequate conceptual tectonic model for Yucca Mountain incorporates the following elements:

Physical Extent–The regional setting in which deformation occurs and the space within which the model applies. This section considers an area within a 100-km (62-mi) radius of Yucca Mountain and a depth of at least 15 km (9 mi). The specific tectonic components relevant to Yucca Mountain comprise the tectonic domain (i.e., the Crater Flat domain).

System Geometry–The shape, orientation, and distribution of tectonic features (e.g., fault and block geometry, volcanic vent distribution).

Boundary Conditions–Bounding structures and stresses at the boundary of the model, character and activity of bounding faults, and bulk physical properties of rock and behavior under stress and heat. Bounding structures define the tectonic domain, as well as its regional setting.

Application of Stress–Stress imposed by crustal motion, chiefly extensional stresses that generate the system geometry and its structural features and that account for timing, magnitude, and distribution of disruptive events.

System Response–Distribution and character of extensional effects including strain rates (fault slip) and volcanism, and other deformation (e.g., fault interactions, rupture patterns, distribution of seismic potential effects on groundwater flow and water table elevation).

Yucca Mountain is located within the Crater Flat domain (see Section 3.5.11). Discussion of the model elements of this domain is contained in the following section.

4.1.1.1 Physical Extent

The Crater Flat Domain–The Crater Flat domain is the structurally defined volume of crust within which Yucca Mountain has evolved and presently experiences tectonic deformation (Fridrich 1999 [DIRS 118942], p. 170, Figure 4-1). The Crater Flat domain is characterized chiefly by a system of closely spaced west-dipping normal faults that are best exposed across Yucca Mountain. The faults are described in detail in Section 3.5. Cumulative down-to-the-west displacement across Yucca Mountain has created a basin partly filled by alluvium, called Crater Flat. The normal fault system in Crater Flat is buried by alluvium, but is partly exposed at the northern and southern ends of the basin. The westernmost of the west-dipping faults observed at the surface are the Crater Flat fault (Section 3, Figure 3-20) and an extension, the West Lava fault (Ramelli et al. 1988 [DIRS 106632]). Even though the normal fault system probably extends eastward beneath Jackass Flats, the domain is bounded by the Gravity fault (Figure 4-1).

The northern boundary of the Crater Flat domain is marked by a transition from systematic down-to-the-west normal faults to the southern margin of the Claim Canyon caldera (Minor et al. 1997 [DIRS 100997], p. 8, Figure 4-1).

The southern end of the Crater Flat domain is marked by scarp exposures of a north-dipping, fault-dissected cuesta that dips into Crater Flat basin and the southern termini of ridges bounded by southern extensions of the Fatigue Wash and Paintbrush Canyon faults (Figure 4-1).

Bare Mountain Fault–The western boundary of Crater Flat (and Crater Flat domain) is marked by the Bare Mountain range front, which approximately defines the trace of an east-dipping range front fault, the Bare Mountain fault (Figure 4-1). The deep seismic reflection profile (Crater Flat seismic profile track, Figure 4-1) (Brocher et al. 1998 [DIRS 100022], p. 956) indicates that the southern end of the Bare Mountain fault dips about 65° east to a depth of about 3.5 to 6 km (2 to 4 mi). The fault cannot be projected deeper than 6 km because it is not imaged in the seismic data (Brocher et al. 1998 [DIRS 100022], p. 959). The Bare Mountain fault has been interpreted as both a single, large displacement fault and as a series of faults. Faults synthetic to Bare Mountain fault have been reported from 0.5 to 2 km (0.3 to 1.2 mi) east of it in Crater Flat (Fridrich 1999 [DIRS 118942], p. 176). The Bare Mountain fault has been active in the Pleistocene (Anderson and Klinger 1996 [DIRS 101420], p. 4.12-67) and has shown oblique dextral displacement near the southern end of Bare Mountain where the Bare Mountain fault curves to a northwest strike (Fridrich 1999 [DIRS 118942], p. 177).

Eastern Structural Boundary of Crater Flat Domain–No well-defined structure marks the eastern margin of the Crater Flat domain, but it is clear that the domain boundary lies west of the Striped Hills and western flank of Little Skull Mountain (Figure 4-1), which exhibit structures not found at Yucca Mountain. A feature identified by gravity surveys, and referred to as the Gravity fault (Winograd and Thordarson 1975 [DIRS 101167], p. C-75), is part of the eastern domain boundary. It is inferred to be a normal fault having down-to-the-west displacements ranging from 150 m (500 ft) to about 1,000 m (3,200 ft). It strikes north beneath surficial deposits along the west side of the Striped Hills (Figure 4-1). The footwall includes the east-striking Striped Hills and Little Skull Mountain. The Gravity fault cannot be traced north of Little Skull Mountain using gravity or aeromagnetic data; therefore, the northeastern boundary of the Crater Flat domain is uncertain.

4.1.1.2   System Geometry

Yucca Mountain Fault System–In general, the faults of Yucca Mountain comprise two major populations: a block-bounding set of west-dipping normal faults that extends into the pre-Tertiary basement that floors the Crater Flat structural basin, and a secondary set that includes northwest-striking and intrablock faults that splay from and/or connect the block-bounding faults (Day et al. 1996 [DIRS 124302], p. 2-2). A third minor population comprises fractures and small faults resulting from cooling and alteration of the bedrock shortly after its deposition by volcanic eruption. The exposed rocks of Yucca Mountain were extended west-northwestward by as much as 40 percent during middle and late Miocene time (Fridrich et al. 1999 [DIRS 107333], p. 197) by normal faulting. The extension apparently began prior to deposition of the Tiva Canyon Tuff (Fridrich 1999 [DIRS 118942], p. 189; Scott 1990 [DIRS 106751], p 268). Major faulting and tilting occurred between the eruptions of the Tiva Canyon Tuff (12.7 Ma) and Rainier Mesa Tuff (11.6 Ma) (Day et al. 1998 [DIRS 100027], pp. 17 to 18).

The relationship of Yucca Mountain faults to faults in the Paleozoic/Precambrian basement is uncertain. Block-bounding faults, such as the Solitario Canyon and Paintbrush Canyon faults (Figure 4-1), penetrate deeply into the basin. Evidence for deep penetration includes relatively high groundwater temperatures measured in wells close to these faults, suggesting upward leakage of warm groundwater from the deep carbonate aquifer (Sass et al. 1995 [DIRS 101288], p. 165). Another indication of deep penetration of the Solitario Canyon fault is the presence of a basalt dike approximately 10 Ma (Carr and Parrish 1985 [DIRS 101093], p. 30) located along part of the fault plane exposed in trench 10 (see location T10 in CRWMS M&O 2000 [DIRS 151945], Figure 4.4-3), where it is offset by the fault.

Structure of Crater Flat–Crater Flat has the structure of a half-graben controlled by the Bare Mountain fault. Because it is covered by alluvium, the structure of Crater Flat is largely inferred from geophysical data and exposures in the surrounding hills. Isostatic gravity maps and profiles (McCafferty and Grauch 1997 [DIRS 104768]; Healey et al. 1987 [DIRS 106118]; Snyder and Carr 1982 [DIRS 106876], Plate 1) show that Crater Flat is underlain by a structural basin about 4 km deep (Blakely et al. 1999 [DIRS 149763], p. 12). Seismic and gravity data indicate that the Crater Flat basin is deepest on the west side (Snyder and Carr 1984 [DIRS 106877], Plate 1; Majer et al. 1996 [DIRS 104685], pp. 45 and 46; Brocher et al. 1996 [DIRS 101495], p. 31). A deep seismic reflection profile (Crater Flat Seismic Profile, Figure 4-1) shows that Crater Flat

structural basin is asymmetric, deepening westward toward the Bare Mountain fault (Brocher et al. 1998 [DIRS 100022], p. 960, Figure 10). This conclusion is supported by the general westward thickening of units exposed along the basin's southern and northern margins (Fridrich 1999 [DIRS 118942], p. 177). There is some evidence of a low longitudinal arch near the basin axis, a feature interpreted as a rollover above the Bare Mountain fault (Faulds et al. 1994 [DIRS 105126]). A narrow zone (0.5 to 2 km [0.3 to 1.2 mi]) along the basin's westernmost edge contains east-dipping faults (Fridrich 1999 [DIRS 118942], p. 176).

The Crater Flat structural basin widens and deepens northward toward the Timber Mountain/Claim Canyon caldera complex (Blakely et al. 1999 [DIRS 149763], p. 11). The caldera complex appears to be a large intrusive/extrusive igneous mass emplaced within a basement trough several kilometers deep. North of the caldera complex, the pattern and style of normal faults expressed in Pahute Mesa are aligned with the fault pattern of the Crater Flat domain, suggesting a link between the two areas (Figure 4-2) (Carr 1990 [DIRS 104669], pp. 291 and 293). The pre-Timber Mountain Group volcanics (12.7 Ma) are tilted northeastward 2° to 4° in the subsurface of Pahute Mesa (Warren et al. 1985 [DIRS 107171], p. 6). The Rainier Mesa Tuff (11.6 Ma) is considerably thicker across down-to-the-west faults on the western side of Pahute Mesa than it is on the east side, indicating greater extension toward the west in the 12.7 to 11.6 Ma interval (Fridrich 1998 [DIRS 101098], p. 15). Fault offsets in the Rainier Mesa Tuff also increase from east to west across Pahute Mesa, similar to the pattern of increase to the west seen in the Crater Flat domain (Fridrich 1998 [DIRS 101098], p. 15). Fault activity at Pahute Mesa declined after the 11.6-Ma volcanic pulse, as is true in Crater Flat (Fridrich 1998 [DIRS 101098], p. 16). The similarities of fault style, attitude, and timing suggest a common genetic relationship that has been attributed to extension localized within the Kawich-Greenwater rift (Carr 1990 [DIRS 104669], pp. 284 and 286) (Figure 4-3).

Vertical Axis Rotation–Changes in strike, dip, and displacement of faults at Yucca Mountain indicate increasing crustal extension toward the south (Fridrich et al. 1999 [DIRS 107333], p. 208). Paleomagnetic data (Rosenbaum et al. 1991 [DIRS 106708], p. 1964; Hudson et al. 1994 [DIRS 100986], p. 270) show that toward the south, Yucca Mountain has been progressively rotated clockwise 25° to 30° following deposition of the Tiva Canyon Tuff (12.7 Ma). Virtually no rotation has occurred at the north end of Yucca Mountain.

Vertical axis rotation appears to have begun approximately 11.6 Ma (Minor et al. 1997 DIRS 100997], p. 20). The cause of late Miocene vertical axis rotation is uncertain. It has been ascribed to dextral shear at or near the south end of Yucca Mountain (Sonder et al. 1994 [DIRS 106881], p. 769; Burchfiel 1965 [DIRS 102052], p. 186) or the influence of a strain gradient resulting from differential extension above a detachment fault (Wernicke and Axen 1988 [DIRS 107238], p. 850; Hagstrum and Gans 1989 [DIRS 105884], p. 1840; Scott 1990 [DIRS 106751], pp. 275 and 279). Rotation has also been attributed to the extension of Crater Flat as a pull-apart basin (Fridrich 1999 [DIRS 118942], p. 210), an increase in listric faulting toward the south, and development of relay ramp slices between fault segments (Stamatakos and Ferrill 1998 [DIRS 113903], p. 158).

Basaltic Volcanism–The history, evolution, and character of Pliocene-Pleistocene basaltic volcanism proximal to Yucca Mountain (within 25 km [16 mi] of the repository) are extensively

described by Crowe et al. (1995 [DIRS 100110]) and summarized in Section 4.2, as well as in CRWMS M&O (2000 [DIRS 151945], Section 12.2).

The episodic nature of basaltic eruptions (11.3 Ma, 3.7 Ma, 1.0 Ma, 77 ka), aligned series of volcanic centers (Figure 4-1), and generally consistent alkalic compositions of the basalts indicate that volcanism is recurrent. Volcanism involves conditions in the entire thickness of the crust and part of the upper mantle beneath the basin (Crowe et al. 1995 [DIRS 100110], pp. 5-1 and 5-14).

4.1.1.3   Boundary Conditions

Tectonic Boundaries–The pattern of gravity and magnetic anomalies affords the best indication of tectonic domain boundaries, but with the exception of the Death Valley-Furnace Creek fault (Figure 4-3), these boundaries are not well expressed in observable structures. Consequently, bounding structures that afford boundary conditions to be fixed for a tectonic model of Yucca Mountain are difficult to determine. The eastern margin of the Walker Lane (Figure 4-3; and Section 2.2.1) forms a structurally complex, poorly defined tectonic boundary. To the north, the Timber Mountain-Oasis Valley caldera complex (Figure 4-2; also the Timber Mountain-Claim Canyon caldera complex, or the Timber Mountain caldera complex) forms a tectonic constraint of deep crustal roots to extension at Yucca Mountain, but this is an intrusive, mantle-derived feature, not part of the fault-defined extensional framework. Furthermore, faulting at Pahute Mesa (Figure 4-2) suggests that the Crater Flat domain may be tectonically continued north to the edge of the Walker Lane. A genetic link would imply that faulting at Pahute Mesa may provide constraints on tectonic models for the Crater Flat domain.

The overall tectonic pattern of the Great Basin indicates that well-defined northern and southern structural constraints, or regional tectonic boundaries for the Yucca Mountain setting, do not exist. The eastern edge of the northwest-trending Walker Lane may constitute a northern constraint, and the southeast projection of the Funeral Mountains may be the southern constraint. Both these features imply influence of right-lateral shear to the north and south.

4.1.1.4   Application of Stress

Contemporary and Paleo-Stress–In the Yucca Mountain area, the least principal stress vector (σ_3), which controls the extension direction, is essentially horizontal and trends N50° to 70°W (Carr 1974 [DIRS 104659], p. 1; USGS 1984 [DIRS 101305], p. 4; Zoback and Zoback 1980 [DIRS 108658], p. 523; Minster and Jordan 1987 [DIRS 106379], p. 4801; Wernicke et al. 1988 [DIRS 149959], p. 1752; Zoback 1989 [DIRS 108651], p. 7105). Analysis of faults near Yucca Flat and in the Basin and Range to the east indicate that the present stress regime originated around 9 Ma. Prior to that time, σ_3 was oriented in a more westerly or southwesterly direction (Zoback et al. 1981 [DIRS 108663], p. 189; Minor 1995 [DIRS 106373], Figure 9). The stress field in the Yucca Mountain region rotated clockwise as much as 65° in the 11- to 8.5-Ma interval (Minor 1995 [DIRS 106373], p. 10,527). The relative magnitudes of σ_1 and σ_2 attained their present values during Plio-Pleistocene time (Bellier and Zoback 1995 [DIRS 101649], p. 588).

Measured σ_3 values from boreholes at Yucca Mountain are low, near values at which normal faults that strike N25° to 30°E, and have a coefficient of static friction between 0.6 and 1.0 might be expected to experience frictional sliding (USGS 1984 [DIRS 101305], p. 59; Stock and Healy 1988 [DIRS 101022], p. 92). These local stress measurements, obtained within 2,000 m of the surface, may not reflect conditions at seismogenic depths where strike-slip and oblique-slip focal mechanisms are common (Rogers et al. 1987 [DIRS 100176], p. 1). Because strike-slip and dip-slip mechanisms occur throughout the uppermost 15 km (9 mi) of the crust, the relative magnitudes of σ_1 and σ_2 (greatest and intermediate principal stress vector, respectively) at depth must be nearly equal, a relationship described as axially symmetric (Rogers et al. 1987 [DIRS 100176], p. 66). Additional discussion of in situ stress measurements in the Exploratory Studies Facility (ESF) is provided in Section 3.7.5.

Contemporary Strain–The northern Basin and Range (north of latitude 37°N) appears to be moving by means of crustal extension at 4.9 ± 1.3 mm/yr (0.19 ± 0.05 in./yr) west-northwest (S82°W $\pm$ 13°) with respect to the continental interior and southern Great Basin (Savage et al. 1995 [DIRS 104553], p. 20,265). The relatively high strain rate of the northern Basin and Range is at least partly accommodated by the central Nevada seismic zone (Figure 2-3). The southern Basin and Range (south of latitude 37°N) has an extension rate of 3 mm/yr (0.1 in./yr) or less (Sauber 1989 [DIRS 104546], p. 123). The boundary between these two regions of differing extension, the intermountain seismic zone, is at about 37°N latitude (Harmsen and Rogers 1986 [DIRS 106092], p. 1561; Smith and Arabasz 1991 [DIRS 105406], p. 192, Figure 7). The intermountain seismic zone accommodates the differential extension between the northern and southern Basin and Range provinces; the slip rate in this zone is estimated at about 3.2 mm/yr (0.12 in./yr) (Savage et al. 1995 [DIRS 104553], p. 20,267).

The Crater Flat domain is located outside the zones of high strain rate defined by the central Nevada seismic zone and intermountain seismic zone. A 50 km (31 mi) aperture trilateration network, centered on Yucca Mountain and operated from 1983 to 1993, showed a strain accumulation of less than 2 mm/yr (0.08 in./yr) in the Crater Flat domain (Savage et al. 1994 [DIRS 103457], p. 18,106; Savage et al. 1999 [DIRS 118952], p. 17,627). The low strain rate (Savage et al. 1995 [DIRS 104553], p. 20,263, Figure 9) and low seismicity levels (Rogers et al. 1987 [DIRS 100176], p. 82) (Section 4.3) in the Crater Flat domain suggest that Yucca Mountain is in a tectonic domain that may be isolated from zones of high strain to the west and north.

Anomalous strain accumulation in the Crater Flat domain was reported by Wernicke et al. (1998 [DIRS 103485]) based on Global Positioning System surveys conducted from 1991 to 1997. The data indicated uniform north-northwest crustal extension across the Crater Flat domain at a rate of 1.7 ± 0.3 mm/yr, or 50 ± 9 nanostrain/yr. This strain rate was considered anomalous on the basis of comparatively very low slip rates for the Bare Mountain fault and for faults at Yucca Mountain (Wernicke et al. 1998 [DIRS 103485], p. 2099). In establishing this strain rate, Wernicke et al. (1998 [DIRS 103485]) minimized the effect of coseismic deformation of the Little Skull Mountain earthquake, by assuming a northwest-dipping nodal plane and discounting strain effects of the Death Valley-Furnace Creek fault. The anomalous strain was considered to reflect extension entirely within the Crater Flat domain.

The strain rate data of Wernicke et al. (1998 [DIRS 103485]) were questioned on the basis of possible monument instability and misinterpretation of the Little Skull Mountain fault plane dip (Savage et al. 1998 [DIRS 145359]). A radar interferometry study (Pezzopane et al. 1999 [DIRS 158691]) confirmed the southeast dip of the Little Skull Mountain nodal plane and demonstrated an associated area of subsidence of approximately 8 by 10 km, centered on Little Skull Mountain, having as much as 25 ± 5 mm (1 ± 0.2 in.) subsidence.

A subsequent strain analysis incorporating geodetic data from 1983, 1984, 1993, and 1998 was presented by Savage et al. (1999 [DIRS 118952]). After removing coseismic effects of the 1992 Little Skull Mountain earthquake, the extensional strain from 1983 to 1998 was found to be 1 ± 12 nanostrain/yr (or -2 ± 12 nanostrain/yr at N65°W). Almost half of the engineering strain rate ($\sim 23 \pm 10$ nanostrain/yr) can be attributed to strain on the Death Valley-Furnace Creek fault and the Hunter Mountain-Panamint Valley fault. Hence, extensional strain accumulation within the Crater Flat domain is insignificant.

Strain measurements in the Crater Flat domain from 1999 to 2001 (Marks 2001 [DIRS 156302]) indicate a pattern of increasing north component of velocity with distance toward the west. Marks (2001 [DIRS 156302]) concluded that the strain velocity field in the Crater Flat Domain is dominated by dextral shear averaging 20 to 26 nanostrain/yr rather than north-northwest extension at 50 ± 9 nanostrain/yr previously reported by Wernicke et al. (1998 [DIRS 103485]). The anomalous high strain rate reported by Wernicke et al. (1998 [DIRS 103485]) is now interpreted as a postseismic transient motion attributed to the 1992 Little Skull Mountain earthquake (Marks 2001 [DIRS 156302]).

4.1.1.5 System Response

The dynamic and long-term effects of extensional stress and heat flow on the Yucca Mountain tectonic system are detailed in different sections of this report (Section 8.4, Long-Term Stability of the Water Table and Flow System; Section 4.2, Igneous Activity and Volcanic Hazards; Section 4.3, Seismicity and Seismic Hazards). This quantitative information details the system response relevant to the critical regulatory period of the repository. Tectonic models must represent the system response and account for the relative rates, sequences, and magnitudes of the deforming events, thereby providing a viable framework for hazards analyses.

4.1.2 Evaluations of Tectonic Models

In this subsection, the various tectonic models that have been proposed for the Yucca Mountain vicinity or the surrounding region are described and evaluated. These models vary considerably in detail. Many were designed to explain a relatively narrow data set or hypothesis but in some cases, boundary conditions and driving forces are not addressed. Hence, each model is discussed primarily in terms of its structural elements and the hypothesized mechanism of deformation. The model's ability to explain the various data sets obtained for site characterization is assessed. Each of the models has limitations, and thus far, no single model has been described that satisfies all the data. The larger the area of a proposed model, the more likely it is that one will find local inconsistencies.

The U.S. Nuclear Regulatory Commission (NRC) identified five viable models (NRC 1999 [DIRS 135621], pp. C1 to C4):

1. Half-Graben with Moderate Depth Detachment Model
2. Half-Graben with Deep Depth Detachment Model
3. Elastic-Viscous Model
4. Crater Flat Pull-Apart Basin Model
5. Lateral Shear Model.

To facilitate a discussion, the models are grouped by style of deformation, similar to the NRC groupings above. The groups are:

- Detachment fault models (simple shear model).

- Rift/graben (elastic-viscous) models (pure shear model).

- Lateral-shear/pull-apart basin models (lateral shear model).

- A unique model based on volcanism (the Crater Flat-Prospector Pass caldera model; Carr 1988 [DIRS 105385]; 1990 [DIRS 104669]; Carr et al. 1986 [DIRS 104670]) does not fit in these categories; it is discussed first. In the following sections, each model type is discussed in the same format: brief description, evidence for, and evidence against.

4.1.2.1 Crater Flat-Prospector Pass Caldera Model

The Crater Flat-Prospector Pass caldera model was formulated (Carr 1982 [DIRS 101519], p. 9; Carr 1984 [DIRS 101037], pp. 2, 3, and 70, Figure 9; Carr 1988 [DIRS 105385], p. 41, Figure 4-2) to account for: (1) the unknown source for tuff of the Crater Flat Group and (2) the form and structure of the Crater Flat basin. Briefly, the model postulates that Crater Flat basin reflects the structure of subsided (now buried) calderas (the Crater Flat caldera and the Prospector Pass caldera) from which the tuffs of the Crater Flat Group were erupted.

Evidence for the Crater Flat-Prospector Pass Caldera Model–The caldera model is based on the following general relationships:

- A thick sequence of welded tuff of the Crater Flat Group was penetrated in drill hole USW VH-1 (Figure 4-1), within the area of a broad positive aeromagnetic anomaly thought to indicate the presence of a thick, circular volcanic rock body representing a resurgent dome of the Crater Flat caldera (Figure 4-2).

- The negative gravity anomaly of Crater Flat is indicative of an underlying graben-like structure; the basin outline appears to conform to a caldera shape.

- The location of several structural and volcanic features (including the Bare Mountain fault, and some Yucca Mountain faults, and the Lathrop Wells basalt cone) could be controlled by an inferred caldera rim.

Two buried calderas were inferred to lie farther north of the inferred Crater Flat caldera: the Tram caldera (postulated by Carr et al. 1984 [DIRS 101522], p. 32), also referred to as the Prospector Pass Segment of the Crater Flat caldera, and an older-tuffs caldera beneath Yucca Mountain (Carr 1982 [DIRS 101519], p. 11). The Tram caldera was inferred based on:

- Arcuate dikes in Bare Mountain that seem to correspond in age and composition to lava beneath the Tram Tuff; the lavas are thought to represent early eruptions from the Tram caldera.

- Thick Tram Tuff (457 m [1,500 ft]) in Beatty Wash (Figure 4-2).

- Truncation of the Tram Tuff in northern Crater Flat by a fault that may be a caldera wall (Carr 1982 [DIRS 101519], p. 10).

Evidence against the Crater Flat Caldera Model–The caldera model is not supported by recently acquired data. For example:

- Paleomagnetic studies (Rosenbaum et al. 1991 [DIRS 106708]; Hudson et al. 1994 [DIRS 100986]) explain the curvature of faults at Yucca Mountain (which form part of the proposed caldera outline) as having been partly a result of vertical axis rotation that occurred about 12.7 Ma and later.

- Analysis of aeromagnetic data indicates that the prominent positive anomaly in Crater Flat originated within the Precambrian or Paleozoic section rather than from structures within the Tertiary section (Brocher et al. 1996 [DIRS 101495], p. 39; Langenheim and Ponce 1995 [DIRS 104561], p. 15).

- A seismic reflection profile across Crater Flat gives no evidence for deformation in Crater Flat apart from block faulting of broadly warped, essentially conformable Tertiary strata (Brocher et al. 1998 [DIRS 100022], Figure 6).

The caldera model places peak tectonic activity in Crater Flat at about 14 Ma and requires that all subsequent fault deformation be guided by relict caldera rim structures. This hypothesis does not address the origins and mechanism of Late Neogene and Quaternary strain effects, such as distributed and recurrent faulting at Yucca Mountain; the origins and impetus for basaltic volcanism in Crater Flat; the mechanisms for vertical axis rotation at the southern half of Yucca Mountain and strike-slip component of faulting; the post-10 Ma uplift of Bare Mountain; evidence for Quaternary faulting at Busted Butte; and the fact that styles of faulting similar to those at Yucca Mountain in Mid Valley, Yucca Flat, and Pahute Mesa have originated independent of any relict guiding caldera structures.

4.1.2.2   Detachment Fault Models

A detachment fault is a regionally extensive normal fault with shallow dip (less than 30°). Above a detachment fault at shallow crustal levels, subparallel sets of concave-upward (listric) normal faults merge into the detachment and form elongate fault blocks that are all steeply tilted in the same direction. Rollover of the beds in the hanging walls (or upper plate) of listric faults

is a characteristic of listric faulting and is caused by the curvature of such faults. Older rocks in the footwall (or lower plate) may not be involved in the extensional faulting (hence the name "detachment") as upper plate faulting appears detached from the lower plate. Extension is thus accomplished in the shallow crust by multiple normal faults that jointly separate and rotate upper plate blocks in a common direction. In the upper crust, this deformation mode is simple shear, in which one geometric axis of the deforming body rotates out of its original orientation.

Evidence for Detachment Fault Models–Detachment models (Figures 4-4, 4-5, 4-6, 4-7) have been applied largely on the strength of four major arguments to Yucca Mountain and its tectonic setting:

1. Proximity–Late Miocene detachment faulting occurred west of Yucca Mountain at Bare Mountain, Bullfrog Hills, and Funeral Mountains (Ransome et al. 1910 [DIRS 166373]; Hoisch 1995 [DIRS 106161]).

2. Geometry–Resemblance of Yucca Mountain faults to tilted dominos with rollover (local increase of hanging wall dip toward the footwalls) suggests that they are listric faults (fault-plane dips that become shallower with depth) that accompany detachment faulting (Fox and Carr 1989 [DIRS 105435], p. 37; Scott 1990 [DIRS 106751], p. 251).

3. Field Observation–Detachments were reported at the Tertiary-Paleozoic contact in places east and south of Yucca Mountain. An interpreted detachment fault at the Tertiary-Paleozoic contact in the Calico Hills, Rock Valley, and Point of Rocks led to the conclusion that a detachment fault forms the Tertiary-Paleozoic contact beneath Yucca Mountain at a depth of 1.5 to 2.5 km (1 to 1.5 mi) (Figure 4-5) (Scott 1990 [DIRS 106751], p. 258, Figure 4).

4. Regional Tectonic Interpretation–A major deep detachment has been proposed to extend from near the Sheep Range, Nevada, west to Death Valley, California (Death Valley breakaway fault zone [Wernicke et al. 1988 [DIRS 149959], pp. 1746 and 1747], Sheep Range detachment [Guth 1981 [DIRS 105817], p. 763]).

Various detachment fault models have been proposed for Yucca Mountain (Hamilton 1988 [DIRS 100037], p. 62; Scott 1990 [DIRS 106751], p. 273; Wernicke et al. 1988 [DIRS 149959], pp. 1746 and 1747; Fox and Carr 1989 [DIRS 105435], p. 37; Ferrill et al. 1996 [DIRS 105309], p. 6-4; Oliver and Fox 1993 [DIRS 106439], p. 1812; Ofoegbu and Ferrill 1995 [DIRS 106427], p. 1-1; and McKague et al. 1996 [DIR 105028], p. 4-5). The original detachment fault model for Yucca Mountain included a regional "rolling hinge." According to this model, detachment faulting reduces vertical confining stress on the lower plate, which then rises by isostatic ductile deformation to form an exposed metamorphic core complex. The detachment plane may be partly preserved across the uplift, because it is in the Funeral Mountains. Thus, Bare Mountain constitutes the uplifted footwall, and the east-sloping flank of Bare Mountain was interpreted to be the exhumed detachment plane (Figure 4-4) (Hamilton 1988 [DIRS 100037], p. 62). The chronology of uplift at Bare Mountain implies that if a detachment exists at Yucca Mountain, it would have ceased slip at about 10 Ma (Fridrich 1999 [DIRS 118942], p. 192).

Two model variants referred to profiles across Yucca Mountain (Figure 4-7a) were based on syntheses of previous proposals. A mid-crustal model (Figure 4-7b) assumes that the Yucca Mountain faults developed as the headwall of the Bullfrog Hills detachment system, which was thought to accommodate as much as 275 percent west-vergent extension (Ferrill et al. 1996 [DIRS 105309], p. 6-4). According to this model, Yucca Mountain faults were isolated from the Bullfrog Hills system by rise of the Bare Mountain block along the Bare Mountain fault, which truncated the Yucca-Bullfrog detachment (Figure 4-4). Continued motion of the Bare Mountain fault led to formation of a deeper, east-directed detachment plane. According to this model, the older, shallower, west-directed detachment accounts for the imbricate faulting at Yucca Mountain; the younger, deeper, east-directed detachment accounts for hanging wall collapse into rollover and formation of Crater Flat basin. A deep-crustal model (Figure 4-7c) links hanging wall rollover and imbricate faulting at Yucca Mountain directly to the Bare Mountain fault. The Yucca Mountain faults are simply antithetic to the deep, master, east-directed Bare Mountain detachment (Ferrill et al. 1996 [DIRS 105309], p. 6-4). These two models may explain the westward subsidence of Crater Flat with time. They are compatible with a succession of relatively young east-dipping faults in Crater Flat (Brocher et al. 1998 [DIRS 100022], Figure 18), even though the model cross sections do not explicitly show such faults. These models also obviate the problem of termination of fault activity after 10 Ma implied by the rolling hinge model (Hamilton 1988 [DIRS 100037]).

Detachment fault models adequately explain the distributed normal fault system at Yucca Mountain and hanging wall rollover exhibited by each fault block. These models also adequately explain vertical axis rotation at Yucca Mountain as a consequence of differential slip rate rather than profound crustal shear mechanisms linked to deformation of the Walker Lane. Because all rotated normal faults of the upper plate are rooted in a common slip plane (the detachment), all faulting is necessarily distributed.

Evidence against Detachment Fault Models–Detailed geologic mapping shows that the Tertiary-Paleozoic contact (Scott 1990 [DIRS 106751], p. 276, Figure 15; Figure 4-5) is not a detachment surface. Tertiary-Paleozoic contacts exposed east and south of Yucca Mountain are erosional contacts, not slip surfaces (Simonds and Scott 1996 DIRS 106809], p. 20), and interpretation of the deep seismic reflection profile across Yucca Mountain (Brocher et al. 1998 [DIRS 100022], p. 967) shows that high-angle faults offset the Tertiary-Paleozoic contact, thus precluding a shallow detachment at the mountain.

Detachment models that incorporate the Bare Mountain fault or that involve a deformation scheme within and west of Bare Mountain (Hamilton 1988 [DIRS 100037], p. 55; Scott 1990 [DIRS 106751], p. 276, Figure 15; McKague et al. 1996 [DIRS 105028], p. 3-11, Figure 3-6) are limited in timing and geometry. Uplift of Bare Mountain (and creation of Crater Flat basin) occurred within the 1.1 m.y. period from 12.7 to 11.6 Ma. By this time, Bare Mountain was already an elevated range that had shed metamorphic rock debris as early as Crater Flat Group time (prior to 13 Ma) (Fridrich 1999 [DIRS 118942], p. 192). The Bare Mountain fault dips steeply to a depth of about 3.5 km (2.2 mi) and possibly as deep as 6 km (3.7 mi) (Brocher et al. 1998 [DIRS 100022], p. 966). Displacement on the Bare Mountain fault would have severed detachments at crustal depths above about 6 km (3.7 mi) at about 12.7 Ma. Furthermore, any regional deep crustal detachment slip at or above the brittle-ductile transition was terminated by about 14 Ma, when dike intrusion and differential uplift along the Bare Mountain front

isolated any deep crustal connection Bare Mountain may have had with detachment farther east. The Bullfrog Hills detachment heads along the west flank of Tram Ridge (Fridrich 1999 [DIRS 118942], p. 173, Figure 3; Figure 4-1). No structural continuity between the Bullfrog Hills and Crater Flat faults can be found that supports a model with detachment that extended through the Bullfrog Hills and Yucca Mountain (McKague et al. 1996 [DIRS 105028], p. 3-11, Figure 3-6). Any shallow detachment that occurred west of the Fluorspar Canyon fault after 14 Ma was isolated from any comparable deformation in Crater Flat east of Tram Ridge (Fridrich et al. 1999 [DIRS 107333], p. 181, Figure 6).

Deep detachment faults (or systems) projected west of the Sheep Range by Guth (1981 [DIRS 105817]) and Wernicke et al. (1988 [DIRS 149959], pp. 1746 and 1747) are incompatible with structures mapped at the Nevada Test Site because they ignore the significant strike-slip faulting within the Spotted Range-Mine Mountain structural zone and east-vergent extension east of the CP Hills (see Section 2 for geographic and structural details). They are not comparable to structure exposed in the Funeral Mountains, Bullfrog Hills, or Bare Mountain. Models of east-vergent detachment do not accommodate the tectonic style and deformation history of Little Skull Mountain and strike-slip dominated faulting to the east.

The deformation history of the Crater Flat basin is incompatible with detachment fault models. The Yucca Mountain faulting pattern does not reflect a systematic vergence to the west and the rate and progress of extension across Crater Flat is diachronous (Fridrich 1999 [DIRS 118942], p. 193; Brocher et al. 1996 [DIRS 101495], p. 955; Simonds et al. 1995 [DIRS 101929]). The structural style of the Crater Flat basin has progressively changed during its tectonic evolution, and the area of active tectonism in the basin has been progressively shrinking toward the southwest corner (Fridrich 1999 [DIRS 118942], p. 192). Crater Flat is young relative to Yucca Mountain and its structural style varies from the 12.7 to 11.6 Ma fault style of Yucca Mountain (Fridrich 1999 [DIRS 118942], p. 190). The low cuesta along the southern flank of the basin formed after about 10 Ma and involved tilting of the strata as much as 10°N into the basin, a style of deformation that is not a continuation of earlier structural patterns (Fridrich 1999 [DIRS 118942], p. 190).

No detachment fault models address lateral boundary conditions to extension in Crater Flat. For example, immediately north of Yucca Mountain, a large volume of magma resided in the crust (Broxton et al. 1989 [DIRS 100024], p. 5983) throughout the period of maximum detachment activity. The effects of large volumes of molten or near-molten rock on the detachment mechanism have not been addressed. The models assume that detachment occurred within brittle rock having no rheological perturbations.

Detachment faulting could have occurred during the period of peak east-west extension at Yucca Mountain as a short-lived local phase of deformation. However, there is no evidence for a widely extended, long-lived system linked to tectonic activity outside the Crater Flat domain, and there is no evidence for any such activity in post-late Miocene time. These models are significantly deficient in that they do not accord with local structural variations and domain boundaries, and they do not accord with the post-late Miocene history of deformation, including basaltic volcanism, recurrent fault slip, contemporary seismicity, and local deformation trends within the Crater Flat domain.

4.1.2.3   Rift-Graben (Elastic-Viscous) Models

Rift-graben models (the elastic-viscous models of NRC [1999 [DIRS 135621], pp. C-1 to C-4]) assume a mobile, viscous middle crust that is overlain by an internally deformable, passive, brittle upper crust. The dominant mode of deformation approximates pure shear, wherein the orientations of geometric axes of the deforming body remain unchanged during deformation. For example, a cube may become stretched or flattened, but its shape is not rotated or skewed from its original rectilinear shape. In the rift-graben models, the result is a variety of rift-like or graben-like elongate basins in the upper crust that have their long axes normal to the extension direction.

Two general rift-graben models (Figures 4-8 and 4-9) have been applied to the Crater Flat domain: a half-graben model and a rift model. These models are also called planar fault models because faults do not change dip (become listric) with depth. In the half-graben model, Crater Flat basin is the hanging wall of the Bare Mountain fault. Slip on the fault controls basin subsidence, and the block-bounding faults of Yucca Mountain are antithetic to the Bare Mountain fault. In the rift model, a master fault is not required; rather, behavior of internal fault sets determines the structural configuration. In this model, Crater Flat is underlain by an axial fracture zone and widening is normal to the fracture. The basin is a lateral propagation of the deep axial fracture zone rather than hanging wall subsidence bounded by a master footwall fault.

Evidence for Rift-Graben Models–Rift-graben models are consistent with Basin and Range structure.   Deep seismic reflection profiles (Hauge et al. 1987 [DIRS 100180], p. 329) and refraction profiles (Catchings and Mooney 1991 [DIRS 102497], p. 6250) across central Nevada support rift-graben models. Seismic data reveal a layered crust. The seismic velocity structure implies that the crust as a whole is extending laterally in boudinage fashion, compatible with a pure shear mechanism (Catchings 1992 [DIRS 102496], p. 1189). An elastic-viscous rift-graben mechanism explains the fundamental graben-like structure of Crater Flat basin. Seismicity suggests that present-day extension occurs throughout most of the southern Great Basin as normal-faulting earthquakes along steeply dipping faults originating at depths approaching 19 km (Doser and Smith 1989 [DIRS 102805], p. 1385). Rift-graben models are consistent with Crater Flat domain earthquakes that exhibit steep fault planes and occur at various depths in the seismogenic brittle crust. The model is also consistent with the locations and genesis of basaltic intrusions in Crater Flat and elsewhere in the Amargosa trough.

Crater Flat basin has been interpreted as a sector graben caused by evacuation of a body of magma from the base of the crust within the Kawich-Greenwater rift (Carr 1990 [DIRS 104669], p. 300; Figure 4-3). This interpretation accords well with the timing and magnitude of initial faulting of Yucca Mountain, as well as the basin shape and position. This rift-graben model implies that Pleistocene extensional faulting at Yucca Mountain is not a function of antithetic slip controlled by the Bare Mountain fault, but is instead controlled by axial fractures within the deepest part of the Crater Flat basin. It implies that any future tectonic activity will be concentrated toward the southern tip of the basin. The model provides a mechanism for recurrent basaltic volcanism within the rift confines and it accounts for a population of east-vergent faults beneath Crater Flat (Brocher et al. 1998 [DIRS 100022], Figure 18).

A rift model for Yucca Mountain, as part of the Amargosa Desert rift zone, was described by Brocher et al. (1998 [DIRS 100022], p. 968) as a kind of evolved pull-apart model that depends on changing behavior of the brittle crust in response to its changing thickness through time. The rift zone was divided into two subdomains based on fault block tilt: a west-tilted Crater Flat domain and an east-tilted Yucca Mountain domain (Brocher et al. 1998 [DIRS 100022], p. 950; Figure 4-9). The fault configuration was interpreted entirely on the basis of a seismic reflection profile and aeromagnetic anomalies that indicate the presence of east-side-down faults in Crater Flat (Brocher et al. 1998 [DIRS 100022], p. 961). The longitudinal extent of the east-dipping faults is unknown.

The Brocher et al. (1998 [DIRS 100022], Figure 18) model geometry implies that as the brittle crust thickens (i.e., becomes cooler with time) and the basin widens, east-dipping faults synthetic to the Bare Mountain fault should slip, and those antithetic to the Solitario Canyon fault that are unable to slip should be cut by new west-dipping faults. This model is too specifically tied to the seismic profile to be applied to the whole Crater Flat basin. If Crater Flat basin is a pull-apart basin, it differs from those in Death Valley (Blakely et al. 1999 [DIRS 149763], p. 12) or others modeled as a rhomb-shaped graben or half-graben that are linked genetically to strike-slip faults (Sims et al. 1999 [DIRS 145327], p. 549).

The rift-graben models account for both uplift and subsidence of block faulted crust. These models can be modified to include vertical axis rotation, which is not easily accounted for in detachment fault models. Rift-graben models imply that faulting and volcanism are coupled processes, that any future volcanism will either penetrate the Bare Mountain fault or focus on deep fault intersections at the southern end of the basin, and that faulting in Crater Flat may precede and accompany volcanism. The rift-graben models allow post-middle Miocene faulting and vertical axis rotation to be unique to the Crater Flat domain.

Evidence against Rift-Graben Models–The half-graben model is adequate only near the central latitudinal axis of the Crater Flat domain. It fails to account for the decreased throw and splitting of the Bare Mountain fault in the vicinity of the caldera complex also does not account for the structural style at the southern end of Crater Flat. The half-graben model also fails to account for a cumulative Pleistocene dip slip on the Bare Mountain fault that is less than that measured across Yucca Mountain.

The rift-graben model does not explain the origin of the cuesta that bounds the southern rim of Crater Flat basin, which shows no evidence of axial symmetry. The model also does not account for hanging wall rollover if, as the model implies, each block-bounding fault at Yucca Mountain extends as an independent plane through the brittle crust. The model does not account for the asymmetry of Crater Flat basin, for uplift of Bare Mountain, or for vertical axis rotation in Crater Flat.

4.1.2.4   Lateral-Shear/Pull-Apart Basin Models

Lateral-shear models apply horizontal shear stress to create translation (lateral offset) as well as tension (pull-apart basins). In this model, Crater Flat is described as having been opened (pulled apart) between linked strike-slip and dip-slip faults. Crater Flat was characterized as a type of half graben known as a rhombochasm (a pull-apart basin modified by distributed dextral shear)

or as a sphenochasm (a pull-apart anchored at one end, so that the basin opens like a fan) (Fridrich 1999 [DIRS 118942], p. 193).

Evidence for Lateral-Shear and Pull-Apart Basin Models–Displacement of Bare Mountain relative to the Striped Hills, now separated by about 20 km (12 mi) (Caskey and Schweickert 1992 [DIRS 102407], p. 1324) to more than 30 km (18 mi) (Schweickert and Lahren 1994 [DIRS 106747], p. A-250; 1997 [DIRS 101012], p. 25), implies a transcurrent north-northwest-striking dextral strike-slip fault zone beneath Yucca Mountain and Crater Flat. The inferred fault zone was defined as the Amargosa fault system by Schweickert and Lahren (1994 [DIRS 106747], A-250; 1997 [DIRS 101012], p. 25) (Figure 4-10), a system that comprises the Stewart Valley, Pahrump Valley, Stateline, and Ivanpah faults for a total length of about 250 km (155 mi). Evidence for the fault system includes gravity, seismic, structural, stratigraphic, and paleomagnetic data; the distribution of springs and basaltic volcanic centers; and patterns of late Quaternary surface faulting (Schweickert and Lahren 1997 [DIRS 101012], p. 25). Vertical axis rotation and centers of Quaternary and Neogene basaltic volcanism inside and outside Crater Flat are explained by action of the shear zone that passes through Crater Flat.

The projected contours of rotation across Crater Flat imply presence of a zone of diffuse dextral shear that is aligned with and perhaps part of a larger belt of clockwise rotation and dextral shear that extends at least 60 km (37 mi) farther to the northwest (Hudson et al. 1996 [DIRS 106194], A-451; Minor et al. 1997 [DIRS 100997], p. 20). The data imply that middle Miocene normal extension was essentially confined to the Crater Flat domain and may have been associated with caldera magmatism (Minor et al. 1997 [DIRS 100997], p. 28), whereas later vertical axis rotation was imposed from outside the domain via dextral shear associated with evolution of the Walker Lane (Minor et al. 1997 [DIRS 100997], p. 33).

A discrete shear zone that passes through Crater Flat would account for vertical axis rotation and for the centers of Quaternary and Neogene basaltic volcanism inside and outside Crater Flat. This model implies that future volcanism in Crater Flat will be narrowly confined. The model is not only compatible with detachment faulting, it requires detachment to hide the transcurrent shear zone in the lower crust. The model implies that slip on the buried strike-slip fault could activate listric faulting across Yucca Mountain.

Evidence against Lateral-Shear and Pull-Apart Basin Models–Crater Flat basin appears to have formed by orthogonal extension. The lateral shear was imposed on the basin during a subsequent episode of deformation (Minor et al. 1997 [DIRS 100997], p. 33). It is uncertain whether the lateral shear was diffuse or more narrowly confined. The amount of vertical axis rotation within the Crater Flat basin cannot accommodate 20 km (12 mi) of dextral offset postulated by Caskey and Schweickert (1992 [DIRS 102407]). A best-fit profile across the inferred shear zone in Crater Flat suggests that only 10 km (6 mi) of lateral offset can be accounted for by vertical axis rotation (Stamatakos and Ferrill 1998 [DIRS 113903], p. 154). None of the post-Miocene features between the Sleeping Butte basalts and Stewart Valley accounts for any significant dextral offset.

Although lateral shear is well-documented at Yucca Mountain, it is insufficient to account for a dextral shear zone of regional extent cutting through Crater Flat basin. The sense of structural displacement and extension in terrain north and south of Crater Flat basin is primarily east-west

(e.g., Oasis Valley, the Amargosa trough). Aeromagnetic data (Figure 4-11) show primarily east-northeast and west-northwest anomaly alignments south of Crater Flat rather than north-northeast alignments expected for a pull-apart mechanism or for a transcurrent shear zone. Paleomagnetic studies (Hudson et al. 1994 [DIRS 100986], p. 258) suggest dextral shear affected the Yucca Mountain region in discrete zones that were discontinuous in length and diachronous in age. Nonsystematic distributions of vertical axis rotations in time and space in the Yucca Mountain region imply that individual basins responded uniquely to distributed northwest-oriented dextral shear driven by post-12.7 Ma extension south of Yucca Mountain and west of the Spring Mountains (Brocher et al. 1993 [DIRS 102002], p. 44; Hudson et al. 1994 [DIRS 100986], p. 274).

4.1.3   Application of Tectonic Models to Hazard Analysis

Two kinds of disruptive events that are potential hazards to a nuclear waste repository at Yucca Mountain are brought about by tectonism: volcanism (including intrusion) and earthquakes. The geologic record provides clear evidence that both volcanoes and earthquakes have occurred in the vicinity of Yucca Mountain during the Quaternary period (1.8 m.y.). The youngest nearby volcano (the Lathrop Wells Cone) erupted approximately 80 ka (Heizler et al. 1999 [DIRS 107255], p. 767). The interval between successive earthquakes on active faults ranges from thousands to tens of thousands of years, with the smaller recurrence intervals applying to faults found more than 50 km (31 mi) west of Yucca Mountain. In part because of the low rate of activity, characterization of geologic parameters that are needed to assess the potential for future activity at Yucca Mountain is subject to significant uncertainties.

Basaltic volcanism and earthquakes are treated separately in the following sections, but the presentation formats are similar. The geologic history and features of the disruptive events are characterized on the basis of field observations, the magnitude and locations of future events are assessed in the context of applicable tectonic models, and spatial and temporal uncertainties of recurrence and distribution are analyzed numerically as probabilities by Probabilistic Seismic Hazard Analysis (PSHA) (see Section 4.3).

In evaluating volcanic hazards, a panel of experts concluded that magma ascent is related to extension (CRWMS M&O 1996 [DIRS 100116]). A pull-apart basin controlled by local, deep-seated normal faults was the most commonly cited model, and strike-slip faulting related to the Walker Lane was acknowledged as a possible factor. No panel member cited detachment faulting in relation to volcanism. The experts' use of tectonic models is summarized in Section 4.2.

For PSHA, six teams of experts evaluated various tectonic models and assigned each a weight (CRWMS M&O 1998 [DIRS 103731]). The expert teams assigned the greatest weight to the planar fault (i.e., rift-graben) model in combination with a component of dextral shear (a pull-apart basin model). The detachment model was assigned lower weight, and the lateral-shear model was assigned the least weight. The expert teams did not consider the Crater Flat-Prospector Pass caldera model viable (CRWMS M&O 1998 [DIRS 103731]).

4.2 BASALTIC VOLCANISM AND VOLCANIC HAZARDS

Basaltic volcanic eruption poses a potential hazard to a waste repository at Yucca Mountain. Assessment of that hazard is founded on the history and character of late Tertiary and Quaternary volcanic activity in the Yucca Mountain area. This section summarizes data obtained on basaltic extrusive rocks by the site characterization program. The data include mineralogical and chemical characteristics of the eruptive rocks, timing, style, and volumes of eruptions, as well as the locations and physical aspects of the volcanic centers. In instances where requisite information concerning intrusive or extrusive phenomena could not be obtained directly, data from analog sites or from experimental evidence was considered. The physical and chemical characteristics of the basalts near Yucca Mountain formed the constraints on appropriate analogs. Based on these data, a Probabilistic Volcanic Hazards Analysis (PVHA) was carried out to assess the frequency of a basalt intrusion penetrating the volume of the waste repository (CRWMS M&O 1996 [DIRS 100116]). The PVHA defined the volcanic hazard at the site as the annual probability of intersection of the repository by a basaltic dike.

The data were also used to formulate models of the consequences of an unlikely eruption through a repository at Yucca Mountain. Studies of eruptive and subsurface features and processes associated with basaltic volcanoes, used to develop additional background material and parameter distributions for the analysis of the consequences of volcanic eruptions through the repository, are discussed in the analysis report *Characterize Eruptive Processes at Yucca Mountain, Nevada* (BSC 2001 [DIRS 160130]). Analyses that were performed to complete the description of the volcanic hazard and effects are provided in analysis and modeling reports supporting the *Disruptive Events Process Model Report* (CRWMS M&O 2000 [DIRS 151950]).

4.2.1 Distribution of Basaltic Volcanism in the Yucca Mountain Region

4.2.1.1 Temporal and Spatial Distribution of Basaltic Volcanic Centers

Following terminal eruption of the Ammonia Tanks caldera at about 11.4 Ma (Fridrich 1999 [DIRS 118942]; Figure 4-1), basalts were erupted in the Yucca Mountain region during two major episodes. The most voluminous episode, the basalt of the silicic episode, erupted between about 11 and 8.5 Ma, and is spatially and temporally associated with the waning of silicic volcanism (CRWMS M&O 1998 [DIRS 135988], pp. 2-12 to 2-13, Figure 2.4). The second episode, the post-caldera basalt, erupted from about 8.5 Ma into the late Quaternary (CRWMS M&O 1998 [DIRS 135988], p. 2-17, Figure 2.5). Post-caldera basalt in the Yucca Mountain region can be divided into two episodes: Miocene (eruptions between ~9 and 7.2 m.y.) and post-Miocene (eruptions between ~4.8 and 0.08 m.y.). The time interval of about 2.5 m.y. between these episodes is the longest eruptive hiatus of basalt in the Yucca Mountain region during the last 9 m.y. (CRWMS M&O 1998 [DIRS 105347], Chapter 3, Table 3.1). This eruptive hiatus also marks a distinct shift in the locus of postcaldera basaltic volcanism in the Yucca Mountain region to the southwest (Figure 4-12).

The Plio-Pleistocene basalts were formed during at least six volcanic events (based on age and spatial groupings) that occurred within 50 km (31 mi) of the repository (Figure 4-12). These six events, in order of decreasing age are: (1) basalt of Thirsty Mesa, (2) Pliocene Crater Flat and Amargosa Valley, (3) Buckboard Mesa, (4) Quaternary Crater Flat, (5) Hidden Cone and Little

Black Peak (the Sleeping Butte centers), and (6) Lathrop Wells. Three of these events at approximately 3.7, approximately 1, and 0.08 Ma (Figure 4-12) are in or near Crater Flat, within 20 km of Yucca Mountain. The seven (or eight if counting Little Cones, Figure 4-12, as two volcanoes) Quaternary volcanoes in the Yucca Mountain region occur to the south, west, and northwest of Yucca Mountain in a roughly linear zone defined as the Crater Flat volcanic zone (Crowe and Perry 1990 [DIRS 100973], p. 328; Figure 4-12). Models that attempt to relate volcanism and structural features in the Yucca Mountain region have emphasized the Crater Flat basin because of the frequency of volcanic activity associated with Crater Flat and its proximity to the Yucca Mountain repository (e.g., Smith et al. 1990 [DIRS 101019], p. 84; Connor and Hill 1995 [DIRS 102646], pp. 10 and 122).

4.2.1.2   Results from Interpretation of Geophysical Data

Several aeromagnetic anomalies in the Amargosa Valley have characteristics that indicate buried basaltic volcanic centers (Langenheim et al. 1993 [DIRS 148622], p. 1840). One of these anomalies (anomaly B of Langenheim et al. 1993 [DIRS 148622]; Figure 4-11) was drilled and basalt cuttings were dated at 3.85 Ma using the $^{40}Ar/^{39}Ar$ method (CRWMS M&O 1998 [DIRS 123196], Table 2.B). The most reliable and detailed data available for magnetic anomalies in the Yucca Mountain region are presented in Conner et al. (1997 [DIRS 102647]) and Magsino et al. (1998 [DIRS 147781]). Collectively, these ground magnetic surveys represent a comprehensive assessment of aeromagnetic anomalies nearest the repository site and provide confidence that the geologic record of basaltic volcanism near Yucca Mountain is adequately understood. Four of the 14 surveys provide evidence of buried volcanic centers (Connor et al. 2000 [DIRS 149935], Plate 3).

A high-resolution aeromagnetic survey conducted in 1999 (Blakely et al. 2000 [DIRS 151881]) recorded a number of small dipole anomalies in Crater Flat and the northern Amargosa Desert (Figure 4-11). Potential-field modeling indicated that isolated, small-volume magnetic bodies embedded within the alluvial deposits of both areas produce the anomalies. Physical sources of the magnetic anomalies were modeled by bodies having volumes, forms, and magnetic susceptibilities comparable to those of the basaltic volcanoes exposed in the vicinity of Yucca Mountain (O'Leary et al. 2002 [DIRS 158468]). The physical characteristics of the modeled bodies and the fact that they tend to be aligned along major structural trends indicate that the anomalies could represent small-volume basaltic volcanic centers (Figure 4-11, Table 4-1) buried at depths between 150 and 350 m (500 and 1,200 ft).

4.2.1.3   Structural Controls on Basaltic Volcanism

Most researchers conclude that (1) volcanism is correlated with zones of past or present crustal extension and (2) once dikes feeding volcanoes enter the shallow upper crust, their location and orientation is influenced by the orientation of the local stress field and the presence of faults that may locally control vent location and alignment. The evidence cited for these two conclusions includes several northeast-oriented vent alignments in the Yucca Mountain region and the association of eruptive centers with known or inferred faults (Smith et al. 1990 [DIRS 101019], p. 83; Connor et al. 1997 [DIRS 102647], p. 78; Fridrich et al. 1999 [DIRS 107333], p. 211).

When considering different scales, regional and local, of spatial control on volcanism, it is important to distinguish between deep (mantle source) and shallow (upper crustal structure and stress field) processes. Volcanism is seen as occurring in the Yucca Mountain region, on a regional scale, because of melting processes in the upper lithospheric mantle that produce small volumes of alkali basalt, a basalt type generated by relatively small percentages of mantle melting compared to other basalt types (CRWMS M&O 1996 [DIRS 100116], Appendix E; CRWMS M&O 1998 [DIRS 106491], p. 4-4). The exact mechanism of mantle melting in the Yucca Mountain region is poorly understood but may be controlled by a complex combination of processes, including the effect of residual heat in the lithospheric mantle from previous episodes of volcanism and the presence of a plate subduction system, local variations in volatile (water) content, variations in mantle mineralogy and chemistry, and the effect of regional lithospheric extension (CRWMS M&O 1996 [DIRS 100116], Appendix E). Researchers who have analyzed magmatic processes in the Yucca Mountain region generally agree that the magnitude of mantle melting has drastically decreased since the middle Miocene and that all melts in the past few million years have been generated within relatively cool (compared to asthenospheric mantle) ancient lithospheric mantle (Farmer et al. 1989 [DIRS 105284], p. 7893; Reamer 1999 [DIRS 119693], p. 47), a factor that may contribute to the relatively small volume of basaltic melt erupted in the Yucca Mountain region since the Miocene (e.g., CRWMS M&O 1996 [DIRS 100116], Appendix E, p. RC-2).

4.2.2 Rates of Basaltic Volcanism in the Yucca Mountain Area

4.2.2.1 Age of Basaltic Volcanism

Extensive studies to establish ages for post-Miocene basalts of the Yucca Mountain region were carried out using the K-Ar method (Fleck et al. 1996 [DIRS 105337], Table 1) and the $^{40}Ar/^{39}Ar$ method (CRWMS M&O 1998 [DIRS 123196], Tables 2.B and 2.C; Heizler et al. 1999 [DIRS 107255], p. 767). Mean age comparisons are generally good for basalt events between 1 and 5 Ma, with a maximum difference in mean age determinations of about 8 percent for the basalt of Buckboard Mesa. However, there is uncertainty regarding the true age distribution of a given volcanic event. For example, the Quaternary basalt centers of Crater Flat can be interpreted as all having the same age of about 1 Ma or, alternatively, there may be a systematic decrease in eruption age from north to south in Crater Flat (Figure 4-13). Age agreement for the two youngest volcanic episodes (Sleeping Butte and Lathrop Wells) is poorer (about 20-30 percent difference), which is considered to reflect the difficulty of obtaining ages for young basalts using these methods. In the case of the Sleeping Butte centers, only a few age determinations have been attempted, and the data are insufficient to assess which age determination is more correct (CRWMS M&O 1998 [DIRS 123196], p. 2-39).

The age of the Lathrop Wells volcanic center has been debated for a number of years (Turrin et al. 1991 [DIRS 101030]; Wells et al. 1990 [DIRS 107207]; Wells et al. 1992 [DIRS 107015]). Recent $^{40}Ar/^{39}Ar$ ages (Heizler et al. 1999 [DIRS 107255], p. 767) on both basalt whole-rock samples and tuff xenolith sanidine samples are reproducible and indicate an age of about 80 ka. This age is consistent with ^3He ages (CRWMS M&O 1998 [DIRS 123196], Table 2.4) and ^{36}Cl ages (Zreda et al. 1993 [DIRS 108617], Table 1) measured at Lathrop Wells, indicating that the true age of the Lathrop Wells center is between approximately 70 and 90 ka.

4.2.2.2   Origin of Basaltic Magma: Waxing or Waning Processes

Teleseismic data give some insight into the physical state of upper mantle basalt sources beneath the Yucca Mountain region. Low upper mantle seismic velocities beneath much of the Basin and Range Province suggest that the upper mantle contains a small percentage of partial melt. Biasi (1996 [DIRS 105358], p. 2) reported new teleseismic data and teleseismic tomography interpretations that do not require magma to exist within the crust beneath Yucca Mountain or Crater Flat.   However, small amounts of partial melt within the mantle (greater than 45 km [28 mi] deep) cannot be ruled out beneath southern Crater Flat and adjacent portions of Amargosa Valley.

The mechanism of mantle melting in the Yucca Mountain region is poorly understood, but may be controlled by a complex combination of processes. These include the effects of residual heat in the lithospheric mantle from previous episodes of volcanism and presence of a plate subduction system, local variations in volatile (water) content, variations in mantle mineralogy and chemistry, and the effect of regional lithospheric extension (CRWMS M&O 1996 [DIRS 100116], Appendix E). Extension may facilitate basalt intrusion by promoting deep crustal fracture propagation in areas where basalt magma is present. Extension also produces tectonic basins partially filled with relatively low-density alluvium and Tertiary volcanic deposits. On this basis, Connor et al. (2000 [DIRS 149935], p. 420) infer that a broad crustal density contrast created by extension and basinal subsidence across the Crater Flat domain and Amargosa trough is sufficient to initiate small-volume decompression melting in the upper mantle. The area of potential decompression melting is inferred to extend at least 50 km (31 mi) east of the Bare Mountain fault (Connor et al. 2000 [DIRS 149935], p. 420), thus including both Crater Flat and Yucca Mountain in a zone of potential future volcanism.

The volume of basalt erupted through time has decreased from approximately 1.5 km^3 in the oldest cycle to 0.1 km^3 at the youngest center, Lathrop Wells (CRWMS M&O 1998 [DIRS 135988], Table 3.1). The volume of individual episodes has decreased progressively through time, with the three Pliocene episodes having volumes of approximately 1 to 3 km^3 each and the three Quaternary episodes having a total volume of only about 0.5 km^3 (Table 4-2). All of the Quaternary volcanoes are similar in that they are of small volume, about 0.15 km^3 or less (Table 4-2). The total volume of the post-Miocene basalts is approximately 6 km^3. The relatively long lifetime of the Crater Flat field, combined with the small volume of erupted material, results in one of the lowest eruptive rates of any basaltic volcanic field in the southwestern United States (CRWMS M&O 1998 [DIRS 106491], Figure 4.2).

Researchers who have analyzed magmatic processes in the Yucca Mountain region generally agree that the magnitude of mantle melting has drastically decreased since the middle Miocene, and that all melts in the past few million years have been generated within relatively cool (compared to asthenospheric mantle) ancient lithospheric mantle (Farmer et al. 1989 [DIRS 105284], p. 7893; Reamer 1999 [DIRS 119693], p. 47). This factor may contribute to the relatively small volume of basaltic melt erupted in the Yucca Mountain region since the Miocene (e.g., CRWMS M&O 1996 [DIRS 100116], Appendix E, p. RC-2).   The combination of decreasing eruptive volume through time and geochemical data discussed in Section 4.2.3 indicates that the intensity of mantle melting processes beneath the Yucca Mountain region has waned over the past 5 Ma (Perry and Crowe 1992 [DIRS 106488], p. 2359). Fleck et al. (1996

[DIRS 105337], p. 8225) observed that the waning volcanism through time is also valid when the time frame is extended to include basalts of Miocene age (less than 11 Ma). They concluded that a general decrease through time in the amount of partial melting of the mantle source is the most reasonable explanation.

In contrast to models of waning volcanism, Smith et al. (2002 [DIRS 158735]) hypothesize that a deep asthenospheric melt source of increasing temperature and volume may exist in the Yucca Mountain region (Smith et al. 2002 [DIRS 158735]; Wang et al. 2002 [DIRS 158736]). The hypothesis of widespread increasing magmatism links episodes of volcanism to periods of rapid extensional strain accumulation (Smith et al. 2002 [DIRS 158735], p. 4). Smith et al. (2002 [DIRS 158735]) argued a tectonic link between Crater Flat basin and Plio-Pleistocene volcanism in the Lunar Crater volcanic field, located 130 km northeast of Yucca Mountain in the Basin and Range province. The combined recurrence intervals at these two volcanic fields and correlations in volcanic style and basalt compositions, along with an interpretation of anomalously high strain rate for the Crater Flat domain (Wernicke et al. 1998 [DIRS 103485]), led Smith et al. (2002 [DIRS 158735], p. 4) to conclude that volcanic recurrence rates at Yucca Mountain may be underestimated. The interpretation of anomalously hot mantle beneath the central Basin and Range is based on temperature estimates that rely on the analysis of experimental data representing dry asthenospheric mantle (Wang et al. 2002 [DIRS 158736], p. ECV5-17), while most researchers agree that the source of basalt in the Yucca Mountain region is hydrous and relatively cool lithospheric mantle (e.g., Farmer et al. 1989 [DIRS 105284]). The extremely low volume of basalt erupted in the Yucca Mountain region during the Quaternary (<1 km^3), combined with the generally low volumes of basalt erupted within the central Basin and Range compared to the margins (Perry et al. 1998 [DIRS 144335], pp. 4-3 to 4-7]), do not support the hypothesis that the mantle source beneath the Yucca Mountain region is anomalously hot or prone to produce increasing volumes or rates of volcanism in the future. In addition, the longevity (> 5 Ma) of basaltic volcanic activity in the Yucca Mountain region is typical of the total lifetime of many basaltic volcanic fields in the western United States. This suggests that basaltic volcanism in the region has completed a major portion of its overall evolution and that the nature of volcanic activity (low volume, low recurrence rate) is unlikely to fundamentally change over short periods of geologic time (Perry and Crowe 1992 [DIRS 106488], p. 2356).

4.2.2.3 Evidence for Simultaneous Faulting and Volcanic Eruption

In an extensional tectonic environment, magma may ascend through the crust along fractures that serve as pathways. In the case of basaltic volcanism, the formation of fracture pathways releases seismic energy that typically results in earthquakes with a maximum magnitude of M 4.0 to 5.0 (Yokoyama and de la Cruz-Reyna 1990 [DIRS 108740], pp. 274, 280). Volcanogenetic earthquakes may, however, trigger larger tectonic earthquakes on nearby faults that have sufficient strain accumulation.

In the Yucca Mountain region, basaltic ash has been found as a minor to dominant component in fissure fillings and stratabound alluvial horizons exposed by trenching of several faults near Yucca Mountain. (The basaltic ash consists of 0.1- to 0.5-mm glass shards containing phenocrysts of olivine and microcrystals of plagioclase; the glass shards have sharp edges, indicating minimal abrasion from surface transportation [CRWMS M&O 1998 [DIRS 106491], Figure 4.19]). Correlation of these ashes, or ash to the contemporary eruptive source has been

used to constrain the age of the ash and, therefore, provide information about the slip history of a fault (CRWMS M&O 1998 [DIRS 106491], Chapter 4, Section VI-C). The most concentrated occurrence of ash in a trenched fault exposure was found in Trench 8, across the trace of the Solitario Canyon fault (Ramelli et al. 1996 [DIRS 101106], p. 4.7-14). This ash occurs at the bottom in a 65-cm- [26-in-] wide fissure that represents the largest recorded Quaternary displacement event (more than 1 m) on the Solitario Canyon fault (Ramelli et al. 1996 [DIRS 101106], p. 4.7-15).

Pure ash separates were analyzed for trace elements by Instrumental Neutron Activation Analysis and compared to the composition of all Quaternary eruptive centers in the Yucca Mountain region (CRWMS M&O 1998 [DIRS 106491], Section VI-C). These geochemical comparisons leave little doubt that the ash found in the Solitario Canyon fault (Trench 8), the Windy Wash fault (Trench CF3), the Fatigue Wash fault (Trench CF1), and the Stagecoach Road fault (Trench T1) originated from the eruption of the Lathrop Wells volcanic center, south of Yucca Mountain (CRWMS M&O 1998 [DIRS 106491], Section VI-C). Based on geochronology results from Lathrop Wells, the age of this ash is about 80 k.y. (CRWMS M&O 1998 [DIRS 106491], Section VI-C). This conclusion is consistent with geochronology results from stratigraphic units exposed in Solitario Canyon fault Trench 8 (Ramelli et al. 1996 [DIRS 101106], p. 4.7-15).

In contrast to the above interpretation, a direct age of the ash sample from Solitario Canyon fault Trench 8 using the Argon-40/Argron-39 method yielded an apparent plateau age of 0.86 ± 0.16 m.y. (CRWMS M&O 1998 [DIRS 106491], Section VI-C, Figure 4.18). This age is consistent with ages of the Quaternary basalt centers in Crater Flat, all of which have ages near 1 m.y., but not with that of the Lathrop Wells Center. Examination of the ash sample by scanning electron microscope, however, shows that about 0.5 percent of the dated sample consists of Miocene, high-K rhyolitic glass (CRWMS M&O 1998 [DIRS 106491], Section VI-C) that is optically cloudy and difficult to distinguish from the basaltic glass. It is likely that this high-K contaminant is the cause of the erroneously old Argon-40/Argon-39 age.

4.2.3 Characterization of Eruptive Processes

4.2.3.1 Style of Eruption

Each Pleistocene basaltic volcanic center typically consists of a single main scoria cone surrounded by a small field of basalt flows, which commonly extend about 1 km from the scoria cone. Quaternary basalts of the Yucca Mountain region display facies that indicate a range of eruptive processes (BSC 2001 [DIRS 160130], Section 6.3). Eruptive styles in the Yucca Mountain region range from violent Strombolian-type on one end of the spectrum to quiescent aa lava on the other (BSC 2001 [DIRS 160130], Section 6.3).

Strombolian-type eruptions are characterized by short duration bursts that throw relatively coarse fragments out along ballistic trajectories. Fragments consist of both melt and solidified lava. Most of the fragments are deposited close to the vent, with only a very small fraction of finer particles rising higher and being dispersed by wind to form minor fallout sheets. Violent Strombolian-type eruptions are characterized by vertical expulsion of a high-speed jet of a gas-ash mixture. As the eruptive mixture rises in the jet, it entrains and heats air, which in turn

reduces the bulk mixture density until the jet becomes buoyant and continues to rise as a plume. The plume rises to an altitude of neutral buoyancy compared to the enclosing atmosphere, in which it then spreads laterally as an anvil or "umbrella" cloud that is transported downwind. Ash falls out from both the vertical eruption column and from the umbrella cloud according to settling velocities. Settling velocity in air depends on the bulk density (the melt density corrected for the porosity or vesicularity of the ash fragments), shape, and size.

The Lathrop Wells volcano is a good example of a range of eruptive processes recorded by a single volcano (BSC 2001 [DIRS 160130], Section 6.3). The surface of the main cone is composed mainly of loose scoria of relatively high vesicularity. The cone is surrounded by a fallout blanket up to about 3 m (10 ft) thick (within 1 km [0.6 mi] of the cone) composed of loose scoria. Remnants of this fallout deposit are exposed as far as 2 km [1.2 mi] north of the crater. About 20 km [12 mi] north of the crater, the reworked equivalent of the fallout deposit is observed in trenches cut into the Solitario Canyon fault. These features all suggest a relatively high-energy eruption (violent Strombolian-type) having an ash column that rose kilometers into the air so that finer ash was dispersed widely by winds. Other parts of the Lathrop Wells volcano, for example the mounds of coarse, partially welded spatter, indicate local, relatively low-energy Strombolian-type eruption (BSC 2001 [DIRS 160130], Section 6.3). Recent quarry exposures in the main cone show welded scoria and agglutinate, typical of Strombolian-type eruption, suggesting that only the late stages of the cone-forming eruptions were violent Strombolian-type. Thick, stubby aa flows suggest short-duration, high-mass-flux effusive eruption. Other volcanoes of the Yucca Mountain region are less well preserved, but they seem to exhibit a similar range in eruptive styles at individual centers.

Eruption duration is difficult to estimate and during formation of a volcanic center, it is likely that eruptive discharge rates varied substantially. BSC 2001 ([DIRS 160130], Section 6.3.4) provides a discussion of estimates of total eruption duration (formation of the entire volcano) and volume for expected basaltic eruptions in the Yucca Mountain region.

4.2.3.2 Geochemistry and Petrology of Yucca Mountain Region Basalts

The compositions of Yucca Mountain region basalts gives insight into mantle source characteristics, the fraction of melt generated in the mantle as a function of time, and ascent history. Basalts of the Yucca Mountain region are classified as alkali olivine basalts, as are most post-Miocene basalts in the interior of the Great Basin. Alkali olivine basalts have high (about 4 to 5 weight percent) total alkalis ($Na_2O + K_2O$; Table 4-3) and are generated at relatively great depths by small degrees of partial melting (less than 15 percent) (Jaques and Green 1980 [DIRS 106220], p. 304, Figure 9). Experimental data (Takahashi 1980 [DIRS 106964], p. 272; Takahashi and Kushiro 1983 [DIRS 106965], Figure 15, Table 3) indicate that alkalic basalts compositionally similar to those of the Great Basin equilibrated at pressures of 14 to 20 kb, equivalent to a depth of 45 to 65 km (28 to 40 mi). Magnesium/iron ratios of basalts in the Yucca Mountain region are relatively low, indicating significant fractionation of olivine and pyroxene en route to the surface. On average, Pliocene basalts have slightly higher magnesium/iron ratios than Quaternary basalts (CRWMS M&O 1998 [DIRS 106491], Figure 4.5). If this difference is significant, it indicates that higher extension rates in the Pliocene favored more rapid transit to the surface with less opportunity for fractional crystallization.

Pliocene basalt lavas in the Yucca Mountain region contain phenocrysts of plagioclase, olivine, and clinopyroxene, whereas Pleistocene lavas contain only olivine phenocrysts. The lack of plagioclase phenocrysts in the younger lavas indicates fractionation at high pressure, within the upper mantle. This interpretation implies a decreased generation rate for basaltic magma in the Quaternary because a decreased magma flux into the crust could not sustain shallower magma chambers (Fleck et al. 1996 [DIRS 105337], Figure 4, p. 8223).

A large geochemical database that includes major elements, trace elements, and radiogenic isotopes exists for basalts of the Yucca Mountain region (Vaniman et al. 1982 [DIRS 101031], Table 2; Perry and Straub 1996 [DIRS 106490]; Bradshaw and Smith 1994 [DIRS 101996], Table 1; Fleck et al. 1996 [DIRS 105337], Tables 3 and 4; CRWMS M&O 1998 [DIRS 106491], Chapter 4, Sections V and VI). An important observation concerning the genesis of basalts in the Yucca Mountain region is that basalts younger than approximately 3 Ma have higher concentrations of many trace elements (e.g., strontium, thorium, uranium, lanthanum, cerium) than older basalts (Vaniman et al. 1982 [DIRS 101031], pp. 351 to 353; Farmer et al. 1989 [DIRS 105284], pp. 7887 and 7888; Fleck et al. 1996 [DIRS 105337], p. 8223). Incompatible trace elements are those that are not easily incorporated into common mantle mineral structures. Thus, upon melting, they are the first released into the melt. For melting of mantle source rocks, elements such as lanthanum and thorium are diagnostic of relative degrees of partial melting (e.g. a relatively low concentration of lanthanum and thorium indicates a relatively large volume of partial melt). The three Pliocene basalt centers (Thirsty Mesa, southeast Crater Flat, Buckboard Mesa) (Figure 4-12) have generally lower lanthanum and thorium concentrations than Quaternary centers, implying larger degrees of partial melting of the mantle source, an interpretation that is consistent with their higher eruption volumes (CRWMS M&O 1998 [DIRS 106491], Figure 4.6). However, the geochemical criteria can only be used as a broad guideline, since source heterogeneity also has to be taken into account.

The high $^{87}Sr/^{86}Sr$ (about 0.707) and low δNd (about -10) of the basalts from the Yucca Mountain and adjacent region are unusual for alkali basalts of the western United States and are interpreted as reflecting the isotopic composition of a lithospheric mantle source (Farmer et al. 1989 [DIRS 105284], p. 7893; Fleck et al. 1996 [DIRS 105337], p. 8224). A lithospheric source is consistent with a relatively shallow generation depth of 45 to 65 km (28 to 40 mi), as previously discussed.

4.2.3.3 Physical Characteristics of Eruption

The physical characteristics of eruption are controlled primarily by volatile content (which is dominated by water) and the rate at which volatiles are exsolved from the magma. The observed eruptive styles indicate a large range in volatile content of Yucca Mountain region magmas.

The solubilities of volatiles such as H_2O and CO_2 in basaltic magmas are proportional to pressure (Table 4-4). As magma ascends through the crust under decreasing lithostatic pressure, it becomes over saturated and volatiles exsolve as bubbles. Rapid rise results in increasing numbers and sizes of bubbles. The combined exsolution of volatiles and decompression and coalescent growth of the bubbles increase the specific volume of the magma and, as a consequence, its ascent velocity also increases (according to conservation of mass). Explosive eruption occurs when, at shallow depths, the magma reaches a foamy state. At this point, the

bubble-charged magma fragments, switching from a melt with dispersed bubbles to a gas with dispersed fragments or clots of melt. Fragmentation depths modeled for magma having the range of initial volatile content (0 to 4 percent) considered for the Yucca Mountain region range from about 0 to 900 m (0 to 3,000 ft) (BSC 2001 [DIRS 160130], Section 6.3.2). At and above the fragmentation depth, the gas-melt mixture accelerates rapidly until it leaves the volcanic vent at speeds of tens to a few hundreds of meters per second.

Experimental data for basalts similar in composition to those of the Yucca Mountain region indicate that any future basaltic activity in the Yucca Mountain region should involve magma having from 0 to 4 percent water, with values approaching 4 percent being uncommon (BSC 2001 [DIRS 160130], Section 6.2.2).

The physical and chemical properties of the magmas play roles in determining eruptive processes. The ranges of magmatic temperatures are well known for magmas as a function of critical melt parameters (i.e., pressure and water content). Calculated water saturation pressures and corresponding temperatures for Lathrop Wells lavas (Table 4-4) are consistent with a long, well-established body of experimental data (BSC 2001 [DIRS 160130], Section 6.2.4). Calculated liquidus temperatures are between 1,169 and 1,046°C, for water content ranging from 0 to 4 percent by weight, at equilibrium saturation pressures ($pH_2O = pT$).

Corrosive gases released from an igneous event will play a role in the performance of the waste packages. A survey of data compilations from the literature, including volcanoes from convergent, divergent, and hot-spot tectonic settings, was used to estimate the mole percent of constituents in volcanic gas (BSC 2001 [DIRS 160130], Section 6.2.3). Species with the largest mole percent concentrations are, in decreasing order, H_2O, CO_2, and SO_2. Concentrations for minor species, which are corrosive, have large uncertainties relative to mean values.

4.2.3.4   Characteristics of Eruptive Conduits, Dike Widths, and Dike Swarms

Most observed basaltic eruptions begin as fissure eruptions, which rapidly become focused into conduit eruptions. Because of the effect of (1) the conduit diameter and (2) depth (to which a conduit extends before merging into a simple feeder dike) on the number of waste packages disrupted by a potential eruption at Yucca Mountain, it is important to constrain both these variables.

It may be assumed that any future basaltic volcanic eruption will be similar in character to Quaternary basaltic eruptions in the Yucca Mountain region, particularly with respect to the eruptive styles and composition recorded at the Lathrop Wells volcano, the most recent in the region. Doubik and Hill (1999 [DIRS 115338], pp. 60 and 61) argued, based on an analogy between the Lathrop Wells volcano and Tobalchik (Kamchatka, Russia) volcano, that the Lathrop Wells conduit may have been as wide as 50 m (164 ft) at the depth of the repository. The 50 m estimate of conduit diameter is large, considering that Doubik and Hill (1999 [DIRS 115338], p. 59) calculated a 48 m (157 ft) diameter for a Tobalchik conduit developed during an eruption much larger than that of the Lathrop Wells cone (BSC 2001 [DIRS 160130], p. 25). A conduit diameter value of 150 m (500 ft) has been estimated for the Grants Ridge conduit/plug in New Mexico (CRWMS M&O 1998 [DIRS 123201], p. 5-60).

Each volcano in the Yucca Mountain region is thought to be fed by one main dike along which a central cone and other vents may form, but subsidiary dikes may also be present. For example, the Lathrop Wells volcano may be underlain by three dikes: the dike that fed the main cone, a dike that fed spatter and scoria mounds in a parallel chain just to the east of the main dike, and possibly a dike that fed scoria vents near the northern edge of the volcano (CRWMS M&O 1998 [DIRS 123196], Appendix 2-M). In addition, there may be small dikes that radiate outward from the main cone's feeder conduit.

4.2.3.5   Potential Effects of Basalt Intrusion on Country Rock: Analog Studies

The Plio-Pleistocene volcanic centers near Yucca Mountain provide limited data pertaining to bedrock contact phenomena and other aspects of volcanism needed to assess hazard. To supplement the locally available data, studies of appropriate volcanic analogs were carried out. Analog studies also encompass results of published experimental work concerning basalt compositions comparable to the alkali-olivine basalts erupted near Yucca Mountain.

The extent of alteration or other damage caused by basalt magma intruding rock of the repository block can be assessed from basalt dike contacts in comparable settings. Such studies constrain the type and spatial scale of alteration that would accompany a basaltic intrusion into the repository. Two sites provided good analogs for the various rocks in the vadose zone at Yucca Mountain: (1) the Slanted Buttes area of Pahute Ridge, eastern Nevada Test Site, where variably vitric and zeolitized silicic tuffs (some of which correlate to those at Yucca Mountain, some 40 km away) were intruded by basaltic dikes and sills; and (2) Grants Ridge, New Mexico, where a thick sequence of rhyolite ignimbrite, fallout, and reworked volcaniclastic deposits were intruded by a basaltic plug. Erosion of the Grants Ridge site has since produced a natural cross section through the scoria cone, its feeding system, and the pyroclastic host rocks.

Slanted Buttes (Pahute Ridge) Site–Localized contact metamorphic zones were formed in vitric and zeolitized tuffs of middle-Miocene age by shallow intrusions of high-alumina alkali basalt at Slanted Buttes in the northeastern part of the Nevada Test Site (CRWMS M&O 1998 [DIRS 123201], p. 5-42). Two dikes, each of similar width (about 9 m [30 ft] wide), produced contact metamorphic zones from 0.5 to about 4 m (1.6 to about 13 ft) wide on either side of the dikes (CRWMS M&O 1998 [DIRS 123201], pp. 5-43 to 5-44). A localized aureole about 5 m (15 ft) wide formed along the lower contact of a 45 m (150 ft) thick basalt sill. The sill and dikes were probably intruded into a shallow, unsaturated environment a few hundred meters from the paleosurface, as indicated by reconstruction of stratigraphy above the intrusions (CRWMS M&O 1998 [DIRS 123201], p. 5-42). The depth of intrusion at this site is comparable to the repository environment at Yucca Mountain.

Basalt dike intrusion caused devitrification and/or fusion of silicic and zeolitized tuffs within the contact zone. Contact alteration of the Ammonia Tanks Tuff of the Timber Mountain Group resulted in the vitric component being totally replaced by feldspar, quartz, and cristobalite. The Tiva Canyon Tuff of the Paintbrush Group beneath the sill was found to contain a vitrophyre and a devitrified zone side by side.

Grants Ridge Site–Despite the size of the basaltic intrusion at Grants Ridge (about 150 m [500 ft] wide), it formed a contact metamorphic zone only about 5 m (15 ft) wide. The non- to

partially-welded ash-flow tuff along the contact aureole is baked, fused, deformed, and injected with basalt lava. Variation in color and degree of compaction of the silicic ash-flow tuff provide evidence for the localized nature of the thermal effect (CRWMS M&O 1998 [DIRS 123201], pp. 5-71, 5-72, and 5-74).

Variations in mineralogical and geochemical compositions are consistent with the changes in color and densification of the silicic rocks. The amount of recrystallized minerals and the alkali contents are higher closer to the contact whereas the volcanic glass, water content, fluorine, chlorine, and iron contents increase away from the intrusion (CRWMS M&O 1998 [DIRS 123201], pp. 5-72 and 5-74).

Devitrification generally is enhanced by presence of pore water and hydrated minerals in the host rock. The field and laboratory data suggest that the effect of the intrusion on the unwelded pumice-rich ash-flow tuff was minimal. The abundance of volcanic glass within a short distance (about 5 m [15 ft]) from the intrusion suggests a dry environment. Thus, in an unsaturated host rock, the width of the contact metamorphic aureole generally is confined to a narrow zone regardless of the size of the intrusion (CRWMS M&O 1998 [DIRS 123201], pp. 5-71 to 5-74).

The two natural analogs described above showed limited alteration caused by hydrothermal circulation, no brecciation nor other deformation related to basaltic intrusion into the vitric and zeolitized tuffs. Field and analytical evidence from the localized contact metamorphic aureoles and devitrification of the silicic tuffs adjacent to the intrusion, minimal hydrothermal alteration, and presence of low-temperature minerals close to the intrusions also suggest insignificant thermal and chemical effects of the shallow basaltic intrusions on the vitric and zeolitized tuffs (CRWMS M&O 1998 [DIRS 123201], p. 5-57).

4.2.4   Probabilistic Volcanic Hazard Analysis

The PVHA was conducted to assess the probability of a future volcanic event intersecting the repository at Yucca Mountain, details of which can be found in CRWMS M&O (1996 [DIRS 100116]). The analysis focused on the volcanic hazard, which is defined as the annual probability of intersection of the repository by a basaltic dike. The hazard analysis provides input to an assessment of volcanic risk, which expresses the probability of dose to the public resulting from dike intersection with the repository.

4.2.4.1   Temporal and Spatial Aspects of Probability Models

A variety of calculation methods were available to the PVHA experts to quantify volcanic hazard models. The calculation methods were used to create probability models that describe temporal and spatial distributions of events. Temporal models include homogeneous and nonhomogeneous models that describe the frequency of occurrence of volcanic activity through time. A homogeneous Poisson model defines the temporal occurrence of volcanic events, based on a uniform rate of volcanism derived from the number of volcanic events that occurred during a fixed time period. Nonhomogeneous models consider the possibility that volcanic events are clustered in time. They describe the possible waning or waxing of volcanic activity in the region during the recent geologic past.

Spatial models predict the spatial distribution of future volcanic activity. Three types of models that were used include: 1) spatially homogeneous distributions, which define source zones on the basis of the observed distribution of volcanic centers, structurally controlled (tectonic) provinces, geochemical characteristics, and other measurable criteria; 2) nonhomogeneous parametric spatial distributions, which assume a bivariate Gaussian distribution based on the locations of volcanoes in Crater Flat; and 3) nonhomogeneous, nonparametric spatial distributions, which apply a kernel density function and a smoothing parameter based on the locations of volcanoes. Details of model selection and application are discussed in CRWMS M&O 2000 ([DIRS 151551], Section 6.3.2).

4.2.4.2   Probabilistic Volcanic Hazards Analysis Results

Although the PVHA assumed volcanic events to have both an extrusive and intrusive component (volcano and dike), the output of the PVHA was the annual frequency of intersection of the repository footprint by an intrusive basaltic dike (CRWMS M&O 1996 [DIRS 100116], Section 4.3).

Each of the 10 experts independently arrived at a probability distribution that typically spanned about two orders of magnitude of the annual probability of intersection. From these individual probability distributions, an aggregate probability distribution was computed that reflects the uncertainty across the entire expert panel (CRWMS M&O 1996 [DIRS 100116], Figure 4-32). The distributions were combined using equal weights to obtain a composite distribution. The mean value of the aggregate probability distribution is 1.5×10^{-8} intersections/yr, with a 90 percent confidence interval of 5.4×10^{-10} to 4.9×10^{-8} (CRWMS M&O 1996 [DIRS 100116], Section 4.3). The composite distribution spans about three orders of magnitude of intersection frequency. The computed mean frequency of intersection for the individual experts' models spans about one order of magnitude, indicating that most of the uncertainty in characterizing the hazard arises from uncertainty in defining the parameters of the hazard model rather than from differences in scientific interpretations. The probability distribution arrived at by the PVHA accounted for undetected events (buried volcanic events or intrusive events that never reached the surface). The undetected event frequency ranged from one to five times that of observed events, with most estimates in the range of 1.1 to 1.5 (CRWMS M&O 1996 [DIRS 100116], Figure 3-62).

The PVHA results indicate that the statistical uncertainty in estimating the event rate is the largest component of intra-expert uncertainty (CRWMS M&O 1996 [DIRS 100116], Figure 4-33). The next largest uncertainty is uncertainty in the appropriate spatial model. Other important uncertainties include the spatial smoothing distance, time period of interest, event counts at the northwest Crater Flat center, and frequency of hidden events (CRWMS M&O 1996 [DIRS 100116], Figure 4-33).

Results of the PVHA (CRWMS M&O 1996 [DIRS 100116], Section 4.3) were recalculated to account for the Site Recommendation footprint of the repository (*Enhanced Design Alternative II Report* [CRWMS M&O 1999] [DIRS 103962]), and included the probability of an eruption within the repository footprint, conditional on a dike intersection (CRWMS M&O 2000 [DIRS 151551], Section 6.5). Figures 4-14 and 4-15 show the individual probability distributions and aggregate probability distribution for the intersection of a basaltic dike with the

repository configuration. Values for the recalculated annual frequency of intersection of the repository footprint by a dike associated with a volcanic event and the annual frequency of a volcanic event producing one or more eruptive centers within the repository are presented in Table 4-5. Spatial distribution of volcanic hazard defined by the probabilistic volcanic hazard analysis expert panel is shown in Figure 4-16.

4.2.4.3 Eruptive Processes Parameters for Consequence Models

Information about natural volcanic systems and the parameters that can be used to model their behavior is presented in BSC 2001 ([DIRS 160130]). Studies of the eruptive and subsurface effects of basaltic volcanism provide information used to develop parameter-value distributions appropriate for analysis of the consequences of potential volcanic eruptions through the repository at Yucca Mountain (BSC 2001 [DIRS 160130]; CRWMS M&O 2000 [DIRS 151551]). The following topics are relevant to potential hazards posed by basaltic volcanism (BSC 2001 [DIRS 160130]).

- The geometry of volcanic feeder systems, which are of primary importance in predicting how much of the repository would be affected by an eruption

- The physical and chemical properties of the magmas, which influence both eruptive styles and mechanisms for interaction with radioactive material

- Eruptive processes, including the ascent velocity of magma at depth, onset of bubble nucleation and growth in the rising magmas, magma fragmentation, and velocity of the resulting gas-particle mixture

- The duration of eruptions, their power output, and mass discharge rates

- Geologic constraints regarding the interaction between magma and waste packages

- The bulk grain size produced by relevant explosive eruptions and grain shapes.

Of particular interest are estimates of the amount of debris that would be entrained by magma rising through the repository and the effects such magma would have on the geochemical and geohydrological processes operating in its vicinity.

4.3 SEISMICITY AND SEISMIC HAZARDS

The assessment of seismic hazards at Yucca Mountain focuses on characterizing the potential vibratory ground motion and fault displacement that will be associated with future earthquake activity in the vicinity of the site. The evaluation of these hazards serves as a basis to define inputs for the preclosure seismic design of a geologic repository (BSC 2003 [DIRS 166274]). The evaluation also provides information that can be used to assess the impact of future seismic activity on the ability of the repository to meet the performance objectives for the postclosure period.

Seismic hazards at Yucca Mountain are assessed probabilistically (YMP 1997 [DIRS 100522]). The assessment is founded on the evaluation of a large set of data pertaining to earthquake

sources, fault displacement, and ground motion propagation in the Yucca Mountain region (Table 4-6). The data set contains information about prehistoric earthquakes on nearby Quaternary faults. The historical earthquake record and information on the attenuation of ground motion are also important components of this data set. Tectonic models that have been proposed for the Yucca Mountain area and information from analog sites in the Basin and Range Province provide the basis to characterize the patterns and amounts of fault displacement. The probabilistic assessment explicitly incorporates uncertainties in the characterization of seismic sources, fault displacement, and ground motion. The resulting hazard calculations thus represent a sound basis for seismic design and performance assessment by reflecting the interpretations that are supported by data, along with the associated uncertainties in those interpretations.

Site characterization activities that focus on understanding vibratory ground motion and fault displacement hazard at Yucca Mountain have included:

- Compilation of a historical catalog of earthquakes to support the analyses of earthquake recurrence rates and magnitude distributions

- Establishment of a network of seismic stations and strong-motion instruments to monitor and characterize contemporary seismicity

- Reconnaissance geologic surveys of known and suspected Quaternary faults within 100 km (60 mi) of the site to characterize their extent and rates of activity

- Paleoseismic studies of known and suspected Quaternary faults in the immediate vicinity of Yucca Mountain to provide information on past earthquakes, including their number, size, extent, and timing

- Geophysical surveys to identify and characterize the orientation of subsurface faults

- Analysis of ground motion data from local earthquakes to evaluate site attenuation

- Analysis of ground motion data from extensional tectonic regimes to provide information on the regional rate of attenuation.

This section presents the data and interpretations that support the PSHA, followed by a brief description of the hazard assessment and its results. The section begins by describing the historical seismicity of the Yucca Mountain region. Next, information on prehistoric earthquakes is presented. This is followed by a discussion of data and analyses carried out to understand seismic ground motion and its attenuation in the region surrounding Yucca Mountain. The integration of interpretations based on these data into a PSHA concludes the section.

4.3.1 Historical Seismicity of the Yucca Mountain Region

Seismic hazard evaluations rely on a description of the temporal and spatial distribution of earthquakes (both prehistoric and historical), their magnitudes and other source parameters, their associations with active faults, and their relationship to the seismotectonic processes of the region. The temporal and spatial occurrence of earthquakes for a given region is evaluated from

two sources: historical (instrumental records and reported effects) and prehistoric (paleoseismic data). Information on the historical record of earthquakes near Yucca Mountain is reported in this section, while information on paleoseismic (prehistoric) earthquakes is presented in Section 4.3.2.

The region of interest for assessing probabilistic seismic hazards at Yucca Mountain is a function of earthquake magnitude and the rate of earthquake occurrence. Because earthquake ground motions attenuate with distance, the farther an earthquake occurs from Yucca Mountain, the larger it must be to contribute significantly to the hazard at the site. At a distance of 100 km from Yucca Mountain, earthquakes must reach a size on the order of[1] M_w 8 to produce median peak horizontal ground accelerations of 0.1 g (98 cm/s^2) at the site (Pezzopane 1996 [DIRS 106524], Figure 11.3). If distant earthquakes are infrequent, ground motions from closer events of similar or lesser size will be more significant to the probabilistic hazard at the site. Thus, as distance from Yucca Mountain increases, seismic hazard studies focus on the longer and more active faults because longer active faults are generally considered capable of producing larger earthquakes.

Although the focus of the hazard studies is the area within 100 km (60 mi) of Yucca Mountain, the historical seismicity within 300 km (186 mi) of Yucca Mountain is considered and described in this section. This examination allows the seismicity of the Yucca Mountain vicinity to be evaluated within a broader regional context and provides an appropriate basis for the characterization of "background" earthquakes as part of the PSHA.

The discussion of historical seismicity in the Yucca Mountain region begins with a history of seismographic monitoring. The distribution and type of operating seismographs determines the completeness of the instrumentally documented record. Next, the catalog of historical earthquakes is discussed. Information on these events is derived from instrumental recordings and from field investigations of fault surface ruptures. The section finishes with a description of areas of general seismicity in the Yucca Mountain region.

4.3.1.1 History of Seismographic Network Monitoring

Seismic monitoring of the southern Great Basin began in the early 1900s with isolated stations installed and operated by the University of California, Berkeley, and the University of Nevada, Reno. In the late 1950s and early 1960s, a global network (the Worldwide Standardized Seismograph Network) came into existence, thereby providing the capability to record earthquakes larger than about M 4 in the southern Great Basin. Later, networks of stations were installed to monitor and study specific areas such as the Nevada Test Site and portions of the western United States. Milestones in monitoring are presented in Table 4-7.

Seismic monitoring specifically to characterize the Yucca Mountain region began when a 47-station network was installed in 1978 and 1979. The network extended out to a distance of 160 km (100 mi) from the site (Figure 4-17a) and employed the analog technology of the day. In 1981, six seismograph stations in the immediate vicinity of Yucca Mountain were added to the

---

[1] When referring to earthquake magnitudes, the following scales are cited and abbreviated as follows: M_L indicates Richter local, M_w indicates moment, M_s indicates surface wave, m_b indicates body wave, M_c or M_d indicates coda duration, M_I indicates intensity-based, and M indicates unspecified.

network. In 1995, seismic monitoring in the vicinity of Yucca Mountain was reconfigured with the establishment of a network based on digitally recorded and telemetered data. The digital network, which is still in operation, spans a radius of 50 km (30 mi) out from Yucca Mountain (Figure 4-17b) and, in 2001, consisted of 30 stations. The higher quality data obtained from the digital network has enabled the detection of smaller magnitude earthquakes and has resulted in improved accuracy of earthquake location.

In addition to the high-dynamic-range seismograph network, 10 strong-motion accelerometers also monitor Yucca Mountain. These stations are designed to record larger ground motions from nearby moderate to large earthquakes. Nine of the strong-motion instruments are located at the surface and one is sited in Alcove 5 of the ESF.

More details on the history of seismic monitoring in the Southern Great Basin is found in CRWMS M&O (2000 [DIRS 151945], Section 12.3.3.1) and von Seggern and Smith (1997 [DIRS 159532]).

4.3.1.2   Historical Seismicity Catalog for the Yucca Mountain Region

As part of the probabilistic seismic hazard analyses project, a catalog of historical and instrumental earthquakes was compiled for the region within 300 km of the repository site at Yucca Mountain (CRWMS M&O 1998 [DIRS 103731], Appendix G). The resulting combined catalog contains 271,223 earthquakes of approximately M_L 1 and greater from 1868 to 1996. All known magnitudes are listed in the catalog. Figure 4-18 shows events in the catalog with magnitude greater than M_w 3.5. The figure also shows seismicity that occurred in 1997 and 1998 and the earthquakes associated with the 1999 Hector Mine event, which had a magnitude of M_w 7.1. The earthquake catalog for Yucca Mountain was compiled from several sources, including the catalogs of Meremonte and Rogers (1987 [DIRS 106352]); Decade of North American Geology (Engdahl and Rinehart 1988 [DIRS 105267]); University of Nevada, Reno; University of California, Berkeley; California Institute of Technology; and USGS for eastern California and Great Basin (CRWMS M&O 1998 [DIRS 103731], Appendix G). Catalog completeness has improved significantly with time, but the catalog is still considered to be complete only for historical events of M_w 5.5 and larger within the 100 km radius around Yucca Mountain since 1868 (Rogers et al. 1991 [DIRS 106702], p. 166).

The accuracy of information in the historical catalog is affected by several variables (e.g., accuracy of historical accounts, detection capability, instrumental precision), especially the variability in seismic network coverage as a function of time. The spatial distribution of seismicity in the 300 km catalog depends both on the density of inhabitants and the density of seismographic network coverage in a particular region over time, and is somewhat an artifact of the more thoroughly represented aftershock sequences of the modern period. For example, a significant portion of the catalog is derived from a recent series of moderate-sized earthquakes, aftershock sequences, and volcanic swarm activity in the Mammoth Lakes, California area. Although these events figure prominently in terms of the number of earthquakes in the catalog, they represent an insignificant portion of the total moment release along the western Basin and Range Province in the past two decades.

Fault Displacement from Historical Seismic Events in the Extensional Cordillera of the Western United States–In addition to analyzing vibratory ground motion from future earthquakes, the analysis of seismic hazards at Yucca Mountain also addresses possible future fault displacement at the repository site. Thus, information on 100 historical earthquakes that occurred in the extensional cordillera of the western United States was compiled and evaluated by Pezzopane and Dawson (1996 [DIRS 103265]). They focused their evaluation on the amounts and patterns of both primary and distributed fault displacements, the minimum magnitude at which an earthquake may produce surface faulting, and the maximum magnitude at which an earthquake does not displace the surface.

For the minimum magnitude earthquake that can produce surface faulting, Pezzopane and Dawson (1996 [DIRS 103265], pp. 9-40 to 9-42) determined a magnitude of 5.2 ± 0.2. They noted that for some regions of the extensional cordillera of the western United States, the magnitude of the minimum magnitude earthquake may be as large as 6.3 ± 0.2. For the maximum magnitude earthquake that does not produce a surface displacement, Pezzopane and Dawson (1996 [DIRS 103265], pp. 9-42 to 9-44) determined a magnitude of 6.1 to 6.6, depending on the time period and region examined.

Examination of historical surface displacements revealed a general correlation of their extent and amplitude with earthquake size, seismotectonic setting, hypocentral depth, fault geometry, and style of slip (Pezzopane and Dawson 1996 [DIRS 103265], p. 9-108). The historical data set is also characterized by considerable variability.

Earthquake Magnitude Scale–Since the Yucca Mountain catalog was compiled from several source catalogs, each using a variety of different magnitude scales that also changed with time, a uniform magnitude scale was required to compute the earthquake recurrence for the region. In addition, it was necessary to assign magnitudes to historical earthquakes that occurred prior to calibrated seismographic instrumentation. Such magnitude estimates are usually based on the felt area or the maximum Modified Mercalli intensity. This is particularly problematic in the Basin and Range Province, where settlement and population growth have been erratic and sparse due to the boom and bust nature of mining operations and rugged environment. For each earthquake in the catalog, M_w was estimated from the best available magnitude. When available, published relationships between seismic moment (M_o) and M_w and M_L were used. A detailed description can be found in CRWMS M&O (1998 [DIRS 103731], Appendix G).

Identification of Nevada Test Site Explosions and Induced Seismicity–Nevada Test Site explosions and their induced earthquake aftershocks and reservoir-induced seismicity events at Lake Mead were identified in the earthquake catalog. Nuclear explosions were identified and flagged in the catalog. Nevada Test Site aftershocks were identified and flagged using a space-time window. Nuclear explosions and related aftershocks were excluded from the catalog for purposes of calculating seismicity recurrence rates. The Lake Mead area-induced seismicity (Anderson and O'Connell 1993 [DIRS 101472]; Rogers and Lee 1976 [DIRS 106699]) was identified but not removed from the catalog. It is unlikely that earthquakes in the Lake Mead area will contribute significantly to ground motion hazard at the Yucca Mountain site.

4.3.1.3 Regional Seismicity

The historical and instrumental earthquake record within 300 km of Yucca Mountain (Figure 4-18) includes the reported earthquakes of the southern Basin and Range Province and portions of the southern Sierra Nevada and Mojave Desert in California. The catalog contains all reported felt and instrumentally located earthquakes since 1868, including a few events of greater than M_w 5 that are located slightly outside of the 300 km radius region. These are included because they are associated with surface ruptures that form important historical analogs for assessing fault displacement hazards at the repository site (Pezzopane and Dawson 1996 [DIRS 103265]).

The larger earthquakes documented in the historical catalog occurred within the central Nevada seismic zone (Wallace 1984 [DIRS 107126]) and eastern California shear zone, 100 to 300 km (60 to 185 mi) to the northwest, west, southwest, and south of Yucca Mountain (Figure 4-18). These zones of activity include the 1872 Owens Valley, California, earthquake (M_w 7.8); 1932 Cedar Mountain, Nevada, earthquake (M_w 7.1); 1954 Fairview Peak and Dixie Valley, Nevada, earthquakes (M_w 7.1 and M_w 6.8); 1992 Landers, California, earthquake (M_w 7.3); and 1999 Hector Mine, California, earthquake (M_w 7.1) (north of Landers, 1992 event and not shown on Figure 4-18). Rupture zones for these events ranged in length from about 50 to 100 km (30 to 60 mi). They exhibited primarily right-lateral strike-slip faulting, with the exception of the Dixie Valley earthquake, which was primarily a normal faulting event (Beanland and Clark 1994 [DIRS 104458]; Gianella and Callaghan 1934 [DIRS 105502]; dePolo et al. 1994 [DIRS 104868]; Doser 1986 [DIRS 102803]; 1988 [DIRS 102804]; Caskey et al. 1996 [DIRS 102408]; Sieh et al. 1993 [DIRS 106802]; Jones 2000 [DIRS 149960]).

Three events during the historical period of greater than M_w 5.5 are located within 100 km of Yucca Mountain (Figure 4-19). The largest event is the 1916 M_w 6.1 earthquake that occurred in Death Valley. These events also include the 1992 M_w 5.6 earthquake that occurred near Little Skull Mountain, about 15 km (9 mi) southeast of Yucca Mountain, and an event in 1910 about 85 km (53 mi) to the northwest (Figure 4-19).

Another trend of seismicity, to the southwest of Yucca Mountain, occurs along the Garlock fault and southern Sierra Nevada in southeastern California. This band of activity includes the 1952 Kern County, California, earthquake (M_w 7.5) (Ellsworth 1990 [DIRS 105259], p. 163), activity near Ridgecrest, California, and the Coso volcanic field (Roquemore et al. 1996 [DIRS 106707], p. 106). Earthquakes of M_w 5.2 and 5.3 occurred in the Ridgecrest area in 1995.

Within the southern Great Basin, Rogers et al. (1991 [DIRS 106702], p. 154) identified the Southern Nevada Seismic Belt extending in an east-west direction between latitudes 36° and 38°N. Part of the activity within this belt is associated with the Pahranagat shear zone, extending east-northeast between the northern Nevada Test Site and the area of the 1966 Clover Mountains earthquake sequence (Figure 4-18). This zone has been a repeated source of M 3 to 4 earthquakes over the recent period of seismic monitoring. High-angle, strike-slip focal mechanisms are consistently reported in this region. The 1966 Clover Mountains (M_w 5.7), 1992 St. George (M_w 5.9), and 1902 Pine Valley (M_w 6) earthquakes and Pahranagat shear zone activity constitute most of the events located within the eastern half of the Southern Nevada Seismic Belt.

The northern region of the Nevada Test Site has experienced considerable earthquake activity associated with nuclear testing, in contrast to seismicity that is tectonic in origin in the southern part of the Nevada Test Site. Discriminating naturally occurring earthquake activity from events associated with underground nuclear explosions is problematic. The relative number of artificial and induced earthquakes in the areas where nuclear testing has occurred (Vortman 1991 [DIRS 107120], Appendix T) suggests that the natural seismicity of the region is close to the background activity of the southern Basin and Range Province. In 1979 and 1983, several swarms of microearthquakes occurred in the region, which were apparently unrelated to the underground nuclear explosions.

The Southern Nevada Seismic Belt also includes seismicity in the northern Amargosa Valley-Sarcobatus Flat area immediately to the west of Yucca Mountain. Activity is distributed in the vicinity of Beatty and the Bullfrog Hills; some of this activity may be related to mining. In Sarcobatus Flat, earthquakes have occurred in four clusters since the beginning of instrumental monitoring (Rogers et al. 1987 [DIRS 100176], p. 43). These clusters, which lie 10 to 20 km (6 to 12 mi) apart, trend north along the length of the valley. Focal mechanisms for the three southern clusters suggest right-lateral slip along northeast-trending structures. The fourth cluster, in the northern part of the valley, shows normal faulting on a northeast-trending fault (Rogers et al. 1987 [DIRS 100176], p. 47).

Significant historical earthquakes ($M_w > 5$) in the 300 km radius of the Yucca Mountain region are listed in Table 4-8. A more complete description of seismicity within 300 km (186 mi) of Yucca Mountain is found in CRWMS M&O (2000 [DIRS 151945], Section 12.3.3.3).

4.3.1.4 Characteristics of the Instrumentally Recorded Seismicity in the Southern Great Basin

Instrumentally recorded seismicity over about the past 20 years provides information on the characteristics of earthquakes that occur in the southern Great Basin. In addition to helping to define the extent and rate of recurrence for seismic source zones, the data also can be used to understand the thickness of the seismogenic crust in the Yucca Mountain vicinity. This thickness is one factor taken into account in evaluating the maximum magnitude for a seismic source. For some events, the data allow focal mechanisms to be determined. Focal mechanisms provide information on the state of stress in the Yucca Mountain region, which can be helpful in assessing the potential activity of faults.

4.3.1.4.1 Depths at which Earthquakes Occur

Various analyses have shown that earthquakes in the southern Great Basin occur predominantly between depths of 2 and 12 km (1 and 7 mi) (e.g., Rogers et al. 1987 [DIRS 100176], pp. 55 to 56; Harmsen and Bufe 1992 [DIRS 105108], pp. 42 to 43). Evaluations of data since 1992 are dominated by the aftershock sequence following the Little Skull Mountain earthquake (e.g., von Seggern et al. 2001 [DIRS 156297], p. 35, Figure 3-15). To address this situation, recent evaluations of data from the Southern Great Basin Digital Seismic Network (von Seggern et al. 2001 [DIRS 156297], pp. 35 to 37, Figure 3-15; von Seggern and Smith 2001 [DIRS 158461], pp. 26 to 27, Figure 3-6) segregate the catalog into earthquakes that occurred within the Little Skull Mountain aftershock zone and those that did not. Earthquakes that are not

part of the Little Skull Mountain sequence have depths primarily within a range of 4 to 12 km (2.5 to 7 mi) (Figure 4-20). Earthquakes within the Little Skull Mountain aftershock zone are more narrowly distributed between 8 and 12 km (5 and 7 mi). von Seggern and Smith (2001 [DIRS 158461], p. 26) note that earthquakes with depths less than 4 km were probably contaminated by a significant number of events whose depth was not well determined. However, they also note that many earthquakes in the Rock Valley area, south of Little Skull Mountain, are known to have very shallow depths (e.g., Shields et al. 1995 [DIRS 106772]).

Information on the depths of larger earthquakes that have occurred in the Basin and Range Province is of interest in assessing maximum magnitudes for hazard analysis. Because most of these events occurred during periods of less dense seismic network coverage, their depths are not well constrained. Several larger magnitude earthquakes are reported to have nucleated deeper than 15 km (9 mi) (Doser and Smith 1989 [DIRS 102805], pp. 1394 and 1397). Nucleation depths ranging from 10 to 20 km have been determined from waveform modeling for several major earthquakes in the Basin and Range Province, including the 1954 Dixie Valley earthquake; 1959 Hebgen Lake, Montana, earthquake; and 1983 Borah Peak, Idaho, earthquake. All three of these earthquakes are associated with surface faulting on range-bounding normal faults (Doser and Smith 1989 [DIRS 102805], p. 1388).

4.3.1.4.2   Focal Mechanisms

Focal mechanisms of recent earthquakes within the southern Great Basin indicate that right-lateral slip on northerly-trending faults is the predominant mode of stress release near the site (Pezzopane et al. 1996 [DIRS 106526], p. 7-3). Normal and oblique-slip faulting is also observed. Focal mechanisms for the period 1971 through 1992 indicate roughly equal proportions of strike-slip and normal faulting (Pezzopane et al. 1996 [DIRS 106526], p. 7-38, Table 7-3). The principal extensional (minimum compression) stress axes inferred from earthquake mechanisms trend northwest and plunge approximately horizontal (Figure 4-21). The principal compressional (maximum compression) stress axes from earthquake mechanisms are concentrated along a belt (girdle) that sweeps from vertical (normal faulting) to northeast and horizontal (strike-slip faulting). Thus, regional stress orientations indicate north-south and east-west orientations for high-angle fault planes, with right-lateral slip on the north-striking and left-lateral slip on the east-west striking surfaces. Normal and oblique slips are indicated on fault surfaces with orientations intermediate to these directions. The style of faulting determined from the focal mechanisms is not a function of depth (Rogers et al. 1987 [DIRS 100176], p. 64).

Harmsen and Rogers (1986 [DIRS 106092]) analyzed the stress field from a set of regional earthquake focal mechanisms. The presence of both strike-slip and dip-slip mechanisms in particular localities was interpreted to indicate an axially symmetric stress field, in which the intermediate and maximum compressive stresses are nearly equal (Harmsen and Rogers 1986 [DIRS 106092], p. 1560). They suggested that because no large earthquakes were present in the data set, movement along a variety of fault plane orientations was accommodated by an ample number of small preferably oriented faults. Rogers et al. (1987 [DIRS 100176], pp. 60 to 70); 1991 [DIRS 106702]) and Bellier and Zoback (1995 [DIRS 101649]) also discuss and analyze the modern stress field in regions of Nevada near Yucca Mountain.

4.3.1.5   Seismicity in the Vicinity of Yucca Mountain

While the southern portion of the Nevada Test Site, southeast of Yucca Mountain, is one of the more seismically active regions in the southern Great Basin (Figure 4-19), the area immediately around Yucca Mountain itself is rather aseismic. Gomberg (1991 [DIRS 105604], pp. 16411 to 16412; 1991 [DIR 105606], pp. 16397 to 16398) and Brune et al. (1992 [DIRS 104611], p. 164) showed that the Yucca Mountain zone of quiescence is a real feature of the seismicity and not an artifact of network design or detection capability. An experiment in high-resolution monitoring of seismicity at the site by Brune et al. (1992 [DIRS 104611]) also confirmed the existence of the quiescent zone. Modeling of the strain field in southern Nevada by Gomberg (1991 [DIRS 105606], pp. 16396 to 16397) suggests that this area is not accumulating significant strain and that Yucca Mountain is an isolated block within the structural framework of the southern Great Basin. Earthquakes located in the immediate vicinity of Yucca Mountain by the Southern Great Basin Digital Seismic Network are shown in Figure 4-22.

Several earthquakes that historical catalogs show as located at Yucca Mountain have been reexamined and shown to be located elsewhere. Two M 3.5 earthquakes in 1948, which were initially reported as being at Yucca Mountain, were reevaluated by von Seggern and Brune (1994 [DIRS 124621], pp. 16 to 20). Von Seggern and Brune found the waveforms and S-wave minus P-wave arrival times at the regional stations operating in 1948 were more consistent with a source near the Rock Valley fault zone than at Yucca Mountain. Gross and Jaumé (1995 [DIRS 105100], pp. 77 to 78) analyzed a number of small events from 1978 to 1992 that were in the historical catalog and reported to be in the Yucca Mountain block. By reviewing the archived waveform data, they determined that some of the events were incorrectly identified as earthquakes.

Figure 4-22 shows micro-earthquakes that have occurred within 10 km (6 mi) of Yucca Mountain between October 1995 and September 2002. The events ranged from M about -1 to 1 in size. These micro-earthquakes occurred throughout the Yucca Mountain block and had focal depths between about 3 and 13 km (2 and 8 mi). Short-period focal mechanisms were determined for some of the events and are consistent with normal to normal-oblique-slip on faults with orientations similar to several Quaternary faults mapped at the surface.

While the immediate Yucca Mountain area has been quiescent during the historical period, note that paleoseismic evidence (Section 4.3.2) indicates active Quaternary faults exist near the site. Paleoseismic events exhibit very long times between events from many thousands of years to more than 100,000 years. Little or no microseismicity may occur on the faults during this long time period. Many faults in the Great Basin with paleoseismic evidence for prehistoric surface-rupture earthquakes have little or no associated historical seismicity.

Seismicity to the east and southeast of Yucca Mountain is spatially associated with the Rock Valley, Mine Mountain, and Cane Springs fault zones. This activity forms a wide, northeast-trending zone that includes the 1973 Ranger Mountain sequence, 1992 Little Skull Mountain sequence, 1993 Rock Valley sequence, 1999 Frenchman Flat sequence, and other earthquake clusters (Harmsen 1993 [DIRS 105106]; 1994 [DIRS 106090]; 1994 [DIRS 105107]; Meremonte et al. 1995 [DIRS 106354]; Shields et al. 1995 [DIRS 106772], von Seggern et al. 2001 [DIRS 156297]) (Figure 4-19). The main shocks from the Little Skull Mountain and

Frenchman Flats sequences, near the ends of the seismicity zone, exhibited normal faulting on northeasterly-striking planes. The Rock Valley sequence in the middle of the zone exhibited strike-slip faulting. Some seismicity in the Yucca Mountain area is also spatially associated with the southern boundary of the Timber Mountain caldera.

1992 Little Skull Mountain Sequence–The largest earthquake recorded by the Southern Great Basin Seismic Network since its establishment in 1978 was the June 29, 1992, M_w 5.6 Little Skull Mountain earthquake (von Seggern and Smith 2001 [DIRS 158461] Figures 3-2 and 3-3). This event (Figure 4-19) produced a peak horizontal ground acceleration of 0.21 g at Lathrop Wells, about 11 km (7 mi) from the epicenter (Anderson et al. 1993 [DIRS 104754], p. 165). The earthquake caused minor damage to the Yucca Mountain Field Operations Center in Jackass Flats, which was located on the surface projection of the buried fault. The event was felt throughout the region. The earthquake appears to have been triggered by the 1992 Landers event that occurred approximately 20 hours earlier (e.g., Anderson et al. 1994 [DIRS 129941]; Bodin and Gomberg 1994 [DIRS 101469]; Gomberg and Bodin 1994 [DIRS 105608]). It occurred in an area of persistent recent seismicity, present throughout the recording period of the Southern Great Basin Seismic Network (Harmsen 1994 [DIRS 106090], p. 1485).

The Little Skull Mountain earthquake initiated at a depth of 11.8 km (7.3 mi), and the rupture was confined between depths of 6 and 12 km (4 and 7.5 mi) (Smith et al. 2000 [DIRS 158466], p. 2). There was no evidence of primary or secondary surface rupture. Rockfalls along the south-facing cliffs of Little Skull Mountain were observed shortly after the earthquake. The distribution of rockfalls was found to be consistent with the ground shaking predicted from the source model and provided a means of calibrating the distribution of ground shaking in the epicentral region (Brune and Smith 1996 [DIRS 102022], p. A-193). The earthquake occurred on a northeast-striking fault plane dipping steeply to the southeast (Harmsen 1994 [DIRS 106090], p. 1485; Meremonte et al. 1995 [DIRS 106354], p. 1039) and involved normal slip with a small left-slip component.

Three aftershocks of M_L greater than 4 occurred, not on the main shock fault plane but on adjacent off-fault structures accommodating the stress change from main shock rupture (Smith et al. 2000 [DIRS 158466], p. 8). The first M_L 4 aftershock occurred too soon after the main shock for its signal to be discriminated on the recorded seismograms from that of the larger, earlier main shock. The location of this aftershock could only be constrained to be east of the main shock epicenter. Focal mechanisms for two of the four M_L 4+ events show northeast-trending, southeast-dipping fault plane solutions.

The Little Skull Mountain earthquake could not be correlated with any mapped faults, although the aftershocks coincide with the projections of the Wahmonie, Cane Springs, and Mine Mountain fault systems near the Rock Valley fault zone. This area may be a zone of stress concentration, accommodating strain from fault systems throughout the south-central Nevada Test Site area (Smith et al. 2000 [DIRS 158466], p. 13). Dip angles determined for the main shock fault plane from the short-period focal mechanisms vary from 70°, consistent with the early aftershock activity, to 56° (Harmsen 1994 [DIRS 106090], p. 1485; Smith et al. 2000 [DIRS 158466], Table 1).

The aftershock sequence was recorded on a number of portable digital seismographs deployed in the epicentral area (Meremonte et al. 1993 [DIRS 106353]; Sheehan et al. 1994 [DIRS 105396]). These data were used to develop high-quality locations for aftershock studies (e.g., Smith et al. 2000 [DIRS 158466]) and contributed to ground motion modeling efforts (Schneider et al. 1996 [DIRS 103270]) that were considered in the PSHA.

1993 Earthquakes in the Rock Valley Fault Zone–Following the Little Skull Mountain earthquake in 1992, earthquake activity in the southern Rock Valley fault zone increased (e.g., Smith et al. 2000 [DIRS 158467], p. 2). Between 1978 and the occurrence of the Little Skull Mountain earthquake, only one M 3+ earthquake was located in this area by the Southern Great Basin Seismic Network. Since the Little Skull Mountain earthquake, a number of M 3.5+ earthquakes and a sequence of very shallow, small-magnitude (M_L less than or equal to 3.7) earthquakes occurred in southern Rock Valley.

The shallow sequence of earthquakes in 1993 was recorded on a near-source portable digital instrument. This station recorded more than 600 earthquakes, of which only 140 triggered the regional seismic network and could be located (Smith et al. 2000 [DIRS 158467], p. 3). S-wave minus P-wave arrival times for the events averaged about 0.5 seconds at this station, and relocations of the earthquakes place them at a depth of only about 2 km (~1 mi). The largest event of the sequence (M_L 3.7) also occurred at a 2 km depth. A cluster of earthquake activity also occurred southeast of the Rock Valley fault zone in the Spotted Range in late 1993 (Smith et al. 2000 [DIRS 158467], p. 9). This cluster of seismicity was the most active in the region east of the Nevada Test Site since the 1973 Ranger Mountain sequence, but was confined to a small volume; it included several earthquakes greater than M 3.

1999 Frenchman Flat Earthquake Sequence–The January 27, 1999, M_w 4.7 Frenchman Flat earthquake was the largest event within the Nevada Test Site since the M_L 5.6 Little Skull Mountain earthquake in 1992. Both events were located near the Rock Valley fault zone, but the distribution of aftershocks and focal mechanisms indicated that the Rock Valley fault system was not involved in either event (Smith 2000 [DIRS 150194]). The Little Skull Mountain earthquake occurred near the western end of Rock Valley. The Frenchman Flat event took place at its eastern end where the Rock Valley fault zone appears to terminate into the basin at Frenchman Flat. The Frenchman Flat main shock was preceded by an extended fore shock sequence that included a M_L 4.2 earthquake. Portable instrumentation was installed shortly after the main shock to provide better constraint on aftershock locations. The main shock appears to have resulted from normal slip on a northeast-striking fault (Smith 2000 [DIRS 150194]).

1999 Scotty's Junction Earthquake Sequence–The M_L 5.7 Scotty's Junction earthquake occurred on August 1, 1999, about 11 km (7 mi) north of Scotty's Junction, Nevada. The earthquake involved primarily normal faulting on a moderately dipping, north-northeast-striking fault plane (Smith 2000 [DIRS 150194]). The aftershock distribution shows a slight alignment with the Sarcobatus Flat fault bordering the volcanic tuffs to the east of the main shock. Main shock depth is estimated to be at about 7 km (4 mi), although permanent station coverage in the epicentral area is poor. The main shock was preceded by a fore shock sequence that included 13 events with M_L greater than 2 beginning on July 31, 1999. Two aftershocks of M_L 4.8 and 4.9 occurred within the first two days after the main shock (Smith 2000 [DIRS 150194]).

4.3.2   Prehistoric Earthquakes at Yucca Mountain

The identification and documentation of earthquakes occurring prior to historical times is possible by studying the geologic record of past events. Larger events that rupture to the surface often leave geological evidence in the form of offset strata and characteristic earthquake-related deposits. Geologic fault studies at Yucca Mountain reveal that the recurrence times of large-magnitude earthquakes are on the order of tens of thousands of years (Keefer et al. 2003 [DIRS 159419]), much longer than the 130 yr historical earthquake record of the Yucca Mountain region. Thus, the prehistoric earthquake history of the Yucca Mountain site spans at least the past several hundred thousand years. This history is particularly important for probabilistic seismic hazard assessments because it extends the record for larger magnitude events.

Geologic studies of faulted deposits are the basis for identifying the occurrence of large-magnitude, surface-rupturing earthquakes and evaluating their size, age, and occurrence rate. Aerial photographs were examined to locate and map evidence of Quaternary surface faulting, such as fault scarps or small slope changes produced by faulting of geologically young colluvial and alluvial deposits or geomorphic surfaces. Typically these deposits and surfaces are Quaternary in age, which spans approximately the past 2 m.y. At the most promising locations, trenches were excavated across the fault scarps, and the late-to-middle Quaternary soils and stratigraphy were mapped specifically to document the size and age of surface-faulting displacement events. The ages of critical deposits were determined where possible, using appropriate geochronologic techniques, to assess the timing of past earthquakes. Fault slip rates were estimated from the age of offset geological deposits and the amount of fault displacement. The prehistoric earthquake record has been constructed from the results of these paleoseismic and geochronologic studies.

Investigations were conducted to identify faults in the Yucca Mountain area that have evidence of Quaternary displacements (Reheis 1991 [DIRS 102916], 1992 [DIRS 106652]; Reheis and Noller 1991 [DIRS 102891]; Dohrenwend et al. 1991 [DIRS 124370]; Dohrenwend et al. 1992 [DIRS 124376]; Anderson et al. 1995 [DIRS 101422], Anderson et al. 1995 [DIRS 105345]; Piety 1996 [DIRS 106540]). These studies were reconnaissance in nature, consisting of a combination of literature research, aerial photographic interpretation, and field traverses to evaluate offset geomorphic surfaces and fault scarps. These studies identified 105 faults with known or suspected Quaternary activity within a 100 km (60 mi) radius of the repository site at Yucca Mountain (Figure 4-23).

Studies, including detailed field mapping, have also been conducted of faults at and near Yucca Mountain with known or suspected Quaternary activity (Faulds et al. 1994 [DIRS 105126]; Simonds et al. 1995 [DIRS 101929]; Whitney and Taylor 1996 [DIRS 107309]; Keefer et al. 2003 [DIRS 159419]). This work identified the location and surface characteristics of the mapped faults and identified locations where Quaternary displacement is evident. Specific physiographic and structural evidence for Quaternary displacements was identified and mapped. Geologic and structural information on the major faults in the Yucca Mountain vicinity is summarized in Section 3.5.

Displaced or deformed alluvial and colluvial deposits record late Quaternary faulting along nine local faults in the Yucca Mountain area. These faults include, from west to east, the Northern Crater Flat, Southern Crater Flat, Windy Wash, Fatigue Wash, Solitario Canyon, Iron Ridge, Stagecoach Road, Bow Ridge, and Paintbrush Canyon faults. Estimates of several paleoseismic parameters for local site faults, including information on fault lengths, probable rupture lengths, and geometric relations between faults, are primarily based on the map compilation of Simonds et al. (1995 [DIRS 101929]). Paleoseismic investigations of these faults are described briefly in Section 3.5, and, in more detail, in Whitney and Taylor (1996 [DIRS 107309]) with references cited therein. Keefer et al. (2003 [DIRS 159419]) provide an updated interpretation of the fault trench data in which some new sample ages are taken into account. While some slip rates and recurrence intervals have been modified from the original interpretations presented in Whitney and Taylor (1996 [DIRS 107309]), the overall conclusions are similar.

Prehistoric earthquakes are interpreted on the basis of displacement of Quaternary deposits and timing of surface ruptures at specific locations. A total of 52 exploratory trenches and natural exposures have been excavated, cleaned, and logged in the past 20 years as part of seismotectonic investigations in the Yucca Mountain site area (Swadley et al. 1984 [DIRS 102917]; Whitney and Taylor 1996 [DIRS 107309]; Keefer et al. 2003 [DIRS 159419]). Forty of these trenches and exposures are located across the nine local Quaternary faults described above. In the central repository block, the remaining 12 trenches are situated across bedrock faults, which lack direct evidence for Quaternary activity. Twenty-eight trenches display clear evidence for displacement of Quaternary deposits across the fault traces. The other trenches lack evidence of Quaternary displacement, either because the trench did not intersect a fault in surficial deposits or because undisturbed deposits were found to overlie a bedrock fault. Trenches that expose unfaulted Quaternary deposits above bedrock faults also provide constraints on the maximum possible length of prehistoric surface ruptures during the Quaternary age.

An additional 11 trenches were excavated across the nearby Bare Mountain and Rock Valley faults, located within a 20-km (12-mi) radius of the site. All of these trenches exposed displaced Quaternary deposits.

Paleoseismic data provide the basis for interpretations made as part of the PSHA. Such data, which were collected or interpreted from trench sites, include fault geometry, character and ages of faulted and unfaulted Quaternary surficial deposits and soils, number and ages of individual surface displacement events, displacement amounts, earthquake recurrence, and fault slip rates. Paleoseismic data available at the time of the PSHA are described in Whitney and Taylor (1996 [DIRS 107309]). A summary of data, based on updated interpretations and data from Keefer et al. (2003 [DIRS 159419]), is provided in Table 4-9.

4.3.2.1   Fault Slip Rates

Fault slip rate is the time-averaged rate of displacement on a fault in millimeters per year. Slip rate is an important paleoseismic parameter and is a standardized measure of activity on the fault, which can be directly used for comparing the activity of many different faults. Fault slip rates are calculated by dividing the amount of cumulative net slip by the age of a specific faulted

deposit or horizon. Fault slip rates were computed at each trench site from measurements of the observed net displacement of one or more dated units. Minimum, maximum, and preferred slip rates were calculated at each site. These rates vary over a large range of values. The range of slip rates reflects uncertainties in both age control and displacement measurements.

Meaningful slip rates should span at least several seismic cycles, encompassing multiple displacement events. This is particularly important for long recurrence, low slip-rate faults such as those observed at Yucca Mountain. At Yucca Mountain, slip rates are averaged values derived from the oldest faulted units with adequate age control, which typically are displaced by two, and commonly three or more, events.

The spatial distribution of fault slip-rate measurements for local faults at Yucca Mountain is determined by the distribution of trench sites with suitable paleoseismic data. One to four slip-rate determinations were computed for nine of the Quaternary faults at Yucca Mountain, as well as the nearby Bare Mountain and Rock Valley faults. The level of study of known and suspected Quaternary faults at distances greater than about 25 km (15 mi) from Yucca Mountain is lower, except for the large, high slip-rate Death Valley and Furnace Creek faults. Trench-derived paleoseismic data, most suitable for slip-rate calculations, are not available for most regional faults. Instead, estimates, with large uncertainties, are derived from the observed offset of geomorphic surfaces using generalized ages based on soil development (Whitney and Taylor 1996 [DIRS 107309], p. 4.0-12).

Estimates of slip rates for faults at Yucca Mountain vary from 0.001 to 0.07 mm/yr (Table 4-9). Preferred slip rates, when determined, are on the order of 0.002 to 0.05 mm/yr.

Even given the uncertainties in slip-rate estimation, the slip rates at Yucca Mountain are low to very low. For example, faults with slip rates of 0.01 mm/yr or less are associated with extremely low rates of activity in a classification of active faulting developed by Slemmons and dePolo (1986 [DIRS 106815]). The slip rates observed at Yucca Mountain fall within the moderately low to low activity fault classification in a regional scheme developed by dePolo (1994 [DIRS 104855], p. 49). This scheme uses slip rates to categorize the activity of normal faults in the Basin and Range Province. The slip rates on faults at Yucca Mountain are equal to, or less than, the lowest values in a regional compilation of slip rates developed by McCalpin (1995 [DIRS 104770]) from fault studies in the entire Basin and Range Province. It should be noted that paleoseismic investigations capable of providing slip rates are rarely conducted on faults with these low rates of activity.

For faults at Yucca Mountain, slip rates are generally lowest at northern sites, intermediate at central sites, and highest at the southernmost sites. This southern increase in the level of Quaternary tectonism resembles other late Cenozoic tectonic patterns at Yucca Mountain. For example, the cumulative offset of bedrock units generally increases to the south along faults at Yucca Mountain (Scott 1990 [DIRS 106751]). Similarly, in the Yucca Mountain area, the total amount of extension across all of the faults increases to the south (Fridrich et al. 1996 [DIRS 105086]). Also, the amount of paleomagnetic rotation of volcanic rocks increases southward (Rosenbaum et al. 1991 [DIRS 106708]; Hudson et al. 1994 [DIRS 100986]).

4.3.2.2　Per-Event Displacements

Per-event displacements are an important paleoseismic parameter for estimating the maximum magnitude of prehistoric earthquakes. The most precise per-event displacements were estimated directly from trench log data. Up to eight measurements of per-event displacement are available for faults at and adjacent to the Yucca Mountain area (CRWMS M&O 2000 [DIRS 151945], Table 12.3-8). Fewer data on per-event displacements are available for regional faults, and the estimates generally are less precise. They are based primarily on the projected measurement of geomorphic surfaces across topographic scarps or the surface trace of the faults.

Per-event displacement data are obtained from trench logging in the following manner. Where possible, displacements associated with each faulting event are determined directly by measuring the apparent offset of marker horizons across the fault, and then subtracting the amount of offset related to any younger events identified higher in the stratigraphic section. This procedure cannot be used if different deposits are present on opposite sides of the fault. For example, at some sites, late Quaternary deposits on the hanging-wall block are faulted against much older deposits or bedrock on the footwall block. Several other methods are used in this situation. In some cases, rupture amounts are derived from the thickness of fault-related colluvial wedges, which may result in minimum estimates that are 50 to 80 percent of the actual surface displacement (e.g., Swan et al. 1980 [DIRS 106954], p. 1441). An alternative method involves measuring vertical separation between a displaced event horizon in the hanging-wall block and the stratigraphically highest faulted unit on the footwall block. Subtracting from this measurement the offsets related to events stratigraphically higher in the hanging-wall block results in displacements per event. A similar technique uses the stratigraphic thickness of deposits between successive event horizons on the hanging-wall block as a maximum estimate for the displacement associated with the stratigraphically lower event. Measurement uncertainties, inherent in all of these methods, are included in the range of displacements reported. The resolution of per-event displacement measurements generally decreases with increasing age because of the propagation of measurement error for successively older displacements in an event sequence.

Dip-slip values for single-event displacements are adjusted to derive net-slip estimates wherever possible. The amount of normal-oblique slip is calculated for any site that contains possible slip indicators. Examples of slip indicators include Quaternary slickensides on bedrock shears or, less reliably, fault striations on carbonate coatings. At some sites, units in the hanging wall are deformed near the main fault zone either by backtilting towards the fault surface or by development of antithetic grabens. The effects of this secondary deformation are removed by projection of displaced horizons into the fault zone from undeformed sections of the hanging wall and footwall prior to measuring displacements on the main fault. All measurement uncertainties are incorporated in derivations of net single-event displacements. Slip indicators clearly associated with Quaternary displacements were rarely observed. Consequently, studies in Whitney and Taylor (1996 [DIRS 107309]) often report dip-slip estimates of single displacements that do not consider modest components of lateral slip. The few slip indicators observed increased displacement amounts by factors of 1.1 to 1.7 above values determined assuming pure dip-slip movement.

Data on fault displacement per event were available for the PSHA are described in Whitney and Taylor (1996 [DIRS 107309]). Table 4-9 summarizes the most recent interpretations of displacement per event for each fault (Keefer et al. 2003 [DIRS 159419]). Most of the uncertainty in the estimates results from measurement uncertainties noted above. Preferred values are based on additional geologic constraints and/or the judgment of the investigator. Preferred per-event displacements vary from near 0 to 257 cm. Fracture events with no detectable offsets are also sometimes identified. Displacements per event are larger (80 to <362 cm) for the Rock Valley and Bare Mountain faults relative to the block-bounding faults at Yucca Mountain. Available estimates of single-event displacements for regional faults are in the general range of those for site faults, with the exception of displacements of 240 to 470 cm on the Death Valley-Furnace Creek fault system.

Single-event displacements are also tabulated for nine scenarios of distributive faulting at Yucca Mountain (CRWMS M&O 2000 [DIRS 151945], Table 12.3-10). Paleoseismic displacements are compiled and plotted as a function of position along the faults, providing a crude slip distribution for each scenario earthquake (Pezzopane et al. 1996 [DIRS 106528]). A method is used to project length along fault traces and paleoseismic study sites onto a north-south plane using a join line at 36°50'N. Displacements associated with each rupture scenario are plotted at the projected position onto this line. Generally, several scenarios exhibit asymmetrically shaped slip distributions, with displacements increasing to the south.

4.3.2.3 Rupture Lengths

Coseismic surface-rupture length is an important parameter used to define the maximum magnitudes of prehistoric earthquakes. Determination of rupture lengths for prehistoric earthquakes can be limited by the availability of surficial mapping data, the locations of trenches, and displacement-event timing data. As noted previously, trench sites generally are located for purposes other than defining paleorupture length. The length of a rupture is determined by the lateral extent a given event can be identified along one or more faults. In some cases, this identification is accomplished via event correlations between sites using similarities in ages and other supportive geologic criteria. Surface-rupture lengths may be equivalent to the total fault length or may be restricted to a specific portion, or segment, of the fault, as discussed below.

Lengths of individual local faults and regional faults in the Yucca Mountain area have been measured along their curvilinear traces. For local faults, maximum, minimum, and preferred lengths are given. These variations in length reflect the manner in which specific disconnected sections of mapped fault traces could be linked together. Individual local fault lengths vary from about 1 to 25 km. Fault lengths in the region surrounding the site range from several kilometers to more than 300 km for the Death Valley-Furnace Creek-Fish Lake fault system. Except for very long, likely segmented faults (see following discussion), the total measured length of a fault represents its maximum rupture potential. This interpretation is considered reasonable, especially for the relatively short faults at Yucca Mountain based on the relationships identified by Wells and Coppersmith (1994 [DIRS 107201]) and Pezzopane and Dawson (1996 [DIRS 103265]).

Fault lengths determined from their mapped surface traces do not always correspond to the length of coseismic surface rupture. Coseismic surface rupture may be segmented; i.e., confined

to a particular section of the fault because of geometric irregularities, physical characteristics of the fault zone, or by the magnitude of the associated earthquake (Aki 1979 [DIRS 101456], 1984 [DIRS 101457]; Schwartz and Coppersmith 1984 [DIRS 104574], 1986 [DIRS 104575]; Schwartz 1988 [DIRS 104573]). Segmentation of fault rupture can be proposed only when analysis of timing constraints on displacement events from multiple sites along a fault or system of faults is used. Even then, resolution of chronologic methods is not sufficient to preclude multiple closely timed events. Rupture segmentation is considered likely on most of the long regional faults, although adequate timing data for faulting events generally are not available to precisely define segment boundaries and lengths.

The presence of rupture segmentation on local Yucca Mountain faults is not well established. However, based on geometric complexities, possible fault segments are identified on at least three local faults: Paintbrush Canyon, Solitario Canyon, and Windy Wash faults. The distribution and resolution of event data are not sufficient to uniquely constrain any rupture segmentation on these three faults. Most of the geometric segments are short (5 to 10 km) and are, therefore, considered unlikely to rupture independently. However, the displacement-timing data suggest that the entire lengths of the faults may not have ruptured in all displacement events. To account for possible rupture segmentation on local faults, minimum rupture lengths are determined for each scenario rupture based on the distribution of paleoseismic sites that contain a given event.

Maximum and minimum lengths are estimated for nine rupture scenarios that have been proposed for distributed faulting on local faults (Table 4-10). The scenarios are based on information available in 1996. The fault trace lengths and locations of paleoseismic study sites associated with each scenario are projected into a common plane, using the projection technique developed for scenario displacements. This method provides a way to obtain composite rupture lengths for scenario events that span more than a single fault at Yucca Mountain. This projection method has inherent distortion that may overestimate rupture length by 1 to 2 km.

Minimum rupture lengths are derived from the northernmost and southernmost trenches that contain the same displacement event associated with a particular scenario. In instances where no trench data are available to constrain the surface-rupture extent, the endpoints of ruptures along nearby faults with trench data are used. In most cases, this results in a partial rupture length relative to the entire length of the projected fault system. Note that on some faults, estimates of minimum rupture length are based on paleoseismic evidence indicating that an event at a site did not occur. This results in a rupture length that is shorter than would be obtained using the trench-to-trench length method. Maximum rupture lengths are estimated by using the longest fault or combination of faults based on the preferred fault length measurements (CRWMS M&O 2000 [DIRS 151945], Table 12.3-8). Maximum-scenario rupture lengths are derived by assuming that an entire fault ruptured if any study site had evidence for the scenario event. As with the minimum-rupture-length estimates, the maximum-scenario rupture length using the entire fault length can be superseded when paleoseismic data preclude the occurrence of a particular scenario event. Thus, in a few cases, the maximum rupture length is shorter than the length of any individual fault involved in the scenario rupture.

4.3.2.4   Recurrence Intervals

Recurrence interval is defined as the time interval between successive surface-rupture earthquakes. It is an important temporal measure of fault behavior in seismic hazard analysis. Recurrence intervals are calculated for individual faults at all relevant sites using paleoseismic data of the number and timing of coseismic surface-rupture events. Individual recurrence intervals are estimated in cases for which there is adequate age control to isolate the timing between specific pairs of events. Recurrence interval errors are smaller when dated units are colluvial wedges or fissures that can be directly tied to faulting events. Unfortunately, this condition is rare in the study trenches. More commonly, deposition occurred at an unknown time prior to or following an event. Thus, the ages for events bracketed by the poorly dated deposits are uncertain. In these cases, an average recurrence interval is calculated by dividing the time bracketed with the age estimates by the number of potential events. Uncertainties in both the dating of units and the number of possible events are incorporated into the reported ranges of recurrence intervals. Late Quaternary recurrence intervals typically are shorter than those of older (greater than 100 to 200 k.y.) events because small displacement events are better preserved in younger deposits and these deposits are more likely to have better age control.

Ages of faulted and unfaulted units and soils are based on geochronologic studies (Paces et al. 1994 [DIRS 106473], 1995 [DIRS 101352]; Whitney and Taylor 1996 [DIRS 107309]). Two basic absolute dating techniques are used: thermoluminescence analysis of fine-grained, polymineralic sediment; and U-Th disequilibrium series (U-series) analyses of pedogenic carbonate-silica laminae and clast rinds, matrix soil carbonate, and rhizoliths (carbonate-replaced root casts). These techniques have undergone extensive testing, development, and refinement during the course of the studies.

Additional geochronologic constraint is provided by correlation of trench deposits and soils with a composite Quaternary chronosequence of surficial deposits in Yucca Mountain (Section 3.3.7) (Whitney et al. 1996 [DIRS 107317]; Taylor 1986 [DIRS 102864]; Peterson 1988 [DIRS 106512]; Hoover 1989 [DIRS 101247]; Wesling et al. 1992 [DIRS 107290]; Lundstrom et al. 1993 [DIRS 106327]; Peterson et al. 1995 [DIRS 106519]). Age assignments for map units in this regional chronosequence are based on a number of geochronologic techniques, including ^{14}C dating of charcoal, thermoluminescence dating, and U-series and U-trend dating of soil carbonate. Some age-dating techniques that were used earlier in the project, such as U-trend dating of soil carbonate, have since been found to be unreliable (e.g., Latham 1995 [DIRS 107482]).

At least one, and commonly two or more, recurrence-interval estimates are made along individual faults at Yucca Mountain (Whitney and Taylor 1996 [DIRS 107309]; Keefer et al. 2003 [DIRS 159419]). Based on the most recent interpretations (Keefer et al. 2003 [DIRS 159419]), average recurrence intervals of individual faults range from 5 to 270 k.y.; preferred average recurrence intervals for all events range from 20 to 140 k.y. (Table 4-9). Recurrence interval information available at the time the PSHA was carried out is described in Whitney and Taylor 1996 [DIRS 107309]. The long recurrence intervals likely result from relatively small numbers of observed displacements in middle Pleistocene deposits.

Ages of regional fault displacement events have been estimated from one or more geomorphic characteristics. These characteristics include the surface expression of the fault, fault scarp morphology, and relationship of the fault to adjoining Quaternary surfaces and deposits, with age assignments based on surface morphology or soil development. Estimates of recurrence intervals for regional faults are, in general, based on limited paleoseismic data. Recurrence intervals vary from up to 100 k.y. to as little as 0.5 to 1.5 k.y. for the Death Valley and Furnace Creek faults.

Nine rupture scenarios were developed for the main Quaternary faults at Yucca Mountain (Table 4-10) based on information available in 1996. The scenarios accommodate distributed displacements on more than one fault during a single prehistoric earthquake. Methods for identifying scenarios and the characteristics of each scenario are described by Pezzopane et al. (1996 [DIRS 106528]). The scenarios are based on correlations of event timing data within the past 150 k.y. between individual trench sites on each of the faults. The scenario correlations are developed from simple probability distribution plots with three basic shapes (boxcar, triangle, and trapezoid), which represent the minimum, maximum, and preferred timing constraints for a given event at each site. The event timing distributions are superposed upon one another and a simple average is calculated from the number and sum of the overlapping distributions. Peaks in the cumulative probability density function occur at times when more than one event's distribution function overlaps another event's timing. At times when two or more events overlap, the cumulative average is higher than when no events overlap. Thus, the shape and overall range of the cumulative distribution characterizes the resultant event correlations and their timing distributions for the different recurrences. Scenarios identified in this manner are then tested for reasonableness using other geologic constraints, such as correlations of deposits and soils offset by the event at the trench sites involved in the scenario, the spatial association of these sites, and the structural and geophysical relationships of faults in the scenario. Preferred ages for all of the nine rupture scenarios thus identified are listed in Table 4-10. The correlations are rated also as high, moderate, or low on the basis of both geochronologic and geologic constraints.

4.3.3 Vibratory Ground Motion

To the extent possible, the vibratory ground motions adopted for the seismic design of the repository and analysis of its postclosure performance should incorporate the effects of the seismic sources, propagation path, and local site geology specific to the Yucca Mountain region and site. Ideally, recorded ground motions from earthquakes in the Yucca Mountain region or Basin and Range Province would be used to develop attenuation relations for application at Yucca Mountain, but such data are small in amount and are not sufficient to adequately constrain empirical models. The few data recorded in the Yucca Mountain region and Basin and Range Province and the geophysical and seismological properties derived for the region do, nevertheless, provide valuable information for estimating ground motions at the repository site. This information forms part of the basis for the expert interpretations and assessments of uncertainty that were part of the PSHA for Yucca Mountain.

Characterizing ground motions at Yucca Mountain using existing attenuation relations involves resolving whether (and to what extent) those relations for the western United States (primarily California) are applicable to the Basin and Range Province, in general, and to Yucca Mountain,

in particular. The seismological questions asked must include whether differences in the factors that influence ground motions in the Yucca Mountain region and in the western United States would lead to significant differences in ground motion estimates for the two regions. These factors include seismic source properties, regional crustal properties, and shallow geologic site properties at the repository. Generally, comparisons must be made between Yucca Mountain factors and average factors inherent in the strong motion database for the western United States.

To address these issues, four ground motion studies were carried out as part of site characterization activities. The first study was an empirical analysis of worldwide ground motion data from extensional regimes (Spudich et al. 1996 [DIRS 110503]). Use of data from beyond the Basin and Range Province was necessary to build up a large enough database to yield statistically significant results. The second study comprised numerical modeling of selected scenario earthquakes near Yucca Mountain in which ground motion was estimated using seismological models of the source, path, and site effects (Schneider et al. 1996 [DIRS 103270]). The numerical modeling allowed the region-specific crustal structure and site-specific rock properties to be incorporated in the ground motion estimates. The third study used weak motion recordings to characterize the near-surface attenuation at Yucca Mountain (Su et al. 1996 [DIRS 100087]). The fourth study (CRWMS M&O 1998 [DIRS 103731]) is the ground motion characterization performed as part of the PSHA (Section 4.3.4) and is the most comprehensive of the four. It incorporated results from the other three studies and resulted in ground motion attenuation relations specific to Yucca Mountain. The results of these four studies are described in the following sections.

4.3.3.1 Key Seismologic Parameters

Several key seismologic parameters are integral to ground motion studies for the Yucca Mountain region. Insofar as they form the input to the various analyses, the parameters, and often their uncertainties, must be adequately quantified. The following discussion presents the current understanding of several of these parameters.

Path Seismic Quality Factor (Q) and Geometrical Spreading—The attenuation properties for the southern Great Basin (including Yucca Mountain) vary widely, depending upon the data set and the analysis method. Several studies have observed the ground motion attenuation rate with distance, which includes the combined effects of geometrical spreading and damping parameter "Q." In a study of Modified Mercalli intensities for the 1952 Kern County earthquake, Evernden (1975 [DIRS 105274], p. 1297) concluded that the ground motion decay rate toward the southern Great Basin was slightly lower than in southern California. On the other hand, Chavez and Priestley (1985 [DIRS 102558], p. 1596) found slightly greater attenuation in the southern Great Basin than in southern California from an evaluation of the M_L scale.

Considering Q alone, and taking $Q(f) = Q_o f^\eta$ where Q_o and η are model parameters and f is frequency, various investigators have found significant differences in Q_o and η. Computed values of Q_o at 1 Hz vary between about 140 and over 750, with η values ranging from 0.04 to 1.05 (Schneider et al. 1996 [DIRS 103270], Table 5.1).

Influences of the following factors contribute to these differences:

- Assumptions about geometrical spreading and scattering
- Other source, path, and site effects
- Widely varying frequency bands, source-receiver distances, and regions of coverage
- Scattering versus anelastic Q
- Vertical versus horizontal component records
- Earthquake versus explosion sources.

Although the apparent differences in Q can be quite large, it is likely that a significant portion of these differences have origins in one or more of these factors.

For ground motion estimation at Yucca Mountain, uncertainty in Q has a relatively small impact on ground motion variability, because of the dominance of close-in sources. Deaggregation of the probabilistic seismic hazard results for Yucca Mountain indicates that most of the hazard for short-period structural response frequencies is derived from sources at distances less than 15 km. For longer-period frequencies, contributions to hazard come from both near-by sources and sources at a distance of about 50 km (CRWMS M&O 1998 [DIRS 103731], Figures 7-15 and 7-16). However, the uncertainty is a factor at very high frequencies, for very low Q values, and for long travel paths (e.g., 50 to 100 km).

Two-Dimensional Crustal Structure–Many underground nuclear explosions have been recorded at Yucca Mountain and in the surrounding region. Walck and Phillips (1990 [DIRS 107122]) have analyzed some of these data. The data constitute 1,829 recordings from 109 events. Of the recordings, 429 are from Yucca Mountain, including 128 downhole recordings.

Based on these data, Walck and Phillips (1990 [DIRS 107122]) developed two-dimensional velocity profiles from Pahute Mesa to Yucca Mountain and from Yucca Flat to Yucca Mountain. The two-dimensional structure is more prominent from Yucca Flat to Yucca Mountain than from Pahute Mesa to Yucca Mountain. For very shallow sources, such as underground nuclear explosions, this structure can have a significant effect on the ground motion. However, the effect on ground motions from earthquake sources at typical seismogenic depths (5 to 15 km) was not evaluated in this study.

Site Attenuation–Recordings of regional earthquakes at Yucca Mountain were used by Su et al. (1996 [DIRS 100087]) to evaluate the near-surface attenuation (or spectral decay) parameter kappa at 12 sites. Their data set comprises broadband digital recordings of 20 aftershocks of the 1992 Little Skull Mountain earthquake. These aftershocks occurred southeast of Yucca Mountain at distances of about 20 to 30 km, had focal depths of 9 to 12 km, and ranged in magnitude from M_L 2.6 to 4.5 (Su et al. 1996 [DIRS 100087], Figure 1, Table 2). The recording sites are located generally east and southeast of Yucca Mountain.

The computational approach involves simultaneous least-squares fitting of kappa, seismic moment, and corner frequency to the S-wave spectra (Anderson and Humphrey 1991 [DIRS 105304]). The analysis assumes that the source spectrum corresponds to a Brune pulse, with the displacement spectrum falling off proportional to ω^{-2} (ω is circular frequency), and that

geometric spreading is 1/R (R is distance). All other differences between the source and site spectra, including all path and site effects, are included in the estimate of kappa.

The values of site kappa vary between a minimum of 0.005 s at a station on Paleozoic rock and a maximum of 0.03 s for a station on soil over Tertiary rock (Su et al. 1996 [DIRS 100087], Table 4). Kappa measured at a tuff site on the Yucca Mountain crest is 0.023 s, and on the flank on a tuff is 0.014 s. The median kappa for all sites is 0.015 s, with a median standard deviation of the computed kappas of about 0.003 s. The average kappa of the two tuff sites is 0.018 s. These values are lower than those for typical California soft rock (0.03 to 0.04 s). Therefore, at low levels of shaking, damping from the tuff is less than that for California soft rock conditions, leading to larger high-frequency ground motion on the tuff as compared to that on California soft rock, assuming that all other parameters are the same. The results of Su et al. (1996 [DIRS 100087]) were used to provide a kappa value for the Yucca Mountain PSHA.

Biasi and Smith (1998 [DIRS 129113], pp. 2 and 3) measured kappa values from very small earthquakes in the Yucca Mountain vicinity. Kappa was determined by fitting the displacement spectra, which was assumed to be flat in the frequency band of interest for these very small magnitude events. Thus, the shape of the source spectrum did not have to be assumed. Results from approximately 250 earthquakes indicate kappa ranges from about 0.022 to 0.056 s, a significantly larger value than obtained by Su et al. (1996 [DIRS 100087]). The higher value of kappa would imply lower ground motions, at least at high frequencies. To explain the difference, Biasi and Smith suggest that the source model used in the Su et al. study underestimates the average radiated high-frequency energy.

Although these results pertain to conditions in the Yucca Mountain region, the values obtained are limited by the data set available for interpretation. The data are deficient in large-magnitude earthquakes (M_w 6.5 and larger). The smaller magnitudes limit the strains that develop in the rock and consequently limit any potential nonlinear site effects. The data are also limited in the range of source-to-site recording distances and geometries. Most data come from the Little Skull Mountain aftershock zone. Variations in properties caused by deeper structure, which would be sampled by earthquakes at longer distances, and those caused by any azimuthal differences in structure, cannot be evaluated.

Local Seismic Velocity Structure–Recent site characterization activities (BSC 2002 [DIRS 157829]) have supplemented earlier work (Majer et al. 1996 [DIRS 106330]) to provide information on the local velocity structure at Yucca Mountain. The earlier work was not conducted to measure near-surface values, and the results are not generally reliable within the uppermost several hundred meters from the earth's surface. In addition to information on seismic velocity, the recent studies have also included testing to determine shear modulus reduction and damping as a function of shear strain (BSC 2002 [DIRS 157829]).

Vertical seismic profile surveys were performed in Boreholes USW G-2, USW G-4, USW NRG-6, USW SD-12, and USW WT-2 by Majer et al. (1996 [DIRS 104685]) and in UE-25 UZ#16 by Balch and Erdemir (1996 [DIRS 105351]). Testing in Boreholes USW G-4 and USW SD-12 used a hammer source, which adequately samples shallow strata. Testing in the remaining boreholes and other testing in USW SD-12 used a vibroseis source. The deepest depth sampled was about 671 m in Borehole USW G-2. The vertical seismic profile field

measurements were processed to obtain P- and S-wave interval velocities (Majer et al. 1996 [DIRS 104685]).

Geotechnical investigations reported by BSC (2002 [DIRS 157829]) also describe testing to gather information on seismic velocities. Testing techniques included downhole seismic velocity surveys and suspension seismic surveys in boreholes, and spectral-analysis-of-surface-wave (SASW) surveys carried out along the ground surface and in the ESF. At the potential site of repository surface facilities, the borehole techniques were employed in 16 "UE-25" Boreholes (UE-25 RF#13 through UE-25 RF#29) and 40 SASW surveys were carried out. Borehole depths ranged from 30 to 203 m. The goal of the SASW surveys was to characterize velocities in the upper 46 m, although some surveys provided data at larger depths. Mean shear-wave velocity from the various techniques ranged from about 305 m/s at the surface to about 1,524 m/s at a depth of 198 m (BSC 2002 [DIRS 157829], Figures 22, 30, and 89).

To characterize the repository block, downhole velocity surveys were carried out in Boreholes USW UZ-N27, USW UZ-N33, USW UZ-N46, USW UZ-N64, USW UZ-N66, USW UZ-N71, USW UZ-N75, and USW UZ-N94. Survey depths ranged from 9 to 55 m. Also within the repository block, data from 36 SASW surveys were collected. Some SASW surveys were designed to measure shear-wave velocity structure to depths of about 152 to 213 m; others targeted velocities in the upper 46 to 61 m. The range of velocities measured was similar to that seen at the surface facilities site (BSC 2002 [DIRS 157829], Figures 192 and 212).

These velocity data are used to develop velocity profiles that serve as an input to analyses of ground motion site response. The ground motion site response forms the basis for developing ground motion design values (e.g., response spectra, time histories) for engineering analyses.

Earthquake Stress Drop–Stress drop is the difference in stress across the fault before and after an earthquake. Stress drop affects high-frequency ground motion. If stress drops in the Yucca Mountain region are greater than the typical value for western United States earthquakes, then larger high frequency motions would be expected at Yucca Mountain relative to motions determined from western United States empirical attenuation relations. To provide data to assess this potential effect, an evaluation of stress drops for earthquakes in extensional regimes was performed in support of the ground motion characterization effort in the PSHA project (CRWMS M&O 1998 [DIRS 103731], p. 5-11).

The analysis used a data set composed of earthquake records from extensional tectonic regimes (Spudich et al. 1997 [DIRS 100082]), including both normal and strike-slip. These data were supplemented with data from the 1995 Dinar, Turkey, earthquake, which were not available to Spudich et al. (1997 [DIRS 100082]). The final data set comprised 210 horizontal components from 140 sites in 24 earthquakes, a magnitude range of M_w 5.1 to 6.9, and distances from 0 to 102 km. The data were fit to a standard earthquake source model. A two-step inversion process was adopted to decouple the inversions for kappa and for stress drop. Stress drops computed for each earthquake were weighted to yield a median value for each mechanism.

The median stress drop for normal-faulting earthquakes was about 45 bars (4.5 MPa), and the value for strike-slip earthquakes (in extensional regimes) was about 55 bars (5.5 MPa). In comparison, stress drops for western United States earthquakes are about 70 to 100 bars (7 to

10 MPa) (e.g., Atkinson 1995 [DIRS 149964], p. 1341). These differences in stress drop contribute to lower high-frequency motions in extensional regimes compared to compressional regimes, such as coastal California. This information was considered in the ground motion characterization component of the PSHA for Yucca Mountain.

4.3.3.2   Attenuation of Strong Motion in Extensional Regimes

Spudich et al. (1996 [DIRS 110503]) conducted an empirical study of strong ground motions recorded in extensional regimes to assess whether the attenuation was different from standard attenuation models for shallow crustal earthquakes in other tectonic regimes, particularly California. They also developed a new set of attenuation relations based solely on these extensional regime data.

The earthquakes used in their study were all located in extensional tectonic regimes. Because the number of events in the entire Basin and Range Province is limited, the database includes ground motion recorded worldwide. Earthquakes with normal dip-, oblique-, and strike-slip mechanisms were evaluated together. A total of 373 recordings (253 horizontal and 120 vertical recordings) is included in the final database. These data represent earthquakes between M_w 5.1 and 6.9, and distances up to about 100 km.

Extensional Data and Western U.S. Empirical Attenuation Relations–Several representative attenuation relations based on western United States data were compared to the extensional data by Spudich et al. (1996 [DIRS 110503]). The attenuation relations were those of Boore et al. (1994 [DIRS 124240]); Idriss (1991 [DIRS 105517]); Sadigh et al. (1993 [DIRS 104537]); Campbell (1989 [DIRS 104648]; 1990 [DIRS 104649]); Campbell and Bozorgnia (1994 [DIRS 104651]); and Sabetta and Pugliese (1996 [DIRS 104529]). These relations generally represent the state of the art in ground motion attenuation studies at the time of the Spudich et al. (1996 [DIRS 110503]) study.

The mean residual, or bias, was computed for each attenuation relation and indicated whether that model systematically under-predicts or over-predicts the extensional strong motion data. In general, the computed residuals indicated that the standard western United States attenuation relations over-predict ground motions from extensional regimes by about 15 to 35 percent on average (Spudich et al. 1996 [DIRS 110503], Table 9; Abrahamson and Becker 1996 [DIRS 101419], Figure 10.5-3). At Yucca Mountain, near-fault ground motion is important because of the hazard contributions from local faults (CRWMS M&O 1998 [DIRS 103731], p. 7-22). Therefore, the bias was computed for a subset of the extensional data that included only sites at distances less than 20 km (Spudich et al. 1996 [DIRS 110503], Table 9; Abrahamson and Becker 1996 [DIRS 101419], Figure 10.5-5). For this distance range, the over-prediction is somewhat greater than for the full data set, although the standard deviations of the residuals are also larger.

The standard errors of the western United States models were compared to the standard errors computed from the extensional regime database for all distances and for distances less than 20 km (Spudich et al. 1996 [DIRS 110503], Tables 9 and 12; Abrahamson and Becker 1996 [DIRS 101419], Figures 10.5-11 and 10.5-12). For all distances, the computed standard errors are consistent with the range of standard errors from the attenuation models. For distances less

than 20 km, the computed standard errors are toward the lower end of the range of the attenuation model standard errors, but the uncertainty in the estimated standard error is much larger. The standard errors in the western United States attenuation models appear to be comparable and thus applicable to extensional regimes.

Spudich et al. (1996 [DIRS 110503]) also evaluated the distance and magnitude scaling inherent in the western United States relations against the extensional data. They found that the distance attenuation represented by the extensional data set is weaker than in the western United States attenuation models. No systematic difference was found in the magnitude scaling of events in the extensional database as compared to the western United States models.

Extensional Regime Attenuation Relation–Spudich et al. (1996 [DIRS 110503]; 1997 [DIRS 100082]) developed a new attenuation relation (SEA96) to estimate ground motions in extensional regimes. The model is based on a functional form developed by Boore et al. (1994 [DIRS 124240]) in which ground motion amplitude is dependent on moment magnitude, distance to the event, and site type (rock or soil).

The extensional regime data set is rather sparse in terms of the magnitudes represented and has little data from rock sites at distances less than 10 km. Consequently, in the regression analysis several model parameters were fixed to values determined by Boore et al. (1994 [DIRS 124240]). The results of the analysis are listed in Spudich et al. (1997 [DIRS 100082], Table 3).

Comparisons of median predictions from this model with those from several western United States attenuation models illustrate their differences. As an example, Figure 4-24 compares median acceleration response spectra for a rock site on the footwall of a dipping fault (57.5°) at a rupture distance of 10 km for M_w 5, 6, and 7 events (Abrahamson and Becker 1996 [DIRS 101419], Figure 10.6-1). In general, at short to moderate periods the Spudich et al. (1997 [DIRS 100082]) model predictions are less than, or lie at the lower limit of, the western United States values. At long periods, the Spudich et al. (1997 [DIRS 100082]) model is similar to the western United States models. Notably, however, the Spudich et al. (1997 [DIRS 100082]) model has a much larger standard deviation at long periods than is usual for the western United States relations.

Spudich et al. (1999 [DIRS 158509]) update the attenuation relation for extensional tectonic regimes using a larger data set and corrected minor errors in the data set used for the earlier analysis. At short distances (5 to 30 km), ground motions predicted by the new relation (SEA99) are up to 20 percent higher than those predicted by the SEA96 relation, while at longer periods (1.0 to 2.0 s) and larger distances (40 to 100 km) they are about 20 percent lower (Spudich et al. 1999 [DIRS 158509], p. 1156). When compared to ground motions determined from the relation of Boore et al. (1994 [DIRS 124240]), results average about 20 percent lower, except for short distances at periods around 1.0 s. For this combination, the ground motions from SEA99 exceed those determined from the Boore et al. (1994 [DIRS 124240]) relation by up to 10 percent.

4.3.3.3 Ground Motions from Yucca Mountain Scenario Earthquakes

Because of the lack of near-fault strong motion data from earthquakes in the Basin and Range Province (including the Yucca Mountain region), a study was carried out to estimate vibratory ground motion for several earthquake scenarios potentially affecting Yucca Mountain (Schneider et al. 1996 [DIRS 103270]). Participants in the study used established numerical modeling methods to simulate ground motions that were appropriate to the specific conditions at Yucca Mountain. As part of the modeling exercise, both median ground motion and its variability were estimated for each earthquake scenario.

Six earthquake scenarios were evaluated (CRWMS M&O 2000 [DIRS 151945], Table 12.3-16) based on two criteria: (1) the postulated sources are likely to have generated significant earthquakes in the past and (2) they are considered likely to produce ground motions that would impact seismic hazard estimates at Yucca Mountain. The six scenarios include four normal faulting events (M_w 6.3 to 6.6) at source-to-site distances of 1 to 15.5 km, and two strike-slip faulting events (M_w 6.7 and 7.0) at distances of 25 and 50 km, respectively.

Six modeling approaches were included in the study. In the model, the seismic source is prescribed only by the rupture geometry, seismic moment, and hypocenter. The manner in which the seismic slip is distributed and released on the fault plane varies between methods. The methods also vary significantly in their assumptions of wave propagation, site response, and overall level of complexity, but all the methods accommodate the essential aspects of seismic energy being generated from a finite source and propagated along a path to a site at the Earth's surface. Differences in resulting predictions capture an important component of the uncertainty in ground motions in these scenario earthquakes that can be applied to the variability of other simulations. A complete description of each modeling method is provided in Schneider et al. (1996 [DIRS 103270], Section 3.4).

Model Validation–The study referenced above includes a validation phase in which the six modeling teams incorporated various Yucca Mountain source, path, and site parameters to calibrate their models to best fit ground motions from five sites that recorded the Little Skull Mountain earthquake. Most of the six methods had also been previously calibrated against recordings from other earthquakes.

The computed 5-percent-damped response spectra for each of the six modeling teams are plotted in Figure 4-25, along with an observed spectrum from the Little Skull Mountain earthquake. The comparisons are for the recording site (Lathrop Wells) nearest to the Little Skull Mountain main shock source. The mean residual and standard deviation for all five sites were computed for each model. The models produced ground motion estimates that were comparatively unbiased for periods less than 1 s (CRWMS M&O 2000 [DIRS 151945], Figure 12.3-27), indicating that they are applicable to estimating ground motions in the Basin and Range Province. However, the bias for periods greater than 1 s indicates that the numerical simulation models do not work well for the 1992 Little Skull Mountain earthquake at long periods.

Computed Ground Motion–Using the Little Skull Mountain calibrated models, the six teams proceeded to compute motions for the six faulting scenarios. Five of the teams whose models were numerical simulations (i.e., all except the empirical underground nuclear explosion model)

ran multiple realizations of the source process and computed a mean spectrum for each scenario. Nonlinear site response effects were incorporated in the scenario ground motions (Schneider et al. 1996 [DIRS 103270], Section 7) based on data for tuffs at Los Alamos, New Mexico (Wong et al. 1995 [DIRS 105550], Section 6.2.3).

The computed median horizontal spectral accelerations for the scenario events based on the team's models are shown on Figure 4-26. Ground motions computed for the normal faulting scenario events at close distances (Bow Ridge, Solitario Canyon, and Paintbrush Canyon faults) are large (Schneider et al. 1996 [DIRS 103270], Figure 10-10); 34-Hz spectral accelerations range from 0.5 to 1.0 g (490 to 981 cm/s^2) at distances of 1 to 3 km. The more distant normal faulting and strike-slip scenario earthquakes (Bare Mountain and Rock Valley faults) resulted in ground motions with 34-Hz spectral accelerations from 0.2 to 0.3 g (196 to 294 cm/s^2). The scenario event at farthest distance (Furnace Creek fault, a strike-slip scenario) produced the lowest high-frequency motion (less than 0.1 g [98 cm/s^2] at 34 Hz). Its long period motions are comparable to the Bare Mountain and Rock Valley fault scenario events as a result of the larger magnitude of the Furnace Creek fault event.

Comparisons with Western United States Attenuation Relations–The model simulations were compared with several western United States empirical attenuation relations (Sadigh et al. 1993 [DIRS 104537]; Boore et al. 1994 [DIRS 124240]). The simulated median ground motions for the four normal faulting scenario events exceed western United States predictions by about 60 percent at distances less than 5 km and by about 20 percent at 15 km (Abrahamson and Becker 1996 [DIRS 101419], p. 10-39). The differences are largest at high frequencies, attributable primarily to low site attenuation (kappa effects) in the shallow rock at Yucca Mountain and to larger crustal amplification for the Basin and Range Province. At long periods, the difference is attributed to the larger crustal amplification and directivity effects (stronger ground motion in the direction of rupture propagation than in other directions from the earthquake source).

For the more distant strike-slip faulting earthquakes, the simulated median ground motions are greater than the western United States attenuation predictions by about 30 percent at a distance of 25 km, also at the high frequencies (Abrahamson and Becker 1996 [DIRS 101419], p. 10-40). This increase is similarly attributed to low kappa and larger crustal amplification. At 50 km, the simulated longer period ground motions are consistent with western United States empirical attenuation predictions because the effect of kappa is not as significant.

The simulated higher ground motions at high frequencies are consistent with records from the 1992 Little Skull Mountain earthquake. The high-frequency ground motions from this event were significantly larger than those predicted by western United States empirical attenuation relations.

The variability of the simulated motions is also greater than that computed for western United States empirical attenuation relations. The standard error is about 0.15 natural log units larger than that found for empirical attenuation relations.

Ground Motion Variability–The variability in ground motion was estimated in the modeling study, including modeling, method, parametric, and geometric variability (Schneider et al. 1996

[DIRS 103270]). The total variability is the combination of these sources of uncertainty. Two types of uncertainty are considered: (1) aleatory, representing random variations and captured in the standard deviation, and (2) epistemic, representing scientific uncertainty due to limited data. Epistemic uncertainty is inherent in both median estimates and their aleatory variability.

The model variability (aleatory) is estimated from comparisons of the model predictions with recordings from actual earthquakes. In the modeling study, this was captured in the Little Skull Mountain validation exercise and other validations each investigator had performed. Method variability (epistemic) is the uncertainty in the median ground motion introduced by the inability to know which numerical model will provide estimates closest to the correct median. Parametric variability (aleatory) is caused by variations in ground motion for future earthquakes caused by variations in source, path, and site parameters in those events. It is computed by varying these parameters (optimized in the validation exercise) in other simulations. Geometric variability (epistemic) results from the inability to know the true geometry of a source. For example, for a single fault it is the uncertainty in the dip of that fault. In the modeling study, geometric variability was included only in the computation of the total uncertainty, depending on the details of the individual simulations. The uncertainty computed for all the simulations is included in Schneider et al. (1996 [DIRS 103270], Section 10). In general, the total uncertainty (combination of model, method, parametric, and geometric variability) increases with period and the greatest contribution to the total uncertainty is the model variability.

4.3.3.4 Implications for Vibratory Ground Motion from Studies of Precarious Rocks at Yucca Mountain

The existence of precariously balanced rocks in the Yucca Mountain region puts some constraints on the level of vibratory ground motion experienced at the site over the past several tens of thousands of years. Precariously balanced rocks provide evidence that past levels of strong vibratory ground motion have been insufficient to topple them. In areas where strong ground motions are known to have occurred historically, precarious rocks are not observed. For example, based on reconnaissance field surveys in southern California, Brune (1996 [DIRS 154300], p. 43) concluded that no precarious rocks are found within 15 km of zones of high-energy release of historic large earthquakes. Laboratory physical modeling, numerical modeling, and field tests provide confidence that rough estimates of the accelerations required to topple precarious rocks can be made without extensive controlled testing (Brune 2000 [DIRS 154301], p. 1107; Anooshehpoor and Brune 2000 [DIRS 154302], pp. 2 to 4). Brune and Whitney (2000 [DIRS 154573], p. 18) noted that numerous precarious rocks exist along Solitario Canyon and argued that accelerations at Yucca Mountain have not exceeded about 0.3 g at the surface during the past 75,000 to 80,000 years. This inference is consistent with information indicating that the last significant surface offset on the Solitario Canyon fault occurred 15,000 to 30,000 years ago (CRWMS M&O 2000 [DIRS 151945], Table 12.3-8b). Vibratory ground motions at the depth of potential waste emplacement would be less than those at the Earth's surface.

Precarious rocks have also been used to test ground motion attenuation relations. Brune (2000 [DIRS 154301], p. 1107) notes that, in contrast to observations in the vicinity of strike-slip faults, precarious and semi-precarious rocks are found nearly to the fault trace on the footwall side of normal faults in Nevada and California. Comparison of estimated toppling accelerations

with accelerations predicted by a ground motion attenuation relation based largely on data for strike-slip earthquakes suggests that the attenuation relation may be conservative. The attenuation relation overestimates accelerations on the footwall of normal faults at near distances (Brune 2000 [DIRS 154301], Figure 2). This result is consistent with results from dynamic foam rubber models of strike-slip and normal faulting earthquakes (Brune and Anooshehpoor 1999 [DIRS 154303]). That is, the models indicate that ground motions near the fault trace are less for normal faulting earthquakes than for strike-slip earthquakes. The implication of this observation is that seismic hazard estimates using ground motion attenuation curves based largely on data from strike-slip earthquakes may result in conservative values of hazard for sites such as Yucca Mountain, where normal faulting dominates.

4.3.4   Probabilistic Seismic Hazard Analysis

To assess the seismic hazards of vibratory ground motions and fault displacement at Yucca Mountain, a PSHA was performed (CRWMS M&O 1998 [DIRS 103731]; CRWMS M&O 2000 [DIRS 142321]). The PSHA provided quantitative hazard results to support an assessment of the repository's long-term performance with respect to waste containment and isolation and to form the basis for developing seismic design criteria for the license application. The hazard results were in the form of annual frequencies for the exceedance of various levels of fault displacement at selected locations at and near Yucca Mountain and various levels of vibratory ground motion at a hypothetical rock outcrop.

The PSHA consisted of four primary activities:

- Identification, evaluation, and characterization of seismic sources that contribute to the fault displacement and vibratory ground motion hazard at Yucca Mountain

- Evaluation and characterization of fault displacement for seismic sources based on faults, including both primary and secondary faulting

- Evaluation and characterization of vibratory ground motion attenuation, including earthquake source, wave propagation path, and rock site effects

- Based on the characterizations of seismic sources, fault displacement and ground motion attenuation, analyses of probabilistic seismic hazards caused by both fault displacement and vibratory ground motion.

Both the preclosure and postclosure performance periods of the repository were addressed in the study.

By necessity, evaluations of seismic source characteristics, earthquake ground motions, and fault displacement involve interpretations of data. These interpretations have associated uncertainties related to the ability of data to fully resolve various hypotheses and models. In the PSHA, a formal expert elicitation process was used to develop inputs that specifically included both estimates of parametric variability and uncertainty in the interpretations. Six teams of three experts each, who together provided composite expertise in the seismicity, tectonics, and geology of the Yucca Mountain site and region, made seismic source characterizations. Seven

individual experts made the ground motion assessments. A deliberate process was followed in facilitating interactions among the experts, in training them to express their uncertainties, and in eliciting their interpretations.

Source and ground motion interpretations, and associated assessments of uncertainty, were made by the experts on the basis of data available in 1996 and 1997. The interpretations and assessments incorporate the experts' evaluations of those data, which may differ from those of the scientists who originally collected and interpreted the data. Thus, it is not expected that the experts' interpretations and those expressed in project reports of site characterization activities should, in all cases, be identical. The technical bases for the experts' interpretations and assessments are provided in CRWMS M&O (1998 [DIRS 103731], Appendices E and F).

4.3.4.1 Probabilistic Seismic Hazard Analysis Methodology

The PSHA methodology for vibratory ground motions was first developed by Cornell (1968 [DIRS 102731]; 1971 [DIRS 102734]) and has become standard practice in evaluating seismic hazards. Use of the methodology results in calculated annual frequencies with which various measures of vibratory ground motion (e.g., peak horizontal acceleration) will be exceeded at a site (Figure 4-27). The resulting seismic hazard curve represents the integration over all earthquake sources and magnitudes of the probability of future earthquake occurrence and, given an occurrence, its effect at a site of interest. The methodology for evaluating fault displacement hazard probabilistically is very similar to that for vibratory ground motions.

The calculation of probabilistic ground motion hazard requires three basic inputs (Figure 4-27):

- Identification of relevant seismic sources and characterization of their source geometry

- Rate of earthquake occurrence for each seismic source and its magnitude distribution

- Attenuation relationships that provide for the estimation of a specified ground motion parameter as a function of magnitude, source-to-site distance, local site conditions, and in some cases, seismic source characteristics.

For evaluating fault displacement hazard, the ground motion attenuation relationships are replaced by relationships that describe the distribution, sense, and amounts of displacement with earthquake occurrence. Both primary and secondary fault displacements are addressed.

An important aspect of the probabilistic seismic hazard calculations is the treatment of uncertainty. For the above inputs, uncertainties are quantified by the experts and included in their models. These uncertainties are propagated throughout the probabilistic analyses using a logic tree methodology resulting in a suite of hazard curves typically showing the mean, median, and various percentile curves.

4.3.4.1.1 Seismic Source Characterization

A seismic source is defined as a region of the earth's crust that has relatively uniform seismicity characteristics, is distinct from those of neighboring sources, and can be used in approximating the locations of future earthquakes. Two main types of seismic sources were characterized by

the seismic source expert teams: fault sources and areal source zones. Fault sources are used to represent the occurrence of earthquakes along a known or suspected fault. Uncertainty in the definition of fault sources is expressed by considering alternative rupture lengths, alternative fault dips, and possible linkages with other faults. In addition, an evaluation is made of the probability that a particular fault is active.

Areal source zones represent regions of distributed seismicity that are not associated with specific known faults, such as "background earthquakes." The events are considered to be occurring on unidentified faults or structures whose areal extents are best characterized by zones. Uncertainty in defining areal zones was typically expressed by considering alternative zonations of the region surrounding the Yucca Mountain site.

Two types of fault sources were considered in the PSHA: regional faults and local faults. Regional faults were defined by most teams as Quaternary faults within 100 km of Yucca Mountain, but outside the local vicinity of the site, that were judged to be capable of generating earthquakes of M_w 5 and greater. Local faults were defined as being located within about 15 km of Yucca Mountain. The specific faults that required detailed characterization were determined based on factors including fault length and location relative to Yucca Mountain, displacement of Quaternary deposits, direct relationship with seismicity, structural relationship to other Quaternary faults, orientation within the contemporary tectonic stress regime, and considerations of alternative tectonic models. Faults that had short lengths or no significant Quaternary displacement were considered, but judged not relevant to the hazard analysis. The faults included in the PSHA are listed in Table 4-11.

The number of regional faults considered by the expert teams ranged from 11 to as many as 36. This reflected, in part, the judgments of the teams regarding the activity of various faults as well as the decision by some teams to also include potentially active faults. For the characterization of local faults, varying behavioral and structural models were employed by the expert teams to represent the full range of possible rupture patterns and fault interactions. Some type of simultaneous rupture of multiple faults was included in all models. In general, preferred models for multiple fault rupture included two to four coalescing fault systems.

Areal source zones were defined by all teams to account for background earthquakes. For each source zone, the expert teams characterized the zone's maximum magnitude, its rate of earthquake occurrence, and the magnitude distribution of those earthquakes. Summaries of the source-zone characterization performed by the six expert teams can be found in CRWMS M&O (2000 [DIRS 151945], Section 12.3.10.2.3). More complete descriptions are found in CRWMS M&O (1998 [DIRS 103731], Appendix E). Four teams included alternative interpretations in their characterization of the areal zones within a 100-km radius of the Yucca Mountain site. Three teams considered interpretations that included one to three areal zones. Four teams defined areal zones that extend beyond 100 km of the Yucca Mountain site. Four teams defined a site region or zone solely for assigning a lower maximum magnitude to the area where more detailed investigations have been conducted and the inventory of fault sources is more complete.

Seismicity related to volcanic processes (specifically to basaltic volcanoes and dike-injection) was considered by all six expert teams, but explicitly characterized as distinct source zones by only two expert teams. Volcanic-related earthquakes were not modeled as a separate seismic

source by the other four teams because the low magnitude and frequency of volcanic-related seismicity was assumed to be accounted for by earthquakes in the areal zones.

Maximum Earthquake Magnitude–A maximum earthquake magnitude (M_{max}) was determined for each source by each expert team to represent the largest earthquake that the source is capable of generating, regardless of how frequently it may occur. Two basic approaches were used to assess maximum magnitude. The primary approach, which was used for faults, was based on estimates of the maximum dimensions of fault rupture. Multiple sources of uncertainties were considered in estimating physical dimensions of maximum rupture on faults, including uncertainties in rupture length, rupture area, and displacement per event. The second approach considered historical data on the seismicity of the region. This approach was used primarily for areal source zones. For each of the faults included in the PSHA, the range of M_{max} values assigned by the teams is indicated in Table 4-11.

Earthquake Recurrence–Earthquake recurrence relationships express the rate or annual frequency of different magnitude earthquakes occurring on a seismic source. Methods for developing these relationships are usually different for fault sources than for areal sources. The expert teams used two approaches to estimate the earthquake recurrence relationships for fault sources. These approaches are based on estimates of fault slip rates and the average slip per event, and on seismic moment rates. Recurrence models considered were the characteristic, truncated exponential, modified truncated exponential, and maximum magnitude models. The experts favored the characteristic model for the fault sources although two or more models were usually weighted and used by the teams. For each of the faults included in the PSHA, the ranges of the slip rate and recurrence rate values assigned by the teams are indicated in Table 4-11. For areal sources, earthquake recurrence relationships were determined from the catalog of historical and instrumental earthquakes within a 300-km radius of Yucca Mountain. The truncated exponential recurrence model was adopted for the areal source zones.

For faults, recurrence models were also required. The recurrence models, which specify the shape of the recurrence relationship, considered were the characteristic, truncated exponential, modified truncated exponential and maximum magnitude. The experts favored the characteristic model for the fault sources although two or more models were usually weighted and used by the teams. The truncated exponential model was adopted for the areal source zones.

4.3.4.1.2 Fault Displacement Characterization

Several original approaches to characterize the fault displacement potential were developed by the seismic source expert teams. These approaches were based primarily on empirical observations of the pattern of faulting at the site during past earthquakes determined from data collected during fault studies at Yucca Mountain. Empirical data were fit by statistical models to allow use by the experts (CRWMS M&O 1998 [DIRS 103731], Appendix H).

The potential for fault displacement was categorized as either principal or distributed faulting. Principal faulting is the faulting along the main plane (or planes) of crustal weakness responsible for the primary release of seismic energy during the earthquake. Where the principal fault rupture extends to the surface, it may be represented by displacement along a single narrow trace or over a zone that can be a few to many meters wide. Distributed faulting is defined as rupture

that occurs on other faults in the vicinity of the principal rupture in response to the principal displacement. Distributed faulting may or may not be the source of seismic energy release, but it is assumed insignificant compared to the principal fault. It is expected that distributed faulting will be discontinuous in nature and occur over a zone that may extend outward several tens of meters to many kilometers from the principal rupture. A fault that can produce principal rupture may also undergo distributed faulting in response to principal rupture on other faults.

Both principal and distributed faulting are important to the assessment of the fault displacement hazard at the Yucca Mountain site. Nine locations at or near Yucca Mountain were identified to demonstrate the fault displacement methodology (CRWMS M&O 2000 [DIRS 151945], Figure 12.3-47). These locations were chosen to represent the range of potential faulting conditions. Some of these locations lie on faults that may experience both principal faulting and distributed faulting. The other points are sites of only potential distributed faulting.

The approaches developed by the seismic source expert teams for characterizing the frequency of displacement events can be divided into two categories: displacement approach and earthquake approach. The displacement approach provides an estimate of the frequency of displacement events directly from observed feature-specific or point-specific data. The earthquake approach involves relating the frequency of slip events to the frequency of earthquakes on the various seismic sources defined by the seismic source characterization models for the ground motion assessment. Both approaches are used for assessing the fault displacement hazard for principal faulting and distributed faulting. Details of the approaches and results for the PSHA fault displacement characterization are documented in CRWMS M&O 1998 ([DIRS 103731], Sections 4.2 and 4.3.2).

4.3.4.1.3   Ground Motion Characterization

The goal of the ground motion evaluation for the Yucca Mountain PSHA was to formulate attenuation models describing vibratory ground motion at the repository. Seven experts evaluated various proponent models (CRWMS M&O 1996 [DIRS 100116]). The experts provided point estimates of ground motion for a suite of prescribed faulting cases, and these point estimates were subsequently regressed to attenuation equations. The ground motions constituted response spectral values (horizontal and vertical components) for specified spectral periods. The point estimates constituted an estimate of the median ground motion, its variability (aleatory variability), and the uncertainty in each (epistemic uncertainty). Each faulting case corresponded to a particular magnitude earthquake, fault geometry, and source-site distance. The cases were designed to sample the magnitude-distance-faulting space in sufficient detail to provide a robust regression.

The ground motion estimates and, thus, resulting attenuation relations, were developed for a reference rock outcrop. This reference rock outcrop was defined to have geotechnical conditions identical those at the depth of the buried repository, not those at the ground surface. The reference rock outcrop was used because site-specific data on the velocities and dynamic properties of the upper 300 m of rock and soil were limited at the time of the PSHA. For design analyses and analyses supporting performance assessment, the effect on ground motion of the rock between the waste emplacement level and the ground surface (site response) needs to be taken into account.

Proponent Models–The experts computed their ground motion point estimates by considering existing proponent models. The proponent models fell into several classes: empirical attenuation relations, hybrid empirical, point-source numerical simulations, finite-fault numerical simulations, and blast models (CRWMS M&O 2000 [DIRS 151945], Table 12.3-14).

Because no empirical attenuation models exist for the Yucca Mountain region or Basin and Range Province, the empirical models used in this study resulted from regression analyses of strong motion records primarily from California earthquakes. Thus, all empirical relations required adjustments so they would better fit conditions in the Yucca Mountain region. The hybrid empirical model is derived from these relations and implicitly includes conversion factors that must be separately applied to the empirical relations.

The blast models are based on empirical records from underground nuclear explosions at the Nevada Test Site (Schneider et al. 1996 [DIRS 103270], pp. 3-15 to 3-17). Three blast models were assessed, each with a different approach to account for differences in earthquake sources and explosion sources.

The numerical simulations were tailored to Yucca Mountain conditions and required no adjustments. The point-source models are the simplest numerical models and also the best understood. The finite-fault numerical simulations were derived from the six models evaluated in the modeling study previously described (Section 4.3.3.3). The experts chose three model approaches for their analyses:

- Stochastic method with ω^2 subevents
- Composite fractal source method
- Broadband Green's function method.

Conversion Models–Depending on the nature of the data sets upon which they were based, the empirical relations often represented source, path, and site conditions different from those encountered at Yucca Mountain. Suites of conversion factors were consequently computed as part of the study. They were developed using the results of numerical finite-fault simulations, stochastic point-source simulations, and empirical attenuation relations. Complete summaries of the conversion factors are presented in CRWMS M&O 1998 ([DIRS 103731], Section 5). The factors included corrections for the following:

- Source: western United States transpressional seismic sources to Yucca Mountain extensional seismic sources

- Crust: western United States crust to Yucca Mountain crust

- Site: Reference rock outcrop conditions to Yucca Mountain surface.

Additionally, many of the proponent models did not include the full range of ground motion parameters required (e.g., not all the empirical models included vertical ground motions). Thus, a variety of scaling factors was also developed and applied in the same manner as the conversion models.

Attenuation Relations–Each expert developed a set of point estimates for the defined cases covering different faulting styles, event magnitudes, source geometries, and source-site distances. The estimates comprised median ground motion, its variability, and the uncertainty in both. The estimates were derived directly from the models, the conversion factors, the adjustment factors described above, and other judgments by the experts. These estimates were then parameterized using attenuation relations.

The seven sets of attenuation relations predict median ground motion that differs by less than a factor of 1.5. The experts' horizontal aleatory estimates, the epistemic uncertainties in their median estimates, and the epistemic uncertainties in their aleatory estimates all vary by less than approximately 0.1 natural log unit (CRWMS M&O 1998 [DIRS 103731], p. 6-4).

4.3.4.2 Results of the Probabilistic Seismic Hazard Analysis

The vibratory ground motion and fault displacement hazard results derived from the PSHA are described below.

4.3.4.2.1 Vibratory Ground Motion Hazard

Vibratory ground motion hazard was computed at a defined reference rock outcrop having the properties of tuff at a waste emplacement depth of 300 m below the ground surface at Yucca Mountain. Ground motion was computed at this reference location as a control motion for later determination of seismic design bases motions for surface and potential waste-emplacement level locations.

Based on equally-weighted inputs from the six seismic source expert teams and the seven ground motion experts, the probabilistic hazard for vibratory ground motion was calculated for horizontal and vertical peak acceleration (defined at 100 Hz), spectral accelerations at frequencies of 0.3, 0.5, 1, 2, 5, 10, and 20 Hz, and peak velocity, and is expressed in terms of hazard curves (e.g., Figure 4-28). The hazard is also expressed in terms of uniform hazard spectra. Peak ground acceleration, 0.3 Hz and 1.0 Hz spectral values, and peak velocity are summarized in Table 4-12 for the annual exceedance probabilities of 10^{-3} and 10^{-4}. The largest source of epistemic uncertainty in the hazard results is in the ground motion characterization.

Deaggregation of the mean hazard for an annual exceedance probability of 10^{-4} shows that at 5 to 10 Hz (or other high frequencies), ground motions are dominated by earthquakes of smaller than M_w 6.5 occurring at distances less than 15 km from Yucca Mountain (Figure 4-29a). Dominant events for low-frequency ground motion, such as at 1 to 2 Hz, display a bimodal distribution that includes large nearby events and M_w 7 and larger earthquakes beyond distances of 50 km (Figure 4-29b). The latter contribution is mainly a result of the contributions from the Death Valley and Furnace Creek faults which have relatively higher activity rates.

Extensive evaluations of parametric sensitivities of the ground motion hazard were performed (CRWMS M&O 1998 [DIRS 103731], Section 7.4). The recurrence approach (either slip rates or recurrence intervals) and recurrence model (e.g., characteristic, exponential, or maximum moment) are the parameters that contribute the most to uncertainty in the ground motion hazard for annual exceedance probabilities of 10^{-3} and 10^{-4}. Maximum magnitude has a small effect on uncertainty, especially for 10 Hz spectral acceleration, because a large fraction of the hazard at

this probability comes from more frequent moderate-magnitude events. Geometric fault parameters (e.g., rupture lengths, dips, maximum depths) are minor contributors to uncertainty. These parameters have a moderate effect on the locations of earthquakes and on maximum magnitude, but do not affect earthquake recurrence. Although the seismic-source expert teams' results varied, the dominant sources for seismic hazard at 10 Hz ground motions are the Paintbrush Canyon-Stagecoach Road and Solitario Canyon faults (or coalesced fault systems including these two faults) and the host areal seismic source zone. For 1 Hz ground motions, the dominant seismic sources are the Death Valley and Furnace Creek faults and the same three sources mentioned above. Multiple-rupture interpretations of the type with comparable seismic moment release on more than one fault (i.e., those requiring modification of the attenuation equations) make a small contribution to the total hazard. Buried strike-slip faults, volcanic seismicity, and seismogenic detachments contribute negligibly to the total hazard.

The major contributor to epistemic uncertainty in the ground motion hazard is the within-expert epistemic uncertainty in ground motion amplitude. Additional contributions to epistemic uncertainty arise from moderate differences among the seismic source expert teams and ground motion experts, as well as from uncertainties expressed by the seismic source logic trees.

4.3.4.2.2   Fault Displacement Hazard

The probabilistic fault displacement hazard was calculated for nine demonstration sites located at or near Yucca Mountain (CRWMS M&O 1998 [DIRS 103731], Figure 4-9, Section 8). Two of the sites have four hypothetical conditions representative of the features encountered within the ESF. The integrated results provide a representation of fault displacement hazard and its uncertainty at the nine sites, based on the interpretations and parameters developed by the six seismic-source expert teams. Separate results were obtained for each site in the form of summary hazard curves (e.g., Figure 4-30). Table 4-13 summarizes the mean displacement hazard results for annual exceedance probabilities of 10^{-4} and 10^{-5} at the nine demonstration sites.

With the exception of the block-bounding Bow Ridge and Solitario Canyon faults (Sites 1 and 2, respectively), the mean displacements are 0.1 cm or less at 10^{-5} annual exceedance probability. At 10^{-5} annual frequency, the mean displacements are 7.8 and 32 cm, respectively, for these two faults (Table 4-13).Thus, for sites not located on a block-bounding fault, such as the potential waste emplacement area, the average recurrence interval for displacements exceeding 0.1 cm is 100 k.y. or more.

The fault displacement hazard results display significant uncertainty. This uncertainty is indicative of the state of practice in PSHA for fault displacement, which is less mature than probabilistic analysis for ground motions. Nonetheless, the results obtained here are considered robust by virtue of the large amount of empirical data for the site, extensive efforts at expert elicitation and feedback, as well as the methodological developments that were undertaken as part of this study. Sites with the highest fault displacement hazard show uncertainties comparable to those obtained in ground motion PSHA. Sites with low hazard show much higher uncertainties.

Also, an expected correlation exists between the amount of geologic data available at a site and the uncertainty in the calculated hazard at that site. For sites with significant geologic data, the team-to-team uncertainty is less than one order of magnitude. For sites with little or no data, the individual team curves span three orders of magnitude. The larger uncertainty at these sites is considered to be due to data uncertainty.

4.4 REFERENCES

The following is a list of the references cited in this document. Column 1 represents the unique six digit numerical identifier, which is placed in the text following the reference callout (e.g., BSC 2002 [DIRS 157829]). The purpose of these numbers is to assist the reader in locating a specific reference. Within the reference list, multiple sources by the same author (e.g., CRWMS M&O 2000) are sorted alphabetically by title.

4.4.1 Documents Cited

101419   Abrahamson, N.A. and Becker, A.M. 1996. "Estimation of Vibratory Ground Motion at Yucca Mountain." Chapter 10 of *Seismotectonic Framework and Characterization of Faulting at Yucca Mountain, Nevada.* Whitney, J.W., ed. Milestone 3GSH100M. Denver, Colorado: U.S. Geological Survey. TIC: 237980. ACC: MOL.19970129.0041.

101456   Aki, K. 1979. "Characterization of Barriers on an Earthquake Fault." *Journal of Geophysical Research, 84*, (B11), 6140-6148. Washington, D.C.: American Geophysical Union. TIC: 234253.

101457   Aki, K. 1984. "Asperities, Barriers, and Characteristic Earthquakes and Strong Motion Prediction." *Journal of Geophysical Research, 89*, (B7), 5867-5872. Washington, D.C.: American Geophysical Union. TIC: 234631.

105304   Anderson, J.G. and Humphrey, J.R., Jr. 1991. "A Least Squares Method for Objective Determination of Earthquake Source Parameters." *Seismological Research Letters, 62*, (3-4), 201-209. El Cerrito, California: Seismological Society of America. TIC: 243235.

104754   Anderson, J.G.; Brune, J.N.; dePolo, D.; Gomberg, J.; Harmsen, S.C.; Savage, M.K.; Sheehan, A.F.; and Smith, K.D. 1993. "Preliminary Report: The Little Skull Mountain Earthquake, June 29, 1992." *Dynamic Analysis and Design Considerations for High-Level Nuclear Waste Repositories, San Francisco, California, August 19-20, 1992.* Hossain, Q.A., ed. Pages 162-175. New York, New York: American Society of Civil Engineers. TIC: 233289.

129941   Anderson, J.G.; Brune, J.N.; Louie, J.N.; Zeng, Y.; Savage, M.; Yu, G.; Chen, Q.; and dePolo, D. 1994. "Seismicity in the Western Great Basin Apparently Triggered by the Landers, California, Earthquake, 28 June 1992." *Bulletin of the Seismological Society of America, 84*, (3), 863-891. El Cerrito, California: Seismological Society of America. TIC: 246338.

101472   Anderson, L.W. and O'Connell, D.R. 1993. *Seismotectonic Study of the Northern Portion of the Lower Colorado River, Arizona, California and Nevada*. USBR SR 93-4. Denver, Colorado: U.S. Department of the Interior, Bureau of Reclamation. TIC: 237904.

101420   Anderson, L.W. and Klinger, R.E. 1996. "Quaternary Faulting on the Bare Mountain Fault." Chapter 4.12 of *Seismotectonic Framework and Characterization of Faulting at Yucca Mountain, Nevada*. Whitney, J.W., ed. Milestone 3GSH100M. Denver, Colorado: U.S. Geological Survey. TIC: 237980. ACC: MOL.19970129.0041.

163106   Anderson, L.W. and Klinger, R.E. 2003. "Quaternary Faulting on the Bare Mountain Fault." Chapter 12 of *Quaternary Paleoseismology and Stratigraphy of the Yucca Mountain Area, Nevada*. U.S. Geological Survey Digital Data Series. Keefer, W.R.; Whitney, J.W.; and Taylor, E.M., eds. Denver, Colorado: U.S. Geological Survey. ACC: MOL.20031208.0113. TBV-5659

101422   Anderson, R.E.; Bucknam, R.C.; Crone, A.J.; Haller, K.M.; Machette, M.N.; Personius, S.F.; Barnhard, T.P.; Cecil, M.J.; and Dart, R.L. 1995. *Characterization of Quaternary and Suspected Quaternary Faults, Regional Studies, Nevada and California*. Open-File Report 95-599. Denver, Colorado: U.S. Geological Survey. ACC: MOL.19960924.0562.

105345   Anderson, R.E.; Crone, A.J.; Machette, M.N.; Bradley, L-A.; and Diehl, S.F. 1995. *Characterization of Quaternary and Suspected Quaternary Faults, Amargosa Area, Nevada and California*. Open-File Report 95-613. Denver, Colorado: U.S. Geological Survey. TIC: 246589.

154302   Anooshehpoor, A. and Brune, J.N. 2000. *Annual Report, Precarious Rock Methodology for Seismic Hazard*. Reno, Nevada: University of Nevada, Reno. ACC: MOL.20000824.0562.

149964   Atkinson, G.M. 1995. "Attenuation and Source Parameters of Earthquakes in the Cascadia Region." *Bulletin of the Seismological Society of America, 85*, (5), 1327-1342. El Cerrito, California: Seismological Society of America. TIC: 247913.

105351   Balch, A.H. and Erdemir, C. 1996. *A Nine-Component, Multiple-Offset Vertical Seismic Profile at the UE-25 UZ#16 Borehole, Nevada Test Site, Nye County, Nevada: Taking VSPs to a New Level*. Milestone 3GUP622M. Denver, Colorado: U.S. Geological Survey. ACC: MOL.19990831.0049.

104458   Beanland, S. and Clark, M.M. 1994. *The Owens Valley Fault Zone, Eastern California, and Surface Faulting Associated with the 1872 Earthquake*. Bulletin 1982. Denver, Colorado: U.S. Geological Survey. TIC: 234443.

101649   Bellier, O. and Zoback, M.L. 1995. "Recent State of Stress Change in the Walker Lane Zone, Western Basin and Range Province, United States." *Tectonics, 14*, (3), 564-593. Washington, D.C.: American Geophysical Union. TIC: 233037.

105358   Biasi, G.P. 1996. *Teleseismic Tomographic Imaging of the Yucca Mountain Region.* Draft. Reno, Nevada: University of Nevada, Reno, Seismological Laboratory. TIC: 242401.

129113   Biasi, G.P. and Smith, K.D. 1998. *Project Report: Site Effects for Seismic Monitoring Stations in the Vicinity of Yucca Mountain, Nevada.* Deliverable SPT38BM4. Reno, Nevada: University of Nevada, Reno, Mackay School of Mines. ACC: MOL.20010605.0279.

149763   Blakely, R.J.; Jachens, R.C.; Calzia, J.P.; and Langenheim, V.E. 1999. "Cenozoic Basins of the Death Valley Extended Terrane as Reflected in Regional-Scale Gravity Anomalies." *Cenozoic Basins of the Death Valley Region.* Wright, L.A. and Troxel, B.W., eds. Special Paper 333. Pages 1-16. Boulder, Colorado: Geological Society of America. TIC: 248054.

151881   Blakely, R.J.; Langenheim, V.E.; Ponce, D.A.; and Dixon, G.L. 2000. *Aeromagnetic Survey of the Amargosa Desert, Nevada and California: A Tool for Understanding Near-Surface Geology and Hydrology.* Open-File Report 00-188. Denver, Colorado: U.S. Geological Survey. TIC: 248767.

101469   Bodin, P. and Gomberg, J. 1994. "Triggered Seismicity and Deformation Between the Landers, California, and Little Skull Mountain, Nevada, Earthquakes." *Bulletin of the Seismological Society of America, 84*, (3), 835-843. El Cerrito, California: Seismological Society of America. TIC: 234274.

104525   Bolt, B.A. and Miller, R.D. 1975. *Catalogue of Earthquakes in Northern California and Adjoining Areas 1 January 1910 - 31 December 1972.* Berkeley, California: University of California, Berkeley. TIC: 245759.

124240   Boore, D.M.; Joyner, W.B.; and Fumal, T.E. 1994. *Estimation of Response Spectra and Peak Accelerations from Western North American Earthquakes: An Interim Report, Part 2.* Open-File Report 94-127. Menlo Park, California: U.S. Geological Survey. TIC: 246666.

101996   Bradshaw, T.K. and Smith, E.I. 1994. "Polygenetic Quaternary Volcanism at Crater Flat, Nevada." *Journal of Volcanology and Geothermal Research, 63*, 165-182. Amsterdam, The Netherlands: Elsevier. TIC: 224980.

102002   Brocher, T.M.; Carr, M.D.; Fox, K.F., Jr.; and Hart, P.E. 1993. "Seismic Reflection Profiling Across Tertiary Extensional Structures in the Eastern Amargosa Desert, Southern Nevada, Basin and Range Province." *Geological Society of America Bulletin, 105*, 30-46. Boulder, Colorado: Geological Society of America. TIC: 224981.

101495   Brocher, T.M.; Hart, P.E.; Hunter, W.C.; and Langenheim, V.E. 1996.
                Hybrid-Source Seismic Reflection Profiling Across Yucca Mountain, Nevada:
                Regional Lines 2 and 3. Open-File Report 96-28. Menlo Park, California: U.S.
                Geological Survey. ACC: MOL.19970310.0094; MOL.19970310.0107.

100022   Brocher, T.M.; Hunter, W.C.; and Langenheim, V.E. 1998. "Implications of
                Seismic Reflection and Potential Field Geophysical Data on the Structural
                Framework of the Yucca Mountain-Crater Flat Region, Nevada." *Geological*
                Society of America Bulletin, 110, (8), 947-971. Boulder, Colorado: Geological
                Society of America. TIC: 238643.

100024   Broxton, D.E.; Warren, R.G.; Byers, F.M.; and Scott, R.B. 1989. "Chemical and
                Mineralogic Trends Within the Timber Mountain–Oasis Valley Caldera Complex,
                Nevada: Evidence for Multiple Cycles of Chemical Evolution in a Long-Lived
                Silicic Magma System." *Journal of Geophysical Research, 94*, (B5), 5961-5985.
                Washington, D.C.: American Geophysical Union. TIC: 225928.

104611   Brune, J.N.; Nicks, W.; and Aburto, A. 1992. "Microearthquakes at Yucca
                Mountain, Nevada." *Bulletin of the Seismological Society of America, 82*, (1),
                164-174. El Cerrito, California: Seismological Society of America. TIC: 212563.

154300   Brune, J.N. 1996. "Precariously Balanced Rocks and Ground-Motion Maps for
                Southern California." *Bulletin of the Seismological Society of America, 86*, (1A),
                43-54. El Cerrito, California: Seismological Society of America. TIC: 249711.

102022   Brune, J.N. and Smith, K.D. 1996. "Precarious Rocks and Seismic Shaking During
                and Before the 1992 M 5.6 Little Skull Mountain Earthquake." *Abstracts with*
                Programs - Geological Society of America, 28, (7), A-193. Boulder, Colorado:
                Geological Society of America. TIC: 234316.

154303   Brune, J.N. and Anooshehpoor, A. 1999. "Dynamic Geometrical Effects on Strong
                Ground Motion in a Normal Fault Model." *Journal of Geophysical Research, 104*,
                (B1), 809-815. Washington, D.C.: American Geophysical Union. TIC: 249707.

154301   Brune, J.N. 2000. "Precarious Rock Evidence for Low Ground Shaking on the
                Footwall of Major Normal Faults." *Bulletin of the Seismological Society of*
                America, 90, (4), 1107-1112. El Cerrito, California: Seismological Society of
                America. TIC: 249712.

154573   Brune, J.N. and Whitney, J.W. 2000. "Precarious Rocks and Seismic Shaking at
                Yucca Mountain, Nevada." Chapter M of *Geologic and Geophysical*
                Characterization Studies of Yucca Mountain, Nevada, a Potential High-Level
                Radioactive-Waste Repository. Version 1.0. DDS-058. Denver, Colorado: U.S.
                Geological Survey. TIC: 249438.

160130   BSC (Bechtel SAIC Company) 2001. *Characterize Eruptive Processes at Yucca Mountain, Nevada*. ANL-MGR-GS-000002 REV 00 ICN 01. Las Vegas, Nevada: Bechtel SAIC Company. ACC: MOL.20020327.0498.

157829   BSC 2002. *Geotechnical Data for a Potential Waste Handling Building and for Ground Motion Analyses for the Yucca Mountain Site Characterization Project*. ANL-MGR-GE-000003 REV 00. Las Vegas, Nevada: Bechtel SAIC Company. ACC: MOL.20021004.0078.

163769   BSC (Bechtel SAIC Company) 2003. *Characterize Framework for Igneous Activity at Yucca Mountain, Nevada*. ANL-MGR-GS-000001 REV 01. Las Vegas, Nevada: Bechtel SAIC Company. ACC: DOC.20040106.0003.

166274   BSC 2003. *Development of Earthquake Ground Motion Input for Preclosure Seismic Design and Postclosure Performance Assessment of a Geologic Repository at Yucca Mountain, NV*. MDL-MGR-GS-000003 REV 00. Las Vegas, Nevada: Bechtel SAIC Company. ACC: DOC.20031201.0001.

102052   Burchfiel, B.C. 1965. "Structural Geology of the Specter Range Quadrangle, Nevada, and Its Regional Significance." *Geological Society of America Bulletin, 76*, 175-192. Boulder, Colorado: Geological Society of America. TIC: 217853.

104648   Campbell, K.W. 1989. *Empirical Prediction of Near-Source Ground Motion for the Diablo Canyon Power Plant Site, San Luis Obispo County, California*. Open-File Report 89-484. Denver, Colorado: U.S. Geological Survey. TIC: 246582.

104649   Campbell, K.W. 1990. *Empirical Prediction of Near-Source Soil and Soft-Rock Ground Motion for the Diablo Canyon Power Plant Site, San Luis Obispo County, California*. Evergreen, Colorado: Dames & Moore. TIC: 245324.

104651   Campbell, K.W. and Bozorgnia, Y. 1994. "Near-Source Attenuation of Peak Horizontal Acceleration from Worldwide Accelerograms Recorded from 1957 to 1993." *Earthquake Awareness and Mitigation Across the Nation, Proceedings of the Fifth U.S. National Conference on Earthquake Engineering, July 10-14, 1994, Chicago, Illinois. III*, 238-292. Oakland, California: Earthquake Engineering Research Institute. TIC: 239121.

104659   Carr, W.J. 1974. *Summary of Tectonic and Structural Evidence for Stress Orientation at the Nevada Test Site*. Open-File Report 74-176. Denver, Colorado: U.S. Geological Survey. TIC: 201381.

101519   Carr, W.J. 1982. *Volcano-Tectonic History of Crater Flat, Southwestern Nevada, as Suggested by New Evidence from Drill Hole USW-VH-1 and Vicinity*. Open-File Report 82-457. Denver, Colorado: U.S. Geological Survey. ACC: NNA.19870518.0057.

101037   Carr, W.J. 1984. *Regional Structural Setting of Yucca Mountain, Southwestern Nevada, and Late Cenozoic Rates of Tectonic Activity in Part of the Southwestern Great Basin, Nevada and California.* Open-File Report 84-854. Denver, Colorado: U.S. Geological Survey. ACC: NNA.19870325.0475.

101522   Carr, W.J.; Byers, F.M., Jr.; and Orkild, P.P. 1984. *Stratigraphic and Volcano-Tectonic Relations of Crater Flat Tuff and Some Older Volcanic Units, Nye County, Nevada.* Open-File Report 84-114. Denver, Colorado: U.S. Geological Survey. ACC: NNA.19870518.0075.

101093   Carr, W.J. and Parrish, L.D. 1985. *Geology of Drill Hole USW VH-2, and Structure of Crater Flat, Southwestern Nevada.* Open-File Report 85-475. Denver, Colorado: U.S. Geological Survey. ACC: HQS.19880517.1918.

104670   Carr, W.J.; Byers, F.M., Jr.; and Orkild, P.P. 1986. *Stratigraphic and Volcano-Tectonic Relations of Crater Flat Tuff and Some Older Volcanic Units, Nye County, Nevada.* Professional Paper 1323. Denver, Colorado: U.S. Geological Survey. TIC: 216598.

105385   Carr, W.J. 1988. "Volcano-Tectonic Setting of Yucca Mountain and Crater Flat, Southwestern Nevada." Chapter 4 of *Geologic and Hydrologic Investigations of a Potential Nuclear Waste Disposal Site at Yucca Mountain, Southern Nevada.* Carr, M.D. and Yount, J.C., eds. Bulletin 1790. Denver, Colorado: U.S. Geological Survey. TIC: 203085.

104669   Carr, W.J. 1990. "Styles of Extension in the Nevada Test Site Region, Southern Walker Lane Belt; An Integration of Volcano-Tectonic and Detachment Fault Models." Chapter 13 of *Basin and Range Extensional Tectonics Near the Latitude of Las Vegas, Nevada.* Wernicke, B.P., ed. Memoir 176. Boulder, Colorado: Geological Society of America. TIC: 222540.

104671   Carr, W.J.; Grow, J.A.; and Keller, S.M. 1995. *Lithologic and Geophysical Logs of Drill Holes Felderhoff Federal 5-1 and 25-1, Amargosa Desert, Nye County, Nevada.* Open-File Report 95-155. Denver, Colorado: U.S. Geological Survey. TIC: 218310.

102407   Caskey, S.J. and Schweickert, R.A. 1992. "Mesozoic Deformation in the Nevada Test Site and Vicinity: Implications for the Structural Framework of the Cordilleran Fold and Thrust Belt and Tertiary Extension North of Las Vegas Valley." *Tectonics, 11,* (6), 1314-1331. Washington, D.C.: American Geophysical Union. TIC: 232936.

102408   Caskey, S.J.; Wesnousky, S.G.; Zhang, P.; and Slemmons, D.B. 1996. "Surface Faulting of the 1954 Fairview Peak (Ms=7.2) and Dixie Valley (Ms=6.8) Earthquakes, Central Nevada." *Bulletin of the Seismological Society of America, 86,* (3), 761-787. El Cerrito, California: Seismological Society of America. TIC: 234277.

102497   Catchings, R.D. and Mooney, W.D. 1991. "Basin and Range Crustal and Upper Mantle Structure, Northwest to Central Nevada." *Journal of Geophysical Research, 96*, (B4), 6247-6267. Washington, D.C.: American Geophysical Union. TIC: 237584.

102496   Catchings, R.D. 1992. "A Relation Among Geology, Tectonics, and Velocity Structure, Western to Central Nevada Basin and Range." *Geological Society of America Bulletin, 104*, 1178-1192. Boulder, Colorado: Geological Society of America. TIC: 234317.

102558   Chavez, D.E. and Priestley, K.F. 1985. "M_L Observations in the Great Basin and M_o Versus M_L Relationships for the 1980 Mammoth Lakes, California Earthquake Sequence." *Bulletin of the Seismological Society of America, 75*, (6), 1583-1598. El Cerrito, California: Seismological Society of America. TIC: 234275.

159410   Coe, J.A. 2003. "Quaternary Faulting on the Northern Crater Flat Fault." Chapter 11 of *Quaternary Paleoseismology and Stratigraphy of the Yucca Mountain Area, Nevada*. U.S. Geological Survey Digital Data Series. Keefer, W.R.; Whitney, J.W.; and Taylor, E.M., eds. Denver, Colorado: U.S. Geological Survey. ACC: MOL.20031208.0113. TBV-5659

159411   Coe, J.A.; Oswald, J.; Vadurro, G.; and Lundstrom, S.C. 2003. "Quaternary Faulting on the Fatigue Wash Fault." Chapter 8 of *Quaternary Paleoseismology and Stratigraphy of the Yucca Mountain Area, Nevada*. U.S. Geological Survey Digital Data Series. Keefer, W.R.; Whitney, J.W.; and Taylor, E.M., eds. Denver, Colorado: U.S. Geological Survey. ACC: MOL.20031208.0113. TBV-5659

163092   Coe, J.A.; Yount, J.C.; O'Leary, D.W.; and Taylor, E.M. 2003. "Paleoseismic Investigations in the Rock Valley Fault System." Chapter 13 of *Quaternary Paleoseismology and Stratigraphy of the Yucca Mountain Area, Nevada*. U.S. Geological Survey Digital Data Series. Keefer, W.R.; Whitney, J.W.; and Taylor, E.M., eds. Denver, Colorado: U.S. Geological Survey. ACC: MOL.20031208.0113. TBV-5659

102646   Connor, C.B. and Hill, B.E. 1995. "Three Nonhomogeneous Poisson Models for the Probability of Basaltic Volcanism: Application to the Yucca Mountain Region, Nevada." *Journal of Geophysical Research, 100*, (B6), 10,107-10,125. Washington, D.C.: American Geophysical Union. TIC: 237682.

102647   Connor, C.B.; Lane-Magsino, S.; Stamatakos, J.A.; Martin, R.H.; LaFemina, P.C.; Hill, B.E.; and Lieber, S. 1997. "Magnetic Surveys Help Reassess Volcanic Hazards at Yucca Mountain, Nevada." *Eos, Transactions, 78*, (7), 73, 77, 78. Washington, D.C.: American Geophysical Union. TIC: 234580.

149935   Connor, C.B.; Stamatakos, J.A.; Ferrill, D.A.; Hill, B.E.; Ofoegbu, G.I.; Conway, F.M.; Sagar, B.; and Trapp, J. 2000. "Geologic Factors Controlling Patterns of Small-Volume Basaltic Volcanism: Application to a Volcanic Hazards Assessment at Yucca Mountain, Nevada." *Journal of Geophysical Research, 105*, (B1), 417-432. Washington, D.C.: American Geophysical Union. TIC: 247906.

102731   Cornell, C.A. 1968. "Engineering Seismic Risk Analysis." *Bulletin of the Seismological Society of America, 58*, (5), 1583-1606. El Cerrito, California: Seismological Society of America. TIC: 237493.

102734   Cornell, C.A. 1971. "Probabilistic Analysis of Damage to Structures Under Seismic Loads." Chapter 27 of *Dynamic Waves in Civil Engineering*. Howells, D.A.; Haigh, I.P.; and Taylor, C., eds. New York, New York: Wiley-Interscience. TIC: 241003.

100110   Crowe, B.; Perry, F.; Geissman, J.; McFadden, L.; Wells, S.; Murrell, M.; Poths, J.; Valentine, G.A.; Bowker, L.; and Finnegan, K. 1995. *Status of Volcanism Studies for the Yucca Mountain Site Characterization Project*. LA-12908-MS. Los Alamos, New Mexico: Los Alamos National Laboratory. ACC: HQO.19951115.0017.

100973   Crowe, B.M. and Perry, F.V. 1990. "Volcanic Probability Calculations for the Yucca Mountain Site: Estimation of Volcanic Rates." *Proceedings of the Topical Meeting on Nuclear Waste Isolation in the Unsaturated Zone, FOCUS '89, September 17-21, 1989, Las Vegas, Nevada*. Pages 326-334. La Grange Park, Illinois: American Nuclear Society. TIC: 212738.

100116   CRWMS M&O (Civilian Radioactive Waste Management System Management and Operating Contractor) 1996. *Probabilistic Volcanic Hazard Analysis for Yucca Mountain, Nevada*. BA0000000-01717-2200-00082 REV 0. Las Vegas, Nevada: CRWMS M&O. ACC: MOL.19971201.0221.

123196   CRWMS M&O 1998. "Geology and Geochronology of Basaltic Volcanism in the Yucca Mountain Region." Chapter 2 of *Synthesis of Volcanism Studies for the Yucca Mountain Site Characterization Project*. Deliverable 3781MR1. Las Vegas, Nevada: CRWMS M&O. ACC: MOL.19990511.0400.

106491   CRWMS M&O 1998. "Petrologic and Geochemical Constraints on Basaltic Volcanism in the Great Basin." Chapter 4 of *Synthesis of Volcanism Studies for the Yucca Mountain Site Characterization Project*. Deliverable 3781MR1. Las Vegas, Nevada: CRWMS M&O. ACC: MOL.19990511.0400.

123201   CRWMS M&O 1998. "Physical Processes of Magmatism and Effects on the Potential Repository: Synthesis of Technical Work through Fiscal Year 1995." Chapter 5 of *Synthesis of Volcanism Studies for the Yucca Mountain Site Characterization Project*. Deliverable 3781MR1. Las Vegas, Nevada: CRWMS M&O. ACC: MOL.19990511.0400.

103731   CRWMS M&O 1998. *Probabilistic Seismic Hazard Analyses for Fault Displacement and Vibratory Ground Motion at Yucca Mountain, Nevada.* Milestone SP32IM3, September 23, 1998. Three volumes. Las Vegas, Nevada: CRWMS M&O. ACC: MOL.19981207.0393.

105347   CRWMS M&O 1998. *Synthesis of Volcanism Studies for the Yucca Mountain Site Characterization Project.* Deliverable 3781MR1. Las Vegas, Nevada: CRWMS M&O. ACC: MOL.19990511.0400.

135988   CRWMS M&O 1998. "Tectonic Setting of the Yucca Mountain Region: Relationship to Episodes of Cenozoic Basaltic Volcanism." Chapter 3 of *Synthesis of Volcanism Studies for the Yucca Mountain Site Characterization Project.* Deliverable 3781MR1. Las Vegas, Nevada: CRWMS M&O. ACC: MOL.19990511.0400.

103962   CRWMS M&O 1999. *Enhanced Design Alternative II Report.* B00000000-01717-5705-00131 REV 00. Las Vegas, Nevada: CRWMS M&O. ACC: MOL.19990712.0194.

151551   CRWMS M&O 2000. *Characterize Framework for Igneous Activity at Yucca Mountain, Nevada.* ANL-MGR-GS-000001 REV 00 ICN 01. Las Vegas, Nevada: CRWMS M&O. ACC: MOL.20001221.0001.

142321   CRWMS M&O 2000. *Characterize Framework for Seismicity and Structural Deformation at Yucca Mountain, Nevada.* ANL-CRW-GS-000003 REV 00. Las Vegas, Nevada: CRWMS M&O. ACC: MOL.20000510.0175.

151950   CRWMS M&O 2000. *Disruptive Events Process Model Report.* TDR-NBS-MD-000002 REV 00 ICN 01. Las Vegas, Nevada: CRWMS M&O. ACC: MOL.20000727.0085.

150640   CRWMS M&O 2000. *Yucca Mountain Historical Earthquake Catalog from 1868 to 1998.* Las Vegas, Nevada: CRWMS M&O. ACC: MOL.20000623.0302.

151945   CRWMS M&O 2000. *Yucca Mountain Site Description.* TDR-CRW-GS-000001 REV 01 ICN 01. Las Vegas, Nevada: CRWMS M&O. ACC: MOL.20001003.0111.

124302   Day, W.C.; Potter, C.J.; Sweetkind, D.S.; Dickerson, R.P.; and Keefer, W.R. 1996. "Structural Geology of the Central Block of Yucca Mountain." Chapter 2-I of *Seismotectonic Framework and Characterization of Faulting at Yucca Mountain, Nevada.* Whitney, J.W., ed. Milestone 3GSH100M. Denver, Colorado: U.S. Geological Survey. TIC: 237980. ACC: MOL.19970129.0041.

100027   Day, W.C.; Dickerson, R.P.; Potter, C.J.; Sweetkind, D.S.; San Juan, C.A.; Drake, R.M., II; and Fridrich, C.J. 1998. *Bedrock Geologic Map of the Yucca Mountain Area, Nye County, Nevada.* Geologic Investigations Series I-2627. Denver, Colorado: U.S. Geological Survey. ACC: MOL.19981014.0301.

104855   dePolo, C.M. 1994. "Estimating Fault Slip Rates in the Great Basin, USA." *Proceedings of the Workshop on Paleoseismology, 18-22 September, 1994, Marshall, California.* Prentice, C.S.; Schwartz, D.P.; and Yeats, R.S., eds. Open-File Report 94-568. Pages 48-49. Menlo Park, California: U.S. Geological Survey. TIC: 234812.

104868   dePolo, C.M.; Ramelli, A.R.; and Bell, J.W. 1994. "The 1932 Cedar Mountain Earthquake, Central Nevada, U.S.A.: A Major Basin and Range Province Earthquake that had a Widely Distributed Surface Faulting Pattern." *Proceedings of the Workshop on Paleoseismology, 18-22 September, 1994, Marshall, California.* Prentice, C.S.; Schwartz, D.P.; and Yeats, R.S., eds. Open-File Report 94-568. Pages 50-52. Menlo Park, California: U.S. Geological Survey. TIC: 234666.

155943   DOE (U.S. Department of Energy) 2002. *Yucca Mountain Science and Engineering Report.* DOE/RW-0539, Rev. 1. Washington, D.C.: U.S. Department of Energy, Office of Civilian Radioactive Waste Management. ACC: MOL.20020404.0042.

124370   Dohrenwend, J.C.; Menges, C.M.; Schell, B.A.; and Moring, B.C. 1991. *Reconnaissance Photogeologic Map of Young Faults in the Las Vegas 1° by 2° Quadrangle, Nevada, California, and Arizona.* Miscellaneous Field Studies Map MF-2182. Denver, Colorado: U.S. Geological Survey. ACC: NNA.19940524.0079.

124376   Dohrenwend, J.C.; Schell, B.A.; McKittrick, M.A.; and Moring, B.C. 1992. *Reconnaissance Photogeologic Map of Young Faults in the Goldfield 1° by 2° Quadrangle, Nevada and California.* Miscellaneous Field Studies Map MF-2183. Denver, Colorado: U.S. Geological Survey. ACC: NNA.19940524.0080.

102803   Doser, D.I. 1986. "Earthquake Processes in the Rainbow Mountain-Fairview Peak-Dixie Valley, Nevada, Region 1954-1959." *Journal of Geophysical Research, 91*, (B12), 12,572-12,586. Washington, D.C.: American Geophysical Union. TIC: 223278.

102804   Doser, D.I. 1988. "Source Parameters of Earthquakes in the Nevada Seismic Zone, 1915-1943." *Journal of Geophysical Research, 93*, (B12), 15,001-15,015. Washington, D.C.: American Geophysical Union. TIC: 238889.

102805   Doser, D.I. and Smith, R.B. 1989. "An Assessment of Source Parameters of Earthquakes in the Cordillera of the Western United States." *Bulletin of the Seismological Society of America, 79*, (5), 1383-1409. El Cerrito, California: Seismological Society of America. TIC: 236846.

115338   Doubik, P. and Hill, B.E. 1999. "Magmatic and Hydromagmatic Conduit Development During the 1975 Tolbachik Eruption, Kamchatka, with Implications for Hazards Assessment at Yucca Mountain, NV." *Journal of Volcanology and Geothermal Research, 91*, 43-64. Amsterdam, The Netherlands: Elsevier. TIC: 246029.

105259   Ellsworth, W.L. 1990. "Earthquake History, 1769-1989." Chapter 6 of *The San Andreas Fault System, California*. Professional Paper 1515. Denver, Colorado: U.S. Geological Survey. TIC: 234474.

105267   Engdahl, E.R. and Rinehart, W.A. 1988. *Seismicity Map of North America*. Continent-Scale Map-004. Boulder, Colorado: Geological Society of America. TIC: 240261.

105274   Evernden, J.F. 1975. "Seismic Intensities, 'Size' of Earthquakes and Related Parameters." *Bulletin of the Seismological Society of America, 65*, (5), 1287-1313. El Cerrito, California: Seismological Society of America. TIC: 240820.

105284   Farmer, G.L.; Perry, F.V.; Semken, S.; Crowe, B.; Curtis, D.; and DePaolo, D.J. 1989. "Isotopic Evidence on the Structure and Origin of Subcontinental Lithospheric Mantle in Southern Nevada." *Journal of Geophysical Research, 94*, (B6), 7885-7898. Washington, D.C.: American Geophysical Union. TIC: 201800.

105126   Faulds, J.E.; Bell, J.W.; Feuerbach, D.L.; and Ramelli, A.R. 1994. *Geologic Map of the Crater Flat Area, Nevada*. Geophysical Investigations Map 101. Reno, Nevada: University of Nevada, Reno. TIC: 211484.

105309   Ferrill, D.A.; Stirewalt, G.L.; Henderson, D.B.; Stamatakos, J.A.; Morris, A.P.; Spivey, K.H.; and Wernicke, B.P. 1996. *Faulting in the Yucca Mountain Region: Critical Review and Analyses of Tectonic Data from the Central Basin and Range*. NUREG/CR-6401. Washington, D.C.: U.S. Nuclear Regulatory Commission. TIC: 231665.

105337   Fleck, R.J.; Turrin, B.D.; Sawyer, D.A.; Warren, R.G.; Champion, D.E.; Hudson, M.R.; and Minor, S.A. 1996. "Age and Character of Basaltic Rocks of the Yucca Mountain Region, Southern Nevada." *Journal of Geophysical Research, 101*, (B4), 8205-8227. Washington, D.C.: American Geophysical Union. TIC: 234626.

105435   Fox, K.F., Jr. and Carr, M.D. 1989. "Neotectonics and Volcanism at Yucca Mountain and Vicinity, Nevada." *Radioactive Waste Management and the Nuclear Fuel Cycle, 13*, 37-50. New York, New York: Harwood Academic Publishers. TIC: 200232.

105086 Fridrich, C.J.; Whitney, J.W.; Hudson, M.R.; Keefer, W.R.; and Crowe, B.M. 1996. "Space-Time Patterns of Extension, Vertical-Axis Rotation, and Volcanism in the Crater Flat Basin." Chapter 2.II of *Seismotectonic Framework and Characterization of Faulting at Yucca Mountain, Nevada*. Whitney, J.W., ed. Milestone 3GSH100M. Denver, Colorado: U.S. Geological Survey. TIC: 237980. ACC: MOL.19970129.0041.

101098 Fridrich, C.J. 1998. *Tectonic Evolution of the Crater Flat Basin, Yucca Mountain Region, Nevada*. Open-File Report 98-33. Denver, Colorado: U.S. Geological Survey. ACC: MOL.19981014.0298.

118942 Fridrich, C.J. 1999. "Tectonic Evolution of the Crater Flat Basin, Yucca Mountain Region, Nevada." Chapter 7 of *Cenozoic Basins of the Death Valley Region*. Wright, L.A. and Troxel, B.W., eds. Special Paper 333. Boulder, Colorado: Geological Society of America. TIC: 248054.

107333 Fridrich, C.J.; Whitney, J.W.; Hudson, M.R.; and Crowe, B.M. 1999. "Space-Time Patterns of Late Cenozoic Extension, Vertical Axis Rotation, and Volcanism in the Crater Flat Basin, Southwest Nevada." Chapter 8 of *Cenozoic Basins of the Death Valley Region*. Wright, L.A. and Troxel, B.W., eds. Special Paper 333. Boulder, Colorado: Geological Society of America. TIC: 248054.

105502 Gianella, V.P. and Callaghan, E. 1934. "The Cedar Mountain, Nevada, Earthquake of December 20, 1932." *Bulletin of the Seismological Society of America, 24*, (4), 345-377. El Cerrito, California: Seismological Society of America. TIC: 217009.

105604 Gomberg, J. 1991. "Seismicity and Detection/Location Threshold in the Southern Great Basin Seismic Network." *Journal of Geophysical Research, 96*, (B10), 16,401-16,414. Washington, D.C.: American Geophysical Union. TIC: 212627.

105606 Gomberg, J. 1991. "Seismicity and Shear Strain in the Southern Great Basin of Nevada and California." *Journal of Geophysical Research, 96*, 16,383-16,399. Washington, D.C.: American Geophysical Union. TIC: 225033.

105608 Gomberg, J. and Bodin, P. 1994. "Triggering of the Ms = 5.4 Little Skull Mountain, Nevada, Earthquake with Dynamic Strains." *Bulletin of the Seismological Society of America, 84*, (3), 844-853. El Cerrito, California: Seismological Society of America. TIC: 240825.

105100 Gross, S. and Jaume, S. 1995. *Historical Seismicity in the Southern Great Basin of Nevada and California*. Denver, Colorado: U.S. Geological Survey. ACC: MOL.19980219.0840.

105817 Guth, P.L. 1981. "Tertiary Extension North of the Las Vegas Valley Shear Zone, Sheep and Desert Ranges, Clark County, Nevada." *Geological Society of America Bulletin, Part I, 92*, (10), 763-771. Boulder, Colorado: Geological Society of America. TIC: 217559.

105884   Hagstrum, J.T. and Gans, P.B. 1989. "Paleomagnetism of the Oligocene Kalamazoo Tuff: Implications for Middle Tertiary Extension in East Central Nevada." *Journal of Geophysical Research, 94*, (B2), 1827-1842. Washington, D.C.: American Geophysical Union. TIC: 234444.

100037   Hamilton, W.B. 1988. "Detachment Faulting in the Death Valley Region, California and Nevada." Chapter 5 of *Geologic and Hydrologic Investigations of a Potential Nuclear Waste Disposal Site at Yucca Mountain, Southern Nevada*. Carr, M.D. and Yount, J.C., eds. Bulletin 1790. Denver, Colorado: U.S. Geological Survey. TIC: 203085.

106092   Harmsen, S.C. and Rogers, A.M. 1986. "Inferences About the Local Stress Field from Focal Mechanisms: Applications to Earthquakes in the Southern Great Basin of Nevada." *Bulletin of the Seismological Society of America, 76*, (6), 1560-1572. El Cerrito, California: Seismological Society of America. TIC: 237978.

105108   Harmsen, S.C. and Bufe, C.G. 1992. *Seismicity and Focal Mechanisms for the Southern Great Basin of Nevada and California: 1987 through 1989*. Open-File Report 91-572. Denver, Colorado: U.S. Geological Survey. ACC: NNA.19920408.0001.

105106   Harmsen, S.C. 1993. *Seismicity and Focal Mechanisms for the Southern Great Basin of Nevada and California in 1991*. Open-File Report 92-340. Denver, Colorado: U.S. Geological Survey. ACC: NNA.19920629.0129.

105107   Harmsen, S.C. 1994. *Preliminary Seismicity and Focal Mechanisms for the Southern Great Basin of Nevada and California: January 1992 through September 1992*. Open-File Report 93-369. Denver, Colorado: U.S. Geological Survey. ACC: NNA.19931215.0008.

106090   Harmsen, S.C. 1994. "The Little Skull Mountain, Nevada, Earthquake of 29 June 1992: Aftershock Focal Mechanisms and Tectonic Stress Field Implications." *Bulletin of the Seismological Society of America, 84*, (5), 1484-1505. El Cerrito, California: Seismological Society of America. TIC: 237937.

100180   Hauge, T.A.; Allmendinger, R.W.; Caruso, C.; Hauser, E.C.; Klemperer, S.L.; Opdyke, S.; Potter, C.J.; Sanford, W.; Brown, L.; Kaufman, S.; and Oliver, J. 1987. "Crustal Structure of Western Nevada from COCORP Deep Seismic-Reflection Data." *Geological Society of America Bulletin, 98*, 320-329. Boulder, Colorado: Geological Society of America. TIC: 234449.

106118   Healey, D.L.; Harris, R.N.; Ponce, D.A.; and Oliver, H.W. 1987. *Complete Bouguer Gravity Map of the Nevada Test Site and Vicinity, Nevada*. Open-File Report 87-506. Menlo Park, California: U.S. Geological Survey. TIC: 203192.

156296   Hector Mine Earthquake Geologic Working Group. 2000. "Surface Rupture, Slip Distribution, and Other Geologic Observations Associated with the M7.1 Hector Mine Earthquake of 16 October 1999." *Seismological Research Letters, 71*, (1), 224. El Cerrito, California: Seismological Society of America. TIC: 250813.

107255   Heizler, M.T.; Perry, F.V.; Crowe, B.M.; Peters, L.; and Appelt, R. 1999. "The Age of Lathrop Wells Volcanic Center: An $^{40}Ar/^{39}Ar$ Dating Investigation." *Journal of Geophysical Research, 104*, (B1), 767-804. Washington, D.C.: American Geophysical Union. TIC: 243399.

105513   Hileman, J.A.; Allen, C.R.; and Nordquist, J.M. 1973. *Seismicity of the Southern California Region 1 January 1932 to 31 December 1972*. Pasadena, California: California Institute of Technology, Seismological Laboratory. TIC: 242404.

106161   Hoisch, T.D. 1995. "Conditions of Metamorphism in Lower-Plate Rocks at Bare Mountain, Nevada - Implications for Extensional Faulting." Chapter 2 of *Characterization of Detachment Faults in the Yucca Mountain Region*. Denver, Colorado: U.S. Geological Survey. ACC: MOL.19960305.0440.

101247   Hoover, D.L. 1989. *Preliminary Description of Quaternary and Late Pliocene Surficial Deposits at Yucca Mountain and Vicinity, Nye County, Nevada*. Open-File Report 89-359. Denver, Colorado: U.S. Geological Survey. ACC: NNA.19900403.0406.

100986   Hudson, M.R.; Sawyer, D.A.; and Warren, R.G. 1994. "Paleomagnetism and Rotation Constraints for the Middle Miocene Southwestern Nevada Volcanic Field." *Tectonics, 13*, (2), 258-277. Washington, D.C.: American Geophysical Union. TIC: 232935.

106194   Hudson, M.R.; Minor, S.A.; and Fridrich, C.J. 1996. "The Distribution, Timing, and Character of Steep-Axis Rotations in a Broad Zone of Dextral Shear in Southwestern Nevada." *Abstracts with Programs - Geological Society of America, 28*, (7), A-451. Boulder, Colorado: Geological Society of America. TIC: 234723.

105517   Idriss, I.M. 1991. "Earthquake Ground Motions at Soft Soil Sites." *Second International Conference on Recent Advances in Geotechnical Earthquake Engineering and Soil Dynamics, March 11-15, 1991*. Prakash, S., ed. III, 2265-2272. Rolla, Missouri: University of Missouri-Rolla. TIC: 241773.

106220   Jaques, A.L. and Green, D.H. 1980. "Anhydrous Melting of Peridotite at 0-15 Kb Pressure and the Genesis of Tholeiitic Basalts." *Contributions to Mineralogy and Petrology, 73*, 287-310. New York, New York: Springer-Verlag. TIC: 225050.

149960   Jones, L.M. 2000. "Overview of the Mw7.1 Hector Mine, California Earthquake of October 16, 1999." *Seismological Research Letters, SSA 2000, Abstracts of the 95th Annual Meeting, 71*, (2), 205. El Cerrito, California: Seismological Society of America. TIC: 247896.

159419   Keefer, W.R.; Whitney, J.W.; and Taylor, E.M., eds. 2003. *Quaternary Paleoseismology and Stratigraphy of the Yucca Mountain Area, Nevada.* U.S. Geological Survey Digital Data Series. Denver, Colorado: U.S. Geological Survey. ACC: MOL.20031208.0113.   TBV-5659

106292   King, K.W.; Bayer, K.C.; and Brockman, S.R. 1971. *Earthquakes On and Around the Nevada Test Site 1950 - 1971.* CGS-746-12. Washington, D.C.: U.S. Department of Commerce, National Oceanic and Atmospheric Administration. TIC: 204588.

148622   Langenheim, V.E.; Kirchoff-Stein, K.S.; and Oliver, H.W. 1993. "Geophysical Investigations of Buried Volcanic Centers Near Yucca Mountain, Southwest Nevada." *High Level Radioactive Waste Management, Proceedings of the Fourth Annual International Conference, Las Vegas, Nevada, April 26-30, 1993. 2,* 1840-1846. La Grange Park, Illinois: American Nuclear Society. TIC: 208542.

104491   Langenheim, V.E. 1995. *Magnetic and Gravity Studies of Buried Volcanic Centers in the Amargosa Desert and Crater Flat, Southwest Nevada.* Open-File Report 95-564. Menlo Park, California: U.S. Geological Survey. ACC: MOL.19970331.0063.

104561   Langenheim, V.E. and Ponce, D.A. 1995. *Ground Magnetic Studies Along a Regional Seismic-Reflection Profile Across Bare Mountain, Crater Flat and Yucca Mountain, Nevada.* Open-File Report 95-834. Menlo Park, California: U.S. Geological Survey. ACC: MOL.19990406.0379.

107482   Latham, A.G. 1995. "On the Principles of the U-Trend Method for Dating Quaternary Sediments, I: Model, Experimental Procedures and Data." *Quaternary Science Reviews (Quaternary Geochronology), 14,* (4), 409-420. New York, New York: Pergamon Press. TIC: 237026.

106327   Lundstrom, S.C.; Wesling, J.R.; Swan, F.H.; Taylor, E.M.; and Whitney, J.W. 1993. "Quaternary Allostratigraphy of Surficial Deposit Map Units at Yucca Mountain, Nevada: A Progress Report." *Abstracts with Programs - Geological Society of America, 25,* (5), A-112. Boulder, Colorado: Geological Society of America. TIC: 237811.

147781   Magsino, S.L.; Connor, C.B.; Hill, B.E.; Stamatakos, J.A.; La Femina, P.C.; Sims, D.A.; and Martin, R.H. 1998. *CNWRA Ground Magnetic Surveys in the Yucca Mountain Region, Nevada (1996-1997).* CNWRA 98-001. San Antonio, Texas: Center for Nuclear Waste Regulatory Analyses. TIC: 247807.

104685   Majer, E.L.; Feighner, M.; Johnson, L.; Daley, T.; Karageorgi, E.; Lee, K.H.; Williams, K.; and McEvilly, T. 1996. *Surface Geophysics.* Volume I of *Synthesis of Borehole and Surface Geophysical Studies at Yucca Mountain, Nevada and Vicinity.* Milestone OB05M. Berkeley, California: Lawrence Berkeley National Laboratory. ACC: MOL.19970610.0150.

106330   Majer, E.L.; Feighner, M.; Johnson, L.; Daley, T.; Williams, K.; Karageorgi, E.; and McEvilly, T. 1996. *Level 4 Milestone Letter Report on Surface Geophysics Synthesis: Data Processing*. Berkeley, California: Lawrence Berkeley National Laboratory. ACC: MOL.19971224.0006.

156302   Marks, S.L. 2001. "First Report on Results from Geodetic Monitoring of the Yucca Mountain Region Using Continuous GPS Measurements - Task 1." Letter from S.L. Marks (UNLV) to R. James (DOE), August 16, 2001, with enclosures. ACC: MOL.20010924.0030.

104768   McCafferty, A.E. and Grauch, V.J.S. 1997. *Aeromagnetic and Gravity Anomaly Maps of the Southwestern Nevada Volcanic Field, Nevada and California*. Geophysical Investigations Map GP-1015. Denver, Colorado: U.S. Geological Survey. TIC: 243156.

104770   McCalpin, J.P. 1995. "Short Notes Frequency Distribution of Geologically Determined Slip Rates for Normal Faults in the Western United States." *Bulletin of the Seismological Society of America, 85*, (6), 1867-1872. El Cerrito, California: Seismological Society of America. TIC: 236669.

105028   McKague, H.L.; Stamatakos, J.A.; and Ferrill, D.A. 1996. *Type I Faults in the Yucca Mountain Region*. CNWRA 96-007, Rev. 1. San Antonio, Texas: Center for Nuclear Waste Regulatory Analyses. TIC: 232061.

159412   Menges, C.M.; Taylor, E.M.; Wesling, J.R.; Swan, F.H.; Coe, J.A.; Ponti, D.J.; and Whitney, J.W. 2003. "Summary of Quaternary Faulting on the Paintbrush Canyon, Stagecoach Road, and Bow Ridge Faults." Chapter 5 of *Quaternary Paleoseismology and Stratigraphy of the Yucca Mountain Area, Nevada*. U.S. Geological Survey Digital Data Series. Keefer, W.R.; Whitney, J.W.; and Taylor, E.M., eds. Denver, Colorado: U.S. Geological Survey. ACC: MOL.20031208.0113. TBV-5659

106352   Meremonte, M.E. and Rogers, A.M. 1987. *Historical Catalog of Southern Great Basin Earthquakes 1868-1978*. Open-File Report 87-80. Denver, Colorado: U.S. Geological Survey. TIC: 203189.

106353   Meremonte, M.E.; Cranswick, E.; Gomberg, J.; Worley, D.; Carver, D.; Brooks, J.; Banfill, R.; Overturf, D.; and Bice, T. 1993. *Report on the Seismological Field Investigations of the 29 June 1992 Little Skull Mountain Earthquake*. Open-File Report 93-555. Denver, Colorado: U.S. Geological Survey. ACC: NNA.19931117.0008.

106354   Meremonte, M.E.; Gomberg, J.; and Cranswick, E. 1995. "Constraints on the 29 June 1992 Little Skull Mountain, Nevada Earthquake Sequence Provided by Robust Hypocentral Estimates." *Bulletin of the Seismological Society of America, 85*, (4), 1039-1049. El Cerrito, California: Seismological Society of America. TIC: 236659.

106373   Minor, S.A. 1995. "Superposed Local and Regional Paleostresses: Fault-Slip Analysis of Neogene Extensional Faulting Near Coeval Caldera Complexes, Yucca Flat, Nevada." *Journal of Geophysical Research, 100*, (B6), 10,507-10,528. Washington, D.C.: American Geophysical Union. TIC: 236631.

100997   Minor, S.A.; Hudson, M.R.; and Fridrich, C.J. 1997. *Fault-Slip Data, Paleomagnetic Data, and Paleostress Analyses Bearing on the Neogene Tectonic Evolution of Northern Crater Flat Basin, Nevada*. Open-File Report 97-285. Denver, Colorado: U.S. Geological Survey. TIC: 242295.

106379   Minster, J.B. and Jordan, T.H. 1987. "Vector Constraints on Western U.S. Deformation from Space Geodesy, Neotectonics, and Plate Motions." *Journal of Geophysical Research, 92*, (B6), 4798-4804. Washington, D.C.: American Geophysical Union. TIC: 234809.

135621   NRC (U.S. Nuclear Regulatory Commission) 1999. *Issue Resolution Status Report Key Technical Issue: Structural Deformation and Seismicity*. Rev. 2. Washington, D.C.: U.S. Nuclear Regulatory Commission. ACC: MOL.19991214.0623.

106435   O'Leary, D.W. 1996. "Synthesis of Tectonic Models for the Yucca Mountain Area." Chapter 8 of *Seismotectonic Framework and Characterization of Faulting at Yucca Mountain, Nevada*. Whitney, J.W., ed. Milestone 3GSH100M. Denver, Colorado: U.S. Geological Survey. TIC: 237980. ACC: MOL.19970129.0041.

158468   O'Leary, D.W.; Mankinen, E.A.; Blakely, R.J.; Langenheim, V.E.; and Ponce, D.A. 2002. *Aeromagnetic Expression of Buried Basaltic Volcanoes Near Yucca Mountain, Nevada*. Open-File Report 02-020. Denver, Colorado: U.S. Geological Survey. ACC: MOL.20020627.0225.

106427   Ofoegbu, G.I. and Ferrill, D.A. 1995. *Finite Element Modeling of Listric Normal Faulting*. CNWRA 95-008. San Antonio, Texas: Center for Nuclear Waste Regulatory Analyses. TIC: 240263.

106439   Oliver, H.W. and Fox, K.F. 1993. "Structure of Crater Flat and Yucca Mountain, Southeastern Nevada, as Inferred from Gravity Data." *High Level Radioactive Waste Management, Proceedings of the Fourth Annual International Conference, Las Vegas, Nevada, April 26-30, 1993. 2*, 1812-1817. La Grange Park, Illinois: American Nuclear Society. TIC: 208542.

106473   Paces, J.B.; Menges, C.M.; Widmann, B.; Wesling, J.R.; Bush, C.A.; Futa, K.; Millard, H.T.; Maat, P.B.; and Whitney, J.W. 1994. "Preliminary U-Series Disequilibrium and Thermoluminescence Ages of Surficial Deposits and Paleosols Associated with Quaternary Faults, Eastern Yucca Mountain." *High Level Radioactive Waste Management, Proceedings of the Fifth Annual International Conference, Las Vegas, Nevada, May 22-26, 1994. 4*, 2391-2401. La Grange Park, Illinois: American Nuclear Society. TIC: 210984.

101352   Paces, J.B.; Mahan, S.A.; Ludwig, K.R.; Kwak, L.M.; Neymark, L.A.; Simmons, K.R.; Nealey, L.D.; Marshall, B.D.; and Walker, A. 1995. *Progress Report on Dating Quaternary Surficial Deposits*. Milestone 3GCH510M. Final Draft. Denver, Colorado: U.S. Geological Survey. ACC: MOL.19960611.0220.

106488   Perry, F.V. and Crowe, B.M. 1992. "Geochemical Evidence for Waning Magmatism and Polycyclic Volcanism at Crater Flat, Nevada." *High Level Radioactive Waste Management, Proceedings of the Third International Conference, Las Vegas, Nevada, April 12-16, 1992. 2*, 2356-2365. La Grange Park, Illinois: American Nuclear Society. TIC: 204231.

106490   Perry, F.V. and Straub. K.T. 1996. *Geochemistry of the Lathrop Wells Volcanic Center*. LA-13113-MS. Los Alamos, New Mexico: Los Alamos National Laboratory. ACC: MOL.19961015.0079.

144335   Perry, F.V.; Crowe, B.M.; Valentine, G.A.; and Bowker, L.M., eds. 1998. *Volcanism Studies: Final Report for the Yucca Mountain Project*. LA-13478. Los Alamos, New Mexico: Los Alamos National Laboratory. TIC: 247225.

106512   Peterson, F.F. 1988. "Consultant's Report: Soil-Geomorphology Studies in the Crater Flat, Nevada, Area." Appendix B of *Quaternary Geology and Active Faulting at and Near Yucca Mountain*. Reno, Nevada: Nevada Bureau of Mines and Geology. TIC: 222315.

106519   Peterson, F.F.; Bell, J.W.; Dorn, R.I.; Ramelli, A.R.; and Ku, T.L. 1995. "Late Quaternary Geomorphology and Soils in Crater Flat, Yucca Mountain Area, Southern Nevada." *Geological Society of America Bulletin, 107*, (4), 379-395. Boulder, Colorado: Geological Society of America. TIC: 235112.

106524   Pezzopane, S.K. 1996. "Relevant Earthquake Sources." Chapter 11 of *Seismotectonic Framework and Characterization of Faulting at Yucca Mountain, Nevada*. Whitney, J.W., ed. Milestone 3GSH100M. Denver, Colorado: U.S. Geological Survey. TIC: 237980. ACC: MOL.19970129.0041.

106526   Pezzopane, S.K.; Bufe, C.G.; Dawson, T.E.; Wong, I.G.; and Bott, J.D.J. 1996. "Historical Seismicity in the Yucca Mountain Region." Chapter 7 of *Seismotectonic Framework and Characterization of Faulting at Yucca Mountain, Nevada*. Whitney, J.W., ed. Milestone 3GSH100M. Denver, Colorado: U.S. Geological Survey. TIC: 237980. ACC: MOL.19970129.0041.

103265   Pezzopane, S.K. and Dawson, T.E. 1996. "Fault Displacement Hazard: A Summary of Issues and Information." Chapter 9 of *Seismotectonic Framework and Characterization of Faulting at Yucca Mountain, Nevada*. Whitney, J.W., ed. Milestone 3GSH100M. Denver, Colorado: U.S. Geological Survey. TIC: 237980. ACC: MOL.19970129.0041.

106528   Pezzopane, S.K.; Whitney, J.W.; and Dawson, T.E. 1996. "Models of Earthquake Recurrence and Preliminary Paleoearthquake Magnitudes at Yucca Mountain." Chapter 5 of *Seismotectonic Framework and Characterization of Faulting at Yucca Mountain, Nevada*. Whitney, J.W., ed. Milestone 3GSH100M. Denver, Colorado: U.S. Geological Survey. TIC: 237980. ACC: MOL.19970129.0041.

158691   Pezzopane, S.K.; Carande, R.E.; and Smith, K.D. 1999. "Preliminary Surface Displacement of the 1992 Little Skull Mountain Earthquake Measured by Satellite Radar Interferometry of the Yucca Mountain Region, Nevada." *Eos (Supplement), 80*, (17), S1. Washington, D.C.: American Geophysical Union. TIC: 252669.

106540   Piety, L.A. 1996. *Compilation of Known or Suspected Quaternary Faults Within 100 km of Yucca Mountain, Nevada and California*. Open-File Report 94-112. Denver, Colorado: U.S. Geological Survey. ACC: MOL.19971009.0003.

106632   Ramelli, A.R.; Bell, J.W.; and dePolo, C.M. 1988. "Evidence for Distributive Faulting at Yucca Mountain, Nevada." *Abstracts with Programs - Geological Society of America, 20*, (7), A383. Boulder, Colorado: Geological Society of America. TIC: 217691.

101106   Ramelli, A.R.; Oswald, J.A.; Vadurro, G.; Menges, C.M.; and Paces, J.B. 1996. "Quaternary Faulting on the Solitario Canyon Fault." Chapter 4.7 of *Seismotectonic Framework and Characterization of Faulting at Yucca Mountain, Nevada*. Whitney, J.W., ed. Milestone 3GSH100M. Denver, Colorado: U.S. Geological Survey. TIC: 237980. ACC: MOL.19970129.0041.

159413   Ramelli, A.R.; Oswald, J.A.; Vadurro, G.; Menges, C.M.; and Paces, J.B. 2003. "Quaternary Faulting on the Solitario Canyon Fault." Chapter 7 of *Quaternary Paleoseismology and Stratigraphy of the Yucca Mountain Area, Nevada*. U.S. Geological Survey Digital Data Series. Keefer, W.R.; Whitney, J.W.; and Taylor, E.M., eds. Denver, Colorado: U.S. Geological Survey. ACC: MOL.20031208.0113. TBV-5659

166373   Ransome, F.L.; Emmons, W.H.; and Garrey, G.H. 1910. *Geology and Ore Deposits of the Bullfrog District, Nevada*. U.S. Geological Survey Bulletin 407. Washington, D.C.: Government Printing Office. ACC: NNA.19901130.0014.

119693   Reamer, C.W. 1999. "Issue Resolution Status Report (Key Technical Issue: Igneous Activity, Revision 2)." Letter from C.W. Reamer (NRC) to Dr. S. Brocoum (DOE/YMSCO), July 16, 1999, with enclosure. ACC: MOL.19990810.0639.

102916   Reheis, M.C. 1991. *Aerial Photographic Interpretation of Lineaments and Faults in Late Cenozoic Deposits in the Eastern Parts of the Saline Valley 1:100,000 Quadrangle, Nevada and California, and the Darwin Hills 1:100,000 Quadrangle, California*. Open-File Report 90-500. Denver, Colorado: U.S. Geological Survey. ACC: NNA.19910507.0001.

102891   Reheis, M.C. and Noller, J.S. 1991. *Aerial Photographic Interpretation of Lineaments and Faults in Late Cenozoic Deposits in the Eastern Part of the Benton Range 1:100,000 Quadrangle and the Goldfield, Last Chance Range, Beatty, and Death Valley Junction 1:100,000 Quadrangles, Nevada and California*. Open-File Report 90-41. Denver, Colorado: U.S. Geological Survey. ACC: NNA.19901031.0001.

106652   Reheis, M.C. 1992. *Aerial Photographic Interpretation of Lineaments and Faults in Late Cenozoic Deposits in the Cactus Flat and Pahute Mesa 1:100,000 Quadrangles and the Western Parts of the Timpahute Range, Pahranagat Range, Indian Springs, and Las Vegas 1:100,000 Quadrangles, Nevada*. Open-File Report 92-193. Denver, Colorado: U.S. Geological Survey. ACC: NNA.19940524.0085.

106699   Rogers, A.M. and Lee, W.H.K. 1976. "Seismic Study of Earthquakes in the Lake Mead, Nevada-Arizona Region." *Bulletin of the Seismological Society of America, 66*, (5), 1657-1681. El Cerrito, California: Seismological Society of America. TIC: 218413.

100176   Rogers, A.M.; Harmsen, S.C.; and Meremonte, M.E. 1987. *Evaluation of the Seismicity of the Southern Great Basin and Its Relationship to the Tectonic Framework of the Region*. Open-File Report 87-408. Denver, Colorado: U.S. Geological Survey. ACC: HQX.19880315.0004.

106702   Rogers, A.M.; Harmsen, S.C.; Corbett, E.J.; Priestly, K.; and dePolo, D. 1991. "The Seismicity of Nevada and Some Adjacent Parts of the Great Basin." Chapter 10 of *The Geology of North America Decade Map*. Volume 1. Boulder, Colorado: Geological Society of America. TIC: 243190.

106707   Roquemore, G.R.; Simila, G.W.; and Mori, J. 1996. "The 1995 Ridgecrest Earthquake Sequence: New Clues to the Neotectonic Development of Indian Wells Valley and the Coso Range, Eastern California." *Abstracts with Programs - Geological Society of America, 28*, (5), 106. Boulder, Colorado: Geological Society of America. TIC: 236678.

106708   Rosenbaum, J.G.; Hudson, M.R.; and Scott, R.B. 1991. "Paleomagnetic Constraints on the Geometry and Timing of Deformation at Yucca Mountain, Nevada." *Journal of Geophysical Research, 96*, (B2), 1963-1979. Washington, D.C.: American Geophysical Union. TIC: 225126.

104529   Sabetta, F. and Pugliese, A. 1996. "Estimation of Response Spectra and Simulation of Nonstationary Earthquake Ground Motions." *Bulletin of the Seismological Society of America, 86*, (2), 337-352. El Cerrito, California: Seismological Society of America. TIC: 241042.

104537   Sadigh, K.; Chang, C.-Y.; Abrahamson, N.A.; Chiou, S.J.; and Power, M.S. 1993. "Specification of Long-Period Ground Motions: Updated Attenuation Relationships for Rock Site Conditions and Adjustment Factors for Near-Fault Effects." *Proceedings of ATC 17-1 Seminar on Seismic Isolation, Passive Energy Dissipation, and Active Control, San Francisco, California, March 11-12, 1993. 1*, 59-70. Redwood City, California: Applied Technology Council. TIC: 238494.

101288   Sass, J.H.; Dudley, W.W., Jr.; and Lachenbruch, A.H. 1995. "Regional Thermal Setting." Chapter 8 of *Major Results of Geophysical Investigations at Yucca Mountain and Vicinity, Southern Nevada*. Oliver, H.W.; Ponce, D.A.; and Hunter, W.C., eds. Open-File Report 95-74. Menlo Park, California: U.S. Geological Survey. ACC: MOL.19980305.0122.

104546   Sauber, J. 1989. *Geodetic Measurement of Deformation in California*. NASA Technical Memoir 100732. Washington, D.C.: National Aeronautics and Space Administration. TIC: 242343.

103457   Savage, J.C.; Lisowski, M.; Gross, W.K.; King, N.E.; and Svarc, J.L. 1994. "Strain Accumulation Near Yucca Mountain, Nevada, 1983-1993." *Journal of Geophysical Research, 99*, (B9), 18,103-18,107. Washington, D.C.: American Geophysical Union. TIC: 235681.

104553   Savage, J.C.; Lisowski, M.; Svarc, J.L.; and Gross, W.K. 1995. "Strain Accumulation Across the Central Nevada Seismic Zone, 1973-1994." *Journal of Geophysical Research, 100*, (B10), 20,257 to 20,269. Washington, D.C.: American Geophysical Union. TIC: 236811.

145359   Savage, J.C.; Connor, C.B.; Stamatakos, J.A.; Ferrill, D.A.; Hill, B.E.; Davis, J.L.; Wernicke, B.P.; and Bennett, R.A. 1998. "Detecting Strain in the Yucca Mountain Area, Nevada." *Science, 282*, (5391), 1007b. Washington, D.C.: American Association for the Advancement of Science. TIC: 243445.

118952   Savage, J.C.; Svarc, J.L.; and Prescott, W.H. 1999. "Strain Accumulation at Yucca Mountain, Nevada, 1983-1998." *Journal of Geophysical Research, 104*, (B8), 17627-17631. Washington, D.C.: American Geophysical Union. TIC: 245645.

103270   Schneider, J.F.; Abrahamson, N.A.; and Hanks, T.C. 1996. *Ground Motion Modeling of Scenario Earthquakes at Yucca Mountain, Final Report for Activity 8.3.1.17.3.3*. Volume 1. Denver, Colorado: U.S. Geological Survey. ACC: MOL.19980617.0477.

104574   Schwartz, D.P. and Coppersmith, K.J. 1984. "Fault Behavior and Characteristic Earthquakes: Examples from the Wasatch and San Andreas Fault Zones." *Journal of Geophysical Research, 89*, (B7), 5681-5698. Washington, D.C.: American Geophysical Union. TIC: 235753.

104575   Schwartz, D.P. and Coppersmith, K.J. 1986. "Seismic Hazards: New Trends in Analysis Using Geologic Data." Chapter 14 of *Active Tectonics*. Washington, D.C.: National Academy Press. TIC: 209251.

104573   Schwartz, D.P. 1988. "Geologic Characterization of Seismic Sources: Moving Into the 1990s." *Earthquake Engineering and Soil Dynamics II—Recent Advances in Ground-Motion Evaluation, June 27-30, 1988, Park City, Utah.* Von Thun, J.L., ed. Geotechnical Special Publication No. 20. Pages 1-42. New York, New York: American Society of Civil Engineers. TIC: 235723.

106747   Schweickert, R.A. and Lahren, M.M. 1994. "Amargosa Fault System Near Yucca Mountain, Nevada." *Abstracts with Programs - Geological Society of America, 26,* (7), A250. Boulder, Colorado: Geological Society of America. TIC: 246689.

101012   Schweickert, R.A. and Lahren, M.M. 1997. "Strike-Slip Fault System in Amargosa Valley and Yucca Mountain, Nevada." *Tectonophysics, 272,* (1), 25-41. Amsterdam, The Netherlands: Elsevier. TIC: 238429.

106751   Scott, R.B. 1990. "Tectonic Setting of Yucca Mountain, Southwest Nevada." Chapter 12 of *Basin and Range Extensional Tectonics Near the Latitude of Las Vegas, Nevada.* Wernicke, B.P., ed. Memoir 176. Boulder, Colorado: Geological Society of America. TIC: 222540.

105396   Sheehan, A.F.; Smith, K.D.; and Savage, M.K. 1994. *Data Package on Seismological Field Investigations of the 29 June 1992 Little Skull Mountain Earthquake.* Reno, Nevada: University of Nevada, Reno. ACC: NNA.19940608.0276.

106772   Shields, G.; Smith, K.; and Brune, J. 1995. "Source Parameters of a Sequence of Very Shallow Earthquakes in the Rock Valley Fault Zone, Southern Nevada Test Site." *Transactions of the American Geophysical Union, 76,* F426. Washington, D.C.: American Geophysical Union. TIC: 235738.

106802   Sieh, K.; Jones, L.; Hauksson, E.; Hudnut, K.; Eberhart-Phillips, D.; Heaton, T.; Hough, S.; Hutton, K.; Kanamori, H.; Lilje, A.; Lindvall, S.; McGill, S.F.; Mori, J.; Rubin, C.; Spotila, J.A.; Stock, J.; Thio, H.K.; Theiman, J.; Wernicke, B.; and Zachariasen, J. 1993. "Near-Field Investigations of the Landers Earthquake Sequence, April to July 1992." *Science, 260,* 171-176. Washington, D.C.: American Association for the Advancement of Science. TIC: 235760.

145316   Simonds, F.W. and Hamilton, W.B. 1995. "A Synthesis of Detachment Fault Studies in the Yucca Mountain Region." Chapter 1 of *Characterization of Detachment Faults in the Yucca Mountain Region.* Administrative Report. Denver, Colorado: U.S. Geological Survey. ACC: MOL.19960305.0440.

101929 Simonds, F.W.; Whitney, J.W.; Fox, K.F.; Ramelli, A.R.; Yount, J.C.; Carr, M.D.; Menges, C.M.; Dickerson, R.P.; and Scott, R.B. 1995. *Map Showing Fault Activity in the Yucca Mountain Area, Nye County, Nevada.* Miscellaneous Investigations Series Map I-2520. Denver, Colorado: U.S. Geological Survey. TIC: 232483.

106809 Simonds, F.W. and Scott, R.B. 1996. *Geology and Hydrothermal Alteration at Calico Hills, Nye County, Nevada.* Milestone 3GTD018M. Denver, Colorado: U.S. Geological Survey. TIC: 238069.

145327 Sims, D.; Ferrill, D.A.; and Stamatakos, J.A. 1999. "Role of Ductile Decollement in the Development of Pull-Apart Basins: Experimental Results and Natural Examples." *Journal of Structural Geology, 21*, (5), 533-554. New York, New York: Pergamon. TIC: 247766.

106816 Slemmons, D.B.; Jones, A.E.; and Gimlett, J.I. 1965. "Catalog of Nevada Earthquakes, 1852-1960." *Bulletin of the Seismological Society of America, 55*, (2), 519-566. El Cerrito, California: Seismological Society of America. TIC: 217161.

106815 Slemmons, D.B. and dePolo, C.M. 1986. "Evaluation of Active Faulting and Associated Hazards." Chapter 3 of *Active Tectonics.* Studies in Geophysics. Washington, D.C.: National Academy Press. TIC: 209251.

101019 Smith, E.I.; Feuerbach, D.L.; Naumann, T.R.; and Faulds, J.E. 1990. "The Area of Most Recent Volcanism Near Yucca Mountain, Nevada: Implications for Volcanic Risk Assessment." *High Level Radioactive Waste Management, Proceedings of the International Topical Meeting, Las Vegas, Nevada, April 8-12, 1990. 1*, 81-90. La Grange Park, Illinois: American Nuclear Society. TIC: 202058.

158735 Smith, E.I.; Keenan, D.L.; and Plank, T. 2002. "Episodic Volcanism and Hot Mantle: Implications for Volcanic Hazard Studies at the Proposed Nuclear Waste Repository at Yucca Mountain, Nevada." *GSA Today, 12*, (4), 4-10. Boulder, Colorado: Geological Society of America. TIC: 253146.

150194 Smith, K. 2000. "Scotty's Junction and Frenchman Flat Earthquakes." E-mail from K. Smith (UNR) to R. Quittmeyer (CRWMS M&O), June 7, 2000, with attachment. ACC: MOL.20000609.0302.

158466 Smith, K.D.; Brune, J.N.; dePolo, D.; Savage, M.K.; Anooshehpoor, R.; and Sheehan, A.F. 2000. "The 1992 Little Skull Mountain Earthquake Sequence, Southern Nevada Test Site." Chapter K of *Geologic and Geophysical Characterization Studies of Yucca Mountain, Nevada, a Potential High-Level Radioactive-Waste Repository.* Version 1.0. DDS-058. Denver, Colorado: U.S. Geological Survey. TIC: 249438.

158467   Smith, K.D.; Shields, G.; and Brune, J.N. 2000. "A Sequence of Very Shallow Earthquakes in the Rock Valley Fault Zone, Southern Nevada Test Site." Chapter L of *Geologic and Geophysical Characterization Studies of Yucca Mountain, Nevada, a Potential High-Level Radioactive-Waste Repository*. Version 1.0. DDS-058. Denver, Colorado: U.S. Geological Survey. TIC: 249438.

105406   Smith, R.B. and Arabasz, W.J. 1991. "Seismicity of the Intermountain Seismic Belt." Chapter 11 of *Neotectonics of North America*. Slemmons, D.B.; Engdahl, E.R.; Zoback, M.D.; and Blackwell, D.D., eds. The Geology of North America Decade Map Volume I. Boulder, Colorado: Geological Society of America. TIC: 240998.

106876   Snyder, D.B. and Carr, W.J. 1982. *Preliminary Results of Gravity Investigations at Yucca Mountain and Vicinity, Southern Nye County, Nevada*. Open-File Report 82-701. Menlo Park, California: U.S. Geological Survey. ACC: HQS.19880517.1481.

106877   Snyder, D.B. and Carr, W.J. 1984. "Interpretation of Gravity Data in a Complex Volcano-Tectonic Setting, Southwestern Nevada." *Journal of Geophysical Research, 89*, (B12), 10,193-10,206. Washington, D.C.: American Geophysical Union. TIC: 203255.

106881   Sonder, L.J.; Jones, C.H.; Salyards, S.L.; and Murphy, K.M. 1994. "Vertical Axis Rotations in the Las Vegas Valley Shear Zone, Southern Nevada: Paleomagnetic Constraints on Kinematics and Dynamics of Block Rotations." *Tectonics, 13*, (4), 769-788. Washington, D.C.: American Geophysical Union. TIC: 232894.

110503   Spudich, P.; Fletcher, J.B.; Hellweg, M.; Boatwright, J.; Sullivan, C.; Joyner, W.B.; Hanks, T.C.; Boore, D.M.; McGarr, A.; Baker, L.M.; and Lindh, A.G. 1996. *Earthquake Ground Motions in Extensional Tectonic Regimes*. Open-File Report 96-292. Menlo Park, California: U.S. Geological Survey. TIC: 245279.

100082   Spudich, P.; Fletcher, J.B.; Hellweg, M.; Boatwright, J.; Sullivan, C.; Joyner, W.B.; Hanks, T.C.; Boore, D.M.; McGarr, A.; Baker, L.M.; and Lindh, A.G. 1997. "SEA96–A New Predictive Relation for Earthquake Ground Motions in Extensional Tectonic Regimes." *Seismological Research Letters, 68*, (1), 190-198. El Cerrito, California: Seismological Society of America. TIC: 234935.

158509   Spudich, P.; Joyner, W.B.; Lindh, A.G.; Boore, D.M.; Margaris, B.M.; and Fletcher, J.B. 1999. "SEA99: A Revised Ground Motion Prediction Relation for Use in Extensional Tectonic Regimes." *Bulletin of the Seismological Society of America, 89*, (5), 1156-1170. El Cerrito, California: Seismological Society of America. TIC: 253393.

138819   Stamatakos, J.A.; Connor, C.B.; and Martin, R.H. 1997. "Quaternary Basin Evolution and Basaltic Volcanism of Crater Flat, Nevada, from Detailed Ground Magnetic Surveys of the Little Cones." *Journal of Geology, 105*, 319-330. Chicago, Illinois: University of Chicago. TIC: 245108.

113903   Stamatakos, J.A. and Ferrill, D.A. 1998. "Strike-Slip Fault System in Amargosa Valley and Yucca Mountain, Nevada - Comment." *Tectonophysics, 294*, 151-160. Amsterdam, The Netherlands: Elsevier. TIC: 245112.

101022   Stock, J.M. and Healy, J.H. 1988. "Stress Field at Yucca Mountain, Nevada." Chapter 6 of *Geologic and Hydrologic Investigations of a Potential Nuclear Waste Disposal Site at Yucca Mountain, Southern Nevada*. Carr, M.D. and Yount, J.C., eds. Bulletin 1790. Denver, Colorado: U.S. Geological Survey. TIC: 203085.

100087   Su, F.; Anderson, J.G.; Brune, J.N.; and Zeng, Y. 1996. "A Comparison of Direct S-Wave and Coda-Wave Site Amplification Determined from Aftershocks of the Little Skull Mountain Earthquake." *Bulletin of the Seismological Society of America, 86*, (4), 1006-1018. El Cerrito, California: Seismological Society of America. TIC: 236585.

102917   Swadley, W C; Hoover, D.L.; and Rosholt, J.N. 1984. *Preliminary Report on Late Cenozoic Faulting and Stratigraphy in the Vicinity of Yucca Mountain, Nye County, Nevada*. Open-File Report 84-788. Denver, Colorado: U.S. Geological Survey. ACC: NNA.19870519.0104.

106954   Swan, F.H.; Schwartz, D.P.; and Cluff, L.S. 1980. "Recurrence of Moderate to Large Magnitude Earthquakes Produced by Surface Faulting on the Wasatch Fault Zone, Utah." *Bulletin of the Seismological Society of America, 70*, (5), 1431-1462. El Cerrito, California: Seismological Society of America. TIC: 221557.

106964   Takahashi, E. 1980. "Melting Relations of an Alkali-Olivine Basalt to 30 Kbar, and Their Bearing on the Origin of Alkali Basalt Magmas." *Carnegie Institution of Washington, Year Book 79*, 271-276. Washington, D.C.: Carnegie Institution of Washington. TIC: 234936.

106965   Takahashi, E. and Kushiro, I. 1983. "Melting of a Dry Peridotite at High Pressures and Basalt Magma Genesis." *American Mineralogist, 68*, 859-879. Washington, D.C.: Mineralogical Society of America. TIC: 225157.

102864   Taylor, E.M. 1986. *Impact of Time and Climate on Quaternary Soils in the Yucca Mountain Area of the Nevada Test Site*. Master's thesis. Boulder, Colorado: University of Colorado. TIC: 218287.

159414   Taylor, E.M. 2003. "Quaternary Faulting on the Southern Crater Flat Fault." Chapter 10 of *Quaternary Paleoseismology and Stratigraphy of the Yucca Mountain Area, Nevada*. U.S. Geological Survey Digital Data Series. Keefer, W.R.; Whitney, J.W.; and Taylor, E.M., eds. Denver, Colorado: U.S. Geological Survey. ACC: MOL.20031208.0113. TBV-5659

106993   Townley, S.D. and Allen, M.W. 1939. "Descriptive Catalog of Earthquakes of the Pacific Coast of the United States 1769 to 1928." *Bulletin of the Seismological Society of America, 29*, (1), 1-297. Berkeley, California: University of California Press. TIC: 239409.

101030   Turrin, B.D.; Champion, D.; and Fleck, R.J. 1991. "^{40}Ar/^{39}Ar Age of the Lathrop Wells Volcanic Center, Yucca Mountain, Nevada." *Science, 253*, (5020), 654-657. Washington, D.C.: American Association for the Advancement of Science. TIC: 225167.

101305   USGS (U.S. Geological Survey) 1984. *A Summary of Geologic Studies Through January 1, 1983, of a Potential High-Level Radioactive Waste Repository Site at Yucca Mountain, Southern Nye County, Nevada*. Open-File Report 84-792. Menlo Park, California: U.S. Geological Survey. ACC: NNA.19891009.0305.

101031   Vaniman, D.T.; Crowe, B.M.; and Gladney, E.S. 1982. "Petrology and Geochemistry of Hawaiite Lavas from Crater Flat, Nevada." *Contributions to Mineralogy and Petrology, 80*, 341-357. Berlin, Germany: Springer-Verlag. TIC: 201799.

158461   von Seggern, D. and Smith, K. 2001. *Seismicity in the Vicinity of Yucca Mountain, Nevada, for the Period October 1, 1999, to September 30, 2000*. TR-00-001. Reno, Nevada: University of Nevada, Reno, Nevada Seismological Laboratory. ACC: MOL.20020126.0106.

124621   von Seggern, D.H. and Brune, J.H. 1994. "Seismicity in the Southern Great Basin, 1868-1992." *Yucca Mountain Tectonics Workshop, January 24-26, 1994*. Draft. Reno, Nevada: University of Nevada-Reno, Seismological Laboratory. ACC: MOL.19960318.0596.

159532   von Seggern, D.H. and Smith, K.D. 1997. *Seismicity in the Vicinity of Yucca Mountain, Nevada, for the Period October 1, 1995, to September 30, 1996*. Milestone Report SPT38AM4. Reno, Nevada: University of Nevada, Reno, Seismological Laboratory. ACC: MOL.19981124.0334.

149993   von Seggern, D.H. and dePolo, D.M. 1998. *Seismicity in the Vicinity of Yucca Mountain, Nevada, for the Period October 1, 1996, to September 30, 1997*. Milestone Report SP32BTM4. Reno, Nevada: University of Nevada, Reno, Seismological Laboratory. ACC: MOL.19990503.0147.

156297   von Seggern, D.H.; Smith, K.D.; and Biasi, G.P. 2001. *Seismicity in the Vicinity of Yucca Mountain, Nevada for the Period October 1, 1997, to September 30, 1999*. Reno, Nevada: University of Nevada, Reno, Nevada Seismological Laboratory. ACC: MOL.20010731.0293.

107120   Vortman, L.J. 1991. *An Evaluation of the Seismicity of the Nevada Test Site and Vicinity*. SAND86-7006. Albuquerque, New Mexico: Sandia National Laboratories. ACC: NNA.19911118.0084.

107122   Walck, M.C. and Phillips, J.S. 1990. *Two-Dimensional Velocity Models for Paths from Pahute Mesa and Yucca Flat to Yucca Mountain*. SAND88-3033. Albuquerque, New Mexico: Sandia National Laboratories. ACC: NNA.19901005.0051.

107126   Wallace, R.E. 1984. "Patterns and Timing of Late Quaternary Faulting in the Great Basin Province and Relation to Some Regional Tectonic Features." *Journal of Geophysical Research, 89*, (B7), 5763-5769. Washington, D.C.: American Geophysical Union. TIC: 218113.

158736   Wang, K.; Plank, T.; Walker, J.D.; and Smith, E.I. 2002. "A Mantle Melting Profile Across the Basin and Range, SW USA." *Journal of Geophysical Research, 107*, (B1), ECV5-1 through ECV5-21. Washington, D.C.: American Geophysical Union. TIC: 253145.

107171   Warren, R.G.; Byers, F.M., Jr.; and Orkild, P.P. 1985. "Post-Silent Canyon Caldera Structural Setting for Pahute Mesa." *Proceedings, Third Symposium on Containment of Underground Nuclear Explosions, Idaho Falls, Idaho, September 9-13, 1985*. Olsen, C.W. and Donohue, M.L., eds. CONF-850953. Volume 2. Pages 3-30. Idaho Falls, Idaho: Department of Energy, Idaho Operations Office. TIC: 227143.

107201   Wells, D.L. and Coppersmith, K.J. 1994. "New Empirical Relationships Among Magnitude, Rupture Length, Rupture Width, Rupture Area, and Surface Displacement." *Bulletin of the Seismological Society of America, 84*, (4), 974-1002. El Cerrito, California: Seismological Society of America. TIC: 226273.

107207   Wells, S.G.; McFadden, L.D.; and Harden, J. 1990. "Preliminary Results of Age Estimations and Regional Correlations of Quaternary Alluvial Fans Within the Mojave Desert of Southern California." *At the End of the Mojave: Quaternary Studies in the Eastern Mojave Desert*. Reynolds, J., ed. Pages 45-53. Redlands, California: San Bernardino County Museum Association. TIC: 246793.

107015   Wells, S.G.; Crowe, B.M.; McFadden, L.D.; Turrin, B.D.; Champion, D.E.; and Fleck, R.J. 1992. "Measuring the Age of the Lathrop Wells Volcanic Center at Yucca Mountain." *Science, 257*, 555-558. Washington, D.C.: American Association for the Advancement of Science. TIC: 225168.

107238   Wernicke, B. and Axen, G.J. 1988. "On the Role of Isostasy in the Evolution of Normal Fault Systems." *Geology, 16*, 848-851. Boulder, Colorado: Geological Society of America. TIC: 233006.

149959   Wernicke, B.; Axen, G.J.; and Snow, J.K. 1988. "Basin and Range Extensional Tectonics at the Latitude of Las Vegas, Nevada." *Geological Society of America Bulletin, 100*, (11), 1738-1757. Boulder, Colorado: Geological Society of America. TIC: 233007.

103485   Wernicke, B.; Davis, J.L.; Bennett, R.A.; Elosegui, P.; Abolins, M.J.; Brady, R.J.; House, M.A.; Niemi, N.A.; and Snow, J.K. 1998. "Anomalous Strain Accumulation in the Yucca Mountain Area, Nevada." *Science, 279*, 2096-2100. New York, New York: American Association for the Advancement of Science. TIC: 235956.

107290   Wesling, J.R.; Bullard, T.F.; Swan, F.H.; Perman, R.C.; Angell, M.M.; and Gibson, J.D. 1992. *Preliminary Mapping of Surficial Geology of Midway Valley Yucca Mountain Project, Nye County, Nevada Interim Data Report.* SAND91-0607. Albuquerque, New Mexico: Sandia National Laboratories. ACC: NNA.19920410.0053.

107309   Whitney, J.W. and Taylor, E.M., eds. 1996. "Quaternary Paleoseismology and Stratigraphy of the Yucca Mountain Site Area." Chapter 4 of *Seismotectonic Framework and Characterization of Faulting at Yucca Mountain, Nevada.* Whitney, J.W., ed. Milestone 3GSH100M. Denver, Colorado: U.S. Geological Survey. TIC: 237980. ACC: MOL.19970129.0041.

107317   Whitney, J.W.; Taylor, E.M.; and Wesling, J.R. 1996. "Quaternary Mapping and Stratigraphy." Chapter 4.1 of *Seismotectonic Framework and Characterization of Faulting at Yucca Mountain, Nevada.* Whitney, J.W., ed. Milestone 3GSH100M. Denver, Colorado: U.S. Geological Survey. TIC: 237980. ACC: MOL.19970129.0041.

159416   Whitney, J.W.; Simonds, F.W.; Shroba, R.R.; and Murray, M. 2003. "Quaternary Faulting on the Windy Wash Fault." Chapter 9 of *Quaternary Paleoseismology and Stratigraphy of the Yucca Mountain Area, Nevada.* U.S. Geological Survey Digital Data Series. Keefer, W.R.; Whitney, J.W.; and Taylor, E.M., eds. Denver, Colorado: U.S. Geological Survey. ACC: MOL.20031208.0113. TBV-5659

101167   Winograd, I.J. and Thordarson, W. 1975. *Hydrogeologic and Hydrochemical Framework, South-Central Great Basin, Nevada-California, with Special Reference to the Nevada Test Site.* Geological Survey Professional Paper 712-C. Washington, D.C.: United States Government Printing Office. ACC: NNA.19870406.0201.

105550   Wong, I.; Kelson, K.; Olig, S.; Kolbe, T.; Hemphill-Haley, M.; Bott, J.; Green, R.;
            Kanakari, H.; Sawyer, J.; Silva, W.; Stark, C.; Haraden, C.; Fenton, C.; Unruh, J.;
            Gardner, J.; Reneau, S.; and House, L. 1995. *Seismic Hazards Evaluation of the
            Los Alamos National Laboratory*. Volume 1. Oakland, California:
            Woodward-Clyde Federal Services. TIC: 247191.

100522   YMP (Yucca Mountain Site Characterization Project) 1997. *Methodology to Assess
            Fault Displacement and Vibratory Ground Motion Hazards at Yucca Mountain*.
            Topical Report YMP/TR-002-NP, Rev. 1. Las Vegas, Nevada: Yucca Mountain
            Site Characterization Office. ACC: MOL.19971016.0777.

108740   Yokoyama, I. and de la Cruz-Reyna, S. 1990. "Precursory Earthquakes of the 1943
            Eruption of Paricutin Volcano, Michoacan, Mexico." *Journal of Volcanology and
            Geothermal Research, 44,* 265-281. Amsterdam, The Netherlands: Elsevier.
            TIC: 234990.

108658   Zoback, M.L. and Zoback, M. 1980. "State of Stress in the Conterminous United
            States." *Journal of Geophysical Research, 85*, (B11), 6113-6156. Washington,
            D.C.: American Geophysical Union. TIC: 218504.

108663   Zoback, M.L.; Anderson, R.E.; and Thompson, G.A. 1981. "Cenozoic Evolution of
            the State of Stress and Style of Tectonism of the Basin and Range Province of the
            Western United States." *Philosophical Transactions of the Royal Society of
            London, Series A*, (300), 407-434. London, United Kingdom: Royal Society of
            London. TIC: 218137.

108651   Zoback, M.L. 1989. "State of Stress and Modern Deformation of the Northern
            Basin and Range Province." *Journal of Geophysical Research, 94*, (B6),
            7105-7128. Washington, D.C.: American Geophysical Union. TIC: 225191.

108617   Zreda, M.G.; Phillips, F.M.; Kubik, P.W.; Sharma, P.; and Elmore, D. 1993.
            "Cosmogenic ^{36}Cl Dating of a Young Basaltic Eruption Complex, Lathrop Wells,
            Nevada." *Geology, 21*, (1), 57-60. Boulder, Colorado: Geological Society of
            America. TIC: 225192.

4.4.2   Data Listed by Data Tracking Number

166575   GS960783117361.004. Historical Seismicity in the Yucca Mountain Region.
            Submittal date: 08/08/1996.

147725   LA000000000099.002. Major Element, Trace Element, Isotopic, and Mineral
            Chemistry Data from Lathrop Wells. Submittal date: 08/02/1995.

149593   LA0004FP831811.002. Volume of Volcanic Centers in the Yucca Mountain
            Region. Submittal date: 04/14/2000.

164714   LA0009FP831811.002. Summary Frequencies of Disruptive Volcanic Events. Submittal date: 09/05/2000.

164713   LA0307BY831811.001. Characterize Igneous Framework Additional Output. Submittal date: 07/29/2003.

144279   LAFP831811AQ97.001. Chemical and Geochronology Data for the Revision and Final Publication of the Volcanism Synthesis Report. Submittal date: 08/29/1997.

148234   MO0002PVHA0082.000. Probabilistic Volcanic Hazard Analysis for Yucca Mountain, Nevada. Submittal date: 02/17/2000.

166581   MO0006COV00226.000. Coverage: QUAKECNSS. Submittal date: 06/26/2000.

166583   MO0007COV00207.000. Coverage: SEISWSTS. Submittal date: 07/12/2000.

166390   MO0205UCC012DV.008. Seismic Catalog for FY01 in the Vicinity of Yucca Mountain. Submittal date: 05/02/2002.

166391   MO0305UCC012DV.014. Catalog of Earthquakes in the Vicinity of Yucca Mountain, Nevada for 10/01/2001 to 09/30/2002. Submittal date: 04/15/2003.

166379   MO0312SEPSDMGA.000. Magnetic Anomalies, Crater Flat Basin and Northern Amargosa Desert, Nevada. Submittal date: 12/13/2003.

166375   MO0312SEPSDPQF.000. Summary of Paleoseismic Data for Quaternary Faults in the Yucca Mountain Area. Submittal date: 12/13/2003.

166380   MO0312SEPSDWPT.000. Weights of Probability for Tectonic Models of Yucca Mountain. Submittal date: 12/13/2003.

150037   MO970483117412.002. Seismicity in the Vicinity of Yucca Mountain, Nevada for the Period October 1, 1995 to September 30, 1996. Submittal date: 04/02/1997.

166582   MO9906COV99279.000. Coverage Name: QUAKEU. Submittal date: 06/29/1999.

166387   MO9906SEISYMNV.000. Seismicity in the Vicinity of Yucca Mountain, Nevada, for the Period 10/01/1996 to 09/30/1997. Submittal date: 06/22/1999.

166388   UN0007SPA012DV.002. Earthquake Catalog for October 1, 1997, to September 30, 1999, in the Vicinity of Yucca Mountain. Submittal date: 07/20/2000.

166389   UN0106SPA012JB.001. Earthquake Catalog for October 1, 1999, to September 30, 2000, in the Vicinity of Yucca Mountain. Submittal date: 06/12/2001.
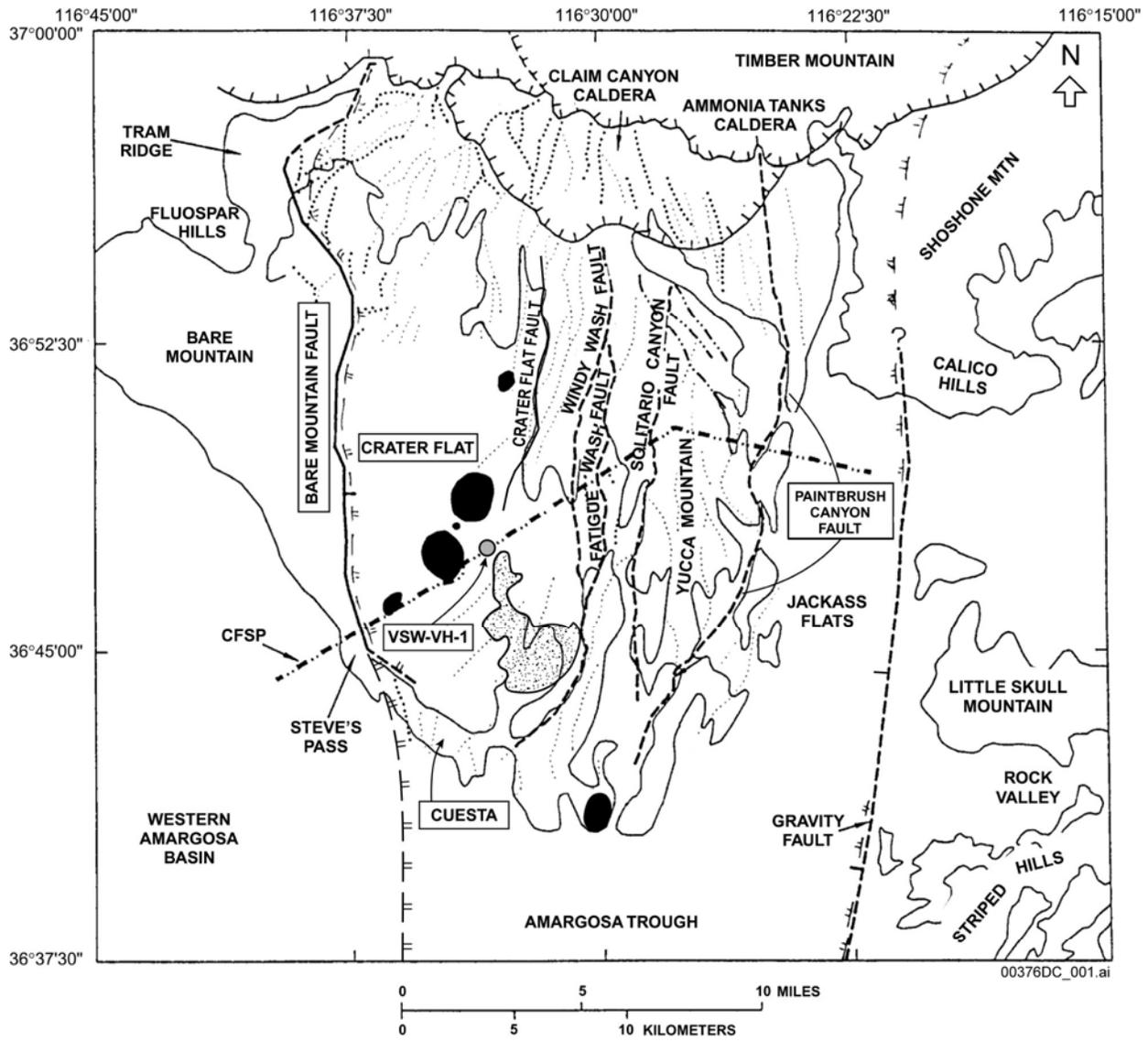
Source: Fridrich 1999 [DIRS 118942], Figure 3

NOTE: The Gravity fault forms the eastern boundary and the Bare Mountain fault forms the western boundary of the Crater Flat Domain. The Paintbrush Canyon fault is considered to be the eastern limit of the normal fault system that characterizes Yucca Mountain.

Figure 4-1. Crater Fault Domain and Its Inferred Bounding Structures
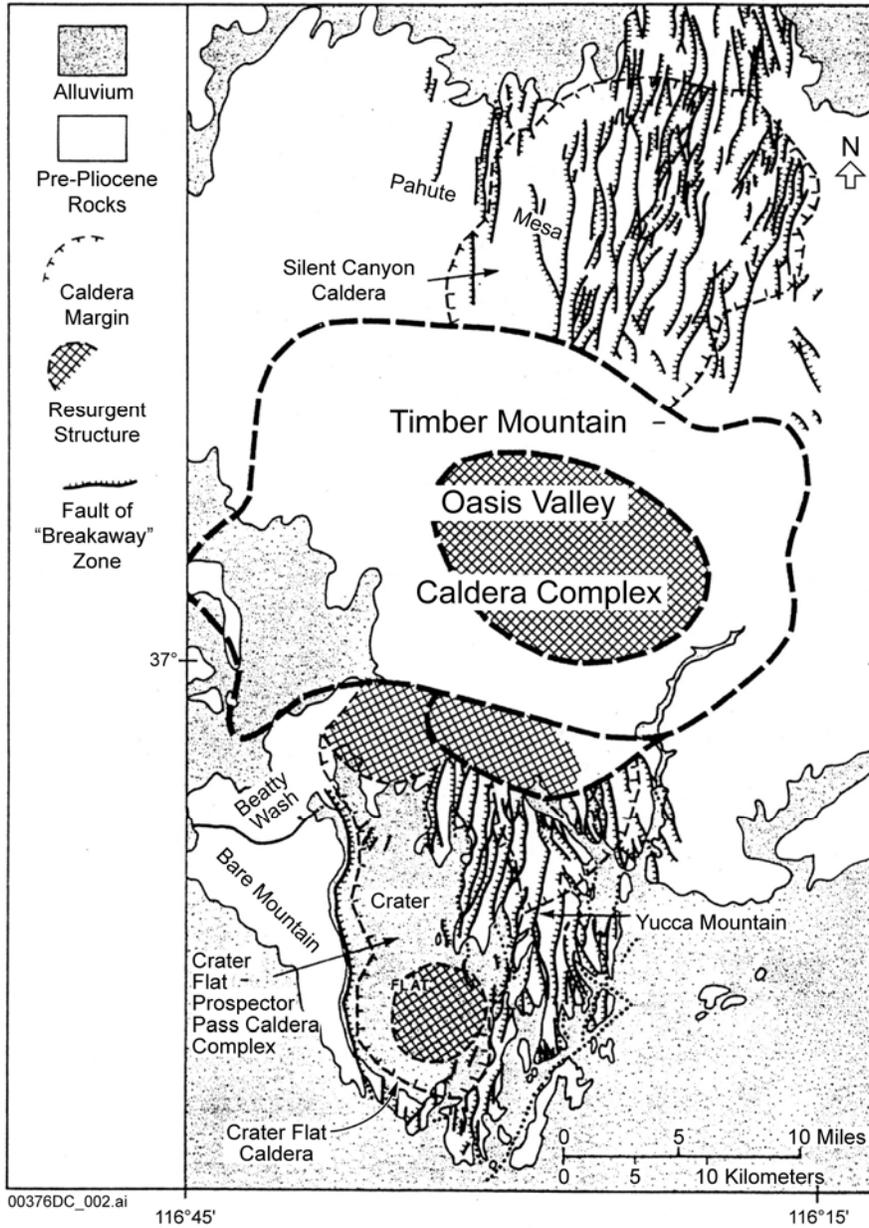
Source: Carr 1990 [DIRS 104669], p. 293

NOTE: "Crater Flat–Prospector Pass Caldera Complex" and "Crater Flat Caldera" are features relevant to the caldera model of Carr 1990 [DIRS 104669].

Figure 4-2. Coaxial Fault Sets of Yucca Mountain and Pahute Mesa Separated by Caldera Complex
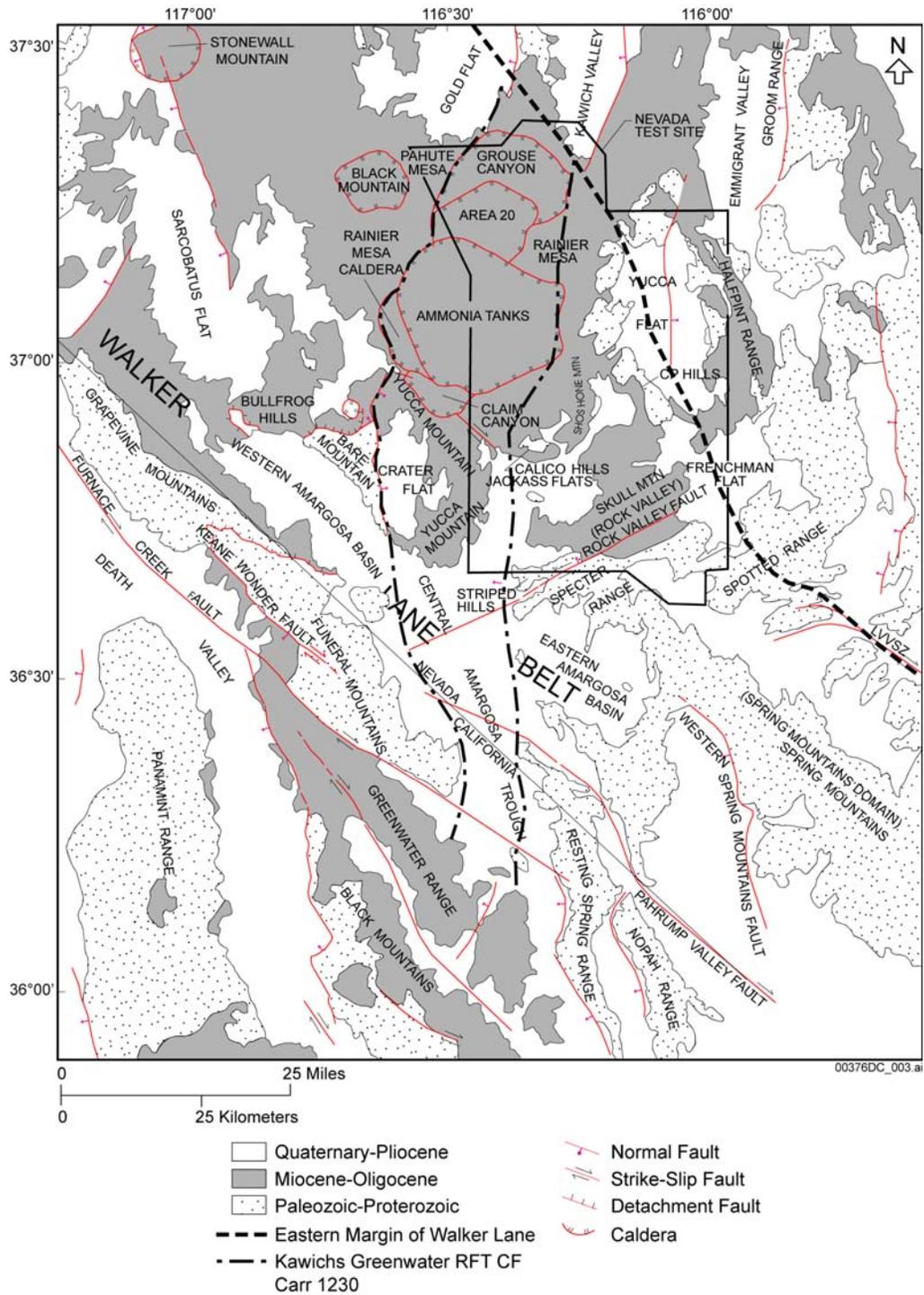
Source: Modified from Minor et al. 1997 [DIRS 100997], Figure 1

NOTE: Heavy dashed line indicates eastern border of Walker Lane.

Figure 4-3. Eastern Border of Walker Lane
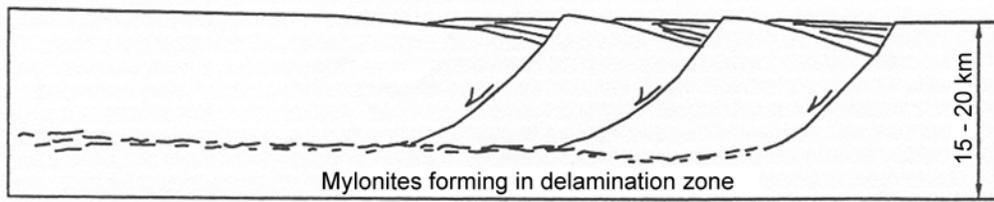
A   At onset of delamination (detachment)
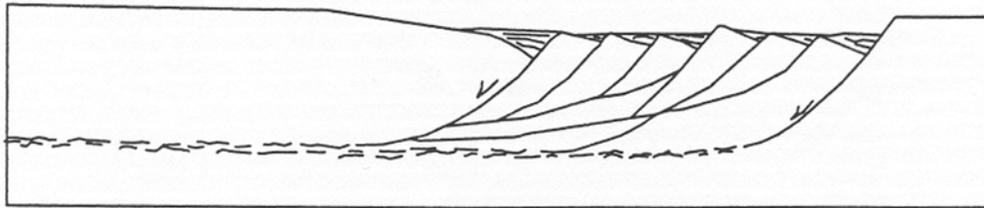
B   Low-angle normal faults "fire" from delaminating layer
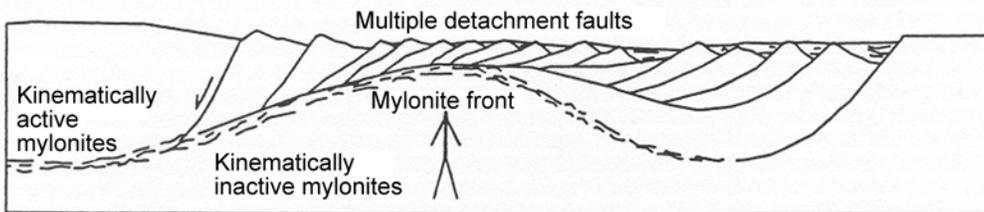
C   Lower Rate bows upwards
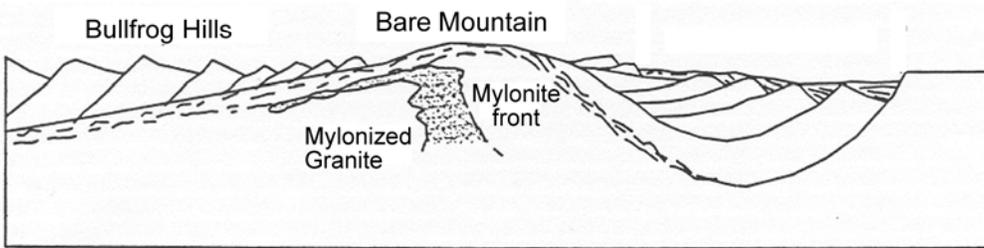
D   Metamorphic core complex in lower plate culmination

Source: Simonds and Hamilton 1995 [DIRS 145316], Figure 1-4

Figure 4-4. Rolling Hinge Model with Reference to Bare Mountain and Crater Flat
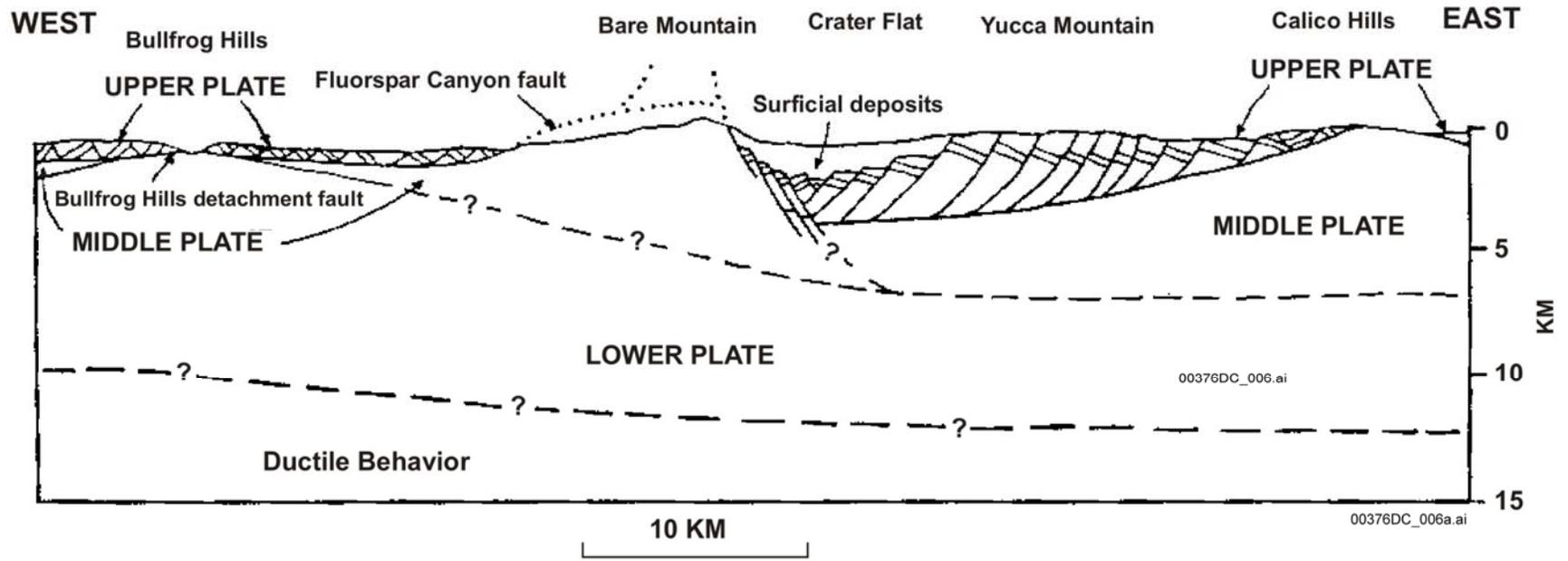
Source: Scott 1990 [DIRS 106751], Figure 4 and Figure 3

Figure 4-5. Cross Sections of Yucca Mountain Showing Inferred Shallow Detachment Fault

Figure 4-6. Conceptual Cross Section Showing Inferred Levels of Detachment beneath Yucca Mountain
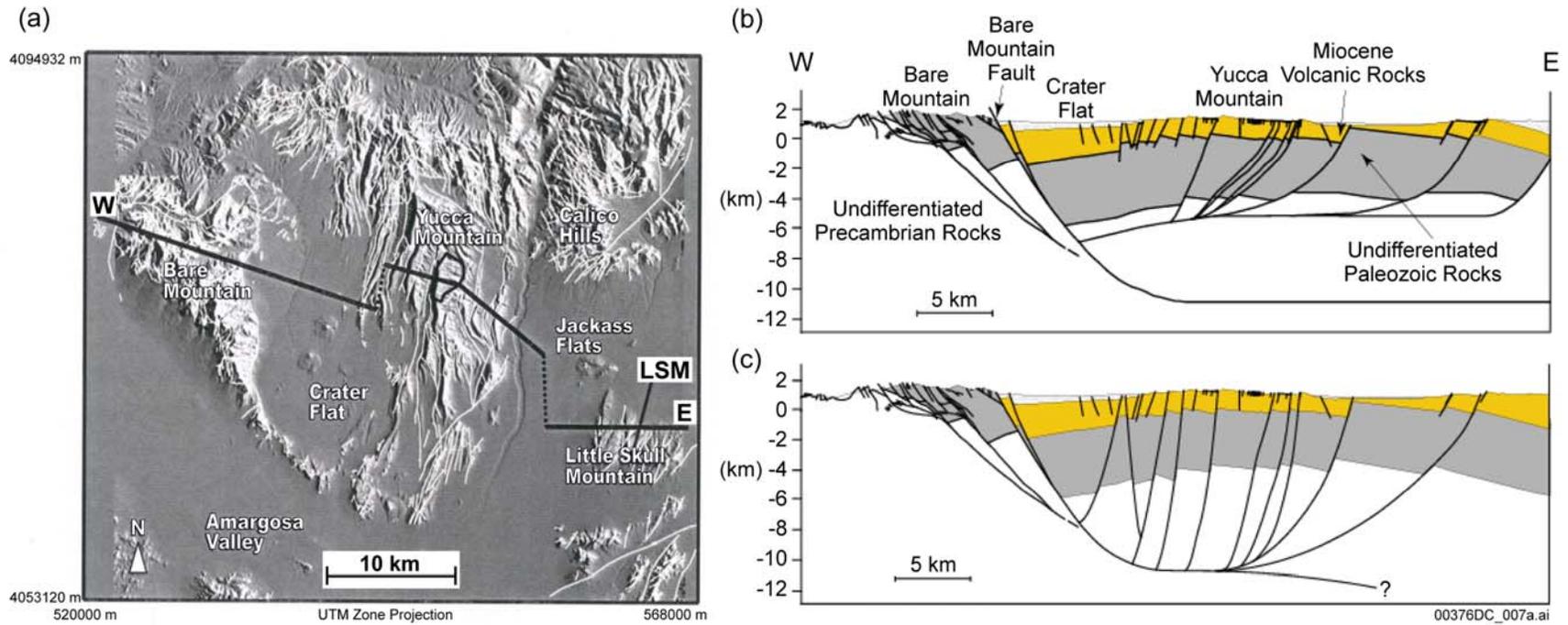
Source: McKague et al. 1996 [DIRS 105028], pp. 3-4 and 3-11

NOTES: Part (a) is a digital elevation map of the Crater Flat domain. The line segments (W-E) show composite trace of cross sections illustrated in Parts (b) and (c). Map coordinates are UTM. Part (b) shows the shallow detachment fault system. Part (c) shows the deep detachment fault system.

Figure 4-7. Alternative Interpretive Cross Sections across Crater Flat Domain
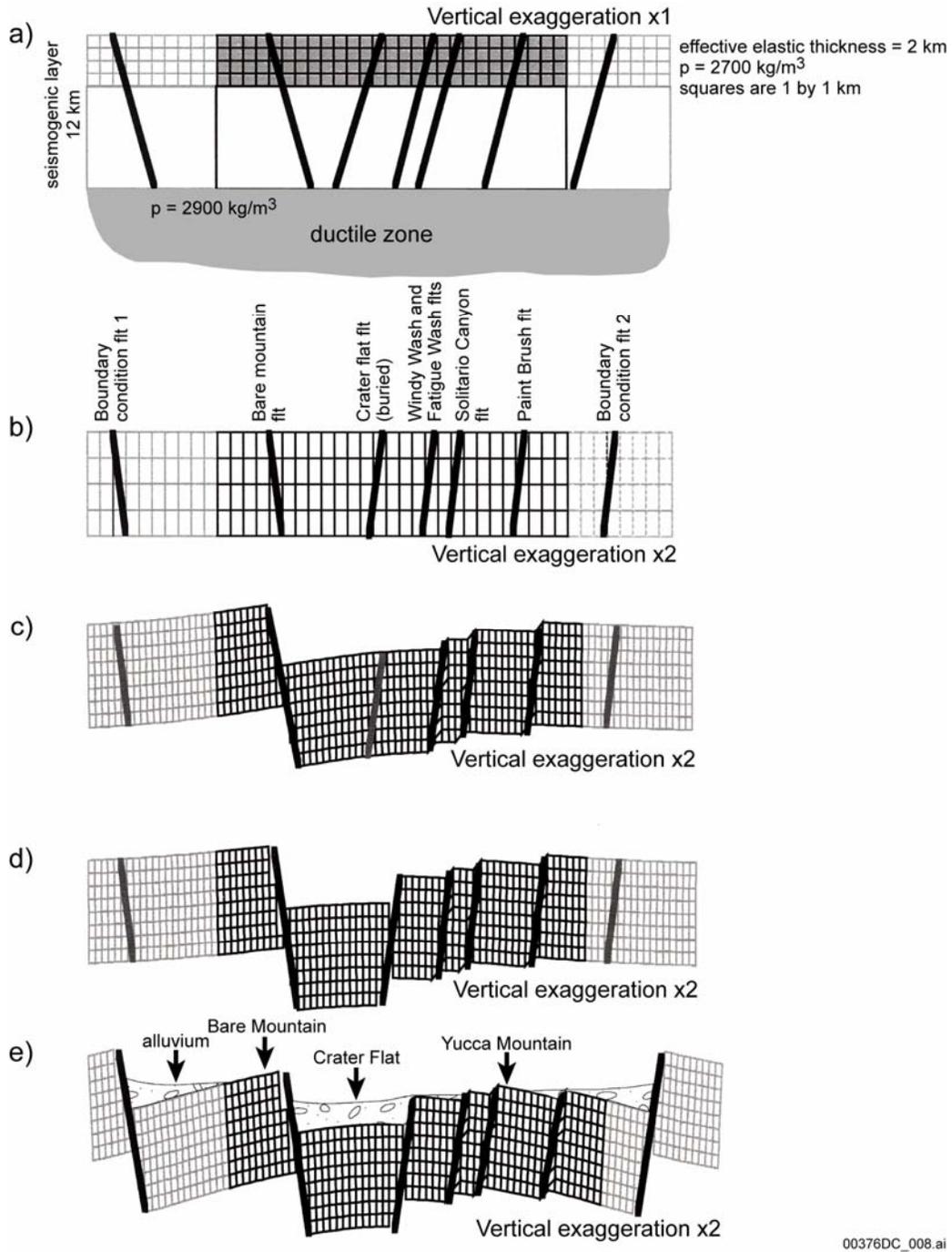
Source: O'Leary 1996 [DIRS 106435], Figure 8.28

NOTES: Boundary condition fault 1 = inferred fault in Amargosa Valley; boundary condition fault 2 = Gravity fault. Panels b-e show brittle crust only; e shows that slip on boundary condition faults provides for appropriate relief for Yucca Mountain

P = density; flt = fault

Figure 4-8. Simplified East-West Cross Section of the Crater Flat Domain Depicted as a Complex Half-Graben
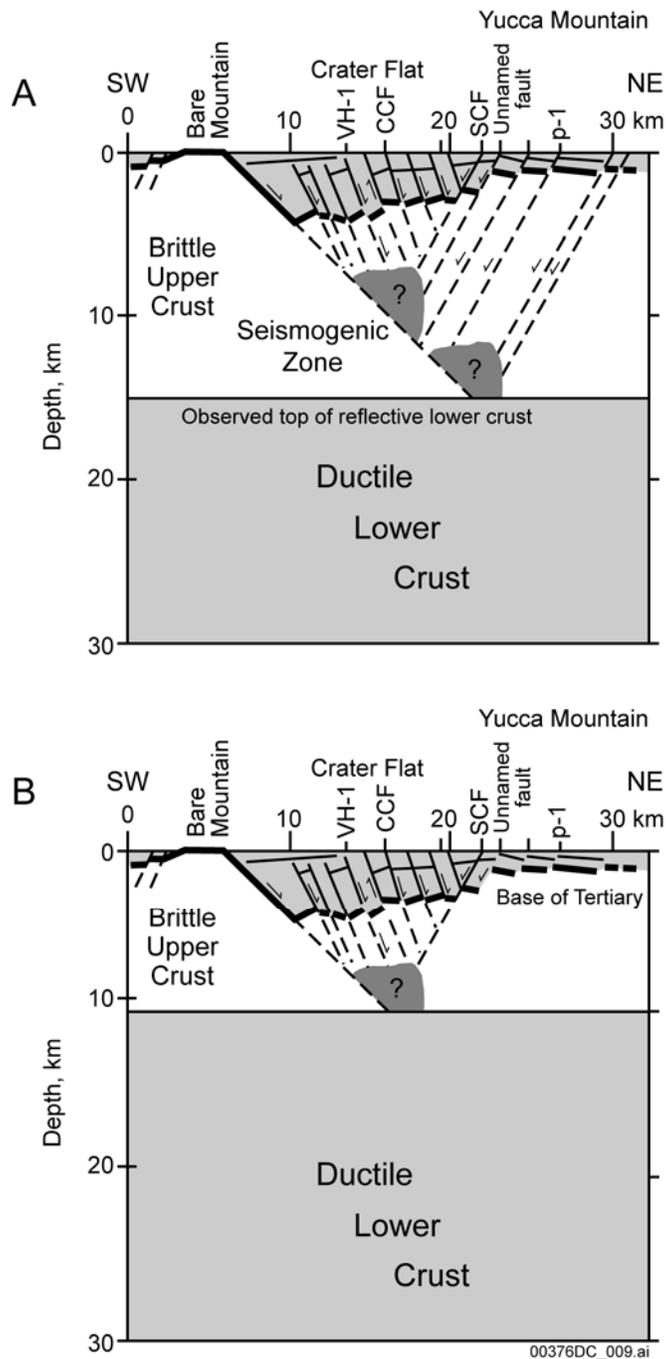
Source: Brocher et al. 1998 [DIRS 100022], p. 968

NOTES: This tectonic model of Crater Flat basin is based on the seismic reflection profile interpretation of CRWMS M&O 2000 [DIRS 151945], Figure 4.3-17. Part (A) depicts present fault configuration. Part (B) depicts Middle Miocene fault configuration. (Black areas in brittle crust are not explained by Brocher et al. 1998 [DIRS 100022]).

VH-1 = location of VH-1 borehole; CCF = Central Crater Flat fault; SCF = Solitario Canyon fault; p-1 = location of p#1 borehole.

Figure 4-9. Tectonic Rift Model of Crater Flat Basin Based on Seismic Reflection Profile Interpretation
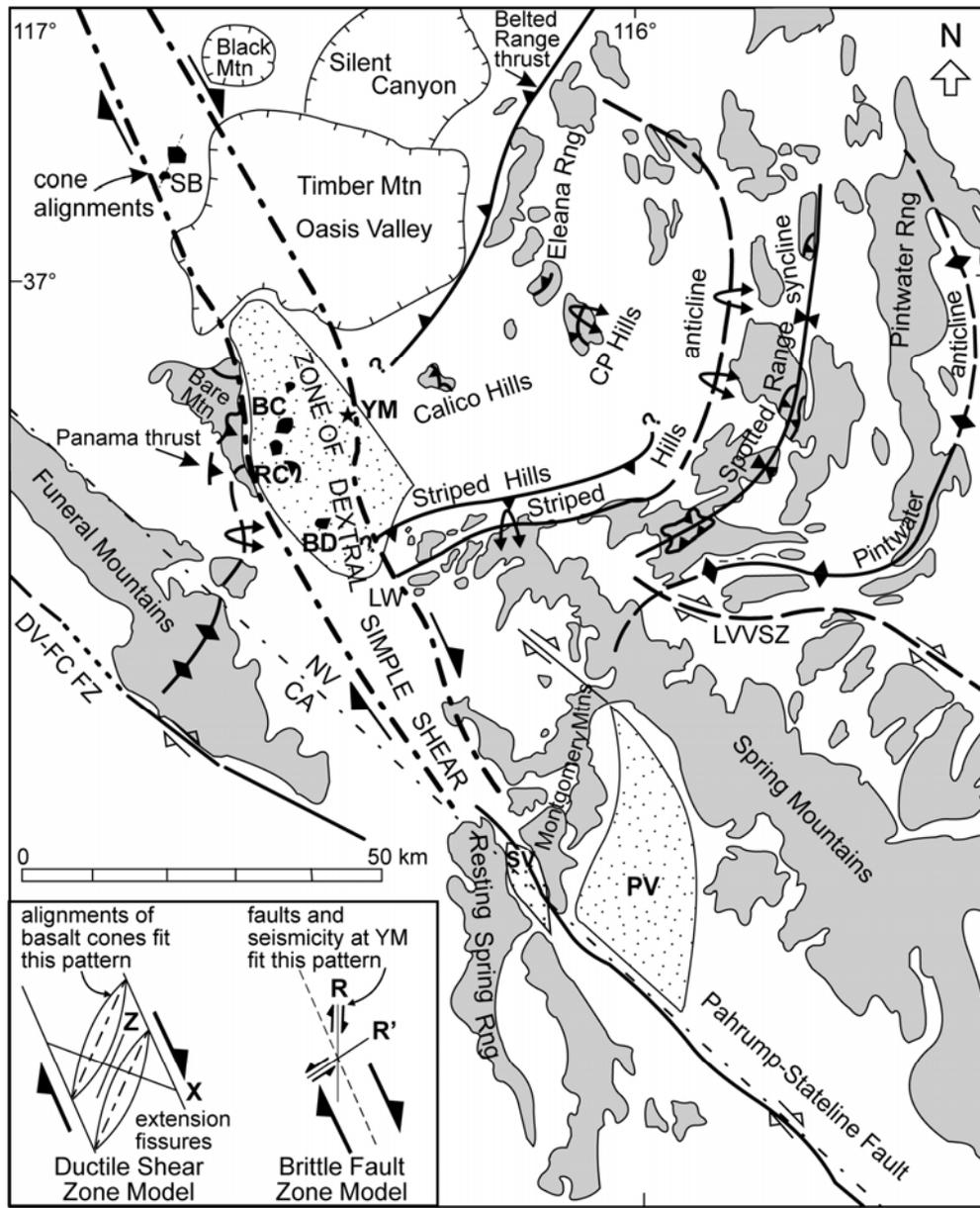
Source: Schweickert and Lahren 1997 [DIRS 101012], Figure 1

NOTES: BC = Black Cone; LVVSZ = Las Vegas Valley Shear Zone; PV = Pahrump Valley; RC = Red Cone;
SB = Sleeping Butte; YM = Yucca Mountain; BD = Big Dune Cone; LW = Lathrop Wells cone;
DV-FCFZ = Death Valley-Furnace Creek fault zone.

Figure 4-10.   Amargosa Desert Fault System
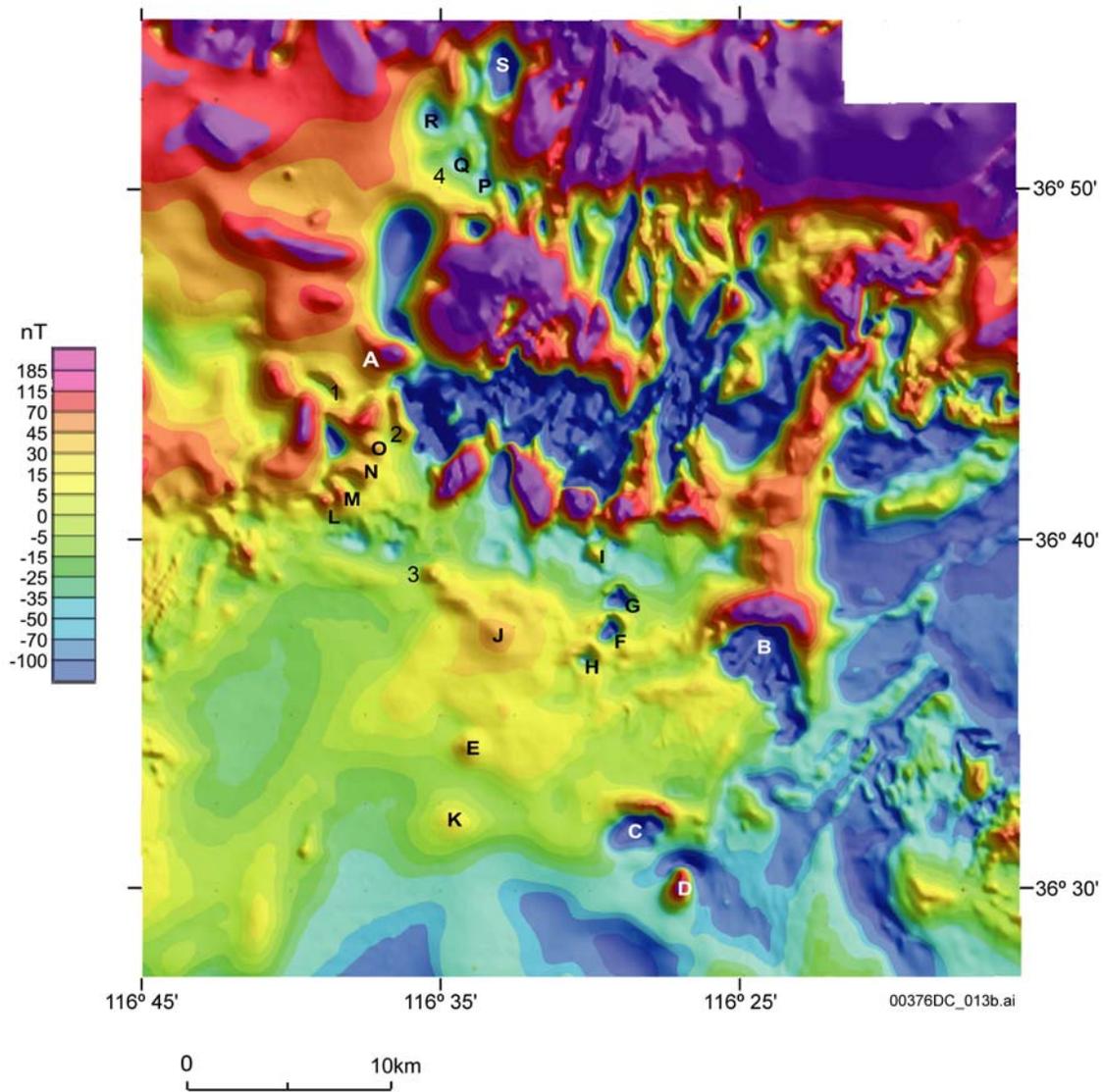
Sources: O'Leary et al. 2002 [DIRS 158468]; Blakely et al. 2000 [DIRS 151881]

NOTES: Colors represent magnetic field intensities relative to the International Geomagnetic Field (Map created by R.J. Blakely, USGS); blue = negative magnetization; purple = positive magnetization. Letters identify anomalies listed in Table 4-1.

Figure 4-11. Magnetic Anomalies, Crater Flat Basin and Northern Amargosa Desert, Nevada
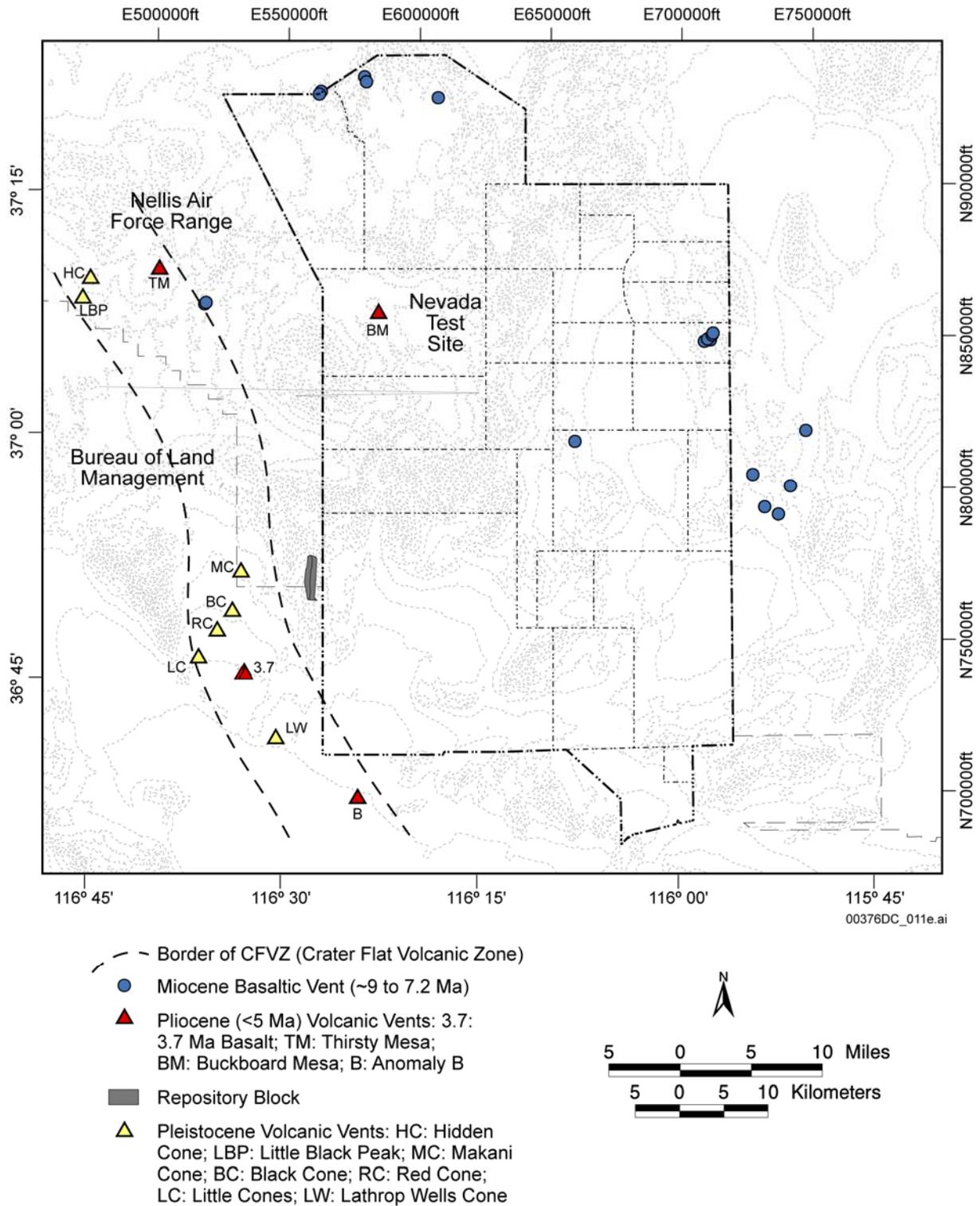
Source: Modified from CRWMS M&O 1998 [DIRS 135988], Figure 3.14

Figure 4-12.   Location of Miocene and Post-Miocene Basaltic Vents of the Yucca Mountain Region
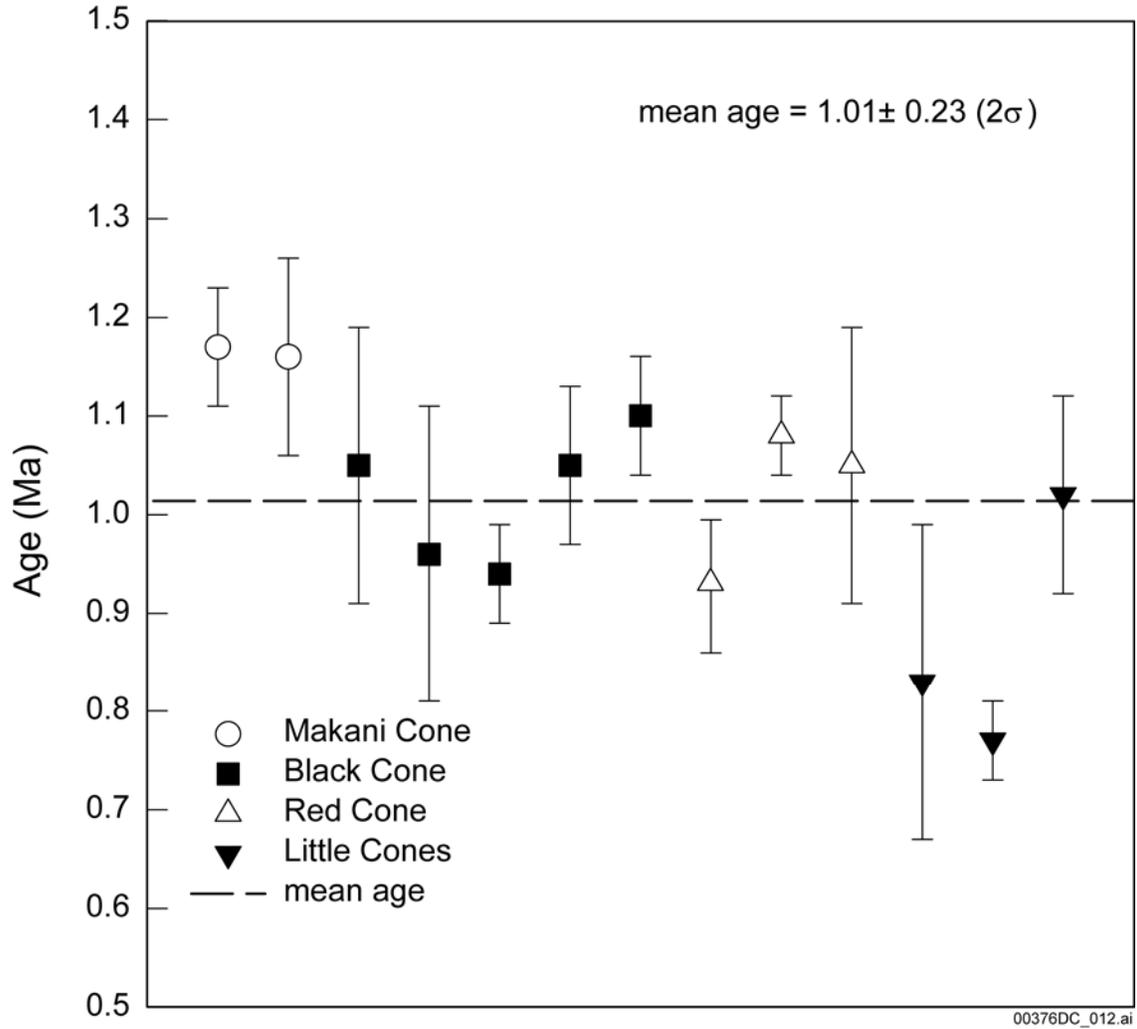
Source: CRWMS M&O 1998 [DIRS 123196], Table 2.B, p. 2-13

NOTE: Left to right on the figure corresponds to north to south for the location of basalt centers within Crater Flat.

Figure 4-13. Argon-40/Argon-39 Ages from Quaternary Basalt Centers of Crater Flat
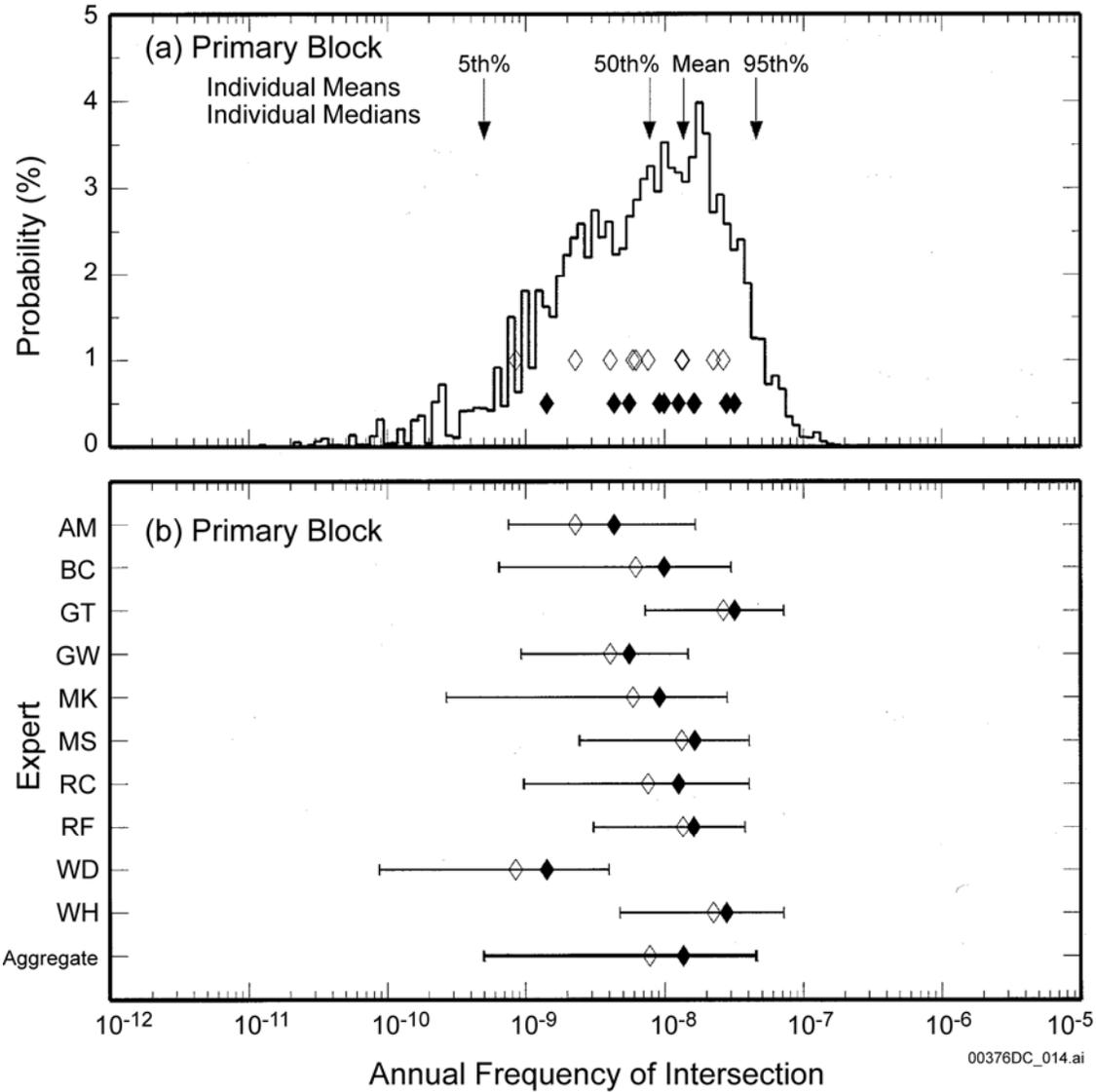
DTN: MO0002PVHA0082.000 [DIRS 148234]

Sources: CRWMS M&O 2000 [DIRS 151551], Figure 20

NOTES: (a) Aggregate distribution and median and means for individual probabilistic volcanic hazard analysis expert hazard models for the primary block case. (b) Range for 5th and 95th percentiles for results from individual probabilistic volcanic hazard analysis expert hazard models compared to range for aggregate distribution for the primary block case. Two-letter code indicates initials of experts identified in Table 12.2-6 of CRWMS M&O 2000 [DIRS 151945].

Figure 4-14. Annual Frequency of Intersecting the Site Recommendation Repository Footprint for the Primary Block Case

Sources: CRWMS M&O 2000 [DIRS 151551], Figure 21

NOTES: (a) Aggregate distribution and median and means for individual probabilistic volcanic hazard analysis expert interpretations for the primary + contingency blocks case. (b) Range for 5th and 95th percentiles for results from individual probabilistic volcanic hazard analysis expert interpretations compared to range for aggregate distribution for the primary + contingency blocks case. Two-letter code indicates initials of experts identified in Table 12.2-6 of CRWMS M&O 2000 [DIRS 151945].

Figure 4-15. Annual Frequency of Intersecting the Site Recommendation Repository Footprint for the Primary Plus Contingency Block Case

(a) Map of Mean Volcanic Event Frequency

(b) Map of Spatial Disaggregation of Intersection Frequency
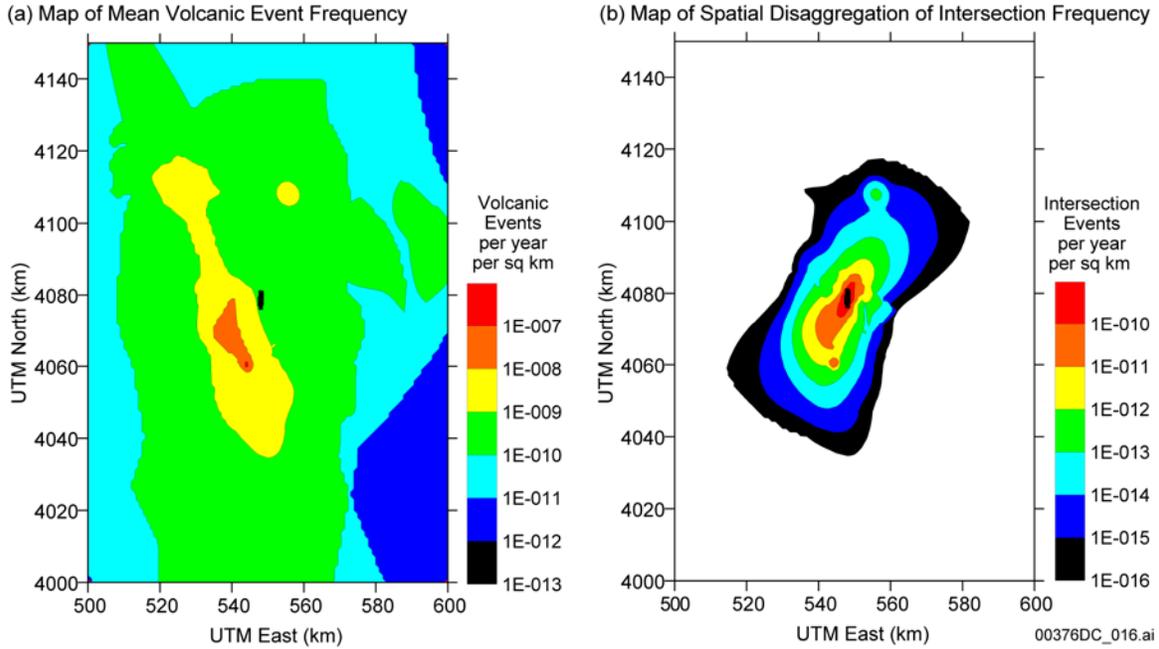
DTN: LA0009FP831811.002 [DIRS 164714]

Sources: CRWMS M&O 1996 [DIRS 100116], Appendix E; CRWMS M&O 2000 [DIRS 151551], Figure 17

NOTES: The maps represent the mean results averaged over 10 experts and over each expert's logic tree. Black area in center of maps is the repository footprint.

Figure 4-16. Spatial Distribution of Volcanic Hazard Defined by the Probabilistic Volcanic Hazard Analysis Expert Panel

(a) and (b) maps showing Digital Stations, Analog Stations, and Other Digital Stations across Nevada, California, Utah, and Arizona, with Nevada Test Site and YMP Site labeled.
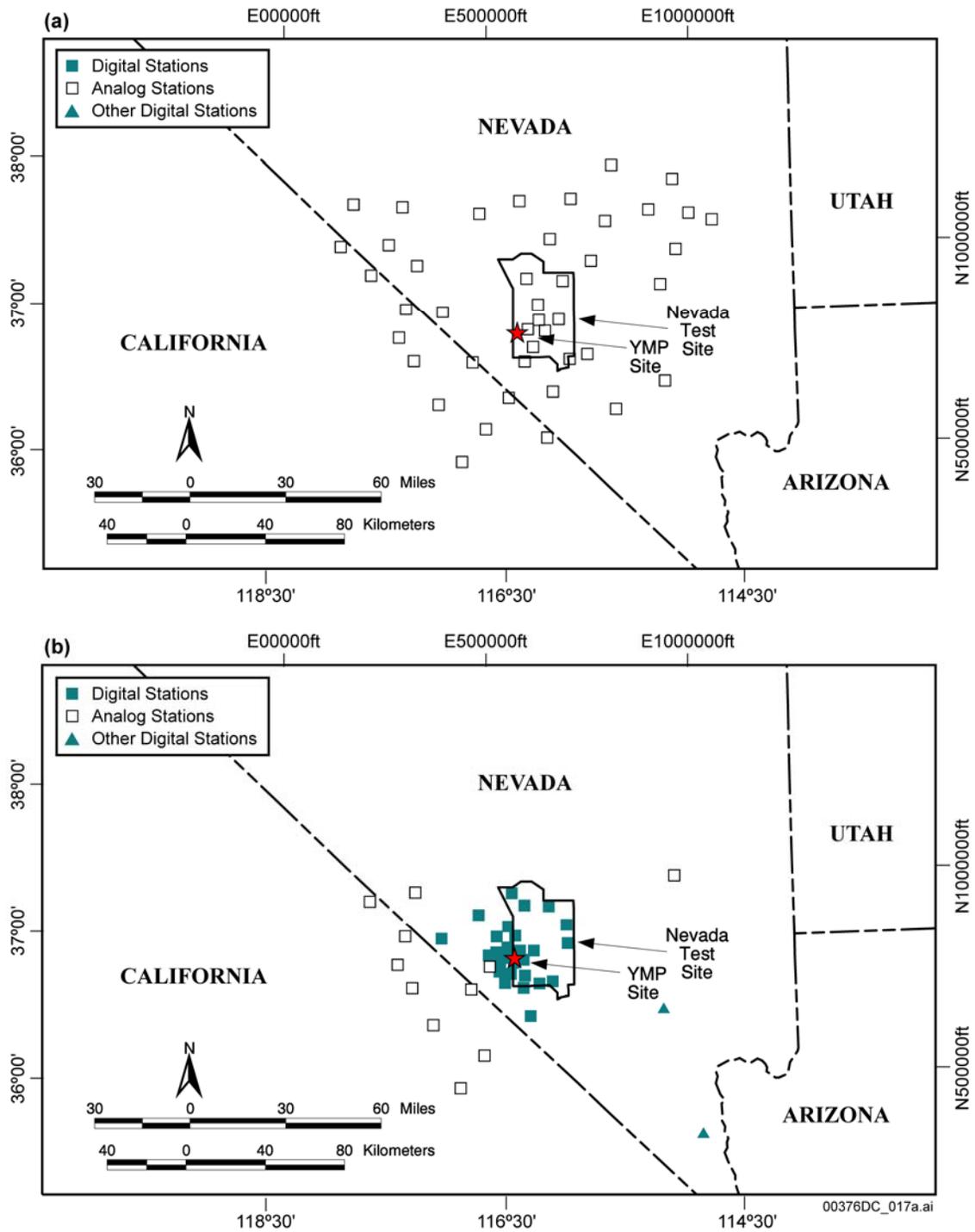
DTN: MO0007COV00207.000 [DIRS 166583]

Figure 4-17.   Seismograph Stations Operating in the Southern Great Basin
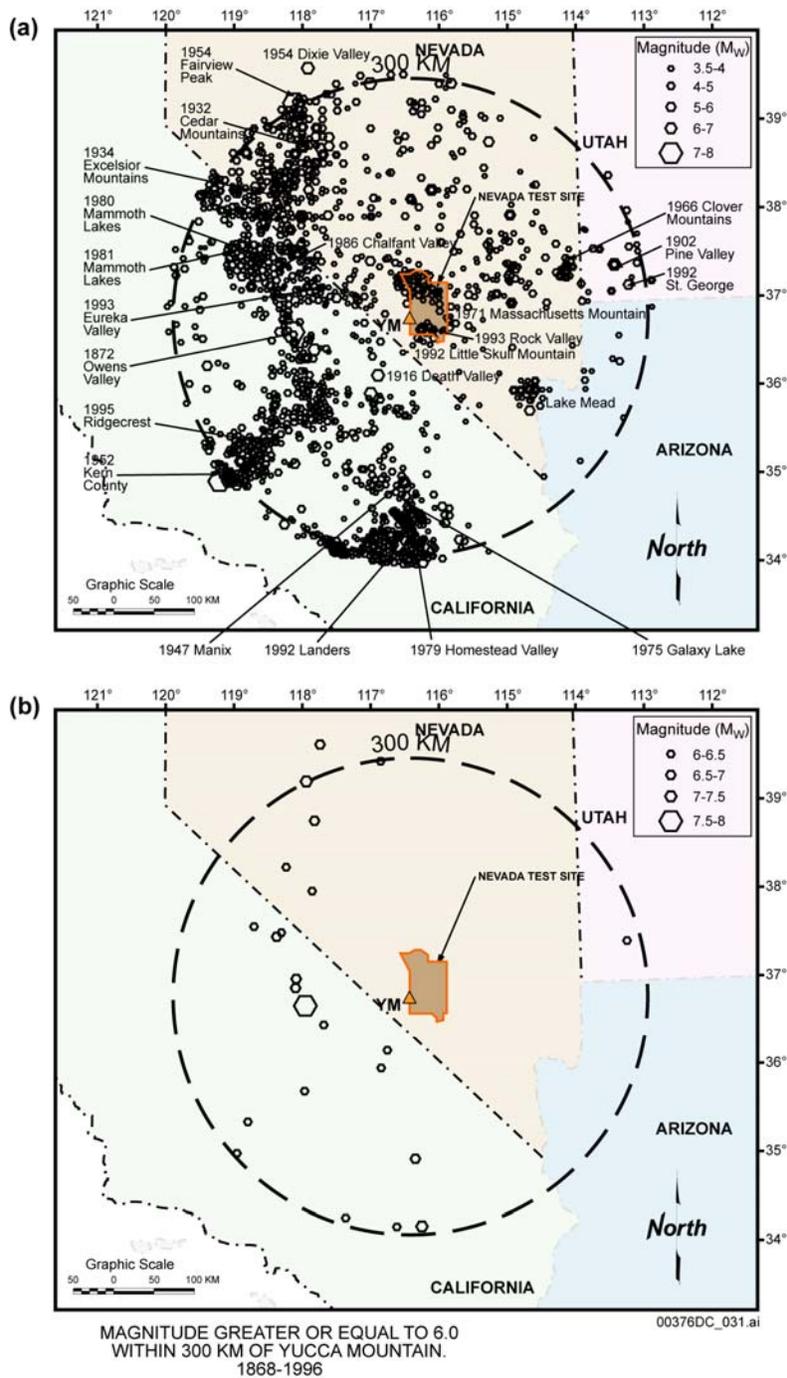
DTNs: MO9906COV99279.000 [DIRS 166582]; MO0006COV00226.000 [DIRS 166581]

Source: DOE 2002 [DIRS 155943], Figure 4-162

NOTES: Shown are earthquakes from 1868 to 1996. This seismicity catalog was compiled from a variety of sources. Coverage of older seismicity is sparse because of the absence or limited availability of seismographic coverage in the late 1800s and early 1900s. The cluster of earthquakes near the southern boundary of the Nevada Test Site represents the 1992 Little Skull Mountain earthquake and its numerous aftershocks. Many of the events in the northern part of the Nevada Test Site occurred in response to underground nuclear weapons tests. Significant earthquakes are labeled with year of occurrence.

Figure 4-18. Historical Earthquake Epicenters within 300 km of Yucca Mountain
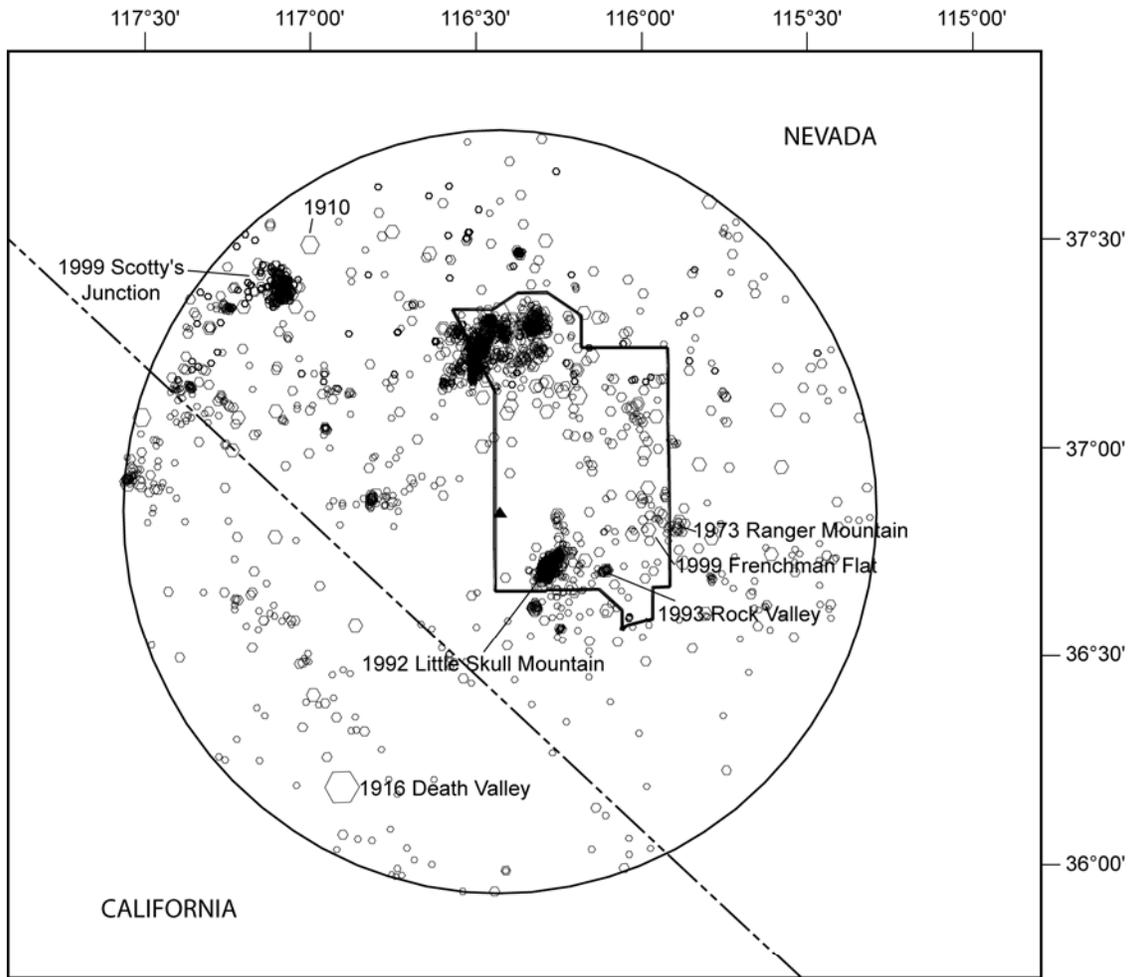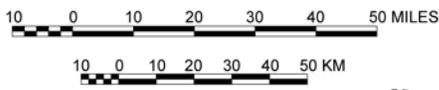
DTNs: MO9906COV99279.000 [DIRS 166582]; MO0006COV00226.000 [DIRS 166581]

Source: CRWMS M&O 2000 [DIRS 151945]

NOTES: Shown are earthquakes from 1904 to 1998. Earthquakes associated with the 1999 Scotty's Junction and 1999 Frenchman Flat sequences are also shown. Significant earthquakes or earthquake sequences are shown with years of occurrence. Activity in the northwestern corner of the Nevada Test Site is related to underground nuclear testing.

Figure 4-19. Historical Earthquake Epicenters within 100 km of Yucca Mountain
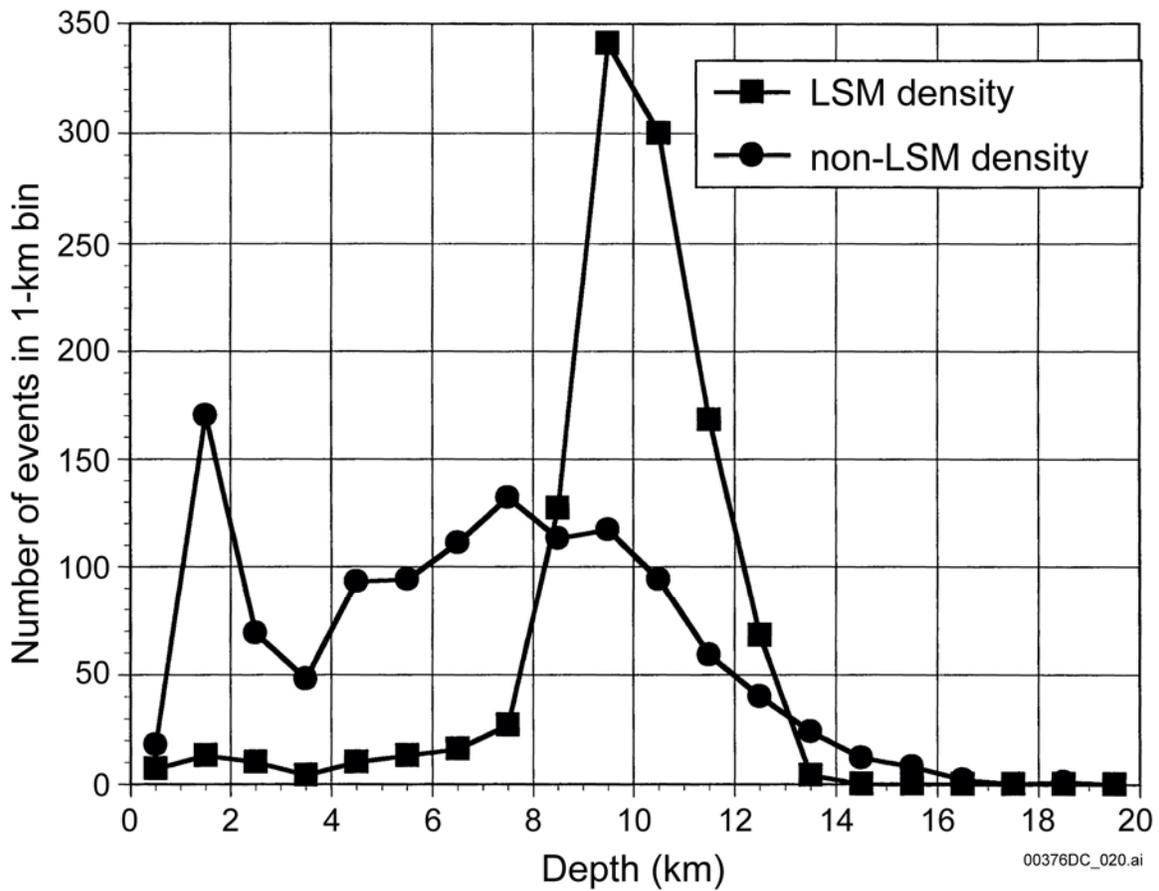
DTN: UN0106SPA012JB.001 [DIRS 166389]

Source: von Seggern and Smith 2001 [DIRS 158461], Figure 3-6

NOTE: The density has been computed separately for "LSM" = Little Skull Mountain and "non-LSM" = all other earthquakes.

Figure 4-20. Focal Depth Distribution of Earthquakes in the Yucca Mountain Vicinity for Fiscal Year 2000
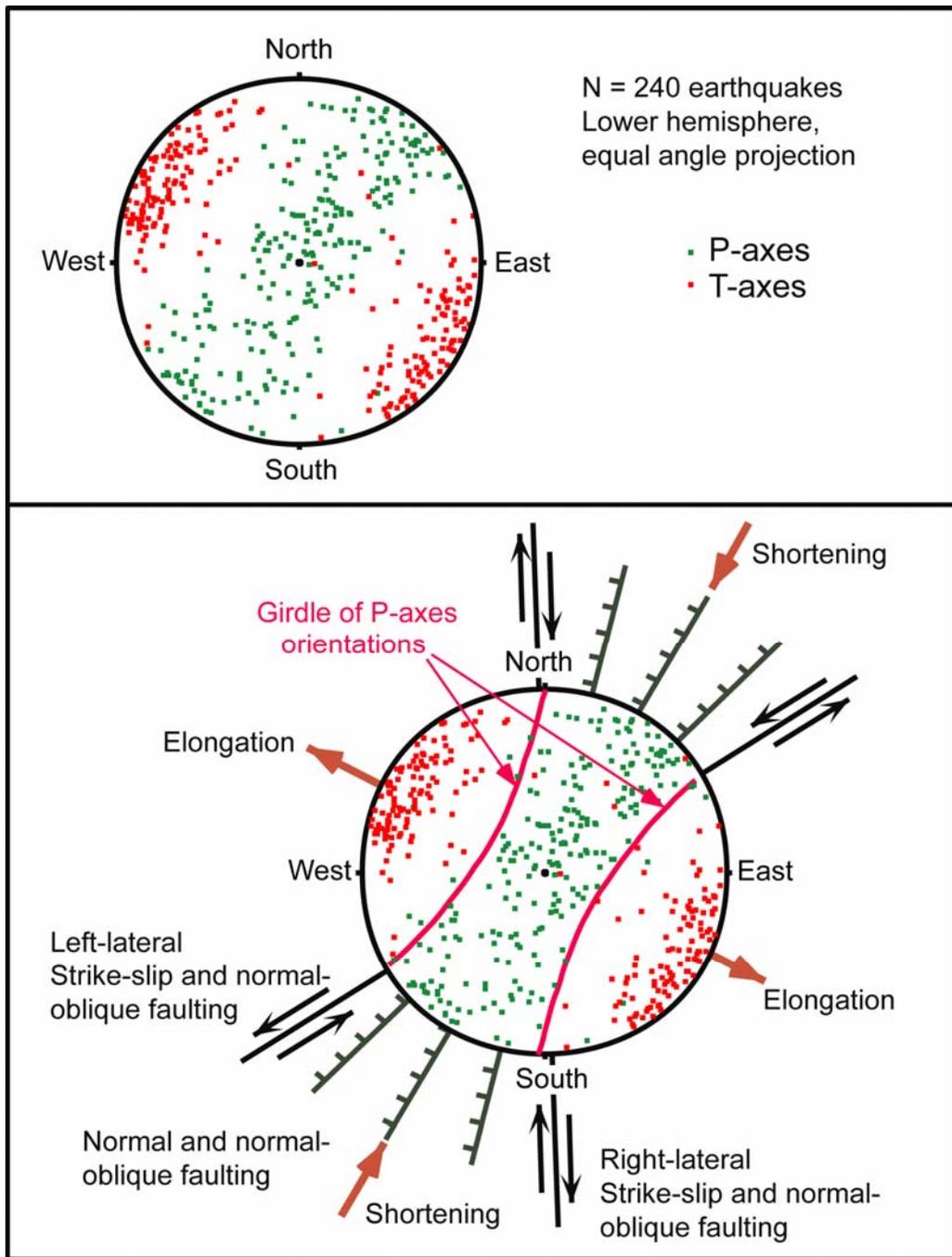
DTN: GS960783117361.004 [DIRS 166575]

Source: Pezzopane et al. 1996 [DIRS 106526], Figure 7-5

NOTES: Lower hemisphere equals angle projection of the principal stress axes. Upper plot shows the data and the lower plot shows the inferred orientations of faulting consistent with the stress orientations. Maximum relative compression (P) axes form a girdle from vertical to northeast-southwest orientation, whereas extensional (minimum relative compression) (T) axes trend northwest-southeast.

Figure 4-21. Focal Mechanisms for Earthquakes in the Vicinity of Yucca Mountain
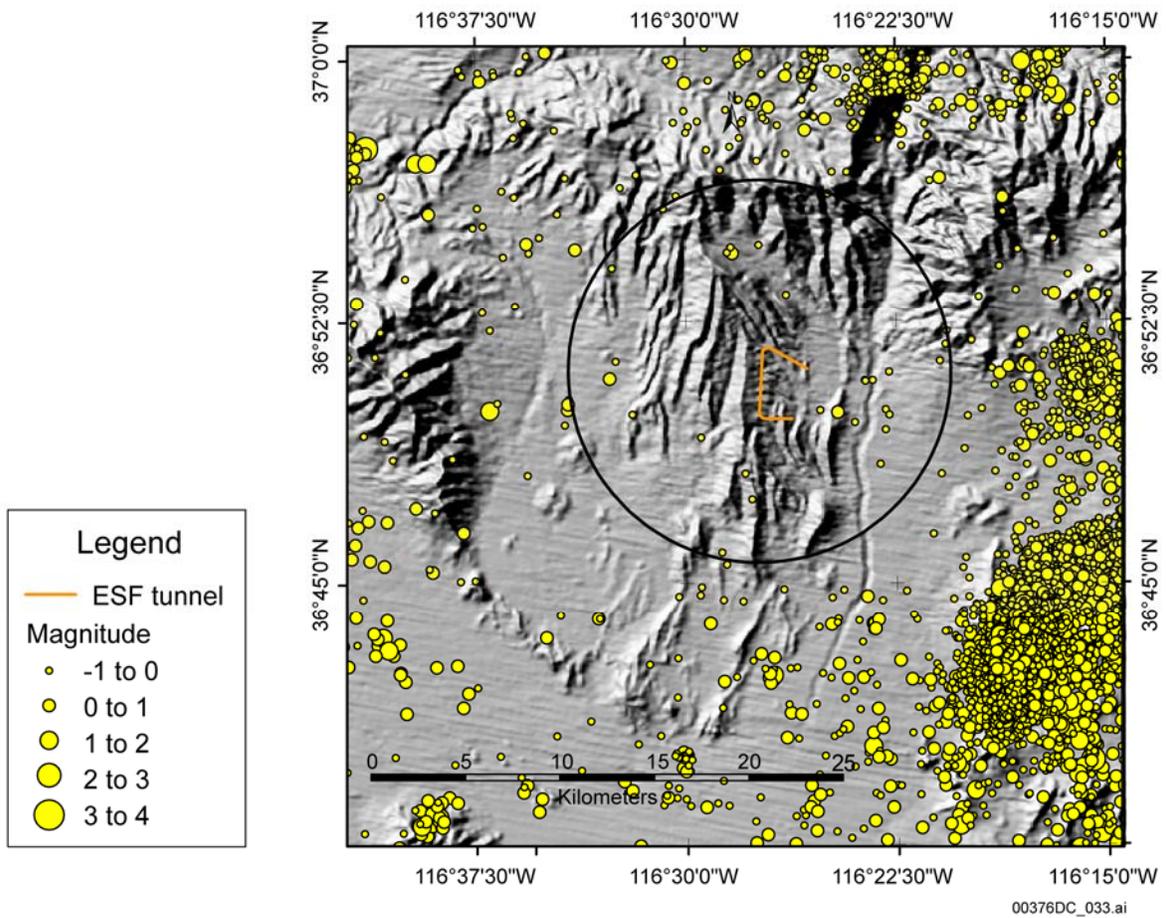
DTNs: MO970483117412.002 [DIRS 150037]; MO9906SEISYMNV.000 [DIRS 166387];
UN0007SPA012DV.002 [DIRS 166388]; UN0106SPA012JB.001 [DIRS 166389];
MO0205UCC012DV.008 [DIRS 166390]; MO0305UCC012DV.014
[DIRS 166391]

Figure 4-22.   Seismicity at Yucca Mountain from October 1, 1995, to September 30, 2002
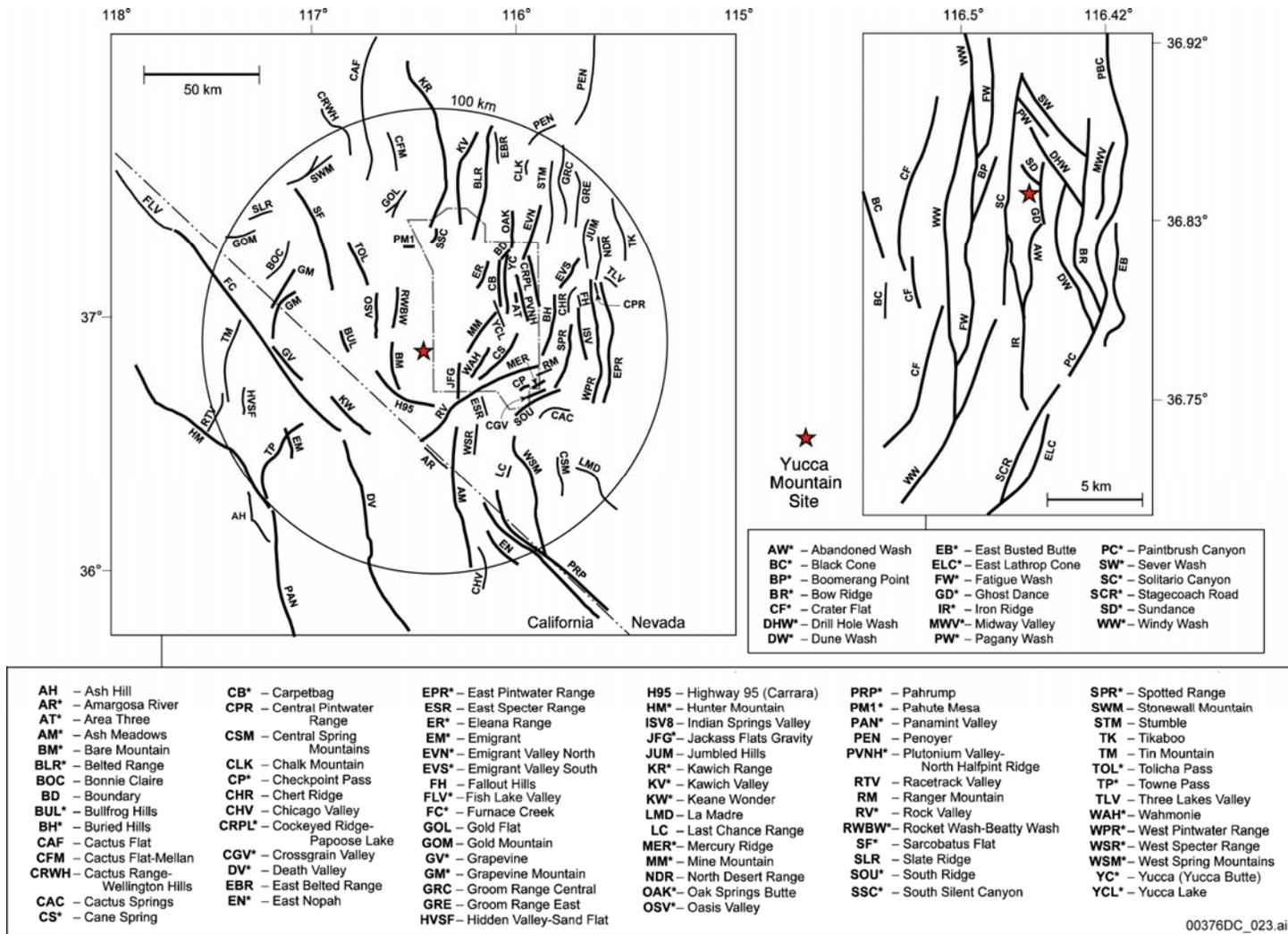
Source: Faults included in the probabilistic seismic hazard analyses (CRWMS M&O 1998 [DIRS 103731]) and/or considered relevant by Pezzopane (1996 [DIRS 106524], Table 11-1)

Figure 4-23.   Known or Suspected Quaternary Faults and Other Notable Local Faults within 100 km of Yucca Mountain
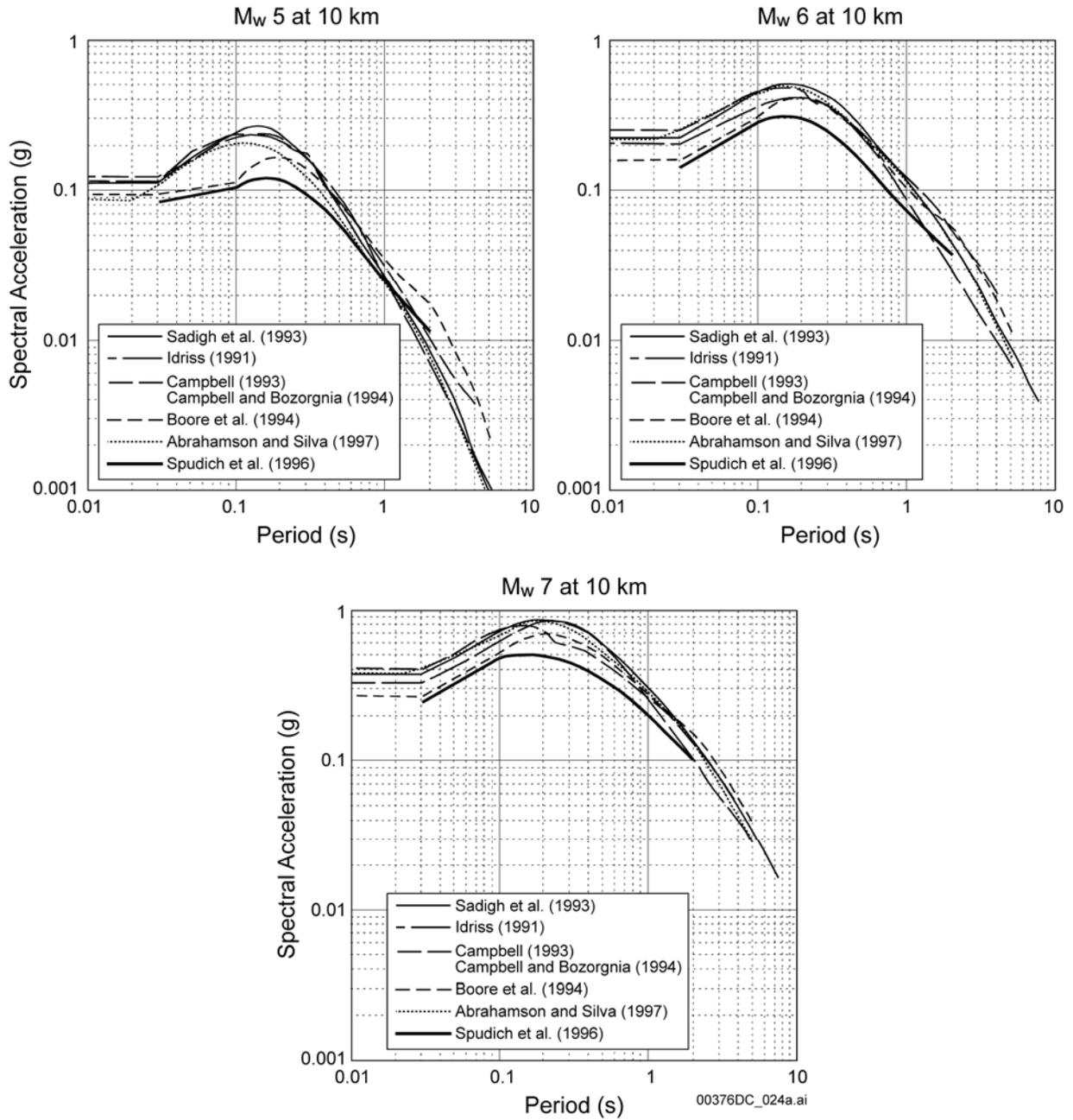
Source: Modified from Abrahamson and Becker 1996 [DIRS 101419], Figure 10.6-1

NOTE: Example shown is for median spectral accelerations for rock on the footwall of a normal fault.

Figure 4-24.   Comparison of Strong Ground Motion Attenuation Relation for Extensional Regimes with Other Selected Relations
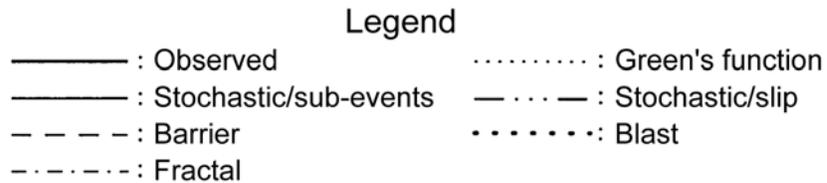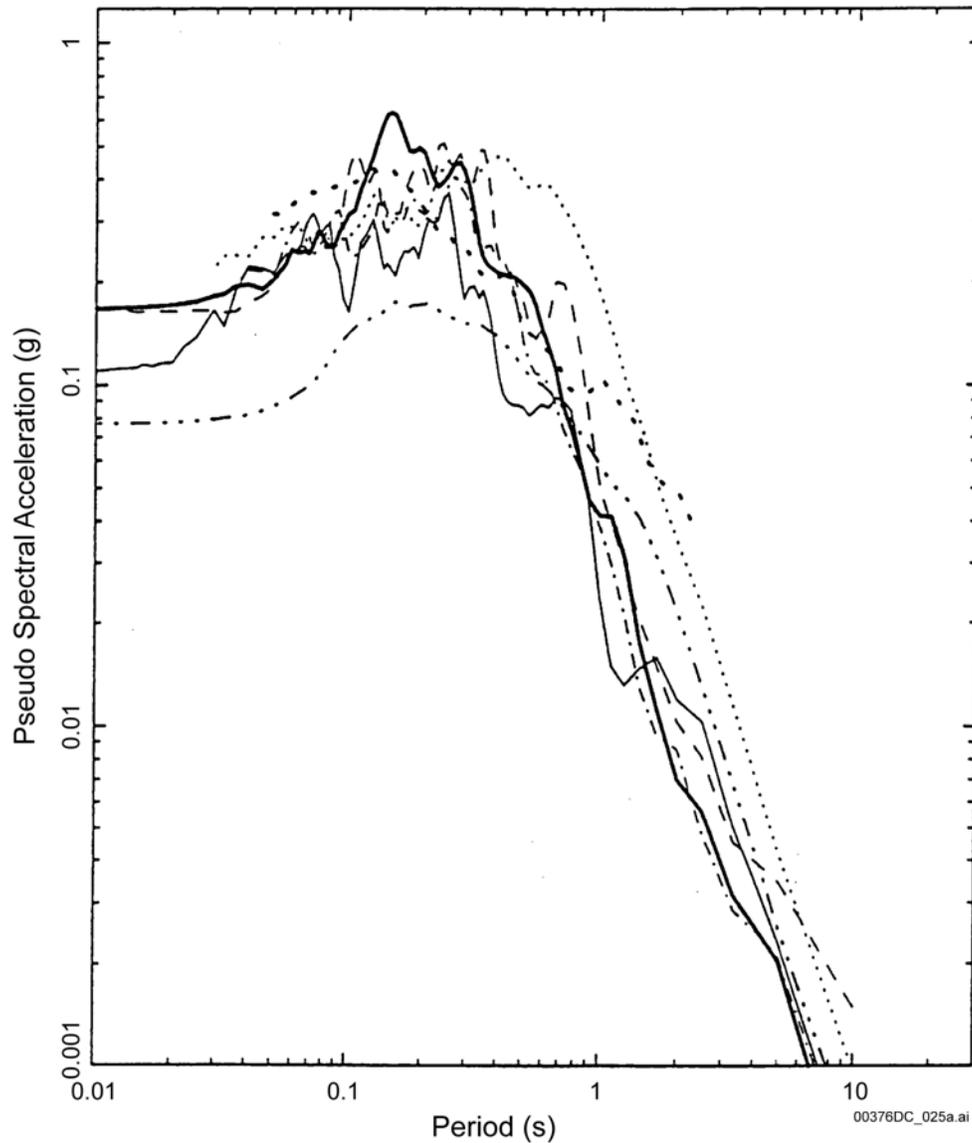
Source: Abrahamson and Becker 1996 [DIRS 101419], Figure 10.7-4a

NOTE: Shown is an observed spectrum (5% damping) for a recorded motion from the Little Skull Mountain earthquake (Lathrop Wells Station) and spectra calculated by six teams using different modeling methods.

Figure 4-25.   Comparison of Calculated Response Spectrum Using Different Modeling Approaches to the Observed Response Spectrum from the Little Skull Mountain Earthquake
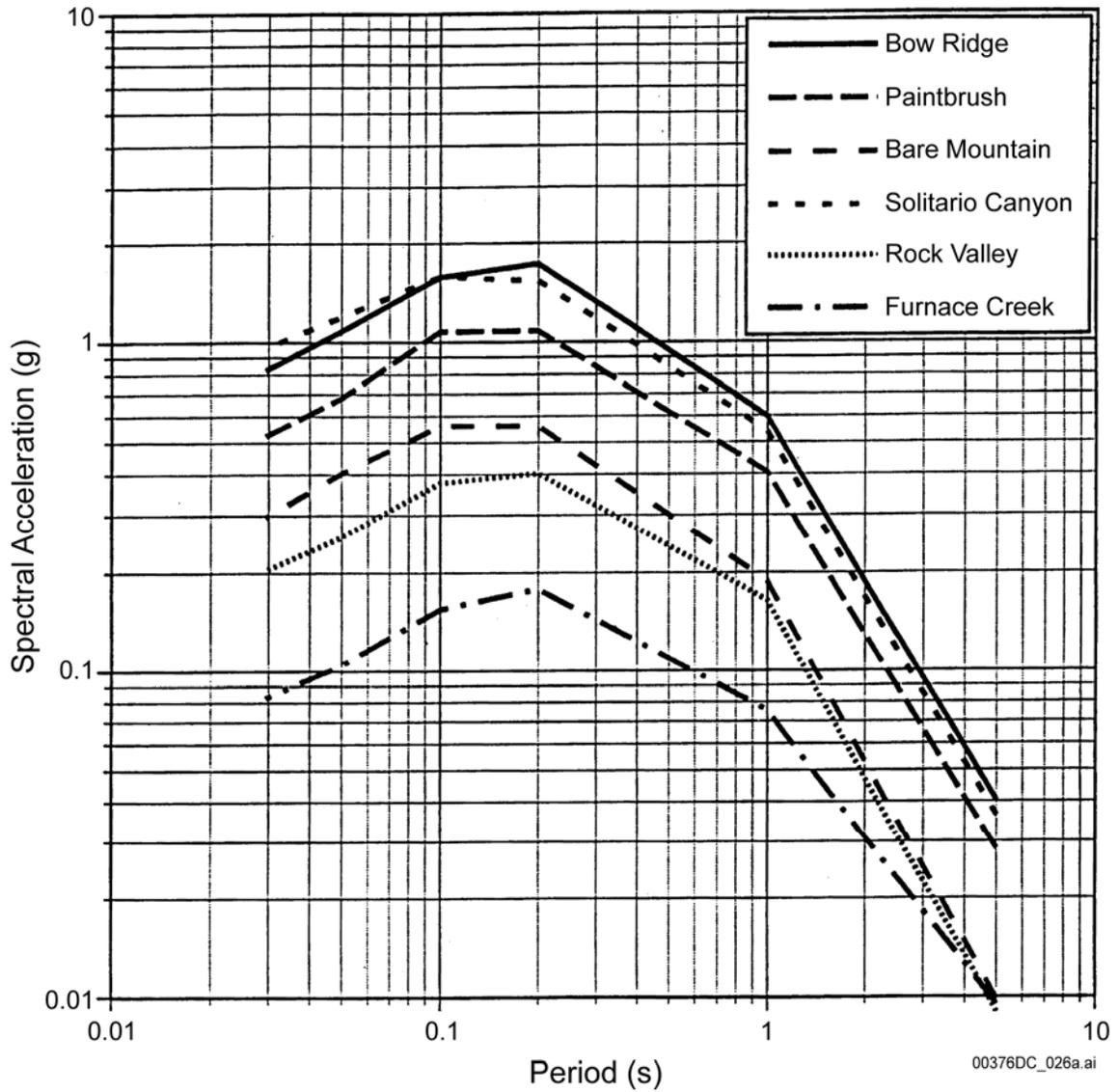
Source: Abrahamson and Becker 1996 [DIRS 101419], Figure 10.8-15

Figure 4-26.   Median Spectral Acceleration of Scenario Earthquakes in the Yucca Mountain Region

a) Seismic source i
   Earthquake locations in space (and magnitude-dependent rupture dimensions) lead to a distributions of distance

   $f_{R(i)|M(i)}(r;m)$
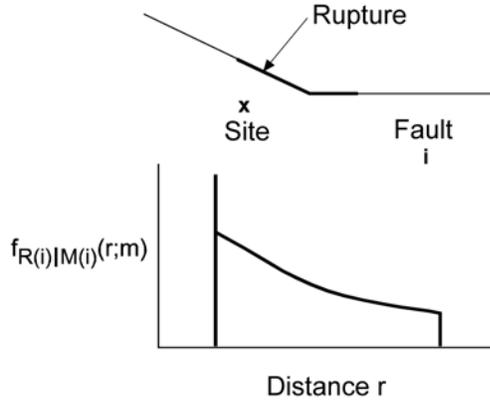
b) Magnitude distribution and rate of occurrence for source i

   $f_{M(i)}(m), \nu_i$
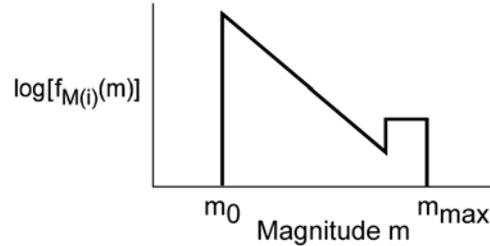
c) Ground-motion attenuation equation

   $G_{A|m,r}(a^*)$
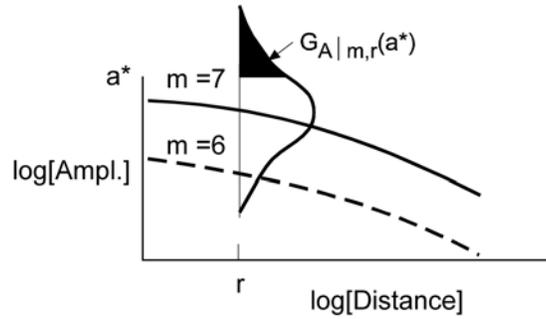
d) Probability analysis: annual exceedance probability

   $\approx \sum_i \nu_i \int_r \int_m G_{A|m,r}(a^*)\, f_{M(i)}(m)\, f_{R(i)|M(i)}(r;m)\, \delta m\, \delta r$
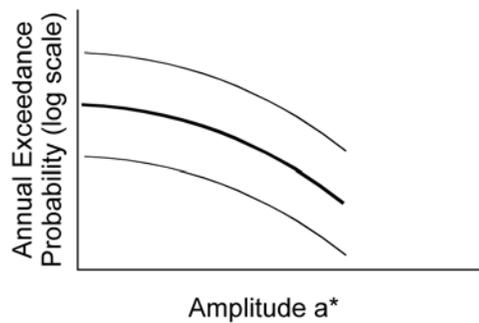
Source: CRWMS M&O 1998 [DIRS 103731], Figure 7-1

Figure 4-27.   Schematic Diagram of the Elements of a Probabilistic Seismic Hazard Analysis
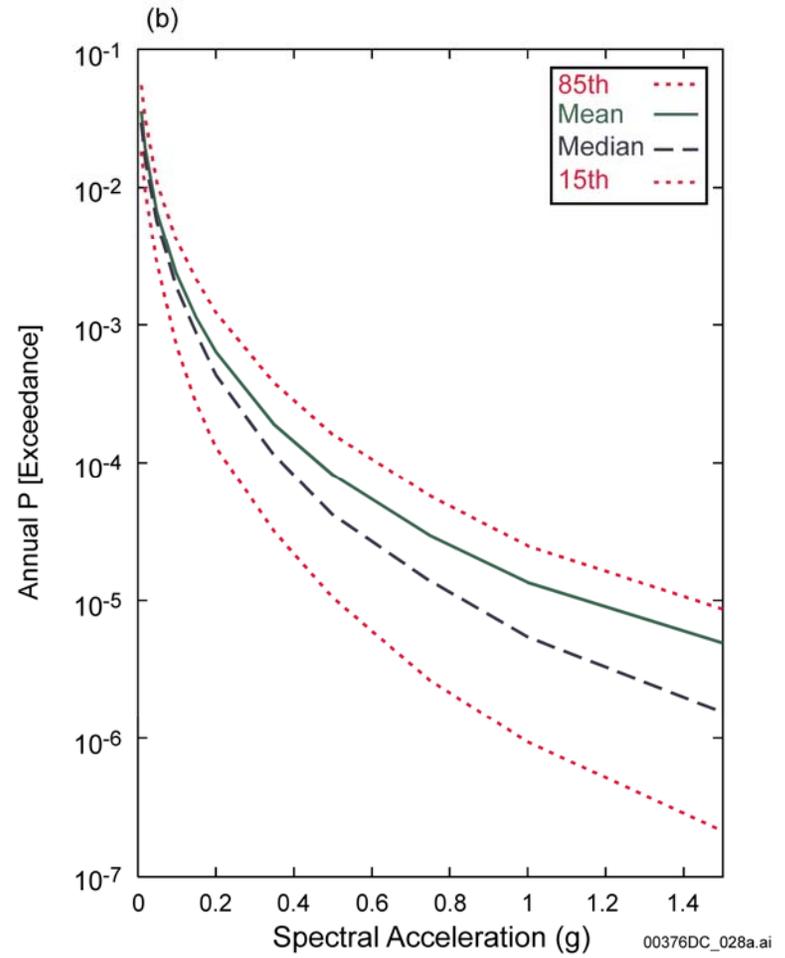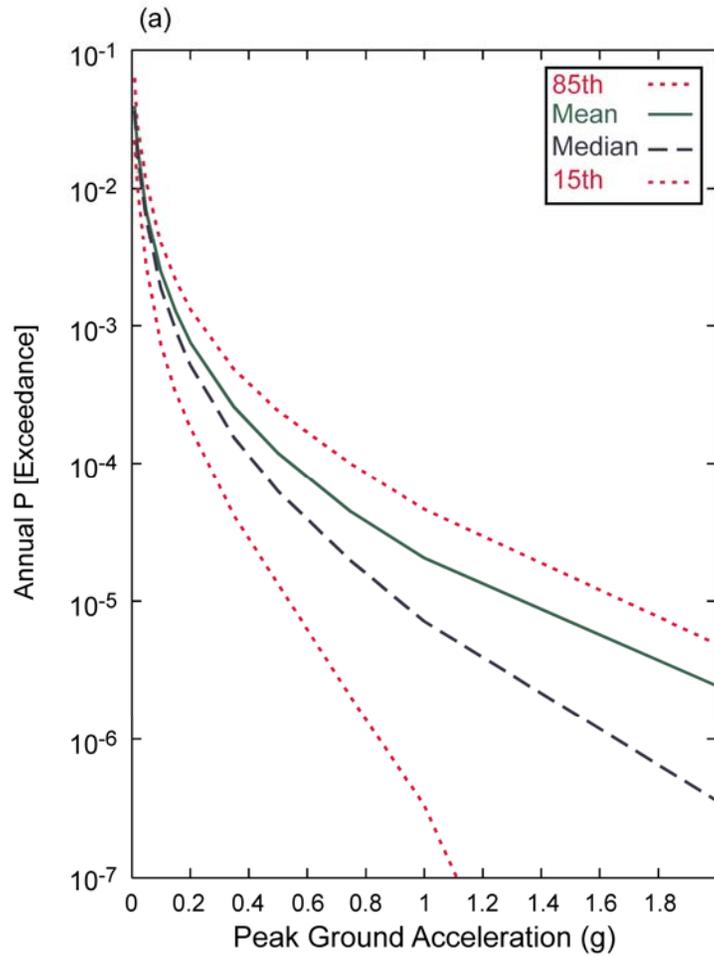
Source: CRWMS M&O 1998 [DIRS 103731], Figures 7-10 and 7-12

NOTES: Plot (a) shows horizontal peak ground acceleration; plot (b) shows 1-Hz spectral acceleration.

Figure 4-28. Summary Ground Motion Hazard Curves for Yucca Mountain
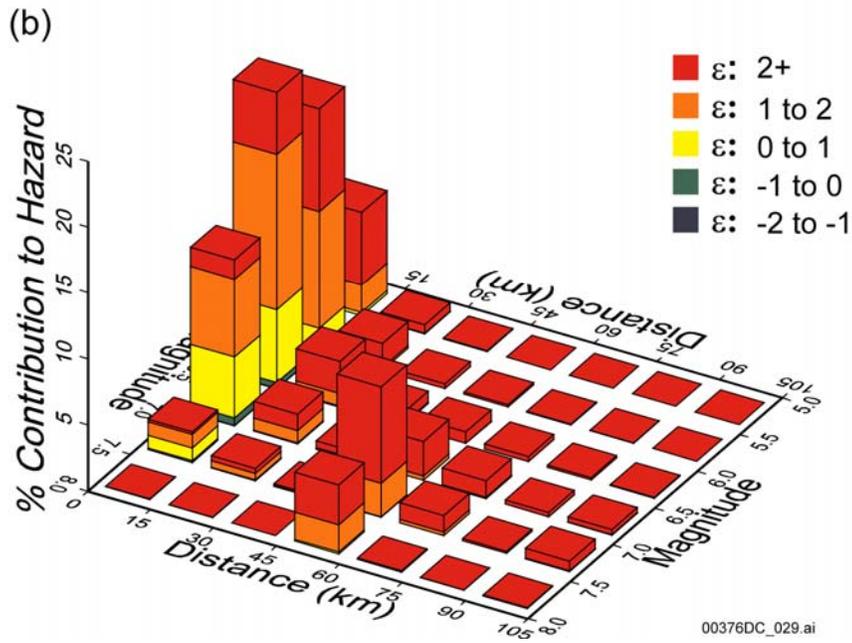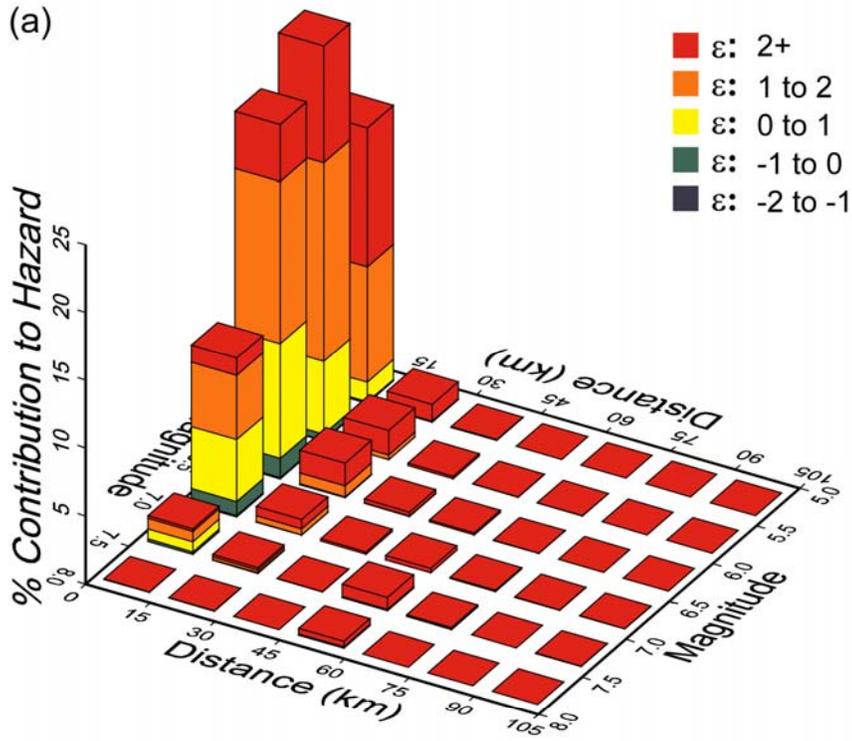
Source: CRWMS M&O 1998 [DIRS 103731], Figures 7-15 and 7-16

NOTES: Graph (a) is for 5- to 10-Hz horizontal spectral acceleration; graph (b) is for 1- to 2-Hz horizontal spectral acceleration.

Figure 4-29.   Deaggregation of Mean Seismic Hazard for Horizontal Spectral Acceleration at 10^{-4} Annual Exceedance Probability
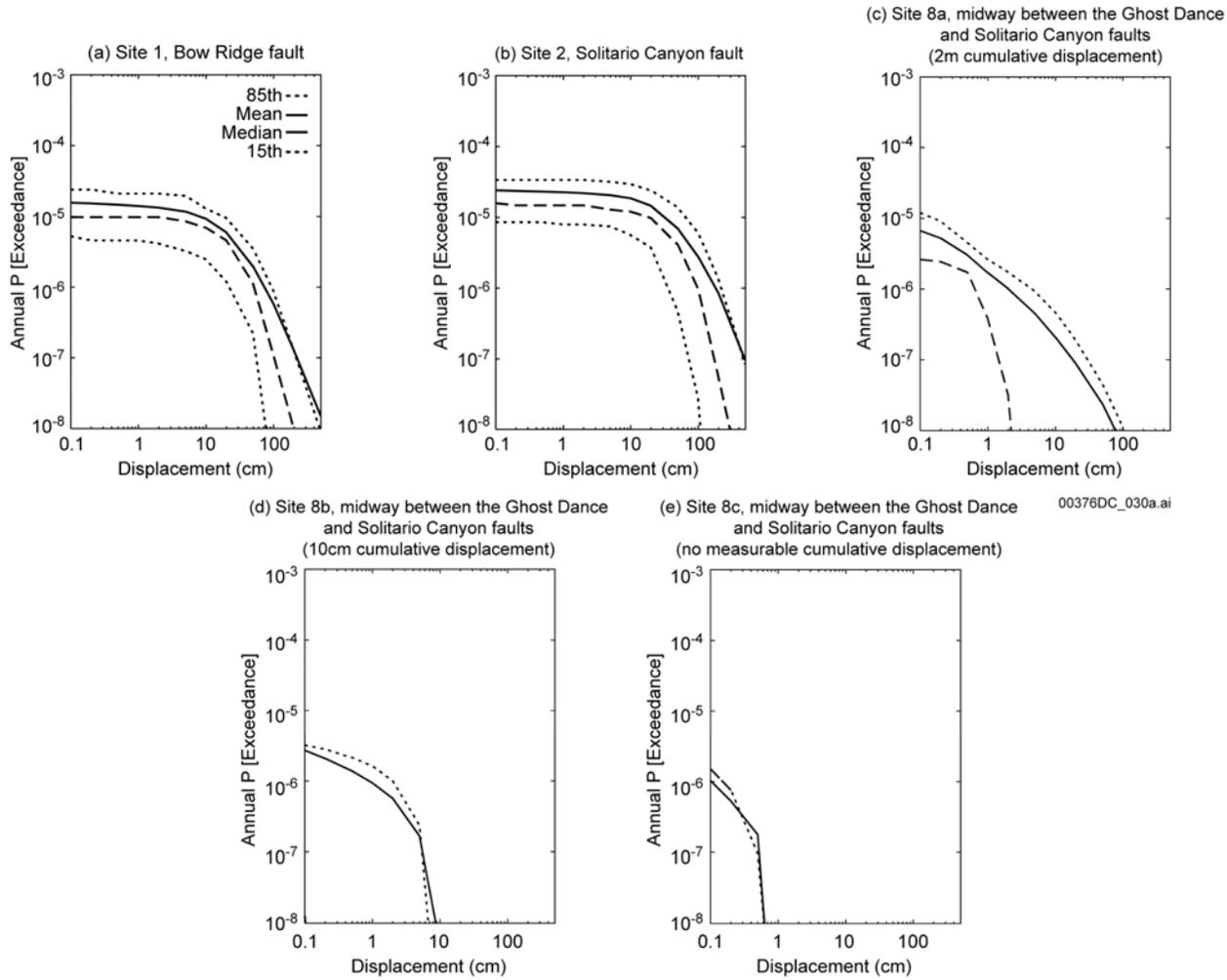
Source: CRWMS M&O 1998 [DIRS 103731], Figures 8-2, 8-3, 8-12, 8-13, and 8-11

Figure 4-30.   Example Summary Fault Displacement Hazard Curves for Yucca Mountain

Table 4-1. Tabulated Labels and Features of the Magnetic Anomalies Thought to Represent Buried Volcanic Centers in Crater Flat and Amargosa Desert Area, Nevada

Rank	Anomaly label				Location (lat-lon coords N, W)		Polarization	Amplitude, nT (ground level)	Depth to top, m	Anomaly/body characteristics
	1	2	3	4						
1	A	A	A	F	36° 45.27'	116° 36.48'	+	~1000	~206 (Langenheim 1995 [DIRS 104491])	Extends NW, has double peak
Conf.	B	B	AAB	B	36° 36.7'	116° 24.14'	-	912 and -1247	≤150 (Langenheim et al. 1993 [DIRS 148622]); 73 (Carr et al. 1995 [DIRS 104671])	~77m thick (Carr et al. 1995 [DIRS 104671])
1	C	C	AAC	C	36° 31.82'	116° 28.27'	-	600	~200 (Langenheim 1995 [DIRS 104491])	
1	D	D	AAD	D	36° 30.02'	116° 26.94'	+	850	~175 (Langenheim 1995 [DIRS 104491])	
2	E	E	AAE	E	36° 34.06'	116° 34.03'	+			
1	F	F	AAA		36° 37.36'	116° 29.20'	-	70-150		F, G, H form NE alignment
1	G	G	AAA		36° 38.23'	116° 29.00'	-	70-150	~250	
1	H				36° 36.56'	116° 30.06'	-	70-150		
2	I				36° 39.52'	116° 29.78'	+		~300	
3	J				36° 37.32'	116° 33.15'	+			
3	K				36° 31.97'	116° 34.50'	+			
3	L				36° 41.09'	116° 38.87'	+		~240	L, M, N, O form NE alignment
3	M				36° 41.26'	116° 38.27'	+		~240	
3	N				36° 41.98'	116° 37.71'	+		~350	
3	O				36° 42.60'	116° 37.24'	+		~250	
4	P				36° 50.22'	116° 33.41'	-			
4	Q		C		36° 50.76'	116° 34.31'	-			
4	R				36° 51.98'	116° 35.16'	-			
4	S				36° 53.43'	116° 32.81'	-			

DTNs: MO0312SEPSDMGA.000 [DIRS 166379]; MO0312SEPSDWPT.000 [DIRS 166380]

Source: O'Leary et al. 2002 [DIRS 158468]

NOTES: Anomaly label numbers indicate sources: 1: O'Leary et al. 2002 [DIRS 158468]; 2: CRWMS M&O 1996 [DIRS 100116]; 3: Connor et al. 2000 [DIRS 149935]; 4: Langenheim 1995 [DIRS 104491]. Column labeled Rank indicates author confidence that anomalies have basalt sources: Conf: confirmed; 1: high confidence; 2: probable; 3: equivocal; 4: low confidence.

Table 4-2. Estimated Volume and Argon-40/Argon-39 Age of Quaternary Volcanoes in the Yucca Mountain Region

Volcano	Volume (km^3)[a]	Volume (km^3)[b]	Age (m.y.)[c]
Makani Cone	0.006	-	1.16 to 1.17
Black Cone	0.105	0.07	0.94 to 1.10
Red Cone	0.105	-	0.92 to 1.08
Little Cones	0.002	>0.01[d]	0.77 to 1.02
Hidden Cone	0.03	-	0.32 to 0.56
Little Black Peak	0.03	-	0.36 to 0.39
Lathrop Wells Cone	0.14	-	0.074 to 0.084

DTNs: LA0004FP831811.002 [DIRS 149593]; LAFP831811AQ97.001 [DIRS 144279]

Source: CRWMS M&O 2000 [DIRS 151551], Table 4

NOTES: [a] CRWMS M&O 1998 [DIRS 135988], Chapter 3, Table 3.1

[b] Stamatakos et al. 1997 [DIRS 138819], p. 327

[c] Range of ages from CRWMS M&O 1998 [DIRS 123196], Table 2.B. Lathrop Wells ages (Heizler et al. 1999 [DIRS 107255], Table 3) represent the range of plateau ages measured, except for sample LW157, a statistical outlier. ^{40}Ar/^{39}Ar dates provide the most complete and self-consistent chronology data set for Quaternary volcanoes of Yucca Mountain.

A full discussion of other chronology methods used to date basaltic rocks in the repository can be found in CRWMS M&O 1998 [DIRS 123196]. Other chronology methods may not provide consistent or accurate estimates of the time of eruption.

[d] Accounts for volume of buried flows detected by ground magnetic surveys.

To convert km^3 to mi^3, multiply by 0.240.

Table 4-3. Lathrop Wells Lava Chemistry with Associated Statistics

Parameter	SiO_2	TiO_2	Al_2O_3	Fe_2O_3T [a]	Fe_2O_3 [b]	FeO [b]	MnO	MgO	CaO	Na_2O	K_2O	P_2O_5
Mean	48.50	1.93	16.74	11.63	1.74	8.90	0.17	5.83	8.60	3.53	1.84	1.22
Standard Error	0.09	0.01	0.03	0.03	0.00	0.02	0.00	0.02	0.03	0.01	0.01	0.00
Median	48.57	1.93	16.75	11.58	1.74	8.86	0.17	5.83	8.55	3.55	1.84	1.22
Mode	48.55	1.97	16.87	11.56	1.73	8.84	0.17	5.88	8.41	3.59	1.84	1.21
Standard Deviation	0.58	0.06	0.22	0.22	0.03	0.17	0.00	0.11	0.22	0.09	0.04	0.03
Sample Variance	0.34	0.00	0.05	0.05	0.00	0.03	0.00	0.01	0.05	0.01	0.00	0.00
Count	45	45	45	45	45	45	45	45	45	45	45	45

DTN: LA000000000099.002 [DIRS 147725]

Source: BSC 2001 [DIRS 160130], Table 2

NOTES: [a] Total iron is reported as Fe_2O_3T.
[b] Fe_2O_3 and FeO were recalculated assuming a 0.15 mole fraction of ferric iron (Fe_2O_3).
Values are in weight percent (excluding count).

Table 4-4. Calculated Saturation Pressures, Temperatures, Viscosities, and Densities as a Function of Water Content for Lathrop Wells Magmas

Water Content (wt. %)	Saturation Pressure (Pa)	Temperature (°C)	Viscosity (log poise)	Density (kg/m^3)
0	1×10^5	1169	2.678	2,663
0.5	9.0×10^6	1153	2.572	2,633
1	2.4×10^7	1137	2.472	2,605
2	6.5×10^7	1106	2.284	2,556
3	1.2×10^8	1076	2.112	2,512
4	1.7×10^8	1046	1.957	2,474

DTN: LA000000000099.002 [DIRS 147725]

Source: BSC 2001 [DIRS 160130], Table 4

NOTES: C = Celsius; F = Fahrenheit
To convert Pa to lb./in.^{2}, multiply by 1.450 x 10^{-4}.
To convert kg/m^3 to lb./ft^3, multiply by 0.0624.
To convert °C to °F, use the formula: °F = (°C x 1.8) + 32.

Table 4-5. Summary Frequencies of Disruptive Volcanic Events for the License Application Footprint

Annual Frequency of Intersection of Repository by a Volcanic Event	Composite Conditional Probability of at Least One Eruptive Center	Annual Frequency of Occurrence of One or More Eruptive Centers within Repository
7.4×10^{-10} (5th percentile)	0.75	5.6×10^{-10}
1.7×10^{-8} (mean)	0.78	1.3×10^{-8}
5.5×10^{-8} (95th percentile)	0.77	4.3×10^{-8}

DTN: LA0307BY831811.001 [DIRS 164713]

Source: BSC 2003 [DIRS 163769], Table 22

NOTE: Results presented in this table were rounded to two significant digits after calculation.

Table 4-6. Relation between Site Characterization Investigations and the Activities Comprising the Probabilistic Seismic Hazard Analyses for Yucca Mountain

Investigation	Activity Supporting Probabilistic Seismic Hazard Analyses					
	Evaluate Possible Tectonic Models	Identify Source of Future Earthquakes	Evaluate Recurrence Rate	Evaluate Maximum Magnitude	Evaluate Amplitude and Attenuation of Ground Motion	Evaluate Amount of Primary and Secondary Fault Displacement
Seismic Monitoring • Detect and locate earthquakes • Determine earthquake size • Determine earthquake style of faulting • Record seismograms	X	X	X	X	X	
Regional Fault Studies • Document Quaternary offset and determine its extent • Determine average rate of fault slip	X	X	X	X		
Local Fault Studies • Document Quaternary offset and determine its extent • Determine average rate of fault slip • Determine fault displacement for individual paleoearthquakes • Determine time of occurrence for individual paleoearthquakes	X	X	X	X		X
Historical Earthquake Catalog • Compile earthquake locations, magnitudes, and time of occurrence based on instrumental records • Compile earthquake locations, magnitudes, and time of occurrence based on felt reports and geologic investigations	X	X	X	X		

Table 4-6. Relation between Site Characterization Investigations and the Activities Comprising the Probabilistic Seismic Hazard Analyses for Yucca Mountain (Continued)

Investigation	Activity Supporting Probabilistic Seismic Hazard Analyses					
	Evaluate Possible Tectonic Models	Identify Source of Future Earthquakes	Evaluate Recurrence Rate	Evaluate Maximum Magnitude	Evaluate Amplitude and Attenuation of Ground Motion	Evaluate Amount of Primary and Secondary Fault Displacement
Geophysical Surveys • Seismic reflection surveys • Gravity surveys	X	X		X		
Tectonic Model Analysis • Compilation of proposed tectonic models • Development of tectonic models	X	X	X			
Ground Motion Studies • Analysis of site attenuation • Analysis of earthquake stress drops • Analysis of scenario earthquakes					X	
Analog Studies • Analysis of ground motion attenuation in extensional tectonic regimes • Compilation of relations between earthquake size and fault rupture parameters • Compilation of ground motion attenuation relations from other regions • Compile information on the distribution of primary and secondary faulting in the Great Basin				X	X	X

Source: Summarized from YMP 1997 [DIRS 100522], Appendix C

Table 4-7. Key Milestones for Earthquake Reporting in the Southern Great Basin

Date	Milestone
Pre-1925	Historical compilations (Townley and Allen 1939 [DIRS 106993]; Slemmons et al. 1965 [DIRS 106816]; Meremonte and Rogers 1987 [DIRS 106352]); no systematic reporting, some low-gain seismographs (e.g., at Reno, Nevada; Mt. Hamilton and Berkeley, California; and Tucson, Arizona) with detection capability of larger events ($M_L > 5.5$) in the southern Great Basin (e.g., 1916 Death Valley earthquake). The University of California, Berkeley, began systematic reporting of western Nevada earthquakes north of 37° latitude in 1910 (Bolt and Miller 1975 [DIRS 104525]).
1925	U.S. Coast and Geodetic Survey began systematic compilation of earthquake felt reports.
1932	Felt reports and instrumental locations for larger earthquakes computed by California Institute of Technology. First seismograph station installed in the southern Great Basin at Tinemaha in Owens Valley, California, by California Institute of Technology in 1931 (Hileman et al. 1973 [DIRS 105513]). Four stations installed (1938-1941) by U.S. Bureau of Reclamation in vicinity of Lake Mead, Nevada, to monitor for reservoir induced seismicity. Detection threshold reduced to about M_L 4.0 in southern Great Basin (Anderson and O'Connell 1993 [DIRS 101472]).
1960	Worldwide Standardized Seismographic Network in operation-location capability (routine operations) (Engdahl and Rinehart 1988 [DIRS 105267]) and detection threshold about M_L 3.5 for southern Nevada.
1961	Regional network installed around the Nevada Test Site by U.S. Coast and Geodetic Survey, Earth Science Laboratories, to monitor Nevada Test Site activity (King et al. 1971 [DIRS 106292]). No significant improvement in detection threshold.
1968	Short-duration local networks sponsored by the U.S. Department of Defense in and around the Nevada Test Site. Detection threshold decreased to about M_L 2.5 (Rogers et al. 1991 [DIRS 106702]).
1972	Regional network installed and operated by the Seismological Laboratory at the University of Nevada, Reno, for the State of Nevada; however, no seismographs installed in southern Nevada (Rogers et al. 1991 [DIRS 106702]). No significant change in detection threshold.
1978	The U.S. Geological Survey Southern Great Basin network began operation-location capability (routine operations) about $M_L < 1.0$ in the vicinity of Yucca Mountain and M_L 1.3 regionally (Gomberg 1991 [DIRS 105604]). Network operation taken over by University of Nevada, Reno, in 1992 (CRWMS M&O 1998 [DIRS 103731], p. G-5).
1995	University of Nevada, Reno, installed 3-component high-dynamic-range digital network and redesigned station configuration-detection capability M_L -0.5 in Yucca Mountain block and M_L 1.0 regionally (von Seggern and dePolo 1998 [DIRS 149993], pp. 40 and 41).

NOTE: M_L = Local Magnitude

Table 4-8. Significant Earthquakes (M_w>5.0) within 300 Kilometers of Yucca Mountain

Date	Origin Time (GMT) (hr:min:sec)	Latitude (degrees)	Longitude (degrees)	Depth (km)	Magnitude (M_w)	Location
March 26, 1872	10:30:00	36.70	-118.10	-	7 3/4	Owens Valley, CA
November 17, 1902	19:50:00	37.39	-113.52	-	6	Pine Valley, NV
November 10, 1916	09:11:00	36.20	-116.90	-	6.1	Death Valley, CA
December 21, 1932	06:10:04	38.80	-117.98	-	6.8	Cedar Mountain, NV
January 30, 1934	20:16:35	38.28	-118.37	-	6.1	Excelsior Mountain, NV
April 10, 1947	15:58:06	34.98	-116.55	-	6.5	Manix, CA
December 16, 1954	11:07:11	39.28	-118.12	15	7.1	Fairview Peak, CA
December 16, 1954	11:11:00	39.67	-117.90	12	6.8	Dixie Valley, NV
September 22, 1966	18:57:34	37.37	-114.18	7	5.7	Clover Mountain, NV
June 1, 1975	01:38:49	34.52	-116.50	4.5	5.2	Galway Lake, CA
March 15, 1979	21:07:17	34.33	-116.44	2.5	5.5	Homestead Valley, CA
May 25, 1980	16:33:44	37.59	-118.85	10.2	6.2	Mammoth Lakes, CA
May 25, 1980	16:49:27	37.67	-118.92	8.9	5.9	Mammoth Lakes, CA
May 25, 1980	20:35:48	37.63	-118.84	8.2	5.6	Mammoth Lakes, CA
May 27, 1980	14:50:57	37.49	-118.81	16.1	5.9	Mammoth Lakes, CA
September 30, 1981	11:53:26	37.59	-118.87	5.7	5.6	Mammoth Lakes, CA
November 23, 1984	18:08:25	37.46	-118.61	11.5	5.8	Round Valley, CA
July 20, 1986	14:29:45	37.57	-118.44	6.7	5.8	Chalfant Valley, CA
July 21, 1986	14:42:26	37.54	-118.44	10.5	6.3	Chalfant Valley, CA
July 21, 1986	14:51:09	37.49	-118.43	11.8	5.5	Chalfant Valley, CA
July 31, 1986	07:22:40	37.47	-118.37	8.1	5.5	Chalfant Valley, CA
June 28, 1992	11:57:34	34.20	-116.44	1.0	7.3	Landers, CA
June 29, 1992	10:14:20	36.72	-116.29	11.8	5.6	Little Skull Mountain, NV
September 2, 1992	10:26:19	37.17	-113.33	9.6	5.9	St. George, UT
May 17, 1993	23:20:50	37.18	-117.83	9.1	6.1	Eureka Valley, CA
August 17, 1995	22:39:58	35.77	-117.65	10.5	5.2	Ridgecrest, CA
September 20, 1995	23:27:36	35.75	-117.64	8.3	5.3	Ridgecrest, CA
August 1, 1999	16:06:22	37.39	-117.08	7.6	5.7	Scotty's Junction, NV
October 16, 1999	09:46:44	34.59	-116.27	5.0	7.1	Hector Mine, CA

DTNs: MO9906COV99279.000 [DIRS 166582]; MO0006COV00226.000 [DIRS 166581]

Sources: CRWMS M&O 2000 [DIRS 150640]; Hector Mine Earthquake Geologic Working Group 2000 [DIRS 156296], p. 11

NOTES: GMT = Greenwich Mean Time; M_w = moment magnitude. To convert km to mi, multiply by 0.621.

Table 4-9. Summary of Paleoseismic Data for Quaternary Faults in the Yucca Mountain Area

Fault	Displacement/Event (cm)		Average Recurrence Interval (k.y.)		Slip Rate (mm/yr)	
	Range	Preferred Value	Range	Preferred Value	Range	Preferred Value
Bare Mountain	80-300[a]	100-150[a]	10's to 100's[a]	-	<0.01-0.02[a]	0.01 or less[a]
Bow Ridge	1-80[b]	13-44[b]	75-215[c]	100-140[c]	0.002-0.007[c]	0.003[c]
Northern Crater Flat	0-45[d]	-	124-165[e]	-	<0.0024[e]	-
Southern Crater Flat	5-32[f]	10-20[f]	5-90[f]	-	0.002[f]	-
Fatigue Wash	0-63[g]	-	30-140[h]	-	0.003-0.007[h]	-
Iron Ridge	0-130[i]	5-100[j]	-	-		-
Paintbrush Canyon	0-257[b]	6-167[b]	20-270[c]	50-120[c]	0.001-0.03[c]	0.002-0.015[c]
Rock Valley	0-<362[j]	-	9-170[k]	-	0.1[k]	-
Solitario Canyon	0-130[l]	-	35-100[m]	-	0.01-0.02[m]	-
Stagecoach Road	28-79[b]	40-67[b]	5-55[c]	20-50[c]	0.006-0.07[c]	0.02-0.05[c]
Windy Wash	-	4-88[n]	40-57[n]	40-45[n]	0.01-0.0116[n]	0.011[n]

DTN: MO0312SEPSDQF.000 [DIRS 166375]

Sources:

[a] Anderson and Klinger 2003 ([DIRS 163106], pp. L-32 to L-35).

[b] Menges et al. 2003 ([DIRS 159412], Table 8). Net-slip, except for MVT-T4 (middle value).

[c] Menges et al. 2003 ([DIRS 159412], Table 11).

[d] Coe et al. 2003 ([DIRS 163092], Table 30).

[e] Coe 2003 ([DIRS 159410], pp. K-4 to K-6).

[f] Taylor 2003 ([DIRS 159414], pp. J-4 to J-8). Recurrence interval is minimum, not average. No preferred displacement given for Event Z.

[g] Coe et al. 2003 ([DIRS 159411], pp. H-10 to H-12).

[h] Coe et al. 2003 ([DIRS 159411], pp. H-13 to H-14).

[i] Menges et al. 2003 ([DIRS 159412], pp. E-1 to E-2, E-34).

[j] Coe et al. 2003 ([DIRS 163092], Table 42) For displacement, total net displacement is used.

[k] Coe et al. 2003 ([DIRS 163092], pp. M-17 to M-20) Range of recurrence intervals, not average recurrence intervals.

[l] Ramelli et al. 2003 ([DIRS 159413], pp. G-36 to G-40).

[m] Ramelli et al. 2003 ([DIRS 159413], pp. G-42 to G-43). This is mid-to-late Q rate. Longer term rate over 900 ka is 0.002 - 0.003 mm/yr.

[n] Whitney et al. 2003 ([DIRS 159416], pp. I-23 to I-24).

NOTES: To convert cm to in., multiply by 0.394.
To convert mm/yr to in./yr, multiply by 0.0394.

Table 4-10. Summary of Possible Distributed Faulting Scenarios for the Yucca Mountain Site

Scenario	Faults[a]	Preferred Age[b] (ka)	Correlation Confidence[c]	Rupture Length[d] (km) Min.	Rupture Length[d] (km) Max.	Rupture Displacement[e] (cm)	Estimated Magnitude[f] Min. RL	Estimated Magnitude[f] Max. RL	Estimated Magnitude[f] Displ.	Preferred Scenario Magnitude[g]
Z	WW, SCF, NCF	5 ± 2	H	8.5	22	18	6.16	6.64	6.16	6.2
Y	PC, SCR	13 ± 3	H	18.5	25.5	43	6.55	6.71	6.43	6.5
X	SC, SCR, IR	26 ± 5	M	15	24	59	6.44	6.68	6.53	6.4
W	BM, WW, FW	40 ± 5	M	10	22	150	6.24	6.64	6.82	6.8
V	PC, SCR	59 ± 5	M	9	15.5	57	6.19	6.46	6.52	6.5
U	SCF, WW, FW, SC, BR, PC	75 ± 10	H	10.5	23	120	6.26	6.66	6.75	6.7 - 6.9[h]
T	PC, SCR	99 ± 10	M	14	20	98	6.41	6.59	6.68	6.6
S	PC, SCR	120 ± 13	L-M	9.5	19.5	40	6.21	6.58	6.41	6.6
R	WW, BR	140 ± 10	L	8.5	22	42	6.16	6.64	6.42	6.5

Source: Pezzopane et al. 1996 [DIRS 106528], Table 5-3

NOTES: [a] Fault abbreviations are as follows: BM = Bare Mountain; BR = Bow Ridge; FW = Fatigue Wash; IR = Iron Ridge; NCF = Northern Crater Flat; PC = Paintbrush Canyon; SC = Solitario Canyon; SCF = Southern Crater Flat; SCR = Stagecoach Road; WW = Windy Wash.

[b] Preferred age is the estimated age (in ka) of each rupture scenario based on the overlap of the timing distributions. The preferred age and a standard error are given; however, a better description of the age uncertainties is provided by the cumulative timing curves shown in the different plots of Figure 5-6 of Pezzopane et al. 1996 [DIRS 106528].

[c] Correlation confidence is a subjective assessment of confidence in the correlation of individual paleoevents to form a rupture scenario: H = high, M = moderate, L = low.

[d] Minimum (Min.) and maximum (Max.) rupture lengths are derived for each scenario on the basis of the trench locations with evidence of correlative events, as well as locations that lack evidence of the correlative event.

[e] Rupture displacement is the largest preferred displacement value (in centimeters) measured on an individual fault or at a single site involved in each rupture scenario.

[f] Estimated magnitudes (moment magnitude) are derived from scenario rupture lengths (Max. RL = maximum rupture length; Min. RL = minimum rupture length) and rupture displacements (Displ. = rupture displacement; see Note "e") using the appropriate empirical relation of Wells and Coppersmith 1994 [DIRS 107201].

[g] Preferred scenario magnitude (moment magnitude) is the preferred magnitude for the scenario rupture.

[h] Preferred value based on maximum rupture length is M 6.7. If slip is summed across all west-side faults (assumes surface faults merge to a single rupture plane at seismogenic depth), a value of M 6.9 is preferred.

To convert km to mi, multiply by 0.621.

To convert cm to in., multiply by 0.394.

Table 4-11. Summary of Fault Parameters from Probabilistic Seismic Hazard Analysis Seismic Source Characterization

Parameter [1]	Probability of Activity	Maximum Magnitude	Slip Rate	Recurrence Interval (k.y.)
Regional Faults				
Amargosa River fault zone	1.0	6.4-7.5	0.005-0.2	10-128
Ash Meadows fault	1.0	6.2-8.1	0.001-0.1	10-180
Bare Mountain fault	1.0	6.5-7.3	0.01-0.28	42-143
Belted Range fault	1.0	6.1-7.7	0.02-0.1	9-90
Buried Hills faults	1.0	6.4-7.3	-	-
Cane Spring fault	0.6-1.0	5.8-7.7	0.002-0.07	20-146
Carpetbag fault system	0.8-1.0	6.5-7.6	0.005-0.05	-
Carrara (Highway 95) fault	0.1-0.85	6.3-7.7	0.01-0.12	10-69
Death Valley fault	1.0	6.4-7.6	0.08-11.5	0.5-5
Death Valley-Furnace Creek	1.0	6.7-8.3	3.0-8.0	0.5-1.0
East Pintwater Range fault	1.0	6.8-7.8	-	-
East Specter Range fault	1.0	6.4-6.7	0.004-0.021	10-128
Eleana Range fault	1.0	6.4-7.4	0.00006-0.2	20-146
Emigrant Valley North fault	1.0	6.5-7.4	-	10-69
Furnace Creek fault zone	1.0	6.6-7.9	2.3-10.0	0.5-1.0
Grapevine fault	1.0	7.0	0.003-0.02	0.6-0.8
Grapevine Mountains fault	1.0	6.7-7.4	-	-
Hunter Mt.-Panamint Valley faults	1.0	7.0-7.6	1.1-3.2	-
Jackass Flats (Gravity) fault	0.9	6.7-7.7	-	-
Kawich Range fault zone	1.0	6.5-8.0	0.001-0.07	-
Keane Wonder fault zone	0.6-0.8	6.5-7.7	0.001-0.01	-
Mine Mountain fault zone	0.6-1.0	6.6-7.7	0.002-0.06	20-146
Oaks Spring Butte faults	1.0	6.1-7.2	0.01-0.2	-
Oasis Valley fault zone	0.4-0.8	5.8-7.7	0.001-0.01	-
Pahute Mesa faults	0.8	6.2-7.1	-	-
Pahrump fault zone	1.0	6.1-8.2	0.005-0.2	-
Panamint Valley fault	1.0	7.2-7.7	1.57-3.15	-
Peace Camp fault	1.0	6.3-7.3	0.02-0.16	-
Rock Valley fault zone	1.0	6.1-7.8	0.003-0.16	33-195
South Silent Canyon fault	0.8	6.2-7.1	-	-
Spotted Range faults	1.0	6.5-7.4	-	-
Towne Pass fault	1.0	6.8-7.6	0.004-0.03	-
Wahmonie fault	0.8-1.0	5.6-7.3	0.002-0.08	20-146
West Pintwater Range fault	1.0	6.3-7.9	0.002-0.2	-
West Specter Range fault	1.0	6.2-7.5	0.001-0.021	10->128
West Spring Mountains fault	1.0	6.2-7.8	0.02-0.2	20-128
Yucca fault	1.0	6.0-7.7	0.001-0.2	20-146
Yucca-Butte fault	1.0	6.7-7.4	-	-
Yucca Lake fault	0.5-1.0	6.3-7.6	0.001-0.034	20-146

Table 4-11. Summary of Fault Parameters from Probabilistic Seismic Hazard Analysis Seismic Source Characterization (Continued)

Parameter [1]	Probability of Activity	Maximum Magnitude	Slip Rate	Recurrence Interval (k.y.)
Local Faults				
Bare Mountain fault	1.0	5.8-7.5	0.005-0.25	20-200
Black Cone fault	0.8	5.0-7.0	0.001-0.005	-
Bow Ridge fault	0.4-1.0	5.2-7.0	0.002-0.007	40-350
Crater Flat fault system	1.0	5.3-7.0	0.001-0.003	-
Central Crater Flat fault	0.6	5.3-7.0	0.001-0.005	-
So. Crater Flat fault	1.0	5.4-7.0	0.002-0.02	40-180
No. Crater Flat fault	1.0	5.5-7.0	0.001-0.005	120-160
Dune Wash fault	0.1	4.9-7.2	0.0001-0.001	-
East Busted Butte fault	0.4	4.5-7.2	0.0005-0.003	-
East Lathrop Cone fault	1.0	4.6-6.9	0.005-0.003	-
Fatigue Wash fault	1.0	5.5-7.3	0.002-0.02	50-250
Fatigue Wash-Windy Wash	1.0	5.6-7.2	0.005-0.024	-
Ghost Dance fault zone	0.05-0.1	4.5-7.0	0.0001-0.002	-
Iron Ridge fault	0.1-1.0	5.1-7.0	0.001-0.005	-
Iron Ridge-Solitario Canyon	1.0	5.5-7.2	0.005-0.024	-
Midway Valley fault	0.1	4.9-7.1	0.0001-0.001	-
Paintbrush Canyon fault	1.0	5.9-7.4	0.002-0.03	20-270
Paintbrush Canyon-Stagecoach Road	1.0	5.6-7.3	0.009-0.05	15-120
Paintbrush-Stagecoach Road-Bow Ridge	1.0	5.5-7.6	0.005-0.02	10-75
Solitario Canyon fault	1.0	5.6-7.4	0.002-0.04	35-180
Stagecoach Road fault	1.0	5.3-7.1	0.01-0.07	5-75
Windy Wash fault	1.0	6.6-7.5	0.01-0.027	35-100
South Windy Wash fault	1.0	5.7-7.1	0.01-0.04	20-60
North Windy Wash fault	1.0	5.6-7.2	0.001-0.005	-

Source: Summarized from CRWMS M&O 1998 [DIRS 103731], Appendix E

NOTE: [1] Parameter ranges developed from all teams reporting (i.e., 1 to 6 teams); all parameter ranges were provided as probability distributions.

Table 4-12. Mean Ground Motion Hazard at 10^{-3} and 10^{-4} Annual Exceedance Probability

Frequency (Hz)	Horizontal		Vertical	
	10^{-3}	10^{-4}	10^{-3}	10^{-4}
PGA	0.169 g	0.534 g	0.112 g	0.391 g
0.3	0.051 g	0.168 g	0.029 g	0.105 g
1.0	0.162 g	0.471 g	0.073 g	0.222 g
PGV	15.3 cm/s	47.6 cm/s	7.4 cm/s	23.4 cm/s

Source: CRWMS M&O 1998 [DIRS 103731], Table 7-1

NOTE: PGA = peak ground acceleraton; PGV = peak ground velocity.
To convert g to cm/s^2, multiply by 980.7.
To convert cm/s to in./s, multiply by 0.394.

Table 4-13. Mean Displacement Hazard at Nine Demonstration Sites

Site	Location	Mean Displacement (cm)	
		Annual Exceedance Probability	
		10-4	10-5
1	Bow Ridge fault	<0.1	7.8
2	Solitario Canyon fault	<0.1	32
3	Drill Hole Wash fault	<0.1	<0.1
4	Ghost Dance fault	<0.1	<0.1
5	Sundance fault	<0.1	<0.1
6	Unnamed fault west of Dune Wash	<0.1	<0.1
7	100 m east of Solitario Canyon fault		
7a	2-m small fault	<0.1	<0.1
7b	10-cm shear	<0.1	<0.1
7c	Fracture	<0.1	<0.1
7d	Intact rock	<0.1	<0.1
8	Between Solitario Canyon and Ghost Dance faults		
8a	2-m small fault	<0.1	<0.1
8b	10-cm shear	<0.1	<0.1
8c	Fracture	<0.1	<0.1
8d	Intact rock	<0.1	<0.1
9	Midway Valley	<0.1	0.1

Source: CRWMS M&O 1998 [DIRS 103731], Table 8-1

NOTE: To convert cm to in., multiply by 0.394.

INTENTIONALLY LEFT BLANK

5. CONDITIONS AND PROCESSES AFFECTING RADIONUCLIDE TRANSPORT

5.1 INTRODUCTION

The geochemistry of the rocks and fluids in the natural system will influence the long-term behavior of components of an engineered barrier system and the ability of any radionuclides that are eventually released to migrate away from the repository. The geochemistry also provides evidence of how geologic and hydrologic processes have operated during the past. An understanding of these processes provides a basis for evaluating the long-term performance of a repository at Yucca Mountain.

Section 5 presents the geochemical conditions and processes affecting radionuclide transport at the site. The petrologic geochemistry of the volcanic sequence is summarized in Section 3.3.5. Section 5.2.1 describes rock geochemistry pertinent to transport—the mineralogy of minerals in faults and fractures, and implications for fluid geochemistry and flow. Section 5.2.2 describes the geochemistry of fluids at the site and in the surrounding area. Section 5.3 discusses factors that affect radionuclide transport, including solubility, sorption, matrix diffusion, and colloids. Section 5.4 deals with the effect of repository heat on coupled hydrologic, chemical, and mechanical processes, and in turn, the effect of a repository and its introduced components on radionuclide transport. The topics covered in Section 5 provide a framework for understanding transport in the unsaturated zone (covered in Section 7) and the saturated zone (covered in Section 8).

5.2 GEOCHEMICAL FRAMEWORK

Section 5.2 describes the lithologic and mineralogic influences on the geochemical environment at Yucca Mountain, and describes the geochemistry and variability of fluids—pore waters, groundwaters, and gasses—in the unsaturated and saturated zones.

5.2.1 Fracture and Matrix Interactions

Faults and associated shear fractures (see Section 3.5.8) can be either transmissive or non-transmissive features, depending on the rock types juxtaposed across the faults and the nature of the alteration mineralogy within the faults. Although any radionuclide transport is likely to be predominantly through fractures or faults in welded units, diffusion into the tuff matrix will also be a significant factor in radionuclide-mineral interactions. Therefore, the mineralogy of fault and fracture coatings and fillings and the rock matrix are all-important to radionuclide retardation.

5.2.1.1 Fracture Minerals at Yucca Mountain

Unsaturated zone fractures contain a highly variable suite of minerals, ranging from early syngenetic to late diagenetic phases. A brief description of these minerals is presented here—see Vaniman et al. (1996 [DIRS 105946], Section 5, pp. 5 and 6) for more detailed descriptions. Though volumetrically minor, fracture minerals, especially clays, zeolites, and manganese and iron oxides, may play an important role in retarding radionuclide transport through ion exchange or surface complexation reactions (Vaniman et al. 1996 [DIRS 105946], Section 4, p. 1).

The silica mineralogy of devitrified-vitric transition zones includes quartz (often occurring as chalcedony), amorphous opal-A, opal-CT (with short-range cristobalite and tridymite ordering), and rare mogonite, a monoclinic form of crystalline silica. Although the most common fracture coatings in the lower vitrophyre of the Topopah Spring Tuff are smectite, opal-CT, and manganese oxide dendrites, fractures may also contain heulandite, mordenite, or other zeolites that are uncommon at Yucca Mountain, such as phillipsite and erionite.

Clinoptilolite and mordenite both occur in fractures within the zeolitized Calico Hills Formation and in the upper Crater Flat Group, wherever zeolites are common in the adjacent tuff matrix. These occurrences are located in the lower unsaturated zone and into the upper saturated zone. Unlike the matrix alteration, which is commonly dominated by clinoptilolite, mordenite is the principal fracture-lining zeolite.

Smectite is nearly ubiquitous in fractures throughout the volcanic sequence at Yucca Mountain. Kaolinite is much less common. The chain-structure clay minerals palygorskite and sepiolite occur sporadically in fractures in the Paintbrush Group, above the middle of the Topopah Spring Tuff.

Manganese oxide minerals occur in fractures in the moderately welded to densely welded vitric and devitrified tuffs throughout the pyroclastic sequence at Yucca Mountain, and are less common in zeolitic zones. Manganese oxide minerals lining fractures in volcanic units underlying Yucca Mountain are known from past studies to contain variable but trace amounts of elemental metals such as lead and zinc, and sometimes also serve as a sink for cerium (Carlos et al. 1993 [DIRS 105210], pp. 51 to 57; Vaniman et al. 1996 [DIRS 105946], Section 4.1.3.1). The layer-structured manganese oxide lithiophorite (lithium-bearing and aluminum-bearing hydrous manganese oxide) and rancieite (calcium-bearing hydrous manganese oxide) are the principal manganese oxide minerals in fractures coatings in the unsaturated zone. Pyrolusite is a rarer manganese oxide phase in the unsaturated zone (Vaniman et al. 1996 [DIRS 105946], Section 5.5.5, p. 11), and is texturally associated with calcite precipitation. Trace levels of arsenic may occur in association with iron oxide minerals (Wilkie and Herig 1996, [DIRS 156570], pp. 97-110), which are known to occur within fratures in the unsaturated zone at Yucca Mountain. Experimental evidence suggests that some naturally-occuring oxides (e.g., manganese oxides) have a capacity for sorbing mercury (Tiffreau and Trocellier 1998 [DIRS 156566], p. 311). Manganese oxides on fracture surfaces in the Tiva Canyon and Topopah Spring tuffs in the unsaturated zone contain less than one percent levels of lead (Vaniman et al. 1996 [DIRS 105946], Appendix 5.2). Data from microautoradiography show that manganese oxides such as rancieite, which can oxidize and remove cerium from solution, have a similar capacity for removing plutonium from solution (Duff et al. 1999 [DIRS 150344]). The iron oxide hematite also occurs as a fracture mineral and is also effective at sorbing and coprecipitating radionuclides (see Section 5.3.3.1) and trace elements. See Section 5.3.3.1 "Minerals and Lithologies that are of Importance to Radionuclide Sorption" for additional information on iron, manganese oxides, and hydroxides, and their relationship to sorption of radionuclides.

Calcite commonly occurs in fractures as well as in lithophysal cavities. It is most common in the densely welded and devitrified portions of the Tiva Canyon and Topopah Spring tuffs in the unsaturated zone (Whelan et al. 1994 [DIRS 100091], pp. 2738 and 2740). Most calcites were

deposited incrementally during the past 10 million years (m.y.) (Paces et al. 1997 [DIRS 100070], pp. E-3 to E-4).

Fine-grained fluorite has been identified in lithophysal cavities, and more rarely, in fractures, in several drill cores, where it commonly occurs under the younger calcite and opal coatings (BSC 2003 [DIRS 166347], p. 6.14-40). It is most abundant, although not limited to, the Paintbrush Group, and its abundance varies laterally across Yucca Mountain (Carlos et al. 1995 [DIRS 101326], p. 7).

Unsaturated Zone Fracture Minerals–Secondary (low temperature) fracture mineral coatings provide a record of past water percolation through the connected fracture network. The deposits are predominantly calcite, interlayered with lesser amounts of silica phases, including opal, chalcedony, and quartz. Other phases may also be present in minor amounts, including fluorite, clay minerals, zeolites, and manganese oxides; however, these are mostly present in older parts of the coatings (BSC 2003 [DIRS 166347], p. 6.14-40). They are present in the form of 0.1-cm to 6-cm-thick coatings, typically towards the lower end of that range, on the footwalls of fractures with apertures exceeding several millimeters, and on floors of lithophysal cavities intersected by fractures. Calcite is commonly present as blocky prisms on high-angle fracture surfaces and as bladed crystals in lithophysal cavities and in low-angle fractures. Opal typically forms water-clear solid hemispheres, botryoidal masses, or it forms thin sheets coating calcite. Both opal and calcite are finely layered (micron-to-submicron) and commonly are intimately intergrown (BSC 2003 [DIRS 166347], p. 6.14-40). Calcite/silica deposits are present in only a small fraction (<10 percent) of all fractures or lithophysae (Paces et al. 2001 [DIRS 156507], p. 11; Whelan et al. 2002 [DIRS 160442], p. 738). This observation is considered strong evidence that secondary mineral deposits are related to fracture flow and seepage rather than to percolation through the matrix of the welded tuffs. The overall abundance of minerals in the welded tuffs is low. Modal fracture mineral abundances have been determined by mineral line surveys in the Exploratory Studies Facility (ESF) main drift and the Enhanced Characterization of the Repository Block (ECRB) Cross-Drift—visual estimation of fracture mineral abundances along a horizontal band on the drift walls—showed that mineral abundances are logarithmically distributed around a mean value of 0.034 percent (BSC 2003 [DIRS 166347], p. 6.14-43). In the Topopah Spring welded (TSw), mineral abundances are not correlated with fracture frequency (BSC 2003 [DIRS 166347], Figure 6.14.4-4), possibly because many of the fractures are strata-bound features that formed during cooling of the volcanic rock, and are unlikely to have the long-range continuity that would facilitate unsaturated zone flow.

There is strong stratigraphic control on secondary calcite deposition (BSC 2003 [DIRS 166347], pp. 6.14-50 to 6.14-51). It is most abundant in the upper parts of Tiva Canyon welded (TCw), decreasing rapidly with depth, probably reflecting larger amounts of amounts of gas flow and consequent rates of evaporation in the shallow, fractured tuffs. Reduced gas fluxes in the Paintbrush Tuff nonwelded (PTn) are a likely cause for lower calcite concentrations. Calcite is more abundant in the TSw, albeit not as common as in the TCw. This is probably due to decreased amounts of gas flow below the PTn. Conceptual models for both calcite and silica deposition rely on interactions between independently migrating gas and liquid phases (Paces et al. 2001 [DIRS 156507]; Whelan et al. 2002 [DIRS 160442]).

Dating of fracture minerals by various methods, each of which is useful for various time intervals, suggests they have accumulated over long time periods (Section 7.7.2). Outer layers generally show younger apparent ages than underlying deposits. For outermost growth surfaces, radiocarbon dates from calcite range from 16 ka to 44 ka, the maximum for that method given the sample sizes available. ^{230}Th/U ages for calcite and opal range from 28 ka to 500 ka (again, the method-maximum), and ^{207}Pb/^{235}U ages range from about 100 ka (the method-minimum) to 1 Ma. Ages from underlying earlier deposits range from 4 to 10 Ma (BSC 2002 [DIRS 160247], Section 6.10.1; ^{14}C data: DTNs: GS960808315215.006 [DIRS 145785]; GS970208315215.003 [DIRS 107347]; thorium and uranium isotopes: DTNs: GS960908315215.014 [DIRS 145804]; GS970208315215.001 [DIRS 107341]; GS970808315215.012 [DIRS 145921]; ^{207}Pb/^{235}U: DTNs: GS970208315215.002 [DIRS 145897]; GS040108315215.001 [DIRS 168529]). Because of slow mineral growth rates, the mineral fractions analyzed represent multi-age materials (many fine growth laminae), and these ages are average values.

Although small aperture fracture may be completely filled with calcite, most secondary minerals are present in fractures and lithophysae with substantial open space. The potential sealing of fractures by secondary minerals can be evaluated by isotopic studies. Tritium isotopic studies within the unsaturated Topopah Spring Tuff (BSC 2003 [DIRS 166347], pp. 6.14-14 to 6.14-18) suggest that fast paths have transmitted surface infiltration to the depth of the potential repository host rock during the past 50 years (yr) (see Section 5.2.2.5.2). This indicates the amount of secondary-mineral deposition in major fault zones has been insufficient to significantly decrease the transmissivities of these fault zones. The locations of the samples showing elevated ^{3}H (tritium) concentrations suggest that these fast paths may be associated with fault zones that cut through the Paintbrush nonwelded hydrogeologic unit and that are fed by sufficiently high surface infiltration rates to sustain a component of fracture flow through it. Apparently, the rates of calcite and opal deposition during the past 10 m.y. have been too low to plug all of the flow paths within the fault zones (see Section 7.7.2).

Chlorine-36 studies completed in the mid-1990s also showed evidence of fast-path transport, although the locations with elevated values did not necessarily coincide with those where tritium was elevated. However, recent attempts to reproduce the earlier ^{36}Cl signatures (Paces et al. 2003 [DIRS 162738], pp. 348-356; BSC 2003 [DIRS 166347], Table 6.14.2-1; DTNs: LL030408023121.027 [DIRS 162949]; LL031200223121.036 [DIRS 168531]) have yielded mixed results. In addition, strontium isotope and uranium (U)-series equilibrium studies (Marshall and Futa 2003 [DIRS 162717]; Gascoyne et al. 2002 [DIRS 154800]) showed that fluids in fault zones and in the adjacent intact tuff matrices are in isotopic equilibrium, suggesting that fluid residence times in the fault zones are similar to those in the unsaturated matrix. The isotopic evidence for fast paths is discussed in detail in Section 5.2.2.5.

Fracture Minerals in the Saturated Zone–Tridymite and cristobalite do not commonly occur in fractures of the saturated zone. These polymorphs are the more soluble of the anhydrous silica polymorphs and are commonly supplanted by opal-CT, which occurs with mordenite and clinoptilolite in the Calico Hills Formation and Crater Flat Group, whether in the saturated zone or unsaturated zone. In the devitrified intervals of the saturated zone, quartz is the common silica polymorph. Lithophysal-type fracture coatings occur in the Bullfrog and Tram tuffs of the Crater Flat Group; although the tridymite morphology has been preserved, the silica mineral is now quartz (Carlos et al. 1995 [DIRS 101326], p. 24). Quartz-lined fractures often contain

manganese oxide minerals and may also contain calcite or mordenite. Mordenite is generally the only zeolite found in fractures in the devitrified Crater Flat Group and is most common, as a fracture mineral, in the southernmost drill holes. This contrasts with the absence of mordenite in zeolitized matrix within the Crater Flat Group at these locations (Carlos et al. 1995 [DIRS 101326], pp. 5 and 8 to 11). Analcime occurs in saturated zone fractures zone at the northern end of Yucca Mountain, where analcime of similar composition also occurs in the altered tuff matrix (Carlos et al. 1995 [DIRS 101326], p. 23). Clinoptilolite-heulandite can also occur in fractures at these depths and may coexist in the matrix with analcime.

Over most of Yucca Mountain, manganese and iron oxides/oxyhydroxides, quartz, and calcite, are the most common fracture coatings in devitrified intervals of the Crater Flat Group below the water table. Hematite is the dominant iron oxide mineral; rarely, goethite occurs in association with the hematite. Cryptomelane-hollandite is the most common manganese oxide mineral throughout the Crater Flat Group below the static water level. Clays have also been identified as fracture filling minerals below the water table. Smectite and mordenite occur together in some fractures in the devitrified intervals in the Crater Flat Group. Several occurrences of green clay (illite) have been identified in the deeper tuffs of the saturated zone; illite associated with calcite and hematite is the most abundant fracture-filling mineral association in the deepest parts of the Tram Tuff, where clinoptilolite gives way to analcime in the tuff matrix (Carlos et al. 1995 [DIRS 101326], pp. 8 to 12 and 23).

Calcite is unevenly distributed, but is locally a common fracture filling in the Crater Flat Group. It is the most common fracture filling in extensively analcime-altered or albite-altered tuffs of the deep saturated zone. It also occurs, usually in association with manganese oxide minerals, in transmissive fractures over restricted depth intervals in the devitrified tuffs of the shallow saturated zone (Carlos et al. 1995 [DIRS 101326], p. 24). In most of these shallower saturated zone occurrences, the calcite is pitted or corroded and shows evidence of alteration to calcium-mordenite (Vaniman and Chipera 1996 [DIRS 100089], p. 4423).

Fault Mineralogy–Fault mineralogy can be a critical component in evaluating flow and transport. Faults can operate as highly transmissive features, particularly if the faults contain no mineralization, or if mineralization along the fault is limited. Alternatively, faults or shear zones filled with non-permeable minerals (e.g., calcite or opal), or minerals with very high effective surface areas such as clays and zeolites, can be transport barriers. Fault minerals may have different effects on flow along the fault plane and flow perpendicular to the fault, as even very thin minerals coatings may inhibit cross-flow and diffusion into and out of the fault zone. Calcite, smectite, and zeolite have all been observed as fault-filling minerals at Yucca Mountain.

Surface exposures of a fault at Busted Butte provide evidence of mineralization along a fault in the unsaturated zone that juxtaposes vitric nonwelded tuff against welded devitrified tuff. The result here is the most thorough zeolitization (98 percent) of vitric tuff yet observed in any sample from Yucca Mountain, with the zeolitization strictly confined to the fault zone (Broxton et al. 1993 [DIRS 107386], p. 10). This fault mineralization apparently resulted from delivery of water through the fractured, devitrified tuff to the nonwelded vitric tuff at the fault interface. The very restricted penetration of zeolitization into the vitric tuff usefully illustrates limited unsaturated zone transport through this rock type.

Fracture and Matrix Systems Compared–Existing differences in fracture and matrix mineralogy and geochemistry are the result of rock-water interactions during the last ~12 m. y. The chemical constituents of fracture coatings and fracture-surface alteration were derived from the rock matrix and from the percolating waters. The nature and degree of the mineralogic differences that develop between fracture and matrix vary with lithology, thermal history, rock hydrologic properties, saturation conditions, and percolation rates.

In low-porosity tuffs, which are exemplified by the densely welded vitric and devitrified units, evidence of short-range (decimeter scale) fluid and solute transport between matrix and fractures is a common attribute of the syngenetic alteration described in Section 3.3.5.1.1. This transport is thought to have occurred at temperatures slightly above ambient (Levy and O'Neil 1989 [DIRS 116960], Table 1) and over time scales of hundreds to thousands of years.

In the moderately welded to nonwelded tuffs, syngenetic alteration is largely absent. Wherever exposure to groundwater has been pervasive (below the present-day water table and for about 100 m above the water table), diagenetic zeolites have replaced most of the matrix glass in nonwelded tuffs. Textural studies suggest that the pervasive zeolitization occurred early in the diagenetic history of Yucca Mountain (Bish et al. 1984 [DIRS 106336], pp. 67 to 76). The fracture minerals in these zeolitized horizons are dominated by the same types of zeolites that occur in the matrix (Carlos et al. 1995 [DIRS 101326], p. 28). Evidence discussed in Section 5.2.2.7 indicates that groundwater interacts effectively with matrix zeolites in these tuffs.

Correlation of fracture-lining zeolites just above and below the water table with degree and type of zeolitization of the high-porosity host tuff suggests that the fracture coatings may have formed at the same time as the tuff alteration. The similarity of chemical compositions of matrix and fracture-lining clinoptilolite supports this hypothesis. An increase in degree of alteration from clinoptilolite/mordenite to analcime in both fractures and matrix toward the north of Yucca Mountain suggests that this alteration may have been a result of hydrothermal activity related to the Timber Mountain volcanism, constraining the age of the zeolites to >9 Ma or older (Bish and Aronson 1993 [DIRS 100006], pp. 154 to 156). The net evidence, from both matrix and fracture minerals in high-porosity tuffs, is thus indicative of early pervasive alteration, overprinted at critical boundaries (particularly within the glass-to-zeolite transition in the unsaturated zone) by subsequent cation exchange. Although zeolites might still be forming at Yucca Mountain, the evidence shows that rates of formation are presently very low, and the principal impact of zeolites on site processes is through ion exchange.

Combined Data from Pumping Tests and Mineralogy that Bear on Fracture/Matrix Interactions–Evidence of fracture flow beneath the water table is provided by comparison of mineralogical and geochemical data with the location of transmissive zones determined by pumping of packed-off intervals (Benson et al. 1983 [DIRS 100727], pp. 11 and 16, Figures 4, 5, 6 and 11). The data indicate that most flow beneath the static water level occurs in the devitrified tuffs between zeolitized layers (Figure 5-1). Fractures in these devitrified layers of the saturated zone often have Liesegang banding extended a centimeter or more into the matrix away from the fracture walls. This is a graphic indication of long-term rock-water interaction in transmissive fractures. Microautoradiography studies (Section 5.3.3.1.3) and fracture-flow dynamic transport experiments (Section 5.3.4.4) indicate that actinide sorption and retardation is associated with smectites and manganese oxides that line some of these fractures.

Within zeolitic intervals, fracture minerals tend to be zeolites similar to those in the host rock. Between the zeolitic intervals, where tuffs are largely devitrified, cryptomelane-group manganese oxides are typically found in fractures of the more welded portions. Mordenite is also locally abundant in some of the saturated zone fractures.

Most transmissivity in the saturated zone occurs in rocks with few zeolites and clays, except for transmissive zone T5 in the zeolitic, bedded interval at the base of the Bullfrog Tuff in UE-25 b#1 (as shown in Figure 5-1). The fate of any radionuclide that passes into the saturated zone will thus be determined by the combined processes of transport through transmissive zones, sorption and desorption on fracture-wall minerals within the transmissive zones, and dispersion into the surrounding tuff matrix, where radionuclides will be retarded by mineral surface processes (sorption) in devitrified tuffs or cation exchange in zeolitic tuffs.

The saturated transmissive zones tend to be restricted to discrete intervals less than 20 m thick within the devitrified, nonzeolitic tuffs. Exceptions to this tendency, however, exist. The transmissive zones are at least in part determined by intervals of abundant shear fractures (e.g., the zone at approximately 900 m depth in USW G-4 and the zone at approximately 480 to 500 m depth in UE-25 p#1) (Figure 5-1). However, mineralogy may also play a role in delimiting transmissive zones, as in UE-25 b#1 at approximately 810 to 820 m depth, where a transmissive zone is capped by an exceptionally smectite-rich zone in devitrified tuffs. This example illustrates the role of mineralogic aquitards in restricting flow paths within the saturated zone.

Zielinski (1983 [DIRS 106657], p. 14) and Zielinski et al. (1986 [DIRS 108836], pp. 374 to 377) have proposed that abundances of manganese oxide minerals can be used as a guide to the extent of past rock-water interaction. This conclusion appears to be borne out in the single, prominent transmissive zone in drill hole USW G-4 (Figure 5-1, see quartz-latitic zone). This zone, at a depth of 892 to 902 m, occurs in an interval of intense shear fracturing (878 to 893-m depth) (Spengler and Chornack 1984 [DIRS 101357], pp. 40 to 43). The manganese oxide minerals cryptomelane and hollandite are also concentrated in this interval. In addition, Spengler and Rosenbaum (1991 [DIRS 146279], p. A119) suggested that a 40- to 60-m-thick breccia zone, within the Tram Tuff and dipping 15° northwest, accounts for much of the transmissivity between wells about 2 km southeast of the repository. The clasts in this breccia are cemented by quartz, calcite, and hematite. Steeply dipping shear fractures within the breccia zone are hematite-coated. The combined observations of Zielinski (1983 [DIRS 106657]), Zielinski et al. (1986 [DIRS 108836]), and Spengler and Rosenbaum (1991 [DIRS 146279]) suggest an important role for both manganese oxides and hematite in indicating present and past transport pathways and contributing to the retardation of possible waste movement by surface complexation of heavy metals, as discussed in Section 5.3.3.5.

5.2.1.2   Links between Rock and Fluid Geochemistry

Minerals that have precipitated from or reacted with groundwater provide a record of the chemical species that were carried in solution as well as some evidence related to groundwater composition (e.g., Eh). In general, the most effective mineralogic recorders are those that occur in fractures, particularly in zones where much of the communication between water and rock is related to fracture flow.

Evidence of both dissolution (e.g., solution pits and etchings) and precipitation (e.g., growth steps) can be found among the unsaturated zone calcites, generally without apparent stratigraphic significance (Vaniman and Chipera 1996 [DIRS 100089]). In contrast to the apparently random distribution of dissolution or precipitation textures in the upper unsaturated zone, there is a "barren zone" of few calcite occurrences that extends from approximately 100 to 300 m above to approximately 400 m below the water table. The barren zone contains very deeply etched calcites in the unsaturated zone at the top of the lower vitrophyre of the Topopah Spring Tuff and throughout the saturated zone above the deep carbonate-near field, where manganese calcites of different origins are abundant. The origins of these deep manganese calcites are linked to release of calcium from Ca-bearing zeolites (clinoptilolite and mordenite) in the formation of analcime and albite.

Very low strontium concentrations (as little as 1 µg/g strontium) can occur in calcites from the barren interval. Although these calcites occur in both unsaturated and saturated environments, they share a common association with zeolites and smectites. Zeolites and smectites accumulate strontium by ion exchange, depleted it from the waters that precipitated the strontium r-poor barren zone calcites.

5.2.1.2.1 Trace-Element Signatures in Minerals Precipitated from Groundwater

Fractures of the unsaturated zone in the densely welded tuffs of the Paintbrush Group contain a generally calcic suite of minerals, including calcite, calcium-zeolites (stellerite, heulandite, and mordenite), calcium-smectite, and rancieite, along with silica polymorphs and lithiophorite. Pore water extracts from parts of the Paintbrush Group above the static water level (Yang 1992 [DIRS 100840]) have chemistry different from that of groundwater from the Paintbrush Group below the static water level (Benson et al. 1983 [DIRS 100727], Table 1 [well J-13]), with increased calcium, magnesium, potassium, and strontium above the static water level. The higher calcium, magnesium, and strontium contents of the pore waters, compared with the composition of groundwater below the static water level, are reflected in the fracture-lining mineral assemblages in the Paintbrush Group.

Lanthanide element patterns in Yucca Mountain calcites point strongly to leaching from local quartz latite or rhyolite as the source for many of the constituents deposited from waters of the unsaturated zone. The preponderance of calcite with lanthanide element patterns inherited from rhyolitic rather than quartz-latitic sources is consistent with the much greater abundance of rhyolitic tuffs at the site. Moreover, the calcites with inherited quartz-latitic lanthanide patterns occur directly beneath the most extensive body of quartz-latitic and quartz-latite-like glass (Topopah Spring Tuff quartz latite and Pah Canyon low-silica rhyolite) at the site.

Figure 5-2 illustrates how the compositions of fracture calcites reflect the local lithology in unsaturated zone groundwaters. The key distinctive feature of lanthanide-element patterns in quartz-latitic tuffs, aside from higher light lanthanide (lanthanum to samarium) content, is the absence of any significant europium anomaly in chondrite-normalized plots, in contrast to the characteristic and strong negative europium anomaly in rhyolitic tuffs (Figure 5-2a). When the chondrite-normalized lanthanide-element patterns of fracture calcites are plotted against their stratigraphic position (Figure 5-2b), it can be seen that calcites with lanthanide element patterns resembling the quartz-latites (no europium anomaly) are largely restricted to horizons where

glassy quartz-latitic rocks occur within an otherwise rhyolitic series of tuffs. This shows that lanthanide elements dissolved from source rocks tend to be deposited locally with very little down-section transport. It is also notable however that many calcites with europium anomalies intermediate between rhyolites and quartz latites occur in the quartz-latitic horizon. Some transport of groundwaters with the overwhelmingly predominant rhyolitic signature does occur into the quartz-latitic horizons.

5.2.1.2.2   Mineralogic Record of Groundwater Redox Processes

Lanthanide-element data for the calcites of Yucca Mountain indicate at least two distinct depositional environments: an upper system in which solutions are cerium-depleted through removal of Ce^{3+} oxidized to Ce^{4+}, and a deeper carbonate-altered system in which all of the lanthanide-series elements are Ln^{3+} (Vaniman et al. 1996 [DIRS 105946], Section 4, pp. 33 to 36). The deeper carbonate-altered system occurs at depths greater than 400 m below the present water table (Vaniman and Chipera 1996 [DIRS 100089], Figure 2) and is of little consequence for transport systems at Yucca Mountain. The shallower carbonate-altered system, with evidence of cerium oxidation and segregation from the other lanthanide elements, is highly relevant. Figure 5-3 illustrates the mechanism by which cerium is segregated from the other lanthanide elements (Figure 5-3a) and the consequences of this process as recorded in fracture calcites from several different stratigraphic horizons (Figure 5-3b). Data collected from mineral separates (Vaniman and Chipera 1996 [DIRS 100089]) and surveys for cerium in fracture samples (Carlos et al. 1993 [DIRS 105210], pp. 56 and 57, Tables 2 and 4) reveal strong correlations of cerium with certain manganese oxide minerals. These cerium accumulations are most prominent in rancieite and can readily account for the corresponding depletion of cerium in those solutions from which calcite has precipitated (Figure 5-3a).

Characteristic negative cerium anomalies in calcites of the oxidizing system are present in both unsaturated zone and upper saturated zone rocks. Manganese oxide minerals, particularly rancieite but possibly others, appear to provide the single most important sink for Ce^{4+} at Yucca Mountain. The virtually universal negative cerium anomalies of oxidizing-zone calcites show that all flow paths in the upper 1 km of Yucca Mountain have some effective contact with manganese oxides. Studies specific to Yucca Mountain point to the potentially significant retardation of radionuclides by manganese oxides. At Yucca Mountain, the universal record of cerium depletions in calcites of the subsurface oxidizing zone, which includes the proximal portions of all transport pathways for radioactive waste, provides a strong indication that fluids do interact with these minerals, despite their low abundance. The calcite data show that even trace minerals, particularly those along fractures, will play an important role in radionuclide interactions.

5.2.1.2.3   Zeolites and Groundwater Conditioning

Zeolitization of vitric tuff results in an initial mobilization of elements at the time of alteration. However, the zeolites thus formed can also be subsequently modified by cation exchange. White et al. (1980 [DIRS 101166]) noted that groundwaters increase in sodium and decrease in calcium and magnesium after passing through zeolitic tuffs in the unsaturated zone at Rainier Mesa, located 50 km north-northeast of Yucca Mountain. The authors concluded that zeolites (and perhaps clays) selectively removed bivalent cations from the groundwater system. Analyses of

vitric and zeolitic tuffs in close proximity and of a single homogeneous depositional unit allow determination of the net effects of both initial chemical alteration and subsequent cation exchange. Generally, the zeolitized samples show gains in calcium, magnesium, and strontium with losses in sodium, potassium, and silicon in the alteration from glass to zeolites. However, aside from strontium, trace elements are less affected. Broxton et al. (1986 [DIRS 100023], p. 20) showed that zeolitized tuffs are enriched in strontium, whereas they are depleted in rubidium and uranium relative to source glasses. Later, Broxton et al. (1993 [DIRS 107386]) showed there is little or no difference in lanthanide-element patterns between vitric sources and zeolitic products.

The strontium increase noted by Broxton et al. (1986 [DIRS 100023], p. 20) is not a general phenomenon but is restricted to the tops of zeolitic horizons at Yucca Mountain (Figure 5-4a). This concentration of strontium provides evidence that laboratory models of strong strontium selectivity and short-range dispersion through sorption/desorption are indeed supported by natural site data. The occurrence of strontium retention profiles at the tops of zeolitized horizons provides evidence of generally downward flow in the unsaturated zone, although lateral flow along the tops of relatively impermeable zeolitic rocks may also occur. The pronounced concentrations of strontium that occur at the tops of zeolitized zones beneath the potential host rock provide direct evidence of the effective extraction of strontium from downward-flowing solutions at Yucca Mountain since the time of zeolite formation (Vaniman et al. 1999 [DIRS 129785], p. S5).

5.2.2 Fluid Geochemistry of Yucca Mountain and Vicinity

An extensive database of geochemical and isotopic characteristics has been established for pore waters and gases from the unsaturated zone, perched water, and saturated zone waters in the Yucca Mountain area. This compilation of water and gas compositions, and a detailed analysis of the data, is described in BSC (2002 [DIRS 160247]). The development of this database has been driven by diverse needs of the Yucca Mountain Project (YMP), process modeling, and performance assessment communities. Water and gas chemistries influence the sorption behavior of radionuclides and the solubilities of the radionuclide compounds that form. The chemistry of waters that may infiltrate the repository will be determined in part by that of water present in the unsaturated zone above the current repository horizon, whereas pore water compositions beneath the current repository horizon will influence the sorption behavior of the radionuclides transported toward the water table. However, more relevant to the discussion in this section, development and testing of conceptual flow and transport models for the Yucca Mountain hydrologic system are strengthened through the incorporation of natural environmental tracer data into the process. Chemical and isotopic data are used to establish bounds on key hydrologic parameters and to provide corroborative evidence for model assumptions and predictions. Examples of specific issues addressed by these data include spatial and temporal variability in net fluxes, lateral diversion in specific stratigraphic units, the role of faults in controlling flow paths, fracture-matrix interactions, the age and origin of perched water, and the distribution of water travel times. This section summarizes the types of data available and their implications for key hydrologic processes at Yucca Mountain.

5.2.2.1 Water and Gas Chemical and Isotopic Compositions and Their Relevance to Site Characterization and Evaluation

A summary of unsaturated zone geochemical and isotopic data available from Yucca Mountain boreholes is provided. Surface-based boreholes from which water and gas samples were collected are shown in Figure 5-5. Additional hydrochemical sampling was conducted in subsurface boreholes in the Busted Butte field test facility; niches, alcoves, and drifts in the ESF; and the ECRB Cross- Drift (Figures 5-5 and 5-6). Additional information on sampling locations, collection methods, and analytical methods is available in the previous version of the *Yucca Mountain Site Description* (REV 01) (CRWMS M&O 2000 [DIRS 151945], Section 5.3.3).

5.2.2.2 Chemical Composition of Precipitation

Waters in the unsaturated zone at Yucca Mountain originate as infiltration of surface precipitation, and knowledge of the initial chemical and isotopic composition of that precipitation is important in evaluating the extent and type of water-rock interactions that occur as the water moves downward through the unsaturated zone and into the saturated zone. Chloride concentrations in local and regional precipitation, along with associated precipitation quantities, are primary input data that provide the basis for estimating infiltration rates by the chloride mass-balance method (Section 5.2.2.2.2) (also discussed in Section 7.1). These precipitation trend data provide a baseline for use in interpreting the chemical compositions of the various sources of water at Yucca Mountain (Section 5.2.2.4.2).

5.2.2.2.1 Processes Controlling Precipitation Chemistry

The initial composition of Yucca Mountain groundwater is largely established by that of local precipitation and dry fallout. Once the precipitation enters the soil zone the absolute and relative concentrations of the various constituents are shifted to varying degrees by evapotranspiration and by interactions with minerals, organic matter, and the gas phase. The effects of these processes are described in subsequent sections. Isotopic data for precipitation are discussed in Section 5.2.2.5.

The composition of precipitation and dry fallout is controlled by many processes, which include:

- **The relative proportion of wet and dry deposition processes**–Between one-third and two-thirds of the chlorine deposition in southern Nevada is from dry deposition (dry fallout) of aerosols and particulates (Eriksson 1960 [DIRS 105533], p. 82; Dettinger 1989 [DIRS 105384], p. 62).

- **The source of salts in aerosols and particulates**–e.g., ocean-derived aerosols are dominantly sodium and chloride-rich, whereas terrestrial dust contributes more to calcium and magnesium concentrations.

- **Anthropogenic activities**–e.g., acid rain resulting from industrial releases of sulfur; the effects of industrial gases (e.g., chloro-fluoro-carbon compounds, and CO_2) on global climate and on chemical reaction rates in the atmosphere; and fallout of radioactivity from aboveground nuclear tests.

- **Atmospheric processes**–e.g., the chemical formation or transformation of molecular species in the atmosphere.

- **Evaporation**–Prior to deposition, evaporation will concentrate many solutes, as well as affecting the fractionation of hydrogen and oxygen isotopes in moisture.

- **Air temperature**–Air temperature affects hydrogen and oxygen isotopic fractionation and controls gas solubilities.

- **Precipitation patterns**–Season, frequency, and cycles of precipitation events.

5.2.2.2.2   Present-Day Regional Characteristics of Precipitation

Within the YMP the National Atmospheric Deposition Program/National Trends Network regional database has been used to characterize chloride deposition rates in the southwestern United States. Chloride behaves conservatively in Yucca Mountain groundwaters, insofar as its origin is strongly dominated by atmospheric sources—the contribution from rock-water interactions generally appears to be negligible, and saturation with respect to chloride phases is never reached. Increases in subsurface concentrations of chloride relative to that in precipitation and dry fallout are attributed to evapotranspiration in the soil zone, including sublimation of snow.

Chloride concentrations in pore water have also been used as a surrogate measure of infiltration rates using the chloride mass-balance method (Scanlon 1991 [DIRS 107233], p. 138), in which total chloride deposition is a key parameter. An estimate of the contribution of dry fallout to total chloride deposition rates in southern Nevada indicates that dry fallout comprises about 70 percent of the total fallout in this area (BSC 2002 [DIRS 160247]).

5.2.2.2.3   Present-Day Site Characteristics of Precipitation

Precipitation represents the starting point in the evolution of groundwater chemistry. The isotopic and chemical composition of precipitation at the Yucca Mountain site is largely inferred from measurements made at other local sites (McKinley and Oliver 1994 [DIRS 101263], pp. 1 to 3; 1995 [DIRS 101264], pp. 1 to 3). Data from two precipitation chemistry monitoring stations in 3-Springs Basin, at 3-Springs Creek and Kawich Peak (BSC 2002 [DIRS 160247], Figure 5, p. II-5) were used to derive average annual weighted concentrations for major chemical constituents in local precipitation. Additional chemical data for precipitation are available for Red Rock Canyon, the desert observation station closest to Yucca Mountain in the National Atmospheric Deposition Program/National Trends Network. This site is about 120 km southeast of Yucca Mountain. The record used for the analysis by Fabryka-Martin et al. (1996 [DIRS 101003], Section 4.1.2.2) spans 12 yr. The water compositions from these two sites differ in both absolute as well as relative concentrations of major ions. The Red Rock Canyon data provide a comparatively long (12 yr) record, with details available for individual storms if desired. In addition, only wet deposition chemistry is measured. The 3-Springs Basin data, although further removed from Yucca Mountain and representing a shorter time period (7 yr), have reduced urban influence and include both wet and dry deposition data. Compositional data

for precipitation is presented in Figures 5-8 to 5-12, along with data for other water types at Yucca Mountain. For detailed chemical analyses, see BSC (2002 [DIRS 160247], Section 6.3).

The chemical and isotopic composition of future precipitation may differ significantly from the present-day values due to global climate change and its effects on carbon-dioxide levels, rainfall patterns, and dust levels and sources.

5.2.2.3   Chemical Composition of Surface Waters

Three types of surface water chemistry exist, depending on the water source:

- Relatively dilute waters from runoff during precipitation or snowmelt
- Relatively saline waters from groundwater discharge at springs
- A mixture of the two preceding types.

Once precipitated water contacts the ground the chemistry of ephemeral surface waters is modified by interactions with rock and soil. The chemical and isotopic compositions of the surface waters may be relevant to flow and transport modeling for two major reasons. First, infiltration of surface runoff into the beds of large channels such as Fortymile Wash may contribute significantly to local recharge and may thereby influence the chemistry of saturated zone fluids (Section 8.3.6). Second, infiltration from runoff events collected from small channels above the repository, at locations where soil cover is negligible, may contribute to seepage directly into the repository.

Surface water samples were collected to the northeast, east, and southeast of Yucca Mountain, at distances from a few km to about 60 km. Water quality data are also taken from a compilation of hydrochemical data collected in the Death Valley region from 1910 to 1990, including baseline data from rivers, playas, springs, and wells (Perfect et al. 1995 [DIRS 101053], pp. 1 and 3). Additional description of the database is provided in BSC 2002 ([DIRS 160247], Section 6.4). The sampling sites fall into three general categories: channel flow from runoff events and surface runoff, channel flow fed by springs and seeps, and overland runoff mixed with spring discharge.

Between 1984 and 1995 data were collected during three series of runoff events from 15 locations within 15 km of Yucca Mountain, along its eastern side. These data are tabulated in Table 5-1, and summarized in the trilinear diagram presented in Figure 5-7. The runoff samples are chemically similar in that they are very dilute (<125 mg/L TDS), the dominant cation is Ca^{+2}, and the dominant anion is carbonate.

Water quality data were also collected at springs in 3-Springs Basin and East Stewart Basin, sites that are considered representative of potential recharge areas in central Nevada (McKinley and Oliver 1994 [DIRS 101263], pp. 1 to 3; 1995 [DIRS 101264], pp. 1 to 3). The two basins were studied as analog sites to Yucca Mountain during wetter and cooler periods. Springs in the basins are probably above the regional groundwater system and do not represent discharge from large groundwater basins, in contrast to springs at Ash Meadows in the Amargosa Desert. The water chemistry of the spring discharges does reflect modification due to water movement through unsaturated volcanic rock layers in the basins. These waters are very similar to the

Yucca Mountain runoff samples with respect to their relative proportions of the major ions; that is, they are calcium-bicarbonate waters with a significant component of sodium. However, they have slightly higher proportions of sodium and chlorine, and lower proportions of calcium and carbonate species, than the Yucca Mountain waters.

The surface waters are plotted with other Yucca Mountain waters in Figures 5-8 to 5-12, and comparison with precipitated waters reveals changes in water chemistry in response to evaporation, dissolution of dry-fall salts accumulated since the last infiltration event, and rock-water interactions. The sulfate:chloride ratio is similar in precipitation and surface waters, although the surface waters are more concentrated. Since chloride is believed to behave conservatively, this suggests that sulfate also behaves conservatively and that its abundance in surface waters is mostly a function of evaporative concentration and dissolution of dry-fall salts. In contrast, both Na^+/Cl^- and Ca^{2+}/Cl^- ratios are considerably higher in the surface waters relative to the precipitation, suggesting that sodium and calcium concentrations are increased by dissolution of carbonate minerals and weathering reactions of soil minerals. Dissolution of carbonate minerals also leads to a large gain in bicarbonate concentrations in the surface runoff. Finally, the most dramatic constituent increase is observed for silica, which increases by two orders of magnitude over its concentration in precipitation due to fast dissolution of unstable amorphous silica minerals in the soil (Chadwick et al. 1987 [DIRS 105224], p. 977).

Another source of chemical data for surface water samples is compiled from analyses of springs and tunnel seeps from Rainier Mesa (McKinley et al. 1991 [DIRS 116222], pp. 26 to 33). Because of similar geologic settings for Yucca Mountain and Rainier Mesa, these samples expand the database used to develop a conceptual model for the early stages of the geochemical evolution of waters contacting tuff. However, these waters have interacted sufficiently with the tuff to have similar compositions to those of perched waters at Yucca Mountain. Water chemical data from this site are not included in Figures 5-8 to 5-12 but can be found in BSC (2002 [DIRS 160247], Figure 11).

5.2.2.4 Chemical Composition of Unsaturated Zone Pore Waters and Perched Water

5.2.2.4.1 Processes Controlling the Chemistry of Unsaturated Zone Waters

The compositions of unsaturated zone waters, including both pore waters and perched waters, are influenced by many factors, including the composition of the infiltrating precipitation and surface waters; soil zone and unsaturated zone processes including rock-water interactions, water-air interactions, and microbial influences; infiltration paths and rates; and the temperature and pressure at the location of interest.

Perched waters occur above the regional water table in areas where the rocks are locally saturated. The presence of perched water implies that, at some time in the past, the percolation rate through the unsaturated zone has exceeded the saturated hydraulic conductivity of the perching layer. The perched water reservoir may be a remnant of a time when percolation rates were higher or may reflect long-term steady-state conditions.

Perched water has been identified below the current repository horizon in six boreholes in the Yucca Mountain area (Figure 5-5): USW UZ-1, USW UZ-14, and USW NRG-7a in Drill Hole

Wash; and USW SD-7, USW SD-9, and USW SD-12 (Rousseau et al. 1999 [DIRS 102097], pp. 170 to 171; O'Brien 1997 [DIRS 101277], p. 23; Rautman and Engstrom 1996 [DIRS 101008], p. 8; 1996 [DIRS 100642], p. 32). The perched water bodies are at elevations significantly below (100 to 200 m) (330 to 660 ft) the current repository horizon. In all cases, perched water accumulates on either the basal vitrophyre of the Topopah Spring Tuff or the vitric-zeolitic boundary in the Calico Hills Formation, in areas where a lateral structural barrier is present (Rousseau et al. 1999 [DIRS 102097], pp. 171 to 172). Although not detected in all boreholes, perched water beneath the site area seems to be a common occurrence and is probably nearly everywhere near the base of the Topopah Spring Tuff in the vicinity of the north ramp (Rousseau et al. 1999 [DIRS 102097], p. 170).

5.2.2.4.2   Major Constituents in Unsaturated Zone Pore Waters and Perched Waters

The compositions of pore waters in and above the current repository horizon are significant to transport modeling because they represent the waters that are present in the near field of the repository, and will influence the composition of potential seepage into the repository. They can also be used to constrain models for the rock and mineral-water-gas interactions that occur in the soil zone and the unsaturated zone above the current repository horizon. Such models can be used to derive estimates of future variations in unsaturated zone water chemistry. Data on major constituents can also be used to evaluate potential flow paths for flow modeling.

Major element concentration data are plotted in Figures 5-13 to 5-16 for perched waters and for pore waters from the TCw, PTn, TSw, and CHn hydrogeologic units. These concentrations are compared against data for precipitation, surface waters, perched waters, and saturated zone waters to elucidate general trends in Figures 5-8 to 5-12.

Major-Ion Chemistry

The composition of unsaturated zone pore waters is summarized in Table 5-2. Pore waters extracted from bedded tuff of the PTn unit are calcium chloride- or calcium sulfate-type waters. This characteristic becomes less pronounced for samples collected deeper within the PTn unit. In general, TSw waters have uniform concentrations of sodium (83.5 ± 26.4 mg/L) and calcium (116 ± 55 mg/L), with less magnesium (15.8 ± 8.2 mg/L) (Peterman and Marshall 2002 [DIRS 162992]); the dominant anion is bicarbonate, with a much smaller proportion of sulfate than is typical of PTn unit waters (Figures 5-14 and 5-15). In terms of relative proportions of anions, the chemical composition of TSw waters is intermediate between those of the PTn and CHn units. Pore waters extracted from the CHn unit are sodium carbonate-bicarbonate-type waters (Figure 5-16). Waters become more strongly sodium carbonate-bicarbonate types with increasing depth within the Calico Hills Formation.

The concentration of constituents in pore waters is highly variable and is often greater near contacts than in the middle of stratigraphic units (Yang et al. 1996 [DIRS 100194], p. 24). Pore waters from surface-based boreholes have significantly larger concentrations of total dissolved solids than either perched water (Tables 5-3 and 5-4) or saturated zone water (Benson and McKinley 1985 [DIRS 101036], p. 5). The concentrations of chloride and sulfate (generally conservative constituents in oxidizing groundwater) in many pore water samples from surface-based boreholes are one to two orders of magnitude greater than those of either perched

water or saturated zone water. Chloride concentrations of deep-perched waters lie between 4.1 and 15.5 mg/L (Table 5-3; DTN: MO0012WTRIONCO.000 [DIRS 153397]) with a mean of 6.8 mg/L, which is similar to that of the saturated zone water from the volcanic rocks beneath Yucca Mountain (9.5 mg/L). In contrast, the chloride concentration of matrix pore water from surface-based boreholes ranges from 10 to 245 mg/L with a mean of about 49 mg/L (BSC 2002 [DIRS 160247], Table 6). The larger concentration of chloride in pore water implies that pore waters and perched waters have distinctly different histories of geochemical evolution. Evapotranspiration near the surface could account for the larger concentrations, but this can only have a limited effect because it is not supported by the stable isotope data (see Section 5.2.2.5.5). A greater degree of rock-water interaction could also account for the high concentrations, which could indicate prolonged contact of percolating water with silicate rocks.

Figure 5-9 shows that sulfate concentrations are similarly elevated in PTn unit pore waters relative to those for the other waters plotted. The higher proportions of chloride and sulfate concentrations in PTn unit pore waters relative to the other waters at the site are also evident by comparing the trilinear diagrams, Figure 5-13 to Figure 5-17.

Silica is low in precipitation water, but substantially higher in surface waters (Figure 5-10). By the time precipitation and surface waters infiltrate into the unsaturated zone, the silica concentrations have reached a limit, presumably as a result of saturation with a silica phase, as discussed later in this section.

The concentrations of sodium and calcium are also elevated in pore waters relative to other waters at the site (Figures 5-11 and 5-12). Sodium is elevated in most of the pore water samples, whereas calcium is elevated only in the PTn and TSw unit samples. Figure 5-14 shows that PTn unit pore water compositions extend to higher calcium proportions than observed in either precipitation compositions or surface water compositions (Figure 5-12). This enhancement presumably reflects water-soil/rock reactions that preferentially release calcium to solution. The pore waters in the Calico Hills (Figure 5-16) and lower units show high proportions of sodium. This shift in dominance from divalent to monovalent cations primarily reflects the ion-exchange reactions with zeolites in the CHn unit. The zeolites preferentially take up calcium and magnesium while releasing sodium to the water.

The chemical composition of pore waters within the nonwelded units does not change in a simple or predictable fashion in a given borehole. Chloride and sulfate show large concentration changes within the CHn unit by as much as a factor of two for samples separated by less than 0.5 m. Similar large contrasts are noted for sodium and total carbonate within the PTn unit. These data may indicate some component of lateral flow within the nonwelded units.

However, Vaniman et al. (2001 [DIRS 157427], p. 3422) analyzed zeolites from three different boreholes and reached a different conclusion. In each of the boreholes examined, the zeolitized horizons in the unsaturated zone were strongly enriched in the divalent cations magnesium, calcium, and strontium, and, as shown for strontium in Figure 5-4, the divalent ion concentrations are highest at the top of each horizon and decrease downward through the zeolitized layer. These clearly indicate that the direction of flow though the zeolitized units has been dominantly downward. They noted, however, that the composition of the zeolites varied markedly from hole to hole, resulting from a varying degree of ion exchange or exchange with

waters of differing compositions. This is consistent with ponding and lateral flow on less permeable horizons in the unsaturated zone, although the local-scale heterogeneities in pore water composition and in zeolite composition could also indicate the presence of waters of differing compositions due to varying recharge rates or degrees of soil/rock-water interaction.

Geochemical Evolution

A convenient method for assessing the magnitude and direction of rock/mineral-water interactions experienced by percolating infiltration waters transported through the soil and unsaturated zone is to normalize the concentrations of the major constituents in these waters relative to a conservative constituent (i.e., a highly soluble and nonsorbing constituent) such as chloride. In the absence of other geochemical processes, evaporation or transpiration of a given water will result in proportional increases in all constituent concentrations; thus, constituent:chloride ratios do not change. If processes other than evapotranspiration significantly influence the concentration of a particular constituent, the proportion of that element relative to chloride will change. The selection of chloride as the normalizing constituent assumes that its concentration is not affected significantly by leakage from fluid inclusions or by geochemical reactions along the flow path.

Calcium and Bicarbonate–When compared to precipitation data, both calcium and bicarbonate are generally depleted in PTn pore waters to chloride (BSC 2002 [DIRS 160247], Figures 24 and 25). This observation implies that calcium and bicarbonate were lost from these waters relative to chloride. Given the fact that soils on Yucca Mountain contain abundant caliche horizons, this loss likely reflects the precipitation of calcite as the result of evapotranspiration and possibly other reactions in the soil zone.

Pore waters from the Calico Hills and Prow Pass units show even greater depletions of calcium relative to the trend predicted by simple evapotranspiration-related concentration of surface precipitation (BSC 2002 [DIRS 160247], Figure 24). These greater depletions likely reflect ion-exchange processes in which sodium in the ion-exchanger phase (e.g., zeolite or clay) was replaced by calcium from the water. Unlike the PTn unit pore waters, many Calico Hills Formation and Prow Pass Tuff pore waters are enriched in bicarbonate relative to the precipitation trend (BSC 2002 [DIRS 160247], Figure 25). This fact most likely reflects carbonic acid weathering reactions.

Sodium–In the weathering of aluminosilicate rocks and minerals, weathering reactions include the exchange of the hydrogen ions produced in the carbonic acid reaction with sodium or other cations on the rock or mineral. This step leads to an increase in sodium as well as bicarbonate concentrations in the water. Sodium concentrations in pore waters from the Calico Hills and Prow Pass units are generally well above the precipitation trend (BSC 2002 [DIRS 160247], Figure 26). This result is attributed to the Na^+/H^+ ion-exchange reaction and to reactions involving calcium, magnesium, and sodium ion exchange on zeolites and clays.

In contrast, sodium is depleted in PTn unit pore waters relative to the precipitation trend. Several explanations could account for this:

- The average Na^+/Cl^- ratios in precipitation may have been lower in the past than present-day ratios measured in 3-Springs Basin.

- Sodium may be taken up by some unidentified rock-water interaction.

- Sodium may have been sequestered in the soil zone as some other sodium salt such as sodium sulfate.

The last hypothesis could also account for the observed depletion in sulfate relative to chloride for PTn unit pore waters, as discussed below.

Sulfate–Pore waters show sulfate-to-chloride ratios consistently lower than the ratios observed in recent precipitation (BSC 2002 [DIRS 160247], Figure 27). Because all the pore water analyses are grossly undersaturated with chloride phases and with gypsum and other possible sulfate phases involving the major cations, it is unlikely that solid chloride or sulfate phases are precipitated in the unsaturated zone (Triay et al. 1997 [DIRS 100422], p. 29).

Drever and Smith (1978 [DIRS 105467], p. 1452) presented a model that offers one potential explanation for the low sulfate-to-chloride ratios in the unsaturated zone pore waters (Triay et al. 1997 [DIRS 100422], p. 29). Their model involves drying and wetting cycles in the soil zone. During the drying phase, concentrations of dissolved solutes are increased in soil waters by evapotranspiration to the degree that phases such as calcite, gypsum, silica, and the more soluble salts precipitate. During occasional heavy rains, the phases precipitated during the drying phase are partially redissolved. Because the dissolution rates for highly soluble salts, such as sodium chloride, are higher than the rates for less soluble salts, such as calcite, gypsum, and silica, a portion of the less soluble salts may remain undissolved after the occasional heavy rains infiltrate through the soil zone. In terms of sulfate and chloride concentrations, this process could lead to soil waters with lower sulfate-to-chloride ratios than those observed in precipitation (Drever and Smith 1978 [DIRS 105467], p. 1452).

Silica–Most pore water samples from the Yucca Mountain area are enriched in silica relative to the precipitation trend (BSC 2002 [DIRS 160247], Figure 28). This result suggests that a process other than evapotranspiration is contributing to increased silica concentrations in these waters. According to Gifford and Frugoli (1964 [DIRS 105641], pp. 386 to 388) and Chadwick et al. (1987 [DIRS 105224], p. 977), silica is added to soil waters as a result of dissolution of solid silicic acid (an unstable silica phase) in soil horizons in arid regions. This explanation would be consistent with the presence of amorphous silica (e.g., opal) in Yucca Mountain soils and opal deposits on fracture surfaces exposed in the ESF. It is also consistent with surface waters having much higher silica concentrations than precipitation compositions (Figure 5-10).

pH–pH values shift from slightly acidic values for precipitation (pH 6), to increasingly basic values with depth in the unsaturated zone (pH 9 or higher for the deepest pore water samples). Controls on pH in ambient unsaturated zone pore waters and perched waters are dominated by the carbonic acid system and the interaction of hydrogen ions with the host rock/mineral. As

discussed above, hydrogen ions can replace sodium ions in the host rock/mineral (e.g., volcanic glass, feldspar) under most conditions. As hydrogen ions are used up, carbonic acid dissociation produces additional hydrogen ions and bicarbonate ions. If H^+/Na^+ exchange is inhibited, the pH of a given pore water sample will depend primarily on the partial pressure of CO_2 in the gas phase in contact with the water and on whether the gas phase has equilibrated with the water phase. This process will buffer the pH of the (dilute) pore waters at nearly neutral levels. If calcite is present, it will also act to buffer the pH, in conjunction with gas-phase CO_2.

Because the sodium-versus-chloride concentration data for pore waters from units above the CHn unit (BSC 2002 [DIRS 160247], Figure 26) suggest little or no evidence for the H^+/Na^+ ion-exchange reaction, the pH of these pore waters likely is controlled in part by the CO_2 partial pressure with which they are in contact. Measured pH values in PTn unit pore waters average 7.2. In contrast, the CHn unit pore waters and perched waters show clear evidence of Na^+/H^+ ion exchange. The average pH values for these waters are 8.1 for perched water, 8.3 for pore waters from the CHn unit above the Prow Pass Tuff, and 9.0 for pore waters from the Prow Pass Tuff and below (BSC 2002 [DIRS 160247], Figure 23). Analytical uncertainties in pH measurements are between 0.2 and 0.3 pH units. Whether the higher pH values for deeper samples reflect the cation/hydrogen-ion exchange rate or simply a lower partial pressure of CO_2 in the gas phase has not yet been resolved.

Redox State–The oxidation/reduction (redox) state of unsaturated zone waters is likely dominated by the presence of oxygen in the unsaturated zone gas phase. At the two locations where such measurements have been made, the unsaturated zone gas phase has atmospheric levels of oxygen: 21 percent reported for USW UZ-6S gas in Thorstenson et al. (1990 [DIRS 100831], p. 256) and 18.5 to 21.1 percent reported for USW UZ-1 gas (BSC 2002 [DIRS 160247], p. 54; Yang et al. 1996 [DIRS 100194], p. 42). These results confirm that unsaturated zone pore waters would generally be oxidizing. Measured Eh would typically be high (400 to 600 mV), but it is possible that lower redox potentials could be present locally (i.e., in microenvironments) as a result of microbial activity or the presence of a reducing mineral species (e.g., pyrite).

Microbial Activity–The influence of microbes on the unsaturated zone water chemistry is not well defined. At a minimum, microbes could produce organic acids and locally alter pH and redox states. Microbial activity could also affect concentrations of sulfate, bromide, and other dissolved species, as well as fractionate isotopes of light elements, such as carbon. According to Kieft et al. (1997 [DIRS 100767], p. 3128), microbial cell counts and microbial biomasses were low at all the locations sampled in the ESF. Kieft et al. (1997 [DIRS 100767], p. 3128) suggest that this result was likely due to low water content and low nutrient availability. However, they note that the potential for microbial activity was high. That is, microbial populations were present but not active. They concluded that if sufficient water and nutrients were added to the system, microbial populations could increase dramatically.

Perched Waters–Perched water compositions are generally distinct from pore water compositions although they are very similar to saturated zone water compositions (Section 5.2.2.7). These relationships are readily seen by comparing the trilinear plots of perched water (Figure 5-13), unsaturated zone pore waters (Figures 5-14 to 5-16), and groundwater (Figure 5-17). Perched water and saturated zone water $^{234}U/^{238}U$ values are also

similar and differ from the pore water values, as discussed in Section 5.2.2.5.7. The similarity of perched and saturated zone water compositions suggests that these waters are subject to similar rock-water interactions. As discussed in Section 5.2.2.7, these reactions predominantly involve mineral/rock dissolution and ion exchange.

The compositional variations of pore waters and perched waters in the unsaturated zone at Yucca Mountain reflect a variety of infiltration rates, rock-water interactions, gas-water interactions, and other effects. The range of these processes and effects is unlikely to change greatly within the potential range of climatic regimes, but their relative importance may change. The local-scale compositional variability displayed by these waters is currently not well understood.

5.2.2.5   Isotopic Composition of Fluids

Aqueous phase isotopic data provide constraints for water and solute transport rates and mechanisms, and a variety of isotopic studies of unsaturated zone fluid and rock samples have been carried out, utilizing both anthropogenic and naturally-occurring isotopes.

5.2.2.5.1   Overview of Isotopic Methods

Isotopic studies fall into several categories as described below, with each method yielding different types of information. This large suite of different approaches has been critical to the development and testing of conceptual models for flow and transport through the unsaturated zone.

Use of Anthropogenic Radionuclides As Groundwater Tracers–This category of environmental tracers includes radioactive species present in global fallout from nuclear weapons testing and from releases from nuclear fuel reprocessing plants. ^{3}H, ^{14}C, and ^{36}Cl produced in the atmosphere during aboveground nuclear testing, primarily between 1952 and 1963, have been widely used in hydrologic studies. The presence of these nuclides at levels above background in subsurface fluids is generally accepted as a clear indication that some proportion of the water was transported to that depth in less than 50 yr. In an arid environment were infiltration rates are low the presence of global fallout nuclides at depths of greater than a few meters implies a component of fracture flow. Hence, these isotopic data provide a means for constraining the importance of fracture flow, and the extent to which solute transport is retarded by diffusion from fractures into the adjacent matrix. Fission products ^{99}Tc and ^{129}I in a subsurface sample (above natural background) would also provide a clear indication of a component of recent water. However, a robust analytical protocol for these species in unsaturated zone fluids has not yet been developed. Other radionuclides in global fallout, such as ^{137}Ce and plutonium isotopes, sorb strongly onto most mineral surfaces and hence are largely immobilized in the near-surface soil. ^{3}H, ^{36}Cl, and ^{14}C data are discussed in Sections 5.2.2.5.2, 5.2.2.5.3, and 5.2.2.5.4, respectively.

Use of Naturally-Occurring Atmospheric Radionuclides as Groundwater Tracers–^{3}H, ^{36}Cl, and ^{14}C are also produced naturally in the atmosphere as the result of the interactions of cosmic rays with atmospheric gases. To the extent that the original concentrations in the infiltrating surface water can be reconstructed, these radionuclides are useful indicators of water residence times, with water ages based on the extent of radioactive decay of the atmospheric component.

Use of Stable Isotopes in Climatic Reconstruction–Stable isotopic compositions of hydrogen and oxygen can be used to infer paleoclimatic conditions (Section 5.2.2.5.5).

Isotopic Evaluation of Water Residence Times and Rock-Water Interactions–Groundwater is commonly out of chemical and isotopic equilibrium with the rocks through which it moves (Davis and Murphy 1987 [DIRS 105814], Section 8). The extent of disequilibrium provides a qualitative method for establishing flow paths and flow chronologies. Furthermore, if the kinetics of chemical or isotopic exchange between the water and minerals along its flow path are well known, then semiquantitative estimates of water travel times may be calculated. Strontium isotopes and uranium decay series isotopes have been used to evaluate rock-water interactions at Yucca Mountain (Sections 5.2.2.5.6 and 5.2.2.5.7, respectively).

Borehole, tunnel, and alcove sampling locations are plotted in Figures 5-5 and 5-6. Isotopic studies of samples from the underground tunnels began in 1995 and continued throughout the mid-to-late 1990s. Early results from these characterization efforts indicated fast paths were present in the tuffs and that surface water could reach the level of the repository in 50 yr or less. Because of the hydrologic implications of "fast paths" with respect to repository performance, a validation study was performed by the USGS, to verify the previously measured isotopic results. In the validation study, samples were collected from those areas in the ESF, where anomalous ^{36}Cl had been reported. The samples were analyzed for ^{36}Cl and ^{3}H, and for strontium and U-series isotopes. Additional samples, from the ECRB Cross-Drift, have also been analyzed for ^{3}H (and in a few cases ^{36}Cl), but these samples were not analyzed as duplicates. The results of the validation study were in some cases inconsistent with the earlier isotopic data, and are discussed in detail in the following sections.

5.2.2.5.2 Tritium

Background

Natural tritium (^{3}H or T) is produced in the upper atmosphere by the bombardment of nitrogen by the flux of neutrons in cosmic radiation (Clark and Fritz 1997 [DIRS 105738], p. 174):

$$^{14}_{7}N + ^{1}_{0}n \Rightarrow ^{12}_{6}C + ^{3}_{1}H \qquad \text{(Eq. 5-1)}$$

where n is a neutron. Once produced, tritium oxidizes rapidly to tritiated water (HTO). Transfer of tritium to the troposphere occurs during spring in midlatitude zones. Tritiated water has a short residence time in the troposphere (less than one yr) and is eventually removed from the atmosphere in precipitation or through isotopic exchange. Tritium values in precipitation prior to the 1950s were between 2 and 25 TU (Yang et al. 1996 [DIRS 100194], p. 51). Because of the relatively short half-life of tritium (12.3 yr; Parrington et al. 1996 [DIRS 103896], p. 18), groundwater infiltrating prior to 1952 with an initial tritium content of 10 TU would have a present-day content of 0.7 TU or less.

Above ground testing of nuclear devices in the northern hemisphere between 1952 and 1963 produced significant amounts of tritium in the earth's atmosphere. Bomb-pulse tritium overwhelmed natural background levels by as much as several orders of magnitude (Figure 5-18). It is possible that venting of tritium from subsurface nuclear detonations on the

Nevada Test Site may also have contributed to tritium in precipitation at Yucca Mountain. Seasonal variations in post-bomb tritium concentrations in precipitation are quite significant (Davis and Murphy 1987 [DIRS 105814], pp. 36 to 37; Clark and Fritz 1997 [DIRS 105738], pp. 177 to 178). These variations are caused by changes in atmospheric circulation between the troposphere and the stratosphere, which is a major reservoir of tritium. Consequently, the seasonal timing of precipitation is a critical determinant of the magnitude of the tritium signal introduced into the subsurface.

As a result of the nuclear test ban treaty of 1963, tritium concentrations have gradually decreased in precipitation. Precipitation samples from 3-Springs Basin in central Nevada, slightly north of the Nevada Test Site, showed slightly lower tritium concentrations in samples collected between 1985 and 1991, ranging from 6 to 22 TU (McKinley and Oliver 1994 [DIRS 101263], pp. 27 and 74). Annual mean values and monthly maximum values for monitoring stations in states surrounding Nevada likewise were in this range (i.e., still elevated above pre-1952 background levels) from 1988 to 1993 (Yang et al. 1996 [DIRS 100194], p. 51). In January and February 1993, the tritium content of surface runoff collected from several sites in the vicinity of Yucca Mountain ranged from 3 to 10 TU (Emett et al. 1994 [DIRS 105532], p. 550; Savard 1996 [DIRS 101290], p. 28); tritium values during the winter are typically the lowest of the year.

The extent to which detectable quantities of tritium enter the subsurface depends on spatial and temporal variations in precipitation. If precipitation is insufficient to lead to net infiltration following a storm event then the tritium is lost back to the atmosphere by evapotranspiration. Consequently, because Yucca Mountain experienced below average levels of precipitation from 1958 to 1964 (French 1986 [DIRS 110645], pp. 52 to 56), it is entirely possible that much of the peak tritium concentrations were never transported into the bedrock at Yucca Mountain. In this regard, the behavior of tritium as a tracer of modern water differs substantially from that of ^{36}Cl.

Yucca Mountain Site Characterization Project Tritium Results

Pre-2000 Results—Tritium was analyzed in more than 800 pore water fluids extracted from unconsolidated material in shallow surface-based boreholes, from drill core from deep surface-based boreholes, and from ESF drill holes (Table 5-5). Analyses are also available for water samples bailed and pumped from perched water bodies (Table 5-4) and from the saturated zone. Detectable levels of tritium have been observed in the Bow Ridge fault zone in ESF Alcove 2 and in pore waters extracted from core samples from surface-based boreholes. These detections occur within the TCw, PTn, and TSw units, and also in some samples from the CHn unit, as deep as the Prow Pass Tuff member of the Crater Flat Group.

Because of the implications of the tritium data for the presence of fast transport paths and large fluxes, it is important to define the threshold at which a given signal can be considered as being above background. The analytical uncertainty in these ^{3}H studies was 4 TU (for 1 standard deviation) based on counting statistics, other factors contributed to a larger uncertainty in the measured value. Chauvenet's criterion for identifying outliers was the basis of the statistical test used to establish the minimum tritium activity that would indicate the presence of elevated ^{3}H levels in a sample (Bevington and Robinson 1992 [DIRS 147076], p. 58). Using Chauvenet's criterion, all values above 25 TU were considered to lie outside the range of the population of background samples (BSC 2002 [DIRS 160247], Figure 30). The limitation of this approach is

that, in this case, background includes post-bomb waters that have returned to pre-bomb tritium levels.

Following this simple statistical analysis, Table 5-5 summarizes the distribution of pore water samples in each borehole, according to the total number of samples analyzed for each hydrogeologic unit and the number that exceeded the threshold of 25 TU. Of the 718 samples included in this summary of the pre-2000 results (DTNs: GS961108312271.002 [DIRS 121708]; MO0012TRITUNSZ.000 [DIRS 153751]; GS991108312272.004 [DIRS 145680]; GS961108312261.006 [DIRS 107293]) 51 had contents above 25 TU.

The largest concentrations of tritium within the unsaturated zone at Yucca Mountain were those associated with the Bow Ridge fault. A concentration of 155 TU was measured for pore water 3.4 m west of the fault within the pre-Rainier Mesa Tuff (LeCain et al. 1997 [DIRS 100156], p. 40). Values of 118 and 128 TU were found in pore waters within the fault breccia. The high values indicate minimal mixing of the percolating fluids with older fluids. No other samples from the ESF had tritium contents above 25 TU, including seven core samples from a drill hole transecting the Ghost Dance fault in the northern Ghost Dance fault access drift (Alcove 6) (LeCain and Patterson 1997 [DIRS 100529], pp. 16 to 17).

Tritium data for the unsaturated zone boreholes show several inversions (larger tritium concentrations located below smaller tritium concentrations in a vertical profile) (Yang et al. 1996 [DIRS 100194], p. 31). Post-bomb tritium concentrations were observed down to bedded tuff or Pah Canyon Tuff in many surface-based boreholes. The occurrence of detectable tritium in waters below nontritium-bearing water (i.e., older water) in a vertical profile is strong evidence of fracture and lateral flow occurring at Yucca Mountain. An alternative hypothesis would be that the inversion results from piston flow of the atmospheric input signal, with the 1960s peak remaining higher than the 1980s input.

Tritium concentrations have been measured in perched water from four Yucca Mountain boreholes (Table 5-4). None of the tritium analyses were above the 25 TU threshold indicating the presence of elevated tritium concentrations.

Validation Study Results—As part of the validation study (BSC 2003 [DIRS 166347], Section 6.14), core samples were taken from 48 four-meter-long (13.1 ft) and 2 10-meter-long (32.8 ft) boreholes drilled in the walls of the ESF at the localities previously identified as having anomalous amounts of ^{36}Cl. Additional samples were analyzed from three preexisting cores from boreholes in Niche 1, from boreholes in the south ramp of the ESF, and boreholes in the ECRB Cross-Drift. The boreholes were dry-drilled, and core samples for ^{3}H analysis were collected from the deepest parts of the boreholes, sealed, and refrigerated until processing. Pore waters used for ^{3}H analysis were extracted using vacuum distillation. A total of 141 samples were collected. Eleven samples from Alcove 2 were analyzed by the USGS, and have 25 TU detection limits, similar to the earlier samples. The remaining samples were analyzed at the University of Miami using a low-level analytical technique incorporating a pre-concentration 7step. The accuracy and detection limits of this technique are much better than the earlier method. Accuracy is 0.1 TU or 3.5 percent, whichever is greater, and the detection limit is less than 1 TU. Given the low natural production rates for ^{3}H, and the radioactive decay rates of tritium in waters entering the unsaturated zone prior to nuclear weapons testing, measured tritium

activities in excess of 1-2 TU are indicative of waters that entered the unsaturated zone within the last 50 yr.

Samples were collected from several locations within the ESF and ECRB, concentrating in areas where previous studies had indicated the presence of fast pathways. These include samples from:

- Boreholes crossing the Bow Ridge Fault in Alcove 2, off the north ramp of the ESF

- The north ramp of the ESF, including the Drill Hole Wash fault

- The Sundance fault area within the main drift of the ESF

- The northern Ghost Dance fault access drift and alcove, and the southern Ghost Dance fault access drift along the main drift of the ESF

- The southern ramp of the ESF

- The ECRB.

The results of the validation study tritium analyses are presented in BSC (2003 [DIRS 166347]) and Patterson (2000 [DIRS 154827]; DTNs: GS020408312272.002 [DIRS 162342]; GS021208312272.005 [DIRS 162934]; GS030208312272.001 [DIRS 162935]). In the north ramp of the ESF the only elevated tritium activities were found in samples from the Bow Ridge fault in Alcove 2. These samples are from the Tiva Canyon Tuff, above the Paintbrush Group nonwelded units. Samples of the Topopah Spring Tuff from the Drill Hole Wash fault and from the vicinity of the Ghost Dance fault contained no tritium activities significantly above the 2 TU threshold, and only one of the samples from the Sundance fault area did (2.6 TU). In the south ramp of the ESF, over half of the samples contained tritium activities significantly over 2 TU, including samples from both above and below the Paintbrush Group nonwelded units. In the ECRB several samples of the Topopah Spring Tuff, especially from the upper lithophysal unit, had tritium activities greater than 2 TU. However, attempts to reproduce the results with adjacent core samples yielded mixed results, possibly reflecting the difficulty in obtaining homogeneous material for testing and the likelihood that if fast-paths are present, they are heterogeneously distributed over small distances.

To summarize, the validation study confirmed the presence of elevated tritium associated with the Bow Ridge fault in units above the Paintbrush Group nonwelded units. Elevated tritium was also found in Topopah Spring Tuff samples from the south ramp of the ESF, where the Paintbrush Group nonwelded units are thinnest, faulted, and the most offset. These occurrences are probably linked to the absence of the Paintbrush Group nonwelded units or the inability of those units to impede downward percolation of young water at these locations (BSC 2003 [DIRS 166347]; Patterson 2000 [DIRS 154827]). It is unclear what features provide pathways for young water in the ECRB, and an investigation into these results is currently in progress.

5.2.2.5.3 Chlorine-36

Background

Measurements of chloride concentrations and ^{36}Cl/Cl for salts extracted from water, soil, and rocks have been used to provide information on characteristics of water movement and solute transport through the unsaturated zone at Yucca Mountain (Fabryka-Martin et al. 1997 [DIRS 100145], pp. 75 and 77 to 79; 1998 [DIRS 100570], p. 93; 1998 [DIRS 146355], p. 264; Wolfsberg et al. 1998 [DIRS 146442], p. 81). ^{36}Cl is a radioactive isotope of chlorine, with a half-life of 3.01×10^5 yr (Parrington et al. 1996 [DIRS 103896], p. 22), and in nature it occurs primarily as the chloride anion. As such, it is relatively inert in the subsurface environment and behaves conservatively. This radionuclide is present in infiltrating waters as a natural tracer produced mainly in the upper atmosphere by the bombardment of argon (Ar) by cosmic radiation (Clark and Fritz 1997 [DIRS 105738], p. 232):

$$^{40}Ar + p \Rightarrow {}^{36}Cl + n + \alpha$$
$$^{36}Ar + n \Rightarrow {}^{36}Cl + p$$

(Eq. 5-2)

where n is a neutron, p is a proton, and α is an alpha particle. Common chlorine (^{35}Cl) in the atmosphere is also irradiated by the atmospheric neutron flux to produce ^{36}Cl and gamma (γ) radiation:

$$^{35}Cl + n \Rightarrow {}^{36}Cl + \gamma$$

(Eq. 5-3)

The relatively long half-life of ^{36}Cl (~300,000 yr) theoretically permits the detection of travel times up to several hundred thousand years. To normalize the data for the variable effects of evapotranspiration, the ^{36}Cl concentration is generally reported relative to that of stable chlorine. Expressed in this manner, the present-day background level of ^{36}Cl/Cl is $502\ (\pm\ 53) \times 10^{-15}$ (BSC 2002 [DIRS 160247], Table 25).

Global fallout from thermonuclear tests conducted, primarily in the Pacific Proving Grounds, resulted in a ^{36}Cl bomb pulse with maximum meteoric ratios in excess of $200,000 \times 10^{-15}$ (Figure 5-18). These extremely high values were diluted by mixing processes in the soil zone and subsurface and are not observable today. Nevertheless, high ^{36}Cl/Cl ratios (those greater than about $1,250 \times 10^{-15}$) indicate some ^{36}Cl-enriched component, and their appearance in an environmental sample signals the presence of at least a small component of anthropogenic ^{36}Cl. Present-day ^{36}Cl/Cl ratios in Yucca Mountain surface soils generally range from $1,500 \times 10^{-15}$ to $3,000 \times 10^{-15}$ (CRWMS M&O 1998 [DIRS 104878], pp. 3 to 5). In subsurface water, similar high ratios suggest travel times from the ground surface of 50 yr or less.

Although the existence of bomb-pulse ^{36}Cl enables the study of solute transport with travel times of 50 yr or less, the natural cosmogenic background permits analysis of much longer term transport processes. However, the use of ^{36}Cl/Cl for dating older waters is not as straightforward as the case for bomb-pulse signals due to the time-varying input signal. Both theoretical considerations as well as measurements of soil profiles and fossil urine from ancient pack-rat middens support the hypothesis that the present-day background ratio has remained relatively

constant during the Holocene (the last 10 k.y.) (Plummer et al. 1997 [DIRS 107034], Figure 3B, p. 539). Expected lower rates of stable chlorine deposition during the Pleistocene (2 Ma to 10 ka), in combination with higher rates of cosmogenic ^{36}Cl deposition as a result of southern shifts in the jet stream would have led to higher local meteoric ^{36}Cl/Cl values relative to those that were present throughout the Holocene (Plummer et al. 1997 [DIRS 107034], p. 540). Superimposed on this effect are varying atmospheric ^{36}Cl production rates caused by variations in the earth's magnetic field. Based on these two factors, the meteoric ^{36}Cl/Cl at Yucca Mountain has been reconstructed for the last 1.8 m.y. (Fabryka-Martin et al. 1997 [DIRS 100145], pp. 4 to 5). Analyses of ^{36}Cl/Cl in ^{14}C-dated pack-rat midden samples are generally consistent with the reconstruction, although these data can only cover the last 40 k.y. due to the comparatively short half-life of ^{14}C (Figure 5-19).

Clorine-36 is also produced in rocks by the low but ubiquitous neutron flux resulting from the decay of uranium and thorium isotopes and their daughters and the spallation of ^{40}Ca, but these background levels are low relative to those measured in Yucca Mountain water samples (Fabryka-Martin et al. 1997 [DIRS 100145], pp. 8 and 13).

Together, the elevated ^{36}Cl record and the long-term reconstruction allow ^{36}Cl/Cl observations in subsurface fluids at Yucca Mountain to be divided into four classes:

- Ratios over $1{,}250 \times 10^{-15}$ suggest bomb-pulse influence, and may indicate the presence of some rapid transport pathways (Fabryka-Martin et al. 1997 [DIRS 100145], p. 18).

- Ratios near the present-day value of 500×10^{-15} suggest Holocene precipitation of pre-nuclear-age (from 1950, extending back to about 10 ka) (Figure 5-19a). A value of 500×10^{-15} is very unlikely to indicate extremely young (post-1980) precipitation because bomb-pulse ^{36}Cl is still widely prevalent in surface soils at Yucca Mountain, based on analyses of surface soils and surface runoff.

- Ratios that are elevated above present-day background but less than $1{,}250 \times 10^{-15}$ cannot be interpreted unambiguously in terms of water travel time, in the absence of additional geochemical or isotopic information. These may be attributed to Pleistocene water that is not so old as to unequivocally demonstrate radioactive decay (note elevated ratios at the end of the Pleistocene) (Fabryka-Martin et al. 1997 [DIRS 100145], pp. 4 to 5, Figure 31b). Alternatively, these ratios may reflect the presence of a small component of bomb-pulse ^{36}Cl, possibly as low as 1 percent of the total flow.

- Ratios significantly less than 350×10^{-15} may show the effects of radioactive decay of ^{36}Cl, or may indicate the effects of mixing with a low ^{36}Cl/Cl source, such as rock chloride. Actual estimates of water age depend on the past meteoric ratios, which must be considered highly speculative for the period before the earliest pack-rat data (40 k.y.). However, based on the current reconstruction, these ratios imply ages in excess of 200 k.y.

More than 900 ^{36}Cl measurements have been conducted thus far for the YMP. Analyzed samples include surface soils and soil profiles; rock samples collected from surface-based boreholes, the ESF, and the cross-drift; water samples, including surface runoff, unsaturated zone pore water,

perched water, and saturated zone water; and fossilized urine from pack-rat middens. Observations from these sample analyses are summarized in Table 5-6 and discussed below.

Chlorine-36 in Shallow Samples

Analyses of bomb-pulse ^{36}Cl and chlorine profiles in soil and alluvial profiles show that thick alluvium is generally effective at reducing net infiltration to levels less than 1 mm/yr (Fabryka-Martin et al. 1996 [DIRS 101003], Section 5.1.2; see data in DTNs: LAJF831222AQ95.006 [DIRS 145633]; LAJF831222AQ96.006 [DIRS 145635]). Exceptions to this generalization may be in channels and at the base of sideslopes, as illustrated by the penetration of bomb-pulse ^{36}Cl into the soil exposed at the NRG-5 drill pad and in samples as deep as 3.3 m in the soil-test pit NRSF-TP-19 at the North Portal (DTNs: LAJF831222AQ95.005 [DIRS 145632]; LAJF831222AQ97.006 [DIRS 145647]). In contrast, where alluvial cover is thin (i.e., less than a few meters thick) or missing, water is able to readily enter bedrock fractures, as shown by the detection of bomb-pulse ^{36}Cl measurements in some bedrock samples (DTNs: LAJF831222AQ96.008 [DIRS 145638]; LAJF831222AQ96.009 [DIRS 145639]; LAJF831222AQ96.011 [DIRS 145642]; LAJF831222AQ96.013 [DIRS 145644]). For example, fast transport through the TCw unit is indicated by bomb-pulse ^{36}Cl/Cl ratios measured in several boreholes that intersect the PTn unit, which lies below the TCw unit. Elevated levels of ^{36}Cl were also observed in drill core samples from the top of the Calico Hills unit in the shallow Busted Butte Field Transport Facility (DTN: LA9909JF831222.005 [DIRS 145630]).

Chlorine-36 in the Exploratory Studies Facility and Cross Drift

Pre-2000 Studies—Evidence for fast pathways that persist into the TSw unit is provided by bomb-pulse ^{36}Cl/Cl ratios measured at locations in the ESF tunnel and the cross-drift (Figure 5-20, Table 5-7). More than 250 samples have been analyzed from the ESF tunnel. Of these, more than 40 had ^{36}Cl levels sufficiently elevated as to be interpreted as unambiguous evidence for the presence of elevated ^{36}Cl (Fabryka-Martin et al. 1996 [DIRS 144839]; 1997 [DIRS 100145]; 1998 [DIRS 162737]; DTNs: LAJF831222AQ98.004 [DIRS 107364]; LAJF831222AQ98.009 [DIRS 145650]; LA9909JF831222.010 [DIRS 122733]). For example, elevated ^{36}Cl was detected in the Drill Hole Wash fault zone, in the vicinity of the Sundance fault zone in the main drift and ESF Niche 1, and near the Sundance fault zone and the Ghost Dance fault zone where they were intersected by the northern Ghost Dance fault access drift (Alcove 6). Similar to the ESF results, 5 out of 15 cross-drift samples had ratios above $1,250 \times 10^{-15}$, and nine were above $1,000 \times 10^{-15}$ (DTN: LA0307RR831222.001 [DIRS 164091]).

The correlation of the elevated ^{36}Cl measurements with the surface expression of faulting indicates that the pathway and travel time may involve locally modified PTn unit fracture properties (Fabryka-Martin et al. 1997 [DIRS 100145], p. 78; 1997 [DIRS 100144], pp. 6-22 and 8-18). These data support the hypothesis that faulting or other disturbances increase PTn unit fracture permeability, thereby generating a local environment in the PTn unit that supports fracture flow and hence rapid transport of solutes. Once through the PTn unit, flux distributions favor fracture flow in the TSw unit, thereby providing a continuous pathway to the sampled depths.

Most of the ESF sample analyses had ratios less than the threshold for indicating bomb-pulse ^{36}Cl (Figure 5-20). In the southern part of the ESF, beyond Station 45+00, most samples had ^{36}Cl/Cl ratios typical of Holocene water, which could suggest travel times of less than 10 k.y. to this depth. A number of samples from this part of the system also had ^{36}Cl signals that were significantly below the present-day background value, suggesting the possible presence of zones of relatively stagnant water.

Many samples from the northern part of the ESF, up to Station 45+00, had ^{36}Cl/Cl ratios variably above the present-day background, providing a striking contrast to the nearly constant ratios measured in its southern part (Figure 5-20). The largest signals—those above a ratio of $1,250 \times 10^{-15}$—are attributed to global fallout ^{36}Cl. Fabryka-Martin et al. (1997 [DIRS 100145], pp. 19 and 21) discuss alternative hypotheses to account for these highly elevated signals and rule out sample contamination as well as in situ production of ^{36}Cl either at the surface or deeper in the profile. They conclude that fast hydrologic paths capable of conducting bomb-pulse ^{36}Cl to the level of the ESF are more prevalent in the northern part of the ESF. With regard to those intermediate samples with ratios greater than present-day background but less than $1,250 \times 10^{-15}$, it is not presently possible to assess whether these intermediate signals indicate the presence of a very small component of bomb-pulse ^{36}Cl or whether the elevated signals reflect travel times exceeding 10 k.y., the most recent time when the signal in infiltrating water would have been high enough (Figure 5-19) to provide these ^{36}Cl/Cl signatures.

The pre-2000 ^{36}Cl results were used to develop a conceptual model for flow through the unsaturated zone at Yucca Mountain (Campbell et al. 2003 [DIRS 162745]). In order for bomb-pulse ^{36}Cl to have reached the level of the repository in less than 50 yr, a thin alluvial cover (less than a few meters) must be present, because thick alluvium slows infiltration. Flow generally occurs as fracture-flow through the welded Tiva Canyon and Topopah Spring tuffs, but matrix flow in the Paintbrush tuff nonwelded hydrogeologic unit. Rapid transport through the nonwelded tuff occurs only in areas where it is faulted, and only in these areas has bomb-pulse ^{36}Cl reached the repository level. Away from PTn-cutting faults, the ages of water samples at the ESF appear to be a function of the thickness of the non-welded tuff between the ground-surface and the ESF.

Validation Study Results—As part of the validation study (BSC 2003 [DIRS 166347], Section 6.14), samples were collected from areas in the ESF where elevated levels of ^{36}Cl had been previously reported. Core samples were collected from systematically-spaced boreholes in the ESF along a 165 meter wide zone associated with the Sundance fault (earlier studies had collected samples by excavation into the drift wall), and from a borehole in Niche 1, also associated with the Sundance fault (BSC 2003 [DIRS 166347]). A small subset of samples from Niche 1 was sent for analysis to Los Alamos National Laboratory (LANL), where the original ^{36}Cl work was performed. The measured ^{36}Cl/Cl values for these samples varied from $1,016 \times 10^{-15}$ to $8,558 \times 10^{-15}$, which are comparable to the pre-1999 results (DTNs: LL031200223121.036 [DIRS 168531]; LL030408023121.027 [DIRS 162949]). The majority of the samples were prepared at the USGS laboratories in Denver, using a "passive" leaching method, where samples were leached with deionized water for one hour at a water/rock ratio of about one, without agitation. The leachate was analyzed for ^{36}Cl at Lawrence Livermore National Laboratory. The results are summarized and compared to the pre-2000 results in Figure 5-21 (BSC 2003 [DIRS 166347] Figure 6.14.2-1; Paces et al. 2003 [DIRS 162738]). The

USGS validation study results, including additional samples from Niche 1, show no evidence of bomb-pulse ^{36}Cl along the Sundance fault, and do not indicate evidence for increased ^{36}Cl production rates during the Pleistocene. Only a few of the ^{36}Cl/Cl ratios measured in the validation study exceeded the concentrations in modern pre-bomb precipitation, and none exceeded the range of values proposed for Pleistocene precipitation.

High tritium and ^{36}Cl/Cl values are typically not correlated. The validation study tritium results for samples from the Sundance and Drill Hole Wash fault zones show no evidence of percolation of young water (there is no bomb signature). This is consistent with the USGS ^{36}Cl validation study results for the Sundance fault, and inconsistent with LANL ^{36}Cl results for both fault zones. The tritium data also indicate the presence of fast paths in the Topopah Spring Tuff in the south ramp of the ESF; pre-2000 ^{36}Cl data showed no evidence for fast path behavior (there is no validation study ^{36}Cl data from this area).

The differences in the ^{36}Cl measurements obtained by LANL and those obtained by the USGS are currently the focus of further investigation. Some of the inconsistencies may be due to the use of different sampling strategies in the pre-2000 studies and the validation study. Early LANL studies used a "feature-based" sampling strategy—collecting samples from faults, breccias, and fractures on the tunnel wall. Such a strategy might be expected to yield more ^{36}Cl "hits" than the systematic sampling done in the validation study, in which boreholes were evenly spaced across broad structural features (the Sundance and Drill Hole Wash fault zones). However, adjacent samples from Niche 1 borehole cores yielded elevated ^{36}Cl when analyzed by LANL and did not when analyzed by the USGS/Lawrence Livermore National Laboratory. Thus, if fast-paths are present, they are heterogeneously distributed over very small distances.

Chlorine-36 in Deep Boreholes

Measured ^{36}Cl/Cl ratios for samples of moderately to densely welded tuff from boreholes are systematically lower than the values for ESF samples. This apparent discrepancy is probably attributable to differences in sample collection techniques (Fabryka-Martin et al. 1996 [DIRS 101003], Section 6.2). Borehole samples are obtained from ream cuttings. Rock chlorine is released to the cuttings during drilling and is subsequently leached together with the pore water chlorine during sample preparation for ^{36}Cl analysis. This source of chlorine has a ^{36}Cl/Cl ratio on the order of 40×10^{-15}. The extent to which rock chlorine contributes to the total amount of chlorine leached from the rock can be estimated from its Br/Cl ratio (Fabryka-Martin et al. 1997 [DIRS 100145], pp. 30 to 32; 1996 [DIRS 101003], Section 6.2.1). Because of the low ^{36}Cl/Cl of the rock chlorine, the ^{36}Cl/Cl calculated for the meteoric component of chlorine in the borehole samples is always equal to or higher than the measured ratio. Samples collected from tunnel walls are not as greatly affected by rock chlorine, as are borehole samples because the manual collection method used in the tunnel does not pulverize the rock, as does the ream bit. Differences between uncorrected ^{36}Cl/Cl ratios for borehole samples from welded units and those from the ESF demonstrate the importance of recognizing the magnitude of the influence of rock chlorine to the ^{36}Cl/Cl values measured for borehole samples. After correcting for this effect, the two sets of analyses are consistent (Fabryka-Martin et al. 1997 [DIRS 100145], p. 33). None of the few ^{36}Cl/Cl measurements available for samples collected below the current repository horizon are sufficiently high to suggest the presence of bomb-pulse ^{36}Cl (Table 5-6, observations for TSw and CHn samples). The maximum ratio measured for a surface-based borehole sample

in or below the Tptpul unit was 843×10^{-15} for USW SD-12 (1,940 to 1,941 ft (abut 600 m), Tcp2 unit; DTN: LAJF831222AQ97.007 [DIRS 145648]).

5.2.2.5.4 Carbon Isotopes

Background

The best developed isotopic method for dating groundwater is that using ^{14}C, which is produced naturally in the upper atmosphere by bombardment of N by the secondary neutron flux (Clark and Fritz 1997 [DIRS 105738], p. 202):

$$\,^{14}_{7}N + \,^{1}_{0}n \Rightarrow \,^{14}_{6}C + \,^{1}_{1}p \qquad\qquad (Eq.\ 5\text{-}4)$$

The modern atmospheric activity of ^{14}C is set by convention to 13.56 decays per minute per gram of carbon in 1950 and is considered to have an activity of 100 percent modern carbon (Clark and Fritz 1997 [DIRS 105738], p. 18). Based on a half-life of 5,715 yr (Parrington et al. 1996 [DIRS 103896], p. 19), this specific activity corresponds to a $^{14}C/C$ ratio of about 1.2×10^{-12}. The above ground testing of nuclear devices temporarily increased the ^{14}C content by as much as a factor of two (Figure 5-18). The decrease since 1964 is due to the exchange of ^{14}C for nonradioactive carbon from the biosphere and hydrosphere, predominantly the ocean. Other secondary influences on the atmospheric ^{14}C inventory are releases of ^{14}C from nuclear fuel reprocessing plants and dilution by releases of nonradioactive carbon from the burning of fossil fuels.

Despite its extensive use in hydrologic studies, numerous processes related to carbon geochemical reactions complicate the interpretation of ^{14}C analyses in water. These processes involve the isotopic exchange between carbonate species dissolved in pore water, carbonates in soil and fracture minerals along the flow path, and CO_2 in the gas phase. Hence, the successful use of ^{14}C to date groundwater depends on a thorough understanding of geochemical reactions involving carbon species in the hydrologic system.

Stable carbon isotope ratios are invaluable for evaluating the likelihood and magnitude of subsurface reactions involving carbon. Stable carbon isotope data are presented as $\delta^{13}C$ values, defined as:

$$\delta^{13}C_{Sample} = \left(\left(^{13}C/^{12}C_{Sample} \div \,^{13}C/^{12}C_{Reference}\right) - 1\right) \times 1000 \qquad\qquad (Eq.\ 5\text{-}5)$$

where $^{13}C/^{12}C_{Sample}$ is the ratio in the sample and $^{13}C/^{12}C_{Reference}$ is the ratio is a reference standard (the commonly used one for carbon is the Pee Dee Formation Belemnite). Thus, $\delta^{13}C$ values are reported as parts per thousand (‰) difference from the reference. A $\delta^{13}C$ ‰ value that is positive has more ^{13}C than the reference, while one that is negative has less.

^{14}C and stable carbon isotopes have been analyzed in perched waters, unsaturated zone gases, and pore waters extracted from drill core from surface-based boreholes and from four alcoves in the ESF (Tables 5-8 and 5-9) (Yang et al. 1996 [DIRS 100194], pp. 27 to 34, 37, 38, 40, 42, 44 to 48; Yang et al. 1998 [DIRS 101441], pp. 16 to 23; LeCain and Patterson 1997 [DIRS 100529], pp. 3, 4, 11, 14; LeCain et al. 1997 [DIRS 100156], pp. 18 to 20, 37 to 39).

Carbon-14 in Pore Water Samples

As is the case for tritium, post-bomb levels of ^{14}C have been observed in a few samples collected above and within the PTn hydrogeologic unit. None of the pore water samples from surface-based boreholes have shown post-bomb levels of ^{14}C, that is, activities above 100-percent modern carbon. Activities range from 53.1 to 97.7 percent of modern carbon (BSC 2002 [DIRS 160247], Tables 15 and 16). However, it is possible that the presence of a relatively small volume of post-bomb water could be obscured by mixing with a large volume of old water, such that the resulting mixture would have an activity less than 100 percent modern carbon. A histogram of the pore water data from the PTn and CHn units (Figure 5-22) shows that the PTn unit values cluster tightly about the range of 80 to 90 percent modern carbon, whereas the CHn unit values spread more evenly across the range, presumably reflecting a larger spread in groundwater travel times to this depth, as would be expected if fracture flow were mixing to variable extents with slower matrix flow. Stable carbon isotope ratios for these same pore waters show a wide range in both hydrogeologic units (Figure 5-22), which may be a consequence of a variety of processes but which is also consistent with spatially and temporally variable infiltration rates and mixing between fast fracture flow and slow matrix flow.

The ^{14}C pore water data do not show any trend in activity with stratigraphic depth (BSC 2002 [DIRS 160247], Table 15). These irregular profiles are consistent with a conceptual model in which fracture flow and perhaps lateral flow occur in some of the stratigraphic units at Yucca Mountain (Yang et al. 1996 [DIRS 100194], p. 32; Yang et al. 1998 [DIRS 101441], p. 23). In general, ^{14}C activities in PTn and CHn unit pore waters suggest apparent ages that are less than 6 ka. Apparent ages are based on the assumption that the initial ^{14}C activity is 100 percent modern carbon and that the carbon isotopic composition of the sample has not been significantly altered by any geochemical processes, such that changes relative to the initial atmospheric activity are solely the result of radioactive decay. This assumption is supported by high ^{14}C activities measured in the annulus of shallow boreholes. These values ranged from 90.4 to 125.6 percent of modern carbon, with 13 of 16 samples yielding activities greater than 100 percent of modern carbon (BSC 2003 [DIRS 166347], Table 17).

Detailed evaluations of the various processes that could affect ^{14}C activities and stable carbon isotope ratios in Yucca Mountain pore waters are presented in Yang et al. (1996 [DIRS 100194], pp. 31 to 34) and in Yang et al. (1998 [DIRS 101441], pp. 21 and 23).

Carbon-14 in Gas Samples

Unsaturated zone gas samples were collected from open surface-based, two instrumented surface-based boreholes, and from USW SD-12. In addition, gas samples from ESF drill holes were collected after CO_2 and SF_6 concentrations had stabilized.

Uncorrected radiocarbon ages for gas samples from open surface-based boreholes range from modern to 2.6 ka in the TCw unit, modern to 3.1 ka in the PTn unit, 650 yr to 7.2 ka in the upper lithophysal and middle nonlithophysal zones of the Topopah Spring Tuff; and modern to 11.2 k.y. in the CHn unit (BSC 2002 [DIRS 160247], Tables 18 and 19). Radiocarbon profiles generally do not show any clear trend with depth.

Carbon-14 data from samples from instrumented boreholes are the most reliable indicators of in situ conditions. Data were collected from two instrumented boreholes and are presented in Table 5-8. Uncorrected radiocarbon ages for USW UZ-1 are modern at the probe near the top of the PTn unit, about 3.6 ka at the probe closest to the base of the PTn unit, about 7 ka in the middle nonlithophysal unit of the Topopah Spring Tuff, and about 7.8 ka and 16 ka at the bottom two probes, in the lower lithophysal zone of the Topopah Spring Tuff (DTN: MO0012CARB1314.000 [DIRS 153398]). Uncorrected ages for USW SD-12 are of similar magnitude although the profile is not as smooth. The gas age is about 1 ka at the top of the PTn unit and about 2.1 ka. at its base. The age increases to nearly 8 ka in the upper lithophysal zone of the Topopah Spring Tuff and to about 11 ka at probe B near the top of the CHn unit (DTN: MO0012CO2UNSZO.004 [DIRS 153756]); however, these ages are greater than those measured for pore waters from the CHn, as discussed above. Pore-water ^{14}C data are not considered representative of the pore-water residence time because of the contamination by atmospheric $^{14}CO_2$ during drilling (Yang 2002 [DIRS 160839], Section 4.1.2; BSC 2002 [DIRS 160247], Section 6.6.4.2) and by exchange processes with the gas phase, which have not been quantified.

Samples were also collected from instrumented boreholes in ESF alcoves. Samples from three boreholes in Alcove 1, all tapping intervals within the TCw unit, contained 93, 101, and 107 percent modern carbon (DTN: GS960208312261.002 [DIRS 121680]). Ten samples from the Alcove 6 borehole, which penetrated the Ghost Dance fault zone in the TSw unit, ranged from 75.1 to 58.1 percent modern carbon, corresponding to uncorrected ^{14}C ages of 2.4 to 4.5 ka (DTN: GS990983122410.003 [DIRS 145908]), somewhat younger than those obtained for similar stratigraphic depths in USW UZ-1 and USW SD-12.

Additional discussion of the carbon isotope data for gas samples is presented in Section 5.2.2.6.3.

Carbon-14 and Delta Carbon-13 in Perched Waters

Carbon-14 activities and $\delta^{13}C$ values of perched waters are shown in Table 5-4. The ^{14}C values range from 67 to 27 percent modern carbon, corresponding to apparent ^{14}C ages of about 3.3 to 11 k.y. (DTN: MO0012CARB1314.001 [DIRS 153394]; also Yang et al. 1996 [DIRS 100194], p. 34). Water ^{14}C ages can be affected by the dissolution of older carbon in the carbonate minerals, which would result in anomalously old apparent ages. Reaction with or incorporation of gas-phase CO_2 from deep in the unsaturated zone can also result in an anomalous apparent age.

The $\delta^{13}C$ values measured for perched water are quite variable, ranging from -9.2 to -16.6‰ (Table 5-4; DTN: MO0012CARB1314.001 [DIRS 153394]). A weak correlation is observed between these values and the surface material in which the drill hole is located. Perched water in USW SD-7, a borehole that is essentially started in bedrock, has heavy values of about -9.5‰, only slightly lighter than atmospheric CO_2. In contrast, perched water from USW NRG-7a, which was drilled through soil, has the lightest value of -16.6‰. This observation is similar to that made for strontium isotopic data, which show a less radiogenic input for bedrock and fracture coatings where there is no soil and for pore waters from a drill hole that was started in bedrock (Section 5.2.2.5.6). In summary, $\delta^{13}C$ data show that most of the bicarbonate in

unsaturated zone matrix pore fluids originated in the soil zone. In contrast, most of the perched water bodies and groundwater in the Yucca Mountain area have heavier (less negative) $\delta^{13}C$ values that do not show the same degree of soil influence as do the unsaturated zone pore waters (Figure 5-23).

5.2.2.5.5   Stable Hydrogen and Oxygen Isotopes

Background

As with carbon, δ values are commonly used to describe hydrogen and oxygen isotopic data. δD and $\delta^{18}O$ are defined, respectively, as:

$$\delta D_{\text{Sample}} = ((^2H/^1H_{\text{Sample}} \div {}^2H/^1H_{\text{Reference}}) - 1) \times 1000 \qquad \text{(Eq. 5-6)}$$

and

$$\delta^{18}O_{\text{Sample}} = ((^{18}O/^{16}O_{\text{Sample}} \div {}^{18}O/^{16}O_{\text{Reference}}) - 1) \times 1000 \qquad \text{(Eq. 5-7)}$$

where the commonly used reference for each is Standard Mean Ocean Water (SMOW).

Isotopic fraction in water arises from phase changes that do not go to completion, that is, partial evaporation, condensation, crystallization, or melting (Davis and Murphy 1987 [DIRS 105814], p. 119). Such incomplete processes are typical of rainfall, snowfall, evapotranspiration, and sublimation of snow and ice. As a consequence, regional differences arise in surface waters as a function of elevation, distance from water sources (i.e., the ocean), orographic (rain shadow) effects, degree of evaporation, and air temperature during precipitation.

If the first four of these factors stay relatively constant for a given location, then variations in δD and $\delta^{18}O$ in infiltrating water may be related to temperature variations during precipitation events. Factors that might complicate simple interpretations of such data at Yucca Mountain include shifts in $\delta^{18}O$ in pore waters due to alteration, dissolution, or precipitation of minerals containing oxygen; isotopic exchange; and sorption of water by clays and zeolites (Yang et al. 1998 [DIRS 101441], p. 24).

Stable Isotope Characteristics of Precipitation, Surface Water, Perched Water, and Groundwater

Stable isotope data are commonly presented by plotting δD versus $\delta^{18}O$, as has been done on Figure 5-24 for precipitation, surface water, perched water, and regional groundwater. The following observations are made from this figure:

- Precipitation data from 3-Springs Basin and Stewart Basin (Figure 5-24a) illustrate how fractionation of oxygen and hydrogen isotopes in atmospheric moisture results in a well-defined correlation line, called the "meteoric water line." Based on its lower elevation and warmer temperatures at Yucca Mountain, modern precipitation there is generally expected to fall along the upper end of the range shown, with heavier (less

negative) compositions, as demonstrated by four local precipitation samples plotted on Figure 5-24.

- Surface water data from 3-Springs Basin and Stewart Basin (Figure 5-24b) illustrate how stable isotopes reflect average climatic conditions prevailing during infiltration events. The cooler climate at Stewart Basin results in lighter (more negative) δ values. The isotopic data plot on the meteoric line indicates that these surface waters have not undergone much evaporation. Such a conclusion is supported by the dilute chemical compositions of these waters (Section 5.2.2.3). Data for two Yucca Mountain surface runoff samples, both collected in February 1993, also show negligible evaporation. Their heavy isotopic signatures overlap with those of the four precipitation samples collected at Yucca Mountain in 1984 (Figure 5-24a).

- Stable isotopic data of the perched water are generally between -12.8 and -13.8‰ for $\delta^{18}O$ and -94‰ and -99.8‰ for δD (Table 5-4). These values are slightly greater than those for the saturated zone values and similar to values for pore waters. They are generally close to the Yucca Mountain precipitation line, indicating little evaporation before infiltration (Figure 5-24c). Evaporation under equilibrium conditions would cause the water compositions to move back up the meteoric water line; however, evaporation is rarely an equilibrium process in natural systems, and generally results in waters moving off and below the meteoric water line. All perched water stable isotope values are similar to modern precipitation and are therefore consistent with recharge during the Holocene, as suggested by the ^{14}C data and ^{36}Cl data for these samples.

- Groundwaters beneath Fortymile Wash (Figure 5-24d) have stable isotope values similar to those for perched water beneath Yucca Mountain. Both data sets are consistent with recharge during the Holocene (i.e., post-glacial climate), as suggested by the ^{14}C data for these waters (Figures 5-23c and d).

- Among the groundwaters in the Yucca Mountain area, the lightest waters are from wells in the southwesternmost portion of the site (e.g., USW WT-10 and USW H-3). Local groundwaters with the heaviest isotopic values overlap with the values measured for perched waters and for wells in Fortymile Wash.

- Groundwaters from Pahute Mesa have lighter isotopic values than do the perched waters and groundwaters from Fortymile Wash. This difference is more consistent with recharge of the Pahute Mesa waters under colder climatic conditions than those that prevailed for the perched waters and samples from Fortymile Wash and with subsequent modification of the Pahute Mesa waters by rock-water interactions that shift $\delta^{18}O$ to heavier values. Although isotopic shifts due to evaporative loss cannot be altogether ruled out, this process seems unlikely to be significant for the Pahute Mesa recharge waters.

Stable Isotope Characteristics of Pore Waters

In contrast with the data for saturated zone water, perched water, and surface waters, hydrogen and oxygen isotope data for unsaturated zone pore waters are more difficult to interpret, possibly due to complications related to fluid extraction methods.

Data for unsaturated zone pore water samples obtained by uniaxial compression of the core plot on or slightly below the meteoric precipitation line, indicating minor evaporative loss (Figure 5-25). This evaporation may have occurred either prior to recharge or during drilling. Alternatively, the shift away from the meteoric water line may reflect oxygen isotopic exchange with the host rock.

In contrast, the composition of the CHn unit pore waters extracted by vacuum distillation is significantly lighter than that of the PTn unit pore waters (Figure 5-25a). Yang et al. (1998 [DIRS 101441], pp. 41 to 43) concluded that these extremely light oxygen isotopic signatures are not representative of in situ pore waters but rather are caused by isotopic fractionation induced by the distillation technique.

Comparison of isotopic compositions of unsaturated zone pore waters (Figure 5-25b) with those of the saturated zone groundwaters (Figure 5-24d) beneath Yucca Mountain show that the CHn unit pore waters are similar to the heaviest (least negative δD and δ^{18}O values) groundwaters in the Yucca Mountain area, whereas the PTn unit pore waters are significantly heavier (less negative) than either data set. Again, this difference is consistent with recharge of the CHn unit pore waters and Yucca Mountain groundwaters occurring under colder climatic conditions than recharge for the PTn unit pore waters. In the TSw unit basal vitrophyre, δD values in pore water from three Boreholes (USW SD-7, USW SD-9, and USW SD-12) are consistently shifted to more negative values, implying that waters were infiltrated during the colder climate of the last ice age (Yang et al. 1998 [DIRS 146443], p. 27, Figure 2). The δD values in pore waters from the underlying CHn unit are heavier than those for pore waters from the basal vitrophyre and similar to those for waters above the basal vitrophyre zone, indicating post-ice age water.

5.2.2.5.6   Strontium Isotopes

Strontium is a trace element in calcite, with concentrations generally tens to hundreds of micrograms per gram. A fraction of stable ^{87}Sr forms by decay of ^{87}Rb. Because calcite contains very little rubidium and the half-life of the ^{87}Rb parent is 4.9×10^{10} yr (Parrington et al. 1996 [DIRS 103896], p. 29), ^{87}Sr/^{86}Sr ratios of calcite record the ratio in the water from which the calcite precipitated. (In a closed system, dissolution and reprecipitation do not alter strontium isotopic compositions.) Thus, in the absence of other sources of strontium, the strontium ratios along a flow path are expected to preserve variations inherited from strontium in the soil zone (Marshall et al. 1998 [DIRS 146444], pp. 55 to 56).

Strontium isotope ratios are reported as differences from modern seawater in parts per thousand using

$$\delta^{87}Sr = ((^{87}Sr/^{86}Sr \div 0.7092) - 1) \times 1000 \qquad \text{(Eq. 5-8)}$$

Strontium isotope compositions in the host volcanic rocks differ significantly from those of the pore waters, indicating that pore water has not reached isotopic equilibrium with the tuffs. Pore water strontium data obtained from USW SD-12 core (Figure 5-26) are remarkable in their systematic variation with depth and their distinction from whole rock compositions. At the top of the core, the δ^{87}Sr value in the pore water is similar to that of soil carbonates from the area. The δ^{87}Sr values increase with depth; this increase is especially evident within the PTn unit and is only slightly discernible in the underlying TSw unit.

Although the data preclude local equilibrium between pore water and rock, the rock data can predict the strontium isotope composition of the pore water if recalculated as a downhole cumulative value weighted according to strontium content of the rock samples and the associated depth interval. An additional weighting factor that takes into account the higher reactivity of the PTn unit provides a close match to observed pore water strontium values throughout most of the TSw unit. The deviation of pore water δ^{87}Sr values from the predicted values is likely due to the presence of clays or zeolites, which may contain a long-lived record of pore water strontium compositions and could have been partially leached in the laboratory.

A working model assumes that strontium is added to infiltrating water by dissolution of calcite in the soil zone (Marshall et al. 1998 [DIRS 146444], pp. 55 to 56). During times of increased surface vegetation, soil waters are more acidic and volcanic detritus in the soil zone can contribute radiogenic strontium into infiltrating water, thus increasing the ^{87}Sr/^{86}Sr ratio in the thick calcretes formed during these times.

Water infiltrating into welded tuff (Tiva Canyon Tuff or Topopah Spring Tuff) tends to retain the strontium isotope composition of the overlying soil. However, the pore water data indicate that water infiltrating into or percolating through nonwelded tuff (e.g., the PTn unit) reacts readily and acquires a strontium isotope signature reflecting interaction with this unit. The strontium isotope composition of the volcanic rocks changes systematically over millions of years due to the decay of ^{87}Rb. As a result, pore waters interacting with these rocks would have δ^{87}Sr values that decrease linearly with age. δ^{87}Sr values of pore waters in the TSw unit are predicted to change from a modern value of 4.9 to about 0.4 at the time of TSw unit emplacement (12.7 Ma). The observation that δ^{87}Sr values vary with microstratigraphic position within thick calcite coatings that occur on fractures in the TSw unit and the match between these ratios and the predicted values strongly suggests that the calcite coatings derive their strontium from the same source as the pore water. In other words, both pore water and the fracture water leading to calcite deposition within the TSw unit derive strontium from rock-water interaction in the overlying section, dominantly in the nonwelded units. This model indicates that pore waters in the PTn unit are redistributed between pore and fracture water that subsequently percolates through the TSw unit.

As part of the ^{36}Cl Validation Study to evaluate "fast pathways" to the repository level, pore water samples were extracted from borehole cores from Niche 3566 in the ESF, an area previously identified on the basis of ^{36}Cl isotopes as having a component of young water and representing a fast path. The strontium isotope composition of the pore waters in this area fell within the range of other TSw pore waters (Marshall and Futa 2003 [DIRS 162717]). This indicates that the pore water in this area interacted with the overlying rocks (especially PTn) to the same degree as other pore water samples from the current repository horizon. This extent of

water-rock interaction requires the long travel times inferred for the unsaturated zone in general, indicating that the core samples from this area do not show evidence for faster flow paths through the unsaturated zone, despite the presence of faults through the overlying nonwelded tuff units (Marshall and Futa 2003 [DIRS 162717]).

5.2.2.5.7   Uranium Isotopes

Uranium isotopic ratios have been used to address the question of local recharge to the water table through the unsaturated zone at Yucca Mountain and the prevalence and frequency of fracture flow. The presence of calcite and opal lining fractures and cavities in the lowest units of the TSw unit exposed in the ECRB Cross-Drift and in core from underlying unsaturated zone units suggests that water moving through fractures has reached these depths. Flow through the matrix also accounts for some portion of the total infiltration. However, the fraction of the shallow groundwater beneath Yucca Mountain that is locally versus regionally derived and the ratio of fracture flow versus matrix flow contributing to local recharge are poorly known. Uranium isotopic compositions of unsaturated zone fracture minerals, pore water, perched water, and shallow groundwater contribute to the conceptualization of these issues (Paces et al. 1998 [DIRS 100072], pp. 187 to 188; Paces and Peterman 1999 [DIRS 127004], pp. 134 to 138), which is summarized in this section.

Unlike oxygen, carbon, and strontium isotope signatures, which are largely inherited during infiltration through soils, uranium isotopic compositions of percolating water are significantly modified from values observed in soil water and surface water, which usually have $^{234}U/^{238}U$ activity ratios from 1.4 to 1.8 (BSC 2002 [DIRS 160247], Table 23; Muhs et al. 1990 [DIRS 105140], Table 24, Figure 3; Paces et al. 1994 [DIRS 106473], p. 2400; Paces et al. 1995 [DIRS 101352], Figures 9, 10, 13, 16, 17, 20, 21, 25, 26, 27, 32, 36, 39, 42, 45, 46, and 53), to ratios as large as 9 at the current repository horizon (Paces et al. 1996 [DIRS 100171], Figure 3.7; Paces et al. 1997 [DIRS 100070], Figure D3). As a consequence of radioactive decay, ^{234}U is preferentially enriched relative to ^{238}U in migrating groundwater (Osmond and Cowart 1992 [DIRS 145190], Figure 9.1). The primary causes for this enrichment are the greater solubility of ^{234}U due to radiation damage of crystal lattice sites containing ^{234}U atoms (Szilard-Chalmers effect) and the greater probability that these ^{234}U atoms have been converted to the more soluble uranyl ion due to the effects of radiation-induced ionization (Gascoyne 1992 [DIRS 127184], Section 2.5.1). In addition, decay of ^{238}U can cause the displacement of the intermediate ^{234}Th daughter (which rapidly decays to ^{234}U) off crystal surfaces into the adjacent water by alpha-recoil processes. The amount of excess ^{234}U relative to ^{238}U is controlled by ^{234}U decay, water/rock ratios, flow path length, and the amount of bulk rock dissolution in the aquifer.

Meteoric water interacts with readily soluble soil components, resulting in infiltration containing relatively large amounts of both ^{234}U and total uranium (BSC 2002 [DIRS 160247], Table 23) derived from bulk dissolution of soil minerals. As infiltrating water descends through the fracture network, small amounts of ^{234}U that have become available from radioactive decay will be incorporated into these solutions. If water fluxes are large, then the $^{234}U/^{238}U$ ratio will remain relatively unchanged from its initial infiltration value. If water fluxes are small and only occur infrequently, ^{234}U can build up in sufficient amounts along the fracture surface between infiltration events such that the $^{234}U/^{238}U$ activity ratio in the water becomes elevated. The large

^{234}U/^{238}U ratios in unsaturated zone waters at Yucca Mountain imply that percolation volumes are small relative to shallow environments that receive larger amounts of percolation.

Data supporting this conceptual model of ^{234}U/^{238}U evolution were obtained from water samples collected during the Single Heater Test (SHT) conducted in the Thermal Test Facility (ESF Alcove 5) (Figure 5-27). Water derived from the welded tuffs proximal to the heater was mobilized and flowed through a connected fracture network for six months into a nearby borehole. Uranium concentrations decreased in that time, and in the same samples, ^{234}U/^{238}U activity ratios dropped. These data are interpreted as evidence that the fracture pathways used by mobilized water during the test had not experienced recent natural flow and had built up substantial amounts of leachable ^{234}U on their surfaces. Fracture water mobilized during the early stages of the test incorporated the more labile ^{234}U en route to the collection site. The most readily leached components dissolved early, so uranium concentrations and ^{234}U/^{238}U activity ratios decreased with time. A similar pattern of decreasing values with time was observed in water mobilized from volumes of rock much larger than the SHT (BSC 2002 [DIRS 160247], Figure 40). This pattern illustrates, in a qualitative sense, the likelihood that frequent flushing of fracture surfaces may not allow sufficient accumulation of ^{234}U on fracture surfaces to substantially alter the ^{234}U/^{238}U ratios in fracture water.

Uranium isotope data from springs discharging from perched water zones in other areas of the Nevada Test Site support the conclusion that small fluxes and infrequent flux events are required to attain the large ^{234}U/^{238}U ratios observed at Yucca Mountain. These springs and seeps have ^{234}U/^{238}U activity ratios ranging between 1.9 and 3.8 (Paces et al. 1995 [DIRS 101352]). These waters have relatively large volume-to-path-length ratios and either continuous or frequent flow that does not permit accumulation of substantial excess ^{234}U on solid surfaces along flow paths. As a result, uranium in water from these systems has isotopic compositions that are only slightly greater than values observed in the infiltrating water. In contrast, these values are much lower than ^{234}U/^{238}U ratios of waters perched within the welded TSw unit at Yucca Mountain (5.2 to 8.4, from Table 5-4; DTNs: GS010808312322.004 [DIRS 156007]; GS010808312322.005 [DIRS 156008]), as well as the initial ^{234}U/^{238}U ratios in young calcite and opal from the repository horizon in the ESF (Paces et al. 1996 [DIRS 100171], Figure 5.1).

Groundwater from the saturated zone beneath Yucca Mountain also has elevated ^{234}U/^{238}U activity ratios compared to well water in adjacent areas (compare Figures 5-28 and 5-29) (Ludwig et al. 1993 [DIRS 101141], Figure 2; Paces et al. 1998 [DIRS 100072], p. 185). Regional saturated zone groundwater in carbonate rock, alluvial, and Precambrian rock aquifers from Oasis Valley, Amargosa Valley, Spring Mountains, and the easternmost Nevada Test Site have ^{234}U/^{238}U activity ratios between 1.5 and 4. Groundwater ^{234}U/^{238}U activity ratios from volcanic rock aquifers in the region are commonly between 4 and 6; however, shallow saturated zone groundwater beneath Yucca Mountain has anomalously large ^{234}U/^{238}U activity ratios between 6 and 8 (Paces et al. 2002 [DIRS 158817], p. 760).

The anomalous uranium isotopic compositions of shallow saturated zone water beneath Yucca Mountain are similar to the elevated initial ^{234}U/^{238}U compositions measured for deep unsaturated zone minerals and perched water bodies within the welded TSw unit. The similarity of the unsaturated zone and saturated zone uranium reservoirs at Yucca Mountain is interpreted as an indication of a genetic linkage between the two. Therefore, some component of recharge

through the thick unsaturated zone at Yucca Mountain is required. Local recharge is considered an important component to the saturated zone immediately below Yucca Mountain; however, this component does not contribute significantly to the regional water budget in the Fortymile Wash or Crater Flat hydrologic flow systems. These conclusions are consistent with major ion data, as well as δD, $\delta^{18}O$, and $\delta^{87}Sr$ data from the shallow groundwaters at Yucca Mountain that are interpreted to indicate kilometer-scale heterogeneities over the same areas (Peterman and Patterson 1998 [DIRS 101150], pp. 277 to 278; Paces and Peterman 1999 [DIRS 127004], p. 137).

As part of the ^{36}Cl Validation Study (BSC 2003 [DIRS 166347], Section 6.14), seventy tuff core samples from ESF boreholes in the vicinity of the Sundance and Drill Hole Wash faults, and from "unfractured" rock in the ECRB, were analyzed for uranium-series isotopic compositions. Most samples were slightly out of secular equilibrium, having a small deficiency of ^{234}U, and a small excess of ^{230}Th, indicating that ^{234}U had been removed from the rocks in the last ~350 ka, probably by migrating pore fluids (Gascoyne et al. 2002 [DIRS 154800]). Both fractured and unfractured tuffs show approximately the same deficiency of ^{234}U, indicating that pore fluids are moving equally through both. Thus, the U-series isotopic compositions of the fractured and unfractured rock suggest that the fractured rock is not a preferential pathway for groundwater flow.

5.2.2.6   Chemical and Isotopic Composition of Gases

5.2.2.6.1   Processes Controlling Gas Chemistry

The composition of air is the primary control on unsaturated zone gas chemistry. However, soil-zone processes, such as plant respiration and microbial activity can alter the chemistry of gases that diffuse into the unsaturated zone. Carbon dioxide partial pressures are particularly susceptible to modification by these processes.

Once gases diffuse from the soil zone into the unsaturated zone, the gas-phase composition will tend to equilibrate with the waters present in the unsaturated zone. Variations in total gas pressure can influence the composition of unsaturated zone waters through their effect on the partial pressures of separate gases in the gas phase. More significant, however, is its effect on gas flow patterns, including water vapor transport.

Gases of non-atmospheric composition can also migrate upward through the unsaturated zone along concentration, temperature, and pressure gradients, and mix with the indigenous gases in the unsaturated zone to alter the overall gas composition.

Temperature influences the kinetics of reactions that control the composition of the gas phase. In addition, temperature controls the equilibrium fractionation of light stable isotopes, particularly oxygen.

5.2.2.6.2   Gas Compositions

Gas composition data were obtained from the instrumented Borehole USW UZ-1 (Yang et al. 1996 [DIRS 100194], Table 8) as well as several other boreholes. To a depth of 368 m (1,207 ft) in USW UZ-1, the concentrations of oxygen, nitrogen, and argon are within analytical

error of atmospheric compositions (BSC 2002 [DIRS 160247], p. 81). According to Thorstenson et al. (1990 [DIRS 100831], p. 260), all gas samples from USW UZ-6S, USW UZ-6, and the neutron boreholes collected to date also show concentrations of O_2, N_2, and argon that are identical to the concentrations of these gases in atmospheric air to the limits of analytical precision. The authors report that all soil gases sampled on and near Yucca Mountain showed methane concentrations that were depleted relative to the atmospheric value of about 1.7 ‰ by volume, but still greater than 0.5 ‰ by volume (Thorstenson et al. 1990 [DIRS 100831], p. 267). In contrast, neutron hole and USW UZ-6S gases generally showed methane concentrations near zero, ranging up to a maximum value of 0.5 ($\pm$ 0.1) ‰ by volume, suggesting that methane consumption occurs in the subsurface, even below the soil zone (Thorstenson et al. 1990 [DIRS 100831], Figure 4).

Carbon dioxide concentrations are generally larger in the rock gas (about 0.1 percent) than in air (0.034 percent). Carbon dioxide gas concentrations in boreholes ranged from 0.01 to 1.3 percent by volume (Thorstenson et al. 1990 [DIRS 100831], Figure 4; Yang et al. 1996 [DIRS 100194], Table 8). Yang et al. (1996 [DIRS 100194], Table 9) published several analyses for the partial pressure of CO_2 in USW NRG-6 and USW NRG-7a in which CO_2 concentrations ranged from 0.05 to 0.19 percent by volume. Some of these data are also listed in Table 5-8. Note that essentially all the data indicate that the partial pressure of CO_2 in the unsaturated zone gas phase is higher by factors of three or more than that in the atmosphere.

5.2.2.6.3   Carbon Isotopes in Gases

Carbon isotopes were monitored at different sampling depths in USW UZ-1 starting in 1984 (Yang et al. 1996 [DIRS 100194], Figures 19 and 20). Most values for $\delta^{13}C$ lie within the range of -16 to -22‰ (Table 5-8 and Figure 5-30). USW SD-12 gases are lighter, with values ranging from -20 to -25‰). Slightly heavier $\delta^{13}C$ values, ranging from -13.5 to -16.5‰, were obtained for gas samples from boreholes in ESF Alcoves 1 and 6 (BSC 2002 [DIRS 160247], Table 21). There is little overlap between the $\delta^{13}C$ values for USW UZ-1 and USW SD-12 gases and those obtained for the gases from the ESF boreholes. However, the slightly heavier $\delta^{13}C$ values observed in the ESF alcoves are likely to be due to contamination by atmospheric CO_2 as a result of ESF ventilation. Hence, the USW UZ-1 $\delta^{13}C$ values that were obtained before the excavation of the ESF are considered to be more representative of in situ rock gas $\delta^{13}C$ values.

The ^{14}C data for USW UZ-1 have been very consistent for the last 7 yr of monitoring, with a gradual decrease in ^{14}C activity with depth to about 23 percent modern carbon at 368 m (Figure 5-30). The ^{14}C profile shows an abrupt change in the slope within the Pah Canyon interval of the PTn unit. The gas transport velocity (^{14}C concentration gradient over distance) within the PTn unit is smaller than the transport velocity in the TSw unit (Yang et al. 1993 [DIRS 100838], p. 404), perhaps because of a greater degree of water saturation in this unit. An estimate of the minimum travel time of gas in the TSw unit based on the apparent ^{14}C ages and depths in the borehole yields gas movement of 3.26 cm/yr. This rate, as well as results of gas transport modeling (Yang et al. 1996 [DIRS 100194], pp. 47 and 49), is consistent with downward movement of atmospheric CO_2 by simple Fickian diffusion. The fact that the ^{14}C values of rock gas in the closed (i.e., instrumented) borehole decrease steadily with depth indicates that inhalation and exhalation of gases in response to changes in atmospheric pressure, as observed in open boreholes, is not a significant process under undisturbed conditions.

Although diffusion may not be the only mechanism for gas movement in the TSw unit at USW UZ-1, it seems to be the dominant mechanism and can account for the observed distribution of gaseous ^{14}C with depth.

The ^{14}C activity of gas in Borehole USW SD-12 is similar to that of USW UZ-1 in that there is a decrease from surface to depth, but there are some large deviations from the trend (Table 5-8). Another difference is the markedly lighter carbon in USW SD-12 and the strong correlation between δ^{13}C and ^{14}C activities. Rousseau et al. (1997 [DIRS 100178], p. 64) noted that the pneumatic pressures in the two deepest stations of USW SD-12 (both within the CHn unit) were lower than predicted by extrapolation of the static pressure profile developed across the overlying TSw unit. This gas pressure deficiency could be due to the presence of hydrocarbons. The oxidation of hydrocarbons, such as methane, could account for the anomalously light carbon in the drill hole and the low ^{14}C activity of the sample at 407 m (1,335 ft).

Although the results from these two boreholes are consistent in showing decreasing ^{14}C activity with depth, it should be noted that there is little data to evaluate this on a site-wide scale. Less extensive data for open surface-based boreholes yield different results from the instrumented Boreholes USW UZ-1 and USW SD-12 (Table 5-8). In the open surface-based drill holes, ^{14}C activity does not appear to decrease with depth and, in fact, some show post-bomb carbon. However, leakage of air through poor sealing of the packer system against the borehole wall could account for these large ^{14}C activities.

The extent to which rock gas is in isotopic equilibrium with the pore waters is not clear. Although no data exist for gas and pore water extracted from the same sample, Table 5-9 compares samples that were collected from the same general depth ranges in Yucca Mountain boreholes. At equilibrium, carbon in bicarbonate in water should be about 8.5‰ heavier than carbon in CO_2 in the gas phase at 25°C (Clark and Fritz 1997 [DIRS 105738], Figure 5-4, p. 120, Table 5.3, p. 521). For these samples, the differences for δ^{13}C in gas and pore water are much less than 8.5‰ for all but a couple of samples from the CHn unit in USW UZ-14. It is inconceivable that CO_2 gas in the pore spaces would not be in isotopic equilibrium with the pore water after coexisting for hundreds, or even thousands, of years. The apparent disequilibrium between the two phases is probably a consequence of the drilling or sampling technique, such that the pore water may have been contaminated by drilling air or the sampled gas may not be derived from the immediate vicinity of the packed-off interval.

5.2.2.7 Chemical and Isotopic Composition of Saturated Zone Groundwater

The chemistry discussed in this section is based in large part on water collected from the upper tens of meters of the saturated zone. The chemical and isotopic data at greater depth are sparse (see Section 8).

5.2.2.7.1 Processes that Control Saturated Zone Water Chemistry

The chemistry of saturated zone waters is determined by processes that are linked in space and time. The similarities in compositions between groundwater and perched water suggest that similar geochemical processes control their compositions and that these processes differ from

those controlling the geochemistry of unsaturated zone pore waters. The chemistries of local saturated zone waters and perched waters are compared in Section 5.2.2.7.3.

The main processes that determine groundwater chemistry along its flow paths are:

- The quantity and compositions of precipitated secondary minerals (Section 5.2.1.1)

- Surface water compositions and infiltration rates (Section 5.2.2.3)

- Soil zone processes at recharge areas and along flow paths between recharge areas and the accessible environment

- Rock-water-gas interactions in the unsaturated zone at recharge areas and at Yucca Mountain (Sections 5.2.1.2 and 5.2.2.4)

- Rock-water interactions in the saturated zone along flow paths between the recharge areas and the accessible environment

- Temperature and pressure conditions along flow paths between recharge areas and the accessible environment

- Mixing of groundwaters from different flow systems.

The primary recharge areas for saturated zone waters in Yucca Mountain are located to the northeast of Yucca Mountain, as discussed in Section 8.2. The rock types dominating the recharge areas are silicic and basaltic volcanic units (Byers et al. 1976 [DIRS 104639], pp. 6, 7 and 19). Although Paleozoic limestones and other sedimentary units are present at depth, they do not appear to have a major effect on the compositions of waters that occur in the saturated volcanic units beneath Yucca Mountain (Section 8.3.6). However, some samples near faults have a slightly elevated $\delta^{13}C$, which could suggest a contribution from the carbonate aquifer (Stuckless et al. 1991 [DIRS 101159]). Such an interpretation is consistent with the greater hydraulic head at depth in UE-25 p#1 (Craig and Johnson 1984 [DIRS 101039]).

The northern recharge area receives more precipitation, is cooler on average than Yucca Mountain, and supports a greater abundance of vegetation. Accordingly, infiltration rates in the northern recharge area are also expected to be higher than infiltration rates on Yucca Mountain. Higher infiltration rates imply that dissolved salts and other constituents that may accumulate in the soil zone as a result of evapotranspiration of infiltrating waters will have shorter residence times in this zone. Also, waters infiltrating into the saturated zone will have lower salt and silica concentrations than waters at Yucca Mountain. This dilute composition makes these waters more reactive with respect to the rock units through which they may subsequently migrate.

Because the waters percolating downward from the soil zones in recharge areas are likely to be more reactive than soil waters percolating into the unsaturated zone at Yucca Mountain, dissolution reactions are likely to be more important in the unsaturated zones of the recharge areas. The dominant changes to the water compositions that result from these reactions are

major increases in silica, sodium, and bicarbonate (White et al. 1980 [DIRS 101166], pp. Q15 to Q17).

Once the water has undergone the initial dissolution reactions, the rate of change in water composition would likely decrease. This decrease occurs because the rate of dissolution is a function of the degree to which the water has approached thermodynamic equilibrium with the rock units it contacts. The closer the water is to thermodynamic equilibrium with the host rock, the slower the reaction rate.

The dominant rock-water reactions that impact the water chemistry after the initial dissolution reactions are silica precipitation reactions and ion-exchange reactions involving minerals such as zeolites and clays. The cation/H^+ ion-exchange reaction will also continue to be of significance. The ion-exchange reactions will tend to lead to increased sodium concentrations and decreased calcium, magnesium, and potassium concentrations in the waters. However, changes in the concentrations of these ions will occur only if zeolites and/or clays are present in adequate quantities in rock units through which the waters migrate. The Na^+/H^+ ion-exchange reaction will continue to increase the sodium content of the waters until thermodynamic equilibrium is achieved with the host rock (although the formation of metastable phases may cause the approach to equilibrium to be very slow).

The degree to which alteration reactions involving silicates and aluminosilicates in the host rock control water compositions is unclear. For example, volcanic glass is thermodynamically unstable in contact with water at ambient conditions, and given enough time, it will alter to secondary minerals such as clays, zeolites, silica polymorphs, and other minerals. However, glass is still present in great abundance in the volcanic units that make up Pahute Mesa and Rainier Mesa (Byers et al. 1976 [DIRS 104639], pp. 6, 7 and 19). Although glass alteration reactions are taking place, the rate at which this happens appears to be much slower than the rate of the initial dissolution reactions and ion-exchange reactions. For purposes of predicting water compositions, restricting the discussion to the latter reaction is probably adequate.

Controls on the pH of groundwaters in the saturated zone are similar to those discussed in Section 5.2.2.4.2. In brief, the primary controls on pH are the partial pressure of CO_2 and the rate at which hydrogen ions are consumed by the rock/mineral matrix. In the saturated zone, access to the CO_2 reservoir in the gas phase of the unsaturated zone becomes progressively more difficult with depth. Therefore, unless a secondary source of carbonic acid or another source of acidity (i.e., sulfide minerals) exist in the saturated zone, the reaction of hydrogen ions with the rock/mineral matrix will eventually consume the available acidity, leading to increased pH. The high pH value observed in USW H-3 (pH 9.4) (Ogard and Kerrisk 1984 [DIRS 100783], p. 9) likely reflects this process.

Controls on redox states in the saturated zone are more difficult to define. Potential redox reactions in the saturated zone include various redox couples such as oxygen/water, ferrous/ferric iron, sulfide/sulfate, nitrite/nitrate, and other couples. If dissolved oxygen is higher than approximately 0.1 mg/L, it could produce a relatively high redox potential (Eh greater than 600 mV). The redox state of saturated zone waters as calculated from the concentrations or activities for respective couples may or may not be at equilibrium.

In summary, the dominant processes that are likely to control water compositions along the flow paths from recharge areas to the saturated zone beneath Yucca Mountain are dissolution reactions, silica and calcite precipitation reactions, and ion-exchange reactions. The pH of these waters will be controlled primarily by the partial pressure of CO_2 and the rate at which the rocks consume hydrogen ions. Controls on the redox state in the saturated zone are poorly defined at the present time.

5.2.2.7.2   Present-Day Regional Characteristics

The available data on saturated zone waters from the potential recharge areas for Yucca Mountain consist primarily of analyses of the major constituents, although a limited number of isotopic analyses have been reported. Relative major-ion abundances in saturated zone waters from eastern Pahute Mesa and southern Rainier Mesa are shown in Figure 5-31. These waters are dominated by sodium bicarbonate; have pH values ranging from 7.4 to 8.2, and total dissolved solids ranging from 169 to 578 mg/L. Claassen (1985 [DIRS 101125], p. F13) noted that these waters are chemically relatively evolved (i.e., the ratio of sodium to other major cations is high). Because these waters occur in the recharge area (i.e., they are the youngest waters in the flow system), this is an important observation.

The locations of wells in the vicinity of Yucca Mountain from which groundwater samples were taken to obtain geochemical data are shown on Figure 5-32. The relative abundances of major ionic constituents in saturated zone waters from these wells are plotted in Figure 5-17. Comparison of Figures 5-31 and 5-17 shows saturated zone waters from volcanic aquifers in the recharge area and in the vicinity of Yucca Mountain to be very similar. Data for downgradient waters directly overlap data points for Yucca Mountain area saturated zone waters. The downgradient waters show a pH range from 7.5 to 8.2 and a range in total dissolved solids from 217 to 233 mg/L (Oliver and Root 1997 [DIRS 100069], Excel file yucca.xls). The fact that the downgradient waters are even farther from the recharge areas than those in the Yucca Mountain area again suggests these waters are close to equilibrium with their host rocks.

5.2.2.7.3   Present-Day Characteristics of Groundwaters in the Yucca Mountain Area

Analyses of groundwater from drill holes that penetrate the host rock and other volcanic units in the area of Yucca Mountain indicate that they are principally sodium-bicarbonate waters (Figure 5-17) with low contents of total dissolved solids (200 to 400 mg/L) (Oliver and Root 1997 [DIRS 100069], Excel file yucca.xls). Compared to waters in the recharge areas, the Yucca Mountain area waters show a greater range in pH values, from 6.6 to 9.2, and total dissolved solids range from 181 to 887 mg/L (Oliver and Root 1997 [DIRS 100069], Excel file yucca.xls).

Plots of the major cations versus chloride show that saturated zone waters (as well as perched waters, based on data from Section 5.2.2.4) are generally distinct from unsaturated zone pore waters in the Yucca Mountain area in several ways:

- Saturated zone waters and perched waters have much lower chloride concentrations than the pore waters (Figure 5-8). This result suggests the saturated zone and perched waters were subject to less evapotranspiration than the pore waters.

- Saturated zone waters have higher sulfate-to-chloride ratios than precipitation (BSC 2002 [DIRS 160247], Figure 27), suggesting that they gained sulfate, perhaps by dissolving sulfate mineral(s) such as gypsum. Among the unsaturated zone pore waters, only some samples from the PTn unit show a similarly high SO_4^{2-}/Cl^- ratio. The vast majority of pore waters plot well below the trend line.

- Unlike unsaturated zone waters, all of the perched waters and a significant proportion of the saturated zone waters have elevated Ca/Cl ratios relative to precipitation (BSC 2002 [DIRS 160247], Figure 24). This suggests that most of these waters gained calcium. Nearly all of these waters gained bicarbonate (BSC 2002 [DIRS 160247], Figure 25) suggesting that the calcium gained may have come from the dissolution of calcite. The loss of calcium likely reflects ion-exchange reactions in clays and zeolites. This possibility is supported by the fact that these waters have all gained sodium (BSC 2002 [DIRS 160247], Figure 26).

- Silica concentrations in these saturated zone waters are slightly lower than those measured in most pore waters. However, nearly all waters are oversaturated with alpha-cristobalite (BSC 2002 [DIRS 160247], Figure 28), suggesting that a different silica phase may control their concentrations.

On trilinear diagrams, local groundwater and perched waters show distributions of major ions that are quite similar to one another (Figures 5-17 and 5-13, respectively) and considerably different from those of unsaturated zone pore waters. The relative abundances of cations in saturated zone waters show considerable variation from east to west across Yucca Mountain, with perched water being most like groundwater from wells in Fortymile Wash (e.g., J-13). Wells on Yucca Mountain and just to the west (USW H-3, USW H-5, and USW H-6) plot nearest the sodium apex of CRWMS M&O (2000 [DIRS 151945], Figure 5.3-27). Wells on the eastern slopes and washes (USW H-1, USW H-4, USW G-4, J-13, and UE-25 b#1) show increasing levels of calcium. The Na+K/Ca+Mg molar ratio increases from 3.8 in J-12 to 263 in H-3. This result most likely reflects ion-exchange reactions involving the zeolites and clays in the saturated zone units beneath Yucca Mountain and the Na^+/H^+ ion-exchange reaction. The fact that bicarbonate concentrations also increase from east to west suggests a significant contribution from the latter reaction.

The anionic constituents of the Yucca Mountain groundwaters show a relatively uniform distribution in all the wells, with about 80 percent bicarbonate and the remainder as sulfate and chloride (usually present in nearly equal molar concentrations) and fluoride (in varying concentrations). Perched waters have a slightly higher molar proportion of bicarbonate (about 85 percent of total anions) and more than twice the proportion of sulfate relative to chloride (Figure 5-13).

The consistency in saturated zone water chemistry discussed previously suggests that climatic influences on saturated zone water chemistry are damped in the flow system. Future climatic change could involve higher infiltration rates in the recharge areas but would not likely involve lower rates. Higher rates would result in more dilute water compositions (e.g., lower chloride).

5.2.2.8 Groundwater Geochemistry: Implications for Flow and Transport Processes in the Unsaturated Zone

Major element and isotopic compositions of unsaturated and saturated zone groundwaters at Yucca Mountain provide valuable information on flow mechanisms and pathways from the surface to the repository level, and flow and transport processes controlling migration of radionuclides from the repository to the water table. Chloride data are especially useful, as it behaves conservatively in the groundwater system.

Chloride pore water concentrations obtained from unsaturated core samples serve several purposes.

- Chlorine concentrations provide independent corroboration of surface infiltration rates estimated by modeling using the chloride mass-balance method (see Section 7.1).

- The pore water chloride data helps constrain the various hypotheses on the derivation of perched water.

- Chlorine, bromine, and sulphate pore water concentrations indicate the extent to which water chemistry is homogenized as it percolates through the nonwelded Paintbrush unit, or is not homogenized along fast fracture and fault pathways. Fracture-dominated flow in the overlying low-permeability, highly fractured TCw unit is expected to transition to matrix-dominated flow in the high-permeability, comparatively unfractured PTn unit (Wolfsberg et al. 1998 [DIRS 146442], p. 82).

- Variability in chlorine, bromine, and SO_4 pore water concentrations can be used to assess the extent to which water may be laterally diverted due to contrasting hydrologic properties of the various stratigraphic units above the current repository horizon (it is recognized that this aspect may be obscured by climatic variability in the chemistry of infiltrating surface waters).

- To the extent that the chlorine pore water database can be extended to a large spatial and stratigraphic coverage, it is a valuable data set for site-scale modelers to use in calibrating flow and transport models of Yucca Mountain.

- Unsaturated zone pore waters are geochemically different than saturated zone and perched waters. Saturated zone and perched waters are similar except for isotopes.

In undisturbed minerals older than several million years, the abundances of ^{238}U and its intermediate alpha-decay product, ^{234}U, reach a state of secular equilibrium where the decay rate of the shorter lived ^{234}U daughter is equal to the production rate from its longer lived ^{238}U parent. Under these conditions, the $^{234}U/^{238}U$ activity ratio will equal unity. Bulk dissolution of most rocks yields dissolved U with a $^{234}U/^{238}U$ AR near 1. However, ^{234}U is commonly more soluble than ^{238}U as the result of several mechanisms related to its origin by radioactive decay. These mechanisms include direct alpha-recoil of short-lived ^{234}Th from mineral surfaces, preferential access to ^{234}U atoms occupying radiation-damaged crystal-lattice sites, and radiation-induced oxidation of ^{234}U to a more soluble hexavalent valance state (Kigoshi 1971 [DIRS 162822];

Gascoyne 1992 [DIRS 127184]; Osmond and Ivanovich 1992 [DIRS 145190]). As a result, natural waters typically are enriched in ^{234}U with $^{234}U/^{238}U$ AR between 1 and 10.

Perched water and saturated zone waters are chemically similar with respect to major constituents (Section 5.2.2.4.2) and uranium isotopes, but are isotopically distinct with respect to strontium. The $\delta^{13}C$ values, $\delta^{87}Sr$ values, and $^{234}U/^{238}U$ activity ratios for perched waters generally differ from those obtained for saturated zone waters. Further, there are consistent trends in $\delta^{13}C$ values, $\delta^{87}Sr$ values, and $^{234}U/^{238}U$ activity ratios in water and secondary mineral samples from the soil zone down through the unsaturated zone and into the uppermost-saturated zone (Section 5.2.2.5). These observations strongly suggest that the waters in the perched zones originated at the surface of Yucca Mountain and do not represent upwelling from the saturated zone.

Analyses of major chemical constituents in perched water samples and pore waters squeezed from core samples indicate that these two water types are generally different in composition. The pore waters contain higher concentrations of most constituents compared to the perched water samples (Table 5-3, Figures 5-8 to 5-12). This difference suggests that these two water types represent different infiltration mechanisms. The higher ionic strength of the pore waters can be explained by higher rates of evapotranspiration at the infiltration points for these waters as compared to the locations at which perched waters infiltrate the subsurface. Thus, perched waters appear, on average, to have spent less time in the near-surface zones than did unsaturated zone pore waters.

The mechanism proposed to explain the chemical differences in pore waters and perched waters is one in which pore waters flow primarily through the rock matrix, whereas perched waters accumulate from flow that occurred primarily through the fractures in the host rock. For perched waters, isotopic data suggest that the flux of water through fractures is likely episodic and of small volume compared to the hydraulic conductivity of the fracture. The high activity ratios in perched waters would be most readily produced when there are episodic fluxes through many small fractures. Under these conditions of rare episodic fracture flow, ^{234}U that has accumulated on the fracture surfaces between fracture flow events is preferentially leached into the water relative to ^{238}U. If the original concentration of uranium in the water is small, or if the flux of water is small, a high $^{234}U/^{238}U$ activity ratio can be produced in the percolating water. Clearly, the higher the fracture surface area to water volume ratio, the higher the resulting $^{234}U/^{238}U$ activity ratio, assuming all other factors remain constant.

The identification of bomb-pulse constituents at depth within Yucca Mountain (Section 5.2.2.5) suggests that flow along fractures can be rapid. However, the absence of a clear bomb-pulse signal for any of these radionuclides in perched water samples (Table 5-4) indicates that the flux of water from the surface downward through fractures to perched water bodies must be small.

Data on major-ion concentrations in unsaturated zone waters beneath the current repository horizon are of great significance as corroborative data for radionuclide transport calculations. For example, the fact that pore waters in the lower portions of the zeolitized Calico Hills Tuff have negligibly low calcium and magnesium concentrations compared to pore waters in the overlying units indicates that ion-exchange processes operate on the pore waters that percolate through the zeolitic tuffs. These processes tend to remove calcium and magnesium from the

percolating waters, replacing them with molar equivalent concentrations of sodium. When combined with ^{14}C age data suggesting relatively young ages (up to 100 percent modern carbon) for CHn unit pore waters, these data indicate that ion-exchange processes operate on vertically migrating young pore waters in the CHn unit. This suggests ion-exchange processes would also operate on radionuclides released from the repository into aqueous solutions that migrate vertically into the zeolitic CHn unit.

5.3 LABORATORY EXPERIMENTS OF RADIONUCLIDE SOLUBILITY, SORPTION, AND COLLOIDS

5.3.1 Introduction

Radionuclide migration from the repository would be mitigated by several barriers, including geochemical retardation in the natural system due to solubility-limited precipitation from waters that infiltrate the repository or due to sorption onto minerals in the surrounding host rock. The solubility of key radionuclides (e.g., neptunium, plutonium, americium, and technetium) is controlled by solution speciation and by the solubility-limiting actinide-bearing solid. This section summarizes the results of laboratory investigations into radionuclide solubility and speciation, sorption (including effects of organics), matrix diffusion, and colloid-facilitated radionuclide transport through the natural system, and the conceptual models that describe these phenomena in transport codes.

5.3.1.1 Key Radionuclides

For spent nuclear fuel, the chief sources of radioactivity from 1 k.y. to 10 k.y. are americium and plutonium isotopes (Langmuir 1997 [DIRS 100051], Figure 13.18). From roughly 10 k.y. to 10 m.y. ^{237}Np is the greatest contributor to the radioactivity of the waste (Langmuir 1997 [DIRS 100051], Figure 13.18). Therefore, studies have concentrated on the geochemical mobility of these three elements. ^{233}U, ^{234}U, ^{129}I, ^{99}Tc, and other radionuclides have also been included in total system performance assessment (TSPA), especially those radionuclides that are soluble and sorb weakly onto geological media. The radionuclides discussed in this section (technetium, uranium, neptunium, plutonium, and americium), include the most important species for the first 10 m.y. (Choi and Pigford 1981 [DIRS 105286]; Langmuir 1997 [DIRS 100051]).

Although the fission products ^{90}Sr and ^{137}Cs will dominate the radioactive inventory in the short term (Choi and Pigford 1981[DIRS 105286]), the half lives of approximately 30 yr mean that these radionuclides will have decayed by the time the metal waste packages are projected to fail as a result of corrosion (Langmuir 1997 [DIRS 100051]). Therefore, less emphasis is given here to studies of the retardation of these radioactive elements.

The following sections focus on the geochemistry and solubility of the long-lived radionuclides with thorough discussions on relevant issues to Yucca Mountain.

Technetium–Technetium the most important radioactive waste β-emitter existing in the greater than 1 k.y. time frame (CRWMS M&O 1994 [DIRS 100111], Table C-3a). Because the waters at Yucca Mountain are generally oxidizing, technetium is expected to exist in the technetium

(VII) state as TcO$_4^-$. This species is highly soluble, and because of its low charge density and anionic character, it sorbs only weakly to mineral sorption sites, most of which are also negatively charged at neutral pH. Interaction with reduced minerals, or with more reducing waters, may reduce the technetium to a lower oxidation state, technetium [IV], which is orders of magnitude less soluble and more sorptive (Lieser and Bauscher 1988 [DIRS 106683]). However, it is conservative to assume that technetium will be present in the oxidized form, and to calculate released quantities of technetium such that they are not significantly limited by solubility.

Iodine–Iodine occurs as iodate (IO$_3^-$) in highly oxidizing waters and as iodide (I$^-$) under less-oxidizing conditions, including most groundwaters (Pourbaix 1966 [DIRS 119532], Figure 1, p. 621; Langmuir 1997 [DIRS 100051], p. 520). Iodide salts are less soluble than iodate salts but are still too soluble to limit maximum possible iodine concentrations in groundwaters emanating from a repository.

Uranium–In aqueous solutions, only uranium (IV) and uranium (VI) are the important oxidation states of uranium, as uranium (V) quickly disproportionates (Newton 1975 [DIRS 106871]). Spent nuclear fuel from commercial nuclear power plants that will be disposed of in the repository, is largely in the form of UO$_2$. Uranium (IV) is stable in solution only at very reducing potentials, with the principal associated minerals being uraninite (crystalline UO$_2$), pitchblende (amorphous UO$_2$), and coffinite (USiO$_4$) (Langmuir 1997 [DIRS 100051], p. 495). In the absence of aqueous carbonate species, the predominant uranium (IV) species in equilibrium with uraninite/pitchblende at pH values greater than 4 is U(OH)$_4{}^0{}_{(aq)}$. (Ryan and Rai 1983 [DIRS 107190]; Parks and Pohl 1988 [DIRS 107004]; Rai et al. 1990 [DIRS 107064], p. 263; Yajima et al. 1995 [DIRS 108814], p. 1142). Coffinite should have a comparable solubility based on the value of its formation constant (Langmuir 1997 [DIRS 100051], pp. 502 and 503). The tetrahydroxide uranium (IV) complex is more stable in solution than uranium (IV) carbonate complexes (Grenthe et al. 1992 [DIRS 101671], pp. 120 to 122, 306 to 333), so uranium (IV) carbonate complexes do not need to be considered further.

In the more oxidizing regions of the uraninite (excluding pitchblende) stability field, the solution species in equilibrium over the uranium (IV) solid can be a uranium (VI) solution species, either a uranyl aquo/hydroxide species or a carbonate species (Langmuir 1997 [DIRS 100051], Figures 13.8 to 13.9). In fact, several mixed-oxidation-state solids are stable at groundwater-relevant pHs before the uranium (VI) solid phases (schoepite (β-UO$_3$·2H$_2$O) and [or] other uranyl phases) predominate in the higher Eh values of the Eh/pH stability diagram. In order of ascending Eh, important uranium solids formed in carbonate-free, near-neutral pH water include UO$_2$, β-U$_4$O$_9$, β-U$_3$O$_7$, U$_3$O$_8$, and UO$_3$ (Langmuir 1997 [DIRS 100051], Figure 13.10). Important uranyl solution species in Yucca Mountain waters (e.g., UE-25 J-13, referred to henceforth as J-13) include, with increasing pH, UO$_2{}^{2+}$, UO$_2$OH$^+$, UO$_2$CO$_3{}^0$, (UO$_2$)$_3$(OH)$_5{}^+$, (UO$_2$)$_2$(CO$_3$)(OH)$_3{}^-$, UO$_2$(CO$_3$)$_2{}^{2-}$, and UO$_2$(CO$_3$)$_3{}^{4-}$ (Grenthe et al. 1992 [DIRS 101671], pp. 98 to 130, 306 to 330; Waite et al. 1994 [DIRS 108746]). Langmuir (1997 [DIRS 100051], Figure 13.5) plotted the uranyl solubility as a function of pH with schoepite as the solubility-controlling solid for two P_{CO_2} cases. With no carbonate present, the solubility reached a minimum of slightly greater than 10^{-7} M at a pH value of just over 7. At pH values of 8.5 and 5.5, on each side of the minimum, the solubility increases to 10^{-6} M. With

$P_{CO_2} = 10^{-2}$ bar, the minimum solubility shifts to a pH of approximately 6.3 and to a value of about 10^{-6} M, and increases by an order of magnitude at pH values of 5 and 8. Typical Yucca Mountain waters (e.g., J-13) would produce solubilities intermediate between these two P_{CO_2} cases. The presence of other potential solid uranyl phases, such as rutherfordine or $Na_2(UO_2)(CO_3)_2$, was not considered. This fact implies that the present estimate is conservative, as a more stable uranyl carbonate solid would lower the solubility values, and less stable phases would convert to the schoepite.

Secondary uranium mineral phases that might occur include uranyl silicates (e.g., uranophane and soddyite), phosphates (e.g., autunite), vanadates (e.g., carnotite), or carbonates (e.g., rutherfordine), depending on what anions are available. The formation of some of these secondary phases would further limit the solubility of uranium relative to that of schoepite. For instance, uranophane is the solubility-limiting phase at Peña Blanca, and uranium solubility is limited to approximately 10^{-7} M (Langmuir 1997 [DIRS 100051], pp. 513 to 514). The Peña Blanca deposit in northern Mexico occurs in an unsaturated and oxidized tuff located in an arid region (Pearcy et al. 1994 [DIRS 100486]), and is a natural analog for Yucca Mountain. Uranyl silicates are readily produced experimentally; Wilson (1990 [DIRS 100793], p. 425) produced Ca-U (VI) silicate solids similar to uranophane by leaching spent nuclear fuel with J-13 water. Similarly, Wronkiewicz et al. (1996 [DIRS 102047], p. 89-93) intermittently exposed UO_2 pellets to a simulated silica-bicarbonate groundwater for 8 yr, and observed the formation of the uranium silicate minerals uranophane, soddyite, and boltwoodite.

Neptunium–TSPA calculations for the Yucca Mountain site have considered neptunium to be the most hazardous radionuclide for repository times beyond 10 k.y. (CRWMS M&O 2000 [DIRS 153246], Section 4, Figure 4.1-25). In natural waters, neptunium (IV) is expected to be the dominant oxidation state under reducing conditions, while neptunium (V) is the dominant oxidation state in oxidizing waters (Katz et al. 1986 [DIRS 106312]; Lieser and Muhlenweg 1988 [DIRS 106684], Section 2; Hobart 1990 [DIRS 106040], p. 407). Although oxidizing conditions are generally expected to prevail in the unsaturated zone within Yucca Mountain, reducing conditions may exist in the saturated zone (Sections 5.3.6 and 5.3.7) or in micro-environments in the drift. Theoretical calculations using different thermodynamic data bases predict that the solubility-limiting solid phase would be either a neptunium (IV) or neptunium (V) compound, depending upon the redox state of the water (Wilson and Bruton 1990 [DIRS 102154]; Hakanen and Lindberg 1991 [DIRS 105905]; Janecky et al. 1995 [DIRS 101338]; Janecky et al. 1997 [DIRS 106265], p. 2). The solubility is several orders of magnitude less under reducing conditions, when the neptunium (IV) phase is the solubility-limiting solid. For neptunium (IV), solubility-controlling solids include $Np(OH)_{4(am)}$ and, especially, $NpO_{2(c)}$. Important solution species include $Np(OH)_4^0$ in low carbonate solutions (for pH greater than 3) and $Np(OH)_3CO_3^-$ in higher carbonate solutions (e.g., total carbonate $= 10^{-2}$ M, similar to UE-25 water, and a pH range from 5 to 11). When neptunium (IV) is the stable oxidation-reduction (redox) state, the solubility in water, at total carbonate concentrations of up to 10^{-2} M, is expected to be lower than 10^{-8} M (Langmuir 1997 [DIRS 100051]).

The stability field for $NpO_{2(c)}$ extends into the Eh region in which neptunium (V) solution species may also exist (Langmuir 1997 [DIRS 100051]). Neptunium (V) solubility-limiting solids include $Np_2O_{5(c)}$, $NpO_2OH_{(am)}$, and in high ionic-strength carbonate media, the so-called double carbonate salts $Na_{2x-1}NpO_2(CO_3)_x$ (where $x = 1$ to 3) (Volkov et al. 1980 [DIRS 141723];

1981 [DIRS 141712]; Neck et al. 1994 [DIRS 106861]; 1995 [DIRS 106858]). In the absence of carbonate, the solution speciation of neptunium (V) is dominated by the highly soluble NpO_2^+, which does not hydrolyze readily below a pH of 10 (Moskvin 1971 [DIRS 106811]; Rosch et al. 1987 [DIRS 107156]; Itagaki et al. 1992 [DIRS 106254], Figure 2; Neck et al. 1992 [DIRS 106857], Figure 3, p. 29; Tait et al. 1996 [DIRS 101359], pp. 34 to 49). In J-13 type waters, where the complexes containing multiple carbonate groups do not predominate even at higher temperatures, the neptunium (V) carbonate species of importance is $NpO_2CO_3^-$ (Tait et al. 1996 [DIRS 101359], p. 41). The solubility of neptunium has been shown to vary several orders of magnitude in oxidizing environments (Efurd et al. 1996 [DIRS 105538]).

Plutonium–Plutonium is an important radionuclide because of its large inventory in the proposed radioactive waste repository and its high mobility in oxidized form. Unlike most metal cations, plutonium can exist in multiple oxidation states simultaneously. The III, IV, V, and VI states of plutonium are readily attainable under ambient conditions, and therefore redox conditions do not necessarily preclude a low release. In general, the solid phases are plutonium (IV), specifically $PuO_{2(c)}$, $Pu(OH)_{4(am)}$, and radiocolloids (suspended PuO_2 polymer). The aging of plutonium solubility-limiting solids might start with the formation of radiocolloids, which gradually dehydrate/polymerize to mixtures of $Pu(OH)_{4(am)}$ and (or) $PuO_{2(am)}$. These mixtures eventually form $PuO_{2(c)}$ (Hobart et al. 1990 [DIRS 141452], pp. 118 to 124; Clark 1994 [DIRS 101332], p. 9). The final aged form of the solid should be $10^{6.6}$ times less soluble than $Pu(OH)_{4(am)}$, but modeling suggests that even aged $PuO_{2(c)}$ contains $Pu(OH)_{4(am)}$ units on its surface (Efurd et al. 1996 [DIRS 105538], p. 7, Table 2). The mobility of the suspended radiocolloid and of plutonium sorbed onto pseudocolloids can be significant, especially in highly fractured media in which filtration and redox reactions are of low importance (Penrose et al. 1990 [DIRS 100811]; Triay et al. 1995 [DIRS 100789]). Oxidation states can redistribute through disproportionation (e.g., plutonium [V] disproportionates to plutonium [IV] and plutonium [VI] in acidic conditions at a rate inversely proportional to $[pH]^4$ (Newton 1975 [DIRS 106871]) and from radiolysis effects. These radiolysis effects can cause either reduction (Cleveland 1979 [DIRS 105752], 1979 [DIRS 105754]) or oxidation (Runde and Kim 1994 [DIRS 107170]) to occur, depending on the initial plutonium oxidation state and the chemical composition of the solution. As with americium, plutonium solubility measurements can be complicated as a result of radiation damage of the solubility-limiting solid.

Dilute plutonium solutions in the environment are likely to have a distribution of oxidation states dominated by the +5 oxidation state, although Langmuir (1997 [DIRS 100051], Figure 13.30) shows a large region of predominance for $Pu(OH)_{4(aq)}$ in the Eh-pH diagram for dilute plutonium. As with neptunium (V), PuO_2^+ does not readily hydrolyze (Bennett et al. 1992 [DIRS 104911], p. 18) in sharp contrast to the other oxidation states (Lemire and Tremaine 1980 [DIRS 101705]; Lemire and Garisto 1989 [DIRS 106580]; Langmuir 1997 [DIRS 100051]). The other plutonium oxidation states hydrolyze readily, and are fully hydrolyzed by a pH of 5 for PuO_2^{2+}, a pH of approximately 1.5 for plutonium (IV), and a pH of approximately 8 for plutonium (III). Plutonium (IV) has been reported to undergo extremely strong hydrolysis, leading to the universally seen formation of radiocolloids at neutral pHs and plutonium concentrations greater than approximately 10^{-7} M (Nitsche et al. 1993 [DIRS 155218]). All oxidation states have strong complexes with carbonate (Langmuir 1997 [DIRS 100051]), approaching the Pu^{3+} and $Pu(OH)_4^0$ predominance zones even at relatively low total carbonate concentration (10^{-2} M).

Americium–As noted above, in the 1- to 10-k.y. period, americium is the largest contributor to the radioactivity of the nuclear waste. Unlike other transuranic species, americium exists primarily in one oxidation state, as americium (III) (Silva et al. 1995 [DIRS 102087], p. 73). At least two complicating factors exist for interpreting americium solubility data. Like plutonium, americium can also exist in colloidal form (Penrose et al. 1990 [DIRS 100811]; Bates et al. 1992 [DIRS 100704]), so phase separation of truly soluble americium species is problematic, and americium colloids provide another route for radionuclide migration. Furthermore, because ^{241}Am is intensely radioactive, it is difficult to form a well-crystallized solid as the solubility-controlling phase.

Americium (III) forms strong hydroxo and carbonato aqueous complexes. As solids, it forms mixed hydroxo-carbonato species (Silva et al. 1995 [DIRS 102087], pp. 151 to 166). Important aqueous species at a P_{CO_2} of $10^{-3.5}$ bars (atmospheric CO_2 and pH values from 6 to 9 include Am^{3+}, $AmOH^{2+}$, $AmCO_3^+$, $Am(OH)_2^+$, and $Am(CO_3)^{2-}$. Above a pH of 9, $Am(CO_3)_3^{3-}$ becomes important (Silva et al. 1995 [DIRS 102087]). The only solid found in Yucca Mountain experiments in J-13 water was $AmOHCO_3$ (Nitsche et al. 1993 [DIRS 155218]), consistent with the large stability field of this solid over different values of pH and P_{CO_2} (Silva et al. 1995 [DIRS 102087]). Other important solids include $Am(OH)_{3(c)}$ (P_{CO_2} less than 10^{-4} bars, pH greater than 7.5) and $Am_2(CO_3)$ (P_{CO_2} greater than 10^{-1} bars, neutral pH) (Runde et al. 1992 [DIRS 107173]). Thermodynamic studies of $AmOHCO_{3(c)}$ at room temperature and $P_{CO_2} = 10^{-3.5}$ bar by Felmy et al. (1990 [DIRS 105566], p. 196, Figure 2) show a solubility of $10^{-7.5}$ to $10^{-8.5}$ M for pH values from 6.5 to 9. Above a pH of 9, the solubility increases due to the formation of $Am(CO_3)_3^{3-}$ in solution.

5.3.2 Solubility and Speciation Studies of the Radionuclides of Concern

Measurements (Efurd et al. 1996 [DIRS 105538], Table I) have shown that the bulk solubility of neptunium in J-13 water ranges from 6×10^{-6} to 1×10^{-3} M. These results are generally an order of magnitude lower than those of earlier reports (Nitsche et al. 1993 [DIRS 155218], Table VI). This difference has been attributed to the higher ionic strength in the earlier studies. Some models, depending on the neptunium solubility and thermodynamic data employed, have predicted neptunium (IV) as the predominant oxidation state in Yucca Mountain waters. If true, it would lower the ultimate solubility of neptunium by several orders of magnitude (Efurd et al. 1996 [DIRS 105538]). However, the Efurd et al. (1996 [DIRS 105538]) study still points to neptunium (V) as the predominant oxidation state, albeit a different solid than reported in the earlier study (Nitsche et al. 1993 [DIRS 155218]). Whether this neptunium (V) solid is the equilibrium state or a kinetically controlled state has not been determined. Similarly, the more refined solubility measurements of Efurd et al. (1996 [DIRS 105538], Table V) found less variability and lower plutonium solubility in J-13 water, although the difference between the two studies was less pronounced than for neptunium. The solubility data for neptunium and plutonium from Efurd et al. (1996 [DIRS 105538]) are considered more reliable than those of Nitsche et al. (1993 [DIRS 155218]) because the solutions had an ionic strength closer to that expected for groundwater at Yucca Mountain and because the solids were better characterized.

For americium, the existing solubility and sorption data are difficult to interpret, in part because they were performed in Yucca Mountain conditions using americium as a tracer in Np/Am

solutions (Nitsche et al. 1993 [DIRS 155218]; 1995 [DIRS 100163]). Radiation damage of a pure americium solid may preclude the formation of the stable crystalline solid indicated in the Yucca Mountain studies. Trivalent actinides are known to be more soluble than the analogous lanthanide (III) compounds (Runde et al. 1992 [DIRS 107173]) (although their sorptive behavior may limit mobility as discussed below).

5.3.2.1 Radionuclide Solubility in Yucca Mountain Relevant Waters

Radionuclide concentrations in water passing through the repository emplacement drifts can be limited by three mechanisms: (1) low dissolution rates of the solid waste form, (2) solubility of individual radionuclides, and (3) sorption of these radionuclides onto geological media. Radionuclide solubility limits provide an upper bound on radionuclide concentrations in solution and a basis for extrapolation to long-term behavior. The rate of groundwater flow through the waste is expected to be sufficiently slow to permit saturation of water with some, if not all radionuclides liberated from the waste form. Dissolution limited by saturation will provide maximum concentration limits. Therefore, an assessment of radionuclide release rates using a saturation-limited dissolution model represents a conservative approach possible for solution transport (Dozol and Hageman 1993 [DIRS 105464], Sections 1 to 2).

Ambient water compositions at Yucca Mountain (controlling solubility and speciation) are generally anticipated to be in the pH range from 6 to 8.5, but contact with cement-affected waters may increase the pH locally to as high as 11. J-13 and UE-25 p#1 waters are low-ionic-strength waters that are considered to be representative of some potential Yucca Mountain waters (Ogard and Kerrisk 1984 [DIRS 100783]). However, repository thermal loading might cause groundwaters to reflux, increasing the extent of water/rock interactions and affecting the composition and ionic strength of the waters that could contact the waste. Thermally perturbed water is discussed in Section 5.4.4.

The solubilities of neptunium and plutonium in J-13 groundwater from the Yucca Mountain region at three temperatures and three hydrogen-ion concentrations were studied by Efurd et al. (1996 [DIRS 105538]). The actinide solubilities were determined from oversaturation at 25°, 60°, and 90°C and initial pH values at 6.0, 7.0, and 8.5. Tables 5-10 and 5-11 summarize the results. Sample evaporation was minimized to maintain the ionic strength of the solutions as close to that of J-13 water as practical for the duration of the experiments. The pH of each solution was adjusted at the start of the solubility experiments, and was not readjusted during the year that the solubility experiments were conducted. In general, results showed that the neptunium solubilities decreased with increasing pH and temperature. X-ray diffractometry identified a mixture of neptunium compounds, including crystalline Np_2O_5 and a sodium salt of neptunium. Plutonium was less soluble than neptunium. In general, plutonium solubility decreased with pH and decreasing temperature. The solubility-controlling, steady-state solids produced X-ray diffraction patterns indicative of a mixture of amorphous and crystalline materials. The relative amount of crystalline solid (PuO_2) increased with temperature. Nitsche et al. (1995 [DIRS 100163]) performed similar experiments on neptunium and plutonium in UE-25 p#1 water, but only at 25°C and 60°C.

The solution behavior of the element plutonium is the most complicated of all the radionuclides of interest. According to Nitsche et al. (1992 [DIRS 101350], Figures 19, 20, 21, and Table 17)

and Nitsche et al. (1995 [DIRS 100163]), plutonium will be present in the +3, +4, +5, and +6 oxidation states, for chemical conditions present in the repository system at Yucca Mountain. The +5 and +6 oxidation states should predominate in solution at redox potentials in the range of 230 to 350 mV. In J-13 and UE-25 p#1 waters, the +5 oxidation states should be dominant (60 to 80 percent) at 25°C. Most of the remaining plutonium in solution is in the +6 oxidation state in J-13 water and the +4 oxidation state in UE-25 p#1 water.

Experimentally determined plutonium solubilities range from 9.0×10^{-9} to 1.0×10^{-6} M at 25°C in J-13 and UE-25 p#1 waters (Table 5-11; Nitsche et al. 1995 [DIRS 100163], Table II). The solubility-controlling solids were found to be mixtures of polymeric plutonium (IV) and smaller amounts of plutonium carbonates. The solubilities measured at pH values of 6 and 7 are consistent with the data reported by Rai et al. (1980 [DIRS 107069]). However, the solubilities measured for a pH of 8.5 exceed those reported by Rai et al. (1980 [DIRS 107069], Table 2) for amorphous $Pu(OH)_4$ in 0.0015 M $CaCl_2$. This result suggests that carbonate complexation of plutonium is significant at a pH of 8.5 in Yucca Mountain groundwaters.

At 60°C, the +6 oxidation state was dominant (more than 80 percent) in the UE-25 p#1 water at all three pH values. In J-13 water, the +5 and +6 oxidation states were present in nearly equal amounts (50 percent) at a pH of 7, whereas the +5 state dominated (60 percent) at a pH of 8.5 and the +6 state dominated (70 percent) at a pH of 6.

Experimentally determined solubilities at 60°C in J-13 water ranged from 9.0×10^{-9} M at a pH of 6 to 6.2×10^{-9} M at a pH of 8.5 (Table 5-11). For UE-25 p#1 water, the solubilities ranged from 9.1×10^{-8} M at a pH of 7 to 9.3×10^{-7} M at a pH of 8.5 (Nitsche et al. 1995 [DIRS 100163]). The solubility-controlling solids at 60°C were found to be amorphous plutonium (IV) polymer and PuO_2.

Finally, there are americium solubility values for Yucca Mountain site-specific conditions as well (Nitsche et al. 1993 [DIRS 155218]). As noted above, these experiments were done ultimately at high ionic strength and with americium as a tracer in a Nd-Am mixture. Given that the solubility-limiting solid state is $AmOHCO_3$, the effect of the ionic-strength differences should be relatively small, and these numbers (Table 5-12) are the best site-specific values available. However, some outliers, especially at 60°C, should be viewed with caution. In general, though, these site-specific numbers are similar to or slightly less than the values predicted by Felmy et al. (1990 [DIRS 105566], pp. 196 to 198) for $P_{CO_2} = 10^{-3.5}$ atm.

According to Nitsche et al. (1993 [DIRS 155218], Table XXI) and Nitsche et al. (1995 [DIRS 100163], Table III), the solubilities of americium are approximately 1×10^{-9} to 2×10^{-9} M in J-13 water and 3×10^{-7} to 3×10^{-6} M in UE-25 p#1 water at 25°C, the larger values corresponding to higher pH. At 60°C, the solubilities of americium compounds were 1×0^{-8} to 2.5×10^{-6} M in J-13 water and 7×10^{-10} to 3×10^{-9} M in UE-25 p#1 water, with solubilities lowest at neutral pH. The solubility-controlling solids were found to be hexagonal and orthorhombic forms of $AmOHCO_3$. Modeling calculations with the speciation code EQ3 suggest that carbonate complexes dominate in both J-13 and UE-25 p#1 waters at 25°C and 60°C (Ogard and Kerrisk 1984 [DIRS 100783]).

5.3.2.2 Solid Phase and Solution Speciation

The solubility-limiting solids in the solubility experiments described in Section 5.3.2.1 were characterized with X-ray diffraction, Raman vibrational, and X-ray absorption techniques. For neptunium, Nitsche et al. (1993 [DIRS 155218]) identified sodium neptunyl carbonate solid phases, but these are likely artifacts of the high ionic strength in those tests, and are unlikely to form in the low-ionic-strength J-13 water. Other neptunium (V) solids, including Np_2O_5 and/or $NpO_2OH_{(am)}$, have been identified as the solubility-limiting solid phase in J-13 water (Efurd et al. 1996 [DIRS 105538], Table VII). Thermodynamic modeling suggests that NpO_2 is the most stable solid. In J-13 water, the solution species are dominated by NpO_2^+ and $NpO_2CO_3^-$, in about equal proportions at a pH of 8.5. For plutonium, the solid phase is best described as poorly crystalline PuO_2, with higher crystallinity for the higher-temperature solutions (Efurd et al. 1996 [DIRS 105538], Section 5.4). The presence of $Pu(OH)_{4(am)}$ is also possible, especially on the surface of the precipitate, as is the presence of a binary oxide containing plutonium (VI) (Stakebake et al. 1993 [DIRS 145111]; Haschke and Ricketts 1997 [DIRS 105926], p. 148). The solution phase contains several oxidation states (Nitsche et al. 1993 [DIRS 155218]), including a plutonium colloid with an unknown plutonium oxidation state. Much of the colloid was filtered out of the solution before counting and was therefore not included in the soluble plutonium concentration figures. Finally, the precipitated americium solid has been reported to be $AmOHCO_3$ (Nitsche et al. 1993 [DIRS 155218]), although the presence of two different phases (orthorhombic and hexagonal) may require further scrutiny. It is noted that americium was only present as a tracer in these experiments—the Nd solid was the only phase identified.

5.3.2.3 Thermodynamic Modeling

The solublilities of neptunium, plutonium, and americium in J-13 water have been modeled using thermodynamic speciation codes (BSC 2003 [DIRS 163152], Section 6). NpO_2 is always the most thermodynamically stable solid in J-13 water for pH values from 6 to 9 and temperatures from 20° to 90°C (Janecky et al. 1997 [DIRS 106265], p. 2; 1995 [DIRS 101338]; Efurd et al. 1996 [DIRS 105538]). This stability extends to an ionic strength of 0.1 M, at which point, for concentrated J-13 water, the sodium neptunyl carbonate becomes stabilized. Other solids that are predicted to occur are (in decreasing importance) $Np(OH)_4$ (the hydrated amorphous form of NpO_2), $NpO_2OH_{(am)}$, and Np_2O_5 (the observed bulk solid). More recent calculations show that Np_2O_5 is a more reasonable choice for the solubilities actually measured and that neptunium (IV) solids do not have to be invoked to explain the solubility data (Efurd et al. 1996 [DIRS 105538]; 1998 [DIRS 108015]).

For plutonium, the measured solubility differs by orders of magnitude relative to that predicted for equilibrium with $PuO_{2(c)}$ (Efurd et al. 1996 [DIRS 105538]), and is consistent with the predicted solubility of $Pu(OH)_{4(am)}$. It may be that although the bulk of the precipitate is $PuO_{2(c)}$, the surface is coated to some extent with $Pu(OH)_4$, and this is the solubility-controlling solid phase depending on the time-scale of observation (BSC 2003 [DIRS 163152], Section 6.5).

Calculations of americium solubility have added uncertainty, because any real americium solid (as well as solids containing plutonium isotopes) would suffer radiation damage, therefore affecting its solubility. However, modeling shows that $AmOHCO_{3(c)}$ is nearly at saturation for the experimental conditions reported by Nitsche et al. (1993 [DIRS 155218]), whereas

Am(OH)$_{3(c)}$ and Am(OH)$_{3(am)}$ are both significantly undersaturated (Janecky et al. 1997 [DIRS 106265], p. 2; BSC 2003 [DIRS 163152], Section 6.9).

The values quoted in Tables 5-11 to 5-12 represent a summary of best-available site-specific solubilities for plutonium and americium. The values chosen were from Nuclear Energy Agency sources (Grenthe et al. 1992 [DIRS 101671]; Silva et al. 1995 [DIRS 102087]), YMP quality assurance sources tested with specific-ion interaction theory (e.g., Tait et al. 1996 [DIRS 101359]), and literature sources (e.g., Langmuir 1997 [DIRS 100051], Sections 13.4 to 13.5). Note that the use of Efurd et al. (1996 [DIRS 105538]) values for neptunium and plutonium gives more consistent and smaller values than those of Nitsche et al. (1993 [DIRS 155218]).

The solubility of uranium depends on the solid phase that will precipitate. Langmuir (1997 [DIRS 100051]) suggests that uranium solubility will be limited by the formation of uranophane (Ca(H$_3$O)$_2$(UO$_2$)$_2$(SiO$_4$)$_2$·3H$_2$O$_{(c)}$) at about 10^{-7} M at Yucca Mountain. Other phases could also potentially controls uranium concentrations. For example, in the high-silica groundwaters of Yucca Mountain, the solubility-controlling compound for uranium could be haiweeite (Ca(UO$_2$)$_2$(Si$_6$O$_{15}$)(H$_2$O)$_5$), according to available thermodynamic data (Bruton 1991 [DIRS 105961], p. 11). However, leaching experiments on uranium-oxide pellets (Bates et al. 1990 [DIRS 104900], Table II) at 90°C using J-13 water produced a variety of phases on reacted surfaces that did not include haiweeite. More recent modeling (BSC 2003 [DIRS 163152], Section 6.7) has chosen schoepite as the controlling solid for conditions representing Yucca Mountain Waters.

For technetium and iodine, in oxidizing waters such as those expected at Yucca Mountain, radionuclide concentrations cannot reasonably be limited by solubility.

For purposes of modeling radionuclide transport, radionuclide solubilities can be abstracted to simple terms. Table 5-13 gives examples of selected solubility for which values for radionuclides of concern. The elements listed include radionuclides for which concentrations in Yucca Mountain waters could be solubility limited. The values used are from expert elicitations, primarily as cited by Triay et al. (1997 [DIRS 100422]) and Langmuir (1997 [DIRS 100051], Sections 13.4 to 13.5) but also Rechard (1995 [DIRS 102059]). These values have been updated with some new experimental data from Efurd et al. (1996 [DIRS 105538]).

5.3.3   Sorption Studies

Radionuclide migration from the repository would be impeded by interactions between the mobile water phase, and immobile mineral phases. Sorption coefficients for radionuclides of interest have been experimentally determined using water and rock samples from the Yucca Mountain site. Batch experiments have been performed at several pH levels to evaluate the impact of pH variations on sorption coefficients. In general, conditions were oxidizing in all the experiments. The potential effects of organics on actinide sorption were evaluated in batch experiments with model organic compounds in water and rock samples from the site. Models were developed to explain the sorption coefficient data and to allow prediction of coefficient values under a wider range of anticipated conditions.

5.3.3.1 Minerals and Lithologies that are of Importance to Radionuclide Sorption

Zeolites–As discussed in Section 3.3.5, zeolitization, primarily at the margins of ash flows, is one of the dominant modes of alteration in Yucca Mountain tuffs. Both sodium and calcium in clinoptilolite exchange readily with a wide range of potential radionuclides, including cesium, rubidium, strontium, and barium (Ames 1960 [DIRS 144954]; Breck 1984 [DIRS 144977], pp. 529 to 588). Potassium is more difficult to remove from the clinoptilolite structure, exchanging well with cesium and rubidium but exchanging poorly with strontium and barium (Ames 1960 [DIRS 144954]). Although mineral compositional effects are most important for sorption of simple cations in solution, studies for the Yucca Mountain Project have focused on the utility of zeolitic horizons in retarding transport of complex transuranic species, most of which sorb poorly.

The large sorption capacity of zeolites for certain cations provided part of the initial impetus for considering tuffs for the disposal of radioactive waste. Radioactive alkali and alkaline-earth cations (strontium and cesium) in particular, are strongly selected for in exchange reactions with loosely held sodium, calcium, and potassium in the zeolites clinoptilolite and mordenite. Work summarized by Thomas (1987 [DIRS 101361], pp. 16 to 21) confirmed that these zeolites have a high sorption capacity for strontium and cesium, but also indicated a much lower sorptive capability for the longer-lived transuranic elements (especially plutonium and neptunium). Nevertheless, ^{135}Cs is a radioactive isotope that may be abundant in the emplaced waste and has a long half-life (3 m.y.) warranting consideration of ion exchange in the site description.

As described in Section 3.3.5, clinoptilolite and mordenite are the most abundant zeolites at Yucca Mountain. Also present are chabazite, which locally comprises up to 9 percent of the rock in some parts of the Calico Hills Formation; heulandite and stellerite, common in fractures of the Topopah Spring Tuff; phillipsite and erionite, which have a very restricted occurrence in the zone of alteration at the top of the basal vitrophyre of the Topopah Spring Tuff, as well as in the adjacent unsaturated fractures (Carlos et al. 1991 [DIRS 101576]; Bish and Chipera 1991 [DIRS 101860], pp. 437 to 444); laumontite, occurring in very small amounts (less than 4 percent) in deep, altered tuffs of drill hole UE-25 p#1 and perhaps in USW G-1 (Bish and Chipera 1989 [DIRS 101195], p. 1, abstract); and analcime a prograde alteration product, occurring only at depths that are so great that little interaction with radionuclides released by the waste is likely. The zeolitic intervals are strongly controlled by tuff stratigraphy.

Temperature can be an important factor affecting radionuclide exchange in zeolites. In dilute solutions, sorption increases with increasing temperatures (Meijer 1990 [DIRS 100780], p. 17). This result is consistent with predicted cation-exchange behavior based on measurements of zeolite electrical properties at various temperatures and salinities (Olhoeft 1986 [DIRS 145087]). However, Olhoeft's (1986 [DIRS 145087]) study of clinoptilolite conductivity behavior also indicated that the increase in cation-exchange capacity with temperature is reversed at high salinities. Other thermal effects (e.g., zeolite dehydration or rehydration, weakening of heated zeolitic rocks) may therefore be important in evaluating the ion exchange behavior of zeolites in the host rock affected by repository heating.

Clay Minerals–Smectite occurs in virtually all samples, typically in amounts less than two percent. However, above the water table, there are two continuously mappable zones in the

Paintbrush Group containing 75 percent smectite: one near the top of the vitric nonwelded base of the Tiva Canyon Tuff and one at the top of the basal vitrophyre of the Topopah Spring Tuff. These clay-rich layers typically have non-expandable illite contents of 10 to 20 percent.

Iron, Manganese Oxides and Hydroxides–Hematite is the most ubiquitous oxide mineral at Yucca Mountain. It occurs in several forms and associations, principally within matrices of glassy, devitrified, and zeolitized tuffs, but also within fractures. Typical abundances in most tuff samples are about one percent by weight in tuff matrices, with locally greater abundance in many fractures (Carlos et al. 1991 [DIRS 101576]). Although studies with pure synthetic hematite can result in high sorption of actinides, experiments with iron oxides from Yucca Mountain show little actinide sorption, probably because of "passivation" of surface sorption sites by other metal cations (Triay et al. 1993 [DIRS 145123]). However, in microautoradiography studies of a sample from the upper part of the rhyolitic, devitrified Topopah Spring Tuff, the oxide minerals account for less than 1 percent of the tuff but hold 60 percent of the plutonium track concentrations. The oxide minerals that retain plutonium have track clusters that are concentrated around the mineral edges and along internal fractures (distributions of tracks along fractures within these opaque grains can be seen in reflected light, through the film coating). This observation should be considered along with other evidence showing that grain-edge and vein alteration, in part due to manganese oxides that may be largely amorphous, is common around magnetite/maghemite phenocrysts. As with altered orthopyroxenes of the devitrified Prow Pass Tuff (discussed below), it is this peripheral and likely amorphous alteration rather than the original trace minerals that accounts for plutonium accumulation.

In contrast with the evidence for general passivation of iron oxides at Yucca Mountain, microautoradiography studies of manganese oxides from Yucca Mountain indicate a significant role for these minerals. Most manganese oxides have structures that allow only limited cation exchange (Bish and Post 1989 [DIRS 144973], pp. 184 to 185), and these minerals are more likely to interact with radionuclide wastes by surface reaction mechanisms (Means et al. 1978 [DIRS 106741], p. 1764). Although not volumetrically abundant, a large variety of manganese oxides occur in the Yucca Mountain tuffs. They are most widely distributed in fractures (Carlos et al. 1990 [DIRS 101324], Tables 1 and 11; 1991 [DIRS 101576]), but also occur within the groundmass of devitrified tuffs, mostly encircling and along microcracks radiating from oxidized magnetite and ilmenite phenocrysts. Above the water table, the principal manganese oxides are lithiophorite, rancieite, and todorokite; the principal cations in these minerals include sodium, potassium, calcium, barium, and cerium. Below the water table, cryptomelane-group minerals (hollandite, cryptomelane, and coronadite) and lesser amounts of todorokite and pyrolusite occur. The principal cations in the cryptomelane-group minerals include potassium, barium, lead, strontium, sodium, and calcium. The abundance and variety of exchangeable constituents in these minerals beneath the water table is evidence of their effective collection and retention of heavy elements, perhaps by surface complexation with later structural incorporation. This mineral group in particular is a key recorder of past water-rock interaction. Studies by Zielinski (1983 [DIRS 106657], p. 7) and Zielinski et al. (1986 [DIRS 108836]) showed a strong correlation of leachable uranium with leachable manganese at Yucca Mountain; the correlation of leachable uranium with leachable iron was much poorer, perhaps suggesting a greater heavy-metal adsorptive capacity for the manganese oxides than for the iron oxide minerals. However, it should be noted that some experiments (Milton and Brown 1987 [DIRS 145077],

p. 1327) have found that uranium is strongly retained by amorphous iron-oxyhydroxide, and desorption of uranium from these phases is limited.

Other Phases and Other Processes–Evidence of recent formation of opal, calcite, and perhaps some other phases (e.g., manganese oxides) suggests that even under ambient conditions, coprecipitation is a possible radionuclide interaction (Section 5.2.1.1). Fracture calcite is also found with intergrowths of sepiolite, kaolinite, calcium-zeolite, and manganese oxides; palygorskite within fractures may also have formed relatively recently. The paragenesis of fracture deposition suggest that calcite, opal, and some zeolites, clays, and manganese oxides were deposited under a variety of conditions beginning soon after tuff emplacement, but that deposition of calcite and some of these other minerals are recent and ongoing, or possibly associated with hydrologic conditions during the last Pluvial.

Some radionuclides leached from canisters could be coprecipitated with calcite under ambient conditions at Yucca Mountain. Those elements that substitute readily for calcium in the calcite structure at low temperature are limited to the divalent metals that are smaller than calcium (principally magnesium, iron, manganese, cadmium, zinc, cobalt, and nickel). Alkaline earth metals (strontium and barium) are incorporated in defects or upon transformation from orthorhombic carbonate structures. (Note: no evidence of orthorhombic carbonates has been found at Yucca Mountain). The abundances of these other elements, which are not defined by stoichiometry, can be sensitive to crystallization rate and to solution compositions. In aqueous solution, the partitioning of strontium into calcite can shift from distribution coefficients less than 1 to coefficients greater than 1 as the crystallization rate increases (Lorens 1981 [DIRS 145042], p. 557). Cations that form carbonate complexes may also be readily incorporated; carbonate-complexed transuranic radionuclides can coprecipitate with calcite (Penrose et al. 1990 [DIRS 100811]). Meece and Benninger (1993 [DIRS 145075], pp. 1455 to 1457) found that plutonium sorbs readily onto calcite with little sensitivity to plutonium oxidation state; their experiments also indicated that americium can be similarly incorporated into calcite. In experiments using Yucca Mountain samples and water compositions, calcite was found to be an important factor in retarding the transport of lanthanides, americium, plutonium, and, to a lesser extent, neptunium (GCX 1994 [DIRS 144994], pp. 4 to 6).

Because calcite saturation is strongly temperature-dependent, the consequences of radioactive decay heating can be considerable, for even a small heat rise. At higher temperature, the calcite that forms is also likely to be more defect-rich, leading to increased incorporation of nonstoichiometric heavy metals, including lanthanides and the radioactive actinides that behave analogously to lanthanides. Under conditions of active calcite precipitation, entrapment of transuranics may become a significant process (Meece and Benninger 1993 [DIRS 145075], pp. 1447 to 1458). With heating at constant pH, SiO_2 solubility increases, and the least stable SiO_2 phases (opal, cristobalite/tridymite, then quartz) progressively dissolve. Conversely, Ca^{2+} concentrations are reduced by heating, through the precipitation of carbonates (or calcium-zeolites, if aluminum activity is sufficient).

Opals in fractures of the unsaturated zone at Yucca Mountain are U-rich (Szabo and Kyser 1990 [DIRS 109172], p. 1715; Paces et al. 2001 [DIRS 156507], p. 25, Figure 12). Coprecipitation of waste elements with silica might be a consequence, not of ongoing natural processes, but of silica dissolution and reprecipitation that is expected to occur in the thermal aureole surrounding

the repository. Dissolution of silica polymorphs or feldspar, the principal constituents of devitrified tuff, or dissolution of vitrophyre glass might be a consequence of the migration of a condensation front through the host rock under a repository-induced thermal load (Section 5.4). Incorporation of uranium and other waste species into opaline precipitates may occur if radionuclides are released while silica precipitation is occurring, particularly as part of the cooling process beneath the repository. Rimstidt et al. (1989 [DIRS 142190], p. 587) tested a boiling water-vapor system in which silicon and iron were leached from the condensation zone and transported with the condensed liquid. Opal and iron-oxyhydroxide were precipitated near the condensation zone, but thicker deposits of these minerals with small amounts of stilbite and perhaps clay formed adjacent to the underlying heat source. In a heated column experiment of crushed tuff, Lowry (2001 [DIRS 157900], Section 5.3.3) also observed that predominantly amorphous silica (i.e., opal-A) and smaller quantities of opal-CT, quartz and feldspar deposited from refluxed water near the heated bottom of the column.

Amorphous materials occur in the tuffs of Yucca Mountain and might have significant sorption capabilities. Amorphous iron-rich materials in altered orthopyroxene microphenocrysts are particularly active in plutonium retention, accounting for less than 1 percent of the devitrified Prow Pass Tuff but holding 11 percent of the plutonium track concentrations in this sample as determined by microautoradiography (Section 5.3.3.1.3). Microautoradiography data from unaltered orthopyroxenes of the vitric Calico Hills Formation show no accumulation of plutonium.

5.3.3.1.1 Impacts of Zeolite Composition on Radionuclide Transport

Modeling by Robinson et al. (1995 [DIRS 100414]) illustrated the cumulative importance of thick zeolitic horizons in neptunium sorption; moreover, data indicate that the compositions of zeolitic rocks may also be an important factor in retardation, with sodium-potassium clinoptilolite providing about twice the neptunium sorption capability of calcium clinoptilolite. Robinson et al. (1995 [DIRS 100414]) assumed a neptunium distribution coefficient (K_d) (as defined in Section 5.3.3.2.1) range of 1.1 to 3.9 mL/g for zeolitic rock in the unsaturated zone. A later report (Triay et al. 1997 [DIRS 100422], pp. 85 to 86) assigned the most effective (i.e., larger) neptunium K_d values to iron oxides anticipated to form by corrosion of a multipurpose container, and assigned the smallest maximum neptunium K_d for the natural site lithologies in the unsaturated zone to zeolitic tuff (unsaturated zone neptunium maximum K_d values were assigned as 15, 6, and 3 mL/g for vitric, devitrified, and zeolitic tuff, respectively [Triay et al. 1997 [DIRS 100422], pp. 85 to 100]). Despite differences in the assignment of K_d values for these different lithologies in various models, the dependence of model results on lithologic type remains.

In the unsaturated zone, exchangeable cations within clinoptilolites on the western side of the exploratory block consist primarily of sodium and potassium (Broxton et al. 1986 [DIRS 100023], p. 22), while clinoptilolites on the eastern side of the block have mixed Na-K and Ca-K compositions. In the saturated zone, clinoptilolite compositions tend to become more sodic with depth on the western side of Yucca Mountain and more calcic with depth to the east (Broxton et al. 1986 [DIRS 100023], p. 22). In this case, the initial results for neptunium (Robinson et al. 1995 [DIRS 100414]) suggest that the western part of Yucca Mountain might have more effective zeolite barriers than the eastern part of Yucca Mountain.

Ultimately, transport modeling at Yucca Mountain must also consider the possible formation of alteration minerals over time, which may affect the way in which radionuclides will interact with the rock. Present rates of mineral alteration at Yucca Mountain are probably low. Geopetal and stable-isotope studies indicate that the major zeolitic intervals near and below the water table formed in the Miocene soon after tuff eruption (Levy 1984 [DIRS 104577]; 1991 [DIRS 100053]) and have probably altered little since. The effects of coupled thermal-hydrologic-geochemical processes on host rock mineralogy and hydraulic properties, and on water chemistry, are discussed in Section 5.4.

5.3.3.1.2 Mineralogy of Samples Used in Sorption Experiments

Yucca Mountain rock samples used in sorption studies can be categorized into three principal rock types, according to quantitative x-ray diffraction analyses:

(1) Devitrified tuff, characterized by prominent feldspar associated with tridymite, cristobalite, and/or quartz, often with minor amounts of hematite and smectite (for reasons discussed in this section, the composition of the devitrified tuffs (rhyolitic or quartz latitic) should also be distinguished).

(2) Zeolitic tuff, generally characterized by abundant clinoptilolite, less often associated with abundant mordenite, and rarely by chabazite and/or one of several lesser zeolites (Section 3.3.5) (zeolitic tuff may be partially vitric in the basal Topopah Spring Tuff, Calico Hills Formation, and upper Prow Pass Tuff and typically contains opal-CT with lesser amounts of feldspar, quartz, and smectite).

(3) Vitric tuff, which is distinguished by its glass component and lesser amounts of smectite, zeolites, silica polymorphs, and hematite. There is a fourth type of sample used in sorption experiments, obtained from surface soils and distinguished by the presence of variable amounts of opaline material, calcite, sepiolite, smectite, quartz, and feldspar.

In addition to these rock samples, pure mineral phases were used in batch-sorption and column-sorption experiments. These studies were pursued because natural materials are multicomponent mixtures of minerals, and it is often difficult to determine which mineral or minerals were responsible for the observed sorption.

Because neptunium does not interact strongly with most rocks and minerals representative of Yucca Mountain, a more extensive suite of batch sorption samples was tested for neptunium than for most other radionuclides.

The samples used in the radionuclide batch-sorption experiments are the most comprehensive of any sample suite used in sorption studies (Triay et al. 1997 [DIRS 100422], pp. 55 to 108). In general, the batch-sorption results show that the lithologies at Yucca Mountain can be broadly considered as the three major types described above: devitrified, zeolitic, and vitric. However, the distinctions between these lithologies are blurred in the sorption affinities of some radionuclides (e.g., americium, which sorbs readily regardless of lithology) and require finer subdivision to explain the sorption behavior of other radionuclides such as neptunium. By splitting out the quartz-latitic from the rhyolitic devitrified and vitric samples, it can be seen that

the lowest K_d values (less than 0.5) are associated only with quartz-latitic compositions, whether vitric or devitrified. The reassessment of neptunium sorption along these lines, based on geochemistry as well as lithology, allows interpretation of the data as follows:

- Neptunium K_d values for zeolitic samples: approximately 1 to 5 mL/g

- Neptunium K_d values for devitrified rhyolitic samples: approximately 1 to 2 mL/g

- Neptunium K_d values for vitric rhyolitic samples: approximately 0.5 to 2.2 mL/g

- Any neptunium K_d values less than 0.5 mL/g are in quartz-latitic devitrified or vitric samples.

This analysis of the neptunium data provides an approach to assessments of neptunium transport that can be linked to the site stratigraphy as well as to lithology, because the quartz-latitic tuffs are all above the repository horizon (Section 3.3.5). More recent sorption data are discussed in Section 5.3.3.2.

In the dynamic transport column experiments (see Section 5.3.4), the devitrified lithologies tested were quartz-latitic, and sorption of neptunium is minimal in this rock type, as discussed above. This was the result observed, with highest K_d values in the zeolitic samples (1.7 to 2.1 mL/g) and K_d values of less than 0.1 mL/g in the devitrified quartz-latitic samples. The vitric rhyolitic samples also had relatively low K_d values in the column experiments (0.1 to 0.2 mL/g), but these values were still higher than those recorded for the quartz-latitic samples. Results for plutonium at different flow rates indicate significant sorption by vitric and zeolitic tuffs but with distinct kinetic effects. Plutonium breakthrough in the columns of devitrified quartz-latitic tuffs was rapid, but it is not known whether the breakthrough would have been any slower in columns of devitrified rhyolitic tuff.

For fracture-flow experiments, only devitrified tuff samples were used. In these samples, natural fractures were identified by their mineral coatings (stellerite, iron-oxides, hollandite, romanechite) although some apparently drilling-induced fractures were tested as well. The results of the fracture transport experiments showed high neptunium affinity for the manganese oxide minerals hollandite and romanechite; these results were confirmed in batch-sorption studies using pure mineral samples.

The fracture-transport experiments show very rapid breakthrough of technetium (consistent with anion exclusion from matrix diffusion), relatively rapid breakthrough of ^{3}H with somewhat more matrix retention across the hollandite + romanechite fracture lining, and markedly strong retention of neptunium by hollandite + romanechite relative to stellerite + iron-oxides. The neptunium results are backed by batch-sorption results indicating very high neptunium K_d values (600 to 700 mL/g) with pure mineral experiments using hollandite and romanechite. These batch-sorption K_d values are much greater than obtained with bulk-rock experiments (K_d values less than 5 mL/g in J-13 water). The combined data make it evident that manganese-oxides significantly retard neptunium movement. These laboratory results should be considered in conjunction with the field evidence of significant interaction between groundwater and manganese oxides in Yucca Mountain fractures (Section 5.2.1.2). The latter data provide a

strong indication that the interactions observed in the laboratory will indeed occur on the field scale at Yucca Mountain, even with manganese oxide minerals that exist as intermittent linings along fractures.

Diffusion studies were pursued to test the movement of radionuclides through matrix diffusion. These experiments were conducted in two forms (see Section 5.3.5). In the first experiment, rock beakers were prepared with drilled-out cavities of 2.8-cm diameter and 2.5-cm depth. The beakers were surrounded with J-13 water and radionuclide-containing solutions of J-13 water were introduced into the drilled-out cavities. In the beaker experiments, the solution introduced into the drilled-out cavity was sampled over time to determine the progressive loss of radionuclides by diffusion through the rock beaker. Radionuclides used in the beaker experiments included ^{3}H, ^{95m}Tc, ^{237}Np, ^{241}Am, ^{85}Sr, ^{137}Cs, and ^{133}Ba. In these beaker experiments, only devitrified tuffs were tested.

The second type of diffusion experiment used diffusion cells with a simpler geometry, measuring the diffusion across a planar slab of tuff (see Section 5.3.5.3). In these experiments, two chambers were separated by a slab of tuff approximately 1 cm thick. The radionuclide tracer solution was emplaced on one side and groundwater without radionuclides was introduced on the other side. Both J-13 and synthetic carbonate aquifer waters were used. Aliquots were periodically sampled from the untraced solution, and the radionuclide activity was measured. As aliquots were removed, the untraced side of the cell was replenished with groundwater to maintain volume and avoid the development of a hydraulic head, which would force the tracer solution through the sample. Radionuclides used in the diffusion-cell experiments included ^{3}H, technetium, uranium, plutonium, and neptunium for devitrified and zeolitic tuffs, using both groundwaters. Mixed solutions of ^{3}H-U-Pu and Tc-Np were studied with devitrified and vitric tuffs. Results of these experiments show that diffusion is slower in devitrified than in zeolitic tuff, but plutonium was not observed in the sampled side of the cell for either lithology over time spans of more than 2,000 hr.

Results of the diffusion experiments agree well with batch-sorption data. For sorbing tracers such as cesium, the diffusion out of the rock beakers was faster than predicted from assumptions of reversible, instantaneous, and linear sorption (Triay et al. 1997 [DIRS 100422], pp. 189 to 203). The dispersal of sorbing species into the matrix thus appears to be more effective than these simplified assumptions would suggest. In the diffusion cell experiments, results indicated that diffusion of nonsorbing tracers (^{3}H) is more rapid in zeolitic than in devitrified tuff. Sorbing species (such as uranium) with K_d values of the order of 10 mL/g or less also diffused more rapidly through the zeolitic tuff, but more highly sorbing species (plutonium) diffused only slowly through either rock type (Triay et al. 1997 [DIRS 100422], p. 196, Figure 133).

5.3.3.1.3 Microautoradiography

Microautoradiography studies of Yucca Mountain samples focused on the three principal rock types—devitrified, vitric, and zeolitic—that underlie the site. In a round of experiments with plutonium (Kitten et al. 1997 [DIRS 101340]), optical analysis of the distributions of ^{239}Pu α-decay tracks in these three types of samples showed only four definitive mineral types that are associated with enhanced affinity for plutonium. All of these associations are with trace minerals. Two of these associations are very restricted in stratigraphic occurrence: the altered

orthopyroxenes of the devitrified Prow Pass Tuff and the altered opaque oxides of the upper Topopah Spring Tuff. The two other associations, however, are with smectites and manganese oxyhydroxides that are much more widely distributed across virtually all stratigraphic levels, albeit generally in trace amounts.

These results provide a valuable comparison to the more quantitative data obtained in sorption studies. However, certain caveats must be considered when using the electron microprobe technique in microautoradiography. First, the use of planar thin sections provides a two-dimensional view of what is essentially a three-dimensional process. Second, the variability in silver emulsion content and thickness and in random α-track occurrences is a minor problem. Third, the size of the electron beam (in this study, $10~\mu m$) might be larger than the individual minerals of interest (e.g., clays) making accurate resolution sorption questionable.

The accuracy of clay/zeolite radionuclide distribution factors determined by electron microbeam methods may be affected by (1) the large ($10~\mu m$) electron beam size relative to the size of the clay bodies being analyzed, and (2) the incorporation of epoxy into parts of the thin section that had originally been occupied by clay. Together, these effects probably lead to underestimates of clay/zeolite radionuclide distribution factors. Nevertheless, in zeolitic rocks such as those in the Calico Hills Formation, smectites that account for less than 10 percent of the rock mass can provide approximately 90 percent of plutonium retardation, particularly where the smectites are concentrated along microfractures.

The microautoradiography data provide information on retardation mechanisms, with insights into phase preferences that may explain the sensitivity of sorption to changes in water composition for some lithologies. Microautoradiography experiments on the three major lithologies from Yucca Mountain (devitrified, vitric, and zeolitic) to three actinide elements (americium, plutonium, uranium) in two different waters (J-13 and UE-25 p#1), provide some insight into the mechanisms that account for variability in batch-sorption results. Batch-sorption analysis of the three lithologies used shows a general ranking of effective retardation for all three actinides in all rock types and both waters with retention of $Am \gg Pu \geq U$. The use of microautoradiography to measure differential retention of these actinides by specific minerals shows that plutonium is particularly strongly concentrated over smectite + manganese oxide associations in zeolitic rocks (regardless of water composition). However, plutonium is concentrated in smectite in vitric samples only when synthetic UE-25 p#1 water is used because the major element chemistry is more concentrated in calcium and sulfate than J-13 water (J-13 water does not lead to any notable smectite preference in the vitric tuff). Phase preferences with americium and uranium were also tested in the zeolitic lithology. For both of these actinides, a significantly higher preference for smectite + manganese oxide phases was observed in synthetic UE-25 p#1 water, but there was little or no preference for specific minerals with J-13 water. The implications of enhanced phase preference in UE-25 p#1 water for explaining shifts in retardation factors may be best illustrated by the behavior of americium in p#1 versus J-13 water. All lithologies exposed to americium in p#1 water have batch-sorption distribution coefficients ranging from 5 to 7 times (in devitrified and vitric rocks) to 55 times (in zeolitic rocks) the batch-sorption values in J-13 water. The strong phase preference for trace but widely dispersed smectite and manganese oxides in zeolitic rocks with UE-25 p#1 water might account for much of this shift, with the much larger shift in zeolitic rock attributable principally to the presence of the manganese oxide mineral rancieite, which strongly sorbs plutonium (Figure 5-33).

Figure 5-33 also shows, however, that not all manganese oxide minerals can be treated similarly in terms of sorptive potential; in this example, a sample with fracture-lining cryptomelane shows no effective plutonium retention.

5.3.3.2   Description of Batch-Sorption Data

5.3.3.2.1   Introduction

For radionuclides present in the aqueous phase, sorption onto the surrounding tuffs becomes an important mode of retardation. "Sorption" actually describes several physicochemical processes, including ion exchange, physical adsorption, and chemisorption. Evaluating the retardation effectiveness of sorption requires theoretical and quantitative understanding of this process. The primary input data used for sorption modeling and radionuclide transport studies (BSC 2003 [DIRS 167208], Attachment I; BSC 2003 [DIRS 163228], Attachment I) are laboratory results of radionuclide sorption experiments using waters collected from Yucca Mountain or synthesized to reflect Yucca Mountain waters, and rock or mineral samples either collected from the field or synthesized in the laboratory.

The use of batch-sorption experiments to obtain sorption distribution coefficients and to identify sorption mechanisms is relatively fast, and inexpensive compared to other methods. A disadvantage is that such experiments are static in nature, whereas transport of radionuclides through the site is dynamic. However, batch-sorption experiments are useful for bounding sorption behavior, and a major part of the experimental effort was devoted to such measurements.

In the experiments, batch-sorption distribution coefficients were determined as functions of variables representing conditions expected outside of the region disturbed by waste emplacement. The variables included mineralogy, groundwater chemistry, sorbing element concentration, atmospheric conditions, and temperature. The sorption behavior of individual pure minerals found in Yucca Mountain tuffs, such as zeolites and manganese or iron oxyhydroxides, was also examined. This approach was designed to allow estimation of sorption coefficients along flow paths with known mineral abundance.

The Distribution Coefficient–The batch-sorption distribution coefficient, K_d, is calculated using

$$K_d = \frac{F}{C} = \frac{\text{moles of radionuclide per gram of solid phase}}{\text{moles of radionuclide per milliliter of solution}} \qquad \text{(Eq. 5-9)}$$

K_d values thus have units of mL/g.

The determination of very small or very large batch-sorption distribution coefficients results in large uncertainties in the K_d values calculated. Because of these uncertainties, most K_d values are only reported to one significant figure.

The sorption distribution coefficient, K_d, for the species being sorbed is the ratio of its concentration in the solid phase, F, to its concentration in the solution phase, C, which implies a linear relationship between the concentrations. Besides linearity, the use of sorption distribution

coefficients in transport calculations assumes instantaneous and reversible sorption behavior. Part of the research discussed in this section was an attempt to assess the validity of using the linear distribution coefficients as opposed to other isotherm functional forms, such as the nonlinear Freundlich and Langmuir isotherms, to describe retardation by sorption in transport calculations (Equation 5-9).

Experimental Procedures–Over the last 25 years, several sets of radionuclide batch sorption experiments have been run, mostly at LANL. A similar procedure was used in all cases. The experiments were performed at room temperature and either under atmospheric conditions or inside glove boxes with a carbon dioxide overpressure. Generally, one gram of crushed rock (usually the 75-500 µm fraction) was added to 20 mL groundwater. Two groundwaters were used. J-13 water was pumped from a volcanic unit, the Topopah Spring Tuff, while UE-25 p#1 water is pumped from a carbonate aquifer. The pH values for the J-13 and p#1 waters under atmospheric conditions were approximately 8.5 and 9, respectively; inside the glove boxes, the pH was 7 (Triay et al. 1997 [DIRS 100422]). The results of these experiments are discussed below for each radionuclide.

5.3.3.2.2   Plutonium

Data from Sorption Experiments Reported in the Literature–Allard (1982 [DIRS 104512], Sections 4 to 5) reported results on experiments involving plutonium sorption on quartz, apatite, attapulgite, montmorillonite, and various minerals rich in ferrous iron in a dilute groundwater containing plutonium at 1.8×10^{-11} M. For all the minerals, the sorption coefficients were greater than 10^3 mL/g over a pH range of 4 to 9. Apatite, attapulgite, biotite, and montmorillonite showed sorption coefficients greater than 10^4 mL/g over this pH range. Torstenfelt et al. (1988 [DIRS 142200], Tables 17 to 25) presented data for plutonium sorption on feldspars, clays, and granite in contact with J-13 water. The sorption coefficients reported by Torstenfelt et al. (1988 [DIRS 142200], Tables 17 to 25) are generally between 100 to 200 mL/g in neutral to alkaline solutions. Data indicating high affinity of plutonium for ferric oxyhydroxide, manganese oxide, and carbonate mineral surfaces were presented by Means et al. (1978 [DIRS 106741]), Keeney-Kennicutt and Morse (1985 [DIRS 106313]), and Sanchez et al. (1985 [DIRS 107213]). Means et al. (1978 [DIRS 106741], pp. 1771 to 1772) noted that manganese oxides sorb plutonium more strongly than ferric oxyhydroxides in natural environments (presumably as a result of redox reactions on the manganese oxide surface).

Data from Laboratory Sorption Experiments with Yucca Mountain Rock and Water Samples–Measurements of plutonium sorption coefficients involving Yucca Mountain rock samples and J-13 groundwater were summarized by Thomas (1987 [DIRS 101361], p. 20). The values measured for the plutonium sorption coefficient range from 20 to greater than 4,500 mL/g, with most values lying between 100 to 2,000 mL/g within a pH range of 8.2 to 8.8. The coefficients determined during desorption experiments were occasionally in the range of the sorption coefficient values, but, more typically, they were 10 to 20 times larger, reflecting the irreversibility of the sorption reactions. Zeolitic samples typically had lower sorption-coefficient values than vitric or devitrified samples. It appears that rocks that have essentially no reduction capacity remaining (i.e., samples lacking ferrous iron or sulfide) show the lowest sorption coefficients for plutonium. Samples with calcite or clay showed the largest sorption coefficients (greater than 4,500 mL/g for samples with 30 percent calcite).

Sorption coefficients for plutonium varied by up to a factor of 12 as a function of groundwater composition. Water from well UE-25 p#1 was associated with the largest values (240 to 540 mL/g, sorption-desorption) with waters from wells H-3 and J-13 showing the lowest values (20 to 230 mL/g) (DTN: LA0010JC831341.006 [DIRS 153318]). The higher values obtained with UE-25 p#1 water might reflect calcite precipitation. The sorption coefficient did not vary systematically with pH over the range from 7 to 9, although the available data are limited. Finally, the measured sorption coefficient varied by less than a factor of four with radionuclide concentration, over the plutonium range from 10^{-9} to 10^{-12} M.

In additional experiments, plutonium sorption coefficients have been measured on a variety of solid samples in contact with Yucca Mountain groundwaters UE-25 J-13 and p#1 under atmospheric conditions (i.e., oxidizing conditions and pH equal to 8.2 to 8.6). The data (Table 5-14; DTN: LA0010JC831341.006 [DIRS 153318]) show that plutonium sorption coefficients will be greater than 100 mL/g for vitric and zeolitic tuffs under these conditions. For devitrified tuffs, sorption coefficients will be less than 100 mL/g in both water compositions (BSC 2001 [DIRS 160828], Section 6.4.4.1.4.1).

The sorption of plutonium onto the three main types of tuff in J-13 water at a pH of 7 was studied using a carbon dioxide overpressure to maintain a pH of 7. These experiments were also conducted under oxidizing conditions (i.e., atmospheric oxygen concentrations). The affinity of tuffs for plutonium at pH = 7, with CO_2 overpressure is, in decreasing order, zeolitic > vitric > devitrified (Triay et al. 1997 [DIRS 100422], Figure 37). Compared to the data presented in Table 5-14, plutonium appears to sorb somewhat less at a pH of 7.0 than at atmospheric P_{CO2} values and pH values from 8.2 to 8.6, particularly on devitrified tuff (K_d less than 10 mL/g).

To investigate which minerals in tuffs were responsible for most plutonium sorption, sorption experiments were also carried out with pure mineral separates. The minerals investigated included hematite, clinoptilolite, albite, and quartz. The results of the batch-sorption experiments for plutonium on these minerals are shown in Table 5-14. The relative affinities of these minerals for plutonium are, in decreasing order, hematite > montmorillonite > clinoptilolite > calcite >> gibbsite > albite ≥ quartz. These data suggest that montmorillonite (a smectite clay) and zeolite minerals are likely responsible for most of the plutonium sorption onto the bulk tuffs. The trace amounts of hematite found in the tuffs do not appear to have a significant impact based on other data (Triay et al. 1997 [DIRS 100422], pp. 65 to 73). However, the presence of calcite in the tuffs can have a significant impact depending on the amounts present and on the surface area of the calcite present.

To investigate the shape of the plutonium sorption isotherms with increasing Pu concentration, experiments were conducted over a range of solution concentrations with various rock and water combinations. The data obtained indicate that the plutonium sorption isotherm is generally nonlinear on tuffs from Yucca Mountain (Triay et al. 1997 [DIRS 100422], pp. 69 to 73). The cause of the nonlinearity is not known. The solution concentrations in these experiments range from 3×10^{-10} to 2×10^{-7} M. Because the upper limit of this range is close to the solubility of plutonium in Yucca Mountain groundwaters, the concentration of aqueous plutonium transported in the flow system will likely not exceed this value. Experiments conducted with concentrations at the low end of the range produce sorption coefficients that are higher than experiments conducted with solution concentrations at the high end of the range.

The sorption of plutonium onto tuffs and minerals in J-13 and synthetic UE-25 p#1 water under atmospheric conditions was studied as a function of time and initial plutonium solution concentration. The resulting data (Triay et al. 1997 [DIRS 100422], p. 69) indicate that it takes a long time for the plutonium sorption reactions to reach a steady state. Even after 32 days, a steady-state concentration in solution was not achieved in these experiments.

Comparing data for plutonium sorption coefficients to similar data for neptunium and uranium indicates that significant plutonium sorption occurred in tuffs and minerals that exhibit very small sorption coefficients for neptunium (V) and uranium (VI). This result is puzzling; if plutonium in J-13 well water is predominantly plutonium (V) and plutonium (VI) (Nitsche et al. 1993 [DIRS 155218]), it is expected that its sorption behavior would have been similar to that observed for neptunium (V) and uranium (VI). There are several possible explanations for this apparent discrepancy:

- The Nitsche et al. (1993 [DIRS 155218]) data for the oxidation states are incorrect, and the predominant plutonium oxidation state in J-13 well water at a pH of 7 is plutonium (IV), not plutonium (V) and plutonium (VI).

- The plutonium (IV) species is what sorbs from J-13 water, but a reequilibration in the solution phase produces more plutonium (IV) to maintain equilibrium (which implies that the kinetics of plutonium speciation in solution are fast, but are slow on the solid).

- Plutonium (V) and plutonium (VI) reduce to plutonium (IV) at solid surfaces (as a result of changes in the solution redox potential in the presence of the solid phases).

The impact of the slow sorption kinetics on predictions of transport rates of plutonium in Yucca Mountain is that the sorption coefficients from the batch tests should generally result in conservative predictions.

Recent additional work has assessed available data on radionuclide sorption from laboratory testing relevant to conditions in the unsaturated and saturated zones at Yucca Mountain, to develop uncertainty distributions for sorption coefficients (BSC 2003 [DIRS 163228], Attachment I; 2003 [DIRS 167208], Attachment I). The sorption coefficient data on which the distributions were based are primarily those discussed and cited previously in this section, obtained in laboratory experiments in which crushed rock samples from the Yucca Mountain site were contacted with groundwaters or simulated groundwaters, spiked with one or more radioelements of interest. Crushed rock materials were grouped into devitrified tuff, zeolitic tuff, and alluvium categories for description of sorption behavior. Solutions consisted mainly of J-13 water, or simulated water from calcic formation conditions in well UE-25 p#1. Sorption experiments have been carried out as functions of time, element concentration, CO_2 fugacity, reactive surface area, and temperature. In some cases, the crushed-rock solids remaining from sorption experiments were contacted with unspiked groundwater in desorption experiments. The sorption and desorption experiments together provided information on the equilibration rates of the forward and backward sorption reactions. For elements that sorb primarily through surface complexation reactions, the experimental data were evaluated using model calculations (BSC 2003 [DIRS 163228], Section I.6; 2003 [DIRS 167208], Section I.1). The development addressed the detailed characteristics of mineral surfaces in rock units at Yucca Mountain, and

other primary controls on sorption behavior of the elements of interest in the unsaturated and saturated flow systems.

A large range in plutonium sorption coefficients was measured in devitrified tuffs, which could be explained if plutonium is active in more than one oxidation state. However, in the absence of definitive data for the oxidation state of plutonium on rock/mineral surfaces, a wide range of experimentally determined values was used to develop uncertainty distributions. The plutonium sorption-coefficient uncertainty distribution for devitrified tuff in the saturated zone is presented as a beta distribution with range of 50 to 300 mL/g, mean of 100 mL/g, and a standard deviation of 15 mL/g (BSC 2003 [DIRS 167208], Section I.8.4.1). The limited data for p#1 water yielded results that lay within the range for J-13 water. The low end of the selected uncertainty range is based on the minimum value observed in long-term experiments (> 40 days), and also captures the potential impacts from variations in surface area among samples, variations in water chemistry, and variations in plutonium concentrations. The upper end of the distribution was chosen to conservatively represent the potential impacts of sorption kinetics during longer term transport (BSC 2003 [DIRS 167208], Section I.8.4.1). Similar results were estimated for unsaturated transport (BSC 2003 [DIRS 163228], Section I.8.D), but with smaller sorption coefficients, recognizing the likelihood of more rapid transport through the unsaturated zone.

The uncertainty distributions adopted for plutonium sorption on zeolitic tuff in the unsaturated and saturated zones are the same as, or very similar to those for devitrified tuff because experimentally derived sorption-coefficient values show similar ranges and sensitivities (BSC 2003 [DIRS 163228], Section I.8.D). For sorption on alluvium in the saturated zone, the identical uncertainty distribution for devitrified tuff was used because: (1) the alluvium had a similar tuffaceous source, and (2) disaggregation of tuffaceous rocks during weathering and transport to form alluvium, has increased the available surface area for sorption (BSC 2003 [DIRS 163228], Attachment I).

Conclusions Regarding Sorption Behavior of Plutonium in the Yucca Mountain Flow System–Based on information in the previous sections, it appears the most important factors controlling the sorption of plutonium from oxidizing groundwater onto Yucca Mountain tuffs are the abundances of montmorillonitic clays and zeolite minerals. Calcite, if present, may also result in high plutonium sorption coefficients. The affinity of Yucca Mountain tuffs for plutonium is highest in zeolitic tuffs, slightly lower in vitric tuffs, and lowest in devitrified tuffs. Groundwater compositional parameters that appear to have the most impact on plutonium sorption behavior are redox potential (i.e., Eh) and pH. Under less-oxidizing redox potentials than those maintained in the batch experiments, plutonium sorption coefficients would be larger. Therefore, the sorption coefficients reported here will result in conservative predictions of plutonium transport rates. The change in sorption coefficients that may result from variations in groundwater composition and pH are accounted for using surface complexation modeling, as described in a later section. Similarly, the impact of potential variations in plutonium concentration will also result in conservative predictions of plutonium transport rates. Although the kinetics of the plutonium sorption reactions appears to be relatively slow compared to elements with simpler solution chemistry (e.g., cesium), the sorption coefficients reported here should result in conservative predictions of plutonium transport rates.

5.3.3.2.3   Cesium, Radium, and Strontium

Behavior in Solutions Representative of Yucca Mountain Groundwaters–These elements (cesium, radium, and strontium) show relatively simple solution behavior in typical groundwaters and are not subject to changes in oxidation state in the groundwater compositions expected in Yucca Mountain. Radium and cesium are invariably present as Ra^{2+} and Cs^+ cations in the expected groundwater compositions (Ogard and Kerrisk 1984 [DIRS 100783]). Strontium exists primarily as the Sr^{2+} ion in these waters, but may also be present as the neutral aqueous species $SrSO_4$, at concentrations of a few percent of the total strontium solution concentration (Ogard and Kerrisk 1984 [DIRS 100783]).   The data of Langmuir and Riese (1985 [DIRS 106457]) indicated that $RaSO_4(_{aq})/Ra^{2+}$ will be greater than or equal to 0.6 when the sulfate ion concentration is greater than 10^{-3} M. These numbers suggest that $RaSO_4(_{aq})$ will be a significant species ($RaCO_3(_{aq})$ and $SrCO_3(_{aq})$ may also be significant).

Literature Data–The sorption behavior of these radionuclides is largely controlled by ion-exchange   reactions   (Bolt   and   Bruggenwert 1978   [DIRS 113856]),   although surface-complexation reactions involving these elements have also been discussed (Balistrieri and Murray 1982 [DIRS 104809]).   The selectivity of most clays and zeolites for cesium, radium, and strontium is greater than the selectivities for the major cations in solution. Strontium K_d values are strongly influenced by ionic strength of the solution, decreasing with increasing ionic strength (Mahoney and Langmuir 1991 [DIRS 166020], pp. 139 to 144; Nisbet et al. 1994 [DIRS 166021], pp. 145 to 154); calcium and natural strontium are especially effective at competing with radioactive strontium. Clay minerals such as illite, smectites, and vermiculite exhibit a high selectivity for cesium (Cornell 1993 [DIRS 166022], pp. 483 to 500). The selectivity is a function of the low hydration energy of cesium; once it is sorbed into clay interlayers, it loses its hydration shell and the interlayer collapses. Magnesium and calcium do not shed their hydration shells and cannot compete for the interlayer sites. Potassium is able to enter the interlayer and competes strongly for exchange sites. Because it causes collapse of the interlayers, cesium does not readily desorb from vermiculite and smectite and may in fact be irreversibly sorbed (Ohnuki and Kozai 1994 [DIRS 166023], pp. 327 to 331; Khan et al. 1994 [DIRS 166024], pp. 629 to 642). Uptake by illitic clay minerals does not occur by ion exchange but rather by sorption onto frayed edge sites (Cremers et al. 1988 [DIRS 166025], pp. 247 to 249; Smith and Comans 1996 [DIRS 166026], pp. 995 to 1004), which are highly selective for cesium. Although illite has a higher selectivity for cesium, it has a much lower capacity than smectites because cesium cannot enter the interlayer sites.

The pH does not have a significant effect on the sorption behavior of these elements over the pH range of interest at Yucca Mountain.

Data from Laboratory Sorption Experiments with Yucca Mountain Rock and Water Samples–Sorption coefficients for cesium, radium, and strontium were reviewed by Daniels et al. (1983 [DIRS 101333], Table 14, pp. 39 to 40), Thomas (1987 [DIRS 101361], p. 4), Meijer (1990 [DIRS 100780], p. 20) and BSC (2003 [DIRS 163228], Attachment I). For cesium at low concentrations (10^{-8} M), sorption coefficients are greater than 100 mL/g for all water-rock combinations tested except UE-25 p#1 water in contact with vitric tuff (BSC 2003 [DIRS 163228],   Attachment I;   DTNs: LA0309AM831341.003   [DIRS 165524]; LA0305AM831341.001 [DIRS 163789]).   At higher cesium concentrations, the K_d values

obtained ranged from 10 to 100 mL/g. There was little or no impact of water chemistry on the cesium sorption in devitrified-tuff. For zeolitic tuffs, sorption coefficients are greater.

Radium appears to have a somewhat higher affinity for sorption onto Yucca Mountain tuffs than cesium (BSC 2003 [DIRS 163228], Attachment I). In addition, the solubility of radium sulfate (RaSO$_4$) limits the concentrations in solution to trace levels (2.9×10^{-7} to 10^{-8} M, DTN: LA0306AM831343.001 [DIRS 164949]). At concentrations below the solubility limit for RaSO$_4$, sorption coefficients for radium are generally in the range of 100-1000 mg/L in devitrified tuff, greater in zeolitic tuff, and smaller in the vitric tuff. (DTNs: LA0309AM831341.002 [DIRS 165523]; LA0305AM831341.001 [DIRS 163789]). There is a limited or no clear dependence on water chemistry in the devitrified or zeolitic tuff. In the vitric tuff, the K_d value was greater with the J-13 water than with the UE-25 p#1 water (BSC 2003 [DIRS 163228], Attachment I).

Strontium sorption behavior is more sensitive to mineral and water compositions than cesium and radium discussed above. For devitrified tuffs, sorption coefficients for the higher ionic-strength waters (e.g., UE-25 p#1) are significantly greater than for lower ionic-strength waters such as J-13. The K_d values generally range between 50 10 to 50 mL/g (BSC 2003 [DIRS 163228], Attachment I; DTNs: LA0309AM831341.006 [DIRS 165527]; LA0305AM831341.001 [DIRS 163789]). These sorption coefficients decrease as the solution concentration of strontium increases above approximately 10^{-5} M (Thomas 1987 [DIRS 101361], Appendix). However, the strontium concentration in solution is limited by the solubility limit for strontianite (SrCO$_3$), which ranges from approximately 9.9×10^{-7} to 2.7×10^{-5} M (DTN: LA0306AM831343.001 [DIRS 164949]). Strontium sorption is more pronounced in zeolitic tuffs, and less significant in vitric tuff.

Conclusions Regarding Sorption Behavior with Respect to Expected Variations in Groundwaters–The existing sorption-coefficient database for cesium, radium, and strontium adequately describe radionuclide interactions with tuff material. However, if the concentration of total cesium in the solution phase in contact with devitrified and vitric tuffs is greater than 10^{-5} M, then an appropriate value for the sorption coefficient might be less than 100 mL/g. The sorption coefficients for strontium in devitrified and vitric tuffs will be as small as 10 to 30 mL/g in higher ionic-strength waters.

5.3.3.2.4 Neptunium

Neptunium, protactinium, and uranium share a common characteristic in that they all tend to show small values for sorption coefficients in the rock-water systems expected within Yucca Mountain under oxidizing conditions. Under more reducing conditions, they would all have much lower solubilities and higher sorption affinities in Yucca Mountain groundwaters. In solutions representative of oxidized water compositions expected within the Yucca Mountain flow system, neptunium will be predominantly in a +5 oxidation state. In this oxidation state, neptunium is quite soluble when compared to lower oxidation states. If reducing conditions are encountered along the flow path between the repository and the accessible environment, neptunium could be reduced to the +4 oxidation state.

Data from Sorption Experiments Reported in the Literature–The results of neptunium sorption experiments with pure mineral separates were reported by Allard (1982 [DIRS 104512], Sections 4 to 5), Meijer et al. (1990 [DIRS 106758]), and others. On the basis of these results, it is evident that in oxidizing solutions, neptunium has a high affinity for ferric oxides and oxyhydroxides, apatite, and attapulgite (a Mg-rich clay). It has a somewhat lower affinity for carbonates (e.g., calcite), sulfates (e.g., anhydrite), and manganese minerals (e.g., cryptomelane). It has a low affinity for most silicate minerals. Neptunium also shows high affinities for minerals that contain ferrous iron (e.g., pyrite, olivine, augite, magnetite, hornblende, epidote, biotite, and chlorite). This affinity is likely due to the reduction of neptunium (V) to neptunium (IV) by ferrous iron on the surfaces of these minerals. Although ferrous Fe-bearing minerals are minor species in Yucca Mountain tuffs (Bish and Chipera 1989 [DIRS 101195]), they could be of considerable significance to neptunium sorption where present in the flow system.

The pH is also an important parameter in neptunium sorption. In general, neptunium sorption increases with increasing pH. This effect is particularly evident in the experiments with ferric-oxyhydroxides (Combes et al. 1992 [DIRS 105758]). However, similar behavior is evident in the sorption experiments with silicate minerals (Allard 1982 [DIRS 104512], Section 4.1, Figure 9). In the latter case, the sorption edge (as a function of pH) is located at a higher pH (8 to 9) than the edge associated with the ferric-oxyhydroxides (a pH of 6 to 7). Neptunium does not appear to have a high affinity for ion-exchange reactions on clays and zeolites (Allard 1982 [DIRS 104512], Figure 16; Triay et al. 1993 [DIRS 125972], p. 1505). This phenomenon might be due to the small charge-to-radius ratio and the large size of the neptunyl cation.

Data from Laboratory Sorption Experiments with Yucca Mountain Rock and Water Samples–The results of neptunium sorption experiments involving Yucca Mountain rock and water samples were reported by Daniels et al. (1982 [DIRS 105803]), Thomas (1987 [DIRS 101361], p. 20 Appendix; 1988 [DIRS 106529]), and Triay et al. (1993 [DIRS 125972], p. 1505). These experiments indicate that neptunium exhibits K_d values of 0 to 5 mL/g for the surfaces in Yucca Mountain tuffs over most of the pH range and water compositions expected in the Yucca Mountain flow system (DTNs: LA0309AM831341.004 [DIRS 165525]; LA0305AM831341.001 [DIRS 163789]). The sorption mechanisms are apparently not entirely reversible, as coefficients obtained from desorption experiments are commonly larger than those obtained from sorption experiments, even though the isotherms are linear in the concentration range covered by these experiments. There is some indication of increased sorption coefficients (5 to 40 mL/g) at the highest pH values (8.5 to 9.0). Torstenfelt et al. (1988 [DIRS 142200], p. 115) suggested that this result reflects increased hydrolysis of the neptunyl ion, resulting in an increase in surface-adsorption reactions.

In the pH range from 6.5 to 8.5, the small but consistent affinity of neptunium for the tuffs most likely reflects the existence of a limited number of favorable sorption sites for neptunium. This number apparently does not involve ion-exchange sites because zeolitic rock samples also show low sorption coefficients. Some zeolitic, vitric, and devitrified tuff samples have almost no affinity for neptunium over the pH range from 6.5 to 8.5, whereas other samples with similar proportions of major minerals show sorption coefficients in the range of 5 to 10 mL/g. This result suggests that the favorable sites are associated with some minor primary or secondary

phase, such as hematite or calcite that has variable abundance. Alternatively, neptunium may be sorbed (through reduction to Np^{4+}) by the small amounts of ferrous Fe-bearing minerals present in the rock samples used in the sorption experiments.

The greater sorption of neptunium on tuffaceous samples known to contain calcite suggests this mineral is of considerable potential significance to neptunium sorption on Yucca Mountain tuffs. For vitric units lacking iron oxides and calcite, neptunium may not be sorbed at all (BSC 2001 [DIRS 160828], Section 6.4.4.1.4.2).

Sorption coefficients for neptunium (V) on samples of vitric, devitrified, and zeolitic tuff under atmospheric conditions (pH = 8.2 to 8.6; oxidizing, $P_{CO2} = 10^{-3.5}$) are shown in Figure 5-34. Note that the sorption coefficients for all samples are less than 5.0 mL/g. The values less than 1.0 are generally for vitric and devitrified samples, and those greater than 1.0 are for zeolitic samples.

Zeolitic tuffs show substantial variation in the neptunium sorption from sample to sample, and under different pH conditions (Figure 5-35). The explanation likely involves the zeolite mineralogy and content of each sample. In J-13 water, neptunium sorbs only sparingly onto devitrified and vitric tuffs at both pH values (7 and 8.5).

Experiments with pure clinoptilolite indicate that sorption increases with decreasing pH for neptunium (V). Table 5-15 shows measured and predicted values of K_a (K_d divided by the solid-phase surface area) for several clinoptilolite-rich tuffs measured at pH 7. Similar calculations (Table 5-15) were made for a series of tuff samples containing various amounts of clinoptilolite for which the surface area had been measured. The values in this table indicate that reasonable predictions can be made based on neptunium sorption data for pure clinoptilolite (assuming clinoptilolite is the only sorptive mineral).

The sorption of neptunium onto zeolitic tuffs and clinoptilolite appears to be linear in the concentration range from 1×10^{-7} to 3×10^{-5} M, and can be fitted using a constant K_d (DTN: LA0010JC831341.007 [DIRS 153319]). In a zeolite-rich tuff at a pH of 7.0, the K_d was 3.0 mL/g, whereas at a pH of 8.5, the K_d was 1.5 mL/g (Figure 5-36). Similar results were obtained with a pure zeolite sample (Figure 5-37). The higher sorption of neptunium onto zeolites at a pH of 7 might be explained by the larger amount of NpO_2^+ relative to $NpO_2CO_3^-$ in J-13 well water at a pH value of 7 compared to that at a pH of 8.5.

The relatively small amount of sorption observed in the zeolitic tuffs, given the large cation-exchange capacity of zeolites, suggests that the mechanism for neptunium sorption onto clinoptilolite is a surface reaction involving only the cation sites accessible on the zeolite surface. One possible explanation for this behavior is that the shape and large size of the neptunyl cation prevents it from entering the pores in the zeolite structure.

The sorption of neptunium onto pure iron oxides (hematite) in J-13 water was also measured (DTN: LA0010JC831341.007 [DIRS 153319]). The measured values of K_d for hematite range from 100 to 2,000 mL/g. Although the sorption onto pure hematite is very large, neptunium sorption onto devitrified tuffs, which have traces of hematite (1 percent $\pm$ 1), is close to zero. This result could be due to differences in the surface chemistry of pure hematite compared to

hematite in tuff. For example, it could be due to passivation of the hematite surfaces in the tuff by elements (e.g., the rare earths) that have a higher affinity for hematite than neptunium and, thus, occupy the sorption sites.

The sorption kinetics of neptunium onto tuffs and clinoptilolite appears to be fast (steady state in 5 to 7 days). No significant differences are observed in neptunium sorption as a function of time for the tuffs studied and for clinoptilolite. This is not the case for pure minerals that tend to sorb by means of a co-precipitation mechanism (e.g., calcite) or by surface complexation (e.g., hematite).

Neptunium sorption onto tuffs and zeolites is very limited (K_d less than 1 mL/g) in UE-25 p#1 water regardless of conditions (pH and neptunium concentration). If clinoptilolite is the only mineral affecting neptunium sorption, and if ion exchange at the surface is the dominating mechanism, it could be that the reason for the lack of neptunium sorption on clinoptilolite is the formation of the neptunium carbonato complex ($NpO_2CO_3^-$) in UE-25 p#1 water to the exclusion of the neptunyl cation. However, the data reported by Nitsche et al. (1995 [DIRS 100163]) do not support this conclusion; the relative amount of neptunyl in UE-25 p#1 water is larger than that in J-13 water at a pH of 7. One possibility is that there is more competition for sorption sites in the higher ionic strength UE-25 p#1 water relative to the J-13 water.

Figures 5-38 and 5-39 summarize the sorption of neptunium under atmospheric conditions for tuffs and minerals as a function of water type. Sorption onto zeolitic tuffs is considerably lower in the UE-25 p#1 water, which is more carbonate-rich and has a higher ionic strength (Figure 5-38). Figure 5-39 shows that calcite and hematite have high affinities for neptunium, particularly in UE-25 p#1 water.

Recent additional work has assessed available data on radionuclide sorption from laboratory testing relevant to conditions in the unsaturated and saturated zones at Yucca Mountain, to develop uncertainty distributions for sorption coefficients (BSC 2003 [DIRS 163228], Attachment I; 2003 [DIRS 167208], Attachment I). The sorption coefficient data on which the distributions were based are primarily those discussed and cited previously in this section, obtained in laboratory experiments in which crushed rock samples from the Yucca Mountain site were contacted with groundwaters or simulated groundwaters, spiked with one or more radioelements of interest. Crushed rock materials were grouped into devitrified tuff, zeolitic tuff, and alluvium categories for description of sorption behavior. Solutions consisted mainly of J-13 water or simulated water from calcic formation conditions in well UE-25 p#1. Sorption experiments have been carried out as functions of time, element concentration, CO_2 fugacity, reactive surface area, and temperature. In some cases, the crushed-rock solids remaining from sorption experiments were contacted with unspiked groundwater in desorption experiments. The sorption and desorption experiments together provided information on the equilibration rates of the forward and backward sorption reactions. For elements that sorb primarily through surface complexation reactions, the experimental data were evaluated using model calculations (BSC 2003 [DIRS 163228], Section I.6; 2003 [DIRS 167208], Section I.1). The development addressed the detailed characteristics of mineral surfaces in rock units at Yucca Mountain, and other primary controls on sorption behavior of the elements of interest in the unsaturated and saturated flow systems.

A wide range of experimentally determined values for neptunium sorption coefficients was used to develop uncertainty distributions. The neptunium sorption-coefficient uncertainty distribution for devitrified tuff in the saturated zone is presented as an exponential distribution with range of 0 to 2 mL/g, mean of 0.69 mL/g, and a standard deviation of 0.707 mL/g (BSC 2003 [DIRS 167208], Section I.8.3.1). The low end of the selected uncertainty range is based on the minimum values observed in short-term experiments (up to 21 days). The upper end of the distribution was chosen to conservatively represent sorption with neptunium concentration near the solubility limit, and results from experiments at pH near 7.0 (BSC 2003 [DIRS 167208], Section I.8.3.1). Similar results were estimated for unsaturated transport (BSC 2003 [DIRS 163228], Section I.8.C). The uncertainty distributions adopted for neptunium sorption on zeolitic tuff in the unsaturated and saturated zones are similar to those for devitrified tuff (BSC 2003 [DIRS 163228], Section I.8.C).

For neptunium sorption on alluvium in the saturated zone, a t-distribution was selected with a mean of 6.3 mL/g and standard deviation of 0.81 mL/g (BSC 2003 [DIRS 163228], Attachment I). This distribution was thought to capture spatial variability in the results obtained with samples from several wells. In addition, other sources of uncertainty were incorporated to address representativeness of the experimental conditions, potential competitive sorption effects among radionuclides, affect of oxidation state on sorption behavior, variability in water composition and lithology, and the potential for complexation by other ligands (e.g., organics).

Conclusions Regarding Neptunium Sorption Behavior with Respect to Expected Variations in Groundwaters–The mechanisms by which neptunium appears to sorb onto mineral surfaces in the Yucca Mountain flow system appear to be ion exchange or surface complexation on zeolitic phases and co-precipitation and surface adsorption involving carbonate minerals. The ion exchange/surface-complexation mechanism appears to be responsible for the 0.5 to 5.0 mL/g range in sorption-coefficient values consistently measured in zeolitic rock samples. The high end of this range may reflect other mechanisms such as the presence of trace minerals with high affinities for neptunium.

5.3.3.2.5   Protactinium

Behavior in Solutions Representative of Yucca Mountain Groundwaters–In aqueous systems, protactinium appears to exist dominantly in the +5 oxidation state, although the +4 state may occur in reducing environments (Brookins 1988 [DIRS 105092]). In both oxidation states, protactinium is strongly hydrolyzed and forms highly insoluble compounds (Cotton and Wilkinson 1988 [DIRS 105732], pp. 1002 and 1003). This result implies that the +5 solution chemistry of protactinium is more akin to that of niobium (V) than to other actinides in +5 oxidation states, such as PuO_2^+ or NpO_2^+. In this case, the solution parameter of greatest importance to protactinium sorption behavior is pH.

Because protactinium forms such insoluble compounds, it is generally assumed to be immobile in the surficial environment.

Data from Laboratory Sorption Experiments With Yucca Mountain Rock and Water Samples–Rundberg et al. (1985 [DIRS 101355], p. 63, Table 17) report protactinium sorption coefficients in the range from 3.7 to 8.2 mL/g for a zeolitic tuff in contact with J-13 water spiked

with 10^{-11} to 10^{-14} M protactinium at pH values of 6.3 to 6.7 (DTN: LA0305AM831341.001 [DIRS 163789]). Combined with the data reported by Allard (1982 [DIRS 104512]), these data suggest that protactinium cations sorb by a surface-complexation mechanism, and that there is a rather steep sorption edge for protactinium at a pH value of approximately 7.

Conclusions Regarding Sorption Behavior with Respect to Expected Variations in Groundwaters–Batch-sorption data for protactinium suggest that sorption coefficients for this element will be small (less than 10 mL/g) at lower pH values (BSC 2003 [DIRS 167208], Figure I-31). There is limited spatial distribution for pH data at Yucca Mountain.

5.3.3.2.6   Uranium

Behavior in Solutions Representative of Yucca Mountain Groundwaters–Under the redox potentials expected in Yucca Mountain groundwaters, particularly in the unsaturated zone, uranium should be in the +6 oxidation state. In this oxidation state, uranium will be present in solution in a variety of complexes, including $(UO_2)_2CO_3(OH)_3^-$, $UO_2(CO_3)_2^{2-}$, $UO_2(CO_3)_3^{4-}$, $UO_2(OH)_{2(aq)}$, $UO_2(CO_3)_{(aq)}$, and other minor species. Phosphate, fluoride, or sulfate species will not be significant within the concentration ranges for these anions and the pH range expected in Yucca Mountain groundwaters.

Qualitative Evidence for Behavior in the Surficial Environment–Data on the behavior of uranium in the surficial environment are available from various sources. Several types of uranium ore deposits have been studied as natural analogs to repository settings. Other sources of data include studies of uranium mill-tailings piles, waste-stream outfalls, and other uranium ore deposits. Only the natural analog studies are discussed in this section.

The deposits that were studied as natural analogs include those at Oklo, Gabon, the Alligator Rivers region in Australia, Cigar Lake in Canada, Poças de Caldas in Brazil, and Peña Blanca in Mexico. These natural analogs are discussed in BSC (2002 [DIRS 160405]). Each deposit was studied in considerable detail to define the geochemical behavior of uranium and its daughter products in the environments in which the ore deposits are found. Although none of the environments is completely analogous to the Yucca Mountain site, the Peña Blanca deposit is at least situated in Tertiary volcanic tuffs similar to those present at Yucca Mountain. These natural analogs are discussed in BSC (2002 [DIRS 160405]).

A critical aspect of any analog for potential uranium migration at the Yucca Mountain site is that the uranium source must be subject to redox potentials similar to those expected at Yucca Mountain, particularly in the unsaturated zone. This fact eliminates data from the Cigar Lake and probably the Oklo deposits (Goodwin et al. 1989 [DIRS 105714], Appendix B.3.4; Cramer and Sargent 1994 [DIRS 105768], p. 2238; Brookins 1983 [DIRS 105091], pp. 206 to 207) from detailed consideration.

The Alligator Rivers deposits are exposed to oxidizing conditions in a surficial environment (Giblin and Snelling 1983 [DIRS 105643], p. 37). Uranium isotope-disequilibrium studies at this site indicate that uranium migration has occurred relatively recently (Snelling and Dickson 1979 [DIRS 142100]). However, evidence for recent transport does not by itself provide an estimate of the transport rate and, more importantly, of the chemical controls on this rate.

At the Koongarra deposit, uranium migration is significantly retarded by the precipitation of uranyl phosphate minerals (Snelling 1980 [DIRS 126708]). Significant phosphate concentrations are found in the country rocks in minerals such as apatite and phosphate concentrates in local groundwater is in the range 0.01 to 0.1 mg/L. The phosphate in the rocks is apparently redistributed locally by groundwater, resulting in the precipitation of uranyl phosphate minerals within the zone of weathering (Snelling 1980 [DIRS 126708]). This retardation mechanism is not expected to be important at Yucca Mountain, given the low phosphate concentrations found in Yucca Mountain rock units and associated waters (Broxton et al. 1986 [DIRS 100023]).

Uranium in the zone of weathering at Alligator Rivers also appears to be associated with, and is probably retarded by, ferric iron compounds (Payne et al. 1990 [DIRS 107008]). Experiments involving uranium sorption were carried out on whole-rock samples from the Alligator River site and on pure mineral samples (Payne et al. 1990 [DIRS 107008]). These experiments suggest that ferric oxyhydroxides are strong sorbers of uranium in this system over a pH range of 5 to 9. Similar results on ferric oxyhydroxides have been reported by others (e.g., Hsi and Langmuir 1985 [DIRS 106131], p. 1931).

The Peña Blanca uranium deposits in Mexico provide a potentially more appropriate analog site in relation to Yucca Mountain. The primary uranium deposits at this site are hydrothermal in origin and were emplaced in structural features associated with Tertiary silicic volcanic tuffs that overlie Mesozoic carbonate strata (George-Aniel et al. 1991 [DIRS 105636], pp. 234 to 236). In addition to the hydrothermal deposits, which contain sulfide minerals as well as uranium oxides, supergene deposits have formed locally through the leaching of uranium from the volcanic rocks and subsequent precipitation as uranyl silicate minerals, including uranophane (Murphy 1992 [DIRS 106833], p. 20). The supergene deposits are hosted by kaolinitic and silicified rhyolite and do not appear to contain sulfide minerals. The absence of sulfide minerals is important because sulfides, such as pyrite, oxidize readily in the surficial environment to produce acidic conditions unlike those expected within Yucca Mountain. The supergene deposits are thought to have formed in a near-surficial environment (George-Aniel et al. 1991 [DIRS 105636], p. 246), and their study may offer useful insight into the potential for migration of uranium from the repository within Yucca Mountain.

A qualitative study by Rosholt et al. (1971 [DIRS 106712]) established that uranium was leached from devitrified tuff samples, but not from hydrated glassy samples obtained from a given geologic unit. These and other data presented suggest devitrification makes the uranium in tuffs more mobile in the surficial environment. Zielinski et al. (1986 [DIRS 108836]) and Flexser and Wollenberg (1992 [DIRS 105597], abstract, pp. 1593 to 1598) observed that uranium in Yucca Mountain devitrified tuffs was commonly associated with manganese oxides. This fact suggests that, although uranium may be mobile in the unsaturated devitrified tuffs in Yucca Mountain, it could be retarded to the extent that there are manganese oxides present along the flow path with sufficient capacity to sorb the potential flux of uranium from the current repository horizon. Given the amount of uranium to be emplaced in the repository, it would seem the sorption capacity of the manganese oxides present in the mountain (Bish and Chipera 1989 [DIRS 101195]) would be rapidly saturated. Nonetheless, manganese oxides may significantly retard the movement of uranium in some of the fracture-flow scenarios.

Data from the Literature–Data have been presented in the literature on the sorption of uranium as uranium (VI) onto a variety of pure mineral phases in simple electrolytes. Among the solid phases investigated are goethite (Hsi and Langmuir 1985 [DIRS 106131]), hematite (Ho and Miller 1986 [DIRS 106039]), silica gel (Zielinski 1980 [DIRS 108833]), clays (Tsunashima et al. 1981 [DIRS 141990]), and zeolites (Ames et al. 1983 [DIRS 104522], Table 2). The results reported are sometimes difficult to reconcile. For example, Hsi and Langmuir (1985 [DIRS 106131], Figure 2) reported that hematite sorbs very little of the uranium in solutions with 5×10^{-5} M uranium and 1×10^{-3} M total carbonate, whereas Ho and Miller (1986 [DIRS 106039], Figure 1) reported that hematite sorbs up to 100 percent of the uranium in their experiments with similar uranium and bicarbonate solution concentrations. Both sets of experiments had similar hematite surface areas. The main difference was that the solution phase in the Hsi and Langmuir (1985 [DIRS 106131]) experiments also contained 0.1 M $NaNO_3$. Why there is a difference in these results is unclear. One possibility is that the surface characteristics of the solid phases used were not the same in the two sets of experiments.

Silica gel appears to have a clear affinity for uranium as established by the results of laboratory experiments and by observations on the association of uranium with opals in nature (Zielinski 1980 [DIRS 108833]). According to Maya (1982 [DIRS 106722]), the uranium is adsorbed to silica gel as the uranyl ion, free of carbonate ligands. Zielinski (1980 [DIRS 108833]) has shown that sorption of uranium onto silica gel is sensitive to the total carbonate concentration of the solution phase when this concentration is above 0.01 M. Experiments carried out at elevated temperatures (65° to 80°C) resulted in somewhat higher sorption coefficients.

Sorption of uranium by clays was investigated in some detail. Borovec (1981 [DIRS 105012], Figure 2, Table 111) presented data that indicate montmorillonite has a high selectivity for uranyl ions relative to divalent ions of zinc, manganese, calcium, magnesium, cobalt, cadmium, and nickel at a pH value of 6 in chloride solutions. However, Tsunashima et al. (1981 [DIRS 141990]) found montmorillonite has a greater selectivity for calcium, magnesium, and barium ions than for uranyl ions in nitrate solutions over the pH range from 4.0 to 4.5. Montmorillonite was found to have a greater selectivity for the uranyl ion than for sodium and potassium ions in the same solutions. Ames et al. (1983 [DIRS 104522], Tables 5 to 7) found that uranium was strongly sorbed to montmorillonite from 0.01 M NaCl solutions but weakly sorbed from 0.01 M $NaHCO_3$ solutions in the pH range from 8 to 9.

Because groundwaters in Yucca Mountain contain significant concentrations of bicarbonate, calcium, and magnesium ions, these data suggest overall that uranyl ions may not compete favorably for exchange sites on clay minerals in Yucca Mountain, although quantitative prediction of the extent of exchange would require more detailed analysis.

Data available on uranium sorption on zeolitic minerals are very limited. Ames et al. (1983 [DIRS 104522], pp. 329 to 331) report that clinoptilolite has a low affinity for trace levels of uranium in the pH range from 8 to 9 in 0.01 M $NaHCO_3$. Doi et al. (1975 [DIRS 105439], p. 637) found that uranium at concentrations of 10^{-6} g per gram of solution was strongly sorbed onto clinoptilolite from perchlorate solutions in the pH range from 4 to 8.5.

Data from Laboratory Sorption Experiments with Yucca Mountain Rock and Water Samples–Data on uranium sorption coefficients for Yucca Mountain rock-water systems were reported by Thomas (1987 [DIRS 101361], p. 20, Appendix) and discussed by Meijer (1990 [DIRS 100780]; 1992 [DIRS 100467]), and in BSC (2003 [DIRS 163228], Attachment I; DTNs: LA0101AM831341.001 [DIRS 163043]; LA0305AM831341.001 [DIRS 163789]; LA0309AM831341.007 [DIRS 165528]). The affinity of the devitrified and vitric tuffs for trace levels of uranium is generally small (K_d less than 5 mL/g) over the pH range from 6 to 9 in J-13 water. For zeolitic tuffs, the K_d is near zero at a pH of 9 but increases with decreasing pH to approximately 25 mL/g at a pH of 6 in J-13 water. This behavior suggests the uranyl cations can exchange with the major cations in zeolites.

In UE-25 p#1 water, uranium batch-sorption experiments were only carried out in the pH range from 8.3 to 9.3 with the result that measured sorption coefficients were small (0 to 2.7 mL/g) (Thomas 1988 [DIRS 106529], Table 4, p. 26). A devitrified sample showed the largest sorption coefficient. In the pH range from 6 to 8, it is expected that the sorption coefficients for uranium in UE-25 p#1 water will increase with decreasing pH (because of predominant $UO_2CO_3^0$ at higher pH values), but they will likely be smaller than the coefficients obtained for the same rock samples in J-13 water over this pH range. In groundwater from well H-3, sorption coefficients were also low for zeolitic and devitrified rock types over the pH range from 9.2 to 9.3, presumably reflecting the elevated carbonate content of this water. However, data for a vitric sample showed a value of 6.2 mL/g for the uranium sorption coefficient at a pH value of 9. This relatively high value was not explained.

The sorption of uranium (VI) onto samples of the three types of tuff in J-13 water (under oxidizing conditions) at the two pH values (7 and 8.5) was studied. However, to identify the sorbing minerals in the tuffs, sorption onto the pure minerals hematite, clinoptilolite, albite, and quartz was also studied. It was found that uranium in J-13 water does not sorb onto devitrified and vitric tuffs, albite, and quartz (Table 5-16). For the experimental conditions cited, uranium sorption onto zeolitic tuffs and clinoptilolite is nonlinear and can be fitted with Freundlich and Langmuir isotherms (Figures 5-40 and 5-41).

For the clinoptilolite-rich zeolitic tuff sample G4-1510, the scatter in the data makes it impossible to conclude whether there is a significant difference between the experiments performed under a carbon-dioxide overpressure and a pH of 7 or at atmospheric conditions and a pH of 8.5 (Figure 5-40). However, the experiments with pure clinoptilolite indicate that sorption increases with decreasing pH for uranium (VI) (Figure 5-41), as is the case for neptunium (V). Because the major constituent of tuff sample G4-1510 is clinoptilolite, predictions of the K_a were made for uranium sorption onto this tuff by assuming that clinoptilolite is the only sorbing phase. Inspection of Table 5-17 indicates that reasonable predictions are obtained with this assumption for a pH of 7 but not for a pH of 8.5. In all cases, predictions based on clinoptilolite sorption are conservative.

The sorption of uranium onto pure iron oxides (e.g., hematite) is very large (and large uncertainties in the K_d values result from measuring the small amounts of radionuclide left in solution after sorption). Although the measured sorption of uranium onto pure hematite is very large, sorption onto devitrified tuffs, which appear to have traces of hematite (1 percent ± 1), is essentially zero. As with neptunium, this result could be due to differences in the surface of pure

hematite compared to hematite in tuff, or it could be due to passivation of the hematite surfaces in the tuff by elements (e.g., the rare earths) that have a higher affinity for hematite than uranium and, thus, occupy the sorption sites.

Conclusions Regarding Sorption Behavior with Respect to Expected Variations in Groundwaters–The dominant groundwater compositional controls on the sorption behavior of uranium on Yucca Mountain rock samples will likely be pH, carbonate content, and the concentrations of calcium and magnesium ions in solution. The pH and carbonate contents influence the sorption largely as a result of the decrease in carbonate complexation of uranium with decreasing pH. These two parameters are therefore not entirely independent. However, different water compositions can have different carbonate contents at a given pH. The expectation is that waters with higher carbonate contents will be associated with lower sorption coefficients. This trend applies to both ion-exchange and surface-complexation sorption mechanisms. For a given rock-water system, the degree of uranium sorption will also depend on the concentrations of competing ions, such as calcium and magnesium. For high calcium and magnesium waters, the competitive effects will be substantial. Because unsaturated zone waters are relatively enriched in calcium and magnesium, uranium sorption coefficients in the unsaturated zone may be on the low end of the range reported to date (Thomas 1987 [DIRS 101361], p. 29; 1988 [DIRS 106529], Table 4, p. 28).

5.3.3.2.7   Carbon, Chlorine, Iodine, and Technetium

Carbon, chlorine, and iodine are unlikely to sorb significantly in the rock-water systems expected at Yucca Mountain. For ^{14}C, the most robust retardation mechanism will be isotopic exchange with stable carbon isotopes in groundwater and on carbonate mineral surfaces (Meijer 1993 [DIRS 106757], abstract, p. 110).

Chloride and iodide ions will have no significant retardation in Yucca Mountain rock-water systems and may even have slightly enhanced migration rates due to anion-exclusion effects (Ogard and Vaniman 1985 [DIRS 101351], p. 7).

Technetium appears to show nonzero, although minimal, retardation in Yucca Mountain rock-water systems (Ogard and Vaniman 1985 [DIRS 101351], p. 44, Table 10; Rundberg et al. 1985 [DIRS 101355], pp. 65 to 69; Thomas 1988 [DIRS 106529], p. 31). However, the cause of this retardation was not identified.

5.3.3.3   Effects of Organics on Actinide Sorption

A wide variety of naturally occurring organic compounds are known to chelate actinides, including citrate, oxalate, humates, fulvic compounds, and siderophores, and that the compounds used in the experimental work were intended to represent the suite of naturally-occurring compounds that are likely to be present. The interaction between organic materials and mineral surfaces in the natural environment is important to mineral surface geochemistry. Sorption of organic material onto mineral surfaces affects not only the solubility and surface charge of the organic materials in solution but also the properties of the mineral surfaces, such as their charge and hydrophobicity, thereby altering the reactivity of the mineral toward metal ions. Therefore, studies were carried out to examine the effect of the presence of organic compounds on

radionuclide sorption. Catechol, alanine, dihydroxyphenylalanine (DOPA), and Nordic aquatic fulvic acid (NAFA) were used as model organic materials. Alanine is an amino acid that will complex with the hard acid type of metal ions in solution. Catechol is a phenolic compound that may chelate with metal ions and undergo redox reaction with the metal. DOPA, a naturally occurring amino acid commonly found in plant seedlings, pods, and broad beans, was chosen because it contains well-defined organic functional groups, such as carboxylic acid, amine, and phenols.

Under the experimental conditions used in this work, the plutonium and neptunium are expected to exist as the chemical species PuO_2^+ and NpO_2^+, respectively. Synthetic boehmite, goethite, hematite, ferrihydrite, and a crushed natural tuff material from Yucca Mountain served as model sorbents (Kung and McBride 1989 [DIRS 106443]; 1989 [DIRS 106445]; 1991 [DIRS 106446], pp. 702 to 703).

5.3.3.3.1 Neptunium

The sorption behavior for neptunium on different iron oxides is shown in Figure 5-42. The sorption of neptunium on model iron oxides follows the order of hematite > ferrihydrite > goethite. However, it should be noted that the surface areas of these iron oxides were different. The sorption of neptunium on these iron oxides was not compared on a unit surface area basis. For ferrihydrite and goethite, the surface areas are around 90 m^2/g. The surface area of hematite is about 40 m^2/g. Higher surface areas are expected to have higher sorptions. Also, the sorption experiment with ferrihydrite was conducted at pH 6.2, while the experiments with hematite and goethite were conducted at pH 6.9.

The pH affects sorption of both radionuclide and organic compounds. Experimental data showed that neptunium sorption by goethite increased as the pH increased from 6.2 to 6.9. DOPA sorption onto all of the oxides examined also increased with increasing pH.

First, the potential effects of naturally-occurring organic materials were evaluated by examining neptunium sorption by crushed tuff and crushed tuff that had been treated with hydrogen peroxide to oxidize the organic matter (a standard treatment; Kunze and Dixon 1986 [DIRS 106448], pp. 95 to 97). Sorption isotherms for both materials did not vary significantly, suggesting that either organic material is not present in the tuff, or that it does not affect sorption of neptunium onto tuff material. To evaluate this, DOPA was added to both treated and untreated crushed tuff materials, and the neptunium sorption isotherms for these systems were compared. The addition of DOPA had no effect on neptunium sorption on either treated or untreated crushed tuff materials, supporting the premise that the presence of organic material does not affect neptunium sorption onto the tuff.

Because this experiment did not rule out the possibility that the lack of an observable effect was a result of the intrinsically low sorption of tuff materials, the experiment was also carried out with iron and aluminum oxides, which sorb neptunium more strongly. Sorption was examined in the presence and absence of DOPA, catechol, and alanine. The organic compounds had no effect of neptunium sorption (BSC 2001 [DIRS 160828], Section 6.4.4.2). Although both catechol and alanine may complex with neptunium in solution, the organic-metal complexes are apparently not strong enough to affect the neptunium sorption.

In another set of experiments to study the effect of naturally occurring organic material on neptunium sorption, NAFA (Nordic aquatic humic acid, a naturally occurring humic material) served as a model fulvic material. NAFA had little effect on neptunium sorption in all systems (Triay et al. 1997 [DIRS 100422], Figures 89, 90, 65 and 66).

Thus, it is concluded that neither simple low-molecular-weight organics nor naturally-occurring fulvic organic material affects neptunium sorption. The lack of detectable effects is possibly attributed to the stable redox state of neptunium (V) in solution and to low complexation between neptunium ions and organic chemicals.

5.3.3.3.2   Plutonium

Sorption of plutonium onto iron oxides also followed the order of hematite $>$ ferrihydrite $>$ goethite (Triay et al. 1997 [DIRS 100422], p. 157), and, as with neptunium, sorption onto goethite increased as the pH increased from 6.6 to 6.9. This suggests that sorption is controlled by a surface-complexation process, because goethite has a positive surface charge at neutral pH, and plutonium is expected to be dominated by the cationic species PuO_2^+ under neutral and slightly acidic conditions.

Sorption isotherms for plutonium onto ferrihydrite, goethite, and hematite were measured in the presence and absence of catechol and alanine, and clearly indicate that the sorption of plutonium onto goethite and ferrihydrite was affected by the presence of the organic materials. Alanine suppressed the plutonium sorption on goethite and ferrihydrite, probably by lowering the free plutonium ion activity in solution by formation of an alanine- plutonium complex. Conversely, plutonium sorption onto goethite and ferrihydrite was higher in the presence of catechol. The presence of catechol and alanine had little effect on the sorption of plutonium onto hematite probably because of the intrinsically high sorption of plutonium onto hematite. Any small enhancement or suppression of sorption due to catechol and alanine was too minor to be expressed.

The isotherms for sorption of plutonium on ferrihydrite and goethite in the absence of DOPA and in its presence at three concentration levels (1×10^{-6}, 1×10^{-7}, and 1×10^{-8} M) clearly demonstrate that sorption is affected by this compound. Plutonium sorption was higher in systems that contained DOPA than in systems that did not contain DOPA, and sorption increased as the initial DOPA concentration increased from 1×10^{-8} to 1×10^{-6} M. This result is likely attributed to the formation of stable surface DOPA plutonium ternary complexes and a redox reaction between DOPA and plutonium. Reduction of plutonium (V) to lower oxidation states will enhance the sorption/precipitation of plutonium. DOPA had little effect on neptunium sorption onto goethite, boehmite, and tuff material suggesting that it does not complex with neptunium in solution, and/or that DOPA cannot reduce neptunium (V) to lower oxidation states.

The sorption of plutonium (V) on three Yucca Mountain tuff materials, vitric tuff (Gu3-1496), devitrified tuff (G4-275), and zeolitic tuff (G4-1529), in natural J-13 and synthetic UE-25 p#1 groundwater, was examined in the presence of NAFA. The results indicate that plutonium (V) sorption onto these tuff materials was not conclusively affected by the presence of this organic compound.

The plutonium (V) species were not stable in the presence of fulvic and humic acids in natural J-13 and synthetic UE-25 p#1 groundwaters (Triay et al. 1997 [DIRS 100422], pp. 158 to 159). However, plutonium (V) is relatively more stable in the presence of organic materials in synthetic p#1 groundwater than in natural J-13 water. Because it is not known why plutonium (V) disappears from solution phase in these groundwater environments, control concentrations for each organic and water condition were used to obtain the sorption data discussed here. It should be noted that plutonium (V) was stable in the sorption experiments conducted in a 0.1 M KCl solution.

5.3.3.3.3   Summary of Effects of Organics on Actinide Sorption

From the sorption data, the following conclusions can be drawn concerning the effect of natural organic materials on neptunium and plutonium sorption by iron and aluminum oxides and crushed tuff material:

- The amount of neptunium sorption was not affected by any of the organic materials (alanine, catechol, DOPA, and NAFA) that were studied. This lack of an observable effect is presumably a result of the weak complexation between neptunium and the model organics.

- The sorption of plutonium was influenced by the presence of DOPA on goethite and ferrihydrite. Increasing the amount of DOPA resulted in higher sorption of plutonium on goethite and ferrihydrite. Alanine decreased the sorption of plutonium, probably by lowering the free Pu-ion activity in solution by formation of an alanine-Pu complex. Plutonium sorption was increased by the presence of catechol, probably due to reduction of plutonium (V) to plutonium (IV) by the organic. Organics had no observable effect on plutonium sorption in the hematite system, probably due to the relatively high affinity of plutonium for the hematite surface.

5.3.3.4   Adsorption of Radionuclides by Alluvium

The migration behavior of sorbing radionuclides in the saturated alluvium south of Yucca Mountain has been studied in a series of laboratory-scale tests (Ding et al. 2003 [DIRS 164737]). The alluvium consists primarily of materials of volcanic origin similar to those found at Yucca Mountain (with some enrichment of clays and zeolites relative to common volcanic tuffs, plus secondary mineral coatings on the detritus).

Experiments conducted using alluvial materials focused on the transport characteristics of ^{129}I, ^{99}Tc, ^{237}Np, and ^{233}U. The first two were determined to be nonsorbing on tuff rocks, while the second two were moderately sorbed on tuff rocks. The goal of these experiments was to determine the sorption coefficient of the alluvial materials under conditions relevant to the field. To achieve these objectives, many batch sorption, batch desorption, and flow-through column experiments were carried out under ambient conditions to determine the sorption coefficients of these radionuclides between groundwater and alluvium from different boreholes.

The alluvium samples used in the experiments (Table 5-23) were obtained at various depths from three Nye County Boreholes (NC-EWDP-19IM1A, NC-EWDP-10SA, and NC-EWDP-22SA).

The alluvium samples used for batch experiments were dry sieved and size fractions of less than 75 μm, 75 to 500 μm, and 75 to 2,000 μm were used in different experiments. For column experiments, alluvium samples within a particle size range of 75 to 2,000 μm were wet sieved to remove fine particles that would clog the columns. Groundwater used in the experiments was obtained from Borehole NC-EWDP-19D (Zones 1 and 4) and NC-EWDP-10SA. Mineral characterization of alluvium used in the experiments was determined by quantitative X-ray diffraction. Although the dominant minerals in the alluvium are quartz, feldspar, and plagioclase, considerable amounts of the sorbing minerals smectite (ranging from 3 to 8 percent) and clinoptilolite (ranging from 4 to 14 percent) were identified in the alluvial samples (Table 5-24).

5.3.3.4.1   Iodine and Technetium Sorption

The results of the batch sorption tests indicate there is negligible sorption of iodine and technetium onto the alluvium (Ding et al. 2003 [DIRS 164737]). Measured K_d values were in the range of 0.0 ± 0.25. The scatter of the results around zero is representative of the degree of precision of the testing method (e.g., the negative K_d values do not necessarily suggest anion exclusion).

5.3.3.4.2   Uranium Sorption

Uranium sorbed rapidly onto the alluvium, showing little change with continued exposure beyond one day (Figure 5-43). The higher K_d value from sample 22SA may be due to its higher smectite and clinoptilolite content (Table 5-24). The experimentally determined K_d values of neptunium and uranium in alluvium are presented in Figure 5-44. The results suggest that sorption coefficients in the alluvium range from about 3 to 13 mL/g for neptunium, and from about 3 to 9 mL/g for uranium.

Tests were conducted to determine whether uranium sorption behavior differs with groundwater composition, using two groundwater samples from different pumped zones in the same Borehole (e.g., NC-EWDP-19D, Zone 1 and Zone 4). Chemically, Zone 4 water is slightly higher pH, and contains less divalent cations. K_d values for uranium measured in Zone 4 water were less than those from Zone 1 (Figure 5-45). These differences may be a result of greater uranium complexation by carbonate in Zone 4 water, or less competition for sorption sites because of the lower divalent cation content.

In addition to the batch experiments described above, column experiments were conducted with ^{233}U and tritium as a nonsorbing tracer. The observed retardation is consistent with the sorption coefficients measured in the batch experiments. An example is given in Figure 5-46.

5.3.3.4.3   Neptunium Sorption

Experimentally determined K_d values for neptunium range from about 4 to 500 ml/g (Figure 5-47), varying widely with sieve fraction used. Smaller sieve fractions have correspondingly higher K_d values, and may contain greater amounts of highly sorptive minerals such as smectites and zeolites.

Sorption experiments were performed on the same alluvial materials with groundwater from two Boreholes, NC-EWDP-3S and NC-EWDP-19D. Although these waters differ in major ion concentrations, they have similar pH values, and therefore similar ratios of carbonate and bicarbonate in solution. The water composition had a negligible effect on the sorption coefficients of neptunium (Figure 5-48), suggesting that pH, and the corresponding carbonate concentration, may be more important than inorganic ion concentrations or the presence of trace amounts of drilling materials (which were found in NC-EWDP-3S water but not in NC-EWDP-19D water) in determining neptunium K_d values.

Sorption is generally dependent on the surface properties of the materials. In general, the larger the surface area of the sample, the larger K_d value under the same experimental conditions. Clay and zeolite minerals have larger surface areas than the primary minerals such as quartz and feldspar that compose the bulk of the alluvium. Therefore, alluvium, which contains large amounts of clay and zeolites, will generally have larger K_d values than the volcanic tuffs. Neptunium K_d values correlate with sample surface area and smectite plus clinoptilolite ratio, with the exception that two high K_d samples do not have correspondingly high smectite and clinoptilolite content (Ding et al. 2003 [DIRS 164737]). These results suggest that trace amount of minerals such as amorphous iron and manganese oxides may affect the sorption of neptunium in alluvium. Additional studies of neptunium sorption to vitric tuffs of Busted Butte indicated that sorption of radionuclides increases with increasing levels of smectite, iron oxide, and manganese oxide in the rock (BSC 2003 [DIRS 164633]). In summary, neptunium is sorptive on the porous materials of the alluvial aquifer, with sorption strongly dependent on the presence of clay minerals and iron and magnesium oxides that have large surface areas available for sorption.

5.3.3.5   Cation Exchange and Surface Complexation

Sorption processes include both ion exchange and surface complexation.

5.3.3.5.1   Cation Exchange

Description of Cation Exchange Sites in Yucca Mountain Tuff–Measurements of the mineralogy of Yucca Mountain tuffs have shown an abundance of minerals known to have both pH-independent cation exchange sites (that is, tetrahedral aluminum sites) and surface complexation sites (e.g., clay edge sites) for outer-sphere surface-complex formation. The most abundant minerals found in Yucca Mountain tuffs (Bish et al. 1983 [DIRS 141826], Figure 2; Daniels et al. 1982 [DIRS 105803]) with a high cation exchange capacity are listed in Table 5-18. In addition to these minerals, feldspars may be important cation exchangers in the devitrified tuffs. Cation exchange capacity for feldspar is not an intrinsic property because only the external surfaces are available for exchange. Thus, the number of sites may depend on the crystal size and morphology.

State of Knowledge of Cation Exchange with Respect to Yucca Mountain Tuffs–As early as 1983 (Daniels et al. 1982 [DIRS 105803]), it was shown that the sorption distribution coefficient, K_d, for the sorption of cesium onto Yucca Mountain tuffs could be predicted to within a factor of three using literature data for the cation exchange on the minerals in Table 5-18 with the addition of analcime. (These predictions only considered competition with sodium.)

The relative contribution of cation exchange to the sorption of neptunyl onto the zeolitic tuff sample G4-1506 from a sodium-bicarbonate solution was determined (Triay et al. 1997 [DIRS 100422], pp. 123 to 127). The experiment was based partly on the method of Baeyens and Bradbury (1995 [DIRS 104677]; 1995 [DIRS 104678]). The surface complexation of neptunyl was shown to be inner sphere and noncharging. Therefore, the surface complexation of neptunium is expected to be largely independent of sodium-ion concentration. The results show a linear decrease in K_d with sodium concentration at low sodium concentrations, which is consistent with cation exchange. At high sodium concentrations, the K_d asymptotically approaches 2.5 mL/g, consistent with surface complexation. The ion-exchange component is larger than the surface-complexation component, which corresponds to a K_d of about 10 in 0.0022 M sodium bicarbonate. The relatively low K_d for neptunyl in a zeolitic tuff is likely due to the large ion size and high hydration number. The K_d in pure sodium bicarbonate solution is larger than that observed in J-13 water; this effect is due to competition with the additional cations in J-13 water of calcium, magnesium, and potassium. A model that describes these data and predicts neptunium sorption in the zeolitic tuff of Calico Hills is described in the next section.

5.3.3.5.2   Surface Complexation

In addition to the experimental data, sorption of each radionuclide has been evaluated using surface complexation modeling—predicting the partitioning of the radionuclide between the solid and the aqueous phases using thermodynamic data (BSC 2003 [DIRS 163228], Attachment I; 2003 [DIRS 167208], Attachment I)—and the modeling results were considered in developing the K_d ranges and distributions. Two examples of this modeling, for neptunium and uranium, are given below.

Modeling of Neptunium Sorption onto Zeolitic Tuff–A surface-complexation reaction for neptunium sorption onto the zeolitic tuff sample G4-1506 was developed to fit the sodium-concentration dependence. The reaction incorporated a simple ion-exchange mechanism:

$$AlO^-Na^+ + NpO_2^+ \leftrightarrow AlO^-NpO_2^+ + Na^+ \qquad \text{(Eq. 5-10)}$$
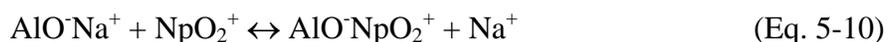
and the formation of an inner-sphere surface complex with octahedral alumina (edge sites) or hematite:

$$AlOH + NpO_2^+ \leftrightarrow AlONpO_2 + H^+ \qquad \text{(Eq. 5-11)}$$
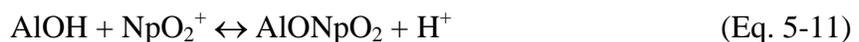
The number of cation exchange sites available to neptunium (tetrahedral aluminum site density of 2×10^{-4} eq/kg [Triay et al. 1997 [DIRS 100422], Table 55]) was based on the apparent saturation of sites observed in a neptunium sorption isotherm measured for tuff sample G4-1608 in a carbon dioxide atmosphere (Thomas 1987 [DIRS 101361], pp. 57 to 58). The neptunium exchange capacity is four orders of magnitude smaller than the cation exchange capacity of clinoptilolite (Table 5-18). This difference can be explained by the large size of the hydrated neptunyl ion. If no sorption occurs in the intracrystalline channels of the clinoptilolite, the maximum exchange capacity will be on the order of a micromole per gram, assuming a 3-μm crystal diameter. The selectivity for neptunium was used as an adjustable parameter, and was fit

to the results of the sodium-ion dependence of neptunium sorption onto tuff sample G4-1506. The inner-sphere surface complexation of neptunium was represented, assuming that surface complexation occurs primarily on clay-edge sites or iron oxide surfaces.

A surface complexation and cation exchange reaction was also developed for pH dependence of uranium sorption onto crushed devitrified tuff. This treatment was similar to that used for neptunium sorption, except that the cation exchange capacity for uranium was not known (i.e., there was no sorption isotherm) and a cation exchange with the monohydroxy-uranyl complex was included. The parameters used are listed in Table 5-19. Sorption site density was much greater than for the zeolitic tuff. The possible reason for this is the exposure of fresh surfaces of feldspar and quartz combined with the lack of exposure to a complex groundwater.

The results of this exercise are shown in Figure 5-49 and are in agreement with the results of Leckie and his students (Davis et al. 1978 [DIRS 105808], pp. 492 to 497). The equilibrium concentration of uranium at pH values of 9 and higher is above the solubility limit for uranium hydroxide. The effect of precipitation was evident in the experimental data.

State of Knowledge of Surface Complexation with Respect to Yucca Mountain–Surface complexation modeling is a useful tool for understanding sorption mechanisms and extending experimental sorption results to full condition. The pH dependence of actinide sorption, and the effects from changes in groundwater composition, can be readily explained with a combined surface-complexation and ion-exchange model.

The modeling of actinide sorption shows that high carbonate concentrations will considerably reduce the ability to form surface complexes on tuff. For actinides, ion exchange reactions appear to dominate under normal conditions over surface complexation. Furthermore, divalent cations are found to be strong competitors for cation exchange sites found in Yucca Mountain tuffs.

5.3.3.6   Summary of Sorption Results

Sorption is a function of water chemistry and lithology at Yucca Mountain (BSC 2003 [DIRS 167208], Attachment I; 2003 [DIRS 163228], Attachment I). Waters from wells J-13 and UE-25 p#1 (and a synthetic equivalent), representing the volcanic- and carbonate-hosted waters, respectively, exemplify the chemistry of the groundwaters at Yucca Mountain. The number of rock types considered can be reduced by placing stratigraphic units into petrographically-similar groups (Thomas 1987 [DIRS 101361]). This reduces the number of sorption-coefficient distributions required to represent radionuclide transport behavior to as few as four: devitrified, vitric, and zeolitic tuff (Wilson et al. 1994 [DIRS 100191]), and alluvial material (Ding et al. 2003 [DIRS 164737]).

The K_d ranges and associated uncertainty distributions that have been developed on probabilistic risk assessment are based on several sources of information. These include the experimentally-measured sorption data, the results of the surface complexation and cation exchange modeling, and expert judgment (BSC 2003 [DIRS 163228], Attachment I; 2003 [DIRS 167208], Attachment I). Surface complexation modeling is used to help account for the many variations in rock properties, mineralogy, and water chemistry that can and will occur

throughout the flow paths to the accessible environment. The developed ranges are more conservative than many experimental sorption data. Summaries of the batch sorption data used for this purpose are presented in BSC (2003 [DIRS 163228], Attachment I) and BSC (2003 [DIRS 167208], Attachment I), for the unsaturated and saturated zones, respectively.

The ranges and uncertainty distributions for K_d values for the different lithologies in the unsaturated zone are presented in Table 5-20. Those for the saturated zone are presented in Table 5-21. The two sets differ because the water compositions differ in the two zones (the pore water in the unsaturated zone has higher ionic strength), affecting the choice of experimental data to include in each set, and the results of the surface complexation and ion exchange modeling.

Though Table 5-21 contains data for different types of tuff, the spatial resolution of the stratigraphy in the saturated zone does not permit breaking the volcanic units down into different lithologies (zeolitic, vitrified, devitrified), so a composite value is applied to the volcanic section as a whole. Also, stochastic modeling on a 500 meter grid suggests that scaling effects result in slightly different K_d ranges and distributions (BSC 2003 [DIRS 167208], Attachment III). Table 5-22 incorporates these factors, and presents the composite K_d ranges and distributions for volcanic and alluvial units in the saturated zone.

5.3.3.7 Effects of Temperature Perturbations on Sorption of Radionuclides

Increased temperature will affect the solubilities of existing phases, the precipitation of new phases, the generation and stability of colloids, and the overall aqueous geochemistry of the drift and near-field environments. Temperature will affect sorption (K_d values) by shifting equilibria among solution species, by changing the zero point of charge of the substrate surfaces, and by changing the ratio of adsorbed to solution-phase species. The magnitude can be modeled with standard thermodynamic relationships if solution and sorption enthalpy data are available (Machesky 1990 [DIRS 145046]). Relationships such as the van't Hoff equation and Boltzmann functions can be used to predict the effect of temperature. There is general agreement that increasing temperature increases the sorption of cations and decreases the sorption of anions (Machesky 1990 [DIRS 145046]; Beckman et al. 1988 [DIRS 144956]). The few data that exist support this assertion. Machesky used the van't Hoff equation to predict a doubling of K_d values with every increase of 20°C.

Beckman et al. (1988 [DIRS 144956], Figure 2, pp. 11 to 12) presented data that showed that barium sorption onto tuff was increased by an order of magnitude, from 25° to 70°C, and describes similar effects for cerium, europium, cesium, and strontium. They also concluded that temperature effects are overwhelmingly more important than effects of concentration or particle size.

The effect of temperature on sorption coefficients was also reviewed by Meijer (1990 [DIRS 100780], p. 17). Again, measured sorption coefficients onto tuffs were higher at elevated temperatures for all elements studied: americium, barium, cerium, cesium, europium, plutonium, strontium, and uranium. Consequently, a conclusion is drawn that for given water and mineral compositions, sorption coefficients measured at ambient temperatures should be generally

conservative when applied to describing aqueous transport of cationic species even at elevated temperatures.

The effect of temperature in a repository will increase sorption of cationic species and decrease sorption of anionic species. Since anions do not adsorb very well at ambient temperatures, a conservative estimate is their K_d values at higher temperatures will be zero. However, the K_d values of cationic species at higher temperatures will increase significantly over those listed in Table 5-20, by as much as 10 times at repository temperatures above 70°C (Meijer 1990 [DIRS 100780], p. 17).

5.3.4 Dynamic Transport Studies in the Laboratory

5.3.4.1 Introduction

The primary input data used for dynamic transport studies are described in (BSC 2001 [DIRS 160828], Table 16) and include laboratory results of radionuclide experiments using waters collected from Yucca Mountain or synthesized to represent Yucca Mountain waters and materials either collected from the field or synthesized in the laboratory. Parameters used in this section are the radionuclide concentration and either percent sorbed onto various substrates or percent eluted through a column as a function of time. The types of experiments performed involved crushed rock, solid rock, fractured rock, and alluvium.

5.3.4.2 Crushed-Rock Columns

Approach–Crushed tuff column studies were performed to verify the results of earlier batch-sorption measurements under flowing conditions without significantly changing the surface properties of the tuff. By comparing differences with the batch-sorption measurements, such studies would be most sensitive to multiple-species formation, colloid formation, and other geochemical reactions (e.g., changes in surface reactivity due to agitation) not fully described by experimentally derived batch-sorption distribution coefficients. In the crushed-tuff column experiments, mass-transfer kinetics was investigated by studying radionuclide migration as a function of water velocity.

Column elution curves can be characterized by two parameters: the time of arrival of the radionuclide eluted through the column and the broadness (dispersion) of the curve. The arrival time depends on the retardation factor, R_f, which for soluble radionuclides depends in turn on the sorption distribution coefficient together with the water content and bulk density of the solid phase. In column testing, significant deviations (larger than expected based on sampling variability) in arrival time from that predicted on the basis of the batch-sorption distribution coefficients indicate one or more of the following:

- The presence of more than one chemical species that are not readily exchanged and that have different selectivities in tuff minerals

- The presence of the radionuclide in colloid form

- Sluggish sorption kinetics

- Irreversibility of the sorption process

- Solubility effects due to the solution mineral equilibria

- Complete saturation of porous column with reacting solution

- Other possible experimental artifacts.

The broadness, or apparent dispersion, of the curve depends on:

- The kinetics and reversibility of sorption

- Diffusion into and out of rock fragments in the crushed-rock column

- The linearity of the isotherm that describes the dependence of sorption on radionuclide concentration.

The main goal of the study was to test the necessary assumptions made in using values of the sorption distribution coefficient, K_d (determined by batch-sorption measurements) to describe hydrologic transport in the field there is a direct relationship between the retardation coefficient and the sorption distribution coefficient. These assumptions are:

- Microscopic equilibrium is attained between the solution species and the adsorbate.

- Only one soluble chemical species is present (or if more than one is present, they interchange rapidly).

- The radionuclides in the solid phase are adsorbed on mineral surfaces (i.e., they are not precipitated).

- The dependence of sorption on concentration is described by a linear isotherm.

5.3.4.2.2 Experimental Conditions

Because the J-13 and UE-25 p#1 well waters used to represent Yucca Mountain groundwaters are both oxidizing (Ogard and Kerrisk 1984 [DIRS 100783]), all the batch-sorption and column experiments were performed under oxidizing conditions. In the column experiments, J-13 water (filtered) and a sodium-bicarbonate buffer that simulated UE-25 p#1 groundwater (because of the unavailability of water from this well) were used.

As in the batch-sorption experiments, all tuff samples were crushed and wet-sieved to obtain particle sizes ranging from 75 to 500 μm.

Relationship Between Column and Batch Experiments–If equilibrium is achieved between a single aqueous chemical species and the species adsorbed on the solid phase, the rate at which a radionuclide moves through a column can simply be related to the sorption distribution coefficient, K_d. The relationship between the retardation factor, R_f, obtained from

column-transport experiments, and the values of K_d, obtained from batch-sorption experiments, is generally given by:

$$R_\text{f} = \frac{V_{gw}}{V_{sp}} = 1 + \rho_d \frac{K_d}{\varepsilon}$$ (Eq. 5-12)

where V_{gw} is the velocity of carrier fluid, V_{sp} is the velocity of the species, ρ_d is the dry bulk density (including pores) and ε is the porosity of the column (Hiester and Vermeulen (1952 [DIRS 106037], p. 514). To test these assumptions, the radionuclide solution used in the batch-sorption measurements was eluted through columns containing tuff samples that came from the same drill hole and depth interval and that had been crushed and sieved to the same size fraction as samples used in the batch-sorption studies.

5.3.4.2.3   Results and Discussion

Neptunium Results–Using crushed-rock columns, the retardation of [237]Np by zeolitic, devitrified, and vitric tuffs in sodium-bicarbonate waters under oxidizing conditions (at room temperature, under atmospheric conditions, and using different water velocities) was studied. Elution of neptunium (V) was measured as a function of water velocity through zeolitic, devitrified, and vitric-crushed tuff in columns with J-13 well water and with synthetic UE-25 p#1 water. The elution curves were published by Triay et al. (1996 [DIRS 101024], Appendix A). Values of R_f were then calculated for the column experiments by dividing the free column volume into the volume of neptunium solution that had to be eluted to recover 50 percent of the injected [237]Np. From these values of R_f, Equation 5-12 was used to calculate the column sorption-distribution coefficients listed in Table 5-25.

Inspection of Table 5-25 indicates good agreement between the values of K_d obtained by the batch-sorption (Triay et al. 1996 [DIRS 101023]; 1996 [DIRS 101016]) and column approaches, which means that the arrival time of [237]Np can be predicted from a value for K_d. The column and batch distribution coefficients agreed well for all tuffs regardless of the groundwater studied and the water velocity used for the column experiments. Charge exclusion does not appear to exclude neptunium aqueous species from the tuff pores. On the other hand, the transport cannot be completely described using a sorption distribution coefficient. The broad, dispersive shape of the elution curves indicates that sorption of neptunium onto zeolitic and vitric tuffs appears to be nonlinear, nonreversible, or noninstantaneous. Previous work has found that sorption of neptunium onto clinoptilolite-rich tuffs is rapid (Triay et al. 1996 [DIRS 101023], p. 18) and can be fit with a linear isotherm (Triay et al. 1996 [DIRS 101016], Figure 4.5). Consequently, the degree of reversibility of neptunium sorption onto zeolitic and vitric tuffs might be the most likely reason for the apparent dispersivity in the tuff-column elution curves.

The elution curves also reveal that, regardless of the water being studied, the elution of [237]Np does not precede the elution of tritium for any of the tuffs. This observation is important because if charge-exclusion effects were to cause the neptunyl-carbonato complex (an anion) to elute faster than neutral tritiated water molecules, significant neptunium releases could occur at Yucca Mountain. Another important observation that can be drawn from these experiments is that values of K_d can be used to obtain suitable estimates for calculation of neptunium transport

through Yucca Mountain tuffs. This conclusion assumes that transport of radionuclides through the unsaturated zone from the repository would occur homogeneously through tuff. The general trends previously observed for neptunium sorption using batch-sorption experiments were: corroborated by these column experiments neptunium sorption onto devitrified and vitric tuffs is minimal, and neptunium sorption onto zeolitic tuffs decreases as the amount of sodium and bicarbonate/carbonate in the groundwaters increases.

Plutonium and Technetium Results–The elution of plutonium (V) through zeolitic, devitrified, and vitric-crushed tuff was measured in columns with J-13 well water and with synthetic UE-25 p#1 water. The elution curves for these experiments (Figures 5-50 to 5-52) indicate that vitric and zeolitic tuffs sorb plutonium significantly, which is probably due to their clay content. The shape of the elution curves for plutonium indicates that use of K_d values to predict plutonium transport through Yucca Mountain tuffs will predict plutonium releases conservatively. Results by Triay et al. (1995 [DIRS 100789], pp. 12 to 13) indicate that plutonium sorption onto tuffs is a slow process and probably due to a redox reaction occurring at the tuff surfaces. To verify these batch-sorption results, which suggest that plutonium sorption, even to the lowest sorbing tuff type (devitrified), could be significant, the migration of plutonium as a function of flow velocity was measured in devitrified tuff using J-13 and UE-25 p#1 waters. Inspection of these elution curves (Figures 5-53 and 5-54) confirms the trends observed using batch-sorption techniques; the elution curves observed for these columns are consistent with slow sorption kinetics.

The elution of pertechnetate was also studied in devitrified, vitric, and zeolitic tuffs in J-13 and synthetic UE-25 p#1 waters as a function of flow velocity. Inspection of the elution curves (Figures 5-55 to 5-57) indicate that anion-exclusion effects for pertechnetate in crushed tuff are essentially negligible except in the case of technetium transport through zeolitic tuff in J-13 well water (Figure 5-57). In this case, the anion-exclusion effect is small but measurable.

5.3.4.3 Solid-Rock Columns

Direct measurements of transport parameters in actual subsurface materials under subsurface conditions are necessary for defensible modeling of contaminant transport in host rocks and engineered barriers surrounding radioactive and hazardous waste repositories. The hydraulic conductivity, K, and the retardation factor, R_f, along with the associated distribution coefficient, K_d, are poorly known transport parameters for real systems, but are key input parameters to existing and developing contaminant release models. Unsaturated R_f and K were experimentally determined for core samples of Yucca Mountain vitric-member tuff, and zeolitic nonwelded tuff from G-Tunnel, Bed 5, with respect to J-13 well water with a selenium concentration (as selenite) of 1.31 mµ/g at 23ºC. The intent was to demonstrate that a method in which flow is induced with an ultracentrifuge could rapidly and directly measure R_f and K in whole-rock tuff cores, and then to compare these directly measured unsaturated R_f values with those calculated from K_d values obtained through traditional batch tests on the same materials.

5.3.4.3.1 Experimental Approach

Retardation–Retardation factors can be determined in flow experiments where R_f for a particular species is the ratio of the solution velocity to the species velocity. The retardation

factor for that species is given by in Equation 5-12. If none of a particular species is lost to the solid phase, then $K_d = 0$ and $R_f = 1$ for that species. In column experiments, a breakthrough curve is obtained for the particular species and R_f is determined as the pore volume at which the concentration of the species in the solution that has passed through the column is 50 percent of the initial concentration ($C/C_0 = 0.5$). It is now generally assumed that, for unsaturated systems, $\varepsilon = \theta$, where θ is the volumetric water content (Bouwer 1991 [DIRS 105056], p. 42; Conca and Wright 1992 [DIRS 105756], pp. 1553 to 1554). The study described in this section experimentally addresses this concern under unsaturated conditions in whole rock, and evaluates the use of data from batch experiments in determining R_f in whole rock.

Hydraulic Conductivity–One way to drive fluid through rock is to use centripetal acceleration as the driving force. This approach was used with a new technology (unsaturated flow apparatus) to produce hydraulic steady state, to control temperature, degree of saturation, and flow rates in all retardation experiments, and to measure the hydraulic conductivity. A specific advantage of this approach is that centripetal acceleration is a whole-body force similar to gravity that acts simultaneously over the entire system and independently of other driving forces, such as gravity or matrix suction (Conca and Wright 1992 [DIRS 105756], p. 1546).

The unsaturated flow apparatus instrument consists of an ultracentrifuge with a constant, ultralow flow-rate pump that provides fluid to the sample surface. Accelerations up to 20,000 g are attainable at temperatures from 150º to 220ºC and flow rates as low as 0.001 mL/hr.

Numerous studies have compared use of the unsaturated flow apparatus approach with traditional methods of analysis in soils and clays, and the agreement is excellent (Conca and Wright 1992 [DIRS 100436], Figure 14; Nimmo et al. 1987 [DIRS 106888]).

The unsaturated flow apparatus technology is effective because it allows the operator to set the variables in Darcy's Law, which can then be used to determine hydraulic conductivity. Under a centripetal acceleration in which water is driven by both the potential gradient, $d\psi/dr$, and the centrifugal force per unit volume, $\rho\omega^2 r$, Darcy's Law is

$$q = -K(\psi) \left[\frac{d\psi}{dr} - \rho\omega^2 r \right] \qquad \text{(Eq. 5-13)}$$

where q is the flux density into the sample; K, the hydraulic conductivity, is a function of the matric suction, ψ, and, therefore, of water content, θ; r is the radius from the axis of rotation; ρ is the fluid density; and ω is the rotation speed. When multicomponent and multiphase systems are present in the unsaturated flow apparatus instrument, each component reaches its own steady state with respect to each phase, as occurs in the field. Appropriate values of rotation speed and flow rate into the sample are chosen to obtain desired values of flux density, water content, and hydraulic conductivity in the sample. Above speeds of about 300 rpm, depending upon the material and providing that sufficient flux density exists, $d\psi/dr \ll \rho\omega^2 r$. Under these conditions, Darcy's Law is given by $q = -K(\psi)[-\rho\omega^2 r]$. Rearranging the equation and expressing hydraulic conductivity as a function of water content, Darcy's Law becomes

$$K(\theta) = \frac{q}{\rho\omega^2 r} \qquad \text{(Eq. 5-14)}$$

As an example, a whole-rock core of Topopah Spring member tuff accelerated to 7,500 rpm, with a flow rate into the core of 2 mL/hr, achieved hydraulic steady state in 30 hr with a hydraulic conductivity of 8.3×10^{-9} cm/s at a volumetric water content of 7.0 percent. Previous studies verified the linear dependence of K on flux and the squared dependence on rotation speed (Conca and Wright 1992 [DIRS 105756], p. 1546; Nimmo et al. 1987 [DIRS 106888], Figure 11). Because the unsaturated flow apparatus method can directly and rapidly control the hydraulic conductivity, fluid content, temperature, and flow rates, other transport properties can then be measured as a function of fluid content, by associated methods, either inside or outside the unsaturated flow apparatus instrument during the overall run.

Fundamental physics issues involving flow in an acceleration field have been raised and successfully addressed by previous research and in numerous forums (Conca and Wright 1992 [DIRS 105756], p. 1547; 1992 [DIRS 100436], p. 8; Nimmo et al. 1987 [DIRS 106888]; Nimmo and Akstin 1988 [DIRS 106879]; Nimmo and Mello 1991 [DIRS 106882]).

5.3.4.3.2   Results and Discussion for Vitric and Zeolitic Tuff

Column Breakthrough Test Results–For these experiments (BSC 2001 [DIRS 160828]), the rotation speed was set at 2,000 rpm with a flow rate into each sample of 0.2 mL/hr. The experiment was run for 9 days with an initial selenium concentration of 1.31 mg/L. Figure 5-58 shows the breakthrough curves for selenite (C/C_o is given for selenium as selenite) in the Yucca Mountain vitric member at 62.6 percent saturation and in the zeolitic nonwelded tuff at 52.8 percent saturation. The experiment was stopped before full breakthrough in the zeolitic nonwelded tuff, but the $C/C_o = 0.5$ point was reached. The retardation factor for each tuff sample is 2.5. For the Yucca Mountain vitric-member tuff $K_d = 0.14$ mL/g, and for the zeolitic nonwelded tuff, $K_d = 0.26$ mL/g.

During these experiments, the unsaturated hydraulic conductivity K for each sample at these water contents was 2.5×10^{-8} cm/s for the Yucca Mountain vitric-member tuff and 1.2×10^{-8} cm/s for the zeolitic nonwelded tuff. Figure 5-59 gives the characteristic curves $K(\theta)$ for these tuffs determined in separate experiments, as well as measurements for other tuffs and materials for comparison.

Batch-Sorption Test Results–Batch-sorption tests were conducted using the same J-13 well water with the slightly lower selenium concentration of 1.1 μg/g and the same zeolitic nonwelded tuff from G-Tunnel, Bed 5, as in the unsaturated flow apparatus column breakthrough test. The sorption distribution coefficients obtained are given in Table 5-26. The Eh of all solutions, measured after the sorption experiments, varied from 140 to 150 mV.

The data presented in Table 5-26 and Figure 5-58 indicate agreement between the column and the batch-sorption experiments. At a selenium concentration of about 1 μg/g, no sorption of the selenium by the tuff is observed for the zeolitic tuff used in batch experiments, and minimal sorption (K_d of 0.8 mL/g) is observed for the zeolitic tuff used in the unsaturated column experiments (Triay et al. 1997 [DIRS 100422], p. 190).

Conclusions–This study used unsaturated flow apparatus technology to rapidly and directly measure retardation factors and hydraulic conductivities in whole-rock cores of tuff under the unsaturated conditions that exist in the field. The batch sorption technique is not well suited for measuring K_d in weakly sorbing solutes, requiring the use of new techniques, including the unsaturated flow apparatus approach. In the unsaturated flow apparatus column breakthrough tests, the retardation factor for the selenite species, at a concentration of 1.1 μg/g selenium in J-13 water was only 2.5 μg/g in Yucca Mountain vitric member tuff at 62.6 percent saturation and in zeolitic nonwelded tuff from G-tunnel at 52.8 percent saturation. In batch tests on the same material with an initial selenium concentration of 1.1 μg/g, the average K_d was 0.08 ± 0.2 mL/g, which gives retardation factors that are slightly lower than those from the unsaturated flow apparatus column breakthrough experiments. This finding suggests that using batch-sorption coefficients to predict radionuclide transport through unsaturated tuff will yield conservative results.

In addition, unsaturated hydraulic conductivities were derived during the experiments of 2.5×10^{-8} cm/s for the Yucca Mountain vitric-member tuff and 1.2×10^{-8} cm/s for the zeolitic nonwelded tuff.

5.3.4.4 Radionuclide Transport Through Fractures

5.3.4.4.1 Overview

The transport of radionuclides through fractures from Yucca Mountain was examined to assess the retardation that can be provided by radionuclide diffusion into the matrix and sorption onto the minerals coating the Yucca Mountain fractures. Radionuclide transport calculations often assume that radionuclides can travel through fractures unimpeded; this assumption is simplistic and leads to conservative predictions of radionuclide releases to the accessible environment. It ignores two main mechanisms by which retardation of radionuclides migrating through fractures can occur: diffusion of the radionuclides from the fractures into the rock matrix and sorption of radionuclides onto the minerals coating the fractures.

Minerals coating the fracture walls are generally different from the host-rock mineralogy due to a variety of factors ranging from precipitation of hydrothermal waters or meteoric waters to alteration of the preexisting minerals. A review of the literature (Carlos 1985 [DIRS 101574]; 1987 [DIRS 101204]; 1989 [DIRS 101575]; Tables I and II, 1994 [DIRS 101325]; Table I;

Carlos et al. 1993 [DIRS 105210]; 1990 [DIRS 101324]) has provided a list of the minerals lining the fractures found at Yucca Mountain (Table 5-27).

5.3.4.4.2 Experimental Conditions

The groundwaters used for the experiments presented in this section were waters from well J-13 (filtered through a 0.05-μm filter) and two sodium bicarbonate buffers that simulated the water chemistry of the groundwaters from wells UE-25 J-13 and UE-25 p#1.

The tuff samples that were chosen were recovered from drill holes at Yucca Mountain and had natural fractures. The matrix of all samples consisted of devitrified tuff, and the minerals lining the fractures were stellerite, magnetite, hollandite, and romanechite. The sampling criteria required that the cores had natural fractures with secondary mineral coatings, and that the core fragments forming the fracture walls could be disassembled for examination and then repositioned in their original orientation. Table 5-28 gives the characteristics of the four columns used in the experiments.

Batch-**Sorption Experiments**–For comparison with the fractured-column experiments, batch-sorption tests of neptunium onto the fracture minerals stellerite, hollandite, romanechite, and magnetite were conducted. These tests were performed under atmospheric conditions using J-13 well water with a neptunium (V) concentration of 6.7×10^{-7} M. The pH of the water in these experiments was approximately 8.5.

5.3.4.4.3 Results and Discussion

As discussed earlier, neptunium sorbs poorly onto devitrified tuff (Triay et al. 1996 [DIRS 101016], p. 12), which constitutes the matrix of all the fractures studied. Retardation during fracture flow occurs by diffusion of the radionuclides into the tuff matrix or by sorption of the radionuclides onto the minerals coating the fractures. Table 5-29 lists the results of batch-sorption experiments describing the sorption of neptunium onto natural minerals.

Although the extrapolation from these experiments to Yucca Mountain tuffs containing the same minerals is not direct, the data of Table 5-29 show some important trends. Neptunium has a high affinity for hollandite and romanechite, whereas sorption onto the zeolite stellerite is not significant. If ion exchange is the main mechanism for neptunium sorption onto stellerite, changing the water from J-13 to p#1 will only result in less sorption (due to the formation of a larger amount of the neptunyl-carbonato complex and the competitive effects as a result of the higher ionic strength of the UE-25 p#1 water). Neptunium sorption onto magnetite does not appear to be significant either. As shown in Table 5-29, the magnetite sample used in the study contains hematite and goethite, which could account for the entire observed sorption.

Because no secondary minerals were observed on the fractures in the G1-1941 sample (Table 5-28, column 1, and Figure 5-60), it can be concluded that the retardation of neptunium observed for that column is due to diffusion into the matrix.

The total neptunium recovery of 70 percent in the UE-25 UZ#16 919 fractured sample (Table 5-28, column 2, and Figure 5-61) could be due to sorption onto the stellerite and magnetite coating the fracture surface, or due to diffusion into the matrix. It is important to note

that in changing the water for this column from synthetic J-13 to synthetic UE-25 p#1, the speciation of neptunium changes from a mixture of neptunyl and neptunyl-carbonato complex to almost 100 percent neptunyl-carbonato complex (which may be excluded from tuff pores due to size and charge).

Neptunium seems to be significantly retarded even during fracture flow in the G4-2981 fractured sample (Table 5-28, column 3, and Figure 5-62) that is coated with hollandite and romanechite. The recovery of neptunium in this fracture is less than 10 percent, and its first appearance is delayed with respect to tritium and technetium.

Inspection of Figures 5-62 and 5-63 (columns 3 and 4 of Table 5-28) indicates that diffusion from the fracture into the matrix has taken place because recovery of tritium was only 80 percent compared to 90 percent for technetium. This trend agrees with diffusion data that were previously obtained for ^{3}H and ^{95m}Tc in devitrified tuff and water from well J-13. These data were fitted to the diffusion equation (Triay et al. 1993 [DIRS 145123]), which yielded diffusion coefficients for saturated devitrified tuffs that were of the order of 10^{-6} cm^2/s for tritiated water and 10^{-7} cm^2/s for technetium. Thus, anion exclusion, in which the large pertechnetate anion is excluded from tuff pores due to its size and charge, was previously observed.

The radionuclide elution data through fractured media was analyzed by Robinson et al. (1995 [DIRS 100414]). Their analyses of ^{237}Np elution through fractured rock made it clear that the data are consistent with very large values of K_d, at least compared to the typical value of 2.5 for ^{237}Np on zeolitic tuff. They also expressed the possibility that minerals present in trace quantities in the bulk rock that do not contribute significantly to sorption may be quite effective at retarding ^{237}Np transport when concentrated on fracture surfaces.

The most significant conclusion of the work presented here is that fracture flow does not necessarily result in a fast pathway for actinide migration through the tuff. Actinide migration through fractures could be significantly retarded by sorption onto minerals coating the fractures and by diffusion into the tuff matrix.

5.3.5   Diffusion Transport Studies in the Laboratory

5.3.5.1   Introduction

The Nitao (1991 [DIRS 106893]) model provides a framework for assessing the importance of matrix diffusion at Yucca Mountain. Neretnieks (1990 [DIRS 106864], Section 6) concluded that most rocks (even dense rocks, such as granites) have small fissures between the crystals that interconnect the pore system containing water. Small molecules of radioactive materials can diffuse in and out of this pore system. The inner surfaces in the rock matrix are much larger than the surfaces in the fractures through which the water flows. The volume of water in the microfissures is much larger than the volume in fractures. Therefore, over a long time, diffusion can play an important role in radionuclide retardation.

The objective of diffusion experiments was to provide diffusion information for nonsorbing neutral molecules, anions, and sorbing radionuclides. Because the uptake of radionuclides by tuff is measured as a function of time, the experiments also yield information on the kinetics of sorption.

The primary input data used for diffusion transport studies described in BSC (2001 [DIRS 160828]) include laboratory results of radionuclide experiments using waters collected from Yucca Mountain or synthesized to reflect Yucca Mountain waters and materials either collected from the field or synthesized in the laboratory.

5.3.5.2 Rock-Beaker Experiments

5.3.5.2.1 Experimental Conditions

The radionuclides used in these experiments were ^{3}H, [95]Tc, [237]Np, [241]Am, [85]Sr, ^{137}Cs, and [133]Ba. A solution (prepared with groundwater from well J-13) containing the radionuclide of interest was placed in the cavity of a rock beaker and then aliquots of the solution from the beaker for the remaining radionuclide concentration were analyzed as a function of time. Batch-sorption experiments were also performed with J-13 water and the tuffs under study.

5.3.5.2.2 Data Analysis

The results of the rock/beaker experiments were analyzed using numerical simulation (Travis and Birdsell 1991 [DIRS 125724]; BSC 2001 [DIRS 160828]). The concentration profiles of the diffusing tracer are fitted to the transport equation (de Marsily 1986 [DIRS 100439], Chapter 10):

$$\nabla \cdot (\varepsilon d \nabla C) = \varepsilon \frac{\partial C}{\partial t} + Q$$

(Eq. 5-15)

where ε is the total porosity of the tuff, d is the diffusion coefficient through the tuff, C is the concentration of the diffusing tracer in solution, and the source term, Q, is zero for a nonreactive tracer, but for a sorbing solute

$$Q = \rho_b \frac{\partial F}{\partial t}$$

(Eq. 5-16)

where F is the amount of tracer sorbed per unit mass of solid and ρ_b is the bulk tuff density ($\rho_b = (1 - \varepsilon)\rho_s$, where ρ_s is the density of the solid particles).

As discussed in previous sections, the mechanism of sorption determines the relationship between F and C. When sorption is linear, reversible, and instantaneous, the relationship between F and C is given by the sorption distribution coefficient

$$K_d = \frac{F}{C}$$

(Eq. 5-17)

Substitution of this equation and Equation 5-16 into Equation 5-15 yields

$$\nabla \cdot (\varepsilon d \nabla C) = \varepsilon R_f \frac{\partial C}{\partial t}$$

(Eq. 5-18)

where, once again, the retardation factor, R_f, is given by

$$R_f = 1 + \frac{\rho_b}{\varepsilon} K_d \qquad \text{(Eq. 5-19)}$$

Equation 5-19 provides a means of comparing results for sorption coefficients obtained under diffusive conditions with sorption coefficients obtained from batch-sorption experiments and is valid only if sorption is linear, reversible, and instantaneous.

Consequently, the effective diffusion coefficient can be determined by fitting concentration profiles for the nonsorbing tracers, and sorption parameters, such as K_d, can be determined by fitting concentration profiles for the sorbing tracers.

5.3.5.2.3 Results and Discussion

Figure 5-64 shows an example of a set of diffusion data for a rock-beaker experiment (BSC 2001 [DIRS 160828]) in which the feldspar-rich tuff G4-737 and solutions of tracers in J-13 water were used. The concentration of tracer, C, remaining in the solution inside the cavity of the rock beaker divided by the initial concentration, C_o, is plotted as a function of elapsed time.

The solid lines in Figure 5-65 are a numerical fit of these same data to the diffusion equation (Equation 5-15) for the two nonsorbing radionuclides, ^{3}H, and ^{95}Tc. The diffusion coefficients obtained in this manner for these radionuclides for all the tuff samples studied (Table 5-30) agree well with previous results (Rundberg et al. 1987 [DIRS 106481]). These two tracers diffuse essentially as tritiated water and the pertechnetate anion, TcO_4^-. Large anions are excluded from tuff pores because of their size and charge, which can account for the lower diffusivity of TcO_4^-.

Figure 5-66 shows the diffusion curves for several radionuclides through devitrified tuff G4-737, calculated using K_d values measured in batch systems and the measured diffusion coefficient for tritiated water (BSC 2001 [DIRS 160828]). Comparing of the calculated curves with the actual measured data (see the results for cesium in Figure 5-67) shows that concentration of the sorbing radionuclides remaining in the rock beaker drops faster than predicted on the basis of a linear K_d. This result indicates that the diffusion of the sorbing radionuclides could not be fitted by assuming reversible, instantaneous, and linear sorption. These results also indicate that transport calculations using a batch-sorption K_d value and the diffusion coefficient measured for tritiated water will result in conservative predictions for the transport of sorbing radionuclides.

The results obtained from rock-beaker (BSC 2001 [DIRS 160828]) experiments agree with previous results (Rundberg 1987 [DIRS 106477], Tables VI and VII). Experiments were performed on the uptake of sorbing radionuclides by tuff, and it was found that rate constants for uptake of the sorbing cations from solution onto tuff were consistent with a diffusion-limited model in which diffusion occurs in two stages. In the first stage, the cations diffuse into rock through water-filled pores; in the second stage, they diffuse into narrower intracrystalline channels. This diffusion model yielded sorption coefficients for cesium, strontium, and barium that agree well with the sorption coefficients determined by batch techniques.

5.3.5.3 Diffusion-Cell Experiments

5.3.5.3.1 Experimental Conditions and Data Analysis

Diffusion cells were constructed with two chambers containing groundwater separated by a slab of tuff. After radioactive tracers were added to one of the chambers, the untraced chamber was periodically monitored for the presence of radioactivity by taking an aliquot of the solution in the chamber and then replenishing that chamber with untraced groundwater.

The only driving force in this experimental setup is the chemical concentration gradient; thus, the solute flux is purely diffusive. The apparent time of arrival depends on the porosity, the heterogeneity of the pore structure, the retardation factor for a given radionuclide, and the sensitivity of radionuclide measurements. The rate of concentration increase in the untraced chamber depends on the ionic diffusivity, the tuff porosity, and the tuff tortuosity/constrictivity factor. Thus, by measuring the movement of sorbing and nonsorbing tracers through tuff slabs as a function of time, the rock-dependent diffusion parameters can be measured.

The two major rock types used for the diffusion-cell experiments were zeolitic (UE-25 1362) and devitrified (G4-287). The zeolitic tuff had a porosity of 0.4 and a bulk density of 1.5 g/mL. The devitrified tuff had a porosity of 0.2 and a bulk density of 2.3 g/mL. The major component of the zeolitic tuff was clinoptilolite; the major component of the devitrified tuff was alkali feldspar.

The actinide concentration of the solutions used for the diffusion experiments was very close to the solubility limit of the actinides in the groundwaters. The experimentally determined solubilities (Nitsche et al. 1993 [DIRS 155218]; 1995 [DIRS 100163]) of plutonium range from 2×10^{-7} M (J-13 water at a pH of 7) to 1×10^{-6} M (UE-25 p#1 water at a pH of 8.5) and of neptunium range from 7×10^{-6} M (UE-25 p#1 water at a pH of 8.5) to 5×10^{-3} M (J-13 water at a pH of 6) (BSC 2001 [DIRS 160828]).

The experimental setup for the diffusion cells can be described by a one-dimensional diffusion model. See CRWMS M&O (2000 [DIRS 151945]) for derivation of the analytical solution and boundary conditions.

5.3.5.3.2 Results and Discussion

The diffusion of ^{3}H, ^{95m}Tc, natural uranium (VI), ^{237}Np (V), and ^{239}Pu (V) through devitrified and zeolitic tuffs was studied using water from well J-13 and synthetic UE-25 p#1 water. (Note that ^{95m}Tc refers to the metastable version of ^{95}Tc.) The radionuclides ^{3}H, natural uranium (VI), and ^{239}Pu (V) were studied together in four diffusion cells (devitrified and vitric tuff cells, each with both types of water). Likewise, the radionuclides ^{95m}Tc and ^{237}Np (V) were studied together in another four diffusion cells. Typical results for these experiments are shown in Figures 5-68 to 5-70.

The results indicate that the diffusion of nonsorbing radionuclides into saturated tuff (illustrated by the diffusion of tritiated water in Figures 5-68 to 5-70) is slower in devitrified tuffs than in zeolitic tuffs. Large anions such as pertechnetate (which are excluded from the tuff pores by size and charge) diffuse slower through the pores than ^{3}H regardless of the groundwater or tuff type (as also observed in the rock-beaker experiments). The migration of plutonium through tuff

under diffusive conditions is controlled by sorption. The migration of neptunium (V) and uranium (VI) through tuff depends on tuff type and water chemistry. In cases, such as tuff G4-287, for which the reported sorption of neptunium is essentially zero (Triay et al. 1996 [DIRS 101016]; 1996 [DIRS 101023]), the diffusion of neptunium through the tuff is slower than the diffusion of ^{3}H but comparable to the diffusion of a nonsorbing, large anion, such as pertechnetate (Figure 5-69).

5.3.5.3.3   Summary of Matrix Diffusion Investigation

Matrix diffusion coefficients from reviews of the literature and the results described above are as follows. For anions, the average matrix diffusion coefficient is 3.2×10^{-11} m^2/s (3.2×10^{-7} cm^2/s) with a standard deviation of 1×10^{-11} m^2/s, a minimum value of zero and a maximum value of 10^{-9} m^2/s (10^{-5} cm^2/s) with a beta distribution. For cations, the average matrix diffusion coefficient is 1.6×10^{-10} m^2/s (1.6×10^{-6} cm^2/s) with a standard deviation of 0.5×10^{-10} m^2/s, a minimum value of zero and a maximum value of 10^{-9} m^2/s (10^{-5} cm^2/s) with a beta distribution.

5.3.6   Colloid-Facilitated Radionuclide Transport

5.3.6.1   Introduction

Recently, generation and mobilization of colloids have become important issues for contaminant transport (Kersting et al. 1999 [DIRS 103282]), particularly facilitated transport of radionuclides as intrinsic colloids (e.g., colloidal plutonium (V)), or as radionuclide-bearing pseudocolloids (e.g., ^{239}Pu, ^{237}Np, ^{243}Am, and ^{247}Cm from high-level radioactive wastes, or ^{137}Cs, ^{90}Sr, and ^{60}Co from low-level radioactive wastes) (Triay et al. 1996 [DIRS 100421], p. 16; Buddemeier and Hunt 1988 [DIRS 100712]; Kaplan et al. 1994 [DIRS 108203]; McCarthy and Degueldre 1993 [DIRS 108215], pp. 250 to 260). Radionuclide-bearing pseudocolloids consist of radionuclides adsorbed onto nonradioactive colloids, such as clays or oxides. New colloids can be generated or activated by perturbations in the hydrogeochemistry of the aquifer system, particularly by waste disposal activities (McCarthy and Degueldre 1993 [DIRS 108215], p. 304). Colloids exist naturally in groundwater in almost all subsurface environments, with the composition and concentration of colloids being site specific and determined by the geologic nature of the subsurface. According to McCarthy and Degueldre (1993 [DIRS 108215], Table 6), the size of natural colloids ranges from 0.01 to 1.0 μm, and concentrations range from 0.1 to 100 μg/g. The large surface area of colloids (10^4 to 5×10^5 m^2/kg) can significantly sorb radionuclides, even for relatively low mass concentrations of colloidal particles in the aquifer (Vilks and Degueldre 1991 [DIRS 108245]; Penrose et al. 1990 [DIRS 100811]). Triay et al. (1996 [DIRS 100421]) studied the generation and stability of colloids in Yucca Mountain groundwater and found that colloids of clays, silicon, and iron oxides were generated in the groundwater, and strong sorption of radionuclides onto these colloids occurred. The stability of clay and silica colloids was a function of the ionic strength. Triay et al. (1997 [DIRS 100422]) found that hematite and goethite colloids rapidly sorbed soluble plutonium (V) as well as colloidal plutonium (IV) in groundwater. However, the desorption of ^{239}Pu from these two iron oxide colloids is much slower than the sorption process (BSC 2001 [DIRS 160828], Section 6.7.3), suggesting that once sorbed onto mobile colloids, radionuclides could be transported great distances before they desorb.

Under most geologic conditions, transport of radionuclides via iron oxide or clay colloids dominates over transport of radionuclides by true polymerized radiocolloids (McCarthy and Zachara 1989 [DIRS 100778]). Champ et al. (1982 [DIRS 101124], pp. 749 to 751) reported that almost 75 percent of the plutonium was associated with colloidal particles and rapidly transported when groundwater was pumped through otherwise undisturbed aquifer cores. In porous media, where the sizes of colloids are smaller than the pores, colloids can migrate over long distances. O'Melia (1990 [DIRS 108227], pp. 447 to 457) reported in one study that colloidal particles with sizes ranging from 0.1 to 1.0 μm were the most mobile during natural gradient flow through a sandy porous medium (unconsolidated), with larger and smaller colloids being preferentially removed. Therefore, these mobile colloids may enhance the transport of the strongly sorbing radionuclides along flow paths. At the Nevada Test Site, transition metals and lanthanide radionuclides associated with inorganic colloids were recovered from groundwater 300 m from a nuclear detonation cavity (Buddemeier and Hunt 1988 [DIRS 100712]). Americium and lead were transported in the vadose zone with organic and inorganic colloids. Penrose et al. (1990 [DIRS 100811]) reported that plutonium and americium were associated with siliceous colloids in a near-surface alluvial aquifer at Los Alamos National Laboratory. The actual plutonium transport velocity was nearly 1,200 times greater than the predicted transport velocity based solely on partitioning between dissolved and stationary solid phases. Kersting et al. (1999 [DIRS 103282]) showed that plutonium associated with colloids had migrated 1.3 km from the 1968 Benham underground nuclear test site, a significant finding for Yucca Mountain.

Experimental studies on colloid transport through soil or rock under partially saturated or highly unsaturated conditions are few, but do indicate that colloids can migrate even under relatively dry conditions, although migration rates exhibit strong dependence upon colloid size as the system desaturates (McGraw 1996 [DIRS 108218]; Wan and Tokunaga 1997 [DIRS 108285]). To examine the influence of colloid size on transport, McGraw (1996 [DIRS 108218], pp. 61 to 68) used five different colloid sizes between 20 and 1,900 nm, under both saturated and unsaturated conditions in quartz sand. The results indicated that under saturated conditions, the breakthrough of each colloid at $C/C_o = 50$ percent was the same as that of the breakthrough of KBr, the nonreactive tracer, indicating no relationship of colloid size to migration under saturated conditions. However, the breakthrough of the colloids under highly unsaturated conditions exhibited a strong relationship between the colloid breakthrough and the colloid size, with a fairly complete breakthrough of the 20-nm colloid and little or no breakthrough of the 1,900-nm colloid.

In another set of experiments, McGraw (1996 [DIRS 108218], pp. 68 to 101) compared four sets of hydrophobic and hydrophilic colloids. Results indicated that transport of hydrophobic colloids depends on colloid size, water film thickness, and colloid charge density. In contrast, hydrophilic colloids were not affected by these variables and were rapidly transported through the system, even under very low moisture contents. McGraw concluded that the unsaturated zone is not an effective barrier to colloid migration, even for large colloids, although it will somewhat retard larger colloids.

Information from the recent advances in this field is presented chronologically, ending with the most recent results for attachment or detachment of plutonium and americium on colloids of hematite, goethite, montmorillonite, and silica in natural and synthetic groundwater.

The primary input data used for colloid-facilitated radionuclide transport studies are described in BSC (2001 [DIRS 160828], Section 6.7) include laboratory results of colloid experiments using waters collected from Yucca Mountain or synthesized to reflect Yucca Mountain waters and colloidal materials either collected from the field or synthesized in the laboratory.

5.3.6.2 Global Approach to Colloid Stability

In natural groundwaters, there is a continuum between inorganic colloids (clay, oxide), inorganic colloids coated with organic material, organic colloids associated with inorganic phases, and organic colloids. Colloid data (e.g., concentration) for shallow as well as deep groundwater systems were published by McCarthy and Degueldre (1993 [DIRS 108215]). Key factors affecting colloid stability were identified as pH, redox potential, salt (sodium, calcium) concentrations (Degueldre et al. 1996 [DIRS 100723], p. 692), the presence of dissolved organics (O'Melia and Tiller 1993 [DIRS 106996], pp. 374, 380 and 383), and the status of the system at steady state.

Conceptual models describing the colloid occurrence take into account their generation and disappearance, aggregation and disaggregation, and attachment and detachment on the rock or substrate. In the aquifer, the balance between generation and disappearance may be postulated for the undisturbed saturated zone. However, it is considered that the stability of the colloid phase is a function of the disappearance rate by attachment, which determines the colloid concentration in the aquifer. Because attachment parameters are defined in stationary conditions, this concept must be extended for flowing conditions or nonisothermal conditions. This extension might justify larger colloid concentrations during hydrogeochemical transients in the aquifer.

The general consensus about contaminant transport by colloid-facilitated processes is the need to understand the colloid generation mechanisms to evaluate a contamination hazard or to design remediation when required. It is necessary to discuss and define rules for evaluating colloid properties in natural systems or systems modified by the presence of contaminants and to sketch a conclusion on a non-site-specific basis. This type of general study, based on recent results obtained from selected hydrogeochemical systems, allows the development of a global approach. Addition of Yucca Mountain-specific data or relevant data from analog sites then increases confidence.

Data were collected for systems ranging from various crystalline to sedimentary geological formations. The crystalline systems comprise recent granitic systems (e.g., the Central European Basement with studies in the Black Forest, South Germany, and the northern part of Switzerland, as well as in the Alpine area, Grimsel, Switzerland) and older granitic systems (e.g., the Scandinavian or Canadian shield). Their organic content is quite low.

The Swiss crystalline studies (Degueldre et al. 1996 [DIRS 100723]; 1996 [DIRS 105377]) selected systems ranging from shallow to deep aquifers. The sites are the Menschenchwand uranium prospect, the Bad Säckingen spring, the Zurzach thermal well, the Leuggern borehole, and, in the Alps, both the Grimsel Test Site and the Transitgas tunnel. The depth ranges from about 100 to 1,680 m in 600 Ma granite. In Sweden, two systems were considered in 2,000 -Ma granite: Äspö, the Experimental Underground Laboratory at a depth of 70 m below the surface

(Laaksoharju et al. 1995 [DIRS 106449]), and the Laxemar deep borehole, with a 1,420- to 1,705-m depth. In Canada, Vilks et al. (1991 [DIRS 108255]) investigated waters at the Whiteshell Research area, underlain by the Lac du Bonnet granite batholith, located in southeastern Manitoba, at depths down to 1,150 m.

At Yucca Mountain the original rock constituent of the silicic ash-flow tuff was predominantly volcanic glass, but high-temperature devitrification and lower-temperature alteration produced mineral assemblages now dominated by feldspar, zeolites, and various silica polymorphs with low organic content. Crystallized accumulations of former colloidal material, produced during rock alteration, are present in the pores of some tuff layers as clay deposits (Levy 1992 [DIRS 100770], p. 79).

Morro do Ferro, Brazil, is an altered (weathered) formation, with some organic content that formed by volcanic activities in a subtropical area. The rocks are predominantly carbonatites deeply weathered to laterites (rich in gibbsite, illite, and kaolinite).

Partially metamorphic and nonmetamorphic sedimentary systems were also considered. They generally contain more organic compounds than the previously mentioned formations.

The Wellenberg system (Degueldre et al. 1994 [DIRS 120929]) in central Switzerland comprises a slightly metamorphic marl formation. The investigated aquifer lies in this marl formation at a 360-m depth, but another system of interest lies at a depth of 1,600 m below the marl formation in a chalk (limestone) layer.

Longworth et al. (1989 [DIRS 108211]) investigated colloids from the Triassic Sandstone aquifer (120-m depth) at the Markham, United Kingdom site, 50 km north of Nottingham. At Gorleben, central Germany, Kim et al. (1992 [DIRS 106387]) investigated a system composed of porous sediments with lignite intercalations. The aquifers there are located at a depth between 50 and 300 m and are composed of glacial sand, silt, marl, and clay.

The Cigar Lake uranium deposit is a sandstone-hosted ore body located in northern Saskatchewan, Canada (Vilks et al. 1993 [DIRS 108261]). The sandstone formation lies at a depth of 432 m below the surface. Finally, the Bangombé fossil reactor zone, Gabon, is located some 30 km south of the Oklo deposit. The sandstones are overlain by a thick series of marine-derived, organic-rich pelites and limestones. These formations were also slightly metamorphic (Pedersen 1996 [DIRS 107013]).

These groundwaters range from oxic to anoxic, sodium (Bad Säckingen) or sodium-calcium-rich (Äspö), K-rich (Poços de Caldas) or with a large magnesium component (Markham, Wellenberg), and organic- depleted (Zurzach) to organic-rich (Gorleben). The groundwater types vary from shallow Ca-HCO_3 (Transitgas tunnel, zone 3) to more complex Na-SO_4-HCO_3-Cl (Zurzach) or K-SO_4-F (Poços de Caldas). For the waters considered, the salt concentrations range over four orders of magnitude, the total hardness of the water over two orders of magnitude, and the pH from 6 to 10. Total organic carbon is low in most of the groundwaters—less than 10^{-5} M in waters from the Swiss crystalline site and on the order of 6×10^{-5} M in the sedimentary waters (e.g., Wellenberg). Its concentration in the Gorleben

system may reach the 10^{-2} M level, because the waters originate from a brown coal formation (nonmetamorphic system).

Steady-state conditions in the aquifers do not exist in some cases. For example, mixing of Na-Ca-HCO$_3$-Cl and Na-Ca-(Mg)-Cl-HCO$_3$ waters is observed at Äspö. A similar situation is also locally observed at Bad Säckingen. An important assessment of the status of the aquifer is the comparison of water temperature with the temperature estimated by geothermometry (T&T$_{geo}$), which may give information about the status of the thermal steady state of the water. For example, large differences between the actual water temperature at the source and that indicated by geothermometry (based on the isotopic composition of the water and chemical species it contains) are noted in the hydrothermal waters collected in zone 2 of the Transitgas tunnel.

5.3.6.2.1   Results and Discussion of Global Studies

Colloid occurrences in aquifers are a consequence of the colloid stability in the hydrogeochemical system. The systems are first supposed to be at steady state (no hydrogeochemical changes). Colloid phases range from clay (Grimsel Test Site, Wellenberg), to SiO$_2$ (Yucca Mountain), Fe-organic-rich phases (Morro do Ferro), clay-coated with organics (Äspö), and clay associated with organic phases (Gorleben).

All results are presented for the 100-nm size range for comparison purposes and for consistency. Factors resulting in decreased colloid stability are an increase of salt (Na$^+$, K$^+$) concentration and of water total hardness (Ca^{2+}, Mg^{2+}). The trend of colloid concentrations as a function of salt concentration and water hardness is shown in Figure 5-71. Strong coagulants (e.g., Fe^{3+}, Al^{3+}) are quasi-insoluble in the groundwater, limiting their action in the aquifer. The effect of calcium may be diminished (Seaman et al. 1995 [DIRS 108234]) in weakly acidic oxic water loaded with positively charged iron-oxyhydroxy colloids, for which cations are not able to act as a coagulant. This effect was observed in the Poços de Caldas mine where iron-oxyhydroxide colloids are stabilized at pH values from 3 to 5 in surface waters acidified by pyrite oxidation. The calcium does not act as a coagulant for Fe-rich colloids in these waters. It must be noted that degassing during water sampling may generate artifacts such as calcite, a particular problem in Ca-rich water. For this reason, data from Laxemar, Whiteshell, and Äspö are absent from Figure 5-71.

The apparent trend observed in Figure 5-71 must be justified on the basis of the physicochemical properties of alkali and alkaline-earth elements with respect to the stability of model colloids. This basis was tested for montmorillonite colloids, selected as an example of clay colloids. The attachment factor (a) of these colloids, a measure of coagulation, increases towards a value of a=1 with increasing alkali and alkaline-earth element concentrations (Figure 5-72). The attachment factor of these clay colloids reaches about a=1 for alkali concentrations of about $10^{-1.5}$ M and alkaline-earth element concentrations around $10^{-3.5}$ M. This test clearly demonstrates that the salinity and hardness of the water play an important role in colloid stability.

Factors increasing colloid stability and, therefore, their mobility, include the presence of organics or changes in the hydrogeochemical state in the aquifer. The effect of organics on the colloid phase stability was studied in detail by O'Melia and Tiller (1993 [DIRS 106996]). They

confirmed that increases in dissolved organic concentration and changes in pH can enhance colloid stability. This result contributes to the large colloid concentration observed in Gorleben. Also studied were systems subject to chemical or dynamic changes that are not at steady state with respect to the hydrothermal signature (e.g., zone 2 in the Transitgas tunnel, Bad Säckingen, and Yucca Mountain) or with colloid populations consisting of amorphous components (vitrified tuff from Yucca Mountain) or in which the chemistry is variable (e.g., the mixing waters at Äspö). In zone 2 from the Transitgas tunnel, the colloid concentration remains large, because the hardness of these waters is low.

5.3.6.2.2   Conclusions from Global Studies

Colloid concentration in a given aquifer is a function of the colloid phase stability in the hydrochemical system. Stability is a function of the chemical composition of the water as well as of the hydrogeochemical steady state of the aquifer. For an aquifer in a steady-state situation, decreases of the concentration of alkali elements below 10^{-2} M and of alkali-earth elements below 10^{-4} M contribute to an increase in the colloid stability and concentration. Water mixing and large concentrations of colloidal or dissolved forms of organic carbon also contribute to an increase in the colloid stability and concentration. In addition, the presence of transient situations, such as changes of temperature, flow rate, or chemistry (pH, salt, or redox potential) in the aquifer, can induce larger colloid concentrations.

5.3.6.3   Recent Experimental Studies

In a study by Noell et al. (1998 [DIRS 106920]) an idealized laboratory setup was used to examine the influence of amorphous silica colloids on the transport of cesium. The intent of these experiments was to establish data, for ideal circumstances, that show the influence of silica colloids on the migration of radionuclides through porous media. This goal was accomplished by using synthetic groundwater and saturated glass-bead columns so that the amount of natural colloidal material in the columns was minimized. Cesium-137 was used as a model radionuclide because of its detectability and simple chemistry. Colloidal silica was examined because of its abundance in many groundwaters, including those expected in the repository situation.

The sorption of cesium to the amorphous silica colloids was found to be significant and fully reversible. In independent batch-sorption experiments, it was determined that a Freundlich isotherm adequately described the partitioning of cesium to the amorphous silica colloids at equilibrium. Nonlinear Freundlich isotherms also best described the sorption of cesium to the glass beads.

It was also determined that the first-order desorption rate coefficient for cesium from silica colloids was approximately eight times greater than the first-order sorption rate coefficient.

By finding kinetic sorption rates between various radionuclides and naturally occurring colloidal material, it is possible to determine which radionuclides have the lowest desorption rates from natural colloids. This information is important in predicting their migration, because radionuclides that are irreversibly sorbed to colloids are most likely to be transport-facilitated.

5.3.6.3.1 Reversibility of Radionuclide Sorption onto Colloids: Plutonium onto Iron Oxides

Triay et al. (1997 [DIRS 100422], pp. 65 to 72) examined sorption for one type of pseudocolloids expected to occur at Yucca Mountain, namely plutonium sorbed onto iron oxide colloids. A natural groundwater and a filtered carbonate-rich synthetic groundwater (0.05-µm membrane) were used as media in this study. Laboratory batch-sorption experiments were performed to evaluate sorption of plutonium as a function of different iron oxide colloid mineralogy and different oxidation states of plutonium and to examine the sorption kinetics of plutonium (IV) colloids (hydrous plutonium oxide) and soluble plutonium (V) onto these iron oxide colloids.

The preliminary results showed that sorption varied depending upon the use of plutonium (IV) colloids or soluble plutonium (V), hematite or goethite substrate, and natural or synthetic J-13 groundwater. Sorption of both the plutonium (IV) colloid and soluble plutonium (V) onto the hematite and goethite colloids varied as a function of time. Iron oxide colloids sorbed more soluble plutonium (V) than plutonium (IV) and also sorbed more plutonium from synthetic J-13 groundwater than from natural J-13 groundwater. The results also showed that the hematite colloids sorbed more plutonium than the goethite colloids. This result was due to differences in surface characteristics. Results indicated that plutonium (IV) colloids, as well as soluble plutonium (V), can be rapidly adsorbed by hematite or goethite colloids in natural or synthetic groundwater, whereas desorption of both forms occurs more slowly.

Thermodynamic calculations show that plutonium (V) is a stable oxidation state in solution in the pH range of 5 to 7 at a pH of 12 and that plutonium (VI) is the most stable oxidation state at higher pH values (Sanchez et al. 1985 [DIRS 107213], p. 2297). It was assumed that sorption of plutonium (IV) onto suspended colloids is due to the interaction of the strongly hydrolyzable plutonium (IV) with the surfaces of natural particulate matter (Sanchez et al. 1985 [DIRS 107213], p. 2305). Keeney-Kennicutt and Morse (1985 [DIRS 106313]) found that PuO_2^+ can be adsorbed from diluted solution and seawater by goethite, aragonite, calcite, and δ-MnO_2. The sorption behavior of PuO_2^+ is influenced by redox reactions occurring on the mineral surface. Sorption of PuO_2^+ on goethite results in a disproportionation reaction in which plutonium (IV) and plutonium (VI) form on the mineral surface. The plutonium (VI) is slowly reduced to plutonium (IV), leaving plutonium (IV) as the dominant surface plutonium species (Keeney-Kennicutt and Morse 1985 [DIRS 106313]). Sanchez et al. (1985 [DIRS 107213]) studied sorption of soluble plutonium (IV) and plutonium (V) on goethite from a sodium-nitrate solution and found that redox transformations are an important aspect of plutonium sorption chemistry. The sorption behavior of plutonium on goethite is related to the different hydrolytic character of these two oxidation states in the solution. The sorption edge of the more strongly hydrolysable plutonium (IV) is in the pH range of 3 to 5, whereas that for plutonium (V) is at pH 5 to 7.

Information on affinity, kinetics, and reversibility of sorption is needed for evaluation of the significance of colloids to plutonium transport. Studies, performed in three phases, have focused on the sorption affinity, kinetics, and reversibility for soluble plutonium (V) and plutonium (IV) colloids onto iron oxide, silica, and clay colloids and on the effect of different plutonium oxidation states with different forms (e.g., colloidal or soluble form) on these two oxidation

states in natural and synthetic groundwater. In this phase of the study, laboratory batch-sorption experiments were performed using a natural groundwater and a carbonate-rich synthetic groundwater as media, to evaluate the following:

- The sorption of plutonium as a function of two different iron oxide colloids (hematite and goethite)

- Sorption of plutonium as a function of two different oxidation states with different forms [plutonium (IV) colloid and soluble plutonium (V)]

- Sorption kinetics of plutonium (IV) colloid and soluble plutonium (V) onto these iron oxide colloids

- Desorption of plutonium from plutonium-loaded iron oxide colloids as a function of time over a long period (approximately one yr).

5.3.6.3.2 Sorption of Plutonium (IV) and Plutonium (V) onto Hematite Colloids

Sorption of plutonium onto the hematite and goethite colloids was investigated as a function of time (BSC 2001 [DIRS 160828], Section 6.73; Triay et al. 1997 [DIRS 100422], Section IV.B). The amounts of plutonium adsorbed varied among the two iron oxides and two solutions. The sorption of plutonium also exhibited different patterns between the plutonium (IV) colloid and the soluble plutonium (V).

Hematite sorbed more soluble plutonium (V) than plutonium (IV) colloids (Table 5-31) (Triay et al. 1997 [DIRS 100422], Section VII.D). Sorption of plutonium also shows different patterns for the two solutions (natural J-13 groundwater and synthetic J-13 groundwater). In both natural and synthetic groundwater, the sorption of plutonium (IV) colloids occurs rapidly, in a single step. After 10 minutes of contact period, about 60 percent of the plutonium (IV) colloids were adsorbed by hematite colloids. At the end of the experiments (5,760 minutes), about 60 to 66 percent of the plutonium (IV) colloids were adsorbed by hematite colloids in both natural and synthetic groundwater. Thus, plutonium (IV) colloids can be readily adsorbed by hematite colloids in both natural and synthetic groundwater.

However, sorption of aqueous plutonium (V) onto hematite colloids varied between the two solutions (Triay et al. 1997 [DIRS 100422], Sections IV.B and VII.D). Generally, hematite colloids sorbed more plutonium (V) in the synthetic groundwater than in the natural groundwater. In the synthetic groundwater, the sorption of soluble plutonium (V) showed a two-step mechanism. The first step was a fast process that occurred in the first 10 minutes of contact. About 82 percent of the plutonium (V) was sorbed during this short period (Table 5-31). The second step was a slower process that continued for 5,750 minutes. Only an additional 5 percent of plutonium (V) was adsorbed during this period.

In natural groundwater, the sorption of plutonium (V) showed a positive correlation with time (Triay et al. 1997 [DIRS 100422], Sections IV.B and VII.D). The amount of plutonium (V) adsorbed gradually increased from 44 to 76 percent as the sorption time increased from 10 to

5,760 minutes (Table 5-31). These data did not distinguish whether the sorption of plutonium (V) in natural water was a one-step or a two-step mechanism.

Desorption of plutonium from hematite is much slower than sorption (Triay et al. 1997 [DIRS 100422], Sections IV.B and VII.D). After 30 days of desorption, aqueous plutonium (V) had not desorbed from hematite, and less than 0.01 percent of plutonium (IV) colloid had desorbed.

5.3.6.3.3 Sorption of Plutonium (IV) and Plutonium (V) Onto Goethite Colloids

Generally, goethite sorbed less plutonium (IV) and plutonium (V) than hematite did in both natural and synthetic groundwater (Triay et al. 1997 [DIRS 100422], Sections IV.B and VII.D). The kinetics of plutonium sorption onto goethite colloids varied with the use of plutonium (IV) colloids and soluble plutonium (V). Sorption of plutonium also varied depending upon the solution (natural or synthetic groundwater).

In the synthetic groundwater, sorption of plutonium (IV) onto goethite colloids was slower than onto hematite colloids. With plutonium (V), goethite also sorbed more of the plutonium (V) in the synthetic groundwater than in the natural groundwater. In the natural groundwater, the sorption of soluble plutonium (V) onto goethite also showed a positive correlation with time.

These results indicate that plutonium (IV) colloids and soluble plutonium (V) can be rapidly adsorbed by goethite colloids in natural or synthetic groundwaters. However, desorption of plutonium (V) and plutonium (IV) from plutonium-loaded goethite colloids did not occur during the first three days of the desorption process (Triay et al. 1997 [DIRS 100422], Sections IV.B and VII.D). After 30 days of desorption, less than 0.01 percent of plutonium (V) and less than 0.1 percent of plutonium (IV) desorbed from the goethite. Desorption of plutonium was much slower than sorption.

The results show that hematite colloids sorbed more plutonium than goethite (Tables 5-31 and 5-32) (Triay et al. 1997 [DIRS 100422], Sections IV.B and VII.D). This result may be due to differences in the surface characteristics and the purity of the mineral materials. The hematite material contained 99.6 percent Fe_2O_3; the goethite material contained 86 percent Fe_2O_3 (in terms of oxides, not mineralogy). Because the usual crystal morphology of synthetic hematite particles is hexagonal plates and the crystal morphology of synthetic goethite particles is acicular, hematite colloids may have larger surface areas than goethite when the particle sizes of both iron oxide colloids are the same.

Both iron oxide colloids sorbed more plutonium in the synthetic groundwater than in the natural groundwater (Triay et al. 1997 [DIRS 100422], Sections IV.B and VII.D). The zero-point-of-charge of synthetic hematite and goethite ranged in pH value from 7.95 to 8.01 in both groundwaters, indicating a similar surface activity with regard to the Fe-OH groups for the two iron-oxides. However, the surface electrical potential of iron-oxide colloids in the synthetic groundwater was higher than in the natural groundwater.

Sorption of soluble plutonium (V) may be a chemisorption process in which the soluble plutonium (V) or its hydrolysis species bind to hydroxyl (OH^-) groups on the hematite or goethite surface. Assuming that plutonium (V) binds to hematite or goethite surface (OH^-)

groups analogous to aqueous coordination reactions, the sorption of plutonium (V) to both iron oxide colloids can be chemically described as exchange of the cationic plutonium species with hydrogen on protonated surface sites. Following sorption, reduction of plutonium (V) to plutonium (IV) may occur. The hydrolysis constants for sorption of plutonium (V) onto iron oxides are not well known (Sanchez et al. 1985 [DIRS 107213], p. 2301).

However, sorption of plutonium (IV) colloids onto iron oxide colloids may have different mechanisms, although the sorption mechanism of plutonium (IV) colloids onto hematite or goethite colloids is not well understood. During the experiments of Triay et al. (1997 [DIRS 100422], Section IV.B), precipitation of plutonium (IV) colloids did not occur. The sorption of plutonium (IV) colloids onto iron oxide colloids may be electrostatic in nature. In the natural or the synthetic groundwater with pH of 8.4 to 8.6, the surface electrical potential of hematite and goethite colloids ranged from 27.1 to 35.4 mV. Therefore, the negatively charged surfaces of iron oxide colloids may electrostatically bind positively charged plutonium (IV) colloids.

5.3.6.4 Reversibility of Sorption onto Colloids

The mechanism that dominates the sorption of actinide contaminants onto oxides or hydroxides in a solid/aqueous interface system is surface complexation (Fuger 1992 [DIRS 108201]). This results in the formation of actinide-hydroxide complexes on the surface of silica, clay, or iron oxide colloids. However, iron oxide colloids have different types of surface hydroxyl groups than do clay colloids or silica colloids. The predominant mechanism of surface complexation reactions of actinide with surface hydroxyl may be different among iron oxide, clay, and silica.

Keeney-Kennicutt and Morse (1985 [DIRS 106313]) found that PuO_2^+ could be adsorbed from diluted solution and seawater on goethite, aragonite, calcite, and δ-MnO_2. The sorption behavior of PuO_2+ is influenced by redox reactions occurring on the mineral surface. Sorption of PuO_2^+ on goethite resulted in a reaction in which plutonium (IV) and plutonium (VI) are formed on the mineral surface. The plutonium (VI) is slowly reduced to plutonium (IV), leaving plutonium (IV) as the dominant plutonium surface species (Keeney-Kennicutt and Morse 1985 [DIRS 106313]). Sanchez et al. (1985 [DIRS 107213]) found that sorption behavior of plutonium onto goethite is related to the different hydrolytic character of these two oxidation states in the solution. The sorption edge of the more strongly hydrolyzable plutonium (IV) occurred in the pH range of 3 to 5, whereas for plutonium (V), it occurred in the pH range of 5 to 7.

Information on affinity, kinetics, and reversibility, which is critical to evaluate the colloid-facilitated transport of radionuclides, is largely unavailable for groundwater particles. There is no information on the sorption of true polymerized radiocolloids (e.g., plutonium (IV) colloids) onto colloids of iron oxide, clays, and silica in groundwater. Laboratory batch-sorption experiments were conducted to evaluate: (1) sorption of ^{239}Pu and ^{243}Am onto different colloids (e.g., hematite, goethite, montmorillonite, and silica), (2) sorption kinetics of ^{239}Pu and ^{243}Am onto these colloids, (3) the effect of colloidal concentrations on the sorption of soluble plutonium (V) and ^{243}Am, (4) the stability of colloidal plutonium (IV) in groundwater, and (5) desorption of ^{239}Pu or ^{243}Am from ^{239}Pu -loaded or ^{243}Am-loaded colloids as a function of time.

5.3.6.4.1 Water, Colloidal Solution, and Tracer

Water from well J-13 and simulated water were used in these studies. The J-13 water had a pH of 8.2 and an ionic strength of 0.005 M. The simulated water had a pH of 8.47, an alkalinity of 25 meq/L, and an ionic strength of 0.005 M (Triay et al. 1997 [DIRS 100422], Section VII.D).

The man made colloidal solutions include pairs of solutions in J-13 and in simulated water for hematite, goethite, montmorillonite, silica-ST-ZL, and silica-PST-1. The average particle size of colloids in the solutions was 416 nm for hematite, 334 nm for montmorillonite, and 139 nm for ST-ZL and PST-1. Approximately 97 percent of goethite colloidal particles were in the size range of 100 to 200 nm.

5.3.6.4.2 Sorption/Desorption Procedure

Three sorption experiments, referred to as sorption 1, sorption 2, and sorption 3, were performed in duplicate at room temperature. Sorption 1 examined the sorption kinetics of soluble plutonium (V) and colloidal plutonium (IV) onto colloids of hematite, goethite, montmorillonite, silica ST-ZL, and silica PST-1. Sorption 2 was performed to evaluate the sorption kinetics of ^{243}Am onto colloids of hematite, montmorillonite, silica ST-ZL, and silica PST-1. Sorption 3 was conducted to examine the effect of colloidal concentration on the sorption of plutonium (V) and ^{243}Am onto colloids of hematite, montmorillonite, silica ST-ZL, and silica PST-1.

The ^{239}Pu-loaded colloidal particles were collected from a 96-hour sorption process. After the wet weights of the colloids were obtained, the colloids were extracted successively with plutonium-free J-13 or simulated water. Desorption was allowed to proceed from 2 to 150 days. Further details are provided by CRWMS M&O (2000 [DIRS 151945], Section 10.3).

5.3.6.4.3 Results

Sorption Kinetics of Colloidal ^{239}Pu onto Colloids–The following discussion is abstracted from CRWMS M&O (2000 [DIRS 151945], Section 10.6.4.4.1).

Sorption of Colloidal ^{239}Pu onto Hematite Colloids–Sorption of colloidal plutonium (IV) onto hematite was rapid in both natural and simulated groundwaters (Figure 5-73). During the first 10 min., approximately 95 percent of plutonium (IV) was adsorbed. The initial rate was 16.4 pCi/mg/min. Thereafter, the amount of sorbed plutonium (IV) increased gradually with time. By the end of the sorption process, the value of the sorption distribution coefficient, K_d, reached 2×10^6 mL/g in natural groundwater and 7×10^5 mL/g in simulated groundwater. Sorption of soluble plutonium (V) by hematite colloids involved two phases in both waters: a fast phase, which occurred in the first 10 min., followed by a slow phase that lasted 95.8 hr. At the end of the sorption process, the K_d value of plutonium (V) on hematite colloids was 10^5 mL/g in both natural and simulated groundwaters.

Sorption of Colloidal ^{239}Pu onto Goethite Colloids–Goethite colloids sorbed approximately 75 percent of plutonium (IV) in natural groundwater during the first 10 minutes (Figure 5-74). After 10 minutes, the amounts of sorbed colloidal plutonium (IV) reached a maximum (approximately 92 percent) at 1 hour; then it decreased gradually during the remaining 95 hr. This result indicates that partial desorption of colloidal plutonium (IV) from goethite colloids

occurs after 1 hour. In the simulated water, approximately 76 percent of plutonium (IV) was sorbed during the first 10 minutes. The initial sorption rate was 12.0 pCi/mg/min. Thereafter, the amount of sorbed plutonium (IV) increased, reaching a maximum (approximately 96 percent) at 6 hours, and then remained at this level during the remaining 90 hours.

Goethite colloids sorbed 56 percent soluble plutonium (V) in natural groundwater during the first 10 min. (Figure 5-74). In the simulated water, approximately 89 percent of plutonium (V) was sorbed during the first 10 minutes. After 10 minutes, the amount of sorbed plutonium (V) increased with time, and an additional 39 percent of plutonium (V) in natural groundwater and 10 percent additional plutonium (V) in the simulated water were adsorbed during the remaining 95.8 hours.

Sorption of ^{239}Pu onto Montmorillonite Colloids–Montmorillonite colloids sorbed 69 percent of plutonium (IV) in natural groundwater during the first 10 minutes (Figure 5-75). After 10 minutes, the amount of sorbed plutonium (IV) increased and reached a maximum (approximately 86 percent) at 4 hours and then it decreased slowly throughout the remaining 236 hours. This result indicates that release of plutonium (IV) occurred after 4 hours in natural groundwater. At the end of the sorption process, the K_d value of plutonium (IV) was 3×10^3 mL/g, which was an order of 10^2 lower than the K_d value on hematite colloid. In simulated water, montmorillonite colloids sorbed 98 percent of plutonium (IV) during the first 10 minutes. The initial rate was 18.1 pCi/mg/min. At the end of the sorption process, the K_d value was 2×10^5 mL/g, which was almost 10^2 times higher than the K_d value in natural groundwater, and was the same value on hematite colloids.

Montmorillonite colloids sorbed 54 percent of plutonium (V) in both natural and simulated groundwater during the first 10 minutes. (Figure 5-75). After 10 minutes, the amount of sorbed plutonium (V) increased with time in both waters. At the end of the sorption process, approximately 90 percent of plutonium (V) in natural groundwater and 97 percent in the simulated water was adsorbed. The K_d value of plutonium (V) was 10^4 mL/g in both waters.

Sorption of ^{239}Pu onto Silica Colloids–Generally, silica colloids sorbed less ^{239}Pu in both natural and simulated waters than iron oxide and montmorillonite colloids did. Silica-PST-1 colloids sorbed 69 percent of plutonium (IV) in natural groundwater and 76 percent in the simulated water during the first 1 hour (Figure 5-76). By the end of the sorption process, approximately 78 percent of plutonium (IV) in natural groundwater and approximately 95 percent in simulated groundwater were adsorbed. The K_d value was 5×10^3 mL/g in natural groundwater and 3×10^4 mL/g in the simulated water.

Sorption Kinetics of ^{243}Am onto Colloids–Generally, sorption of ^{243}Am by colloids was in the order of hematite > montmorillonite > silica in both natural and simulated groundwater. The amount of americium sorbed by these three types of colloids was not significantly different between natural and simulated groundwater. The following discussion is abstracted from CRWMS M&O (2000 [DIRS 151945], Section 10.6.4.4.2).

Sorption of ^{243}Am onto Hematite Colloids–Hematite colloids sorbed almost 100 percent of americium in both natural and simulated groundwater during the first 1 hour (Figure 5-77). The initial rate was 6.1 pCi/mg/min. in natural groundwater and 3.9 pCi/mg/min. in the simulated

water. After 1 hour, the amount of sorbed americium decreased gradually during the remaining 239 hr in natural groundwater. However, in the simulated water, sorption of americium showed a fluctuation with time. The amount of sorbed [234]Am decreased slightly during the period from 1 to 48 hours, and then it increased up to the original sorption level (approximately 100 percent) at 96 hours. Thereafter, the amount of sorbed americium decreased during the remaining 144 hours. This result indicates that partial desorption of americium from hematite colloids occurs after 1 hour in both waters. At the end of the sorption process, approximately 90 percent of americium in the natural groundwater and approximately 93 percent in the simulated water were adsorbed. The K_d value was 10^5 mL/g in both natural and simulated groundwaters.

Sorption of [243]Am onto Montmorillonite Colloids–Montmorillonite colloids sorbed approximately 61 percent of americium in natural groundwater and 79 percent in the simulated groundwater during the first hour (Figure 5-77). The initial rate was 3.8 pCi/mg/min. in natural groundwater and 3.2 pCi/mg/min. in the simulated water. After 1 hour, the amount of sorbed americium increased and reached a maximum at 96 hours in natural and simulated groundwater. After 96 hours, the amount of sorbed americium decreased during the remaining 144 hours. This result indicates that partial desorption of americium from montmorillonite occurs after 96 hours of the sorption. At the end of the sorption process, approximately 63 percent of americium in natural groundwater and 73 percent in the simulated water were adsorbed. The K_d value was 10^4 mL/g in both natural and simulated groundwater, which was 10 times lower than the K_d value on hematite.

Sorption of [243]Am onto Silica Colloids–Generally, silica colloids sorbed less [243]Am in both natural and simulated waters than iron-oxide and montmorillonite colloids did. Silica-PST-1 colloids sorbed 28 percent of americium in both natural and simulated groundwater during the first hour (Figure 5-77). The initial rate was 1.7 pCi/mg/min. in natural groundwater and 1.1 pCi/mg/min. in the simulated water. After 1 hour, the amount of sorbed americium increased and reached a maximum at 48 hr, and then it decreased gradually during the remaining 192 hours in the simulated water. However, in the simulated water, sorption of americium shows a fluctuation with time. The amount of sorbed [234]Am decreased to 35 percent at 96 hours, and then it increased up to 60 percent at the end of sorption process. The K_d values were 10^4 mL/g in natural groundwater and 5×10^3 mL/g in the simulated water.

The Effect of Colloidal Concentration on the Sorption of Plutonium (V)–To examine the effect of colloidal concentration on the sorption of plutonium (V) onto colloids of hematite, montmorillonite, and two types of silica, an additional experiment was conducted. The results show that, per unit of colloid, sorption of plutonium (V) was much higher at low colloid concentrations than at high colloid concentrations (Figure 5-78). Silica colloids also show a similar pattern, as montmorillonite colloids did. Therefore, the results from silica colloids are not presented here (CRWMS M&O 2000 [DIRS 151945], Section 10.6.4.4.3).

Desorption of [239]Pu From Colloids–Little plutonium was desorbed from hematite colloids after 150 days, even under vigorous shaking conditions (Figure 5-79) (CRWMS M&O 2000 [DIRS 151945], Section 10.6.4.4.4). As much as 0.5 percent of colloidal plutonium (IV) and 0.8 percent of soluble plutonium (V) were desorbed from goethite colloids. Desorption of [239]Pu from montmorillonite or silica colloids was faster and higher than from hematite and goethite colloids. As much as 8 percent of colloidal plutonium (IV) and 0.7 percent of soluble

plutonium (V) were desorbed from montmorillonite colloids after 150 days. However, as much as 20 percent of colloidal plutonium (IV) and 6 percent of soluble plutonium (V) were desorbed from silica colloids (Figure 5-79). The results suggest that desorption of ^{239}Pu from colloids of hematite, goethite, or montmorillonite in groundwater is much slower than the sorption process.

Therefore, colloids of iron oxide and clay in groundwater may enhance the transport of ^{239}Pu along the potential flow paths.

5.3.6.4.4 Summary of Most Recent Results

Sorption of radionuclides onto colloids of iron oxide, clays, and silica in groundwater may play an important role in their transport. Laboratory batch-sorption experiments (further details see CRWMS M&O 2000 [DIRS 151945], Section 10.6.4.5) were conducted to evaluate (1) sorption of ^{239}Pu and ^{243}Am onto different colloids (e.g., hematite, goethite, montmorillonite, and silica), (2) sorption kinetics of ^{239}Pu and ^{243}Am onto these colloids, (3) effect of colloidal concentrations on the sorption of soluble plutonium (V) and ^{243}Am, (4) stability of colloidal plutonium (IV) in groundwater, and (5) desorption of ^{239}Pu or ^{243}Am from ^{239}Pu-loaded or ^{243}Am-loaded colloids as a function of time. Natural groundwater and carbonate-rich-simulated groundwater were used.

The results show that colloidal plutonium (IV) and soluble plutonium (V) were rapidly sorbed by colloids of hematite, goethite, montmorillonite, and silica in both natural and synthetic groundwater. The initial sorption rates of plutonium onto these colloids are summarized in Table 5-33. Sorption of plutonium (V) per unit colloid was higher at low colloidal concentrations than at high colloidal concentrations. At high colloidal concentrations, the K_d values of plutonium (V) range from 10^3 to 10^5 mL/g for hematite colloid and from 10^2 to 10^3 mL/g for montmorillonite colloid. At low colloid concentrations, the K_d values of plutonium (V) range from 10^4 to 10^5 mL/g for hematite and from 10^2 to 10^3 mL/g for montmorillonite.

Desorption of ^{239}Pu from colloids of hematite, goethite, and montmorillonite was much slower than the sorption process. Desorption of ^{239}Pu from silica colloids was faster than from the other three types of colloids. Tables 5-33 and 5-34 summarize the initial sorption and desorption rates from plutonium-loaded colloids.

Sorption of ^{243}Am by hematite colloids was faster and greater than by montmorillonite and silica colloids. Maximum sorption of ^{243}Am occurred at 1 hour for hematite, 48 hours for silica, and 96 hours or more for montmorillonite. After these time periods, partial desorption of ^{243}Am from colloids occurred. With the maximum sorption, the sorption distribution coefficient, K_d, for ^{243}Am was of the order of 10^4 mL/g for silica, and 10^5 mL/g for hematite and montmorillonite.

5.3.6.5 Mineralogy of Colloids

The following discussion was abstracted from CRWMS M&O (2000 [DIRS 151945], Section 10.6.5). Colloid researchers define upper size limits of 1 to 10 μm for colloidal particles. For these studies, colloids are adequately defined as fine particulates that were transported and deposited in aqueous suspension. The selection of a particular size limit is not so important for alteration history studies because the relict colloidal materials preserved in Yucca Mountain

rocks have been texturally modified by recrystallization. Most of the colloidal deposits identified in alteration history studies existed locally at some time as gels, semisolid colloid-water systems, with the macroscopic appearance and behavior of a jelly or paste. Liquid rich gels have been observed in underground workings at Rainier Mesa, north of Yucca Mountain, and dried or crystallized gels have been identified in drill cores and in the ESF at Yucca Mountain itself.

X-ray diffraction analysis of dried gel from Rainier Mesa reveals a very pure, well-crystallized smectite. In addition to the smectite, there are fragments and clast coatings of silica-rich-dried gels. Mineral phases identified by morphology and energy-dispersive x-ray spectra include silica, barite, copper-iron sulfides or sulfates, and possible zeolites, as well as the smectite (Levy 1992 [DIRS 100770], pp. 83 to 84).

Liquid rich free gels (as distinguished from gel layers on hydrated glass surfaces) have not yet been found at Yucca Mountain, in either drill cores or the ESF. Prominent dried smectite gels are present in the Tiva Canyon Tuff exposed by the ESF north ramp box cut and starter tunnel. Laminated deposits of smectite, up to several centimeters thick, coat fractures and fill the bottoms of lithophysal cavities. The abundance of this material gradually diminishes inward from the portal. Although this diminution corresponds to increasing depth below the surface in the ESF, the smectite probably is not derived from present-day surficial deposits, because clay coatings are absent from the Tiva Canyon Tuff exposed at the ESF South Portal.

A clay-rich fracture filling from the Topopah Spring Tuff in the ESF offers a dramatic example of particulate transport. The wall rock is densely welded, devitrified tuff, but the fracture filling consists of devitrified rock fragments in a fine-grained matrix of Topopah Spring glass pyroclasts. Several sequences of graded bedding are preserved within the fillings. The glassy constituents had to come from tens of meters higher in the stratigraphic section.

Of the former gels and colloidal accumulations observed in altered rocks at Yucca Mountain, those in altered basal Topopah Spring Tuff vitrophyre are especially relevant because the alteration conditions may represent a natural analog to a radioactive waste repository environment. The chief hydrous products of glass alteration are smectite and heulandite-clinoptilolite. Smectite commonly crystallized as spherical aggregates, 2 to 50 µm across, adhering to each other, with a small amount of intergrown, extremely fine-grained zeolite. Perhaps because of this growth habit, there is little evidence of free smectite gels in this altered zone. Relict colloidal accumulations of silica also fill dissolution cavities in altered vitrophyre and primary and secondary pores in moderately welded tuffs below the vitrophyre. Some of these are uraniferous opal deposits, with relevance to radionuclide transport.

The most common examples of former gels at Yucca Mountain are microscopic geopetal deposits in pores of the zeolitized nonwelded tuffs. Layers within silica deposits are distinguished by color, by variations in incipient birefringence related to differences in crystallinity, or by differences in granularity. Zeolite and silica occur commonly in separate layers, with the zeolite lowermost. Another variety of relict gel fills only primary pores and is a major cementing constituent in certain well-sorted bedded tuffs that originally contained little or no fine-grained ash; heulandite-clinoptilolite and opal, in variable proportions, are the main constituents. The infilling of virtually all primary porosity, but only primary porosity, by gel in

this kind of tuff indicates that the gel constituents were externally derived and transported into the bedded tuff by moving water before the tuff itself began to be altered.

5.4 INTEGRATED NATURAL SYSTEM RESPONSE TO THERMAL LOADING

This section presents the results of site characterization activities aimed at understanding the thermally-induced coupled processes, resulting from the emplacement of radioactive wastes in the repository, that form the integrated natural system response to thermal loading. Among the responses are thermal-hydrologic effects, such as rock drying or wetting, changes in relative humidity, and redistribution of water flux; thermomechanical effects on fractures; and thermal-chemical alteration of heated rock and seepage composition. These processes take place in the near field, an environment of great importance to the degradation of waste packages and the waste form and to the subsequent transport of released radionuclides into the unaltered host rock of the unsaturated zone below the repository.

This section describes the thermal-hydrology (Section 5.4.2), geomechanics (Section 5.4.3), geochemistry (Section 5.4.4), and associated field-testing (Section 5.4.5) at Yucca Mountain. This discussion was based originally on *Near Field Environment Process Model Report* (CRWMS M&O 2000 [DIRS 146589]), *Unsaturated Zone Flow and Transport Model Process Model Report* (CRWMS M&O 2000 [DIRS 145774]), and *Engineered Barrier System Degradation, Flow, and Transport Process Model Report* (CRWMS M&O 2000 [DIRS 145796]); and has been updated to incorporate more recent work appearing in *Multiscale Thermohydrologic Model Report* REV 01 (BSC 2003 [DIRS 163056]), *Thermal Testing Measurements Report* (BSC 2002 [DIRS 160771]), *Drift-Scale Coupled Processes (DST and THC Seepage) Models* (BSC 2003 [DIRS 162050]), and *Engineered Barrier System: Physical and Chemical Environment Model* REV 02 (BSC 2003 [DIRS 167461]).

5.4.1 Overview

5.4.1.1 Definitions of Thermally Affected Zones in the Natural System

The near field environment is defined as the area and conditions within the repository region including the rock immediately surrounding the drifts outward to a distance that encompasses significant heating-related processes or excavation-related changes in rock properties (DOE 2002 [DIRS 155943], p. G-20). "Significant" refers to the effect on the repository system performance.

Interactions between the natural system and radioactive wastes could cause both permanent and transient property changes within a region that extends for a considerable distance into the rock mass (BSC 2003 [DIRS 166512]; 2003 [DIRS 164890]; 2003 [DIRS 162050]; 2003 [DIRS 166498]). Beyond this near field lies the far field (i.e., unaltered host rock of the unsaturated zone and saturated zone), where only minor changes may occur, such as slightly elevated temperatures. The near field may extend considerably farther for some processes than for others (BSC 2003 [DIRS 162050] Figure 6.8-40; 2003 [DIRS 164890] Figure 7.4.3-2), ranging from tens of meters to 100 m or more outward from the emplacement drift (BSC 2003 [DIRS 162050], Section 6; 2003 [DIRS 164890], Figure 7.4.3; 2003 [DIRS 166498],

Sections 6.2 and 6.3). The near field also evolves as the rate of heat generation from the decay of the radioactive waste decreases over time.

5.4.1.2 Waste Isolation Performance Considerations

The near field is important to waste isolation because it is the environment that directly impacts the waste packages and the waste form. The impact of the near field environment on waste isolation depends largely on three factors:

- The preemplacement natural system—that is, the rock mass. The most important characteristic of the rock mass around the repository is that it is unsaturated, which will limit seepage of water into the emplacement drifts and promote oxidizing conditions.

- Radioactive decay heat from the waste, and the processes associated with that heat.

- Design aspects of the repository that control the postclosure conditions, including thermal loading, introduced materials, and operation of the repository during the preclosure period.

Thermally-driven coupled processes within the near field can affect water distribution, and cause changes in rock porosity and permeability, which in turn can affect water contact with the waste. These processes can also modify the mineralogy, resulting in changed sorption capacities of the near field.

The thermal characteristics of the waste are described in BSC (2003 [DIRS 163056]). An exponentially declining release of heat is a fundamental characteristic. Although heat output will persist for hundreds of thousands of years, the exponential decline will render additional effects on the repository negligible within a few tens of thousands of years. Along with the unsaturated nature of the site, heating is one of the major determinants of site response.

The unsaturated zone is a key factor that determines the amount and composition of water (seepage) that enters the near field environment. The quantity and chemistry of seepage (including their spatial and temporal evolution) are discussed in BSC (2003 [DIRS 165564]) and BSC (2003 [DIRS 162050]), respectively. The waste form contributes to isolation of radionuclides mainly by limiting the rate at which the waste can be released. The near-field environment factors that influence the rate of release are the amount, temperature, and chemical content of water that contacts the waste. The properties of the waste that determine this rate are discussed in Stout and Leider (1997 [DIRS 100419], Section 2). The near field will be a major factor in the release rates from the waste form because the quantity, temperature, and chemicals in the water contacting the waste will be dominated by the near-field environment (BSC 2003 [DIRS 167461]).

Radionuclide release from the engineered barrier system requires two conditions:

- A breach or failure of the metal barriers of the waste package.

- Contact of the waste form by liquid water, which can dissolve or suspend radionuclides and transport them through the failed waste package and other elements of the

engineered barrier system to the rock below the drifts. (Gaseous radionuclides, such as $^{14}CO_2$, are not included in these near-field environment discussions.)

Breach of the outer barrier is determined by its corrosion rate (the potential effect of mechanical stress on container breach is discussed in Section 5.4.3). Manufacturing defects can also lead to juvenile failure of the waste package. The corrosion rate is a function of near-field conditions (humidity or liquid water contacting packages) and stresses induced by seismic and or volcanic events. Some of the rate parameters also depend strongly on the chemical composition of solids (dust, salts from evaporated seepage) on the waste package (BSC 2003 [DIRS 167461]).

Postemplacement cladding failure will be controlled by the temperature within the waste package and the amount of O_2 that is able to contact the cladding; both factors will be affected by the near field environment. Other factors that can impact postemplacement cladding failure include existing flaws and stress. Waste package temperature will depend on the rate of heat transfer between the waste package and its surroundings.

Even if a waste package fails, the release of radioactive material will be limited unless liquid water is advected into the drift, into the breached waste package, onto the waste form, and back into the rock surrounding the repository. All of these aspects of repository performance may be affected by changes within the near field involving:

- Interactions with introduced materials and their degradation products

- Mineralogical changes (alteration, mineral dissolution/precipitation) that influence near-field hydrologic properties and water chemistry

- Coupled thermal-mechanical-hydrologic-chemical processes within the near field that may change the flow fields above and below the repository.

Such processes could alter the physical and geochemical environment in the near field that controls waste package performance and the transport of radionuclides in the unsaturated and saturated zones.

5.4.1.3 Emplacement and Repository Concepts

The current design (Williams 2003 [DIRS 162731]) features drift spacing of 81 m (265 ft), line-load waste package spacing, and approximately 50 years of drift ventilation prior to permanent closure. The waste packages will be spaced closely together so that they act as a variable, linear heat source. Ventilation will remove heat generated by the waste as it ages within the repository during the pre-closure period, and reduces thermal changes in the near field after closure. Prior to closure, drip shields will be placed over the waste packages.

5.4.1.4 Repository Performance Terminology

The following terminology associated with the design, construction, and operation of the repository is used in the discussion of coupled processes.

Construction–excavation of rock, ventilation, and fluids and materials introduced during drilling, excavation, and construction.

Rock Excavation–alteration of rock stresses and concomitant changes in rock properties, discussed in Section 5.4.3.

Ventilation–causes rock matrix drying surrounding the emplacement drifts, shafts, ramps, and access drifts by removing moisture from the rock (Section 5.4.2).

Introduction of Materials during Construction–may include crushed rock, engine exhaust, rubber products and other polymers, metals, and concretes.

Materials Introduced during Waste Emplacement–these include the container materials and engineered barrier system packing materials, including dust.

Heat Output–waste package heat output will decline continuously due to radioactive decay. The heat output will be at a maximum during the preclosure period (50 yr), and the emplacement drifts will be ventilated during this period to remove much of this heat (BSC 2003 [DIRS 164576]). Warming of ventilation air will ensure that preclosure conditions are dry, especially where in-drift temperatures are greatest.

At permanent closure, ventilation will cease and the drift-wall rock temperature will increase sharply within a few decades (BSC 2003 [DIRS 163056], Section 6.3.1). The maximum postclosure temperature of a waste package at any location will be determined by the history of heat output, the resistance to dissipation of heat in the host rock, heat transfer from the waste package to the drift wall, and the relationship to other nearby heat sources.

Closure–major activities associated with closure will include installation of drip shields, cessation of ventilation, and installation of seals and plugs.

Climate Changes–conditions in the repository and near field will be affected by potential long-term climate changes. Percolation flux in the near-field environment will depend on changes in net infiltration, which is related to climate. Thermal-hydrologic response to climate changes is addressed in Section 5.4.2.

5.4.1.5 Processes Influencing Ambient Seepage

Water enters the unsaturated zone from above as net infiltration, then drains or percolates downward through the host rock under the impetus of gravity, principally through the fractures and to a lesser extent through the relatively impermeable rock matrix. Underground openings in unsaturated rock have a tendency to divert the percolating water around them because of the capillary barrier effect, as illustrated in Figure 5-80. This effect is well known in soils, and arises when coarse-grained soils are overlain by fine-grained soils (Ross 1990 [DIRS 141790]; Oldenburg and Pruess 1993 [DIRS 141594]). The stronger negative capillary pressure developed in the fine-grained material prevents water from entering the larger pores of the underlying coarse-grained material (Birkholzer et al. 1999 [DIRS 105170]). If a drift is conceptualized as "very coarse grained" with essentially zero capillarity, seepage into the drift can only occur if the capillary pressure in the rock close to the drift walls becomes zero (i.e., the

fractured rock becomes locally saturated). The rock can become locally saturated by disturbance to the flow field, which is caused by the presence of the drift opening (Philip et al. 1989 [DIRS 105743]) and more importantly by spatial heterogeneity that promotes channelized flow and local ponding (Birkholzer et al. 1999 [DIRS 105170]).

Seepage is defined as the movement of liquid water into an underground opening and does not include movement of water vapor or condensation within openings. Seepage flux is the rate of seepage per unit flow area. Seepage percentage is defined as the ratio of the seepage flux to the percolation flux in the host rock. The seepage threshold is a critical percolation flux below which seepage in the opening is unlikely to occur, as demonstrated in field tests (BSC 2003 [DIRS 162267]). Where seepage occurs, the water evaporates, follows the inclined rough wall of the opening as flow in a thin film, or forms a drop that grows and eventually detaches (Or and Ghezzehei 2000 [DIRS 144773]).

For an emplacement drift of a given shape, the seepage threshold and the amount of seepage once this threshold is exceeded depend on the local flow conditions in the near field (Figure 5-80). These conditions are mainly influenced by the local percolation flux reaching the opening and by the local hydrologic properties of the host rock (principally the capillary strength and relative permeability of the fracture network) (BSC 2003 [DIRS 165564], Section 6.3.1). Small-scale heterogeneity of hydrologic properties (i.e., fracture characteristics) increases the likelihood of seepage (Birkholzer et al. 1999 [DIRS 105170]). Effects from small-scale heterogeneity are included in the field data sets that have been used to calibrate the ambient seepage model (BSC 2003 [DIRS 165564], Section 6.4.1.1). In addition, intermediate-scale and mountain-scale variability in hydrologic properties and flow paths within Yucca Mountain produces spatial variability in the percolation flux, which is accommodated through the estimation of flow focusing (BSC 2003 [DIRS 165564], Section 6.3.1). The drift opening cross-sectional shape and size also affect seepage in the manner originally discussed by Philip et al. (1989 [DIRS 105743]).

5.4.1.6 Processes Influencing Thermal-Hydrologic-Chemical Processes in the Near-Field and In-Drift Environments

Thermal-Hydrologic Processes in the Host Rock–Heat output from waste emplacement gives rise to above-boiling temperature conditions inside the drifts and in the fractured rock surrounding them. The ensuing TH processes have been examined theoretically and experimentally for the fractured welded tuffs at Yucca Mountain and similar sites since the early 1980s (Pruess et al. 1984 [DIRS 144801]; 1990 [DIRS 100819]; Buscheck and Nitao 1993 [DIRS 100617]; Pruess 1997 [DIRS 144794]; Kneafsey and Pruess 1998 [DIRS 145636]; Tsang and Birkholzer 1999 [DIRS 137577]; Birkholzer and Tsang 2000 [DIRS 154608]; Buscheck et al. 2002 [DIRS 160749]). Key TH processes occurring around a drift are shown schematically in Figure 5-81 (BSC 2003 [DIRS 166512]). The figure indicates that heating of the rock causes pore water in the rock matrix to boil and vaporize. The vapor moves away from the drift through the permeable fracture network, driven primarily by pressure increase caused by boiling. In cooler regions away from the drift, the vapor condenses in the fractures, where it can drain either toward the heat source from above or away from the drift into the zone below the heat source.

Condensed water can also imbibe from fractures into the matrix, leading to increased liquid saturation in the rock matrix. With continuous heating, a hot dryout zone may develop closest to the heat source, separated from the condensation zone by a nearly isothermal zone maintained at about the boiling temperature. This nearly isothermal zone is characterized by a continuous process of boiling, vapor transport, condensation, and migration of water back towards the heat source (either by capillary forces or gravity drainage), and often referred to as a heat pipe (Pruess et al. 1990 [DIRS 100819]). For the current repository design at Yucca Mountain, the dryout zone around drifts extends to a maximum distance of approximately 5 to 10 m from the drift wall (BSC 2003 [DIRS 166512], Sections 6.2.2 and 6.2.3). This zone forms a barrier to water drainage since the above-boiling temperatures cause water to vaporize. The current repository design has parallel emplacement drifts that are separated by 81 m from center to center and a drift radius of 2.75 m (Williams 2003 [DIRS 163765]). The drift spacing is large compared to the dryout zone, indicating that water above the repository can drain between drifts where the rock remains below boiling. This process of pillar drainage is important for performance, because it reduces the potential amount of water buildup above drifts.

TH processes occur at different physical scales. During the early part of the heating period, important TH processes are expected to occur near the emplacement drifts. At the drift scale, variability in heat output from individual waste packages and different times of waste emplacement may give rise to variability in the extent of dryout, rewetting, and water flux along drifts and at different drift locations. At later times, heat-driven coupled processes are at the mountain scale. These include repository edge effects, large-scale enhanced water and gas flow, and potential alteration of perched-water bodies.

Thermal seepage refers to seepage during the time period that the flow around drifts is perturbed from heating. This effect is particularly important for above-boiling temperature conditions where a hot dryout region develops in the vicinity of a drift. This hot dryout zone provides an additional barrier preventing seepage, since percolating water can be entirely vaporized prior to reaching the drift wall. Therefore, thermal seepage is unlikely as long as boiling conditions exist. On the other hand, condensed water forms a zone of elevated water saturation above the rock dryout zone. Water from this zone may be mobilized to flow rapidly down towards the drift. This effect may promote seepage. The combined effect of TH perturbation, vaporization barrier, and capillary barrier formation is investigated in BSC (2003 [DIRS 166512], Sections 6.2 and 6.3).

Thermal-Hydrological Processes in Emplacement Drifts–Two important factors influence the TH conditions within the emplacement drifts (BSC 2003 [DIRS 163056], Section 6.1.4). The first is whether or not temperatures at the drift wall are above the boiling point, which affects whether the relative humidity in the near-field host rock is reduced relative to ambient (humid) conditions as well as the likelihood of water seeping into the drift. The second is the temperature difference between the waste package and drift wall, which strongly affects how much lower relative humidity is on the waste package than on the drift wall.

Dissolution and Precipitation of Minerals–Geochemical processes will be coupled with TH processes (BSC 2003 [DIRS 162050]). Where and when dryout occurs, the dominant processes will be vapor flow and associated chemical exchanges. Where temperatures reach boiling, the rock will undergo drying, which will result in the deposition of nonvolatile dissolved salts in

rock pores and fractures. As complete dryout occurs, the last remaining aqueous solutions will be highly concentrated but volumetrically limited salt solutions. Studies have shown that, in addition to salt deposition, mineralogical changes can result from rock-water interactions at elevated temperatures (BSC 2003 [DIRS 162050]). During the cooling stage, salt minerals in the rock and on the waste package may deliquesce (a liquid phase will be present) and begin to dissolve at temperatures as high as 140°C (see Sections 5.4.4.2.2 and 5.4.4.3).

Thermal-Mechanical Processes Induced by Stress Changes–The largest effect on the geomechanical behavior of the near-field environment is expected to be from thermal expansion and contraction during the thermal cycle as the rock heats and then slowly cools.

Deformations within the rock mass can affect the hydrologic flow system. Greater impact often results from shear rather than normal deformations (Bandis et al. 1983 [DIRS 100003]; Barton et al. 1985 [DIRS 100005]). This is especially true once stresses are removed, as would be the case for the repository once the thermal pulse has decayed. This has been observed in field studies (Wilder 1987 [DIRS 100189]).

5.4.2 Thermal Hydrology

5.4.2.1 Conceptual Description of Thermal-Hydrological Processes in the Near Field

Heating of the host rock will produce the greatest movement of moisture and liquid water after permanent closure (DOE 2002 [DIRS 155943], Section 4.2.2). Much of the heat will be transported away from the drifts by thermal conduction through the rock. A portion of the heat will be transported as latent heat by water that vaporizes near the drift and condenses in cooler rock farther away. These processes are depicted in Figure 5-81, which represents the conceptual understanding of TH processes occurring around a drift as derived from the Drift Scale Test (DST) and other field-scale thermal tests.

Given the projected heat output of the waste and the host rock characteristics, the near field host rock will be heated to above-boiling temperatures (i.e., greater than 96°C at the repository elevation) for several hundred years (BSC 2003 [DIRS 163056], Section 6.3.1). Where temperatures exceed boiling, substantially all of the water will be evaporated from the rock (dryout zone in Figure 5-81). The duration and extent of dryout will depend on the history of local heat generation, the percolation flux in the host rock, and host rock properties such as thermal conductivity. Thermal evolution of a particular waste package will also depend on its location in the repository layout (i.e., whether it is near the center or the edge). As the waste heat output decreases with time, the dryout zone will eventually shrink back to the drift wall, cooling to below-boiling temperatures. Waste package temperatures will follow the evolution of the local drift-wall temperature but will be as much as 10° to 20°C warmer because of thermal resistance across the drip shield and the in-drift air spaces (BSC 2003 [DIRS 163056], Section 6.3, Table 6.3-4). This temperature difference will approach zero at later times as the heat output declines.

Condensation controls the relative humidity on the waste package surfaces, because relative humidity will be very close to 100 percent where the condensation occurs. Water vapor is readily dispersed in the gas phase of the host rock, so the water vapor fraction in the gas phase

varies little over the few meters from the drift wall to the location of condensation. Accordingly, if the in-drift temperatures (e.g., on the waste package and the drift wall) are greater than boiling, then the relative humidity will be less than 100 percent near those surfaces. Thus, the condensation of water vapor in the host rock, and the difference in temperature compared to the waste package determine the evolution of dew-point temperatures/relative humidity at the waste package and drip shield surfaces.

Thermally driven movement of water, as liquid and vapor, will be strongest when the host rock forms a dryout zone at above-boiling temperature. In other words, boiling temperatures are required to dewater the rock matrix where most of the formation water resides. In the rock at the outer margin of the dryout zone, water vapor will coexist with liquid condensate (Pruess et al. 1990 [DIRS 100818], p. 1,235) (Figure 5-81). Reflux will occur if the condensate flows back toward the dryout zone under gravity or capillarity, but the condensate water may also drain away from the dryout zone and be removed from further consideration as potential seepage. Reflux activity has been observed during thermal testing at Yucca Mountain, and occurs only when and where the rock temperature is at boiling (BSC 2003 [DIRS 166512], Section 7). Studies show that rewetting occurs at a much slower rate than drying. If most condensate drained away from the repository, rewetting would depend mostly on percolation flux from surface precipitation and might take thousands of years (Buscheck et al. 1996 [DIRS 131789]; Buscheck and Nitao 1993 [DIRS 100655]).

Another mechanism for transport involves migration of some vapor back into the emplacement drifts, where it will be transported along the open drifts. Along a particular emplacement drift, vapor will be produced mainly in the region of the drift where the rock temperature is above boiling, and condensation will occur mainly in unheated portions of the drift (e.g., at the ends where there are no waste packages). Waste packages near the edge of the repository layout will be exposed to increased relative humidity and slightly increased temperature, but dripping condensation is unlikely because there will be much cooler, unheated rock available. Condensation effects associated with large-scale variations in temperature and humidity within the emplacement drifts are currently under investigation.

Thermal seepage for temperatures at or above boiling will be prevented by vigorous boiling in the hot, dry rock of the dryout zone (BSC 2003 [DIRS 166512], Section 6.2.1.1.2). The dryout zone (Figure 5-81) will form a vaporization barrier that prevents thermal seepage by completely evaporating any liquid water that enters the zone from above, before it reaches the drift wall. Thermal seepage is unlikely because of this evaporation barrier, as long as above-boiling temperatures persist. In addition, the intensity of reflux activity is directly related to heat output, which will be strongest early in the thermal evolution when the dryout zone has its greatest extent. By the time the host rock cools and the dryout zone shrinks, the magnitude of the reflux activity will be attenuated because the heat output of the repository will have decayed.

Relatively large liquid fluxes (compared with the natural percolation flux) may impinge on the dryout zone because of reflux, possibly associated with episodic reflux events. Such episodic events have been observed (BSC 2001 [DIRS 157330], Section 6.2.4.1) for test conditions similar to the repository host rock. Liquid flow in the dryout zone will be prevented by the vaporization barrier; moreover, the capillary barrier will also be effective, even at elevated temperatures (see Section 7.10). It is reasonable to use the same conceptual basis for the

capillary barrier at elevated temperature that was developed for ambient seepage (BSC 2003 [DIRS 166512], Section 6.2.1.1.2).

5.4.2.2   Natural System Factors that Influence the Near-Field Thermal-Hydrologic Response

The TH environment of the near field host rock will be influenced by key factors (BSC 2003 [DIRS 163056], Section 1; 2003 [DIRS 166512], Section 6.2.2):

- **Percolation Flux**–The magnitude of the percolation flux is a key factor determining seepage and thermal-hydrologic responses to heating. Percolation flux varies significantly over the repository footprint. The flux is greatest beneath the crest of Yucca Mountain and lowest along the flanks and in the alluvial-filled washes. Percolation flux also varies temporally as a result of short-term fluctuations and long-term climatic changes.

- **Hydrologic Properties in the Repository Horizon Host-Rock Unit**–The most important properties are those governing capillarity, especially in the host rock. The capillary properties of the matrix govern how quickly matrix imbibition rewets the dryout zone. The capillary properties of fractures also affect the tendency for water to seep into drift openings.

- **Thermal Properties in the Repository Horizon Host-Rock Unit**–The repository intersects several different subunits of the Topopah Spring Tuff; these subunits have different thermal conductivity.

- **Overburden Thickness**–The depth of the current repository horizon below the ground surface translates to thickness of insulating rock between the repository and the ground surface, a constant-temperature boundary, which acts like a heat sink.

Of these factors, the host-rock thermal conductivity and percolation flux above the repository horizon are the most important for TH behavior at the repository (BSC 2003 [DIRS 163056], Section 6.1.6).

5.4.2.3   In-Drift Thermal-Hydrological Conditions

This section summarizes the analyses and interpretation of in-drift conditions from results of the DST (BSC 2003 [DIRS 166512]), and discusses in-drift observations during the ESF moisture monitoring and liquid release seepage tests (BSC 2003 [DIRS 166347]; 2003 [DIRS 162267]).

Results of the Drift Scale Test–Selected temperatures from the DST are presented in Figure 5-82. The temperature profiles and temperature history plots show reflux behavior (deflections near 100°C) in measured responses. In addition to temperature measurements, TH processes are also monitored by tracking the time-varying location of the dryout zone and the associated condensation front, in response to heating. This was done using geophysical methods that respond to liquid saturation changes in the matrix, and by periodic air-injection tests that respond to liquid saturation changes in the fractures (BSC 2003 [DIRS 166512],

Figure 7.4.3.2-3). These observed trends are in general agreement with predictions of the DST TH model (BSC 2003 [DIRS 166512], Section 7), which provides confidence that the model accurately represents the relevant TH processes of moisture redistribution. In addition, the DST is one of three heater tests of different scales and geometry that have been conducted at Yucca Mountain. The successful modeling analyses performed for the SHT and the Large Block Test provide additional confidence in the capability to predict TH conditions for the Yucca Mountain repository (Tsang and Birkholzer 1999 [DIRS 137577]; BSC 2001 [DIRS 157330]; Mukhopadhyay and Tsang 2002 [DIRS 160788]).

Wet Zones Observed in the ESF Moisture Monitoring and Liquid Release Seepage Tests– Part or all of the water reaching the ceiling of the opening may evaporate, depending on the evaporation potential in the drift and the wet area exposed to evaporation. The evaporation potential depends on the relative humidity in the opening and the thickness of a diffusive boundary layer at the drift surface, which in turn is governed by the air velocity in the opening.

Wetting of the drift ceiling also depends on the formation properties and the spreading mechanism along the drift surface. Under conditions prevailed in the ESF, evaporation in ventilated openings prevents wetting at the drift surface and thus prevents seepage. However, the development of wetting and its relation to in-drift conditions has been studied during the seepage tests conducted in several niches and along the ECRB Cross-Drift (BSC 2003 [DIRS 166347], Section 6.10.2).

If evaporation is significantly reduced, wetting of the drift surface is expected. Wet surfaces and film flow are an integral part of the capillary barrier concept, providing evidence that the capillary barrier is engaged. Wet surfaces were observed in the closed-off sections of the ECRB Cross-Drift (BSC 2003 [DIRS 166347], Section 6.10.2). These observations provide information regarding potential seepage and in-drift moisture redistribution. The observations of moisture on impervious (nonporous) surfaces suggest that, at least partially, the moisture originated from condensation. The near 100 percent relative humidity in the ECRB Cross-Drift and local thermal gradients (partly induced by electrical equipment in the closed-off drift sections) are the likely causes for the observed condensation. Although it is possible that the dripping may have resulted from seepage of formation water, geochemical analyses (BSC 2003 [DIRS 166347], Section 6.10.2) support the conclusion that this is most likely condensation water.

It is useful to qualitatively compare the observations made in the ECRB Cross-Drift and Alcove 7, with the representation of seepage in the abstraction model for TSPA (BSC 2003 [DIRS 165564], Section 6.8.1). The abstraction model for drift seepage shows that approximately eight percent of waste packages (averaged over the entire repository layout area) are predicted to experience seepage, for the mean infiltration case and present-day climate conditions (BSC 2003 [DIRS 165564], Table 6.8-1). In addition, the seepage abstraction results in an average of 1.7 L/yr per waste package, or about 20 L/yr per waste package with a seep. Percolation flux is greater in some parts of the site area (BSC 2003 [DIRS 163045], Section 6.6, Figure 6.6-6) and is above average in the host rock under Yucca Crest that is traversed by the ECRB Cross-Drift. Accordingly, the seepage abstraction model predicts at least an 8 percent likelihood that seepage will occur (at rates of about 20 L/yr) in any 5.1-m long drift interval, through several hundred meters of the cross-drift. Similar statements were made in the test

planning for the ECRB Cross-Drift passive monitoring test (BSC 2001 [DIRS 158187], Section 6.1). These results are consistent with the possibility that the source of liquid water in the ECRB is seepage. However, it is probable that these observations are the result of condensation from the humid air in the drift. This humid air was primarily derived from moisture in the form of water vapor coming into the drift following the cessation of ventilation. Although not explicitly quantified in the seepage model (which assumes 100 percent relative humidity at the drift wall), this moisture flux is generally a small fraction of the seepage amount for relative humidities approaching 100 percent (BSC 2003 [DIRS 162267], Figure 33).

5.4.3 Thermal-Mechanical Near-Field Processes

The stress field in the repository near-field environment (i.e., the rock surrounding the waste emplacement drifts) will be altered by excavation effects and thermal stresses from the heat generated by radioactive decay. The thermal stress will produce changes in rock characteristics that affect flow in fractures and drift opening stability.

The Large Block Test, the SHT, and the DST have investigated coupled thermal-mechanical and thermal-mechanical-hydrologic processes in fractured tuff under conditions that approximate those of an actual repository. In addition, a number of laboratory tests have been conducted on samples ranging from a few millimeters to 0.5 m in scale. The laboratory tests have provided essential data on rock properties and insight into the coupled thermal-mechanical-hydrologic behavior of the rock under well-controlled conditions.

This section describes the thermal-mechanical properties and coupled thermal-mechanical-hydrologic behavior of the Topopah Spring Tuff, which forms the current repository horizon at Yucca Mountain.

5.4.3.1 Ambient Site Geomechanical Characteristics

A detailed geologic description of the rock and associated geologic units is given in Section 3.3. The current repository horizon is located at a depth of about 300 m (984 ft) in the TSw2 unit of the Topopah Spring Tuff consisting of, in order of proportion, the lower lithophysal (Tptpll or tsw35), the middle nonlithophysal (Tptpmn, tsw34), the upper lithophysal (Ttptul or tsw33), and the lower nonlithophysal (Tptpln or tsw36) units (BSC 2003 [DIRS 165572]).

In Situ Stress–Magnitudes and orientations for the principal in situ stresses at the current repository horizon have been determined from measurements in drill holes USW G-1, USW G-2, and USW G-3 (Stock et al. 1985 [DIRS 101027], p. 8697). The maximum principal stress at the current repository horizon is vertical and has been estimated at 7.0 MPa, on average. Horizontal stresses are low. The ratios of minimum and maximum horizontal stresses to vertical stress and their bearings are given in CRWMS M&O (2000 [DIRS 151945], Table 11.3-1). The maximum horizontal stress is oriented in a northeasterly direction. In situ stresses at Yucca Mountain are also discussed in Section 3.7.5.

Hydraulic fracturing tests were conducted in the TSw2 unit at a depth of approximately 250 m (820 ft) as part of the DST block characterization (Lee and Haimson 1999 [DIRS 129667], p. 749). The tests yielded principal horizontal stresses of 2.9 ± 0.4 MPa oriented N15°E ± 14°

(maximum horizontal stress) and 1.7 ±0.1 MPa oriented N75°W ± 14° (minimum horizontal stress). The vertical stress at this level was calculated to be 4.7 MPa.

Rock-Mass Strength–Rock-mass strength is discussed in Section 3.7.4.

5.4.3.2 Thermal Properties

Thermal Conductivity–The thermal properties of tuff samples from Yucca Mountain have been the subject of several laboratory studies, which are reviewed in BSC (2002 [DIRS 160319], Section 4.1.3 and Attachment III). In addition, two recent tests also provided in situ bulk thermal conductivity values (BSC 2002 [DIRS 160319], Section 4.1.4). Thermal conductivity was found to depend strongly on water saturation and weakly on temperature. For thermal-mechanical unit TSw2, thermal conductivity measurements were performed on wet samples at low temperatures (25° to 70°C) and on dry samples at temperatures between 110° and 290°C (Brodsky et al. 1997 [DIRS 100653]). Additionally, wet and dry thermal conductivity measurements were made on 6 samples from Alcove 5 in the Tptpmn unit (BSC 2002 [DIRS 160319], Attachment III). Modeling analyses of these data gave average thermal conductivities for the repository host-rock units Tptpul, Tptpmn, Tptpll, and Tptpln (BSC 2002 [DIRS 160319], Table 7-10). Similar analyses yielded thermal conductivity values for non-repository lithostratigraphic layers (BSC 2003 [DIRS 166242], Table 6-13).

A comparison of observed and predicted temperatures for the SHT suggests that the laboratory thermal conductivities form effective upper and lower bounds for in situ thermal conductivities. The laboratory thermal conductivity values, $C_{dry} = 1.67$ W/mK and $C_{wet} = 2.0$ W/mK, were used in numerical simulations of the SHT to provide interpolated estimates of rock-mass thermal conductivity as a function of saturation (CRWMS M&O 1999 [DIRS 129261], Table 8-11). Results showed very good agreement between predicted and observed temperatures in the SHT (CRWMS M&O 1999 [DIRS 129261], Section 8.7.3).

Thermal Expansion–Laboratory measurements of linear thermal expansion have been made on many tuff samples from Yucca Mountain. These measurements are discussed at length in CRWMS M&O (2000 [DIRS 151945], Section 4.7.4.2.2) and the data are archived in the Yucca Mountain Project Reference Information Base. Thermal expansion coefficients for TSw2 tuff show moderate temperature dependence below 100°C and stronger temperature dependence above 100°C. The increase in thermal expansivity with temperature is partly attributed to microcracks, induced largely along grain boundaries by differences in constituent mineral thermal expansion properties, and near 200°C, to phase changes in tridymite and cristobalite. In contrast to temperature, confining pressure has little effect on the coefficient of thermal expansion (Martin et al. 1996 [DIRS 100057]). Brodsky et al. (1997 [DIRS 100653], Tables 4-4 and 4-5) provides the linear coefficient of thermal expansion for TSw2 tuff over a range of temperatures at atmospheric pressure.

Field measurements of thermal expansion indicate that the laboratory values discussed above may be too high to describe rock-mass expansion in situ. Results of the SHT indicate that the coefficient of thermal expansion for the rock mass heated in this test is as much as 50 percent lower than that measured for laboratory samples (CRWMS M&O 1999 [DIRS 129261], pp. 12-1 and 9-11). The reduction in the coefficient of thermal expansion at the field scale is likely due to

the closure of fractures, which would thereby accommodate a portion of the thermal expansion. Lower thermal expansion values will reduce stress estimates for the rock surrounding the emplacement drifts.

5.4.3.3 Mechanical Properties

Deformation Modulus and Rock Strength–Many laboratory measurements have been made to determine the mechanical properties of intact samples from the repository host rock units (see Section 3.7). These data indicate that the intact nonlithophysal rock is strong, with a uniaxial compressive strength of 168 MPa (BSC 2003 [DIRS 166346], Table V-11) and a Young's modulus of approximately 33 GPa (BSC 2003 [DIRS 166346], Table V-5). Uncracked samples have stress-strain curves that show nearly linearly elastic behavior until failure (CRWMS M&O 1997 [DIRS 103564]). Samples with cracks exhibit nonlinear stress-strain behavior, as expected when stress is above 50 percent of the failure stress. Stress-strain curves for 50.8-mm (2 in.) diameter saturated samples tested under drained conditions are presented by Price (1986 [DIRS 106589], Figure 5). Most of the tests for compressive strength were conducted on samples that were saturated with water and tested under drained conditions. This represents a minimum value for the rock matrix, as rocks are generally weaker when saturated with water. Rock compressive strength typically decreases with increase of temperature. Price et al. (1987 [DIRS 100173]) report that, for samples from the current repository horizon, Young's modulus and the mean ultimate strength both decreased by an average of 16 percent as temperature is raised from 22° to 150°C. This result was based on tests conducted at both 0 and 5 MPa confining pressures.

Larger rock specimens almost invariably contain more heterogeneities than smaller core samples tested in most laboratory work; hence, compressive strengths tend to be lower when larger specimens are tested. This scale effect has been well documented for intact Topopah Spring Tuff specimens by Price (1986 [DIRS 106589]), who found both uniaxial compressive strength and axial strain at failure to be inversely related to specimen diameter. Specimen diameters exceeding 250 mm (10 in.) are apparently required to avoid such size effects, even for intact samples. Young's modulus and Poisson's ratio, on the other hand, were found by Price (1986 [DIRS 106589]) to be largely independent of specimen diameter. Uniaxial compressive tests performed on a 0.5-m (1.6 ft) scale block of Topopah Spring Tuff by Blair and Berge (1997 [DIRS 101369], Section 4.2) obtained an overall Young's modulus of about 3 GPa at axial stresses below 4 MPa, which increased to 6 GPa above 4 MPa. Young's moduli measured across individual fractures were generally below 1 GPa. In portions of the block lacking visible vugs or fractures, Young's modulus varied between 7 and 31 GPa.

Discernible mechanical anisotropy is correlated with the ash-flow fabric. Similar blocks were loaded perpendicular to the rock fabric by Blair and Berge (1997 [DIRS 101369], p. 24) and parallel to the rock fabric by Costantino et al. (1998 [DIRS 152436], p. 2-21). Costantino et al. (1998 [DIRS 152436], p. 2-17) found a Young's modulus of 40 GPa for axial stresses of 4 to 8 MPa, about twice that found by Blair and Berge (1997 [DIRS 101369], Section 4.2) for the perpendicular loading for intact portions of their block. The anisotropy in Young's modulus is a minimum of 25 percent and can be much greater when vuggy zones exist.

Field tests of rock deformation modulus have shown a wide range of values. A plate-loading test conducted in association with the DST indicated a modulus of 30 GPa on one side of the alcove and 11 GPa on the other side. Goodman jack tests in the same vicinity produced much lower moduli, in the range of 3 to 6 GPa, whereas estimates of modulus based on rock-mass quality were in the range of 15 to 34 GPa (CRWMS M&O 1998 [DIRS 108306], pp. 6-18 and 6-27).

A series of laboratory and field experiments have been conducted on small diameter 1-in. to 2-in (25-mm to 50-mm) cores of lithophysal rocks to provide basic elastic and strength data, including: (1) Uniaxial compression and Brazilian tensile strength tests on 2-in. (50-mm) cores from north ramp geotechnical boreholes; (2) Uniaxial compression tests on 10.5-in (413-mm) diameter core samples of Tptpul from Busted Butte; (3) Uniaxial compression tests on 11.5-in diameter core samples from the Tptpul and Tptpll drilled from exposures in the ESF main loop and ECRB Cross-Drift; and (4) In situ slot uniaxial compression tests on 1 m rock samples of the Tptpul and Tptpll conducted in the walls and floor in the ESF main loop and ECRB Cross-Drift (BSC 2003 [DIRS 166346], Section 7.4.1). The small diameter cores do not accurately reflect the true strength or elastic properties of the lithophysal rock; therefore, reliance is placed on measurements from large samples that contain multiple lithophysal cavities in a given sample. The results of compression testing on samples from the Tptpul and Tptpll from the ESF main loop and ECRB Cross-Drift and from the Tptpul at Busted Butte are provided in (BSC 2003 [DIRS 166346], Table V-8). The mean ultimate strength value for these tests is 17.8 MPa. The mean Young's modulus is 10.1 GPa (BSC 2003 [DIRS 166346], Section 7.4.1).

5.4.3.4 Time-Dependent Properties

Martin et al. (1995 [DIRS 100159]) investigated creep (i.e., time-dependent strain developing with constant stress) in laboratory samples of Topopah Spring Tuff at ambient and elevated temperatures. The observed creep deformation was consistent with a time-dependent crack growth mechanism, particularly at stresses above 90 percent of the rock's uniaxial compressive strength. The stress necessary to produce failure appeared to decrease with increasing temperature, but the data were not sufficient to quantify that effect. Temperature did cause a reduction in strength (Martin et al. 1995 [DIRS 100159], pp. 18 to 20). Blair and Berge (1997 [DIRS 101369], p. 26) found that imposing low levels of compressive stress for periods of a few days on 0.5-m (1.6 ft) scale blocks of Topopah Spring Tuff caused time-dependent, inelastic crack closure.

Subcritical crack growth is of concern because the slow formation, growth, and coalescence of microcracks over long time periods would contribute to excavation damage and thereby alter rock physical, hydrologic, and geochemical properties in the near-field environment. Time-dependent rock mass strength data from static-fatigue tests for Lac du Bonnet granite (Schmidtke and Lajtai 1985 [DIRS 164774]; Lau et al. 2000 [DIRS 164769]) and Yucca Mountain nonlithophysal tuff (Martin et al. 1997 [DIRS 165960]) were used in BSC (2003 [DIRS 166346], Attachment XIX) to predict the evolution of the drift profile. The PFC stress corrosion model (Potyondy 2003 [DIRS 165550]) was used to assess the influence of confinement and lithophysal void porosity on the static-fatigue curves of lithophysal rock, and to generate curves of damage increase as a function of time for static-fatigue tests performed at different load levels. These curves were then used in prediction of time-dependent damage and rockfall. The analyses of the available static-fatigue test data for Yucca Mountain indicate that

an approximate 40 percent reduction in cohesive strength occurs over a 20,000-yr period. The nominal case for drift degradation (i.e., considering thermal and time-dependent effects, but excluding seismic effects) results in only partial collapse of the drift at 20,000 yr (BSC 2003 [DIRS 166346], Attachment XIX).

5.4.3.5 Thermal-Mechanical Effects on Fracture Flow

As normal stresses increase, fracture apertures close and fluid flow is reduced. Thus, as the general level of compressive stress in the repository rises with heating, the apertures of many fractures may be reduced, lowering permeability. Thermal-mechanical effects are more complicated though, in that heating may also increase shear stresses on favorably oriented fractures and cause shear displacements. Olsson and Brown (1994 [DIRS 100169], pp. 5 to 6) and others have shown that shear displacements along fractures tend to increase fracture apertures and thus increase permeability.

Field measurements from heater tests at G-Tunnel, located in the northeast portion of the Nevada Test Site, indicated that rock-mass permeability increased during heating and did not return to initial levels upon cooldown, indicating that a mechanism other than normal closure of fractures dominated fracture flow behavior (Lee and Ueng 1991 [DIRS 129664], p. 6). More recently, Barton et al. (1997 [DIRS 100004]) have presented evidence that hydraulically conductive fractures in the Dixie Valley geothermal field are critically stressed, potentially active normal faults. The implication is that slip on critically stressed fractures can increase permeability. The work of Barton et al. (1997 [DIRS 100004]) provides a means to predict which fractures are likely to become more hydraulically conductive.

Fracture flow and uniaxial compression tests were conducted on a heated 0.3 by 0.3 by 0.6 m (1 by 1 by 2 ft) block of Topopah Spring Tuff containing an artificial, horizontal fracture (Costantino et al. 1998 [DIRS 152436], p. 2-21). Fracture surface profiles, performed before the flow tests, indicated a large number of millimeter-sized channels were aligned with the ash-flow fabric. Flow tests showed low imbibition of water through the fracture surfaces and little storage of water in connected porosity. These results are consistent with a similar finding from the SHT, which indicates that fracture flow dominates fluid movement upon initial heating, with limited communication between fractures and the matrix (CRWMS M&O 1999 [DIRS 129261]). The tests also showed fluid movement in the fracture plane to be anisotropic, with more flow parallel to the rock fabric, and to be independent of normal stress to 8 MPa. These results suggest that flow was primarily through channels that remained open and connected over a fairly wide range of applied stress. Hence, fractures having uncorrelated surfaces can be very conductive and very stiff at the same time. These results indicate that fracture permeability may not decrease significantly as compressive stresses rise in the host rock with heating.

5.4.3.6 Field Observations of Thermal-Mechanical Effects

Efforts to understand and characterize coupled processes in a fractured rock mass at Yucca Mountain include the SHT, the Large Block Test, and the DST.

Single Heater Test–A primary objective of the SHT was to study the in situ thermal-mechanical behavior of densely welded, nonlithophysal Topopah Spring Tuff. A single 5-m (16 ft) long,

linear heat source supplied heat to a pillar at the ESF over approximately 9 months. Temperature, water saturation, mechanical deformation, and other rock responses were monitored during the heating phase and for an additional nine months during cooldown. Rock displacements were measured with multiple point borehole extensometers in three boreholes parallel to and a single borehole perpendicular to the heater. Further experimental details of the extensometer system are given in CRWMS M&O (1999 [DIRS 129261], Section 9.1). Plan and cross-sectional views of the SHT geometry are shown on Figures 5-83 and 5-84.

The thermal-mechanical data obtained during the SHT include estimates of rock mass thermal expansion, rock mass modulus, and rock bolt loading. The thermal expansion coefficient of the SHT rock mass below 200°C was as much as 50 percent lower than that given by laboratory measurements on small core samples. The lower in situ value is attributed in part to open fractures that accommodate a large portion of the thermal expansion in the field.

The rock modulus was measured using a Goodman jack in a single horizontal borehole emplaced perpendicular to the heater, 5.5 m from the west face of the SHT block (Figures 5-83 and 5-84). Additional details are given in CRWMS M&O (1999 [DIRS 129261], Section 9.2). The measured modulus values range from 3.7 to 23 GPa, with most values below 10 GPa (CRWMS M&O 1999 [DIRS 129261], Table 9-6). The highest value was obtained at 6.2 m (20 ft) near the heater and may be a result of fracture closure during heating. The modulus values are considerably lower than intact moduli obtained from laboratory tests on small core samples of Topopah Spring Tuff, as expected, because small core samples typically exclude visible fractures. No information is available on rock modulus anisotropy because the tests were limited to a single borehole.

The objective of the rockbolt load tests (Figures 5-83 and 5-84) was to evaluate the effect of elevated temperature on the long-term performance of this type of rock anchorage. Loads were found to decrease over time in all rockbolt load cells, with larger losses of load occurring for the rockbolts on the heated side of the test alcove, particularly for the two rockbolts nearest the heater (CRWMS M&O 1999 [DIRS 129261], Table 9-8). The loss of load may have resulted from the greater thermal expansion of carbon steel than tuff or may be due to creep of the rockbolt anchorage. The rockbolt load tests are discussed in CRWMS M&O (1999 [DIRS 129261], Section 9.3).

Large Block Test–The objective of the Large Block Test was to create a planar, horizontal boiling zone in a fractured rock mass to observe coupled thermal-hydrologic-mechanical-chemical behavior (Lin et al. 2001 [DIRS 159069]). Specific aims of the Large Block Test were to study the dominant heat-transfer mechanism, condensate refluxing, rewetting of the dryout zone following the cooldown of the block, displacement of fractures, and rock-water interactions. One particular goal was to assess how episodes of normal and shear fracture displacements relate to changes in the TH behavior of the rock mass.

The Large Block was exposed from an outcrop of nonlithophysal Topopah Spring Tuff at Fran Ridge by excavating the surrounding rock, leaving a rectangular prism 3 m × 3 m in cross section and 4.5 m (14.7 ft) high (Figure 5-85; Blair and Lin 1997 [DIRS 150392], p. 2). Two subvertical sets of fractures and one set of subhorizontal fractures intersect the block. The subvertical fracture sets are approximately orthogonal, with a spacing of 0.25 to 1 m (1 to 3 ft) and are

oriented generally in the northeast-southwest and northwest-southeast directions. A major subhorizontal fracture is located approximately 0.5 m (2 ft) below the top surface (Figure 5-85). Heaters were placed in five horizontal boreholes 1.75 m (6 ft) above the base of the block. A steel plate fitted with heating/cooling coils was mounted on top of the block to provide temperature control for the top surface. The vertical sides of the block were insulated. The geomechanical response of the rock to heating was monitored using multiple-point borehole extensometers and surface-mounted fracture gauges.

Heating started on February 27, 1997 and ended on March 10, 1998. Temperatures near the center of the heater plane (Figure 5-86) increased from ambient to 90°C in the first few hundred hours of heating. The overall temperature history is consistent with conduction-dominated heat flow in the block, except for the temperature excursions when opening and sliding of fractures were also observed that appeared to be associated with episodes of increased water infiltration.

Thermal expansion of the block began a few hours after the heating started, and horizontal expansion was consistent with the opening of vertical fractures. The overall horizontal deformation of the block revealed similar amounts of expansion in both the east-west and north-south directions.

Fractures generally opened during the test. Aperture changes reveal that several of the fractures opened more than 0.1 mm (0.004 in.), and partial closure of only a few fractures was observed (Figure 5-87). Shear displacements both parallel and perpendicular to the faces are both fewer and smaller than normal displacements across the fractures (Blair and Lin 1997 [DIRS 150392], Figure 6).

Drift Scale Test–The cooldown phase of the DST is now under way in Alcove 5 of the ESF. The principal objective of the DST is to study coupled thermal-hydrologic-mechnical chemical-l processes at the repository horizon in the middle nonlithophysal unit of the Topopah Spring Tuff (BSC 2002 [DIRS 160771]). The test geometry includes a heated drift, an access/observation drift, and a short connecting drift (Figure 5-88). The heated drift is horizontal, oriented approximately east-west, and has a diameter of 5 m. It consists of an 11-m long entry, which includes a plate-loading niche, and a 47.5-m long test drift. The pillar between the heated drift and the access/observation drift is approximately 30 m thick. The surrounding rock mass is heated by nine electrical resistance heater canisters in the heated drift and 50 wing heaters in horizontal boreholes, 25 on either side of the heated drift (Figure 5-89). Drift-wall temperatures were maintained at 200°C during the heating phase of the test. Thermal-mechanical measurements and results of the heating phase of the DST relevant to the analysis of thermal-mechanical effects are described in Section 5.4.5.3.

5.4.3.7   Mechanical Loading Conditions on Waste Packages

Several underground mechanisms have been identified that could lead to mechanical loading on the waste packages or drip shields. These mechanisms include:

- **Creep**–convergence of drift walls.
- **Block Failures**–the most credible loading scenario.
- **Seismic Loading Fault Displacements**–rock burst failures are unlikely.

- **Hydrostatic Loading**–implausible because the rock is unsaturated.

The types of loading that would result from these failures will be different, as discussed below.

Creep–If sufficient long-term strength degradation of the rock mass takes place to collapse the openings around the waste packages entirely, then the full lithostatic load might be imposed. In this case, rock displacements will not be uniform because of the rock structure and the anisotropy of the stress field. The analyses of the available static-fatigue test data for Yucca Mountain indicate that an approximate 40 percent reduction in cohesive strength occurs over a 20,000-yr period. The nominal case for drift degradation (i.e., considering thermal and time-dependent effects, but excluding seismic effects) results in only partial collapse of the drift at 20,000 years (BSC 2003 [DIRS 166346], Attachment XIX). There is no indication that full lithostatic loading is likely to be imposed. Natural openings in other rock types have remained open over long periods (e.g., limestone caves and lava tubes), and evidence from these suggests that drifts would remain open at Yucca Mountain over the 10,000 year regulatory time frame (BSC 2002 [DIRS 160405], Section 3.1).

Block Failures–The size of blocks that could fall into drift openings depends on the fracture spacing and the opening dimensions that result after ground support failure. Four fracture sets were identified for the ESF main drift by Albin et al. (1997 [DIRS 101367], pp. 33 to 39) based on orientation. Two fracture sets are steeply dipping, a third set dips about 30°, and the fourth set has an intermediate dip. Given the orientation of one fracture set (about 18° to the drift orientation), tabular blocks up to 16-m-long could theoretically fall within the drift. However, a more realistic value estimated from the average spacing for the three prominent fracture sets indicates that if a block fell into the drift, it could range in mass from 20,000 to 360,000 kg. It is less likely that a single block 45 m (150 ft) high would fail; therefore, the 360,000 kg block represents a conservative upper limit.

A statistical description of the probable block sizes formed by fractures around the emplacement drifts has been developed for the middle non-lithophysal unit (Tptpmn) of the repository host horizon (BSC 2003 [DIRS 166346], Attachment IV). The static condition (i.e., upon excavation) and the effect of seismic events on rockfall were also analyzed. Block size distributions and drift profiles were determined for two seismic levels, including a 1,000 year event and a 10,000 year event. This analysis involved the use of a distinct element code and probabilistic key block theory through numerical code. In general, the static key block results presented are representative of the observed key block occurrence in the ESF (i.e., the Tptpmn [middle non-lithophysal] unit). The key block analysis was based primarily on results of laboratory and field experiments conducted on small diameter cores from the Tptpmn unit (BSC 2003 [DIRS 166346]).

The analysis (BSC 2003 [DIRS 166346], Attachment IV) concluded that the available fracture data were suitable for supporting a detailed key block analysis of the repository host horizon rock mass. The seismic effect on the rockfall size distribution for all events analyzed would be relatively minor. Time-dependent and thermal effects also showed minor impact on rockfall.

The results of the key block study (BSC 2003 [DIRS 166346], Attachment IV) show that key blocks are most predominant in the Tptpmn unit, which agrees with field observations. The size

of key blocks observed in the field is generally less than 1 m^3 (35 ft^3), which agrees with the simulated distribution of block sizes presented in the analysis.

Based on additional data from in situ slot uniaxial compression tests conducted in the lower lithophysal unit, more recent analyses of drift degradation with improved numerical models of nonlithophysal rockfall and of lithophysal rockfall show primarily minor drift damages to structure-controlled rockfall in the nonlithophysal tuff with some likelihood for severe spalling (BSC 2003 [DIRS 166346]). This is consistent with the previous results obtained with the Discrete Region Key Block Analysis approach. For the lithophysal tuff, however, the new analyses show that drift degradation is primarily controlled by stress conditions, and that postclosure ground motion could result in complete collapse of the drift, with fragmented rock particle sizes on the order of centimeters to decimeters. Thermal and time-dependent effects will result in localized to significant areas of rock failure, depending on the selection of the degree of strength loss of the rock mass with time. The analyses of the available static-fatigue test data indicate that an approximate 40 percent reduction in cohesive strength occurs over a 20,000 year period. The nominal case for drift degradation (i.e., considering thermal and time-dependent effects, but excluding seismic effects) results in only partial collapse of the drift at 20,000 years. Additional work is under way to better understand the time-dependence of drift degradation.

Seismic Loading/Fault Displacements–Description of the assessment of seismic loading and fault displacements can be found in Section 4.3.4.

Hydrostatic Loading–No hydrostatic loading is anticipated because the repository horizon is unsaturated. Any water that might be introduced inadvertently into the system may drain away before any appreciable head can develop.

5.4.3.8 Radiation Effects of Waste Emplacement on Geomechanical Properties

The effect of radiation on the geomechanical properties of the host rock, though uncertain, is likely to be limited. The radiation field is expected to affect only rock exposed on the surface of excavated drifts and to penetrate only a few centimeters into the rock. The waste package itself will form a radiation barrier. Moreover, radiation is expected to have a negligible effect on rock mechanical properties based on the work of Durham et al. (1986 [DIRS 129649], p. 168) who conducted a series of unconfined compression tests on intact cylindrical specimens of Climax quartz monzonite and Westerly granite. The tests showed no statistically significant difference in unconfined compressive strength, Young's modulus, or Poisson's ratio between the two groups of irradiated and nonirradiated specimens. Durham et al. (1986 [DIRS 129649], p. 168) concluded that gamma irradiation has no measurable effect on the mechanical properties of either rock type.

A similar series of uniaxial compression tests was performed by Blair et al. (1996 [DIRS 129637]) on 44 specimens of Topopah Spring Tuff collected from a surface outcrop at Fran Ridge, part of the welded lithophysae-poor layer that overlies the current repository horizon. The specimens were divided into two matched groups based on the presence of small cracks and infilled vugs, then half of each group were exposed to a 9.5-MegaGray dose of gamma radiation over a 47-day period. The radiation dose was found to have no discernible effect on the unconfined compressive (peak) strength or Young's modulus of the homogeneous,

uncracked specimens. However, specimens that contained partially healed, preexisting vertical or subvertical cracks may have suffered some degradation of mechanical strength and Young's modulus, suggesting that exposure to radiation may have weakened the largely carbonate cementing material in the cracks. The cementing material is thought to be largely composed of carbonates, and the authors discussed two possible mechanisms that could weaken the cementing material when it is exposed to radiation: (1) degradation of the carbonate cement by nitric acid formed by irradiation of moist air in the pore space of the rock; and (2) alteration of hydrated minerals in the cement through radiolysis of the waters of crystallization (Blair et al. 1996 [DIRS 129637], p. 13).

5.4.3.9 Natural Analogs for THM Effects

The impact of thermal-hydrologic-mechanical (THM) processes (such as excavation and heating) on the performance of repository host rocks has been assessed through field studies at a variety of underground sites (BSC 2003 [DIRS 164890], Section 7.8). These studies indicate that the effects of excavation on rock stability tend to be highly site-specific, depending on rock physical properties, the presence and orientation of faults and fractures, and the local stress regime. Excavation often leads to localized increases in permeability. Heating generally results in an increase in stress and a reduction in permeability. The results of THM experiments conducted at the Nevada Test Site and the Stripa underground laboratory in Sweden are summarized in the following subsection.

5.4.3.9.1 Nevada Test Site Thermal-Hydrological-Mechanical Experiments

Four thermal-mechanical (TM)/THM experiments relating to high-level nuclear waste research were conducted at the G-tunnel in Rainier Mesa. These tests included a single borehole heater test, a small-diameter heater test, a heated block test, and a prototype engineered-barrier-system field test. One objective of the heated block test was to measure rock-mass mechanical and TM properties of welded ash-flow tuff under controlled thermal- and stress-loading conditions. The block was subjected to maximum temperatures ranging from 76° to 130°C and equal biaxial stresses with magnitudes up to 10.6 MPa (Zimmerman et al. 1986 [DIRS 145625]). The effective modulus of deformation ranged from 0.4 to 0.83 times the intact rock measurements, depending on the number of joints included and their apertures. A slight dependence of modulus on stress was indicated, but no significant temperature effects on modulus were identified.

A second objective of the heated block test was to determine the effects of excavation, stress, and temperature changes on the permeability of a single joint. The permeability of a single near-vertical fracture was measured using three vertical boreholes in a linear array. The largest changes in permeability were associated with excavation of the block, when the apparent permeability increased from 76 to 758 microdarcies. Subsequent compressive loading decreased the permeability but did not completely reverse the unloading conditions, and the apparent permeability ranged from 252 to 332 microdarcies over a stress range of 3.1 to 10.6 MPa (Hardin and Chesnut 1997 [DIRS 100534], p. 4-6). Increased temperature under biaxial confinement decreased the fracture aperture, lowering the apparent permeability from 234 to 89 microdarcies during heating caused by rock thermal expansion. These observations are consistent (i.e., of the same order of magnitude) with the Yucca Mountain THM modeling and field studies described in BSC (2003 [DIRS 164890]). That is, fracture permeability increases about one order of

magnitude as a result of unloading during excavation and decreases by less than one order of magnitude during heating.

5.4.3.9.2 Underground Testing at Stripa

A time-scaled heater test was performed at Stripa to investigate the long-term TM response to thermal loading (Chan et al. 1980 [DIRS 154672]). Analysis showed that, in the full-scale and time-scale heater tests, heat flow conformed to linear conduction theory and was not affected by fractures or other discontinuities. Thermal-elastic deformation of the rock mass was nonlinear and less than expected. Early in the tests, measured displacements were much less than predicted by linear thermal-elasticity. Later, the displacements increased uniformly, but in fixed proportions to predicted levels. This was likely a result of the closing of fractures in response to thermal expansion. Fracture closure was confirmed by observation of diminished water inflow to the heater and instrument boreholes (Nelson et al. 1981 [DIRS 150092], p. xi) and by increased compressional wave velocity during heating (Paulsson et al. 1980 [DIRS 154570], p. 4). The closing of fractures (and resulting changes in fracture permeability due to thermal input) is consistent with the results of the Yucca Mountain studies described in BSC (2003 [DIRS 164890]).

5.4.3.9.3 DECOVALEX Findings at Fanay-Augeré and Kamaishi Mine Heater Tests

The results in BSC (2003 [DIRS 164890]) can also be compared to findings in the international cooperative project DECOVALEX (DEvelopment of COupled Models and their VALidation against EXperiments in nuclear waste isolation). Model validation against in situ tests such as Fanay-Augeré (Rejeb 1996 [DIRS 162589]) and Kamaishi Mine (Rutqvist et al. 2001 [DIRS 162586]) demonstrates that the temperature field can be predicted with confidence because it is mainly governed by heat conduction through rock masses, with little influence from discrete fractures. Rock-mass deformation measured along extensometers between anchors placed several meters apart can also be predicted reasonably well in trends and magnitudes. This is because the bulk thermal expansion of the rock is dominated by the thermal expansion of the matrix rock, while fractures have a secondary effect that appears as a reduction of the rock-mass thermal expansion coefficient. It can also be concluded from these two heater tests that the general thermal expansion of the rock mass is essentially elastic for measurements conducted over several meters of fractured rock. However, although the bulk thermal expansion of the rock mass is essentially elastic and reversible, the displacement and aperture changes measured over individual fractures are generally irreversible. That is, there is a remaining change in fracture aperture after the rock mass has cooled down to ambient conditions. Furthermore, it is generally much more difficult to predict the responses of individual fractures than to predict the overall rock-mass thermal expansion. This might be important for predicting changes in hydraulic permeability, which critically depend on the aperture changes of fractures.

5.4.3.9.4 Geothermal Reservoir Temperature-Permeability Correlation

In addition to field studies of coupled THM processes that provide direct evidence of how a repository at Yucca Mountain would perform, corroborative results for coupled THM effects may be found in the geothermal literature. A survey of geothermal reservoir properties worldwide (Björnsson and Bodvarsson 1990 [DIRS 154606], pp. 19 to 21) showed a correlation

between permeability and temperature for various geothermal systems (BSC 2003 [DIRS 164890], Figure 7.8.4-1). The values are scattered, but they indicate a trend toward decreasing permeability with increasing temperatures. The low permeability at temperatures around 300°C and above is more likely caused by geochemical effects. THM effects may be present at lower temperatures.

5.4.3.9.5 Coupled THM Analyses of the Yucca Mountain Drift Scale Test within DECOVALEX III

The TM and THM responses of the Yucca Mountain DST are independently analyzed by the participants of the DECOVALEX III project, which is an international research project "to develop coupled models and their validation against experiments." The outcome of the analyses by the DECOVALEX participants, generally corroborative of the drift-scale THM model (BSC 2003 [DIRS 164890]), were presented in the GeoProc2003 conference held in Stockholm, Sweden, in October 2003 and will be published in a special issue of the *International Journal of Rock Mechanic*s.

5.4.4 Near-Field and In-Drift Geochemical Environments

5.4.4.1 Near-Field Geochemical Environment under Ambient Conditions

The repository host rock geologic environment under ambient conditions is described in Section 3.3.5. The host rock and near field geochemical environment under ambient conditions, including chemical compositions of percolation water, porewater, perched water, and gases is described in Section 5.2.2, with additional details provided in BSC (2003 [DIRS 162050], Section 6.2.2). In addition, results of various mineralogy studies can be found in Vaniman et al. (1996 [DIRS 105946]) and Peterman and Cloke (2002 [DIRS 162576]).

5.4.4.2 Near-Field Geochemical Environment under Thermally Perturbed Conditions

Geochemical processes in the thermally perturbed near field, which occurs following waste emplacement, will be affected by the heat transferred into the rock surrounding the emplacement drifts and the hydrologic regime associated with that heat. As shown in Figure 5-90, elevated temperatures couple (see yellow arrows) to mineralogy and rock properties by means of several geochemical processes. These processes include dehydration, rock-water interactions, and changes in the mass and chemistry of water that is available for geochemical reaction.

5.4.4.2.1 Thermally-Driven Processes Affecting Seepage Chemistry

Conceptually the present-day mineralogy and mineral distributions in the volcanic units at Yucca Mountain show the effects of thermally-driven post-depositional alteration processes that are expected to be similar to postclosure alteration processes. The repository host rock horizon, the Topopah Spring Tuff, has not been significantly altered by these processes (see Section 5.2), but through the study of other units at Yucca Mountain showing alteration, inferences can be made concerning the impact that heating and the resulting water movement will have on the host rock. The study of other natural analogs, outcome from field and laboratory tests, and computer simulations supported by existing data are combined to provide an understanding of the changes to the natural system from the repository.

Geochemical processes and their effects on rock properties will vary with distance from the repository. Generally, strong thermal gradients will exist in the near field (closer to the source of heat) and create a dynamic environment. Here, the predominant geochemical processes will be evaporation and boiling, mineral dissolution/precipitation and dehydration-hydration, and solid-vapor interactions. Beyond the boiling zone, thermally driven circulation of hot waters and gasses, and circulation of waters chemically modified by reactions near the repository, will create an alteration halo that may extend for some distance into the surrounding rock. The boiling front is the boundary between these two regions and will be dynamic, expanding outward during the initial heating stage and the collapsing inwards as the radioactivity and heat generated by the waste decrease with time. Thus, the geochemical effects of high temperatures in the near field may be overprinted by later sub-boiling reactions as the repository cools.

The geochemical evolution of the thermally perturbed Yucca Mountain will be intimately coupled with the thermal-hydrologic processes (boiling, condensation, and drainage) discussed in Section 5.4.2 and BSC (2003 [DIRS 162050], Section 6.2.1.2). The distribution of boiling and condensation zones in the fracture system will determine where mineral precipitation and dissolution can occur and where there can be direct interaction (via diffusion) between matrix pore waters and fracture waters. For the near-field environment, Figure 5-91 shows schematically the relationships between themohydrologic and geochemical processes in the zones of boiling, condensation, and drainage in the rock mass surrounding the drift.

The effects of TH processes on water chemistry depend on the intrinsic characteristics of the dissolved species and the types of chemical reactions in which they are involved. Conservative species (i.e., nonreactive and nonvolatile) such as chloride become concentrated in waters undergoing vaporization or boiling, but are essentially absent from the vapor condensing in the fractures. Therefore, the concentrations of conservative species in condensate waters are determined by the extent of mixing with background fracture waters and matrix pore waters. In addition, the concentrations of more reactive aqueous species such as calcium are affected by mineral dissolution or precipitation reactions and by exchange or alteration reactions involving zeolites, clays, or feldspars.

Mineral Solubilities–At the higher expected near-field environment temperatures, as long as cristobalite is still present, the concentration of dissolved silica will be closely controlled by equilibrium with this mineral. At lower temperatures (near ambient), the concentration of dissolved silica may be somewhat lower than cristobalite solubility and instead be a near steady-state value controlled by the dissolution rates of metastable silicate minerals and the growth rates of stable ones. Nevertheless, as the near-field environment goes through the initial heating stage, the concentration of dissolved silica will increase.

Calcite ($CaCO_3$) is the major mineral in the fractures throughout the repository block (Section 5.2.1.1). Calcite has retrograde solubility (it is less soluble at higher temperature), while most other minerals, such as silica, exhibit prograde solubility (they are more soluble at higher temperatures). This results in differences in the distribution of calcite and silica phases. Because of its retrograde solubility, additional calcite will be precipitated from aqueous solution in the near-field environment during the initial heating stage. Calcite also forms by carbonation (CO_2 addition) of concrete (Lichtner and Pabalan 1997 [DIRS 157740]; Steefel and Lichtner 1998 [DIRS 156714]). Although concrete was an important component in early

repository designs, the current design has significantly reduced the volume of this introduced material. The relevance of concrete in the repository is discussed in BSC (2003 [DIRS 165675]). Precipitation of amorphous silica or a similar phase tends to be confined to a narrow zone where evaporative concentration exceeds the solubility (BSC 2003 [DIRS 162050], Section 6.8.5.4). In contrast, calcite tends to precipitate in regions where elevated temperature has resulted in CO_2 exsolution, and tends to dissolve where there is lower pH. Alteration of feldspars to clays and zeolites tends to be most rapid in the boiling zone because of the increased solubility (as well as having higher dissolution and precipitation rates) at higher temperatures (Lasaga 1998 [DIRS 117091], p. 66).

Mineral Stability–Unaltered glass and metastable silica polymorphs in the Topopah Spring Tuff will have a prominent role in the mineral evolution that occurs in the thermally perturbed environment. The alteration of volcanic glass to an assemblage of secondary minerals will necessarily be accompanied by a volume change, which in turn will affect porosity. Quartz and the metastable silica polymorphs (cristobalite, tridymite, and opal-CT) are all found in the unsaturated zone at Yucca Mountain (Carlos et al. 1995 [DIRS 101326]). Cristobalite is the primary silica polymorph within the current repository horizon, and it is known to undergo a displacive phase transformation at about 250°C that is accompanied by a volume increase of a few percent.

The silica activity in pore fluids is a particularly important geochemical parameter with regard to repository performance. Repository performance can be affected in two ways: (1) the activity of silica in pore waters affects mineral stabilities, and (2) redistribution of silica depends on the silica activity. In the first case, mineral equilibria are affected through the stabilization and destabilization of mineral species. For example, clinoptilolite, mordenite, and smectite are stabilized by high silica activity, whereas analcime and illite are stabilized by low silica activity. In the second case, elevated silica concentrations in pore fluids potentially cause silica deposition, whereas lower values are likely to result in dissolution of metastable silica polymorphs.

A practical, conceptual model of Yucca Mountain mineral evolution under various thermal and hydrologic conditions may be developed with the integrated use of natural analogs and available thermodynamic and kinetic studies, as described (BSC 2002 [DIRS 160405], Section 11.2). Based on natural analogs and theoretical studies, four potential mineralogical reactions are recognized which may be accelerated at Yucca Mountain by a thermal pulse from radioactive waste. The possible reactions include:

- Volcanic glass → clinoptilolite ± smectite ± opal-CT
- Tridymite, cristobalite, opal-CT → quartz
- Clinoptilolite, mordenite → analcime + quartz ± calcite
- Smectite → illite.

In predicting mineral evolution at Yucca Mountain, evidence of past alteration in the Tpt unit serves as a model for the geochemical and hydrologic conditions of interest. Thus, in considering natural analogs to compare with the evolving potential repository environment, Yucca Mountain itself may serve as one of the useful analogs. The reported diagenetic alteration observed there today includes the formation of zeolites, opal-CT, smectite, the smectite-to-illite

transition, and the loss of volcanic glass and metastable silica polymorphs (Carlos et al. 1995 [DIRS 101326]). For example, vitric tuffs containing unaltered volcanic glass are found with minor smectite, opal-CT, heulandite, and calcium-rich clinoptilolite. Glass loss is associated with the formation of significant amounts of clinoptilolite and mordenite. Another alteration reaction is the disappearance of metastable silica polymorphs at depths generally corresponding to the appearance of secondary quartz (presumably through dissolution-precipitation) and the appearance of analcime. The transformation of silica polymorphs is the rate-limiting step in the reaction of the sorptive zeolites clinoptilolite and mordenite to analcime-bearing assemblages (Carlos et al. 1995 [DIRS 101326]). Furthermore, tridymite is not observed below the water table and is presumed lost to dissolution.

Under all likely repository conditions, cristobalite and opal-CT are unstable with respect to quartz. The rate of reaction to quartz, however, is expected to be negligible in the unsaturated zone. Observations of mineral distribution under ambient Yucca Mountain conditions support slow reaction kinetics; that is, tridymite, glass, cristobalite, opal-CT, clinoptilolite, and mordenite have survived (some 10 m.y.) (Carlos et al. 1995 [DIRS 101326]). Reactions rates for saturated conditions may be bounded by applying dissolution-precipitation rate data from Renders et al. (1995 [DIRS 107088]) for an upper bound and the rate data of Ernst and Calvert (1969 [DIRS 105535]) for a lower bound. Alternatively, the Yucca Mountain self-analog studies may be used to infer a value of 100°C as the temperature by which all cristobalite and opal-CT are reacted to quartz under saturated conditions. Thus, under saturated conditions and the present-day geothermal gradient, the metastable phases may persist for times on the order of 10 m.y.; for temperatures greater than 100°C, times of 1 m.y. or less are expected (Carlos et al. 1995 [DIRS 101326]).

Zeolites and smectites are important reaction products from volcanic glass at Yucca Mountain. The sorptive zeolites, clinoptilolite and mordenite, have been studied in natural analogs, including Yucca Mountain and the Yellowstone caldera. For unsaturated conditions, these zeolites are expected to have a negligible tendency to break down. For saturated conditions, and in the presence of cristobalite and opal-CT, these minerals may be stable to at least a temperature of 100°C. Thus, the current conceptual model has clinoptilolite and mordenite stable in the presence of cristobalite and opal-CT, but following the loss of the metastable silica polymorphs, these zeolites are expected to break down at temperatures exceeding 90°C. In addition, the stability of the sorptive zeolites may also depend on pH, so that under conditions of substantially lower pH than present-day Yucca Mountain, the reaction may proceed at even lower temperatures (Carlos et al. (1995 [DIRS 101326]). Summary of hydration-dehydration studies may be found in Hardin and Chesnut (1997 [DIRS 100534], pp. 2-29 to 2-31).

Smectite reportedly develops through reactions that consume volcanic glass but is itself transformed progressively to illite with increasing temperature and/or decreasing aqueous silica activity. The transformation of smectite to illite occurs under saturated conditions and is favored by high temperatures and lower values of aqueous silica activity (Bish et al. 1996 [DIRS 101430]; Chipera et al. 1995 [DIRS 100025]). Here, two possible end-member models for the reaction process are formulated. The transformation to illite occurs only if cristobalite and opal-CT are lost and if the silica activity is controlled by quartz. The transformation to illite is also temperature-dependent and requires 0.1 m.y. at 75°C for activation energy of 19.6 kcal/mole, based on the kinetic model of Eberl and Hower (1976 [DIRS 105489]).

Fracture-Matrix Disequilibrium–When chemical species are transported in fracture waters at rates greater than the rate of equilibration with the rock matrix, the result is disequilibrium between waters in fractures and matrix. The disequilibrium can result in differences in the stable mineral assemblage and in reaction rates in the two locations. Because the system is unsaturated and undergoes boiling, the transport of gaseous species is important. To evaluate the near field geochemical environment, the separate yet interacting geochemical, hydrologic, and thermal processes in the fractures and the rock matrix are incorporated into a dual-permeability modeling approach. In this approach, each location in the model is represented by both matrix and fracture grid blocks, each with its own pressure and temperature, liquid saturation, water and gas chemistry, and mineralogy (BSC 2003 [DIRS 162050], Section 6.2.1.5).

Gas-Phase Interaction–An aspect of the chemical system that is particularly important to simulation of thermal testing and repository heating is the exsolution of CO_2 from liquid water as temperature increases. Where boiling occurs, exsolution of CO_2 causes a local increase in pH. Where vapor enriched in CO_2 is transported and condenses, there is a decrease in pH. The extent to which the pH shifts depends on the rate of mineral-water reactions that can buffer the change. Because the diffusivities of gaseous species are several orders of magnitude greater than those of aqueous species, and because the advective transport of gases is more rapid than that of liquids in the unsaturated environment, the region where CO_2 exsolution affects water and gas chemistry will be larger than the region affected by the transport of aqueous species (BSC 2003 [DIRS 166498], Section 6.4.3.3).

Effects of Infiltration and Climate Changes–Early in the thermal evolution of the repository (i.e., the dryout regime described in Section 5.4.2), the chemistry of the host rock around the emplacement drifts will be strongly influenced by the chemistry of ambient matrix pore water, affected by boiling, condensation, and mineral-water-gas reactions. Once the peak rock temperatures have subsided (transition and low-temperature regimes), natural percolation flux will mix with the condensate above the drifts will eventually rewet the dryout zone. The composition of the rewetting waters could be similar to that presently found in the host rock as matrix pore water, or it could be more dilute reflecting wetter climates. Rewetting will redissolve and mobilize any soluble salts deposited in fractures of the dryout zone. Future changes in the percolation flux also affect the extent of mineral precipitation and dissolution, because of dilution effects and changes in the fluxes of dissolved species to the near-field (BSC 2003 [DIRS 162050], Section 6.2.1.3).

Hydrologic Property Changes in Fractures and Matrix–Mineral precipitation and dissolution in the fractures and matrix have the potential to modify the porosity, permeability, and unsaturated hydrologic properties of the host rock (BSC 2003 [DIRS 162050], Section 6.2.1.4). Because the molar volumes of minerals created by hydrolysis reactions (e.g., feldspars reacting with water to form zeolites or clays) are commonly greater than the molar volumes of the reactant minerals, the reactions lead to porosity reduction. The extent of mineral-water reaction is controlled by the surface areas of the mineral phases in contact with water, which is sensitive to heterogeneity in the distribution of minerals in the fractures. Therefore, changes in porosity and permeability may also be heterogeneously distributed. Other factors that could lead to variability in the degree to which hydraulic properties are modified by water-rock interactions are the distribution of liquid saturation in fractures and the proportion of fractures having actively flowing water.

Porosity and Permeability–Silica is expected to be redistributed (e.g., cristobalite dissolution in one place, followed by amorphous silica precipitation in another) and the redistribution may alter, create, and close off (or reduce) fluid transport pathways. Hydrothermal plug-flow reactor experiments of Topopah Spring tuff reacted with de-ionized water have demonstrated significant dissolution and some precipitation of silica phases (Johnson et al. 1998 [DIRS 101630]). A laboratory fracture sealing experiment of two saw-cut blocks of welded rhyolite ash-flow tuff, separated to create a vertical planar fracture, showed that amorphous silica was deposited from injected water at temperatures exceeding 100°C (BSC 2003 [DIRS 162050], Section 7.3). Fracture sealing occurred after 5 days of injection, with 1.2 to 4.7 percent of the total porosity filled with solid precipitate. Bridging structures of amorphous silica that formed during the experiment in both the saw-cut fracture and a natural fracture appear to obstruct fluid flow within the fracture system.

Although other chemical constituents may similarly be redistributed (e.g., aluminum, sodium, calcium, potassium, and magnesium), it is the silica dissolution and precipitation that dominate the changes. The impact of some additional phases, although much less significant in overall abundance, may nonetheless be important in other processes. For example, calcite ($CaCO_3$) is a major mineral in the fractures of the potential repository zone and the dissolution and precipitation of calcite may impact fluid chemistry (pH, in particular). The retrograde solubility of calcite is expected to lead to its precipitation in the near-field environment during initial heating stages, which subsequently leads to an increase in pH. However, as boiling and evaporation drive the water vapor and CO_2 into cooler regions, the vapor condensation and CO_2 dissolution will decrease pH, favoring calcite dissolution in the condensation and drainage zones. Smectite formation along preferred flow paths is potentially significant for subsequent radionuclide retardation, owing to high sorption capacities (including ion exchange) and possibly high concentrations of these phases.

The net effect of the mineral precipitation and dissolution reactions is expected to be changes in hydrologic properties (e.g., reduction in fracture porosity and permeability). This conceptual understanding is consistent with results of recent thermal-hydrologic-chemical (THC) simulations using the composition of water sample HD-PERM from the Tptmn unit in Alcove 5 (BSC 2003 [DIRS 162050], Section 6.8.5.4) showing that a zone of higher liquid saturation formed 7 to 8 meters above the drift, with partial diversion of flow. This "umbrella" effect results from a thin region of lower permeability created predominately by mineral deposition of amorphous silica at the boiling front, during the boiling period. In this case, the permeability decreased by a factor of about 10, and liquid saturations at the drift crown are less than for the TH prediction. Similar results were obtained using other waters as the initial composition, with the permeability decreasing by as much as two to three orders of magnitude.

Other THC simulations using the HD-PERM water and two fixed infiltration rates of 6 and 25 mm/y, and a simulation neglecting vapor-pressure lowering, also predict the "umbrella" effect above the drift (BSC 2003 [DIRS 162050], Figure 6.8-42b). The magnitude of permeability change may also be controlled by the rate of rewetting of the near-field host rock during cooldown (controlled by hydrologic properties and vapor pressure lowering) and the homogeneity of the fracture permeability. However, because the zone of precipitation is thin and located several meters above the drift crown, any focusing of flow in the zone is not anticipated

to increase vertical fluxes at the drift crown much beyond what is predicted without considering thermal-hydrologic-chemical processes.

In these simulations, the permeability decrease results primarily from the precipitation of amorphous silica and, to a lesser extent, calcite (BSC 2003 [DIRS 162050], Figures 6.8-43 through 6.8-46). Gypsum precipitation is significant only with two of the starting waters, the HD-PERM water and water sample ECRB-SYS-CS500/12.0-16.7/UC from the Tptpll, because these waters initially contain a higher proportion of calcium. The fracture porosity is predicted to decrease by approximately 4 to 7 percent depending on the simulation. The maximum porosity decrease occurs in a thin zone during refluxing at the edge of the dryout zone, before the collapse of this zone around the drift.

5.4.4.2.2 Overview of Processes Affecting In-Drift Chemical Conditions

The factors affecting the near-field environment water chemistry are depicted in the interaction matrix presented in Figure 5-92. The key parameters of the near-field environment are shown along the diagonal (blue shading); the coupled processes (the interactions that occur between parameters) are shown off the diagonal. Yellow arrows in clockwise and counterclockwise directions represent forward and backward coupling, respectively. The overall process is complex but understandable within the context of thermodynamic modeling (Wolery et al. 1990 [DIRS 100098]; Wolery 1992 [DIRS 100835]; 1992 [DIRS 100836]; Daveler and Wolery 1992 [DIRS 103803]; Wolery and Daveler 1992 [DIRS 100097]) and reactive transport modeling (Steefel and Lasaga 1994 [DIRS 101480]; Steefel and Yabusaki 1996 [DIRS 100827]).

To determine the composition of water that might contact the waste packages, the possible evolution of waters throughout the thermally perturbed region is considered. As the near-field environment heats up, ambient waters will be subjected to evaporation and to mineral-water interactions. One important trend expected during heating is the degassing of CO_2 and the effects on the solution pH. Heating and evaporation will liberate CO_2 gas, which will move away into cooler regions, causing the pH in the heated region to increase. The solution also becomes increasingly concentrated by the loss of H_2O. Dissolved salts may then raise the boiling temperature slightly, and higher-temperature mineral-water interactions are possible. Eventually, salt minerals (e.g., NaCl, $NaNO_3$, $CaSO_4$) will precipitate, and the remaining liquid water will disappear.

Where humid air reaches cooler temperature rock, condensate will form. Compositionally, the condensing water is essentially distilled water, but it will rapidly react with minerals lining the fractures, as well as CO_2, which was degassed from waters closer to the heat source. Thus, the condensate will have a dilute chemistry (depending on the extent of water-rock interactions) and somewhat lower pH values than observed in ambient waters.

Condensate waters and natural percolation will be mobile as fracture flow above drift openings. Studies demonstrate that the composition of fracture waters will likely be dominated by interaction of condensate and fracture-lining minerals, as observed in thermal field test samples (BSC 2003 [DIRS 162050], Section 7.1.11.1). A review of rock-water studies may also be found in Hardin (1998 [DIRS 100123], pp. 6-3 to 6-12).

Within the drift, the temperature will be greater and waters originating from the host rock will continue to evolve. Seepage water falling on waste package and drip shield surfaces will evaporate and may form highly concentrated brines and deposited salts. In addition, the salts in dust that accumulates on waste package and drip shield surfaces during repository operation and postclosure ventilation may deliquesce, forming brines even when host rock temperature is too high to allow seepage water to enter the drift or when relative humidity is significantly below 100 percent.

Deliquescence and seepage evaporation will be the dominant processes affecting solution composition on the drip shield and waste package. Deliquescent minerals absorb water from the air, and either incorporate this liquid as waters of hydration within their mineral structure, or dissolve within it to form a saturated solution at a given temperature and pressure. Deliquescent minerals in dust have the potential to change the microscale liquid environment as they absorb water vapor from the air. The brine composition that forms and the temperature conditions at which a solution will be present are a function of the composition and relative abundance of salt minerals present in the dust and of the relative humidity within the repository drift.

As shown in Figure 5-93, the evaporative process is the reverse of deliquescence. As seepage waters evaporate, minerals precipitate and the relative concentrations of dissolved components will change. As explained by Drever (1988 [DIRS 118564], p. 235): "whenever a binary salt is precipitated during evaporation, and the effective ratio of the two ions in the salt is different from the ratio of these ions in solution, further evaporation will result in an increase in the concentration of the ion present in greater relative concentration in solution and a decrease in the concentration of the ion present in lower relative concentration." Thus, a chemical divide develops each time a mineral precipitates—waters with proportionally more of the cation will diverge chemically from waters containing proportionally more of the anion. There are six common geochemical divides for natural lakes (Drever 1988 [DIRS 118564]) (see Figure 5-94). These geochemical divides largely control the types of waters that can develop in these lakes. Analogous evaporite minerals are commonly found on desert playa lakes in Nevada as the result of evaporative concentration of relatively dilute and low-solute-content rainwater and snow melt (Papke 1976 [DIRS 162274], Table 1).

The thermal seepage constraints indicate that there can be no seepage at drift temperatures above about 100°C. This is supported by the results of the DST, which indicate that there should be no macro scale liquid water available in the host rock at temperatures above about 105°C (see Figure 5-95). Thus, the seepage evaporation scenario is not expected to be important above those temperatures. Dust deliquescence, however, potentially occurs whenever seepage is not present on waste packages, irrespective of temperature conditions.

5.4.4.3 Evolution of In-Drift Water Chemistry

Within the drift, the geochemical environment on the surfaces of the drip shield and waste package can affect corrosion processes. As discussed earlier, aqueous solutions on the drip shield and waste package surfaces may originate by deliquescence of dust minerals or by seepage.

Aqueous Conditions Associated with Dust–Dust deliquescence is considered because it allows brine formation even at temperatures too high to allow seepage water to enter the drift. In order to

evaluate the effects of this process, a field-sampling program was undertaken to characterize repository dust (Peterman 2001 [DIRS 165976]; Peterman et al. 2002 [DIRS 165975]; Peterman et al. 2003 [DIRS 162819]). In 2001 and 2002 the USGS collected dust samples from tunnel walls, service pipes, and other flat surfaces at 37 sites in the ESF. These samples were sieved and split, and aliquots of each were analyzed for bulk chemical composition. A second aliquot of dust was leached with deionized water to determine the concentrations of water-soluble cations and anions present in the dust. It is these water-soluble salts could potentially deliquesce, producing aqueous fluids on the surface of the waste package.

The major element compositions of the bulk dust samples were very similar to that of the repository host rock, indicating that the dust is dominated by finely comminuted rock produced during tunnel excavation and construction activities (Peterman et al. 2003 [DIRS 162819]). Enrichments relative to the tuff wall rock in CaO, MgO, MnO, fluorine, and CO_2 are interpreted to be due to preferential comminution of fracture and cavity coatings (carbonates, manganese oxides hydroxides, fluorite) relative to the bulk tuff (Peterman et al. 2003 [DIRS 162819]). The enrichment of chlorine is likely related to salts derived from native pore water and construction water. Ferrous iron is enriched in the dust due to construction-related ferrous metal particulates. Finally, all measured organic carbon, up to a few percent of the total mass, has non-rock sources (soot and aerosols from diesel exhaust, abraded rubber and fiber from the conveyer belts, aerosols of hydraulic fluid, oil and greases, etc.).

Water soluble anions and cations comprise only a tiny fraction of the bulk material, less than 0.5 percent of the total. Calcium, sodium, and potassium are the major cations in descending order of concentration, and sulfate, nitrate, and chloride are the major anions (carbonate was not analyzed). These compositions represent salts derived from evaporation of both native pore water and construction water. The construction water can be identified by the presence of LiBr, which was used as tracer in this fluid (Peterman et al. 2003 [DIRS 162819]). Bromide was also observed as a soluble constituent of dust. The compositions of the dust leachate are used in BSC (2003 [DIRS 167461]) as input for determining the compositions of brines that might form by deliquescence on the drip shield and waste package, and under what conditions (relative humidity, temperature) those brines will occur.

Evolution of Seepage Waters–The liquid waters entering the near-field environment will include natural percolation, condensate, and mixtures thereof. As these waters move through the near-field environment and enter the drifts, they may pick up salts (e.g., NaCl, $NaNO_3$, $CaSO_4$) left in and near the drift openings when ambient waters are boiled. Within the drifts, these waters may interact with man-made materials, now altered by heat, that were introduced during construction and waste emplacement. Such materials will include iron and/or steel (CRWMS M&O 2000 [DIRS 146589]).

The chemical consequences of evaporation are distinct from those of boiling. An important distinction arises from the contrast in behavior of dissolved gases during the two processes. In evaporation, the dissolved gases are generally in a state of near-equilibrium with an overlying atmosphere, whereas in boiling systems the dissolved gaseous components are quickly removed. Gaseous CO_2 is related to pH, an important variable in aqueous systems. Equilibrium with an overlying atmosphere may tend to keep the dissolved CO_2 nearly constant, and thus buffer the

pH.   The loss of CO_2 from typical formation water tends to increase the pH, as discussed previously.

The presence of man-made materials in the near-field environment will influence the geochemical reactions that may occur. The metal present in the waste canisters and the engineered barrier system may give rise to chemically significant corrosion products. Possible chemical interactions with introduced materials in the drift environment have been evaluated (BSC 2003 [DIRS 167461]).

Microbially-mediated chemical processes can significantly alter the geochemical environment and have direct impacts on potential repository materials. Microbes are capable of using a wide range of organic compounds to serve as energy sources of carbon to satisfy carbon requirements for synthesis of cellular materials. Similarly, oxygen or a wide array of inorganic compounds may be used as a terminal electron sink. The nutrient supply, rate of nutrient transport, and identity of the potential microbial community in the repository will govern the specific types of metabolic activities that occur. Bacteria can also bind metals, secrete metal-complexing compounds, and modify metal ions speciation, capabilities that may affect the transport of radionuclides from the near-field environment (Hardin 1998 [DIRS 100123], Chapter 7).

5.4.4.4 Geochemical and Mineralogical Studies of the Near Field Beyond the Boiling Zone

In comparison to the proximal near field, water-rock interactions beyond the boiling zone are simpler. Related discussions of site geochemistry and mineral stability are presented in Section 5.2 of this report and BSC (2003 [DIRS 167461], Section 6).

5.4.4.4.1 Hydrothermal Alteration of Devitrified and Vitric Tuffs

A series of hydrothermal experiments were conducted in which samples of Topopah Spring tuff (vitric and devitrified tuffs) were reacted with J-13 well water (Knauss et al. 1985 [DIRS 100150]; Knauss and Peifer 1986 [DIRS 100151]; Knauss et al. 1987 [DIRS 100152]; Knauss 1987 [DIRS 100050]). In these experiments, temperatures ranged between 90° and 350°C for exposure times up to 303 days. Detailed analyses were made of the evolving fluid chemistry (fluid samples were taken during the runs) and of the mineralogy and chemistry of the reacted tuffs (analyzed after completion of the runs). Zeolites were identified as alteration products in most of the runs at 150° and 250°C (mordenite and dachiardite in runs with devitrified tuff, clinoptilolite in runs with vitric tuff). No zeolites were observed in runs at 90°C. Reaction of naturally zeolitized tuff at 90° and 150°C resulted in a change in the composition of the zeolite heulandite. This became more K-rich, but did not show evidence of dissolution. Below 90°C zeolites appear to be slow to form in the laboratory. The most prominent change in the water chemistries was the increase in the concentration of aqueous silica. In systems with devitrified tuff, this concentration appears to be controlled by cristobalite solubility. In systems with vitric tuff, the aqueous silica concentrations were higher, approaching the solubility of amorphous silica.

5.4.4.4.2 Evaporation Experiments

A series of open system evaporation experiments were conducted under various temperature and relative humidity conditions using synthetic J-13 water (Rosenberg et al. 1999 [DIRS 125338]); CRWMS M&O 2000 [DIRS 146460]). Similar evaporation experiments were also conducted with Topopah Spring tuff pore water (Rosenberg et al. 1999 [DIRS 125339]) and seawater (McCaffrey et al. 1987 [DIRS 164481]).

Subboiling temperatures were maintained and evaporation was permitted both in the presence and absence of crushed tuff. Solution samples were collected and chemically analyzed to document the evaporative chemical evolution, and solids were characterized by mineral identification. In one experiment, 30 L of synthetic J-13 well water was evaporated to approximately 30 mL. The analyzed solids were identified by x-ray diffraction to be amorphous silica, aragonite, and calcite (Rosenberg et al. 1999 [DIRS 125338]). The solution was then allowed to completely evaporate, and analysis of the solids revealed that halite, niter, thermonatrite, and possibly gypsum, anhydrite, and hectorite had also precipitated. The solution analyses, after concentrating by a factor of about 1,000, indicated that calcium and magnesium had been largely removed by mineral precipitation, presumably as carbonates, while Na^+, K^+, and SiO_2 largely remained in solution, and Cl^-, F^-, NO_3^-, and SO_4^{2-} remained in solution in nearly identical proportions as in the starting water (they behaved conservatively). The solution pH stabilized at about 10. The presence of tuff appeared to have little effect on the relative distribution of the anions in solution, except for possibly fluorine, which had a relatively lower concentration ratio. The SiO_2 was lower in the solutions with tuff present, suggesting that the tuff enhances SiO_2 precipitation. In the experiments with Topopah Spring tuff pore water, XRD analysis detected gypsum, and after complete evaporation, tachyhydrite (Rosenberg et al. 1999 [DIRS 125338]).

McCaffrey et al. (1987 [DIRS 164481]) sampled and analyzed the chemical compositions of the evolving seawater at the Morton Bahamas solar salt production facility on Great Inagua Island in the Bahamas, and found that gypsum began to precipitate after the seawater had been evaporatively concentrated by a factor of around 3.8, but did not observe precipitation of potassium-bearing phases up to a concentration factor of 80.

5.4.4.4.3 Natural Analogs to Gain Confidence in Geochemical Modeling

Natural analogs help constrain predictions that are based on experimental results and kinetic and thermodynamic modeling. In BSC (2002 [DIRS 160405], Section 11), the Yellowstone caldera and the Paiute Ridge intrusive complex (located on the northeastern boundary of the Nevada Test Site, Nye County, Nevada) are discussed as analogs for future behavior of a repository. Bruton et al. (1995 [DIRS 117033]) discuss the potential for using geothermal areas, such as those in the Taupo Volcanic Zone in New Zealand, as natural analogs to many of the processes that are anticipated to occur in the postemplacement environment at Yucca Mountain. The ability of the EQ3/6 software and associated thermodynamic databases (Wolery 1992 [DIRS 100835]; 1992 [DIRS 100836]; Daveler and Wolery 1992 [DIRS 103803]; Wolery and Daveler 1992 [DIRS 100097]) to simulate groundwater-tuff interactions in the postemplacement environment at the potential Yucca Mountain repository was tested in high-temperature (greater than 200°C) systems using comparisons between observed equilibria and simulations of field relations in the

Wairakei geothermal system. High-temperature systems were chosen in the initial studies because those systems are generally considered to be in equilibrium, but the magnitude and types of observed water-rock-gas interactions in these systems do not represent conditions of the Yucca Mountain system. These analogs are generally high temperature and full liquid saturation, and the Yucca Mountain repository would be in the unsaturated zone with lower temperatures. Nevertheless, once confidence is gained in the ability to model equilibrium systems, the codes can be tested for lower temperature systems in which reaction kinetics are introduced as an additional variable.

Wairakei Geothermal Field–The work addresses mineral equilibria and fluid chemistry in the Wairakei geothermal field at temperatures of about 250°C. Petrologic studies by Reyes et al. (1994 [DIRS 146636]) of mineral relations and fluid chemistry at 100° to 200°C at the Wairakei and Kawerau geothermal fields revealed a variety of zeolites (e.g., clinoptilolite, mordenite, stilbite, and dachiardite) that would enable further testing of the codes and thermodynamic databases at lower temperatures. Such simulations are especially required because of the need to address kinetic constraints on mineral precipitation and dissolution in lower temperature systems, and to resolve discrepancies in predicting zeolite stability in relation to nonzeolite aluminosilicates (Viani and Bruton 1992 [DIRS 101407]).

Trends in water and gas chemistries and well discharge characteristics through time were analyzed. A set of representative water and gas analyses were identified from 250°C production zones in three wells. The most common vein minerals at this temperature are wairakite, adularia, epidote, quartz, albite, chlorite, calcite, and prehnite (Reyes et al. 1993 [DIRS 146638]).

Geochemical calculations with EQ3/6 using measured aluminum concentrations and thermodynamic data for aluminum aqueous species from Pokrovskii and Helgeson (1995 [DIRS 101699]) combined with quartz solubility data from Fournier (1983 [DIRS 146639]) suggest that vein minerals are presently in equilibrium with subsurface fluids (Glassley 1996 [DIRS 140011], Figure 3.4-21) in Wairakei producing zones. Good agreement is indicated when the affinity-temperature curves of observed minerals converge on zero at the measured downhole temperature. Matrix replacement minerals, although of much greater variety and number than vein minerals owing to variations in initial rock mineralogy (Reyes et al. 1993 [DIRS 146638]), are consistent with calculated mineral stabilities at downhole temperatures.

One of the greatest areas of uncertainty in predicting the stability of aluminosilicate minerals involves the aluminum system and measurements of aluminum concentration in natural waters, as well as the thermodynamic data for aluminum aqueous complexes. The temperatures of the geothermal systems at Wairakei are sufficiently high to yield significant, measurable quantities of aluminum in solution. Combined with the observed stability of varied aluminosilicate minerals, these data can be used to test available thermodynamic data for aluminum aqueous complexes. Simulations were made using the SUPCRT92 (Johnson et al. 1992 [DIRS 101632]) and Pokrovskii and Helgeson (1995 [DIRS 101699]) databases. Aluminum data from Pokrovskii and Helgeson (1995 [DIRS 101699]) reproduced observed mineral equilibria quite well; those of SUPCRT92 did not. Measured aluminum concentrations were used in these calculations; they were not automatically set using mineral equilibria as is often done (Bowers and Burns 1990 [DIRS 105057]; Chipera et al. 1995 [DIRS 100025]).

5.4.4.4.4 Kinetics of Amorphous Silica Precipitation

Dissolution of silica (SiO_2) in response to water movement at elevated temperatures and subsequent precipitation of silica on cooling may affect local porosity and permeability. Amorphous silica will play an important role in the evolution of the Yucca Mountain system (Wilder 1996 [DIRS 100792]). Carroll et al. (1998 [DIRS 124275]) measured the precipitation rate of this substance at the Wairakei geothermal borefield in New Zealand. The same report summarizes measured rates of amorphous silica precipitation in the laboratory at 60° to 120°C over a range of silica concentrations. The measured field rates were compared to predictions based on the laboratory studies. Amorphous silica precipitation rates appeared to be controlled by different mechanisms in laboratory and field studies. Rates from the Wairakei field study were 10 to 300 times higher than those predicted from laboratory experiments. The deviation in rates increased with the degree of supersaturation and may have been influenced by the presence of dissolved solutes, such as aluminum. The field rates may be accelerated by surface defect/surface nucleation effects associated with the incorporation of trace amounts of aluminum into the precipitate.

5.4.5 Field Thermal Tests

Three field thermal tests have been conducted to obtain a more in-depth understanding of the thermal-hydrologic-mechanical-chemical coupled processes and to provide data for enhancing confidence in the model analyses. Those tests are the Large Block Test, the SHT, and the DST. While all three tests were conducted in the Tptpmn unit, the SHT and the DST were conducted in situ (at Alcove 5 of the ESF) and the Large Block Test was conducted in a nearby outcrop located at Fran Ridge. Detailed descriptions of the Large Block Test, the SHT, and the DST can be found in Lin et al. (2001 [DIRS 159069]). A detailed description of the SHT can be found in CRWMS M&O (1999 [DIRS 129261]); and CRWMS M&O (1997 [DIRS 146917]; 1998 [DIRS 111115]), respectively. These tests are briefly described below to facilitate discussion of the test results. Additional discussions of the test results and analyses of the data can be found in analysis/model reports (BSC 2002 [DIRS 160771]; 2003 [DIRS 162050]).

5.4.5.1 The Large Block Test

The primary purpose of the Large Block Test was to investigate coupled THMC processes in a controlled heating condition so that the test results could be readily compared with model calculations (BSC 2002 [DIRS 160771], Section 6.1). A freestanding 3 by 3 by 4.5 m (10 by 10 by 15 ft) column of Topopah Spring Tuff was isolated at the outcrop at Fran Ridge, Nevada. The block correlates with the nonlithophysal unit of the Topopah Spring Tuff in the repository horizon in Yucca Mountain. Fractures in the block were mapped on the five exposed surfaces and in the boreholes, which were drilled to install instruments. Five heaters were installed in the block to form a horizontal heater plane at a depth of 2.74 m (9 ft) from the top. Instruments were installed in the boreholes to measure temperature, gas pressure, relative humidity, moisture content (using neutron logging), and deformation. In addition, instruments installed on the block surface included electrodes for electrical resistance tomography, fracture gauges, and resistance temperature devices to monitor the near-surface temperature gradients. Labeled native microbes were introduced into the heater boreholes and other boreholes so that their survivability and migration could be studied. Four observation boreholes were constructed near the bottom of the

block to conduct qualitative observations of fracture flows and microbial migrations. Coupons of candidate waste package materials were placed at designated locations within the block. The four vertical sides of the block were coated with a moisture barrier and then insulated. Water vapor was allowed to leave the block through the top. A heat exchanger was installed on the top to control the top boundary temperature (BSC 2002 [DIRS 160771], Section 6.1).

The heaters were energized to their full power (450 W each) on February 28, 1997. The temperature on the top was allowed to rise to 60°C, and then the heat exchanger was activated to maintain 60°C on the temperature. When the temperature near the heater horizon reached 140°C, the heater power was adjusted to keep the temperature between 135° and 140°C. The heating phase of the Large Block Test was terminated on March 10, 1998 (9,000 hr or approximately 1 yr). The monitoring of the Large Block Test was terminated on September 16, 1998 (13,899 hr or approximately 1.6 yr) (BSC 2002 [DIRS 160771], Section 6.1).

Description of the temperature data for the Large Block Test and DTN links to the data can be found in BSC (2002 [DIRS 160771], Section 6.1.1). Figures 5-96 and 5-97 show the highest temperatures measured along the two vertical Boreholes, TT1 and TT2, respectively, as a function of time for the entire test history. Temperature measurements show that the block was heated nearly one-dimensionally.

The sudden drops of temperature at TT1-14 at 2,525 hours (June 13, 1997) (Figure 5-96) and at TT2-14 at 4,475 hours (September 2, 1997) (Figure 5-97) and the subsequent temperature fluctuations were caused by thermal-hydrologic processes. During the event, temperatures at these locations converged to boiling, then increased followed by fluctuations. Close examination of the data indicates that the behavior was caused by condensate refluxing. The June 13, 1997 (2,525 hr), thermal-hydrologic event and the subsequent temperature fluctuations were associated with rain-water that infiltrated into the block. Heavy rain occurred at Fran Ridge on the night before this event. All measured temperatures along TT1 showed a decrease at the onset of this event; which indicates the influence of rain-water.

Deformations within the block were measured by multiple-point borehole extensometers for the bulk displacements within the block, and by fracture gauges for the deformations across fractures on the block surfaces (Wilder et al. 1997 [DIRS 125467], p. 19; Lin et al. 2001 [DIRS 159069], Section 7.1.1). Description of the thermal-mechanical observations can be found in Section 5.4.3.6.

In summary, the Large Block Test performed as intended (Lin et al. 2001 [DIRS 159069]). A uniform dryout zone was created at the heater horizon. Moisture distributions above and below the dryout zone varied, probably due to the heterogeneity of the block. Refluxing of condensate was observed. There was some indication of coupling between block deformations and the thermal-hydrologic processes. The labeled microbes, which had been placed in the heater holes before the heating, were found in the observation holes about 1.7 m (5.6 ft) below the heater holes during the heating phase of the test. This indicates that the microbes survived the heating, and that water drained from the heater holes.

5.4.5.2 Single Heater Test

The SHT was the first in situ thermal tests conducted underground at Yucca Mountain. The overall objective was to gain a more in-depth understanding of the coupled thermal, mechanical, hydrologic, and chemical processes that will affect the rock-mass surrounding the repository. The test included pre-test predictions using existing models and subsequently refining or modifying the models, on the basis of comparative and interpretive analyses of the measurements and predictions.

Another objective of the SHT was to prove the various instruments, equipment, and procedures that would be used in the larger, more complex, longer duration DST (see Section 5.4.5.3).

Heating and cooling of the test block were carried out between August 1996 and January 1998. Post cooling characterization, laboratory testing, modeling, analysis, and documentation culminated in *Single Heater Test Final Report* (CRWMS M&O 1999 [DIRS 129261]).

Key findings and observations of SHT are described below:

- Conduction was the dominant heat transfer mechanism in the SHT block, although the pore water in the rock had a role via convection, both in the liquid and gas phases.

- Based on the regions of increased and decreased matrix saturations as monitored by electrical resistivity tomography, neutron logging, and ground penetrating radar, and the locations of those regions predicted by the models, the dual permeability model is considered to be more effective than the equivalent continuum model in simulating the thermal-hydrologic responses of fractured tuff.

- Electrical resistivity tomography and ground penetrating radar measurements showed that condensate drained by fracture flow to below the heated region, and did not remain perched above it.

- Borehole pneumatic measurements indicated that air-permeability in certain regions of the test block, some distance away from the heater, decreased by a factor of two to five during the heating phase due to condensation of mobilized moisture in fractures. Permeability rebounded when the heating stopped, as the supply of mobilized moisture ended and liquid water drained down in the fractures by gravity.

- Electrical resistivity tomography and neutron logging measurements showed good agreement with each other in tracking the growth of the dryout regions.

- Temperature measurements in the neutron boreholes indicated that the rock began to dry out at approximately 60°C.

- The coefficient of thermal expansion of the rockmass below 200°C, as derived from measured displacements and temperatures, is as much as 50 percent smaller than that measured in the laboratory using small samples. This was caused by fractures, which tend to accommodate part of the thermal expansion of the rock.

- Based on comparative analyses of predicted and measured temperatures, the SHT indicates that the bulk thermal conductivity of the rock in situ is substantially greater than that of dried rock, because the presence of moisture.

- Chemical analysis of samples of water mobilized by heating and subsequent modeling demonstrated that gas-phase reactions play an important role in the thermal-chemical response of the rock.

- Reactive-transport simulations, based on the chemical compositions of water samples from Borehole 16, leads to the conclusion that the Borehole 16 water resulted from condensation in fractures. The mildly acidity of the water reflected the dissolution of gaseous CO_2 during condensation.

- Post-test mineralogic analyses of samples obtained by overcoring found calcite, gypsum and amorphous silica. The distribution and textural attributes of these minerals suggest that they formed through evaporation of residual water during the post-heating (cooling phase) of the test.

- Strontium and uranium analyses of water samples indicated that the concentrations of these cations were comparable to those of pore water. The $^{87}Sr/^{86}Sr$ ratios remained essentially constant and well within the range measured on pore water from these strata.

- Post-cooling air-permeability measurements showed an increase in permeability ranging from 20 percent to a factor of 3.5 compared to the pre-heating values. This increase was the result of the opening of fractures due to heating and/or cooling.

- All the test specimens or coupons of carbon steel left in the two hydrology boreholes before the start of heating underwent various degrees of corrosion. The corrosion products were generally goethite (α-FeO(OH)) and magnetite (Fe_3O_4). The chloride containing mineral akaganeite (β-FeO(OH,Cl)) was identified in one coupon.

- The copper tubing protecting the heating elements was found to be covered with oxidation products upon withdrawal after heating and cooling. The oxidation minerals included tenorite, cuprite, paratacamite, and atacamite.

A number of the findings of the SHT are consistent with findings from the Large Block Test and the DST. The following are two most significant, findings that can be applied to the assessment of the repository's performance.

- The dual permeability model is the preferred conceptual model for simulating the thermal-hydrologic responses of the near-field rock mass in the drift-scale. The dual permeability model is also the preferred model for simulating THM responses.

- All three thermal tests indicate that the rock porewater mobilized by the heat tends to drain by gravity, via the fractures, to below the heated region rather than staying perched above it. This means that condensate refluxing resulting in seepage into the emplacement drifts is less likely to occur during the postclosure period.

5.4.5.3   Drift Scale Test

The DST was designed to collect data of in situ drift-scale coupled thermal-mechanical-hydrologic-chemical processes. Figures 5-88 and 5-89 show the general drift configurations and borehole layout of the DST. The objectives and design of the DST are described in detail in CRWMS M&O (1997 [DIRS 146917], Sections 2 and 3). The drift configuration consisted of an observation drift, a connection drift, and a heated drift (Figure 5-88). The observation drift connected with the main ESF tunnel at about 2.88 km (1.79 mi) from the North Portal of the main tunnel. The heated drift was about 47.5 m (156 ft) long, starting from a thermal bulkhead located near the intersection of the connection drift (Figure 5-88). The heat sources included nine canister heaters lined up on the heated drift floor and 25 wing heaters on each side. Each canister heater was about 4.7 m (15 ft) long and 1.7 m (5.6 ft) in diameter. Each wing heater was placed in a horizontal wing heater borehole that was 11.5 m (38 ft) long and drilled into the heated drift side wall about 0.25 m (0.8 ft) below the springline.

At the initiation of the heating phase, the total power of the canister heaters and wing heaters was approximately 54 kW and 140 kW, respectively. Each wing heater consisted of two sections of heating elements. The outer (farther away from the heated drift) element had a rated power output of about 1.7 kW; the inner section had about 1.1 kW. Temperature was measured in boreholes arranged radially from the heated drift and in longitudinal boreholes parallel to the heated drift (BSC 2002 [DIRS 160771], Figure 6.3-3). Electrical resistance tomography was conducted in vertical planes parallel to the heated drift and in two vertical planes perpendicular to the heated drift from the observation drift (BSC 2002 [DIRS 160771], Figure 6.3-8). Neutron logging was conducted in two sets of boreholes from the access/observation drift (BSC 2002 [DIRS 160771], Figure 6.3-6). Each neutron borehole set (five boreholes) forms a fan-shaped vertical plane perpendicular to the heated drift, with three boreholes above and two below.

Gas sampling ports and water absorbing pads were installed in the membrane in situ sampling technology system in two sets of chemistry boreholes, which were drilled from the access/observation drift (BSC 2002 [DIRS 160771], Figure 6.3-7). As with the neutron boreholes, each chemistry borehole set formed a fan-shaped vertical plane perpendicular to the heated drift, with three boreholes above it and two under it. The hydrology borehole arrangement was the same as for the membrane in situ sampling technology boreholes (BSC 2002 [DIRS 160771], Figure 6.3-4). In addition, two more hydrology boreholes were drilled from the observation drift at 44.8 m from the bulkhead: one above the heated drift and one under it.

Rock mass displacement was measured by multiple-point borehole extensometers (BSC 2002 [DIRS 160771], Figure 6.3-5). All instrumentation boreholes, except for those containing the multiple-point borehole extensometer, and the hydrology boreholes were sealed by casing, cement grout, packers, or a membrane.

The heaters in the DST were energized on December 3, 1997. The heating phase ended approximately four years later on January 14, 2002. The test is currently in the middle of its planned four-year cooling phase.

5.4.5.3.1 Thermal-Hydrological-Mechanical Measurements: Drift Scale Test

The DST data collection system recorded thermal, some hydrologic, and some mechanical data, on an hourly basis (BSC 2002 [DIRS 160771], Section 6.3). Scientific notebooks provide additional details of measurements including calibration information. These data form the basis of the summary of DST measurements listed in BSC (2002 [DIRS 160771], Table 4-3).

5.4.5.3.2 Chemical Measurements: Drift Scale Test

Aqueous Chemistry

Field Measurements and Observations–Aqueous samples collected for chemical analyses have been acquired from several hydrology boreholes during the four years of heating (BSC 2002 [DIRS 160771], Section 6.3.4.1). The first samples were collected six months after heating began, with subsequent sampling activities about every two to three months (more or less frequently as indicated). A summary of the water samples, the field data, and important observations for samples collected up to January 14, 2002 is presented in BSC (2002 [DIRS 160771], Table 6.3.4.1-1).

Laboratory Analyses–Water samples collected from the hydrology boreholes are prioritized for several analytical tests, including major ion chemistry and certain isotope analyses. The major ion data compiled for the samples analyzed are presented in BSC (2002 [DIRS 160771], Table 6.3.4.1-2); values for pH and HCO_3^- (measured in the field) are included for convenience.

Chemical analyses have been reported from water samples collected from each of the three borehole arrays (BSC 2002 [DIRS 160771], Table 6.3.4.1-1) and from boreholes located both above and below the heated drift. Most of the aqueous samples collected and analyzed fall into two main groups:

1. Water samples for which chemistries have been consistent with mineral/water interactions, particularly fracture lining minerals such as silica polymorphs and calcium carbonate. Intervals from which these waters derive are below and up to boiling (~96°C) temperatures.

2. Very dilute water samples obtained from intervals near or above boiling that were consistent with derivation from condensed moisture in the sampling line.

Some trends may be observed among the first group of samples. First, measured pH values range from ~6.1 to 8.3. Concentrations for specific analytes were variable, but the trends were similar. In general, SO_4^{2-} and Cl^- were the dominant anions; Si^{4+} is the principal cation, followed by Ca^{2+} and Na^+ (having similar concentrations to each other). Present, but in lower concentrations, were K^+, Mg^{2+}, $Sr^{2+,}$ and NO_3^-. (These data were different from chemistry of the baseline pore water samples and were unrelated to construction water, which had a bromide tracer of ~20 ‰.) This class included a small number of water samples with very distinctive, concentrated water. Borehole 59-4 (sampled during 11/98 and 01/99) in particular appeared to exhibit evaporatively concentrated water, and Boreholes 59-2 (08/99) and 76-3 (10/99) had somewhat higher concentrations of the principal analytes observed.

Some samples could be recognized in the field and by laboratory analyses as deriving from condensed vapor and generally showing little or no water/rock interaction. The samples generally had lower pH values (approximately 4.0-6.0) and low total dissolved solids (TDS) and electrical conductivity. These samples were collected from borehole intervals, which were at boiling or hotter. The analytical results from the samples indicate the compositions are consistent with relatively pure water. (These analyses were generally of little interest; they were, therefore, not routinely submitted to the Technical Data Management System.) On the other hand, condensates from the highest temperature intervals (>140°C) exhibited lower pH values (<4.0) than might be expected from the effect of CO_2-bearing steam condensation alone. These samples also exhibit values of TDS and electrical conductivity that are not negligible and have unusually high fluoride concentrations of 5 to 66 mg/L. Further field-testing was carried out to investigate the cause of the unexpected fluoride concentration for these water samples (BSC 2002 [DIRS 160771], Section 6.3.4.1.2).

Unlike most water samples, some samples showed relatively high concentrations of dissolved solids and low pH values relative to background values (YMP 2002 [DIRS 158176]; Williams 2003 [DIRS 163765]). The samples were limited to regions where the rock was well above the boiling temperature, and generally above 140°C. A series of field and laboratory tests confirmed that the source of elevated fluoride was due to the packer materials and not due to thermal response of the host rock. The laboratory tests also showed that the volcanic tuff is not a source of hydrofluoric gas. Laboratory tests further demonstrated that neoprene could release significant quantities of chloride, especially when reacted with a higher temperature vapor system.

Gas Chemistry

Gas samples were periodically collected from the hydrology boreholes during the heating phase from December 3, 1997 through January 14, 2002 (BSC 2002 [DIRS 160771], Section 6.3.4.2). These samples were collected to measure the concentration and carbon isotope ratio of CO_2 and the hydrogen and oxygen isotope ratios of water vapor. The concentration and isotopic composition of CO_2 in the heated drift and the observation drift were also measured during the test. In addition, to provide data on the background concentration and isotopic composition of CO_2 in the rock, two gas samples were collected in August 1997 from Borehole 182 (one of the ambient testing boreholes drilled on the opposite side of the connecting drift across from the DST block). The CO_2 concentrations and isotope compositions for both the gas samples and the condensate samples collected from 16 sampling trips during the heating phase can be found in BSC (2002 [DIRS 160771], Table 6.3.4.2-1).

The hydrogen and oxygen isotope compositions of the vapor-condensate samples were measured to gain an estimate of the isotopic composition of the pore water in the rock (BSC 2002 [DIRS 160771], Table 6.3.4.2-3). The isotopic composition of the pore water can be calculated from the isotopic composition of the vapor (Horita and Wesolowski 1994 [DIRS 159108]), assuming that the pore water is in isotopic equilibrium with the vapor in the gas samples at the temperature of the rock. This information can provide valuable insights into the degree of dryout in the rock and the extent of vapor transport.

Mineralogy

Ambient Pre-Test Mineralogy–Systematic data on natural, pre-heating fracture-mineral coverage were collected from the drill core of Borehole ESF-HD-TEMP-2, a horizontal borehole that runs parallel to the heated drift. The drill core is 196.5 ft (60 m) long, but the first 25 ft (7.6 m) of the core are well outside the heated drift and were excluded from study. The number of fractures in the relevant length of core was too large for all to be included in the characterization. Therefore, a conceptual model of fracture attributes was developed to guide the selection of a subset of fractures for mineralogic analysis. The conceptual model was based on a simplification of the criteria used to define subzones of the middle nonlithophysal zone (Buesch and Spengler 1998 [DIRS 101433], pp. 18 and 20).

The rock traversed by ESF-HD-TEMP-2 consisted of intervals dominated by vapor-phase features and intervals where vapor-phase features are not prominent. Reconnaissance examination of the drill core suggested that the fracture coatings are different in the vapor-phase and nonvapor-phase intervals, an observation that was confirmed by detailed study. Based on this observation, detailed fracture-mineral studies were performed each type of interval. Mineral abundances on the fracture surfaces were determined for stellerite, manganese minerals, crystalline silica and feldspar (combined), clay (probably also including minor mordenite), and calcite. The results are presented in BSC (2002 [DIRS 160771], Table 6.3.4.3-1). For the minerals included in the inventory, differences in abundance of crystalline silica plus feldspar, and in calcite between the vapor-phase and nonvapor-phase intervals, were documented. The greater abundance of crystalline silica plus feldspar in the vapor-phase interval is expected because these minerals are among the defining characteristics of vapor-phase void spaces. Additional natural minerals observed in very small quantities or in local concentrations by scanning electron microscope of pre-heating core include mordenite, pyrite, and possible hematite.

Sidewall Core Mineralogy–Sidewall cores collected during the DST revealed new mineral deposits on borehole surfaces and on the surfaces of fractures that intersect the boreholes. New mineral deposits are common on the borehole surfaces because the boreholes act as preferential pathways for fluid flow. Deposits are less common and quantities of new minerals less abundant on the natural fractures within the core samples.

Mineral deposition within the boiling zone is documented by samples from Borehole ESF-HD-CHE-3 (Borehole 54). The three products observed so far are tentatively identified as amorphous silica, gypsum, and calcite (DTN: LA0201SL831225.001 [DIRS 158426]; BSC 2002 [DIRS 160771]). The tentative identifications of gypsum and calcite are based on identifications of these phases by XRD as products of the SHT (DTN: LA0009SL831151.001 [DIRS 153485]). The silica deposits exhibit considerable textural heterogeneity, perhaps because some were deposited when the collection site was in the condensation zone and others deposited when boiling-zone dryout conditions were reached.

Examples of possible condensation zone silica deposition above the heated drift have been identified. In one example, a fracture surface is completely coated by terrace-like silica deposits up to a few micrometers thick. In another example, several discoid silica deposits (up to about 20 micrometers across) rest on a surface of earlier-deposited discs cemented and largely

obscured by silica particles about one or two micrometers across. In both examples, the deposits were built up during multiple episodes of silica deposition, perhaps during the passage of numerous pulses of silica-saturated water.

Very thin (less than 0.5 µm thick) curled silica sheets may be products of final dryout in the boiling zone. There is no textural evidence of successive buildup in the silica sheets. Also lying atop the earlier silica deposits or on pre-heating fracture surfaces are scattered deposits of prismatic gypsum and rounded mounds of calcite.

Studies of pre-heating core from the SHT showed that some of the natural fracture minerals have experienced dissolution caused by ancient or ongoing geochemical processes. This complicates the effort to document mineral dissolution resulting specifically from the DST (BSC 2002 [DIRS 160771], Section 6.3.4.3.3; CRWMS M&O 1999 [DIRS 129261], Sections 6.4.1.2 and 6.4.2).

Among the dissolution features observed were corroded forms of vapor-phase feldspar crystals in lithophysal cavities. These were encrusted with irregular 10 µm long potassium-rich feldspar crystals. Also observed were occurrences of open fractures containing stellerite, both lying on top of other fracture minerals and intergrown with, or overgrown by potassium-rich feldspar crystals mostly 10 µm across, accompanied by smectite and silica (CRWMS M&O 1999 [DIRS 129261], Sections 6.4.2.1 to 6.4.2.3).. To provide documentation of natural alteration, samples of pre-heating drill core from approximately the same locations as sidewall samples were examined by scanning electron microscopes. Images of the typical morphologies of natural fracture-coating minerals and rock-fracture surfaces were recorded. The majority of such documentation was devoted to stellerite because it is the single most abundant fracture-coating mineral.

The natural stellerite fracture coatings in pre-heating samples did not show clear evidence of dissolution. Stellerite in the sidewall core samples also showed no evidence of dissolution. The lone exception occurred on one fracture from the 66.5 ft (20-m) depth in Borehole ESF-HD-CHE-3. In this location, a highly corroded stellerite crystal, several slightly to moderately corroded stellerite crystals, and a moderately corroded silica crystal were adjacent to or within a lobate deposit of amorphous silica (DTN: LA0201SL831225.001 [DIRS 158426]; BSC 2002 [DIRS 160771]). At the time of sample collection, this sample came from within the boiling zone. However, the sampled rock volume had previously been within the condensation zone before the boiling zone moved to its farthest position away from the heaters. It is possible that the observed mineral dissolution and, perhaps, deposition, occurred when the rock volume was in the condensation zone.

Strontium and Uranium in Water Samples

Measurements of strontium and uranium concentrations and isotopic compositions in a subset of water samples provided information on mineral reactions and water flow paths occurring as the block was heated during the test. In addition, isotopic analyses can provide unequivocal evidence of interaction of test-produced water with the engineered materials introduced into the test block during construction. This section discusses data obtained from waters sampled from five DST hydrology Boreholes: 60, 186, 59, 76, and 80. Uranium and strontium concentrations

were determined by isotope dilution. Uranium and strontium isotopic ratios were determined by thermal-ionization mass spectrometry. The data can be found in DTNs: GS011108312322.008 [DIRS 159136] and GS011108312322.009 [DIRS 159137].

Uranium concentrations and $^{234}U/^{238}U$ activity ratios in DST waters, as well as values obtained for pore water from upper lithophysal and middle nonlithophysal units of the Topopah Spring Tuff (Tpt) and values for water perched in the base of Tpt are presented in BSC (2002 [DIRS 160771], Figure 6.3.4.4-1). Uranium concentrations in DST samples vary from 0.003 to 0.65 µg/L and are typically lower than concentrations observed in pore water extracted by ultracentrifugation from the same units. The $^{234}U/^{238}U$ activity ratios (AR) in DST samples vary from 1.14 to 5.68, and unlike uranium concentrations, typically overlap the $^{234}U/^{238}U$ AR values observed in pore water. Samples from individual DST sites obtained at different times during the heating phase of the test have uranium concentrations that show a fairly systematic decrease with time (BSC 2002 [DIRS 160771], Figure 6.3.4.4-2). Zone 60-3 water shows a 10-fold decrease in uranium concentration between 6/4/98 and 5/25/99 to a value of 0.01 µg/L. Zone 59-3 water shows an even greater decrease from 0.015 to 0.0003 µg/L. Temporal changes in $^{234}U/^{238}U$ are not as systematic. Zone 60-3 water decreases significantly from values of 3.6 to 4.1 in 1998 to a value of 1.4 in May 1999. In contrast, the sample collected from Borehole 80 in October 1999 has substantially higher $^{234}U/^{238}U$ AR than samples collected in April of the same year. Samples from 59-2 collected between October 1999 and January 2001 show nearly constant $^{234}U/^{238}U$ AR.

The fact that DST water samples show distinctly lower Uranium concentrations implies that condensate was incorporated into water collected during the heating phase of the experiment. Three different water-rock interaction scenarios could give rise to the resulting DST-water Uranium-234/Uranium-238 AR ratios: 1) bulk dissolution of Uranium from wall rocks by chemically aggressive condensate would result in lowering of Uranium-234/Uranium-238 AR values towards the values inherent in the rocks, 2) flow of less-chemically aggressive water along pathway surfaces with Uranium-234 that is more soluble than ^{238}U due to alpha-recoil-related processes would lead to higher Uranium-234/Uranium-238 AR ratios in DST samples, and 3) pore water mobilized during the heating phase may experience little water-rock interaction, but may be diluted by condensate resulting in no change of the isotopic composition of Uranium. Available data do not allow characterization of the dominant hydrochemical process.

The general trends of decreasing uranium concentration with time are consistent with increasing proportions of condensate mixed in with pore water that was mobilized during the DST heating phase. The wide range in uranium concentrations observed in Tpt pore waters makes it difficult to estimate the amount of condensate added; however, all but two samples with uranium concentrations >0.15 µg/L appear to contain at least some condensate. Samples with uranium concentrations <0.01 µg/L probably consist of more than 90 percent condensate. Even though these samples are particularly susceptible to contamination, most still have $^{234}U/^{238}U$ AR within the range observed in porewater.

Similar to uranium, the strontium concentrations in the test waters approach the values estimated for pore water and decrease with time. Borehole 60-3 water reached a strontium concentration of 0.2 µg/L in June 1999, about 1,000 times less than this zone produced initially. BSC (2002

[DIRS 160771], Figure 6.3.4.4-3) shows the variation of strontium isotopic compositions in the test waters compared to various reservoirs of strontium in the DST block. The orange and red bands show the strontium isotopic compositions of the Topopah Spring Tuff (middle nonlithophysal and upper lithophysal zones) today and at the time of their deposition, respectively. The green band is the range of $^{87}Sr/^{86}Sr$ in pore water; these data are from Borehole USW SD-9, which is the closest vertical borehole to the DST block. Grout introduced into the DST block during emplacement of borehole instrumentation has also been measured and is shown by the black line at an $^{87}Sr/^{86}Sr$ value of 0.7086. The grout contains over 800 μg/g strontium, providing a potentially important added source.

Borehole 59, zone 4 was sampled in November 1998 and showed a very unusual chemistry (approximately 1,200 mg/L chloride) that was initially interpreted as probable contamination. This sample was analyzed for strontium isotopic composition, and the result plots in the field of pore water (BSC 2002 [DIRS 160771], Figure 6.3.4.4-3). Similarly, the $^{234}U/^{238}U$ AR for this sample is in the range of observed porewaters and higher than other samples from Borehole 59 (BSC 2002 [DIRS 160771], Figure 6.3.4.4-1) unlike samples with low $^{234}U/^{238}U$ suspected of contamination. Based on these results, the 59-4 sample is unlikely to be contaminated with grout or other anthropogenic materials. Rather, this sample may represent pore water that has become isolated and evaporated either through natural processes or due to the heat during the test. This is a potentially important sample because it exhibits relatively higher concentrations of sulfate and fluoride.

5.4.5.3.3 Analyses of Drift Scale Test Data

TH Processes in the Drift Scale Test

Measured data relevant to the evaluation of TH processes in the DST include the following: (1) Temperatures measured at numerous sensor locations; (2) Changes in matrix saturation estimated from geophysical measurements conducted at periodic intervals through the duration of the DST; and (3) Changes in fracture saturation estimated from air-permeability measurements conducted at periodic intervals through the duration of the DST (BSC 2002 [DIRS 160771], Section 6.3.2).

Measured temperatures from the DST showed interesting thermal behaviors (BSC 2002 [DIRS 160771], Figures 6.3.1.2-2 and 6.3.1.2-3). BSC (2002 [DIRS 160771], Figure 6.3.1.2-2) shows a significant flattening in Borehole 79 temperatures at 96°C due to reflux activity. Measured temperatures also indicated the influence of fractures in maintaining temperatures close to boiling through moisture movement (BSC 2002 [DIRS 160771], Section 6.3.1.2.1).

While the temperature rise in the test block is dominated by heat conduction, evidence of TH coupling is manifested in heat-pipe signatures in the temperature data, indicating the presence of liquid water at the boiling point (BSC 2003 [DIRS 166512]). The main phenomenon of TH coupling was the redistribution of moisture via condensed vapor in the rock mass. Zones of increased or decreased water saturation in fractures and matrix (compared to preheat baseline data) were monitored in the DST by periodic geophysical methods and air-permeability measurements.

For example, BSC (2002 [DIRS 160771], Figure 6.3.2.3-2) shows that the water content in the rock remained nearly constant within 8-14 percent until temperatures near boiling were reached. Thereafter, significant reduction in water content occurred between 90°C and 105°C where it approached1 percent. Water content in the rock continued to decrease, as it approached zero at approximately 150°C. Although some anomalously low water content was measured in the sub-boiling regime, most of the water content data were reasonably consistent for the range of temperatures considered (25-190°C) (BSC 2002 [DIRS 160771], Section 6.3.2.3.1).

Temperature rise in the rock from heating was predominantly controlled by heat conduction, which is a linear process (BSC 2003 [DIRS 166512], Section 7.4.3). Therefore, the coupling between TH processes, which are nonlinear in nature, is evidenced in subtle signals in the temperature data. Typically, effects of TH coupling appear as a flat region in temperature profiles (or temperature evolution plots) at the nominal boiling point of water (heat-pipe signature), indicating boiling conditions with presence of both liquid water and vapor. Heat-pipe signals can be seen in both measured and simulated responses for all time snapshots depicted in BSC (2003 [DIRS 166512], Figures 7.4.3.1-1a through 7.4.3.1-1d).

Changes in permeability as a ratio to baseline permeability estimates was used to indicate changes in fracture liquid saturation (BSC 2002 [DIRS 160771], Figure 6.3.2.4-4). In general the decrease in air permeability indicated a gradual build-up in fracture liquid saturation during heating (BSC 2002 [DIRS 160771], Section 6.3.2.4.1). Some decrease in bulk permeability was also attributed to mechanical closure of fractures (BSC 2003 [DIRS 164890], Section 7).

Some uncertainty remains in the understanding of TH coupled processes from analyses of the DST data alone. First, no seepage of liquid water has been observed in the heated drift of the DST. The DST results allow for a unique model validation with respect to the near-field TH conditions in the rock mass, but offer no seepage data (observed seepage rates) that can be used directly for thermal seepage validation purposes. Direct validation of thermal seepage would require a heater test operated at artificially enhanced percolation fluxes, in order to observe the seepage potential for extreme flow conditions. Without such testing, validation of the seepage part of the TH Seepage Model is indirect. Second, all three thermal tests have been conducted in the Tptpmn unit at Yucca Mountain; so far, there has been no testing in the Tptpll unit. Therefore, some uncertainty remains about the rock properties in this unit and the influence of lithophysal cavities.

By taking these limitations into account, the conceptual model developed in the TH Seepage Model (BSC 2003 [DIRS 166512]) was tested by performing blind predictions of seepage rates for niche liquid release tests that had not been used for model calibration and that were conducted in a different drift section. It was demonstrated that the measured ambient seepage data (seepage threshold and seepage rate) were accurately represented by the simulated results. Validation of the coupled TH processes with the rock mass (using the DST data) together with validation of the ambient seepage conceptual model (using liquid-release data) provides confidence in the thermal seepage results of the TH Seepage Model.

Uncertainties regarding the effectiveness of the vaporization barrier have been addressed in BSC (2003 [DIRS 166512], Section 6.3) where an alternative conceptual model of water flow in the superheated rock environment was introduced. This alternative model conceptualizes that

the thermally perturbed downward flux from the condensation zone towards the drift, through superheated rock drains in episodic finger-flow patterns. The effectiveness of the vaporization barrier is then tested for these extreme conditions where downward flux is focused and large in magnitude compared to average flow, and where vaporization is limited by the small cross-sectional area between the narrow finger and the rock surface.

THM Processes in the Drift Scale Test

Understanding of THM Processes Understood from the DST–The Drift-Scale THM Model was developed to analyze the impact of coupled THM processes in the repository located in the Tptpmn unit or in the Tptpll unit (BSC 2003 [DIRS 164890], Sections 6.5 and 6.6). The following conclusions can be drawn from this modeling analysis (BSC 2003 [DIRS 164890], Section 8.1).

The maximum THM effects would occur when the temperature in the rock mass at the repository level reaches its maximum. The primary effects are thermally induced and excavation-induced changes in the stress field that would act on pre-existing fractures, thereby causing fracture closure or opening with accompanying changes in fracture permeability and capillary pressure.

Thermal stresses in the horizontal direction would increase significantly, whereas the vertical stresses will remain almost unchanged through the thermal period. The analysis indicates that horizontal stresses will increase by more than 10 MPa at the repository level (BSC 2003 [DIRS 164890], Figure 6.5.3-1). As a result, the vertical intrinsic permeability would decrease in a zone extending several hundred meters above and below the repository (BSC 2003 [DIRS 164890], Figure 6.5.4-1). Using a conservative (more sensitive) stress-permeability relationship, the permeability in the Tptpmn unit would decrease at most to a factor of 0.03 of its original permeability. In the Tptpll unit, vertical permeability is estimated to decrease to a factor of 0.5 of its original value.

The maximum principal compressive stress would occur at the drift crown and is estimated to be about 31 MPa (BSC 2003 [DIRS 164890], Figure 6.5.3-4). An analysis of the observed rock scaling at the crown of the DST shows that a maximum principal stress of about 60 MPa would be required to initiate limited rock scaling. Thus, the model shows that thermal stress is not likely to induce failure at a repository located in the Tptpmn unit.

The analysis indicates that the impact of stress-induced changes in hydrologic properties on the flow field was small to moderate, with the strongest impact occurring in the Tptpmn unit, mainly on the dryout zone near the repository drift. When stress-induced changes in hydrologic properties were considered, the extent of the dryout zone was slightly smaller, and consequently, water would reach the drift wall sooner (BSC 2003 [DIRS 164890], Figure 6.5.5-4). At 10,000 yr, vertical permeability was still significantly reduced, especially immediately above the repository drift. The impact of this reduction in permeability tends to prevent vertical flux from reaching the drift wall at the drift crown (BSC 2003 [DIRS 164890], Figure 6.5.5-5).

The impact of stress-induced changes in hydraulic properties on the flow field around a repository in the Tptpll unit is similar to those for a repository in the Tptpmn unit, but the

magnitude of impact is much smaller, owing to larger initial stresses and initial fracture permeability in the Tptpll unit.

THM Effects on Hydrology–The Drift-Scale THM Model Report (BSC 2003 [DIRS 164890], Section 7.4.3) presents recent analyses to separate effects of TM processes on hydrology from the TH effects. The model is validated for THM processes by comparing calculated vs. measured changes in intrinsic (pneumatic) permeability. The measured change in air permeability reflects two simultaneous processes: TM-induced changes in intrinsic permeability and TH-induced changes in relative permeability for airflow. TM-induced changes in intrinsic permeability result from thermal stresses associated with the heating of the rock mass. Thermal stresses act upon existing fractures, changing their aperture, which in turn may either increase or decrease the intrinsic fracture permeability. TH-induced changes are associated with thermally driven changes of moisture content in fractures. Wetting and drying in fractures (in other words, increase and decrease of liquid saturation) gives rise to changes in relative permeability for airflow.

The calculated permeability changes are compared to air-permeability measurements in the DST in Figure 5-98 (BSC 2003 [DIRS 164890], Figure 7.4.3-4). In borehole intervals closet to the drift ($z = 6$ m), the air permeability first decreased with time to reach a minimum at about 24 months. Thereafter, the permeability increased slightly in three of four boreholes sections and increased dramatically in the fourth (Figure 5-98a). The figure compares measured changes in air permeability at the four borehole sections with calculated changes in permeability. The solid line indicates the calculated changes in air permeability, which are the product of the intrinsic permeability (TM effect) and gas relative permeability (TH effect). The figure shows that the solid line representing the combined TH and TM effects matches three of four measurements best. In the fourth section, the measured changes appear to match a pure TH response the best.

Further away ($z = 12$ m), the measured responses in these three boreholes are very consistent, with an initial increase in air permeability during the first nine months, followed by a gradual decrease with time until the end of heating (Figure 5-98b). The decrease in permeability can be interpreted either as a change in intrinsic permeability (TM), or as a change in relative permeability (TH), or a combination of the two (THM). However, the initial increase during the first 9 months can only be explained as a TM response.

For the measurements located farthest away from the drift—74:4 and 57:4 at approxamately 18 m—there was an increase in air permeability caused solely by TM-induced changes in intrinsic permeability (TM in Figure 5-98c). At this location, far away from the heated drift, no effect from TH-induced changes appears until about 36 months, when a slight wetting began. The overall simulated changes in air permeability using those parameters are in agreement with the measured changes. The simulated changes in air permeability are in the correct direction and within an order of magnitude.

THC Processes in the Drift Scale Test

CO_2 Degassing and Accompanying Changes in Aqueous Chemistry–Measured CO_2 gaseous concentrations from repeat samples from the same borehole intervals between February 1998 and January 2002 are analyzed for trends of CO_2 evolution (BSC 2003 [DIRS 162050],

Section 7.1.10.3). The increase of CO_2 concentrations during the heating phase clearly resulted from the degassing of CO_2 caused by boiling and its outward transport from the heated drift. The measured data were compared to the DST THC model predictions. Model predicted locations of high CO_2 concentration and range of CO_2 concentration agrees reasonably well with observed. The model also accurately predicted the evolution of the CO_2 concentration in the heating phase, but in the later months of heating and early phase of cooling, the model predictions did not agree as well (BSC 2003 [DIRS 162050], Section 7.1.10.3). A correction was needed to account for the effects of water-vapor condensation during sample collection.

Similar comparison was made for the pH and aqueous concentrations of major cations and anions including Na^+, K^+, Ca^{2+}, Mg^{2+}, SiO_2, Cl^-, SO_4^{2-}, HCO_3^-, NO_3^-, and F^- (BSC 2003 [DIRS 162050], Section 7.1.11). The overriding effects manifested in measured aqueous concentrations are predominately those of the TH processes (i.e., boiling or condensation). The analysis interpreted the dilution of concentrations in fractures as being due to condensation and drainage below the heaters, and slow imbibition of the condensate water into the matrix (BSC 2003 [DIRS 162050]). During heating pH decreased to approximately 7.2 in the condensation zone. The pH in the condensate water was related closely to the CO_2 concentration. The pH in waters collected near the dryout zone increases from the initial porewater condition, due to boiling, degassing, and outward transport of CO_2. Dissolution of certain minerals such as feldspars also results in an increase of pH. For conservative species such as Cl^- and SO_4^{2-}, the main effect of heating is a marked decreased in concentrations within fractures in the condensation and drainage zones; in the matrix, there is significant dilution in the condensation zones with a corresponding increase in concentration near the edge of the dryout zone.

Secondarily, water-rock interactions also contribute to behavior of the more reactive species. For example, the extent of dilution of Na^+ and K^+ is less than Cl^-, indicating some contribution of water-rock interaction from alkali feldspars. More sensitive species include Ca^{2+}, whose concentration (which would decrease) is strongly affected by calcite with a fast reaction rate and low solubility at high temperatures. Silica concentrations increased, likely due to accelerated reaction for silica phase (possibly opal-CT) or reaction of "fresh" mineral surfaces (i.e., cristobalite and quartz) in the borehole walls. Sharp drops in Mg^{2+} concentration were caused by dilution from the condensate and the precipitation of magnesium-rich minerals. The comparisons involving NO_3^- and F^- are less conclusive because of uncertainties in their initial concentrations.

Mineral Precipitation and Dissolution–Extent of mineral precipitation during the DST was assessed through side-wall core sampling from above-boiling zones and X-ray diffraction analyses (BSC 2003 [DIRS 162050], Section 7.1.12). Direct evidence of mineral precipitation from migrating fluids was obtained from side-wall samples drilled into the walls of pre-test boreholes. The side-wall samples were taken towards the end of the heating phase of the DST. X-ray diffraction analyses of these samples provided mineral distribution and abundance in the pre-test rock under ambient conditions, and a means for assessing mineralogic changes while the test was in process. The results identify precipitation of amorphous silica as the dominant phase, followed by lesser amounts of calcite and gypsum, (Borehole 54). These data also have been qualitatively compared to the DST THC model, and the agreement increases confidence that the model adequately captures the dominant THC processes.

Porosity and Permeability Changes–Laboratory studies of fracture heating indicate that smoothing of the fracture asperities by dissolution and precipitation can effectively change the permeability (Daily et al. 1987 [DIRS 131816], p. 7861). The laboratory fracture sealing experiment showed that amorphous silica was deposited from injected fluid at temperatures exceeding 100°C (BSC 2003 [DIRS 162050], Section 7.3). Fracture sealing occurred after 5 days of injection, with 1.2 to 4.7 percent of the total porosity filled with solid precipitate. Bridging structures of amorphous silica that formed during the experiment in both the saw-cut fracture and a natural fracture appear to obstruct fluid flow within the fracture system.

The DST THC model simulations showed potentially significant deposition of amorphous silica in fractures (BSC 2003 [DIRS 162050], Section 7.1.12). BSC (2003 [DIRS 162050], Figure 7.1 to 7.40) shows the simulated change in fracture porosity after four years of heating in the DST. The areas above the heated drift and near the edges of the wing heaters show the greatest reduction in fracture porosity, reaching somewhat less than -0.8 percent.

Changes in matrix porosity after four years of heating in the DST have also been calculated (BSC 2003 [DIRS 162050], Figure 7.1-41). Reductions in matrix porosity are limited solely to the dryout zone where mineral precipitation accompanied boiling of the in situ pore water. Increases in matrix porosity are actually greater than the reductions and are evident throughout the condensation zones, where imbibition of dilute water must have led to mineral dissolution. Areas of fracture drainage around the outer edges of the heated zone apparently produced the highest level of matrix imbibition and mineral dissolution in the matrix. The porosity increase in the matrix is, however, approximately two orders of magnitude less than the porosity decrease in the fractures.

Fracture permeability changes resulting from mineral precipitation and dissolution are tied to changes in porosity and more directly to fracture aperture changes. For the heating phase of the DST changes in fracture porosity of less than one percent of the original value would have a correspondingly small effect on fracture permeability (BSC 2003 [DIRS 162050], Section 7.1.13). These results are consistent with the observations of limited changes in air permeability during the DST, which have been attributed predominantly to water saturation changes (mostly in the condensation zones, where mineral precipitation is negligible) (BSC 2002 [DIRS 160771], p. 6.3-15). For a simulation period of 2,400 years the fracture porosity was estimated to decrease by approximately four to seven percent in the Tptpll unit (BSC 2003 [DIRS 162050], Section 6.8.5.4, p. 230). Accordingly, the estimated permeability reduction would be on the order of 12 to 20 percent using the Carmen-Kozeny equation (BSC 2003 [DIRS 162050], Section 6.4.4, Equation 6.4 to 6.17). The estimated permeability reduction is within the order of magnitude natural variability observed in this host rock unit (BSC 2003 [DIRS 161773], Table 6).

5.5 REFERENCES

The following is a list of the references cited in this document. Column 1 represents the unique six digit numerical identifier, which is placed in the text following the reference callout (e.g., CRWMS M&O 2000 [DIRS 144054]). The purpose of these numbers is to assist the reader in locating a specific reference. Within the reference list, multiple sources by the same author (e.g., CRWMS M&O 2000) are sorted alphabetically by title.

5.5.1 Documents Cited

101367   Albin, A.L.; Singleton, W.L.; Moyer, T.C.; Lee, A.C.; Lung, R.C.; Eatman, G.L.W.; and Barr, D.L. 1997. *Geology of the Main Drift - Station 28+00 to 55+00, Exploratory Studies Facility, Yucca Mountain Project, Yucca Mountain, Nevada.* Milestone SPG42AM3. Denver, Colorado: Bureau of Reclamation and U.S. Geological Survey. ACC: MOL.19970625.0096.

104512   Allard, B. 1982. *Sorption of Actinides in Granitic Rock.* SKB TR-82-21. Stockholm, Sweden: Svensk Kärnbränsleförsörjning A.B. TIC: 205892.

144954   Ames, L.L., Jr. 1960. "The Cation Sieve Properties of Clinoptilolite." *American Mineralogist, 45*, 689-700. Washington, D.C.: Mineralogical Society of America. TIC: 235507.

104522   Ames, L.L., Jr.; McGarrah, J.E.; and Walker, B.A. 1983. "Sorption of Trace Constituents from Aqueous Solutions onto Secondary Minerals: 1. Uranium." *Clays and Clay Minerals, 31*, (5), 321-334. Long Island City, New York: Pergamon Press. TIC: 238914.

104677   Baeyens, B. and Bradbury, M.H. 1995. *A Quantitative Mechanistic Description of Ni, Zn and Ca Sorption on Na-Montmorillonite, Part I: Physico-Chemical Characterization and Titration Measurements.* PSI Bericht 95-10. Villigen, Switzerland: Paul Scherrer Institute. TIC: 237271.

104678   Baeyens, B. and Bradbury, M.H. 1995. *A Quantitative Mechanistic Description of Ni, Zn and Ca Sorption on Na-Montmorillonite, Part II: Sorption Measurements.* PSI Bericht 95-11. Villigen, Switzerland: Paul Scherrer Institute. TIC: 237272.

104809   Balistrieri, L.S. and Murray, J.W. 1982. "The Adsorption of Cu, Pb, Zn, and Cd on Goethite from Major Ion Seawater." *Geochimica et Cosmochimica Acta, 46*, 1253-1265. New York, New York: Pergamon Press. TIC: 238913.

100003   Bandis, S.C.; Lumsden, A.C.; and Barton, N.R. 1983. "Fundamentals of Rock Joint Deformation." *International Journal of Rock Mechanics and Mining Science & Geomechanics Abstracts, 20*, (6), 249-268. New York, New York: Pergamon Press. TIC: 224201.

100004   Barton, C.A.; Hickman, S.; Morin, R.; Zoback, M.D.; Finkbeiner, T.; Sass, J.; and Benoit, D. 1997. "Fracture Permeability and Its Relationship to In Situ Stress in the Dixie Valley, Nevada, Geothermal Reservoir." *Proceedings, Twenty-Second Workshop on Geothermal Reservoir Engineering, January 27-29, 1997.* Pages 210-215. Stanford, California: Stanford University. TIC: 237673.

100005   Barton, N.R.; Bandis, S.; and Bakhtar, K. 1985. "Strength, Deformation, and Conductivity Coupling of Rock Joints." *International Journal of Rock Mechanics and Mining Science & Geomechanics Abstracts, 22*, (3), 121-140. New York, New York: Pergamon Press. TIC: 217135.

100704   Bates, J.K.; Bradley, J.P.; Teetsov, A.; Bradley, C.R.; and Buchholtz ten Brink, M. 1992. "Colloid Formation During Waste Form Reaction: Implications for Nuclear Waste Disposal." *Science, 256*, 649-651. Washington, D.C.: American Association for the Advancement of Science. TIC: 239138.

104900   Bates, J.K.; Tani, B.S.; Veleckis, E.; and Wronkiewicz, D.J. 1990. "Identification of Secondary Phases Formed During Unsaturated Reaction of UO_2 with EJ-13 Water." *Scientific Basis for Nuclear Waste Management XIII, Symposium held November 27-30, 1989, Boston, Massachusetts*. Oversby, V.M. and Brown, P.W., eds. 176, 499-506. Pittsburgh, Pennsylvania: Materials Research Society. TIC: 203658.

144956   Beckman, R.; Thomas, K.; and Crowe, B. 1988. *Preliminary Report on the Statistical Evaluation of Sorption Data: Sorption as a Function of Mineralogy, Temperature, Time, and Particle Size*. LA-11246-MS. Los Alamos, New Mexico: Los Alamos National Laboratory. ACC: NNA.19890918.0500.

104911   Bennett, D.A.; Hoffman, D.; Nitsche, H.; Russo, R.E.; Torres, R.A.; Baisden, P.A.; Andrews, J.E.; Palmer, C.E.A.; and Silva, R.J. 1992. "Hydrolysis and Carbonate Complexation of Dioxoplutonium(V)." *Radiochimica Acta, 56*, 15-19. München, Germany: R. Oldenbourg Verlag. TIC: 224778.

104370   Benson, L. and Klieforth, H. 1989. "Stable Isotopes in Precipitation and Ground Water in the Yucca Mountain Region, Southern Nevada: Paleoclimatic Implications." *Aspects of Climate Variability in the Pacific and the Western Americas*. Peterson, D.H., ed. Geophysical Monograph 55. Pages 41-59. Washington, D.C.: American Geophysical Union. TIC: 224413.

101036   Benson, L.V. and McKinley, P.W. 1985. *Chemical Composition of Ground Water in the Yucca Mountain Area, Nevada, 1971-84*. Open-File Report 85-484. Denver, Colorado: U.S. Geological Survey. ACC: NNA.19900207.0281.

100727   Benson, L.V.; Robison, J.H.; Blankennagel, R.K.; and Ogard, A.E. 1983. *Chemical Composition of Ground Water and the Locations of Permeable Zones in the Yucca Mountain Area, Nevada*. Open-File Report 83-854. Denver, Colorado: U.S. Geological Survey. ACC: NNA.19870610.0028.

147076   Bevington, P.R. and Robinson, D.K. 1992. *Data Reduction and Error Analysis for the Physical Sciences*. 2nd Edition. New York, New York: McGraw-Hill. TIC: 243514.

105170   Birkholzer, J.; Li, G.; Tsang, C-F.; and Tsang, Y. 1999. "Modeling Studies and Analysis of Seepage into Drifts at Yucca Mountain." *Journal of Contaminant Hydrology, 38*, (1-3), 349-384. New York, New York: Elsevier. TIC: 244160.

154608   Birkholzer, J.T. and Tsang, Y.W. 2000. "Modeling the Thermal-Hydrologic Processes in a Large-Scale Underground Heater Test in Partially Saturated Fractured Tuff." *Water Resources Research, 36*, (6), 1431-1447. Washington, D.C.: American Geophysical Union. TIC: 248278.

100006   Bish, D.L. and Aronson, J.L. 1993. "Paleogeothermal and Paleohydrologic Conditions in Silicic Tuff from Yucca Mountain, Nevada." *Clays and Clay Minerals, 41*, (2), 148-161. Long Island City, New York: Pergamon Press. TIC: 224613.

106336   Bish, D.L.; Broxton, D.E.; Byers, F.M., Jr.; Caporuscio, F.A.; Carlos, B.A.; Levy, S.S.; and Vaniman, D.T. 1984. "Petrofabric Constraints of the Age of Zeolitization at Yucca Mountain." Chapter VIII, Section C of *Research and Development Related to the Nevada Nuclear Waste Storage Investigations, July 1—September 30, 1983*. Bryant, E.A. and Vaniman, D.T., eds. LA-10006-PR. Los Alamos, New Mexico: Los Alamos National Laboratory. ACC: HQS.19880517.1962.

101430   Bish, D.L.; Carey, J.W.; Levy, S.S.; and Chipera, S.J. 1996. *Mineralogy-Petrology Contribution to the Near-Field Environment Report*. Milestone LA3668. Los Alamos, New Mexico: Los Alamos National Laboratory. ACC: MOL.19971111.0588.

101195   Bish, D.L. and Chipera, S.J. 1989. *Revised Mineralogic Summary of Yucca Mountain, Nevada*. LA-11497-MS. Los Alamos, New Mexico: Los Alamos National Laboratory. ACC: NNA.19891019.0029.

101860   Bish, D.L. and Chipera, S.J. 1991. "Detection of Trace Amounts of Erionite Using X-Ray Powder Diffraction: Erionite in Tuffs of Yucca Mountain, Nevada, and Central Turkey." *Clays and Clay Minerals, 39*, (4), 437-445. Long Island City, New York: Pergamon Press. TIC: 203789.

144973   Bish, D.L. and Post, J.E. 1989. "Thermal Behavior of Complex, Tunnel-Structure Manganese Oxides." *American Mineralogist, 74*, 177-186. Washington, D.C.: Mineralogical Society of America. TIC: 222519.

141826   Bish, D.L.; Vaniman, D.T.; Rundberg, R.S.; Wolfsberg, K.; Daniels, W.R.; and Broxton, D.E. 1983. *Natural Sorptive Barriers in Yucca Mountain, Nevada, for Long-Term Isolation of High-Level Waste*. IAEA-CN-43/461. Vienna, Austria: International Atomic Energy Agency. TIC: 228652.

154606   Bjornsson, G. and Bodvarsson, G. 1990. "A Survey of Geothermal Reservoir Properties." *Geothermics, 19*, (1), 17-27. New York, New York: Pergamon Press. TIC: 249741.

101369   Blair, S.C. and Berge, P.A. 1997. *Geomechanical Properties of Topopah Spring Tuff at the 0.5-m Scale: Preliminary Results of Compression Tests at Elevated Temperature*. UCRL-ID-125089. Livermore, California: Lawrence Livermore National Laboratory. TIC: 236600.

129637   Blair, S.C.; Kelly, J.M.; Pine, O.; Pletcher, R.; and Berge, P.A. 1996. *Effect of Radiation on the Mechanical Properties of Topopah Spring Tuff*. UCRL-ID-122899. Livermore, California: Lawrence Livermore National Laboratory. ACC: MOL.19961021.0132.

150392   Blair, S.C. and Lin, W. 1997. *Thermal-Mechanical Behavior of a Heated 3m Block of Fractured Tuff*. UCRL-JC-128350. Livermore, California: Lawrence Livermore National Laboratory. TIC: 248080.

113856   Bolt, G.H. and Bruggenwert, M.G.M., eds. 1978. *Soil Chemistry, A. Basic Elements*. Developments in Soil Science 5A. 2nd Revised Edition. New York, New York: Elsevier. TIC: 243742.

105012   Borovec, Z. 1981. "The Adsorption of Uranyl Species by Fine Clay." *Chemical Geology, 32*, 45-58. Amsterdam, The Netherlands: Elsevier. TIC: 237323.

105056   Bouwer, H. 1991. "Simple Derivation of the Retardation Equation and Application to Preferential Flow and Macrodispersion." *Ground Water, 29*, (1), 41-46. Dublin, Ohio: Water Well Publishing Company. TIC: 224079.

105057   Bowers, T.S. and Burns, R.G. 1990. "Activity Diagrams for Clinoptilolite: Susceptibility of this Zeolite to Further Diagenetic Reactions." *American Mineralogist, 75*, 601-619. Washington, D.C.: Mineralogical Society of America. TIC: 235378.

144977   Breck, D.W. 1984. "Ion Exchange Reactions in Zeolites." Chapter 7 of *Zeolite Molecular Sieves, Structure, Chemistry, and Use*. Malabar, Florida: Robert E. Krieger Publishing Company. TIC: 245213.

100653   Brodsky, N.S.; Riggins, M.; Connolly, J.; and Ricci, P. 1997. *Thermal Expansion, Thermal Conductivity, and Heat Capacity Measurements for Boreholes UE25 NRG--4, UE25 NRG-5, USW NRG-6, and USW NRG-7/7A*. SAND95-1955. Albuquerque, New Mexico: Sandia National Laboratories. ACC: MOL.19980311.0316.

105091   Brookins, D.G. 1983. "Migration and Retention of Elements at the Oklo Natural Reactor." *Environmental Geology, 4*, 201-208. New York, New York: Springer-Verlag. TIC: 239003.

105092   Brookins, D.G. 1988. *Eh-pH Diagrams for Geochemistry*. New York, New York: Springer-Verlag. TIC: 237943.

107386   Broxton, D.E.; Chipera, S.J.; Byers, F.M., Jr.; and Rautman, C.A. 1993. *Geologic Evaluation of Six Nonwelded Tuff Sites in the Vicinity of Yucca Mountain, Nevada for a Surface-Based Test Facility for the Yucca Mountain Project*. LA-12542-MS. Los Alamos, New Mexico: Los Alamos National Laboratory. ACC: NNA.19940224.0128.

100023   Broxton, D.E.; Warren, R.G.; Hagan, R.C.; and Luedemann, G. 1986. *Chemistry of Diagenetically Altered Tuffs at a Potential Nuclear Waste Repository, Yucca Mountain, Nye County, Nevada*. LA-10802-MS. Los Alamos, New Mexico: Los Alamos National Laboratory. ACC: MOL.19980527.0202.

105961   Bruton, C.J. 1991. "Equilibrium Controls of Radionuclide Concentrations in Nevada Test Site Waters: Preliminary Results for Th, U, Np, Pu, Am, Sr, Ra and Pb." Appendix D of *Waste Inventory and Preliminary Source Term Model for the Greater Confinement Disposal Site at the Nevada Test Site*. Chu, M.S.Y. and Bernard, E.A., eds. SAND91-0170. Albuquerque, New Mexico: Sandia National Laboratories. ACC: MOL.19990211.0489.

117033   Bruton, C.J.; Glassley, W.E.; and Meike, A. 1995. *Geothermal Areas as Analogues to Chemical Processes in the Near-Field and Altered Zone of the Potential Yucca Mountain, Nevada Repository*. UCRL-ID-119842. Livermore, California: Lawrence Livermore National Laboratory. ACC: MOV.19980504.0002.

158187   BSC (Bechtel SAIC Company) 2001. *Test Plan for: Moisture Monitoring in the ECRB Bulkheaded Cross Drift*. SITP-02-UZ-001 REV 00. Las Vegas, Nevada: Bechtel SAIC Company. ACC: MOL.20011018.0011.

157330   BSC 2001. *Thermal Tests Thermal-Hydrological Analyses/Model Report*. ANL-NBS-TH-000001 REV 00 ICN 02. Las Vegas, Nevada: Bechtel SAIC Company. ACC: MOL.20011116.0025.

160828   BSC 2001. *Unsaturated Zone and Saturated Zone Transport Properties (U0100)*. ANL-NBS-HS-000019 REV 00 ICN 02. Las Vegas, Nevada: Bechtel SAIC Company. ACC: MOL.20020311.0017.

160247   BSC 2002. *Analysis of Geochemical Data for the Unsaturated Zone*. ANL-NBS-HS-000017 REV 00 ICN 02. Las Vegas, Nevada: Bechtel SAIC Company. ACC: MOL.20020314.0051.

160405   BSC 2002. *Natural Analogue Synthesis Report*. TDR-NBS-GS-000027 REV 00 ICN 02. Las Vegas, Nevada: Bechtel SAIC Company. ACC: MOL.20020520.0288.

160319   BSC 2002. *Thermal Conductivity of the Potential Repository Horizon Model Report*. MDL-NBS-GS-000005 REV 00. Las Vegas, Nevada: Bechtel SAIC Company. ACC: MOL.20020923.0167.

160771   BSC 2002. *Thermal Testing Measurements Report*. ANL-NBS-HS-000041
            REV 00. Las Vegas, Nevada: Bechtel SAIC Company. ACC:
            MOL.20021004.0314.

165564   BSC 2003. *Abstraction of Drift Seepage*. MDL-NBS-HS-000019 REV 00 ICN 01.
            Las Vegas, Nevada: Bechtel SAIC Company. ACC: DOC.20031112.0002.

161773   BSC 2003. *Analysis of Hydrologic Properties Data*. MDL-NBS-HS-000014
            REV 00. Las Vegas, Nevada: Bechtel SAIC Company.
            ACC: DOC.20030404.0004.

165675   BSC 2003. *Committed Ground Support Materials for LA Design*. 800-K0C-WIS0-
            00100-000-00B. Las Vegas, Nevada: Bechtel SAIC Company.
            ACC: ENG.20031009.0012.

163152   BSC 2003. *Dissolved Concentration Limits of Radioactive Elements*. ANL-WIS-
            MD-000010 REV 02. Las Vegas, Nevada: Bechtel SAIC Company.
            ACC: DOC.20030624.0003.

166346   BSC 2003. *Drift Degradation Analysis*. ANL-EBS-MD-000027 REV 02 ICN 01C.
            Las Vegas, Nevada: Bechtel SAIC Company. ACC: MOL.20031210.0125.
            TBV-5654

164890   BSC 2003. *Drift Scale THM Model*. MDL-NBS-HS-000017 REV 00 ICN 01.
            Las Vegas, Nevada: Bechtel SAIC Company. ACC: DOC.20031014.0009.

162050   BSC 2003. *Drift-Scale Coupled Processes (DST and THC Seepage) Models*.
            MDL-NBS-HS-000001 REV 02. Las Vegas, Nevada: Bechtel SAIC Company.
            ACC: DOC.20030804.0004.

166512   BSC 2003. *Drift-Scale Coupled Processes (DST and TH Seepage) Models*.
            MDL-NBS-HS-000015 REV 00C. Las Vegas, Nevada: Bechtel SAIC Company.
            ACC: MOL.20030910.0160. TBV-5666

166347   BSC 2003. *In Situ Field Testing of Processes*. ANL-NBS-HS-000005 REV 02.
            Las Vegas, Nevada: Bechtel SAIC Company. ACC: DOC.20031208.0001.

166498   BSC 2003. *Mountain-Scale Coupled Processes (TH/THC/THM)*. MDL-NBS-HS-
            000007 REV 01. Las Vegas, Nevada: Bechtel SAIC Company.
            ACC: DOC.20031216.0003.

163228   BSC 2003. *Radionuclide Transport Models Under Ambient Conditions*.
            MDL-NBS-HS-000008 REV 01. Las Vegas, Nevada: Bechtel SAIC Company.
            ACC: DOC.20031201.0002.

162267   BSC 2003. *Seepage Calibration Model and Seepage Testing Data*. MDL-NBS-HS-000004 REV 02. Las Vegas, Nevada: Bechtel SAIC Company. ACC: DOC.20030408.0004.

167208   BSC 2003. *Site-Scale Saturated Zone Transport.* MDL-NBS-HS-000010 REV 01. Las Vegas, Nevada: Bechtel SAIC Company. ACC: DOC.20040126.0003.

166242   BSC 2003. *Thermal Conductivity of Non-Repository Lithostratigraphic Layers*. MDL-NBS-GS-000006 REV 00. Las Vegas, Nevada: Bechtel SAIC Company. ACC: DOC.20030815.0001.

165572   BSC 2003. *Underground Layout Configuration*. 800-P0C-MGR0-00100-000-00E. Las Vegas, Nevada: Bechtel SAIC Company. ACC: ENG.20031002.0007.

163045   BSC 2003. *UZ Flow Models and Submodels*. MDL-NBS-HS-000006 REV 01. Las Vegas, Nevada: Bechtel SAIC Company. ACC: DOC.20030818.0002.

164576   BSC 2003. *Ventilation Model and Analysis Report*. ANL-EBS-MD-000030 REV 03 ICN 01. Las Vegas, Nevada: Bechtel SAIC Company. ACC: DOC.20030804.0003.

167461   BSC 2004. *Engineered Barrier System: Physical and Chemical Environment Model*. ANL-EBS-MD-000033 REV 02. Las Vegas, Nevada: Bechtel SAIC Company. ACC: DOC.20040212.0004.

163056   BSC 2004. *Multiscale Thermohydrologic Model.* ANL-EBS-MD-000049 REV 01. Las Vegas, Nevada: Bechtel SAIC Company. ACC: DOC.20040301.0004.

100712   Buddemeier, R.W. and Hunt, J.R. 1988. "Transport of Colloidal Contaminants in Groundwater: Radionuclide Migration at the Nevada Test Site." *Applied Geochemistry, 3*, 535-548. Oxford, England: Pergamon Press. TIC: 224116.

101433   Buesch, D.C. and Spengler, R.W. 1998. "Character of the Middle Nonlithophysal Zone of the Topopah Spring Tuff at Yucca Mountain." *High-Level Radioactive Waste Management, Proceedings of the Eighth International Conference, Las Vegas, Nevada, May 11-14, 1998*. Pages 16-23. La Grange Park, Illinois: American Nuclear Society. TIC: 237082.

100617   Buscheck, T.A. and Nitao, J.J. 1993. "Repository-Heat-Driven Hydrothermal Flow at Yucca Mountain, Part I: Modeling and Analysis." *Nuclear Technology, 104*, (3), 418-448. La Grange Park, Illinois: American Nuclear Society. TIC: 224039.

100655   Buscheck, T.A. and Nitao, J.J. 1993. *The Impact of Repository Heat on Thermo-Hydrological Performance at Yucca Mountain*. UCRL-JC-114791. Livermore, California: Lawrence Livermore National Laboratory. ACC: NNA.19940121.0144.

131789   Buscheck, T.A.; Nitao, J.J.; and Ramspott, L.D. 1996. *Near-Field Thermal-Hydrological Behavior for Alternative Repository Designs at Yucca Mountain*. UCRL-JC-124629. Livermore, California: Lawrence Livermore National Laboratory. ACC: MOL.19971217.0341.

160749   Buscheck, T.A.; Rosenberg, N.D.; Gansemer, J.; and Sun, Y. 2002. "Thermohydrologic Behavior at an Underground Nuclear Waste Repository." *Water Resources Research, 38*, (3), 10-1 through 10-19. Washington, D.C.: American Geophysical Union. TIC: 253566.

104639   Byers, F.M., Jr.; Carr, W.J.; Orkild, P.P.; Quinlivan, W.D.; and Sargent, K.A. 1976. *Volcanic Suites and Related Cauldrons of Timber Mountain-Oasis Valley Caldera Complex, Southern Nevada*. Professional Paper 919. Washington, D.C.: U.S. Geological Survey. TIC: 201146.

162745   Campbell, K.; Wolfsberg, A.; Fabryka-Martin, J.; and Sweetkind, D. 2003. "Chlorine-36 Data at Yucca Mountain: Statistical Tests of Conceptual Models for Unsaturated-Zone Flow." *Journal of Contaminant Hydrology, 62-63*, 43-61. New York, New York: Elsevier. TIC: 254205.

101574   Carlos, B.A. 1985. *Minerals in Fractures of the Unsaturated Zone from Drill Core USW G-4, Yucca Mountain, Nye County, Nevada*. LA-10415-MS. Los Alamos, New Mexico: Los Alamos National Laboratory. ACC: NNA.19920506.0037.

101204   Carlos, B.A. 1987. *Minerals in Fractures of the Saturated Zone from Drill Core USW G-4, Yucca Mountain, Nye County, Nevada*. LA-10927-MS. Los Alamos, New Mexico: Los Alamos National Laboratory. ACC: NNA.19900222.0149.

101575   Carlos, B.A. 1989. *Fracture-Coating Minerals in the Topopah Spring Member and Upper Tuff of Calico Hills from Drill Hole J-13*. LA-11504-MS. Los Alamos, New Mexico: Los Alamos National Laboratory. TIC: 202383.

101325   Carlos, B.A. 1994. *Field Guide to Fracture-Lining Minerals at Yucca Mountain, Nevada*. LA-12803-MS. Los Alamos, New Mexico: Los Alamos National Laboratory. ACC: MOL.19950717.0113.

101324   Carlos, B.A.; Bish, D.L.; and Chipera, S.J. 1990. *Manganese-Oxide Minerals in Fractures of the Crater Flat Tuff in Drill Core USW G-4, Yucca Mountain, Nevada*. LA-11787-MS. Los Alamos, New Mexico: Los Alamos National Laboratory. ACC: NNA.19900206.0163.

101576   Carlos, B.A.; Bish, D.L.; and Chipera, S.J. 1991. "Fracture-Lining Minerals in the Lower Topopah Spring Tuff at Yucca Mountain." *High Level Radioactive Waste Management, Proceedings of the Second Annual International Conference, Las Vegas, Nevada, April 28-May 3, 1991. 1*, 486-493. La Grange Park, Illinois: American Nuclear Society. TIC: 204272.

105210   Carlos, B.A.; Chipera, S.J.; Bish, D.L.; and Craven, S.J. 1993. "Fracture-Lining Manganese Oxide Minerals in Silicic Tuff, Yucca Mountain, Nevada, U.S.A." *Chemical Geology, 107*, 47-69. Amsterdam, The Netherlands: Elsevier. TIC: 208629.

101326   Carlos, B.A.; Chipera, S.J.; and Bish, D.L. 1995. *Distribution and Chemistry of Fracture-Lining Minerals at Yucca Mountain, Nevada*. LA-12977-MS. Los Alamos, New Mexico: Los Alamos National Laboratory. ACC: MOL.19960306.0564.

124275   Carroll, S.; Mroczek, E.; Alai, M.; and Ebert, M. 1998. "Amorphous Silica Precipitation (60 to 120°C): Comparison of Laboratory and Field Rates." *Geochimica et Cosmochimica Acta, 62*, (8), 1379-1396. New York, New York: Elsevier. TIC: 243029.

105224   Chadwick, O.A.; Hendricks, D.M.; and Nettleton, W.D. 1987. "Division S-5—Soil Genesis, Morphology, and Classification, Silica in Duric Soils: I. A Depositional Model." *Soil Science Society of America Journal, 51*, 975-982. Madison, Wisconsin: Soil Science Society of America. TIC: 236964.

101124   Champ, D.R.; Merritt, W.F.; and Young, J.L. 1982. "Potential for the Rapid Transport of Plutonium in Groundwater as Demonstrated by Core Column Studies." *Scientific Basis for Nuclear Waste Management V, Proceedings of the Materials Research Society Fifth International Symposium held June 7-10, 1982, Berlin, Germany*. Lutze, W., ed. *11*, 745-754. New York, New York: North-Holland. TIC: 204398.

154672   Chan, T.; Binnall, E.; Nelson, P.; Stolzman, R.; Wan, O.; Weaver, C.; Ang, K.; Braley, J.; and McEvoy, M. 1980. *Thermal and Thermomechanical Data from In Situ Heater Experiments at Stripa, Sweden*. LBL-11477. Berkeley, California: Lawrence Berkeley Laboratory. TIC: 211543.

100025   Chipera, S.J.; Bish, D.L.; and Carlos, B.A. 1995. "Equilibrium Modeling of the Formation of Zeolites in Fractures at Yucca Mountain, Nevada." Natural *Zeolites '93: Occurrence, Properties, Use, Proceedings of the 4th International Conference on the Occurrence, Properties, and Utilization of Natural Zeolites, June 20-28, 1993, Boise, Idaho*. Ming, D.W. and Mumpton, F.A., eds. Pages 565-577. Brockport, New York: International Committee on Natural Zeolites. TIC: 243086.

105286   Choi, J.S. and Pigford, T.H. 1981. "Water Dilution Volumes for High-Level Wastes." *Transactions of the American Nuclear Society Winter Meeting, San Francisco, California, 1981, 39*, 176-177. La Grange Park, Illinois: American Nuclear Society. TIC: 236930.

101125   Claassen, H.C. 1985. *Sources and Mechanisms of Recharge for Ground Water in the West-Central Amargosa Desert, Nevada—A Geochemical Interpretation*. U.S. Geological Survey Professional Paper 712-F. Washington, D.C.: United States Government Printing Office. TIC: 204574.

101332   Clark, D.L. 1994. *Letter Report on the Status of Pu(IV) Colloid Studies*. Milestone 4026. Draft. Los Alamos, New Mexico: Los Alamos National Laboratory. ACC: MOL.19951002.0234.

105738   Clark, I.D. and Fritz, P. 1997. *Environmental Isotopes in Hydrogeology*. Boca Raton, Florida: Lewis Publishers. TIC: 233503.

105752   Cleveland, J.M. 1979. "Critical Review of Plutonium Equilibria of Environmental Concern." Chapter 16 of *Chemical Modeling in Aqueous Systems, Speciation, Sorption, Solubility, and Kinetics*. Jenne, E.A., ed. ACS Symposium Series 93. Washington, D.C.: American Chemical Society. TIC: 208922.

105754   Cleveland, J.M. 1979. *The Chemistry of Plutonium*. La Grange Park, Illinois: American Nuclear Society. TIC: 10231.

105758   Combes, J.M.; Chisholm-Brause, C.J.; Brown, G.E., Jr.; Parks, G.A.; Conradson, S.D.; Eller, P.G.; Triay, I.R.; Hobart, D.E.; and Meijer, A. 1992. "EXAFS Spectroscopic Study of Neptunium(V) Sorption at the a-FeOOH/Water Interface." *Environmental Science & Technology, 26*, (2), 376-382. Washington, D.C.: American Chemical Society. TIC: 224053.

105756   Conca, J.L. and Wright, J. 1992. "A New Technology for Direct Measurements of Unsaturated Transport." *Proceedings of the International Topical Meeting on Nuclear and Hazardous Waste Management, Spectrum '92, August 23-27, 1992, Boise, Idaho. 2*, 1546-1555. La Grange Park, Illinois: American Nuclear Society. TIC: 205023.

100436   Conca, J.L. and Wright, J. 1992. "Diffusion and Flow in Gravel, Soil, and Whole Rock." *Applied Hydrogeology, 1*, 5-24. Hanover, Germany: Verlag Heinz Heise GmbH. TIC: 224081.

166022   Cornell, R.M. 1993. "Adsorption of Cesium on Minerals: A Review." *Journal of Radioanalytical and Nuclear Chemistry, Articles, 171*, (2), 483-500. Lausanne, Switzerland: Elsevier. TIC: 226328.

152436   Costantino, M.S.; Carlson, S.R.; and Blair, S.C. 1998. *Results of a Coupled Fracture-Flow Test at the 0.5-m Scale*. UCRL-ID-131493. Livermore, California: Lawrence Livermore National Laboratory. ACC: MOL.20001002.0156.

105732   Cotton, F.A. and Wilkinson, G. 1988. *Advanced Inorganic Chemistry*. 5th Edition. New York, New York: John Wiley & Sons. TIC: 236867.

101039   Craig, R.W. and Johnson, K.A. 1984. *Geohydrologic Data for Test Well UE-25p#1, Yucca Mountain Area, Nye County, Nevada*. Open-File Report 84-450. Denver, Colorado: U.S. Geological Survey. ACC: NNA.19870406.0256.

101040   Craig, R.W. and Robison, J.H. 1984. *Geohydrology of Rocks Penetrated by Test Well UE-25p#1, Yucca Mountain Area, Nye County, Nevada*. Water-Resources Investigations Report 84-4248. Denver, Colorado: U.S. Geological Survey. ACC: NNA.19890905.0209.

105768   Cramer, J.J. and Sargent, F.P. 1994. "The Cigar Lake Analog Study: An International R&D Project." *High Level Radioactive Waste Management, Proceedings of the Fifth Annual International Conference, Las Vegas, Nevada, May 22-26, 1994. 4*, 2237-2242. La Grange Park, Illinois: American Nuclear Society. TIC: 210984.

166025   Cremers, A.; Elsen, A.; De Preter, P.; and Maes, A. 1988. "Quantitative Analysis of Radiocaesium Retention in Soils." *Nature, 335*, (6633), 247-249. London, England: Macmillan Publishing. TIC: 255181.

100111   CRWMS M&O (Civilian Radioactive Waste Management System Management and Operating Contractor) 1994. *Total System Performance Assessment - 1993: An Evaluation of the Potential Yucca Mountain Repository*. B00000000-01717-2200-00099 REV 01. Las Vegas, Nevada: CRWMS M&O. ACC: NNA.19940406.0158.

146917   CRWMS M&O 1997. *Drift Scale Test Design and Forecast Results*. BAB000000-01717-4600-00007 REV 01. Las Vegas, Nevada: CRWMS M&O. ACC: MOL.19980710.0155.

100401   CRWMS M&O 1997. *Summary Report Geochemistry/Transport Laboratory Tests*. Deliverable SP23QM3. Las Vegas, Nevada: CRWMS M&O. ACC: MOL.19980122.0053.

103564   CRWMS M&O 1997. *Yucca Mountain Site Geotechnical Report*. B00000000-01717-5705-00043 REV 01. Two volumes. Las Vegas, Nevada: CRWMS M&O. ACC: MOL.19971017.0736; MOL.19971017.0737.

111115   CRWMS M&O 1998. *Drift Scale Test As-Built Report*. BAB000000-01717-5700-00003 REV 01. Las Vegas, Nevada: CRWMS M&O. ACC: MOL.19990107.0223.

108306   CRWMS M&O 1998. *Drift Scale Test Progress Report No. 1*. BAB000000-01717-5700-00004 REV 01. Las Vegas, Nevada: CRWMS M&O. ACC: MOL.19990209.0240.

104878   CRWMS M&O 1998. *Evaluation of Flow and Transport Models of Yucca Mountain, Based on Chlorine-36 and Chloride Studies for FY98*. BA0000000-01717-5700-00007 REV 00. Las Vegas, Nevada: CRWMS M&O. ACC: MOL.19981208.0119.

129261   CRWMS M&O 1999. *Single Heater Test Final Report*. BAB000000-01717-5700-00005 REV 00 ICN 1. Las Vegas, Nevada: CRWMS M&O. ACC: MOL.20000103.0634.

145796   CRWMS M&O 2000. *Engineered Barrier System Degradation, Flow, and Transport Process Model Report*. TDR-EBS-MD-000006 REV 00. Las Vegas, Nevada: CRWMS M&O. ACC: MOL.20000324.0558.

146460   CRWMS M&O 2000. *Environment on the Surfaces of the Drip Shield and Waste Package Outer Barrier*. ANL-EBS-MD-000001 REV 00. Las Vegas, Nevada: CRWMS M&O. ACC: MOL.20000328.0590.

146589   CRWMS M&O 2000. *Near Field Environment Process Model Report*. TDR-NBS-MD-000001 REV 00. Las Vegas, Nevada: CRWMS M&O. ACC: MOL.20000421.0034.

153246   CRWMS M&O 2000. *Total System Performance Assessment for the Site Recommendation*. TDR-WIS-PA-000001 REV 00 ICN 01. Las Vegas, Nevada: CRWMS M&O. ACC: MOL.20001220.0045.

145774   CRWMS M&O 2000. *Unsaturated Zone Flow and Transport Model Process Model Report*. TDR-NBS-HS-000002 REV 00. Las Vegas, Nevada: CRWMS M&O. ACC: MOL.20000320.0400.

151945   CRWMS M&O 2000. *Yucca Mountain Site Description*. TDR-CRW-GS-000001 REV 01 ICN 01. Las Vegas, Nevada: CRWMS M&O. ACC: MOL.20001003.0111.

131816   Daily, W.; Lin, W.; and Buscheck, T. 1987. "Hydrological Properties of Topopah Spring Tuff: Laboratory Measurements." *Journal of Geophysical Research, 92*, (B8), 7854-7864. Washington, D.C.: American Geophysical Union. TIC: 226512.

101333   Daniels, W.R.; Erdal, B.R.; and Vaniman, D.T., eds. 1983. *Research and Development Related to the Nevada Nuclear Waste Storage Investigations, July 1— September 30, 1982*. LA-9577-PR. Los Alamos, New Mexico: Los Alamos National Laboratory. ACC: NNA.19870406.0180.

105803   Daniels, W.R.; Wolfsberg, K.; Rundberg, R.S.; Ogard, A.E.; Kerrisk, J.F.; Duffy, C.J.; Newton, T.W.; Thompson, J.L.; Bayhurst, B.P.; Bish, D.L.; Blacic, J.D.; Crowe, B.M.; Erdal, B.R.; Griffith, J.F.; Knight, S.D.; Lawrence, F.O.; Rundberg, V.L.; Skyes, M.L.; Thompson, G.M.; Travis, B.J.; Treher, E.N.; Vidale, R.J.; Walter, G.R.; Aguilar, R.D.; Cisneros, M.R.; Maestas, S.; Mitchell, A.J.; Oliver, P.Q.; Raybold, N.A.; and Wanek, P.L. 1982. *Summary Report on the Geochemistry of Yucca Mountain and Environs*. LA-9328-MS. Los Alamos, New Mexico: Los Alamos National Laboratory. ACC: NNA.19870406.0243.

103803   Daveler, S.A. and Wolery, T.J. 1992. *EQPT, A Data File Preprocessor for the EQ3/6 Software Package: User's Guide and Related Documentation (Version 7.0)*. UCRL-MA-110662 PT II. Livermore, California: Lawrence Livermore National Laboratory. TIC: 205240.

105808   Davis, J.A.; James, R.O.; and Leckie, J.O. 1978. "Surface Ionization and Complexation at the Oxide/Water Interface: I. Computation of Electrical Double Layer." *Journal of Colloid and Interface Science, 63*, (3), 480-499. New York, New York: Academic Press. TIC: 223904.

105814   Davis, S.N. and Murphy, E. 1987. *Dating Ground Water and the Evaluation of Repositories for Radioactive Waste*. NUREG/CR-4912. Washington, D.C.: U.S. Nuclear Regulatory Commission. ACC: NNA.19900522.0260.

101557   Day, W.C.; Potter, C.J.; Sweetkind, D.S.; Dickerson, R.P.; and San Juan, C.A. 1998. *Bedrock Geologic Map of the Central Block Area, Yucca Mountain, Nye County, Nevada*. Miscellaneous Investigations Series Map I-2601. Washington, D.C.: U.S. Geological Survey. ACC: MOL.19980611.0339.

100439   de Marsily, G. 1986. *Quantitative Hydrogeology: Groundwater Hydrology for Engineers*. San Diego, California: Academic Press. TIC: 208450.

105377   Degueldre, C.; Grauer, R.; Laube, A.; Oess, A.; and Silby, H. 1996. "Colloid Properties in Granitic Groundwater Systems. II: Stability and Transport Study." *Applied Geochemistry, 11*, 697-710. Oxford, England: Elsevier. TIC: 236569.

120929   Degueldre, C.; Laube, A.; and Scholtis, A. 1994. *WLB: A Study of Colloids in Ground-Waters at the Wellenberg Site: Status Report*. Interner Bericht 94-41. Wettingen, Switzerland: Nationale Genossenschaft für die Lagerung Radioaktiver Abfalle. TIC: 246054.

100723   Degueldre, C.; Pfeiffer, H.R.; Alexander, W.; Wernli, B.; and Bruetsch, R. 1996. "Colloid Properties in Granitic Groundwater Systems. I: Sampling and Characterization." *Applied Geochemistry, 11*, 677-694. Oxford, England: Elsevier. TIC: 236886.

105384   Dettinger, M.D. 1989. "Reconnaissance Estimates of Natural Recharge to Desert Basins in Nevada, U.S.A., by Using Chloride-Balance Calculations." *Journal of Hydrology, 106*, 55-78. Amsterdam, The Netherlands: Elsevier. TIC: 236967.

164737   Ding, M.; Reimus, P.W.; Ware, S.D.; and Meijer, A. 2003. "Experimental Studies of Radionuclide Migration in Yucca Mountain Alluvium." *Proceedings of the 10th International High-Level Radioactive Waste Management Conference (IHLRWM), March 30-April 2, 2003, Las Vegas, Nevada*. Pages 126-135. La Grange Park, Illinois: American Nuclear Society. TIC: 254559.

155943   DOE (U.S. Department of Energy) 2002. *Yucca Mountain Science and Engineering Report*. DOE/RW-0539, Rev. 1. Washington, D.C.: U.S. Department of Energy, Office of Civilian Radioactive Waste Management. ACC: MOL.20020404.0042.

105439   Doi, K.; Hirono, S.; and Sakamaki, Y. 1975. "Uranium Mineralization by Groundwater in Sedimentary Rocks, Japan." *Economic Geology, 70*, 628-646. El Paso, Texas: Economic Geology Publishing. TIC: 236987.

105464   Dozol, M. and Hageman, R. 1993. "Radionuclide Migration in Groundwaters: Review of the Behaviour of Actinides." *Pure and Applied Chemistry, 65*, (5), 1081-1102. Oxford, United Kingdom: Blackwell Scientific Publishers. TIC: 236897.

118564   Drever, J.I. 1988. *The Geochemistry of Natural Waters*. 2nd Edition. Englewood Cliffs, New Jersey: Prentice-Hall. TIC: 242836.

105467   Drever, J.I. and Smith, C.L. 1978. "Cyclic Wetting and Drying of the Soil Zone as an Influence on the Chemistry of Ground Water in Arid Terrains." *American Journal of Science, 278*, 1448-1454. New Haven, Connecticut: Yale University, Kline Geology Laboratory. TIC: 237357.

150344   Duff, M.C.; Newville, M.; Hunter, D.B.; Bertsch, P.M.; Sutton, S.R.; Triay, I.R.; Vaniman, D.T.; Eng, P.; and Rivers, M.L. 1999. "Micro-XAS Studies with Sorbed Plutonium on Tuff." *Journal of Synchrotron Radiation, 6*, (3), 350-352. Copenhagen, Denmark: Munksgaard International Booksellers and Publishers. TIC: 248072.

129649   Durham, W.B.; Beiriger, J.M.; Axelrod, M.; and Trettenaro, S. 1986. "The Effect of Gamma Radiation on the Strength and Elasticity of Climax Stock and Westerly Granites." *Nuclear and Chemical Waste Management, 6*, 159-168. New York, New York: Pergamon Journals. TIC: 236715.

105489   Eberl, D. and Hower, J. 1976. "Kinetics of Illite Formation." *Geological Society of America Bulletin, 87*, 1326-1330. Boulder, Colorado: Geological Society of America. TIC: 223629.

152135 Eckhardt, R.C. 2000. "Site Description, Sec. 5 & 10, Selected Tables and Figures." Letter from R.C. Eckhardt (LANL) to A. Simmons (LBNL), EES-13-06-00-176, June 27, 2000, with enclosures. ACC: MOL.20000808.0058.

108015 Efurd, D.W.; Runde, W.; Banar, J.C.; Janecky, D.R.; Kaszuba, J.P.; Palmer, P.D.; Roensch, F.R.; and Tait, C.D. 1998. "Neptunium and Plutonium Solubilities in a Yucca Mountain Groundwater." *Environmental Science & Technology, 32*, (24), 3893-3900. Easton, Pennsylvania: American Chemical Society. TIC: 243857.

105538 Efurd, D.W.; Runde, W.; Banar, J.C.; Roensch, F.R.; Palmer, P.D.; Clark, D.L.; and Tait, C.D. 1996. *Measured Solubilities and Speciation of Neptunium and Plutonium in J-13 Groundwater*. Milestone 3411. Los Alamos, New Mexico: Los Alamos National Laboratory. TIC: 237839.

105532 Emett, D.C.; Hutchinson, D.D.; Jonson, N.A.; and O'Hair, K.L. 1994. *Water Resources Data, Nevada, Water Year 1993*. Water-Data Report NV-93-1. Carson City, Nevada: U.S. Geological Survey. TIC: 236836.

105533 Eriksson, E. 1960. "The Yearly Circulation of Chloride and Sulfur in Nature: Meteorological, Geochemical, and Pedalogical Implications. Part II." *Tellus, 12*, (1), 63-109. Stockholm, Sweden: Swedish Geophysical Society. TIC: 236893.

105535 Ernst, W.G. and Calvert, S.E. 1969. "An Experimental Study of the Recrystallization of Porcelanite and Its Bearing on the Origin of Some Bedded Cherts." *American Journal of Science, 267A*, 114-133. New Haven, Connecticut: Yale University, Kline Geology Laboratory. TIC: 224645.

100144 Fabryka-Martin, J.T.; Flint, A.L.; Sweetkind, D.S.; Wolfsberg, A.V.; Levy, S.S.; Roemer, G.J.C.; Roach, J.L.; Wolfsberg, L.E.; and Duff, M.C. 1997. *Evaluation of Flow and Transport Models of Yucca Mountain, Based on Chlorine-36 Studies for FY97*. LA-CST-TIP-97-010. Los Alamos, New Mexico: Los Alamos National Laboratory. ACC: MOL.19980204.0916.

101003 Fabryka-Martin, J.T.; Turin, H.J.; Wolfsberg, A.V.; Brenner, D.; Dixon, P.R.; and Musgrave, J.A. 1996. *Summary Report of Chlorine-36 Studies*. LA-CST-TIP-96-003. Draft. Los Alamos, New Mexico: Los Alamos National Laboratory. ACC: MOL.19970103.0037.

162737 Fabryka-Martin, J.T.; Turin, H.J.; Wolfsberg, A.V.; Brenner, D.L.; Dixon, P.R.; and Musgrave, J.A. 1998. *Summary Report of Chlorine-36 Studies as of August 1996*. LA-13458-MS. Los Alamos, New Mexico: Los Alamos National Laboratory. ACC: MOL.20031119.0395.

144839   Fabryka-Martin, J.; Wolfsberg, A.V.; Dixon, P.R.; Levy, S.; Musgrave, J.; and Turin, H.J. 1996. *Summary Report of Chlorine-36 Studies: Sampling, Analysis and Simulation of Chlorine-36 in the Exploratory Studies Facility.* Milestone 3783M. Los Alamos, New Mexico: Los Alamos National Laboratory. ACC: MOL.19970103.0047.

100145   Fabryka-Martin, J.T.; Wolfsberg, A.V.; Dixon, P.R.; Levy, S.S.; Musgrave, J.A.; and Turin, H.J. 1997. *Summary Report of Chlorine-36 Studies: Sampling, Analysis, and Simulation of Chlorine-36 in the Exploratory Studies Facility.* LA-13352-MS. Los Alamos, New Mexico: Los Alamos National Laboratory. ACC: MOL.19980812.0254.

146355   Fabryka-Martin, J.T.; Wolfsberg, A.V.; Roach, J.L.; Winters, S.T.; and Wolfsberg, L.E. 1998. "Using Chloride to Trace Water Movement in the Unsaturated Zone at Yucca Mountain." *High-Level Radioactive Waste Management, Proceedings of the Eighth International Conference, Las Vegas, Nevada, May 11-14, 1998.* Pages 264-268. La Grange Park, Illinois: American Nuclear Society. TIC: 237082.

100570   Fabryka-Martin, J.T.; Wolfsberg, A.V.; Levy, S.S.; Roach, J.L.; Winters, S.T.; Wolfsberg, L.E.; Elmore, D.; and Sharma, P. 1998. "Distribution of Fast Hydrologic Paths in the Unsaturated Zone at Yucca Mountain." *High-Level Radioactive Waste Management, Proceedings of the Eighth International Conference, Las Vegas, Nevada, May 11-14, 1998.* Pages 93-96. La Grange Park, Illinois: American Nuclear Society. TIC: 237082.

105566   Felmy, A.R.; Rai, D.; and Fulton, R.W. 1990. "The Solubility of $AmOHCO_3(c)$ and the Aqueous Thermodynamics of the System Na^+-Am^{3+}-HCO_3^--CO_3^{2-}-OH^--H_2O." *Radiochimica Acta, 50,* 193-204. München, Germany: R. Oldenbourg Verlag. TIC: 236870.

105597   Flexser, S. and Wollenberg, H.A. 1992. "Radioelements and Their Occurrence with Secondary Minerals in Heated and Unheated Tuff at the Nevada Test Site." *High Level Radioactive Waste Management, Proceedings of the Third International Conference, Las Vegas, Nevada, April 12-16, 1992. 2,* 1593-1598. La Grange Park, Illinois: American Nuclear Society. TIC: 204231.

100394   Flint, L.E. and Flint, A.L. 1995. *Shallow Infiltration Processes at Yucca Mountain, Nevada—Neutron Logging Data 1984-93.* Water-Resources Investigations Report 95-4035. Denver, Colorado: U.S. Geological Survey. ACC: MOL.19960924.0577.

146639   Fournier, R.O. 1983. "A Method of Calculating Quartz Solubilities in Aqueous Sodium Chloride Solutions." *Geochimica et Cosmochimica Acta, 47,* 579-586. New York, New York: Pergamon Press. TIC: 236664.

110645   French, R.H. 1986. *Daily, Seasonal, and Annual Precipitation at the Nevada Test Site, Nevada*. DOE/NV/10384-01. Las Vegas, Nevada: Desert Research Institute, Water Resources Center. TIC: 206773.

108201   Fuger, J. 1992. "Thermodynamic Properties of Actinide Aqueous Species Relevant to Geochemical Problems." *Radiochimica Acta, 58/59*, (I), 81-91. Munchen, Germany: R. Oldenbourg Verlag. TIC: 245944.

127184   Gascoyne, M. 1992. "Geochemistry of the Actinides and Their Daughters." Chapter 2 of *Uranium-Series Disequilibrium: Applications to Earth, Marine, and Environmental Sciences*. Ivanovich, M. and Harmon, R.S., eds. 2nd Edition. New York, New York: Oxford University Press. TIC: 234680.

154800   Gascoyne, M.; Miller, N.H.; and Neymark, L.A. 2002. "Uranium-Series Disequilibrium in Tuffs from Yucca Mountain, Nevada, as Evidence of Pore-Fluid Flow Over the Last Million Years." *Applied Geochemistry, 17*, (6), 781-792. New York, New York: Elsevier. TIC: 251901.

144994   GCX 1994. *Ground Water Compositional Parameters Most Critical to the Sorption Behavior of Radionuclides-of-Concern to the Yucca Mountain Project*. Milestone 4032. Draft. Albuquerque, New Mexico: GCX. ACC: MOL.19950630.0308.

105636   George-Aniel, B.; Leroy, J.L.; and Poty, B. 1991. "Volcanogenic Uranium Mineralizations in the Sierra Pena Blanca District, Chihuahua, Mexico: Three Genetic Models." *Economic Geology, 86*, (2), 233-248. El Paso, Texas: Economic Geology Publishing. TIC: 237050.

105643   Giblin, A.M. and Snelling, A.A. 1983. "Application of Hydrogeochemistry to Uranium Exploration in the Pine Creek Geosyncline, Northern Territory, Australia." *Journal of Geochemical Exploration, 19*, 33-55. Amsterdam, The Netherlands: Elsevier. TIC: 237423.

105641   Gifford, R.O. and Frugoli, D.M. 1964. "Silica Source in Soil Solutions." *Science, 145*, 386-388. Washington, D.C.: American Association for the Advancement of Science. TIC: 239118.

140011   Glassley, W.E. 1996. "Equilibrium Bounds on Water Chemistry and Mineralogical Changes Produced by Near-Field Relative Humidity Changes." Chapter 3 Section 3.4.1 of *Near-Field and Altered-Zone Environment Report*. Wilder, D.G., ed. UCRL-LR-124998, Volume II. Livermore, California: Lawrence Livermore National Laboratory. ACC: MOL.19961212.0122.

105714   Goodwin, B.W.; Cramer, J.J.; and McConnell, D.B. 1989. "The Cigar Lake Uranium Deposit: An Analogue for Nuclear Fuel Waste Disposal." Appendix B of *Natural Analogues in Performance Assessments for the Disposal of Long Lived Radioactive Wastes*. Technical Reports Series 304. Vienna, Austria: International Atomic Energy Agency. TIC: 7851.

101671   Grenthe, I.; Fuger, J.; Konings, R.J.M.; Lemire, R.J.; Muller, A.B.; Nguyen-Trung, C.; and Wanner, H. 1992. *Chemical Thermodynamics of Uranium*. Volume 1 of *Chemical Thermodynamics*. Wanner, H. and Forest, I., eds. Amsterdam, The Netherlands: North-Holland Publishing Company. TIC: 224074.

105905   Hakanen, M. and Lindberg, A. 1991. "Sorption of Neptunium Under Oxidizing and Reducing Groundwater Conditions." *Radiochimica Acta, 52/53*, 147-151. Munchen, Germany: R. Oldenbourg Verlag. TIC: 237041.

100123   Hardin, E.L. 1998. *Near-Field/Altered-Zone Models Report*. UCRL-ID-129179. Livermore, California: Lawrence Livermore National Laboratory. ACC: MOL.19980630.0560.

100534   Hardin, E.L. and Chesnut, D.A. 1997. *Synthesis Report on Thermally Driven Coupled Processes*. Milestone SPL8BM4. Livermore, California: Lawrence Livermore National Laboratory. ACC: MOL.19980113.0395.

105926   Haschke, J.M. and Ricketts, T.E. 1997. "Adsorption of Water on Plutonium Dioxide." *Journal of Alloys and Compounds, 252*, 148-156. Lausanne, Switzerland: Elsevier. TIC: 241047.

116809   Hevesi, J.A.; Flint, A.L.; and Istok, J.D. 1992. "Precipitation Estimation in Mountainous Terrain Using Multivariate Geostatistics. Part II: Isohyetal Maps." *Journal of Applied Meteorology, 31*, (7), 677-688. Boston, Massachusetts: American Meteorological Society. TIC: 225248.

106037   Hiester, N.K. and Vermeulen, T. 1952. "Saturation Performance of Ion-Exchange and Adsorption Columns." *Chemical Engineering Progress, 48*, (10), 505-516. New York, New York: American Institute of Chemical Engineers. TIC: 224052.

106039   Ho, C.H. and Miller, N.H. 1986. "Adsorption of Uranyl Species from Bicarbonate Solution onto Hematite Particles." *Journal of Colloid and Interface Science, 110*, (1), 165-171. New York, New York: Academic Press. TIC: 226326.

106040   Hobart, D.E. 1990. "Actinides in the Environment." Chapter XIII of *Proceedings of the Robert A. Welch Foundation Conference on Chemical Research XXXIV, Fifty Years with Transuranium Elements, Houston, Texas, October 22-23, 1990*. Houston, Texas: Robert A. Welch Foundation. TIC: 237030.

141452   Hobart, D.E.; Morris, D.E.; Palmer, P.D.; and Newton, T.W. 1990. "Formation, Characterization, and Stability of Plutonium(IV) Colloid: A Progress Report." *Proceedings of the Topical Meeting on Nuclear Waste Isolation in the Unsaturated Zone, FOCUS '89, September 17-21, 1989, Las Vegas, Nevada*. Pages 118-124. La Grange Park, Illinois: American Nuclear Society. TIC: 212738.

159108   Horita, J. and Wesolowski, D.J. 1994. "Liquid-Vapor Fractionation of Oxygen and Hydrogen Isotopes of Water from the Freezing to the Critical Temperature." *Geochimica et Cosmochimica Acta, 58*, (16), 3425-3437. New York, New York: Elsevier. TIC: 240153.

106131   Hsi, C-K.D. and Langmuir, D. 1985. "Adsorption of Uranyl onto Ferric Oxyhydroxides: Application of the Surface Complexation Site-Binding Model." *Geochimica et Cosmochimica Acta, 49*, 1931-1941. New York, New York: Pergamon Press. TIC: 224090.

106254   Itagaki, H.; Nakayama, S.; Tanaka, S.; and Yamawaki, M. 1992. "Effect of Ionic Strength on the Solubility of Neptunium(V) Hydroxide." *Radiochimica Acta, 58/59*, 61-66. München, Germany: R. Oldenbourg Verlag. TIC: 240833.

106265   Janecky, D.R.; Duffy, C.J.; Tait, C.D.; and Clark, D. 1997. *Letter Report on Thermochemical Data on Actinides for Modeling*. Milestone 4025. Los Alamos, New Mexico: Los Alamos National Laboratory. TIC: 243470.

101338   Janecky, D.R.; Enter, J.; Duffy, C.; and Tait, C.D. 1995. *Modeled Actinide Solubilities and Speciation*. Milestone 3463. Draft. Los Alamos, New Mexico: Los Alamos National Laboratory. ACC: MOL.19960417.0131.

101630   Johnson, J.W.; Knauss, K.G.; Glassley, W.E.; DeLoach, L.D.; and Tompson, A.F.B. 1998. "Reactive Transport Modeling of Plug-Flow Reactor Experiments: Quartz and Tuff Dissolution at 240°C." *Journal of Hydrology, 209*, 81-111. Amsterdam, The Netherlands: Elsevier. TIC: 240986.

101632   Johnson, J.W.; Oelkers, E.H.; and Helgeson, H.C. 1992. "SUPCRT92: A Software Package for Calculating the Standard Molal Thermodynamic Properties of Minerals, Gases, Aqueous Species, and Reactions from 1 to 5000 Bar and 0 to 1000°C." *Computers & Geosciences, 18*, (7), 899-947. New York, New York: Pergamon Press. TIC: 234273.

108203   Kaplan, D.I.; Bertsch, P.M.; Adriano, D.C.; and Orlandini, K.A. 1994. "Actinide Association with Groundwater Colloids in a Coastal Plain Aquifer." *Radiochimica Acta, 66/67*, 181-187. Munchen, Germany: R. Oldenbourg Verlag. TIC: 245939.

106312   Katz, J.J.; Seaborg, G.T.; and Morss, L.R., eds. 1986. *The Chemistry of the Actinide Elements*. 2nd Edition. Two volumes. New York, New York: Chapman and Hall. TIC: 243942.

106313   Keeney-Kennicutt, W.L. and Morse, J.W. 1985. "The Redox Chemistry of $Pu(V)O_2^+$ Interaction with Common Mineral Surfaces in Dilute Solutions and Seawater." *Geochimica et Cosmochimica Acta, 49*, (12), 2577-2588. New York, New York: Pergamon. TIC: 237000.

103282   Kersting, A.B.; Efurd, D.W.; Finnegan, D.L.; Rokop, D.J.; Smith, D.K.; and Thompson, J.L. 1999. "Migration of Plutonium in Ground Water at the Nevada Test Site." *Nature, 397*, (6714), 56-59. London, England: Macmillan Journals. TIC: 243597.

166024   Khan, S.A.; Rehman, Riaz-ur-; and Kahn, M.A. 1994. "Sorption of Cesium on Bentonite." *Waste Management, 14*, (7), 629-642. New York, New York: Pergamon. TIC: 255184.

100767   Kieft, T.L.; Kovacik, W.P., Jr.; Ringelberg, D.B.; White, D.C.; Haldeman, D.L.; Amy, P.S.; and Hersman, L.E. 1997. "Factors Limiting Microbial Growth and Activity at a Proposed High-Level Nuclear Repository, Yucca Mountain, Nevada." *Applied and Environmental Microbiology, 63*, (8), 3128-3133. Washington, D.C.: American Society for Microbiology. TIC: 236444.

162822   Kigoshi, K. 1971. "Alpha-Recoil Thorium-234: Dissolution into Water and the Uranium-234/Uranium-238 Disequilibrium in Nature." *Science, 173,* 47-48. Washington, D.C.: American Association for the Advancement of Science. TIC: 254208.

106387   Kim, J.I.; Zeh, P.; and Delakovitz, B. 1992. "Chemical Interactions of Actinide Ions with Groundwater Colloids in Gorleben Aquifer Systems." *Radiochimica Acta, 58/59*, 147-154. München, Germany: R. Oldenbourg Verlag. TIC: 236935.

101340   Kitten, J.; Vaniman, D.; Triay, I.; and Thompson, J. 1997. *Comparative Microautoradiography and Batch Sorption Experiments on Three Principal Lithologies from Yucca Mountain, Nevada*. Milestone SP341CM4. Los Alamos, New Mexico: Los Alamos National Laboratory. ACC: MOL.19990211.0486.

100050   Knauss, K.G. 1987. "Zeolitization of Glassy Topopah Spring Tuff Under Hydrothermal Conditions." *Scientific Basis for Nuclear Waste Management X, Symposium held December 1-4, 1986, Boston, Massachusetts*. Bates, J.K. and Seefeldt, W.B., eds. 84, 737–745. Pittsburgh, Pennsylvania: Materials Research Society. TIC: 203663.

100152   Knauss, K.G.; Beiriger, W.J.; and Peifer, D.W. 1987. *Hydrothermal Interaction of Solid Wafers of Topopah Spring Tuff with J-13 Water at 90 and 150°C Using Dickson-Type, Gold-Bag Rocking Autoclaves: Long-Term Experiments*. UCRL-53722. Livermore, California: Lawrence Livermore National Laboratory. ACC: NNA.19870713.0081.

100150   Knauss, K.G.; Beiriger, W.J.; Peifer, D.W.; and Piwinskii, A.J. 1985. *Hydrothermal Interaction of Solid Wafers of Topopah Spring Tuff with J-13 Water and Distilled Water at 90, 150, and 250°C, Using Dickson-Type, Gold-Bag Rocking Autoclaves*. UCRL-53645. Livermore, California: Lawrence Livermore National Laboratory. ACC: NNA.19900207.0282.

100151   Knauss, K.G. and Peifer, D.W. 1986. *Reaction of Vitric Topopah Spring Tuff and J-13 Ground Water Under Hydrothermal Conditions Using Dickson-Type, Gold-Bag Rocking Autoclaves.* UCRL-53795. Livermore, California: Lawrence Livermore National Laboratory. ACC: NNA.19891102.0117.

145636   Kneafsey, T.J. and Pruess, K. 1998. "Laboratory Experiments on Heat-Driven Two-Phase Flows in Natural and Artificial Rock Fractures." *Water Resources Research, 34*, (12), 3349-3367. Washington, D.C.: American Geophysical Union. TIC: 247468.

106443   Kung, K-H. and McBride, M.B. 1989. "Adsorption of Para-Substituted Benzoates on Iron Oxides." *Soil Science Society of America Journal, 53*, 1673-1678. Madison, Wisconsin: Soil Science Society of America. TIC: 237036.

106445   Kung, K-H. and McBride, M.B. 1989. "Coordination Complexes of p-Hydroxybenzoate on Fe Oxides." *Clay and Clay Minerals, 37*, (4), 333-340. Boulder, Colorado: Clay Minerals Society. TIC: 236863.

106446   Kung, K-H.S. and McBride, M.B. 1991. "Bonding of Chlorophenols on Iron and Aluminum Oxides." *Environmental Science & Technology, 25*, (4), 702-709. Washington, D.C.: American Chemical Society. TIC: 236864.

106448   Kunze, G.W. and Dixon, J.B. 1986. "Pretreatment for Mineralogical Analysis." Chapter 5 of *Method of Soil Analysis, Part 1, Physical and Mineralogical Methods.* Klute, A., ed. 2nd Edition. Madison, Wisconsin: Soil Science Society of America. TIC: 217566.

106449   Laaksoharju, M.; Degueldre, C.; and Skarman, C. 1995. *Studies of Colloids and Their Importance for Repository Performance Assessment.* SKB TR-95-24. Stockholm, Sweden: Svensk Kärnbränsleförsörjning A.B. TIC: 223428.

100051   Langmuir, D. 1997. Aqueous Environmental Geochemistry. Upper Saddle River, New Jersey: Prentice Hall. TIC: 237107.

106457   Langmuir, D. and Riese, A.C. 1985. "The Thermodynamic Properties of Radium." Geochimica et Cosmochimica Acta, 49, 1593-1601. New York, New York: Pergamon Press. TIC: 241035.

117091   Lasaga, A.C. 1998. Kinetic Theory in the Earth Sciences. Princeton, New Jersey: Princeton University Press. TIC: 246279.

164769   Lau, J.S.O.; Gorski, B.; Conlon, B.; and Anderson, T. 2000. *Long-Term Loading Tests on Saturated Granite and Granodiorite.* Report No. 06819-REP-01300-10016 R00. Toronto, Ontario, Canada: Ontario Power Generation, Nuclear Waste Management Division. TIC: 254970.

100529   LeCain, G.D. and Patterson, G.L. 1997. "Milestones — Submittal of Milestone SPH35EM4." Memorandum from G.D. LeCain and G.L. Patterson (USGS) to R. Craig (USGS-TPO), March 11, 1997, with attachment. ACC: MOL.19980224.0146.

100156   LeCain, G.D.; Patterson, G.L.; and Severson, G.R. 1997. *Results from Pneumatic Monitoring, Hydrochemistry Sampling, Air-Injection, and Tracer Testing in the Upper Tiva Canyon, and Bow Ridge Fault Alcoves, Yucca Mountain, Nevada, November, 1994 to July, 1996*. Milestone 3GUS619M-1996. Denver, Colorado: U.S. Geological Survey. ACC: MOL.19970415.0387.

129664   Lee, K.H. and Ueng, T-S. 1991. *Air-Injection Field Tests to Determine the Effect of a Heat Cycle on the Permeability of Welded Tuff*. UCRL-ID-105163. Livermore, California: Lawrence Livermore National Laboratory. ACC: NNA.19910912.0001.

129667   Lee, M.Y. and Haimson, B.C. 1999. "Initial Stress Measurements in the Exploratory Studies Facility Yucca Mountain, Nevada." *Rock Mechanics for Industry, Proceedings of the 37th U.S. Rock Mechanics Symposium, Vail, Colorado, USA, 6-9 June 1999*. Amadei, B.; Kranz, R.L.; Scott, G.A.; and Smeallie, P.H., eds. *2*, 743-750. Brookfield, Vermont: A.A. Balkema. TIC: 245246.

106580   Lemire, R.J. and Garisto, F. 1989. *The Solubility of U, Np, Pu, Th and Tc in a Geological Disposal Vault for Used Nuclear Fuel*. AECL-10009. Pinawa, Manitoba, Canada: Atomic Energy of Canada Limited. TIC: 213161.

101705   Lemire, R.J. and Tremaine, P.R. 1980. "Uranium and Plutonium Equilibria in Aqueous Solutions to 200°C." *Journal of Chemical and Engineering Data, 25*, (4), 361-370. Washington, D.C.: American Chemical Society. TIC: 222175.

104577   Levy, S.S. 1984. "Studies of Altered Vitrophyre for the Prediction of Nuclear Waste Repository-Induced Thermal Alteration at Yucca Mountain, Nevada." *Scientific Basis for Nuclear Waste Management VII, Symposium held November 14-17, 1983, Boston, Massachusetts*. McVay, G.L., ed. *26*, 959-966. New York, New York: Elsevier. TIC: 204393.

100053   Levy, S.S. 1991. "Mineralogic Alteration History and Paleohydrology at Yucca Mountain, Nevada." *High Level Radioactive Waste Management, Proceedings of the Second Annual International Conference, Las Vegas, Nevada, April 28-May 3, 1991. 1*, 477-485. La Grange Park, Illinois: American Nuclear Society. TIC: 204272.

100770   Levy, S.S. 1992. "Natural Gels in the Yucca Mountain Area, Nevada, USA." *Applied Clay Science, 7*, (1-3), 79-85. Amsterdam, The Netherlands: Elsevier. TIC: 225196.

116960   Levy, S.S. and O'Neil, J.R. 1989. "Moderate-Temperature Zeolitic Alteration in a Cooling Pyroclastic Deposit." *Chemical Geology, 76*, (3/4), 321-326. Amsterdam, The Netherlands: Elsevier. TIC: 237819.

157740   Lichtner, P.C. and Pabalan, R.T. 1997. *Preliminary Evaluation of the Effects of Alkaline Plume Migration on the Near-Field Environment of a High-Level Waste Geologic Repository*. Washington, D.C.: U.S. Nuclear Regulatory Commission. TIC: 242056.

106684   Lieser, K.H. and Muhlenweg, U. 1988. "Neptunium in the Hydrosphere and in the Geosphere, I. Chemistry of Neptunium in the Hydrosphere and Sorption of Neptunium from Groundwaters on Sediments Under Aerobic and Anaerobic Conditions." *Radiochimica Acta, 43*, 27-35. Munchen, Germany: R. Oldenbourg Verlag. TIC: 236783.

106683   Lieser, K.H. and Bauscher, C. 1988. "Technetium in the Hydrosphere and in the Geosphere, II. Influence of pH, of Complexing Agents, and of Some Minerals on the Sorption of Technetium." *Radiochimica Acta, 44/45*, 125-128. Munchen, Germany: R. Oldenbourg Verlag. TIC: 237071.

159069   Lin, W.; Blair, S.C.; Wilder, D.; Carlson, S.; Wagoner, J.; DeLoach, L.; Danko, G.; Ramirez, A.L.; and Lee, K. 2001. *Large Block Test Final Report*. UCRL-ID-132246, Rev. 2. Livermore, California: Lawrence Livermore National Laboratory. TIC: 252918.

101050   Lobmeyer, D.H. 1986. *Geohydrology of Rocks Penetrated by Test Well USW G-4, Yucca Mountain, Nye County, Nevada*. Water-Resources Investigations Report 86-4015. Lakewood, Colorado: U.S. Geological Survey. ACC: NNA.19890918.0510.

105457   Lobmeyer, D.H.; Whitfield, M.S., Jr.; Lahoud, R.G.; and Bruckheimer, L. 1983. *Geohydrologic Data for Test Well UE-25b#1, Nevada Test Site, Nye County, Nevada*. Open-File Report 83-855. Denver, Colorado: U.S. Geological Survey. ACC: NNA.19890922.0285.

108211   Longworth, G.; Ross, C.A.M.; Degueldre, C.; and Ivanovich, M. 1989. *Interlaboratory Study of Sampling and Characterization Techniques for Groundwater Colloids*. AERE-R 13393. Oxfordshire, United Kingdom: Harwell Laboratory. TIC: 242340.

145042   Lorens, R.B. 1981. "Sr, Cd, Mn and Co Distribution Coefficients in Calcite as a Function of Calcite Precipitation Rate." *Geochimica et Cosmochimica Acta, 45*, 553-561. New York, New York: Pergamon. TIC: 247351.

157900   Lowry, W.E. 2001. *Engineered Barrier Systems Thermal-Hydraulic-Chemical Column Test Report*. TDR-EBS-MD-000018 REV 00. Las Vegas, Nevada: Bechtel SAIC Company. ACC: MOL.20020102.0206.

101141   Ludwig, K.R.; Peterman, Z.E.; Simmons, K.R.; and Gutentag, E.D. 1993. "$^{234}U/^{238}U$ as a Ground-Water Tracer, SW Nevada-SE California." *High Level Radioactive Waste Management, Proceedings of the Fourth Annual International Conference, Las Vegas, Nevada, April 26-30, 1993. 2*, 1567-1572. La Grange Park, Illinois: American Nuclear Society. TIC: 208542.

145046   Machesky, M.L. 1990. "Influence of Temperature on Ion Adsorption by Hydrous Metal Oxides." Chapter 22 of *Chemical Modeling of Aqueous Systems II*. ACS Symposium Series 416. Melchior, D.C. and Bassett, R.L., eds. Washington, D.C.: American Chemical Society. TIC: 241139.

166020   Mahoney, J.J. and Langmiur, D. 1991. "Adsorption of Sr on Kaolinite, Illite and Montmorillonite at High Ionic Strengths." *Radiochimica Acta, 54*, 139-144. München, Germany: R. Oldenbourg Verlag. TIC: 255180.

162717   Marshall, B.D. and Futa, K. 2003. "Strontium in Pore Water from the Topopah Spring Tuff, Yucca Mountain, Nevada." *Proceedings of the 10th International High-Level Radioactive Waste Management Conference (IHLRWM), March 30-April 2, 2003, Las Vegas, Nevada*. Pages 373-376. La Grange Park, Illinois: American Nuclear Society. TIC: 254204.

146444   Marshall, B.D.; Futa, K.; and Peterman, Z.E. 1998. "Hydrologic Inferences from Strontium Isotopes in Port Pore Water from the Unsaturated Zone at Yucca Mountain, Nevada." *Proceedings of FTAM: Field Testing and Associated Modeling of Potential High-Level Nuclear Waste Geologic Disposal Sites, Lawrence Berkeley National Laboratory, December 15-16, 1997*. Bodvarsson, G.S., ed. LBNL-42520. Pages 55-56. Berkeley, California: Lawrence Berkeley National Laboratory. TIC: 243019.

100057   Martin, R.J.; Noel, J.S.; Boyd, P.J.; and Price, R.H. 1996. "Thermal Expansion as a Function of Confining Pressure for Welded Tuff from Yucca Mountain." *Rock Mechanics Tools and Techniques, Proceedings of the 2nd North American Rock Mechanics Symposium, NARMS '96, A Regional Conference of ISRM, Montreal, Quebec, Canada, 19-21 June, 1996*. Aubertin, A.; Hassani, F.; and Mitri, H., eds. *2*, 1659-1666. Rotterdam, The Netherlands: A.A. Balkema. TIC: 237844.

165960   Martin, R.J.; Noel, J.S.; Boyd, P.J.; and Price, R.H. 1997. "Creep and Static Fatigue of Welded Tuff from Yucca Mountain, Nevada." *International Journal of Rock Mechanics and Mining Sciences, 34*, (3-4), Paper No. 190. New York, New York: Pergamon. TIC: 255298.

100159   Martin, R.J., III; Price, R.H.; Boyd, P.J.; and Noel, J.S. 1995. *Creep in Topopah Spring Member Welded Tuff*. SAND94-2585. Albuquerque, New Mexico: Sandia National Laboratories. ACC: MOL.19950502.0006.

106722   Maya, L. 1982. "Sorbed Uranium(VI) Species on Hydrous Titania, Zirconia, and Silica Gel." *Radiochimica Acta, 31*, 147-151. München, Germany: R. Oldenbourg Verlag. TIC: 236887.

164481   McCaffrey, M.A.; Lazar, B.; and Holland, H.D. 1987. "The Evaporation Path of Seawater and the Coprecipitation of Br^- and K^+ with Halite." *Journal of Sedimentary Petrology, 57*, (5), 928-937. Tulsa, Oklahoma: Society of Economic Paleontologists and Mineralogists. TIC: 254627.

108215   McCarthy, J.F. and Degueldre, C. 1993. "Sampling and Characterization of Colloids and Particles in Groundwater for Studying Their Role in Contaminant Transport." *Environmental Particles*. Buffle, J. and van Leeuwen, H.P., eds. Environmental Analytical and Physical Chemistry Series Volume 2. Pages 247-315. Boca Raton, Florida: Lewis Publishers. TIC: 245905.

100778   McCarthy, J.F. and Zachara, J.M. 1989. "Subsurface Transport of Contaminants." *Environmental Science & Technology, 23*, (5), 496-502. Easton, Pennsylvania: American Chemical Society. TIC: 224876.

108218   McGraw, M.A. 1996. *The Effect of Colloid Size, Colloid Hydrophobicity, and Volumetric Water Content on the Transport of Colloids Through Porous Media*. Ph.D. dissertation. Berkeley, California: University of California. TIC: 245722.

116222   McKinley, P.W.; Long, M.P.; and Benson, L.V. 1991. *Chemical Analyses of Water from Selected Wells and Springs in the Yucca Mountain Area, Nevada and Southeastern California*. Open-File Report 90-355. Denver, Colorado: U.S. Geological Survey. ACC: NNA.19901031.0004.

101263   McKinley, P.W. and Oliver, T.A. 1994. *Meteorological, Stream-Discharge, and Water-Quality Data for 1986 through 1991 from Two Small Basins in Central Nevada*. Open-File Report 93-651. Denver, Colorado: U.S. Geological Survey. ACC: NNA.19940114.0099.

101264   McKinley, P.W. and Oliver, T.A. 1995. *Meteorological, Stream-Discharge, and Water-Quality Data for Water Year 1992 from Two Basins in Central Nevada*. Open-File Report 94-456. Denver, Colorado: U.S. Geological Survey. ACC: MOL.19950124.0284.

106741   Means, J.L.; Crerar, D.A.; and Borcsik, M.P. 1978. "Adsorption of Co and Selected Actinides by Mn and Fe Oxides in Soils and Sediments." *Geochimica et Cosmochimica Acta, 42*, 1763-1773. New York, New York: Pergamon Press. TIC: 218336.

145075   Meece, D.E. and Benninger, L.K. 1993. "The Coprecipitation of Pu and Other Radionuclides with $CaCO_3$." *Geochimica et Cosmochimica Acta, 57*, (7), 1447-1458. New York, New York: Pergamon. TIC: 247349.

100780   Meijer, A. 1990. *Yucca Mountain Project Far-Field Sorption Studies and Data Needs*. LA-11671-MS. Los Alamos, New Mexico: Los Alamos National Laboratory. ACC: MOL.19980508.1113.

100467   Meijer, A. 1992. "A Strategy for the Derivation and Use of Sorption Coefficients in Performance Assessment Calculations for the Yucca Mountain Site." *Proceedings of the DOE/Yucca Mountain Site Characterization Project Radionuclide Adsorption Workshop at Los Alamos National Laboratory, September 11-12, 1990*. Canepa, J.A., ed. LA-12325-C. Pages 9-40. Los Alamos, New Mexico: Los Alamos National Laboratory. ACC: NNA.19920421.0117.

106757   Meijer, A. 1993. "Far-Field Transport of Carbon Dioxide: Retardation Mechanisms and Possible Validation Experiments." *Proceedings of the Topical Meeting on Site Characterization and Model Validation, FOCUS '93, September 26-29, 1993, Las Vegas, Nevada*. Pages 110-112. La Grange Park, Illinois: American Nuclear Society. TIC: 102245.

106758   Meijer, A.; Triay, I.; Knight, S.; and Cisneros, M. 1990. "Sorption of Radionuclides on Yucca Mountain Tuffs." *Proceedings of the Topical Meeting on Nuclear Waste Isolation in the Unsaturated Zone, FOCUS '89, September 17-21, 1989, Las Vegas, Nevada*. Pages 113-117. La Grange Park, Illinois: American Nuclear Society. TIC: 212738.

145077   Milton, G.M. and Brown, R.M. 1987. "Adsorption of Uranium from Groundwater by Common Fracture Secondary Minerals." *Canadian Journal of Earth Sciences, 24*, 1321-1328. Ottawa, Ontario, Canada: National Research Council of Canada. TIC: 247350.

106811   Moskvin, A.I. 1971. "Hydrolytic Behavior of Neptunium (IV,V,VI)." *Soviet Radiochemistry, 13*, (1), 700-705. New York, New York: Consultants Bureau. TIC: 245661.

105140   Muhs, D.R.; Whitney, J.W.; Shroba, R.R.; Taylor, E.M.; and Bush, C.A. 1990. "Uranium-Series Dating of Secondary Carbonates Near Yucca Mountain, Nevada: Applications to Tectonic, Paleoclimatic, and Paleohydrologic Problems." *High Level Radioactive Waste Management, Proceedings of the International Topical Meeting, Las Vegas, Nevada, April 8-12, 1990. 2*, 924-929. La Grange Park, Illinois: American Nuclear Society. TIC: 202058.

160788   Mukhopadhyay, S. and Tsang, Y.W. 2002. "Understanding the Anomalous Temperature Data from the Large Block Test at Yucca Mountain, Nevada." *Water Resources Research, 38*, (10), 28-1 through 28-12. Washington, D.C.: American Geophysical Union. TIC: 253867.

106833   Murphy, W.M. 1992. "Natural Analog Studies for Geologic Disposal of Nuclear Waste." *Technology Today*, Pages 16-21. San Antonio, Texas: Southwest Research Institute. TIC: 238853.

106857   Neck, V.; Kim, J.I.; and Kanellakopulos, B. 1992. "Solubility and Hydrolysis Behavior of Neptunium(V)." *Radiochimica Acta, 56*, 25-30. Munich, Germany: R. Oldenbourg Verlag. TIC: 224093.

106858   Neck, V.; Runde, W.; and Kim, J.I. 1995. "Solid-Liquid Equilibria of Neptunium(V) in Carbonate Solutions of Different Ionic Strengths: II. Stability of the Solid Phases." *Journal of Alloys and Compounds, 225*, 295-302. Lausanne, Switzerland: Elsevier. TIC: 237061.

106861   Neck, V.; Runde, W.; Kim, J.I.; and Kanellakopulos, B. 1994. "Solid-Liquid Equilibrium Reactions of Neptunium(V) in Carbonate Solution at Different Ionic Strength." *Radiochimica Acta, 65*, 29-37. München, Germany: R. Oldenbourg Verlag. TIC: 237467.

150092   Nelson, P.H.; Rachiele, R.; Remer, J.S.; and Carlsson, H. 1981. *Water Inflow into Boreholes During the Stripa Heater Experiments*. LBL-12574. Berkeley, California: Lawrence Berkeley Laboratory. TIC: 228851.

106864   Neretnieks, I. 1990. *Solute Transport in Fractured Rock — Applications to Radionuclide Waste Repositories*. SKB TR-90-38. Stockholm, Sweden: Svensk Kärnbränsleförsörjning A.B. TIC: 208618.

106871   Newton, T.W. 1975. *The Kinetics of the Oxidation-Reduction Reactions of Uranium, Neptunium, Plutonium, and Americium in Aqueous Solutions*. TID-26506. Oak Ridge, Tennessee: U.S. Energy Research and Development Administration. TIC: 239297.

106879   Nimmo, J.R. and Akstin, K.C. 1988. "Hydraulic Conductivity of a Sandy Soil at Low Water Content After Compaction by Various Methods." *Soil Science Society of America Journal, 52*, (2), 303-310. Madison, Wisconsin: Soil Science Society of America. TIC: 224083.

106882   Nimmo, J.R. and Mello, K.A. 1991. "Centrifugal Techniques for Measuring Saturated Hydraulic Conductivity." *Water Resources Research, 27*, (6), 1263-1269. Washington, D.C.: American Geophysical Union. TIC: 224084.

106888   Nimmo, J.R.; Rubin, J.; and Hammermeister, D.P. 1987. "Unsaturated Flow in a Centrifugal Field: Measurement of Hydraulic Conductivity and Testing of Darcy's Law." *Water Resources Research, 23*, (1), 124-134. Washington, D.C.: American Geophysical Union. TIC: 216671.

166021   Nisbet, A.F.; Mocanu, N.; and Shaw, S. 1994. "Laboratory Investigation into the Potential Effectiveness of Soil-Based Countermeasures for Soils Contaminated with Radiocaesium and Radiostrontium." *The Science of the Total Environment, 149*, (3), 145-154. New York, New York: Elsevier. TIC: 255183.

106893   Nitao, J.J. 1991. "Theory of Matrix and Fracture Flow Regimes in Unsaturated, Fractured Porous Media." *High Level Radioactive Waste Management, Proceedings of the Second Annual International Conference, Las Vegas, Nevada, April 28-May 3, 1991. 1*, 845-852. La Grange Park, Illinois: American Nuclear Society. TIC: 204272.

101350   Nitsche, H.; Gatti, R.C.; Standifer, E.M.; Lee, S.C.; Muller, A.; Prussin, T.; Deinhammer, R.S.; Maurer, H.; Becraft, K.; Leung, S.; and Carpenter, S.A. 1992. *Measured Solubilities and Speciations of Neptunium, Plutonium, and Americium in a Typical Groundwater (J-13) from the Yucca Mountain Region*. LBL-30958. Berkeley, California: Lawrence Berkeley National Laboratory. ACC: MOL.19960701.0272.

155218   Nitsche, H.; Gatti, R.C.; Standifer, E.M.; Lee, S.C.; Müller, A.; Prussin, T.; Deinhammer, R.S.; Maurer, H.; Becraft, K.; Leung, S.; and Carpenter, S.A. 1993. *Measured Solubilities and Speciations of Neptunium, Plutonium, and Americium in a Typical Groundwater (J-13) from the Yucca Mountain Region*. LA-12562-MS. Los Alamos, New Mexico: Los Alamos National Laboratory. ACC: NNA.19930507.0136.

100163   Nitsche, H.; Roberts, K.; Prussin, T.; Muller, A.; Becraft, K.; Keeney, D.; Carpenter, S.A.; and Gatti, R.C. 1995. *Measured Solubilities and Speciations from Oversaturation Experiments of Neptunium, Plutonium and Americium in UE25p#1 Well Water from the Yucca Mountain Region*. LA-12563-MS. Los Alamos, New Mexico: Los Alamos National Laboratory. ACC: MOL.19951006.0171.

106920   Noell, A.L.; Thompson, J.L.; Corapcioglu, M.Y.; and Triay, I.R. 1998. "The Role of Silica Colloids on Facilitated Cesium Transport Through Glass Bead Columns and Modeling." *Journal of Contaminant Hydrology, 31*, (1-2), 23-56. Amsterdam, The Netherlands: Elsevier. TIC: 245510.

101277   O'Brien, G.M. 1997. *Analysis of Aquifer Tests Conducted in Boreholes USW WT-10, UE-25 WT#12, and USW SD-7, 1995-96, Yucca Mountain, Nevada*. Water-Resources Investigations Report 96-4293. Denver, Colorado: U.S. Geological Survey. ACC: MOL.19980219.0822.

108227   O'Melia, C.R. 1990. "Kinetics of Colloid Chemical Processes in Aquatic Systems." Chapter 16 of *Aquatic Chemical Kinetics, Reaction Rates of Processes in Natural Waters*. Stumm, W., ed. Pages 447-474. New York, New York: John Wiley & Sons. TIC: 245726.

106996   O'Melia, C.R. and Tiller, C.L. 1993. "Physicochemical Aggregation and Deposition in Aquatic Environments." *Environmental Particles*. Buffle, J. and van Leeuwen, H.P., eds. Environmental Analytical and Physical Chemistry Series Volume 2. Pages 353-386. Boca Raton, Florida: Lewis Publishers. TIC: 238504.

100783   Ogard, A.E. and Kerrisk, J.F. 1984. *Groundwater Chemistry Along Flow Paths Between a Proposed Repository Site and the Accessible Environment.* LA-10188-MS. Los Alamos, New Mexico: Los Alamos National Laboratory. ACC: HQS.19880517.2031.

101351   Ogard, A.E. and Vaniman, D.T., eds. 1985. *Research and Development Related to the Nevada Nuclear Waste Storage Investigations, July 1–September 30, 1984.* LA-10299-PR. Los Alamos, New Mexico: Los Alamos National Laboratory. ACC: NNA.19920922.0014.

166023   Ohnuki, T. and Kozai, N. 1994. "Sorption Characteristics of Radioactive Cesium and Strontium on Smectite." *Radiochimica Acta, 66/67*, 327-331. München, Germany: R. Oldenbourg Verlag. TIC: 255179.

141594   Oldenburg, C.M. and Pruess, K. 1993. "On Numerical Modeling of Capillary Barriers." *Water Resources Research, 29*, (4), 1045-1056. Washington, D.C.: American Geophysical Union. TIC: 238834.

145087   Olhoeft, G.R. 1986. "Electrical Conductivity." *Eighth Workshop on Electromagnetic Induction in the Earth and Moon, Review Papers, Working Group 1-3, International Association of Geomagnetism and Aeronomy, August 25, 1986.* Pages 2-1 to 2-13. Neuchatel, Switzerland: Universite de Neuchatel, Observatoire Cantonal de Neuchatel. TIC: 247674.

100069   Oliver, T. and Root, T. 1997. *Hydrochemical Database for the Yucca Mountain Area, Nye County, Nevada.* Denver, Colorado: U.S. Geological Survey. ACC: MOL.19980302.0367.

100169   Olsson, W.A. and Brown, S.R. 1994. *Mechanical Properties of Seven Fractures from Drillholes NRG-4 and NRG-6 at Yucca Mountain, Nevada.* SAND94-1995. Albuquerque, New Mexico: Sandia National Laboratories. ACC: MOL.19941007.0081.

144773   Or, D. and Ghezzehei, T.A. 2000. "Dripping into Subterranean Cavities from Unsaturated Fractures under Evaporative Conditions." *Water Resources Research, 36*, (2), 381-393. Washington, D.C.: American Geophysical Union. TIC: 246982.

145190   Osmond, J.K. and Cowart, J.B. 1992. "Ground Water." Chapter 9 of *Uranium-Series Disequilibrium: Applications to Earth, Marine, and Environmental Sciences.* Ivanovich, M. and Harmon, R.S., eds. 2nd Edition. New York, New York: Oxford University Press. TIC: 234680.

158817   Paces, J.B.; Ludwig, K.R.; Peterman, Z.E.; and Neymark, L.A. 2002. "^{234}U/^{238}U Evidence for Local Recharge and Patterns of Ground-Water Flow in the Vicinity of Yucca Mountain, Nevada, USA." *Applied Geochemistry, 17*, (6), 751-779. New York, New York: Elsevier. TIC: 252809.

100072   Paces, J.B.; Ludwig, K.R.; Peterman, Z.E.; Neymark, L.A.; and Kenneally, J.M. 1998. "Anomalous Ground-Water ^{234}U/^{238}U Beneath Yucca Mountain: Evidence of Local Recharge?" *High-Level Radioactive Waste Management, Proceedings of the Eighth International Conference, Las Vegas, Nevada, May 11-14, 1998.* Pages 185-188. La Grange Park, Illinois: American Nuclear Society. TIC: 237082.

101352   Paces, J.B.; Mahan, S.A.; Ludwig, K.R.; Kwak, L.M.; Neymark, L.A.; Simmons, K.R.; Nealey, L.D.; Marshall, B.D.; and Walker, A. 1995. *Progress Report on Dating Quaternary Surficial Deposits.* Milestone 3GCH510M. Final Draft. Denver, Colorado: U.S. Geological Survey. ACC: MOL.19960611.0220.

100070   Paces, J.B.; Marshall, B.D.; Whelan, J.F.; and Neymark, L.A. 1997. "Submission of Milestone: SPC23FM4, Due March 14, 1997." Memorandum from J.B. Paces, B.D. Marshall, J.F. Whelan, and L.A. Neymark (USGS) to R.W. Craig, March 14, 1997, with attachment, "Progress Report on Unsaturated Zone Stable and Radiogenic Isotope Studies." ACC: MOL.19980224.0119.

106473   Paces, J.B.; Menges, C.M.; Widmann, B.; Wesling, J.R.; Bush, C.A.; Futa, K.; Millard, H.T.; Maat, P.B.; and Whitney, J.W. 1994. "Preliminary U-Series Disequilibrium and Thermoluminescence Ages of Surficial Deposits and Paleosols Associated with Quaternary Faults, Eastern Yucca Mountain." *High Level Radioactive Waste Management, Proceedings of the Fifth Annual International Conference, Las Vegas, Nevada, May 22-26, 1994. 4*, 2391-2401. La Grange Park, Illinois: American Nuclear Society. TIC: 210984.

100171   Paces, J.B.; Neymark, L.A.; Marshall, B.D.; Whelan, J.F.; and Peterman, Z.E. 1996. *Letter Report: Ages and Origins of Subsurface Secondary Minerals in the Exploratory Studies Facility (ESF).* Milestone 3GQH450M, Results of Sampling and Age Determination. Las Vegas, Nevada: U.S. Geological Survey. ACC: MOL.19970324.0052.

156507   Paces, J.B.; Neymark, L.A.; Marshall, B.D.; Whelan, J.F.; and Peterman, Z.E. 2001. *Ages and Origins of Calcite and Opal in the Exploratory Studies Facility Tunnel, Yucca Mountain, Nevada.* Water-Resources Investigations Report 01-4049. Denver, Colorado: U.S. Geological Survey. TIC: 251284.

127004   Paces, J.B. and Peterman, Z.E. 1999. "Isotope Hydrology of Ground-Water Flow Systems, Southern Nevada." *Proceedings of the International Symposium on Dynamics of Fluids in Fractured Rocks Concepts and Recent Advances, February 10-12, 1999.* Faybishenko, B., ed. LBNL-42718. Pages 134-138. Berkeley, California: Lawrence Berkeley National Laboratory. ACC: MOL.20000106.0492.

162738   Paces, J.B.; Peterman, Z.E.; Neymark, L.A.; Nimz, G.J.; Gascoyne, M.; and Marshall, B.D. 2003. "Summary of Chlorine-36 Validation Studies at Yucca Mountain, Nevada." *Proceedings of the 10th International High-Level Radioactive Waste Management Conference (IHLRWM), March 30-April 2, 2003, Las Vegas, Nevada*. Pages 348-356. La Grange Park, Illinois: American Nuclear Society. TIC: 254253.

162274   Papke, K.G. 1976. *Evaporites and Brines in Nevada Playas*. Nevada Bureau of Mines and Geology Bulletin 87. Reno, Nevada: University of Nevada, Reno, Mackay School of Mines. TIC: 211869.

107004   Parks, G.A. and Pohl, D.C. 1988. "Hydrothermal Solubility of Uraninite." *Geochimica et Cosmochimica Acta, 52*, 863-875. New York, New York: Pergamon Press. TIC: 240879.

103896   Parrington, J.R.; Knox, H.D.; Breneman, S.L.; Baum, E.M.; and Feiner, F. 1996. *Nuclides and Isotopes, Chart of the Nuclides*. 15th Edition. San Jose, California: General Electric Company and KAPL, Inc. TIC: 233705.

154827   Patterson, G.L. 2000. "Low-Level Measurements of Tritium in the Unsaturated Zone from the Exploratory Studies Facility Beneath Yucca Mountain, Nevada." *Abstracts with Programs - Geological Society of America, 32*, (7), A-479–A-480. Boulder, Colorado: Geological Society of America. TIC: 249113.

154570   Paulsson, B.N.P.; King, M.S.; and Rachiele, R. 1980. *Ultrasonic and Acoustic Emission Results from the Stripa Heater Experiments*. Parts I & II. LBL-10975. Berkeley, California: Lawrence Berkeley National Laboratory. TIC: 211547.

107008   Payne, T.E.; Davis, J.A.; and Waite, T.D. 1990. "Modeling of Uranium Sorption to Substrates from the Weathered Zone in the Vicinity of the Koongarra Ore Body." *Alligator Rivers Analogue Project, First Annual Report 1988-89*. Duerden, P., ed. Menai, New South Wales, Australia: Australian Nuclear Science and Technology Organisation. TIC: 244780.

100486   Pearcy, E.C.; Prikryl, J.D.; Murphy, W.M.; and Leslie, B.W. 1994. "Alteration of Uraninite from the Nopal I Deposit, Pena Blanca District, Chihuahua, Mexico, Compared to Degradation of Spent Nuclear Fuel in the Proposed U.S. High-Level Nuclear Waste Repository at Yucca Mountain, Nevada." *Applied Geochemistry, 9*, 713-732. New York, New York: Elsevier. TIC: 236934.

107013   Pedersen, K. 1996. *Bacteria, Colloids, and Organic Carbon in Groundwater at the Bangombe Site in the Oklo Area*. SKB TR-96-01. Stockholm, Sweden: Svensk Kärnbränsleförsörjning A.B. TIC: 225494.

100811   Penrose, W.R.; Polzer, W.L.; Essington, E.H.; Nelson, D.M.; and Orlandini, K.A. 1990. "Mobility of Plutonium and Americium Through a Shallow Aquifer in a Semiarid Region." *Environmental Science & Technology, 24*, 228-234. Washington, D.C.: American Chemical Society. TIC: 224113.

101053   Perfect, D.L.; Faunt, C.C.; Steinkampf, W.C.; and Turner, A.K. 1995. *Hydrochemical Data Base for the Death Valley Region, California and Nevada.* Open-File Report 94-305. Denver, Colorado: U.S. Geological Survey. ACC: MOL.19940718.0001.

165976   Peterman, Z. 2001. "Letter Report on Dust Geochemistry." Letter from Z. eterman (USGS) to N. Kramer, September 7, 2001, with attachment. ACC: MOL.20011004.0234.

162576   Peterman, Z.E. and Cloke, P.L. 2002. "Geochemistry of Rock Units at the Potential Repository Level, Yucca Mountain, Nevada (includes Erratum)." *Applied Geochemistry, 17*, (6, 7), 683-698, 955-958. New York, New York: Pergamon. TIC: 252516; 252517.

165975   Peterman, Z.E.; Hudson, D.; and Harrington, B. 2002. *Analyses of Water Soluble Anions and Cations in Dust from the Exploratory Studies Facility (Supplement to Letter Report of September 7, 2001).* Denver, Colorado: U.S. Geological Survey. ACC: MOL.20020430.0259.

162992   Peterman, Z.E. and Marshall, B.D. 2002. "Geochemistry of Pore Water from Densely Welded Topopah Spring Tuff at Yucca Mountain, Nevada." *GSA Abstracts with Programs, 34*, (6), 308. Boulder, Colorado: Geological Society of America. TIC: 254868.

162819   Peterman, Z.E.; Paces, J.B.; Neymark, L.A.; and Hudson, D. 2003. "Geochemistry of Dust in the Exploratory Studies Facility, Yucca Mountain, Nevada." *Proceedings of the 10th International High-Level Radioactive Waste Management Conference (IHLRWM), March 30-April 2, 2003, Las Vegas, Nevada.* Pages 637-645. La Grange Park, Illinois: American Nuclear Society. TIC: 254559.

101150   Peterman, Z.E. and Patterson, G. 1998. "Isotopes Aid in Understanding the Yucca Mountain Flow System." *High-Level Radioactive Waste Management, Proceedings of the Eighth International Conference, Las Vegas, Nevada, May 11-14, 1998.* Pages 182-184. La Grange Park, Illinois: American Nuclear Society. TIC: 237082.

105743   Philip, J.R.; Knight, J.H.; and Waechter, R.T. 1989. "Unsaturated Seepage and Subterranean Holes: Conspectus, and Exclusion Problem for Circular Cylindrical Cavities." *Water Resources Research, 25*, (1), 16-28. Washington, D.C.: American Geophysical Union. TIC: 239117.

107034   Plummer, M.A.; Phillips, F.M.; Fabryka-Martin, J.; Turin, H.J.; Wigand, P.E.; and Sharma, P. 1997. "Chlorine-36 in Fossil Rat Urine: An Archive of Cosmogenic Nuclide Deposition During the Past 40,000 Years." *Science, 277*, 538-541. Washington, D.C.: American Association for the Advancement of Science. TIC: 237425.

101699   Pokrovskii, V.A. and Helgeson, H.C. 1995. "Thermodynamic Properties of Aqueous Species and the Solubilities of Minerals at High Pressures and Temperatures: The System Al_2O_3-H_2O-NaCl." *American Journal of Science, 295*, 1255-1342. New Haven, Connecticut: Yale University, Kline Geology Laboratory. TIC: 236803.

165550   Potyondy, D.O. 2003. "PFC Stress Corrosion Model." Annex 11.4 of *Seismic Validation of 3-D Thermo-Mechanical Models for the Prediction of the Rock Damage Around Radioactive Spent Fuel Waste*. Project No. FIKW-2001-00200. Liverpool, England: University of Liverpool. TIC: 254978.

119532   Pourbaix, M. 1966. *Atlas of Electrochemical Equilibria in Aqueous Solutions*. Long Island City, New York: Pergamon Press. TIC: 240774.

106589   Price, R.H. 1986. *Effects of Sample Size on the Mechanical Behavior of Topopah Spring Tuff*. SAND85-0709. Albuquerque, New Mexico: Sandia National Laboratories. ACC: NNA.19891106.0125.

100173   Price, R.H.; Connolly, J.R.; and Keil, K. 1987. *Petrologic and Mechanical Properties of Outcrop Samples of the Welded, Devitrified Topopah Spring Member of the Paintbrush Tuff*. SAND86-1131. Albuquerque, New Mexico: Sandia National Laboratories. ACC: NNA.19870601.0013.

100819   Pruess, K.; Wang, J.S.Y.; and Tsang, Y.W. 1990. "On Thermohydrologic Conditions Near High-Level Nuclear Wastes Emplaced in Partially Saturated Fractured Tuff, 2. Effective Continuum Approximation." *Water Resources Research, 26*, (6), 1249-1261. Washington, D.C.: American Geophysical Union. TIC: 224854.

144801   Pruess, K.; Tsang, Y.W.; and Wang, J.S.Y. 1984. *Numerical Studies of Fluid and Heat Flow Near High-Level Nuclear Waste Packages Emplaced in Partially Saturated Fractured Tuff*. LBL-18552. Berkeley, California: Lawrence Berkeley Laboratory. TIC: 211033.

100818   Pruess, K.; Wang, J.S.Y.; and Tsang, Y.W. 1990. "On Thermohydrologic Conditions Near High-Level Nuclear Wastes Emplaced in Partially Saturated Fractured Tuff, 1. Simulation Studies with Explicit Consideration of Fracture Effects." *Water Resources Research, 26*, (6), 1235-1248. Washington, D.C.: American Geophysical Union. TIC: 221923.

144794   Pruess, K. 1997. "On Vaporizing Water Flow in Hot Sub-Vertical Rock Fractures." *Transport in Porous Media, 28*, (3), 335-372. Boston, Massachusetts: Kluwer Academic Publishers. TIC: 238922.

107064   Rai, D.; Felmy, A.R.; and Ryan. J.L. 1990. "Uranium(IV) Hydrolysis Constants and Solubility Product of $UO_2.xH_2O$(am)." *Inorganic Chemistry, 29*, 260-264. Washington, D.C.: American Chemical Society. TIC: 237466.

107069   Rai, D.; Serne, R.J.; and Moore, D.A. 1980. "Solubility of Plutonium Compounds and Their Behavior in Soils." *Soil Science Society of America Journal, 44*, 490-495. Madison, Wisconsin: Soil Science Society of America. TIC: 219108.

100642   Rautman, C.A. and Engstrom, D.A. 1996. *Geology of the USW SD-12 Drill Hole Yucca Mountain, Nevada*. SAND96-1368. Albuquerque, New Mexico: Sandia National Laboratories. ACC: MOL.19970613.0101.

101008   Rautman, C.A. and Engstrom, D.A. 1996. *Geology of the USW SD-7 Drill Hole Yucca Mountain, Nevada*. SAND96-1474. Albuquerque, New Mexico: Sandia National Laboratories. ACC: MOL.19971218.0442.

102059   Rechard, R.P., ed. 1995. *Executive Summary*. Volume 1 of *Performance Assessment of the Direct Disposal in Unsaturated Tuff of Spent Nuclear Fuel and High-Level Waste Owned by U.S. Department of Energy*. SAND94-2563/1. Albuquerque, New Mexico: Sandia National Laboratories. TIC: 237101.

162589   Rejeb, A. 1996. "Mathematical Simulations of Coupled THM Processes of Fanay-Augères Field Test by Distinct Element and Discrete Finite Element Methods." *Developments in Geotechnical Engineering, 79*, 341-368. New York, New York: Elsevier. TIC: 254247.

107088   Renders, P.J.N.; Gammons, C.H.; and Barnes, H.L. 1995. "Precipitation and Dissolution Rate Constants for Cristobalite from 150 to 300°C." *Geochimica et Cosmochimica Acta, 59*, 77-85. New York, New York: Elsevier. TIC: 226987.

146638   Reyes, A.G.; Giggenbach, W.F.; and Christenson, B.W. 1993. *First Report, EQ3-EQ6 Code Validation Contract*. Client Report 722305.15A. Taupo, New Zealand: Institute of Geological & Nuclear Sciences. TIC: 241764.

146636   Reyes, A.G.; Giggenbach, W.F.; and Christenson, B.W. 1994. *Third Report, EQ3-EQ6 Code Validation Contract*. Client Report 724305.15C. Taupo, New Zealand: Institute of Geological & Nuclear Sciences. TIC: 241763.

142190   Rimstidt, J.D.; Newcomb, W.D.; and Shettel, D.L., Jr. 1989. "A Vertical Thermal Gradient Experiment to Simulate Conditions in Vapor Dominated Geothermal Systems, Epithermal Gold Deposits, and High Level Radioactive Repositories in Unsaturated Media." *Proceedings of the 6th International Symposium on Water-Rock Interaction, WRI-6, Malvern, United Kingdom, 3-8 August 1989*. Miles, D.L., ed. Pages 585-588. Rotterdam, The Netherlands: A.A. Balkema. TIC: 241868.

100414   Robinson, B.A.; Wolfsberg, A.V.; Zyvoloski, G.A.; and Gable, C.W. 1995. *An Unsaturated Zone Flow and Transport Model of Yucca Mountain*. Milestone 3468. Draft. Los Alamos, New Mexico: Los Alamos National Laboratory. ACC: MOL.19960415.0218.

107156   Rosch, F.; Milanov, M.; Hung, T.K.; Ludwig, R.; Buklanov, G.V.; and Khalkin, V.A. 1987. "Electromigration of Carrier-Free Radionuclides, 5. Ion Mobilities and Hydrolysis of Np(V) in Aqueous Perchlorate Solutions." *Radiochimica Acta, 42*, (1), 43-46. München, Germany: R. Oldenbourg Verlag. TIC: 245662.

125338   Rosenberg, N.D.; Knauss, K.G.; and Dibley, M.J. 1999. *Evaporation of J13 Water: Laboratory Experiments and Geochemical Modeling*. UCRL-ID-134852. Livermore, California: Lawrence Livermore National Laboratory. TIC: 246322.

125339   Rosenberg, N.D.; Knauss, K.G.; and Dibley, M.J. 1999. *Evaporation of Topopah Spring Tuff Pore Water*. UCRL-ID-135765. Livermore, California: Lawrence Livermore National Laboratory. TIC: 246231.

106712   Rosholt, J.N.; Prijana; and Noble, D.C. 1971. "Mobility of Uranium and Thorium in Glassy and Crystallized Silicic Volcanic Rocks." *Economic Geology, 66*, 1061-1069. El Paso, Texas: Economic Geology Publishing. TIC: 219186.

141790   Ross, B. 1990. "The Diversion Capacity of Capillary Barriers." *Water Resources Research, 26*, (10), 2625-2629. Washington, D.C.: American Geophysical Union. TIC: 225235.

102097   Rousseau, J.P.; Kwicklis, E.M.; and Gillies, D.C., eds. 1999. *Hydrogeology of the Unsaturated Zone, North Ramp Area of the Exploratory Studies Facility, Yucca Mountain, Nevada*. Water-Resources Investigations Report 98-4050. Denver, Colorado: U.S. Geological Survey. ACC: MOL.19990419.0335.

100178   Rousseau, J.P.; Loskot, C.L.; Thamir, F.; and Lu, N. 1997. *Results of Borehole Monitoring in the Unsaturated Zone Within the Main Drift Area of the Exploratory Studies Facility, Yucca Mountain, Nevada*. Milestone SPH22M3. Denver, Colorado: U.S. Geological Survey. ACC: MOL.19970626.0351.

106477   Rundberg, R.S. 1987. *Assessment Report on the Kinetics of Radionuclide Adsorption on Yucca Mountain Tuff*. LA-11026-MS. Los Alamos, New Mexico: Los Alamos National Laboratory. ACC: NNA.19930405.0075.

101355   Rundberg, R.S.; Ogard, A.E.; and Vaniman, D.T., eds. 1985. *Research and Development Related to the Nevada Nuclear Waste Storage Investigations, April 1-June 30, 1984*. LA-10297-PR. Los Alamos, New Mexico: Los Alamos National Laboratory. ACC: NNA.19920922.0018.

106481   Rundberg, R.S.; Partom, I.; Ott, M.A.; Mitchell, A.J.; and Birdsell, K. 1987. *Diffusion of Nonsorbing Tracers in Yucca Mountain Tuff*. Milestone R524. Los Alamos, New Mexico: Los Alamos National Laboratory. ACC: NNA.19930405.0074.

107170   Runde, W. and Kim, J.I. 1994. *Chemisches Verhalten von Drei- und Funfwertigem Americium in Salinen NaCl-Losungen*. RCM 01094. Garching, Germany: Technische Universitat Munchen. TIC: 241857.

107173   Runde, W.; Meinrath, G.; and Kim, J.I. 1992. "A Study of Solid-Liquid Phase Equilibria of Trivalent Lanthanide and Actinide Ions in Carbonate Systems." *Radiochimica Acta, 58/59*, 93-100. München, Germany: R. Oldenbourg Verlag. TIC: 237409.

162586   Rutqvist, J.; Börgesson, L.; Chijimatsu, M.; Nguyen, T.S.; Jing, L.; Noorishad, J.; and Tsang, C.-F. 2001. "Coupled Thermo-Hydro-Mechanical Analysis of a Heater Test in Fractured Rock and Bentonite at Kamaishi Mine — Comparison of Field Results to Predictions of Four Finite Element Codes." *International Journal of Rock Mechanics & Mining Sciences, 38*, (1), 129-142. New York, New York: Pergamon. TIC: 254246.

107190   Ryan, J.L. and Rai, D. 1983. "The Solubility of Uranium(IV) Hydrous Oxide in Sodium Hydroxide Solutions Under Reducing Conditions." *Polyhedron, 2*, (9), 947-952. Oxford, United Kingdom: Pergamon Press. TIC: 236941.

107213   Sanchez, A.L.; Murray, J.W.; and Sibley, T.H. 1985. "The Adsorption of Plutonium IV and V on Goethite." *Geochimica et Cosmochimica Acta, 49*, (11), 2297-2307. New York, New York: Pergamon Press. TIC: 224091.

101290   Savard, C.S. 1996. *Selected Hydrologic Data from Fortymile Wash in the Yucca Mountain Area, Nevada, Water Years 1993-94*. Open-File Report 95-709. Denver, Colorado: U.S. Geological Survey. ACC: MOL.19980226.0548.

107233   Scanlon, B.R. 1991. "Evaluation of Moisture Flux from Chloride Data in Desert Soils." *Journal of Hydrology, 128*, 137-156. Amsterdam, The Netherlands: Elsevier. TIC: 224126.

164774   Schmidtke, R.H. and Lajtai, E.Z. 1985. "The Long-Term Strength of Lac du Bonnet Granite." *International Journal of Rock Mechanics and Mining Science & Geomechanics Abstracts, 22*, (6), 461-465. New York, New York: Pergamon. TIC: 254874.

108234   Seaman, J.C.; Bertsch, P.M.; and Miller, W.P. 1995. "Chemical Controls on Colloid Generation and Transport in a Sandy Aquifer." *Environmental Science & Technology, 29*, (7), 1808-1815. Washington, D.C.: American Chemical Society. TIC: 237337.

102087   Silva, R.J.; Bidoglio, G.; Rand, M.H.; Robouch, P.B.; Wanner, H.; and Puigdomenech, I. 1995. *Chemical Thermodynamics of Americium*. Volume 2 of *Chemical Thermodynamics*. Amsterdam, The Netherlands: Elsevier. TIC: 237106.

166026   Smith, J.T. and Comans, R.N.J. 1996. "Modelling the Diffusive Transport and Remobilisation of ^{137}Cs in Sediments: The Effects of Sorption Kinetics and Reversibility." *Geochimica et Cosmochimica Acta, 60*, (6), 995-1004. New York, New York: Pergamon. TIC: 255182.

126708   Snelling, A.A. 1980. "Uraninite and Its Alteration Products, Koongarra Uranium Deposit." *Uranium in the Pine Creek Geosyncline, Proceedings of International Uranium Symposium on the Pine Creek Geosyncline, Jointly Sponsored by the Bureau of Mineral Resources, Geology and Geophysics and the CSIRO Institute of Earth Resources in Co-Operation with the International Atomic Energy Agency and held in Sydney, Australia, 4–8 June 1979*. Ferguson, J. and Goleby, A.B., eds. Pages 487-498. Vienna, Austria: International Atomic Energy Agency. TIC: 236806.

142100   Snelling, A.A. and Dickson, B.L. 1979. "Uranium/Daughter Disequilibrium in the Koongarra Uranium Deposit, Australia." *Mineralium Deposita, 14*, 109-118. New York, New York: Springer-Verlag. TIC: 237067.

101357   Spengler, R.W. and Chornack, M.P. 1984. *Stratigraphic and Structural Characteristics of Volcanic Rocks in Core Hole USW G-4, Yucca Mountain, Nye County, Nevada with a Section on Geophysical Logs by D.C. Muller and J.E. Kibler*. Open-File Report 84-789. Denver, Colorado: U.S. Geological Survey. ACC: NNA.19890804.0012.

146279   Spengler, R.W. and Rosenbaum, J.G. 1991. "A Low-Angle Breccia Zone of Hydrologic Significance at Yucca Mountain, Nevada." *Abstracts with Programs - Geological Society of America, 23*, (5), A119. Boulder, Colorado: Geological Society of America. TIC: 247113.

145111   Stakebake, J.L.; Larson, D.T.; and Haschke, J.M. 1993. "Characterization of the Plutonium-Water Reaction II: Formation of a Binary Oxide Containing Pu(VI)." *Journal of Alloys and Compounds, 202*, 251-263. Lausanne, Switzerland: Elsevier. TIC: 241265.

101480   Steefel, C.I. and Lasaga, A.C. 1994. "A Coupled Model for Transport of Multiple Chemical Species and Kinetic Precipitation/Dissolution Reactions with Application to Reactive Flow in Single Phase Hydrothermal Systems." *American Journal of Science, 294*, (5), 529-592. New Haven, Connecticut: Yale University, Kline Geology Laboratory. TIC: 235372.

156714   Steefel, C.I. and Lichtner, P.C. 1998. "Multicomponent Reactive Transport in Discrete Fractures II: Infiltration of Hyperalkaline Groundwater at Maqarin, Jordan, a Natural Analogue Site." *Journal of Hydrology, 209*, (1-4), 200-224. New York, New York: Elsevier. TIC: 251162.

100827   Steefel, C.I. and Yabusaki, S.B. 1996. *OS3D/GIMRT Software for Modeling Multicomponent-Multidimensional Reactive Transport User Manual & Programmer's Guide*. PNL-11166. Richland, Washington: Pacific Northwest Laboratory. TIC: 240572.

101027   Stock, J.M.; Healy, J.H.; Hickman, S.H.; and Zoback, M.D. 1985. "Hydraulic Fracturing Stress Measurements at Yucca Mountain, Nevada, and Relationship to the Regional Stress Field." *Journal of Geophysical Research, 90*, (B10), 8691-8706. Washington, D.C.: American Geophysical Union. TIC: 219009.

100419   Stout, R.B. and Leider, H.R., eds. 1997. *Waste Form Characteristics Report Revision 1*. UCRL-ID-108314. Version 1.2. Livermore, California: Lawrence Livermore National Laboratory. ACC: MOL.19980512.0133.

101159   Stuckless, J.S.; Whelan, J.F.; and Steinkampf, W.C. 1991. "Isotopic Discontinuities in Ground Water Beneath Yucca Mountain, Nevada." *High Level Radioactive Waste Management, Proceedings of the Second Annual International Conference, Las Vegas, Nevada, April 28-May 3, 1991. 2*, 1410-1415. La Grange Park, Illinois: American Nuclear Society. TIC: 204272.

109172   Szabo, B.J. and Kyser, T.K. 1990. "Ages and Stable-Isotope Compositions of Secondary Calcite and Opal in Drill Cores from Tertiary Volcanic Rocks of the Yucca Mountain Area, Nevada." *Geological Society of America Bulletin, 102*, 1714-1719. Boulder, Colorado: Geological Society of America. TIC: 221927.

101359   Tait, C.D.; Clark, D.L.; Neu, M.P.; and Hobart, D.E. 1996. *Specific Ion Interaction Theory Studies*. Milestone 3792M. Los Alamos, New Mexico: Los Alamos National Laboratory. ACC: MOL.19961231.0094.

101361   Thomas, K.W. 1987. *Summary of Sorption Measurements Performed with Yucca Mountain, Nevada, Tuff Samples and Water from Well J-13.* LA-10960-MS. Los Alamos, New Mexico: Los Alamos National Laboratory. ACC: NNA.19900604.0045.

106529   Thomas, K.W. 1988. *Research and Development Related to the Nevada Nuclear Waste Storage Investigations, October 1-December 31, 1984.* LA-11443-PR. Los Alamos, New Mexico: Los Alamos National Laboratory. ACC: NNA.19920131.0372.

100831   Thorstenson, D.C.; Weeks, E.P.; Haas, H.; and Woodward, J.C. 1990. "Physical and Chemical Characteristics of Topographically Affected Airflow in an Open Borehole at Yucca Mountain, Nevada." *Proceedings of the Topical Meeting on Nuclear Waste Isolation in the Unsaturated Zone, Focus '89, September 17-21, 1989, Las Vegas, Nevada.* Pages 256-270. La Grange Park, Illinois: American Nuclear Society. TIC: 212738.

156566   Tiffreau, C. and Trocellier, P. 1998. "Modelling the Sorption of Mercury (II) on (Hydr)oxides: Application of Ion Beam Analysis to Sorption Processes." *Nuclear Instruments and Methods in Physics Research B: Beam Interactions with Materials and Atoms, 136-138,* (1-4), 308-312. New York, New York: Elsevier. TIC: 251346.

142200   Torstenfelt, B.; Rundberg, R.S.; and Mitchell, A.J. 1988. "Actinide Sorption on Granites and Minerals as a Function of pH and Colloids/Pseudocolloids." *Radiochimica Acta, 44/45*, 111-117. München, Germany: R. Oldenbourg Verlag. TIC: 237496.

125724   Travis, B.J. and Birdsell, K.H. 1991. *TRACR3D: A Model of Flow and Transport in Porous Media, Model Description and User's Manual.* LA-11798-M. Los Alamos, New Mexico: Los Alamos National Laboratory. TIC: 201398.

145123   Triay, I.R.; Birdsell, K.H.; Mitchell, A.J.; and Ott, M.A. 1993. "Diffusion of Sorbing and Non-Sorbing Radionuclides." *High Level Radioactive Waste Management, Proceedings of the Fourth Annual International Conference, Las Vegas, Nevada, April 26-30, 1993. 2*, 1527-1532. La Grange Park, Illinois: American Nuclear Society. TIC: 208542.

101023   Triay, I.R.; Cotter, C.R.; Huddleston, M.H.; Leonard, D.E.; Weaver, S.C.; Chipera, S.J.; Bish, D.L.; Meijer, A.; and Canepa, J.A. 1996. *Batch Sorption Results for Neptunium Transport Through Yucca Mountain Tuffs.* LA-12961-MS. Los Alamos, New Mexico: Los Alamos National Laboratory. ACC: MOL.19980924.0050.

101016   Triay, I.R.; Cotter, C.R.; Kraus, S.M.; Huddleston, M.H.; Chipera, S.J.; and Bish, D.L. 1996. *Radionuclide Sorption in Yucca Mountain Tuffs with J-13 Well Water: Neptunium, Uranium, and Plutonium*. LA-12956-MS. Los Alamos, New Mexico: Los Alamos National Laboratory. TIC: 226117.

100421   Triay, I.R.; Degueldre, C.; Wistrom, A.O.; Cotter, C.R.; and Lemons, W.W. 1996. *Progress Report on Colloid-Facilitated Transport at Yucca Mountain*. LA-12959-MS. Los Alamos, New Mexico: Los Alamos National Laboratory. TIC: 225473.

101024   Triay, I.R.; Furlano, A.C.; Weaver, S.C.; Chipera, S.J.; and Bish, D.L. 1996. *Comparison of Neptunium Sorption Results Using Batch and Column Techniques*. LA-12958-MS. Los Alamos, New Mexico: Los Alamos National Laboratory. ACC: MOL.19980924.0049.

100422   Triay, I.R.; Meijer, A.; Conca, J.L.; Kung, K.S.; Rundberg, R.S.; Strietelmeier, B.A.; and Tait, C.D. 1997. *Summary and Synthesis Report on Radionuclide Retardation for the Yucca Mountain Site Characterization Project*. Eckhardt, R.C., ed. LA-13262-MS. Los Alamos, New Mexico: Los Alamos National Laboratory. ACC: MOL.19971210.0177.

125972   Triay, I.R.; Robinson, B.A.; Lopez, R.M.; Mitchell, A.J.; and Overly, C.M. 1993. "Neptunium Retardation with Tuffs and Groundwaters from Yucca Mountain." *High Level Radioactive Waste Management, Proceedings of the Fourth International Conference, Las Vegas, Nevada, April 26-30, 1993. 2*, 1504-1508. La Grange Park, Illinois: American Nuclear Society. TIC: 208542.

100789   Triay, I.; Simmons, A.; Levy, S.; Nelson, S.; Nuttall, H.; Robinson, B.; Steinkampf, W.; and Viani, B. 1995. *Colloid-Facilitated Radionuclide Transport at Yucca Mountain*. LA-12779-MS. Los Alamos, New Mexico: Los Alamos National Laboratory. ACC: NNA.19930628.0067.

137577   Tsang, Y.W. and Birkholzer, J.T. 1999. "Predictions and Observations of the Thermal-Hydrological Conditions in the Single Heater Test." *Journal of Contaminant Hydrology, 38*, (1-3), 385-425. New York, New York: Elsevier. TIC: 244160.

141990   Tsunashima, A.; Brindley, G.W.; and Bastovanov, M. 1981. "Adsorption of Uranium from Solutions by Montmorillonite: Compositions and Properties of Uranyl Montmorillonites." *Clays and Clay Minerals, 29*, (1), 10-16. Boulder, Colorado: Clay Minerals Society. TIC: 236914.

164633   Turin, H.J.; Groffman, A.R.; Wolfsberg, L.E.; Roach, J.L.; and Strietelmeier, B.A. 2002. "Tracer and Radionuclide Sorption to Vitric Tuffs of Busted Butte, Nevada." *Applied Geochemistry, 17*, (6), 825-836. New York, New York: Pergamon. TIC: 254046.

105946   Vaniman, D.T.; Bish, D.L.; Chipera, S.J.; Carlos, B.A.; and Guthrie, G.D., Jr. 1996. *Chemistry and Mineralogy of the Transport Environment at Yucca Mountain.* Volume I of *Summary and Synthesis Report on Mineralogy and Petrology Studies for the Yucca Mountain Site Characterization Project.* Milestone 3665. Los Alamos, New Mexico: Los Alamos National Laboratory. ACC: MOL.19961230.0037.

129785   Vaniman, D.T.; Carey, J.W.; Bish, D.L.; and Chipera, S.J. 1999. "Cation Profiles Generated by Downward Transport Into Unsaturated Zeolitic Strata at Yucca Mountain, Nevada." *Eos, Transactions (Supplement), 80*, (17), S5. Washington, D.C.: American Geophysical Union. TIC: 246464.

100089   Vaniman, D.T. and Chipera, S.J. 1996. "Paleotransport of Lanthanides and Strontium Recorded in Calcite Compositions from Tuffs at Yucca Mountain, Nevada, USA." *Geochimica et Cosmochimica Acta, 60*, (22), 4417-4433. New York, New York: Pergamon Press. TIC: 231351.

157427   Vaniman, D.T.; Chipera, S.J.; Bish, D.L.; Carey, J.W.; and Levy, S.S. 2001. "Quantification of Unsaturated-Zone Alteration and Cation Exchange in Zeolitized Tuffs at Yucca Mountain, Nevada, USA." *Geochimica et Cosmochimica Acta, 65*, (20), 3409-3433. New York, New York: Elsevier. TIC: 251574.

101407   Viani, B.E. and Bruton, C.J. 1992. *Modeling Fluid-Rock Interaction at Yucca Mountain, Nevada: A Progress Report.* UCRL-ID-109921. Livermore, California: Lawrence Livermore National Laboratory. ACC: NNA.19920805.0002.

108261   Vilks, P.; Cramer, J.J.; Bachinski, D.B.; Doern, D.C.; and Miller, H.G. 1993. "Studies of Colloids and Suspended Particles, Cigar Lake Uranium Deposit, Saskatchewan, Canada." *Applied Geochemistry, 8*, (6), 605-616. London, England: Pergamon Press. TIC: 237449.

108245   Vilks, P. and Degueldre, C. 1991. "Sorption Behavior of ^{5}Sr, ^{31}I and ^{37}Cs on Colloids and Suspended Particles from the Grimsel Test Site, Switzerland." *Applied Geochemistry, 6*, 553-563. London, England: Pergamon Press. TIC: 236931.

108255   Vilks, P.; Miller, H.G.; and Doern, D.C. 1991. "Natural Colloids and Suspended Particles in the Whiteshell Research Area, Manitoba, Canada, and Their Potential Effect on Radiocolloid Formation." *Applied Geochemistry, 6*, (5), 565-574. London, England: Pergamon Press. TIC: 237339.

141712   Volkov, Y.F.; Visyashcheva, G.I.; Tomilin, S.V.; Kapshukov, I.I.; and Rykov, A.G. 1981. "Study of Carbonate Compounds of Pentavalent Actinides with Alkali-Metal Cations. X. Composition and Crystal Structure of Carbonates." *Radiokhimiya (English Translation), 23*, (2), 200-204. New York, New York: Plenum Publishing Corporation. TIC: 239010.

141723   Volkov, Y.F.; Visyashcheva, G.I.; Tomilin, S.V.; Spiryakov, V.I.; Kapshukov, I.I.; and Rykov, A.G. 1980. "Carbonate Compounds of Pentavalent Actinides with Alkali Metal Cations. VII. Synthesis and Crystal Structure of Hydrate Compounds with the Composition $Na_{0.6}NpO_2(CO_3)_{0.8} \bullet nH_2O$." *Radiokhimiya (English Translation), 21*, (5), 583-590. New York, New York: Plenum Publishing Corporation. TIC: 240213.

108746   Waite, T.O.; Davis, J.A.; Payne, T.E.; Waychunas, G.A.; and Xu, N. 1994. "Uranium(VI) Adsorption to Ferrihydrite: Application of a Surface Complexation Model." *Geochimica et Cosmochimica Acta, 58*, (24), 5465-5478. Oxford, England: Elsevier. TIC: 226322.

108285   Wan, J. and Tokunaga, T.K. 1997. "Film Straining on Colloids in Unsaturated Porous Media: Conceptual Model and Experimental Testing." *Environmental Science & Technology, 31*, (8), 2413-2420. Washington, D.C.: American Chemical Society. TIC: 234804.

160442   Whelan, J.F.; Paces, J.B.; and Peterman, Z.E. 2002. "Physical and Stable-Isotope Evidence for Formation of Secondary Calcite and Silica in the Unsaturated Zone, Yucca Mountain, Nevada." *Applied Geochemistry, 17*, (6), 735-750. New York, New York: Elsevier. TIC: 253462.

100091   Whelan, J.F.; Vaniman, D.T.; Stuckless, J.S.; and Moscati, R.J. 1994. "Paleoclimatic and Paleohydrologic Records from Secondary Calcite: Yucca Mountain, Nevada." *High Level Radioactive Waste Management, Proceedings of the Fifth Annual International Conference, Las Vegas, Nevada, May 22-26, 1994. 4*, 2738-2745. La Grange Park, Illinois: American Nuclear Society. TIC: 210984.

101166   White, A.F.; Claassen, H.C.; and Benson, L.V. 1980. *The Effect of Dissolution of Volcanic Glass on the Water Chemistry in a Tuffaceous Aquifer, Rainier Mesa, Nevada. Geochemistry of Water*. Geological Survey Water-Supply Paper 1535-Q, Washington, D.C.: U.S. Government Printing Office. TIC: 221391.

100189   Wilder, D.G. 1987. *Influence of Stress-Induced Deformations on Observed Water Flow in Fractures at the Climax Granitic Stock*. UCRL-95539, Rev. 1. Livermore, California: Lawrence Livermore National Laboratory. ACC: NNA.19880425.0044.

100792   Wilder, D.G., ed. 1996. *Volume II: Near-Field and Altered-Zone Environment Report*. UCRL-LR-124998. Livermore, California: Lawrence Livermore National Laboratory. ACC: MOL.19961212.0121; MOL.19961212.0122.

100190   Wilder, D.G. 1997. *Technical Bases for EBS Design*. Volume I of *Near-Field and Altered-Zone Environment Report*. UCRL-LR-107476, Rev. 1. Livermore, California: Lawrence Livermore National Laboratory. ACC: MOL.19980107.0365.

125467   Wilder, D.G.; Lin, W.; Blair, S.C.; Buscheck, T.; Carlson, R.C.; Lee, K.; Meike, A.; Ramirez, A.L.; Wagoner, J.L.; and Wang, J. 1997. *Large Block Test Status Report*. UCRL-ID-128776. Livermore, California: Lawrence Livermore National Laboratory. ACC: MOL.19980508.0727.

156570   Wilkie, J.A. and Hering, J.G. 1996. "Adsorption of Arsenic onto Hydrous Ferric Oxide: Effects of Adsorbate/Adsorbent Ratios and Co-Occurring Solutes." *Colloids and Surfaces A: Physicochemical and Engineering Aspects, 107*, 97-110. New York, New York: Elsevier. TIC: 250392.

163765   Williams, N.H. 2003. "Contract No. DE-AC28-01RW1210 – Transmittal of White Paper, Effects of Neoprene on Water in the Drift Scale Test." Letter from N.H. Williams (BSC) to J.D. Ziegler (DOE/ORD), February 4, 2003, 0129035843, with enclosure. ACC: MOL.20030206.0211.

162731   Williams, N.H. 2003. "Thermal Inputs for Evaluations Supporting TSPA-LA, Supplement." Interoffice memorandum from N.H. Williams (BSC) to Distribution, April 4, 2003, 0205035938, with enclosures. ACC: MOL.20030501.0081.

100793   Wilson, C.N. 1990. *Results from NNWSI Series 3 Spent Fuel Dissolution Tests*. PNL-7170. Richland, Washington: Pacific Northwest Laboratory. ACC: NNA.19900329.0142.

102154   Wilson, C.N. and Bruton, C.J. 1990. "Studies on Spent Fuel Dissolution Behavior Under Yucca Mountain Repository Conditions." *Nuclear Waste Management III, Proceedings of the Fourth International Symposium on Ceramics in Nuclear Waste Management, held in Indianapolis, Indiana, April 24-26, 1989*. Pages 423-442. Westerville, Ohio: American Ceramic Society. TIC: 235673.

100191   Wilson, M.L.; Gauthier, J.H.; Barnard, R.W.; Barr, G.E.; Dockery, H.A.; Dunn, E.; Eaton, R.R.; Guerin, D.C.; Lu, N.; Martinez, M.J.; Nilson, R.; Rautman, C.A.; Robey, T.H.; Ross, B.; Ryder, E.E.; Schenker, A.R.; Shannon, S.A.; Skinner, L.H.; Halsey, W.G.; Gansemer, J.D.; Lewis, L.C.; Lamont, A.D.; Triay, I.R.; Meijer, A.; and Morris, D.E. 1994. *Total-System Performance Assessment for Yucca Mountain – SNL Second Iteration (TSPA-1993)*. SAND93-2675. Executive Summary and two volumes. Albuquerque, New Mexico: Sandia National Laboratories. ACC: NNA.19940112.0123.

100835   Wolery, T.J. 1992. *EQ3/6, A Software Package for Geochemical Modeling of Aqueous Systems: Package Overview and Installation Guide (Version 7.0)*. UCRL-MA-110662 PT I. Livermore, California: Lawrence Livermore National Laboratory. TIC: 205087.

100836   Wolery, T.J. 1992. *EQ3NR, A Computer Program for Geochemical Aqueous Speciation-Solubility Calculations: Theoretical Manual, User's Guide, and Related Documentation (Version 7.0)*. UCRL-MA-110662 PT III. Livermore, California: Lawrence Livermore National Laboratory. ACC: MOL.19980717.0626.

100097   Wolery, T.J. and Daveler, S.A. 1992. *EQ6, A Computer Program for Reaction Path Modeling of Aqueous Geochemical Systems: Theoretical Manual, User's Guide, and Related Documentation (Version 7.0)*. UCRL-MA-110662 PT IV. Livermore, California: Lawrence Livermore National Laboratory. ACC: MOL.19980701.0459.

100098   Wolery, T.J.; Jackson, K.J.; Bourcier, W.L.; Bruton, C.J.; Viani, B.E.; Knauss, K.G.; and Delany, J.M. 1990. "Current Status of the EQ3/6 Software Package for Geochemical Modeling." Chapter 8 of *Chemical Modeling in Aqueous Systems II*. ACS Symposium Series 416. Washington, D.C.: American Chemical Society. TIC: 225589.

146442   Wolfsberg, A.V.; Fabryka-Martin, J.T.; Roemer, G.J.C.; and Robinson, B.A. 1998. "Modeling Flow and Transport Pathways to the Potential Repository Horizon at Yucca Mountain." *High-Level Radioactive Waste Management, Proceedings of the Eighth International Conference, Las Vegas, Nevada, May 11-14, 1998*. Pages 81-84. La Grange Park, Illinois: American Nuclear Society. TIC: 237082.

102047   Wronkiewicz, D.J.; Bates, J.K.; Wolf, S.F.; and Buck, E.C. 1996. "Ten-Year Results from Unsaturated Drip Tests with UO_2 at 90°C: Implications for the Corrosion of Spent Nuclear Fuel." *Journal of Nuclear Materials, 238*, (1), 78-95. Amsterdam, The Netherlands: North-Holland. TIC: 243361.

108814   Yajima, T.; Kawamura, Y.; and Ueta, S. 1995. "Uranium(IV) Solubility and Hydrolysis Constants Under Reduced Conditions." *Scientific Basis for Nuclear Waste Management XVIII, Symposium held October 23-27, 1994, Kyoto, Japan*. Murakami, T. and Ewing, R.C., eds. *353*, 1137-1142. Pittsburgh, Pennsylvania: Materials Research Society. TIC: 216341.

100840   Yang, I.C. 1992. "Flow and Transport Through Unsaturated Rock – Data from Two Test Holes, Yucca Mountain, Nevada." *High Level Radioactive Waste Management, Proceedings of the Third International Conference, Las Vegas, Nevada, April 12-16, 1992. 1*, 732-737. La Grange Park, Illinois: American Nuclear Society. TIC: 204231.

160839   Yang, I.C. 2002. "Percolation Flux and Transport Velocity in the Unsaturated Zone, Yucca Mountain, Nevada." *Applied Geochemistry, 17*, (6), 807-817. New York, New York: Elsevier. TIC: 253605.

100838   Yang, I.C.; Peters, C.A.; and Thorstenson, D.C. 1993. "Carbon Isotopic Data from Test Hole USW UZ-1, Yucca Mountain, Nevada." *High Level Radioactive Waste Management, Proceedings of the Fourth Annual International Conference, Las Vegas, Nevada, April 26-30, 1993. 1*, 401-406. La Grange Park, Illinois: American Nuclear Society. TIC: 208542.

146443   Yang, I.C.; Rattray, G.W.; and Scofield, K.M. 1998. "Carbon and Hydrogen Isotopic Compositions for Pore Water Extracted from Cores at Yucca Mountain, Nevada." *High-Level Radioactive Waste Management, Proceedings of the Eighth International Conference, Las Vegas, Nevada, May 11-14, 1998.* Pages 27-32. La Grange Park, Illinois: American Nuclear Society. TIC: 237082.

100194   Yang, I.C.; Rattray, G.W.; and Yu, P. 1996. *Interpretation of Chemical and Isotopic Data from Boreholes in the Unsaturated Zone at Yucca Mountain, Nevada.* Water-Resources Investigations Report 96-4058. Denver, Colorado: U.S. Geological Survey. ACC: MOL.19980528.0216.

101441   Yang, I.C.; Yu, P.; Rattray, G.W.; Ferarese, J.S.; and Ryan, J.N. 1998. *Hydrochemical Investigations in Characterizing the Unsaturated Zone at Yucca Mountain, Nevada.* Water-Resources Investigations Report 98-4132. Denver, Colorado: U.S. Geological Survey. ACC: MOL.19981012.0790.

158176   YMP (Yucca Mountain Site Characterization Project) 2002. *Effects of Introduced Materials in the Drift Scale Test.* North Las Vegas, Nevada: Yucca Mountain Site Characterization Office. ACC: MOL.20020304.0044.

108833   Zielinski, R.A. 1980. "Uranium in Secondary Silica: A Possible Exploration Guide." *Economic Geology, 75,* 592-602. Lancaster, Pennsylvania: Economic Geology Publishing. TIC: 237418.

106657   Zielinski, R.A. 1983. *Evaluation of Ash-Flow Tuffs as Hosts for Radioactive Waste: Criteria Based on Selective Leaching of Manganese Oxides.* Open-File Report 83-480. Denver, Colorado: U.S. Geological Survey. ACC: HQS.19880517.1582.

108836   Zielinski, R.A.; Bush, C.A.; Spengler, R.W.; and Szabo, B.J. 1986. "Rock-Water Interaction in Ash-Flow Tuffs (Yucca Mountain, Nevada, U.S.A.) – The Record from Uranium Studies." *Uranium, 2,* 361-386. Amsterdam, The Netherlands: Elsevier. TIC: 222472.

145625   Zimmerman, R.M.; Blanford, M.L.; Holland, J.F.; Schuch, R.L.; and Barrett, W.H. 1986. *Final Report, G-Tunnel Small-Diameter Heater Experiments.* SAND84-2621. Albuquerque, New Mexico: Sandia National Laboratories. ACC: HQS.19880517.2365.

5.5.2 Data, Listed by Data Tracking Number

153407   GS000608312271.001. Pore-Water Hydrochemistry and Isotopic Data for Boreholes USW NRG-6, USW NRG-7A, USW SD-7, USW SD-9, USW SD-12, USW UZ-14 and UE-25 UZ#16 from 10/1/96 to 1/31/97. Submittal date: 06/23/2000.

156187   GS010608315215.002. Uranium and Thorium Isotope Data for Waters Analyzed Between January 18, 1994 and September 14, 1996. Submittal date: 06/26/2001.

156375   GS010708312272.002. Chemical Data for Pore Water from Tuff Cores of USW NRG-6, USW NRG-7/7A, USW UZ-14, USW UZ-N55 and UE-25 UZ#16. Submittal date: 09/05/2001.

156007   GS010808312322.004. Uranium and Uranium Isotopic Data for Water Samples from Wells and Springs in the Yucca Mountain Vicinity Collected Between December 1996 and December 1997. Submittal date: 08/29/2001.

156008   GS010808312322.005. Uranium and Uranium Isotope Data for Water Samples from UE-25 J-12/J-13 Storage Tank Collected Between October 1996 and November 1997. Submittal date: 08/29/2001.

163555   GS010908312332.002. Borehole Data from Water-Level Data Analysis for the Saturated Zone Site-Scale Flow and Transport Model. Submittal date: 10/02/2001.

159136   GS011108312322.008. Uranium Concentrations and ^{234}U/^{238}U Activity Ratios Analyzed between February 1, 1999, and August 1, 2001 for Drift-Scale Heater Test Water Collected between June 1998 and April 2001, and Pore Water Collected between March 1996 and April 1999. Submittal date: 12/19/2001.

159137   GS011108312322.009. Strontium Isotope Ratios and Strontium Concentrations in Water Samples from the Drift Scale Test Analyzed from March 16, 1999 to June 27, 2001. Submittal date: 02/07/2002.

162342   GS020408312272.002. Tritium Abundance Data from Pore-Water in Core Samples from Yucca Mountain ESF Boreholes for the Period of April 30, 1998 through March 21, 2001. Submittal date: 05/08/2002.

160899   GS020408312272.003. Collection and Analysis of Pore Water Samples for the Period from April 2001 to February 2002. Submittal date: 04/24/2002.

166569   GS020808312272.004. Analysis of Water-Quality Samples for the Period from July 1999 to July 2002. Submittal date: 09/18/2002.

162934   GS021208312272.005. Tritium Abundance Data from Pore-Water in Core Samples from Yucca Mountain ESF ECRB. Submittal date: 12/19/2002.

162935   GS030208312272.001. Gas and Water Vapor Chemistry Data in Yucca Mountain ESF ECRB Bulkheads. Submittal date: 03/11/2003.

165226   GS030408312272.002. Analysis of Water-Quality Samples for the Period from July 2002 to November 2002. Submittal date: 05/07/2003.

166570   GS031008312272.008. Analysis of Pore Water and Miscellaneous Water Samples for the Period from December 2002 to July 2003. Submittal date: 11/13/2003.

168529   GS040108315215.001. Uranium-Lead Isotope Data for ESF Secondary Minerals from July 12, 1997 to August 24, 1997. Submittal date: 02/09/2004.

148105   GS920508312321.004. Chemical Analyses of Water from Selected Wells and Springs in the Yucca Mountain Area, Nevada and Southeastern California. Submittal date: 05/28/1992.

145525   GS930108315213.004. Uranium Isotopic Analyses of Groundwaters from SW Nevada – SE California. Submittal date: 01/21/1993.

145583   GS930108315214.004. Chemical Analysis of Surface-Water, Spring, and Precipitation Samples Collected from Kawich and Stewart Creek Basins from May, 1989, to September, 1991. Submittal date: 11/18/1992.

145530   GS930308312323.001. Chemical Composition of Groundwater and the Locations of Permeable Zones in the Yucca Mountain Area. Submittal date: 03/05/1993.

121639   GS930508312271.021. Analysis of Gaseous-Phase Stable and Radioactive Isotopes in the Unsaturated Zone, Yucca Mountain, Nevada. Submittal date: 04/30/1993.

145543   GS930908315214.030. Chemical Analysis of Surface-Water, Spring, and Precipitation Samples Collected from Kawich and Stewart Creek Basins from February, 1992, to September, 1992. Submittal date: 09/30/1993.

145582   GS940308312133.002. Water Quality Data for Samples Taken in Fortymile Wash, Nevada, During the 1993 Water Year. Submittal date: 03/02/1994.

148110   GS940308312322.001. Hydrochemical Data Base for the Death Valley Region. Submittal date: 03/08/1994.

153678   GS940408312271.005. Laboratory Results of Carbon 14 Analysis of Gas Samples from Borehole USW UZ-1 Collected 12/3/93 - 12/8/93. Submittal date: 03/25/1994.

121653   GS941208312261.008. Carbon Dioxide, Methane, Carbon 14, and Carbon 13/12 Data from USW NRG-6 and USW NRG-7 for May and June 1994; and Carbon 14 Data from USW Wells NRG#5, UZ-6S, UZ-N27, UZ-N62, UZ-N64, UZ-N93, UZ-N94, and UZ-N95 from March 1994. Submittal date: 12/16/1994.

106513   GS950708315131.001. Woodrat Midden and Pollen Core Radiocarbon (C14). Submittal date: 07/21/1995.

106515   GS950708315131.002. Woodrat Midden Contents Comprised of Raw Counts of Plant Macrofossils from Northern and Southern Nevada. Submittal date: 07/21/1995.

106516   GS950708315131.003. Woodrat Midden Age Data in Radiocarbon Years Before Present. Submittal date: 07/21/1995.

121680   GS960208312261.002. Carbon-14 Results from Gas Samples Collected; Carbon Dioxide, Carbon 13/12, Oxygen 18/16, and Carbon-14 Results from Gas Samples Collected; and Carbon Dioxide, Methane, Carbon 13/12 and Oxygen 18/16 Results from Gas Samples Collected. Submittal date: 02/16/1996.

145606   GS960308312133.001. Water Quality Data from Samples Collected in the Fortymile Wash Watershed, Yucca Mountain Area, Nevada, Water Year 1995. Submittal date: 03/27/1996.

106517   GS960308315131.001. Woodrat Midden Radiocarbon (C14). Submittal date: 03/07/1996.

145785   GS960808315215.006. 14-Carbon Analyses of Calcite from Exploratory Studies Facility (ESF) Fracture Coatings, 12/95 - 2/96. Submittal date: 08/21/1996.

145804   GS960908315215.014. Uranium and Thorium Isotope Data for ESF Secondary Minerals Collected Between March 1996 and July 1996. Submittal date: 09/25/1996.

107293   GS961108312261.006. Gas Chemistry, ESF Alcoves 2 and 3, 11/95 - 4/96; Water Chemistry, Alcove 2 (Tritium), Alcove 3, and ESF Tunnel; and Pneumatic Pressure Response from Boreholes in Exploratory Studies Facility Alcoves 2 and 3, 10/95-5/96. Submittal date: 11/12/1996.

121708   GS961108312271.002. Chemical and Isotopic Composition of Pore Water and Pore Gas, 1994–96, from Boreholes USW UZ-1, USW UZ-14, UE-25 UZ#16, USW NRG-6, USW NRG-7A, USW SD-7, USW SD-9, ESF-AL#3-RBT#1, and ESF-AL#3-RBT#4, and ESF Rubble. Submittal date: 12/04/1996.

109775   GS970108312232.001. Sulfur Hexafluoride Gas Chemistry Data and Shut-in Pressure Monitoring Data from the Radial Boreholes in Alcove 1 of the ESF, 4/95; and Tritium Data from Borehole ESF-AL#2-HPF#1 in Alcove 2. Submittal date: 01/09/1997.

107341   GS970208315215.001. Uranium and Thorium Isotope Data Collected Between September 1996 and February 1997 from Secondary Minerals in the ESF. Submittal date: 03/06/1997.

145897   GS970208315215.002. Uranium-Lead Isotope Data for ESF Secondary Minerals from Sep. 96 to Feb. 97. Submittal date: 03/06/1997.

107347   GS970208315215.003. 14-Carbon Analyses of Calcite from ESF Fracture Coatings, February 1997. Submittal date: 02/27/1997.

121745   GS970283122410.002. Gas and Water Chemistry Data from Samples Collected at Boreholes UE-25 NRG#5 and USW SD-7 on Yucca Mountain, Alcove 5, and Borehole ESF-NAD-GTB#1A in Alcove 6, ESF, between 8-11-96 and 1-14-97. Submittal date: 02/21/1997.

145713   GS970508312272.001. Uranium Isotopic Data from ESF Alcove 5 Pore-Water Leaches and UZ Heater-Test Water Collected Between April and May, 1997. Submittal date: 05/30/1997.

145609   GS970608312272.005. Tritium Data from ESF Alcove #5 Cores for Single Heater Test. Submittal date: 06/06/1997.

145405   GS970708312323.001. Delta 18-O and Delta D Stable Isotope Analyses of a Bore-Hole Waters from GEXA Well 4 and VH-2. Submittal date: 07/22/1997.

145921   GS970808315215.012. Uranium and Thorium Isotope Data from Secondary Minerals in the ESF Collected Between 02/15/97 and 09/15/97. Submittal date: 09/17/1997.

111467   GS970908312271.003. Unsaturated Zone Hydrochemistry Data, 2-1-97 to 8-31-97, Including Chemical Composition and Carbon, Oxygen, and Hydrogen Isotopic Composition: Porewater from USW NRG-7A, SD-7, SD-9, SD-12 and UZ-14; and Gas from USW UZ-14. Submittal date: 09/08/1997.

146064   GS980108312322.004. Strontium Isotope Ratios and Strontium Concentrations in Water Samples from USW WT-24 and UE-25 J-13 Collected in October 1997. Submittal date: 01/26/1998.

146065   GS980208312322.006. Uranium Isotopic Data for Saturated- and Unsaturated-Zone Waters Collected by Non-YMP Personnel Between May 1989 and August 1997. Submittal date: 02/03/1998.

156242   GS980708315215.012. Uranium and Thorium Isotope Data from UE-25 a#1 Altered Tuff, and UE-25 J-13 and UE-25 ONC#1 Waters Analyzed from 3/23/94 through 10/25/95. Submittal date: 07/17/1998.

118977   GS980908312322.009. Uranium Concentrations and ^{234}U/^{238}U Ratios from Spring, Well, Runoff, and Rain Waters Collected from the Nevada Test Site and Death Valley Vicinities and Analyzed between 01/15/1998 and 08/15/1998. Submittal date: 09/23/1998.

153677   GS981008312272.004. Analysis for Chemical Composition of Pore Water from Boreholes USW UZ-7A, USW WT-24, USW SD-6, USW SD-7, and USW SD-12 During FY 1997 and 1998. Submittal date: 10/28/1998.

146134   GS990208312272.001. Analysis for Chemical Composition of Pore Water from Borehole USW UZ-14 and UE-25 UZ#16 and Groundwater from UE-25 UZ#16. Submittal date: 02/23/1999.

145711   GS990308315215.004. Strontium Isotope Ratios and Strontium Concentrations in Rock Core Samples and Leachates from USW SD-9 and USW SD-12. Submittal date: 03/25/1999.

145611   GS990608312133.001. Ground-Water Quality Data. Submittal date: 06/09/1999.

145908   GS990983122410.003. Carbon-14 Data from ESF/NAD/GTB#1A Gas. Submittal date: 09/30/1999.

145680   GS991108312272.004. Analysis of Tritium Concentrations in Pore Water During FY98 and FY99. Submittal date: 11/24/1999.

166677   LA000000000012.002. Measured Solubilities and Speciations of Neptunium, Plutonium, and Americium in a Typical Groundwater (J-13) from the Yucca Mountain Region. Submittal date: 03/26/1993.

148602   LA000000000034.001. Diffusion of Sorbing and Non-Sorbing Radionuclides. Submittal date: 01/22/1993.

148603   LA000000000034.002. Diffusion of Sorbing and Non-Sorbing Radionuclides. Submittal date: 06/22/1993.

145613   LA000000000062.002. Halide and Chlorine-36 Analyses of Cuttings from Borehole USW UZ-N27. Submittal date: 09/01/1993.

138456   LA000000000106.001. Report on the Study of Kinetic Effects Using Crushed Tuff Columns: Neptunium in Sodium Bicarbonate Waters. Submittal date: 11/01/1994.

145251   LA0001JC831361.001. Radionuclide Transport Through Saturated Fractures. Submittal date: 01/14/2000.

145253   LA0001JC831361.002. Radionuclide Transport Through Saturated Fractures. Submittal date: 01/14/2000.

145903   LA0001JF12213U.001. Reconstructed Annual Record of Tritium in Atmospheric Moisture for Albuquerque, New Mexico, 1946-1993. Submittal date: 01/07/2000.

147081   LA0002JC831341.001. Depth Intervals and Bulk Densities of Alluviums. Submittal date: 03/08/2000.

147083   LA0002JC831341.002. Quantitative X-Ray Diffraction (QXRD) Results of Three Alluviums. Submittal date: 03/08/2000.

147088   LA0002JC831361.002. Column Studies Using G4-268 Devitrified Tuff with Synthetic UE-25 p#1 Water and Radionuclides (H-3 and Pu-239). Submittal date: 03/16/2000.

147089   LA0002JC831361.003. Column Studies Using G4-268 Devitrified Tuff with J-13 Well Water and Radionuclides (H-3 and Tc-95m). Submittal date: 03/16/2000.

147091   LA0002JC831361.004. Column Studies Using GU3-1414 Vitric Tuff with J-13 Well Water and Radionuclides (H-3 and Tc-95m). Submittal date: 03/16/2000.

147092   LA0002JC831361.005. Column Studies Using G4-1533 Zeolitic Tuff with J-13 Well Water and Radionuclides (H-3 and Tc-95m). Submittal date: 03/16/2000.

147234   LA0003JF12213U.001. Precipitation-Weighted Average Monthly Concentrations (MG/L) of Precipitation in Red Rock Canyon, Nevada, 1985 to 1998. Submittal date: 03/13/2000.

149172   LA0003NL831352.001. Experimental Data on Sorption and Desorption Amounts for Plutonium Onto Clay Colloids. Submittal date: 03/16/2000.

149987   LA0004JC831224.001. Preliminary Unsaturated Hydraulic Conductivities of Tuffs from Yucca Mountain Boreholes, Tunnel Bed 5 (G-Tunnel) and Bandelier Tuff (Los Alamos). Submittal date: 05/01/2000.

149397   LA0004JC831361.001. Preliminary Retardation Data for Selenium Transport Through Unsaturated Tuffs. Submittal date: 04/19/2000.

150272   LA0004NL831352.001. Pu(IV) and Pu(V) Sorption on Hematite and Goethite Colloids with Natural and Synthetic J-13 Water (1997-98 Data). Submittal date: 04/04/2000.

166674   LA0004NL831352.002. PU(IV) and PU(V) Sorption and Desorption Studies with Iron Colloids, Utilizing Natural and Synthetic J-13 Water (1997-98 Data). Submittal date: 04/04/2000.

150273   LA0004NL831352.003. Pu(IV) and Pu(V) Sorption and Desorption Studies with Silica Colloids, Utilizing Natural and Synthetic J-13 Water (1997-98 Data). Submittal date: 04/04/2000.

168530   LA0006JC831341.008. Selenium Batch Adsorption on Nonwelded Zeolitic Tuff. Submittal date: 07/21/2000.

153485   LA0009SL831151.001. Fracture Mineralogy of the ESF Single Heater Test Block, Alcove 5. Submittal date: 09/28/2000.

153320   LA0010JC831341.005. Radionuclide Retardation Measurements of Sorption Distribution Coefficients for Uranium. Submittal date: 10/19/2000.

153318   LA0010JC831341.006. Radionuclide Retardation Measurements of Sorption Distribution Coefficients for Plutonium. Submittal date: 10/19/2000.

153319   LA0010JC831341.007. Radionuclide Retardation Measurements of Sorption Distribution Coefficients for Neptunium. Submittal date: 10/19/2000.

163042   LA0012AM831341.002. NP Sorption onto Clinoptilolite-Rich Tuff in J-13 Water Under Atmospheric Conditions. Submittal date: 12/19/2000.

163043   LA0101AM831341.001. Uranium Sorption Coefficients for Minerals and Tuffs Under Oxidizing Conditions in J-13 Water. Submittal date: 01/23/2001.

156870   LA0109MD831341.001. Adsorption of NP-237 in Three Types of Alluvium as a Function of Time and Stratigraphic Position. Submittal date: 09/14/2001.

158426   LA0201SL831225.001. Chemical, Textural, and Mineralogical Characteristics of Sidewall Samples from the Drift Scale Test. Submittal date: 01/10/2002.

162575   LA0302AM831341.002. Unsaturated Zone Distribution Coefficients (KDS) for U, NP, PU, AM, PA, CS, SR, RA, and TH. Submittal date: 02/04/2003.

163784   LA0302MD831341.003. Neptunium-237 Sorption in Alluvium from NC-EWDP Wells 19IM1A, 10SA, and 22SA Under Ambient Conditions. Submittal date: 02/11/2003.

163785   LA0302MD831341.004. Uranium Sorption in Alluvium from NC-EWDP Wells 19IM1A, 10SA, and 22SA Under Ambient Conditions. Submittal date: 02/11/2003.

163789   LA0305AM831341.001. 1977 to 1987 Sorption Measurements of AM, BA, CS, NP, PU, PA, SR, TH, and U with Yucca Mountain Tuff Samples. Submittal date: 05/21/2003.

164949   LA0306AM831343.001. Modeling Calculations of Radionuclide Sorption via Surface-Complexation Reactions. Submittal date: 06/09/2003.

164091   LA0307RR831222.001. Chloride, Bromide, Sulfate, and Chlorine-36 Analyses of Salts Leached from Cross Drift Rock Samples in FY99 and FY00. Submittal date: 07/09/2003.

165523   LA0309AM831341.002. Batch Sorption Coefficient Data for Barium on Yucca Mountain Tuffs in Representative Water Compositions. Submittal date: 09/25/2003.

165524 LA0309AM831341.003. Batch Sorption Coefficient Data for Cesium on Yucca Mountain Tuffs in Representative Water Compositions. Submittal date: 09/25/2003.

165525 LA0309AM831341.004. Batch Sorption Coefficient Data for Neptunium on Yucca Mountain Tuffs in Representative Water Compositions. Submittal date: 09/25/2003.

165527 LA0309AM831341.006. Batch Sorption Coefficient Data for Strontium on Yucca Mountain Tuffs in Representative Water Compositions. Submittal date: 09/25/2003.

165528 LA0309AM831341.007. Batch Sorption Coefficient Data for Uranium on Yucca Mountain Tuffs in Representative Water Compositions. Submittal date: 09/25/2003.

165891 LA0310AM831341.002. Saturated Zone Distribution Coefficients (KDs) for U, Np, Pu, Cs, Am, Pa, SR, Th, Ra, C, Tc, and I. Submittal date: 10/21/2003.

166697 LA0401MD831341.001. Batch Study of NP-237 Adsorption on to Alluvium as Function of Sample Depth, Particle Size, and Liquid to Solid Ratio Under Ambient Condition. Submittal date: 01/08/2004.

166696 LA0401MD831361.001. U-233 Column Tests Performed on Alluvium from NC-EWDP Wells 19IM1A, 10SA, and 22SA Under Ambient Conditions. Submittal date: 01/08/2004.

166726 LA0401PR831361.001. Column Studies Using G4-268 Devitrified Tuff with J-13 Well Water and Radionuclides (H-3 and Pu-239). Submittal date: 01/13/2004.

145630 LA9909JF831222.005. Chlorine-36 Analyses of ESF and Busted Butte Porewaters in FY99. Submittal date: 09/29/1999.

122733 LA9909JF831222.010. Chloride, Bromide, Sulfate, and Chlorine-36 Analyses of ESF Porewaters. Submittal date: 09/29/1999.

142389 LA9910SK831341.004. Effects of Alanine and Catechol on Neptunium (V) Sorption on Ferrihydrite, Goethite, and Hematite. Submittal date: 12/07/1999.

145655 LA9912JF831222.001. Halide and Chlorine-36 Analyses of Drillcore from USW UZ-N55. Submittal date: 12/16/1999.

166676 LADT831351AQ98.001. Neptunium and Plutonium Solubilities in a Yucca Mountain Groundwater. Submittal date: 04/27/1999.

138447   LAIT831361AQ95.001. Crushed Rock Column Data to Obtain Sorption Coefficients for Pu(IV), Np, Tc-95m Using J-13 and UE-25 p#1, Waters Yucca Mountain, Nevada. Submittal date: 09/29/1995.

107090   LAIT831361AQ95.003. Transport Data of H3, Np, and Tc-95M Collected to Calculate Retardation Coefficients Using J-13 and UE-25 p#1 Waters. Submittal date: 08/20/1997.

107098   LAIT831362AQ95.001. Solid Rock Diffusion Data Collected to Determine Rate of Movement for Np, U, and HTO through an Unsaturated Tuff. Submittal date: 09/29/1995.

146237   LAJF831222AN97.008. Halide, Sulfate and 36CL Analyses of Cuttings from Borehole ONC#1. Submittal date: 09/26/1997.

146238   LAJF831222AN97.012. Halide, Sulfate and 36CL Analyses of Surface Soils. Submittal date: 09/26/1997.

146240   LAJF831222AN98.013. Chloride, Bromide, Sulfate, and Chlorine-36 Analyses of Groundwater from USW UZ-1, UE#25-p1, UE25 UZN#2, and USW VH-1. Submittal date: 09/09/1998.

145585   LAJF831222AQ95.003. Halide Analyses of Rainwater from Yucca Mountain. Submittal date: 09/26/1995.

145632   LAJF831222AQ95.005. Halide and Chlorine-36 Analyses of Soils from the UE25 NRG#5 Drillpad. Submittal date: 09/26/1995.

145633   LAJF831222AQ95.006. Halide and Chlorine-36 Analyses of Soils Collected from Midway Valley Pits and Trenches. Submittal date: 09/26/1995.

146246   LAJF831222AQ95.007. Halide and Chlorine-36 Analyses of Soils from Test Cell C, NTS Area 25. Submittal date: 09/26/1995.

145634   LAJF831222AQ96.005. Halide and Chlorine-36 Analyses of Cuttings from Boreholes UE25 NRG -4, USW NRG -6, and USW NRG-7A. Submittal date: 09/30/1996.

145635   LAJF831222AQ96.006. Halide and Chlorine-36 Analyses of Soil from Midway Valley Pit MWV-P2. Submittal date: 09/30/1996.

145638   LAJF831222AQ96.008. Halide and Chlorine-36 Analyses of Cuttings from Boreholes USW UZ-N15, USW UZ-N16, USW UZ-N17, USW UZ-N36, USW UZ-N38, UE25 UZ-N39, USW UZ-N61, USW UZ-N62, and USW UZ-N64. Submittal date: 09/30/1996.

145639   LAJF831222AQ96.009. Halide and Chlorine-36 Analyses of Cuttings from Borehole USW UZ-N11. Submittal date: 09/30/1996.

145640   LAJF831222AQ96.010. Halide and Chlorine-36 Analyses of Cuttings from Borehole USW UZ-N37. Submittal date: 09/30/1996.

145642   LAJF831222AQ96.011. Halide and Chlorine-36 Analyses of Cuttings from Borehole USW UZ-N53. Submittal date: 09/30/1996.

145643   LAJF831222AQ96.012. Halide and Chlorine-36 Analyses of Cuttings from Borehole USW UZ-N54. Submittal date: 09/30/1996.

145644   LAJF831222AQ96.013. Halide and Chlorine-36 Analyses of Cuttings from Borehole USW UZ-N55. Submittal date: 09/30/1996.

145645   LAJF831222AQ96.014. Halide and Chlorine-36 Analyses of Cuttings from Borehole UE25 UZ#16. Submittal date: 09/30/1996.

145646   LAJF831222AQ96.015. Halide and Chlorine-36 Analyses of Cuttings from Borehole USW UZ-14. Submittal date: 09/30/1996.

145401   LAJF831222AQ97.002. Chlorine-36 Analyses of Packrat Urine. Submittal date: 09/26/1997.

145647   LAJF831222AQ97.006. Halide, Sulfate and Chlorine-36 Analyses of Soils from Midway Valley Soil Pits MWV-P31 and NRSF-TP-19. Submittal date: 09/26/1997.

145648   LAJF831222AQ97.007. Halide, Sulfate and 36CL Analyses of Cuttings from Borehole SD-12. Submittal date: 09/26/1997.

146310   LAJF831222AQ98.003. Chloride, Bromide, Sulfate, and Chlorine-36 Analysis of Construction Water. Submittal date: 09/09/1998.

107364   LAJF831222AQ98.004. Chloride, Bromide, Sulfate, and Chlorine-36 Analyses of Salts Leached from ESF Rock Samples. Submittal date: 09/10/1998.

145649   LAJF831222AQ98.005. Chloride, Bromide, Sulfate, and Chlorine-36 Analyses of Soils Collected Above the ESF South Ramp. Submittal date: 09/09/1998.

122730   LAJF831222AQ98.007. Chloride, Bromide, and Sulfate Analyses of Salts Leached from ECRB-CWAT#1, #2, and #3 Drill Core. Submittal date: 09/09/1998.

145650   LAJF831222AQ98.009. Chlorine-36 Analyses of Salts Leached from ESF Niche 3566 (Niche #1) Drillcore. Submittal date: 09/09/1998.

145402   LAJF831222AQ98.011. Chloride, Bromide, Sulfate and Chlorine-36 Analyses of Springs, Groundwater, Porewater, Perched Water and Surface Runoff. Submittal date: 09/10/1998.

160897   LB0208AIRKDSTH.001. Air Permeability Data for the Heating Phase of the DST. Submittal date: 08/09/2002.

166675   LB0303DSCPDSTV.001. Drift-Scale Coupled Process Model Validation: Simulation Files. Submittal date: 03/20/2003.

166342   LB0306DSTTHMVL.002. DST and Niche THM Model Validation: Summary Plots Values. Submittal date: 06/26/2003.

159551   LL020710223142.024. Moisture Content of Rock from Neutron Logging Activities in the Drift Scale Test (DST): August 1997 through May 2002. Submittal date: 08/20/2002.

162949   LL030408023121.027. Cl Abundance and Cl Ratios of Leachates from ESF Core Samples. Submittal date: 04/17/2003.

168531   LL031200223121.036. CL ABUNDANCE AND CL RATIO OF LEACHATES FROM ESF CORE SAMPLES. Submittal date: 12/03/2003.

135872   LL980918904244.074. Temperature, Relative Humidity and Gas Pressure Results During the Large Block Test FY 98. Submittal date: 09/29/1998.

153836   MO0001SEPDSTPC.000. Drift Scale Test (DST) Temperature, Power, Current, and Voltage Data for June 1, 1999 through October 31, 1999. Submittal date: 01/12/2000.

152554   MO0004QGFMPICK.000. Lithostratigraphic Contacts from MO9811MWDGFM03.000 to be Qualified Under the Data Qualification Plan, TDP-NBS-GS-000001. Submittal date: 04/04/2000.

153767   MO0005CL3SPRGS.000. Dissolved Chloride, 3 Springs Basin. Submittal date: 05/22/2000.

153768   MO0005CLESTWRT.000. Dissolved Chloride, East Stewart Basin. Submittal date: 05/22/2000.

153769   MO0005CLKAWICH.000. Dissolved Chloride, Kawich Peak. Submittal date: 05/22/2000.

151501   MO0007GNDWTRIS.011. Isotopic Content of Groundwater from Selected Boreholes Not Drilled for the Yucca Mountain Project Extracted from ANL-NBS-HS-000021, Geochemical and Isotopic Constraints on Groundwater Flow Directions, Mixing and Recharge at Yucca Mountain, Nevada. Submittal date: 07/28/2000.

151504 MO0007GNDWTRIS.013. Isotopic Content of Perched Groundwater from Yucca Mountain Project Boreholes Extracted from ANL-NBS-HS-000021, Geochemical and Isotopic Constraints on Groundwater Flow Directions, Mixing and Recharge at Yucca Mountain, Nevada. Submittal date: 07/28/2000.

153707 MO0007SEPDSTPC.001. Drift Scale Test (DST) Temperature, Power, Current, and Voltage Data for November 1, 1999 through May 31, 2000. Submittal date: 07/13/2000.

153398 MO0012CARB1314.000. Water - Carbon 13 and Carbon 14 Abundance. Submittal date: 12/01/2000.

153394 MO0012CARB1314.001. Water - Carbon 13 and Carbon 14 Isotope Abundance. Submittal date: 12/01/2000.

153408 MO0012CARBON13.000. Water - Carbon 13 Isotope Ratio. Submittal date: 12/01/2000.

153758 MO0012CO13UNSZ.000. Carbon 13 Data for Unsaturated Zone Borehole. Submittal date: 12/21/2000.

153780 MO0012CO13UNSZ.001. Carbon 13 Data for Unsaturated Zone Borehole. Submittal date: 12/21/2000.

153781 MO0012CO13UNSZ.002. Carbon 13 Data for Unsaturated Zone Borehole. Submittal date: 12/21/2000.

153757 MO0012CO13UNSZ.003. Carbon 13 Data for Unsaturated Zone Borehole USW UZ-1. Submittal date: 12/22/2000.

153766 MO0012CO14UNSZ.002. Carbon 14 Data for Unsaturated Zone Borehole. Submittal date: 12/21/2000.

153756 MO0012CO2UNSZO.004. Carbon Dioxide Abundance in Unsaturated Zone Borehole USW UZ-1 Collected from 02/06/1995 to 02/10/1995. Submittal date: 12/22/2000.

153679 MO0012MAJIONIS.000. Water-Major Ion and Isotope Data. Submittal date: 12/01/2000.

153708 MO0012SEPDSTPC.002. Drift Scale Test (DST) Temperature, Power, Current, and Voltage Data for June 1, 2000 through November 30, 2000. Submittal date: 12/19/2000.

153751 MO0012TRITUNSZ.000. Tritium Data for Unsaturated Zone Borehole. Submittal date: 12/21/2000.

153384   MO0012URANISOT.000. Water - Selected Uranium Abundance and Isotope Ratios. Submittal date: 12/06/2000.

153397   MO0012WTRIONCO.000. Water - Ionic Concentrations Water. Submittal date: 12/05/2000.

153858   MO0102UNSZHYCM.000. Preliminary Unsaturated Zone Borehole Hydrochemistry Data. Submittal date: 02/02/2001.

158321   MO0107SEPDSTPC.003. Drift Scale Test (DST) Temperature, Power, Current, and Voltage Data for December 1, 2000 through May 31, 2001. Submittal date: 07/06/2001.

158320   MO0202SEPDSTTV.001. Drift Scale Test (DST) Temperature, Power, Current, and Voltage Data for June 1, 2001 through January 14, 2002. Submittal date: 02/28/2002.

161767   MO0208SEPDSTTD.001. Drift Scale Test (DST) Temperature Data for January 15, 2002 through June 30, 2002. Submittal date: 08/29/2002.

166480   MO0312SEPSDC14.000. Carbon-14 Versus Stable Carbon for Yucca Mountain Waters and Gases. Submittal date: 12/16/2003.

166478   MO0312SEPSDCHV.000. Chemical Variability in Drill Core Data for High-Silica Rhyolite. Topopah Spring Tuff. Core UE-25 UZ#16 (Normalized Anhydrous). Submittal date: 12/16/2003.

166442   MO0312SEPSDCNL.000. Primary Differences in Chondrite-Normalized Lanthanide-Element Patterns for Rhyolite and Quartz-Latitic Source Rocks. Submittal date: 12/15/2003.

166443   MO0312SEPSDDCA.000. Development of Cerium Anomalies in Fracture-Lining Manganese Oxides and Calcites. Submittal date: 12/15/2003.

166481   MO0312SEPSDDHO.000. Delta Hydrogen-2 and Delta Oxygen-18 Compositions of Yucca Mountain Waters. Submittal date: 12/16/2003.

166482   MO0312SEPSDMIC.000. Histograms for Major Ion Concentrations in Precipitation, Surface Water, and the Unsaturated Zone, Perched Water, and the Saturated Zone at Yucca Mountain. Submittal date: 12/16/2003.

166479   MO0312SEPSDTRD.000. Trilinear Diagram for Yucca Mountain Groundwaters. Submittal date: 12/16/2003.

166444   MO0312SEPSDZSA.000. Profiles of Zeolites and Strontium Abundance. Submittal date: 12/15/2003.

113644   MO9807DSTSET01.000. Drift Scale Test (DST) Temperature, Power, Current, Voltage Data for November 7, 1997 through May 31, 1998. Submittal date: 07/09/1998.

113662   MO9810DSTSET02.000. Drift Scale Test (DST) Temperature, Power, Current, Voltage Data for June 1 through August 31, 1998. Submittal date: 10/09/1998.

113673   MO9906DSTSET03.000. Drift Scale Test (DST) Temperature, Power, Current, Voltage Data for September 1, 1998 through May 31, 1999. Submittal date: 06/08/1999.

109059   MO9906GPS98410.000. Yucca Mountain Project (YMP) Borehole Locations. Submittal date: 06/23/1999.

INTENTIONALLY LEFT BLANK
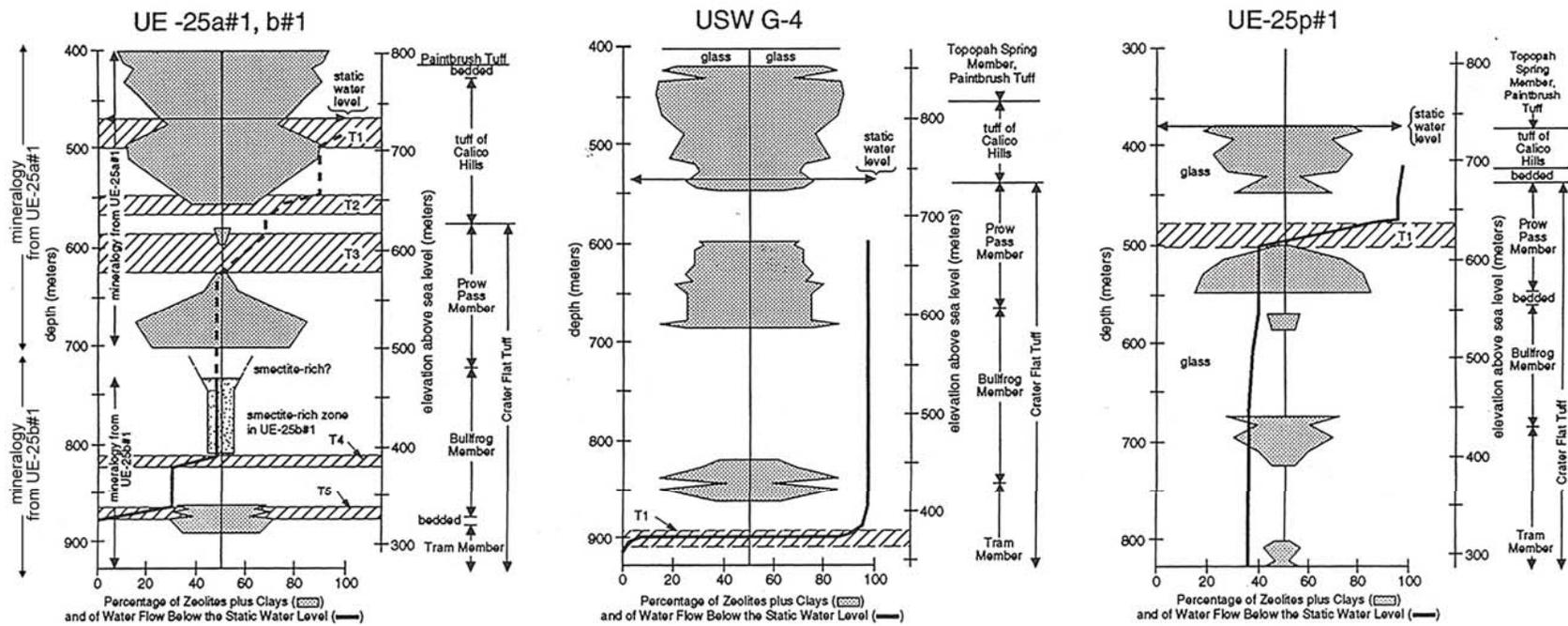
00377DCa_007.ai

Sources: Bish and Chipera 1989 [DIRS 101195]; Craig and Johnson 1984 [DIRS 101039]; Craig and Robison 1984 [DIRS 101040]; Lobmeyer 1986 [DIRS 101050]; Lobmeyer et al. 1983 [DIRS 105457], Figure 8, p.25

NOTES: Intervals of abundant shear fractures are shown by fractured pattern. Stippled patterns show zones with abundant zeolite (close stipples in all three plots) or abundant smectite (widely spaced stipples in UE-25 b#1). Solid lines show percent of total flow in numbered transmissive zones (e.g., T1, T2). Horizontal scale applies to both mineral abundances (measured across the width of the stippled patterns) and cumulative percentage of total flow.

Figure 5-1. Transmissive Zones below the Water Table in Three Drill Holes at Yucca Mountain
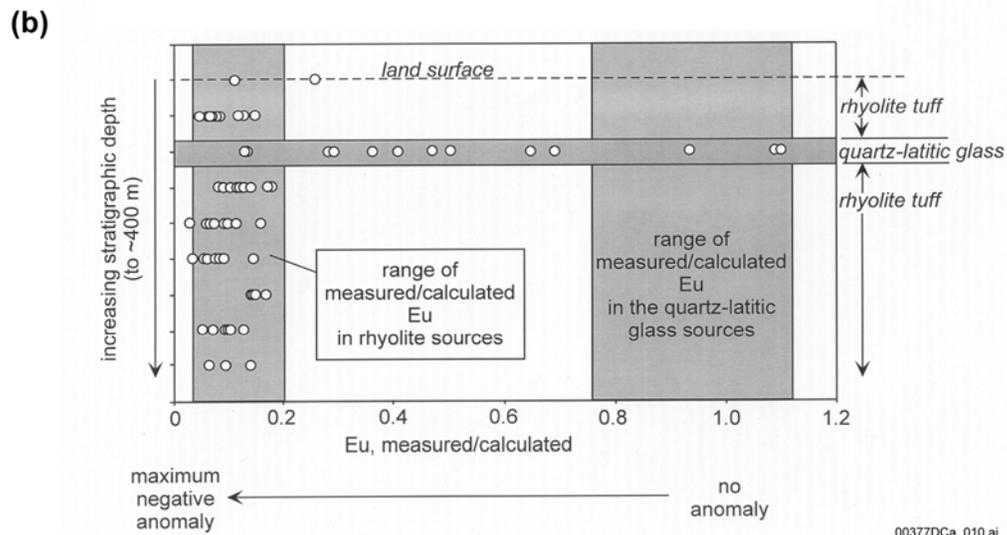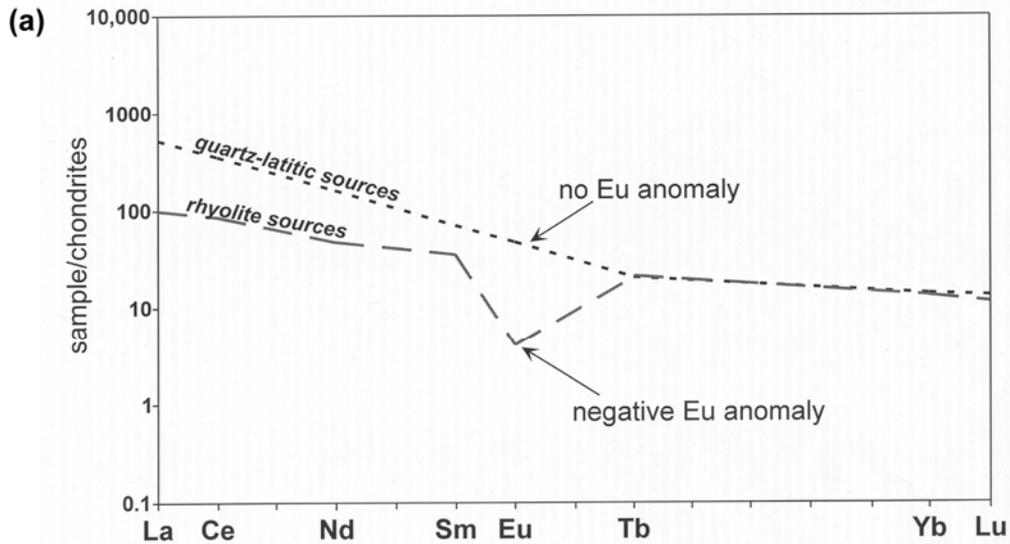
DTN: MO0312SEPSDCNL.000 [DIRS 166442]

Source: Eckhardt 2000 [DIRS 152135]; see also Vaniman and Chipera 1996 [DIRS 100089], Figure 4

NOTES: Part (a) Lanthanide element patterns for Yucca Mountain rhyolitic rocks have a well-defined negative europium anomaly, which is absent from quartz-latitic sources. Part (b) The magnitude of europium anomalies in calcites from the land surface (calcretes) and at eight stratigraphic horizons of the unsaturated zone. The europium anomaly is diminished or absent only where glassy quartz-latitic rocks, also lacking a europium anomaly, occur.

Figure 5-2. Chondrite-Normalized Lanthanide-Element Patterns for Rhyolite and Quartz-Latitic Source Rocks, and for Calcites in the Soil and the Unsaturated Zone

(a)

(b)
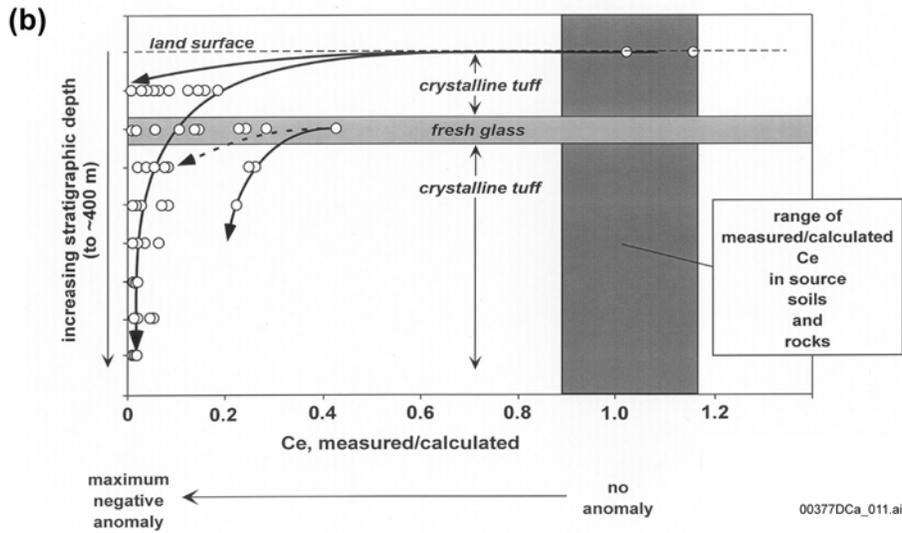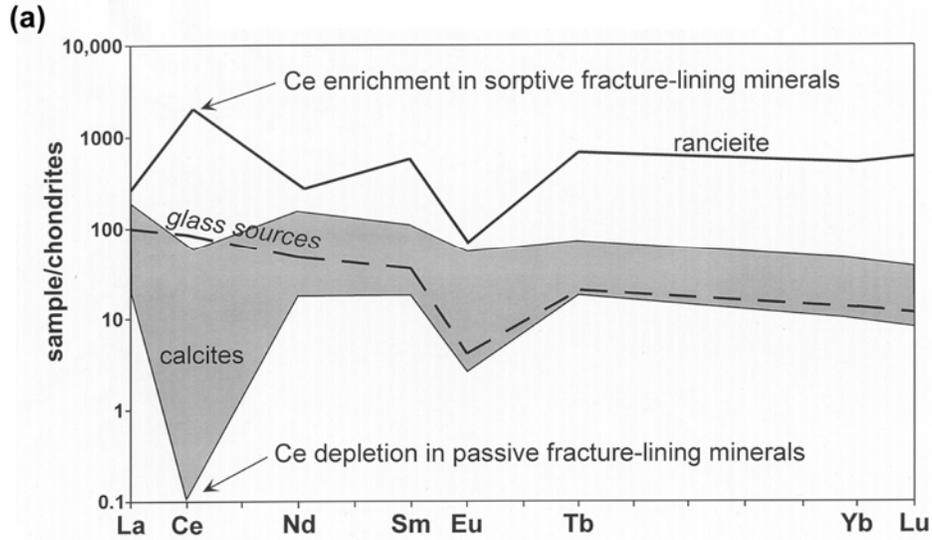
DTN: MO0312SEPSDDCA.000 [DIRS 166443]

Source: Eckhardt 2000 [DIRS 152135]; see also Vaniman and Chipera 1996 [DIRS 100089], Figure 4

NOTES: Part (a): With only very rare exceptions at the north end of Yucca Mountain, glass sources lack any cerium anomaly (Figure 5-4), but such anomalies are generated through fracture transport and accumulation of cerium in manganese oxides (example rancisite), leaving calcite-depositing solutions cerium-depleted. Part (b) illustrates the loss of cerium and development of negative cerium anomalies in fracture calcites of stratigraphic horizons immediately below the glassy layer where dissolution and fresh input of lanthanide elements without cerium anomaly occurs (a process driven by interaction with fracture minerals).

Figure 5-3. Development of Cerium Anomalies in Fracture-Lining Manganese Oxides and Calcites
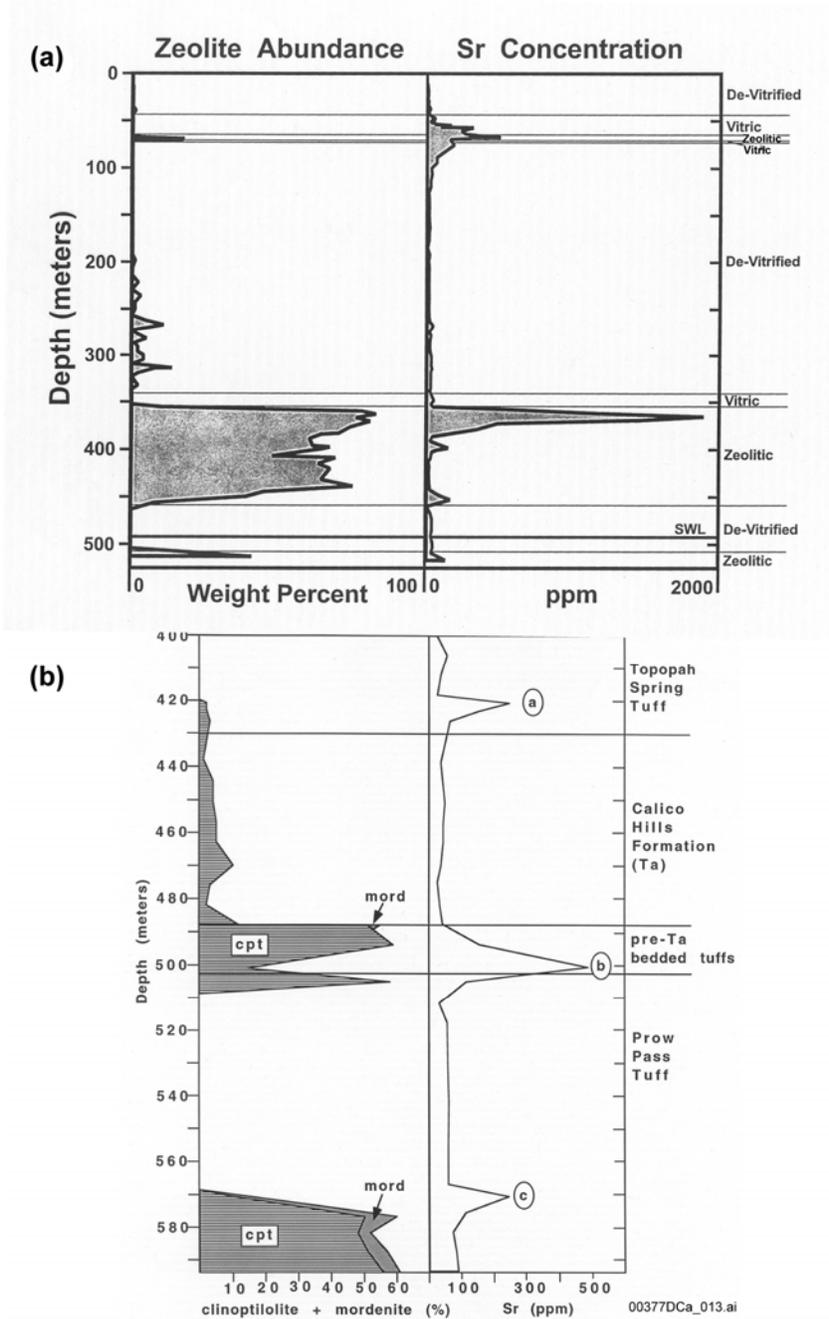
DTN: MO0312SEPSDZSA.000 [DIRS 166444]

Source: Eckhardt 2000 [DIRS 152135]; see also Vaniman et al. 2001 [DIRS 157427], Figure 4

NOTES: Part (a) shows abundances in UE-25 UZ#16. Part (b) shows abundances in USW SD-12. Strontium concentrations are particularly high at the top of the major zeolitized horizon in UZ#16. Lesser strontium accumulations are evident at positions (a) and (c) in SD-12, at the tops of the two zeolitized horizons that occur above the water table. Note that the strontium spike at position (b) in the lower panel reflects a depositional accumulation of strontium-rich feldspar, rather than later accumulation of strontium in zeolites by cation exchanges.

Figure 5-4.   Profiles of Zeolite and Strontium Abundance in the Unsaturated Zone
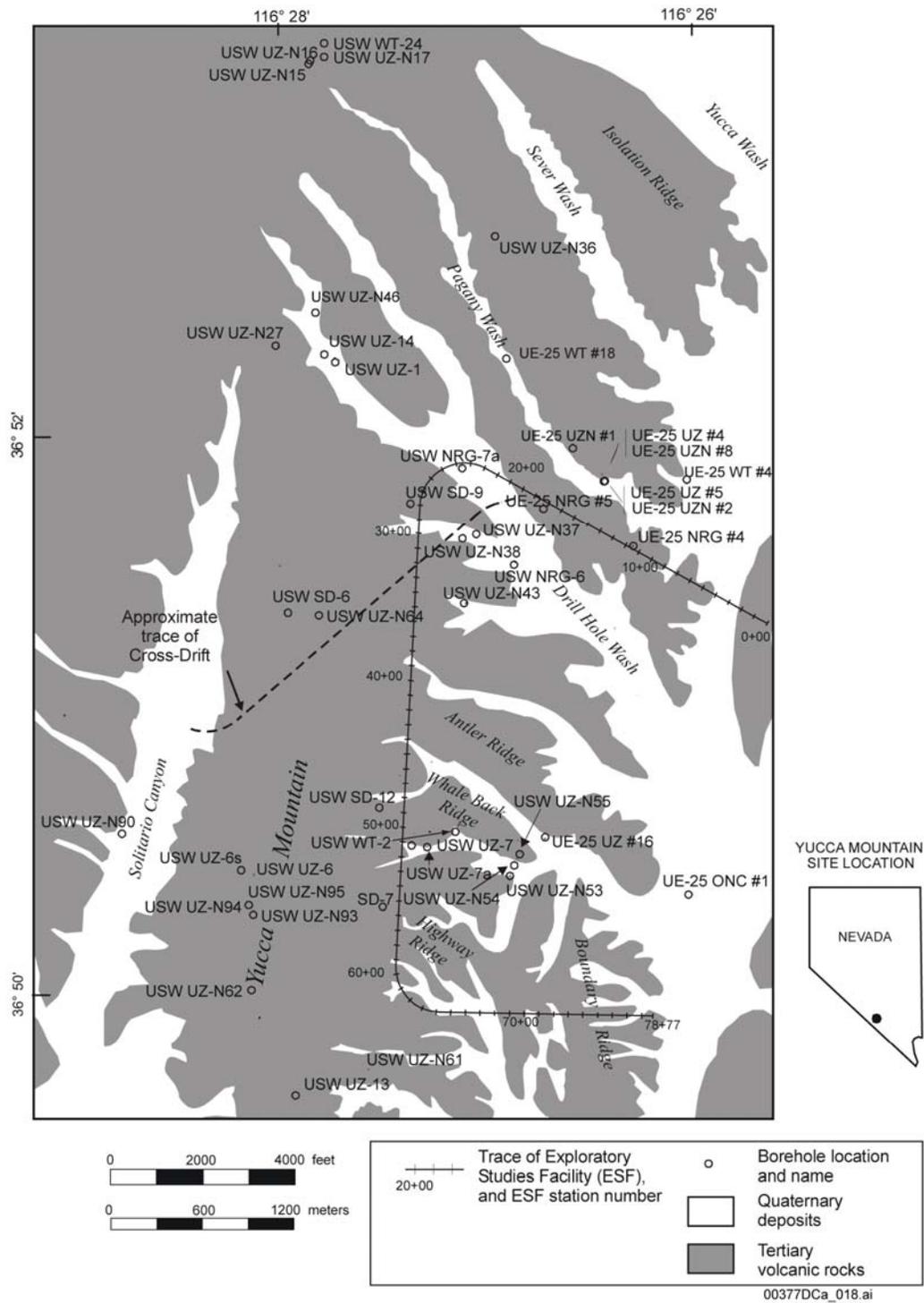
DTN: MO0312SEPSDDCA.000 [DIRS 166443]

Source: BSC 2002 [DIRS 160247], Figure 3

NOTE: This map shows the locations of surface-based boreholes for which isotopic and geochemical data are available for water and gas samples. Boreholes that are not shown because they are outside the map area are UZ N11, UZ N#39, and UZN #91.

Figure 5-5. Yucca Mountain Site Characterization Project Boreholes
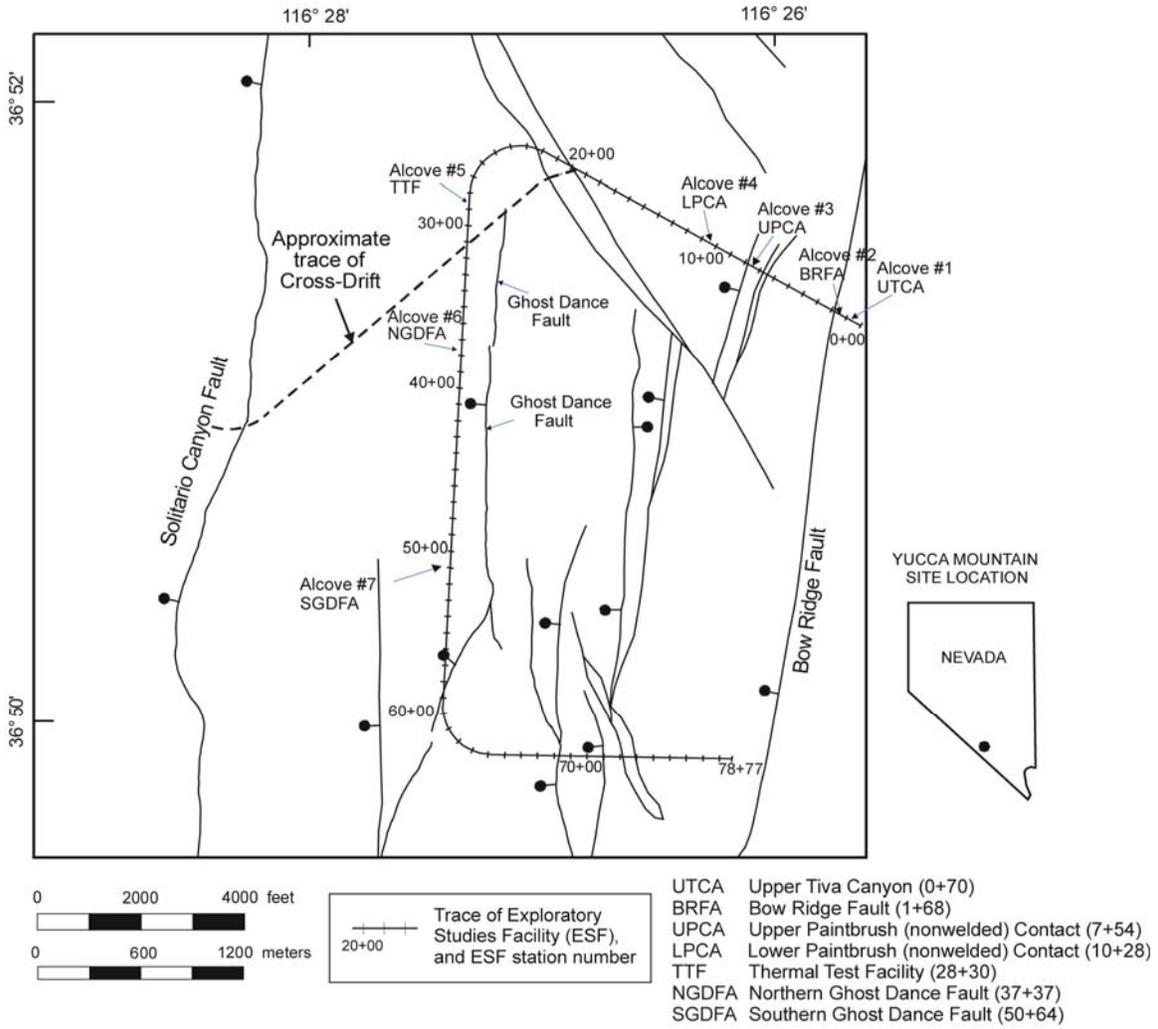
Source: BSC 2002 [DIRS 160247], Figure 4

NOTE: Alcove locations are shown relative to faults (ball-and-bar symbols on downdropped side) mapped at the surface by Day et al. (1998 [DIRS 101557], Plate 1). Not all faults on that map are shown here.

Figure 5-6. Locations of Exploratory Studies Facility Test Alcoves

Figure 5-7. Trilinear Diagram for Surface Runoff from the Yucca Mountain Area

Source: BSC 2002 [DIRS 160247], Figure 8, p. II-9

NOTE: This plot shows the extent to which different water samples are similar or dissimilar in composition. For those waters that are very similar (i.e., data symbols overlap), it is not important to be able to discern individual points.
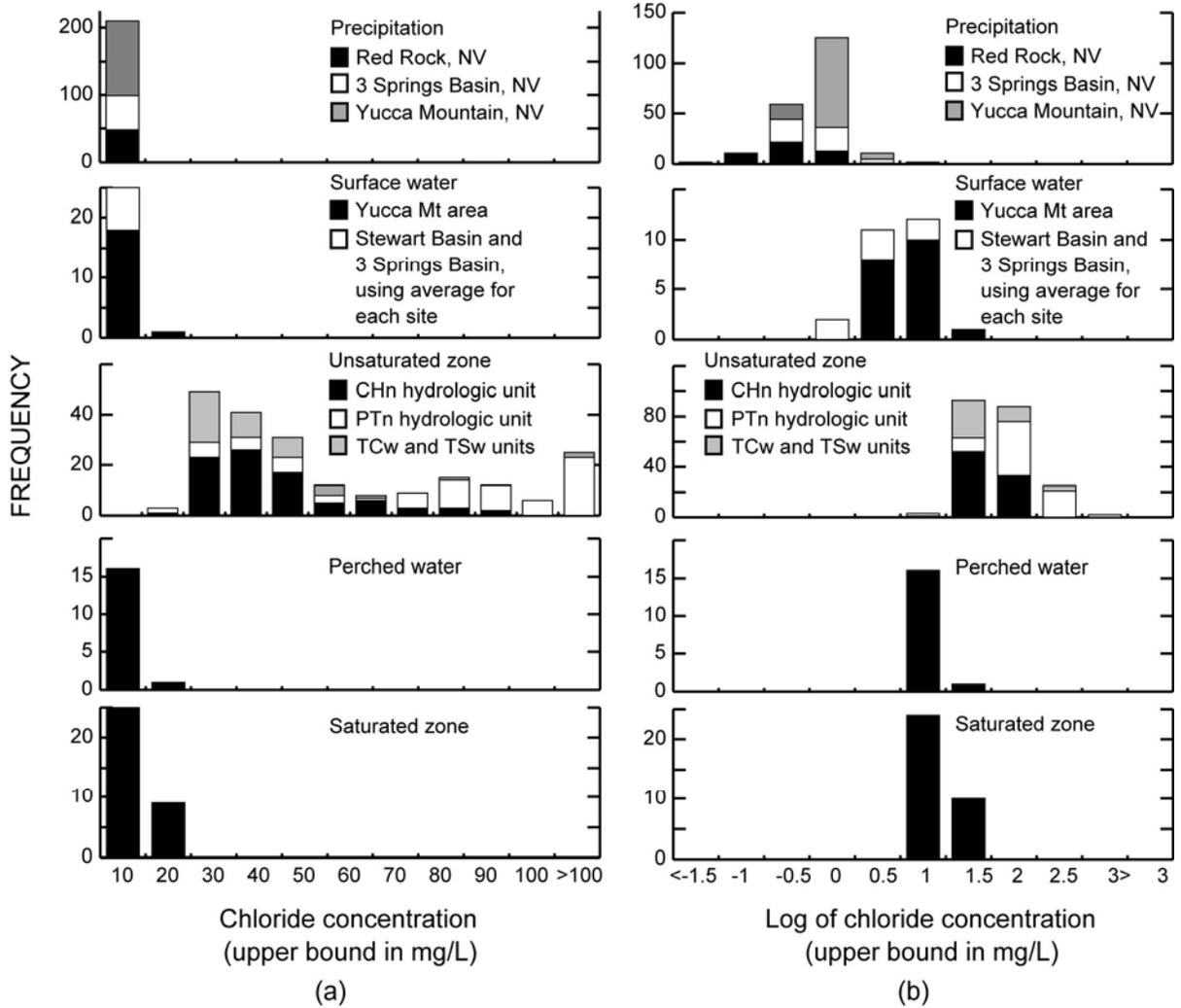
00377DCb_005.ai

DTNs: MO0005CL3SPRGS.000 [DIRS 153767]; MO0005CLESTWRT.000 [DIRS 153768];
MO0005CLKAWICH.000 [DIRS 153769]; GS930108315214.004 [DIRS 145583];
GS930908315214.030 [DIRS 145543]; LA0003JF12213U.001 [DIRS 147234];
LAJF831222AQ95.003 [DIRS 145585]; GS940308312133.002 [DIRS 145582];
GS960308312133.001 [DIRS 145606]; GS010708312272.002 [DIRS 156375];
GS961108312271.002 [DIRS 121708]; GS000608312271.001 [DIRS 153407];
GS970908312271.003 [DIRS 111467]; GS981008312272.004 [DIRS 153677];
GS990208312272.001 [DIRS 146134]; MO0012WTRIONCO.000 [DIRS 153397];
MO0312SEPSDMIC.000 [DIRS 166482]
(includes data from Oliver and Root 1997 [DIRS 100069])

Source: BSC 2002 [DIRS 160247], Figure 18, p. II-20

NOTE: Histograms are of chloride concentrations in precipitation, surface water, unsaturated zone pore water, perched water, and saturated zone groundwater. Part (a) shows chloride concentrations. Part (b) shows log of chloride concentrations.

Figure 5-8.   Histograms of Chloride Concentrations for Yucca Mountain Water Types

Figure 5-9.   Histograms of Sulfate Concentrations

DTNs: MO0005CL3SPRGS.000 [DIRS 153767]; MO0005CLESTWRT.000 [DIRS 153768];
MO0005CLKAWICH.000 [DIRS 153769]; GS930108315214.004 [DIRS 145583];
GS930908315214.030 [DIRS 145543]; LA0003JF12213U.001 [DIRS 147234];
GS940308312133.002 [DIRS 145582]; GS960308312133.001 [DIRS 145606];
GS010708312272.002 [DIRS 156375]; GS961108312271.002 [DIRS 121708];
GS000608312271.001 [DIRS 153407]; GS970908312271.003 [DIRS 111467];
GS981008312272.004 [DIRS 153677]; GS990208312272.001 [DIRS 146134];
MO0012WTRIONCO.000 [DIRS 153397]; MO0312SEPSDMIC.000 [DIRS 166482]
(includes data from Oliver and Root 1997 [DIRS 100069])

Source: BSC 2002 [DIRS 160247], Figure 19, p. II-21

NOTE: Histograms are of sulfate concentrations in precipitation, surface water, unsaturated zone pore water, perched water, and saturated zone groundwater. Part (a) shows sulfate concentrations. Part (b) shows log of sulfate concentrations.

Figure 5-9.   Histograms of Sulfate Concentrations
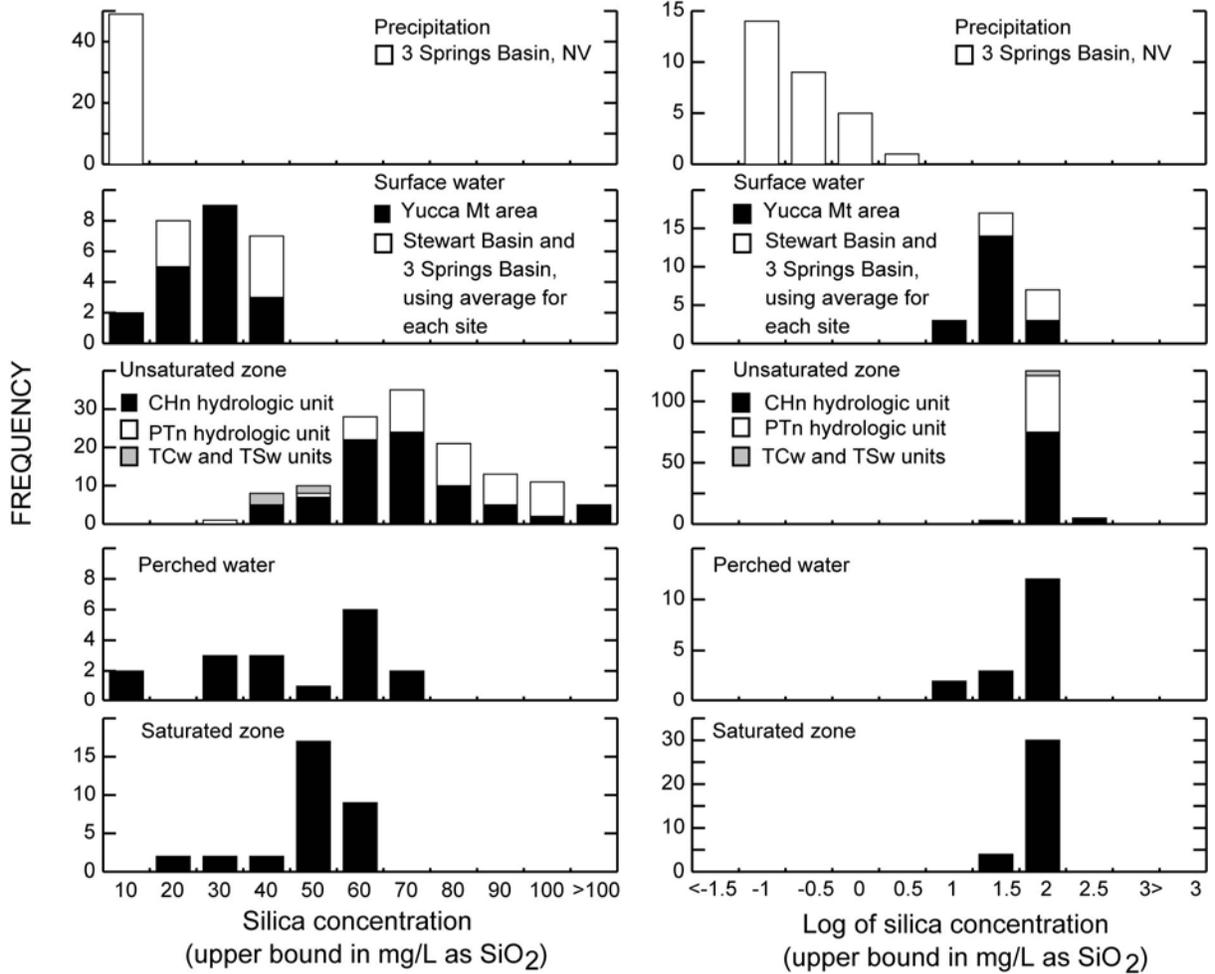
(a)

(b)

00377DCb_007.ai

DTNs: MO0005CL3SPRGS.000 [DIRS 153767]; MO0005CLESTWRT.000 [DIRS 153768];
MO0005CLKAWICH.000 [DIRS 153769]; GS930108315214.004 [DIRS 145583];
GS930908315214.030 [DIRS 145543]; GS940308312133.002 [DIRS 145582];
GS960308312133.001 [DIRS 145606]; GS010708312272.002 [DIRS 156375];
GS961108312271.002 [DIRS 121708]; GS000608312271.001 [DIRS 153407];
GS970908312271.003 [DIRS 111467]; GS981008312272.004 [DIRS 153677];
GS990208312272.001 [DIRS 146134]; MO0012WTRIONCO.000 [DIRS 153397],
MO0312SEPSDMIC.000 [DIRS 166482]
(includes data from Oliver and Root 1997 [DIRS 100069])

Source: BSC 2002 [DIRS 160247], Figure 20, p. II-22

NOTE: Histograms are of silica concentrations in precipitation, surface water, unsaturated zone pore water, perched water, and saturated zone groundwater. Part (a) shows silica concentrations. Part (b) shows log of silica concentrations.

Figure 5-10. Histograms of Silica Concentrations
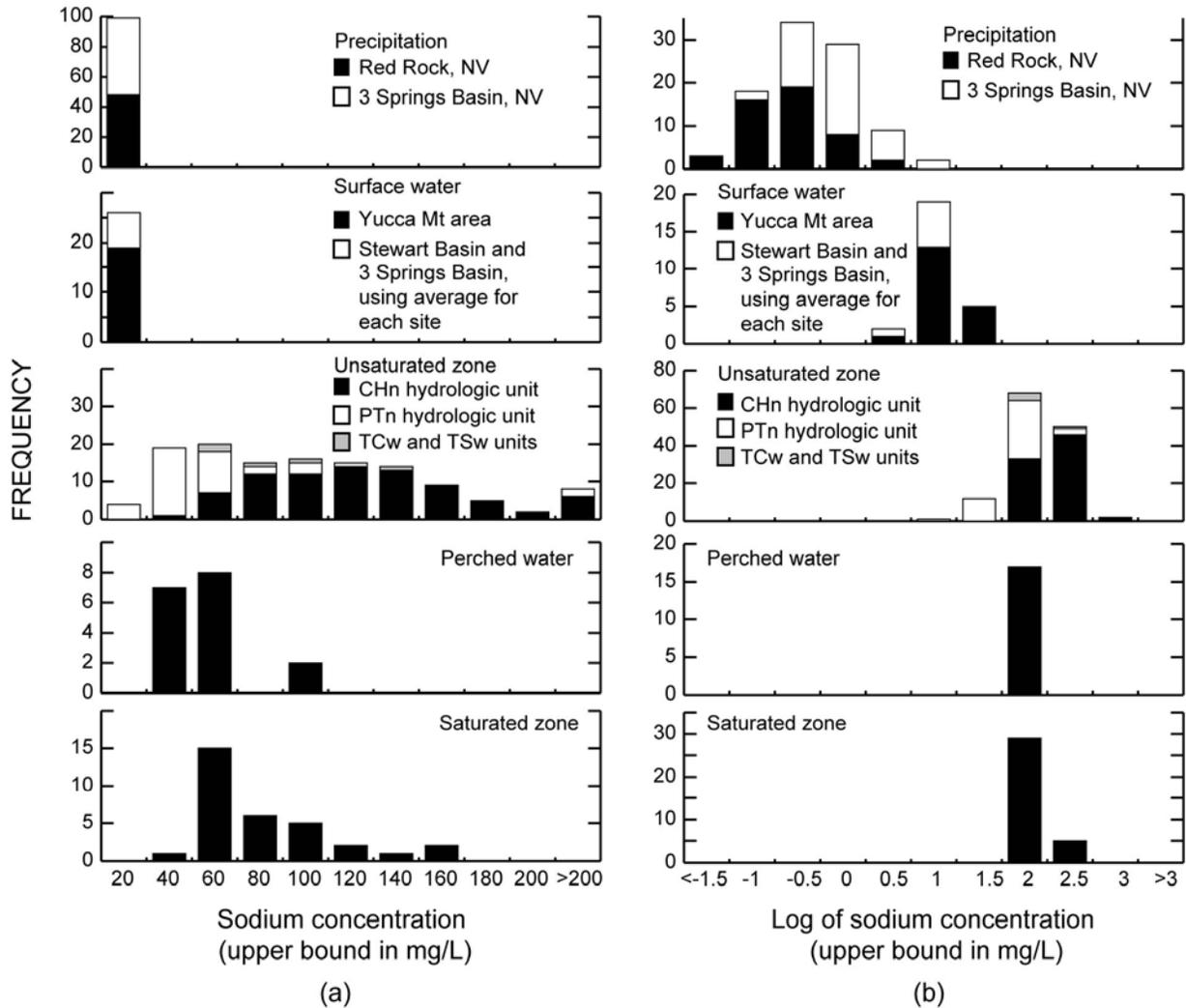
00377DCb_008.ai

DTNs: MO0005CL3SPRGS.000 [DIRS 153767]; MO0005CLESTWRT.000 [DIRS 153768];
MO0005CLKAWICH.000 [DIRS 153769]; GS930108315214.004 [DIRS 145583];
GS930908315214.030 [DIRS 145543]; LA0003JF12213U.001 [DIRS 147234];
GS940308312133.002 [DIRS 145582]; GS960308312133.001 [DIRS 145606];
GS010708312272.002 [DIRS 156375]; GS961108312271.002 [DIRS 121708];
GS000608312271.001 [DIRS 153407]; GS970908312271.003 [DIRS 111467];
GS981008312272.004 [DIRS 153677]; GS990208312272.001 [DIRS 146134];
MO0012WTRIONCO.000 [DIRS 153397]; MO0312SEPSDMIC.000 [DIRS 166482]
(includes data from Oliver and Root 1997 [DIRS 100069])

Source: BSC 2002 [DIRS 160247], Figure 21, p. II-23

NOTE: Histograms are of sodium concentrations in precipitation, surface water, unsaturated zone pore water, perched water, and saturated zone groundwater. Part (a) shows sodium concentrations. Part (b) shows log of sodium concentrations.

Figure 5-11. Histograms of Sodium Concentrations
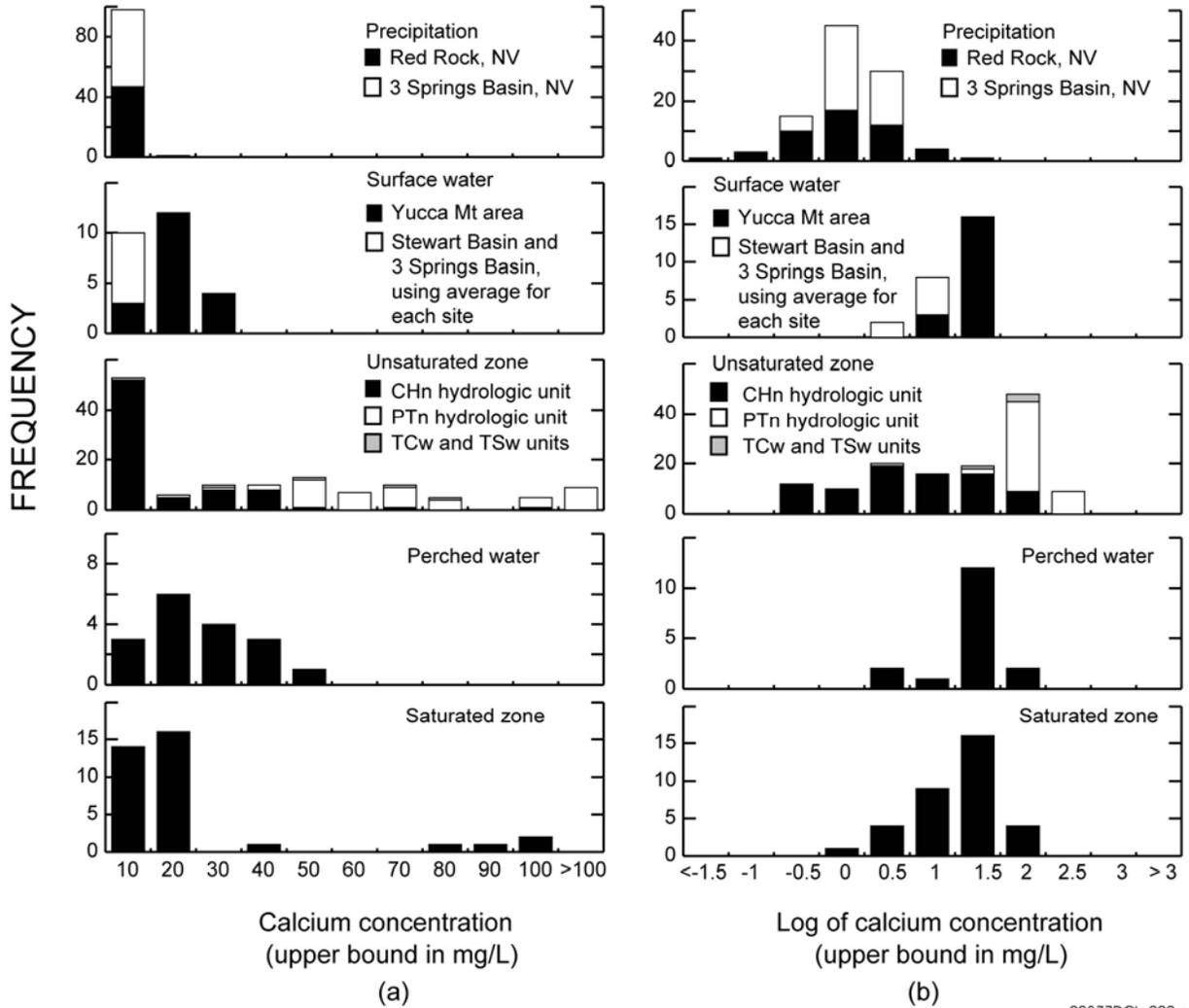
DTNs: MO0005CL3SPRGS.000 [DIRS 153767]; MO0005CLESTWRT.000 [DIRS 153768];
MO0005CLKAWICH.000 [DIRS 153769]; GS930108315214.004 [DIRS 145583];
GS930908315214.030 [DIRS 145543]; LA0003JF12213U.001 [DIRS 147234];
GS940308312133.002 [DIRS 145582]; GS960308312133.001 [DIRS 145606];
GS010708312272.002 [DIRS 156375]; GS961108312271.002 [DIRS 121708];
GS000608312271.001 [DIRS 153407]; GS970908312271.003 [DIRS 111467];
GS981008312272.004 [DIRS 153677]; GS990208312272.001 [DIRS 146134];
MO0012WTRIONCO.000 [DIRS 153397] MO0312SEPSDMIC.000 [DIRS 166482] (
includes data from Oliver and Root 1997 [DIRS 100069])

Source: BSC 2002 [DIRS 160247], Figure 22, p. II-24

NOTE: Histograms are of calcium concentrations in precipitation, surface water, unsaturated zone pore water, perched water, and saturated zone groundwater. Part (a) shows calcium concentrations. Part (b) shows log of calcium concentrations.

Figure 5-12. Histograms of Calcium Concentrations
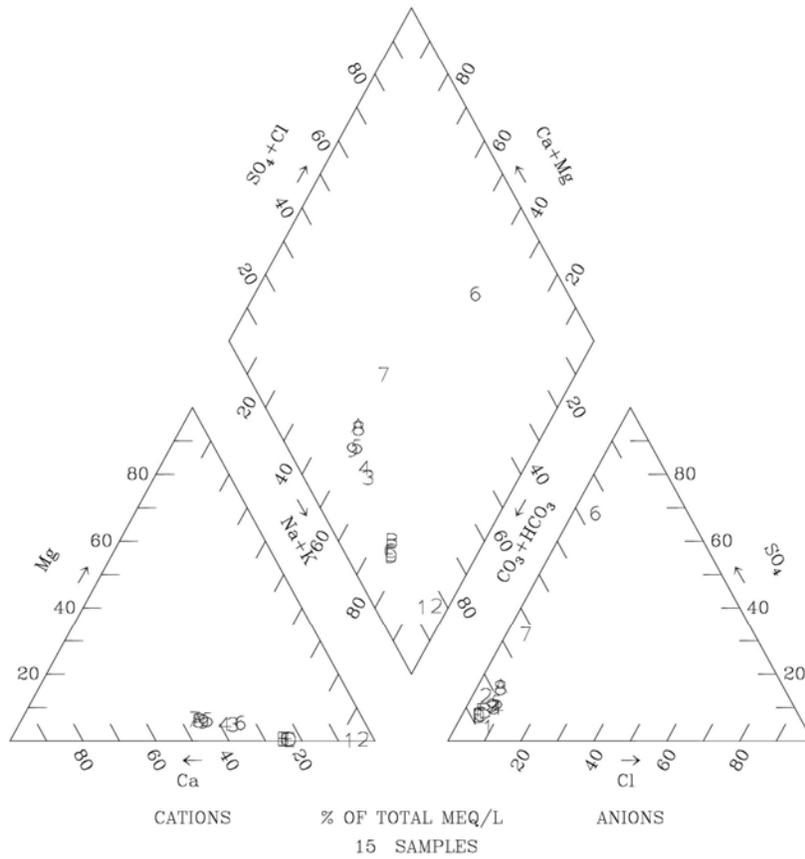
Legend

List of Plotted Points, Borehole Identifiers, and Sampled Depths (feet)

1	NRG7A	460.25	6	UZ14 C	390.75	B	SD7 (3/8/95)	479.76
2	SD9/TS	453.85	7	UZ14 PT1	390.75	C	SD7 (3/16/95)	488.29
3	UZ14 A	384.6	8	UZ14 PT2	390.75	D	SD7 (3/17/95)	488.29
4	UZ14 A2	384.6	9	UZ14 PT4	390.75	E	SD7 (3/20/95)	488.29
5	UZ14 B	387.68	A	UZ14 D	390.75	F	SD7 (3/21/95)	488.29

00377DCb_012.ai

DTN: MO0012WTRIONCO.000 [DIRS 153397]

Source: BSC 2002 [DIRS 160247], Figure 17, p. II-19

NOTE: Data are listed in Table 5-5. This plot shows the extent to which different water samples are similar or dissimilar in composition. For those waters that are very similar (i.e., data symbols overlap), it is not important to be able to discern individual points.

Figure 5-13. Trilinear Diagram for Perched Water near Yucca Mountain

CATIONS   % OF TOTAL MEQ/L   ANIONS
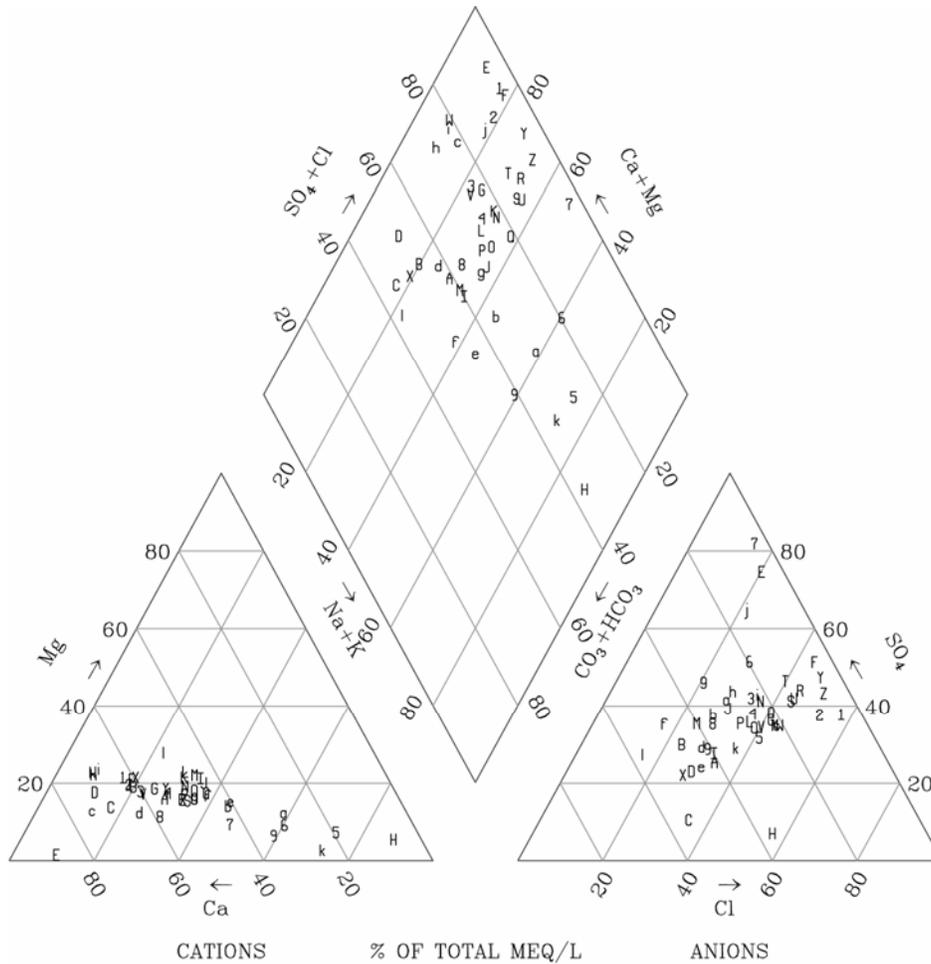
Legend

List of Plotted Points, Borehole Identifiers, and Tops of Sampled Intervals (feet)

1	NRG6-158.2	A	SD12-265.8	J	UZ14-91	S	UZ14-178.1	b	SD9-251.8
2	NRG6-160.8	B	SD12-278.6	K	UZ14-95.5	T	UZ14-215.7	c	UZN55-195.3
3	NRG6-171	C	SD12-296.1	L	UZ14-96.2	U	UZ14-225.9	d	UZN55-199.0
4	NRG6-175.6	D	SD7-339.7	M	UZ14-100.4	V	UZ14-235.1	e	SD6-430.3
5	NRG6-219.9	E	SD7-370.3	N	UZ14-114.8	W	UZ14-245.5	f	SD6-443.2
6	NRG6-244.6	F	SD9-94.2	O	UZ14-135.5	X	UZ16-180.9	g	SD6-443.5
7	NRG6-255.9	G	SD9-154	P	UZ14-144.8	Y	SD9-114.1	h	UZ7a-203.3
8	NRG7A-165.8	H	UZ14-45	Q	UZ14-147.8	Z	SD9-135.1	i	UZ7a-220.2
9	NRG7A-258	I	UZ14-85.2	R	UZ14-177.6	a	SD9-176.2	j	UZ7a-241.4
								k	UZ14-240.8
								l	UZ16-163.5

00377DCb_014a.ai

DTNs: GS961108312271.002 [DIRS 121708]; GS000608312271.001 [DIRS 153407]; GS981008312272.004 [DIRS 153677]; GS970908312271.003 [DIRS 111467]; GS010708312272.002 [DIRS 156375]

Source: BSC 2002 [DIRS 160247], Figure 12, p. II-14

NOTE: This plot shows the extent to which different water samples are similar or dissimilar in composition. For those waters that are very similar (i.e., data symbols overlap), it is not important to be able to discern individual points.

Figure 5-14.   Trilinear Diagram for Pore Waters from the Paintbrush Tuff Nonwelded Hydrogeologic Unit

CATIONS   % OF TOTAL MEQ/L   ANIONS
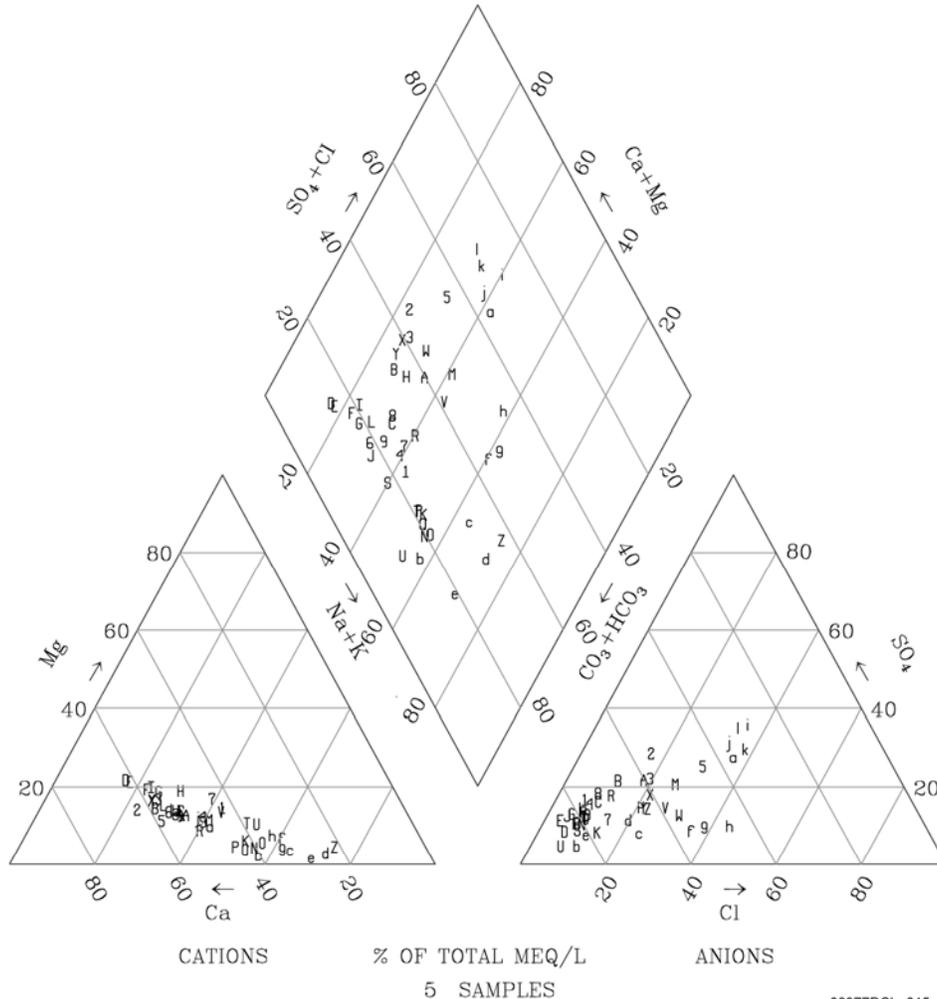
5 SAMPLES

00377DCb_015a.ai

Legend
List of Plotted Points, Borehole Identifiers, and Tops of Sampled Intervals (feet)

ECRB-SYS-CS:						ESF-SAD-GTB:				
1	400/5.6	B	950/4.8	L	1250/3.4	V	#1/119.4	Z	NRG-7/7A/839.3
2	450/5.3	C	950/5.2	M	1500/10.0	W	#1/123.1	a	SD-9/669.1
3	500/12.0	D	1000/10.9	N	2000/16.3	X	#1/194.2	b	SD-9/990.4
4	600/3.6	E	1000/11.1	O	2000/16.5	Y	#1/195.4	c	SD-9/1184.0
5	750/6.2	F	1000/12.9	P	2000/3.3			d	SD-9/1184.7
6	800/4.9	G	1000/15.6	Q	2000/3.95	ESF-THERMALK:		e	SD-9/1184.8
7	850/5.1	H	1000/5.4	R	2150/5.5	i	017/22.3	f	SD-9/1236.4
8	900/2.8	I	1000/7.3	S	2250/5.2	j	017/26.5	g	SD-9/1275.6
9	900/3.5	J	1100/3.7	T	2300/4.3	k	019/19.5	h	SD-9/1330.4
A	900/5.4	K	1150/3.2	U	2300/6.1	l	017/22.9		

DTN: GS010708312272.002 [DIRS 156375]

Source: BSC 2002 [DIRS 160247], Figure 13, p. II-15

NOTE: Sample UZN55-166.1 is from the Tiva Canyon welded unit; all other samples are from the Topopah Spring welded unit.

Figure 5-15. Trilinear Diagram for Pore Waters from the Tiva Canyon Welded and Topopah Spring Welded Hydrogeologic Units

CATIONS   % OF TOTAL MEQ/L   ANIONS

33 SAMPLES
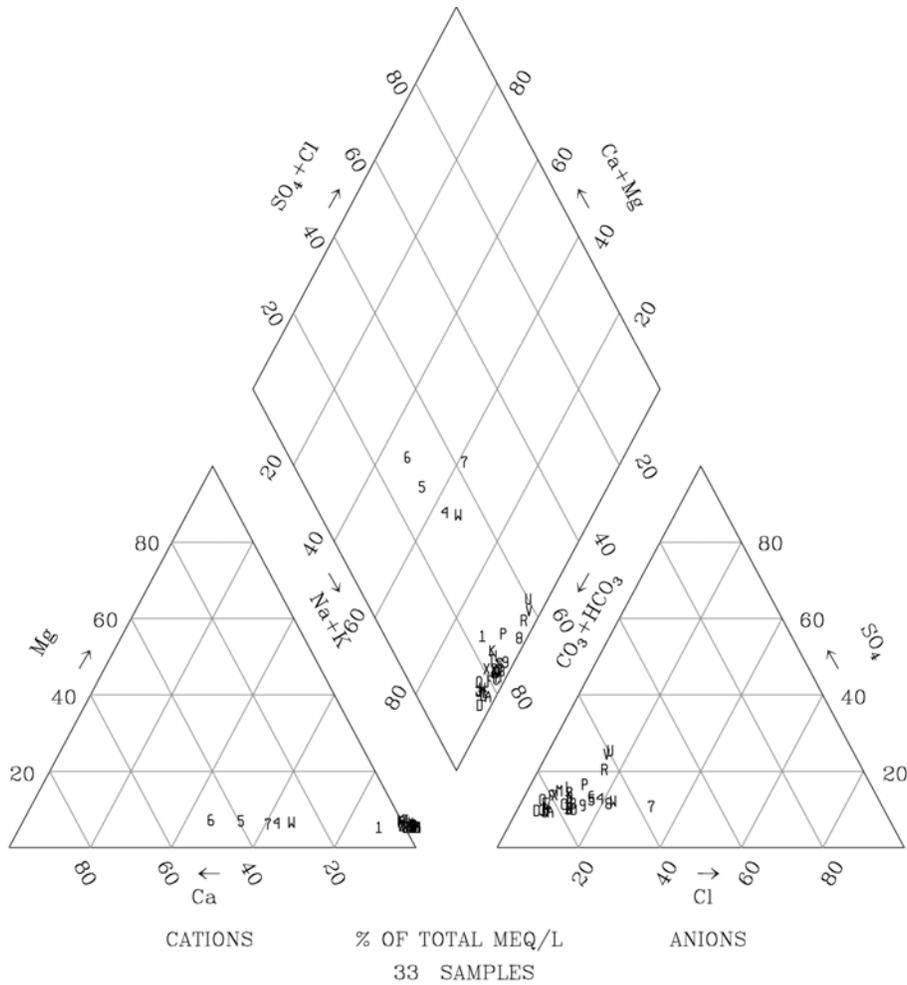
Legend

List of Plotted Points, Borehole Identifiers, and Tops of Sampled Intervals (feet)

1	SD12-1517	9	SD9-1661.1	H	UZ14-1585.3	P	UZ16-1389.4
2	SD12-1600.6	A	SD9-1741	I	UZ14-1605.9	Q	UZ16-1398.5
3	SD12-1636.8	B	SD9-1741.7	J	UZ14-1644.3	R	UZ16-1412.9
4	SD7-1498.4	C	SD9-1800.7	K	UZ14-1674.8	S	UZ16-1428.1
5	SD7-1524.6	D	UZ14-1563.6	L	UZ14-1695.4	T	UZ16-1442.8
6	SD7-1558.4	E	UZ14-1564.6	M	UZ14-1715	U	SD12-1558.9
7	SD7-1617	F	UZ14-1564.9	N	UZ14-1734.5	V	SD12-1582.5
8	SD9-1619.9	G	UZ14-1585	O	UZ14-1735.3	W	SD7-1600.1
						X	UZ16-1395.5

00377DCb_017a.ai

DTNs: GS961108312271.002 [DIRS 121708]; GS000608312271.001 [DIRS 153407];
GS981008312272.004 [DIRS 153677]; GS990208312272.001 [DIRS 146134];
GS010708312272.002 [DIRS 156375]

Source: BSC 2002 [DIRS 160247], Figure 15, p. II-17

NOTE: This plot shows the extent to which different water samples are similar or dissimilar in composition. For those waters that are very similar (i.e., data symbols overlap), it is not important to be able to discern individual points.

Figure 5-16. Trilinear Diagram for Pore Waters below the Top 200 Feet of the Calico Hills Nonwelded Hydrogeologic Unit and above the Prow Pass Lithostratigraphic Unit

Figure 5-17. Trilinear Diagram for Yucca Mountain Groundwater

DTNs: GS930308312323.001 [DIRS 145530]; MO0012MAJIONIS.000 [DIRS 153679]; GS990608312133.001 [DIRS 145611]; MO0312SEPSDTRD.000 [DIRS 166479] (includes data from Oliver and Root 1997 [DIRS 100069])

Source: BSC 2002 [DIRS 160247], Figure 48, p. II-50

NOTE: The trilinear diagram is for groundwater from the vicinity of Yucca Mountain. Well locations are shown in Figure 5-57. This plot shows the extent to which different water samples are similar or dissimilar in composition. For those waters that are very similar (i.e., data symbols overlap), it is not important to be able to discern individual points.

Part (A): 36Cl /Cl ratio (x 10^-15) vs year, 1950–1985. Predicted 36Cl/Cl ratio for global fallout at Yucca Mountain (Background = 500 x 10^-15). One-year residence time in soil zone; Ten-year residence time in soil zone.

Part (B): Tritium Units (TU) vs year, 1950–1985. Atmospheric tritium in Albuquerque, NM (Background = 6 TU). measured; decay-corrected to 1990.

Part (C): % Modern Carbon (pmc) vs year, 1950–1985. Atmospheric 14C in northern troposphere (Background = 100 pmc).

00377DCc_007.ai

DTN: LA0001JF12213U.001 [DIRS 145903]

Source: BSC 2002 [DIRS 160247], Figure 29, p. II-31

NOTE: Part (A) shows estimated chlorine-36/chlorine ratio for global fallout at Yucca Mountain as a function of average residence time in the soil zone, Part (B) shows tritium in atmospheric moisture in Albuquerque, New Mexico, and Part (C) shows atmospheric concentrations of bomb-pulse carbon-14 for the northern hemisphere.

Figure 5-18.   Input Functions for Bomb-Pulse Nuclides

(a)

Legend: ■ Paranagut Range □ Owl Canyon ▨ Little Skull Mountain ● Stockade Wash

(b)
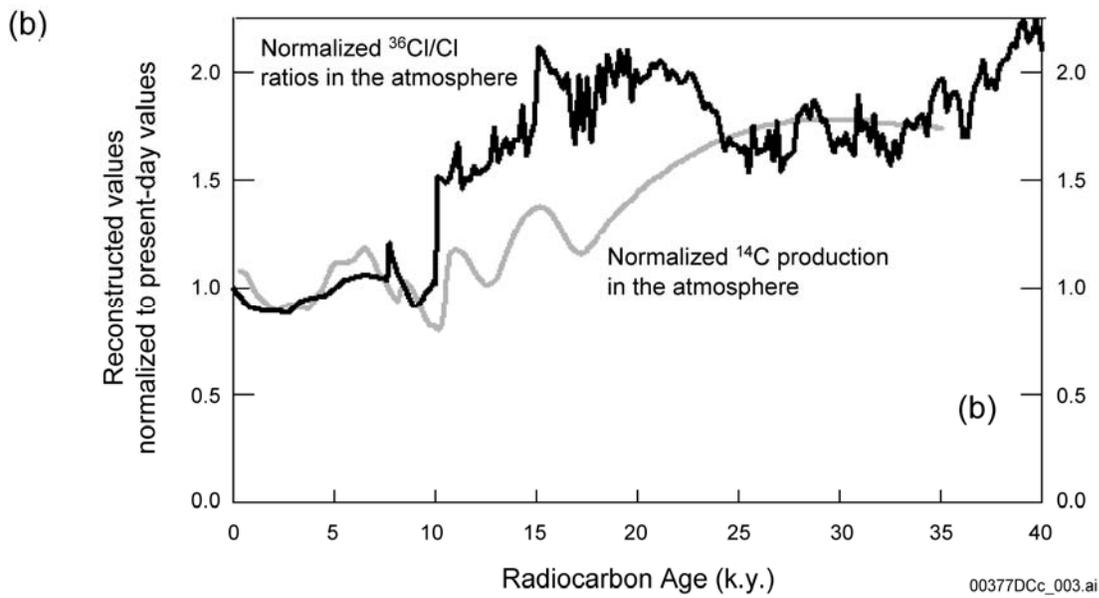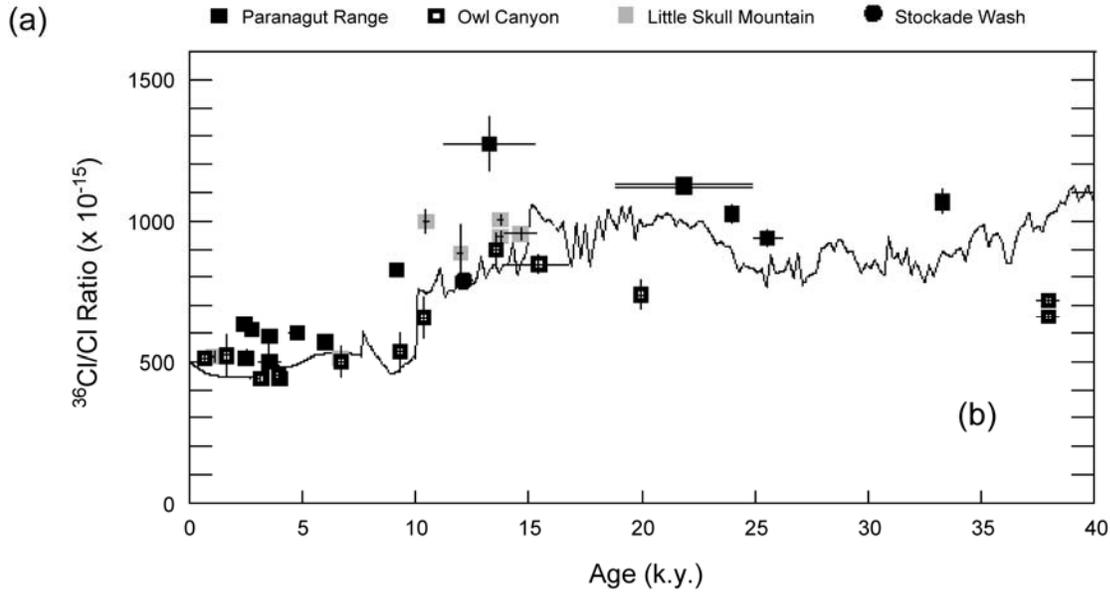
DTNs: LAJF831222AQ98.007 [DIRS 122730]; GS950708315131.003 [DIRS 106516];
GS960308315131.001 [DIRS 106517]; GS950708315131.001 [DIRS 106513];
GS950708315131.002 [DIRS 106515]

Source: BSC 2002 [DIRS 160247], Figure 31, p. II-33

NOTE: The top plot (a) compares the reconstructed $^{36}Cl/Cl$ ratio to measured $^{36}Cl/Cl$ ratios for fossilized pack-rat urine from southern Nevada (based on Plummer et al. 1997 [DIRS 107034], Figure 2). The bottom plot (b) compares the reconstructed $^{36}Cl/Cl$ ratio (normalized to a present-day value of 500×10^{-15}) to the reconstructed ^{14}C activity of Plummer et al. (1997 [DIRS 107034], Figure 3B).

Figure 5-19. Reconstructed Atmospheric $^{36}Cl/Cl$ Ratio
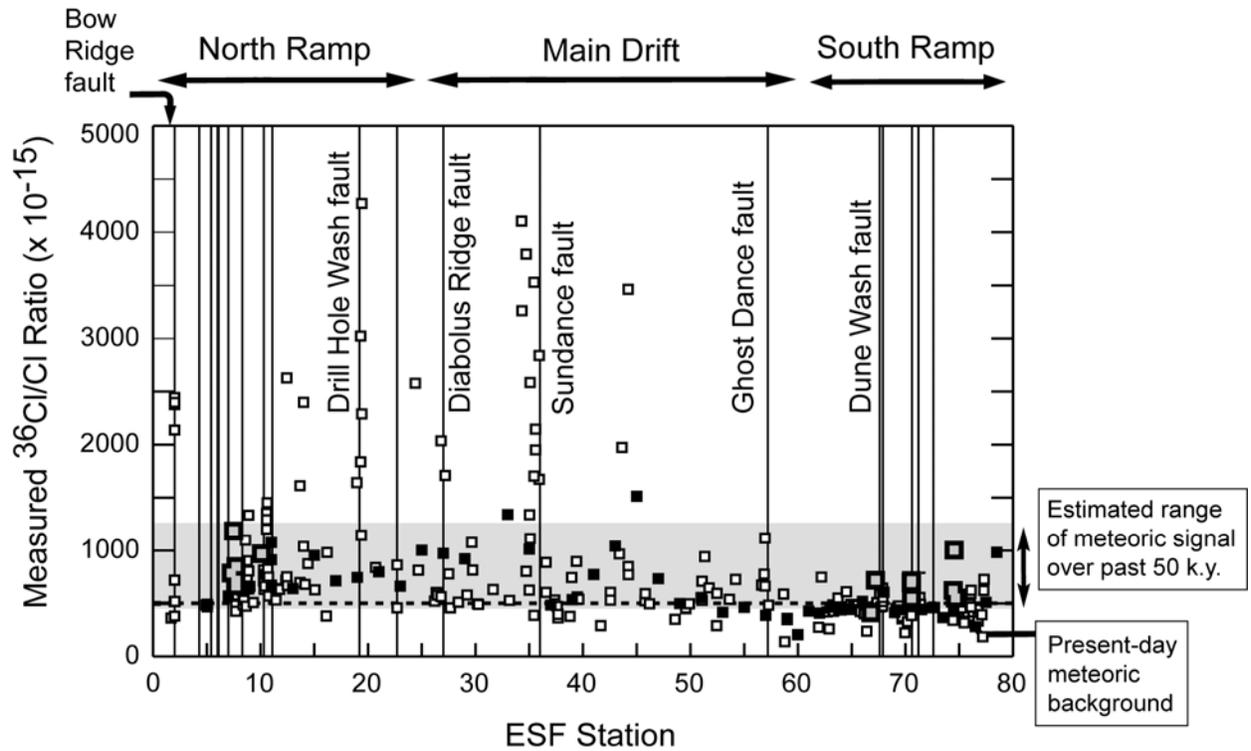
Figure 5-20.   Distribution of ^{36}Cl/Cl in the Exploratory Studies Facility (pre-2000 data)

DTNs: LAJF831222AQ98.004 [DIRS 107364]; LA9909JF831222.005 [DIRS 145630];
LA9909JF831222.010 [DIRS 122733]

Source: BSC 2002 [DIRS 160247], Figure 32, p. II-34

NOTE: This plot shows the distribution of ^{36}Cl/Cl ratios measured for leachates from rock samples in the Exploratory Studies Facility. Faults in the Exploratory Studies Facility that correlate with mapped faults at the surface are shown. Exploratory Studies Facility stations are labeled in 100-meter increments. Analytical uncertainties are less than 10 percent.

DTNs: LAJF831222AQ98.004 [DIRS 107364]; LAJF831222AQ98.009 [DIRS 145650]

Source: BSC 2003 [DIRS 166347], Figure 6.14.2-1, p. 6.14-9

NOTE: Although the main trace of the Sundance fault (shaded broad dashes) is exposed at a distance of 3,593 from the ESF North Portal, the entire zone between about 3,400 and 3,650 meters is pervasively fractured. Analytical errors (2σ) are shown as vertical lines if they are larger than the size of the symbol. The USGS-LLNL validation-study samples are shown as filled circles. Previously published LANL data (Fabryka-Martin et al. 1996 [DIRS 144839]; 1997 [DIRS 100145]; 1998 [DIRS 162737]) are shown as open squares. Ranges for different chlorine-36/chlorine signatures are from Fabryka-Martin et al. (1996 [DIRS 144839]; 1997 [DIRS 100145]).

Figure 5-21. Comparison of ^{36}Cl/Cl Ratios Obtained by Pre-2000 and Validation Studies for the Sundance Zone
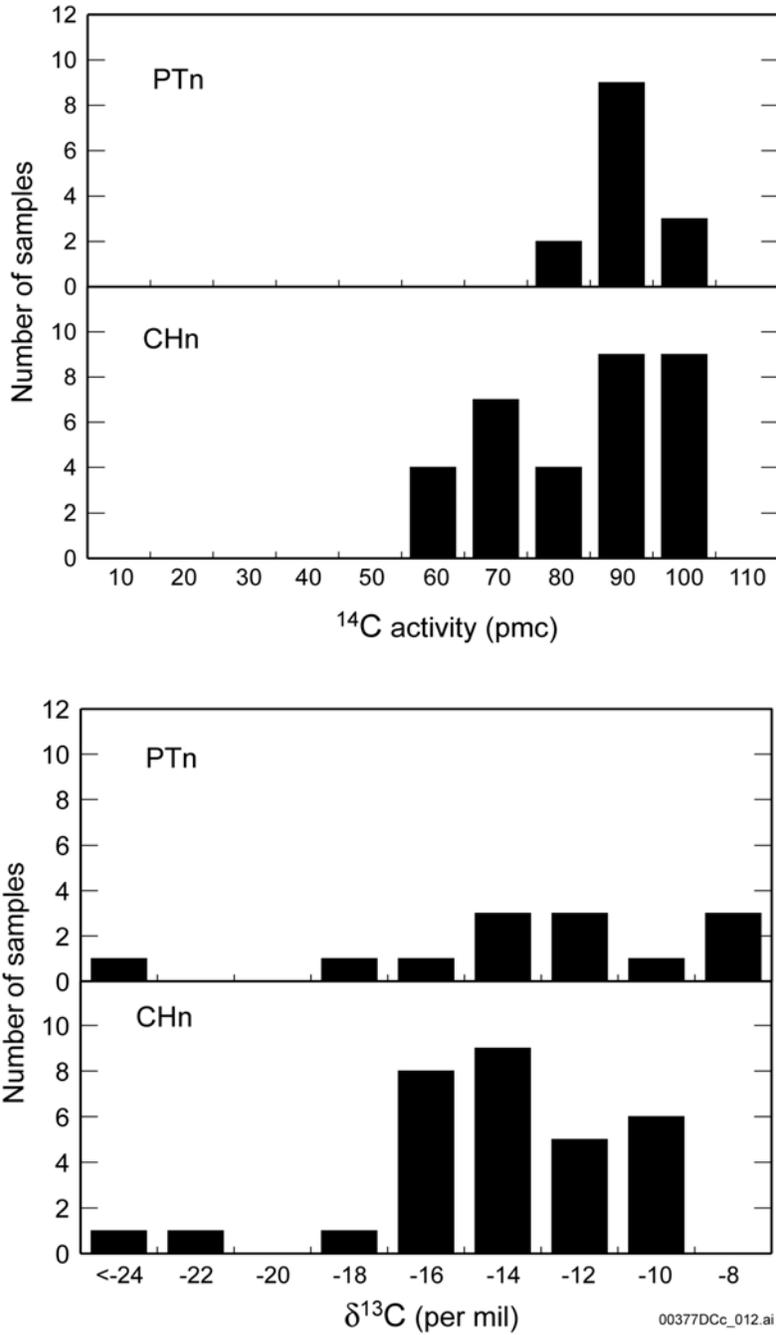
DTNs: MO0012CARB1314.001 [DIRS 153394]; MO0102UNSZHYCM.000 [DIRS 153858];
MO0012CARBON13.000 [DIRS 153408]; GS961108312271.002 [DIRS 121708];
GS000608312271.001 [DIRS 153407]

Source: BSC 2002 [DIRS 160247], Figure 34, p. II-36

NOTE: Frequency histograms comparing the distribution of ^{14}C activities and δ^{13}C values of unsaturated zone pore waters in the Paintbrush Group nonwelded and Calico Hills nonwelded hydrogeologic units of Yucca Mountain.

Figure 5-22.   Histogram of Carbon Isotopes in Pore Waters

(a) Unsaturated zone porewaters

(c) Perched water

(b) Unsaturated zone gases

(d) Saturated zone groundwaters

δ¹³C (per mil)
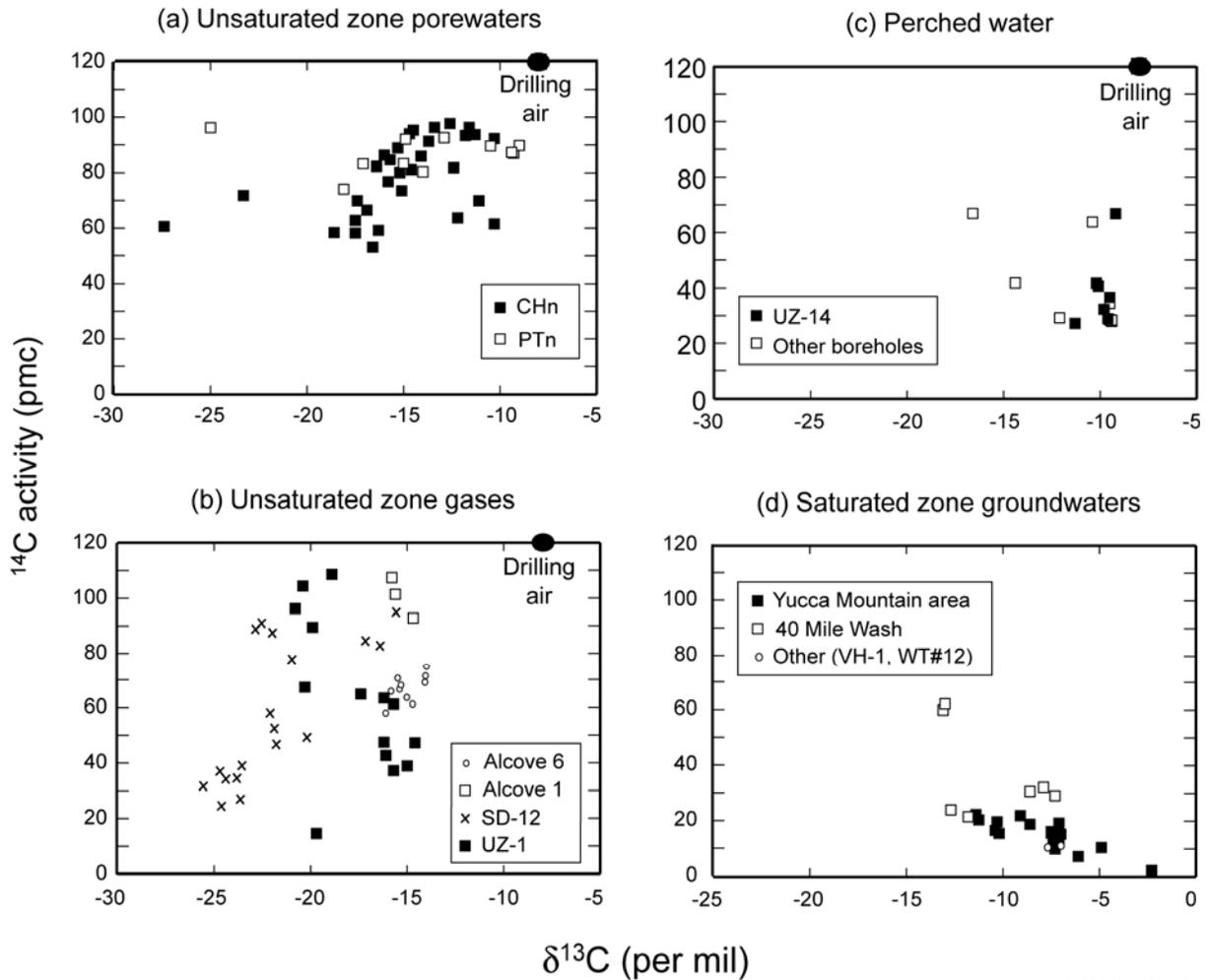
00377DCc_013.ai

DTNs: MO0012CARB1314.001 [DIRS 153394]; MO0102UNSZHYCM.000 [DIRS 153858];
GS961108312271.002 [DIRS 121708]; GS000608312271.001 [DIRS 153407];
MO0012CARBON13.000 [DIRS 153408]; MO0012CARB1314.000 [DIRS 153398];
GS960208312261.002 [DIRS 121680]; GS970283122410.002 [DIRS 121745];
GS990983122410.003 [DIRS 145908]; GS930308312323.001 [DIRS 145530];
MO0312SEPSDC14.000 [DIRS 166480]
(includes data from Oliver and Root 1997 [DIRS 100069])

Source: BSC 2002 [DIRS 160247], Figure 35, p. II-37

NOTE: Plots show ¹⁴C activity versus δ¹³C values for (a) pore waters from the unsaturated zone, (b) gas from the unsaturated zone, (c) perched water, and (d) saturated zone groundwaters. The reference standard for δ¹³C is the Pee Dee Formation Belemnite.

Figure 5-23. ¹⁴C Activity versus δ¹³C Values for Yucca Mountain Waters and Gases
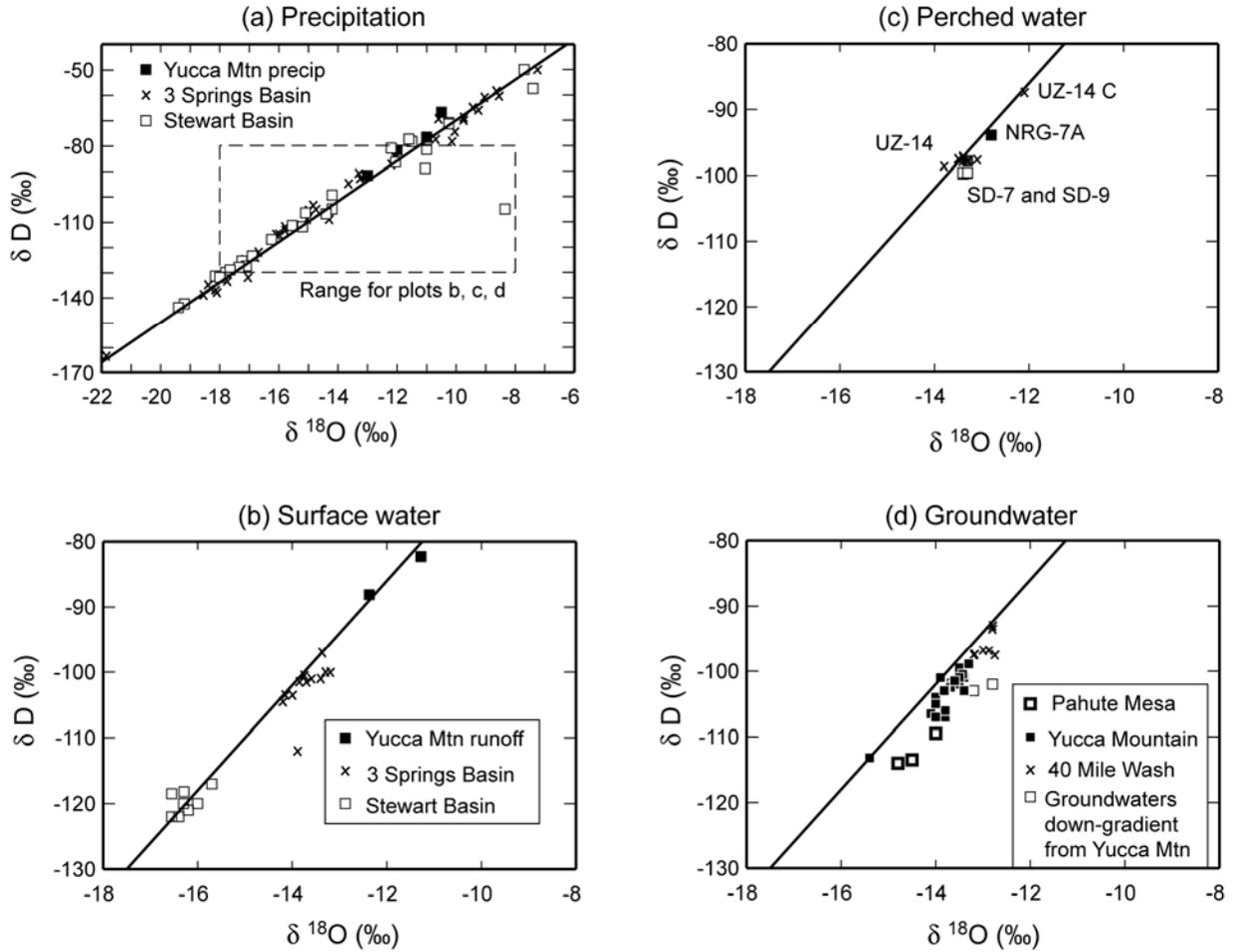
Figure 5-24. δD and δ¹⁸O Values for Yucca Mountain Waters

Source: BSC 2002 [DIRS 160247], Figure 36, p. II-38

NOTE: This plot shows δD and δ¹⁸O values of (a) local precipitation, (b) local surface water, (c) perched water, and (d) Yucca Mountain groundwaters. Both δ¹⁸O and δD are calculated relative to standard mean ocean water (SMOW). The solid line on each plot is the best-fit regression line for the precipitation data.

Figure 5-24. δD and δ¹⁸O Values for Yucca Mountain Waters

(a) UZ-14 porewater, distilled

(b) UZ-14 porewater, squeezed
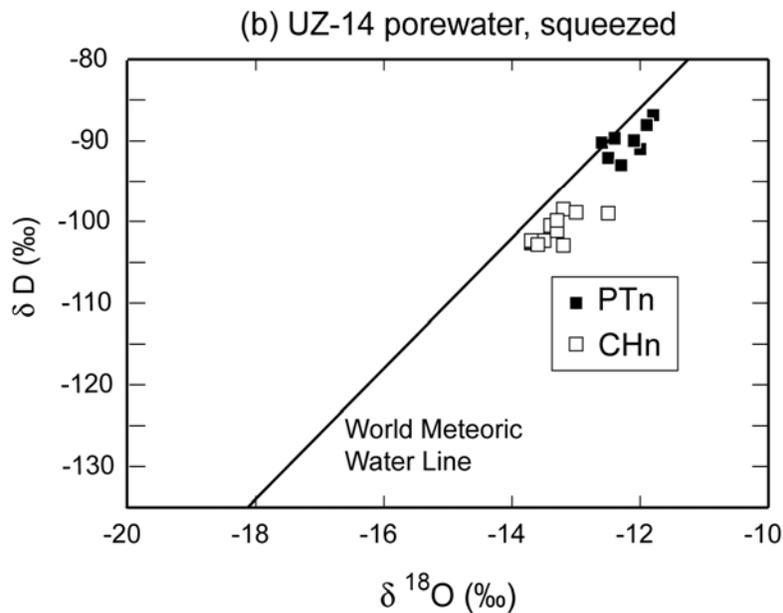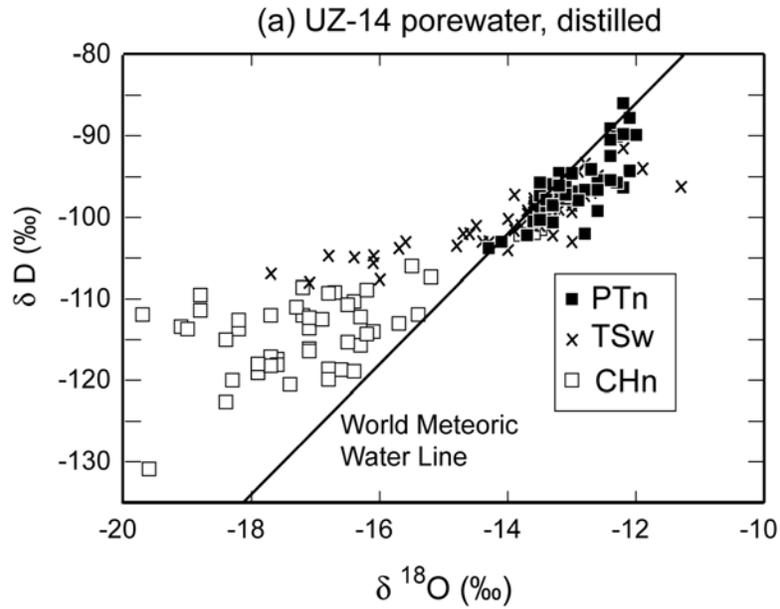
00377DCc_015a.ai

DTN: MO0102UNSZHYCM.000 [DIRS 153858]

Source: BSC 2002 [DIRS 160247], Figure 37, p. II-39

NOTE: This plot contrasts the stable isotopic signatures obtained for pore waters extracted using two different methods of extraction: (a) pore water extracted by vacuum distillation and (b) pore water extracted by uniaxial compression squeezing. The solid line on each plot is the best-fit regression line for the precipitation data

Figure 5-25. Plot of δD versus δ^{18}O for Pore Water Compositions in UZ-14
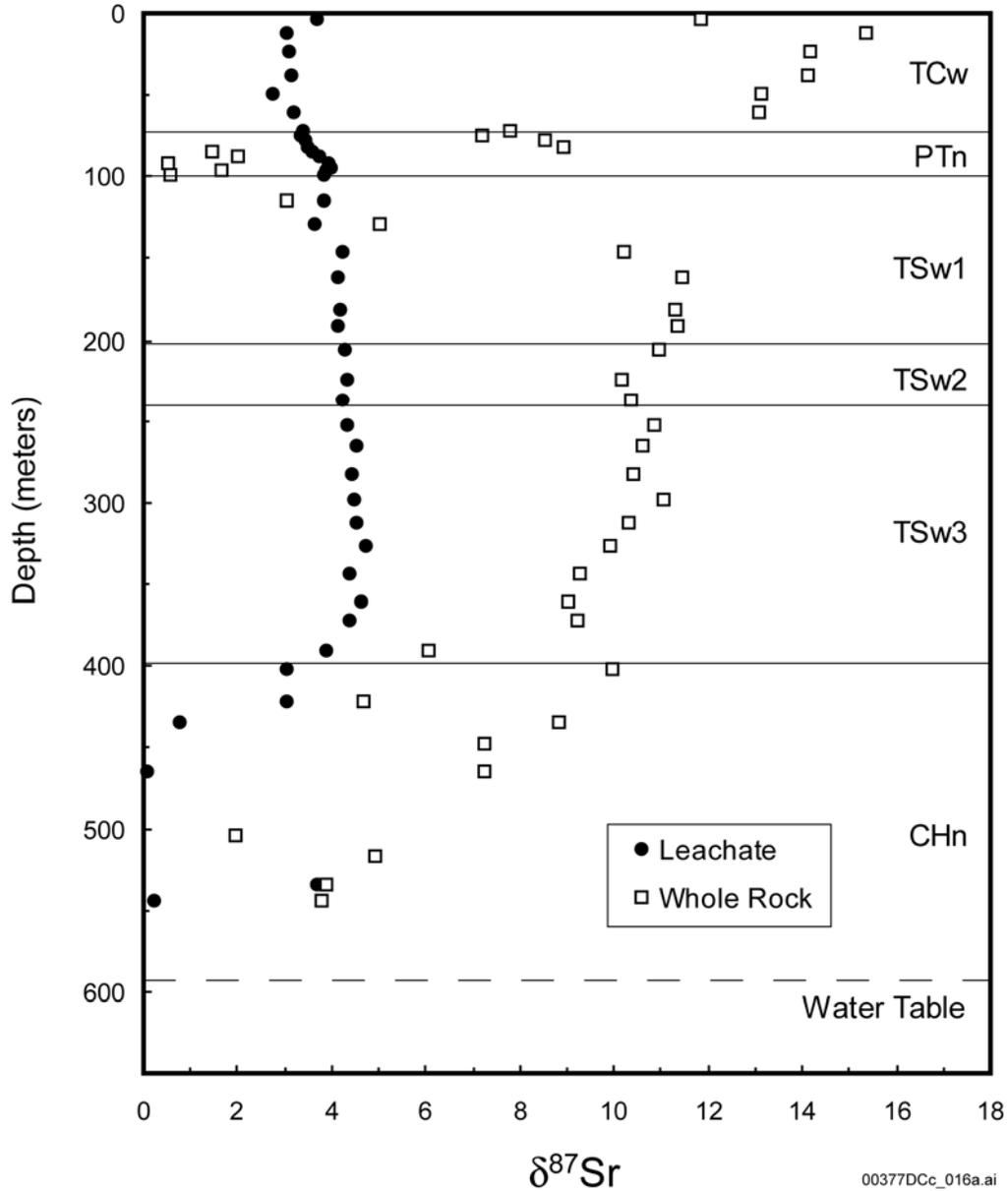
DTNs: GS990308315215.004 [DIRS 145711]; MO0004QGFMPICK.000 [DIRS 152554];
GS010908312332.002 [DIRS 163555]

NOTE: δ^{87}Sr (per mil) of rock leachate (black dots) and calcite fracture coatings (boxes) in USW SD-12 as a function of depth are shown. For rock leachate fractions, material was crushed, sieved, and leached with water to extract strontium present in pore water and soluble salts. Leachate (and presumable pore water strontium isotope compositions in USW SD-12 vary as a function of depth because of water-rock interaction, especially within the Paintbrush Tuff nonwelded hydrogeologic unit.

Figure 5-26. δ^{87}Sr in USW SD-12 Pore Waters and Calcites

Uranium concentration and isotopic composition for water collected from the Single Heater Test.
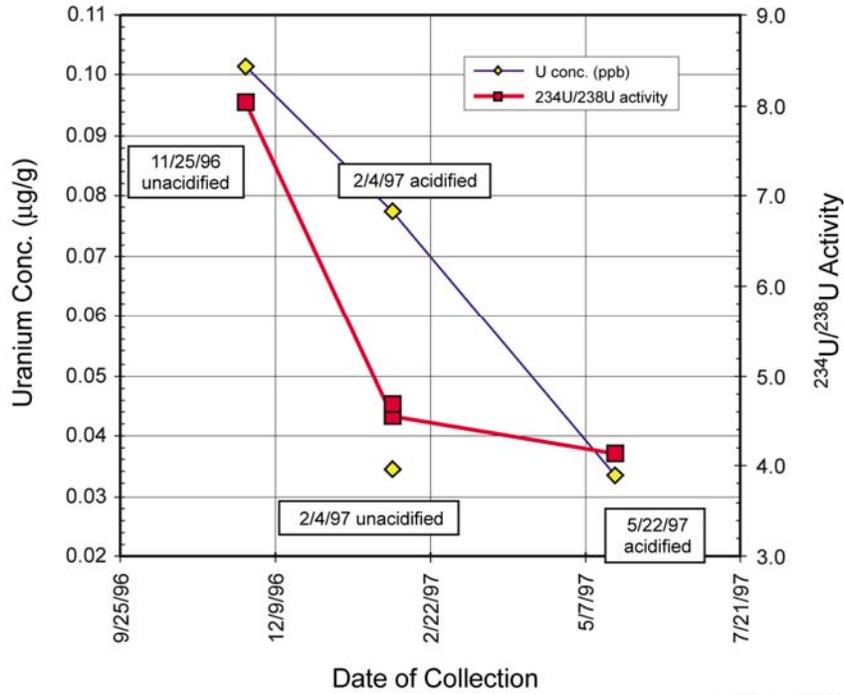
00377DCc_017.ai

DTNs: GS970508312272.001 [DIRS 145713]; GS980908312322.009 [DIRS 118977]

Source: BSC 2002 [DIRS 160247], Figure 39, p. II-41

NOTE: Plot shows uranium concentrations and ^{234}U/^{238}U activity ratios in water collected from Borehole ESF-TMA-NEU2, zone 4, associated with the Single Heater Test, Exploratory Studies Facility Alcove 5.

Figure 5-27.   Uranium Concentrations and ^{234}U/^{238}U Activity Ratios of Waters from the Single Heater Test
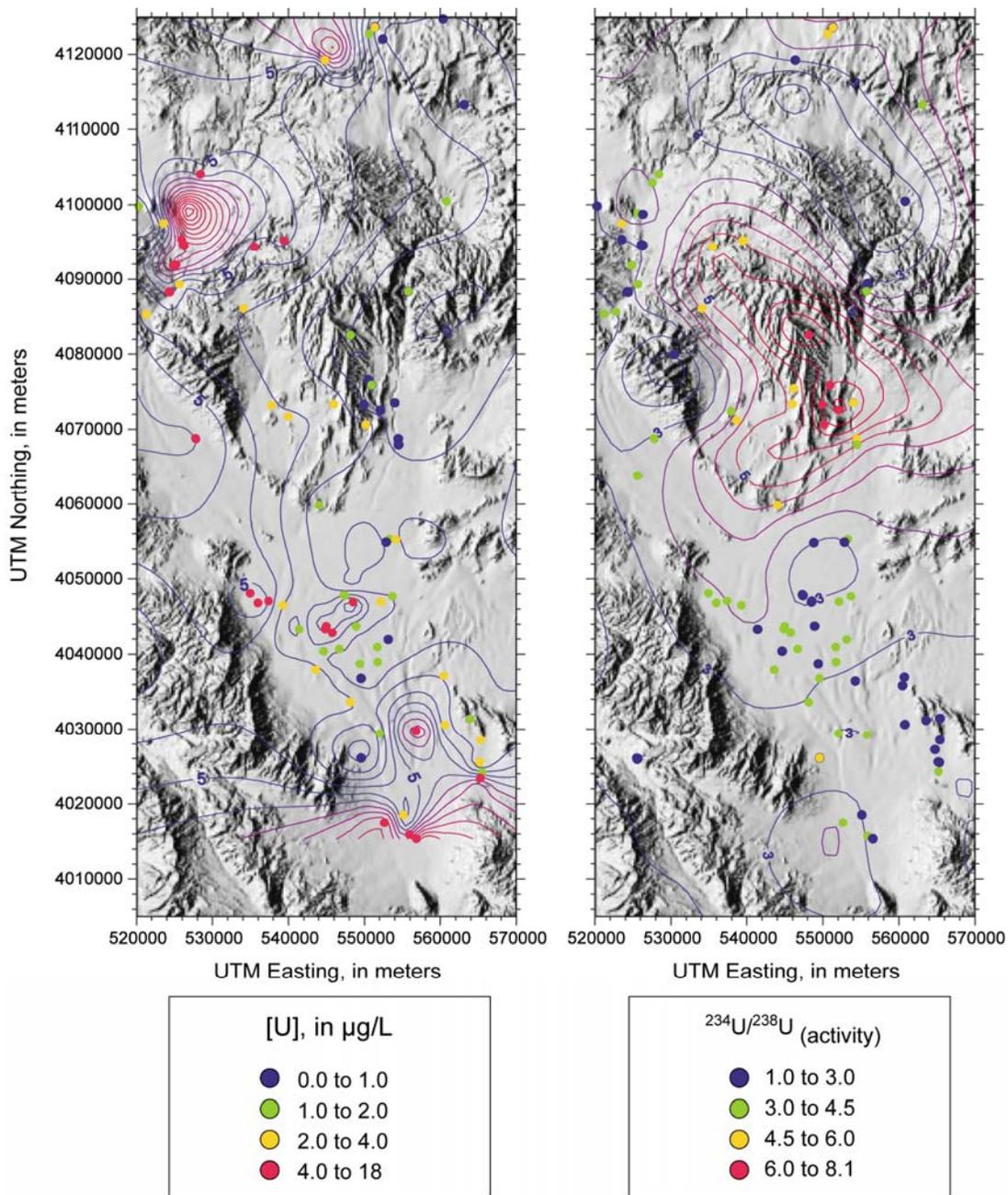
DTNs: GS930108315213.004 [DIRS 145525]; GS010608315215.002 [DIRS 156187];
GS980708315215.012 [DIRS 156242]; GS010808312322.004 [DIRS 156007];
GS010808312322.005 [DIRS 156008]; GS980208312322.006 [DIRS 146065];
GS980908312322.009 [DIRS 118977]

Source: BSC 2002 [DIRS 160247], Figure 42, p. II-44

NOTE: Uranium concentrations and $^{234}U/^{238}U$ activity ratios of saturated zone groundwater samples from the vicinity of the Nevada Test Site are shown. The highest activity ratios (right hand Figure) are beneath and slightly east of Yucca Mountain.

Figure 5-28. Uranium Concentrations and $^{234}U/^{238}U$ Activity Ratios in Regional Groundwater Samples
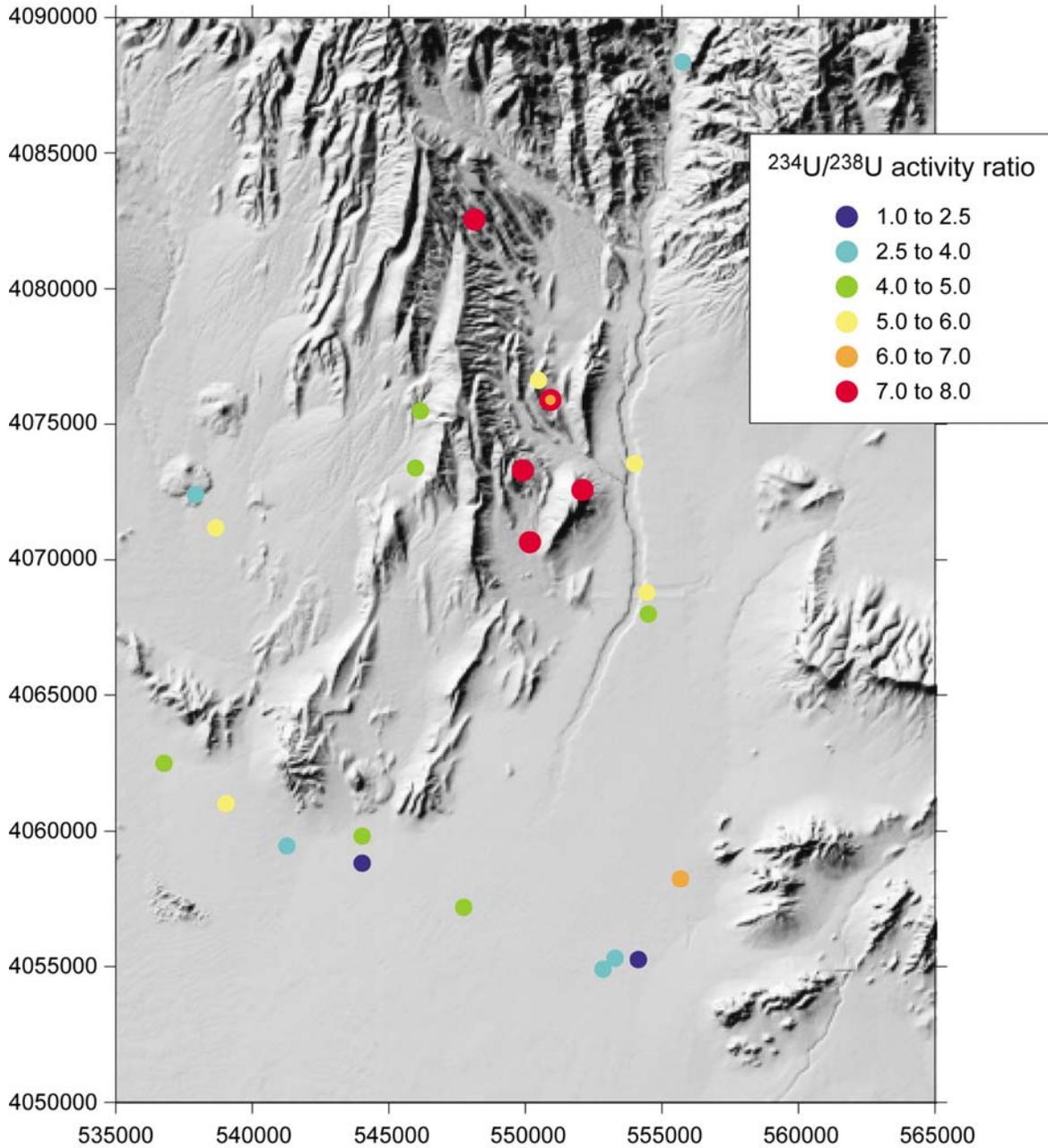
DTNs: GS930108315213.004 [DIRS 145525]; GS010608315215.002 [DIRS 156187];
GS010808312322.004 [DIRS 156007]; GS980208312322.006 [DIRS 146065];
GS980908312322.009 [DIRS 118977]; MO0012URANISOT.000 [DIRS 153384]

Source: BSC 2002 [DIRS 160247], Figure 43, p. II-45

NOTE: Uranium isotopic compositions of regional saturated zone groundwater samples from the Yucca Mountain vicinity are shown. Yucca Mountain is the long ridge slightly west of the cluster of samples with the highest activity ratios on this map.

Figure 5-29. $^{234}U/^{238}U$ Activity Ratios of Groundwater in the Yucca Mountain Vicinity
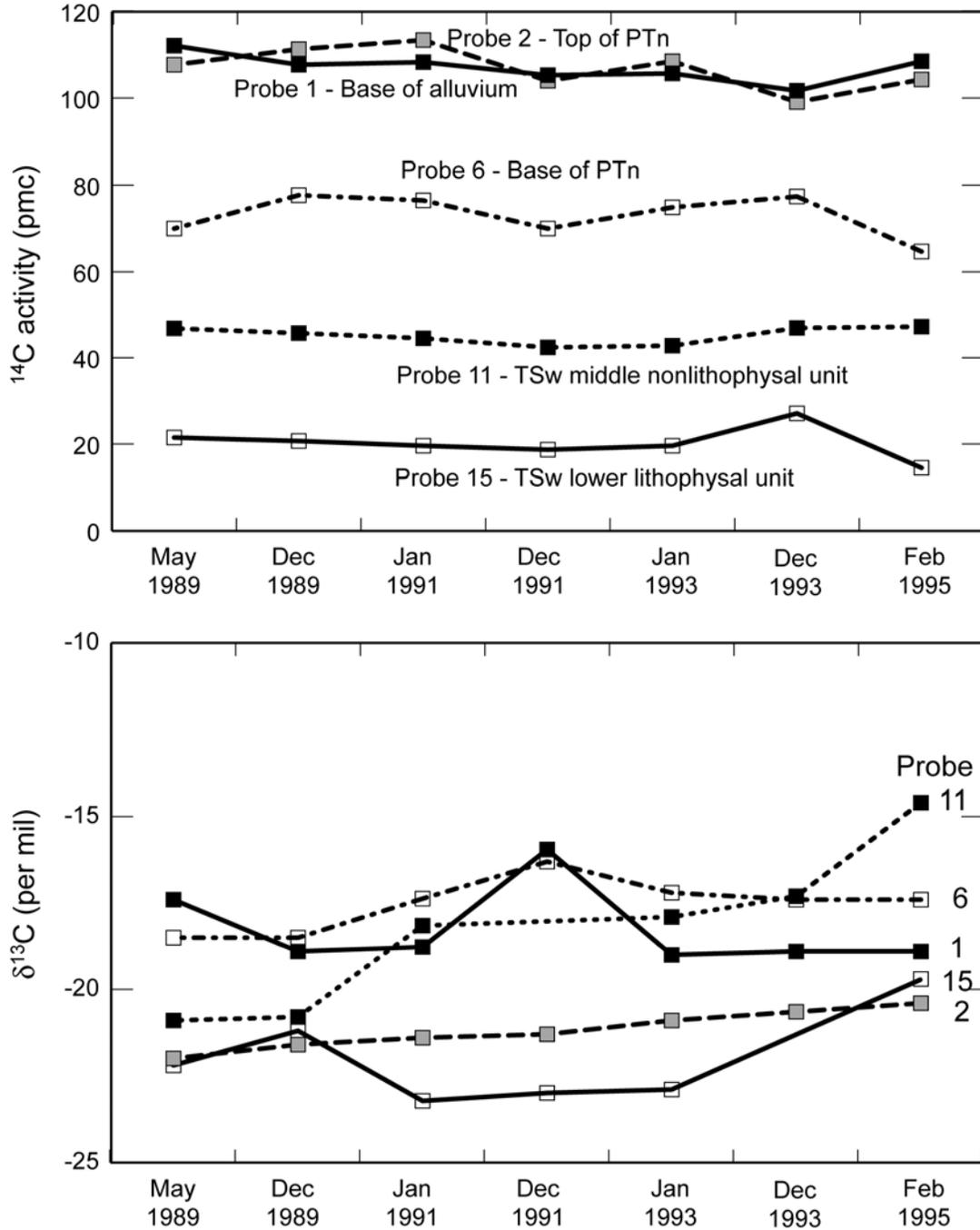
Figure 5-30. Carbon Isotopes in UZ-1 Gases

Source: BSC 2002 [DIRS 160247], Figure 44, p. II-46

Figure 5-31. Trilinear Diagram for Upgradient Groundwaters
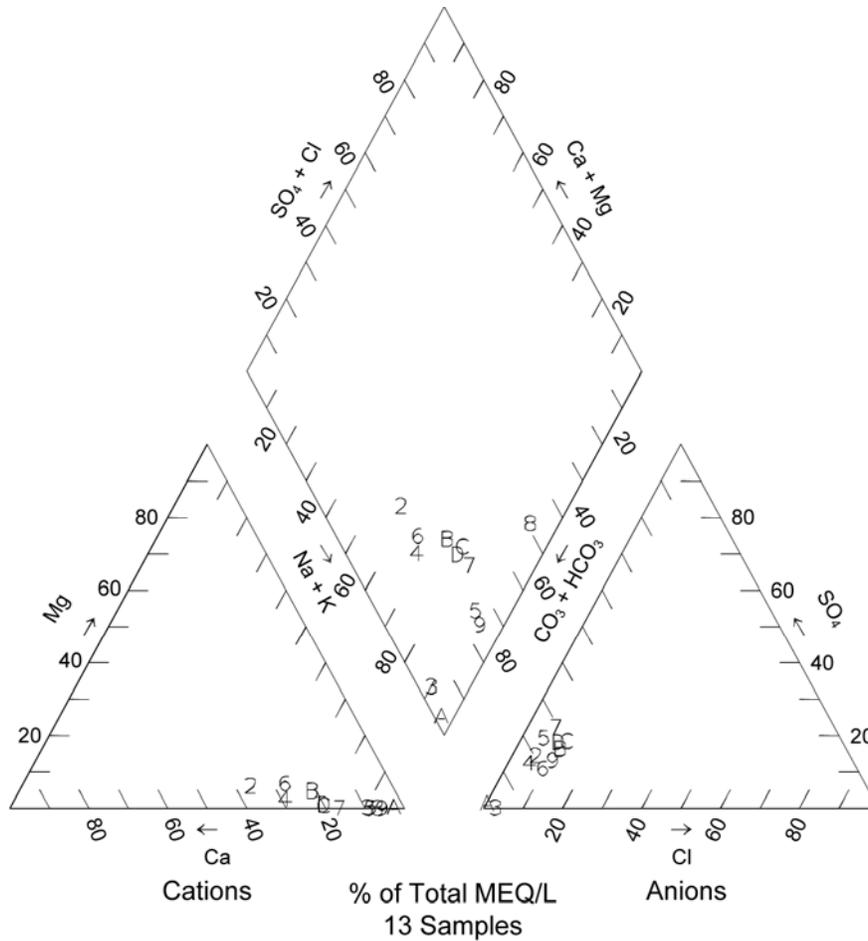
Legend
List of Plotted Points, Site Numbers, and Borehole Identifiers

1	152: U-20a#2	6	165: UE-19fs	B	198: Water Well 8
2	161: UE-19b#1	7	166: UE-19gs	C	181: UE-29 a#2 (250-355 m)
3	162: UE-19c	8	167: UE-19i	D	182: UE-29 a#2 (87-213 m)
4	163: UE-19d	9	141: TW-1 (0-171 m)		
5	164: UE-19e	A	142: TW-1 (0-1282 m)		

00377DCc_022.ai

DTNs: GS930308312323.001 [DIRS 145530]; GS920508312321.004 [DIRS 148105]
(includes data from McKinley et al. 1991 [DIRS 116222], Table 6)

Source: BSC 2002 [DIRS 160247], Figure 47, p. II-49

NOTE: This trilinear diagram is for groundwaters upgradient of Yucca Mountain, (Pahute Mesa and Rainier Mesa, Nevada). This plot shows the extent to which different water samples are similar or dissimilar in composition. For those waters that are very similar (i.e., data symbols overlap), it is not important to be able to discern individual points.

Source: BSC 2002 [DIRS 160247], Figure 46, p. II-48

NOTE: This map shows the locations of selected wells in the vicinity of Yucca Mountain for which geochemical data for groundwater samples are available. H-5 and H-3 mark the ridgeline of Yucca Mountain.

Figure 5-32. Location of Selected Wells in the Vicinity of Yucca Mountain
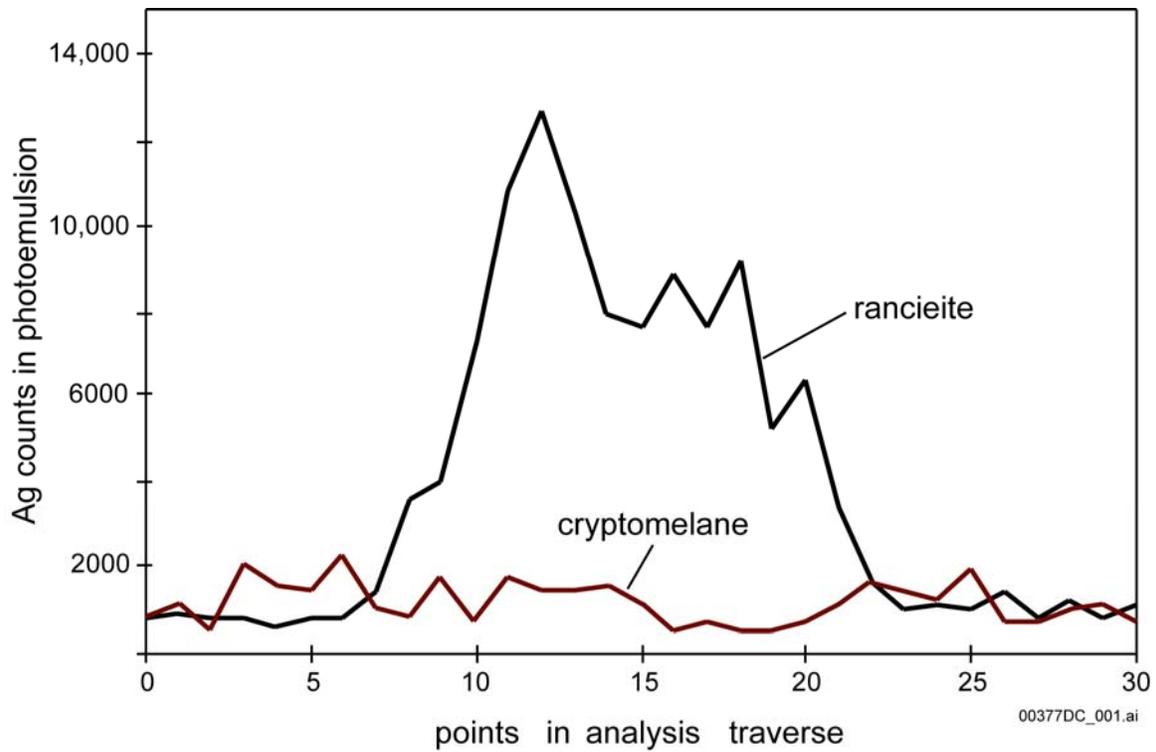
Source: Eckhardt 2000 [DIRS 152135]

NOTE: The linescans cross two different manganese oxide bodies exposed to similar plutonium-bearing solutions: (1) a rancieite body with zeolitic tuff and (2) cryptomelane lining a fracture in devitrified tuff (both linescans collected with a 10 μm beam, 15 s/point, and 12 μm between analytical points).

Figure 5-33.   Electron Microprobe Linescans for Silver in Two Microautoradiography Photoemulsions
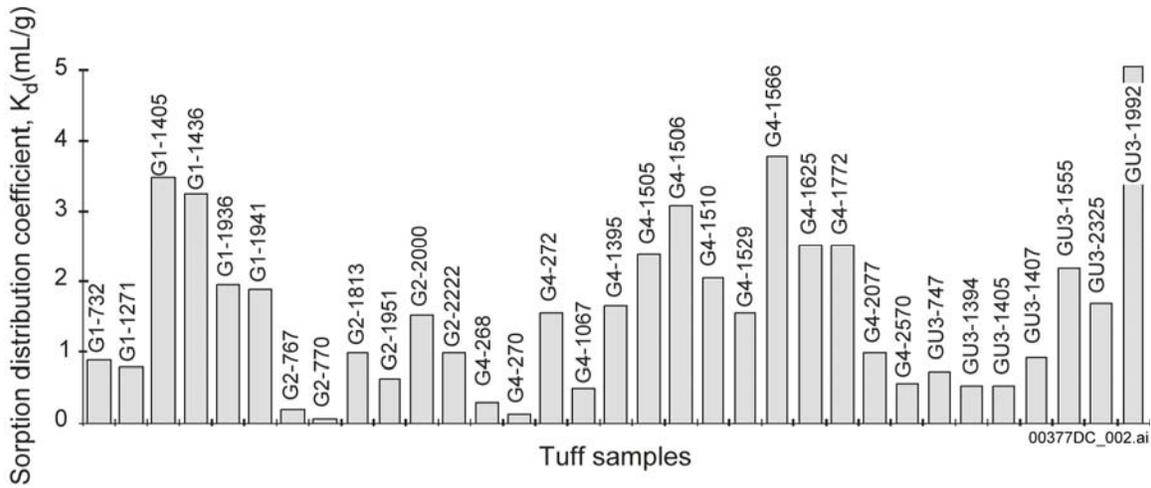
DTN: LA0010JC831341.007 [DIRS 153319]

Source: BSC 2001 [DIRS 160828], Figure 1

NOTE: These values of the batch sorption distribution coefficient, K_d, illustrate the limited sorption of neptunium onto a large range of Yucca Mountain tuffs in J-13 well water under atmospheric conditions. The initial neptunium concentration ranged from 6 to 8×10^{-7} M. The tuffs were wet-sieved to particle sizes that ranged from 75 to 500 µm. The pretreatment period was 2 to 14 days; the sorption period was 3 to 23 days.

Figure 5-34.   Neptunium Sorption in J-13 Well Water
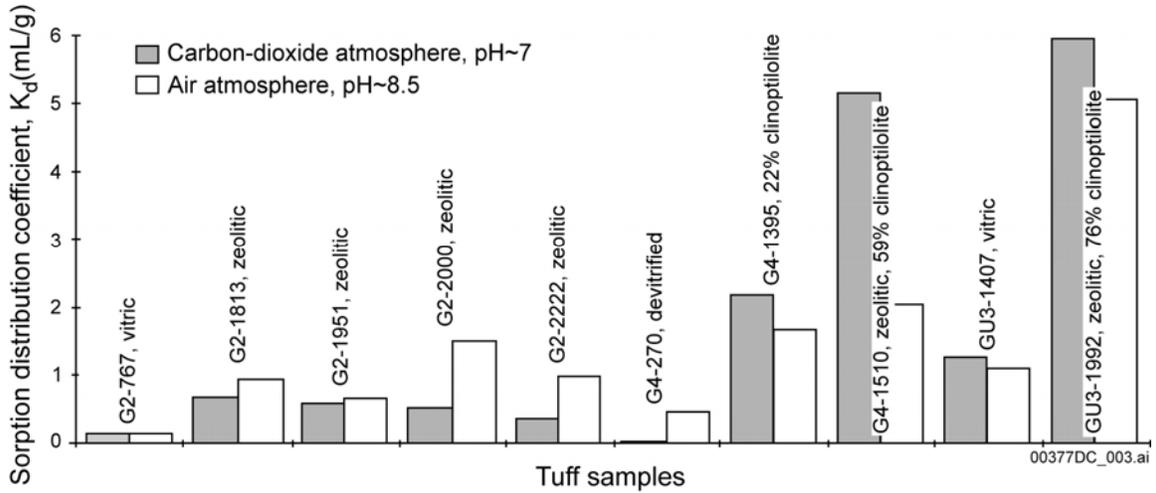
DTN: LA0010JC831341.007 [DIRS 153319]

Source: BSC 2001 [DIRS 160828], Figure 2

NOTE: Experimental values of K_d for the sorption of neptunium onto tuffs in J-13 water at initial concentrations of 6 to 7×10^{-7} M are compared for atmospheric conditions (pH of about 8.5) and a carbon-dioxide overpressure (pH of about 7). Tuffs were wet-sieved (75 to 500 µm); the pretreatment period was 2 to 3 days; the sorption period was 3 to 5 days.

Figure 5-35.   The pH Dependence of Neptunium Sorption onto Tuffs at 10^{-7} M
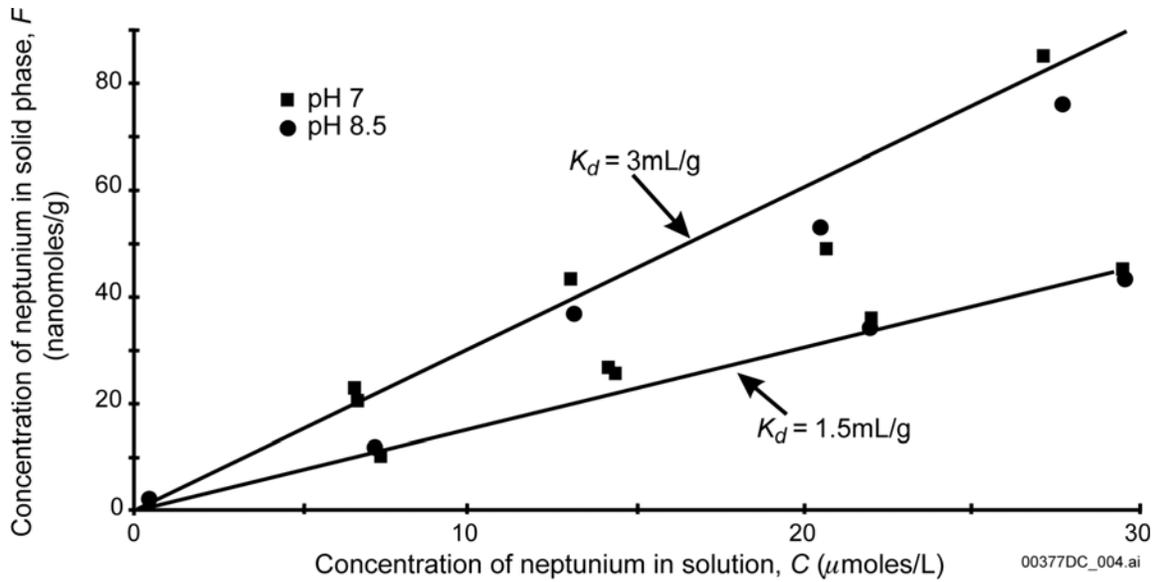
Source: BSC 2001 [DIRS 160828], Figure 3

NOTE: A plot is shown of the concentration, *F*, of neptunium in the solid phase of the clinoptilolite-rich tuff G4-1510 versus the concentration, *C*, of neptunium in the solution phase of J-13 well water and linear (*K$_d$*) fits to the data for two values of pH.

Figure 5-36. Neptunium Sorption onto Clinoptilolite-Rich Tuff
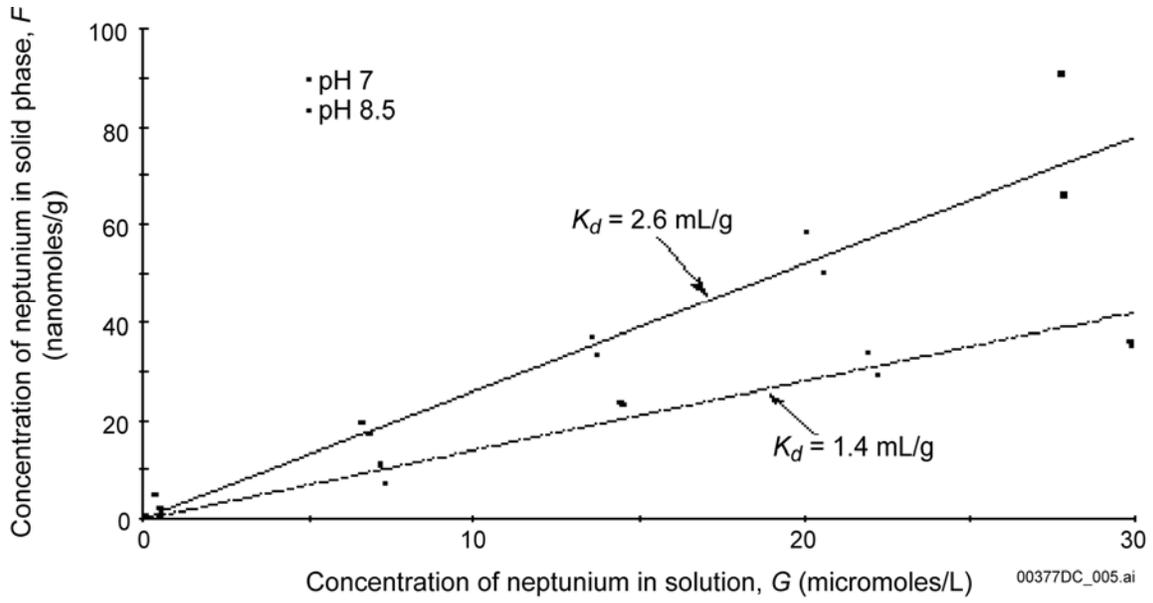
DTN: LA0010JC831341.007 [DIRS 153319]

Source: BSC 2001 [DIRS 160828], Figure 4

NOTE: A plot is shown of the concentration, F, of neptunium in the solid phase of the clinoptilolite-rich tuff G4-1510 versus the concentration, C, of neptunium in the solution phase of J-13 well water and linear (K_d) fits to the data for two values of pH.

Figure 5-37. Neptunium Sorption onto Clinoptilolite
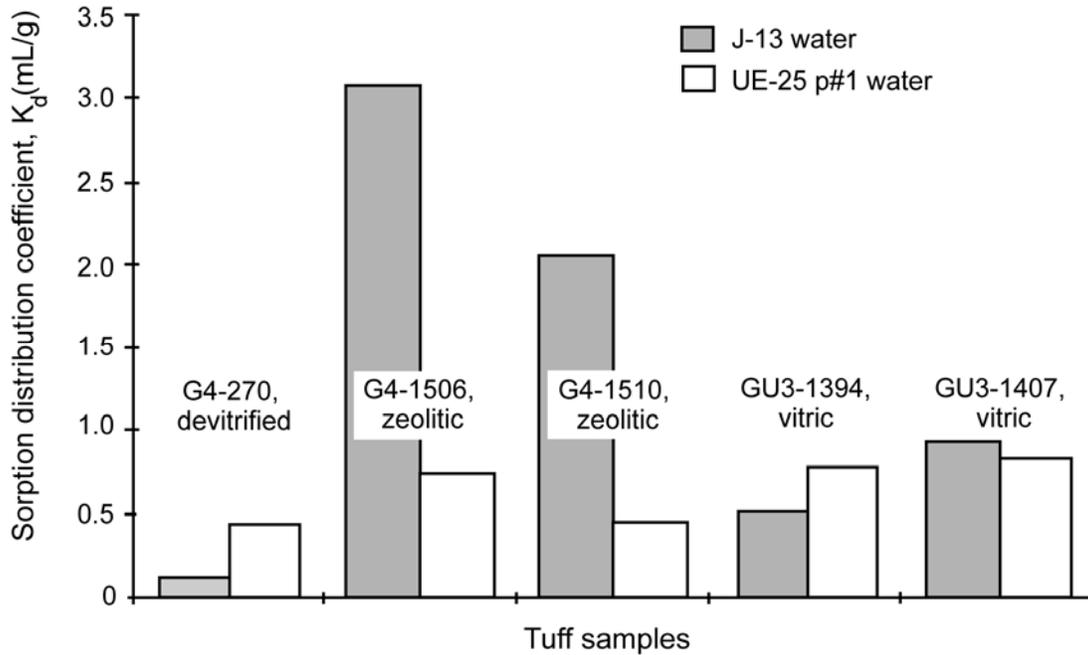
DTN: LA0010JC831341.007 [DIRS 153319]

Source: BSC 2001 [DIRS 160828], Figure 5

NOTE: Values of K_d for sorption of neptunium onto several tuffs that allow comparison of sorption (under atmospheric conditions) for the two types of groundwaters. The initial neptunium concentration ranged from 6×10^{-7} to 8×10^{-7} M. The tuffs were wet-sieved to particle sizes ranging from 75 to 500 μm. The pretreatment period was 2 to 14 days; the sorption period was 3 to 23 days.

Figure 5-38.   Comparison of Neptunium Sorption onto Tuffs
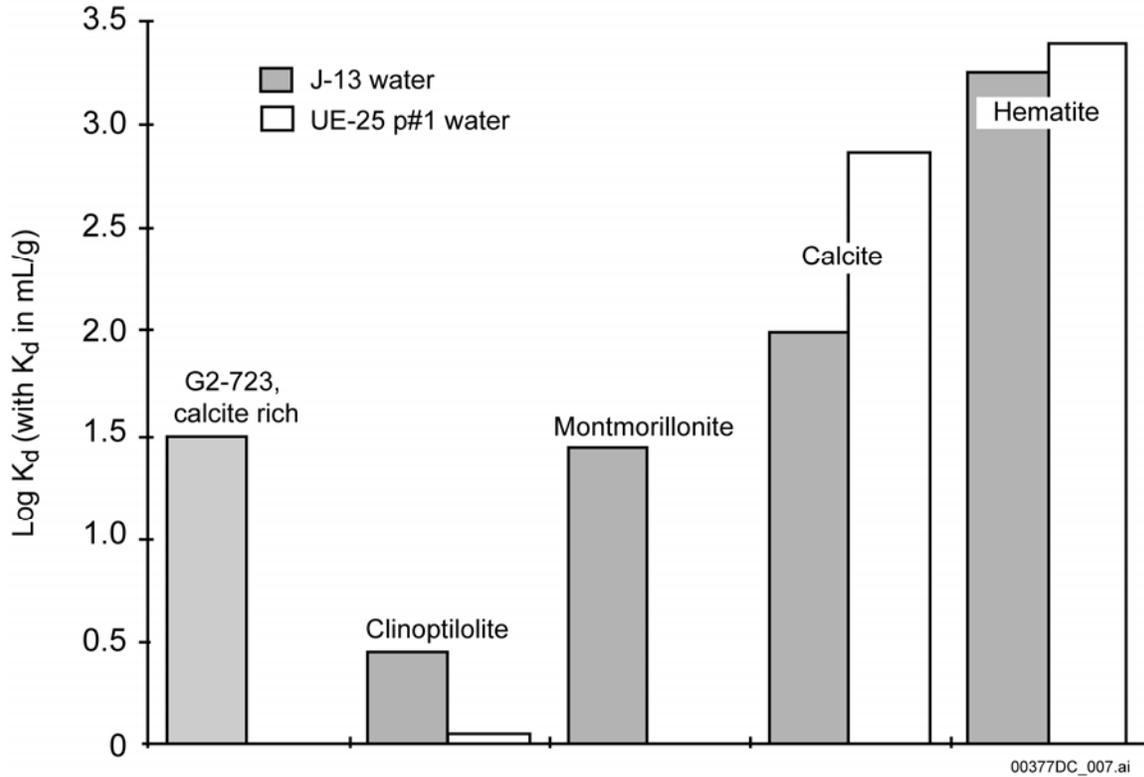
DTN: LA0010JC831341.007 [DIRS 153319]

Source: BSC 2001 [DIRS 160828], Figure 6

NOTE: Values of K_d for neptunium onto several minerals and a calcite-rich tuff that allow comparison of sorption (under atmospheric conditions) for the two types of groundwaters. The initial neptunium concentration ranged from 6×10^{-7} to 8×10^{-7} M. The tuff and the calcite were wet-sieved to particle sizes ranging from 75 to 500 µm; the montmorillonite was dry-sieved; the clinoptilolite and hematite were not sieved; the sorption period was 17 to 22 days. (Note the use of log units on y axis.)

Figure 5-39. Dependence of Water for Neptunium Sorption onto Minerals

Source: BSC 2001 [DIRS 160828], Figure 7

NOTE: This is a log-log plot of the concentration of uranium in the solid phase, F1, of the clinoptilolite-rich tuff G4-1510 versus the concentration of uranium in the solution phase, C, of J-13 well water. The tuff was wet-sieved to give particles that ranged in size from 70 to 50 μm. The period of pretreatment was 2 to 4 days; the sorption period was 3 to 4 days. The data for a pH of 7 have been fitted with a Langmuir isotherm. The data for a pH of 8.5 have been fitted with a Freundlich Isotherm.

Figure 5-40. Uranium Sorption onto Clinoptilolite-Rich Tuff

Log of the concentration (µg/g) of uranium in solid phase, log F

- pH 7
- pH 8.5

Langmuir isotherm
$K_1 = 23$, $K_2 = 0.7$

Langmuir isotherm
$K_1 = 9.5$, $K_2 = 0.5$

Log of the concentration (ppm) of uranium in solution, log C
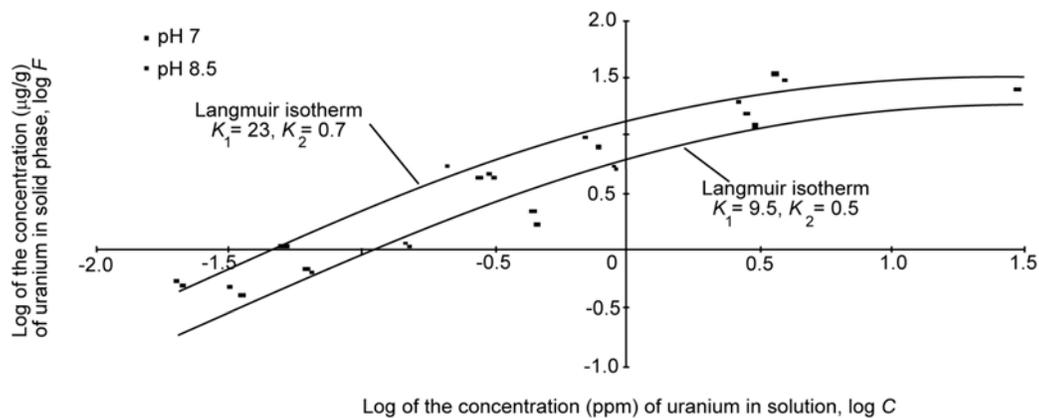
00377DC_009.ai

DTN: LA0010JC831341.005 [DIRS 153320]

Source: BSC 2001 [DIRS 160828], Figure 8

NOTE: This is a log-log plot of the concentration of uranium in the solid phase, F1, of the clinoptilolite versus the concentration of uranium in the solution phase, C, of J-13 well water. The mineral was unsieved. The period of pretreatment was 2 to 4 days; the period of sorption was 3 to 4 days. The data for a pH (7 and 8.5) have been fitted with a Langmuir isotherm.

Figure 5-41.   Uranium Sorption onto Clinoptilolite
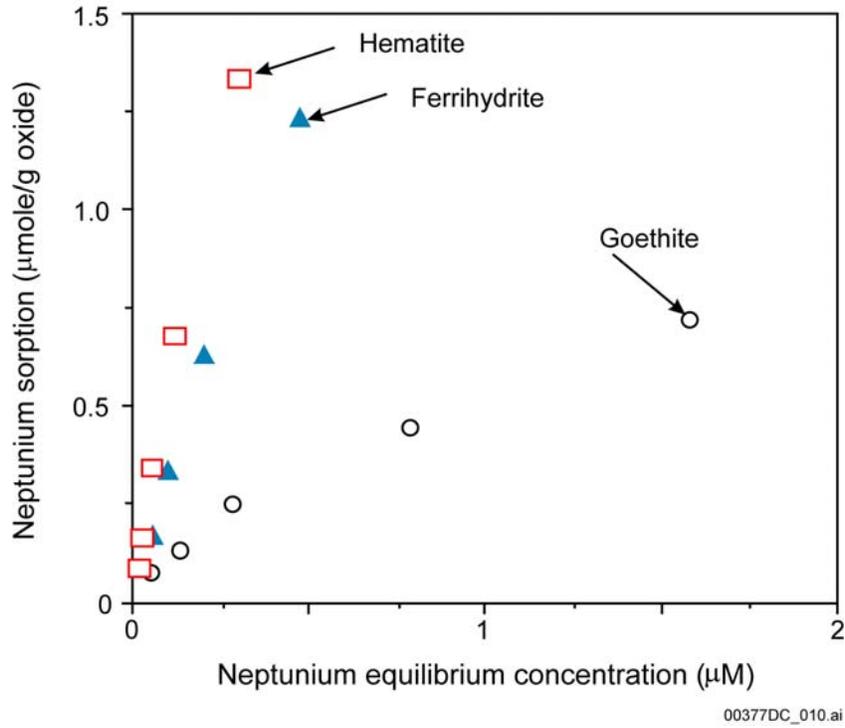
DTN: LA9910SK831341.004 [DIRS 142389]

Source: Triay et al. 1997 [DIRS 100422], Figure 67, p. 110

NOTE: The plot shows isotherms for the sorption of neptunium on three different iron oxides, calculated on the basis of unit mass.

Figure 5-42.   Neptunium Sorption per Unit Mass on Iron Oxides
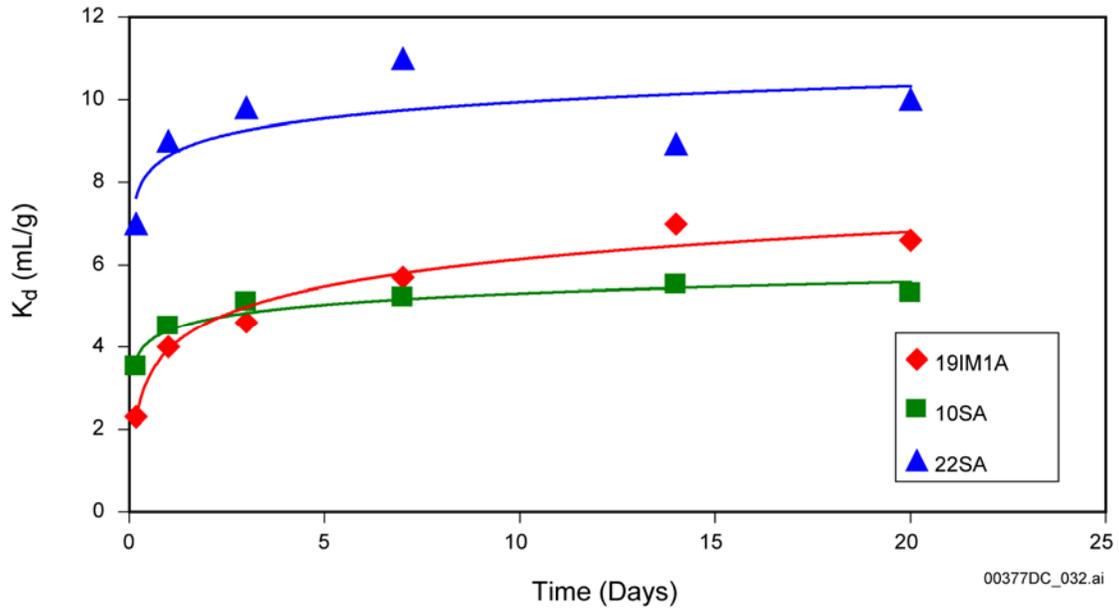
DTNs: LA0302MD831341.003 [DIRS 163784]; LA0302MD831341.004 [DIRS 163785]

NOTE: Borehole names refer to Nye County EWDP boreholes.

Figure 5-43.   Sorption of Uranium onto Alluvium as a Function of Time
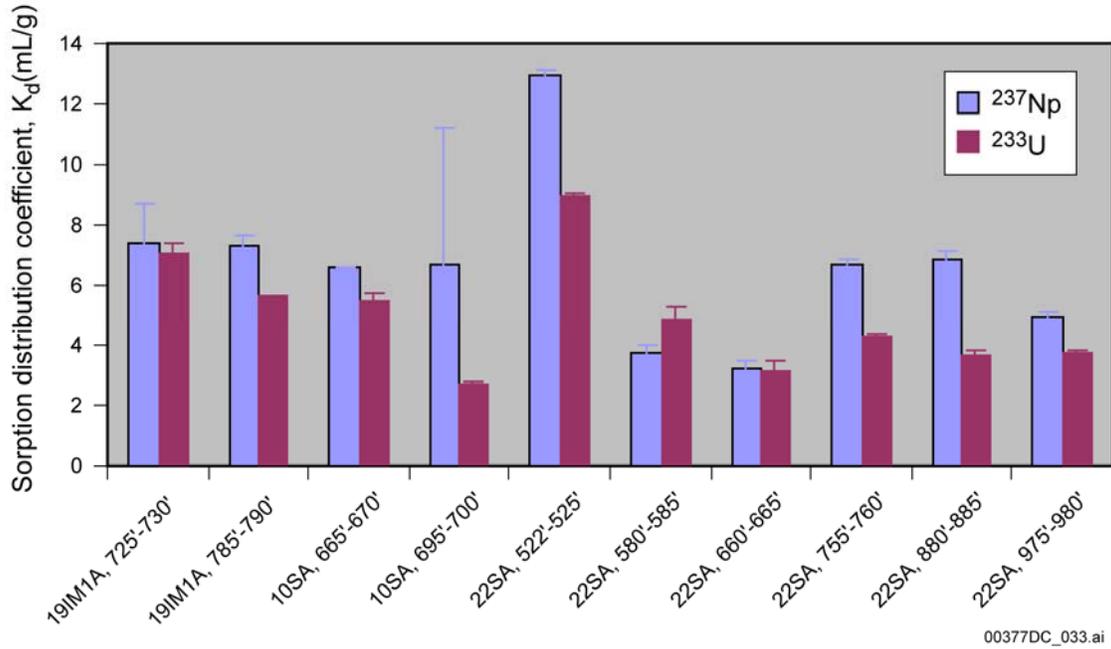
DTNs: LA0302MD831341.003 [DIRS 163784]; LA0302MD831341.004 [DIRS 163785]

Source: Ding et al. 2003 [DIRS 164737], Attachment B

NOTE: Borehole names refer to Nye County EWDP boreholes.

Figure 5-44.   Sorption Coefficients of ^{237}Np and ^{233}U in Alluvium

NOTE: Borehole names refer to Nye County EWDP boreholes.

Figure 5-45.   Sorption of Uranium in NE-EWDP-19D Zone 1 and Zone 4 Waters
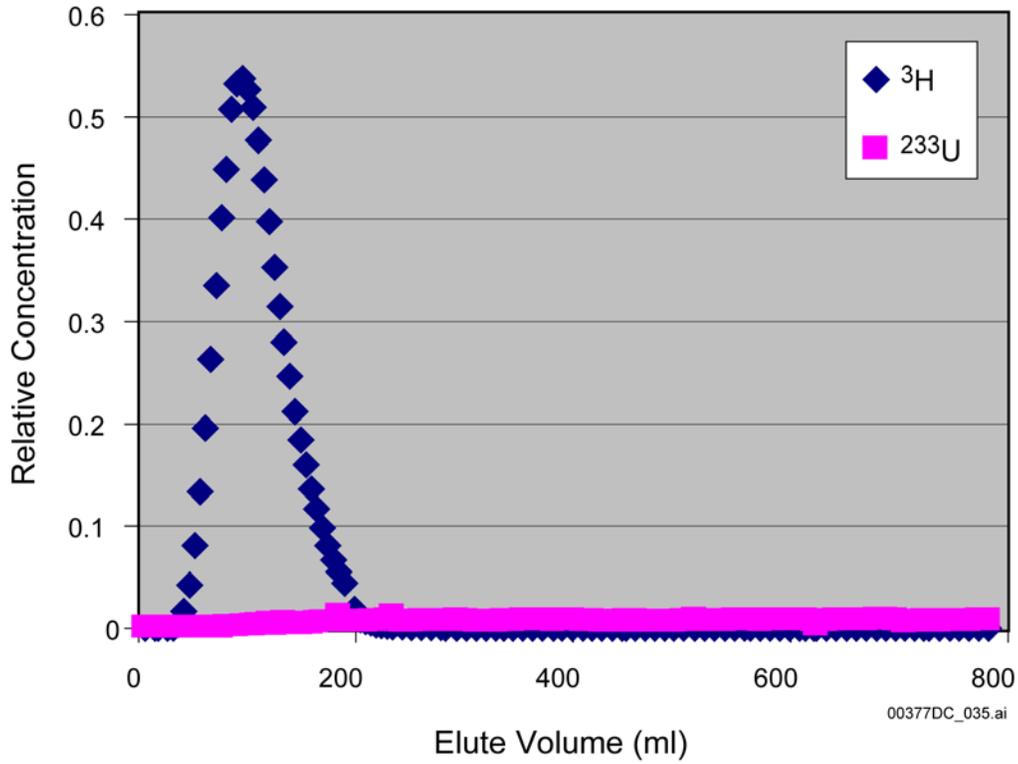
DTN: LA0401MD831361.001 [DIRS 166696]

Source: Ding et al. 2003 [DIRS 164737]

NOTE: The total recovery of tritium is about 94 percent and that of ^{233}U is about 10 percent. Flow rate is 10 ml/h.

Figure 5-46. Tritium and Uranium Breakthrough Curves for a Column Test
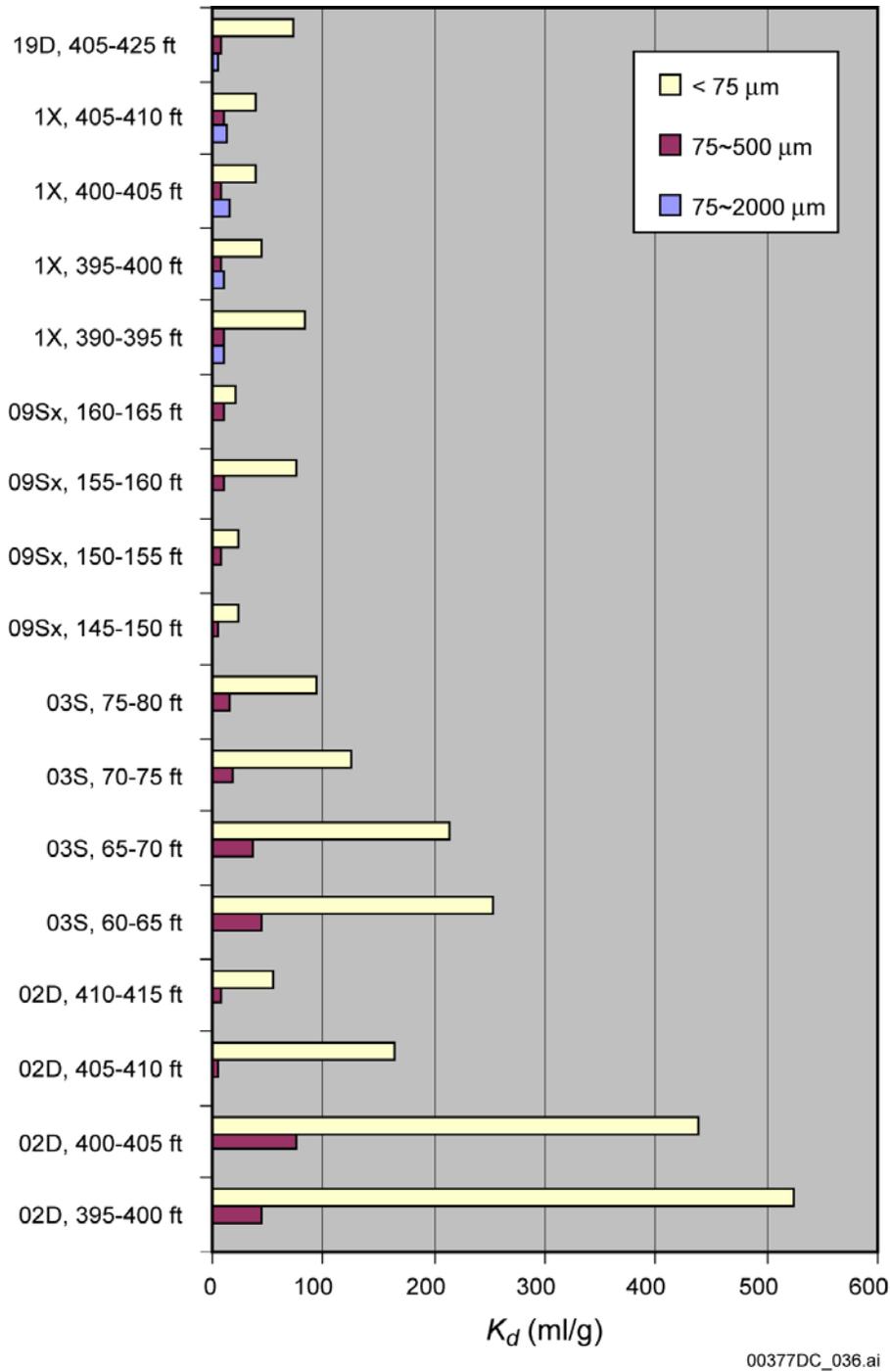
DTN: LA0109MD831341.001 [DIRS 156870]; DTN: LA0401MD831341.001 [DIRS 166697]

Source: Ding et al. 2003 [DIRS 164737], Figure 2

NOTE: Borehole names refer to Nye County Early Warning Drilling Programs boreholes.

Figure 5-47. Sorption Coefficients of ^{237}Np (V) as a Function of Test Interval and Size Fraction Determined from Batch Experiments

Figure caption and chart content:

K_d (mL/g) axis from 0 to 300

Legend: ■ 3S, □ 19D2

Categories:
- 2D, 410-415 ft, 75-500um
- 9Sx, 160-165 ft, 75-500um
- 3S, 75-80 ft, 75-500 um
- 2D, 410-415 ft, < 75 um
- 9Sx, 155-160 ft, < 75 um
- 3S, 60-65 ft, < 75 um
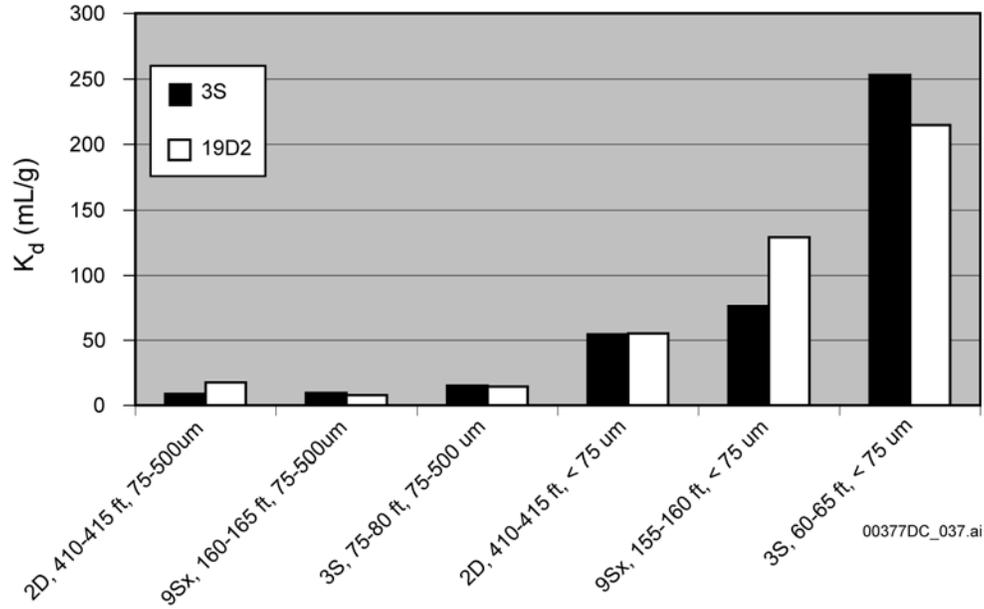
00377DC_037.ai

DTN: LA0109MD831341.001 [DIRS 156870]

Source: Ding et al. 2003 [DIRS 164737], Attachments A and C

NOTE: Borehole names refer to Nye County EWDP boreholes.

Figure 5-48.   Sorption of Neptunium (V) on Alluvium
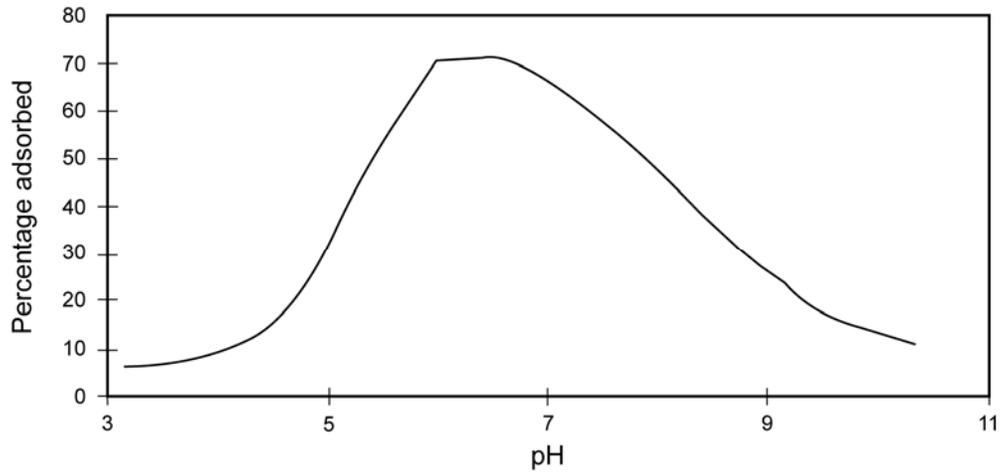
Source: Triay et al. 1997 [DIRS 100422], Figure 95, p. 133

NOTE: The curve above shows the predictions of the FITEQL code for the adsorption of uranium onto crushed devitrified tuff from a 0.1 M NaCl solution in a controlled atmosphere with an initial uranium concentration of 1×10^{-6} M.

Figure 5-49. Modeled Uranium Adsorption

Figure. Normalized cumulative activity vs. Cumulative volume (mL). Plot shows ^{3}H at 2.76 ml/hr (open diamonds) and ^{239}Pu at 2.77 ml/hr (filled squares). Inset label: G4-268, devitrified J-13 well water. 00377DC_039.ai
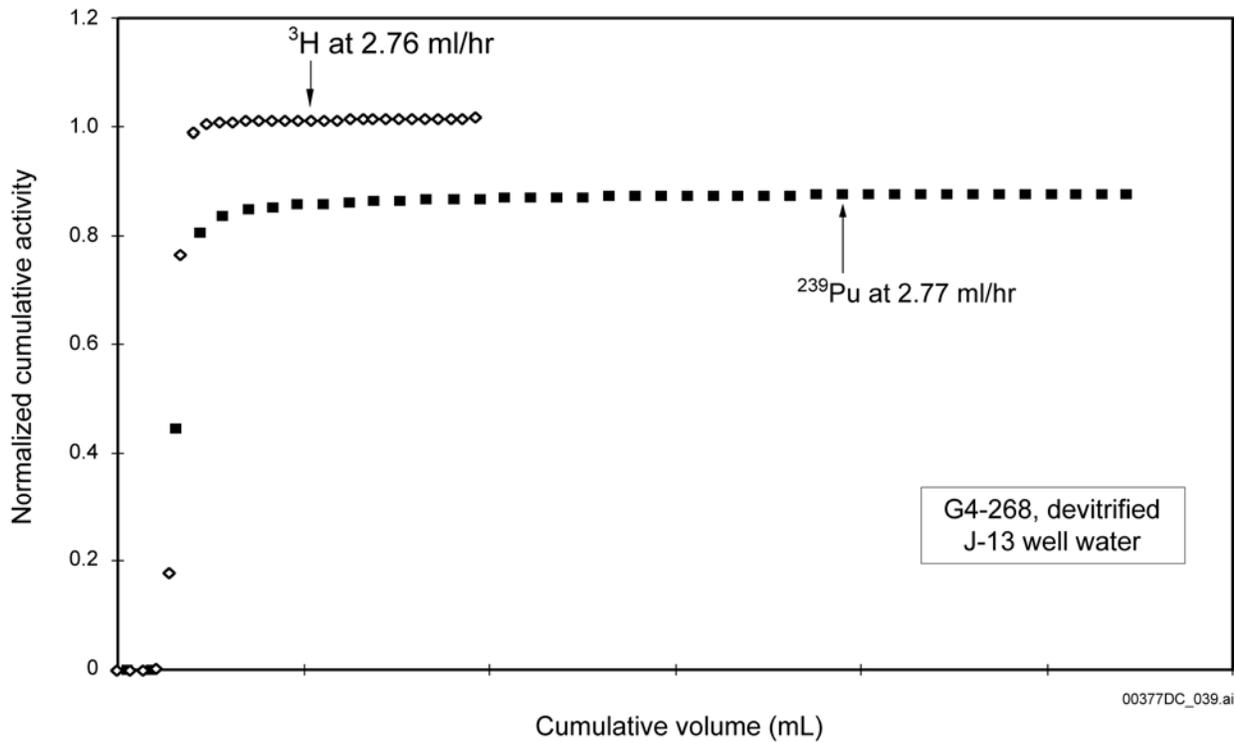
DTN: LAIT831361AQ95.001 [DIRS 138447]

Source: Triay et al. 1997 [DIRS 100422], Figure 98, p. 144

NOTE: This plot shows the elution curves for tritium and ^{239}Pu through devitrified tuff sample G4-268 with J-13 well water. Cumulative concentration (in Figures 5-50 to 5-57) is the total activity of the recovered tracer divided by the total activity injected initially. As seen by the variation of the final part of the curves, this variable has an experimental error of about ± 20 percent.

Figure 5-50.   Plutonium through Devitrified Tuff

Source: BSC 2001 [DIRS 160828], Figure 14

NOTE: This plot shows the elution curves for tritium and [239]Pu through vitric tuff sample GU-1405 with J-13 well water.

Figure 5-51.   Plutonium through Vitric Tuff
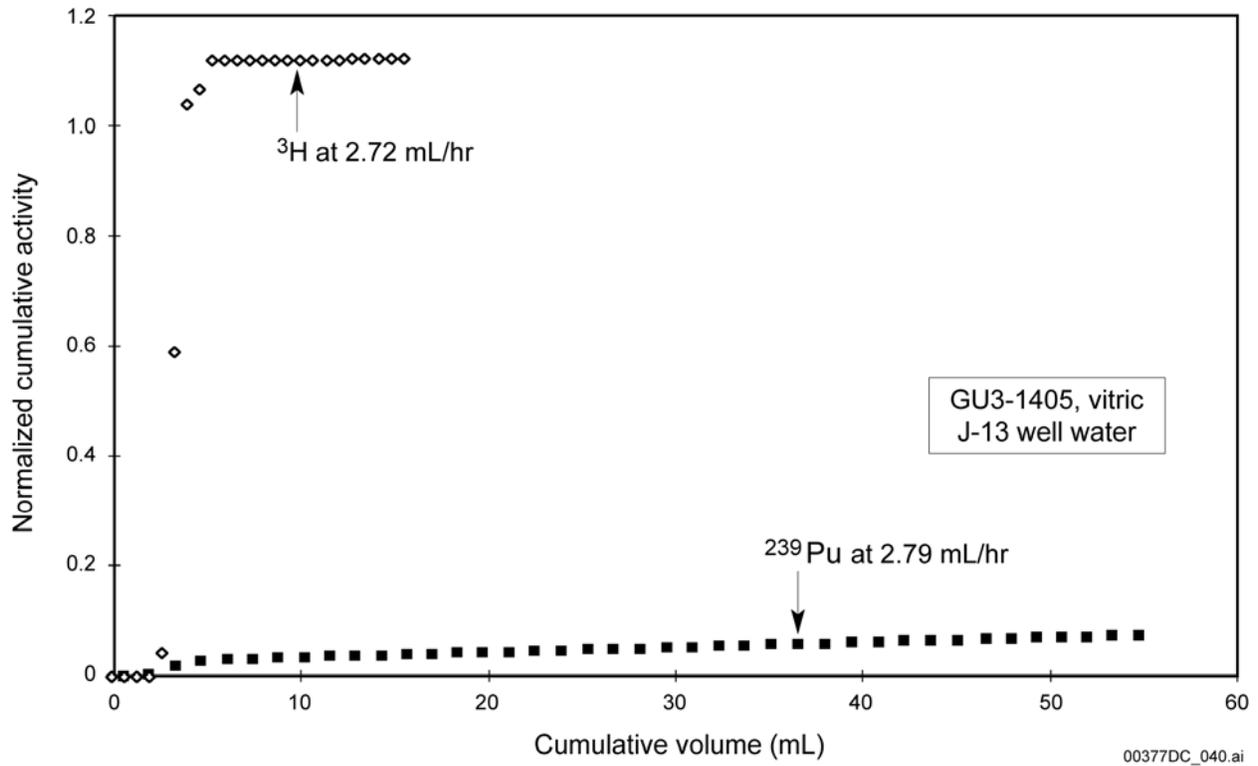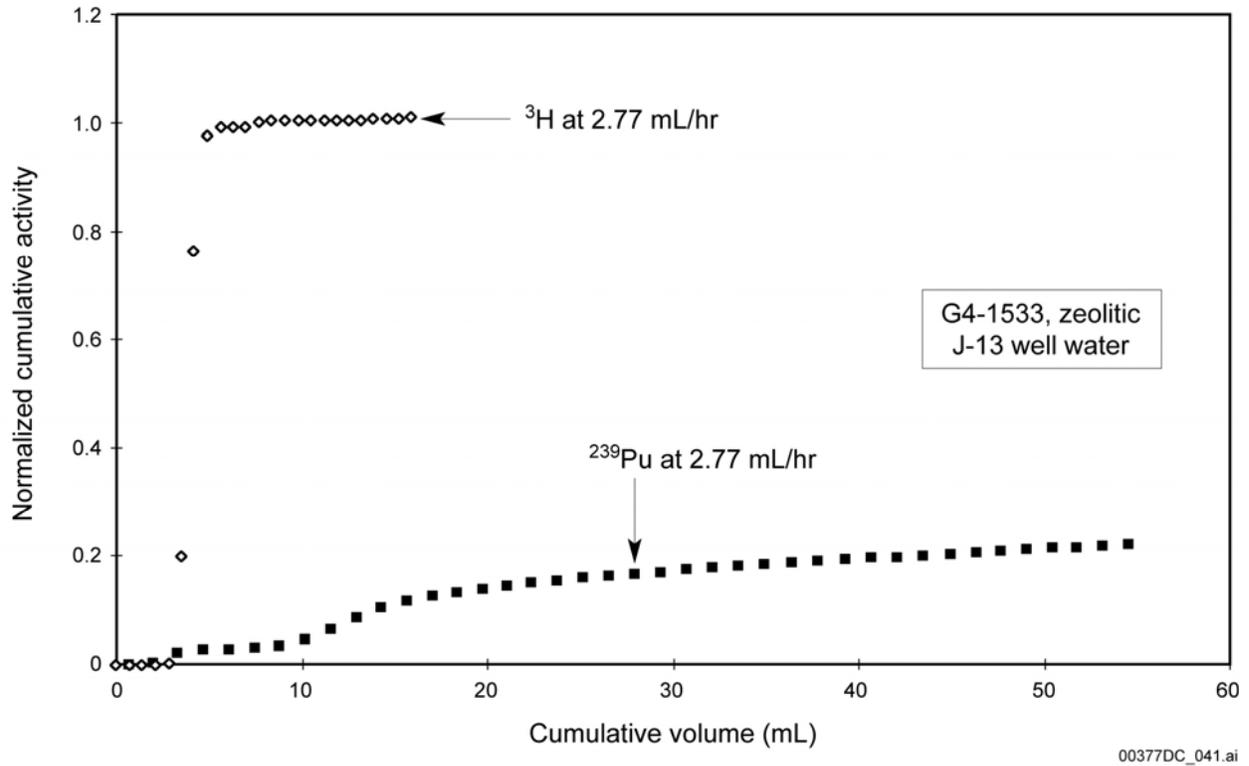
DTN: LAIT831361AQ95.001 [DIRS 138447]

Source: BSC 2001 [DIRS 160828], Figure 15

NOTE: This plot shows the elution curves for tritium and ^{239}Pu through zeolitic tuff sample G4-1533 with J-13 well water.

Figure 5-52. Plutonium through Zeolitic Tuff
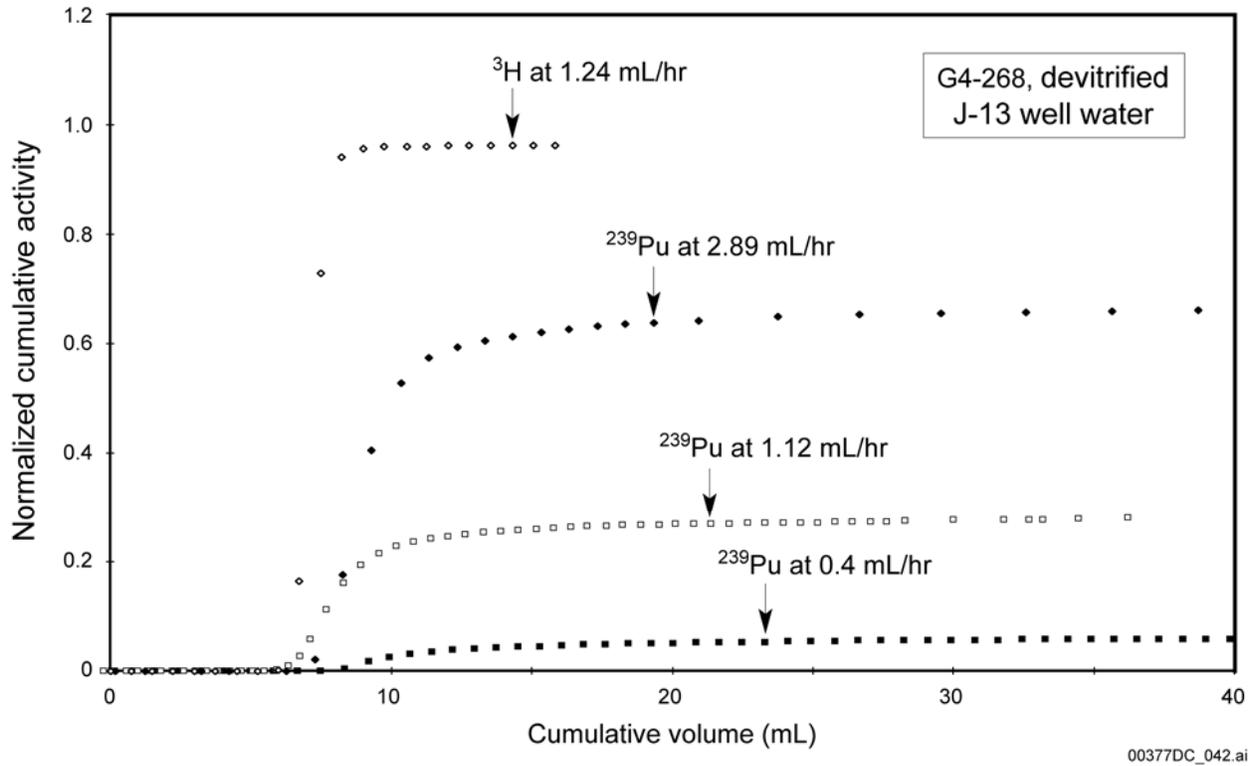
DTN: LA0401PR831361.001 [DIRS 166726]

Source: BSC 2001 [DIRS 160828], Figure 16

NOTE: This plot shows the elution curves for tritium and [239]Pu at different flow rates with J-13 water through devitrified tuff G4-268.

Figure 5-53.   Plutonium in Devitrified Tuff (J-13 Well Water) at Various Flow Rates
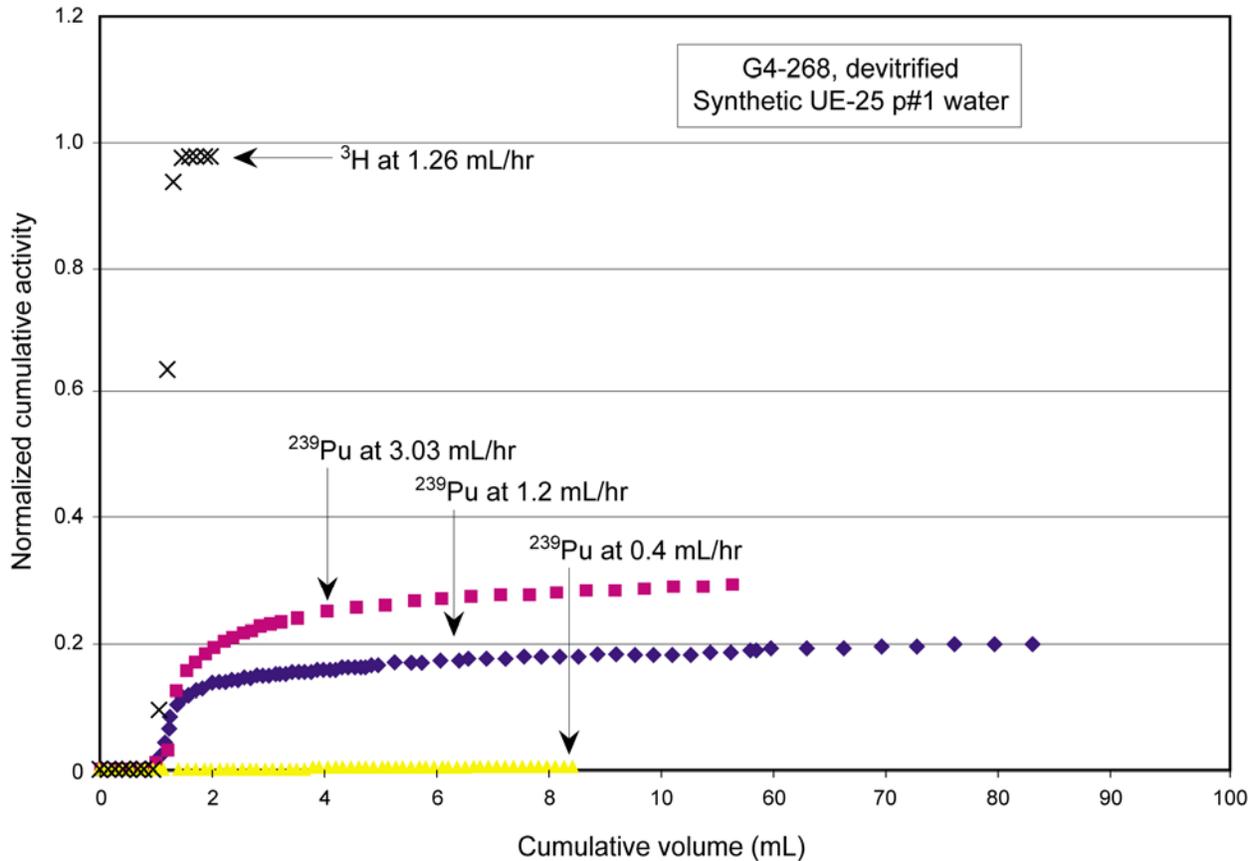
DTN: LA0002JC831361.002 [DIRS 147088]

Source: BSC 2001 [DIRS 160828], Figure 17

NOTE: This plot shows the elution curves for tritium and [239]Pu at different flow rates in synthetic UE-25 p#1 water and tuff G4-268.

Figure 5-54. Plutonium in Devitrified Tuff (UE-25 p#1 Water) at Various Flow Rates

Figure caption area:
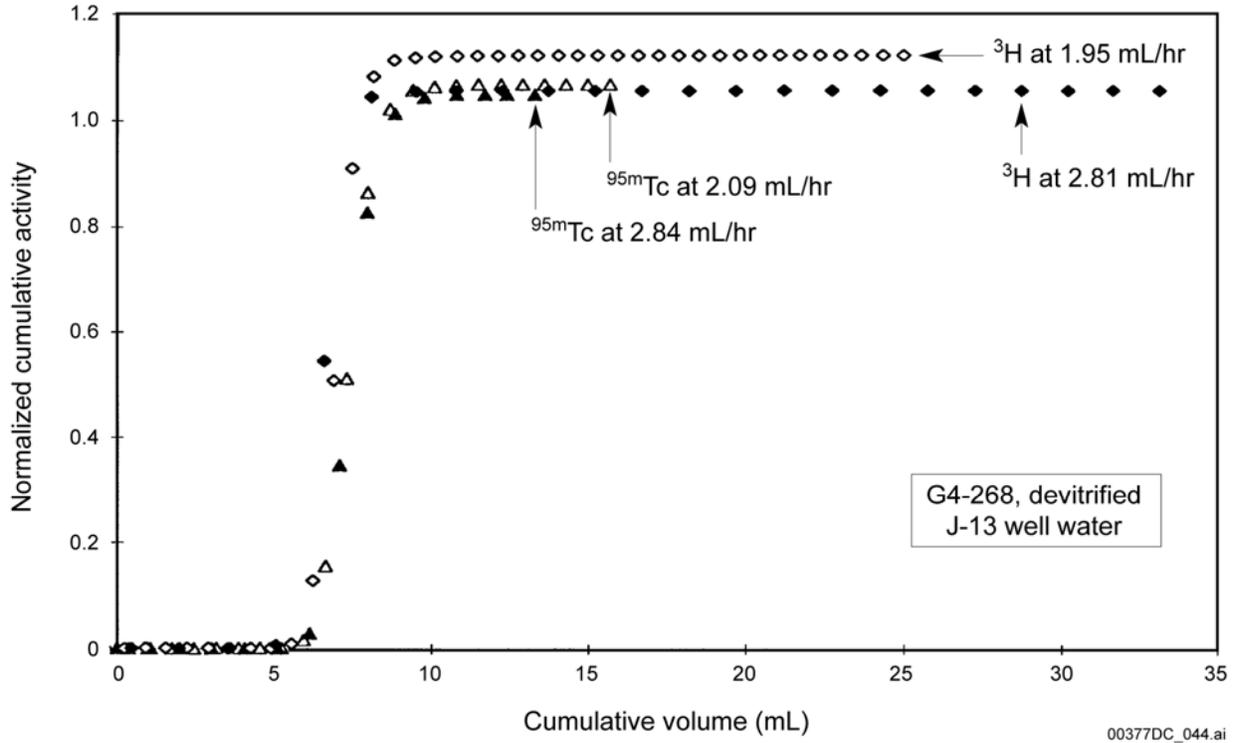
DTN: LA0002JC831361.003 [DIRS 147089]

Source: BSC 2001 [DIRS 160828], Figure 18

NOTE: This plot shows the elution curves for tritium and ^{95m}Tc at different flow rates with J-13 well water through devitrified tuff sample G4-268.

Figure 5-55.   Technetium in Devitrified Tuff at Various Flow Rates
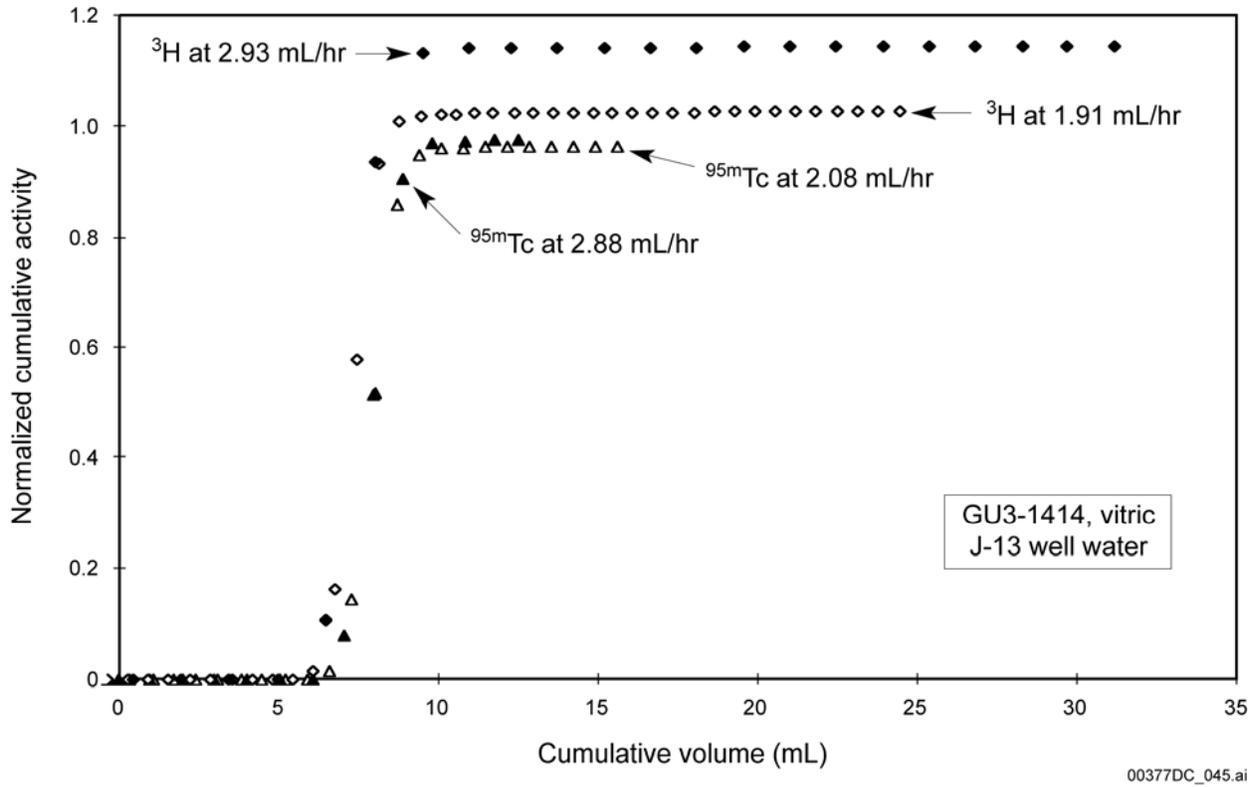
DTN: LA0002JC831361.004 [DIRS 147091]

Source: BSC 2001 [DIRS 160828], Figure 19

NOTE: This plot shows the elution curves for tritium and ^{95m}Tc at different flow rates with J-13 well water through vitric tuff sample GU3-1414.

Figure 5-56.   Technetium in Vitric Tuff at Various Flow Rates
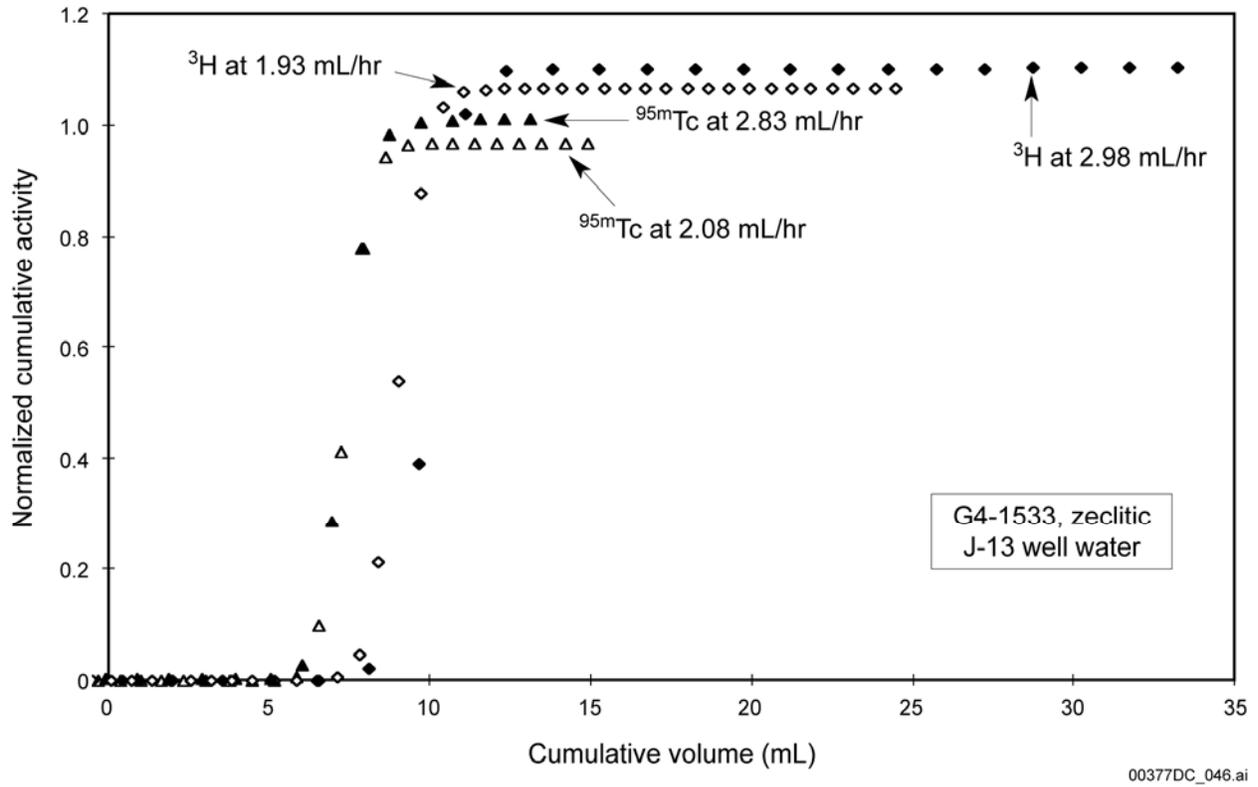
DTN: LA0002JC831361.005 [DIRS 147092]

Source: BSC 2001 [DIRS 160828], Figure 20

NOTE: This plot shows the elution curves for tritium and ^{95m}Tc at different flow rates with J-13 well water through zeolitic tuff sample G4-1533.

Figure 5-57.   Technetium in Zeolitic Tuff at Various Flow Rates

Figure with axes: y-axis "C/C₀ for selenium" ranging 0.0 to 1.6, x-axis "Pore volume, θ" ranging 0 to 15.

Legend:
□ Zeolitized nonwelded G-tunnel tuff (1.21 g/cm^3; 52.8% saturation; $K = 1.2 \times 10^{-8}$ cm/s)
◇ Yucca Mountain vitric-member tuff (1.54 g/cm^3; 62.6% saturation; $K = 2.5 \times 10^{-8}$ cm/s)

00377DC_047.ai
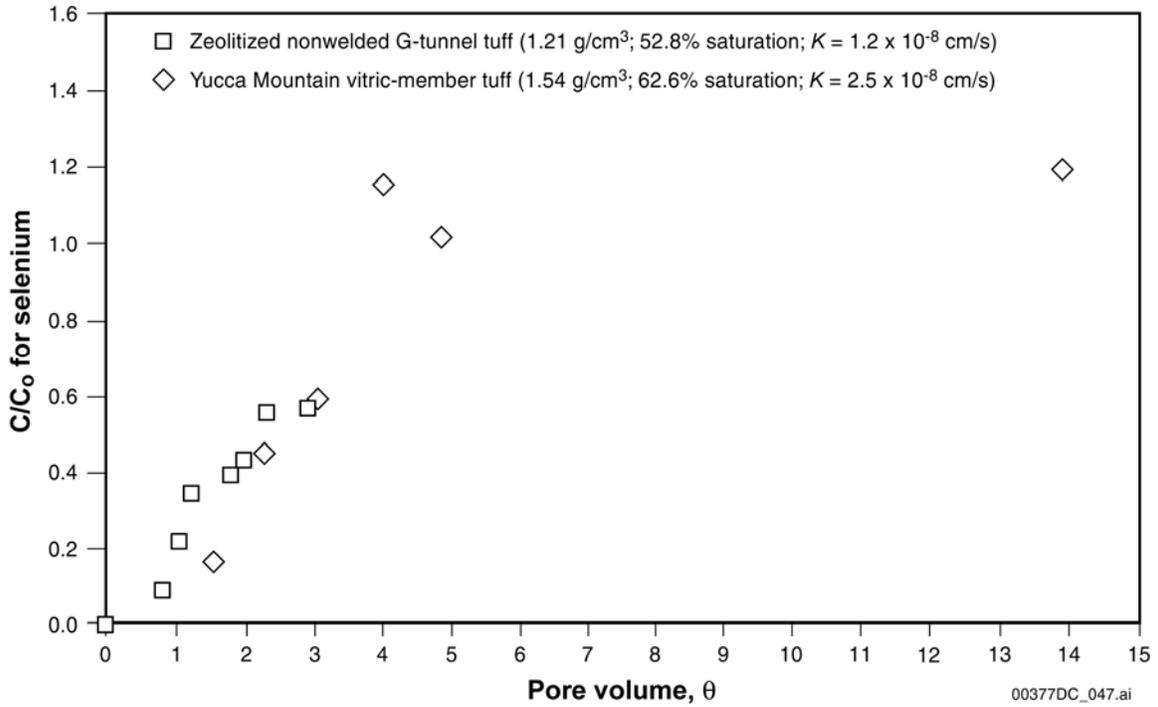
DTN: LA0004JC831361.001 [DIRS 149397]

Source: BSC 2001 [DIRS 160828], Figure 21

NOTE: The unsaturated flow apparatus column data plotted here for a Yucca Mountain tuff retardation experiment show the breakthrough curves for selenium. The initial concentration, C_o, of selenium (as selenite), was 1.31 ‰ in J-13 well water.

Figure 5-58.   Selenium Breakthrough Curves

Yucca Mountain tuffs
— □ — Calico Hills zeolitized tuff (1.45 g/cm³)
— ■ — Topopah Spring welded tuff (2.41 g/cm³)
···■··· Vitric tuff (1.54 g/cm³)

Bandelier tuffs and basalt
— ○ — Nonwelded vitric tuff (SHB-1-520, 1.30 g/cm³)
— × — Densely welded tuff (SHB-1-168, 1.86 g/cm³)
— △ — Nonwelded devitrified tuff (SHB-2-30, 1.56 g/cm³)
···□··· Vesicular basalt (SHB-1-661, 2.28 g/cm³)

00377DC_048.ai
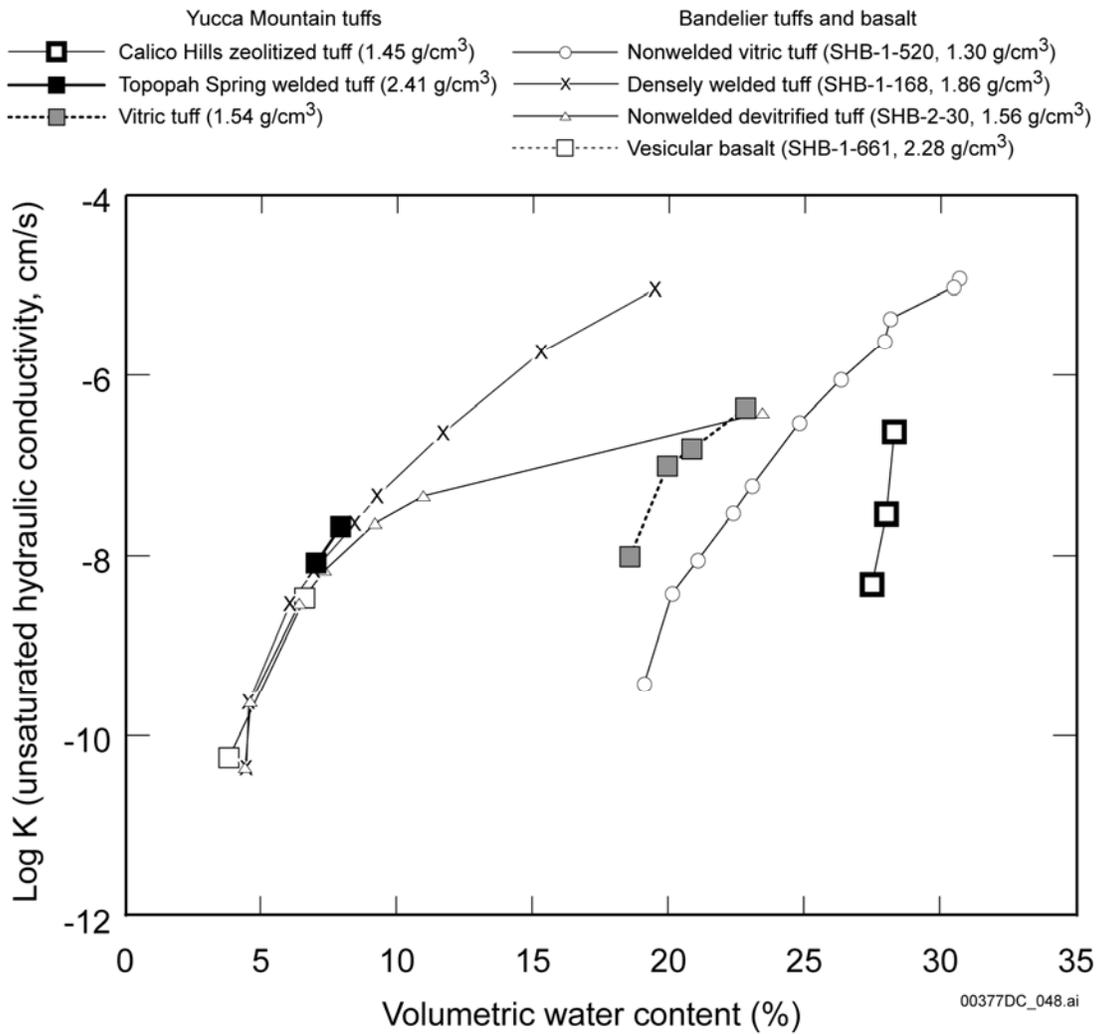
DTN: LA0004JC831224.001 [DIRS 149987]

Source: BSC 2001 [DIRS 160828], Figure 22

NOTE: The unsaturated flow apparatus column data for various Yucca Mountain and Bandelier tuffs and other soil samples show the unsaturated hydraulic conductivity, K, as a function of volumetric water content. The name and the density of each tuff are given in the legend.

Figure 5-59. Unsaturated Hydraulic Conductivity
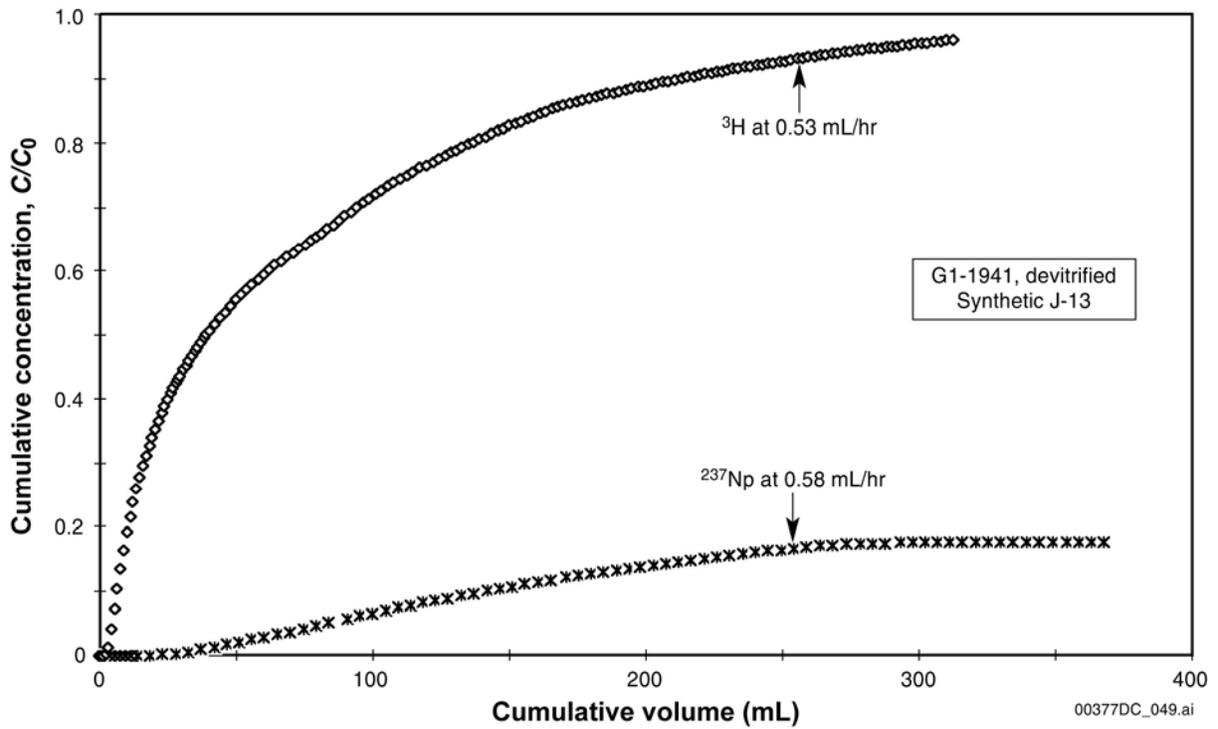
DTN: LA0001JC831361.001 [DIRS 145251]

Source: BSC 2001 [DIRS 160828], Figure 23

NOTE: This plot shows the elution curves for tritium and [237]Np in synthetic J-13 water through a fractured column of devitrified tuff sample G1-1941.

Figure 5-60.   Neptunium in Fractured Tuff G1-1941
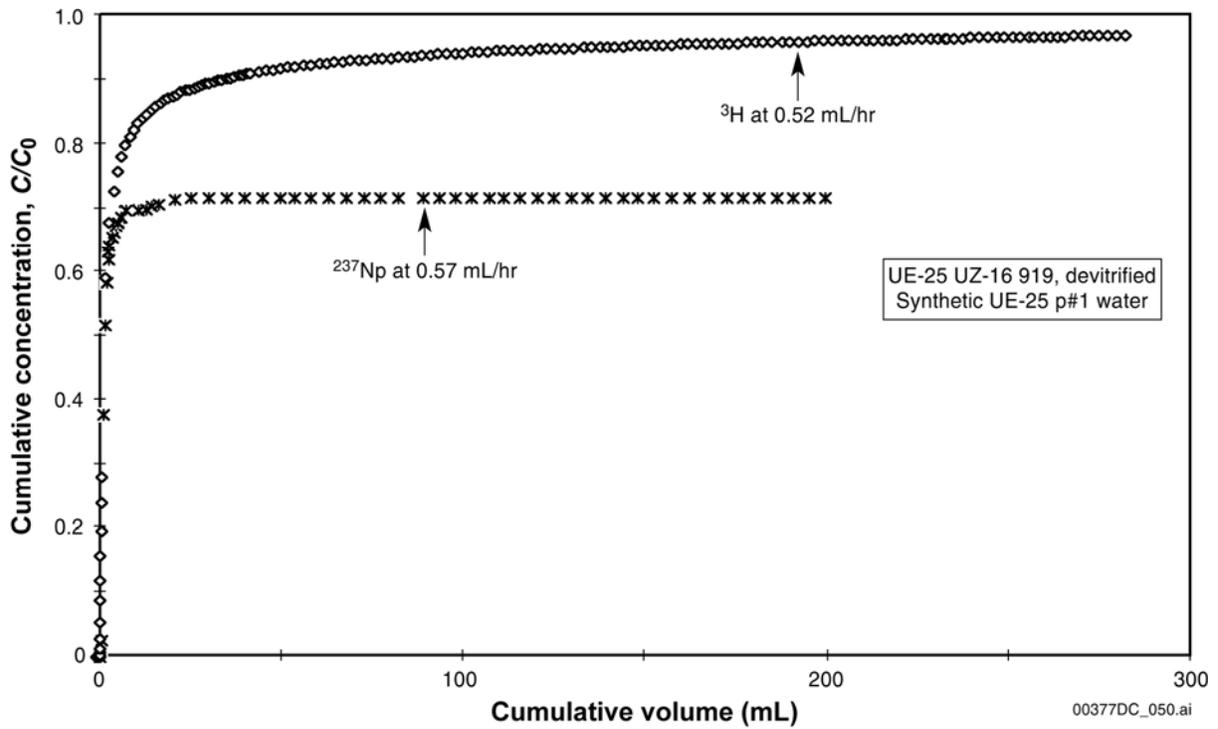
DTN: LA0001JC831361.001 [DIRS 145251]

Source: BSC 2001 [DIRS 160828], Figure 24

NOTE: This plot shows the elution curves for tritium and ^{237}Np in synthetic UE-25 p#1 water through a fractured column of devitrified tuff sample UE-25 UZ-16 919.

Figure 5-61. Neptunium in Fractured Tuff UZ-16 919
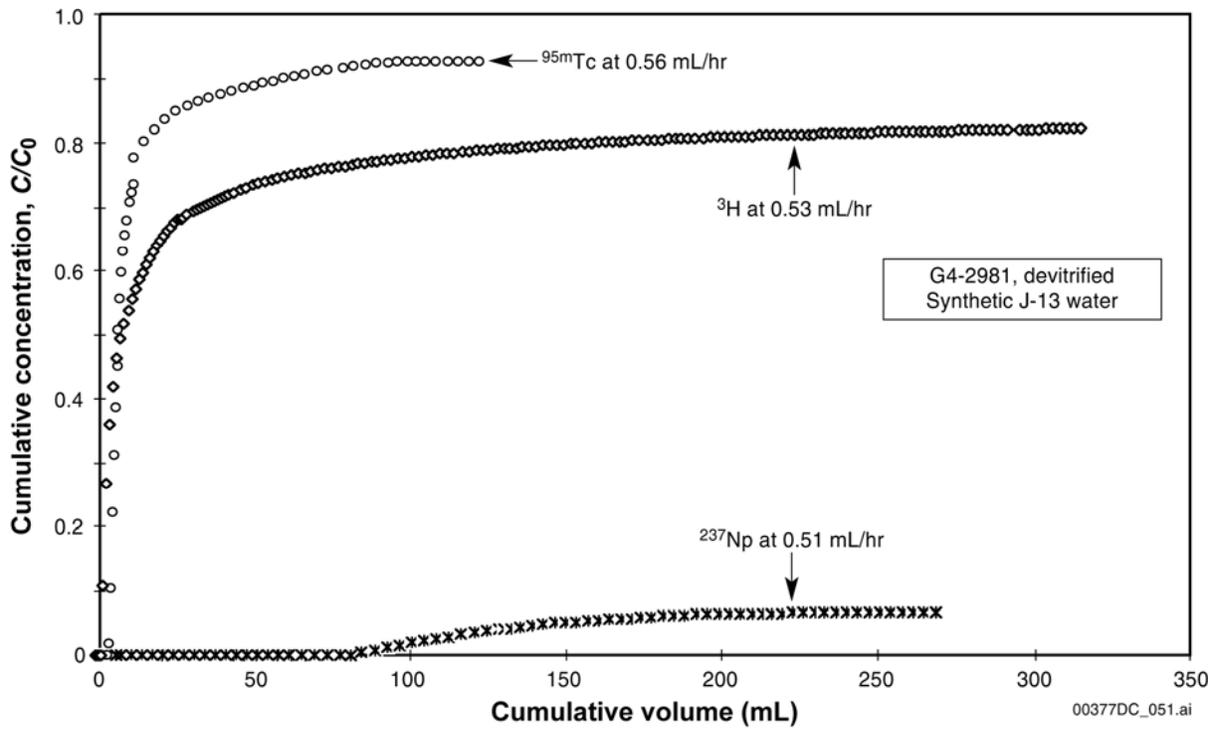
Figure 5-62 plot showing cumulative concentration curves.

DTNs: LA0001JC831361.001 [DIRS 145251]; LA0001JC831361.002 [DIRS 145253]

Source: BSC 2001 [DIRS 160828], Figure 25

NOTE: This plot shows the elution curves for tritium, ^{237}Np, and ^{95m}Tc in synthetic J-13 water through a fractured column of tuff G4-2981.

Figure 5-62.   Neptunium and Technetium in Fractured Tuff G4-2981
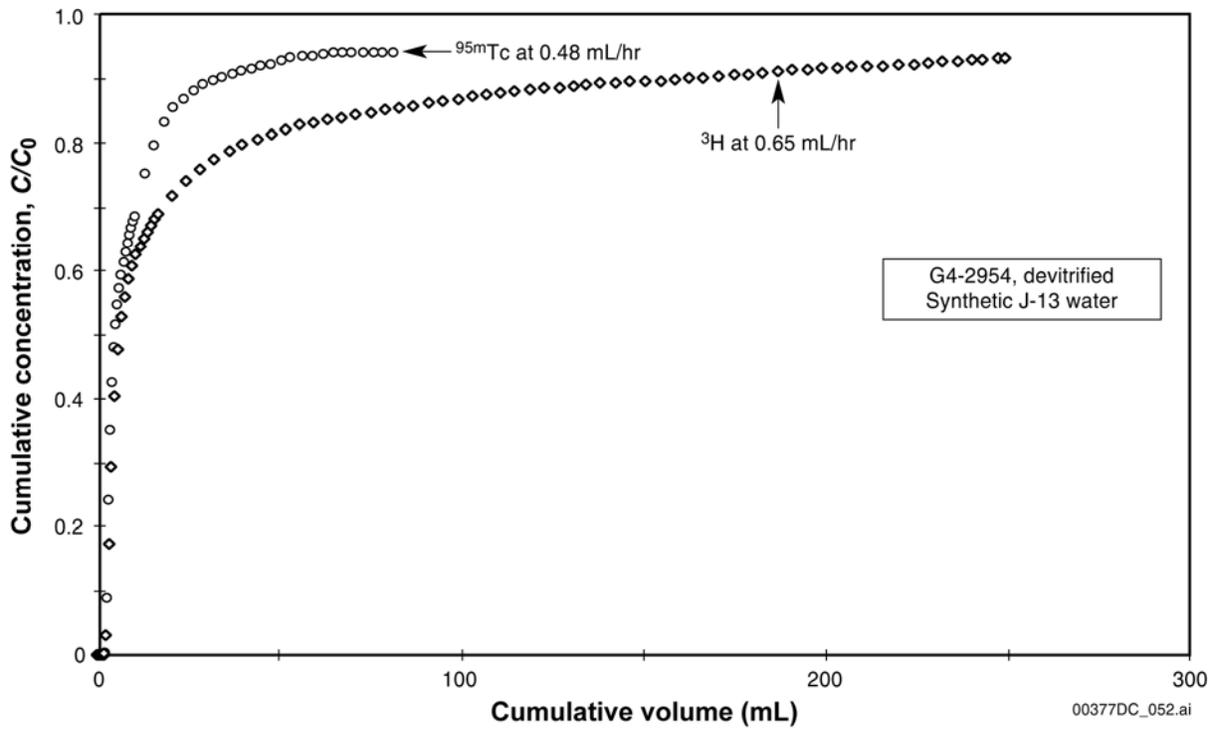
DTNs: LA0001JC831361.001 [DIRS 145251]; LA0001JC831361.002 [DIRS 145253]

Source: BSC 2001 [DIRS 160828], Figure 26

NOTE: This plot shows the elution curves for ^{95m}Tc and tritium in synthetic J-13 water through a fractured column of devitrified tuff G4-2954.

Figure 5-63.   Technetium in Fractured Tuff G4-2954
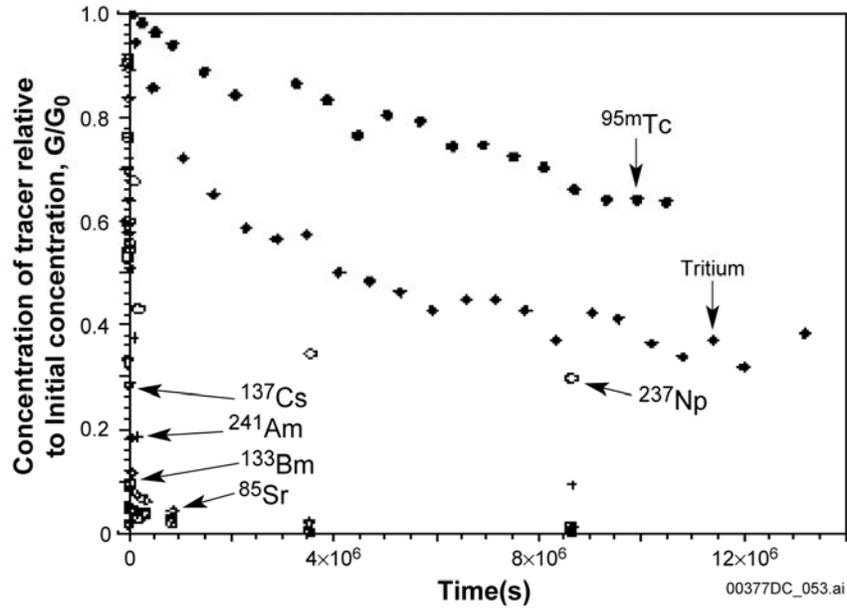
Source: BSC 2001 [DIRS 160828], Figure 27

NOTE: These data for diffusion of tracers in J-13 water and in rock beakers made of tuff G4-737 show the concentration, *C*, of tracer (relative to the initial concentration, C_0) remaining in the beaker as a function of elapsed time.

Figure 5-64.   Diffusion Data
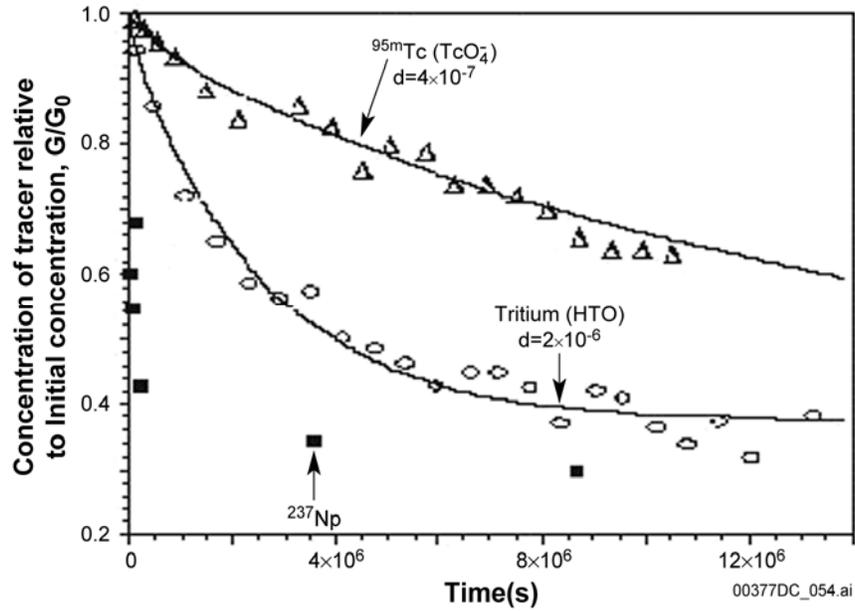
Source: BSC 2001 [DIRS 160828], Figure 28

NOTE: The solid curves are fits to the diffusion data by the TRACRN V.10 code for the nonsorbing tracers tritium and technetium in the rock-beaker experiments with tuff G4-737. Units of d are in cm^2 sec^{-1}.

Figure 5-65.   Diffusion Data Curve Fits
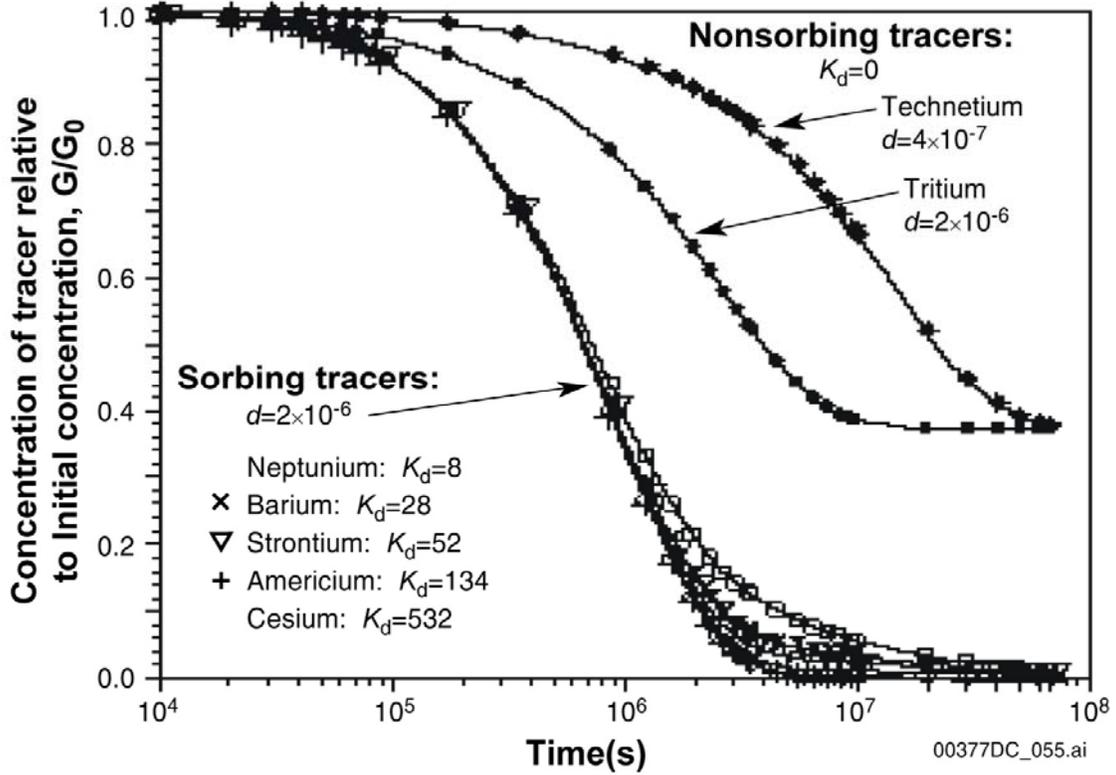
Source: BSC 2001 [DIRS 160828], Figure 29

NOTE: These curves were calculated for tuff G4-737 using the diffusion coefficient, d, measured from tritiated water and the batch-sorption coefficients, K_d, measured for the sorbing radionuclides. Diffusion curves for tritium and technetium are also shown. Units of d are in $cm^2 sec^{-1}$; units of K_d are mL g^{-1}.

Figure 5-66. Calculated Diffusion Curve
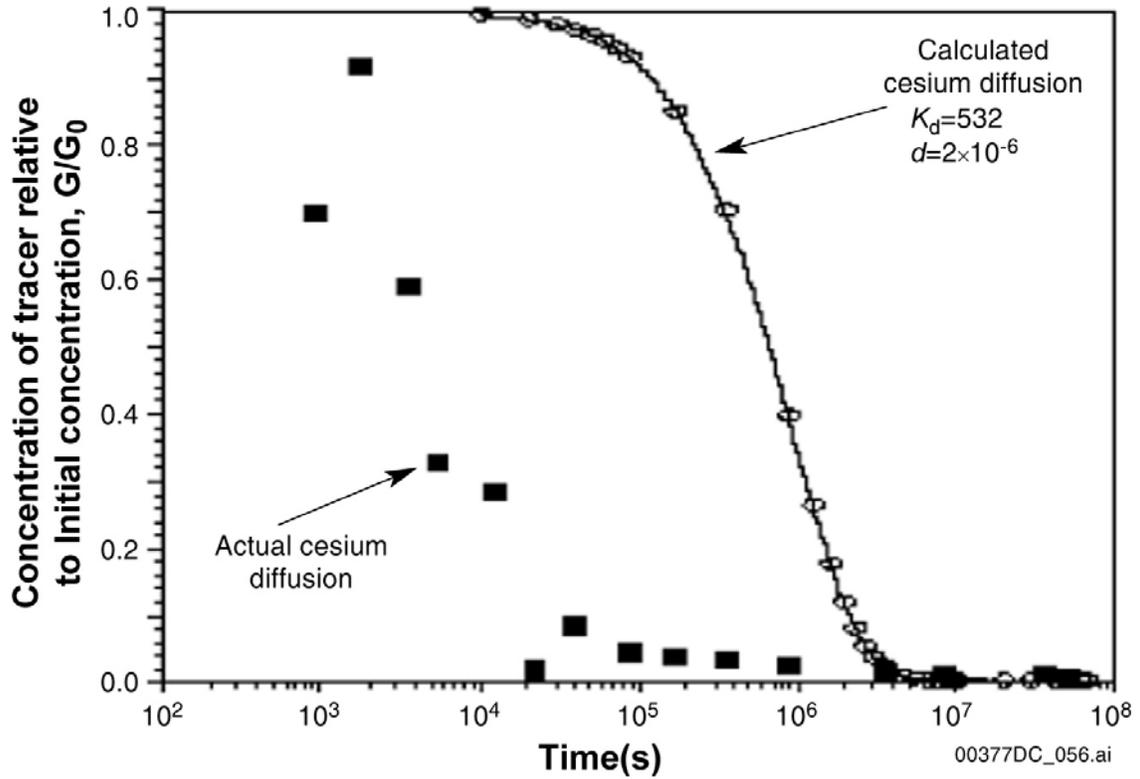
Source: BSC 2001 [DIRS 160828], Figure 30

NOTE: The solid curve is the diffusion curve calculated for cesium using a K_d value and the diffusion coefficient for tritium (Figure 5-65 and 5-66); the squares are the actual diffusion data for cesium with tuff G4-737. Units of d are in $cm^2 sec^{-1}$; units of K_d are mL g^{-1}.

Figure 5-67.   Comparison of Calculated and Actual Diffusion Data

Source: BSC 2001 [DIRS 160828], Figure 31

NOTE: The data show the concentration in synthetic UE-25 p#1 water of tritium, ^{239}Pu (V), and natural uranium (VI) (relative to the concentration in the traced cell, C/C_0) diffusing through devitrified tuff G4-287 into the untraced cell as a function of time.

Figure 5-68.   Tritium, Plutonium, and Uranium Diffusion through Devitrified Tuff

Source: BSC 2001 [DIRS 160828], Figure 32

NOTE: The data show the concentration in synthetic UE-25 p#1 water of ^{95m}Tc and ^{237}Np (relative to the concentration in the traced cell, C/C_0) diffusing through devitrified tuff G4-287 into the untraced cell as a function of time.

Figure 5-69.   Technetium and Neptunium Diffusion through Devitrified Tuff

Figure 5-70. Tritium, Plutonium, and Uranium Diffusion through Zeolitic Tuff
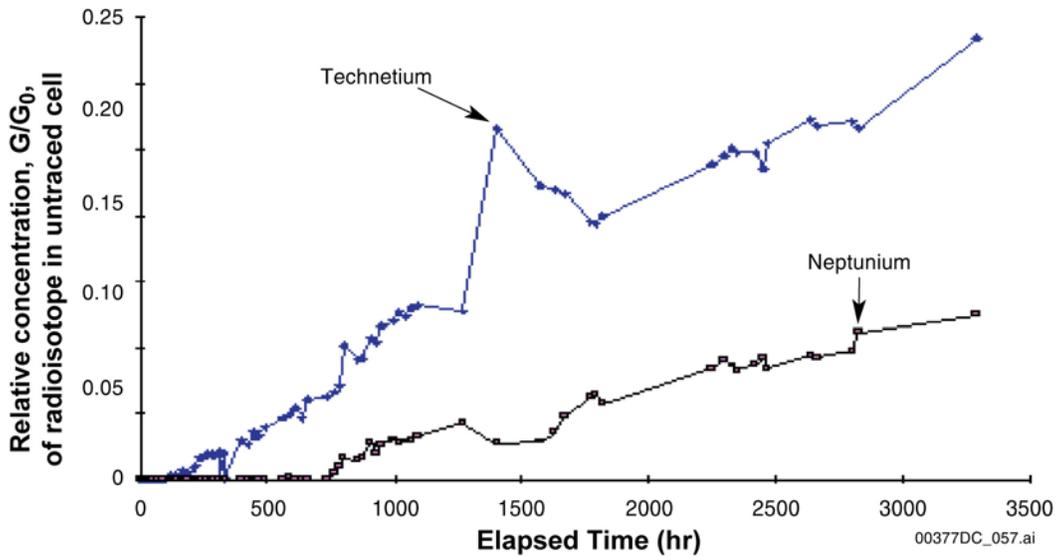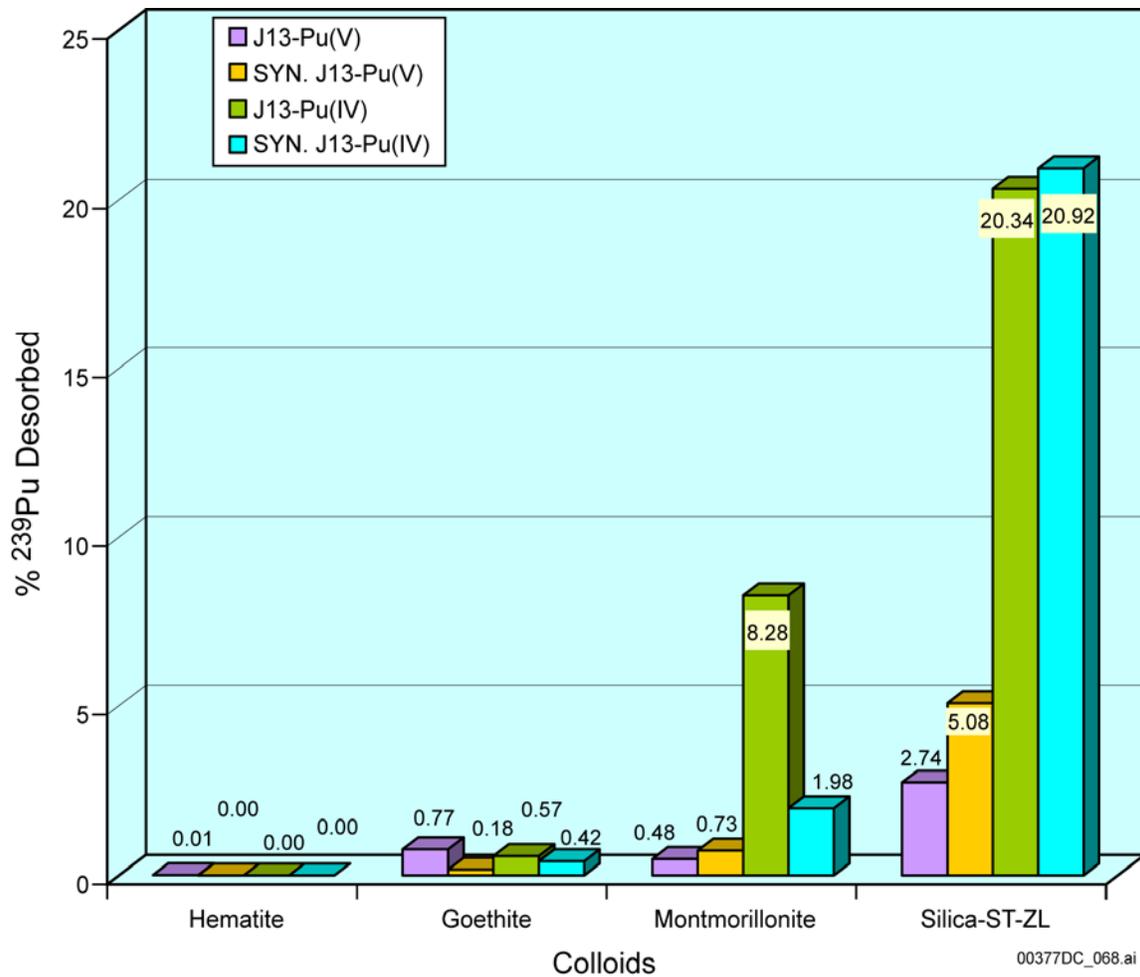
DTN: LAIT831362AQ95.001 [DIRS 107098]

Source: BSC 2001 [DIRS 160828], Figure 33

NOTE: The data show the concentration in synthetic UE-25 p#1 water of tritium, ^{239}Pu (V), and natural uranium (VI) (relative to the concentration in the traced cell, C/C_0) diffusing through zeolitic tuff UE-25 1362 into the untraced cell as a function of time.
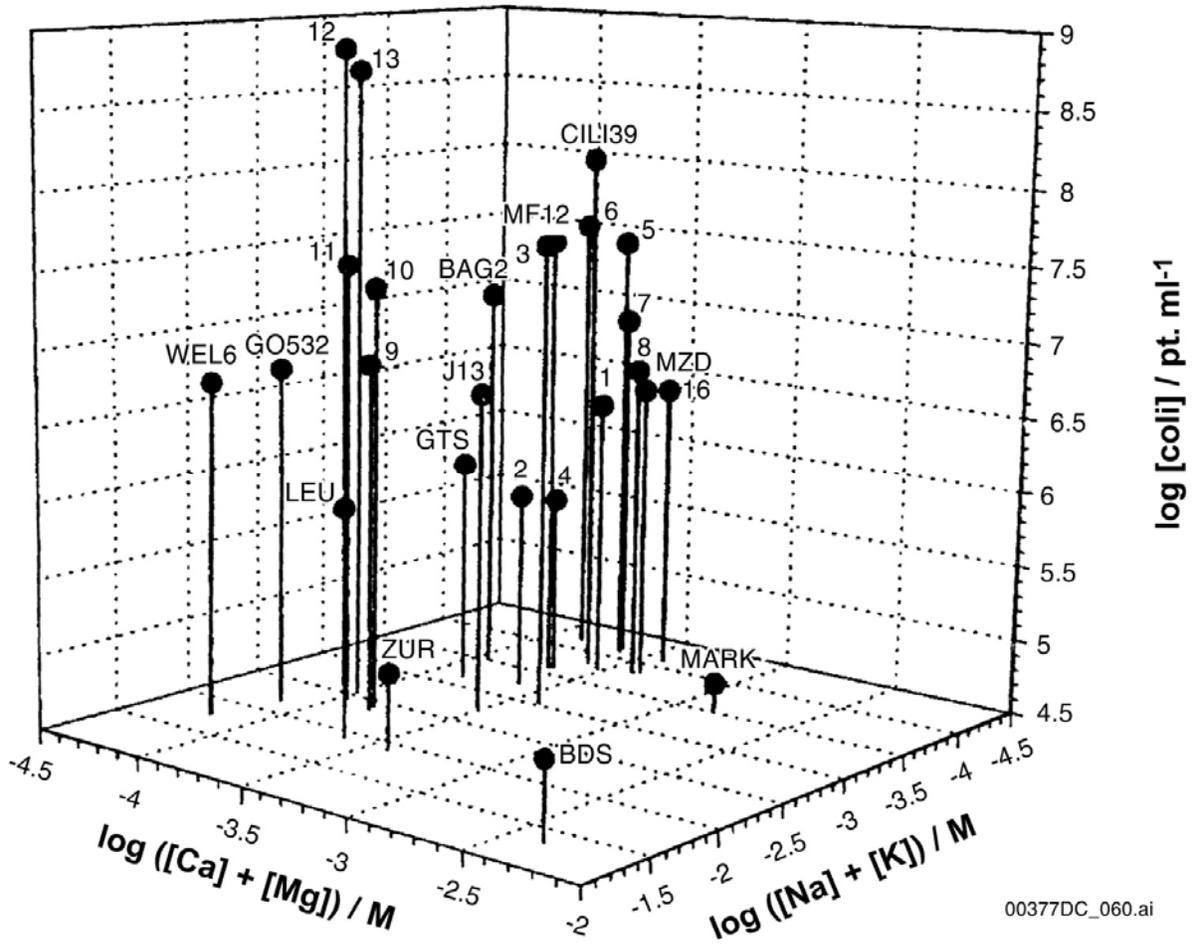
Source: CRWMS M&O 1997 [DIRS 100401], Chapter VIIA, Figure 1

NOTE: Concentrations of colloids are compared on the basis of alkali and alkaline-earth element concentration for colloid size greater than 100 nm.

Figure 5-71.   Colloid Concentrations as a Function of Salt Concentration and Hardness
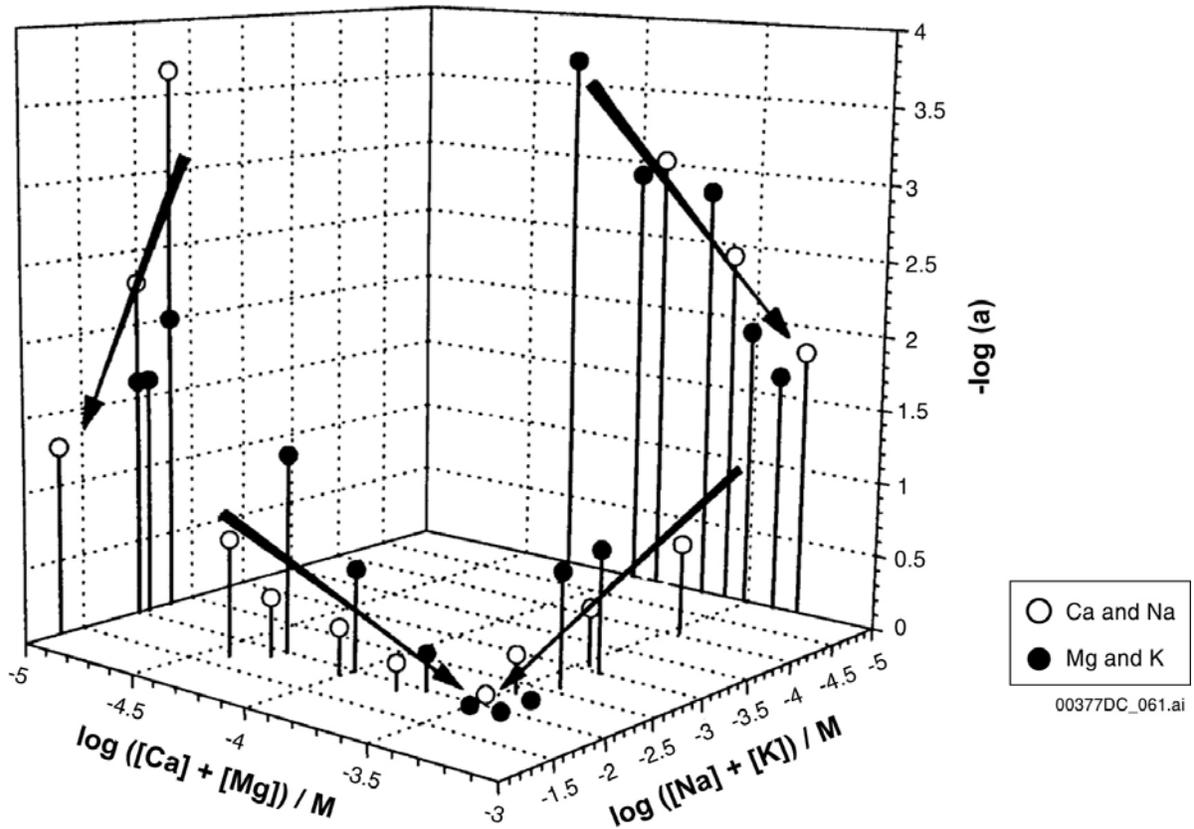
Source: CRWMS M&O 1997 [DIRS 100401], Chapter VIIA, Figure 2

NOTE: This plot shows the effect of calcium + magnesium and sodium + potassium on the colloid attachment factor at a pH of 8 for montmorillonite colloids of size greater than 100 nm with total organic carbon less than 5×10^{-5} M.

Figure 5-72.   Colloid Attachment as a Function of Salt Concentration and Hardness
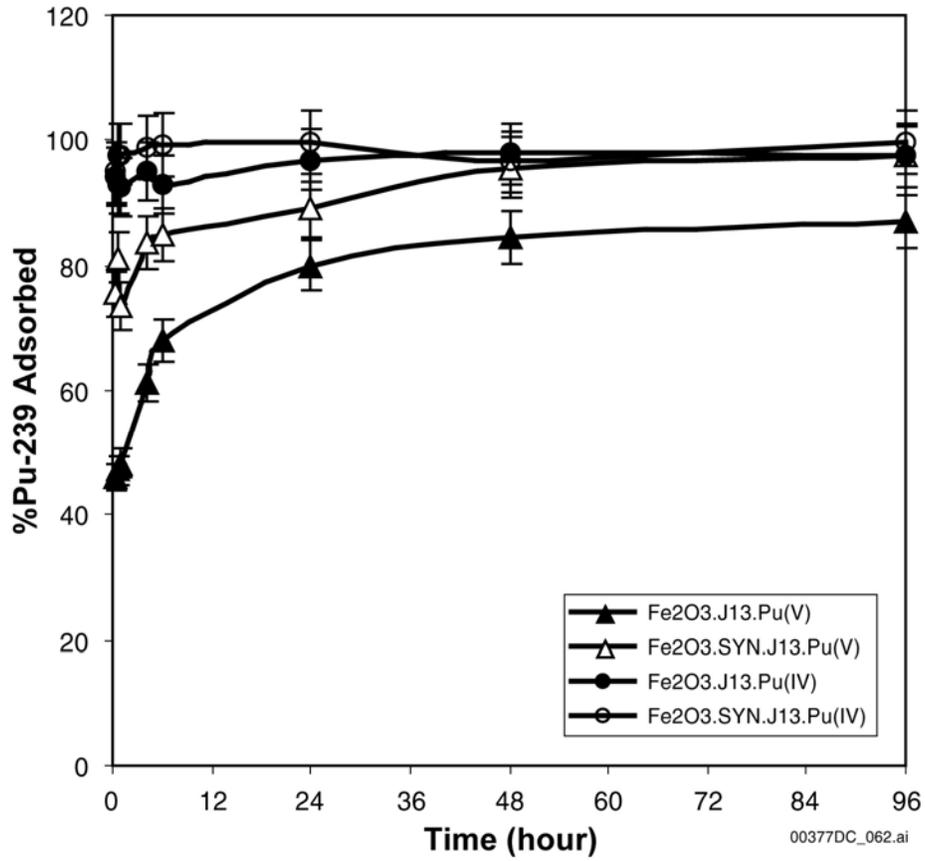
DTN: LA0004NL831352.002 [DIRS 166674]

Source: CRWMS M&O 1997 [DIRS 100401], Chapter VIID, Figure 1

Figure 5-73. Sorption of [239]Pu onto Hematite Colloids as a Function of Time in Natural and Simulated Groundwater
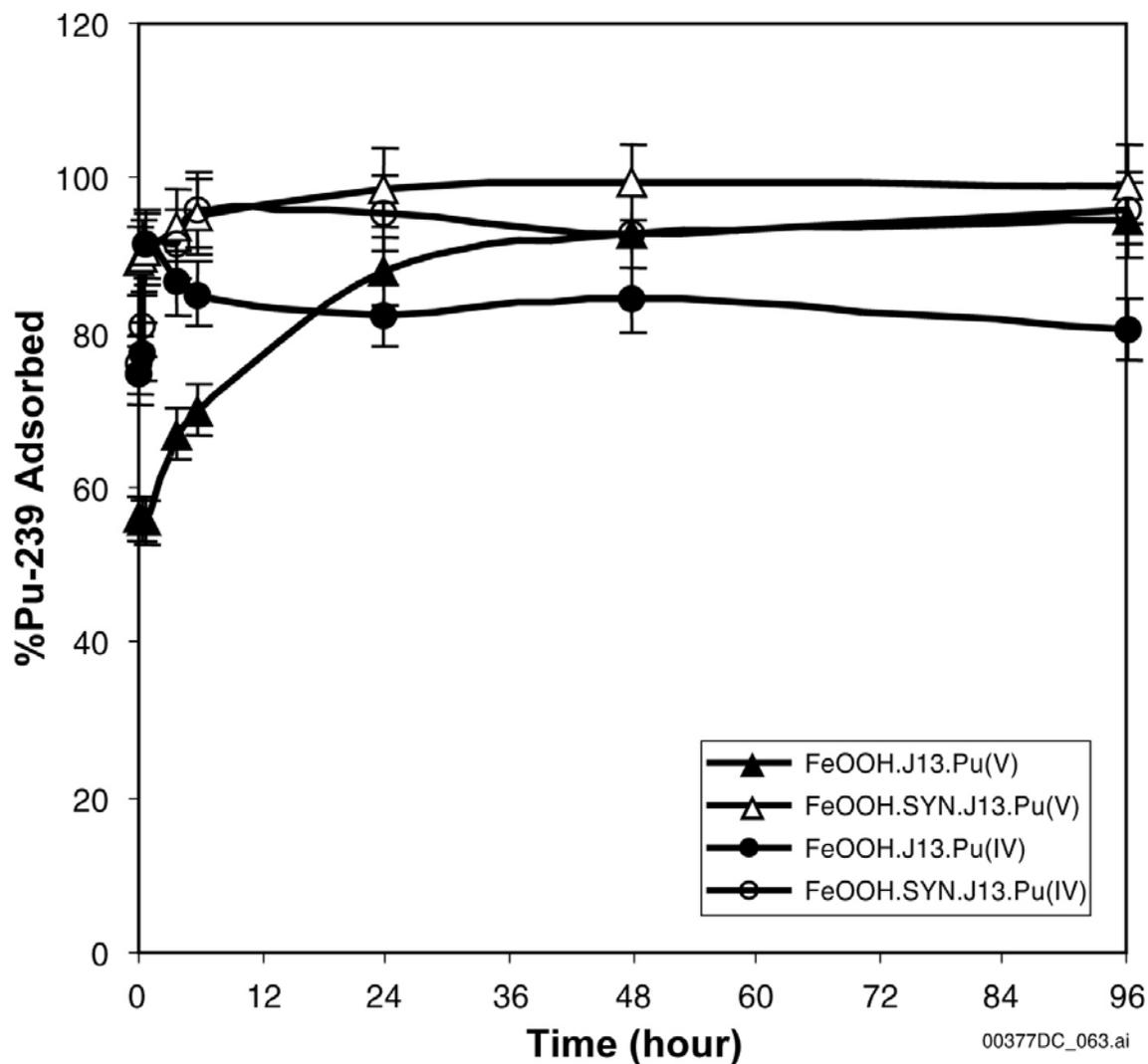
DTN: LA0004NL831352.002 [DIRS 166674]

Source: CRWMS M&O 1997 [DIRS 100401], Chapter VIID, Figure 1

Figure 5-74. Sorption of ^{239}Pu onto Goethite Colloids as a Function of Time in Natural and Simulated Groundwater
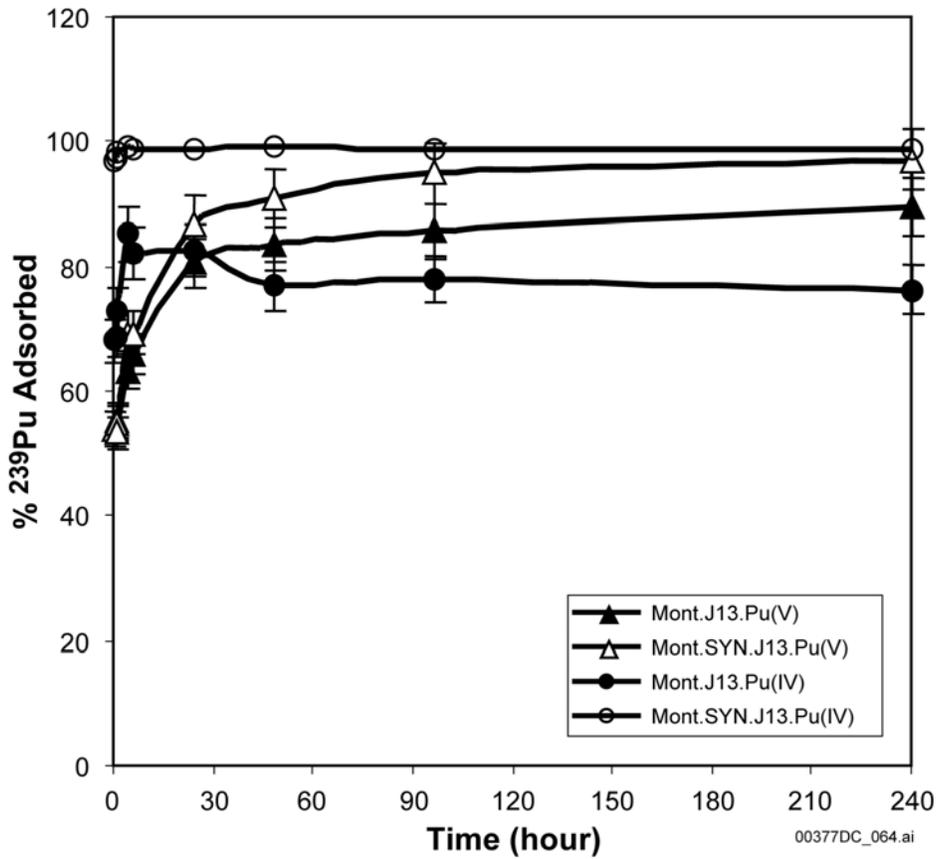
DTN: LA0004NL831352.001 [DIRS 150272]

Figure 5-75. Sorption of ^{239}Pu onto Montmorillonite Colloids as a Function of Time in Natural and Simulated Groundwater
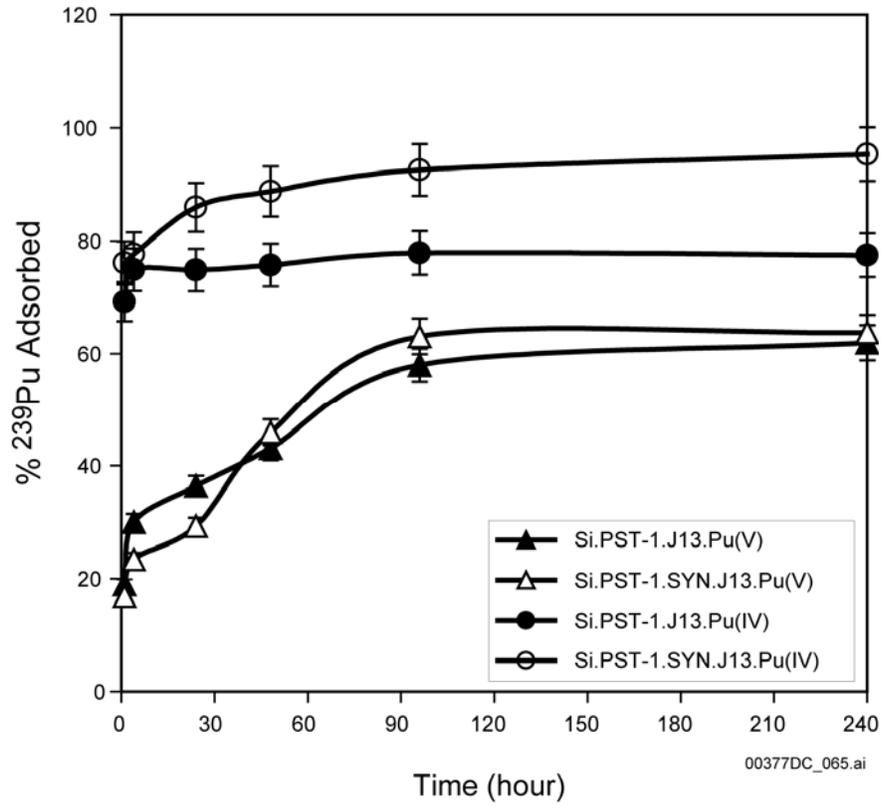
Figure 5-76. Sorption of [239]Pu onto Silica-PST-1 Colloids as a Function of Time in Natural and Simulated Groundwater
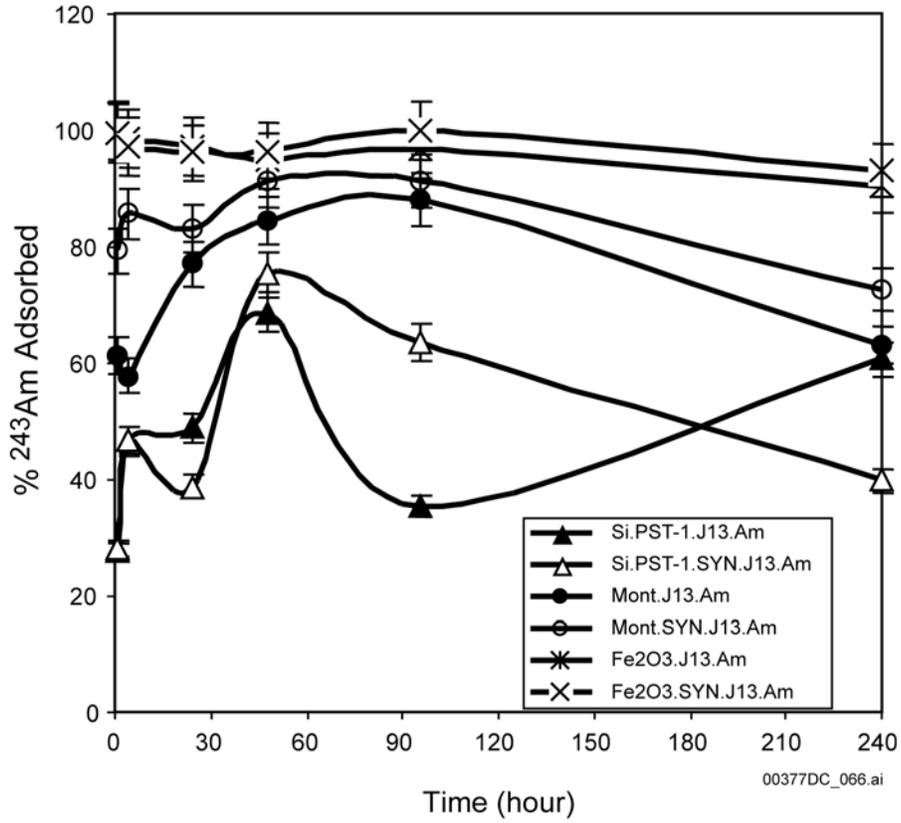
DTN: LA0004NL831352.001 [DIRS 150272]

Figure 5-77. Percentage of ^{243}Am Adsorbed onto Colloids of Hematite, Montmorillonite, and Silica-PST-1 as a Function of Time in Natural and Simulated Groundwater
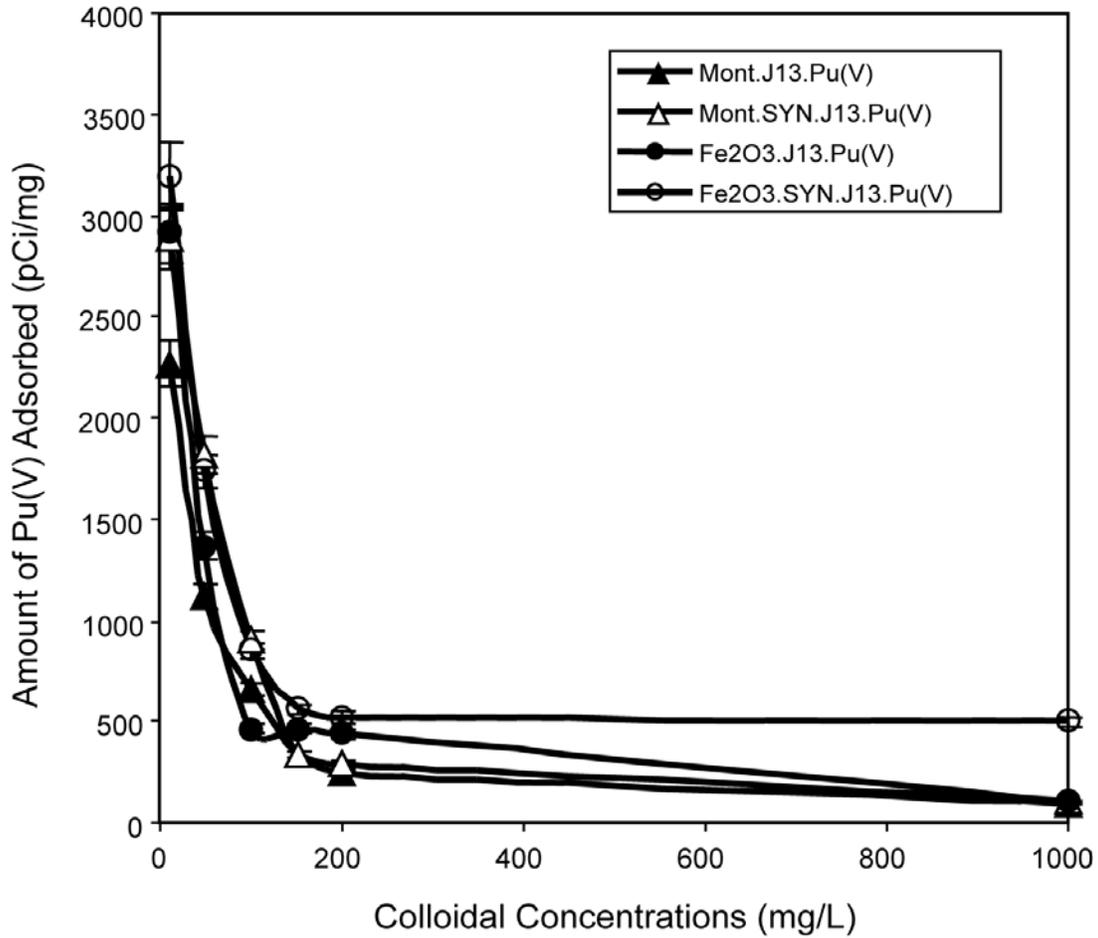
00377DC_067.ai

DTN: LA0004NL831352.001 [DIRS 150272]

Figure 5-78. Amount of Plutonium (V) Adsorbed onto Hematite and Montmorillonite as a Function of Colloidal Concentrations in Natural and Simulated Groundwater after 240 Hours
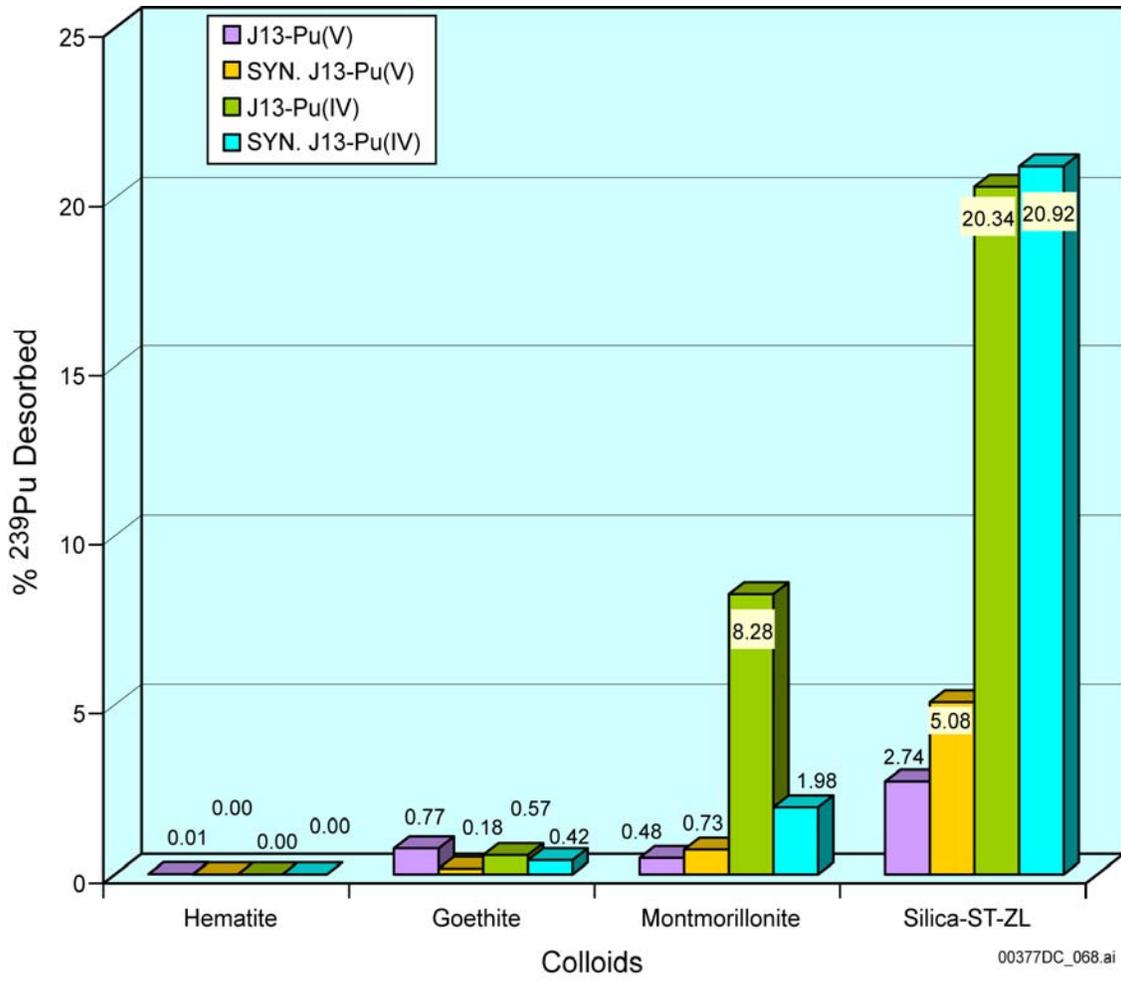
Figure 5-79. Desorption of [239]Pu from Colloids of Hematite, Goethite, Montmorillonite, and Silica in Natural and Simulated Groundwater after 150 Days

1. Capillary-Barrier Effect
2. Local Percolation Flux Distribution
3. Fracture Network
4. Drift Geometry
5. Excavation-Disturbed Zone/Dryout Zone

00357DCf_014.ai
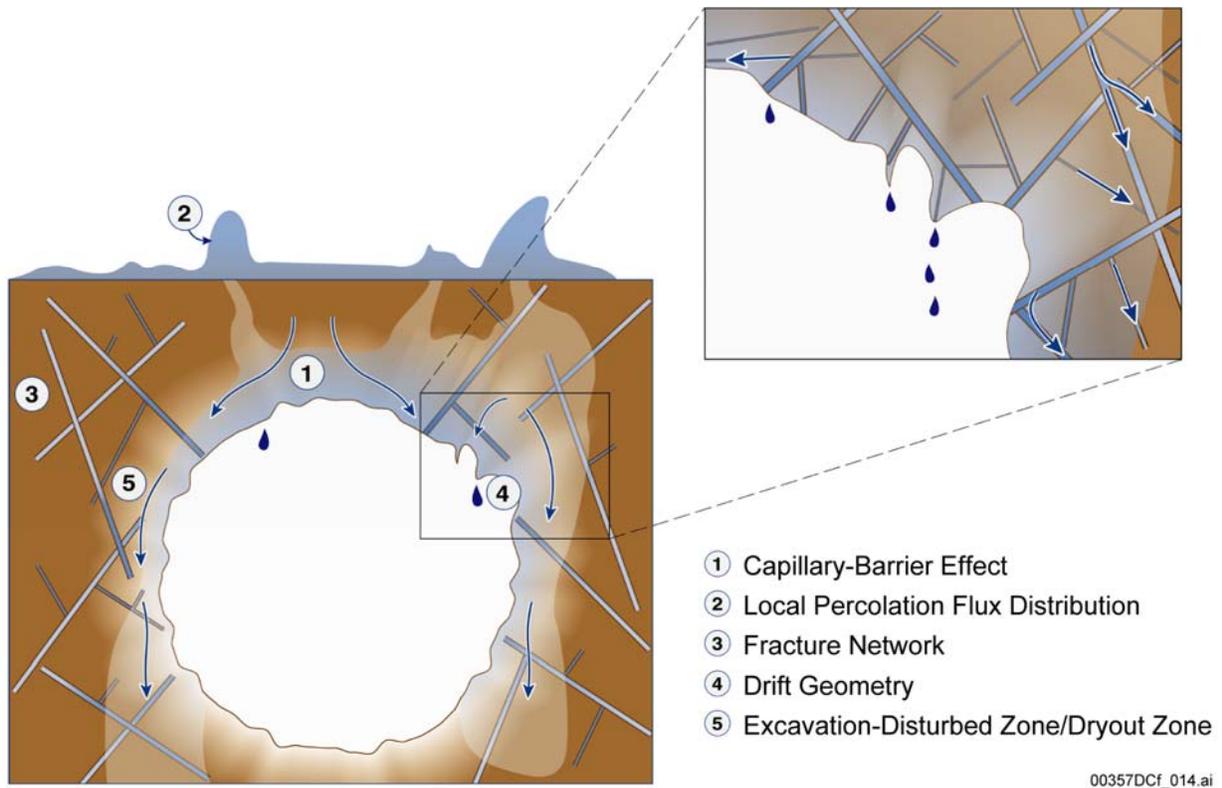
Source: BSC 2003 [DIRS 165564], Figure 6.3-1

Figure 5-80.   Phenomena and Processes Affecting Drift Seepage
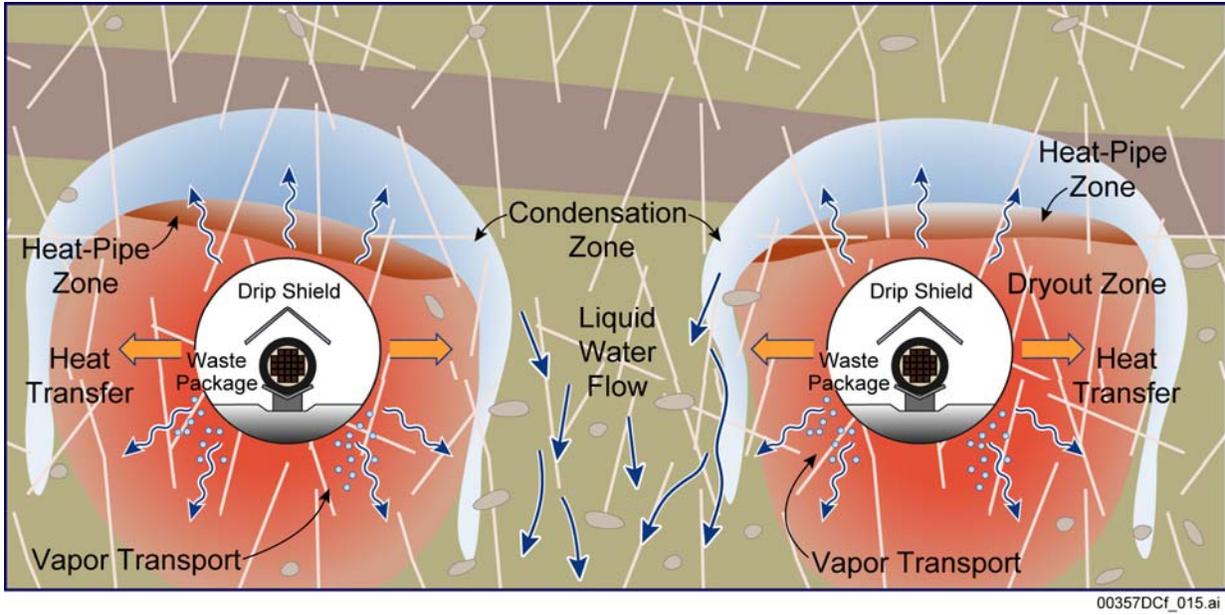
Source: Adapted from BSC 2003 [DIRS 166512], Figure 6.1-1

Figure 5-81.   Thermal-Hydrologic Processes at the Drift Scale
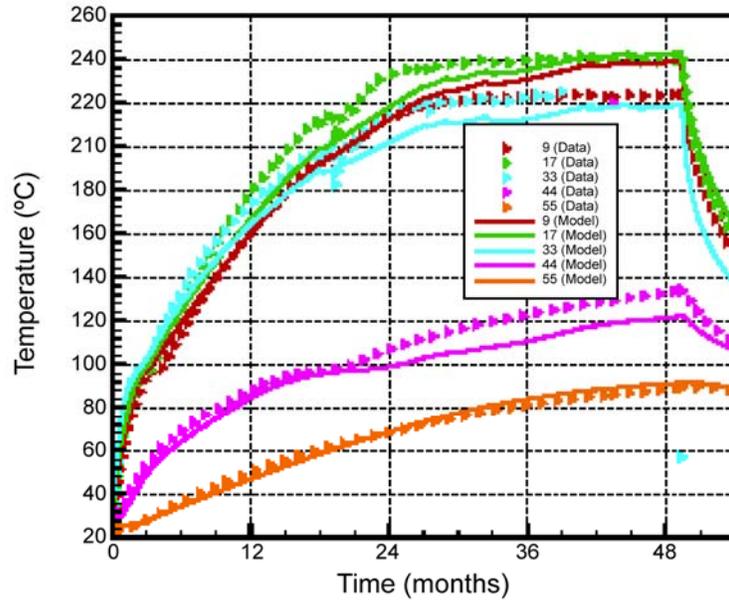
(a)
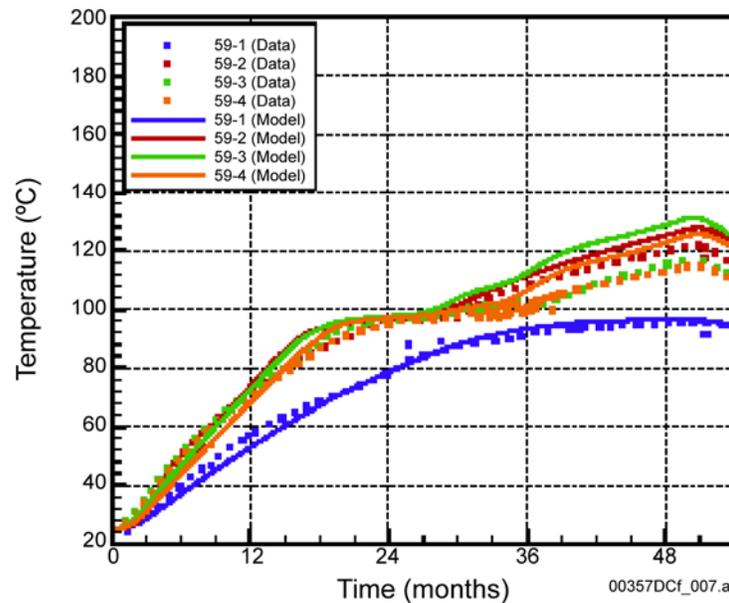
(b)

DTN (for Figures 7.4.3.1-3a through 3c): LB0303DSCPDSTV.001 [DIRS 166675]
DTNs (for Figures 7.4.3.1-3a through 3c): MO9807DSTSET01.000 [DIRS 113644],
MO9810DSTSET02.000 [DIRS 113662], MO9906DSTSET03.000 [DIRS 113673],
MO0001SEPDSTPC.000 [DIRS 153836], MO0007SEPDSTPC.001 [DIRS 153707],
MO0012SEPDSTPC.002 [DIRS 153708], MO0107SEPDSTPC.003 [DIRS 158321],
MO0202SEPDSTTV.001 [DIRS 158320]; MO0208SEPDSTTD.001 [DIRS 161767]

Source: BSC 2003 [DIRS 166512], Figure 7.4.3.1-3

NOTE: (a) Borehole 160 (horizontal); (b) Borehole 59 (subhorizontal, above and perpendicular to the heated drift).

Figure 5-82.   Temporal Evolution of Temperature at Selected Borehole Sensors, in Horizontal Temperature Boreholes That Traverse the Drift Scale Test
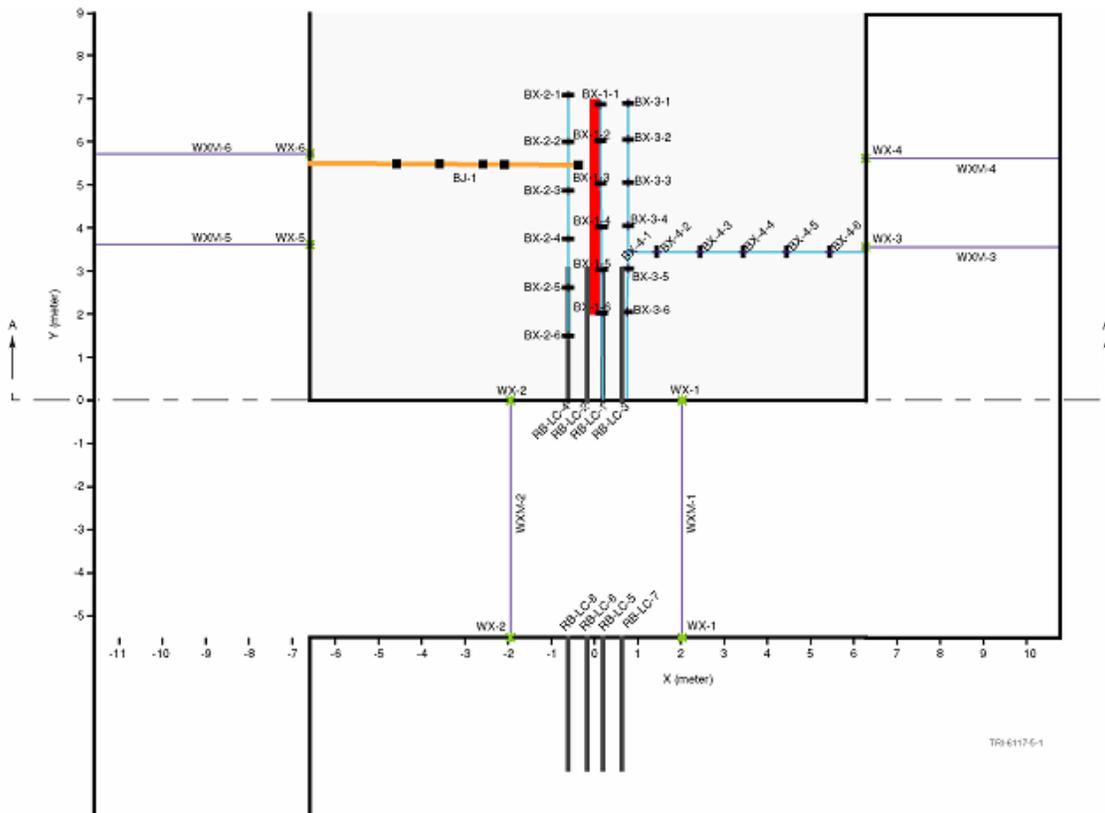
Source: CRWMS M&O 1999 [DIRS 129261], Figure 9-1

NOTE: Based on Figure 1 of Björnsson and Bodvarsson 1990 [DIRS 154606]

Figure 5-83. Plan View of the Single Heater Test Block Showing Monitoring Locations
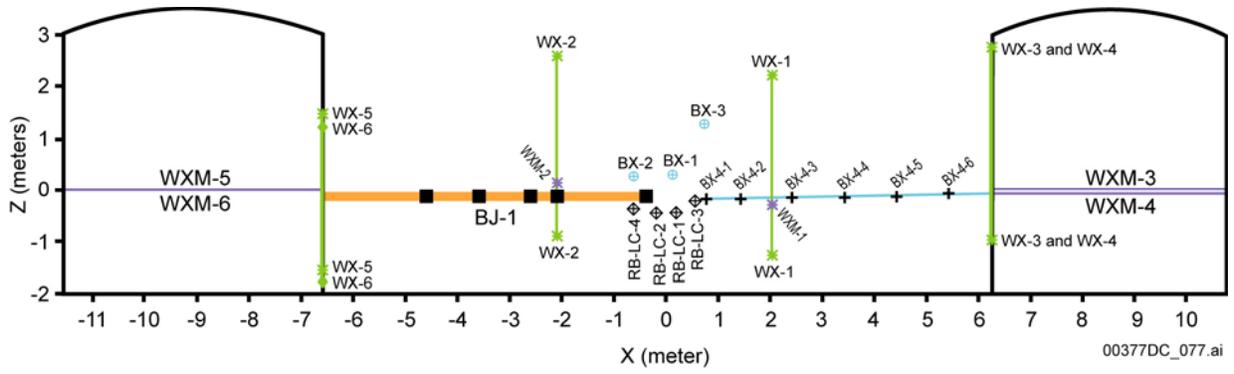
Source: CRWMS M&O 1999 [DIRS 129261], Figure 9-2

Figure 5-84.   Cross Section of the Single Heater Test Block Showing Monitoring Locations

00377DC_074.ai

Source: Wilder et al. 1997 [DIRS 125467], Figure 2-5

NOTE: The upper portion of the block is exposed, while the lower portion of the block is supported with bracing. T-shaped grooves on the face of the block are the locations of fracture monitors.

Figure 5-85. Photograph of the Large Block
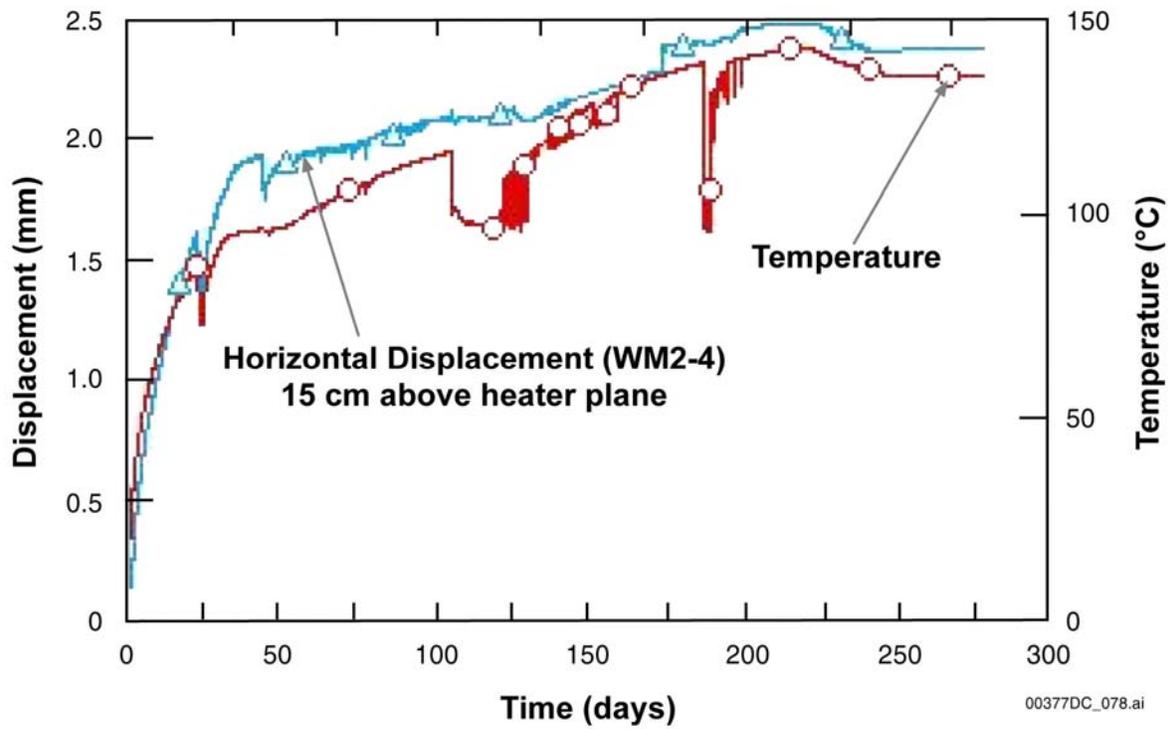
DTN: N/A

Source: Adapted from Blair and Lin 1997 [DIRS 150392], Figure 4

Figure 5-86.   Temperature History near the Heater Plane for the Large Block Test

WM-2

Start Date: 2/27/97
End Date: 12/5/97

00377DC_079.ai
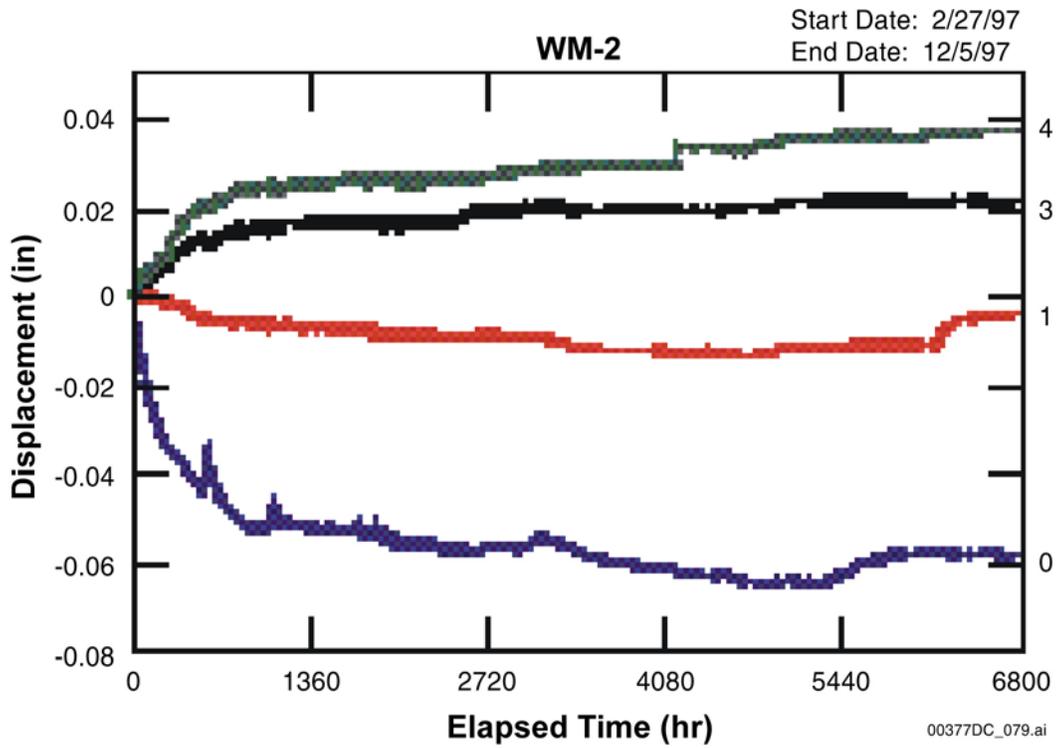
DTN: N/A

Source: Blair and Lin 1997 [DIRS 150392], Figure 5

NOTE: Numbers (0 through 4) represent anchors.

Figure 5-87. East-West Deformation Recorded with a Multiple-Point Borehole Extensometer Referenced to the Center of the Large Block
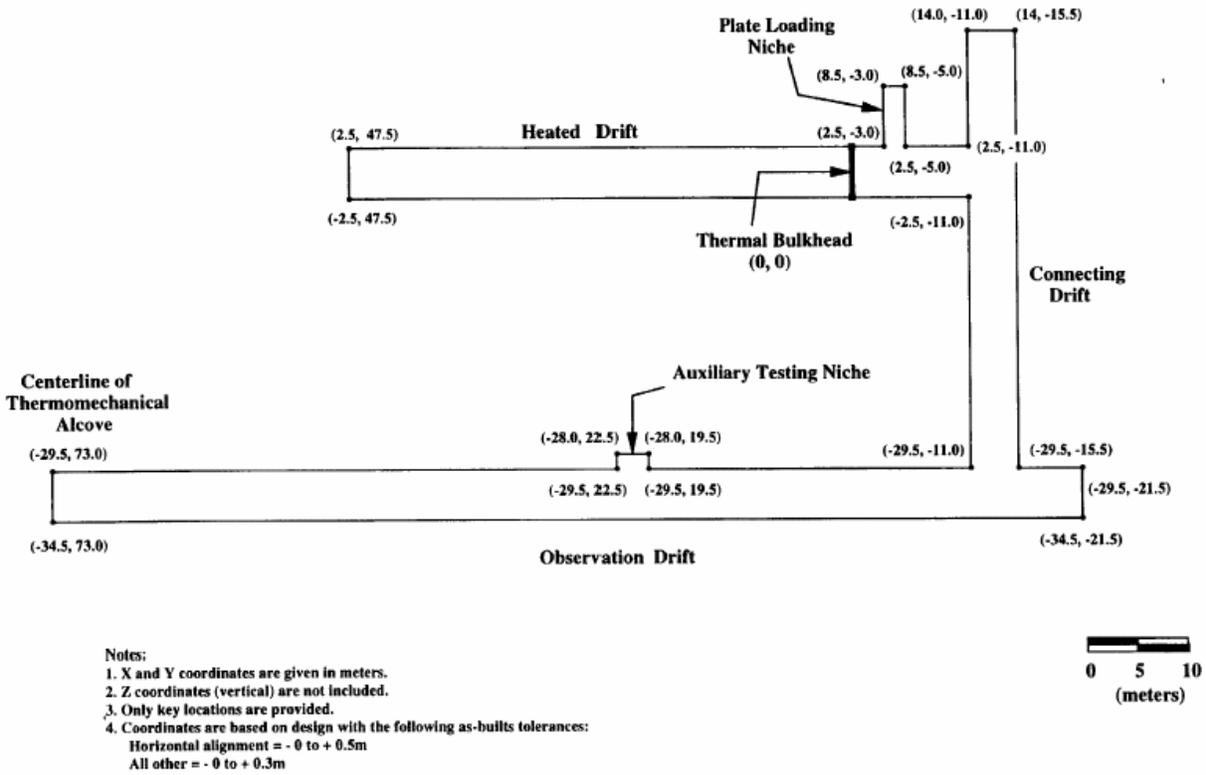
Source: BSC 2002 [DIRS 160771], Figure 6.3-1

Figure 5-88.   DST As-Built Plan View with Two-Dimensional Coordinates of Key Locations
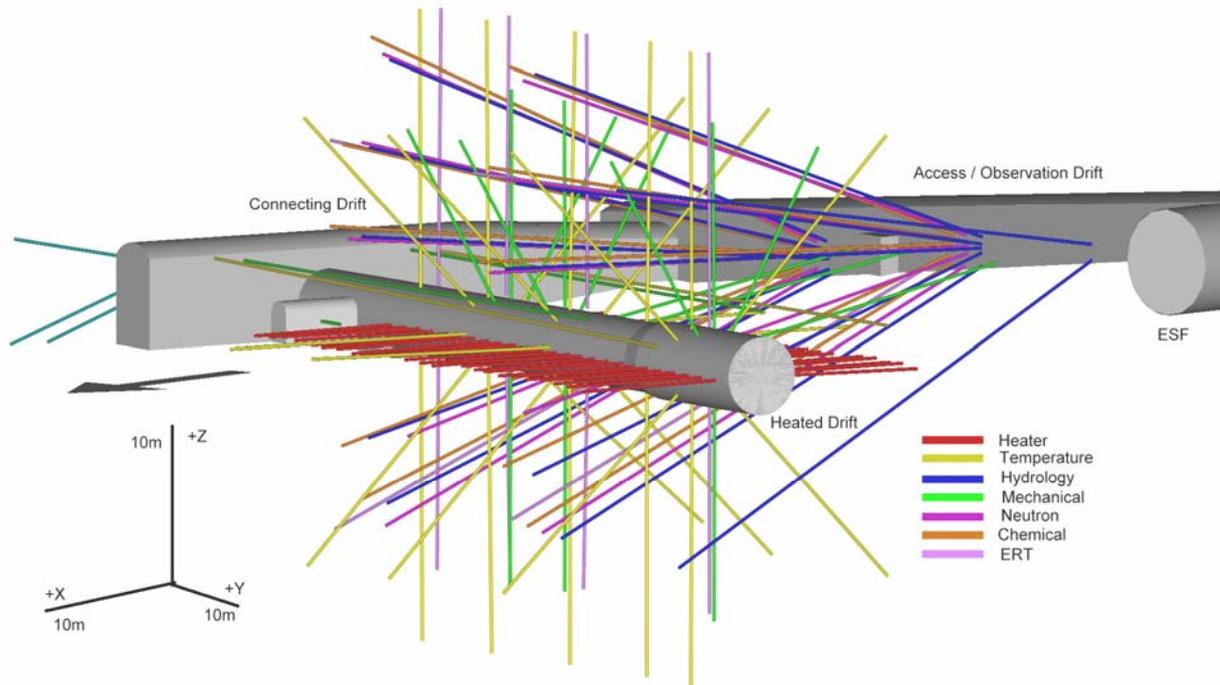
Source: BSC 2002 [DIRS 160771], Figure 6.3-2

Figure 5-89.   Perspective View Showing Drifts and Boreholes of the DST

Source: Wilder 1997 [DIRS 100190], Figure 5-15

NOTE: Yellow arrows indicate elevated temperature coupling.

Figure 5-90. Matrix of Coupled Geochemical and Mineralogical Processes

Source: BSC 2003 [DIRS 162050], Figure 6.2-2

Figure 5-91. Diagram of Fracture-Matrix Interface, Showing the Relation between Thermal-Hydrologic Processes and Geochemical Processes

Ambient percolation flux	Latent heat convection						
	Rock-mass temperature	Dryout/ evaporation	· Dryout/ evaporation · Vapor/water mobilization	· Dryout/ evaporation · Heat of vaporization · Buoyancy		· Rock-water interaction · Mineral dehydration	· Rock-water interaction · Mineral dehydration
		Moisture in pores	· Saturation gradients · Imbibition · Condensation · Capillary/ gravity equil.	Vapor diffusion	· Moisture mobilization · Imbibition · Rock-water interaction	· Primary minerals water interaction · Buffering · Pore-water chemistry	
	· Convection · Latent heat · Heat pipe (refluxing)		Moisture in fractures	Vapor equilibrium	Condensate drainage	· Secondary minerals water interaction · Fracture water chemistry	
	· Heat pipe · Vapor heat redistribution · Heat release · Condensation	Vapor resaturation	Vapor resaturation	Vapor in fractures	Vapor escape from system	Vapor rock interaction	
	Imbibition	· Mixing · Dilution			Net percolation flux	· Mixing · Buffering	
	Changes in boiling point	Changes in boiling point	Changes in vapor pressure			Water chemistry	Rock-water interaction
			Changes in vapor pressure			· Chemical reactions · Rock-water interaction · Buffering	Mineral changes

00377DCa_026.ai

Source: Wilder 1997 [DIRS 100190], Figure 4-9

NOTE: Yellow arrows in clockwise and counterclockwise directions represent forward and backward coupling, respectively. Key parameters are shown along the diagonal in blue. Coupled processes are shown off-diagonal.

Figure 5-92.   Matrix of Coupled Processes in the Near-Field Environment Related to Water Chemistry
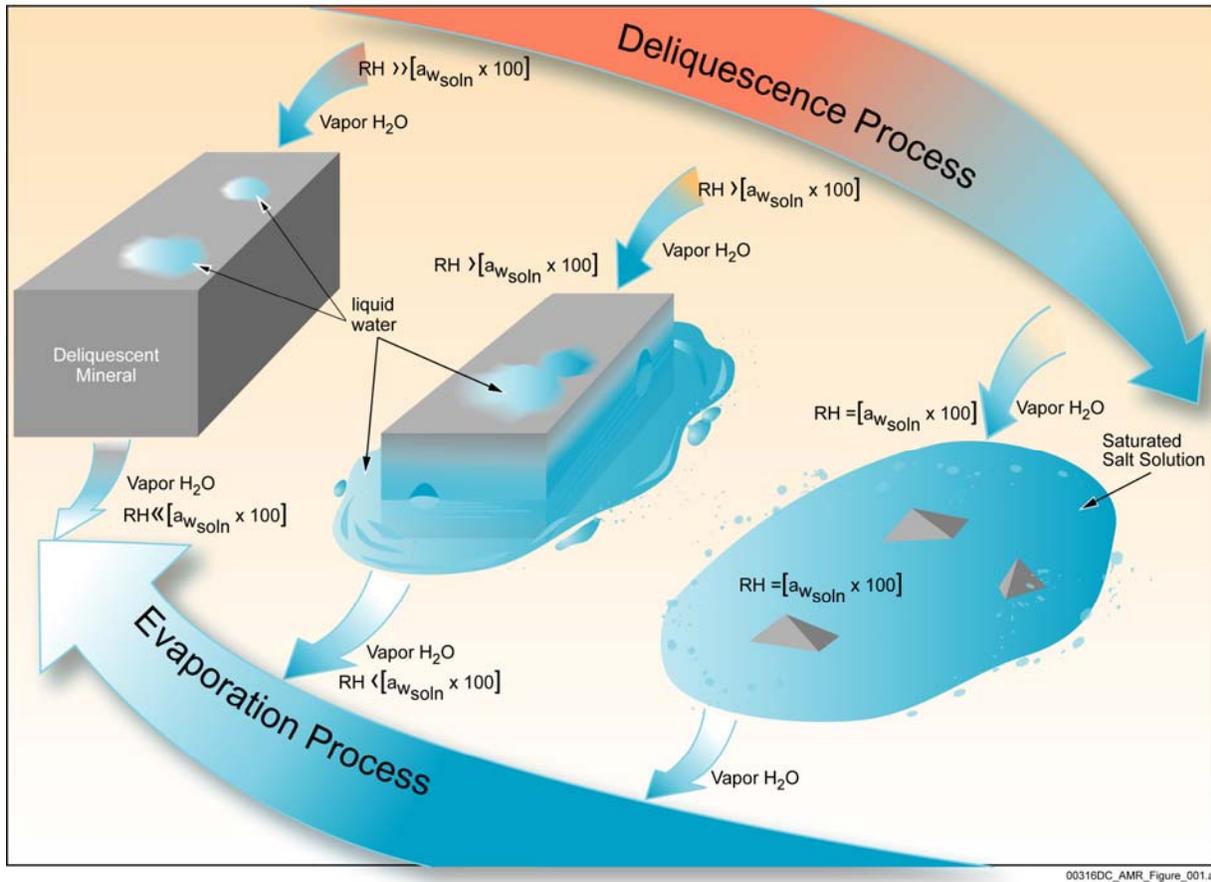
Source: BSC 2003 [DIRS 167461], Figure 6.2-2

Figure 5-93. Schematic Illustration of Deliquescence and Evaporation
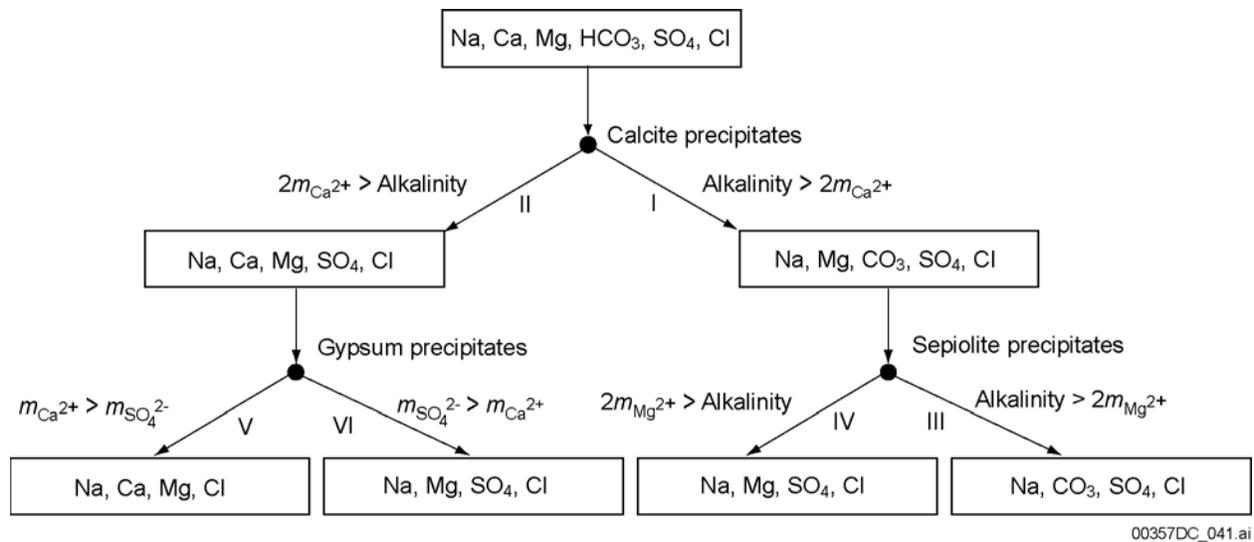
Source: Drever 1988 [DIRS 118564], p. 236

Figure 5-94. Simplified Chemical Divides Diagram Based on Evaporative Concentration of Dilute Starting Waters to Form a Suite of Naturally Occurring Lake Waters
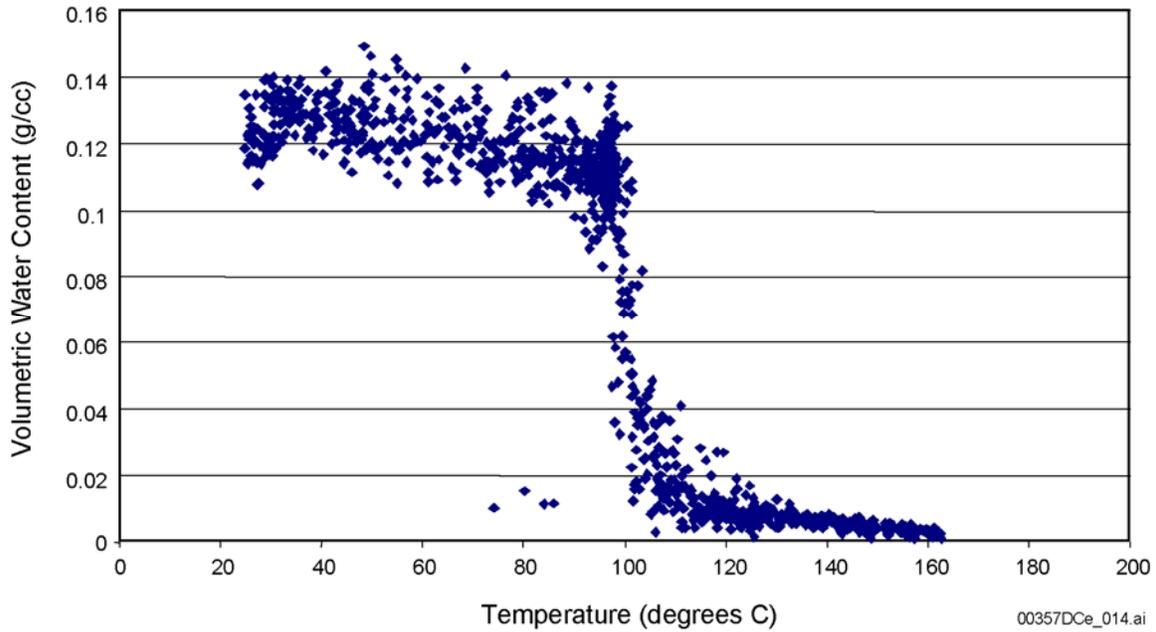
DTNs: MO9807DSTSET01.000 [DIRS 113644], MO9810DSTSET02.000 [DIRS 113662], MO9906DSTSET03.000 [DIRS 113673], MO0001SEPDSTPC.000 [DIRS 153836], MO0007SEPDSTPC.001 [DIRS 153707], and LL020710223142.024 [DIRS 159551]

Source: BSC 2003 [DIRS 161963], Figure 6.2-4

NOTE: This borehole is almost level over an instrumented 40 meter section, almost parallel and 9.5 meter offset from the center of the drift, and about 3.5 meters above the wing heaters that simulate the heat from a waste package. The test was conducted from February 1998 to May 2000.

Figure 5-95. Experimental Relationship between Borehole Temperature and Volumetric Water Content for Borehole 79 during the Drift Scale Test over a Two-Year Period during Heating
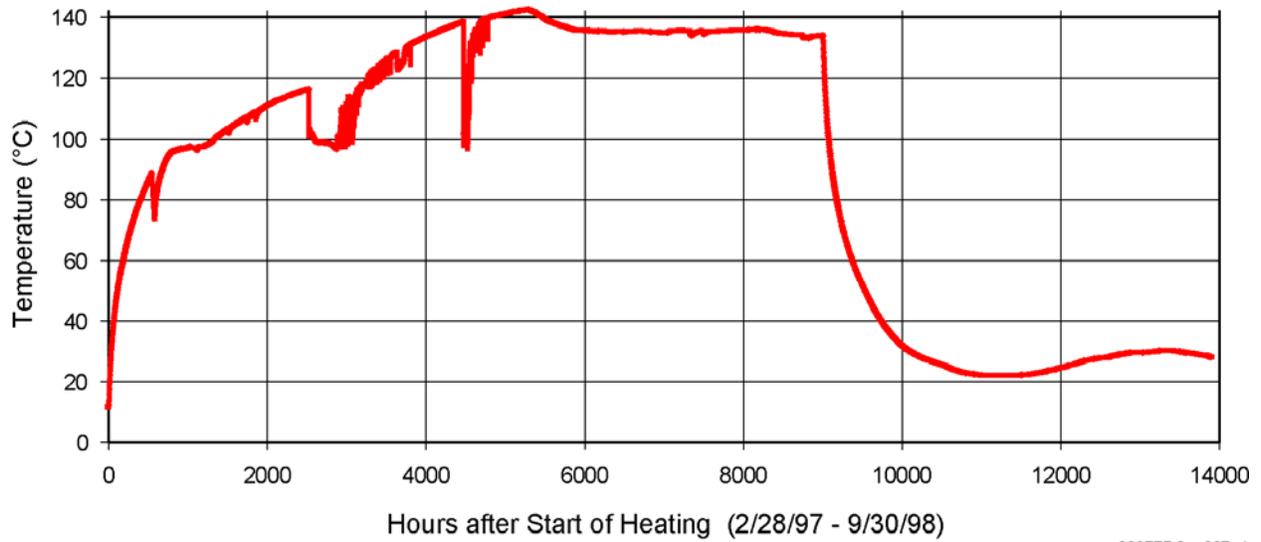
Source: Modified from CRWMS M&O 2000 [DIRS 146589], Figure 3-29

Figure 5-96.   Temperature at Sensor 14 in Borehole TT1 of the Large Block Test as a Function of Time
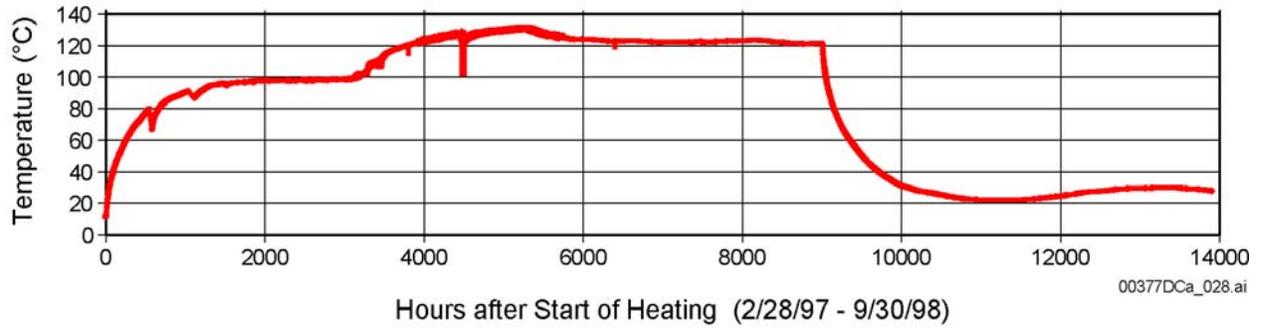
Source: Modified from CRWMS M&O 2000 [DIRS 146589], Figure 3-30

Figure 5-97. Temperature at Sensor 14 in Borehole TT2 of the Large Block Test as a Function of Time
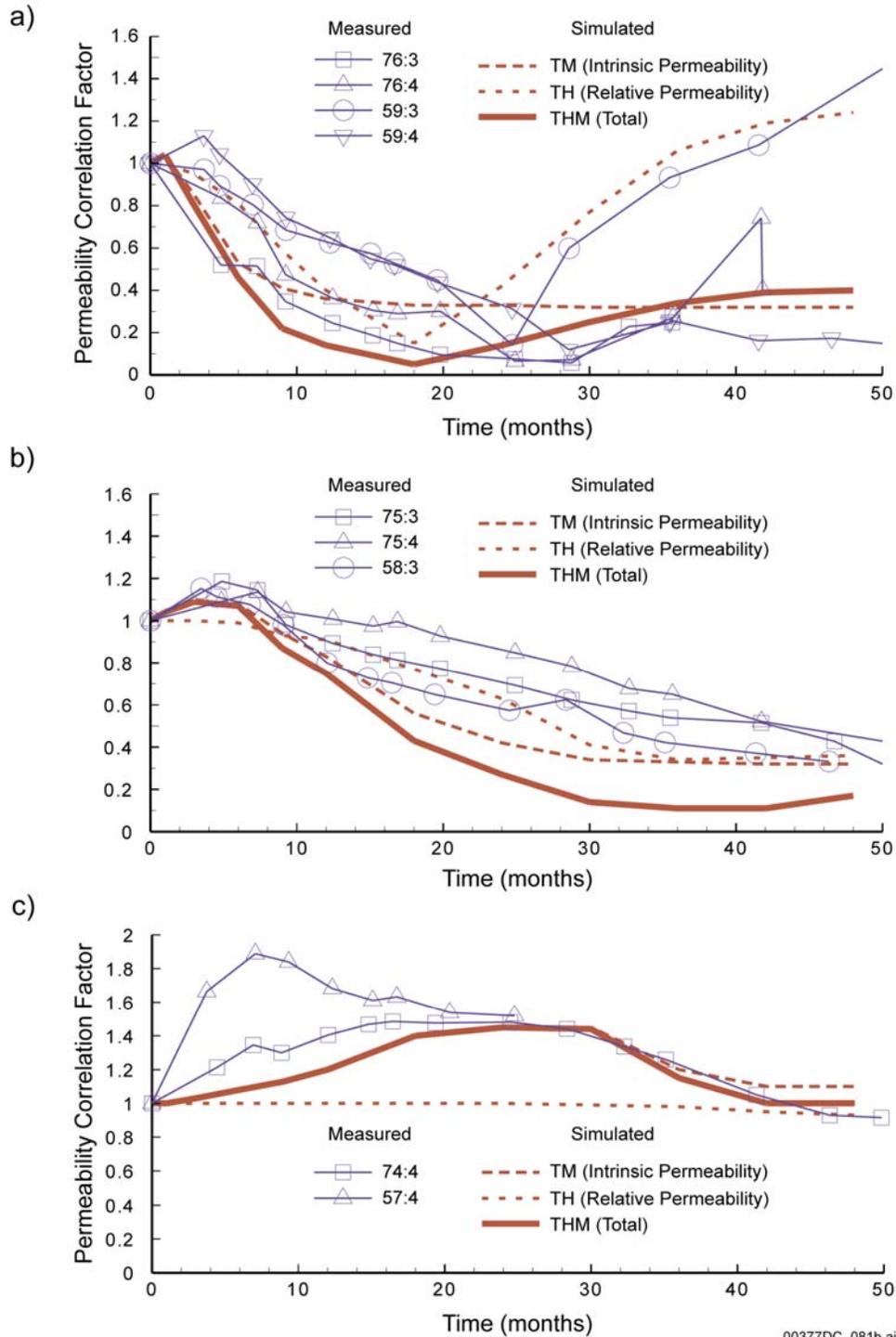
DTN: LB0208AIRKDSTH.001 [DIRS 160897]; LB0306DSTTHMVL.002 [DIRS 166342]

Source: BSC 2003 [DIRS 164890], Figure 7.4.3-3

Figure 5-98. Measured and Simulated Evolution of Permeability Correction Factors ($F_k=k/k_i$) for Three Groups Located at Various Distances above the Heated Drift $b_{max}=150\mu m$, $\alpha=0.6MPa^{-1}$

Table 5-1.   pH, Specific Conductivity and Major Ion Concentrations of Surface Waters in the Yucca Mountain Region

Location	Location on BSC 2002 [DIRS 160247], Figure 7	Sample Collection date	pH	Spec Cond µS/cm	Ca, mg/L	Mg, mg/L	Na, mg/L	K, mg/L	Cl, mg/L	SO$_4$, mg/L	F, mg/L	HCO$_3$, mg/L	SiO$_2$, mg/L	TDS, mg/L
Busted Butte Wash	60	8/14/84	8.3	120	12	1.8	7	8.1	1.7	7.9	0.3	57	23	100
Delerium Canyon @ mouth	55	2/9/93	7.8	118	12	2.4	7.6	-	3.2	7.8	0.3	48	33	-
Drill Hole Wash @ mouth	58	8/14/84	8.3	100	9.5	1.3	8.6	7.4	2.2	12	0.3	51	20	92
Fortymile Wash @ H Rd	59	8/15/84	8.0	170	21	2.9	8.2	9.1	1.4	10	0.2	91	24	122
Fortymile Wash @ J-12	61	8/14/84	8.2	59	6.7	0.7	2.4	6.3	2	6.3	<0.1	32	4.5	45
Fortymile Wash above Drill Hole	57	8/14/84	8.4	70	8.1	0.9	4.1	5.6	1.3	6.2	<0.1	44	8.7	-
Overland near Fortymile Canyon	56	1/24/95	8.1	164	20	2.9	8.4	4.5	2.6	8.5	0.2	72	23	-
Overland near Pah	52	1/6/95	7.8	134	15	2.8	4.9	3.7	3.4	7.8	0.1	34	18	-
Pagany Wash #1 near UZ-4	29	12/7/92	-	218	21	2.1	13	4.6	10	24	0.2	na	14	-
Pah Canyon	52	2/23/93	8.0	140	14	2.6	9.3	-	4.3	10	0.3	54	34	-
Pah Canyon	52	1/26/95	7.9	145	16	2.9	8.2	4.3	4	7.6	0.3	55	30	100
Split Wash below Quac Wash	33	1/25/95	8.2	199	24	3.4	9.3	8.8	3.7	8.7	0.2	88	19	-
Stockade Wash	23	2/10/93	-	122	15	3.1	6.4	4.3	3.1	6.5	<0.1	55	24	90
Unnamed Tributary	22	1/22/93	-	134	14	2.8	10	3.2	5.1	8.4	0.1	54	20	90
Unnamed Tributary	22	3/23/93	-	164	16	3.6	11	5.2	4.3	9	0.2	76	36	123
Wren Wash @ Yucca Mtn	31	1/25/95	8.2	258	28	3.9	16	11	5.8	16	0.2	109	21	-
Yucca Wash near mouth	26	1/18/93	-	133	15	2.3	11	4.1	4.4	6	0.2	55	24	94
Yucca Wash near mouth	26	1/26/95	8.1	117	15	2.1	5.8	4.1	2	4.1	0.2	53	22	-

DTN: MO0312SEPSDCHV.000 [DIRS 166478] (includes data from Emett et al. 1994 [DIRS 105532], p. 550; Perfect et al. 1995 [DIRS 101053], attached file; Savard 1996 [DIRS 101290], p. 28)

NOTES: TDS = total dissolved solids.
- = not analyzed or not calculated.

Table 5-2. pH, Specific Conductivity and Major Ion Concentrations of Unsaturated Zone Pore Waters at Yucca Mountain

Sample Name	Unit	pH	SC µs/ cm	Ca mg/L	Mg mg/L	Na mg/L	K mg/L	Cl mg/L	SO$_4$ mg/L	HCO$_3$ mg/L	F mg/L	NO$_3$ mg/L	SiO$_2$ mg/L	TDS Calc mg/L
ECRB-SYS-CS400/5.6-6.2/UC	Tptpul	7.0	920	85	15.4	89	9.7	21	64	415	1.7	8.5	55	555.3
ECRB-SYS-CS450/5.3-6.0/UC	Tptpul	6.7	1460	190	22.9	68	17.0	66	147	388	1.1	4.8	54	763.3
ECRB-SYS-CS500/12.0-16.7/UC	Tptpul	8.0	520	120	19.3	57	10.3	54	78	286	4.8	6.1	49	540.5
ECRB-SYS-CS600/3.6-4.0/UC	Tptpul	7.5	1000	81	10.6	67	10.4	22	50	346	2	3.3	44	462.5
ECRB-SYS-CS750/6.2-6.5/UC	Tptpul	7.6	900	130	12.9	70	8.5	73	78	191	1.2	<0.2	40	508.9
ECRB-SYS-CS800/4.9-5.6/UC	Tptpul	7.4	840	92	11.9	53	6.6	20	32	357	1.6	0.0	53	447.1
ECRB-SYS-CS850/5.1-5.6/UC	Tptpul	8.1	560	63	13.1	59	5.9	32	30	280	2.9	1.6	46	392.6
ECRB-SYS-CS900/2.8-3.0/UC	Tptpul	NA	NA	142	17.7	90	8.7	25	63	349	0.52	1.2	45	568.8
ECRB-SYS-CS900/3.5-4.1/UC	Tptpul	7.5	1240	210	25.8	140	13.6	53	88	775	2.0	1.9	65	985.6
ECRB-SYS-CS900/5.4-5.9/UC	Tptpul	7.7	770	110	14.0	79	6.9	37	56	216	1.7	1.3	54	468.4
ECRB-SYS-CS950/4.8-5.5/UC	Tptpul	7.1	1030	170	22.6	84	7.1	30	67	286	4.9	11	58	597.7
ECRB-SYS-CS950/5.2-5.3/UC	Tptpul	7.1	670	98	13.6	66	6.2	19	37	239	1.9	0.27	58	419.0
ECRB-SYS-CS1000/10.9-11.1/UC	Tptpul	NA	NA	275	53.5	72	18.7	29	45	700	0.87	4.3	64	910.3
ECRB-SYS-CS1000/11.1-11.6/UC	Tptpul	7.3	1830	280	54.1	79	21.3	18	65	714	0.59	5.6	57	935.7
ECRB-SYS-CS1000/12.9-14.0/UC	Tptpul	7.8	990	120	21.9	47	9.9	22	35	405	2.0	17	50	525.5
ECRB-SYS-CS1000/15.6-15.8/UC	Tptpul	NA	NA	240	44.2	110	24.8	29	82	741	1.3	9.6	61	969.3
ECRB-SYS-CS1000/5.4-6.1/UC	Tptpul	8.0	730	105	21.6	64	13.5	48	41	258	1	5.9	50	478.3
ECRB-SYS-CS1000/7.3-7.7/UC	Tptpul	7.6	570	94	18.1	39	7.6	21	36	333	3.4	2.6	42	428.8
ECRB-SYS-CS1100/3.7-3.8/UC	Tptpmn	7.1	1150	170	23.3	110	9.0	17	55	525	0.65	24	54	725.0
ECRB-SYS-CS1150/3.2-3.8/UC	Tptpmn	NA	NA	96	6.3	130	8.8	33	22	323	1.9	24	70	552.3
ECRB-SYS-CS1250/3.4-4.0/UC	Tptpmn	7.5	930	160	23.5	83	13.7	25	60	464	2.1	1.3	54	652.8
ECRB-SYS-CS1500/10.0-12.1./CU	Tptpll	8.1	770	130	16.4	120	11.1	97	97	349	1.4	0.52	46	692.5
ECRB-SYS-CS2000/16.3-16.5/UC	Tptpll	7.4	740	81	3.3	120	6.1	24	31	362	6.0	0.41	42	493.5
ECRB-SYS-CS2000/16.5-21.1/UC	Tptpll	7.4	810	82	5.3	130	10.6	26	39	382	11	4.2	48	545.7
ECRB-SYS-CS2000/3.3-3.8/UC	Tptpll	NA	NA	170	7.1	204	20.3	38	76	639	3.9	0	64	901.9
ECRB-SYS-CS-2000/3.95-4.1/UC	Tptpll	7.8	1340	88	2.8	116	11.1	20	35	329	7.7	2.0	39	485.2
ECRB-SYS-CS2150/5.5-6.1/UC	Tptpll	7.6	770	98	8.3	83	6.9	27	48	265	5.3	1.2	52	461.4
ECRB-SYS-CS2250/5.2-5.6/UC	Tptpll	8.0	710	87	10.1	74	9.1	24	27	384	1.1	1.3	54	477.5
ECRB-SYS-CS2300/4.3-4.9/UC	Tptpll	7.9	700	73	10.2	98	12.5	23	34	340	1.7	0.9	43	464.6
ECRB-SYS-CS2300/6.1-6.7/UC	Tptpll	8.2	610	65	9.3	96	12.7	20	13	434	1.0	1.4	49	481.9
ESF-NR-MS#10/4.9-5.1/UC	Tpbt3	7.6	510	24	7.0	83	3.0	24	35	169	4	1.1	72	337.1

Table 5-2. pH, Specific Conductivity and Major Ion Concentrations of Unsaturated Zone Pore Waters at Yucca Mountain (Continued)

Sample Name	Unit	pH	SC μs/cm	Ca mg/L	Mg mg/L	Na mg/L	K mg/L	Cl mg/L	SO$_4$ mg/L	HCO$_3$ mg/L	F mg/L	NO$_3$ mg/L	SiO$_2$ mg/L	TDS Calc mg/L
ESF-SAD-GTB#1/119.4-120.0/UC	Tptpmn/ Tptpll	NA	NA	73	12.0	69	19.2	69	46	266	1.5	3.9	51	476.4
ESF-SAD-GTB#1/123.1-123.4/UC	Tptpll	NA	NA	170	23.3	100	22.4	133	66	427	1.2	6.2	54	788.4
ESF-SAD-GTB#1/194.2-195.2/UC	Tptpll	8.0	1740	230	35.5	97	24.7	110	115	545	1.5	1.5	66	952.8
ESF-SAD-GTB#1/195.4-196.7/UC	Tptpll	7.6	1120	190	29.0	81	21.2	97	79	501	1.4	3.7	62	813.4
ESF-SR-MS#22/4.3-4.5/UC	Tpbt2	NA	NA	303	38.2	68	13.8	123	139	147	0.57	10	64	834.5
ESF-SR-MS#22/5.8-6.0/UC	Tpbt2	NA	NA	105	22.9	55	10.8	134	160	156	0.61	13	62	NC
ESF-SR-MS#22/6.0-6.3/UC	Tpbt2	7.5	770	108	23.1	55	9.6	113	140	154	0.85	15	69	610.7
ESF-SR-MS#23/6.3-6.7/UC	Tpbt2	NA	NA	183	41.6	125	23.6	176	191	511	1.3	8.6	55	1059.2
ESF-SR-MS#23/14.5-14.6/UC	Tpbt2	NA	NA	89	19.7	52	9.2	119	111	141	0.86	29	66	NC
ESF-SR-MS#23/14.6-14.9/UC	Tpbt2	7.7	900	90	19.6	47	9.3	109	116	133	0.83	37	62	NC
ESF-THERMALK-017/22.3-22.9/UC	Tptpmn	NA	NA	60	7.8	48	14.1	65	86	95	1.5	41	51	421.5
ESF-THERMALK-017/26.5-26.9/UC	Tptpmn	7.7	690	62	7.9	45	14.4	67	82	126	1.4	44	52	438.1
ESF-THERMALK-019/19.5-19.7/UC	Tptpmn	NA	NA	71	9.1	44	13.2	82	82	124	0.6	50	59	472.4
ESF-THERMALK-017/22.9-23.0/UC	Tptpmn	7.9	710	72	9.9	37	14.5	69	94	116	1.1	46	55	456.1
NRC-7/7A/1504.2-1504.3/UC	Tac	7.5	460	22	<0.8	64	8.6	41	34	104	2.1	27	59	NC
NRG7/7A/1504.3-1504.6/UP-1/BOTTOM	Tac	7.8	440	20	<0.8	53	8.2	35	29	85	2.1	22	57	NC
NRG7/7A/1504.3-1504.6/UP-1/TOP	Tac	7.4	490	21	<0.8	59	9.1	39	33	101	2.5	24	58	295.4
NRG7/7A/1504.3-1504.6/UP-2/BOTTOM	Tac	9.3	370	16	<0.8	47	7.2	26	22	85	1.9	17	63	NC
NRG7/7A/1504.3-1504.6/UP-2/TOP	Tac	8.3	420	16	<0.8	55	8.4	32	26	85	2.7	20	58	NC
NRG-7/7A/839.3-839.8/UC	Tptpmn	7.9	520	19	1.6	67	6.9	31	24	151	2.8	25	41	293.1
SD-9/58.5-58.8/UC	Tpcpv2	6.7	980	150	26.9	47	8.1	233	271	24	0.3	8.9	74	832.2
SD-9/93.3-93.4/UC	Tpbt4	7.3	1580	199	40.5	56	12.7	234	393	56	1.1	17	76	1058.7
SD-9/134.2-134.4/UC	Tpy	7.4	1080	121	21.5	46	8.4	143	213	50	1.5	14	72	666.1
SD-9/252.9-253.0/UC	Tpbt2	7.6	390	33	6.1	36	2.6	27	49	99	0.91	18	81	NC
SD-6/501.3-501.4/UC	Tpbt2	NA	NA	45	9.2	52	1.6	25	57	165	3.6	29	69	NC
SD-6/501.3-501.6/UC	Tpbt2	7.7	610	50	9.9	51	1.5	27	63	167	3.7	34	65	NC
SD-9/669.1-669.2/UC	Tptpul	NA	NA	66	6.9	61	6.3	76	75	136	1.2	29	49	437.9
SD-9/990.4-991.7/UC	Tptpll	7.9	630	56	0.9	84	7.9	23	10	313	2.5	17	50	405.9
SD-9/1184.0-1184.2/UC	Tptpln	7.7	610	44	1.9	92	7.6	44	17	221	1.7	17	45	379.5
SD-9/1184.7-1184.8/UC	Tptpln	8.2	350	19	0.7	59	4.8	23	16	142	2.2	16	42	NC

Table 5-2. pH, Specific Conductivity and Major Ion Concentrations of Unsaturated Zone Pore Waters at Yucca Mountain (Continued)

Sample Name	Unit	pH	SC µs/cm	Ca mg/L	Mg mg/L	Na mg/L	K mg/L	Cl mg/L	SO$_4$ mg/L	HCO$_3$ mg/L	F mg/L	NO$_3$ mg/L	SiO$_2$ mg/L	TDS Calc mg/L
SD-9/1184.8-1185.0/UC	Tptpln	7.9	450	24	<0.4	62	5.4	16	12	196	0.84	12	47	276.0
SD-9/1236.4-1236.8/UC	Tptpln	7.5	700	51	4.9	100	8.4	77	21	210	3.6	12	54	436.0
SD-9/1275.6-1276.0/UC	Tptpln	7.5	590	42	2.5	81	7.7	61	20	146	3.7	8.5	38	336.8
SD-9/1330.4-1330.7/UC	Tptpln	7.2	1010	73	7.5	130	9.5	133	35	245	5	15	55	584.7
SD-9/1452.1-1452.2/UC	Tptpv1	8.1	330	2	<0.4	57	5.4	8.6	9.8	124	2.8	12	77	NC
SD-9/1535.0-1535.1/UC	Tac	8.1	380	1	<0.4	85	5.4	11	22	150	3.8	14	81	NC
SD-9/1661.3-1661.4/UC	Tac	8.1	420	<0.4	<0.4	93	4.5	25	18	162	3.1	9.9	67	300.4
SD-9/1880.35-1880.45/UC	Tcp	8.3	740	7	<0.4	171	9.1	25	35	365	2.7	17	38	NC

DTNs: GS020408312272.003 [DIRS 160899]; GS020808312272.004 [DIRS 166569]; GS030408312272.002 [DIRS 165226]; GS031008312272.008 [DIRS 166570]

NOTES: Porewater data are found in DTNs: GS020408312272.003 [DIRS 160899] and GS031008312272.008 [DIRS 166570]

NA: Not analyzed

NC: Not calculated

TDS calc : Calculated total dissolved solids

See DTNs for trace element data

Table 5-3.   pH, Specific Conductivity and Major Ion Concentrations of Deep Perched Water at Yucca Mountain

| Borehole and Sample Identifier | Average Depth (m) | Date | Temperature (°C) | pH | Specific Conductivity (µS/cm) | Concentration (mg/L) | | | | | | | | | | | Charge Balance[a] |
						Al	Ca	Mg	K	Na	SiO$_2$	HCO$_3$	CO$_3$	Cl	NO$_3$	SO$_4$	
NRG-7A	460.25	03-07-94	-	8.7	224	0.0	3	0	6.8	42	9	114	-	7	1	4	-0.4
SD-9/TS	453.85	07-17-94	27.0	8.6	445	2.1	2.9	0.2	9.8	98	64.2	197	10	5.6	3.3	27.6	7.6
UZ-14 A	384.60	08-02-93	27.1	7.6	312	0.7	23	1.8	5.6	39	34.2	150	0	7.9	8.6	14.3	0.3
UZ-14 A2	384.60	08-02-93	27.1	7.8	308	1.0	24	1.8	3.9	38	36.4	148.8	0	9.1	12.5	13.8	-1.4
UZ-14 B	387.68	08-03-93	23.8	8.1	335	6.1	31	2.7	4.4	40	51.4	147.6	0	8.3	16.9	16.3	5.2
UZ-14 C	390.75	08-05-93	24.2	8.3	518	0.0	45	4.1	5.8	88	7.7	106.1	0	15.5	0	223	-1.9
UZ-14 PT-1	390.75	08-17-93	-	-	-	0.0	37	3.1	6.3	40	21.4	144	0	7.2	12.7	57.3	0.5
UZ-14 PT-2	390.75	08-19-93	-	-	-	0.0	30	2.4	3.3	35	25.7	144	0	7.0	15.4	22.9	0.3
UZ-14 PT-4	390.75	08-27-93	-	-	-	0.0	27	2.1	1.8	34	32.1	141.5	0	6.7	14.5	14.1	0.2
UZ-14 D	390.75	08-31-93	-	7.8	-	0.0	31	2.5	4.1	35	40.7	146.4	0	7.0	17.1	24.2	0.1
SD-7(3/8)	479.76	03-08-95	-	-	-	0.28	14.2	0.13	5.3	45.5	62.3	112	0	4.4	33.8	9.1	2.5
SD-7(3/16)	488.29	03-16-95	21.8	8.1	239	0.44	13.3	0.13	5.3	45.3	57.4	128	0	4.1	33.8	9.1	-2.9
SD-7(3/17)	488.29	03-17-95	22.6	8.2	285	0	12.8	0.08	5.5	45.8	50.9	130	0	4.1	22.8	8.6	-0.3
SD-7(3/20)	488.29	03-20-95	23.3	8.0	265	0	12.9	0.07	5.4	45.5	55	127	0	4.1	13.4	8.5	3.3
SD-7(3/21)	488.29	03-21-95	23.2	8.2	259	0	13.5	0.08	5.5	44.6	55.9	128	0	4.1	13.2	10.3	2.2

DTN: MO0012WTRIONCO.000 [DIRS 153397]

Source: BSC 2002 [DIRS 160247], Table 8, p. I-22

NOTES: [a]Charge balance calculated from data shown using the following formula: (meq cation - meq anion)/(meq cation + meq anion)*100.

- = data not available; 0 = values below detection limit

Table 5-4. Isotopic Composition of Hydrogen, Carbon, Strontium, and Uranium in Perched Water at Yucca Mountain

Borehole and Sample Identity	Depth (m)	Date	$\delta^{13}C$ (‰)	^{14}C (pmc)	^{14}C Age[a] (yr)	^3H (TU)	δD (‰)	$\delta^{18}O$ (‰)	$^{234}U/^{238}U$ Activity Ratio	$\delta^{87}Sr$ (‰)	$^{36}Cl/Cl$ (x 10^{-15})
SD-7	479.76	03-08-95	-10.4	34.4	8,798	6.2	-99.8	-13.4	-	-	511
	488.29	03-16-95	-9.4	28.6	10,321	-	-99.7	-13.3	-	-	-
	488.29	03-17-95	-9.5	28.4	10,379	-	-99.6	-13.4	3.50	-	657
	488.29	03-20-95	-9.5	27.9	10,525	-	-99.6	-13.4	3.58	-	-
	488.29	03-21-95	-9.5	28.4	10,379	-	-99.6	-13.3	3.69	-	609, 635
SD-9	-	03-07-94	-14.4	41.8	7,192	0	-97.8	-13.3	-	-	-
	-	07-07-94	-	-		-	-	-	2.42[b]	-	-
	453.85	07-17-94	-14.4	41.8	7,192	0	-97.8	-13.3	-	-	449
	-	09-12-94	-	-		-	-	-	2.42[b]	5.92	-
UZ-14 A	384.60	08-02-93	-10.2	41.7	7,212	0.3	-98.6	-13.8	-	4.51	559
UZ-14 A2	384.60	08-02-93	-10.1	40.6	7,432	3.1	-97.5	-13.5	-	4.47	538
UZ-14 B	387.68	08-03-93	-9.5	36.6	8,287	0	-97.1	-13.4	-	4.34	566
UZ-14 C	390.75	08-05-93	-9.2	66.8	3,327	0.4	-87.4	-12.1	-	4.37	389
UZ-14 PT-1	390.75	08-17-93	-9.8	32.3	9,318	1.8	-97.8	-13.3	-	3.91-4.30	644
UZ-14 PT-2	390.75	08-19-93	-	28.9	10,235	3.1	-97.9	-13.4	-	3.51-4.19	656
UZ-14 PT-4	390.75	08-27-93	-9.6	27.2	10,735	0	-97.3	-13.4	7.55	4.45-4.49	675
UZ-14 D	390.75	08-31-93	-11.3	29.2	10,150	0	-97.6	-13.1	-	-	690
WT-24	-	10-06-97 10-16-97 10-17-97 10-22-97	- -	- -	- -	- -	- -	- -	4.36[b] 6.58[b] 8.33 8.37	4.08 2.61 3.88 4.00	- - 586
NRG-7a	- 460.25 -	03-04-94 03-07-94 03-08-94	-- 16.6 --	- 66.9 --	- 3,314 --	- 10.4 --	-- 93.9 --	-12.8 -- --	5.17[b] - -	4.94 2.54-2.91 11.68	518 474 -
UZ-1[c]	382	07-07-83 to 07-21-83	-12.1	64.0	3,680	1.0	-102	-13	-	-	999
UZN#91	28.7	03-05-92	-	-	-	-	-	-	-	-	880
UZN#2	15.2	04-09-91 02-22-95									2,012[c] 3,150

DTNs: MO0012CARB1314.001 [DIRS 153394]; MO0007GNDWTRIS.013 [DIRS 151504]; MO0012TRITUNSZ.000 [DIRS 153751]; GS010808312322.004 [DIRS 156007]; GS010608315215.002 [DIRS 156187]; GS980108312322.004 [DIRS 146064]; LAJF831222AQ98.011 [DIRS 145402]; LAJF831222AN98.013 [DIRS 146240]

Sources: BSC 2002 [DIRS 160247], Table 9, pp. I-22 and I-23; Rousseau et al. 1999 [DIRS 102097]

NOTES: [a] Uncorrected carbon-14 age calculated using the radioactive decay equation: $t = (t1/2 / \ln 2) \ln (A/A0)$, where $t1/2$ is the half-life for carbon-14 (5,715 yr), A is the measured carbon-14 activity, and A_0 is the initial carbon-14 activity (100 pmc).

[b] This result is not representative of in situ conditions because of sample contamination.

[c] Data are unqualified because samples were collected prior to the establishment of a formal quality assurance program.

- = not available

Table 5-5.   Summary of Tritium Analyses in Unsaturated Zone Pore Waters at Yucca Mountain

ESF or Borehole Location	Geomorphic Location	Collar Elevation (ft)	TCw and Above		PTn		TSw		CHn Above Tcp		TCp and Below		Total	
			Above 25 TU	Total	Above 25 TU	Total	Above 25 TU	Total	Above 25 TU	Total	Above 25 TU	Total	Above 25 TU	Total
ESF Alcove 2	Bow Ridge fault zone	-	8	9	-	-	-	-	-	-	-	-	8	9
ESF Alcove 3	-	-	-	-	-	3	-	7	-	-	-	-	-	10
ESF Alcove 5	-	-	-	-	-	-	-	7	-	-	-	-	-	7
ESF Alcove 6	Ghost Dance fault zone	-	-	-	-	-	-	7	-	-	-	-	-	7
ESF North Ramp	-	-	-	3	-	-	-	2	-	-	-	-	-	5
ESF Main Drift	-	-	-	-	-	-	-	4	-	-	-	-	-	4
Subtotals, ESF			8	12	-	3	-	27	-	-	-	-	8	42
UZ#16	Terrace, large wash	4,000	1	5	-	3	11	51	2	27	-	13	14	99
NRG-6	Hillslope	4,092	-	-	6	13	-	-	-	-	-	-	6	13
NRG-7A	Hillslope	4,207	-	4	-	9	1	22	-	9	-	-	1	44
UZ-7a	Small wash bottom	4,228	-	-	-	1	-	13	-	-	-	-	-	14
SD-9	Small wash bottom	4,273	-	2	-	15	-	22	-	26	-	3	-	68
SD-12	Small wash bottom	4,343	-	13	-	10	-	27	-	18	1	7	1	75
UZ-1	Large channel (Drill Hole Wash)	4,425	-	1	-	5	1	9	-	-	-	-	1	15
UZ-14	Large channel (Drill Hole Wash)	4,425	-	-	1	35	-	53	-	35	-	14	1	137
SD-7	Ridgetop	4,472	-	10	-	7	-	15	-	18	-	-	-	50
WT-24	Ridgetop	4,900	-	-	-	-	7	10	-	-	5	58	12	68
SD-6	Small wash bottom	4,905	-	6	-	17	3	22	-	11	4	37	7	93
Subtotals, Boreholes			1	41	7	115	23	244	2	144	10	132	43	676
Total, All Samples			9	53	7	118	23	271	2	144	10	132	51	718

DTNs: GS961108312271.002   [DIRS 121708];   MO0012TRITUNSZ.000   [DIRS   153751];   GS991108312272.004   [DIRS 145680];   GS961108312261.006   [DIRS 107293]; GS970108312232.001 [DIRS 109775]; GS970283122410.002 [DIRS 121745]; GS970608312272.005 [DIRS 145609]; GS970908312271.003 [DIRS 111467]

Source: BSC 2002 [DIRS 160247], Table 10, pp. I-24

NOTES: Borehole elevations (DTN: MO9906GPS98410.000 [DIRS 109059]) are listed to provide a rough surrogate for average annual precipitation, which typically increases as a function of elevation (Hevesi et al. 1992 [DIRS 116809], Figure 7, p. 685).

The threshold for indicating the unambiguous presence of bomb-pulse or post-bomb tritium is 25 tritium units, based on the application of Chauvenet's criterion (BSC 2002 [DIRS 160247], Figure 2-30, p. 2-32). This statistical test was applied to the 803 samples, including 75 duplicate analyses but excluding Exploratory Studies Facility data that were reported more than once. Where duplicate analyses exist, the sample results were only tallied once for this table.

Table 5-6. Summary of the Distribution of ^{36}Cl in the Unsaturated Zone at Yucca Mountain

Location	Relevant Sample Sets	Observed Chlorine-Distribution
Soil	Surface soils[a] Surface runoff Soil profiles Alluvial profiles for UZ-N37, UZ-N39, UZ-N54, UZ-N61, UZ-14, UZ#16	In areas with sufficiently thick soil cover, elevated ^{36}Cl is almost completely retained within the uppermost 2 to 3 m of soil. For thinner soils, some fraction of the bomb-pulse signal has moved down into the underlying bedrock. Elevated $^{36}Cl/Cl$ ratios in shallow soils and surface runoff show that residual elevated ^{36}Cl is still present on the surface.
TCw	Bomb-pulse in TCw: UZ-N11, UZ-N15, UZ-N16, UZ-N17, UZ-N27, UZ-N36, UZ-N38, UZ-N53, UZ-N55, UZ-N64; No bomb-pulse in TCw: UZ-N37, UZ-N54, UZ#16 ESF North Ramp ESF South Ramp	Based on borehole data, elevated ^{36}Cl appears to be widely present in the fractured welded TCw unit where it is overlain by thin soil cover (ridgetops and sideslopes) and absent where the soil thickness is at least 3 m. Fracture transport is also indicated by UZ-N53 neutron logging data, which have shown changes in moisture content down to a depth of 12 m, well into the TCw (Flint and Flint 1995 [DIRS 100394], p. 29). The North Ramp data provide evidence of transport of elevated ^{36}Cl through the TCw.
PTn	Bomb-pulse in PTn: UZ-N11, UZ-N53, UZ-N55 ESF North Ramp[b] No bomb-pulse in PTn: most of PTn in UZ-N37, UZ-N53, UZ-N54, UZ#16, UZ-14 ESF North Ramp ESF South Ramp	Evidence for fast transport of water into the PTn is shown by elevated $^{36}Cl/Cl$ ratios from this interval in boreholes with thin soil cover. Elevated ^{36}Cl has also been measured in the PTn unit in several ESF samples from the North Ramp.[b] No unambiguous evidence of elevated ^{36}Cl is seen in the South Ramp despite infiltration rates and soil thicknesses that are similar to those over the North Ramp.
TSw	ESF Main Drift, Alcove #6, ESF Niche#1 Cross Drift UE-25 NRG#4 UE-25 NRG#5 USW NRG-7a Perched water: UZ-14, NRG-7A, SD-7, SD-9	Elevated ^{36}Cl has been observed at several locations in the ESF and Cross Drift in the pre-2000 studies, and appears to be associated with faults.[b] No elevated levels of ^{36}Cl were found by the USGS Validation Study. No unambiguous levels of elevated ^{36}Cl are observed in any of the perched-water bodies at the base of this unit or at the top of the CHn; values for these samples are at or slightly above present-day background. Borehole ^{36}Cl (from ream-bit cuttings) for this unit are usually too diluted by rock chlorine to provide a reliable indication of the presence or lack of elevated ^{36}Cl.
CHn	UZ-14 UZ#16 SD-12	No unambiguous levels of elevated ^{36}Cl have been observed in the CHn in surface-based boreholes. Measured $^{36}Cl/Cl$ ratios are generally at or somewhat above present-day background. The highest ratios have been measured in SD-12, to a maximum value of 843×10^{-15}.
Saturated Zone	C#3, G-2, SD-7, J-13, SD-9, WT-10, WT-12	The $^{36}Cl/Cl$ ratio is uniformly at present-day background in the aquifer underlying the site, independent of location or depth.

DTNs: LA000000000062.002 [DIRS 145613]; LA0307RR831222.001 [DIRS 164091]; LA9909JF831222.005 [DIRS 145630]; LA9909JF831222.010 [DIRS 122733]; LAJF831222AQ95.005 [DIRS 145632]; LAJF831222AQ95.006 [DIRS 145633]; LAJF831222AQ95.007 [DIRS 146246]; LAJF831222AQ96.005 [DIRS 145634]; LAJF831222AQ96.006 [DIRS 145635]; LAJF831222AQ96.008 [DIRS 145638]; LAJF831222AQ96.009 [DIRS 145639]; LAJF831222AQ96.010 [DIRS 145640]; LAJF831222AQ96.011 [DIRS 145642]; LAJF831222AQ96.012 [DIRS 145643]; LAJF831222AQ96.013 [DIRS 145644]; LAJF831222AQ96.014 [DIRS 145645]; LAJF831222AQ96.015 [DIRS 145646]; LAJF831222AQ97.002 [DIRS 145401]; LAJF831222AQ97.006 [DIRS 145647]; LAJF831222AQ97.007 [DIRS 145648]; LAJF831222AQ98.003 [DIRS 146310]; LAJF831222AQ98.004 [DIRS 107364]; LAJF831222AQ98.005 [DIRS 145649]; LAJF831222AQ98.009 [DIRS 145650; LAJF831222AQ98.011 [DIRS 145402]; LA9912JF831222.001 [DIRS 145655]; LAJF831222AN97.012 [DIRS 146238]; LAJF831222AN98.013 [DIRS 146240]; LAJF831222AN97.008 [DIRS 146237]

Source: BSC 2002 [DIRS 160247], Table 13, p. I-28

NOTES: [a] Numerous analyses of ^{36}Cl in surface soil samples from Yucca Mountain confirm the continued presence of the bomb-pulse signal.

[b] Numerous analyses of ^{36}Cl in tunnel construction water confirm that this potential source of contamination cannot be the source of the elevated $^{36}Cl/Chlorine$ used to identify the presence of bomb-pulse.

Table 5-7. ^{36}Cl in Faults and Fault Zones in the Cross Drift

Cross Drift Station (m)	Sampling Criterion	Description of Sampled Feature	^{36}Cl/Cl x 10$^{-15(a)}$		
CS1135.5	Systematic fault transect	Breccia from Sundance fault zone	347	±	16
CS1137	Systematic fault transect	Fractured wallrock adjacent to Sundance fault zone	1,206	±	98
CS1317	Systematic fault transect	Breccia	587	±	42
CS1318	Systematic fault transect	Breccia in fault zone	342	±	29
CS2154	Systematic fault transect	Breccia in fault zone	918	±	49
CS2154.5	Systematic fault transect	Breccia in fault zone	4,890	±	174
CS2238	Other through-going fault	Breccia in fault zone	2,361	±	106
CS2348	Other through-going fault	Fault with 3-m offset	1,052	±	38
CS2530.5	Systematic fault transect	Fractured rock between two faults	1,122	±	45
CS2545	Opportunistic	Highly fractured bedrock within Solitario Canyon fault zone	854	±	43
CS2550	Opportunistic	Fractured rock and gouge within Solitario Canyon fault zone	324	±	24
CS2570	Systematic fault transect	Solitario Canyon fault zone	2,158	±	87
CS2580	Systematic fault transect	Solitario Canyon fault zone	890	±	55
CS2585	Other through-going fault	Brecciated footwall of fault	2,460	±	103
CS2586.5	Other through-going fault	Brecciated hanging wall of fault	1,233	±	41
CS2590	Systematic fault transect	Solitario Canyon fault zone	1,379	±	58
CS2621	Other through-going fault	Solitario Canyon fault zone	974	±	50

DTN: LA0307RR831222.001 [DIRS 164091]

Source: BSC 2002 [DIRS 160247], Table 14, p. I-29

NOTES: [a] Measured ^{36}Cl/Cl ratios have been adjusted to correct for the presence of construction water, as estimated from the measured bromine/chlorine ratio.

Table 5-8. Carbon Dioxide and Carbon Isotope Profiles in Unsaturated Zone Gases from Instrumented Boreholes USW UZ-1 and USW SD-12

Borehole	Depth	Probe or Station	Hydrogeologic and Lithostratigraphic Unit[a]		CO_2 (vol. %)[b]	$\delta^{13}C$ (‰)	^{14}C (pmc)	Uncorrected ^{14}C Age[b] (yr)
USW UZ-1	42 ft	1	Qtac	UO	0.535	-18.9	108.5	Modern
	62 ft	2	PTn	Tpy	0.581	-20.4	104.3	Modern
	93 ft	3	PTn	Tpbt3	0.307	-20.8	96.2	319
	131 ft	4	PTn	Tpp	0.428	-19.9	89.4	924
	201 ft	5	PTn	Tpp	0.230	-20.3	67.2	3,277
	266 ft	6	PTn	Tptrv3	0.205	-17.4	64.7	3,590
	348 ft	7	TSw	Tptrn	0.104	-16.2	63.3	3,770
	421 ft	8	TSw	Tptrn	0.092	-15.7	61.1	4,062
	501 ft	9	TSw	Tptpul	0.082	-16.2	47.4	6,155
	621 ft	10	TSw	Tptpul	0.051	-16.1	42.6	7,036
	747 ft	11	TSw	Tptpmn	0.094	-14.6	47.2	6,190
	871 ft	12	TSw	Tptpll	0.121	-15.7	37.1	8,175
	998 ft	13	TSw	Tptpll	0.042	-16.9	-	-
	1,100 ft	14	TSw	Tptpll	0.091	-15.0	38.8	7,806
	1,207 ft	15	TSw	Tptpll	0.216	-19.7	14.5	15,921
USW SD-12	24.7 m	P	TCw	Tpcpmn/ Tpcpll	-	-22.55	90.98	779
	43.9 m	O	TCw	Tpcplnh	-	-20.20	49.17	5,853
	65.2 m	N	TCw	Tpcplnc	-	-21.99	87.39	1,111
	91.7 m	L	PTn	Tptrv1	-	-16.41	82.71	1,565
	107.0 m	K	TSw	Tptrn	-	-20.98	77.75	2,075
					-	-15.58	94.91	431
	128.9 m	J	TSw	Tptrn	-	-22.11	57.95	4,498
	171.0 m	I	TSw	Tptpul	-	-23.57	38.95	7,774
	208.2 m	H	TSw	Tptpmn	-	-24.71	36.92	8,215
	236.8 m	G	TSw	Tptpmn	-	-25.57	31.57	9,506
	256.6 m	F	TSw	Tptpll	-	-24.40	34.13	8,863
	285.0 m	E	TSw	Tptpll	-	-21.89	52.41	5,327
	322.5 m	D	TSw	Tptpln	-	-21.79	46.65	6,287
					-	-23.83	34.43	8,791
	385.6 m	C	TSw	Tptpln	-	-22.86	88.69	990
	407.2 m	B	CHn	Tptpv2	-	-24.63	24.43	11,620
					-	-23.65	26.89	10,829
	435.9 m	A	CHn	Tac4	-	-17.17	84.47	1,392

DTNs: MO0012CARB1314.000 [DIRS 153398]; MO0012CO2UNSZO.004 [DIRS 153756]

Source: BSC 2002 [DIRS 160247], Table 20, p. I-39

NOTES: [a] Hydrologic and lithographic nomenclature from Tables 3-5 and 8-3. UZ-1 stratigraphy and UZ-1 probe depths from DTN: GS930508312271.021 [DIRS 121639].

[b] Uncorrected ^{14}C age calculated using the radioactive decay equation: $t = (t_{1/2} / \ln 2) \ln (A/A_0)$, where $t_{1/2}$ is the half-life for carbon-14 (5,715 yr), A is the measured ^{14}C activity, and A_0 is the initial ^{14}C activity (100 percent modern carbon).

- = not available

Table 5-9. Comparison of Carbon Isotopes in Pore Water and Gas Samples Collected from Similar Borehole Intervals

Borehole	Pore-Water Results					Gas Results				
	Stratigraphic Unit		Depth (m)	δ13C (‰)	^{14}C (pmc)	Stratigraphic Unit		Depth (m)	δ^{13}C (‰)	^{14}C (pmc)
USW NRG-6	PTn	Tpbt2	71.6	-14.9	92.1	PTn	Tpp	61	-14.1 to -14.9	91.0
USW SD-7	PTn	Tpbt3	103	-18.1	74.1	PTn	Tpp	107	-14.1 to -16.4	91.4
USW SD-9	CHn	Tac3	468	-15.3	88.9	CHn	Tac3	454	-19.1	51.0
	CHn	Tac2	494 to	-14.5	95.3		to	to	to	
	CHn	Tacbt	506	-16.4	82.3		Tcp4	560	-19.8	
			549							
USW SD-12	PTn	Tpbt4	82	-14	80.3	PTn	Tptrv1	92	-16.4	82.7
	CHn	Tac3	462	-17.4	69.9	CHn	Tac4	436	-17.2	84.5
USW UZ-14	CHn	Tac3	436	-11.1	69.9	CHn	Tac3	440	Variable	99.2
	CHn	Tac3	445	-13.4	96.3	CHn	Tac3	454	-19.45	50.4
	CHn	Tac2	465	-11.8	93.4	CHn	Tac2	469	-8.42	48.8
	CHn	Tac2	477	-15.8	76.8	-	-	-	-	-
	CHn	Tac2	477	-15.2	80.0	-	-	-	-	-
	CHn	Tac2	483	-11.3	93.7	CHn	Tac2	485	-9.3	99.2
	CHn	Tac2	490	-14.6	81.1	-	-	-	-	-
	CHn	Tac2	501	-16	86.3	CHn	Tac2	500	-9.24	100.9
	CHn	Tac1	510	-13.7	91.3	CHn	Tac1	515	-20.89	67.8
	CHn	Tacbt	517	-10.3	92.3	CHn	Tacbs	530	-20.05	80.1
	CHn	Tacbt	523	-11.6	96.3	-	-	-	-	-
USW UZ-14 pore water (compared with USW UZ-1 gas from similar depth)	PTn	Tpbt3	26	-17.1	83.2	PTn	Tpbt3	28	-20.8	96.2
	PTn	Tpbt3	29	-15.0	83.3	-	-	-	-	-
	PTn	Tpp	45	-13.0	84.9	PTn	Tpp	40	-19.9	89.4
	PTn	Tpp	67	-25.0	96.2	PTn	Tpp	61	-20.3	67.2

DTNs: MO0012CARB1314.001 [DIRS 153394]; MO0012CARB1314.000 [DIRS 153398]; GS941208312261.008 [DIRS 121653]; GS970283122410.002 [DIRS 121745]; GS970908312271.003 [DIRS 111467]; GS961108312271.002 [DIRS 121708]

Source: BSC 2002 [DIRS 160247], Table 22, p. I-41

NOTE: - = not available.

Table 5-10. Summary of Results for Solubility Experiments on Neptunium in J-13 Groundwater

	Steady-State Concentration (M)		
pH	25°C	60°C	90°C
6.0	$(6.5 \pm 1.1) \times 10^{-4}$	$(9.4 \pm 1.2) \times 10^{-4}$	$(9.1 \pm 1.8) \times 10^{-4}$
7.0	$(3.1 \pm 0.2) \times 10^{-5}$	$(1.6 \pm 0.6) \times 10^{-5}$	$(8.6 \pm 2.3) \times 10^{-6}$
8.5	$(1.5 \pm 0.6) \times 10^{-5}$	$(1.7 \pm 0.9) \times 10^{-5}$	$(5.8 \pm 2.5) \times 10^{-6}$

DTN: LADT831351AQ98.001 [DIRS 166676]

Source: Efurd et al. 1996 [DIRS 105538], Table I

Table 5-11. Summary of Results for Solubility Experiments on Plutonium in J-13 Groundwater

	Steady-State Concentration (M)		
pH	25°C	60°C	90°C
6.0	$(4.7 \pm 1.1) \times 10^{-8}$	$(9.0 \pm 2.0) \times 10^{-6}$	$(4.3 \pm 2.1) \times 10^{-9}$
7.0	$(2.4 \pm 1.2) \times 10^{-8}$	$(8.2 \pm 0.7) \times 10^{-9}$	$(3.6 \pm 1.1) \times 10^{-9}$
8.5	$(9.4 \pm 1.6) \times 10^{-9}$	$(6.2 \pm 1.8) \times 10^{-9}$	$(4.2 \pm 1.1) \times 10^{-9}$

DTN: LADT831351AQ98.001 [DIRS 166676]

Source: Efurd et al. 1996 [DIRS 105538], Table II

Table 5-12. Summary of Results for Solubility Experiments on Americium in J-13 Groundwater (Americium Tracer in Neodymium)

	Steady-State Concentration (M)		
pH	25°C	60°C	90°C
6.0	$(1.8 \pm 0.6) \times 10^{-9}$	$(2.5 \pm 0.7) \times 10^{-9}$	$(1.7 \pm 0.9) \times 10^{-9}$
7.0	$(1.2 \pm 0.3) \times 10^{-9}$	$(9.9 \pm 9.2) \times 10^{-9}$	$(3.1 \pm 1.7) \times 10^{-10}$
8.5	$(2.4 \pm 1.9) \times 10^{-9}$	$(1.2 \pm 1.3) \times 10^{-8}$	$(3.4 \pm 2.1) \times 10^{-10}$

DTN: LA000000000012.002 [DIRS 166677]

Source: Nitsche et al. 1993 [DIRS 155218], Table XXI

Table 5-13. Extractions of Solubility Values for Total System Performance Assessment

Element	Minimum Value (M)	Maximum Value (M)	Expected Value (M)	Coefficient of Variation	Distribution
Americium	10^{-10}	10^{-6}	5×10^{-7}	-	uniform
Plutonium	$3 \times 10^{-9(a)}$	10^{-6}	5.1×10^{-7}	-	uniform
Uranium	10^{-8}	10^{-2}	3.2×10^{-5}	0.20	log beta
Thorium	10^{-10}	10^{-7}	-	-	log uniform
Radium	10^{-9}	10^{-5}	10^{-7}	0.10	log beta
Lead	10^{-8}	10^{-5}	$10^{-6.5}$	0.08	log beta
Neptunium	5×10^{-6}	$10^{-3(a)}$	1.4×10^{-4}	0.20	log beta
Protactinium	10^{-10}	10^{-5}	-	-	log uniform
Actinium	10^{-10}	10^{-6}	-	-	uniform
Tin	10^{-11}	10^{-7}	-	-	uniform
Nickel	10^{-6}	10^{-1}	$10^{-2.7}$	0.25	log beta
Strontium	10^{-6}	10^{-3}	10^{-4}	0.12	log beta
Samarium	10^{-10}	10^{-6}	-	-	uniform
Zirconium	10^{-12}	10^{-7}	-	-	log uniform
Niobium	10^{-9}	10^{-7}	-	-	log uniform

Source: Triay et al. 1997 [DIRS 100422], Table 45

NOTE: Values are from expert elicitations, except where updated by new experimental data from Efurd et al. 1996 [DIRS 105538].

- = no data available

Table 5-14. Plutonium Sorption Distribution Coefficients (Under Atmospheric Conditions)

Solid Phase	K_d Range in UE-25 J-13 Water (mL/g)	K_d Range in Synthetic UE-25 p#1 Water (mL/g)
Vitric tuff	600-2,000	100-400
Zeolitic tuff	300-500	100-400
Devitrified tuff	40-100	20-70
Synthetic hematite	> 10,000	> 10,000
Montmorillonite	> 10,000	> 10,000
Clinoptilolite	600-3,000	2,000-5,000
Calcite	200-1,000	100-800
Gibbsite	0-10	10-90
Albite	3-10	< 10
Quartz	< 10	< 10

DTN: LA0010JC831341.006 [DIRS 153318]

Source: BSC 2001 [DIRS 160828], Table 4

Table 5-15. Neptunium Sorption onto Clinoptilolite-Rich Tuffs in J-13 Water

Tuff Sample	Measured K_a (m)	Predicted K_a (m)	Clinoptilolite %
G1-1405	1×10^{-7}	1×10^{-7}	68 ± 7
G4-1505	9×10^{-8}	1×10^{-7}	74 ± 7
G4-1506	1×10^{-7}	1×10^{-7}	62 ± 7
G4-1510	8×10^{-8}	1×10^{-7}	59 ± 7
G4-1529	7×10^{-8}	1×10^{-7}	59 ± 8
G4-1625	9×10^{-8}	1×10^{-7}	61 ± 7
G4-1772	1×10^{-7}	1×10^{-7}	63 ± 5
G4-2077	5×10^{-8}	8×10^{-8}	51 ± 8

DTN: LA0012AM831341.002 [DIRS 163042]

Source: BSC 2001 [DIRS 160828], Table 6, p. 60

NOTE: Atmospheric conditions; initial neptunium concentrations ranged from 6 to 8 x 10^{-7} M; tuffs were wet-sieved to particle sizes ranging from 75 to 500 mm; the pretreatment period was 2 to 14 days; and the sorption period was 3 to 23 days.

Table 5-16. Uranium Sorption in J-13 Water under Oxidizing Conditions

Solid Phase	pH	K_d (mL/g)[a, b]
G4-268, devitrified tuff	7	2×10^{-1}
	8.5	7×10^{-1}
GU3-1405, vitric tuff	7	-5×10^{-1}
	8.5	6×10^{-1}
Quartz	7	1×10^{-1}
	8.5	7×10^{-2}
Albite	7	-5×10^{-2}
	8.5	-1×10^{-1}

DTN: LA0101AM831341.001 [DIRS 163043]

Source: BSC 2001 [DIRS 160828], Table 7, p. 72

NOTE: [a] The uncertainties in the data are ± 3 mL/g.

[b] Negative values are the results of analytical error for the case of very little sorption (i.e., a small) number obtained as the difference of two large numbers).

Table 5-17. Prediction of Uranium Sorption on Clinoptilolite-Rich G4-1510 Tuff in J-13 Water

Initial Concentration (M)	pH	Measured K_a (m)	Predicted K_a (m)[a]
2×10^{-7} to 4×10^{-7}	7	8×10^{-7}	8×10^{-7}
	8.5	8×10^{-7}	4×10^{-7}

DTNs: LA0101AM831341.001 [DIRS 163043]; LA0012AM831341.002 [DIRS 163042]

Source: BSC 2001 [DIRS 160828], Table 8, p. 73

NOTE: [a] prediction assumes clinoptilolite is the only sorbing mineral in the tuff.

Table 5-18. Minerals in Yucca Mountain Tuff with High Caution Exchange Capacities

Mineral	Maximum Abundance	Capacity (meq/g)
Clinoptilolite	90%	2.3
Mordenite	60%	2.3
Montmorillonite	40%	0.8-1.5
Illite	20%	0.13-0.42

Source: Triay et al. 1997 [DIRS 100422], Table 20, p. 126

NOTE: CPM = counts per minute.

Table 5-19. Additional Equations and Parameters Used to Model Uranium Sorption onto Devitrified Tuff

Type of Reaction	Equilibrium Reaction	log K
Aqueous reactions	$UO_2^{2+} + H_2O \leftrightarrow UO_2OH^+ + H^+$	-5.8
	$UO_2^{2+} + 2H_2O \leftrightarrow UO_2(OH)_2 + 2H^+$	-12.5
	$2UO_2^{2+} + 2H_2O \leftrightarrow (UO_2)_2(OH)_2^{2+} + 2H^+$	-5.62
	$3UO_2^{2+} + 5H_2O \leftrightarrow (UO_2)_3(OH)_5^+ + 5H^+$	-15.63
Uranyl adsorption reactions	$2t\text{-}Al^-Na^+ + UO_2^{2+} \leftrightarrow (t\text{-}Al^-)_2UO_2^{2+} + 2Na^+$	1.8
	$t\text{-}Al^-Na^+ + UO_2^{2+} + H_2O \leftrightarrow t\text{-}Al^-UO_2OH^+ + Na^+ + H^+$	-1.5
	$MOH + UO_2^{2+} \leftrightarrow MOUO_2^+ + H^+$	0.60
	$MOH + UO_2^{2+} + Cl^- \leftrightarrow MOUO_2^+Cl^- + H^+$	2.8
	$2MOH + UO_2^{2+} \leftrightarrow (MO)_2UO_2 + 2H^+$	-2.8
Parameters	**Type of site**	**Site density (eq/kg)**
	Tetrahedral(t) aluminum	2×10^{-2}
	Octahedral aluminum (edge)	2×10^{-3}

Source: Triay et al. 1997 [DIRS 100422], Table 24, p. 133

Table 5-20. Summary of K_ds for the Unsaturated Zone, Based on Laboratory Data and Surface Complexation Modeling

Element	Unit/lithology	Parameter Value Range (ml/g)	Distribution type
U	Zeolitic	0 - 30	Cumulative
	Devitrified	0 - 4	Cumulative
	Alluvium	0 - 3	Cumulative
Np	Zeolitic	0 - 6	Cumulative
	Devitrified	0 - 6	Cumulative
	Alluvium	0 - 3	Cumulative
Pu	Zeolitic	10 - 200	Cumulative
	Devitrified	10 - 200	Cumulative
	Alluvium	10 - 200	Cumulative
Cs	Zeolitic	425 - 20,000	Cumulative
	Devitrified	1 - 15	Uniform
	Alluvium	0 - 100	Cumulative
Am	Zeolitic	100 - 1000	Uniform
	Devitrified	100 - 2000	Uniform
	Alluvium	100 - 1000	Cumulative
Pa	Zeolitic	1,000 - 20,000	Uniform
	Devitrified	1,000 - 20,000	Uniform
	Alluvium	1,000 - 20,000	Uniform
Sr	Zeolitic	50 - 2000	Uniform
	Devitrified	10 - 70	Uniform
	Alluvium	0 - 50	Uniform
Th	Zeolitic	1,000 - 30,000	Uniform
	Devitrified	1,000 - 10,000	Uniform
	Alluvium	1,000 - 10,000	Uniform
Ra	Zeolitic	1,000 - 5,000	Uniform
	Devitrified	100 - 1000	Uniform
	Alluvium	50 - 600	Uniform
C/Tc/I	Volcanics/Alluvium	0	Constant

DTN: LA0302AM831341.002 [DIRS 162575]

Source: BSC 2003 [DIRS 163228], Attachment I

NOTE: Development of the K_d distributions can be found in BSC 2003 [DIRS 163228].

Table 5-21. Summary of K_ds for Saturated Zone Lithologies, Developed on the Basis of Laboratory Data and Surface Complexation Modeling

Element	Unit/lithology	Parameter Value Range (ml/g)	Distribution type
U	Zeolitic	5 - 20	Normal
	Devitrified	0 - 4	Normal
	Alluvium	1.7 - 8.9	Cumulative
Np	Zeolitic	0 - 6	Normal
	Devitrified	0 - 2	Exponential
	Alluvium	1.8 - 13	Cumulative
Pu	Zeolitic	50 - 300	Beta
	Devitrified	50 - 300	Beta
	Alluvium	50 - 300	Beta
Cs	Zeolitic	4,000 - 42,000	Exponential
	Devitrified	100 - 1000	Normal
	Alluvium	100 - 1000	Normal
Am	Zeolitic	1000 - 10,000	Truncated normal
	Devitrified	1000 - 10,000	Truncated normal
	Alluvium	1000 - 10,000	Truncated normal
Pa	Zeolitic	1,000 -10,000	Truncated normal
	Devitrified	1,000 -10,000	Truncated normal
	Alluvium	1,000 -10,000	Truncated normal
Sr	Zeolitic	100 - 90,000	Cumulative
	Devitrified	20 - 400	Uniform
	Alluvium	20 - 400	Uniform
Th	Zeolitic	1,000 - 10,000	Truncated normal
	Devitrified	1,000 - 10,000	Truncated normal
	Alluvium	1,000 - 10,000	Truncated normal
Ra	Zeolitic	1,000 - 250,000	Truncated log-normal
	Devitrified	100 - 1,000	Normal
	Alluvium	100 - 1,000	Normal
C/Tc/I	Volcanics/Alluvium	0	Constant

DTN: LA0310AM831341.002 [DIRS 165891]

Source: BSC 2003 [DIRS 167208], Attachment I

NOTE: Development of the K_d distributions can be found in BSC 2003 [DIRS 166220].

Table 5-22. Summary of Composite K_ds for the Saturated Zone, Based on Laboratory Data and Large-Scale Stochastic Modeling

Element	Unit/lithology	Parameter Value Range (ml/g)	Distribution type
U	Composite (volcanics)	0 - 20	Cumulative
	Alluvium	1.7 - 8.9	Cumulative
Np	Composite (volcanics)	0 - 6	Cumulative
	Alluvium	1.8 - 13	Cumulative
Pu	Composite (volcanics)	10 - 300	Cumulative
	Alluvium (devitrified)	50 - 300	Beta
Cs	Composite (volcanics)	100 - 6,783	Cumulative
	Alluvium (devitrified)	100 - 1,000	Truncated normal
Am/Th/Pa	Volcanics and Alluvium	1,000 - 10,000	Truncated normal
Sr	Volcanics and Alluvium	20 - 400	Uniform
Ra	Volcanics and Alluvium	100 - 1000	Uniform
C/Tc/I	Volcanics and Alluvium	0	Constant

DTN: LA0310AM831341.002 [DIRS 165891]

Source: BSC 2003 [DIRS 166220], Attachment III

NOTE: Development of the K_d distributions can be found in BSC 2003 [DIRS 166220].

Table 5-23. Depth Intervals and Bulk Densities of Alluvium Samples

Borehole-02D		Borehole-09Sx		Borehole-03S	
Depth (ft)	Density (g/cm^3)	Depth (ft)	Density (g/cm^3)	Depth (ft)	Density (g/cm^3)
395-400	1.3	145-150	1.3	60-65	1.3
400-405	1.2	150-155	1.3	65-70	1.2
405-410	1.3	155-160	1.3	70-75	1.3
410-415	1.3	160-165	1.2	75-80	1.2

DTN: LA0002JC831341.001 [DIRS 147081]

Source: BSC 2001 [DIRS 160828], Table 9

Table 5-24.   Quantitative X-Ray Diffraction Results of Three Alluviums

Minerals	Samples		
	NC-EWDP-2D 410-415 ft, 75-500 mm	**NC-EWDP-3S 75-80 ft, 75-500 mm**	**NC-EWDP-9Sx 160-165 ft, 75-500 mm**
Smectite	2 ± 1	1 ± 1	6 ± 2
Kaolinite	1 ± 1	1 ± 1	-
Clinoptilolite	4 ± 1	13 ± 1	3 ± 1
Tridymite	3 ± 1	-	1 ± 1
Cristobalite	16 ± 1	10 ± 1	18 ± 1
Quartz	18 ± 1	17 ± 1	14 ± 1
Feldspar	54 ± 8	53 ± 8	58 ± 8
Calcite	-	4 ± 1	-
Mica	Trace	1 ± 1	Trace
Hematite	1 ± 1	-	Trace
Hornblende	Trace	Trace	-
Unidentified Phases	Trace	-	-
Total	99 ± 8	100 ± 8	100 ± 8

DTN: LA0002JC831341.002 [DIRS 147083]

Source: BSC 2001 [DIRS 160828], Table 10

NOTE: - = no data available

Table 5-25. Comparison of Neptunium K_d Values from Batch and Column Measurements

Column Number	Tuff Sample	Water Type	Batch K_d (mL/g)	Column K_d (mL/g)
1	G4-1508, zeolitic	J-13	1.7 ± 0.4 (G4-1510)	1.7
2	G4-1508, zeolitic	J-13	1.7 ± 0.4 (G4-1510)	1.2
3	G4-1505, zeolitic	J-13	2.1 ± 0.4	2.8
4	G4-1505, zeolitic	Syn. UE-25 p#1	0.2 ± 0.3 (G4-1506)	0.4
5	G4-1505, zeolitic	Syn. UE-25 p#1	0.2 ± 0.3 (G4-1506)	0.2
6	G4-1505, zeolitic	Syn. UE-25 p#1	0.2 ± 0.3 (G4-1506)	0.2
7	G4-268, devitrified	J-13	-0.04 ± 0.2	0.07
8	G4-268, devitrified	J-13	-0.04 ± 0.2	0.01
9	G4-268, devitrified	J-13	-0.04 ± 0.2	0.02
10	G4-268, devitrified	J-13	-0.04 ± 0.2	0.01
11	G4-272, devitrified	Syn. UE-25 p#1	0.2 ± 0.3 (G4-270)	0.06
12	G4-268, devitrified	Syn. UE-25 p#1	0.2 ± 0.3 (G4-270)	0.03
13	G4-268, devitrified	Syn. UE-25 p#1	0.2 ± 0.3 (G4-270)	0.03
14	GU3-1407, vitric	J-13	0.1 ± 0.5	0.2
15	GU3-1407, vitric	J-13	0.1 ± 0.5	0.1
16	GU3-1405, vitric	J-13	0.03 ± 0.2	0.1
17	GU3-1405, vitric	Syn. UE-25 p#1	0.2 ± 0.4 (GU3-1407)	0.1
18	GU3-1405, vitric	Syn. UE-25 p#1	0.2 ± 0.4 (GU3-1407)	0.1
19	GU3-1405, vitric	Syn. UE-25 p#1	0.2 ± 0.4 (GU3-1407)	0.1

DTNs: LA000000000106.001 [DIRS 138456]; LA0010JC831341.007 [DIRS 153319]

Source: BSC 2001 [DIRS 160828], Table 11, p. 98

Table 5-26. Selenium Batch Adsorption on Nonwelded Zeolitic Tuff

Pretreatment Period (days)	Sorption Period (days)	K_d (mL/g)
6.9	0.04	-0.2
6.9	0.04	0.3
6.8	13.9	0.0
6.8	13.9	0.2

DTN: LA0006JC831341.008 [DIRS 168530]

Source: BSC 2001 [DIRS 160828], Table 12, p. 108

NOTE: Experimental conditions: J-13 water; 20°C; 75 to 500 millimeter tuff particle sizes; 1.1 parts per million initial selenium concentration; solution pH after sorption of 8.4; and samples from the same location in G-Tunnel, Bed-5, as the tuff used in the column experiments.

Table 5-27. Minerals Coating Fracture Walls in Yucca Mountain Tuffs

Zeolites	
Heulandite↔Clinoptilolite	$Ca_4Al_8Si_{28}O_{72} \cdot 24H_2O \leftrightarrow (Na, K)_6Al_6Si_{30}O_{72} \cdot 24H_2O$
(range of compositions with arbitrary division of Si/Al < 4.4 for heulandite and Si/Al > 4.4 for clinoptilolite)	
Mordenite	$(Ca,Na_2,K_2)4Al_8Si_{40}O_{96} \cdot 28H_2O$
Analcime	$NaAlSi_2O_6 \cdot H_2O$
Chabazite	$CaAl_2Si_4O_{12} \cdot 6H_2O$
Phillipsite	$(K_2,Na_2,Ca)Al_2Si_4O_{12} \cdot 4\text{-}5H_2O$
Erionite	$(Ca,Na_2,K_2)_4Al_8Si_{28}O_{72} \cdot 27H_2O$
Stellerite	$CaAl_2Si_7O_{18} \cdot 7H_2O$

Silica	
Quartz	SiO_2—low-temperature polymorph of silica
Tridymite	SiO_2—high-temperature polymorph of silica
Cristobalite	SiO_2—highest-temperature polymorph of silica
Opal	$SiO_2 \cdot nH_2O$
Feldspars	
Plagioclase (albite)	Solid solutions of albite ($NaAlSi_3O_8$) and anorthite ($CaAl_2Si_2O_8$)
K-feldspar (sanidine)	Solid solutions of orthoclase ($KAlSi_3O_8$) and albite ($NaAlSi_3O_8$)

Clays	
Smectite family:	
Dioctahedral (montmorillonite)	$(Na,K,Mg_{0.5},Ca_{0.5}, \text{possibly others})_{0.33}Al_{1.67}Mg_{0.33}Si_4O_{10}(OH)_2 \cdot nH_2O$
Trioctahedral (saponite)	$(Ca_{0.5},Na)_{0.33}(Mg,Fe)_3(Si_{3.67}Al_{0.33})O_{10}(OH)_2 \cdot 4H_2O$
Sepiolite	$Mg_4(Si_2O_5)_3(OH)_2 \cdot 6H_2O$
Palygorskite	$(Mg,Al)_2Si_4O_{10}(OH) \cdot 4H_2O$
Illite	$(H_3O,K)_y(Al,Fe,Mg_{1\text{-}1.5})_4(Si_{8\text{-}y}Al_y)O_{20}(OH)_4 \cdot 2H_2O$

Manganese Oxides/Hydroxides		
Pyrolusite	MnO_2	(1x1 tunnel structure)
Cryptomelane family:	$A_{0\text{-}2}(Mn^{4+},Mn^{3+})_8(O,OH)_{16}$	(2x2 tunnel structure)
Cryptomelane	A = K	
Hollandite	A = Ba	
Coronadite	A = Pb	
Romanechite	$(Ba,H_2O)_2Mn_5O_{10}$	
Todorokite	$(Na,Ca,Ba,Sr)_{0.3\text{-}0.7}(Mn,Mg,Al)_6O_{12} \cdot 3.2\text{-}4.5H_2O$	(2x3 tunnel structure)
Aurorite	$(Mn^{2+},Ag,Ca)Mn_3O_7 \cdot 3H_2O$	(3x3 tunnel structure)
Lithiophorite	$m\{Al_{0.5}Li_{0.5}MnO_2(OH)_2\} \cdot n\{Al_{0.667}(Mn^{4+},Co,Ni,Mn^{2+})O_2(OH)_2\} \cdot pH_2O$	
Rancieite	$(Ca,Mn^{2+})(Mn^{4+})_4O_9 \cdot 3H_2O$	

Iron Oxides/Hydroxides	
Hematite	Fe_2O_3
Magnetite	$(Fe,Mg)Fe_2O_4$

Carbonates	
Calcite	$CaCO_3$
Halides	
Fluorite	CaF_2

Source: BSC 2001 [DIRS 160828], Table 13

Table 5-28. Characteristics of Fractured Devitrified-Tuff Columns

Characteristics	Column 1	Column 2	Column 3	Column 4
Sample Identifier	G1-1941	UE-25 UZ-16 919	G4-2981	G4-2954
SMF Barcode Number	N/A	0029365	0029366	0029368
Major Minerals in Tuff Matrix	Alkali Feldspar and Quartz	Alkali Feldspar and Quartz	Alkali Feldspar and Opal CT	Alkali Feldspar and Opal CT
Minerals Coating the Fracture	None (apparent	Stellerite	Hollandite	Hollandite
	Induced fracture)	Magnetite	Romanechite	Romanechite
Water Type	Synthetic J-13	Synthetic p#1	Synthetic J-13	Synthetic J-13
pH	8.6	8.8	8.6	8.6
Concentration of ^{237}Np (M)	1.4×10^{-5}	4.8×10^{-6}	1.4×10^{-5}	1.4×10^{-5}
Length (cm)	12.6	6.1	6.0	Not determined
Diameter (cm)	6.1	5.2	5.2	Not determined
Volumetric Flow Rate (mL/hr.)	0.5	0.5	0.5	0.5

DTN: LAIT831361AQ95.003 [DIRS 107090]

Source: BSC 2001 [DIRS 160828], Table 14

NOTE: SMF = Sample Management Facility.

Table 5-29. Batch-Sorption Results for ^{237}Np in J-13 Well Water

Major Mineral in Solid Phase	K_d (mL/g)	Solid-Phase Composition[a]
Stellerite	~ 0	N/A
Hollandite	700	100% Hollandite
Romanechite	600	N/A
Magnetite	7	85% Magnetite
		12% Hematite
		3% Goethite

DTN: LAIT831361AQ95.003 [DIRS 107090]

Source: BSC 2001 [DIRS 160828], Table 15

NOTE: [a] Determined by x-ray-diffraction analysis.

Table 5-30. Rock-Beaker Diffusion Results for Nonsorbing Radioisotopes and Devitrified Tuffs

Tuff Sample	Major Minerals	Porosity	Diffusion Coefficient, d (cm^2/s)	
			HTO	TcO4-
G4-737	Alkali feldspar 68% Cristobalite 28%	0.07	2.2×10^{-6}	3.9×10^{-7}
GU3-304 #1	Alkali feldspar 75% Cristobalite 25%	0.06	1.5×10^{-6}	3.0×10^{-7}
GU3-304 #2			1.6×10^{-6}	3.0×10^{-7}
GU3-433	Alkali feldspar 76% Cristobalite 15%	0.10	3.5×10^{-6}	
GU3-1119	Alkali feldspar 70% Quartz 19%	0.10	2.0×10^{-6}	4.9×10^{-7}
Topopah outcrop	Alkali feldspar 59% Cristobalite 23% Quartz 12%	0.07	1.0×10^{-6}	1.0×10^{-7}

DTN: LA000000000034.002 [DIRS 148603]

Source: BSC 2001 [DIRS 160828], Table 16, p. 120

Table 5-31. Percentage of ^{239}Pu Adsorbed onto Hematite Colloids in Natural Groundwater and Synthetic Groundwater

Time (min.)e	Fe2O3 J-13 Pu (V)%	Fe2O3 J-13 Pu (IV)%	Fe2O3 Syn. J-13 Pu (V)%	Fe2O3 Syn. J-13 Pu (IV)%
10	43.5	56.9	81.8	65.9
30	45.2	58.8	84.2	66.0
60	45.1	59.7	83.3	65.6
240	54.7	59.7	87.2	65.5
360	59.0	59.7	86.9	65.8
1,440	70.4	59.7	86.7	65.5
2,880	73.5	59.8	87.1	65.8
5,760	76.4	60.3	86.9	65.8

Source: CRWMS M&O 1997 [DIRS 100401], Chapter VIID, Table 2, p. VIID-6

NOTE: Data in table are corroborating data only.

Table 5-32. Percentage of [239]Pu Adsorbed onto Goethite Colloids in Natural Groundwater and Synthetic Groundwater

Time(min.)	FeOOH J-13 Pu (V)%	FeOOH J-13 Pu (IV)%	FeOOH Syn. J-13 Pu (V)%	FeOOH Syn. J-13 Pu (IV)%
10	19.2	28.5	63.3	34.2
30	20.5	31.0	63.0	36.9
60	23.5	45.1	63.8	48.0
240	35.6	40.3	68.4	48.0
360	40.5	38.9	70.0	52.6
1,440	53.2	37.2	74.2	52.2
2,880	58.6	39.2	74.8	49.4
5,760	61.8	34.4	74.1	52.8

Source: CRWMS M&O 1997 [DIRS 100401], Chapter VIID, Table 3, p. VIID-9

NOTE: Data in table are corroborating data only.

Table 5-33. Initial Forward (Sorption) Rate (k_f) of [239]Pu onto Colloids of Hematite, Goethite, Montmorillonite, and Silica

Minerals	k_f for Pu (V) (pCi/mg colloid/min.)		k_f for Pu (IV) (pCi/mg colloid/min.)	
	J-13	Syn. J-13	J-13	Syn. J-13
Hematite	7.28 ± 0.36	12.55 ± 1.59	12.69 ± 0.03	16.17 ± 0.09
Goethite	7.74 ± 1.64	13.43 ± 0.47	8.66 ± 1.19	11.88 ± 1.96
Montmorillonite	8.30 ± 0.03	10.11 ± 0.09	8.51 ± 0.04	18.06 ± 0.17
Silica-PST-1	0.55 ± 0.02	0.49 ± 0.04	1.74 ± 0.07	2.17 ± 0.05
Silica-ST-ZL	0.58 ± 0.005	0.59 ± 0.02	1.96 ± 0.00	2.19 ± 0.07

DTNs: LA0004NL831352.001 [DIRS 150272], LA0003NL831352.001 [DIRS 149172], LA0004NL831352.003 [DIRS 150273].

NOTES: k_f values for hematite, goethite, and smectite were calculated from the data collected from the first 10 minutes. After 10 minutes, additional small amounts of plutonium were adsorbed during the remaining 95.8 hour. The k_f values for silica were calculated from the data collected from the first hour (there was no 10-minute and 30-minute sorption for silica). After 1 hour, the amounts of plutonium sorbed by silica colloids increased with time. Therefore, k_f values reported here are the minimum values.

Table 5-34. Initial Backward (Desorption) Rate (k_b) for ^{239}Pu from Colloids, Hematite, Goethite, Montmorillonite, and Silica

Minerals	k_b for Pu (V) (pCi/mg colloid/min)		k_b for Pu (IV(pCi/mg colloid/min)	
	J-13	Syn. J-13	J-13	Syn. J-13
Hematite	9.7×10^{-7} ± (5.8×10^{-7})	6.9×10^{-8} ± (0.0)	-8.7×10^{-8} ± (1.3×10^{-8})	0.0000
Goethite	3.8×10^{-5} ± (3.1×10^{-7})	1.8×10^{-5} ± (1.5×10^{-6})	1.9×10^{-5} ± (1.0×10^{-6})	3.5×10^{-5} ± (1.2×10^{-6})
Smectite	2.1×10^{-5} ± (2.9×10^{-6})	1.9×10^{-5} ± (6.2×10^{-6})	9.0×10^{-4} ± (8.3×10^{-5})	8.7×10^{-5} ± (9.3×10^{-6})
Silica-PST-1	9.6×10^{-4} ± (2.3×10^{-4})	3.5×10^{-4} ± (6.3×10^{-5})	2.0×10^{-3} ± (1.4×10^{-4})	2.2×10^{-3} ± (1.3×10^{-3})
Silica-ST-ZL	2.7×10^{-4} ± (1.2×10^{-5})	5.1×10^{-4} ± (4.0×10^{-5})	4.2×10^{-3} ± (7.2×10^{-4})	3.6×10^{-3} ± (4.0×10^{-4})

DTNs: LA0004NL831352.001 [DIRS 150272], LA0003NL831352.001 [DIRS 149172], LA0004NL831352.003 [DIRS 150273].

NOTES: k_b values were calculated using the data collected from the first two days' desorption process. After two days, additional small amounts of plutonium were desorbed from colloids during the remaining 266 days. Therefore, k_b values reported here are the highest values.

INTENTIONALLY LEFT BLANK

Yucca Mountain Site Description

Volume II: Sections 6 – 8

6. CLIMATE: PAST, PRESENT, AND FUTURE

Climatology and meteorology studies in the Yucca Mountain area have resulted in the following key observations and conclusions:

- The present-day arid climate of the Yucca Mountain area can be understood in terms of global-scale atmospheric circulation and regional-to-local physiographic features. In general terms, the area is under the influence of mid-latitude westerly winds and associated storm systems during the cool part of the year, and is under the influence of moist air advected from the eastern tropical Pacific Ocean and Gulf of California during the summer. Temperature and precipitation data from Nevada regions 3 and 4 (southern Nevada) between 1895 and 1998 suggest a mean annual temperature of 13.4°C and a mean annual precipitation of 125 mm at 1,524 m (5,000 ft) elevation (Thompson et al. 1999 [DIRS 109470], Figures 13 and 14, pp. 27 and 28).

- Climate change over the past several hundred thousand years can be partially understood in terms of changes in these atmospheric circulation patterns, physiographic features, and predictable variations in the earth's orbital characteristics.

- Past climate change can be timed using the earth's orbital parameters: eccentricity and precession. This implies that some past climate or aspects of past climate will recur in the future because future eccentricity and precession can be calculated.

- Regional and local evidence indicates that the Yucca Mountain site has experienced, over the past several hundred thousand years, many different climate states ranging from glacial to interglacial periods. Glacial and intermediate climate periods were periods of sustained greater effective moisture, commonly defined as precipitation minus evaporation. Greater effective moisture does not necessarily signify increased precipitation. Low temperatures can play a critical role in determining effective moisture; hence, greater effective moisture can occur under conditions of very low temperatures and low precipitation. Greater infiltration and recharge occurred during periods of greater effective moisture, the glacial and intermediate climate periods, than during interglacial (i.e., modern) periods. Although Yucca Mountain experienced glacial climates, it did not experience glaciation.

- For the purposes of this report, long-term past climate proxy data were simplified into four climate states (i.e., interglacial, monsoon, intermediate, glacial), each with a different level of effective moisture. Climate states typical of the past 500,000 years (yr) are thought likely to recur in the next 500,000 yr. These climate states, their duration, and magnitude are based on the assumptions and methods used and discussed herein.

- Six glacial stages are forecast to occur over the next 500,000 yr. They may range between 8,000 and 38,000 yr in duration and encompass about 19 percent (95,000 yr) of the next 500,000 yr. These glacial stages will vary in magnitude, ranging from relatively warm and wet to cold and dry.

- Future glacial period upper bound (most conservative) estimates for mean annual temperature and mean annual precipitation in the Yucca Mountain area are 0°C and 513 mm, respectively. Glacial period lower bound estimates for mean annual temperature and mean annual precipitation in the Yucca Mountain area are approximately 9°C and 430 mm/yr, respectively. Published estimates of past temperature and precipitation for the Yucca Mountain area and western Great Basin during glacial periods range from 4 to 15°C colder than today and precipitation from 1.4 to 3 times modern.

- The intermediate and intermediate/monsoon climate states are estimated to encompass over 68 percent of the next 500,000 yr (>340,000 yr). Intermediate climate state bounds range from approximately 9 to 10°C and 200 to 430 mm/yr.

- Monsoon climate states, which tend to occur between interglacial and intermediate climate states, are estimated to occur 3 percent of the time over the next 500,000 yr during the intermediate/monsoon climate state. Monsoon climate state bounds range from about 13 to 17°C and 125 to 400 mm/yr.

- Interglacial (e.g., modern) climate is the warmest and driest of all climate states. This climate state has been dominant in the Yucca Mountain area, for only the last seven to eight thousand years (ka). The interglacial climate state is estimated to occur about 13 percent (65,000 yr) of the time during the next 500,000 yr. Mean annual temperature and precipitation are estimated to be about 13°C and 125 mm/yr.

- Present-day meteorological stations were selected to represent the four past climate states.

6.1 INTRODUCTION

To understand the past, present, and future climate of Yucca Mountain, it is necessary to investigate how climate patterns function not only in and around Yucca Mountain, but also on a broader geographic and temporal scale because the Yucca Mountain region is not isolated from change in the global climate. Climate in the Yucca Mountain area is influenced by many factors from local topography that can produce microclimates, to El Niño Southern Oscillation (ENSO) events that can affect climate on multi-year time frames, to astronomical parameters that can affect climate on millennial time scales.

Because the climate of the Yucca Mountain region affects groundwater infiltration and the elevation of the water table, knowledge of the past and present climate of the site is crucial to the development of infiltration and atmospheric dispersion models and aids in environmental analyses of repository design facilities. The future period of interest for performance of the repository is 10 k.y. (40 CFR Part 197 [DIRS 155238]), although longer time periods up to 1 m.y. are also of interest for supplementary analyses and to examine performance sensitivities.

This chapter discusses forcing mechanisms that help drive climate into different states (Section 6.2). These include extraterrestrial and terrestrial mechanisms functioning on very different time scales that have operated in the same way for many hundred thousands of years.

Present climate, including planetary-scale and synoptic (storm)-scale atmospheric features and meteorological conditions, is described in Section 6.3, along with the Yucca Mountain regional and site climatology. Section 6.4 documents the timing, duration, magnitude, and character of past climates in the Yucca Mountain area, and establishes the rationale for projecting such changes into the future. Section 6.5 integrates the material from the previous sections, establishing timing relations between calculated earth-orbital parameters and past climate cycles to forecast the potential timing and magnitude of future climate changes.

This forecast is an estimate of likely future climate scenarios under four key assumptions set forth by the U.S. Geological Survey (USGS 2001 [DIRS 158378], p. 19):

1. Climate is cyclical over 400,000-yr periods, and the earth is entering into the next 400,000-yr cycle. Climate cyclicity is important for forecasting future climate because it implies some past climate or aspects of past climate will recur in the future (Section 6.5.3).

2. Past climate change can be timed with an earth-orbital clock of precession and eccentricity, so the timing of future climate change can also be estimated using the orbital clock. Timing climate change with a clock that can be set accurately in the future is important for forecasting climate, because it allows for an assessment of future climate durations used as input by total system performance assessment and infiltration models (Section 6.5.3).

3. Past glacial and interglacial climates differ from each other, and the nature of particular past climates should repeat themselves in a predetermined order. Thus, the analysis can focus on one particular climate sequence rather than all past climates and need not take the most conservative approach of using the climates that generate the highest infiltration as being those expected throughout the future (Section 6.5.3.5).

4. Long-term earth-based climate-forcing functions, such as tectonic change, have remained relatively constant over the past 500,000 yr and will remain relatively constant for approximately the next 500,000 yr. This is important to forecasting because climate beyond the next 500,000 yr may change in noncyclic ways because of such forcing functions (Section 6.5.3.3).

New information since Revision 01 of the *Yucca Mountain Site Description* (YMSD) (CRWMS M&O 2000 [DIRS 151945]) includes a more detailed description of modern climate, the addition of estimates of the timing and magnitude of climate states beyond 10,000 yr after present, a section on the potential consequences of anthropogenic warming, and updated modern meteorological data and references.

6.2 FORCING MECHANISMS

More than 99.9 percent of the energy that heats the earth comes from solar radiation (Lutgens and Tarbuck 1998 [DIRS 108899], p. 23). Changes in the radiative budget of the earth are associated with solar output (irradiance) and varying orbital parameters of the earth; the former influences the total energy received annually by the earth, and the latter influences its spatial and seasonal distribution. Thus, solar radiation is a key factor in understanding past, present, and

future climate. However, it is important to remember that the earth itself is a dynamic system that responds to changes in solar radiation received at the earth's surface (insolation), with complex terrestrial interrelations that profoundly affect climate.

In this section climatic forcing mechanisms are divided into four subsections:

- Astronomical (extraterrestrial) changes affecting the solar insolation received by the earth (Section 6.2.1)

- Terrestrial changes involving the physical and biological environment (Section 6.2.2)

- Unpredictable events which can affect climate, such as volcanic eruptions and asteroid impacts (Section 6.2.3)

- Uncertainties associated with these forcing mechanisms (Section 6.2.4).

6.2.1 Astronomical Forcing Mechanisms

The earth is very nearly in radiational equilibrium with space. The earth receives radiation from the sun and adjusts its temperature structure until it emits as much radiation as it receives. Solar insolation is largely received in the visible part of the electromagnetic spectrum from the hot sun (5,600 Kelvin [K]), and radiated out to space in the infrared part of the spectrum (long wave) from the relatively cool earth (288 K). Therefore, the atmosphere selectively passes a larger percentage of incoming shortwave energy than it passes outgoing long wave energy, thus heating the surface of the earth. This difference in radiation wavelengths has a profound effect on terrestrial interactions and forcing mechanisms.

Incoming solar insolation at the top of earth's atmosphere can change in two basic ways: (1) solar source variability (changes in total solar irradiance) (Section 6.2.1.1), and (2) earth receptor variability (changes in the latitudinal and seasonal distribution of solar insolation arising from variations in earth's orbital parameters) (Section 6.2.1.2).

6.2.1.1 Solar Source Variability

The energy delivered to the earth from the sun is not constant but changes a fraction of a percent in relation to solar magnetic activity (Barry and Chorley 1992 [DIRS 108902], pp. 17 and 18). Variability in solar activity (the number and distribution of turbulent and calm areas on the sun's surface) occurs in short-term cycles, ranging from the familiar "sunspot cycles" of quasi-periodicity (having an 11-yr duration) to longer periods of greater or lesser activity (Muller and MacDonald 2002 [DIRS 160236], pp. 186 to 188; Sharma 2002 [DIRS 160143], p. 469). The full 22-yr cycle includes the magnetic pole reversal in sunspot clusters each successive 11-yr cycle.

Changes in solar irradiance may impact climate globally (Eddy 1976 [DIRS 108978], p. 1199; Willson 1997 [DIRS 109184], p. 1963). For example, Willson and Hudson (1988 [DIRS 109185], p. 810) suggest that a decrease in total solar irradiance during the Maunder Minimum (a period of very low sunspot activity between 1650 and 1715 A.D.) may have been a contributing factor to the Little Ice Age (~1450 to ~1850), a climate event that coincided with

expansion of glaciers throughout much of northwestern Europe (Grove 1988 [DIRS 109113], pp. 117 and 354) and a general lowering of temperature of about 1°C. Similarly, colder and moister climates indicated by tree ring chronologies in the White Mountains in eastern California (LaMarche 1974 [DIRS 109123], Figure 5, p. 1046) and in the southern Sierra Nevada, east of Fresno, California, (Graumlich 1993 [DIRS 161150], p. 249) correlate to the time of Little Ice Age environments in Europe. Pollen records from Lower Pahranagat Lake, about 110 km northeast of Yucca Mountain (Wigand 1997 [DIRS 109182], p. 73), suggest persistent submillennial-scale gains in precipitation and reduction in temperature that correspond in time to the Little Ice Age-style climate changes seen in tree ring records.

A small change in irradiation is considered by many to be insufficient to force significant climate change. However, total solar irradiance and other factors may affect climate through cosmic radiation and its role in cloud formation and enhancement of precipitation (Muller and McDonald 2002 [DIRS 160236], p. 187). At present, the earth is experiencing a trend of increasing solar irradiance (Willson 1997 [DIRS 109184], p. 1963) that may be part of a 250- to 350-yr cycle (Wigley and Kelly 1990 [DIRS 109183], p. 557).

6.2.1.2 Earth Receptor Variability Due to Orbital Parameters

Earth receptor variability is a function of change in the earth-sun distance, the orientation of the earth's axis of rotation relative to its orbit, or the position of its orbit relative to the center of mass of the solar system or some other non-earth reference. These cyclical and systematic changes in the distance and orientation of the earth relative to the sun, and the resulting changes in insolation the earth receives, seem small. Based on long-term climate records, however, these changes are significant and show a relation with glacial and interglacial periods. Berger and Loutre (1991 [DIRS 108910], pp. 298 to 304) and Muller and MacDonald (2002 [DIRS 160236], pp. 28 to 45) describe the behavior and timing of earth-orbital parameters and the criteria to calculate these parameters, past and future. Calculating the past timing of these parameters permits their comparison with climate proxy records, such as the Devils Hole isotope record (Winograd et al. 1992 [DIRS 100094], p. 255).

Three of the earth's orbital parameters vary on a cyclical basis (Berger and Loutre 1991 [DIRS 108910], p. 297; Muller and MacDonald 2002 [DIRS 160236], p. 28; Crowley and North 1991 [DIRS 121811], pp. 132 and 133): eccentricity (the variation in the shape of the earth's elliptical orbit), precession (the slow migration of the earth's axis that traces out a cone coupled with the rotation of the axis of the earth's orbit), and obliquity (the angle of tilt of the earth's axis of rotation). Eccentricity changes the annual total radiation received at the top of the earth's atmosphere via variations in earth-sun distance. Precession and obliquity change the seasonal and latitudinal distribution of insolation at the top of the earth's atmosphere, but not the total insolation. Because eccentricity, precession, and obliquity vary with different frequencies, they will act collectively to sometimes reinforce or sometimes dampen insolation departures from average, as can be seen by inspection of long-term insolation curves for different earth latitudes. For example, high eccentricity amplifies the seasonal effects of precession (Crowley and North 1991 [DIRS 121811], p. 134). Each of these three parameters and their effect on insolation are described in the following paragraphs. For a depiction of orbital parameters, see Figure 14-8 in Lutgens and Tarbuck (1998 [DIRS 108899], p. 331).

Eccentricity–The ellipticity of the orbit, as measured by eccentricity, plays a key role in the nature of earth's insolation (Hartmann 1994 [DIRS 152035], p. 303). The shape of the earth's orbit varies from nearly circular (e=0.004) to more elliptical (e=0.06) over approximately 100 k.y. cycles. Four 100 k.y. cycles form a 400 k.y. cycle (Berger and Loutre 1991 [DIRS 108910], Figure 4a, p. 309). If the earth's orbit were circular, and centered on the sun, incoming solar radiation over the tropics would be the same in all months because the earth-sun distance is constant. Also, energy input to the northern and southern hemispheres would be seasonally symmetrical (i.e., the northern hemisphere would receive the same amount of energy in summer [June] as the southern hemisphere in its equivalent summer season [December]). The present value, e=0.017, accounts for a variation of 3.3 percent in sun-earth distance (Muller and MacDonald 2002 [DIRS 160236], pp. 30 and 31) between perihelion (closest approach) and aphelion (furthest distance); about 7 percent difference in radiation because of the inverse square law. Therefore, when the orbit is elliptical, energy input to the northern and southern hemispheres is not seasonally equal. Eccentricity modulates the amplitude of precession cycles; high eccentricity produces a strong precessional cycle.

Precession–The climatic effect of precession is to change the distance between the earth and sun at any given season. This changes the distribution of incoming solar radiation on the earth. Two components make up the "precession index," which is basically a measure of the earth-sun distance on June 21, the summer solstice in the northern hemisphere and winter solstice in the southern hemisphere. The first component, axial precession, is the "wobble" of the earth about an axis of symmetry resulting in the North Pole describing a circle in space, much like the axis of a spinning top. The second component, elliptical precession, is the axis of the orbital ellipse slowly rotating in the opposite direction of axial precession. These two effects together are called precession of the equinoxes, and these changes occur on 19,000 and 23,000-yr cycles.

A decrease in the earth-sun distance at any given season causes an increase in radiation during that season. For example, perihelion occurs presently in northern winter. Consequently, portions of the winter hemisphere receive as much as 10 percent more solar radiation at present than they will 11,000 yr from now when perihelion will occur in the summer (Crowley and North 1991 [DIRS 121811], p. 134).

Obliquity–Obliquity is the angle of tilt of the earth's axis of rotation (between 22° and 25°) toward the sun relative to the plane of its orbit. Presently, it is 23.5°. Obliquity changes the distribution of incoming radiation and simultaneously amplifies the seasonal cycle in high latitudes of both hemispheres. Increase in tilt concentrates radiation toward the poles and reduces the amount received each year at low latitudes. Obliquity serves to increase or decrease the polar energy deficit relative to the tropics and, in this way, increases or decreases the strength of planetary atmospheric circulations. It operates over an approximately 41 to 44 k.y. cycle (Crowley and North 1991 [DIRS 121811], pp. 134 to 136).

Although orbital inclination is another parameter that could influence climate change (Muller and MacDonald 2002 [DIRS 160236], pp. 215 to 229), it is not considered in the following analysis. Orbital inclination is the angle between a selected reference plane and the plane of the earth's orbit (Muller and MacDonald 2002 [DIRS 160236], p. 42). Using the reference plane (the "invariable plane") selected by Muller and MacDonald (2002 [DIRS 160236], p. 44), orbital inclination has a periodicity of about 100,000 yr. They suggest that the angle of inclination

affects the accretion of interplanetary dust, which alters climate through its effect on cloud cover and ozone. With continued research, this hypothesis may further our understanding of the mechanisms of climate change.

The orbital parameters of eccentricity, precession, and obliquity operate on a multimillennial scale to alter the total amount and global distribution of insolation. Seasonal variations in insolation at the equator and in the northern and southern hemispheres drive global atmospheric circulation. A change in insolation has the potential to change climate on a global scale in a sustained manner, not just temporarily perturb it (e.g., following volcanic eruptions). Because insolation is calculated from known principles of celestial mechanics, future values of insolation may be calculated (Section 6.5.5, Figures 6-10a and 6-10b). The next 100 k.y. eccentricity cycle will produce a relatively circular, rather than elliptical, orbit (Berger and Loutre 2002 [DIRS 160153], p. 1287). The last time a relatively circular orbit occurred was 400 ka, so it is expected that insolation for the next 100 k.y. will be similar to that between 400 and 300 ka (compare Figure 6-7a to 6-7d and Figure 6-10a to 6-10b).

6.2.2 Terrestrial Interactions and Forcing Mechanisms

The earth's response to insolation and to changes in insolation is governed by the individual properties of, and interactions among, the four terrestrial spheres (Lutgens and Tarbuck 1998 [DIRS 108899], p. 3):

1. Lithosphere—the solid earth
2. Atmosphere—the gaseous envelope that surrounds the earth
3. Hydrosphere—the earth's waters: fresh and salt, liquid and frozen
4. Biosphere—the earth's life forms.

Some interactions among these spheres are fairly well known. For example, the lithosphere affects the global circulation of the atmosphere and oceanic currents because of the location of mountains and continents; the atmosphere affects insolation and redistribution of heat; the hydrosphere affects the amount of energy absorbed by the atmosphere, as well as the distribution of heat on earth via latent heat effects; and the biosphere and lithosphere affect CO_2 uptake and loss in terrestrial and oceanic systems.

Greatly simplified, global climate may be thought of as processes operating within the atmosphere and hydrosphere to minimize temperature differences arising from unequal reception of energy in different locations and seasons. As a consequence of the insolation imbalance, energy is transported toward the poles from the equator by both air and ocean circulation. Atmospheric energy transport interacts in complex ways with the hydrosphere, lithosphere, and biosphere, resulting in the observed features of global and synoptic circulation described in Sections 6.3.1 and 6.3.2, respectively. As discussed in Section 6.2.1, changes in the earth's insolation over millennia result in changes in the energy budget between the equatorial regions and poles. As the energy budget changes, so does climate (Barry and Chorley 1992 [DIRS 108902], pp. 318 to 320; Imbrie et al. 1992 [DIRS 109430], p. 701).

The lowest level of the atmosphere, the troposphere, interacts with the other three spheres resulting in local-to-global effects, which are discussed in the following bullets.

- Volcanic eruptions–Sulfur derived from volcanic eruptions can form sulfuric-acid aerosols, which can cause atmospheric cooling by backscattering and absorbing incident solar radiation. Eruptions can also release CO_2 into the atmosphere (lithosphere and atmosphere interaction).

- Atmospheric dust–Dust, especially if it resides in the stratosphere where it cannot rain out, is thought to play a role in the atmospheric energy budget by reflecting incoming shortwave energy back out to space, thereby cooling the troposphere and the earth's surface (lithosphere and atmosphere interaction).

- Greenhouse gas (GHG)–The greenhouse effect occurs because atmospheric GHG and water vapor absorb some outbound long-wave radiation, resulting in a gain in atmospheric energy (heat) (atmosphere and biosphere interaction).

- Snow cover–Snow and ice cover affect reflective characteristics (albedo) of the surface and energy transfer to the atmosphere. Snow cover increases the reflective characteristics of the earth's surface and increases outbound, reflected short-wave radiation, resulting in greater energy (heat) loss. Snow cover can also act as a heat sink because it takes 80 cal/g to melt snow. Therefore, the growth and loss of glaciers during different climate periods can have a large effect (hydrosphere and atmosphere interaction).

- Oceanic processes–Gain or loss of energy between the oceans and atmosphere affects atmospheric circulation because the oceans typically receive heat in the tropics and give off heat at high latitude. Such exchanges represent important and complex atmospheric energy-budget interactions. Changes in sea level, ocean basin shape, salinity, abyssal circulation, and ENSO events also affect the terrestrial sphere (hydrosphere, atmosphere, and biosphere interaction).

- Precipitation–Changes in precipitation can lead to changes in plant density and composition (hydrosphere, atmosphere, biosphere, and lithosphere interaction).

- Land features–Tectonic change can alter regional climate. For example, mountain-building can create a rain-shadow on the lee side of a mountain range, such as on the east side of the Sierra Nevada today. The creation of a rain shadow over time can affect vegetation (lithosphere, atmosphere, and biosphere interaction).

- Natural (dust, volcanic emissions) and anthropogenic (inorganic and organic species [i.e., sulfates, black carbon, organic carbon]) aerosols–These aerosols can create a net effect of cooling the climate system by enhancing scattering and absorption of solar radiation (Kaufman et al. 2002 [DIRS 161923], p. 215; Ramanathan et al. 2001 [DIRS 160999], p. 2119) (atmosphere and biosphere interaction).

These are a few examples of the processes interacting among spheres. Thus, the tropospheric energy budget has a variety of interaction mechanisms. Sometimes the effects may be small or self-canceling. However, effects can be additive, creating significant changes in precipitation and temperature.

6.2.3   Unpredictable Forcing Events

The foregoing sections addressed astronomical and terrestrial climatic forcing mechanisms. In addition to the forcing mechanisms discussed above, unpredictable occurrences such as volcanism and asteroid impacts may affect climate on differing time scales.

Volcanic eruptions can indirectly affect climate through CO_2, particulate, and aerosol emissions. Although periodicities in the number and size of volcanic eruptions occur (Bryson 1989 [DIRS 108942], Figure 16, p. 117), they appear related to crustal movements caused by tectonism. Consequently, although the climatic effects of volcanic eruptions can be considered in future climate scenarios, the timing and magnitude of the effects cannot be accurately predicted.

Estimates vary on the type, size, quantity, and statistical threat of comet and asteroid impacts that could cause climate change. Rabinowitz et al. (2000 [DIRS 161194], p. 165) report that 1,000 to 2,000 near-earth objects large enough to cause climate change upon impact (diameters greater than 1 km) exist. However, the expected repeat rate of impact events like those associated with Cretaceous-Tertiary and Eocene-Oligocene transitions is on the order of ten million years or longer (Bottomley et al. 1997 [DIRS 161205], p. 368). Thus, in consideration of the shorter timeframe for Yucca Mountain performance assessment, and given the uncertain stochastic statistical nature postulated for volcanic eruptions and near-earth objects events, these potential climatic-change forcing mechanisms are not included in our estimates of future climate.

6.2.4   Uncertainties in Current Understanding of Climatic Forcing Mechanisms

The preceding sections have addressed climatic forcing mechanisms on the astronomical (solar system) and terrestrial scales. Not all of these mechanisms are presently well understood, and some of these forcing mechanisms may be coincidental (or correlative) responses to some larger, presently unknown causal phenomenon rather than original causal mechanisms themselves. The uncertainties affecting our current understanding are listed here.

Uncertainty in the present:

- The unpredictability and chaotic nature of the climate system on both short and long time scales

- Understanding of the role and mechanisms of global oceanic circulation

- Understanding of the role and global effects of land use and land surface variations

- The role of biological and chemical processes.

Uncertainty in the past:

- The accuracy of paleoecologic and paleoclimatic reconstructions

- Determining the thickness and elevation and, therefore, the influence of ice sheets on the atmosphere

- The accurate dating of past events

- The assumption that past climate can serve as an analog for future climate.

Uncertainty in the future:

- Future events that we are unable to predict, such as volcanic eruptions, meteor showers, asteroid impacts, changes in solar activity, and tectonic change

- The effects of ocean-atmosphere interactions

- Factors influencing the onset and timing of climate cycles

- Indirect effects of human activity on climate and geologic activities.

Interactions among the above sources of uncertainty could create either a larger or a smaller uncertainty. There is no straightforward way of assessing the nature of uncertainty as it might apply to future climate change.

6.3 MODERN CLIMATE

"Climate" can be considered to consist of the time-averaged properties and time-varying behavior of the atmosphere. The appropriate averaging time depends on the questions of interest although an averaging period of 30 yr is conventional. However, climate issues associated with the Yucca Mountain Project would more properly define modern climate on a millennial scale. Instrumental climate records in the western United States typically span only years to decades and, at most, a century.

Climate, by its nature, is constantly fluctuating, and thus is never fully in an equilibrium state. This characterization of modern climate in the Yucca Mountain area is based on a random sample spanning the past several decades, for which there are direct physical measurements. The set of physical measurements recorded at a single point, such as a Yucca Mountain climate station, is the result of processes ranging over spatial dimensions from the size of the components in the measuring device, on up to the size of the earth. However, this record cannot be fully understood without reference to the full range of time and space scales, even though we have only a partial understanding of how climate operates, and why it varies at some of these time and space scales. The causal chains have been incompletely worked out, and many of them are not even known.

This discussion of Yucca Mountain climate reflects the range of climatic influences, and is organized from the largest down to the smallest scales. Important effects can occur at each scale.

Planetary-scale features occupy areas with horizontal dimensions of several thousand kilometers and have durations of a week or more whereas synoptic-scale horizontal dimensions are smaller, several hundred to a few thousand kilometers, with durations from a few days to a few weeks (Ahrens 1994 [DIRS 107641], pp. 248 and 249). At still smaller scales are local hills and valleys, drainage channels, rock outcrops and cliffs, hill slopes, and similar sized features.

6.3.1 Planetary-Scale Atmospheric Features and Processes

The principal factors which govern the average conditions of the atmosphere at the larger (planetary) dimensions include the spherical shape of the earth, fact that it spins, tilt of this rotational axis with respect to the plane of its orbit, distribution of the oceans and continents, effects of constituents in the atmosphere on the flow of energy in the form of radiation (all wavelengths) through the system, and absorption and emission of this energy at interfaces such as those separating the atmosphere from the hydrosphere and lithosphere. At time scales of centuries to millennia, significant variations in climate can result from the seemingly subtle effects of shifts in the exact angle of the tilt, and in the place in the orbit where the axis is most directly pointed toward or away from the sun. The sun's energy output itself may also vary (independently) during the orbital variations.

The circulation of the atmosphere is ultimately driven by the uneven distribution of heating and cooling, from flow the size of a candle plume to the largest planetary waves. The sequence is as follows: unbalanced energy flows (more arrives than leaves a selected location, or vice versa) lead to uneven heating rates, which lead to differing temperatures between locations, which produce air parcel density differences, which produce pressure differences, which cause air to move and result in wind.

In broad outline, effects stemming from the rotation of the earth, atmospheric heating and moisturizing, and surface friction lead to a vertical circulation approximately symmetrical about the equator. Near the equator, air rises primarily in organized systems of towering thunderstorms and then spreads laterally and poleward, at upper levels, until cooling processes cause it to sink around 30° to 35°N and S latitude. Precipitation at these latitudes is thereby suppressed, as in the southwest United States. Dynamic processes create a region between about 30° and 60˚ latitude where westerly winds predominate, and most of the rising motion takes place in large horizontal storm systems. The tropical cells (in latitudinal cross section) to the north and south of the equator are referred to as Hadley cells (warm air rising and cool air sinking).

To describe winds, meteorologists use a coordinate system that is fixed to the earth and rotates with it. In the northern hemisphere, any moving object (e.g., a baseball, train, air molecule) experiences a force to the right along the direction of motion. In the absence of complicating factors, dynamic balance results in air that moves clockwise around high-pressure systems, and counterclockwise around low-pressure systems.

As previously stated, air rises near the equator, sinks near 30° to 35°N and S latitude, and returns toward the equator. The earth's spin exerts its effect on those returning winds, and the result is the Trade Winds, the steadiest winds on earth. In the northern hemisphere they blow from northeast toward southwest nearly constantly, in the latitude band from about 5° to 15°N. To the north, in roughly the band from 30° to 60°N, westerly winds predominate, although specific

locations, and some topographically affected sites, show that winds from all directions can occur. As altitude increases, winds from the west become more and more dominant. In regions poleward of 60°N latitude, light easterly surface winds are common; however, as altitude increases, winds become stronger from the west. The zone between easterly and westerly winds migrates northward in the summer and southward in the winter. A generalized view of atmospheric circulation is presented in Figure 2 of USGS (2001 [DIRS 158378], p. 24).

Air density depends on temperature. In warm, tropical latitudes, the air column is expanded vertically; in cool, polar latitudes, the air column is contracted. So at a given distance above sea level, more air is found below that height in a cold climate (higher density) than in a warm climate (lower density). Thus, a latitudinal pressure difference exists at upper altitudes, with low pressure (less air remaining above) in the polar regions. Alternatively, one may say that the height above sea level at which a barometer will show a particular pressure will be higher in the tropics than over the pole.

Dynamic processes tend to concentrate this broad belt of winds into a ribbon called the jet stream. This feature is usually transitory in nature lasting from a few hours to days or weeks. Strongest winds are typically found about 10 to 12 kilometers (km) above the ground. The jet stream constantly adjusts and fluctuates, strengthening and expanding in the winter and weakening and contracting in the summer. The jet stream causes storms and is caused by storms, giving energy to them and then taking it back and, thus, delineates the approximate paths of storms: the storm track. Yucca Mountain lies under this influence more often in winter and much less often in summer.

The position of the jet stream and the storm track depends on geographic and topographic influences (e.g., ocean and land, mountains and valleys) as well as season. The average position of the storm track can change slowly at decadal to millennial scales, remain more or less stationary for long periods of time, or change abruptly.

The polar front usually oriented east-west, lies approximately beneath the polar jet stream and is the zone that usually separates cool northern air from warm southern air. Its many undulations are more prominent when the north-south latitudinal temperature gradient is weak, and are fewer in number when the gradient is strong. High and low pressure systems (at the surface) and wavy upper-level counterparts called ridges and troughs (at 5 to 10 km above the surface) regularly traverse along this belt, bringing all the familiar types of mid-latitude weather. The equator-to-pole temperature difference is much larger in winter than summer. In the winter the polar front moves as far south as 30°N, retreating poleward in summer to near 50°N (Lutgens and Tarbuck 1998 [DIRS 108899], pp. 173 and 174). Yucca Mountain is at about 37°N (Figure 6-1). Thus, this area receives more precipitation as the polar front with its active storm track expands southward in winter, and less precipitation as the front contracts northward in summer.

As spring transitions into summer, an east-west ridge of higher pressure forms at upper levels, essentially creating a western extension of the subtropical Bermuda High in the Atlantic. Through early summer, this feature migrates slowly north. On its southern side, the east to west flow helps steer low-latitude atmospheric disturbances in a generally westward direction. By July 4, this feature has typically moved far enough north to about the Four Corners area (the

intersection of the states of Utah, Colorado, New Mexico, and Arizona), to permit the northward intrusion of very moist tropical air into the southwest United States. The often abrupt arrival of this southwest monsoon is accompanied by greatly decreased vertical stability and numerous, and often heavy, thunderstorms. The areas most affected by the monsoon include New Mexico, Arizona, desert California, southern Nevada, Utah, and Colorado. The western boundary of this humid southerly flow shows a systematic westward progression through July into August and early September. It is during this time that the incidence of thunderstorms in southern Nevada increases dramatically. Yucca Mountain lies in a transition zone, where the influence of the monsoon is significant, although this influence decreases steadily to the north and west along the California-Nevada diagonal boundary. At Yucca Mountain, the heaviest showers of the year usually occur during July and August. Less commonly, in September and sometimes October, remnant moisture exported northeastward from dying tropical storms off Baja California can also produce very heavy precipitation.

In the lower atmosphere, areas hundreds of kilometers in size and possessing similar air properties (e.g., temperature, moisture) are formed as a consequence of physical modification processes involving the atmosphere and its surface substrate. These can be thought of as three-dimensional air masses that show a change of properties at their boundaries. Complex fluid-dynamic processes tend to concentrate the boundaries between such air masses into narrow zones called fronts. Air mass properties across these frontal zones can change very abruptly in space.

As we move from the realm of weather to that of climate, the number of factors that can change increases. From day to day, glaciers and forest boundaries can be held fixed, and thus "external" to the system. Over longer time scales, these and other features can vary, according to the state of the system, and thus become regarded as "internal" to the system, and as participants in and determinants of its evolution.

The flows of energy that drive the behavior of the climate system span numerous scales, and result in a highly interconnected climate system. This connectivity ensures that the climates of individual locations, such as Yucca Mountain, are affected by influences around the entire earth, including the world's oceans, its vegetation and biology, and polar and mountain snow and ice. These large-scale influences set the stage for more regional processes that, in turn, produce their own effects, in a cascading manner down to very tiny scales. However, in a corresponding manner, the large-scale influences are usually the integrated effects of numerous small-scale processes and, therefore, one scale is not more important than another.

6.3.2 Description of Synoptic-Scale Features and Processes

This section presents a general description of large-scale atmospheric features that influence the Yucca Mountain area. The day-to-day manifestations of these systems appear in upper-level meteorological pressure charts as ridges and troughs, in surface weather maps as high- and low-pressure centers and fronts, and in satellite imagery as cloud patterns (Bluestein 1992 [DIRS 107644], pp. 5 to 7; Ahrens 1994 [DIRS 107641], pp. 248 and 249).

The temperature and humidity properties of most synoptic-scale atmospheric systems depend largely on the land or ocean properties underlying the system air mass. Certain semi-permanent

atmospheric pressure features over and near the United States play dominant roles in controlling the present-day synoptic weather patterns that affect the southwest. These are the Bermuda High (western north Atlantic), Pacific High (eastern north Pacific), Aleutian Low (Gulf of Alaska; winter), and summertime thermal low (southwestern United States) (Ahrens 1994 [DIRS 107641], Figure 11.3, pp. 288 and 289). Seasonal changes in position and strength of these centers of action influence winds and the movement of storms.

The Pacific High strengthens and moves closer to the west coast in summer, and produces persistent northerly winds. These, in turn, lead to strong upwelling, cool ocean temperatures, and cool foggy maritime climates along the coast. During summer, traveling disturbances in more northerly latitudes tend to be steered around the perimeters of the high pressure systems, although occasionally the stronger disturbances travel through when the high pressure systems break down slightly.

The westward extension of the Bermuda High steers tropical moisture and embedded disturbances over the Gulf of Mexico toward and into the southwest, increasingly from early to mid summer. This flow generally recurves toward the north and back toward the east in the central and northern Rockies.

In the winter, the eastward extension of the Pacific High steers most cyclonic storms away from the southwestern United States by deflecting the jet stream toward more northerly latitudes[1]. Thus, the desert southwest region experiences relatively few storm passages and tends to have mild, dry winter weather. On occasion, the Pacific High weakens or moves, and the jet stream shifts to help bring storms, precipitation, and cooler air into the southwest (Mock 1996 [DIRS 109138], pp. 1111 and 1113). Though relatively infrequent, these storms are a very important contributor to the annual recharge and stream flow in the southwest. Many pacific cyclones affecting Yucca Mountain form in the vicinity of the Aleutian Low and arrive from the west or northwest, often on a trajectory that curves around or over the southern end of the Sierra Nevada.

Great Basin precipitation arises primarily from three airflow trajectories and moisture origins in the Pacific, Gulf of Mexico, and continental regions. The most important to the Yucca Mountain area is the Pacific trajectory, followed to a lesser extent by the continental and gulf trajectories (Benson and Klieforth 1989 [DIRS 104370], pp. 52 and 53). Much of the observed fine-scale spatial variation in precipitation in the mountainous western United States (Mock 1996 [DIRS 109138], p. 1111; Blumen 1990 [DIRS 108936], pp. 243 and 244) arises from the way that terrain influences flow patterns, on both large and small scales. The Sierra Nevada and Transverse Mountains can either block or impede atmospheric moisture transport from the Pacific Ocean to Yucca Mountain, especially during winter, leading to a rain-shadow effect. In summer, moisture usually arrives from the south, where blockage is less effective.

---

[1] The simultaneous behaviors exhibited by the jet stream, storm track, and various surface pressure features constitute a mutually determined and self-consistent solution to the equations of motion. To say that entrenched high pressure "deflects" an approaching front on one occasion and that the front "displaces" or "destroys" high pressure on another, that one is cause and the other is effect, gives undue emphasis to one feature. These connected systems co-evolve and their components react jointly to the same overall physical circumstances. The forces that cause the jet stream to change also cause the associated surface pressure patterns to change.

6.3.3 Regional and Site Climatology

Yucca Mountain is on the climate gradient associated with the rise from the low elevation Mojave Desert to the higher elevation Great Basin Desert. Depending on their elevation, geographic features in the vicinity of Yucca Mountain exhibit qualities of those two regimes. Because of its latitude, the Yucca Mountain area alternates between two main influences during the annual cycle. During the cool portions of the year, the area is under the influence of the mid-latitude westerly winds and associated storm systems. In summer, this band of upper air (i.e., tropospheric) winds weakens and retreats toward the United States Canadian border, leaving the Yucca Mountain area under the influence of the southwest monsoon described above.

The Sierra Nevada west of Yucca Mountain forms a significant impediment to the movement of air. Eastward-moving air from the west must either ascend the Sierra Nevada, which is high at this latitude (numerous 4,270-m peaks), or skirt the range to the south, or (only occasionally) follow a more northerly trajectory. In any case, intervening mountain ranges can remove much of the moisture that might have originally been in the air. Nearly all precipitation is from "imported" moisture. The southern Nevada region is too arid to resupply much moisture back to the overlying atmosphere from vegetation and other local surface sources.

Winter disturbances are typically frontal storms exhibiting large-scale organization and structure, on the order of hundreds to over a thousand kilometers in horizontal dimensions. The cool season storms help to equalize horizontal temperature differences between the tropics and the polar latitudes, which radiative processes continually recreate. The storms usually have a warm sector, with southerly or southwesterly winds in advance (east) of the core of the storm, and a trailing (west) cool sector, with northerly to northwesterly winds. The transition between sectors manifests itself as a wind shift as the storm passes. Storms occurring in summer typically have smaller dimensions, the size of individual thunderstorms, with horizontal dimensions of just a few kilometers. On occasion, individual storms can merge into larger scale assemblages that last longer and produce heavier rains.

Topography provides a significant influence regionally and locally, at scales down to that recorded by the measurement stations. Terrain can channel, accelerate, or block the movement of air and affect the vertical component of air motion, and thus precipitation mechanisms. During large-scale storms in the cool season, the effect of mountains on precipitation dynamics is related to the altitude of cloud bases, which is, in turn, correlated with relative humidity. High relative humidity in an atmospheric column typically results in low cloud bases. Mountains often serve to initiate convection (the vertical overturning of air) in favorable locations, especially in summer when they act as elevated regions supplying (sensible, as opposed to latent) heat to the atmosphere. Mountains perform this role differently according to the time of year, the direction of moisture inflow, and other immediate circumstances.

6.3.3.1 Effects of the El Niño Southern Oscillation and Pacific Decadal Oscillation

Up to this point the emphasis has been on the influences that are present each year. We now consider why years, decades, or centuries should be different from each other. During one traverse around the sun, the astronomical factors (Section 6.2.1) that most significantly affect climate through incoming solar radiation return to almost precisely the same state with very

small differences. However, the rest of the world climate system is not in exactly the same state as it was 365.24 days ago, exhibiting a variety of random and systematic differences (Ahrens 1994 [DIRS 107641], pp. 299 and 300). These differences affect the use and disposition of solar energy supply, and also govern differences in patterns of energy loss back to space. A variety of mechanisms can both dampen and enhance the effect of these differences on climate behavior. Thus, the annual progression of the seasons, while exhibiting an overall general regularity, nonetheless shows great variability from one year to the next, and indeed from one decade, century, and millennium to the next.

One mechanism influencing Yucca Mountain climate is the water temperature of the tropical Pacific Ocean, especially the area that closely straddles the equator between the coast of Peru and International Date Line. Warm-ocean, El Niño, and cool-ocean, La Niña, conditions with respect to long-term average temperatures alternate in intervals typically of two to seven years. Occurring with El Niño/La Niña conditions is a pattern of pressure variability with oceanic and atmospheric aspects called ENSO, a convention that minimizes the importance of La Niña. During the northern hemisphere cool season, approximately October through March, La Niña is associated with drier than usual conditions, and El Niño is associated with wetter than usual conditions in southern Nevada. These surface effects are expressions of major shifts in the storm tracks to other latitudes as the jet stream responds to changes in atmospheric temperature and heat content produced by El Niño and La Niña.

During La Niña, the dry conditions in the southwest and in southern Nevada have been consistent over the past 70 yr. During El Niño winters, however, although the likelihood of heavy precipitation events and higher-than-usual runoff increases in the southwest (Cayan et al. 1999 [DIRS 161154], p. 2881; Woolhiser et al. 1993 [DIRS 161149], p. 1287), such winters have been dry or simply average in about a third of all cases (Redmond and Koch 1991 [DIRS 161153], Figure 4, p. 2389). Evidence suggests that tropical storms are a little more likely to strike (very rare) or influence (common) the southwest during the autumn months when El Niño is present. In addition, annual stream flow, especially in spring, shows a similar preponderance of high values following El Niño winters (Cayan et al. 2001 [DIRS 161156], p. 399). Such heavy precipitation events and higher than usual stream flows are both important sources of groundwater recharge.

El Niño is closely associated with flood frequency and heavy precipitation in the southwest (Redmond et al. 2002 [DIRS 161157], pp. 33 and 34) and therefore variations in the rate of recurrence of El Niño are of great importance and relevance to Yucca Mountain. Analyses of high-resolution proxy records of climate, including tree rings, corals, ice cores, and varved sediments, have made it possible to establish the recurrence interval of ENSO events. Of relevance to Yucca Mountain are data that suggest variability in the intensity and frequency of past ENSO events. For example, Anderson (1992 [DIRS 108850], p. 193) statistically examined historical ENSO records to show that the frequency of the warm ocean El Niño phase varied on preferred time scales of 90, 50, and 22 yr, and that during the Medieval Warm Period (~600 to 1,000 A.D.), El Niño events were less common. Farther back in time, paleoenvironmental records from Australia and South America suggest that in early Holocene time (10 to 7.5 k.y.), ENSO events were either of much reduced amplitude or were of different expression because of altered climatic and oceanic boundary conditions (McGlone et al. 1992 [DIRS 109134], p. 436). Proxy records from tree rings and other sources show that there have

been significant variations in southwestern United States precipitation during the past 1,500 yr with the recent century among the wettest in that time period (Redmond et al. 2002 [DIRS 161157], p. 38; Figure 9, p. 32).

Tree ring studies of southern California forests, including the White Mountains, have been integrated with other tree ring records in the western United States to track potential ENSO periodicities (Meko 1992 [DIRS 109135], p. 227). The results show that southwest tree-ring-width variations are highly correlated with the characteristic ENSO time scales (2.8 to 10.2 yr). However, the tree-ring-width series is also well correlated at longer and shorter periodicities, indicating that not only ENSO affects regional tree growth. In fact, even correlations within the characteristic ENSO time scales cannot be unambiguously related to ENSO, because many other climate-controlled factors also operate within the ENSO band (Meko 1992 [DIRS 109135], p. 238).

The variable role that the ENSO has played in past climate is likely to continue into the future, especially as boundary conditions change because of slowly varying insolation and ocean circulation. It is reasonable to assume that Yucca Mountain will be affected by these changes, and, consequently, predictions of future climate in southern Nevada eventually may incorporate the natural variability of climate in response to processes like ENSO. For example, abundant winter precipitation in the local Yucca Mountain area in response to the 1969 and 1993 ENSO events caused sufficient flow in the Amargosa River to form shallow lakes in Death Valley (Grasso 1996 [DIRS 101216], p. 30). During the 1983 ENSO event, both winter and summer precipitation events were so large that the Amargosa flow gauge at Tecopa, California (35°53'N, 116°14'W), 100 km south of Yucca Mountain, was destroyed by flooding (Grasso 1996 [DIRS 101216], p. 13; Figure 2, p. 6).

On longer time scales, periods of warmer or wetter climate lasting decades and longer have been documented. Most of these are natural in origin, although they may be increasingly human-aided during the last 100 yr (Section 6.5.5.1 includes discussion on anthropogenic warming). Among the former is a large-scale, slowly varying pattern of ocean temperatures in the central and northern Pacific called the Pacific Decadal Oscillation (PDO). The PDO appears to modulate the effect of El Niño on the southwest United States (Mantua et al. 1997 [DIRS 161155], pp. 1077 and 1078). The cause of the PDO is not known, although it appears to be related to El Niño and La Niña.

The southwestern region has recently experienced a period with above-normal precipitation, the wettest in the past century, from the late 1970s through the mid-1990s. The PDO was consistently in the positive, or warm, phase during this time. The southwest has subsequently experienced significant drought for much of the last decade, the first wide-scale drought in the west and southwest in a half-century. The period from the late 1940s to 1977 was also quite dry, and encompassed the severe drought of the 1950s. During both of these periods, the PDO was consistently negative, or in the cool phase. This pattern suggests that during the twentieth century, slow variations in the north Pacific have affected winter precipitation in the southwest, including the Yucca Mountain area, and that recent short-term precipitation records should be interpreted with reference to these possible external influences. At the same time, temperatures have been rising in southern Nevada for the past 30 to 40 yr, for unknown reasons. A variety of indicators (direct thermometer measurements, plant blooming dates, spring runoff dates) are

showing that winter and spring appear to be warming much more than summer or fall (Cayan et al. 2001 [DIRS 161156], p. 399) in the western United States.

Tree ring data from southern and Baja California suggest that PDO reversals from positive to negative have occurred throughout the last 400 yr (Biondi et al. 2001 [DIRS 161151], p. 9). The known major PDO reversals of 1947 and 1977 are matched by reversals in tree growth time series from these sites. These records also suggest that more pronounced climate transitions occur when transitions from El Niño to La Niña coincide with PDO reversals (Biondi et al. 2001 [DIRS 161151], p. 8). Longer-term data sets imply that the representativeness of the relatively short instrumental records, used to base the understanding of "modern" climate, may need to be reconsidered. They also bring into question how long those records must be to establish such representativeness.

6.3.3.2   Station-Specific Climate Characteristics

The following sections on temperature, precipitation, humidity, wind, solar radiation, evaporation, air quality, and atmospheric dispersion rely, in part, on data from Regional Meteorological Stations (Table 6-1) and U.S. Department of Energy (DOE) Meteorological Monitoring Sites (Table 6-2; Figure 6-2a). Data such as temperature, precipitation, barometric pressure, humidity, and wind speed and direction from these stations are compiled in Tables 6-3 to 6-23. Figure 6-2a illustrates stations in close proximity to Yucca Mountain whereas Figure 6-2b illustrates some of the stations more distant. Stations listed in Table 6-1 but not shown on Figures 6-2a and 6-2b are located beyond the areas shown on the maps. Figure 6-2a shows the 9 Met stations and 3 precipitation stations listed in Table 6-2.

The DOE Monitoring Sites were established to provide representative data regarding meteorological conditions in topographically diverse settings at and around Yucca Mountain and to provide data for the purpose of making atmospheric dispersion estimates for evaluating the consequences of potential airborne releases. Sites 1 to 5 of the DOE Meteorological Monitoring Sites were installed in December 1985 as part of an environmental monitoring network. Sites 6 to 8 were added in July 1992, and Site 9 was added in January 1993 primarily to provide localized airflow characteristics related to the Exploratory Studies Facility. Five of the nine sites (3, 5, 6, 7, and 8) were downgraded to precipitation sites in 1999 with accompanying temperature and humidity measurements. Seventeen supplementary precipitation sites (401 to 417) were added to the monitoring network in 1997 to extend the precipitation data collection. Sites 405 and 415 have all season and storage precipitation gages. Site 401 was downgraded to only a storage gage October 30, 2001. The remaining supplementary precipitation sites have calibrated tipping bucket rain gages and are maintained by the University and Community College System of Nevada.

Monitoring equipment installed at the sites varies (Table 6-24). Onsite data loggers record meteorological conditions including mean, extreme, standard deviation, and total summaries using a range of time periods. Wind gusts occurring in a 3-second period and extreme daily 1-minute average wind speed and temperature values are recorded. The main summaries of all measurements are made for 10-minute and 1-hour time periods, with some daily summary values recorded (CRWMS M&O 1999 [DIRS 115672], pp. 1-8 and 1-9). All sites have two precipitation gages: one records by increments of 0.01 inch; the other is a standard storage gage.

The recording gage at Site 1 is heated to capture snowfall as it occurs. Site 1 has a 60-m tower, instrumented at two levels with wind and temperature sensors at 10 and 60 m above ground level (agl). Horizontal wind speed and direction are measured at both levels, and vertical wind speed is measured at 10 agl. Site 1 temperature, relative humidity, and pyranometers (used for measuring solar radiation) are located at 2 agl, and barometric pressure is nominally located at the surface. Sites 2, 4, and 9 include towers instrumented at 10 agl with wind and temperature sensors virtually the same as the 10 agl at Site 1. These sites also record temperature, relative humidity, and solar radiation at 2 agl. Barometric pressure is recorded at the surface. Sites 3, 5, 6, 7, and 8 have temperature and relative humidity sensors at 2 agl. Site 5 includes a barometer at the surface.

6.3.3.2.1   Temperature

Temperatures range from cool in the winter to hot in summer. Average monthly and annual temperatures are higher at lower elevations. The modest elevation (1,000 to 1,500 m) at Yucca Mountain is enough to prevent occurrence of the extremely hot temperatures reached in other, lower, southwestern deserts. At Site 1 (elevation 1,143 m; Table 6-6), temperatures rarely exceed 40°C, whereas at Site 9 (840 m; Table 6-14) temperatures can reach over 45°C. In the dry and cloudless air, surfaces cool efficiently by radiation, and daily ranges can be large.

Low humidity and clear skies allow surface temperatures to decrease significantly with elevation, especially during daylight hours. This is less true at night, and depends on local (sometimes very local) exposure and station site geometry. Unless it is cloudy or windy, surface-based temperature inversions form nearly every night, with warmer air aloft overlying cooler air near the surface. Such situations are stable and usually persist until daybreak. These conditions lead to surface heating, particularly in the summer with its high sun, which disrupts this vertical layering and soon produces temperatures that decrease with elevation. For this reason, sites on the sides or tops of even small hills often have warmer minimums than sites in adjoining low spots. Atmospheric moisture absorbs the infrared radiation emitted by the ground as it cools. In the very dry desert air, water vapor is not available to absorb this upward flux and re-radiate it back down toward the surface, so the surface cools very rapidly. Only in July and August, when the southwest monsoon brings extremely moist air to the Yucca Mountain area on occasion, is the humidity enough to significantly reduce the rate at which the atmosphere cools. Well into late spring or early summer, with sufficiently dry air, the high desert can sometimes cool to or below the freezing point.

6.3.3.2.2   Precipitation

Annual precipitation is low and occurs in two main seasons, during the winter months and the southwest monsoon in July and August. On rare occasions tropical storm remnants can supply precipitation in early autumn. As elevation increases, annual precipitation increases, and the seasonal cycle gradually changes to a regime increasingly dominated by winter precipitation. Elevated topography is associated with increased precipitation for three main reasons: (1) more precipitation-bearing clouds are formed than over lower elevations, (2) clouds and storm systems that already exist are augmented and assisted in producing more precipitation, and (3) lower evaporation losses are associated with reduced fall distances. Therefore, even heavy thunderstorms may deposit little precipitation on low elevation surfaces. In areas with arid

climates, the relative variability of aggregated precipitation totals is very large on all time scales, from daily to decadal. Relative variability is a measure of statistical dispersion of the frequency distribution (e.g., standard deviation), divided by the mean. Temperature data do not show such high variability. Longer records are thus needed for precipitation data than for temperature data to obtain a "representative" mean.

Another feature of arid climates is that much of the annual precipitation falls in just a few concentrated episodes. Typically, in this part of the United States, the wettest day brings about a quarter to a third of the annual mean precipitation, and about once in 50 to 100 yr the wettest annual day rivals the mean annual total in the driest locations. Previous estimates from Atlas 2 by the National Oceanic and Atmospheric Administration (Miller et al. 1973 [DIRS 109141]) have been updated by the National Weather Service Hydrometeorological Design Studies Center and placed online (www.nws.noaa.gov/ohd/hdsc). Because the values from 1973 are in such widespread use, both old and new estimates (following in brackets) for this area (36.904°N, 116.481°W, 5,206 ft elevation) are given here. They show that in a 6-hour period, about 19 mm [20 mm] will fall in a randomly placed gage about 50 times in 100 yr and that about 43 mm [63 mm] would fall about once in a hundred years. For a 24-hour period, about 28 mm [30 mm] is expected about every other year and about 71 mm [96 mm] could be expected during a randomly selected 100-yr period. The newer values are higher than the previous values in part because the region experienced a somewhat wetter precipitation regime from the mid 1970s to the mid 1990s.

A maximum annual total precipitation value of 36.7 cm was recorded in 1998 for the period of record 1986 to 2001 (Minwalla 2003 [DIRS 161362], pp. 247 and 248). This was measured at the 60 agl tower at Site 1. A survey of hourly precipitation records at Yucca Mountain from 1986 through 2000 indicated that the maximum observed hourly precipitation event amounted to 3.15 cm per hour at Site 7 in 1999 (Minwalla 2003 [DIRS 161362], p. 248). A maximum daily precipitation value of 13 cm per day and precipitation intensities of 5.8 cm per hour for a 50-yr return period and 6.6 cm per hour for a 100-yr return period were developed as design criteria from YMP station precipitation values (Minwalla 2003 [DIRS 161362], pp. 247 and 248).

The Mercury Desert Rock Airport period of record, 1984 to 2001, elevation 1005.8 m (3,300 ft), records maximum daily snowfall at 15 cm; maximum daily snow depth at 10 cm and maximum monthly snowfall at 17 cm (Minwalla 2003 [DIRS 161362], p. 247).

6.3.3.2.3   Humidity

The atmosphere in southern Nevada is characterized by very low relative and absolute humidity, especially in summer. Absolute humidity refers to the number of water molecules as a fraction of the total air molecules. Relative humidity refers to what the air could contain. The ability of air to "hold" water vapor (its moisture-bearing capacity) doubles about every 10°C. Thus, for the same amount of moisture, relative humidity is low in mid-afternoon and higher at night, and is higher in winter than in summer for the same part of the day, and on a daily average. Although absolute humidity is usually very low, occasionally, during the monsoon (mostly July and August), short episodes of high absolute humidity can occur with dew points reaching 23°C. In

the lower atmosphere, relative humidity increases with elevation, reflecting the decrease of temperature with height, whereas absolute humidity typically decreases with elevation.

Table 6-23 shows upper-air statistics based on twice daily radiosonde ascents at 0000 and 1200 Greenwich Mean Time at the National Oceanic and Atmospheric Administration station in Desert Rock, Nevada.

6.3.3.2.4 Wind

Wind is one of the most variable atmospheric elements, in both time and space. Winds have local and large-scale origins, ranging from small-scale heating differences on the scale of millimeters up to the size of the globe. In a typical desert environment, the surface and upper flows are much more strongly coupled during daytime and often completely decoupled at night. Wind speeds usually increase with elevation, but there are many exceptions to this generalization. Topographic effects, such as channeling, steering, waves, rotors, accelerations, quiet zones, cold air trapping, and other phenomena, are common. In the free atmosphere, winds increase with elevation in winter. In the summer, July winds decrease away from the surface, in part reflecting the low-level northward transport associated with the monsoon. No matter how hard the wind is blowing, wind velocity always goes to zero at the surface. Therefore, a larger variation exists within a few vertical meters for wind than for almost any other atmospheric parameter.

Wind velocity is also a vector quantity, which complicates the task of formulating simple or adequate summaries of wind effects. Scalar properties suffice for some processes. For example, evaporation depends on wind speed and is not affected by wind direction, unless the moving air mass carries a directionally varying property, such as temperature or moisture content. For other processes, the information on wind speed and direction must be summarized with probability distributions. The strongest winds in southern Nevada are likely to be associated with thunderstorms. In the dry desert air, very strong downdrafts can develop through evaporative cooling of drops falling in concentrated rain shafts. The strongest thunderstorm winds will preferentially be in the direction of storm movement, which is from southern and western quadrants. Wind is also a major factor in removal of moisture near the surface after recent wetting by a rainstorm. When such moisture is available, evaporative losses are considerably increased by strong winds.

Wind patterns are a result of local topography and synoptic- and regional-scale weather patterns (CRWMS M&O 1997 [DIRS 101215], p. 3-1). The primary influence on local wind is topography because it channels winds along the axes of valleys and generates diurnal winds due to air density differences over varying elevations.

Local topography can generate winds because the common diurnal wind cycle of airflow is toward higher terrain in the daytime, and away from higher terrain at night. This movement of air is caused by air pressure differences that arise from air density differences (caused by temperature differences between the air and earth's surface at equal elevations over higher and lower terrain). The diurnal cycle occurs most often during clear sky conditions, which are characteristic of the Great Basin climate. The downslope winds occurring during nighttime hours are frequently called drainage winds, because they typically follow the directions of

hydrologic drainage in complex terrain. Daytime wind patterns are often from the south and nighttime winds are often from the north; however, these patterns can be influenced by regional scale weather systems (CRWMS M&O 1997 [DIRS 101215], p. 3-9).

Synoptic and regional scale weather systems can overpower or enhance the local airflow mechanisms and create airflow occurring from directions different from the typical diurnal cycles. Data from the DOE sites show that airflow is typically from the south during the day and from the north during the night through Jackass Flats and Midway Valley (CRWMS M&O 1999 [DIRS 102877], pp. 8, 9, and 11). Airflow is apparently channeled by the north-south alignments of Fran Ridge and Yucca Mountain. However, ridge-top winds on Yucca Mountain are less channeled than those at lower elevations in the valley and wash areas. These winds are spread over a wider range from the southeast through the southwest. The data also show frequent occurrences of northeasterly winds during daytime hours, which are driven by regional scale weather patterns rather than the slope wind mechanisms (CRWMS M&O 1997 [DIRS 101215], p. 3-17). The most important factors appear to be cloud cover and wind speeds resulting from pressure gradients associated with these regional weather systems. Both factors tend to minimize the slope flows by altering the surface heating and cooling mechanisms (CRWMS M&O 1997 [DIRS 101215], p. 3-63).

Seasonal wind patterns are also common in the Yucca Mountain area. Stronger and more variable winds exist in winter than in summer. This corresponds to the greater number of frontal passages through northern and central Nevada in winter than in summer. Frontal passage periods can have wind forces strong enough to override the upslope and downslope topographic mechanisms (CRWMS M&O 1997 [DIRS 101215], p. 4-2). More cold air in the winter can enhance the downslope portion of the wind while suppressing some of the upslope wind compared to summer months.

Northerly winds dominate in the winter at night (CRWMS M&O 1997 [DIRS 101215], p. 3-34). The nighttime winds at Site 1 are from the northwest and north-northwest during all seasons, typically with speeds less than 3.3 meters per second (m/s). The corresponding winds at Site 9 are from the NNE and NE, typically with speeds greater than 3.3 m/s. The nighttime summer wind rose data from Site 1 show about twice the frequency of southerly winds than occur during the winter. The summer nighttime data show the fewest occurrences of winds greater than 5.4 m/s, indicating the least amount of strong weather patterns during the summer (CRWMS M&O 1997 [DIRS 101215], p. 3-34). Nighttime winds appear to be channeled by local topography more than the daytime winds. The summer months at DOE Sites 1 and 9 show notably more frequent southerly winds with speeds typically between 3.3 and 8.5 m/s (CRWMS M&O 1997 [DIRS 101215], p. 3-21). The northwest and north-northwest directions during winter and spring usually occur with speeds greater than 5.4 m/s (CRWMS M&O 1997 [DIRS 101215], p. 3-34).

Wind speed is one measure of the kinetic energy of the airflow. Higher wind speeds correspond to more kinetic energy and less channeling through topography (CRWMS M&O 1997 [DIRS 101215], p. 3-2). Table 6-25 shows the maximum-recorded daily one-minute and one-second gust wind speeds for the nine meteorological sites (CRWMS M&O 1997 [DIRS 100117], Table 4-4, p. 4-22; Table 4-6, p. 4-25). The projection at Site 1 is based on one year of data (1996) and the projections for the other sites are based on either three or four years

data (1993 or 1994 to 1996). In 1996, the average network wind speeds were highest during April, and lowest during November (CRWMS M&O 1999 [DIRS 115672], p. 3-1). The highest gusts in 1996 occurred in the beginning of the frontal passage season in October while the highest gusts in 1997 occurred in January and continued through the winter frontal system season (CRWMS M&O 1999 [DIRS 115672], p. 3-2).

Return values for these sites were derived from wind speed data. A 50-yr return value of 45 m/s was derived from Site 1, and a 50-yr return value of 54.11 m/s, the upper bounding value for all locations, was based on data recorded at Site 4, an exposed location at 1,234 m (4,050 ft) elevation (Minwalla 2003 [DIRS 161362], p. 248). Sites 3 and 5 through 9 show 100-yr return period values less than about 36 m/s (CRWMS M&O 1997 [DIRS 100117], p. 4-22). The maximum recorded daily 1-minute wind speed values (18.6 m/s at Site 3 to 33.16 m/s at Site 4) are about 63 to 76 percent of the 100-yr return period estimates (CRWMS M&O 1997 [DIRS 100117], p. 4-22). The record of extreme wind occurrences in the 1986 to 2000 period indicates that the return values continue to be viable estimates (Minwalla 2003 [DIRS 161362], p. 248).

Maximum wind speeds generally come from northerly and southerly directions at most of the sites (CRWMS M&O 1997 [DIRS 100117], p. 4-23). At Site 5, 30 percent of the daily one-minute maximum winds were from the north and 27 percent were from the south-southeast to south directions. Sites 3 and 6, those near confined topography, show channeling of the maximum winds along the axes of nearby topography. Site 2, on the ridge, recorded south-southeast and southwest to west-southwest winds. Site 4 recorded two well-defined north-northeast and south direction categories that contained over 50 percent of the daily maximum values (CRWMS M&O 1997 [DIRS 100117], p. 4-23). The distributions of the maximum wind speeds show that the daily maximum one-minute speeds were mostly greater than 5.4 m/s. All the sites except for Site 3 had daily maximum one-minute speeds over 11 m/s on at least 24 percent of the days.

6.3.3.2.5   Solar Radiation

Southern Nevada experiences abundant sunshine, and with relatively few additional sources to absorb or redirect ("scatter") light, the atmosphere is a little more transparent in the Yucca Mountain area than in urbanized regions to the south and west. This radiant energy is absorbed at the air-soil interface and converted primarily to the physical heating of the atmosphere. It is also readily available to evaporate whatever water exists at the surface.

The DOE monitoring sites are providing representative data on solar radiation within the (dispersion) model area. Table 6-26 shows mean daily and mean monthly solar radiation averages in megajoules (MJ) per square meter (m^2) for the period 1992 to 1997. Mean daily network averages for the period 1992 to 1997 ranged from a low of 8.9 megajoules per square meter per day ($MJ/m^2/d$) in January at Site 6 to 30.6 $MJ/m^2/d$ in June at Site 2. Differences in solar radiation measured between DOE monitoring sites were small during most months. The difference in mean monthly average solar radiation values reported for Sites 1 and 2 during the month of July, over the monitoring period of record, represents the largest recorded difference: 816.0 $MJ/m^2/d$ at Site 1 to 930.7 $MJ/m^2/d$ at Site 2. The yearly average for the period 1992 to

1997 ranged from a low of 583.4 MJ/m^2/d at Site 1 to a high of 621.4 MJ/m^2/d at Site 2 (CRWMS M&O 1999 [DIRS 102877], Appendix A, pp. A-1 to A-10).

6.3.3.2.6 Evaporation

Evaporation is important to the Yucca Mountain project because it is one factor that helps to determine the moisture content of the soil and, hence, groundwater recharge. The rates of water loss are strong functions of wind, atmospheric humidity, temperature, and to a lesser extent, solar radiation. There are few direct local measurements of actual or potential evaporation. However, the station at Boulder City, Nevada shows a long term average (1931 to 2000) of 2,947 mm/yr from a standard National Weather Service evaporation pan, kept full so that water availability is not a limiting factor (DTN: UN0201SPA021SS.007 [DIRS 161588]) (Section 7.1.5.3).

Transpiration from desert plants is relatively small because of a shortage of water to evaporate and the high efficiency of desert plant life in uptaking water. Moisture is lost from the soil directly and by the wicking action of plants. Plants uptake water from a deep, long taproot, or from extensive, shallow roots. Taproots can be many tens of meters long and draw moisture from deep in the soil while shallow roots uptake water during rare rain episodes.

6.3.3.2.7 Atmospheric Stability

Atmospheric stability is an indicator of the potential strength of the horizontal and vertical atmospheric mixing processes. Stability can be thought of as a measure of the tendency of the air to react to vertical displacement (CRWMS M&O 1997 [DIRS 101215], p. 3-2). Data from DOE Sites 1 to 9 indicate that stability ranges from very stable (category F, restricted mixing conditions occurring during nights with little cloud cover and low wind speed) to extremely unstable (category A, vigorous mixing conditions occurring during days with strong to moderate insolation and low wind speed). The neutral category is associated with moderate mixing conditions, occurring during either night or day with moderate to high wind speeds. The stable periods minimize vertical mixing and dilution of airborne pollutants (CRWMS M&O 1997 [DIRS 101215], p. 3-34). Stable air tends to return to its original level following a vertical displacement, so stable airflow is more likely to flow around obstacles than up and over them. Neutral or unstable air is less channeled because it is more likely to flow over obstacles (CRWMS M&O 1997 [DIRS 101215], p. 3-2). The less stable the air, the greater the horizontal and vertical spread compared to more stable periods (CRWMS M&O 1997 [DIRS 101215], p. 3-34).

Stability data are important so that the atmospheric dispersion of airborne material can be modeled. Atmospheric dispersion refers to the mixing and transport of momentum, kinetic energy, or a contaminant (heat, particles or gas) by the atmospheric processes of molecular diffusion, turbulent diffusion, and advection. Wind is the dominant meteorological parameter related to characterizing atmospheric dispersion because airflow controls the transport pathway and dilution of airborne material. However, wind patterns are influenced by topographic channeling, overprinted by regional airflow, and by diurnal and seasonal cycles at Yucca Mountain. Stability categories could also include factors such as these, in addition to wind speed, wind direction, and percentage occurrence of wind direction.

The Yucca Mountain area typically exhibits unstable and neutral atmospheric stability conditions during daytime hours and stable conditions typically during the nighttime hours (CRWMS M&O 1997 [DIRS 101215], p. 3-34).

Heating of the ground surface (through solar radiance), during the largely cloudless daytime periods contributes to instability, thus effectively enhancing mixing conditions by creating large negative vertical temperature gradients. Conversely, the clear sky during the nighttime hours allows the ground surface to cool leading to positive vertical temperature gradients (temperatures increasing with height) that suppress vertical mixing. The resulting density differences at higher-elevation air levels (elevated terrain) compared to lower-elevation air levels (adjacent valleys) during the nighttime hours create a downslope (generally southward-moving) drainage wind in contrast to typical northward-moving winds observed during daytime hours (CRWMS M&O 1997 [DIRS 101215], pp. 3-9 and 5-1).

The most stable periods typically occur with airflow downslope from the east side of Yucca Mountain through Fortymile Wash toward Amargosa Valley (CRWMS M&O 1997 [DIRS 101215], p. 3-10).

Extremely unstable conditions (category A) occur most often with winds from the southerly direction, which is generally upslope or up valley at all the DOE meteorological sites. The first few hundred meters above ground level are well mixed, and the transport direction is usually toward the north. Strong vertical mixing occurs during unstable conditions, which tends to cause winds above the surface to be similar to the winds near the surface. Transition periods from northerly nighttime to southerly daytime flow also produce unstable conditions (CRWMS M&O 1997 [DIRS 101215], pp. 3-36 and 5-1).

Local topography influences stability categories. The direction and dispersion (spread or distribution) varies among DOE Meteorological Monitoring Sites. For example, hilltop Sites 2 and 4 show fewer occurrences of the extremely unstable (A) and extremely stable (F) categories, with proportionally more occurrences in the neutral category (D). This may result from generally greater wind speeds and fewer occurrences of steady drainage winds at these hilltop sites compared to valley floor locations. Valley floor locations (Sites 5, 6, and 9) generally show fewer hours of extremely stable (F) and extremely unstable (A) categories with more hours in the slightly stable (E) or neutral (D) categories. This may be a result of steady-flow downslope drainage winds (CRWMS M&O 1997 [DIRS 101215], p. 3-36).

6.3.3.2.8 Air Quality

The Yucca Mountain Project ambient air quality monitoring program includes total suspended particulate matter and inhalable particulate matter (PM_{10}) sampling. Carbon monoxide, nitrogen dioxide, ozone, sulfur dioxide, nitric oxide, and the oxides of nitrogen were monitored from October 1991 through September 1995. Particulate matter monitoring began at Sites 1 and 5 in 1989 and at Sites 6 and 9 in 1992 (CRWMS M&O 1999 [DIRS 102877], pp. 7 and 8). The air quality monitoring program consistently showed levels well below the applicable National Ambient Air Quality Standards. The highest PM_{10} concentration measured was 67 μg/m^3, which is 45 percent of the applicable standard concentration level (CRWMS M&O 1999 [DIRS 102877], p. 9).

6.4 PAST CLIMATE

Climate change operates over a wide range of time scales. Geologic-scale or long-term forcing mechanisms, such as differing land and ocean configurations resulting from continental drift and the location and height of mountain ranges, occur over thousands of millennia (Barry and Chorley 1992 [DIRS 108902], p. 321) and operate over time scales outside of regulatory interest. However, intermediate to short-term climate forcing mechanisms, such as the earth's orbital cycle or solar output cycles, function within multi-millennial to decadal time frames that are within timescales of regulatory interest. These intermediate to shorter-term climate driving factors have the potential to affect the long-term performance of a repository system within Yucca Mountain. Therefore, climate change on the century-through-millennium to tens-of-millennia time scales is of regulatory interest because a repository must isolate or impede radionuclide transport during the postclosure period.

Most of these intermediate to short-term climate forcing mechanisms have operated throughout the earth's history, but extremely different climates occurred (e.g., global aridity during the Triassic period or tropical humidity of the Cretaceous period) because the configuration of land and ocean on the earth has changed over time (Barry and Chorley 1992 [DIRS 108902], p. 321). However, changes in land, mountain, and ocean configuration have been minimal for at least the past 500 k.y. and are expected to change little during the next 500 k.y. (USGS 2001 [DIRS 158378], p. 19). Therefore, the climate for the next 500 k.y., like that of the past 500 k.y., should be largely determined by changes in the intermediate to shorter-term climate driving factors. Furthermore, climates typical of the recent past are likely to recur in the future.

A variety of sources of information contribute to developing an understanding of the paleoclimate in the Yucca Mountain area. Data can be classified as providing long regional records of Quaternary climate change (Section 6.4.1), a local record of late Quaternary climate change (Section 6.4.2), or information on site climate change (Section 6.4.3). The primary records of past climate change come from stratigraphic successions of plant and animal fossils, and stable oxygen (δ^{18}O) and carbon (δ^{13}C) isotopes. Equally important age relations of the climate records are derived from U-series disequilibria (^{230}Th/U), and radiocarbon (^{14}C) dating, tephrochronology, paleomagnetic polarity stratigraphy, and stratigraphic position.

Regional records are from outside the Yucca Mountain area, but within approximately 162 km (100 mi) of Yucca Mountain. Long-term records of regional climate are available from Devils Hole in the Ash Meadows area of Nevada; Owens Lake, California; and Death Valley, California (Figure 6-1). The regional records can identify the rate and timing of climate change, as well as the duration of climate states, but the magnitude of that change may or may not apply precisely to the Yucca Mountain area.

Local records, by contrast, are within the Yucca Mountain area and include plant macrofossil data collected from packrat middens and wetland and spring deposits. These records span shorter periods of time than the long regional records, and may be short and discontinuous, but they identify the timing and often the magnitude of different climate states.

Site records are those on and within Yucca Mountain. They include data sets collected from calcite and silica precipitated in fractures within Yucca Mountain and calcite precipitated in the soils on or near Yucca Mountain.

This section documents the timing, magnitude, and character of past climate change in the Yucca Mountain area to establish the background and rationale for projecting such changes into the future. The linkage of past climate, especially parameters such as mean annual temperature (MAT) and mean annual precipitation (MAP), with past Yucca Mountain hydrology provides a basis for bounding the relation between climate and hydrology in the future. Wetter and cooler climates that persisted for centuries or millennia are of the greatest interest, because such climates produce more infiltration and percolation, resulting in higher water tables and increased groundwater discharge relative to present hydrologic conditions (Section 6.4.2.2).

An important factor influencing past Yucca Mountain glacial climate is the presence, size, and height of the North American continental glaciers. Atmospheric circulation models strongly suggest that the presence of Pleistocene ice sheets over the northern United States and southern Canada deflected the average polar front position southward (Kutzbach et al. 1993 [DIRS 119269], Figures 4.16 and 4.17, pp. 56 to 59), bringing cold and wet weather to southern Nevada for decades, centuries, or longer. During glacial maxima, the presence of an ice sheet as far south as the latitude of present-day Tacoma, Washington, (approximately 46°N latitude) led to a steepening of the pole-to-equator temperature and pressure gradients relative to present values. This steepened gradient displaced the polar cell, now largely confined in the winter to latitudes above 55°N latitude, southward to approximately 35°N (Kutzbach and Guetter 1986 [DIRS 109122], Figure 13, p. 1748). Yucca Mountain is about 37°N. This polar air mass was more extensive and much more vigorous than what we experience today. The presence of the North American ice sheets allowed the polar air mass to persist in the Yucca Mountain region year-round so summers were cool and wet and winter storms made landfall in California rather than in the Pacific Northwest.

Therefore, ice sheets largely account for the substantial increase in precipitation evident in glacial-age paleoclimatic records in the Yucca Mountain region (Thompson et al. 1993 [DIRS 149936], pp. 501 to 505). Furthermore, the existence of extensive continental and mountain glaciers sustained the polar air mass throughout the northern hemisphere summer, unlike present conditions in which solar input warms land areas at high latitude because there is no cold sink of ice and snow resulting in a weak and poorly defined polar air mass in summer. During glacial periods stronger year-round polar air masses existed with minimal tropical air mass penetration into middle and high latitudes, again unlike modern climate conditions.

6.4.1 Long Regional Records of Quaternary Climate Change

Long regional records of Quaternary climate change are critical for understanding the timing, magnitude, and frequency of past climates in the Yucca Mountain region. Long records provide the linkages between orbital parameters (Section 6.2.1.2), which force, or at least time, climate change and interpretable climate records. Such records, close to Yucca Mountain, have the advantage of identifying global climate cyclicity within a temporal framework and specific patterns of past regional climate changes relevant to the repository site. Comparison and integration of these climate proxy data provide a local and regional picture of variation in past

temperature, precipitation, and hydrology in both glacial and interglacial climate regimes. These past climate proxy records, when linked to global circulation patterns and orbital parameters, illuminate the process, timing, and potential drivers of past climate and provide insight on potential future climate change.

Three sites with long climate records are located within about 160 km (100 mi) of Yucca Mountain. The first site, Devils Hole, Nevada is a large, open extensional fracture within the carbonate aquifer, located in the Ash Meadows discharge area. Over the past 600 k.y., the fracture has generally maintained the opening and calcite has slowly precipitated on the fracture walls, leaving a stable isotope record of the water in the aquifer. Because of its well-constrained chronology (Ludwig et al. 1992 [DIRS 104631], Tables 1 and 2, pp. 285 and 286; Landwehr et al. 1997 [DIRS 109124], pp. 1 and 2), Devils Hole provides an absolute timing of global climate change applicable to the Yucca Mountain local area. The isotope record from Devils Hole does not, however, provide a clear sense of past change in air temperature and precipitation.

The second site, Owens Lake, California occupies a structural graben immediately east of the Sierra Nevada and contains an 800 k.y. proxy record of precipitation and runoff from the Sierra Nevada (Smith and Bischoff 1997 [DIRS 100077], p. 1). The Owens Lake record provides a sense of past changes in temperature and precipitation, but the timing of those changes are constrained by a relative chronology or potentially correlative chronology (Smith et al. 1997 [DIRS 109170], pp. 152 and 153; Litwin et al. 1999 [DIRS 109440], pp. 1161 to 1163).

The third site with a long paleoclimate record comes from Death Valley, California (Li et al. 1996 [DIRS 100054], p. 179). This fault-controlled basin, which today lies 86 m below sea level, contained deep freshwater and saline lakes that were supported by flow in the Amargosa River and its tributaries, such as Fortymile Wash adjacent to Yucca Mountain.

6.4.1.1 Devils Hole, Nevada

The Devils Hole record is significant for studies at Yucca Mountain because it provides an absolute chronology for past glacial and interglacial periods recorded in the Yucca Mountain region. The principal research at Devils Hole (Winograd et al. 1992 [DIRS 100094], p. 255; Winograd et al. 1988 [DIRS 109186], p. 1275) has focused on the excellent chronology of recorded isotopic changes. The chronology is now well established, using thermal-ionization mass-spectrometric uranium-series and protactinium-231 analyses (Ludwig et al. 1992 [DIRS 104631], p. 284; Edwards et al. 1997 [DIRS 166420], p. 782).

Devils Hole, located about 60 km southeast of Yucca Mountain (Figure 6-1), lies within the Yucca Mountain precipitation basin. It contains an accurately dated calcite vein that records the isotopic variation in atmospheric precipitation in the recharge area of the regional aquifer (Winograd et al. 1992 [DIRS 100094], p. 255) from approximately 568,000 to 60,000 yr before present.

Because the light isotopes of O and H are preferentially enriched in the vapor phase during evaporation or condensation of water, an enrichment that increases as temperature decreases, they can be used as tracers of precipitation air-mass sources and recharge conditions. Thus, higher $\delta^{18}O$ (and δD) values are indicators of warmer seasons or climates, or tropical air mass

sources, and lower values are indicators of cooler seasons or climates, or higher latitude air mass sources. Hence, $\delta^{18}O$ values are lower in glacial periods and higher in interglacial periods. Because the precipitation pathways reflect the relative dominance of polar (glacial) versus tropical (interglacial) circulation, then the absolute chronology of the Devils Hole $\delta^{18}O$ record provides a climate change chronology.

The Devils Hole $\delta^{18}O$ isotope curve (Figures 6-3a to 6-3c) shows cyclic fluctuations between isotopically lower and higher values that, respectively, track a progression of glacial and interglacial climates (Winograd et al. 1988 [DIRS 109186], p. 1276). The published records of cores from Devils Hole (DH-11 and DH-2) end at about 60 ka (DH-11) or 51 ka (DH-2), leaving the last glacial episode as yet undocumented. Significantly for Yucca Mountain studies, the shape of the Devils Hole $\delta^{18}O$ isotopic curve compares well with other major $\delta^{18}O$ isotope records. Comparisons include composite records from the global oceans established by the Spectral Mapping Project (Imbrie et al. 1993 [DIRS 109118], p. 531), the $\delta^{18}O$ values of ice from cores taken in Antarctica (Vostok) (Landwehr and Winograd 2001 [DIRS 160145], p. 31856) and Greenland (Taylor Dome) (Grootes et al. 2001 [DIRS 160979], Figure 4, p. 293), and other paleoclimatic records reflecting glacial and interglacial climate states (Landwehr et al. 1997 [DIRS 109124], pp. 3 to 8; Smith et al. 1997 [DIRS 109170], p. 153; Jannik et al. 1991 [DIRS 109434], p. 1158; Lowenstein et al. 1999 [DIRS 149904], p. 5; Ku et al. 1998 [DIRS 109438], p. 272; Morrison 1999 [DIRS 138393], p. 333; Prokopenko et al. 2001 [DIRS 160507], p. 126; Petit et al. 1999 [DIRS 109450], p. 430).

A time lag between atmospheric precipitation and the deposition of calcite adds uncertainty to the Devils Hole record (Winograd et al. 1992 [DIRS 100094], p. 256), as does the sampling interval. One sample represents about 1,800 yr (Winograd et al. 1992 [DIRS 100094], p. 255). Consequently, specific paleoclimatic interpretations of past climate scenarios from this record have not been made. However, the generalized conditions that lead to observed isotopic trend patterns within the Devils Hole record can be understood and described. For example, as continental glaciers expand, the polar front and the latitudinal position of the associated storm tracks move southward. The seasonal or annual southerly position of polar air steepens the thermal gradient between the Devils Hole recharge areas and the largely tropical and subtropical oceanic moisture source areas thousands of kilometers west and south of Yucca Mountain.

The Devils Hole record and climate proxy records from both hemispheres provide critical evidence that orbital dynamics (Section 6.2.1.2), at a minimum, represent a clock that signals the beginning of glacial periods. Although changes in insolation (related to changes in orbital parameters) are commonly cited as a primary cause of climate change, the specific causes of both the origins and terminations of glacial periods remain unknown. They probably involve complex interactions between orbital, solar, marine, and terrestrial climate-forcing functions that operate in different ways. The importance, or result, of a particular forcing function will vary according to its distance and relation to the proxy studied. Regardless, the existence of a chronology of past climate change specific to the Yucca Mountain region provides a crucial bounding parameter needed to estimate future climate for Yucca Mountain site characterization.

6.4.1.2   Owens Lake, California

The Owens Lake record is important to the understanding of past climate and hydrology in the Yucca Mountain area because it provides a record of snowpack in the Sierra Nevada above Owens Lake; hence the nature, rate of change, and duration of past glacial and interglacial periods.

Owens Lake is a present-day playa (elevation 1,081 m) in Inyo County, about 160 km west of Yucca Mountain (Figure 6-1). The sill, or spillway, of Owens Lake is at 1,145 m, so a 64 m lake depth likely occurred during a Pleistocene high stand (Smith and Bischoff 1997 [DIRS 100077], p. 2). The playa contains a thick sequence of lacustrine deposits, which includes diatom, ostracode, pollen, and geochemical proxies for paleohydrology and climate. Three cores were drilled to a total depth of 322.86 m in the south-central part of the playa (Smith and Bischoff 1997 [DIRS 100077], p. 6). The composite core represents 80 percent of the section. Three other cores provide additional sediment for a high-resolution study of the upper part of the Owens Lake section (Benson et al. 1996 [DIRS 108908], p. 746; 1997 [DIRS 108909], p. 263).

The cored record of Owens Lake spans the past 850 k.y. (Sarna-Wojcicki et al. 1997 [DIRS 109161], p. 79; Bischoff et al. 1997 [DIRS 108913], p. 91; Benson et al. 1996 [DIRS 108908], Figure 2, p. 747; Benson et al. 1997 [DIRS 108909], Figure 2, p. 264). The chronology for the Owens Lake record is derived largely from an age model based on a sediment accumulation rate (Bischoff et al. 1997 [DIRS 108913], p. 94), unlike the Devils Hole stable isotope record, which has a chronology derived from direct radiometric dating, or the Spectral Mapping Project (Imbrie et al. 1984 [DIRS 100047], pp. 269 to 305), which has a chronology derived from correlation of a composite marine record to the known orbital chronology based on the assumption of causality. As with any age model based on sediment-mass accumulation rates, it is expected that some events will be assigned ages that are too young or too old simply because natural sediment-accumulation rates are not constant.

However, Litwin et al. (1999 [DIRS 109440], p. 1151) provide a 230,000 yr-duration radiometrically calibrated climate proxy record for the Owens Lake cores based on pollen profiles that better resolves the earlier chronology (Bischoff et al. 1997 [DIRS 108913], p. 94) for this period. Both records show some intervals that can be attributed to glacial periods and other intervals that can be attributed to interglacial periods. These glacial and interglacial periods most likely correspond to the Devils Hole (Smith et al. 1997 [DIRS 109170], pp. 152 to 155) and Death Valley climate records (Lowenstein et al. 1999 [DIRS 149904], p. 6). Therefore, just as the undated Spectral Mapping Project marine record was synchronized to an orbital time scale, the Owens Lake record is synchronized here to the Devils Hole chronology**.**

6.4.1.2.1   Owens Lake Hydrology Linkage to Climate

The Owens Lake region lies in a winter-wet climate regime. During the winter, as westerly flow intensifies because of the southward migration of the polar front, numerous storms move into the southern California area. As these storms, pushed by the energized westerlies, rise over the Sierra Nevada, they commonly deliver large quantities of snow and rain to the higher elevations. Some storms are strong enough to deliver moisture to the Owens Lake Basin, but, more commonly, the prominent rain shadow effect of the Sierra Nevada isolates the Owens Lake

Basin from westerly storms. Whereas the crest of the Sierra Nevada often receives 150 cm or more of precipitation, typically as snow, Owens Lake proper averages only about 14 cm, most of which occurs in winter (Smith and Bischoff 1997 [DIRS 100077], p. 2). The persistence and location of the Aleutian low can influence the amount of tropical moisture in the westerlies, resulting in strong westerly flow and exceptionally wet California winters. Conversely, dry California winter conditions occur when the polar front is situated in a more northerly or, possibly, a still more southerly position. Eighty percent of the year-to-year variation in precipitation at Owens Lake is a function of the strength of the westerly (winter) flow (Bell and Basist 1994 [DIRS 108906], Figure 18c, pp. 1595 and 1597).

Summer precipitation is typically limited. It is usually related to monsoonal activity (Hansen and Schwarz 1981 [DIRS 109114], Figure 2.2, pp. 7, 8, and 60; Kay 1982 [DIRS 109121], pp. 76 and 77) that brings moisture from the Gulf of California and the Pacific Ocean into the Owens Valley. Higher levels of summer precipitation often occur in years when winter precipitation is low.

Owens Lake records hydrochemical change, which is directly related to precipitation in the Sierra Nevada. During glacial periods, water in the Owens River is dilute and dominated by runoff derived from extensive snowpack. During interglacial periods, water in the Owens River is less dilute and dominated by base flow. The high-flow glacial regimes maintain a dilute lake with a low residence time and through-flow, whereas the interglacial regimes store water in the lake with outflow primarily as vapor (evaporation) resulting in a saline lake.

Although the waters in the basin are chemically diverse, they may be divided into two groups, based on the total alkalinity to dissolved Ca (alk/Ca) ratio (Forester et al. 1999 [DIRS 109425], p. 19). Surface water from high elevations typically has a low alk/Ca ratio, whereas base flow water at low elevations typically has a high alk/Ca ratio. The solute content (total dissolved solids [TDS] and alk/Ca ratio) in Owens Lake at any time will depend on the volume of flow from high elevations. If flow is very high and persistent from year to year, then the solute composition in Owens Lake will move to the high-elevation chemical signature, low alk/Ca ratio. That signature will be further maintained by the lake rising to its outlet and overflowing, resulting in decreased residence time and lower TDS.

If, at the other end of the spectrum, flow from high elevations is very low, then the solute composition in Owens Lake will move to the low-elevation chemical signature and high alk/Ca ratio. Low flow and high evaporation will prevent the lake from rising to its outlet, further concentrating the solutes from increased residence time. Little is known about the geohydrological characteristics of the aquifer that supports the high alk/Ca ratio base flow, (Hollett et al. 1991 [DIRS 109115], pp. B47 and B53 to B55), but its water content is ultimately dependent on high-elevation recharge that would be reduced during extended dry periods. Based on diatom and ostracode assemblages recovered from sediment representing the last 50,000 yr, the saline springwater discharge into Owens Lake played an important role in determining lake hydrochemistry during arid climatic periods (Bradbury and Forester 2002 [DIRS 161595], p. 171). The combination of high evaporation and little or no base flow in the Owens River results in a dry, saline, mineral-rich Owens Lake bed.

The Owens Lake solute budget, therefore, offers a way of identifying the climate characteristics of the basin. When the polar front moves south in winter, or more permanently during glacial periods, westerly flow is energized (Barry and Chorley 1992 [DIRS 108902], p. 164). Energized westerly flow brings numerous storms into southern California (Smith and Bischoff 1997 [DIRS 100077], Table 1, p. 3), and those storms produce a large snowpack at higher elevations in the Sierra Nevada. Upon melting, that snowpack provides sufficient flow to the Owens River; thus, high-elevation solute chemistry retains its signature on the valley floor and within Owens Lake. Conversely, a weak polar front results in less snowpack and flow in the Owens River will be reduced; thus, Owens Lake solute composition moves toward the valley-bottom chemical signature.

The latitudinal position of the polar front affects Yucca Mountain as well as Sierra Nevada climate. Although at a much lower elevation than the upper reaches of the Owens River, the Yucca Mountain area experiences cool and wet weather when the Sierra Nevada receives abundant snowfall and the polar front moves to its southerly position (Section 6.3.1). Because the Owens Lake drainage occupies the same latitudinal zone as that of Yucca Mountain, approximately 150 km (93 mi) to the east, it is assumed that variations in one can be related to variations in the other.

The variability of solute composition, particularly the alk/Ca ratio, and TDS in Owens Lake water then becomes a measure of the variability of the climate system within the region. If, for example, the alk/Ca ratio and TDS fluctuate widely in tandem from decade to decade, high variability in the climate system is indicated. Such variability might occur if there are a few years with strong polar fronts in combination with strong ENSO years, which alternate with correspondingly dry periods as a result of opposite atmospheric conditions. Conversely, a low variation in solute chemistry and TDS implies a system with low variability. Low variability and a continuously high alk/Ca ratio and high TDS imply dominance by weak westerly flow and a consistent retreat of the average polar front location to the north. However, low variability, a low alk/Ca ratio, and low TDS imply persistent dominance of the polar front and westerly storm tracks.

6.4.1.2.2   Microfossils as Proxy Records of Climate

In broad terms, the fossil diatoms and ostracodes in the Owens Lake cores reflect the spectrum of water chemistry found in the Owens River drainage. The low TDS and low alk/Ca waters are characterized by freshwater planktonic diatoms, such as *Stephanodiscus*, which indicate large, deep, freshwater lakes (Fritz et al. 1993 [DIRS 109054], Table 2, pp. 1848 and 1853), or ostracodes, such as *Cytherissa lacustris*, which today live in dilute cold lakes situated in the Canadian boreal forest (Delorme 1970 [DIRS 108953], p. 1257). The high TDS and high alk/Ca waters host shallow water diatoms, such as *Campylodiscus clypeus*, which are tolerant of waters with high electrical conductivity (Fritz et al. 1993 [DIRS 109054], Table 2, pp. 1850 and 1851), and ostracode taxa, such as *Limnocythere sappaensis* (Forester 1983 [DIRS 109023], p. 436, Table 1; 1986 [DIRS 109024], Figure 1, p. 797). Other diatom and ostracode species are sensitive to the spectrum of alk/Ca ratios and TDS conditions that could occur under all other possible flow conditions between these extremes.

The microfossil record can be translated into a chronological progression of climate-induced hydrochemical environments (Bradbury and Forester 2002 [DIRS 161595], p. 171). The translation requires the standard assumption common to paleoenvironmental reconstructions from fossils, in that abundances of the fossil species reflect their habitat ecology and are proportional to the type of environments that existed at the locality when those species were alive. For example, an abundance of modern taxa that today live in cold, low alk/Ca, fresh water would imply the persistent existence of a polar front situated in a southerly position. As a consequence of this paleoclimatic scenario, MAT in the region, including Yucca Mountain, would be lowered and MAP elevated. Change is recorded in the characteristics of the paleolake as some (or all) species comprising a particular assemblage become rare or disappear and others appear and become common in a stratigraphic series of samples.

The rate of climate change can be estimated from the stratigraphy and chronology within which key environmental indicator species' abundances change. Similarly, the persistence of key environmental indicator species provides an estimate of the duration of a climate state. Diatom and ostracode assemblages recovered from Owens Lake dating from about the last 50,000 yr suggest that at about 52,000 yr ago, the lake transitioned from a closed to an open basin in less than 300 yr, and that at about 10,000 yr ago, it transitioned from fresh to saline in less than 100 yr (Bradbury and Forester 2002 [DIRS 161595], p. 171). The apparent rapidity and magnitude of climate changes at Owens Lake, therefore, implies that the small changes in the Devils Hole isotopic record from groundwater interglacial to glacial conditions (Section 6.4.1.1) reflect substantial changes in ambient temperature and/or moisture characteristics within the region. Thus, the stratigraphic profiles of microfossil abundances from the Owens Lake sedimentary record provide a proxy for the nature, rate of change, and duration of climate states in this region in the past.

For the purposes of this report, the paleoclimate record of Owens Lake is based primarily on the stratigraphic distribution and abundances of diatoms and ostracodes in cores taken from the basin. However, interpretation of the lake record using ostracode and diatom data is generally consistent with interpretations using other Owens Lake climate proxy records such as pollen, chemical, mineralogical, and geophysical data (Smith et al. 1997 [DIRS 109170], Figures 1 and 2, pp. 145 and 146). Five key ostracode species were recovered from the Owens Lake sediment core. The occurrence of each species suggests a different climate scenario, because these microfossils track climate-induced water chemistry and temperature of the lacustrine habitats in which they have lived for the past 400 k.y. (CRWMS M&O 2000 [DIRS 151945], pp. 6.3-15 to 6.3-17).

The climate and limnologic relations of the microfossils are summarized below from USGS (2001 [DIRS 158378], pp. 50, 53, 54, 55, 56, 58, and 65) and Bradbury and Forester (2002 [DIRS 161595], pp. 156, 161, 162, and 166). In all cases, the expected change for climate varying from glacial to interglacial and back to glacial is observed in diatom and ostracode assemblages. The first five scenarios (A through E) are developed from the occurrence of these five ostracode species and coeval diatoms. The last scenario, F, is based on the rarity of ostracodes and diatoms and the intermittent occurrence of brine shrimp, which indicate very saline or intermittent playa conditions, or both. The following five scenarios are ordered from the coldest, wettest, and most stable conditions to the warmest, driest, and most variable conditions at Owens Lake.

Scenario A–Full glacial, cold, and wet. Scenario A is identified by the modern day boreal ostracode *Cytherissa lacustris*. Diatoms in Owens Lake under such climates are low-light, freshwater species of *Stephanodiscus* and *Cyclostephanos* that bloom during the short open-water season. This climate scenario is one in which the polar front resides near or south of the latitude of Owens Lake. This cold frontal boundary directs westerly storm tracks to the Sierra Nevada and maintains cold and seasonally stable temperatures, relative to today. The resulting cold climate supports extensive valley glaciers in the Sierra Nevada and increased snowpack runoff relative to today, greatly increasing annual effective moisture. Continental glaciers are both large and extensive, thus maintaining polar air and, possibly, arctic air at Yucca Mountain latitudes during winter and perhaps throughout the year. In response to this climate type, Owens Lake contains cold and dilute through-flowing water, with low-alk/Ca water throughout the year.

Scenario B–Full glacial, cold, and wet, but not as cold as Scenario A. The ostracode assemblage in Scenario B is dominated by *Candona caudata*, which lives today in the Owens Lake drainages at higher elevations and north into Canada, and *Cytherissa lacustris*, which is rare or absent in the Owens system drainage. The diatom assemblage is characterized by planktonic species that bloom in the late summer or fall, as well as species prospering in the early open-water season. This scenario represents the persistent residence of the polar front during each winter, year after year, but this frontal boundary may retreat northward during most summers. The seasonal cold and wet winter conditions may promote the growth of regional valley glaciers during the waxing phase of continental ice sheets, or the retreat or loss of valley glaciers during the waning phase of a continental ice sheet. Continental ice sheets are less extensive than in Scenario A. Owens Lake is large, fresh, and overflowing with low-alk/Ca water. Seasonality in temperature, and perhaps limited seasonality in chemistry, occurs.

Scenario C–Intermediate, cold, and drier than Scenario A or B. *Limnocythere ceriotuberosa* characterizes this climatic environment, but depending on whether the system is at a wet or dry end of its range, other taxa are also present, such as *Candona caudata* (wet) or *Limnocythere sappaensis* (dry). The diatom flora of Owens Lake under this climate regime exhibit similar variability. Dry decadal-scale intervals support saline planktonic diatoms or summer-blooming freshwater planktonic species, depending on the net hydrologic balance in the lake. Scenario C represents an intermediate climate state between the glacial state described in Scenario B and the interglacial state described in Scenario D. This climate scenario is characterized by a relatively common movement of the polar front to Owens Lake latitudes during most, but not all, winters. Continental ice sheets are either in the early stages of growth or nearing the final stages of retreat. Mountain glaciers probably exist in the high cirques and may expand or contract on decadal or century scales. Although the polar front is present in most years in this scenario, it may not be as persistent or consistently resident for the entire winter as in Scenario B. During some winters, the polar front resides to the north of Owens Lake, but it is still close enough to ensure ample precipitation to provide the lake with regular seasonal discharge. The relatively freshwater lake could either overflow seasonally or not spill at all, shifting seasonally to a slightly saline (a few grams per liter) lake in which the alk/Ca ratio is elevated. Summer seasons are warm to hot, and Owens Lake becomes smaller because of evaporation and reduced flow in the Owens River. TDS increase during the summer.

Scenario D–Interglacial or modern climate regime. *Limnocythere sappaensis*, an ostracode of moderately to highly alkaline and saline lakes, dominates in Scenario D. Saline benthic diatoms document the shallowness of the lake and the variably high salinity. Diatom preservation is often poor because of corrosion and breakage in shallow, alkaline water. Scenario D represents Holocene-like (modern) climate conditions in which the average position of the polar front varies from year to year. Westerly atmospheric flow brings snow to the Sierra Nevada, but in most years snowpack is not especially deep, resulting in modest to low flow in the Owens River and a lake that rarely overflows. Continental ice sheets are small, like those of today. Evaporative water loss in summer sustains saline, high-alk/Ca water. Climate in this scenario can be variable, with greater snowpack occasionally occurring either from strong ENSO conditions or from a cold period similar to the Little Ice Age. Flow in the Owens River is proportional to available snowpack and, in years comparable to 1968 and 1969, flow is very high and freshens the saline lake.

Scenario E–Monsoon, warmer, and wetter than the current climate. *Limnocythere bradburyi*, an ostracode that commonly occurs under current climatic conditions in central Mexico, represents wetter, and perhaps warmer, climates than today at Owens Lake. Although the climate is likely to be warmer during a monsoon state, temperatures may be moderated by increased cloud cover relative to modern cloud cover. The presence of this ostracode in the Owens Lake stratigraphic record implies an Owens Lake source water derived from strong summer monsoon climate episodes that likely were brought northward from the gulfs of California and/or Mexico (USGS 2001 [DIRS 158378], p. 56) or eastern tropical Pacific Ocean. Monsoon climates in the Yucca Mountain area can be characterized by summer rain generated by incursions of moisture originating within subtropical easterlies or marine vapor flowing into a well-developed thermal low. Winter precipitation most likely did not dominate the MAP during monsoon intervals because winter storms would have been less frequent than at the present. Monsoon climate states were most likely wetter and perhaps warmer in summer than today, with much of the precipitation lost to evapotranspiration and evaporation.

Scenario F–Hotter, drier than today. Neither diatom nor ostracode populations persist in Scenario F long enough to leave a significant record. During rare flood events, redeposition of fossils from high-stand lake deposits is possible, but generally the sediments are barren of microfossils. In this scenario, the average position of the polar front is typically north of the Owens Lake latitudes, and westerly flow is weak, making snowpack typically negligible. Any summer precipitation is used by valley-bottom plant communities. These conditions may be common for centuries, or even a few millennia, with only infrequent reversals to wetter conditions. The middle Holocene, beginning about 8 ka, was a recent period when these dry conditions were common (inferred from Bradbury 1997 [DIRS 108938], p. 109). Because snowpack is limited, recharge is also limited, and, consequently, base flow in the Owens River eventually falls to a very low level, or the river goes dry. Because of limited surface flow and, eventually, base flow, Owens Lake becomes a dry and perhaps deflating playa, at least seasonally and probably for decades at a time.

6.4.1.2.3   Past Climate Inferred from the Owens Lake Record

The Owens Lake microfossil record shows that the region has undergone significant climate change on the millennial time scale and suggests rapid changes from interglacial to glacial

stages. These rapid transitions occur within one or two millennia to as little as a few centuries. The past climates differed from those of today because the predominant circulation pattern of the atmosphere was different from that which typifies the modern world. An alternative viewpoint is presented by Davis (1989 [DIRS 160138], p. 621) and Zielinski and McCoy (1987 [DIRS 160136], p. 133) who argue that the position of some major atmospheric circulation features did not change during the late Quaternary epoch. Such rapid changes from warm and dry to cold and wet climates at Owens Lake suggest a southerly shift in the average position and strengthening of the polar front and associated polar jet stream. The present atmospheric circulation pattern and a significant rain-shadow effect are the reasons for today's arid to semiarid climate in the Yucca Mountain region (Section 6.3.3).

During the past 400 k.y. microfossils from the Owens Lake core document five major cool and/or wet periods, called marine isotope stages (MIS), which are also documented in other climate proxy records: MIS 10, 8, 6, 4, and 2^2. The MIS numbers were established from studies using marine carbonate $\delta^{18}O$ records reflecting change in $\delta^{18}O$ values of ocean water as continental ice sheets expanded and contracted (Imbrie et al. 1984 [DIRS 100047], pp. 288 to 293; Shackleton and Opdyke 1973 [DIRS 109163], Figure 7, pp. 45 and 41 to 44). Even-numbered MIS represent glacial stages, whereas odd-numbered MIS represent interglacial stages. MIS dates vary with the proxy record and location.

The occurrence of the ostracode *Cytherissa lacustris* in the MIS 6 and MIS 2 glacial periods in Owens Lake suggests climate Scenario A, whereas its absence in the first two glacial stages (MIS 10 and MIS 8) in the 400 k.y. orbital cycle suggests climate Scenario B. Additionally, the persistence and commonness of *C. lacustris* during MIS 6 relative to MIS 2 suggests MIS 6 had much greater effective moisture, the so-called "superpluvial" period within the long (400 k.y.) orbital cycle, than MIS 2. The abundance and duration of juniper pollen in the Owens Lake record between 170 and 120 ka relative to other glacial periods (Litwin et al. 1997 [DIRS 109126], Figure 4, pp. 134 and 138) also indicates that MIS 6 had much higher effective moisture than other glacial stages.

The present interglacial period, the Holocene (MIS 1), may be the most arid of the past 800 k.y., based, in part, on the presence of oolites, which form in shallow, moderately saline water and are unique to the uppermost levels of Owens Lake deposits (Smith et al. 1997 [DIRS 109170], p. 151). This stratigraphic interval is commonly barren of microfossils, suggesting climate Scenario F. Sediment cores from other lakes in the Owens drainage system also show extreme aridity in the Holocene. Jannik et al. (1991 [DIRS 109434], p. 1159) suggest that if "borne out by further investigations, it will imply that the Holocene is not a good model for reconstruction of paleoecological patterns during previous interpluvial periods." Similarly, Bradbury and Forester (2002 [DIRS 161595], p. 170) report overflow conditions at Owens Lake from about 50 to 10 ka, and that the lake remained below its spill level for long periods of time during the last 10,000 yr.

---

[2] The onset and termination of MIS inferred from climate proxy data vary depending on type and location of record. Estimated dates of mid-glacial stages for the Yucca Mountain area (using Figure 6-3b and c; Table 6-28; and Jannik et al. 1991 [DIRS 109434], Figure 10, p. 1158) are as follows: MIS 18 (~675 ka), MIS 16 (~600 ka), MIS 14 (~520 ka), MIS 12 (~430 ka), MIS 10 (~370 ka), MIS 8 (~260 ka), MIS 6 (~160 ka), MIS 4 (~70 ka), and MIS 2 (~20 ka).

The presence of a glacial and interglacial biostratigraphy within the Owens Lake microfossil record implies that, like the Devils Hole record, the Owens Lake record is relatively continuous and can be interpreted in terms of global climate changes that are correlated with orbital parameters. This linked evidence allows the Owens Lake record to serve as a guide to future climate changes there and at nearby Yucca Mountain.

6.4.1.3   Death Valley, California

Death Valley, California also records a sequence of climate events similar to the Devils Hole and Owens Lake records, further documenting the regional character of climate change in the Yucca Mountain region. The Death Valley lake record is important to the Yucca Mountain paleohydrology and paleoclimate story because a combination of low temperatures and surface and groundwater sources were maintaining the 175 to 300 m-deep lake during glacial periods. Therefore, the glacial period effective moisture was very different than modern effective moisture. Death Valley is potentially fed by three major sources of water: (1) drainage from the Sierra Nevada via the Owens River and through Owens Lake, China Lake, Searles Lake, Panamint Valley, and ultimately to Death Valley; (2) the Mojave River flowing from the Transverse Mountains into the southern side of Death Valley; and (3) the Amargosa River draining the highlands north of Yucca Mountain via Fortymile Wash and flowing into Death Valley on the southeast margin of the basin (Figure 6-1).

Sediment and shoreline deposits in Death Valley, Owens Lake, Searles Valley, and Panamint Valley suggest that increased precipitation in the Amargosa and Mojave River drainages, rather than runoff from the Owens River drainage, was the primary source of water for the 18 ka and 12 ka (MIS 2) Death Valley lake high stands (Anderson 1999 [DIRS 150236], pp. 124 and 130; Anderson and Wells 2003 [DIRS 162062], p. 115). The Amargosa River provides the only significant water to Death Valley today and is likely to have been a major contributor to the basin in the past. Evidence for Mojave or Owens River overflow into Death Valley during the 26 ka highstand does not exist, so it is thought that this highstand resulted entirely from local Amargosa River runoff (Anderson and Wells 2003 [DIRS 162062], p. 115). Because the Amargosa River does not have high mountain ranges like the Sierra Nevada in its drainage area, deep lakes in Death Valley support the reconstructions of cold and relatively wet climates derived from climate proxy data in the Yucca Mountain area. If the Amargosa River supported a large lake in Death Valley, Fortymile Wash was likely a permanent stream requiring a groundwater system to support it (Anderson and Wells 2003 [DIRS 162062], p. 127).

These periods of increased effective moisture during MIS 2 and other glacial periods suggest that the summer subtropical high presently occurring over southern Nevada was not present so summer temperatures were lower and infiltration was greater than today. Silver Lake Playa, in the Mojave River drainage just south of Death Valley, currently floods only during high-intensity storms. These storms occur when the winter storm track is in a southerly position over the eastern north Pacific, directing tropical moisture into southern California (Enzel and Wells 1997 [DIRS 160157], p. 223). Thus, the presence of large Pleistocene lakes in the southern California and southern Nevada region suggests that the storm tracks may have been displaced southward during glacial episodes.

The Death Valley paleohydrologic and paleoclimatic data are primarily from a 186 m core (DV93-1) from lake deposits (surface elevation below sea level) in the Badwater Basin (36°14'N, 116°48'W) of Death Valley located about 80 km (50 mi) from Yucca Mountain (Figure 6-1). The core consists of interbedded silty muds and evaporites deposited during the past 200 k.y. Sedimentary structures of muds and evaporites, evaporite mineralogy, and analysis of fluid inclusions from this and other cores (Li et al. 1996 [DIRS 100054], p. 179; Roberts and Spencer 1995 [DIRS 109156], p. 3929; Roberts and Spencer 1998 [DIRS 160208], p. 367; Spencer and Roberts 1998 [DIRS 160207], p. 378; Lowenstein et al. 1998 [DIRS 160388], pp. 243 and 244; Anderson 1999 [DIRS 150236], pp. 124 to 126; and Lowenstein 2002 [DIRS 161594], p. 109) provide a paleolimnologic and temperature history for the Death Valley Basin that can be compared to other proxy data from the Owens Lake core, the Devils Hole oxygen isotope record, and other lacustrine records in the Mojave Desert.

Studies of Death Valley sediments deposited over the last 200,000 yr identify four distinct playa or lake environments: dry mud flats, playa salt pans, layered halite of permanent saline lakes, and black mud with sedimented halite representing large saline lakes receiving allochthonous detrital materials from the drainage basin. These four sediment types correspond to progressively deeper and more persistent saline lacustrine environments that occupied the Death Valley Basin in the past (Roberts et al. 1994 [DIRS 109157], p. 61). The chronology of these depositional environments has been established by U-series dates of bedded salts (Roberts and Spencer 1995 [DIRS 109156], Figure 7, p. 3935; Li et al. 1996 [DIRS 100054], pp. 187 and 188).

Shallow to deep permanent saline lakes characterize the MIS 6 and MIS 2 glacial periods, whereas dry mud flats and salt pans represent the last interglacial and Holocene arid environments (MIS 3 and MIS 1). Four shoreline tufas located 73 to 90 m above sea level with ages of 194 to 216 k.y. are older than sediments from core DV93-1. The oldest tufas suggest a third paleolake highstand in Death Valley existed at about 200 ka (Lowenstein 1999 [DIRS 130132], p. 143; Ku et al. 1998 [DIRS 109438], p. 261).

Lake Manly formed in Death Valley between approximately 186 to 120 ka during glacial period MIS 6 (Roberts 1996 [DIRS 109155], pp. 168 to 169). It was large and estimates of its depth range from 175 m to more than 300 m, with a high stand 90 m above sea level (Roberts and Spencer 1998 [DIRS 160208], pp. 365 to 367; Ku et al. 1998 [DIRS 109438], pp. 261 to 269). Over 30 m of black mud were deposited in the lake during this interval (Ku et al. 1998 [DIRS 109438], p. 271). Lake salinity may have varied from less than 10,000 to less than 3,000 ppm, based on the ostracode record (Lowenstein et al. 1999 [DIRS 149904], p. 4; Lowenstein 2002 [DIRS 161594], p. 118). The existence of a deep lake in Death Valley during MIS 6 is consistent with evidence discussed by Morrison (1999 [DIRS 138393], pp. 332 to 336) indicating that Tecopa Valley, California, harbored high lake stands from MIS 10 to MIS 6. The Owens Lake and Searles Lake records also suggest high stands during this time period (Smith et al. 1997 [DIRS 109170], Figure 6, p. 150).

The highest stands of Lake Manly during MIS 6 occurred between ~185 to 160 ka, which also corresponds to the lightest (cold) oxygen isotope values between 170 to 155 ka in the Devils Hole record (Ku et al. 1998 [DIRS 109438], p. 273). The high stand at about 200 ka, which was comparable in size to the MIS 6 lake (Ku et al. 1998 [DIRS 109438], p. 261), may correspond to

Stage 7b in the Devils Hole record. An increase in spring-fed groundwater along lake shorelines during MIS 6 in southern Death Valley is based on U content of tufa (Ku et al. 1998 [DIRS 109438], p. 261). Tufa often originates from Ca-rich springs. This suggests greatly increased precipitation and recharge relative to today. Spencer and Roberts (1998 [DIRS 160207], p. 378) suggest that the loss of this lake in Death Valley was due to a reduction in precipitation rather than just warming.

According to a U-series date on halite precipitated from lake water, the initial transition between glacial period MIS 6 and interglacial period MIS 5e began at about 128 ka. The end of the perennial lake in Death Valley occurred at about 120 ka, with a moderate lake existing between these time periods. At about 120 ka, the Owens Lake drainage closed (Roberts and Spencer 1998 [DIRS 160208], p. 367). However, these dates are problematic (too young), because other climate proxy data suggest that less effective moisture in the area at this time could not support a moderate lake. The ages are derived from $^{234}U/^{238}U$ and $^{230}Th/^{234}U$ ratios, (Ku et al. 1998 [DIRS 109438], Table 2, p. 267) and low ratios such as these are considered to be unreliable (Muhs et al. 2002 [DIRS 161012], p. 1359) and thus, may have large errors. Arid conditions, similar to modern climate, occurred between 120 and 60 ka; however, fresher lake phases lasting a few thousand years occurred between about 154 to 146 ka, 129 to 127 ka, and 123 to 121 ka (Ku et al. 1998 [DIRS 109438], p. 261; Lowenstein et al. 1999 [DIRS 149904], p. 4), provided that the dating is accurate.

Death Valley contained saline pans with ephemeral salt lakes between 60 and 35 ka, (Lowenstein et al. 1998 [DIRS 160388], p. 237). Then, between 35 and 10 ka (MIS 2), a perennial saline lake, occasionally between 80 and 90 m deep with fluctuating salinities and lake levels, existed (Ku et al. 1998 [DIRS 109438], p. 272; Lowenstein 2002 [DIRS 161594], pp. 117 and 118; Lowenstein et al. 1999 [DIRS 149904], p. 4; Lowenstein 1997 [DIRS 109129], Figure Core DV-93; Li et al. 1996 [DIRS 100054], Figure 5, pp. 179 and 187; Anderson 1999 [DIRS 150236], p. 128). Anderson (1999 [DIRS 150236], pp. 129 and 130) suggests that the Mojave River contributed significant volumes of water to Death Valley during MIS 2, based on sediment cores in Death Valley and lake stands at Lake Mojave (~18.4 to 16.6 ka and ~13.7 to 11.4 ka) and Lake Dumont (30 to 25.3 ka and ~19.4 to 18 ka), which are along the Mojave River drainage up-drainage from Death Valley. She postulates that the high stand in Death Valley at approximately 18 ka owed its existence to precipitation in the headwaters area of the Mojave River in the Transverse Mountains (Anderson 1999 [DIRS 150236], p. 130). Subsequently, mudflats and saline pans have predominated over the last 10 k.y. (Lowenstein et al. 1998 [DIRS 160388], p. 237).

The Death Valley core contains halite crystals precipitated from lake water. Fluid inclusions in the halite crystals recorded surface brine temperatures at the time of halite precipitation. The inclusions were studied using the methodology described by Roberts and Spencer (1995 [DIRS 109156], p. 3930) and Lowenstein et al. (1998 [DIRS 160388], pp. 228 to 233). The resulting maximum homogenization temperatures of halite fluid inclusions (Th_{MAX}) reflect the maximum water temperature at which the halite precipitated (Roberts and Spencer 1995 [DIRS 109156], p. 3929; Roberts and Spencer 1998 [DIRS 160208], pp. 364, 367; Spencer and Roberts 1998 [DIRS 160207], p. 378; Lowenstein et al. 1998 [DIRS 160388], p. 223; CRWMS M&O 2000 [DIRS 151945], Figure 6.3-14, p. F6.3-14).

Spencer and Roberts (1998 [DIRS 160207], p. 378) suggest 10°C colder-than-modern summer and winter maximum air temperatures between 192 to 186 ka (MIS 7) and 15°C colder-than-modern summer and winter maximum air temperatures between 128 and 120 ka (MIS 5). Lowenstein et al. (1998 [DIRS 160388], p. 243; Lowenstein et al. 1999 [DIRS 149904], pp. 5 and 6) found that fluid-inclusion homogenization temperatures for virtually all of the last 100,000 yr were lower than modern temperatures. Halites dated about 100 ka had the highest Th_{MAX} values in the 100,000-yr record: between 23 and 35°C, with four values 30°C or above. The higher values are similar to the modern spring time temperatures at Yucca Mountain. Halites dated between 60 and 35 ka had brine temperatures 6 to 11°C below modern temperatures (23 to 28°C). Halites dated from the last glacial period (MIS 2), between 35 and 10 ka, had brine temperatures ~4 to 15°C below modern temperatures (19 to 30°C). Estimates based on ^2H and $\delta^{18}O$ isotopes in groundwater in the west-central Amargosa desert support these temperature estimates; MAT was about 8°C less than the present value about 17 ka (Claassen 1986 [DIRS 160155], p. 323). This study also suggests that summer precipitation was high enough to recharge groundwater.

Cold periods identified in the Death Valley fluid inclusion paleotemperature record coincide with cold periods in the Devils Hole calcite record between ~100 to 60 ka and from ~186 to 150 ka. However, the fluid inclusion record does not show warming at 146 ka and between 128 to 120 ka, as does the Devils Hole record and other climate records. The colder-than-modern summer and winter maximum temperatures in MIS 7 and MIS 5 are not consistent with other climate data during these interglacial periods. This suggests that these data are proxy dependent (Lowenstein et al. 1999 [DIRS 149904], p. 6), or that the dates in the Death Valley core are wrong. For MIS 2, the range of brine temperature values is consistent with and supportive of the temperature reconstructions based on packrat midden and ostracode data sets (Sections 6.4.2.1 and 6.4.2.2.1).

6.4.1.4 Comparison of Regional Records to Other Records

Other climate proxy data record climate episodes similar in magnitude and timing to the Owens Lake and Death Valley sediment core data. Lake and glacial records in the region and records as far away as Greenland, Antarctica, Siberia, and Europe also show that climate varied synchronously and substantively over time.

Jannik et al. (1991 [DIRS 109434], p. 1146) established the chronology of environmental change in the Owens River system for the last 2 m.y. based on dated lake sediment using ^{36}Cl, U/Th, ^{14}C, and magnetostratigraphy. Lakes in the entire Owens system (Owens, China, Searles, Panamint) were overflowing between 1.2 to 1.0 Ma and Searles Lake was the terminal sink for most of the last 1 m.y. with possible overflow events periodically occurring.

The ^{36}Cl record for the last 700 k.y. in the Owens system supports very high lake phases at times during MIS 16 and MIS 6 (Jannik et al. 1991 [DIRS 109434], pp. 1156 and 1157). Overflow also occurred during MIS 12 (Jannik et al. 1991 [DIRS 109434], pp. 1156 and 1157). Between 700 and 600 ka, Searles Lake overflowed into Panamint Valley at least twice, probably causing Panamint Lake to overflow into Death Valley (Figure 6-1). Other overflow events occurred between 440 to 400 ka, 380 to 350 ka, and 150 to 120 ka (Jannik et al. 1991 [DIRS 109434], p. 1157). The existence of halite layers dated by ^{36}Cl at 392 +/- 90 and

175 +/- 74 ka suggest Panamint Lake desiccated after the 440 to 400 ka overflow event and before the 150 to 120 ka overflow event, further supporting this chronology and overflow history (Jannik et al. 1991 [DIRS 109434], p. 1156). Searles Lake desiccated around 290 ka, fluctuated as a shallow lake between 100 and 24 ka, and desiccated from 10 ka to the present (Jannik et al. 1991 [DIRS 109434], p. 1158). Both Jannik et al. (1991 [DIRS 109434], p. 1158) and Smith (1984 [DIRS 109168], p. 1) report a 400 k.y. periodicity in the Owens River system lake records.

Morrison (1999 [DIRS 138393], p. 301) reports exposed lake sediments about 100 km south of Yucca Mountain, in the Tecopa Valley, California (400 to 700 m elevation; Figure 6-1). According to Morrison, the climatic history of pluvial and interpluvial cycles over the last 1 m.y. records significant increases in effective precipitation, stream flow, flood magnitude, erosion rate, groundwater recharge, water tables and potentiometric surfaces relative to modern values, until Lake Tecopa was breached, approximately 186 ka (Morrison 1999 [DIRS 138393], pp. 335 and 336). These proxy climate records in the Tecopa Valley include groundwater discharge deposits correlating with periods of higher lake stands representing periods of greater effective moisture (Morrison 1999 [DIRS 138393], p. 337). Increased effective moisture leads to increased groundwater recharge and ultimately to increased groundwater discharge to springs and lakes. Increased inflow to lakes by surface water and precipitation on the lake surface also raised lake levels.

Lakes along the present-day Mojave River drainage also record high stands during MIS 14, 12, 8, 6, and 4 (Jefferson 2003 [DIRS 162063], p. 57). Lake Manix covered approximately 236 km^2 of the central Mojave Desert during high lake stands and most of the lacustrine sediments preserved in the Afton basin were deposited during MIS 6 (Jefferson 2003 [DIRS 162063], pp. 43 and 56).

Reheis 1999 ([DIRS 109454], Figure 1, p. 197), Reheis 2000 ([DIRS 161023], p. A-503) and Reheis et al. 2002 ([DIRS 161593], p. 53) report lake highstands 25 to 70 m above late Pleistocene highstands shortly after 660 ka in the northwestern Great Basin. At the 70 m above-late-Pleistocene highstand, submerged basins thought to have been previously isolated were part of an extensive Lake Lahontan. Reheis suggests that to reach the highest levels of Lake Columbus-Rennie (located in present-day Columbus Salt Marsh and Fish Lake Valley, Nevada, 180 km [112 mi] northwest of Yucca Mountain), a 2 to 3 times increase in precipitation and a temperature decrease of 8ºC would have been required (Reheis 1999 [DIRS 109454], p. 202). Ancient Lake Russell, where Mono Lake stands today, records a minimum of three large-lake periods in the early-to-middle Pleistocene with levels between 250 and 330 m higher than the present 1,950 m elevation of Mono Lake (Reheis et al. 2002 [DIRS 161010], p. 991, abstract). Estimates using modern groundwater recharge suggest that drainage additions account for only a small part of these high lake levels. The lakes progressively decreased in size, suggesting a long-term drying trend from early to late Pleistocene (Reheis et al. 2002 [DIRS 161593], p. 53). Conversely, Morrison (1999 [DIRS 138393], p. 336) reports that a strengthening of pluvial climates has occurred since the middle Pleistocene, based on the increasing depths of Lake Tecopa during the last 1 m.y. until it was breached.

Fresh and saline lake phases in both Death Valley and Owens Lake are essentially synchronous over the past 200 k.y., the length of the Death Valley record. Glacial advances, recorded by high plagioclase feldspar content in the Owens Lake core, overlap with times of glacial advance

established in the Sierra Nevada by Phillips et al. (1996 [DIRS 160978], Table 1, p. 751) based on ^{36}Cl dates on glacial moraines (Lowenstein et al. 1999 [DIRS 149904], p. 6). Chemical analyses of sediment in Owens Lake show a rock-flour record with two major ice advances during MIS 6 and major advances during MIS 4, 3, and 2, which also correspond to ^{36}Cl dates on alpine glacial moraines in the Sierra Nevada (Bischoff et al. 1997 [DIRS 160217], pp. 314 and 324).

Benson (1999 [DIRS 160213], p. 203) provides a comparison of lake cycles to glacial-interglacial events in the western Great Basin. He concludes that alpine glacial periods were generally wet and interglacial periods were generally dry, although both glacial and interglacial periods included dry and wet intervals (Benson 1999 [DIRS 160213], p. 208; Figure 8, p. 212). During the last alpine glacier interval, cold-dry stades alternated with warm-wet interstades on millennial time scales (Benson 1999 [DIRS 160213], p. 222). High variability between 52,600 and 40,000 radiocarbon years before present is recorded in Owens Lake sediments. Wet periods lasting approximately 5,000 yr occurred during the last interpluvial, and interstades lasting approximately 5,000 yr occurred during glacial intervals (Benson 1999 [DIRS 160213], Figure 2, p. 207; Figure 8, p. 212; p. 219). Sediment in Owens and Pyramid lakes shows at least 20 stadial-interstadial oscillations occurring on a frequency of less than or equal to 1,900 yr in the Sierra Nevada, between 52,600 and 14,000 radiocarbon years before present (Benson et al. 1998 [DIRS 160977], p. 113), suggesting that millennial scale oscillations occurred in California and Nevada during most of this time.

Based on total organic carbon and δ^{18}O in Owens Lake sediments, alpine glacial stades were characterized by *relatively* (emphasis by Benson 1999 [DIRS 160213], p. 212) dry climates within the very wet period between 52,600 and 40,000 radiocarbon years before present. This is supported by pronounced δ^{18}O maxima during this time, representing dry, closed-basin environments rather than very cold precipitation-condensation temperatures (Benson 1999 [DIRS 160213], pp. 209 and 212). Benson (1999 [DIRS 160213], p. 212) estimates that late Pleistocene MIS 2 condensation air temperatures were only a few degrees colder than today. However, an abrupt decrease in δ^{18}O values in Owens Lake sediment at about 13,000 yr before present indicates a "profound increase in wetness" (Benson et al. 1996 [DIRS 108908], p. 747). Jayko et al. (2002 [DIRS 161019]) report a large saline lake associated with a high water table in Panamint Valley during MIS 2, indicating that it was supported by a high groundwater table.

Glaciated mountain ranges near the Yucca Mountain area include the White Mountains and possibly the Spring Range (Figure 6-1). The White Mountains supported relatively large glaciers likely dating MIS 2, whereas the Spring Range may or may not have supported glaciers (Osborn and Bevis 2001 [DIRS 160199], pp. 1384 and 1385). However, Van Hoesen et al. (2000 [DIRS 161021], p. A-16) argue that cirques and two morainal deposits in the Spring Range near Las Vegas, Nevada are evidence for glaciation, although the age of the deposits is not known. Controversy exists as to whether these are indeed morainal deposits; they may be fluvial (for a discussion of soil properties and previous work see Reheis et al. 1992 [DIRS 106661], Figure 3, pp. 309, 308, and 320). Regardless of whether these deposits are morainal or fluvial as suggested by Reheis et al. 2002 [DIRS 161593], at an elevation of 7,500 feet above mean sea level, it implies a much colder and wetter climate than is found there today.

Prolonged lake highstands lasting between 2,000 and 3,000 yr recorded in the Mojave River basin beginning as early as 22 ka were produced by episodic large-scale floods resulting from significantly increased precipitation relative to today (Wells et al. 2003 [DIRS 162060], p. 79). Values of stream discharge reaching Afton Canyon are estimated to have been two to three times larger than modern extremes (Wells et al. 2003 [DIRS 162060], p. 80). These values were calculated using a precipitation-discharge-evaporation model that infers either a 50 percent increase in precipitation in headwater catchment area resulting in annual flood events or a 100 percent increase in precipitation catchment area with a 50 percent decrease from modern climate evaporation combined with annual flood events reaching Afton Canyon. Lake Dumont also records periods of shallow lakes and spring discharge during MIS 2, the source likely being local streams and springs from the Avawatz Mountains and Kingston Wash prior to Lake Mojave overflow (Anderson and Wells 2003 [DIRS 162061], p. 140).

Controversy exists as to the age and extent of a highstand in the Lake Manly-Silver-Soda Lake basins (Figure 6-1) in MIS 5e/6 (Hooke 1999 [DIRS 160219], p. 328; Hooke 2002 [DIRS 160983], pp. 177 to 179; Enzel et al. 2002 [DIRS 160991], pp. 67 to 74). Hooke argues for a highstand about 186,000 yr ago, whereas Enzel et al. counter that the highstand to which Hooke is referring dates between 30,000 and 9,000 yr ago. Enzel provides an excellent overview of past work in this geographic area.

Figure 6-4 compares the Devils Hole isotopic record with lake sediment core records in California and Lake Baikal, Siberia, and with the Vostok, Antarctica, ice core record. The Devils Hole, Baikal, and Vostok records are plotted so that the glacial periods are peaks and the interglacial periods troughs. The timing of some events in these and other global records is strikingly similar, suggesting a global forcing mechanism to which these different climate proxies are responding.

The biogenic silica record from Lake Baikal, Siberia, (Prokopenko et al. 2001 [DIRS 160507], pp. 123 and 124; Figure 3, p. 128), covering the last 800,000 yr to MIS 19, records substages e through a for MIS 9, 7, and 5, and possibly substages e and a in MIS 15. The authors suggest these interglacial stages correspond to precessional insolation peaks (Prokopenko et al. 2001 [DIRS 160507], p. 123; Figure 2, p. 126). Additionally, the climate change record, based on pollen in sediment cores from Owens and Searles Lake, is similar to a number of proxy climate records in France, Greece, western North America, and marine sediment cores off the southern California coast (Litwin et al. 1999 [DIRS 109440], pp. 1163 to 1168).

Sulfate minerals in the Death Valley core record patterns of oxygen isotopic change that correlate to the SPECMAP record of marine carbonate and global ice volume variation and Summit Ice Core in Greenland (Yang et al. 1999 [DIRS 160216], Figure 5, p. 152). Yang et al. conclude that the regional records of Death Valley, Owens Lake, and Devils Hole are responding to the same climatic changes, but manifesting them differently (Yang et al. 1999 [DIRS 160216], p. 148). Phillips et al. (1994 [DIRS 160158], pp. 1115 and 1117) discuss a correspondence between Searles Lake and Summit, Greenland. Low water episodes at Searles Lake are synchronous with the interstadial episodes determined by $\delta^{18}O$ values at Summit, with both records recording relatively long stadials punctuated by brief interstadials. Phillips et al. (1994 [DIRS 160158], p. 1117) suggest that both records are responding to climatic forcing. Finally,

the 400,000-yr δ^{18}O record from Taylor Dome, Antarctica, and δD Vostok record are similar in timing (Grootes et al. 2001 [DIRS 160979], Figure 3, p. 292).

6.4.2 Local Records of Past Climate

Local records of climate change are common throughout the Yucca Mountain region and include packrat middens as well as paleowetland and paleospring deposits. Although these records are, by their nature, discontinuous, they provide important insights into the timing and magnitude of local climate change in the Yucca Mountain region. Packrat midden records are temporally discontinuous relative to the time scales considered here, although site-specific records can approach 7 k.y. in length (Spaulding 1985 [DIRS 106883], p. 35). Paleo-wetland and spring deposits are discontinuous records as well, because most basins within the Yucca Mountain precipitation area are situated well above the regional groundwater table. Therefore, their stratigraphic records tend to capture only episodes representing high water tables. Erosion of these deposits may occur during ensuing dry climate episodes, thus forming an even more discontinuous sedimentary record.

6.4.2.1 Packrat Middens

Packrat middens, common in the deserts of western North America, are an important source of paleoenvironmental information. Packrats, rodents of the genus *Neotoma*, are widespread and share the trait of collecting large amounts of vegetal material and caching it in their dens. Packrat middens are accumulations of organic debris typically rich in plant fragments. When located in a sheltered situation such as a cave, they can be preserved for tens of thousands of years. The subfossil plant remains from the middens represent species that grew close to the midden site, and because they are often identifiable to the species level, they offer a means of determining what species were present at a given time in the past, determined by radiocarbon dating of the remains. Packrat middens have been used to reconstruct past vegetation and climates in the region since the 1960s (Betancourt et al. 1990 [DIRS 128131], pp. 3 and 4). Because midden data rely on radiocarbon dating, plant assemblages older than about 45 ka are generally at the limit of radiocarbon dating, and therefore the utility of these data in understanding glacial climates is restricted to late MIS 3 and MIS 2 times.

The composition of modern plant communities of the Yucca Mountain region changes in response to elevation-dependent variation in temperature and precipitation regimes. At the lowest elevations below about 1,000 m (3,280 ft) and in most arid habitats, desert scrub vegetation is predominant, typified by such heat-loving plants as creosote bush (*Larrea tridentata*) and white bursage (*Ambrosia dumosa*). These communities give way to mixed desert scrub (hopsage, *Grayia spinosa*; Desert thorn*, Lycium andersonii*) above about 1,200 m (4,000 ft) elevation. At even higher elevations above about 1,300 m (4,265 ft), semi-arid habitats most often support scrub vegetation dominated by blackbrush (*Coleogyne ramosissima*). Pigmy conifer woodland, dominated by Utah juniper (*Juniperus osteosperma*) and piñon (*Pinus monophylla*), occurs above approximately 1,800 m (5,906 ft) elevation. On higher mountains in the region, montane conifer forest, typified by white fir (*Abies concolor*) and ponderosa pine (*Pinus ponderosa*), occurs above approximately 2,200 m (7,218 ft), while subalpine conifer forest characteristically dominated by bristlecone pine (*Pinus longaeva*) occurs above

approximately 2,700 m (8,858 ft) elevation (Beatley 1976 [DIRS 102221], pp. 29 to 52, 115, and 116; Spaulding 1990 [DIRS 100078], pp. 166 to 168).

Desert scrub in the vicinity of Yucca Mountain contains many plant species that are frost sensitive or frost intolerant, as well as drought hardy. Creosote bush, for example, is excluded from habitats where cold air collects during winter nights (Beatley 1975 [DIRS 103356], p. 57). Plant communities at progressively higher elevations, as well as those to the north, contain species that are more tolerant of low temperatures and require more water to survive. These relationships between individual plant-species distributions and limiting climatic conditions have been key in employing the packrat midden record to reconstruct temperature and precipitation changes in the Yucca Mountain area over the past 50 k.y. (Spaulding 1985 [DIRS 106883], p. 1; Thompson 1990 [DIRS 109174], Figure 10.6, p. 211; Forester et al. 1999 [DIRS 109425], pp. 32 and 33).

To understand how past climates differed from those of the present, a large data set, including the macrofossil assemblages from 200 radiocarbon-dated packrat midden samples, was compiled from studies conducted throughout southern Nevada (Forester et al. 1999 [DIRS 109425], p. 31; Spaulding 1985 [DIRS 106883], Table 6, pp. 18 and 19; Wigand and Rhode 2002 [DIRS 161596], pp. 332 to 342). The packrat midden data set indicates that woodland was common from about 35 to 12 ka in contrast to the desert scrub vegetation currently widespread in the area. The most common tree species in MIS 2 packrat middens from the area were Utah juniper and limber pine (*Pinus flexilis*) (Spaulding 1985 [DIRS 106883], pp. 37 and 38). White fir and bristlecone pine were found in midden samples from a number of higher elevation sites. Bristlecone pine was restricted to calcareous rocks, as it is today (Spaulding 1990 [DIRS 100078], Figure 9.15, p. 183; Thompson 1990 [DIRS 109174], p. 212). Limber pine grew at elevations as low as 1,600 m, about 1,000 m below its modern elevation in the Sheep and Spring ranges (Wigand and Rhode 2002 [DIRS 161596], p. 333). Piñon, common throughout the woodland of the region today, is rare in midden samples from the Yucca Mountain area and during late MIS 3 and most of MIS 2 apparently occurred no farther north than the Amargosa Desert at 36°38'N latitude (Spaulding 1990 [DIRS 100078], p. 176). Cold-tolerant shrubs typical of Great Basin desert and woodland, indicating relatively cold and dry conditions, were common in MIS 2 assemblages (Thompson 1990 [DIRS 109174], p. 210; Spaulding 1985 [DIRS 106883], pp. 31, 33, and 37).

The distribution of common plant species during MIS 3 and MIS 2, both within and outside the Yucca Mountain region, indicates a climate different from that of today. Warm-desert shrubs and succulents, such as creosote bush, were restricted to more southerly latitudes in the present Sonoran Desert (Spaulding 1990 [DIRS 100078], p. 191). At these southerly latitudes, south of 34°N latitude, pigmy conifer woodland supported a wide array of tree and succulent species, whereas the Yucca Mountain area supported fewer such species and a wider array of shrubs, presently growing in semi-arid habitats, such as blackbrush and snowberry (*Symphoricarpos longiflorus*) (Spaulding 1990 [DIRS 100078], pp. 191 and 192). Subalpine woodland, which presently exists only on the highest mountains of the region, descended to elevations of about 1,800 m (5,906 ft) (Thompson 1990 [DIRS 109174], p. 215), and all the way to the valley floors (on rocky substrates, at least) farther north in the Great Basin (Spaulding 1985 [DIRS 106883], p. 1; Spaulding 1990 [DIRS 100078], pp. 190 and 191). Wells and Woodcock (1985

[DIRS 160204], p. 11) report an elevational displacement of 1,200 to 1,500 m of Utah juniper below modern elevations between 19 and 13 ka on the mountain flanks of Death Valley.

The relative displacement of plant species downslope and to more southerly latitudes during MIS 3 and MIS 2 indicates colder and wetter conditions relative to modern times, just as those plant species grow in colder and wetter conditions at higher elevations and in more northerly latitudes today. Climate during MIS 2 must have involved cold, perhaps snowy winters and cool, probably dry summers. This interpretation is consistent with interpretations of past climate from the Owens Lake core (Section 6.4.1.2) and other climate proxy records.

Quantitative estimates of past temperatures and precipitation, indicated by plant species in packrat middens, can be made by examining the current range of these species in "climate space" (Thompson et al. 1999 [DIRS 109470], p. 2). These authors chose four time periods for climatic reconstruction, based on data availability in the Yucca Mountain area and the objective of reconstructing climatic variability during late MIS 3 and MIS 2. Employing the quantitative techniques described by Thompson et al. (1999 [DIRS 109470], pp. 4 to 10), these authors describe the following reconstructed climatic parameters (Thompson et al. 1999 [DIRS 109470], p. 34):

- 35 to 30 ka–MAT about 4°C colder than present, and MAP 1.5 times that of present
- 27 to 23 ka–MAT about 5°C colder than present, MAP 2.2 times that of present
- 20.5 to 18 ka–MAT about 8°C colder than present, MAP 2.4 times that of present
- 14 to 11.5 ka–MAT about 5.5°C colder than present, MAP 2.6 times that of present.

Thompson et al. (1999 [DIRS 109470], pp. 16 and 25) note that while their reconstructed last glacial maximum (20.5 to 18 ka) temperatures and those reconstructed by Spaulding (1985 [DIRS 106883], p. 39) do not differ greatly (MAT 8°C and 7°C lower than present, respectively), the difference in reconstructed precipitation is substantial. Thompson et al. (1999 [DIRS 109470], p. 25) arrive at a full-glacial MAP of 2.1 to 2.6 times current MAP, compared to 1.4 times current MAP reconstructed by Spaulding (1985 [DIRS 106883], p. 40) for that time. They show that the difference in precipitation estimates lies in the baseline data selected by Spaulding, which reflected much wetter modern climatic conditions than the baseline data used in their analysis (Thompson et al. 1999 [DIRS 109470], pp. 25, 26, and 34). Consequently, the relative change in precipitation reflected in Spaulding's reconstruction was substantially lower.

6.4.2.2 Wetland and Spring Deposits

Wetland and spring discharge is rare in southern Nevada today because the climate is arid and effective moisture is low. Spring discharge at elevations typically above about 2,000 m (6,562 ft) is supported by winter storms and snowpack on the higher mountains (Winograd and Riggs 1984 [DIRS 108884], p. 698). Spring discharge at low elevation typically comes from water in the regional carbonate or volcanic aquifers (Winograd and Thordarson 1975 [DIRS 101167], pp. C1 and C92) that is recharged at high elevation and over large areas. However, sedimentary deposits on the valley floors throughout the southern Nevada region show evidence of increased spring discharge such as wet meadows, seeps, flowing springs, streams,

and wetlands during times of greater effective moisture than today (Quade et al. 2003 [DIRS 161592], p. 165).

During MIS 2 the springs and wetlands on the valley floors supported abundant aquatic vegetation (sedge and cattails), fauna (ostracodes, diatoms, and mollusks), and waterfowl (ducks and wading birds) (Mehringer 1967 [DIRS 149909], pp. 170 and 172; Figure 36, p. 182) (Mawby 1967 [DIRS 149919], p. 108; Taylor 1967 [DIRS 149920], p. 399; Quade et al. 1995 [DIRS 100074], pp. 214 to 216). A diverse vertebrate community from large mammals such as mammoths and camels, to small mammals such as pikas, marmots, and ground squirrels, also lived on the valley floors (Grayson 1993 [DIRS 104089], Table 7-1, pp. 156 and 157; Table 7-12, p. 177). The existence of fossils of small mammals (which today live at either the upper tree line or in the northern United States) found in sediments, packrat middens, and caves in the northern Las Vegas Valley and nearby localities supports the temperature reconstructions from the plant macrofossils discussed above (Grayson 1993 [DIRS 104089], pp. 177 to 181).

Relying on exposed stratigraphy plus U-series, luminescence, and radiocarbon geochronology, Lundstrom et al. (1999 [DIRS 160387], p. 110) document multiple episodes of groundwater discharge in the northern Las Vegas Valley, Pahrump Valley, and Amargosa Desert over the last ~120 k.y. Although dates are discontinuous, fan deposition and aggradation occurred during 120-50 ka. An extensive period of discharge occurred between 40 to 25 ka. This period overlapped and preceded major fanhead incision in watersheds that include the highest portions of the Spring Range and the Timber Mountain area. Alluvial fan sedimentation overlapped a less extensive period of discharge between 13 and 8 ka. Lundstrom et al. conclude that climate conditions were responsible for these periods of fan deposition. Furthermore, fanhead incision required concentrated runoff and low sediment yield and was probably dominated by snowmelt. The penultimate period of extensive fan deposition and aggradation similar to that in the Holocene occurred between 120 and 50 ka, probably in response to high-intensity rainfall, runoff, and erosion of uplands.

The existence and annual persistence of groundwater discharge and permanent through-flowing wetlands at low elevation require that the past levels of effective moisture were much higher than today (Quade et al. 1995 [DIRS 100074], p. 228). However, the inference of past water table rises exceeding 100 m, although valid when made by Quade et al. (1995 [DIRS 100074], Table 5, p. 226), is not supported by more recent data collected through the Nye County Early Warning Drilling Program. Data from wells located south of Yucca Mountain along potential groundwater flow paths suggest that the maximum Pleistocene groundwater table rise was only 17 to 30 m (56 to 98 ft) (Paces and Whelan 2001 [DIRS 154724]). Presently, the regional groundwater table is less than 20 m below the Lathrop Wells Spring discharge sediments (Paces and Whelan 2001 [DIRS 154724]). The estimated water table elevations in the Yucca Mountain area vary with the characteristics of the aquifer involved. For example, systems with greater transmissivity have greater flow-through and, hence, rise less than systems with lower transmissivity, given equal amounts of recharge. Hence, a small rise in the water table of a transmissive aquifer could reflect a change to a much wetter climate.

Three discharge records that provide insight into the nature of past climate are discussed below. These records include: an ostracode record from Corn Creek Flat, a well-dated section in the Las Vegas Valley; an isotope record from Cactus Springs, a well-dated section north of the

Las Vegas Valley; and the diatomaceous deposits near Lathrop Wells, north of U.S. Highway 95 and south of Crater Flats, down the regional flow gradient from Yucca Mountain (Figure 6-1).

6.4.2.2.1   Corn Creek Flat Section (Site OCI-11 and LPM-34) Ostracode Data

Corn Creek Flat (Figure 6-1) lies near the center of the upper Las Vegas Valley at an elevation of 840 m. Two sections of wetland sediments approximately 200 m apart (OCI-11 and LPM-34) have been analyzed (Quade 1986 [DIRS 109151], p. 340; Quade and Pratt 1989 [DIRS 109152], p. 368; Quade et al. 2003 [DIRS 161592], p. 166), CRWMS M&O 2000 [DIRS 151945], pp. 6.3-25 to 6.3-28). Three informal stratigraphic units, denoted B, D, and E, which were described by Haynes (1967 [DIRS 147123], pp. 34 to 39) and Quade (1986 [DIRS 109151], p. 340) are found in these sections and in other localities in southern Nevada. Unit B is much more extensive than unit D, and unit D is often inset into unit B. These units are distinguished from each other by a variety of sedimentary features, such as bed forms, grain size, color, rhizolith content, and fossils (Quade 1986 [DIRS 109151], Figure 2, p. 342; Quade and Pratt 1989 [DIRS 109152], Figure 4, p. 359; Quade et al. 1995 [DIRS 100074], Table 1, p. 215). Sediments comprising units B and D occur throughout the Las Vegas Valley, indicating they were deposited in extensive wetlands (Quade 1986 [DIRS 109151], pp. 340 and 355; Quade and Pratt 1989 [DIRS 109152], p. 351).

Based on ostracode assemblages, deposition of unit B_2 of OCI-11, dating >41,000 yr old, continued through three environmental settings: a wetland with a regional water table higher and discharging at a higher rate than today, a stream and flowing spring, and a wet meadow (Quade et al. 2003 [DIRS 161592], pp. 170 and 171). The basal section of B_2 represents a wetland environment with TDS most likely below 1,000 mg/L, with summer water temperatures likely between 12°C and 18°C (Quade et al. 2003 [DIRS 161592], pp. 172 and 173). The next youngest unit, B_3 with an estimated age >33,780, likely represents an ephemeral wetland, similar to the topmost subunit in B_2, that evolved into a more permanent wetland by the time the top of the unit was deposited (Quade et al. 2003 [DIRS 161592], pp. 173 and 174). The upper subunit of B_3 contained species not common in the older sediments, implying a higher regional water table with active discharge and warmer summer water temperatures than the older subunit environments. Summer water temperatures (in degrees Celsius) may have been between the high teens and low twenties during two or more months of the year. Winter water temperatures remained cool, possibly below ~12°C (Quade et al. 2003 [DIRS 161592], p. 174).

Unit D represents a complex of relatively permanent flowing springs and wetlands. An estimated date from the middle of the section is at least 17,770 +/- 90 ^{14}C yr before present, but no older than 19,380 +/- 110 ^{14}C yr before present (Quade et al. 2003 [DIRS 161592], p. 174). TDS remained low, probably below 750 mg/L, summer water temperatures were similar to the top of unit B_3, and winter water temperatures were likely below 12°C (Quade et al. 2003 [DIRS 161592], p. 174).

Unit E_1, with a basal date of ~12,800 ^{14}C yr before present probably represents wetland, wet meadow, and cold-flowing stream conditions at different times with a TDS below 300 mg/L. Water temperature may have been <15°C (Quade et al. 2003 [DIRS 161592], pp. 174 and 175). Based on sediment characteristics and ostracode assemblages, the other section, LPM-34, is most likely equivalent to OCI-11 units D and E. In this section, basal unit D was a wetland, but then

transitioned to a wet meadow at the unit D to E transition. Quade et al. postulate that this could have resulted from either a hydrofacies shift or climatic change (Quade et al. 2003 [DIRS 161592], p. 176).

Forester and Smith (1994 [DIRS 109040], Figure 1, p. 2556; pp. 2559 and 2560) also estimated temperature and precipitation based on ostracodes from LPM-34 and nearby sections. They suggested late Pleistocene MAP was four times wetter than today and possibly as much as 10°C colder. Their precipitation value is most likely an overestimation because they did not recognize the importance of flow through the wetlands. The flow through these wetlands was probably low, but sufficient to keep the waters relatively fresh and cool. Flowing water is usually less thermally and evaporatively coupled to the atmosphere than is standing water (Forester 1987 [DIRS 109033], p. 262). Therefore, MAP estimates from flowing water could be lower than MAP estimates from standing water. The higher MAP levels of 400 to 600 mm reported by Forester and Smith (1994 [DIRS 109040], Table 6, p. 2559) probably did exist in this area, but at higher elevation, where present MAP is also higher.

Quade et al. (2003 [DIRS 161592], p. 165) tentatively correlate deposits in the Las Vegas Valley dating >41 ^{14}C ka with MIS 6 and a series of discharge events between <26.3 and 16.4, ~13.9 to 13.5, and 11.6 to ~9.5 ^{14}C ka as MIS 2 and early Holocene. Units D and E, originally defined by Haynes (1967 [DIRS 147123], p. 17) at Tule Springs, may be correlative with the lake highstand chronologies of Lake Manly in Death Valley, Silver Lake, and to a certain extent, Searles Lake. Based on δ^{18}O of fossil ostracodes, Quade et al. (2003 [DIRS 161592], p. 166) estimate that the MAT during MIS 6 (unit B$_2$) was at least 10.8°C colder than today and at least 5.6°C colder during the last glacial maximum (unit D). If a vital effect[3] (biologically precipitated calcite not formed in isotopic equilibrium with the water) of 0.8 to 1.0 percent on ostracode valves is assumed, then valley bottom temperatures were warmer than their MIS 2 estimate by ~2 to 3°C. However, warmer temperatures are not consistent with other data.

6.4.2.2.2   Cactus Springs Ostracode and Fossil Mollusk Data

Quade et al. (2003 [DIRS 161592], p. 176) report on ostracode assemblages in LPM-35, from the Cactus Springs locality (Figure 6-1). These deposits probably represent the upper part of unit D or more likely unit E. Dates on the middle of unit D/E$_1$ range from 13,690+/-80 to 13,350+/-60 ^{14}C yr before present and are thought to span the period of most effective moisture in this section. The section represents a wet meadow environment in the basal unit, flowing springs possibly derived from valley aquifer fill, but without extensive discharge of regional groundwater in the middle and a transition to a drier environment in unit E$_2$, which has a date of 10,030 ^{14}C yr before present.

Oxygen isotopic compositions of fossil bivalves from Cactus Springs were compared to modern bivalve δ^{18}O values of shell carbonate (Sharpe et al. 1994 [DIRS 109165], p. 2538). Oxygen isotope data from the bivalve *Pisidium* spp., living in Cold Creek Spring at 1,940 m and found as

---

[3] Some ostracodes make a shell with isotopic values higher than for inorganic calcite precipitated in equilibrium with the same water. However, some ostracodes make a shell that is in, or close to, isotopic equilibrium with their host water. Therefore, vital effects can vary by taxa and may account for some of the range of isotope values measured from a particular assemblage (Quade et al. 2003 [DIRS 161592], p. 181).

a fossil in the Cactus Springs (930 m) section (CRWMS M&O 2000 [DIRS 151945], Figure 6.3-18, p. F6.3-18), offer a way to compare modern data from high-elevations to data from low-elevation fossil localities without concern for different vital effects. The $\delta^{18}O$ values for living *Pisidium* spp. from the Cold Creek Spring locality averaged about 18.7‰ (n = 8), and the fossil site sample values averaged 19.6‰ (n = 6). The $\delta^{18}O$ values of water collected from a small pond receiving flow from the Cold Creek Spring averaged about -14‰, and so the modern bivalve values are about 32.7‰ higher than the water values (Sharpe et al. [DIRS 109165] p. 2341). Because the $\delta^{18}O$ value of a bivalve is determined by both the isotopic composition and the temperature of the water in which the organism lived, the fossil data cannot be directly converted into a $\delta^{18}O$ value for the paleowater. However, the similarity between the modern and fossil bivalve $\delta^{18}O$ values suggests that the paleowater $\delta^{18}O$ and temperature at the fossil site on the valley bottom may have been comparable to those found today at the Cold Creek Spring locality at an elevation of 1,940 m. Modern recharge to the Spring Mountains occurs primarily from winter precipitation with values of approximately -14‰ (Winograd and Riggs 1984 [DIRS 108884], p. 698). The low $\delta^{18}O$ values of paleowaters on the valley bottom, as indicated by the fossil bivalves, are, therefore, consistent with the expansion of the polar cell into this region during glacial times.

6.4.2.2.3 Lathrop Wells Ostracode and Diatomite Microfossil and Isotope Data

The Lathrop Wells diatomite deposits occur at the southern margin of Crater Flat, approximately 18 km southwest of Yucca Mountain at an elevation of 792.5 m (2,600 ft) (Figure 6-1). These spring deposits originated from discharge from the regional water table and are comprised of pale-green mudstones, local secondary carbonate, silicious rhizoliths, and diatomite (Quade et al. 1995 [DIRS 100074], p. 226). Diatomite is sediment composed primarily of the opaline frustules of diatoms (single-celled algae). Various studies provide the basis for interpreting the stratigraphy, ostracode paleontology, and paleohydrology and age of these deposits. Paces et al. (1993 [DIRS 106474], p. 1573; Paces et al. 1996 [DIRS 100171], p. 3; Paces et al. 2001 [DIRS 156507], p. 1) and Quade et al. (1995 [DIRS 100074], p. 213) reconstruct the site's paleohydrology based on fossil and isotope data. Quade et al. (2003 [DIRS 161592], p. 177) report on the stratigraphy, ^{14}C dating, and ostracode paleontology of the site.

Brennan and Quade (1997 [DIRS 108940], p. 329) discuss the importance of radiocarbon data collected at this site in understanding changes in travel time within the regional groundwater system in the area including Yucca Mountain. Evidence for the age of these deposits is discussed in detail in Paces et al. (1993 [DIRS 106474], pp. 1573 to 1580), Quade et al. (1995 [DIRS 100074], Table 2, p. 215), and Brennan and Quade (1997 [DIRS 108940], Table 1, pp. 332 to 333).

Although Swadley and Carr (1987 [DIRS 101300], I-1767 map) believed these deposits are Pliocene to lower Quaternary based on fission-track and K-Ar dating, the bulk of the reported dates and vertebrate fossils recovered primarily from the diatomite in these deposits imply MIS 6 to MIS 2 ages for the deposits (Paces et al. 1993 [DIRS 106474], pp. 1578 and 1579; Paces et al. 1997 [DIRS 109148], Figure 18; and Quade et al. 2003 [DIRS 161592], Figure 6, p. 178; Table 1, p. 172).

Isotopic evidence (Paces et al. 1993 [DIRS 106474], p. 1577) suggests that the Lathrop Wells diatomite deposits were derived from a regional groundwater source and not from surface water or a perched aquifer (Paces and Whelan 2001 [DIRS 154724]). Strontium and uranium isotopic ratios for authigenic materials in these deposits are similar to those from regional groundwater sampled nearby. These data exclude a surface water source, and $^{234}U/^{238}U$, $\delta^{87}Sr$, and $\delta^{13}C$ data from authigenic materials in the deposit are inconsistent with perched water compositions expected from interactions with local rock sources.

The reconstruction of climate from aquatic microfossils and from stable isotope data in the Las Vegas and Indian Springs Valleys (CRWMS M&O 2000 [DIRS 151945]) at Corn Creek Flat, Cactus Springs, and Lathrop Wells is consistent with the packrat midden and plant macrofossil climate reconstruction. However, because the Las Vegas and Indian Springs valleys are bounded by some of the highest mountains in the region, their hydrological response to Pleistocene climate change may have been accentuated by local upland recharge relative to that in the immediate Yucca Mountain flow system. The Lathrop Wells diatomite, by contrast, represents the response of the Yucca Mountain paleohydrological system to climate change without significant effects of local high-mountain recharge.

6.4.2.3 Summary of Local Records

The climate interpretations based on the terrestrial and aquatic records discussed above collectively show increased MAP and lower MAT relative to modern levels during all of the past glacial periods. Table 6-27 summarizes various temperature and precipitation estimates from the different past climate proxies discussed above. Estimates include air temperature, brine temperatures, and condensation of air temperature, as well as sites with different elevations and microclimates. However, it is clear that the MAT was lower and the MAP was substantially higher than modern MAT and MAP for sustained periods at numerous times over the last 500,000 yr. MAT is estimated to have varied from 4°C to as much as 10° or 15°C below modern temperature, and precipitation may have been from 1.4 to 3 times modern precipitation during certain periods.

6.4.3 Site Records of Climate Change

Site records of past climate are those within or on Yucca Mountain. Data from secondary minerals, mainly low-temperature calcite and opal, in fractures and cavities can be used to evaluate hydrological conditions in the unsaturated zone and the response of the hydrogeologic system to climatic change over time (Paces et al. 1998 [DIRS 107408], p. 36). Secondary mineral data from Yucca Mountain do not provide high-resolution paleoclimatic data, although some studies corroborate conclusions from other climate proxy data. These conclusions are summarized here. Section 7.7 discusses the paleohydrological conditions within the local Yucca Mountain area using the physical morphology, geochronology, and chemical and isotopic composition of secondary minerals.

Isotopic and chemical data from unsaturated zone minerals support their source from descending meteoric water (Whelan et al. 1994 [DIRS 100091], p. 2738; Vaniman et al. 2001 [DIRS 157427], p. 3420). Based on chloride simulations and data collected by Sonnenthal and Bodvarsson (1998 [DIRS 162120], p. 131) perched waters appear to contain a substantial

component of older waters from a period of higher precipitation, which may date to late Pleistocene or early Holocene time periods. However, at the scale sampled, the isotopic data show no evidence of a cyclic pattern within the younger parts of the deposits that could be related to climate variation over the last 500 k.y.

6.4.4 Summary of Past Climate Records

Comparison and integration of climate proxy data provide a local and regional picture of variations in past temperature, precipitation, and hydrology in both glacial and interglacial climate regimes. These past climate proxy records, when linked to global circulation patterns and orbital parameters, illuminate the cyclicity, process, timing, and potential drivers of past climate and provide insight on potential future climate change.

These climate proxy data suggest:

1. Numerous climate states occurred during the last 500,000 yr ranging from warm interglacial periods (modern climate) to cool or cold and wet glacial periods. The last 500,000 yr contained glacial periods of different magnitudes ranging from cold and very wet to cool and dry. The glacial maximum temperature in MIS 2 is estimated to have been between 4 and 8°C colder than present (13°C) with a MAP between 1.8 to 2.4 times that of present. This glacial period is considered to have been cool and dry compared to previous glacial periods.

2. Past climate states contained periods of high variability with warmer periods occurring in glacial stages and cool episodes occurring in warm climate periods.

3. The modern climate is the least common of climate states.

4. The modern climate is one of less effective moisture compared to other climate states.

5. Past climates resulted in infiltration and percolation within Yucca Mountain.

6.5 FUTURE CLIMATE

Numerous computer-generated models have predicted future climate on varying time scales (Berger and Loutre 2002 [DIRS 160153], pp. 1287 and 1288; Loutre and Berger 2000 [DIRS 160117], pp. 84 and 85; Berger et al. 1991 [DIRS 160237], p. 161; Watson et al. 2001 [DIRS 162081], Figure 5.2, p. 89). These models integrate factors affecting the earth's climate into a time-series numeric model, and then the model is run for selected future times under predetermined boundary conditions. However, present-day science cannot explain with certainty why climate changes, or numerically describe the change in climate systems in a time series, nor is there widespread agreement about future boundary conditions.

The future climate for the Yucca Mountain area is forecast here by identifying a past climate sequence rather than developing a computer-generated model. Part of the reasoning behind this approach is that the evaluation of past climate is the only defensible source of future climate information. Therefore, the relation between calculated earth-orbital parameters and past climate

cycles is established here, and the timing and nature of these events are used to identify a past-climate time series analog. Once identified, this sequence is projected into the future.

This forecast methodology was devised and developed by R.M. Forester, USGS, who suggested a specific linkage between the Devils Hole chronology, a pattern of climate change, and the relation of eccentricity to precession (USGS 2001 [DIRS 158378], p. 35). This methodology, based on USGS (2001 [DIRS 158378]) and Sharpe (2003 [DIRS 161591]), quantifies estimates of temperature and precipitation over time to be used as input to models of the infiltration process (USGS 2001 [DIRS 154674], p. 13). Other forecast methodologies might develop a different rationale or select other past climates, resulting in a different future climate scenario.

Uncertainties using this approach to forecast future climate include the possibility that change in orbital parameters may be correlated with some other factor that independently causes climate change. These factors could include solar variability (Gauthier 1999 [DIRS 109427], p. 764; Sharma 2002 [DIRS 160143], p. 469; Jouzel 2001 [DIRS 160196], p. F1; Shackleton 2000 [DIRS 160156], p. 1897; Bond et al. 2001 [DIRS 160522], p. 2130; Rind 2002 [DIRS 160513], pp. 676 and 677), the content of atmospheric carbon dioxide (Cuffey and Vimeux 2001 [DIRS 160144], p. 523), the effects of wind and tidal forcing on the ocean's mass flux (Wunsch 2002 [DIRS 160993], p. 1179), or a threshold, such as radiation windows (Shaffer et al. 1996 [DIRS 109164], p. 1017; Figure 2, p. 1019), or ice sheet volume and behavior coupled with CO_2 levels (Loutre and Berger 2000 [DIRS 160117], p. 69; Helmke et al. 2002 [DIRS 160997], p. 55). None, some, or all of these factors may be involved. This methodology assumes that the nature and sequencing of climate state characteristics are similar and repeated over time.

6.5.1 Approach

The approach used in this analysis of future climate is described as follows:

1. Identifies the sequencing and duration of past climate states (glacial, interglacial, monsoon, and intermediate) suggested by the Owens Lake, California, paleoenvironmental record (Section 6.5.2)

2. Compares the relation of the Devils Hole reconstructed climate interval (approximately 568 to 60 ka) to calculated orbital parameters based on astronomical forcing to identify a pattern of past climate (Section 6.5.3)

3. Selects present-day meteorological stations to represent these past climate states so that the record of daily temperature and precipitation from these stations can represent future temperature and precipitation (Section 6.5.4)

4. Projects this pattern into the future to establish the nature and timing of future climate change (Section 6.5.5).

6.5.2 Identifying the Nature and Timing of Climate States Using the Owens Lake Record

Four basic climate states[4] (interglacial, monsoon, intermediate, and glacial) occurring in the past 400,000 yr were identified, based on the modern geographic and climatic distributions of ostracode and diatom taxa recovered from the Owens Lake sedimentary record (CRWMS M&O 2000 [DIRS 151945], pp. 6.3-15 to 6.3-17; USGS 2001 [DIRS 158378], Figure 11, p. 50; pp. 53 to 73; Sharpe 2003 [DIRS 161591], pp. 20 and 21). The modern distribution of ostracodes is related to the TDS, solute composition, and temperature of the water, among other factors, in which they live (Forester 1983 [DIRS 109023], pp. 437 and 438; Forester 1985 [DIRS 109423], pp. 13 and 14; Forester 1986 [DIRS 109024], Figures 1, 2, and 3, pp. 797 and 798) (Sections 6.4.1.2.1 and 6.4.1.2.2). Because these variables are commonly correlated with climate (Forester 1987 [DIRS 109033], pp. 261 to 267), as in the case of Owens Lake, modern ostracode geographical distributions can be linked to climate and, hence, the atmospheric circulation patterns that affect regional climate. Therefore, change in the ostracode assemblage at Owens Lake is commonly linked to climate change, which may have resulted from a major shift in atmospheric circulation.

6.5.2.1 Identifying Climate States

Based on ostracode and diatom assemblages from the Owens Lake sediment core, Figure 6-5 shows the sequence of the four climate states. The sequence is cyclical, moving from interglacial to glacial climate states and back again. The transitions between these states are termed intermediate with bursts of monsoonal activity (designated intermediate/monsoon climate states) lasting 1,000 to 2,000 yr. Figure 6-6 shows how the Owens Lake ostracode assemblages represent these different combinations of temperature and precipitation, which represent different climate states. Climate states have different levels of effective moisture, which is a combination of temperature and precipitation. Greater effective moisture does not necessarily occur with only increased precipitation. Very cold temperatures and low precipitation can produce levels of effective moisture equal to climates with warm temperatures and high precipitation. The modern climate is the warmest and driest (low effective moisture) compared to the other climate states.

The interglacial climate state is comparable to our relatively warm present climate state; the monsoon climate state is characterized by hotter summers with increased summer rainfall relative to today; the intermediate climate state has cooler and wetter summers and winters relative to today. Although USGS (2001 [DIRS 158378], pp. 54 and 67) referred interchangeably to a glacial-transition or intermediate climate, Sharpe (2003 [DIRS 161591], p. 7) uses only the term intermediate climate. Both reports define this state as that climate period transitioning from a glacial state to an interglacial state or visa versa, and the term used hereafter is intermediate climate state. Glacial states (climates cooler and wetter than today) were not included in USGS (2001 [DIRS 158378]) because the forecast time frame for the next 10,000 yr did not include a glacial state. Sharpe (2003 [DIRS 161591], Figure 6-8, p. 59) forecast the next 1,000,000 yr and predicted glacial states would occur during that time frame. Glacial states are of particular importance to the licensing and design of the proposed underground radioactive

---

[4] Climate *states* are defined here as the *type* of dominant climate (glacial, interglacial, monsoon, or intermediate); whereas, marine isotope *stage* refers to a period of time associated with a glacial or interglacial climate state.

nuclear waste repository because periods of substantially cooler and wetter climate relative to today will increase infiltration.

Future climate will undoubtedly include many more climate states than the four identified here. Climate states were limited to four in this analysis to simplify model simulations of net infiltration. However, these four climate states represent four conditions of differing effective moisture, either increasing precipitation and decreasing temperature (more effective moisture) or decreasing precipitation and increasing temperature (less effective moisture), which will likely encompass the range of future climate states. For example, the interglacial climate state has low effective moisture, so infiltration would be less than in the glacial climate state, which has the greatest effective moisture of these four selected climate states.

6.5.2.2   Determining the Timing of Past Climate States

Table 6-28 shows different climate states based on the Owens Lake ostracode record. The first column refers to MIS 12 through 1, with MIS 12 being the oldest and MIS 1 being the youngest. The time series is based on the Devils Hole $\delta^{18}O$ chronology beginning in MIS 12 through MIS 5 and into MIS 4, where the published Devils Hole data ends. MIS 3 to the present is based on the δD data from the Vostok Ice Core (Petit et al. 1999 [DIRS 109450], Figure 1, p. 430) because it is also a continental record of climate change and the Vostok curve shows a strong similarity to the Devils Hole curve (Winograd et al. 1992 [DIRS 100094], Figure 3, p. 257; Landwehr and Winograd 2001 [DIRS 160145], p. 31,860; Landwehr 2002 [DIRS 161926], pp. 2 and 3). Data sets were combined to complete the time-series analysis by graphically scaling the Vostok record to the Devils Hole curve. The superimposed curves resulted in a near identical agreement through the 450-60 ka interval.

The timing between MIS listed in Table 6-28 was determined by locating the inflection points on the Devils Hole and Vostok isotope records. Once the MIS isotope-stage boundaries were delineated in this manner, the ages at which the curves reverse direction denote the general centers of glacial or interglacial periods. The uppermost peaks in the curve (high $\delta^{18}O$ or δD values) represent interglacial periods, and the troughs represent glacial periods.

The length of time that the glacial or interglacial periods lasted was based on change in the slope of the isotope curves near the reversal peaks or troughs. A one-value cutoff-point designating all glacial or all interglacial periods could not be chosen because each individual glacial or interglacial event had its own set of values particular to the preceding climate interval and factors associated with climate and groundwater mechanisms. However, the estimated durations of glacial and interglacial states, based on a change in slope in the Devils Hole isotope curve, are generally consistent with the timing of glacial and interglacial onset and duration reported in the literature. Portions of the isotope record falling between the glacial and interglacial periods were designated intermediate or monsoon climate states.

6.5.3   The Relation of Devils Hole Record to Calculated Orbital Parameters

Once past climate states and their timing were identified using the Owens Lake record, a method for forecasting future climate was established. USGS (2001 [DIRS 158378], pp. 35 to 37) identified a pattern linking precession, eccentricity, and terminations in glacial and interglacial

cycles during the last 400,000 yr of the Devils Hole record. A comparison of the Devils Hole record with orbital parameters revealed that terminations of glacial periods followed eccentricity minima. Further comparison suggested that the initiation of glacial conditions could be directly related to the precession index. Interglacial periods also followed a pattern linked to the interplay of eccentricity and precession. These relations provide the basis for forecasting future climate, because each 400 k.y. cycle can be divided into glacial, interglacial, and intermediate climate states based on eccentricity and precession. These datasets also support the first two assumptions discussed in Section 6.1, that (1) climate is cyclical; therefore, the past can be used to forecast the future; and (2) a relation exists between the timing of (inter) glacial cycles and the timing of changes in certain earth-orbital parameters. Briefly, these two datasets are described as follows.

6.5.3.1   Orbital Parameters

Past and future timing of the earth's orbital parameters (obliquity, eccentricity, and precession; Section 6.2.1.2) can be accurately constructed from celestial mechanics calculations, assuming there are no perturbations from any large bodies passing through the solar system (Hartmann 1994 [DIRS 152035], pp. 307 and 308). Figure 6-7a to d shows the magnitude and timing of precession and eccentricity for the last 1,000,000 yr, derived from basic celestial mechanics (Berger 1978 [DIRS 121783], p. 2362; Berger 2000 [DIRS 152040]; Berger and Loutre 1991 [DIRS 108910], p. 297; DTN: GS000900005121.004 [DIRS 153822]).

As discussed in Section 6.2.1.2, eccentricity (dashed curve in Figure 6-7a to d) is the degree to which the orbit of the earth departs from a circle (Hartmann 1994 [DIRS 152035], p. 303). Precession (solid curve in Figure 6-7a to d) affects the latitudinal and seasonal redistribution of solar radiation at the top of the atmosphere (Crowley and North 1991 [DIRS 121811], pp. 134 and 135). Obliquity influences the seasonal cycle in high latitudes (Crowley and North 1991 [DIRS 121811], p. 133). No consistent relation between obliquity and the Devils Hole record has been established (USGS 2001 [DIRS 158378], p. 33); therefore, it is not shown in Figure 6-7a to d.

In Figures 6-7a to 6-7d, the small letter "m" denotes the eccentricity minimum (more circular orbit), and the large letter "T" ("T" = initiation of transition to interglacial climate) marks the first summer northern hemisphere solar radiation maximum after the eccentricity minimum. Dates for these events are shown toward the bottom of the graph. The precession index maxima near the numbers 1 through 4 or 5 at the top of Figures 6-7a to 6-7d indicate summer-solar-radiation maxima in the southern hemisphere. Conversely, the precession index minima near the numbers 1 through 4 or 5 at the bottom of the graph indicate summer solar radiation maxima in the northern hemisphere. The letter "I" ("I" = initiation of transition to glacial climate) marks the second southern hemisphere precession peak after the "T" event. USGS (2001 [DIRS 158378], p. 42) suggests invoking a 30,000-yr constant measured forward in time from each "T" event to locate the "I" events. Sharpe (2003 [DIRS 161591], p. 39) suggests that the 30,000-yr interval is not necessary because all the "I" events designated in USGS (2001 [DIRS 158378], Figures 7a and 7b, pp. 38 and 39) for the past 400,000 yr are located two southern hemisphere maxima-precession-peaks forward in time from each "T" event. The span from one "I" event to the next encompasses a precession sequence. The number of precession peaks in past sequences is randomly either four or five.

6.5.3.2 Devils Hole Calcite Record

The Devils Hole record (Landwehr et al. 1997 [DIRS 109124], pp. 1 to 8) contains the most robust information and most accurate dates about climate change in the region (Section 6.4.1.1). It is the only essentially continuously dated long climate record. Other long, dated climate records exist, but typically the chronology for those records is not well dated and/or relies on extensive interpolation between dates. Because of this drawback, the chronology of continental climate records is often derived from marine climate records that are derived from correlation with orbital properties. For these reasons, Devils Hole provides the climate-linked chronology that forms the basis for this analysis of future climate. The high $\delta^{18}O$ values in the Devils Hole record interglacial climates and the low values record glacial and what is termed herein as intermediate climates (inferred from Winograd et al. 1992 [DIRS 100094], pp. 255 and 256; Landwehr and Winograd 2001 [DIRS 160145], p. 31,854). Changes in the Devils Hole $\delta^{18}O$ calcite values record are thought to reflect changes in isotopic values of infiltration in the recharge area.

6.5.3.3 Comparing the Datasets – The Precession Methodology

By comparing the Devils Hole $\delta^{18}O$ and age data (Landwehr et al. 1997 [DIRS 109124], Table 1, pp. 3 to 8) with orbital parameter and age data (Berger and Loutre 1991 [DIRS 108910], p. 297), USGS (2001 [DIRS 158378], p. 35), a formal relation between the timing of climate change and precession was established. That relation between climate change and precession in the past provides the basis to use a precessional clock to time climate change in the future.

The Devils Hole record is shown in Figures 6-3a to 6-3c along with the precession parameter. As in Figures 6-7a to 6-7d, the "I" and "T" events are shown. The "I" events correspond to times when high Devils Hole $\delta^{18}O$ values (interglacials and other warm periods) are changing towards low values, whereas "T" events in Devils Hole $\delta^{18}O$ values (glacial periods) correspond to times when low values are changing toward high values. Furthermore, a substantial amount of time elapses from these primary reversals, which begin a change to the next climate state, before the next climate state is reached and smaller reversals occur within each general trend. The interglacial climates (defined by $\delta^{18}O$ values that increase and reach a plateau following a glacial period in the Devils Hole record) generally reach those plateaus of $\delta^{18}O$ values about 20,000 to 25,000 yr after the glacial reversals (USGS 2001 [DIRS 158378], p. 42). Selecting reversal points at the ends of interglacials and glacial periods to mark the beginnings and ends of (inter) glacial periods is not conventional (Winograd et al. 1997 [DIRS 100096], pp. 141 and 142; Kukla et al. 2002 [DIRS 160981], p. 6), but better suits the purposes of this study. By relating the pattern of variation in orbital parameters to the climate records for Owens Lake (Table 6-28) and Devils Hole (Figures 6-3a to 6-3c), the following observations and definitions are evident:

1. The last northern hemisphere solar radiation maximum in the summer sequence, #4 or #5, just prior to the "I" event, begins the interglacial climate state. This interglacial state lasts to the "I" event (southern hemisphere maximum #1).

2. From the "I" event to about halfway between the southern hemisphere solar radiation maximum #3 and northern hemisphere solar radiation maximum #3, a combination of intermediate and monsoon climate states occurs. The end of the intermediate climate

state is defined as being the point where the precession curve crosses the 0 precession mark, just beyond the southern hemisphere solar radiation maximum #3.

3. The glacial climate is defined as beginning where the intermediate climate ends in #2 above. The end of the glacial is defined as the point where the precession curve crosses the 0 precession mark just forward in time following a "T" event (the northern hemisphere solar radiation maximum precession #3 [if a 4-sequence] or #4 [if a 5-sequence]).

4. An intermediate climate is defined to exist following the first 0 precession mark after a "T" event until the northern hemisphere precession maxima before the next "I."

For example, the eccentricity minimum at 269 ka noted as heavy vertical line segment marked "m" on Figure 6-7c is followed moving forward in time at 267 ka by a minimal precession value noted as "T" on Figure 6-7c. This point generally corresponds in time with minimal $\delta^{18}O$ values in the Devils Hole record (Figure 6-3b), signaling a shift from a glacial toward an interglacial climate. This relation, discernible from the end of the interglacial period around 400,000 yr ago, consistently identifies all of the primary reversals in the available Devils Hole record. New work at Devils Hole has extended the record from about 50,000 to about 9,000 yr ago, but those data are not yet available.

The largest discrepancy between an interglacial period designated by high $\delta^{18}O$ values in the Devils Hole record and precession ("I" event) occurs at the end of interglacial stage 5e. The isotope peak is at 126.7 ka in the Devils Hole record and the "I" event occurs at 116 ka (Figure 6-3c). However, when sea level records are considered, the timing of the "I" event is consistent with a change from an interglacial period.

Records from sediments and corals from the Bahamas, Barbados, New Guinea, and eastern Pacific Rise (Henderson Island) suggest a sea-level high stand occurred about 135,000 yr ago, (Henderson and Slowey 2000 [DIRS 160234], p. 62; Gallup et al. 2002 [DIRS 160218], p. 312; Esat et al. 1999 [DIRS 160517], pp. 197 and 201; Stein et al. 1993 [DIRS 160504], p. 2541) consistent with the Devils Hole chronology suggesting that Stage 5e began at about this time. Muhs (2002 [DIRS 161006], p. 39) reports that U-series' dates on corals from Bermuda, Bahamas, Hawaii, and Australia indicate that the last interglacial period had a sea level at least as high as present from ~128 to 116 ka before present. Speleothems from northwestern Europe also suggest that the initiation of this deglaciation may have been underway as early as 145 ka and certainly by 133 ka (Winograd 2002 [DIRS 160982], p. 7a). Therefore, warming was underway at least 10 k.y. prior to ice sheet melting as indicated by benthic $\delta^{18}O$ marine records (Landwehr and Winograd 2001 [DIRS 160145], p. 31,854; Kukla et al. 2002 [DIRS 160981], pp. 6 and 7). If these dates are used, all of the precession ages and available Devils Hole reversal point ages are within 2,500 yr or less of each other, a good agreement between the two sets of data.

The general nature of (inter) glacial climate does not change precisely at the primary reversal points, instead the reversals begin a trend toward an (inter) glacial climate. Also, climate does not necessarily move continuously towards an (inter) glacial. The Devils Hole $\delta^{18}O$ profile shows a relatively smooth curve, indicating a continuous transition toward and into (inter) glacial climates, because each Devils Hole data point integrates approximately 1,800 yr (Winograd et al.

1992 [DIRS 100094], p. 255). Examination of a higher resolution curve, such as the deuterium record of the last 420,000 yr from Antarctica (Petit et al. 1999 [DIRS 109450], Figure 1, p. 430), shows a pattern of numerous small-magnitude climate reversals that occur on decade and century time scales not recorded in the Devils Hole record.

The correspondence between the timing of "I" events (high $\delta^{18}O$ values representing warmer and/or drier conditions in the recharge area) in the latter part of the Devils Hole record and maximum precession (increased summer solar radiation) in the southern hemisphere summer (Figures 6-3a to 6-3c) suggests that northern hemisphere climate begins a cooling trend when heat is being added to the southern hemisphere. Although it is possible that no causal relationship exists between these two variables, this relation suggests that a linkage between (inter) glacial periods and tropical insolation may exist.

Mechanisms and linkages for orbital forcing, a tropical moisture source, and short and long-term climatic events are discussed in Winograd 2001 ([DIRS 160147], pp. 302 to 304); Landwehr and Winograd 2001 ([DIRS 160145], p. 31854); Cane 1998 ([DIRS 160521], pp. 59 to 61); Kerr 2001 ([DIRS 160516], pp. 660 and 661); Cane and Evans 2000 ([DIRS 160520], p. 1108); Clement et al. 2001 ([DIRS 160518], pp. 2370 and 2373); Clement and Cane 1999 ([DIRS 160525], abstract, p. 363); Cane and Clement 1999 ([DIRS 160506], p. 373); Seager et al. 2000 ([DIRS 160512], abstract, p. 2144); Clement and Seager 1999 ([DIRS 160519], p. 3399); Kukla et al. 2002 ([DIRS 160980], p. 27); Pierrehumbert 1999 ([DIRS 160139], p. 339); and Khodri et al. 2001 ([DIRS 160225], p. 570). Furthermore, Kukla et al. 2002 ([DIRS 160981], p. 11), in a comprehensive paper on interglacial climates, suggest "the orbital shift to the warming of the tropics and cooling of the high latitudes in autumn is strongly indicated as the primary cause of the interglacial decline."

Note the lower variability in the Devils Hole record prior to approximately 470,000 yr before present (Figures 6-3a and 6-3b). Although glacial period MIS 14 may be recorded at the "T" event at about 528,000 yr before present, the $\delta^{18}O$ curve is relatively flat across the estimated interglacial climate state. The relative invariability of these $\delta^{18}O$ values could mean:

- The site did not record a change in recharge

- The glacial and interglacial pattern established by the Devils Hole record subsequent to 470,000 yr before present is coincidental

- The dates are not accurate based on the uncertainty this far back in the record

- The climate signal is lost in the regional aquifer from mixing of waters having different ages and isotopic values or hydrologic head relations between recharge and discharge change

- The climate did not accentuate the differences in the isotopic value of snow by increasing and decreasing thermal gradient between source area and recharge area

- The earliest part of the Devils Hole record was influenced by a shift in climate, earth processes, or some other factor.

Shifts in climate have been documented in basins in the Atlantic and/or Pacific oceans between 1,500,000 and 600,000 yr ago (Rutherford and D'Hondt 2000 [DIRS 160224], p. 72); between 1,200,000 and 1,000,000 yr ago (Berger et al. 1994 [DIRS 160205], p. 465); between 900,000 and 600,000 yr ago (Williams et al. 1988 [DIRS 100093], p. 221); about 640,000 yr ago (Mudelsee and Schulz 1997 [DIRS 160200], p. 121); and between 870,000 and 450,000 yr ago (Hall et al. 2001 [DIRS 160235], p. 810). These datasets show that the response of the earth to orbital forcing has varied considerably over the last million years, and supports Assumption 4 (Section 6.1) that long-term earth-based climate-forcing functions have remained relatively constant only over the past 500,000 yr.

6.5.3.4   Describing the Patterns

The timing and pattern of interglacial to glacial periods in the Devils Hole record show a remarkable consistency during the last eccentricity cycle (~400,000 yr). As discussed above, the ends of interglacial episodes correspond with the "I" events when $\delta^{18}O$ values in Devils Hole calcite become lower moving forward in time. The path taken by Devils Hole $\delta^{18}O$ from an "I" to a "T" event is oscillatory in nature reflecting a climate path of cold and warm events until the initiation of the glacial period. This complex climate change path is also known from numerous long records around earth. Cold episodes during an interglacial are termed sub-stages "d" and "b," and the warmer intervals are termed substages "e," "c," and "a." Sub-stage e is always the oldest and sub-stage a is always the youngest (Figure 6-3c).

In the period between 250 and 60 ka, the interglacial periods MIS 7 and 5 contain cold episodes occurring during sub-stages 7d, 7b, 5d, and 5b. These cold episodes are recorded as troughs in the Devils Hole isotopic record at about 223, 200, 112, and 88 ka, respectively (Figure 6-3c). Troughs in the Devils Hole isotopic record also occur during MIS 11 (388 and 377 ka), and during MIS 9 (314 and 296 ka [Figure 6-3b]).

Warm episodes occur after each of these troughs during the substages 7c, 7a, 5c, and 5a (Figure 6-3c). This pattern is also evident in the earlier interglacials, MIS 9 and 11. Prokopenko et al. (2001 [DIRS 160507], Figure 3, p. 128; p. 127) designate the peaks in biogenic silica (indicating warm climatic periods) at about 333 ka and 287 ka (9e and 9a, respectively); whereas Landwehr and Winograd (2001 [DIRS 160145], Figure 1a, p. 31,856) label the interglacial in the Devils Hole record at approximately 330 ka as 9c rather than 9a (Figure 6-3b). The MIS 11 climatic optimum in the Lake Baikal record is provisionally labeled 11e by Prokopenko et al. (2001 [DIRS 160507], pp. 127 and 128). This interglacial period corresponds to 11c at approximately 400 ka in the Devils Hole record (Figure 6-3b). The interglacial substages 11c, centered at about 410 ka, and 9c, centered at about 330 ka, (after Winograd et al. 1997 [DIRS 100096], Figure 2, p. 143), correspond to "e" events and not "c" events following this pattern.

Warm substages generally occur between the southern hemisphere summer radiation maxima 1 and 2 and between 2 and 3. The last 400,000 yr of the Owens Lake ostracode record (Table 6-28) based on the Devils Hole chronology also largely supports this pattern. This pattern is not as pronounced in the Devils Hole record prior to about 420,000 yr ago, possibly due to reasons discussed above. However, cold and warm episodes associated with the numbered sub-stages also appear in other paleoenvironmental records worldwide (Woillard 1978

[DIRS 152155], p. 16; Litwin et al. 1999 [DIRS 109440], Figure 3a, p. 1158; Adam 1988 [DIRS 152163], Figure 1, p. 85; Shackleton and Opdyke 1973 [DIRS 109163], Figure 8, p. 47, Figure 9, p. 48; Prokopenko et al. 2001 [DIRS 160507], Figure 3, p. 128).

After the warm peak near each of the "I" events, climate moves toward a glacial period (Figures 6-3b and 6-3c). Each "I" to "I" event encompasses a precession sequence. The timing, pattern, and magnitude of each glacial period correspond with the number of precession cycles in a precession sequence. Glacial cycles in precession sequences with 5 cycles generally fall between northern hemisphere summer radiation maxima 3 and 4. The precession sequences with 5 cycles have a glacial period with two cold troughs (MIS 12, 6, 4). The cycles with 4 precession periods have a single trough (MIS 10, 8) near the southern hemisphere summer radiation maxima 3. The lightest isotopic values for single trough glacials are about 13‰ and double trough glacials are about 13.5‰. The magnitude of past glacial states based on proxy data is discussed in Sections 6.4.1.2.2 and 6.4.1.2.3.

The published Devils Hole record ends at about 60,000 yr ago, and until the data from the youngest part of the core are published, it is unclear how MIS 2 (which occurred approximately between 25,000 to 12,000 yr before present in southern Nevada) will be recorded. However, if the past glacial and interglacial patterns shown in the Devils Hole record continue to repeat, the Devils Hole record should show a dip (lower values) at about northern hemisphere summer radiation maxima 4 and then begin a trend to higher interglacial values.

The repetitive pattern of the Devils Hole isotope record suggests that MIS 4, 3, and 2 could be combined into a single longer segment for the purposes of this analysis. Both the Owens Lake and the Devils Hole records contain patterns that support combining these 3 MIS. Each precession sequence ("I" to "I" event) between 425,000 and 60,000 yr ago, in the Devils Hole chronology, begins with an event in an interglacial period ("I" event), moves into a glacial period, and then moves toward another interglacial period as it nears the next "I" event (Figures 6-3a to 6-3c). If glacial MIS 4 and 2 are defined as separate MIS in the last precession sequence, this sequence would be the only sequence containing three interglacial (MIS 5, 3, and 1) and two glacial periods (MIS 4 and 2).[5] If MIS 2 is considered to be the second dip in the double trough MIS 4 glacial, the four precession sequences over the last 400,000 yr display a similar pattern. Therefore, MIS 2 and 4 are considered here as one "type" of glacial with a magnitude of MIS 2. This sequence simplifies the specification of estimated future climate states and largely preserves the cycle of precession sequences for the last 425,000 yr.

6.5.3.5   Characteristics and Repetition of Past Climate

The last 800,000 yr include two full eccentricity cycles, each approximately 400,000 yr long. At present, the earth is at the end of the 400 to 0 ka cycle and poised to begin a new 400,000-yr cycle by repeating orbital parameter relations that pertained 400,000 yr ago[6] (USGS 2001

---

[5] Muller and MacDonald (2002 [DIRS 160236], p. 232) include a short account of Nicholas Shackleton recounting Cesare Emiliani's designation of MIS 3. Apparently, Emiliani based its designation on the 41,000-year obliquity cycle (41,000 years prior to MIS 2), even though the MIS 3 warming was not as pronounced as in previous interglacial periods.

[6] To compare Stages 11 and 1 in oceanic records, see Hodell et al. 2000 [DIRS 160511]; Bauch et al. 2000 [DIRS 160524]; Kindler and Hearty 2000 [DIRS 160509]; and Murray et al. 2000 [DIRS 160508].

[DIRS 158378], pp. 59, 62, and 63; Loutre and Berger 2000 [DIRS 160117], p. 64; Poore and Dowsett 2001 [DIRS 160201], Figure 3, p. 73). If a general relation can be determined to exist between the characteristics and magnitude of past glacial and interglacial climates and the repetition of those climates in different 400,000-yr earth-orbital cycles, then this relation provides a criterion for selecting a particular past climate cycle as an analog of future climate (Assumption 3 in Section 6.1).

Support for this assumption depends on interpreting paleoenvironments from the penultimate 400,000-yr cycle; data from that cycle are limited. However, if temperature and precipitation characteristics of past glacial and interglacial climates differ from each other in a systematic way throughout the last 400,000-yr cycle, then this relation provides a criterion for selecting particular past climates as analogs for future climates in the next 400,000 yr at Yucca Mountain. Although a strict repetition of climate characteristics is not expected or implied from the available data, the general characteristics of future precipitation and temperature for a particular interglacial and glacial couplet can be estimated. Thus, the nature of various interglacial and glacial couplets during the last 400,000-yr orbital cycle serve as analogs for future climates during the next 400,000 yr. If this assumption were not accepted, then the bounding estimates for future climate at Yucca Mountain would be based on the extreme estimates of temperature (very cold) and precipitation (very wet) from the entire previous 400,000-yr cycle, instead of based on a range of values designated for each of the four forecast climate states.

Section 6.5.3.4 described precession sequences containing either four or five precession cycles and how patterns of the Devils Hole isotope record corresponded to the varying number of precession cycles in a sequence. The lake record in the western Great Basin suggests that MIS in precession sequences with five cycles had larger lakes than MIS in precession sequences with four cycles. The absolute size of a lake in a particular basin is a function of many climatic and nonclimatic factors, but MIS 16, 12, 6, 4/2 (all precession sequences with five cycles) suggest high effective moisture generated by some combination of increased precipitation and/or lowered temperature relative to the other MIS. As mentioned earlier, effective moisture does not necessarily reflect precipitation; cold, dry glacial periods can have greater effective moisture than warm, wet glacial periods.

MIS 16 and 6 were the glacials with the highest effective moisture in the last two eccentricity cycles (USGS 2001 [DIRS 158378], p. 60). However, MIS 16 (centered about 600,000 yr before present and lasting for approximately 30,000 yr) appears to have had greater effective moisture than MIS 6. The MIS 16 lakes identified by Reheis (1999 [DIRS 109454], Figure 1, p. 197) in the northern Great Basin were much larger and deeper than those in the same basins during MIS 6. Evidence also exists for a large lake during MIS 12, but not as large as the one during MIS 16 (Reheis 1999 [DIRS 109454], Figure 3, p. 200). Oviatt et al. (1999 [DIRS 109448], p. 180) present chronological and environmental evidence of a lake in the Great Salt Lake Basin during MIS 16 and MIS 12, but no others during the older long climate cycle. Precession sequences containing five precession cycles with high amplitude (MIS 6 and 16 over the last 1,000,000 yr) appear to have colder, wetter glacial periods than those with lesser amplitudes.

A number of other studies suggest that MIS 16 had very high effective moisture (Knott 1999 [DIRS 109436], p. 92; Jannik et al. 1991 [DIRS 109434], p. 1146; Smith and Bischoff 1997 [DIRS 100077], p. 123; Whitney and Harrington 1993 [DIRS 107303], p. 1016; Reheis 1999

[DIRS 109454], p. 196; Morrison 1999 [DIRS 138393], p. 304). However, uncertainties exist in this time frame because tectonic activity may have affected topography and, hence, climate. For example, Lake Clyde, a tectonically dammed lake in the Central Valley of California, could have recharged Pacific air masses that could have increased the rain and snowfall on the Sierra Nevada during MIS 16 time (Reheis et al. 2002 [DIRS 161593], p. 101). It is also possible that a shifting of the center of mass of the continental ice sheets from the west in the older glacials to the east in the younger glacials may have significantly impacted the Great Basin climate over this time period. Nonetheless, because MIS 16 appears to have had the greatest effective moisture of any glacial period over the last 800,000 yr, estimates of temperature and precipitation during this time are used as an upper-bound glacial-climate parameter.

Death Valley MIS 6 had larger lakes than during MIS 2 (Ku et al. 1998 [DIRS 109438], Figure 6, p. 272). The MIS 2 lake in Death Valley was large (approximately 70 m deep), but smaller than the MIS 6 lake (at least 175 m deep) (Ku et al. 1998 [DIRS 109438], p. 261). Jannik et al. (1991 [DIRS 109434], Figure 10, p. 1158) suggest that the Owens drainage lakes filled and may have flowed into Panamint Valley during parts of MIS 16, 12, 10, and 6, but not in MIS 2 (Figure 6-4).

The marine isotope record, providing a general proxy for ice volume (although ocean temperature appears to play an important role), also suggests that MIS in precession sequences with five cycles had larger ice sheets than MIS in precession sequences with four cycles. For example, the largest ice sheets recorded by the marine isotope record over the last 800,000-yr interval occurred during MIS 16, 12, 6, and 2 (all found in precession sequences with five cycles), although these sheets varied in their relative size (indicating that these glacial periods were not of the same magnitude) (USGS 2001 [DIRS 158378], p. 61; Crowley and North 1991 [DIRS 121811], Figure 6.1, p. 111; Oviatt et al. 1999 [DIRS 109448], Figure 2, p. 183).

The marine isotope record for the last 800,000 yr suggests that glacial MIS 18, 14, 10, 8, and 4 had smaller and/or lower ice sheets than other glacial MIS. With the exception of MIS 4, these are all found in precession sequences with four cycles. If MIS 4 and 2 are considered one glacial in a 5-cycle precession sequence, the previous pattern is preserved. This may indicate that the record of relatively smaller lakes in Nevada was created during glacial periods with less effective moisture relative to MIS 16, 12, 6, and 4/2 (USGS 2001 [DIRS 158378], pp. 60 and 61; Sharpe 2003 [DIRS 161591], pp. 22 to 25). These smaller lakes could have been created by less effective moisture even if the overall climate was very wet, but the temperature was warm. In the Bonneville Basin four deep-lake cycles corresponding to MIS 16, 12, 6, and 2 occurred (Oviatt et al. 1999 [DIRS 109448], Table 2, p. 182). The authors suggest that lakes formed only at these times because these were the most extensive of the northern hemisphere glaciations.

It is possible that MIS with very large ice sheets could produce climates with greater effective moisture in the vicinity of Yucca Mountain relative to MIS with smaller ice sheets. As continental ice sheets expand in the area and become higher in elevation, they tend to deflect dry and very cold arctic high-pressure air masses southward during the entire year (an annual cold and dry climate state), or just during the winter if high pressure cells retreat northward in summer (Kutzbach et al. 1993 [DIRS 119269], Figures 4.16 and 4.17, pp. 56 to 59).

The warm climate states in each 400,000-yr cycle also have similarities. Based on the Owens Lake ostracode and diatom record, the warm, dry climate periods were occasionally punctuated by warm, wet, but low effective moisture, tropical-dominated climates. Extensive periods occurred when climate characteristics were intermediate between full-glacial high effective moisture and interglacial low effective moisture. The change between the various climate states was rapid, apparently occurring on a decade to century time scale.

6.5.4 Selecting Present-Day Meteorological Stations as Analogs to Past Climate States

Establishing the nature of past climate states using paleoenvironmental data allows the selection of present-day meteorological stations representing those past climate states. The continuous daily temperature and precipitation values from present-day meteorological stations are used to calculate model-derived infiltration estimates. The meteorological stations chosen to represent past climate states were selected, in part, based on the limiting hydrologic and physical factors estimated from the modern distributions of fossil ostracode and diatom assemblages recovered from the Owens Lake record (USGS 2001 [DIRS 158378], pp. 68 to 75).

Stations based on geographic location rather than on elevation in the Yucca Mountain area were chosen as analog climate sites because the shifting of atmospheric circulation patterns over time manifests itself more in terms of latitude and longitude than elevation. Because of the atmospheric circulation patterns described above, present-day meteorological stations positioned with respect to the seasonal location of the polar front and associated low and high pressure zones were selected as analogs for past climate. These stations better represent the seasonal distribution of temperature, precipitation, snowfall, and humidity than stations located on an elevational gradient in southern Nevada.

In particular, the present-day late spring through early autumn season in the Yucca Mountain region is characterized by the residence of a tropical high-pressure system whereby sinking air and clear skies help create the high summer temperatures. Evidence from many sources described above indicates that the subtropical high-pressure system was not resident during glacial and intermediate climate states. Therefore, evaporation would have been much lower and so infiltration was likely much higher than at present during those climates when the tropical high-pressure system was not resident. Hence, if stations were selected based on elevation alone, they would represent only modern atmospheric circulation patterns with the same annual distribution of temperature and precipitation as the present day.

Table 6-29 lists the regional meteorological stations representing analogs of future climate states, and Figure 6-8 shows their locations (USGS 2001 [DIRS 158378], pp. 69 to 71; Sharpe 2003 [DIRS 161591], pp. 30 and 31). Only meteorological stations with relatively complete and long records were considered as analogs for past climates (Sharpe 2003 [DIRS 161591], p. 28). Stations were chosen to represent upper (wetter) and lower (drier) bounds. The number of past climate states and representative meteorological stations were limited to facilitate and simplify model simulations of net infiltration.

The present-day climate state is represented by regional meteorological stations in the Yucca Mountain area. Modern climate in the Yucca Mountain region averages 13.4 C MAT and

125 mm MAP[7] (Thompson et al. 1999 [DIRS 109470], Table 4, p. 24). Currently, precipitation minus open-water evaporation is -100 cm/yr (Winter 1990, Plate 2 [DIRS 166505]). The monsoon climate state is represented by Nogales, Arizona, and Hobbs, New Mexico, for an upper bound and the Yucca Mountain regional stations as a lower bound (USGS 2001 [DIRS 158378], pp. 71 and 72). Precipitation minus open-water evaporation is about -120 cm/yr at these stations (Winter 1990, Plate 2 [DIRS 166505]). The intermediate climate state is represented by three stations in Washington: Rosalia, St. John, and Spokane for an upper bound, and Beowawe, Nevada, and Delta, Utah, for a lower bound (USGS 2001 [DIRS 158378], pp. 72 to 75). Upper bound precipitation minus open-water evaporation is approximately 0 cm/yr at these stations (Winter 1990, Plate 2 [DIRS 166505]). The lower bound precipitation minus open-water evaporation is -60 cm/yr at these stations (Winter 1990, Plate 2 [DIRS 166505]). Three magnitudes of glacial climate (cold-wet, cold-dry, and warm-wet relative to each other) are designated by MIS stages (Sharpe 2003 [DIRS 161591], pp. 29 and 32) and have upper and lower bounds represented by stations in Wyoming, Montana, Nevada, and Washington. Precipitation minus open-water evaporation ranges from +25 cm/yr (upper bound) to -60 cm/yr (lower bound) (Winter 1990, Plate 2 [DIRS 166505]).

Ostracode species in the Owens Lake stratigraphic profiles provided information about the nature and magnitudes of climate states, based on inferences about the linkage between climate and the paleolimnology of Owens Lake (Forester 1983 [DIRS 109023], pp. 436 and 437; Forester 1985 [DIRS 109423], pp. 10 and 11; Forester 1986 [DIRS 109024], pp. 797 and 798) (Section 6.4.1.2). Then, approximate values of MAT and MAP were established for the Yucca Mountain area using the present day climate from the Yucca Mountain region and the reconstructed climate for MIS 2 based on packrat middens (Thompson et al. 1999 [DIRS 109470], Table 4, p. 24).

Thompson et al. (1999 [DIRS 109470], Table 4, p. 24) estimate MIS 2 MAP and MAT at Yucca Mountain were 266 to 321 mm and 7.9 to 8.5°C, respectively. These values agree fairly well with the MAP and MAT values estimated by Mensing (2001 [DIRS 161011], p. 61) from pollen assemblages in Owens Lake between 16,200 and 15,000 calendar years before present: 308 to 370 mm and 9.4°C. Mensing (2001 [DIRS 161011], p. 61]) estimates a greater than 80 percent increase in effective moisture and a 4 to 5°C decrease in MAT compared to modern MAT. Owens Lake, at about 1,085 m, is lower in elevation and would, therefore, have warmer temperatures than Yucca Mountain at 1,500 to 1,930 m in elevation (4,920 to 6,330 ft). The differences in rainfall at Owens Lake relative to Yucca Mountain are well within estimation errors and consistent with expected regional variability in MAP.

Based on the Owens Lake ostracode assemblages and other climate proxy data in the Yucca Mountain region, MIS 10 was wetter and warmer than either MIS 2 or 6. Therefore, MIS 10 likely had a MAP much greater than 300 mm and a MAT greater than about 8°C. If MIS 6 was colder, but with a similar MAP to MIS 2, it may have been colder than 8°C with a MAP of 300 mm or more. With the intermediate climates drier and warmer than MIS 2, but wetter and cooler than present day, MAP for the intermediate climates may have been more than 125 mm,

---

[7] These values integrate a number of meteorological stations throughout the Yucca Mountain region (Nevada Divisions 3 and 4) over a 30-year period.

but less than about 275 mm, and MAT may have been between 8 and 13°C (USGS 2001 [DIRS 158378], p. 58).

Based on climate proxy records, the full-glacial MIS 6 climate seems to have had greater effective moisture than MIS 2 or MIS 10, with a MAP of 300 mm or more and a MAT colder than 8°C. Greater effective moisture does not necessarily signify increased precipitation. Low temperatures can play a critical role in determining effective moisture; hence, increased effective moisture can occur under conditions of very low temperatures and low precipitation. MIS 16 appeared to have more effective moisture than MIS 6; therefore, meteorological stations with values colder and wetter than MIS 2 were sought for the 6/16 analog climate station.

The ostracode *Cytherissa lacustris* is currently found only in a few localities in the United States. It has been collected in Lake Yellowstone, Wyoming, a very fresh and cold lake. Because this region is dominated by polar air masses, it was chosen as the upper bound for the full glacial MIS 6/16 analog climate state. The MAT at this station is very cold (0°C) because of its high elevation and latitude and, therefore, provides a lower bounding estimate on the coldest temperature. The lower bound MIS 6/16 analog stations, Browning and Simpson, Montana, are slightly more in line with estimated MIS 6 temperatures (4.4 and 5.0°C, respectively) and average slightly above the estimated 300 mm MIS 2 MAP, even though *Cytherissa lacustris* has not been reported in this locality.

The lower bound for the full-glacial MIS 6/16 climate (the Montana stations) was also chosen as the upper bound of the full-glacial MIS 2/4 because estimates based on packrat middens put the MAP for MIS 2 between 266 and 321 mm and MAT between 7.9 and 8.5°C (Thompson et al. 1999 [DIRS 109470], Table 4, p. 24). Again, this is an upper bounding estimate because average annual temperatures for these stations are 3 to 4°C below the MIS 2/4 temperature estimates. Elko, Nevada, was selected as the lower bound for full-glacial MIS 2/4 with a MAP of about 240 mm and a MAT of about 8°C (Table 6-29, Figure 6-9). Elko was selected because it can experience cold, wet, and snowy winters, influenced by either Polar lows or Arctic highs, and cool and dry summers resulting from both the presence of cool westerly flows and the absence of subtropical highs in the region.

The area east of the Cascade mountain range in the state of Washington was chosen as the lower bound full-glacial MIS 8/10 analog and the average upper bound analog for the intermediate climate state. This choice was made because the region:

- Is east of a high mountain range in a rain shadow similar to the Yucca Mountain region
- Is winter-precipitation dominated
- Is under the influence of the polar front during the winter
- Is situated near the average position of the polar front throughout the year
- Does not experience extended dominance by cold Arctic high-pressure air.

Ostracodes recovered from the full glacial MIS 8 and 10 in the Owens Lake core also occur at present in eastern Washington, supporting the link between ostracode distribution and climate. The Spokane, Rosalia, and St. John climate stations were selected to represent the upper bound intermediate (glacial-transition) climate in USGS (2001 [DIRS 158378], Table 2, p. 66).

Because the full glacial MIS 8/10 upper bound required wetter and slightly cooler climate than MIS 2, Chewelah, Washington, was selected, based on geographic criteria and the fact that it has a MAP of approximately 537 mm and a MAT of approximately 8°C. Beowawe, Nevada, and Delta, Utah, were chosen for the intermediate lower bound climate analogs in USGS (2001 [DIRS 158378], Table 2, p. 66) because they represent cool, winter wet seasons, warm to cool and dry summers, and lie on the east sides of large mountain ranges (USGS 2001 [DIRS 158378], pp. 73 to 75).

Nogales, Arizona, and Hobbs, New Mexico, were chosen as the monsoon average upper bound climate analogs in USGS (2001 [DIRS 158378], Table 2, p. 66) and, herein, because the ostracode *Limnocythere bradburyi*, recovered from the Owens Lake record, implies an Owens Lake source water derived from summer rain rather than snowmelt. The presence of this ostracode in Owens Lake can be best explained by an expansion and intensification of the summer rain system (monsoons) from moisture sources originating in the Gulf of California or Gulf of Mexico (USGS 2001 [DIRS 158378], pp. 71 and 72). Stations in both Arizona and New Mexico were chosen to represent the monsoon climate state because monsoonal precipitation appears to vary depending on if the air mass originates in the Gulf of California or tropical eastern Pacific Ocean (Mitchell et al. 2002 [DIRS 161001], p. 2271). The monsoon climate analog average lower bound and modern (interglacial) climate state are represented by the Yucca Mountain regional climate stations. These stations average 13.4°C and 125 mm precipitation per year (Thompson et al. 1999 [DIRS 109470], Table 4, p. 24).

Figure 6-9 portrays the temperature and precipitation values (Table 6-29) for each of the climate-state upper and lower bounds. If an upper or lower bound is represented by more than one climate station, the values are averaged to show a general comparison among the climate states. For example, the full glacial MIS 6/16 lower-bound Browning and Simpson, Montana, values are averaged; these values are cooler and wetter than modern values except for the monsoon temperature upper bound. Infiltration is greater during cooler and wetter climate states.

6.5.5 Forecasting Future Climate

Past climate states and their timing have been identified (Section 6.5.2), the relation of Devils Hole chronology and isotopic data to orbital parameters was examined (Section 6.5.3), and analog meteorological stations were selected to represent past climate states. This was done so that daily temperature and precipitation values (Section 6.5.4) could be used as input to models of the infiltration process. This section uses the above information to forecast climate first for the upcoming 10,000 yr and then for the next 400,000 yr.

Future eccentricity and precession cycles for the next 500,000 yr are graphed in Figures 6-10a and 6-10b. As in the previous figures showing orbital parameters, "m," "I," and "T" events are designated. A flattening of the eccentricity cycle occurs at 95,500 yr after present, as eccentricity remains almost constant for approximately 40,000 yr. This affects the magnitude of the corresponding precession sequence because eccentricity amplifies or dampens precession. The precession sequence here is the only one containing three precession peaks, rather than four or five, in the entire 1,500,000-yr time span evaluated in this analysis. Because no previous pattern for a three-precession cycle sequence was available, the intermediate/monsoon climate states were determined to be one precession cycle shorter, lasting through southern hemisphere

maximum two rather than three. This adjustment makes the durations of the glacial and following intermediate climate states similar to past durations, so that consistency with the methodologies described above was maintained. If the intermediate/monsoon climate state continued to just beyond the southern hemisphere summer radiation maximum as in previous cycles, then the glacial, intermediate, and interglacial states would be compressed into 17,000 yr in less than one precession cycle. Also the next 500,000 yr has only one precession sequence containing five precession cycles from 241,000 to 355,000 yr after present.

6.5.5.1   The Near Future-Anthropogenic Warming

Human-caused increases in the so-called greenhouse gases (collectively, GHG: carbon dioxide, methane, nitrous oxide, hydrofluorocarbons, perfluorocarbons, sulfur hexafluoride) have generated much scientific and public concern because higher levels of atmospheric GHG act as a trap for outbound long-wave radiation; thus, warming the earth (Baede et. al. 2001 [DIRS 163810], pp. 87 and 88). The consequences of a warmer earth will almost certainly increase the amount of water vapor in the atmosphere; thus, enhancing the hydrologic cycle. Warmth and an energized hydrological cycle will likely lead to greater climate variability from region to region. Some disagreement exists as to whether recent climate variability results from rising GHG levels, beginning with the widespread use of coal during the Industrial Revolution, or from the variable impacts of other factors, such as solar input and volcanic dust (Crowley 2000 [DIRS 160214], p. 270).

Natural levels of CO_2 varied significantly in the past, particularly between glacial and interglacial periods, as a function of ocean characteristics (e.g., circulation, chemistry, productivity, temperature), terrestrial vegetation cover, volcanism, and other factors. Low CO_2 levels during glacial periods were succeeded by higher preindustrial levels over the course of millennia in some ice cores (Neftel et al. 1988 [DIRS 109139], Figure 3, p. 611), and rapid (50 yr or less) changes of smaller magnitude occurred during both glacial and interglacial periods (Stauffer et al. 1984 [DIRS 109171], Figure 1, pp. 160 and 162). The basic individual mechanisms underlying CO_2 variations are known, but the details and dynamics of the overall changes are not (Siegenthaler 1991 [DIRS 109166], p. 257). It is not known whether climate changes affected CO_2 levels or vice versa. Changes in the carbon budget, to the extent that they affect climate, have already had and will, in the future, have some effect on the climate of Yucca Mountain.

The Intergovernmental Panel on Climate Change was established in 1988 by the World Meteorological Organization and United Nations Environment Programme (Watson et al. 2001 [DIRS 162081], p. vii). The Intergovernmental Panel on Climate Change has produced a series of reports and papers assessing the available information of the science, impacts, and economics of climate change. They conclude that, "the Earth's climate system has demonstrably changed on both global and regional scales after the preindustrial era, with some of these changes attributable to human activities" (Watson et al. 2001 [DIRS 162081], p. 4). Among the observed changes occurring during this time frame are increased greenhouse gases likely resulting from the combustion of fossil fuels, agriculture, and land-use change. Crowley (2000 [DIRS 160214], abstract, p. 270) maintains that global warming projections for the next 100 yr far exceed the natural variability of temperature for the past 1,000 yr.

During the twentieth century, global mean surface temperature increased by 0.6 ± 0.2°C. Also during this time, continental precipitation increased by 5 to 10 percent in the northern hemisphere; cold or frost days decreased for nearly all land areas; the duration of ice cover of rivers and lakes decreased by about two weeks in mid and high latitudes in the northern hemisphere, and snow cover decreased in area by 10 percent since the 1960s (Watson et al. 2001 [DIRS 162081], Table SPM-1, pp. 5 and 6). The confidence levels associated with these weather indicators are placed at a 90 to 99 percent chance that the above measured results are true (Watson et al. 2001 [DIRS 162081], p. 5). Twentieth century weather change indicators with a confidence interval of 66 to 90 percent include an increase in northern hemisphere surface temperatures greater than during any other century in the last 1,000 yr with (Watson et al. 2001 [DIRS 162081], Table SPM-1, pp. 5 and 6):

- 1990 being the warmest decade of the millennium

- A decrease in the diurnal land-surface temperature range over the years 1950 to 2000 with nighttime minimum temperatures increasing at twice the rate of daytime maximum temperatures

- An increase in hot days

- An increase in heavy precipitation events at mid- and high latitudes

- An increase in the frequency and severity of drought in some areas

- Thinning of and decrease in arctic sea ice.

Uncertainty in the Intergovernmental Panel on Climate Change reports is discussed in Reilly et al. (2001 [DIRS 160514], pp. 430 to 433) and Allen et al. (2001 [DIRS 160515], pp. 430 to 433).

These changes are consistent with a warming of climate near the earth's surface. Whether the changes are human-induced or not, their implication for the Yucca Mountain area is that the observed historical climate patterns from recent decades are not representative of century- or millennial-scale past climate and may not be representative of future climate.

Cohen et al. (2001 [DIRS 162088], Figure 15-1, p. 746) project a change in snowpack and the timing of runoff from mountain areas, possible declines in groundwater recharge, increased water temperatures, and increased frequency of intense precipitation events in the southwestern United States from projected climate change. The Intergovernmental Panel on Climate Change models[8] for western North America show increased summer and winter temperatures, a small increase in winter precipitation, and disagreement of model predictions for summer precipitation (Giorgi et al. 2001 [DIRS 162084], Figures 10.4 and 10.6, pp. 596, 598, 862, and 864). Because

---

[8] Results from different models were based on conditions of a 1 percent/year increasing CO_2 (mean for 2071 to 2100 A.D.) without and with sulphate forcing. Model results were averaged to a single case, and "agreement" was defined as having at least four of the five CO_2-only and three of the four increased CO_2-with-sulphate-aerosol cases agreeing (Giorgi et al. 2001 [DIRS 162084], Figures 10. 3 and 10. 4, pp. 595 and 596).

these estimates cover large geographic areas and many types of terrain, it is unrealistic to extract specific values for the Yucca Mountain area from these estimates. However, Thompson et al. (1998 [DIRS 160523], Figure 3, p. 7) estimate climate change for the western United States resulting from a doubling of GHG. In this report, January temperatures are estimated to increase 2 to 3°C and July temperatures are estimated to increase 3 to 4°C; January and July precipitation are expected to decrease 10 to 30 mm in the Yucca Mountain area. Regarding the inconsistency of climate change forecasts, the general consensus is that temperature effects are more likely to be correctly forecast than are precipitation effects (Giorgi et al. 2001 [DIRS 162084], Figures 10.4 and 10.6, pp. 596 and 598). If an average annual warmer and drier climate occurs, then less annual infiltration than modern annual infiltration should result.

If GHG emissions peak and decrease within the next 100 yr, the climate system will not respond immediately. It is estimated that temperature and CO_2 emissions will stabilize in a few centuries (Watson et al. 2001 [DIRS 162081], Figures 5-1 and 5-2, pp. 88 and 89). However, because the climate system, particularly the oceans and cryosphere[9], has a long response time, it could be thousands to tens of thousands of years before sea level and ice caps reach equilibrium (Watson et al. 2001 [DIRS 162081], Figures 5-1 and 5-2, pp. 88 and 89)[10]. How these long-term responses will be manifested in climate in the Yucca Mountain region is not known. Therefore, GHG forced climate change was not considered in selecting future climate analog stations, although the kinds of climate change estimated from elevated levels of GHG may share some characteristics of the monsoonal climates that are believed to occur at the ends of the interglacial climates.

6.5.5.2   The Next 10,000 Years

The initial step in determining what point in MIS 11 was the equivalent to our modern climate was to select a past/present analog point of 403,970 yr before present in the MIS 11 sequence at Owens Lake between the occurrence of ostracodes *Limnocythere sappaensis* and *L. bradburyi* (inferred from CRWMS 2000 [DIRS 151945], Figure 6.4-10; USGS 2001 [DIRS 158378], p. 63). The large *L. sappaensis* abundance peak in MIS 11 reflects a mid-stage warm and dry climate (similar to present day) and the enhanced monsoon reflecting the *L. bradburyi* abundance peak had and has yet to occur. Because the present interglacial is nearing its end, the analog point was placed closer to the monsoon climate indicator than to the interglacial climate indicator

---

[9] The cryosphere is the component of the climate system consisting of all snow, ice, and permafrost on and beneath the surface of the earth and ocean (Watson et al. 2001 [DIRS 162081], p. 370).

[10] Loutre and Berger (2000 [DIRS 160117], p. 61) suggest that the present interglacial will last about 50,000 years with an interstadial at about 60,000 years in the future and a glacial maximum at about 100,000 years in the future using CO_2 concentrations ranging from 210 to 290 parts per million by volume (ppmv). They also warn that anthropogenic disturbance may significantly affect the northern hemisphere ice sheet for approximately the next 50,000 years. Berger and Loutre (2002 [DIRS 160153], p. 1287) provide an overview of the results from different future climate models. Models using a human-induced concentration of 750 (ppmv) CO_2 predict an interglacial lasting from about 5,000 years ago to 50,000 years into the future with the next glacial maximum occurring in 100,000 years. In this article, Berger and Loutre suggest that "an irreversible greenhouse effect" could become the climate of the future if CO_2 concentrations increase to 750 ppmv over the next 200 years and return to natural levels (~225 ppmv) by 1,000 years from now. Hence, the next glacial could be postponed.

at an Owens Lake chronology age of ~404,000 yr ago[11] (USGS 2001 [DIRS 158378], Section 6.6.1, pp. 62 to 66, for a complete discussion of analog placement point).

This timing, using a sediment accumulation rate of 63 cm per 1,000 yr (Litwin et al. 1999 [DIRS 109440], p. 1161), leads to the prediction of three climate states at Yucca Mountain over the next 10,000 yr (USGS 2001 [DIRS 158378], Table 2, p. 66): a modern-like climate for 400 to 600 yr, then a monsoon climate for about 900 to 1,400 yr, and finally a glacial-transition climate that will persist through the remainder of the period (USGS 2001 [DIRS 158378], Table 2, p. 66).

In contrast, Sharpe (2003 [DIRS 161591], p. 54) suggests that the monsoon climate state has already begun, which is ~1,600 yr ahead of the USGS estimate (2001 [DIRS 158378], p. 76). Sharpe's evaluation (2003 [DIRS 161591], p. 48) is based on the precession methodology described in Section 6.5.3.3, so this timing is based on orbital parameters rather than past climate proxy data. The intermediate/monsoon climate state is estimated to have begun at the "I" event 1,000 yr ago and will last 500 yr into the future for a total of 1,500 yr (Sharpe 2003 [DIRS 161591], Table 6-6, p. 56).

In this methodology, monsoon climate states were incorporated into the intermediate states based on the monsoon intervals suggested by the ostracode assemblages in the Owens Lake record (Sharpe 2003 [DIRS 161591], p. 47). Based on this record, individual monsoon events lasted approximately from 1,000 to 2,000 yr during MIS interglacial stages 11, 7, and 5 (Table 6-28). The total cumulative duration of the monsoon states during each MIS stage was about 3,000 yr. Sharpe divides this 3,000-yr cumulative duration into two monsoon intervals, each 1,500 yr long, evenly distributed within the intermediate climate state moving from interglacial to glacial states. This artificial construct was used to time the monsoon climate states for future climate estimates. Although it is an oversimplification of the past climate that the ostracode record suggests, it includes the climatic events represented by the monsoon intervals while simplifying input to be used for modeling infiltration.

---

[11] The timing of the analog point (~404,000) falls within the *Limnocythere bradburyi* event (405,000 to 403,000 years before present) in Table 6-28. That is, it appears that *L. bradburyi* arrived "sooner" (by about 1,000 years) than it should have. However, the timing of the analog point was chosen using the isotope values and timing of the Devils Hole chronology. The analog point had to correspond to a point in the Devils Hole record where the isotopic values were increasing in response to monsoonal flow, after 405,400 years before present. Since the sampling interval of the Devils Hole calcite represents an average time interval of about 1,800 years at 2 σ (Winograd et al. 1992 [DIRS 100094], p. 255), the timing discrepancy falls within this uncertainty.

Table 6-30 compares the two analyses with respect to the estimated timing[12] of climate states. Both USGS (2001 [DIRS 158378], pp. 48 and 67) and Sharpe (2003 [DIRS 161591], p. 56) agree that an interglacial climate state has occurred from at least 9,000 yr ago to the present. However, three timing differences occur over the next ~20,000 yr between the two future climate estimates:

1. Transition from modern to monsoon climate states, maximum difference is 1,600 yr between 600 yr after present and 1,000 yr before present.

2. Transition from monsoon to intermediate climate states, difference is 1,500 yr between 2,000 yr after present and 500 yr after present.

3. A 1,500-yr monsoon climate state occurring between 18,500 yr after present and 20,000 yr after present.

The difference in timing between USGS (2001 [DIRS 158378]) and Sharpe (2003 [DIRS 161591]) is considered to be insignificant. Both estimates use the Devils Hole record chronology. Each Devils Hole sample integrates a particular thickness of carbonate in a continuous sample series and represents about 1,800 yr (Winograd et al. 1992 [DIRS 100094], p. 255). Therefore, the differences of 1,600 yr and 1,500 yr for the first two timing differences are less than the Devils Hole sample resolution of 1,800 yr. The duration of the 1,500-yr monsoon interval is also less than the Devils Hole sampling error. Since the monsoon is between two intermediate states of long durations (18,500 yr), the uncertainties of timing for both the beginning and the end of monsoon are dominated by the uncertainties of the intermediate states. Therefore, the timing of future climate estimated in Sharpe (2003 [DIRS 161591], p. 55) confirms the timing suggested in USGS (2001 [DIRS 158378], p. 76).

6.5.5.3   The Next 400,000-Year Eccentricity Cycle

USGS (2001 [DIRS 158378], Table 2, p. 66) and Sharpe (2003 [DIRS 161591], Table 6-6, p. 56) are in relatively close agreement for the onset and length of the next glacial state after the intermediate (glacial-transition) climate state concludes. USGS (2001 [DIRS 158378], pp. 48 and 57) forecasts that intermediate climates will begin in southern Nevada about 2,000 yr from now and will end about 30,000 yr from now based on the analogy with Owens Lake record. Sharpe (2003 [DIRS 161591], Table 6-6, p. 56) estimates intermediate climates will begin about 500 yr from now and persist for approximately the next 38,000 yr based on the precession methodology. This timing includes a 1500-yr monsoon state. USGS (2001 [DIRS 158378], p. 48) estimates the next glacial state will begin about 30,000 and end before 50,000 yr after present, and Sharpe (2003 [DIRS 161591], Table 6-6, p. 56) estimates that it will occur 38,000 to 49,000 yr after present.

The predicted sequence and durations of climate states for the next 500,000 yr taken from Sharpe (2003 [DIRS 161591], Table 6-5, p. 55) are listed in Table 6-31. This table was generated using

---

[12] USGS (2001 [DIRS 158378], Table 2, p. 66) reported durations of modern climate for 400 to 600 years; monsoon climate for 900 to 1,400 years; and glacial transition (intermediate) climate for 8,000 to 8,700 years. However, Table 6-30 uses 600 years and 2,000 years after present selected by USGS (2001 [DIRS 154674], p. 57) as the timing for these changes in climate states.

values from the precession methodology described in Section 6.5.3.3 with the values used to generate Figures 6-10a and 6-10b. As described in Section 6.5.2.1, four climate states are considered to comprise the sequence of climate states during the next million years: intermediate/monsoon alternating between monsoon and intermediate climate states, glacial, intermediate, and interglacial.

Future glacial stages are based on the pattern of glacial stages over the last 400,000 yr: MIS 10 to 8 to 6 to 4/2 as in USGS (2001 [DIRS 158378], p. 48) and Sharpe (2003 [DIRS 161591], pp. 22 to 25)[13]. MIS 2 and 4 are combined for the purpose of this analysis (Section 6.5.3.4) and the magnitude is based on the magnitude of MIS 2. Glacial stages that were similar (8 and 10, or 6 and 16) were combined as one type of glacial state (8/10 and 6/16).

Table 6-32 was created by using the information in Tables 6-28 and 6-31. It compares the estimated durations of past climate states based on the fossil and isotope records with the durations of glacial and interglacial stages based on the timing of orbital parameters for the past and future 500,000 yr (with MIS 4 and 2 combined). This table was generated using values from the precession methodology.

The durations are fairly consistent for both past and future stages. Interglacial states, which are comparable to our relatively warm modern climate state, last between 10,000 and 12,000 yr. Monsoon/intermediate states are highly variable in duration and last between 29,000 to 52,000 yr. This climate state alternates between hot summers with increased rainfall relative to the present (monsoon) and periods of time that have cooler and wetter summers and winters relative to today (intermediate). Glacial states last between 8,000 and 39,000 yr, and these states are much cooler and wetter than the present. Intermediate states moving forward in time from glacial to interglacial last between 13,000 and 23,000 yr. Notice that the duration of certain climate states for particular MIS tend to be fairly consistent. For example, the durations of the monsoon/intermediate state in MIS 11 and its future equivalents range from 39,000 to 46,000 yr. Similarly, the durations of the intermediate states in MIS 10 range from 13,000 to 16,000 yr.

Total durations and percent of each of the major climate states during the past 410,000 yr and the next 507,000 yr are listed in Table 6-33. The values for the precession method are the sums of the rows in Table 6-32. For example, the past 500,000 yr of interglacial climate is the sum of the row of past interglacial climate in Table 6-32. Differences in the duration for each climate state are evident when comparing the Owens Lake record and precession methodology. The total time period for each column differs slightly. Glacial states are the most consistent occurring 19 to 23 percent of past and future time. Interglacial climates are recorded at Owens Lake 20 percent

---

[13] An alternate method of sequencing future glacial states can be based on the number of precession cycles in a sequence (see Sections 6. 5. 3. 4 and 6. 5. 3. 5). Based on paleoenvironmental data, precession sequences with four precession cycles host warmer, wetter glacial periods (MIS 8/10); precession sequences with five high-amplitude precession cycles host colder glacials (MIS 6/16); and precession sequences with five low-amplitude precession cycles host cooler drier glacials. The differences in the order of glacial magnitude over the next 500,000 years between Table 6-31 and the precession-cycle method discussed in this footnote occur in the third (~200,000 to 213,000) and fourth (291,000 to 329,000) glacial periods after present. The precession-cycle method estimates the third glacial period is to be of MIS 8/10 magnitude, and the fourth glacial period is to be of MIS 6/16 magnitude; whereas the magnitudes herein are estimated to be MIS 6/16 and MIS 4/2, respectively.

of the time compared with only 13 percent for the precession methodology. Intermediate/monsoon climates occurred between 59 and 68 percent of the time, with Owens Lake recording the low of 59 percent. Although the difference in duration for these different climate states is almost 10 percent, the discrepancy is likely reasonable, considering that sediment deposition rates are not constant and may contribute to inconsistencies with the times chosen for beginning and ending climate states using the precession methodology.

Six glacial stages are estimated to occur over the next 500,000 yr. They may range between 8,000 and 38,000 yr in length and comprise about 19 percent (95,000 yr) of the next 500,000 yr. These glacials will be different in magnitude, varying from relatively warm and wet to cold and dry. The upper bound for the most conservative estimates (MIS 6/16 equivalent) for MAT and MAP is 0°C and 513 mm, respectively. The lower bound for the warmest and wettest estimate (MIS 8/10 equivalent) for MAT and MAP is approximately 9°C and 430 mm, respectively. The intermediate, and intermediate/monsoon, climate states may comprise over 68 percent of the total next 500,000 yr (>347,000 yr). Intermediate climate state bounds range from approximately 9 to 10°C MAT and 430 to 200 mm MAP per year. Monsoon climate states are calculated to occur 3 percent of the time within the intermediate/monsoon climate state. Monsoon climate state bounds range from about 13 to 17°C MAT and 125 to 400 mm MAP per year. Interglacial (modern-like) climate is estimated to occur about 13 percent (65,000 yr) of the time during the next 500,000 yr with estimated MAT and MAP to be about 13°C and 125 mm, respectively.

6.6 REFERENCES

6.6.1 Documents Cited

152163   Adam, D.P. 1988. "Correlations of the Clear Lake, California, Core CL-73-4 Pollen Sequence with Other Long Climate Records." *Late Quaternary Climate, Tectonism, and Sedimentation in Clear Lake, Northern California Coast Ranges*. Sims, J.D., ed. Special Paper 214. Pages 81-95. Boulder, Colorado: Geological Society of America. TIC: 248627.

107641   Ahrens, C.D. 1994. *Meteorology Today, An Introduction to Weather, Climate, and the Environment*. 5th Edition. St. Paul, Minnesota: West Publishing. TIC: 237196.

160515   Allen, M.; Raper, S.; and Mitchell, J. 2001. "Climate Change: Uncertainty in the IPCC's Third Assessment Report." *Science, 293*, (5529), 430-431, 430. Washington, D.C.: American Association for the Advancement of Science. TIC: 253530.

150236   Anderson, D. 1999. "Latest Quaternary (<30 ka) Late High-Stand Fluctuations and Evolving Paleohydrology of Death Valley." *Proceedings of Conference on Status of Geologic Research and Mapping in Death Valley National Park, Las Vegas, Nevada, April 9-11, 1999*. Slate, J.L., ed. Open-File Report 99-153. Pages 124-131. Denver, Colorado: U.S. Geological Survey. TIC: 245245.

162062 Anderson, D.E. and Wells, S.G. 2003. "Latest Pleistocene Lake Highstands in Death Valley, California." *Paleoenvironments and Paleohydrology of the Mojave and Southern Great Basin Deserts*. Enzel, Y.; Wells, S.G.; and Lancaster, N., eds. Special Paper 368. Pages 115-128. Boulder, Colorado: Geological Society of America. TIC: 255307.

162061 Anderson, K.C. and Wells, S.G. 2003. "Latest Quaternary Paleohydrology of Silurian Lake and Salt Spring Basin, Silurian Valley, California." *Paleoenvironments and Paleohydrology of the Mojave and Southern Great Basin Deserts*. Enzel, Y.; Wells, S.G.; and Lancaster, N., eds. Special Paper 368. Pages 129-141. Boulder, Colorado: Geological Society of America. TIC: 255307.

108850 Anderson, R.Y. 1992. "Long-Term Changes in the Frequency of Occurrence of El Nino Events." Chapter 9 of *El Nino, Historical and Paleoclimatic Aspects of the Southern Oscillation*. Diaz, H.F. and Markgraf, V., eds. New York, New York: Cambridge University Press. TIC: 239178.

163810 Baede, A.P.M.; Ahlonsou, E.; Ding, Y.; Schimel, D.; Bolin, B.; and Pollonais, S. 2001. "The Climate System: An Overview." Chapter 1 of *Climate Change 2001: The Scientific Basis, Contribution of Working Group I to the Third Assessment Report of the Intergovernmental Panel on Climate Change*. New York, New York: Cambridge University Press. TIC: 251101.

108902 Barry, R.G. and Chorley, R.J. 1992. *Atmosphere, Weather and Climate*. 6th Edition. New York, New York: Routledge. TIC: 243554.

160524 Bauch, H.A.; Erlenkeuser, H.; Helmke, J.P.; and Struck, U. 2000. "A Paleoclimatic Evaluation of Marine Oxygen Isotope Stage 11 in the High-Northern Atlantic (Nordic Seas)." *Global and Planetary Change, 24*, (1), 27-39. New York, New York: Elsevier. TIC: 253536.

103356 Beatley, J.C. 1975. "Climates and Vegetation Pattern Across the Mojave/Great Basin Desert Transition of Southern Nevada." *American Midland Naturalist, 93*, (1), 53-70. Notre Dame, Indiana: University of Notre Dame. TIC: 241488.

102221 Beatley, J.C. 1976. *Vascular Plants of the Nevada Test Site and Central-Southern Nevada: Ecologic and Geographic Distributions*. TID-26881. Oak Ridge, Tennessee: Energy Research and Development Administration. TIC: 204727.

108906 Bell, G.D. and Basist, A.N. 1994. "Seasonal Climate Summary, The Global Climate of December 1992–February 1993. Part I: Warm ENSO Conditions Continue in the Tropical Pacific; California Drought Abates." *Journal of Climate, 7*, 1581-1605. Boston, Massachusetts: American Meteorological Society. TIC: 236883.

104370   Benson, L. and Klieforth, H. 1989. "Stable Isotopes in Precipitation and Ground Water in the Yucca Mountain Region, Southern Nevada: Paleoclimatic Implications." *Aspects of Climate Variability in the Pacific and the Western Americas*. Peterson, D.H., ed. Geophysical Monograph 55. Pages 41-59. Washington, D.C.: American Geophysical Union. TIC: 224413.

108909   Benson, L.; Burdett, J.; Lund, S.; Kashgarian, M.; and Mensing, S. 1997. "Nearly Synchronous Climate Change in the Northern Hemisphere During the Last Glacial Termination." *Nature, 388*, 263-265. New York, New York: Nature America. TIC: 236823.

160213   Benson, L. 1999. "Records of Millennial-Scale Climate Change from the Great Basin of the Western United States." *Mechanisms of Global Climate Change at Millennial Time Scales*. Clark, P.U.; Webb, R.S.; and Keigwin, L.D., eds. Geophysical Monograph 112. Pages 203-225. Washington, D.C.: American Geophysical Union. TIC: 253298.

108908   Benson, L.V.; Burdett, J.W.; Kashgarian, M.; Lund, S.P.; Phillips, F.M.; and Rye, R.O. 1996. "Climatic and Hydrologic Oscillations in the Owens Lake Basin and Adjacent Sierra Nevada, California." *Science, 274*, 746-749. Washington, D.C.: American Association for the Advancement of Science. TIC: 236824.

160977   Benson, L.V.; May, H.M.; Antweiler, R.C.; Brinton, T.I.; Kashgarian, M.; Smoot, J.P.; and Lund, S.P. 1998. "Continuous Lake-Sediment Records of Glaciation in the Sierra Nevada between 52,600 and 12,500 ^{14}C yr B.P." *Quaternary Research, 50*, (2), 113-127. New York, New York: Academic Press. TIC: 253661.

160237   Berger, A.; Gallée, H.; and Mélice, J.L. 1991. "The Earth's Future Climate at the Astronomical Timescale." *Future Climate Change and Radioactive Waste Disposal, Proceedings of the International Workshop held at UEA, Norwich, 1-3 November 1989*. Goodess, C.M. and Palutikof, J.P., eds. Pages 148-165. Norwich, England: University of East Anglia, School of Environmental Sciences, Climatic Research Unit. TIC: 253447.

108910   Berger, A. and Loutre, M.F. 1991. "Insolation Values for the Climate of the Last 10 Million Years." *Quaternary Science Reviews, 10*, 297-317. Oxford, United Kingdom: Pergamon Press. TIC: 234261.

152040   Berger, A. 2000. "Orbital Data Question." E-mail from A. Berger (Universite Catholique de Louvain) to S. Sharpe, May 22, 2000. ACC: MOL.20000920.0551.

160153   Berger, A. and Loutre, M.F. 2002. "An Exceptionally Long Interglacial Ahead?" *Science, 297*, (5585), 1287-1288. Washington, D.C.: American Association for the Advancement of Science. TIC: 253328.

121783   Berger, A.L. 1978. "Long-Term Variations of Daily Insolation and Quaternary Climate Changes." *Journal of the Atmospheric Sciences, 35*, (12), 2362-2367. Boston, Massachusetts: American Meteorological Society. TIC: 225333.

160205   Berger, W.H.; Yasuda, M.K.; Bickert, T.; Wefer, G.; and Takayama, T. 1994. "Quaternary Time Scale for the Ontong Java Plateau: Milankovitch Template for Ocean Drilling Program Site 806." *Geology, 22*, (5), 463-467. Boulder, Colorado: Geological Society of America. TIC: 253312.

128131   Betancourt, J.L.; Van Devender, T.R.; and Martin, P.S., eds. 1990. *Packrat Middens, The Last 40,000 Years of Biotic Change*. Tucson, Arizona: University of Arizona Press. TIC: 237983.

161151   Biondi, F.; Gershunov, A.; and Cayan, D.R. 2001. "North Pacific Decadal Climate Variability Since 1661." *Journal of Climate, 14*, (1), 5-10. Boston, Massachusetts: American Meteorological Society. TIC: 253745.

160217   Bischoff, J.L.; Menking, K.M.; Fitts, J.P.; and Fitzpatrick, J.A. 1997. "Climatic Oscillations 10,000–155,000 yr B.P. at Owens Lake, California Reflected in Glacial Rock Flour Abundance and Lake Salinity in Core OL-92." *Quaternary Research, 48*, (3), 313-325. New York, New York: Academic Press. TIC: 253334.

108913   Bischoff, J.L.; Stafford, T.W., Jr.; and Rubin, M. 1997. "A Time-Depth Scale for Owens Lake Sediments of Core OL-92: Radiocarbon Dates and Constant Mass-Accumulation Rate." Chapter 8 of *An 800,000-Year Paleoclimatic Record from Core OL-92, Owens Lake, Southeast California*. Smith, G.I. and Bischoff, J.L., eds. Special Paper 317. Boulder, Colorado: Geological Society of America. TIC: 236857.

107644   Bluestein, H.B. 1992. *Principles of Kinematics and Dynamics*. Volume I of *Synoptic-Dynamic Meteorology in Midlatitudes*. New York, New York: Oxford University Press. TIC: 241142.

108936   Blumen, W., ed. 1990. "Atmospheric Processes Over Complex Terrain." *Meteorological Monographs, 23*, (45), 1-323. Boston, Massachusetts: American Meteorological Society. TIC: 237113.

160522   Bond, G.; Kromer, B.; Beer, J.; Muscheler, R.; Evans, M.N.; Showers, W.; Hoffmann, S.; Lotti-Bond, R.; Hajdas, I.; and Bonani, G. 2001. "Persistent Solar Influence on North Atlantic Climate During the Holocene." *Science, 294*, (5549), 2130-2136. Washington, D.C.: American Association for the Advancement of Science. TIC: 253535.

161205   Bottomley, R.; Grieve, R.; York, D.; and Masaitis, V. 1997. "The Age of the Popigai Impact Event and its Relation to Events at the Eocene/Oligocene Boundary." *Nature, 388*, (6640), 365-368. New York, New York: Macmillan Publishers. TIC: 253740.

108938   Bradbury, J.P. 1997. "A Diatom-Based Paleohydrologic Record of Climate Change for the Past 800 k.y. from Owens Lake, California." Chapter 9 of *An 800,000-Year Paleoclimatic Record from Core OL-92, Owens Lake, Southeast California*. Smith, G.I. and Bischoff, J.L., eds. Special Paper 317. Boulder, Colorado: Geological Society of America. TIC: 236857.

161595   Bradbury, J.P. and Forester, R.M. 2002. "Environment and Paleolimnology of Owens Lake, California: A Record of Climate and Hydrology for the Last 50,000 Years." *Great Basin Aquatic Systems History*. Hershler, R.; Madsen, D.B.; and Currey, D.R., eds. Smithsonian Contributions to the Earth Sciences, Number 33. Pages 145-173. Washington, D.C.: Smithsonian Institution Press. TIC: 254006.

108940   Brennan, R. and Quade, J. 1997. "Reliable Late-Pleistocene Stratigraphic Ages and Shorter Groundwater Travel Times from 14C in Fossil Snails from the Southern Great Basin." *Quaternary Research, 47*, 329-336. New York, New York: Academic Press. TIC: 237063.

108942   Bryson, R.A. 1989. "Late Quaternary Volcanic Modulation of Milankovitch Climate Forcing." *Theoretical and Applied Climatology, 39*, 115-125. New York, New York: Springer-Verlag. TIC: 237005.

160506   Cane, M. and Clement, A.C. 1999. "A Role for the Tropical Pacific Coupled Ocean-Atmosphere System on Milankovitch and Millennial Timescales. Part II: Global Impacts." *Mechanisms of Global Climate Change at Millennial Time Scales*. Clark, P.U.; Webb, R.S.; and Keigwin, L.D., eds. Geophysical Monograph 112. Pages 373-383. Washington, D.C.: American Geophysical Union. TIC: 253525.

160521   Cane, M.A. 1998. "A Role for the Tropical Pacific." *Science, 282*, (5386), 59-61. Washington, D.C.: American Association for the Advancement of Science. TIC: 253439.

160520   Cane, M.A. and Evans, M. 2000. "Do the Tropics Rule?" *Science, 290*, (5494), 1107-1108. Washington, D.C.: American Association for the Advancement of Science. TIC: 253534.

161154   Cayan, D.R.; Redmond, K.T.; and Riddle, L.G. 1999. "ENSO and Hydrologic Extremes in the Western United States." *Journal of Climate, 12*, (9), 2881-2893. Boston, Massachusetts: American Meteorological Society. TIC: 253743.

161156   Cayan, D.R.; Kammerdiener, S.A.; Dettinger, M.D.; Caprio, J.M.; and Peterson, D.H. 2001. "Changes in the Onset of Spring in the Western United States." *Bulletin of the American Meteorological Society, 82*, (3), 399-415. Boston, Massachusetts: American Meteorological Society. TIC: 253747.

160155 Claassen, H.C. 1986. "Late-Wisconsin Paleohydrology of the West-Central Amargosa Desert, Nevada, U.S.A." *Chemical Geology (Isotope Geoscience Section), 58*, 311-323. New York, New York: Elsevier. TIC: 219986.

160519 Clement, A. and Seager, R. 1999. "Climate and the Tropical Oceans." *Journal of Climate, 12*, (12), 3383-3401. Boston, Massachusetts: American Meteorological Society. TIC: 253533.

160525 Clement, A.C. and Cane, M. 1999. "A Role for the Tropical Pacific Coupled Ocean-Atmosphere System on Milankovitch and Millennial Timescales. Part I: A Modeling Study of Tropical Pacific Variability." *Mechanisms of Global Climate Change at Millennial Time Scales*. Clark, P.U.; Webb, R.S.; and Keigwin, L.D., eds. Geophysical Monograph 112. Pages 363-371. Washington, D.C.: American Geophysical Union. TIC: 253537.

160518 Clement, A.C.; Cane, M.A.; and Seager, R. 2001. "An Orbitally Driven Tropical Source for Abrupt Climate Change." *Journal of Climate, 14*, (11), 2369-2375. Boston, Massachusetts: American Meteorological Society. TIC: 253532.

162088 Cohen, S.; Miller, K.; Duncan, K.; Gregorich, E.; Groffman, P.; Kovacs, P.; Magaña, V.; McKnight, D.; Mills, E.; and Schimel, D. 2001. "North America." Chapter 15 of *Climate Change 2001: Impacts, Adaptation, and Vulnerability, Contribution of Working Group II to the Third Assessment Report of the Intergovernmental Panel on Climate Change*. McCarthy, J.J.; Canziani, O.F.; Leary, N.A.; Dokken, D.J.; and White, K.S., eds. New York, New York: Cambridge University Press. TIC: 253549.

121811 Crowley, T.J. and North, G.R. 1991. *Paleoclimatology*. New York, New York: Oxford University Press. TIC: 245421.

160214 Crowley, T.J. 2000. "Causes of Climate Change Over the Past 1000 Years." *Science, 289*, (5477), 270-277. Washington, D.C.: American Association for the Advancement of Science. TIC: 253299.

100117 CRWMS M&O (Civilian Radioactive Waste Management System Management and Operating Contractor) 1997. *Engineering Design Climatology and Regional Meteorological Conditions Report*. B00000000-01717-5707-00066 REV 00. Las Vegas, Nevada: CRWMS M&O. ACC: MOL.19980304.0028.

103155 CRWMS M&O 1997. *Meteorological Monitoring Program 1996 Summary Report*. B00000000-01717-5705-00072 REV 00. Las Vegas, Nevada: CRWMS M&O. ACC: MOL.19980210.0202.

101215 CRWMS M&O 1997. *Regional and Local Wind Patterns Near Yucca Mountain*. B00000000-01717-5705-00081 REV 00. Las Vegas, Nevada: CRWMS M&O. ACC: MOL.19980204.0319.

102877   CRWMS M&O 1999. *Environmental Baseline File for Meteorology and Air Quality*. B00000000-01717-5705-00126 REV 00. Las Vegas, Nevada: CRWMS M&O. ACC: MOL.19990302.0186.

115672   CRWMS M&O 1999. *Meteorological Monitoring Program 1997 Summary Report*. B00000000-01717-5705-00107 REV 00. Las Vegas, Nevada: CRWMS M&O. ACC: MOL.19990804.0287.

151945   CRWMS M&O 2000. *Yucca Mountain Site Description*. TDR-CRW-GS-000001 REV 01 ICN 01. Las Vegas, Nevada: CRWMS M&O. ACC: MOL.20001003.0111.

160144   Cuffey, K.M. and Vimeux, F. 2001. "Covariation of Carbon Dioxide and Temperature from the Vostok Ice Core After Deuterium-Excess Correction." *Nature, 412*, (6846), 523-527. London, England: Macmillan Journals. TIC: 253329.

160138   Davis, O.K. 1989. "The Regionalization of Climatic Change in Western North America." *Paleoclimatology and Paleometeorology: Modern and Past Patterns of Global Atmospheric Transport, Proceedings of the NATO Advanced Research Workshop, Oracle, Arizona, U.S.A., November 17-19, 1987*. Leinen, M. and Sarnthein, M., eds. NATO ASI Series. Series C: Mathematical and Physical Sciences - Volume 282. Pages 617-636. Boston, Massachusetts: Kluwer Academic Publishers. TIC: 253286.

108953   Delorme, L.D. 1970. "Freshwater Ostracodes of Canada. Part IV. Families Ilyocyprididae, Notodromadidae, Darwinulidae, Cytherideidae, and Entocytheridae." *Canadian Journal of Zoology, 48*, (6), 1251-1259. Ottawa, Ontario, Canada: National Research Council of Canada. TIC: 234265.

108978   Eddy, J.A. 1976. "The Maunder Minimum." *Science, 192*, (4245), 1189-1201. Washington, D.C.: American Society for the Advancement of Science. TIC: 237060.

166420   Edwards, R.L.; Cheng, H.; Murrell, M.T.; and Goldstein, S.J. 1997. "Protactinium-231 Dating of Carbonates by Thermal Ionization Mass Spectrometry: Implications for Quaternary Climate Change." *Science, 276*, (5313), 782-786. Washington, D.C.: American Association for the Advancement of Science. TIC: 255358.

160157   Enzel, Y. and Wells, S.G. 1997. "Extracting Holocene Paleohydrology and Paleoclimatology Information from Modern Extreme Flood Events: An Example from Southern California." *Geomorphology, 19*, (3-4), 203-226. New York, New York: Elsevier. TIC: 253318.

160991   Enzel, Y.; Knott, J.R.; Anderson, K.; Anderson, D.E.; and Wells, S.G. 2002. "Is There Any Evidence of Mega-Lake Manly in the Eastern Mojave Desert During Oxygen Isotope Stage 5e/6? A Comment on Hooke, R.L. (1999). Lake Manly(?) Shorelines in the Eastern Mojave Desert, California, Quaternary Research 52, 328-336." *Quaternary Research, 57*, (1), 173-176. New York, New York: Academic Press. TIC: 253662.

160517   Esat, T.M.; McCulloch, M.T.; Chappell, J.; Pillans, B.; and Omura, A. 1999. "Rapid Fluctuations in Sea Level Recorded at Huon Peninsula During the Penultimate Deglaciation." *Science, 283*, (5399), 197-201. Washington, D.C.: American Association for the Advancement of Science. TIC: 253437.

109023   Forester, R.M. 1983. "Relationship of Two Lacustrine Ostracode Species to Solute Composition and Salinity: Implications for Paleohydrochemistry." *Geology, 11*, (8), 435-438. Boulder, Colorado: Geological Society of America. TIC: 222805.

109423   Forester, R.M. 1985. "Limnocythere bradburyi N. SP.: A Modern Ostracode from Central Mexico and a Possible Quaternary Paleoclimatic Indicator." *Journal of Paleontology, 59*, (1), 8-20. Tulsa, Oklahoma: Society of Economic Paleontologists and Mineralogists. TIC: 225826.

109024   Forester, R.M. 1986. "Determination of the Dissolved Anion Composition of Ancient Lakes from Fossil Ostracodes." *Geology, 14*, 796-798. Boulder, Colorado: Geological Society of America. TIC: 223180.

109033   Forester, R.M. 1987. "Late Quaternary Paleoclimate Records from Lacustrine Ostracodes." Chapter 12 of *North America and Adjacent Oceans During the Last Deglaciation*. Ruddiman, W.F. and Wright, H.E., Jr., eds. Volume K-3. Boulder, Colorado: Geological Society of America. TIC: 209437.

109040   Forester, R.M. and Smith, A.J. 1994. "Late Glacial Climate Estimates for Southern Nevada, the Ostracode Fossil Record." *High Level Radioactive Waste Management, Proceedings of the Fifth Annual International Conference, Las Vegas, Nevada, May 22-26, 1994. 4*, 2553-2561. La Grange Park, Illinois: American Nuclear Society. TIC: 210984.

109425   Forester, R.M.; Bradbury, J.P.; Carter, C.; Elvidge-Tuma, A.B.; Hemphill, M.L.; Lundstrom, S.C.; Mahan, S.A.; Marshall, B.D.; Neymark, L.A.; Paces, J.B.; Sharpe, S.E.; Whelan, J.F.; and Wigand, P.E. 1999. *The Climatic and Hydrologic History of Southern Nevada During the Late Quaternary*. Open-File Report 98-635. Denver, Colorado: U.S. Geological Survey. TIC: 245717.

109054   Fritz, S.C.; Juggins, S.; and Battarbee, R.W. 1993. "Diatom Assemblages and Ionic Characterization of Lakes of the Northern Great Plains, North America: A Tool for Reconstructing Past Salinity and Climate Fluctuations." *Canadian Journal of Fisheries and Aquatic Sciences, 50*, 1844-1856. Ottawa, Ontario, Canada: Canadian Department of Fisheries and Oceans. TIC: 234180.

160218   Gallup, C.D.; Cheng, H.; Taylor, F.W.; and Edwards R.L. 2002. "Direct Determination of the Timing of Sea Level Change During Termination II." *Science, 295*, (5553), 310-313. Washington, D.C.: American Association for the Advancement of Science. TIC: 253302.

109427   Gauthier, J.H. 1999. "Unified Structure in Quaternary Climate." *Geophysical Research Letters, 26*, (6), 763-766. Washington, D.C.: American Geophysical Union. TIC: 245706.

162084   Giorgi, F.; Hewitson, B.; Christensen, J.; Hulme, M.; Von Storch, H.; Whetton, P.; Jones, R.; Mearns, L.; and Fu, C. 2001. "Regional Climate Information – Evaluation and Projections." Chapter 10 of *Climate Change 2001: The Scientific Basis, Contribution of Working Group I to the Third Assessment Report of the Intergovernmental Panel on Climate Change*. New York, New York: Cambridge University Press. TIC: 251101.

101216   Grasso, D.N. 1996. *Hydrology of Modern and Late Holocene Lakes, Death Valley, California*. Water-Resources Investigations Report 95-4237. Denver, Colorado: U.S. Geological Survey. ACC: MOL.19970204.0218.

161150   Graumlich, L.J. 1993. "A 1000-Year Record of Temperature and Precipitation in the Sierra Nevada." *Quaternary Research, 39*, (2), 249-255. New York, New York: Academic Press. TIC: 253744.

104089   Grayson, D.K. 1993. *The Desert's Past: A Natural Prehistory of the Great Basin*. Washington, D.C.: Smithsonian Institution Press. TIC: 211247.

160979   Grootes, P.M.; Steig, E.J.; Stuiver, M.; Waddington, E.D.; Morse, D.L.; and Nadeau, M-J. 2001. "The Taylor Dome Antarctic ^{18}O Record and Globally Synchronous Changes in Climate." *Quaternary Research, 56*, (3), 289-298. New York, New York: Academic Press. TIC: 253683.

109113   Grove, J.M. 1988. *The Little Ice Age*. New York, New York: Methuen. TIC: 238258.

160235   Hall, I.R.; McCave, I.N.; Shackleton, N.J.; Weedon, G.P.; and Harris, S.E. 2001. "Intensified Deep Pacific Inflow and Ventilation in Pleistocene Glacial Times." *Nature, 412*, (6849), 809-812. New York, New York: Macmillan Publishers. TIC: 253363.

109114   Hansen, E.M. and Schwarz, F.K. 1981. *Meteorology of Important Rainstorms in the Colorado River and Great Basin Drainages*. Hydrometeorological Report No. 50. Silver Spring, Maryland: U.S. Department of Commerce, National Oceanic and Atmospheric Administration. TIC: 234708.

152035   Hartmann, D.L. 1994. *Global Physical Climatology*. Volume 56 in the International Geophysics Series. San Diego, California: Academic Press. TIC: 248393.

147123   Haynes, C.V. 1967. "Quaternary Geology of the Tule Springs Area, Clark County, Nevada." Part 1 of *Pleistocene Studies in Southern Nevada*. Wormington, H.M. and Ellis, D., eds. Anthropological Papers No. 13. Carson City, Nevada: Nevada State Museum. TIC: 225671.

160997   Helmke, J.P.; Schulz, M.; and Bauch, H.A. 2002. "Sediment-Color Record from Northeast Atlantic Reveals Patterns of Millennial-Scale Climate Variability During the Past 500,000 Years." *Quaternary Research, 57*, (1), 49-57. New York, New York: Academic Press. TIC: 253675.

160234   Henderson, G.M. and Slowey, N.C. 2000. "Evidence from U-Th Dating Against Northern Hemisphere Forcing of the Penultimate Deglaciation." *Nature, 404*, (6773), 61-66. New York, New York: Macmillan Publishers. TIC: 253362.

160511   Hodell, D.A.; Charles, C.D.; and Ninnemann, U.S. 2000. "Comparison of Interglacial Stages in the South Atlantic Sector of the Southern Ocean for the Past 450 kyr: Implifications for Marine Isotope Stage (MIS) 11." *Global and Planetary Change, 24*, (1), 7-26. New York, New York: Elsevier. TIC: 253527.

109115   Hollett, K.J.; Danskin, W.R.; McCaffrey, W.F.; and Walti, C.L. 1991. *Geology and Water Resources of Owens Valley, California*. Water-Supply Paper 2370-B. Denver, Colorado: U.S. Geological Survey. TIC: 234646.

160219   Hooke, R.L. 1999. "Lake Manly (?) Shorelines in the Eastern Mojave Desert, California." *Quaternary Research, 52*, (3), 328-336. New York, New York: Academic Press. TIC: 253207.

160983   Hooke, R.L. 2002. "Is There Any Evidence of Mega-Lake Manly in the Eastern Mojave Desert During Oxygen Isotope Stage 5e/6?" *Quaternary Research, 57*, (1), 177-179. New York, New York: Academic Press. TIC: 253681.

100047   Imbrie, J.; Hays, J.D.; Martinson, D.G.; McIntrye, A.; Mix, A.C.; Morley, J.J.; Pisias, N.G.; Prell, W.L.; and Shackleton, N.J. 1984. "The Orbital Theory of Pleistocene Climate: Support from a Revised Chronology of the Marine $\delta^{18}O$ Record." *Milankovitch and Climate, Understanding the Response to Astronomical Forcing*. Berger, A.; Imbrie, J.; Hays, J.; Kukla, G.; and Saltzman, B., eds. Pages 269-305. Boston, Massachusetts: D. Reidel Publishing Company. TIC: 225740.

109430   Imbrie, J.; Boyle, E.A.; Clemens, S.C.; Duffy, A.; Howard, W.R.; Kukla, G.; Kutzbach, J.; Martinson, D.G.; McIntyre, A.; Mix, A.C.; Molfino, B.; Morley, J.J.; Peterson, L.C.; Pisias, N.G.; Prell, W.L.; Raymo, M.E.; Shackleton, M.J.; and Toggweiler, J.R. 1992. "On the Structure and Origin of Major Glaciation Cycles, 1. Linear Responses to Milankovitch Forcing." *Paleoceanography, 7*, (6), 701-738. Washington, D.C.: American Geophysical Union. TIC: 245699.

109118   Imbrie, J.; Mix, A.C.; and Martinson, D.G. 1993. "Milankovitch Theory Viewed from Devils Hole." *Nature, 363*, (6429), 531-533. London, England: Macmillan Journals. TIC: 234192.

109434   Jannik, N.O.; Phillips, F.M.; Smith, G.I.; and Elmore, D. 1991. "A 36Cl Chronology of Lacustrine Sedimentation in the Pleistocene Owens River System." *Geological Society of America Bulletin, 103*, 1146-1159. Boulder, Colorado: Geological Society of America. TIC: 245705.

161019   Jayko, A.S.; Forester, R.M.; and Yount, J.C. 2002. "Distribution and Character of Late Pleistocene Lacustrine and Spring Deposits Panamint Valley, California." *Abstracts with Programs - Geological Society of America, 34*, (6), 395. Boulder, Colorado: Geological Society of America. TIC: 253665.

162063   Jefferson, G.T. 2003. "Stratigraphy and Paleontology of the Middle to Late Pleistocene Manix Formation, and Paleoenvironments of the Central Mojave River, Southern California." *Paleoenvironments and Paleohydrology of the Mojave and Southern Great Basin Deserts.* Enzel, Y.; Wells, S.G.; and Lancaster, N., eds. Special Paper 368. Pages 43-60. Boulder, Colorado: Geological Society of America. TIC: 255307.

160196   Jouzel, J. 2001. "Milankovitch and Ice Core Records." *Eos, Transactions (Supplement), 82*, (47), F1. Washington, D.C.: American Geophysical Union. TIC: 253333.

161923   Kaufman, Y.J.; Tanré, D.; and Boucher, O. 2002. "A Satellite View of Aerosols in the Climate System." *Nature, 419*, (6903), 215-223. New York, New York: Macmillan Publishers. TIC: 253958.

109121   Kay, P.A. 1982. "Perspective on Great Basin Paleoclimates." *Man and Environment in the Great Basin.* Madsen, D.B. and O'Connell, J.F., eds. SAA Paper No. 2. Pages 76-81. Washington, D.C.: Society of American Archaeology. TIC: 234650.

160516   Kerr, R.A. 2001. "The Tropics Return to the Climate System." *Science, 292*, (5517), 660-661. Washington, D.C.: American Association for the Advancement of Science. TIC: 253531.

160225   Khodri, M.; Leclainche, Y.; Ramstein, G.; Braconnot, P.; Marti, O.; and Cortijo, E. 2001. "Simulating the Amplification of Orbital Forcing by Ocean Feedbacks in the Last Glaciation." *Nature, 410*, (6828), 570-574. New York, New York: Macmillan Magazines. TIC: 253303.

160509   Kindler, P. and Hearty, P.J. 2000. "Elevated Marine Terraces from Eleuthera (Bahamas) and Bermuda: Sedimentological, Petrographic and Geochronological Evidence for Important Deglaciation Events During the Middle Pleistocene." *Global and Planetary Change, 24*, (1), 41-58. New York, New York: Elsevier. TIC: 253540.

109436   Knott, J.R. 1999. "Quaternary Stratigraphy and Geomorphology of Death Valley." *Proceedings of Conference on Status of Geologic Research and Mapping in Death Valley National Park, Las Vegas, Nevada, April 9-11, 1999.* Slate, J.L., ed. Open-File Report 99-153. Pages 90-96. Denver, Colorado: U.S. Geological Survey. TIC: 245245.

109438   Ku, T-L.; Luo, S.; Lowenstein, T.K.; Li, J.; and Spencer, R.J. 1998. "U-Series Chronology of Lacustrine Deposits in Death Valley, California." *Quaternary Research, 50*, 261-275. New York, New York: Academic Press. TIC: 245707.

160981   Kukla, G.J.; Bender, M.L.; de Beaulieu, J-L.; Bond, G.; Broecker, W.S.; Cleveringa, P.; Gavin, J.E.; Herbert, T.D.; Imbrie, J.; Jouzel, J.; Keigwin, L.D.; Knudsen, K-L.; McManus, J.F.; Merkt, J.; Muhs, D.R.; Müller, H.; Poore, R.Z.; Porter, S.C.; Seret, G.; Shackleton, N.J.; Turner, C.; Tzedakis, P.C.; and Winograd, I.J. 2002. "Last Interglacial Climates." *Quaternary Research, 58*, (1), 2-13. New York, New York: Academic Press. TIC: 253671.

160980   Kukla, G.J.; Clement, A.C.; Cane, M.A.; Gavin, J.E.; and Zebiak, S.E. 2002. "Last Interglacial and Early Glacial ENSO." *Quaternary Research, 58*, (1), 27-31. New York, New York: Academic Press. TIC: 253682.

109122   Kutzbach, J.E. and Guetter, P.J. 1986. "The Influence of Changing Orbital Parameters and Surface Boundary Conditions on Climate Simulations for the Past 18,000 Yrs." *Journal of the Atmospheric Sciences, 43*, (16), 1726-1759. Boston, Massachusetts: American Meteorological Society. TIC: 221722.

119269   Kutzbach, J.E.; Guetter, P.J.; Behling, P.J.; and Selin, R. 1993. "Simulated Climatic Changes: Results of the COHMAP Climate-Model Experiments." Chapter 4 of *Global Climates Since the Last Glacial Maximum.* Wright, H., Jr.; Kutzbach, J.; Webb, T., III; Ruddiman, W.; Street-Perrott, F.; and Bartlein, P., eds. Minneapolis, Minnesota: University of Minnesota Press. TIC: 234248.

109123   LaMarche, V.C., Jr. 1974. "Paleoclimatic Inferences from Long Tree-Ring Records." *Science, 183*, (4129), 1043-1048. Washington, D.C.: American Association for the Advancement of Science. TIC: 225741.

109124   Landwehr, J.M.; Coplen, T.B.; Ludwig, K.R.; Winograd, I.J.; and Riggs, A.C. 1997. *Data for Devils Hole Core DH-11.* Open-File Report 97-792. Reston, Virginia: U.S. Geological Survey. TIC: 245712.

160145   Landwehr, J.M. and Winograd, I.J. 2001. "Dating the Vostok Ice Core Record by Importing the Devils Hole Chronology." *Journal of Geophysical Research, 106*, (D23), 31,853-31,861. Washington, D.C.: American Geophysical Union. TIC: 253325.

161926   Landwehr, J.M. 2002. *Ice Core Depth-Age Relation for Vostok äD and Dome Fuji ä* ^{18}*O Records Based on the Devils Hole Paleotemperature Chronology.* Open-File Report 02-266. Reston, Virginia: U.S. Geological Survey. TIC: 253910.

100054   Li, J.; Lowenstein, T.K.; Brown, C.B.; Ku, T-L.; and Luo, S. 1996. "A 100 Ka Record of Water Tables and Paleoclimates from Salt Cores, Death Valley, California." *Palaeogeography, Palaeoclimatology, Palaeoecology, 123*, (1-4), 179-203. Amsterdam, The Netherlands: Elsevier. TIC: 236544.

109126   Litwin, R.J.; Adam, D.A.; Frederiksen, N.O.; and Woolfenden, W.B. 1997. "An 800,000-Year Pollen Record from Owens Lake, California: Preliminary Analyses." Chapter 12 of *An 800,000-Year Paleoclimatic Record from Core OL-92, Owens Lake, Southeast California.* Smith, G.I. and Bischoff, J.L., eds. Special Paper 317. Boulder, Colorado: Geological Society of America. TIC: 236857.

109440   Litwin, R.J.; Smoot, J.P.; Durika, N.J.; and Smith, G.I. 1999. "Calibrating Late Quaternary Terrestrial Climate Signals: Radiometrically Dated Pollen Evidence from the Southern Sierra Nevada, USA." *Quaternary Science Reviews, 18*, 1151-1171. New York, New York: Pergamon Press. TIC: 245700.

160117   Loutre, M.F. and Berger, A. 2000. "Future Climatic Changes: Are We Entering an Exceptionally Long Interglacial?" *Climatic Change, 46*, (1-2), 61-90. Boston, Massachusetts: Kluwer Academic Publishers. TIC: 250895.

130132   Lowenstein, T. 1999. "200-K.Y. Paleoclimate Record from Core DV 93-1, Badwater Basin, Death Valley, California." *Proceedings of Conference on Status of Geologic Research and Mapping in Death Valley National Park, Las Vegas, Nevada, April 9-11, 1999.* Slate, J.L., ed. Open-File Report 99-153. Pages 142-144. Denver, Colorado: U.S. Geological Survey. TIC: 245245.

109129   Lowenstein, T.K. 1997. "Death Valley Salt Core: 200,000 Year Paleoclimate Record from Sedimentary Structures, Saline Mineralogy, Fluid Inclusions in Halite, and Ostracodes." *GBASH 97, Great Basin Aquatic System History, Fifty Years of Geologic, Biologic, and Hydroclimatic Progress in Lake Cenozoic Aquatic System History, September 17-20, 1997, Salt Lake City, Utah.* Salt Lake City, Utah: University of Utah. TIC: 247450.

160388   Lowenstein, T.K.; Li, J.; and Brown, C.B. 1998. "Paleotemperatures from Fluid Inclusions in Halite: Method Verification and a 100,000 Year Paleotemperature Record, Death Valley, CA." *Chemical Geology, 150*, (3-4), 223-245. New York, New York: Elsevier. TIC: 253394.

149904   Lowenstein, T.K.; Li, J.; Brown, C.; Roberts, S.M.; Ku, T-L.; Luo, S.; and Yang, W. 1999. "200 K.Y. Paleoclimate Record from Death Valley Salt Core." *Geology, 27*, (1), 3-6. Boulder, Colorado: Geological Society of America. TIC: 247905.

161594 Lowenstein, T.K. 2002. "Pleistocene Lakes and Paleoclimates (0 to 200 Ka) in Death Valley, California." *Great Basin Aquatic Systems History*. Hershler, R.; Madsen, D.B.; and Currey, D.R., eds. Smithsonian Contributions to the Earth Sciences, Number 33. Pages 109-120. Washington, D.C.: Smithsonian Institution Press. TIC: 254006.

104631 Ludwig, K.R.; Simmons, K.R.; Szabo, B.J.; Winograd, I.J.; Landwehr, J.M.; Riggs, A.C.; and Hoffman, R.J. 1992. "Mass-Spectrometric ^{230}Th-^{234}U-^{238}U Dating of the Devils Hole Calcite Vein." *Science, 258*, 284-287. Washington, D.C.: American Association for the Advancement of Science. TIC: 237796.

160387 Lundstrom, S.C.; Paces, J.B.; Mahan, S.A.; Page, W.R.; and Workman, J.B. 1999. "Quaternary Geologic Mapping and Geochronology of the Las Vegas 1:100,000 Sheet and Yucca Mountain Area—Geomorphic and Hydrologic Response to Climate Change Near Death Valley." *Proceedings of Conference on Status of Geologic Research and Mapping in Death Valley National Park, Las Vegas, Nevada, April 9-11, 1999*. Slate, J.L., ed. Open-File Report 99-153. Pages 110-111. Denver, Colorado: U.S. Geological Survey. TIC: 245245.

108899 Lutgens, F.K. and Tarbuck, E.J. 1998. *The Atmosphere, An Introduction to Meteorology*. 7th Edition. Upper Saddle River, New Jersey: Prentice-Hall. TIC: 245656.

161155 Mantua, N.J.; Hare, S.R.; Zhang, Y.; Wallace, J.M.; and Francis, R.C. 1997. "A Pacific Interdecadal Climate Oscillation with Impacts on Salmon Production." *Bulletin of the American Meteorological Society, 78*, (6), 1069-1079. Boston, Massachusetts: American Meteorological Society. TIC: 253746.

149919 Mawby, J.E. 1967. "Fossil Vertebrates of the Tule Springs Site, Nevada." Part 2 of *Pleistocene Studies in Southern Nevada*. Wormington, H.M. and Ellis, D., eds. Anthropological Papers No. 13. Carson City, Nevada: Nevada State Museum. TIC: 225671.

109134 McGlone, M.S.; Kershaw, A.P.; and Markgraf, V. 1992. "El Nino/Southern Oscillation Climatic Variability in Australasian and South American Paleoenvironmental Records." Chapter 21 of *El Nino, Historical and Paleoclimatic Aspects of the Southern Oscillation*. Diaz, H.F. and Markgraf, V., eds. New York, New York: Cambridge University Press. TIC: 239178.

149909 Mehringer, P.J., Jr. 1967. "Pollen Analysis of the Tule Springs Site, Nevada." Part 3 of *Pleistocene Studies in Southern Nevada*. Wormington, H.M. and Ellis, D., eds. Anthropological Papers No. 13. Carson City, Nevada: Nevada State Museum. TIC: 225671.

109135   Meko, D.M. 1992. "Spectral Properties of Tree-Ring Data in the United States Southwest as Related to El Nino/Southern Oscillation." Chapter 12 of *El Nino, Historical and Paleoclimatic Aspects of the Southern Oscillation*. Diaz, H.F. and Markgraf, V., eds. New York, New York: Cambridge University Press. TIC: 239178.

161011   Mensing, S.A. 2001. "Late-Glacial and Early Holocene Vegetation and Climate Change Near Owens Lake, Eastern California." *Quaternary Research, 55*, (1), 57-65. New York, New York: Academic Press. TIC: 253660.

147129   Mifflin, M.D. and Wheat, M.M. 1979. *Pluvial Lakes and Estimated Pluvial Climates of Nevada*. Bulletin 94. Reno, Nevada: Nevada Bureau of Mines and Geology. TIC: 200724.

109141   Miller, J.F.; Frederick, R.H.; and Tracey, R.J. 1973. *Precipitation-Frequency Atlas of the Western United States*. NOAA Atlas 2. Volume VII–Nevada. Silver Spring, Maryland: U.S. Department of Commerce, National Oceanic and Atmospheric Administration. TIC: 206081.

161362   Minwalla, H.J. 2003. *Project Design Criteria Document*. 000-3DR-MGR0-00100-000-001. Las Vegas, Nevada: Bechtel SAIC Company. ACC: ENG.20030402.0001.

161001   Mitchell, D.L.; Ivanova, D.; Rabin, R.; Brown, T.J.; and Redmond, K. 2002. "Gulf of California Sea Surface Temperatures and the North American Monsoon: Mechanistic Implications from Observations." *Journal of Climate, 15*, (17), 2261-2281. Boston, Massachusetts: American Meteorological Society. TIC: 253716.

109138   Mock, C.J. 1996. "Climatic Controls and Spatial Variations of Precipitation in the Western United States." *Journal of Climate, 9*, 1111-1125. Boston, Massachusetts: American Meteorological Society. TIC: 237443.

138393   Morrison, R.B. 1999. "Lake Tecopa: Quaternary Geology of Tecopa Valley, California, A Multimillion-Year Record and Its Relevance to the Proposed Nuclear-Waste Repository at Yucca Mountain, Nevada." *Cenozoic Basins of the Death Valley Region*. Wright, L.A. and Troxel, B.W., eds. Special Paper 333. Pages 301-344. Boulder, Colorado: Geological Society of America. TIC: 246719.

160200   Mudelsee, M. and Schulz, M. 1997. "The Mid-Pleistocene Climate Transition: Onset of 100 ka Cycle Lags Ice Volume Build-Up by 280 ka." *Earth and Planetary Science Letters, 151*, (1-2), 117-123. New York, New York: Elsevier. TIC: 253309.

161006   Muhs, D.R. 2002. "Evidence for the Timing and Duration of the Last Interglacial Period from High-Precision Uranium-Series Ages of Corals on Tectonically Stable Coastlines." *Quaternary Research, 58*, (1), 36-40. New York, New York: Academic Press. TIC: 253673.

161012 Muhs, D.R.; Simmons, K.R.; and Steinke, B. 2002. "Timing and Warmth of the Last Interglacial Period: New U-Series Evidence from Hawaii and Bermuda and a New Fossil Compilation for North America." *Quaternary Science Reviews, 21*, (12-13), 1355-1383. New York, New York: Elsevier. TIC: 253666.

160236 Muller, R.A. and MacDonald, G.J. 2002. *Ice Ages and Astronomical Causes, Data, Spectral Analysis and Mechanisms.* Springer-Praxis Books in Environmental Sciences. New York, New York: Springer. TIC: 253395.

160508 Murray, R.W.; Knowlton, C.; Leinen, M.; Mix, A.C.; and Polsky, C.H. 2000. "Export Production and Terrigenous Matter in the Central Equatorial Pacific Ocean During Interglacial Oxygen Isotope Stage 11." *Global and Planetary Change, 24*, (1), 59-78. New York, New York: Elsevier. TIC: 253436.

109139 Neftel, A.; Oeschger, H.; Staffelbach, T.; and Stauffer, B. 1988. "CO_2 Record in the Byrd Ice Core 50,000—5,000 Years BP." *Nature, 331*, (6157), 609-611. London, England: Macmillan Journals. TIC: 236205.

160199 Osborn, G. and Bevis, K. 2001. "Glaciation in the Great Basin of the Western United States." *Quaternary Science Reviews, 20*, (13), 1377-1410. New York, New York: Elsevier. TIC: 253308.

109448 Oviatt, C.G.; Thompson, R.S.; Kaufman, D.S.; Bright, J.; and Forester, R.M. 1999. "Reinterpretation of the Burmester Core, Bonneville Basin, Utah." *Quaternary Research, 52*, (2), 180-184. San Diego, California: Academic Press. TIC: 245885.

106474 Paces, J.B.; Taylor, E.M.; and Bush, C. 1993. "Late Quaternary History and Uranium Isotopic Compositions of Ground Water Discharge Deposits, Crater Flat, Nevada." *High Level Radioactive Waste Management, Proceedings of the Fourth Annual International Conference, Las Vegas, Nevada, April 26-30, 1993. 2*, 1573-1580. La Grange Park, Illinois: American Nuclear Society. TIC: 208542.

100171 Paces, J.B.; Neymark, L.A.; Marshall, B.D.; Whelan, J.F.; and Peterman, Z.E. 1996. *Letter Report: Ages and Origins of Subsurface Secondary Minerals in the Exploratory Studies Facility (ESF).* Milestone 3GQH450M, Results of Sampling and Age Determination. Las Vegas, Nevada: U.S. Geological Survey. ACC: MOL.19970324.0052.

109148 Paces, J.B.; Whelan, J.F.; Forester, R.M.; Bradbury, J.P.; Marshall, B.D.; and Mahan, S.A. 1997. *Summary of Discharge Deposits in the Amargosa Valley.* Milestone SPC333M4. Denver, Colorado: U.S. Geological Survey. ACC: MOL.19981104.0151.

107408   Paces, J.B.; Neymark, L.A.; Marshall, B.D.; Whelan, J.F.; and Peterman, Z.E. 1998.
"Inferences for Yucca Mountain Unsaturated-Zone Hydrology from Secondary
Minerals." *High-Level Radioactive Waste Management, Proceedings of the Eighth
International Conference, Las Vegas, Nevada, May 11-14, 1998.* Pages 36-39.
La Grange Park, Illinois: American Nuclear Society. TIC: 237082.

156507   Paces, J.B.; Neymark, L.A.; Marshall, B.D.; Whelan, J.F.; and Peterman, Z.E. 2001.
*Ages and Origins of Calcite and Opal in the Exploratory Studies Facility Tunnel,
Yucca Mountain, Nevada.* Water-Resources Investigations Report 01-4049. Denver,
Colorado: U.S. Geological Survey. TIC: 251284.

154724   Paces, J.B. and Whelan, J.F. 2001. "Water-Table Fluctuations in the Amargosa
Desert, Nye County, Nevada." *"Back to the Future - Managing the Back End of the
Nuclear Fuel Cycle to Create a More Secure Energy Future," Proceedings of the 9th
International High-Level Radioactive Waste Management Conference (IHLRWM),
Las Vegas, Nevada, April 29-May 3, 2001.* La Grange Park, Illinois: American
Nuclear Society. TIC: 247873.

109450   Petit, J.R.; Jouzel, J.; Raynaud, D.; Barkov, N.I.; Barnola, J.-M.; Basile, I.; Bender,
M.; Chappellaz, J.; Davis, M.; Delaygue, G.; Delmotte, M.; Kotlyakov, V.M.;
Legrand, M.; Lipenkov, V.Y.; Lorius, C.; Pepin, L.; Ritz, C.; Saltzman, E.; and
Stievenard, M. 1999. "Climate and Atmospheric History of the Past 420,000 Years
from the Vostok Ice Core, Antarctica." *Nature, 399*, (6735), 429-436. London,
England: Macmillan Magazines. TIC: 245695.

160158   Phillips, F.M.; Campbell, A.R.; Smith, G.I.; and Bischoff, J.L. 1994. "Interstadial
Climatic Cycles: A Link Between Western North America and Greenland?"
Geology, 22, (12), 1115-1118. Boulder, Colorado: Geological Society of America.
TIC: 253317.

160978   Phillips, F.M.; Zreda, M.G.; Benson, L.V.; Plummer, M.A.; Elmore D.; and Sharma,
P. 1996. "Chronology for Fluctuations in Late Pleistocene Sierra Nevada Glaciers and
Lakes." *Science, 274*, (5288), 749-751. Washington, D.C.: American Association for
the Advancement of Science. TIC: 253700.

160139   Pierrehumbert, R.T. 1999. "Subtropical Water Vapor as a Mediator of Rapid Global
Climate Change." *Mechanisms of Global Climate Change at Millennial Time Scales.*
Clark, P.U.; Webb, R.S.; and Keigwin, L.D., eds. Geophysical Monograph 112.
Pages 339-361. Washington, D.C.: American Geophysical Union. TIC: 253287.

160201   Poore, R.Z. and Dowsett, H.J. 2001. "Pleistocene Reduction of Polar Ice Caps:
Evidence from Cariaco Basin Marine Sediments." *Geology, 29*, (1), 71-74. Boulder,
Colorado: Geological Society of America. TIC: 253310.

160507   Prokopenko, A.A.; Karabanov, E.B.; Williams, D.F.; Kuzmin, M.I.; Shackleton, N.J.; Crowhurst, S.J.; Peck, J.A.; Gvozdkov, A.N.; and King, J.W. 2001. "Biogenic Silica Record of the Lake Baikal Response to Climatic Forcing During the Brunhes." *Quaternary Research, 55*, (2), 123-132. New York, New York: Academic Press. TIC: 253435.

109151   Quade, J. 1986. "Late Quaternary Environmental Changes in the Upper Las Vegas Valley, Nevada." *Quaternary Research, 26*, (3), 340-357. New York, New York: Academic Press. TIC: 218889.

109152   Quade, J. and Pratt, W.L. 1989. "Late Wisconsin Groundwater Discharge Environments of the Southwestern Indian Springs Valley, Southern Nevada." *Quaternary Research, 31*, (3), 351-370. New York, New York: Academic Press. TIC: 223977.

100074   Quade, J.; Mifflin, M.D.; Pratt, W.L.; McCoy, W.; and Burckle, L. 1995. "Fossil Spring Deposits in the Southern Great Basin and Their Implications for Changes in Water-Table Levels Near Yucca Mountain, Nevada, During Quaternary Time." *Geological Society of America Bulletin, 107*, (2), 213-230. Boulder, Colorado: Geological Society of America. TIC: 234256.

161592   Quade, J.; Forester, R.M.; and Whelan, J.F. 2003. "Late Quaternary Paleohydrologic and Paleotemperature Change in Southern Nevada." *Paleoenvironments and Paleohydrology of the Mojave and Southern Great Basin Deserts*. Enzel, Y.; Wells, S.G.; and Lancaster, N., eds. Special Paper 368. Pages 165-188. Boulder, Colorado: Geological Society of America. TIC: 255307.

161194   Rabinowitz, D.; Helin, E.; Lawrence, K.; and Pravdo, S. 2000. "A Reduced Estimate of the Number of Kilometre-Sized Near-Earth Asteroids." *Nature, 403*, (6766), 165-166. New York, New York: Macmillan Magazines. TIC: 253742.

160999   Ramanathan, V.; Crutzen, P.J.; Kiehl, J.T.; and Rosenfeld, D. 2001. "Aerosols, Climate, and the Hydrological Cycle." *Science, 294*, (5549), 2119-2124. Washington, D.C.: American Association for the Advancement of Science. TIC: 253718.

161153   Redmond, K.T. and Koch, R.W. 1991. "Surface Climate and Streamflow Variability in the Western United States and Their Relationship to Large-Scale Circulation Indices." *Water Resources Research, 27*, (9), 2381-2399. Washington, D.C.: American Geophysical Union. TIC: 239212.

161157   Redmond, K.T.; Enzel, Y.; House, P.K.; and Biondi, F. 2002. "Climate Variability and Flood Frequency at Decadal to Millennial Time Scales." *Ancient Floods, Modern Hazards, Principles and Applications of Paleoflood Hydrology*. House, P.K.; Webb, R.H.; Baker, V.R.; and Levish, D.R., eds. Water Science and Application 5. Pages 21-45. Washington, D.C.: American Geophysical Union. TIC: 253726.

106661 Reheis, M.C.; Sowers, J.M.; Taylor, E.M.; McFadden, L.D.; and Harden, J.W. 1992. "Morphology and Genesis of Carbonate Soils on the Kyle Canyon Fan, Nevada, U.S.A." *Geoderma, 52*, 303-342. Amsterdam, The Netherlands: Elsevier. TIC: 224418.

109454 Reheis, M. 1999. "Highest Pluvial-Lake Shorelines and Pleistocene Climate of the Western Great Basin." *Quaternary Research, 52*, (2), 196-205. New York, New York: Academic Press. TIC: 245885.

161023 Reheis, M. 2000. "Great Big Lakes in the Western Great Basin." *Abstracts with Programs - Geological Society of America, 32*, (7), A-503. Boulder, Colorado: Geological Society of America. TIC: 249113.

161593 Reheis, M.C.; Sarna-Wojcicki, A.M.; Reynolds, R.L.; Repenning, C.A.; and Mifflin, M.D. 2002. "Pliocene to Middle Pleistocene Lakes in the Western Great Basin: Ages and Connections." *Great Basin Aquatic Systems History*. Hershler, R.; Madsen, D.B.; and Currey, D.R., eds. Smithsonian Contributions to the Earth Sciences, Number 33. Pages 53-108. Washington, D.C.: Smithsonian Institution Press. TIC: 254006.

161010 Reheis, M.C.; Stine, S.; and Sarna-Wojcicki, A.M. 2002. "Drainage Reversals in Mono Basin During the Late Pliocene and Pleistocene." *Geological Society of America Bulletin, 114*, (8), 991-1006. Boulder, Colorado: Geological Society of America. TIC: 253669.

160514 Reilly, J.; Stone, P.H.; Forest, C.E.; Webster, M.D.; Jacoby, H.D.; and Prinn, R.G. 2001. "Uncertainty and Climate Change Assessments." *Science, 293*, (5529), 430-431, 433. Washington, D.C.: American Association for the Advancement of Science. TIC: 253766.

160513 Rind, D. 2002. "The Sun's Role on Climate Variations." *Science, 296*, (5568), 673-677. Washington, D.C.: American Association for the Advancement of Science. TIC: 253529.

109157 Roberts, S.M.; Spencer, R.J.; and Lowenstein, T.K. 1994. "Late Pleistocene Saline Lacustrine Sediments, Badwater Basin, Death Valley, California." *Lacustrine Reservoirs and Depositional Systems, Society of Economic Petrologists and Mineralogists (SEPM), Core Workshop No. 19, Denver, Colorado, June 12, 1994*. Lomando, A.J.; Schreiber, B.C.; and Harris, P.M., eds. Pages 61-103. Tulsa, Oklahoma: Society for Sedimentary Geology. TIC: 237003.

109156 Roberts, S.M. and Spencer, R.J. 1995. "Paleotemperatures Preserved in Fluid Inclusions in Halite." *Geochimica et Cosmochimica Acta, 59*, (19), 3929-3942. New York, New York: Pergamon Press. TIC: 236546.

109155   Roberts, S.M. 1996. *Paleoclimate of Death Valley, California (100-200 ka): A Record from Cored Sediments, Homogenization Temperatures of Fluid Inclusions in Halite, and Stable Isotopes of Fluid Inclusions.* Ph.D. dissertation. Calgary, Alberta, Canada: University of Calgary, Alberta. TIC: 240208.

160208   Roberts, S.M. and Spencer, R.J. 1998. "A Desert Responds to Pleistocene Climate Change: Saline Lacustrine Sediments, Death Valley, California, USA." *Quaternary Deserts and Climatic Change, Proceedings of the International Conference on Quaternary Deserts and Climatic Change, Al Ain, United Arab Emirates, 9-11 December 1995.* Alsharhan, A.S.; Glennie, K.W.; Whittle, G.L.; and Kendall, C.G.St.C., eds. Pages 357-370. Brookfield, Vermont: A.A. Balkema. TIC: 253315.

160224   Rutherford, S. and D'Hondt, S. 2000. "Early Onset and Tropical Forcing of 100,000-Year Pleistocene Glacial Cycles." *Nature, 408,* (6808), 72-75. New York, New York: Macmillan Publishers. TIC: 253304.

109161   Sarna-Wojcicki, A.M.; Meyer, C.M.; and Wan, E. 1997. "Age and Correlation of Tephra Layers, Position of the Matuyama-Brunhes Chron Boundary, and Effects of Bishop Ash Eruption on Owens Lake, as Determined from Drill Hole OL-92, Southeast California." Chapter 7 of *An 800,000-Year Paleoclimatic Record from Core OL-92, Owens Lake, Southeast California.* Smith, G.I. and Bischoff, J.L., eds. Special Paper 317. Boulder, Colorado: Geological Society of America. TIC: 236857.

160512   Seager, R.; Clement, A.C.; and Cane, M.A. 2000. "Glacial Cooling in the Tropics: Exploring the Roles of Tropospheric Water Vapor, Surface Wind Speed, and Boundary Layer Processes." *Journal of the Atmospheric Sciences, 57,* (13), 2144-2157. Boston, Massachusetts: American Meteorological Society. TIC: 253528.

109163   Shackleton, N.J. and Opdyke, N.D. 1973. "Oxygen Isotope and Palaeomagnetic Stratigraphy of Equatorial Pacific Core V28-238: Oxygen Isotope Temperatures and Ice Volumes on a 10^5 and 10^6 Year Scale." *Quaternary Research, 3,* 39-55. New York, New York: Academic Press. TIC: 225720.

160156   Shackleton, N.J. 2000. "The 100,000-Year Ice-Age Cycle Identified and Found to Lag Temperature, Carbon Dioxide, and Orbital Eccentricity." *Science, 289,* (5486), 1897-1902. Washington, D.C.: American Association for the Advancement of Science. TIC: 253324.

109164   Shaffer, J.A.; Cerveny, R.S.; and Dorn, R.I. 1996. "Radiation Windows as Indicators of an Astronomical Influence on the Devil's Hole Chronology." *Geology, 24,* (11), 1017-1020. Boulder, Colorado: Geological Society of America. TIC: 237308.

160143   Sharma, M. 2002. "Variations in Solar Magnetic Activity During the Last 200000 Years: Is There a Sun–Climate Connection?" *Earth and Planetary Science Letters, 199,* (3-4), 459-472. Amsterdam, The Netherlands: Elsevier. TIC: 253331.

161591   Sharpe, S. 2003. *Future Climate Analysis—10,000 Years to 1,000,000 Years After Present*. MOD-01-001 REV 01. Reno, Nevada: Desert Research Institute. ACC: MOL.20030407.0055.

109165   Sharpe, S.E.; Whelan, J.F.; Forester, R.M.; and McConnaughey, T. 1994. "Molluscs as Climate Indicators: Preliminary Stable Isotope and Community Analysis." *High Level Radioactive Waste Management, Proceedings of the Fifth Annual International Conference, Las Vegas, Nevada, May 22-26, 1994. 4*, 2538-2544. La Grange Park, Illinois: American Nuclear Society. TIC: 210984.

109166   Siegenthaler, U. 1991. "Glacial-Interglacial Atmospheric CO_2 Variations." *Global Changes of the Past, Papers Arising from the 1989 OIES Global Change Institute, Snowmass, Colorado, 24 July – 4 August 1989*. Bradley, R.S., ed. Pages 245-260. Boulder, Colorado: University Corporation for Atmospheric Research. TIC: 237911.

109168   Smith, G.I. 1984. "Paleohydrologic Regimes in the Southwestern Great Basin, 0-3.2 my Ago, Compared with Other Long Records of 'Global' Climate." *Quaternary Research, 22*, 1-17. New York, New York: Academic Press. TIC: 219152.

100077   Smith, G.I. and Bischoff, J.L. 1997. "Core OL-92 from Owens Lake: Project Rationale, Geologic Setting, Drilling Procedures, and Summary." Chapter 1 of *An 800,000-Year Paleoclimatic Record from Core OL-92, Owens Lake, Southeast, California*. Smith, G.I. and Bischoff, J.L., eds. Special Paper 317. Boulder, Colorado: Geological Society of America. TIC: 236857.

109170   Smith, G.I.; Bischoff, J.L.; and Bradbury, J.P. 1997. "Synthesis of the Paleoclimatic Record from Owens Lake Core OL-92." Chapter 13 of *An 800,000-Year Paleoclimatic Record from Core OL-92, Owens Lake, Southeast California*. Smith, G.I. and Bischoff, J.L., eds. Special Paper 317. Boulder, Colorado: Geological Society of America. TIC: 236857.

162120   Sonnenthal, E.L. and Bodvarsson, G.S. 1998. "Percolation Flux Estimates from Geochemical and Thermal Modeling." *High-Level Radioactive Waste Management, Proceedings of the Eighth International Conference, Las Vegas, Nevada, May 11-14, 1998*. Pages 130-132. La Grange Park, Illinois: American Nuclear Society. TIC: 237082.

106883   Spaulding, W.G. 1985. *Vegetation and Climates of the Last 45,000 Years in the Vicinity of the Nevada Test Site, South-Central Nevada*. Professional Paper 1329. Washington, D.C.: U.S. Geological Survey. TIC: 203210.

100078   Spaulding, W.G. 1990. "Vegetational and Climatic Development of the Mojave Desert: The Last Glacial Maximum to the Present." Chapter 9 of *Packrat Middens, The Last 40,000 Years of Biotic Change*. Betancourt, J.L.; Van Devender, T.R.; and Martin, P.S., eds. Tucson, Arizona: University of Arizona Press. TIC: 237983.

160207   Spencer, R.J. and Roberts, S.M. 1998. "Magnitude of Climate Change in Death Valley, California, USA Between 100 and 200 ka BP: Comparison with Modern Systems." *Quaternary Deserts and Climatic Change, Proceedings of the International Conference on Quaternary Deserts and Climatic Change, Al Ain, United Arab Emirates, 9-11 December 1995*. Alsharhan, A.S.; Glennie, K.W.; Whittle, G.L.; and Kendall, C.G.St.C., eds. Pages 371-380. Brookfield, Vermont: A.A. Balkema. TIC: 253314.

109171   Stauffer, B.; Hofer, H.; Oeschger, H.; Schwander, J.; and Siegenthaler, U. 1984. "Atmospheric CO_2 Concentration During the Last Glaciation." *Annals of Glaciology, 5*, 160-164. Cambridge, Cambridgeshire, United Kingdom: International Glaciological Society. TIC: 237454.

160504   Stein, M.; Wasserburg, G.J.; Aharon, P.; Chen, J.H.; Zhu, Z.R.; Bloom, A.; and Chappell, J. 1993. "TIMS U-Series Dating and Stable Isotopes of the Last Interglacial Event in Papua New Guinea." *Geochimica et Cosmochimica Acta, 57*, (11), 2541-2554. New York, New York: Pergamon Press. TIC: 253539.

101300   Swadley, W C and Carr, W.J. 1987. *Geologic Map of the Quaternary and Tertiary Deposits of the Big Dune Quadrangle, Nye County, Nevada, and Inyo County, California*. Miscellaneous Investigations Series Map I-1767. Denver, Colorado: U.S. Geological Survey. TIC: 203089.

149920   Taylor, D.W. 1967. "Late Pleistocene Molluscan Shells from the Tule Springs Area." Part 8 of *Pleistocene Studies in Southern Nevada*. Wormington, H.M. and Ellis, D., eds. Anthropological Papers No. 13. Carson City, Nevada: Nevada State Museum. TIC: 225671.

109174   Thompson, R.S. 1990. "Late Quaternary Vegetation and Climate in the Great Basin." Chapter 10 of *Packrat Middens, The Last 40,000 Yrs of Biotic Change*. Betancourt, J.L.; Van Devender, T.R.; and Martin, P.S., eds. Pages 200-239. Tucson, Arizona: University of Arizona Press. TIC: 237983.

149936   Thompson, R.S.; Whitlock, C.; Bartlein, P.J.; Harrison, S.P.; and Spaulding, W.G. 1993. "Climatic Changes in the Western United States Since 18,000 yr B.P." Chapter 18 of *Global Climates Since the Last Glacial Maximum*. Wright, H., Jr.; Kutzbach, J.; Webb, T., III; Ruddiman, W.; Street-Perrott, F.; and Bartlein, P., eds. Minneapolis, Minnesota: University of Minnesota Press. TIC: 234248.

160523   Thompson, R.S.; Hostetler, S.W.; Bartlein, P.J.; and Anderson, K.H. 1998.
*A Strategy for Assessing Potential Future Changes in Climate, Hydrology, and
Vegetation in the Western United States.* Circular 1153. Denver, Colorado:
U.S. Geological Survey. TIC: 253442.

109470   Thompson, R.S.; Anderson, K.H.; and Bartlein, P.J. 1999. *Quantitative
Paleoclimatic Reconstructions from Late Pleistocene Plant Macrofossils of the Yucca
Mountain Region.* Open-File Report 99-338. Denver, Colorado: U.S. Geological
Survey. ACC: MOL.19991015.0296.

158378   USGS (U.S. Geological Survey) 2001. *Future Climate Analysis.* ANL-NBS-GS-
000008 REV 00 ICN 01. Denver, Colorado: U.S. Geological Survey.
ACC: MOL.20011107.0004.

154674   USGS 2001. *Simulation of Net Infiltration for Modern and Potential Future Climates.*
ANL-NBS-HS-000032 REV 00 ICN 01. Denver, Colorado: U.S. Geological Survey.
ACC: MOL.20010405.0002.

161021   Van Hoesen, J.G.; Orndorff, R.L.; and Saines, M. 2000. "Evidence for Pleistocene
Glaciation in the Spring Mountains, Nevada." *Abstracts with Programs - Geological
Society of America, 32*, (7), A-16. Boulder, Colorado: Geological Society of
America. TIC: 249113.

157427   Vaniman, D.T.; Chipera, S.J.; Bish, D.L.; Carey, J.W.; and Levy, S.S. 2001.
"Quantification of Unsaturated-Zone Alteration and Cation Exchange in Zeolitized
Tuffs at Yucca Mountain, Nevada, USA." *Geochimica et Cosmochimica Acta, 65*,
(20), 3409-3433. New York, New York: Elsevier. TIC: 251574.

162081   Watson, R.T.; Albritton, D.L.; Barker, T.; Bashmakov, I.A.; Canziani, O.; Christ, R.;
Cubasch, U.; Davidson, O.; Gitay, H.; Griggs, D.; Halsnaes, K.; Houghton, J.; House,
J.; Kundzewicz, Z.; Lal, M.; Leary, N.; Magadza, C.; McCarthy, J.J.; Mitchell, J.F.B.;
Moreira, J.R.; Munasinghe, M.; Noble, I.; Pachauri, R.; Pittock, B.; Prather, M.;
Richels, R.G.; Robinson, J.B.; Sathaye, J.; Schneider, S.; Scholes, R.; Stocker, T.;
Sundararaman, N.; Swart, R.; Taniguchi, T.; and Zhou, D. 2001. "Summary for
Policymakers." *Climate Change 2001: Synthesis Report, An Assessment of the
Intergovernmental Panel on Climate Change.* Watson, R.T., ed. New York,
New York: Cambridge University Press. TIC: 253925.

160204   Wells, P.V. and Woodcock, D. 1985. "Full-Glacial Vegetation of Death Valley,
California: Juniper Woodland Opening to Yucca Semidesert." *Madroño, 32*, (1),
11-23. San Francisco, California: California Botanical Society. TIC: 234252.

162060   Wells, S.G.; Brown, W.J.; Enzel, Y.; Anderson, R.Y.; and McFadden, L.D. 2003.
         "Late Quaternary Geology and Paleohydrology of Pluvial Lake Mojave, Southern
         California." *Paleoenvironments and Paleohydrology of the Mojave and Southern
         Great Basin Deserts*. Enzel, Y.; Wells, S.G.; and Lancaster, N., eds. Special Paper
         368. Pages 79-114. Boulder, Colorado: Geological Society of America.
         TIC: 255307.

100091   Whelan, J.F.; Vaniman, D.T.; Stuckless, J.S.; and Moscati, R.J. 1994. "Paleoclimatic
         and Paleohydrologic Records from Secondary Calcite: Yucca Mountain, Nevada."
         *High Level Radioactive Waste Management, Proceedings of the Fifth Annual
         International Conference, Las Vegas, Nevada, May 22-26, 1994. 4*, 2738-2745.
         La Grange Park, Illinois: American Nuclear Society. TIC: 210984.

107303   Whitney, J.W. and Harrington, C.D. 1993. "Relict Colluvial Boulder Deposits as
         Paleoclimatic Indicators in the Yucca Mountain Region, Southern Nevada."
         Geological Society of America Bulletin, 105, 1008-1018. Boulder, Colorado:
         Geological Society of America. TIC: 208099.

109182   Wigand, P.E. 1997. "A Late Holocene Pollen Record from Lower Pahranagat Lake,
         Southern Nevada, USA: High-Resolution Paleoclimatic Records and Analysis of
         Environmental Responses to Climate Change." *Proceedings of the Thirteenth Annual
         Pacific Climate (PACLIM) Workshop, Asilomar, California, April 14-17, 1996*.
         Isaacs, C.M. and Tharp, V.L., eds. Technical Report 53. Sacramento, California:
         California Department of Water Resources. TIC: 247036.

161596   Wigand, P.E. and Rhode, D. 2002. "Great Basin Vegetation History and Aquatic
         Systems: The Last 150,000 Years." *Great Basin Aquatic Systems History*. Hershler,
         R.; Madsen, D.B.; and Currey, D.R., eds. Smithsonian Contributions to the Earth
         Sciences, Number 33. Pages 309-367. Washington, D.C.: Smithsonian Institution
         Press. TIC: 254006.

109183   Wigley, T.M.L. and Kelly, P.M. 1990. "Holocene Climate Change, 14C Wiggles and
         Variations in Solar Irradiance." *Philosophical Transactions of the Royal Society of
         London, Series A, 330*, (1615), 547-560. London, England: Royal Society of London.
         TIC: 237434.

100093   Williams, D.F.; Thunell, R.C.; Tappa, E.; Rio, D.; and Raffi, I. 1988. "Chronology of
         the Pleistocene Oxygen Isotope Record: 0-1.88 m.y. B.P." *Palaeogeography,
         Palaeoclimatology, Palaeoecology, 64*, 221-240. Amsterdam, The Netherlands:
         Elsevier. TIC: 236879.

109185   Willson, R.C. and Hudson, H.S. 1988. "Solar Luminosity Variations in Solar
         Cycle 21." *Nature, 332*, (6167), 810-812. London, England: Macmillan Journals.
         TIC: 240841.

109184   Willson, R.C. 1997. "Total Solar Irradiance Trend During Solar Cycles 21 and 22." *Science, 277*, 1963-1965. Washington, D.C.: American Association for the Advancement of Science. TIC: 237442.

101167   Winograd, I.J. and Thordarson, W. 1975. *Hydrogeologic and Hydrochemical Framework, South-Central Great Basin, Nevada-California, with Special Reference to the Nevada Test Site*. Geological Survey Professional Paper 712-C. Washington, D.C.: United States Government Printing Office. ACC: NNA.19870406.0201.

108884   Winograd, I.J. and Riggs, A.C. 1984. "Recharge to the Spring Mountains, Nevada: Isotopic Evidence." *Abstracts with Programs - Geological Society of America. 16*, 698. Boulder, Colorado: Geological Society of America. TIC: 217345.

109186   Winograd, I.J.; Szabo, B.J.; Coplen, T.B.; and Riggs, A.C. 1988. "A 250,000-Year Climate Record from Great Basin Vein Calcite: Implications for Milankovitch Theory." *Science, 242*, 1275-1280. Washington, D.C.: American Association for the Advancement of Science. TIC: 222215.

100094   Winograd, I.J.; Coplen, T.B.; Landwehr, J.M.; Riggs, A.C.; Ludwig, K.R.; Szabo, B.J.; Kolesar, P.T.; and Revesz, K.M. 1992. "Continuous 500,000-Year Climate Record from Vein Calcite in Devils Hole, Nevada." *Science, 258*, 255-260. Washington, D.C.: American Association for the Advancement of Science. TIC: 237563.

100096   Winograd, I.J.; Landwehr, J.M.; Ludwig, K.R.; Coplen, T.B.; and Riggs, A.C. 1997. "Duration and Structure of the Past Four Interglaciations." *Quaternary Research, 48*, 141-154. New York, New York: Academic Press. TIC: 236777.

160147   Winograd, I.J. 2001. "The Magnitude and Proximate Cause of Ice-Sheet Growth Since 35,000 yr B.P." *Quaternary Research, 56*, (3), 299-307. New York, New York: Academic Press. TIC: 253330.

160982   Winograd, I.J. 2002. "Evidence from Uranium-Series-Dated Speleothems for the Timing of the Penultimate Deglaciation of Northwestern Europe." *Quaternary Research, 58*, (1), 60-61. New York, New York: Academic Press. TIC: 253679.

166505   Winter, T.C. 1990. "Distribution of the Difference Between Precipitation and Open-Water Evaporation in North America." Plate 2 of *Surface Water Hydrology*. Wolman, M.G. and Riggs, H.C., eds. Volume O-1. Boulder, Colorado: Geological Society of America. TIC: 255382.

152155   Woillard, G.M. 1978. "Grande Pile Peat Bog: A Continuous Pollen Record for the Last 140,000 Years." *Quaternary Research, 9*, 1-21. New York, New York: Academic Press. TIC: 248803.

161149   Woolhiser, D.A.; Keefer, T.O.; and Redmond, K.T. 1993. "Southern Oscillation Effects on Daily Precipitation in the Southwestern United States." *Water Resources Research, 29*, (4), 1287-1295. Washington, D.C.: American Geophysical Union. TIC: 253725.

165987   WRCC (Western Regional Climate Center) 2002. *Western U.S. Historical Summaries by State Arizona, California, Idaho, Nevada, New Mexico, Oregon, Utah, and Washington*. Reno, Nevada: Western Regional Climate Center, Desert Research Institute. TIC: 253357.

160993   Wunsch, C. 2002. "What is the Thermohaline Circulation?" *Science, 298*, (5596), 1179-1181. Washington, D.C.: American Association for the Advancement of Science. TIC: 253722.

160216   Yang, W.; Krouse, H.R.; Spencer, R.J.; Lowenstein, T.K.; Hutcheon, I.E.; Ku, T-L.; Li, J.; Roberts, S.M.; and Brown, C.B. 1999. "A 200,000-Year Record of Change in Oxygen Isotope Composition of Sulfate in a Saline Sediment Core, Death Valley, California." *Quaternary Research, 51*, (2), 148-157. San Diego, California: Academic Press. TIC: 246724.

160136   Zielinski, G.A. and McCoy, W.D. 1987. "Paleoclimatic Implications of the Relationship Between Modern Snowpack and Late Pleistocene Equilibrium-Line Altitudes in the Mountains of the Great Basin, Western U.S.A." *Arctic and Alpine Research, 19*, (2), 127-134. Boulder, Colorado: Institute of Arctic and Alpine Research, University of Colorado at Boulder. TIC: 253284.

6.6.2   Codes, Standards, Regulations, and Procedures

155238   40 CFR 197. 2001. Protection of Environment: Public Health and Environmental Radiation Protection Standards for Yucca Mountain, Nevada. Readily available.

6.6.3   Data, Listed by Data Tracking Number

146819   GS000200005121.003. Radiometric Dating and [18]O Data from Devils Hole, Nevada. Submittal date: 03/06/2000.

153822   GS000900005121.004. Numerical Values of the Elements of the Earth's Orbit from 5,000,000 YBP to 1,000,000 YAP. Submittal date: 02/05/2001.

168533   GS031108315121.003. Supplementary Data to Ostracode Data from Owens Lake 1984-1992 Cores. Submittal date: 02/09/2004.

106508   GS970708315121.002. Ostracode Data from Owens Lake 1984-1992 Cores. Submittal date: 07/31/1997.

149892   MO0004YMP98129.002. Locations of the Regional Meteorological Stations.
          Submittal date: 04/19/2000.

163595   MO0302UCC021SS.009. Upper Air Statistics for Desert Rock, NV, for May 1978
          through December 1997. Submittal date: 02/10/2003.

163597   MO0302UCC021SS.011. Durations of Glacial and Interglacial Oxygen Isotope
          Stages in Thousands of Years, for Past and Future Climate Based on the Precession
          Methodology. Submittal date: 02/11/2003.

163599   MO0303UCC021SS.014. Time Bias Corrected Divisional Temperature-Precipitation-
          Drought Index Data. Submittal date: 03/13/2003.

167116   MO0312SEPQ1997.001. Data Collected at Meteorological Monitoring Sites 1-9,
          Yucca Mountain, Area 25, Nevada Test Site, Las Vegas, Nevada, From 01/01/1997
          Through 12/31/1997. Submittal date: 12/24/2003.   TBV-5689

148887   MO9811DEDCRMCR.000. Data Reported in the Engineering Design Climatology
          and Regional Meteorology Conditions Report. Submittal date: 11/12/1998.

116056   MO9903CLIMATOL.001. Climatological Tables from 1986-1997 Meteorological
          Data from Site 1 through Site 9 EFPD Meteorological Sites. Submittal date:
          03/23/1999.

163709   MO9907COV99282.000. Coverage Name: Metmons. Submittal date: 07/27/1999.

166372   TM000000000001.103. 1996 Annual Meteorological Summary Report. Submittal
          date: 04/29/1997.

160118   UN0104SPA021SS.001. Vostok Ice Core Deuterium Values. Submittal date:
          04/11/2001.

160119   UN0112SPA021SS.004. Western Regional Climate Summaries Through December
          31, 2000. Submittal date: 12/13/2001.

161588   UN0201SPA021SS.007. Mean Annual Temperature and Precipitation for Select
          Western Regional Climate Locations. Submittal date: 01/11/2002.
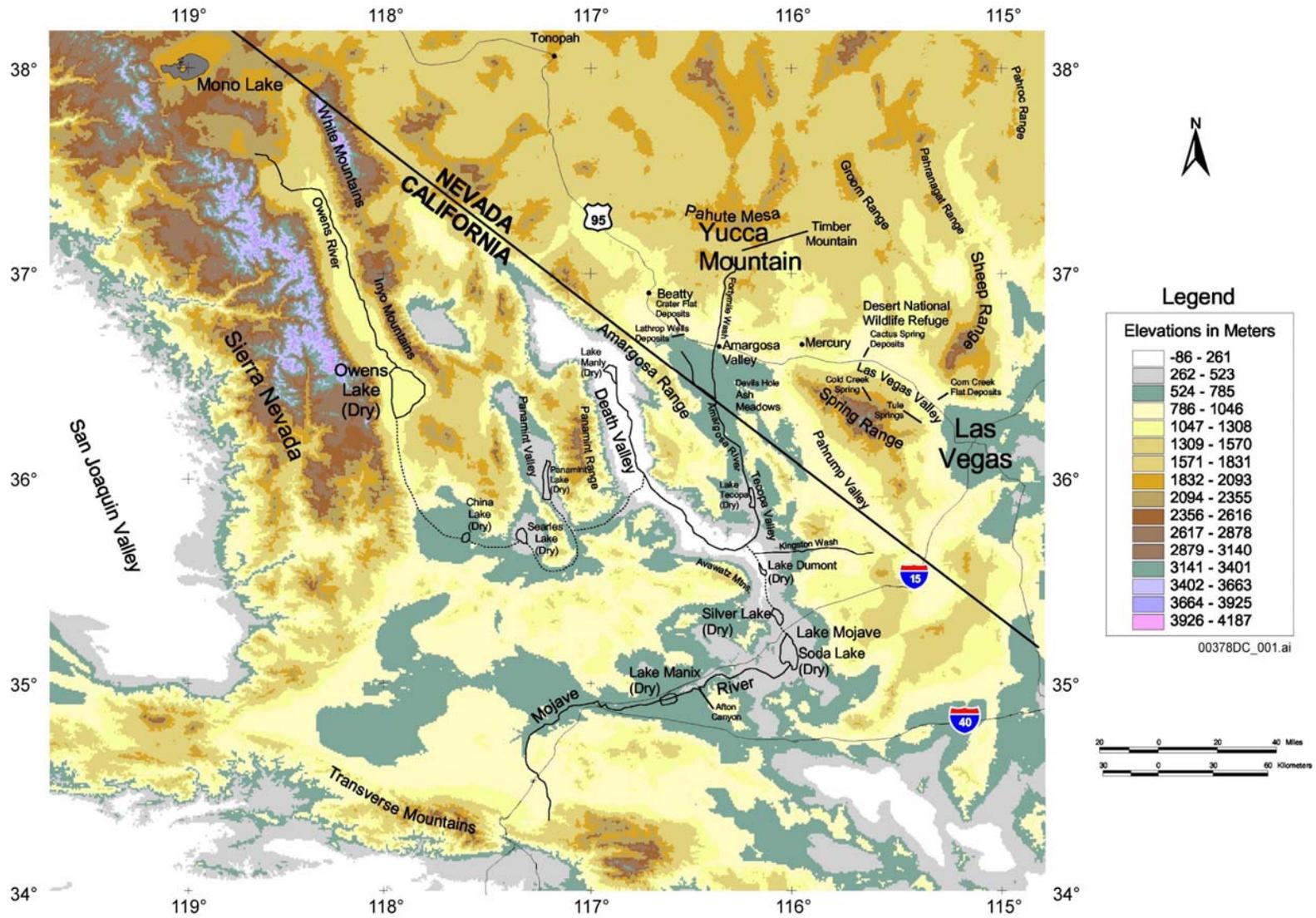
Source: Modified from USGS 1984 [DIRS 158378], Figure 1

Figure 6-1. Localities Important to Past and Future Climate Estimates in the Yucca Mountain Area
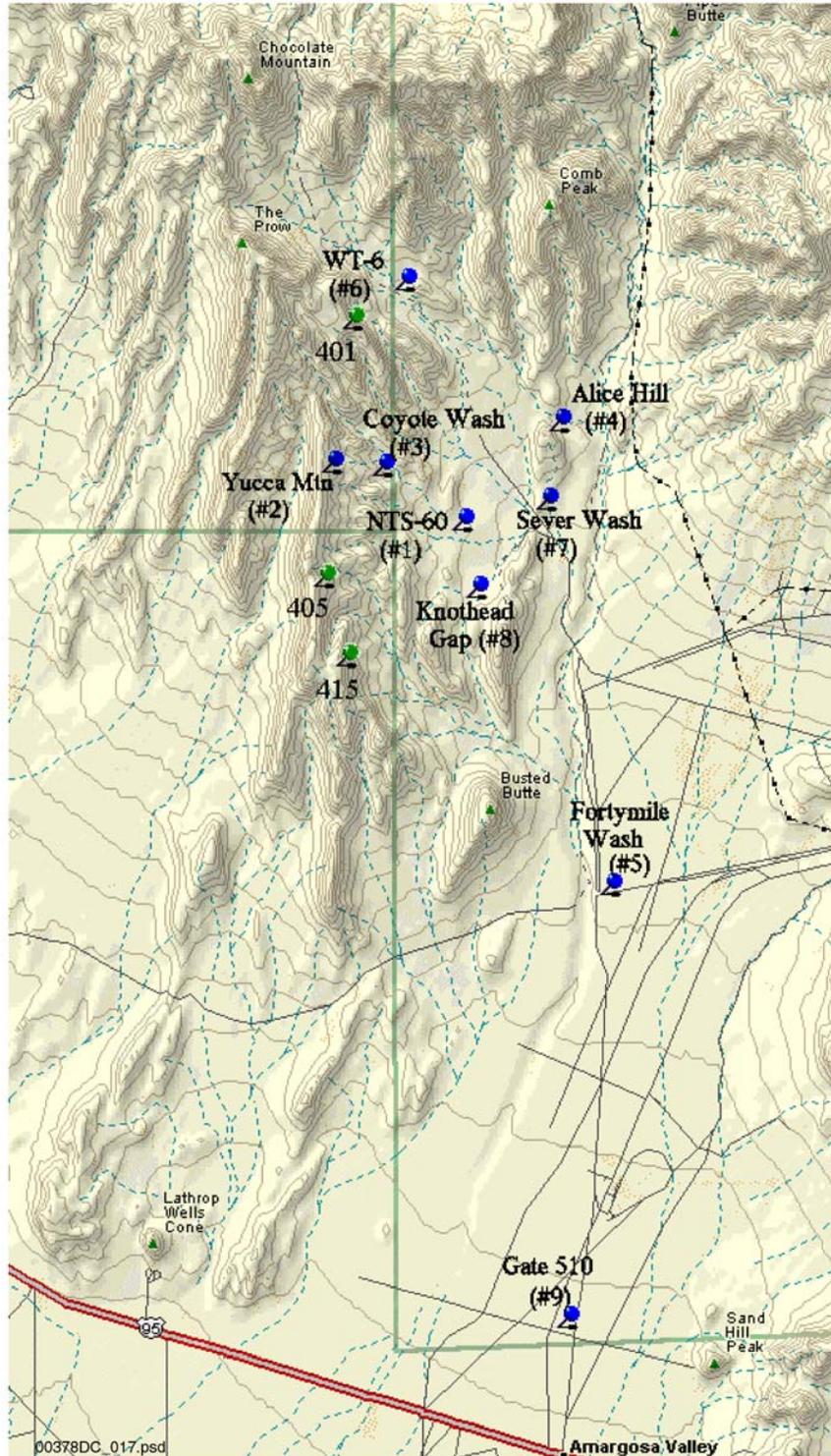
Source: CRWMS M&O 1997 [DIRS 100117], Figure 2-1, p. 2-2; CRWMS M&O 1999 [DIRS 115672], Figure 1-1, p. 1-3

NOTE: Blue pins are DOE Meteorological Monitoring Sites; Green pins are Precipitation-only sites.

Figure 6-2a. Yucca Mountain Modern Meteorological Stations

Figure 6-2b. Locations of the Regional Meteorological Stations
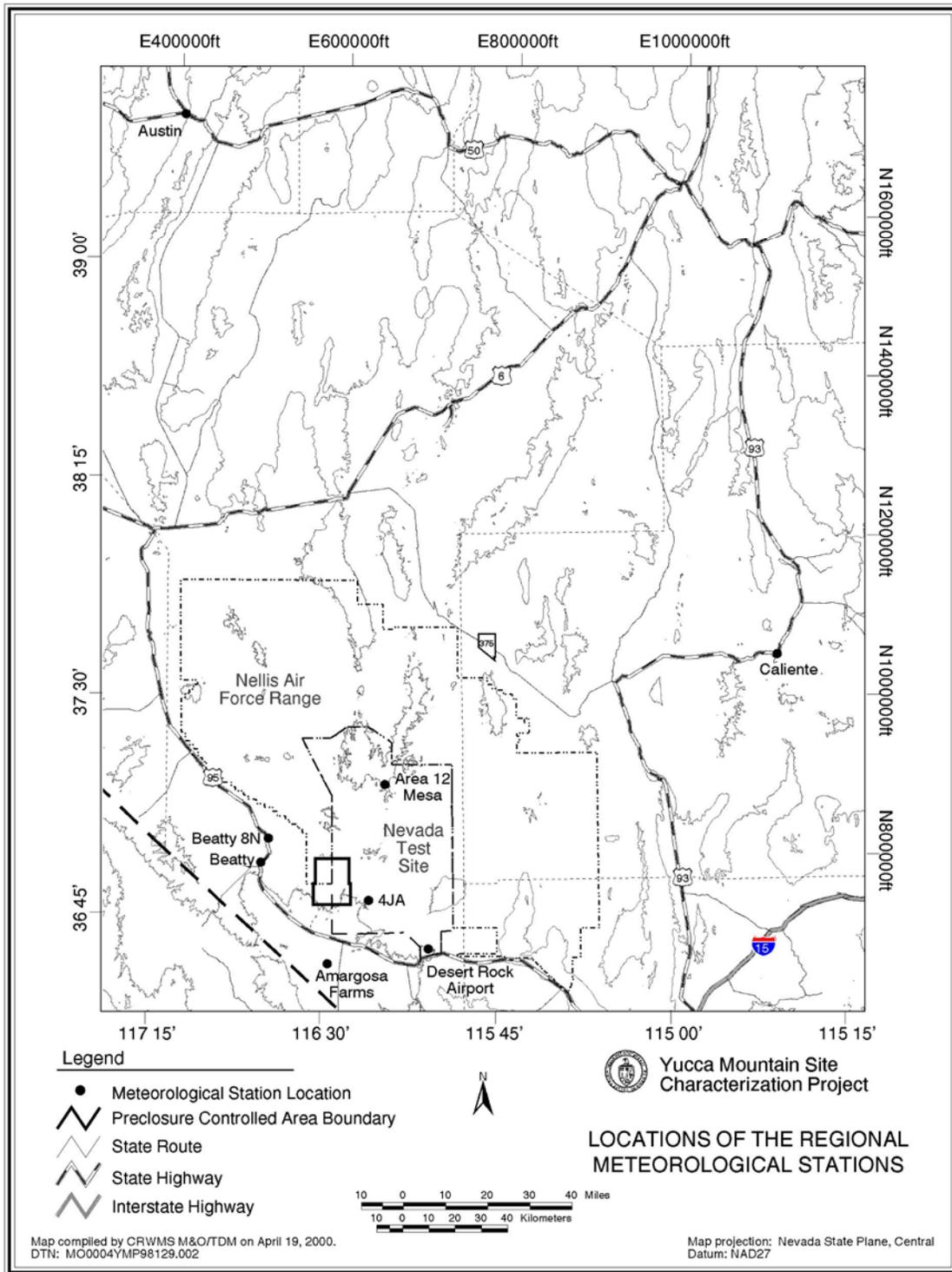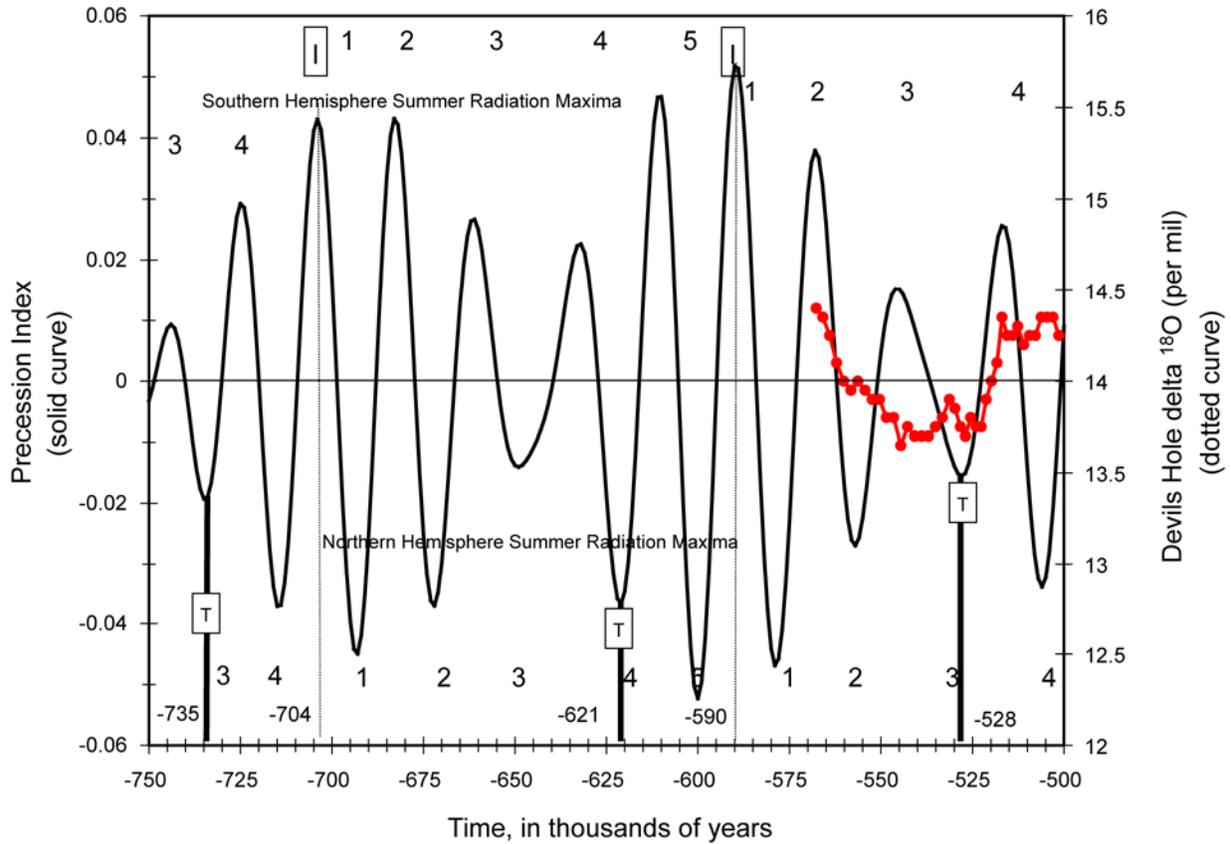
DTN: MO0004YMP98129.002 [DIRS 149892]

DTN: GS000200005121.003 [DIRS 146819]

Source: Sharpe 2003 [DIRS 161591], Figure 6-6a through c, pp. 41 to 43

NOTES: Stable isotope data (closed circles) are reported relative to VSMOW. I = initiation of transition to glacial climate; T = initiation of transition to interglacial climate; and the I to I event equals a precession sequence. Ages for I and T are shown near the bottom of the graph. Numbers 1 through 4 or 5 = summer solar radiation maxima; numbers at the top of the graph are summer solar radiation maxima in the southern hemisphere; numbers at the bottom of the graph are summer solar radiation maxima in the northern hemisphere. MIS = Marine Isotope Stage. Continuation of the diagram is given as Figures 6-3b and c.

Figure 6-3a.   Relation of Precession to the Devils Hole Stable Isotope Climate Proxy Record during the Last 568,000 Years (-500 to -750)
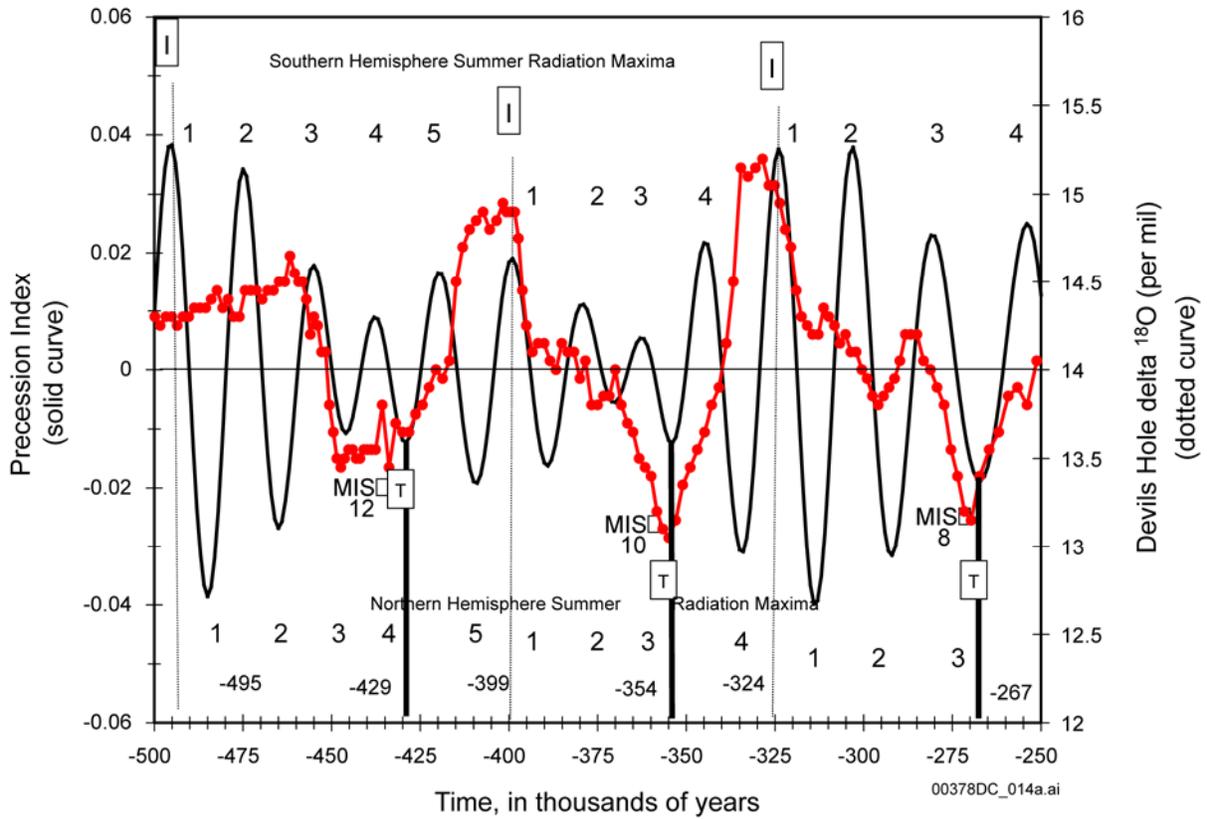
DTN: GS000200005121.003 [DIRS 146819]

Source: Sharpe 2003 [DIRS 161591], Figure 6-6a through c, pp. 41 to 43

Figure 6-3b. Relation of Precession to the Devils Hole Stable Isotope Climate Proxy Record during the Last 568,000 Years (-250 to -500)
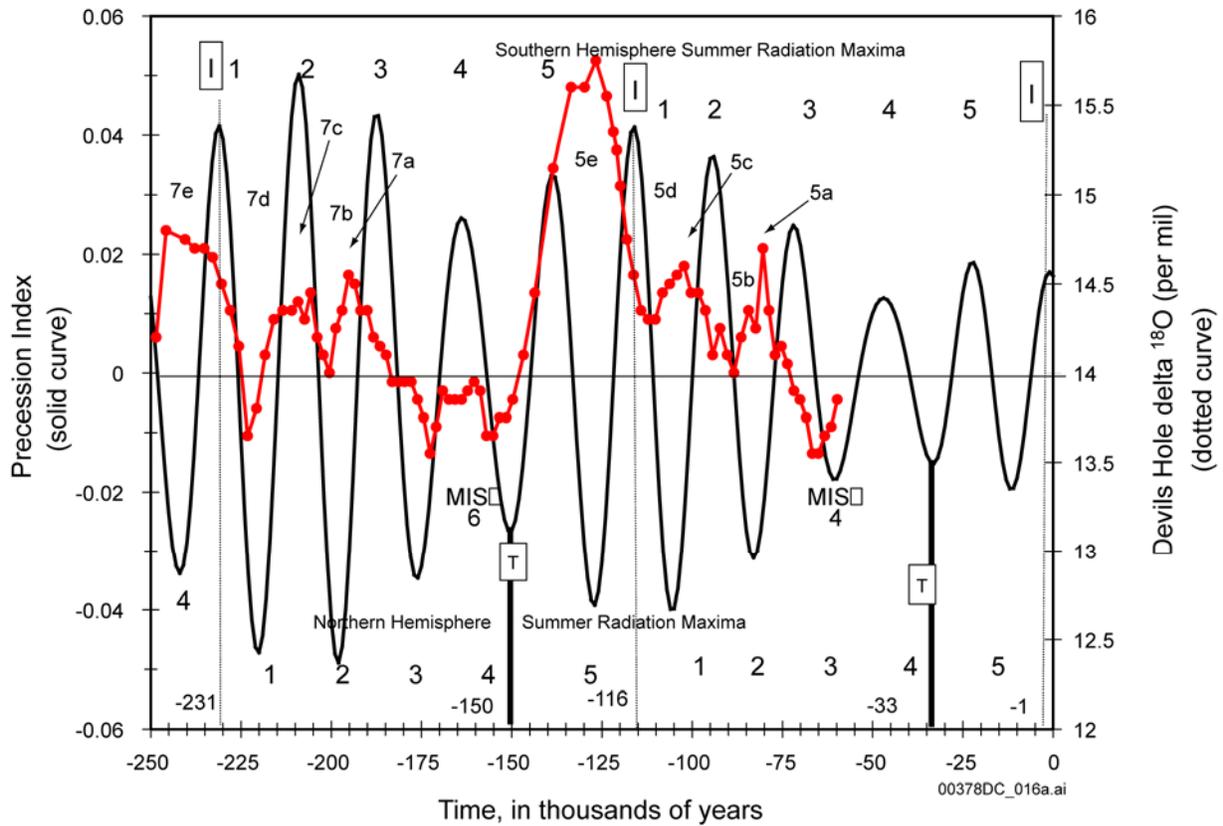
DTN: GS000200005121.003 [DIRS 146819]

Source: Sharpe 2003 [DIRS 161591], Figure 6-6a through c, pp. 41 to 43

Figure 6-3c.   Relation of Precession to the Devils Hole Stable Isotope Climate Proxy Record during the Last 568,000 Years (0 to -250)
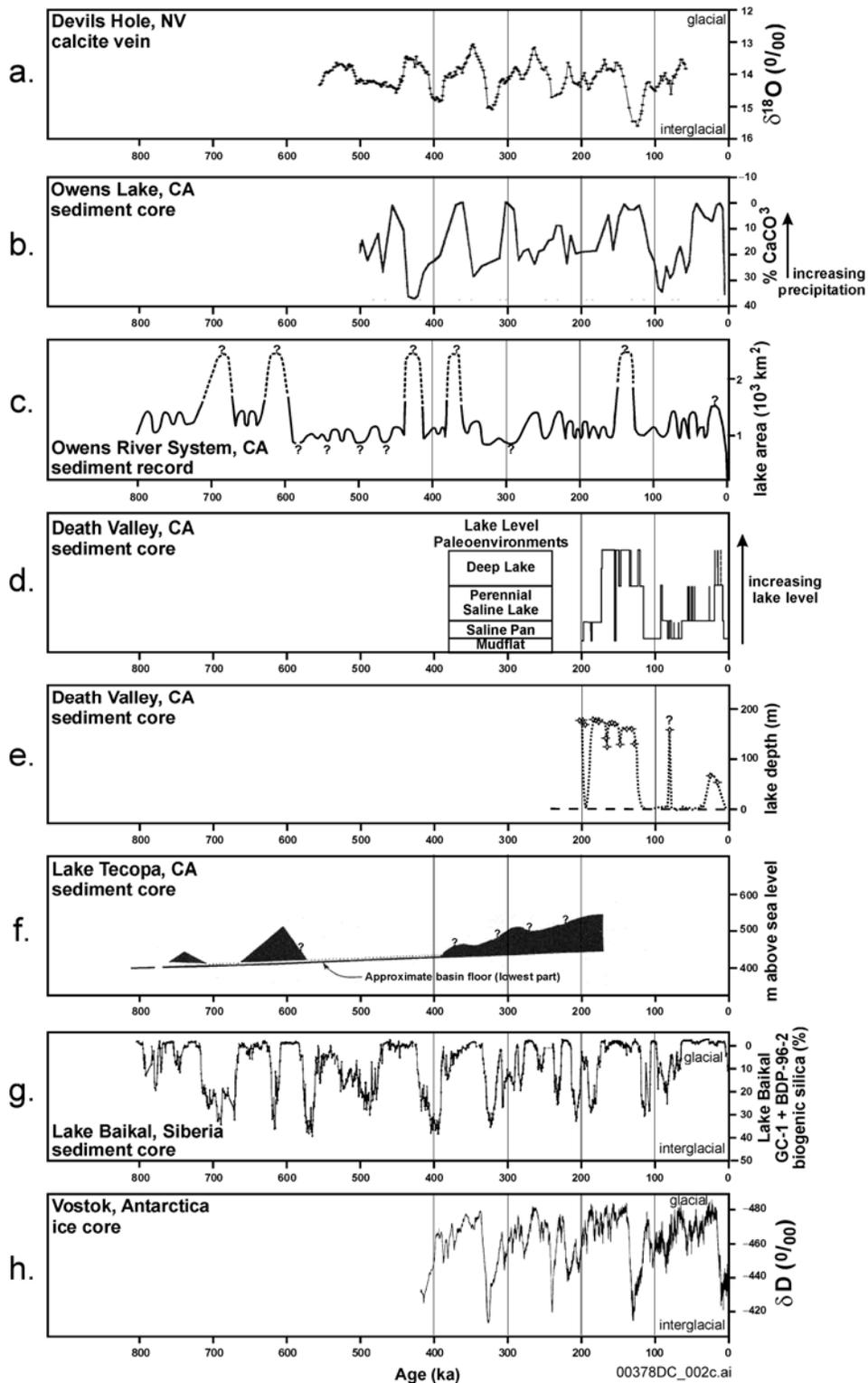
Sources: a) Landwehr et al. 1997 [DIRS 109124], pp. 3 to 8; b) Smith et al. 1997 [DIRS 109170], p. 153; c) Jannik et al. 1991 [DIRS 109434], p. 1158; d) Lowenstein et al. 1999 [DIRS 149904], p. 5; e) Ku et al. 1998 [DIRS 109438], p. 272; f) Morrison 1999 [DIRS 138393], p. 333; g) Prokopenko et al. 2001 [DIRS 160507], p. 126; h) Petit et al. 1999 [DIRS 109450], p. 430

Figure 6-4. Comparison of Proxy Records for Glacial and Interglacial Climate
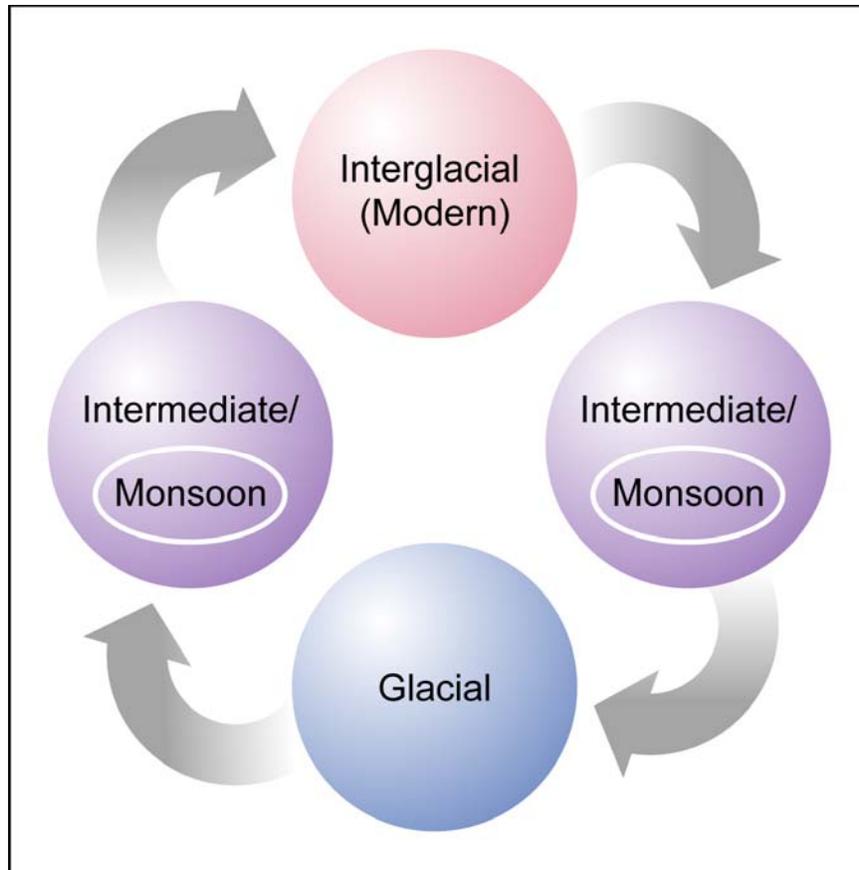
00378DC_003.ai

Source: Sharpe 2003 [DIRS 161591], Figure 6-1, p. 16

Figure 6-5. Simplified Climate State Sequence
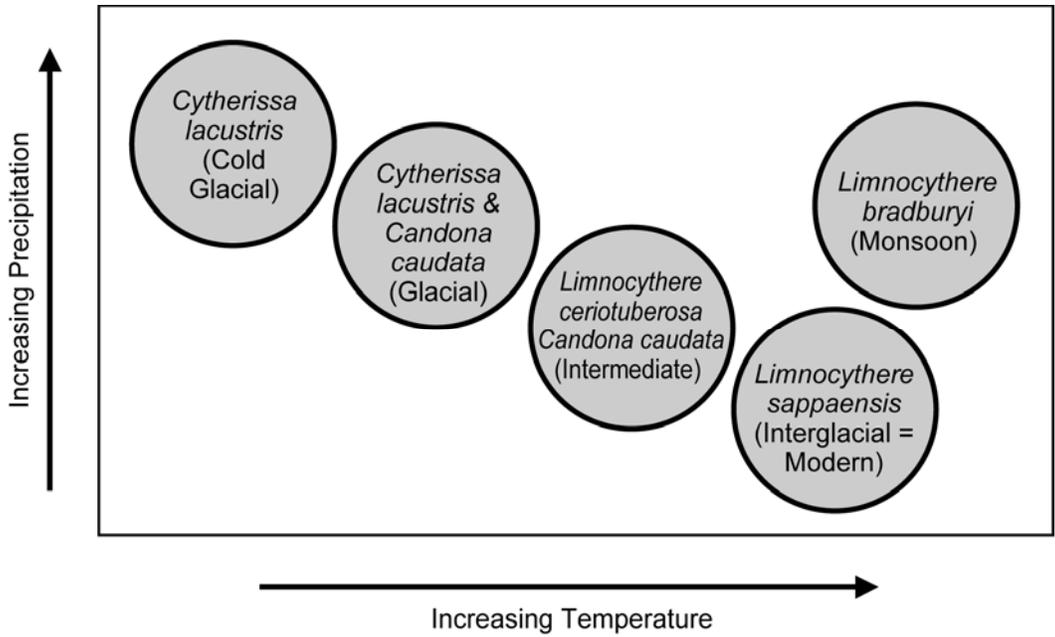
Source: Sharpe 2003 [DIRS 161591], Figure 6-2, p. 17

Figure 6-6. Climate State and Relative Magnitude of Associated Parameters Based on the Owens Lake Ostracode Record
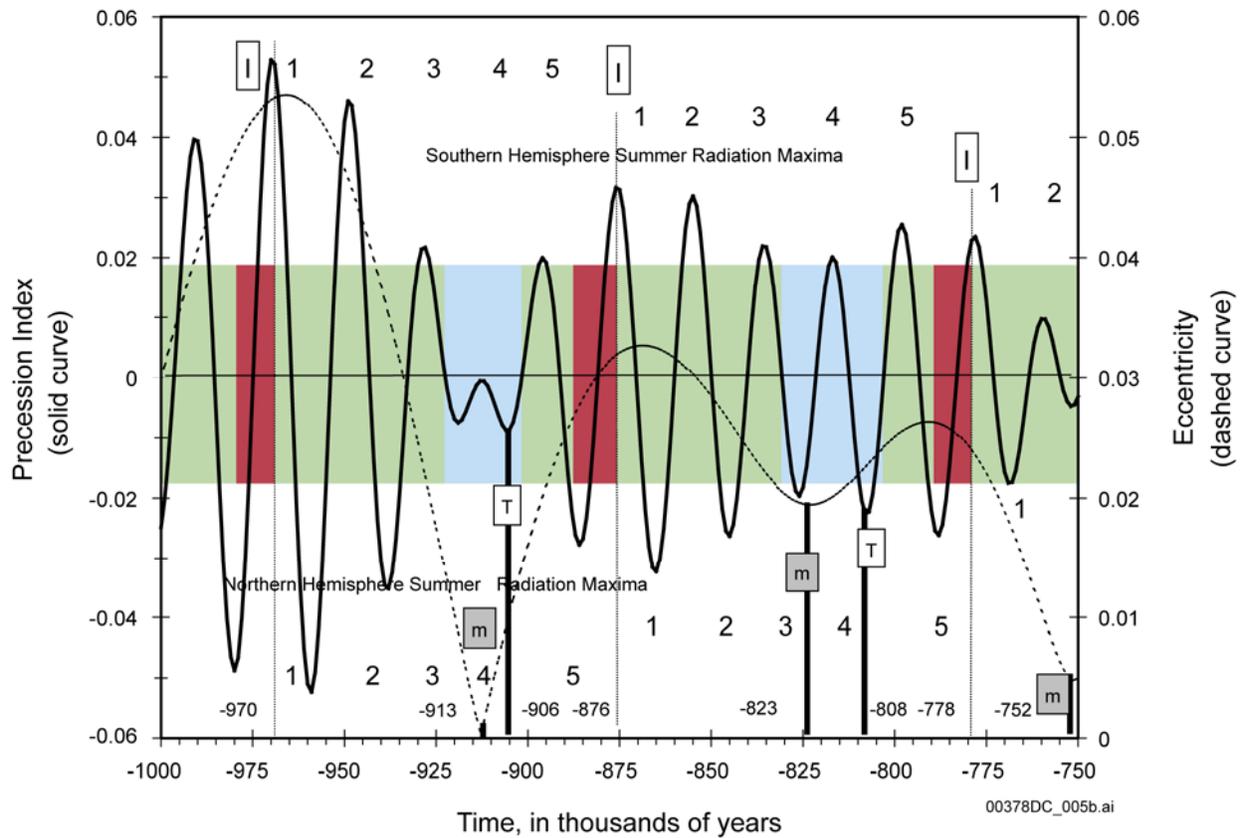
DTN: GS000900005121.004 [DIRS 153822]

Source: Sharpe 2003 [DIRS 161591], Figure 6.5a through d, pp. 35 to 38

NOTE: I = initiation of transition to glacial climate; T = initiation of transition to interglacial climate; m = minimum eccentricity value; numbers 1 through 4 or 5 = summer solar radiation maxima; numbers at the top of the graph are summer solar radiation maxima in the southern hemisphere; numbers at the bottom of the graph are summer solar radiation maxima in the northern hemisphere. The I to I event equals a precession sequence. Ages for I, T, and m are shown near the bottom of the graph. Continuation of the diagram is given as Figures 6-7b, 6-7c, and 6-7d.

Figure 6-7a. Precession, Eccentricity, and Obliquity for the Last 1,000,000 Years
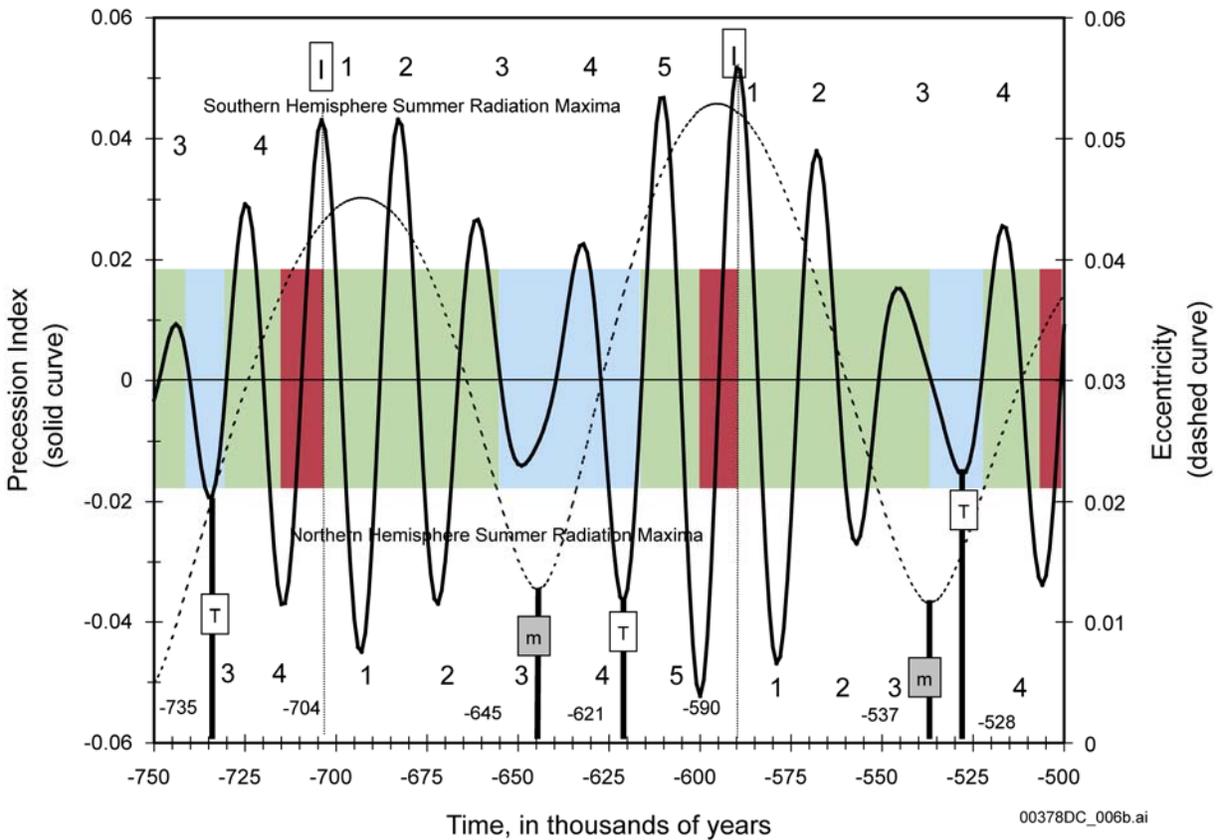
Source: Sharpe 2003 [DIRS 161591], Figures 6.5a through d., pp. 35 to 38

Figure 6-7b. Precession, Eccentricity, and Obliquity for the Last 1,000,000 Years
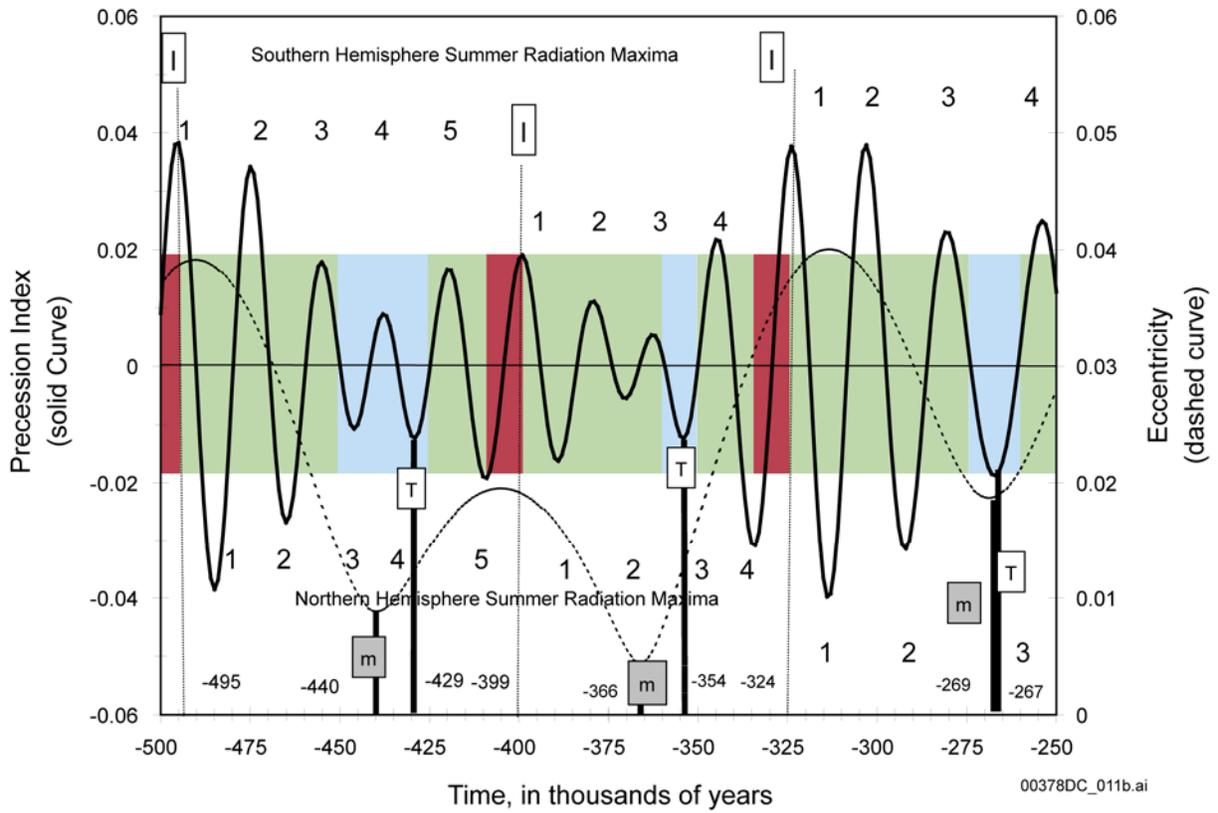
Source: Sharpe 2003 [DIRS 161591], Figures 6.5a through d, pp. 35 to 38

Figure 6-7c. Precession, Eccentricity, and Obliquity for the Last 1,000,000 Years
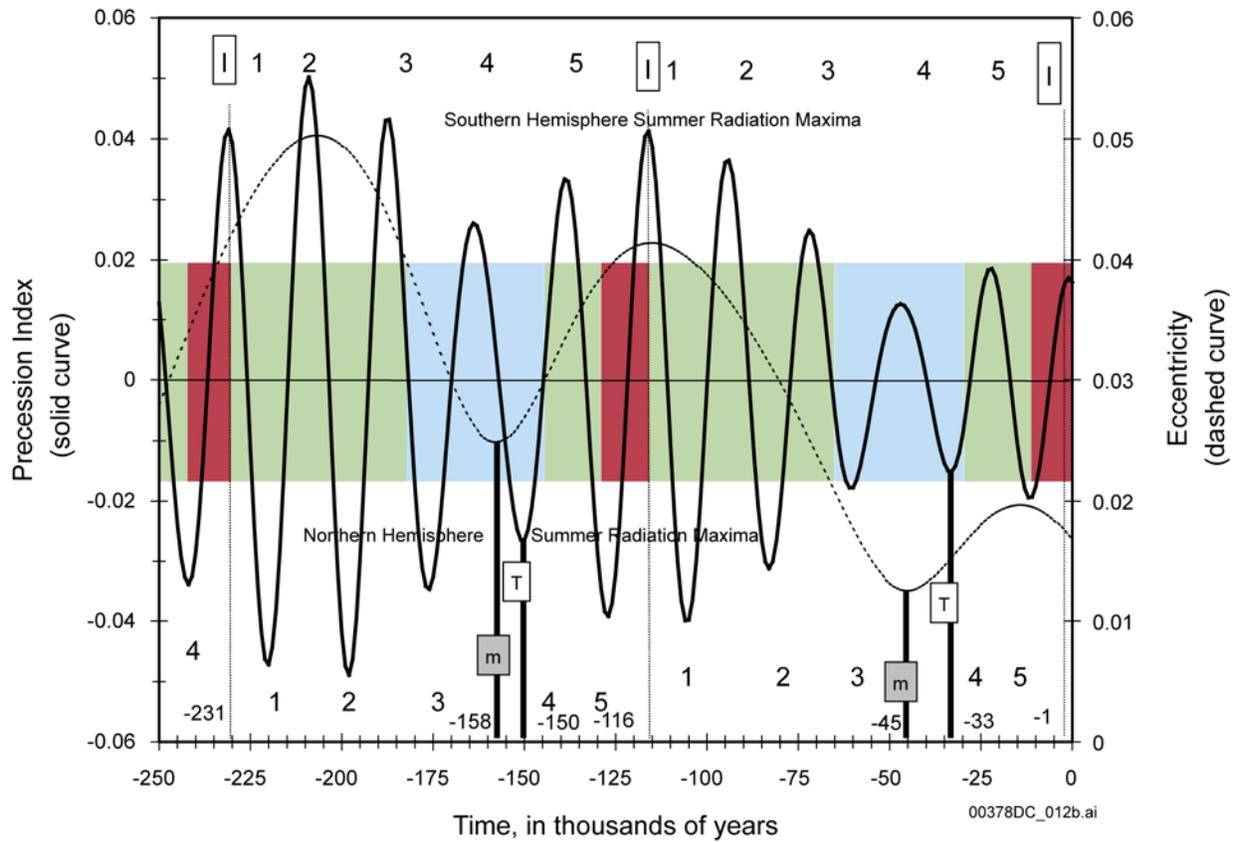
Source: Sharpe 2003 [DIRS 161591], Figures 6.5a through d, pp. 35 to 38

Figure 6-7d. Precession, Eccentricity, and Obliquity for the Last 1,000,000 Years
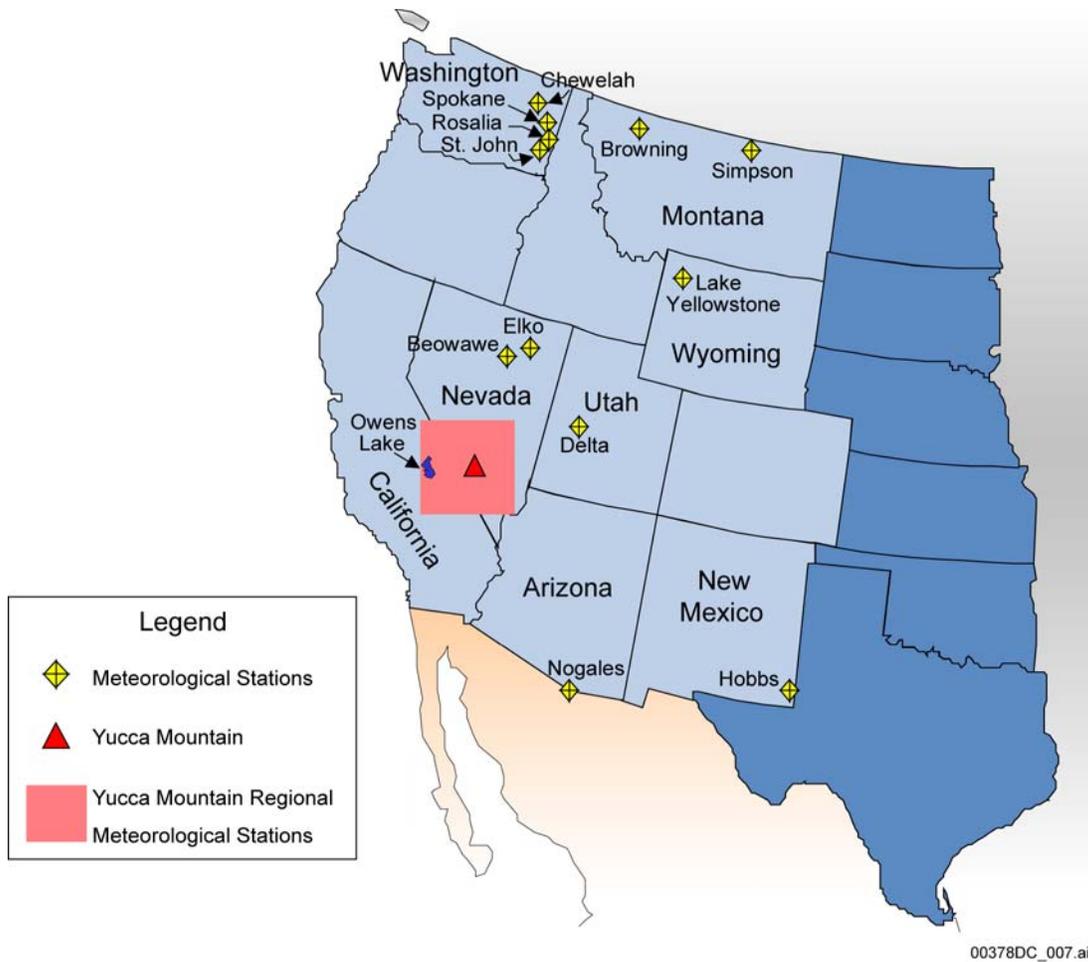
Source: Sharpe 2003 [DIRS 161591], Figure 6-3, p. 30

Figure 6-8. Modern Meteorological Stations Used as Future Climate Analogues
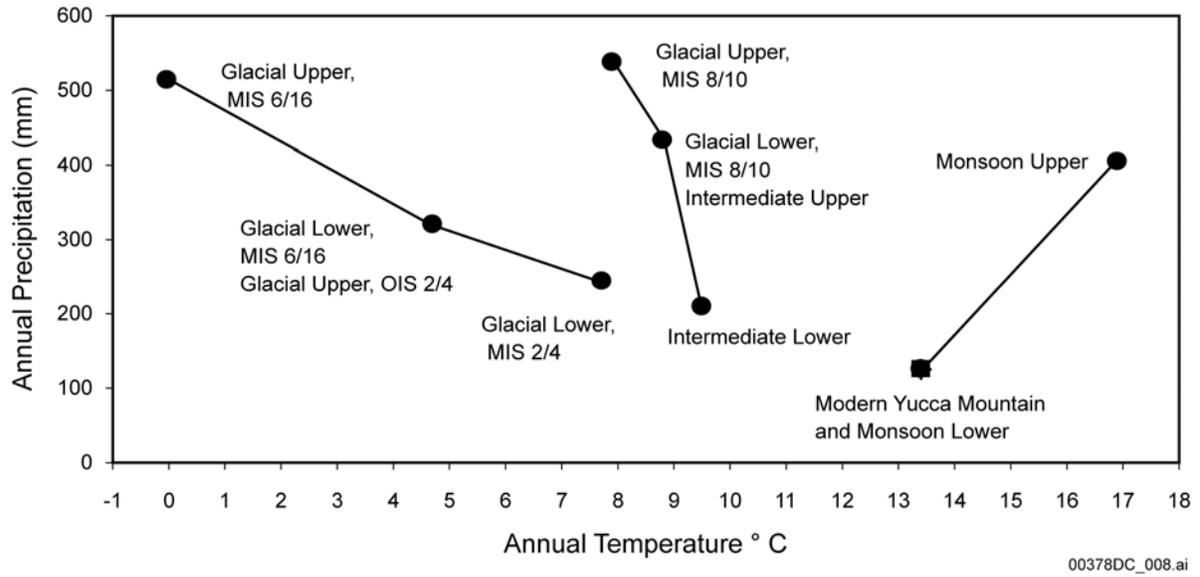
Source: Sharpe 2003 [DIRS 161591], Figure 6-4, p. 33

Figure 6-9. Modern Meteorological Station Mean Annual Temperature and Precipitation
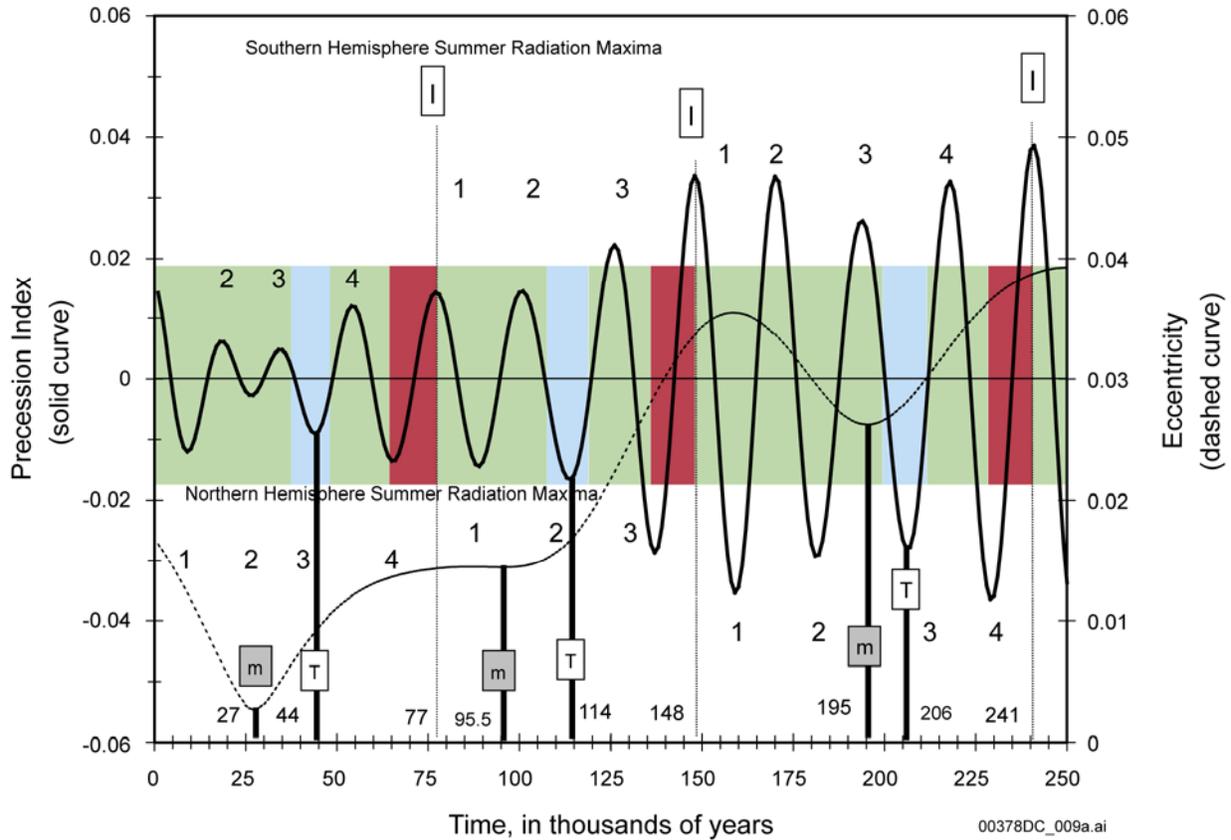
DTN: GS000900005121.004 [DIRS 153822]

Source: Sharpe 2003 [DIRS 161591], Figure 6-7a and b, pp. 50 and 51

NOTES: I = initiation of transition to glacial climate; T = initiation of transition to interglacial climate; m = minimum eccentricity value; numbers 1 through 4 or 5 = summer solar radiation maxima; numbers at the top of the graph are summer solar radiation maxima in the southern hemisphere; numbers at the bottom of graph are summer solar radiation maxima in the northern hemisphere. The I to I event equals a precession sequence. Ages for I, T, and m are shown near the bottom of the graph. Continuation of the diagram is given as Figure 6-10b.

Figure 6-10a. Relation between Precession and Eccentricity from Present to 500,000 Years after Present
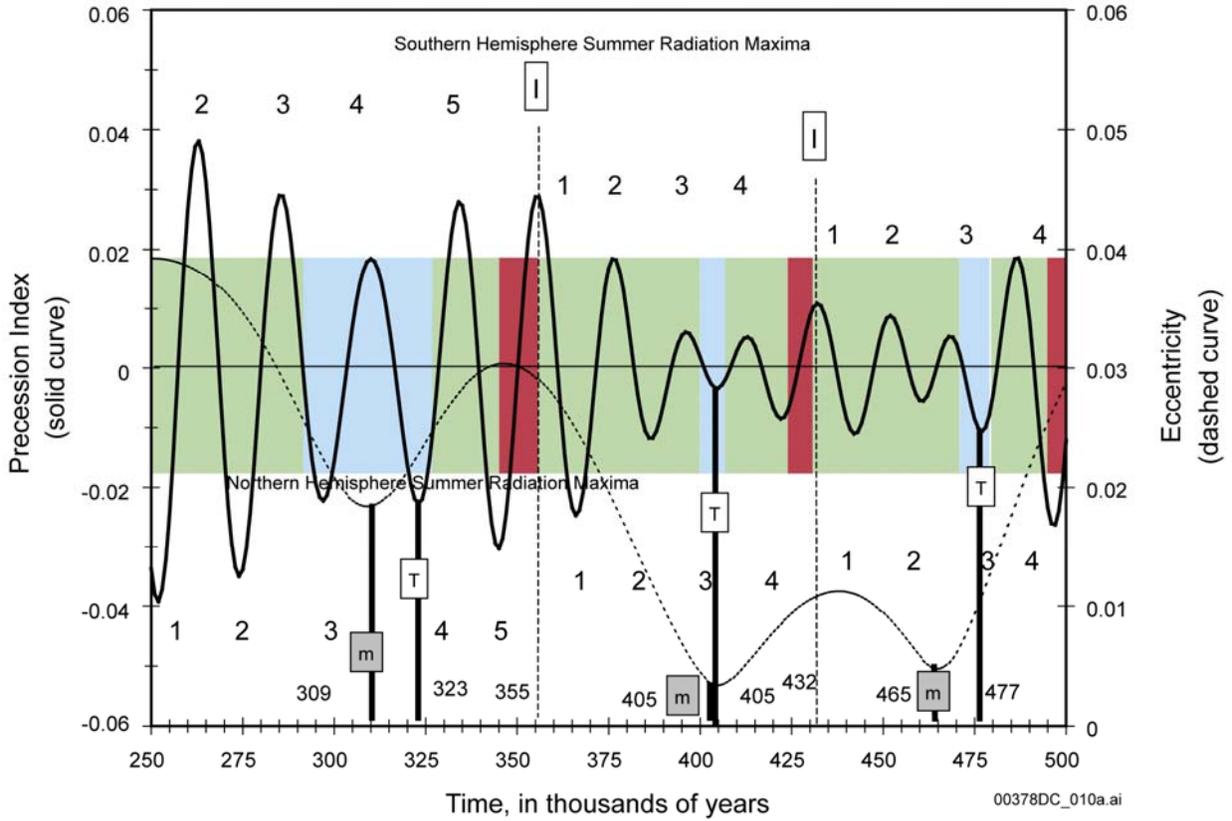
Source: Sharpe 2003 [DIRS 161591], Figure 6-7a and b, pp. 50 and 51

Figure 6-10b. Relation between Precession and Eccentricity from Present to 500,000 Years after Present

INTENTIONALLY LEFT BLANK

Table 6-1. Regional Meteorological Stations

Station Name	Latitude Longitude (deg° min')	Elevation (m [ft])	Overall Period of Station Operation	Approximate Distance and Direction from Yucca Mountain
Amargosa Farms Garey	36°34'N 116°28'W	746.8 [2449.5]	1965 to Present	30 km [19 mi] S
Austin	39°30'N 117°05'W	2013.2 [6603.3]	1890 to Present	290 km [180 mi] NNW
Battle Mountain	40°37'N 116°54'W	1383.8 [4538.9]	1944 to Present	410 km [255 mi] NNW
Beatty	36°55'N 116°45'W	1007.1 [3303.3]	1948 to 1972	25 km [16 mi] WNW
Beatty 8 N	37°00'N 116°43'W	1082.0 [3549.0]	1972 to Present	25 km [16 mi] WNW
Caliente	37°37'N 114°31'W	1341.1 [4398.8]	1928 to Present	170 km [106 mi] NE
Desert National Wildlife Range	36°26'N 115°22'W	890.0 [2919.2]	1948 to Present	109 km [68 mi] ESE
Elko Municipal Airport	40°50'N 115°47'W	1548.4 [5078.8]	1890 to Present	425 km [264 mi] NNE
Ely Yelland Field	39°17'N 114°51'W	1908.7 [6260.5]	1948 to Present	300 km [186 mi] NE
Indian Springs	36°35'N 115°41'W	951.9 [3122.2]	1948 to 1964	76 km [47 mi] ESE
Las Vegas McCarran International Airport	36°05'N 115°10'W	648.2 [2160.0]	1937 to Present	150 km [93 mi] SE
Mercury Desert Rock Airport	36°37'N 116°01'W	1006.1 [3300.0]	1984 to Present	45 km [28 mi] SE
Pahranagat Wildlife Refuge	37°16'N 115°07'W	1036.3 [3399.1]	1964 to Present	128 km [80 mi] ENE
Pioche	37°56'N 114°27'W	1883.7 [6178.5]	1948 to Present	215 km [133 mi] NE
Ruby Lake	40°12'N 115°30'W	1831.8 [6008.3]	1948 to Present	381 km [287 mi] NNE
Snowball Ranch	39°04'N 116°12'W	2182.4 [7158.3]	1966 to Present	243 km [151 mi] N
Tonopah	38°04'N 117°14'W	1856 [6090]	1928 to 1954	140 km [87 mi] NW

Table 6-1. Regional Meteorological Stations (Continued)

Station Name	Latitude Longitude (deg° min')	Elevation (m [ft])	Overall Period of Station Operation	Approximate Distance and Direction from Yucca Mountain
Tonopah Airport	38°04'N 117°05'W	1655.1 [5428. 7]	1954 to Present	140 km [87 mi] NW
Winnemucca Municipal Airport	40°54'N 117°48'W	1309.7 [4295.8]	1897 to Present	464 km [228 mi] NNW
4JA	36°47'N 116°17'W	1043 [3422]	1967 to Present	15 km [9 mi] ESE
Area 12 Mesa	37°11'N 116°13'W	2283 [7490]	1959 to 1993	44 km [27 mi] NNE

DTNs: MO9907COV99282.000 [DIRS 163709]; UN0201SPA021SS.007 [DIRS 161588]

Source: CRWMS M&O 1997 [DIRS 100117], Table 2-2

NOTES: All except the last two stations in the table are National Weather Service Primary or Cooperative stations. The last two stations were established as part of the NOAA Air Resources Laboratory, the Special Operations and Research Division network to monitor meteorological conditions on the Nevada Test Site. Some stations have moved slightly during their period of operation. Latitude, longitude, and elevation are given for the most current location. Data availability is the time range for which some "Summary of the Month Cooperative" data are available (for National Weather Service stations); however, for most stations, availability is discontinuous for this range. For some analyses reported in this section, data from nearby stations were combined to create a longer period of record. Stations listed in Table 6-1 but not shown on Figures 6-2a and 6-2b are locted beyond the areas shown on the maps.

Table 6-2. Department of Energy Meteorological Monitoring Site

Site	Latitude (deg° min' sec")	Longitude (deg° min' sec")	Elevation (above mean sea level)	Overall Period of Station Operation
Site 1 (NTS-60)	36°50'34"N	116°25'50"W	3,750 ft [1,143 m]	1985-present
Site 2 (Yucca Mountain)	36°51'19"N	116°27'56"W	4,850 ft [1,478 m]	1985-present
Site 3 (Coyote Wash)	36°51'17"N	116°27'06"W	4,195 ft [1,279 m]	1985-present
Site 4 (Alice Hill)	36°51'51"N	116°24'15"W	4,050 ft [1,234 m]	1985-present
Site 5 (Fortymile Wash)	36°45'52"N	116°23'26"W	3,125 ft [953 m]	1985-present
Site 6 (WT-6)	36°53'40"N	116°26'45"W	4,315 ft [1,315 m]	1992-present
Site 7 (Sever Wash)	36°50'49"N	116°24'28"W	3,545 ft [1,081 m]	1992-present
Site 8 (Knothead Gap)	36°49'42"N	116°25'35"W	3,710 ft [1,131 m]	1992-present
Site 9 (Gate-510)	36°40'17"N	116°24'17"W	2,750 ft [838 m]	1993-present
Site 401 (Bleach Bone Ridge)	36°53'16"N	116°27'42"W	5,125 ft 1,562 m	1997-present
Site 405 (Yucca Mt-WX46)	36°49'50"N	116°28'03"W	4,882 ft 1,488 m	1997-present
Site 415 (Yucca Mt SE 01 E01 G-3)	36°48'47"N	116°27'39"W	4,725 ft 1,440 m	1997-present

DTN: MO9907COV99282.000 [DIRS 163709]

Source: CRWMS M&O 1997 [DIRS 100117], Table 2-1

Table 6-3. Annual Precipitation Statistics for Three Stations (1986 to 1996)

Parameter	Site 1	Beatty 8N	Mercury Desert Rock Airport
Mean	4.97 in. [126.24 mm]	5.63 in. 143.00 mm]	5.67 in. [144.02 mm]
Maximum (year occurred)	9.17 in. [232.92 mm] (1995)	8.45 in. [214.63 mm] (1995)	8.56 in. [217.42 mm] (1987)
Minimum (year occurred)	1.44 in. [36.58 mm] (1989)	2.43 in. [61.72 mm] (1989)	1.25 in. [31.75 mm] (1989)
Standard Deviation	2.22 in. [56.39 mm]	1.74 in. [44.20 mm]	2.13 in. [54.10 mm]

DTN: M09811DEDCRMCR.000 [DIRS 148887]

Source: CRWMS M&O 1997 [DIRS 100117], Table 4-2

NOTE: R/EFPD = Radiological and Environmental Field Programs Department. The number in parentheses indicates year occurred.

Table 6-4. Annual Precipitation Statistics for Two Stations (1966 to 2002)

Parameter	Amargosa Farms Garey	Beatty/Beatty 8N
Mean	4.29 in. [109 mm]	5.82 in. [148 mm]
Maximum (year occurred)	10.37 in. [263 mm] (1983)	12.62 in. [321 mm] (1998)
Minimum (year occurred)	0.45 in. [11 mm] (2002)	0.46 in. [12 mm] (2002)
Standard Deviation	2.75 in. [70 mm]	2.53 in. [64 mm]

DTN: M09811DEDCRMCR.000 [DIRS 148887]

Source: Calculated from data presented in Table 6-21

NOTE: The number in parentheses indicates year occurred.

Table 6-5. Average Monthly Temperature for Five Stations

Month	Statistic (°C)	Site 1 1986-1996	Site 5 1986-1996	Mercury Desert Rock Airport Jan 1985-1995 July 1984-1995	Austin 1921-1995	Caliente 1929-1995
January	Mean Max	10.9	12.6	12.4	4.9	7.8
	Mean Min	2.4	1.8	0.4	-7.4	-8.2
July	Mean Max	34.2	36.3	36.9	30.6	35.3
	Mean Min	22.1	21.8	21.3	12.1	13.6

DTN: M09811DEDCRMCR.000 [DIRS 148887]

Source: CRWMS M&O 1997 [DIRS 100117], Tables A-1, A-5, A-11, and A-12

Table 6-6.   Monthly and Annual Climatological Summaries: Department of Energy Site 1

Parameter	Jan.	Feb.	Mar.	Apr.	May	Jun.	Jul.	Aug.	Sep.	Oct.	Nov.	Dec.	Year
Temperature (°C) (1986-1996)													
Extreme Maximum[a]	20.5	26.3	26.2	31.7	36.0	39.8	40.9	40.3	37.3	34.7	26.2	20.3	40.9
Mean Maximum[a]	10.9	13.4	16.1	21.1	24.9	31.0	34.2	33.7	29.0	23.5	15.5	10.6	22.0
Mean[a]	6.3	8.7	11.3	15.9	19.5	25.3	28.6	27.9	23.5	18.0	10.4	6.0	16.8
Mean Minimum[a]	2.4	4.4	6.5	10.2	13.4	18.6	22.1	21.7	17.7	12.8	5.9	2.1	11.5
Extreme Minimum[a]	-7.0	-11.1	-3.9	-0.8	0.3	4.5	10.9	13.9	6.9	-0.3	-6.1	-11.7	-11.7
Number of Days (1986-1996)													
Precipitation 0.01 in. or more	4.5	4.3	5.2	2.9	4.2	2.7	1.9	3.2	2.8	3.5	2.8	3.8	41.8
Temperature[a] 32°C (90°F) and above	0	0	0	0	3	13.8	22.9	21.5	6.4	2.7	0	0	70.3
0°C (32°F) and below	7.2	6	2.6	0	0	0	0	0	0	0	3.7	10.1	29.6
Barometric Pressure (mb) (1986-1996) Mean[a]	888.4	886.7	884.6	884.2	882.4	883.1	885.1	885.7	885.7	886.7	888.4	888.8	885.8
Mean Relative Humidity (%) (1986-1996) Hour 0400 (PST) [a]	44.6	45.3	41.5	32.3	31.5	22.8	23.5	25.5	25.9	28.0	37.2	45.9	33.7
Hour 1000[a]	39.8	40.0	34.7	25.4	22.7	18.3	18.0	20.0	21.2	22.4	30.3	38.7	27.6
Hour 1600[a]	33.1	30.9	26.2	18.8	17.1	13.0	13.4	14.3	14.8	18.1	25.1	31.9	21.4
Hour 2200[a]	41.9	40.6	35.5	25.8	23.8	16.8	17.3	19.2	20.1	24.5	33.4	42.8	28.5
Precipitation (in.) (1986-1996)													
Max 1 hr total	0.19	0.16	0.58	0.21	0.27	0.12	0.47	0.66	0.12	0.19	0.40	0.23	0.66
Max 6 hr total[b]	0.77	0.49	0.84	0.71	0.42	0.16	0.86	1.18	0.39	0.48	0.66	0.70	1.18
Max 24 hr total[b]	1.39	0.76	1.33	1.32	0.46	0.24	1.22	1.18	0.44	0.62	1.29	1.00	1.39
Total	0.92	0.61	0.90	0.25	0.39	0.09	0.25	0.53	0.09	0.25	0.24	0.45	4.97
Wind Mean Speed (m/s)[a] **(1986-1996)**	2.8	3.2	3.7	4.0	4.0	3.9	3.7	3.5	3.3	3.0	3.2	2.8	3.4
Fastest 1 min[c] **(1986-1996)** Speed (m/s) **(1986-1996)**	n/a	n/a	n/a	n/a	n/a	n/a	n/a	n/a	n/a	n/a	n/a	n/a	n/a
Direction (deg) **(1986-1996)**	n/a	n/a	n/a	n/a	n/a	n/a	n/a	n/a	n/a	n/a	n/a	n/a	n/a
Peak 1s Gust (m/s) **(1986-1996)**	n/a	n/a	n/a	n/a	n/a	n/a	n/a	n/a	n/a	n/a	n/a	n/a	n/a

Source: CRWMS M&O 1997 [DIRS 100117], Table A-1

NOTES: [a] Values are derived from 1-s data averaged over 1 hr.
            [b] A continuous running period that may encompass more than one calendar day.
            [c] Values are derived from 1-s data averaged over 1 min.
            n/a = no data available; To convert in. to mm, multiply by 25.4.
            PST = Pacific Standard Time.
            To convert m/s to mi/hr, multiply by 2.24.

Table 6-7.   Monthly and Annual Climatological Summaries: Department of Energy Site 2

Parameter	Jan.	Feb.	Mar.	Apr.	May	Jun.	Jul.	Aug.	Sep.	Oct.	Nov.	Dec.	Year
Temperature (°C) (1986-1996)													
Extreme Maximum[a]	18.5	23.6	24.0	29.8	34.2	39.9	39.7	39.1	36.1	33.5	24.3	18.9	39.9
Mean Maximum[a]	8.6	11.0	14.0	19.0	22.9	29.1	32.3	31.6	27.1	21.0	13.0	8.3	19.8
Mean[b]	5.6	7.4	10.2	14.6	18.2	23.9	27.1	26.7	22.7	17.1	9.5	5.5	15.7
Mean Minimum[a]	2.9	4.3	6.9	10.5	13.7	19.1	22.4	22.4	18.6	13.6	6.5	2.9	12.0
Extreme Minimum[a]	-10.1	-12.5	-3.7	-0.6	-1.2	2.4	10.2	12.7	5.6	-1.5	-7.3	-12.3	-12.5
Number of Days													
Precipitation 0.01 in. or more	5.4	5.7	5.4	1.4	2.3	1.0	1.1	1.1	1.0	1.4	1.7	3.7	31.4
Temperature[b]													
32°C (90°F)and above	0	0	0	0	0.2	6.7	16.2	12.4	2.6	0.1	0	0	38.2
0°C (32°F) and below	7.3	5.6	2	0.3	0.2	0.1	0	0	0	0.3	2.9	6.7	25.4
Barometric Pressure (mb) (1989-1996) Mean[b]	851.5	850.8	849.7	849.1	848.3	849.8	852.1	852.6	852.6	852.1	852.6	851.5	851.1
Mean Relative Humidity (%) (1986-1996)													
Hour 0400 (PST)[b]	45.6	42.3	40.1	28.5	27.5	16.0	18.5	22.2	23.2	27.4	35.9	41.4	30.7
Hour 1000[b]	43.2	41.2	38.0	25.5	22.9	13.6	14.9	19.2	19.8	25.1	33.0	38.7	27.9
Hour 1600b	38.8	33.5	29.5	18.2	16.5	8.6	10.6	13.2	13.8	19.9	27.1	34.3	22.0
Hour 2200b	43.8	39.4	34.7	23.7	22.0	12.3	14.4	17.9	18.4	24.5	32.4	39.9	27.0
Precipitation (in.) (1989-1996)													
Max 1 hr total	0.31	0.21	0.32	0.13	0.21	0.36	0.20	0.50	0.17	0.12	0.26	0.23	0.50
Max 6 hr total[c]	0.63	0.64	0.92	0.22	0.37	0.58	0.26	0.56	0.34	0.42	0.71	1.03	1.03
Max 24 hr total[c]	1.31	1.20	1.70	0.48	0.45	0.67	0.28	0.56	0.34	0.75	1.17	1.78	1.78
Total	1.29	1.51	1.55	0.14	0.22	0.14	0.11	0.23	0.09	0.23	0.31	0.74	6.56
Wind Mean Speed (m/s)[b] **(1986-1996)**	3.6	4.1	4.5	5.0	4.8	4.6	4.2	4.6	4.2	4.1	4.0	3.8	4.3
Fastest 1 min[a] **(1993-1996)**	23.2	26.3	28.7	28.9	21.6	30.0	23.0	19.7	20.9	29.4	25.0	26.1	30.0
Direction (deg) **(1993-1996)**	326	312	307	237	285	324	99	268	316	325	269	319	239
Peak 3s Gust (m/s) **(1993-1996)**	27.2	31.0	34.8	38.2	27.2	33.4	28.5	25.2	24.1	33.3	31.9	31.6	38.2

Source: CRWMS M&O 1997 [DIRS 100117], Table A-2

NOTES: [a] Values are derived from 1-s data averaged over 1 min.
[b] Values are derived from 1-s data averaged over 1 hr.
[c] A continuous running period that may encompass more than one calendar day.
PST = Pacific Standard Time.
To convert in. to mm, multiply by 25.4.
To convert m/s to mi/hr, multiply by 2.24.

Table 6-8.   Monthly and Annual Climatological Summaries: Department of Energy Site 3

Parameter	Jan.	Feb.	Mar.	Apr.	May	Jun.	Jul.	Aug.	Sep.	Oct.	Nov.	Dec.	Year
Temperature (°C) (1986-1996)													
Extreme Maximum[a]	19.5	24.9	25.0	30.9	34.6	40.4	39.9	39.6	36.6	33.6	25.2	19.7	40.4
Mean Maximum[a]	9.9	12.5	15.1	20.3	23.8	30.0	33.0	32.5	28.2	22.1	14.4	9.5	20.9
Mean[b]	6.3	8.6	10.8	15.6	19.0	24.8	28.0	27.5	23.4	17.8	10.3	5.9	16.5
Mean Minimum[a]	3.0	4.9	6.4	10.5	13.6	18.8	22.2	22.1	18.4	13.4	6.4	2.5	11.8
Extreme Minimum[a]	-7.9	-10.7	-4.3	-0.3	0.1	4.2	10.5	14.3	7.2	0.3	-5.9	-12.2	-12.2
Number of Days													
Precipitation 0.01 in. or more	5.1	4.6	5.3	1.4	3.3	1.1	1.3	1.3	1.6	1.4	2.3	4.6	33.3
Temperature[b]													
32°C (90°F) and above	0	0	0	0	0.5	9.6	17.5	16.6	4.5	0.3	0	0	49.0
0°C (32°F) and below	6.8	4.1	1.9	0.1	0	0	0	0	0	0	1.9	8.2	23.0
Barometric Pressure (mb) (1989-1996)													
Mean[b]	872.9	871.8	870.1	869.6	867.9	868.7	870.8	871.3	871.6	872.0	873.2	872.7	871.0
Mean Relative Humidity (%) (1986-1996)													
Hour 0400 (PST)[b]	45.1	44.5	43.4	33.9	33.1	21.9	22.9	26.2	28.9	31.4	37.6	45.4	34.5
Hour 1000[b]	39.4	39.6	37.3	27.2	24.7	16.8	16.8	20.8	22.3	25.1	30.8	38.3	28.3
Hour 1600[b]	35.4	31.8	29.6	19.9	18.4	12.4	13.0	15.1	16.4	21.4	26.5	34.7	22.9
Hour 2200[b]	42.9	40.8	38.0	26.9	25.2	16.6	17.1	20.3	22.5	27.9	33.8	42.9	29.6
Precipitation (in.) (1989-1996)													
Max 1 hr total	0.32	0.20	0.43	0.14	0.23	0.29	0.18	0.31	0.27	0.17	0.57	0.26	0.57
Max 6 hr total[c]	0.74	0.61	1.13	0.21	0.36	0.60	0.18	0.62	0.27	0.53	0.77	0.77	1.13
Max 24 hr total[c]	1.53	1.22	1.89	0.31	0.41	0.67	0.18	0.67	0.27	0.79	1.60	1.12	1.89
Total	1.33	1.29	1.57	0.14	0.33	0.14	0.09	0.20	0.15	0.31	0.39	0.75	6.70
Wind													
Mean Speed (m/s)[b] **(1986-1996)**	2.2	2.4	2.7	2.8	2.8	2.8	2.6	2.4	2.4	2.4	2.6	2.3	2.5
Fastest 1 min[a] **(1993-1996)**	16.3	15.9	16.0	17.0	13.7	17.3	18.6	11.7	13.9	18.0	15.2	14.6	18.6
Direction (deg) **(1993-1996)**	300	306	309	302	290	299	107	294	89	307	310	302	107
Peak 3s Gust (m/s) **(1993-1996)**	23.3	21.8	25.2	24.5	19.2	24.3	21.0	17.3	19.5	26.2	21.5	22.0	26.2

Source: CRWMS M&O 1997 [DIRS 100117], Table A-3

NOTES: [a] Values are derived from 1-s data averaged over 1 min.
[b] Values are derived from 1-s data averaged over 1 hr.
[c] A continuous running period that may encompass more than one calendar day.
PST = Pacific Standard Time.
To convert in. to mm, multiply by 25.4.
To convert m/s to mi/hr, multiply by 2.24.

Table 6-9.   Monthly and Annual Climatological Summaries: Department of Energy Site 4

Parameter	Jan.	Feb.	Mar.	Apr.	May	Jun.	Jul.	Aug.	Sep.	Oct.	Nov.	Dec.	Year
Temperature (°C) (1986-1996)													
Extreme Maximum[a]	20.7	25.3	26.5	32.3	36.8	42.3	41.6	41.0	38.0	34.8	26.5	20.4	42.3
Mean Maximum[a]	10.4	12.8	15.8	20.6	24.4	30.5	33.7	33.5	28.9	22.6	14.7	10.0	21.5
Mean[b]	6.5	8.6	11.2	15.6	19.2	25.2	28.4	28.1	23.6	17.6	10.3	6.2	16.7
Mean Minimum[a]	2.9	4.5	6.8	10.3	13.8	19.2	22.7	22.5	18.1	12.5	6.2	2.6	11.8
Extreme Minimum[a]	-7.3	-11.0	-4.1	0.0	-0.3	4.0	11.2	14.1	7.4	0.0	-6.0	-12.6	-12.6
Number of Days													
Precipitation 0.01 in. or more	5.8	4.6	5.4	1.6	2.4	1.4	0.9	1.3	0.9	1.6	2.2	4.0	32.0
Temperature[b]													
32°C (90°F) and above	0	0	0	0	1	11.2	20.3	18.5	6	0.4	0	0	57.4
0°C (32°F) and below	5.3	4.3	1.4	0.1	0.1	0	0	0	0	0	1.4	6.3	18.9
Barometric Pressure (mb) (1989-1996)													
Mean[b]	877.7	876.5	874.5	873.9	872.2	873.2	875.3	876.0	876.4	876.5	878.3	878.1	875.7
Mean Relative Humidity (%) (1986-1996)													
Hour 0400 (PST)[b]	46.5	46.0	43.0	30.4	30.2	18.9	20.4	22.7	25.1	30.9	37.8	45.1	33.1
Hour 1000[b]	43.7	42.7	37.7	24.4	22.3	14.7	15.5	18.0	20.3	24.9	32.9	40.0	28.1
Hour 1600[b]	36.2	33.2	28.3	17.3	15.7	9.9	12.6	12.7	14.1	19.4	26.1	33.1	21.6
Hour 2200[b]	44.0	42.1	37.3	24.2	22.3	13.9	15.3	17.6	19.9	26.8	33.3	42.4	28.3
Precipitation (in.) (1989-1996)													
Max 1 hr total	0.29	0.22	0.33	0.17	0.14	0.12	0.33	0.38	0.24	0.19	0.42	0.23	0.42
Max 6 hr total[c]	0.69	0.61	0.95	0.35	0.31	0.43	0.36	0.53	0.49	0.43	0.81	0.81	0.95
Max 24 hr total[c]	1.19	1.13	1.76	0.53	0.50	0.49	0.37	0.56	0.58	0.74	1.51	1.86	1.86
Total	1.49	1.16	1.43	0.21	0.22	0.12	0.16	0.17	0.11	0.32	0.37	0.84	6.57
Wind													
Mean Speed (m/s)[b] **(1986-1996)**	3.7	4.2	4.6	5.2	5.1	4.8	4.3	4.1	4.1	4.1	4.5	3.7	4.4
Fastest 1 min[a]													
Speed (m/s) **(1993-1996)**	24.4	25.3	27.8	29.3	24.6	26.8	25.1	19.9	22.9	33.2	25.6	23.7	33.2
Direction (deg) **(1993-1996)**	340	339	2	351	10	338	37	33	329	345	342	344	345
Peak 3s Gust (m/s) **(1993-1996)**	28.0	29.2	31.4	32.2	29.3	30.0	28.3	28.5	24.9	37.2	29.8	27.9	37.2

Source: CRWMS M&O 1997 [DIRS 100117], Table A-4

NOTES: [a] Values are derived from 1-s data averaged over 1 min.
            [b] Values are derived from 1-s data averaged over 1 hr.
            [c] A continuous running period that may encompass more than one calendar day.
            PST = Pacific Standard Time.
            To convert in. to mm, multiply by 25.4.
            To convert m/s to mi/hr, multiply by 2.24.

Table 6-10. Monthly and Annual Climatological Summaries: Department of Energy Site 5

Parameters	Jan.	Feb.	Mar.	Apr.	May	Jun.	Jul.	Aug.	Sep.	Oct.	Nov.	Dec.	Year
Temperature (°C) (1986-1996)													
Extreme Maximum[a]	22.9	27.9	28.6	34.6	38.8	43.6	43.5	42.8	39.9	36.9	28.3	22.2	43.6
Mean Maximum[a]	12.6	15.3	18.4	23.4	27.2	33.1	36.3	35.7	31.3	25.6	17.5	12.3	24.1
Mean[b]	6.8	9.5	12.5	17.0	20.9	26.4	29.6	28.9	24.5	18.8	11.2	6.4	17.7
Mean Minimum[a]	1.8	4.3	6.5	10.2	13.6	18.3	21.8	21.4	17.4	12.6	5.7	1.4	11.2
Extreme Minimum[a]	-7.1	-11.8	-4.7	-0.5	1.4	2.6	11.1	13.0	5.5	-0.7	-6.6	-13.1	-13.1
Number of Days													
Precipitation 0.01 in. or more	4.7	4.6	4.9	1.6	2.7	0.9	1.0	1.3	0.7	1.1	1.4	3.3	28.1
Temperature[b] 32°C (90°F) and above	0.0	0.0	0.0	0.6	3.1	18.8	27.4	25.0	13.3	2.8	0.0	0.0	91.0
0°C (32°F) and below	7.5	3.7	0.7	0.0	0.0	0.0	0.0	0.0	0.0	0.1	2.0	8.5	22.6
Barometric Pressure (mb) (1989-1996) Mean[b]	908.1	906.7	904.5	903.5	901.5	901.9	903.6	904.5	904.8	905.9	908.2	908.2	905.1
Mean Relative Humidity (%) (1986-1996) Hour 0400 (PST)[b]	49.1	47.3	46.1	33.2	34.0	21.4	22.5	25.4	25.8	29.2	36.8	44.4	34.6
Hour 1000[b]	40.7	38.0	34.5	23.2	21.9	14.4	15.1	18.4	18.7	21.1	27.5	34.6	25.7
Hour 1600[b]	32.2	28.8	26.3	16.6	15.8	9.4	10.5	12.4	12.5	15.9	20.7	26.6	19.0
Hour 2200[b]	47.1	43.9	40.1	27.2	25.0	15.2	16.4	19.0	20.4	25.6	32.6	41.9	29.5
Precipitation (in.) (1989-1996)													
Max 1 hr total	0.23	0.26	0.16	0.22	0.10	0.19	0.50	0.38	0.33	0.25	0.16	0.23	0.50
Max 6 hr total[c]	0.50	0.59	0.53	0.26	0.25	0.50	0.72	0.53	0.74	0.49	0.70	0.78	0.78
Max 24 hr total[c]	1.02	0.89	0.94	0.26	0.49	0.53	0.72	0.53	0.84	0.97	1.05	1.63	1.63
Total	1.14	0.94	0.89	0.12	0.20	0.10	0.15	0.12	0.14	0.26	0.23	0.79	5.10
Wind													
Mean Speed (m/s)[b] **(1986-1996)**	3.7	4.1	4.3	4.6	4.6	4.5	4.3	4.3	4.3	4.1	4.2	3.9	4.2
Fastest 1 min[a] **(1993-1996)** Speed (m/s)	17.2	19.7	19.7	21.6	20.3	20.9	18.4	16.7	16.7	25.3	18.2	18.4	25.3
Direction (deg) **(1993-1996)**	350	185	349	346	317	344	82	227	178	337	336	178	337
Peak 3s Gust (m/s) **(1993-1996)**	20.7	23.1	24.9	26.4	24.8	25.1	26.5	20.0	20.7	30.4	21.7	22.1	30.4

Source: CRWMS M&O 1997 [DIRS 100117], Table A-5

NOTES: [a] Values are derived from 1-s data averaged over 1 min.
[b] Values are derived from 1-s data averaged over 1 hr.
[c] A continuous running period that may encompass more than one calendar day.
PST = Pacific Standard Time.
To convert in. to mm, multiply by 25.4.
To convert m/s to mi/hr, multiply by 2.24.

Table 6-11.   Monthly and Annual Climatological Summaries: Department of Energy Site 6

Parameter	Jan.	Feb.	Mar.	Apr.	May	Jun.	Jul.	Aug.	Sep.	Oct.	Nov.	Dec.	Year
Temperature (°C) (1993-1996)													
Extreme Maximum[a]	19.8	23.1	24.5	30.4	34.7	39.6	39.6	41.9	36.3	33.7	25.5	18.5	41.9
Mean Maximum[a]	9.8	12.3	16.2	19.8	24.2	30.5	33.9	33.9	29.1	22.1	14.2	10.0	21.3
Mean[b]	4.7	6.8	10.1	13.4	17.5	23.3	27.4	26.6	22.0	15.5	8.3	5.1	15.1
Mean Minimum[a]	0.2	1.5	4.1	6.4	9.9	14.6	18.4	18.3	14.5	9.4	2.7	0.1	8.3
Extreme Minimum[a]	-9.9	-9.9	-6.9	-1.4	-0.3	2.3	11.0	12.0	6.2	-1.0	-7.8	-7.2	-9.9
Number of Days													
Precipitation 0.01 in. or more	7.5	5.8	4.3	1.5	4.0	1.5	1.0	1.0	1.3	1.0	2.3	3.5	34.5
Temperature[b]													
32°C (90°F) and above	0.0	0.0	0.0	0.0	0.8	12.3	23.0	22.0	5.8	0.5	0.0	0.0	64.3
0°C (32°F) and below	12.3	10.8	3.0	0.0	0.0	0.0	0.0	0.0	0.0	0.0	6.0	13.3	45.3
Barometric Pressure (mb) (1993-1996)													
Mean[b]	867.4	866.5	866.5	865.2	864.4	866.3	868.3	868.2	867.9	867.4	868.9	868.9	867.1
Mean Relative Humidity (%) (1993-1996)													
Hour 0400 (PST)[b]	61.7	61.2	55.2	41.7	45.8	30.4	29.8	30.4	31.6	36.0	45.8	56.2	43.8
Hour 1000[b]	49.2	45.3	38.7	26.3	26.2	18.3	16.5	17.3	18.7	23.8	31.4	39.6	29.3
Hour 1600[b]	46.4	37.7	29.5	18.5	19.3	11.6	11.4	11.4	12.8	18.8	27.7	36.2	23.4
Hour 2200[b]	59.3	57.9	47.1	33.4	34.9	22.0	20.3	21.5	23.2	31.0	41.9	53.0	37.1
Precipitation (in.) (1993-1996)													
Max 1 hr total	0.44	0.27	0.25	0.19	0.34	0.27	0.31	0.28	0.28	0.17	0.25	0.24	0.44
Max 6 hr total[c]	1.24	0.56	1.16	0.40	0.39	0.58	0.40	0.61	0.36	0.39	0.87	1.10	1.24
Max 24 hr total[c]	1.54	1.27	2.14	0.51	0.41	0.69	0.40	0.64	0.38	0.76	1.45	1.78	2.14
Total	2.35	1.50	1.52	0.34	0.38	0.25	0.21	0.26	0.17	0.36	0.68	0.68	8.69
Wind (1993-1996)													
Mean Speed (m/s)[b]	3.4	3.6	4.1	4.6	4.2	4.2	4.1	4.0	4.0	3.8	3.8	3.6	4.0
Fastest 1 min[a]													
Speed (m/s)	17.6	18.4	20.2	21.4	19.7	22.7	17.5	16.0	19.1	19.8	19.9	20.8	22.7
Direction (deg)	336	335	346	147	145	341	114	142	135	345	337	337	149
Peak 3s Gust (m/s)	21.5	25.7	26.1	28.7	26.5	28.8	23.6	21.1	24.0	27.0	26.7	23.6	28.8

Source: CRWMS M&O 1997 [DIRS 100117], Table A-6

NOTES: [a] Values are derived from 1-s data averaged over 1 min.
[b] Values are derived from 1-s data averaged over 1 hr.
[c] A continuous running period that may encompass more than one calendar day.
PST = Pacific Standard Time.
To convert in. to mm, multiply by 25.4.
To convert m/s to mi/hr, multiply by 2.24.

Table 6-12.   Monthly and Annual Climatological Summaries: Department of Energy Site 7

Parameter	Jan.	Feb.	Mar.	Apr.	May	Jun.	Jul.	Aug.	Sep.	Oct.	Nov.	Dec.	Year
Temperature (°C) (1993-1996)													
Extreme Maximum[a]	22.2	25.3	27.1	33.3	37.8	42.3	42.8	42.3	39.3	36.1	27.8	20.5	42.8
Mean Maximum[a]	11.9	14.7	18.9	22.6	27.3	33.5	36.9	36.8	32.0	24.5	16.3	11.9	24.0
Mean[b]	5.0	7.4	11.1	14.7	18.9	24.5	28.4	27.6	22.6	15.6	8.5	5.1	15.8
Mean Minimum[a]	-1.6	0.0	2.8	5.3	8.9	13.0	16.9	16.8	12.4	6.7	0.2	-2.4	6.6
Extreme Minimum[a]	-11.3	-10.8	-6.6	-1.7	-0.8	0.2	10.6	9.2	3.8	-5.0	-9.7	-12.8	-12.8
Number of Days													
Precipitation 0.01 in. or more	5.8	5.3	4.8	1.5	3.5	1.3	1.0	1.0	1.0	1.8	3.3	2.8	32.8
Temperature[b]													
32°C (90°F) and above	0.0	0.0	0.0	0.3	2.0	19.3	30.3	28.5	14.0	2.3	0.0	0.0	96.5
0°C (32°F) and below	17.3	11.5	3.5	0.8	0.3	0.0	0.0	0.0	0.0	0.3	10.8	18.8	63.0
Barometric Pressure (mb) (1993-1996)													
Mean[b]	893.1	891.9	891.6	890.2	888.8	890.0	891.7	891.7	891.9	892.2	893.8	894.0	891.7
Mean Relative Humidity (%) (1993-1996)													
Hour 0400 (PST)[b]	66.9	67.5	59.9	44.9	48.8	32.9	31.8	31.4	33.5	39.5	50.4	62.5	47.5
Hour 1000[b]	48.7	44.6	35.6	23.2	23.3	15.8	14.2	15.1	16.3	21.0	29.3	39.1	27.2
Hour 1600[b]	41.9	34.3	25.9	16.4	16.5	9.4	9.1	9.4	10.5	16.2	23.8	31.5	20.4
Hour 2200[b]	62.5	62.2	49.9	34.5	34.2	21.5	20.2	21.4	23.5	31.4	44.2	56.2	38.5
Precipitation (in.) (1993-1996)													
Max 1 hr total	0.41	0.23	0.24	0.15	0.18	0.12	0.59	0.33	0.05	0.20	0.40	0.28	0.59
Max 6 hr total[c]	0.97	0.52	0.94	0.26	0.24	0.46	0.60	0.50	0.07	0.48	0.81	0.93	0.97
Max 24 hr total[c]	1.18	1.25	1.69	0.37	0.35	0.49	0.60	0.55	0.08	0.73	1.49	2.15	2.15
Total	1.90	1.32	1.11	0.30	0.28	0.16	0.22	0.19	0.03	0.36	0.57	0.74	7.17
Wind													
Mean Speed (m/s)[b] (1993-1996)	2.5	2.8	3.3	3.9	3.6	3.6	3.4	3.3	3.1	2.9	2.9	2.5	3.2
Fastest 1 min[a] (1993-1996)													
Speed (m/s) (1993-1996)	15.8	16.7	18.1	21.3	18.9	18.5	15.6	15.2	16.9	23.2	18.0	17.1	23.2
Direction (deg) (1993-1996)	320	328	329	331	163	162	165	152	218	331	333	162	333
Peak 3s Gust (m/s) (1993-1996)	20.5	20.7	22.3	25.5	23.0	24.8	23.5	21.5	26.9	27.7	21.9	20.6	27.7

Source: CRWMS M&O 1997 [DIRS 100117], Table A-7

NOTES: [a] Values are derived from 1-s data averaged over 1 min.
            [b] Values are derived from 1-s data averaged over 1 hr.
            [c] A continuous running period that may encompass more than one calendar day.
            PST = Pacific Standard Time.
            To convert in. to mm, multiply by 25.4.
            To convert m/s to mi/hr, multiply by 2.24.

Table 6-13.   Monthly and Annual Climatological Summaries: Department of Energy Site 8

Parameter	Jan.	Feb.	Mar.	Apr.	May	Jun.	Jul.	Aug.	Sep.	Oct.	Nov.	Dec.	Year
Temperature (°C) (1993-1996)													
Extreme Maximum[a]	21. 2	24. 7	26. 2	32. 8	37. 1	41. 9	42. 0	41. 3	38.2	35.6	27.2	19.7	42.0
Mean Maximum[a]	11.4	14.1	18.3	21.9	26.6	32.8	36.2	36.2	31.3	24.0	15.8	11.5	23.4
Mean[b]	5.2	7.5	11.1	14.6	19.0	24.7	28.7	27.9	23.0	15.8	8.8	5.5	16.0
Mean Minimum[a]	-0.5	1.0	3.8	6.3	10.1	14.4	18.5	18.4	14.0	8.3	1.7	-0.7	7.9
Extreme Minimum[a]	-9.9	-9.5	-6.6	-1.0	0.0	2.5	12.0	11.1	5.9	-3.1	-8.0	-9.6	-9.9
Number of Days													
Precipitation 0.01 in. or more	6.0	5.0	4.8	1.5	3.3	1.3	1.3	1.5	1.3	1.0	2.5	2.8	32.0
Temperature[b]													
32°C (90°F) and above	0.0	0.0	0.0	0.0	1.5	17.5	29.8	27.8	11.8	1.8	0.0	0.0	90.0
0°C (32°F) and below	11.8	10.5	2.0	0.0	0.0	0.0	0.0	0.0	0.0	0.3	7.5	14.3	46.3
Barometric Pressure (mb) (1993-1996)													
Mean[b]	888.8	887.7	887.1	885.6	883.9	884.8	886.3	886.4	886.8	887.5	889.1	889.4	887.0
Mean Relative Humidity (%) (1993-1996)													
Hour 0400 (PST)[b]	62.7	64.0	57.0	41.6	45.1	30.1	28.9	29.3	31.1	36.8	46.8	58.2	44.3
Hour 1000[b]	47.6	44.4	35.4	22.9	23.2	15.4	13.9	15.2	16.0	20.5	29.0	38.3	26.8
Hour 1600[b]	41.4	34.1	26.2	15.7	16.5	9.1	9.0	9.2	10.2	16.1	23.9	32.0	20.3
Hour 2200[b]	59.2	57.5	47.0	32.2	32.8	20.0	18.8	19.9	21.9	30.1	41.3	52.9	36.1
Precipitation (in.) (1993-1996)													
Max 1 hr total	0.43	0.21	0.22	0.23	0.26	0.14	0.29	0.39	0.04	0.13	0.40	0.23	0.43
Max 6 hr total[c]	1.06	0.47	0.84	0.23	0.31	0.58	0.31	0.69	0.08	0.53	0.76	1.02	1.06
Max 24 hr total[c]	1.18	1.25	1.43	0.29	0.38	0.62	0.31	0.73	0.11	0.84	1.42	2.43	2.43
Total	1.94	1.36	1.14	0.25	0.32	0.19	0.20	0.27	0.04	0.22	0.52	0.56	6.99
Wind													
Mean Speed (m/s)[b] (1993-1996)	2.4	2.7	3.2	3.8	3.6	3.5	3.3	3.2	2.9	2.7	2.7	2.4	3.0
Fastest 1 min[a] (1993-1996) Speed (m/s) (1993-1996)	16.6	18.9	17.7	19.9	17.3	19.7	15.5	15.0	16.7	21.3	16.4	17.1	21.3
Direction (deg) (1993-1996)	327.9	331.1	189.9	204.1	171.1	337.2	322.5	168.2	167.4	332.3	4.1	200.7	220
Peak 3s Gust (m/s) (1993-1996)	20.5	22.6	25.0	27.6	20.7	23.9	20.5	18.9	21.4	27.3	21.9	20.8	27.6

Source: CRWMS M&O 1997 [DIRS 100117], Table A-8

NOTES: [a] Values are derived from 1-s data averaged over 1 min.
[b] Values are derived from 1-s data averaged over 1 hr.
[c] A continuous running period that may encompass more than one calendar day.
PST = Pacific Standard Time.
To convert in. to mm, multiply by 25.4.
To convert m/s to mi/hr, multiply by 2.24.

Table 6-14.   Monthly and Annual Climatological Summaries: Department of Energy Site 9

Parameter	Jan.	Feb.	Mar.	Apr.	May	Jun.	Jul.	Aug.	Sep.	Oct.	Nov.	Dec.	Year
Temperature (°C) (1993-1996)													
Extreme Maximum[a]	22.9	26.6	29.2	35.4	39.5	45.1	44.7	43.8	40.5	37.8	28.5	22.5	45.1
Mean Maximum[a]	13.4	16.5	20.8	24.6	29.2	35.6	39.5	38.9	33.9	26.0	18.2	14.2	25.9
Mean[b]	7.0	9.7	13.3	16.8	21.3	27.6	31.4	30.5	25.4	17.8	10.5	7.1	18.2
Mean Minimum[a]	1.0	3.3	5.9	8.2	12.3	16.4	21.2	21.0	16.4	9.8	3.4	1.2	10.0
Extreme Minimum[a]	-7.6	-5.3	-3.8	0.0	1.2	2.5	12.2	13.8	7.5	0.6	-6.8	-7.7	-7.7
Number of Days													
Precipitation 0.01 in. or more	6.5	5.0	4.5	2.0	3.5	0.8	1.0	0.5	0.3	1.0	1.8	2.5	29.3
Temperature[b]													
32°C (90°F) and above	1.5	1.0	1.3	3.0	8.5	24.5	31.0	30.8	21.0	3.3	1.8	1.3	128.8
0°C (32°F) and below	7.8	5.8	1.0	0.0	0.0	0.0	0.0	0.0	0.0	0.0	6.0	10.8	31.3
Barometric Pressure (mb) (1993-1996) Mean[b]	919.7	918.4	918.2	916.6	914.4	915.0	916.3	916.3	916.5	917.7	919.5	920.5	917.4
Mean Relative Humidity (%) (1993-1996) Hour 0400 (PST)[b]	61.0	59.3	53.9	39.1	42.5	26.4	23.7	24.2	26.6	32.6	44.6	55.1	40.7
Hour 1000[b]	46.9	42.7	34.3	21.1	23.5	14.1	12.6	14.0	15.6	19.2	28.4	37.6	25.8
Hour 1600[b]	39.0	30.9	23.3	14.2	16.0	7.8	7.2	8.2	9.1	14.0	21.2	28.5	18.3
Hour 2200[b]	57.1	53.0	43.6	30.6	30.1	17.0	15.4	16.6	19.0	25.8	37.6	49.5	33.0
Precipitation (in.) (1993-1996)													
Max 1 hr. total	0.13	0.29	0.12	0.16	0.18	0.32	0.02	0.04	0.01	0.19	0.16	0.20	0.32
Max 6 hr total[c]	0.39	0.57	0.40	0.16	0.43	0.68	0.03	0.05	0.02	0.44	0.50	0.42	0.68
Max 24 hr total[c]	0.65	0.94	0.61	0.18	0.57	0.68	0.04	0.05	0.02	0.63	0.63	0.97	0.97
Total	1.11	0.84	0.58	0.15	0.28	0.21	0.02	0.02	0.01	0.27	0.26	0.49	4.20
Wind													
Mean Speed (m/s)[b] (1993-1996)	3.8	4.2	4.4	4.8	4.7	4.7	4.6	4.7	4.4	4.1	4.1	4.0	4.4
Fastest 1 min[a] (1993-1996)													
Speed (m/s) (1993-1996)	16.5	19.3	19.1	19.9	18.5	17.8	19.2	20.5	16.8	19.1	16.7	19.8	20.5
Direction (deg) (1993-1996)	320	182	171	195	163	356	85	137	164	335	335	167	354
Peak 3s Gust (m/s) (1993-1996)	20.2	24.7	22.7	25.4	23.6	26.7	23.2	25.1	20.1	23.0	19.2	23.2	26.7

Source: CRWMS M&O 1997 [DIRS 100117], Table A-9

NOTES: [a] Values are derived from 1-s data averaged over 1 min.
          [b] Values are derived from 1-s data averaged over 1 hr.
          [c] A continuous running period that may encompass more than one calendar day.
          PST = Pacific Standard Time.
          To convert in. to mm, multiply by 25.4.
          To convert m/s to mi/hr, multiply by 2.24.

Table 6-15. Yearly Climatological Data Summary

Parameter	Site 1	Site 2	Site 3	Site 4	Site 5	Site 6	Site 7	Site 8	Site 9
Temperature (°C)									
Extreme Maximum[a]	40.9	39.9	40.4	42.3	43.6	41.9	42.8	42.0	45.1
Mean Maximum[a]	22.0	19.8	20.9	21.5	24.1	21.3	24.0	23.4	25.9
Mean[b]	16.8	15.7	16.5	16.7	17.7	15.1	15.8	16.0	18.2
Mean Minimum[a]	11.5	12.0	11.8	11.8	11.2	8.3	6.6	7.9	10.0
Extreme Minimum[a]	-11.7	-12.5	-12.2	-12.6	-13.1	-9.9	-12.8	-9.9	-7.7
Number of Days									
Precipitation 0.01 in. or more	41.8	31.4	33.3	32.0	28.1	34.5	32.8	32.0	29.3
Temperature (Hourly Averaged) 32°C (90°F) and above	70.3	38.2	49.0	57.4	91.0	64.3	96.5	90.0	128.8
0°C (32°F) and below	29.6	25.4	23.0	18.9	22.6	45.3	63.0	46.3	31.3
Mean Relative Humidity (%)									
Hour 0400 (PST)[b]	33.7	30.7	34.5	33.1	34.6	43.8	47.5	44.3	40.7
Hour 1000[b]	27.6	27.9	28.3	28.1	25.7	29.3	27.2	26.8	25.8
Hour 1600[b]	21.4	22.0	22.9	21.6	19.0	23.4	20.4	20.3	18.3
Hour 2200[b]	28.5	27.0	29.6	28.3	29.5	37.1	38.5	36.1	33.0
Precipitation (in.)									
Max 1 hr total	0.66	0.50	0.57	0.42	0.50	0.44	0.59	0.43	0.32
Max 6 hr total	1.18	1.03	1.13	0.95	0.78	1.24	0.97	1.06	0.68
Max 24 hr total	1.39	1.78	1.89	1.86	1.63	2.14	2.15	2.43	0.97
Total	4.97	6.56	6.70	6.57	5.10	8.69	7.17	6.99	4.20
Wind									
Mean Speed (m/s)[b]	3.4	4.3	2.5	4.4	4.2	4.0	3.2	3.0	4.4
Fastest 1 min[b] Speed (m/s)	n/a	30.0	18.6	33.2	25.3	22.7	23.2	21.3	20.5
Direction (deg)	n/a	239	307	345	337	149	333	220	354
Peak 3s Gust (m/s)	n/a	38.2	26.2	37.2	30.4	28.8	27.7	27.6	26.7

DTN: M09811DEDCRMCR.000 [DIRS 148887]

Source: CRWMS M&O 1997 [DIRS 100117], Table A-10

NOTES: [a] Values are derived from 1-s data averaged over 1 min.
[b] Values are derived from 1-s data averaged over 1 hr.
Site information is listed on Figure 6-2.
n/a = no data available; To convert in. to mm, multiply by 25.4.
PST = Pacific Standard Time.
To convert m/s to mi/hr, multiply by 2.24.

Table 6-16. Climatological Summary for Austin and Battle Mountain Meteorological Stations

Station and Parameter	Jan.	Feb.	Mar.	Apr.	May	Jun.	Jul.	Aug.	Sep.	Oct.	Nov.	Dec.	Year
Austin, NV													
Temperature (°C)													
Extreme Maximum	18.3	21.1	23.3	28.3	32.8	36.1	40.6	37.8	36.1	30.0	23.9	21.1	40.6
Mean Maximum	4.9	6.7	9.1	13.6	18.7	24.7	30.6	29.5	24.5	17.8	9.9	5.9	16.4
Mean Minimum	-7.4	-5.9	-4.1	-0.8	3.2	7.4	12.1	11.3	7.1	2.1	-3.3	-6.4	1.3
Extreme Minimum	-31.7	-27.8	-21.1	-16.1	-11.1	-5.0	2.2	-1.1	-7.8	-16.7	-21.7	-28.9	-31.7
Precipitation (in.)													
Mean Monthly	1.18	1.15	1.61	1.62	1.53	0.97	0.56	0.61	0.60	0.96	1.03	1.20	13.51
Monthly Maximum	4.00	2.95	5.36	5.96	5.85	3.55	2.53	2.45	3.45	3.72	3.73	4.19	22.37
Maximum Daily	1.64	1.60	1.76	2.01	1.57	1.57	1.99	1.25	1.65	2.04	1.18	1.19	2.04
Snowfall (in.)													
Mean Monthly	0.92	0.06	0.00	0.00	0.00	0.00	0.00	0.00	0.00	0.00	0.11	0.05	1.13
Monthly Maximum	16.70	1.40	0.10	0.00	0.00	0.00	0.00	0.00	0.00	0.00	4.00	2.00	16.70
Daily Maximum	24.0	16.8	19.0	22.0	12.0	8.0	0.0	T	9.0	20.0	13.0	10.4	24.0
Battle Mountain, NV													
Temperature (°C)													
Extreme Maximum	19.4	22.2	26.7	32.2	36.1	40.0	42.8	41.1	38.9	33.9	26.7	19.4	42.8
Mean Maximum	4.8	8.8	12.2	17.3	22.7	28.1	33.9	32.8	27.5	20.2	10.9	5.4	18.9
Mean Minimum	-9.6	-6.1	-4.0	-1.2	3.3	7.1	10.4	8.7	3.8	-1.3	-5.6	-9.0	-0.2
Extreme Minimum	-37.2	-31.7	-19.4	-13.3	-10.0	-4.4	-0.6	-2.2	-11.7	-14.4	-22.8	-39.4	-39.4
Precipitation (in.)													
Mean Monthly	0.65	0.58	0.69	0.78	1.01	0.88	0.28	0.32	0.51	0.64	0.68	0.75	7.60
Monthly Maximum	2.22	2.20	2.42	3.02	4.91	3.39	1.62	1.65	2.92	2.83	2.08	2.58	12.50
Maximum Daily	0.75	0.90	0.73	1.00	1.10	1.10	0.70	0.50	0.97	1.10	0.84	1.00	1.10
Snowfall (in.)													
Mean Monthly	7.72	3.09	1.16	0.91	0.12	0.00	0.00	0.00	0.00	0.12	2.35	3.35	18.82
Monthly Maximum	33.00	13.00	5.00	5.00	2.00	0.00	0.00	0.00	0.00	2.00	18.00	10.00	54.00
Daily Maximum	7.8	10.0	7.0	12.0	3.9	T	0.0	0.0	T	3.0	6.0	12.4	12.4

DTN: M09811DEDCRMCR.000 [DIRS 148887]

Source: CRWMS M&O 1997 [DIRS 100117], Table A-11

NOTES: To convert in. to mm, multiply by 25.4.
T = trace amount.

Table 6-17. Climatological Summary for Caliente and Desert Rock Meteorological Stations

Station and Parameter	Jan.	Feb.	Mar.	Apr.	May	Jun.	Jul.	Aug.	Sep.	Oct.	Nov.	Dec.	Year
Caliente, NV													
Temperature (°C)													
Extreme Maximum	21.7	27.2	32.2	33.3	36.7	42.8	42.8	42.2	41.1	34.4	26.7	21.7	42.8
Mean Maximum	7.8	11.3	15.6	20.7	25.8	31.5	35.3	33.9	29.8	23.1	14.8	9.0	21.6
Mean Minimum	-8.2	-5.3	-2.3	1.2	5.5	9.6	13.6	12.9	7.7	1.8	-4.0	-7.3	2.2
Extreme Minimum	-35.0	-28.3	-16.7	-9.4	-4.4	0.6	4.4	1.7	-3.9	-12.2	-17.8	-27.8	-35.0
Precipitation (in.)													
Mean Monthly	0.86	0.84	1.08	0.71	0.61	0.34	0.80	0.96	0.63	0.76	0.76	0.70	8.82
Monthly Maximum	3.47	3.15	4.59	3.71	2.27	1.95	5.36	4.18	3.14	4.29	3.38	3.76	18.73
Maximum Daily	1.41	1.90	1.35	1.15	1.48	0.99	1.51	1.70	1.56	2.13	1.80	2.11	2.13
Snowfall (in.)													
Mean Monthly	3.96	2.42	1.14	0.11	0.01	0.00	0.00	0.00	0.03	0.07	0.83	2.85	13.80
Monthly Maximum	31.00	27.60	9.50	3.70	0.50	0.00	0.00	0.00	2.00	4.00	12.00	20.00	46.60
Daily Maximum	12.0	14.0	8.0	2.5	0.5	0.0	0.0	0.0	2.0	4.0	5.0	11.0	14.0
Mercury Desert Rock Airport, NV													
Temperature (°C)													
Extreme Maximum	22.8	28.3	28.9	33.9	38.9	43.9	44.4	42.8	39.4	35.6	29.4	22.2	44.4
Mean Maximum	12.4	15.5	18.8	23.9	28.2	33.9	36.9	36.1	31.8	25.6	16.8	12.3	24.6
Mean Minimum	0.4	2.6	5.2	8.8	13.0	17.9	21.3	20.7	16.1	10.3	3.4	-0.2	10.2
Extreme Minimum	-8.9	-11.7	-5.0	-1.1	0.6	4.4	11.7	12.8	4.4	0.0	-7.2	-14.4	-14.4
Precipitation (in.)													
Mean Monthly	1.02	0.74	0.67	0.28	0.34	0.08	0.76	0.71	0.25	0.40	0.52	0.65	5.50
Monthly Maximum	3.37	3.29	2.39	1.50	1.94	0.41	3.64	3.14	1.43	1.65	1.76	1.91	8.56
Maximum Daily	0.87	1.15	0.65	0.72	0.92	0.39	2.03	1.10	1.25	0.67	1.48	0.91	2.03
Snowfall (in.)													
Mean Monthly	1.33	0.77	0.15	0.00	0.00	0.00	0.00	0.00	0.00	0.00	0.23	0.83	2.86
Monthly Maximum	5.10	6.00	0.50	0.00	0.00	0.00	0.00	0.00	0.00	0.00	1.50	6.60	8.80
Daily Maximum	4.3	6.0	0.5	0.0	T	0.0	0.0	0.0	0.0	0.0	1.5	4.0	6.0

DTN: M09811DEDCRMCR.000 [DIRS 148887]

Source: CRWMS M&O 1997 [DIRS 100117], Table A-12

NOTES: To convert in. to mm, multiply by 25.4.
    T = trace amount.

Table 6-18. Climatological Summary for Elko and Ely Meteorological Stations

Station and Parameter	Jan.	Feb.	Mar.	Apr.	May	Jun.	Jul.	Aug.	Sep.	Oct.	Nov.	Dec.	Year
Elko Municipal Airport, NV													
Temperature (°C)													
Extreme Maximum	17.8	21.1	25.0	30.0	33.3	40.0	41.7	41.7	37.2	31.1	25.6	18.3	41.7
Mean Maximum	2.2	5.5	9.9	15.3	20.6	26.3	32.5	31.4	26.1	18.8	9.4	3.5	16.8
Mean Minimum	-11.4	-7.9	-4.6	-1.7	2.2	5.8	9.4	8.1	2.9	-2.0	-6.6	-10.2	-1.3
Extreme Minimum	-41.7	-38.3	-22.8	-18.9	-12.2	-5.0	-1.1	-6.7	-12.8	-16.1	-24.4	-38.9	-41.7
Precipitation (in.)													
Mean Monthly	1.09	0.81	0.90	0.81	1.00	0.80	0.35	0.44	0.48	0.69	0.99	1.02	9.38
Monthly Maximum	3.35	2.49	2.39	2.17	4.09	2.61	2.35	4.61	3.22	2.76	2.80	4.21	18.34
Maximum Daily	1.25	0.89	0.79	1.07	1.73	1.05	1.04	4.13	2.25	1.31	1.33	1.60	4.13
Snowfall (in.)													
Mean Monthly	10.05	6.09	5.07	2.29	0.78	0.00	0.00	0.00	0.06	0.70	4.74	7.85	37.75
Monthly Maximum	29.20	26.10	23.20	15.60	11.30	0.00	0.00	0.00	2.00	5.60	20.00	33.20	85.40
Daily Maximum	16.3	9.0	8.2	9.3	7.8	T	T	T	2.0	5.2	10.6	9.3	16.3
Ely Yelland Field, NV													
Temperature (°C)													
Extreme Maximum	20.0	19.4	22.8	27.8	31.7	37.2	37.8	36.1	33.9	28.9	23.9	19.4	37.8
Mean Maximum	3.8	6.1	9.0	14.2	19.3	25.6	30.4	29.2	24.4	17.6	9.6	4.8	16.3
Mean Minimum	-12.7	-9.7	-6.4	-3.3	0.8	4.6	8.7	8.1	3.0	-2.2	-7.6	-11.8	-2.3
Extreme Minimum	-32.8	-34.4	-25.0	-20.6	-13.9	-7.8	-1.1	-4.4	-9.4	-19.4	-26.1	-33.9	-34.4
Precipitation (in.)													
Mean Monthly	0.74	0.66	0.99	0.89	1.17	0.74	0.63	0.75	0.83	0.75	0.62	0.68	9.48
Monthly Maximum	2.08	2.19	2.40	3.41	3.26	3.53	2.30	2.51	4.99	3.67	1.82	2.11	15.98
Maximum Daily	0.88	1.38	0.69	0.80	1.37	1.44	1.20	1.01	2.52	1.09	1.17	0.84	2.52
Snowfall (in.)													
Mean Monthly	9.43	7.27	9.35	6.12	2.67	0.14	0.00	0.00	0.33	2.34	5.31	7.69	50.55
Monthly Maximum	24.80	20.00	25.30	24.50	12.10	1.70	0.00	0.00	6.30	12.10	17.30	22.30	101.30
Daily Maximum	0.88	1.38	0.69	0.80	1.37	1.44	1.20	1.01	2.52	1.09	1.17	0.84	2.52

DTN: M09811DEDCRMCR.000 [DIRS 148887]

Source: CRWMS M&O 1997 [DIRS 100117], Table A-13

NOTES: To convert in. to mm, multiply by 25.4.
    T = trace amount.

Table 6-19. Climatological Summary for Las Vegas and Tonopah Meteorological Stations

Station and Parameter	Jan.	Feb.	Mar.	Apr.	May	Jun.	Jul.	Aug.	Sep.	Oct.	Nov.	Dec.	Year
Las Vegas McCarran International Airport, NV													
Temperature (°C)													
Extreme Maximum	25.0	30.6	32.8	37.2	42.8	46.1	46.7	46.7	45.0	39.4	30.6	25.0	46.7
Mean Maximum	13.4	16.9	20.4	25.6	30.8	36.9	40.1	38.8	34.7	27.4	19.0	13.9	26.6
Mean Minimum	0.9	3.6	6.4	10.6	15.5	20.7	24.6	23.6	19.0	12.2	5.4	1.2	12.0
Extreme Minimum	-13.3	-8.9	-5.0	-0.6	4.4	8.9	15.6	13.3	7.8	-3.3	-6.1	-11.7	-13.3
Precipitation (in.)													
Mean Monthly	0.58	0.47	0.48	0.18	0.20	0.10	0.42	0.48	0.25	0.21	0.40	0.37	4.14
Monthly Maximum	3.00	2.52	4.80	2.44	0.96	0.97	2.48	2.59	1.58	1.22	2.22	1.71	9.88
Maximum Daily	0.74	1.29	1.20	0.97	0.83	0.82	1.36	2.58	1.07	1.05	1.09	0.95	2.58
Snowfall (in.)													
Mean Monthly	0.92	0.06	0.00	0.00	0.00	0.00	0.00	0.00	0.00	0.00	0.11	0.05	1.13
Monthly Maximum	16.70	1.40	0.10	0.00	0.00	0.00	0.00	0.00	0.00	0.00	4.00	2.00	16.70
Daily Maximum	7.4	1.4	0.1	T	T	T	0.0	T	0.0	T	3.0	2.0	7.4
Tonopah Airport, NV													
Temperature (°C)													
Extreme Maximum	19.4	23.9	25.6	31.1	34.4	38.9	40.0	39.4	35.6	32.2	25.0	21.1	40.0
Mean Maximum	6.4	9.6	12.9	17.4	22.7	28.9	32.8	31.6	26.8	20.3	12.1	7.3	19.2
Mean Minimum	-7.6	-4.7	-2.3	0.7	5.5	10.3	13.4	12.5	8.3	2.8	-3.3	-7.0	2.4
Extreme Minimum	-26.1	-22.8	-15.6	-12.8	-7.2	-2.8	4.4	2.8	-3.9	-10.6	-15.6	-25.0	-26.1
Precipitation (in.)													
Mean Monthly	0.40	0.45	0.53	0.38	0.61	0.30	0.55	0.53	0.46	0.37	0.44	0.27	5.33
Monthly Maximum	2.25	2.68	2.38	2.13	2.03	1.67	2.49	2.65	2.05	2.16	2.68	1.02	10.64
Maximum Daily	0.59	0.55	0.67	0.85	0.96	1.06	1.23	1.36	1.13	1.14	0.67	0.62	1.36
Snowfall (in.)													
Mean Monthly	3.22	2.71	2.43	1.14	0.42	0.00	0.00	0.00	0.01	0.07	1.50	1.85	13.53
Monthly Maximum	16.50	13.60	16.40	7.50	5.00	0.00	0.00	0.00	0.40	1.50	9.60	17.00	31.30
Daily Maximum	7.1	9.7	9.0	7.2	5.0	T	0.0	T	0.4	1.0	8.0	7.6	9.7

DTN: M09811DEDCRMCR.000 [DIRS 148887]

Source: CRWMS M&O 1997 [DIRS 100117], Table A-14

NOTES: To convert in. to mm, multiply by 25.4.
T = trace amount.

Table 6-20. Annual Precipitation for National Weather Service Stations: 1921 through 1947

Year	Amargosa Farms Garey	Austin	Beatty	Beatty 8N	Caliente	Desert National Wildlife Range	Elko Municipal Airport	Ely Yelland Field	Indian Springs	Las Vegas McCarran International	Mercury Desert Rock Airport	Pahranagat Wildlife Refuge	Pioche	Ruby Lake	Snowball Ranch	Tonopah	Tonopah Airport	Winnemucca Municipal Airport
1921	–	9.21	–	–	–	–	–	–	–	–	–	–	–	–	–	–	–	–
1922	–	17.86	–	–	–	–	–	–	–	–	–	–	–	–	–	–	–	–
1923	–	10.15	–	–	–	–	–	–	–	–	–	–	–	–	–	–	–	–
1924	–	9.14	–	–	–	–	–	–	–	–	–	–	–	–	–	–	–	–
1925	–	19.08	–	–	–	–	–	–	–	–	–	–	–	–	–	–	–	–
1926	–	4.57	–	–	–	–	–	–	–	–	–	–	–	–	–	–	–	–
1927	–	10.64	–	–	–	–	–	–	–	–	–	–	–	–	–	–	–	–
1928	–	10.44	–	–	–	–	5.17	–	–	–	–	–	–	–	–	2.63	–	5.52
1929	–	10.65	–	–	1.84	–	6.84	–	–	–	–	–	–	–	–	3.36	–	3.85
1930	–	16.67	–	–	3.56	–	13.30	–	–	–	–	–	–	–	–	4.49	–	9.60
1931	–	11.77	–	–	9.49	–	6.07	–	–	–	–	–	–	–	–	6.53	–	4.87
1932	–	12.43	–	–	11.61	–	12.23	–	–	–	–	–	–	–	–	3.88	–	8.70
1933	–	10.16	–	–	8.16	–	6.65	–	–	–	–	–	–	–	–	2.19	–	5.67
1934	–	14.63	–	–	7.14	–	6.72	–	–	–	–	–	–	–	–	3.48	–	9.07
1935	–	16.26	–	–	9.43	–	8.23	–	–	–	–	–	–	–	–	3.40	–	10.59
1936	–	14.91	–	–	11.60	–	10.52	–	–	–	–	–	–	–	–	4.62	–	8.76
1937	–	7.03	–	–	6.84	–	7.12	–	–	–	–	–	–	–	–	4.39	–	9.35
1938	–	16.51	–	–	4.43	–	9.75	–	–	–	–	–	–	–	–	7.71	–	11.98
1939	–	10.46	–	–	9.41	–	7.78	–	–	–	–	–	–	–	–	6.25	–	7.79
1940	–	14.51	–	–	7.49	–	10.76	–	–	–	–	–	–	–	–	4.59	–	11.69
1941	–	19.36	–	–	18.73	–	16.24	–	–	–	–	–	–	–	–	6.29	–	13.24
1942	–	10.81	–	–	6.63	–	12.23	–	–	–	–	–	–	–	–	2.19	–	10.07
1943	–	11.89	–	–	11.70	–	9.58	–	–	–	–	–	–	–	–	6.56	–	6.60
1944	–	10.68	–	–	7.96	–	9.59	–	–	–	–	–	–	–	–	3.49	–	10.34
1945	–	16.31	–	–	11.60	–	12.62	–	–	–	–	–	–	–	–	5.77	–	14.54
1946	–	16.93	–	–	12.36	–	10.18	–	–	–	–	–	–	–	–	10.27	–	10.65
1947	–	6.40	–	–	7.47	–	7.25	–	–	–	–	–	–	–	–	3.66	–	6.24

DTN: M09811DEDCRMCR.000 [DIRS 148887]

Source: CRWMS M&O 1997 [DIRS 100117], Table A-15

NOTE: A dash for a given station and year signifies no data are available.

Table 6-21. Annual Precipitation for National Weather Service Stations: 1948 through 2002

Year	Amargosa Farms Garey	Austin	Beatty	Beatty 8N	Caliente	Desert National Wildlife Range	Elko Municipal Airport	Ely Yelland Field	Indian Springs	Las Vegas McCarran International Airport	Mercury Desert Rock Airport	Pahranagat Wildlife Refuge	Pioche	Ruby Lake	Snowball Ranch	Tonopah	Tonopah Airport	Winnemucca Municipal Airport
1948	–	11.90	–	–	5.23	0.70	7.41	–	–	–	–	–	3.86	4.86	–	6.11	–	7.52
1949	–	9.10	5.43	–	10.03	6.28	7.10	6.88	7.04	4.42	–	–	15.36	10.73	–	5.85	–	6.23
1950	–	10.12	2.05	–	2.92	1.41	14.60	6.03	0.66	2.34	–	–	7.11	18.18	–	5.08	–	10.61
1951	–	11.38	2.60	–	10.15	4.21	7.97	7.29	1.84	2.81	–	–	13.98	12.84	–	4.99	–	8.63
1952	–	10.34	8.36	–	11.52	6.54	7.28	10.98	3.26	5.08	–	–	16.14	10.49	–	7.89	–	10.33
1953	–	6.73	0.69	–	4.66	1.00	6.85	5.22	1.41	0.56	–	–	7.26	10.18	–	2.91	–	6.28
1954	–	9.92	6.44	–	9.31	3.05	6.58	7.89	2.92	4.71	–	–	13.28	8.20	–	–	–	3.13
1955	–	11.02	4.31	–	7.13	3.64	9.52	8.76	1.73	5.40	–	–	14.09	11.92	–	–	4.13	7.28
1956	–	12.30	1.67	–	4.77	0.85	10.04	6.36	1.86	2.04	–	–	3.81	12.98	–	–	2.51	7.29
1957	–	12.70	5.91	–	9.11	5.87	10.10	9.14	4.70	4.98	–	–	17.14	14.54	–	–	5.10	10.02
1958	–	8.93	4.23	–	8.13	5.86	6.40	7.58	4.38	4.52	–	–	15.51	9.39	–	–	3.38	9.61
1959	–	5.91	3.39	–	4.83	3.94	5.51	5.97	3.50	4.17	–	–	10.41	9.76	–	–	2.37	4.07
1960	–	8.49	5.12	–	9.77	4.20	7.84	7.89	5.14	4.40	–	–	12.85	13.81	–	–	3.69	8.11
1961	–	9.38	3.29	–	8.80	5.76	7.60	7.29	2.75	3.17	–	–	9.62	10.98	–	–	2.90	7.79
1962	–	6.96	2.67	–	4.76	1.79	8.24	7.36	2.02	1.45	–	–	7.53	12.20	–	–	5.84	6.83
1963	–	16.61	5.00	–	10.15	4.27	15.03	11.14	2.91	3.87	–	–	12.80	14.35	–	–	6.03	10.86
1964	–	15.62	2.11	–	6.58	1.11	12.14	12.70	–	1.12	–	–	7.88	16.25	–	–	3.88	10.47

Table 6-21. Annual Precipitation for National Weather Service Stations: 1948 through 2002 (Continued)

Year	Amargosa Farms Garey	Austin	Beatty	Beatty 8N	Caliente	Desert National Wildlife Range	Elko Municipal Airport	Ely Yelland Field	Indian Springs	Las Vegas McCarran International Airport	Mercury Desert Rock Airport	Pahranagat Wildlife Refuge	Pioche	Ruby Lake	Snowball Ranch	Tonopah	Tonopah Airport	Winnemucca Municipal Airport
1965	–	19.28	7.33	–	10.61	7.41	11.17	10.77	–	7.96	–	7.80	17.99	13.63	–	–	5.58	7.75
1966	1.28	7.85	3.22	–	6.15	2.34	6.50	6.08	–	1.91	–	3.93	16.04	7.46	–	–	3.00	4.51
1967	1.42	10.22	4.88	–	12.86	4.93	8.62	14.73	–	5.54	–	8.83	14.46	12.14	11.20	–	7.68	7.70
1968	3.00	12.23	4.45	–	6.79	1.47	14.63	10.03	–	1.11	–	6.60	12.38	11.97	8.35	–	6.56	8.48
1969	6.95	15.16	6.53	–	9.76	7.53	9.71	11.45	–	5.09	–	8.35	18.66	15.81	11.14	–	5.16	9.67
1970	–	13.95	3.00	–	8.39	2.60	14.19*	10.69	–	4.29	–	4.41	18.07	13.97	8.37	–	3.11	9.09
1971	–	20.71	1.98	–	8.75	1.50	13.67	9.42	–	2.54	–	3.93	12.88	14.61	8.08	–	3.36	9.17
1972	–	11.85	–	–	7.20	6.57	8.47	6.59	–	4.85	–	5.36	8.99	9.89	6.02	–	5.59	6.62
1973	–	15.71	–	6.72	9.75	4.58	9.10	11.23	–	4.68	–	7.14	12.51	13.07	7.44	–	5.11	7.92
1974	–	10.92	–	5.80	8.01	4.77	4.77	4.22	–	4.52	–	5.45	10.28	5.94	5.32	–	4.43	6.33
1975	–	20.35	–	4.84	7.56	5.15	11.34	9.77	–	3.47	–	5.01	12.22	15.95	8.06	–	4.38	8.59
1976	–	13.58	–	7.82	10.74	6.35	7.10	8.25	–	6.77	–	8.16	11.78	10.24	10.93	–	7.14	7.31
1977	–	12.62	–	6.44	8.51	3.03	6.46	9.19	–	3.97	–	4.03	9.38	12.52	10.43	–	7.34	8.08
1978	–	19.42	–	10.80	16.83	6.88	11.14	12.47	–	7.65	–	9.46	27.29	17.84	11.63	–	10.64	8. 10
1979	2. 16	12.60	–	4.71	9.31	1.95	7.74	7.39	–	6.79	–	0.00	10.60	14.70	7.47	–	5.94	8.73
1980	6.24	12.67	–	6.01	11.67	4.54	12.81	12.78	–	5.63	–	5.58	18.38	19.41	13.16	–	4.18	7.36
1981	3.20	11.84	–	3.73	9.60	3.26	8.78	10.29	–	3.14	–	6.58	11.81	11.22	6.87	–	9.21	8.44
1982	4.30	16.82	–	6.07	12.90	4.87	13.72	15.53*	–	3.99	–	9.87	17.50	16.87	10.57	–	6.19	9.04
1983	10.37	22.37	–	11.49	12.21	6.34	18.34	14.84	–	4.86	–	11.54	18.78	23.86	14.24	–	9.64	14.47
1984	8.80	17.72	–	5.43*	13.11	10.38	10.36	14.84	–	6.85	–	8.86	9.40	17.78	8.27	–	6.95	12.87

Table 6-21. Annual Precipitation for National Weather Service Stations: 1948 through 2002 (Continued)

Year	Amargosa Farms Garey	Austin	Beatty	Beatty 8N	Caliente	Desert National Wildlife Range	Elko Municipal Airport	Ely Yelland Field	Indian Springs	Las Vegas McCarran International Airport	Mercury Desert Rock Airport	Pahranagat Wildlife Refuge	Pioche	Ruby Lake	Snowball Ranch	Tonopah	Tonopah Airport	Winnemucca Municipal Airport
1985	1.00	15.83	–	2.79	7.89	2.58	7.30	9.89	–	1.27	4.77	4.84	12.22	10.84	6.98	–	5.96	7.01
1986	3.75	5.98	–	5.22	7.94	4.66	6.08	8.60	–	2.65	6.92	4.37	11.36	12.00	6.35	–	2.53	5.51
1987	8.18	18.98	–	7.38	12.08	7.21	8.62	12.30	–	6.59	8.56	7.71	17.42	11.20	10.35	–	8.33	9.04
1988	5.59	16.53	–	6.21	6.22	3.12	6.72	8.66	–	2.29	5.84	5.32	7.92*	9.34	10.21	–	5.67	6.73
1989	0.72	10.56*	–	2.43	5.20	1.51	7.88	6.60	–	2.11	1.25	2.23	7.31	10.28	6.18	–	3.00	5.56
1990	2.58	14.00*	–	4.92	8.93	2.82	9.43	8.76	–	3.75	4.88	5.70	–	9.78	7.25	–	5.18	6.37
1991	3.40	14.01	–	5.15	7.49	4.07	7.85	9.98	–	4.06	5.55	5.52	–	11.89	10.14	–	5.79	7.80
1992	6.09	8.83	–	7.37	12.00	8.85	7.56	9.78	–	9.88	6.35	9.66	15.75	10.62	7.30	–	3.30	4.14
1993	5.68	8.00	–	5.71	11.83	4.91	7.66	10.06	–	5.05	7.55	6.82	17.91	13.67	6.66	–	4.45	7.27
1994	2.27	13.47	–	3.44	9.00	3.89	8.32	9.22	–	2.56	3.28	6.27	14.36	12.02	8.76	–	4.10	7.58
1995	5.27	15.42	–	8.45	7.98	4.53	11.46	12.10	–	3.69	7.90	7.53	15.27	18.70	9.75	–	6.75	9.82
1996	2.83	6.44	–	5.60	6.65	2.74	15.24	7.31	–	2.76	–	3.33	15.80	21.48	8.50	–	3.83	10.70
1997	3.33	6.02	–	6.64	7.30	4.40	10.99	9.50	–	3.63	–	5.55	13.19	16.40	9.37	–	4.58	7.88
1998	8.71	22.38	–	12.62	14.13	9.23	12.43	12.23	–	7.35	–	7.71*	26.35	18.03*	11.36	–	9.42	15.61
1999	2.35	6.31	–	4.69*	6.30	3.66	7.55	6.61	–	3.73	–	3.97	8.63	10.20	9.11	–	4.53*	5.33
2000	2.67	10.94	–	7.18	13.55	3.33	8.95	10.12	–	3.47	3.73	5.81*	11.45*	8.34	6.65*	–	6.93	10.11
2001	3.76*	12.30*	–	7.30*	5.95	4.12	8.49	6.70	–	3.94	5.04	–	11.68*	11.19	10.12	–	4.46	4.84
2002	0.47	6.47	–	0.46	2.47	0.69	7.48	4.52	–	1.44	1.99	–	5.52	5.50	–	–	1.42	6.07

DTNs: M09811DEDCRMCR.000 [DIRS 148887]; UN0201SPA021SS.007 [DIRS 161588]

Sources: CRWMS M&O 1997 [DIRS 100117], Table A-16 for 1948-1995

NOTES: A dash for a given station and year signifies no data are available, or record is missing more than 3 months of data.
*Indicates one to three months of data missing.

Table 6-22. American Society of Heating, Refrigeration, and Air-Conditioning Engineers Summary Table for the Radiological and Environmental Field Programs Department Meteorological Sites

Station	Latitude	Longitude	Elev (m)	Winter, °C Design Dry Bulb[a]		Summer, °C Design DryBulb/Mean Coincident Wet Bulb[b]			Mean Daily Range[c]	Design Wet Bulb[d]			Prevailing Winds, mean m/s[e] Winter	Summer	Temp, °C Median of Annual Extreme[f]	
				99%	97.5%	1%	2.5%	5%		1%	2.5%	5%			Max	Min
Site 1 (Nevada Test Site 60)	36°50'34"N	116°25'50"W	1143	-5	-3	37/16	36/16	35/15	12	18	17	16	NNW 3	S	39	-6
Site 2 (Yucca Mountain)	36°51'19"N	116°27'56"W	1478	-6	-4	35/13	34/13	33/13	9	17	16	15	NE 6	WSW	36	-7
Site 3 (Coyote Wash)	36°51'17"N	116°27'06"W	1279	-5	-3	36/15	35/15	34/15	10	19	18	17	WNW 3	SSE	38	-7
Site 4 (Alice Hill)	36°51'51"N	116°24'15"W	1234	-5	-3	37/16	36/16	34/15	10	18	18	17	NNE 5	S	38	-6
Site 5 (Fortymile Wash)	36°45'52"N	116°23'26"W	953	-4	-2	39/15	38/15	37/15	14	20	19	18	N 4	S	41	-9
Site 6 (WT6)	36°53'40"N	116°26'45"W	1315	-4	-2	36/15	35/14	34/14	14	18	17	16	NW 3	SSE	38	-6
Site 7 (Sever Wash)	36°50'49"N	116°24'28"W	1081	-6	-5	39/15	38/15	37/15	18	19	18	17	WNW 1	S	41	-10
Site 8 (Knothead Gap)	36°49'42"N	116°25'35"W	1131	-5	-4	39/15	38/14	36/14	16	18	18	17	NNW 1	S	41	-8
Site 9 (Gate 510)	36°40'17"N	116°24'17"W	838	-3	-2	42/16	40/16	39/16	17	20	19	18	NNE 4	SW	44	-6

DTN: M09811DEDCRMCR.000 [DIRS 148887]

Source: CRWMS M&O 1997 [DIRS 100117], Table A-17

NOTES: [a] = Indicated hourly values are those that have been equaled or exceeded by 99 percent and 97.5 percent of the total hours in December, January, and February.

[b] = Indicated hourly values are those that have been equaled or exceeded by 1 percent, 2.5 percent, and 5 percent of the total hours in June, July, August, and September. The listed wet-bulb temperature is the mean of all wet-bulb temperatures coincident with those dry-bulb temperatures exceeding the given levels (the value preceding the solidus (/)).

[c] = Mean Daily Range is the difference between the average daily maximum and average daily minimum temperatures in degrees Celsius for the warmest month.

[d] = The wet-bulb temperatures in degrees Celsius that have been equaled or exceeded by 1 percent, 2.5 percent, and 5 percent of the total hours in June, July, August, and September.

[e] = The wind direction occurring coincidentally with the 97.5 percent dry-bulb temperature in December, January, and February (winter), the wind direction occurring coincidentally with the 2.5 percent dry-bulb temperature in June, July, August, and September (summer), and the mean wind speed in meters per second occurring coincidentally with the 97.5 percent dry-bulb temperature in December, January, and February.

[f] = The median of the annual extreme maximum and minimum temperature in degrees Celsius.

To convert m to ft, multiply by 3.28.

To convert m/s to mi/hr, multiply by 2.24.

Table 6-23. Desert Rock, Nevada, Upper Air Statistics

| Desert Rock Upper Air Statistics. Surface elevation 1,007 m. May 1978–Dec 1997. | | | | | | | | | | | | |
| Pressure (mb) | January | | | | July | | | | Annual | | | |
	Height (m)	RH (%)	Tdew (°C)	Wind (m/s)	Height (m)	RH (%)	Tdew (°C)	Wind (m/s)	Height (m)	RH (%)	Tdew (°C)	Wind (m/s)
900	1059	38.4	-7.2	1.7	1018	26.5	4.6	1.7	1,039	31.3	-3.2	1.7
850	1506	42.8	-7.5	2.2	1503	23.8	3.5	2.7	1,494	31.0	-3.0	2.6
800	1999	45.6	-9.6	3.0	2034	25.2	0.6	2.9	2,005	33.8	-5.3	3.0
750	2519	44.6	-12.4	3.7	2590	28.4	-1.9	2.8	2,540	36.6	-7.8	3.2
700	3069	41.9	-15.6	4.3	3175	32.4	-4.4	2.8	3,105	38.2	-10.7	3.5

DTN: MO0302UCC021SS.009 [DIRS 163595]

NOTE: By worldwide convention, measurements are made at specified pressure levels. Sea level pressure averages 1013.246 millibars (mb). The height above sea level of these pressure levels varies seasonally. Mean monthly relative humidity, absolute humidity (as indicated by dew point temperature), and wind speed are shown for these heights above the ground.

Table 6-24. Types of Monitoring Equipment Installed in the Field to Measure Various Environmental Parameters

Parameter	Measurement or Calculation
Wind speed	Cup anemometer with photochopper
Wind direction	Vane, with potentiometer at Sites 2 through 9 and resolver at Site 1
Temperature and Delta-temperature	Mechanically aspirated shields with thermistor
Relative humidity	Capacitance sensors at Sites 1 through 9
Barometric pressure	Aneroid wafer
Precipitation	Tipping bucket, 8-inch orifice, 0. 01-inch tip
Solar radiation	Pyranometer
Vertical wind speed	Propeller anemometer with optical chopper

Source: Updated from CRWMS M&O 1999 [DIRS 115672], Table 1-3, p. 1-7

Table 6-25. Summary of Maximum Wind Speeds (m/s)

Location	Maximum Recorded Daily 1-Minute Wind Speeds (m/s) [years covered]	Maximum Recorded 1-Second Gust Wind Speeds (m/s) [years covered]
Site 1 (10 m-agl)	23.26 [1996]	28.29 [1996]
Site 1 (60 m-agl)	27.89 [1996]	34.34 [1996]
Site 2	29.95 [1994-1996]	40.22 [1993-1996]
Site 3	18.6 [1994-1996]	28.37 [1993-1996]
Site 4	33.16 [1994-1996]	40.22 [1993-1996]
Site 5	25.26 [1994-1996]	30.86 [1993-1996]
Site 6	22.65 [1994-1996]	31.29 [1993-1996]
Site 7	23.17 [1994-1996]	28.33 [1993-1996]
Site 8	21.3 [1994-1996]	29.22 [1993-1996]
Site 9	20.5 [1994-1996]	26.77 [1993-1996]

Source: CRWMS M&O 1997 [DIRS 100117], Table 4-4, p. 4-22, and Table 4-6, p. 4-25

Table 6-26. Mean Daily Solar Radiation

Parameter (MJ/m^2/d)[a]	Jan.	Feb.	Mar.	Apr.	May	Jun.	Jul.	Aug.	Sep.	Oct.	Nov.	Dec.	Year
Site 1													
1996[b]	10.8	12.4	20.0	26.0	27.6	31.0	28.3	26.3	22.5	16.1	11.2	8.3	20.0
1997[c]	9.0	14.9	21.1	24.2	26.6	28.5	29.4	26.5	20.9	18.0	10.5	9.6	19.9
Period 1992-1997 mean daily[d]	9.5	13.6	18.4	23.8	26.0	28.7	28.5	26.2	20.8	16.8	11.4	9.1	19.4
Period 1992-1997 mean monthly[d]	294.5	383.2	546.7	712.8	807.3	861.2	816.0	812.9	623.4	520.0	340.1	283.3	583.4
Site 2													
1996[b]	11.6	12.8	21.2	26.6	27.6	31.8	29.3	27.3	23.3	16.5	11.4	8.2	20.6
1997[c]	9.2	15.3	21.6	25.0	28.0	29.4	30.4	27.2	22.2	18.7	11.1	10.0	20.7
Period 1992-1997 mean daily[d]	9.6	14.2	19.7	24.5	26.9	30.6	30.0	27.1	23.0	17.4	12.1	9.5	20.4
Period 1992-1997 mean monthly[d]	298.6	402.0	611.3	735.4	834.7	918.1	930.7	840.4	690.7	538.9	362.2	293.5	621.4
Site 3													
1996[b]	10.8	12.4	20.0	26.0	27.3	31.7	29.1	26.8	22.7	16.1	11.0	7.8	20.1
1997[c]	8.9	15.0	21.0	24.4	27.4	28.8	29.6	26.4	21.3	18.0	10.5	9.7	20.1
Period 1992-1997 mean daily[d]	9.3	13.8	19.1	23.7	26.1	30.0	29.6	26.5	22.2	16.9	11.5	9.1	19.8
Period 1992-1997 mean monthly[d]	288.3	389.4	591.2	704.9	808.6	901.1	917.7	822.2	666.6	523.6	346.0	278.9	603.2
Site 4													
1996[b]	11.1	13.0	20.8	26.7	27.5	31.9	29.0	27.4	23.3	16.8	12.2	8.4	20.7
1997[c]	9.3	15.4	21.7	24.4	28.0	29.1	29.8	26.9	21.7	18.6	10.8	9.9	20.5
Period 1992-1997 mean daily[d]	9.7	14.3	19.7	24.1	26.8	30.3	29.7	26.8	22.7	17.4	11.9	9.4	20.2
Period 1992-1997 mean monthly[d]	300.1	402.7	610.2	717.9	831.9	907.5	919.3	831.9	681.3	540.9	356.7	292.1	616.0
Site 5													
1996[b]	11.2	13.0	20.9	26.1	27.7	31.8	29.5	27.1	23.2	16.5	11.7	8.8	20.6
1997[c]	9.6	15.2	21.1	24.9	28.3	29.2	29.8	26.6	21.9	18.4	11.0	9.6	20.5
Period 1992-1997 mean daily[d]	9.9	14.1	19.7	24.6	26.7	30.4	29.8	26.7	22.8	17.3	12.0	9.6	20.3
Period 1992-1997 mean monthly[d]	306.8	385.4	610.1	736.9	828.0	910.9	925.2	828.4	648.5	537.2	361.4	296.2	614.6

Table 6-26. Mean Daily Solar Radiation (Continued)

Parameter (MJ/m²/d)[a]	Jan.	Feb.	Mar.	Apr.	May	Jun.	Jul.	Aug.	Sep.	Oct.	Nov.	Dec.	Year
Site 6													
1996[b]	10.6	12.5	20.0	26.1	27.4	31.6	28.7	26.9	22.8	16.2	11.2	8.0	20.2
1997[c]	8.9	15.2	21.3	24.8	27.2	29.1	29.8	26.7	21.3	18.0	10.7	9.6	20.2
Period 1992-1997 mean daily[d]	8. 9	13. 2	18. 6	24. 1	26. 7	29. 9	29. 7	26. 7	22. 4	16. 7	11. 8	9. 0	19. 8
Period 1992-1997 mean monthly[d]	274. 8	372. 6	577. 1	724. 4	827. 4	896. 4	920. 2	773. 7	570. 4	518. 9	353. 5	277. 9	590. 6
Site 7													
1996[b]	10. 9	12. 7	20. 1	26. 0	27. 3	31. 3	28. 9	26. 8	22. 6	16. 1	11. 1	8. 3	20. 2
1997[c]	9. 2	15. 2	21. 1	24. 4	27. 5	29. 1	29. 8	26. 7	21. 5	18. 0	10. 6	9. 6	20. 2
Period 1992-1997 mean daily[d]	9. 3	13. 5	18. 9	24. 3	26. 8	29. 7	29. 7	26. 7	22. 3	16. 9	12. 1	9. 3	20. 0
Period 1992-1997 mean monthly[d]	**283. 9**	**381. 4**	**584. 4**	**730.5**	**832.1**	**891.7**	**920.4**	**773.4**	**560.1**	**524.6**	**362.2**	**288.7**	**594.5**
Site 8													
1996[b]	10.9	12.7	20.0	26.3	27.7	31.6	29.0	26.9	22.8	16.6	11.2	8.3	20.3
1997[c]	9.1	15.3	21.2	24.4	27.6	28.9	29.8	26.7	21.6	18.1	10.9	9.8	20.3
Period 1992-1997 mean daily[d]	9.1	13.4	18.8	24.4	26.8	30.1	29.9	26.8	22.3	16.8	11.9	9.2	19.9
Period 1992-1997 mean monthly[d]	278.7	378.8	581.7	730.6	829.3	904.1	921.4	775.9	564.6	512.2	352.8	284.3	592.9
Site 9													
1996[b]	11.3	13.0	20.8	26.6	28.1	31.8	29.7	27.3	23.4	16.8	11.9	8.8	20.8
1997[c]	9.8	15.1	21.5	24.4	28.1	29.0	29.5	26.8	21.3	18.3	11.0	9.8	20.4
Period 1993-1997 mean daily[d]	9.5	13.9	19.4	24.6	27.5	29.9	29.4	27.0	22.6	17.4	11.9	9.6	20.2
Period 1993-1997 mean monthly[d]	295.4	391.4	602.9	739.1	851.4	892.5	906.0	838.5	641.8	539.2	357.6	296.2	612.7

DTN: M09811DEDCRMCR.000 [DIRS 148887]

Sources: CRWMS M&O 1999 [DIRS 115672], Appendix C, pp. C-1 to C-10[c]; CRWMS M&O 1999 [DIRS 102877], Appendix A, pp. A-1 to A-10[d]; CRWMS M&O 1997 [DIRS 103155], Appendix C, pp. C-1 to C-10[b]

NOTES: [a] = values derived from 1-second data averaged over 1 hour; the conversion from Watts per square meter to joules utilizes one Watt-second equivalent to one joule.
[b] = Refers to 1996 data.
[c] = Refers to 1997 data.
[d] = Refers to periods of time.
Mean daily: average of the totaled 1-hour averages.
Mean monthly: average of the mean daily values.

Table 6-27. Temperature and Precipitation Estimates from Published Reports

Age	Location	Elev (m)	MAT < modern °C	MAP x Modern	Proxy Data	Reference
>500	W. Great Basin		8	2 to 3	stratigraphy, geomorphology	Reheis 1999 [DIRS 109454], p. 202
192 to 186 ka	Death Valley	<305	10		fluid inclusion homogenization	Spencer and Roberts 1998 [DIRS 160207], p. 378
186 to 120 ka	Death Valley	<305	10 to 15		fluid inclusion homogenization	Roberts and Spencer 1998 [DIRS 160208], pp. 363 to 364
128 to 120 ka	Death Valley	<305	15		fluid inclusion homogenization	Spencer and Roberts 1998 [DIRS 160207], p. 378
0 to 100 ka	Death Valley	<305	Lower than modern		fluid inclusion homogenization	Lowenstein et al. 1998 [DIRS 160388], p. 243
60 to 35 ka	Death Valley	<305	Brine 6 to 11		fluid inclusion homogenization	Lowenstein et al. 1998 [DIRS 160388], p. 243
35 to 10 ka	Death Valley	<305	Brine 4 to 15		fluid inclusion homogenization	Lowenstein et al. 1998 [DIRS 160388], p. 243
35 to 30 ka	YM area	1,524	4	1.5	vegetation: packrat middens	Thompson et al. 1999 [DIRS 109470], p. 34
27 to 23 ka	YM area	1,524	5	2.2	vegetation: packrat middens	Thompson et al. 1999 [DIRS 109470], p. 34
20. 5 to 18 ka	YM area	1,524	8	2.4	vegetation: packrat middens	Thompson et al. 1999 [DIRS 109470], p. 34
20. 5 to 18 ka	YM area	varies	7 to 8	1.4	vegetation: packrat middens	Spaulding 1985 [DIRS 106883], p. 1
14 to 11. 5 ka	YM area	1,524	6	2.6	vegetation: packrat middens	Thompson et al. 1999 [DIRS 109470], p. 34
> 41 ka	Corn Creek Flat	840	Lower than 10. 8		isotopes on ostracode valves	Quade et al. 2003 [DIRS 161592], p. 183
< 26. 3 to 16. 4	Corn Creek Flat	840	Lower than 5. 6; lower than ~2.9		isotopes on ostracode valves	Quade et al. 2003 [DIRS 161592], p. 183
MIS 2	Nevada	varies	5	1.68	pluvial lake record	Mifflin and Wheat 1979 [DIRS 147129], p. 5
17 ka	W. Central Amargosa	varies	8		isotopes on groundwater	Claassen 1986 [DIRS 160155], p. 323
~16 ka	Owens Lake	1,085	4 to 5	1.8	pollen	Mensing 2001 [DIRS 161011], p. 61
~13 ka	Owens Lake	1,085	Condensation air temp. is a few deg. cooler		isotopes on TOC	Benson 1999 [DIRS 160213], p. 212

DTNs: MO9903CLIMATOL.001 [DIRS 116056]; TM000000000001.103 [DIRS 166372]; MO0312SEPQ1997.001 [DIRS 167116]

NOTE: MAT = Mean Annual temperature; MAP = Mean Annual precipitation; TOC = Total Organic Carbon.

Table 6-28. Correlation between Climate States, Representative Ostracodes, and Marine Isotope Stages for the Owens Lake Core for the Last 400,000 Years

Climate State and Representative Ostracode Marine Isotope Stage/sub-stage	Interglacial (IG) *Limnocythere sappaensis*			Monsoon (M) *Limnocythere bradburyi*			Intermediate (IM) *Limnocythere ceriotuberosa*			Full glacial (G) *Cytherissa lacustris* *Candona caudata*		
	Begin yr B.P.	End yr B.P.	Duration years	Begin yr B.P.	End yr B.P.	Duration years	Begin yr B.P.	End yr B.P.	Duration years	Begin yr B.P.	End yr B.P.	Duration years
12							425,000	410,000	15,000			
11	410.000	405.000	5.000									
11				405,000	403,000	2,000						
11	403,000	398,000	5,000									
11				398,000	397,000	1,000						
11	397,000	397,000	0									
			T: 10,000			T: 3,000						
10							397,000	364,000	33,000			
10										364,000	348,000	16,000
10							348,000	336,000	12,000			
									T: 45,000			
9	336,000	323,000	13,000									
9				323,000	323,000	0						
9							323,000	276,000	47,000			
8										276,000	262,000	14,000
8							262,000	247,000	15,000			
7E				247,000	247,000	0						
7E	247,000	246,000	1,000									
7E				246,000	245,000	1,000						
7E	245,000	244,000	1,000									
7E				244,000	244,000	0						
7E	244,000	243,000	1,000									
7E				243,000	242,000	1,000						
7E	242,000	235,000	7,000									
7E				235,000	234,000	1,000						
7E	234,000	232,000	2,000									
7D							232,000	225,000	7,000			
7D										225,000	219,000	6,000
7C							219,000	210,000	9,000			
7C				210,000	210,000	0						
7C							210,000	201,000	9,000			
7B										201,000	200,000	1,000
7A							200,000	184,000	16,000			
			T: 12,000			T: 3,000			T: 41,000			T: 7,000
6										184,000	147,000	37,000
6							147,000	140,000	7,000			
5E				140,000	138,000	2,000						
5E	138,000	119,000	19,000									
5D							119,000	109,000	10,000			

Table 6-28. Correlation between Climate States, Representative Ostracodes, and Marine Isotope Stages for the Owens Lake Core for the Last 400,000 Years (Continued)

Climate State and Representative Ostracode Marine Isotope Stage/sub-stage	Interglacial (IG) *Limnocythere sappaensis*			Monsoon (M) *Limnocythere bradburyi*			Intermediate (IM) *Limnocythere ceriotuberosa*			Full glacial (G) *Cytherissa lacustris Candona caudata*		
	Begin yr B.P.	**End** yr B.P.	**Duration** years	**Begin** yr B.P.	**End** yr B.P.	**Duration** years	**Begin** yr B.P.	**End** yr B.P.	**Duration** years	**Begin** yr B.P.	**End** yr B.P.	**Duration** years
5C	109,000	95,000	14,000									
5B							95,000	81,000	14,000			
5A	81,000	81,000	0									
5A				81,000	80,000	1,000						
			T: 33,000			T: 3,000			T: 24,000			
4							80,000	70,000	10,000			
4										70,000	60,000	10,000
4							60,000	58,000	2,000			
									T: 12,000			
3	58,000	56,000	2,000									
3							56,000	34,000	22,000			
2							34,000	24,000	10,000			
2										24,000	24,000	0
2							24,000	23,000	1,000			
2										23,000	22,000	1,000
2							22,000	21,000	1,000			
2										21,000	20,000	1,000
2							20,000	19,000	1,000			
2										19,000	19,000	0
2							19,000	18,000	1,000			
2										18,000	18,000	0
2							18,000	12,000	6,000			
									T: 20,000			T: 2,000
1	12,000	0	12,000									

NOTE: T = total years of substages; yr B.P. = years before present; numbers rounded to nearest 1,000 years; durations of 0 years = < 500 years.

Table 6-29. Present-Day Meteorological Stations Selected as Analogues for Climate States

Climate State	Analogue Meteorological Stations[4]	Latitude	Longitude	Elevation, m[1]	MAT ° C	MAP mm/yr
Full Glacial, MIS 6/16–Average upper bound[2]	Lake Yellowstone, WY (485345)[4]	44°33'	110°24'	2,368	0. 0	513
Full Glacial MIS 6/16–Average lower bound[2]	Browning, MT (241202)[4]	48°34'	113°01'	1,329	4.4	380
	Simpson 6NW, MT (247620)[4]	48°59'	110°19'	835	5.0	260
Full Glacial, MIS 2/4–Average upper bound[2]	Browning, MT (241202)[4]	48°34'	113°01'	1,329	4. 4	380
	Simpson 6NW, MT (247620)[4]	48°59'	110°19'	835	5. 0	260
Full Glacial, MIS 2/4–Average lower bound[2]	Elko, WB Airport, NV (262573)[4]	40°50'	115°47'	1,539	7.7	243
Full Glacial, MIS 8/10–Average upper bound[2]	Chewelah, WA (451395)[4]	48°15'	117°43'	509	7.9	537
Full Glacial, MIS 8/10–Average lower bound[2]	Rosalia, WA (457180)[4]	47°14'	117°22'	732	8.3	455
	St. John, WA (457267)[4]	47°06'	117°35'	594	9.1	432
	Spokane, WSO Airport, WA (457938)[4]	47°38'	117°32'	719	8.9	409
Intermediate–Average upper bound[2]	Rosalia, WA (457180)[4]	47°14'	117°22'	732	8.3	455
	St. John, WA (457267)[4]	47°06'	117°35'	594	9.1	432
	Spokane, WSO Airport, WA (457938)[4]	47°38'	117°32'	719	8.9	409
Intermediate–Average lower bound[2]	Beowawe, NV (260795)[4]	40°36'	116°29'	1,433	8.8	217
	Delta, UT (422090)[4]	39°20'	112°35'	1,408	10.1	201
Monsoon–Average upper bound[2]	Nogales, Old Nogales, AZ (025922)[4]	31°20'	110°57'	1,189	17.1	399
	Hobbs, NM (294026)[4]	32°42'	103°08'	1,103	16.6	409
Monsoon–Average lower bound[3]	Yucca Mountain regional stations			1,524	13.4	125
Modern or interglacial climate[3]	Yucca Mountain regional stations			1,524	13.4	125

Sources: Sharpe 2003 [DIRS 161591], Table 6-3, p. 31; WRCC 2002 [DIRS 165987]; USGS 2001 [DIRS 154674], [DIRS 158378]; Thompson et al. 1999
 [DIRS 109470], Table 4, p. 24

NOTES: MAT = mean annual temperature; MAP = mean annual precipitation; MIS = Marine isotope stage.
 [1] Elevations are above mean sea level.
 [2] Using DTN: UN0112SPA021SS.004 [DIRS 160119], MAT is calculated by averaging average annual maximum and average minimum temperature
 (in °F) and then converting to °C; MAP is calculated by converting inches to mm.
 [3] Thompson et al. 1999 [DIRS 109470]. DTN: MO0303UCC021SS.014 [DIRS 163599].
 [4] Station identification numbers in parentheses.

Table 6-30. Comparison between the Two Estimates of the Timing of Future Climate States for the Next ~50,000 Years

USGS Estimate		Sharpe Estimate	
Modern	600 yr A.P. [600]	Interglacial	N/A
Monsoon	600 to 2,000 yr A.P. [1,400]	Monsoon	-1,000 yr B.P. to 500 yr A.P.[1,500]
Glacial-Transition	2,000 to 30,000 yr A.P. [28,000]	Intermediate	500 to 18,500 yr A.P. [18,000]
		Monsoon	18,500 to 20,000 yr A.P. [1,500]
		Intermediate	20,000 to 38,000 yr A.P. [18,000]
Glacial	30,000 ending before 50,000 yr A.P. [<20,000]	Glacial	38,000 to 49,000 yr A.P. [11,000]

Source: USGS 2001 [DIRS 158378], pp. 48, 67; USGS 2001 [DIRS 154674], p. 57; Sharpe 2003 [DIRS 161591], Table 6-6, p. 56

NOTE: yr A.P. = years after present [brackets denote duration in years]; yr B.P. = years before present [brackets denote duration in years].

Table 6-31. Forecast Sequence and Durations of Climate States for the Next 500,000 Years

Climate State	Begin (yr A.P.)	End (yr A.P.)	Duration (years)
IG	-12,000	-1,000	11,000

IM/M = Intermediate and monsoon combination
M = Monsoon
IM = Intermediate
G = Full Glacial
G, 10/8 = Glacial Stage 10 and 8 equivalent
G, 16/6 = Glacial Stage 16 and 6 equivalent
G, 4/2 = Glacial Stage 2 equivalent
IG = Interglacial (modern equivalent)

Climate State	Begin (yr A.P.)	End (yr A.P.)	Duration (years)
IM/M	Combination		
M	-1,000	0	1,000
M	0	500	500
IM	500	18,500	18,000
M	18,500	20,000	1,500
IM	20,000	38,000	18,000
G, 10/8	38,000	49,000	11,000
IM	49,000	65,000	16,000
IG	65,000	77,000	12,000
Sequence Duration			78,000

Climate State	Begin (yr A.P.)	End (yr A.P.)	Duration (years)	Climate State	Begin (yr A.P.)	End (yr A.P.)	Duration (years)
IM/M	Combination			IM/M	Combination		
M	77,000	78,500	1,500	M	355,000	356,500	1,500
IM	78,500	91,500	13,000	IM	356,500	378,000	21,500
M	91,500	93,000	1,500	M	378,000	379,500	1,500
IM	93,000	106,000	13,000	IM	379,500	401,000	21,500
G, 10/8	106,000	120,000	14,000	G, 10/8	401,000	409,000	8,000
IM	120,000	137,000	17,000	IM	409,000	422,000	13,000
IG	137,000	148,000	11,000	IG	422,000	432,000	10,000
Sequence Duration			71,000	Sequence Duration			77,000
IM/M	Combination			IM/M	Combination		
M	148,000	149,500	1,500	M	432,000	433,500	1,500
IM	149,500	174,000	24,500	IM	433,500	451,500	18,000
M	174,000	175,500	1,500	M	451,500	453,000	1,500
IM	175,500	200,000	24,500	IM	453,000	471,000	18,000
G, 16/6	200,000	213,000	13,000	G, 10/8	471,000	482,000	11,000
IM	213,000	229,000	16,000	IM	482,000	497,000	15,000
IG	229,000	241,000	12,000	IG	497,000	507,000	10,000
Sequence Duration			93,000	Sequence Duration			75,000
IM/M	Combination						
M	241,000	242,500	1,500				
IM	242,500	266,000	23,500				
M	266,000	267,500	1,500				
IM	267,500	291,000	23,500				
G, 4/2	291,000	329,000	38,000				
IM	329,000	345,000	16,000				
IG	345,000	355,000	10,000				
Sequence Duration			114,000				

Source: Excerpted from Sharpe 2003 [DIRS 161591], Table 6-6, p. 55

NOTE: Values rounded to nearest 500 years.

Table 6-32. Durations of Glacial and Interglacial Marine Isotope Stage, in Thousands of Years, for Past and Future, Based on the Precession Methodology

MIS ⟶													
Past	11	10	9	8	7	6	5	4	11				
Interglacial (Modern Equivalent)	10		10		11		11		11				
Intermediate and Monsoon Combination	39		50		49		50		1				
Full Glacial		10		14		38		39					
Intermediate		16		18		17		15					
MIS ⟶													
Future	**11**	**10**	**9**	**8**	**7**	**6**	**5**	**4**	**11**	**10**	**9**	**8**	**7**
Interglacial (Modern Equivalent)			12		11		12		10		10		10
Intermediate and Monsoon Combination	38		29		52		50		46		39		
Full Glacial		11		14		13		38		8		11	
Intermediate		16		17		16		16		13		15	

DTN: MO0302UCC021SS.011 [DIRS 163597]

Source: Sharpe 2003 [DIRS 161591], Table 6-7, p. 58

NOTES: Years are in k.y.; past is based on 410,000 years duration; future is based on 507,000 years duration.

MIS 4, 3, and 2 are combined and equal MIS 4. MIS 1 = MIS 11.

Table 6-33. Years and Percentage for Each Climate State

Climate State	Last 409,000 Years Based on Precession Methodology (from Figure 6-7a-c)	%	Last 410,000 Years Based on Owens Lake Ostracodes (from Table 6-28)	%	Future 507,000 Years Based on Precession Methodology (from Table 6-31)	%
Interglacial	54,000	13	82,000	20	65,000	13
Intermediate and Monsoon	260,000	64	242,000	59	347,000	68
Glacial	95,000	23	86,000	21	95,000	19

Sources: Sharpe 2003 [DIRS 161591], Figures 6.5a through d, pp. 35 to 38; Sharpe 2003 [DIRS 161591], Table 6-1, pp. 20 and 21; Excerpted from Sharpe 2003 [DIRS 161591], Table 6-6, p. 55

7. UNSATURATED ZONE HYDROLOGY

The thick unsaturated zone at Yucca Mountain has been designated as the host environment for the nuclear waste repository. A small percentage of the precipitation falling on the ground surface infiltrates into the near-surface rock and percolates through the unsaturated zone to the water table. The amount of water contacting waste packages ultimately affects all aspects of performance, from waste package lifetime to radionuclide movement. The amount of water contacting the waste packages is limited by the seepage into waste emplacement drifts, which depends on the nature of percolation through the repository host rock in the unsaturated zone. Once radionuclides are released from a waste package, the unsaturated zone system beneath the repository delays the movement and reduces the concentration of radionuclides during transport to aquifers beneath the repository. Because of the factors described above, understanding the unsaturated zone flow system at the site is key to assessing how well the repository will perform.

The following hydrologic terms are used in the Yucca Mountain study. "Infiltration" is defined as the flow of surface water downward across the atmosphere-soil or the atmosphere-bedrock interface. "Net infiltration" is the flow of water downward (i.e., drainage) below the zone of evapotranspiration. "Percolation" is the flow of net infiltration through the deep unsaturated zone and is discussed in Sections 7.4 and 7.6. "Recharge" is defined as flow of water from the unsaturated zone downward to the water table where it enters the saturated zone. Estimates of net infiltration for the Yucca Mountain area may not correspond directly to recharge because of the time frame under consideration, the extent to which the thick unsaturated zone attenuates the temporal and spatial variability of net infiltration, and the combined effects of lateral flow and vapor flow on percolation.

In the unsaturated zone, infiltration of precipitation and subsequent percolation to the water table involve dominantly vertical flow, so the area of principal interest is essentially the immediate vicinity of Yucca Mountain, referred to here as the site area (Figures 3-1 and 3-2 [see Section 3]). The location of the repository, as investigated for site recommendation, is in the central block of the site area between the Solitario Canyon and Bow Ridge faults. A geologic map and a cross section of the central block area are shown in Figures 3-1 and 3-21, respectively. Below the surficial alluvium, the five principal hydrogeologic units defined in the unsaturated zone at the site are the Tiva Canyon welded (TCw), Paintbrush nonwelded (PTn), Topopah Spring welded (TSw), Calico Hills nonwelded (CHn), and Crater Flat undifferentiated (CFu) hydrogeologic units (Table 7-1). Figure 7-1 depicts the relation between these hydrogeologic units and the major processes that control water movement in the unsaturated zone: net infiltration, evaporation, percolation to the repository horizon, fracture-matrix interaction, accumulation of perched water, lateral flow, and deep percolation to the water table.

In support of studies of the unsaturated zone, many boreholes have been drilled in the immediate vicinity of Yucca Mountain (Figure 7-2). Boreholes drilled, sampled, tested, and monitored at the site have provided information on the vertical and lateral distribution of hydrogeologic units, hydrologic properties of the rocks, thermal and other geophysical conditions and properties, chemistry of the contained fluids, pneumatic pressure, and water content and potential. Additional data for some of these parameters have been obtained from test alcoves and niches in tunnels for the Exploratory Studies Facility (ESF), the Enhanced Characterization of the

Repository Block (ECRB) Cross-Drift; and at the Busted Butte unsaturated zone test facility. These test locations are shown on Figures 1-3 and 1-4 and the studies are listed in Table 7-2.

Sections 7.1 to 7.10 describe the hydrologic setting of the site unsaturated zone and the characteristics, features, events, and processes of the unsaturated zone that are most important to repository design and performance. The discussion follows the movement of water and gas from the land surface through the unsaturated zone as follows: precipitation at the surface and infiltration into the alluvium and bedrock (Section 7.1); hydrologic properties affecting fluid flow (Section 7.2); gaseous-phase flow (Section 7.3); hydrologic conditions, including occurrences of perched water (Section 7.4); hydrochemical and isotopic indications of fluid flow (Section 7.5); field-scale flow testing and moisture conditions at Yucca Mountain (Section 7.6); paleohydrologic evidence of past percolation (Section 7.7); and field-scale transport testing (Section 7.8). These sections are followed by descriptions of the conceptual models (Section 7.9) and numerical models that have been developed to simulate three-dimensional fluid flow and support site-performance models (Section 7.10).

7.1 SITE INFILTRATION

Quantitative estimates of net infiltration at the Yucca Mountain site under present-day and possible future climatic conditions are used to define the upper boundary condition of unsaturated zone flow models. These models constitute primary input to the total system performance assessment models being used to evaluate the performance of the repository (DOE 1998 [DIRS 101779], Volume 3, Figure 2-1). Data and interpretations from field studies at Yucca Mountain, combined with insights about hydrologic processes documented in the scientific literature, have led to an understanding of the physical processes and properties that control net infiltration. These processes include precipitation, surface runoff and run-on, infiltration, evapotranspiration, and the redistribution of moisture in the shallow subsurface, schematically shown in Figure 7-3.

7.1.1 Surface Water Drainage System

This section characterizes the surface water hydrology of the Yucca Mountain vicinity and surrounding region. Yucca Mountain is located in the Amargosa River drainage basin, the major tributary drainage area to Death Valley, shown in Figure 7-4. Streamflow from Yucca Mountain can extend from local drainages to the Amargosa River and then to Death Valley. Because most of the Amargosa River and its tributaries are ephemeral streams (i.e., they flow only in immediate response to precipitation, and are dry most of the time), flow rarely occurs throughout the entire reach of the drainage system. Surface flow in a stream channel may occur for short distances where groundwater discharges from springs and into the channel. This water is subsequently lost to infiltration and evaporation as the streamflow moves downstream. However, during infrequent flood events, flow occurs throughout the Amargosa River and has filled many square miles of the Death Valley salt pan to depths of 0.3 m (1 ft) or more (Miller 1977 [DIRS 105462], p. 18). The entire surface drainage basin tributary to Death Valley, plus several closed drainage basins are interconnected via the groundwater flow system (see Section 8.2).

7.1.1.1 Surface Drainage

The Amargosa River heads at Pahute Mesa (Figure 7-4) and flows southward through Oasis Valley, where the flow largely infiltrates into stream deposits and dissipates by evapotranspiration. The channel is then joined by Beatty Wash and passes through Amargosa Narrows into the Amargosa Desert. The channel trends southeasterly along the southwestern flank of the Amargosa Desert about 80 km (50 mi) to Alkali Flat (also known as Franklin Lake Playa), a discharge area for the regional groundwater flow system, where it passes through a bedrock narrows to enter the Lower Amargosa Valley. The channel extends 64 km (40 mi) farther south past the southern end of the Black Mountains, then turns westward and enters Death Valley, where it is joined by Salt Creek (from the south). The Amargosa River channel then extends northwesterly 80 km (50 mi), terminating at Badwater, the low point of Death Valley.

As the Amargosa River channel extends southward through the Amargosa Desert, a tributary, Carson Slough (not shown in Figure 7-4), joins the channel system. Carson Slough drains perennial spring flow from the Ash Meadows regional groundwater discharge area in the eastern portion of the Amargosa Desert.

The ephemeral streams at Yucca Mountain are tributary to Fortymile Wash, which also heads at Pahute Mesa (Figure 7-4), and then flows southward (Figure 7-5a) before flowing onto an alluvial fan at the Narrows (data collection site 25, Figure 7-5b). The eastern slope of Yucca Mountain drains via Yucca Wash, Drill Hole Wash, and Dune Wash (earlier termed Busted Butte Wash) to Fortymile Wash (Figure 7-5b). Fortymile Wash spreads out into a distributary system in the Amargosa Desert, and during floods joins the Amargosa River about 21 km (13 mi) northwest of Death Valley Junction, California (Beck and Glancy 1995 [DIRS 104463], p. 3). An ephemeral stream channel in Crater Flat collects drainage from the western slope of Yucca Mountain via Solitario Canyon (Figure 7-5b). This channel also collects drainage from the southern slope of Yucca Mountain, that drains into Windy Wash, which joins the Amargosa River near its confluence with Fortymile Wash. Jackass Flats, where support facilities for Yucca Mountain studies and other Nevada Test Site projects are located, is drained by Topopah Wash (Figure 7-5b). Topopah Wash flows during floods into the Amargosa River in the Amargosa Desert.

Permanent lakes in the vicinity are Crystal Reservoir, Lower Crystal Marsh, Horseshoe Reservoir, and Peterson Reservoir. These lakes are artificial impoundments that store the discharge of springs in Ash Meadows (Figure 7-4). Crystal Reservoir is the largest, with a capacity of 1,837,000 m^3 (1,500 acre-ft) (Giampaoli 1986 [DIRS 105506], Field Reconnaissance Stop 8). Like the streams, the playas shown in Figure 7-4 contain water only after heavy runoff periods. However, some, like Badwater in Death Valley and Alkali Flat in the Amargosa Desert, represent zones of continuous groundwater discharge.

7.1.1.2 Streamflow

There are no perennial streams in the Yucca Mountain region, and even the larger streams are ephemeral. Throughout the Death Valley Basin, perennial flow is only observed downgradient of spring discharges and around the margins of playas and salt pans where the land surface and water table converge.

Surface water flows have been monitored at numerous sites in the Yucca Mountain region, as shown on Figures 7-5a and 7-5b. Peak discharge data recorded at these sites are provided in Table 7-3. The nature of streamflow in the desert terrain of the Amargosa River basin is extremely erratic and sparse.

Streamflow occurred throughout the Fortymile Wash channel system from the Pah Canyon area in Fortymile Canyon (7.1 km [4.4 mi]) north of the Narrows) to the Amargosa Desert in March 1995 (Savard 1998 [DIRS 102213], p. 9). Based on data from gauging stations and miscellaneous sites, streamflow probably occurred throughout the Fortymile Wash system in January and February 1969, March 1983, and July and August 1984 (additional description of the February 1969 flood event is presented in Section 3.4.3). In July 1985, streamflow occurred throughout much of the Fortymile Wash system, but probably not throughout the entire system. In August 1991, February and March 1992, January and February 1993, and January 1995, streamflow occurred in the Fortymile Canyon reach. In February, May, and November 1987, September 1990 and 1991, February and March 1992, and January 1993 and 1995, streamflow occurred in small sections of the Fortymile Wash system in Jackass Flats and in the Amargosa Desert. As a result of infiltration into the channel sediments, groundwater levels rose in boreholes in Fortymile Canyon after the streamflow in 1983, 1992, 1993, and 1995 (Savard 1998 [DIRS 102213], p. 10).

The data analysis of streamflow in the Yucca Mountain region indicates that: (1) the flood of February 24-25, 1969, was the greatest runoff event since recordings of streamflow began in the early 1960s; (2) although the Amargosa River drainage area exceeds that of Fortymile Wash, unit peak discharges commonly are greater in Fortymile Wash; (3) unit peak discharges typically are greater in small drainage basins than in larger basins; and (4) maximum peak discharges do not correlate closely with maximum unit peak discharges.

7.1.2 Infiltration of Streamflow as Source of Groundwater Recharge

Early simulations of groundwater flow in the Yucca Mountain region suggested significant recharge in the Fortymile Wash channel system. For example, Czarnecki and Waddell (1984 [DIRS 101042], p. 12) estimated the recharge to be about 8 million m^3/yr (6,400 acre-ft/yr) in the reach from 5 km (3 mi) upstream of the Pah Canyon confluence to midway between the stream gauges near well J-13 and near Amargosa Valley, Nevada. Savard (1998 [DIRS 102213]) used streamflow data from continuous streamflow gauging stations, crest-stage gauges, and miscellaneous sites during 1969 to 1995, and depth-to-water data in boreholes from 1983 to 1995, to estimate streamflow volumes, infiltration loss, and groundwater recharge in the Fortymile Wash channel system. A long-term groundwater recharge rate was estimated based on the winter/spring and summer/fall groundwater recharge rate for four reaches of the channel system.

For four flow events, Savard (1998 [DIRS 102213], p. 14, Table 2, Figure 7) estimated a streamflow loss of 7,300 m^3/km (9.5 acre-ft/mi) for Fortymile Wash, which was then applied to all known flows from January 25, 1969, to March 15, 1995. The estimated flow losses, together with groundwater records, were used (Savard 1998 [DIRS 102213], p. 20) to establish a minimum infiltration volume of 9,000 m^3 (7.3 acre-ft), below which groundwater recharge did not likely occur.

Groundwater recharge volumes were assumed to increase linearly as a function of infiltration (Savard 1998 [DIRS 102213], Figure 8). This relationship was applied to estimate groundwater recharge volume for all flow events from January 25, 1969, through March 15, 1995, which were identified by reaches and separated into three time periods: from 1969 to 1995, from 1983 to 1995, and from 1992 to 1995 (Savard 1998 [DIRS 102213], Table 4). Because winter/spring and summer/fall precipitation patterns result from different storm patterns, the recharge rates were segregated by season. Combined long-term average annual recharge rates calculated in this manner were 27,000 m^3/yr (22 acre-ft/yr) for the Fortymile Canyon reach, 1,100 m^3/yr (0.90 acre-ft/yr) for the upper Jackass Flats reach, 16,400 m^3/yr (13 acre-ft/yr) for the lower Jackass Flats reach, and 64,300 m^3/yr (52 acre-ft/yr) for the Amargosa Desert reach (Savard 1998 [DIRS 102213], Table 5).

Groundwater recharge has been estimated throughout the Amargosa River basin above Shoshone, California, using a geomorphic/distributed-parameter simulation approach (Osterkamp et al. 1994 [DIRS 100602]). In these calculations, all channel loss was assumed to represent groundwater recharge (Osterkamp et al. 1994 [DIRS 100602], pp. 496 and 497). Osterkamp et al. (1994 [DIRS 100602], Table 2) estimated average annual recharge at 4,220,000 m^3/yr over the entire 95 km (60 mi) course of Fortymile Wash, as compared to the shorter 42 km (26 mi) segment described herein located in the immediate vicinity of Yucca Mountain. Savard's estimates were adjusted to the total infiltration loss by adding long-term average annual recharge to infiltration (not believed to contribute to recharge and ultimately returned to the atmosphere). In Table 7-4, the Osterkamp estimates indicate that the bulk of infiltration occurs in the upper Jackass Flats reach, whereas the Savard estimates show more uniform distribution, with maximum infiltration in the downstream reaches. Both estimates are smaller by more than an order of magnitude than an estimate of about 8 million m^3/yr (6,400 acre-ft/yr) by Czarnecki and Waddell (1984 [DIRS 101042], p. 12) for a comparable reach of Fortymile Wash.

7.1.3 Conceptual Model of Net Infiltration

The schematic of a conceptual model of the hydrologic cycle (see Figure 7-3) provides a framework for the understanding of dominant hydrologic processes, such as precipitation, evaporation, and transpiration; run-on and runoff; infiltration; the redistribution of moisture in the shallow subsurface; and groundwater recharge. Precipitation is mostly dependent on meteorological factors, but also on geographic location, elevation, and physiography. Evapotranspiration is dependent on vegetation, the moisture distribution in the shallow subsurface, and potential evapotranspiration, which is determined by the energy balance. Redistribution of moisture in the shallow subsurface occurs in response to gravity and matric potential gradients and is strongly dependent on soil and bedrock properties. Surface water runoff occurs when the precipitation rate exceeds the infiltration capacity of surficial materials. Run-on and runoff are mostly dependent on the hydraulic properties of surficial materials, topography, and channel geometry.

7.1.3.1   Field Water Balance

The field water balance is a fundamental aspect of conceptual and numerical infiltration models and is based on the principle of conservation of mass for water (Flint et al. 1996 [DIRS 100147], pp. 9 to 11):

$$P+A+U+W_s+S_s+B_s+L_i+R_{on}-R_{off}-D-E-T-L_o-E_x=0 \qquad \text{(Eq. 7-1)}$$

where:

$$
\begin{array}{lll}
P & = & \text{precipitation} \\
A & = & \text{applied water (man-induced)} \\
U & = & \text{upward flow} \\
W_s & = & \text{change in soil-water storage} \\
S_s & = & \text{change in surface-water storage} \\
B_s & = & \text{change in above-ground, biomass-water storage} \\
L_i & = & \text{lateral flow in} \\
R_{on} & = & \text{surface run-on} \\
R_{off} & = & \text{surface runoff} \\
D & = & \text{deep drainage or percolation (net infiltration)} \\
E & = & \text{evaporation} \\
T & = & \text{transpiration} \\
L_o & = & \text{lateral flow out} \\
E_x & = & \text{extraction of water (man-induced)}
\end{array}
$$

Taking into account the spatial and temporal variability of processes, Equation 7-1 must be defined over some arbitrary time-interval (e.g., day or year) and volume (or depth) of the soil. In most cases, the general form of the water-balance equation can be simplified by assuming one or more of the terms to be zero or negligible. For example, the terms B_s, R_{on}, and R_{off} can often be set to zero in cases involving arid and semiarid sites where overland flow occurs only in direct response to relatively infrequent, larger-magnitude precipitation events. In the case of one-dimensional flow with zero or negligible run-on and runoff under current climatic conditions, negligible upward flow ($U=0$) and lateral flow ($L_i=L_o=0$), man-induced fluxes ($A=E_x=0$), and surface storage ($S_s=0$), the water-balance equation becomes:

$$P+W_s-D-E-T=0 \qquad \text{(Eq. 7-2)}$$

This equation (Eq. 7-2) provides a practical starting point for analyzing net infiltration (D). The sum of E and T is usually termed the evapotranspiration (ET). The water balance can provide a method of estimating W_s, ET, and D.

Because net infiltration is assumed to represent the drainage of water below the root zone (which is the upper boundary condition for flux in the unsaturated zone site-wide model), it is not necessarily equivalent to groundwater recharge, which is the flux across the water table. The near-surface (shallow subsurface) flow and transport processes are distinct from those in deeper zones (depths greater than approximately 50 m [160 ft]), because transient and nonequilibrium conditions are likely to exist between soils and bedrock and between bedrock matrix and

fractures at or near the land surface. Annual, seasonal, and diurnal variations in meteorology and vegetation cause temporal variability in net infiltration; while topography, vegetation, soil depth, soil properties, and properties of the underlying bedrock cause spatial variability in net infiltration. Because of the thickness of the unsaturated zone at Yucca Mountain, net infiltration is strongly affected by short-term variability in climatic conditions, whereas recharge is more likely to be affected by longer term, average climatic conditions. The potential ability (or inability) of the thick unsaturated zone to dampen and smooth out spatially and temporally variable net infiltration to a more uniformly distributed flux at the repository level will be discussed in detail below.

Other factors that could affect net infiltration are solar radiation, relative humidity, air temperature, and, to a lesser degree, atmospheric turbidity, ozone, and wind. Along with site-specific parameters, such as slope, aspect, and albedo, these climate variables control the energy balance that determines potential evapotranspiration. Air temperature also determines the occurrence of precipitation as snow and the ability of vegetation to transpire soil moisture.

7.1.3.2   Climatic Factors and Precipitation

The most important climatic factors affecting water-transport processes in the unsaturated zone are solar radiation flux, diurnal and seasonal temperature cycles, relative humidity, and periodic inputs from precipitation, in the form of either rain or snow, followed by extended periods of drought. Evaluation of past climate is needed to assess the impact that climate has on the hydrologic conditions, and, in particular, on net infiltration. Evaluation of current climate is necessary to relate changes in climate to near-surface processes, such as infiltration, runoff, redistribution, and evapotranspiration. One of the primary climatic factors affecting surface hydrology and net infiltration is the regime (timing, frequency, duration, and intensity) of precipitation (Flint et al. 1996 [DIRS 100147], p. 31). Precipitation at the site depends on the synoptic-scale weather circulation pattern (Flint et al. 1996 [DIRS 100147], pp. 12 and 13). Current climatic conditions for the site and the Yucca Mountain region are discussed in detail in Section 6. The Yucca Mountain Project (YMP) environmental program collected site meteorological data using a network of nine automated weather stations (see Figure 6-2).

Average annual precipitation over the area of the Nevada Test Site ranges from a maximum of 370 mm (14.6 in.) in the Belted Range to a minimum of 110 mm (4.33 in.) in the Amargosa Desert (Hevesi and Flint 1995 [DIRS 107413], Table 2). Annual precipitation in the vicinity of Yucca Mountain ranges from a minimum of about 100 mm (~4 in.) at low elevations in the south to a maximum in excess of 300 mm (11 in.) at high elevations in the north (Figure 7-6). Based on the analysis of data from 114 precipitation stations in the Yucca Mountain region having at least eight years of complete records, a strong positive correlation between average annual precipitation and station elevation was found (Hevesi and Flint 1995 [DIRS 107413], p. 63, Figure 9), which is shown in Figure 7-7. These results indicate that the zones of maximum precipitation and maximum infiltration are likely to correspond to the zones of higher elevations of the mountain ranges.

7.1.3.3 Physiographic and Topographic Factors

Yucca Mountain is located within a broad ecological transition zone, referred to as Transition Desert, between the northern boundary of the Mojave Desert and the southern boundary of the Great Basin Desert (Flint et al. 1996 [DIRS 100147], pp. 43 and 44). Topography has an important impact on the spatial distribution of precipitation, potential evapotranspiration, and channeling surface flow (runoff). (A discussion of surface-water hydrology is provided in Section 7.1.1, along with descriptions of drainage and channel networks for the Yucca Mountain area.) The topography at Yucca Mountain can be classified as follows: ridgetops, side slopes, terraces, and channels (Flint and Flint 1995 [DIRS 100394], pp. 2 to 6; Flint et al. 1996 [DIRS 100147], pp. 38 and 39). The ridgetops generally are flat to gently sloping and are higher in elevation than the other topographic zones. They have thin (less than 1 m [3 ft] thick) to no surficial deposits, but are relatively stable morphologically. Where present, soils are fairly well developed, commonly containing thin calcium-carbonate layers. The underlying bedrock on ridgetops is moderately to densely welded and moderately to highly fractured. The higher elevations of the ridgetops and upper slopes (above 1,400 m [4,600 ft]) have a greater potential of sustaining a thin snow cover for up to several weeks during the winter. Side slopes are distinguished from the terraces and channels by depth of deposits and slope. Surficial deposits on hillside slopes are thin to nonexistent, and in most locations, bedrock is densely welded and highly fractured. The side slopes are approximately north-or south-facing in the southern part of the site and, therefore, have different seasonal solar radiation loads. In the northern washes, although the side slopes face more southwestward and northeastward, the steepness of the slopes accentuates seasonal radiation differences. Terraces and channels are located at lower elevations of primary washes and are underlaid by thin deposits in the upper washes and thick deposits farther downstream. Very little bedrock is exposed in the washes. The soil development in terrace and channel deposits has varying degrees of calcium-carbonate cementation that commonly is quite extensive (Section 3.3.7.2). The surfaces of terraces are relatively flat and dissected by old stream channels and active channels. Channels differ from terraces in that the periodic runoff that occurs in the channels in response to extreme precipitation conditions can rework the channel materials. Although channels occupy a very small surface area of the wash, they may contribute significantly to net infiltration during runoff events. Over the area of the site-scale unsaturated zone flow model, ridgetops (including the shoulders) encompass about 5 to 10 percent of the model area, side slopes (including foot slopes) about 45 percent, terraces about 45 percent, and active channels less than 5 percent (Flint et al. 1996 [DIRS 100147], p. 38).

7.1.3.4 Surficial Deposits

The dominant surficial deposits in the general vicinity of Yucca Mountain are fluvial sediments and fluvial debris-flow deposits that are found in the basins, washes, and alluvial fans. These deposits have varying degrees of soil development and thickness and have a gravelly texture, with rock fragments constituting between 20 and 80 percent of the total volume (Section 3.3.7.2). The deposits range from 100 m (330 ft) thick in the valleys to less than 30 m (98 ft) thick in the mouths of the washes. Halfway up the washes, alluvial fill generally is less than 15 m (50 ft) deep in the center of the channels and well-developed, cemented, calcium-carbonate layers are common. More stable surfaces, generally on the ridgetops, have developed soils 0.5 to 2 m (1.6 to 6.6 ft) thick with high clay contents. Overall, deposit thickness was classified into four categories: 0 to less than 0.5 m (1.6 ft), 0.5 m (1.6 ft) to less than 3.0 m (9.8 ft), 3.0 m (9.8 ft) to

less than 6.0 m (20 ft), and greater than or equal to 6.0 m (20 ft), which encompass about 50 percent, 5 percent, 5 percent, and 40 percent of the site area, respectively. The spatial distribution of deposit thickness is determined primarily by topography. The deeper deposits are present on the shallower slopes of the ridgetops, in washes, and underlying alluvial fans; whereas the deposits on the steeper side slopes are thin to absent.

For the infiltration modeling, mapped surficial, unconsolidated deposits were reconfigured into eight surficial "soil types" based on differences in soil texture (Flint et al. 1996 [DIRS 100147], pp. 40 and 41). Two additional soil types were added to the original eight soil types to account for bare rock and disturbed ground, consistent with the geologic mapping.

Soil storage capacity is determined mostly by soil thickness and porosity. Soil thickness tends to be well correlated to local topography, with the upland areas generally having thin soils and the lower washes and alluvial fans having thicker soils (surficial materials). Soil porosity and permeability, along with various other hydrologic properties, such as residual water content and field capacity, can be correlated to soil type (Flint et al. 1996 [DIRS 100147], pp. 39 to 40).

7.1.3.5 Bedrock Geology and Hydrologic Properties of Fractures

The most important (from a hydrologic prospective) bedrock volcanic units in the unsaturated zone at Yucca Mountain are: the Tiva Canyon, Yucca Mountain, Pah Canyon, and Topopah Spring tuffs; the interlayered bedded tuffs; the Calico Hills Formation; and the Prow Pass Tuff. Although the matrix properties (e.g., porosity, bulk density, particle density, saturated hydraulic conductivity (K_s), and moisture retention characteristics) of the bedrock units have been characterized in great detail (see Section 7.2.1), the hydrologic properties of the fracture network are not nearly as well defined.

The density and properties of fractures (Section 3.5.8) are critical to understanding and modeling net infiltration because of the potential for significant infiltration to occur as fracture flow in the shallow subsurface under certain moisture conditions (Flint et al. 1996 [DIRS 100147], pp. 24 and 25). Fracture densities and apertures are not well characterized, but estimates have been made from borehole core logs (Flint et al. 1996 [DIRS 100147], pp. 35 and 36). Hydraulic properties of fractures are dependent on fracture aperture and whether the fractures are open or filled with calcium carbonate or siliceous materials. Estimates of porosity and saturated hydraulic conductivity (K_s) for fractures can be made using estimated density and aperture. Assuming that significant net infiltration through fractures occurs only under saturated or near-saturated conditions, unsaturated flow parameters for fractures are not required to model infiltration by way of fracture flow. Average K_s values for fractures were estimated based on data from fluid-flow experiments conducted in the laboratory on a block of fractured tuff for a range of apertures as follows: for 2.5 μm aperture, $K_s = 410$ millimeters per day (mm/d); for 25 μm, $K_s = 15,700$ mm/d, and for 250 μm, $K_s = 745,000$ mm/d (Flint et al. 1996 [DIRS 100147], p. 36). For fracture-fill materials, an averaged $K_s = 43.2$ mm/d. For fractures, K_s were estimated for each of the 76 lithostratigraphic units identified by Scott and Bonk (1984 [DIRS 104181]) by assigning the appropriate hydraulic conductivity value for the percent of area per square meter of rock, given the fracture density and aperture available for water flow (Flint et al. 1996 [DIRS 100147], p. 36). These values of fracture conductivity then were added to the K_s values of the rock matrix, yielding combined matrix-fracture effective saturated hydraulic

conductivity values for each lithostratigraphic unit for each of six fracture types: open or filled for each of the three aperture classes.

7.1.3.6 Types of Vegetation

The information on plant types and distributions supports estimates of evapotranspiration and modeling of radiation loads over the surface of Yucca Mountain. Yucca Mountain is located near the northern boundary of the Mojave Desert where the vegetation transitions from Mojave Desert flora to combinations of Mojave and Great Basin desert flora. Floral composition in these transition zones is dependent on individual species tolerance limits which are influenced by precipitation, temperature, soil characteristics, and nutrient availability. In the Yucca Mountain area, the transition is gradual and sometimes difficult to distinguish. Plant species typical of the Mojave Desert dominate low elevations. Valleys, alluvial fans, and large washes are dominated by creosote bush (*Larrea tridentata*), white bursage (*Ambrosia dumosa*), Nevada jointfir (*Ephedra nevadensis*), littleleaf ratany (*Krameria erecta*), and pale wolfberry (*Lycium pallidum*) (CRWMS M&O 1998 [DIRS 104589], pp. 5 to 10). Low-elevation hillsides are dominated by similar species, with the addition of shadscale (*Atriplex confertifolia*), California buckwheat (*Eriogonum fasciculatum*), and spiny hopsage (*Grayia spinosa*). Creosote bush drops out at about 1,280 m. Vegetation on the Yucca Mountain crest (about 1,478 m) and upper slopes (1280 m to 1,460 m) primarily support Mojave species with addition of some Great Basin species (CRWMS M&O 1998 [DIRS 104589], pp. 5 to 10). These ridge tops and slopes support vegetation associations that are dominated by one or more of the following species: blackbrush (*Coleogyne ramosissima*), heath goldenrod (*Ericameria teretifolius*), Nevada jointfir, broom snakeweed (*Gutierrezia sarothrae*), green ephedra (*Ephedra viridis*), and California buckwheat. On a few steep north-facing slopes at higher elevations (1,430 m to 1,465 m), big sagebrush (*Artemisia tridentata*) is dominant (CRWMS M&O 1998 [DIRS 104589], pp. 5 to 10).

Distribution, minimum xylem water potential, and rooting depths were the vegetation characteristics most important in evaluating evapotranspiration (Flint et al. 1996 [DIRS 100147], p. 45). Minimum xylem water potential was used to calculate the -6 megapascal (MPa) (−60 bar) lower limit of plant-available water, which amounts to residual water content in terms of evapotranspiration and is equivalent to the wilting point of vegetation. Rooting depths were used to estimate extraction depths for transpiration.

7.1.3.7 Effects of Soil Saturation

Net infiltration at Yucca Mountain occurs as an episodic, transient process that depends primarily on the length of time saturated or near-saturated conditions exist at the soil-bedrock interface and the effective conductivity of the underlying bedrock (Flint et al. 1996 [DIRS 100147], pp. 24 and 25). Saturated soils are primarily established during the winter in response to a series of large storms that tend to occur more frequently during years when the El Niño Southern Oscillation is active. The timing, intensity, and duration of precipitation, the storage capacity of the soil, evapotranspiration, and the hydrogeologic properties of underlying bedrock determine the availability of water for net infiltration (Flint et al. 1996 [DIRS 100147], p. 90). During winter, when potential evapotranspiration is at a minimum, saturated conditions at the soil-bedrock interface can develop (Flint et al. 1996 [DIRS 100147], p. 67). When the storage capacity of the soil reaches its maximum value, and the infiltration rate exceeds the

effective hydraulic conductivity of the underlying bedrock, or when precipitation intensity exceeds the infiltration capacity of the soil, runoff is generated, routing down slopes and into channels. Net infiltration beneath channels in washes, at side slopes, and ridgetops depends on the frequency and magnitude of runoff events.

Differences in the response of the bedrock to the degree of saturation and available moisture in the overlying soil is illustrated by the record of water content and water potential at Borehole USW UZ-N52 (Figure 7-8). The graph indicates the measured change through time of the water content of the soil layer above the soil-bedrock interface from 1984 through 1994 (Flint et al. 1996 [DIRS 100147], p. 24, Figure 6). The air-entry water potentials needed to initiate and maintain fracture flow for both an open and filled fracture are plotted (heavy dashed lines) along with the water potential of the soil calculated using the known moisture characteristic of the soil. The increases in water content of the soil profile correspond to the wetter than average winters of 1988, 1992, and 1993. Net infiltration for both the filled and open fractures occurred only during 1992 and 1993 when the water potential exceeded about 0.1 MPa (1 bar), although the filled fractures came close to initiating infiltration during 1988. During most of the record, the soil above the bedrock interface remained too dry for the infiltration of water into bedrock.

7.1.4 Methods for Determining Net Infiltration and Recharge

Taking into account the complexity of flow processes in the fractured environment at Yucca Mountain, infiltration studies were conducted using a combination of several monitoring techniques, field and laboratory tests, and calculation methods, including the following:

- Flux calculations, using measured hydraulic properties
- Simple water-balance models
- Statistical modeling of measured parameters
- Geochemical methods
- Deterministic water-balance models.

A summary of methods for determining net infiltration is presented in Flint et al. (2002 [DIRS 157411], Table 3).

7.1.4.1 Flux Calculations Using Measured Hydraulic Properties

Calculations of unsaturated flux have been made using measurements or estimates of the vertical water-potential gradient for selected depths and known or estimated moisture-characteristic curves, assuming that lateral-flow components are negligible. Although this approach is of questionable validity in hydrologic settings dominated by fracture flow, it has been successfully applied to sites with thick alluvial deposits, yielding steady-state flux estimates ranging from 0.04 to 2 mm/yr (Flint et al. 1996 [DIRS 100147], p. 7). Spatially distributed estimates of net infiltration for the Yucca Mountain repository site have been made using hydraulic-property measurements of the bedrock matrix underlying the soil. This approach yielded estimates of net infiltration ranging from 0.02 to 13.4 mm/yr for the site (Flint et al. 1996 [DIRS 100147], p. 7 to 8). This approach indicated the high degree of spatial variability in net infiltration caused by the variability of soil and bedrock properties. The weakness of this approach is that steady-state

flow conditions were assumed, limiting the ability to take into account shallow transient flow and fracture flow.

Water potentials for several depths in the soil profile have been obtained at the site using heat dissipation probes (Section 7.1.5.5). From these measurements, in conjunction with the moisture-characteristic curves for the soils, infiltration was estimated as high as 150 mm/mo, following a storm, which agrees with estimates from changes in the water content in nearby neutron boreholes (Flint et al. 1996 [DIRS 100147], p. 68).

7.1.4.2   Simple Water-Balance Models

Estimates of net infiltration and recharge have been made using measurements or estimates of the components of the water-balance equation. However, in arid environments such as Yucca Mountain, the net infiltration is relatively small compared to other water-balance elements. Using basin-wide water-balance studies at Yucca Mountain, based on climatic, vegetation, geologic, streamflow, and groundwater data, the groundwater recharge rate is estimated to range from 0 to 10 mm/yr (Flint et al. 1996 [DIRS 100147], p. 6). The spatial variability of the infiltration rate depends on the variability of mean annual precipitation, which, in turn, depends on elevation.

7.1.4.3   Statistical Modeling of Measured Parameters

Measured changes in water-content profiles at neutron-moisture boreholes (UZN and UZ-N Boreholes shown on Figure 7-2) located in the vicinity of the repository were used to estimate net-infiltration (Flint et al. 1996 [DIRS 100147], p. 8). The developed net infiltration data were modeled through statistical correlation of water-content changes with three variables: average annual precipitation, soil thickness (depth of bedrock), and topographic position, all of which are directly or indirectly dependent on elevation. Estimates of net infiltration obtained for the site vicinity ranged from 0 to 45 mm/yr. The limitations of the analysis are as follows:

- Only the neutron-moisture borehole data were used.

- Differences in geology beneath the soil layer were not taken into account.

- Seasonal variations in precipitation were not taken into account.

- Calculations were limited to the time frame of the water-content measurements and, therefore, could not provide any insight on the effects of climate change on infiltration.

7.1.4.4   Geochemical Methods

A chloride mass-balance method was used to estimate basin-wide recharge in a six-year study of two small, upland watersheds in central and south-central Nevada (Lichty and McKinley 1995 [DIRS 100589]). These watersheds were selected as "analog recharge" sites because they represent the effects of a possible future wetter climate at Yucca Mountain. For the East Stewart Basin, which is the smaller of the two basins, the average estimated recharge was 310 mm/yr, or about 50 percent of the estimated average annual precipitation of 639 mm (Table 7-5). For the

3-Springs Basin, which is more arid, the estimated average infiltration was 33 mm/yr, or about 10 percent of the average annual precipitation of 336 mm.

Flint et al. (1996 [DIRS 100147], Table 7) reported net infiltration estimated at borehole locations within the Yucca Mountain site area using a chloride mass-balance method. The estimated values ranged from 0.02 to 5.9 mm/yr (Table 7-6). The estimates made using the chloride mass-balance method vary considerably, depending on the depth of soil or rock samples and the type of material. For example, at Borehole UE-25 UZ#16, a net infiltration flux of 0.02 mm/yr was determined for a soil sample collected from an alluvial terrace, but fluxes of 3.0 mm/yr and 3.5 mm/yr were estimated for rock samples from the PTn and CHn hydrogeologic units, respectively. Differences between the results obtained using chloride mass-balance method for soil and underlying bedrock (especially the PTn hydrogeologic unit) may indicate that some lateral redistribution of higher fluxes into the nearby side slopes occurs by the time the water reaches the PTn (Flint et al. 1996 [DIRS 100147], p. 64). Thus, point estimates of net infiltration and recharge derived from the chloride mass-balance technique tend to be less robust than basin-wide estimates because of the assumption that only vertical flow occurs. Additional information on application of the chloride mass-balance method to the Yucca Mountain site is provided in CRWMS M&O (2000 [DIRS 151945], Section 5.3.10.2.1). More recent data from Flint et al. (2002 [DIRS 157411], pp. 188 to 189) (Table 7-7) obtained from samples collected from the PTn hydrogeologic unit in the ESF north ramp indicate infiltration rates as high as 9.9 mm/yr. This range of estimated values of net infiltration is corroborated by other methods, including ^{14}C residence times of pore water and water content of core samples (Yang 2002 [DIRS 160839]).

7.1.4.5 Deterministic Water-Balance Models

Deterministic numerical models for estimating net infiltration and recharge are based on the water-balance approach. A deterministic numerical model of net infiltration was developed for the Yucca Mountain site area (Section 7.10.3) to estimate net infiltration as the upper boundary condition for the site-scale unsaturated zone flow model and the total system performance assessment model. The development, calibration, and application of the numerical infiltration model are described in Flint et al. (1996 [DIRS 100147]). In general, the application of this approach requires measurements and estimates of basin-wide precipitation, snowpack depth and density, stream discharge, and meteorological parameters for defining potential evapotranspiration (Lichty and McKinley 1995 [DIRS 100589], pp. 4 to 10). Spatially varying parameters, such as evapotranspiration, canopy cover, snowpack cover and density, and soil characteristics, are also needed. The model was calibrated against the measured streamflow hydrographs for each basin, and model results compared reasonably well with results obtained using chloride mass-balance estimates. It was concluded that the uncertainty associated with the numerical model was greater than that of the chloride mass-balance model because of uncertainties in measured and estimated parameters needed for the model (Lichty and McKinley 1995 [DIRS 100589], pp. 1 and 26).

7.1.5 Collection and Analysis of Data for Incorporation in the Infiltration Model

The numerical model developed to similate infiltration in the Yucca Mountain area is described in USGS (2001 [DIRS 160355]). Various field and laboratory activities were conducted to

collect, analyze, and synthesize pertinent hydrologic data that served as the basis for constructing the net infiltration model (Flint et al. 1996 [DIRS 100147], pp. 46 to 69). These data were also used to test and validate various aspects of the conceptual model, as well as to calibrate the numerical model of net infiltration. The field and laboratory activities, which were conducted over a period of about ten years, included the following: collection of precipitation data (discussed in Section 7.1.3.2); monitoring of surface runoff; laboratory determination of matrix hydrologic properties and hydrochemistry of rock cores from shallow boreholes; measurement of soil hydrologic properties; measurement of evapotranspiration; neutron logging in boreholes, to determine volumetric water content; and measurement of water potential above and at the soil-bedrock interface.

7.1.5.1   Collection and Analysis of Runoff Data

Episodic overland flow as run-on and runoff were monitored at Yucca Mountain from 1984 to 1995 (Flint et al. 1996 [DIRS 100147], pp. 54 to 56). The most significant runoff events involving widespread overland flow and channel flow occurred in 1984, 1991, 1992, and 1995. The 1984 event was caused by an active warm-season El Niño Southern Oscillation. Streamflow data were obtained for several episodes of runoff that occurred in various drainages and subdrainages during the winters of 1991 to 1992, 1992 to 1993, and 1994 to 1995, all of which were years affected by an active cold-season El Niño Southern Oscillation.

7.1.5.2   Laboratory Determination of Matrix Hydrologic Properties and Hydrochemistry of Rock Core and Soil Samples

Matrix hydrologic-properties determinations of core samples from 23 neutron-moisture boreholes were conducted in the laboratory to determine porosity, bulk density, particle density, volumetric water content, saturated hydraulic conductivity, and moisture-retention characteristics (Flint 1998 [DIRS 100033], p. 11, Tables 5 and 7). These measurements were used in conjunction with data obtained from eight deep, surface-based boreholes to define the hydrogeologic framework of the unsaturated zone at Yucca Mountain and to determine mean hydrologic properties for each hydrogeologic unit (see Section 7.2.1). Core samples obtained from the neutron boreholes were also subjected to geochemical and isotopic analyses, including chloride concentration and ^{36}Cl ratios (Flint 1998 [DIRS 100033], p. 11, Tables 5 and 7). The analysis of ^{36}Cl ratios was used to qualitatively assess the vertical and horizontal movement of water in the shallow part of the unsaturated zone.

Field and laboratory analyses of the uppermost 1 ft (0.3 m) of various surficial soil types present at Yucca Mountain were conducted to define the spatial distribution of soil hydrogeologic properties (Flint et al. 1996 [DIRS 100147], pp. 41 to 43). Soil properties determined included field bulk density, grain density, porosity, rock fragment content, and sand, silt, and clay percentages. Soil water-content was determined at –0.01 MPa (-0.1 bar) and -6 MPa (-60 bars) water potentials. Saturated hydraulic conductivity was measured in the field using a double-ring infiltrometer. Porosity of the soil units ranged from 0.28 to 0.37 and saturated hydraulic conductivity ranged from 5.6×10^{-6} m/s to 3.8×10^{-5} m/s (Table 7-8).

7.1.5.3   Evapotranspiration Measurements

Pan evaporation was measured for several years near Yucca Mountain using a Class A evaporation pan (Figure 7-9). Although the data could not be used as a direct measure of potential evapotranspiration, they showed strong advective effects in the arid environment at Yucca Mountain. The data were also used to establish the upper limit of available energy for potential evapotranspiration modeling, given that modeled potential evapotranspiration should not exceed pan evaporation. The potential evapotranspiration ranges from a minimum of 500 mm/yr to a maximum of 900 mm/yr, depending mostly on the land-surface slope and aspect (CRWMS M&O 2000 [DIRS 151945], Section 8.2.5.2). Actual evapotranspiration will be less than the potential evapotranspiration due to limitations on the availability of water. The estimated actual evapotranspiration at Yucca Mountain ranges from 140 to 240 mm/yr (USGS 2001 [DIRS 160355], Section 6.11.1). Minimum values of evapotranspiration occur at locations on steep, northerly, and northeasterly facing slopes, particularly at locations surrounded by blocking topography.

7.1.5.4   Measurements of Water-Content in Neutron-Access Boreholes

A network of 99 shallow boreholes, ranging in depth from 4.6 to 78.0 m (15 to 260 ft), was established for measurement of subsurface volumetric water content by neutron geophysical logging (Flint and Flint 1995 [DIRS 100394], pp. 6 and 7). Measurements were performed at least monthly from 1984 through 1993. (The network of neutron boreholes was monitored through the end of September 1995.) Following major storm events (precipitation depth greater than approximately 25 mm), selected boreholes were also logged weekly and daily. The logs provided a measure of volumetric water content at borehole intervals of 0.1 and 0.3 m (0.3 and 1.0 ft). Most of the neutron boreholes were located on ridgetops, side slopes, and terraces and in active channels (Flint and Flint 1995 [DIRS 100394], pp. 2 to 6). Some boreholes were located to investigate the effect of specific geologic features, such as lithology of the underlying bedrock and fault zones.

As an example, Figure 7-10 shows the distribution of the moisture content with depth and time, indicating propagation of infiltration pulses caused by runoff during 1993 and 1995, and subsequent moisture redistribution in bedrock directly under a channel with thin alluvium (0.7 m [2.3 ft] deep) in Borehole USW UZ-N15, located on a ridge in the headwater part of Pagany Wash. The depth-versus-time profile shows a wetting front moving rapidly to a depth of 7.5 m (25 ft) in 1993 and 10 m (33 ft) in 1995, and then advancing more slowly to a maximum infiltration depth of over 15 m (50 ft) after the 1995 event. Most of the increases in water content depicted by the depth-time profile are assumed to be representative of net infiltration volumes because of the depth of penetration into the bedrock. The total increase in water storage below 3 m (10 ft) was equivalent to 500 mm (20 in.) in 1995. Two nearby Boreholes in the same geologic setting (USW UZ-N36 and USW UZ-N17), indicated similar patterns of water content redistribution, with smaller increases (150 mm and 110 mm [6 and 4 in.], respectively) in water storage below 3 m (10 ft), as no surface runoff occurred at these sites in 1995. Because these estimates of net infiltration are based on measurements of the volumetric water content using a neutron probe, they likely represent water that was imbibed into the rock matrix. Additional water may have penetrated to greater depths through fractures but is not likely detected using neutron-logging.

Shallow infiltration processes could be categorized on the basis of how water content changed with depth and time (Flint et al. 1996 [DIRS 100147], pp. 61 and 62; Flint et al. 2002 [DIRS 157411], pp. 185 and 195). Infiltration at ridgetops is affected by flat to gently sloping conditions, with thin soils mostly developed in places with clays and a higher water-holding capacity that reduces rapid evaporation and drainage. The ridgetops generally are located where the bedrock is moderately to densely welded and, therefore, fractured. These conditions lead to deeper penetration of infiltration pulses than in the other topographic positions, but relatively smaller volumes of water. Infiltration at the side slopes is affected by steep topography, commonly with very shallow to no soil cover, usually developed over welded, fractured tuff. These conditions often result in rapid runoff and low storage capacity of soils, so that the exposure of fractures at the surface can allow small volumes of water to infiltrate to greater depths, especially on slopes with north-facing exposures. If thin soil at the side slopes becomes saturated, flow into the underlying fractures could initiate. Infiltration at soil terraces is determined by flat topography, with broad deposits of rock fragments and fine soil with a large storage capacity. Such infiltration results in little runoff and only shallow penetration of the infiltrating water, which subsequently is almost entirely removed from the soil profile by evapotranspiration. Consequently, terraces contribute the least to net infiltration in the watershed. Infiltration at active channels differs little from that at the terraces except that they collect and concentrate runoff, which, although it occurs infrequently, can then penetrate deeply. However, this mechanism is not considered to be a major contributor to areally distributed net infiltration because of the infrequency of precipitation resulting in runoff and because the channels encompass only about 2 percent (Flint et al. 1996 [DIRS 100147], p. 61) of the Yucca Mountain site area. Nevertheless, significant localized pulses of net infiltration may occur in active channels.

Overall, analyses of changes in water-content profiles indicated deeper penetration and higher net infiltration rates at sites with thin soil cover (Flint et al. 1996 [DIRS 100147], pp. 60 and 61), (Figure 7-11), which tended to be on ridgetops and side slopes, but also included some channels in the upper part of watersheds (Figure 7-12). The deepest penetration of wetting fronts and the highest rates of net infiltration (greater than 60 mm/yr) were observed at sites where surface flow was concentrated or channeled toward locations underlain by fractured bedrock. Such sites include the headwater zones of washes and the lower sections of side slopes. Furthermore, more precipitation infiltrates into the ridgetops during the winter because lower-intensity storms result in little or no runoff, and slowly melting snow results in slow but steady infiltration over a period of several weeks each winter. This slow rate of input over long time periods allows for larger volumes of water to penetrate below the root zone and, thereby, escape the high evapotranspiration rates of the following summer. When surface flow is negligible, the deepest infiltration was observed on the ridgetops and the shallowest infiltration was observed in the washes, although there was little difference in infiltration characteristics between terraces and channels.

7.1.5.5   Continuous Monitoring of Water Potential Using Heat-Dissipation Probes

Heat-dissipation probes were used to obtain continuous water-potential measurements (Flint et al. 1996 [DIRS 100147], pp. 67 and 68). Water-potential measurements, shown in Figure 7-13, were obtained at four depths (7, 15, 36.5, and 73.7 cm [3, 5.9, 14.4, and 29 in.]) near neutron-access Borehole USW UZ-N15, which is on a bedrock ridge, with the deepest

measurement at the soil-bedrock interface. Within two weeks of installation (February 1995), heavy winter precipitation saturated the soil-bedrock interface to within 36 cm (14 in.) of the ground surface. The probe at the soil-bedrock interface indicated saturated conditions until the end of March and then dryout to less than -1 MPa (-10 bars) by September. The probes closer to the ground surface dried out faster, with the near-surface probes wetting up periodically due to summer precipitation events. A series of selected data were chosen and the rate of water loss was calculated based on the changes in water content with time, assuming vertical one-dimensional flow. Based on the calculated rate of water loss, the flow rate in early March was over 10 mm/d, but dropped to less than 2 mm/d within 30 days (Figure 7-14). The evaporation rate was estimated to be less than 2 mm/d, based on potential evapotranspiration calculations using the Priestley-Taylor equation, and yielding a maximum infiltration rate into the bedrock of 8 mm/d (Flint et al. 1996 [DIRS 100147], p. 68). The average infiltration rate for 30 days was 5 mm/d, equaling a total infiltration into the bedrock of 150 mm. The estimate of net infiltration (from analysis of the volumetric water content profile) for the nearby Borehole USW UZ-N17 was 110 mm for the same time period (Flint et al. 1996 [DIRS 100147], p. 68).

7.2   PROPERTIES OF HYDROGEOLOGIC UNITS

Properties of hydrogeologic units in the unsaturated zone were measured directly by use of two distinctly different methods: matrix-properties analysis of rock cores and field-scale air-injection testing. To define a physical and hydrologic properties database adequate for three-dimensional modeling of fluid flow in the unsaturated zone, an intensive study of matrix properties was performed using core samples from 31 boreholes (Flint 1998 [DIRS 100033], p. 11). Nearly 4,900 core samples were analyzed in the laboratory to measure important hydraulic properties. These properties include porosity, bulk density, particle density, water content, water potential, saturated and unsaturated hydraulic conductivity, and moisture retention characteristics. The results of the matrix properties analyses are described in Section 7.2.1. Unsaturated zone air-injection testing measured the bulk (or total) permeability of the rock mass to air (LeCain 1997 [DIRS 100153]; LeCain 1998 [DIRS 100052]). When combined with other information, these data are used to analyze the flow of both water and gas through the rock units in which the repository will be located. Air-injection tests were performed to determine field-scale bulk permeability, porosity, and anisotropy of the major rock units above, below, and within the repository horizon. The results of the air-injection tests are described in Section 7.2.2. Indirect estimates of bulk permeability were derived from the analysis of the pneumatic-pressure response of instrumented boreholes to changes in atmospheric pressure. The results of these pneumatic analyses are described in Section 7.3. In addition, air-injection and tracer testing of the Ghost Dance fault are described in Section 7.2.2.2 and air-injection and liquid-release tests conducted in niches of the ESF main drift for seepage-related studies are summarized in Section 7.6.4.1. Furthermore, fractured rock-mass studies using fracture data from surface exposures, boreholes, and ESF mapping were described in Section 3.5.8. Data from the fractured rock-mass studies were used to help interpret the air-injection tests.

7.2.1   Characterization of Hydrogeologic Units Using Core-Scale Matrix Properties

During the early phases of the YMP, designation of hydrogeologic units for the unsaturated zone encompassed large rock-unit divisions based primarily on the degree of welding (Montazer and Wilson 1984 [DIRS 100161], p. 9). In addition, this system of identification also recognized

other characteristics potentially important to hydrologic properties, such as occurrence of lithophysal cavities, fracturing, bedding, and mineral alteration. Stratigraphic relationships and lithologic characteristics of the geologic formations that comprise the hydrogeologic units are described in Section 3.3; structural characteristics are described in Section 3.5. The detailed designation of hydrogeologic units based on matrix hydrologic properties is described in this section, and the use of stratigraphic, structural, and hydrologic information to construct the site-scale unsaturated zone flow model is described in Sections 7.9 and 7.10.

Matrix properties testing was conducted on 4,892 rock-core samples taken from 31 boreholes (Flint 1998 [DIRS 100033], p. 11). Measurements were made of porosity, bulk density, particle density, volumetric water content, saturated hydraulic conductivity, and moisture retention characteristics. Selected samples also were analyzed for unsaturated hydraulic conductivity. Detailed descriptions of the methods used to measure matrix properties are contained in Flint (1998 [DIRS 100033], pp. 11 to 19) and Conca and Wright (1998 [DIRS 150049]). Additional matrix properties measurements which include data for Boreholes USW SD-6 and USW WT-24, were recently published (Flint 2003 [DIRS 163336], Table 3).

7.2.1.1   Matrix Properties of Detailed Hydrogeologic Units

The distributions of physical properties and hydrologic parameters at the Yucca Mountain site are complex because of the depositional, cooling, and alteration history of the volcanic rock units (Flint 1998 [DIRS 100033], p. 2). This history results in differences in porosity, connectivity and tortuosity of flow paths, water-retention character, heterogeneities, and scales of features that all influence the resulting hydrology of the unsaturated zone at the site. Characterization of matrix properties involves the measurement and description of both small-scale heterogeneities of the rocks and larger-scale features of the hydrogeologic units as a whole. Nevertheless, the definition of detailed hydrogeologic units is based on measurement of rock properties from 7 cm (3 in.) diameter core samples collected during the drilling of boreholes. Thus, matrix properties analysis is limited to features and properties that can be captured on a relatively small scale.

Because water is stored in and flows through the interconnected pores of the rock matrix, porosity is useful for characterizing the hydrologic character of the various rock types. In general, porosity can be related primarily to the depositional features and amount of welding. (A welded tuff was deposited under conditions where the particles making up the rock were heated sufficiently to cohere. In contrast to nonwelded tuff, welded tuff is considered to be denser, less porous, and more likely to be fractured.) Porosity is also directly related to the alteration history of the rocks at Yucca Mountain; clays, zeolites, opal, and calcite form in situ or are deposited in pore spaces, causing a reduction in porosity (Flint 1998 [DIRS 100033], p. 32). However, the occurrence of clay or zeolite zones reduces the measured porosity only slightly because water is stored in clay and zeolite mineral structures rather than in pore spaces. An exception involves smectites, which swell with the incorporation of water to as much as 300 times their original size, thus reducing their porosity. Because clays and zeolites influence pore-size distribution, their presence also affects moisture retention characteristics and permeability. Rocks containing clay or zeolites typically contain a relatively large volume of water, but because the water is held tightly within clay structures and very small pores, the permeability is reduced.

Differences in these characteristics have been used to identify detailed hydrogeologic units within the major hydrogeologic units, as shown in Table 7-9. Distinctions made based on porosity are indicated in parentheses next to the detailed hydrogeologic unit in Table 7-9. Core samples having the lowest porosity were collected from the most densely welded rocks, and the core samples exhibiting the highest porosity were derived from nonwelded and bedded rocks (Table 7-10). For the TCw hydrogeologic unit, porosity variations define most of the boundaries (Table 7-9), with the exception of the boundary between the CUC and CW detailed hydrogeologic units which is defined as the lithostratigraphic contact between the upper lithophysal and middle nonlithophysal zones of the crystal-poor Tiva Canyon Tuff (Tpcpul and Tpcpmn, respectively). For the PTn hydrogeologic unit, porosity is the principal distinction, except the TPP detailed hydrogeologic unit is identified based on its low extent of welding. Distinctions among the detailed hydrogeologic units in the TSw hydrogeologic unit are based on porosity differences associated with the lithophysal and nonlithophysal zones. In the CHn hydrogeologic unit, the detailed hydrogeologic units are defined by the relative vitric and zeolitic mineral content that could be identified through differences in porosity for relative-humidity drying at 60°C and standard 105°C oven drying. For the CFu hydrogeologic unit, the detailed hydrogeologic units are identified on the basis of alteration character (Flint 1998 [DIRS 100033], pp. 19 to 32).

7.2.1.2 Effects of Mineral Alteration and Estimation of Saturated-Hydraulic Conductivity

The altered rocks of the CHn hydrogeologic unit, such as the detailed hydrogeologic units of BT (consisting of the Tacbt and Tacbs lithostratigraphic units), PP4 (Tcp unit 4), and PP1 (Tcp unit 1) units (Table 7-9), have relatively low relative-humidity porosity values (Flint 1998 [DIRS 100033], pp. 32 and 33). However, these rocks also have residual water contents of 5 percent or greater, either because water is bound in the zeolitic minerals or because water is trapped by tridymite and cristobalite (Rautman and Engstrom 1996 [DIRS 101008], Appendix H). It is apparent that the presence of cristobalite alone does not produce this effect, but rather that tridymite is necessary, possibly in combination with cristobalite. These findings indicated that certain vapor-phase alteration minerals have significant effects on the structure and geometry of the pore spaces in the rock, resulting in greater residual water content. The greater tortuosity of the flow channels caused by the presence of clay, zeolites, or vapor-phase minerals also reduces the permeability (Flint 1998 [DIRS 100033], p. 33), as discussed in the following paragraphs. (There is evidence that the very high percentages of opal-CT [a disordered silica phase containing both cristobalite- and tridymite-like structural units] often found in the Tacbt may influence the hydrologic character of rocks by reducing the permeability even more than the presence of zeolites.)

The effects of alteration minerals on the hydrologic properties of the unsaturated rocks at Yucca Mountain were evaluated further by comparing the relative-humidity porosity with the measured saturated hydraulic conductivity (K_s) for 593 samples, collectively representing all unsaturated zone lithostratigraphic units (Flint 1998 [DIRS 100033], p. 38). These comparisons are shown in Figure 7-15. Figure 7-15a shows the relation of the log of K_s to porosity for samples grouped by hydrogeologic unit. The location on the plot of the points representing the zeolitic rocks of the Calico Hills Formation (CHZ detailed hydrogeologic unit) is distinct in that they indicate a relatively high porosity (greater than 0.2) but very low saturated conductivity (most less than

1×10^{-10} m/s). Most samples from the crystal-rich and crystal-poor vitrophyres of the Topopah Spring Tuff (TC and PV3 detailed hydrogeologic units) have very low matrix porosity values (less than 0.1), yet several have relatively high conductivity (1×10^{-8} to 1×10^{-7} m/s) because of the presence of microfractures. Similarly, three crystallized and welded samples from the Topopah Spring Tuff (Tpt) with low porosity and high conductivity contained visible microfractures. It is possible that some of the samples from the TC and the PV3 with low values of K_s had microfractures, but they were filled with alteration minerals.

The correlation between porosity and saturated hydraulic conductivity is indicated clearly in Figure 7-15b, where the porosity and saturated conductivity are plotted by more generalized rock types: vitric/crystallized, altered, and microfractured (Flint 1998 [DIRS 100033], pp. 38 and 39). The microfractured category includes the TC and PV3 detailed hydrogeologic units, plus the three welded samples from the Tpt with the visible microfractures that do not truly represent matrix permeability. The "altered" category includes all lithostratigraphic units below the vitric/zeolitic boundary in the CHn hydrogeologic unit (including the BT1, CHZ, BT, PP4, PP3, PP2, PP1, BF3, and BF2 detailed hydrogeologic units) and the CMW detailed hydrogeologic unit in the Tiva Canyon Tuff. The vitric/crystallized category includes all of the other hydrogeologic units. The altered category is only crudely defined because there are crystallized and unaltered zones within the hydrogeologic units that comprise this category. The hydrogeologic units present at the vitric/zeolitic boundary vary spatially in the vicinity of Yucca Mountain (Flint 1998 [DIRS 100033], p. 39). In the southern part of the site, where the boundary is as much as 140 m below the Tptpv3, the upper parts of the Calico Hills Formation and the Tpbt1, Tptpv1, and Tptpv2 units of the Topopah Spring Tuff are unaltered. This condition was observed in the samples from only two Boreholes, USW SD-7 and USW SD-12. All other boreholes are located to the north and east, where the vitric/zeolitic boundary is typically defined at the base of Tptpv3. Properties for the BT1 detailed hydrogeologic unit, which includes the Tptpv1 and Tpbt1 lithostratigraphic units, have been characterized for both altered (BT1a) and unaltered (BT1) samples.

The location of the vitric/zeolitic boundary seems to be an important factor contributing to formation of perched-water bodies (Rousseau et al. 1999 [DIRS 102097], pp. 171 and 172). High saturations in rocks below the Topopah Spring Tuff indicate that the presence of alteration minerals has reduced the permeability and the capacity of these rocks to transmit water downward. In zones where there is little or no alteration, such as in the vitric rocks of the Calico Hills Formation (CHV detailed hydrogeologic unit) and some of the devitrified and vapor-phase corroded rocks of the Prow Pass Tuff (PP3 detailed hydrogeologic unit), saturations are extremely low because the pores are larger and drain more easily. In the crystallized and minimally vapor-phase-corroded Prow Pass Tuff (PP4, PP2, and PP1 detailed hydrogeologic units), saturations are high because the rocks are welded and have small pores. There is also some evidence that high-temperature alteration products, such as the vapor-phase crystallization minerals tridymite and cristobalite, have influenced the retention of water in this zone (Flint 1998 [DIRS 100033], p. 33).

7.2.1.3 Mean Matrix Property Values for Hydrogeologic Units

Mean values and standard deviations were calculated from the regression analyses for all measured properties (Table 7-10) and for estimated K_s values for each hydrogeologic unit

(Flint 1998 [DIRS 100033], p. 43). In general, the variation in porosity within each detailed hydrogeologic unit was relatively small, with the exception of BT4, BT2, and PV2. Because BT4 is very thin and few samples were collected, substantial variation in properties was expected. The relatively large variation in properties in BT2 resulted from the fact that it is composed of lithostratigraphic units that vary significantly in the amount of mineral alteration, and it includes the moderately welded Tptrv2 lithostratigraphic unit, which rapidly grades downward into low-porosity rocks. The same is true for the PV2, which grades relatively sharply from very low-porosity to relatively high-porosity rocks.

Examination of the means and standard deviations for K_s reveals large statistical variances for many hydrogeologic units (Flint 1998 [DIRS 100033], pp. 43 and 46). In particular, detailed hydrogeologic unit CMW exhibits large variances because the degree of mineral alteration likely is variable vertically within the unit and laterally between boreholes. The large variance in K_s values for detailed hydrogeologic unit TC is likely caused by the random sampling of microfractures.

7.2.1.4   Moisture Retention Characteristics and Unsaturated Hydraulic Conductivity

Moisture retention curves (water potential versus saturation) were developed for representative hydrogeologic units (Flint 1998 [DIRS 100033], p. 40) and are shown in Figure 7-16. The first three data sets for detailed hydrogeologic units CW, BT3, and TR include both laboratory data desorption curves and composite curves combining laboratory data from core samples and all field data. Moisture retention van Genuchten curve-fit parameters (α, n, and m) for each detailed hydrogeologic unit were also calculated (Flint 1998 [DIRS 100033], p. 46) and are listed in Table 7-11.   Two models were developed: one model is associated with the laboratory desorption data (thick lines on Figure 7-16a through 7-16c), and the second model is associated with the composite data set (thin lines on Figure 7-16a through 7-16c).

Notable differences in the moisture retention curves are chiefly a function of the pore-size distributions of the rock types (Flint 1998 [DIRS 100033], p. 40). These different distributions primarily result from the different degrees of welding and are exemplified by comparing the curve for the bedded tuff detailed hydrogeologic unit BT3 to those of the welded tuffs (CW and TUL detailed hydrogeologic units). Moisture retention curve-fit parameters were used to predict unsaturated hydraulic conductivity based on values of saturated conductivity (Flint et al. 1999 [DIRS 107377]) and the relation developed by van Genuchten (1980 [DIRS 100610]).

7.2.1.5   Properties of Fault Zones

Borehole USW UZ-N35 is located in Broken Limb Wash, near USW SD-12 (Figure 7-2), and penetrated the Ghost Dance fault zone at a depth of approximately 30 m (100 ft).   Neutron moisture logging indicated an increase in water content in the footwall associated with precipitation during the winter of 1993 (Flint and Flint 1995 [DIRS 100394], p. 7; Flint et al. 1996 [DIRS 100147], p. 60). One possible interpretation is that the fault provided a fast pathway for infiltration.

Analysis of rock core from a horizontal borehole in the ESF northern Ghost Dance fault alcove indicated that the porosity slightly decreased and the saturation slightly increased in the footwall

east of the main trace of the fault (Figure 7-17). There was no distinctive change in either porosity or saturation for samples collected from the fault zone.

7.2.1.6 Spatial Variability of Matrix Properties

Rock properties vary vertically and laterally as the result of original, depositional processes and subsequent postdepositional alteration. At certain scales and at certain positions within the volcanic rocks at Yucca Mountain, the influence of deterministic geologic processes can be predicted. For example, porosity values are relatively high in the rocks at the base of the ash-flow sheets (Tiva Canyon and Topopah Spring tuffs), where cooling occurred quickly. Progressively lower porosity values occur at higher stratigraphic levels within the ash-flow sheet, and porosity decreases to very low values in the interior of the deposit, where temperatures remained high long enough for compaction and welding to occur (Flint 1998 [DIRS 100033], Figures 3 and 4).

Samples of the Tiva Canyon Tuff were collected along a series of 26 vertical transects on the west-facing slope of Solitario Canyon to examine spatial variability in that unit (Rautman et al. 1995 [DIRS 106645]). The sampling covered a stratigraphic sequence beginning in the moderately welded rocks of the Tiva Canyon Tuff crystal-poor lower nonlithophysal columnar subzone (Tpcplnc), downward through the Tiva Canyon Tuff crystal-poor vitric densely welded subzone (Tpcpv3), Tiva Canyon Tuff crystal-poor vitric moderately welded subzone (Tpcpv2), and Tiva Canyon Tuff crystal-poor vitric nonwelded subzone (Tpcpv1), and terminating in the Pre-Tiva Canyon bedded tuff (Tpbt4). Porosity values were plotted in relation to the scaled thickness from the base of each transect, expressed as a dimensionless proportion (Rautman et al. 1995 [DIRS 106645], Figure 3). Porosity ranged from 0.10 at the top of the stratigraphic sequence to as high as 0.60 at the bottom. The composite plots of porosity and saturated hydraulic conductivity (Figure 7-18) indicate strong vertical trends in porosity and saturated hydraulic conductivity. Analysis of the horizontal trends indicated a lack of substantial spatial correlation. However, because of the obvious vertical trends, vertical models were fit to the data sets to predict properties of the corresponding stratigraphic elevation in other locations (Rautman et al. 1995 [DIRS 106645], Figure 7). (See CRWMS M&O 2000 [DIRS 151945], Section 4.8, for a detailed description of three-dimensional modeling of rock properties.)

The variability of matrix properties of the Topopah Spring Tuff at the repository horizon are shown on Figure 7-19, which lists porosity and saturated hydraulic conductivity values from the Topopah Spring Tuff middle nonlithophysal (Tptpmn). In addition, a lithostratigraphic section encompassing the Tptpmn (detailed hydrogeologic unit TMN in Tables 7-9 and 7-10) and the upper part of the Topopah Spring Tuff crystal-poor lower lithophysal (Tptpll) (TLL) was sampled systematically in the ESF main drift (from ESF construction station 28+00m to 58+00m along the length of the tunnel). A total of 142 rock samples were collected systematically at 20 m (66 ft) spacing and analyzed for physical properties, including porosity (Figure 7-19). Saturated hydraulic conductivity has been measured on 60 of the 142 samples. There is substantial scatter in the Tptpmn (ESF construction station 28+00 to 35+00), and then an increase in the relative-humidity porosity from about 9 percent to about 12 percent midway through the transect, associated with the intensely fractured zone. A visual comparison of saturated hydraulic conductivity and porosity values (Figure 7-19) indicates that the two data sets correlate reasonably well. Mean relative-humidity porosity for the 60-sample subset from the

ESF main drift systematic sampling transect is 0.079 (standard porosity, determined at 105ºC, is 0.099), and mean saturated hydraulic conductivity is 4.7×10^{-12} m/s.

Few of the hydrogeologic units present at Yucca Mountain were penetrated by a sufficient number of surface-based boreholes to determine if areal trends in porosity are present (Flint 1998 [DIRS 100033], pp. 46 to 54). However, a large-scale analysis of areal distribution of porosity was done using kriging for the two detailed hydrogeologic units that were penetrated by the largest number of boreholes—the central, welded, crystal-poor member of the Tiva Canyon Tuff (CW) and the Pre-Pah Canyon/Topopah Spring bedded tuff (BT2) (Flint 1998 [DIRS 100033], pp. 46 and 47). In the vicinity of the repository, CW has a relatively smooth increase in porosity from south (about 0.07) to north (about 0.12), based on data from 17 boreholes (Flint 1998 [DIRS 100033], Figure 16). In contrast, BT2 has a smaller areal distribution and a range in porosity from 0.37 at Borehole USW SD-7 to 0.52 at the northern end of the repository area (Flint 1998 [DIRS 100033], Figure 16), based on data from 15 boreholes. The calculated areal variation in porosity for these two units is in contrast to the lack of lateral trends in the two-dimensional surface transect study of the base of the Tiva Canyon Tuff discussed in the previous paragraph.

Vertical variability of matrix properties within hydrogeologic units can be reasonably described for most of the units (Flint 1998 [DIRS 100033], p. 46). Problematic units are very thin or layered units or those with features larger than core-size samples that dominate the flow of water at the site scale. However, there is a large degree of uncertainty associated with the representations of areal variability of hydrologic properties, because of the high degree of rock heterogeneity and because the bulk of the data is from core-scale-sized samples from one-dimensional boreholes sparsely distributed over the study area. The areal distribution of core scale properties might adequately be represented for large-scale numerical flow models by the correlation of flow properties with surrogates such as porosity, which can be modeled using lithostratigraphic distributions and which has been shown to be related to flow properties. The correlation of porosity with lithology provides a much larger database with which to calculate spatial distributions. Additional information regarding this relationship is provided in the description of rock-property modeling in CRWMS M&O (2000 [DIRS 151945], Section 4.8).

7.2.1.7 Matrix Properties of the Calico Hills Nonwelded Hydrogeologic Unit at the Busted Butte Test Facility

Physical-properties testing of core samples from the Busted Butte test facility have been completed on 80 samples, 59 of which also have been tested for K_s. Mean values of relative-humidity porosity and K_s for the Busted Butte samples are listed in Table 7-12, along with mean values for samples from the two surface-based Boreholes (USW SD-7 and USW SD-12) nearest the repository area that penetrated the same lithostratigraphic units. Also listed are mean values for all surface-based boreholes in the site area. Because lithostratigraphic unit Tpbt1 is not present at Busted Butte, units Tptpv1 and Tpbt1 were combined for the site evaluation. This combination is justified because the properties of these two units are not significantly different (Flint 1998 [DIRS 100033], p. 29).

The porosity of Tptpv2 at Busted Butte is much higher than in Boreholes USW SD-7 and USW SD-12. Similarly, K_s of the Tptpv2 at Busted Butte is 1,000 to 10,000 times greater. Although porosity of the Tptpv1/Tpbt1 rocks is higher at Busted Butte than that in all the surface-based boreholes, K_s is about one-tenth of that in the boreholes, suggesting some alteration not evident in the physical property measurements. Although porosity of the vitric Tac at Busted Butte is about the same as in the boreholes. K_s at Busted Butte is about 100 times greater than in the boreholes. The difference in K_s results most likely from a biasing of the samples collected from the surface-based drilling toward those less friable, given that core recovery in the friable rocks was generally poor (Flint 1998 [DIRS 100033], Table 4).

Unsaturated hydraulic conductivity data (30 samples) and moisture-retention-curve data (52 samples) were determined from cores sampled from the Busted Butte test facility. Measurements of the unsaturated hydraulic conductivity and moisture-retention functions on a representative sample from the Calico Hills Formation is shown in Figure 7-20.

7.2.2   Field-Scale Characterization of Hydrogeologic Units Using Air-Injection Testing

Air-injection testing has been conducted in the Yucca Mountain unsaturated zone to determine the field-scale bulk permeability, porosity, and anisotropy of the rock units that comprise, overlie, and underlie the repository horizon. For the nonwelded and bedded units (such as the PTn hydrogeologic unit), air-injection tests provide field-scale measurements of the matrix permeability and porosity. For the highly fractured units (such as the TSw hydrogeologic unit), air-injection tests provide measurements of the bulk permeability and porosity of the fracture network.

7.2.2.1   Surface-Based Air-Injection Testing

Air-permeability values were determined from 194 single-hole, air-injection tests conducted in four surface-based boreholes (LeCain 1997 [DIRS 100153]). The geologic units tested were the Tiva Canyon, Yucca Mountain, Pah Canyon, and Topopah Spring tuffs; the Calico Hills Formation; and three bedded tuffs within the PTn hydrogeologic unit. Air-injection permeability values were compared to permeability values derived from laboratory tests and pneumatic monitoring. Regression analysis was conducted between air-injection permeability values and fracture density and the presence of lithophysal cavities. Because the air permeability of rock will change with water content, a given permeability also has an associated capillary pressure. Consequently, the relationship between air permeability and water redistribution was also evaluated.

Air-injection measurements were performed in four boreholes. The testing interval ranged from 3.5 to 4.6 m [LeCain 1997 [DIRS 100153], p. 5). Borehole UE-25 UZ#16 extended from the crystal-poor, lower-lithophysal zone of the Tiva Canyon Tuff (Tpcpll) down to the Calico Hills Formation and was the only borehole tested that penetrated the Calico Hills Formation. Borehole USW SD-12 extended from the Tpcpll down to the crystal-poor lower nonlithophysal zone of the Topopah Spring Tuff crystal-poor lower nonlithophysal (Tptpln), but tests in this borehole were limited to the Topopah Spring Tuff. Borehole USW NRG-6 extended from the Tpcpll down to the crystal-poor middle nonlithophysal zone of the Topopah Spring Tuff (Tptpmn). Borehole USW NRG-7a extended from the Tiva Canyon Tuff crystal-poor lower

nonlithophysal (Tpcpln) down to the crystal-poor lower lithophysal zone of the Topopah Spring Tuff (Tptpll).

7.2.2.1.1   Air-Injection Permeability Values Results

Tiva Canyon Tuff–A statistical summary of air-injection permeability values for individual lithostratigraphic units within the Tiva Canyon Tuff is presented in Table 7-13, and a statistical summary for the entire Tiva Canyon Tuff is presented in Table 7-14. All test intervals were located in zones of the crystal-poor member of the Tiva Canyon Tuff, including the lower lithophysal, the lower nonlithophysal, and crystal-poor vitric. The database is small, with only four test intervals in each of Boreholes UE-25 UZ#16, USW NRG-6, and USW NRG-7a. The total number of test intervals in each of the two tables differs because test intervals that straddled two lithostratigraphic units are not included in Table 7-13.   The air-injection permeability values ranged from 2.4×10^{-13} m^2 in USW NRG-7a to 5.4×10^{-11} m^2 in USW NRG-7a. The mean air-injection permeability value for all boreholes was 1.2×10^{-11} m^2. Analysis of variance indicated that the mean permeability values of the four boreholes are not statistically different (LeCain 1997 [DIRS 100153], p. 17).

Paintbrush Nonwelded Hydrogeologic Unit–A statistical summary of the air-injection permeability values for individual lithostratigraphic units within the PTn hydrogeologic unit is presented in Table 7-15, and a summary for the entire PTn is presented in Table 7-16. All values are from Borehole USW NRG-7a. The summary includes test intervals in the Yucca Mountain Tuff, Pah Canyon Tuff, the three bedded tuffs between the base of the Tiva Canyon Tuff and the top of the Topopah Spring Tuff (Tpbt2, Tpbt3, and Tpbt4), and two test intervals in the crystal-poor nonwelded vitric zone of the Tiva Canyon Tuff (Tpcpvl). The nonwelded tuff air-injection permeability values ranged from 1.2×10^{-13} m^2 at the bottom of the Pah Canyon Tuff and the crystal-poor vitric zone of the Tiva Canyon Tuff to 3.0×10^{-12} m^2 in the pre-Yucca Mountain Tuff bedded tuff (Tpbt3).   The mean air-injection permeability value was 5.4×10^{-13} m^2 (LeCain 1997 [DIRS 100153], p. 20). Air-injection permeability values for the PTn hydrogeologic unit with depth are shown on Figure 7-21. The geology and rock-structure log (SNL 1995 [DIRS 101293], p. 7) describes the Tpbt3 as "coarse grained and weakly consolidated," with no fractures, indicating that flow in Tpbt3 is through the matrix. The log describes the Tiva Canyon crystal-poor vitric test interval as a "welding transition zone." The low permeability is probably the result of partial welding. The Yucca Mountain and Pah Canyon tuffs both showed decreased permeability with increased depth. Statistical analysis of the air-injection permeability values for the PTn hydrogeologic unit indicates that, although slightly skewed by the relatively larger values for the pre-Yucca Mountain Tuff bedded tuff (Tpbt3), the distribution is reasonably log normal (LeCain 1997 [DIRS 100153], p. 20).

Topopah Spring Tuff–A statistical summary of air-injection permeability values for individual lithostratigraphic units within the Topopah Spring Tuff is presented in Table 7-17, and a summary for the entire Topopah Spring Tuff by borehole is presented in Table 7-18. Permeability values ranged from 3.3×10^{-11} m^2 in the crystal-rich lithophysal zone of Borehole USW SD-12 to 2.0×10^{-14} m^2 in the crystal-poor middle nonlithophysal zone of Borehole UE-25 UZ#16.   The borehole mean permeability values ranged from 4.0×10^{-13} m^2 in BoreholeUSW NRG-7a to 4.7×10^{-12} m^2 in Borehole USW SD-12. These permeability values

agree with the 10^{-15} to 10^{-11} m^2 permeability range was derived from the Alcove 5 preheating, air-injection testing (BSC 2002 [DIRS 160771], Section 6.3.2.4; Tsang et al. 2000 [DIRS 162593]). Histograms (LeCain 1997 [DIRS 100153], p. 22, Figures 17 and 18) show that the distributions of the air-permeability values for the Topopah Spring Tuff are not normal; however, the natural log permeability values could be considered normally distributed.

7.2.2.1.2   Relation of Fracture Density, Lithophysal Cavities, and Core Recovery to Air-Injection Permeability

Table 7-19 shows that Boreholes UE-25 UZ#16 and USW SD-12 have similar fracture densities in both the Tiva Canyon and Topopah Spring tuffs, whereas in Boreholes USW NRG-6 and USW NRG-7a, fracture densities in Tiva Canyon Tuff are about four times larger than in the Topopah Spring Tuff. The NRG boreholes are both located on the edge of Drill Hole Wash (Rousseau et al. 1999 [DIRS 102097], Figure 20), which has been eroded along the Drill Hole Wash fault (Section 3.5.4.3), whereas Boreholes UE-25 UZ#16 and USW SD-12 are located farther south, and at a distance from block-bounding or intrablock faults (discussed in Sections 3.5.3 and 3.5.4). The differences in fracture density and air-injection permeability between boreholes may be related to their location with respect to these fault structures (Rousseau et al. 1999 [DIRS 102097], pp. 44 to 53).

7.2.2.2   Air-Injection and Supportive Testing in the Exploratory Studies Facility

Air-injection and gaseous tracer tests have been conducted in test alcoves constructed off the north ramp and main drift of the ESF (Figure 1-3). Testing was conducted in Alcove 1 to confirm the gaseous-phase properties of the Tiva Canyon Tuff determined through investigations in surface-based boreholes. Testing in Alcove 2 was intended to determine the properties of the Bow Ridge fault zone and the extent to which it may be a fast pathway for the flow of fluids (gas and water). Testing in Alcove 3 was intended to determine the properties of the transition zone between the TCw and PTn hydrogeologic units. The testing interval ranged from 1 to 3 m (LeCain 1998 [DIRS 100052], p. 5). Testing to ascertain the properties of the Ghost Dance fault was conducted in Alcoves 6 and 7.

7.2.2.2.1   Alcove 1

Alcove 1, at ESF construction station 00+43, was constructed in the Tiva Canyon crystal-poor upper lithophysal unit (Tpcpul), which is moderately to densely welded and fractured (LeCain 1998 [DIRS 100052], p. 13). Air-permeability values derived from single-hole air-injection tests ranged from 2.0×10^{-13} m^2 to 8.5×10^{-11} m^2 (LeCain 1998 [DIRS 100052], p. 15, Tables 1 to 3). The arithmetic means of these measurements range from 1.1×10^{-11} m^2 to 3.85×10^{-11} m^2; the geometric means range from 7.2×10^{-12} m^2 to 2.7×10^{-11} m^2 (Table 7-20).

7.2.2.2.2   Alcove 2

Alcove 2, the Bow Ridge fault test alcove, was constructed at ESF construction station 01+68 on the east side (footwall) of the Bow Ridge fault in the Tiva Canyon crystal-poor middle nonlithophysal zone (Tpcpmn, Table 3-5), which is densely welded and fractured (LeCain 1998 [DIRS 100052], p. 17). The alcove is approximately 48 m (160 ft) long and parallels the Bow

Ridge fault, on the east side of the fault. The strike/dip orientation of the Bow Ridge fault is 180°/75° west. The Bow Ridge fault is a normal fault, with approximately 100 m (330 ft) offset, down to the west. In the ESF exposure, the Tmbt1 (Table 3-5) on the west side of the fault is in contact with the Tiva Canyon Tuff east of the fault. The fault zone is approximately 2 m (7 ft) wide and the brecciated zone is composed of Tiva Canyon Tuff clasts in a pre-Rainier Mesa Tuff matrix. Two test boreholes drilled westward from the alcove penetrated the Tiva Canyon crystal-poor lower lithophysal zone (Tpcpll, Table 3-5), the Bow Ridge fault, and then the pre-Rainier Mesa Tuff bedded tuff (Tmbt1) in the hanging wall of the fault (LeCain 1998 [DIRS 100052], Figure 12).

Temperature Measurements–Temperature measurements from both test boreholes indicated that the heat conduction, which was apparently caused by the alcove ventilation, could affect the temperature regime approximately 6.1 m (20 ft) into the rock. At the same time, the temperature over the Bow Ridge fault remained stable. In interpreting the temperature data, however, the possible effects of changes in the borehole diameter and a downward flux of cooler air or water cannot be completely ruled out. Overall, the temperature data suggest that there was no flow in the Bow Ridge fault zone (LeCain et al. 1997 [DIRS 100156], pp. 34 and 35).

Single-Hole and Crosshole Air-Injection and Tracer Testing–Single-hole and crosshole air-injection and tracer testing was conducted in the Bow Ridge fault test-boreholes. The single-hole air-injection permeability values of the Tpcpmn ranged from 6.0×10^{-12} m^2 to 26.4×10^{-12} m^2, with arithmetic and geometric means of 13.9 and 12.2×10^{-12} m^2, respectively (Table 7-21). Permeability values of the Tpcpll ranged from 0.6×10^{-12} m^2 to 2.0×10^{-12} m^2, with arithmetic and geometric means of 1.3×10^{-12} m^2 and 1.2×10^{-12} m^2. The three permeability values of the Bow Ridge fault breccia range from 8.0×10^{-12} m^2 to 15.8×10^{-12} m^2 (LeCain 1998 [DIRS 100052], Table 5). The two permeability values for the Tmbt1 are 41.3×10^{-12} m^2 and 22.0×10^{-12} m^2 (LeCain 1998 [DIRS 100052], Table 5). The permeability of the Tpcpmn is about 10 times greater than that of the Tpcpll. Comparing the mean permeability values of the Tpcpmn and the Tpcpll with the permeability values of the Bow Ridge fault zone and the Tmbt1, the permeability of the Tpcpll is 5 to 10 times smaller than the other units. This may be due to less intense fracturing of the Tpcpll associated with the Bow Ridge fault, because the lithophysal cavities of the Tpcpll may have absorbed some of the tectonic stress.

Eleven test intervals indicated water redistribution at pressures less than 0.064 MPa (0.64 bars); one test interval had a water-redistribution pressure of less than 0.006 MPa (0.06 bars) (LeCain 1998 [DIRS 100052], Table 5). The absence of water redistribution does not mean that the capillary pressure is greater than the gas injection pressure but may be a function of the fracture apertures intersecting the test interval. Test intervals that showed no water redistribution probably intersect fractures with apertures too large to hold water at the in situ capillary pressures. Overall, the testing indicates that the in situ capillary pressures of the Tpcpmn and Tpcpll are less than one bar (0.1 MPa). Testing in the fault breccia and Tmbt1 indicated low water-saturation, which could have been caused by the increased porosity of the nonwelded Tmbt1 (LeCain 1998 [DIRS 100052], p. 19).

Crosshole air-injection test results agreed with the single-hole results, in that the crosshole values were within 2 or 3 times the single-hole values, and indicated that the scale differences (1 m vs.

3 m [3 ft vs. 10 ft]) did not effect the test results. Table 7-23 shows the permeability and porosity values from crosshole tests 4, 5, and 6 for the spherical-flow type curve analysis (LeCain 1998 [DIRS 100052], p. 21). Comparison of the Tpcpmn air-permeability values to the surface-based values indicates that the Tiva Canyon Tuff is isotropic. Comparison of the Tiva Canyon Tuff lower lithophysal air-permeability values and the surface-based values indicate that the Tpcpll is anisotropic, with a horizontal-to-vertical ratio of approximately 10:1. The crosshole testing also provided pneumatic porosity estimates for the Bow Ridge fault breccia of 0.13 and 0.20, and 0.27 for the Tmbt1 (LeCain et al. 1997 [DIRS 100156], pp. 41 to 47).

Crosshole gas-tracer testing was also conducted by releasing slugs of helium and sulfur hexifloride in isolated injection intervals and sampling in isolated withdrawal intervals. The results of the crosshole tracer testing are presented in Table 7-22. The tracer velocity is an average velocity based on the peak arrival time, and the Darcy velocity is based on the pneumatic permeability and pneumatic gradient. The effective porosity values of the fault zone determined from tests 2 and 3 are larger than their corresponding pneumatic porosity values from crosshole air-injection tests 4 and 5, indicated in Table 7-23. The larger effective porosity values indicate increased tortuosity and/or adsorption of the tracer (LeCain 1998 [DIRS 100052], p. 22).

Chemical Sampling of the Bow-Ridge Fault–Pneumatic monitoring indicated that the Tiva Canyon Tuff, Bow Ridge fault breccia, and the Tmbt1 all have sufficient air permeability to allow essentially instantaneous propagation of the barometric signal, either from the land surface or from the ESF. The high air-permeability is supported by the geochemistry. The δ^{13}C values indicate a large degree of mixing between atmospheric gas or ESF gas and rock gas, which in turn is indicative of the large air-permeability of the Tiva Canyon Tuff, Bow Ridge fault breccia, and Tmbt1. The ^{14}C analysis of the Tiva Canyon Tuff samples yielded apparent ages from 500 to 1,000 years old (94 to 89 percent modern), except for the shallowest sample (3.4-5.8 m [11.1-19.0 ft] from the alcove wall), which was less than 50 years old (113 percent modern). The δ^{13}C values also indicated a large degree of mixing. The ^{14}C analysis of gas from the Bow Ridge fault breccia yielded a significantly older apparent age of 1,745 years (81 percent modern) (LeCain et al. 1997 [DIRS 100156], p. 36).

Two matrix water samples from within the fault breccia had tritium concentrations of 118.3 and 128.1 tritium units (TU), while one sample from the Tmbt1, 3.4 m west of the fault breccia, had a tritium concentration of 154.6 TU. The tritium data indicate that within the last 46 years (postnuclear testing), water has moved down from the surface along the Bow Ridge fault and mixed with older water already resident in the rock matrix pores (LeCain et al. 1997 [DIRS 100156], Table 8).

7.2.2.2.3   Alcove 3

Alcove 3 was constructed in the moderately welded Tiva Canyon Tuff crystal-poor lower nonlithophysal columnar subzone (Tpcplnc), in the vicinity of the contact between the TSw and PTn hydrogeologic units (LeCain 1998 [DIRS 100052], p. 23). Permeability values are summarized in Table 7-24 and range from 4.0×10^{-13} m^2 to 5.7×10^{-11} m^2, with geometric means in the subunits ranging from 3.0×10^{-13} m^2 to 7.0×10^{-12} m^2. The relatively large permeability values of the Tpcpv subzones, compared to the Tpcpln subzones, indicate significant fracturing in the less welded Tpcpv. Twenty-two test intervals in Boreholes ESF-AL#3-RBT#1 and

ESF-AL#3-RBT#4 indicated water redistribution at pressures less than 0.095 MPa (0.95 bars), and one test interval in Borehole ESF-AL#3-RBT#1 had a water pressure of less than 0.005 MPa (0.05 bars) (LeCain 1998 [DIRS 100052], Tables 9 and 10).

7.2.2.2.4   Alcove 6

Geothermal logging, air and core-water chemistry sampling, air-injection testing, and tracer testing were conducted in Alcove 6, the northern Ghost Dance fault test alcove that was constructed off the ESF (LeCain et al. 2000 [DIRS 144612]). The location of Alcove 6 is shown in Figure 1-3; test boreholes that were constructed in the alcove are shown in Figure 7-22. The alcove is located in the middle nonlithophysal unit of the Topopah Spring Tuff (Tptpmn). The goals of the fault testing were to determine air permeability, porosity, gaseous tracer-transport characteristics (transport porosity and longitudinal dispersivity), and ages of water in the volcanic rocks (tuff) that comprise the fault zone, footwall, and hanging wall of the Ghost Dance fault. This section presents the results of testing, sampling, and analysis conducted in Alcove 6, from November 1996 through August 1998.

Geothermal Logging, Pneumatic-Pressure Monitoring, and Chemical Sampling in Borehole ESF-NAD-GTB#1a–Borehole ESF-NAD-GTB#1a was drilled across the trace of the Ghost Dance fault in Alcove 6, along the alignment of the access drift (Figure 7-22), prior to the excavation of the drift across the fault. Geothermal logging, pneumatic-pressure monitoring, and chemical sampling were conducted in Borehole ESF-NAD-GTB#1a using methods and procedures described in LeCain et al. (2000 [DIRS 144612], pp. 7 to 8). Geothermal logs of Borehole ESF-NAD-GTB#1a indicated the effects of ESF ventilation to depths of 3 to 5 m (10 to 16 ft) (LeCain et al. 2000 [DIRS 144612], p. 17).

In situ pneumatic pressures were monitored in Borehole ESF-NAD-GTB#1a from December 19, 1996 to January 10, 1997, using a 30 m (98 ft) long borehole liner and an uphole pressure transducer. Downhole pressures showed minimal barometric pressure attenuation (0.0005 MPa or less) and small time lags (LeCain et al. 2000 [DIRS 144612], p. 18, Figures 8 and 9). Comparison of the downhole pressure fluctuations to the barometric pressure fluctuation indicated that the permeability of the rock is relatively high.

Gas-phase chemistry samples were collected from Borehole ESF-NAD-GTB#1a from December 4, 1996 to January 14, 1997, using the borehole liner. Gas-phase carbon dioxide concentrations ranged from 660 to 1,175 parts per million (LeCain et al. 2000 [DIRS 144612], pp. 18 to 22, Table 2). Carbon dioxide concentrations increased with distance from the northern Ghost Dance fault access drift and indicate that air from the northern Ghost Dance fault access drift had moved a minimum of 13.9 m (45.6 ft) into the tuff. Uncorrected ^{14}C ages of gas samples ranged from 2.4 to 4.5 ka. Downhole pressures showed minimal barometric pressure attenuation and small-time lags, implying that the gas moves readily through the system and is not impeded by lower conductivity zones. The ^{14}C age and the correlation between the ^{14}C age and the gas-pressure attenuation corroborates the conclusion that air from the northern Ghost Dance fault access drift penetrates the tuff through the fracture system.

Chemical Sampling of the Northern Ghost Dance Fault Drill-Room Boreholes–The northern Ghost Dance fault drill room was excavated parallel to and east of the fault (Figure 7-22),

allowing access to drill test boreholes across the fault. Gaseous-phase chemistry samples were collected from Boreholes ESF-NDR-MF#1 and ESF-NDR-MF#2 (Figure 7-22) from August 4 to August 20, 1998, using the borehole liner. Gaseous-phase carbon dioxide concentrations in Boreholes ESF-NDR-MF#1 and ESF-NDR-MF#2 ranged from 711 to 913 parts per million, and uncorrected ^{14}C ages ranged from 2.5 to 3.6 ka (LeCain et al. 2000 [DIRS 144612], Tables 4 and 5). There was no correlation between gaseous-phase chemistry and depth. Overall, the data indicate that the gas samples from the boreholes are a mixture of northern Ghost Dance fault alcove air and rock-gas. The mixing probably resulted from the high permeability of the fault zone, penetration of the fault by the northern Ghost Dance fault access drift, providing a short flow path, and the relatively long time (17 months) between fault penetration and gas sampling.

Single-Hole Air-Injection Testing in Borehole ESF-NAD-GTB#1a–Single-hole air-injection testing was conducted in Borehole ESF-NAD-GTB#1a from January 15 to February 23, 1997 (LeCain et al. 2000 [DIRS 144612], pp. 8 to 10). One-meter-long test intervals were selected from a review of the borehole video logs. Following the selection of a test interval, two pneumatic packers were inserted into the borehole and straddled the selected test interval.

The pressure responses measured in the test intervals usually showed an initial pressure increase followed by a period of decreasing pressure caused by water redistribution. Initial permeability values were calculated for each test, using a modified version of the Hvorslev steady-state solution (Hvorslev 1951 [DIRS 101868]). To evaluate turbulence, which produces non-Darcian flow, multiple tests at variable flow rates were performed on each test interval. A complete explanation of the mathematics used to account for turbulence and calculate air permeability is contained in LeCain et al. (2000 [DIRS 144612], pp. 8 to 10).

Permeability values from the hanging wall (west side) of the Ghost Dance fault generally ranged from 1.0×10^{-13} to 2.5×10^{-12} m^2, with an arithmetic mean of 1.1×10^{-12} m^2 (LeCain et al. 2000 [DIRS 144612], p. 23, Table 7). Air-injection testing indicated a zone of greater permeability encompassing the brecciated zone associated with the main trace of the fault and about 2 m (6.6 ft) of the adjacent, intensely fractured hanging wall. This zone was interpreted as the "fault zone" and had permeability values that ranged from 8.5×10^{-12} to 1.1×10^{-11} m^2, with an arithmetic mean of 1.0×10^{-11} m^2. Permeability of the footwall (east side) of the Ghost Dance fault was very similar to that of the hanging wall, ranging from 2.0×10^{-13} to 2.1×10^{-12} m^2, with an arithmetic mean of 1.0×10^{-12} m^2. Overall, the permeability of the unaffected rock surrounding the fault is very similar to the permeability of the Tptpmn derived from air-injection testing of surface-based boreholes (3.7×10^{-13} to 2.7×10^{-12} m^2), while the fault-zone permeability is several times larger, 5.7×10^{-12} m^2 for a 12 m (39 ft) long test interval that straddled the hanging wall, fault zone, and footwall. A larger permeability of the fault zone in the TSw hydrogeologic unit most likely resulted from more intense fracturing and brecciation associated with the Ghost Dance fault.

Crosshole Air-Injection Testing in the Northern Ghost Dance Fault Drill Room Boreholes– Cross-hole air-injection tests were conducted among the three boreholes in the Northern Ghost Dance fault drill room (Figure 7-22) in three phases, from August 1997 to June 1998 (LeCain et al. 2000 [DIRS 144612], pp. 24 to 26). Crosshole testing consisted of injecting air into an isolated interval of a borehole (injection borehole) and monitoring the pressure response in isolated monitored intervals in other boreholes (monitor boreholes). The injection borehole

was instrumented with the same dual-packer gas-injection system used in the single-hole air-injection testing. The air-injection rate for the crosshole testing was 500 standard liters per minute (SLPM) and was monitored and controlled by mass-flow controllers. Air was injected until the pressure in the injection interval and in the monitor intervals neared steady state, which generally required approximately 3 hours.

The air-injection tests and the test environment were analyzed with an analytical model using type curves, a numerical model using the computer code AIR3D V.22.6.98 (USGS 1999 [DIRS 166193]), and a discrete-feature model using the computer code FRACMAN V.2.511 (USGS 1999 [DIRS 160577]). The analysis was developed to evaluate flow in an equivalent porous medium. Therefore, application of the method to fractured tuff assumes that the fracture-flow system is sufficiently connected and extensive so that the fractured tuff could be treated as an equivalent porous medium. A more detailed discussion of the analytical method is given in LeCain et al. (2000 [DIRS 144612], pp. 26 to 34).

Analysis of Crosshole Air-Injection Tests in the Northern Ghost Dance Fault Drill Room Boreholes–The results based on the type-curve method used are given in Tables 7-25 and 7-26. In the hanging wall, the arithmetic mean permeability and porosity from the crosshole tests are 5.0×10^{-12} m^2 and 0.04, respectively. In the fault zone, the arithmetic mean permeability is 18.1×10^{-12} m^2 and porosity is 0.13. In the footwall, the arithmetic mean permeability and the porosity are 8.7×10^{-12} m^2 and 0.04, respectively (LeCain et al. 2000 [DIRS 144612], pp. 24 and 26).

The mean porosity values derived from the crosshole air-injection testing indicate that the porosity of the fault zone is about three times that of both the hanging wall and the footwall (LeCain et al. 2000 [DIRS 144612], p. 45). Although the pressure responses in the borehole monitored intervals did not indicate a dual-porosity system, and the analysis assumed that the matrix was water-filled, the porosity values were greater than expected and indicate a porosity component in addition to the fracture porosity. Freeze and Cherry (1979 [DIRS 101173], p. 408) state that, in general, fracture porosity ranges from 10^{-2} to 10^{-5}. Visual examination of the extensive fracturing in the Northern Ghost Dance fault access drift led LeCain et al. (2000 [DIRS 144612], p. 26) to state that the fault zone fracture porosity may be larger than 10^{-2}. Possible explanations of the additional porosity include air-filled lithophysal cavities, as well as air-filled matrix pores in direct contact with the fractures.

Modeling of the crosshole air injection tests using continuum and discrete fracture methods is presented in LeCain et al. (2000 [DIRS 144612]).

Crosshole Tracer Testing in the Northern Ghost Dance Fault Drill-Room Boreholes– Crosshole convergent-tracer tests were conducted between intervals that had crosshole pneumatic connections, using the same equipment as in the crosshole air-injection testing, except that the air compressor was replaced with a vacuum pump (LeCain et al. 2000 [DIRS 144612], pp. 14 and 15). The interval isolated by the dual-packer assembly was pumped at approximately 30 SLPM, creating a pneumatic gradient toward the pumped interval. When the flow system reached steady state, a slug of SF$_6$ (0.3 to 0.6 L of 10 percent SF$_6$) and a slug of He (0.3 to 0.6 L of 10 percent He) were released in monitor intervals in a different borehole. The tracers flowed to the pumped interval where the tracer concentrations were measured, using a gas

chromatograph for the SF$_6$ and a mass spectrometer for the He. The pumping rate was regulated by mass-flow controllers, and the pneumatic pressure was monitored by pressure transducers. Because the zone of decreased pressure around the pumped interval was small, the linear distances between the tracer-release interval and the pumped interval generally were less than 7 m (23 ft). Details of tracer-test configuration are described in LeCain et al. (2000 [DIRS 144612], pp. 14 and 15).

Analysis of Crosshole Tracer Tests in the Northern Ghost Dance Fault Drill-Room Boreholes Using Moench-Type Curves–The crosshole tracer tests were analyzed using the Moench-type curve method (Moench 1995 [DIRS 148784]), which assumes that the fracture system can be treated as an equivalent porous medium and is based on mass conservation and Fick's law (LeCain et al. 2000 [DIRS 144612], pp. 15 and 34). A statistical summary of the northern Ghost Dance fault transport porosity and longitudinal dispersivity values by geologic structure is provided in Table 7-27. The wide range of transport porosity and longitudinal-dispersivity values may indicate that the test scale was smaller than the representative elementary volume. An analysis was performed of the three-dimensional orientation (bearing and plunge) of the straight lines connecting the source and sink for all of the tracer tests and the associated calculated transport porosity values (see LeCain et al. 2000 [DIRS 144612], Figure 18). These data indicate no directional control: slow and fast tracer-transport pathways occur along the same orientation.

Modeling of the crosshole tracer injection tests using a discrete fracture method is presented in LeCain et al. (2000 [DIRS 144612]).

7.2.2.2.5   Alcove 7

Alcove 7, the southern Ghost Dance fault test alcove, is located at ESF construction station 50+64 (see Figure 1-3), in the middle nonlithophysal zone of the Topopah Spring Tuff (Tptpmn) west of the fault, and in the lower lithophysal zone (Tptpll) east of the fault. The alcove was constructed at a heading of due east to a distance of 199 m (653 ft). The alcove intersected the Ghost Dance fault at 167 m (548 ft) (DTN: GS980508314224.003 [DIRS 166199]); Kurzmack et al. 2002 [DIRS 162333]).

A borehole temperature log, run in Borehole ESF-SAD-GTB#1 (drilled when the alcove excavation was at approximately 135 m, before penetrating the Ghost Dance fault), showed a 1.5°C temperature drop, centered at the fault at 167 m (548 ft) (DTN: GS970883122410.006 [DIRS 162164]). The temperature drop at the fault could be caused by the downward transport of cooler atmospheric air or infiltrating water moving along the Ghost Dance fault, or by evaporative cooling, both suggesting flow in the Ghost Dance fault. However, the temperature drop could not be duplicated a month later, under different atmospheric condition. The 1.5°C temperature drop may have been due to drilling-induced evaporative cooling, gas-expansion adiabatic cooling, other drilling effects, or possibly the variable borehole diameter (LeCain et al. 2000 [DIRS 144612], p. 17).

Air-injection testing was conducted on two test intervals located in the hanging wall of the Ghost Dance fault (DTN: GS980283122410.004 [DIRS 162166]) when the alcove was excavated to a depth of approximately 150 m. The test interval located in Borehole ESF-SAD-GTB#1 at 153 to

159 m (502 to 522 ft), in the Tptpmn, had an average permeability of 2.2×10^{-12} m^2. This agrees with the average permeability value for the Tptpmn derived from air-injection tests in surface boreholes, documented in Section 7.2.2. Test interval 160 to 166 m (525 to 544 ft), also located in the Tptpmn, had an average permeability of 2.3×10^{-11} m^2, an order of magnitude larger. The increased permeability probably results from an increase in the fracture density associated with the Ghost Dance fault.

As part of the ESF monitoring program, and to assist in the evaluation of the role of the Ghost Dance fault in the flow and transport of fluids through Yucca Mountain, bulkheads were installed in Alcove 7 at distances of 64 m (210 ft) and 132 m (433 ft) from the ESF. Pressure, temperature, and relative-humidity sensors were installed at distances of 4, 57, 72, 126, and 144 m (13, 187, 236, 413, and 472 ft) from the ESF. For the period September 25, 2001, to June 10, 2002, the relative humidity at all stations was drier than 95 percent (<80 bars) (Kurzmack et al. 2002 [DIRS 162333]). The relative-humidity data indicated that, despite the presence of the bulkheads, the ESF ventilation continued to remove water vapor from the alcove, resulting in artificially dry relative-humidity values. Pressure monitoring indicated that the transmission of atmospheric pressure fluctuations across both bulkheads showed minimal dampening (< 5 percent) and short time lags (on the order of hours). The pressure monitoring behind the second bulkhead (monitor interval 132 to 199 m [433 to 653 ft]) showed no effect that could be attributed to the Ghost Dance fault. This probably results from the overwhelming influence of the ESF. Large temperature fluctuations (19.5 to 27.5°C) at a station located 4 m (13 ft) from the ESF reflect the transmission of seasonal temperature fluctuations down the ESF by the ventilation system. Ventilation-driven diurnal temperature fluctuations at the station at 4 m (13 ft) were as large as 1.2°C (Kurzmack et al. 2002 [DIRS 162333]). Temperatures behind the bulkheads indicated no discernible annual fluctuation and diurnal fluctuations of less than 0.05°C. This indicated that although the bulkheads were inefficient at mitigating the ESF pressure fluctuations, they were very efficient at mitigating the ESF temperature fluctuations. However, there were temperature fluctuations behind the bulkheads. Abrupt temperature decreases (as much as 1.0°C) were measured behind the bulkheads and were correlated with the pressure-recovery period following a barometric low-pressure event. One hypothesis is that the system operates similarly to a household evaporative cooler. The rising barometric pressure in front of the bulkhead could force warm, dry ESF air through the fractures around the bulkhead, which would evaporate water, cool the air, and result in the abrupt temperature decreases behind the bulkhead (Kurzmack et al. 2002 [DIRS 162333]).

7.2.2.3   Water-Redistribution Pressures as an Indication of Capillary Pressures

During air-injection tests, occurrence of a "breakover" pressure response, or a decrease in pressure with time, indicates near-field redistribution of water (LeCain 1998 [DIRS 100052], pp. 5 and 6). Water redistribution occurs when the gas-injection pressure exceeds the capillary forces that hold water in the matrix pores and fractures. The air-injection pressure at which water redistribution is identified can be interpreted as an upper estimate of the near-field capillary pressure. Overall, the water-redistribution data from the ESF alcove testing showed that about 20 percent of test intervals had capillary pressures less (wetter) than 0.020 MPa (0.20 bars). This agrees with the water-potential values from the Alcove 3 and 4 boreholes presented in Section 7.4.1 (see Table 7-28). A capillary pressure of 0.020 MPa is equivalent to a

water potential of -0.020 MPa (-0.2 bar), which is somewhat wetter than the -0.30 to -0.10 MPa (-3.0 to -1.0 bars) water potentials measured in surface-based boreholes in the TSw and the PTn hydrogeologic units (Rousseau et al. 1999 [DIRS 102097], pp. 143 to 151). Based on the matrix moisture-retention-characteristics curves presented in Figure 7-16 and discussed in Section 7.2.1.4, the lower capillary pressures indicate that all the matrix pores and the smaller fractures (aperture less than 14 μm) of these intervals are saturated. These wetter capillary pressures could indicate a potential for significant microfracture (apertures of 1 to 14 μm) water flow through the unsaturated zone.

7.2.2.4 Comparison of Laboratory Permeability Values with Surface-Based and Exploratory Studies Facility Air-Injection Permeability Values

Saturated hydraulic conductivity values determined from laboratory analysis of core samples of various hydrogeologic units (Table 7-10) (Flint 1998 [DIRS 100033], Table 7) were converted to the values of permeability and then compared to air-injection permeability values from surface-based boreholes and the ESF (LeCain 1997 [DIRS 100153], pp. 28 and 29). Overall, the surface-based and ESF air-injection permeability values for the TCw and TSw hydrogeologic units are 3 to 6 orders of magnitude greater than the core-scale intrinsic permeability values. Negating the difference in the viscosity of water and air, the air-injection permeability values from the surface-based boreholes and the ESF are larger because they dominantly represent the bulk permeability of the fracture network in the TCw and the TSw hydrogeologic units. As the results of the laboratory tests on core samples represent the permeability of the rock matrix, it is not surprising that the field-scale air-injection tests generated higher values then those from the laboratory core measurements.

The surface-based and ESF air-permeability values for the PTn hydrogeologic unit are much closer to the laboratory core values, falling in the upper range of the core values or differing by no more than a factor of 10. This similarity between the field air-injection and laboratory core permeability values is expected in rock dominated by matrix flow. However, although the permeability of the PTn is much more homogeneous at the two scales than that of the welded units, the PTn nevertheless indicated some fracture permeability (LeCain 1997 [DIRS 100153], p. 29). An alternative explanation is that the laboratory permeability values are skewed toward the lower range because the higher-permeability core samples were destroyed during drilling because of being so friable.

7.2.2.5 Comparison of the Surface-Based, Exploratory Studies Facility, and Pneumatic Monitoring Air-Permeability Values and Estimation of Anisotropy

Comparisons of mean air-permeability values determined from air-injection testing in surface-based boreholes and the ESF, and air-permeability values determined by pneumatic monitoring are shown in Table 7-29. The air-permeability values are the arithmetic means from Sections 7.2.2.1 and 7.2.2.2. The pneumatic-monitoring air-permeability values are derived from Rousseau et al. (1999 [DIRS 102097], pp. 97 to 110; 1997 [DIRS 100178], pp. 52 to 56). Comparison of the pneumatic monitoring and air-injection permeability values may provide some insight into how scale influences the results of these different methods in determining air permeability (LeCain 1997 [DIRS 100153], p. 30 and 31).

The permeability values derived from pneumatic monitoring in the Tiva Canyon Tuff and the PTn hydrogeologic unit generally are within the range of those determined from the surface-based and ESF air-injection boreholes (Table 7-29), with the exception of the larger pneumatic-monitoring values obtained for the Tiva Canyon Tuff from Borehole USW SD-12. This is expected because the Tiva Canyon Tuff and the PTn hydrogeologic unit are relatively heterogeneous. At the scale of the pneumatic monitoring (40 to 200 m [130 to 660 ft] vertically), individual lithostratigraphic intervals must be combined, and the heterogeneity indicated by the range in air-injection values is lost in the pneumatic-monitoring average permeability value. In contrast, the pneumatic-monitoring permeability values for the Topopah Spring Tuff are at least 10 times greater than the surface-based air-injection permeability values (Table 7-29). One possible explanation is that the permeability of the Topopah Spring Tuff is anisotropic (LeCain 1997 [DIRS 100153], p. 31). The apparent anisotropy of the Topopah Spring Tuff has been noted in other studies, including Rousseau et al. (1999 [DIRS 102097], p. 122), which concluded that the ratio of vertical-to-horizontal permeability in the Topopah Spring Tuff is 3:1 to 10:1. Other factors, such as differences in borehole construction and the damage to the near-borehole zone, could have caused the differences in calculated values of rock permeability.

When comparing air-injection and pneumatic-monitoring permeability values, it is important to keep in mind that the pneumatic-monitoring permeability values are derived from a pneumatic-diffusivity model (LeCain 1997 [DIRS 100153], p. 31). Because the pneumatic-diffusivity term has permeability in the numerator and porosity in the denominator, the calculated permeability value will be different for a different assumed value of porosity, while the pneumatic-diffusivity term will remain constant.

7.2.3 Porosity of the Topopah Spring Tuff Lower Lithophysal Zone in the Enhanced Characterization of the Repository Block Cross-Drift

Because a large amount of the repository is located in the crystal-poor, lower lithophysal zone of the Topopah Spring Tuff (Tptpll), a detailed study was made of the lithostratigraphic features in the Tptpll exposed in the ECRB Cross-Drift (DTN: GS021008314224.002 [DIRS 161910]). The data package documents the distribution of size, shape, and abundance of lithophysal cavities, rims, spots, and lithic clasts, and these data can be displayed and analyzed as: (1) local variations, (2) along the tunnel (a critical type of variation), and (3) as values for the total zone. A detailed description of lithophysal abundance and lithophysal characteristics is provided in BSC (2003 [DIRS 162711], Attachment XV).

In addition to the along-the-tunnel variation in the abundance of features, such as lithophysae, there are variations in the sizes, shapes, and distances between features. These types of variations are most easily observed with panel map data (Figure 7-23). Locations of the panel maps were positioned to capture representative variations in the rocks along the tunnel. Additional details on the development of these panel maps are provided in BSC (2003 [DIRS 162711], Attachment XV).

Using the approach described in BSC (2003 [DIRS 162711], Attachment XV), the total porosity of the component features of the lithophysal rock mass (i.e., the porosity of the lithophysal cavities, rims, and spots) has been calculated. The porosity variation along the ECRB Cross-Drift is shown in Figure 7-24, with total porosity typically ranging from 20 to 35 percent,

with some outlines as high as 42 percent. These porosity values, with lithophysal taken into consideration, are two to three times higher than the mean porosity value of 11 percent (Table 7-10, unit TLL), derived from laboratory measurements on rock core samples (Section 7.2.1).

7.3 PNEUMATIC PRESSURE AND GASEOUS-PHASE FLOW IN THE UNSATURATED ZONE

Gas and water vapor movement through the unsaturated zone is driven by changes in barometric pressure, temperature-induced density differences, and wind effects (Rousseau et al. 1999 [DIRS 102097], pp. 55 and 56). Changes in barometric pressure at the land surface result in corresponding changes in pneumatic pressure in the unsaturated zone, which commonly are amplitude-attenuated and time-lagged relative to the pressure change at the surface. The subsurface pressure response to surface barometric changes is controlled by the distribution and interconnectedness of fractures, the presence of faults and their ability to conduct gas and vapor, and the moisture content and matrix permeability of the rock units. Temperature-induced density effects are expected to be significant only in hilly terrain and are dominated by drier, cooler air entering along hillsides and exhausting along hillcrests. This is referred to by mechanical engineers as the "thermosiphon" effect (Patterson et al. 1996 [DIRS 100172], pp. 3 and 4). The purpose of pneumatic monitoring at Yucca Mountain is threefold:

1. To measure in situ pneumatic pressure response to atmospheric pressure changes to determine the influence of lithostratigraphy, bulk properties, and major structural features on the natural gaseous-phase circulation system

2. To use the response of the system at depth to changes in atmospheric pressure to estimate pneumatic diffusivities and, ultimately, effective gas permeabilities of the lithostratigraphic layers

3. To assess the effects of excavation of the ESF on in situ pneumatic pressure and on the overall gaseous-phase circulation system.

7.3.1 Monitoring Well Layout

From 1994 to 1997, 11 deep boreholes were instrumented in the Yucca Mountain unsaturated zone to measure in situ pneumatic pressure, water potential, and temperature at multiple depths (Rousseau et al. 1999 [DIRS 102097], p. 77; 1997 [DIRS 100178], pp. 18 and 19). These Boreholes were UE-25 NRG #5, USW NRG-6, USW NRG-7a, USW SD-7, USW SD-9, USW SD-12, UE-25 UZ #4, UE-25 UZ #5, USW UZ-7a, USW UZ-1, and UE-25 NRG #4 (Figure 7-2). The types of instrumentation and methods of sampling and monitoring are described in Rousseau et al. (1999 [DIRS 102097], pp. 77, 88 and 89; 1997 [DIRS 100178], pp. 18 to 23). The locations of monitoring stations with respect to lithostratigraphy in boreholes are shown in Figure 7-25. The symbols depicting lithostratigraphic units are defined in Figure 7-26. Monitoring in these boreholes began in October 1994 and continued to December 2001. The data collection also included measurements of atmospheric pressure.

7.3.2 Subsurface Pneumatic Pressure Prior to the Excavation of the Exploratory Studies Facility

The computed phase lags and residual amplitudes of the in situ pressure data were determined for four distinct pneumatic systems, corresponding to the major hydrogeologic units (the TCw, PTn, TSw, and CHn) (Rousseau et al. 1999 [DIRS 102097], p. 89).

7.3.2.1 Tiva Canyon Welded Hydrogeologic Unit

Generally, pneumatic-pressure records for the TCw hydrogeologic unit display very little attenuation and lagging of the synoptic pressure signal. Residual amplitudes of the synoptic signal are on the order of 96 percent or greater, and phase lags are less than one hour (Rousseau et al. 1999 [DIRS 102097], p. 89). In many cases, it is not possible to distinguish the atmospheric signal from the downhole pressure signal. The only significant exception to this behavior is the pneumatic pressure record from the Tiva Canyon crystal-poor columnar subzone (instrument station G) in Borehole USW NRG-6, where the residual amplitude of the pressure signal is only 56 percent of the synoptic signal, and its phase lag is 1.8 hour. Unusually high precipitation during late 1994 and early 1995 caused a temporary pneumatic sealing of near-surface fractures by localized infiltrating water, which could explain the small residual amplitudes of pneumatic pressure (Rousseau et al. 1999 [DIRS 102097], p. 93).

7.3.2.2 Paintbrush Nonwelded Hydrogeologic Unit

Across the Yucca Mountain site area, the PTn hydrogeologic unit generally becomes thinner from northwest to southeast (Rousseau et al. 1999 [DIRS 102097], p. 93). Pneumatic-pressure records from monitoring boreholes at different locations within the site area indicated that the attenuation of the synoptic pressure signal across the PTn is greater at boreholes in the northern part of the site area than in the southern part of the site area (Patterson et al. 1996 [DIRS 100172], p. 23). Evaluation of the pneumatic-pressure data from various boreholes indicates that the attenuation in different subunits of the PTn varies from one location to another and that the composite thickness of the PTn is insufficient to uniquely account for these variations (Rousseau et al. 1999 [DIRS 102097], p. 96). These differences are probably reflected by local differences in the saturation of individual units and the presence or absence of open fractures within these subunits. Detailed descriptions of these borehole-to-borehole variations are contained in Rousseau et al. (1999 [DIRS 102097], pp. 93 to 96) and Patterson et al. (1996 [DIRS 100172], pp. 23 to 26).

7.3.2.3 Topopah Spring Welded Hydrogeologic Unit

Regardless of location within the site area, borehole pneumatic-pressure signals in the lithophysal and nonlithophysal units indicate negligible attenuation across the crystal-rich vitric zone of the Topopah Spring Tuff, which encompasses the lowermost part of the PTn hydrogeologic unit and the uppermost part of the TSw hydrogeologic unit (Rousseau et al. 1999 [DIRS 102097], pp. 96 and 97; Patterson et al. 1996 [DIRS 100172], pp. 26 and 27). Pressure signals appear to be transmitted nearly instantaneously throughout most of the vertical section of the TSw hydrogeologic unit. The pressure data from the TSw indicate that the fractures within that unit apparently are very permeable and highly interconnected within both the lithophysal

and nonlithophysal units (Rousseau et al. 1999 [DIRS 102097], pp. 96 and 97). Exceptions to this are the lowermost instrument stations of Boreholes UE-25 NRG#5 (Figure 7-27) and USW SD-12 (Figure 7-28). In Borehole UE-25 NRG#5, the residual amplitude of pneumatic pressure increases from 29 percent at instrument station 9, to 39 percent at station 10, and the phase lag decreases by over 10 hours from station 9 to station 10. (This reversal in the normal trend of increasing attenuation with depth probably results from the barometric-pressure signal bypassing the PTn hydrogeologic unit by traveling preferentially down the Drill Hole Wash fault.) A similar situation exists in Borehole USW SD-12 (Figure 7-28), where station C exhibits a larger residual amplitude and smaller phase lag than the overlying stations; the likely preferential pathway for the pneumatic signal is through the Ghost Dance fault.

7.3.2.4   Calico Hills Nonwelded Hydrogeologic Unit

The pneumatic-pressure measurements in this unit are affected by the presence of perched water, encountered during drilling near the base of the Topopah Spring Tuff in Borehole USW SD-9 and near the base of the Calico Hills Formation in Borehole USW SD-7 (see Section 7.4.2). Although no perched-water reservoir of sufficient magnitude to cause standing water in the borehole was detected during the drilling of USW SD-12, the video camera log of this borehole indicates that a perched-water zone of limited extent probably is present in the densely welded vitric subunit (Tptpv3) of the Topopah Spring Tuff (Rousseau et al. 1997 [DIRS 100178], p. 21, Figure 3.0-1). The pressure records for stations located below perched water indicate that the synoptic barometric signal is almost completely attenuated (Patterson et al. 1996 [DIRS 100172], p. 28). This is consistent with the concept that the presence of a perched-water zone with extremely low permeability to air would effectively impede the downward propagation of the surface barometric signal.

7.3.3   Effects of Excavating the Exploratory Studies Facility Tunnel on Pneumatic Pressure in Boreholes

The effects of ESF excavation on in situ pneumatic pressure were carefully monitored, because such effects offer some insight on how the overall gaseous-phase system in the unsaturated fractured rock could be affected by the exposure to atmospheric pressure from the underground tunnel. Further, monitoring of such effects also presented an opportunity to use the pneumatic stress caused by ESF excavation to determine large-scale pneumatic properties of the rock units and to identify pneumatic fast pathways within the subsurface. Pneumatic pressure-interference effects associated with excavation of the ESF by the tunnel-boring machine have been observed in all monitored boreholes (Rousseau et al. 1999 [DIRS 102097], p. 110; 1997 [DIRS 100178], p. 34; Patterson et al. 1996 [DIRS 100172], p. 40). A possible exception to this general observation may be Borehole USW UZ-7a. Borehole USW UZ-7a was drilled within the disturbed zone of the Ghost Dance fault and, therefore, exhibited only partially attenuated responses to the surface barometric signal, which may effectively mask the detection of any possible effects of ESF excavation (Patterson et al. 1996 [DIRS 100172], pp. 40 and 41). Table 7-30 indicates the event and first occurrence of pneumatic-interference effects for each affected borehole at Yucca Mountain (data from Rousseau et al. (1999 [DIRS 102097], Table 13), Rousseau et al. (1997 [DIRS 100178], Table 4.1-3), and Patterson et al. (1996 [DIRS 100172], Table 5). Detection of the first occurrence of a pneumatic disturbance effect may not coincide exactly with key excavation events in the ESF tunnel, such as penetration of a

fault or pneumatic-impeding layer (Rousseau et al. 1999 [DIRS 102097], p. 110). Many of the recorded dates for pneumatic-interference events appear in the pneumatic record several days after the excavation event. The apparent lag effect can be attributed to two primary causes. First, changes in the frequency and amplitude of the synoptic pressure signal, as it was registered downhole, were used to determine when a tunnel interference effect had occurred. The wavelength of this signal is 96 hours +/-3 hours, depending on the time of year (longer in the summer, shorter in the winter). To observe a change in in situ pressure using this signal requires at least a half wavelength of record (two days or more) before changes in the amplitude and frequency become apparent. Second, the rate of advance of the tunnel-boring machine tends to obscure detection of the first arrival of the pneumatic interference, because this interference is initially propagated as a weak spherical wavefront that gradually evolves into a stronger cylindrical wavefront as the tunnel-boring machine advances closer and closer to the affected borehole. Because all instrument stations in the Topopah Spring welded hydrogeological unit (based on measurements in Borehole USW SD-7) responded simultaneously to barometric signals, both prior to and after ESF interference effects, the vertical permeability of the TSw hydrogeologic unit at the location of Borehole USW SD-7 must be very large.

7.4 DISTRIBUTION OF IN SITU WATER POTENTIAL, TEMPERATURE, AND PERCHED WATER IN THE UNSATURATED ZONE

The goal of this section is to describe the results of in situ measurements of the water potential (which is equivalent to the matric potential), temperature, and the creation of perched-water zones. These hydrologic and thermal conditions are used to provide direct evidence of flow in the PTn hydrogeologic unit and diversion of flow into structural pathways. They also provide evidence for the transition of flow from highly fractured to sparsely fractured rock at the base of the TSw hydrogeologic unit and at the top of the CHn hydrogeologic unit. Perched water is found to be associated with the change in hydraulic characteristics at this unit interface (Rousseau et al. 1999 [DIRS 102097], p. 151). Furthermore, these conditions are necessary information to develop flow and transport models for the unsaturated zone.

7.4.1 In Situ Water Potentials

7.4.1.1 Monitoring Methods and Data Sources

In situ water potentials have been monitored at multiple depths in surface-based instrumented Boreholes USW NRG-6, USW NRG-7a, UE-25 UZ#4, UE-25 UZ#5, USW UZ-7a, and USW SD-12 (Rousseau et al. 1999 [DIRS 102097], pp. 143 to 151; 1997 [DIRS 100178], pp. 39 to 45) using thermocouple psychrometers. In ESF Alcoves 3 and 4 boreholes, monitoring was conducted using heat dissipation probes (LeCain et al. 2002 [DIRS 162337]). Water-potential data were collected from these boreholes (for various periods of time) from November 1994 through December 2001. Water-potential accuracies of the thermocouple psychrometers and the heat dissipation probes were ± 0.2 MPa and ± 0.02 MPa, respectively. In addition, water-potential data were collected in Borehole USW UZ-1 from October 1983 through October 1985, using a prototype borehole instrumentation system. The principal sources of data, analyses, and interpretations of water-potential measurements in the unsaturated zone are summarized by Rousseau et al. (1997 [DIRS 100178]; 1999 [DIRS 102097]), and LeCain et al. (2002 [DIRS 162337]), and also in Table 7-28.

7.4.1.2   Water-Potential Trends and Gradients

Effect of Borehole Construction–The water-potential data from Borehole USW UZ-1 provide important insights into the trend of stabilization of water potential following instrumentation and stemming of deep boreholes in the unsaturated zone (Rousseau et al. 1999 [DIRS 102097], pp. 144 and 145). Observations in Borehole USW UZ-1 indicated an increase in water potentials even after two years (Rousseau et al. 1999 [DIRS 102097], Figure 92). The recovery time for water potentials after the borehole dried out prior to stemming may be caused by the large diameter of the borehole (0.92 m [3 ft] from 12 to 30 m [39 to 98 ft] in depth, 0.45 m [1.5 ft] diameter below 30 m [98 ft]) and the type of stemming materials used. The more rapid recovery of water potentials at instrument stations 4, 7, 11, 14, and 15 correlate with zones of high-fracture density. The resultant water-potential profile for October 25, 1985, indicates that water-potential gradients in all Topopah Spring Tuff units, with the possible exception of the lower lithophysal unit, are very close to zero. Extrapolation of the observed trend in water potentials at stations 12 and 13 from October 1984 to October 1985 indicates that the water-potential gradient throughout the Topopah Spring Tuff is close to zero. Thus, the gravitational potential may be a dominant component of the total hydraulic gradient that is very close to unity (Rousseau et al. 1999 [DIRS 102097], p. 145).

In Borehole USW NRG-6, for the period November 1, 1995, to February 8, 1996, the water potentials in nearly all the instrument stations were nearing steady state after about one year (Rousseau et al. 1999 [DIRS 102097], p. 145). The profile of water potential with depth for November 14, 1995, indicated a near-zero water-potential gradient across the PTn hydrogeologic unit and the upper portion of the TSw hydrogeologic unit (Rousseau et al. 1999 [DIRS 102097], Figure 94). Monitoring indicated that the deeper stations required up to three years to reach steady state. By the time testing ended in Borehole USW NRG-7a in December 2001, the water potentials at all wells had stabilized in a range from 0 to - 0.35 MPa (Table 7-28), with a vertical water-potential gradient close to zero.

Despite the quasi-stability and uniformity of the water-potential profile in Borehole USW NRG-7a, transient moisture-redistribution events apparently occurred sporadically. Moisture redistribution in the fractures of the overlying TCw hydrogeologic unit, accompanied by topographically induced density-driven gas flow, may have caused the unusual water-potential responses observed at station D in this borehole.

Water-potential profiles for Boreholes UE-25 UZ#4 and UE-25 UZ#5 are shown in Figure 7-29 for elapsed-time periods of about three months (September 26, 1995) and six months (December 25, 1995) following instrumentation (Rousseau et al. 1999 [DIRS 102097], p. 149). This figure also shows the results of water-potential measurements made on core samples shortly after the boreholes were drilled in 1984. (Borehole UE-25 UZ#4 is located in the active channel of Pagany Wash, and UE-25 UZ#5 is located on a side slope adjacent to Pagany Wash, approximately 38 m south of UE-25 UZ#4.) Figure 7-29 shows little or no difference between water potentials measured on September 26 and December 25, 1995, at several stations in UE-25 UZ#4 (Rousseau et al. 1999 [DIRS 102097], p. 149). This indicated that water potentials equilibrated fairly rapidly at instrument stations located at the top of the crystal-rich nonlithophysal unit of the TSw hydrogeologic unit and in the upper subunits of the PTn hydrogeologic unit tuff. The wetting trend at these stations indicated that the equilibrated profile

would be very close to that derived from the core samples and that the resulting profile would approximate a zero water-potential gradient across most of the PTn section at this borehole (Rousseau et al. 1999 [DIRS 102097], pp. 183 and 184). By the time the monitoring program ended in December 2001, the water potential at all stations in Borehole UE-25 UZ#4 had stabilized in the -0.06 to -0.16 MPa range, with a water-potential gradient close to zero (Table 7-28). The recovery of the water potential in Borehole UE-25 UZ#5 was slower than that in UE-25 UZ#4 (Rousseau et al. 1999 [DIRS 102097], p. 149). Figure 7-29 also shows that the water-potential profile in this well is nearly zero across the entire PTn section. By December 2001, the water-potential values at all stations in Borehole UE-25 UZ#5 stabilized in the 0 to -0.29 MPa range (Table 7-28).

Borehole USW SD-12, located along the ESF main drift, is the deepest borehole instrumented in the Yucca Mountain unsaturated zone and is the only borehole that has instrument stations in all four major hydrogeologic units (TCw, PTn, the TSw, and CHn) (Rousseau et al. 1997 [DIRS 100178], Figure 3.0-1). Despite some differences in the water-potential recovery patterns during the first six months after instrumentation (Rousseau et al. 1997 [DIRS 100178], p. 41), water potentials measured at all of the USW SD-12 stations stabilized in a fairly narrow range of 0 to -0.19 MPa, and indicated a water-potential gradient close to zero (Table 7-28). Interestingly, the time-series of water potentials for Borehole USW SD-12 within the PTn and TCw hydrogeologic units contrasted markedly with those for deeper stations (Rousseau et al. 1997 [DIRS 100178], Figure 4.2.1-4). The dynamics of barometric pumping are readily apparent in the water-potential record of station L, located near the base of the PTn hydrogeologic unit. This barometric-pumping effect is strongest during the early recovery period and diminishes over time, but never dissipates completely as water-potential equilibrium is reached at about -0.5 MPa (Rousseau et al. 1997 [DIRS 100178], p. 43).

Borehole USW UZ-7a was drilled in the Ghost Dance fault zone about 200 m (660 ft) east of the ESF main drift, near the southern end of the repository area (Figure 7-2). The borehole intersected the easternmost (main) trace of the Ghost Dance fault zone at a depth of about 120 m (390 ft) within the crystal-poor, upper lithophysal unit of the Topopah Spring Tuff (Tptpul), very near the contact with the crystal-rich lithophysal unit (Tptrl) (Rousseau et al. 1997 [DIRS 100178], p. 21). Total estimated displacement across the fault zone is about 24 m (80 ft). According to the time-series water-potential data, during the early time after instrumentation, the recovery period for the deepest station (A) is considerably longer than that of the other two stations (B and C) located below the easternmost trace of the Ghost Dance fault zone (Rousseau et al. 1997 [DIRS 100178], p. 43). Many stations exhibited water-potential oscillations that were directly correlated with the surface barometric-pressure changes. However, water-potential oscillations are conspicuously absent in the three lower stations (A, B, and C) located below the easternmost trace of the Ghost Dance fault zone, but are pronounced at station D, located immediately above the fault trace in this borehole (Rousseau et al. 1997 [DIRS 100178], p. 43). These observations and the analysis of pneumatic pressures in Borehole USW UZ-7a prior to ESF excavation indicated that the pneumatic characteristics of the TSw hydrogeologic unit in the fault zone are much different from anywhere else at Yucca Mountain. Specifically, within the Ghost Dance fault zone, the TSw hydrogeologic unit is much less isolated from the atmosphere than elsewhere, probably caused by higher fracture densities in the PTn hydrogeologic unit tuff. This enhanced connection to the atmosphere and the effects of more deeply penetrating barometric pumping resulted in a more dynamic moisture regime than

elsewhere, because it could be affected by both rapid, focused percolation of liquid water and the drying effects of barometric pumping. By January 1999, the water potentials at all stations in Borehole USW UZ-7a stabilized in the 0 to -0.23 MPa range (Table 7-28), also indicating a water-potential gradient close to zero.

Vertical boreholes drilled from Alcoves 3 and 4, located in the ESF, were instrumented with heat-dissipation probes to measure the water potentials of the nonwelded units of the Paintbrush Group (LeCain et al. 2002 [DIRS 162337]). These units include the nonwelded units of the Tiva Canyon and Topopah Spring tuffs, the Pah Canyon Tuff, and several bedded units. Borehole ESF-UPCA-PTN#1 (hereinafter referred to as Borehole PTN#1), located in Alcove 3 at ESF construction station 7+60 m, penetrated the lower welded Tiva Canyon Tuff, the nonwelded units of the Paintbrush Group, and the upper welded units of the Topopah Spring Tuff. Borehole ESF-LPCA-PTN#2 (hereinafter referred to as Borehole PTN#2), located in Alcove 4 at ESF construction station 10+27 m, penetrated the lower nonwelded units of the Paintbrush Group and the upper welded units of the Topopah Spring Tuff. The boreholes were monitored from April 2000 to March 2001. The heat-dissipation probes required from 3 to 12 months to stabilize. Water-potential values are presented in Table 7-28. The ESF ventilation system caused near-surface drying to a depth of 4.9 m (16.1 ft) in Alcove 3 Borehole PTN#1. Ventilation effects were minimal in Alcove 4 Borehole PTN#2. Interestingly, Alcove 3 was isolated from the ESF ventilation system by a bulkhead, but Alcove 4 was not. Water-potential values from stations below the zone of ventilation effects ranged from -0.01 to -0.17 MPa in the nonwelded units of the Paintbrush Group and from -0.0 to -0.43 MPa in the upper welded units of the Topopah Spring Tuff (Table 7-28). The wettest ESF borehole water-potential value was measured at the Tpbt2/Tptrv3 contact (-0.01 MPa). Water-potential values in the upper welded units of the Topopah Spring Tuff were drier with depth. Water potentials of the nonwelded units of the Paintbrush Group agree with the 0.04 to -0.29 MPa water-potential values measured in surface-based monitoring boreholes (Table 7-28). Several of the Alcove 4 Borehole PTN#2 water potential values from the upper welded units of the Topopah Spring Tuff were drier (-0.14 to -0.43 MPa) than those measured in the same units in the surface-based boreholes (0.0 to -0.23 MPa).

The water potentials of the PTn and TSw hydrogeologic units indicate a nonzero downward percolation flux under equilibrium conditions. The water potential of -0.01 MPa at the Bt2/Tptrv3 contact (Table 7-28) indicates a possibility for ponding and subsequent lateral flow. The relatively large water potentials also indicate that the rock matrix of the TSw hydrogeologic unit is relatively wet (at least near fractures), which might create water flow through the fractures and little imbibition by the low-permeability rock matrix. Across the TCw hydrogeologic unit, water potentials indicate progressively drier conditions with decreasing depth, as exemplified by the in situ water-potential profiles for Boreholes USW UZ-7a and USW SD-12 (Rousseau et al. 1997 [DIRS 100178], p. 45). These drier conditions indicate greater imbibition capacity associated with the TCw hydrogeologic unit and upward matrix flow across this unit. However, these observations do not exclude the possibility of episodic, downward fracture flow across this unit.

7.4.1.3 Effects of Exploratory Studies Facility Excavation on Pneumatic Pressure and Moisture Regime of the Topopah Spring Welded Hydrogeologic Unit

The effect of ESF excavation on the moisture regime can be studied based on the changes in pneumatic pressures and the water potential. In Borehole USW SD-12, the closest approach of the tunnel boring machine was on March 23, 1996 (Table 7-30). The ESF excavation significantly affected the pneumatic pressure in the TSw hydrogeologic unit (Rousseau et al. 1997 [DIRS 100178], pp. 60 and 61). Figures 7-28 and 7-30 are examples of time-series pneumatic pressure before and after the excavation, respectively. From April 1996 to January 1997, residual amplitudes decreased between 7 and 12 percentage points, and phase lags increased between 3.7 and 4.1 hours, with the larger adjustments above the Tptpmn. These changes may be related to drying out the rock mass from ESF excavation, resulting in an increase in the pore-gas saturation and a decrease in the pneumatic diffusivities of the affected units. The pneumatic-pressure fluctuations could have induced some spikes and/or instabilities in measurements using thermocouple psychrometers at some stations in USW SD-12 after the ESF construction, but the recovery was quick, and no long-term changes were identified. Although most of the surface-based borehole moisture monitoring stations did not show any correlation between the water potential and ESF excavation, the effect of ESF excavation on the moisture regime in the TSw hydrogeologic unit was evident in Borehole USW NRG-7a in June 1997. In this borehole, the water potential at station A (approximately 26 m [85 ft] away horizontally from the ESF north ramp) indicated some wetting of the Tptpul from the time of the borehole instrumentation in October 1994 until June 27, 1997. Afterward, the trend was reversed, and the Tptpul surrounding the borehole interval began to dry out. Subsequent monitoring has shown significant fluctuations of the water potential, ranging from -0.1 to -0.2 MPa. Drying out the rock-fracture network could have caused these fluctuations, as the moisture is removed from the ESF tunnel by the ventilation system.

7.4.2 Perched Water in the Site Area

The presence of perched water implies that, at least at some time in the past, the percolation rate through the unsaturated zone had exceeded the discharge through the perching layer or structural or stratigraphic traps, causing percolating water to accumulate. These conditions become an important issue upgradient from the repository, because perched water in close proximity to the waste-emplacement tunnels could become an additional source of water. This water might become mobilized as vapor, resulting from waste-generated heat, a fact that needs to be considered when attempting to analyze the impact of mobilized water on repository performance.

Perched water was identified below the repository horizon in seven boreholes in the Yucca Mountain site area (Rousseau et al. 1999 [DIRS 102097], p. 170; 1997 [DIRS 100178], pp. 21 and 22; CRWMS M&O 1997 [DIRS 107637]). Commonly, identified perched-water bodies at elevations 100 to 200 m (330 to 660 ft) below the repository horizon do not represent obstacles to the repository design or construction. The accumulation of perched water is caused by either the basal vitrophyre of the Topopah Spring Tuff or the vitric-zeolitic boundary in the Calico Hills Formation being in contact with a lateral structural barrier (Rousseau et al. 1999 [DIRS 102097], pp. 171 and 172).

Perched water in Borehole USW UZ-1 (located in Drill Hole Wash and drilled to a depth of 387.1 m [1,269.7 ft]) was encountered at an elevation of 966.7 m (3,170 ft), which is about 190 m (620 ft) above the water table. Perched water in Borehole USW UZ-14 (located about 26 m (85 ft) from Borehole USW UZ-1 in Drill Hole Wash) was encountered at an elevation of 967.7 m (3,175 ft.). The perched water was pumped for about three days at an average rate of about 0.06 L/s, and fully recovered in about 5.6 days after the pumping stopped, indicating that this perched-water reservoir may be extensive. Transmissivity estimates ranged from 0.55 to 0.62 square meters per day (m^2/d) (Striffler et al. 1996 [DIRS 104951], p. 22). In these boreholes, perched water occurs near the upper contact of the Topopah Spring basal vitrophyre (Tptpv), above the relatively unfractured tuffs of the Calico Hills Formation (Rousseau et al. 1999 [DIRS 102097], p. 171). In Borehole USW UZ-14, the rock-fracture density decreases with depth substantially from the perched-water zone into the bedded tuffs (Tpbt1, Tac) (Rousseau et al. 1999 [DIRS 102097], Figure 24). Air-injection permeability data indicate that the permeability of the Calico Hills Formation is about 100 times lower than that of the lower units of the Topopah Spring Tuff (LeCain 1997 [DIRS 100153], p. 15 and Table 6). This suggests that the perched water encountered near the base of the TSw hydrogeologic unit in Boreholes USW UZ-1 and USW UZ-14 may be hydraulically connected with perched waters within the Calico Hills Formation. Another hypothesis explaining the creation of perched waters is the presence of a lateral barrier (Rousseau et al. 1999 [DIRS 102097], p. 172, Figures 108 and 109) that could have been formed by a northeast trending fault (i.e., a splay off the Solitario Canyon fault). The juxtaposition of a more permeable layer (Tptpln or upper Tptpv) west of the fault against a less permeable layer (the lower Tptpv or Tpbt1) east of the fault could form a structural trap. This trap could intercept water flowing downward along the crystal-poor vitric zone (Tptpv) or the zeolitic alteration boundary.

Perched water was first detected in Borehole USW NRG-7a (located in Drill Hole Wash and drilled to a depth of 461.3 m (1,514 ft) into the top of the Calico Hills Formation) at a depth of 460.2 m (1,510 ft), 91 m (298 ft) above the predicted water table elevation (Rousseau et al. 1999 [DIRS 102097], p. 171). The perched water was located below the contact between the Topopah Spring crystal-poor vitric zone (Tptpv) and the Tpbt1. The water level in the borehole then rose about 30 m (98 ft) to a depth of 430 m (1,410 ft) (elevation of 853 m [2,800 ft]). This is about 2 m (6.6 ft) above the base of the Topopah Spring Tuff crystal-poor lower nonlithophysal zone (Tptpln). The perched water was encountered near the contact of a series of highly fractured welded tuffs overlying relatively unfractured, nonwelded tuffs (Rousseau et al. 1999 [DIRS 102097], Figure 25). This is similar to the situation at Boreholes USW UZ-1 and USW UZ-14, where perched water may be trapped in fractures while slowly imbibing into the matrix of the less fractured underlying rock unit.

Standing water in Borehole USW SD-9 (located adjacent to Drill Hole Wash and drilled to a total depth of 677.6 m [2,223 ft]) (Rousseau et al. 1999 [DIRS 102097], p. 171) was first detected at a depth of 448.8 m (1,472 ft). Video camera logs revealed that water seeped through a fracture into the borehole at a depth of 413 m (1,360 ft), which is 3 m (10 ft) above the contact between the Topopah Spring Tuff crystal-poor lower nonlithophysal zone (Tptpln) and the Topopah Spring Tuff crystal-poor vitric zone (Tptpv) and about 157m (515 ft) above the predicted regional water table. The perched-water reservoir is in fractured welded tuff (Tptpv) underlain by less-fractured nonwelded and bedded tuffs that comprise the uppermost part of the

CHn hydrogeologic unit (Rousseau et al. 1999 [DIRS 102097], Figure 24), as illustrated in Figure 7-31.

Although no perched water was detected during drilling, the video camera log of this borehole indicates that a perched-water zone of a limited extent probably is present in the densely welded vitric subunit (Tptpv3) of the Topopah Spring Tuff (Rousseau et al. 1997 [DIRS 100178], p. 21). The video camera log indicates increased light reflectance and shimmering effect in the depth interval between 388.1 m and 403.8 m (1,273 to 1,325 ft), or from the top of the Topopah Spring Tuff densely welded vitric unit (Tptpv3) down to the base of the Topopah Spring Tuff moderately welded vitric unit, Tptpv2 (the top of the CHn hydrogeologic unit). Perched water over this interval is also indicated by the in situ pneumatic pressure responses observed in the instrument station immediately below this zone (see Section 7.3.2).

Perched water in Borehole USW SD-7 (located on the eastern slope of Yucca Mountain near the ESF main drift and near the southern extent of the repository area and drilled to a depth of 815.3 m (2,675 ft) (Rousseau et al. 1997 [DIRS 100178], p. 22), was first observed during coring at a depth of 488 m (1,600 ft) in the bedded tuffs (Tacbt), which is at the base of the Calico Hills Formation (O'Brien 1997 [DIRS 101277], p. 23). This depth is 4.5 m (15 ft) above the top of the Prow Pass Tuff (Rousseau et al. 1997 [DIRS 100178], Figure 3.0-3) and about 143 m (469 ft) above the regional water table. The perched-water level subsequently rose 8.4 m (28 ft) (Rousseau et al. 1997 [DIRS 100178], p. 22). The occurrence of perched water at this depth may be directly related to the bedding layers in the bedded tuff, Tacbt. The matrix hydraulic conductivity of the nonwelded vitric horizon (CHv) is much greater than that of the zeolitized horizon (CHz) beneath it (see Table 7-10). Lateral flow may also contribute to the formation of a perched-water reservoir, because the horizontally fractured sandstone layer could be a water-bearing stratum. A structural trap may also be present near Borehole USW SD-7 (O'Brien 1997 [DIRS 101277], p. 29, Figure 18), as schematically depicted in Figure 7-32.

Based on the results of hydraulic tests conducted in Borehole USW SD-7 in March 1995 (O'Brien 1997 [DIRS 101277], pp. 23 to 34), the mean transmissivity was 8 m^2/d. The recovery of the water level was not complete, with a residual drawdown of 2.3 m (7.5 ft), indicating a limited vertical and lateral extent of a perched-water zone. Analysis of the August 1995 tests resulted in a mean transmissivity estimate of 4 m^2/d. Similarly to the March testing, most of the recovery occurred during the first 20 minutes. Slow recovery, at the rate of about 1 m (3 ft) per six days, continued to show the residual drawdown of 2.9 m (9.5 ft.). Based on the results of these hydraulic tests, the perched-water volume in the vicinity of Borehole USW SD-7 was estimated to be 97,000 L prior to pumping (O'Brien 1997 [DIRS 101277], p. 34).

Two perched-water zones were detected in Borehole USW WT-24, located at the north end of Yucca Mountain on Mile-High Mesa. This is in an area where the potentiometric surface is characterized by a large hydraulic gradient (Luckey et al. 1996 [DIRS 100465], p. 21). The borehole was drilled to a depth of about 863.8 m (2,834 ft). Perched-water bodies were detected at 507 m (1,660 ft) and 654 m (2,150 ft) below land surface. The first perched water body was encountered in the lower subzones of the Topopah Spring welded hydrogeological unit and the pre-Topopah Spring bedded tuff. The second perched-water body was encountered in the Calico Hills Formation. (Because USW WT-24 was not drilled to a sufficient depth, data are not available to adequately define the second perched-water body.) Based on the results of

hydrochemical and isotopic analysis of water samples (Patterson et al. 1998 [DIRS 107402]), the major-ion chemistry of the perched water in Borehole USW WT-24 is very similar to that from the perched water in Borehole USW UZ-14, indicating that the perched water in Borehole USW WT-24 has not been in contact with zeolites. The presence of the uppermost perched-water body in Borehole USW WT-24 is also confirmed by strontium concentrations and isotopic ratios. Also, the results of hydrochemical analyses are consistent with an interpretation of perched water within the basal vitrophyre of the Topopah Spring Tuff (based on comparisons with perched water encountered in Boreholes USW G-2 and USW UZ-14).

7.4.3 Temperature Measurements and Estimation of Heat Flow

7.4.3.1 Temperature Measurements and Gradients

In the 1980s, temperature measurements were made in numerous boreholes within the central block of Yucca Mountain and in the surrounding area (Sass et al. 1988 [DIRS 100644]) as part of a regional heat-flow study. More recently, in situ temperature measurements were made as part of the instrumented borehole-monitoring program at Yucca Mountain (Rousseau et al. 1999 [DIRS 102097], pp. 151 to 161; 1997 [DIRS 100178], pp. 46 to 52). The measured temperature profiles provided a means for calibrating field-scale values of thermal conductivity (Bodvarsson and Bandurraga 1996 [DIRS 100102], Section 9.4), for calculating heat fluxes, from which estimates of percolation flux were made (Rousseau et al. 1999 [DIRS 102097], pp. 56 to 60, 184 to 208; Bodvarsson and Bandurraga 1996 [DIRS 100102], Section 9.5; Bodvarsson et al. 1997 [DIRS 100103], Chapter 11), and for calibrating the unsaturated zone flow model (BSC 2003 [DIRS 163045], Section 6.3).

In situ measurements of temperatures are available from eight instrumented (stemmed or packed-off) boreholes (Rousseau et al. 1999 [DIRS 102097], p. 152; Rousseau et al. 1997 [DIRS 100178], p. 46). Additional data were acquired from 10 open boreholes in the vicinity of the ESF during the early 1980s (Rousseau et al. 1999 [DIRS 102097], p. 152). Temperature profiles for Boreholes UE-25 a#1, UE-25 a#4, UE-25 a#5, UE-25 a#6, UE-25 a#7, USW G-1, USW G-4, USW H-1, UE-25 WT#4, and UE-25 WT#18 are presented in Sass et al. (1988 [DIRS 100644], Appendices 1 and 2). Multiple-temperature profiles were made in these boreholes intermittently between 1980 and 1984. Measurements were made using thermistors lowered either into water-filled tubes inserted into these boreholes (preferred method) or into air-filled access tubes used for water-level monitoring or for supporting the downhole instrumentation bundle in Borehole USW UZ-1. Measurement methodology, data limitations, and an analysis of heat flow within the unsaturated zone at Yucca Mountain based on these data are presented in Sass et al. (1988 [DIRS 100644]).

Temperature measurements made in instrumented boreholes since 1994 confirm the general findings and conclusions presented in the earlier work of Sass et al. (1988 [DIRS 100644], pp. 35 and 42): (1) heat flow in the unsaturated zone primarily is conductive, and (2) temperature gradients in the unsaturated zone vary, but generally consist of multiple linear segments (Rousseau et al. 1999 [DIRS 102097], p. 152).

Temperature profiles in six of the eight instrumented boreholes indicated that temperature gradients in the Topopah Spring welded hydrogeological unit can be approximated by nearly

linear segments that are continuous over large, composite thicknesses of this hydrogeologic unit (Rousseau et al. 1999 [DIRS 102097], p. 156). The gradients vary significantly from one location to another within the study area, and range from a low of 1.59°C per 100 m (330 ft) at Borehole UE-25 a#4 to a high of 2.55°C per 100 m (330 ft) at UE-25 NRG#4 (Rousseau et al. 1999 [DIRS 102097], Table 17). In general, smaller gradients in the Topopah Spring welded hydrogeological unit appear to be associated with active channels or valley floors of major drainages. Larger gradients are present beneath channel margins and hillslopes immediately adjacent to these channels, reaching a maximum beneath ridges (UE-25 NRG#4 located on Azreal Ridge) or in hydrologically inactive areas (UE-25 WT#4 and UE-25 a#6) located on hillslopes that are distant from major drainages. The apparent correlation of temperature gradients with geomorphic setting probably has hydrologic significance, similar to the relation between net infiltration and topography and physiography (see Section 7.1.4.3).

Small temperature gradients in the TSw hydrogeologic unit beneath alluvium-filled channels and large gradients along hillslopes and ridges indicate higher heat flow in the TSw, where the unsaturated zone section is thickest (Rousseau et al. 1999 [DIRS 102097], p. 156). The thermal conductivity of the TSw is well constrained, ranging from 1.61 to 1.82 J/s/m/°C. This cannot explain the large differences in gradient required to maintain a vertical and areally uniform heat-flow field (that is, a 45 percent difference in gradient and a 12 percent difference in thermal conductivity). The above generalization appears to describe the northern part of the site area, which has two major drainages (Drill Hole Wash and Pagany Wash), but it may not be true elsewhere on Yucca Mountain. Sass et al. (1988 [DIRS 100644], p. 35, Figure 16), using a one-dimensional analysis of data from many boreholes outside the site area, determined an inverse correlation between total thickness of the unsaturated zone and heat flow. This inverse relation is consistent with topographically induced heat-flow divergence beneath topographic highs and with heat-flow convergence beneath topographic lows. In contrast, the temperature data from boreholes in the northern part of the site area, with the exception of UE-25 WT#18 (on a very steep ridge), appear to support a direct correlation between heat flow and unsaturated zone thickness.

Changes in temperature gradients occur in all boreholes across the contact between the PTn and TSw hydrogeologic units because of major differences between the thermal conductivities of nonwelded and welded tuffs (Rousseau et al. 1999 [DIRS 102097], pp. 156 and 161). Temperature gradients within the PTn are larger because of the lower thermal conductivities of the nonwelded subunits of the PTn. Gradients across the composite PTn section vary from less than 2°C per 100 m (330 ft) to greater than 4°C to 5°C per 100 m (330 ft) (Rousseau et al. 1999 [DIRS 102097], Table 17). Temperature gradients within the PTn tend to show more geographic variability than gradients within the TSw hydrogeologic unit (see temperature profiles of Sass et al. 1988 [DIRS 100644], Appendices 1 and 2). Variability in the gradient across the PTn can be attributed to a number of factors: (1) differences in heat flow from the underlying TSw hydrogeologic unit; (2) a relatively shallow location of the PTn hydrogeologic unit, which is affected by seasonal temperature variations; (3) the presence or absence of alluvial fill; and (4) differences in thermal conductivity, which is sensitive to variability in porosity and saturation.

Temperature gradients within the TCw hydrogeologic unit tend to be small and are strongly affected by seasonal land-surface temperature variations (Rousseau et al. 1999 [DIRS 102097],

p. 161). Temperature profiles for the instrumented and stemmed boreholes indicate that surface temperature changes are propagated to depths of about 15 m (50 ft). These data also indicate that temperatures at this depth tend to be higher in boreholes located within or near active channels (Rousseau et al. 1999 [DIRS 102097], Table 17) because of the low thermal conductivity of the alluvial fill.

7.4.3.2   Time-Series Temperature Data from Monitored Boreholes

Borehole USW SD-12, which is instrumented in all four principal bedrock hydrogeologic units (TCw, PTn, TSw, and CHn), has yielded the most comprehensive records of temperature data (Figure 7-33). Temperature stations in the shallow part of the TCw hydrogeologic unit, above the depth of 15 m (50 ft), indicated the influence of seasonal surface temperature changes (Rousseau et al. 1997 [DIRS 100178], p. 48). Time-series temperature records for instrument stations located in the deeper part of the TCw in Boreholes USW SD-12 and USW UZ-7a indicate slight temperature declines following what appears to be full recovery to ambient, predisturbed temperatures (Rousseau et al. 1997 [DIRS 100178], pp. 47 and 48).   These temperature reversals, even though slight, are significant because they occurred at depths below the penetration of seasonal surface temperature changes. In Borehole USW SD-12, the temperature reversal has been detected down to 76.2 m (250 ft) and in Borehole USW UZ-7a, to a depth of 45.7 m (150 ft), abruptly terminating near the top of the PTn hydrogeologic unit. The significance of time-varying temperatures in the TCw hydrogeologic unit is discussed in Section 7.4.3.3.

The asymptotic warming trends established at instrument stations in the TSw hydrogeologic unit in Borehole USW SD-12 were interrupted by ESF-excavation pneumatic disturbances in the vicinity of the borehole (Rousseau et al. 1997 [DIRS 100178], pp. 49 and 50). The temperature disturbances consisted of a very subtle increase in the temperature-recovery rates, followed by a reversal from a warming to a cooling trend. There is no evidence of temperature disturbances associated with the tunnel-induced pressure disturbances in Borehole USW NRG-7a, despite the fact that it is closer to the ESF than USW SD-12, and ESF-excavation-induced pressure changes occurred in USW NRG-7a almost 4 months before they occurred in USW SD-12. The lack of temperature disturbance in USW NRG-7a may result from lower fracture densities in the TSw hydrogeologic unit at USW NRG-7a and/or from USW NRG-7a being on the east side of the ESF, and, therefore, on the downgradient or "upwind" side of the pressure disturbances caused by tunnel excavation.

7.4.3.3   Estimation of Heat Flow and Implications for Infiltration, Percolation, and Gas Flow

Heat flow at Boreholes UE-25 UZ#4 and UE-25 UZ#5 in Pagany Wash was estimated based on temperature measurements and estimated gradients (Rousseau et al. 1999 [DIRS 102097], pp. 184 to 186). The possible effect of percolation on the inferred heat-flow distribution was taken into account. Trends in temperature indicated that: (1) overall temperatures at UE-25 UZ#4 are higher than at UE-25 UZ#5; and (2) the vertical temperature gradients across the Yucca Mountain and Tiva Canyon tuffs at UE-25 UZ#4 are large, whereas the gradients across these units at UE-25 UZ#5 are small. Convex upward flexures in isotherms beneath Pagany Wash (Rousseau et al. 1999 [DIRS 102097], Figure 116) indicate that the low thermal

conductivity of the alluvial fill acts as an insulator, trapping heat in the underlying PTn hydrogeologic unit and elevating temperatures at UE-25 UZ#4. The low thermal conductivity of the alluvial fill forces heat flow to diverge away from the channel and converge in the TCw hydrogeologic unit along the margins and hillslopes bordering this channel.

Comparison of calculated and estimated heat flow through the major hydrogeologic units at Boreholes UE-25 UZ#4 and UE-25 UZ#5 indicates a large heat-flow deficit across the contact between the TSw and PTn hydrogeologic units (Rousseau et al. 1999 [DIRS 102097], p. 189, Table 20). The heat flow estimated for the Pah Canyon Tuff (15.5 megajoules per second per square meter (MJ/s/m^2)) is substantially less than the conductive heat flow of 32 to 40 MJ/s/m^2 estimated as typical for the TSw hydrogeologic unit in the northern part of the site area. Heat flow increases with elevation at Borehole UE-25 UZ#5, and, to a lesser extent, at Borehole UE-25 UZ#4, presumably as a result of the lateral divergence of heat around the alluvium toward the more thermally conductive rocks of the TCw hydrogeologic unit. The reduction in heat flow from 32 to 40 MJ/s/m^2 in the TSw to approximately 15.5 MJ/s/m^2 in the Pah Canyon Tuff indicates the presence of heat-consuming processes, such as the downward movement of water from cooler to warmer thermal regimes. This agrees with the work presented by LeCain et al. (2002 [DIRS 158511]), who showed that the 1998 El Niño rainfall at Yucca Mountain resulted in the infiltration and deep percolation of up to 1 meter of water at Borehole UE-25 UZ#4 (LeCain et al. 2002 [DIRS 158511], Table 1).

In the repository block area, steady-state temperature profiles in Boreholes USW NRG-7a, USW SD-12, and USW UZ-7a are nearly linear across most of the TSw hydrogeologic unit (Rousseau et al. 1997 [DIRS 100178], p. 56). Slight convex-upward curvature in the profiles in Boreholes USW SD-12 and USW UZ-7a probably results from an increase in thermal-conductivity-with-depth that is correlated to decreasing matrix porosity and increasing matrix-saturation-with-depth across the TSw hydrogeologic unit. The nearly linear changes in the temperature gradients within the TSw at USW SD-12 and USW UZ-7a indicate that heat flow is primarily conductive (Rousseau et al. 1997 [DIRS 100178], p. 57). The computed vertical, conductive heat flow across the TSw at Boreholes USW NRG-7a, USW UZ-7a, and USW SD-12 is 37 MJ/s/m^2, 37 to 39 MJ/s/m^2, and 32 to 33 MJ/s/m^2, respectively. These estimates compare well with the regional estimates of heat flow of 30 to 40 MJ/s/m^2 (Sass et al. 1988 [DIRS 100644], Tables 5 and 6, Figure 15) for the unsaturated zone in the area of the repository.

The steady-state temperature profiles for Boreholes USW NRG-7a, USW UZ-7a, and USW SD-12 also indicate significant changes in the temperature gradients across the PTn and TCw hydrogeologic units (Rousseau et al. 1997 [DIRS 100178], p. 57). Larger gradients across the PTn are consistent with a decrease in thermal conductivity with depth. In contrast, the nearly isothermal temperature profiles in Boreholes USW UZ-7a and USW SD-12 and the very small gradient at USW NRG-7a indicate significant nonconductive heat-extraction processes. Conductive heat-balance calculations across the PTn and the TCw at these boreholes indicate that the conductive heat-flux deficit ranges from 6.6 MJ/s/m^2 at USW UZ-7a to 8.8 MJ/s/m^2 at USW NRG-7a (Rousseau et al. 1997 [DIRS 100178], pp. 57 and 58, Table 5.1-3). The apparent heat losses can be accounted for by considering the two most significant nonconductive heat-transfer processes in the unsaturated zone: (1) sensible-heat consumption caused by convective downward and/or lateral movement of liquid water from relatively cool, shallow

depths to deeper and warmer depths, and (2) latent-heat consumption due to evaporation sustained by active, convective gas flow that removes vapor-laden air.

The computed conductive heat-flow deficits for latent heat are sufficient to vaporize a water flux equivalent of 0.11 mm/yr at USW NRG-7a, 0.10 mm/yr at USW SD-12, and 0.08 mm/yr at USW UZ-7a (Rousseau et al. 1997 [DIRS 100178], pp. 58 and 59). Alternatively, sensible heat losses would require a downward, liquid infiltration rate of 52 mm/yr at USW NRG-7a, 78 mm/yr at USW SD-12, and 96 mm/yr at USW UZ-7a, if liquid flow were the only nonconductive heat-transfer mechanism. These estimates for vaporization and infiltration represent two end-members of the nonconductive heat-transfer spectrum. Some combination of these processes is supported by other evidence from the borehole monitoring data from USW UZ-7a and USW SD-12. As described in Section 7.4.3.2, the time-series temperature records for all the instrument stations in the TCw hydrogeologic unit indicate a possibility of a very low-amplitude, low-frequency temperature cycle down to depths of 76.2 m (250 ft) at USW SD-12 and 45.7 m (150 ft) at USW UZ-7a (Rousseau et al. 1997 [DIRS 100178], pp. 58 and 59). These depths are much greater than the depth of penetration of seasonal surface temperature changes, 15.2 m (50 ft), and thus cannot logically be attributed to conductive heat transfer from the ground surface. One possible explanation for the cyclic character of these temperatures is evaporation accompanied by active, convective gas flow. However, additional monitoring data are needed to confirm the presence of these deep temperature cycles and their relation to surface temperatures and seasonal temperature changes.

Heat losses caused by a downward infiltration in the range of 52 to 96 mm/yr are extremely unlikely, unless substantial lateral flow occurs within the PTn hydrogeologic unit (Rousseau et al. 1997 [DIRS 100178], p. 59). On the other hand, studies of gas residence times in the TCw hydrogeologic unit indicate that gas circulation through this unit is sufficient to remove the 0.08 to 0.11 mm/yr of liquid flux equivalent needed to sustain the latent-heat process (Rousseau et al. 1997 [DIRS 100178], p. 58). Gas residence times have been estimated using the chemical concentrations of three chlorofluorocarbon species and $^{14}CO_2$ collected from the TCw hydrogeologic unit from Boreholes USW UZ-6s and USW UZ-6 near Yucca Crest (Patterson et al. 1996 [DIRS 100172], pp. 93 and 94). In this analysis, gas residence times were constrained to between 1 and 4 years, with a best estimate of about 2 years. If the average travel distance from the recharge area to the discharge area is 200 m (660 ft), the 2-year residence time requires a gas circulation velocity of 100 m/yr through the TCw hydrogeologic unit, which would be sufficient to sustain a vaporization rate of 0.7 mm/yr.

7.5 HYDROCHEMICAL AND ISOTOPIC INDICATIONS OF FLUID FLOW

Aqueous- and gaseous-phase hydrochemical and isotopic data for water and gas collected from the unsaturated zone are discussed in Sections 5.2.2.4 through 5.2.2.6. Interpretations of these data are used to provide constraints on possible flow mechanisms and residence times of fluids (water and air) in the unsaturated zone (Yang et al. 1996 [DIRS 100194], p. 2; 1998 [DIRS 101441], p. 2). Methods used to collect and process water and gas samples for chemical and isotopic analyses are described in Yang et al. (1996 [DIRS 100194], pp. 6 to 12) and Yang et al. (1998 [DIRS 101441], pp. 4 to 7, pp. 24 to 29).

Aqueous-phase hydrochemical data have been interpreted to determine possible flow mechanisms and residence times for pore water in the unsaturated zone. The data consist of chemical compositions (major cations and anions), discussed in Section 5.2.2.4, and isotopic compositions, including tritium and chlorine isotopes (discussed in Sections 5.2.2.5.2 and 5.2.2.5.3, respectively), the carbon isotopes ^{14}C, and ^{13}C (discussed in Section 5.2.2.5.4), stable isotopes of ^{18}O and deuterium (discussed in Section 5.2.2.5.5), strontium isotopes (discussed in Section 5.2.2.5.6), of pore water in cores obtained from unsaturated zone boreholes. Chemical compositions of pore water in different lithologic units help in understanding the hydrologic relations among the major hydrogeologic units. The chemical and isotopic data have been used to formulate preliminary conceptual hydrologic flow models.

Detailed information about gaseous-phase chemistry and isotopes in unsaturated zone water is provided in Section 5.2.2.6. These data include carbon isotopic data obtained from boreholes.

7.6 HYDROLOGIC CONDITIONS AND TESTING IN THE EXPLORATORY STUDIES FACILITY

Exploratory Studies Facility testing encompasses a wide range of investigations that include collecting and analyzing geologic, hydrologic, geochemical, and geomechanical data to understand the natural processes of rock mechanics and fluid migration. The studies described in this section were designed to collect and analyze pertinent geologic, hydrologic, and chemical data needed to estimate accurately percolation flux and gaseous-phase circulation at the repository horizon, and seepage into emplacement drifts. The underground testing program was recently summarized in Wang and Bodvarsson (2003 [DIRS 163215]).

7.6.1 Effects of Ventilation on Moisture Conditions in the Exploratory Studies Facility

Ventilation of the ESF has affected the surrounding rocks by creating a dryout zone around tunnels and drifts (BSC 2003 [DIRS 166347], Section 6.10.1.2.1). It is therefore anticipated that while the repository is ventilated after the emplacement of waste, the amount of seepage that might occur at the repository horizon will be lessened due to this dryout, during the time period that ventilation is occurring. In this section, the moisture-monitoring study in the ESF is described, along with observations from both the ESF main drift and the ECRB Cross-Drift. Descriptions of dryout in ESF niche boreholes also are included. Table 7-2 summarizes the niches and alcoves that have been constructed in support of unsaturated zone studies, and their locations are shown in Figure 1-3.

7.6.1.1 Exploratory Studies Facility Main Drift Observations

The moisture removal capacity within the ESF system depends on evaporation (BSC 2003 [DIRS 166347], Section 6.10.1.2.1). For a 6,250 m long tunnel with a cross-sectional area of 40 m^2, the humid tunnel-air can contain 2,500 kg of excess water mass, if the tunnel is estimated to have on average 50 percent higher relative humidity than the outside air, with the corresponding vapor density difference on the order of 0.01 kg/m^3. If the tunnel air is ventilated with a flow rate of 47 m^3/s or 100,000 ft^3/min, it will take 5,300 s, or 1.5 hr, to remove and replace the tunnel air. The water removal rate of 2,500 kg over 1.5 hr corresponds to 285 m^3/wk (285 kl/wk or 75,000 gal/wk). Approximating that all the moisture in the tunnel air is from

evaporation, the equivalent evaporation rate from the tunnel walls and inverts (with area approximately 148,000 m^2 (6,250 m long × 23.7 m) is approximately 100 mm/yr (Wang et al. 1996 [DIRS 101309], Section 2.2).

The equivalent evaporation rate of 100 mm/yr is an order of magnitude larger than the ambient average percolation flux averaged over the unsaturated zone flow model domain (BSC 2003 [DIRS 163045], Table 6.1-2). The large evaporation rate could suppress the observations of active seeps and contribute to the apparent dry-tunnel conditions. The results of water potentials near the rock surfaces (which were measured with heat-dissipation probes) and water-potential profiles along boreholes (which were measured by psychrometers in niches and alcoves along the ESF main drift and along the ECRB Cross-Drift) showed that the dryout zone could extend to 1 to 3 m (3 to 10 ft) into the rock, with fractures and faults likely extending the depths of drying influence (BSC 2003 [DIRS 166347], Section 6.10.1.2.1). Rock temperatures near the tunnel boring machine were observed to change spatially and temporally and could be related to evaporation from rock surfaces.

7.6.1.2   Cross-Drift Observations

Conditions in the ECRB Cross-Drift in 1998 were similar to the conditions of the ESF main drift in 1996. High-humidity conditions existed in the new sections just excavated. Relative humidity data from three moisture stations in the ECRB Cross-Drift are illustrated in Figures 7-34 and 7-35 for the month of November 1998, right after the completion of the excavation by the tunnel boring machine. The moisture sensor at ECRB Cross-Drift construction station CD 25+55 (2,555 meters from the ECRB Cross-Drift entrance) is located near the Solitario Canyon fault on the western boundary of the repository block. The other two sensors, at construction stations CD 14+43 and CD 21+40, measured the moisture conditions in the middle part of the ECRB Cross-Drift within the repository block.

The effect of a newly excavated tunnel on the temporal and spatial distributions of relative humidity in the ECRB Cross-Drift is illustrated in Figures 7-34 and 7-35. Relative-humidity gradients, together with the ventilation rates, are needed to calculate the moisture-removal rates. The ECRB Cross-Drift is a simple tunnel system compared to the ESF main drift. There is only one ventilation line operating along the ECRB Cross-Drift, without any secondary branches separating the air flow into side alcoves and niches.

7.6.1.3   Observations of Dryout in Niche Boreholes

Drying processes in the rocks of the ESF main drift were monitored with psychrometers, installed in boreholes in three niches, to measure water potential (BSC 2003 [DIRS 166347], Section 6.8). Niches 1, 2, and 3 (at construction stations 35+66, 36+50, and 31+07) are located on the west side of the ESF main drift (Figure 1-3) in the vicinity of two faults, the Ghost Dance fault and the Sundance fault.

Overall, psychrometer measurements in the ESF indicate significant variability in water potential among the three niches and within each niche (BSC 2003 [DIRS 166347], Section 7.8). The main observations are the following:

- Ventilation effects may have penetrated the rock, possibly greater than 3 m (10 ft).

- Two zones of wetter conditions in Niche 1 appear to be associated with the Sundance fault.

- There was large variability of the water potential (-15 m to -84 m) within the 0.9 m (3 ft) in two boreholes at Niche 3.

- In the zone beyond where ventilation effects of the ESF were observed (i.e., at 10 m depths), the rocks in Niche 1 appeared to be wetter than those in Niche 2.

7.6.2   Distribution and Movement of Water Used in Construction

The use and release of construction water affects the moisture distribution in the rocks surrounding ESF drifts (Finsterle et al. 1996 [DIRS 101223], Section 1.1).   Monitoring and predicting the migration of construction water may provide information on water flow in the fractured, unsaturated tuffs at Yucca Mountain.   The amount of water released, permeability of the fractured formation, continuity of the fracture network, and fracture-matrix interaction are all expected to be sensitive parameters, affecting penetration depths, migration velocity, and flow patterns of a construction-water plume.

7.6.2.1   Detection of Construction-Water Tracers in Cores below the Exploratory Studies Facility Loop

Water used for tunnel construction has been traced by adding a lithium-bromide tracer to it at a concentration of 20 parts per million bromide (Finsterle et al. 1996 [DIRS 101223], Section 3.1). The bromide-to-chloride ratio in this water is 2.9, which is significantly higher than the ratio (about 0.01) in natural infiltrating water at Yucca Mountain.   Hence, construction water is interpreted to be present in a pore-water sample extracted from an ESF drill core, if its bromide-to-chloride ratio is greater than 0.01.   This threshold is supported by statistical analysis performed on the data.

Three slanted Boreholes (ECRB-CWAT#1 at construction station 37+37, ECRB-CWAT#2 at construction station 50+64, and ECRB-CWAT#3 at construction station 63+92) were drilled downwards from the floor of the ESF tunnel, and pore-water salts were extracted from the drill cores for analysis (Finsterle et al. 1996 [DIRS 101223], Sections 1.1 and 2.2).   Based on bromide-to-chloride ratios, the shallowest depth of penetration was in Borehole ECRB-CWAT#3, in which construction water was detected only in the top 2 m (6.6 ft) (Finsterle et al. 1996 [DIRS 101223], Section 3.1).   The deepest penetration was in Borehole ECRB-CWAT#2, in which construction water had reached the bottom of the borehole (30 m [98 ft]). In Borehole ECRB-CWAT#1, construction water was detected in all samples to a depth of 2.4 m (7.9 ft) and in two isolated peaks at depths of 6.7 m (22 ft) and 8.5 m (28 ft), indicating fracture flow.   Differences in migration distances are most likely related to differences in

water-application rates and in hydraulic characteristics of the geologic units at each location (Finsterle et al. 1996 [DIRS 101223], Section 3.1).

These observations provide a minimum estimate for the depth of construction-water penetration during construction of the primary ESF loop (Finsterle et al. 1996 [DIRS 101223], Section 3.1). The water may have migrated considerably farther through the fracture network than indicated by these data, particularly where the water was applied directly onto the Tptpmn (in the cases of Boreholes ECRB-CWAT#1 and ECRB-CWAT#2).

7.6.2.2 Wetting-Front Detection in the Enhanced Characterization of the Repository Block Cross-Drift Starter Tunnel

During excavation of the ECRB Cross-Drift, sensors were placed in a borehole drilled below the starter tunnel, and sensors and water-collection trays were placed along the ESF main drift at the point where the cross-drift crosses over the main drift (BSC 2003 [DIRS 166347], Section 6.9). The migration of water plumes (or wetting fronts) from tunneling activities associated with the ECRB Cross-Drift was monitored. A 30 m (98 ft) long borehole (0.10 m [0.33 ft] inside diameter) was drilled at an angle of 30° from the horizontal along the proposed path of the cross-drift tunnel in the Tptpul unit. Changes in water potential and wetting-front position were monitored along the entire length of the wetting-front monitoring borehole using psychrometers and electrical resistance probes, respectively, as the tunnel boring machine advanced through the rocks above.

Overall analysis of data collected to detect wetting-front migration from the ECRB Cross-Drift starter tunnel resulted in the following conclusions (BSC 2003 [DIRS 166347], Section 7.9):

- Three events were observed along the borehole below the starter tunnel at depths close to 10 m (33 ft). A ponding event that occurred on March 8, 1998, increased water-potential values up to a depth of 8.65 m (28.4 ft) (17.3 m [56.8 ft] along the borehole). During this event, the magnitude of the disturbance decreased farther into the borehole, with an anomaly observed at a depth of 9.4 m (31 ft) where the change in water potentials was significantly larger than the expected trend.

- At different times during the monitoring period, changes in water-potential values occurred at different locations along the borehole. Early in March 1998, the large changes were restricted to locations close to the borehole collar, whereas by early April, large changes were evident at depths between 9.4 and 11.4 m (31 and 37.4 ft).

- One concern that could arise from the use of a slanting borehole to measure wetting-front migration is the possibility of the bore cavity short-circuiting flow paths. For this particular investigation, this short-circuiting does not appear to be happening, as indicated by the analysis of recovery responses observed at the depth of 5.2 m. Here, the response to a wetting event was negligible when compared with other psychrometers close to this location (above and below), suggesting that this zone was well isolated (hydraulically) from the adjacent zones and did not detect the wetting front.

7.6.2.3 Wetting-Front Monitoring at the Main Drift-Cross Drift Crossover Location

Figure 7-36 illustrates the seepage-detection system at the main drift-cross–drift crossover location, showing the location of fluid collection trays hung below the ceiling of the ESF main drift. The seepage monitoring system was used to detect the wetting front in the ESF main drift as the result of releases of traced water in the cross-drift above (BSC 2003 [DIRS 166347], Section 6.9.1.3). Overall analysis of data collected resulted in the following conclusions (BSC 2003 [DIRS 166347], Section 7.9):

- No seepage was observed, nor did a wetting front reach the ESF main drift when the tunnel boring machine crossed over the ESF main drift during excavation of the cross-drift

- The tunnel boring machine apparently released insufficient water to induce seepage into the main drift, 17.5 m (57.4 ft) below

- Confirmation of no seepage at the crossover location establishes the lower limit for drift-to-drift flow and drift-seepage processes associated with construction-water usage.

7.6.3 Fracture-Matrix and Fault-Matrix Interactions for Liquid Flow

7.6.3.1 Fracture-Matrix Flow at Alcove 6

Wetting-front movement, flow-field evolution, and drainage of fracture flow paths were evaluated in a test bed with a slot excavated below a cluster of boreholes. The slotted test bed is located within the Topopah Spring welded tuff (TSw) at Alcove 6 in the ESF at Yucca Mountain, Nevada. Hydraulic parameters such as formation intake rates, flow velocities, seepage rates, and fracture volumes were measured under controlled boundary conditions, using techniques developed specifically for in situ testing of flow in fractured rock.

7.6.3.1.1 The Test Bed

The test bed was located at Alcove 6 in the ESF, lying within the middle nonlithophysal zone of the TSw. The rock was visibly fractured, with predominantly vertical fractures and a few subhorizontal fractures. The relatively wide fracture spacing (on the order of tens of centimeters) facilitated the choice of injection zones, allowing discrete fractures and well-characterized fracture networks to be isolated by packers for localized flow testing.

A horizontal slot and a series of horizontal boreholes are the distinct features of the test bed (BSC 2003 [DIRS 166347], Figure 6.6.1-1b). The slot, located below the test bed, was excavated by an over-coring method. The excavation sequence required (first) the drilling of parallel pilot holes, 0.10 m in diameter, over 4 m in length with a 0.22 m spacing, normal to the alcove wall. The pilot holes were then over-cored by a 0.3 m drill-bit to excavate the 2.0 m wide, 4.0 m deep and 0.3 m high slot located approximately 0.8 m above the alcove floor. Three I-beam supports were installed along the length of the slot for support. Four horizontal boreholes, 0.1 m in diameter and 6.0 m in length, were drilled perpendicular to the alcove wall above the slot. Two boreholes were located 1.6 m above the slot ceiling, while two boreholes

were 0.9 m and 1.0 m above the slot ceiling, respectively, and 0.7 m apart (BSC 2003 [DIRS 166347], Figure 6.6.1-1b).

7.6.3.1.2   Test Operation and Monitoring

Field tests included multiple releases of tracer-laced water in one high-permeability zone (HPZ) and one low-permeability zone (LPZ) along an injection borehole. The permeabilities of these zones were determined from air-permeability measurements conducted over 0.3 m sections along the borehole, using a straddle packer that also was used for liquid releases. The HPZ had an air-permeability value of 6.7×10^{-12} m^2, and the LPZ had an air-permeability value of 2.7×10^{-13} m^2 (Salve 1999 [DIRS 155692], pp. 48 and 49; Cook 2001 [DIRS 156902], pp. 51 to 53). During and following liquid-release events, changes in saturation and water potential in the fractured rock were measured in three monitoring boreholes, with changes continuously recorded by an automated data acquisition system. The water that seeped into the excavated slot below the injection zone was collected, quantified for volumes and rates, and analyzed for tracers.

There were three distinct components to the flow investigation: (1) controlled release of water into isolated zones, (2) borehole monitoring for changes in saturation and water potential, and (3) collection of seepage from the slot ceiling. All the water used in the ESF was spiked with lithium bromide for mining-related activities and for most of the scientific investigations. Additional tracers were added to the water injected into the LPZ and during the first set of experiments in the HPZ (BSC 2003 [DIRS 166347], Table 6.6.1-1). During the tests, water that seeped into the slot was periodically sampled and analyzed for tracer concentrations.

7.6.3.1.3   Observations and Conclusions

With a slot below injection zones, it was possible to quantify both the inflow into the system and outflow at the lower boundary, and to better evaluate the flow field in underground test conditions, as described in BSC (2003 [DIRS 166347], Section 6.6), in Salve et al. (2002 [DIRS 161318]), and in Hu et al. (2001 [DIRS 165413]).

In this field study, techniques developed to investigate flow in fractured welded tuffs were evaluated. Results from field tests suggest that in situ characterization of certain fundamental flow parameters (such as travel times, percolation, and seepage rates) can be achieved with this approach. Alcove 6 is in the middle nonlithophysal TSw unit, with well-defined fracture network through competent welded tuff rock.

The test results revealed aspects of flow in unsaturated, fractured systems and provided insight towards the conceptualization of flow through unsaturated and fractured rock formations. The Alcove 6 test is the first test conducted in the ESF on unsaturated fractured tuff with attempts in taking liquid mass conservation explicitly into account. In field tests, it is frequently difficult to control the boundaries, and liquid can flow to unknown domains. Transient data collected at Alcove 6 also contribute to the evaluation of unsaturated flow in fractured tuffs.

Several sets of liquid-release tests were conducted with localized injections of liquid into an LPZ and into an HPZ along a borehole. The major test results were (BSC 2003 [DIRS 166347], Section 7.6):

- For all injections into both LPZ and HPZ, changes in electrical resistance and psychrometer readings were detected in two monitoring boreholes ~0.6 m below the point of injection.

- For the LPZ tests, water did not seep into the slot located 1.65 m below.

- Liquid-release rate into the LPZ was observed to steadily decrease by two orders of magnitude (from >30 to < 0.1 mL/min) over a period of 24 hours.

- In the HPZ, liquid-release rates under constant-head conditions were significantly higher (~100 mL/min), with intermittent changes observed in the intake rate.

- For injection tests in HPZ, water was observed to drip into the slot in 3 to 7 minutes at high injection rates of ~28 to ~100 mL/min, in 1 hour at the low injection rate of 14 mL/min, and in 5 hours at the lowest rate of 5 mL/min.

- During the course of each test, seepage rates measured in the slot showed intermittent responses despite constant-head or constant-rate conditions imposed at the input boundary.

- The percentage of cumulative volume of water recovered in the slot was observed to increase in most tests, approaching steady-state values after ~10 L of water had been injected.

- A maximum of 80 percent of the injected water was recovered for high-rate injection tests.

- The saturated volumes of fracture flow paths were estimated for each test from measurements of fluid volume before wetting front arrivals and from measurements of drainage volume into the slot after termination of injection. The flow path volumes were found to increase from <0.2 L initially to ~1.0 L during recovery, with some stepped increments of 0.1 to 0.3 L observed.

- Plug-flow processes were observed with tracer analyses. "New" water replaced "old" water from the previous test.

The stepped and intermittent changes could be associated with heterogeneous distribution of storage volumes in the connected fracture flow paths, in the dead-end fractures, and in the rock matrix blocks. The test results from Alcove 6 could be used to evaluate fracture flows and fracture-matrix interactions.

7.6.3.2   Liquid Flow Testing in a Minor Fault in the Nonwelded Paintbrush Hydrogeologic Unit (Alcove 4)

Alcove 4, at construction station 10+28 in the ESF (Figure 1-3), was constructed across a fault in the PTn hydrogeologic unit to evaluate the effect of a fault on fluid flow in a nonwelded unit. These experiments included multiple releases of tracer-laced water in isolated zones along three horizontal boreholes. The zones into which water was released were selected based on air-permeability measurements conducted over 0.3 m (1 ft) sections of borehole (BSC 2003 [DIRS 166347], Section 6.7.1.3). The plumes that developed from these releases were monitored in six separate horizontal boreholes. During, and following, liquid-release events, changes in water potential (measured with an accuracy of 10 Pa) along horizontal monitoring boreholes were continuously recorded by an automated data-acquisition system.

7.6.3.2.1   The Test Bed

The test bed is located at Alcove 4, which transects portions of the lower Pah Canyon Tuff (Tpp) and the upper pre-Pah Canyon bedded tuffs (Tpbt2) of the PTn hydrogeologic unit. The central axis of the alcove has an azimuth of 6°, which coincides with the approximate strike of the lithostratigraphic units in the vicinity. The north face of the alcove, in which the test bed is located, is approximately 6 m (20 ft) wide and 5.3 m (17.4 ft) high (Figure 7-37).

A normal fault with a small offset (0.25 m [0.8 ft]) cuts across the north face of Alcove 4. As mapped along the crown at the end of the alcove (Barr et al. 1996 [DIRS 100029]), full-periphery geologic map OA-46-289 (DTN: GS960908314224.020 [DIRS 106059]) for the crown, but not for the end face), the fault has a strike of approximately 195° and a westward dip of 58°. The fault is open in the ceiling and is closed, with knife-edge thickness, near the invert on the north face. Intersecting the fault near the alcove crown along the north face is a high-angle fracture. The fracture also appears to have a large aperture near the ceiling and a much smaller aperture (eventually becoming undetectable) close to the invert.

Two distinct features that were imposed on the formation define the layout of the field experiment (i.e., a horizontal slot and a series of horizontal boreholes). The slot, located immediately below the test bed, was designed to capture any seepage resulting from gravity drainage. Twelve 6.0 m (19.7 ft) long, approximately 0.1 m (3 in.) diameter boreholes were drilled into the alcove face, as illustrated in Figure 7-38.

7.6.3.2.2   Test Operation and Monitoring

The flow investigation had three distinct components: (1) controlled release of water into isolated zones, (2) borehole monitoring for changes in saturation and water potential, and (3) the monitoring of seepage from the slot ceiling (BSC 2003 [DIRS 166347], Section 6.7.1.2). Because water did not seep into the slot, the seepage monitoring system was not used. The liquid-release experiments required water to be injected into the formation over a 0.3 m section of borehole, with a constant-head boundary condition to determine the maximum rates at which the zone could take in water. In six monitoring boreholes (Boreholes 1, 2, 11, 6, 7, and 8 in Figure 7-38) located above the slot, changes in water potential were continuously recorded during the entire investigation.

A total of 193 L of water was released into Borehole 12 during seven events, under constant-head conditions, between October 21 and November 5, 1998, as summarized in Table 7-31. In Borehole 5, away from the fault, water was released into two zones. In the first zone (located 1.50 to 1.80 m from the collar), 1.37 L of water were released to the zone on October 19, 1998, and the same volume was released on October 20, 1998.

7.6.3.2.3 Observations of Fault Flow

Water was injected into the section of Borehole 12 that intercepted the fault approximately 1.40 m from the collar (BSC 2003 [DIRS 166347], Section 6.7.2.1.1). Here, 193 L of water were released into the formation during seven events that extended over a period of two weeks, as illustrated in Figure 7-39.

When water was introduced into Borehole 12, the time taken for the wetting front to travel 1.07 m along the fault to Borehole 11 varied among the seven tests (BSC 2003 [DIRS 166347], Figure 6.7.2-2, Section 6.7.2.1.2). In the first test, water was detected in the lower borehole ~300 minutes after the first release, while in the second test, the travel time was reduced to ~200 minutes. For the third test, the travel time was ~250 minutes; in the fourth test, water appeared in the fault in Borehole 11 within ~150 minutes. The fastest travel time was observed for the fifth test, when the front arrived in Borehole 11 within ~120 minutes. In the last two tests, the travel times were significantly slower, with increasing saturations observed 400 and 700 minutes after the initial release of water.

7.6.3.2.4 Summary and Conclusions from Alcove 4 Testing

Fault and matrix flow data were collected in a test bed located in the PTn at Alcove 4 in the ESF. Using a series of horizontal boreholes, the intake rates and plume travel times in various locations within the test bed were determined, as described in Section 6.7, in Salve et al. (2003 [DIRS 164470]), and in Salve and Oldenburg (2001 [DIRS 157316]).

These test results revealed aspects of flow in a fault located within the nonwelded tuffs and provided insights into the flow properties of the PTn. With the exception of a well-defined fault trace, no visible fracture traces are evident in the bulk of the test bed in the Paintbrush nonwelded tuff test bed. A series of localized liquid-release tests helped determine that (BSC 2003 [DIRS 166347], Section 7.7):

- Intake rates within a fault located in the PTn decreased as more water was introduced into the release zone (i.e., from an initial value of ~200 mL/min to ~50 mL/min after 193 L of water entered the injection zone).

- The travel time of the wetting front resulting from water released in the fault decreased when the fault was wet (i.e., in closely timed tests, the plume traveled faster in subsequent releases).

- Over time, the hydrologic properties of the fault appear to be altered, with water traveling along the fault at significantly slower rates.

- The matrix adjacent to the fault imbibed water that was introduced into the fault. Changes in saturation were seen more than 1.0 m from the point of release.

- The intake rates and wetting-front travel times in the matrix were significantly slower than in the fault. Water released into the matrix was observed to travel 0.45 m in 14 days.

Uncertainties are also associated with relative short durations in comparison with seepage tests in niches. With a limited number of tests, uncertainties are expected to be larger than tests collecting more data. Not enough water was injected to induce seepage and water collection with the slot below. The tests were conducted to gain understanding of the flow through a nonwelded tuff unit, with large damping capacities for modulating infiltrating pulses.

7.6.4 Estimation of Seepage into Drifts of the Repository

Evaluation of seepage into mined underground openings or drifts is part of a larger ambient field-testing program under way in the ESF. The general objective of the ambient field-testing program is to assess and evaluate the potential waste-emplacement environment and the unsaturated zone natural barriers to radionuclide transport at Yucca Mountain. The evaluations provide the necessary framework to accomplish the following (BSC 2003 [DIRS 166347], Section 6.2):

- Measuring in situ hydrologic properties of the repository host rock for use in *Seepage Calibration Model and Seepage Testing Data* (BSC 2003 [DIRS 162267]) and *Seepage Model for PA Including Drift Collapse* (BSC 2003 [DIRS 163226]).

- Providing a database of liquid-release and seepage data that can be used to evaluate seepage and other related unsaturated zone processes.

- Evaluating drift-scale seepage processes to quantify the extent to which seepage is excluded from entering an underground cavity.

- Determining the seepage threshold below which percolating water will not seep into a drift.

7.6.4.1 Air-Injection and Liquid-Release Tests Conducted in Exploratory Studies Facility Niches

Air-injection tests and liquid-release tests were conducted prior to excavation of the ESF niches to characterize the flow of air and water through relatively undisturbed fractures. Similar tests were conducted after excavation to quantify the effect of excavation on air permeability and water seepage into an underground opening from a small-scale percolation event of known duration and intensity. The niche locations, shown on Figure 1-3, were selected for study based on fracture and hydrologic data collected in the ESF (BSC 2003 [DIRS 166347], Section 6.1.1.1). Four niches were excavated along the main drift of the ESF and a fifth in the ECRB Cross-Drift.

7.6.4.1.1 Preexcavation and Postexcavation Air-Injection Tests

Extensive crosshole air-injection tests were performed in borehole clusters at five niches and at three alcoves to characterize the air-permeability distribution and to select locations for subsequent liquid-release tests (see BSC 2003 [DIRS 166347], Sections 6.1 and 6.2). Air-injection tests consist of injecting compressed air at a constant mass rate into an isolated section of borehole while monitoring the pressure responses in the injection interval and in nearby observation intervals. Two basic types of measurements are readily available from air-injection tests: (1) single-hole air-permeability profiles, which are used for hole-to-hole and site-to-site comparisons of air-permeability values, and (2) crosshole pressure-response data, which enable a determination of fracture or flow-path connectivity between boreholes at a given site. This section focuses on the permeability profiles obtained from four niche sites. Permeability profiles obtained before niche excavation were compared with profiles obtained after niche excavation.

Table 7-32 summarizes the average (arithmetic and geometric) values, standard deviations, and ranges of variations in pre- and postexcavation permeability of individual boreholes and of whole niche sites. Table 7-33 shows similar information for the boreholes above Niche 5 (also referred to as Niche 1620; Table 7-2) in the ECRB Cross-Drift. For assessing the excavation-induced impacts, the analyses in Tables 7-32 and 7-33 are for the upper boreholes only. Drift scale variations along boreholes and among different boreholes within the same niche test-site are larger than differences among different sites.

Each niche has distinct air-permeability values, and the data indicate the difference in permeabilities determined using single-hole (the borehole injection interval is 0.3 m) and crosshole air-injection tests (using borehole clusters of 3 or 7 boreholes, with averaging up to a 100 m^3 volume). The mean and standard deviation of air permeability (log k), determined from studies in niche and alcove boreholes, are presented in Table 7-34. Niche 1 and Niche 3 (also referred to as Niche 3566 and Niche 3107, respectively; Table 7-2) each have a "radial" entry in the table, which indicates boreholes that are drilled from inside the niches after excavation. Permeability values from these boreholes for Niche 3 vary little from those of the preexcavation boreholes, indicative of the uniformity of the formation around Niche 3. For Niche 1, however, the radial boreholes that were tested intersected the brecciated zone of the Sundance fault and so exhibited higher permeability than that for the preexcavation boreholes. Preexcavation means and standard deviations were derived from averaging over all the seven boreholes in each niche cluster. The middle- and lower-level boreholes supplement the upper boreholes to characterize the three-dimensional space in the niche test-beds and locate flow paths under preexcavation conditions. After excavation, with only upper boreholes in a horizontal plane remaining, the air-permeability tests can characterize only the zones above the niche ceilings.

Figure 7-40 illustrates both preexcavation and postexcavation air-permeability values along the three boreholes drilled above Niche 2 (also referred to as Niche 3650; Table 7-2). The data indicate that postexcavation permeabilities are greater than, or equal to, those measured prior to excavation (BSC 2003 [DIRS 166347], Section 6.1.2.2). In general, the preexcavation and postexcavation air-permeability values from tests performed on borehole intervals beyond the end of the niche excavation appear to exhibit smaller changes than those measured directly above the opening. The permeability increases could be interpreted as the opening of existing fractures

induced by stress releases associated with niche excavation (Wang and Elsworth 1999 [DIRS 104366], pp. 752 to 756). Intervals with high preexcavation permeability exhibited the smallest postexcavation permeability changes consistent with the stress-release model. Some of the permeability increases could be caused by the intersection of previously dead-end or long fractures with the constant-pressure boundary condition created by the drift. Alternatively, permeability increases could be caused by the creation of new fractures or extension of existing fractures because of physical damage (i.e., induced fracturing) to the rock caused by mechanical mining.

7.6.4.1.2 Data Obtained from the Liquid-Release and Seepage Tests Conducted at the Niches

The air-permeability data were used to select test intervals for subsequent liquid-release tests (BSC 2003 [DIRS 166347], Section 6.2.1.1). In the same borehole used for air-injection tests, a series of low flow-rate liquid-release tests were conducted prior to niche excavation. A small quantity (about 1 L) of water containing colored or fluorescent dyes was pumped into an isolated section of the borehole (test interval) at a constant rate, with little or no pressure buildup. Various dyes were used during the study to document the flow path traveled by the wetting front.

Subsequently, each niche was excavated dry using an Alpine Miner, to observe and photograph the distribution of fractures and dye within the welded tuff (BSC 2003 [DIRS 166347], Section 6.2.1.2). During the mining of Niche 1 and Niche 2, two types of flow paths were observed based on the pattern of dye, including: (1) flow-through individual or small groups of high-angle fractures; and (2) flow-through several interconnected low- and high-angle fractures, creating a fracture network. Dye was observed along individual fractures and fracture networks to a maximum depth of 2.6 m (8.5 ft) below the release points in the middle nonlithophysal zone (Tptpmn) of the crystal-poor Topopah Spring Tuff (in the TSw hydrogeologic unit). The vertically elongated dye pattern suggests that water is predominantly flowing downwards. An approximately symmetrical (two-dimensional) dye pattern was observed around the release point at Niche 5, located in the lower lithophysal zone (Tptpll) of the TSw hydrogeologic unit. Dye was observed in fractures and lithophysae to a maximum depth of 1.4 m (4.6 ft). Here the dye patterns were more symmetric, with the lateral edges of the wetted area lying about equal distance from the release point.

The mass of water released into each interval was compared to the maximum depth/distance of infiltration, lateral distance traveled by the wetting front, and ratio of depth-to-lateral distance (BSC 2003 [DIRS 166347], Section 6.2.1.2). There was a general trend for the wetting front to move deeper into the rock and farther from the release location as the mass of water released increased. The data showed that water spread laterally over larger distances in the interconnected network of fractures than in high-angle fractures. For the same amount of water injected, the ratio of depth-to-lateral distance traveled shows that the aspect ratio is consistently higher for the high-angle fracture-flow data than for the fracture-network data (CRWMS M&O 2000 [DIRS 141400], Figure 17).

An extensive series of seepage tests was performed at Niche 2, Niche 3, and Niche 4 (also referred to as Niche 4788, Table 2) to quantify the amount of water seeping into the drift from a localized water source of known duration and intensity (BSC 2003 [DIRS 166347],

Section 6.2.1.3). The seepage tests were conducted after the niches were excavated by pumping water into selected-test intervals in Borehole UL (upper left), Borehole UM (upper middle), and Borehole UR (upper right) located above each niche. The distance from the test intervals to the niche ceiling, ranges from 0.58 to 1.23 m for all the niche sites. Water that migrated from the release point to the ceiling of the niche and dripped into the opening was collected and weighed. This was used to determine the seepage percentage, which is the mass of water that dripped into the opening, divided by the mass of water released, and multiplied by 100.

For Niche 2, the seepage percentage ranged from 0 to 56.2 percent. In the early stages of testing at Niche 2, the seepage percentage resulting from two tests were significantly different, even though the tests were conducted at nearly the same liquid-release rate (BSC 2003 [DIRS 166347], Section 6.2.1.3.1). It was determined during the early stages of testing that the memory effect, or wetting history, had a profound impact on seepage. If the liquid-release tests were performed too close together in time, then it was found that the seepage percentage increased dramatically, as one would expect. This is because the fractures contained residual moisture, and their unsaturated conductivity was higher during subsequent tests. The test with seepage percentage of 56.2 percent, the third test in a series of four tests in the same interval, was conducted within 2 hours after the second test with 23.2 percent seepage. In comparison, the first test conducted 20 days before the second test had a fairly consistent result of 22.6 percent seepage (BSC 2003 [DIRS 166347], Section 7.2.2).

For Niche 3, the seepage percentage ranged from 0 percent for zones that did not seep to a maximum of 70.1 percent. The wetting front typically arrived at the niche ceiling directly below the test zone. Most of the water was typically captured in only one or two 0.3×0.3 m cells located directly beneath the test interval. Similar results were found for Niche 4, with the seepage percentage ranging from 0 percent to 68.7 percent.

Tests performed in Niche 5 in the ECRB Cross-Drift indicated that a measurable seepage threshold exists for the Tptpll. Photographic evidence collected in Niche 5 showed the wetted area spreading down the sidewall during the test, providing qualitative evidence that flow was diverted around the niche (BSC 2003 [DIRS 166347], Section 6.2.1.3.5.4).

Predictive modeling of niche tests are given in BSC (2003 [DIRS 162267], Section 7.2.2).

7.6.4.2 Air-Injection and Liquid-Release Tests Conducted in the Enhanced Characterization Repository Block Cross-Drift

The lower lithophysal zone unit of the Topopah Spring Tuff (Tptpll) is intersected by many small fractures (less than 1 m [3 ft] long) and interspersed with many lithophysal cavities (ranging in size from 15 to 100 cm [0.5 to 3.3 ft]) (BSC 2003 [DIRS 166347], Section 6.11). The size and spacing of both the fractures and lithophysal cavities vary appreciably along the drift walls (the drift is 5.0 m [16.4 ft] in diameter) over an 800 m (2,600 ft) distance, the approximate length of the Tptpll exposure in the ECRB Cross-Drift. This indicates that hydrologic characteristics at one particular location may not be representative of the entire unit. Therefore, a systematic approach of testing at regular intervals was adopted to acquire knowledge of the heterogeneous hydrologic characteristics of this unit, in which over 80 percent

of the repository will reside. Systematic hydrologic characterization investigated the hydrologic properties that are important to repository performance. Field measurements include:

- Air-injection tests, which give a measure of fracture permeability

- Liquid-release tests, which determine the ability of the open drift to act as a capillary barrier (diverting water around itself) as well as the potential of the water to seep into the drift

- Crosshole gas-tracer tests, which measure the effective porosity of the rock mass.

7.6.4.2.1   Systematic Borehole Configuration

Figure 7-41 shows a schematic of the arrays of boreholes (all 20 m [65 ft] in length) drilled at regular intervals along the ECRB Cross-Drift. The borehole arrays are divided into three groups (BSC 2003 [DIRS 166347], Section 6.11.1.1). Group I consists of low-angled boreholes drilled into the crown of the 5.0 m (16.4 ft) diameter ECRB Cross-Drift, inclined at 15° from the drift-axis. These boreholes are intended for both air-injection and liquid-release tests, with the spacing of adjacent boreholes from collar-to-collar at 30 m (98 ft). Group II consists of near-vertical boreholes drilled from the crown of the drift, which are intended for air-injection tests to determine the effect of drift excavation on fracture properties. Group III consists of pairs of parallel horizontal boreholes, spaced 3 m (10 ft) apart and drilled into the side of the drift, which are used for gas-tracer tests to determine the effective porosity of the rocks. Group II and III boreholes are in groups of three, spaced 90 m (295 ft) apart, as shown in Figure 7-41. Details of the test equipment and procedures are given in BSC (2003 [DIRS 166347], Section 6.11).

7.6.4.2.2   Test Results

Borehole ECRB-SYBT-LA#2-Borehole ECRB-SYBT-LA#2 (referred to as Borehole LA2) is collared at ECRB Cross-Drift construction station CD 17+26 (Figure 1-3). Three packers isolated the borehole into three zones so that the distance from the middle of the 1.83 m (6 ft) liquid-release zone to drift crown is respectively 1.58 m (5.18 ft), 2.84 m (9.31 ft), and 4.10 m (13.4 ft) for Zone 1, Zone 2 and Zone 3 (BSC 2003 [DIRS 166347], Section 6.11.2.1).

Air-permeability estimates for the three zones from the steady-state pressure-response to constant-flow-rate air-injection tests are tabulated in Table 7-35. The fast rise and decay of the pressure in response to initiation and termination of air injection indicate very little storage effect (BSC 2003 [DIRS 166347], Section 6.11.2.1).

Following the air-injection tests in all three zones, a liquid-release test was conducted in Zone 1 only (BSC 2003 [DIRS 166347], Section 6.11.2.1). A large, liquid-release rate of ~450 mL/min was initiated in zone 1 through one single release point in the 1.83 m (6 ft) long injection zone. No return flow was detected, indicating that all released water was able to enter the rock formation through the injection section.

Liquid-release tests in Zones 2 and 3 show that the seepage rates depend on evaporation in the ECRB Cross-Drift, as seepage rates increase and decrease with the rise and fall of relative humidity (BSC 2003 [DIRS 166347], Section 6.11.2.4). The seepage rate in Zone 3 is higher

than that in Zone 2, reaching a high of about 6 mL/min. This may result from the higher water-release rate in Zone 3 (~38 mL/min, as compared to ~34 mL/min in Zone 2).

Borehole ECRB-SYBT-LA#1 (LA1)-Similar to Borehole LA2, Borehole ECRB-SYBT-LA#1 (referred to as Borehole LA1) is a low-angle, near-horizontal borehole (inclination of 15° from the cross drift axis), drilled from the ECRB Cross-Drift crown (BSC 2003 [DIRS 166347], Section 6.11.2.5). It is collared at ECRB Cross-Drift construction station CD 17+49 m immediately outside of the first bulkhead. Rock fragments that fell into the borehole (postdrilling) caused the borehole to be totally obstructed from 8.2 m (26.9 ft) from the collar to the end of the 20 m (65 ft) long hole. Therefore, only one zone instead of the intended three (as in Borehole LA2) was accessible for fluid testing.

A liquid-release test in Zone 2 of Borehole LA1 was carried out over approximately 62 days. The injection rates varied between 15 to 42 mL/min, with some intermittent interruptions to the injection (BSC 2003 [DIRS 166347], Section 6.11.2.6). Photographs show that the first appearance of a wet spot (water arriving at the drift ceiling) was about 75 hours after initiation of water release. Cumulative water supply and seepage data indicate that about 60 L of water had been introduced into the formation at this time. Data indicate that, in general, the water-release rate needed to be above 20 mL/min for recorded seepage. Seepage was on the order of 10 mL/min for periods when the water-release rate was on the order of 42 mL/min.

Data indicate that the evaporation rate is on the order of 3 mm/d (BSC 2003 [DIRS 166347], Section 6.11.2.5). Coupling this information with the largest (stable) wetted area estimated from photographs of the drift ceiling (~4.5 m^2) would give an upper bound of the evaporation from the wetted drift surface a rate of 9.5 mL/min.

7.6.4.2.3 Participation of Lithophysal Cavities in Storage and Flow Paths

Drift-wall mapping along the ECRB Cross-Drift indicates a mean lithophysal cavity porosity of 0.125 m^3/m^3 in the lower Topopah Spring Tuff lithophysal unit (Mongano et al. 1999 [DIRS 149850]). Gas-tracer measurements of the effective porosity in the middle nonlithophysal units indicate that fracture porosity is on the order of 0.01 (DTN: LB980912332245.002 [DIRS 105593]). Both cavities and fractures are expected to be essentially dry at ambient conditions. Laboratory measurements from 453 samples of surface-based boreholes give the mean matrix porosity of 0.13 m^3/m^3 and a mean saturation of 0.78 m^3/m^3 for the lower lithophysal unit (Flint 1998 [DIRS 100033]). Fourteen measurements on cores from boreholes drilled for systematic testing at ECRB Cross-Drift construction station CD 17+49 (DTN: LB0110COREPROP.001 [DIRS 157169]) give results similar to that of Flint (1998 [DIRS 100033]): mean values of 0.12 m^3/m^3 for matrix porosity and 0.72 m^3/m^3 for liquid saturation. Because of the high-ambient liquid saturation, matrix contributes to only about 0.03 m^3/m^3 of the total porosity that is available for liquid storage from systematic testing. In liquid-release tests, such as those conducted for the systematic testing, it is anticipated that fractures and possibly connected cavities will ultimately be responsible for the steady-state flow behavior, while slow-draining cavities and matrix will most likely contribute to first-time storage (BSC 2003 [DIRS 166347], Section 6.11.3.1).

The estimated effective-porosity values were determined to be 0.013 m^3/m^3 and 0.067 m^3/m^3 for Boreholes LA2 and LA1, respectively, prior to the establishment of fast paths (BSC 2003 [DIRS 166347], Section 6.11.3.1). In the case of Zone 1 in Borehole LA2, when the release rate was as high as 450 mL/min, the fracture porosity was accessed with little imbibition into the matrix at the time of intersection with the drift. Also, for the lithophysal cavities that act as a capillary barrier with the very high release rate, little water would be expected to seep into these cavities. For Borehole LA1, when the release rate was about 30 times slower at 15 mL/min, the flowing water would have time to access the matrix porosity, and less would be diverted around the lithophysal cavities. The difference in effective-porosity results from these two tests could thus be a measure of the component of storage due to matrix and slow-filling cavities. Because cavities are the primary contributor of actual porosity in the system, even a little participation in the flow path would raise the effective porosity. In the case of Borehole LA1, they seem to contribute up to a maximum of about 0.057 (effective minus fracture porosity, not accounting for matrix participation) and a minimum of 0.027 (if all the available matrix porosity participates). These values indicate that only a quarter to one-half of the lithophysal cavity volume (porosity of 0.125) participates in liquid storage (BSC 2003 [DIRS 166347], Section 6.11.3.1).

7.6.4.2.4   Estimation of the Steady-State Nonintersecting Flow around the Drift

A fraction of the water will be diverted around the drift opening because of the nonuniform flow from heterogeneity. At the drift crown, additional lateral flow will be diverted around the drift, resulting from the drift acting as a capillary barrier (BSC 2003 [DIRS 166347], Section 6.11.3.2). The total component of nonintersecting water (from flow channeling and capillary effects) can roughly be thought of as the difference between the rate of injection and the rate of seepage into the drift when the test has reached steady-state conditions, provided that there are no other losses. However, the systematic data (BSC 2003 [DIRS 166347], Sections 6.11.2.3, 6.11.2.4, and 6.11.2.6) show clearly that evaporation contributes to the difference in the recorded injected-and-seeped volume of water. It is thus essential that evaporation be taken into account in any attempt to estimate the nonintersecting component.

The evaporation contribution to the wetted-drift ceiling can be estimated by multiplying the flux from an evaporation pan mounted just below the seep (to get accurate conditions) by the wetted area associated with the seep (BSC 2003 [DIRS 166347], Section 6.11.3.2). All monitoring data for the water-level drop in the evaporation pan show that the evaporation flux is on the order of 3 mm/d, for the wide range (15 to 90 percent) of relative humidity encountered. Trautz and Wang (2002 [DIRS 160335]) show, by gravimetric methods, that evaporation rates range from about 4 to 0.4 mm/d in the ECRB Cross-Drift for relative humidity ranging from 15 to 90 percent. Even greater evaporation rates could occur under windy conditions, such as those present during active ventilation of the tunnel. For Borehole LA2, the evaporation rate was estimated to be 14.4 mL/min. For Borehole LA1, the evaporation rate was estimated to be 9.5 mL/min. The nonintersecting flow was estimated through material balance between injection, evaporation, and seepage collection. From these data, the nonintersecting flow was found to range from 46 to 55 percent of the steady-state flow. Because of the evaporation component and involvement of different flow paths, seepage collection rate is not necessarily proportional to injection rate.

7.6.4.2.5   Minimum Injection Rate Needed to Induce Seepage

At the scale of the drift, flow is more likely to progress along zones of preferential flow, but not as a uniformly spreading front. A borehole line-release occurs locally over the area projection of the borehole zone (BSC 2003 [DIRS 166347], Section 6.11.3.3). This area emulates one of these concentrated regions at a given distance above the drift. During the testing at Borehole LA1 (BSC 2003 [DIRS 166347], Section 6.11.2.5) for the period from December 20 to December 26, 2001, observations (photographs) every half-hour confirmed that at the flow rate of 15 mL/min, with no ventilation, seepage on the ceiling was just observable as a tiny spot on the morning of December 25, 2001. It is postulated that there was little evaporation from the surface because there was no significant area to the spot. The spot stayed small for the remainder of the test, indicating that the system as a whole was approaching steady state. The 15 mL/min of injected flow in this case appear to just barely reach the crown. Thus, the threshold below which seepage into the drift does not occur is less than 15 mL/min (BSC 2003 [DIRS 166347], Section 6.11.3.3). Note that the water-release rate at the borehole does not necessarily correspond to the water-arrival rate at the niche ceiling.

7.6.4.3   Seepage Threshold Evaluation

The seepage threshold flux, defined as the liquid-release flux at, and below, which water will no longer seep into the drift, was determined for a given test interval by performing multiple seepage tests at different liquid-release fluxes (BSC 2003 [DIRS 166347], Section 6.2.2.1). The liquid-release flux is defined as the volumetric rate at which water was released into the borehole, divided by the approximate cross-sectional area of the test interval. Initial tests were conducted at high liquid-release fluxes, with subsequent tests performed at lower fluxes until water no longer seeped into the opening. Individual tests were separated by a two- to four-week inactive period to allow the water within the fracture network to reequilibrate with the surrounding rock matrix.

Figure 7-42 shows a plot of the seepage percentages observed during four tests conducted at different injection rates (q_s) in Borehole UM at the same interval, located 5.5 to 5.8 m (18 to 19 ft) from the borehole collar at Niche 2 (BSC 2003 [DIRS 166347], Section 6.2.2.1). A linear regression was performed on the four data points to compute the equation for the trendline and the R-squared values (R^2) shown in Figure 7-42 and tabulated in Table 7-36. This exercise was repeated for the intervals tested at all the niches to produce the regression data reported in Table 7-36 for all the zones that seeped. The R-squared values were computed separately for each interval and are listed for those intervals where three or more data points are available.

Table 7-36 also summarizes the niche seepage threshold (K_o^*) (BSC 2003 [DIRS 166347], Section 6.2.2.1). The K_o^* values were determined using the regression equations provided in Table 7-36 by setting the seepage percentage, y, equal to 0, then solving for $K_o = K_o^*$ [$K_o^* = K_o(y=0)$]. Here, the symbol K_o is used to denote the liquid-release flux used in the regression model to distinguish it from the liquid-release flux computed using the field data (q_s). In terms of K_o and K_o^*, the niche seepage threshold is defined as follows:

- If the liquid-release flux exceeds the seepage threshold flux ($K_o > K_o^*$) for the given interval, then water will seep into the drift.

- If the liquid-release flux is less than the seepage threshold flux ($K_o < K_o^*$), then water will not enter the cavity.

Figure 7-43 shows a log-log plot of K_o^* versus the saturated hydraulic conductivity (K_l) for 10 test intervals at Niche 2 and three test intervals at Niche 4 where seepage occurred (BSC 2003 [DIRS 166347], Section 6.2.2.1). For each test interval, multiple tests with different release rates were conducted to estimate the niche-seepage threshold. The straight line in Figure 7-43 is derived from an analytic solution (BSC 2003 [DIRS 166347], Section 6.2.2.2).

7.6.4.4 Fracture-Water Characteristic Curves

Seepage into drifts is a result of the interplay between capillary and gravity forces in fractures. Although gravity forces are relatively easy to quantify, capillary forces are a complex function of fracture geometry and water saturation. Therefore, experimental methods to quantify capillary pressure conditions in fractures are needed. Fracture-water characteristic curves provide a functional relationship between the water content of fractures (θ) and its water potential (ψ), the latter of which is the driving force behind the movement of water through the unsaturated zone. Characteristic curves for unconsolidated porous media are typically measured in the laboratory, but even for intact fractures in consolidated rocks, laboratory measurement of characteristic curves can be difficult. Therefore, the fracture-water characteristic curves were defined via an indirect approach using the test data from the niche-seepage tests. The change in volumetric water content was estimated for each seepage experiment using the arrival time for the wetting front observed at the niche ceiling, the distance from the borehole to the niche ceiling, and the liquid-release data from each test (BSC 2003 [DIRS 166347], Section 6.2.2.3). Assuming that the antecedent or residual moisture content is negligible when compared to the average water content, the change in water content is equivalent to the average volumetric water content of the fractures. The water-content values shown in Table 7-37 range from 0.09 to 5.0 percent. Based on these results, the saturated water contents or porosities of the fractures could be as high as 5.0 percent. In turn, these values could influence travel-time calculations computed for the unsaturated zone, since travel time is proportional to water content. Using larger water content for the fractures would result in longer travel times. An indirect measure of the water potential (ψ) was formulated using the α^{-1} values computed earlier, the liquid-release fluxes, and the air-derived saturated hydraulic conductivities. The derived estimated water-potential values ranged from -0.2 to -0.003 m, as shown in Table 7-38.

The volumetric water-content values and their corresponding water-potential values described above are plotted in Figure 7-44 to create a water-characteristic curve (BSC 2003 [DIRS 166347], Section 6.2.2.5). Only those test intervals in which three or more tests were conducted are included in the figure. In addition, data points that were influenced by hysteresis (wetting history) and those from tests conducted below the seepage threshold flux were excluded, unless noted. The data fall into two groups exhibiting similar water-retention characteristics. The first group (N3650 UL 7.62-7.92 m, N3650 UR 6.71-7.01 m, and N3650 4.88-5.18 m) consists of high-permeability fractures that drain over a narrow range of water potentials and appear to have low residual-water contents of about 0.001 to 0.002. The second group (N3650 UM 4.27-4.57 m, N3650 UM 5.49-5.79 m, N4788 UM 6.10-6.40 m, N4788 UL 7.62-7.93 m, and N4788 UR 5.18-5.48 m) consists of lower-permeability fractures

that drain over a relatively larger range of water potentials and appear to have a slightly larger residual water content of about 0.005.

7.6.5   Drift Scale Test Measurements and Analyses

If a geologic repository is constructed at Yucca Mountain, the emplaced radioactive wastes will emit a significant amount of heat from the radioactive decay of the wastes (CRWMS M&O 2000 [DIRS 141187], Section 6.3). This heat will influence hydrologic, mechanical, and chemical conditions in both the near-field (drift scale) and far-field (mountain scale). This section discusses the potential effects of the corresponding coupled processes—thermal-hydrologic, thermal-mechanical, and thermal-chemical—on flow and transport within the Yucca Mountain unsaturated zone. The development of the conceptual model of the coupled processes is closely tied to the field thermal tests described in Section 5.4.5. The Drift-Scale Test (DST) is the largest and latest field thermal test, and the data collection activities and data analyses are further summarized in this section for conceptual understanding of the coupled processes. Mountain-scale coupled-process effects are discussed in Section 7.10.1.4, and drift-scale coupled-process effects are discussed in Sections 7.10.2.2 to 7.10.2.4.

7.6.5.1   Thermal-Hydrologic-Mechanical-Chemical Measurements in the Drift-Scale Test

The DST was designed to collect data of in situ drift-scale coupled thermal-mechanical-hydrologic-chemical processes. Figures 5-88 and 5-89 show the general drift configurations and borehole layout of the DST. The objectives and design of the DST are described in detail in CRWMS M&O (1997 [DIRS 146917], Sections 2 and 3). The drift configuration consisted of an observation drift, a connecting drift, and a heated drift (Figure 5-88). The observation drift connected with the main drift of the ESF at about 2.88 km (1.79 mi) from the North Portal of the main tunnel. The heated drift was about 47.5 m (156 ft) long, starting from a thermal bulkhead located near the intersection of the connecting drift (BSC 2002 [DIRS 160771], Figure 6.3-1). The heat sources included nine canister heaters lined up on the heated drift floor and 25 wing heaters on each side. Each canister heater was about 4.7 m (15 ft) long and 1.7 m (5.6 ft) in diameter. Each wing heater was placed in a horizontal wing heater borehole that was 11.5 m (38 ft) long and drilled into the heated drift side wall about 0.25 m (0.82 ft) below the springline.

At the initiation of the heating phase, the total power of the canister heaters and wing heaters was approximately 54 kW and 140 kW, respectively. Each wing heater consisted of two sections of heating elements. The outer (farther away from the heated drift) element had a rated power output of about 1.7 kW; the inner section had about 1.1 kW. Temperature was measured in boreholes arranged radially from the heated drift and in longitudinal boreholes parallel to the heated drift (Figure 5-89) (BSC 2002 [DIRS 160771], Figure 6.3-3). Electrical resistance tomography was conducted in vertical planes parallel to the heated drift and in two vertical planes perpendicular to the heated drift from the observation drift (Figure 5-89) (BSC 2002 [DIRS 160771], Figure 6.3-8). Neutron logging was conducted in two sets of boreholes from the observation drift (Figure 5-89) (BSC 2002 [DIRS 160771], Figure 6.3-6). Each neutron borehole set (five boreholes) forms a fan-shaped vertical plane perpendicular to the heated drift, with three boreholes above and two below.

Gas sampling ports and water absorbing pads were installed in the membrane in situ sampling technology system in two sets of chemistry boreholes, which were drilled from the observation drift (Figure 5-89) (BSC 2002 [DIRS 160771], Figure 6.3-7). As with the neutron boreholes, each chemistry borehole set formed a fan-shaped vertical plane perpendicular to the heated drift, with three boreholes above it and two under it. The hydrology borehole arrangement was the same as for the chemistry boreholes (Figure 5-89) (BSC 2002 [DIRS 160771], Figure 6.3-4). In addition, two more hydrology boreholes were drilled from the observation drift at 44.8 m from the bulkhead: one above the heated drift and one under it.

Rock mass displacement was measured by multiple-point borehole extensometers in the mechanical boreholes (Figure 5-89) (BSC 2002 [DIRS 160771], Figure 6.3-5). All instrumentation boreholes, except for those containing the multiple-point borehole extensometer, and the hydrology boreholes were sealed by casing, cement grout, packers, or a membrane.

The heaters in the DST were energized on December 3, 1997. The heating phase ended approximately four years later on January 14, 2002. The test is currently in the middle of its planned four year cooling phase.

The DST data collection system recorded thermal, some hydrologic, and some mechanical data, on an hourly basis (BSC 2002 [DIRS 160771], Section 6.3). Scientific notebooks provide additional details of measurements including calibration information. These data form the basis of the summary of DST measurements listed in BSC (2002 [DIRS 160771], Table 4-3).

Aqueous samples collected for chemical analyses have been acquired from several hydrology boreholes during the four years of heating (BSC 2002 [DIRS 160771], Section 6.3.4.1). The first samples were collected six months after heating began, with subsequent sampling activities about every two to three months. A summary of the water samples, the field data, and important observations for samples collected up to January 14, 2002 is presented in BSC (2002 [DIRS 160771], Table 6.3.4.1-1).

Gas samples were periodically collected from the hydrology boreholes during the heating phase from December 3, 1997 through January 14, 2002 (BSC 2002 [DIRS 160771], Section 6.3.4.2). These samples were collected to measure the concentration and carbon isotope ratio of CO_2 and the hydrogen and oxygen isotope ratios of water vapor. The concentration and isotopic composition of CO_2 in the heated drift and the observation drift were also measured during the test. In addition, to provide data on the background concentration and isotopic composition of CO_2 in the rock, two gas samples were collected in August 1997 from Borehole 182 (one of the ambient testing boreholes drilled on the opposite side of the connecting drift across from the DST block). The CO_2 concentrations and isotope compositions for both the gas samples and the condensate samples collected during the heating phase can be found in (BSC 2002 [DIRS 160771], Table 6.3.4.2-1). The hydrogen and oxygen isotope compositions of the vapor-condensate samples were measured to gain an estimate of the isotopic composition of the pore water in the rock (BSC 2002 [DIRS 160771], Table 6.3.4.2-3).

7.6.5.2 Analyses of Drift-Scale Test Data

7.6.5.2.1 Thermal-Hydrologic Processes in the Drift-Scale Test

Measured data relevant to the evaluation of thermal-hydrologic processes in the DST include the following: (1) temperatures measured at numerous sensor locations; (2) changes in matrix saturation estimated from geophysical measurements conducted at periodic intervals through the duration of the DST; and (3) changes in fracture saturation estimated from air-permeability measurements conducted at periodic intervals through the duration of the DST (BSC 2002 [DIRS 160771], Section 6.3.2).

Measured temperatures from the DST showed interesting thermal behaviors (BSC 2002 [DIRS 160771], Figures 6.3.1.2-2 and 6.3.1.2-3). BSC (2002 [DIRS 160771], Figure 6.3.1.2-2) shows a significant flattening in Borehole 79 temperatures at 96°C due to reflux activity. Measured temperatures also indicated the influence of fractures in maintaining temperatures close to boiling through moisture movement (BSC 2002 [DIRS 160771], Section 6.3.1.2.1).

While the temperature rise in the test block is dominated by heat conduction, evidence of thermal-hydrologic coupling is manifested in heat-pipe signatures in the temperature data, indicating the presence of liquid water at the boiling point (BSC 2003 [DIRS 166512], Section 7.4.3.1). The main phenomenon of thermal-hydrologic coupling was the redistribution of moisture via condensed vapor in the rock mass. Zones of increased or decreased water saturation in fractures and matrix (compared to preheat baseline data) were monitored in the DST by periodic geophysical methods and air-permeability measurements.

For example, BSC (2002 [DIRS 160771], Figure 6.3.2.3-2) shows that the water content in the rock remained nearly constant within 8 to 14 percent until near-boiling temperatures were reached. Thereafter, significant reduction in water content occurred between 90°C and 105°C where it approached 1 percent. Water content in the rock continued to decrease, as it approached zero at approximately 150°C. Although some anomalously low water content was measured in the sub-boiling regime, most of the water content data were reasonably consistent for the range of temperatures considered (25°C to 190°C) (BSC 2002 [DIRS 160771], Section 6.3.2.3.1).

Temperature rise in the rock from heating was predominantly controlled by heat conduction, which is a linear process (BSC 2003 [DIRS 166512], Section 7.4.3.1). Therefore, the coupling between thermal-hydrologic processes, which are nonlinear in nature, is evidenced in subtle signals in the temperature data. Typically, effects of thermal-hydrologic coupling appear as a flat region in temperature profiles (or temperature evolution plots) at the nominal boiling point of water (heat-pipe signature), indicating boiling conditions with presence of both liquid water and vapor. Heat-pipe signals can be seen in both measured and simulated responses for all time snapshots depicted in BSC (2003 [DIRS 166512], Figures 7.4.3.1-1a through 7.4.3.1-1d).

Changes in permeability as a ratio to baseline permeability estimates was used to indicate changes in fracture liquid saturation (BSC 2002 [DIRS 160771], Figure 6.3.2.4-4). In general, the decrease in air permeability indicated a gradual build-up in fracture liquid saturation during heating (BSC 2002 [DIRS 160771], Section 6.3.2.4.1). Some decrease in bulk permeability was also attributed to mechanical closure of fractures (see BSC 2003 [DIRS 164890], Section 7).

7.6.5.2.2 Thermal-Hydrologic-Mechanical Processes in the Drift Scale Test

The maximum thermal-hydrologic-mechanical effects would occur when the temperature in the rock mass at the repository level reaches its maximum. The primary effects are thermally-induced and excavation-induced changes in the stress field that would act on preexisting fractures, thereby causing fracture closure or opening with accompanying changes in fracture permeability and capillary pressure.

The calculated permeability changes are compared to air-permeability measurements in the DST in BSC (2003 [DIRS 164890], Figure 7.4.3-3). In borehole intervals closest to the drift (z is approximately 6 m), the air permeability first decreased with time to reach a minimum at about 24 months. Thereafter, the permeability increased slightly in three of four borehole sections and increased dramatically in the fourth. The figure compares measured changes in air permeability at the four borehole sections with calculated changes in permeability. The solid line indicates the calculated changes in air permeability, which are the product of the intrinsic permeability (thermal-mechanical effect) and gas relative permeability (thermal-hydrologic effect). The figure shows that the solid line representing the combined thermal-hydrologic and thermal-mechanical effects matches three of four measurements best. In the fourth section, the measured changes appear to match a pure thermal-mechanical response the best.

Further away (z is approximately 12 m), the measured responses in these three boreholes are very consistent, with an initial increase in air permeability during the first 9 months, followed by a gradual decrease with time until the end of heating. The decrease in permeability can be interpreted either as a change in intrinsic permeability (thermal-mechanical), or as a change in relative permeability (thermal-mechanical), or a combination of the two (thermal-hydrologic-mechanical). However, the initial increase during the first nine months can only be explained as a thermal-mechanical response.

For the measurements located farthest away from the drift (z is approximately 18 m) there was an increase in air permeability caused solely by thermal-mechanical-induced changes in intrinsic permeability. At this location, far away from the heated drift, no effect from thermal-hydrologic-induced changes appears until about 36 months, when a slight wetting began. The overall simulated changes in air permeability using those parameters are in agreement with the measured changes. The simulated changes in air permeability are in the correct direction and within an order of magnitude.

7.6.5.2.3 Thermal-Hydrologic-Chemical Processes in the Drift-Scale Test

CO_2 Degassing and Accompanying Changes in Aqueous Chemistry–Measured CO_2 gaseous concentrations from repeat samples from the same borehole intervals between February 1998 and January 2002, were analyzed for trends of CO_2 evolution (BSC 2003 [DIRS 162050], Section 7.10.2). The increase of CO_2 concentrations during the heating phase clearly resulted from the degassing of CO_2 caused by boiling and its outward transport from the heated drift.

For the pH and aqueous concentrations of major cations and anions, including Na^+, K^+, Ca^{2+}, Mg^{2+}, SiO_2, Cl^-, SO_4^{2-}, HCO_3^-, NO_3^-, and F^- (BSC 2003 [DIRS 162050], Section 7.10.3), the overriding effects manifested in measured aqueous concentrations are predominately those of the

thermal-hydrologic processes (i.e., boiling, condensation). The analysis interpreted the dilution of concentrations in fractures as being due to condensation and drainage below the heaters, and slow imbibition of the condensate water into the matrix (BSC 2003 [DIRS 162050]). During heating, pH decreased to approximately 7.2 in the condensation zone. The pH in the condensate water was related closely to the CO_2 concentration. The pH in waters collected near the dryout zone increases from the initial pore-water condition, due to boiling, degassing, and outward transport of CO_2. Dissolution of certain minerals, such as feldspars, also results in an increase of pH. For conservative species such as Cl^- and SO_4^{2-}, the main effect of heating is a marked decrease in concentrations within fractures in the condensation and drainage zones; in the matrix, there is significant dilution in the condensation zones with a corresponding increase in concentration near the edge of the dryout zone.

Secondarily, water-rock interactions also contribute to behavior of the more reactive species. For example, the extent of dilution of Na^+ and K^+ is less than Cl^-, indicating some contribution of water-rock interaction from alkali feldspars. More sensitive species include Ca^{2+}, whose concentration is strongly affected by calcite with a fast reaction rate and low solubility at high temperatures. Silica concentrations also increased, likely due to accelerated reaction for silica phase (possibly opal-CT) or reaction of "fresh" mineral surfaces (i.e., cristobalite and quartz) in the borehole walls. Sharp drops in Mg^{2+} concentration were caused by dilution from the condensate and the precipitation of Mg-rich minerals.

Mineral Precipitation and Dissolution–Extent of mineral precipitation during the DST was assessed through side-wall core sampling from above-boiling zones and X-ray diffraction analyses (BSC 2003 [DIRS 162050], Section 7.1.12). Direct evidence of mineral precipitation from migrating fluids was obtained from side-wall samples drilled into the walls of pretest boreholes. The side-wall samples were taken towards the end of the heating phase of the DST. X-ray diffraction analyses of these samples provided mineral distribution and abundance in the pretest rock under ambient conditions, and a means for assessing mineralogic changes while the test was in process. The results identify precipitation of amorphous silica as the dominant phase, followed by lesser amounts of calcite and gypsum.

Porosity and Permeability Changes–Laboratory studies of fracture heating indicate that smoothing of the fracture asperities by dissolution and precipitation can effectively change the permeability (Daily et al. 1987 [DIRS 131816], p. 7861). The laboratory fracture sealing experiment showed that amorphous silica was deposited from injected fluid at temperatures exceeding 100°C (BSC 2003 [DIRS 162050], Section 7.3). Fracture sealing occurred after five days of injection, with 1.2 to 4.7 percent of the total porosity filled with solid precipitate. Bridging structures of amorphous silica that formed during the experiment in both the saw-cut fracture and a natural fracture appear to obstruct fluid flow within the fracture system.

Fracture permeability changes resulting from mineral precipitation and dissolution are tied to related changes in porosity and more directly to fracture aperture changes. For the heating phase of the DST changes in fracture porosity of less than 1 percent of the original value would have a correspondingly small effect on fracture permeability (BSC 2003 [DIRS 162050], Section 7.1.13). These results are consistent with the observations of limited changes in air permeability during the DST, which have been attributed predominantly to water saturation

changes (mostly in the condensation zones, where mineral precipitation is negligible) (BSC 2002 [DIRS 160771], Section 6.3.2.4.1).

7.7 EVIDENCE OF PAST PERCOLATION THROUGH THE UNSATURATED ZONE

Deposits of secondary minerals (mainly low-temperature calcite and opal) in fractures and cavities mark pathways of past percolation of water through the unsaturated zone (Paces et al. 2001 [DIRS 156507], p. 2). The physical morphology, geochronology, and composition (both chemical and isotopic) provide a record of the paleohydrologic conditions within Yucca Mountain over the last 12+ million years. In addition, fluid inclusion and oxygen isotope data, along with geochronological constraints, allow an evaluation of the long-term thermal history of the unsaturated zone. Therefore, data from secondary calcite and opal constrain the location and timing of unsaturated fracture flow through the mountain, and provide an independent means of evaluating the unsaturated zone hydrologic models used to represent this flow (Paces et al. 1998 [DIRS 107408], p. 36).

Initial studies of secondary calcite and opal in the unsaturated zone were based on samples of drill-core from surface-based boreholes. Efforts to study these deposits were greatly aided by construction of underground facilities that commenced in 1995, primarily by providing much higher quality samples and the ability to directly make field observations regarding the occurrence and distribution of mineral assemblages on tunnel walls.

7.7.1 Distribution, Morphology, and Paragenesis of Secondary Minerals in the Unsaturated Zone at Yucca Mountain

Most of the secondary mineralization within the unsaturated zone occurs as patchy coatings on the footwalls of fracture cavities or as irregular to hummocky accumulations on the floors of lithophysal cavities. Hanging-wall surfaces and cavity ceilings are almost invariably devoid of calcite/silica deposits (Paces et al. 2001 [DIRS 156507], p. 8 to 11; Whelan et al. 2002 [DIRS 160442], p. 737). Although some small-aperture fractures may be completely filled with calcite, most secondary minerals are present in fractures and lithophysae with substantial open space. Calcite/silica deposits are present in only a small percentage of all fractures or lithophysae; more than 90 percent of the fractures and cavities exposed in the underground workings do not contain secondary minerals (Whelan et al. 2002 [DIRS 160442], p. 738). The overall distribution of secondary calcite/silica deposits in the Yucca Mountain unsaturated zone is consistent with a formation under hydrologically unsaturated conditions and is inconsistent with a formation under even locally saturated conditions (Paces et al. 2001 [DIRS 156507], p. 66; Whelan et al. 2002 [DIRS 160442], p. 735).

Secondary mineral deposits consist of ~1 to ~40 mm (~0.05 to ~1.5 in.) thick irregular coatings of predominantly calcite, interlayered with lesser amounts of silica phases, including opal, chalcedony, and quartz. Other phases may also be present in minor amounts, including fluorite, clay minerals, zeolites, and manganese oxides. However, these phases are mostly present in older parts of the coatings (Paces et al. 2001 [DIRS 156507], p. 8). Textures of secondary minerals have been described in detail (Paces et al. 2001 [DIRS 156507], pp. 11 to 17; Whelan et al. 2002 [DIRS 160442], p. 738) and vary widely in both space and time. Calcite typically forms equant, blocky prisms on high-angle fracture surfaces and unusual, delicately

bladed crystals in lithophysal cavities and in low-angle fractures. Opal typically forms water-clear solid-hemispherical bubbles, botryoidal bubbly masses, or thin sheets coating calcite substrates. Opal commonly occurs at the tops of calcite blades. Both opal and calcite are finely layered (micron to submicron) and commonly are intimately intergrown. Outermost surfaces of both minerals show little evidence of dissolution, although scattered patches of basal porous zones may be related to dissolution of early-formed calcite blades.

Secondary mineral deposits contain characteristic sequences of mineral assemblages and textures (paragenesis) that vary systematically across the coatings (Paces et al. 2001 [DIRS 156507], p. 17 to 19; Whelan et al. 2002 [DIRS 160442], pp. 739 to 741). A generalized paragenesis based on petrographic criteria has been used to distinguish early, intermediate, and late stages of mineral deposition, although samples displaying the complete paragenetic sequence are rare. Separation of depositional events into these three categories is not intended to imply distinct or unique episodes of mineral formation, but to reflect gradual, long-term changes in the depositional environment. The paragenesis based on petrographic features are consistent with differences in other data sets, including chemical compositions, isotopic compositions, and ages.

7.7.2 Ages of Secondary Minerals

Ages of the low-temperature minerals have been investigated using radiocarbon (on calcite), ^{230}Th/U (on calcite and opal), and ^{235}U/^{207}Pb (on opal) methods (Neymark and Paces 2000 [DIRS 127012]; Neymark et al. 2000 [DIRS 154828]; Paces et al. 2001 [DIRS 156507]; Neymark et al. 2002 [DIRS 158673]; Paces et al. 2003 [DIRS 166371]). Outermost calcite-growth surfaces have radiocarbon ages of 20 to 44 ka, whereas thorium-230/uranium (^{230}Th/U) ages for calcite and opal from the same mineral surfaces range from 59 ka to 428 ka (Paces et al. 2001 [DIRS 156507], pp. 28 to 29, Table 1). These surfaces are young compared to the age of the host rocks (12.7 to 12.8 million years, Sawyer et al. 1994 [DIRS 100075], p. 1312). No systematic age differences exist between calcite and opal regardless of depositional setting, indicating that lithophysal cavities are as likely to receive percolating water as the fractures. Multiple subsamples from the same outermost surfaces of a single mineral coating commonly have different ages, with subsamples representing the least number of outer layers often having the youngest ages. Initial ^{234}U/^{238}U activity ratios between 1 and 9.5 show a distinct negative correlation with ^{230}Th/U age and are restricted to values >4 for samples younger than 100 ka (Neymark and Paces 2000 [DIRS 127012]). To explain these data, a depositional model has been proposed in which very thin layers are added, more or less continuously, on a scale finer than sampling techniques can resolve (Neymark and Paces 2000 [DIRS 127012], pp. 154 to 155; Neymark et al. 2000 [DIRS 162710], p. 2921; Paces et al. 2001 [DIRS 156507], pp. 46 to 56). Measured isotopic compositions, therefore, represent mixtures of materials intermediate between older and younger layers present within a subsample. The slow, long-term average rates of deposition (less than about 5 mm (0.2 in.) of mineral per million years) inferred from subsamples of outermost calcite and opal (Paces et al. 2001 [DIRS 156507], p. 49 and Figure 31) are similar to those calculated assuming that of the total thickness of mineral coatings accumulated over 12 million years, and to long-term average rates determined using the ^{235}U/^{207}Pb geochronometer on older materials (see below). Slow, more-or-less uniform rates of Pleistocene mineral growth of less than about 1 mm (0.04 in.) per million year have been confirmed within individual opal hemispheres, using ^{230}Th/U analytical methods capable of

spatial resolution on the order of 2 to 40 μm (Paces et al. 2000 [DIRS 154413]; 2003 [DIRS 166371]).

Ages of opal and chalcedony from interior parts of the secondary mineral coatings have been determined using $^{235}U/^{207}Pb$ dating and indicate that the coatings were formed over long periods of time (Neymark et al. 1998 [DIRS 109140]; 2002 [DIRS 158673]). Typically, $^{235}U/^{207}Pb$ ages range from 0.5 to 9.8 million years and are consistent with microstratigraphy within mineral coatings. The oldest dated opal layers are typically underlain by earlier-formed calcite deposits that may be nearly as old as the host tuffs. The absence of $^{235}U/^{207}Pb$ ages older than 10 million years is consistent with resetting of the $^{235}U/^{207}Pb$ geochronometer by thermal overprinting subsequent to emplacement of the tuffs (Neymark et al. 2002 [DIRS 158673], pp. 729 to 730). Average mineral-growth rates calculated using $^{235}U/^{207}Pb$ ages and measured depths within the coating microstratigraphy, vary between about 1 and 5 mm (0.04 to 0.2 in.) per million years for samples at the repository horizon (Neymark et al. 2002 [DIRS 158673], p. 731). Mineral coatings from the TCw hydrogeologic unit lying above the bedded tuffs of the PTn hydrogeologic unit commonly show absence of Quaternary material, possible open-system behavior of uranium and its daughter products, and faster apparent depositional rates (Neymark et al. 2002 [DIRS 158673], p. 732). This contrasts with the slower, uniform, average-growth rates observed for coatings from the TSw hydrogeologic unit below the PTn hydrogeologic unit. Recently, Pashenko and Dublyansky (2002 [DIRS 163684]) have proposed a theoretical model of radon emanation that involves the possibility that some of the measured ^{207}Pb may be unsupported by ^{235}U present in the sample, resulting in erroneously old $^{235}U/^{207}Pb$ ages for the secondary mineral coatings. In response, Neymark et al. (2003 [DIRS 163681]) demonstrated the ineffectiveness of the radon emanation argument and the veracity of published $^{235}U/^{207}Pb$ ages.

7.7.3 Isotopic Compositions

Stable isotopes of carbon and oxygen, as well as radiogenic strontium and uranium isotopes incorporated into calcite and opal at the time of formation, reflect the isotopic compositions of percolating fluids, which, in turn, relate to sources and climate conditions prevalent at the time of infiltration. Calcite shows a wide range of $\delta^{13}C$ values, from about -9.5 to 10.1 per mil (‰), with corresponding $\delta^{18}O$ values of about 23.0 to 3.2 ‰ (Whelan et al. 2002 [DIRS 160442], p. 742 and Figure 5). Both $\delta^{13}C$ and $\delta^{18}O$ in calcite are negatively correlated so that subsamples with large $\delta^{13}C$ values tend to have small $\delta^{18}O$ values. Systematic microsampling across individual mineral coatings indicates that $\delta^{13}C$ values in calcite shifted from larger values (2 to 9 ‰) early in the depositional history to intermediate values (-3 to 0 ‰) and, finally, to smaller values (-8 to -5‰) over time (Paces et al. 2001 [DIRS 156507], p. 38, Figure 22). Similar results for $\delta^{18}O$ values are obtained, with the largest values obtained from outer calcite and the smallest values from basal calcite. Radiometric ages ($^{230}Th/U$ and $^{207}Pb/^{235}U$) coupled with $\delta^{13}C$ data and petrographic observations allow constraints to be placed on both the timing of carbon-compositional changes in percolating fluids and the general paragenetic sequence (Whelan et al. 2002 [DIRS 160442], Figure 7).

Opal, quartz, and chalcedony also show shifts in both abundance and $\delta^{18}O$ compositions over time (Paces et al. 2001 [DIRS 156507], pp. 39 and 40). The paragenesis of chalcedony followed

by quartz is restricted to early depositional stages, whereas opal is most common in the intermediate and late stages of deposition. Massive chalcedony has the smallest $\delta^{18}O$ values (7.9 to 17.3 per mil), whereas quartz $\delta^{18}O$ values are substantially larger (16.8 to 22.8 ‰) (Paces et al. 2001 [DIRS 156507], p. 40, Figure 23). Opal deposited throughout most of the depositional history of the mineral coatings has $\delta^{18}O$ values that overlap those for quartz, but extends the range of $\delta^{18}O$ to even larger values (18.0 to 27.9 ‰).

Strontium isotope ratios of calcite correlate with microstratigraphic positions within individual mineral coatings and show a general trend of increasing $^{87}Sr/^{86}Sr$ ratios over time (Paces et al. 2001 [DIRS 156507], p. 41). Outer calcite $^{87}Sr/^{86}Sr$ ratios of 0.7115 to 0.7127 overlap values observed in the local pedogenic calcite deposits (Paces et al. 2001 [DIRS 156507], pp. 40 to 43, 58, and Figure 25). Early-stage calcite has the least radiogenic $^{87}Sr/^{86}Sr$ ratios between 0.7105 and 0.7120. Temporal variations in strontium concentrations are less well-defined over time than $^{87}Sr/^{86}Sr$ ratios. However, early- and intermediate-stage calcite typically has concentrations less than about 130 µg/g, whereas late-stage calcite commonly has larger concentrations. Strontium isotope ratios from subsamples across mineral coatings show distinct correlations with carbon and oxygen isotopes that probably are related to a gradual evolution of isotopic compositions in water percolating through fractures (Paces et al. 2001 [DIRS 156507], pp. 43 to 45, and Figure 28). The relatively large amount of scatter observed in these correlations indicate that separate, time-dependent processes most likely control the resulting isotopic composition of fracture water.

Compositions of $\delta^{18}O$, $\delta^{13}C$, and $^{87}Sr/^{86}Sr$ for late-stage calcite vary over limited ranges and are similar to values observed in present-day, calcite-rich soils, once $\delta^{18}O$ is corrected for fractionation due to the geothermal gradient. In contrast, early-stage calcite shows distinct differences in all three isotope systems, including lighter values for $\delta^{18}O$, heavier values for $\delta^{13}C$, and less radiogenic values for $^{87}Sr/^{86}Sr$. The three systems show covariance, indicating that common mechanisms controlled the variations in isotopic compositions of early infiltrating solutions. Data for the earliest calcite indicate that geothermal gradients may have been steeper, methane may have been an important carbon species controlling carbon fractionation in the subsurface, and strontium was derived from a source that was less radiogenic than the current soil or volcanic-rock reservoir. Thus, the unsaturated zone may have changed substantially over 12 million years (m.y.), with the present-day, soil-subsurface system having been established only within the last several million years. These isotopic variations support the concept that the secondary mineral records date back to the early history of flux through the mountain (Marshall and Futa 2001 [DIRS 156503], Figure 3; Whelan et al. 2002 [DIRS 160442], p. 743, Figure 7). At the scale sampled, the isotopic data show no evidence of a cyclic pattern within the younger parts of the deposits that could be related to climate variation over the last 500 k.y.

Calculated initial $^{234}U/^{238}U$ ratios representing the isotopic composition of percolating waters at the time of mineral deposition range from about 4 to 9.4 for minerals that are younger than 100 k.y., and are from the TSw hydrogeologic unit (Paces et al. 2001 [DIRS 156507], p. 31 and Figure 17). In addition, initial $^{234}U/^{238}U$ ratios in minerals and measured $^{234}U/^{238}U$ ratios in pore water show a pronounced shift in mineral coatings collected from tuffs above and below the PTn hydrogeologic unit (Paces and Neymark 2002 [DIRS 163374]). Strontium isotopes in modern pore waters leached from tuffs also show a distinct shift in composition across the bedded PTn

units. Compositions of $\delta^{18}O$ in late-stage calcite also show differences between samples from the TCw and TSw hydrogeologic units. These differences were interpreted to be the result of greater amounts of evaporation in the tuffs above the bedded PTn (Whelan et al. 2002 [DIRS 160442], p. 743). These observations reflect the hydrologic role played by the PTn hydrogeologic unit in affecting liquid flow through the Yucca Mountain unsaturated zone.

Increasing values for initial $^{234}U/^{238}U$ activity ratios (commonly between 6 and 9 within the repository horizon) also indicate modification of uranium isotopic compositions from values typical of surface waters and pedogenic sources (commonly 1.5 to 1.8) (Paces et al. 2002 [DIRS 158817], Table 2; Ludwig and Paces 2002 [DIRS 163682], p. 487) as a consequence of percolation through the unsaturated zone. Elevated initial $^{234}U/^{238}U$ in the repository-horizon secondary minerals are similar to values observed in perched and saturated zone groundwater beneath the mountain (Paces et al. 2002 [DIRS 158817], Tables 1 and 2). The origins of large ^{234}U enrichments in Yucca Mountain unsaturated zone percolation and recharge are discussed elsewhere (Paces et al. 2002 [DIRS 158817], pp. 768 to 769) and imply that percolation fluxes through the Yucca Mountain unsaturated zone were less frequent and involved lower volumes of water than those in other areas.

7.7.4 Depositional Processes

Isotopic and chemical data from unsaturated zone minerals indicate a descending meteoric source of percolating water that has interacted with soil at Yucca Mountain (Whelan et al. 1994 [DIRS 100091], p. 2738; Paces et al. 2001 [DIRS 156507], pp. 56 to 61; Vaniman et al. 2001 [DIRS 157427], pp. 3420 to 3421). Textural gradations in the upper 10 to 30 m (30 to 100 ft) of the unsaturated zone provide a link between fine-grained, detritus-rich, pedogenic deposits and the detritus-free, coarse-grained calcite and opal present in the deeper unsaturated zone. Isotopic compositions of oxygen, carbon, and strontium in outer unsaturated zone calcite also overlap the isotopic compositions of pedogenic calcite. Infiltration rapidly interacts with calcite- and opal-rich materials in surface deposits. Therefore, descending fracture water is likely to be saturated with respect to both calcite and opal (Apps 1997 [DIRS 101368]; Paces et al. 2001 [DIRS 156507], pp. 61 and 62 and Figure 36). Infiltration may reach the network of connected pathways in fractured bedrock where it will become distributed in response to gravity-controlled downward percolation, most likely as thin sheets or films of water on a relatively small number of fracture surfaces (Pruess 1999 [DIRS 104250]; Tokunaga and Wan 1997 [DIRS 139195]). Seepage of percolating water into open cavities connected to active flow paths allows downward-migrating liquid to interact with an independently migrating gas phase, allowing CO_2 and water-vapor loss from solution and precipitation of secondary calcite and silica (Paces et al. 2001 [DIRS 156507], p. 66 to 67; Whelan et al. 2002 [DIRS 160442], p. 743).

Textures indicating preferential mineral growth on crystal tips require a supply of aqueous solutions via capillary flow of films on outer mineral surfaces, because there is no physical evidence that cavities were ever saturated with water (Paces et al. 2001 [DIRS 156507], p. 67). Thinning of water films around the edges of crystal tips results in localized areas of greater vapor pressure (Ho 1997 [DIRS 141521]), favoring increased potential for gas loss and mineral precipitation (Paces et al. 2001 [DIRS 156507], p. 67; Whelan et al. 2002 [DIRS 160442], pp. 744 to 745). Differences in textures between near-horizontal substrates and high-angle fractures indicate that slowing of downward-migrating water is an important factor in influencing

mineral growth (Paces et al. 2001 [DIRS 156507], p. 66; Whelan et al. 2002 [DIRS 160442], p. 744). Rates of water vapor and CO_2-transfer from the unsaturated zone, especially in the deeper parts below the PTn hydrogeologic unit, are likely to be small. However, operation of these processes over long periods of time results in the very slow growth rates observed for calcite and opal in the unsaturated zone (Neymark and Paces 2000 [DIRS 127012], p. 156; Paces et al. 2001 [DIRS 156507], p. 66; Neymark et al. 2002 [DIRS 158673], p. 731).

7.7.5 Seepage Rates Into Lithophysal Cavities

The mineral record can be used to estimate past seepage rates if the distribution of secondary minerals is known in space and time, and if the volumes of water required to account for the mineral deposits can be estimated (Marshall et al. 2003 [DIRS 162891]). Estimates of the abundance of secondary minerals have been made from surveys of lithophysal cavities in the ESF (Paces et al. 1998 [DIRS 107408], Figure 2). Using the median and 95th percentile calcite volumes derived from these surveys and a bounding value for the water-to-calcite volume ratio, a long-term average seepage rate of 0.005 L/yr (based on the median number of seeps per waste package of 13 and a water-to-calcite volume ratio of 4×10^5) was calculated (Marshall et al. 2003 [DIRS 162891], pp. 243 to 245) and compared to values of 0 to 8 L/yr calculated in recent performance assessment models using 5 and 14.6 mm/yr percolation fluxes (DOE 2001 [DIRS 153849]). Using the 95th percentile number of seeps of 52 and a greater water-to-calcite volume ratio of 1×10^6, seepage rates up to 5 L/yr were calculated, compared to the 3.2 to 23 L/yr estimates included in recent performance assessment models (DOE 2001 [DIRS 153849]). Therefore, long-term seepage onto a given waste package is estimated to be significantly less than 5 L/yr, with about half the waste packages being contacted by some seepage. Agreement between seepage rates determined from calcite data, with performance assessment calculations using the smaller value for percolation flux (5 mm/yr), supports use of lower estimates for long-term average percolation flux (Marshall et al. 2003 [DIRS 162891], p. 246). These estimates are limited by the assumption that all seepage locations are marked by the presence of calcite and/or opal; in this respect, the estimates are minimum values.

7.7.6 Fluid Inclusion Studies and Thermal Histories

During the process of slow mineral growth, subsurface calcite commonly incorporates small voids that trap some of the percolating fluids. The resulting fluid inclusions may contain all liquid, all vapor, or a combination of both liquid and vapor. Because of differences in thermal expansion coefficients between the solid and aqueous liquid phases, single-phase liquid inclusions trapped at elevated temperatures will form shrinkage bubbles of water vapor at lower temperatures, resulting in a two-phase fluid inclusion. When reheated, the liquid and vapor phases within an individual inclusion may become rehomogenized at the temperature conditions under which the inclusions initially became closed. Therefore, fluid inclusion geothermometry is an important means of determining the original temperature conditions under which Yucca Mountain secondary minerals were formed.

Shortly after completion of the ESF north ramp, Dublyansky et al. (1996 [DIRS 109204]) demonstrated that subsurface calcite contained two-phase fluid inclusions exhibiting closure temperatures substantially greater than modern unsaturated zone temperatures. Earlier studies of fluid inclusions in unsaturated zone calcite from surface-based boreholes did not identify a suite

of reliable two-phase fluid inclusions (Roedder et al. 1994 [DIRS 109159]), most likely because the inclusions are sensitive to rehomogenization from inadvertent heating during drilling, core storage, and sample preparation (Whelan et al. 2002 [DIRS 160442], p. 746). New studies of fluid inclusions at both the University of Nevada, Las Vegas, and the U.S. Geological Survey confirm the presence of a small percentage of two-phase fluid inclusions, which indicate homogenization temperatures between 30°C and 85°C (Whelan et al. 2001 [DIRS 154773]; Wilson and Cline 2001 [DIRS 155426]). Detailed petrographic studies indicate that two-phase fluid inclusions with closure temperatures >40°C are almost always restricted to early stages of the paragenesis, whereas inclusions indicating temperatures of 30°C to 40°C are locally present within the basal parts of intermediate-stage calcite (Whelan et al. 2002 [DIRS 160442], p. 746; 2003 [DIRS 163590], pp. 359 to 364). Significantly, late-stage calcite characterized by magnesium-rich growth-zoning contains only rare, liquid-only inclusions indicating trapping of fluids at temperatures less than about 35°C (Cline and Wilson 2001 [DIRS 161550], p. 1313; 2001 [DIRS 155426]).

Oxygen isotopic compositions of both silica and calcite are also consistent with elevated temperatures derived from fluid-inclusion geothermometry (Paces et al. 2001 [DIRS 156507], p. 67-69; Whelan et al. 2001 [DIRS 154773]; Whelan et al. 2002 [DIRS 160442], p. 746; 2003 [DIRS 163590]). Early-stage calcite commonly has $\delta^{18}O$ values of 10 to 15‰, which gradually shift towards larger values between about 16 to 21‰ in late-stage calcite (Whelan et al. 2001 [DIRS 154773], Figure 4). A smaller number of early-stage calcite analyses from ESF north and south ramp locations have even lower $\delta^{18}O$ between 3.4 and 10‰ and are consistent with the high fluid-inclusion temperatures (54°C to 85°C) recorded in some of the same samples (Whelan et al. 2001 [DIRS 154773], Table 1). These changes in oxygen isotope composition are more consistent with a pattern of gradually decreasing unsaturated zone temperatures over time, rather than monotonic shifts in the $\delta^{18}O$ composition of infiltrating water over the last 12.8 Ma (Whelan et al. 2001 [DIRS 154773]).

Ages of inclusion-bearing calcite have been bounded by $^{207}Pb/^{235}U$ ages of interlayered opal and chalcedony (Neymark et al. 2001 [DIRS 156889]; Wilson and Cline 2001 [DIRS 155426]). Ages of silica overlying calcite with elevated fluid inclusion temperatures or $\delta^{18}O$ temperatures (calculated from fractionation of $^{18}O/^{16}O$ between measured calcite $\delta^{18}O$ and an assumed water $\delta^{18}O$) range from 1.88 ± 0.05 Ma to 9.7 ± 1.5 Ma, although most values are older than 6 to 8 Ma (Neymark et al. 2001 [DIRS 156889]). The absence of two-phase fluid inclusions in late-stage, magnesium-rich calcite provides strong evidence that temperatures of formation remained below 30°C to 35°C during the most recent depositional history. Estimates of the initiation of late-stage of calcite growth range from 2 to 4 Ma (Wilson and Cline 2001 [DIRS 155426]; Whelan et al. 2002 [DIRS 160442], Figure 7; Whelan et al. 2003 [DIRS 163590], pp. 363 to 364).

Combined fluid-inclusion, $\delta^{18}O$, and geochronology data indicate a prolonged period of monotonically decreasing temperatures in the Yucca Mountain unsaturated zone (Whelan et al. 2003 [DIRS 163590], Figure 4). Temperatures declined from above 80°C shortly after eruption at 12.8 Ma to less than about 30°C to 35°C at about 5 to 6 Ma. This extracted period of cooling is much longer than expected for heat dissipation from the tuff sheet itself (Holt 2002 [DIRS 162326], p. 570) and requires conductive heat input from a large, long-lived

magma body associated with eruptions emanating from the Timber Mountain caldera immediately north of the Yucca Mountain outflow sheet (Whelan et al. 2001 [DIRS 154773]; 2003 [DIRS 163590], p. 363). Two-dimensional conductive/convective thermal modeling of an idealized upper-crustal section at Yucca Mountain indicates that modern geothermal gradients were established by 6 Ma (Marshall and Whelan 2000 [DIRS 154415]). These results are consistent with the cooling history observed in unsaturated zone secondary minerals. Warmer saturated zone groundwater, higher water-table elevations, and greater overburden thickness are also effective at keeping temperatures at the repository horizon higher for longer periods of time (Whelan et al. 2001 [DIRS 154773], Figure 5).

In addition to geothermal information, fluid inclusions also preserve evidence of physical conditions of the unsaturated zone at the time of trapping. Besides all-liquid inclusions and inclusions containing small and consistent vapor-liquid ratios, all-vapor inclusions and two-phase fluid inclusions with highly variable vapor-liquid ratios are present (Whelan et al. 2002 [DIRS 160442], p. 747). Although these types of fluid inclusion assemblages have been interpreted to reflect trapping of a heterogeneous fluid under conditions of boiling or effervescence (Roedder 1984 [DIRS 106675], p. 31), they are also consistent with trapping of a mixture of both liquid and atmospheric gases in unsaturated zone environments at low temperatures (Goldstein 1986 [DIRS 105674], p. 795; Goldstein and Reynolds 1994 [DIRS 126906], p. 8). Because boiling temperatures are not implied by thermal indicators, a vadose zone environment is interpreted as the cause for the complex suite of inclusions in Yucca Mountain unsaturated zone calcite (Whelan et al. 2002 [DIRS 160442], p. 748).

7.7.7 Hydrologic Implications

Data from secondary minerals can be used to evaluate hydrologic conditions in the unsaturated zone and the response of the hydrogeologic system to changes that have occurred over the last 12.8 million years. As noted above, physical evidence indicates that the deposition of low-temperature minerals occurred under unsaturated hydrologic conditions. The distribution of secondary mineral coatings indicate the absence of even local water ponding (Paces et al. 2001 [DIRS 156507], p. 66; Whelan et al. 2002 [DIRS 160442], p. 747). Open space appears to be required for mineral deposition, and the occurrence of secondary mineral coatings on fracture footwalls and cavity floors indicates the strong influence of gravity on water percolating through the unsaturated zone. In addition, the presence of secondary minerals in only a small percentage of all possible depositional sites in highly fractured welded tuffs indicates the absence of saturated conditions during the entire posteruptive history of Yucca Mountain. Fluid-inclusion data also require calcite formation in an unsaturated environment, allowing heterogeneous trapping of both liquid and atmospheric gases (Section 7.7.6 above) (Whelan et al. 2002 [DIRS 160442], p. 747). Oxygen, strontium, and (to at least some degree) carbon isotope data in late-stage unsaturated zone calcite are also indicative of a meteoric water source and are inconsistent with a source associated with a saturated zone source similar to any known groundwater in the Yucca Mountain vicinity (Paces et al. 2001 [DIRS 156507], p. 61). Depositional processes most likely involve water moving down fracture surfaces as thin sheets or films (Tokunaga and Wan 1997 [DIRS 139195]) where solutions may lose both water vapor and CO_2, resulting in the slow growth of calcite and opal, often as intimate admixtures with complex textures (Paces et al. 2001 [DIRS 156507], Figures 7 to 9; Whelan et al. 2002 [DIRS 160442], Figure 4). The absence of secondary deposits from the majority of the lithophysal cavities

indicates that seepage responsible for calcite and silica is related to discrete fracture flow rather than the potentially more voluminous and pervasive pore-water flow through the welded-tuff matrix. The secondary mineral deposits also require the presence of an independently migrating gas phase that transports water vapor and CO_2 upwards in response to the geothermal gradient (Paces et al. 2001 [DIRS 156507], p. 66; Whelan et al. 2002 [DIRS 160442], p. 743).

Geochronological data indicate that growth rates are extremely slow and have remained approximately uniform over long periods of time (Neymark et al. 1998 [DIRS 109140]; Neymark and Paces 2000 [DIRS 127012]; Paces et al. 2000 [DIRS 154413]; Paces et al. 2001 [DIRS 156507]; Neymark et al. 2002 [DIRS 158673]). The mm-per-million-year rates of growth for calcite and silica at Yucca Mountain are up to 10^6 to 10^7 times slower than growth rates commonly reported for deposits in karst environments, and they are more than 10^3 times slower than the slowest reported speleothem growth rates (Paces et al. 2001 [DIRS 156507], p. 66). The average long-term growth rates calculated for Yucca Mountain deposits within the repository horizon have also remained relatively constant from early- through late-stage parts of the coatings (Neymark et al. 2002 [DIRS 158673], p. 731). The U-series data from outermost calcite and silica imply similarly slow growth rates evenly distributed throughout the last 500 k.y., in spite of the known variations in Pleistocene climate in the region (Paces et al. 2001 [DIRS 156507], p. 72). These growth rates are consistent with rates derived by assuming that the cumulative thicknesses of 10 to 20 mm (0.4 to 0.8 in.) of mineral coatings were formed at constant rates over the past 10 to 12.8 million years. This observation, plus the fact that most coatings continued to grow through the Pleistocene, indicate that once established, transmissive fracture pathways appear to be maintained throughout the history of the mountain. These interpretations of slow, uniform growth rates at the same depositional sites over long periods indicate that the unsaturated zone fracture network is capable of maintaining a large degree of hydrologic stability (Neymark et al. 1998 [DIRS 109140]; Paces et al. 2001 [DIRS 156507], p. 72).

Hydrologic stability of the Yucca Mountain unsaturated zone is also implied by the fact that the approximately uniform long-term growth rates have been maintained throughout the Miocene, Pliocene, and Pleistocene epochs. Regional climate conditions in southern Nevada have shifted during the past 10 million years from milder, wetter conditions in the Tertiary, to the more severe, semiarid conditions characteristic of the Quaternary (Thompson 1991 [DIRS 109175], pp. 126 and 127). A shift to increased aridity in the Yucca Mountain vicinity between about 1 and 2 Ma was also inferred from changes in hydrogen isotope compositions of fluid inclusions in calcite veins of Pliocene and Pleistocene age (Winograd et al. 1985 [DIRS 109187]). Changes in carbon isotope signatures observed between middle- and late-stage unsaturated zone calcite likely represent shifts in the make-up of the plant community as it responded to changes in climate conditions (Whelan and Moscati 1998 [DIRS 109179], p. 14). Milder Tertiary climates are likely to have included higher proportions of plants utilizing the C4 photosynthetic pathway (species commonly found in tropical and temperate grasslands), which produce heavier (less negative) $\delta^{13}C$ signatures. The shift to colder, more-arid Quaternary conditions favored plants utilizing the C3 photosynthetic pathway (species dominant in temperate and high-latitude regions), producing lighter (more negative) $\delta^{13}C$ signatures. Mineral growth rates appear less affected by these climate changes, implying that percolation flux rates may be buffered in the deep unsaturated zone (Paces et al. 2001 [DIRS 156507], p. 72). Buffering may be accomplished by a combination of processes, including shifts to a greater biomass, allowing

greater evapotranspiration rates, increased downslope diversion of soil water at the colluvium/tuff boundary, and variable saturation in nonwelded tuffs of the PTn hydrogeologic unit (Paces et al. 2001 [DIRS 156507], p. 72). However, recent U-series age determinations of individual opal hemispheres at greater spatial resolutions (1.5 to 35 μm compared to the 10^2 to 10^3 μm thick samples analyzed previously) may reflect both slower Pleistocene growth rates (<1 mm/m.y.) relative to Miocene rates (1 to 5 mm/m.y.) and variable growth rates throughout the Pleistocene that correlate with climate changes in the past 30 ka. This includes the possibility that percolation fluxes became low enough in the middle Holocene so that seepage into lithophysal cavities ceased (Paces et al. 2003 [DIRS 166371], pp. 19 to 22).

7.7.8 Alternative Hypotheses

An alternative explanation for the origins of the secondary minerals in the Yucca Mountain unsaturated zone has been proposed elsewhere (Hill et al. 1995 [DIRS 106126]; Dublyansky and Szymanski 1996 [DIRS 161545]; Hill and Dublyansky 1999 [DIRS 165606]; Dublyansky 2001 [DIRS 161542]; Smirnov and Dublyansky 2000 [DIRS 154789]; Dublyansky et al. 2001 [DIRS 161543]). This hypothesis is based on earlier speculations (Szymanski 1989 [DIRS 106963]) whereby groundwater from the saturated zone is introduced into the unsaturated zone through a seismic pumping mechanism, forcing groundwater to heights greater than 500 m (1,640 ft) above the present-day water table. Both unsaturated zone and pedogenic calcite deposits have been attributed to this saturated zone hydrogenic source. This interpretation has been strongly rebutted, using a preponderance of evidence in support of a descending meteoric water source (Stuckless 1991 [DIRS 130503]; Stuckless et al. 1991 [DIRS 106947]; National Research Council 1992 [DIRS 105162]; Vaniman et al. 1994 [DIRS 145369]; Monger and Adams 1996 [DIRS 148859]; Stuckless et al. 1998 [DIRS 100086], Vaniman et al. 2001 [DIRS 157427]), by the absence of credible driving mechanisms for large vertical fluctuations of the water table (Carrigan et al. 1991 [DIRS 100967]; Bredehoeft 1992 [DIRS 101122]; Rojstaczer 1999 [DIRS 129750]), by the preservation of fragile $\delta^{18}O$ signatures in paleofumaroles (Holt 2002 [DIRS 162326]), and by evidence from the deposits themselves (Paces et al. 2001 [DIRS 156507], p. 56; Whelan et al. 2002 [DIRS 160442], pp. 746 to 748).

Fluid inclusions with trapping temperatures above those expected from the present-day geothermal gradient were used as a primary argument for the forceful injection of "hydrothermal" water episodically, forming a saturated (phreatic) environment within the otherwise unsaturated zone tuffs (Dublyansky et al. 1996 [DIRS 109204]; Hill and Dublyansky 1999 [DIRS 165606]; Dublyansky 2001 [DIRS 161542]; Dublyansky et al. 2001 [DIRS 161543]). As part of an evaluation of this alternative hypothesis, independent fluid inclusion studies were established at three different institutions (University of Nevada, Las Vegas, Nevada, USA; United Institute of Geology, Geophysics, and Mineralogy, Novosibirsk, Russia; U.S. Geological Survey, Denver, Colorado, USA) using a single suite of Yucca Mountain samples collected and prepared specifically so that two-phase fluid inclusions would not be homogenized prior to laboratory examination.

All three groups identified the presence of inclusions trapped at temperatures above modern conditions. However, only two studies included comprehensive attempts to define and quantify depositional histories, and then place the fluid inclusion results within this framework. Results of these studies (summarized in Section 7.7.6) recognized the temporal evolution of

fluid-inclusion temperatures, noting that most of the inclusions with elevated trapping temperatures are in early- and intermediate-stage calcite (Whelan et al. 2001 [DIRS 154773]), constrained to be mostly older than 6 to 8 Ma (Neymark et al. 2001 [DIRS 156889]). Wilson and Cline (2001 [DIRS 155426]) noted that the "most significant observation is that these elevated temperature fluids were not trapped in the youngest, chemically distinct Mg-enriched growth-zoned calcite, which began precipitating around 2.8 to 1.9 Ma." Dublyansky (2001 [DIRS 161542]) continued to assert the presence of elevated temperatures throughout the paragenesis, but provided no comprehensive documentation of these results or independent age analyses to support the assertion. Whelan et al. (2001 [DIRS 154773]) noted that warmer temperatures do not require flooding of the unsaturated zone, and that the fluid-inclusion assemblages themselves do not support flooding of the host rocks then, or at any other time. Although Yucca Mountain thermal evolution based on these data require that heat dissipation from Miocene magmatic activity extended through longer periods of time than those expected by some (Dublyansky 2001 [DIRS 161542]), results are consistent with heat-flow models involving multiple injections of large magma bodies at shallow crustal levels.

7.8 FIELD-SCALE TRANSPORT TESTING

Field-scale transport testing investigates the factors expected to affect radionuclide transport in the unsaturated zone. Tests have been conducted at the Busted Butte test facility near Yucca Mountain and in the ESF and ECRB underground facilities at Yucca Mountain. Transport in the unsaturated zone is affected by several factors, including advection, fracture-matrix interaction (both advective and diffusive), radionuclide sorption on rock, and colloidal interactions. The studies described in this section were designed to collect data pertinent to these factors to aid in the development of appropriate conceptual and numerical models that are used to represent radionuclide transport in the unsaturated zone.

7.8.1 Busted Butte Unsaturated Zone Transport Test

The Busted Butte unsaturated zone transport test facility is located in Area 25 of the Nevada Test Site approximately 8 km (5 mi) southeast of the Yucca Mountain repository area (Figure 1-4). The site was chosen based on the presence of readily accessible exposures of the lowermost Topopah Spring Tuff (Tpt) and the Calico Hills Formation (Tac), which were not encountered in the ESF or ECRB Cross-Drift (BSC 2003 [DIRS 166347], Section 6.13.1.1). Busted Butte is a small (2.5 km by 1 km [1.5 mi by 0.6 mi]), north-trending mountain block primarily made up of thick ignimbrite deposits of the Paintbrush Group. The Busted Butte facility is located within a small horst on the southeast side of Busted Butte. Geologic units exposed in the vicinity of the test facility include, in ascending order, the Wahmonie Formation, the Calico Hills Formation, and the Topopah Spring Tuff (Figure 7-45). The test facility consists of an underground excavation along a geologic contact between the Topopah Spring Tuff and the Calico Hills Formation. The corresponding hydrogeologic contact between the TSw and the CHn hydrogeologic units occurs between the moderately welded and nonwelded subzones of the basal vitrophyre of the Topopah Spring Tuff, between Tptpv2 and Tptpv1, respectively. More detailed geologic characterization is presented in BSC (2001 [DIRS 160828], Section 6.8.3.1).

7.8.1.1 Overview of the Unsaturated Zone Transport Test

The principal objectives of the unsaturated zone transport test were to address uncertainties associated with flow and transport in the unsaturated zone process models for Yucca Mountain (BSC 2003 [DIRS 166347], Section 6.13). These uncertainties include:

- The effect of heterogeneities on flow and transport in unsaturated and partially saturated conditions near the contact between the TSw and CHn hydrogeologic units; in particular, issues relevant to fracture-matrix interactions and permeability contrast boundaries

- Validation of laboratory sorption experiments of unsaturated Calico Hills Formation samples

- The effect of upscaling from laboratory to field-and-site scales

- Inputs to the three-dimensional site-scale flow and transport-process model used in the performance assessment abstractions for license application

- Migration behavior of colloids in fractured and unfractured Calico Hills rocks.

The unsaturated zone transport test was comprised of three integrated efforts: the field test, a parallel laboratory-scale testing program, and validation and assessment of models used for performance assessment. The field test involved design of the test, analysis of the geology, identification of tracer breakthrough using chemical analyses, in situ imaging of liquid and tracer migration through geophysical techniques, and, ultimately, destructive testing to quantify tracer migration. Laboratory analytical and testing programs in geochemistry, tracer evaluation, hydrology, and mineralogy were designed to help interpret the field results. The flow-and-transport modeling study was the third aspect of the unsaturated zone transport test. The principal objective of the test is to evaluate the validity of the flow-and-transport site-scale process models used in performance assessment abstractions.

7.8.1.2 Test Design

The unsaturated zone transport test facility is comprised of the main adit, which is 75 m (246 ft) in length, and a test alcove, which is 19 m (62 ft) in length. The configuration of the unsaturated zone transport test site is shown in Figures 7-46 and 7-47. Details of the design and construction criteria can be found in SubTerra (1998 [DIRS 147703], pp. 9 to 21, 33 to 44).

The unsaturated zone transport field test was designed as two test phases (BSC 2003 [DIRS 166347], Section 6.13). Test Phase 1 was comprised of two smaller-scale tests, Phase 1A and Phase 1B. Phase 1A was in the Tac and the nonwelded zone (Tptpv1) at the bottom of the basal vitrophyre of the Tpt; and Phase 1B was in the Tptpv2, the moderately welded subzone of the Tpt vitrophyre. Phase 1A was a "blind" single-point injection test, using four boreholes and injection rates of either 1mL/hr or 10 mL/hr rates. Following the injection period, a mini-mineback was done to expose the distribution of the tracer in the rock mass. Phase 1B involved two pairs of injection-and-collection boreholes in Tptpv2. Phase 1B also used two injection rates (1 mL/hr and 10 mL/hr). The 2 m (6.5 ft) long Phase 1B collection boreholes,

immediately below the injection boreholes, were used to capture arrival of tracers. At the culmination of injection, overcoring was done to collect rock samples for tracer analysis. Phase 2 involved a larger (7 m × 10 m × 10 m) block comprising all of the lithologies of Phase 1. Unlike the single-point injection geometries in Phase 1, the injection systems in Phase 2 were designed to activate large surfaces of the block. Phase 2 included eight injection boreholes drilled from the test alcove and distributed in two horizontal, parallel planes. Injection boreholes were placed to test the properties of the lower Topopah Spring Tuff (Tptpv1 and Tptpv2) and the Calico Hills Formation (Tac). In addition, there were 12 collection boreholes drilled from the main adit. Collection holes were perpendicular in plan view to the injection holes and distributed at various distances from the injectors (Figure 7-47).

7.8.1.2.1 Injection, Sampling, and Monitoring

Injection and sampling of the liquid tracers were accomplished by two pneumatically inflated borehole sealing-and-measurement systems (BSC 2003 [DIRS 166347], Section 6.13.1.6). To allow visual inspection of the injection points under both standard and ultraviolet illumination, a transparent packer system was developed for the tracer-injection systems. Moisture sensing and sampling were accomplished using pneumatically emplaced inverting membranes, which were fabricated with mesh pockets to retain absorbent sample pads.

Electrical-resistance moisture sensors were installed to monitor the relative moisture state of the injection pads and the arrival of liquid tracer at the data collection sampling-pad (BSC 2003 [DIRS 166347], Section 6.13.1.7). Ambient pressure, temperature, and relative humidity and wind speed (due to ventilation) data were collected to define environmental conditions. Injection pressure, pumps operations, and relative saturation at injection points, at the face of boreholes, and along sampling membranes were monitored to define experimental control.

7.8.1.2.2 Nonreactive and Reactive Tracers and Microspheres

The behavior of actual radionuclides of concern has been extensively studied in the laboratory, but regulatory and environmental concerns prevent the use of these materials in the field. For the Busted Butte field tests, nonreactive and reactive tracers were used as surrogates for radionuclides. Surrogate nonreactive and reactive tracers and colloids were mixed together to the consistency in the hydrologic conditions for the different tracers. The tracers used in the Busted Butte experiments of Phase 1 are lithium bromide, fluorescent polystyrene latex microspheres, sodium fluorescein, "pyridone" (3-carbomoyl-2(1H)-pyridone), 2,6-difluorobenzoic acid (2,6-DFBA), and pentafluorobenzoic acid (PFBA) (BSC 2003 [DIRS 166347], Section 6.13.1.8) (Table 7-39a).

Phase 2 tracers include those used in Phase 1 but with three additional fluorinated benzoic acids (FBAs) (2,4-DFBA, 2,4,5-triFBA, 2,3,4,5-tetraFBA), iodide, a fluorescent reactive tracer (Rhodamine WT), and additional reactive ions that served as analogs for neptunium, plutonium, and americium, as given in Table 7-39b. The sequence of tracer injections for Phase 2 are described in BSC (2003 [DIRS 166347], Section 6.13.3.1). To minimize the reactivity of the tracer solution with the country rock a synthetic pore water, based on measured in situ composition, was used as a matrix for the tracers in solution (see Section 7.8.1.4).

7.8.1.3 Mineralogy of Busted Butte and Comparison to Rock Units at Yucca Mountain

The mineral abundances for the Calico Hills Formation (Tac) and the Wahmonie Formation surface samples at the Busted Butte site are presented in Table 7-40. These samples are arranged in Table 7-40 by relative depth and show that the lowermost part of the Tac contains appreciable amounts of clinoptilolite. The upper part of the Tac at this site, however, is characterized more by smectite than by zeolite alteration. The mineral constituents in the alcove (especially the low biotite and feldspar components) are characteristic of the Calico Hills Formation, indicating that Wahmonie Formation deposits are more than 4 m (13 ft) below the present alcove floor (BSC 2001 [DIRS 160828], Section 6.8.3.1).

Comparisons were made between hydrologic properties and the extent of zeolitization in the lower Topopah Spring Tuff and upper Calico Hills Formation from drill-core samples from boreholes in the repository block (Carey et al. 1998 [DIRS 109051]). The results suggest that rock texture or fabric may be a significant factor in the ability of samples to retain water within pores. The data also indicate that a statistically useful, direct relationship between hydrous-mineral abundance and porosity properties might be derived for Yucca Mountain samples, with applicability down to very low abundances of hydrous minerals.

A comparison of the Busted Butte and Yucca Mountain rock units (BSC 2003 [DIRS 166347], Attachment VIII) was made using an informal internal lithostratigraphy of the Calico Hills Formation devised by Moyer and Geslin (1995 [DIRS 101269], pp. 5 to 9). These authors divided the Calico Hills Formation into five ash-flow/air-fall tuff units, plus a bedded tuff and volcaniclastic sandstone (sand grains are mostly from volcanic rocks) at the base of the formation (Table 7-41). Moyer and Geslin (1995 [DIRS 101269], p. 5) speculated that each of the pyroclastic units may correspond to one of the five Calico Hills Formation lava flows that are recognized east of Yucca Mountain. The majority of units (other than bedded tuff/sandstones) are laterally discontinuous, but pyroclastic unit 3 is present in most, and perhaps all, of the drill cores examined by Moyer and Geslin (1995 [DIRS 101269], pp. 6, 8, and 9). However, incomplete recovery of core from the vitric intervals Calico Hills Formation has made unit identification ambiguous.

Given that the Busted Butte section appears to contain only one pyroclastic-flow unit, the identification of unit 3 must be based on observable petrographic parameters without recourse to examination of the contacts of a multiunit sequence. The parameters deemed to have the most characteristic values for unit 3 are the total lithic-clast content and the presence of black perlitic lithic clasts. Moyer and Geslin (1995 [DIRS 101269], pp. 6 and 7) found that the lithic-clast content (including crystalline and vitric-lithic clasts) of unit 3 is in the range of 5 to 10 percent (excluding localized zones of higher concentration), higher than the ranges of 1 to 5 percent in units 2 and 4. Based on these data, the section of the Calico Hills Formation exposed in the Busted Butte field test facility does not contain all the informal units of the formation that are present at Yucca Mountain. Given this limitation, correspondence of the Busted Butte test-facility section with unit 3 provides the best possible applicability, because this is the unit of widest occurrence within the Yucca Mountain region. Unit 3 comprises at least one-third of the thickness of the Calico Hills Formation wherever the formation is predominantly vitric, based on the interpretations of Moyer and Geslin (1995 [DIRS 101269], p. 8).

7.8.1.4 Geochemical and Hydrologic Characterization

For the Busted Butte field tests, analog, conservative and reactive tracers are used as surrogates for radionuclides. To validate the use of these tracers and the site-scale use of the minimum-K_d approach for sorption and the processes of matrix diffusion and colloid migration, a series of laboratory batch-sorption studies were conducted (BSC 2001 [DIRS 160828], Section 6.8.5.1).

The results of the sorption studies for Li, Mn, Co, and Ni are presented in Table 7-42. The results indicate that the Tac sample sorbed the metals more strongly than the Tptpv2 sample and that, on both samples, the metals showed a consistent sequence of sorption: Li « Mn « Ni < Co.

Three core samples were selected for detailed sorption and mineralogic characterization (BSC 2001 [DIRS 160828], Table 27). The sorption of Np, Pu, and Am to the three Busted Butte rock samples was measured at three different concentration levels. Average results for each nuclide are summarized in Table 7-43.

Pore-water samples were collected and analyzed from rock cores collected in the Busted Butte Main Adit to develop a recipe for "synthetic" Busted Butte water that closely resembled the in situ chemistry. Results of the chemical analyses are presented here; details of the synthetic pore-water recipe are given in BSC (2001 [DIRS 160828], Section 6.8.2.4.3).

The results in Table 7-44 show that the pore water is a mixed-ion water (Ca-Na-HCO$_3$-SO$_4$) with an average total dissolved solids of approximately 200 mg/L (BSC 2001 [DIRS 160828], Section 6.8.5.1). Sample 3B, from near the adit wall, differs somewhat from the other samples, perhaps due to the influence of construction water and atmospheric CO$_2$ levels. The compositions of the other three pore-water samples were averaged (as shown in the table), and these average values were used to develop the synthetic pore-water recipe.

Samples of the Calico Hills Formation and Topopah Spring Tuff exposed in Busted Butte outcrops were used to determine the hydrologic properties of the formations in the test block. Table 7-45 presents the mean and standard deviation for porosity, saturated conductivity, and van Genuchten parameters for samples taken from the three units at Busted Butte (BSC 2003 [DIRS 166347], Attachment VIII).

7.8.1.5 Field-Scale Tracer Transport: Phase 1

7.8.1.5.1 Test Phase 1A

Test Phase 1A was located in the CHn hydrogeologic unit, spanning both the geologic Calico Hills Formation (Tac) and the nonwelded subzone of the lowermost Topopah Spring Tuff (Tptpv1) (BSC 2003 [DIRS 166347], Section 6.13.2.1). It was a noninstrumented test consisting of four single-point injection boreholes. All Phase 1 boreholes were 2 m (6.5 ft) in length and 10 cm (4 in.) in diameter. The injection point was located 90 cm (35 in.) in from the borehole collar. Injection started on April 2, 1998, and ended on January 12, 1999. Averaged injection rates were approximately 1 mL/hr (Boreholes 2 and 4) and 10 mL/hr (Boreholes 1 and 3). A mixture of nonreactive tracers (bromide, fluorescein, pyridone, and fluorinated benzoic acids

[FBAs]), a reactive tracer (lithium), and fluorescent polystyrene microspheres were used to track nonreactive transport, reactive transport, and colloid migration, respectively.

The field test was completed through excavation by "mineback" and auger sampling (BSC 2003 [DIRS 166347], Section 6.13.2.1). During mineback, as successive layers of the adit wall were removed, digital photographs were taken under visible and ultraviolet illumination, and the exposed face was surveyed. In addition, rock samples were collected by augering, for laboratory analysis of tracer and moisture content.

Observations from the Phase 1A test demonstrated strong capillary-dominated flow for both the 1 and 10 mL/hr injection rates (BSC 2003 [DIRS 166347], Section 6.13.2.1). The plumes were relatively uniformly distributed around the injection sites. Lithologic contacts were shown to influence the flow. The fracture acted as a permeability barrier rather than as a fast path, indicating that fractures have a relatively minor effect on the flow in Tac and Tptpv1 units.

Augered rock samples were analyzed for bromide and moisture content (BSC 2003 [DIRS 166347], Section 6.13.2.1). Table 7-46 reports measured data from these samples. Samples 1 to 4 were collected at increasing distance below Borehole 3. Samples 1 and 2 were collected from above the ash layer (shown on Figure 7-46), while Samples 3 and 4 were located vertically beneath the injector. Samples 5 to 12 were collected at increasing lateral distance from the injection point.

7.8.1.5.2   Test Phase 1B

Test Phase 1B involved both injection of a tracer mixture and collection of pore-water/tracer samples in the lower section of the Topopah Spring Tuff (Tptpv2) (BSC 2003 [DIRS 166347], Section 6.13.2.2). Because of the paucity of data on fracture-matrix interactions in this lithology, this test was designed to provide data on fracture-matrix interactions in the TSw hydrogeologic unit. The results were used to calibrate fracture properties for Phase 2 analysis.

Phase 1B tests were conducted using two, 2 m (6.5 ft) long injection boreholes (Boreholes 5 and 7) and two, 2 m (6.5 ft) long collection boreholes (Boreholes 6 and 8; see Figure 7-47). The tracer mixture was injected at 10 mL/hr in Borehole 5 and at 1 mL/hr in Borehole 7. Phase 1B injection began on May 12, 1998. Borehole 7 injection was terminated on November 9, 1998, and Borehole 5 injection was terminated on November 18, 1998. Throughout the experiment, rock pore-water samples were collected at regular intervals, using collection pads installed in Boreholes 6 and 8.

At the conclusion of the experiment, overcoring of the Phase-1B boreholes was conducted (BSC 2003 [DIRS 166347], Section 6.13.2.2). Moisture pad collection was conducted on collection Borehole 8, directly below injection Borehole 7, until injection shutdown of Borehole 7 on November 9, 1998. Tracer injection and moisture-pad collection were continued in Boreholes 5 and 6, while two, 10-inch-diameter overcores were drilled approximately tangential to one another, with their centerlines in a vertical plane and contained in the area between the top of injection Borehole 7 and the bottom of collection Borehole 8. When injection hole 5 was shut down, three 10-inch-diameter overcores were drilled, approximately tangential to one another, with their centerlines in a vertical plane, and contained in the area between the top

of injection Borehole 5 and 10 inches below the bottom of collection Borehole 6. As soon as
each of the injection holes was turned off, the injection and collection holes were surveyed, and a
video camera and a neutron logger were run in the holes.

There were 176 selected pads extracted for tracers, and the extracts were analyzed by ion
chromatograph, inductively coupled plasma/mass spectroscopy, high-pressure liquid
chromatograph, spectrofluorimetry, and epifluorescent microscopy (BSC 2003 [DIRS 166347],
Section 6.13.2.2). Breakthrough of all five solute tracers was detected in Borehole 6, directly
below the 10 mL/hr injection site in Borehole 5. No breakthrough was detected in
Borehole 8 below the 1 mL/hr injection site in Borehole 7. No clear evidence of microsphere
breakthrough was detected in either borehole, but this may result from analytical difficulties,
discussed below. The Borehole 6 breakthrough results are summarized in Figure 7-48
(a through e), which shows tracer concentration in pad (C) normalized by the input tracer
concentration (C_0) (BSC 2003 [DIRS 166347], Section 6.13.1.9).

All five tracers shown in Figure 7-48 (a through e) give clear evidence of breakthrough by the
end of the experiment (BSC 2003 [DIRS 166347], Section 6.13.2.2). Bromide and 2,6-DFBA,
both nonreactive anionic tracers, show similar and reasonable breakthrough patterns. The peak
measured fluorescein concentration is over twice the injected concentration. This anomaly
reflects analytical difficulties associated with the extremely high concentration of fluorescein
injected. The high concentration succeeded in improving field visualization of the plumes during
mineback and overcore, even though it had adverse effects on laboratory quantification.
The later breakthrough and lower detected concentrations of pyridone may also reflect analytical
difficulties suggesting either sorption or degradation of this tracer. The lithium breakthrough
response, in comparison with nonreactive anionic tracers, is consistent with the expectation that
lithium sorbs on the rock.

During the Phase 1B experiment, even when injection occurs immediately adjacent to a fracture,
water appears to be imbibed quickly into the surrounding matrix (BSC 2001 [DIRS 160828],
Section 6.8.6.3.4). The transport times observed immediately below the injection point were on
the order of 30 days, whereas pure fracture flow would have resulted in travel times of minutes
to hours at this flow rate.

7.8.1.5.3   Field-Scale Tracer Transport: Phase 2

Test Configuration–Phase 2 testing involved a 7 m (23 ft) high, 10 m wide (33 ft), and 10 m
(33 ft) deep block comprising all of the lithologies of Phase 1 (see Figure 7-47) (BSC 2003
[DIRS 166347], Section 6.13.3.1). The injection systems in Phase 2 were designed to activate
large surfaces of the block. The injection points for this phase are distributed in two horizontal,
parallel planes arranged to test the properties of the lower Topopah Spring Tuff (Tptpv2) and the
CHn hydrogeologic unit (represented at this location by the Tptpv1 and Tac lithostratigraphic
units). The natural fracture pattern present in this unit serves as the conduit for tracer migration
into the CHn. The lower horizontal injection plane was located in the Calico Hills Formation
(Tac). Phase 2 included 15 collection boreholes drilled from the Main Adit, perpendicular to the
injection boreholes (BSC 2003 [DIRS 166347], Section 6.13.3). A detailed description of the
injection and collection systems is given in BSC (2003 [DIRS 166347], Section 6.13.3).

Natural infiltration rates at Yucca Mountain vary between 0.01 and 250 mm/yr, with an average of 5 mm/yr (Flint et al. 1996 [DIRS 100147]). Phase 2A injection rates fall within the range of natural, present-day infiltration rates at Yucca Mountain, whereas those for Phase 2B are at the high end of predicted values for a pluvial-climate scenario. Phase 2C infiltration rates are artificially higher-than-expected natural-infiltration rates for the region, but provide for the longest travel distances, given the short duration of the experiment. Further, these high injection-rates may provide insight into system behavior during unnaturally high-flow potentially caused by repository heating.

Additional Coring and Mineback–During February and March 2000, three additional cores were extracted from the Phase 2 collection face. Following termination of tracer injection, five overcores were taken around and below injection holes to analyze the rock for tracers. These overcores were located to obtain the broadest spectrum of information on metals and microspheres, which had not been observed on any collection pads.

The purpose of the mineback was (1) to collect additional information about the geology of the block, particularly faults and permeability contrasts, and (2) to obtain rock samples for tracer analysis that cover a larger portion of the test-block volume than that accessible from the collection boreholes (BSC 2003 [DIRS 166347], Section 6.13.3.3). Observations from the mineback have identified at least one fault. An ash layer was observed in the lower Tptpv1 unit, and at least one of the injection boreholes was fully contained within this layer. Observations of in situ fluorescing tracer indicate that this layer strongly affected flow by impeding movement of injected tracer mix into the remainder of the block.

Phase 2 Results–Pad analyses confirm breakthrough of nonreactive tracers in 14 of the 15 collection boreholes (all except Borehole 10) (BSC 2003 [DIRS 166347], Section 6.13.3.4). Lithium breakthrough has been confirmed in 10 of the 15 collection boreholes (all except Boreholes 10, 11, 47, 49, and 51). No other sorbing tracers were unequivocally detected. The breakthrough of moisture onto the collection pads precedes the breakthrough of tracer (BSC 2003 [DIRS 166347], Figure 6.13.3-3). Initial saturation of the unsaturated zone transport test Phase 2 block was estimated at approximately 16 percent. Because the block was not totally dry, tracer displaced existing water ahead of it as it was injected.

Boreholes 12, 13, 14, and 15 are all equidistant from, and parallel to, the upper injection boreholes. They are all in the same unit. Differences in breakthrough patterns between these boreholes are, thus, a result of heterogeneities in the test block. Noticeable variability in both breakthrough times and concentrations was found for bromide in these boreholes (Figure 7-49). The significant delay between breakthrough in Borehole 12 versus Boreholes 13 and 15 is possibly a result of the presence of a fault in the back of the block. This fault appears to cut between the injection boreholes and Borehole 12.

In each of the injection holes, a mix of a number of tracers was introduced (BSC 2003 [DIRS 166347], Section 6.13.3.8). The tracer mix was the same for all boreholes except with regard to the FBAs. A different FBA was injected in each injection borehole to allow identification of the source of the tracer when collection pads were analyzed. Thus, by looking at tracer breakthrough patterns in a single collection borehole, the extent of lateral dispersion can be assessed. Borehole 16 is 0.7 m (2.3 ft) below the injection boreholes (BSC 2003

[DIRS 166347], Section 6.13.3.8). The breakthrough pattern in Borehole 16 indicates that there is little transverse dispersion or mixing of the tracer being injected at the various injection boreholes (BSC 2003 [DIRS 166347], Figure 6.13.3-6).

The influence of sorption/retardation is analyzed by comparing breakthrough curves for bromide versus lithium at various boreholes (BSC 2003 [DIRS 166347], Section 6.13.3.9). Borehole 16 and Borehole 15 are below the upper-injection boreholes (50 mL/hr), in Tptpv1, 0.7 m (2.3 ft) and 1.3 m (4.3 ft), respectively. Borehole 48 is below the lower-injection boreholes (10 mL/hr), located in the Tac. As expected, lithium breakthrough is retarded with respect to bromide (BSC 2003 [DIRS 166347], Figure 6.13.3-7). Laboratory sorption measurements calculate lithium K_d values between 0.4 and 1.1 (DTN: LA9912WS831372.001 [DIRS 156586]). All of the other reactive tracers being used have significantly higher K_d values and were not found to break through at any of the boreholes.

Tracer transport test modeling for the Busted Butte tests are presented in BSC (2001 [DIRS 160828], Section 6.8.6).

7.8.1.6   Tomographic Studies: Geophysical Techniques at the Busted Butte Unsaturated Zone Test Facility

Geophysical monitoring techniques were used to provide real-time data on the advance of fluid fronts and tracer fronts through the block (BSC 2003 [DIRS 166347], Section 6.13.4). Combining two geophysical techniques enables the collection of detailed, high-resolution, three-dimensional, calibrated, real-time monitoring of moisture and tracer movement through the unsaturated fractured medium. Specifically, electrical resistance tomography provided three-dimensional global coverage, and ground-penetrating radar tomography provided high spatial resolution.

7.8.1.6.1   Busted Butte Ground Penetrating Radar Tomography

The ground-penetrating radar data acquisition was conducted in the Phase 2 test block to monitor the tracer injection, both spatially and temporally, and to investigate the nature of fluid migration through the Calico Hills Formation (BSC 2003 [DIRS 166347], Section 6.13.4.1). All analyzed data were periodically compared to the other available geophysical data (as well as to the tracer breakthrough data) to constrain the interpretation of the fluid/tracer migration within the block.

In the borehole radar method, modified surface radar antennas are emplaced into a rock formation, and high-frequency electromagnetic signals are transmitted through the formation to a receiving antenna (BSC 2003 [DIRS 166347], Section 6.13.4.1.1). The electrical properties of the subsurface material greatly influence the transmitted electromagnetic signal. In particular, the dielectric permittivity (ε_r) of the rock has a strong influence on the propagation of the signal and whether it travels at a high or low velocity. Moisture content affects dielectric permittivity and, hence, has such an effect. The high dielectric permittivity of water (ε_r ~80) or wet rock (ε_r ~20 to 30) in contrast to drier rock (ε_r ~3 to 6) typically results in greatly reduced signal velocities. Changing chemical compositions (i.e., tracers) may also alter the bulk dielectric permittivity of the rock and, hence, the propagation velocity of the radar waves. Because such changes in signal character were measured over the course of the Busted Butte unsaturated zone

transport test, any increase (or decrease) in background moisture-content or chemical composition resulting from the tracer injection (or rock dryout) should result in changes in the received radar velocity. A detailed description of the equipment used, the component specifications, the operating principles, and the ground-penetrating radar survey methodology can be found in Bussod et al. (1998 [DIRS 131513], Section 5.1).

The radar data were acquired in eight of the Phase 2 collection boreholes (Boreholes 9, 11, 13, 15, 16, 46, 47, and 48), which were constructed orthogonal to the direction of the Phase 2 injection boreholes (Boreholes 19 and 22) (BSC 2003 [DIRS 166347], Section 6.13.4.1.3). Additionally, two of the Phase 2 injection boreholes were used to acquire data, one time only, after they were apparently affected by grout infiltration resulting from nearby electrical resistance tomography borehole grouting. The configuration and layout of the boreholes used are illustrated in Figure 7-50. The radar data were acquired in the two-dimensional planes defined by two boreholes, more commonly referred to as well pairs. The well pairs for acquiring data include the following: 13-15, 48-46, 47-11, 46-9, 46-16, and 22-19 (one time only). The decision to acquire data in these particular well pairs was made based on the relative proximity to the injection boreholes. Information on the radar imaging are presented in BSC (2003 [DIRS 166347], Section 6.13.4).

Ground-penetrating radar tomographic data were obtained for well pairs 46-16, 46-9, and 13-15. Decreases in the velocity relative to the baseline data were found surrounding the high- and low-injections boreholes BSC (2003 [DIRS 166347], Section 6.13.4.1.3). Well pair 46-16 represents a vertical slice through the block (Figure 7-50). It images tracer and moisture contributions from both the upper and the lower injection boreholes (BSC 2003 [DIRS 166347], Section 6.13.4.1.3). For this well pair, the zones of decreased velocity can be seen to expand away from the injection boreholes over time, both in a vertical as well as a horizontal direction. Such vertical and horizontal spreading is to be expected as a result of the matrix or capillary-driven flow and was, in fact, confirmed in the Phase 1A excavation. Well pairs 46-9 and 13-15 both represent a horizontal slice through the block, and images the tracer/moisture front associated with the lower-injection boreholes (BSC 2003 [DIRS 166347], Figures 6.13.4-2 and 6.13.4-4). For these well pairs, zones of decreased velocity expand away from the injection boreholes over time in a horizontal direction. Because a horizontal well pair cannot capture the vertical flow of moisture away from the boreholes, only the extent of the horizontal flow can be imaged.

7.8.1.6.2   Electrical-Resistance Tomography

The geophysical imaging technique electrical resistance tomography can be used to map subsurface liquids as flow occurs and to map geologic structure (BSC 2003 [DIRS 166347], Section 6.13.4.2). Electrical resistance tomography is a technique for reconstruction of subsurface electrical resistivity. The result of such a reconstruction is a two- or three-dimensional map of the electrical resistivity distribution underground made from a series of voltage and current measurements from buried electrodes. The electrical resistance tomography approach followed here relies on detection and mapping of the changes in electrical resistivity associated with the movement of a tracer through the test block at the unsaturated zone transport test site.

Sixty electrical resistance tomography electrodes were installed in the test block (BSC 2003 [DIRS 166347], Figure 6.13.4-5). The electrodes were placed in six drilled holes, ERT-1 though ERT-6, and two surface arrays (upper and lower) (BSC 2003 [DIRS 166347], Section 6.13.4.2.1). Data collected from these electrodes provided the three-dimensional sampling of the test-block resistivity, and the three-dimensional inversion algorithm operated on these data to produce a three-dimensional electrical resistance tomography image of the block.

The results presented here consider difference images that compare the resistivity of the block at two points in time. Because the tracer mixture injected during Phase 2 of the unsaturated zone transport test experiment was approximately eight times more conductive than the pore water, resistivity decreases in the images are of interest (BSC 2003 [DIRS 166347], Section 6.13.4.2.1). The different images show regions of resistivity decrease near injection holes 18, 20, and 21, as one would expect from the injection of conductive tracer mixture (BSC 2003 [DIRS 166347], Section 6.13.4.2.3). The electrical resistance tomography tomograms suggest that the movement of conductive water is captured in the measurements. For example, it is apparent in Figure 7-51 that a pronounced resistivity decrease exists in the slice 2.66 m (8.72 ft) from the wall facing the test alcove, which could be associated with water moving downward in the block. The region of the block between 1.33 and 4.0 m (4.36 and 13.1 ft), which contains this slice, also appears to be a low-resistivity region in the absolute image.

7.8.2 Alcove 1

An infiltration-and-tracer transport test was performed in the Alcove 1 of the ESF (CRWMS M&O 2000 [DIRS 122797], Section 6.8.1). Alcove 1 is located near the North Portal of the ESF (see Figure 1-3) in the upper lithophysal zone of the Tiva Canyon Tuff (Tpcpul) unit, corresponding to hydrogeologic unit CUL (Flint 1998 [DIRS 100033], p. 3; Table 7-1). The Tpcpul unit extends above the alcove to the ground surface, with the crown of the drift approximately 30 m (100 ft) below the ground surface. The alcove is about 5.5 m high and 5.8 m wide. In the Alcove 1 tests, water was applied in a plot ~30 m directly above the alcove. The size of the infiltration plot was 7.9×10.6 m (Liu et al. 2003 [DIRS 162470], pp. 174 and 175). Irrigation drip tubing, with 490 drippers uniformly distributed within the infiltration plot, was used to apply the water. The vertical cross section and plan view of the test site is illustrated in Figure 7-52 (Guertal 2001 [DIRS 164070], pp. 29 and 30). At a late stage of the test, a conservative bromide tracer was introduced into the infiltrating water. The seepage into the alcove and the tracer arrival time were recorded. The experimental observations were used for evaluating the parameters of a continuum type unsaturated zone flow and transport model. The test consisted of two phases.

7.8.2.1 Alcove 1 Test Data

Phase I infiltration and seepage is summarized in DTN: GS000308312242.002 [DIRS 156911]. Water was applied at the surface with irrigation drip tubing (March 9, 1998 to August 13, 1998) and collected by a series of 1-foot-square (~0.3 m × 0.3 m) drip trays inside Alcove 1 (May 5, 1998 to August 27, 1998). The irrigated area was 83.7 m^2, and the collection area was 40.2 m^2. The amount of seepage as a percentage of the water applied on the surface depends on the areas chosen for comparison and on the time of observations: 2.9 percent of the total applied water seeped into Alcove 1; 6.1 percent of the water applied directly above the collection area seeped

in Alcove 1; 5.4 percent of the total applied water seeped into Alcove 1 after the rock above Alcove 1 was wetted; and 11.1 percent of the water applied above the collection area seeped into Alcove 1 after the rock above Alcove 1 was wetted.

Both Phase I and Phase II data were used to interpret the test, with calibration using the seepage rate from Phase I of the test and prediction and comparison for Phase II (Liu et al. 2003 [DIRS 162470], Figure 1 for infiltration rates, Figure 3 for seepage rates). The study of LiBr tracer data shows that matrix diffusion may have a significant effect on overall transport behavior in unsaturated fractured rocks.

Models of the Alcove 1 test data are presented in Liu et al. (2003 [DIRS 162470]).

7.8.2.2   Alcove 1 and Pagany Wash Infiltration Comparison

In addition to seepage and transport, the Alcove 1 tests also have implications for the description of net infiltration processes through the bedrock. The ground surface at Yucca Mountain is either exposed bedrock with a thin veneer of soil cover, or is underlain by alluvium, as in washes. The Alcove 1 infiltration plot was on an exposed bedrock surface on a hill slope. In this section, the results of that test are compared to an analysis of infiltration data from Pagany Wash, which is an alluvium-filled wash.

The maintenance of rates at the infiltration plot is related to a controlling factor in determining net infiltration. The range of flux was from 0 to 30 mm/d during February 19, 1999 to December 15, 1999. The range of 18 mm/d to 25 mm/d was maintained from September 21, 1999 to October 15, 1999 before the test with tracer application began. In both the Phase I test (from March 8, 1998 to December 4, 1998) and the Phase II test (from January 29, 1999 to June 20, 2000), water applications were controlled such that no surface runoff occurred. Therefore, infiltration rate over 30 mm/d could induce surface runoff (BSC 2003 [DIRS 166347], Section 6.12.5.2).

This range of infiltration rate (< 30 mm/d) is orders of magnitude smaller than the hydraulic conductivity values for the Tiva Canyon fractured rock, ranging from 169 mm/d to 7.20×10^4 mm/d, with the geometric mean of 1.36×10^4 mm/d. These values are based on measured permeability values from air-injection tests in boreholes drilled from the interior of Alcove 1 (LeCain 1998 [DIRS 100052], p. 1 and Tables 1 to 3). One implication is that the fractures on the surface in the infiltration plot are filled with soils or other in-fill material, and the conductivity is determined by the filling material. At depths below the zone of soil influence, fractures are open, with much higher conductivity values. The net infiltration is controlled by the filled fractures near the surface.

Such a discrepancy between near-surface conductivity and formation conductivity may not exist in alluvium, based on an analysis of the data from Borehole UE-25 UZ #4, located in Pagany Wash. Pagany Wash is an alluvium/colluvium filled channel located northeast of Yucca Mountain (Figures 7-2 and 7-5). An analytical estimation of infiltration was made using the temperature data collected between sensors at 3.0 and 6.1 m (9.8 and 20 ft) below the surface in the borehole (LeCain et al. 2002 [DIRS 158511], Table 1, p. 18). The hydraulic conductivity used in the analysis is 149 mm/d. This value is of the same order of magnitude as the

conductivity value of about 500 mm/d used in the infiltration estimation (Table 7-8; USGS 2001 [DIRS 160355], Section 5). Alluvium can be treated as a porous medium without fractures, based on the relatively close agreement between the alluvium conductivity value and the model parameter used in the interpretation of temperature signal propagation.

Both the Alcove 1 test result and Pagany Wash analysis suggest that surface soils have significant influence on the infiltration process.

7.8.3 Alcove 8 - Niche 3 Drift to Drift Test

This test is aimed at evaluating unsaturated zone flow, seepage response, and matrix-diffusion processes between two drifts (BSC 2003 [DIRS 166347], Section 6.12), and is currently in progress. Alcove 8 (located in the ECRB Cross-Drift) has been excavated to study liquid releases through a fault and a network of fractures. Niche 3 (located at construction station 31+07 in the main drift of the ESF, ~20 m [65 ft] vertically below Alcove 8, and also referred to as Niche 3107) serves as the site for monitoring the wetting-front migration and for collection of seepage originating at Alcove 8. As shown in Figure 7-53, a series of boreholes surrounding Niche 3 have been instrumented with sensors to detect the arrival of a wetting front. The interior of the niche has been instrumented with water-collection trays. Additional boreholes have been drilled in Alcove 8 and Niche 3 for geophysical measurements.

A near-vertical fault trends between Alcove 8 and Niche 3 and is exposed at both locations, providing a unique opportunity to evaluate important hydrologic parameters associated with flow through faults and redistribution of water between fractures and matrix (often called fracture-matrix interaction). A schematic layout of boreholes in Niche 3 is shown in Figure 7-54 (BSC 2003 [DIRS 166347], Section 6.12). This section describes liquid-release tests followed by tracer tests using mixtures of tracers (with both large and small molecular-diffusion coefficients) to evaluate the importance of matrix diffusion from observations of breakthrough times, and the effective fracture-matrix interfacial area. The results of geophysical imaging are also presented.

The major test objectives are (BSC 2003 [DIRS 166347], Section 6.12):

- Quantification of large-scale (~20 m) infiltration and seepage processes along a fault in a repository horizon

- Estimation of relations between relative permeability and water potential for unsaturated flow in faults and through fracture networks

- Evaluation of the importance of matrix diffusion in the unsaturated zone transport processes.

7.8.3.1 Fault Test

The tests were conducted in two phases (BSC 2003 [DIRS 166347], Section 6.12.1.1). During the first phase, water was introduced along the fault under ponded conditions (i.e., with 2 cm (0.75 in.) of water head) until steady seepage was observed in Niche 3. The flow test was followed by the introduction of a finite volume of water containing two tracers with different

molecular-diffusion coefficients (Br and PFBA) into the fault. After the tracer-laced water was released into the fault, more tracer-free water was released. Both tracer-laced and tracer-free releases occurred under the same ponded condition. The second phase of the test involved a series of controlled releases of water with dissolved tracers under nonponded conditions (BSC 2003 [DIRS 166347], Section 6.12.1.1). Liquid release into the fault ranged (in average) from ~25 to ~80 liters/day (L/d) (BSC 2003 [DIRS 166347], Figure 6.12.2-1). The advancing edge of the wetting front was detected 1.9 m (6.2 ft) from the collar of Borehole 10 (BH10 in Figure 7-54) immediately above Niche 3, 34 days after the start of liquid releases along the fault in Alcove 8 (Figure 7-55) (BSC 2003 [DIRS 166347], Section 6.12.2.2). This plume was observed to extend between 1.65 (5.4 ft) and 2.40 m (7.9 ft) from the collar in Borehole 10 over the next seven days. Over the next few weeks, the number of seeps along the fault exposed in Niche 3 gradually increased. The seepage rate from a single seep location suggests that following the first measurable seepage, seepage rates climbed to near-steady values in the next four weeks. As cumulative seepage to the niche increased, measurements of seepage rates at localized zones suggest steady-state conditions.

From the time that the first seep was observed in Niche 3 on April 9, 2001, water samples were periodically collected from the location of the first seep and analyzed for LiBr concentrations. Six months later, when the tracer-mix comprised of LiBr and PFBA was injected with the infiltrating water, seeping water from three locations along the Niche 3 ceiling was sampled. During this sampling, all water seeping from the three locations was collected as discrete 0.5 or 1.0 L samples and analyzed for concentrations of Li, Br, and PFBA.

BSC (2003 [DIRS 166347], Figure 6.12.2-7) shows the concentration of Br measured in the seepage water along with the daily seepage rates for a 1.5 month period following arrival of the wetting front. The Br concentration was initially low (about 3 ppm), increasing gradually with time to a value of 30 ppm (that is the same as that for water applied at the infiltration plot) about 30 days after seepage occurred at Niche 3. This may be an indication of the importance of matrix diffusion. If there is no matrix diffusion at all, the Br arrival would not be developed and Br concentration should be a constant (30 ppm) with time. In addition to matrix diffusion, other mechanisms, such as sorption, may also contribute to the observed retardation of Br transport. However, Br is generally considered conservative, and the potential sorption is expected to play a minor role in the observed retardation.

Figure 7-56 presents the tracer concentration in the seepage water collected from two sampling locations. In tray 7, both bromide and PFBA were first detected three weeks after initial application of the tracers along the fault. In the following month, the concentration of both the tracers gradually increased, with the PFBA concentrations clearly preceding bromide. Peak concentrations of PFBA at this location were observed 61 days after the start of tracer release in Alcove 8. Over the next three months, the concentration of both tracers gradually decreased. During the final month of sampling, the tracer concentrations remained relatively constant.

In Tray 9+23, except for the period between mid-October and late November 2001, when the PFBA concentrations suggest faster travel through the fault zone, both tracers showed a similar temporal recovery pattern. The peak concentrations of tracers at this location were observed 43 days after the start of tracer release in Alcove 8, suggesting a transport velocity of ~ 0.46 meters per day (m/d).

Modeling of the Alcove 8-Niche 3 tests is presented in BSC (2003 [DIRS 163045], Section 7.6) and BSC (2003 [DIRS 163228], Section 7.4).

7.8.3.2 Geophysical Imaging of the Drift-to-Drift Test Block

Images for the test block between Alcove 8 and Niche 3 have been collected with two different techniques: seismic tomography and ground-penetrating radar tomography (BSC 2003 [DIRS 166347], Section 6.12.3). The objective of seismic tomography data acquisition was to acquire baseline data to help monitor the fluid infiltration tests. Both geophysical tomography studies used the slant (near-vertical) boreholes drilled around the test block, as illustrated in Figures 7-53 and 7-54, around a large plot prepared for planar infiltration tests.

Radar data are obtained between pairs of boreholes. All six of the boreholes drilled from Alcove 8 were used for radar measurements. Additionally, two of the boreholes in Niche 3 were used in combination with two of the holes in Alcove 8 (BSC 2003 [DIRS 166347], Section 6.12.3.2). Data were acquired from five borehole pairs in Alcove 8 (Boreholes 1-2, 3-4, 1-3, 2-4, and 5-6), and between Alcove 8 Borehole 1 and Niche 3 Borehole 3, and between Alcove 8 Borehole 4 and Niche 3 Borehole 1 (Figure 7-53).

All of the radar data processed thus far between the boreholes in Alcove 8 show similar results and, as such, are considered together in this section (BSC 2003 [DIRS 166347], Section 6.12.3.2.1, Figures 6.12.3-1a through 1e). The radar velocity images all appear to suggest that the lithologic formation directly underlying Alcove 8 varies little in its dielectric properties. The data suggest that any changes resulting from wetting or fluid flow upon commencement of the infiltration experiment are not expected to follow any particular path. After acquiring the radar data between the boreholes in Alcove 8, additional data were acquired in boreholes between Alcove 8 and Niche 3 (BSC 2003 [DIRS 166347], Section 6.12.3.2.2). The drift-to-drift tests imaged the lithologic contact occurring between the two locations and allowed for monitoring of this contact during the infiltration. The higher-velocity subhorizontal interface near the upper portions of the Niche 3 boreholes is apparent. This region is inferred to be the lithologic contact between the two locations. Results of the seismic tomographic images are presented in Descour et al. (2001 [DIRS 156869]). The seismic images also show a region approximating a lithologic contact between Alcove 8 and Niche 3 at approximately the same location.

7.8.3.3 Summary and Conclusions from Alcove 8–Niche 3 Testing

Fault testing and preliminary stages of the block test in this unique test bed in Alcove 8-Niche 3, resulted in acquiring data that describe the response of the system to releases of water under constant-head conditions. Specifically:

- Infiltration rates along the fault reached quasi-steady-state conditions ~45 days after water was introduced to the infiltration zones, and the infiltration rates varied at different locations along the fault.

- Observations of saturation changes within the fault indicate the velocity of the wetting front vertically along the fault to be ~0.65 m/d.

- Seepage observations indicate that quasi-steady state conditions may have been reached two months after the initial releases into the fault.

- Radar data collected thus far in support of the Alcove 8/Niche 3 infiltration experiment suggest that this method is appropriate for investigating subsurface anomalies that may be related to moisture migration.

- Experimental results indicate that matrix diffusion has an important effect on solute transport.

- Observed low seepage recovery rate from the fault implies good communication between the fault and the surrounding fracture networks.

- Similar tracer arrival times (corresponding to the peak concentration values) for most flow paths suggest that macrodispersion may not be important for solute transport in unsaturated fractured rock.

7.9 CONCEPTUAL MODEL OF FLUID AND GAS FLOW IN THE UNSATURATED ZONE

The conceptual model of flow and transport in the Yucca Mountain unsaturated zone is based to a great extent on the ideas originally presented by Montazer and Wilson (1984 [DIRS 100161], pp. 36 to 49) and has been developed through the evaluation of collected data and the results of modeling studies. For flow, the conceptual model addresses infiltration and flow-partitioning in fractured rock, perched water, faults, transient flow, and gas flow. For transport, the conceptual model addresses advection, fracture-matrix interaction, sorption, and colloid-facilitated transport. For thermal-coupled processes, the conceptual models address mass and energy transfer, phase changes, and thermal-mechanical and thermal-chemical effects on hydrologic properties and processes. The conceptual models for unsaturated zone flow and transport are documented in CRWMS M&O (2000 [DIRS 141187]).

7.9.1 Conceptual Model of Fluid Flow in the Unsaturated Zone

This section documents the conceptual models used for flow (and also transport and coupled processes) within the Yucca Mountain unsaturated zone.

7.9.1.1 Shallow Infiltration

Net infiltration is the ultimate source of percolation flux at the repository horizon and provides the water for flow-and-transport mechanisms that may move radionuclides from the repository to the water table (CRWMS M&O 2000 [DIRS 141187], Section 6.1.1, p. 20). Net infiltration is spatially and temporally variable because of the nature of the storm events that supply precipitation and the variation in soil cover and topography (Section 7.1). Infiltration is believed to be high on side slopes and ridgetops where bedrock crops out, and fracture flow in the bedrock is able to move moisture away from zones of active evapotranspiration.

Near-surface infiltration data suggest that significant net infiltration occurs only every few years. In these years, the amount of net infiltration varies greatly, depending on storm amplitudes,

durations, and frequencies. In very wet years, infiltration pulses may infiltrate into Yucca Mountain during a relatively short time period (Section 7.1.5.4, Figure 7-10). More detailed information about the conceptual model of net infiltration can be found in Section 7.1.3.

7.9.1.2 Downward Percolation through Hydrogeologic Units

As a result of the relatively high density of interconnected fractures and low matrix permeabilities in the TCw hydrogeologic unit (Figure 7-57), net infiltration pulses are expected to move rapidly through the fracture system with little attenuation relative to travel times in the matrix (CRWMS M&O 2000 [DIRS 141187], Section 6.1.2, p. 21). This is partially supported by pneumatic data from sensors in the TSw that show little attenuation of the barometric signal in monitoring boreholes compared with the barometric signal observed at the land surface (Section 7.3). In this case, the flow paths for liquid water should be similar to gas-flow paths. The possible presence of relatively high fractional abundance of ^{36}Cl measured in TCw borehole samples (Section 5.2.2.5.3) also supports this conceptual model regarding liquid-water flow. The source of the elevated levels of (bomb-pulse) ^{36}Cl has been attributed to nuclear testing conducted in the 1950s (Fabryka-Martin et al. 1998 [DIRS 100570], p. 93), and its occurrence in the TCw hydrogeologic unit would indicate the presence of fast pathways for water flow into and through the unit.

Once liquid water leaves the TCw hydrogeologic unit and percolates downward into the PTn hydrogeologic unit, different flow processes are evident (CRWMS M&O 2000 [DIRS 141187], Section 6.1.2, p. 21). Because of the relatively high matrix permeability and porosity, as well as low fracture densities of the PTn, predominantly fracture flow in the TCw becomes dominantly matrix flow in the PTn (Figure 7-57). Pneumatic data are consistent with the concept that fracturing within the PTn is limited. The pneumatic signal is propagated predominantly through the high-storage matrix, leading to significant attenuation of the barometric signal (Section 7.3.2.2). Similarly, much of the moisture flow occurs in the relatively high-porosity matrix in this unit. As a result, the PTn greatly attenuates infiltration pulses, such that liquid-water flow below the PTn is approximately in steady state. This is supported by the modeling study of Wang and Narasimhan (1993 [DIRS 106793], pp. 354 to 361) and BSC (2003 [DIRS 166347], Section 7.7).

The early conceptual model of Yucca Mountain hypothesized that significant lateral flow occurs within the PTn, in response to the capillary-barrier effect and the extremely low net-infiltration (Montazer and Wilson 1984 [DIRS 100161], pp. 45 to 47). Recent numerical modeling results have shown that effective capillary barriers can develop in the PTn. Model results indicate that strong capillary-barrier effects exist for diverting a significant amount of moisture flow through the relatively shallow PTn, with major faults observed at the site serving as major downward pathways for laterally diverted percolation fluxes. Capillary-barrier effects are strongly correlated with surface infiltration rates: lower net infiltration leads to relatively larger lateral flow. Observed field liquid saturation and geochemical isotopic data have been found to be consistent with lateral flow resulting from capillary barriers in the PTn hydrogeologic unit (Wu et al. 2002 [DIRS 161058]).

Unsaturated flow of liquid water in the TSw hydrogeologic unit (Figure 7-57) is primarily through fractures (CRWMS M&O 2000 [DIRS 141187], Section 6.1.2). Assuming a unit

hydraulic gradient, the matrix percolation rate will be the same as the matrix hydraulic conductivity. Using matrix saturated-hydraulic conductivities determined from permeabilities measured in the TSw (Section 7.2.1.3), the calculated matrix percolation rate is a small fraction of the average infiltration rate currently estimated. Therefore, the remainder of the flow must be distributed in the fracture network (Pruess et al. 1999 [DIRS 117112], p. 283). Calcite-coating data show that in the welded units most of the deposition is within fractures or on the floor of lithophysal cavities intersected by fractures (Paces et al. 2001 [DIRS 156507], p. 8 to 11), supporting the hypothesis that fracture water flow is a major flow mechanism within the TSw. Calcite coatings are a signature of liquid-water flow history (Section 7.7).

7.9.1.3   Fracture-Matrix Interaction

Fracture-matrix interaction (caused by water and chemical exchange between the fractures and matrix) is likely limited within welded units at Yucca Mountain (CRWMS M&O 2000 [DIRS 141187], Section 6.1.3; Bodvarsson et al. 1999 [DIRS 120055], p. 13). Chloride concentration data indicate that perched water was derived mainly from fracture flow, with only a small degree of interaction with matrix water (Yang et al. 1996 [DIRS 100194], p. 55). The small degree of interaction between fractures and matrix at locations associated with specific geologic features is also suggested by the possible presence of bomb-pulse ^{36}Cl at the repository level in the ESF (Fabryka-Martin et al. 1998 [DIRS 100570], pp. 93 and 94). Studies by Ho (1997 [DIRS 100584]) evaluated methods of incorporating the conceptual model of fracture-matrix interaction into a dual-permeability model. Results indicated that the calibration with observed matrix saturation and water-potential data was improved using techniques that reduce the fracture-matrix interaction significantly (Ho 1997 [DIRS 100584], p. 409).

The limitation of fracture-matrix interaction at the Yucca Mountain site is consistent with many other independent laboratory tests, as well as theoretical and numerical studies (CRWMS M&O 2000 [DIRS 141187], Section 6.1.3). Laboratory experiments have demonstrated that gravity-driven fingering flow is a common flow-mechanism in individual fractures and can reduce the wetted area in a single fracture to fractions as low as 0.01 to 0.001 of the total fracture area (Glass et al. 1996 [DIRS 139237], pp. 6 and 7). Other theoretical studies have shown that matrix imbibition can increase wetted areas of fingering-flow patterns in individual fractures and reduce the degree of fingering (Abdel-Salam and Chrysikopoulos 1996 [DIRS 132960], pp. 1537 and 1538). Therefore, although fingering flow in individual fractures is an important mechanism for reducing fracture-matrix interaction, its effects may not be as significant as shown in individual fracture experiments that did not incorporate matrix imbibition. Theoretical studies have indicated that the wetted area in a fracture under unsaturated flow conditions is generally smaller than the geometric interface area between fractures and matrix, even when fingering flow is not present (Wang and Narasimhan 1993 [DIRS 106793], pp. 329 and 335). This results from the consideration that liquid water in an unsaturated fracture occurs as saturated segments that cover a portion of the fracture-matrix interface area. Conversely, recent laboratory experiments by Tokunaga and Wan (1997 [DIRS 139195]) demonstrated that water-film flow could be important in unsaturated fractures when the matrix is nearly saturated and water flow occurs from matrix to fractures. Therefore, it can be hypothesized that liquid water generally exists as saturated segments around contact points in unsaturated fractures. The distribution of liquid water in this form will reduce fracture-matrix interaction as compared to the case in which

the whole geometric interface area is considered to contribute to flow-and-transport between fractures and matrix.

Other studies have suggested that in unsaturated, fractured rocks, fingering flow occurs at both a single-fracture scale and at a connected-fracture network scale. Such a phenomenon has been supported by numerical simulations of liquid-water flow in a simple, unsaturated fracture network. These simulations found that a large portion of the connected fracture network played no role in conducting the flow when the fractures do not have uniform apertures. Fingering flow at a fracture-network scale has important effects on large-scale flow-and-transport, and it contributes significantly to the reduction of fracture-matrix interaction (CRWMS M&O 2000 [DIRS 141187], Section 6.1.3).

Studies also have shown that mineral coatings on fracture surfaces might have important effects on fracture-matrix interaction. Experiments on coated and uncoated fractures in tuff have indicated that the low-permeability coatings inhibited matrix imbibition considerably. In contrast, other studies have shown that fracture coatings may, in some cases, increase the fracture-matrix interaction when microfractures develop in the coatings (CRWMS M&O 2000 [DIRS 141187], Section 6.1.3). Because fracture coatings may or may not result in fracture-matrix interaction reduction, coating effects were ignored for modeling flow and transport in the Yucca Mountain unsaturated zone.

Although several mechanisms may limit fracture-matrix interaction in the Yucca Mountain unsaturated zone, fingering flow at a fracture-network scale is considered to be the key mechanism (CRWMS M&O 2000 [DIRS 141187], Section 6.1.3). A new active-fracture model based on this mechanism has been developed and used for modeling fracture-matrix interaction (Section 7.10).

7.9.1.4 Perched Water

Perched water is groundwater in the unsaturated zone that is above or not directly connected to the static water table (CRWMS M&O 2000 [DIRS 141187], Section 6.1.4; Wu et al. 1999 [DIRS 117167], p. 158). Perched water may occur when permeability differences between geologic units are large. Perched-water zones are present at Yucca Mountain in the lower portion of the TSw hydrogeologic unit and the upper portion of the CHn hydrogeologic unit (Figure 7-57) (Section 7.4.2). Field tests indicate that Yucca Mountain perched-water zones have very different water volumes.

The presence of perched water at Yucca Mountain has important implications for the travel times and flow paths of water through the unsaturated zone (CRWMS M&O 2000 [DIRS 141187], Section 6.1.4). First, perched-water ^{14}C data indicate that apparent age estimates of perched-water bodies range from approximately 3.3 to 11 ka (Table 5-4), suggesting a dominant fracture flow in the TSw hydrogeologic unit. Second, the occurrence of perched-water bodies indicates that the basal vitrophyre of the TSw unit, as well as the CHn hydrogeologic unit, serve as barriers to vertical flow and cause downward percolation to be diverted laterally. Although the vitrophyre is extensively fractured, many of the fractures have been filled with zeolitic materials that impede flow. Portions of the Calico Hills Formation have been extensively altered

to zeolites, and the resulting lower fracture permeability has contributed to the formation of perched water bodies.

Carbon-14 ages of the perched-water bodies below the TSw hydrogeologic unit range from 3.3 to 11 ka (see Section 5.2.2.5.4 for a discussion regarding issues pertaining to carbon isotope dating of groundwater), also suggesting fracture-dominated flow in the TSw because the water travel-times from the ground surface to the perched-water zones would be much longer for the liquid water flowing only in the matrix (Bandurraga and Bodvarsson 1999 [DIRS 103949], p. 40, Table 3). Because of the small matrix permeabilities, the perched-water bodies would have much older ages if they had resulted from matrix water flow within the TSw hydrogeologic unit.

The occurrence of perched-water bodies at a number of boreholes in the lower part of the TSw hydrogeologic unit and the upper part of the CHn hydrogeologic unit (Figure 7-57) (Section 7.4.2) indicates that the basal vitrophyre layers of the TSw, as well as the CHn hydrogeologic unit, serve as barriers to vertical flow and cause lateral flow (CRWMS M&O 2000 [DIRS 141187], Section 6.1.2). The main hydrogeologic units below the repository are the CHn and the CFu hydrogeologic units. Both of these units have vitric and zeolitic components that differ by the degree of hydrothermal alteration (Flint 1998 [DIRS 100033], pp. 29 to 33). Because the zeolitic rocks of the CHn and CFu hydrogeologic units have low matrix permeability and some fracture permeability, a relatively small amount of water may flow through the zeolitic units. However, most of the water that percolates to the zeolitic horizon is diverted laterally in the perched-water bodies and then vertically down faults (Figure 7-57). Conversely, but similar to the PTn hydrogeologic unit, the vitric rocks of the CHn and the CFu hydrogeologic units have relatively high matrix porosity and permeability. Thus, mostly porous-medium flow predominates in these rocks. Fracture flow is believed to be limited in these units.

7.9.1.5   Major Faults

Because strike-slip and normal faults with varying amounts of displacement are numerous at Yucca Mountain, it is important to understand how major faults affect flow processes (CRWMS M&O 2000 [DIRS 141187], Section 6.1.5). A fault can act as a transient fast-flow conduit for vertical liquid-water flow, particularly as a result of temporally variable infiltration. Because the major faults cut through the PTn hydrogeologic unit, the damping effect of the PTn on transient infiltration is significantly reduced. Net infiltration into the fault depends upon its hydraulic conductivity at the atmosphere-rock interface and how much fault area is exposed in developed surface-water drainage basins. However, if this transient flow occurs along the major faults, it is expected to carry only a small amount of water and may not be a major liquid-flow mechanism above the repository horizon. This is because of the relatively small cross-sectional areas of the fault zones in the horizontal plane and/or insignificant transient lateral flow to the fault in the unsaturated zone. As discussed in Section 7.10.1.2.1, lateral flow both above and below the repository horizon is believed to be significant.

A fault zone also can act as a barrier to lateral liquid-water flow where it is highly fractured. The resulting coarse openings create a capillary barrier. In addition, a fault can act as a barrier to lateral flow when fault displacement results in a low-permeability unit being juxtaposed against a relatively high-permeability unit within a fault zone. In this case, the fault will act as a

permeability barrier to the lateral flow within the unit with relatively high permeability (CRWMS M&O 2000 [DIRS 141187], Section 6.1.5). Montazer and Wilson (1984 [DIRS 100161], p. 20) conceptualized that permeability would vary along faults, with higher bulk permeability in the brittle, welded units and lower permeability in the nonwelded units where gouge or sealing material may be produced. Whereas a fault sealed with gouge or other fine-grained material will have much higher capillary suction, it will also have low permeability, retarding the movement of liquid water.

In summary, because lateral flow is significant above the repository and focusing infiltration near faults may occur, faults may act as flow paths to significantly alter the percolation pattern from the surface to the repository level (BSC 2003 [DIRS 163045], Section 6.2.2.1). Below the repository, low-permeability layers in the CHn hydrogeologic unit divert some flow to faults that act as conduits to the water table (Figure 7-57). Also, the effects of major faults on gas-flow processes within the unsaturated zone are likely to be significant, as discussed in Section 7.9.1.8.

7.9.1.6 Transient versus Steady-State Flow

In general, flow in the Yucca Mountain unsaturated zone is time-dependent or transient, resulting mainly from the temporal variations in infiltration flux at the land surface (CRWMS M&O 2000 [DIRS 141187], Section 6.1.6). The temporal variation in infiltration may be approximated as occurring over short intervals characterized by changes in weather, resulting in episodic transient flows, or over much longer time periods corresponding to climate change. The PTn hydrogeologic unit greatly attenuates short-term episodic infiltration pulses, so that liquid-water flow below the PTn is approximately in steady state (Wang and Narasimhan 1993 [DIRS 106793], pp. 354 to 361). The attenuation is a result of matrix flow in the PTn and the relatively large storage capacity of the PTn, which results primarily from the relatively low matrix saturation in this unit. However, longer-term climate change, rather than short-term episodic infiltration, has a more pronounced influence on the flow pattern within the mountain and ultimately impacts the entire flow field in the unsaturated zone. In total system performance assessment simulations of radionuclide transport, however, the actual transient period during which the unsaturated zone flow system responds to a climate change has been found to be less significant (DOE 1998 [DIRS 100550], Section 3.6.1.1, p. 3-116). The reason for this is that the change in flow in the fractures, which dominates the flux in most hydrogeologic units, responds relatively quickly to a change in infiltration. It is expected that flow through isolated fast-flow paths that bypass the PTn exhibits a strong transient character, because a significant attenuation mechanism is lacking (CRWMS M&O 2000 [DIRS 141187], Section 6.1.6). However, these isolated flow paths are believed to carry only a small amount of water (Section 7.9.1.7). Therefore, a quasi-steady flow model was used to estimate the effects of climate change on radionuclide transport. In this model, infiltration rate was assumed to change abruptly when climate changes from one steady flow-field to another. Transport calculations simply were restarted when climate changed, with the radionuclides that were present in the unsaturated zone at the end of the previous climate included as an initial condition for the next climate. Based on the results of transport modeling, it is reasonable to assume flow to be in steady state for modeling liquid-water flow in the unsaturated zone.

7.9.1.7   Focusing Flow and Fast-Flow Paths

Depending on geologic conditions and the magnitude of the flux, focusing flow leading to fast pathways across the PTn hydrogeologic unit may occur. Only rock samples associated with localized fault structures that cut through the PTn show bomb-pulse signatures of ^{36}Cl in the lower PTn (Section 5.2.2.5.3). These pathways are possibly responsible for the high levels of ^{36}Cl within the TSw hydrogeologic unit at the repository horizon. However, because bomb-pulse samples were taken at only a few locations, no significant correlation between high matrix saturation and elevated ^{36}Cl levels has been reported. Because these discrete fast paths are not associated with large catchment areas involving large volumes of infiltrating water, it is expected that these fast flow paths probably carry only a very small amount of water. Although a recent analysis of additional samples to validate the ^{36}Cl findings could not duplicate the earlier finding (Section 5.2.2.5.3), the conceptualization of potential fast-flow paths is a conservative approach to modeling flow through the unsaturated zone (DOE 2002 [DIRS 157080], Section 4.3.4).

Fingering flow through the matrix may be an alternative fast-flow mechanism through the PTn hydrogeologic unit (CRWMS M&O 2000 [DIRS 141187], Section 6.1.7). However, it is unlikely that fingering flow is an important flow mechanism for the tuff matrix, because fingering flow is a gravity-driven phenomenon and cannot occur when capillary forces are dominant (see Section 7.9.1.3). One major difference between Yucca Mountain soils and the tuff matrix is that the tuff matrix exhibits much stronger capillary strength than soils (Wang and Narasimhan 1993 [DIRS 106793], pp. 374 to 377), which could significantly reduce the possibility for fingering flow in the tuff matrix.

A variety of observations indicates that the fracture-water flow paths in the TSw hydrogeologic unit are many and widely dispersed. Average measured matrix saturations suggest relatively uniform values within each lithostratigraphic unit for most of the units (Flint 1998 [DIRS 100033], pp. 24 to 30, Figures 5 to 9), and in situ water-potential measurements also show little variability within the TSw for different boreholes (Rousseau et al. 1999 [DIRS 102097], pp. 146 to 151). Additionally, the temperature within the TSw was observed to be fairly uniform (Bodvarsson et al. 1999 [DIRS 120055], p. 13; Rousseau et al. 1999 [DIRS 102097], pp. 151 to 161). The spatial distribution of fracture lining calcite is an indicator of flow focusing (BSC 2003 [DIRS 161773], Section 7). These observations are consistent with a conceptual model in which fracture flow is dispersed, resulting in relatively uniform conditions within the geologic formation.

7.9.1.8   Gas-Flow Processes

Gas flow in the Yucca Mountain unsaturated zone depends mainly on the characteristics of fracture networks (CRWMS M&O 2000 [DIRS 141187], Section 6.1.8). In the PTn hydrogeologic unit, the permeability of the fracture continuum is perceived to be closer to the matrix continuum because of lower liquid saturation and larger pore sizes in the matrix of the PTn (Table 7-10). In the welded units (TCw and TSw hydrogeologic units), the fractures generally are perceived to be much more permeable than the matrix because of larger absolute permeability and lower liquid saturation. Few data exist on gas flow below the bottom of the TSw, although high-liquid saturation and low permeability, such as due to a perched water zone, are likely to significantly reduce gas flow (Section 7.3.2.4).

The ambient gas-flow processes occurring at Yucca Mountain include barometric pumping, wind, and density-driven flow (Section 7.3). Barometric pumping is the response of subsurface pneumatic pressure to changes in atmospheric pressure. Because this is a transient process, both the permeability and storage of the media affect the subsurface response. In the welded units, this translates into little change in the pneumatic-pressure signal with depth.   In the PTn hydrogeologic unit, however, the approximately equal fracture and matrix permeability and the high gas-filled porosity serve to attenuate and lag the response to barometric pumping between the top and the bottom of the unit (Section 7.3.2). Using vertical, one-dimensional inversion models of hydrologic properties, Ahlers et al. (1999 [DIRS 109715], p. 58) showed a close correlation between the thickness of the PTn and pneumatic response below the PTn. However, evaluation of borehole pneumatic-pressure data indicates that the attenuation characteristics of different subunits of the PTn vary spatially and that the composite thickness of the PTn is insufficient to uniquely account for these variations (Rousseau et al. 1999 [DIRS 102097], p. 96). Ahlers et al. (1999 [DIRS 109715], pp. 47 and 59 to 66) also showed that faults are fast pathways for gas flow, particularly in the TSw hydrogeologic unit, but affect subsurface response only on a relatively local scale, confirming the results of pneumatic monitoring (Rousseau et al. 1999 [DIRS 102097], pp. 110 to 115).

Gas flow occurs under ambient conditions as a result of density-driven and wind-driven processes (CRWMS M&O 2000 [DIRS 141187], Section 6.1.8). (The thermosiphon effect is discussed in Section 7.3.) Density-driven flow occurs in the area of steep topography and is a consequence of the differences between the density of dry air in the atmosphere and moist air in the mountain. For example, in winter, the moist, warmer air inside the mountain is lighter and rises in response to the pressure exerted by the heavier, cooler, dry air, causing flow within the mountain from the lower elevations toward the crest. Wind-driven flow occurs because of the higher pressure exerted on the windward side of the mountain and the lower pressure in the lee of the crest. Thus, wind-driven flow will also promote flow toward the crest of Yucca Mountain. Measurement of air flow in an open borehole near the crest of Yucca Mountain shows that density-driven and wind-driven flow occurs primarily in the TCw hydrogeologic unit.

7.9.1.9   Summary of Conceptual Model of Fluid Flow

The conceptual model of fluid flow in the Yucca Mountain unsaturated zone (Figure 7-57) is based on an understanding and integration of the flow processes and issues discussed in Sections 7.9.1.1 to 7.9.1.8 (CRWMS M&O 2000 [DIRS 141187], Section 6.1.9).   Shallow infiltration is highly variable, both spatially and temporally. Infiltration pulses move rapidly through the fractures in the TCw hydrogeologic unit with little attenuation by the matrix. Because of the attenuation effects of the PTn hydrogeologic unit, the liquid-water flow processes below this unit are approximately in steady state under ambient conditions. Lateral flow in the PTn is considered to be significant. Fracture liquid-water flow is dominant in welded units (TCw and TSw hydrogeologic units), and matrix flow is dominant in nonwelded units (PTn and CHn hydrogeologic units), except where the CHn is zeolitic. It is expected that only a limited number of fractures are actively involved in water flow in the welded units in the Yucca Mountain unsaturated zone. Isolated, transient, and fast-flow paths exist, but they carry only a small portion of the total liquid-water flux. The existence of perched-water bodies below the repository horizon introduces three-dimensional lateral flow within the unsaturated zone. Major faults act as flow paths to significantly alter the percolation pattern from the surface to the

repository level. However, below the repository horizon, low-permeability layers in the zeolitic parts of the CHn divert some flow to faults that act as conduits to the water table.

There are differences between the current conceptual model of flow in the unsaturated zone and earlier conceptual models published in the literature (CRWMS M&O 2000 [DIRS 141187], Section 6.1.9). From the mid-1980s to the early 1990s, the prevailing view of the Yucca Mountain unsaturated zone has been that under ambient conditions, water flow occurs mainly through the rock matrix, even in the welded, densely welded, and fractured TSw hydrogeologic unit. Based on capillary theory, it was believed that under unsaturated conditions, liquid water would essentially be excluded from fractures because of the capillary strength of the matrix. However, with much more data available from site characterization, it has become evident that unsaturated flow in the welded units is primarily through the fractures.

Pruess (1999 [DIRS 104250], pp. 1040 to 1042) proposed a conceptual model for flow through thick unsaturated zones in fractured, low-permeability rocks that is applicable to Yucca Mountain. Key elements of this conceptual model are as follows:

- Most of the deep percolation in thick, unsaturated zones of fractured rock proceeds by way of episodic, transient, and localized flow through fractures.

- Liquid-water flow can remain localized, even in the presence of dispersive effects that would tend to cause lateral spreading.

- Several mechanisms combine to severely reduce the effects of matrix imbibition.

Both the model of Pruess (1999 [DIRS 104250], pp. 1040 to 1042) and the current conceptual model argue that fracture-matrix interaction is limited in the unsaturated zone and that only a portion of fractures are active in conducting liquid water (CRWMS M&O 2000 [DIRS 141187], Section 6.1.9). However, the models differ in their description of the spatial distribution and time-dependent character of fracture flow. The Pruess model hypothesizes that fracture flow-paths in unsaturated, fractured rocks are sparse and transient, whereas the current conceptual model argues that liquid-water flow below the PTn hydrogeologic unit is approximately in steady state and that fracture flow-paths are many and dispersed. The assumption of steady state is valid for a time span of thousands of years and provides an average of flow consistent with results showing that the PTn dampens flow to the repository horizon. Over longer periods, transient conditions associated with climate change will have a greater effect on flow. However, for present-day conditions, transient flow at the repository horizon is not supported by the data that currently exist.

7.9.2 Conceptual Model of Transport in the Unsaturated Zone

This section documents the conceptual model of transport used for modeling transport within the Yucca Mountain unsaturated zone (Section 7.10). The conceptual model of transport is presented by addressing important transport processes and issues. Transport is closely tied to flow processes, because flow is a major driving force for transport.

7.9.2.1 Advective Transport

Advective transport (advection) refers to the movement of dissolved or colloidal materials as a result of the bulk flow of fluid (CRWMS M&O 2000 [DIRS 141187], Section 6.2.1). Transport is strongly related to liquid-water flow through advection, and advective transport pathways are consistent with flow pathways discussed in Section 7.9.1. In the welded units, advection through fractures is expected to dominate transport behavior, mainly because liquid water largely flows through fracture networks in these units. Advection is also an important mechanism for transport between fractures and matrix, especially at interfaces between nonwelded and welded units. At these interfaces, transitions occur between dominant fracture-flow and dominant matrix-flow. Liquid-water flow paths below the repository horizon will be critical to the radionuclide transport resulting from advection, particularly in perched water bodies, where lateral transport of radionuclides is likely to occur. Dominant fault-and-fracture flow in the zeolitic part of the CHn hydrogeologic unit (Figure 7-57) provides relatively short travel times for transport to the water table, whereas dominant matrix flow in the vitric part of the CHn provides much longer travel times.

7.9.2.2 Matrix Diffusion

Matrix diffusion refers to solute transport from fracture networks to surrounding matrix blocks resulting from molecular diffusion (CRWMS M&O 2000 [DIRS 141187], Section 6.2.2). Mass transfer between fractures and tuff matrix may play an important role in transport within Yucca Mountain. Because flow velocity in the matrix is much slower than in fractures, transfer of radionuclides from fractures to the matrix can significantly retard the overall transport of radionuclides to the water table. The transfer can result from advection, dispersion, and diffusion processes. Where fracture flow is dominant, advection from fractures to the matrix may not be important because only a relatively small amount of water flows into the matrix, with the rest flowing through fractures. Thus, matrix diffusion is a major mechanism for mass transfer between fractures and the matrix. Furthermore, the diffusion process in the matrix is more important than dispersion because of the slow pore-velocity. Therefore, matrix diffusion probably is the most important physical process in the matrix that contributes to retardation of radionuclide transport when fracture flow is dominant.

The significance of matrix diffusion depends primarily on such factors as effective contact area between fracture and matrix, effective molecular diffusion coefficient, and characteristics of fracture networks (CRWMS M&O 2000 [DIRS 141187], Section 6.2.2). Fracture-matrix interaction is expected to be limited in the welded units, mainly because of fingering flow in fractures, giving rise to a much smaller fracture-matrix interfacial area being available for matrix diffusion than the geometric contact area between fractures and matrix (Section 7.9.1.3). This can reduce the retardation effect of matrix diffusion considerably. The effective molecular-diffusion coefficient is defined as a product of the free water-diffusion coefficient, which is a strong function of solute or radionuclide type, and a factor considering the effects of unsaturated matrix on diffusion. For a given solute or radionuclide type, the effective molecular-diffusion coefficient is dependent mainly on the volumetric water content, which is a function of saturation. For rocks in the Yucca Mountain unsaturated zone, saturation is relatively uniform spatially (Flint 1998 [DIRS 100033], pp. 24 to 30, Figures 5 to 9). Hence, it is reasonable to assume that the effective matrix-diffusion coefficient depends primarily on the

solute or radionuclide type for the unsaturated zone. In general, matrix diffusion can be an important retardation mechanism for a radionuclide or solute with a relatively large molecular-diffusion coefficient but becomes insignificant when the diffusion coefficient is rather small. Matrix diffusion is also affected by characteristics of fracture networks. Because only some of the fractures actively conduct liquid water in the unsaturated zone, the inactive and relatively dry fractures could serve as barriers for flow and transport, including matrix diffusion, between matrix blocks separated by these fractures.

7.9.2.3   Fracture and Matrix Sorption

Sorption is an important process in reactive chemical and radionuclide transport (CRWMS M&O 2000 [DIRS 141187], Section 6.2.3). In the context of total system performance assessment and unsaturated zone transport assessment for Yucca Mountain, sorption is used to describe a combination of chemical interactions between dissolved solutes and the solid phases (immobile rock matrix or colloids), including adsorption, ion exchange, surface complexation, and chemical precipitation. The strength of the sorptive behavior is a function of the chemical element, the rock type involved in the interaction, and the geochemical conditions of the water contacting the rock. Sorption can act to retard the movement of radionuclides in the groundwater. Most radionuclides and other chemical elements that are strongly sorbed to the rock matrix are relatively immobile. However, sorptive interactions may enhance radionuclide transport if the aqueous species sorbs to colloids. (See Section 7.9.2.4.)

The importance of sorption in the different rock types is not only a function of the sorptive strength, but also the degree of exposure that the radionuclides have with the rock matrix during transport through the unsaturated zone (CRWMS M&O 2000 [DIRS 141187], Section 6.2.3). Zeolitic tuff generally has a larger sorptive capacity than vitric tuff, but the matrix flow component in zeolitic tuff is relatively small because of low matrix permeability (DOE 1998 [DIRS 100550], p. 3-118). Thus, sorption in the zeolitic tuff may not be able to effectively retard transport of radionuclides with small molecular diffusion coefficients.

The surfaces of fractures, often lined with minerals that differ from the bulk of the rock matrix, may be capable of sorbing many of the radionuclides (CRWMS M&O 2000 [DIRS 141187], Section 6.2.3). However, characterization of the distributions of the fracture-lining minerals and sorptive interactions with these minerals has been limited. Also, the fracture minerals have a relatively small volume and surface area. For these reasons, a conservative assumption in modeling radionuclide transport is that no sorptive interaction with fracture surfaces occurs and that sorptive interactions are possible for radionuclides only in matrix blocks.

In the transport assessment for Yucca Mountain, sorption is characterized by a sorption or distribution coefficient (K_d). In general, for a given radionuclide and rock type, this coefficient is not a constant, but depends on the temporally and spatially varied chemical composition of both the aqueous and solid phases. As a conservative approach to modeling radionuclide transport through the Yucca Mountain unsaturated zone, a minimum bound for K_d can be used. The minimum K_d represents the smallest reasonable ratio of radionuclides attached to the solid phase versus the aqueous phase.

7.9.2.4 Colloid-Facilitated Transport

Radionuclide transport in the unsaturated zone also involves a colloid-facilitated transport process (CRWMS M&O 2000 [DIRS 141187], Section 6.2.4) (see also Section 5.3). Colloids are particles small enough to become suspended (and thus transportable) in a liquid. They can interact with radionuclides through sorption mechanisms. Unlike sorption of radionuclides to the rock matrix, however, radionuclides sorbed onto colloids are potentially mobile. Therefore, colloids can facilitate radionuclide transport through the unsaturated zone at a faster rate than the aqueous phase alone. Another form of colloidal movement occurs when the radionuclide is an integral component of the colloid structure. In this case, the radionuclide is irreversibly bound to the colloid (DOE 1998 [DIRS 100550], Section 3.5.2.4, Figure 3-53), or the entire component of the colloidal particle (true colloid, PuO_2) is radioactive (BSC 2003 [DIRS 163228], Section 6.18.1).

Colloid-facilitated transport is controlled by several processes, including advection of colloids, matrix diffusion and dispersion of colloids, sorption of radionuclides on colloids, radioactive decay of radionuclides, and filtration of colloid particles (CRWMS M&O 2000 [DIRS 141187], Section 6.2.4). Advective radionuclide transport paths are consistent with liquid-water flow paths below the repository. The advective transport through fractures is enhanced by reduced matrix diffusion and matrix sorption. Colloid particles themselves are not expected to experience any significant matrix diffusion because of the very low diffusion coefficients associated with colloids. Colloids may not be able to move through some of the rock matrix, particularly the welded and zeolitic-rock types, because of their large size. However, movement through the more permeable nonwelded vitric rock in the CHn hydrogeologic unit may be possible. The restriction of matrix particle size on movement of colloid particles is the filtration process. Obviously, the colloid-facilitated transport becomes more important for strongly sorbing radionuclides.

7.9.2.5 Other Transport Processes and Issues

Radioactive decay is a transformation process that affects the concentration of radionuclides during transport through the unsaturated zone (CRWMS M&O 2000 [DIRS 141187], Section 6.2.5). For simple decay, radionuclide concentration decreases exponentially with time, creating stable decay products. Chain decay adds additional complexity because of the ingrowth of new radionuclides created from the decay of a parent radionuclide. One aspect of potential significance with respect to chain decay is that daughter products may have significantly different sorption behavior than the parent radionuclide, therefore exhibiting different transport behavior.

Dispersion is a transport mechanism caused by localized variations in flow velocity (CRWMS M&O 2000 [DIRS 141187], Section 6.2.5). However, it is not expected to play an important role in transport in the Yucca Mountain unsaturated zone. For example, with respect to radionuclide transport from the repository to the water table, the repository emplacement area is very broad relative to the distance to the water table; this ratio tends to suppress dispersion effects. A more important reason for dispersion to become secondary is the explicitly modeled variations in transport velocity caused by the fracture-matrix system. In the rock matrix,

dispersion is also considered to be minor compared with diffusion because of low pore velocity in the matrix, which affects dispersion.

The presence of perched water below the repository horizon may serve as a mechanism to dilute liquid-phase solute and radionuclide concentrations in the unsaturated zone. In the TSw hydrogeologic unit above the perched water, solutes and radionuclides will primarily be carried by many flow channels (active fractures). Once they arrive at perched-water bodies, the fracture water will mix with the perched water, resulting in a decrease in chemical concentrations. The degree of dilution depends on the residence time of chemicals in perched water. Longer residence time corresponds to a larger degree of mixing within the perched-water body, and, therefore, a larger degree of dilution (CRWMS M&O 2000 [DIRS 141187], Section 6.2.5). Sonnenthal and Bodvarsson (1999 [DIRS 117127], p. 118) observed that chloride concentrations in water samples collected during pump tests of the perched-water bodies are not particularly variable, because the water is probably well mixed. Modeling of these data showed that perched-water compositions are best matched by a mixture of Pleistocene-age water and variable amounts of modern water (Sonnenthal and Bodvarsson 1999 [DIRS 117127], p. 151).

7.9.2.6 Summary of the Conceptual Model of Transport

The conceptual model of transport in the Yucca Mountain unsaturated zone is based on an understanding and integration of the transport processes and issues discussed in Sections 7.9.2.1 to 7.9.2.5 (CRWMS M&O 2000 [DIRS 141187], Section 6.2.6). Because flow is the major driving force for transport, the conceptual model of transport is closely tied to the current conceptual model of flow (Section 7.9.1). Advective transport pathways are consistent with flow pathways. Matrix diffusion is a major mechanism for mass transfer between fractures and the matrix, and contributes to retardation of radionuclide transport when fracture-flow is dominant. Sorption can act to retard the movement of radionuclides in the unsaturated zone. However, sorptive interactions may enhance radionuclide transport if the aqueous species sorbs to colloids. Dispersion is not expected to be a major transport mechanism in the unsaturated zone at Yucca Mountain.

7.10 SUMMARY OF MODELING FOR THE UNSATURATED ZONE

Data collected to characterize the unsaturated zone of the site provide information at point locations. Ascertaining the three-dimensional interrelationship of the various collected data sets requires the use of numerical models. Due to computational limitations, the complex flow and transport processes occurring within the unsaturated zone at Yucca Mountain requires simplification of the real-world system. This is done through numerical solution of a set of mathematical equations (representing the behavior of the physical process under investigation) for a modeled volume that has been discretized into a finite number of nodes, or elements, for which certain rock properties are known (as described in the preceding sections) or estimated.

Site-scale unsaturated zone flow, transport, and coupled-process models have been developed to evaluate flow to the drifts through rock units overlying the repository, transport of radionuclides through the unsaturated zone beneath the repository to the water table, and the effects of waste heat on hydrologic, chemical, and mechanical processes. Supporting these models are various other models and analyses that develop components or characterize processes that feed into the

flow and transport model. The site-scale model in turn supports models of unsaturated zone flow and coupled processes at the drift-scale. The analyses and modeling reports that describe these models for the unsaturated zone are:

- **Future Climate Analysis**–develops a prediction of climates in the next 10,000 years (USGS 2001 [DIRS 158378]).

- **Future Climate Analysis–10,000 Years to 1,000,000 Years After Present**–extends the future climate analysis out to 1,000,000 years (Sharpe 2003 [DIRS 161591]).

- **Development of Numerical Grids for Unsaturated Zone Flow and Transport Modeling**–develops the hydrogeologic framework for the unsaturated zone flow and transport models and supporting sub-models (BSC 2003 [DIRS 160109]).

- **Simulation of Net Infiltration for Modern and Future Climates**–provides simulated minimum, mean, and maximum infiltration rates for the unsaturated zone flow model area for three different climate scenarios (USGS 2001 [DIRS 160355]).

- **Analysis of Infiltration Uncertainty**–provides an analysis of the probability distribution for infiltration resulting from uncertainty in the underlying hydrologic properties (BSC 2003 [DIRS 165991]).

- **Analysis of Hydrologic Properties Data**–provides the analysis of field data that establishes values for uncalibrated parameters and initial estimates for parameters calibrated in the calibrated properties model (BSC 2003 [DIRS 161773]).

- **Calibrated Properties Model**–incorporates data from analyses and models into one model to develop a set of calibrated hydrologic properties for each hydrogeologic unit in the unsaturated zone flow model (BSC 2003 [DIRS 160240]).

- **Unsaturated Zone Flow Models and Submodels**–develops the unsaturated zone flow fields to be used in unsaturated zone transport studies, and sets the boundary conditions for drift-scale models (BSC 2003 [DIRS 163045]).

- **Radionuclide Transport Models under Ambient Conditions**–produces breakthrough curves for radionuclides reaching the water table (BSC 2003 [DIRS 163228]).

- **Particle Tracking Model and Abstraction of Transport Processes**–provides a transport methodology for computing radionuclide transport between the repository and the water table suitable for use in the total system performance assessment model (BSC 2003 [DIRS 162730]).

- **Seepage Calibration Model and Seepage Testing Data**–provides estimates of seepage-related parameters, to be used in the seepage model for performance assessment (BSC 2003 [DIRS 162267]).

- **Seepage Model for Performance Assessment Including Drift Collapse**–calculates seepage fluxes at an emplacement drift, under the three climate scenarios, and taking possible drift collapse into consideration (BSC 2003 [DIRS 163226]).

- **Abstraction of Drift Seepage**–provides a treatment of drift seepage, combining ambient and thermal seepage under consideration of the effects of coupled processes; and includes an assessment of uncertainties suitable for use in the total system performance assessment model (BSC 2003 [DIRS 165564]).

- **Drift-Scale Radionuclide Transport**–allocates radionuclide transport between fracture and matrix domains upon exiting waste emplacement drifts (BSC 2003 [DIRS 164889]).

- **Mountain-Scale Coupled Processes**–evaluates the effects of waste heat on hydrologic, chemical, and mechanical processes at the mountain-scale, including feedback between chemical and mechanical processes and hydrologic properties (BSC 2003 [DIRS 166498]).

- **Drift-Scale Coupled Processes (Drift Scale Test and Thermal-Hydrologic Seepage) Models**–predicts the effects of waste heat on hydrologic behavior at the drift scale, particularly drift seepage processes (BSC 2003 [DIRS 166512]).

- **Drift-Scale Coupled Processes (Drift Scale Test and Thermal-Hydrologic-Chemical Seepage) Models**–predicts the chemical evolution of pore waters including the effects of waste heat and the thermal-hydrologic feedback resulting from mineral precipitation/dissolution processes (BSC 2003 [DIRS 162050]).

- **Drift Scale Thermal-Hydrologic-Mechanical Model**–evaluates the effects of waste heat on rock-mechanical processes including the effects of waste heat and the feedback resulting from changes in fracture hydrologic properties (BSC 2003 [DIRS 164890]).

- **Abstraction of Drift-Scale Coupled Processes**–provides an assessment of the Drift-Scale thermal-hydrologic-chemical seepage model with respect to seepage water composition, including an assessment of uncertainties, suitable for use in the total system performance assessment model (BSC 2003 [DIRS 167972]).

The purposes for developing a model of the unsaturated zone of Yucca Mountain and the drift environment are to:

- Estimate groundwater flow magnitude and chemistry of water that may reach the emplacement drifts, and subsequently the saturated zone beneath the repository.

- Characterize the complex three-dimensional behavior of flow through heterogeneous porous and fractured media.

- Identify the potential role of faults as pathways for unsaturated groundwater flow.

- Provide a model of the flow system for subsequent flow, heat, and radionuclide-transport modeling.

- Assess the conceptual model and parameter uncertainties with respect to their influence on total system performance of the Yucca Mountain repository.

The previous version of this document (CRWMS M&O 2000 [DIRS 151945]), and the current analyses and modeling reports listed above, discuss in detail the development of the site scale unsaturated zone flow and transport model, including the model assumptions, data sources, sources of uncertainty, and numerical methods and computer software used. In this document, the focus is on the key results of the modeling, referring the reader to other references for details.

7.10.1 Site-Scale Modeling

The site-scale flow-and-transport behavior in the unsaturated zone at Yucca Mountain are characterized by two important features (CRWMS M&O 2000 [DIRS 151940], Section 3.4.1.3). The first feature is that the isolated fast-flow paths only carry small amounts of water and do not significantly contribute to the overall flow-and-transport patterns in the unsaturated zone, and fracture flow-paths are many and dispersed. This makes the continuum model a reasonable choice for simulations of flow-and-transport in the unsaturated zone at Yucca Mountain. The second feature is the coexistence of matrix-dominant flow-and-transport in nonwelded units and fracture-dominant flow-and-transport in welded units. This feature can be easily handled by continuum models, but not by other models, such as a fracture-network model. The scale of the problem is an important factor for assessing appropriateness of numerical schemes for flow-and-transport in the unsaturated zone. Because continuum models are relatively simple and straightforward to implement, they are preferred for most applications that are encountered in practice (National Research Council 1996 [DIRS 139151], p. 331). Estimates of the number of potentially water-conducting fractures at Yucca Mountain are on the order of 10^9 (Doughty 1999 [DIRS 135997], p. 77). Considering data availability and computational feasibility, it is practically impossible to construct and calibrate a discrete fracture-network, site-scale model with so many fractures.

Based on the above considerations, continuum models are considered appropriate for use in the unsaturated flow-and-transport models at Yucca Mountain. To account for flow in fractures, the fracture network is represented by a separate continuum that is coupled to the rock matrix continuum to represent flow interaction between the fractures and the rock matrix. As a compromise between accuracy and feasibility, dual-permeability models have become the main modeling approach currently used to simulate unsaturated water flow, heat transfer, and chemical transport at Yucca Mountain (CRWMS M&O 2000 [DIRS 151940], Section 3.4.1.3). An active fracture model, documented in CRWMS M&O (2000 [DIRS 141187], Section 6.4.5), accounts for limited fracture-matrix interaction and flow through only a portion of connected fractures.

7.10.1.1 Calibrated Properties Model

The calibrated properties model (BSC 2003 [DIRS 160240]) incorporates many different data from analyses and models into one model to develop calibrated properties for the unsaturated zone flow and transport model that are consistent with all these data. The properties that are

calibrated are fracture and matrix permeability (k_f and k_m), the fracture and matrix van Genuchten α and m parameters (α_f, α_m, m_f, and m_m), and the active fracture parameter (γ) (see CRWMS M&O 2000 [DIRS 141187], Section 6.4.5) for discussion of the active fracture model for which this is the parameter). Except for γ, these are also the properties for which prior information is provided. All other properties are used unchanged from the initial hydrologic properties estimates.

Development of saturation, water potential, and pneumatic data; prior information; and one-dimensional and two-dimensional inversions are documented by BSC (2003 [DIRS 160240], Section 6). The misfit between the ambient conditions calculated by the models and the ambient conditions data as well as the misfit between the prior information and the parameters being calibrated all contribute to the objective function, which is the quantitative measure that is minimized. Saturation and water potential data are evaluated after steady-state conditions are reached. Pneumatic data are evaluated after a 30-day, barometric pumping initialization period (CRWMS M&O 2000 [DIRS 151940], Section 3.6.4).

7.10.1.2 Unsaturated Zone Flow Model

The development and features of the three-dimensional-model grids with the geological model are discussed and documented in *Development of Numerical Grids for UZ Flow and Transport Modeling* (BSC 2003 [DIRS 160109]). In this geological model and the associated numerical grids, the geologic formations within the unsaturated zone have been reorganized into layered hydrogeologic units, based primarily on the degree of welding of the Yucca Mountain tuffs (BSC 2003 [DIRS 160109], Section 6.3).

The three-dimensional unsaturated zone flow model domain is represented using a three-dimensional numerical grid. The model domain is selected to focus on studies at and near the repository area and to investigate effects of different infiltration scenarios and major faults on fluid-and-heat flow and radionuclide migration around and below the repository.

7.10.1.2.1 Flow Patterns in the Unsaturated Zone Flow Model

Comparisons of the calculated repository percolation with those of the surface infiltration maps indicate that percolation fluxes at the repository are very different from surface infiltration patterns. Note that surface infiltration rates and distributions are independent of faults. The major differences in percolation flux at the repository level are (1) flow mainly through faults in the very northern part of the model domain (north of NSP coordinate 237,000 m); (2) flow diverted into or near faults located in the model domain; and (3) about a 500 m (1,640 ft) lateral flow east of the high infiltration zones from south to north along the crest. Lateral flow may also occur eastward from the Solitario Canyon fault, reaching the repository blocks, because the fault is very close to the repository. Overall, percolation results display very different patterns from the surface infiltrations, because of the substantial amount of large-scale lateral flow within the PTn hydrogeologic unit. This indicates that within the PTn, lateral flow has a significant impact on percolation flux distribution in the repository layer. In comparing the simulation results for three different climate scenarios, and the minimum, mean, and maximum infiltration values for each, all flow fields indicate that the lower the infiltration rate, the larger the lateral flow scale. This is because the lower infiltration results in drier conditions with

stronger capillarity (Wu et al. 2002 [DIRS 161058], p. 35-9). On the other hand, the simulation results with nine alternative flow fields show small lateral flow occurrence in the PTn in the area above the repository. These results show that the flow patterns through the PTn have a large impact on percolation flux distribution in the repository horizon (BSC 2003 [DIRS 163045], Section 6.6.3). The model results were used to derive the percentage of fracture-matrix flow components and fault flow at the repository horizon and the water table within the model domain.

These statistics indicate that fracture flow is dominant both at the repository horizon and at the water table. At the repository level, fracture flow consists of more than 90 to 95 percent of the total percolation fluxes. Fracture flow at the water table takes 70 to 80 percent of the total flow. The fault flow percentage increases from about 30 to 40 percent of the fracture flow at the repository to about 60 percent at the water table, except for the case of the present-day, lower-bound infiltration, where the percentages are higher (BSC 2003 [DIRS 163045], Section 6.6.3, Table 6.6-3). Note that according to the active fracture concept (Liu et al. 1998 [DIRS 105729], p. 2635), not all fractures transmit percolation fluxes. Actual active fracture spacings (i.e., fracture flow intervals) in the flow fields are much larger than measured fracture spacings in different units.

The CHn hydrogeologic unit occurs between the repository horizon and the saturated zone. The predominantly nonwelded nature of the CHn makes these initially high-porosity, vitric tuffs susceptible to hydrothermal alteration. Hydrothermal alteration produces low-permeability clays and zeolites that create complex, heterogeneous flow paths within the CHn. The observed widespread alteration within the CHn (Section 3.3.4.6) has important implications for perched water, for groundwater flow paths, and for radionuclide transport because of the reduced permeability and the sorption potential associated with zeolitic and vitric rocks. Modeling results indicate that significant lateral flow or diversion occurs at perched or zeolitic layers when water flows through the layers of the CHn hydrogeologic unit (BSC 2003 [DIRS 163045], Section 8.6).

7.10.1.2.2   Estimation of Percolation Flux in the Unsaturated Zone

Geochemical and thermal data may be used to bound infiltration rates and percolation fluxes at the repository horizon. The geochemical data used are pore-water chloride concentrations and calcite abundances.

The sensitivity of natural conservative tracers such as chloride to infiltration rate is well known, such as implemented by the chloride mass-balance method (Phillips 1994 [DIRS 144787]). The model used for the simulation of chloride considers that its source is the precipitation falling on the surface. A base-case simulation was conducted using the present-day (modern), mean infiltration rate to compare the base-case model with observed chloride data (BSC 2003 [DIRS 163045], Section 6.5). Chloride concentrations from the steady-state transport simulation were compared with measured pore-water chloride concentration data. The measured chloride concentrations show a smaller range than would be predicted for the modern infiltration rates under steady-state conditions (CRWMS M&O 2000 [DIRS 151940], Section 3.8.2).

The chloride profiles from the unsaturated zone flow model can be compared with the present-day mean infiltration rates, and the lower and upper bounds on the infiltration rates (from USGS 2001 [DIRS 160355], Section 7). The results demonstrate that the mean infiltration casehas the closest match between the simulated concentrations and the field-measured chloride data. The upperbound case shows a moderate match; the lower-bound case shows the poorest match (BSC 2003 [DIRS 163045], Section 6.5.2). Because many measured chloride concentrations are fit closely by the model results, it appears that the mean infiltration rate is approximately correct. Use of the mean glacial infiltration scenario generally yields lower chloride concentrations than the present case, upper bound. A special scenario run with the glacial case was conducted. The model was run for 100,000 years to steady state with glacial recharge, and then was switched to present-day recharge for 11,600 years. This run yields a closer match to the measured data than the glacial recharge case (BSC 2003 [DIRS 163045], Figure 6.5-2).

In the above base case (A), the property set for the Paintbrush nonwelded vitric tuff would favor lateral diversion of flow. An alternative model (B) was run, using a different property set for the PTn hydrogeologic unit, one that does not favor large-scale lateral diversion (BSC 2003 [DIRS 163045], Section 6.5.2). Comparison of base-case and alternative flow fields indicate, consistently, that the base-case flow field simulations provide an overall better match with the observed chloride. The main difference between the base-case and alternative flow fields is whether there is large- or small-scale lateral flow within the PTn, with the base-case flow fields predicting relatively large lateral diversion in general. These model calibration results with chloride data further support the conceptual model that large lateral diversion may exist in the PTn. Therefore, pore water chloride may provide key evidence for understanding flow through the PTn hydrogeologic unit, which has a direct impact on chloride transport and distributions.

Hydrogenic calcite deposits in fractures and cavities at Yucca Mountain have been studied to estimate past percolation fluxes, flow pathways, and hydrologic processes (Section 7.7). A series of simulations examining the sensitivity of calcite deposition to: (1) infiltration, (2) the ambient geothermal gradient, (3) gaseous CO_2 diffusive transport and partitioning in liquid and gas phases, (4) fracture-matrix interaction for water flow and chemical constituents (dual permeability), and (5) water-rock interaction are described in BSC (2003 [DIRS 163045], Section 7.9) and Xu et al. (2003 [DIRS 162124]). The dual permeability model can address not only the abundances of calcite with depth, but also its relative abundance in fractures and in the rock matrix as a function of the hydrologic/geochemical processes in each medium, as well as the interaction of water flowing between fractures and matrix. Modeling of calcite deposition in the Yucca Mountain unsaturated zone was performed for one-dimensional simulations at the USW WT-24 Borehole location where measured calcite abundance data in core were available. Generally, the results obtained using the base-case infiltration rate agree better with the measured mineral abundances than those obtained using the other infiltration rates, especially for the PTn hydrogeologic unit. The simulations indicated that some contribution of calcium from the rock is required, especially for the TSw hydrogeologic unit. The simulated calcite abundances in the basal tuff layer of the PTn hydrogeologic unit for the three infiltration simulations are higher than that measured in samples from Borehole USW WT-24. This results from an increase in the temperature gradient resulting in a concomitant decrease in calcite solubility. The relatively larger calcite abundances in the bottom layer of the PTn have been observed at other locations such as in another deep Borehole, USW G-2 (Carey et al. 1998 [DIRS 109051]). The lower

measured calcite abundances may also result for lateral flow not captured in the one-dimensional simulations. Results for the welded TSw hydrogeologic unit (of the most interest to the YMP) generally fall in the wide range of measured calcite data, with a direct correlation between calcite deposition values and infiltration rate.

Because water consumes heat as it moves from cooler, shallow depths to warmer, deeper environments, borehole temperature profiles are potentially a sensitive indicator of the percolation flux. Numerical analysis of borehole temperature data also was conducted (Bodvarsson et al. 1997 [DIRS 100103], pp. 11-11 to 11-18), which incorporates geological layering and the known variability in thermal properties. In the numerical analysis, one-dimensional columns were extracted from the unsaturated zone model, and the percolation rate was varied until a reasonable match was achieved between computed and observed temperature profiles for each borehole. Results indicate that at the crest of Yucca Mountain, percolation flux rates are about 5 mm/yr, with somewhat higher rates (about 10 to 15 mm/yr) at Boreholes USW G-2, USW SD-12, and UE-25 WT#18 (Bodvarsson et al. 1997 [DIRS 100103], Table 11.4 and Figure 11.14).

The analysis of the distribution of percolation fluxes within the repository indicates that the highest flux frequencies have a normalized flux of about 0.5 or less of the averaged infiltration rate for that climate scenario, and occur over about 50 percent of the repository area. The area with normalized percolation fluxes greater than 5 times the averaged infiltration rate comprises less than 1 percent of the total repository area. In general, the modeling results for all of the scenarios show that the percolation flux value with highest areal frequencies is always lower than the average values of the corresponding infiltration rates (BSC 2003 [DIRS 163045], Section 6.6.3).

7.10.1.3 Unsaturated Zone Transport Model

Modeling of radionuclide transport using large-scale three-dimensional grids was documented in BSC (2003 [DIRS 163228], Sections 6.8 to 6.18). Radionuclides of ^{99}Tc, ^{237}Np, and ^{239}Pu were investigated, as well as the important members in the decay chains of ^{241}Am and ^{239}Pu. Transport results for ^{241}Am, ^{233}U, ^{235}U, ^{90}Sr, ^{135}Cs, ^{236}Ra, ^{229}Th, and ^{231}Pa are also included. The grids and flow fields used for present-day infiltration and perched water model #1 were identical to those discussed by BSC (2003 [DIRS 163045], Section 6.2). The release rate of radionuclides at the repository was considered constant over time. Transport parameters such as sorption, diffusion, and dispersion are discussed in BSC (2003 [DIRS 163228], Section 6.1). The treatment of fracture-matrix interactions is a critical issue in the simulation of flow and transport under the two-phase flow conditions of the fractured unsaturated zone rocks (BSC 2003 [DIRS 163228], Section 6.1.5.3). The unsaturated zone transport model closely follows the dual-permeability approach presented in *UZ Flow Models and Submodels* (BSC 2003 [DIRS 163045]).

Model results indicate that the highly conductive Drill Hole Wash fault and Pagany Wash fault are the main pathways of transport (and related to the percolation patterns) for the northern part of the repository. Radionuclides released directly into these faults or reaching them from adjacent areas move rapidly downward to reach the water table at an earlier time. Additionally, the Sundance fault, the Solitario Canyon fault, and the Ghost Dance fault are

transport-facilitating geological features, but their effect becomes significant at later times (BSC 2003 [DIRS 163228], Section 8.2.1). Fractures are the main pathways of radionuclide transport. Sorption and diffusion from the fractures into the matrix are the main retardation processes in radionuclide transport. When radionuclides sorb onto the matrix into which they diffuse, their migration is further retarded. Sorption also leads to retardation in the fractures by resulting in larger concentration gradients (thus enhanced diffusion) between the liquid phases in the fractures and in the matrix (BSC 2003 [DIRS 163228], Section 8.2.1). Colloids may also play a role in overall radionuclide transport. Because fractures are the main transport conduit at Yucca Mountain, the inability of larger colloids to diffuse into the matrix, because of smaller diffusion coefficient values and size exclusion, results in fast transport to the groundwater. Smaller colloidal particles can diffuse more easily into the matrix, and their transport is thus more retarded. Size exclusion at the interfaces of different geologic units leads to colloid concentrations directly above the interface that can be higher than that in the water released from the repository (BSC 2003 [DIRS 163228], Section 8.2.4).

7.10.1.4   Mountain-Scale Coupled Processes Model

7.10.1.4.1   Mountain-Scale Thermal-Hydrologic Model

Unsaturated zone flow and transport will be affected by the heat released from the decay of radioactive waste in emplacement drifts of the repository at Yucca Mountain. The mountain-scale thermal-hydrologic model uses input parameters based on the calibrated properties (BSC 2003 [DIRS 160240]), a spatially varying mean infiltration rate, with varying climates during the thermal loading period (BSC 2003 [DIRS 166498], Section 6.1.4). The simulations were performed using the average initial thermal load of 1.45 kW/m of waste emplacement drift. To account for ventilation, only about 13.7 percent of this heat is used during the first 50 years (BSC 2003 [DIRS 166498], Section 6.1.5). The thermal-hydrologic model boundary and initial conditions and three-dimensional model grid are specified in the same way as for the ambient thermal-hydrologic model (BSC 2003 [DIRS 166498], Sections 6.1.1 and 6.1.2) discussed in *UZ Flow Models and Submodels* (BSC 2003 [DIRS 163045]). A two-dimensional, north-south cross-sectional model is also used for investigating mountain-scale thermal-hydrologic processes.

Higher temperature zones or heated regions around the repository drifts enlarge with time. The thermal-hydrologic models predict that heated zones reach their maximum about 2,000 years after waste emplacement. During the heating period, the temperatures at the middle pillar regions between two drifts are elevated significantly to above 80°C, but never reach the boiling point. At 2,000 years, temperatures at the bottom of the PTn hydrogeologic unit reach their highest values of 40°C to 50°C. At the same time, peak temperatures at the top of CHn hydrogeologic unit are elevated to 70°C. After 5,000 years, the repository and surrounding rock are significantly cooled down, and the thermal-hydrologic effect diminishes (BSC 2003 [DIRS 166498], Section 8.1).

The three-dimensional thermal-hydrologic model predicts that repository heating will have in general only a limited impact on far-field flow fields with ventilation. In this case, thermally enhanced flux zones are no more than 30 m in the regions directly above or below the repository blocks. The thermal-hydrologic model predicts much stronger effects along highly permeable

columns of faults that intersect repository blocks, because of the stronger vapor flow and condensation. The thermal-hydrologic model results also predict that repository heating will have only a small impact on flow through the pillar regions between two drifts. This is because boiling does not occur in these pillar areas, and moisture conditions there are not much changed from ambient status. Simulated vertical fluxes in the pillar regions show little variation with thermal activity at drifts. In fact, flow through the pillar regions is more affected by surface infiltration or climate changes than by repository heating (BSC 2003 [DIRS 166498], Section 8.1).

7.10.1.4.2 Mountain-Scale Thermal-Hydrologic-Chemical Model

Coupled thermal-hydrologic-chemical processes that are caused by variations in geology (structure and lithology), infiltration rate, and temperature at a mountain or repository scale have also been investigated using a coupled thermal-hydrologic-chemical model (BSC 2003 [DIRS 166498], Section 6.4). These are processes that affect the percolation flux to the repository horizon (relevant to seepage), and flow below the repository (relevant to radionuclide transport in the unsaturated zone). The pertinent mineral-water-gas reactions in the host rock, under thermal loading conditions, as they influence the chemistry of water and gas in the mountain and associated changes in mineralogy are captured in the model. The data incorporated in the model include hydrologic properties from the calibrated property sets, geological layering from the unsaturated zone three-dimensional flow and transport model, geochemical data (fracture and matrix mineralogy, aqueous geochemistry, and gas chemistry) derived from various sources, thermodynamic data (minerals, gases, and aqueous species), data for mineral-water reaction kinetics, and transport data. Simulations of thermal-hydrologic-chemical processes included coupling among heat, water, and vapor flow, aqueous and gaseous species transport, kinetic and equilibrium mineral-water reactions, and feedback of mineral precipitation/dissolution on porosity, permeability, and capillary pressure for a dual permeability (fracture-matrix) system. Calculations were carried out on an approximately one-kilometer-long, north-south, vertical cross section (BSC 2003 [DIRS 166498], Figure 6.4-2).

The results of the simulations indicate that mineral precipitation/dissolution will not significantly affect the hydrologic properties and the percolation flux compared to the effects caused by thermal-hydrologic processes alone. Glass-rich layers in the CHn hydrogeologic unit show alteration to zeolites, with clinoptilolite breaking down to form stellerite at elevated temperatures. Changes to water chemistry, mineralogy, and hydrologic properties in the ambient temperature regions are minimal over the 7,000 years of the simulation. The overall range in the aqueous species concentrations at a particular time above the drifts is about one order of magnitude. The CO_2 concentrations in the gas phase differ by about one to two orders of magnitude, with the range decreasing over time after the peak thermal period. The range in pH of about 7 to 9 is strongly linked to changes in gas-phase CO_2 concentrations, relative to the ambient system away from the repository. Differences are smaller in the high-temperature repository center (and the pH is higher) compared to the edges (which have somewhat elevated values and pH values down to approximately 7) (BSC 2003 [DIRS 166498], Section 8.2).

7.10.1.4.3 Mountain-Scale Thermal-Hydrologic-Mechanical Model

The heat generated by the decay of radioactive waste results in elevated rock temperatures for thousands of years after the waste emplacement. These temperatures cause thermal expansion of the rock, with the potential of opening or closing of fractures and thus changing fracture permeability close to the repository. Change in permeability may impact the percolation flux around the repository and thereby impact the performance of the repository.

The flow is computed using a dual-permeability continuum model with interacting fractured and matrix continua consistent with the unsaturated zone flow model and other coupled-processes analyses. Because the fractured porous medium is always in static equilibrium, the three-dimensional stress is equivalent in the fracture and matrix continua. Therefore, the mechanical dual-continuum model reduces to a lumped fracture-matrix continuum model (equivalent continuum model). For fluid and heat transport, the dual continuum stills exists, but with fracture and matrix continua that may not be in equilibrium and hence can have different fluid pressure and temperature (BSC 2003 [DIRS 166498], Section 6.5.3). The model domain is a vertical two-dimensional cross section extending from the ground surface down to the groundwater table (BSC 2003 [DIRS 166498], Figure 6.5.6-1). The thermal and hydrologic properties used are consistent with the properties used for the mountain-scale thermal-hydrologic model. Mechanical properties and couplings are discussed in BSC (2003 [DIRS 166498], Sections 6.5.8 and 6.5.9).

The results show that maximum thermal-hydrologic-mechanical induced changes in hydrologic properties occurs around 1,000 years after emplacement, when average temperature in the mountain peaks. Near the repository level, thermal-elastic stresses tend to tighten vertical fractures to smaller apertures, leading to reduced permeability and increased capillarity. At the ground surface, in a zone extending down about 100 m (330 ft), compressive stresses are completely relieved into tension. In this zone, fractures will open elastically, and fracturing or shear-slip along pre-existing fractures are feasible (BSC 2003 [DIRS 166498], Section 8.3).

7.10.2 Drift-Scale Modeling

A continuum approach is used to calculate drift-scale phenomena such as seepage into drifts and thermally-induced coupled processes in the drift vicinity (BSC 2003 [DIRS 162267]; BSC 2003 [DIRS 166512], Sections 6.2.1.1.1 and 6.3.2; BSC 2003 [DIRS 162050], Section 6.2.1.5; BSC 2003 [DIRS 164890], Section 6.2). This approach is based on the observation that the fracture network in the Topopah Spring Tuff middle nonlithophysal unit at Yucca Mountain is well connected (BSC 2003 [DIRS 163226], Section 6.3). In addition, the synthetic study presented in Finsterle (2000 [DIRS 151875]) demonstrates that simulating seepage into underground openings excavated from a highly fractured formation can be performed using a model that is based on the continuum assumption, provided that the model is calibrated against seepage-relevant data, such as data from a liquid-release test. The appropriateness of using the continuum approach to simulate flow through fractured rock was also studied by Jackson et al. (2000 [DIRS 141523]), using synthetic and actual field data. They concluded that heterogeneous continuum representations of fractured media are self-consistent (i.e., appropriately estimated effective continuum parameters are able to represent the underlying fracture network characteristics).

7.10.2.1 Drift Seepage

Estimating seepage into underground openings excavated in an unsaturated fractured formation requires process understanding on a wide range of scales, from the mountain-scale distribution of percolation flux to the intermediate-scale channeling or dispersion of flow in an unsaturated fracture network, to the small-scale capillary-barrier effect, to the micro-scale phenomena within fractures and, specifically, at the drift wall. Moreover, the thermodynamic environment in the drift (temperature, relative humidity, ventilation regime, etc.) must be considered. The development of a seepage process model and its calibration is described in *Seepage Calibration Model and Seepage Testing Data* (BSC 2003 [DIRS 162267]).

The seepage calibration model is a heterogeneous fracture-continuum model that is developed based on air-permeability and liquid-release-test data from several experiments performed in the ESF and the ECRB Cross-Drift at Yucca Mountain. For each experiment conducted, a geostatistical analysis of postexcavation air-permeability data provides the basis for the generation of a heterogeneous property field, which is mapped onto the model grid. Liquid-release tests are simulated to calibrate the model against measured cumulative-seepage data. The key seepage-relevant parameter to be estimated is the van Genuchten capillary-strength parameter $1/\alpha$. Permeability, k, is fixed at the value estimated from the air-injection tests. The inverse modeling approach used follows the concept described by Carrera and Neuman (1986 [DIRS 104368]) and Finsterle (1999 [DIRS 104367], pp. 1 to 130). The misfit between calculated and measured seepage is evaluated using the least-squares objective function (Finsterle 1999 [DIRS 104367], p. 33). The objective function is minimized using the Levenberg-Marquardt algorithm (Finsterle 1999 [DIRS 104367], pp. 44 and 45). More details about the development of the seepage calibration model can be found in BSC (2003 [DIRS 162267]).

Comparisons of the observed seepage rate used for calibration and the corresponding simulation results obtained with the calibrated seepage calibration model are given in BSC (2003 [DIRS 162267], Figure 31) for the middle nonlithophysal unit of the TSw hydrogeologic unit. Seepage testing and model calibration were also conducted for the lower lithophysal unit of the TSw. The impact of lithophysal cavities on seepage is twofold: (1) they lead to some small-scale flow focusing, and (2) they increase the roughness of the drift wall. Both effects tend to promote seepage (BSC 2003 [DIRS 162267], Section 6.3.3.5). For the tests performed in the TSw, the van Genuchten parameter $1/\alpha$ was estimated during these inversions, and porosity, as the considerably less sensitive parameter, was fixed (BSC 2003 [DIRS 162267], Section 6.6.3.1). Results of the calibration gave similar values for $1/\alpha$ in the lower lithophysal unit and middle nonlithophysal unit of the TSW hydrogeologic unit (BSC 2003 [DIRS 162267], Figure 32).

7.10.2.2 Thermal-Hydrologic Seepage Model

Thermal seepage refers to seepage during the time period that the flow around drifts is perturbed from heating. This effect is particularly important for above-boiling temperature conditions where a large, hot, dryout region develops in the vicinity of a drift. This hot dryout zone provides a barrier preventing seepage, since percolating water can be entirely vaporized prior to reaching the drift wall. Therefore, thermal seepage is unlikely as long as boiling conditions exist. On the other hand, condensed water forms a zone of elevated water saturation above the

rock dryout zone. Water from this zone may be mobilized to flow rapidly down towards the drift. This effect may promote seepage (BSC 2003 [DIRS 166512], Section 6.1.2).

The thermal effects on flow and seepage are found to be negligible for cases in which the rock temperature never reaches boiling. For cases in which boiling occurs in the fractured rock close to waste emplacement drifts, simulation results demonstrate that the thermal perturbation of the flow field—causing increased downward flux from the condensation zone towards the drifts—is strongest during the first few hundred years after closure, corresponding to the time period when rock temperature is highest and the vaporization barrier is most effective. Even for high percolation fluxes into the model domain, and strong flow channeling as a result of fracture heterogeneity, water cannot penetrate far into the superheated rock during the time that rock temperature is above boiling, and model results show no seepage. The majority of the vaporized (and subsequently condensed) matrix water is diverted around the dryout zone and drains away from the drift. The magnitude of percolation affects the temperature conditions in the fracture rock. For a given thermal load, high percolation fluxes tend to cool down the rock temperatures, result in a shorter boiling period, and cause more distinct heat-pipe effects compared to small percolation fluxes (BSC 2003 [DIRS 166512], Section 8.1).

7.10.2.3 Thermal-Hydrologic-Chemical Seepage Model

The thermal-hydrologic-chemical seepage model is used to evaluate the effects of thermal-hydrologic-chemical processes in the rock around emplacement drifts, changes in seepage-water chemistry and gas-phase composition, and the potential effects of thermal-hydrologic-chemical processes on unsaturated zone flow and transport. The effects of mineral dissolution and precipitation; the effects of CO_2 exsolution and transport in the region surrounding the drift; the potential for forming zones of calcite, silica, or other minerals; the resulting changes to porosity and permeability; and the potential effects on seepage were investigated. The thermal-hydrologic-chemical seepage model, and validation of the data and processes using the DST, are described in *Drift-Scale Coupled Processes (DST and THC Seepage) Models* (BSC 2003 [DIRS 162050]).

The CO_2 evolution in the gas phase is a controlling factor for the pH and mineral-water reactions. Carbon dioxide concentrations in fractures drop significantly during dryout and increase again during rewetting (BSC 2003 [DIRS 162050], Section 6.2.1.2). The predicted trend of CO_2 concentrations with time in fracture gas (BSC 2003 [DIRS 162050], Figure 6.5-8) generally shows a large decline during dryout, followed by a steep increase during the initial cooling and rewetting stage. The decrease during dryout is the direct result of displacement by steam upon boiling. The increase after dryout remains below 10,000 ppmv, and concentrations are predicted to return to ambient values after 20,000 to 50,000 years (BSC 2003 [DIRS 162050], Section 6.5.5.2). This rise in CO_2 appears to be caused by the arrival of percolating water with a significantly higher dissolved CO_2 content than the locally decarbonated water (BSC 2003 [DIRS 162050], Section 6.8.5.3.2).

The predicted pH values in fracture water (BSC 2003 [DIRS 162050], Figure 6.8-13) are consistent with modeled trends of CO_2 concentrations. Compared to earlier simulations, the lower temperatures during preclosure (due to higher heat removal efficiency) yield lower CO_2 partial pressures and thus higher pH values (generally by less than a half unit). After closure, the

higher predicted CO_2 concentrations yield lower pH values (mostly by less than a half unit) (BSC 2003 [DIRS 162050], Section 6.8.5.3.1).

Conservative species (i.e., those that are unreactive and nonvolatile), such as chloride, become concentrated in waters undergoing vaporization or boiling, but are essentially absent from the vapor condensing in the fractures. Therefore, the concentration of conservative species (e.g., nitrate, chloride) in the draining condensate waters is determined by mixing with fracture pore waters and diffusive mixing with matrix pore waters (BSC 2003 [DIRS 162050], Section 6.2.1.2). At the time of rewetting, the effect of remobilization of concentrated solutions results in a sharp rise in chloride concentrations. After rewetting, chloride concentrations drop relatively quickly towards ambient values (BSC 2003 [DIRS 162050], Section 6.5.5.2).

The predicted magnitude of fracture porosity change caused by water-rock interaction around waste emplacement drifts depends strongly on the initial fracture porosity (with the largest relative change for the smallest porosity), and results in large part from mineral precipitation directly at the boiling front due to evaporative concentration. Simulation results show a thin zone of predominantly amorphous silica deposition several meters above the drift wall that reduces the percolation flux at the drift wall. This zone has a fracture permeability that is one to two orders of magnitude lower than in the surrounding rock fractures, deflecting some of the percolating water around the drift and significantly extending the shadow zone below the drift. Because the silica solubility decreases with declining temperature, the amorphous silica precipitated in fractures does not dissolve appreciably into percolating water over 100,000 years (BSC 2003 [DIRS 162050], Section 8.2).

7.10.2.4 Thermal-Hydrologic-Mechanical Seepage Model

Coupled thermal-hydrologic-mechanical processes in the fractured rock around a waste emplacement drift can impact the spatial distribution of percolation flux through stress-induced changes in porosity, permeability and capillary pressure. Stress-induced changes can occur as a result of tunneling excavation and heating of the rock mass surrounding the waste emplacement drifts. Tunneling excavation can affect the permeability through opening or closing of existing fractures and potentially through formation of new fractures near the drift wall. After waste emplacement, the heating of the rock mass will induce thermal expansion and thermal stresses that will tend to strain existing fractures, leading to a change in fracture permeability (BSC 2003 [DIRS 164890], Section 6.1). The thermal-hydrologic-mechanical (THM) model and validation of the data and processes using the DST are treated in *Drift-Scale THM Model* (BSC 2003 [DIRS 164890]).

The model simulation found that the hydrologic properties will change around an emplacement drift first as a result of excavation of the drift and then as a result of heating of the rock mass surrounding the drift. The excavation of the drift is predicted to induce a maximum one-order-of-magnitude increase in the horizontal permeability at the drift crown, while the vertical permeability at the same location is predicted to increase much less. The maximum thermal-hydrologic-mechanical effects will occur around 100 to 1,000 years after emplacement of the waste, when the temperature in the rock mass at the repository level reaches its maximum. These effects will last well over 10,000 years, because the temperature over that time is still significantly over ambient. While the thermally-induced permeability changes are strong in the

drift vicinity, the impact of these stress-induced changes in hydrologic properties on the flow field is small to moderate, with the strongest impact occurring for a repository located in the Tptpmn model domain. The reason for a smaller impact in the Tptpll unit is that both the initial stresses and initial fracture permeability are higher in the Tptpll unit than in the Tptpmn unit. While the liquid vertical flux distribution in the fracture continuum is slightly affected, the main impact appears to be on the dryout zone near the repository drift. When stress-induced changes in hydrologic properties are considered, the extent of the dryout zone is slightly smaller, and consequently the liquid water will reach the drift wall in a shorter time. In the longer term, around 10,000 years, vertical permeability is still significantly decreased, especially just above the repository drift. The impact of this reduction in permeability is small, but tends to prevent vertical flux from reaching the drift wall at the drift crown (BSC 2003 [DIRS 164890], Section 8.1).

7.10.3 Infiltration Modeling

7.10.3.1 General Approach

Estimates of net infiltration are based on a primary assumption that water in excess of the field capacity for a given soil type is available for both evapotranspiration and net infiltration. Net infiltration is calculated as a daily rate equal to the effective saturated hydraulic conductivity of the bedrock type assigned to each cell, assuming a unit hydraulic gradient (Flint et al. 1996 [DIRS 100147], p. 83). All drainage from the soil profile into the bedrock is defined as net infiltration. The spatial distribution of the infiltration rate depends on the spatial distribution of soil depth, which is determined primarily by physiographic conditions.

For the estimation of net infiltration at Yucca Mountain for the next 10 k.y., the climatic conditions were derived from analysis and interpretation of paleoclimate records and the earth's orbital parameters (USGS 2000 [DIRS 158378]). The first climate state is a continuation of current, or modern, climate conditions from the present to about 600 years into the future. The second climate state is expected to begin about 600 years from the present and will consist of a monsoon climate with wetter summers than the modern climate. The third climate state is expected to begin about 2 k.y. from the present and will consist of a glacial transition climate, with cooler air temperatures and higher annual precipitation than the modern climate (Section 6.5.5.2). The duration of the glacial transition climate is estimated to extend beyond the required 10 k.y. estimation period (Sharpe 2003 [DIRS 161591], Table 6-6). The potential future monsoon and glacial transition climate states have been represented, in terms of mean annual precipitation, mean annual air temperature, and seasonal distributions of mean annual precipitation and mean annual air temperature, through identification of a set of current-climate analog sites. To account for variability and uncertainty in precipitation and air temperature, lower- and upper-bound climate scenarios have been identified for each climate state. To account for uncertainty in the selection of a single "best" analog site, the lower- and upper-bound climate scenarios are represented using a set of two or three analog sites (USGS 2001 [DIRS 158378], Table 2, Sections 6.6.1 and 6.6.2). Net infiltration is simulated using the climate input developed from the records at each analog site, and the results are averaged to obtain an estimate of net infiltration for a given climate scenario. Net infiltration simulations were done for each of nine climate scenarios using daily climate input parameters and a set of root-zone model coefficients (USGS 2001 [DIRS 160355], Section 6.9). The nine

climate scenarios are represented by a drier lower bound, a wetter upper bound, and an intermediate mean climate scenario for the modern, monsoon, and glacial-transition climate stages.

7.10.3.2   Results of Infiltration Modeling

Results of modeling infiltration for the lower-bound, mean, and upper-bound modern climate scenarios are summarized in USGS (2001 [DIRS 160355], Table 6-8), for the whole 123.7 km^2 infiltration model domain; and USGS (2001 [DIRS 160355], Table 6-10), for a 4.7 km^2 area above the repository (USGS 2001 [DIRS 160355], Section 6.11.1). For the entire flow domain of 123.7 km^2 of the infiltration model, for the mean modern climate scenario, average precipitation is estimated to be 188.5 mm/yr, average outflow as streamflow is 0.2 mm/yr (corresponding to an average stream discharge of 0.03 ft^3/s), and average net infiltration is 3.6 mm/yr. The average net infiltration ranges from 1.2 mm/yr for the lower-bound modern climate to 8.8 mm/yr for the upper-bound modern climate. Net infiltration rates for the areas of the unsaturated zone flow model (BSC 2003 [DIRS 163045]) and the repository are greater than those of the infiltration model domain because these areas have higher average elevations (with higher precipitation, thinner soils, and higher net infiltration) than the infiltration model domain, which covers a much larger area (USGS 2001 [DIRS 160355], Section 6.11.1).

Results of infiltration modeling for the lower-bound, mean, and upper-bound monsoon climate scenarios for the entire domain of the infiltration model (123.7 km^2 [47.8 mi^2]) are summarized in USGS (2001 [DIRS 160355], Table 6-12). As indicated above, results for the lower-bound monsoon scenario are equivalent to the mean modern climate results (see USGS 2001 [DIRS 160355], Tables 6-8 and 6-10). For the mean monsoon climate scenario, average precipitation is 300.5 mm/yr, average outflow as streamflow of 5.1 mm/yr, and average net infiltration is estimated to be 8.6 mm/yr. Calculations for the upper-bound monsoon climate resulted in estimates of average precipitation rate of 412.5 mm/yr, an average outflow as streamflow of 10.0 mm/yr, and an average net infiltration of 13.6 mm/yr. For the area of the repository (USGS 2001 [DIRS 160355], Table 6-14) for the mean monsoon climate scenario, average precipitation is 309.3 mm/yr, average outflow as streamflow is 13.2 mm/yr, and average net infiltration is estimated to be 12.5 mm/yr. For the upper-bound monsoon climate, average precipitation is 421.6 mm/yr, outflow as streamflow is 25.1 mm/yr, and net infiltration is 20.3 mm/yr over the area of the repository.

For the mean glacial transition climate over the entire infiltration model domain (USGS 2001 [DIRS 160355], Table 6-17), average precipitation is 316.1 mm/yr, average snowfall is 45.5 mm/yr, average infiltrated surface-water run-on is 14.6 mm/yr, outflow as streamflow is 1.5 mm/yr, and average net infiltration is estimated to be 13.4 mm/yr. In comparison, the mean net infiltration is 2.2 mm/yr for the lower-bound glacial transition climate and 24.6 mm/yr for the upper-bound glacial climate. Net infiltration is between 20 and 50 mm/yr along most of the crest of Yucca Mountain, with isolated areas of net infiltration exceeding 50 mm/yr (USGS 2001 [DIRS 160355], Section 6.11.3). Within the repository area, maximum net infiltration exceeds 500 mm/yr in the channel of Drill Hole Wash. Comparison with the mean modern climate conditions (USGS 2001 [DIRS 160355], Table 6-8) indicates that significant changes in the overall water balance could occur during the glacial climate. While average annual precipitation for mean glacial transition conditions is about 68 percent greater than for mean modern, net

infiltration is expected to be about 272 percent greater for the glacial transition climate. This will be caused by the cooler temperature and smaller evapotranspiration. In addition, snowfall is expected to become a significant component of the water balance, accounting for 14 percent of annual precipitation. Infiltrated surface-water run-on is expected to exceed 100 mm/yr throughout most of the upper sections of channels, including Pagany Wash, Drill Hole Wash, Solitario Canyon, and sections of all washes draining the eastern slopes of Yucca Mountain (USGS 2001 [DIRS 160355], Section 6.11.3). Within the infiltration model area, maximum infiltrated surface-water run-on is expected to exceed 3,000 mm/yr along isolated sections of Yucca Wash.

These results shows that the greater the annual precipitation, the greater the net infiltration when climate scenarios are compared to one another. However, the relation of net infiltration to precipitation is not uniform because of differences in evapotranspiration caused by differences in temperature, vegetation cover, and thickness of the bedrock root-zone layer. Overall, the greater the annual precipitation, the greater the surface-water outflow, but there are exceptions to this, probably because of differences in the seasonality of precipitation. For example, in each case, the monsoon climate scenarios produce greater surface-water outflow than do the corresponding glacial transition scenarios even though the glacial transition scenarios have greater annual precipitation. This is probably because the monsoon climate scenarios contain a higher frequency of severe summer storms. These storms can result in flash runoff in channels that tends to drain away quickly before infiltrating into the root zone where it can be transpired or become net infiltration. Overall, the differences in results among the climate scenarios illustrate the complexity of flow-and-transport processes in the unsaturated zone and expected sensitivity of predictions to temporal variations in climatic and climate-related factors, such as precipitation, temperature, and vegetation characteristics.

7.11 REFERENCES

The following is a list of the references cited in this section. Column 1 represents the unique six-digit numerical identifier (the Document Input Reference System [DIRS] number), which is placed in the text following the reference callout (e.g., BSC 2002 [DIRS 160405]). The purpose of these numbers is to assist the reader in locating a specific reference. Within the reference list, multiple sources by the same author (e.g., BSC 2002) are sorted alphabetically by title.

7.11.1 Cited Documents

132960   Abdel-Salam, A. and Chrysikopoulos, C.V. 1996. "Unsaturated Flow in a Quasi-Three-Dimensional Fractured Medium with Spatially Variable Aperture." *Water Resources Research, 32*, (6), 1531-1540. Washington, D.C.: American Geophysical Union. TIC: 239861.

109715   Ahlers, C.F.; Finsterle, S.; and Bodvarsson, G.S. 1999. "Characterization and Prediction of Subsurface Pneumatic Response at Yucca Mountain, Nevada." *Journal of Contaminant Hydrology, 38*, (1-3), 47-68. New York, New York: Elsevier. TIC: 244160.

101367   Albin, A.L.; Singleton, W.L.; Moyer, T.C.; Lee, A.C.; Lung, R.C.; Eatman, G.L.W.; and Barr, D.L. 1997. *Geology of the Main Drift - Station 28+00 to 55+00, Exploratory Studies Facility, Yucca Mountain Project, Yucca Mountain, Nevada*. Milestone SPG42AM3. Denver, Colorado: Bureau of Reclamation and U.S. Geological Survey. ACC: MOL.19970625.0096.

101368   Apps, J.A. 1997. "Hydrochemical Analysis." Chapter 14 of *The Site-Scale Unsaturated Zone Model of Yucca Mountain, Nevada, for the Viability Assessment*. Bodvarsson, G.S.; Bandurraga, T.M.; and Wu, Y.S., eds. LBNL-40376. Berkeley, California: Lawrence Berkeley National Laboratory. ACC: MOL.19971014.0232.

103949   Bandurraga, T.M. and Bodvarsson, G.S. 1999. "Calibrating Hydrogeologic Parameters for the 3-D Site-Scale Unsaturated Zone Model of Yucca Mountain, Nevada." *Journal of Contaminant Hydrology, 38*, (1-3), 25-46. New York, New York: Elsevier. TIC: 244160.

100029   Barr, D.L.; Moyer, T.C.; Singleton, W.L.; Albin, A.L.; Lung, R.C.; Lee, A.C.; Beason, S.C.; and Eatman, G.L.W. 1996. *Geology of the North Ramp — Stations 4+00 to 28+00, Exploratory Studies Facility, Yucca Mountain Project, Yucca Mountain, Nevada*. Denver, Colorado: U.S. Geological Survey. ACC: MOL.19970106.0496.

101486   Bauer, D.J.; Foster, B.J.; Joyner, J.D.; and Swanson, R.A. 1996. *Water Resources Data for Nevada Water Year 1995*. Water-Data Report NV-95-1. Carson City, Nevada: U.S. Geological Survey. ACC: MOL.20010721.0049.

101191   Beason, S.C.; Turlington, G.A.; Lung, R.C.; Eatman, G.L.W.; Ryter, D.; and Barr, D.L. 1996. *Geology of the North Ramp - Station 0+60 to 4+00, Exploratory Studies Facility, Yucca Mountain Project, Yucca Mountain, Nevada*. Denver, Colorado: U.S. Geological Survey. ACC: MOL.19970106.0449.

104463   Beck, D.A. and Glancy, P.A. 1995. *Overview of Runoff of March 11, 1995, in Fortymile Wash and Amargosa River, Southern Nevada*. Fact Sheet FS-0xx-95. Draft. Las Vegas, Nevada: U.S. Geological Survey. ACC: MOL.19960715.0133.

100102   Bodvarsson, G.S. and Bandurraga, T.M., eds. 1996. *Development and Calibration of the Three-Dimensional Site-Scale Unsaturated Zone Model of Yucca Mountain, Nevada*. LBNL-39315. Berkeley, California: Lawrence Berkeley National Laboratory. ACC: MOL.19970701.0692.

100103   Bodvarsson, G.S.; Bandurraga, T.M.; and Wu, Y.S., eds. 1997. *The Site-Scale Unsaturated Zone Model of Yucca Mountain, Nevada, for the Viability Assessment*. LBNL-40376. Berkeley, California: Lawrence Berkeley National Laboratory. ACC: MOL.19971014.0232.

120055   Bodvarsson, G.S.; Boyle, W.; Patterson, R.; and Williams, D. 1999. "Overview of Scientific Investigations at Yucca Mountain—The Potential Repository for High-Level Nuclear Waste." *Journal of Contaminant Hydrology, 38*, (1-3), 3-24. New York, New York: Elsevier. TIC: 244160.

101122   Bredehoeft, J.D. 1992. "Response of the Ground-Water System at Yucca Mountain to an Earthquake." Appendix D of *Ground Water at Yucca Mountain: How High Can It Rise?*. Washington, D.C.: National Academy Press. TIC: 233195.

160828   BSC (Bechtel SAIC Company) 2001. *Unsaturated Zone and Saturated Zone Transport Properties (U0100)*. ANL-NBS-HS-000019 REV 00 ICN 02. Las Vegas, Nevada: Bechtel SAIC Company. ACC: MOL.20020311.0017.

159124   BSC 2002. *Geologic Framework Model (GFM2000)*. MDL-NBS-GS-000002 REV 01. Las Vegas, Nevada: Bechtel SAIC Company. ACC: MOL.20020530.0078.

160771   BSC 2002. *Thermal Testing Measurements Report*. ANL-NBS-HS-000041 REV 00. Las Vegas, Nevada: Bechtel SAIC Company. ACC: MOL.20021004.0314.

165564   BSC 2003. *Abstraction of Drift Seepage*. MDL-NBS-HS-000019 REV 00 ICN 01. Las Vegas, Nevada: Bechtel SAIC Company. ACC: DOC.20031112.0002.

161773   BSC 2003. *Analysis of Hydrologic Properties Data*. MDL-NBS-HS-000014 REV 00. Las Vegas, Nevada: Bechtel SAIC Company. ACC: DOC.20030404.0004.

165991   BSC 2003. *Analysis of Infiltration Uncertainty*. ANL-NBS-HS-000027 REV 01. Las Vegas, Nevada: Bechtel SAIC Company. ACC: DOC.20031030.0003.

160240   BSC 2003. *Calibrated Properties Model*. MDL-NBS-HS-000003 REV 01. Las Vegas, Nevada: Bechtel SAIC Company. ACC: DOC.20030219.0001.

160109   BSC 2003. *Development of Numerical Grids for UZ Flow and Transport Modeling*. ANL-NBS-HS-000015 REV 01. Las Vegas, Nevada: Bechtel SAIC Company. ACC: DOC.20030404.0005.

162711   BSC 2003. *Drift Degradation Analysis*. ANL-EBS-MD-000027 REV 02. Las Vegas, Nevada: Bechtel SAIC Company. ACC: DOC.20030709.0003.

162050   BSC 2003. *Drift-Scale Coupled Processes (DST and THC Seepage) Models*. MDL-NBS-HS-000001 REV 02. Las Vegas, Nevada: Bechtel SAIC Company. ACC: DOC.20030804.0004.

166512   BSC 2003. *Drift-Scale Coupled Processes (DST and TH Seepage) Models*. MDL-NBS-HS-000015 REV 00C. Las Vegas, Nevada: Bechtel SAIC Company. ACC: MOL.20030910.0160. TBV-5666

164889   BSC 2003. *Drift-Scale Radionuclide Transport*. MDL-NBS-HS-000016 REV 00.
Las Vegas, Nevada: Bechtel SAIC Company. ACC: DOC.20030902.0009.

164890   BSC 2003. *Drift Scale THM Model*. MDL-NBS-HS-000017 REV 00 ICN 01.
Las Vegas, Nevada: Bechtel SAIC Company. ACC: DOC.20031014.0009.

166347   BSC 2003. *In Situ Field Testing of Processes*. ANL-NBS-HS-000005 REV 02.
Las Vegas, Nevada: Bechtel SAIC Company. ACC: DOC.20031208.0001.

166498   BSC 2003. *Mountain-Scale Coupled Processes (TH/THC/THM)*. MDL-NBS-HS-
000007 REV 01. Las Vegas, Nevada: Bechtel SAIC Company.
ACC: DOC.20031216.0003.

163228   BSC 2003. *Radionuclide Transport Models Under Ambient Conditions*. MDL-NBS-
HS-000008 REV 01. Las Vegas, Nevada: Bechtel SAIC Company.
ACC: DOC.20031201.0002.

162267   BSC 2003. *Seepage Calibration Model and Seepage Testing Data*. MDL-NBS-HS-
000004 REV 02. Las Vegas, Nevada: Bechtel SAIC Company.
ACC: DOC.20030408.0004.

163226   BSC 2003. *Seepage Model for PA Including Drift Collapse*. MDL-NBS-HS-000002
REV 02. Las Vegas, Nevada: Bechtel SAIC Company. ACC: DOC.20030709.0001.

163045   BSC 2003. *UZ Flow Models and Submodels*. MDL-NBS-HS-000006 REV 01.
Las Vegas, Nevada: Bechtel SAIC Company. ACC: DOC.20030818.0002.

167972   BSC 2004. *Errata 001 for Abstraction of Drift-Scale Coupled Processes*.
MDL-NBS-HS-000018 REV 00. Las Vegas, Nevada: Bechtel SAIC Company.
ACC: DOC.20031223.0004; DOC.20040223.0003.

162730   BSC 2004. *Particle Tracking Model and Abstraction of Transport Processes*.
MDL-NBS-HS-000020 REV 00. Las Vegas, Nevada: Bechtel SAIC Company.
ACC: DOC.20040120.0001.

100106   Buesch, D.C.; Spengler, R.W.; Moyer, T.C.; and Geslin, J.K. 1996. *Proposed
Stratigraphic Nomenclature and Macroscopic Identification of Lithostratigraphic
Units of the Paintbrush Group Exposed at Yucca Mountain, Nevada*. Open-File
Report 94-469. Denver, Colorado: U.S. Geological Survey.
ACC: MOL.19970205.0061.

131513   Bussod, G.Y.; Coen, K.; and Eckhardt, R.C. 1998. *LA Testing Status Report: Busted
Butte Unsaturated Zone Transport Test FY 98*. SPU85M4. Los Alamos,
New Mexico: Los Alamos National Laboratory. TIC: 246363.

109051   Carey, J.W.; Chipera, S.J.; Vaniman, D.T.; and Bish, D.L. 1998. *Three-Dimensional Mineralogic Model of Yucca Mountain, Nevada: Rev 2.0.* Deliverable SP32BSM4. Los Alamos, New Mexico: Los Alamos National Laboratory, Earth and Environmental Sciences Division. ACC: MOL.20000110.0159.

104368   Carrera, J. and Neuman, S.P. 1986. "Estimation of Aquifer Parameters Under Transient and Steady State Conditions: 1. Maximum Likelihood Method Incorporating Prior Information." *Water Resources Research, 22*, (2), 199-210. Washington, D.C.: American Geophysical Union. TIC: 245915.

100967   Carrigan, C.R.; King, G.C.P.; Barr, G.E.; and Bixler, N.E. 1991. "Potential for Water-Table Excursions Induced by Seismic Events at Yucca Mountain, Nevada." *Geology, 19*, (12), 1157-1160. Boulder, Colorado: Geological Society of America. TIC: 242407.

161550   Cline, J.S. and Wilson, N.S.F. 2001. "Paragenesis of Secondary Mineralization at Yucca Mountain, Nevada, USA." *Water-Rock Interaction, Proceedings of the Tenth International Symposium on Water-Rock Interaction, WRI-10, Villasimius, Italy, 10-15 July 2001.* Cidu, R., ed. *2*, 1311-1314. Exton, Pennsylvania: A.A. Balkema. TIC: 253823.

150049   Conca, J.L. and Wright, J. 1998. "The UFA Method for Rapid, Direct Measurements of Unsaturated Soil Transport Properties in Soil, Sediment, and Rock." *Australian Journal of Soil Research, 36*, (2), 291-315. Melbourne, Australia: CSIRO Publishing. TIC: 248019.

156902   Cook, P. 2001. Drift Scale Seepage Test. Scientific Notebook YMP-LBNL-JSW-PJC-6.2. ACC: MOL.20011105.0080.

107637   CRWMS M&O (Civilian Radioactive Waste Management System Management and Operating Contractor) 1997. Daily Operations Report: USW WT-24, July 14, 1997 to November 7, 1997. Las Vegas, Nevada: CRWMS M&O. ACC: MOL.19980128.0477.

146917   CRWMS M&O 1997. *Drift Scale Test Design and Forecast Results.* BAB000000-01717-4600-00007 REV 01. Las Vegas, Nevada: CRWMS M&O. ACC: MOL.19980710.0155.

104589   CRWMS M&O 1998. *Classification and Map of Vegetation at Yucca and Little Skull Mountains, Nevada.* B00000000-01717-5705-00083 REV 00. Las Vegas, Nevada: CRWMS M&O. ACC: MOL.19990615.0237.

141187   CRWMS M&O 2000. *Conceptual and Numerical Models for UZ Flow and Transport.* MDL-NBS-HS-000005 REV 00. Las Vegas, Nevada: CRWMS M&O. ACC: MOL.19990721.0526.

141400   CRWMS M&O 2000. *In Situ Field Testing of Processes*. ANL-NBS-HS-000005 REV 00. Las Vegas, Nevada: CRWMS M&O. ACC: MOL.20000504.0304.

151940   CRWMS M&O 2000. *Unsaturated Zone Flow and Transport Model Process Model Report*. TDR-NBS-HS-000002 REV 00 ICN 02. Las Vegas, Nevada: CRWMS M&O. ACC: MOL.20000831.0280.

122797   CRWMS M&O 2000. *UZ Flow Models and Submodels*. MDL-NBS-HS-000006 REV 00. Las Vegas, Nevada: CRWMS M&O. ACC: MOL.19990721.0527.

151945   CRWMS M&O 2000. *Yucca Mountain Site Description*. TDR-CRW-GS-000001 REV 01 ICN 01. Las Vegas, Nevada: CRWMS M&O. ACC: MOL.20001003.0111.

154024   CRWMS M&O 2001. *Unsaturated Zone and Saturated Zone Transport Properties (U0100)*. ANL-NBS-HS-000019 REV 00 ICN 1. Las Vegas, Nevada: CRWMS M&O. ACC: MOL.20010201.0026.

101042   Czarnecki, J.B. and Waddell, R.K. 1984. *Finite-Element Simulation of Ground-Water Flow in the Vicinity of Yucca Mountain, Nevada-California*. Water-Resources Investigations Report 84-4349. Denver, Colorado: U.S. Geological Survey. ACC: NNA.19870407.0173.

131816   Daily, W.; Lin, W.; and Buscheck, T. 1987. "Hydrological Properties of Topopah Spring Tuff: Laboratory Measurements." *Journal of Geophysical Research, 92*, (B8), 7854-7864. Washington, D.C.: American Geophysical Union. TIC: 226512.

156869   Descour, J.M.; Hanna, K.; Conover, D.; and Hoekstra, B. 2001. *Seismic Tomography Technology for the Water Infiltration Experiment*. TDR-EBS-MD-000017 REV 00. Las Vegas, Nevada: Bechtel SAIC Company. ACC: MOL.20010508.0194.

100550   DOE (U.S. Department of Energy) 1998. *Total System Performance Assessment*. Volume 3 of *Viability Assessment of a Repository at Yucca Mountain*. DOE/RW-0508. Washington, D.C.: U.S. Department of Energy, Office of Civilian Radioactive Waste Management. ACC: MOL.19981007.0030.

101779   DOE 1998. *Viability Assessment of a Repository at Yucca Mountain*. DOE/RW-0508. Overview and five volumes. Washington, D.C.: U.S. Department of Energy, Office of Civilian Radioactive Waste Management. ACC: MOL.19981007.0027; MOL.19981007.0028; MOL.19981007.0029; MOL.19981007.0030; MOL.19981007.0031; MOL.19981007.0032.

153849   DOE 2001. *Yucca Mountain Science and Engineering Report*. DOE/RW-0539. Washington, D.C.: U.S. Department of Energy, Office of Civilian Radioactive Waste Management. ACC: MOL.20010524.0272.

157080   DOE 2002. *Site Recommendation Comment Summary Document*. DOE/RW-0548. Washington, D.C.: U.S. Department of Energy, Office of Civilian Radioactive Waste Management. ACC: MOL.20020404.0044.

135997   Doughty, C. 1999. "Investigation of Conceptual and Numerical Approaches for Evaluating Moisture, Gas, Chemical, and Heat Transport in Fractured Unsaturated Rock." *Journal of Contaminant Hydrology, 38*, (1-3), 69-106. New York, New York: Elsevier. TIC: 244160.

161545   Dublyansky, Y.V. and Szymanski, J.S. 1996. "Carbonate Deposits at Yucca Mountain (Nevada, USA) and the Problem of High-Level Nuclear Waste Disposal." *Chemistry for Sustainable Development, 4*, (3), 146-161. Novosibirsk, Siberia, Russia: Russian Academy of Sciences. TIC: 253850.

109204   Dublyansky, Y.; Reutsky, V.; and Shugurova, N. 1996. "Fluid Inclusions in Calcite from the Yucca Mountain Exploratory Tunnel." *Sixth Biennial Pan American Conference on Research in Fluid Inclusions, May 30 - June 1, 1996*. Brown, P.E. and Hagemann, S.G., eds. Madison, Wisconsin: Department of Geology, University of Wisconsin. TIC: 237704.

161542   Dublyansky, Y.V. 2001. "Paleohydrogeology of Yucca Mountain by Fluid Inclusions and Stable Isotopes." *"Back to the Future - Managing the Back End of the Nuclear Fuel Cycle to Create a More Secure Energy Future," Proceedings of the 9th International High-Level Radioactive Waste Management Conference (IHLRWM), Las Vegas, Nevada, April 29-May 3, 2001*. La Grange Park, Illinois: American Nuclear Society. TIC: 247873.

161543   Dublyansky, Y.; Ford, D.; and Reutski, V. 2001. "Traces of Epigenetic Hydrothermal Activity at Yucca Mountain, Nevada: Preliminary Data on the Fluid Inclusion and Stable Isotope Evidence." *Chemical Geology, 173*, (1-3), 125-149. New York, New York: Elsevier. TIC: 253849.

100570   Fabryka-Martin, J.T.; Wolfsberg, A.V.; Levy, S.S.; Roach, J.L.; Winters, S.T.; Wolfsberg, L.E.; Elmore, D.; and Sharma, P. 1998. "Distribution of Fast Hydrologic Paths in the Unsaturated Zone at Yucca Mountain." *High-Level Radioactive Waste Management, Proceedings of the Eighth International Conference, Las Vegas, Nevada, May 11-14, 1998*. Pages 93-96. La Grange Park, Illinois: American Nuclear Society. TIC: 237082.

101223   Finsterle, S.; Bandurraga, T.M.; Doughty, C.; and Bodvarsson, G.S. 1996. "Simulation of Coupled Processes in a Two-Dimensional West-East Cross-Section of Yucca Mountain, Nevada." Chapter 12 of *Development and Calibration of the Three-Dimensional Site-Scale Unsaturated Zone Model of Yucca Mountain, Nevada*. Bodvarsson, G.S. and Bandurraga, T.M., eds. Berkeley, California: Lawrence Berkeley National Laboratory. ACC: MOL.19970211.0176.

104367   Finsterle, S. 1999. *ITOUGH2 User's Guide*. LBNL-40040. Berkeley, California: Lawrence Berkeley National Laboratory. TIC: 243018.

151875   Finsterle, S. 2000. "Using the Continuum Approach to Model Unsaturated Flow in Fractured Rock." *Water Resources Research, 36*, (8), 2055-2066. Washington, D.C.: American Geophysical Union. TIC: 248769.

100147   Flint, A.L.; Hevesi, J.A.; and Flint, L.E. 1996. *Conceptual and Numerical Model of Infiltration for the Yucca Mountain Area, Nevada*. Milestone 3GUI623M. Denver, Colorado: U.S. Geological Survey. ACC: MOL.19970409.0087.

157411   Flint, A.L.; Flint, L.E.; Kwicklis, E.M.; Fabryka-Martin, J.T.; and Bodvarsson, G.S. 2002. "Estimating Recharge at Yucca Mountain, Nevada, USA: Comparison of Methods." *Hydrogeology Journal, 10*, (1), 180-240. Berlin, Germany: Springer-Verlag. TIC: 251765.

100394   Flint, L.E. and Flint, A.L. 1995. *Shallow Infiltration Processes at Yucca Mountain, Nevada—Neutron Logging Data 1984-93*. Water-Resources Investigations Report 95-4035. Denver, Colorado: U.S. Geological Survey. ACC: MOL.19960924.0577.

100033   Flint, L.E. 1998. *Characterization of Hydrogeologic Units Using Matrix Properties, Yucca Mountain, Nevada*. Water-Resources Investigations Report 97-4243. Denver, Colorado: U.S. Geological Survey. ACC: MOL.19980429.0512.

107377   Flint, L.E.; Hudson, D.B.; and Flint, A.L. 1999. "Unsaturated Hydraulic Parameters Determined from Direct and Indirect Methods." *Proceedings of the International Workshop on Characterization and Measurement of the Hydraulic Properties of Unsaturated Porous Media, Part 1, Riverside, California, October 22-24, 1997*. van Genuchten, M.Th.; Leij, F.J.; and Wu, L., eds. Pages 293-302. Riverside, California: University of California. TIC: 247322.

163336   Flint, L.E. 2003. "Physical and Hydraulic Properties of Volcanic Rocks from Yucca Mountain, Nevada." *Water Resources Research, 39*, (5), 1-1 through 1-13. Washington, D.C.: American Geophysical Union. TIC: 254297.

101173   Freeze, R.A. and Cherry, J.A. 1979. *Groundwater*. Englewood Cliffs, New Jersey: Prentice-Hall. TIC: 217571.

149742   Frisbie, H.R.; LaCamera, R.J.; Riek, M.M.; and Wood, D.B. 1984. *Water Resources Data Nevada Water Year 1983*. Water-Data Report NV-83-1. Carson City, Nevada: U.S. Geological Survey. TIC: 221937.

105506   Giampaoli, M.C. 1986. *Trip Report: Hydrologic Field Reconnaissance Led by Robert Coache, Water Resources Division, Nevada Department of Conservation and Natural Resources, April 24, 1986*. M86-GEO-MEG-054. Las Vegas, Nevada: Science Applications International Corporation. TIC: 218738.

139237   Glass, R.J.; Nicholl, M.J.; and Tidwell, V.C. 1996. *Challenging and Improving Conceptual Models for Isothermal Flow in Unsaturated, Fractured Rock Through Exploration of Small-Scale Processes*. SAND95-1824. Albuquerque, New Mexico: Sandia National Laboratories. ACC: MOL.19970520.0082.

105674   Goldstein, R.H. 1986. "Reequilibration of Fluid Inclusions in Low-Temperature Calcium-Carbonate Cement." *Geology, 14*, (9), 792-795. Boulder, Colorado: Geological Society of America. TIC: 237435.

126906   Goldstein, R.H. and Reynolds, T.J., eds. 1994. "Fluid Inclusions and Their Origin." SEPM Short Course 31. *Systematics of Fluid Inclusions in Diagenetic Minerals*. Pages 5-9. Tulsa, Oklahoma: Society for Sedimentary Geology. TIC: 246523.

164070   Guertal, W. 2001. *Seepage into Alcove 1*. Scientific Notebook SN-USGS-SCI-108-V1. ACC: MOL.20011219.0325.

107413   Hevesi, J.A. and Flint, A.L. 1995. *Geostatistical Model for Estimating Precipitation and Recharge for the Yucca Mountain Region, Nevada-California*. Water-Resources Investigations Report. Draft. Denver, Colorado: U.S. Geological Survey. ACC: MOL.19980223.0573.

106126   Hill, C.A.; Dublyansky, Y.V.; Harmon, R.S.; and Schluter, C.M. 1995. "Overview of Calcite/Opal Deposits at or Near the Proposed High-Level Nuclear Waste Site, Yucca Mountain, Nevada, USA: Pedogenic, Hypogene, or Both?" *Environmental Geology, 26*, 69-88. New York, New York: Springer-Verlag. TIC: 222318.

165606   Hill, C.A. and Dublyansky, Y.V. 1999. "Response to Stuckless and Others (1998) on 'Overview of Calcite/Opal Deposits at or Near the Proposed High-Level Nuclear Waste Site, Yucca Mountain, Nevada, USA: Pedogenic, Hypogene, or Both?'" *Environmental Geology, 38*, (1), 77-81. New York, New York: Springer-Verlag. TIC: 255228.

141521   Ho, C.K. 1997. "Evaporation of Pendant Water Droplets in Fractures." *Water Resources Research, 33*, (12), 2665-2671. Washington, D.C.: American Geophysical Union. TIC: 246969.

100584   Ho, C.K. 1997. "Models of Fracture-Matrix Interactions During Multiphase Heat and Mass Flow in Unsaturated Fractured Porous Media." *Proceedings of the ASME Fluids Engineering Division, November 16–21, 1997, Dallas, Texas*. FED-Vol. 244. Pages 401-412. New York, New York: American Society of Mechanical Engineers. TIC: 241082.

162326   Holt, E.W. 2002. "$^{18}O/^{16}O$ Evidence for an Early, Short-Lived (~10 yr), Fumarolic Event in the Topopah Spring Tuff Near the Proposed High-Level Nuclear Waste Repository Within Yucca Mountain, Nevada, USA." *Earth and Planetary Science Letters, 201*, (3-4), 559-573. New York, New York: Elsevier. TIC: 255127.

165413   Hu, Q.; Salve, S.; Stringfellow, W.T.; and Wang, J.S.Y. 2001. "Field Tracer-Transport Tests in Unsaturated Fractured Tuff." *Journal of Contaminant Hydrology, 51*, (1-2), 1-12. New York, New York: Elsevier. TIC: 254969.

101868   Hvorslev, M.J. 1951. *Time Lag and Soil Permeability in Ground-Water Observations*. AEWES Bulletin 36. Vicksburg, Mississippi: U.S. Army Corps of Engineers, Waterways Experiment Station. TIC: 238956.

141523   Jackson, C.P.; Hoch, A.R.; and Todman, S. 2000. "Self-Consistency of a Heterogeneous Continuum Porous Medium Representation of a Fractured Medium." *Water Resources Research, 36*, (1), 189-202. Washington, D.C.: American Geophysical Union. TIC: 247466.

162333   Kurzmack, M.; LeCain, G.D.; and Hudson, D. 2002. "Relative Humidity, Pressure, and Temperature Values from the Ghost Dance Fault Alcove 7, Yucca Mountain, Nevada." *Abstracts with Programs - Geological Society of America, 34*, (6), 59. Boulder, Colorado: Geological Society of America. TIC: 254868.

100153   LeCain, G.D. 1997. *Air-Injection Testing in Vertical Boreholes in Welded and Nonwelded Tuff, Yucca Mountain, Nevada*. Water-Resources Investigations Report 96-4262. Denver, Colorado: U.S. Geological Survey. ACC: MOL.19980310.0148.

100156   LeCain, G.D.; Patterson, G.L.; and Severson, G.R. 1997. *Results from Pneumatic Monitoring, Hydrochemistry Sampling, Air-Injection, and Tracer Testing in the Upper Tiva Canyon, and Bow Ridge Fault Alcoves, Yucca Mountain, Nevada, November, 1994 to July, 1996*. Milestone 3GUS619M-1996. Denver, Colorado: U.S. Geological Survey. ACC: MOL.19970415.0387.

100052   LeCain, G.D. 1998. *Results from Air-Injection and Tracer Testing in the Upper Tiva Canyon, Bow Ridge Fault, and Upper Paintbrush Contact Alcoves of the Exploratory Studies Facility, August 1994 through July 1996, Yucca Mountain, Nevada*. Water-Resources Investigations Report 98-4058. Denver, Colorado: U.S. Geological Survey. ACC: MOL.19980625.0344.

144612   LeCain, G.D.; Anna, L.O.; and Fahy, M.F. 2000. *Results from Geothermal Logging, Air and Core-Water Chemistry Sampling, Air-Injection Testing, and Tracer Testing in the Northern Ghost Dance Fault, Yucca Mountain, Nevada, November 1996 to August 1998*. Water-Resources Investigations Report 99-4210. Denver, Colorado: U.S. Geological Survey. TIC: 247708.

162337   LeCain, G.D.; Ellett, K.M.; and Hudson, D. 2002. "In Situ Water-Potential Values of the Nonwelded Units of the Paintbrush Group, Yucca Mountain, Nevada." *Abstracts with Programs - Geological Society of America, 34*, (6), 59. Boulder, Colorado: Geological Society of America. TIC: 254868.

158511   LeCain, G.D.; Lu, N.; and Kurzmack, M. 2002. *Use of Temperature, Pressure, and Water Potential Data to Estimate Infiltration and Monitor Percolation in Pagany Wash Associated with the Winter of 1997–98 El Niño Precipitation, Yucca Mountain, Nevada*. Water Resources Investigations Report 02-4035. Denver, Colorado: U.S. Geological Survey. TIC: 252641.

100589   Lichty, R.W. and McKinley, P.W. 1995. *Estimates of Ground-Water Recharge Rates for Two Small Basins in Central Nevada*. Water-Resources Investigations Report 94-4104. Denver, Colorado: U.S. Geological Survey. ACC: MOL.19960924.0524.

105729   Liu, H.H.; Doughty, C.; and Bodvarsson, G.S. 1998. "An Active Fracture Model for Unsaturated Flow and Transport in Fractured Rocks." *Water Resources Research, 34*, (10), 2633-2646. Washington, D.C.: American Geophysical Union. TIC: 243012.

162470   Liu, H-H.; Haukwa, C.B.; Ahlers, C.F.; Bodvarsson, G.S.; Flint, A.L.; and Guertal, W.B. 2003. "Modeling Flow and Transport in Unsaturated Fractured Rock: An Evaluation of the Continuum Approach." *Journal of Contaminant Hydrology, 62-63*, 173-188. New York, New York: Elsevier. TIC: 254205.

100465   Luckey, R.R.; Tucci, P.; Faunt, C.C.; Ervin, E.M.; Steinkampf, W.C.; D'Agnese, F.A.; and Patterson, G.L. 1996. *Status of Understanding of the Saturated-Zone Ground-Water Flow System at Yucca Mountain, Nevada, as of 1995*. Water-Resources Investigations Report 96-4077. Denver, Colorado: U.S. Geological Survey. ACC: MOL.19970513.0209.

163682   Ludwig, K.R. and Paces, J.B. 2002. "Uranium-Series Dating of Pedogenic Silica and Carbonate, Crater Flat, Nevada." *Geochimica et Cosmochimica Acta, 66*, (3), 487-506. New York, New York: Pergamon. TIC: 255305.

154415   Marshall, B.D. and Whelan, J.F. 2000. "Isotope Geochemistry of Calcite Coatings and the Thermal History of the Unsaturated Zone at Yucca Mountain, Nevada." *Abstracts with Programs - Geological Society of America, 32*, (7), A-259. Boulder, Colorado: Geological Society of America. TIC: 249113.

156503   Marshall, B.D. and Futa, K. 2001. "Strontium Isotope Evolution of Pore Water and Calcite in the Topopah Spring Tuff, Yucca Mountain, Nevada." *"Back to the Future - Managing the Back End of the Nuclear Fuel Cycle to Create a More Secure Energy Future," Proceedings of the 9th International High-Level Radioactive Waste Management Conference (IHLRWM), Las Vegas, Nevada, April 29-May 3, 2001*. La Grange Park, Illinois: American Nuclear Society. TIC: 247873.

162891   Marshall, B.D.; Neymark, L.A.; and Peterman, Z.E. 2003. "Estimation of Past Seepage Volumes from Calcite Distribution in the Topopah Spring Tuff, Yucca Mountain, Nevada." *Journal of Contaminant Hydrology, 62-63*, 237-247. New York, New York: Elsevier. TIC: 254210.

105462   Miller, G.A. 1977. *Appraisal of the Water Resources of Death Valley, California-Nevada*. Open-File Report 77-728. Menlo Park, California: U.S. Geological Survey. ACC: HQS.19880517.1934.

148784   Moench, A.F. 1995. "Convergent Radial Dispersion in a Double-Porosity Aquifer with Fracture Skin: Analytical Solution and Application to a Field Experiment in Fractured Chalk." *Water Resources Research, 31*, (8), 1823-1835. Washington, D.C.: American Geophysical Union. TIC: 233132.

149850   Mongano, G.S.; Singleton, W.L.; Moyer, T.C.; Beason, S.C.; Eatman, G.L.W.; Albin, A.L.; and Lung, R.C. 1999. *Geology of the ECRB Cross Drift - Exploratory Studies Facility, Yucca Mountain Project, Yucca Mountain, Nevada*. Deliverable SPG42GM3. Denver, Colorado: U.S. Geological Survey. ACC: MOL.20000324.0614.

148859   Monger, H.C. and Adams, H.P. 1996. "Micromorphology of Calcite-Silica Deposits, Yucca Mountain, Nevada." *Soil Science Society of America Journal, 60*, (2), 519-530. Madison, Wisconsin: Soil Science Society of America. TIC: 247738.

100161   Montazer, P. and Wilson, W.E. 1984. *Conceptual Hydrologic Model of Flow in the Unsaturated Zone, Yucca Mountain, Nevada*. Water-Resources Investigations Report 84-4345. Lakewood, Colorado: U.S. Geological Survey. ACC: NNA.19890327.0051.

101269   Moyer, T.C. and Geslin, J.K. 1995. *Lithostratigraphy of the Calico Hills Formation and Prow Pass Tuff (Crater Flat Group) at Yucca Mountain, Nevada*. Open-File Report 94-460. Denver, Colorado: U.S. Geological Survey. ACC: MOL.19941208.0003.

105162   National Research Council. 1992. *Ground Water at Yucca Mountain, How High Can It Rise? Final Report of the Panel on Coupled Hydrologic/Tectonic/Hydrothermal Systems at Yucca Mountain*. Washington, D.C.: National Academy Press. TIC: 204931.

139151   National Research Council. 1996. *Rock Fractures and Fluid Flow, Contemporary Understanding and Applications*. Washington, D.C.: National Academy Press. TIC: 235913.

109140   Neymark, L.A.; Amelin, Y.V.; Paces, J.B.; and Peterman, Z.E. 1998. "U-Pb Age Evidence for Long-Term Stability of the Unsaturated Zone at Yucca Mountain." *High-Level Radioactive Waste Management, Proceedings of the Eighth International Conference, Las Vegas, Nevada, May 11-14, 1998*. Pages 85-87. La Grange Park, Illinois: American Nuclear Society. TIC: 237082.

162710   Neymark, L.A.; Amelin, Y.V.; and Paces, J.B. 2000. "^{206}Pb–^{230}Th–^{234}U–^{238}U and ^{207}Pb–^{235}U Geochronology of Quaternary Opal, Yucca Mountain, Nevada." Geochimica et Cosmochimica Acta, 64, (17), 2913-2928. New York, New York: Pergamon. TIC: 253360.

154828   Neymark, L.A.; Amelin, Y.V.; Paces, J.B.; Whelan, J.F.; and Peterman, Z.E. 2000. "U-Pb Dating of Opal and Chalcedony Above and Below the Modern Water Table at Yucca Mountain, Southern Nevada." *Abstracts with Programs - Geological Society of America, 32*, (7), A-259. Boulder, Colorado: Geological Society of America. TIC: 249113.

127012   Neymark, L.A. and Paces, J.B. 2000. "Consequences of Slow Growth for ^{230}Th/U Dating of Quaternary Opals, Yucca Mountain, NV, USA." *Chemical Geology, 164*, (1-2), 143-160. Amsterdam, The Netherlands: Elsevier. TIC: 246316.

156889   Neymark, L.A.; Amelin, Y.V.; Paces, J.B.; Peterman, Z.E.; and Whelan, J.F. 2001. "Age Constraints on Fluid Inclusions in Calcite at Yucca Mountain." *"Back to the Future - Managing the Back End of the Nuclear Fuel Cycle to Create a More Secure Energy Future," Proceedings of the 9th International High-Level Radioactive Waste Management Conference (IHLRWM), Las Vegas, Nevada, April 29, May 3, 2001.* La Grange Park, Illinois: American Nuclear Society. TIC: 247873.

158673   Neymark, L.A.; Amelin, Y.; Paces, J.B.; and Peterman, Z.E. 2002. "U-Pb Ages of Secondary Silica at Yucca Mountain, Nevada: Implications for the Paleohydrology of the Unsaturated Zone." *Applied Geochemistry, 17*, (6), 709-734. New York, New York: Elsevier. TIC: 252598.

163681   Neymark, L.A.; Paces, J.B.; and Amelin, Y.V. 2003. "Reliability of U-Th-Pb Dating of Secondary Silica at Yucca Mountain, Nevada." *Proceedings of the 10th International High-Level Radioactive Waste Management Conference (IHLRWM), March 30-April 2, 2003, Las Vegas, Nevada.* Pages 1-12. La Grange Park, Illinois: American Nuclear Society. TIC: 254559.

101277   O'Brien, G.M. 1997. *Analysis of Aquifer Tests Conducted in Boreholes USW WT-10, UE-25 WT#12, and USW SD-7, 1995-96, Yucca Mountain, Nevada.* Water-Resources Investigations Report 96-4293. Denver, Colorado: U.S. Geological Survey. ACC: MOL.19980219.0822.

100602   Osterkamp, W.R.; Lane, L.J.; and Savard, C.S. 1994. "Recharge Estimates Using a Geomorphic/Distributed-Parameter Simulation Approach, Amargosa River Basin." *Water Resources Bulletin, 30*, (3), 493-506. Minneapolis, Minnesota: American Water Resources Association. TIC: 237428.

107408   Paces, J.B.; Neymark, L.A.; Marshall, B.D.; Whelan, J.F.; and Peterman, Z.E. 1998.
          "Inferences for Yucca Mountain Unsaturated-Zone Hydrology from Secondary
          Minerals." *High-Level Radioactive Waste Management, Proceedings of the Eighth
          International Conference, Las Vegas, Nevada, May 11-14, 1998.* Pages 36-39.
          La Grange Park, Illinois: American Nuclear Society. TIC: 237082.

154413   Paces, J.B.; Neymark, L.A.; Persing, H.M.; and Wooden, J.L. 2000. "Demonstrating
          Slow Growth Rates in Opal from Yucca Mountain, Nevada, Using Microdigestion and
          Ion-Probe Uranium-Series Dating." *Abstracts with Programs - Geological Society of
          America, 32*, (7), A-259. Boulder, Colorado: Geological Society of America.
          TIC: 249113.

156507   Paces, J.B.; Neymark, L.A.; Marshall, B.D.; Whelan, J.F.; and Peterman, Z.E. 2001.
          *Ages and Origins of Calcite and Opal in the Exploratory Studies Facility Tunnel,
          Yucca Mountain, Nevada.* Water-Resources Investigations Report 01-4049. Denver,
          Colorado: U.S. Geological Survey. TIC: 251284.

158817   Paces, J.B.; Ludwig, K.R.; Peterman, Z.E.; and Neymark, L.A. 2002. "^{234}U/^{238}U
          Evidence for Local Recharge and Patterns of Ground-Water Flow in the Vicinity of
          Yucca Mountain, Nevada, USA." *Applied Geochemistry, 17*, (6), 751-779.
          New York, New York: Elsevier. TIC: 252809.

163374   Paces, J.B. and Neymark, L.A. 2002. "U-Series Isotopes, Water/Rock Interaction, and
          Evidence of Unsaturated-Zone Flow at Yucca Mountain, Nevada." *Abstracts with
          Programs - Geological Society of America, 34*, (6), 308-309. Boulder, Colorado:
          Geological Society of America. TIC: 254868.

166371   Paces, J.B.; Neymark, L.A.; Wooden, J.L.; and Persing, H.M. 2003. *Improved
          Spatial Resolution for U-Series Dating of Opal at Yucca Mountain, Nevada, USA,
          Using Ion-Microprobe and Microdigestion Methods.* Denver, Colorado: U.S.
          Geological Survey. ACC: MOL.20031212.0025. TBV-5658

163684   Pashenko, S.E. and Dublyansky, Y.V. 2002. "The Role of Radon and Colloids in
          Distorting the U-Pb Age Dates of Geologically Young Minerals Deposited in Open
          Cavities." *Geochimica et Cosmochimica Acta, 66*, (15A), A581. New York,
          New York: Elsevier. TIC: 254097.

100172   Patterson, G.L.; Weeks, E.P.; Rousseau, J.P.; and Oliver, T.A. 1996. *Interpretation of
          Pneumatic and Chemical Data from the Unsaturated Zone Near Yucca Mountain,
          Nevada.* Milestone 3GGP605M. Denver, Colorado: U.S. Geological Survey.
          ACC: MOL.19970324.0058.

107402   Patterson, G.L.; Peterman, Z.E.; and Paces, J.B. 1998. "Hydrochemical Evidence for
          the Existence of Perched Water at USW WT-24, Yucca Mountain, Nevada." *High-
          Level Radioactive Waste Management, Proceedings of the Eighth International
          Conference, Las Vegas, Nevada, May 11-14, 1998.* Pages 277-278. La Grange Park,
          Illinois: American Nuclear Society. TIC: 237082.

144787   Phillips, F.M. 1994. "Environmental Tracers for Water Movement in Desert Soils of the American Southwest." *Soil Science Society of America Journal, 58*, 15-24. Madison, Wisconsin: Soil Science Society of America. TIC: 240651.

104250   Pruess, K. 1999. "A Mechanistic Model for Water Seepage Through Thick Unsaturated Zones in Fractured Rocks of Low Matrix." *Water Resources Research, 35*, (4), 1039-1051. Washington, D.C.: American Geophysical Union. TIC: 244913.

117112   Pruess, K.; Faybishenko, B.; and Bodvarsson, G.S. 1999. "Alternative Concepts and Approaches for Modeling Flow and Transport in Thick Unsaturated Zones of Fractured Rocks." *Journal of Contaminant Hydrology, 38*, (1-3), 281-322. New York, New York: Elsevier. TIC: 244160.

106645   Rautman, C.A.; Flint, L.E.; Flint, A.L.; and Istok, J.D. 1995. *Physical and Hydrologic Properties of Outcrop Samples from a Nonwelded to Welded Tuff Transition, Yucca Mountain, Nevada*. Water-Resources Investigations Report 95-4061. Denver, Colorado: U.S. Geological Survey. ACC: MOL.19971212.0129.

101008   Rautman, C.A. and Engstrom, D.A. 1996. *Geology of the USW SD-7 Drill Hole Yucca Mountain, Nevada*. SAND96-1474. Albuquerque, New Mexico: Sandia National Laboratories. ACC: MOL.19971218.0442.

106675   Roedder, E. 1984. *Fluid Inclusions*. Reviews in Mineralogy, Volume 12. Washington, D.C.: Mineralogical Society of America. TIC: 236874.

109159   Roedder, E.; Whelan, J.F.; and Vaniman, D.T. 1994. "Fluid Inclusion Studies of Calcite Veins from Yucca Mountain, Nevada, Tuffs: Environment of Formation." *High Level Radioactive Waste Management, Proceedings of the Fifth Annual International Conference, Las Vegas, Nevada, May 22-26, 1994. 4*, 1854-1860. La Grange Park, Illinois: American Nuclear Society. TIC: 210984.

129750   Rojstaczer, S. 1999. "Stress Dependent Permeability and Its Political Consequences at Yucca Mountain." *Eos, Transactions (Supplement), 80*, (17), S4. Washington, D.C.: American Geophysical Union. TIC: 246513.

100178   Rousseau, J.P.; Loskot, C.L.; Thamir, F.; and Lu, N. 1997. *Results of Borehole Monitoring in the Unsaturated Zone Within the Main Drift Area of the Exploratory Studies Facility, Yucca Mountain, Nevada*. Milestone SPH22M3. Denver, Colorado: U.S. Geological Survey. ACC: MOL.19970626.0351.

102097   Rousseau, J.P.; Kwicklis, E.M.; and Gillies, D.C., eds. 1999. *Hydrogeology of the Unsaturated Zone, North Ramp Area of the Exploratory Studies Facility, Yucca Mountain, Nevada*. Water-Resources Investigations Report 98-4050. Denver, Colorado: U.S. Geological Survey. ACC: MOL.19990419.0335.

155692   Salve, R. 1999. *Fracture Flow, Fracture-Matrix Interaction*. Scientific Notebook YMP-LBNL-JSW-RS-1. ACC: MOL.19991013.0470.

157316   Salve, R. and Oldenburg, C.M. 2001. "Water Flow Within a Fault in Altered Nonwelded Tuff." *Water Resources Research, 37*, (12), 3043-3056. Washington, D.C.: American Geophysical Union. TIC: 251485.

161318   Salve, R.; Wang, J.S.Y.; and Doughty, C. 2002. "Liquid-Release Tests in Unsaturated Fractured Welded Tuffs: I. Field Investigations." *Journal of Hydrology, 256*, (1-2), 60-79. New York, New York: Elsevier. TIC: 253774.

164470   Salve, R.; Oldenburg, C.M.; and Wang, J.S.Y. 2003. "Fault-Matrix Interactions in Nonwelded Tuff of the Paintbrush Group at Yucca Mountain." *Journal of Contaminant Hydrology, 62-63*, 269-286. New York, New York: Elsevier. TIC: 254205.

100644   Sass, J.H.; Lachenbruch, A.H.; Dudley, W.W., Jr.; Priest, S.S.; and Munroe, R.J. 1988. *Temperature, Thermal Conductivity, and Heat Flow Near Yucca Mountain, Nevada: Some Tectonic and Hydrologic Implications.* Open-File Report 87-649. Denver, Colorado: U.S. Geological Survey. TIC: 203195.

102213   Savard, C.S. 1998. *Estimated Ground-Water Recharge from Streamflow in Fortymile Wash Near Yucca Mountain, Nevada.* Water-Resources Investigations Report 97-4273. Denver, Colorado: U.S. Geological Survey. TIC: 236848.

100075   Sawyer, D.A.; Fleck, R.J.; Lanphere, M.A.; Warren, R.G.; Broxton, D.E.; and Hudson, M.R. 1994. "Episodic Caldera Volcanism in the Miocene Southwestern Nevada Volcanic Field: Revised Stratigraphic Framework, ^{40}Ar/^{39}Ar Geochronology, and Implications for Magmatism and Extension." *Geological Society of America Bulletin, 106*, (10), 1304-1318. Boulder, Colorado: Geological Society of America. TIC: 222523.

104181   Scott, R.B. and Bonk, J. 1984. *Preliminary Geologic Map of Yucca Mountain, Nye County, Nevada, with Geologic Sections.* Open-File Report 84-494. Denver, Colorado: U.S. Geological Survey. ACC: HQS.19880517.1443.

161591   Sharpe, S. 2003. *Future Climate Analysis—10,000 Years to 1,000,000 Years After Present.* MOD-01-001 REV 01. Reno, Nevada: Desert Research Institute. ACC: MOL.20030407.0055.

154789   Smirnov, S. and Dublyansky, Y. 2000. "Secondary Mineral Assemblages in Fractures and Lithophysal Cavities at Yucca Mountain, Nevada, USA." *Abstracts with Programs - Geological Society of America, 32*, (7), A-260. Boulder, Colorado: Geological Society of America. TIC: 249113.

101293   SNL (Sandia National Laboratories) 1995. *Yucca Mountain Site Characterization Project Geology and Rock Structure Log, USW NRG-7/7a.* Rev. 1. Albuquerque, New Mexico: Sandia National Laboratories. ACC: MOL.19950327.0095.

117127   Sonnenthal, E.L. and Bodvarsson, G.S. 1999. "Constraints on the Hydrology of the Unsaturated Zone at Yucca Mountain, NV from Three-Dimensional Models of Chloride and Strontium Geochemistry." *Journal of Contaminant Hydrology, 38*, (1-3), 107-156. New York, New York: Elsevier. TIC: 244160.

104951   Striffler, P.; O'Brien, G.M.; Oliver, T.; and Burger, P. 1996. *Perched Water Characteristics and Occurrences, Yucca Mountain, Nevada*. Milestone 3GUS600M. Denver, Colorado: U.S. Geological Survey. ACC: MOL.19980224.0105.

130503   Stuckless, J.S. 1991. "An Evaluation of Evidence Pertaining to the Origin of Vein Deposits Exposed in Trench 14, Nevada Test Site, Nevada." *High Level Radioactive Waste Management, Proceedings of the Second Annual International Conference, Las Vegas, Nevada, April 28-May 3, 1991. 2*, 1429-1438. La Grange Park, Illinois: American Nuclear Society. TIC: 204272.

106947   Stuckless, J.S.; Peterman, Z.E.; and Muhs, D.R. 1991. "U and Sr Isotopes in Ground Water and Calcite, Yucca Mountain, Nevada: Evidence Against Upwelling Water." *Science, 254*, 551-554. Washington, D.C.: American Association for the Advancement of Science. TIC: 224423.

100086   Stuckless, J.S.; Marshall, B.D.; Vaniman, D.T.; Dudley, W.W.; Peterman, Z.E.; Paces, J.B.; Whelan, J.F.; Taylor, E.M.; Forester, R.M.; and O'Leary, D.W. 1998. "Comments on 'Overview of Calcite/Opal Deposits at or Near the Proposed High-Level Nuclear Waste Site, Yucca Mountain, Nevada, USA: Pedogenic, Hypogene, or Both' by C.A. Hill, Y.V. Dublyansky, R.S. Harmon, and C.M. Schluter." *Environmental Geology, 34*, (1), 70-78. New York, New York: Springer-Verlag. TIC: 238097.

147703   SubTerra. 1998. *Final Report, TRW Environmental Safety Systems, Inc., Busted Butte Test Facility*. Project: 97-35. Kirkland, Washington: SubTerra. TIC: 247628.

106963   Szymanski, J.S. 1989. *Conceptual Considerations of the Yucca Mountain Groundwater System with Special Emphasis on the Adequacy of This System to Accommodate a High-Level Nuclear Waste Repository*. Three volumes. Las Vegas, Nevada: U.S. Department of Energy, Nevada Operations Office. ACC: NNA.19890831.0152.

109175   Thompson, R.S. 1991. "Pliocene Environments and Climates in the Western United States." *Quaternary Science Reviews, 10*, 115-132. Oxford, United Kingdom: Pergamon Press. TIC: 234260.

139195   Tokunaga, T.K. and Wan, J. 1997. "Water Film Flow Along Fracture Surfaces of Porous Rock." *Water Resources Research, 33*, (6), 1287-1295. Washington, D.C.: American Geophysical Union. TIC: 242739.

160335   Trautz, R.C. and Wang, J.S.Y. 2002. "Seepage into an Underground Opening Constructed in Unsaturated Fractured Rock Under Evaporative Conditions." *Water Resources Research, 38*, (10), 6-1 through 6-14. Washington, D.C.: American Geophysical Union. TIC: 253348.

162593   Tsang, Y.W.; Huang, K.; and Bodvarsson, G.S. 2000. "Estimation of the Heterogeneity of Fracture Permeability by Simultaneous Modeling of Multiple Air-Injection Tests in Partially Saturated Fractured Tuff." *Dynamics of Fluids in Fractured Rock*. Geophysical Monograph 122. Pages 99-114. Washington, D.C.: American Geophysical Union. TIC: 255306.

149715   USGS (U.S. Geological Survey) 1974. *1973 Water Resources Data for Nevada, Part 1. Surface Water Records, Part 2. Water Quality Records*. Carson City, Nevada: U.S. Geological Survey. TIC: 236232.

158378   USGS 2001. *Future Climate Analysis*. ANL-NBS-GS-000008 REV 00 ICN 01. Denver, Colorado: U.S. Geological Survey. ACC: MOL.20011107.0004.

160355   USGS 2001. *Simulation of Net Infiltration for Modern and Potential Future Climates*. ANL-NBS-HS-000032 REV 00 ICN 02. Denver, Colorado: U.S. Geological Survey. ACC: MOL.20011119.0334.

100610   van Genuchten, M.T. 1980. "A Closed-Form Equation for Predicting the Hydraulic Conductivity of Unsaturated Soils." *Soil Science Society of America Journal, 44*, (5), 892-898. Madison, Wisconsin: Soil Science Society of America. TIC: 217327.

145369   Vaniman, D.T.; Chipera, S.J.; and Bish, D.L. 1994. "Pedogenesis of Siliceous Calcretes at Yucca Mountain, Nevada." *Geoderma, 63*, 1-17. Amsterdam, The Netherlands: Elsevier. TIC: 212060.

157427   Vaniman, D.T.; Chipera, S.J.; Bish, D.L.; Carey, J.W.; and Levy, S.S. 2001. "Quantification of Unsaturated-Zone Alteration and Cation Exchange in Zeolitized Tuffs at Yucca Mountain, Nevada, USA." *Geochimica et Cosmochimica Acta, 65*, (20), 3409-3433. New York, New York: Elsevier. TIC: 251574.

106793   Wang, J.S.Y. and Narasimhan, T.N. 1993. "Unsaturated Flow in Fractured Porous Media." Chapter 7 of *Flow and Contaminant Transport in Fractured Rock*. Bear, J.; Tsang, C-F.; and de Marsily, G., eds. San Diego, California: Academic Press. TIC: 235461.

101309   Wang, J.S.Y.; Flint, A.L.; Nitao, J.J.; Chesnut, D.A.; Cook, P.; Cook, N.G.W.; Birkholzer, J.; Freifeld, B.; Flint, L.E.; Ellet, K.; Mitchell, A.J.; Homuth, E.F.; Griego, G.J.; Cerny, J.A.; and Johnson, C.L. 1996. *Evaluation of Moisture Evolution in the Exploratory Studies Facility*. Milestone TR31K6M. Berkeley, California: Lawrence Berkeley National Laboratory. ACC: MOL.19961231.0089.

104366   Wang, J.S.Y. and Elsworth, D. 1999. "Permeability Changes Induced by Excavation in Fractured Tuff." *Rock Mechanics for Industry, Proceedings of the 37th U.S. Rock Mechanics Symposium, Vail, Colorado, USA, 6-9 June 1999.* Amadei, B.; Kranz, R.L.; Scott, G.A.; and Smeallie, P.H., eds. *2*, 751-757. Brookfield, Vermont: A.A. Balkema. TIC: 245246.

163215   Wang, J.S.Y. and Bodvarsson, G.S. 2003. "Evolution of the Unsaturated Zone Testing at Yucca Mountain." *Journal of Contaminant Hydrology, 62-63,* 337-360. New York, New York: Elsevier. TIC: 254205.

100091   Whelan, J.F.; Vaniman, D.T.; Stuckless, J.S.; and Moscati, R.J. 1994. "Paleoclimatic and Paleohydrologic Records from Secondary Calcite: Yucca Mountain, Nevada." *High Level Radioactive Waste Management, Proceedings of the Fifth Annual International Conference, Las Vegas, Nevada, May 22-26, 1994. 4,* 2738-2745. La Grange Park, Illinois: American Nuclear Society. TIC: 210984.

109179   Whelan, J.F. and Moscati, R.J. 1998. "9 M.Y. Record of Southern Nevada Climate from Yucca Mountain Secondary Minerals." *High-Level Radioactive Waste Management, Proceedings of the Eighth International Conference, Las Vegas, Nevada, May 11-14, 1998.* Pages 12-15. La Grange Park, Illinois: American Nuclear Society. TIC: 237082.

154773   Whelan, J.F.; Roedder, E.; and Paces, J.B. 2001. "Evidence for an Unsaturated-Zone Origin of Secondary Minerals in Yucca Mountain, Nevada." *"Back to the Future - Managing the Back End of the Nuclear Fuel Cycle to Create a More Secure Energy Future," Proceedings of the 9th International High-Level Radioactive Waste Management Conference (IHLRWM), Las Vegas, Nevada, April 29-May 3, 2001.* La Grange Park, Illinois: American Nuclear Society. TIC: 247873.

160442   Whelan, J.F.; Paces, J.B.; and Peterman, Z.E. 2002. "Physical and Stable-Isotope Evidence for Formation of Secondary Calcite and Silica in the Unsaturated Zone, Yucca Mountain, Nevada." *Applied Geochemistry, 17,* (6), 735-750. New York, New York: Elsevier. TIC: 253462.

163590   Whelan, J.F.; Neymark, L.A.; Roedder, E.; and Moscati, R.J. 2003. "Thermochronology of Secondary Minerals from the Yucca Mountain Unsaturated Zone." *Proceedings of the 10th International High-Level Radioactive Waste Management Conference (IHLRWM), March 30-April 2, 2003, Las Vegas, Nevada.* Pages 357-366. La Grange Park, Illinois: American Nuclear Society. TIC: 254368.

155426   Wilson, S.F. and Cline, J.S. 2001. "Paragenesis, Temperature and Timing of Secondary Minerals at Yucca Mountain." *"Back to the Future - Managing the Back End of the Nuclear Fuel Cycle to Create a More Secure Energy Future," Proceedings of the 9th International High-Level Radioactive Waste Management Conference (IHLRWM), Las Vegas, Nevada, April 29-May 3, 2001.* La Grange Park, Illinois: American Nuclear Society. TIC: 247873.

109187   Winograd, I.J.; Szabo, B.J.; Coplen, T.B.; Riggs, A.C.; and Kolesar, P.T. 1985. "Two-Million-Year Record of Deuterium Depletion in Great Basin Ground Waters." *Science, 227*, 519-522. Washington, D.C.: American Association for the Advancement of Science. TIC: 216799.

117167   Wu, Y.S.; Ritcey, A.C.; and Bodvarsson, G.S. 1999. "A Modeling Study of Perched Water Phenomena in the Unsaturated Zone at Yucca Mountain." *Journal of Contaminant Hydrology, 38*, (1-3), 157-184. New York, New York: Elsevier. TIC: 244160.

161058   Wu, Y-S.; Zhang, W.; Pan, L.; Hinds, J.; and Bodvarsson, G.S. 2002. "Modeling Capillary Barriers in Unsaturated Fractured Rock." *Water Resources Research, 38*, (11), 35-1 through 35-12. Washington, D.C.: American Geophysical Union. TIC: 253854.

162124   Xu, T.; Sonnenthal, E.; and Bodvarsson, G. 2003. "A Reaction-Transport Model for Calcite Precipitation and Evaluation of Infiltration Fluxes in Unsaturated Fractured Rock." *Journal of Contaminant Hydrology, 64*, (1-2), 113-127. New York, New York: Elsevier. TIC: 254008.

100194   Yang, I.C.; Rattray, G.W.; and Yu, P. 1996. *Interpretation of Chemical and Isotopic Data from Boreholes in the Unsaturated Zone at Yucca Mountain, Nevada*. Water-Resources Investigations Report 96-4058. Denver, Colorado: U.S. Geological Survey. ACC: MOL.19980528.0216.

101441   Yang, I.C.; Yu, P.; Rattray, G.W.; Ferarese, J.S.; and Ryan, J.N. 1998. *Hydrochemical Investigations in Characterizing the Unsaturated Zone at Yucca Mountain, Nevada*. Water-Resources Investigations Report 98-4132. Denver, Colorado: U.S. Geological Survey. ACC: MOL.19981012.0790.

160839   Yang, I.C. 2002. "Percolation Flux and Transport Velocity in the Unsaturated Zone, Yucca Mountain, Nevada." *Applied Geochemistry, 17*, (6), 807-817. New York, New York: Elsevier. TIC: 253605.

7.11.2   Data Listed by Data Tracking Number

162173   GS000108312232.001. Deep Unsaturated Zone Instrumentation Data from Boreholes USW NRG-7A, UE-25 UZ#4, UE-25 UZ#5, USW UZ-7A and USW SD-12 for 10/01/98 through 03/31/99. Submittal date: 01/03/2000.

146853   GS000308311221.004. Geospatial Input Data for Infil V2.0 FY99. Submittal date: 03/01/2000.

156911   GS000308312242.002. Phase 1 of Water Collection in Alcove 1 from 05/05/98 to 08/27/98. Submittal date: 03/01/2000.

162174   GS000708312232.004. Deep UZ Surface-Based Borehole Instrumentation Program-Interim Data Submittal for Boreholes USW NRG-7A, UE-25 UZ#4, and UE-25 UZ#5. Data Were Collected between 4/1/99 and 3/31/00. Submittal date: 09/13/2000.

162175   GS010908312232.001. Deep Unsaturated Zone Surface-Based Borehole Instrumentation Program-Interim Data Submittal for Boreholes USW NRG-7A, UE-25 UZ#4, and UE-25 UZ#5. Data Were Collected between April 1, 2000 and March 31, 2001. Submittal date: 09/26/2001.

162176   GS021008312232.001. Deep Unsaturated Zone Surface-Based Borehole Instrumentation Program - Final Data Submittal for Boreholes USW NRG-7A, UE-25 UZ#4, and UE-25 UZ#5. Data Were Collected between April 1, 2001 and December 17, 2001. Submittal date: 12/12/2002.

162178   GS021008312242.003. Moisture Monitoring in ESF, Alcoves 3 and 4, from April 1, 2000 through March 31, 2002. Submittal date: 01/15/2003.

161910   GS021008314224.002. Lithophysal Data Study from the Tptpll in the ECRB from Stations 14+44 to 23+26. Submittal date: 01/28/2003.

166517   GS921008312211.008. Geohydrologic Data from Test Holes UE-25 UZ#4 and UE-25 UZ#5, Yucca Mountain Area, Nye County, Nevada. Submittal date: 12/01/1992.

166239   GS940208314224.002. Full Periphery Geologic Map: Yucca Mountain Project, Exploratory Studies Facility, North Ramp - Starter Tunnel. Submittal date: 02/16/1994.

107136   GS940708312212.011. Volumetric Water Content from Neutron Moisture Meter Counts for 99 Boreholes from 5/3/89 or from the Time They Were Drilled Until 12/31/93. Submittal date: 07/13/1994.

166516   GS950108312210.001. Class A Pan Evaporation Depth for 1/1/90 to 9/30/94. Submittal date: 01/18/1995.

105572   GS950208312232.003. Data, Including Water Potential, Pressure and Temperature, Collected from Boreholes USW NRG-6 and USW NRG-7A from Instrumentation through March 31, 1995. Submittal date: 02/13/1995.

108990   GS950308312231.002. Laboratory Measurements of Core from USW SD-12 and Radial Boreholes. Submittal date: 03/02/1995.

108984   GS951108312231.009. Physical Properties, Water Content, and Water Potential for Borehole USW SD-7. Submittal date: 09/26/1995.

106756   GS951108312232.008. Data, Including Water Potential, Pressure and Temperature, Collected from Boreholes UE-25 UZ#4 & UZ#5 from Instrumentation through September 30, 1995, and from USW NRG-6 & NRG-7A from April 1 through September 30, 1995. Submittal date: 11/21/1995.

107131   GS960108312111.001. Geostatistical Model for Estimating Precipitation and Recharge in the Yucca Mountain Region, Nevada - California. Submittal date: 01/23/1996.

105573   GS960308312232.001. Deep Unsaturated Zone Surface-Based Borehole Instrumentation Program Data from Boreholes USW NRG-7A, USW NRG-6, UE-25 UZ#4, UE-25 UZ#5, USW UZ-7A, and USW SD-12 for the Time Period 10/01/95 through 3/31/96. Submittal date: 04/04/1996.

108985   GS960808312231.004. Physical Properties, Water Content and Water Potential for Samples from Lower Depths in Boreholes USW SD- 7 and USW SD-12. Submittal date: 08/30/1996.

108995   GS960808312231.005. Water Permeability and Relative Humidity Calculated Porosity for Samples from Boreholes USW SD-7, USW SD-9, USW SD-12 and USW UZ-14. Submittal date: 08/30/1996.

105974   GS960808312232.004. Deep Unsaturated Zone Surface-Based Borehole Instrumentation Program Data for Boreholes USW NRG-7A, USW NRG-6, UE-25 UZ#4, UE-25 UZ#5, USW UZ-7A and USW SD-12 for the Time Period 4/1/96 through 8/15/96. Submittal date: 08/30/1996.

146872   GS960908312211.004. Heat Dissipation Probe Data: Bleach Bone Ridge 3/95 - 11/95. Submittal date: 09/19/1996.

107065   GS960908312231.004. Characterization of Hydrogeologic Units Using Matrix Properties at Yucca Mountain, Nevada. Submittal date: 09/12/1996.

107228   GS960908312232.014. Unsaturated-Zone Gaseous-Phase (Pneumatic) System, and Overview of the Pneumatic System. Submittal date: 09/18/1996.

166511   GS960908312261.005. Milestone Report 3GGP605M Entitled Interpretation of Pneumatic and Chemical Data from the Unsaturated Zone Near Yucca Mountain, Nevada. Submittal date: 09/24/1996.

106059   GS960908314224.020. Analysis Report: Geology of the North Ramp - Stations 4+00 to 28+00 and Data: Detailed Line Survey and Full-Periphery Geotechnical Map - Alcoves 3 (UPCA) and 4 (LPCA), and Comparative Geologic Cross Section - Stations 0+60 to 28+00. Submittal date: 09/09/1996.

107182   GS970108312231.002. Physical Properties of Surface Samples from the ESF Main Drift (29+00 M to 57+00 M). Submittal date: 01/31/1997.

105975   GS970108312232.002. Deep Unsaturated Zone, Surface-Based Borehole Instrumentation Program - Raw Data Submittal for Boreholes USW NRG-7A, USW NRG-6, UE-25 UZ#4, UE-25 UZ#5, USW UZ-7A, and USW SD-12, for the Period 8/16/96 through 12/31/96. Submittal date: 01/22/1997.

107181   GS970208312231.003. Physical Properties, Water Content and Water Potential on Samples from Boreholes ESF-NAD-GTB#1 and ESF-NAD-GTB#1A from Alcove 6 in the ESF. Submittal date: 02/05/1997.

105675   GS970308312232.003. Results of Borehole Monitoring in the Unsaturated Zone Within the Main Drift Area of the Exploratory Studies Facility, Yucca Mountain, Nevada. Submittal date: 03/12/1997.

107183   GS970708312231.004. Physical Properties of Surface Samples for the ESF Main Drift. Submittal date: 07/18/1997.

105978   GS970808312232.005. Deep Unsaturated Zone Surface-Based Borehole Instrumentation Program Data from Boreholes USW NRG-7A, UE-25 UZ#4, UE-25 UZ#5, USW UZ-7A and USW SD-12 for the Time Period 1/1/97 - 6/30/97. Submittal date: 08/28/1997.

162164   GS970883122410.006. Horizontal Temperature Log Data Collected from Coreholes in Alcoves 2, 3, and 7 in the ESF, April 8-10, 1997. Submittal date: 08/27/1997.

107184   GS971008312231.006. Physical Properties and Saturated Hydraulic Conductivity of Cores from Surface Samples from the ESF Main Drift 29+00 M to 57+00 M. Submittal date: 10/06/1997.

105980   GS971108312232.007. Deep Unsaturated Zone Surface-Based Borehole Instrumentation Program Data from Boreholes USW NRG-7A, UE-25 UZ #4, UE-25 UZ #5, USW UZ-7A and USW SD-12 for the Time Period 7/1/97 - 9/30/97. Submittal date: 11/18/1997.

162166   GS980283122410.004. Pressure, Temperature, and Mass Flow Measurements from Alcove #7, Southern Ghost Dance Fault Drift (SGDFA), Single-Hole Air Injection Tests. Submittal date: 02/10/1998.

105982   GS980408312232.001. Deep Unsaturated Zone Surface-Based Borehole Instrumentation Program Data from Boreholes USW NRG-7A, UE-25 UZ #4, USW NRG-6, UE-25 UZ #5, USW UZ-7A and USW SD-12 for the Time Period 10/01/97 - 03/31/98. Submittal date: 04/16/1998.

166199   GS980508314224.003. Full-Periphery Geotechnical Maps (Drawings OA-46-309 through OA-46-311 and OA-46-313) and Rock Mass Quality Ratings Report for Alcove 7 (SGDFA), Exploratory Studies Facility, Main Drift. Submittal date: 05/08/1998.

156505   GS981208312232.002. Deep UZ Surface-Based Borehole Instrumentation Program Data from Boreholes USW NRG-7A, UE-25 UZ#4, USW NRG-6, UE-25 UZ#5, USW UZ-7A and USW SD-12 for the Time Period 4/1/98 through 9/30/98. Submittal date: 12/03/1998.

107185   GS990308312242.007. Laboratory and Centrifuge Measurements of Physical and Hydraulic Properties of Core Samples from Busted Butte Boreholes UZTT-BB-INJ-1, UZTT-BB-INJ-3, UZTT-BB-INJ-4, UZTT-BB-INJ-6, UZTT-BB-COL-5 and UZTT-BB-COL-8. Submittal date: 03/22/1999.

109822   GS990708312242.008. Physical and Hydraulic Properties of Core Samples from Busted Butte Boreholes. Submittal date: 07/01/1999.

149399   LA0004WS831372.002. Sorption of Np, Pu, and Am on Rock Samples from Busted Butte, NV. Submittal date: 04/19/2000.

156586   LA9912WS831372.001. Sorption of Fluorinated Benzoic Acids and Lithium on Rock Samples from Busted Butte, NV. Submittal date: 02/22/2000.

153155   LB0011AIRKTEST.001. Air Permeability Testing in Niches 3566 and 3650. Submittal date: 11/08/2000.

157169   LB0110COREPROP.001. Lab Measurements of 14 Matrix Cores. Submittal date: 11/12/2001.

158478   LB0204NICH3TRC.001. Fault Infiltration Test Tracer Sampling Apr 2001-Mar 2002. Submittal date: 04/30/2002.

162570   LB0303A8N3LIQR.001. Alcove 8 - Niche 3 Seepage Data Compilation. Submittal date: 03/19/2003.

105593   LB980912332245.002. Gas Tracer Data from Niche 3107 of the ESF. Submittal date: 09/30/1998.

143974   MO0001GSC00001.000. Alcove #4 and Alcove #4 Technical Coordination Office (TCO) Niche Profile Alignments, Exploratory Studies Facility (ESF). Submittal date: 01/20/2000.

152167   MO0003GSC00096.000. Exploratory Studies Facility (ESF) Niche #2 Profile Alignment. Submittal date: 03/01/2000.

152108   MO0003GSC00102.000. Exploratory Studies Facility (ESF) Alcove #6, Drill Bay Profile Alignment. Submittal date: 03/03/2000.

152176   MO0003GSC00103.000. Exploratory Studies Facility (ESF) Niche 3 Profile Alignment. Submittal date: 03/03/2000.

149808   MO0004YMP99055.001. Surface Water Features in the Yucca Mountain Region.
          Submittal date: 03/31/2000.

149812   MO0004YMP99057.001. Surface Water Data Collection Sites in the Yucca Mountain
          Vicinity. Submittal date: 03/31/2000.

153143   MO0005GSC00216.000. Exploratory Studies Facility (ESF) Alcove 1, Profile
          Alignment. Submittal date: 05/25/2000.

152630   MO0006GSC00241.000. Exploratory Studies Facility (ESF) Alcove 8, Profile
          Alignment. Submittal date: 06/30/2000.

150613   MO0006YMP99058.001. Surface Water Data Collection Sites at and Near Yucca
          Mountain Region. Submittal date: 06/07/2000.

154173   MO0008GSC00272.000. Exploratory Studies Facility (ESF) Niche 1, Profile
          Alignment. Submittal date: 08/01/2000.

152626   MO0008GSC00273.000. Exploratory Studies Facility (ESF) Niche 4, Profile
          Alignment. Submittal date: 08/01/2000.

155370   MO0009GSC00332.000. Exploratory Studies Facility (ESF) Niche 5, Plan and
          Profile As-Built. Submittal date: 09/27/2000.

166212   MO0011GSC00385.000. Alcove #7 Profile/Alignment, Southern Ghost Dance Fault,
          Exploratory Studies Facilities (ESF). Submittal date: 11/14/2000.

166213   MO0208GSC01042.001. Alcove #5 Profile/Alignment, Exploratory Studies Facilities
          (ESF). Submittal date: 08/15/2002.

166495   MO0312SEPSDAAR.000. Model Estimates of Average Annual Recharge of
          3-Springs and East Steward Watersheds. Submittal date: 12/14/2003.

166405   MO0312SEPSDAIR.000. Apparent Infiltration Rates Calculated from Representative
          Pore Water Chloride Concentrations at Yucca Mountain. Submittal date: 12/14/2003.

166382   MO0312SEPSDAPM.000. Statistical Summaries of Air Permeability Data by
          Lithostratigraphic and Hydrogeologic Unit, and for the Bow Ridge Fault. Submittal
          date: 12/14/2003.

166483   MO0312SEPSDBBG.000. Busted Butte Geologic Map. Submittal date: 12/16/2003.

166567   MO0312SEPSDBTV.000. Statistical Summary of Permeability Values from the
          Type-Curve Analytical Solutions of Crosshole Air-Injection Testing of the Northern
          Ghost Dance Fault Drill Room Boreholes, Alcove 6. Submittal date: 12/19/2003.

166562   MO0312SEPSDDVT.000. Depth Versus Time Profile of Measured Water Contents in
          Borehole USW UZ-N15 for 1993 through 1995. Submittal date: 12/19/2003.

166386   MO0312SEPSDHYP.000. Statistical Summaries of Hydrologic Properties Resulting from Testing in Alcove 6. Submittal date: 12/14/2003.

166489   MO0312SEPSDIFR.000. Infiltration Rates Calculated by Chloride Mass Balance Method. Submittal date: 12/14/2003.

166564   MO0312SEPSDINP.000. Air-Injection Permeability Values in the Paintbrush Hydrogeologic Unit with Depth in Borehole USW NRG-7A Tuff. Submittal date: 12/19/2003.

166492   MO0312SEPSDNBH.000. List of Neutron Boreholes, Locations, and Altitude, Drilling Dates, Description, Depths, and Lithology at Yucca Mountain. Submittal date: 12/16/2003.

166565   MO0312SEPSDOPD.000. The Ten Largest Observed Peak Discharges in the Yucca Mountain Region. Submittal date: 12/19/2003.

166573   MO0312SEPSDOV6.000. Schematic Diagram (Overhead View) of Alcove 6 (the Northern Ghost Dance Fault Alcove) and Test Boreholes. Submittal date: 12/19/2003.

166568   MO0312SEPSDPIE.000. Summary of Pneumatic-Interference Events at Instrumented Boreholes Caused by Exploratory Studies Facility Excavation. Submittal date: 12/19/2003.

166563   MO0312SEPSDSHC.000. Porosity and Log of Saturated Hydraulic Conductivity of all Samples from 26 Vertical Transects of the Base of the Tiva Canyon. Submittal date: 12/19/2003.

166566   MO0312SEPSDTIL.000. Comparison of Total Infiltration Loss Estimates for Fortymile Wash. Submittal date: 12/19/2003.

166561   MO0312SEPSDWCP.000. Water Content and Water Potential at the Soil-Bedrock Interface at a Depth of 2.1 Meters (6.9 Feet) in Borehole USW UZ-N52. Submittal date: 12/19/2003.

144030   MO9912GSC99493.000. Exploratory Studies Facility (ESF) Alcove #2 Profile Alignment. Submittal date: 12/21/1999.

141489   MO9912GSC99494.000. Exploratory Studies Facilities (ESF) Alcove #3 Profile Alignment. Submittal date: 12/21/1999.

146457   MO9912YMP99069.000. Potential Repository Area Boreholes and Exploratory Studies Facility. Submittal date: 12/01/1999.

7.11.3 Software Codes

166193   USGS 1999. *Software Code: AIR3D*. V22.6.98. PC, DOS. 10134-22.6.98-00.

160577   USGS 1999. *Software Code: FracMAN*. V.2.511. PC Windows NT.
10114-2.511-00.

INTENTIONALLY LEFT BLANK
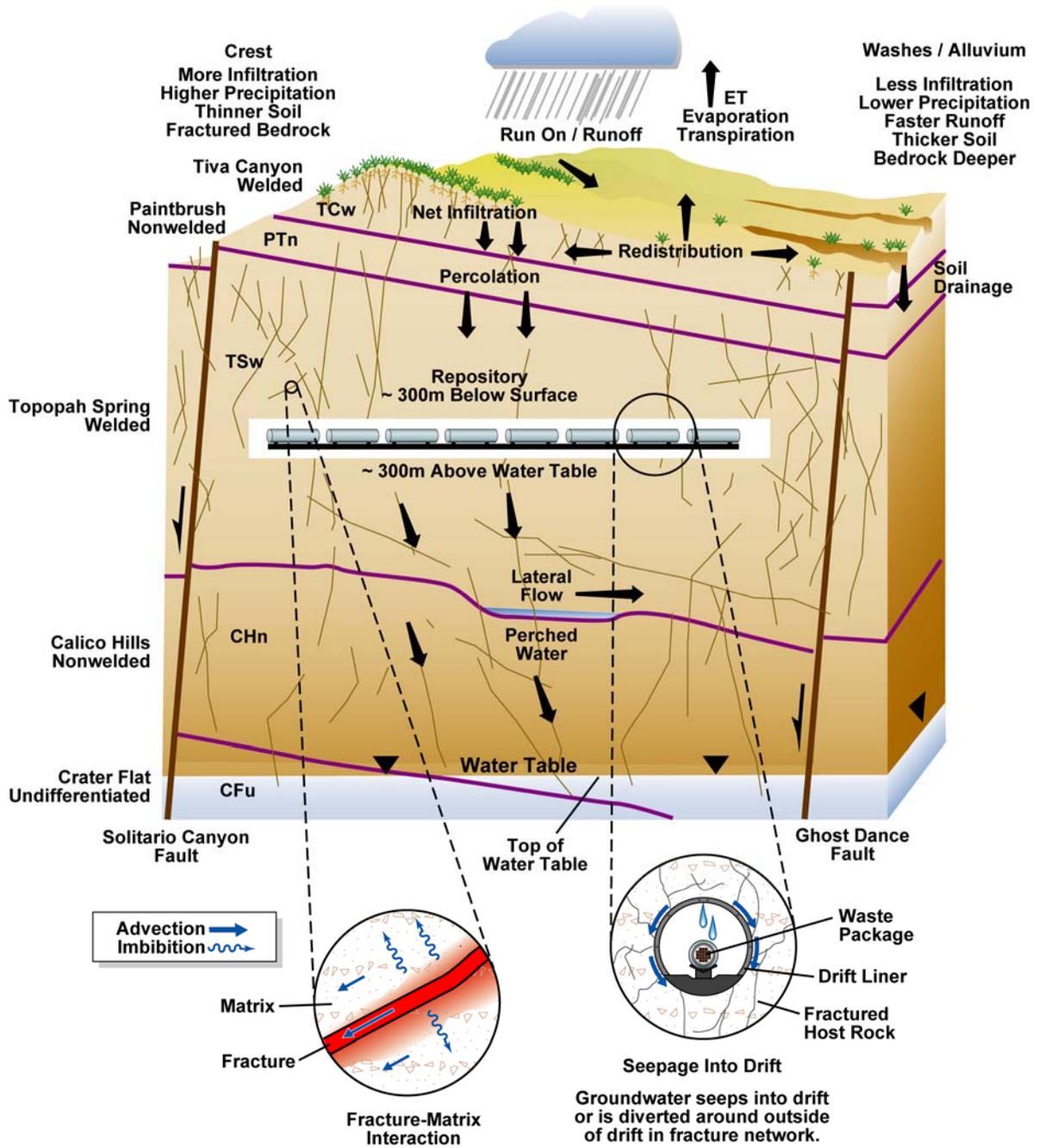
Source: DOE 1998 [DIRS 101779], Volume 1, Figure 2-15

Figure 7-1. Conceptual Drawing of Unsaturated Zone Flow Processes

Source: Modified from DTN: MO9912YMP99069.000 [DIRS 146457]

Figure 7-2. Map Showing Repository Area Boreholes and the Exploratory Studies Facility, and the Enhanced Characterization of the Repository Block Cross Drift
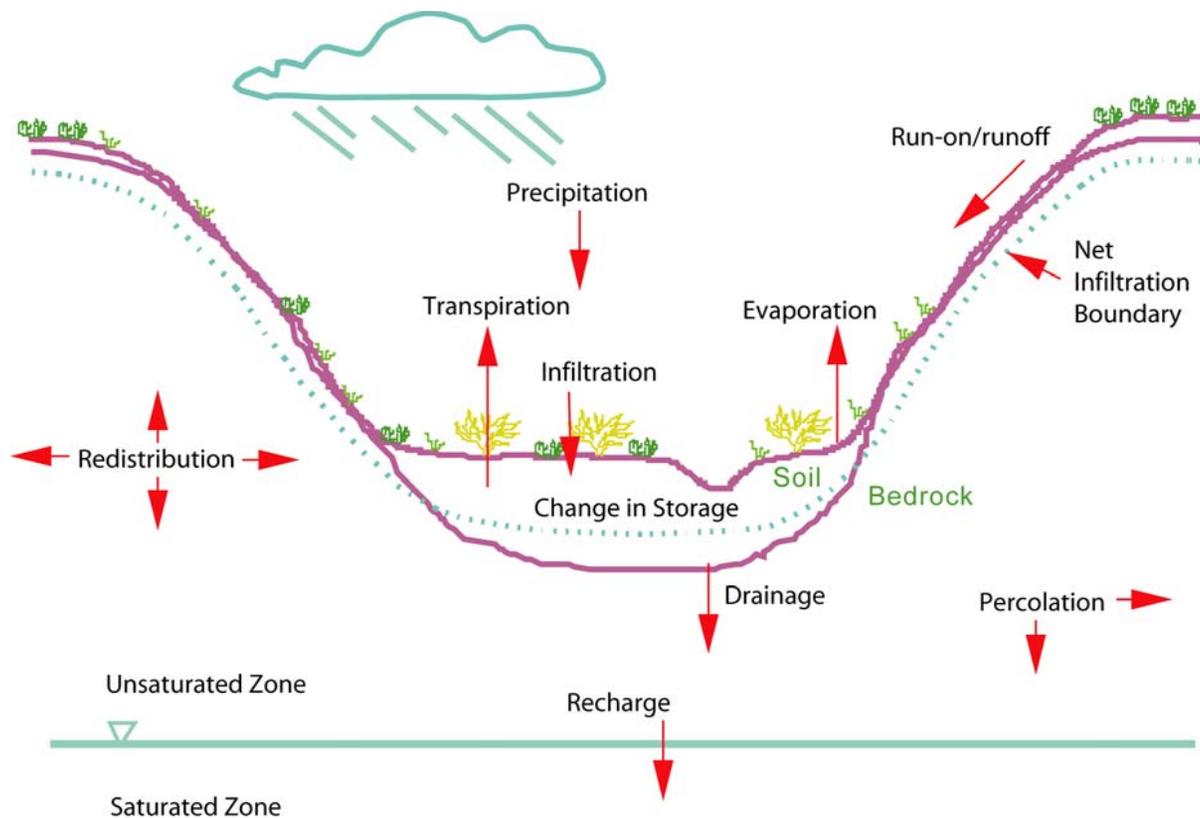
Precipitation + Change in Storage - Drainage-ET-Runoff=0

00379DC_003.ai

Source: Modified from Flint et al. 1996 [DIRS 100147], Figure 3

Figure 7-3. Schematic of Hydrologic Cycle Illustrating Surficial and Subsurface Processes Affecting Net Infiltration and Recharge
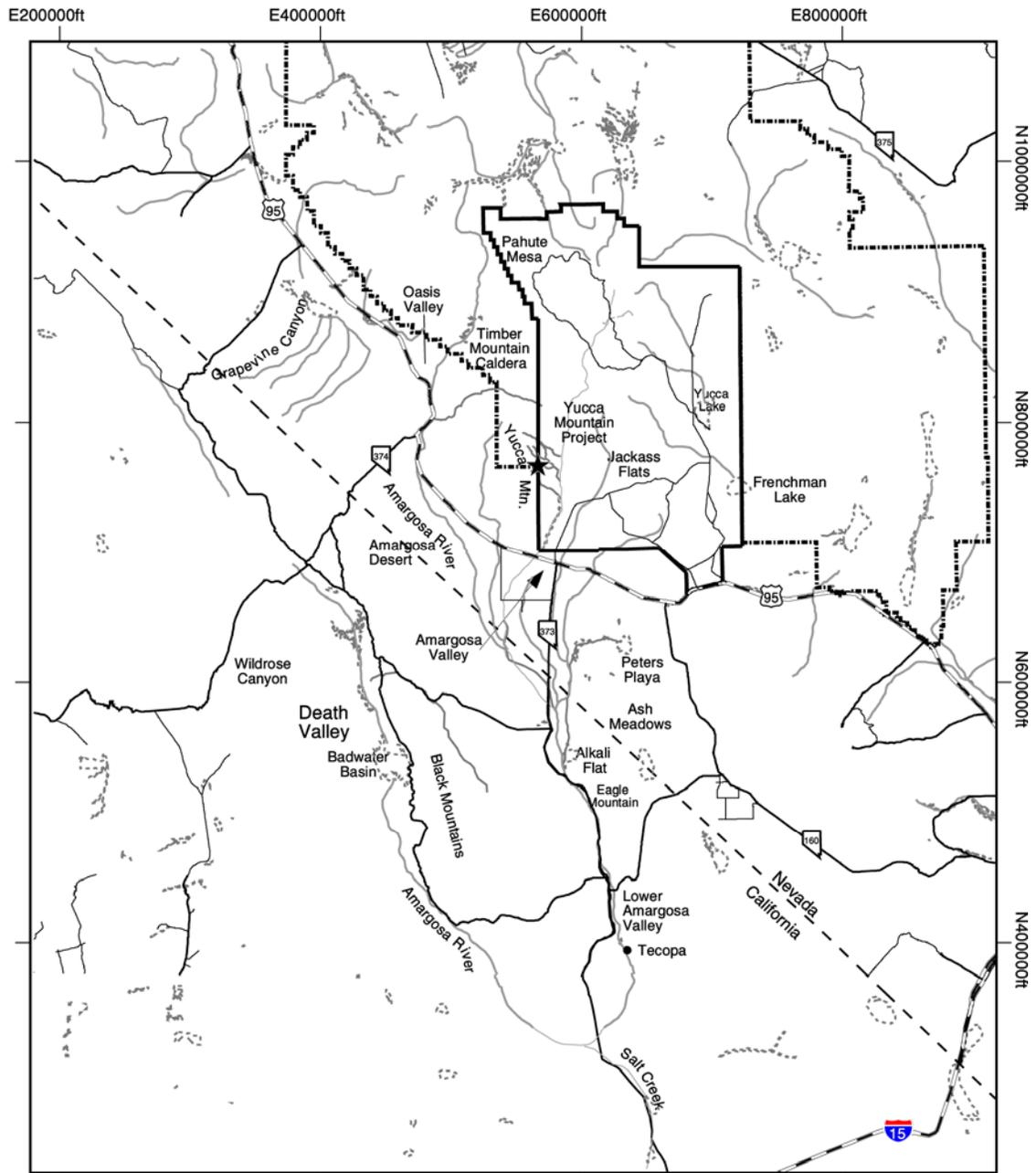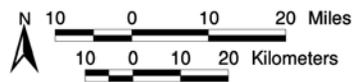
Source: Modified from DTN: MO0004YMP099055.001 [DIRS 149808]

Figure 7-4. Surface Water Features in the Yucca Mountain Region
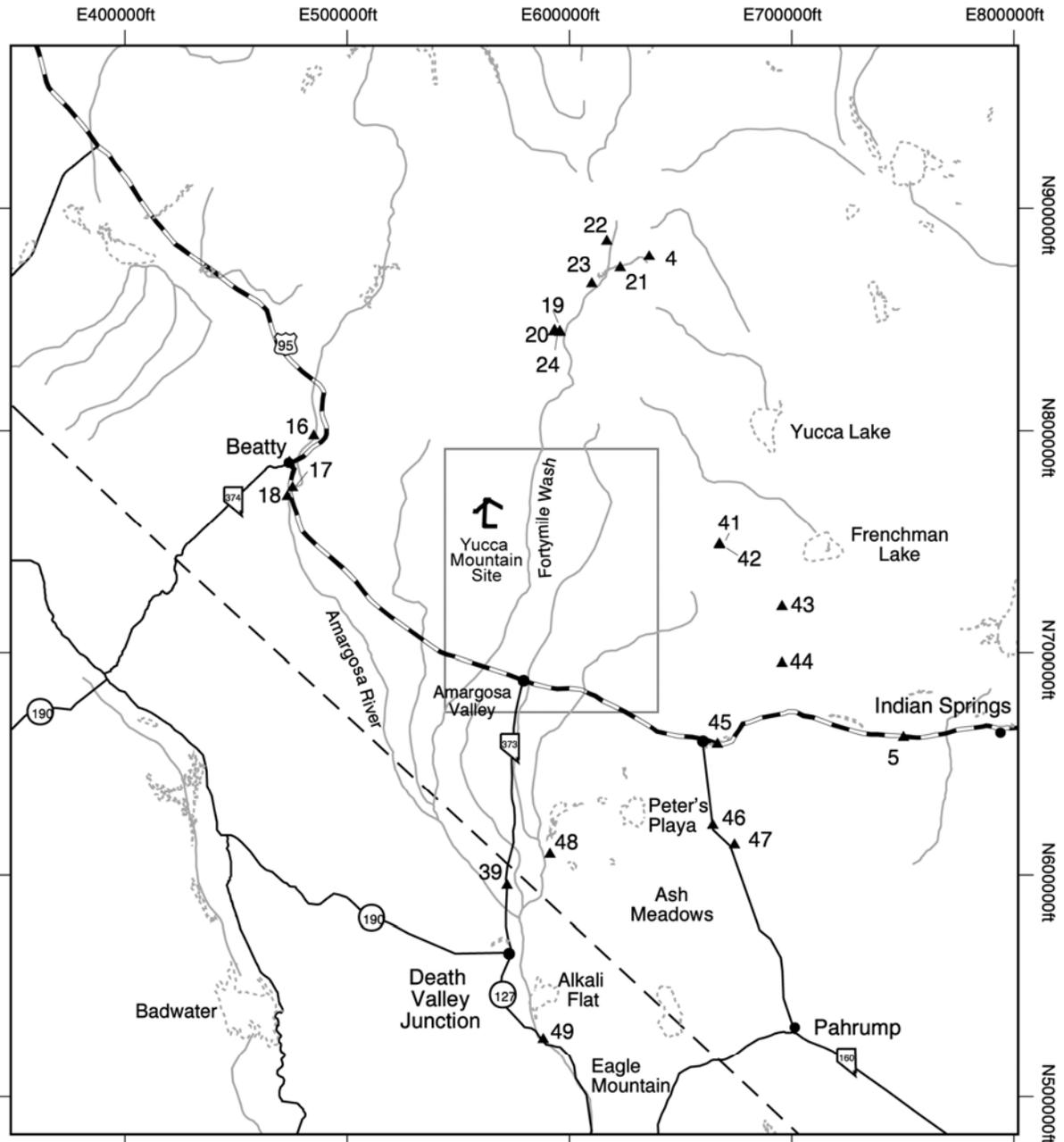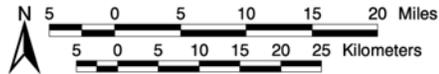
Source: Modified from DTN: MO0004YMP99057.001 [DIRS 149812]

NOTE: Callout area in the vicinity of the Yucca Mountain Site and Fortymile Wash is shown in Figure 7-5b.

Figure 7-5a. Surface Water Data Collection Sites near Yucca Mountain
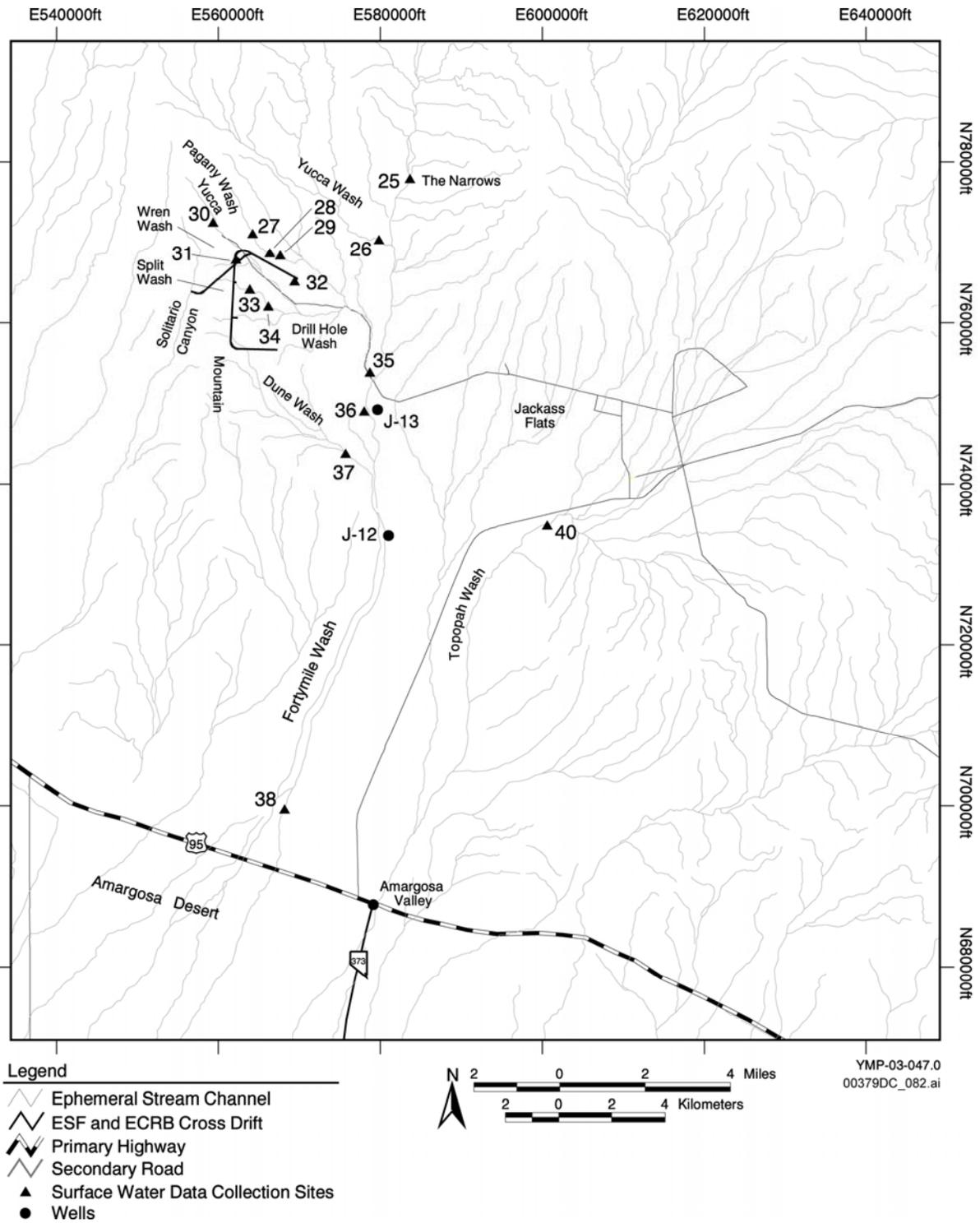
Source: Modified from DTN: MO0006YMP99058.001 [DIRS 150613]

Figure 7-5b. Surface Water Data Collection Sites in the Yucca Mountain Vicinity
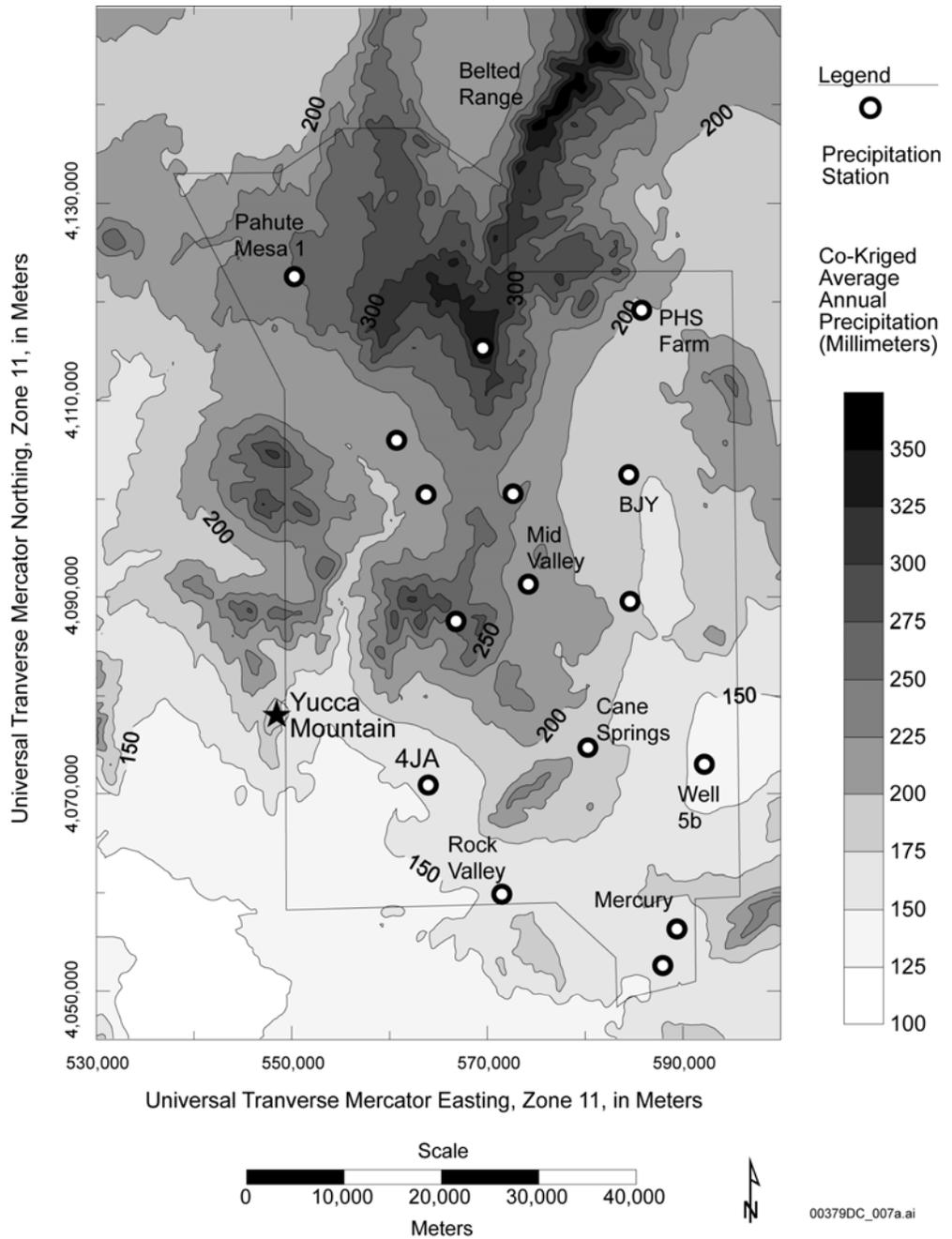
DTN: GS960108312111.001 [DIRS 107131]

Source: Modified from Hevesi and Flint 1995 [DIRS 107413], Figure 22

Figure 7-6. Estimated Average Annual Precipitation for Yucca Mountain and the Nevada Test Site
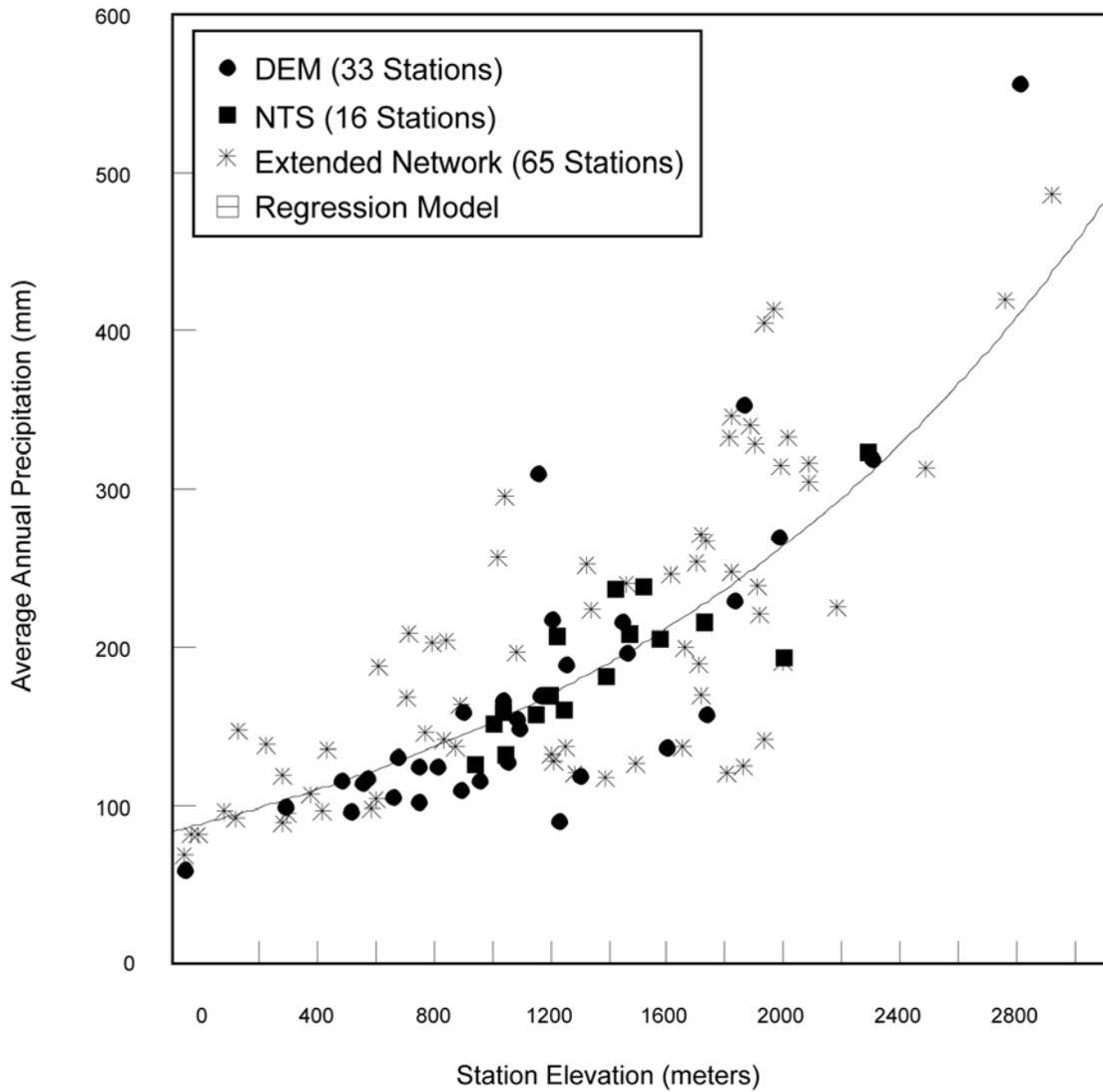
Source: Hevesi and Flint 1995 [DIRS 107413], Figure 9

Figure 7-7.   Average Annual Precipitation versus Elevation for 114 Precipitation Stations in the Yucca
Mountain Region with a Minimum of Eight Complete Years of Record
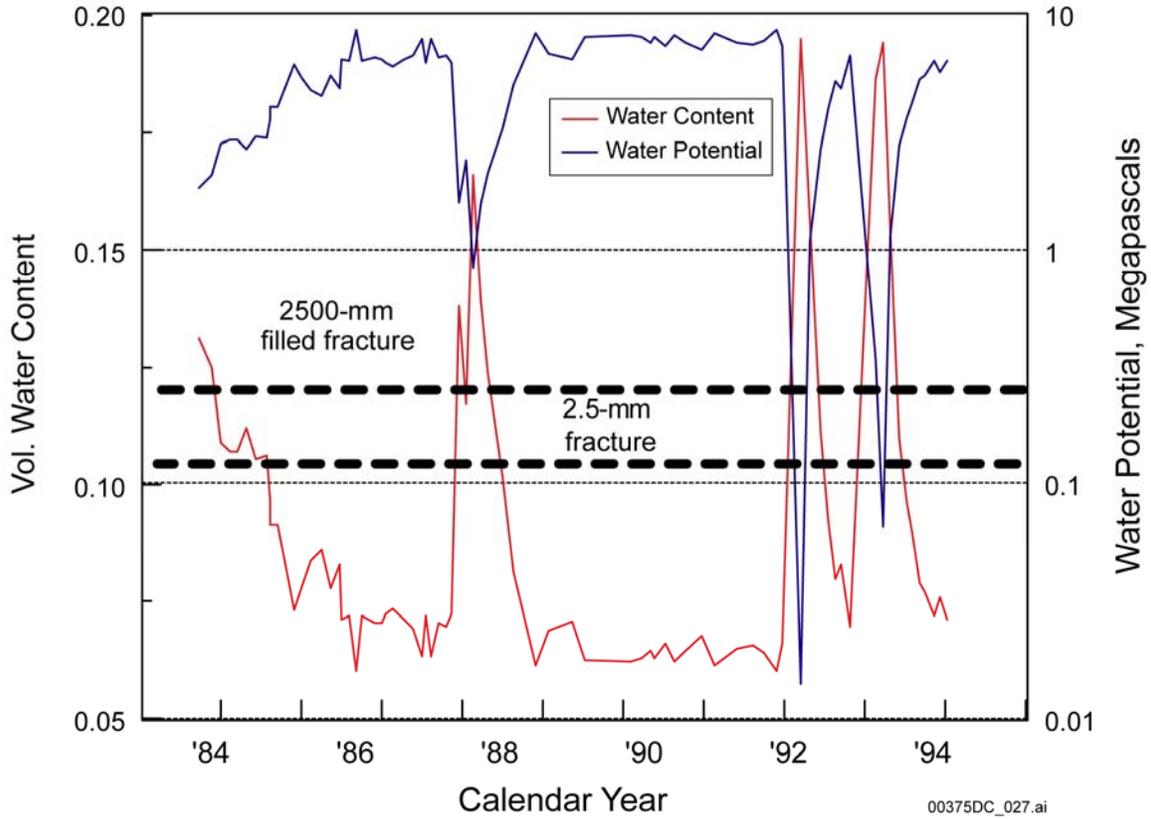
DTN: MO0312SEPSDWCP.000 [DIRS 166561]

Source: Flint et al. 1996 [DIRS 100147], Figure 6

Figure 7-8.   Water Content and Water Potential at the Soil-Bedrock Interface at a Depth of 2.1 Meters
(6.9 Feet) in Borehole USW UZ-N52
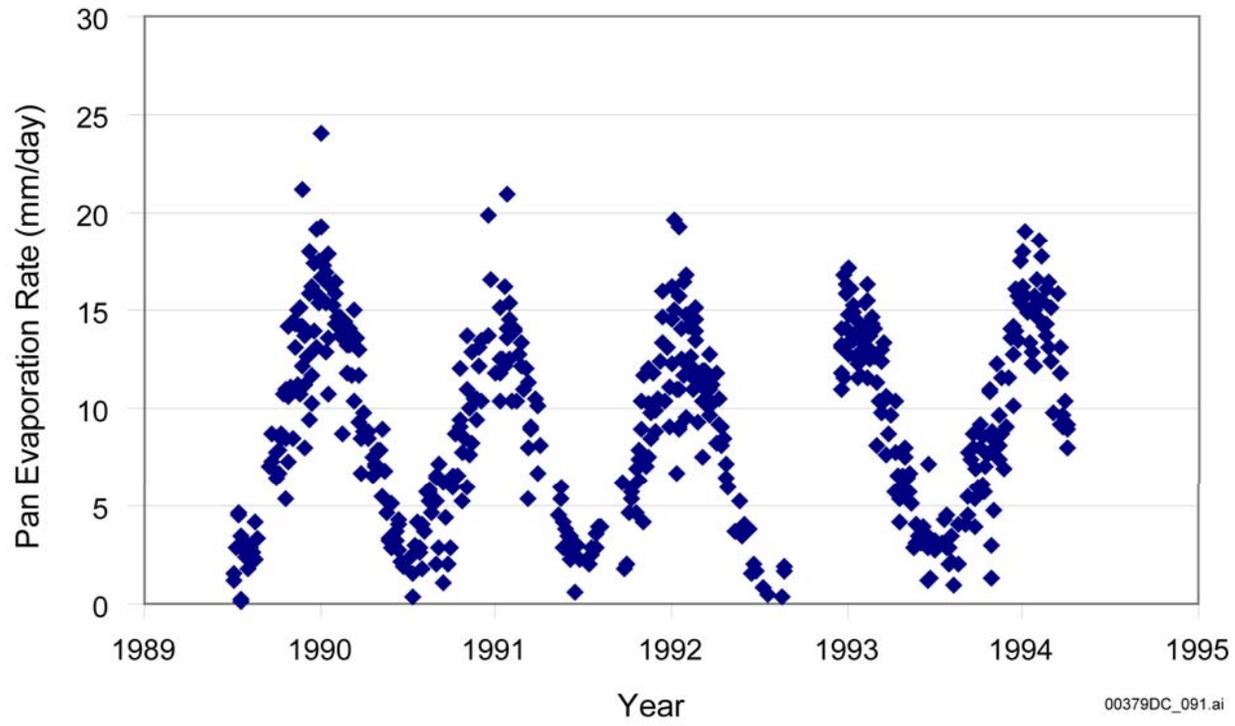
DTN: GS950108312210.001 [DIRS 166516]

Figure 7-9. Measured Evaporation Pan Data for 1990 to 1994
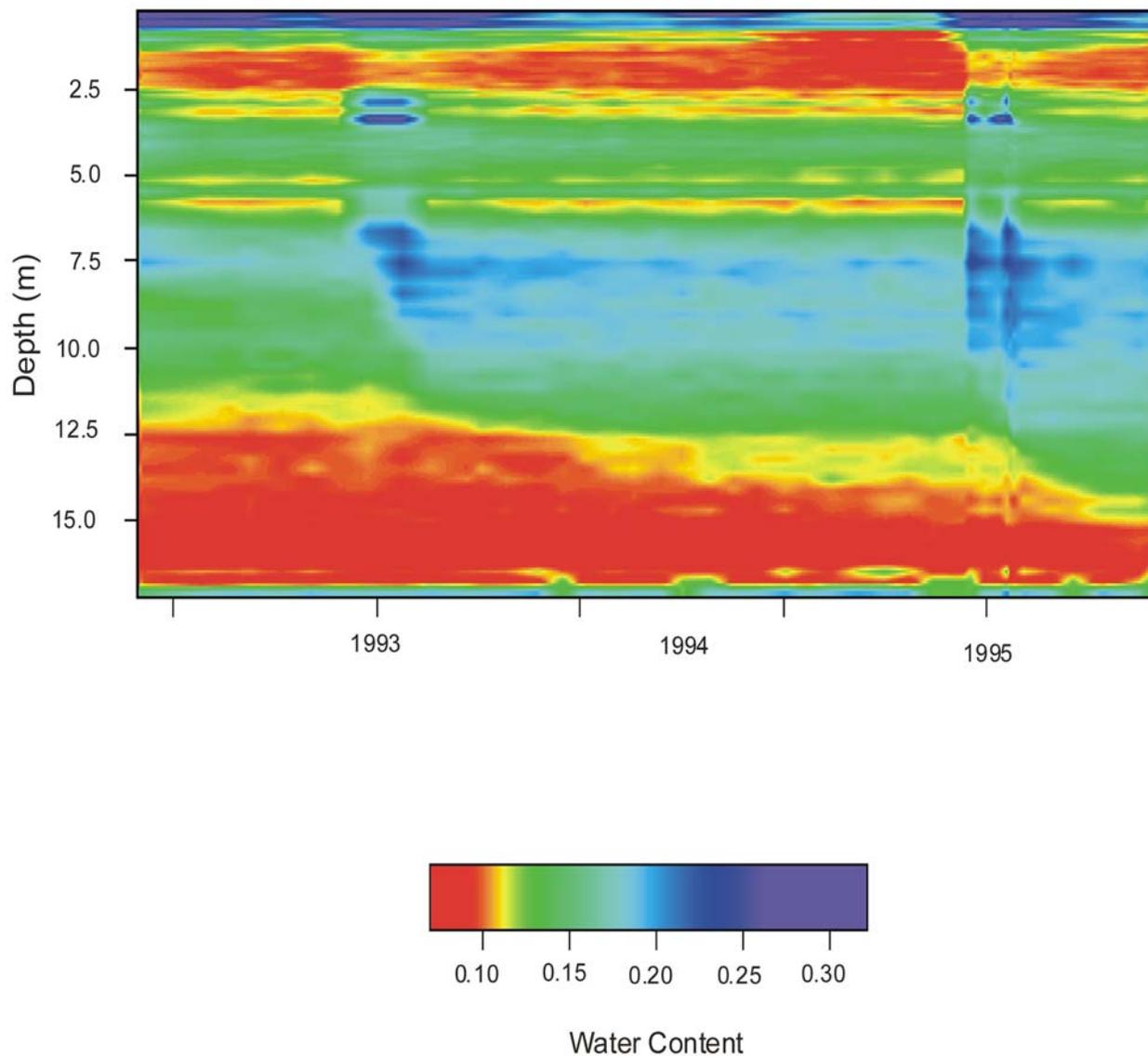
Source: USGS 2001 [DIRS 160355], Figure 6-4

Figure 7-10. Depth versus Time Profile of Measured Water Contents in Borehole USW UZ-N15 for 1993 through 1995
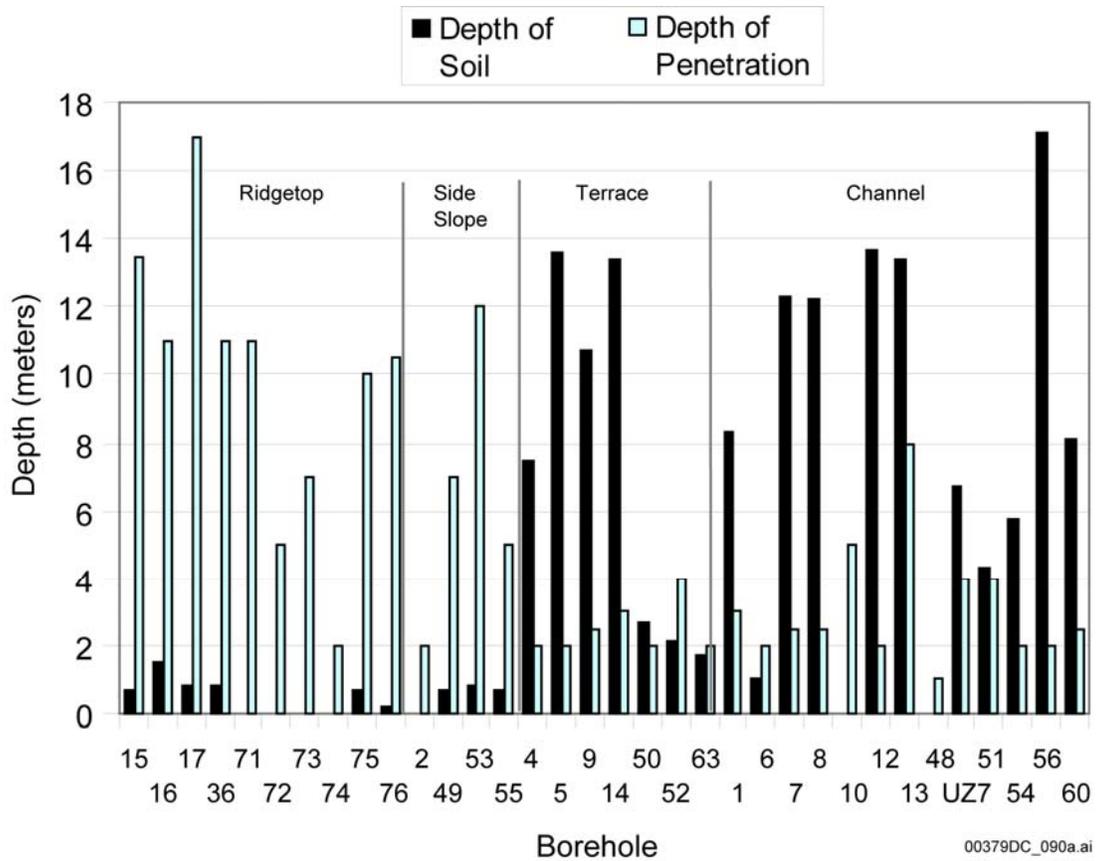
DTN: GS940708312212.011 [DIRS 107136]; MO0312SEPSDNBH.000 [DIRS 166492]

Source: Modified from Flint and Flint, 1995 [DIRS 100394], Figure 7

Figure 7-11.   Average Depth of Penetration of the Wetting Front for Year 1990 to 1993 and Soil Depth for 34 Boreholes
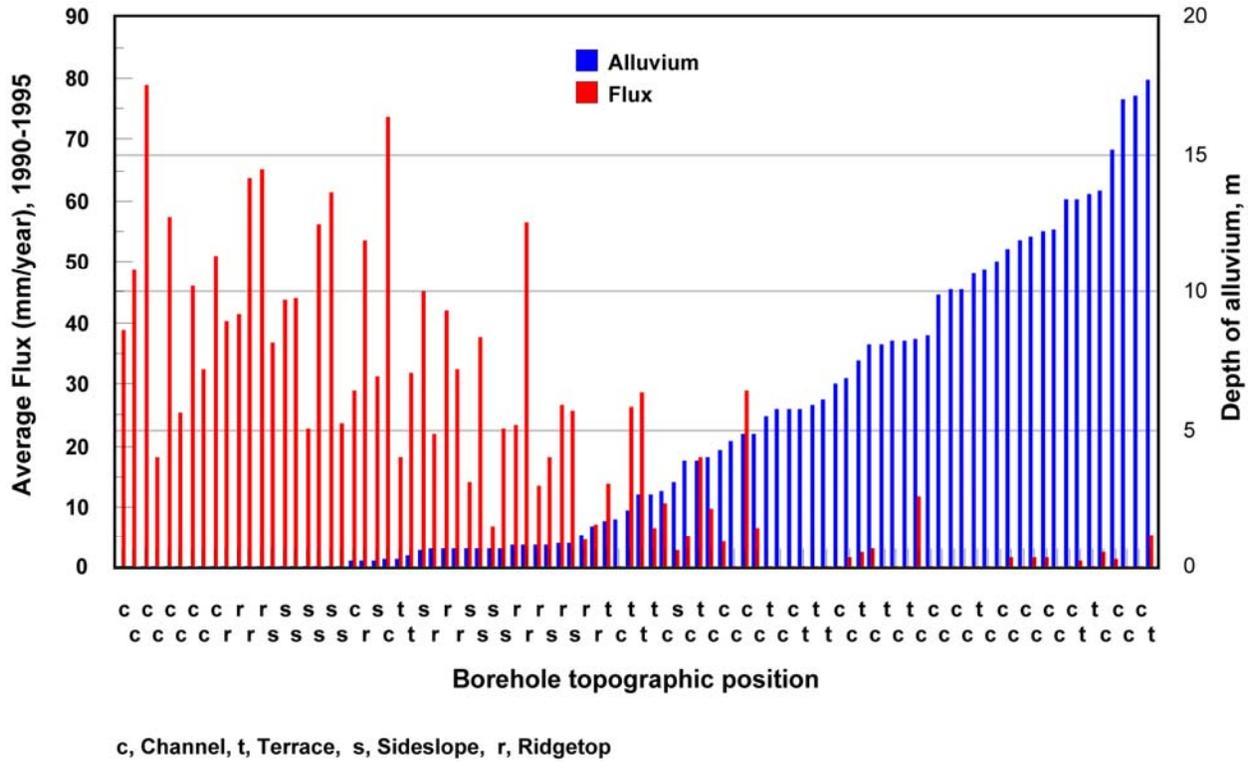
Source: USGS 2001 [DIRS 160355], Figure 6-5

Figure 7-12. Average Annual Infiltration through the Top One Meter of Bedrock at Neutron Boreholes for 1990 through 1995 Compared to Depth of Alluvium
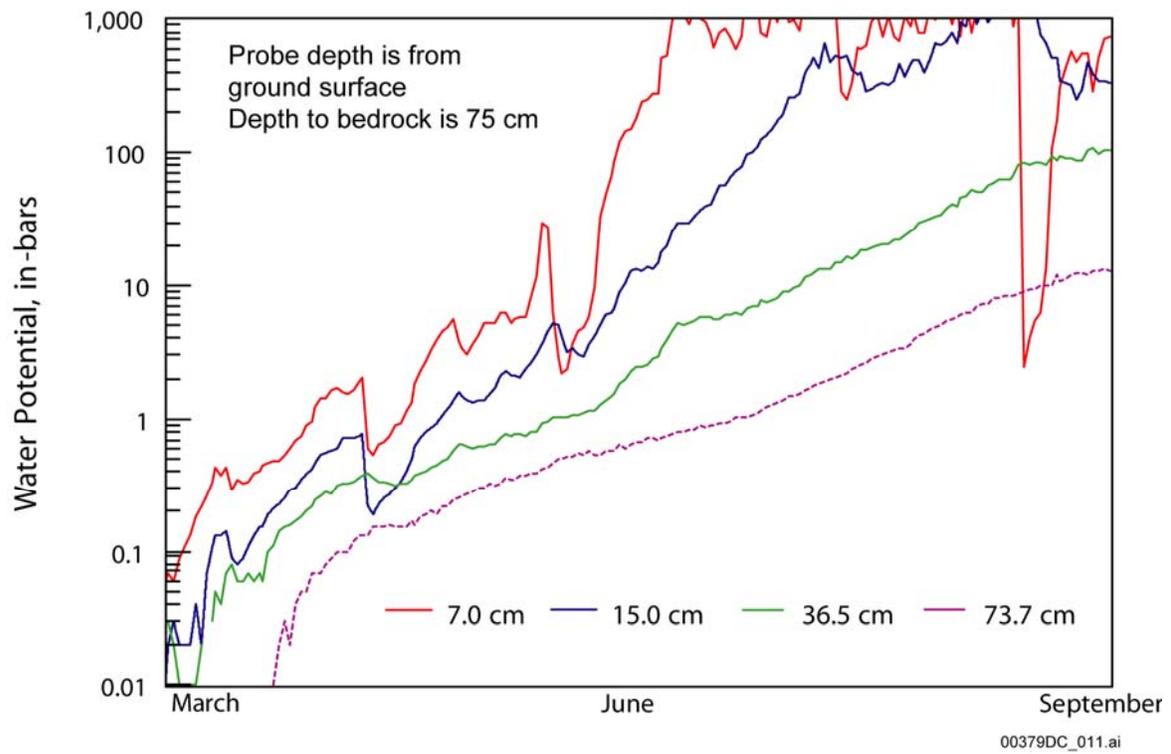
DTN: GS960908312211.004 [DIRS 146872]

Sources: USGS 2001 [DIRS 160355], Figure 6-6

Figure 7-13. Water-Potential Measurements used to Estimate Infiltration Flux
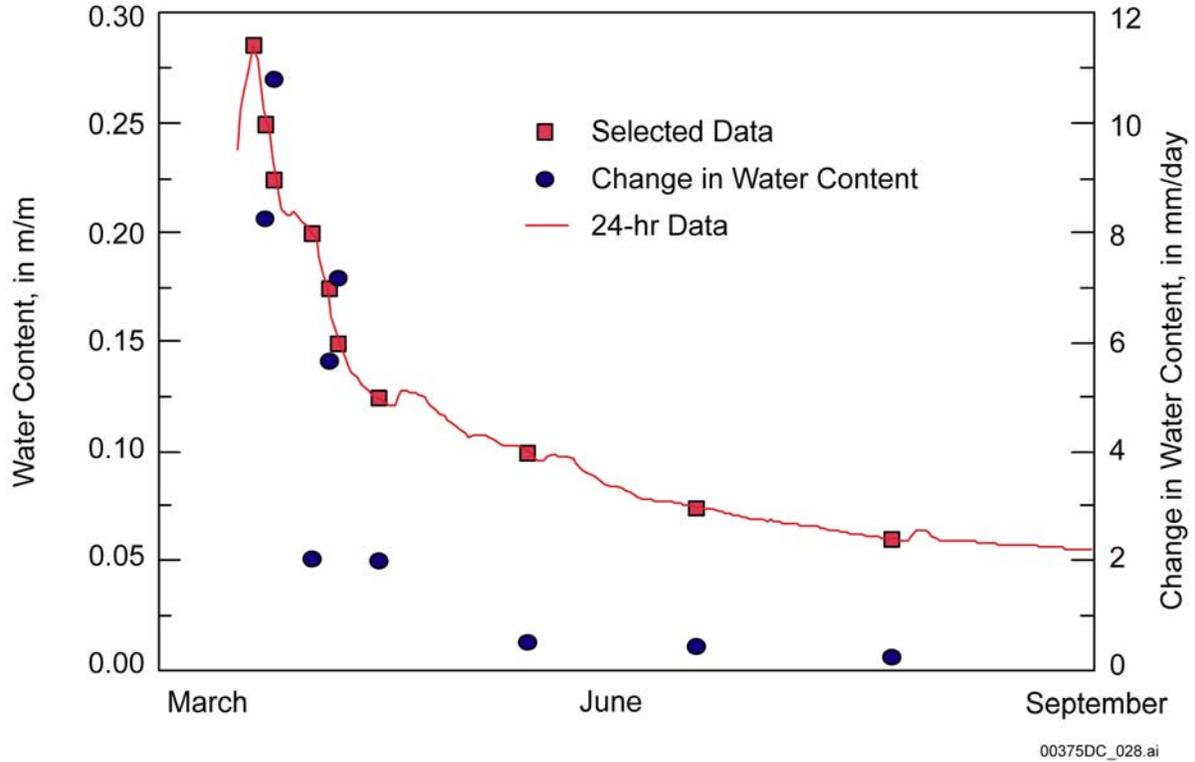
DTN: GS960908312211.004 [DIRS 146872]

Source: Modified from USGS 2001 [DIRS 160355], Figure 6-6

Figure 7-14. Changes in Water Content with Depth near Borehole USW UZ-N15, February to September 1995
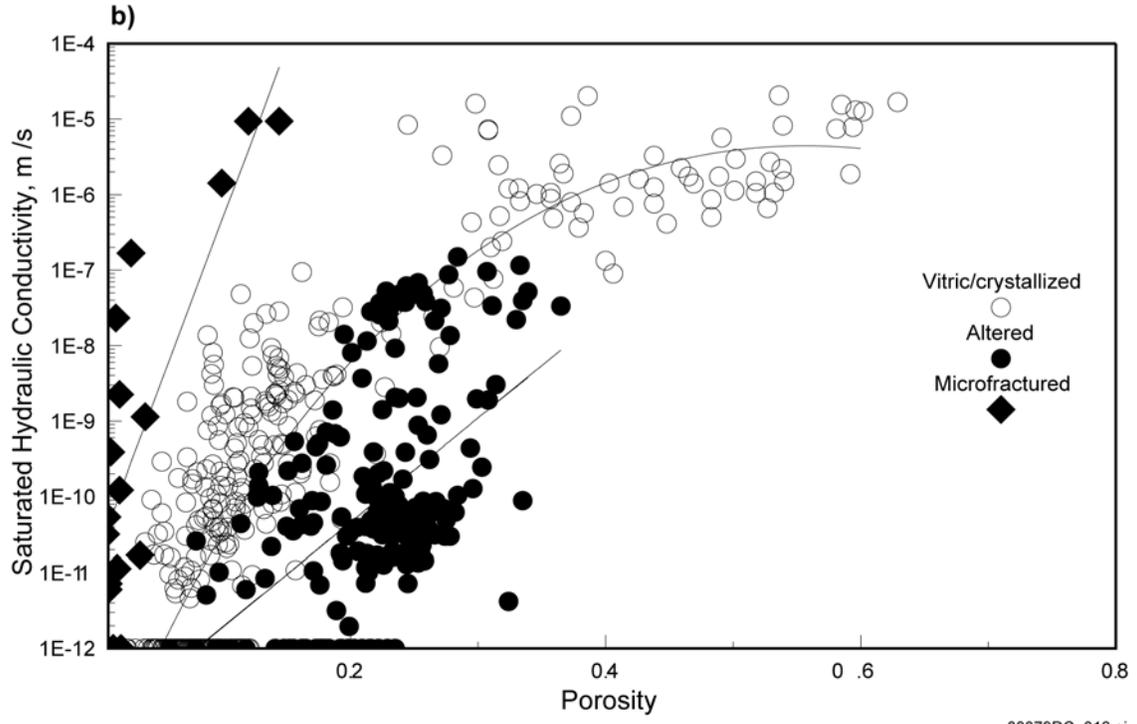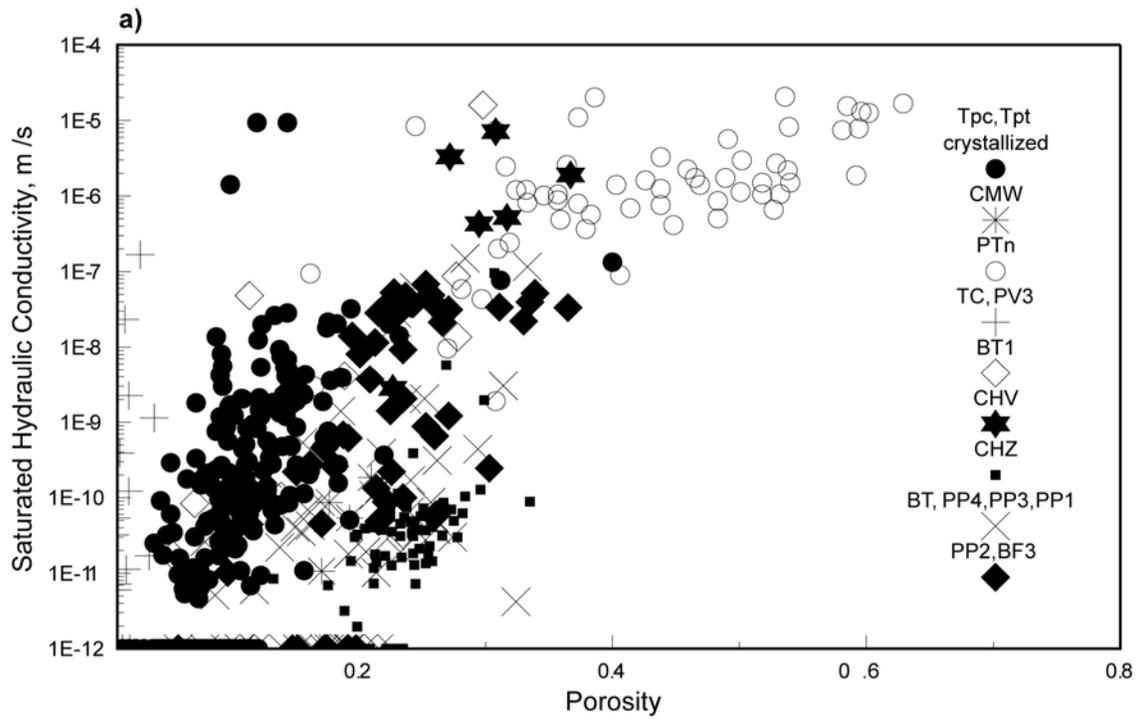
Source: Flint 1998 [DIRS 100033], Figure 12

NOTES: Plot (a) is grouped by hydrologic unit; plot (b) by generalized rock type. Values of 1×10^{-12} m/s are samples that had conductivities too low to measure.

Figure 7-15. Relationship between Porosity and Saturated Hydraulic Conductivity
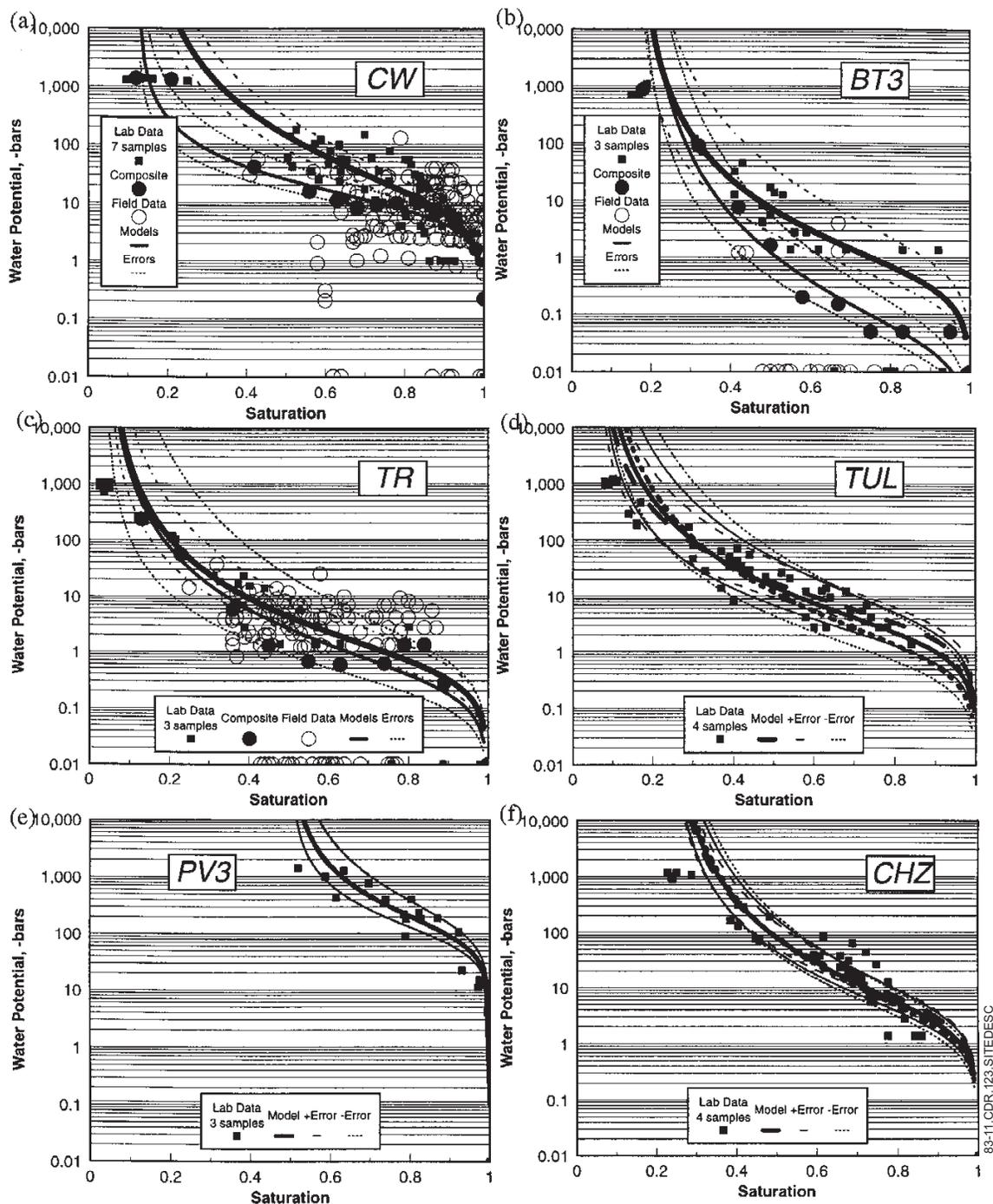
Source: Flint 1998 [DIRS 100033], Figure 13

NOTE: Data sets for all units include laboratory measurements of core, whereas data sets for units CW, BT3, and TR also include field measurements.

Figure 7-16. Moisture Retention Curves for Core Samples from Six Hydrogeologic Units
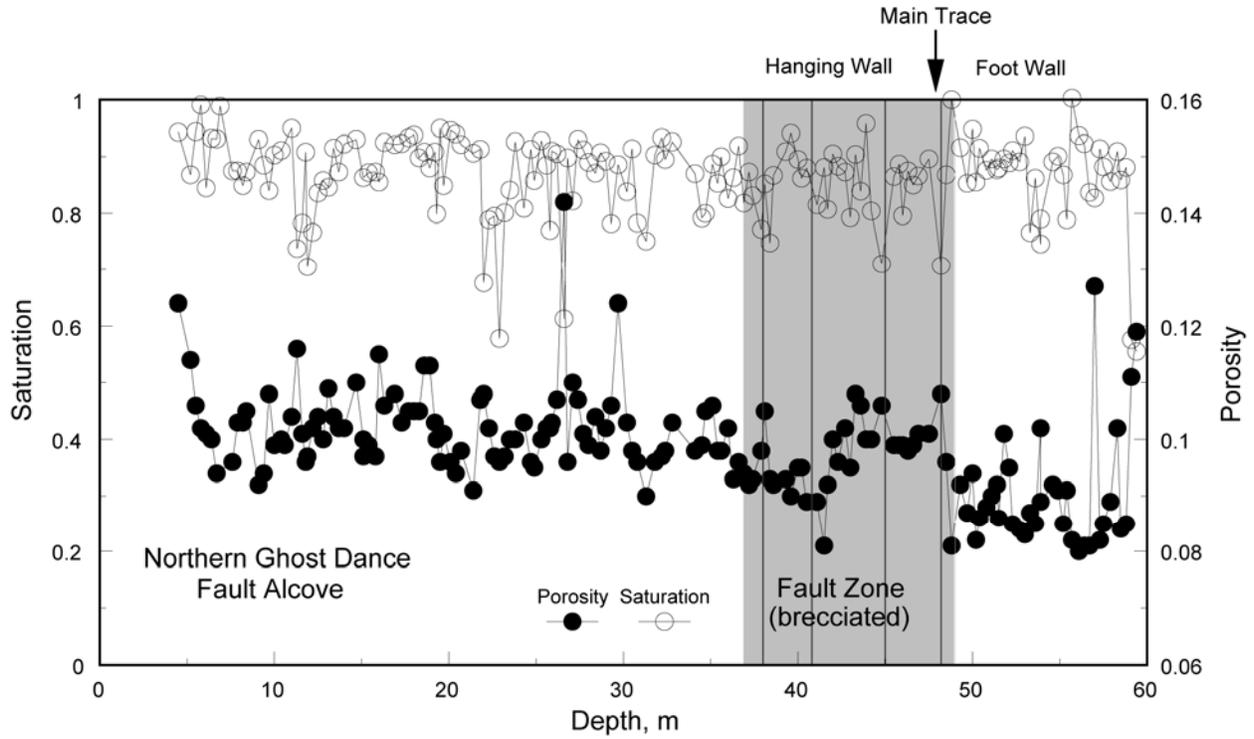
DTN: GS970208312231.003 [DIRS 107181]

Figure 7-17. Porosity and Saturation for Borehole ESF-NAD-GTB#1A in the Exploratory Studies Facility Alcove 6 across the Ghost Dance Fault
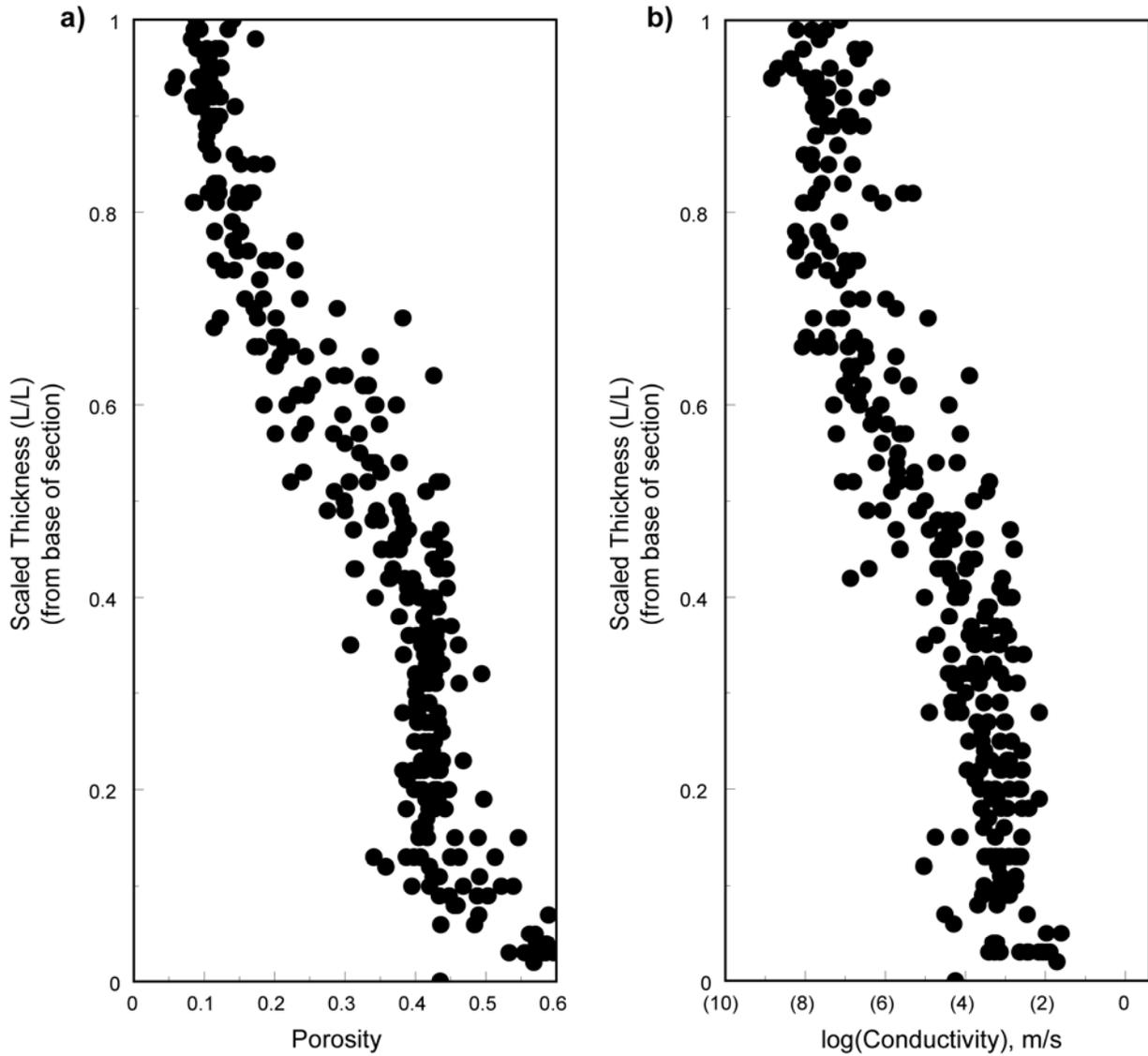
DTN: MO0312SEPSDSHC.000 [DIRS 166563]

Source: Modified from Rautman 1995 [DIRS 106645], Figure 6

Figure 7-18.   (a) Porosity and (b) Log of Saturated Hydraulic Conductivity of all Samples from 26 Vertical Transects of the Base of the Tiva Canyon Tuff
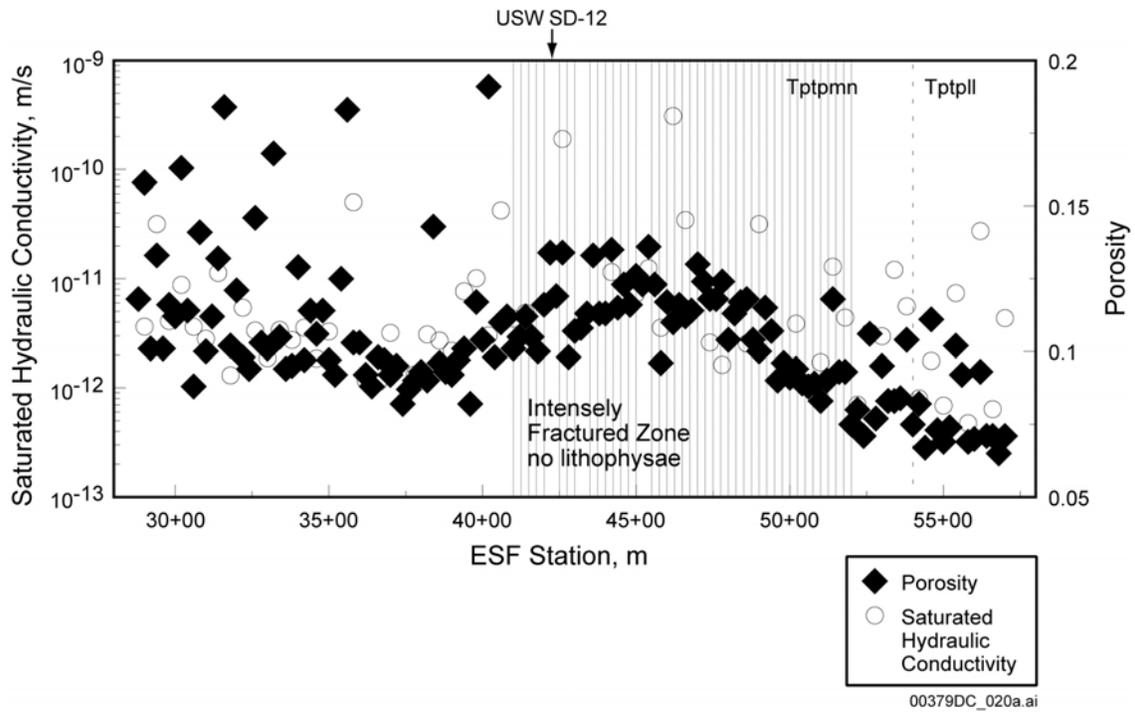
DTNs: GS970708312231.004 [DIRS 107183]; GS971008312231.006 [DIRS 107184];
GS960908312231.004 [DIRS 107065]; GS970108312231.002 [DIRS 107182]

NOTES: Porosity and saturated hydraulic conductivity measured along the systematic-sampling transect in the Exploratory Studies Facility Main Drift.

Figure 7-19. Porosity and Saturated Hydraulic Conductivity for Samples Collection in the Exploratory Studies Facility Main Drift
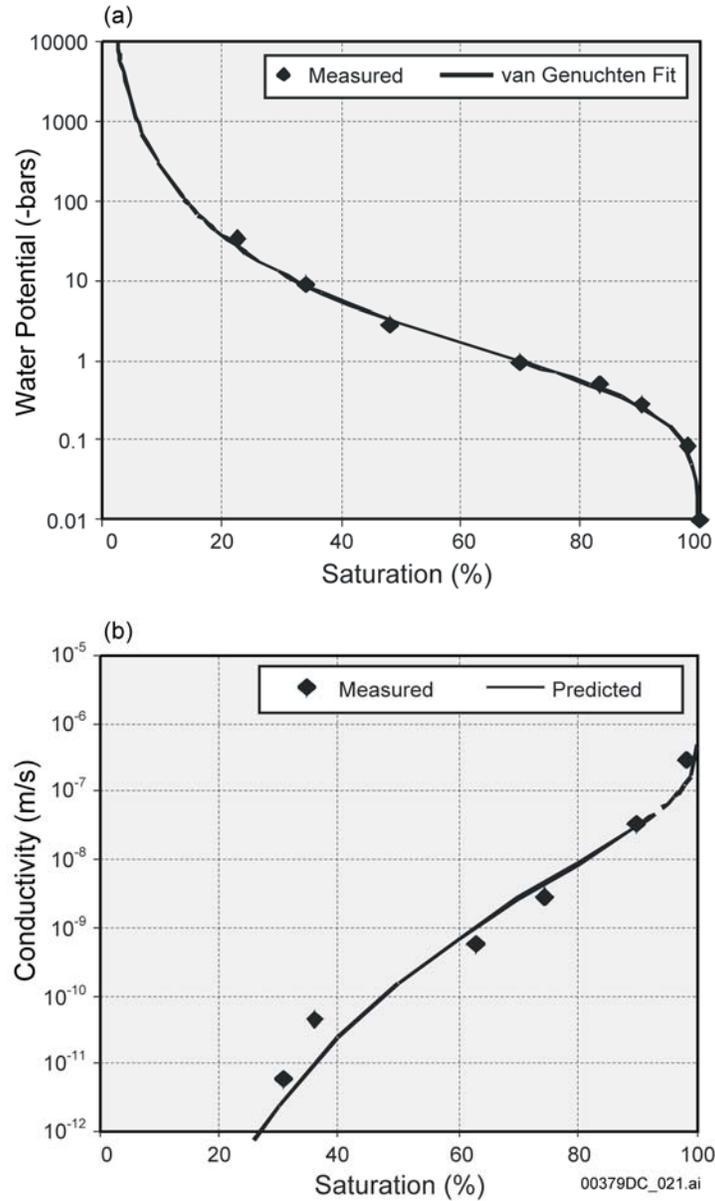
DTNs: GS990308312242.007 [DIRS 107185]; GS990708312242.008 [DIRS 109822]

Figure 7-20. (a) Measured and Model-Predicted Moisture Retention and (b) Unsaturated Hydraulic Conductivity for a Sample of the Vitric Calico Hills Formation (Tac Unit 4) from the Busted Butte Test Facility (Measurements Made Using a Steady-State Centrifuge)
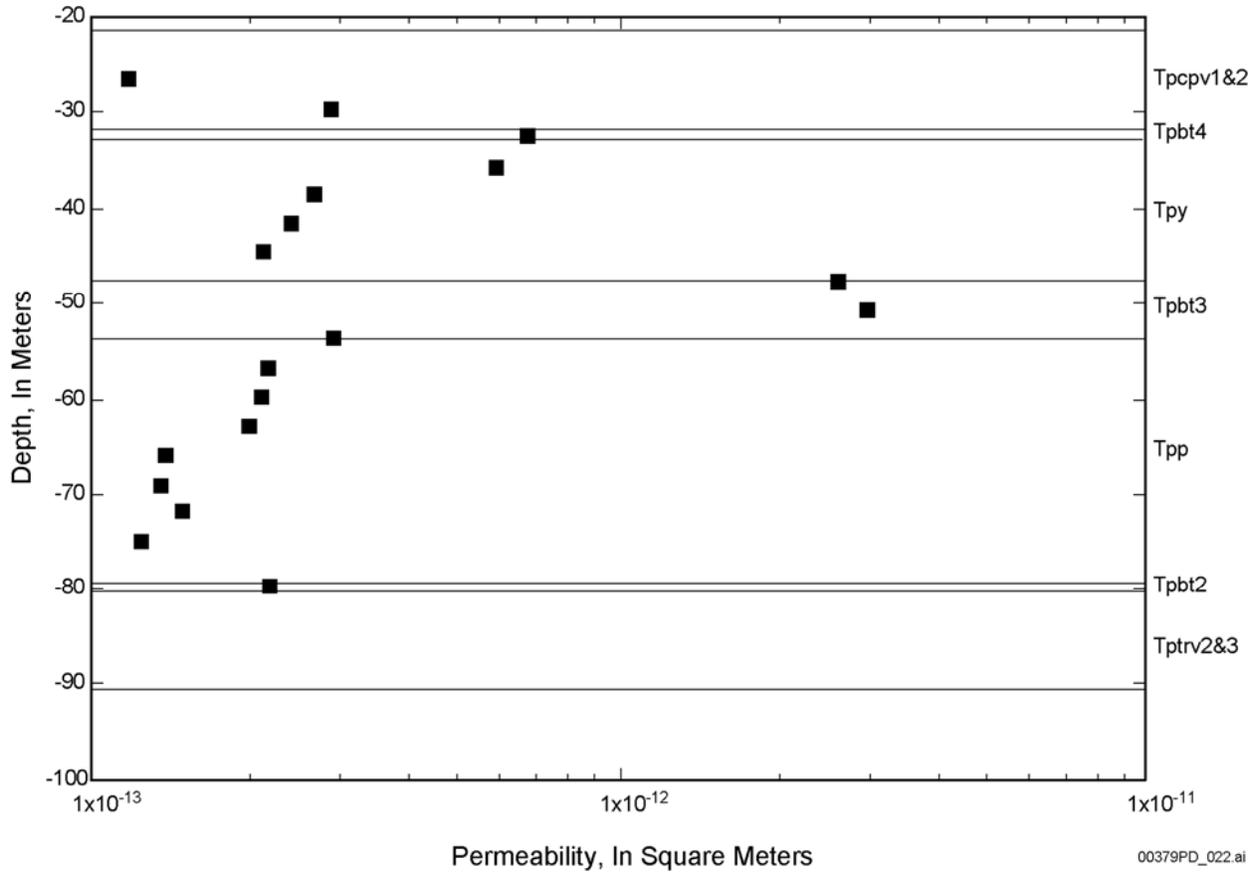
DTN: MO0312SEPSDINP.000 [DIRS 166564]

Source: LeCain 1997 [DIRS 100153], Figure 14

Figure 7-21. Air-Injection Permeability Values in the Paintbrush Nonwelded Hydrogeologic Unit with Depth in Borehole USW NRG-7a

Ghost Dance
Fault Zone
(4 m width)

Fault Zone
Permeability = 18.1 x 10^{-12} m^2
Porosity = 0.13

Northern
Ghost Dance Fault
Drill Room

Hanging Wall
Permeability = 5.0 x 10^{-12} m^2
Porosity = 0.04

Footwall
Permeability = 8.7 x 10^{-12} m^2
Porosity = 0.04

Exploratory Studies Facility Main Drift

BOREHOLE NDR-MF#1

BOREHOLE NDR-MF#3

BOREHOLE NDR-MF#2

Northern Ghost Dance
Fault Access Drift

105 m

Pre-excavation location
of borehole NAD-GTB#1a

164 m

Drawing Not To Scale
00379DC_039a.ai
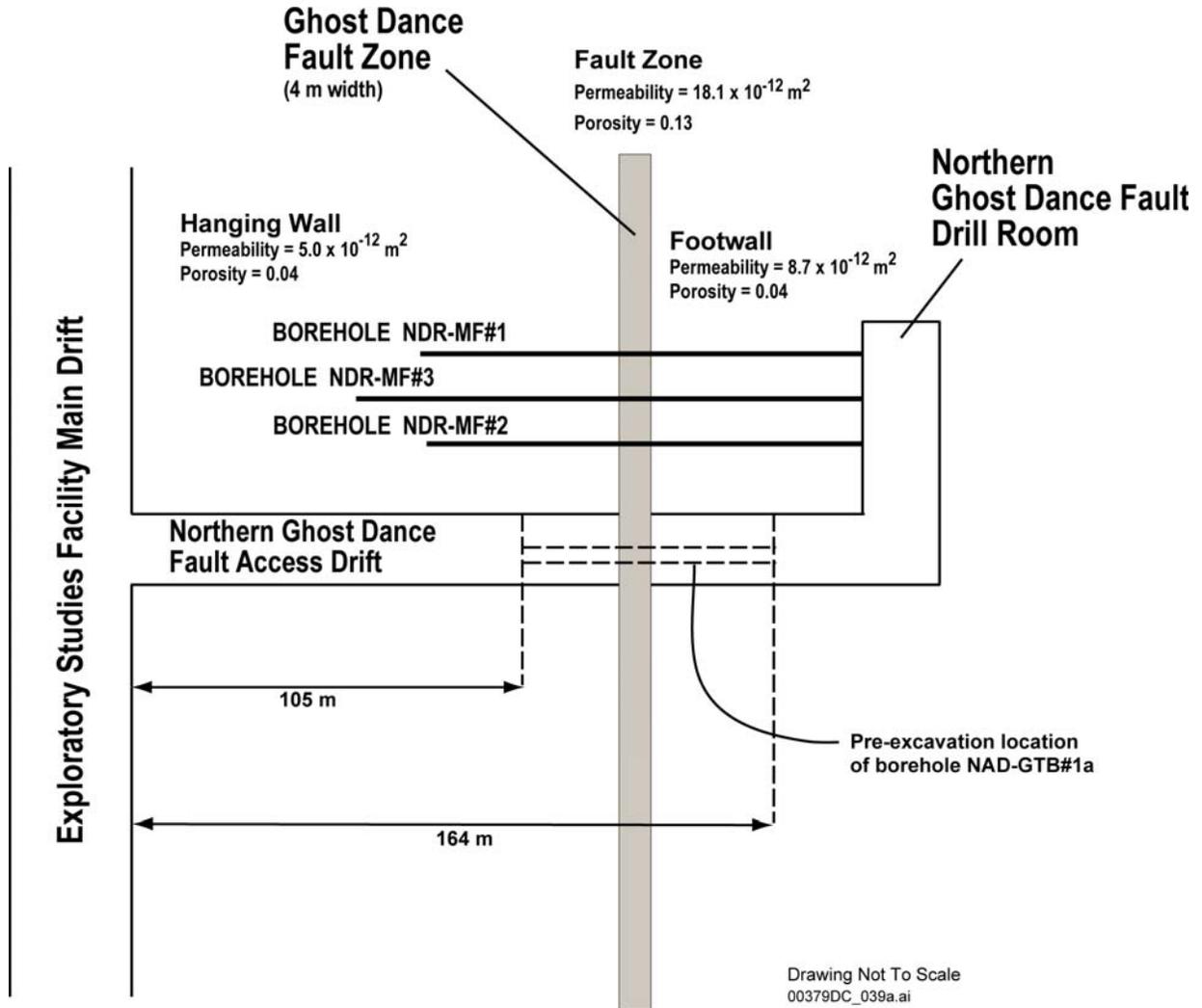
DTN: MO0312SEPSD0V6.000 [DIRS 166573]

Source: Modified from LeCain et al. 2000 [DIRS 144612], Figure 3, p. 24

NOTE: Permeability and porosity values are results of type-curve analysis of crosshole air-injections tests (Section 7.2.2.2.4).

Figure 7-22. Schematic Diagram (Overhead View) of Alcove 6 (the Northern Ghost Dance Fault Alcove) and Test Boreholes
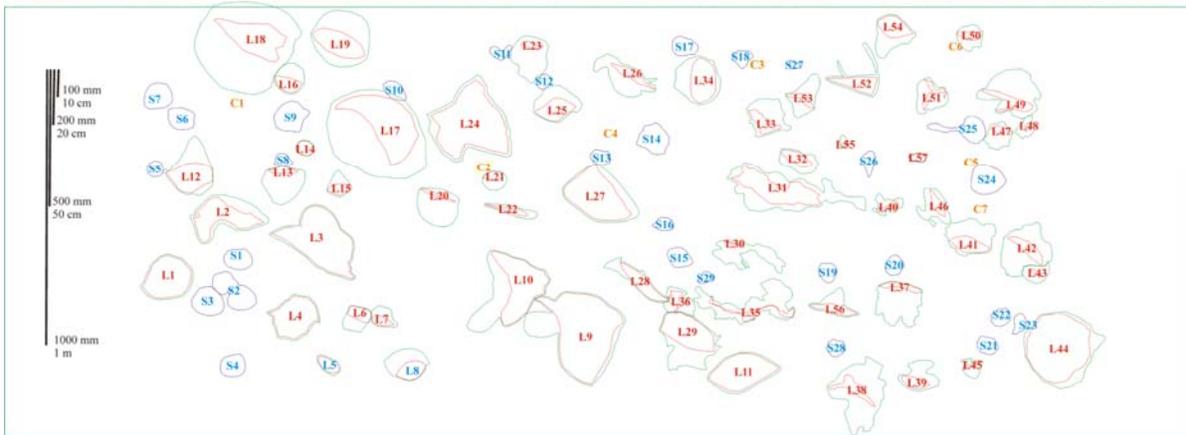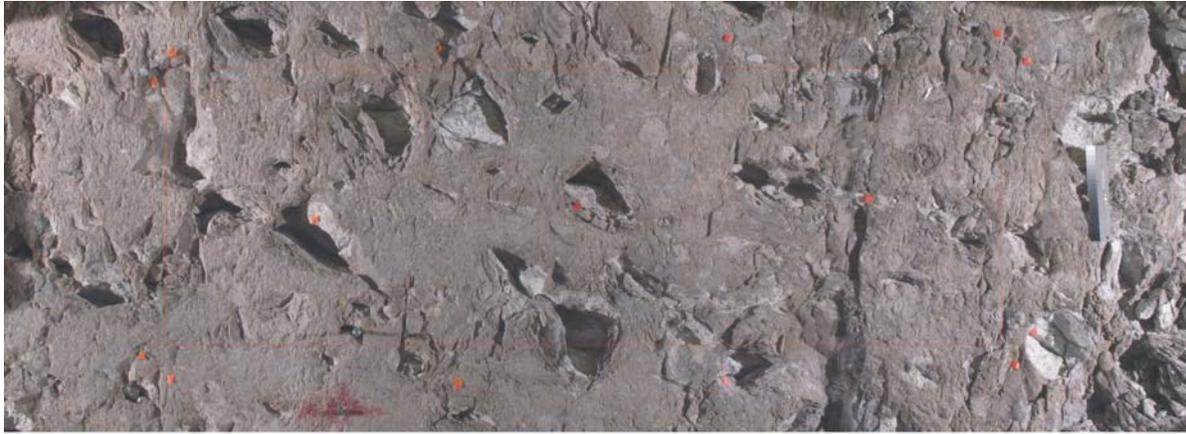
DTN: GS021008314224.002 [DIRS 161910]

Source: BSC 2003 [DIRS 162711], Figure 12

NOTE: Lithophysae have red "L" identifiers with cavities outlined in red and rims in green. Spots have blue "S" identifiers with cyan outlines. Lithic clasts have orange "C" identifiers with gold outlines.

Figure 7-23. Lithophysae, Spots, and Clasts of Tptpll in Panel Map 1493, Located on the Right Rib from Enhanced Characterization of the Repository Block Cross Drift, between Construction Stations 14+93 and 14+96

Source: BSC 2003 [DIRS 162711], Figure 13

NOTE: Porosity of the 5-m averaged large-lithophysae inventory is not included in the total.

Figure 7-24. Calculated Porosity of Lithophysal Cavities, Rims, Spots, Matrix-Groundmass, and the Total Porosity in the Tptpll Exposed along the Enhanced Characterization of the Repository Block Cross-Drift
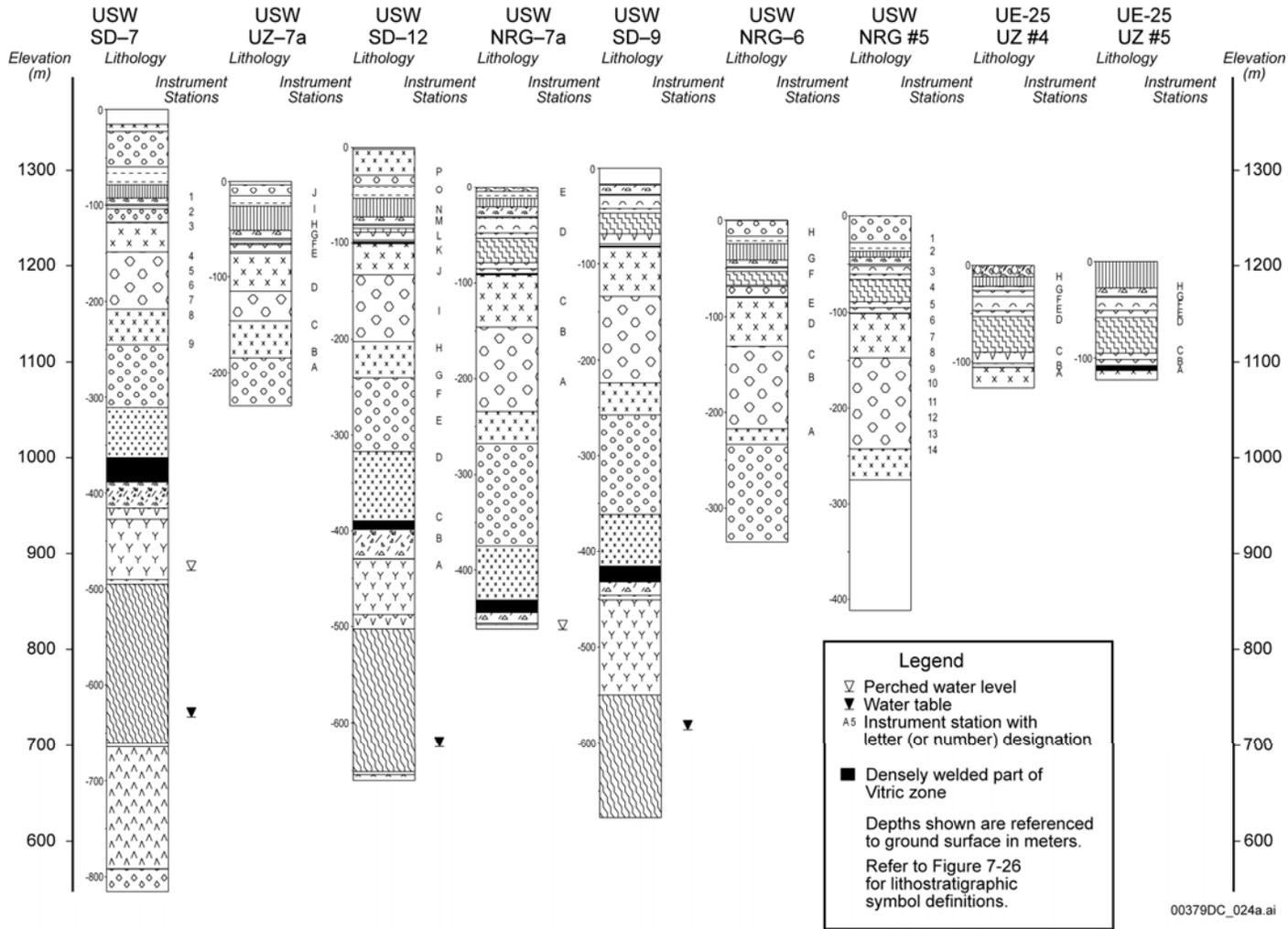
DTN: MO0312SEPSDAPM.000 [DIRS 166382]

Sources: Rousseau et al. 1999 [DIRS 102097], Figure 41; Rousseau et al. 1997 [DIRS 100178], Figure 3.0-1; Patterson et al. 1996 [DIRS 100172], Figure 4

Figure 7-25. Location of Instrument Stations and Lithostratigraphy for Instrumented Boreholes

Lithostratigraphic units	Lithostratigraphic symbol	Hydrogeologic units

Alluvium/Colluvium (QTac)

Post-Tiva Canyon Tuff bedded tuff (Tpbt5)

Tiva Canyon Tuff (Tpc)

    Crystal-rich

        Vitiric (rv)

        Nonlithophysal (rn)

    Crystal-poor

        Upper lithophysal (pul)

        Middle nonlithophysal (pmn)

        Lower lithophysal (pll)

        Lower nonlithophysal (pln)

            Hackly (plnh)

            Columnar (plnc)

        Vitiric (pv3, pv2, pv1)

Pre-Tiva Canyon Tuff bedded tuff (Tpbt4)

Yucca Mountain Tuff (Tpy)

Pre-Yucca Mountain Tuff bedded tuff (Tpbt3)

Pah Canyon Tuff (Tpp)

Pre-Pah Canyon Tuff bedded tuff (Tpbt2)

Topopah Spring Tuff (Tpt)

    Crystal-rich

        Vitiric (rv3, rv2, rv1)

        Nonlithophysal (rn)

        Lithophysal (rl)

    Crystal-poor

        Upper lithophysal (pul)

        Middle nonlithophysal (pmn)

        Lower lithophysal (pll)

        Lower nonlithophysal (pln)

        Vitiric (pv3, pv2, pv1)

Pre-Topopah Spring Tuff bedded tuff (Tpbt1)

Calico Hills Formation

Pre-Calico Hills Formation bedded tuff (Tacbt1)

Prow Pass Tuff

Bullfrog Tuff

Hydrogeologic units:

Unconsolidated Surficial Materials (UO)

Tiva Canyon welded hydrogeologic unit (TCw)

Paintbrush nonwelded hydrogeologic unit (PTn)

Topopah Spring welded hydrogeologic unit (TSw)

Calico Hills nonwelded hydrogeologic unit (CHn)

00379DC_025.ai

Source: Modified from Rousseau et al. 1999 [DIRS 102097], Figure 23

Figure 7-26. Lithostratigraphic and Hydrogeologic Units in the Yucca Mountain Area
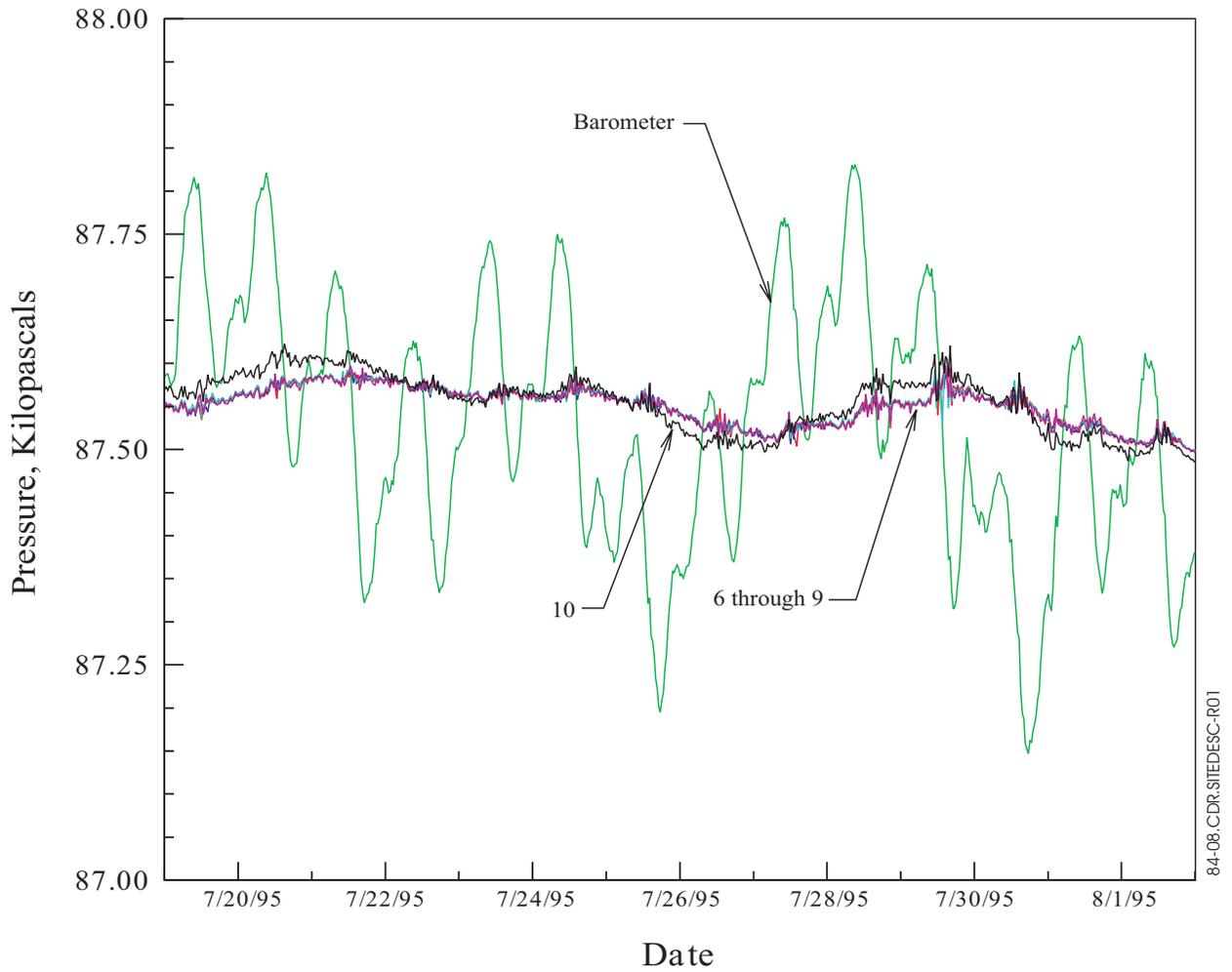
Instrument Station	Depth (meters)	Lithology	Residual Amplitude (percent)	Phase Lag (hours)
6	107.9	Topopah Spring Crystal-Rich Nonlithophysal	30	47.9
7	125.0	Topopah Spring Crystal-Rich Nonlithophysal	29	47.8
8	158.8	Topopah Spring Upper Lithophysal	29	47.9
9	192.9	Topopah Spring Upper Lithophysal	29	48.3
10	226 8	Topopah Spring Upper Lithophysal	39	37 7

DTN: GS960908312261.005 [DIRS 166511]

Source: Patterson et al. 1996 [DIRS 100172], Figure 5b

Figure 7-27. Pneumatic Pressure Record and Results of Cross-Spectral Analysis for Instrument Stations 6 through 10 in Borehole UE-25 NRG#5 Prior to the Exploratory Studies Facility Excavation
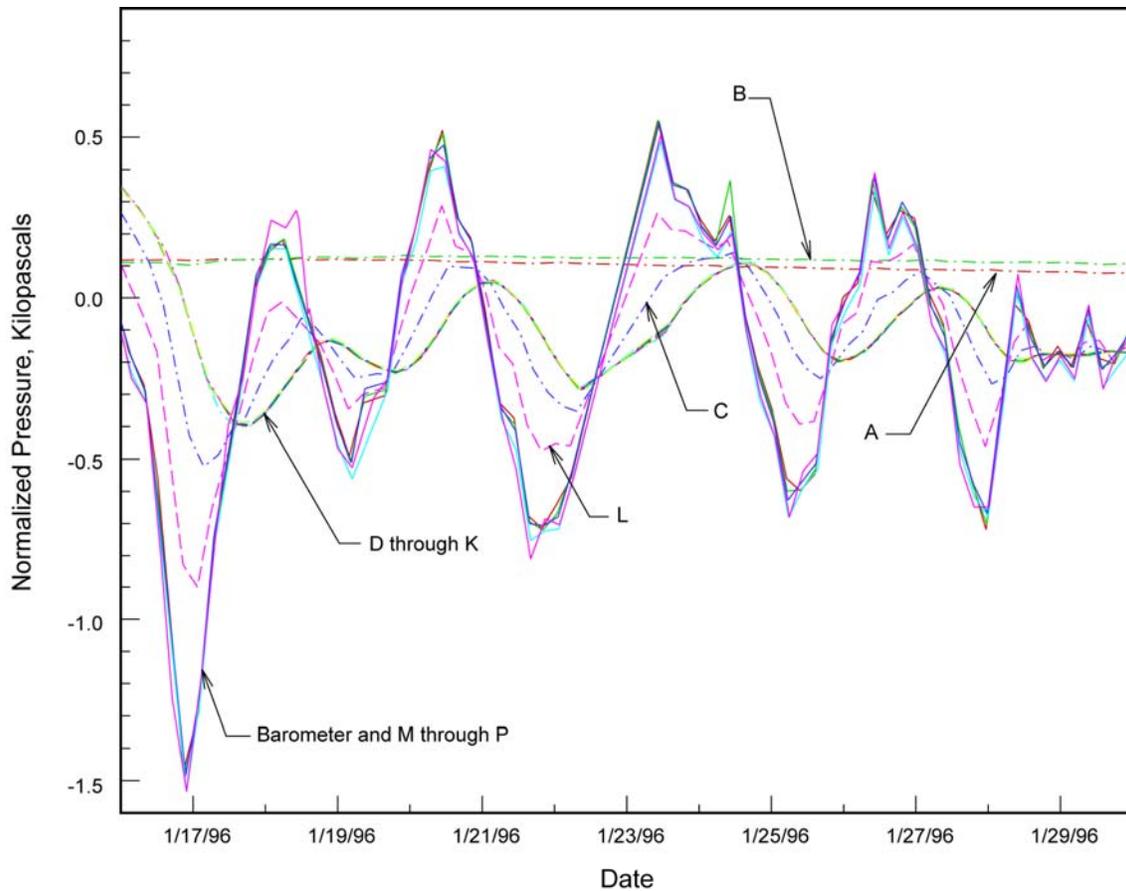
Instrument Station	Depth (meters)	Lithology	Residual Amplitude (percent)	Phase Lag (hours)
M-P	24.6-76.7	Tiva Canyon Tuff	100	N/A
L	91.8	Pre-Pah Canyon Tuff bedded tuff	69	7.4
K	106.8	Topopah Spring Crystal-Rich Nonlithophysal	50	28.0
J	128.9	Topopah Spring Crystal-Rich Nonlithophysal	50	27.9
I	170.8	Topopah Spring Upper Lithophysal	50	28.1
H	208.1	Topopah Spring Middle Nonlithophysal	51	28.1
G	236.8	Topopah Spring Middle Nonlithophysal	51	28.0
F	256.5	Topopah Spring Lower Lithophysal	51	28.8
E	285.1	Topopah Spring Lower Lithophysal	52	29.6
D	322.6	Topopah Spring Lower Nonlithophysal	52	29.7
C	385.7	Topopah Spring Lower Nonlithophysal	57	18.8
A-B	406-433	Topopah Spring Crystal-Poor Vitric	N/A	N/A

N/A = Not analyzed

00379DC_027a.ai

DTNs: GS951108312232.008 [DIRS 106756]; GS960308312232.001 [DIRS 105573]; GS921008312211.008 [DIRS 166517]

Source: Patterson et al. 1996 [DIRS 100172], Figure 10; Figure 7-33 (this report)

Figure 7-28. Pneumatic Pressure Record and the Results of Cross-Spectral Analysis for Borehole USW SD-12 Prior to the Exploratory Studies Facility Excavation
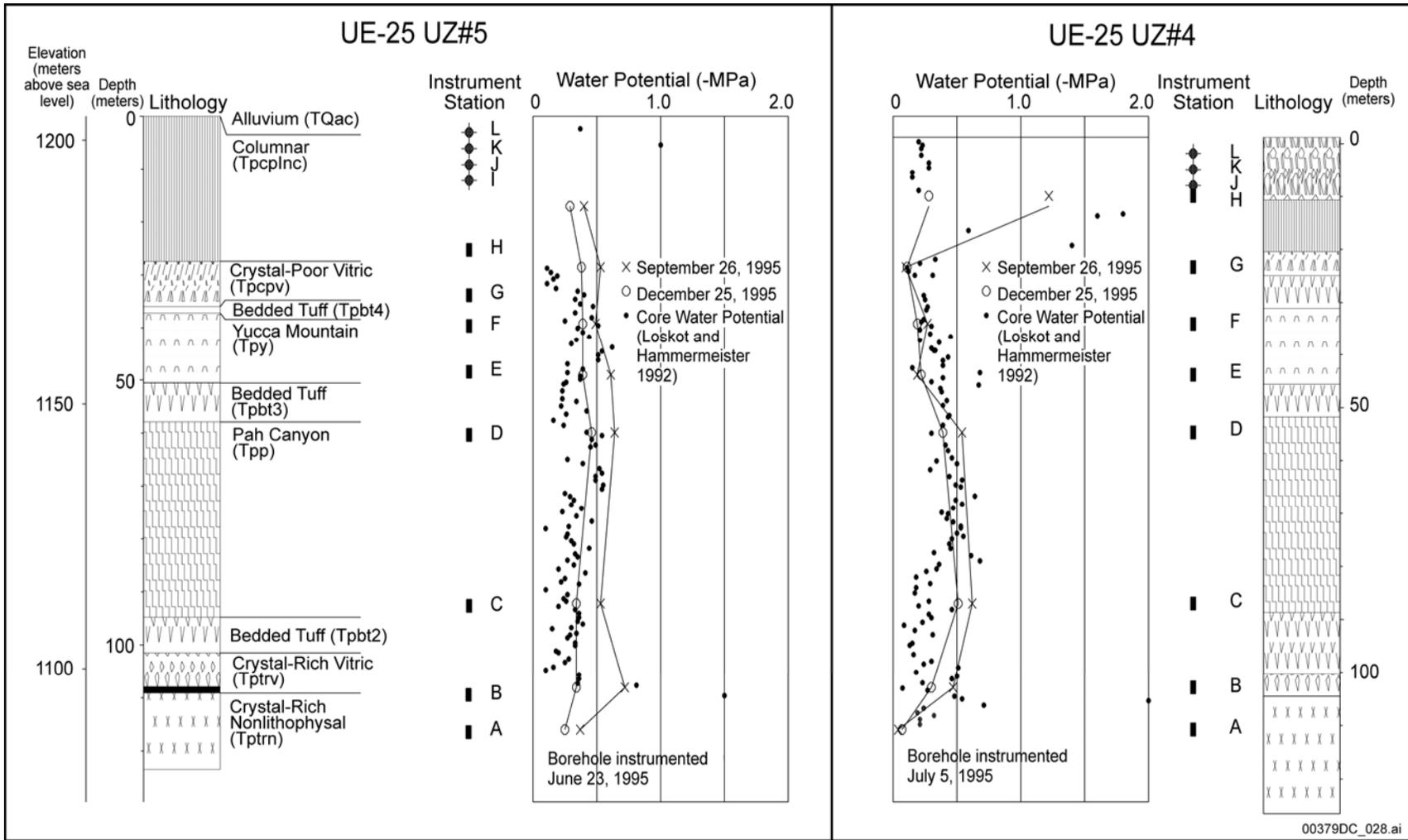
DTNs: GS921008312211.008 [DIRS 166517]; GS951108312232.008 [DIRS 106756]; GS960308312232.001 [DIRS 105573]

Source: Rousseau et al. 1999 [DIRS 102097], Figure 97

Figure 7-29. In Situ and Core Sample Water Potentials for Boreholes UE-25 UZ#4 and UE-25 UZ#5 in Pagany Wash
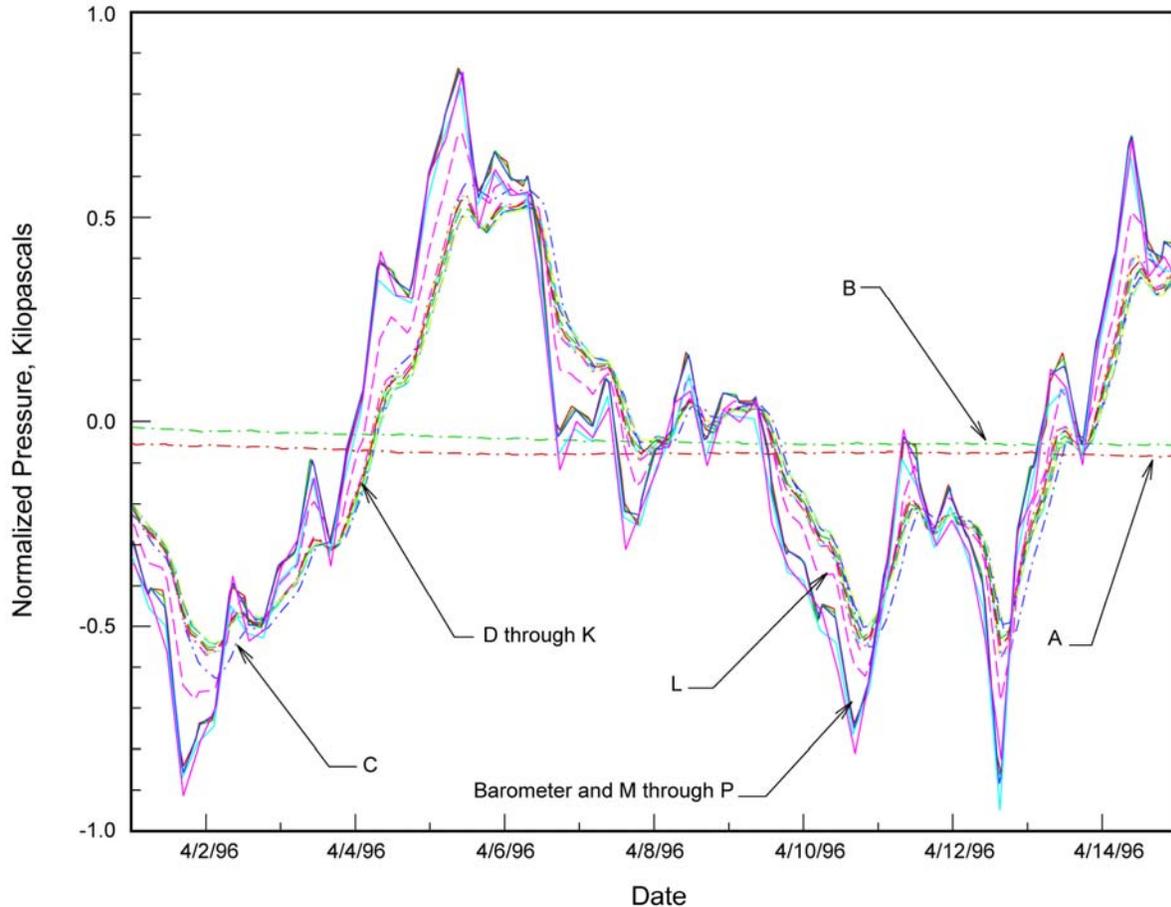
Instrument Station	Depth (meters)	Lithology	Residual Amplitude (percent)	Phase Lag (hours)
N-P	24.6-65.3	Tiva Canyon Tuff	100	0.3
M	76.7	Tiva Canyon Crystal-Poor Vitric	100	0.6
L	91.8	Pre-Pah Canyon Tuff bedded tuff	85	4.4
K	106.8	Topopah Spring Crystal-Rich Nonlithophysal	69	10.3
J	128.9	Topopah Spring Crystal-Rich Nonlithophysal	69	10.4
I	170.8	Topopah Spring Upper Lithophysal	70	10.2
H	208.1	Topopah Spring Middle Nonlithophysal	71	9.3
G	236.8	Topopah Spring Middle Nonlithophysal	72	8.8
F	256.5	Topopah Spring Lower Lithophysal	74	8.2
E	285.1	Topopah Spring Lower Lithophysal	74	8.3
D	322.6	Topopah Spring Lower Nonlithophysal	74	8.6
C	385.7	Topopah Spring Lower Nonlithophysal	80	9.8
A-B	406-433	Topopah Spring Crystal-Poor Vitric	N/A	N/A

00379DC_029.ai

DTN: GS960908312261.005 [DIRS 166511]

Source: Patterson et al. 1996 [DIRS 100172], Figure 26

Figure 7-30. Pneumatic Pressure Record and Results of Cross-Spectral Analysis for Borehole USW SD-12 after the Exploratory Studies Facility Excavation

Figure 7-31. Lithostratigraphy and Fracture Density for Borehole USW SD-9
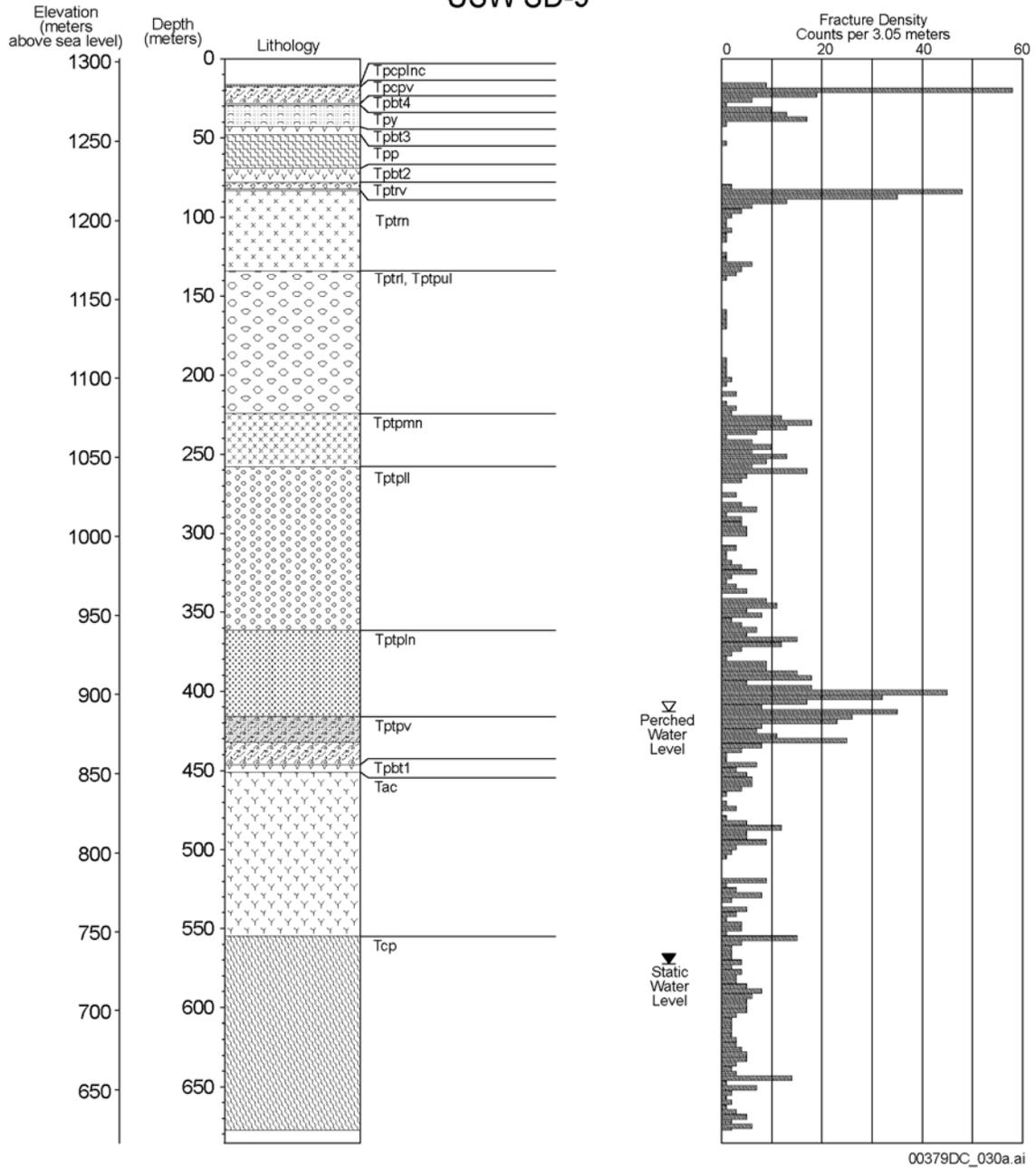
DTN: GS960908312232.014 [DIRS 107228]

Source: Modified from Rousseau et al. 1999 [DIRS 102097], Figure 24
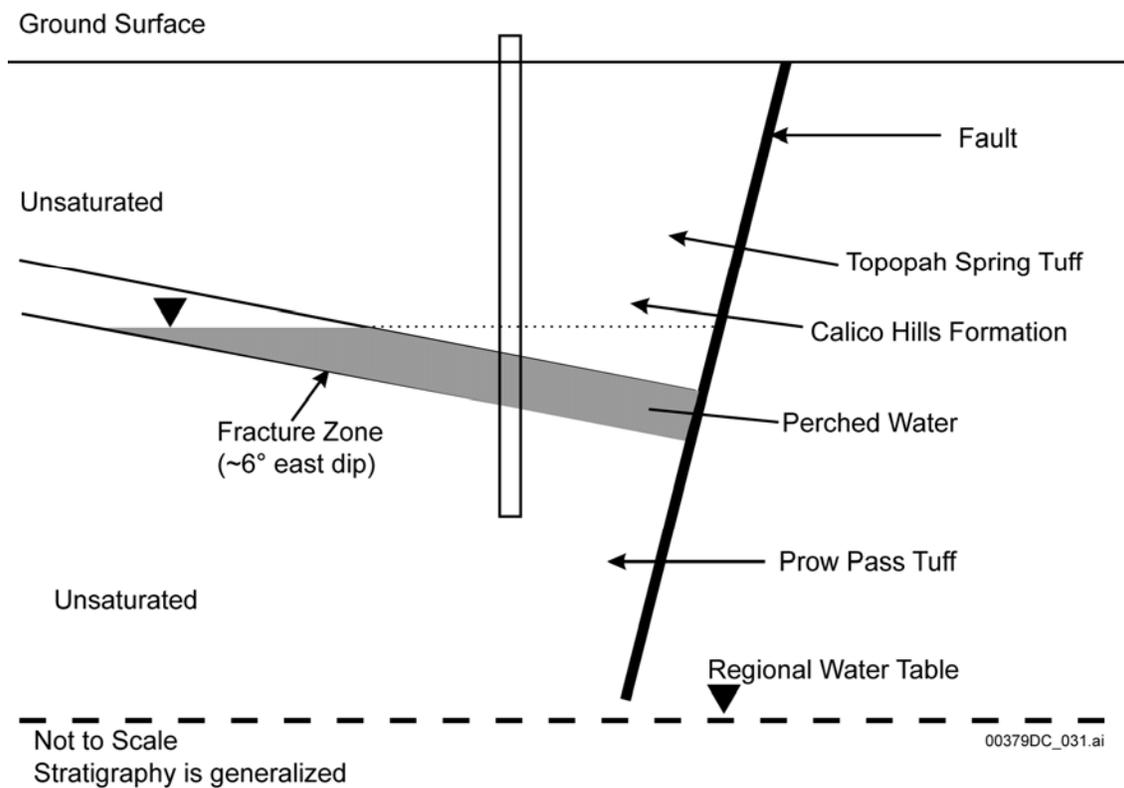
Source: O'Brien 1997 [DIRS 101277], Figure 18

Figure 7-32. Idealized Conceptual Model of the Perched-Water Reservoir at Borehole USW SD-7
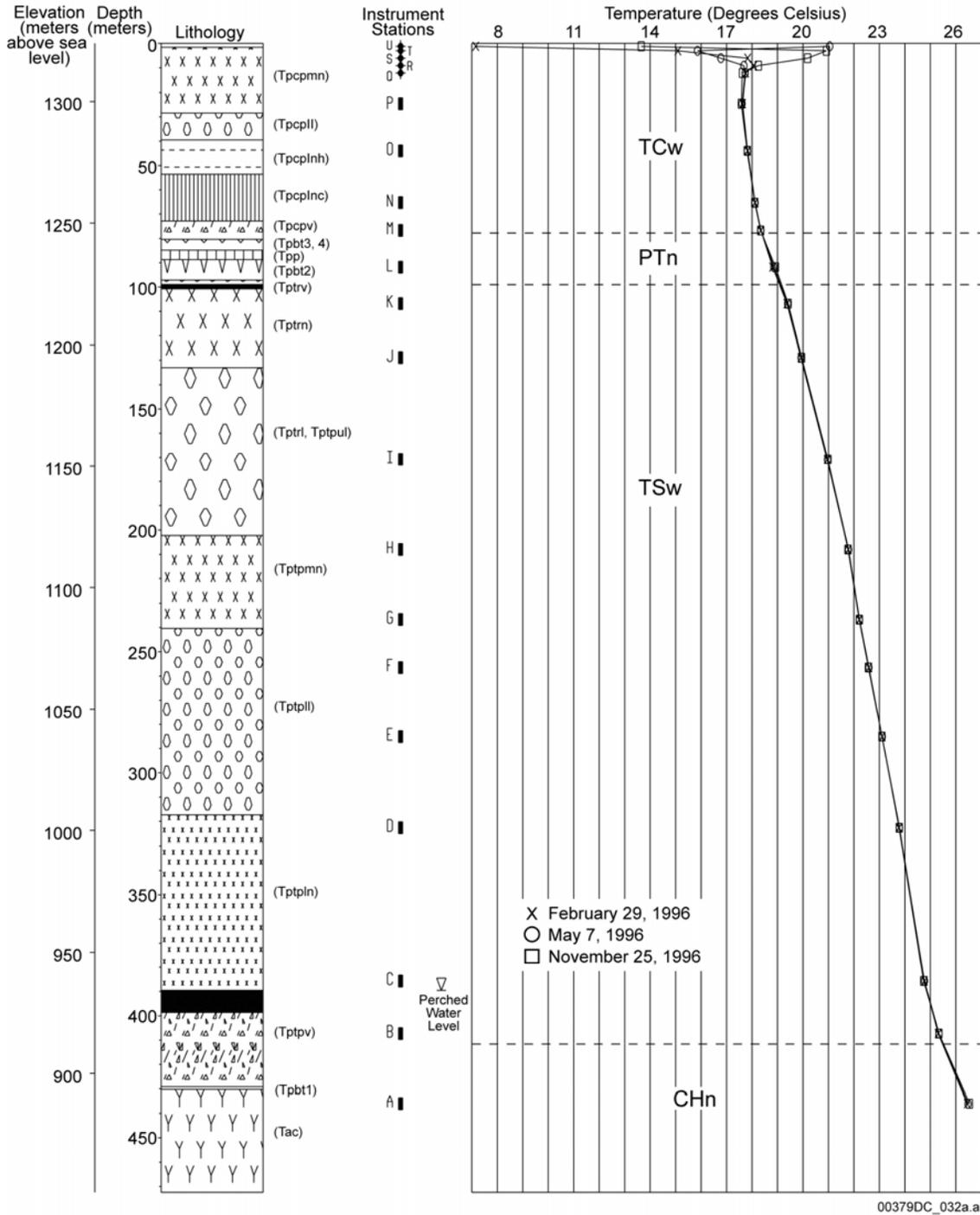
DTN: GS970308312232.003 [DIRS 105675]

Source: Modified from Rousseau et al. 1997 [DIRS 100178], Figure 4.3.2-2

Figure 7-33. Time-Lapse Temperature Profiles for Borehole USW SD-12
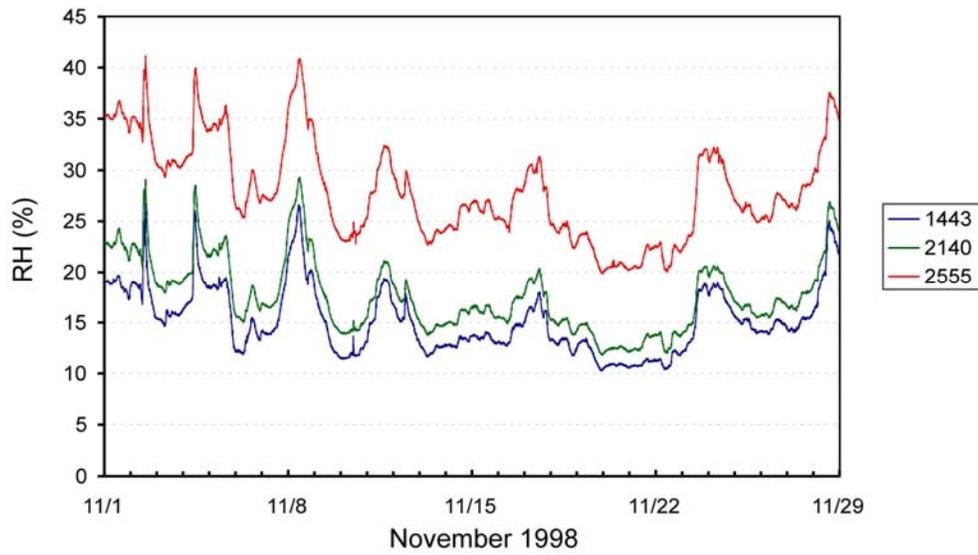
00379DC_036a.ai

Source: BSC 2003 [DIRS 166347], Figure 6.10.1-1

NOTE: The data were collected in November 1998 after completion of excavation. The legends are the distance in meters from the moisture station to the Enhanced Characterization of the Repository Block Cross Drift entrance.

Figure 7-34. Relative Humidity Temporal Variations in the Enhanced Characterization of the Repository Block Cross-Drift
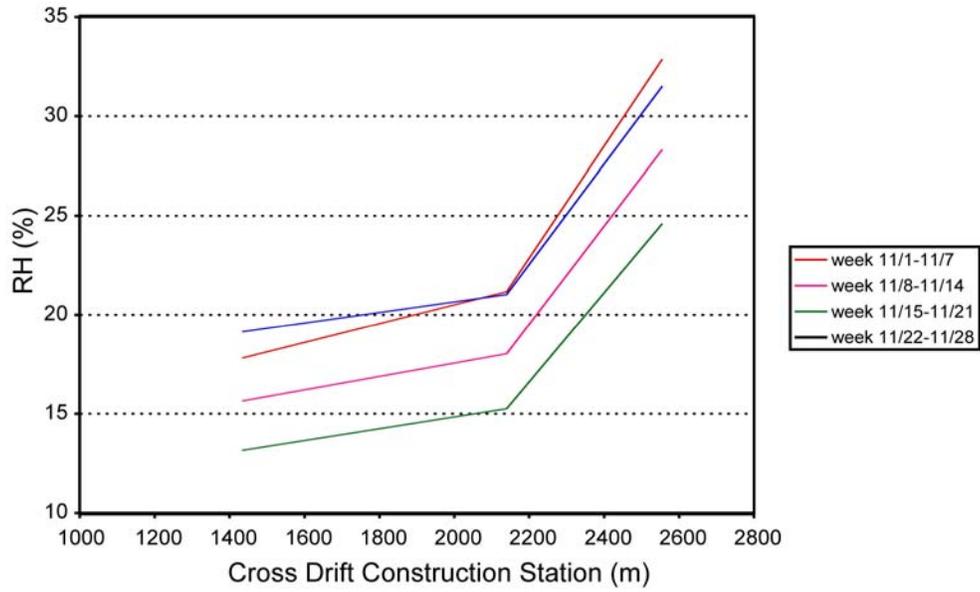
00379DC_037a.ai

Source: BSC 2003 [DIRS 166347], Figure 6.10.1-2

NOTE: The weekly averages of day shift data are presented for November 1998 after completion of excavation.

Figure 7-35.   Relative Humidity Spatial Variations along the Enhanced Characterization of the Repository Block Cross-Drift

Source: Modified from BSC 2003 [DIRS 166347], Figure 6-2

Figure 7-36. Schematic Diagram of the Exploratory Studies Facility Main Drift—Cross-Drift Crossover Point
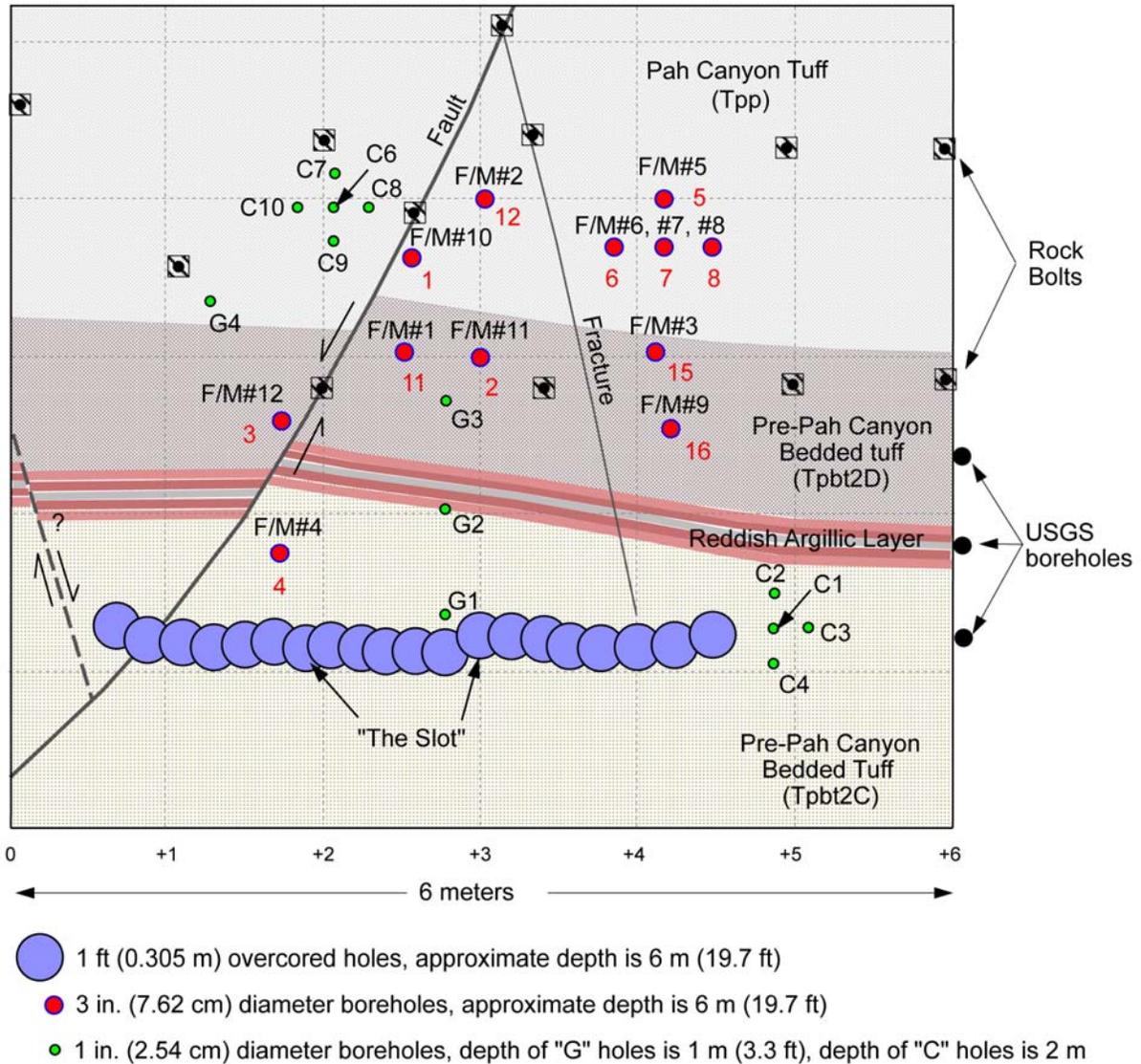
Source: Modified from BSC 2003 [DIRS 166347], Figure 6.7.1-1

NOTE: "F/M#12" refers to full borehole name of ESF-LPCA-FM#12. The second, numerical callouts ("3") for the same borehole are the informal borehole names referred to in the text. The "USGS boreholes" are ESF-LPCA-MOISTSTDY#1, #2, and #3, respectively, from top to bottom.

Figure 7-37. Geological Sketch for the North Face of Alcove 4 in the Exploratory Studies Facility at Yucca Mountain
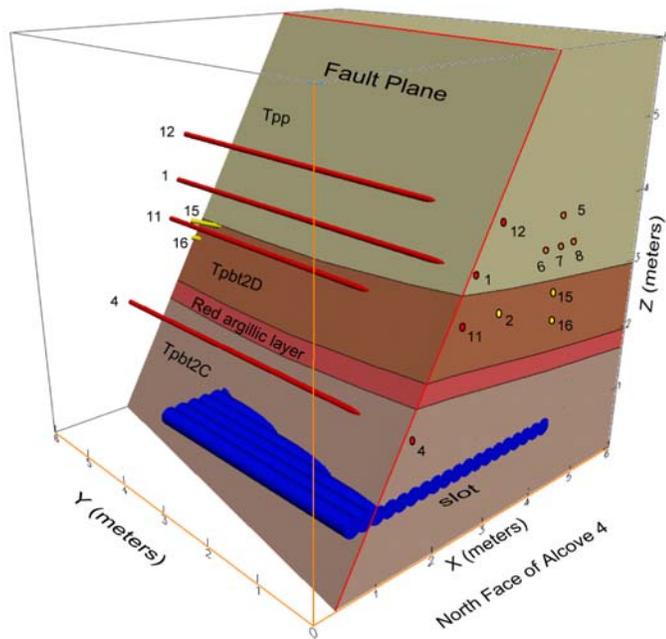
00379DC_041.ai

Source: BSC 2003 [DIRS 166347], Figure 6.7.1-2

Figure 7-38.   Perspective Illustration of Three-Dimensional View of the Boreholes, Slot, and Lithological Unit Contacts in the Alcove 4 Test Bed
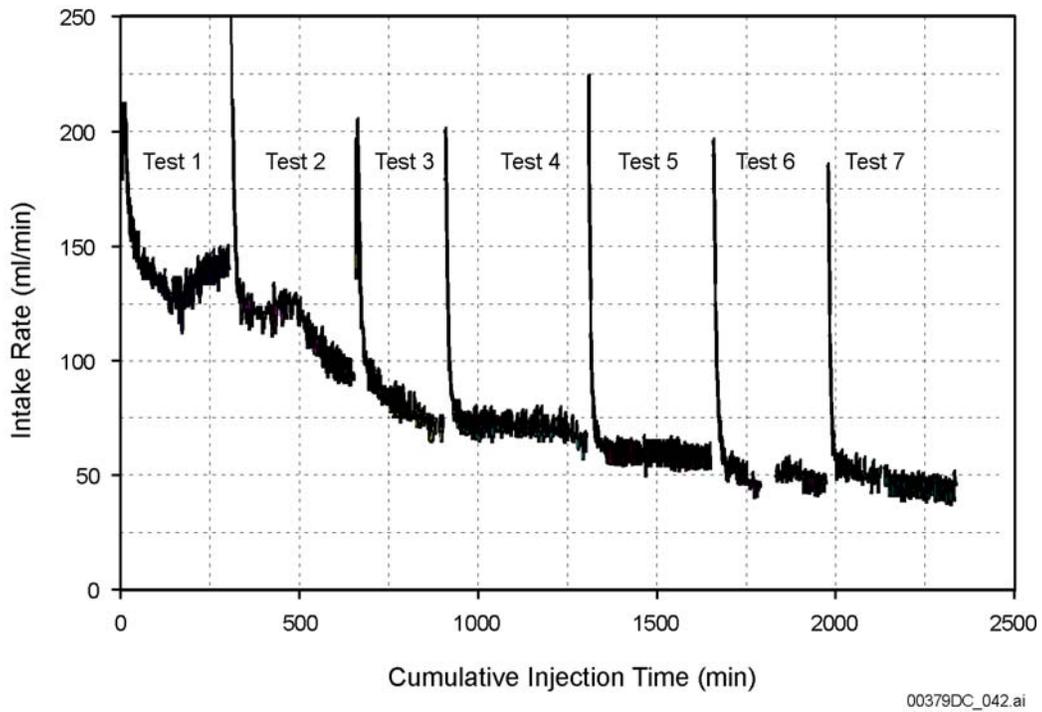
Source: BSC 2003 [DIRS 166347], Figure 6.7.2-1

Figure 7-39. Intake Rates along the 0.3 m Zone Located on the Fault in Borehole 12, in Alcove 4
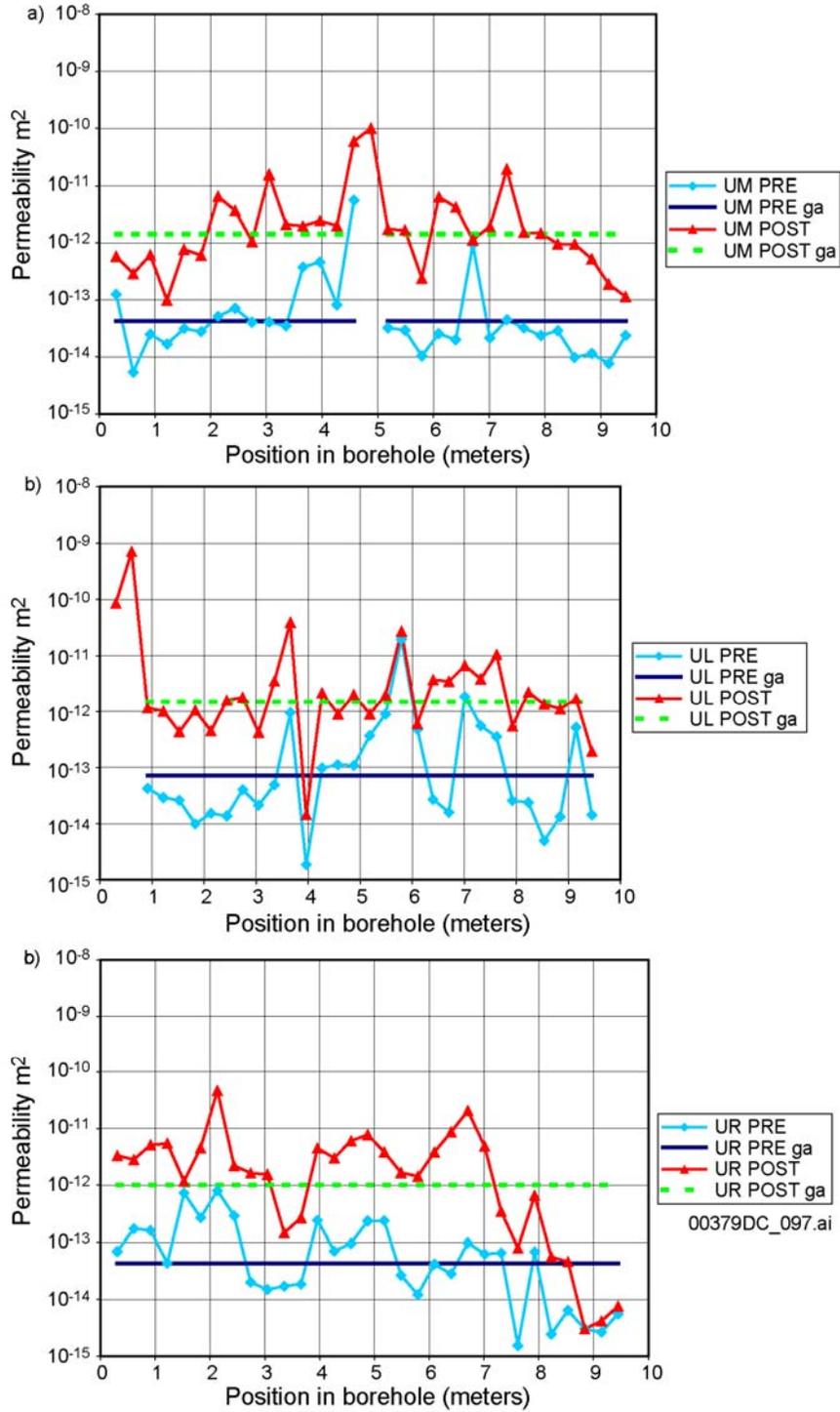
DTN: LB0011AIRKTEST.001 [DIRS 153155]

Source: BSC 2003 [DIRS 166347], Figure 6.1.2-1

NOTE: "ga" is the geometric average, UL = upper left (borehole), UM = upper middle, UR = upper right.

Figure 7-40. Pre- and Post-Excavation Air-Permeability Profiles along Upper Boreholes at Niche 2
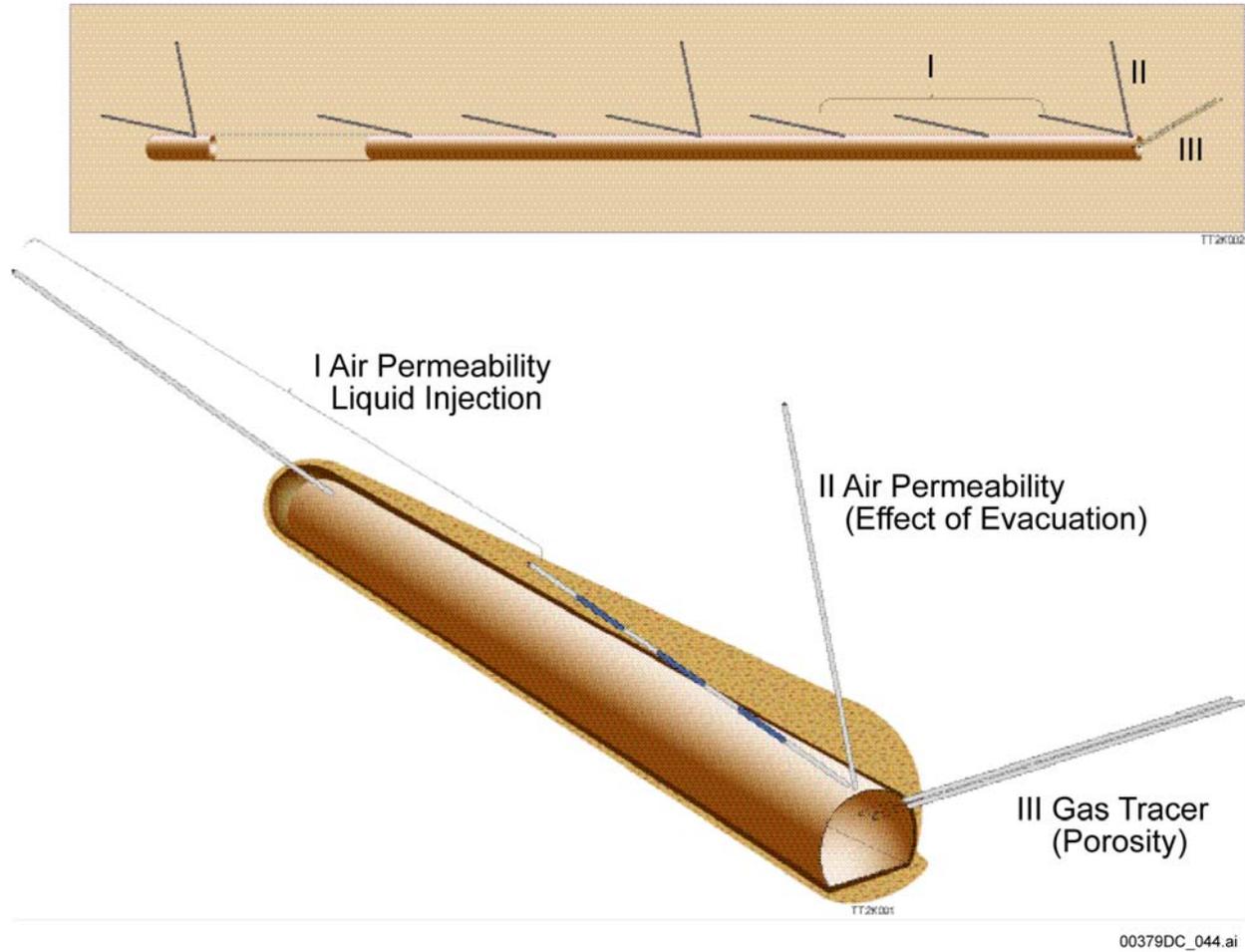
Source: BSC 2003 [DIRS 166347], Figure 6.11.1-1

Figure 7-41. Schematic of Borehole Configuration in the Enhanced Characterization of the Repository Block Cross-Drift for Systematic Characterization of the Topopah Spring Tuff Lower Lithophysal Unit

The figure shows a plot of Seepage Percentage, y (%) on the y-axis (0 to 30) versus Liquid-Release Flux, q_s (m/s) on the x-axis (1.0E-07 to 1.0E-04, logarithmic scale).

Linear Regression
$y = 5.88\ln(K_o) + 87.5$
$R^2 = 0.96$

Seepage Threshold Flux, K_{o*}

Data —— Linear regression
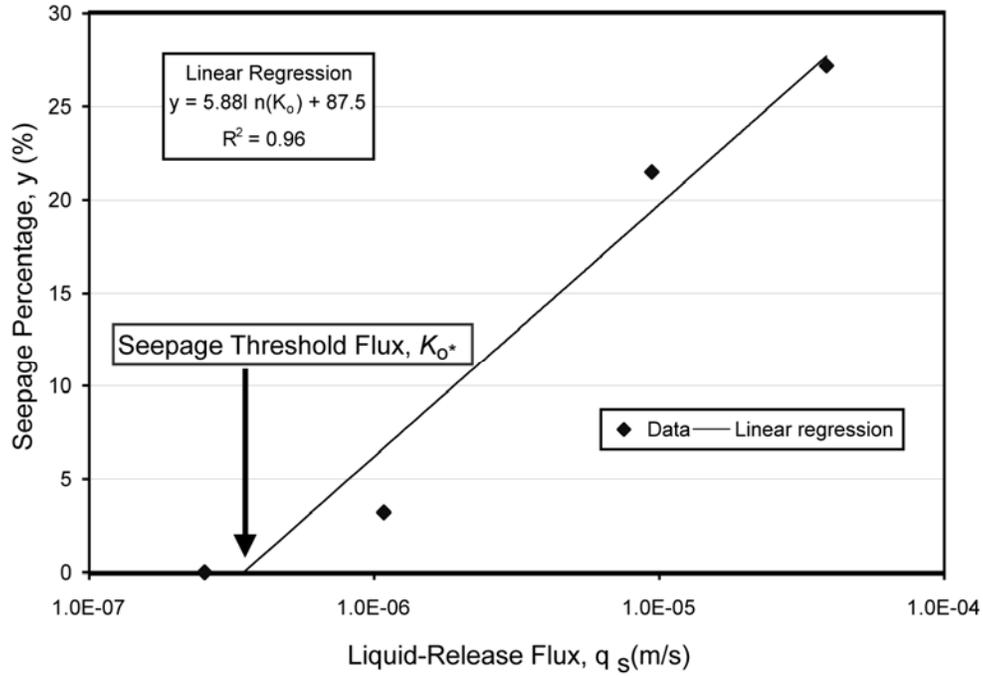
00379DC_045.ai

Source: BSC 2003 [DIRS 166347], Figure 6.2.2-1

NOTE: Seepage tests were conducted for the interval 18 to 19 ft (5.5 to 5.8 m) from the collar for the upper middle borehole at Niche 2.

Figure 7-42. Liquid-Release Flux versus Seepage Percentage, Niche 2
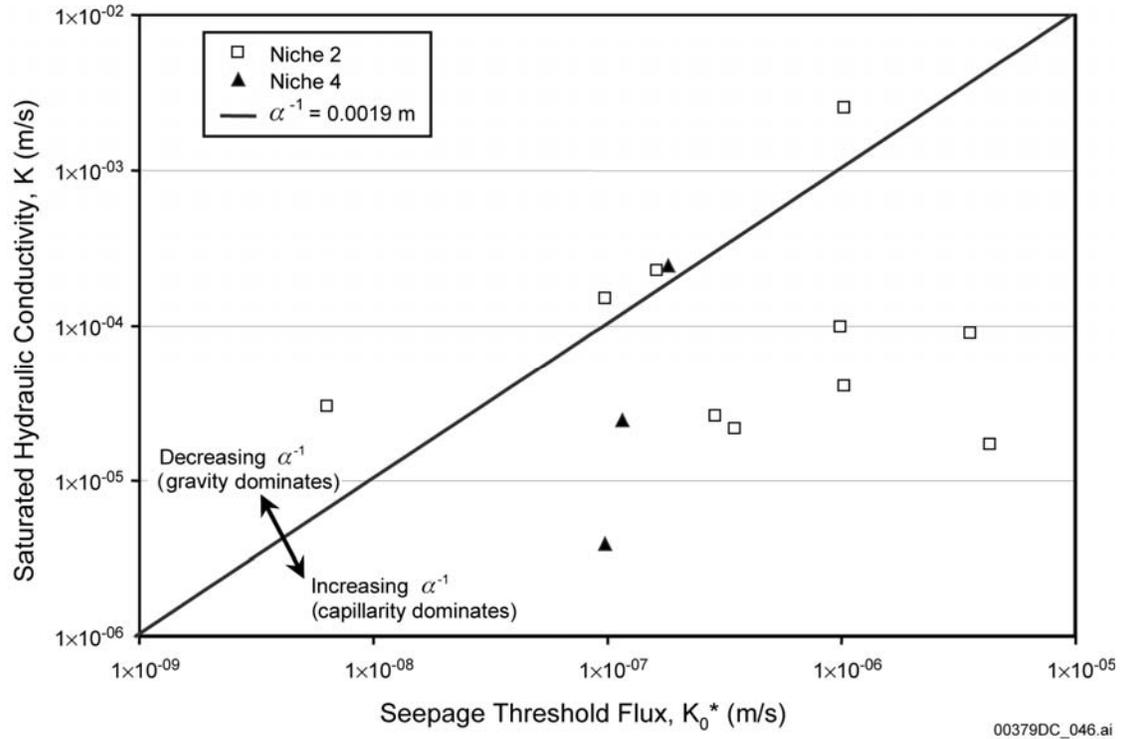
Source: BSC 2003 [DIRS 166347], Figure 6.2.2-2

NOTE: A diagonal line separates zones with gravity and capillary dominated flow.

Figure 7-43. Niche Seepage Threshold (Niches 2 and 4)
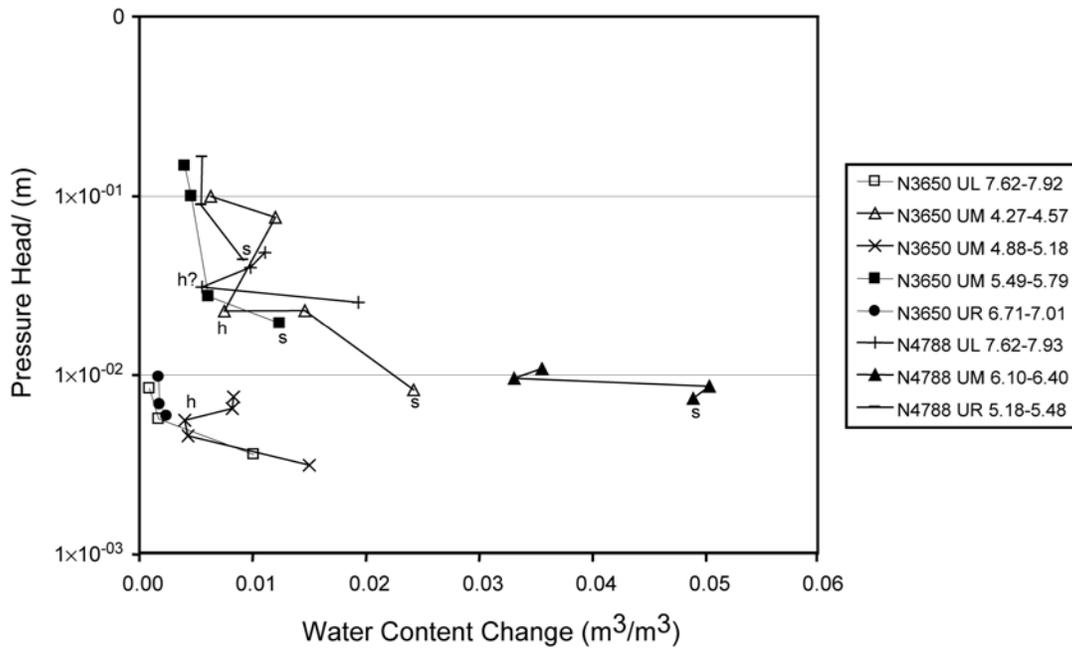
00379DC_047.ai

Source: BSC 2003 [DIRS 166347], Figure 6.2.2-3

NOTE: s = saturated conditions; h = data point influenced by wetting history.

Figure 7-44. Water Retention Curves for Fractures, Based in Niche Tests
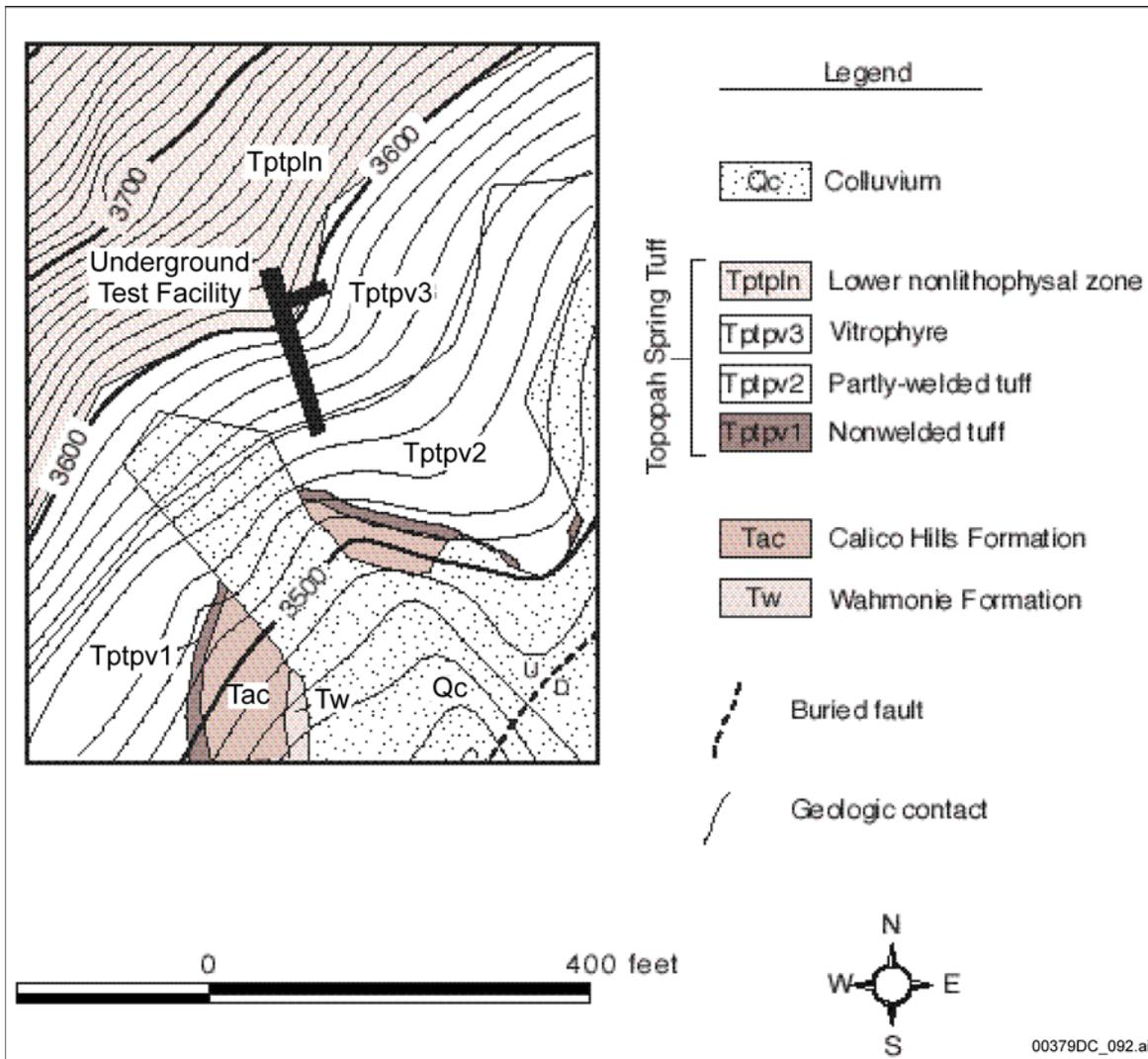
Source: CRWMS M&O 2001 [DIRS 154024], Figure 44

NOTE: The plot is a geologic map of the area around the underground test facility in the southeastern part of Busted Butte. The contour interval is 10 feet. The tunnel entrance is at the southern end of the facility.

Figure 7-45. Busted Butte Geologic Map
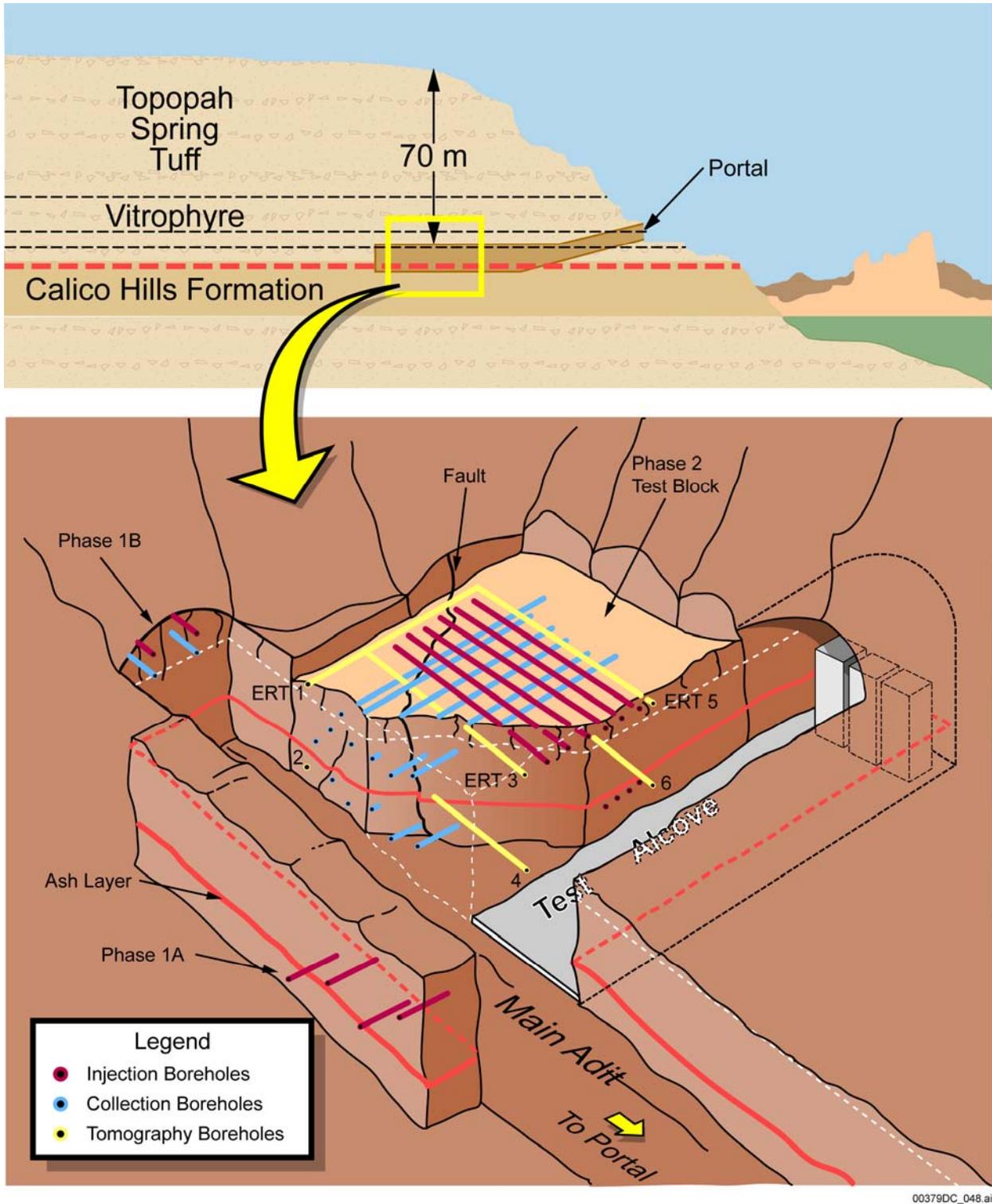
Source: Modified from BSC 2003 [DIRS 166347], Figure 6.13.1-1

NOTE: This schematic shows the relative locations of the different experiment phases and borehole locations.

Figure 7-46. Busted Butte Unsaturated Zone Transport Test Facility
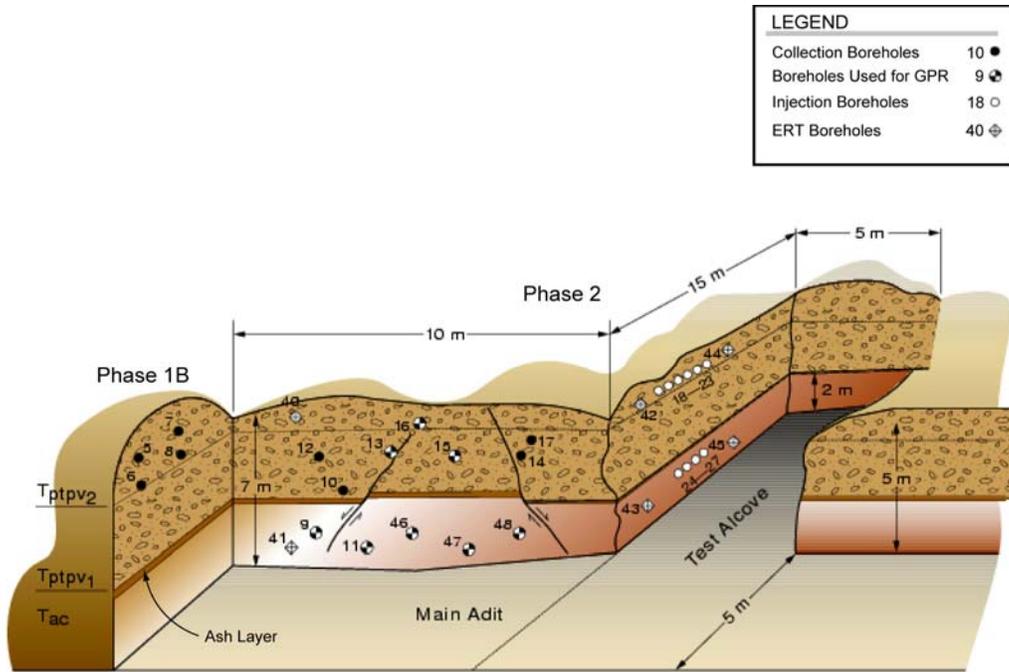
Source: BSC 2003 [DIRS 166347], Figure 6.13.1-4

Figure 7-47. Phase-1B and Phase-2 Boreholes, Busted Butte Unsaturated Zone Transport Test
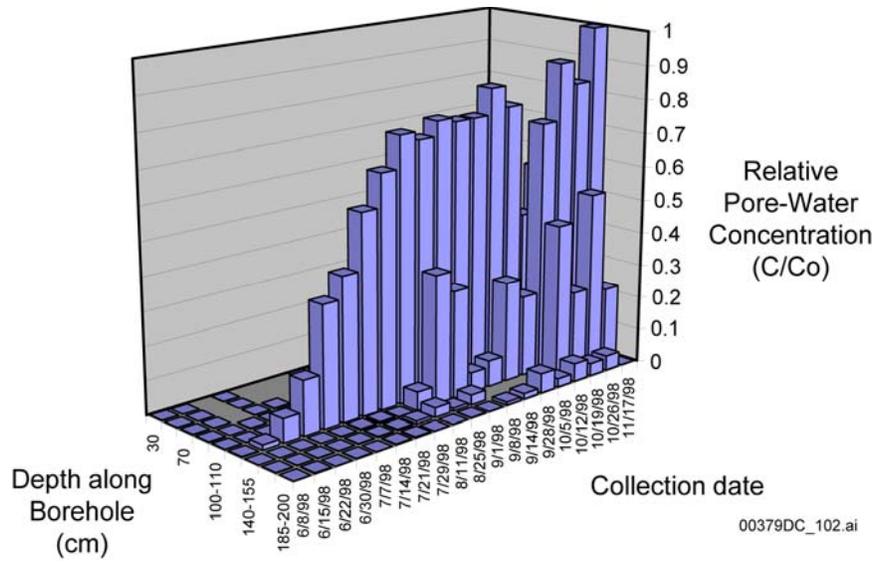
Source: BSC 2003 [DIRS 166347], Figure 6.13.2-4a

Figure 7-48a. Bromide Concentrations in Borehole 6 for Phase-1B, Busted Butte Unsaturated Zone Transport Test
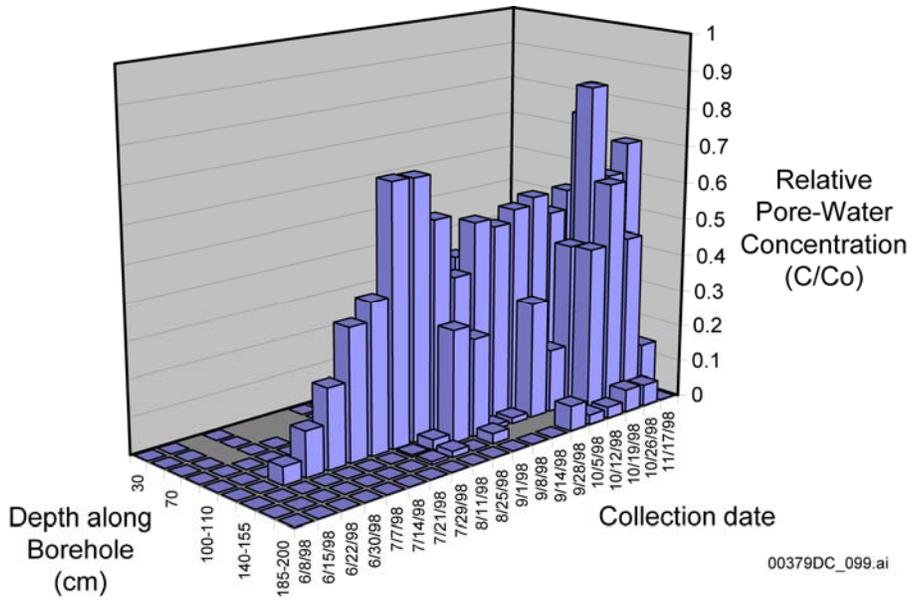
Source: BSC 2003 [DIRS 166347], Figure 6.13.2-4b

Figure 7-48b. 2, 6-DFBA Concentrations in Borehole 6 for Phase-1B, Busted Butte Unsaturated Zone Transport Test
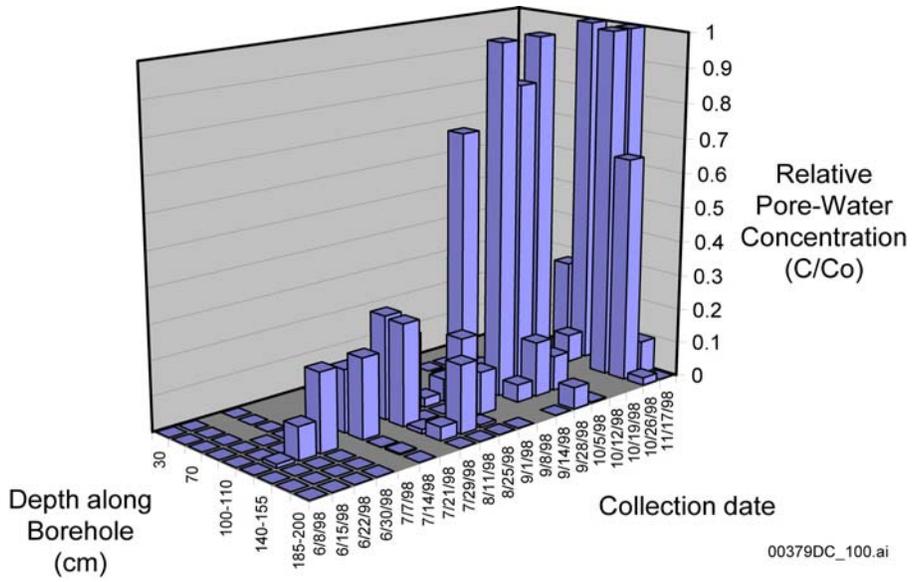
Source: BSC 2003 [DIRS 166347], Figure 6.13.2-4c

Figure 7-48c. Fluorescein Concentrations in Borehole 6 for Phase-1B (maximum values truncated at 1), Busted Butte Unsaturated Zone Transport Test
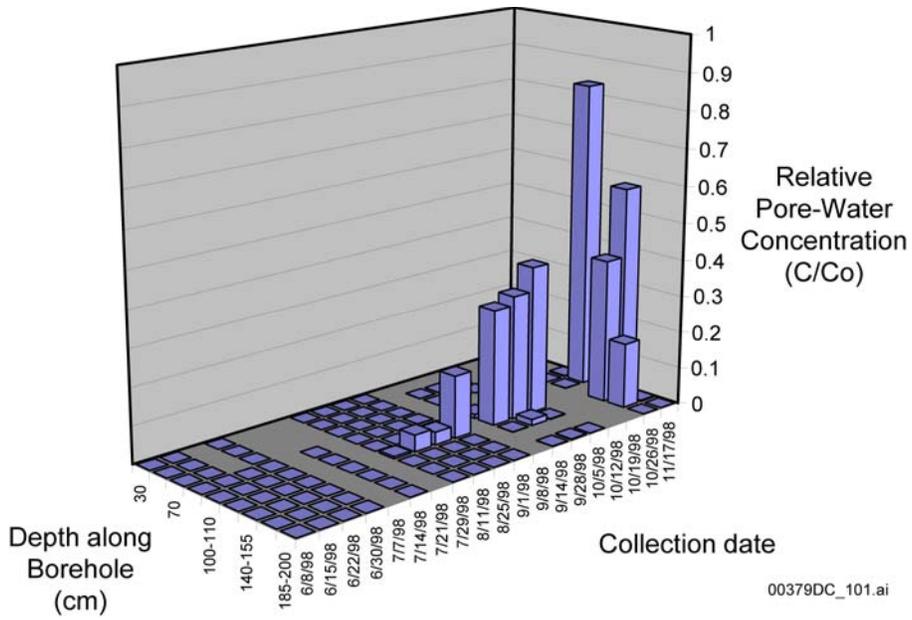
Source: BSC 2003 [DIRS 166347], Figure 6.13.2-4d

Figure 7-48d. Pyridone Concentrations in Borehole 6 for Phase-1B, Busted Butte Unsaturated Zone Transport Test
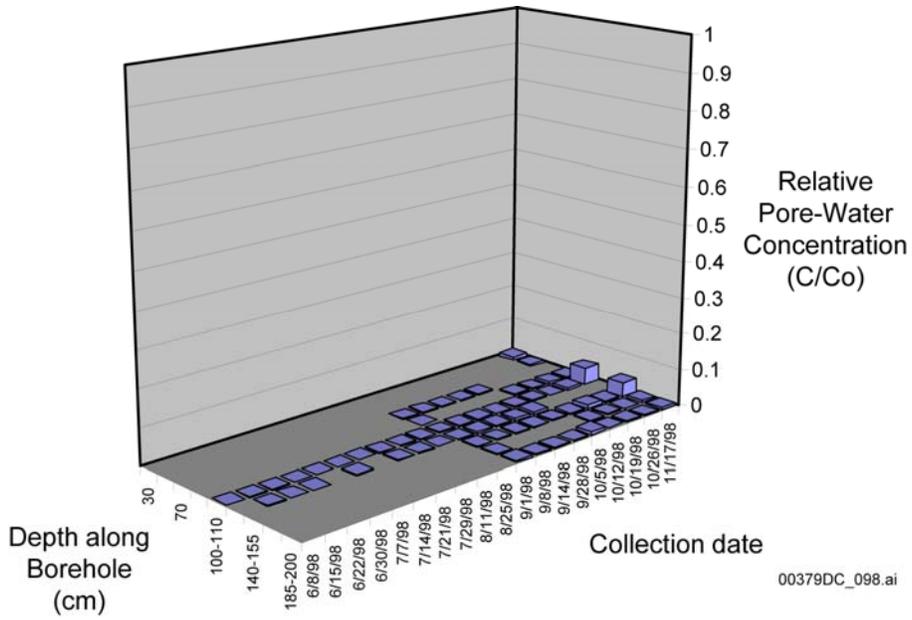
Source: BSC 2003 [DIRS 166347], Figure 6.13.2-4e

Figure 7-48e. Lithium Concentrations in Borehole 6 for Phase-1B, Busted Butte Unsaturated Zone Transport Test
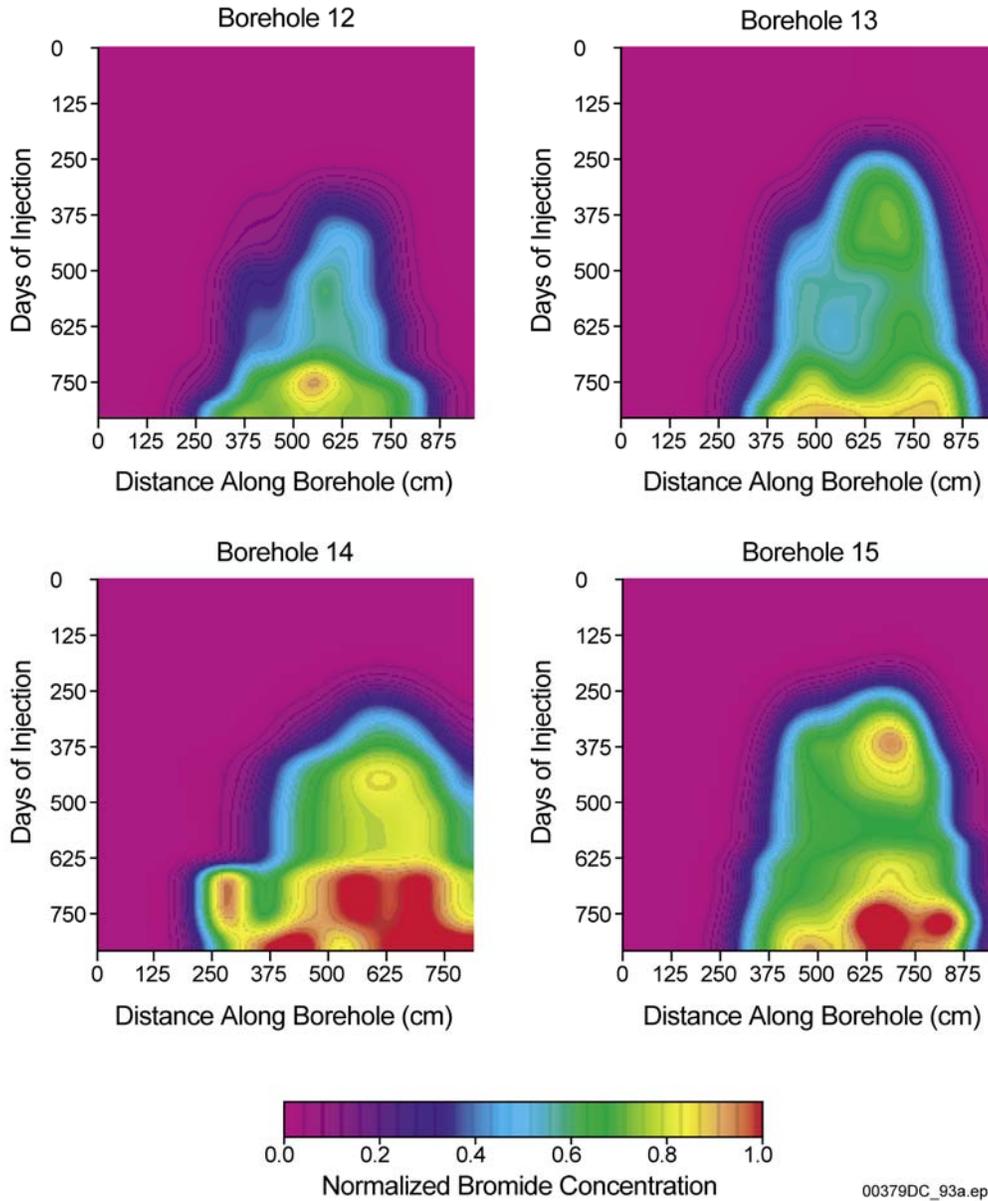
Source: Modified from BSC 2003 [DIRS 166347], Figure 6.13.3-5

Figure 7-49. Influence of Rock Heterogeneity on Tracer Transport in Busted Butte Unsaturated Zone Transport Test Phase-2
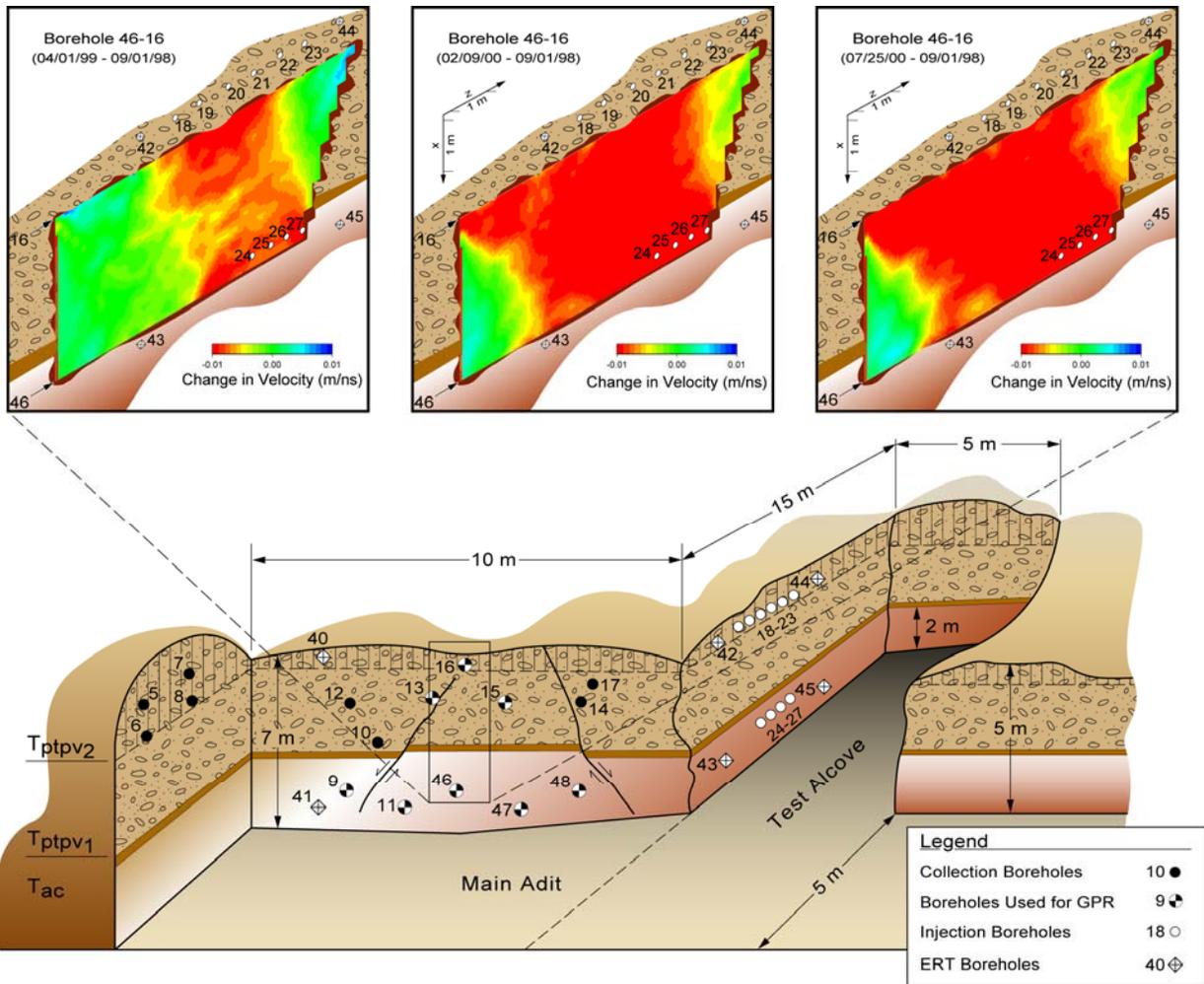
Source: BSC 2003 [DIRS 166347], Figure 6.13.4-1

NOTE: Concentration is presented as a function of vertical distance from the injection point for different two-dimensional sensitivity runs.

Figure 7-50. Tomography (GPR-T) Results from Well Pair 46-16 from December 1998, March 1999, and April 1999, Busted Butte Unsaturated Zone Transport Test
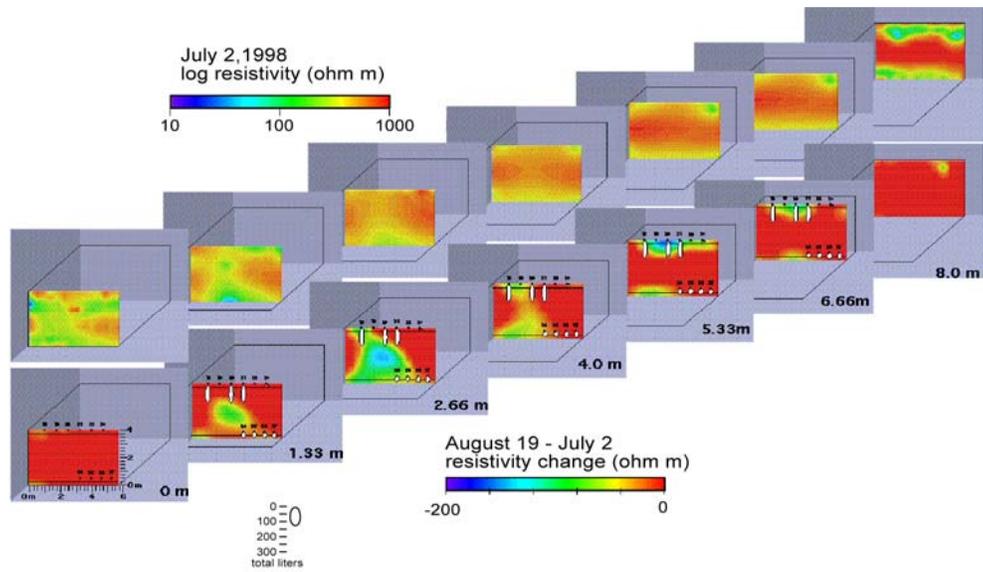
Source: Modified from BSC 2003 [DIRS 166347], Figure 6.13.4-7

NOTES: The diagram shows vertical slices through block at 0, 1.33, 2.66, 4.0, 5.33, 6.66, and 8.0 m (0, 4.36, 8.72, 13.12, 17.48, 21.84, and 26.24 ft). The top series is an absolute image (baseline, July 2, 1998), and the bottom series is the August 19-July 2, 1998 difference images.

Figure 7-51. Electrical-Resistance Tomography Images of the Test Block Viewed from Test Alcove (Perpendicular to the Busted Butte Tunnel): Baseline and August 19-July 2, 1998 Differences
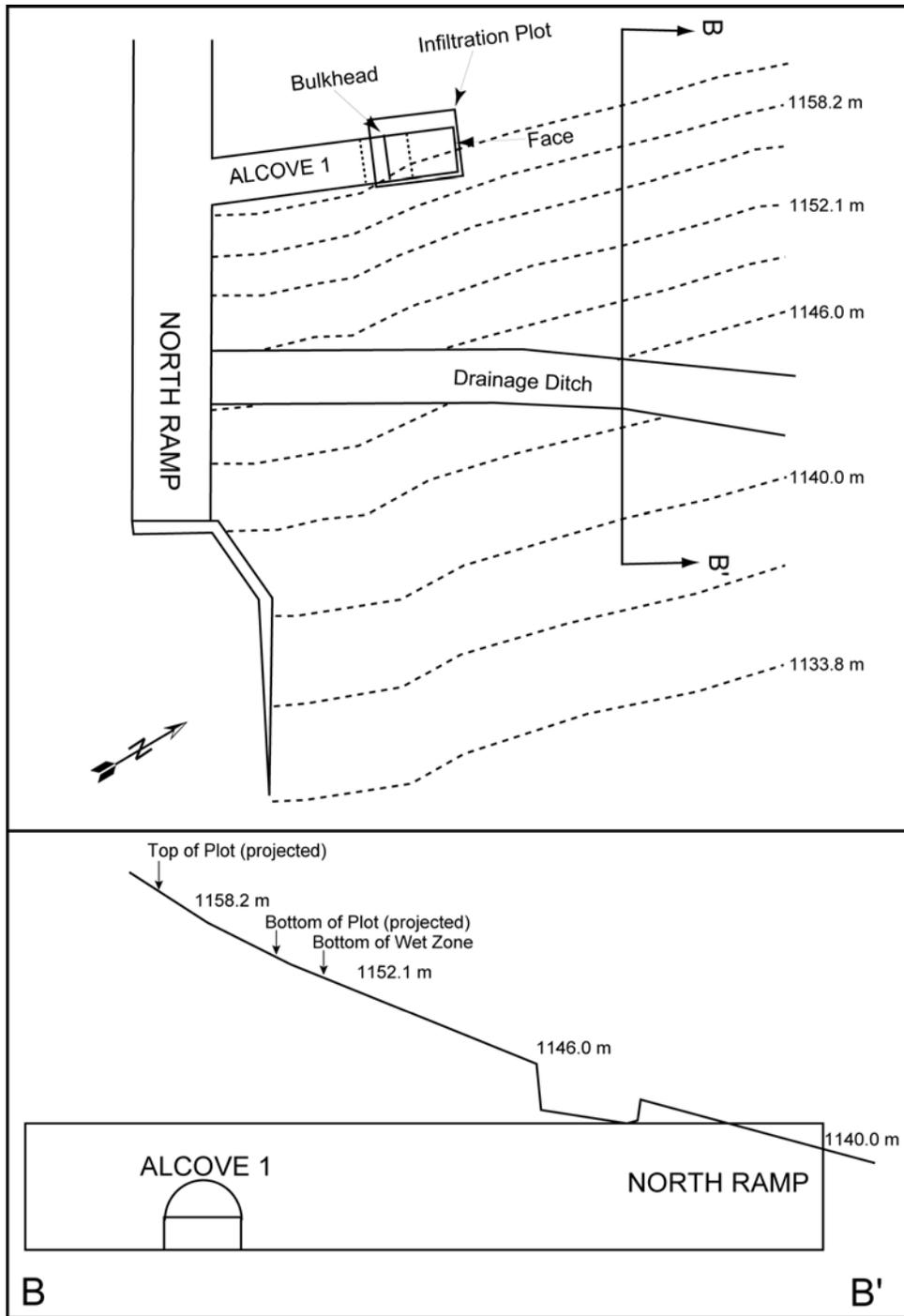
Source: Guertal (2001 [DIRS 164070], pp. 29-30)

Figure 7-52.   Schematic Illustration of Alcove 1 Test Site Inside the Exploratory Studies Facility North Portal
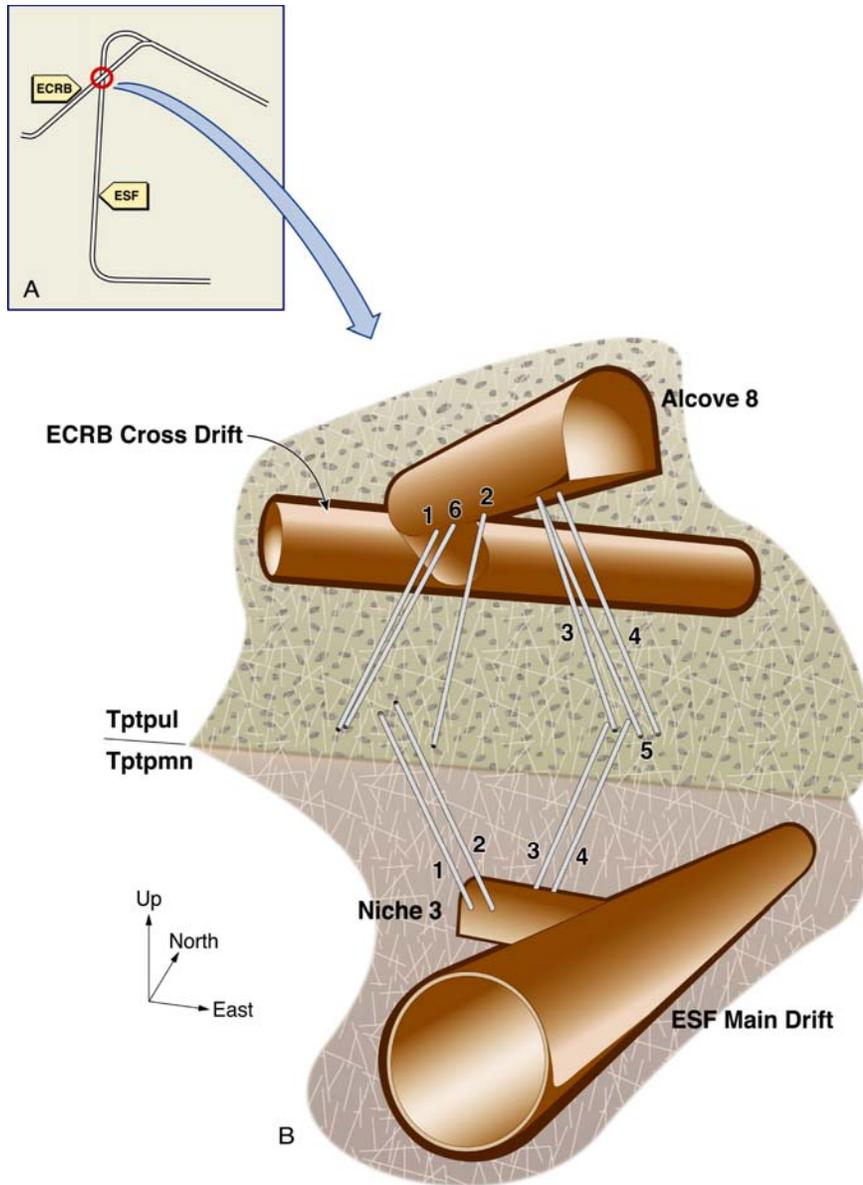
Source: BSC 2003 [DIRS 166347], Figure 6.12.1-2

Figure 7-53. Schematic Illustration of the Test Bed for the Alcove 8-Niche 3 Tests
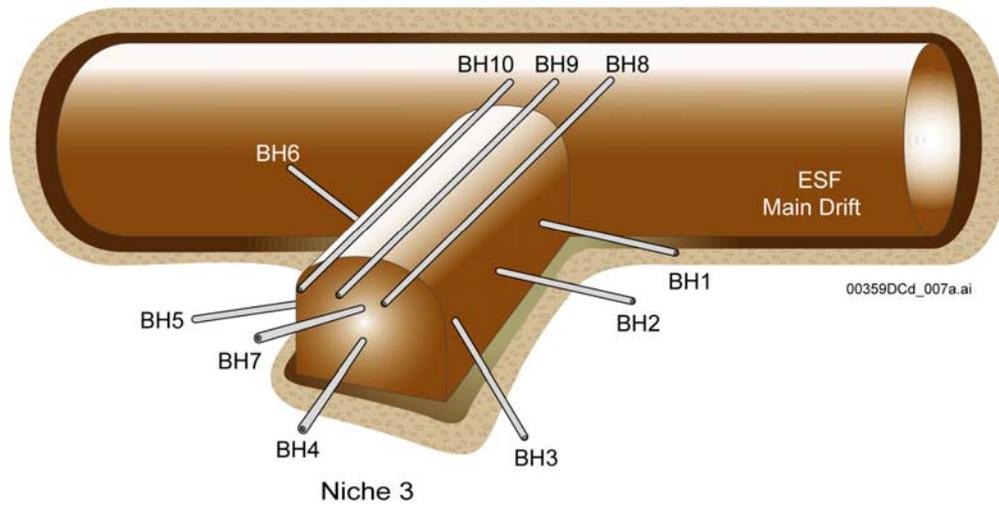
Source: Modified from BSC 2003 [DIRS 166347], Figure 6.12.1-4

Figure 7-54. Schematic Illustration of the Monitoring Boreholes in Niche 3
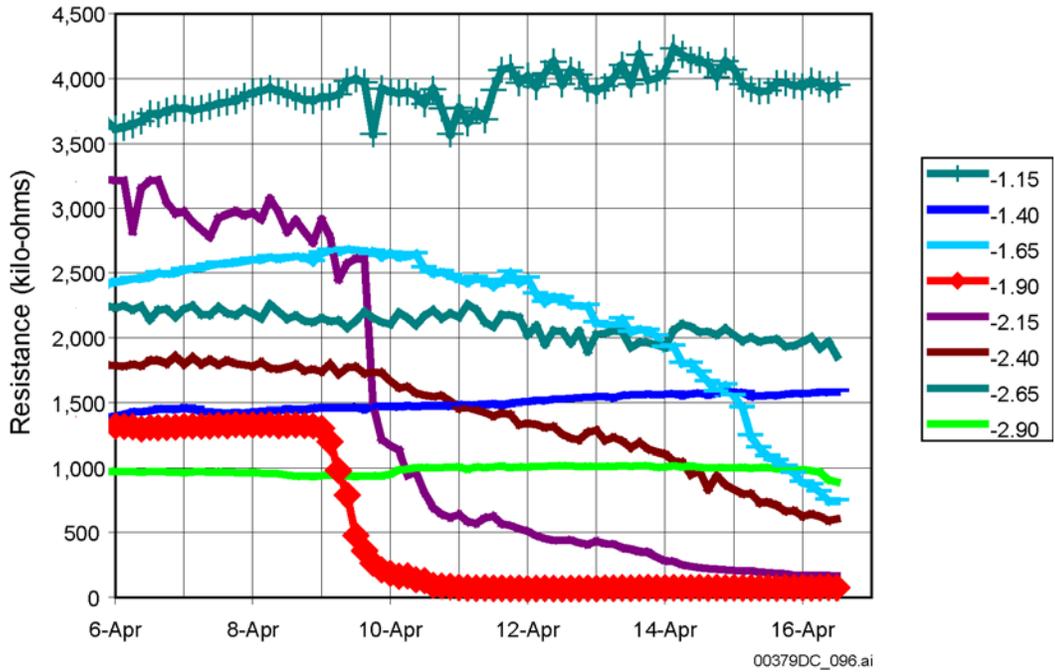
Source: BSC 2001 [DIRS 166347], Figure 6.12.3-2

NOTE: Legend indicates the location of measurement (in meters) from borehole collar.

Figure 7-55. Wetting-Front Arrival Detected in Borehole 10 in Niche 3
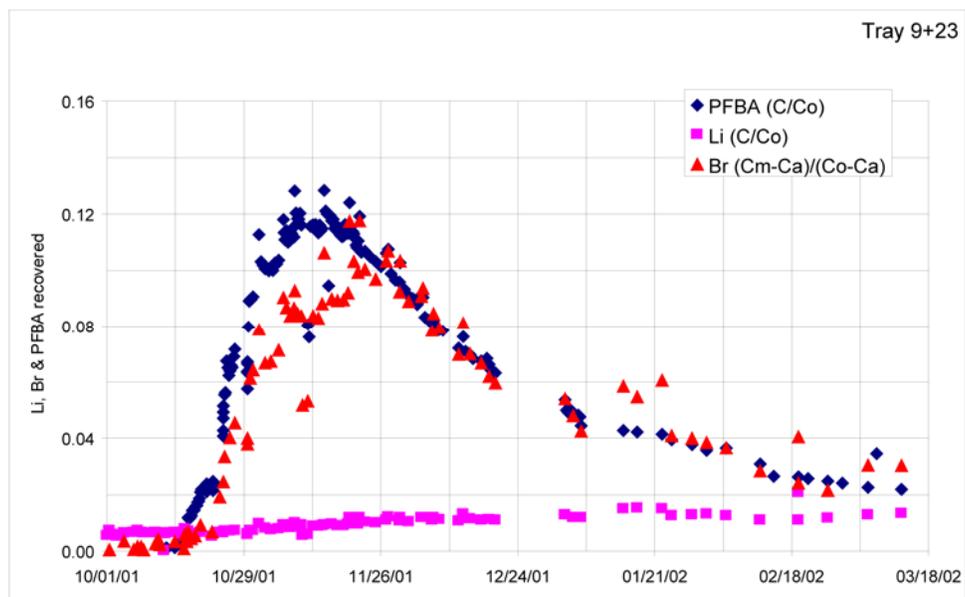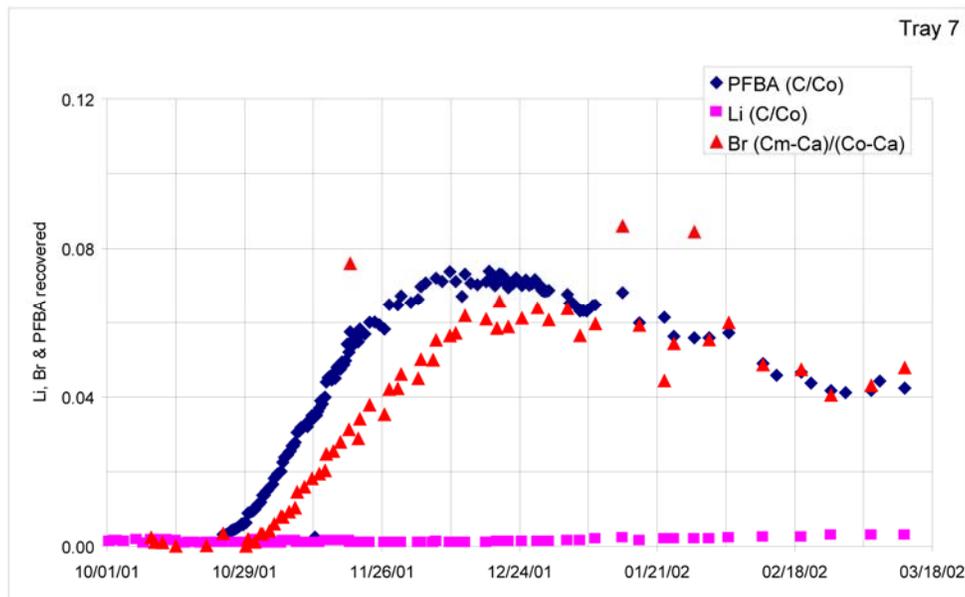
DTNs: LB0204NICH3TRC.001 [DIRS 158478]; LB0303A8N3LIQR.001 [DIRS 162570]

NOTE: C_m is the measured concentration and C_a is the background concentration in the leachate.

Figure 7-56. Relative Mass Recovery of Tracers Measured in Seepage in Niche 3
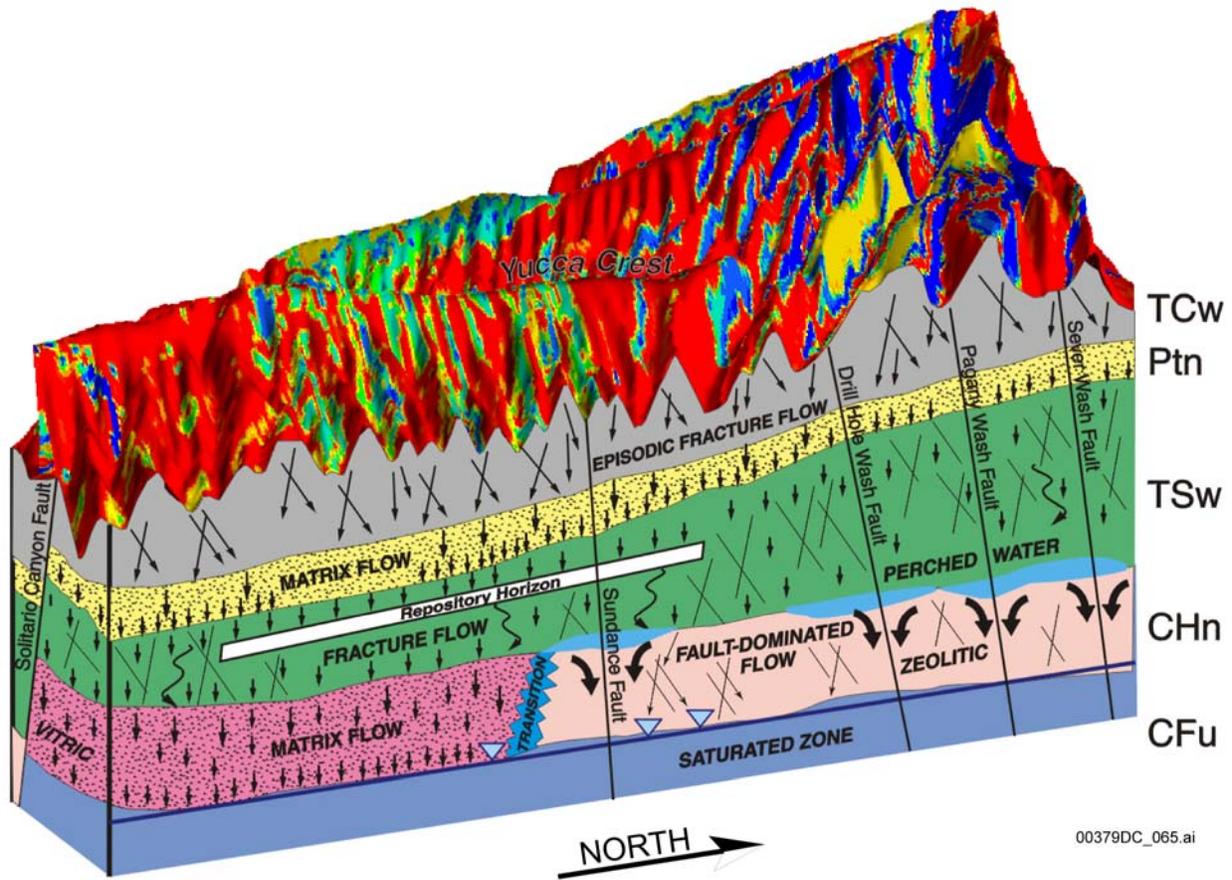
Source: CRWMS M&O 2000 [DIRS 141187], Figure 1

NOTE: Schematic cross section west of the Ghost Dance fault. The color patterns at the top of the diagram represent shallow infiltration flux. Red is the lowest flux; blue is the highest flux; green, yellow, and beige are intermediate fluxes in descending order.

Figure 7-57. Schematic Diagram of Conceptual Model of Liquid Water Flow through the Unsaturated Zone at Yucca Mountain

Table 7-1. Lithostratigraphy, Hydrogeologic Unit, and Unsaturated Zone Flow Model Layer Correlation

Major Hydrogeologic Unit (Modified from Montazer and Wilson 1984 [DIRS 100161], Table 1)	Lithostratigraphic Nomenclature (GFM2000) (BSC 2002 [DIRS 159124], Table 4)	Detailed Hydrogeologic Unit (Flint 1998 [DIRS 100033], Table 1)	UZ Flow Model Layer
Tiva Canyon welded (TCw)	Tpcr	CCR, CUC	tcw11
	Tpcp	CUL, CW	tcw12
	TpcLD		
	Tpcpv3	CMW	tcw13
	Tpcpv2		
Paintbrush nonwelded (PTn)	Tpcpv1	CNW	ptn21
	Tpbt4	BT4	ptn22
	Tpy (Yucca)		
		TPY	ptn23
		BT3	ptn24
	Tpbt3		
	Tpp (Pah)	TPP	ptn25
	Tpbt2	BT2	ptn26
	Tptrv3		
	Tptrv2		
Topopah Spring welded (TSw)	Tptrv1	TC	tsw31
	Tptrn		
		TR	tsw32
	Tptrl, Tptf	TUL	tsw33
	Tptpul, RHHtop		
	Tptpmn	TMN	tsw34
	Tptpll	TLL	tsw35
	Tptpln	TM2 (upper 2/3 of Tptpln)	tsw36
		TM1 (lower 1/3 of Tptpln)	tsw37
	Tptpv3	PV3	tsw38
	Tptpv2	PV2	tsw39 (vit, zeo)
Calico Hills nonwelded (CHn)	Tptpv1	BT1 or BT1a (altered)	ch1 (vit, zeo)
	Tpbt1		
	Tac (Calico)	CHV (vitric) or CHZ (zeolitic)	ch2 (vit, zeo)
			ch3 (vit, zeo)
			ch4 (vit, zeo)
			ch5 (vit, zeo)
	Tacbt (Calicobt)	BT	ch6 (vit, zeo)
	Tcpuv (Prowuv)	PP4 (zeolitic)	pp4
	Tcpuc (Prowuc)	PP3 (devitrified)	pp3

Table 7-1. Lithostratigraphy, Hydrogeologic Unit and Unsaturated Zone Flow Model Layer, and Correlation (Continued)

Major Hydrogeologic Unit (Modified from Montazer and Wilson 1984 [DIRS 100161], Table 1)	Lithostratigraphic Nomenclature (GFM2000) (BSC 2002 [DIRS 159124], Table 4)	Detailed Hydrogeologic Unit (Flint 1998 [DIRS 100033], Table 1)	UZ Flow Model Layer
Calico Hills nonwelded (CHn) (Continued)	Tcpmd (Prowmd)	PP2 (devitrified)	pp2
	Tcplc (Prowlc)		
	Tcplv (Prowlv)	PP1 (zeolitic)	pp1
	Tcpbt (Prowbt)		
	Tcbuv (Bullfroguv)	BF3 (welded)	bf3
Crater Flat undifferentiated (CFu)	Tcbuc (Bullfroguc)		
	Tcbmd (Bullfrogmd)		
	Tcblc (Bullfroglc)		
	Tcblv (Bullfroglv)	BF2 (nonwelded)	bf2
	Tcbbt (Bullfrogbt)		
	Tctuv (Tramuv)		
	Tctuc (Tramuc)	Not Available	tr3
	Tctmd (Trammd)		
	Tctlc (Tramlc)		
	Tctlv (Tramlv)	Not Available	tr2
	Tctbt (Trambt) and below		

Source: Modified from BSC 2003 [DIRS 160109], Table 11

Table 7-2. Underground Unsaturated Zone Test Locations

Name	Construction Station (m)	Geologic Unit[b]	Sources	Hydrogeologic Unit[b]	Process Tested	Feature/Unit Tested	Discussed in
ESF Study Sites[a]							
Alcove 1	00+43	Tpcpul	1, 14	TCw	Gas flow, infiltration, seepage	Upper Tiva Canyon Tuff	Sections 7.2.2.2.1, 7.8.2
Alcove 2	01+68	Tpcpmn	2, 15	TCw	Gas flow	Bow Ridge fault	Sections 7.2.2.2.2
Alcove 3	07+54	Tpcpln	3, 16	TCw / PTn	Gas flow, water potential	Upper PTn contact	Sections 7.2.2.2.3, 7.4.1.2
Alcove 4	10+28	Tpbt2	4, 16	PTn	Fault flow, matrix flow, water potential	Lower PTn contact	Sections 7.4.1.2, 7.6.3.2
Alcove 5	28+27	Tptpmn	5, 17	TSw	Thermal effects	Thermal Test Facility	Section 7.6.5
Alcove 6	37+37	Tptpmn	6, 17	TSw	Fracture and fault flow	Ghost Dance fault (northern alcove)	Sections 7.2.2.2.4, 7.6.3.1
Alcove 7	50+64	Tptpmn, Tptpll	7, 20	TSw	Infiltration, fault flow	Ghost Dance fault (southern alcove)	Section 7.2.2.2.5
Niche 1 (Niche 3566)[c]	35+69	Tptpmn	9, 17	TSw	Gas flow, water potential, seepage	Sundance fault	Section 7.6.4.1
Niche 2 (Niche 3650)[c]	36+53	Tptpmn	10, 17	TSw	Gas flow, water potential, seepage	TSw matrix and fractures	Section 7.6.4.1
Niche 3 (Niche 3107)	31+07	Tptpmn	11, 17	TSw	Gas flow, water potential, seepage	Cross-over of ECRB drift	Sections 7.6.4.1, 7.8.3
Niche 4 (Niche 4788)	47+88	Tptpmn	12, 17	TSw	Gas flow, water potential, seepage	TSw matrix and fractures	Section 7.6.4.1
ECRB Study Sites[a]							
Alcove 8	7+98	Tptpul	8, 18	TSw	Fluid flow	Cross-over of ECRB drift	Section 7.8.3
Niche 5 (Niche CD 1620)[c]	16+18	Tptpll	13, 18	TSw	Gas flow, seepage	TSw matrix and fractures	Section 7.6.4.1
Systematic Testing Boreholes (SYTB)	16+65 to 17+49	Tptpll	19	TSw	Gas and fluid flow, seepage	Boreholes systematically spaced for analysis of lateral variability	Sections 7.6.4.2
Busted Butte Unsaturated Zone Test							
Busted Butte[d]	NA	Tptpv, Tac	20	TSw/CHn	Matrix, fault, fracture flow and transport	TSw, CHn, and TSw/CHn contact	Section 7.8.1

Sources: 1) Alcove 1: MO0005GSC00216.000 [DIRS 153143]; 2) Alcove 2: MO9912GSC99493.000 [DIRS 144030]; 3) Alcove 3: MO9912GSC99494.000 [DIRS 141489]; 4) Alcove 4: MO0001GSC00001.000 [DIRS 143974]; 5) Alcove 5: MO0208GSC01042.001 [DIRS 166213]; 6) Alcove 6: MO0003GSC00102.000 [DIRS 152108]; 7) Alcove 7: MO0011GSC00385.000 [DIRS 166212]; 8) Alcove 8: MO0006GSC00241.000 [DIRS 152630]; 9) Niche 1: MO0008GSC00272.000 [DIRS 154173]; 10) Niche 2: MO0003GSC00096.000 [DIRS 152167]; 11) Niche 3: MO0003GSC00103.000 [DIRS 152176]; 12) Niche 4: MO0008GSC00273.000 [DIRS 152626]; 13) Niche 5: MO0009GSC00332.000 [DIRS 155370]; 14) GS940208314224.002 [DIRS 166239]; 15) Beason et al. 1996 [DIRS 101191], p. 17; 16) Barr et al. 1996 [DIRS 100029], Table 1; 17) Albin et al. 1997 [DIRS 101367], Table 5; 18); Mongano et al. 1999 [DIRS 149850], Table 1; 19) BSC 2003 [DIRS 166347], Section 6.11.1.1; 20) BSC 2003 [DIRS 166347], Section 6.13.1.1

NOTES: [a] Locations are shown on Figure 1-3.
[b] Geologic unit and hydrogeologic unit symbols are defined on Table 7-1.
[c] Niches were named prior to completion of location survey.
[d] Location is shown on Figure 1-4.

Table 7-3. The Ten Largest Observed Peak Discharges in the Yucca Mountain Region

Site	Station Number	Station Name	Drainage Area (km²)	Date mm/dd/yy	Peak Discharge (m³/s)	Unit Peak Discharge (m³/s / km²)
36	10251255	Fortymile Wash near Well J-13, Nevada Test Site, Nevada	787	02/25/69	570	0.724
18	10251220	Amargosa River near Beatty, Nevada	1222	02/24/69	453	0.371
50	10251300	Amargosa River at Tecopa, California	8003	08/18/83	300	0.037
50	10251300	Amargosa River at Tecopa, California	8003	02/26/69	142	0.018
18	10251220	Amargosa River near Beatty, Nevada	1222	08/30/67	120	0.098
45	10251270	Amargosa River tributary near Mercury, Nevada	285	08/01/68	97.1	0.341
38	10251258	Fortymile Wash near Amargosa Valley, Nevada	818	02/25/69	93.5	0.114
19	10251242	Fortymile Wash above East Cat Canyon, Nevada Test Site, Nevada	106	03/11/95	85.0	0.802
25	10251250	Fortymile Wash at Narrows, Nevada Test Site, Nevada	668	03/11/95	85.0	0.127
36	10251255	Fortymile Wash near Well J-13, Nevada Test Site, Nevada	787	03/11/95	85.0	0.108

DTN: MO0312SEPSDOPD.000 [DIRS 166565]

Sources: USGS 1974 [DIRS 149715]); Frisbie et al. 1984 [DIRS 149742]); Bauer et al. 1996 [DIRS 101486]

NOTE: Locations of stations are shown in Figures 7-5a and 7-5b.

Table 7-4. Comparison of Total Infiltration Loss Estimates for Fortymile Wash

Estimator	Fortymile Canyon Reach (7.1 km)	Upper Jackass Flats Reach (10.1 km)	Lower Jackass Flats Reach (16.8 km)	Amargosa Desert Reach (13.9 km)	Total (47.9 km)
Osterkamp et al. (1994)	50,000 m³/yr	510,000 m³/yr	10,000 m³/yr	20,000 m³/yr	590,000 m³/yr (478 a.-ft)
Savard (1998)	36,000 m³/yr	71,100 m³/yr	86,400 m³/yr	104,300 m³/yr	297,800 m³/yr (241 a.-ft)

DTN: MO0312SEPSDTIL.000 [DIRS 166566]

Sources: Savard 1998 [DIRS 102213], pp. 26 to 27; Osterkamp et al. 1994 [DIRS 100602], pp. 496 to 499

NOTE: To obtain infiltration loss estimates in cubic feet per year, multiply the cubic meter per year value by 35.3146.

Table 7-5. Compilation of Observed Data and Model Estimates of Average Annual Recharge for Study Basins

| | Average Annual Values of | | Chloride Mass-Balance Method |
Basin	Basin-Wide Precipitation (mm)	Observed Runoff (mm)	Estimate of Average Annual Recharge (mm)
3-Springs	336.3	10.7	32.8
East Stewart	639.1	330.5	309.9

DTN: MO0312SEPSDAAR.000 [DIRS 166495]

Source: Modified from Lichty and McKinley 1995 [DIRS 100589], Table 15

NOTE: mm = millimeter.

Table 7-6. Infiltration Fluxes Estimated by the Chloride Mass-Balance Method

Borehole	Unit	Depth interval (m)	Apparent flux (mm/yr)
USW UZ-N37	Soil	0-13	0.5
USW-UZ-N53	PTn		3.3
USW-UZ-N54	Soil	0-7.8	0.02
	PTn		3.3
USW-UZ-N55	PTn		2.4
USW-UZ-N11	PTn		3.2
UE-25 UZ#16	Soil	0-7.4	0.02
	PTn	50-55	3.0
	Calico Hills	368-440	3.5
USW-UZ-14	PTn	44-75	1.2
	Calico Hills	470-477	5.9
UE-25 UZ#4	PTn	91-96	1.1
UE-25 UZ#5	PTn	29-36	2.5
	PTn	94-97	1.4

DTN: MO0312SEPSDIFR.000 [DIRS 166489]

Sources: Flint et al. 1996 [DIRS 100147], Table 7

NOTES: m = meter; mm/yr = millimeters per year. Borehole locations are shown on Figure 7-2.

Table 7-7. Apparent Infiltration Rates Calculated from Representative Pore-Water Chloride Concentrations at Yucca Mountain

Borehole Location	Chloride Concentration[a] (mg/L)	Apparent Infiltration Rate[b] (mm/year)
Alluvial samples from depths greater than 5 m (large washes and thick terraces)		
USW UZ-N37	133	0.4
USW UZ-N54	7,400	0.01
USW UZ-14	520	0.1
UE-25 UZ#16	3,700	0.02
Samples from PTn beneath area with thick alluvial cover (large washes and thick terraces)		
UE-25 UZ#4	104	0.6
UE-25 UZ#5	42	1.4
USW UZ-14	44	1.4
UE-25 UZ#16	32	1.8
USW NRG-6	47	1.3
USW SD-9	40	1.5
Samples from PTn beneath area with moderate alluvial cover (terrace or near base of sideslope, soil 0.5 to 3 m thick)		
USW NRG-7a	39	1.5
USW SD-12	46	1.3
USW UZ-7a	60	1.0
Samples from PTn or TSw beneath area with thin alluvial cover (ridgetop or sideslope, soil <0.5 m thick)		
USW SD-6 (PTn)	27	2.2
USW SD-7 (PTn)	77	0.8
USW UZ-N55 (PTn)	77	0.8
ESF North Ramp (PTn)	6	9.9
ESF South Ramp (PTn)	17	3.5
ESF Main Drift (TSw)	16	3.7
ECRB Cross Drift (TSw)	12	5.0

DTN: MO0312SEPSDAIR.000 [DIRS 166405]

Sources: Flint et al. 2002 [DIRS 157411], Table 1

NOTES: [a] Cl concentrations for alluvial samples are averages for depths >5 m in order to ensure that they reflect concentrations below the zone of evapotranspiration. Concentrations cited for pore-water samples from PTn and TSw units are the lowest values of those measured in those stratigraphic units at each location.

[b] Infiltration-rate calculation assumes an average annual precipitation of 170 mm with an average chloride concentration of 0.35 mg/L.

Table 7-8. Summary of Soil Properties

Soil Unit	Saturated Hydraulic Conductivity (simulated, m/s)	Alpha (1/Pa)	n	Porosity (%)	Rock Fragments (%)	Bulk Density (g/cm³)	Water Content at –0.1 Bar Water Potential (%)	Water Content at –60 Bars Water Potential (%)
1	5.6×10^{-6}	0.00052	1.24	36.6	10.5	1.60	24.2	5.4
2	1.2×10^{-5}	0.00062	1.31	31.5	11.6	1.73	17.3	2.3
3	1.3×10^{-5}	0.00066	1.36	32.5	18.7	1.70	16.3	1.7
4	3.8×10^{-5}	0.00087	1.62	28.1	21.9	1.81	7.3	0.2
5	6.7×10^{-6}	0.00056	1.28	33.0	15.2	1.69	20.0	3.5
6	2.7×10^{-5}	0.00074	1.40	33.9	11.7	1.66	15.0	1.1
7	5.6×10^{-6}	0.00055	1.26	37.0	17.1	1.58	23.4	4.6
9	5.7×10^{-6}	0.00055	1.30	32.2	19.1	1.72	18.9	2.8

DTN: GS000308311221.004 [DIRS 146853]

Source: USGS 200l [DIRS 160355], Table IV-4

NOTES: g/cm³ = grams per cubic centimeter; m/s = meters per second; Pa = pascals; % = percent.

Table 7-9. Generalized Lithostratigraphy, Previously Used Informal Stratigraphic Nomenclature, and Corresponding Detailed and Major Hydrogeologic Units at Yucca Mountain

Currently Used Formal and Informal Nomenclature[a], Lithostratigraphic Unit	Previously Used Informal Nomenclature [b]	Hydrogeologic Units Detailed [c]	Hydrogeologic Units Major [d]
PAINTBRUSH GROUP			Tiva Canyon welded (TCw)
Tiva Canyon Tuff (Tpc)			
crystal-rich member (Tpcr)			
vitric zone (rv)			
nonlithophysal zone (rn)			
subvitrophyre transition subzone (rn4)	vitrophyre (ccr)	CCR (< 10%)	
pumice-poor subzone (rn3)	upper cliff (cuc)	CUC (> 9%)	
mixed pumice subzone (rn2)			
crystal transition subzone (rn1)			
lithophysal zone (rl)			
crystal-poor member (Tpcp)			
upper lithophysal zone (pul)	upper lithophysal (cul)	CUL (< 20%)	
middle nonlithophysal zone (pmn)	clinkstone(cks), rounded step(crs)	CW	
lower lithophysal zone (pll)	lower lithophysal (cll)		
lower nonlithophysal zone (pln)			
hackly subzone (plnh)	hackly (ch)		
columnar subzone (plnc)	columnar (cc)		
argillic pumice interval (plnc2)	vitrophyre	CMW (> 15%)	
vitric zone (pv)			
densely welded subzone (pv3v)			
moderately welded subzone (pv2)	nonwelded base (ccs)	CNW (> 28%)	
non- to partially welded subzone (pv1)			Paintbrush nonwelded (PTn)
Pre-Tiva Canyon Tuff bedded tuff (Tpbt4)		BT4	
Yucca Mountain Tuff (Tpy)		TPY (< 30%)	
Pre-Yucca Mountain Tuff bedded tuff (Tpbt3)		BT3	
Pah Canyon Tuff (Tpp)		TPP	
Pre-Pah Canyon Tuff bedded tuff (Tpbt2)		BT2	
Topopah Spring Tuff (Tpt)			
crystal-rich member (Tptr)			
vitric zone (rv)			
nonwelded subzone (rv3)			
moderately welded subzone (rv2)			
densely welded subzone (rv1)	vitrophyre (tc)	TC (< 9%)	Topopah Spring welded (TSw)
nonlithophysal zone (rn)	rounded (tr)		
dense subzone (rn3)			
vapor-phase corroded subzone (rn2)		TR	
lithophysal zone (rl)		TUL	
crystal-poor member (Tptp)			
upper lithophysal zone (pul)	upper lithophysal (tul)		
middle nonlithophysal zone (pmn)	middle nonlithophysal (tmn)	TMN	
lower lithophysal zone (pll)	lower lithophysal (tll)	TLL	
lower nonlithophysal zone (pln)	mottled (tm)	TM2 (upper 2/3)	
		TM1 (lower 1/3)	
vitric zone (pv)			
densely welded subzone (pv3)	basal vitrophyre (tv)	PV3	
moderately welded subzones (pv2)			

Table 7-9. Generalized Lithostratigraphy, Previously Used Informal Stratigraphic Nomenclature, and Corresponding Detailed and Major Hydrogeologic Units at Yucca Mountain (Continued)

Currently Used Formal and Informal Nomenclature [a]	Previously Used Informal Nomenclature [b]	Hydrogeologic Units	
		Detailed [c]	Major [d]
nonwelded subzone (pv1)			Calico Hills nonwelded (CHn)
Pre-Topopah Spring Tuff bedded tuff (Tpbt1)		BT1a (altered)	
		BT1 (unaltered)	
CALICO HILLS FORMATION (Tac)			
Unit 4 Pumiceous pyroclastic flow	Calico Hills vitric (CHv)	CHV (vitric)	
Unit 3 Lithic-rich pyroclastic flow	Calico Hills zeolitized (CHz)	CHZ (zeolitic)	
Unit 2 Pumiceous pyroclastic flow			
Unit 1 Lithic-rich pyroclastic flow			
Bedded tuff (Tacbt)		BT (zeolitic)	
Basal sandstone (Tacbs)			
CRATER FLAT GROUP			
Prow Pass Tuff (Tcp)			
Unit 4 Pyroxene rich		PP4 (zeolitic)	
Unit 3 Welded pyroclastic flow		PP3 (welded, altered)	
		PP2 (welded)	
Unit 2 Lithic-rich pyroclastic flow		PP1 (zeolitic)	
Unit 1 Pumiceous pyroclastic flow			
Pre-Prow Pass bedded tuff (Tcpbt)			
Bullfrog Tuff (Tcb)		BF3 (welded)	
Unit 4			
Unit 3			Crater Flat undifferentiated (Cfu)
Unit 2		BF2 (zeolitic)	
Unit 1			
Pre-Bullfrog Tuff basal sandstone (Tcbbs)			
Tram Tuff (Tct)			

Source: Modified from Flint 1998 [DIRS 100033], Table 1; BSC 2003 [DIRS 160109], Table 11

NOTES: % = percentage of matrix porosity.
   [a] After Buesch, Spengler et al. 1996 [DIRS 100106]; Moyer and Geslin 1995 [DIRS 101269].
   [b] After Scott and Bonk 1984 [DIRS 104181].
   [c] After Flint 1998 [DIRS 100033].
   [d] After Montazer and Wilson 1984 [DIRS 100161].

Table 7-10. Mean Values and Standard Deviations for Measured Core Properties and Estimated Saturated Hydraulic Conductivity for Each Hydrogeologic Unit

Hydrogeologic Unit	Relative Humidity Porosity (v/v)		N	Bulk Density (g/cm³)		Porosity (v/v)		Particle Density (g/cm³)		N	Volumetric Water Content (v/v)		Saturation		N	Water Potential (-bars)		N	Saturated Hydraulic Conductivity (m/s)		Saturated Hydraulic Conductivity (m/s)		N	Estimated Saturated Hydraulic Conductivity (m/s)		N
	Mean	SD		Mean	SD	Mean	SD	Mean	SD		Mean	SD	Mean	SD		Geom. Mean	SD		Geom. Mean	SD	PL Mean	SD		Geom. Mean	SD	
CCR			0	2.39	0.07	0.062	0.020	2.55	0.04	9	0.046	0.015	0.75	0.13	9			0					0	1.5E-12	2.1E-12	9
CUC	0.235	0.025	17	1.91	0.13	0.253	0.060	2.56	0.09	101	0.098	0.048	0.40	0.17	101			0	3.8E-08	2.2E-08	3.3E-08	5.9E-08	3	3.9E-08	1.4E-07	101
CUL	0.126	0.038	31	2.10	0.14	0.164	0.062	2.52	0.03	98	0.094	0.021	0.61	0.15	98			0	1.2E-08		1.2E-08		1	5.7E-10	1.2E-07	98
CW	0.066	0.026	405	2.30	0.06	0.082	0.030	2.51	0.05	599	0.064	0.026	0.80	0.14	599	8.8	8.9	183	5.4E-11	5.2E-12	4.6E-11	1.0E-10	6	3.8E-12	4.1E-09	599
CMW	0.140	0.044	61	1.97	0.14	0.203	0.054	2.47	0.06	90	0.185	0.062	0.90	0.13	90	0.9	16.0	13	5.0E-10	5.6E-08	1.6E-10	4.7E-08	4	8.8E-12	1.0E-11	90
CNW	0.300	0.088	59	1.46	0.17	0.387	0.070	2.38	0.10	101	0.259	0.081	0.69	0.24	101	0.2	0.5	25	3.1E-08	4.1E-06	7.6E-10	4.8E-07	8	2.6E-07	2.2E-06	101
BT4	0.369	0.120	24	1.31	0.29	0.439	0.123	2.34	0.14	33	0.220	0.097	0.51	0.19	33	0.1	0.0	5	1.6E-07	2.4E-04	2.6E-09	6.5E-06	3	4.1E-07	1.8E-05	33
TPY	0.234	0.082	37	1.79	0.23	0.254	0.082	2.40	0.11	43	0.163	0.046	0.68	0.20	43	0.1	0.0	9	3.3E-08	2.0E-07	1.2E-08	2.5E-07	2	1.7E-08	7.4E-07	43
BT3	0.353	0.079	60	1.39	0.18	0.411	0.079	2.37	0.10	85	0.216	0.065	0.54	0.16	85	0.1	0.1	34	5.4E-07	1.2E-06	1.7E-07	2.3E-06	17	7.8E-07	1.1E-06	85
TPP	0.469	0.038	132	1.13	0.09	0.499	0.041	2.26	0.09	164	0.178	0.064	0.36	0.13	156	0.1	0.1	64	8.8E-07	4.2E-07	7.3E-07	6.7E-07	10	3.6E-06	1.2E-06	164
BT2	0.464	0.093	118	1.20	0.26	0.489	0.105	2.37	0.23	171	0.185	0.069	0.39	0.15	171	0.3	0.7	41	3.2E-06	5.6E-06	8.8E-07	9.6E-06	19	1.7E-06	2.9E-06	171
TC	0.042	0.036	50	2.38	0.10	0.054	0.036	2.51	0.04	66	0.034	0.024	0.62	0.17	66	9.4	186.7	21	7.6E-10	7.5E-09	1.5E-10	1.3E-08	3	6.2E-13	7.1E-10	66
TR	0.146	0.034	435	2.15	0.08	0.157	0.030	2.55	0.03	439	0.078	0.019	0.51	0.13	439	1.2	4.5	159	1.7E-09	1.6E-07	8.6E-10	1.4E-06	45	3.9E-10	1.0E-09	439
TUL	0.135	0.032	455	2.13	0.08	0.154	0.031	2.51	0.02	455	0.108	0.022	0.72	0.15	455	1.4	4.7	246	2.0E-10	3.0E-08	9.7E-11	2.5E-07	33	2.3E-10	5.2E-10	455
TMN	0.089	0.021	266	2.25	0.05	0.110	0.020	2.53	0.03	266	0.093	0.019	0.85	0.12	266	8.6	10.1	176	4.0E-11	4.3E-11	2.2E-11	4.4E-10	11	1.5E-11	2.3E-11	266
TLL	0.115	0.032	453	2.21	0.17	0.130	0.031	2.54	0.17	453	0.101	0.024	0.78	0.14	453	1.3	3.6	253	2.3E-10	2.2E-09	8.7E-11	9.3E-09	43	7.0E-11	4.5E-10	453
TM2	0.092	0.033	225	2.27	0.08	0.112	0.031	2.56	0.03	225	0.095	0.026	0.85	0.10	225	3.0	9.2	157	9.6E-10	8.8E-07	1.9E-10	2.4E-06	15	1.8E-11	2.1E-09	225
TM1	0.071	0.019	102	2.30	0.05	0.094	0.019	2.54	0.03	102	0.081	0.016	0.87	0.09	102	12.8	12.8	70	7.5E-11	4.5E-12	6.5E-11	8.2E-11	2	4.8E-12	5.8E-12	102
PV3	0.020	0.018	89	2.27	0.26	0.036	0.039	2.36	0.25	89	0.034	0.039	0.88	0.14	87	4.9	66.2	70	5.0E-11	2.7E-10	2.6E-11	8.5E-10	7	1.5E-13	2.1E-12	89
PV2	0.123	0.079	39	1.96	0.25	0.173	0.106	2.37	0.03	39	0.148	0.107	0.84	0.16	39	3.3	15.9	30	7.3E-10	3.5E-08	1.5E-10	2.4E-08	4	7.4E-11	2.0E-07	39
BT1a	0.193	0.077	36	1.66	0.16	0.288	0.072	2.34	0.05	36	0.267	0.076	0.93	0.16	36	0.3	1.6	29	5.4E-09	1.6E-08	1.4E-09	4.3E-08	4	6.0E-11	8.0E-10	36
BT1	0.265	0.065	43	1.66	0.14	0.273	0.067	2.28	0.07	43	0.083	0.020	0.32	0.10	43	0.1	0.4	43	1.6E-05		1.6E-05		1	6.1E-08	3.2E-07	43
CHV	0.321	0.037	69	1.47	0.06	0.345	0.034	2.24	0.10	69	0.168	0.078	0.50	0.24	69	0.2	0.2	62	5.5E-07	2.9E-06	1.0E-07	3.2E-06	6	2.1E-07	5.5E-07	69
CHZ	0.240	0.049	293	1.57	0.10	0.331	0.039	2.35	0.05	293	0.320	0.041	0.97	0.07	293	0.5	1.8	206	4.5E-11	6.5E-10	3.2E-11	9.9E-08	69	1.1E-10	1.3E-10	293

Table 7-10. Mean Values and Standard Deviations for Measured Core Properties and Estimated Saturated Hydraulic Conductivity for Each Hydrogeologic Unit (Continued)

Hydrogeologic Unit	Relative Humidity Porosity (v/v)		N	Bulk Density (g/cm³)		Porosity (v/v)		Particle Density (g/cm³)		N	Volumetric Water Content (v/v)		Saturation		N	Water Potential (-bars)		N	Saturated Hydraulic Conductivity (m/s)		Saturated Hydraulic Conductivity (m/s)		N	Estimated Saturated Hydraulic Conductivity (m/s)		N
	Mean	SD		Mean	SD	Mean	SD	Mean	SD		Mean	SD	Mean	SD		Geom. Mean	SD		Geom. Mean	SD	PL Mean	SD		Geom. Mean	SD	
BT	0.169	0.050	69	1.79	0.13	0.266	0.041	2.44	0.08	69	0.265	0.040	1.00	0.03	69	0.2	2.3	59	8.4E-11	8.5E-12	7.4E-11	1.0E-07	3	1.4E-11	2.1E-11	69
PP4	0.236	0.055	47	1.62	0.09	0.325	0.045	2.41	0.04	47	0.308	0.051	0.94	0.08	47	0.3	10.9	43	7.5E-11	3.4E-11	5.9E-11	1.0E-07	5	9.6E-11	1.4E-10	47
PP3	0.274	0.053	166	1.79	0.12	0.303	0.043	2.58	0.05	166	0.165	0.092	0.55	0.29	166	0.6	0.8	141	1.9E-08	2.9E-08	3.2E-09	7.0E-08	29	2.9E-10	4.0E-10	166
PP2	0.217	0.060	140	1.85	0.21	0.263	0.072	2.51	0.06	140	0.248	0.081	0.93	0.10	140	0.4	1.7	124	2.8E-10	1.2E-09	1.4E-10	9.9E-08	25	5.6E-11	1.1E-10	140
PP1	0.197	0.055	245	1.74	0.15	0.280	0.053	2.42	0.07	245	0.269	0.051	0.96	0.08	245	0.6	5.5	226	9.4E-11	1.6E-10	5.5E-11	1.0E-07	21	3.1E-11	5.6E-11	245
BF3	0.102	0.038	86	2.28	0.09	0.115	0.040	2.57	0.03	86	0.112	0.039	0.98	0.07	86	0.6	4.5	86	8.7E-11	--	8.7E-11		1	2.1E-12	2.4E-12	86
BF2	0.213	0.083	65	1.79	0.21	0.259	0.084	2.41	0.05	65	0.261	0.089	1.00	0.08	65	0.1	3.4	61	8.8E-10	5.4E-10	5.3E-10	9.8E-08	2	5.0E-11	7.0E-10	65

DTN: GS960908312231.004 [DIRS 107065]

Source: Flint 1998 [DIRS 100033], Table 7

NOTE: N = number of samples; v/v = dimensionless volume; SD = standard deviation; Geom. = geometric; PL = power-law; = no samples.

Table 7-11. Moisture Retention van Genuchten Curve-Fit Parameters (Alpha and n) for Each Hydrogeologic Unit

Hydrogeologic Unit	N	Laboratory Desorption Curves van Genuchten Parameters									Composite Curves van Genuchten Parameters									Residual Saturation (v/v)
		Alpha (1/bars)	SE	95 Percent Confidence Limits Upper	Lower	n	SE	95 Percent Confidence Limits Upper	Lower	m	Alpha (1/bars)	SE	95 Percent Confidence Limits Upper	Lower	n	SE	95 Percent Confidence Limits Upper	Lower	m	
CCR		0.335	0.140			1.254	0.037			0.203										0.20
CUC	3	0.827	0.227	1.290	0.364	1.840	0.221	2.291	1.388	0.457										0.04
CUL	3	1.404	0.462	2.344	0.463	1.529	0.110	1.752	1.306	0.346										0.06
CW	7	0.115	0.029	0.173	0.056	1.300	0.041	1.383	1.219	0.231	0.124	0.024	0.176	0.072	1.690	0.171	2.068	1.321	0.408	0.13
CMW	2	0.023	0.008	0.039	0.007	1.776	0.309	2.417	1.135	0.437	0.028	0.011	0.054	0.002	1.890	0.337	2.692	1.098	0.471	0.33
CNW	4	7.522	6.465	20.610	undef.	1.203	0.047	1.299	1.107	0.169	2.420	1.647	6.197	undef.	1.380	0.124	1.666	1.095	0.275	0.10
BT4	5	3.652	1.930	7.516	undef.	1.285	0.052	1.389	1.181	0.222	17.889	11.110	43.509	undef.	1.233	0.049	1.346	1.120	0.189	0.10
TPY	2	0.756	0.296	1.380	0.131	1.953	0.377	2.747	1.158	0.488	2.638	1.812	7.296	undef.	1.507	0.171	1.947	1.067	0.336	0.14
BT3	3	2.590	1.500	5.659	undef.	1.310	0.067	1.443	1.168	0.237	41.540	19.147	85.691	undef.	1.234	0.044	1.336	1.133	0.190	0.17
TPP	1	3.412	2.145	8.265	undef.	1.427	0.129	1.719	1.136	0.299	40.016	15.204	77.217	2.815	1.494	0.140	1.837	1.151	0.331	0.10
BT2	2	9.800	8.695	27.939	undef.	1.294	0.072	1.445	1.144	0.227	52.638	41.468	148.261	undef.	1.278	0.076	1.454	1.103	0.218	0.10
TC	2	0.335	0.140	0.632	0.039	1.254	0.037	1.332	1.175	0.203	0.885	0.418	1.907	undef.	1.249	0.043	1.354	1.145	0.199	0.11
TR	3	2.037	0.754	3.576	0.499	1.335	0.051	1.439	1.231	0.251	3.776	2.399	9.151	undef.	1.317	0.106	1.553	1.081	0.241	0.04
TUL	4	0.657	0.150	0.958	0.355	1.331	0.032	1.396	1.267	0.249										0.06
TMN	3	0.064	0.013	0.091	0.038	1.470	0.076	1.624	1.316	0.320										0.18
TLL	3	0.273	0.105	0.485	0.060	1.294	0.051	1.398	1.189	0.227										0.08
TM2	1	0.047	0.005	0.060	0.034	1.713	0.078	1.897	1.530	0.416										0.18
TM1	1	0.022	0.002	0.026	0.017	2.141	0.267	2.727	1.554	0.533										0.32
PV3	3	0.010	0.003	0.016	0.004	1.582	0.127	1.845	1.319	0.368										0.50
PV2	1	1.255	0.652	2.797	undef.	1.310	0.075	1.488	1.133	0.237										0.12
BT1a	3	0.019	0.008	0.035	0.003	1.561	0.180	1.931	1.191	0.359										0.36
BT1		9.800	8.695	27.939	undef.	1.294	0.072	1.445	1.144	0.227										0.04
CHV		9.800	8.695	27.939	undef.	1.294	0.072	1.445	1.144	0.227										0.06
CHZ	4	0.394	0.125	0.647	0.142	1.290	0.037	1.365	1.215	0.225										0.20
BT	1	0.015	0.001	0.018	0.012	1.909	0.111	2.151	1.667	0.476										0.33
PP4	1	0.010	0.001	0.009	0.007	3.035	0.404	3.967	2.104	0.671										0.25
PP3	3	1.817	0.599	3.032	0.601	1.455	0.071	1.599	1.311	0.313										0.07
PP2	3	0.072	0.012	0.097	0.046	1.603	0.081	1.768	1.439	0.376										0.10
PP1	2	0.179	0.060	0.305	0.054	1.454	0.078	1.616	1.292	0.312										0.18
BF3	1	0.036	0.010	0.063	0.009	1.680	0.202	2.240	1.119	0.405										0.09
BF2	1	0.012	0.001	0.014	0.010	2.477	0.275	3.353	1.602	0.596										0.19

DTN: GS960908312231.004 [DIRS 107065]

Source: Flint 1998 [DIRS 100033], Table 8

NOTES: SE = standard error; v/v = dimensionless volume; undef. = undefined values of less than or equal to zero on a log scale; N = number of data sets; m = 1-(1n).
Parameters for unit CCR are from unit TC; parameters for units BT1 and CHV are from unit BT2.

Table 7-12. Mean Porosity and Saturated Hydraulic Conductivity for Samples from Busted Butte and Surface-Based Boreholes

Lithostratigraphic Unit[a] and Property		Busted Butte (N)[b]	Borehole USW SD-7 (N)[c]	Borehole USW SD-12 (N)[d]	All Surface-Based Boreholes (N)[e]
Tptpv2	Porosity	0.37 (18)	0.13 (7)	0.15 (11)	0.123 (39)
	K_s (m/s)	3.0E-6 (17)	ND (0)	4.1E-9 (1)	7.3E-10 (4)
Tptpv1/Tpbt1	Porosity	0.42 (26)	0.23 (19)	0.33 (21)	0.265 (43)
	K_s (m/s)	3.0E-6 (20)	1.6E-5 (1)	ND (0)	1.6E-5 (1)
Tac (vitric)	Porosity	0.36 (35)	0.34 (31)	0.35 (30)	0.321 (69)
	K_s (m/s)	1.5E-5 (22)	4.0E-7 (3)	ND (0)	5.5E-7 (6)

Sources: [a] See Table 7-1
[b] DTNs: GS990308312242.007 [DIRS 107185]; GS990708312242.008 [DIRS 109822]
[c] DTNs: GS951108312231.009 [DIRS 108984]; GS960808312231.005 [DIRS 108995]
[d] DTNs: GS950308312231.002 [DIRS 108990]; GS960808312231.004 [DIRS 108985]; GS960808312231.005 [DIRS 108995]
[e] Data from Flint (1998) [DIRS 100033], Table 7

NOTE: N = number of samples; porosity (relative humidity) = cm^3/cm^3; Ks = geometric mean saturated hydraulic conductivity; ND = no data.

Table 7-13. Statistical Summary of Tiva Canyon Tuff Air-Injection Permeability Values by Lithostratigraphic Unit and Borehole

Lithostratigraphic Unit	Borehole UE-25 UZ#16 Mean (#) st. dev.	Borehole USW SD-12 Mean (#) st. dev.	Borehole USW NRG-6 Mean (#) st. dev.	Borehole USW NRG-7a Mean (#) st. dev.
Lower Lithophysal (Tpcpll)	5.5 (1) NA	19.6 (2) 18.7	14.0 (1) NA	-
Lower Nonlithophysal Hackly (Tpcplnh)	-	1.7 (1) NA	28.0 (1) NA	-
Lower Nonlithophysal Columnar (Tpcplnc)	15.0 (1) NA	2.9 (3) 2.2	1.3 (2) 1.0	25.7 (2) 14.9
Crystal-Poor Vitric (Tpcpv)	-	-	-	0.2 (2) 0.1

DTN: MO0312SEPSDAPM.000 [DIRS 166382]

Source: LeCain 1997 [DIRS 100153], Table 2

NOTES: Permeability values are given in 10^{-12} m^2; Mean = arithmetic mean; # = number of test intervals; st. dev. = standard deviation; NA = not applicable; - = no data.

Table 7-14. Statistical Summary of Tiva Canyon Tuff Air-Injection Permeability Values by Borehole

Borehole	Number of Test Intervals	Arithmetic Mean	Geometric Mean	Maximum Value	Minimum Value
UE-25 UZ#16	4	12.3	7.6	27.0	1.5
USW SD-12	11	7.0	3.4	38.0	0.8
USW NRG-6	4	11.2	4.1	28.0	0.3
USW NRG-7a	4	26.6	8.4	54.0	0.24

DTN: MO0312SEPSDAPM.000 [DIRS 166382]

Source: LeCain 1997 [DIRS 100153], Table 1

NOTE: Permeability values are given in 10^{-12} m^2.

Table 7-15. Statistical Summary of the Air-Injection Permeability Values for Individual Lithostratigraphic Units within the Paintbrush Nonwelded Hydrogeologic Unit

Lithostratigraphic Unit	Borehole USW NRG-7a Arithmetic Mean (Number of Intervals) Standard Deviation
Tiva Canyon crystal-poor vitric (Tpcpv1)	0.2 (2) 0.12
Pre-Tiva Canyon Tuff bedded tuff (Tpbt4)	0.2 (1) NA
Yucca Mountain Tuff (Tpy)	0.3 (4) 0.2
Pre-Yucca Mountain Tuff bedded tuff (Tpbt3)	3.0 (1) NA
Pah Canyon Tuff (Tpp)	0.2 (7) 0.04
Pre-Pah Canyon Tuff bedded tuff (Tpbt2)	0.7 (1) NA

DTN: MO0312SEPSDAPM.000 [DIRS 166382]

Source: Modified from LeCain 1997 [DIRS 100153], Table 4

NOTES: Permeability values are given in 10^{-12} m^2. NA = not applicable.

Table 7-16. Statistical Summary of the Air-Injection Permeability Values of the Paintbrush Nonwelded Hydrogeologic Unit

Borehole	Number of Test intervals	Arithmetic Mean	Geometric Mean	Maximum Value	Minimum Value
USW NRG-7a	18[a]	0.54	0.30	3.0	0.12

DTN: MO0312SEPSDAPM.000 [DIRS 166382]

Source: LeCain 1997 [DIRS 100153], Table 3

NOTES: [a]Includes two test intervals from the crystal-poor vitric nonwelded subzone of the Tiva Canyon Tuff, which is considered part of the Paintbrush nonwelded hydrogeologic unit.

Permeability values are given in 10^{-12} m^2.

Table 7-17. Statistical Summary of Topopah Spring Tuff Air-Injection Permeability Values by Lithostratigraphic Unit and Borehole

Lithostratigraphic Unit	Borehole UE-25 UZ#16 Mean (#) st. dev.	Borehole USW SD-12 Mean (#) st. dev.	Borehole USW NRG-6 Mean (#) st. dev.	Borehole USW NRG-7a Mean (#) st. dev.
Crystal-rich vitric (Tptrv)	-	-	-	-
Crystal-rich nonlithophysal (Tptrn)	0.65 (1) NA	5.8 (7) 10.0	2.2 (20) 5.0	0.23 (3) 0.13
Crystal-rich lithophysal (Tptrl)	-	-	0.25 (1) NA	0.15 (3) 0.08
Crystal-poor upper lithophysal (Tptpul)	1.8 (4) 0.34	5.4 (5) 6.6	4.1 (5) 4.4	0.32 (9) 0.10
Crystal-poor middle nonlithophysal (Tptpmn)	0.37 (17) 0.35	2.7 (7) 2.9	1.1 (7) 0.89	0.57 (6) 0.82
Crystal-poor lower lithophysal (Tptpll)	3.2 (16) 2.5	-	-	0.40 (15) 0.27
Crystal-poor lower nonlithophysal (Tptpln)	1.9 (13) 1.5	1.3 (6) 0.40	-	-
Crystal-poor vitric (Tptpv)	-	-	-	-

DTN: MO0312SEPSDAPM.000 [DIRS 166382]

Source: LeCain 1997 [DIRS 100153], Table 6

NOTES: Permeability values are given in 10^{-12} m^2; Mean = arithmetic mean; (#) = number of test intervals; st. dev. = standard deviation; NA = not applicable; - = no data.

Table 7-18. Statistical Summary of Topopah Spring Tuff Air-Injection Permeability Values by Borehole

Borehole	Number of Test Intervals	Arithmetic Mean	Geometric Mean	Maximum Value	Minimum Value
UE-25 UZ#16	54	1.8	0.9	9.5	0.02
USW SD-12	27	4.7	1.7	33.0	0.12
USW NRG-6	34	2.1	0.8	24.0	0.08
USW NRG-7a	38	0.4	0.3	2.4	0.04

DTN: MO0312SEPSDAPM.000 [DIRS 166382]

Source: LeCain 1997 [DIRS 100153], Table 5

NOTE: Permeability values are given in 10^{-12} m^2.

Table 7-19. Average Number of Natural Fractures per Test Interval by Lithostratigraphic Unit and Borehole

Lithostratigraphic or Hydrogeologic Unit	Borehole USW UZ#16 # Fractures (# Intervals)	Borehole USW SD-12 # Fractures (# Intervals)	Borehole USW NRG-6 # Fractures (# Intervals)	Borehole USW NRG-7a # Fractures (# Intervals)
Tiva Canyon Tuff	16 (4)	11 (11)	23 (4)	19 (4)
PTn	- -	- -	- -	2 (18)
Topopah Spring Tuff	14 (54)	16 (27)	6 (34)	4 (38)

DTN: MO0312SEPSDAPM.000 [DIRS 166382]

Source: LeCain 1997 [DIRS 100153], Table 7

Table 7-20. Statistical Summary of Air-Injection Permeability Values for the Tiva Canyon Crystal-Poor Upper Lithophysal Unit in Alcove 1

Borehole Number	Arithmetic Mean (Standard Deviation)	Geometric Mean
ESF-AL#1 RBT#1	11.0 (10.4)	7.2
ESF-AL#1 RBT#2	38.5 (24.0)	27.1
ESF-AL#1 RBT#3	27.8 (26.9)	13.3

DTN: MO0312SEPSDAPM.000 [DIRS 166382]

Source: LeCain 1998 [DIRS 100052], Table 4

NOTE: Units are given in 10^{-12} m^2.

Table 7-21. Statistical Summary of the Air-Injection Permeability Values for the Tiva Canyon Tuff Crystal-Poor Middle Nonlithophysal and Lower Lithophysal Zones in Alcove 1

	Tiva Canyon Tuff Crystal-Poor Middle Nonlithophysal (Tpcpmn)	Tiva Canyon Tuff Crystal-Poor Lower Lithophysal (Tpcpll)
Number of Test Intervals	8	5
Arithmetic Mean and Ranges	13.9 (6 to 26)	1.3 (0.6 to 2.0)
Standard Deviation	8.1	0.6
Geometric Mean	12.2	1.2

DTN: MO0312SEPSDAPM.000 [DIRS 166382]

Source: Modified from LeCain 1998 [DIRS 100052], Table 6

NOTE: Permeability values are given in 10^{-12} m^2.

Table 7-22. Results from Crosshole Gaseous Tracer Tests Conducted across the Bow Ridge Fault from Alcove 2

Alcove Test Number	Pumped Interval HPF #1	Release Interval HPF #2	First Arrival (min.)	Peak Arrival (min.)	Tracer Velocity (10^{-4} m/s)	Darcy Velocity (10^{-4} m/s)	ϕ_{eff}
2	Fault	Fault	16	80	6.5	3.1-3.4	0.48 to 0.52
3	Fault	Fault	16	36	14.4	3.1-3.4	0.22 to 0.24

DTN: MO0312SEPSDAPM.000 [DIRS 166382]

Source: LeCain 1998 [DIRS 100052], Table 8

NOTE: ϕ_{eff} = effective porosity.

Table 7-23. Air Permeability and Porosity Values from Crosshole Pneumatic Tests Conducted across the Bow Ridge Fault from Alcove 2

Test Number	Injection Interval	Monitor Interval	Type Curve Analysis
4	Bow Ridge fault zone	Bow Ridge fault zone	k = 27.8; ϕ = 0.13
5	Bow Ridge fault zone	Bow Ridge fault zone	k = 25.9; ϕ = 0.20
6	pre-Rainier Mesa Tuff bedded tuff #1 (Tmbt1)	pre-Rainier Mesa Tuff bedded tuff #1 (Tmbt1)	k = 23.2; ϕ = 0.27

DTN: MO0312SEPSDAPM.000 [DIRS 166382]

Source: LeCain 1998 [DIRS 100052], Table 7

NOTE: k = permeability given in 10^{-12} m^2; ϕ = porosity.

Table 7-24. Statistical Summary of the Air-Injection Permeability Values for the Basal Tiva Canyon Tuff, from Alcove 3

	Tiva Canyon Crystal-Poor Lower Nonlithophysal Hackly Subzone (Tpcplnh)	Tiva Canyon Crystal-Poor Lower Nonlithophysal Columnar Subzone (Tpcplnc)	Tiva Canyon Crystal-Poor Vitric Subzones 2 and 1 (Tpcpv2 and Tpcv1)
Number of Test Intervals	11	6	12
Arithmetic Mean	3.7	0.7	16.5
Geometric Mean	2.1	0.3	7.0

DTN: MO0312SEPSDAPM.000 [DIRS 166382]

Source: Based on LeCain 1998 [DIRS 100052], Table 11

NOTE: Permeability values are given in 10^{-12} m^2.

Table 7-25. Statistical Summary of Permeability Values from the Type-Curve Analytical Solutions of Crosshole Air-Injection Testing of the Northern Ghost Dance Fault Drill Room Boreholes, Alcove 6

Structural Unit	Permeability Values, Arithmetic Mean	Permeability Values, Range	Permeability Values, Geometric Mean
Hanging wall	5.0	0.7 to 12.8	4.1
Fault zone	18.1	7.0 to 37.9	14.6
Footwall	8.7	1.1 to 34.1	7.8

DTN: MO0312SEPSDBTV.000 [DIRS 166567]

Source: LeCain et al. 2000 [DIRS 144612], Table 13

NOTE: Permeability values are given in 10^{-12} m^2.

Table 7-26. Statistical Summary of Porosity Values from the Type-Curve Analytical Solutions of Crosshole Air-Injection Testing of the Northern Ghost Dance Fault Drill Room Boreholes, Alcove 6

Structural Unit	Range (m^3/m^3)	Arithmetic Mean (m^3/m^3)	Geometric Mean (m^3/m^3)
Hanging wall	0.01 to 0.09	0.04	0.03
Fault zone	0.05 to 0.27	0.13	0.10
Footwall	0.01 to 0.12	0.04	0.03

DTN: MO0312SEPSDHYP.000 [DIRS 166386]

Source: Modified from LeCain et al. 2000 [DIRS 144612], Table 14

Table 7-27. Statistical Summary of Northern Ghost Dance Fault Transport-Porosity and Longitudinal-Dispersivity Values by Geologic Structure

Geologic Structure	Transport-Porosity Range (Arithmetic Mean) (m³/m³)	Longitudinal-Dispersivity Range (Arithmetic Mean) (m)
Footwall	0.003 to 0.032 (0.013)	0.42 to 1.54 (1.03)
Fault zone	0.004 to 0.034 (0.014)	0.37 to 1.38 (0.62)
Hanging wall	0.001 to 0.070 (0.013)	0.06 to 2.63 (0.76)

DTN: MO0312SEPSDHYP.000 [DIRS 166386]

Source: LeCain et al. 2000 [DIRS 144612], Table 19

Table 7-28. Water-Potential Values from Exploratory Studies Facility Alcoves and Selected Surface-Based Boreholes Monitoring Programs

Geologic Unit	Alcove 3 mPa	Alcove 4 mPa	USW UZ-7a mPa	USW SD-12 mPa	USW NRG-7a mPa	UE-25 UZ#4 mPa	UE-25 UZ#5 mPa
Tpcpmn				-0.01			
Tpcpln				-0.12	-0.05		
Tpcpv1/2	-0.35, -2.7		0.0, -0.17	0.0			-0.07
Bt4	-0.17						
Tpy					-0.09, -0.18	-0.12	-0.07, -0.24
Bt3							
Tpp	-0.09, -0.15		-0.21			-0.12, -0.16	-0.16, -0.29
Bt2	-0.08			-0.04, -0.19			
Bt2/Tptrv3	-0.01, -0.03						
Tptrv3		-0.08	-0.13, -0.19			-0.06, -0.14	-0.09
Tptrv3/2	-0.06						
Tptrv2							
Tptrv1/2		0.00					
Tptrv1	-0.08						
Tptrn	-0.13, -0.14	-0.14 to -.043	-0.20, -0.23	0.0 to -0.05	0.0 to -0.11	-0.10, -0.12	0.0
Tptrl							
Tptul					-0.15		
Tptpmn			-0.09, -0.12	0.0, -0.19			
Tptpll			-0.12, -0.15				
Tptpln							
Tptpv				-0.08			
CHn				-0.19			

DTNs: For Alcove 3 and 4 Values: GS021008312242.003 [DIRS 162178]

For Surface-Based Boreholes: GS950208312232.003 [DIRS 105572]; GS951108312232.008 [DIRS 106756]; GS960308312232.001 [DIRS 105573]; GS960808312232.004 [DIRS 105974]; GS970108312232.002 [DIRS 105975]; GS970808312232.005 [DIRS 105978]; GS971108312232.007 [DIRS 105980]; GS980408312232.001 [DIRS 105982]; GS981208312232.002 [DIRS 156505]; GS000108312232.001 [DIRS 162173]; GS000708312232.004 [DIRS 162174]; GS010908312232.001 [DIRS 162175]; GS021008312232.001 [DIRS 162176]

NOTE: Water potential values are in mPa, and all values greater than zero are listed as zero.

Table 7-29. Arithmetic Mean Air Permeability Values for Lithostratigraphic and Hydrogeologic Units from Exploratory Studies Facility Air-Injection Tests, Surface-Based Air-Injection Tests, and Pneumatic Monitoring

Unit	UTCA (ESF)	BRFA (ESF)	UPCA (ESF)	UE-25 UZ#16 (SB)	USW SD-12 (SB)	USW NRG-6 (SB)	USW NRG-7a (SB)	USW NRG-6 (PM)	USW NRG-7a (PM)	USW SD-12 (PM)[b]
Tpcpul	28.6 (27)									
Tpcpmn		13.9 (8)								>100
Tpcpll		1.3 (5)		5.5 (1)	19.6 (2)	14.0 (1)		3.1		>100
Tpcpln			2.6 (17)	15.0 (1)	2.6 (4)	10.2 (3)	25.7 (2)	3.1	1.3	>100
Tpcpv			16.5 (12)				0.20 (2)	0.5-2.1	0.65-1.3	
PTn[a]							0.54 (18)	0.5-2.1	0.65-1.3	1.0
Tptrv								0.5-2.1	0.65-1.3	>10
Tptrn				0.65 (1)	5.8 (7)	2.2 (20)	0.23 (3)	14.7-50.0	>10	>10
Tptrl						0.25 (1)	0.15 (3)	>10	>10	
Tptpul				1.8 (4)	5.4 (5)	4.1 (5)	0.32 (9)	>10	>10	>10
Tptpmn				0.37 (17)	2.7 (7)	1.1 (7)	0.57 (6)			>10
Tptpll				3.2 (16)			0.40 (15)			>10
Tptpln				1.9 (13)	1.3 (6)					>10

DTN: MO0312SEPSDAPM.000 [DIRS 166382]

Sources: LeCain 1998 [DIRS 100052], Tables 1 through 7, 9, and 10; LeCain 1997 [DIRS 100153], Tables 2, 3, and 6; Rousseau et al. 1999 [DIRS 102097], Tables 9 and 10; Rousseau et al. 1997 [DIRS 100178], Table 5.1-1

NOTES: [a] PTn is a composite hydrogeologic unit; all others are lithostratigraphic units (see Table 7-1). Air permeability values are given in 10^{-12} m^2; the number of test intervals is in parentheses. UTCA = Upper Tiva Canyon Alcove (Alcove 1); BRFA = Bow Ridge Fault Alcove (Alcove 2); UPCA = Upper Paintbrush Contact Alcove (Alcove 3); ESF = Exploratory Studies Facility; SB = surface based; PM = pneumatic monitoring.

[b] The analysis method of Rousseau et al. (1999 [DIRS 102097], pp. 55-71) is insensitive at permeability values larger than 10×10^{-12} m^2.

Table 7-30. Summary of Pneumatic-Interference Events at Instrumented Boreholes Caused by Exploratory Studies Facility Excavation

Borehole	Event Producing First Interference (Date)	Position of the TBM, ESF Construction Stations (Distance from North Portal)	Horizontal Distance From TBM Advance Point to Borehole, in meters (feet)	Lithostratigraphic Unit Exposed at the Face of ESF Tunnel
UE-25 NRG#4	Penetration of PTn (06/16/95)	10 + 68.3 (1,068.3 m)	25 (82)	pre-Pah Canyon Tuff (Tpbt2)
UE-25 UZ#4	Crossing of fault zone (08/12/95)	12 + 61.8	415 (1,361)	Topopah Spring Crystal-Rich Nonlithophysal (Tptrn)
UE-25 UZ#5	Crossing of fault zone (08/12/95)	12 + 61.8	377 (1,237)	Topopah Spring Crystal-Rich Nonlithophysal (Tptrn)
UE-25 NRG#5	Close approach of TBM (09/14/95)	16 + 56.3	93 (305)	Topopah Spring Crystal-Rich Nonlithophysal (Tptrn)
USW NRG-6	Crossing of Drill Hole Wash Fault (10/01/95)	20 + 02.1	551 (1,807)	Topopah Spring Upper Lithophysal (Tptrl, Tptpul)
USW NRG-7a	Crossing of Drill Hole Wash Fault (10/21/95)	23 + 46.8	26 (85)	Topopah Spring Upper Lithophysal (Tptrl, Tptpul)
USW SD-9	Close approach of TBM (11/07/95)	26 + 54.7	184 (603)	Topopah Spring Middle Nonlithophysal (Tptpmn)
USW SD-12	Close approach of TBM (03/23/96)	46 + 23.0	49 (161)	Topopah Spring Middle Nonlithophysal (Tptpmn)
USW SD-7	Passage of TBM (06/05/96)	55 + 98.0	106 (348)	Topopah Spring Middle Nonlithophysal (Tptpmn)

DTN: MO0312SEPSDPIE.000 [DIRS 166568]

Sources: Rousseau et al. 1999 [DIRS 102097], Table 13; Rousseau et al. 1997 [DIRS 100178], Table 4.1-3; Patterson et al. 1996 [DIRS 100172], Table 5

Table 7-31. Summary of Liquid Releases into the Fault Zone in Borehole 12, Alcove 4

Test Number	Date (mm/dd/yy)	Volume Injected (l)	Duration (hh:mm)	Average Intake Rate (mL/min)
1	10/21/98	42.90	5:12	138
2	10/22/98	41.44	5:59	115
3	10/26/98	21.34	4:22	81
4	10/27/98	29.53	6:59	70
5	10/28/98	22.16	6:10	60
6	11/04/98	17.08	5:48	49
7	11/05/98	18.85	6:31	48

Source: BSC 2003 [DIRS 166347], Table 6.7.1-1

Table 7-32. Statistical Analyses of Air Permeability along Boreholes above Niches

Borehole	Niche 2			Niche 3			Niche 4		
	Pre-Excavation	Post-Excavation	Post/Pre Ratio*	Pre-Excavation	Post-Excavation	Post/Pre Ratio*	Pre-Excavation	Post-Excavation	Post/Pre Ratio*
Geometric Mean**									
UL	7.26E-14	2.09E-12	20.75	2.22E-14	4.55E-13	20.51	1.41E-13	1.07E-12	7.62
UM	4.29E-14	1.64E-12	33.29	5.81E-14	4.82E-13	8.72	1.81E-13	2.56E-12	11.09
UR	4.27E-14	1.01E-12	23.56	3.32E-14	2.64E-13	8.94	6.27E-14	6.27E-13	9.42
All 3	5.07E-14	1.51E-12	25.38	3.50E-14	3.87E-13	11.69	1.05E-13	1.20E-12	9.42
Arithmetic Mean**									
UL	8.59E-12	2.98E-11	47.06	8.12E-14	1.46E-12	135.48	2.82E-13	2.07E-12	14.28
UM	1.01E-12	7.78E-12	72.98	1.14E-13	1.55E-12	21.36	8.59E-13	6.19E-12	26.43
UR	1.27E-13	4.59E-12	53.62	1.14E-13	1.04E-12	30.95	4.42E-13	3.79E-12	45.09
All 3	3.24E-12	1.40E-11	57.89	1.03E-13	1.35E-12	62.60	5.05E-13	3.99E-12	28.55
Minimum Value**									
UL	1.86E-15	1.45E-14	0.67	1.44E-15	2.90E-15	1.06	9.16E-15	3.57E-14	0.67
UM	5.40E-15	9.88E-14	1.19	4.10E-15	1.24E-14	0.43	8.99E-15	6.56E-14	1.64
UR	1.53E-15	3.02E-15	1.01	1.43E-15	3.72E-15	0.63	8.01E-15	1.98E-14	0.24
All 3	1.53E-15	3.02E-15	0.67	1.43E-15	2.90E-15	0.43	8.01E-15	1.98E-14	0.24
Maximum Value**									
UL	1.27E-10	7.15E-10	271.15	5.32E-13	7.99E-12	1229.23	1.15E-12	8.44E-12	51.54
UM	2.28E-11	1.01E-10	427.91	5.15E-13	1.40E-11	153.02	3.56E-12	2.50E-11	110.52
UR	8.07E-13	4.66E-11	310.67	8.06E-13	5.80E-12	184.13	3.83E-12	2.51E-11	386.90
All 3	1.27E-10	7.15E-10	427.91	8.06E-13	1.40E-11	1229.23	3.83E-12	2.51E-11	386.90
Range of Log									
UL	4.83	4.69	2.61	2.57	3.44	3.06	2.10	2.37	1.89
UM	3.63	3.01	2.56	2.10	3.05	2.55	2.60	2.58	1.83
UR	2.72	4.19	2.49	2.75	3.19	2.47	2.68	3.10	3.21
All 3	4.92	5.38	2.80	2.75	3.68	3.45	2.68	3.10	3.21
Std. Dev. of Log									
UL	1.18	0.84	0.69	0.81	0.83	0.83	0.58	0.57	0.54
UM	0.80	0.70	0.62	0.57	0.71	0.61	0.95	0.70	0.58
UR	0.73	1.05	0.66	0.79	0.90	0.74	0.85	0.94	0.84
All 3	0.93	0.88	0.66	0.74	0.82	0.75	0.79	0.78	0.67

Source: BSC 2003 [DIRS 166347], Table 6.1.2-1

NOTES: * The post/pre ratio is the ratio of post-excavation to pre-excavation permeabilities. This ratio was calculated for each interval in each borehole. Values reported are the statistical measures (maximum, minimum, mean, etc.) of all post/pre ratios calculated for each borehole. For example, mean of (post/pre) ratio is not the same as the ratio of mean(post)/mean(pre).

** Preexcavation and postexcavation permeability values are given as m^2. Where more than one measurement of permeability was made at a position, the lesser value is used in averaging.

Table 7-33. Statistical Analyses of Air Permeability m^2 along Boreholes above Niche 5 in Enhanced Characterization of the Repository Block Cross Drift

	Niche 5		
Borehole	Pre-Evacuation	Post-Evacuation	Post/Pre Evacuation
Geometric Mean			
ML	1.23E-11	2.14E-11	1.75
UL	5.54E-12	5.48E-11	9.89
UM	2.40E-12	3.32E-12	1.38
All 3	3.88E-12	9.19E-12	2.37
Arithmetic Mean			
ML	7.88E-11	5.15E-11	2.93
UL	1.75E-11	5.90E-10	22.75
UM	7.58E-11	4.90E-10	17.84
All 3	6.14E-11	4.44E-10	16.65
Minimum			
ML	1.06E-12	3.30E-12	0.11
UL	1.46E-13	1.19E-12	0.74
UM	9.28E-15	4.82E-14	0.00
All 3	9.28E-15	4.82E-14	0.00
Maximum			
ML	2.86E-10	1.82E-10	7.33
UL	4.53E-11	4.03E-09	115.10
UM	1.19E-09	9.51E-09	354.12
All 3	1.19E-09	9.51E-09	354.12
Range of Log			
ML	2.43	1.74	1.82
UL	2.49	3.53	2.19
UM	5.11	5.30	5.19
All 3	5.11	5.30	5.19
Std Dev of Log			
ML	1.03	0.63	0.57
UL	0.87	1.22	0.63
UM	1.25	1.25	1.19
All 3	1.14	1.27	1.04

Source: BSC 2003 [DIRS 166347], Table 6.1.2-2

Table 7-34. Comparison of Geometric Means and Standard Deviations of Air Permeability Measurements in Niches and Alcoves in the Exploratory Studies Facility at Yucca Mountain

Borehole Cluster	Type of Rocks	log(k) (m^2) Mean	log(k) (m^2) Standard Deviation
Niche 1 Pre-Excavation	Intersects brecciated zone	-13.0	0.92
Niche 1 Radial	Predominantly within brecciated zone	-11.8	0.66
Niche 2 Pre-Excavation	Moderately fractured welded tuff	-13.4	0.81
Niche 2 Post-Excavation	Post-excavation welded tuff	-11.8	0.88
Niche 3 Pre-Excavation	Moderately fractured welded tuff	-13.4	0.70
Niche 3 Post-Excavation	Post-excavation welded tuff	-12.4	0.82
Niche 3 Radial	Moderately fractured welded tuff	-13.8	0.92
Niche 4 Pre-Excavation	Highly fractured welded tuff	-13.0	0.85
Niche 4 Post-Excavation	Post-excavation welded tuff	-11.9	0.78
Alcove 4	Discretely faulted and fractured non-welded tuff	-13.0	0.93
Alcove 6	Highly fractured post-excavation welded tuff	-11.9	0.67

Source: BSC 2003 [DIRS 166347], Table 6.1.2-5

Table 7-35. Air Permeability Estimates for the Three Zones in Borehole LA2

Zone ID	Zone Length (m)	Air Permeability k(m^2), for Packer Inflation at 27.5 PSI	Air Permeability k(m^2), for Packer Inflation at 32.5 PSI
LA2 zone 1	1.83	2.5×10^{-11}	2.3×10^{-11}
LA2 zone 2	1.83	2.7×10^{-11}	2.5×10^{-11}
LA2 zone 3	5.18	1.1×10^{-11}	0.95×10^{-11}

Source: BSC 2003 [DIRS 166347], Table 6.11.2-1

Table 7-36. Seepage Threshold Fluxes (K_o*), from Exploratory Studies Facility Niche Testing

Niche	Borehole and Depth (m)	Linear Regression Equation	Data Points	Correlation Coefficient (R^2)	Niche Seepage Threshold K_o^* (m/s)	Saturated Hydraulic Conductivity K_l (m/s)
3	UM 4.88-5.18	$y = 30.440\ln(K^o) + 456.085$	8	0.820	3.11E-07	NA
2	UL 7.01-7.32	$y = 0.6833\ln(K^o) + 8.5742$	2	NR	3.55E-06	8.98E-05
	UL 7.62-7.92	$y = 5.7394\ln(K^o) + 92.627$	3	0.979	9.80E-08	1.51E-04
	UM 4.27-4.57	$y = 5.2757\ln(K^o) + 79.443$	4	0.921	2.89E-07	2.62E-05
	UM 4.88-5.18	$y = 2.304\ln(K^o) + 31.767$	3	0.975	1.03E-06	2.52E-03
	UM 5.49-5.79	$y = 5.8876\ln(K^o) + 87.528$	4	0.963	3.50E-07	2.16E-05
	UR 4.27-4.57	$y = 0.314\ln(K^o) + 4.3283$	2	NR	1.03E-06	4.08E-05
	UR 4.88-5.18	$y = 0.3165\ln(K^o) + 4.3751$	2	NR	9.92E-07	9.87E-05
	UR 5.49-5.79	$y = 28.419\ln(K^o) + 351.09$	2	NR	4.31E-06	1.71E-05
	UR 6.10-6.40	$y = 4.2169\ln(K^o) + 79.596$	2	NR	6.35E-09	3.01E-05
	UR 6.71-7.01	$y = 10.574\ln(K^o) + 165.28$	3	0.974	1.63E-07	2.28E-04
4	UL 7.62-7.93	$y = 9.273\ln(K^o) + 148.119$	4	0.929	1.16E-07	2.46E-05
	UM 6.10-6.40	$y = 15.697\ln(K^o) + 243.611$	4	0.980	1.82E-07	2.45E-04
	UR 5.18-5.48	$y = 25.415\ln(K^o) + 410.285$	3	0.970	9.75E-08	3.92E-06

Source: BSC 2003 [DIRS 166347], Table 6.2.2-1

NOTES: NA = not applicable, the test could not be completed as planned because of rock properties outside the equipment's measurable range.

NR = not reported because two data points result in perfect correlation (R^2 =1.0), therefore, correlation coefficient is meaningless.

y = predicted seepage percentage (%); K_o = net downward liquid-release flux from regression model (m/s); ln = natural logarithm.

Table 7-37. Estimated Changes in Volumetric Water Content ($\Delta\theta$)

Niche	Depth (m)	Test Name	Liquid Release Flux q_s, (m/s)	Average Water Content Change $\Delta\theta = \theta_{ave} - \theta_n$ (m^3/m^3)
2	UL 7.62-7.92	Test #2 1-6-98	9.49E-06	0.0101
	UL 7.62-7.92	Test #1 2-12-98	1.89E-06	0.0017
	UL 7.62-7.92	Test #1 3-4-98	2.33E-07	0.0009
	UM 4.27-4.57	Test 5 Niche 2 (11-13-97)	3.78E-05	0.0242
	UM 4.27-4.57	Test #1 12-3-97	9.42E-06	0.0146
	UM 4.27-4.57	Test #2 12-3-97	9.47E-06	0.0075
	UM 4.27-4.57	Test #1 1-7-98	8.82E-07	0.0120
	UM 4.27-4.57	Test #2 2-10-98	3.09E-07	0.0063
	UM 4.88-5.18	Test 1 Niche 2 (11-12-97)	5.41E-05	0.0150
	UM 4.88-5.18	Test #1 12-4-97	9.49E-06	0.0043
	UM 4.88-5.18	Test #2 12-5-97	2.70E-06	0.0040
	UM 4.88-5.18	Test #1 1-8-98	8.75E-07	0.0082
	UM 4.88-5.18	Test #1 3-6-98	2.48E-07	0.0083
	UM 5.49-5.79	Test 4 Niche 2 (11-13-97)	3.87E-05	0.0124
	UM 5.49-5.79	Test #2 12-4-97	9.43E-06	0.0061
	UM 5.49-5.79	Test #1 1-9-98	1.08E-06	0.0046
	UM 5.49-5.79	Test #1 2-11-98	2.55E-07	0.0040
	UR 6.71-7.01	Test #1 1-13-98	3.68E-06	0.0024
	UR 6.71-7.01	Test #2 2-3-98	1.91E-06	0.0018
	UR 6.71-7.01	Test #1 3-5-98	2.48E-07	0.0017
4	UL 7.62-7.93	Test #1 11/3/99	1.65E-06	0.0200
	UL 7.62-7.93	Test #1 11-30-99 Niche 4	9.22E-07	0.0057
	UL 7.62-7.93	Test #1 6-26-2000	3.59E-07	0.0101
	UL 7.62-7.93	Test #1 01-24-00	1.46E-07	0.0115
	UM 6.10-6.40	Test #1 Niche 4 11/16/99	1.72E-06	0.0489
	UM 6.10-6.40	Test #1 Niche 4 12-10-99	7.33E-07	0.0503
	UM 6.10-6.40	Test #1 06-08-2000	3.83E-07	0.0331
	UM 6.10-6.40	Test #1 3-14-2000	1.66E-07	0.0355
	UR 5.18-5.48	Test #1 Niche 4 12/7/99	1.69E-06	0.0092
	UR 5.18-5.48	Test #1 1/5/2000	7.11E-07	0.0055
	UR 5.18-5.48	Test #1 02-14-2000	1.65E-07	0.0055

Source: BSC 2003 [DIRS 166347], Table 6.2.2-3

Table 7-38. Estimated Water Potential (ψ) for the Fractures

Niche	Borehole/Depth (m)	Test Name	Absolute Value of the Water Potential ψ (m)
2	UL 7.62-7.92	Test #2 1-6-98	3.59E-03
	UL 7.62-7.92	Test #1 2-12-98	5.68E-03
	UL 7.62-7.92	Test #1 3-4-98	8.39E-03
	UM 4.27-4.57	Test 5 Niche 2 (11-13-97)	8.26E-03
	UM 4.27-4.57	Test #1 12-3-97	2.30E-02
	UM 4.27-4.57	Test #2 12-3-97	2.29E-02
	UM 4.27-4.57	Test #1 1-7-98	7.64E-02
	UM 4.27-4.57	Test #2 2-10-98	1.00E-01
	UM 4.88-5.18	Test 1 Niche 2 (11-12-97)	3.13E-03
	UM 4.88-5.18	Test #1 12-4-97	4.56E-03
	UM 4.88-5.18	Test #2 12-5-97	5.58E-03
	UM 4.88-5.18	Test #1 1-8-98	6.50E-03
	UM 4.88-5.18	Test #1 3-6-98	7.53E-03
	UM 5.49-5.79	Test 4 Niche 2 (11-13-97)	1.95E-02
	UM 5.49-5.79	Test #2 12-4-97	2.77E-02
	UM 5.49-5.79	Test #1 1-9-98	1.00E-01
	UM 5.49-5.79	Test #1 2-11-98	1.48E-01
	UR 6.71-7.01	Test #1 1-13-98	5.90E-03
	UR 6.71-7.01	Test #1 2-3-98	6.84E-03
	UR 6.71-7.01	Test #1 3-5-98	9.76E-03
4	UL 7.62-7.93	Test #1 11/3/99	2.56E-02
	UL 7.62-7.93	Test #1 11-30-99 Niche 4	3.12E-02
	UL 7.62-7.93	Test #1 6-26-2000	4.01E-02
	UL 7.62-7.93	Test #1 01-24-00	4.86E-02
	UM 6.10-6.40	Test #1 Niche 4 11/16/99	7.38E-03
	UM 6.10-6.40	Test #1 Niche 4 12-10-99	8.65E-03
	UM 6.10-6.40	Test #1 06-08-2000	9.61E-03
	UM 6.10-6.40	Test #1 3-14-2000	1.09E-02
	UR 5.18-5.48	Test #1 Niche 4 12/7/99	4.41E-02
	UR 5.18-5.48	Test #1 1/5/2000	8.93E-02
	UR 5.18-5.48	Test #1 02-14-2000	1.66E-01

Source: BSC 2003 [DIRS 166347], Table 6.2.2-4

Table 7-39a. Summary of Tracers and Concentrations Used for Busted Butte Phase-1 Injections

Phase 1A – 10 mL/hr Injection Rate; Boreholes 1 and 3:
500 mg kg^{-1} lithium bromide
500 mg kg^{-1} sodium fluorescein
100 mg kg^{-1} 2,6-DFBA
1 mL kg^{-1} fluorescent polystyrene microspheres
Phase 1A – 1 mL/hr Injection Rate; Boreholes 2 and 4:
500 mg kg^{-1} lithium bromide
500 mg kg^{-1} sodium fluorescein
100 mg kg^{-1} PFBA
1 mL kg^{-1} fluorescent polystyrene microspheres
Phase 1B – 10 mL/hr Injection Rate; Borehole 5:
500 mg kg^{-1} lithium bromide
500 mg kg^{-1} sodium fluorescein
100 mg kg^{-1} 2,6-DFBA
100 mg kg^{-1} pyridone
1 mL kg^{-1} fluorescent polystyrene microspheres
Phase 1B – 1 mL/hr Injection Rate; Borehole 7:
500 mg kg^{-1} lithium bromide
500 mg kg^{-1} sodium fluorescein
100 mg kg^{-1} PFBA
100 mg kg^{-1} pyridone
1 mL kg^{-1} fluorescent polystyrene microspheres

Source: BSC 2003 [DIRS 166347], Table 6.13.1-2

Table 7-39b. Correspondence between Radionuclides and Tracer Analogs Used for Phase-2 Busted Butte Investigation

Radionuclide	Tracer Analog
Neptunium Analogs (NpO$_2^+$m Np(V))	Nickel (Ni^{2+}) Cobalt (Co^{2+}) Manganese (Mn^{2+})
Plutonium Analog (Pu^{3+})	Samarium (Sm^{3+})
Plutonium Analogs (colloidal form)	Polystyrene microspheres
Americium Analog (Am^{3+})	Cerium (Ce^{3+})

Source: BSC 2003 [DIRS 166347], Section 6.13

Table 7-40. Mineral Abundances (Weight Percent) in Surface Samples from Busted Butte

Sample	Smectite	Clinoptilolite	Crist./ Opal-CT	Quartz	Feldspar	Glass	Hematite	Biotite	Total
Vitric Calico Hills Formation									
DEB 3/90-10	1 ± 1	-	-	2 ± 1	11 ± 1	86 ± 2	-	tr	100 ± 2
DEB 3/90-9	6 ± 2	-	-	4 ± 1	15 ± 2	74 ± 3	-	tr	100 ± 3
DTV-97-2	2 ± 1	-	1 ± 1	1 ± 1	2 ± 1	94 ± 2	-	tr	100 ± 2
DEB 3/90-8a	-	-	1 ± 1	1 ± 1	1 ± 1	97 ± 2	-	tr	100 ± 2
DEB 3/90-8b	1 ± 1	-	1 ± 1	4 ± 1	7 ± 1	86 ± 2	-	tr	100 ± 2
DEB 3/90-7	3 ± 1	1 ± 1	1 ± 1	7 ± 1	12 ± 1	76 ± 2	tr	tr	100 ± 2
Zeolitic Calico Hills Formation									
DTV-97-3	-	9 ± 1	1 ± 1	7 ± 1	16 ± 2	64 ± 3	1 ± 1	2 ± 1	100 ± 3
DEB 3/90-6	1 ± 1	12 ± 1	1 ± 1	7 ± 1	16 ± 2	62 ± 3	-	1 ± 1	100 ± 3
Wahmonie Formation									
DEB 3/90-5	5 ± 2	-	-	1 ± 1	26 ± 3	54 ± 5	1 ± 1	9 ± 3	100 ± 5
DEB 3/90-4	4 ± 1	-	-	2 ± 1	24 ± 3	46 ± 6	2 ± 1	17 ± 5	100 ± 6

Source: Modifed from BSC 2001 [DIRS 160828], Table 22

NOTES: - = not detected; tr = trace abundance.

Samples are arranged by relative depth and show that the lowermost part of the Tac contains appreciable amounts of clinoptilolite. The upper part of the Tac at this site, however, is characterized more by smectite than by zeolite alteration. The mineral constituents in alcove rocks (especially the low biotite and feldspar components) are characteristic of the Calico Hills Formation, indicating that Wahmonie Formation deposits are more than 396 cm below the present alcove floor.

Table 7-41. Calico Hills Formation Lithostratigraphy

Unit 5 – Non- to partially welded, pumiceous pyroclastic-flow deposit
Slightly elongated pumice clasts; bimodal distribution of pumice clast sizes; 20 to 30 percent pumice. Light colored pumice clasts; moderate reddish-orange to grayish-pink matrix. Base marked by thinly bedded fall deposits.
Unit 4 – Nonwelded, pumiceous pyroclastic-flow deposit
Volcanic lithic clasts are large (20 to 70 mm), isolated orin swarms; prominent clasts of moderate reddish-orange tuff. Light colored pumice clasts; very pale orange to grayish orange-pink matrix. Lithic-poor sections appear similar to Unit 2. Base marked by a heterolithologic sequence of fall deposits.
Unit 3 – Nonwelded, lithic-rich pyroclastic flow deposit
Lithic clasts comprise 5 to 10 percent, locally 10 to 30 percent (near the base and in several intervals within the unit); predominantly devitrified volcanic rocks with local obsidian. Grayish-orange to grayish-yellow or pinkish-gray matrix. The basal lithic-rich fallout is an excellent stratigraphic marker.
Unit 2 – Nonwelded, pumiceous pyroclastic-flow deposit
20 to 40 percent light colored pumice clasts; moderate pink or moderate orange-pink matrix. The fall deposit at the base of the unit contains porcelaneous ash layers.
Unit 1 – Nonwelded, lithic-rich pyroclastic-flow deposit
Interbedded coarse-grained fallout deposits, pyroclastic-flow deposits (many reworked or with paleosols), and thinly bedded porcelaneous ash-fall deposits. Pyroclastic-flow deposits have 13 to 25 percent phenocrysts.
Bedded tuff unit
Interbedded coarse-grained fallout deposits, pyroclastic-flow deposits (many reworked or with paleosols), and thinly bedded porcelaneous ash-fall deposits. Pyroclastic-flow deposits have 13 to 25 percent phenocrysts.
Basal sandstone unit
Massive to laminated, immature volcaniclastic sandstone; very pale orange to moderate red; medium to coarse grained; accumulations of argillic pumice clasts and rare sedimentary structures, including load casts, pinch-and-swell structures, and flame structures. Locally interbedded with reworked pyroclastic-flow deposits.

Source: Moyer and Geslin (1995 [DIRS 101269], Table 3)

Table 7-42. Preliminary Measured Sorption Coefficients

Rock Sample	Measured K_d (mL/g)			
	Lithium	**Manganese**	**Cobalt**	**Nickel**
Tac (Phase 1, BH #4)	1	16	38	34
Tptpv2 (Phase 1, BH #7)	1	6	14	13

Source: Modified from BSC 2001 [DIRS 160828], Table 26

Table 7-43. Summary of Radionuclide Sorption Results

Sample		Approximate Average K_d (g/g)		
	Geologic Unit	**Neptunium**	**Americium**	**Plutonium**
UZTT-BB-PH1-3	Tptpv1	0.3	380	19
UZTT-BB-PH1-4	Tac	1.4	470	2,500
UZTT-BB-PH1-7	Tptpv2	1.1	460	1,100

DTN: LA0004WS831372.002 [DIRS 149399]

Source: see also BSC 2001 [DIRS 160828], Table 28

Table 7-44. Chemical Composition of Busted Butte Pore Water, with J-13 Groundwater for Comparison

Constituent	Concentrations (mg/L)					
	Sample 3B	Sample 3N	Sample 3Q	Sample 3U	Average 3N3U	J-13 Water
Br	0.06	0.07	0.06	0.06	0.06	-
Ca	17.73	24.35	21.16	19.81	21.77	12.5
Ce	< 0.5	< 0.5	< 0.5	< 0.5	< 0.6	-
Cl	16.13	19.06	17.71	16.74	17.84	6.5
Co	< 1.0	< 1.0	< 1.0	< 1.0	< 1.1	-
F	2.36	1.82	1.85	1.41	1.69	0.53
Fe	< 0.1	< 0.1	< 0.1	< 0.1	< 0.2	< 0.05
HCO_3 (est.)	33.0	52.7	45.6	40.6	46.3	137.2
K	4.14	3.35	3.37	3.44	3.39	4.5
Li	0.11	0.11	0.10	< 0.1	0.10	< 0.1
Mg	3.20	4.13	3.64	3.19	3.66	2.1
Mn	< 0.5	< 0.5	< 0.5	< 0.5	< 0.6	< 0.01
Mo	< 1.0	< 1.0	< 1.0	< 1.0	< 1.1	-
Na	17.67	21.36	19.63	17.89	19.63	44.6
Ni	< 1.0	< 1.0	< 1.0	1.34	1.34	-
NO_3	22.76	26.48	22.62	20.99	23.36	1.3
PO_4	< 0.1	< 0.1	< 0.1	< 0.1	< 0.2	-
Re	< 1.0	< 1.0	< 1.0	< 1.0	< 1.1	-
Si	29.69	31.85	34.10	31.00	32.32	29.6
Sm	< 0.5	< 0.5	< 0.5	< 0.5	< 0.6	-
SO_4	31.29	33.63	31.36	30.08	31.69	18.6
Sr	0.37	0.49	0.42	0.38	0.43	-
TDS	178.5	219.4	201.6	186.9	203.6	257.4
pH	8.20	8.48	8.45	8.28	8.40	7.3-8.4
Gravimetric moisture content	0.123	0.134	0.158	0.109	0.133	N/A

Source: BSC 2001 [DIRS 160828], Table 29

NOTES: N/A = not applicable; TDS = total dissolved solids; - = No sample.

Because the analyses involve a bicarbonate buffer, the bicarbonate numbers listed are estimated by charge balance.

Table 7-45. Hydrogeologic Properties of Busted Butte Units

Unit	# Samples	Porosity Mean	Porosity Std Dev	K_s [m/s] Arith. Mean	K_s [m/s] Std Dev	K_s [m/s] Geom. mean
Tac	35	0.354	0.042	2.363E-05	1.720E-05	1.523E-05
Tptpv1	25	0.420	0.040	1.073E-05	1.853E-05	3.372E-06
Tptpv2	19	0.387	0.032	4.397E-06	4.387E-06	2.651E-06

Unit	# Samples	Van Genuchten alpha [1/m] Mean	Van Genuchten alpha [1/m] Std Dev	Van Genuchten n Mean	Van Genuchten n Std Dev
Tac	35	3.014	2.632	1.279	0.205
Tptpv1	25	0.685	0.365	1.385	0.278
Tptpv2	19	0.633	0.015	1.309	0.109

Source: BSC 2003 [DIRS 166347], Table VIII-6

Table 7-46.   Bromide Concentrations in Phase-1A Samples Collected from the 90 cm Mineback Face at Borehole 3, Busted Butte Unsaturated Zone Test

Sample Name	Gravimetric Moisture Content (g/g)	Bromide C/Co
BBR-990204-3-1-B	0.078	0.74
BBR-990204-3-2-B	0.112	0.49
BBR-990204-3-3-B	0.115	0.00
BBR-990204-3-4-B	0.122	0.00
BBR-990205-3-5-HS	0.064	2.77
BBR-990204-3-6-B	0.081	0.87
BBR-990204-3-7-B	0.077	0.75
BBR-990204-3-8-B	0.074	0.75
BBR-990204-3-9-B	0.077	0.81
BBR-990204-3-10-B	0.078	0.79
BBR-990204-3-11-B	0.074	0.32
BBR-990204-3-12-B	0.077	0.01

Source: BSC 2003 [DIRS 166347], Table 6.13.2-1

NOTES: Samples were analyzed for moisture content and bromide concentration. Sample BBR-990205-3-5-HS was a hand sample and is suspected to have been concentrated by evaporation.

C/Co = measured concentration divided by the released concentration of bromide in the lithium bromide tracer that was injected in Phase-1A, (Table 7-39a).

8. SATURATED ZONE HYDROLOGY

8.1 INTRODUCTION

The saturated zone is the rock, sediment, or soil lying below the unsaturated zone (see Section 7) where the interstitial openings (e.g., pores, cavities, and fractures) are completely filled with water. The water table is commonly considered as the boundary between the saturated and unsaturated zones, and it is defined as the surface on which the interstitial fluid pressure in the saturated medium is equal to atmospheric pressure (Freeze and Cherry 1979 [DIRS 101173], p. 39). The lower boundary of the saturated zone is not defined precisely, but it occurs at a depth below which the intrinsic permeability of the medium becomes negligibly small because lithostatic (overburden) pressure and geochemical processes (e.g., mineral alteration and precipitation) close the interstitial openings. Water in the saturated zone, generally termed groundwater, is of meteoric origin and is supplied to the saturated zone as recharge in areas where rainfall and snowmelt infiltrate and percolate through the unsaturated zone to reach the water table. Within the saturated zone, groundwater can be conceptualized as occupying a continuum of interconnected interstitial openings through which the groundwater moves, however slowly, in response to potentiometric energy gradients induced principally by the combined effects of fluid pressure and gravity.

The importance of the saturated zone for the Yucca Mountain repository is that water moving through the saturated zone below the repository may provide the principal means by which radioactive materials released from the repository could be transported, either as dissolved or suspended constituents, to the accessible environment. Consequently, understanding the saturated zone flow system in the Yucca Mountain area is important for evaluating the capability of the repository for isolating waste, and protecting the environment and public health and safety. The site-scale saturated zone flow system, however, cannot be evaluated in isolation; it must be considered in the context of the regional groundwater flow system in which the site-scale system is embedded.

The construction and application of numerical groundwater flow models are important tools for yielding quantitative representations of groundwater flow into, out of, and through a groundwater flow system, and for synthesizing understanding of the prevailing state of the system and the processes controlling system evolution. Based on the underlying conceptual models which are derived from governing equations and based on the laws of physics, including mass conservation and conservation of momentum, and geologic and hydrologic input data, flow models yield internally self-consistent representations of the flow system that can be calibrated and evaluated against field data. The adequacy and accuracy of the model representations depend on the appropriateness of the conceptual models and the availability of input data, which include, for example, the hydrogeologic framework of the system, locations and rates of water inflows (recharge) to the system and of outflows (discharge) from the system, and the hydraulic properties of the aquifers and transmissive zones within the system. Groundwater flow models have been constructed for the regional and site-scale groundwater flow systems. The site-scale saturated zone flow model additionally provides the basis for developing solute transport models to support quantitative evaluations of possible transport of radioactive materials from the repository to the accessible environment.

Because groundwater tends to acquire the chemical signature of the materials through which it moves, hydrochemical data from boreholes, wells, and springs provide an independent body of data from which groundwater flow patterns and rates of flow can be inferred. These inferences can be used as evidence for testing the conceptual models of groundwater flow for the regional and site-scale hydrologic systems, as well to provide corroborative data to support the results of numerical flow model simulations. Although the areal distribution of data is somewhat restricted, a large amount of major ion, trace element, and isotopic data are available from the Yucca Mountain and downgradient areas that provide a basis for evaluating and refining the current understanding of the groundwater flow system.

The regional hydrologic system, which contains and influences the site-scale system, is described in Section 8.2. The site-scale saturated zone system is described in Section 8.3; it encompasses the hydrologic environment of the repository site and the compliance area that is specified in current regulations. The stability of the hydrologic system in response to past and possible future climate changes is discussed in Section 8.4.

This chapter updates its predecessor (CRWMS M&O 2000 [DIRS 151945], Chapter 9) in the following principal ways:

- The description of the regional flow system reflects post-1998 evolution of the regional hydrogeologic framework and flow models, as well as more current understanding of recharge and discharge in the region.

- Several reports that present the design, input data, calibration, and results of recent site-scale flow and transport modeling are summarized in Section 8.3. The previous *Yucca Mountain Site Description* discussed only flow modeling and presented limited information about transport processes.

- Several boreholes have been completed near the southern end of the site-scale area under the Nye County Early Warning Drilling Program (NC-EWDP). Some of these boreholes provide potentiometric (water-level) and thermal data.

- The Alluvial Testing Complex, a multiple-borehole tracer-testing site in lower Fortymile Wash, is described in Section 8.3, as are the results of early testing at that site. Results of earlier tracer testing in fractured tuffs at the C-Wells Complex are further analyzed and reported.

8.2 REGIONAL GROUNDWATER FLOW SYSTEM

8.2.1 Introduction

The Yucca Mountain repository site is located within the Death Valley regional groundwater flow system (Figure 8-1) in the southern part of the Great Basin subprovince of the Basin and Range physiographic province (Section 2.1). The movement of groundwater into, through, and out of the regional flow system depends on the topography and geology of the region. The topography of the region is expressed by linear, generally northwest-southeast trending, fault bounded mountain ranges that are separated by broad (20 to 30 km) intermontane alluvial valleys

and basins, some of which are identified in Figure 8-2. This characteristic topography resulted from partitioning of the region into faulted and tilted structural blocks in response to Late Cenozoic crustal extension (Grose and Smith 1985 [DIRS 150249], pp. 41 to 43, 45 to 46). The relief between valley floors and adjacent mountains locally exceeds 1,500 m (Bedinger et al. 1989 [DIRS 101118], p. F2), and altitudes in the region range from 86 m below sea level at Badwater in Death Valley to 3,600 m above sea level in the Spring Mountains. Overall, the mountain ranges occupy about 40 to 50 percent of the surface area within the region. The topographic valleys and basins that comprise the remaining area are filled with alluvial and colluvial deposits that, generally, descend from the flanks of the bordering mountain ranges to the valley floors as gently sloping alluvial fans or piedmont slopes. Valley-fill materials commonly attain thicknesses of several hundred meters in the central parts of the basins.

The valley and basin floors are local depositional centers and the basins usually contain playas that act as catchments for surface-water runoff (Grose and Smith 1985 [DIRS 150249], p. 46). Playas occupy about 10 percent of the region (Bedinger et al. 1989 [DIRS 101118], p. F3), and although they are seldom occupied by perennial surface water, numerous playas contain saline deposits that indicate the evaporation of surface water or shallow groundwater from the playa surface.

The hydrology of the region is dominated by the prevailing present-day arid to semi-arid climatic conditions (see Section 6.3) that restrict the quantities of water available to sustain surface-water drainage systems and recharge underlying groundwater flow systems. The Amargosa River and its tributaries (Figure 8-1) constitute the major fluvial system within the region, which, under present-day climatic conditions, is an ephemeral system in which flow occurs only in response to infrequent heavy precipitation events. The surface-water and groundwater flow systems terminate in hydrologic sinks consisting of discharge areas from which water is returned to the atmosphere by evaporation or plant transpiration. The salt pan that occupies the floor of Death Valley is the ultimate discharge area, or sink, for the overall regional hydrologic system.

The Death Valley regional groundwater flow system, as represented here, is defined by the domain of the regional groundwater flow model developed by D'Agnese et al. (2002 [DIRS 158876]). The model is a three-dimensional numerical groundwater flow model that synthesizes the current understanding of the hydrogeology and hydrology of the regional groundwater flow system. As discussed in Section 8.2.8.2.3, the regional boundaries define the flow model boundaries (Figure 8-1). In this way, the major hydrogeologic features are incorporated and determine and control the movement of groundwater into and out of the system (D'Agnese et al. 2002 [DIRS 158876], p. 36).

8.2.2   Overview of the Death Valley Regional Groundwater Flow System

The Death Valley regional groundwater flow system (Figure 8-1) encompasses an area of approximately 70,000 km^2 in Nevada and California. In addition to Death Valley, which is the major hydrologic sink for the region, the region includes several large valleys, such as the Amargosa Desert and Oasis Valley, that are major intermediate discharge areas for the regional flow system. Several major mountain ranges are located in or bound the region. The Panamint Range and the Amargosa Range border Death Valley on the west and the east, respectively, and the Last Chance Range, the Montezuma Range, the Cactus Range, the Kawich Range, the Quinn

Canyon Range, and the Timpahute Range define the northern extent of the region. The East
Pahranagat Range, the Sheep Range, and the Spring Mountains form the eastern boundary, and
the Kingston Range is near the southern boundary. Pahute Mesa is a prominent upland area
extending from Rainier Mesa on the Nevada Test Site westward to Stonewall Mountain, a
distance of about 75 km. With elevations generally exceeding 1,700 m, Pahute Mesa exerts a
major influence on the local climate and, therefore, on recharge to the flow system in the
northern part of the region that includes the Yucca Mountain area.

The eastern and southern parts of the Death Valley region lie within the carbonate-rock province
of the Great Basin (Prudic et al. 1993 [DIRS 103136], pp. 1, 3, and 4, Figure 1), which is
characterized by thick sequences of carbonate rocks. These rocks form a generally deep regional
aquifer within the groundwater flow system and allow interbasin transfer of groundwater in the
Death Valley region (D'Agnese et al. 1997 [DIRS 100131], p. 5). Winograd and Thordarson
(1975 [DIRS 101167], p. C53) attribute the deep water table in the Yucca Flat and Frenchman
Flat areas to be due to groundwater drainage from saturated valley-fill materials into the
underlying and surrounding carbonate rocks. In other valleys, such as the Amargosa Desert,
southern Indian Springs Valley, and possibly eastern Jackass Flats, interbasin movement of
groundwater generally is upward from the deep-lying carbonate rocks into the overlying
valley-fill materials.

The northwestern part of the Death Valley region generally is underlain by Tertiary silicic
volcanic rocks that are part of the southwest Nevada volcanic field (Laczniak et al. 1996
[DIRS 103012], p. 15, Figure 4). The hydraulic properties of the volcanic rocks are governed
chiefly by the mode of eruption and cooling, by the extent of primary and secondary fracturing,
and by the degree to which secondary alteration (crystallization of volcanic glass and zeolite
alteration) have affected primary permeability (Laczniak et al. 1996 [DIRS 103012], p. 15). On
a regional scale, the volcanic rocks generally are in hydraulic connection with overlying
valley-fill materials, and may be in hydraulic connection with underlying carbonate rocks, as
well as laterally from one subbasin to another.

8.2.2.1   Hydrogeology

The Death Valley region has a long and active geologic history, including intermittent marine
and nonmarine sedimentation, large-scale compressive deformation, plutonism, volcanism, and
extensional tectonics (D'Agnese et al. 1997 [DIRS 100131], p. 13; see also Section 2.4).
Consequently, diverse rock types, ages, and deformational structures are often juxtaposed
(Figure 8-3). As a result, subsurface conditions are variable and complex, and knowledge of the
geologic diversity beneath alluvial basins is indirect in most of the Death Valley region.
The regional geology (Section 2.3) can be summarized as consisting of the following major
stratigraphic groups:

- Precambrian and Cambrian clastic and crystalline rocks
- Paleozoic clastic and carbonate rocks
- Clastic and intrusive rocks of Mesozoic age
- Tertiary tuffs, lava flows, and volcaniclastic rocks
- Varied fluvial, paludal, and playa sedimentary deposits of Pliocene age
- Tertiary-Quaternary alluvial, colluvial, eolian, and volcanic deposits.

To facilitate interpretation and description of the groundwater hydrology of a region, it may be possible to group geologically defined stratigraphic units within the regional geologic framework into hydrogeologic units that possess common hydrologic properties (Winograd and Thordarson 1975 [DIRS 101167], pp. C13 to C14). Several investigators have delimited and characterized hydrogeologic units in the Death Valley region. Winograd and Thordarson (1975 [DIRS 101167], Table 1) divided the regional stratigraphy into a set of 10 hydrogeologic units, and Bedinger et al. (1989 [DIRS 101118], Table 1) defined 12 hydrogeologic units for the Death Valley region. Faunt et al. (1997 [DIRS 148957], Table 1) defined 10 hydrogeologic units that were used as the basis for the hydrogeologic framework for the regional groundwater flow model (D'Agnese et al. 1997 [DIRS 100131]).

Belcher et al. (2002 [DIRS 158875]) updated and merged the hydrogeologic framework developed for the regional groundwater flow model (D'Agnese et al. 1997 [DIRS 100131]) with that developed for the underground test area (DOE 1997 [DIRS 103021]) to construct an integrated hydrogeologic framework model to support further development of the regional groundwater flow model (D'Agnese et al. 2002 [DIRS 158876]). In constructing the hydrogeologic framework model, Belcher et al. (2002 [DIRS 158875]) divided the regional hydrogeologic setting into the 28 hydrogeologic units (Table 8-1) that, based on Faunt et al. (1997 [DIRS 148957]), were broadly grouped into the 10 major hydrogeologic units (Figure 8-3). Detailed descriptions of the 28 individual hydrogeologic units are provided in Belcher et al. (2002 [DIRS 158875], pp. 17 to 83).

8.2.2.1.1   Quaternary-Tertiary Valley-Fill Materials

Quaternary-Tertiary Valley-Fill Alluvium–A heterogeneous mixture of fine-grained playa and lakebed deposits containing evaporites of limited areal extent, fluvial deposits, heterogeneous debris flows and fan deposits, and tuffs. Valley-fill alluvium occurs in the valleys between the ranges and has a maximum thickness of 4,600 m in the Pahrump Valley.

Quaternary-Tertiary Valley-Fill Playa Deposits–A relatively homogeneous deposit composed primarily of sand, silt, and clay-sized particles. The unit includes lacustrine limestones and evaporites. The playa deposits were deposited contemporaneously with the younger alluvial sediments, and the deposits grade into each other. Playa deposits occur in the topographically low areas of many basins and have a maximum thickness of 4,200 m in that part of Pahrump Valley that is included in the hydrogeologic framework model for the regional groundwater flow model. Large playas occur primarily in Death Valley, Pahrump Valley, the Amargosa Desert, around Tecopa, and near Indian Springs.

8.2.2.1.2   Quaternary and Tertiary Volcanic Rocks

Tertiary volcanic rocks of the southwest Nevada volcanic field overlie most of the Paleozoic rocks of the Nevada Test Site area and major parts of the Death Valley region. The distribution, thickness, lithology, and degree of welding of the volcanic units differ widely depending on the distance of the units from the source caldera. At most localities, only a partial section is present. Consequently, the volcanic stratigraphy is complex and grouping the volcanic rocks into a consistent regional hydrogeologic framework requires simplification. The volcanic-rock sequence was subdivided into nine hydrogeologic units (Table 8-1).

Undifferentiated Volcanic Rocks–Undifferentiated volcanic rocks include volcanic units of Tertiary and Quaternary age other than those on or very near the Nevada Test Site, including volcanic rocks of the southwest Nevada volcanic field. The Undifferentiated Volcanic Rocks unit has a maximum thickness of 5,300 m in the central Kawich Range.

Southern Nevada Test Site/Yucca Mountain Volcanic Units–Volcanic strata in the southern part of the Nevada Test Site and the Yucca Mountain area have been grouped into two volcanic hydrogeologic units, the volcanic aquifer and the underlying volcanic confining unit. In general, altered (typically zeolitized) volcanic rocks are confining units, and the unaltered rocks constitute aquifers. These two units have approximately the same distribution in Yucca Flat and occur as erosional remnants preserved in the deeper parts of the Tertiary basin. The volcanic aquifer and the volcanic confining unit cover most of the southern Nevada Test Site from Frenchman Flat to Bare Mountain and have a maximum thickness of 1,300 m and 2,100 m, respectively. The maximum thickness of the volcanic aquifer occurs near Skull Mountain, while the maximum thickness for the volcanic confining unit occurs in northern Jackass Flats.

Timber Mountain/Pahute Mesa Volcanic Units–The caldera-related volcanic units complex, as described here, includes the nested calderas that underlie Pahute Mesa and the Timber Mountain caldera complex. The units were defined on the basis of their stratigraphic position within the volcanic pile, lithologic properties related to depositional environment, postdepositional alteration, and degree of welding. From top (stratigraphically) to bottom, the volcanic hydrogeologic units in the Timber Mountain/Pahute Mesa area are: Timber Mountain aquifer, Paintbrush/Calico Hills tuff cone, Bullfrog confining unit, Belted Range aquifer, Basal confining unit, and Basal aquifer. The volcanic hydrogeologic units occurring in the Timber Mountain/Pahute Mesa area have maximum thicknesses ranging from 1,600 m to 4,000 m.

8.2.2.1.3 Tertiary Sediments/Death Valley Section

The Tertiary sediments/Death Valley section is the combination of Tertiary-aged sediments and similar sediments in the Death Valley area. Tertiary sediments and the Death Valley section were mapped together because they are similar deposits and because they are in geographically mutually exclusive areas. The Tertiary sediments include clastic and volcaniclastic sediments of the Horse Spring Formation lithologic equivalent (the Oligocene rocks of Winapi Wash) and the Titus Canyon Formation. In the northern Amargosa Desert area, the Tertiary sediments include sediments and buried, highly distended tectonic blocks of Tertiary volcanic rocks. The Death Valley section consists of the Artist Drive, Furnace Creek, and Funeral Formations, and the Greenwater Volcanics in Death Valley and Furnace Creek areas. In the southern Funeral Mountains, the Tertiary sediments/Death Valley section unit directly overlies the lower carbonate aquifer (LCA) and has a maximum thickness of 2,600 m in southern Death Valley.

8.2.2.1.4 Mesozoic Volcaniclastic and Sedimentary Rocks

The Mesozoic volcaniclastic and sedimentary rocks are predominantly continental fluvial, lacustrine, and eolian deposits, and clastic and carbonate sedimentary rocks in the eastern part of the region, as well as Mesozoic-age volcanic rocks in the southwest part of the region. These rocks form outcrops on the sides of the Spring Mountains where they have been overridden by thrust faulting. Where intensively faulted, these rocks can be highly permeable and locally may

form important aquifers; however, they are not widespread. Limited sections of the Mesozoic volcanic rocks are also found in the southwestern part of the Death Valley region. The Mesozoic volcaniclastic and sedimentary rocks unit primarily occurs in the Spring Mountains and in the southwestern part of the Death Valley region, and it has a maximum thickness of 1,300 m south of the Owlshead Mountains.

8.2.2.1.5 Paleozoic Aquifers and Confining Units

Upper Carbonate Aquifer–The upper carbonate aquifer consists of Paleozoic limestone, dolomite, and calcareous shales. The upper carbonate aquifer is stratigraphically above the upper clastic confining unit and the large-scale thrusted carbonate units primarily in the upper plate of the CP thrust fault in the Calico Hills. The CP thrust fault extends from the Calico Hills northeastward and then northward along the Belted Range. The upper carbonate aquifer unit includes Pennsylvanian and Mississippian carbonate rocks above the Eleana Formation and Chainman Shale, as well as older carbonate rocks traditionally assigned to the LCA contained in the CP thrust. The upper carbonate aquifer occurs primarily in the area of Yucca Flat and has a maximum thickness of 900 m in the area of the hydrogeologic framework model near the Calico Hills.

Upper Clastic Confining Unit–The upper clastic confining unit is composed of the Eleana Formation and the Chainman Shale. The Eleana Formation, composed mostly of relatively impermeable argillites and shales, forms a locally important clastic confining unit. The argillites and shales tend to deform plastically, probably by shearing and tight folding. Thus, open fractures are unlikely to occur at depth in this formation. The Eleana Formation, where present, may be thousands of meters thick. The presence of this unit, which has low transmissivity, may account for many of the large hydraulic gradients observed in the region.

Lower Carbonate Aquifer–The LCA is the most important regional aquifer because of its wide distribution and large hydraulic conductivity. Limestone, dolomite, and calcareous shales of Paleozoic age underlie many valleys and crop out along the flanks of and throughout some mountains. The geologic units included in the LCA include all Devonian-, Silurian-, and Ordovician-aged strata, plus the Cambrian Nopah Formation, the Bonanza King Formation, and the upper two-thirds of the Carrara Formation. The LCA also includes Pennsylvanian and Mississippian carbonate rocks where the upper clastic confining unit does not separate the Paleozoic carbonate rocks into an upper and lower aquifer. These carbonate rocks cover an extensive part of the area around Death Valley, extending to the north and the east. They are commonly interbedded with siltstones and shales, and are locally interrupted by volcanic intrusions in the north. These carbonate rocks have an aggregate thickness of about 8,000 m. Where hydraulically connected, they provide an avenue for interbasinal flow. The LCA has a maximum thickness of 6,100 m in that part of the Timpahute Range that is included in the hydrogeologic framework model for the regional groundwater flow model. In the Yucca Mountain area, the LCA is covered by volcanic rock (volcanic aquifer and volcanic confining unit), and the extent to which the LCA is present beneath the volcanic cover is uncertain. Borehole UE-25 p #1, which is located near the eastern flank of Yucca Mountain, penetrates the LCA, and is taken as evidence to suggest that the LCA underlies the volcanic rocks throughout the Yucca Mountain area.

Thrust faults within the LCA unit complicate the flow patterns in the groundwater system. Where a repeated stratigraphic section occurs due to thrust faults, the LCA is incorporated in the regional groundwater flow model (Section 8.2.8) as separate units. The area between the southern Funeral Mountains and the Spring Mountains contains separately defined thrust-fault areas (representing the Schwaub Peak, Specter Range, and the Wheeler Pass thrusts) in which the lower clastic confining unit overlies the LCA. The LCA units in these thrusts are included in the lower and upper plates of these thrust systems. Other hydrologically important thrusts in the region include the Lee Canyon thrust in the Spring Mountains and the Gass Peak thrust in the Sheep Range. The Belted Range thrust is represented implicitly in the LCA unit as a thickened section.

Lower Clastic Confining Unit–Late Proterozoic to early Paleozoic siltstone, quartzite, shale, sandstone, and some metamorphic rocks form clastic confining units, which are designated as the lower clastic confining unit, although in areas where it is intensely fractured it may act locally as an aquifer. Regionally, these rocks vary in aggregate thickness, with a maximum thickness of about 3,500 m. These rocks permit negligible interstitial groundwater movement but frequently are highly fractured and locally brecciated. At shallow depths, the fractures and breccias can be conduits for flow, converting the clastic rocks into locally important shallow aquifers.

In the hydrogeologic framework model (USGS 2002 [DIRS 165615]), the lower clastic confining unit is present as four explicitly thrusted units: the lower clastic confining unit, the combined upper and lower plates of the Specter Range/Wheeler Pass thrust in the Amargosa Desert area, and the Gass Peak thrust in the Sheep Range.

8.2.2.1.6   Precambrian Granites and Metamorphic Rocks

Crystalline metamorphic and igneous rocks of Middle Proterozoic age and metamorphosed Late Proterozoic sedimentary rocks are widespread throughout the southern part of the region, cropping out in many mountain ranges and underlying most of the area at depth. Groundwater is present only locally in these crystalline bodies where the rock is fractured. Because the fractures are poorly connected, these rocks act mostly as confining units or barriers to flow. The Late Proterozoic sedimentary rocks form the base of the hydrogeologic framework model (which extends to 4,000 m below sea level), and constitutes the ultimate basement complex for the region. These units have a thickness of 5,600 m in the southern part of the Panamint Range that is included in the regional model domain.

8.2.2.1.7   Tertiary-Jurassic Intrusives

Crystalline granitic rocks of Mesozoic and Tertiary age are widespread throughout the southern part of the region and occur as isolated plutonic bodies in the northern part of the regional model domain. They crop out in many mountain ranges and underlie most of the southern part of the region at depth. Groundwater is likely to be present in these crystalline rocks only where they are fractured, and, in general, these rocks are considered to be confining units that are barriers to groundwater flow. The unit has a maximum thickness of 6,500 m in the southern Panamint Range.

8.2.2.2   Hydraulic Properties of the Hydrogeologic Units

Bedinger et al. (1987 [DIRS 150241]) compiled and analyzed hydraulic-property data from the literature for the Basin and Range Province and for rocks with similar characteristics outside the province. They tabulated ranges of values for hydraulic conductivity and porosity (Bedinger et al. 1987 [DIRS 150241], Table 1), and calculated the distributions of expected hydraulic conductivity values for 14 rock types (Bedinger et al. 1987 [DIRS 150241], Figure 2).

Based partly on the analyses of these hydraulic properties (Bedinger et al. 1987 [DIRS 150241]), Faunt et al. (1997 [DIRS 148957], Table 3, p. 16) assigned approximate hydraulic conductivity values to 10 hydrogeologic units in the Death Valley region, including the effects of depth, fracturing, and weathering.

Based on data from aquifer tests, Belcher et al. (2001 [DIRS 158458], Table 2) estimated mean values and statistical ranges for hydraulic conductivity and storativity (or specific yield). The hydrogeologic units defined by Belcher et al. (2001 [DIRS 158458]) and shown in Table 8-2, differ somewhat from those shown in Table 8-1, mainly due to D'Agnese et al. combining some of the units for their analyses. The means and ranges (Table 8-2) represent properties of the generalized hydrogeologic units in the Death Valley region and support the development of transient groundwater flow models for the region.

The permeabilities and hydraulic conductivities of the rocks in the Death Valley region are variable within and among rock types. The faulted and karstic Paleozoic carbonate aquifer units tend to have the largest hydraulic conductivities, but the alluvial and fractured volcanic units also may exhibit large hydraulic conductivity values. Unfaulted Paleozoic carbonate rocks tend to have smaller hydraulic conductivity values than the faulted and fractured carbonate rocks. Of the volcanic units, the tuff breccias tend to be the most permeable, and the ash-flow tuffs, bedded tuffs, and lava flows tend to be the least permeable. The hydraulic conductivities of the welded, usually fractured tuffs tend to be greater than those of the nonwelded tuffs. Analyses of regression and covariance show a weak, but quantitatively indeterminate, relation between hydraulic conductivity and depth (Belcher et al. 2001 [DIRS 158458], p. 1, Figure 4).

8.2.2.3   Overview of Regional Groundwater Flow

Groundwater movement in the regional flow system generally originates as interbasinal underflow across the lateral boundaries of the system, and as asymmetric radial flow from recharge from precipitation on mountains and other highlands that are located principally along the periphery of the system. The overall flow system, therefore, can be conceptualized as consisting of a set of relatively shallow localized flow systems that are superimposed on a deeper regional system (Freeze and Cherry 1979 [DIRS 101173], Figure 6.3). Within the system, the overall movement of groundwater is from the source areas near the margins of the system to the regional hydrologic sink in the floor of Death Valley.

The geographic distribution of rainfall and snowfall is principally a function of land surface altitude, so the highland areas receive most of the precipitation and provide most of the recharge to the groundwater flow system. This distribution of recharge is reflected as highs in the potentiometric surface (Figure 8-4). The most prominent recharge mound in the region is

associated with the Spring Mountains (Figure 8-4, location No. 1) in the eastern part of the flow system, where the piezometric surface altitude is estimated to exceed 2,300 m. At the regional sink in Death Valley (Figure 8-4, location No. 12), the piezometric altitude is almost 100 m below sea level, providing about 2,400 m of total relief on the regional potentiometric surface. Regional groundwater flow also discharges at intermediate areas as spring flow (such as at Ash Meadows), evapotranspiration at playas and valley floors (such as at Alkali Flat and Oasis Valley), and pumping near Pahrump and in the Amargosa Desert. The regional potentiometric surface is discussed further in Section 8.2.6.

Groundwater flow from the Panamint Range on the western boundary of the regional system is generally east to northeast. Progressing clockwise from the northwestern end of Death Valley, the regional flow directions change from south to southwest, then to approximately west from the Spring Mountains and the southeast quadrant of the system.

Groundwater in the Yucca Mountain area, especially in the Fortymile Wash drainage system to the east of Yucca Mountain, probably originates primarily as recharge in easternmost Pahute Mesa, Rainier Mesa, Timber Mountain, and Shoshone Mountain, which are the principal uplands of the northern Fortymile Canyon area (Section 8.3.8.1.4). Hydrochemical and isotopic evidence (Sections 8.2.7 and 8.3.6.1.2) suggests that recharge to the groundwater system underlying Yucca Mountain has occurred predominantly as downward percolation of water through the overlying unsaturated zone with relatively little contribution by subsurface inflow from the volcanic highlands to the north. Based on the configuration of the potentiometric surface (Figure 8-4), groundwater in the Yucca Mountain area is considered to flow generally southward through the aquifers of the volcanic sequence underlying Crater Flat, Yucca Mountain, and Jackass Flats and, ultimately, into valley-fill material in the Amargosa Desert. Flow in the vicinity of Yucca Mountain and into the Amargosa Desert is discussed in greater detail in Section 8.3.

Fractures and faults within the hydrogeologic units constitute the dominant pathways for regional groundwater flow. The presence, orientation, and type of faults provide major controls on groundwater flow according to three principles (Faunt 1997 [DIRS 100146], pp. 24 to 31):

1. Large-scale folding and block faulting have formed the major topographic features and sedimentary basins that define the groundwater recharge and discharge areas.

2. Faulting and intense folding have induced fracturing in the rock masses and have created highly permeable channels that have been enhanced by dissolution in the carbonate aquifers.

3. Faulting and folding in some rock types have created barriers to groundwater flow by displacing permeable strata against low-permeability strata and by emplacing low-permeability materials within faults and fractures. These circumstances locally may cause groundwater to be forced to the surface as springs and diffuse discharge.

Tensional faults and fracture zones develop parallel to the major stress direction (i.e., normal to regional extension, or least-stress direction), enhancing large-scale permeability in that direction. Compressional and shear features intersect the major stress direction at moderate to large angles,

and they commonly are associated with mechanical and chemical effects that produce low-permeability gouge in and near faults. In the northern and central parts of the Death Valley regional groundwater flow system, the north-south to northeast-southwest orientation of the major normal faults is approximately perpendicular to the least stress, enhancing southward flow that is already predisposed by the regional topographic slope.

8.2.3 Boundaries of Death Valley Regional Flow System and Subregions

8.2.3.1 Regional Flow System

Three principal sets of flow boundaries (upper, lower, and lateral) were defined for the saturated zone in the Death Valley region. These flow system boundaries are either physical boundaries (caused by changes in bedrock conditions) or hydraulic boundaries (caused by potentiometric-surface configurations). The upper bounding surface of the Death Valley groundwater flow system is the water table (D'Agnese et al. 2002 [DIRS 158876], p 14). Under natural, or predevelopment conditions, groundwater moves vertically downward into the flow system across this boundary as regional groundwater recharge, or vertically upward out of the system across this boundary at natural groundwater discharge sites (e.g., springs, evapotranspiration areas, and wet playas). The lower boundary surface is at a depth where groundwater flow is dominantly horizontal or parallel to the lower surface and moves with such small velocities that the volumes of water involved do not greatly affect regional flow estimates. The depth of this surface may vary and generally corresponds with the upper surface of low-permeability basement rock.

Lateral boundaries of the Death Valley regional groundwater flow system, defined by Harrill and Prudic (1998 [DIRS 149377]), are shown in Figure 8-1. These boundaries may be flow boundaries or no-flow boundaries (D'Agnese et al. 2002 [DIRS 158876], p. 14). Under steady-state conditions, no-flow boundaries occur where groundwater movement across the boundary is impeded because of physical (e.g., low-permeability) barriers, because the interpreted flow paths are parallel to the boundary, or because flow paths diverge to create a groundwater divide. Under steady-state conditions, the location of no-flow boundaries that originate from alignment of flow paths parallel to boundaries or groundwater divides remains fixed, but under transient conditions these boundaries may change over time in response to changing environmental conditions (e.g., future climate change) or imposed stress (e.g., groundwater withdrawals by pumping).

Most of the lateral boundaries of the Death Valley regional flow system are no-flow boundaries that arise from the presence of low-permeability bedrock. Flow boundaries, however, occur where bedrock is permeable enough to allow considerable groundwater fluxes to enter the flow system and where a hydraulic gradient directed into the system is present across the boundary (Figure 8-1). Lateral boundaries that may provide groundwater inflow include southern Railroad Valley, Reveille Valley, Stone Cabin Valley, Mud Lake (Ralston Valley), Fish Lake and Eureka Valley, Saline Valley, Panamint Valley, Pilot Knob Valley, Pahranagat Valley, and North Las Vegas Valley (D'Agnese et al. 2002 [DIRS 158876], p. 14).

8.2.3.2   Subregional Flow Systems

To facilitate development of the regional groundwater flow model, D'Agnese et al. (2002 [DIRS 158876]) used the system and subregion boundaries defined by Harrill and Prudic (1998 [DIRS 149377]), which divides the regional system into the three subregions (Figure 8-1). The boundaries of these subregions generally conform with the boundaries defined by Harrill and Prudic (1998 [DIRS 149377]), but they were modified to include areas within the underground test area model domain (DOE 1997 [DIRS 103021]) and to include certain other small areas on the boundary (D'Agnese et al. 2002 [DIRS 158876], p. 36). D'Agnese et al. (2002 [DIRS 158876]) used the boundaries of the Death Valley regional groundwater flow system of Harrill and Prudic (1998 [DIRS 149377]) to refine the boundaries of the subregions defined by D'Agnese et al. (1997 [DIRS 100131]) and to locate flow paths into the system across the lateral system boundaries (Figure 8-1).

D'Agnese et al. (1997 [DIRS 100131], p. 62) originally defined the subregions based on where they discharge into Death Valley (D'Agnese et al. 2002 [DIRS 158876], pp. 18 to 26) and include:

- The Northern Death Valley subregion, which discharges into the northern part of Death Valley at Grapevine and Staininger springs, and at Mesquite Flat, with some intermediate discharge along the flow path at Sarcobatus Flat and Coyote Hole playas (D'Agnese et al. 2002 [DIRS 158876], Figure 10).

- The Central Death Valley subregion (Figure 8-5), which includes Yucca Mountain, discharges predominantly into the main Death Valley salt pan at Cottonball, Middle, and Badwater basins. This subregion also discharges at springs in the Furnace Creek area (e.g., Travertine, Texas, and Nevares springs).

- The Southern Death Valley subregion, which discharges at the Saratoga Springs area in southern Death Valley, with some intermediate discharge along the flow path as spring flows and as evapotranspiration between Shoshone and Tecopa (D'Agnese et al. 2002 [DIRS 158876], Figure 12).

8.2.4   Groundwater Discharge

8.2.4.1   Introduction

Characterizing the groundwater discharge component of the hydrologic cycle is an important step in developing an understanding of a groundwater flow system. The contributions to discharge at land surface arguably can be measured more easily and accurately than the recharge component, so the comparison of the two in a water budget provides enhanced understanding of recharge as well. Although Death Valley is recognized to be the ultimate discharge area for the regional groundwater flow system (e.g., D'Agnese et al. 1997 [DIRS 100131], p. 43), intermediate areas of groundwater discharge occur because of human activity and as a result of topographic, geomorphic, stratigraphic, or structural controls. Consequently, discharge from the Death Valley region includes groundwater withdrawals from wells, spring flow, and evapotranspiration by phreatophytes and from wet playas, moist soils, and surface water. One

difficulty in assessing discharge is that evapotranspiration, which is the most difficult component to determine, includes vaporization of soil moisture replenished by capillarity from the water table and by reinfiltration of spring flow and pumpage used for irrigation.

8.2.4.2 Spring Discharge and Evapotranspiration

Numerous springs in the Death Valley region are present as localized small discharges in many of the mountain ranges (D'Agnese et al. 1997 [DIRS 100131], p. 44). These spring discharges derive from nearby local groundwater sources, and the locations of these springs are controlled by permeability variations in the rocks and water levels related to land-surface altitude, which cause the water to discharge at the surface. These springs, which have small (less than 25 m^3/d) to moderate yields (25 m^3/d to more than 2,200 m^3/d), commonly represent perched or semiperched local groundwater flow systems associated with regional recharge areas. These springs commonly emerge from consolidated rock within the mountains or ridges flanking valleys and are characterized by highly variable discharge rates and by variable temperature, usually less than 21°C (Winograd and Thordarson 1975 [DIRS 101167], p. C50).

Springs that discharge from the regional groundwater flow system are distinct from the group of localized springs. Regional springs typically emerge from the valley fill or the adjacent consolidated rocks at low elevations along valley borders or on valley floors (Winograd and Thordarson 1975 [DIRS 101167], p. C50). D'Agnese et al. (1997 [DIRS 100131], p. 44) consider the locations of the regional springs to result from:

- Intersections of the water table with land surface

- High permeability faults or fractures that act as conduits, directing regional groundwater to the surface

- Stratigraphic contacts of high permeability material with low permeability material, which forces flow paths to arc toward the land surface

- Structural contacts caused by the juxtaposition of high permeability material with low permeability material, causing an abrupt change in groundwater flow paths.

The regional springs are characterized by large and uniform discharge, and by uniform temperatures that typically range from 24°C to 35°C (Winograd and Thordarson 1975 [DIRS 101167], p. C50). The major regional springs in the Death Valley region generally are west and south of Yucca Mountain (Figure 8-6, shown as areas of phreatophytes and evapotranspiration), and discharge ranges from 411 to 30,421 m^3/d (D'Agnese et al. 2002 [DIRS 158876], Table 3). Ash Meadows, a broad discharge zone, is shown on Figure 8-5.

In the Death Valley region, direct discharge of groundwater to the surface as springs or stream base flow, generally, is consumed locally, usually by evapotranspiration. There is no flow out of Death Valley itself by either groundwater or surface water. Even within the groundwater basins and subbasins of the Death Valley regional groundwater system, surface-water flow sustained over large distances is almost nonexistent. Springs and their outlet channels are bordered by dense growths of phreatophytes, giving way downstream to a succession of salt-tolerant shrubs

and grasses that ultimately consume the flow. In Ash Meadows in the late 1960s and early 1970s, phreatophytes were eradicated over large areas to preserve the spring flow for agricultural and domestic use, both of which return the moisture to the atmosphere.

The most recent and comprehensive study of evapotranspiration in the Death Valley region was conducted by Laczniak et al. (2001 [DIRS 165609]). The primary focus of this study was to estimate, in a consistent manner, the average annual evapotranspiration from the major areas of natural groundwater discharge (Figure 8-6). Laczniak et al. (2001 [DIRS 165609]) used satellite spectral data to identify and delimit the evapotranspiration discharge areas and divided each area into evapotranspiration units that represent a unique combination of soil and vegetation conditions. An average annual rate of evapotranspiration was estimated for each identified evapotranspiration unit within a discharge area based on micrometeorological data that were collected within the local area over a multiyear period. In estimating the groundwater component of annual evapotranspiration, they accounted for and subtracted the contribution of water that originated from local precipitation. Their estimates of groundwater evapotranspiration rates and spatial distributions of evapotranspiration units were used to develop the overall estimate of groundwater discharge within the Death Valley region presented by D'Agnese et al. (2002 [DIRS 158876], Table 3). For discharge areas not evaluated by Laczniak et al. (2001 [DIRS 165609]), evapotranspiration distributions or average volumetric discharge from regional springs were developed from other data (e.g., the distribution of phreatophytes and spectral imagery) and in-progress studies (D'Agnese et al. 2002 [DIRS 158876], pp. 39 to 40).

8.2.4.3 Evaluation of Groundwater Pumpage

To characterize the amount of human-induced water use in the basin, a data set of water-producing wells was developed. Estimates of water use for the Death Valley region have been reported on a somewhat discontinuous basis. These estimates are reported by use (commercial, irrigation, mining, and domestic) for each hydrographic area. Unfortunately, such records did not exist for all of the hydrographic areas in the Death Valley region. Pumpage varies from year to year so some adjustment is needed to get a single rate for use in the steady-state simulation. To account for these factors, pumpage rates were reduced by a factor of 50 percent to calculate an overall average annual rate. Although these average rates are based on different time periods and different years, they offer the best available estimate of annual pumping over historical time.

Groundwater withdrawals from 1913 through 1998 from the Death Valley Regional Flow System have been compiled to support a regional, three-dimensional, transient groundwater flow model (Moreo et al. 2003 [DIRS 168008]). Withdrawal locations and depths of production intervals were estimated and associated errors were reported for 9,300 wells. Locations of about 97 percent of wells in the study area were mapped to within 1,000 ft and have reported completion intervals. About 90 percent of all groundwater withdrawal in the study area was from basin-fill deposits in Pahrump Valley, Amargosa Desert, Penoyer Valley, and Mesquite Valley.

Withdrawals were categorized into three general classes: mining, public supply, and commercial water use; domestic water use; and irrigation water use. Water-use categories were based on the method of estimating pumpage. Mining, public-supply, and commercial wells typically were

metered and withdrawals ranged from 2 to 13 percent of annual withdrawals from the study area. Withdrawals for domestic water use, estimated as the number of domestic wells times a consumption rate, ranged from 1 to 7 percent of total annual withdrawals. Irrigation was estimated as the product of acreage and application rates and accounted for more than 80 percent of all withdrawals in Death Valley Regional Flow System during any year (Moreo et al. 2003 [DIRS 168008], p. 22).

8.2.5 Groundwater Recharge

The major source of recharge to the Death Valley regional groundwater flow system is from precipitation on the higher mountains (D'Agnese et al. 2002 [DIRS 158876], p. 29). The regional system also receives interbasin flow, recharge due to recycled irrigation and domestic waters, and seepage of spring discharge back into the groundwater system (Rice 1984 [DIRS 101284], p. 25). However, these recycled components are negligible compared to regional infiltration and interbasinal flux (Waddell 1982 [DIRS 101062], p. 14).

8.2.5.1 Previous Recharge Estimates

Empirical, water-balance, and distributed-parameter methods have been used to characterize the locations and rates of recharge from precipitation in the Death Valley region. Each method attempts to characterize the complex array of factors controlling recharge, but each method has limitations.

Empirical Methods–The Maxey-Eakin method (described by D'Agnese et al. 1997 [DIRS 100131], p. 51) is an empirical precipitation-recharge relationship based on water mass-balance estimates for basins in southern and eastern Nevada that does not account for differences in lithology, soils, climate, vegetation, or topographic factors. Using this method, the amount of precipitation and the percentage of precipitation that becomes recharge increases with increasing altitude. Depending on the valley, the method assumes that no recharge occurs if mean precipitation is less than about 200 mm/yr or if the altitude is lower than 1,524 m (5,000 ft). Above 1,524 m in altitude, an increasing percentage of the precipitation (from 3 to 25 percent) becomes recharge over a series of 305 m (1,000 ft) altitude intervals.

D'Agnese et al. (1997 [DIRS 100131]) used comparative hydrogeologic data sets to enhance the Maxey-Eakin method. Several recharge indicators were identified, including: altitude, slope aspect, rock type, and vegetation. These data sets were classified into four maps describing recharge potential on a five point scale, where 1 represents low recharge potential and 5 represents high recharge potential. The four recharge potential maps were then grouped to develop a final map containing six classes: high, high-moderate, moderate, moderate-low, low and no recharge potential. The areas most likely to have high recharge potential were those that possessed favorable conditions for all four recharge indicators.

The six recharge potential classes were used in a groundwater flow model to represent a percent of average annual precipitation that is recharged (D'Agnese et al. 1997 [DIRS 100131]). However, during calibration of the model, parameter sensitivities indicated that only four zones representing high, moderate, and low recharge potential could be estimated given the model constraints derived from hydraulic head and spring flow data. In the regional model, recharge

was represented as occurring in zones of 0, 1, 3, and 23 percent average annual precipitation (D'Agnese et al. 1997 [DIRS 100131]). Total simulated recharge for the model area was 338,000 m^3/d, which is somewhat greater that the total recharge estimated by the modified Maxey-Eakin method (312,300 m^3/d) (D'Agnese et al. (1997 [DIRS 100131], Table 17).

For the regional model developed for the underground test area (DOE 1997 [DIRS 103021], pp. 5-21 to 5-30, pp. 7-13 and 7-40), recharge was calculated using a modification of the Maxey-Eakin method. In and near the Nevada Test Site, the recharge was modified to account for runoff and recharge below stream channels and in distributary fan deposits. This primarily resulted in simulated recharge beneath Fortymile Canyon and Fortymile Wash. The Maxey-Eakin coefficients and ranges were then adjusted to produce a recharge rate equal to the algebraic sum of the other model fluxes, while producing recharge in lower elevation areas such as Shoshone Mountain and the Bullfrog Hills.

Water-Balance Methods–Rice (1984 [DIRS 101284]) developed a detailed recharge calculation as part of a regional modeling study. Rice (1984 [DIRS 101284], Appendix A) employed a water-balance method that used average annual precipitation distributions derived from regressions (Quiring 1965 [DIRS 150255]). These computations showed that recharge occurs if the altitude is greater than 5,500 ft and the annual precipitation is greater than 254 mm. Because these two criteria meet the requirements of pinyon pine and juniper, Rice (1984 [DIRS 101284], p. A.23) placed the area of recharge to coincide with the pinyon-juniper plant zone and plant zones of higher altitude and moisture. More recent investigations by West (1989 [DIRS 108861]) have placed the lower altitude limits of regional recharge at the mixed shrub-transition zone where blackbrush flourishes. West (1989 [DIRS 108861], p. 2112) noted that these communities represent the altitudinal zone in which winter soil moisture is normally balanced by summer evapotranspiration loss. Therefore, in wet years some recharge may occur in these areas.

Distributed-Parameter Methods–Lichty and McKinley (1995 [DIRS 100589]) and Leavesley et al. (1983 [DIRS 105399]) used distributed-parameter precipitation-runoff models to estimate groundwater recharge in several hydrographic basins of the Death Valley region. These models simulate the processes in the soil-plant-atmosphere system through a series of integrated modules. For basins that contain surface-water and groundwater components, monthly or storm-based water-balance simulations can be modeled. However, although successful simulations have been conducted using these models for various regions of the United States, the use of such models has proven difficult in arid environments where little surface water is present (D'Agnese et al. 1997 [DIRS 100131], p. 51).

8.2.5.2 Current Recharge Estimates

Estimates of recharge for the Death Valley region are listed in D'Agnese et al. (2002 [DIRS 158876], Table 30), which presents a comparison between inflow and outflow components of the regional water budget that were simulated using the regional groundwater flow model and estimates of recharge that were derived from the numerical distributed-parameter net-infiltration model (INFIL; Hevesi et al. 2002 [DIRS 158877]). INFIL is a quasi-three-dimensional numerical model that is based on mass-balance processes and uses real or stochastically simulated values of precipitation, parameters describing the physical setting,

and hydrologic properties of the Death Valley region to approximate actual conditions. The model was calibrated by matching simulated daily mean stream discharge rates to the measured daily mean discharge resulting from episodic runoff events in calibration basins. In addition to measured stream discharge, the model was calibrated using volumetric water content data from neutron boreholes that were used to calculate net-infiltration flux. The model generated a spatial distribution of net infiltration for the region that incorporates a conceptual model of net infiltration based on the physical setting and hydrologic properties of the region. The modeled distribution of regional net infiltration can be used to represent regional groundwater recharge by assuming that water that is simulated to infiltrate past the root zone continues to percolate vertically downward through the unsaturated zone and ultimately becomes groundwater recharge. Net infiltration rates distributed over the region (derived from INFIL results) ranged from less than 1 to 200 mm/yr (Figure 8-7).

Net infiltration based on INFIL (less than 969,200 m^3/d; D'Agnese et al. 2002 [DIRS 158876], Table 30), however, suggests that estimated recharge in the Death Valley region exceeds the estimated groundwater discharge for the basin (295,500 m^3/d) by a factor of about 3.3 (D'Agnese et al. 2002 [DIRS 158876], Table 30). Limitations of the net infiltration model that may contribute to this overestimation, include (D'Agnese et al. 2002 [DIRS 158876], p. 32):

- Processes between the root zone and the water table are not taken into account.

- Defined bedrock permeability could be unrealistically large.

- Evapotranspiration of soil water was underestimated in upland areas with thin soil.

- Precipitation records used in the model (1980 to 1995) were higher than the long-term average.

- Rainfall extrapolation algorithm overestimated rainfall in many areas.

- Soil moisture properties were overly generalized.

- Errors in estimates of saturated and unsaturated hydraulic-conductivity might have affected certain soil types and climate conditions.

- All of the natural processes and conditions could not be simulated, and many of these processes could reduce infiltration.

Ultimately, net infiltration rates could be overestimated because large amounts of water might be impeded or redistributed in the unsaturated zone before reaching the water table. During construction of the regional flow model, the INFIL rates were modified by a factor that depended on the rock type at the water table (D'Agnese et al. 2002 [DIRS 158876], pp. 40 to 42) to represent processes that might redirect infiltrating waters between the root zone and the water table. Calibration of the model required other modifications to the calculated INFIL rates that generally lowered the rates (D'Agnese et al. 2002 [DIRS 158876], pp. 50 to 52). Parameter estimation methods indicate that the total recharge generated from INFIL by Hevesi et al. (2002 [DIRS 158877]) may overestimate total recharge by a factor of as much as four (D'Agnese et al.

2002 [DIRS 158876], p. 50). The recharge value (312,300 m^3/d) estimated by D'Agnese et al. (1997 [DIRS 100131], Table 17) using a modified Maxey-Eakin method may be a closer approximation to the actual recharge value in the Death Valley region.

8.2.6 Potentiometric Surface and Hydraulic Gradients

A number of potentiometric-surface maps have been developed for basins within the Death Valley region (D'Agnese et al. 1998 [DIRS 103006], p. 3). Several are generalized contour maps of shallow basin-fill aquifers, such as those for Sarcobatus Flat and Oasis Valley (Malmberg and Eakin 1962 [DIRS 106695], pp. 13 and 23), the Amargosa Desert (Walker and Eakin 1963 [DIRS 103022], pp. 16 to 17), and the Pahrump Valley (Malmberg 1967 [DIRS 101260], p. 25). Kilroy (1991 [DIRS 103010], pp. 9, 11 and 16) summarized groundwater data collected in the Amargosa Desert from 1952 to 1987, with special attention given to the 1986 to 1987 data. Winograd and Thordarson (1975 [DIRS 101167]) provide several potentiometric maps of basins, or parts of basins, in the Nevada Test Site area.

A regional potentiometric-surface map (Figure 8-4) was constructed to aid in conceptualizing the Death Valley regional groundwater flow system and for developing the numerical regional groundwater flow model.

8.2.6.1 Present-Day Potentiometric Surface

The regional potentiometric-surface map (Figure 8-4) was generated primarily from regional water-level data. However, where needed, these data were supplemented by additional comparative information derived from the hydrographic data, hydrogeologic map, and interpretations of the distribution of regional discharge and recharge to improve interpolations in areas of sparse borehole data. Details of map construction are given by D'Agnese et al. (1998 [DIRS 103006]).

The regional potentiometric surface is controlled primarily by topography, lithology, and geologic structure (D'Agnese et al. 1998 [DIRS 103006], p. 10). Potentiometric-surface mounds, depressions, and troughs, commonly bordered by zones of large hydraulic gradient, are among the dominant features in the regional potentiometric surface that result from important geologic and structural controls.

Potentiometric-Surface Mounds and Depressions–Mounds in the potentiometric surface are commonly associated with groundwater recharge areas (Figure 8-4). Several recharge mounds are inferred where water-level data are not available, because recharge conditions and low permeability rocks occur in these areas (suggesting that recharge mounds are likely to exist) (D'Agnese et al. 1998 [DIRS 103006], p. 10). Mounds are associated with areas recharging the regional flow system, and also indicate recharge to subregional and local flow systems. The most prominent mound (and the largest recharge area) is located beneath the Spring Mountains; smaller recharge mounds are present beneath 10 other mountains or mountain ranges (Figure 8-4, Features 1 through 11).

Depressions in the potentiometric surface are indicators of groundwater discharge areas (D'Agnese et al. 1998 [DIRS 103006], p. 11). The largest depression occurs in Death Valley (Figure 8-4). This depression, controlled mainly by topography, forms the terminus of the

regional groundwater flow system. Smaller depressions in the potentiometric surface occur at Mesquite Lake, Stonewall Flats, and Sarcobatus Flat (Figure 8-4).

Potentiometric-Surface Troughs–Two prominent troughs are controlled by geologic structure (D'Agnese et al. 1998 [DIRS 103006], p. 12). A trough north of the Spring Mountains (Figure 8-4) has been described as the result of high-permeability, faulted, and fractured rock present along the axis of the Spotted Range-Mine Mountain structural zone (Faunt 1997 [DIRS 100146], Plate 1, Figure 3). The trough located at Pahute Mesa is the result of a linear feature believed to be a fault. Less prominent troughs that may be structurally controlled occur at Amargosa Desert, Grapevine Canyon, and Stonewall Pass. Troughs that may be controlled by topography and lithology are located at Yucca Flat and Emigrant Valley. A trough that may be associated with all three controls is located at Fortymile Canyon, although specific geologic or structural controls have been sought but not found.

Large Hydraulic Gradients–Large hydraulic gradients (gradients larger than 0.1) may be controlled by recharge, lithology, topography, structure, or by a combination of these factors (D'Agnese et al. 1998 [DIRS 103006], p. 13). Large hydraulic gradients are a common feature of the Death Valley regional groundwater flow system.

Two regional-scale domains of large hydraulic gradients are present in the Death Valley region. One domain separates Death Valley from adjoining areas to the northeast and east (Figure 8-4). This abrupt drop in water-table altitude is associated with contacts between low-permeability rocks in the Amargosa Range and higher permeability rocks in Death Valley, which are associated with the Death Valley fault zone. This large hydraulic gradient also may result from the large elevation change between the Amargosa Desert (land-surface altitude about 700 m) and Death Valley (land-surface altitude about –80 m). The second domain of large hydraulic gradient occurs along the northern and western margins of the Spring Mountains (Figure 8-4). The large hydraulic gradient in this area is associated with low-permeability clastic aquitard present in the northwestern Spring Mountains (Figure 8-3). North of the Spring Mountains, the large hydraulic gradient also appears to be related to the Las Vegas Valley shear zone and may be due to low-permeability fault gouge developed in this major structural zone.

A zone of large hydraulic gradient begins on the east side of the southern Grapevine Mountains, crosses Yucca Mountain, and extends northeastward to Emigrant Valley and the Groom Range. This hydraulic gradient may be the result of three or more large-scale features, including:

- A largely buried contact of less-permeable rocks to the north and thick, permeable units to the south.

- A generally southward topographic decrease of altitude that is mirrored approximately by the regional potentiometric surface.

- Large regional recharge areas to the north and west, for example, from the vicinity of Pahute Mesa to the Groom Range.

The large hydraulic gradient zone beneath northern Yucca Mountain is characterized by a gradient of 0.13 and possibly as large as 0.15 (Luckey et al. 1996 [DIRS 100465], p. 21).

However an alternative interpretation (that water levels in this area reflect perched water bodies) results in a smaller gradient of 0.06 to 0.07 (USGS 2002 [DIRS 165615]). Characteristics of this gradient and its possible causes are discussed in Section 8.3.4.4.

8.2.6.2   Vertical Hydraulic Gradients

Vertical hydraulic gradients are natural consequences of groundwater flow. In recharge areas, water flow must have a downward component, and in discharge areas, water generally moves upward from depth towards land surface. This simple concept is sometimes complicated by hydrogeologic heterogeneity, as well as by the fact that recharge may be distributed along an entire flow path. In arid to semiarid environments, however, most recharge occurs in upland areas that are separated by arid land from most of the topographically lower discharge areas.

In the Ash Meadows groundwater basin, part of the Central Death Valley subregion (Figure 8-5), the highly transmissive LCA is relatively isolated from the overlying shallow groundwater flow systems. Water-table altitudes in saturated valley-fill materials in basins upgradient from Ash Meadows (e.g., Yucca Flat, Frenchman Flat, and eastern Emigrant Valley; Figure 8-5) and beneath the intervening topographic divides are higher than the potentiometric surface in the LCA (Winograd and Thordarson 1975 [DIRS 101167], p. C93). This indicates that these valleys may contribute recharge to the underlying LCA by downward vertical leakage. However, the vertical permeabilities of the volcanic and valley fill units are small, and these units are expected to impede downward flow. From measurements of hydraulic heads in boreholes in Yucca Flat, Winograd and Thordarson (1975 [DIRS 101167], pp. C54 to C57) suggest that the maximum vertical gradient is about 0.2 and that downward leakage into the LCA in Yucca Flat amounts only to about 31,000 m^3/yr.

Water levels in 17 boreholes in the Yucca Mountain area indicate vertical gradients (USGS 2002 [DIRS 165615], pp. 19 to 23). These water-level data can be used to calculate the difference in hydraulic heads between different monitored intervals. Upward (head increases with depth) and downward (head decreases with depth) vertical gradients have been observed. A number of the boreholes that exhibit positive (upward) head differences are located near Yucca Mountain, and the remainder are located south and southwest of Yucca Mountain. The latter group of Boreholes (e.g., NC-EWDP-2DB/2D, -4PB/4P, -12PC/PB/PA, and -19D/P) indicates upward vertical head differences of about 0.1 to 7.6 m. There were fewer downward gradients (5 of 17) than upward gradients (12 of 17). Upward vertical head differences range from 0.1 to almost 55 m (gradients generally less than 0.01, but as large as 0.13), and downward vertical head differences range from 0.5 to 38 m (gradients generally less than 0.01, but as large as 0.09). Site-scale vertical hydraulic gradients are described further in Section 8.3.4.3.

Upward gradients are commonly observed in the eastern and southern portions of the Amargosa Desert (Kilroy 1991 [DIRS 103010], pp. 11 and 16, Table 3, Plate 4). Downward gradients occur at several localities, but particularly near the Amargosa River east of the Funeral Mountains (western Amargosa Desert). Kilroy (1991 [DIRS 103010]) considered that upward gradients imply hydraulic connection with the LCA, while downward gradients imply hydraulic isolation from it. In several boreholes (or sets of boreholes), upward gradients exceed 0.1, and one extreme value of 1.2 is given (Kilroy 1991 [DIRS 103010], Table 3). Downward gradients are as large as 0.4.

Dudley and Larson (1976 [DIRS 103415], Table 3, Figure 17) report numerous flowing wells at Ash Meadows, which is to be expected in a major regional discharge area that contains many large springs. Dudley and Larson (1976 [DIRS 103415], Figure 10) also provide a contour map of the water table showing a groundwater mound beneath the Devils Hole hills, which are composed of faulted and intensely fractured Paleozoic carbonate rocks that receive little recharge. The warm temperature of the water in and discharging from these rocks, 33°C to 34.5°C (Dudley and Larson 1976 [DIRS 103415], Table 2, p. 24), implies that the groundwater mound is supported by upward flow of water that has circulated deeply within the regional flow system.

8.2.7 Hydrochemical and Isotopic Indicators of Regional Flow

8.2.7.1 Introduction

Hydrochemical and isotopic data from analyses of groundwater samples collected in boreholes, wells, and springs in the Yucca Mountain region provide an independent set of data from which groundwater flow patterns and rates of flow can be inferred and used to test the conceptual basis of the regional groundwater flow model. The hydrochemical signature of groundwater depends on factors such as host rock composition, mineral precipitation and dissolution processes, pH, oxidation potential, partial pressure of carbon dioxide, flow path length, and groundwater flux. Consequently, the inorganic chemistry of groundwaters, including major-ion chemistry, isotopic composition, and trace-element abundances, can be used to characterize chemical reactions between the water and host rocks, identify source areas for recharge, delineate flow paths, evaluate lateral and vertical mixing of groundwaters, and locate areas of evapotranspiration and groundwater discharge.

Controls on the isotopic composition of groundwaters differ from those that apply to the major-ion chemistry. The stable isotopes of hydrogen and oxygen (deuterium and ^{18}O) are conservative (nonreactive) and concentrations are virtually unchanging in groundwater, and they are valuable paleoclimatic indicators of time, location, and environment of recharge, plus the direction (path) of groundwater flow. The decay rates for radioactive isotopes tritium, ^{36}Cl, and ^{14}C are known, and can be used to indicate modern nuclear-age recharge as well as to date the time of prenuclear-age recharge. Major-ion chemistry and isotopic chemistry of groundwaters represent complementary approaches as indicators of regional flow and paleohydrologic conditions. There is considerable variability in the spatial distribution of the data; however, a large amount of information is available regarding the abundances of deuterium, ^{18}O, ^{14}C, and ^{13}C in the region.

A detailed review of fluid geochemical and isotopic parameters and their relevance to site characterization and site evaluations are presented in Section 5. Precipitation, unsaturated zone pore water, perched water, unsaturated zone gases, and groundwater are also summarized in Section 5. Discussions include present conditions, as well as isotopic interpretations indicating past conditions. This section summarizes information on data sources, regional flow patterns, groundwater flow paths, and possible regional recharge areas. Most of the data were collected in the Central Death Valley subregion (Figure 8-5), and the discussion focuses on this subregion. Yucca Mountain is located in the Central Death Valley subregion, and hydrochemical data that

provide evidence for flow paths and processes near Yucca Mountain are discussed in Section 8.3.6.

8.2.7.2 Data Sources

As reflected in the references used in this section, numerous authors have described the hydrochemical and isotopic characteristics of groundwater in the Death Valley region. BSC (2001 [DIRS 158606]) provides updated chemical and isotopic information. Additionally, Stetzenbach et al. (2001 [DIRS 158819]) provide data on concentrations of major ions, several trace elements, and rare earth elements, and Paces et al. (2002 [DIRS 158817]) present data on uranium characteristics in groundwater from springs and wells in southern Nevada, including some of the boreholes drilled as part of the NC-EWDP.

A number of limitations are associated with interpreting the hydrochemical data and restrict the use of these data for inferring regional groundwater flow paths. Although the data set is large (Oliver and Root 1997 [DIRS 100069]; Perfect et al. 1995 [DIRS 101053]), there are a number of deficiencies. For example, cation-anion charge balances have not been calculated for many of the samples because of incomplete analyses (Perfect et al. 1995 [DIRS 101053], p. 9). Many analyses did not differentiate between field and laboratory measurements of pH and inorganic carbon values (bicarbonate, carbonate, alkalinity) (Perfect et al. 1995 [DIRS 101053], p. 9). The representativeness of any given sample has not been assured in most cases because typically a suite of samples was not collected to determine if a steady state composition had been reached during sampling. The number of borehole volumes of water withdrawn prior to sampling generally was not recorded. The data are not uniformly distributed (i.e., they tend to be clustered in the Oasis Valley, Yucca Mountain, and Amargosa Desert areas). In addition, there are few three-dimensional data and water composition in each aquifer generally is taken to be homogeneous with depth; however, this is not always the case (Benson and McKinley 1985 [DIRS 101036], p. 1). Finally, there is no single chemical or isotopic species that varies everywhere throughout the region sufficiently to serve as a common delineator of groundwater flow paths (BSC 2001 [DIRS 158606], Section 6.5.2).

Allowing for these limitations, however, the hydrochemical and isotopic data provide a body of evidence for interpreting regional groundwater flow paths and flow processes. The relative concentrations of conservative constituents, such as chloride and stable isotopes of deuterium and oxygen, provide information useful for constraining possible flow paths. Additionally, systematic variations of other hydrochemical parameters, including strontium isotopic data, uranium concentrations, $^{234}U/^{238}U$ activity ratios, and the concentrations of trace and rare earth elements, provide complementary data and corroborative information to further define patterns in regional groundwater chemistry and delineate regional groundwater flow paths.

8.2.7.3 Hydrochemistry of the Central Death Valley Subregion

The Central Death Valley subregion (Section 8.2.3.2) is divided, based on differences in hydrogeologic characteristics, into groundwater basins that, in turn, are further subdivided into sections (Figure 8-5). The groundwater basin and section nomenclature shown in Figure 8-5 is used in the following discussion to identify specific hydrochemical domains and sampling sites. Saturated zone hydrochemistry of the Yucca Mountain area, which is on the boundary between

the Fortymile Canyon and the Crater Flat sections of the Alkali Flat-Furnace Creek groundwater basin, is discussed in Section 8.3.6.

A classification of groundwaters based on the spatial distribution of hydrochemical facies provides a generalized description of the major-ion chemistry of groundwaters in the Central Death Valley subregion. (Winograd and Thordarson 1975 [DIRS 101167], pp. C98 to C102):

- A dominantly calcium-magnesium bicarbonate facies is characteristic of groundwater from the LCA that dominates the hydrogeology of the eastern part of the subregion (and is presumed to underlie most of the subregion at depth) and from valley-fill materials composed predominantly of carbonate rock detritus.

- A sodium-potassium bicarbonate facies is characteristic of groundwater from the Tertiary volcanic rocks in the northern part of the subregion, including Yucca Mountain, and from valley-fill materials composed of volcanic detritus.

- A mixed calcium-magnesium-sodium bicarbonate facies is characteristic of water from the valley-fill materials and may indicate areas of groundwater mixing in which, for example, there may be upward leakage from the LCA into overlying valley-fill materials.

- A playa facies of variable hydrochemical character is characteristic of near-surface groundwaters in areas where groundwater is discharged by evapotranspiration.

- A sodium-sulfate bicarbonate facies is characteristic of groundwater discharged from the regional flow system in Furnace Creek area springs at the southern end of the Funeral Mountains in Death Valley.

Although this classification of groundwaters places the regional hydrochemical regime in broad perspective, there are differences in detail that result principally from the controls placed on individual flow paths by the complex geologic framework traversed by groundwater as it moves from upgradient source areas to downgradient discharge areas.

Stetzenbach et al. (2001 [DIRS 158819], Section 4) reported the results of a principal components analysis that are in keeping with the hydrochemical facies classification of Winograd and Thordarson (1975 [DIRS 101167], C97 to C112). Principal component scores, plotted for four major cations (calcium, magnesium, sodium, and potassium), showed that groundwater from the Tertiary volcanic aquifers and aquitards in the Nevada Test Site and Yucca Mountain areas cluster into a group, while groundwater from springs discharging from the LCA at Ash Meadows fall into a separate cluster (with the exception of two spring samples excluded due to postdischarge modifications attributed to evaporative concentration, evapotranspiration, or both). The separation of the volcanic aquifer and aquitard groundwaters from the LCA groundwaters reflects the relatively higher sodium and potassium concentrations of the volcanic groundwaters and the higher calcium and magnesium concentrations of the carbonate groundwaters (e.g., Peterman and Patterson 1998 [DIRS 101150], p. 183).

Pahute Mesa-Oasis Valley Groundwater Basin–The Pahute Mesa-Oasis Valley groundwater basin (Figure 8-5) occupies the northernmost part of the Central Death Valley subregion. The northern half of the groundwater basin is divided into two sections that consist of two large internally drained, high desert basins: Kawich Valley on the east and Gold Flat on the west. The southern half of the groundwater basin corresponds generally to the Amargosa River drainage basin upstream from the Amargosa Narrows. The southward flowing Amargosa River is aligned with the topographic axis of Oasis Valley and is joined by tributary ephemeral washes that drain adjacent uplands.

Throughout the basin, groundwater compositions are of a sodium-potassium bicarbonate type (White 1979 [DIRS 101165]; Blankennagel and Weir 1973 [DIRS 101233]) and are consistent with water chemistry derived from the tuffaceous volcanic rocks that underlie the basin. These data imply that groundwater at the northern boundary of the basin moves southerly towards Pahute Mesa and then southwesterly into Oasis Valley, where considerable spring discharge occurs, mainly along the Amargosa River channel (White 1979 [DIRS 101165], p. E6). Many of the springs discharge directly from volcanic rocks, but some discharge from alluvium in the valley floor. The spring discharge infiltrates surficial alluvium and follows flow paths along the principal drainage channels to the Amargosa River channel, and then it follows this channel southward (White 1979 [DIRS 101165], Figure 3). Most of the spring flow is consumed by evapotranspiration along the Amargosa River, but residual subsurface groundwater flows southward beneath the Amargosa River channel and discharges into the Amargosa Desert (White 1979 [DIRS 101165], p. E6).

These conclusions are supported by isotopic data based on analyses of 22 groundwater sources from the Oasis Valley area and 3 wells on Pahute Mesa (White and Chuma 1987 [DIRS 108871]). The isotopically lightest (i.e., most depleted in delta-deuterium [δ^2H] and ^{18}O with respect to standard mean ocean water [SMOW]) occur beneath Pahute Mesa and in the upgradient part of Oasis Valley, which supports the earlier conclusion by White (1979 [DIRS 101165], p. E24) that the major-ion chemistry indicates the Oasis Valley groundwater represents flow largely from Pahute Mesa. Other inferences from the δD and $\delta^{18}O$ data include (White and Chuma 1987 [DIRS 108871], p. 573) that the isotopically light nature of Pahute Mesa groundwater is consistent with recharge derived from the high altitude and prevailing cold condensation temperature on Pahute Mesa, that groundwater moving downgradient in Oasis Valley becomes isotopically heavier and reflects mixing of Pahute Mesa groundwater with local sources and the effects of evapotranspiration, and that deuterium in the sampled groundwaters is depleted by about 5‰ relative to modern precipitation. These are similar to the results of Benson and Klieforth (1989 [DIRS 104370], pp. 48 and 57), who interpreted this to indicate a change in the relative humidity of the moisture source area in the eastern Pacific Ocean prior to 9,000 yrs before present. If evapotranspiration has occurred to any great degree, δD would show a more pronounced effect than $\delta^{18}O$, and would plot below the meteoric water line. White and Chuma (1987 [DIRS 108871], pp. 574, 578 and 579) also used two methods (based on applying $\delta^{13}C$ age corrections and using a reaction-path model of groundwater composition) to estimate corrected ^{14}C ages for Oasis Valley groundwaters. Age estimates, depending on the correction method applied, ranged from about 2,000 to 17,000 yrs and, together with the δD data, are consistent with groundwater recharge during late Pleistocene and early Holocene under climatic conditions different from present-day conditions. This information indicates the groundwater in

the discharge areas of the Pahute Mesa/Oasis Valley flow system is old (late Pleistocene) and represents older climatic conditions. This suggests that present day recharge may not be occurring near the discharge areas, or the transport time from the present recharge area on Pahute Mesa is many thousands of years. These findings have not been verified.

Shale-normalized rare earth element patterns in groundwater samples from wells and springs tested in Oasis Valley do not resemble the typically flat, shale-normalized rare earth element patterns found in groundwaters discharging from the LCA at Ash Meadows (Johannesson et al. 2000 [DIRS 165610], p. 2704). With the exception of a deep water well sample from a well immediately adjacent to an outcrop of Tertiary felsic volcanic rocks, the Oasis Valley wells and springs also have shale-normalized rare earth element patterns that differ from those in perched groundwaters (e.g., Tippipah Spring and Topopah Spring discharge waters from volcanic rock aquifers on the Nevada Test Site (Johannesson et al. 2000 [DIRS 165610], Table 2 and p. 2704; Stetzenbach et al. 2001 [DIRS 158819], Table 1). However, the Oasis Valley groundwater samples, taken in alluvial units composed of materials derived from weathering of the local tuffaceous rocks, exhibit large negative europium values that are also characteristic of felsic volcanic rocks. This is in contrast to rocks of the LCA that do not exhibit distinct shale-normalized negative europium anomalies. This contrast reflects the interaction of groundwater in this area with the (europium-depleted) rhyolitic shallow alluvial aquifer materials (Johannesson et al. 2000 [DIRS 165610], p. 2704).

Ash Meadows Groundwater Basin–The Ash Meadows groundwater basin includes somewhat more than the eastern half of the Central Death Valley subregion (Figure 8-5). This basin is almost entirely underlain by the LCA (Section 8.2.2.1). Hydrogeologic and hydrochemical evidence (Thomas 1996 [DIRS 131259], p. 46) suggests that groundwater in this basin moves predominantly from the Spring Mountains (on the south) and Pahranagat Valley (on the northeast) towards the major spring discharge area at Ash Meadows (Figure 8-5). Thomas 1996 [DIRS 131259] deemed this interpretation to be reasonable given that the central core of thick, continuous carbonate rock extends from Pahranagat Valley to Ash Meadows (Thomas 1996 [DIRS 131259], Figure 17). Comparing the chemistries of different groundwater systems that are separated by tens of kilometers and that are known to exhibit variability of composition could be suspect or uncertain. Based on the deuterium content of water discharged at Ash Meadows, Thomas (1996 [DIRS 131259], p. 46) calculated that the water consists of a blend of 40 percent Pahranagat Valley water and 60 percent Spring Mountain water, which represents a small increase in the contribution from Pahranagat Valley over the estimate by Winograd and Friedman (1972 [DIRS 108880]). Other sources contributing to the spring discharge appear to be minor (Thomas 1996 [DIRS 131259], p. C38), although Winograd and Thordarson (1975 [DIRS 101167], p. C94) estimate that as much as five percent of the discharge may be contributed by water moving into the LCA from the Tertiary volcanic rocks in the northwestern part of the Ash Meadows groundwater basin. Based on principal components analysis, however, Stetzenbach et al. (2001 [DIRS 158819], pp. 263 to 264) suggest that the Ash Meadows groundwater is more similar to the volcanic-rock groundwaters of the western Nevada Test Site and Yucca Mountain areas and the carbonate-rock groundwaters from the Pahranagat Valley than to groundwaters from the carbonate rocks of the Spring Mountains.

The Ash Meadows spring line is a nearly linear array of oases, salt meadows, and springs that extend southward from Fairbanks Spring for about 15 km to Bole Spring (Dudley and Larson

1976 [DIRS 103415], Figure 3). This is the principal discharge area from the LCA in the Ash Meadows groundwater basin (Dudley and Larson 1976 [DIRS 103415], p. 1). The springs emerge from relatively flat-lying Quaternary lake beds (clays and marls) and local travertine deposits apparently as a result of water upwelling along the trace of an inferred normal fault that has displaced low-permeability Tertiary rocks against the transmissive rocks of the LCA and acts as a barrier to lateral groundwater flow (Winograd and Thordarson 1975 [DIRS 101167], pp. C78 and C81). Waters discharged from the springs exhibit a generally uniform major-ion chemistry and are predominantly of a calcium-magnesium-sodium bicarbonate type. This composition is consistent with water upwelling from the LCA that, however, has been converted from a carbonate-rock calcium-magnesium bicarbonate facies to the calcium-magnesium-sodium bicarbonate facies by downward leakage of sodium- and sulfate-rich water from the volcanic rocks that overlie the LCA in the central part of the Ash Meadows groundwater basin (Winograd and Thordarson 1975 [DIRS 101167], p. C107). Although the Ash Meadows spring line constitutes the major discharge area from the Ash Meadows groundwater basin, Winograd and Thordarson (1975 [DIRS 101167], p. C85) acknowledge that water may cross the spring line as underflow into the southern part of the Alkali Flat-Furnace Creek groundwater basin.

Analyses of the trace element and rare earth element concentrations of groundwater discharging from the LCA at Ash Meadows have also been conducted (e.g., Hodge et al. 1996 [DIRS 101135]; Johannesson et al. 1996 [DIRS 103476]; Johannesson et al. 1997 [DIRS 101137]; Johannesson et al. 2000 [DIRS 165610]; Stetzenbach et al. 2001 [DIRS 158819]). Rare earth elements investigated as part of these studies, in order of increasing atomic elements include: (1) lanthanum and rhenium; (2) the lanthanides cerium, neodymium, samarium, europium, gadolinium, terbium, dysprosium, holmium, erbium, ytterbium, and lutetium; and (3) the actinide thorium. Other trace elements studied include: lithium, strontium, titanium, vanadium, chromium, copper, zinc, arsenic, rubidium, molybdenum, tin, barium, and uranium. The rare earth element analyses were performed as part of a number of regional studies of trace element and rare earth element concentrations in wells and springs in southern Nevada to provide additional information to further evaluate possible regional patterns of groundwater hydrochemistry. This additional information includes the identification of groundwater "provenances" (the combination of aquifer rock type and associated groundwater composition) and the delineation of potential groundwater flow paths. The rare earth element data obtained from these studies are considered useful indicators of groundwater flow paths because results of previous studies suggest that groundwaters and some surface waters can inherit aqueous rare earth element signatures from the host materials through which the water flows and interacts (e.g., Johannesson et al. 1997, [DIRS 101137]; p. 807; Stetzenbach et al. 2001, [DIRS 158819] p. 256).

Results of the above studies indicate that the groundwaters discharging at Ash Meadows exhibit rare earth element patterns that mimic rare earth element patterns in the LCA host rocks (Johannesson et al. 2000 [DIRS 165610], p. 249). The LCA host rocks have overall lower rare earth element values than volcanic rocks analyzed in southern Nevada (Johannesson et al. 2000 [DIRS 165610], p. 247). Johannesson et al. (2000 [DIRS 165610], p. 249) also indicate that rocks of the LCA typically exhibit flat rare earth element patterns when normalized to shale. The trace element and rare earth element concentrations in these discharge samples exhibit many similarities to those reported in modern seawater (e.g., Stetzenbach et al. 2001, [DIRS 158819], Table 1). For example, analysis of nine Ash Meadows spring discharge samples indicates a

mean concentration of rhenium in of about 40.7 picomoles/kilogram (pmol/kg) (Stetzenbach et al. 2001, [DIRS 158819], Table 1), which is similar to the rhenium value (39.8 ± 0.2 pmol/kg) reported for seawater (Hodge et al. 1996 [DIRS 101135]; p. 3203). Additionally, concentrations of neodymium in the groundwaters discharging at Ash Meadows range from approximately 3.6 to 23.3 pmol/kg, with a mean concentration of about 9.2 pmol/kg (Stetzenbach et al. 2001, [DIRS 158819], Table 1), similar to neodymium values reported for seawater (Johannesson et al. 1997 [DIRS 101137], p. 811).

In principle, ^{14}C can be used to estimate the time taken for groundwater to travel from the recharge area to a discharge area. Apparent (uncorrected) ^{14}C ages of waters discharged from the major springs at Ash Meadows indicate average times of recharge that range from about 18,000 to 30,000 yrs (Winograd and Pearson 1976 [DIRS 108882], p. 1131). Winograd and Pearson (1976 [DIRS 108882], p. 1140) applied corrections to the apparent ages to account for dilution of ^{14}C by dead carbon derived from the dissolution of ancient marine carbonate rocks that form the LCA. Adjusted ages for water discharged from Crystal Pool, which is the largest spring in the Ash Meadows area, ranged from 8,000 to 13,000 yrs; adjusted ages for other sampled springs ranged from 19,000 to 28,000 yrs. Winograd and Pearson (1976 [DIRS 108882], p 1141) attributed the variability in estimated ^{14}C ages along the spring line to the presence of megascale flow channeling within the LCA and may indicate that, other chemical indicators notwithstanding, the water being discharged from the springs is not well mixed throughout the discharge area.

Alkali Flat-Furnace Creek Groundwater Basin–The Alkali Flat-Furnace Creek groundwater basin is divided into four sections (Figure 8-5). Yucca Mountain forms the drainage divide that separates the Crater Flat and the Fortymile Canyon sections of the groundwater basin, and although discussed here in the context of the regional flow system, much of the data available for these two sections have been obtained to support evaluation of the Yucca Mountain repository (Section 8.3.6). The Amargosa River section of the groundwater basin is essentially coincident with the Amargosa Desert, which is a broad intermontane basin extending about 85 km from the western flanks of the Spring Mountains to the Bullfrog Hills west of Beatty, Nevada. Numerous wells and boreholes have been drilled into the valley-fill aquifers in the Amargosa Desert, most of which supply water for domestic and agricultural use. The Funeral Mountains section of the groundwater basin includes the regional hydrologic sink in Death Valley.

The major-ion composition of groundwater in the Alkali Flat-Furnace Creek groundwater basin transitions from north to south. In the north, the groundwater is characteristic of a dominantly sodium-potassium bicarbonate facies, which is characteristic of the volcanic aquifers at Yucca Mountain (Benson and McKinley 1985 [DIRS 101036], Figure 3; Thomas 1996 [DIRS 131259]). To the south, the groundwater is characteristic of a calcium-magnesium-sodium bicarbonate facies in the valley-fill aquifers of the Amargosa Desert (Winograd and Thordarson 1975 [DIRS 101167], Table 8; Claassen 1985 [DIRS 101125], Figures 4 to 7). This interpretation is supported by the hydrochemistry of groundwaters sampled from most of the NC-EWDP Boreholes (e.g., NC-EWDP-9S, -19P, -15P, -3S, -5S, -4PB, -12PB, -12PA, and -1D), which typically represent a sodium-potassium bicarbonate facies (Farnham et al. 2002 [DIRS 165612], Section 8.1). The NC-EWDP boreholes are located along the boundary between the Amargosa River section and the Crater Flat and Fortymile Canyon sections of the Alkali Flat-Furnace Creek groundwater basin. These boreholes generally penetrate saturated intervals

composed of volcanic detrital material that locally overlies indurated volcanic rocks. In accordance with the facies classification of Winograd and Thordarson (1975 [DIRS 101167]), the hydrochemistry of these groundwaters is consistent with water that has interacted chemically with felsic volcanic rocks, such as the rhyolites and quartz latites of the Timber Mountain caldera complex to the north, or with sedimentary rocks (volcaniclastics) and alluvial deposits composed of weathered fragments of these volcanic rocks.

In the Amargosa Desert to the south of the NC-EWDP boreholes, Claassen (1985 [DIRS 101125], pp. F13 to F14) concluded, based on a comparison of the hydrochemical character of Amargosa Desert groundwaters with that of representative groundwaters from the Nevada Test Site, that the water in the valley-fill aquifers was not derived from recharge in the upland volcanic areas to the north via subsurface flow, but rather that it was recharged by direct surface runoff during the Pleistocene and early Holocene. White and Chuma (1987 [DIRS 108871], p. 578) provide a somewhat different interpretation, arguing that groundwater in the northern Amargosa Desert (near the present-day Fortymile Wash drainage) evolved chemically from groundwater that had recharged upgradient in Fortymile Canyon with only selective modification by reaction with alluvium. Additionally, Claassen (1985 [DIRS 101125], p. F18) interpreted hydrochemical data from near the potentiometric high at the western end of the Specter Range (near the boundary between the Alkali Flat-Furnace Creek and Ash Meadows groundwater basins) to imply the occurrence of upward leakage of water into the valley-fill materials from the LCA coupled with direct surface inflow (Claassen 1985 [DIRS 101125], Figure 2). This interpretation is in accord with that reached by Winograd and Thordarson (1975 [DIRS 101167], pp. C84 to C85) based on potentiometric arguments. The Gravity fault/Specter Range Thrust fault intersection and the inferred role of the Gravity fault in facilitating upward movement may be consistent with these results.

A conspicuous feature of the areal distribution of chloride concentrations within the Alkali Flat-Furnace Creek groundwater basin is the presence of a north-to-south trending trough of chloride concentration that is essentially coincident with the Fortymile Canyon section of the groundwater basin, including Yucca Mountain, and extends southward into the Amargosa Desert (BSC 2001 [DIRS 158606], Figure 12.4-5). Chloride concentrations generally are less than 10 mg/L along this trough, which to the north is underlain by Tertiary volcanic rocks and to the south by valley-fill materials consisting primarily of volcanic detritus. The extension of the depression into the northern Amargosa Desert may be consistent with the interpretation that the water entering the Amargosa Desert along the Fortymile Wash drainage has derived from recharge upgradient in Fortymile Canyon (White and Chuma 1987 [DIRS 108871]). The chloride data, however, do not exclude the possibility that the low chloride concentrations in the northern Amargosa Desert reflects local recharge, as proposed by Claassen (1985 [DIRS 101125], pp. F13 to F14), coupled with subsurface inflow from upgradient sources in Fortymile Canyon (BSC 2001 [DIRS 158606], p.110).

Isotopic data from groundwaters in the northern Amargosa Desert appear to favor the hypothesis of local recharge to the valley-fill material from surface-water flow under Pleistocene and early Holocene pluvial conditions (Claassen 1985 [DIRS 101125], pp. F13 to F14). Benson and Klieforth (1989 [DIRS 104370], Figure 14) showed that a plot of δD versus $\delta^{18}O$ for modern precipitation in the Yucca Mountain area is close to the world meteoric trend line $\delta D = 8\delta^{18}O + 10$ (Craig 1961 [DIRS 104753]). Groundwaters in the Amargosa Desert,

Fortymile Wash, and Yucca Mountain areas, however, plot below the world meteoric trend (BSC 2001 [DIRS 158606], Figure 26), which Benson and Klieforth (1989 [DIRS 104370], p. 57) interpreted to be due to a change in relative humidity over the eastern Pacific moisture source area during the period 18,500 to 9,000 yr before present. The δD values in groundwater near Fortymile Wash in the Amargosa Desert are lower than the δD values in groundwater near Fortymile Wash east of Yucca Mountain (BSC 2001 [DIRS 158606], Figure 26), implying different origins or different ages of groundwaters (BSC 2001 [DIRS 158606], p. 110). Because the deuterium excess (the additive constant in the meteoric trend line) decreases with increasing relative humidity in the moisture source area, and because higher relative humidity would be expected over the eastern Pacific Ocean under the cooler climatic conditions that prevailed during the Pleistocene, the observation that the low-chloride Amargosa Desert groundwaters appear to fall along or below a meteoric trend line with a smaller deuterium excess ($\delta D = 8\delta^{18}O + 5$) (BSC 2001 [DIRS 158606], Figure 26) than the modern meteoric trend line may reflect a predominantly Pleistocene origin for these groundwaters (BSC 2001 [DIRS 158606], p. 110). Additionally, the Amargosa Desert groundwaters exhibit appreciable dispersion in a plot of δD versus $\delta^{18}O$ (BSC 2001 [DIRS 158606], Figure 26; Benson and Klieforth 1989 [DIRS 104370], Figure 9). Benson and Klieforth (1989 [DIRS 104370], p. 48) attributed this dispersion to the effects of evaporation during or after infiltration of the relatively shallow waters, which is consistent with the interpretation that recharge in the northern Amargosa Desert mainly resulted from infiltration of surface-water flows (Claassen 1985 [DIRS 101125], pp. F13 and F14). As discussed below, Paces et al. (2002 [DIRS 158817], p. 766) suggest that observed trends of uranium concentrations and $^{234}U/^{238}U$ activity ratios in groundwaters from boreholes along the lower reaches of the Fortymile Wash drainage system support the interpretation of surface-water recharge to the valley-fill material in the northern and central Amargosa Desert.

Paces et al. (2002 [DIRS 158817], Figures 5 and 8) grouped data for uranium concentrations and $^{234}U/^{238}U$ activity ratios in groundwaters in the Central Death Valley subregion into three geographic domains. These domains reflect the extent of hydrochemical differentiation of groundwaters within the subregion and have implications for possible groundwater flow paths. The Yucca Mountain domain underlies and extends southward from Yucca Mountain, and it is associated with groundwaters within the Tertiary volcanic aquifers that are characterized by intermediate uranium concentrations and high $^{234}U/^{238}U$ activity ratios between 6 and 8 (Paces et al. 2002 [DIRS 158817], p. 760). The Fortymile domain is defined by the Fortymile Wash drainage system and extends southward into the central Amargosa Desert area. This domain encompasses groundwaters associated with the Tertiary volcanic aquifers in the upper and middle reaches of Fortymile Wash and with the valley-fill aquifer in the lower reaches of Fortymile Wash and the Amargosa Desert. These groundwaters have low to intermediate uranium concentrations (values greater than 2.5 μg) and low to intermediate $^{234}U/^{238}U$ activity ratios (Paces et al. 2002 [DIRS 158817], p. 760). The third domain consists of groundwaters from the Tertiary volcanic aquifers and the valley-fill aquifers in the Pahute Mesa-Oasis Valley groundwater basin and the western and southwestern margins of the Amargosa Desert in the Alkali Flat-Furnace Creek groundwater basin. Groundwaters in this area are characterized by low to intermediate $^{234}U/^{238}U$ activity ratios (less than about 5.5) that are similar to groundwaters in the Fortymile domain, but they have substantially larger uranium concentrations (Paces et al. 2002 [DIRS 158817], p. 760).

Hydrochemical implications for groundwater flow near Yucca Mountain are discussed in Section 8.3.6 and Section 5, but the results reported by Paces et al. (2002 [DIRS 158817]) for the Yucca Mountain domain carry regional implications. In particular, Paces et al. (2002 [DIRS 158817], pp. 767 and 768) interpret the high $^{234}U/^{238}U$ activity ratios to imply that the groundwater flow system in the saturated zone beneath Yucca Mountain is effectively isolated from subsurface inflow and is supplied by local recharge through the overlying unsaturated zone with only limited quantities of water entering the system from the regional volcanic aquifers to the north. Despite the apparent low recharge rates and apparent relative isolation of the groundwater flow system beneath Yucca Mountain, Paces et al. (2002 [DIRS 158817], p. 769) conclude that groundwater outflow from the system is likely. Paces et al. (2002 [DIRS 158817], pp. 769 and 770) point out that Borehole NC-EWDP-2D, which penetrates the valley-fill aquifer about 20 km south of Yucca Mountain, has a $^{234}U/^{238}U$ activity ratio of 4.77, which is greater than that of groundwater in nearby boreholes in the adjacent Fortymile domain, and may be evidence of a natural flow path oriented north-south from central Yucca Mountain.

The Fortymile domain is coincident with the Fortymile Wash drainage system, and Paces et al. (2002 [DIRS 158817], p. 765) point out that there is evidence suggesting that at least the upper and middle reaches of the drainage system are structurally controlled with the result that the flow of groundwater in the underlying saturated Tertiary volcanic rocks is aligned with the overlying surface-water system. Between observation Borehole UE-25 JF#3, which penetrates the Tertiary volcanic rock aquifer in the middle reach of Fortymile Wash, and Highway 95 to the south, groundwater moving south beneath Fortymile Wash flows out of the Tertiary volcanic rocks and into the valley-fill materials. Groundwaters from boreholes that penetrate valley-fill materials downgradient from Borehole UE-25 JF#3 along the Fortymile Wash drainage system show a trend of progressively increasing uranium concentrations and decreasing $^{234}U/^{238}U$ activity ratios (Paces et al. 2002 [DIRS 158817], Figure 8) that Paces et al. (2002 [DIRS 158817], p. 766) suggest could result from groundwater from the upland Tertiary volcanic rocks mixing with surface-water recharge from channel-bed infiltration in the lower reaches of Fortymile Wash. Paces et al. (2002 [DIRS 158817], p.766) show that a binary mixing model that uses the measured uranium concentrations and $^{234}U/^{238}U$ activity ratios in groundwaters from boreholes in the central Amargosa Desert and from observation Borehole UE-25 JF#3 as endpoints can account for the observed trend of uranium characteristics along the lower reach of the Fortymile Wash drainage system.

The hydrochemical and isotopic evidence is consistent with the hypothesis that the apparent structural control imposed on the Fortymile Wash drainage system has resulted in progressive downgradient interaction between groundwaters in the shallow volcanic-rock and valley-fill aquifers with groundwater in the underlying LCA. Under this hypothesis, groundwater in the northern Amargosa Desert represents a hydrochemical composite derived from groundwater moving southward along the drainage system in the volcanic-rock and valley-fill aquifers and groundwater leaking vertically upward from the LCA with an admixture of surface-water infiltration along the lower reaches of the drainage system.

The Funeral Mountains section of the Alkali Flat-Furnace Creek groundwater basin includes Death Valley, which is the hydrologic sink for the regional groundwater flow system. Areas of groundwater discharge in the Funeral Mountains section include evapotranspiration from the floor of Death Valley and outflow from high- and low-discharge springs along the western

margin of the Amargosa Range. This includes the Funeral Mountains and the Grapevine Mountains, which forms the eastern boundary of Death Valley. A group of large springs, with discharge rates ranging from 16 to 75 L/s (Miller 1977 [DIRS 105462], p. 27), discharge in eastern Death Valley on the western flank of the Funeral Mountains in the Furnace Creek area. These springs, which include Texas, Nevares, and Travertine springs, are notable for their steady flow, nearly identical hydrochemistry, and unchanging water temperatures that are higher than the local ambient air temperature. Miller (1977 [DIRS 105462], p. 26) interprets these characteristics to imply that the springs are supplied by a common source. Although Pistrang and Kunkel (1964 [DIRS 103115], p. Y20) attributed the water source to recharge from precipitation over the Furnace Creek Wash drainage area, Winograd and Thordarson (1975 [DIRS 101167], p. C95) and Miller (1977 [DIRS 105462], pp. 28 to 30) interpret the evidence to suggest that the more likely source is groundwater moving southward through the Amargosa Desert (underflow through the LCA beneath the Funeral Mountains).

Hydrochemically, waters discharging from the Furnace Creek area springs constitute a sodium-sulfate bicarbonate facies that is distinct from the hydrochemical facies associated with the principal aquifers in the Central Death Valley subregion (e.g., Winograd and Thordarson 1975 [DIRS 101167], Figure 38). Winograd and Thordarson (1975 [DIRS 101167], p. C112) suggest that the spring water may represent a mixture (with addition of sulfate and chloride) of water that is moving southward from Oasis Valley along the western side of Amargosa Desert with water moving westward from Ash Meadows. With regard to possible sulfate and chloride enrichment, Winograd and Thordarson (1975 [DIRS 101167], p. C112) point out that groundwaters sampled from three boreholes along the Amargosa River in the Amargosa Desert exhibit relatively elevated sulfate and chloride concentrations, and Claassen (1985 [DIRS 101125], pp. F20 to F23) observed that, compared to modern precipitation, groundwaters along the upper reach of the Amargosa River in the Amargosa Desert have been concentrated by a factor of 200 in sulfate and chloride. Although it is plausible that downward flow of water from the overlying valley-fill aquifer into the LCA with subsequent movement towards Death Valley may be the source of water discharged from the Furnace Creek area springs, Winograd and Thordarson (1975 [DIRS 101167], p. C112) point out that this possibility cannot be evaluated until the hydraulic head relationships between the two aquifers in the central and southern part of the Amargosa Desert have been determined.

Miller (1977, [DIRS 105462] pp. 28 to 32) presented various geologic and hydrologic discussions germane to the question of the source of the water discharging from the springs at the west end of Furnace Creek Wash. Miller concluded that the consensus of the information indicated the water discharging at these springs likely flows from the basins to the north and east, through the southern part of the Funeral Mountains. Carr (1984, [DIRS 101037] p. 61) suggested that water discharging at both Ash Meadows and the Furnace Creek springs derives from groundwater flowing through the Spotted-Range-Mine Mountain structural zone. Carr (1984, [DIRS 101037] p. 11, p. 30) further described several other northeast-trending structural zones in the Walker Lane Belt, some of which terminate at the Fish-Lake-Death Valley-Furnace Creek fault zone (Figure 2-12).

Steinkampf and Werrell (2001 [DIRS 158818]) used hydrochemical data from analyses of water samples collected from springs, including the Furnace Creek area springs, in and along the western flank of the Amargosa Range and hydrogeologic arguments to infer likely flow

pathways for groundwater moving towards the regional hydrologic sink in Death Valley. They note that the water chemistries of the Furnace Creek area springs are more calcic than waters that have reacted solely with volcanic rocks or volcanic detritus, and they conclude that the water chemistries have been influenced by volcanic and carbonate rocks (Steinkampf and Werrell 2001 [DIRS 158818], p. 25). They further suggest, however, that the waters discharged from these springs bear chemical and isotopic resemblance to the Ash Meadows spring group to the east of the Furnace Creek area springs and likely are representative of water that has moved through the valley-fill aquifer in the Amargosa Desert into the southern Funeral Mountains (Steinkampf and Werrell 2001 [DIRS 158818], p. 33). They point out that the Ash Meadows spring group and the Furnace Creek springs are associated with the Spotted Range-Mine Mountain structural zone (Section 2.2.1), a zone of dominantly northeast-striking left-lateral faults that may provide preferential conduits to direct groundwater flow from the Ash Meadows groundwater basin to the southwest across the Amargosa River section of the Alkali Flat-Furnace Creek groundwater basin and provide a drain through the Paleozoic carbonate rocks beneath the Funeral Mountains (Steinkampf and Werrell 2001 [DIRS 158818], p. 33).

Isotopic data (e.g., δD and $\delta^{18}O$,) from the Furnace Creek area springs are virtually identical (Rose et al. 1997 [DIRS 144725], Table 5; Steinkampf and Werrell 2001 [DIRS 158818], Table 2) and support the inference that the spring waters derive from a common source. The δD and $\delta^{18}O$ values are comparable to those reported by Claassen (1985 [DIRS 101125], Table 6) for the high sulfate-chloride groundwaters from boreholes in the western Amargosa Desert. Steinkampf and Werrell (2001 [DIRS 158818], p. 25) indicate that a simple mixing calculation produces a composite water closely approximating the compositions of the Travertine and Nevares Spring discharge water. The calculation uses water representative of water in wells in the Amargosa Desert Wells that are completed in tuff and tuff detritus alluvium (area depicted on Claassen 1985 [DIRS 101125], Figures 1 and 3), with water from Amargosa Desert wells completed in mixed tuff-plus-carbonate alluvium (Steinkampf and Werrell 2001 [DIRS 158818], Figure 4), and with water from one of the Ash Meadows springs (Thomas 1996 [DIRS 131259], Appendix B). The authors inferred that the computed composition, having a chloride value slightly lower than the Travertine and Nevares Spring values, could be reconciled through further augmentation of chloride levels during flow through the southern Funeral Mountains. They further inferred that some additional flow component to and through the southern Funeral Mountains may occur through fractured, likely Paleozoic, carbonates, that underlie the Amargosa Desert alluvium, with the flow path most likely following the southwest end of the Spotted Range-Mine Mountain structural zone, as discussed above.

Johannesson et al. (2000 [DIRS 165610], Table 1 and p. 249) present data demonstrating that the rare earth element signatures of Ash Meadows groundwaters are similar to those of springs in the Furnace Creek area of Death Valley. The data also demonstrate that the groundwaters discharging at both Ash Meadows and Furnace Creek Wash exhibit rare earth element patterns that mimic rare earth element patterns in rocks from the LCA in southern Nevada. For example, the relatively low neodymium concentrations in the Ash Meadows springs (mean concentration of about 27 pmol/kg reported for six samples) and the Furnace Creek Wash springs (mean concentration of about 27 pmol/kg reported for three samples) are virtually the same which are similar to values reported for seawater (Johannesson et al. 1997 [DIRS 101137], p. 811). By contrast, groundwater samples from Tippipah Spring and Topopah Spring which discharge from a Tertiary volcanic tuff unit at the base of Shoshone Mountain on the Nevada Test Site northeast

of Yucca Mountain, exhibit shale-normalized rare earth element signatures that are similar to the local felsic volcanic rocks, including having substantially higher concentrations (1,576 and 863 pmol/kg, respectively) of neodymium (Stetzenbach et al. 2001 [DIRS 158819], Table 1) and substantial negative europium anomalies of -0.4 and -0.39, respectively (Johannesson et al. 2000 [DIRS 165610], p. 249).

8.2.7.4 Regional Groundwater Flow Inferred from Hydrochemical Evidence

Major-ion and isotopic chemistry of groundwaters in the Death Valley region provide complementary information on regional groundwater flow and recharge. Major-ion chemistry is indicative mainly of rock-water interactions that occur along a groundwater flow path, including, for example, such processes as the dissolution and precipitation of mineral matter and ion-exchange reactions. Isotopic chemistry, which generally is subject to controls that differ from those imposed on major-ion chemistry, provides information regarding location, timing, and environment of groundwater recharge; near-surface evaporation processes in areas of groundwater discharge; and mixing of groundwaters within and between different aquifer systems. Radiogenic isotopes also provide evidence for rock-water interactions, for example, the abundance of ^{87}Sr, which is enriched in groundwaters that have flowed through the Precambrian cores of the Spring or Funeral Mountains or through alluvial materials derived from these rocks.

The major-ion chemistry of groundwaters in the region indicate the existence of two principal hydrochemical facies: a relatively dilute sodium-potassium bicarbonate facies associated with the Tertiary volcanic-rock aquifers and with volcanic-rock detritus derived from the volcanic rocks, and a more concentrated calcium-magnesium bicarbonate facies associated with the underlying Paleozoic carbonate-rock aquifers and detrital material derived from these rocks. Where these two hydrochemical facies mix, for example in the valley-fill aquifers, the groundwaters tend to transition to a calcium-magnesium-sodium bicarbonate facies. In addition, a playa facies of variable hydrochemistry associated with near-surface evaporation processes is recognized locally within groundwaters in the valley-fill aquifers, and a distinct sodium-sulfate bicarbonate facies is recognizable in waters that are discharged from the regional system in springs in Death Valley.

The principal isotopic data include the δD and δ^{18}O contents of groundwaters, which are indicative of groundwater recharge processes and environments; ^{14}C and, to a lesser extent, tritium contents, which are indicators of the time since recharge; the δ^{13}C content, which is indicative of the degree to which ^{14}C in groundwater has been diluted by the uptake into solution of nonradioactive carbon; and uranium concentrations and ^{234}U/^{238}U activity ratios that can be used to define different groundwater types, or facies, and characterize groundwater flow and downgradient dilution and dispersion processes.

Major findings that emerge from the hydrochemical and isotopic data for groundwaters in the Central Death Valley subregion include:

- Under present-day climatic conditions, recharge is confined largely to infiltration of precipitation in upland areas, such as the volcanic highlands of Pahute Mesa and the carbonate-rock massif of the Spring Mountains, with subsequent decrease in the amount

of infiltration water downward due to permeability reduction caused by precipitation of minerals from the water.

- A number of processes affect the chemistry of groundwater as it moves through a flow system. These processes include, for example, chemical precipitation of less soluble mineral phases in response to increasing water temperature, changes in pH, and ion-exchange reactions; concentration of dissolved constituents through near-surface evaporation processes; and adsorption of dissolved or suspended constituents on exposed surfaces in the rocks and detrital materials through which the water moves. The groundwater chemistries produced through these processes are consistent with the general conceptual model of groundwater flow in the Central Death Valley subregion. This conceptual model considers groundwater to enter the flow system as recharge in upland areas and as inflow across subregional boundaries with subsequent downgradient flow along flow paths directed towards the regional hydrologic sink in Death Valley.

- Deuterium and $\delta^{18}O$ appear to be conservative constituents in the regional groundwater flow system that are indicative of the conditions under which recharge from land-surface precipitation occurred. These constituents are sensitive to the temperature prevailing at the time when arriving water vapor condensed to produce rain or snow and may be a consequence of land-surface altitude or an effect of climatic conditions in the source area producing the moisture. The values for δD and $\delta^{18}O$ from groundwater in the Death Valley region differ markedly from the values for modern precipitation in the region. This difference is interpreted to indicate that major recharge to the flow system from precipitation occurred under pluvial conditions that prevailed during the Pleistocene and early Holocene when humidity in the eastern Pacific Ocean likely would have been higher than present-day conditions.

- Uranium concentrations and $^{234}U/^{238}U$ activity ratios measured in groundwaters in the Yucca Mountain area, together with potentiometric data and inferences based on the hydrochemistry and isotopic composition of groundwaters along the Fortymile Wash drainage system, support the interpretation that the groundwater flow system in the Tertiary volcanic rocks beneath Yucca Mountain is relatively isolated hydrologically from the regional groundwater flow system.

- A major area of groundwater discharge from the eastern half of the Central Death Valley subregion consists of the apparently structurally controlled upwelling of water from the LCA along the Ash Meadows spring line; however, locally and at depth, groundwater in the LCA may bypass the spring line and move southwesterly into the Amargosa Desert.

- The hydrochemical and isotopic compositions of the water discharged from the major springs in Furnace Creek Wash area on the eastern flank of Death Valley suggest that these springs constitute a major subsurface drain for regional groundwaters flowing southwestward through the LCA from upgradient recharge areas including the Spring Mountains, Pahranagat Valley, and the White River Flow System. These regional groundwaters may have mixed with waters in the southern central Amargosa Desert derived from shallow groundwater flowing southwestward from the western Amargosa Desert and/or groundwater flowing through fractured, probably Paleozoic carbonates

underlying the Amargosa Desert alluvium. The flow path for the groundwater discharging in the Furnace Creek Wash springs area likely follows the southwest end of the Spotted Range-Mine Mountain structural zone, passing through the southern Funeral Mountains, and appears to be subject to further controls exerted by the Furnace Creek and Keane Wonder fault zones and the synclinal structure of the sedimentary fill in Furnace Creek Wash.

Overall, the regional hydrochemical and isotopic data support the conceptual model for regional groundwater flow that provides the basis for the numerical regional groundwater flow model (D'Agnese et al. 2002 [DIRS 158876].

In addition to the major-ion chemistry and isotopic composition of groundwater in the region, studies of the concentrations of 13 trace elements and 14 rare earth elements in groundwater from springs and boreholes in the region provide corroborative information for evaluating regional patterns of groundwater hydrochemistry, including the identification of groundwater "provenances" (the combination of aquifer rock type and associated groundwater composition) and the delineation of potential groundwater flow paths.

Results of these studies suggest that groundwaters and some surface waters inherit aqueous rare earth element signatures from the host materials through which the water flows and interacts (e.g., Johannesson et al. 1997 [DIRS 101137], p. 807; Stetzenbach et al. 2001 [DIRS 158819], p. 256). Furthermore, depending on characteristics of the groundwater and the host material, solution and complexation of various rare earth elements in the water also can exert controls on the rare earth element concentrations (Johannesson et al. 1997 [DIRS 101137], p. 815). The rare earth elements are primarily complexed with carbonate ions in the groundwaters of south-central Nevada and Death Valley, California, such that typically greater than 90 percent and up to greater than 99 percent of each rare earth element is present in solution as rare earth element-carbonate complexes (Johannesson et al. 1997 [DIRS 101137], p. 815). Data indicate the following patterns with respect to rare earth element concentrations in the Tertiary volcanic rock aquifers and the LCA in the Yucca Mountain region:

- Groundwaters in southern Nevada and Death Valley generally exhibit mild enrichments in the heavier rare earth elements compared to the lighter rare earth elements when normalized to shale rare earth element levels (Johannesson et al. 1997 [DIRS 101137], p. 816).

- Shale-normalized rare earth element concentrations in groundwaters from the Tertiary volcanic aquifer and the LCA are similar to rare earth element concentrations in the host rock unit (Johannesson et al. 2000 [DIRS 165610], p. 247).

- Rare earth element concentrations sampled in the Tertiary volcanic rocks and the rocks of the LCA vary by less than an order of magnitude, with the carbonate rock samples having lower values overall for each rare earth element than the volcanic rocks (Stetzenbach et al. 2001 [DIRS 158819]). Rocks of the LCA typically have flat rare earth element patterns when normalized to shale (Stetzenbach et al. 2001 [DIRS 158819]).

- Groundwaters that discharge at Ash Meadows and at the springs in the Furnace Creek area exhibit rare earth element patterns that mimic rare earth element patterns in rocks from the LCA (Stetzenbach et al. 2001 [DIRS 158819]).

- Felsic volcanic rocks of the type underlying Yucca Mountain and the Nevada Test Site exhibit substantial negative, shale-normalized europium anomalies ($Eu/Eu^* = -0.46 \pm 0.01$, where Eu/Eu^* represents the logarithm of the ratio of twice the shale-normalized europium concentration to the sum of the shale-normalized concentrations of samarium and gadolinium).

- Based on nine samples, the mean rare earth element concentration in groundwaters discharging from the LCA at Ash Meadows (Stetzenbach et al. 2001 [DIRS 158819], Table 1) is 40.7 pmol/kg, which is similar to the rare earth element value $(39.8 \pm 0.2$ pmol/kg) reported for seawater (Hodge et al. 1996 [DIRS 101135], p. 3197).

- Groundwater samples from Tippipah Spring and Topopah Springs (Stetzenbach et al. 2001 [DIRS 158819], Figure 1), which discharge from a Tertiary tuff unit at the base of Shoshone Mountain northeast of Yucca Mountain, exhibit shale-normalized rare earth element signatures that are similar to the local felsic volcanic rocks, including having substantial negative europium anomalies. Values for Tippipah Spring and Topopah Springs are -0.4 and -0.39, respectively (Johannesson et al. 2000 [DIRS 165610], p. 249). Water from Tippipah and Topopah springs also have higher rare earth element concentrations than those in groundwater from the LCA, especially for neodymium (concentrations of 1,576 and 863 pmol/kg, respectively), compared to neodymium concentrations of 3.6 to 23.3 pmol/kg in groundwaters discharging from the LCA at Ash Meadows (Stetzenbach et al. 2001 [DIRS 158819], Table 1). The low neodymium concentrations from the Ash Meadows and Furnace Creek areas are similar to values for seawater (Johannesson et al. 1997 [DIRS 101137], p. 811).

Based on similar, flat shale-normalized rare earth element patterns of the groundwaters discharged from springs at Ash Meadows and Furnace Creek, and work by previous investigators (Winograd and Robertson 1982 [DIRS 165605]) demonstrating that groundwaters from the regional LCA are well oxygenated and, therefore, are not likely to be subject to large changes in redox chemistry, Johannesson et al. (1997 [DIRS 101137]) postulate that the groundwater responsible for the springs at Ash Meadows also likely contributes to the groundwater discharging from the springs in Furnace Creek area, whereas the shallow groundwater in the Amargosa Desert is likely to be of minor importance as a potential source of water to the Furnace Creek area springs. Under this conceptual model, discharge from the Furnace Creek area springs is interpreted to be predominantly flow-through Ash Meadows-like groundwater that may or may not include a smaller component of shallow Amargosa Desert groundwater.

Although the data are not well distributed over the region, the results of the trace element and rare earth elements analyses generally are consistent with the results of the major-ion and isotopic analyses. With regard to the sources of water for the Furnace Creek area springs, however, the interpretation of Johannesson et al. (1997 [DIRS 101137]) accords with that of Steinkampf and Werrell (2001 [DIRS 158818], p. 33), but it is at variance with the interpretation of Winograd and Thordarson (1975 [DIRS 101167], p. C112).

8.2.8 Analysis and Modeling of the Regional Groundwater Flow System

A number of numerical, computer-based groundwater flow models have been developed for the Death Valley region in attempts to simulate regional hydrologic processes and conditions. The model domains have encompassed parts of, as well as the entirety of, the Death Valley regional groundwater flow system.

Most recently, D'Agnese et al. (2002 [DIRS 158876]) simulated predevelopment regional groundwater flow conditions for the overall Death Valley groundwater flow system. This model updated the previous model of the regional groundwater flow system (D'Agnese et al. 1997 [DIRS 100131]). The fundamental conceptual models on which these numerical models are based were derived from a synthesis of known geologic and hydrologic conditions within the region. Key parameters used for developing the conceptual and numerical groundwater flow models include:

- Estimated magnitudes and rates of regional surface recharge
- Estimated magnitudes and rates of regional subsurface flux
- Locations and estimated rates of regional groundwater discharge
- Definition of the estimated boundaries of the subregional and local flow systems
- The hydrogeologic framework of the flow system
- Hydraulic properties of the hydrogeologic units
- Potentiometric levels within the hydrogeologic units.

Although the other sources of groundwater discharge were considered, no explicit allowance was made for groundwater withdrawals from pumping wells in developing the current regional groundwater flow model. Instead, natural, predevelopment steady-state conditions are simulated with recharge being set equal to discharge from springs and evapotranspiration recharge is simulated as infiltration of precipitation and spring flows and as underflows from adjacent basins (D'Agnese et al. 2002 [DIRS 158876], pp. 26, 32, and 34).

The discussions of the conceptual analysis of the regional flow system and of the numerical modeling of the regional groundwater flow system that follow are based primarily on the reports by D'Agnese et al. (1997 [DIRS 100131]) and D'Agnese et al. (2002 [DIRS 158876]) that provide details of the model conceptualization, assumptions, construction and solution methods, and results.

8.2.8.1 Conceptualization of the Regional Groundwater Flow System

A conceptual model for the Death Valley regional groundwater flow system was developed by D'Agnese et al. (1997 [DIRS 100131]) by integrating interpretations of specific flow-system components. Discussion of the flow-system dynamics includes defining regional, subregional, and groundwater basin boundaries as well as identifying and describing the source, occurrence, and movement of groundwater within the system. Groundwater movement in the Death Valley region generally is complexly interrelated by structural and topographic features that are superimposed on an underlying hydrogeologic framework composed of hydrogeologic units with differing hydraulic properties.

8.2.8.1.1 Source and Movement of Groundwater

D'Agnese et al. (2002 [DIRS 158876], Figures 7, 10, 11, and 12) divided the Death Valley regional groundwater flow system into three major subregional flow systems (Northern, Central, and Southern Death Valley subregions) (Figure 8-1). The Central Death Valley subregion was subdivided into three groundwater basins, which were further subdivided into sections (Figure 8-5). Although they were defined based on generalized topographic controls, the groundwater basins and sections are used primarily for descriptive purposes only and do not define discrete independent flow systems.

Northern Death Valley Subregion–The Northern Death Valley subregion defined by D'Agnese et al. (2002 [DIRS 158876]) differs from the previously defined subregional area of D'Agnese et al. (1997 [DIRS 100131]) in that it has been enlarged to include the Cottonwood Mountains on the western edge of the subregion and an area south of Mesquite Flats between the Cottonwood and Panamint Mountains (D'Agnese et al. 2002 [DIRS 158876], Figure 10).

Groundwater in the Northern Death Valley subregion is derived from precipitation on the Montezuma Range and the Palmetto, Gold, and Stonewall Mountains (D'Agnese et al. 2002 [DIRS 158876], p 18). Some groundwater may enter the subregion across the system boundary from Mud Lake (Ralston Valley), Fish Lake and Eureka Valleys, and Saline Valley. Groundwater recharged on the mountains in the northwest part of this subregion is interpreted to move toward the central axes of adjacent valleys. In this subregion, water levels indicate that much of the groundwater flow appears to be controlled by the northeast-southwest trending structural zones described by Carr (1984 [DIRS 101037]). Deep regional inter-basinal flow is unlikely because the subregion is mostly underlain by relatively impermeable shallow Tertiary intrusive granites and crystalline Proterozoic rocks. The regional carbonate aquifer is believed to be extensive and continuous only in the southeastern part of the subregion (Grose 1983 [DIRS 148960], Plate NC-T2) near western Pahute Mesa and southern Sarcobatus Flat.

Groundwater in the Northern Death Valley subregion discharges as evapotranspiration at Sarcobatus Flat, Coyote Hole playa, and Mesquite Flat; as major spring discharge at Grapevine and Staininger springs; as discharge at Sand Spring; and as underflow to northern Death Valley beneath Mesquite Flat.

Central Death Valley Subregion–The Central Death Valley subregion defined by D'Agnese et al. (2002 [DIRS 158876]) differs from the subregional area defined previously by D'Agnese et al. (1997 [DIRS 100131]) in that it includes part of the Panamint Range on the western side of Death Valley and Railroad Valley in the northern part of the subregion (Figure 8-5).

Of the three subregions, the hydrogeology of the Central Death Valley subregion is the best characterized and is subdivided into three large groundwater basins (Figure 8-5). The Pahute Mesa-Oasis Valley groundwater basin drains the northwestern part of the subregion, and the Ash Meadows basin drains the eastern part. The third basin, the Alkali Flat-Furnace Creek groundwater basin, lies between the lower reaches of the first two and extends below their downgradient limits, where it receives surface overflow and subsurface underflow from the other two subregions. The Alkali Flat-Furnace Creek groundwater basin is of primary hydrologic

importance because it includes the Yucca Mountain repository site and incorporates that part of the saturated zone hydrologic system that could be the principal means for groundwater transport of radioactive materials from the repository to the accessible environment.

The Ash Meadows groundwater basin is the largest of the three groundwater basins, extending to recharge areas in the mountains along the northern and eastern boundaries of the Death Valley regional groundwater flow system (D'Agnese et al. 2002 [DIRS 158876], p. 23). The LCA underlies most of the Ash Meadows groundwater basin, and the basin boundaries are controlled to a large degree by structural features that disrupt the distribution of the carbonate rocks. The southern boundary of the Ash Meadows basin coincides with the axis of the prominent recharge mound beneath the crest of the Spring Mountains, which reflects the high precipitation and subsequent recharge in the mountains and the exposed or shallow presence of the lower clastic aquitard. The boundary continues southwest from the Spring Mountains, following the general trace of the lower clastic aquitard, to the southern Amargosa Desert. The basin terminates in the west at a major fault, the Gravity fault, in the eastern Amargosa Desert, where much of the regional flow is forced to the surface and discharged at springs along the Ash Meadows spring line. Westward underflow of groundwater across the spring line through the down-faulted carbonate rocks is likely but unproven (Winograd and Thordarson 1975 [DIRS 101167], p. C85). As discussed in Section 8.2.7, north of Ash Meadows, flow across the fault into the valley fill is indicated hydrochemically by the mixed carbonate-volcanic nature of the groundwater in the northeast and east-central Amargosa Desert (Claassen 1985 [DIRS 101125], pp. F16 to F19).

In the northern part of the Central Death Valley subregion, the western boundary of the Ash Meadows groundwater basin is defined by a prominent potentiometric divide extending from the Belted Range, through Rainier Mesa, and southward to Shoshone Mountain (Figure 8-4). This is the approximate boundary between the carbonate-rock province and the southwest Nevada volcanic field. The potentiometric divide loses clear definition beneath Jackass Flats, but the boundary generally continues southward to the inferred Gravity fault in the northeastern Amargosa Desert.

The Pahute Mesa-Oasis Valley groundwater basin occupies the northwestern part of the Central Death Valley subregion. It is recharged principally at Pahute Mesa and, further north, in the Belted and Kawich Ranges (D'Agnese et al. 2002 [DIRS 158876], p. 23). Additional recharge may occur as regional groundwater flows across system boundaries from southern Railroad, Reveille, and Stone Cabin Valleys.

Groundwater discharge in the Pahute Mesa-Oasis Valley groundwater basin takes place mainly by evapotranspiration and spring flows in Oasis Valley (D'Agnese et al. 2002 [DIRS 158876], p. 23), but some groundwater flows out of the basin across its southern boundary. A small flux of water passes from Oasis Valley through sediments in the Amargosa River channel south of Beatty, providing inflow to the Alkali Flat-Furnace Creek groundwater basin. Additional discharge from the basin probably occurs as underflow beneath the northern Bare Mountain area into Crater Flat.

The northern part of the Alkali Flat-Furnace Creek groundwater basin lies between the Ash Meadows and Pahute Mesa-Oasis Valley groundwater basins, and the southern part broadens to

truncate the two flanking basins (Figure 8-5). The volcanic terrain of Pahute Mesa and Timber Mountain lie along the northern and northeastern boundaries of the basin and are the principal recharge areas. Shoshone Mountain to the east and the Funeral Mountains and Grapevine Mountain to the south also are likely recharge areas and define the eastward, southern, and southward continuation of the boundary of this basin into Jackass Flats and to the northern Amargosa Desert, respectively. From eastern Pahute Mesa, the northwestern basin boundary trends to the southwest across Timber Mountain to Bare Mountain, and then extends westward across southern Oasis Valley to the western boundary of the Central Death Valley subregion. In addition to recharge from precipitation in upland areas, recharge to the basin also may occur as interbasinal flow across basin boundaries from Sarcobatus Flat, Oasis Valley, and Ash Meadows.

The prevailing conceptual model (D'Agnese et al. 2002 [DIRS 158876], p. 24) of groundwater flow in the upper part of the Alkali Flat-Furnace Creek groundwater basin, which includes the Yucca Mountain area, considers that water is recharged locally in the northern volcanic highlands, moves laterally southward through the underlying fractured volcanic rock aquifers into the valley-fill deposits that occupy the floors of the intermontane basins adjacent to Yucca Mountain and, ultimately, is discharged as spring flow or evapotranspiration in areas in the southern part of the basin. In the northwestern part of the basin, subregional groundwater flow is dominantly lateral and downward into the underlying regional LCA; Sinton 1987 [DIRS 103019]; Kilroy 1991 [DIRS 103010]). Near Yucca Mountain, however, hydraulic gradients may be upward from the LCA into the overlying volcanic units (Luckey et al. 1996 [DIRS 100465], pp. 27 to 29), which implies that water could (if connected) tend to move upward from the carbonate rocks into the overlying volcanic rocks. As discussed in Section 8.2.7.3, hydrochemical and isotopic evidence suggests that the groundwater flow system immediately beneath Yucca Mountain may be relatively isolated from the regional groundwater flow system. In the south-central part of the basin, near the Nevada-California border, groundwater flow is dominantly upward from the LCA into the subregional system and toward discharge areas along the Amargosa River, Carson Slough, and Alkali Flat (Czarnecki and Waddell 1984 [DIRS 101042], p. 7). These inferences imply that the regional LCA is hydraulically connected with and exerts control on the potentiometric surface configuration in the overlying alluvial and volcanic rock aquifers throughout the groundwater basin.

The lower part of the Alkali Flat-Furnace Creek groundwater basin lies between the Gravity fault in the eastern Amargosa Desert and Death Valley on the west. A potentiometric divide in the southern Grapevine Mountains separates Death Valley (the Funeral Mountains section) from the Amargosa River section of the groundwater basin (Figure 8-5). A major intermediate discharge area occurs at Alkali Flat, a playa at the southern edge of the Alkali Flat-Furnace Creek groundwater basin. Groundwater and intermittent surface flow breach the southern boundary along the Amargosa River, providing inflow to the southern Death Valley subregion. Beyond the springs at Furnace Creek, groundwater flows toward the salt pan on the floor of Death Valley and is discharged either by stands of mesquite on the lower part of the Furnace Creek fan or by evapotranspiration from the Death Valley salt pan (D'Agnese et al. 2002 [DIRS 158876], p. 24).

Southern Death Valley Subregion–The Southern Death Valley subregion defined by D'Agnese et al. (2002 [DIRS 158876], pp. 24 to 26) differs from the subregional area defined previously by D'Agnese et al. (1997 [DIRS 100131]) in that it includes Shadow Valley, Valjean Valley, Silurian Valley, Salt Springs Hills, the Avawatz Mountains, and the Owlshead

Mountains in the southern and southwestern parts of the subregion (D'Agnese et al. 2002 [DIRS 158876], Figure 12).

In general, groundwater in the Southern Death Valley subregion is derived primarily from infiltration on the Spring Mountains and small inputs from the Nopah, Kingston, and Greenwater Ranges. Minor amounts of groundwater may flow into this subregion across the boundary from the Alkali Flat-Furnace Creek groundwater basin south of Alkali Flat and further south from Pilot Knob Valley.

Groundwater recharged on the Spring Mountains moves toward Pahrump Valley. Historically, groundwater discharged from Manse and Bennett springs along the base of the broad alluvial fans at the foot of the Spring Mountains; however, pumping of groundwater in the valley has caused these springs to cease flowing. More recently (late 1990s), Manse Spring has begun to flow again, perhaps due to changes in agricultural practices in the valley. Groundwater in the Pahrump Valley section flows dominantly along subregional flow paths either to the west toward Stewart Valley and the northern end of Chicago Valley, or to the southwest toward California Valley. Some of the groundwater flowing toward the north and west is discharged at Stewart and Pahrump Valley playas, and some of this groundwater may discharge at the southern end of Ash Meadows (Winograd and Thordarson 1975 [DIRS 101167], p. C91; Peterman and Stuckless 1993 [DIRS 106495], p. 70; Peterman and Stuckless 1994 [DIRS 165681], p. 712). Groundwater flow that continues toward Chicago Valley, within the Shoshone-Tecopa section, mixes with groundwater flowing from south of Alkali Flat, and ultimately discharges as spring flows and evapotranspiration in an area between the towns of Shoshone and Tecopa. Groundwater that does not discharge in the Shoshone-Tecopa area may continue flowing to the southwest into the Ibex Hills section to be discharged as spring flow and evapotranspiration in the Saratoga Springs area. Some additional groundwater may enter the basin from Valjean and Shadow Valleys into California Valley and discharge at Saratoga Springs. Small volumes of groundwater may continue north past Saratoga Springs to discharge at the Badwater Basin salt pan. Additional groundwater entering southern Death Valley as under-flow from Pilot Knob Valley may discharge at the salt pan.

8.2.8.1.2   Regional Flow System Water Budget

Historically, water budgets have been estimated for local areas within the Death Valley region (Malmberg and Eakin 1962 [DIRS 106695]; Walker and Eakin 1963 [DIRS 103022]; Miller 1977 [DIRS 105462]; Malmberg 1967 [DIRS 101260]; Winograd and Thordarson 1975 [DIRS 101167]; Harrill 1986 [DIRS 148961]). These budgets were based on estimates of recharge and discharge using the Maxey-Eakin method, evapotranspiration and spring discharge, and estimated interbasin underflow, which was calculated from the difference between rainfall recharge and evapotranspiration.

A lumped-value water budget of the Death Valley regional groundwater flow system, for early 1990s conditions, was produced by D'Agnese et al. (1997 [DIRS 100131], p. 69, Table 13, and Table 17) for the regional groundwater flow model. Each component of the water budget (inflow from recharge, precipitation, and groundwater inflow; outflow from evapotranspiration, spring discharge, groundwater outflow, and groundwater withdrawals from wells) was generally defined as a lumped value, instead of discrete regional, subregional, or groundwater basin values.

More recently, D'Agnese et al. (2002 [DIRS 158876], Table 30) estimated water-budget components for the Death Valley region for predevelopment conditions. The water budgets for these two models are not directly comparable because of differences in estimation methods, areal extent of the model domains, and differences in how budget components were combined.

The large size of the Death Valley region precludes an accurate assessment of all inflows and outflows. However, the major estimated groundwater inflows and outflows can be summarized.

Inflow–The main source of regional recharge is through infiltration of precipitation (Figure 8-7). Recharge to the system was estimated at 312,300 m^3/d using the modified Maxey-Eakin approach (D'Agnese et al. 1997 [DIRS 100131], Table 17). Using the infiltration modeling approach of Hevesi et al. (2002 [DIRS 158877]), recharge to the system was estimated at less than 969,200 m^3/d (D'Agnese et al. 2002 [DIRS 158876], Table 30). The discrepancy between the estimates are due to limitations of the infiltration model (Section 8.2.5.2). The amount of recharge simulated in the updated regional flow model, 266,800 m^3/d, is closer to the previously estimated value (D'Agnese et al. 1997 [DIRS 100131], Table 17).

Additional inflow to the Death Valley region occurs as boundary inflow at various locations; however, the amount of inflow (estimated as greater than 23,400 m^3/d) is small compared to the inflow from infiltration of precipitation (D'Agnese et al. 2002 [DIRS 158876], Table 30).

Outflow–Most natural groundwater discharges from the region as evapotranspiration or spring flow (Figure 8-6). Total estimated discharge is 295,500 m^3/d, and the largest discharge areas are the Death Valley salt pan (92,200 m^3/d) and the Ash Meadows area (60,800 m^3/d) (D'Agnese et al. 2002 [DIRS 158876], Table 30). A small amount of groundwater (about 23,400 m^3/d) flows out of the region as underflow across system boundaries (D'Agnese et al. 2002 [DIRS 158876], Table 30). D'Agnese et al. 1997 ([DIRS 100131], p. 47-50 characterized human-induced water use in the base, Table 4). For example, estimates for Amargosa Valley averaged 351 m^3/d. Most other basins, except Pahrump, were much lower.

8.2.8.2   Development of the Regional-Scale Groundwater Flow Model

Based on this conceptualization of the regional flow system, D'Agnese et al. (2002 [DIRS 158876]) developed an updated regional groundwater flow model. The updated model synthesizes two previous models: the earlier regional model (D'Agnese et al. 1997 [DIRS 100131]) and the underground test area model (DOE 1997 [DIRS 103021]). The updated regional model is a three-dimensional, multilayer model that uses finite-difference numerical methods to solve the governing groundwater flow equations under imposed boundary and initial conditions. The model was designed to simulate predevelopment groundwater conditions. The regional models have been used to provide boundary conditions for the site-scale models. Details of model construction, model geometry, boundary conditions (including external and internal boundaries, and recharge), model calibration, and an evaluation of the model results and limitations are presented in D'Agnese et al. (2002 [DIRS 158876]).

8.2.8.2.1   Regional-Scale Model Simplifications

Simplifications and assumptions must be used to adapt the complex conceptual model for numerical simulation (D'Agnese et al. 2002 [DIRS 158876], p. 32-34). The assumptions and simplifications used to develop the Death Valley Region Flow System model include the following:

- Groundwater in the region flows through fractures and solution openings of consolidated rocks, as well as in porous valley-fill alluvium. However, fracture-flow simulation is impractical at a regional scale; therefore, a porous medium simulation is used.

- The model simulation assumes steady-state conditions prior to development, in which estimates of recharge equal estimates of natural discharge prior to groundwater development. That is, the model does not include groundwater withdrawals. Whether current recharge equals natural discharge is unknown.

- Horizontal isotropy within each model cell is used. This assumption is reasonable for cells corresponding to basin fill, but may be unreasonable for cells corresponding to consolidated rocks. Where flow is through fractures, the fractures may have a preferred orientation that could produce a greater hydraulic conductivity in one direction. Because the region contains numerous regional fracture patterns, it was concluded that no single orientation was dominant over the entire model domain.

8.2.8.2.2   Regional Scale Model Results

Good fit to observed hydraulic heads (residuals with absolute values less than 10 m) generally was obtained in areas of flat hydraulic gradient. Reasonable fit to observed heads (residuals with absolute values of 10 to 20 m) was obtained in areas of moderate hydraulic gradient. Poorer fit to observed heads (residuals with absolute values of greater than 20 m) was obtained in large hydraulic gradient areas. Poorest fit to observed hydraulic heads occurs in the vicinity of Indian Springs, western Yucca Flat, and the southern Bullfrog Hills. Most of these discrepancies can be attributed to insufficient representation of the hydrogeology in the hydrogeologic framework model, misinterpretation of water levels, and model inaccuracy associated with grid cell size.

The model results indicate a fairly random distribution of groundwater discharge residuals with a slight bias toward being negative, which indicates that simulated flows in these areas are less than observed flows. The largest unweighted groundwater discharge residuals occur at Ash Meadows, Sarcobatus Flat, Death Valley, Penoyer Valley, and Pahrump Valley. The two major discharge areas that would contribute the largest volumetric error to the model are Ash Meadows and Death Valley. Ash Meadows is one of the largest discharge areas in the Death Valley region; therefore, moderate percentages of error in the simulated discharge could result in large volumetric errors. Overall, the flow model adequately represents the total estimated natural groundwater discharge conditions in each major regional discharge area. In particular, the sum of all simulated groundwater discharge is 286,800 m^3/d and the sum of observed (i.e., estimated) groundwater discharge is 295,500 m^3/d (D'Agnese et al. 2002 [DIRS 158876], Table 30).

8.2.8.2.3   Regional-Scale Model Limitations

Two basic limitations are inherent to the regional flow model: the representation of the hydrogeologic framework and the representation of the prevailing hydrologic state of the system (D'Agnese et al. 2002 [DIRS 158876], p. 105). These limitations are manifested as:

- Discretization and abstraction inherent to the hydrogeologic framework model impose limitations on the ability of the flow model to resolve accurately local-scale geologic complexity and heterogeneity, especially at the 1,500-m grid-cell spacing necessitated by the regional scale of the flow model domain.

- Because little data are available in areas defined as lateral flow-system boundaries, the imposed boundary conditions are uncertain. Also, in imposing these boundary conditions on a steady-state flow model, boundary conditions are effectively limited to no-flow or constant-head.

- The inability to calculate groundwater recharge accurately based on numerical modeling of net infiltration or based on empirical estimation methods places limits on establishing an accurate overall water budget for the model. Consequently, the water budget imposed on the model is controlled principally by the estimated rates and distribution of groundwater discharge from the system that, under steady-state conditions, must be supplied to the system as areally distributed recharge over the model domain and as inflow to the system across lateral system boundaries.

The updated regional flow model provides a representation of the overall regional groundwater flow system that is consistent with hydrogeologic data for the Death Valley region, in spite of these limitations.

8.2.9   Summary of Regional Flow Patterns and Flow Model

The regional groundwater flow system constitutes a partially closed groundwater basin that is underlain by surficial Quaternary alluvial and valley-fill deposits, Tertiary volcanic rocks (principally tuffs), Mesozoic volcaniclastic and sedimentary rocks, and Paleozoic carbonate and clastic rocks that, in turn, overlie Precambrian granitic and metamorphic basement rocks.

The stratigraphic units define the principal aquifers and confining units that control the movement of groundwater within the flow system. In particular, highly transmissive carbonate rocks of Lower Paleozoic age are pervasive in the subsurface and in outcrops throughout the region, and define the LCA that exerts major control on the overall regional groundwater flow system.

The region is partitioned structurally into a complex of tilted fault blocks that juxtapose hydrogeologic units of differing hydrologic properties, leading to heterogeneity in the flow system. Consequently, groundwater flow paths within the regional flow system are complex.

The prevailing conceptual model considers that water enters the system as interbasinal underflow and as recharge from precipitation in upland areas. Because of present-day arid conditions, present-day recharge is restricted to the higher altitudes with virtually no recharge or perennial

surface-water flow occurring in the lowlands and valley floors. Groundwater flow paths within the system diverge from the highlands and are superimposed on deeper regional flow paths that are controlled largely by flow in the LCA. The overall direction of flow is towards the hydrologic sink in Death Valley, although there are a number of localized discharge areas.

The understanding of the regional groundwater flow system has been synthesized through the development of a numerical three-dimensional groundwater flow model that simulates the flow system under present-day climatic conditions and assumed steady-state flow conditions. The hydrogeologic setting was incorporated into the model through a separate hydrogeologic framework model. Boundary conditions were imposed through analysis of likely conditions along the lateral boundaries of the model and by independent construction of a net-infiltration model to estimate the spatial distribution of groundwater recharge. Finite-difference numerical techniques are used to solve the groundwater flow equations, and nonlinear regression techniques were used to estimate model parameter values and to calibrate the model. The model results were evaluated through comparisons of simulated values of hydraulic head and groundwater discharge against observed or estimated values. The resulting numerical model yields a quantitative, internally consistent representation of the overall regional flow system.

8.3 FLOW AND TRANSPORT WITHIN THE YUCCA MOUNTAIN AREA

8.3.1 Overview of Hydrogeology and Flow

The Yucca Mountain area generally is coincident with the domain of the site-scale saturated zone flow model (BSC 2001 [DIRS 155974]). Boundaries of the model domain extend from central Jackass Flats on the east (longitude 116°18') to western Crater Flat on the west (longitude 116°37'30"), and from the headwaters of Beatty Wash on the north (latitude 36°56') to the northern Amargosa Desert on the south (latitude 36°34') (Figure 8-8). The southern boundary is about 30 km south of the repository.

Yucca Mountain is located within the Alkali Flat–Furnace Creek groundwater basin, which is part of the Central Death Valley subregion (Figure 8-5). Groundwater flow in the saturated zone beneath Yucca Mountain is part of the dominant regional north to south flow within the western part of the Alkali Flat–Furnace Creek Groundwater Basin.

The Yucca Mountain repository site occupies an intermediate position between regional areas of recharge (Figure 8-7) and discharge (Figure 8-6; see also Sections 8.2.4 and 8.2.5). The aridity and small average rate of recharge produce a correspondingly small groundwater flux, which is readily transmitted through the well-fractured rocks that compose most of the region. Consequently, the average regional hydraulic gradient is small, resulting in a water table that generally is deep beneath the land surface, particularly beneath prominent ridges such as Yucca Mountain.

Infiltration through the unsaturated zone to the water table contributes some recharge to the saturated zone. However, most of the groundwater flux in the saturated zone beneath the repository probably is throughflow which, in a regional context, generally is from north to south. At Yucca Mountain, the local saturated zone flow direction is southeast toward Jackass Flats, but it turns southward as it approaches Fortymile Wash (within a few kilometers of the mountain).

Yucca Mountain is a north-trending ridge formed by an eastward-tilted, fault-bounded block of layered volcanic rocks (Figure 3-1) near the southern limit of Miocene volcanics that blanket much of southern Nevada (Figure 8-3 and 8-9). The volcanic rocks, mainly ash-flow tuffs and lavas, are thickest in the northern source areas and decrease in thickness to the south. They are about 2 km thick beneath Yucca Mountain. Southward from the repository area, depositional thinning and post-Miocene erosion combine to produce an increasingly discontinuous distribution of the volcanics into the northern Amargosa Desert, allowing exposure of the underlying Paleozoic and Proterozoic rocks at the surface or beneath surficial valley fill sediments (Figure 3-1). Numerous faults occur near the site (Figures 3-2 and 8-9). The north-striking faults that border and intersect the site are part of a more extensive set that forms additional ridges to the east and west of the site and that underlies the intervening valleys. Northwest-striking faults occur just north, south, and southeast of the site. Northeast-striking faults are regionally important to the east and south of the site, projecting into the southern part of the saturated zone study area. The faults probably greatly influence the movement of groundwater, either as preferential pathways or impediments to flow.

The upper part of the Miocene volcanic sequence and the surficial Quaternary-Tertiary sediments comprise an unsaturated zone that is 400 to 750 m thick in the Yucca Mountain area, owing principally to topographic irregularity above a relatively flat water table. From west to east between block-bounding faults, the generally eastward dip of the layered volcanic rocks causes successively younger strata to be submerged beneath the more gently sloping water table.

The principal stratigraphic units, correlative hydrogeologic units, and their general distributions in the unsaturated and saturated zones in the vicinity of Yucca Mountain are listed in Table 8-3. The descriptions of the hydrogeologic units presented below are taken from Faunt et al. (1997 [DIRS 148957], pp. 12 to 14).

> **Playa Deposits of Quaternary Age (Qp)**–The lacustrine confining beds, lake-bed sediments of Quaternary age, are a relatively homogeneous deposit composed of mainly clay-sized particles. The unit includes fine-grained playa deposits, lacustrine limestone, and evaporites. Accordingly, the unit can exhibit matrix flow from the permeable unconsolidated deposits and fault- and fracture-controlled flow in consolidated deposits. The lacustrine beds were deposited contemporaneously with the younger alluvial sediments. As a result, the deposits grade into each other. In some of the valleys, the lacustrine confining beds are several hundred meters thick.

> **Valley Fill of Quaternary-Tertiary–Age (QTvf)**–The alluvial sediments of Quaternary-Tertiary age are a heterogeneous mixture of volcanic and sedimentary rock detritus ranging from clay to boulder size. The heterogeneous mixture includes units of fine-grained playa and lake beds containing evaporites (of limited areal extent), boulder-cobble-pebble debris flow and fan deposits, and volcanic tuffs. Accordingly, they may exhibit matrix flow in the permeable unconsolidated materials, but fault- and fracture-controlled flow in more indurated materials. The valley fill (including fluvial deposits) accumulated largely in structural basins. As a result, the valley-fill deposits range in thickness from zero at margins of valleys to several hundred meters in valley lowlands. The

fill in many basins is greater than 1,300 m thick and may be as thick as 2,000 m. The basin fill forms the major aquifer system in many of the valleys.

These basin-fill aquifers constitute a regional system because of the similarities between basins and because they are the most developed source of groundwater in the region. Some basins are topographically and hydraulically closed by low-permeability bedrock, while others are part of multibasin flow systems connected by perennial streams or by flow through the basin fill or permeable bedrock. Well yields within the basin fill seem to be related to physiographic setting. The hydrologic properties of these deposits can differ greatly over short distances, both laterally and vertically, because of abrupt changes in grain size, and the degree of sorting and consolidation.

Volcanic Rocks of Quaternary-Tertiary Age (QTv)–The volcanic rocks, including lava flows and undifferentiated volcanic rocks of Tertiary and Quaternary age, underlie the valleys and crop out extensively in many of the mountains. The lava flows are primarily basalts, andesites, and rhyolites of Tertiary and Quaternary age. Columnar jointing and platy fractures are common in the flows, which vary from vesicular to dense. Secondary openings are developed along fractures and bedding planes. Individual flows generally are less than 33 m thick; some are less than 1 m thick. Aggregate thicknesses are as much as 1,000 m.

Volcanic Rocks of Tertiary Age (Tv)–These volcanic rocks include tuffs and undifferentiated volcanic rocks of Tertiary and Quaternary age. They underlie the valleys and crop out extensively in northern and central portions of the Death Valley region, including the Yucca Mountain area, where tuffs of Tertiary age are widespread. These units have an aggregate thickness of more than 4,000 m. The composition and structure of these volcanic tablelands, and their position and mode of emplacement, drastically affect regional groundwater flow by altering flowpaths, providing numerous avenues of recharge, and altering water-table gradients.

This hydrogeologic unit includes densely welded to nonwelded, bedded, reworked, and air-fall tuffs. Welded ashflow tuffs characteristically have an interstitial porosity of about 5 percent or less; thus, the commonly moderate to large hydraulic conductivity of welded ashflow tuffs is largely a function of secondary openings along joints, bedding planes, and partings within the flows. Where these welded tuffs are not fractured or jointed, they tend to form confining beds; thus, welded tuffs can only transmit significant quantities of water where they are fractured.

In contrast, nonwelded ashflow tuffs may have a large interstitial porosity, but low hydraulic conductivity, and can function as confining beds. Fractures and joints are virtually absent in nonwelded ashflow tuffs. Hence, the nonwelded tuffs generally act as confining units. These nonwelded tuffs, however, have limited areal extent.

Volcanic and Volcaniclastic Rocks of Tertiary Age (Tvs)–Clastic and tuffaceous aquifers and confining beds comprise tuffs and associated sedimentary rocks. They include up to 1,500 m of a variety of nonwelded to welded ashflow tuff, ashfall tuff, tuff breccia, breccia flow deposits, tuffaceous sandstone, siltstone, mudstone, freshwater limestone, and minor amounts of densely welded tuff. Despite the widely differing origins of these rocks, this unit usually has matrices consisting of zeolite or clay minerals, which results in low hydraulic conductivity. Some of the limestone and densely welded tuff may not have zeolitic or clayey matrices, but are believed to have low hydraulic conductivity. These rocks usually separate the more permeable volcanic rocks (Tv) from the Paleozoic carbonate rocks (P2).

Granitic Rocks of Tertiary-Late Jurassic Age (TJg)–Crystalline granitic rocks of Mesozoic and Tertiary age are widespread throughout the southern portion of the region. They outcrop in many mountain ranges and underlie most of the southern portion of the region at depth. Groundwater is thought to occur in these crystalline rocks only where they are fractured. Because the fractures are poorly connected, these rocks are believed to act mostly as confining units.

Sedimentary and Metavolcanic Rocks of Mesozoic Age (Mvs)–The clastic rocks of Mesozoic age are predominantly continental fluvial, lacustrine, and eolian deposits, and clastic and carbonate sedimentary rocks. These rocks form extensive outcrops on the sides of the Spring Mountains where they have been thrusted. The rocks have a variable thickness due to the extensive thrust faulting and are some of the more permeable rocks in the Death Valley region; however, they are not widespread. Some of these rocks are also found in the southwestern portion of the Death Valley region.

Carbonate Rocks of Paleozoic Age (P2)–Limestone, dolomite, and calcareous shales of Paleozoic age underlie many valleys and outcrop along the flanks of and throughout some mountains. These carbonate rocks cover an extensive portion of the area around Death Valley, extending to the north and east. They are often interbedded with siltstones and shales, and are locally interrupted by volcanic intrusions in the north. These carbonate rocks, which have an aggregate thickness of about 8,000 m, are probably the most permeable rocks in the area. Where hydraulically connected, they contribute significantly to interbasinal movement of water. This interbasinal movement includes movement of water within the groundwater basin between topographic basins, and the entrance of groundwater from basins to the northeast of the Death Valley regional flow system. Many of the springs in the area are associated with the carbonate rocks. Intergranular flow is not significant in these rocks; the large transmissivity is primarily due to fractures and solution channels. Hydraulic tests of carbonate-rock aquifers throughout eastern and southern Nevada indicate that faults can increase their transmissivity by factors of 25 times or more.

Clastic Rocks of Paleozoic-Precambrian Age (P1)–Siltstone, quartzite, shale, sandstone, and some metamorphic rocks of later Precambrian and Paleozoic age

form clastic confining units. These rocks vary in aggregate thickness with a maximum thickness of about 3,500 m. These rocks have negligible interstitial groundwater movement but frequently are highly fractured and locally brecciated. At shallow depths, these fractures and breccias can be conduits to flow, converting these clastic rocks into locally important shallow aquifers.

Clastic rocks in the region differ hydrologically from carbonate rocks in two important ways. First, secondary porosity rarely develops along bedding planes in any of the clastic rocks because of the low solubility of their constituents, including quartz, mica, and clay minerals. Second, the clastic rocks deform more plastically than the carbonates and, as a result, fractures may become sealed or isolated during deformation. In these rocks, the fractures may be sealed by continued deformation caused by the same process that formed them or by later plastic deformation. Open fractures in interbedded competent rocks may be sealed by plastic deformation of the less competent interbedded strata.

Igneous and Metamorphic Rocks of Precambrian Age (pCgm)–Crystalline metamorphic and igneous rocks of Precambrian age are widespread throughout the southern part of the region, cropping out in many mountain ranges and underlying most of the area at depth. Hydrologically, this unit behaves similarly to the other crystalline rocks in the region (TJg). Groundwater is thought to occur only locally in these crystalline bodies where the rock is fractured. Because the fractures are poorly connected, these rocks are believed to act mostly as confining units.

8.3.2   Data and Information Sources

Much of the information pertaining to the hydrogeology and hydrology of Yucca Mountain area has been compiled by Luckey et al. (1996 [DIRS 100465]). Luckey et al. (1996 [DIRS 100465]) restrict their discussion to the hydrogeology of the Tertiary volcanic rocks in the vicinity of the repository site. Czarnecki et al. (1997 [DIRS 141643]) include a description and classification of the deeper volcanic aquifers and confining units between the repository area and the northern Amargosa Desert. Although regional in scope, a description of the possible hydraulic effects of faults and fracture zones of the Death Valley region (Faunt 1997 [DIRS 100146]) is useful in conceptualizing the hydrogeology of the Yucca Mountain area.

Geldon (1996 [DIRS 100396]) and Geldon et al. (1997 [DIRS 100397]) present analyses of multiborehole tests at the C-Wells Complex, as well as the effects of long-term pumping on observation boreholes 1 km away. BSC (2003 [DIRS 167209]) presents preliminary test results from the Alluvial Testing Complex, along with analyses of hydraulic and tracer tests performed at the C-Wells Complex.

The results of a decade (1985 to 1995) of water-level monitoring in the Yucca Mountain area are presented by Graves et al. (1997 [DIRS 101046]). The immediate (seismic-phase) and short-term effects of the Landers, California, and Little Skull Mountain earthquakes in June 1992 on potentiometric levels near Yucca Mountain were described by O'Brien (1993 [DIRS 101276]).

An early site-scale potentiometric map was produced by Tucci and Burkhardt (1995 [DIRS 101060]) which includes Crater Flat, Jackass Flats, and the large hydraulic gradient area north of Yucca Mountain. The current site-scale potentiometric map, which presents an alternative concept of the large hydraulic gradient area north of Yucca Mountain, is provided by USGS (2002 [DIRS 165615], Figure 6-1. The current map also updates the potentiometric surface to the south using information from Phases I and II of the NC-EWDP Wells.

Sass et al. (1988 [DIRS 100644]) provide the principal source of data on the geothermal environment of Yucca Mountain, including subsurface temperature profiles, thermal conductivity of the rocks, and calculated conductive heat flow. Sass et al. (1995 [DIRS 101288]) provide supplemental data and an expanded interpretation of the data, whereas Sass (1998 [DIRS 148805]) offers a different interpretation of one particularly enigmatic data set.

In addition to this research, additional analyses are presented in various reports, including an updated hydrogeologic framework (BSC 2003 [DIRS 160109], p. 38 to 50), an analysis of water-level data (USGS 2002 [DIRS 165615]), a calibrated site-scale flow model (BSC 2001 [DIRS 155974]), and a synthesis of the hydrochemistry data (BSC 2001 [DIRS 158606]). Other reports synthesize site-scale data on flow and transport collected in the past two decades. Finally, Nye County is drilling and testing a series of boreholes in the southern site-scale area.

8.3.3   Hydraulic Properties

Hydraulic properties most commonly estimated are porosity and hydraulic conductivity at the rock-matrix scale (tests on core samples), plus transmissivity at the rock-mass scale (tests in boreholes). In addition, a few multiple-borehole tests provide information on storage and large-scale permeability. The discussion in this section emphasizes field-scale measurements in the site-scale area. Additional details of the core-scale data are presented in the previous version of this document (CRWMS M&O 2000 [DIRS 151945]).

8.3.3.1   Test Methods

Several methods have been used to determine the hydraulic properties of the saturated zone. Field tests to estimate transmissivity and storativity include:

- Single-borehole, constant rate discharge tests (i.e., pumping tests)
- Multiple-borehole pumping tests, in which observation boreholes were used
- Constant-rate injection tests in single-borehole and multiple-borehole configurations
- Single-borehole, variable rate discharge tests
- Single-borehole, slug-injection, and slug-withdrawal tests
- Single-borehole, pressure-injection tests.

Borehole flow and temperature surveys during pumping provide information on the vertical distribution of the hydraulic properties. Because of the depth of the saturated zone at Yucca Mountain, most of the tests in the volcanic tuffs were single-borehole tests of the entire open interval or of specific depth intervals in a borehole. Multiple-borehole tests have been conducted mainly at the C-Wells Complex (Geldon et al. 1998 [DIRS 129721]), but tests of borehole pairs (UE-25 a #1 and UE-25 b #1) also have been conducted in Drill Hole Wash (Moench 1984

[DIRS 148783], pp. 831 to 846). Testing was performed in the valley-fill alluvium at the Alluvial Testing Complex (BSC 2003 [DIRS 167209]). Additional details on the types of hydraulic tests, analytical methods, and references are listed in the previous revision of this report (CRWMS M&O 2000 [DIRS 151945], Table 9.3-3).

A single-borehole pumping test provides an estimate of the transmissivity, the integrated water conducting capability of the entire saturated section to which the borehole is open. The principal limitations are that:

- No information regarding the vertical distribution of permeability or the degree of anisotropy is obtained directly, although a flow survey mitigates the former.

- Head losses close to the pumping borehole occur due to turbulent flow and plugging of openings near the borehole during drilling (skin effect). These are a large part, sometimes the major part, of the drawdown, causing transmissivity to be underestimated and diminishing the sensitivity of drawdown to hydraulic properties of the more distant reaches of the affected rock mass.

- Storativity cannot be determined reliably from pumped-borehole drawdown data.

Using an observation borehole eliminates the skin effect and the turbulent flow factors, which provides a more reliable drawdown value, although only in the direction connecting the pumping and observation boreholes. Multiple observation boreholes located on intersecting axes give a more accurate record of the directional aspects of drawdown, allowing evaluation of anisotropy as well as the transmissivity and storativity where hydrogeologic conditions are favorable. The following list of tests presents the test methods used; additional details on the characteristics of each hydraulic test procedure, and their relative strengths and limitations, were discussed in the previous version of this report (CRWMS M&O 2000 [DIRS 151945]).

Slug Tests–Single-borehole tests that involve measuring rising or falling heads as a function of time over relatively short periods of time.

Pumping Tests–Extraction of water at a known rate with pressure transducers set at one or more intervals. Changes in hydraulic head are recorded during pumping.

Flow and Temperature Surveys–Surveys conducted in conjunction with constant-rate pumping tests to detect transmissive intervals that provide inflow to the borehole and to estimate the relative contributions of each interval to the total production. Changes in fluid flow velocity along the borehole and inflections in the temperature profiles are interpreted to identify and quantify the flow under pumping or ambient conditions.

Packer Tests–Inflatable packers used to isolate specific intervals within a borehole for testing or to measure head at various depths. Transducers generally are set within the isolated intervals to monitor the hydraulic-head response to the applied stress. Falling head or pressure injection tests are used to stress the aquifer and measure the response to obtain hydraulic properties.

Swabbing Tests–Water withdrawal and monitoring from deep boreholes by lowering swab cups below the water level inside internal-flush tubing or drill pipe, and raising the water column in the tube above the swab.

Multiple-Borehole Tests at the C-Wells Complex (Figure 8-10)–Multiple-borehole constant discharge (pumping) tests were conducted in March, May, and October to December 1984; May and June 1995; February 1996; from May 1996 to November 1997; and June to September 1998. In these tests, a borehole or an isolated interval within a borehole was pumped, and hydraulic responses in nearby observation boreholes were monitored. In preliminary hydraulic tests conducted at the C-Wells Complex in 1984, shortly after completion of drilling, Boreholes UE-25 c #2 and UE-25 c #3 were pumped and monitored in a variety of configurations using several testing methods. Detailed descriptions of the 1984 tests and interpretations of the results are provided by Geldon (1996 [DIRS 100396]), Geldon et al. (2002 [DIRS 161163]), and BSC (2003 [DIRS 167209]). The hydraulic test conducted in May 1995 involved pumping Borehole UE-25 c #3, while observing drawdown and recovery in UE-25 c #1 and UE-25 c #2; no packers were used, so the pumping and observation boreholes were open to the composite saturated sections (Geldon et al. 1998 [DIRS 129721]). Hydraulic tests conducted in June 1995 involved pumping UE-25 c #3, again without packers, and observing drawdown and recovery in six isolated intervals in UE-25 c #1 and UE-25 c #2 (Geldon et al. 1998 [DIRS 129721]).

In February 1996, an interval including the lower Bullfrog Tuff and upper Tram Tuff was isolated in Borehole UE-25 c #3 and pumped for five days to establish a gradient for a tracer test. The Calico Hills, Prow Pass, upper Bullfrog, and Bullfrog-Tram Tuff intervals in Boreholes UE-25 c #1 and UE-25 c #2 were monitored. In 1996 and 1997 (18 months), the lower Bullfrog Tuff interval was isolated and pumped in Borehole UE-25 c #3, and the Calico Hills, Prow Pass, and upper and lower Bullfrog Tuff intervals in UE-25 c #1 and UE-25 c #2 were monitored. Five additional Boreholes (UE-25 ONC-1, USW H-4, UE-25 WT #3, UE-25 WT #14, and UE-25 p #1) were monitored to evaluate heterogeneity and scale effects in the volcanic rocks and to determine any possible hydraulic connection between the volcanics and the underlying Paleozoic carbonate rocks. Additional details of the hydraulic tests conducted at the C-Wells Complex during 1995 to 1997 are provided by Geldon et al. (2002 [DIRS 161163]).

On June 2, 1998, pumping in Borehole UE-25 c #2 was initiated to create a forced hydraulic gradient for tracer tests in the Prow Pass interval at the C-Wells Complex. Injection of water into UE-25 c #3 to expedite tracer transport began on June 11 and continued without interruption until September 2. Tracers were injected into Boreholes UE-25 c #3 and UE-25 c #1. Responses in Boreholes UE-25 c #1, UE-25 c #3, and UE-25 ONC #1 to pumping, in advance of the tracer tests, were analyzed as a constant-rate withdrawal test. After water injection into Borehole UE-25 c #3 began, the superimposed effects of pumping water from UE-25 c #2, injecting water into UE-25 c #3, injecting tracers into UE-25 c #3 and UE-25 c #1, intermittently operating a mixing pump in c#3, and mechanical problems that affected pumping and injection rates made it difficult to quantitatively analyze data. However, Borehole UE-25 ONC #1 was far enough away from the pumping and injection boreholes that the water-level rise in UE-25 ONC #1, resulting from injecting water into UE-25 c #3, could be separated from the relatively minor drawdown caused by pumping UE-25 c #2. The water-level rise in UE-25 ONC #1 from June 11 to September 1 was analyzed as a constant-rate injection test.

Multiple-Borehole Tests at the Alluvial Testing Complex–On July 7, 2000, a single-borehole hydraulic test of the alluvial aquifer to a depth of 812 ft (247.5 m) below land surface was initiated in NC-EWDP-19D1 (Figure 8-10) to determine the transmissivity and hydraulic conductivity of the alluvium. The borehole was pumped for seven days, with production coming from the upper four screened intervals, or all of the intervals completed in the alluvium (a packer was inflated below the fourth screen to isolate the alluvium from the underlying tuffs). The water depth just before the test was about 349 ft (106.4 m) below land surface, and the effective alluvium thickness tested was about 446 ft (135.9 m) (distance from water table to the bottom of the fourth screened interval; total saturated alluvium thickness is 463 ft [141.1 m]). Recovery data were collected for 14 days after pumping stopped. The test will be used to constrain the hydraulic parameters obtained from isolated-interval testing. During this test, four Boreholes (NC-EWDP-15P, NC-EWDP-4PA, NC-EWDP-4PB, and Washburn-1x) and the nearby piezometer NC-EWDP-19P were also monitored.

After the combined interval test, the four intervals in NC-EWDP-19D1 were isolated and tested to estimate transmissivity and storativity. These tests provided data on hydraulic property heterogeneity over the thickness of the alluvium at NC-EWDP-19D1. These data help in determining the conceptual model of flow in the saturated alluvium south of Yucca Mountain. Details of these experiments are given in BSC (2003 [DIRS 167209]).

8.3.3.2   Matrix Properties

Matrix properties in the saturated volcanic tuffs are important for basic characterization information. However, most of the water transmitted over large distances in the saturated zone is through fractures and faults. Therefore, measurements of rock matrix properties play a relatively small role in understanding the large-scale flow system. However, estimates of fluid storage must account for the volume in the rock matrix, and diffusion into the pore space within the rock matrix is an important mechanism for solute transport. A summary of the matrix properties is presented in this section, emphasizing matrix porosity and solute diffusion coefficients; additional details are provided in the previous revision of this report (CRWMS M&O 2000 [DIRS 151945]). Also, a more complete discussion of the matrix properties, including permeabilities, determined from field tests in the unsaturated zone, is presented in Section 7, the Unsaturated Zone section, because matrix properties exert greater control on the behavior of the hydrologic system under unsaturated conditions.

Porosity provides a reasonable surrogate for inferring flow properties of various rock units in the Yucca Mountain area because it has been measured in most core samples, and because it is well correlated with saturated hydraulic conductivity and with the moisture-retention characteristic curve for a given hydrogeologic unit (Flint 1998 [DIRS 100033], p. 54). The correlation of porosity with lithology and the alteration character of the rock units permits a larger database of hydrogeologic unit properties with which to evaluate spatial distribution of hydraulic properties and potential heterogeneity in hydraulic properties.

Porosity has been used as a primary determinant for discriminating between different lithostratigraphic units underlying the Yucca Mountain area and for defining horizontal boundaries between the units. Vitric and bedded tuffs, and nonwelded ash-flow tuffs of the Paintbrush Tuff nonwelded hydrogeologic unit, vary in mean porosity between about 39 and

50 percent, as shown in Tables 7-10 and 7-11. By comparison, mean porosities in the Topopah Spring Tuff hydrogeologic units within the crystal-poor, welded member of the Topopah Spring Tuff, the host rock for the repository, range from about 9 to 13 percent, also shown in Tables 7-10 and 7-11. Although the Topopah Spring Tuff is present in the saturated zone in the southern portion of the Yucca Mountain, area where it constitutes the upper volcanic aquifer, it is present in the unsaturated zone flow system over most of the area (Section 7). The core data confirm that the matrix porosity of the Topopah Spring Tuff generally decreases with increased degree of welding of the rock strata, and fracture porosity generally increases with degree of welding. Recent information is presented in Flint (2003 [DIRS 163336]).

Matrix porosities in the Calico Hills Formation, which is part of the upper volcanic confining unit, range between 18 and 44 percent, with mean porosity values of about 34, 32, and 22 percent for the vitric-zeolitic unit, zeolitic units, and bedded tuff and basal sandstone hydrogeologic units, respectively (Flint 2003 [DIRS 163336], Table 3). In the tuffs that compose the Crater Flat Group (Prow Pass, Bullfrog, and Tram Tuffs), mean porosity values range between about 12 and 28 percent (Flint 2003 [DIRS 163336], Table 3), with individual values varying from 6 to 46 percent (Flint 1998 [DIRS 100033], Tables 4 and 7 and Appendix). All volcanic hydrogeologic units below the Topopah Spring Tuff have moderate to relatively high mean porosity (about 21 to 34 percent) except for the welded upper portion of the Bullfrog Tuff lithostratigraphic unit, which has a mean porosity of about 12 percent (Flint 2003 [DIRS 163336], Table 3). In the deeper tuffs of the lower volcanic confining unit, the mean porosity is estimated to be approximately 15 to 16 percent. Rocks of the LCA exhibit the smallest values of matrix porosity, with values ranging from about 5 percent in the Lone Mountain Dolomite to 0.3 percent in the Roberts Mountain Formation (Anderson 1991 [DIRS 101183], Table 5). The general trend through the volcanic strata in a descending order below the Topopah Spring Tuff, then, is to transition from the most porous unit in the upper interval in the saturated zone, through the less porous tuffs, including the Crater Flat Group and Lithic Ridge Tuff.

Porosity values for selected volcanic tuff samples have been used to estimate diffusion coefficients for tracers in the tuff matrices. Porosity (and estimated permeability) values and diffusion coefficients for two tracers at the C-Wells Complex are presented in Section 8.3.7.

8.3.3.3   Rock Mass Properties, Including Faults

The capability of rock to transmit or store water depends on the properties of the matrix and the fractures. Ideally, rock-mass hydraulic characteristics are determined for a hydrogeologic unit (usually an aquifer) of stratigraphically defined thickness, but commonly they are determined for the thickness of tested interval, whether that is the saturated zone depth penetrated by a borehole or the thickness of a specific interval.

More than 150 hydraulic tests have been conducted in boreholes on and around Yucca Mountain. Most were single-borehole tests in specific depth intervals, but a few multiple-borehole tests were conducted at the C-Wells Complex and in Drill Hole Wash. The hydraulic parameters discussed in the following section were determined mostly from single-borehole tests, although some results from the C-Wells Complex are included. Because multiple-borehole tests provide more information and at a larger scale, these tests are discussed in Section 8.3.7.

8.3.3.3.1 Single-Borehole Tests

Tests were conducted to estimate hydraulic conductivity values for hydrogeologic units near Yucca Mountain (Table 8-4). Apparent hydraulic conductivity values were based on single-borehole hydraulic tests and generally were calculated by dividing the total transmissivity of the tested interval by its thickness in the borehole. Hydraulic conductivity values for individual intervals in a borehole could differ by several orders of magnitude, depending on whether or not transmissive fractures were present. In intervals without open fractures, hydraulic conductivity tended to be low (generally less than 0.01 m/d), reflecting the hydraulic conductivity of the rock matrix or of tiny fractures. In intervals with transmissive fractures, the apparent hydraulic-conductivity values may be somewhat misleading. Most, if not all, of the water produced in such an interval could have been produced by a few thin, highly conductive fractures in an otherwise thick, essentially less permeable rock matrix. Therefore, hydraulic conductivity so determined is an effective or bulk value representing the overall ability of the medium to transmit fluid.

Upper Volcanic Aquifer–Hydraulic properties of the upper volcanic aquifer were estimated from tests in three boreholes (Table 8-4). In Borehole USW WT-10, O'Brien (1997 [DIRS 101277], p. 14) reported a mean transmissivity of 1,600 m^2/d, which was estimated from the results of a series of tests performed using different durations and pumping rates. Assuming an aquifer thickness of 83 m (saturated thickness tested), the apparent hydraulic conductivity was 19 m/d. In Borehole UE-25 WT #12, O'Brien (1997 [DIRS 101277], p. 22) estimated a mean transmissivity of 7 m^2/d for the saturated interval tested. Of the interval tested, 41 m were completed in the upper volcanic aquifer and 12 m were completed in the upper volcanic confining unit. The low transmissivity could indicate the very lowest limit of transmissivity values for the upper volcanic aquifer, or the degree of fracturing was very low in the interval of the upper volcanic aquifer tested and the transmissivity is more representative of the upper volcanic confining unit (O'Brien 1997 [DIRS 101277], pp. 22 to 23). Assuming a saturated thickness of 53 m, the apparent hydraulic conductivity was 0.13 m/d. Thordarson (1983 [DIRS 101057], Table 12 and pp. 27 to 29) reported a transmissivity of 120 m^2/d for geologic units that correspond to the upper volcanic aquifer in Borehole UE-25 J-13. The apparent hydraulic conductivity estimated for Borehole UE-25 J-13 was 1.0 m/d.

The upper volcanic aquifer also was tested at Borehole USW VH-1 (Thordarson and Howells 1987 [DIRS 103172]); however, the tests were conducted over the entire saturated interval, which includes the lower volcanic aquifer. Most of the water produced by the borehole may be from a small part of the lower volcanic aquifer (Thordarson and Howells 1987 [DIRS 103172], p. 9). Transmissivity ranged from 450 to 2,400 m^2/d (Thordarson and Howells 1987 [DIRS 103172], pp. 14 to 18), and apparent hydraulic conductivity values ranged from 0.8 to 4.2 m/d for five tests in this borehole (Luckey et al. 1996 [DIRS 100465], p. 35). Because of uncertainty about which aquifer was tested, these values are not included in Table 8-4.

Upper Volcanic Confining Unit–Hydraulic properties of the upper volcanic confining unit were estimated from tests at the C-Wells Complex and in four other Boreholes (UE-25 b #1, UE-25 J-13, and USW G-2 [Table 8-4]; also see comments above regarding uncertainty for Borehole UE-25 WT #12). Transmissivity values for the upper volcanic confining unit ranged

from 2.0 to 26 m^2/d, and apparent hydraulic conductivity values ranged from 0.02 to 0.26 m/d (Luckey et al. 1996 [DIRS 100465], p. 35; O'Brien 1998 [DIRS 101278], p. 7).

Lower Volcanic Aquifer–Hydraulic properties of the lower volcanic aquifer were estimated from tests in nine boreholes and C-Wells Complex. For the boreholes, transmissivity values of the lower volcanic aquifer ranged from less than 1.1 to 589 m^2/d. The arithmetic mean of the transmissivity values was about 152 m^2/d, and the geometric mean was about 43 m^2/d. Apparent hydraulic-conductivity values for the lower volcanic aquifer ranged from less than 3.7×10^{-3} to 1.4 m/d (Table 8-4). The arithmetic mean of the apparent hydraulic conductivity values was 0.49 m/d, and the geometric mean was 0.15 m/d. In Borehole USW H-1, apparent hydraulic conductivity of individual intervals ranged 4×10^{-5} to 18 m/d in single borehole tests (Rush et al. 1984 [DIRS 101054], Table 14; Luckey et al. 1996 [DIRS 100465], p. 35).

Little data exist from single-borehole aquifer tests, and therefore early responses from multiple-borehole aquifer tests conducted at the C-Wells Complex in May and June 1995 were used in place of single-borehole tests. The early responses gave a range of transmissivities from 1,600 to 3,200 m^2/d, and a range of hydraulic conductivities of 6.5 to 13 m/d (Table 8-4). It is assumed that these values of transmissivity and hydraulic conductivity are dominated by the lower volcanic aquifer. However, pumping and monitoring boreholes were completed in saturated sections of the lower volcanic aquifer and lower volcanic confining unit (Geldon et al. 1998 [DIRS 129721], p. 1). Detailed information on the multiple-borehole testing at the C-Wells Complex is provided in Section 8.3.3.3.2.

Lower Volcanic Confining Unit–Hydraulic properties of the lower volcanic confining unit were estimated from tests in seven boreholes (Table 8-4). Transmissivity values ranged from less than 3.0×10^{-3} to 23 m^2/d. The arithmetic mean of the transmissivity values was 3.7 m^2/d, and the geometric mean was 0.20 m^2/d. Apparent hydraulic-conductivity values for the lower volcanic confining unit ranged from 5.5×10^{-6} to 0.11 m/d. The arithmetic mean of the apparent hydraulic conductivity values was 1.7×10^2 m/d, and the geometric mean was 1.3×10^{-3} m/d (Luckey et al. 1996 [DIRS 100465], p. 35).

Lower Carbonate Aquifer–Data for the LCA in the vicinity of Yucca Mountain are only available for Borehole UE-25 p #1. Hydraulic data presented by Craig and Robison (1984 [DIRS 101040], Table 5, p. 52 to 53) for Borehole UE-25 p #1 indicated a transmissivity of 108 m^2/d.

Alluvium–Hydraulic properties for the alluvium were determined from single-borehole and cross-hole hydraulic tests conducted in Borehole NC-EWDP-19D1 (Table 8-5). These results are preliminary because a complete accounting of wellbore pressure losses has not been performed. The hydraulic conductivity of the alluvium is similar to that of the volcanic tuff aquifers. Same results from the NC-EWDP are reported in *Nye County Nuclear Waste Repository Project Office* (2001 [DIRS 156115]).

Anisotropic Conditions–In fractured-rock aquifers, hydraulic conductivity probably is anisotropic. Long-term hydraulic testing at the C-Wells Complex (Section 8.3.3.3.2) resulted in an elliptical pattern in drawdown, oriented northwest-southeast (Geldon et al. 1997 [DIRS 100397], Hydraulit Tests, pp. 42 to 44). This pattern may indicate anisotropic conditions

in that orientation. In an alternative interpretation of the C-Wells pumping data, Ferrill et al. (1999 [DIRS 118941], pp. 6 to 7) used data obtained from three observation boreholes located northwest, northeast, and southeast of Borehole UE-25 c #3 to estimate a horizontal anisotropy having a maximum principal direction of north-northeast to south-southwest.

Aquifer Storage–Storativity at the C-Wells Complex was 0.0005 (Geldon 1996 [DIRS 100396], Table 9, p. 71) and 0.001 to 0.003 (Geldon et al. 1998 [DIRS 129721]), and specific yields ranged from 0.003 to 0.07 (Geldon 1996 [DIRS 100396], Table 9, p. 71) and 0.01 to 0.2 (Geldon et al. 1998 [DIRS 129721]). These boreholes penetrate the upper volcanic confining unit, the lower volcanic aquifer, and the upper part of the lower volcanic confining unit. Storativity for Borehole USW H-1 ranged from 6×10^{-6} to 6×10^{-3} for the lower volcanic aquifer and from 6×10^{-4} to 2×10^{-3} for the lower volcanic confining unit (Rush et al. 1984 [DIRS 101054], Table 12). Barr (1985 [DIRS 101187], Table 3) used the same data and obtained similar results. Storativity for Borehole USW H-3 ranged from 4×10^{-6} to 7×10^{-6} for the entire saturated interval (Thordarson et al. 1985 [DIRS 105670], Table 2.). Specific yields for Borehole USW H-5 ranged from 0.15 to 0.28 for the entire saturated interval (Robison and Craig 1991 [DIRS 101286], p. 24); however, more than 95 percent of the water in the borehole was produced from fractures in the upper part of the lower volcanic aquifer (Robison and Craig 1991 [DIRS 101286], Figure 6). Storativity for nine intervals in the lower volcanic aquifer in Borehole USW G-4 ranged from 1×10^{-5} to 8×10^{-6} (Luckey et al. 1996 [DIRS 100465], p. 37).

Flow Surveys–Flow surveys were conducted in most of the deeper boreholes at Yucca Mountain. Flow surveys are useful for determining the intervals, and possibly the fractures, that produce water. Most of the flow surveys were conducted using a tool developed for oil-field use that releases small quantities of radioactive ^{131}I (Blankennagel 1967 [DIRS 103092], pp. 15 to 19). As the ^{131}I moves up or down the borehole, it is sensed by gamma-ray detectors. Most surveys are done while water is being pumped from or injected into the borehole. Static tests were occasionally conducted (Luckey et al. 1996 [DIRS 100465], p. 37).

Flow surveys are useful for determining the parts of the borehole that produce (or accept) the most flow. The information is useful when subdividing a system into aquifers and confining units and for assessing the distribution of flow within a unit. Flow surveys for seven boreholes are shown in Figure 8-11. For comparison, the depths for the surveys were adjusted to a standard thickness of 524.3 m for the lower volcanic aquifer, which is the estimated thickness of this aquifer in Borehole USW G-1, but it is not necessarily representative of the thickness of the aquifer elsewhere (Luckey et al. 1996 [DIRS 100465], p. 37). The flow surveys generally indicated that production (or acceptance) of water occurred in a few intervals. For example, in Borehole USW H-1, 64 percent of the production came from a 1-m interval, whereas in Borehole USW H-5, 73 percent of the production came from a 42-m interval.

Flow and transport modeling must consider the geometry of the flowing intervals to provide credible assessment of the migration rates of radionuclides through the saturated zone. An analysis was performed to derive the flowing interval spacing from flow survey data (BSC 2001 [DIRS 156965]). The analysis accounts for the sampling issue associated with the potential to miss a large number of flowing intervals in a vertical borehole if the fractures transmitting the water are near vertical. From the flow-survey data, this study found a distribution of flowing interval spacings with a mean value of about 20 m. This result indicates that within the fractured

volcanic tuffs, flow is focused in a relatively small proportion of the rock volume. These intervals of locally enhanced permeability might be individual fractures, but they likely are rubblized zones of enhanced fracturing. This explanation is reasonable given the hydrogeologic setting at Yucca Mountain.

8.3.3.3.2 Multiple-Borehole Tests

The main results of multiple-borehole hydraulic tests conducted at the C-Wells Complex are summarized in this section. These are the most complete set of data for examining larger scale behavior at Yucca Mountain. Multiple-borehole tests conducted at the Drill Hole Wash Complex are summarized elsewhere (CRWMS M&O 2000 [DIRS 151945]).

The C-Wells Boreholes (UE-25 c #1, UE-25 c #2, and UE-25 c #3; Figure 8-10) were drilled to a depth of 914.4 m in 1983 and 1984. The water table is 400 to 402 m deep at the site. The C-Wells penetrate the Calico Hills Formation and the Crater Flat Group. A northerly trending fault, the Paintbrush Canyon or Midway Valley fault, and an offsetting northwesterly trending fault intersect the C-Wells at the bottom of the Bullfrog and top of the Tram Tuffs. The proximity of these boreholes to one another and to others in the vicinity (UE-25 ONC-1, USW H-4, UE-25 WT #14, UE-25 WT #3, and UE-25 p #1) allowed for the use of multiple-well analysis techniques. The focus of the summary in this section is the larger scale results obtained from long-term pump tests and observations in the surrounding boreholes. The complete history of hydraulic testing at the C-Wells is presented in Geldon et al. (1997 [DIRS 100397]), Geldon et al. (1998 [DIRS 129721]), Geldon, et al. (2002 [DIRS 161163]), and BSC (2003 [DIRS 167209]).

Six hydrogeologic intervals were identified at the C-Wells Complex: Calico Hills, Prow Pass, Upper Bullfrog, Lower Bullfrog, Upper Tram, and Lower Tram. Flow within these intervals comes from diversely oriented fractures and the interstices of variably welded ash-flow, ash-fall, and reworked tuff. During hydraulic tests, the Lower Bullfrog interval contributes about 70 percent of the flow, the Upper Tram interval contributes about 20 percent of the flow, and all of the other intervals contribute the remaining 10 percent. Because these hydrogeologic intervals are defined by spatially related faults and fracture zones, their existence and hydraulic properties cannot be extended beyond the immediate vicinity of the C-Wells Complex. However, the results of hydraulic tests at the C-Wells Complex imply that the transmissivity of a rock mass is relatively large close to faults and associated fracture zones, and decreases with distance from these features. Although this result is based on observations at the C-Wells Complex in the vertical direction, it is believed that the same principle can be applied areally.

The hydrogeologic intervals at the C-Wells Complex were isolated and tested separately, and the results indicated layered heterogeneity. The Calico Hills interval responded as an unconfined unit. The Prow Pass and Upper Bullfrog intervals responded as confined units. The Lower Bullfrog interval behaved as a fissure-block aquifer. However, during the four hydraulic tests conducted at the C-Wells Complex from 1995 to 1997, drawdown occurred in all monitored intervals of the C-Wells and other observation boreholes, regardless of the geologic interval being pumped. This hydraulic connection across geologic and lithostratigraphic contacts is believed to result from interconnected faults, fractures, and intervals with large matrix permeability. Therefore, at larger scales, the Miocene tuffaceous rocks appear to be a single

aquifer in the structural block bounded on the east by the Paintbrush Canyon fault, on the south by the Dune Wash fault, and on the west by faults cutting Boundary Ridge, at least as far north as lower Midway Valley. This conclusion is supported by the ability to combine the drawdown from observation boreholes completed in different Miocene geologic units in the same analytical solution of drawdown as a function of time, or of drawdown as a function of distance. These hydraulic results suggest that formal designation of aquifers and confining units within the Miocene tuffaceous sequence at Yucca Mountain may not be justified in areas containing interconnected faults and fractures. Alternatively, it might be reasonable to retain such hydrogeologic designations as long as the influence of faults is incorporated separately.

There was no response in Borehole UE-25 p #1 to pumping at the C-Wells Complex. If there had been a response, it would indicate that tuffaceous rocks were hydraulically connected to the Paleozoic carbonate aquifer, which is about 455 m below the bottom of the C-Wells boreholes. This result, combined with the 22 m difference in hydraulic head between the Paleozoic carbonate rocks and the Miocene tuffaceous rocks at UE-25 p #1, probably means that there are confining units between the two systems with little hydraulic connectivity. Therefore, the pumping at the C-Wells Complex probably drew laterally from the tuffaceous rocks. Although communication with the carbonate aquifer may exist, the large storage capacity dampened the response to the point where it was undetectable.

Based on comparisons of single-borehole and multiple-borehole results, hydraulic conductivity appears to be scale-dependent (Figure 8-12). Geldon (1996 [DIRS 100396]) reported that transmissivity and apparent hydraulic-conductivity values determined using multiple-borehole hydraulic tests tend to be one to two orders of magnitude higher than values reported for single-borehole tests conducted at the same borehole. For example, a single-borehole test at Borehole UE-25 c #3 resulted in a transmissivity value of 27.9 m^2/d, but results of a multiple-borehole test for the same interval indicated a transmissivity value of 1,860 m^2/d. Geldon (1996 [DIRS 100396], p. 69) concluded that multiple-borehole tests generally sample a larger volume of the aquifer material and incorporate a larger number of transmissive fractures than single-borehole tests. Because most transmissivity and hydraulic-conductivity values at Yucca Mountain were obtained from single-borehole tests, the values listed in Table 8-4 are more appropriate for scales less than tens to hundreds of meters (Luckey et al. 1996 [DIRS 100465], pp. 36 to 37), and the permeability at larger scales should be higher, or the role of faults should be explicitly considered.

Geldon et al. (1997 [DIRS 100397], Figure 38) used data from four observation boreholes surrounding the C-Wells Complex to estimate a northwest-southeast oriented elliptical anisotropic transmissivity pattern. This indicates a fault-related hydraulic connection between the observation boreholes and the C-Wells across geologic contacts and relatively large distances. They inferred that the drawdown results could have been influenced by northwesterly and northerly trending faults. In contrast, Ferrill et al. (1999 [DIRS 118941], pp. 6 to 7) used data obtained from three observation Boreholes (ONC-1, UE-25 WT #14, and UE-25 WT #3, respectively located 843 m northwest, 3,526 m northeast, and 2,249 m southeast of Borehole UE-25 c #3) to estimate a horizontal anisotropy having a maximum principal direction of north-northeast to south-southwest. Ferrill et al. (1999 [DIRS 118941], p. 6) did not consider data from Borehole USW H-4 because the borehole could have been affected by a fault system between it and the pumped borehole. Despite the differences, both analyses suggest that at the

larger scale, there are preferential directions for flow that are correlated with known faulting in the area. This basic conclusion probably can be extended throughout the tuff aquifers in the site-scale saturated zone model domain.

8.3.3.4 Synthesis and Interpretation of Hydraulic Data

The specific discharge downgradient from the repository, along with effective transport porosity, determines the rate at which groundwater moves beneath and away from Yucca Mountain. The specific discharge, in turn, is a function of the permeability of the rocks and alluvium, and the hydraulic gradient in this area. Permeability data from single- and multiple-borehole hydraulic tests at Yucca Mountain and single-borehole tests elsewhere at the Nevada Test Site were compared to permeabilities estimated during calibration of the site-scale saturated zone flow model (Figure 8-12).

The mean permeability for the Calico Hills Formation from single-borehole tests ($k = 7.8 \times 10^{-13}$ m^2) is larger than that estimated from cross-borehole tests ($k = 1.7 \times 10^{-13}$ m^2). This observation indicates that factors other than the test method and the scale of the test influence the results. One factor might be proximity to faults. Several of the single-borehole tests in the Calico Hills Formation were done in the highly faulted area at Borehole UE-25 b #1, whereas faults were present only at deeper stratigraphic horizons at the C-Wells Complex where the cross-borehole tests were done. Nonetheless, geologic contacts with open partings may have enhanced permeability in the Calico Hills Formation at the C-Wells Complex (Geldon et al. 1998 [DIRS 129721]). Secondly, both estimates of the mean Calico Hills Formation permeability are either larger than the mean permeability estimated for the carbonate aquifer from Yucca Mountain data ($k = 7.2 \times 10^{-14}$ m^2) or comparable to mean permeabilities estimated for the carbonate aquifer from Nevada Test Site data ($k = 6.0 \times 10^{-13}$ m^2) (BSC 2001 [DIRS 155974], Tables 9 and 10). Although the permeability of the Calico Hills Formation may be higher locally than the mean permeability of the carbonate aquifer, it is unlikely that this relation between the two formation permeabilities can exist in general. The carbonate aquifer, along with the alluvial aquifers, is widely viewed as a major water-supply source in southern Nevada (e.g., Dettinger 1989 [DIRS 154690]). Mean hydraulic conductivity values for the LCA in the Death Valley region are much higher than those of Calico Hills (Belcher et al. 2001 [DIRS 158458]) Table 2. In contrast, the Calico Hills Formation has properties similar to those of rocks deemed suitable for nuclear weapons tests below the water table at Pahute Mesa. The rocks at Pahute Mesa had properties (low intrinsic permeability due to zeolitization and sparse, poorly connected fractures) that were predicted, and later observed, to result in only small amounts of seepage into open test chambers during their construction (Blankennagel and Weir 1973 [DIRS 101233], pp. B30 to B31). Similar rocks in the unsaturated zone at Rainier Mesa produced perched water from isolated fault zones during construction of tunnels into the mesa; however, because the fault zones drained quickly and fault zones intersected later during tunneling also initially produced water, the fault zones were inferred to be relatively isolated horizontally and vertically (Thordarson 1965 [DIRS 106585], p. 42 to 43). At Yucca Mountain, the apparently widespread presence of perched water on top of the zeolitic Calico Hills Formation in northern Yucca Mountain (Patterson 1999 [DIRS 158824]) indicates that the formation generally has low permeability compared to the rate of water percolation through the unsaturated zone.

Information from permeability measurements based on air, rather than water, allows a larger data set to be synthesized. A caveat is that although in theory the intrinsic permeability should not depend on the flowing fluid (air versus water), in practice, experimental conditions might yield different estimates of permeability due to complexities associated with the distribution of air and water in the medium, as well as scale effects (Rasmussen et al. 1993 [DIRS 154688]; Vesselinov et al. 2001 [DIRS 154706]). Nevertheless, it is assumed that permeabilities calculated from air-injection test data in the unsaturated zone probably provide good approximations to the water permeabilities, particularly in the densely welded intervals where drained fractures dominate the overall air permeability. Surface-based tests in four boreholes at Yucca Mountain showed that the highest air permeabilities (up to 54.0×10^{-12} m^2) were present at depths less than 50 m in the Tiva Canyon Tuff, presumably because low lithostatic stresses at these depths allowed fractures to open (LeCain 1997 [DIRS 100153], Figures 7 to 10). However, permeabilities in the Tiva Canyon Tuff typically decreased rapidly with depth, so that the permeabilities at depths greater than 50 m were less than 1×10^{-11} m^2. The geometric mean permeabilities of the Tiva Canyon Tuff in the four boreholes varied between 3.4×10^{-12} and 8.4×10^{-12} m^2 (LeCain 1997 [DIRS 100153], Table 1), with an overall geometric mean permeability of 4.7×10^{-12} m^2 based on 23 tests. Geometric mean permeabilities of the Topopah Spring Tuff at the four boreholes ranged from 0.3×10^{-12} to 1.7×10^{-12} m^2 (LeCain 1997 [DIRS 100153], Table 5) with an overall geometric mean permeability of 0.75×10^{-12} m^2 based on 153 tests.

Cross-borehole air injection tests conducted in and adjacent to the Ghost Dance fault resulted in geometric mean permeability values of 4.1×10^{-12} m^2 for the hanging wall of the fault, 14.6×10^{-12} m^2 for the main fault zone (defined by a zone of higher fracture density), and 7.8×10^{-12} m^2 for the footwall (LeCain et al. 2000 [DIRS 144612], Table 13). These permeabilities were several times higher than permeabilities measured in the same units elsewhere from the surface-based boreholes, and they were 2 to 5 times higher than permeabilities estimated for the Ghost Dance fault and adjacent rock from single-borehole tests (LeCain et al. 2000 [DIRS 144612], p. 26). Air permeabilities also have been estimated using subsurface pneumatic pressure changes that occur in response to barometric changes at the land surface (Kwicklis 1999 [DIRS 157414], pp. 97 to 110; Ahlers et al. 1999 [DIRS 109715]). These studies yielded results similar to those presented here.

Water and air permeability measurements were plotted to examine depth-dependent trends in permeability (Figure 8-13). The results are consistent with trends expected from a conceptual model in which higher lithostatic stresses and more intense hydrothermal alteration close fractures at increasing depths. Conversely, permeabilities measured from cross-borehole tests at the C-Wells Complex indicate trends that reflect proximity to the Midway Valley fault. Therefore, except for the Calico Hills Formation, the single-borehole permeabilities probably reflect the true permeabilities of the hydrogeologic units in unfaulted areas and can be used to represent the hydrogeologic unit permeabilities in specific discharge calculations or in numerical models, provided the effects of faults are considered. The geometric mean permeability estimated for the Calico Hills Formation was probably unduly biased toward that of faulted locations by data from Boreholes UE-25 b #1 and UE-25 J-13. In unfaulted areas, the Calico Hills Formation permeability is probably several orders of magnitude less than the geometric mean permeability calculated from the single-borehole tests. The similarity of geometric mean permeability values from cross-borehole air-permeability testing in the Ghost Dance fault (k = 14.6×10^{-12} m^2) and the maximum permeabilities from cross-borehole testing at the C-Wells

Complex (54.0×10^{-12} m^2) indicate that values of 10.0×10^{-12} to 50.0×10^{-12} m^2 may be appropriate as fault zone properties in numerical models so long as the modeled width reflects the true width of the fault; otherwise, the permeabilities in the model should be adjusted to preserve the overall transmissivity of the faults.

In summary, permeability data from the Yucca Mountain site exhibits a range of values depending on scale, lithology, and proximity to faults and fractures (Figure 8-12). On this figure, the approximate ranges of permeability values for the core, single-borehole, and cross-borehole tests are marked. These marks indicate the role of scale and fracturing on the permeabilities measured or estimated for the Yucca Mountain tuffs. Matrix permeability, obtained from cores, spans a range of values that extends to considerably lower values than field-scale permeability measurements. This means that at field scales, the unfractured rock is unlikely to transmit large quantities of fluid compared to the larger scale measurement. In the figure, the range labeled "Single-Hole Tests" indicates the range of single-borehole permeability data, thought to encompass a larger scale, with single fractures and fracture networks controlling the bulk permeability. Because some of these experiments were undoubtedly performed in regions of low fracture transmissivity, the range overlaps with the core measurements. In the figure, the category "Cross-Hole Tests" spans the range of cross-borehole data from the C-Wells Complex, as well as values estimated through calibration of the site-scale saturated zone flow model. Overlap of the single- and cross-borehole data is reasonable, given that some single-borehole tests were performed in zones containing considerable fracturing and in close proximity to faults. Mostly by design, the model calibration permeability estimates fall in the range of the cross-borehole tests. The modeling approach gave weight to matching the cross-borehole test data, under the assumption that faults are likely to be important at the scale of kilometers, which is the scale of the numerical model.

Hydrologic properties of faults near Yucca Mountain are largely unknown. Faunt, 1997 [DIRS 100146] summarized the understanding of the effect of faulting on groundwater movement in the Death Valley Region. From her analysis, she applied the three following principles in development of the hydrogeologic framework model.

1. Large scale folding and block faulting form major topographic features and sedimentary basins (influencing recharge and discharge areas)

2. Faulting and intense folding cause fracturing and create highly permeable channels that are enhanced by dissolution in the carbonate aquifer

3. Faulting and folding in rock types create barriers to groundwater movement due to displacing strata and create low permeability materials within the faulted and fractured rocks. As a result, groundwater is forced to the surface as springs and diffuse discharge.

Bredehoeft 1997 [DIRS 100007] concluded that the deep carbonate aquifer has a good tidal response at UE-25 p #1, indicating that the fault zones which cut through the rocks beneath the valley that borders Yucca Mountain on the east must be relatively impermeable. The hydraulic conductivity of the Fran Ridge fault zone assuming a 3-m width is approximately 10^{-6} m/s, slightly higher that that of the overlying tuff aquifer. Varying the width of the fault would have

an inverse effect on the calculated permeability; the flux of the water would remain the same. Upwelling of the carbonate water along the major fault zones in the vicinity of Yucca Mountain is consistent with the water table temperature (Bredehoeft 1997 [DIRS 100007]).

8.3.4 Potentiometric Characteristics

8.3.4.1 Data Collection

Since 1981, water-level data in the Yucca Mountain area have been collected and reported for a number of boreholes and depth intervals (Figure 8-10). Water level data have also been collected by the NC-EWDP. Information concerning the Nye County boreholes and the water-level data for those boreholes can be found on their website, http://www.nyecounty.com.

8.3.4.2 Potentiometric Levels and Stability

8.3.4.2.1 Potentiometric Levels

Water levels in the Yucca Mountain area generally have been stable (Luckey et al. 1996 [DIRS 100465], p. 29). Graves et al. (1997 [DIRS 101046]) analyzed water-level data from 28 boreholes monitoring 36 depth intervals collected during 1985 to 1995 (Table 8-6). The maximum water-level change was 12.22 m and the minimum change was 0.31 m. In 31 of the 36 depth intervals monitored, the range of water-level change was less than 1 m. Generally, water-level fluctuations can be attributed to barometric and Earth-tide changes.

Potentiometric Trends–Trends in groundwater water-level changes in the Yucca Mountain area have been discussed by Rice et al. (1990 [DIRS 148780]), Ervin et al. (1994 [DIRS 100633]), Tucci and Burkhardt (1995 [DIRS 101060], p. 12 to 13), and Graves et al. (1997 [DIRS 101046]).

Rice et al. (1990 [DIRS 148780]) analyzed 1983 to 1986 water-level data from eight boreholes to evaluate whether the data contained periodic (cosine) components. They concluded that there may be periodic components in five of the boreholes. The periodic behavior had a spatial distribution, with boreholes west of Yucca Mountain having periods and phase shifts that were different from boreholes on and east of Yucca Mountain. The spatial distribution may be due to physical causes and the periodic fluctuations may be due to recharge related to periodicity in precipitation (Rice et al. 1990 [DIRS 148780]).

Ervin et al. (1994 [DIRS 100633]) analyzed water-level data collected from 23 boreholes during 1986 to 1989 for yearly trends (excluding shorter-term changes). Water levels in five boreholes exhibited positive trends (rising 0.07 to 0.6 m/yr) that were statistically significant (Ervin et al. 1994 [DIRS 100633], Table 2).

Tucci and Burkhardt (1995 [DIRS 101060], pp. 12 to 13) analyzed trends in water-level data collected from 1986 to 1993. Water-level data from three of 22 boreholes exhibited statistically significant positive trends, rising 0.004 to 0.01 m/yr (Tucci and Burkhardt 1995 [DIRS 101060], Table 4). Ervin et al. (1994 [DIRS 100633]) and Tucci and Burkhardt (1995 [DIRS 101060]) did not find trends in the same boreholes.

Graves et al. (1997 [DIRS 101046]) analyzed water-level data collected during 1985 to 1995 and discussed periods of rising, declining, or stable water levels. In comparing these data, few uniform water-level trends were detected. Graves et al. (1997 [DIRS 101046], pp. 58 to 68) concluded that:

- Seasonal water-level trends were not detected

- Regional groundwater withdrawals did not appear to cause water-level changes

- Most water-level fluctuations can be attributed to barometric and Earth-tide changes

- With the exception of three boreholes in Crater Flat, no uniform water-level changes were observed in boreholes located in the same general area or with the same general water-table altitude.

Fenelon and Moreo (2002 [DIRS 164662], pp. 64 to 66) summarized trend-analysis of water-level data collected from 1992 to 2000. They found that from 1992 to 2000, statistically significant upward trends were determined for 12 water-level sites and statistically significant downward trends were determined for 14 water-level sites and one spring-discharge site. No statistically significant upward or downward trend was observed at the remaining sites. In general, the magnitude of change in water levels from 1992 to 2000 was small (less than 2 ft), except where influenced by pumping or affected by local aquifer conditions near a well site.

Seasonal trends are superimposed on some of the long-term trends in water levels and spring discharge. Causes for seasonal trends include seasonal changes in barometric pressure, evapotranspiration, and pumping. The magnitude of seasonal change in water level can vary from as little as 0.05 ft in regional aquifers to greater than 5 ft in monitoring wells near large supply wells in the Amargosa Farms area. Seasonal fluctuations in water levels (corrected for instantaneous effects of barometric pressure), ranging in magnitude from about 0.05 to 0.2 ft, were observed in several wells in the carbonate- or volcanic-rock aquifers. These small seasonal fluctuations are attributed to the effects of a lagged response to barometric pressure that was not removed during the barometric correction.

Evapotranspiration within the study area occurs primarily in discharge areas, where depths to groundwater are shallow. The primary natural discharge areas in the study area are Ash Meadows, Alkali Flat, and Death Valley. Four wells in the network for this study had water levels that appeared to be responding to evapotranspiration—three in Ash Meadows and one near Death Valley Junction.

Groundwater withdrawals from several regional sources, including Las Vegas Valley, Pahrump Valley, the Amargosa Farms area, and the Nevada Test Site, may account for long-term water-level declines in the Ash Meadows area. Withdrawals from Las Vegas Valley and Pahrump Valley have been considerable since the early 1900s, whereas large withdrawals from Amargosa Farms and the Nevada Test Site began in the mid-1950s to early 1960s. Additionally, incomplete recovery from local pumping in the Ash Meadows area that ended in 1982 may account for some of the long-term decline in water levels at Devils Hole and site AD-6.

Water levels in six wells adjacent to Fortymile Wash in Jackass Flats were monitored. Five of these wells are completed in volcanic rocks and one well is completed in the Paleozoic carbonate-rock aquifer. Groundwater is withdrawn from Jackass Flats to support several DOE activities, including Yucca Mountain site characterization. From 1992 to 2000, water levels in wells JF-1, JF-2, and JF-2a had statistically significant upward trends, whereas water levels in wells J-12, J-13, and JF-3 showed no statistically significant upward or downward trends. Wells J-12 and J-13 are water-supply wells. The maximum change in smoothed water level from 1992 to 2000 for wells in the volcanic-rock aquifers ranged from 0.5 to 0.9 ft, whereas for well JF-2a (the carbonate-rock well), the water level rose about 2.2 ft.

The largest area of consistent trends in the study area is in the Amargosa Farms area, where water levels declined from about 3 ft to more than 15 ft from 1992 to 2000, and from 10 ft to 30 ft from 1964 to 2000. The Amargosa Farms area is the largest center of pumping in the study area and one of the major regional pumping centers. Water levels in some parts of the Amargosa Farms area have declined since the mid- to late 1950s, about the same time as large-scale pumping began in the area. Water-level declines accelerated in the early 1990s as pumping rates more than doubled. Pumping in the Amargosa Farms area may affect water levels in some wells as far away as 5 to 14 mi.

8.3.4.2.2   Earthquake Effects

Section 4 provides details on the subject of the tectonic setting of the Yucca Mountain area. Earthquakes have caused water-level fluctuations in the Yucca Mountain area. On June 28, 1992, earthquakes occurred in California near Landers (magnitude 7.5) and Big Bear (magnitude 6.6) (both about 300 km south of Yucca Mountain) (O'Brien 1993 [DIRS 101276], Figure 1, Table 1). On June 29, 1992, an earthquake occurred at Little Skull Mountain (about 23 km from Yucca Mountain) with a magnitude of 5.6 (O'Brien 1993 [DIRS 101276], Figure 1, Table 1). Boreholes USW H-5 and USW H-6 were monitored continuously at that time, producing records of effects of seismic ground motion on water levels (upper intervals) and fluid pressures (lower intervals) (O'Brien 1993 [DIRS 101276], Figures 2 and 3, respectively).

The confined pressure responses in the lower intervals of both boreholes exceeded the recording scales, although only slightly in Borehole USW H-5 for the Little Skull Mountain earthquake. The double-amplitude pressure ranged from 0.6 to 1.5 m in Borehole USW H-5, and from 1.1 to 2.2 m in Borehole USW H-6 (O'Brien 1993 [DIRS 101276], Table 1). Water-level responses in the upper intervals ranged from 0.2 to 0.9 m in USW H-5, and from 0.06 to 0.6 m in USW H-6 (O'Brien 1993 [DIRS 101276], Table 1).

The earthquakes caused short-term (less than 2-hour) responses in 17 depth intervals of 14 boreholes that were being monitored hourly. These responses were small and of short duration (O'Brien 1993 [DIRS 101276], p. 1). Longer-term effects on water-level fluctuations from the earthquakes (Figure 8-14) were thought to have occurred in Boreholes UE-25 WT #4, UE-25 WT #6, USW WT-11, and UE-25 p #1 (Graves et al. 1997 [DIRS 101046], pp. 59 and 61), which included:

- In Borehole UE-25 WT #4, the water-level rose about 0.25 m and then, within about 42 days, returned back to a water level consistent with levels prior to the earthquakes.

Because the measurements for Borehole UE-25 WT #4 during this time were periodic, the maximum rise and fall in water level and the actual response times are not known.

- In Borehole UE-25 WT #6, there was a maximum recorded rise in water level of about 1.07 m followed by a decline in water level of about 2.66 m within about 85 days of the earthquakes. The water level continued to decline in Borehole UE-25 WT #6 through October 16, 1992 (declining another 0.07 m). Because the measurements for Borehole UE-25 WT #6 during this time were periodic, the maximum rise and fall in water level and the actual response times are not known.

- In Borehole USW WT-11, the water level initially increased 0.03 m and then decreased 0.07 m by July 2, 1992. This quick change was followed by a slow decrease in water level from July through November 1992, with a maximum change in water level of 0.24 m. Following this low, by April 1993, the water level slowly rose back to levels seen before the earthquake. Hourly data were collected for Borehole USW WT-11 during 1992.

- In Borehole UE-25 p #1, the water level declined about 0.53 m on June 28. Following this decline, the water level began to rise and had fully recovered from the effects of the earthquakes within about 191 days. Hourly data were collected for Borehole UE-25 p #1 during 1992.

An alternative view of the effects of the June 1992 earthquakes has been suggested. Davies and Archambeau (1997 [DIRS 103180], p. 26) state that in response to the Little Skull Mountain earthquake, a long-term increase in water-level change was observed, with a maximum increase of about 5 m. The water-level data presented by Davies and Archambeau (1997 [DIRS 103180]) were reviewed and compared to water-level data collected by the U.S. Geological Survey for the same boreholes and for the same period of time. Comparison of the two data sets (CRWMS M&O 2000 [DIRS 151945], p. 9.4-22 to 9.4-23) indicates that the data presented by Davies and Archambeau (1997 [DIRS 103180]) were flawed.

Earthquakes prior to the June 1992 events also affected water levels in the Yucca Mountain area. Four earthquakes in California during late April 1992 produced small water-level fluctuations (0.26 to 0.53 m) in Borehole USW H-5 (O'Brien 1992 [DIRS 101275]) that generally lasted less than 2 hr. No long-term effects on water-level fluctuations were seen in other boreholes in the Yucca Mountain area due to the April earthquakes. Short-term effects could have occurred in other boreholes, but only Borehole USW H-5 was instrumented to monitor for earthquake activity during this time.

Fenelon and Moreo (2002 [DIRS 164662], p. 54) have provided the most recent analysis of water level trends. For seismic events they found that earthquakes are known to affect spring discharge and water levels in the Yucca Mountain region, including Ash Meadows. Some of these effects, observed in discharge records for the carbonate-rock aquifer, appear to last for years. For example, after an abrupt increase in discharge at Travertine Springs in Death Valley following the Landers/Little Skull Mountain earthquakes in 1992, discharge declined for about 8 years. Discharge from Travertine Springs at the end of 2000 was similar to discharge prior to the Landers/Little Skull Mountain earthquakes; however, it is not clear whether discharge will

continue to decline. Closer to Ash Meadows, water levels at site AD-6 (Tracer Well 3) rose approximately 120 mm to 150 mm following the Landers/Little Skull Mountain earthquakes. Water levels in this well declined for 4 years but did not approach levels seen before the earthquakes until the end of 2000. In Devils Hole and Devils Hole Well, water levels were affected by Landers/Little Skull Mountain earthquakes for more than a year. Water levels in Devils Hole abruptly dropped following the June 1992 earthquakes, then rose through June 1993 above the levels seen before the earthquakes, finally returning to normal in 1994.

8.3.4.2.3   Potentiometric Surface

Several potentiometric maps of the Yucca Mountain area have been constructed. This section summarizes these more recent maps while focusing on the two most recent maps (USGS 2001 [DIRS 154625] p. 8; USGS 2002 [DIRS 165615]).

Tucci and Burkhardt (1995 [DIRS 101060], Figure 4) constructed a potentiometric-surface map using 1993 average water levels that defined the potentiometric surface in the Yucca Mountain area in greater detail than did an earlier map (Ervin et al. 1994 [DIRS 100633]), extending contours farther east into Jackass Flats and west into Crater Flat. Czarnecki et al. (1997 [DIRS 141643], pp. 25 to 26, Figure 5) used water levels collected from 1952 to 1996 to produce a computer-generated potentiometric surface map, which was then used to develop a preliminary three-dimensional groundwater flow model of the site-scale saturated zone area.

The USGS (2001 [DIRS 154625]) produced a site-scale potentiometric map using all water-level data within the model area, including data from NC-EWDP boreholes and information from large-scale geologic mapping for contour control (Figure 8-15). For this map, it was implicitly assumed that the saturated zone groundwater system is a hydraulically well-connected water body. Locally, the map may include perched water levels where the possibility of perching cannot be ruled out. To some extent, water levels used in compiling the site-scale potentiometric map represent composite heads in more than one zone; however, it is believed that the surface reasonably represents water table conditions in the model area.

This site-scale potentiometric map uses 25 m contour intervals, which permits definition of the large and medium hydraulic gradient areas; however, the 25-m interval is too coarse to allow the small hydraulic gradient to be adequately portrayed on the map. The map was constructed to represent the early 1990s, which was consistent with data used for the regional-scale map (D'Agnese et al. 1997 [DIRS 100131], Figure 27). Pre-1990 data were used, however, to provide better areal coverage.

Faults are assumed to have an important effect on saturated zone flow, and in the fault blocks to the east and west of the Solitario Canyon fault, the map indicates nearly level hydraulic gradients extending about 10 km west and south of the repository to a fault approximately paralleling U.S. Highway 95. This interpreted groundwater contour pattern suggests that the conditions similar to those in the area of the small hydraulic gradient previously defined between Fortymile Wash and Yucca Mountain extend southward over a large area.

The large hydraulic gradient is portrayed as representing the water table rather than a perched condition.

The USGS (2002 [DIRS 165615]) developed an alternative conceptual model of the large hydraulic gradient and updated the potentiometric surface south of Yucca Mountain (Figure 8-16). This alternative is based on the assumption that perched conditions exist north of Yucca Mountain at Boreholes USW G-2 and UE-25 WT #6. The area covered by this potentiometric-surface map is the same as the earlier map (Figure 8-15), and most of the water-level data used to construct the maps were the same. Updated information and water levels from Borehole USW WT-24 (north of Yucca Mountain) and five NC-EWDP boreholes (south of Yucca Mountain) were included in the updated map.

Overall, the two potentiometric maps (Figures 8-15 and 8-16) are similar; however, they differ in several important ways. The portrayal of the large hydraulic gradient is different. In the updated map, water levels in Boreholes USW G-2 and UE-25 WT #6 were assumed to represent perched conditions, and data from those boreholes were excluded. This reduced the large hydraulic gradient from about 0.11 (Tucci and Burkhardt 1995 [DIRS 101060], p. 9) to between 0.06 to 0.07. Another difference is that the contours are no longer offset where they cross faults. Such offsets (Figure 8-15) would not be expected where the contours are perpendicular or nearly perpendicular to fault traces. Direct evidence of offset, which would be provided by boreholes that straddle the fault, does not exist at Yucca Mountain. Faults were used, however, to help in the placement of contours oriented parallel or approximately parallel to faults. The concept used to represent the impact of faults on potentiometric contours is that groundwater flow across a fault (or fault zone) is impeded by the fault, and groundwater flow parallel to a fault is not impeded by the fault. The contour intervals used for the two maps differ. In the older map (Figure 8-15), the contour interval is a uniform 25 m. In the updated map (Figure 8-16), the contour intervals are not uniform, and an interval of 50 m is used for contours greater than 800 m, and an interval of 25 m is used for contours less than 800 m. Two additional contours, 730 m and 720 m, are included in the updated map. These help in visualizing the effect of the fault along U.S. Highway 95 on the groundwater flow system.

The alternative interpretation (USGS 2002 [DIRS 165615] map (Figure 8-16) also shows a moderate- to large-gradient (0.01 to 0.05) area southwest of Yucca Mountain (along Highway 95 near southern Crater Flat), where water levels range from 720 to 775 m. This feature, which is discussed more in Section 8.3.4.4.2, is not present in the older map (Figure 8-15).

8.3.4.3   Vertical Potentiometric Gradients

Within the site-scale saturated zone flow model area, 17 boreholes monitor, or have historically monitored, water levels in more than one vertical interval (Table 8-7). Water-level data from these boreholes can be used to calculate the difference in potentiometric heads at each monitored interval. Upward (head increases with depth) and downward (head decreases with depth) vertical gradients have been observed. Fewer downward gradients (5) are observed than upward gradients (12). Upward vertical head differences range from 0.1 m to almost 55 m, and downward vertical head differences range from 0.5 to 38 m. The monitored intervals were selected to either monitor water levels between different geologic units or between different permeable intervals within the same geologic unit.

Only two Boreholes (UE-25 p #1 and NC-EWDP-2D/2DB) provide information on vertical gradients between volcanic rocks and the underlying Paleozoic carbonate rocks. At UE-25 p #1,

water levels currently are monitored only in the carbonate aquifer; however, water-level data were obtained from the volcanic rocks as the borehole was drilled and tested. At this site, water levels in the Paleozoic carbonate rocks are about 20 m higher than those in the overlying volcanic rocks. Borehole NC-EWDP-2DB penetrated Paleozoic carbonate rocks toward the bottom of the borehole (USGS 2002 [DIRS 165615], p 19). Water levels measured within the deep part of the borehole are about 7.2 m higher than levels measured in volcanic rocks.

Water levels monitored in boreholes that penetrate to the lower part of the volcanic-rock sequence also are higher than levels monitored in the upper part of the volcanics. Boreholes USW H-1 (tube 1) and USW H-3 (lower interval) monitor water levels in the lower part of the volcanic-rock sequence, and upward gradients are observed at these boreholes (head differences of 54.7 m, and 28.9 m, respectively; Table 8-7). The gradient at USW H-3 is not completely known because water levels in the lower interval had been continuously rising before the packer that separates the upper and lower intervals failed in 1996.

An upward gradient (head difference 5.3 m) was observed between the alluvial deposits monitored in Borehole NC-EWDP-19P and underlying volcanic rocks monitored in Borehole NC-EWDP-19D (Table 8-7). However, data for NC-EWDP-19D represent a composite water level for alluvium and volcanics, so the true head difference between the units is not completely known.

Downward gradients also were observed (Table 8-7). The largest downward gradient was between deep and shallow intervals at Borehole NC-EWDP-1DX (head difference of 38 m). The depth to water at this site was only 17 m and within Tertiary spring deposits. Other downward gradients have smaller magnitudes.

Four boreholes with three or more monitoring intervals (Table 8-7; Boreholes USW H-1, USW H-6, UE-25 J-13, NC-EWDP-9SX) had head differences that were in different directions on both sides of the intermediate interval. For example, at Borehole USW H-1, the head difference between the uppermost (tube 4) and next lower interval (tube 3) is –0.2 m, indicating a small downward gradient; however, the head difference between tube 3 and the next lower interval (tube 2) is 5.3 m, indicating an upward gradient. The importance of the mixed gradients on overall groundwater flow paths is not known.

8.3.4.4   Potentiometric Surface and Lateral Gradients

The potentiometric surface is characterized by four areas with differing overall gradients (Figure 8-17). The hydraulic gradient is small to the east and south of Yucca Mountain. To the east and southeast, the gradient ranges from 0.0001 to 0.0004 (Tucci and Burkhardt 1995 [DIRS 101060], p. 9), and water levels range from about 728 to 732 m. In the Amargosa Desert, south of Yucca Mountain, the gradient also is small (0.001 to 0.0004) and water levels range from about 720 to about 690 m. To the west of Yucca Mountain, the hydraulic gradient is moderate (0.02 to 0.04; Tucci and Burkhardt (1995 [DIRS 101060], p. 9), and water levels range from about 740 to 800 m. There is a moderate- to large-gradient (0.01 to 0.05) southwest of Yucca Mountain between U.S. Highway 95 and Crater Flat, where water levels range from 720 to 775 m (USGS 2002 [DIRS 165615], p. 28). Finally, there is a large-gradient (0.06 to 0.07,

USGS 2002 [DIRS 165615], p.28; 0.11, Tucci and Burkhardt 1995 [DIRS 101060], p. 9) area north of Yucca Mountain, where water levels range from about 738 to 1,188 m.

8.3.4.4.1   Large Hydraulic Gradient

Luckey et al. (1996 [DIRS 100465], p. 21) and Czarnecki et al. (1997 [DIRS 141643], pp. 27 to 29) reviewed water-level data from the areas north and beneath Yucca Mountain, and present hypotheses to explain the large hydraulic gradient (Figure 8-17) Luckey et al. (1996 [DIRS 100465], p. 21, 24) summarize the possible causes, stating that the large hydraulic gradient may:

- Result from flow through the upper-volcanic confining unit

- Represent perched or semiperched conditions

- Represent a drain into a fault zone that moves water from the volcanic aquifers to the LCA

- Result from a deeply buried fault that marks the effective northern limit of the lower volcanic aquifer (i.e., the spillway hypothesis)

- Result from the presence, at depth, of the Eleana Formation, which is part of the Paleozoic upper clastic confining unit

- Reflect an area of decreased permeability due to fracture-closing crustal stress (least principal stress); this hypothesis, however, has been studied and rejected (Luckey et al. 1996 [DIRS 100465], p. 45).

The USGS (2002 [DIRS 165615]) present an alternative concept that, similar to that of Ervin et al. (1994 [DIRS 100633]), assumes the water levels in Boreholes USW G-2 and UE-25 WT #6 represent perched conditions. Although perched water has previously been proposed for Borehole USW G-2, conclusive evidence is lacking. This alternative concept also assumes that water levels in USW WT-24 represent the regional potentiometric level. During drilling of USW WT-24, a water-bearing fracture was encountered at about 760 m below land surface and water rose in the borehole to an altitude of about 840 m above sea level. Drilling continued for another 104 m below the water-bearing fracture with little change in the water level (USGS 2002 [DIRS 165615], p. 15). Because the potentiometric level persisted as the borehole was deepened, and because the water level remained relatively stable after completion, the 840 m level was assumed to represent the regional potentiometric level.

If the water levels in Boreholes USW G-2 and UE-25 WT #6 represent perched conditions, then the magnitude of the large hydraulic gradient is reduced to about 0.07. If those water levels represent regional potentiometric levels, then the hydraulic gradient between USW WT-24 and USW G-2 is about 0.2, and the gradient between USW WT-24 and the small hydraulic-gradient area is about 0.11.

8.3.4.4.2   Moderate Hydraulic Gradients

There are moderate hydraulic gradients west and southwest of Yucca Mountain (Figure 8-17). Ervin et al. (1994 [DIRS 100633]) described the moderate hydraulic gradient west of Yucca Mountain, and the USGS (2002 [DIRS 165615]) described the moderate hydraulic gradient southwest of Yucca Mountain along U.S. Highway 95.

The moderate hydraulic gradient west of Yucca Mountain is defined by boreholes with altitudes of the potentiometric surface ranging from about 732 to 775 m (Luckey et al. 1996 [DIRS 100465], p. 25). The Solitario Canyon fault is believed to act as a barrier to west-east groundwater flow along the west side of Yucca Mountain, causing water levels to build up along the fault (BSC 2001 [DIRS 155974], Table 6; USGS 2003 [DIRS 165176], Section 6.3.3). The moderate hydraulic gradient could also be interpreted as a southward extension of the large hydraulic gradient, with or without the Solitario Canyon fault causing the moderate gradient.

The second area of moderate hydraulic gradient occurs southwest of Yucca Mountain between U.S. Highway 95 and Crater Flat. Water levels are about 730 to 775 m above sea level on the north side of this area, and they are less than 720 m above sea level on the south side. The cause of this gradient is not known, but it has been proposed that a buried fault may act as a barrier to north-south groundwater flow (USGS 2002 [DIRS 165615], p. 27).

8.3.4.4.3   Small Hydraulic Gradient

There is a small hydraulic gradient beneath Yucca Mountain and much of the area east and south of Yucca Mountain (Figure 8-17). Water levels in this area range from less than 700 to 732 m above mean sea level. The small hydraulic gradient is bounded on the north by Boreholes USW H-1 and UE-25 WT #14 and on the west by Boreholes USW H-1, USW H-3, and USW WT-11. Ervin et al. (1993 [DIRS 102524], p. 1558) stated that the small hydraulic gradient could indicate highly transmissive rocks, limited groundwater flow through the system, or a combination of both phenomena.

8.3.5   Thermal Characteristics

The geothermal gradient in the Basin and Range province is relatively large, owing mainly to the tectonically thinned crust that separates the mantle from the land surface. Decay of radioactive elements within the crust, friction produced by tectonic processes, and intrusions of magma produce additional heat, locally increasing the geothermal gradient and flow of heat toward the surface.

Heat flow in the province is typically between about 60 mW/m^2 and about 100 mW/m^2, but large areas have considerably lower or higher heat flows. A large area of subnormal heat flow, less than 1.5 heat-flow units (63 mW/m^2), located between Eureka and Mercury in southeastern Nevada, was termed the Eureka Low by Sass et al. (1971 [DIRS 104545], pp. 6409 to 6411). They attributed this geothermal feature to "hydrologic decoupling" of the thermal regime by interbasin flow of groundwater at depths as great as a few kilometers. The use of heat-flow units has declined in favor of mW/m^2, and the definition of "normal" heat flow in the province has evolved to range from 60 to 100 mW/m^2 (e.g., Sass et al. 1995 [DIRS 101288], pp. 157 to 159).

Sass and Lachenbruch (1982 [DIRS 103145], Table 1) reported heat flow measurements for 15 deep boreholes in the Nevada Test Site area, nine of which were more than 60 mW/m^2 (Figure 8-18). High heat flows were found in two boreholes in the north-central Nevada Test Site area, and in six boreholes in the southern Nevada Test Site area. Borehole USW TW-5 (near the southern border of the Nevada Test Site) penetrates the Precambrian confining unit and provides the only direct measurement of crustal heat flow (84 mW/m^2) in the vicinity of Yucca Mountain beneath the advective water flow in the LCA. Heat flow values from three boreholes at Yucca Mountain are lower than 60 mW/m^2 (Figure 8-18). Borehole UE-25 p #1, with a heat flow value of 61 mW/m^2, is located just outside the 60 mW/m^2 contour. A larger and more recent data set (Sass et al. 1988 [DIRS 100644], Table 5) indicates that saturated zone heat flow in the repository area generally ranges between 30 and 70 mW/m^2, comparable to that in the Eureka Low.

Sass et al. (1988 [DIRS 100644], Tables 1 and 2) reported temperatures in 18 boreholes drilled deeply into the saturated zone in the vicinity of Yucca Mountain, as well as in 17 boreholes drilled to the water table. Additionally, they provided average values for thermal conductivities of the major rock units (Sass et al. 1988 [DIRS 100644], Table 3) and individual measurements of thermal conductivity on core from five deep geologic boreholes at the repository site (Sass et al. 1988 [DIRS 100644], Appendix 3, Tables 3-1 through 3-5). Heat-flow estimates (Sass et al. 1988 [DIRS 100644], Table 5, Figure 17), the products of thermal gradients and conductivity, were calculated for boreholes or segments of boreholes in which the thermal gradients were sufficiently uniform to be represented as least-squares approximations or as linear segments of measured gradients (Sass et al. 1988 [DIRS 100644], pp. 34 to 42). Where intra-borehole flow of water can be shown to be absent or minimal, generally in the deepest part of the borehole, the linear-segment method provides an estimate of conductive heat flow at that depth and location. The least-squares method yields an apparent heat flux, which includes conductive and convective components.

8.3.5.1   Water Table Temperature

Temperatures at the water table (Sass et al. 1995 [DIRS 101288], Figure 8.4) near Yucca Mountain range from about 28°C to 38°C (Figure 8-19). There are high-temperature anomalies associated with Solitario Canyon and Midway Valley, which overlie zones of north-trending faults. This indicates a relationship between faulting and temperature anomalies at the water table.

Temperature gradients at the water table reach about 5°C/km on the east and west sides of the north-trending high-temperature anomalies (Figure 8-19). Between the anomalies (i.e., within the faulted-bounded structural blocks), gradients parallel to the north-south structural trend are small. The water table generally warms southward from 31°C at USW G-1 to 33°C at UE-25 WT #12 (a distance of about 10 km), but the trend is not uniform. The depth to the water table decreases over the same distance from 572 m to 345 m. About 15 km farther south, in the vicinity of U.S. Highway 95, the shallower water table ranges in temperature from the near-surface mean-annual temperature (about 18°C) to about 30°C (Paces and Whelan 2001 [DIRS 154724], p. 2).

8.3.5.2 Temperature Profiles and Heat Flow

Sass et al. (1988 [DIRS 100644], Appendix 1) measured temperatures in boreholes that deeply penetrated the saturated zone near Yucca Mountain. Temperature logs for six boreholes are shown in Figure 8-20. Heat-flow estimates were made for most of the deep boreholes (Table 8-8), although confidence in the estimates varies. Where distortion of the temperature profiles by intra-borehole flows prevented low-confidence heat-flow estimates, values are provided for the overlying unsaturated zone from Sass et al. (1988 [DIRS 100644], Table 5). Temperature-log segments that appear to be conductive generally occur in the deepest parts of the boreholes, where inflow and outflow are limited by rock permeability rather than fractures.

Boreholes USW G-1 and USW H-1 were both drilled to a depth of approximately 1,800 m in Drill Hole Wash near the northern border of the repository. They provided very similar, long intervals of apparently conductive conditions and thermal gradients of about 30°C/km below approximately 1,100 m depth (Figure 8-20). Hydraulic testing in Borehole USW H-1 (Rush et al. 1984 [DIRS 101054]) showed that permeability largely was restricted to zones shallower than about 750 m, consistent with the uniform temperature profile. Thermal conductivities were measured on 45 core samples from the saturated zone in Borehole USW G-1. Heat flows were calculated to be 53 mW/m^2 for Borehole USW G-1 and 54 mW/m^2 for Borehole USW H-1 (Table 8-8).

The lowest heat flows (Table 8-8) were calculated for Boreholes USW G-3 (36 mW/m^2) and USW H-3 (32 mW/m^2). These boreholes are on the crest of Yucca Mountain, penetrate similar stratigraphy, and have similar temperature profiles that appear to be relatively undistorted by intra-borehole flow. The core from Borehole USW G-3 provided thermal-conductivity values (Sass et al. 1988 [DIRS 100644], Table 3-3), and hydraulic tests were conducted in USW H-3 (Thordarson et al. 1985 [DIRS 105670], pp. 9, 17 to 30). The potentiometric head below a depth of 1,125 m in USW H-3 was about 21 m greater than the composite head above 1,125 m, indicating possible upward flow, but the permeability of the deep zone was low and yielded little flow.

Figure 8-20 also shows the temperature log for depths beneath about 750 m in USW G-2, drilled in the northern part of Yucca Mountain. Based on the deepest linear segment (1,125 to 1,250 m) that was accessible after the borehole was bridged subsequent to the September 1982 log, USW G-2 has the highest apparently conductive heat flow in the Yucca Mountain area, about 65 mW/m^2. From December 1981 until June 1984, eight similar temperature logs showed apparent downward flow from the static water level (depth about 530 m) to a depth of about 750 m. The profiles were nearly isothermal between 615 m and 750 m. When the borehole was logged again in 1995, the isothermal step had partly dissipated, the temperature beneath the step had increased about 1°C, and the static water level had dropped about 12m. These changes are consistent with depletion of a perched water body by downward drainage (Czarnecki et al. 1995 [DIRS 103371]).

Boreholes UE-25 b #1 and USW H-4 are located within faulted and fractured rocks that border the repository on the east, whereas USW H-5 was drilled close to splinters of the Solitario Canyon fault on the west side. The logs for these boreholes indicate active intra-borehole flow.

Borehole USW H-6 penetrates the hanging-wall block on the west side of the Solitario Canyon fault. Sass et al. (1988 [DIRS 100644], Table 5) report an apparent heat flow of 51 mW/m^2, calculated from the least-squares thermal gradient through the entire saturated zone interval, the upper part of which apparently has active groundwater convection (Figure 8-20). However, the deepest 400 meters of the borehole displays a uniform thermal gradient of about 37°C/km. The relatively high conductive heat flow, 65 mW/m^2, in this deeper zone is probably a local consequence of high-temperature water in the fault below the borehole.

The effects of local hydrogeologic features are evident on the October 1983 temperature profile for UE-25 p #1 (Figure 8-20). From the water table downward to a depth of about 650 m, the log displays several small higher-temperature excursions and one sharp excursion that corresponds with an unnamed fault at a depth of about 490 m. This excursion was caused by the loss of upward-flowing warm water from the borehole into the fault zone before the borehole was cased through the Tertiary rocks (Craig and Robison 1984 [DIRS 101040], p. 10). A log obtained almost 7 years later (Sass et al. 1995 [DIRS 101288], p. 164) showed that the short-wavelength excursions had dissipated but that the broad, convex-upward excursion above 650 m had persisted. The prominent anomaly culminating in a nearly isothermal segment between 1,200 m and 1,400 m corresponds to the fault zone, probably the Paintbrush Canyon fault, that separates the Tertiary volcanic rocks from the underlying Paleozoic carbonate rocks (Carr et al. 1986 [DIRS 102046], pp. 23 to 25). This excursion was nearly unchanged in the later log.

The basic shape of the persistent temperature profile in UE-25 p #1, which is dominated by positive excursions at shallow and deep fault zones, makes it difficult to assign any part of the log to a conductive thermal gradient, and the heat flow in the saturated zone is, therefore, indeterminate. However, a conductive temperature profile, unperturbed by faulting, can be approximately reconstructed by connecting temperatures from the bottom of the borehole and the surface, varying the slope of the profile according to the thermal conductivities of the rocks. The resulting heat flow is about 42 mW/m^2 (Sass et al. 1995 [DIRS 101288], p. 166).

8.3.5.3   Implications for Groundwater Flow

The thermal environments in Boreholes USW G-1 (which is within a relatively unfaulted block) and UE-25 p #1 (which penetrates one of the more important faults in the area and at least one other hydrologically important fault) differ (Figure 8-20). The log for Borehole USW G-1 is dominated by apparently conductive sections, whereas the log for Borehole UE-25 p #1 exhibits temperature excursions associated with the shallower and deeper faults. The log for Borehole USW G-1 probably represents the ambient temperature distribution in a large volume of rock around the borehole, as well as southward through the central Yucca Mountain area. The log for Borehole UE-25 p #1 is influenced by the ambient temperature, by the anomalous high temperatures in the fault zones, and by the varying proximity of the borehole to the faults.

Temperature isotherms were plotted in vertical profile for the area near Borehole UE-25 p #1 (Figure 8-21). Mounding of the isotherms near Borehole UE-25 p #1 implies that southward flow along the faults is accompanied by vertical mixing of warm water within the fault zones, followed by a reversal deeper in the borehole and cooler below, but it does not necessarily imply large upward water flux within the faults. Bredehoeft (1997 [DIRS 100007], pp. 2461 to 2463) estimated that, for an assumed width of 3 m for the deeper fault, a fault-zone hydraulic

conductivity through the saturated tuffs of about 0.1 m/d would provide sufficient mass and heat transfer to approximate the water-table temperature anomaly, while still providing sufficient confinement of the LCA to produce the observed earth-tide response in the borehole. The pattern of isotherms also is consistent with the downward reversal of the temperature gradient within the carbonate aquifer. In this interpretation, the temperature between the two fault zones through most of the saturated Tertiary rocks trends toward a cooler ambient, as it does below the deeper fault, but it remains somewhat elevated.

The hypothesis by Fridrich et al. (1994 [DIRS 100575], pp. 162 to 165), that a fault underlying the large hydraulic gradient provides a path for introducing downflow of cool water into the Paleozoic rocks, is conceptually consistent with this general concept. In the northern reach of the large hydraulic gradient, heat flow at USW G-2, 65 mW/m^2 or greater, is marginally within the normal range for the Basin and Range province. Values of about 53 mW/m^2 at USW G-1 and USW H-1 occur near the toe of the large hydraulic gradient, whereas the lowest heat flows, about 34 mW/m^2, were determined for the southernmost Boreholes, USW H-3 and USW G-3. The decrease of deep, primarily conductive heat flow southward from the large gradient is not consistent with a simple model of cool recharge to the LCA and southward warming of that flow as heat is collected. However, a somewhat more realistic, three-dimensional model might prove to be consistent with the observations. No alternative for introducing cool water to the deep aquifer has been proposed.

The linear temperature anomalies that correlate spatially with the Solitario Canyon fault and with faults in Midway Valley clearly indicate that lateral flow is influenced by the north-south trending faults. Fridrich et al. (1994 [DIRS 100575], pp. 155 to 157) and Sass et al. (1995 [DIRS 101288], pp. 165 to 166) suggest that the faults also may provide permeable pathways for upward seepage to the volcanic aquifers from a deeper aquifer, tentatively the Paleozoic carbonate aquifer.

The heat-flow deficiency in the Yucca Mountain area extends at least to near the base of the Tertiary volcanic rocks, based on logs for deep boreholes (e.g., USW G-1, USW H-3, and USW G-3). The tentatively reconstructed heat flow in the LCA at UE-25 p #1, about 42 mW/m^2, may indicate that the anomaly penetrates deeply into the Paleozoic rocks. Based on these considerations, Sass et al. (1988 [DIRS 100644], p. 48) concluded that flow in the LCA intercepts crustal heat flow, transporting it laterally toward discharge areas. From the repository area, the deep carbonate aquifer becomes shallower southward. At the northern edge of the Amargosa Desert, it reaches its shallowest position before it is dislocated by a major fault, becoming deep again beneath the broad valley of the Amargosa Desert (Section 8.2). Although discharge to the surface is not presently occurring, nonemergent discharge into younger Tertiary volcanic rocks and the valley fill sediments is probable in this hydrogeologic setting. Heat being transported in the regional groundwater system should be revealed by anomalously high geothermal gradients, groundwater temperatures, and heat flow. Evidence that this is the case is presently developing.

To date, drilling for the NC-EWDP has been concentrated at the northern edge of the Amargosa Desert along U.S. Highway 95, but additional boreholes are planned between there and the repository site where hydrologic and thermal data are sparse (Nye County Nuclear Waste Repository Project Office 2001 [DIRS 156115], pp. 24 to 25).

Temperature logs for three of the NC-EWDP boreholes demonstrate larger geothermal gradients than are present below the water table at the repository site. These boreholes, their maximum measured temperatures, and the depths of measurement are: NC-EWDP-1DX, 52°C at 762 m; NC-EWDP-2DB, 67°C at 762 m; and NC-EWDP-3D, 62°C at 579 m (Nye County Nuclear Waste Repository Project Office 2001 [DIRS 156115], p. 55). The computed average gradients are 45°C/km, 64°C/km, and 76°C/km, respectively. Rather than being attributed to a shallow heat source associated with the nearby Lathrop Wells volcanic center, "these higher temperature gradients more likely reflect the regional temperature regime. For example, at NC-EWDP-1DX, the temperature log confirms that warm water is upwelling via fracture flow and that the carbonate aquifer underlying the valley-fill sediments is the source of the warm water" (Nye County Nuclear Waste Repository Project Office 2001 [DIRS 156115], p. 30).

8.3.5.4 Geothermal Features of the Surrounding Area

One objective of the Yucca Mountain studies was to determine if natural resources might be precluded from development by the development of a nuclear-waste repository. Because of the importance of geothermal resources in northern Nevada, the geothermal potential of the Yucca Mountain area was evaluated (Flynn et al. 1996 [DIRS 112530]). Citing geologic, geophysical, and geochemical findings, as well as chemical geothermometry and the low thermal gradient, they concluded that "the evaluation clearly indicates that there is no potential for geothermal development in this area" and "the absence of a geothermal anomaly and the extreme depth to low-temperature fluids essentially rules out geothermal exploration or development on a commercial scale in the Yucca Mountain area" (Flynn et al. 1996 [DIRS 112530], p. 92).

In discussing the tectonic and geothermal framework of Yucca Mountain, Hill et al. (1995 [DIRS 106126], p. 71) cite thermal springs as being characteristic of the region and heat flow "as high as 130 mW/m^2" as being characteristic of the Yucca Mountain site. Descriptions of thermal springs in Nevada (Garside and Schilling 1979 [DIRS 105478], Plate 1) and in Nye County (Nye County Nuclear Waste Repository Project Office 2001 [DIRS 156115], pp. 54 to 55, Figure 5.1-1) show that thermal springs and temperatures in boreholes in southern Nye County are classified as low-temperature (between the mean-annual surface temperature and 90°C). Stuckless et al. (1998 [DIRS 100086], p. 70) observe that the highest spring temperatures in the vicinity of Yucca Mountain occur in Oasis Valley, west of Crater Flat, where deeply circulating groundwaters from Pahute Mesa and Timber Mountain emerge with a maximum temperature of 41°C. That is only about 25°C warmer than the mean-annual surface temperature. It is evident from the several temperature logs (Figure 8-20) that temperatures of 40°C to 60°C are attainable within 1 to 2 km of the surface in an area of deficient heat flow.

Heat flow of 130 mW/m^2 (Hill et al. 1995 [DIRS 106126], p. 71) occurs in Borehole UE-25 a #3 (Sass et al. 1980 [DIRS 103147]), which is several kilometers east of Yucca Mountain (Figure 8-18). This borehole penetrates argillite of the Eleana Formation before entering carbonate rocks that probably are part of the LCA, which is structurally high beneath the Calico Hills. It is likely that the high heat flow in the argillite is a local anomaly driven by deeper warm water rising along a fault zone, as is apparent in UE-25 p #1, and now becoming evident at the northern edge of the Amargosa Desert.

8.3.6 Saturated Zone Hydrochemistry of Yucca Mountain

Section 5 provides a detailed review of fluid geochemical and isotopic parameters and their relevance to site characterization and site evaluations. Readers are directed to this section, which discusses and summarizes precipitation, unsaturated zone pore water, perched water, unsaturated zone gases and groundwater. Discussions include present conditions, as well as isotopic interpretations indicating past conditions. In this section, the focus is on hydrochemical characteristics of the Crater Flat and Fortymile Canyon sections of the Alkali Flat-Furnace Creek groundwater basin in comparison to other flow systems in the Death Valley groundwater flow system. Hydrochemical and isotopic evidence for mixing and compartmentalization of flow domains in the saturated zone beneath Yucca Mountain also are examined.

It should be noted that the characterization of groundwater, especially for minor and trace elements and isotopes in the Death Valley Region and at Yucca Mountain is limited in most places to the shallow groundwater encountered in wells. At a few locations, information for major-ion chemistry has been collected at multiple depths, but for the most part, we have a two dimensional view of conditions in a three-dimensional system. As such, some anomalous results may have more to do with upgradient waters traveling below local recharge sampled at a location, or perturbations on the system caused by long term or high-yield pumping, such as at UE-25 J-12 and UE-25 J-13. In addition, many of the analyses of mixing include a mix of dependent and independent variables that can increase the uncertainty of the evaluation. As such, the understanding of mixing relationships in the vicinity of Yucca Mountain, although explored by many investigators over time, is tenuous. The results are presented as described by the investigators, even though each may seem to be contradictory of other investigations. Some of this apparent disagreement in conclusions is the result of different comparisons either areally or using different indicators.

The hydrochemistry and isotopic hydrology of waters of the Yucca Mountain-Fortymile Wash flow system provide complementary information on recharge and regional groundwater flow. The major-ion chemistry mainly indicates rock-water interactions (i.e., dissolution of mineral matter, precipitation, and ion-exchange reactions), while isotopic chemistry provides information on the location and environment of recharge, on mixing of groundwater from different sources, and on the time of recharge.

Taken together, the hydrochemistry indicates two basic chemical types of water: a relatively dilute sodium-bicarbonate water of high silica content associated with volcanic rocks and derivative sediments, and a more concentrated calcium-magnesium bicarbonate water of low silica content associated with carbonate rocks. Where these two rock types are mixed, as in alluvial valleys, a water of calcium-magnesium-sodium bicarbonate composition commonly results. In addition, some alluvial groundwater reflects concentration of the chemical constituents due to evaporation; these waters are distinguished by relatively higher proportions of sulfate and chlorine ions in ratios similar to that observed in regional precipitation.

The only groundwaters that appear to be highly anomalous with respect to the ratio of deuterium and ^{18}O are from boreholes near Fortymile Wash. This evidence, together with hydrogeologic and isotopic evidence of nuclear bomb period water (as indicated by tritium and ^{36}Cl content) in

the water of UE-29 a #2, suggests that the water represents a blend of ancient groundwater with modern recharge.

Unusually high $^{234}U/^{238}U$ activity ratios in some Yucca Mountain perched water and in underlying groundwater indicate that some shallow groundwaters at Yucca Mountain were derived almost entirely from local recharge. The anomalously high ratios appear to result from small, but intermittent pulses of water along fractures and faults in the unsaturated zone. The presence and persistence of the elevated ratios suggest the hydraulic isolation of this groundwater by faults and other hydrologic barriers in upgradient areas west and north of the repository. The plume of groundwater with high $^{234}U/^{238}U$ activity ratios cannot be traced downgradient from Yucca Mountain, possibly because of mixing with other groundwaters or because of the incorporation of other sources of uranium.

Most of the isotopic evidence suggests there has been little mixing of waters from the carbonate aquifer with those of the volcanic aquifer. Most of the groundwater at Yucca Mountain appears to represent late Pleistocene-early Holocene recharge, suggesting that groundwater recharge and throughflow have been minimal in the present climate.

8.3.6.1   Crater Flat and Fortymile Canyon Flow System

Hydrogeologic data for the Crater Flat and Fortymile Canyon sections of the Alkali Flat-Furnace Creek groundwater basin (Figure 8-5) were summarized by Luckey et al. (1996 [DIRS 100465], pp. 21 to 27). The data indicate the potential for groundwater flow toward the repository from the large hydraulic gradient to the north and from Crater Flat to the west, and then flow from the repository toward Fortymile Wash to the east. Luckey et al. (1996 [DIRS 100465], pp. 27 to 29) also discussed the potential for upward flow from the LCA to the volcanic aquifers. However, major conceptual uncertainties remain regarding the quantity of groundwater flow in the saturated zone (Luckey et al. 1996 [DIRS 100465], pp. 52 to 53).

8.3.6.1.1   Major-Ion Chemistry

Water in the volcanic aquifers and confining units is a relatively dilute sodium bicarbonate type in which the cations derive from reaction with volcanic glass, primary minerals, soils, and probably with secondary phase minerals such as calcite (Luckey et al. 1996 [DIRS 100465], p. 44). In general, the calcium/sodium ratio increases from west to east, with the lowest values being west of and near the Solitario Canyon fault. Luckey et al. (1996 [DIRS 100465], p. 4) speculate that the relatively higher calcium/sodium ratio to the east may indicate recharge from Fortymile Wash. An alternative explanation, and one that does not require groundwater flowing counter to the direction indicated by the existing hydraulic gradient, is that the west to east increase in the calcium/sodium ratio reflects the increasing contribution of chemically unevolved local recharge at Yucca Mountain. This recharge, which is represented by deep perched water at Yucca Mountain (BSC 2001 [DIRS 158606], Table 7, Figure 19) has calcium and sodium concentrations that are comparable to those measured in boreholes along Fortymile Wash.

The major-ion content of waters from Borehole UE-25 p #1, which taps the LCA, differs from the content of boreholes that tap the volcanic aquifers (BSC 2001 [DIRS 155950], Table 6.3.1.5.2; Triay et al. (1997 [DIRS 100422], Table 3). Borehole UE-25 p #1 samples two depth zones: an upper zone (0 to 1,200 m) in volcanic rocks, and a lower zone (1,300 to 1,800 m) in the LCA. Water temperature and major-ion concentrations (CRWMS M&O 1998 [DIRS 100353], Table 6.2-18) of samples from the two zones are virtually identical. Because the hydraulic head of the lower zone is about 21 m higher than that of the shallower volcanic aquifer (Luckey et al. 1996 [DIRS 100465], Table 3), it appears that the water chemistry of the upper zone is affected by inflow from the lower zone. It is assumed that the sample from the lower zone is representative of the LCA.

Comparison of the lower zone sample (CRWMS M&O 1998 [DIRS 100353], Table 6.2-18) with median values of samples of all boreholes in the Yucca Mountain-Fortymile Wash area indicates the lower zone sample is enriched in calcium, sodium, bicarbonate, sulfate, chloride, and total dissolved solids, and depleted in silica. This comparison suggests that only small amounts of mixing, if any, have occurred between the LCA and the overlying volcanic aquifer.

8.3.6.1.2 Isotope Chemistry

Isotopic data for Yucca Mountain (CRWMS M&O 1998 [DIRS 100353], Table 6.2-19) consist of analyses for deuterium, ^{18}O, tritium, ^{13}C, and ^{14}C of samples from most boreholes, and ^{36}Cl, ^{234}U/^{238}U, and ^{87}Sr/^{86}Sr from a few selected borings. The latter isotopes are not available for deeper portions of the saturated zone. Benson and Klieforth (1989 [DIRS 104370]) integrated the groundwater isotopic data with stable isotope (deuterium and ^{18}O) data on precipitation to arrive at a paleoclimatic interpretation of late Pleistocene-Holocene conditions. Section 5 provides additional discussion of more recent interpretations of these data and how they relate to the geochemical description of Yucca Mountain and related fluids and gases.

8.3.6.1.3 Characterization of Saturated Zone Water Chemistry at Yucca Mountain

In Yucca Mountain area groundwaters, sodium is the primary cation, and carbonate (as carbonic acid, bicarbonate, and carbonate) is the primary anion (Benson et al. 1983 [DIRS 100727], p. 11; Ogard and Kerrisk 1984 [DIRS 100783], p. 16; Benson and McKinley 1985 [DIRS 101036]). Other major cations are calcium, potassium, and magnesium; other major anions are sulfate and chloride, with lesser quantities of fluoride and nitrate. Yucca Mountain is located near Jackass Flats and Amargosa Valley that are represented by mixed and volcanic aquifer signatures, based on groundwater chemical signatures in the Death Valley groundwater basin (Schoff and Moore 1964 [DIRS 150257]).

Saturated zone waters, along with perched waters and pore waters from the Calico Hills, have elevated carbonic acid-chloride ratios and sodium-chloride ratios relative to ratios observed in recent precipitation, which supports the hypothesis that these waters have been subject to hydrolysis reactions. Triay et al. (1997 [DIRS 100422], p. 38) calculated that about 95 percent of the excess sodium in solution is from hydrolysis reactions, with about 5 percent from ion exchange. This is consistent with the amounts of calcium and magnesium lost from saturated zone waters relative to precipitation.

8.3.6.2 Evaluation of Flow Paths and Domains

General flow paths and recharge domains in the Yucca Mountain area have been evaluated using a variety of techniques involving analysis of hydrochemical and isotopic data. The data are used to constrain rates and directions of groundwater flow near Yucca Mountain and to estimate the timing and magnitude of recharge. In this section, the geochemical and isotopic data analyses completed in support of characterizing the site-scale saturated zone are examined. The sources of recharge, recharge rates and volumes, the composition and age of recharge, and the composition of flow domains are considered.

8.3.6.2.1 Isotopic Evidence for Recharge Areas to Yucca Mountain

Sources of Recharge–Sources of water that enter the volcanic aquifers and confining units in the Yucca Mountain area potentially include inflow from upgradient volcanic aquifers and confining units, local recharge from Fortymile Wash, precipitation that infiltrates the surface of Yucca Mountain, and upward flow from the carbonate aquifer (Luckey et al. 1996 [DIRS 100465], p. 39). The magnitude of most of the inflow to the volcanic system has not been quantified. Where vertical gradients have been measured, they generally are upward, indicating a potential for upward groundwater flow (Luckey et al. 1996 [DIRS 100465], p. 28).

Potentiometric data from boreholes upgradient from Yucca Mountain indicate that groundwater probably flows south from upland recharge areas (Luckey et al. 1996 [DIRS 100465], p. 51). However, the concept of inflow from upgradient regions is based on limited data, particularly between Yucca Mountain and Pahute Mesa. The higher sulfate concentration (McKinley et al. 1991 [DIRS 116222], Table 5) and lighter deuterium content (Thomas 1996 [DIRS 131259], Appendix A) of groundwater at western Pahute Mesa compared to Yucca Mountain (McKinley et al. 1991 [DIRS 116222], Table 1; Benson and Klieforth 1989 [DIRS 104370], Table 1a) indicate Pahute Mesa groundwater is not an important source of recharge for the shallow saturated zone beneath Yucca Mountain. Yucca Mountain area groundwater is characterized by low sulfate and chloride concentrations compared to surrounding areas. Conversely, data from McKinley et al. (1991 [DIRS 116222], Table 6 [site numbers 141 to 150]) indicate recharge from Rainier Mesa could be present in Yucca Mountain area groundwater. Groundwater mixing calculations made on the basis of uranium concentrations and $^{234}U/^{238}U$ activity ratios indicate that no more than 20 percent of Pahute Mesa groundwater could be present beneath Yucca Mountain, but up to 55 percent of groundwater like that at eastern Timber Mountain (Water Well 8) could be present beneath Yucca Mountain (Paces et al. 2002 [DIRS 158817], p. 768).

Based on rising water levels in three boreholes in Fortymile Canyon following local precipitation and runoff, recharge from Fortymile Wash probably occurred in 1983, 1992, 1993, and 1995 (Savard 1998 [DIRS 102213], pp. 25 to 27).

At least some of the shallow groundwater beneath Yucca Mountain appears to have been recharged on Yucca Mountain, based on the anomalously high $^{234}U/^{238}U$ activity ratios found in some perched groundwater and in underlying groundwater (Paces et al. 2002 [DIRS 158817]).

Amount of Recharge from Streamflow Infiltration–The estimate of average annual recharge from the infiltration of streamflow in Fortymile Wash of 1.1×10^5 m³/yr by Savard (1998 [DIRS 102213], Table 5) is lower than estimates of recharge from Fortymile Canyon and Fortymile Wash by Czarnecki and Waddell (1984 [DIRS 101042], Table 1, p. 12) of 8×10^6 m³/yr, by Campana and Byer (1996 [DIRS 126814], p. 476) of 6.57×10^6 m³/yr, and by Osterkamp et al. (1994 [DIRS 100602], Table 6) of 4.22×10^6 m³/yr based on simulation modeling.

Recharge Rates from Infiltration of Precipitation–Because it appears that groundwater at Boreholes USW G-2, UE-25 c #3, UE-25 WT #17, UE-25 WT #3, and UE-25 WT #12 originated solely from Yucca Mountain recharge, the chloride concentrations in these boreholes can be used to estimate recharge rates during the late Pleistocene (see Sections 5.2.2, 7.1.4.4, and 7.10.1.2.2). Based on regional precipitation data, the chloride concentration in present-day precipitation at Yucca Mountain has been estimated as 0.35 mg/L, and the average precipitation at Yucca Mountain is presently about 170 mm/yr (Flint et al. 2002 [DIRS 157411], p. 188). Average infiltration rates in the late Pleistocene, calculated using chloride mass balance calculations, were between 7.6 and 9.9 mm/yr, or about twice the average infiltration rates estimates for the repository area under the present-day climate (Flint et al. 2002 [DIRS 157411], p. 195).

Isotopic Composition of Recharge–The ratio of deuterium and ^{18}O from samples from Borehole UE-29 a #2 provided the most definitive data of the stable isotope content of modern recharge in the Yucca Mountain area. The only groundwaters that appear to be significantly different with respect to ratio of deuterium and ^{18}O from the rest of the saturated zone are from boreholes near Fortymile Wash (i.e., production Boreholes UE-25 J-12 and UE-25 J-13, and Borehole UE-29 a #2). The waters of Borehole UE-29 a #2 had unadjusted ^{14}C ages of 3,800 and 4,100 yrs, and deuterium values of −93.5‰ and −93.0‰, which are lower than the waters of UE-25 J-12 and UE-25 J-13. Moreover, deuterium from UE-29 a #2 is similar to that of modern precipitation. Comparable deuterium values (greater than -95‰) have been reported from Rainier Mesa north of the headwaters of Fortymile Wash, east of Fortymile Wash at Shoshone Mountain, and in recently completed boreholes at Timber Mountain west of Fortymile Canyon (Figure 8-5), indicating that considerable recharge may occur in those areas (Figure 8-22). Pore water samples from nonwelded tuffs in the upper part of Borehole USW UZ-14, that may also represent modern infiltration, have δD values that average about −90‰ (Yang et al. 1998 [DIRS 101441], Table 9). There are a few other occurrences of anomalous values outside of the site-scale boundary. The rationale for these values is not understood.

Age of Recharge–Hydrochemical data (Benson and Klieforth 1989 [DIRS 104370], Table 1, p. 41) indicate that water in the volcanic aquifer beneath Yucca Mountain and Crater Flat was recharged during wetter climatic conditions approximately 12,000 to 18,500 yrs, based on apparent ^{14}C ages. However, these data do not preclude that some modern recharge occurs. ^{14}C dating of perched waters at Yucca Mountain indicated that the perched waters were recharged generally between 7,000 and 11,000 yrs before present, although waters as young as 3,300 yrs

were found in Borehole USW NRG-7a and in one interval of Borehole USW UZ-14 (BSC 2001 [DIRS 158606], p. 100). Actual ages may be younger than apparent ages; the water probably is a mixture from recharge events that spanned at least a number of millennia, and the apparent age is influenced by input of dead carbon from calcite and dust in the surface environment.

Summarizing the hydrochemical analysis (BSC 2001 [DIRS 158606], Sections 7.2 to 7.5), the following was concluded regarding the source and timing of recharge and flow paths:

- Miller (1977 [DIRS 105462] pp. 28 to 32) presented various geologic and hydrologic discussions germane to the question of the source of the water discharging from the springs at the west end of Furnace Creek Wash. He concluded that the consensus of the information indicated the water discharging at these springs flows likely from the basins to the north and east, through the southern part of the Funeral Mountains. Carr (1984, [DIRS 101037] p. 61) suggested that water discharging at both Ash Meadows and the Furnace Creek springs derives from groundwater flowing through the Spotted-Range-Mine Mountain structural zone. Carr (1984, [DIRS 101037] p. 11, p. 30) further described several other northeast-trending structural zones in the Walker Lane Belt, some of which terminate at the Fish Lake-Death Valley-Furnace Creek fault zone (Figure 2-12).

- Carbon-14 data suggest that the best estimate of true age of the saturated zone waters at Yucca Mountain is about 2,000 yrs less than the uncorrected ages of predominantly 7,000 to 11,000 yrs.

- Hydrochemical data suggest a small amount of mixing between water from the LCA with water in the volcanic aquifers.

- Uranium isotope activity ratios and other isotopic and hydrochemical evidence suggest that at least the upper portions of the saturated zone groundwater at Yucca Mountain originated largely from local infiltration via perched water zones during late Pleistocene-early Holocene.

8.3.6.2.2   Uses of Chemical and Isotopic Trends to Discern Flow Paths and Domains

White and Chuma (1987 [DIRS 108871], pp. 571 to 582) used environmental isotopes and carbon chemistry to differentiate various recharge areas, flow paths, and groundwater ages in Oasis Valley and Fortymile Canyon. The isotope distribution data support a conclusion that groundwater beneath Pahute Mesa discharges to Oasis Valley and that groundwater in tuff in Fortymile Canyon is of local origin. This conclusion is supported by the Feeney et al. (1987 [DIRS 150756]) deuterium model of the western Nevada Test Site and by the Sadler et al. (1992 [DIRS 145202]) calibrated stable isotope model of the region. As discussed in the previous section, $^{234}U/^{238}U$ activity ratios and other hydrochemical data support a local origin for much of the shallow groundwater at Yucca Mountain.

To the west of Yucca Mountain, the uranium characteristics of groundwaters (Paces et al. 2002 [DIRS 158817], Figure 6) are consistent with a conceptual model of groundwaters originating in the volcanic highlands to the north and generally flowing southerly into the western Amargosa

Desert. This pattern is implied by the relatively high $^{234}U/^{238}U$ activity ratios in groundwaters from the Tertiary volcanic rocks in Pahute Mesa, Crater Flat, and Beatty Wash. The smaller activity ratio values are typical of groundwaters in the Oasis Valley and the southwestern Amargosa Desert (Paces et al. 2002 [DIRS 158817], p. 760). Alternatively, the smaller activity ratios typical of water west of Yucca Mountain may exist at depth if the waters that cover these deeper waters were recharged through the mountain.

The uranium characteristics of groundwaters from two boreholes west of the Solitario Canyon fault (USW WT-10 and a well at the Lathrop Wells cinder cone) provide evidence that this fault acts as a barrier for groundwater flow. The fault appears to prevent groundwater from moving eastward into the saturated zone beneath Yucca Mountain; rather, the groundwater flows southward along the fault and its southerly extensions (Paces et al. 2002 [DIRS 158817], p. 765). The apparent absence of communication between groundwaters on opposite sides of the Solitario Canyon fault, together with the southward movement of groundwater in the Fortymile Wash drainage system, further supports the high $^{234}U/^{238}U$ activity ratio evidence that flow in the saturated volcanic rocks beneath Yucca Mountain is effectively isolated from the regional flow system.

The calcium-sodium ratio in the groundwater increases by an order of magnitude from west to east across Yucca Mountain. The increase in this ratio may indicate that the chemical evolution of the water has progressed farther in water to the west. This possible evolution could be the combined effect of the Solitario Canyon fault that acts as a barrier to flow from the west, the unidentified geologic features that cause the large hydraulic gradient (acting as a barrier to flow from the north), and the less evolved local recharge that moves from Yucca Mountain toward Fortymile Wash.

The $^{87}Sr/^{86}Sr$ ratio for saturated zone waters from the volcanic aquifer ranges from 0.7093 to 0.7119 (Marshall et al. 1993 [DIRS 101142]). The ratio for saturated zone fracture-filling calcites is 0.70894, which is close to the ratio of 0.709 for the carbonate aquifer. In contrast, unsaturated zone fracture fillings have a ratio of 0.7119, and pedogenic calcites have a ratio of 0.7124. Thus, the values for saturated zone waters are bracketed by ratios for the carbonate aquifer and the unsaturated zone calcites. The $^{87}Sr/^{86}Sr$ ratio does not change systematically across the site. However, strontium concentrations decrease from the west (Crater Flat), across the Solitario Canyon fault, to the east (Fortymile Wash).

8.3.6.3 Mixing

Various approaches have been used to attempt to discern whether groundwater compositions at Yucca Mountain reflect mixing of waters of different sources. Some of these methods include investigation of conservative trace elements, rare earth elements, and isotopic ratios in the groundwater, as well as compositions of fracture-filling minerals deposited by the groundwater.

Vaniman and Chipera (1996 [DIRS 100089]) showed that lanthanide ratios and strontium contents of fracture-filling calcites record the chemical evolution of waters flowing through the unsaturated zone and upper saturated zone. A 300 to 400 m "barren zone," where calcite fracture fillings are sparse, straddles the water table. Carbon and oxygen isotopes of the calcites provide evidence that most of the calcite is derived from surface sources in the upper unsaturated zone

above the barren zone, whereas carbonates of the deep saturated zone volcanic aquifer contain carbon and oxygen, consistent with deviation from fluids that were in contact with Paleozoic carbonates. The barren zone could act as a large region of "mixing corrosion" (Ford and Williams 1989 [DIRS 148968]), where meteoric, tuffaceous aquifer, and carbonate-alteration zone waters mix and interact with zeolites and clays to provide variable water compositions and cause calcite to be unstable. From this line of evidence, it appeared to Vaniman and Chipera (1996 [DIRS 100089]) that, over a very long time period, vertical mixing on the scale of hundreds of meters may have occurred around the water table.

Whelan et al. (1998 [DIRS 108865], pp. 179 to 180) analyzed the secondary calcite from the unsaturated and saturated zones. They concluded that most of the rare calcite from the barren zone, including that within the upper 300 m of the current saturated zone, resembles unsaturated zone mineralization that allows for an interpretation that the water table was lower at some time in the past.

Stetzenbach et al. (2001 [DIRS 158819]) used a multivariate statistical analysis to show that the trace element chemistry of water from Boreholes UE-25 J-12 and UE-25 J-13 was more like the trace element chemistry of water from the carbonate aquifer (Ash Meadows), the Spring Mountains, and the Pahranagat Valley than it was like water from Tippipah Spring and Topopah Spring, which discharge from the volcanic aquifer northeast of Yucca Mountain. On this basis, they state that the trace element signature of water from Boreholes UE-25 J-12 and UE-25 J-13 indicates that the waters primarily originate from the carbonate aquifer, which suggests upwelling of waters from the Paleozoic carbonates to these boreholes (Stetzenbach et al. (2001 [DIRS 158819], p. 266). Again, however, it is unlikely that important upwelling from the carbonate aquifer has affected groundwater at UE-25 J-12 or UE-25 J-13 based on the similarity of groundwater chloride, sulfate, and bicarbonate concentrations at these boreholes to those at UE-29 a #2 (a likely recharge area for these groundwater in Fortymile Canyon), and the higher concentrations of these constituents in the carbonate aquifer. It should be noted that these two wells are completed near the carbonate aquifer and have had large amounts of water extracted from them for many years.

Uranium isotopes suggest some degree of mixing of waters of different sources to produce signatures of water at Yucca Mountain, but the degree of mixing is hard to quantify. Three major components of mixing were suggested by Ludwig et al. (1993 [DIRS 101141]): one with high $^{234}U/^{238}U$ and low $\delta^{87}Sr$ that is present mostly in Tertiary volcanic aquifers, a second with low $^{234}U/^{238}U$ and high $\delta^{87}Sr$ that is present mostly in the Paleozoic aquifer, and a third with low $^{234}U/^{238}U$ and $\delta^{87}Sr$ that is present in both. Boreholes from Fortymile Wash show an unusually high dispersion in $^{234}U/^{238}U$, at nearly constant $\delta^{87}Sr$ compositions. Variable but small amounts of contamination from the Paleozoic aquifer (represented by UE-25 p #1) would be sufficient to cause this dispersion, as UE-25 p #1 has the highest uranium content of the analyzed waters. However, if this is the case, other sources must come into play in addition to UE-25 p #1, because it does not form a straight line end member with the Fortymile Wash samples (Ludwig et al. 1993 [DIRS 101141]).

Strontium isotope data do not support mixing hypotheses. Values of $\delta^{87}Sr$ increase progressively from +0.5 to +2 beneath Yucca Mountain, to larger values to the southwest and southeast (Peterman and Stuckless 1993 [DIRS 101149]). All of the groundwater samples from the

volcanic aquifer at and north of Amargosa Valley have δ^{87}Sr values (-0.4 to 5.4) within the range of values for the volcanic rock units (-0.4 to 9.6). The total Topopah Spring Tuff has a δ^{87}Sr value of 5.7. The Prow Pass Tuff of the Crater Flat Group has a δ^{87}Sr value of 3.6, whereas the Bullfrog Tuff has 0.5 and the Tram Tuff, 0.8 (Peterman and Stuckless 1993 [DIRS 101149], p. 1563 and Table 1). In the vicinity of Yucca Mountain, the δ^{87}Sr values of the groundwater are typically intermediate between the bulk rock values for the Crater Flat Group through younger units and those units older than the Crater Flat Group (with slightly negative to 0.5 values). Delta ^{87}Sr values also increase from north to south (downgradient) in the Cenozoic aquifer flow system beneath the Yucca Mountain region (Peterman and Stuckless 1993 [DIRS 101149], p. 1559). This flow path is tens of kilometers long, making conclusions tenuous.

The enrichment of deuterium and ^{18}O in groundwater from UE-25 J-12, UE-25 J-13, and UE-29 a #2 relative to all other samples from the Yucca Mountain region (δDof -93.5 to -97.5‰ SMOW and δ^{18}O of -12.8 to -13.0‰ SMOW [Stuckless et al. 1991 [DIRS 101159], Table 1]) indicates that groundwater from the upper reaches of Fortymile Canyon is closer to the modern global meteoric water line, suggesting local, relatively recent recharge (e.g., at lower elevations during the summer months). This evidence suggests little communication between the Tertiary aquifers beneath Fortymile Canyon and those to the west under Yucca Mountain (White and Chuma 1987 [DIRS 108871], p. 573; Stuckless et al. 1991 [DIRS 101159], pp. 1411 to 1412). Alternatively, however, the distinct isotopic compositions of water from Yucca Mountain and Fortymile Wash may indicate that groundwater flow from Yucca Mountain is more directly south than is indicated by the present-day hydraulic gradient.

Geochemical information obtained during long-term pump testing conducted at the C-Wells Complex does not support upwelling of water from the Lower Carbonate Aquifer to the volcanic aquifers or the possibility of a hydraulic connection between these two aquifer within the area of influence during the pump testing. The data obtained on the chemistry of water samples collected from well UE-25 c #3 over an extended period of pumping at the C-Wells Complex, which, when compared to the chemistry of water characteristic of the water in UE-25 p #1, are not supportive of such a hydraulic connection in the C-Wells Complex vicinity (Geldon et al. 2002 [DIRS 161163], pp. 51 to 54).

8.3.7 Field Scale Transport Testing

Field-scale transport tests have been conducted in the fractured tuff and alluvial aquifer systems in or near the groundwater pathways downgradient from the repository. In the fractured tuffs, a series of multiborehole tracer tests carried out between 1996 and 1999 provide data on which the conceptual model for transport in the tuffs is based. For the alluvium, only single-borehole, injection-pumpback experiments have been conducted. Similar to the synthesis of hydraulic data, the tracer testing provides experimental validation of the conceptual models used in the numerical model of the site, and provides guidance on the proper parameters. The main results are summarized in the following sections; details are provided by BSC (2003 [DIRS 167209]).

8.3.7.1 Tracer Tests in Fractured Tuff

Conservative tracer tests were conducted in the hydrogeologic units exposed at the C-Wells Complex, and the results of the analyses (BSC 2003 [DIRS 167209], Section 6) are consistent

with conclusions from tests in which multiple tracers were used simultaneously. Only the results of the multiple tracer tests are presented here. The first test was conducted in the Bullfrog member between Boreholes UE-25 c #2 and UE-25 c #3, using UE-25 c #2 as the tracer injection borehole and UE-25 c #3 the production borehole. The second test, conducted in the Prow Pass tuff, used UE-25 c #3 as the injection borehole and UE-25 c #2 as the production borehole. Prior to injection of tracers, a flow field was established by reinjecting a small fraction of the produced fluid into the injection boreholes. Water samples were collected and analyzed to measure the concentration of injected tracers.

For the Bullfrog tracer test, in which three tracers were used (BSC 2003 [DIRS 167209], Section 6.3), curves were plotted as normalized concentration versus time (Figure 8-23). Two peaks were observed on the curves that were caused by the presence of two flowing zones, which gave rise to two distinct flow paths and overlapping transport times. For the conservative tracers, the tracer with the lower molecular diffusion coefficient (pentafluorobenzoic acid) exhibited a higher peak concentration than did bromide, an observation that is consistent with a dual-porosity model in which tracers travel in fractures and diffuse into the rock matrix. Lithium, a weakly sorbing tracer, exhibited further attenuation, but the arrival time was similar to the other two tracers. A matrix diffusion model also explains this observation more completely than does a single continuum model, which would predict delayed arrival times for a sorbing tracer.

In addition to the three tracers, 360-nm-diameter carboxylate-modified polystyrene microspheres were injected during the Bullfrog tracer test (BSC 2003 [DIRS 167209], Section 6.3) to examine how finite-sized particles transport through the fractured tuffs (microspheres provide insight into the behavior of colloids). Microspheres transported through the medium at the scale of this test, but the concentrations were attenuated compared to the conservative solute (Figure 8-24). This was probably due to filtration in the medium, although the possibility of settling could not be ruled out. There was a suggestion that the microspheres arrived earlier than the conservative tracer, implying that the microspheres may have preferentially moved in the higher velocity flow paths in the system.

The Prow Pass tracer test (BSC 2003 [DIRS 167209], Section 6.3) exhibited many of the same characteristics as the Bullfrog test, suggesting that the transport mechanisms in these units were similar, despite differences in the hydrologic properties (Figure 8-25). The coincident arrivals times and relative heights of the tracer peaks were consistent with the Bullfrog results. During these tests, the flow field was interrupted three times. During the interruptions, tracer that had diffused into the matrix partially diffused back into the fractures, and when pumping resumed, increased concentrations were observed for short periods of time. These observations further confirmation the dual-porosity transport model of fracture flow and matrix diffusion.

Analysis of these and earlier tests are presented in BSC (2003 [DIRS 167209]). These analyses, in addition to confirming the dual-porosity behavior, were used to derive field-scale transport parameters such as longitudinal dispersivity and the matrix diffusion mass transfer coefficient.

8.3.7.2 Tracer Testing in Alluvium

Three single-borehole injection-withdrawal tracer tests were conducted in saturated alluvium at the Alluvial Testing Complex (BSC 2003 [DIRS 167209], Section 6.5). In each test, two nonsorbing solute tracers with different diffusion coefficients were injected simultaneously. The experimental conditions were similar, except for the time that was allowed to elapse between the cessation of tracer and chase water injection and the initiation of pumping. The rest period in the three tests was about 0.5 hr, about 2 days, and about 30 days. This allowed for the tracers to diffuse into the stagnant water in the flow system and to migrate with the natural groundwater flow. Tests were interpreted by comparing the responses of different tracers in the same test, as well as the responses of similar tracers in different tests. Differences in the responses of the tracers injected in the same test provided information on diffusion into the stagnant water, while differences in the responses of tracers injected in different tests provided information on tracer drift during the rest periods.

In the short-term test (BSC 2003 [DIRS 167209], Section 6.5) the two solute tracers had essentially identical responses (Figure 8-26), which is consistent with a single porous continuum model (i.e., little diffusion between flowing and stagnant water). Flow interruptions during the tailing portions of two longer tests also showed minimal diffusion. The results for the microspheres, which provided information on colloid filtration and detachment rates in the flow system, differed for the fractured tuff and alluvium. In contrast to the tuffs, the alluvium exhibited behavior more like that of a porous continuum model (i.e., less diffusion into stagnant fluids). This result may be scale dependent, such that over longer transport times, diffusion becomes more important.

The single-borehole test results were used to estimate specific discharge near borehole NC-EWDP-19D1 (BSC 2003 [DIRS 167209], Section 6.5.4). Because different drift durations were used in the tracer tests, the results (combined with an idealized model of groundwater flow near the borehole) could be used to estimate specific discharge, which ranged from 1.3 to 9.4 m/yr depending on model assumptions and parameter uncertainties (BSC 2003 [DIRS 167209], Table 6.5-7). This range of values agrees with those calculated using the calibrated site-scale saturated zone flow model (Section 8.3.9).

8.3.8 Conceptual Model of Flow and Transport

8.3.8.1 Site-Scale Saturated Zone Groundwater Flow

8.3.8.1.1 General Description

Groundwater flow at Yucca Mountain primarily occurs in a sequence of fractured volcanic rocks and underlying carbonate rocks. Where the volcanic rocks pinch out to the south of Yucca Mountain, groundwater also flows in Tertiary alluvial and carbonate deposits. The volcanic sequence is divided into two aquifers (the upper and middle aquifers) and two confining units (the upper and middle volcanic confining units). Generally, only a small number of intervals within the aquifers, usually associated with fractures or faults, produce water. The confining units also may transmit water, but to a lesser extent than the aquifers. For the volcanic tuff units, groundwater flow is considered to occur primarily through fractures, while flow in the alluvium

is through the porous matrix. In less transmissive units (e.g., Calico Hills Formation), a larger proportion of the flow probably occurs in the matrix.

The carbonate aquifer appears to underlie the middle volcanic confining unit beneath Yucca Mountain. The units of the lower volcanic aquifer and confining unit are found elsewhere in the region but are likely absent at Yucca Mountain. Several lines of evidence indicate that the middle volcanic confining unit effectively isolates the carbonate aquifer from the volcanic aquifers. However, the altered mineralogy of the tuffs, particularly in Borehole UE-25 p #1, indicates past influx of deeper water, possibly localized along faults (Carr et al. 1986 [DIRS 102046], p. 24). Higher water table temperatures aligned along existing faults may indicate upwelling, probably from the carbonate aquifer (Fridrich et al. 1994 [DIRS 100575]). Beneath the northern part of Yucca Mountain, the carbonate aquifer may also be confined by the Eleana Formation. If the volcanic aquifers were essentially isolated from the carbonate aquifer, then the potentiometric surface in the volcanic aquifer would be independent of the potentiometric surface in the carbonate aquifer. If, however, the confinement is breached by faults, the potentiometric surface in one system may affect the potentiometric surface in the other system. An analysis of fault permeability at Borehole UE-25 p #1 indicates that the carbonate aquifer is well confined by a layer of low-hydraulic conductivity (Bredehoeft 1997 [DIRS 100007], p. 2459). However, the modeling analysis also supports the concept of upward flow from the carbonate aquifer along faults.

On a regional scale, flow generally is from north of Yucca Mountain (higher mountains and plateaus) to south of the mountain (lower desert valleys), and then continuing south and westward to lower areas of discharge in Death Valley (Figure 8-6). Flow paths through the Timber Mountain area are not clear because of a lack of potentiometric data. To evaluate likely flow paths beneath Yucca Mountain, hydrochemical and isotopic data were analyzed to identify areas with similar concentrations of conservative species. Chloride data, as well as other chemical and isotopic data, suggest that groundwater from beneath the repository site may flow initially southeastward, then generally south-southwestward. For areas downgradient from the repository, flow paths simulated using the site-scale flow and transport model (Figure 8-27) are generally consistent with the flow paths estimated from hydrochemical data (BSC 2001 [DIRS 158606], Figure 17). The flow paths inferred from hydrochemical data for areas south of the repository also are consistent with the potentiometric surface map (Figure 8-15).

In the area of small hydraulic gradient (Figure 8-17), the potentiometric surface is a continuous, almost flat surface that does not change noticeably as it passes through the various faults east of the Solitario Canyon fault. The potentiometric surface slopes gently to the east at a relatively constant gradient (0.0001 to 0.0003), which is consistent with earlier maps by Ervin et al. (1994 [DIRS 100633], 1993 [DIRS 102524]). Tucci and Burkhardt (1995 [DIRS 101060], p. 7 to 11, Figure 4) also show this type of surface and gradient. Lehman and Brown (1996 [DIRS 149173], pp. 24 to 36) present an alternative potentiometric surface that appears to be influenced by northwest-southeast-trending structures on the east side of Yucca Mountain; however, analysis of the map and data indicates that the map is probably not valid.

The potentiometric surface in the area of small hydraulic gradient also does not seem to change as it transects aquifers and confining units. Beneath the crest of Yucca Mountain, flow is entirely in the lower volcanic aquifer and deeper units. However, at Fortymile Wash, the upper

volcanic aquifer dips beneath the water table and dominates the flow system. There is no obvious break in the slope of the potentiometric surface in the transition area, which must be somewhere in Midway Valley (the valley at the foot of Yucca Mountain on the east side). In the vicinity of the large hydraulic gradient (Figure 8-17), the potentiometric surface may or may not reflect a change in hydrogeologic units, depending on the interpretation of the cause of the large hydraulic gradient.

Vertical hydraulic gradients could influence the analysis of the effectiveness of the saturated zone as a barrier to radionuclide transport. Based on limited data (five boreholes), an areally extensive upward gradient can be inferred between the carbonate and volcanic aquifers, which may indicate that, at least for the immediate Yucca Mountain area, radionuclide transport would be restricted to the volcanic system.

Potentiometric levels have been measured at multiple depth intervals in several boreholes (Table 8-7). Differences in potentiometric levels at different depths in the same borehole ranged from 0.1 to almost 5m. Potentiometric levels generally are higher in the lower intervals of the volcanic rocks than in the upper intervals, indicating a potential for upward flow. However, in some boreholes (Section 8.3.4.3 and Table 8-7), potentiometric levels in the volcanic rocks were higher in the uppermost intervals than in the next lower intervals. Potentiometric levels in the Paleozoic carbonate aquifer at Borehole UE-25 p #1 are about 21 m higher than levels in the lower volcanic aquifer (Craig and Johnson 1984 [DIRS 101039], p. 12), indicating the potential for upward groundwater flow.

The volume of groundwater that flows beneath Yucca Mountain is unknown. Most conceptual models, and in fact the numerical model of the site-scale flow and transport system, interpret the large gradient as a region of small groundwater flux caused by a local or distributed zone of low permeability. It then follows that the low-gradient region downgradient from Yucca Mountain is due to low groundwater flow rates. However, because there is no direct way to measure groundwater flow, resolution of the possible causes of the small hydraulic gradient depends on indirect evidence.

8.3.8.1.2 Large Hydraulic Gradient Area

Several hypotheses have been proposed for the cause of the large hydraulic gradient (Section 8.3.4). Simulation of this feature in groundwater flow models has typically been through the use of low-permeability features, such as large areas of low permeability (Barr and Miller 1987 [DIRS 101189]; Lehman and Brown 1996 [DIRS 149173]; Haws 1990 [DIRS 148778]; Cohen et al. 1997 [DIRS 101038], p. 65 to 71; BSC (2003 [DIRS 166262]) or a low-permeability barrier (Czarnecki and Waddell 1984 [DIRS 101042], p. 7 to 8; Czarnecki et al. 1997 [DIRS 141643], p. 26 to 29).

A panel of five experts reviewed data and arguments in support of the hypothesized causes of the large hydraulic gradient and chose two credible concepts (CRWMS M&O 1998 [DIRS 100353], pp. 3 to 5). In the saturated zone hypothesis, the large hydraulic gradient was interpreted to result from a steeply inclined water table within a fully saturated flow system. Factors such as topography, recharge, and geology probably contribute to the slope of the feature. In the perched water hypothesis, the flow system consists of a (semi-perched) saturated interval overlying a

wedge of unsaturated rocks, which, in turn, overlies the regional water table. The panelists considered both hypotheses to be about equally credible, with a slight preference toward the perched water model. The experts agreed that the issue was mainly one of technical credibility, that the probability of long-term transient readjustment of gradients was low, and that the probability of large transient change in the configuration of the large gradient was low (CRWMS M&O 1998 [DIRS 100353]).

8.3.8.1.3   Influence of Faults

Some faults have been described as barriers to groundwater flow, while others have been described as conduits. The influence of faults on groundwater movement in the Death Valley region has been characterized and related their influence to crustal stress, fracture mechanics, and structural geologic data (Faunt 1997 [DIRS 100146]). In the regional groundwater model, some faults were considered barriers (features trending northwest to southeast) to groundwater flow (D'Agnese et al. 2002 [DIRS 158876], p. 82). Locally at Yucca Mountain, however, the features trending northwest to southeast may not be barriers to flow, at least not in the trend direction. Hydraulic and tracer tests in Drill Hole Wash (Lahoud et al. 1984 [DIRS 101049]; Ogard et al. 1983 [DIRS 103114]) indicated that the underlying structure, whether it was a fault or a fracture zone, provides continuous, permeable flow paths. Also, Geldon et al. (1997 [DIRS 100397]) inferred from drawdown in observation boreholes while pumping at the C-Wells Complex, that northwest-southeast structure could provide a permeable connection to Borehole USW H-4.

Most researchers have concluded that the Solitario Canyon fault is a barrier to west-to-east groundwater flow (Luckey et al. 1996 [DIRS 100465], pp. 25 to 26; Czarnecki et al. 1997 [DIRS 141643], p. 84) and is a probable cause for the moderate hydraulic gradient (Luckey et al. 1996 [DIRS 100465], pp. 25 to 26; Ervin et al. 1994 [DIRS 100633]; Tucci and Burkhardt 1995 [DIRS 101060], p. 9). However, the Solitario Canyon fault may also provide a conduit for upward flow to the Tertiary volcanic aquifers from the underlying Paleozoic carbonate aquifer (Fridrich et al. 1994 [DIRS 100575]). Other north-trending faults at Yucca Mountain may also provide conduits for upward flow, particularly where they correspond to linear anomalies in water temperature (Fridrich et al. 1994 [DIRS 100575]; Sass et al. 1995 [DIRS 101288], p. 165; Lehman and Brown 1996 [DIRS 149173]; Bredehoeft 1997 [DIRS 100007], pp. 2462 to 2463). The apparent roles of the Solitario Canyon fault (as a barrier to flow across the fault and as a conduit for flow parallel to it) indicate the likelihood that the fault zone itself may be poorly permeable but that the well-fractured hanging-wall rocks are highly permeable.

Several other investigators have discussed the role of faults and other structural features as possible conduits or preferential pathways for groundwater flow at Yucca Mountain (Luckey et al. 1996 [DIRS 100465], pp. 25 to 26, 60; Lehman and Brown 1996 [DIRS 149173]; Cohen et al. 1997 [DIRS 101038], pp. 49 to 65; Geldon 1996 [DIRS 100396]; Geldon et al. 1997 [DIRS 100397]; Ferrill et al. 1999 [DIRS 118941]). As summarized in Section 8.3.3.3.2, the relatively large hydraulic conductivity at the C-Wells Complex is strongly influenced by the presence of faults and fractures that intersect the borehole (Geldon et al. 1997 [DIRS 100397]). The distribution of drawdown in response to extensive pumping at the C-Wells Complex is believed to be related to the location of nearby structural features, and the areal distribution of hydraulic conductivity in the area may be related to the presence or absence of faults

(Geldon et al. 1997 [DIRS 100397]). Little information is available, however, concerning hydraulic properties within the saturated zone of individual faults in the area.

8.3.8.1.4   Recharge and Discharge

Recharge in the Yucca Mountain area is assumed to be from four sources:

- Downward and possible lateral recharge from episodic flooding of Fortymile Wash. Based on field studies of stream loss, the total recharge in Fortymile Wash is estimated at about 108,000 m^3/yr (Savard 1998 [DIRS 102213], Table 5, p. 26). This estimate represents a minimum value based on the inability to account for all reaches of Fortymile Wash, which may have received unobserved runoff and recharge, coupled with the minimum period of streamflow observations.

- Throughflow from Pahute and Rainier mesas, and from the northwestern part of the Amargosa Desert. Few data constrain the conceptual models or the numerical values for this recharge.

- Minor recharge from episodic flooding of the Amargosa River channel. Streamflow in the Amargosa Farms area generally is limited (Osterkamp et al. 1994 [DIRS 100602]). Based on channel-morphology measurements, the composite average recharge is estimated to be 0.2×10^6 m^3/yr along the 15.9-km length of the Amargosa River from Ashton to Big Dune, an area near the site-scale model area (Osterkamp et al. 1994 [DIRS 100602]). Recharge is assumed to be negligible along the few kilometers of the Amargosa River in the southwestern portion of the model.

- Net infiltration from precipitation that becomes recharge to the saturated zone groundwater beneath Yucca Mountain is conceptualized to be derived from infiltration from precipitation that occurs primarily along the northern part of Yucca Mountain (Czarnecki et al. 1997 [DIRS 141643], p. 43; USGS 2001 [DIRS 160355], pp. 63 to 66).

A detailed description of net infiltration to the water table at Yucca Mountain has been developed (USGS 2001 [DIRS 160355]). In general, recharge to the saturated zone is highest at the northern end of Yucca Mountain and below some of the major surface water drainages (BSC 2001 [DIRS 164648], Figure 6.1.3-2). Net infiltration is an episodic process at Yucca Mountain that tends to occur only under wetter than average conditions or in response to isolated but intense storms (USGS 2001 [DIRS 160355], Section 6.1.5). During an average precipitation year (approximately 170 mm annual precipitation), an average annual net infiltration rate of 3.6 mm/yr has been estimated for modern climate scenarios over the 123.7-km^2 area considered in the Yucca Mountain infiltration model domain (USGS 2001 [DIRS 160355], Table 6-8).

Based on regional recharge to the unsaturated zone flow model, recharge to the saturated zone near Yucca Mountain was estimated using the chloride mass balance method (BSC 2003 [DIRS 163045], Section 6.5). For groundwater in the immediate vicinity of Yucca Mountain, chloride concentrations range from 5 to 9 mg/L (BSC 2001 [DIRS 158606], Figure 17), from which local recharge rates were estimated at approximately 7 to 14 mm/yr. These values are consistent with values from unsaturated zone models (BSC 2003 [DIRS 163045], Figure 6.1-2).

Natural surface discharge does not occur near Yucca Mountain. The nearest natural discharge areas connected to the saturated zone flow system beneath Yucca Mountain are Franklin Lake playa (also known as Alkali Flat), and possibly the major springs at Furnace Creek and the floor of Death Valley. Although most regional models (D'Agnese et al. 1997 [DIRS 100131], pp. 113 to 116; Rice 1984 [DIRS 101284], Figures 6, and 12; Czarnecki and Waddell 1984 [DIRS 101042], Plate 2) required a groundwater flow path from Yucca Mountain to Death Valley, Czarnecki and Wilson (1991 [DIRS 148760]) postulated that this was unsubstantiated by (but not inconsistent with) the data. They suggested that groundwater from Yucca Mountain ultimately discharges at Franklin Lake playa through evapotranspiration.

Within the domain of the site-scale saturated zone flow model, groundwater withdrawals occur in the Amargosa Desert (for agricultural and domestic use) and in Jackass Flat (industrial use). In the Amargosa Desert, most discharge occurs in the southwestern corner of the site-scale model domain (D'Agnese et al. 1997 [DIRS 100131]). Pumpage from Boreholes UE-25 J-12 and UE-25 J-13, just east of Yucca Mountain, was about 1,200,000 m^3 from each borehole from 1985 to 1995 (Graves et al. 1997 [DIRS 101046], pp. 40 to 41).

8.3.8.2   Site Saturated Zone Transport

8.3.8.2.1   General Description

The subcomponents (i.e., geologic modeling, field tests, and modeling to match field observations and all forward predictions) listed in this section contributed to establishing the conceptual model of saturated zone transport. The fluid-flow behavior discussed in the previous section sets the overall transport framework on which the modeling of radionuclide migration is based. Conceptual model elements specific to the transport of radionuclides in the saturated zone are the focus of this section.

- Radionuclides enter the saturated zone via groundwater percolating through the unsaturated zone. The exact nature of unsaturated zone transport should not exert a great influence on the site-scale saturated zone flow and transport model; thus, the models can be developed independently.

- The radionuclide transport pathways follow those predicted by the calibrated flow model, with the uncertainties implied by the analyses and data limitations described for the flow model. Flow occurs within the highly fractured portions of the Tertiary tuffs near Yucca Mountain and in the alluvium for the last 6 to 7 km at the south of the model domain near the water table. Upward gradients from the Paleozoic carbonate aquifer to the volcanic tuffs and alluvium imply that there probably would be little tendency for radionuclides to migrate into the deeper units in the regional system, within the Yucca Mountain site-scale model domain.

- In the fractured tuffs, transport pathways are southeasterly, transitioning to southerly along or to the west of Fortymile Wash. Approximately 12 to 13 km from the site, the water table may transition from being in the volcanic tuffs to being in the alluvium. Therefore, conceptual models of tuff and alluvium transport are required.

- Dispersion in the aquifers is governed by local variations in fluid velocity due to heterogeneities in the fractured tuffs and alluvium. Standard theory on the role of heterogeneities on transport behavior and dispersion is assumed to be applicable.

- Contact of radionuclides with rock surfaces can result in sorption and the retardation of radionuclide movement. Some radionuclides (e.g., strontium, cesium, and plutonium) undergo strong sorption, whereas others (e.g., technetium, carbon, and iodine) experience no sorption. Laboratory-derived sorption coefficients, when combined with the field-scale transport model, form the basis for predicting the migration of various radionuclides.

- Colloid-facilitated transport is possible for radionuclides that tend to sorb because the mechanisms that result in sorption to the mineral surfaces also result in sorption onto potentially mobile colloids. Colloids undergo transport via advection, dispersion, and filtration. The resulting affect on transport is uncertain, but most observations are consistent with the general conclusion that strongly sorbing radionuclides, if available, can be transported over large distances.

8.3.8.2.2   Transport Through Fractured Volcanic Tuff

In the fractured volcanic tuffs, the data are consistent with a dual-porosity transport model consisting of fracture flow and matrix diffusion. The hydraulic conductivity of the matrix is lower than the flowing fractures (2 to 6 orders of magnitude lower), and therefore the matrix conducts small amounts of water under natural groundwater flow conditions. However, a large amount of fluid is stored in the pore space of the matrix, and this is important to radionuclide migration because radionuclides can diffuse out of the fractures and into the matrix (BSC 2003 [DIRS 164870]; BSC 2003 [DIRS 167209]; Section 8.3.7.1). Diffusion into the matrix slows the radionuclide travel velocity because the radionuclides are essentially immobile in the nearly stagnant pore water.

Sorbing radionuclides that diffuse into the matrix will be further retarded by sorption onto the large mineral surface area. The system parameters of greatest importance in this conceptual transport model are the relative volumes of flowing and near-stagnant water that radionuclides experience as they move through the fractured tuffs, and the radionuclide sorption parameters onto fracture and matrix minerals. The matrix porosities of interest are those of the rock within fractured regions. Fractures generally are found within moderately to densely welded tuffs, so the range of matrix porosities of these tuffs (0.06 to 0.09 for densely welded and 0.11 to 0.28 for moderately welded) more accurately reflects the fluid storage of interest than the wider ranges of values found within a specific lithologic member. Field data from tracer testing at the C-Wells Complex are consistent with this conceptual model (Section 8.3.7.1), and interpretations and analyses presented in BSC (2003 [DIRS 167209]) provide plausible ranges of ratios of flowing to near-stagnant water volumes derived from tracer testing. Sorption parameters onto fracture and matrix minerals have been reported by Triay et al. (1997 [DIRS 100422]).

8.3.8.2.3　　Transport through Alluvium

The most likely conceptual model of flow and transport in the alluvium is that of a porous continuum. The limited field data from single borehole tracer testing in the alluvium is consistent with this conceptual model (Section 8.3.7.2). Therefore, even though the medium is heterogeneous, effective properties can be established at the site-scale that captures the behavior of the system. This does not mean that transport through the alluvium is homogeneous. It is likely that a radionuclide plume reaching the alluvium would follow preferential flow paths, with the surrounding medium being available for diffusion into dead-end pore spaces. However, in contrast to the fractured tuffs, the effective flow porosity of the alluvium is likely to be greater than the fracture porosity of the tuffs, and the impact of diffusion into the stagnant pore waters will be less pronounced.

The alluvium probably can be treated as a continuum with an effective porosity dictated by the degree of preferential channeling and the intrinsic porosity of the high-permeability pathways. This effective porosity is likely to result in lower predicted transport velocities in the alluvium compared to the fractured tuffs, and sorption is likely to be more effective at retarding radionuclides. The alluvium could be treated as a dual-porosity system; however, observations in the single-borehole tracer tests showed no evidence of dual-porosity behavior. This conceptual model uncertainty remains because the time and spatial scales of the tracer testing are sufficient only to bound the amount of diffusion possible, rather than eliminating the possibility altogether.

8.3.9　　Summary of Site-Scale Flow and Transport Modeling

A site-scale saturated zone flow model (BSC 2001 [DIRS 155974]) was developed to evaluate the movement of groundwater from beneath the repository. The site-scale saturated zone flow model was used to:

- Estimate groundwater flow directions and magnitudes

- Characterize the complex three-dimensional behavior of flow through heterogeneous porous and fractured media

- Identify the potential role of faults as barriers or conduits to groundwater flow

- Provide a model of the flow system for subsequent flow, heat, and radionuclide transport modeling

- Assess the conceptual model and parameter uncertainties with respect to their influence on total system performance of the Yucca Mountain repository.

The modeling report (BSC 2001 [DIRS 155974], Section 6) presents details of this model. Example flow paths predicted by the site-scale saturated zone flow model are shown in Figure 8-27. The site-scale flow model was calibrated to water levels observed in wells, and the residual head differences are shown in Figure 8-28.

The modeling of radionuclide transport in the saturated zone is carried out with a particle tracking method that captures the key conceptual model elements, which include advection, dispersion, matrix diffusion, sorption, and colloid-facilitated transport (BSC 2003 [DIRS 167208]). Uncertainties in site characteristics affecting transport are handled using a Monte Carlo approach.

The saturated zone will affect the performance of the repository in two principal ways. First, the saturated zone will delay the arrival of radionuclides at the compliance boundary, providing more time for radionuclide decay. Second, radionuclide concentrations will be attenuated during transport to the compliance boundary (this effect may not be important to regulatory compliance depending on how dilution at the biosphere is calculated).

8.3.9.1   Site-Scale Model Simplifications

A number of important assumptions were made during development of the site-scale saturated zone flow model (BSC 2001 [DIRS 155974], Section 5).

- The hydrogeologic framework model is an acceptable representation of the hydrogeologic units of the saturated zone flow system. Underlying this assumption is the idea that it is valid to treat the hydrologic properties of a hydrogeologic unit cell as uniform.

- Hydrostratigraphic units and faults influence the magnitude and direction of groundwater flow, and stratigraphic units can be simplified into hydrostratigraphic units.

- On the scale represented by the model, the site is well represented by an effective-continuum flow model.

- Groundwater flow conditions in the saturated zone are approximately steady state.

- A confined aquifer solution is adequate and allows for recharge to be modeled as distributed inflow onto the top layer.

- Horizontal anisotropy in permeability is adequately represented by a permeability tensor that is oriented in the north-south and east-west directions, and a vertical to horizontal anisotropy ratio of 0.1 is appropriate for most of the hydrogeologic units.

- Fluid in the matrix of volcanic rocks is stagnant.

- Changes in the water table elevation due to future climate changes will have a negligible effect on the direction of the groundwater flow.

- Boundary fluxes, provided by the regional flow model, are similar enough to actual fluxes so that any inaccuracies in the calculated regional fluxes do not adversely impact site scale flow and transport calculations.

8.3.9.2   Site-Scale Model Results

The calibrated site-scale saturated zone flow model was used to predict the potentiometric surface. The largest residuals (about 100-m) were in the northern part of the model domain in the high head gradient area near the east-west barrier. These head residuals are largely the result of the low weighting (i.e., not a likely pathway leaving the repository) assigned to these calibration targets and of the uncertainty in these measurements due to the perched conditions that may exist in this area. The next highest group of head residuals borders the east-west barrier and Solitario Canyon fault.

Flow paths from the repository were predicted using the calibrated site-scale model. From the repository area, the pathways generally travel south-southeasterly to near Fortymile Wash, then trend south-southwest and generally follow Fortymile Wash southward. Some of the pathways follow fault zones along Fortymile Wash. These predicted paths are in general agreement with the flow paths interpreted from the hydrochemistry data (Section 8.3.6).

Specific discharge values of 1m/yr, 2m/yr and 2 m/yr were estimated for a nominal fluid path leaving the repository area and traveling 5, 20, and 30 km, respectively. These values were in good agreement with those estimated by the expert elicitation panel, which estimated a specific discharge of 0.7 m/yr at a distance of 5-km (CRWMS M&O 1998 [DIRS 100353], Figure 3-e). The single-borehole tracer tests in the alluvium (Section 8.3.7.2) yielded estimates ranging from 1.3 to 9.4 m/yr, which compare favorably with the values predicted by the calibrated model, although the uncertainty is large.

8.4   LONG-TERM STABILITY OF THE WATER TABLE AND FLOW SYSTEM

8.4.1   Introduction

Changes in hydrologic conditions that have occurred in the Yucca Mountain region during the last few-hundred thousand years are important for assessing the long-term performance of the repository. Proxy records of past climates from the southern Great Basin demonstrate that, relative to modern conditions, episodes of higher effective moisture dominated during the last 400,000 yrs (Sharpe and Forester 2001 [DIRS 160238]; also see Section 6.3). Paleowetlands that have been inferred as sites of former discharge of the regional groundwater system indicate that the lower water-table elevations observed today might be typical only for relatively short, drier interglacial periods. Based on the data, the water table has been higher in the past and would likely rise during future pluvial (glacial) cycles. A rise of the water table could affect performance of the repository adversely by reducing the thickness of the unsaturated zone below the repository and could increase the hydraulic gradient in the saturated zone.

In this section, natural features, isotopic data, and mineralogical data that provide information on past potentiometric levels in the Yucca Mountain region are summarized, and simulations conducted to estimate a realistic upper limit to expected water-table rise are discussed. Additional details of related topics, such as Quaternary climates and the origin of features within the overlying unsaturated zone that some have proposed as evidence of tectonically driven upwelling of water from great depths, are discussed in the previous revision of this report (CRWMS M&O 2000 [DIRS 151945]).

8.4.2   Paleohydrologic Features at the Surface

Several types of paleohydrologic evidence provide information on the elevation attained locally by water tables of the region during Pleistocene time. The evidence consists of tufas, spring orifices, calcitic veins, and cylindrical calcite-lined tubes that mark the routes of former groundwater flow to springs; former water levels marked by calcite cave deposits in the Browns Room of Devils Hole (a fault-controlled cavern in Ash Meadows); and widespread marsh deposits formed at former groundwater discharge sites.

Fossil spring deposits in the southern Great Basin are described by Quade et al. (1995 [DIRS 100074]). They attributed these deposits to the presence of elevated water tables and increased groundwater discharge during the Pleistocene. Estimated changes in water level since the last glacial maximum ranged from 10 to 95 m (Quade et al. 1995 [DIRS 100074], Table 5). Based on the nature and position of the fossil spring deposits, the water table during the Pleistocene might have been from 15 m to at most 115 m higher than present levels (Quade et al. 1995 [DIRS 100074], p. 226). More recent findings, however, limit the maximum to about 70 m higher than present (Paces and Whelan 2001 [DIRS 154724]), because current water levels are not as deep as assumed by Quade et al. 1995 [DIRS 100074]. Recent results from drilling at the paleodischarge sites by Nye County indicate very shallow depth to water (NC-EWDP-7S, 7C, NC-EWDP-ID, 1DX, 1S and NC-EWDP-9S, 95X).

In the carbonate hydrogeologic terrain of the Ash Meadows basin and eastern Death Valley, the paleodischarge deposits consist largely of calcite that forms tufa mounds, travertine terraces, and stratiform deposits, the latter indicating deposition in shallow marshes or ponds, or along the shores of lakes. Contemporaneous deposits in Crater Flat and the Amargosa Desert (Sections 8.4.2.2, 8.4.2.3, and 8.4.2.4) record discharge from basin-fill deposits derived primarily from volcanic rocks. Consequently, the amount of carbonate material is less.

8.4.2.1   Ash Meadows Basin

Devils Hole (DH on Figure 8-29) is located about 50 km southeast of Yucca Mountain, at the terminus of the Ash Meadows groundwater basin (Section 8.2). Analysis of petrographic and morphological characteristics of calcite deposits precipitated at or near the present water table provides a chronology of water table fluctuations for the past 120,000 yrs (Szabo et al. 1994 [DIRS 100088]). Relative to the present position, the water table was more than 5 m higher between about 116,000 to 53,000 yrs ago, fluctuated between about 5 and 9 m higher during the period between about 44,000 and 20,000 yrs ago, and declined from 9 m higher to its present level during the past 20,000 yrs (Szabo et al. 1994 [DIRS 100088], p. 59). These water-level fluctuations generally correlate in time with other Great Basin proxy paleoclimatic data. Based on the rapidity of the water-level fluctuations, they considered climate change, particularly the previous occurrence of wetter and drier episodes in the Great Basin, to be the dominant determinant of these water table fluctuations.

Tufas and carbonate-lined paleodischarge paths of unknown age as much as 14 km north and northeast of Devils Hole occur in the eastern extension of Amargosa basin (Amargosa Flats) at elevations up to about 760 to 770 m, about 40 to 50 m higher than the presumed present potentiometric level in the LCA that underlies the area at depth (Winograd and Doty 1980

[DIRS 107320], pp. 64 to 65). However, an intensive search for such deposits on the ground and by small aircraft showed that they occur at scattered, isolated localities but are generally absent at similar elevations elsewhere within the basin and along its margins. The localities are associated with known or suspected faults, including the Gravity fault that controls modern discharge areas in Ash Meadows and northward. The modern water table in the Cenozoic valley-fill sediments of Amargosa Flats is about 9 m lower than the potentiometric level of the deeper Paleozoic carbonate aquifer (Winograd and Doty 1980 [DIRS 107320], p. 76). In the more active hydrologic regime associated with Pleistocene climates, the potentiometric difference was probably greater. Where paleodischarge deposits are apparently associated with faults, it is possible, perhaps probable, that upflow along faults produced scattered potentiometric mounding and discharge to the surface at elevations higher than the surrounding water table.

8.4.2.2 Southern Crater Flat Area

Paleospring deposits are located on the north and south sides of the unnamed ridge that defines the southern edge of Crater Flat (Figure 8-29). These deposits, located about 15 to 18 km southwest of Yucca Mountain, are the closest unequivocal groundwater discharge deposits to Yucca Mountain (Quade et al. 1995 [DIRS 100074], p. 226). On the north side of the unnamed ridge, the Crater Flat Deposit occurs at an elevation of about 840 m. On the south side of the unnamed ridge, there are two paleospring deposits. The Lathrop Wells Diatomite occurs at elevations ranging from 790 to 800 m, and the Crater Flat Wash deposit occurs at an elevation of about 790 m. The paleospring deposits also are referred to by earlier names: the Crater Flat Deposit formerly was Site 199, the Lathrop Wells Diatomite formerly was the Horse Tooth Deposit, and the Crater Flat Wash deposit formerly was the Root Cast Deposit.

The lithologic characteristics of these deposits are similar to the State Line Deposits and the Indian Pass Deposit (SLD and IPD on Figure 8-29). The particle size distribution within the discharge deposits is dominated by finesand and silt fractions. Bedding typically is massive, punctuated by occasional laterally discontinuous layers of authigenic materials such as carbonate-rich nodules or mat-like layers, casts of insect burrows or plant petrifactions. Authigenic calcite and lesser silica produce a wide range of cementation from soft, barely calcareous silt to contorted hard nodules to dense limestone containing regularly spaced, nearly vertical tube-like voids that are probably plant-stem molds. Much of the layered or nodular limestone typically contains fine-grained clays. A 1- to 2- m thick bed of white to whitish gray diatomite is unique to the Lathrop Wells Diatomite deposit (Paces et al. 1996 [DIRS 107002], p. 3).

Paces et al. (1993 [DIRS 106474]) reported uranium-series disequilibrium ages of the Crater Flat Deposit and Lathrop Wells Diatomite paleospring deposits, and additional ages were determined for samples taken from these and other paleospring deposits within the vicinity, adding ^{14}C and thermal-luminescent techniques to the uranium-series dating (Paces et al. 1996 [DIRS 107002]). Results of the three methods generally were consistent with stratigraphic characterization of these sites and others in the vicinity. They indicate that, beginning about 60,000 yrs ago, spring deposits formed above the modern water table until about 15,000 yrs ago at up-gradient sites, and until about 9,000 to 10,000 yrs ago at lower sites. An older episode occurred between 90,000 and 180,000 yrs before present (Paces et al. 1996 [DIRS 107002], p. 1). Discharge

activity during this time was consistent with a regional phenomenon rather than isolated activity related to local hydrologic conditions (Forester et al. 1996 [DIRS 100148], p. 56).

Based on a regional potentiometric map (Winograd and Thordarson 1975 [DIRS 101167], Plate 1), the Crater Flat Deposit was estimated to be 98 to 116 m above the potentiometric surface (Paces et al. 1993 [DIRS 106474], p. 1578). The authors inferred that the water table had risen to that maximum height during the late Quaternary and may have fluctuated repeatedly. No similar deposits were found at higher elevations in the region, implying that these values represent maximum water-table excursions. The Lathrop Wells Diatomite and Crater Flat Wash sites were estimated to be 79 to 85 m above the current potentiometric surface (Paces et al. 1993 [DIRS 106474], p. 1578). For the southern Crater Flat area, the late Pleistocene water table has, until recently, been represented by all investigators of the area to have been 80 m to 120 m above the modern level. Water levels at NC-EWDP-75 and 75C are about 7 to 8 m. At NC-EWDP-1DX near Highway 95, the depth to water is about 17 m; at NC-EWDP-95X, it is about 31 m.

Data on groundwater levels from the NC-EWDP boreholes have revealed that water levels at the Lathrop Wells Diatomite and Crater Flat Wash sites are at elevations of about 787 m and 767 m, respectively (LWD and CFW on Figure 8-29). Water temperatures at the shallowest depths are 27°C to 30°C (Paces and Whelan 2001 [DIRS 154724], p. 2), probably indicating that regional, deep flow is rising in this area and is possibly controlled by the Highway 95 fault, north-striking faults (e.g., Windy Wash and Solitario Canyon), or a combination of these. An even higher water level (830 m) is indicated for Borehole NC-EWDP-7S (near the Crater Flat Deposit), but this tentatively is considered to be perched. Rather than the previously accepted requirement for potentiometric rises as large as 120 m to produce surface discharge, the new data indicate necessary rises of only 17 to 30 m for the two southern sites (Paces and Whelan 2001 [DIRS 154724], p. 4) and not more than 70 m, but possibly as little as 10 m, at the Crater Flat Deposit site.

8.4.2.3   State Line Deposits

Paleodischarge deposits similar to those at the Crater Flat sites occur along the Nevada California state line near the confluence of Fortymile Wash and the Amargosa River (Figure 8-29). The water table is shallow along this reach of the river, and extensive carbonate-capped terrace deposits indicate that discharge occurred as much as 6 m above the river bottom (which is likely only a few meters above the water table) between 30,000 and 50,000 yrs (Paces et al. 1996 [DIRS 101281], p. 10). Other samples from more limited exposures yield uranium-series and thermal-luminescence ages as great as 100,000 yrs, and radiocarbon dates as young as about 10,000 yrs (Paces et al. 1996 [DIRS 101281], p. 11). These findings are consistent with the belief that the Amargosa River system was a major source for Lake Manly in Death Valley until about 10,000 yrs ago (Anderson 1999 [DIRS 150236]; see also Chapter 6).

8.4.2.4   Indian Pass Deposit

An exposure of paleodischarge deposits occurs at an elevation of about 780 m near the toe of the northeast-facing slope of the Funeral Mountains (Figure 8-29) that are similar to the Crater Flat

and State Line deposits. Limited sampling and uranium-series and thermal-luminescence geochronology indicate that they are comparable in age to the 10,000 to 60,000 yr episode of discharge to the surface at several localities in the southern Great Basin.

8.4.2.5 Fortymile Canyon Packrat Middens

Ancient packrat middens in the middle reaches of Fortymile Canyon, approximately 12 km northeast of Yucca Mountain have been studied. One midden site is located near the confluence of Pah and Fortymile canyons, where the present water table is about 30 m deep (approximately 1,185 m above mean sea level). Two assemblages from this site provide radiocarbon dates of more than 52,000 yrs and about 47,000 yrs (Spaulding 1997 [DIRS 147841], p. 1). The midden site preserves plant species that indicate damp soil conditions and the presence of a nearby former water table, as well as one that is restricted to the sandy, disturbed floors of washes above the water table. Based on the midden location, current water-table elevations in the area, and the plant species identified, and taking into account estimated magnitudes of geomorphic changes in this part of the canyon area since the time the midden was formed, the estimated water table was formerly a minimum of about 50 m higher at this location and could have been a maximum of about 80 m higher during early to middle Wisconsin time (Spaulding 1997 [DIRS 147841]).

Figure 2 in Spaulding (1994 [DIRS 148867]) shows two springs located near FMC-7. One spring ~700 m to the north at an elevation of ~4300 ft and a seep ~900 m to the WNW at an elevation of ~4100 ft. The midden is at an elevation of ~4150 ft (Spaulding 1997 [DIRS 147841]). Spaulding uses a value of 1,185 m (~3885 ft) for the present elevation of the water table. If that is the case, then these modern day springs are perched. Given that perched springs are found in this area under current climatic conditions (demonstrating conditions conducive to perching), it is probable that under wetter conditions perched springs would be more abundant and perched springs could occur near FMC-7 and not require an elevated regional water table. Spaulding did not consider the possibility of perched springs, but that is an alternative explanation for the results.

8.4.2.6 Sources of Surface Discharge

Based on ratios of isotopic compositions (initial $^{234}U/^{238}U$, $^{87}Sr/^{86}Sr$, and $^{13}C/^{14}C$), the source or sources of water for the Crater Flat and State Line paleodischarge deposits could not have been surface water or perched water within the present unsaturated zone. The compositions of the deposits are consistent with water from the regional volcanic and alluvial aquifers and possibly, but less likely, the regional carbonate aquifer (Paces et al. 1995 [DIRS 106465], pp. 17 to 19, Tables 14 and 15).

8.4.3 Past Water Table Elevations at Yucca Mountain

Although there are no definitive data for past water table elevations beneath Yucca Mountain, several lines of evidence suggest that the water table elevation has never been more than 100 m higher than exist today.

Glass within the nonwelded tuffs occurs above and below the welded zone in the Topopah Spring Member of the Paintbrush Tuff (Bish and Vaniman 1985 [DIRS 101196]). Bish and Vaniman (1985 [DIRS 101196], p. 8) state "the lower nonwelded vitric zone thins and

disappears to the east where stratigraphic dip and structural displacements bring the basal Topopah Spring Member glassy zone closer to the static water level. The vitric nonwelded material may have paleohydrologic importance because the preservation of open shards and pumice made of nonwelded glass is rare below past water levels (Hoover 1968 [DIRS 106046])." The minor glass that does exist below past zones of saturation may do so because of armoring by alteration products (Bish and Chipera 1989 [DIRS 101195], p. 11). Where present, the base of the lower nonwelded vitric tuff occurs about 80 to 100 m above the present water table. Based on mineralogy, Bish and Vaniman (1985 [DIRS 101196], p. 10) concluded, "The only apparent change in phase assemblage near the water table in Yucca Mountain is the alteration of vitric tuff of Calico Hills and lower Topopah Spring Member." These observations suggest that past water levels beneath Yucca Mountain may never have been more than 100 m higher than the modern water levels.

Levy (1991 [DIRS 100053]) re-evaluated the base of the vitric tuff as a paleohydrologic indicator in the light of structures and uplift that occurred after devitrification. It was noted that some of the devitrified tuff, which occurred farthest above the current water table, was not coplanar with the water table and apparently had formed prior to tilting of the tuffs. Thus, some of the devitrification must have occurred more than 13 million yrs ago. Other past water table elevations must be younger and postdate major tectonic events. The occurrence of such a stand probably cannot be dated, but it might have occurred several million to several thousand years ago. Even in the absence of a date for the alteration, the base of the nonwelded vitric tuff shown on the cross-sections of Bish and Vaniman (1985 [DIRS 101196], Appendix B) is tens of meters to more than 100 m below the base of the repository horizon. Thus, a possible maximum (although undated) water table stand is lower than the repository horizon under consideration. If the structural interpretations proposed by Levy (1991 [DIRS 100053]) are taken into account, the maximum rise in the water table, for a long enough period of time to cause devitrification, is 60 m. Levy (1991 [DIRS 100053]) reported that the time required to form zeolites from glass can be from thousands to millions of years where meta-stable minerals prevail, and thus, larger short-term fluctuations are not precluded by the elevation of the devitrified tuff.

There was almost no drill-core information for the central and southern part of the exploration block (Levy 1991 [DIRS 100053]), but drill cores from Boreholes USW SD-12 and USW SD-7 provide data in this area. The new data generally support the previous findings, but do not provide an unequivocal limit of water table rise.

Studies of secondary minerals in samples from the Exploratory Studies Facility and the Enhanced Charaterization Repository Block (ECRB) Cross-Drift show no evidence that the saturated zone ever extended to the elevation of these tunnels, and it was concluded that all secondary minerals precipitated in an unsaturated environment (Paces et al. 2001 [DIRS 156507], p. 73 to 75; Wilson and Cline 2001 [DIRS 155426]; Whelan et al. 2001 [DIRS 154773]; Whelan et al. 2002 [DIRS 160442]). The physical evidence for formation in an unsaturated environment includes the location of secondary calcite and silica, which is generally on the floors of lithophysal cavities and footwalls of fractures, and that over 90 percent of the fractures and cavities exposed in the Exploratory ECRB Cross-Drift do not contain secondary minerals (Whelan et al. 2002 [DIRS 160442], p. 737 to 738). Deposition in a saturated environment would result in coatings on both sides of fractures, no preferential deposition on the floors of cavities, and approximately the same amount of mineralization in all cavities.

Geochronologic studies have shown that unsaturated conditions at this level have persisted for the last 10 million years (Neymark et al. 2002 [DIRS 158673], p. 732).

Deposition of calcite and silica at constant temperature within the unsaturated zone is caused by loss of a gas phase (either carbon dioxide for calcite or water vapor for silica). The greater percentage of secondary silica in the Tiva Canyon Tuff than in the Topopah Spring Tuff is consistent with precipitation in the unsaturated zone because the former has better communication with the atmosphere, and therefore, a better chance for loss of water vapor by evaporation (Paces et al. 2001 [DIRS 156507], pp. 66, 67, and 75). Larger openings favor gas loss in the unsaturated zone, which is consistent with the observed distribution of fracture coatings. Secondary minerals are rare in fractures and apertures smaller than about 2 mm (Whelan et al. 2002 [DIRS 160442], p. 743). Paces et al. (2001 [DIRS 156507]) have suggested that the morphology of the secondary minerals is consistent with precipitation within the unsaturated zone. In their model, water is drawn by surface tension to the tips of crystals where gas loss causes precipitation and consequent elongated crystals.

Early studies of secondary minerals obtained from outcrops and boreholes lead to inferences on past water table elevations.

Strontium and carbon isotopic compositions of calcite were similar to compositions found in soils in the vicinity of Yucca Mountain to depths within 85 m of the water table. This leads to a model of downward percolating meteoric water through the unsaturated zone with minor chemical interaction of the water and the rocks through which it passed. This model is still the preferred one; however, studies of secondary minerals from the Exploratory Studies Facility and the ECRB Cross-Drift have shown that calcite is zoned as a function of time (strontium becoming more radiogenic and carbon becoming lighter with decreasing age). Without age control for the early analyses, it can only be concluded that the secondary minerals with compositions similar to modern soil were formed in the unsaturated zone, but this does not preclude excursions of the water table without leaving a mineralogic record.

Calcite from the unsaturated zone fluoresces bright white to pale purple, whereas calcite from the saturated zone fluoresces in hues of orange to pink (Whelan and Stuckless 1992 [DIRS 108863]). In addition, saturated zone calcite exhibits strong phosphorescence. The fluorescence analyses did not show zoning, and are thus a good indication for a maximum rise in the water table beneath Yucca Mountain of less than 85 m.

Chemical anomalies, such as low abundances of transition elements and prominent negative cerium and europium anomalies in the unsaturated zone calcites, have been noted in Boreholes USW G-2 and USW GU-3/G-3 (Vaniman 1994 [DIRS 108813]). These anomalies are not as definitive in USW G-4 (Vaniman 1993 [DIRS 145240]). The change in calcite chemistry appears to be near the present water table elevation. In a study of minerals in fractures in the same borehole (Carlos 1987 [DIRS 101204]), it was noted that mineralogy and mineral morphology did not change at or near the current water table, but rather about 118 m above it. These studies reported no age control on samples and were completed prior to the discovery of the long-term growth and consequent zoning of calcite deposits.

Studies of fluid inclusions within calcites from drill cores support an unsaturated zone origin for these minerals (Roedder et al. 1994 [DIRS 109159]). Crushing of the fluid inclusions shows that they formed at low (essentially atmospheric) pressures. Had they formed under saturated conditions with saturation existing all the way to the surface of the earth, the overlying water column would have generated as much as 30 atmospheres of pressure for the deepest sample investigated.

Fluid inclusion studies show that the early calcites were deposited at temperatures of 35°C to 85°C (Whelan et al. 2002 [DIRS 160442], p. 746). Similar temperatures were reported by Wilson and Cline (2001 [DIRS 155426]) and Dublyansky et al. (2001 [DIRS 161543]). The latter authors, together with Hill and Dublyansky (1999 [DIRS 165606]) and Dublyansky and Szymanski (1996 [DIRS 161545]) argued that the elevated temperatures indicated an origin from upwelling hydrothermal fluids. However, there are abundant physical, chemical, and isotopic data that conflict with this theory (e.g., Stuckless et al. 1991 [DIRS 101159]; Stuckless et al. 1998 [DIRS 100086]; Vaniman 1993 [DIRS 145240]; Whelan et al. 1994 [DIRS 100091]; Whelan et al. 2001 [DIRS 154773]; Paces et al. 1998 [DIRS 100072]; and Paces et al. 2001 [DIRS 156507]). Furthermore, there is no credible mechanism for rapidly raising the water table hundreds of meters above its current position (National Research Council 1992 [DIRS 105162]; Rojstaczer 1999 [DIRS 129750]). Because the fluid inclusions with liquid and water phases (indicating formation above ambient temperatures) are largely restricted to early calcite and lacking from late-stage calcite, the elevated temperatures are best explained by the long cooling history of the Timber Mountain Caldera (Marshall and Whelan 2001 [DIRS 163591]). Additional details on these arguments are summarized in the previous revision of this report (CRWMS M&O 2000 [DIRS 151945], Section 4.4.4).

8.4.4 Numerical Models as Predictors of Water Table Elevations Given Future Climate Assumptions

A number of modeling simulations have been conducted to evaluate the effects of past and hypothetical future changes in climate on the height of the water table in the Yucca Mountain region. This section describes and summarizes the results of these simulations.

Czarnecki (1984 [DIRS 101043]) evaluated the effects of increased precipitation (similar to past pluvial conditions) on the groundwater system in the vicinity of Yucca Mountain using a two-dimensional finite-element groundwater flow model of the region. Input parameters and initial conditions for the model were based on previous modeling (Czarnecki and Waddell 1984 [DIRS 101042]) to derive a baseline potentiometric surface (current water-table levels). A 100-percent increase over modern precipitation was assumed, based on previous investigations performed by Spaulding et al. (1984 [DIRS 106503]), resulting in a 15-fold increase in recharge over the model domain. At Yucca Mountain, recharge increased from the then-estimated modern rate of 0.5 mm/yr to a simulated rate of about 8 mm/yr. Results from the model showed a maximum increase in water table elevation of about 130 m beneath the site of the repository (Czarnecki 1984 [DIRS 101043], p. 21). Among the conservative assumptions was that half of the calculated recharge flux in the model was applied directly east of the repository site along a short segment of Fortymile Wash, which caused about 75 percent of the computed water table rise. Despite the limitations imposed by computers and models at the time, as well as by less complete hydrogeologic data than now exist, the results are similar to those from later modeling

(Czarnecki 1985 [DIRS 160149]). They are commonly cited as being consistent with water-table rises estimated from studies of paleodischarge deposits and subsurface mineralogy. However, more complete hydrologic properties data and new potentiometric surface data at the Nye County paleodischarge sites show that such a rise is highly unlikely.

Another flow model was developed by Ahola and Sagar (1992 [DIRS 103622]), who used a regional groundwater flow model to evaluate the effect of a 10-fold increase in recharge within the Yucca Mountain area, including Fortymile Wash. Simulations indicated that the water table might rise about 75 to 100 m; however, the model was preliminary, required the use of interpolated data based on previous calibrated models, and was not fully calibrated.

D'Agnese et al. (1999 [DIRS 120425]) modeled the effects of climate change on the Death Valley regional groundwater flow system using a past climate representative of the late Pleistocene full glacial condition (21,000 yrs ago), for which maximum water-table levels are documented by studies of paleodischarge sites and mineralogic characteristics in the subsurface at Yucca Mountain. An initial simulation was evaluated by comparing the results to observed paleodischarge sites around the region. The cooler and wetter conditions present 21,000 yrs ago were also considered to represent a wet climate that might occur in the future during the operational life of the repository (D'Agnese et al. 1999 [DIRS 120425], p. 4).

A second simulation was performed in which recharge to the Death Valley regional groundwater flow system was increased assuming a wetter and warmer future climate due to increased carbon dioxide concentrations in the atmosphere.

In each of these, the changes in climatic conditions were simulated by changing the distribution and rates of groundwater recharge over the model grid. Average annual precipitation maps for past-climate and future-climate scenarios were reassigned to the model grid. Results of the simulations were evaluated through analyses of simulated discharge areas, water-level changes, potentiometric surface configurations, and water budgets. The simulation for the past climate (21,000 yrs ago) was estimated to have increased recharge five-fold, which led to an increase in elevation of the potentiometric surface near Yucca Mountain between approximately 60 and 150 m. These changes presumed a much greater depth to water at the Nye County paleodischarge sites than is now known to exist.

For the past-climatic condition, the most substantial water-level rises in the Yucca Mountain area occurred to the north and northeast of Yucca Mountain in the Timber and Shoshone Mountain areas. The model predicted enough groundwater in the system to maintain paleolake levels in the northern parts of the model domain and at Lake Manly in Death Valley. Groundwater discharge occurred at most of the observed paleodischarge sites, which indicated that the recharge distribution used in the simulation generally was valid. Higher water table levels that were predicted to occur between Rainier Mesa and Yucca Flat north of Yucca Mountain increased the areal extent and steepness of the present-day large hydraulic gradient in this area. However, the large gradient appeared to remain fixed geographically, that is, it did not migrate southward toward the repository block (D'Agnese et al. 1999 [DIRS 120425], p. 27).

Under future-climate conditions, simulated recharge increased and decreased throughout the model domain (D'Agnese et al. 1999 [DIRS 120425], p. 2). The configuration of the simulated

potentiometric surface changed slightly relative to simulated present-day conditions to indicate depressions at discharging playas. Simulated discharge to these playas, however, was not as great as during the full-glacial (past) climate, and perennial lakes probably would not be supported at these locations. Simulated discharge increased over present-day discharge at Ash Meadows, Oasis Valley, and Death Valley. Under future-climate conditions, large hydraulic gradients were maintained and enhanced in some areas, but they did not migrate in position. Simulated recharge throughout the modeled area increased by a factor of about 1.8 compared to simulated present-day recharge levels, causing the water table beneath the repository to rise about 50 m. There are numerous limitations in evaluating the effects of climate change on regional groundwater flow systems when using numerical models (D'Agnese et al. 1999 [DIRS 120425]). Limitations relevant in estimating future water table elevations are:

- The predictive simulations can be no more accurate than the present-day, steady-state regional groundwater flow model on which they are based.

- Paleohydrologic evidence is critical to the validity of the assumptions, and this evidence, including evidence of past-discharge areas, is subject to interpretation.

- The size of the model grid from which the average annual precipitation distributions for past-climate and future-climate conditions were extracted was greater than the size of the grid required for the regional groundwater flow model.

Based on these considerations, the simulated effects of climate change should be considered conceptual in nature and should be used only to estimate the magnitudes, not to predict values, of potential increases of regional groundwater levels relative to the present-day water table.

8.4.5 Summary of Paleohydrologic Evidence

Investigators have analyzed paleohydrologic evidence and conducted numerical simulations to evaluate the effects that various past and potential future climates on water-table elevations at and near Yucca Mountain.

In the carbonate terrain of the eastern Amargosa Desert, the evidence indicates that the Late Pleistocene water level in Devils Hole was at most 9 m higher than at present. As far as 14 km upgradient in the Ash Meadows groundwater basin, potentiometric levels were as much as 50 m above modern. As noted earlier, the current depth to water is poorly constrained and the age of the deposits is unknown.

In the Amargosa River at the Nevada-California state line, within the Alkali Flat-Furnace Creek groundwater basin, late Pleistocene water levels reached more than 6 m above the present river channel. At the ridge dividing the Amargosa Valley and Crater Flat sections of the Alkali Flat-Furnace Creek groundwater basin, about 15 to 18 km south of the repository site, water levels reached 10 to less than 30 m above the present water table, although the rise was at least somewhat limited below this potential maximum by discharging at the land surface.

At the repository site south of the large hydraulic gradient, subsurface mineralogic evidence suggests a rise during the Quaternary of at most 60 m above the present water table, although a

rise of 100 m cannot be ruled out. North of the large hydraulic gradient, isotope compositions in a drillcore may indicate a maximum rise of 85 m, and packrat midden data in nearby Fortymile Wash suggests late Pleistocene discharge to the surface at about 80 m above the present water table.

Modeling of the regional groundwater system under climatic conditions reconstructed to have existed during the glacial maximum at about 21,000 yrs results in estimated water-table levels beneath Yucca Mountain that are 60 to 150 m higher than present (D'Agnese et al. 1999 [DIRS 120425]). Given the uncertainties in such simulations, these estimates are quite consistent with the field evidence.

Although there is mineralogic evidence for a water table rise beneath Yucca Mountain of as much as 100 m, the age of such a rise is poorly constrained and may represent conditions from 10 million years ago. Other reported large rises at paleodischarge sites assumed greater depth to water than is now known to exist, and in some cases involved deposits of unknown age. The most reliably dated paleospring deposits (where depth to water is known) suggest groundwater table rises of only 10 to 30 m in the last 15,000 years.

8.5   GROUNDWATER USAGE

8.5.1   Historical Groundwater Usage

Historical groundwater use in the immediate vicinity of Yucca Mountain primarily was a result of the Nevada Test Site and the YMP activities, including construction of the Exploratory Studies Facility (ESF). Groundwater development in the immediate vicinity of the Yucca Mountain area began in the 1950s. Wells UE-25 J-12 and UE-25 J-13, located southeast of Yucca Mountain in the western part of Jackass Flats (Figure 8-10), were developed for water supply during the early 1960s (Luckey et al. 1996 [DIRS 100465], p. 41). Wells UE-25 J-12 and UE-25 J-13 have total depths of 347 and 1,066 m (1,139 and 3,498 ft), respectively. Well UE-25 J-12 is perforated in the welded tuff aquifer within the Topopah Spring Tuff of the Paintbrush Group; well UE-25 J-13 is perforated in the Topopah Spring Tuff of the Paintbrush Group, the Tram Tuff of the Crater Flat Group, and the upper part of the Lithic Ridge Tuff (Graves et al. 1997 [DIRS 101046], pp. 95 to 96). The well capacities for wells UE-25 J-12 and UE-25 J-13 are and 48 and 43 L/s (760 and 680 gpm), respectively (DOE 1996 [DIRS 101811], Table 4-3). Information describing the drilling and testing of well UE-25 J-13 is presented in Thordarson (1983 [DIRS 101057]).

Between 1962 and 1967, wells UE-25 J-12 and UE-25 J-13 were pumped extensively to supply water for a nearby rocket development station (Young 1972 [DIRS 103023]). The annual average pumping rate from these two wells during this time period is estimated to be 690,000 m^3/yr (560 acre-ft/yr) (Luckey et al. 1996 [DIRS 100465], p. 41). The 1983 to 1997 average annual pumping rate from well UE-25 J-12 ranged from 47,450 m^3/yr (38.43 acre-ft/yr) to 181,405 m^3/yr (146.94 acre-ft/yr), and averaged 107,310 m^3/yr (87 acre-ft/yr) (Tucci and Faunt 1999 [DIRS 145962], p. 5). The 1983 to 1996 average annual pumping rate from well UE-25 J-13 ranged from 62,415 m^3/yr (50.56 acre-ft/yr) to 184,325 m^3/yr (149.30 acre-ft/yr), and averaged 116,800 m^3/yr (95 acre-ft/yr) (Tucci and Faunt 1999 [DIRS 145962], p. 5). Table 8-9 presents a historical summary of the pumping that has occurred in wells UE-25 J-12 and

UE-25 J-13. Well UE-25 J-11, also located in Jackass Flats, was completed in 1957. However, this well was not used for water supply because of poor water quality and a well casing problem (Luckey et al. 1996 [DIRS 100465], p. 41).

Within the Yucca Mountain area, groundwater has been pumped intermittently from various Boreholes for hydraulic testing purposes, including wells UE-25 J-12, UE-25 J-13, C-Holes Complex in Basin 227A, and Boreholes USW VH-1 and USW H-6 in Crater Flat. Wells at the C-Holes Complex were pumped for short periods of time (days to weeks) intermittently for hydraulic testing in the mid-1980s, 1995, and early 1996 (Tucci and Faunt 1999 [DIRS 145962], p. 5). During a multi-borehole pumping test conducted in November 1984, the pumping rate at Borehole UE-25 c #1 (one of the wellbores at the C-Holes Complex) was about 32,000 m^3 (26 acre-ft) (Luckey et al. 1996 [DIRS 100465], p. 41). At the same borehole complex, water was pumped from well UE-25 c #3 from May 1996 through November 1997 for the purpose of hydraulic and tracer tests (Tucci and Faunt 1999 [DIRS 145962], p. 5). During 1997, the average pumping rate from well UE-25 c #3 was 773 m^3/day (0.63 acre-ft/day) (Tucci and Faunt 1999 [DIRS 145962], p. 5).

Groundwater withdrawal for the purpose of hydraulic testing generally is not classed as groundwater development. However, long-term testing resulting in the discharge of large quantities of groundwater requires that temporary applications to appropriate (i.e., formally obtain permits for future usage of water) be filed with the Nevada State Engineer. This was the method used, for example, in conjunction with the well testing conducted at the C-Holes Complex, in Hydrographic Basin 227A. Table 8-10 presents a summary of the historical annual groundwater withdrawals in Basin 227A. The approximate boundary of Hydrographic Basin 227A, and the boundaries of adjacent Hydrographic Basins 227B (Buckboard Mesa), 228 (Oasis Valley), 229 (Crater Flat), and 230 (Amargosa Desert), are depicted on Figure 8-30.

In Crater Flat (Basin 229), water has been occasionally pumped from Borehole USW VH-1 (Figure 8-10) at low rates (Luckey et al. 1996 [DIRS 100465], p. 41). The volume of water pumped from Borehole USW H-6 during pumping tests in 1982 and 1984 was 25,000 m^3 (20 acre-ft) (Luckey et al. 1996 [DIRS 100465], p. 41). Groundwater was also pumped elsewhere in Crater Flat in support of private mining operations. Committed groundwater resources by water permits and certificates for Basin 229, as of January 9, 1999, were 1.43×10^6 m^3/yr (1,160.83 acre-ft/yr) (CRWMS M&O 2000 [DIRS 145966]). Approximately 95 percent of this amount—1.36×10^6 m^3/yr (1,100 acre-ft/yr)—was committed for mining use, and the remainder—75,000 m^3/yr (61.38 acre-ft/yr)—was committed for industrial use.

Water use on the Nevada Test Site has varied considerably over the history of the facility. The groundwater withdrawal rate has ranged from 1 to 4.2×10^6 m^3/yr (800 to 3,400-acre-ft/yr) (DOE 1996 [DIRS 101811], p. 5-29). The total pumping capacity is estimated to be about 8.6×10^6 m^3/yr (7,000 acre-ft/yr) based on the Nevada Test Site Environmental Impact Statement report (DOE 1996 [DIRS 101811], Table 4-3). This potential capacity is much greater than the historical pumping rate.

8.5.2 Recent Groundwater Pumpage in Basin 227A

Table 8-10 summarizes annual withdrawal (if available) during the period of 1961 to 1992. Wells UE-25 J-12 and UE-25 J-13 are currently used to supply the water needs of the YMP and other uses at the Nevada Test Site. Between 1993 and 1997, the combined amount of water pumped from wells UE-25 J-12 and UE-25 J-13 averaged 281,000 m^3/yr (228 acre-ft/yr) (CRWMS M&O 2000 [DIRS 145966], p. 25). During this same time period, the amount of water pumped from the C-Holes Complex ranged from 0 (1993 and 1994) to a high of 238,000 m^3/yr (193 acre-ft/yr) in 1997, with an annual average withdrawal rate of 97,400 m^3/yr (79 acre-ft/yr) (CRWMS M&O 2000 [DIRS 145966], p. 25). An average of 191,000 m^3/yr (155 acre-ft/yr) of this diverted water was supplied to the YMP (CRWMS M&O 2000 [DIRS 145966], p. 25). The balance of the water (an average of 187,000 m^3/yr [152 acre-ft/yr]) was used on the Nevada Test Site. Table 8-11 summarizes water pumping rates from Basin 227A between 1993 and 1997.

8.5.3 Development of Water Resources in the Region

Groundwater is the principal source of water for agricultural, mining, industrial, municipal, and domestic uses within the Death Valley region. By contrast, surface water, which is sparsely distributed and occurs generally at small and unreliable rates of flow, is a very minor component of the region's water resource inventory. Most of the groundwater-resource development in the central Death Valley subregion has occurred in Nevada, although minor development has taken place in the extreme southwestern Amargosa Desert near Death Valley Junction, California. In the Furnace Creek area of Death Valley National Park, spring discharge supplies the small domestic and commercial use. The quality of groundwater in the region is marginally suitable for agricultural use, and in most respects is suitable for industrial uses and for potable drinking water. A notable exception to the latter is the fluoride content, which typically exceeds state and federal limits in groundwater supplied to areas near Beatty and Lathrop Wells (Amargosa Valley).

Most of the producing wells in the region are completed in the alluvial sands and gravels in the upper 90 to 150 m (300 to 500 ft) of the basin-fill (valley-fill aquifer) sediments in the Amargosa Desert. These permeable deposits are most prevalent in the north-central part of the structural basin, where tributaries of Fortymile Wash have washed in vast quantities of sand and gravel. This is known as the "Amargosa Farms area" and it contains among the densest concentrations of wells in the region. These sediments are capable of yielding large discharge rates (well yields from 6.3 to 130 L/s [100 to 2,000 gpm]). The valley-fill aquifer provides water for irrigation, mining, commercial, and domestic use in the western Amargosa Desert and Oasis Valley, and the support of operations of the Nevada Test Site in Mercury Valley, Frenchman Flat, and Yucca Flat.

Paleozoic (carbonate aquifer) rock units currently provide productive quantities of water for commercial/domestic use at a few locations within the region. The capacity of a well installed within this aquifer depends primarily on the number and condition of fractures present in the carbonate rocks that are intersected by the well. Due to the relatively great depth of the carbonate aquifer in the Amargosa Desert—as much as 760 m (2,500 ft) in the Amargosa Farms area—where water is most in demand, and because of the unpredictability of encountering

productive zones, there is currently little interest in developing the carbonate aquifer for private use.

Numerous wells on the Nevada Test Site and Oasis Valley produce water from volcanic rocks. Volcanic rocks have also been tested in numerous exploratory holes drilled at Yucca Mountain. Two wells in Crater Flat currently produce water from the tuff aquifer. Fractured welded tuffs and, to a lesser degree, lavas are the principal aquifers within the Tertiary volcanic suite of rocks underlying the Yucca Mountain region, although some nonwelded tuffs may also be moderately productive. The Topopah Spring Tuff, a formation within the Paintbrush Group, is the transmissive aquifer developed in the current Jackass Flats production wells, UE-25 J-12 and UE-25 J-13. These wells have reported well yields of about 48 and 43 L/s (760 and 680 gpm).

8.5.4   Summary

Groundwater is the principal source of water for agricultural, mining, industrial, municipal, and domestic uses within the Death Valley region. Most of the producing wells in the region that are capable of yielding large discharge rates are completed in the alluvial sands and gravels in the upper 90 to 150 m (300 to 500 ft) of the basin-fill (valley-fill aquifer) sediments in the Amargosa Desert. The quality of groundwater in the region is generally suitable for agricultural use, industrial uses, and for potable drinking water. Fractured welded tuffs and, to a lesser degree, lavas are the principal aquifers within the Tertiary volcanic suite of rocks underlying the Yucca Mountain region, although some nonwelded tuffs may also be moderately productive.

An extensive (10-plus yr) record of well pumping data from existing water supply wells UE-25 J-12 and UE-25 J-13, located southeast of Yucca Mountain, and the results of independent modeling simulations, suggest that if wells UE-25 J-12 and UE-25 J-13 (along with the nearby C-Holes) were to be pumped at a level equal to that proposed (531,000 m^3/yr [430 acre-ft/yr]) in permanent water rights applications recently filed by the DOE, the magnitude of water level effects in the surrounding water table would be very small to negligible at distances beyond the immediate vicinity of the pumping wells.

8.6 REFERENCES

8.6.1 Documents Cited

109715   Ahlers, C.F.; Finsterle, S.; and Bodvarsson, G.S. 1999. "Characterization and Prediction of Subsurface Pneumatic Response at Yucca Mountain, Nevada." *Journal of Contaminant Hydrology, 38*, (1-3), 47-68. New York, New York: Elsevier. TIC: 244160.

103622   Ahola, M. and Sagar, B. 1992. *Regional Groundwater Modeling of the Saturated Zone in the Vicinity of Yucca Mountain, Nevada, Iterative Performance Assessment – Phase 2*. NUREG/CR-5890. Washington, D.C.: U.S. Nuclear Regulatory Commission. TIC: 232662.

150236   Anderson, D. 1999. "Latest Quaternary (<30 ka) Late High-Stand Fluctuations and Evolving Paleohydrology of Death Valley." *Proceedings of Conference on Status of Geologic Research and Mapping in Death Valley National Park, Las Vegas, Nevada, April 9-11, 1999*. Slate, J.L., ed. Open-File Report 99-153. Pages 124-131. Denver, Colorado: U.S. Geological Survey. TIC: 245245.

101183   Anderson, L.A. 1991. *Results of Rock Property Measurements Made on Core Samples from Yucca Mountain Boreholes, Nevada Test Site, Nevada. Part 1. Boreholes UE25A-4, -5, -6, and -7. Part 2. Borehole UE25p#1*. Open-File Report 90-474. Denver, Colorado: U.S. Geological Survey. ACC: NNA.19910411.0081.

101187   Barr, G.E. 1985. *Reduction of the Well Test Data for Test Well USW H-1, Adjacent to Nevada Test Site, Nye County, Nevada*. SAND84-0637. Albuquerque, New Mexico: Sandia National Laboratories. ACC: NNA.19870407.0324.

101189   Barr, G.E. and Miller, W.B. 1987. *Simple Models of the Saturated Zone at Yucca Mountain*. SAND87-0112. Albuquerque, New Mexico: Sandia National Laboratories. ACC: NNA.19870811.0058.

150241   Bedinger, M.S.; Langer, W.H.; and Reed, J.E. 1987. "Synthesis of Hydraulic Properties of Rocks with Reference to the Basin and Range Province, Southwestern United States." *Selected Papers in the Hydrologic Sciences 1986*. Subitzky, S., ed. Water-Supply Paper 2310. Pages 35-43. Reston, Virginia: U.S. Geological Survey. TIC: 248073.

101118   Bedinger, M.S.; Langer, W.H.; and Reed, J.E. 1989. "Ground-Water Hydrology." *Studies of Geology and Hydrology in the Basin and Range Province, Southwestern United States, for Isolation of High-Level Radioactive Waste—Characterization of the Death Valley Region, Nevada and California*. Bedinger, M.S.; Sargent, K.A.; and Langer, W.H., eds. Professional Paper 1370-F. Denver, Colorado: U.S. Geological Survey. ACC: NNA.19920131.0251.

158458   Belcher, W.R.; Elliot, P.E.; and Geldon, A.L. 2001. *Hydraulic-Property Estimates for use with a Transient Ground-Water Flow Model of the Death Valley Regional Ground-Water Flow System, Nevada and California*. Water-Resources Investigations Report 01-4210. Carson City, Nevada: U.S. Geological Survey. TIC: 252585.

158875   Belcher, W.R.; Faunt, C.C.; and D'Agnese, F.A. 2002. *Three-Dimensional Hydrogeologic Framework Model for Use with a Steady-State Numerical Ground-Water Flow Model of the Death Valley Regional Flow System, Nevada and California*. Water-Resources Investigations Report 01-4254. Denver, Colorado: U.S. Geological Survey. TIC: 252875.

104370   Benson, L. and Klieforth, H. 1989. "Stable Isotopes in Precipitation and Ground Water in the Yucca Mountain Region, Southern Nevada: Paleoclimatic Implications." *Aspects of Climate Variability in the Pacific and the Western Americas*. Peterson, D.H., ed. Geophysical Monograph 55. Pages 41-59. Washington, D.C.: American Geophysical Union. TIC: 224413.

100727   Benson, L.V.; Robison, J.H.; Blankennagel, R.K.; and Ogard, A.E. 1983. *Chemical Composition of Ground Water and the Locations of Permeable Zones in the Yucca Mountain Area, Nevada*. Open-File Report 83-854. Denver, Colorado: U.S. Geological Survey. ACC: NNA.19870610.0028.

101036   Benson, L.V. and McKinley, P.W. 1985. *Chemical Composition of Ground Water in the Yucca Mountain Area, Nevada, 1971-84*. Open-File Report 85-484. Denver, Colorado: U.S. Geological Survey. ACC: NNA.19900207.0281.

101196   Bish, D.L. and Vaniman, D.T. 1985. *Mineralogic Summary of Yucca Mountain, Nevada*. LA-10543-MS. Los Alamos, New Mexico: Los Alamos National Laboratory. ACC: MOL.19950412.0041.

101195   Bish, D.L. and Chipera, S.J. 1989. *Revised Mineralogic Summary of Yucca Mountain, Nevada*. LA-11497-MS. Los Alamos, New Mexico: Los Alamos National Laboratory. ACC: NNA.19891019.0029.

103092   Blankennagel, R.K. 1967. *Hydraulic Testing Techniques of Deep Drill Holes at Pahute Mesa, Nevada Test Site*. Interagency Report: Special Studies I-1. Washington, D.C.: U.S. Geological Survey. ACC: NNA.19870729.0095.

101233   Blankennagel, R.K. and Weir, J.E., Jr. 1973. *Geohydrology of the Eastern Part of Pahute Mesa, Nevada Test Site, Nye County, Nevada*. Professional Paper 712-B. Washington, D.C.: U.S. Geological Survey. TIC: 219642.

100007   Bredehoeft, J.D. 1997. "Fault Permeability Near Yucca Mountain." *Water Resources Research, 33*, (11), 2459-2463. Washington, D.C.: American Geophysical Union. TIC: 236570.

155974   BSC (Bechtel SAIC Company) 2001. *Calibration of the Site-Scale Saturated Zone Flow Model*. MDL-NBS-HS-000011 REV 00 ICN 01. Las Vegas, Nevada: Bechtel SAIC Company. ACC: MOL.20010713.0049.

155950   BSC 2001. *FY 01 Supplemental Science and Performance Analyses, Volume 1: Scientific Bases and Analyses*. TDR-MGR-MD-000007 REV 00 ICN 01. Las Vegas, Nevada: Bechtel SAIC Company. ACC: MOL.20010801.0404; MOL.20010712.0062; MOL.20010815.0001.

158606   BSC 2001. *Geochemical and Isotopic Constraints on Groundwater Flow Directions, Mixing, and Recharge at Yucca Mountain, Nevada*. ANL-NBS-HS-000021 REV 00 ICN 2. Las Vegas, Nevada: Bechtel SAIC Company. ACC: MOL.20020128.0434.

156965   BSC 2001. *Probability Distribution for Flowing Interval Spacing*. ANL-NBS-MD-000003 REV 00 ICN 02. Las Vegas, Nevada: Bechtel SAIC Company. ACC: MOL.20010625.0304.

164648   BSC 2001. *Recharge and Lateral Groundwater Flow Boundary Conditions for the Saturated Zone Site-Scale Flow and Transport Model*. ANL-NBS-MD-000010 REV 00 ICN 01. Las Vegas, Nevada: Bechtel SAIC Company. ACC: MOL.20020129.0093.

158198   BSC 2002. *Test Plan for Alluvial Testing Complex – Single-Well, Multi-Well, and Laboratory Studies*. SITP-02-SZ-003 REV 01. Las Vegas, Nevada: Bechtel SAIC Company. ACC: MOL.20020404.0081.

160109   BSC 2003. *Development of Numerical Grids for UZ Flow and Transport Modeling*. ANL-NBS-HS-000015 REV 01. Las Vegas, Nevada: Bechtel SAIC Company. ACC: DOC.20030404.0005.

167209   BSC 2003. *Saturated Zone In-Situ Testing*. ANL-NBS-HS-000039 REV 00. Las Vegas, Nevada: Bechtel SAIC Company. ACC: DOC.20040128.0003.

166262   BSC 2003. *Site-Scale Saturated Zone Flow Model.* MDL-NBS-HS-000011 REV 01. Las Vegas, Nevada: Bechtel SAIC Company. ACC: DOC.20040126.0004.

167208   BSC 2003. *Site-Scale Saturated Zone Transport.* MDL-NBS-HS-000010 REV 01. Las Vegas, Nevada: Bechtel SAIC Company. ACC: DOC.20040126.0003.

164870   BSC 2003. *SZ Flow and Transport Model Abstraction*. MDL-NBS-HS-000021 REV 00. Las Vegas, Nevada: Bechtel SAIC Company. ACC: DOC.20030818.0007.

163045   BSC 2003. *UZ Flow Models and Submodels*. MDL-NBS-HS-000006 REV 01. Las Vegas, Nevada: Bechtel SAIC Company. ACC: DOC.20030818.0002.

167211   BSC 2004. *Geochemical and Isotopic Constraints on Groundwater Flow Directions, Mixing, and Recharge at Yucca Mountain.* ANL-NBS-HS-000021 REV 01. Las Vegas, Nevada: Bechtel SAIC Company. ACC: DOC.20040212.0003.

126814   Campana, M.E. and Byer, R.M., Jr. 1996. "A Conceptual Evaluation of Regional Ground-Water Flow, Southern Nevada-California, USA." *Environmental and Engineering Geoscience, II*, (4), 465-478. Boulder, Colorado: Geological Society of America. TIC: 246651.

101204   Carlos, B.A. 1987. *Minerals in Fractures of the Saturated Zone from Drill Core USW G-4, Yucca Mountain, Nye County, Nevada.* LA-10927-MS. Los Alamos, New Mexico: Los Alamos National Laboratory. ACC: NNA.19900222.0149.

102046   Carr, M.D.; Waddell, S.J.; Vick, G.S.; Stock, J.M.; Monsen, S.A.; Harris, A.G.; Cork, B.W.; and Byers, F.M., Jr. 1986. *Geology of Drill Hole UE25p#1: A Test Hole Into Pre-Tertiary Rocks Near Yucca Mountain, Southern Nevada.* Open-File Report 86-175. Menlo Park, California: U.S. Geological Survey. ACC: HQS.19880517.2633.

101037   Carr, W.J. 1984. *Regional Structural Setting of Yucca Mountain, Southwestern Nevada, and Late Cenozoic Rates of Tectonic Activity in Part of the Southwestern Great Basin, Nevada and California.* Open-File Report 84-854. Denver, Colorado: U.S. Geological Survey. ACC: NNA.19870325.0475.

101125   Claassen, H.C. 1985. *Sources and Mechanisms of Recharge for Ground Water in the West-Central Amargosa Desert, Nevada—A Geochemical Interpretation.* U.S. Geological Survey Professional Paper 712-F. Washington, D.C.: United States Government Printing Office. TIC: 204574.

101038   Cohen, A.J.B.; Oldenburg, C.M.; Simmons, A.M.; Mishra, A.K.; and Hinds, J. 1997. S4Z: *Sub-Site Scale Saturated Zone Model for Yucca Mountain.* Milestone SP25UM4. Berkeley, California: Lawrence Berkeley National Laboratory. ACC: MOL.19971204.0732.

104753   Craig, H. 1961. "Isotopic Variations in Meteoric Waters." *Science, 133*, 1702-1703. Washington, D.C.: American Association for the Advancement of Science. TIC: 236943.

101039   Craig, R.W. and Johnson, K.A. 1984. *Geohydrologic Data for Test Well UE-25p#1, Yucca Mountain Area, Nye County, Nevada.* Open-File Report 84-450. Denver, Colorado: U.S. Geological Survey. ACC: NNA.19870406.0256.

101040   Craig, R.W. and Robison, J.H. 1984. *Geohydrology of Rocks Penetrated by Test Well UE-25p#1, Yucca Mountain Area, Nye County, Nevada.* Water-Resources Investigations Report 84-4248. Denver, Colorado: U.S. Geological Survey. ACC: NNA.19890905.0209.

101206   Craig, R.W. and Reed, R.L. 1991. *Geohydrology of Rocks Penetrated by Test Well USW H-6, Yucca Mountain, Nye County, Nevada.* Water-Resources Investigations Report 89-4025. Denver, Colorado: U.S. Geological Survey. ACC: NNA.19900615.0030.

100353   CRWMS M&O (Civilian Radioactive Waste Management System Management and Operation) 1998. *Saturated Zone Flow and Transport Expert Elicitation Project.* Deliverable SL5X4AM3. Las Vegas, Nevada: CRWMS M&O. ACC: MOL.19980825.0008.

145966   CRWMS M&O 2000. *Numerical Modeling of Groundwater Flow in the Death Valley Hydrographic Region: Basins 225-230.* Las Vegas, Nevada: CRWMS M&O. ACC: MOL.20000228.0518.

151945   CRWMS M&O 2000. *Yucca Mountain Site Description.* TDR-CRW-GS-000001 REV 01 ICN 01. Las Vegas, Nevada: CRWMS M&O. ACC: MOL.20001003.0111.

101043   Czarnecki, J.B. 1984. *Simulated Effects of Increased Recharge on the Ground-Water Flow System of Yucca Mountain and Vicinity, Nevada-California.* Water-Resources Investigations Report 84-4344. Denver, Colorado: U.S. Geological Survey. ACC: HQS.19880517.1750.

101042   Czarnecki, J.B. and Waddell, R.K. 1984. *Finite-Element Simulation of Ground-Water Flow in the Vicinity of Yucca Mountain, Nevada-California.* Water-Resources Investigations Report 84-4349. Denver, Colorado: U.S. Geological Survey. ACC: NNA.19870407.0173.

160149   Czarnecki, J.B. 1985. *Simulated Effects of Increased Recharge on the Ground-Water Flow System of Yucca Mountain and Vicinity, Nevada-California.* Water-Resources Investigations Report 84-4344. Denver, Colorado: U.S. Geological Survey. TIC: 203222.

148760   Czarnecki, J.B. and Wilson, W.E. 1991. "*Conceptual Models of Regional Ground-Water Flow and Planned Studies at Yucca Mountain, Nevada.*" Hydrological Science and Technology, 7, (1-4), 15-25. St. Paul, Minnesota: American Institute of Hydrology. TIC: 225946.

103371   Czarnecki, J.B.; Nelson, P.H.; O'Brien, G.M.; Sass, J.H.; Thapa, B.; Matsumoto, Y.; and Murakami, O. 1995. "Testing in Borehole USW G-2 at Yucca Mountain: The Saga Continues." *Eos, 76,* (46), 191-192. Washington, D.C.: American Geophysical Union. TIC: 240933.

141643   Czarnecki, J.B.; Faunt, C.C.; Gable, C.W.; and Zyvoloski, G.A. 1997. *Hydrogeology and Preliminary Three-Dimensional Finite-Element Ground-Water Flow Model of the Site Saturated Zone, Yucca Mountain, Nevada.* Milestone SP23NM3. Denver, Colorado: U.S. Geological Survey. ACC: MOL.19990812.0180.

100131   D'Agnese, F.A.; Faunt, C.C.; Turner, A.K.; and Hill, M.C. 1997. *Hydrogeologic Evaluation and Numerical Simulation of the Death Valley Regional Ground-Water Flow System, Nevada and California.* Water-Resources Investigations Report 96-4300. Denver, Colorado: U.S. Geological Survey. ACC: MOL.19980306.0253.

103006   D'Agnese, F.A.; Faunt, C.C.; and Turner, A.K. 1998. *An Estimated Potentiometric Surface of the Death Valley Region, Nevada and California, Developed Using Geographic Information System and Automated Interpolation Techniques.* Water-Resources Investigations Report 97-4052. Denver, Colorado: U.S. Geological Survey. TIC: 237331.

120425   D'Agnese, F.A.; O'Brien, G.M.; Faunt, C.C.; and San Juan, C.A. 1999. *Simulated Effects of Climate Change on the Death Valley Regional Ground-Water Flow System, Nevada and California.* Water-Resources Investigations Report 98-4041. Denver, Colorado: U.S. Geological Survey. TIC: 243555.

158876   D'Agnese, F.A.; O'Brien, G.M.; Faunt, C.C.; Belcher, W.R.; and San Juan, C. 2002. *A Three-Dimensional Numerical Model of Predevelopment Conditions in the Death Valley Regional Ground-Water Flow System, Nevada and California.* Water-Resources Investigations Report 02-4102. Denver, Colorado: U.S. Geological Survey. TIC: 253754.

103180   Davies, J.B. and Archambeau, C.B. 1997. "Geohydrological Models and Earthquake Effects at Yucca Mountain, Nevada." *Environmental Geology, 32,* (1), 23-35. New York, New York: Springer-Verlag. TIC: 237118.

154690   Dettinger, M.D. 1989. *Distribution of Carbonate-Rock Aquifers in Southern Nevada and the Potential for Their Development, Summary of Findings, 1985-88.* Summary Report No. 1. Carson City, Nevada: State of Nevada. ACC: NNA.19940412.0056.

101811   DOE (U.S. Department of Energy) 1996. *Final Environmental Impact Statement for the Nevada Test Site and Off-Site Locations in the State of Nevada.* DOE/EIS-0243. Las Vegas, Nevada: U.S. Department of Energy, Nevada Operations Office. ACC: MOL.20010727.0190; MOL.20010727.0191.

103021   DOE 1997. *Regional Groundwater Flow and Tritium Transport Modeling and Risk Assessment of the Underground Test Area, Nevada Test Site, Nevada.* DOE/NV-477. Las Vegas, Nevada: U.S. Department of Energy. ACC: MOL.20010731.0303.

161543   Dublyansky, Y.; Ford, D.; and Reutski, V. 2001. "Traces of Epigenetic Hydrothermal Activity at Yucca Mountain, Nevada: Preliminary Data on the Fluid Inclusion and Stable Isotope Evidence." *Chemical Geology, 173*, (1-3), 125-149. New York, New York: Elsevier. TIC: 253849.

161545   Dublyansky, Y.V. and Szymanski, J.S. 1996. "*Carbonate Deposits at Yucca Mountain (Nevada, USA) and the Problem of High-Level Nuclear Waste Disposal.*" Chemistry for Sustainable Development, 4, (3), 146-161. Novosibirsk, Siberia, Russia: Russian Academy of Sciences. TIC: 253850.

103415   Dudley, W.W., Jr. and Larson, J.D. 1976. *Effect of Irrigation Pumping on Desert Pupfish Habitats in Ash Meadows, Nye County, Nevada.* Professional Paper 927. Washington, D.C.: U.S. Geological Survey. ACC: MOL.20010724.0312.

102524   Ervin, E.M.; Luckey, R.R.; and Burkhardt, D.J. 1993. "Summary of Revised Potentiometric-Surface Map for Yucca Mountain and Vicinity, Nevada." *High Level Radioactive Waste Management, Proceedings of the Fourth Annual International Conference, Las Vegas, Nevada, April 26-30, 1993.* 2, 1554-1558. La Grange Park, Illinois: American Nuclear Society. TIC: 208542.

100633   Ervin, E.M.; Luckey, R.R.; and Burkhardt, D.J. 1994. *Revised Potentiometric-Surface Map, Yucca Mountain and Vicinity, Nevada.* Water-Resources Investigations Report 93-4000. Denver, Colorado: U.S. Geological Survey. ACC: NNA.19930212.0018.

165612   Farnham, I.M.; Johannesson, K.H.; Hodge, V.F.; and Singh, A.K. 2002. *Preliminary Geochemical Evaluation of Groundwaters from Wells of the Nye County Early Warning Drilling Program.* TR-02-004, Rev. 0. Washington, D.C.: U.S. Department of Energy. ACC: MOL.20030910.0174.

100146   Faunt, C.C. 1997. *Effect of Faulting on Ground-Water Movement in the Death Valley Region, Nevada and California.* Water-Resources Investigations Report 95-4132. Denver, Colorado: U.S. Geological Survey. ACC: MOL.19980429.0119.

148957   Faunt, C.C.; D'Agnese, F.A.; and Turner, A.K. 1997. *A Hydrogeologic Map of the Death Valley Region, Nevada and California, Developed Using GIS Techniques.* Water-Resources Investigations Report 95-4016. Denver, Colorado: U.S. Geological Survey. TIC: 235009.

150756   Feeney, T.A.; Campana, M.E.; and Jacobson, R.L. 1987. *A Deuterium-Calibrated Groundwater Flow Model of the Western Nevada Test Site and Vicinity.* DOE/NV/10384-16. Reno, Nevada: Desert Research Institute, Water Resources Center. TIC: 206775.

164662   Fenelon, J.M. and Moreo, M.T. 2002. Trend Analysis of Ground-Water Levels and Spring Discharge in the Yucca Mountain Region, Nevada and California, 1960–2000. Water-Resources Investigations Report 02-4178. Carson City, Nevada: U.S. Geological Survey. ACC: MOL.20030812.0306.

118941   Ferrill, D.A.; Winterle, J.; Wittmeyer, G.; Sims, D.; Colton, S.; Armstrong, A.; and Morris, A.P. 1999. "Stressed Rock Strains Groundwater at Yucca Mountain, Nevada." *GSA Today, 9,* (5), 1-8. Boulder, Colorado: Geological Society of America. TIC: 246229.

157411   Flint, A.L.; Flint, L.E.; Kwicklis, E.M.; Fabryka-Martin, J.T.; and Bodvarsson, G.S. 2002. "*Estimating Recharge at Yucca Mountain, Nevada, USA: Comparison of Methods*." Hydrogeology Journal, 10, (1), 180-240. Berlin, Germany: Springer-Verlag. TIC: 251765.

100033   Flint, L.E. 1998. *Characterization of Hydrogeologic Units Using Matrix Properties, Yucca Mountain, Nevada*. Water-Resources Investigations Report 97-4243. Denver, Colorado: U.S. Geological Survey. ACC: MOL.19980429.0512.

163336   Flint, L.E. 2003. "Physical and Hydraulic Properties of Volcanic Rocks from Yucca Mountain, Nevada." *Water Resources Research, 39*, (5), 1-1 through 1-13. Washington, D.C.: American Geophysical Union. TIC: 254297.

112530   Flynn, T.; Buchanan, P.; Trexler, D.; Shevenell, L.; and Garside, L. 1996. *Geothermal Resource Assessment of the Yucca Mountain Area, Nye County, Nevada*. BA0000000-03255-5705-00002. Las Vegas, Nevada: University and Community College System of Nevada. ACC: MOL.19960903.0027.

148968   Ford, D.C. and Williams, P.W. 1989. *Karst Geomorphology and Hydrology*. Boston, Massachusetts: Unwin Hyman. TIC: 248029.

100148   Forester, R.M.; Bradbury, J.P.; Carter, C.; Elvidge, A.B.; Hemphill, M.L.; Lundstrom, S.C.; Mahan, S.A.; Marshall, B.D.; Neymark, L.A.; Paces, J.B.; Sharpe, S.E.; Whelan, J.F.; and Wigand, P.E. 1996. *Synthesis of Quaternary Response of the Yucca Mountain Unsaturated and Saturated Zone Hydrology to Climate Change*. Milestone 3GCA102M. Las Vegas, Nevada: U.S. Geological Survey. ACC: MOL.19970211.0026.

101173   Freeze, R.A. and Cherry, J.A. 1979. *Groundwater*. Englewood Cliffs, New Jersey: Prentice-Hall. TIC: 217571.

100575   Fridrich, C.J.; Dudley, W.W., Jr.; and Stuckless, J.S. 1994. "Hydrogeologic Analysis of the Saturated-Zone Ground-Water System, Under Yucca Mountain, Nevada." *Journal of Hydrology, 154*, 133-168. Amsterdam, The Netherlands: Elsevier. TIC: 224606.

105478   Garside, L.J. and Schilling, J.H. 1979. *Thermal Waters of Nevada*. Bulletin 91. Reno, Nevada: Nevada Bureau of Mines and Geology. TIC: 219499.

100396   Geldon, A.L. 1996. *Results and Interpretation of Preliminary Aquifer Tests in Boreholes UE-25c #1, UE-25c #2, and UE-25c #3, Yucca Mountain, Nye County, Nevada*. Water-Resources Investigations Report 94-4177. Denver, Colorado: U.S. Geological Survey. ACC: MOL.19980724.0389.

100397   Geldon, A.L.; Umari, A.M.A.; Fahy, M.F.; Earle, J.D.; Gemmell, J.M.; and Darnell, J. 1997. *Results of Hydraulic and Conservative Tracer Tests in Miocene Tuffaceous Rocks at the C-Hole Complex, 1995 to 1997, Yucca Mountain, Nye County, Nevada*. Milestone SP23PM3. Las Vegas, Nevada: U.S. Geological Survey. ACC: MOL.19980122.0412.

129721   Geldon, A.L.; Umari, A.M.A.; Earle, J.D.; Fahy, M.F.; Gemmell, J.M.; and Darnell, J. 1998. *Analysis of a Multiple-Well Interference Test in Miocene Tuffaceous Rocks at the C-Hole Complex, May-June 1995, Yucca Mountain, Nye County, Nevada*. Water-Resources Investigations Report 97-4166. Denver, Colorado: U.S. Geological Survey. TIC: 236724.

161163   Geldon, A.L.; Umari, A.M.A.; Fahy, M.F.; Earle, J.D.; Gemmell, J.M.; and Darnell, J. 2002. *Results of Hydraulic Tests in Miocene Tuffaceous Rocks at the C-Hole Complex, 1995 to 1997, Yucca Mountain, Nye County, Nevada*. Water-Resources Investigations Report 02-4141. Denver, Colorado: U.S. Geological Survey. TIC: 253755.

101046   Graves, R.P.; Tucci, P.; and O'Brien, G.M. 1997. *Analysis of Water-Level Data in the Yucca Mountain Area, Nevada, 1985-95*. Water-Resources Investigations Report 96-4256. Denver, Colorado: U.S. Geological Survey. ACC: MOL.19980219.0851.

155411   Graves, R.P. 1998. *Water Levels in the Yucca Mountain Area, Nevada, 1996*. Open-File Report 98-169. Denver, Colorado: U.S. Geological Survey. ACC: MOL.19981117.0340.

148960   Grose, T.L.T. 1983. *Thirty-Two Geologic Cross-Sections, Clark, Esmeralda, Lincoln, Mineral, and Nye Counties, Nevada, and Adjacent Areas in California*. Open-File Report 83-13. Reno, Nevada: Nevada Bureau of Mines and Geology. TIC: 237882.

150249   Grose, T.L.T. and Smith, G.I. 1985. "Geology." *Studies of Geology and Hydrology in the Basin and Range Province, Southwestern United States, for Isolation of High-Level Radioactive Waste; Characterization of the Death Valley Region, Nevada and California*. Bedinger, M.S.; Sargent, K.A.; and Langer, W.H., eds. Open-File Report 84-743. Denver, Colorado: U.S. Geological Survey. ACC: HQS.19880517.2612.

148961 Harrill, J.R. 1986. *Ground-Water Storage Depletion in Pahrump Valley, Nevada-California, 1962-75*. Water-Supply Paper 2279. Denver, Colorado: U.S. Geological Survey. TIC: 226027.

149377 Harrill, J.R. and Prudic, D.E. 1998. *Aquifer Systems in the Great Basin Region of Nevada, Utah, and Adjacent States - Summary Repor*t. Professional Paper 1409-A. Denver, Colorado: U.S. Geological Survey. TIC: 247432.

148778 Haws, S.J. 1990. *The Distribution of Vertical Groundwater Flow in the Saturated Zone of the Yucca Mountain Area: A Cross-Sectional Finite Element Model. Master's thesis*. Las Vegas, Nevada: University of Nevada, Las Vegas. TIC: 237284.

158877 Hevesi, J.A.; Flint, A.L.; and Flint, L.E. 2002. *Preliminary Estimates of Spatially Distributed Net Infiltration and Recharge for the Death Valley Region, Nevada–California.* Water-Resources Investigations Report 02-4010. Sacramento, California: U.S. Geological Survey. TIC: 253392.

106126 Hill, C.A.; Dublyansky, Y.V.; Harmon, R.S.; and Schluter, C.M. 1995. "Overview of Calcite/Opal Deposits at or Near the Proposed High-Level Nuclear Waste Site, Yucca Mountain, Nevada, USA: Pedogenic, Hypogene, or Both?" *Environmental Geology, 26*, 69-88. New York, New York: Springer-Verlag. TIC: 222318.

165606 Hill, C.A. and Dublyansky, Y.V. 1999. "Response to Stuckless and Others (1998) on 'Overview of Calcite/Opal Deposits at or Near the Proposed High-Level Nuclear Waste Site, Yucca Mountain, Nevada, USA: Pedogenic, Hypogene, or Both?' *Environmental Geology, 38*, (1), 77-81. New York, New York: Springer-Verlag. TIC: 255228.

101135 Hodge, V.F.; Johannesson, K.H.; and Stetzenbach, K.J. 1996. "Rhenium, Molybdenum, and Uranium in Groundwater from the Southern Great Basin, USA: Evidence for Conservative Behavior." G*eochimica et Cosmochimica Acta, 60*, (17), 3197-3214. New York, New York: Elsevier. TIC: 236469.

106046 Hoover, D.L. 1968. "*Genesis of Zeolites*." Nevada Test Site. Eckel, E.B., ed. Memoir 110. Boulder, Colorado: Geological Society of America. TIC: 221562.

103476 Johannesson, K.H.; Stetzenbach, K.J.; Kreamer, D.K.; and Hodge, V.F. 1996. "Multivariate Statistical Analysis of Arsenic and Selenium Concentrations in Groundwaters from South-Central Nevada and Death Valley, California." *Journal of Hydrology, 178*, 181-204. Amsterdam, The Netherlands: Elsevier. TIC: 240432.

101137 Johannesson, K.H.; Stetzenbach, K.J.; Hodge, V.F.; Kreamer, D.K.; and Zhou, X. 1997. "Delineation of Ground-Water Flow Systems in the Southern Great Basin Using Aqueous Rare Earth Element Distributions." *Ground Water, 35*, (5), 807-819. Worthington, Ohio: Water Well Journal Publishing. TIC: 236540.

165610   Johannesson, K.H.; Zhou, X.; Guo, C.; Stetzenbach, K.J.; and Hodge, V.F. 2000. "Origin of Rare Earth Element Signatures in Groundwaters of Circumneutral pH from Southern Nevada and Eastern California, USA." *Chemical Geology, 164*, (3-4), 239-257. New York, New York: Elsevier. TIC: 254993.

103010   Kilroy, K.C. 1991. *Ground-Water Conditions in Amargosa Desert, Nevada-California, 1952-87.* Water-Resources Investigations Report 89-4101. Carson City, Nevada: U.S. Geological Survey. TIC: 209975.

157414   Kwicklis, E.M. 1999. "Determination of Pneumatic Diffusivity." *Hydrogeology of the Unsaturated Zone, North Ramp Area of the Exploratory Studies Facility, Yucca Mountain, Nevada.* Rousseau, J.P.; Kwicklis, E.M.; and Gillies, D.C., eds. Water-Resources Investigations Report 98-4050. Denver, Colorado: U.S. Geological Survey. ACC: MOL.19990419.0335.

103012   Laczniak, R.J.; Cole, J.C.; Sawyer, D.A.; and Trudeau, D.A. 1996. *Summary of Hydrogeologic Controls on Ground-Water Flow at the Nevada Test Site, Nye County, Nevada.* Water-Resources Investigations 96-4109. Carson City, Nevada: U.S. Geological Survey. TIC: 226157.

165609   Laczniak, R.L.; Smith, J.L.; Elliott, P.E.; DeMeo, G.A.; Chatigny, M.A.; and Roemer, G.J. 2001. *Ground-Water Discharge Determined from Estimates of Evapotranspiration, Death Valley Regional Flow System, Nevada and California.* Water-Resources Investigations Report 01-4195. Carson City, Nevada: U.S. Geological Survey. TIC: 255215.

101049   Lahoud, R.G.; Lobmeyer, D.H.; and Whitfield, M.S., Jr. 1984. *Geohydrology of Volcanic Tuff Penetrated by Test Well UE-25b #1, Yucca Mountain, Nye County, Nevada.* Water-Resources Investigations Report 84-4253. Denver, Colorado: U.S. Geological Survey. ACC: NNA.19890511.0117.

105399   Leavesley, G.H.; Lichty, R.W.; Troutman, B.M.; and Saindon, L.G. 1983. *Precipitation-Runoff Modeling System: User's Manual.* Water-Resources Investigations Report 83-4238. Denver, Colorado: U.S. Geological Survey. ACC: MOL.19950105.0009.

100153   LeCain, G.D. 1997. *Air-Injection Testing in Vertical Boreholes in Welded and Nonwelded Tuff, Yucca Mountain, Nevada.* Water-Resources Investigations Report 96-4262. Denver, Colorado: U.S. Geological Survey. ACC: MOL.19980310.0148.

144612   LeCain, G.D.; Anna, L.O.; and Fahy, M.F. 2000. *Results from Geothermal Logging, Air and Core-Water Chemistry Sampling, Air-Injection Testing, and Tracer Testing in the Northern Ghost Dance Fault, Yucca Mountain, Nevada, November 1996 to August 1998.* Water-Resources Investigations Report 99-4210. Denver, Colorado: U.S. Geological Survey. TIC: 247708.

149173 Lehman, L.L. and Brown, T.P. 1996. *Summary of State of Nevada - Funded Studies of the Saturated Zone at Yucca Mountain, Nevada, Performed by L. Lehman & Associates, Inc*. Burnsville, Minnesota: L. Lehman and Associates. TIC: 231894.

100053 Levy, S.S. 1991. "Mineralogic Alteration History and Paleohydrology at Yucca Mountain, Nevada." *High Level Radioactive Waste Management, Proceedings of the Second Annual International Conference, Las Vegas, Nevada, April 28-May 3, 1991. 1, 477-485*. La Grange Park, Illinois: American Nuclear Society. TIC: 204272.

100589 Lichty, R.W. and McKinley, P.W. 1995. *Estimates of Ground-Water Recharge Rates for Two Small Basins in Central Nevada*. Water-Resources Investigations Report 94-4104. Denver, Colorado: U.S. Geological Survey. ACC: MOL.19960924.0524.

101050 Lobmeyer, D.H. 1986. *Geohydrology of Rocks Penetrated by Test Well USW G-4, Yucca Mountain, Nye County, Nevada*. Water-Resources Investigations Report 86-4015. Lakewood, Colorado: U.S. Geological Survey. ACC: NNA.19890918.0510.

100465 Luckey, R.R.; Tucci, P.; Faunt, C.C.; Ervin, E.M.; Steinkampf, W.C.; D'Agnese, F.A.; and Patterson, G.L. 1996. *Status of Understanding of the Saturated-Zone Ground-Water Flow System at Yucca Mountain, Nevada, as of 1995*. Water-Resources Investigations Report 96-4077. Denver, Colorado: U.S. Geological Survey. ACC: MOL.19970513.0209.

101141 Ludwig, K.R.; Peterman, Z.E.; Simmons, K.R.; and Gutentag, E.D. 1993. "^{234}U/^{238}U as a Ground-Water Tracer, SW Nevada-SE California." *High Level Radioactive Waste Management, Proceedings of the Fourth Annual International Conference, Las Vegas, Nevada, April 26-30, 1993. 2, 1567-1572*. La Grange Park, Illinois: American Nuclear Society. TIC: 208542.

106695 Malmberg, G.T. and Eakin, T.E. 1962. *Ground-Water Appraisal of Sarcobatus Flat and Oasis Valley, Nye and Esmeralda Counties, Nevada*. Ground-Water Resources – Reconnaissance Series Report 10. Carson City, Nevada: State of Nevada, Department of Conservation and Natural Resources. TIC: 208666.

101260 Malmberg, G.T. 1967. *Hydrology of the Valley-Fill and Carbonate-Rock Reservoirs Pahrump Valley Nevada-California*. Water Supply-Paper 1832. Washington, D.C.: U.S. Geological Survey. ACC: NNA.19870406.0430.

101142 Marshall, B.D.; Peterman, Z.E.; and Stuckless, J.S. 1993. "Strontium Isotopic Evidence for a Higher Water Table at Yucca Mountain." *High Level Radioactive Waste Management, Proceedings of the Fourth Annual International Conference, Las Vegas, Nevada, April 26-30, 1993. 2, 1948-1952*. La Grange Park, Illinois: American Nuclear Society. TIC: 208542.

163591   Marshall, B.D. and Whelan, J.F. 2001. "Simulating the Thermal History of the Unsaturated Zone at Yucca Mountain, Nevada." *Abstracts with Programs - Geological Society of America, 33*, (6), A-375. Boulder, Colorado: Geological Society of America. TIC: 252701.

116222   McKinley, P.W.; Long, M.P.; and Benson, L.V. 1991. *Chemical Analyses of Water from Selected Wells and Springs in the Yucca Mountain Area, Nevada and Southeastern California.* Open-File Report 90-355. Denver, Colorado: U.S. Geological Survey. ACC: NNA.19901031.0004.

105462   Miller, G.A. 1977. *Appraisal of the Water Resources of Death Valley, California-Nevada.* Open-File Report 77-728. Menlo Park, California: U.S. Geological Survey. ACC: HQS.19880517.1934.

148783   Moench, A.F. 1984. "Double-Porosity Models for a Fissured Ground-Water Reservoir with a Fracture Skin." *Water Resources Research, 20,* (7), 831-846. Washington, D.C.: American Geophysical Union. TIC: 218689.

100161   Montazer, P. and Wilson, W.E. 1984. *Conceptual Hydrologic Model of Flow in the Unsaturated Zone, Yucca Mountain, Nevada.* Water-Resources Investigations Report 84-4345. Lakewood, Colorado: U.S. Geological Survey. ACC: NNA.19890327.0051.

168008   Moreo, M.T.; Halford, K.J.; La Camera, R.J.; and Laczniak, R.J. 2003. *Estimated Ground-Water Withdrawals from the Death Valley Regional Flow System, Nevada and California, 1913–98.* Water-Resources Investigations Report 03-4245. Carson City, Nevada: U.S. Geological Survey. ACC: MOL.20040304.0087.

105162   National Research Council. 1992. *Ground Water at Yucca Mountain, How High Can It Rise? Final Report of the Panel on Coupled Hydrologic/Tectonic/ Hydrothermal Systems at Yucca Mountain.* Washington, D.C.: National Academy Press. TIC: 204931.

158673   Neymark, L.A.; Amelin, Y.; Paces, J.B.; and Peterman, Z.E. 2002. "U-Pb Ages of Secondary Silica at Yucca Mountain, Nevada: Implications for the Paleohydrology of the Unsaturated Zone." *Applied Geochemistry, 17,* (6), 709-734. New York, New York: Elsevier. TIC: 252598.

156115   Nye County Nuclear Waste Repository Project Office 2001. *Nye County Nuclear Waste Repository Project Office Independent Scientific Investigations Program Final Report, Fiscal Years 1996—2001.* NWRPO-2001-04. Pahrump, Nevada: U.S. Department of Energy, Nye County Nuclear Waste Repository Project Office. ACC: MOL.20010906.0199.

101275   O'Brien, G.M. 1992. *Earthquake-Induced Water-Level Fluctuations at Yucca Mountain, Nevada, April, 1992.* Open-File Report 92-137. Denver, Colorado: U.S. Geological Survey. ACC: NNA.19920626.0001.

101276   O'Brien, G.M. 1993. *Earthquake-Induced Water-Level Fluctuations at Yucca Mountain, Nevada, June 1992.* Open-File Report 93-73. Denver, Colorado: U.S. Geological Survey. ACC: NNA.19930326.0022.

101277   O'Brien, G.M. 1997. *Analysis of Aquifer Tests Conducted in Boreholes USW WT-10, UE-25 WT#12, and USW SD-7, 1995-96, Yucca Mountain, Nevada.* Water-Resources Investigations Report 96-4293. Denver, Colorado: U.S. Geological Survey. ACC: MOL.19980219.0822.

101278   O'Brien, G.M. 1998. *Analysis of Aquifer Tests Conducted in Borehole USW G-2, 1996, Yucca Mountain, Nevada.* Water-Resources Investigations Report 98-4063. Denver, Colorado: U.S. Geological Survey. ACC: MOL.19980904.0095.

103114   Ogard, A.E.; Aguilar, R.A.; Griffith, J.F.; Maestas, S.; Mitchell, A.J.; and Wanek, P.L. 1983. "Groundwater Chemistry." Chapter III. A. *of Research and Development Related to the Nevada Nuclear Waste Storage Investigations, July 1— September 30, 1982.* Daniels, W.R.; Erdal, B.R.; and Vaniman, D.T., eds. LA-9577-PR. Los Alamos, New Mexico: Los Alamos National Laboratory. ACC: NNA.19870406.0180.

100783   Ogard, A.E. and Kerrisk, J.F. 1984. *Groundwater Chemistry Along Flow Paths Between a Proposed Repository Site and the Accessible Environment.* LA-10188-MS. Los Alamos, New Mexico: Los Alamos National Laboratory. ACC: HQS.19880517.2031.

100069   Oliver, T. and Root, T. 1997. *Hydrochemical Database for the Yucca Mountain Area, Nye County, Nevada.* Denver, Colorado: U.S. Geological Survey. ACC: MOL.19980302.0367.

100602   Osterkamp, W.R.; Lane, L.J.; and Savard, C.S. 1994. "Recharge Estimates Using a Geomorphic/Distributed-Parameter Simulation Approach, Amargosa River Basin." *Water Resources Bulletin, 30,* (3), 493-506. Minneapolis, Minnesota: American Water Resources Association. TIC: 237428.

106465   Paces, J. 1995. "Letter Report on FY1995 Studies of Paleodischarge Deposits." Internal memorandum from J. Paces (USGS) to Chief, Yucca Mountain Project Branch (USGS), June 26, 1995. ACC: MOL.19960702.0134.

106474   Paces, J.B.; Taylor, E.M.; and Bush, C. 1993. "Late Quaternary History and Uranium Isotopic Compositions of Ground Water Discharge Deposits, Crater Flat, Nevada." *High Level Radioactive Waste Management, Proceedings of the Fourth Annual International Conference, Las Vegas, Nevada, April 26-30, 1993.* 2, 1573-1580. La Grange Park, Illinois: American Nuclear Society. TIC: 208542.

101281 Paces, J.B.; Forester, R.M.; Whelan, J.F.; Mahan, S.A.; Bradbury, J.P.; Quade, J.; Neymark, L.A.; and Kwak, L.M. 1996. *Synthesis of Ground-Water Discharge Deposits Near Yucca Mountain*. Milestone 3GQH671M. Las Vegas, Nevada: U.S. Geological Survey. ACC: MOL.19970205.0007.

107002 Paces, J.B.; Neymark, L.A.; Kwak, L.M.; and Peterman, Z.E. 1996. "U-Series Dating of Secondary Minerals in Unsaturated-Zone Tuffs Indicating Low Paleo Water Flux Through Yucca Mountain, Nevada." Abstracts with Programs - *Geological Society of America, 28,* (7), A139-140. Boulder, Colorado: Geological Society of America. TIC: 235053.

109148 Paces, J.B.; Whelan, J.F.; Forester, R.M.; Bradbury, J.P.; Marshall, B.D.; and Mahan, S.A. 1997. *Summary of Discharge Deposits in the Amargosa Valley*. Milestone SPC333M4. Denver, Colorado: U.S. Geological Survey. ACC: MOL.19981104.0151.

100072 Paces, J.B.; Ludwig, K.R.; Peterman, Z.E.; Neymark, L.A.; and Kenneally, J.M. 1998. "Anomalous Ground-Water ^{234}U/^{238}U Beneath Yucca Mountain: Evidence of Local Recharge?" *High-Level Radioactive Waste Management, Proceedings of the Eighth International Conference, Las Vegas, Nevada, May 11-14, 1998*. Pages 185-188. La Grange Park, Illinois: American Nuclear Society. TIC: 237082.

156507 Paces, J.B.; Neymark, L.A.; Marshall, B.D.; Whelan, J.F.; and Peterman, Z.E. 2001. *Ages and Origins of Calcite and Opal in the Exploratory Studies Facility Tunnel, Yucca Mountain, Nevada*. Water-Resources Investigations Report 01-4049. Denver, Colorado: U.S. Geological Survey. TIC: 251284.

154724 Paces, J.B. and Whelan, J.F. 2001. "Water-Table Fluctuations in the Amargosa Desert, Nye County, Nevada." *"Back to the Future - Managing the Back End of the Nuclear Fuel Cycle to Create a More Secure Energy Future," Proceedings of the 9th International High-Level Radioactive Waste Management Conference (IHLRWM), Las Vegas, Nevada, April 29-May 3, 2001*. La Grange Park, Illinois: American Nuclear Society. TIC: 247873.

158817 Paces, J.B.; Ludwig, K.R.; Peterman, Z.E.; and Neymark, L.A. 2002. "^{234}U/^{238}U Evidence for Local Recharge and Patterns of Ground-Water Flow in the Vicinity of Yucca Mountain, Nevada, USA." *Applied Geochemistry, 17,* (6), 751-779. New York, New York: Elsevier. TIC: 252809.

158824 Patterson, G.L. 1999. "Occurrences of Perched Water in the Vicinity of the Exploratory Studies Facility North Ramp." *Hydrogeology of the Unsaturated Zone, North Ramp Area of the Exploratory Studies Facility, Yucca Mountain, Nevada*. Rousseau, J.P.; Kwicklis, E.M.; and Gillies, D.C., eds. Water-Resources Investigations Report 98-4050. Denver, Colorado: U.S. Geological Survey. ACC: MOL.19990419.0335.

101053   Perfect, D.L.; Faunt, C.C.; Steinkampf, W.C.; and Turner, A.K. 1995. *Hydrochemical Data Base for the Death Valley Region, California and Nevada.* Open-File Report 94-305. Denver, Colorado: U.S. Geological Survey. ACC: MOL.19940718.0001.

101149   Peterman, Z.E. and Stuckless, J.S. 1993. "Isotopic Evidence of Complex Ground-Water Flow at Yucca Mountain, Nevada, USA." *High Level Radioactive Waste Management, Proceedings of the Fourth Annual International Conference, Las Vegas, Nevada, April 26-30, 1993. 2,* 1559-1566. La Grange Park, Illinois: American Nuclear Society. TIC: 208542.

106495   Peterman, Z.E. and Stuckless, J.S. 1993. "Application of Strontium and Other Radiogenic Tracer Isotopes to Paleohydrologic Studies." *Paleohydrogeological Methods and Their Applications, Proceedings of an NEA Workshop, Paris (France), 9-10 November 1992.* Pages 59-84. Paris, France: Organisation for Economic Co-operation and Development. TIC: 225213.

165681   Peterman, Z.E. and Stuckless, J.S. 1994. "Strontium Isotope Characterization of Flow Systems in Southern Nevada." *Mineralogical Magazin, 58A*, 711-712. London, England: Mineralogical Society. TIC: 255126.

101150   Peterman, Z.E. and Patterson, G. 1998. "Isotopes Aid in Understanding the Yucca Mountain Flow System." *High-Level Radioactive Waste Management, Proceedings of the Eighth International Conference, Las Vegas, Nevada, May 11-14, 1998.* Pages 182-184. La Grange Park, Illinois: American Nuclear Society. TIC: 237082.

103115   Pistrang, M.A. and Kunkel, F. 1964. *A Brief Geologic and Hydrologic Reconnaissance of the Furnace Creek Wash Area, Death Valley National Monument California.* Water-Supply Paper 1779-Y. Washington, D.C.: U.S. Geological Survey. ACC: HQS.19880517.1819.

103136   Prudic, D.E.; Harrill, J.R.; and Burbey, T.J. 1993. *Conceptual Evaluation of Regional Ground-Water Flow in the Carbonate-Rock Province of the Great Basin, Nevada, Utah, and Adjacent States.* Open-File Report 93-170. Carson City, Nevada: U.S. Geological Survey. ACC: MOL.19950105.0016.

100074   Quade, J.; Mifflin, M.D.; Pratt, W.L.; McCoy, W.; and Burckle, L. 1995. "Fossil Spring Deposits in the Southern Great Basin and Their Implications for Changes in Water-Table Levels Near Yucca Mountain, Nevada, During Quaternary Time." *Geological Society of America Bulletin, 107,* (2), 213-230. Boulder, Colorado: Geological Society of America. TIC: 234256.

150255   Quiring, R.F. 1965. *Annual Precipitation Amount as a Function of Elevation in Nevada South of 38 1/2 Degrees Latitude.* Las Vegas, Nevada: U.S. Geological Survey. TIC: 221202.

154688   Rasmussen, T.C.; Evans, D.D.; Sheets, P.J.; and Blanford, J.H. 1993. "Permeability of Apache Leap Tuff: Borehole and Core Measurements Using Water and Air." *Water Resources Research, 29*, (7), 1997-2006. Washington, D.C.: American Geophysical Union. TIC: 245278.

148780   Rice, J.; Lehman, L.; and Keen, K. 1990. "Cosine Components in Water Levels at Yucca Mountain." *Waste Management '90, "Working Towards a Cleaner Environment," Waste Processing, Transportation, Storage and Disposal, Technical Programs and Public Education, Proceedings of the Symposium on Waste Management, Tucson, Arizona, February 25-March 1, 1990.* Post, R.G., ed. 2, 557-564. Tucson, Arizona: University of Arizona. TIC: 204390.

101284   Rice, W.A. 1984. *Preliminary Two-Dimensional Regional Hydrologic Model of the Nevada Test Site and Vicinity.* SAND83-7466. Albuquerque, New Mexico: Sandia National Laboratories. ACC: NNA.19900810.0286.

105536   Robison, J.H.; Stephens, D.M.; Luckey, R.R.; and Baldwin, D.A. 1988. *Water Levels in Periodically Measured Wells in the Yucca Mountain Area, Nevada, 1981-87.* Open-File Report 88-468. Denver, Colorado: U.S. Geological Survey. ACC: NNA.19890306.0113.

101286   Robison, J.H. and Craig, R.W. 1991. *Geohydrology of Rocks Penetrated by Test Well USW H-5, Yucca Mountain, Nye County, Nevada.* Water-Resources Investigations Report 88-4168. Denver, Colorado: U.S. Geological Survey. ACC: NNA.19900110.0400.

109159   Roedder, E.; Whelan, J.F.; and Vaniman, D.T. 1994. "Fluid Inclusion Studies of Calcite Veins from Yucca Mountain, Nevada, Tuffs: Environment of Formation." *High Level Radioactive Waste Management, Proceedings of the Fifth Annual International Conference, Las Vegas, Nevada, May 22-26, 1994. 4,* 1854-1860. La Grange Park, Illinois: American Nuclear Society. TIC: 210984.

129750   Rojstaczer, S. 1999. "Stress Dependent Permeability and Its Political Consequences at Yucca Mountain." *Eos, Transactions (Supplement), 80,* (17), S4. Washington, D.C.: American Geophysical Union. TIC: 246513.

144725   Rose, T.P.; Kenneally, J.M.; Smith, D.K.; Davisson, M.L.; Hudson, G.B.; and Rego, J.H. 1997. *Chemical and Isotopic Data for Groundwater in Southern Nevada.* UCRL-ID-128000. Livermore, California: Lawrence Livermore National Laboratory. TIC: 243649.

101054   Rush, F.E.; Thordarson, W.; and Pyles, D.G. 1984. *Geohydrology of Test Well USW H-1, Yucca Mountain, Nye County, Nevada.* Water-Resources Investigations Report 84-4032. Denver, Colorado: U.S. Geological Survey. ACC: NNA.19870518.0067.

145202   Sadler, W.R.; Campana, M.E.; Jacobson, R.L.; and Ingraham, N.L. 1992. *A Deuterium-Calibrated, Discrete-State Compartment Model of Regional Groundwater Flow, Nevada Test Site and Vicinity*. DOE/NV/10845-9. Las Vegas, Nevada: U.S. Department of Energy, Nevada Field Office. TIC: 248076.

104545   Sass, J.H.; Lachenbruch, A.H.; Munroe, R.J.; Greene, G.W.; and Moses, T.H., Jr. 1971. "Heat Flow in the Western United States." *Journal of Geophysical Research, 76,* (26), 6376-6413. Washington, D.C.: American Geophysical Union. TIC: 218845.

103147   Sass, J.H.; Lachenbruch, A.H.; and Mase, C.W. 1980. *Analysis of Thermal Data from Drill Holes UE25a-3 and UE25a-1, Calico Hills and Yucca Mountain, Nevada Test Site*. Open-File Report 80-826. Denver, Colorado: U.S. Geological Survey. ACC: HQS.19880517.1429.

103145   Sass, J.H. and Lachenbruch, A.H. 1982. *Preliminary Interpretation of Thermal Data from the Nevada Test Site*. Open-File Report 82-973. Denver, Colorado: U.S. Geological Survey. ACC: NNA.19870406.0040.

100644   Sass, J.H.; Lachenbruch, A.H.; Dudley, W.W., Jr.; Priest, S.S.; and Munroe, R.J. 1988. *Temperature, Thermal Conductivity, and Heat Flow Near Yucca Mountain, Nevada: Some Tectonic and Hydrologic Implications*. Open-File Report 87-649. Denver, Colorado: U.S. Geological Survey. TIC: 203195.

101288   Sass, J.H.; Dudley, W.W., Jr.; and Lachenbruch, A.H. 1995. "Regional Thermal Setting." Chapter 8 of *Major Results of Geophysical Investigations at Yucca Mountain and Vicinity, Southern Nevada*. Oliver, H.W.; Ponce, D.A.; and Hunter, W.C., eds. Open-File Report 95-74. Menlo Park, California: U.S. Geological Survey. ACC: MOL.19980305.0122.

148805   Sass, J.H. 1998. "Thermal Tracking of Water Flow Under Yucca Mountain." *High-Level Radioactive Waste Management, Proceedings of the Eighth International Conference, Las Vegas, Nevada, May 11-14, 1998*. Pages 269-271. La Grange Park, Illinois: American Nuclear Society. TIC: 237082.

102213   Savard, C.S. 1998. *Estimated Ground-Water Recharge from Streamflow in Fortymile Wash Near Yucca Mountain, Nevada*. Water-Resources Investigations Report 97-4273. Denver, Colorado: U.S. Geological Survey. TIC: 236848.

150257   Schoff, S.L. and Moore, J.E. 1964. *Chemistry and Movement of Ground Water, Nevada Test Site*. TEI-838. Washington, D.C.: U.S. Geological Survey. ACC: HQS.19880517.1842.

160238   Sharpe, S.E. and Forester, R.M. 2001. "Reconstructing Past and Forecasting Future Climate at Yucca Mountain, Nevada." *"Back to the Future - Managing the Back End of the Nuclear Fuel Cycle to Create a More Secure Energy Future," Proceedings of the 9th International High-Level Radioactive Waste Management Conference (IHLRWM), Las Vegas, Nevada, April 29-May 3, 2001.* La Grange Park, Illinois: American Nuclear Society. TIC: 247873.

103019   Sinton, P.O. 1987. *Three-Dimensional, Steady-State, Finite-Difference Model of the Ground-Water Flow System in the Death Valley Ground-Water Basin, Nevada-California.* Master's thesis. Golden, Colorado: Colorado School of Mines. TIC: 236959.

147841   Spaulding, G. 1997. *"Recalculation of the Elevation of the Fortymile Canyon-7 Packrat Midden Site."* Memorandum from G. Spaulding (Dames & Moore) to Fans of Fortymile Paleohydrology, June 7, 1997. TIC: 247789.

106503   Spaulding, W.G.; Robinson, S.W.; and Paillet, F.L. 1984. *Preliminary Assessment of Climatic Change During Late Wisconsin Time, Southern Great Basin and Vicinity, Arizona, California, and Nevada.* Water-Resources Investigations Report 84-4328. Denver, Colorado: U.S. Geological Survey. ACC: NNA.19910221.0114.

148867   Spaulding, W.G. 1994. *Paleohydrologic Investigations in the Vicinity of Yucca Mountain: Late Quaternary Paleobotanical and Palynological Records.* NWPO-TR-022-94. Carson City, Nevada: State of Nevada, Agency for Nuclear Projects/Nuclear Waste Project Office. TIC: 215002.

158818   Steinkampf, W.C. and Werrell, W.L. 2001. *Ground-Water Flow to Death Valley, as Inferred from the Chemistry and Geohydrology of Selected Springs in Death Valley National Park, California and Nevada.* Water-Resources Investigations Report 98-4114. Denver, Colorado: U.S. Geological Survey. TIC: 251734.

158819   Stetzenbach, K.J.; Hodge, V.F.; Guo, C.; Farnham, I.M.; and Johannesson, K.H. 2001. "Geochemical and Statistical Evidence of Deep Carbonate Groundwater Within Overlying Volcanic Rock Aquifers/Aquitards of Southern Nevada, USA." *Journal of Hydrology, 243,* (3-4), 254-271. New York, New York: Elsevier. TIC: 252814.

101159   Stuckless, J.S.; Whelan, J.F.; and Steinkampf, W.C. 1991. "Isotopic Discontinuities in Ground Water Beneath Yucca Mountain, Nevada." *High Level Radioactive Waste Management, Proceedings of the Second Annual International Conference, Las Vegas, Nevada, April 28-May 3, 1991.* 2, 1410-1415. La Grange Park, Illinois: American Nuclear Society. TIC: 204272.

100086   Stuckless, J.S.; Marshall, B.D.; Vaniman, D.T.; Dudley, W.W.; Peterman, Z.E.; Paces, J.B.; Whelan, J.F.; Taylor, E.M.; Forester, R.M.; and O'Leary, D.W. 1998. "Comments on 'Overview of Calcite/Opal Deposits at or Near the Proposed High-Level Nuclear Waste Site, Yucca Mountain, Nevada, USA: Pedogenic, Hypogene, or Both' by C.A. Hill, Y.V. Dublyansky, R.S. Harmon, and C.M. Schluter." *Environmental Geology, 34,* (1), 70-78. New York, New York: Springer-Verlag. TIC: 238097.

100088   Szabo, B.J.; Kolesar, P.T.; Riggs, A.C.; Winograd, I.J.; and Ludwig, K.R. 1994. "Paleoclimatic Inferences from a 120,000-Yr Calcite Record of Water-Table Fluctuation in Browns Room of Devils Hole, Nevada." *Quaternary Research, 41,* (1), 59-69. New York, New York: Academic Press. TIC: 234642.

131259   Thomas, J.M. 1996. *Geochemical and Isotopic Interpretation of Groundwater Flow, Geochemical Processes, and Age Dating of Groundwater in the Carbonate-Rock Aquifers of the Southern Basin and Range.* Ph.D. dissertation. Reno, Nevada: University of Nevada, Reno. TIC: 247758.

106585   Thordarson, W. 1965. *Perched Ground Water in Zeolitized-Bedded Tuff, Rainier Mesa and Vicinity, Nevada Test Site, Nevada.* TEI-862. Washington, D.C.: U.S. Geological Survey. ACC: NN1.19881021.0066.

101057   Thordarson, W. 1983. *Geohydrologic Data and Test Results from Well J-13, Nevada Test Site, Nye County, Nevada.* Water-Resources Investigations Report 83-4171. Denver, Colorado: U.S. Geological Survey. ACC: NNA.19870518.0071.

105670   Thordarson, W.; Rush, F.E.; and Waddell, S.J. 1985. *Geohydrology of Test Well USW H-3, Yucca Mountain, Nye County, Nevada.* Water-Resources Investigations Report 84-4272. Lakewood, Colorado: U.S. Geological Survey. ACC: HQS.19880517.1852.

103172   Thordarson, W. and Howells, L. 1987. *Hydraulic Tests and Chemical Quality of Water at Well USW VH-1, Crater Flat, Nye County, Nevada.* Water-Resources Investigations Report 86-4359. Lakewood, Colorado: U.S. Geological Survey. ACC: NNA.19870515.0019.

100422   Triay, I.R.; Meijer, A.; Conca, J.L.; Kung, K.S.; Rundberg, R.S.; Strietelmeier, B.A.; and Tait, C.D. 1997. *Summary and Synthesis Report on Radionuclide Retardation for the Yucca Mountain Site Characterization Project.* Eckhardt, R.C., ed. LA-13262-MS. Los Alamos, New Mexico: Los Alamos National Laboratory. ACC: MOL.19971210.0177.

101060   Tucci, P. and Burkhardt, D.J. 1995. *Potentiometric-Surface Map, 1993, Yucca Mountain and Vicinity, Nevada.* Water-Resources Investigations Report 95-4149. Denver, Colorado: U.S. Geological Survey. ACC: MOL.19960924.0517.

145962   Tucci, P. and Faunt, C.C. 1999. *Simulated Effects of Potential Withdrawals from Wells Near Yucca Mountain, Nevada.* Water-Resources Investigations Report 99-4166. Denver, Colorado: U.S. Geological Survey. ACC: MOL.19991112.0127.

160355   USGS (U.S. Geological Survey) 2001. *Simulation of Net Infiltration for Modern and Potential Future Climates.* ANL-NBS-HS-000032 REV 00 ICN 02. Denver, Colorado: U.S. Geological Survey. ACC: MOL.20011119.0334.

157611   USGS 2001. *Water-Level Data Analysis for the Saturated Zone Site-Scale Flow and Transport Model.* ANL-NBS-HS-000034 REV 01. Denver, Colorado: U.S. Geological Survey. ACC: MOL.20020209.0058.

154625   USGS 2001. *Water-Level Data Analysis for the Saturated Zone Site-Scale Flow and Transport Model.* ANL-NBS-HS-000034 REV 00 ICN 01. Denver, Colorado: U.S. Geological Survey. ACC: MOL.20010405.0211.

165615   USGS 2002. *Water-Level Data Analysis for the Saturated Zone Site-Scale Flow and Transport Model, with Errata.* ANL-NBS-HS-000034 REV 01. Denver, Colorado: U.S. Geological Survey. ACC: MOL.20020209.0058; MOL.20020917.0136.

165176   USGS 2003. *Errata, Hydrogeologic Framework Model for the Saturated-Zone Site-Scale Flow and Transport Model.* ANL-NBS-HS-000033 REV 00 ICN 02. Denver, Colorado: U.S. Geological Survey. ACC: DOC.20030319.0002; MOL.20011112.0070.

145240   Vaniman, D.T. 1993. "*Calcite Deposits in Fractures at Yucca Mountain, Nevada.*" *High Level Radioactive Waste Management, Proceedings of the Fourth Annual International Conference, Las Vegas, Nevada, April 26-30, 1993. 2,* 1935-1939. La Grange Park, Illinois: American Nuclear Society. TIC: 208542.

108813   Vaniman, D.T. 1994. *Calcite Deposits in Drill Cores USW G-2 and USW GU-3/G-3 at Yucca Mountain, Nevada: Preliminary Report.* LA-12720-MS. Los Alamos, New Mexico: Los Alamos National Laboratory. TIC: 210807.

100089   Vaniman, D.T. and Chipera, S.J. 1996. "Paleotransport of Lanthanides and Strontium Recorded in Calcite Compositions from Tuffs at Yucca Mountain, Nevada, USA." *Geochimica et Cosmochimica Acta, 60,* (22), 4417-4433. New York, New York: Pergamon Press. TIC: 231351.

154706   Vesselinov, V.V.; Illman, W.A.; Hyun, Y.; Neuman, S.P.; Di Federico, V.; and Tartakovsky, D.M. 2001. "Observation and Analysis of a Pronounced Permeability and Porosity Scale-Effect in Unsaturated Fractured Tuff." *Fractured Rock 2001, An International Conference Addressing Groundwater Flow, Solute Transport, Multiphase Flow, and Remediation in Fractured Rock, March 26-28, 2001, Toronto, Ontario, Canada*. Kueper, B.H.; Novakowski, K.S.; and Reynolds, D.A., eds. Smithville, Ontario, Canada: Smithville Phase IV. TIC: 249909.

101062   Waddell, R.K. 1982. *Two-Dimensional, Steady-State Model of Ground-Water Flow, Nevada Test Site and Vicinity, Nevada-California*. Water-Resources Investigations Report 82-4085. Denver, Colorado: U.S. Geological Survey. ACC: NNA.19870518.0055.

103022   Walker, G.E. and Eakin, T.E. 1963. *Geology and Ground Water of Amargosa Desert, Nevada-California*. Ground-Water Resources – Reconnaissance Series Report 14. Carson City, Nevada: State of Nevada, Department of Conservation and Natural Resources. TIC: 208665.

108861   West, N.E. 1989. *"Intermountain Deserts, Shrub Steppes, and Woodlands."* Chapter 7 of *North American Terrestrial Vegetation*. Barbour, M.G. and Billings, W.D., eds. New York, New York: Cambridge University Press. TIC: 241505.

108863   Whelan, J.F. and Stuckless, J.S. 1992. "Paleohydrologic Implications of the Stable Isotopic Composition of Secondary Calcite Within the Tertiary Volcanic Rocks of Yucca Mountain, Nevada." *High Level Radioactive Waste Management, Proceedings of the Third Annual International Conference, Las Vegas, Nevada, April 12-16, 1992. 2, 1572-1581*. La Grange Park, Illinois: American Nuclear Society. TIC: 204231.

100091   Whelan, J.F.; Vaniman, D.T.; Stuckless, J.S.; and Moscati, R.J. 1994. "Paleoclimatic and Paleohydrologic Records from Secondary Calcite: Yucca Mountain, Nevada." *High Level Radioactive Waste Management, Proceedings of the Fifth Annual International Conference, Las Vegas, Nevada, May 22-26, 1994. 4, 2738-2745*. La Grange Park, Illinois: American Nuclear Society. TIC: 210984.

108865   Whelan, J.F.; Moscati, R.J.; Roedder, E.; and Marshall, B.D. 1998. "Secondary Mineral Evidence of Past Water Table Changes at Yucca Mountain, Nevada." *High-Level Radioactive Waste Management, Proceedings of the Eighth International Conference, Las Vegas, Nevada, May 11-14, 1998*. Pages 178-181. La Grange Park, Illinois: American Nuclear Society. TIC: 237082.

154773   Whelan, J.F.; Roedder, E.; and Paces, J.B. 2001. "Evidence for an Unsaturated-Zone Origin of Secondary Minerals in Yucca Mountain, Nevada." *Back to the Future - Managing the Back End of the Nuclear Fuel Cycle to Create a More Secure Energy Future," Proceedings of the 9th International High-Level Radioactive Waste Management Conference (IHLRWM), Las Vegas, Nevada, April 29-May 3, 2001.* La Grange Park, Illinois: American Nuclear Society. TIC: 247873.

160442   Whelan, J.F.; Paces, J.B.; and Peterman, Z.E. 2002. "Physical and Stable-Isotope Evidence for Formation of Secondary Calcite and Silica in the Unsaturated Zone, Yucca Mountain, Nevada." *Applied Geochemistry, 17,* (6), 735-750. New York, New York: Elsevier. TIC: 253462.

101165   White, A.F. 1979. *Geochemistry of Ground Water Associated with Tuffaceous Rocks, Oasis Valley, Nevada.* Professional Paper 712-E. Washington, D.C.: U.S. Geological Survey. TIC: 219633.

108871   White, A.F. and Chuma, N.J. 1987. "Carbon and Isotopic Mass Balance Models of Oasis Valley - Fortymile Canyon Groundwater Basin, Southern Nevada." *Water Resources Research, 23,* (4), 571-582. Washington, D.C.: American Geophysical Union. TIC: 237579.

101067   Whitfield, M.S., Jr.; Eshom, E.P.; Thordarson, W.; and Schaefer, D.H. 1985. *Geohydrology of Rocks Penetrated by Test Well USW H-4, Yucca Mountain, Nye County, Nevada.* Water-Resources Investigations Report 85-4030. Denver, Colorado: U.S. Geological Survey. ACC: NNA.19870407.0328.

155426   Wilson, S.F. and Cline, J.S. 2001. "Paragenesis, Temperature and Timing of Secondary Minerals at Yucca Mountain." *"Back to the Future - Managing the Back End of the Nuclear Fuel Cycle to Create a More Secure Energy Future," Proceedings of the 9th International High-Level Radioactive Waste Management Conference (IHLRWM), Las Vegas, Nevada, April 29-May 3, 2001.* La Grange Park, Illinois: American Nuclear Society. TIC: 247873.

108880   Winograd, I.J. and Friedman, I. 1972. "Deuterium as a Tracer of Regional Ground-Water Flow, Southern Great Basin, Nevada and California." *Geological Society of America Bulletin, 83,* (12), 3691-3708. Boulder, Colorado: Geological Society of America. TIC: 217734.

101167   Winograd, I.J. and Thordarson, W. 1975. *Hydrogeologic and Hydrochemical Framework, South-Central Great Basin, Nevada-California, with Special Reference to the Nevada Test Site.* Geological Survey Professional Paper 712-C. Washington, D.C.: United States Government Printing Office. ACC: NNA.19870406.0201.

108882   Winograd, I.J. and Pearson, F.J., Jr. 1976. "Major Carbon 14 Anomaly in a Regional Carbonate Aquifer: Possible Evidence for Megascale Channeling, South Central Great Basin." *Water Resources Research, 12*, (6), 1125-1143. Washington, D.C.: American Geophysical Union. TIC: 217731.

107320   Winograd, I.J. and Doty, G.C. 1980. *Paleohydrology of the Southern Great Basin, with Special Reference to Water Table Fluctuations Beneath the Nevada Test Site During the Late(?) Pleistocene*. Open-File Report 80-569. Reston, Virginia: U.S. Geological Survey. ACC: NNA.19870518.0073.

165605   Winograd, I.J. and Robertson, F.J. 1982. "Deep Oxygenated Ground Water: Anomaly or Common Occurrence?" *Science, 216*, 1227-1230. Washington, D.C.: American Association for the Advancement of Science. TIC: 224602.

101441   Yang, I.C.; Yu, P.; Rattray, G.W.; Ferarese, J.S.; and Ryan, J.N. 1998. *Hydrochemical Investigations in Characterizing the Unsaturated Zone at Yucca Mountain, Nevada*. Water-Resources Investigations Report 98-4132. Denver, Colorado: U.S. Geological Survey. ACC: MOL.19981012.0790.

103023   Young, R.A. 1972. *Water Supply for the Nuclear Rocket Development Station at the U.S. Atomic Energy Commission's Nevada Test Site*. Water-Supply Paper 1938. Washington, D.C.: U.S. Geological Survey. ACC: NNA.19870519.0070.

8.6.2   Data, Listed by Data Tracking Number

155307   GS010608312332.001. Potentiometric-Surface Map, Assuming Perched Conditions North of Yucca Mountain, in the Saturated Site-Scale Model. Submittal date: 06/19/2001.

166523   GS031008312316.002. Hydraulic Parameters from Analysis of Hydraulic Tests Conducted in the Alluvium at the Alluvial Testing Complex (ATC), and Total Porosity from Grain-Size Distribution and from Background Monitoring. Submittal date: 10/09/2003.

148168   GS920408312314.009. Geohydrology of Rocks Penetrated by Test Well UE-25p#1 (UE-25 p#1), Yucca Mountain Area, Nye County, Nevada. Submittal date: 04/27/1992.

145763   GS930208318523.001. Temperature and Thermal Conductivity in Wells Near Yucca Mountain. Submittal date: 02/16/1993.

129625   GS930408312132.007. Geohydrologic Data and Test Results from Well J-13, Nevada Test Site, Nye County, Nevada. Submittal date: 04/23/1993.

148665   GS930408312312.015. Water Levels in the Yucca Mountain Area, Nevada, 1990-91. Submittal date: 04/28/1993.

148668   GS931008312312.025. Water Levels in Periodically Measured Wells in the Yucca Mountain Area, Nevada, 1981-87. Submittal date: 04/23/1993.

105063   GS960908312312.010. Analysis of Water-Level Data in the Yucca Mountain Area, Nevada, 1985-1995. Submittal date: 09/19/1996.

155272   GS980308312312.004. Water Levels in the Yucca Mountain Area, Nevada, 1996. Submittal date: 03/31/1998.

156043   LA0007PR831231.001. Bullfrog Reactive Tracer Test Data. Submittal date: 07/21/2000.

162431   LA0207PR831352.001. Microsphere Data from Single-Well Tracer Testing at NC-EWDP-19D1 (ATC). Submittal date: 07/30/2002.

166546   LA0309RR831233.001. Regional Groundwater Hydrochemical Data in the Yucca Mountain Area Used as Direct Inputs for ANL-NBS-HS-000021, REV 01. Submittal date: 09/05/2003.

166548   LA0309RR831233.002. Regional Groundwater Hydrochemical Data in the Yucca Mountain Area Used as Corroborative Data for ANL-NBS-HS-000021, REV 01. Submittal date: 09/05/2003.

150285   MO0004YMP00019.000. Hydrographic Basins in the Vicinity of Yucca Mountain. Submittal date: 04/04/2000

155456   MO0008WTRALTG4.000. Water-Table-Altitude Data for Well USW G-4, Yucca Mountain Area, Nye County, Nevada. Submittal date: 08/24/2000.

155271   MO0103COV01031.000. Coverage: BORES3Q. Submittal date: 03/22/2001.

157173   MO0111DQRWLNYE.003. Water Level Data from Westbay Instrumented Borehole NC-EWDP-3S. Submittal date: 11/29/2001.

157174   MO0111DQRWLNYE.004. Water Level Data from Westbay Instrumented Borehole NC-EWDP-9SX. Submittal date: 11/29/2001.

157175   MO0112DQRWLNYE.005. Well Completion Diagram for Borehole NC-EWDP-4PA. Submittal date: 12/03/2001.

157176   MO0112DQRWLNYE.006. Well Completion Diagram for Borehole NC-EWDP-4PB. Submittal date: 12/04/2001.

157180   MO0112DQRWLNYE.010. Well Completion Diagram for Borehole NC-EWDP-12PA. Submittal date: 12/04/2001.

157181   MO0112DQRWLNYE.011. Well Completion Diagram for Borehole NC-EWDP-9SX. Submittal date: 12/04/2001.

157182   MO0112DQRWLNYE.012. Well Completion Diagram for Borehole NC-EWDP-12PB. Submittal date: 12/04/2001.

157183   MO0112DQRWLNYE.013. Well Completion Diagram for Borehole NC-EWDP-12PC. Submittal date: 12/04/2001.

157184   MO0112DQRWLNYE.014. Well Completion Diagram for Borehole NC-EWDP-19P. Submittal date: 12/04/2001.

157200   MO0112DQRWLNYE.015. Well Completion Diagram for Borehole NC-EWDP-3S. Submittal date: 12/04/2001.

157185   MO0112DQRWLNYE.016. Well Completion Diagram for Borehole NC-EWDP-3D. Submittal date: 12/04/2001.

157186   MO0112DQRWLNYE.017. Well Completion Diagram for Borehole NC-EWDP-1DX. Submittal date: 12/05/2001.

157187   MO0112DQRWLNYE.018. Well Completion Diagram for Borehole NC-EWDP-19D. Submittal date: 12/05/2001.

157188   MO0112DQRWLNYE.019. Multi-Level Monitoring Port Depths in Nye County Boreholes NC-EWDP-1S, -3S and -9SX. Submittal date: 12/05/2001.

157199   MO0112DQRWLNYE.020. Water Level Depth Data for Nye County Boreholes NC-EWDP-2D and -2DB. Submittal date: 12/05/2001.

157189   MO0112DQRWLNYE.021. Multilevel Piezometer Casing Log for Borehole NC-EWDP-9SX. Submittal date: 12/05/2001.

157190   MO0112DQRWLNYE.022. Multilevel Piezometer Casing Log for Borehole NC-EWDP-3S. Submittal date: 12/05/2001.

157192   MO0112DQRWLNYE.024. EWDP Phase I Manual Water Level Measurements. Submittal date: 12/06/2001.

157193   MO0112DQRWLNYE.025. EWDP Phase II Manual Water Level Measurements. Submittal date: 12/06/2001.

166551   MO0312SEPSDAMH.000. Estimated Apparent Mean Hydraulic Conductivity Values from Single-Borehole Tests. Submittal date: 12/19/2003.

166550   MO0312SEPSDHCU.000. Statistical Distributions for the Hydraulic Conductivity of Generalized Hydrogeologic Units in the Death Valley Region. Submittal date: 12/19/2003.

166381   MO0312SEPSDHFC.000. Heat Flows Calculated for Deep Boreholes at Yucca Mountain. Submittal date: 12/13/2003.

166494   MO0312SEPSDHTF.000. Heat Flows for Boreholes in the Nevada Test Site Area. Submittal date: 12/16/2003.

166544   MO0312SEPSDWLA.000. Water-Level Altitudes in Boreholes that may have been Affected by the June 1992 Earthquakes. Submittal date: 12/19/2003.

166384   MO0312SPESDFLS.000. Flow Surveys for Selected Boreholes in the Yucca Mountain Area. Submittal date: 12/13/2003.

166383   MO0312SPESDTWT.000. Temperatures at the Water Table. Submittal date: 12/13/2003.

168534   MO0401COV03168.000. Coverage: NCEWDPS. Submittal date: 01/27/2004.

129714   SNT05082597001.003. TSPA-VA (Total System Performance Assessment-Viability Assessment) Saturated Zone (SZ) Base Case Modeling Analysis Results. Submittal date: 02/03/1998.

162442   UN0109SPA008IF.006. Concentration Dataset for Tracers (2,4-Difluorobenzoic Acid and Chloride) Used for the 30-Day Shut in Tracer Test at the Alluvial Tracer Complex in Nye County Nevada. Submittal date: 09/28/2001.
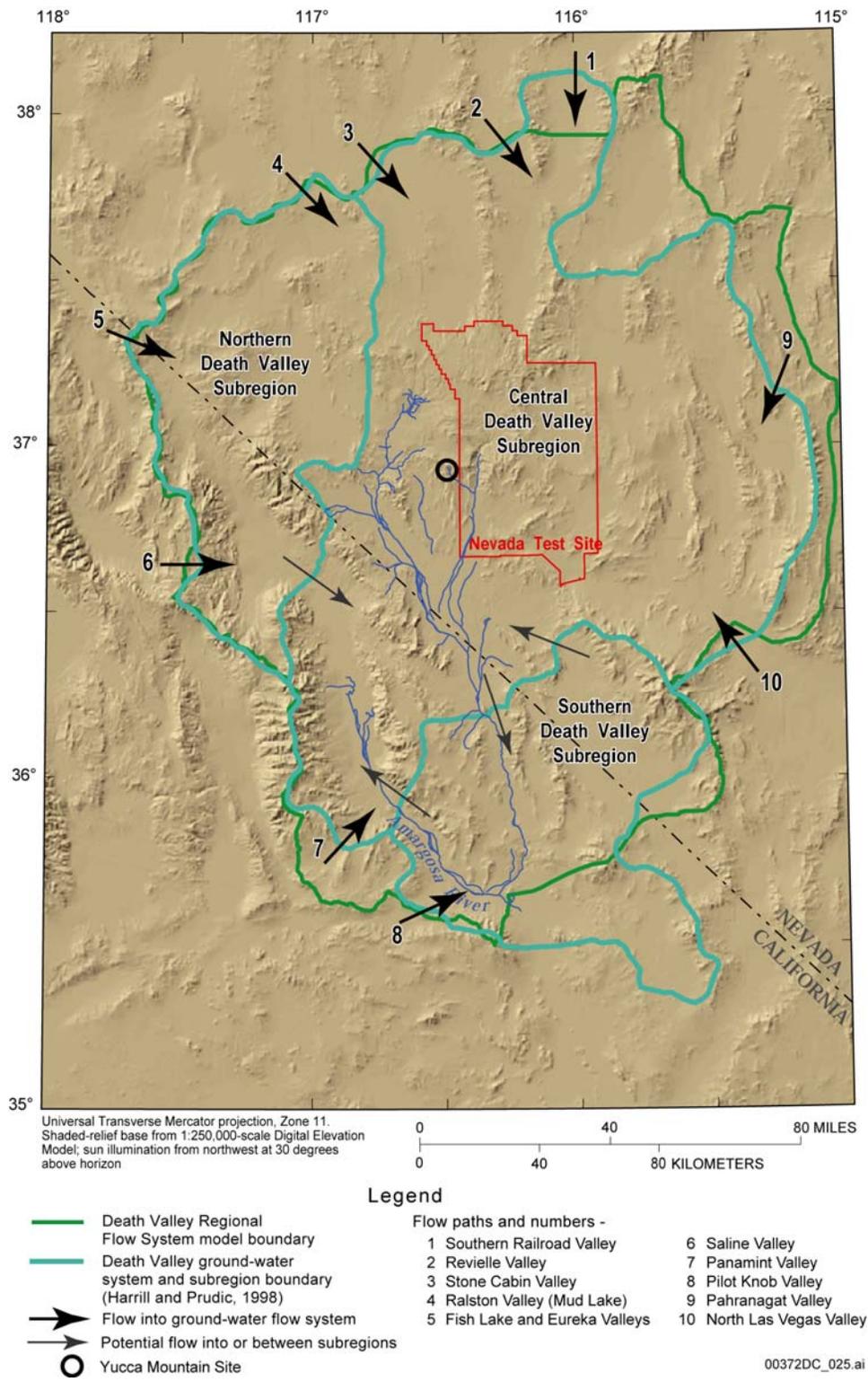
Source: D'Agnese et al. 2002 [DIRS 158876], Figure 7

Figure 8-1. Subregions and Flow Paths for the Death Valley Regional Groundwater Flow System
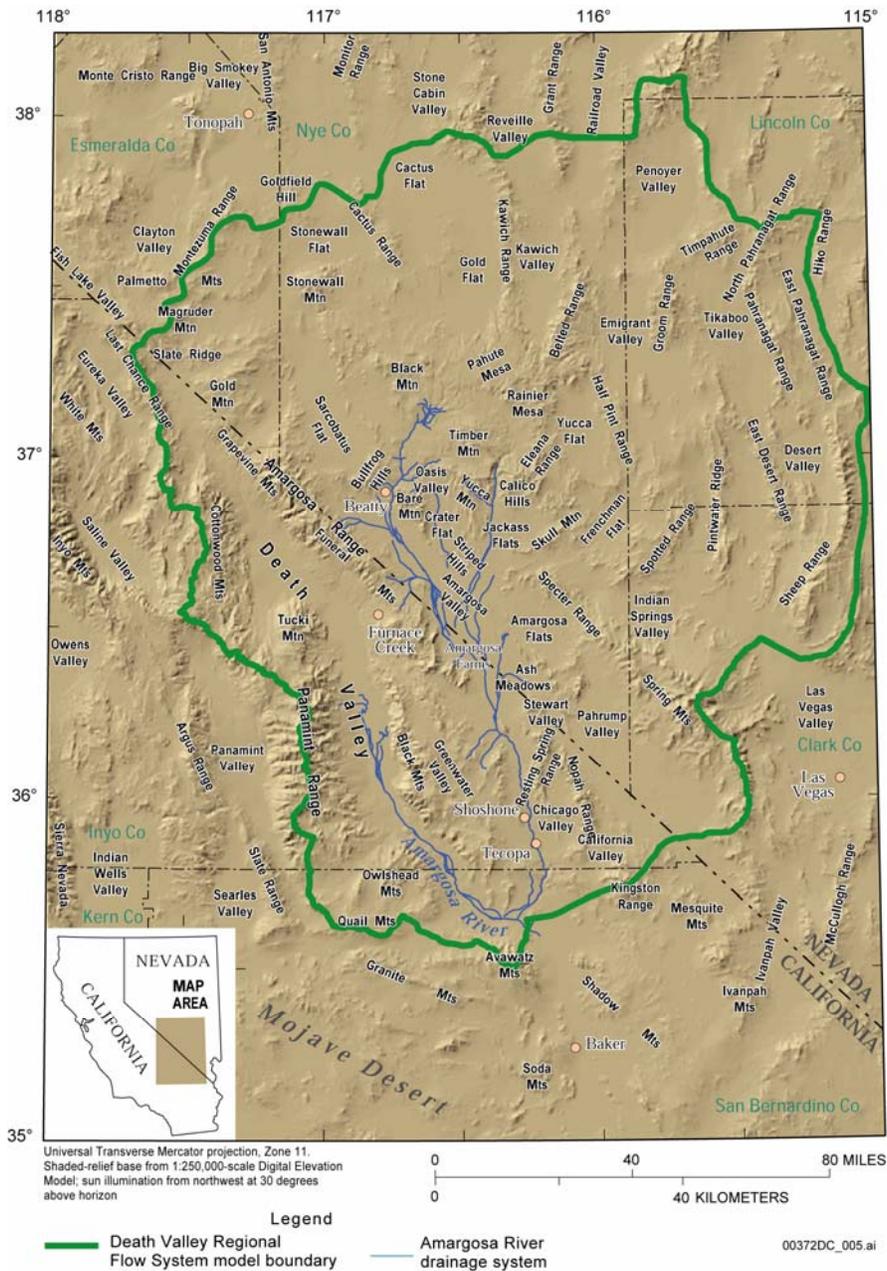
Source: D'Agnese et al. 2002 [DIRS 158876], Figure 1

Figure 8-2. Geographic and Prominent Topographic Features of the Death Valley Region
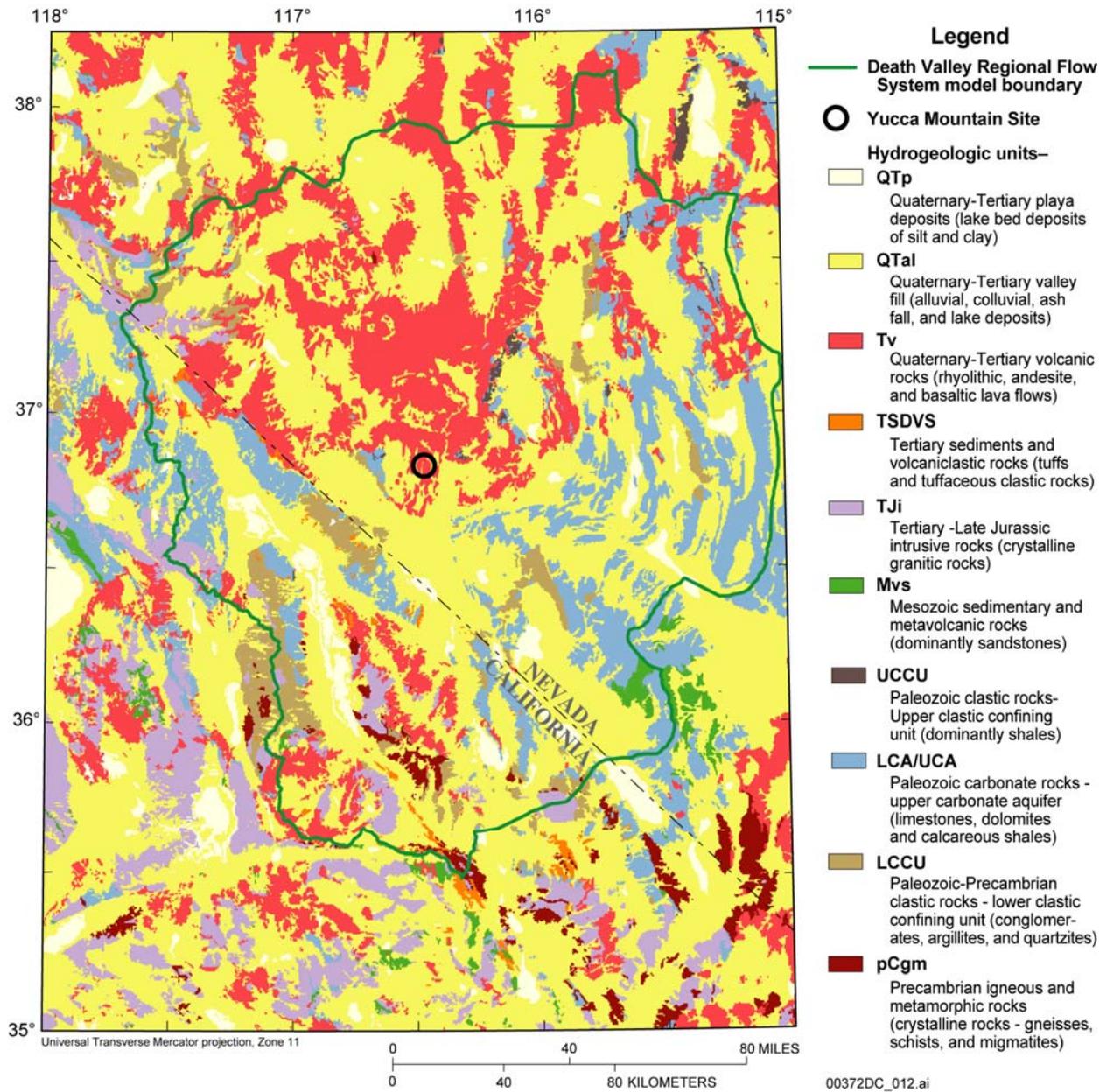
Source: Modified from Belcher et al. 2002 [DIRS 158875], Figure 4

Figure 8-3. Hydrogeologic Units of the Death Valley Region
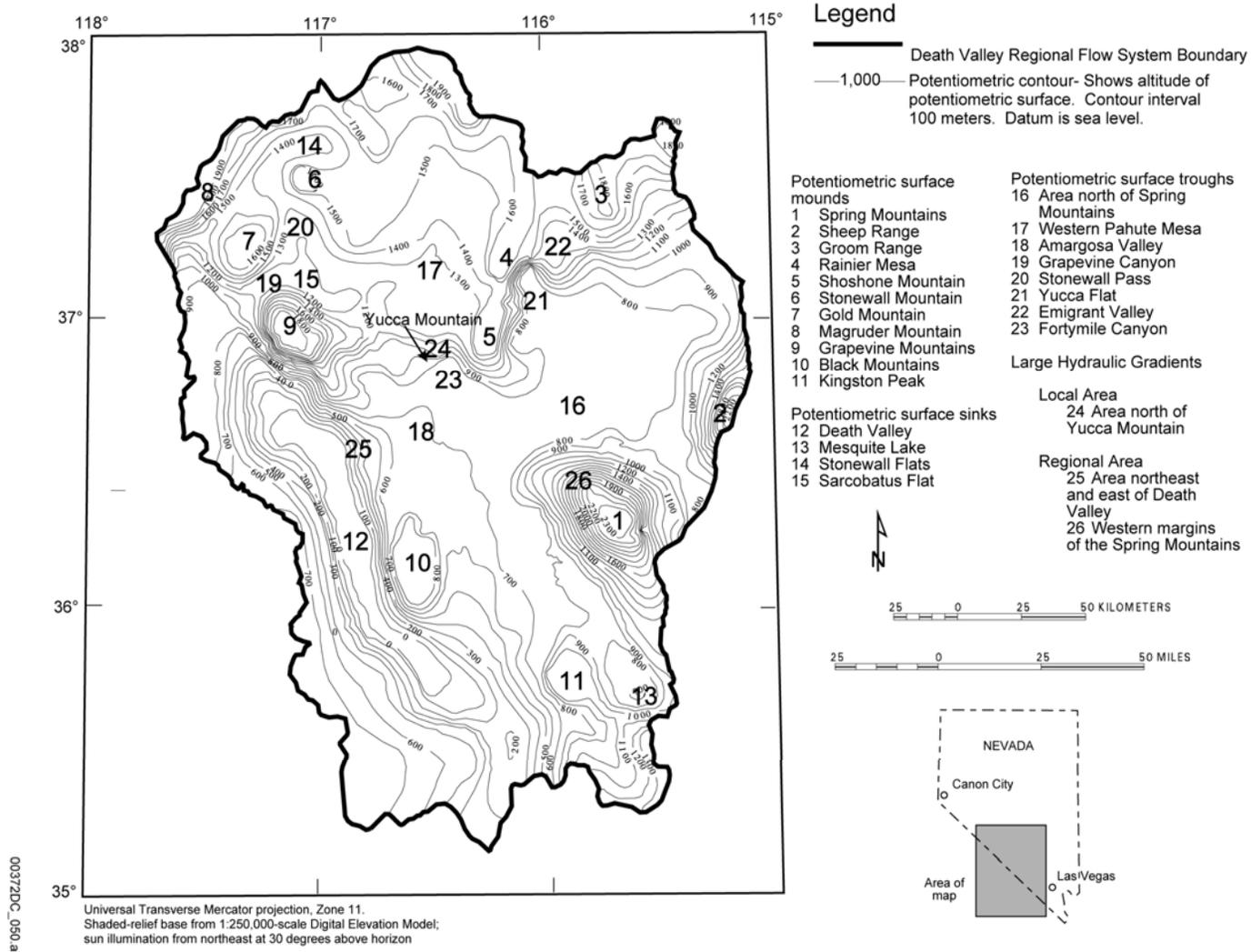
Source: D'Agnese et al. 1998 [DIRS 103006], Plate 1

Figure 8-4. Potentiometric Surface of the Death Valley Region with Locations of Major Potentiometric Features

Source: D'Agnese et al. 2002 [DIRS 158876], Figure 11

Figure 8-5. Central Death Valley Subregion
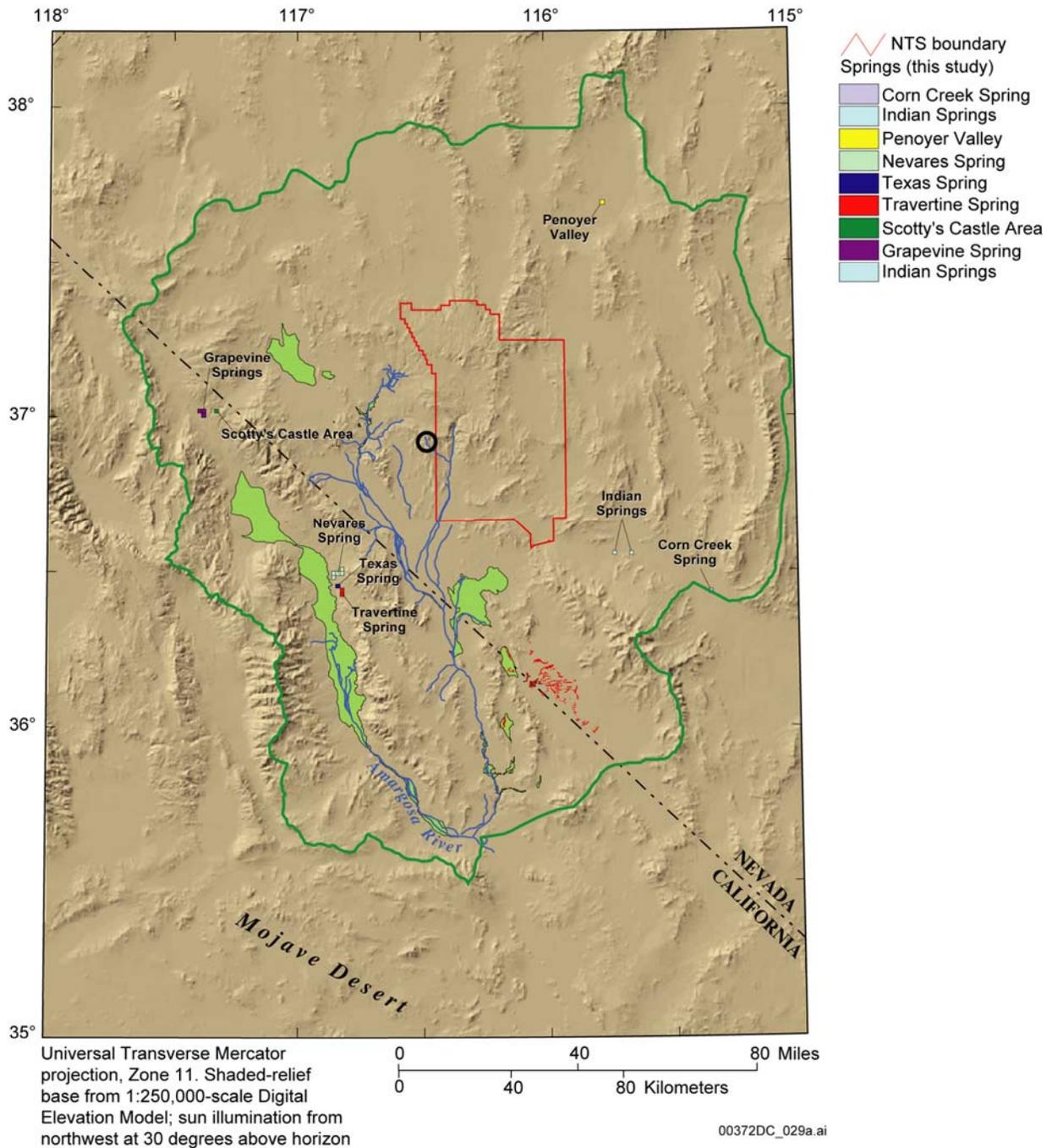
Source: D'Agnese et al. 2002 [DIRS 158876], Figure 13

Figure 8-6. Groundwater Discharge Areas in the Death Valley Region
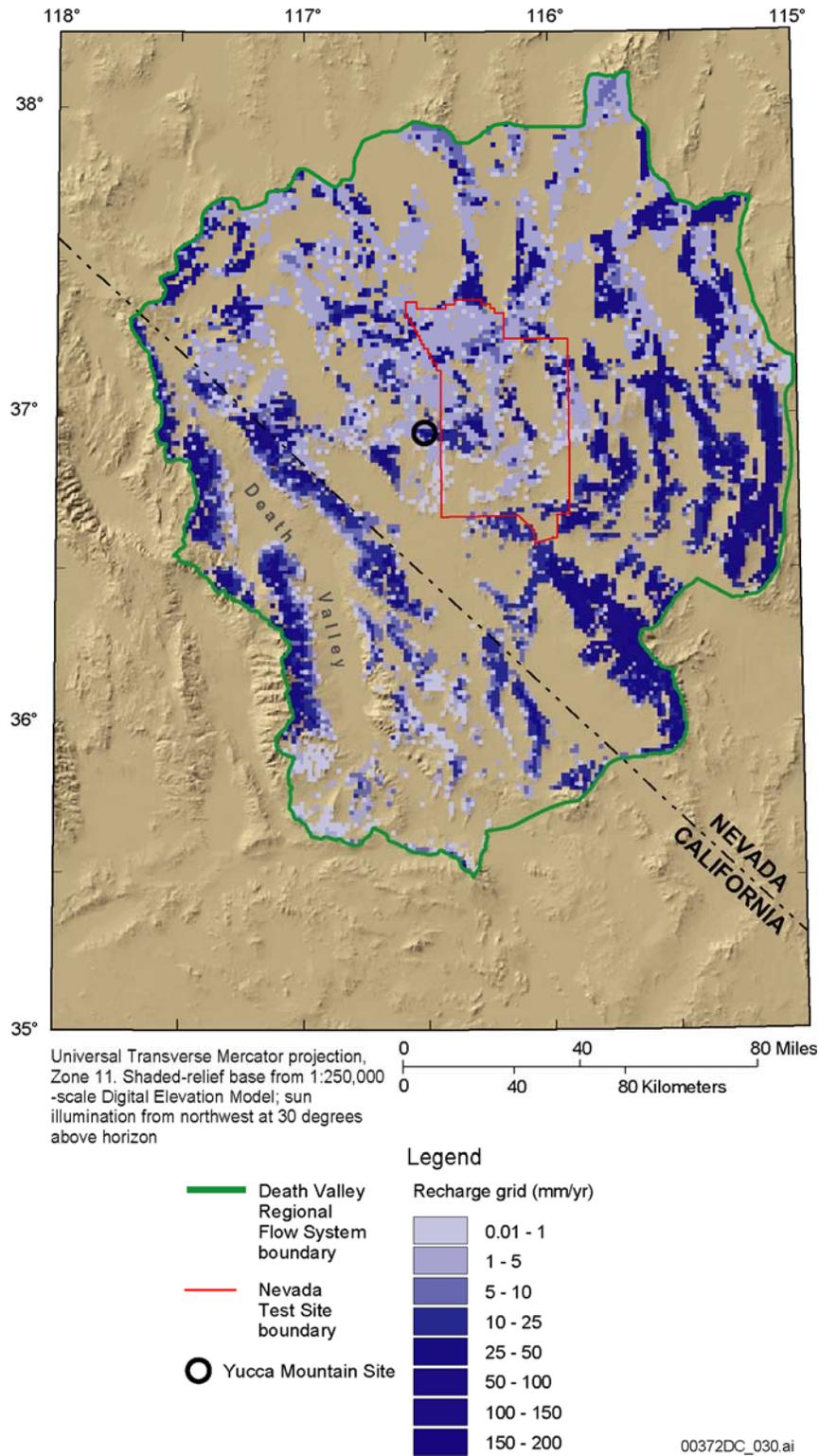
Source: D'Agnese et al. 2002 [DIRS 158876], Figure 14

NOTE: Estimates based on INFIL modeling.

Figure 8-7. Net Infiltration for the Death Valley Region
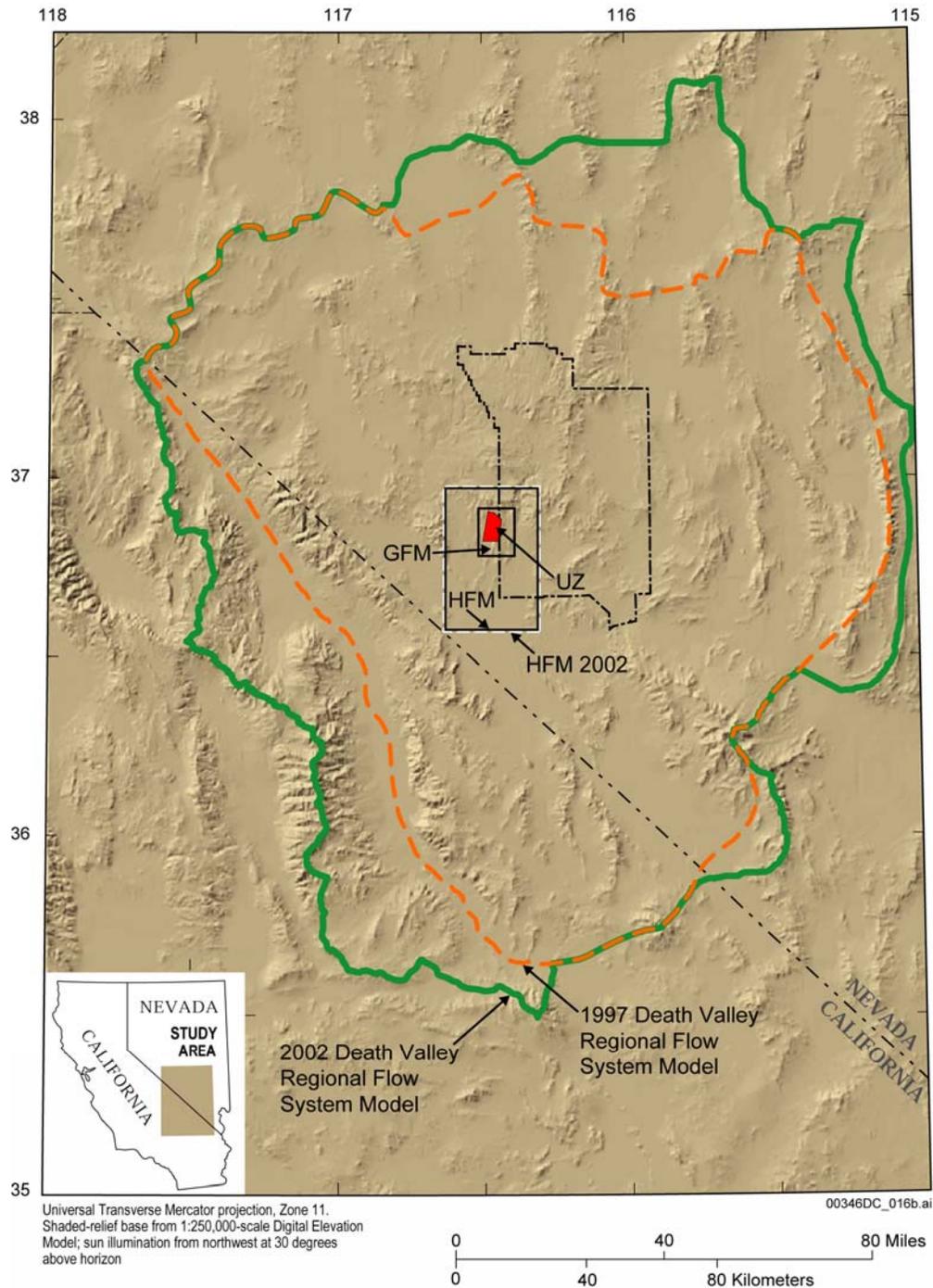
Source: Adapted from D'Agnese et al. 2002 [DIRS 158876], Figure 1

NOTE: HFM 2002 shows the site-scale saturated zone model domain.

Figure 8-8. Boundaries of Models in the Yucca Mountain Area
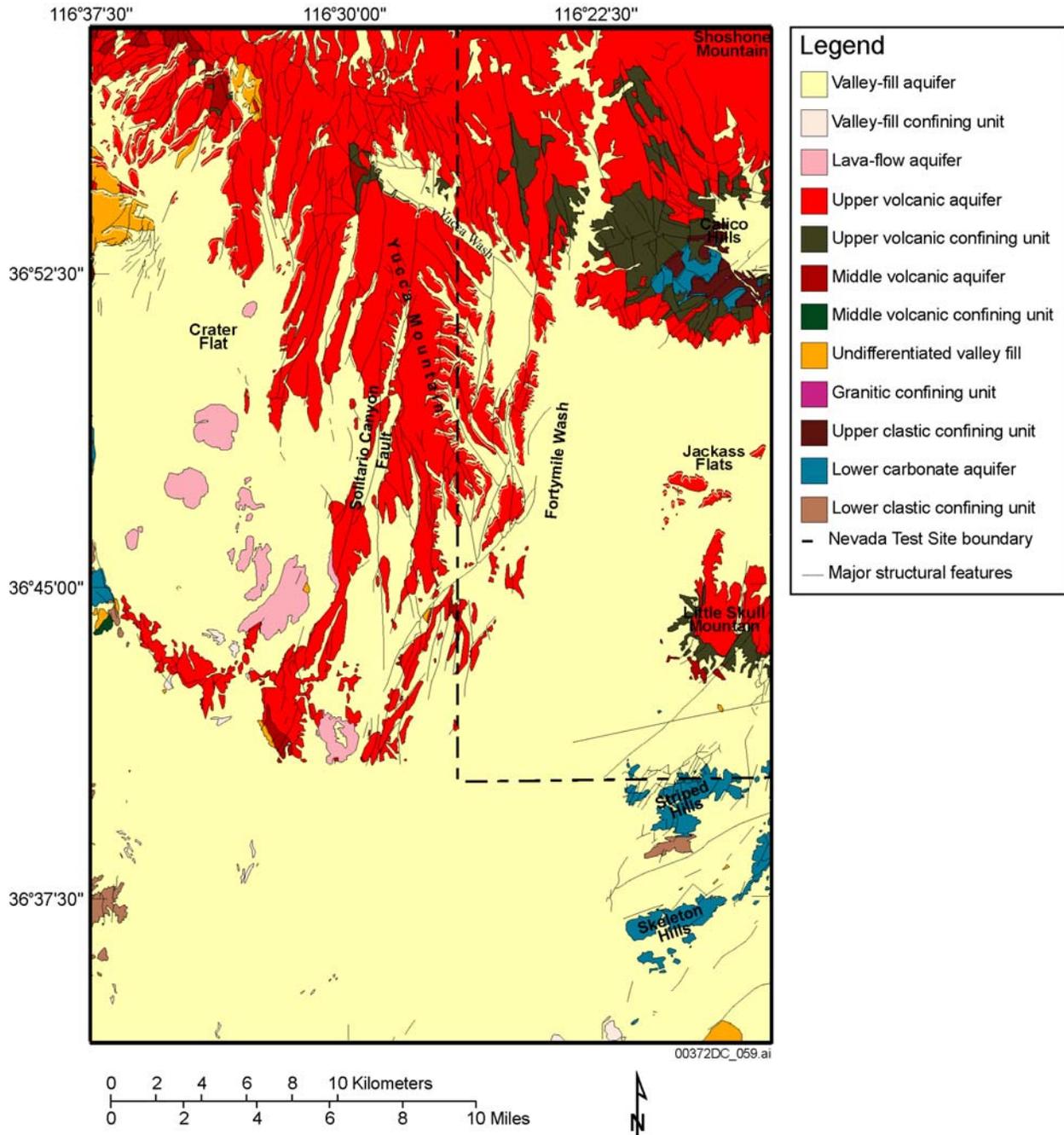
Source: Based on Czarnecki et al. 1997 [DIRS 141643], Figure 3b

Figure 8-9. Generalized Hydrogeologic Map of Site Saturated Zone Study Area with Major Faults
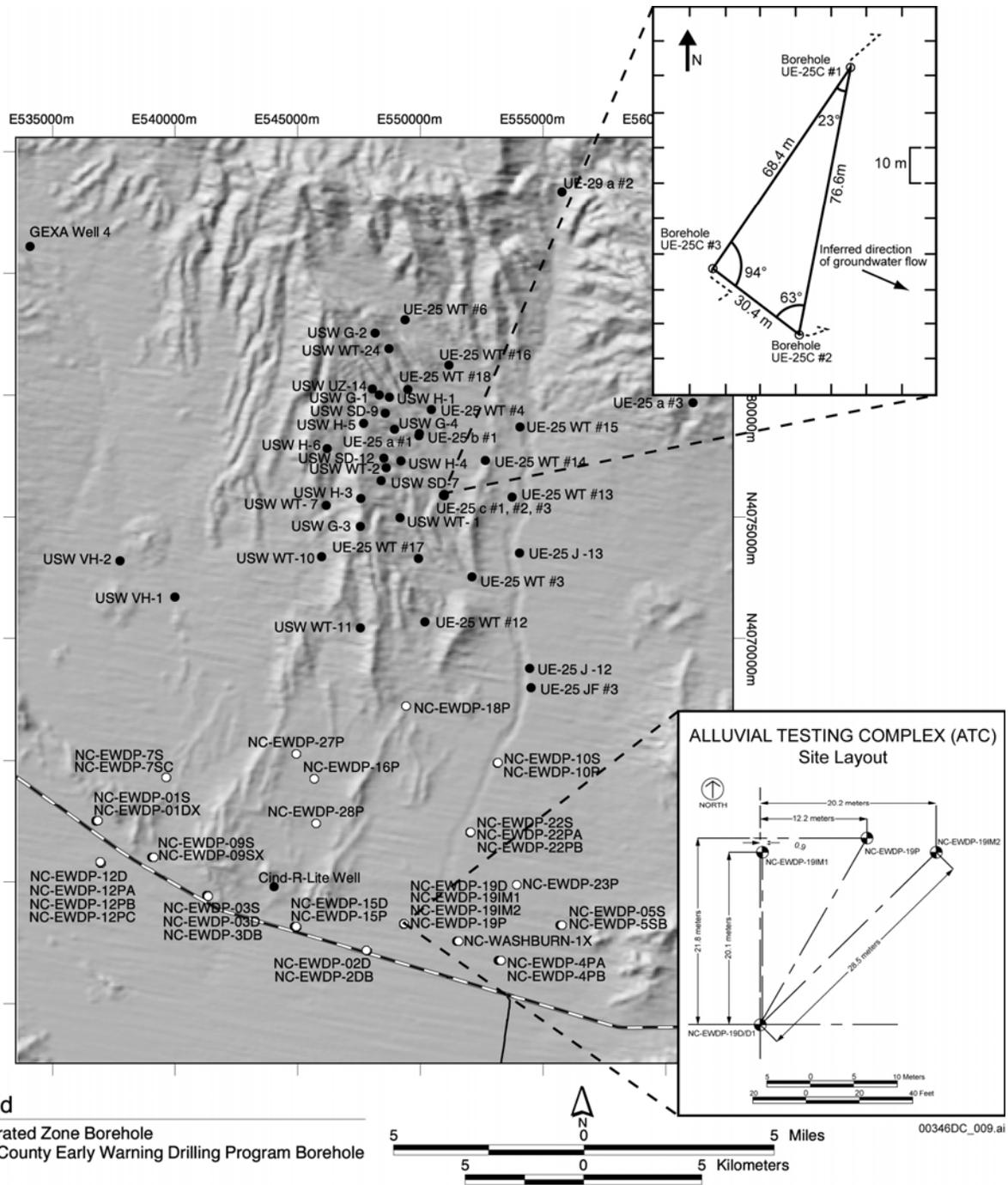
Source: C-Wells Layout: BSC 2003 [DIRS 167209], Figure 6.1-1; Alluvial Testing Complex layout: BSC 2002 [DIRS 158198], Figure 2, p. 34; Borehole location DTNs: GS010608312332.001 [DIRS 155307]; MO0401COV03168.000 [DIRS 168534]; MO0103COV01031.000 [DIRS 155271].

Figure 8-10. Location of the C-Wells Complex and the Alluvial Testing Complex
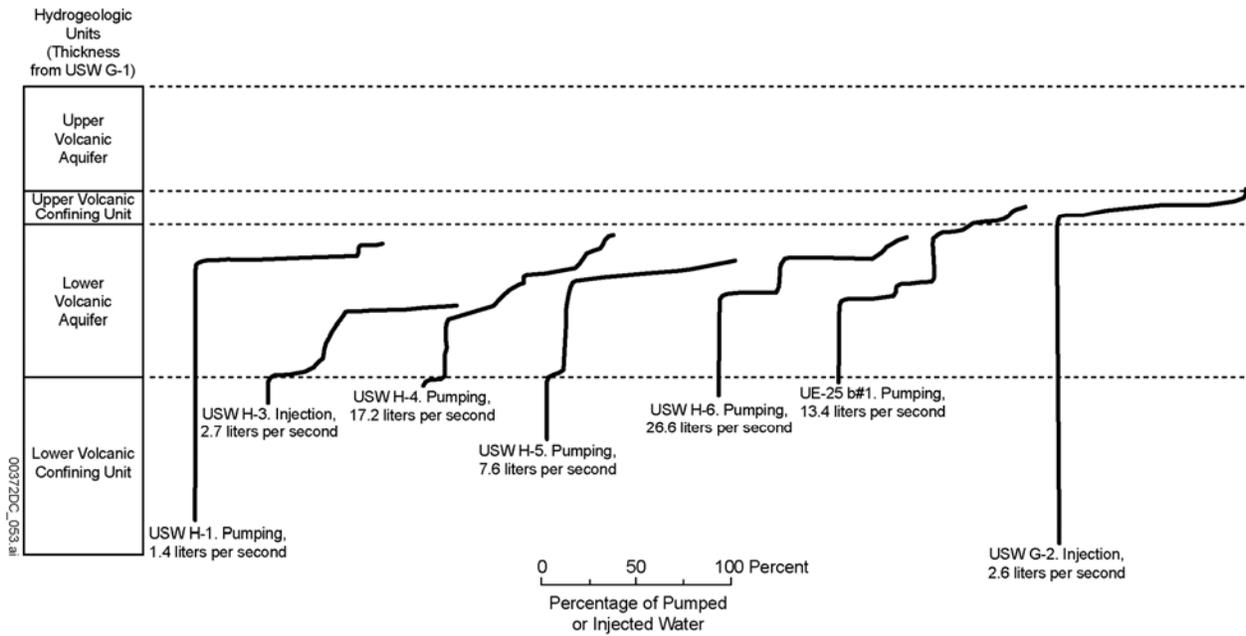
DTN: MO0312SPESDFLS.000 [DIRS 166384]

Source: Luckey et al. 1996 [DIRS 100465], Figure 15, p. 38

NOTE: Flow surveys adjusted to a standard thickness of 524.3 m in the lower volcanic aquifer and a standard thickness of 121.3 m in the upper confining unit, the thickness of the units in Borehole USW G-1. All flow surveys are from 0 to 100 percent of total pumping or injection.

Figure 8-11. Flow Surveys for Selected Boreholes in the Yucca Mountain Area

DTN: SNT05082597001.003 [DIRS 129714]
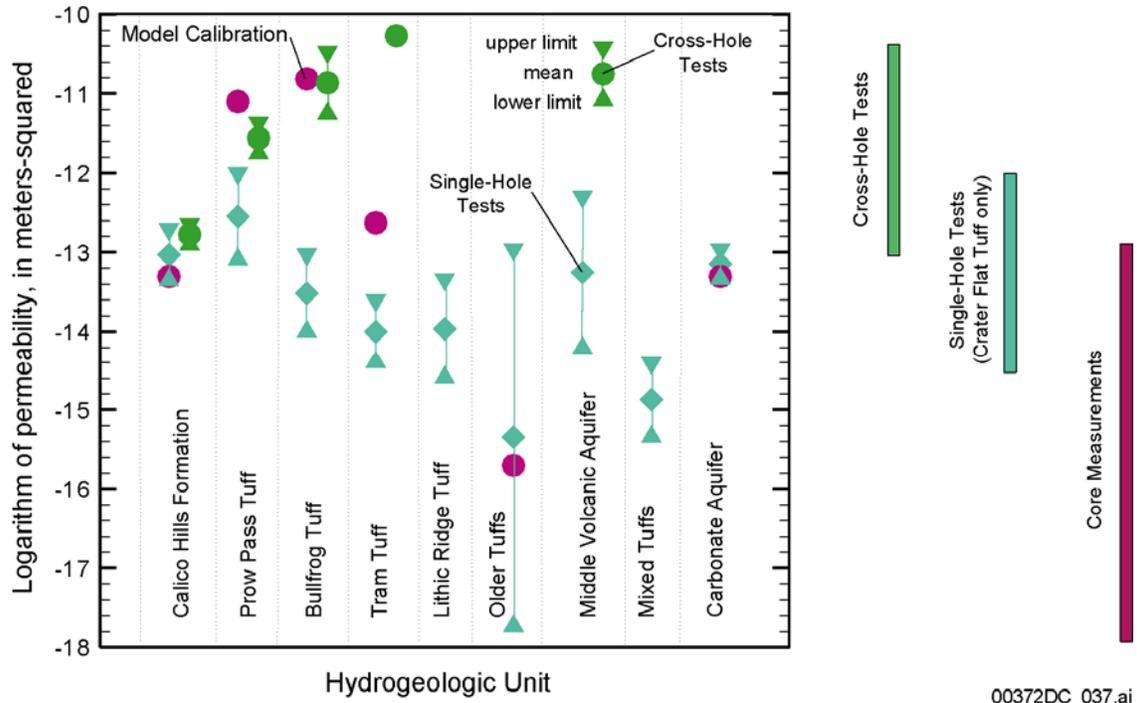
Source: Adapted from BSC 2001 [DIRS 155974], Figure 14

Figure 8-12. Measured and Model-Calibrated Permeabilities in the Fractured Volcanic Tuffs
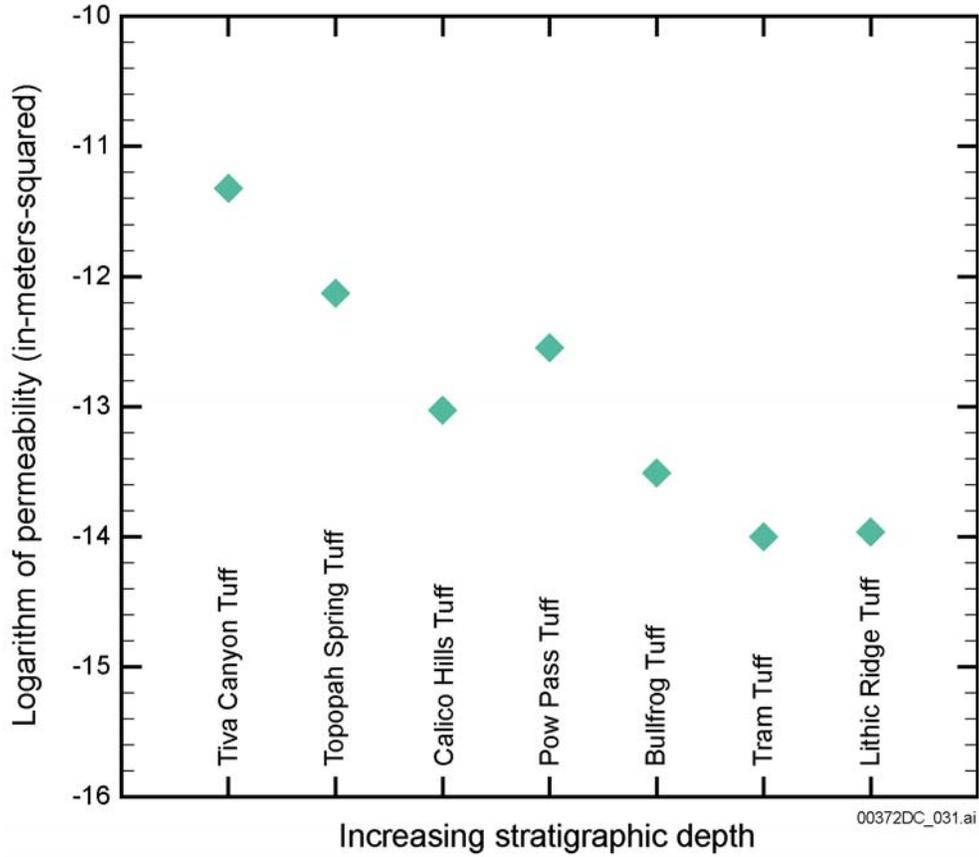
DTN: SNT05082597001.003 [DIRS 129714]

Source: Based on BSC 2001 [DIRS 155974], Table 9; except Tiva Canyon Tuff data from Section 6.7.7.6

Figure 8-13. Permeabilities Measured for Fractured Volcanic Tuffs in the Unsaturated and Saturated Zones
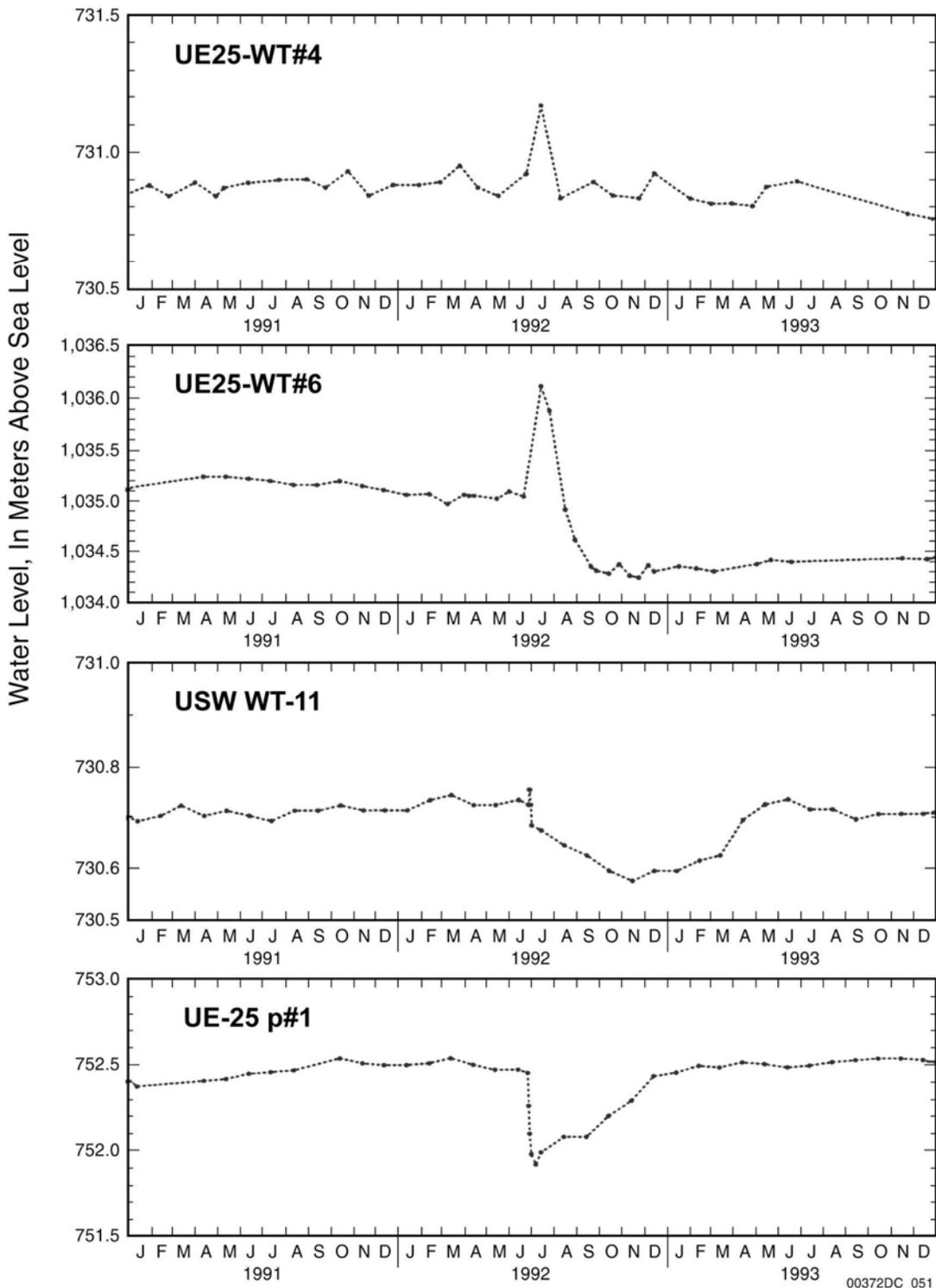
DTN: MO0312SEPSDWLA.000 [DIRS 166544]

Source: Based on Graves et al. 1997 [DIRS 101046], Figure 39

Figure 8-14. Water-Level Altitudes in Boreholes That May Have Been Affected by the June 1992 Earthquakes
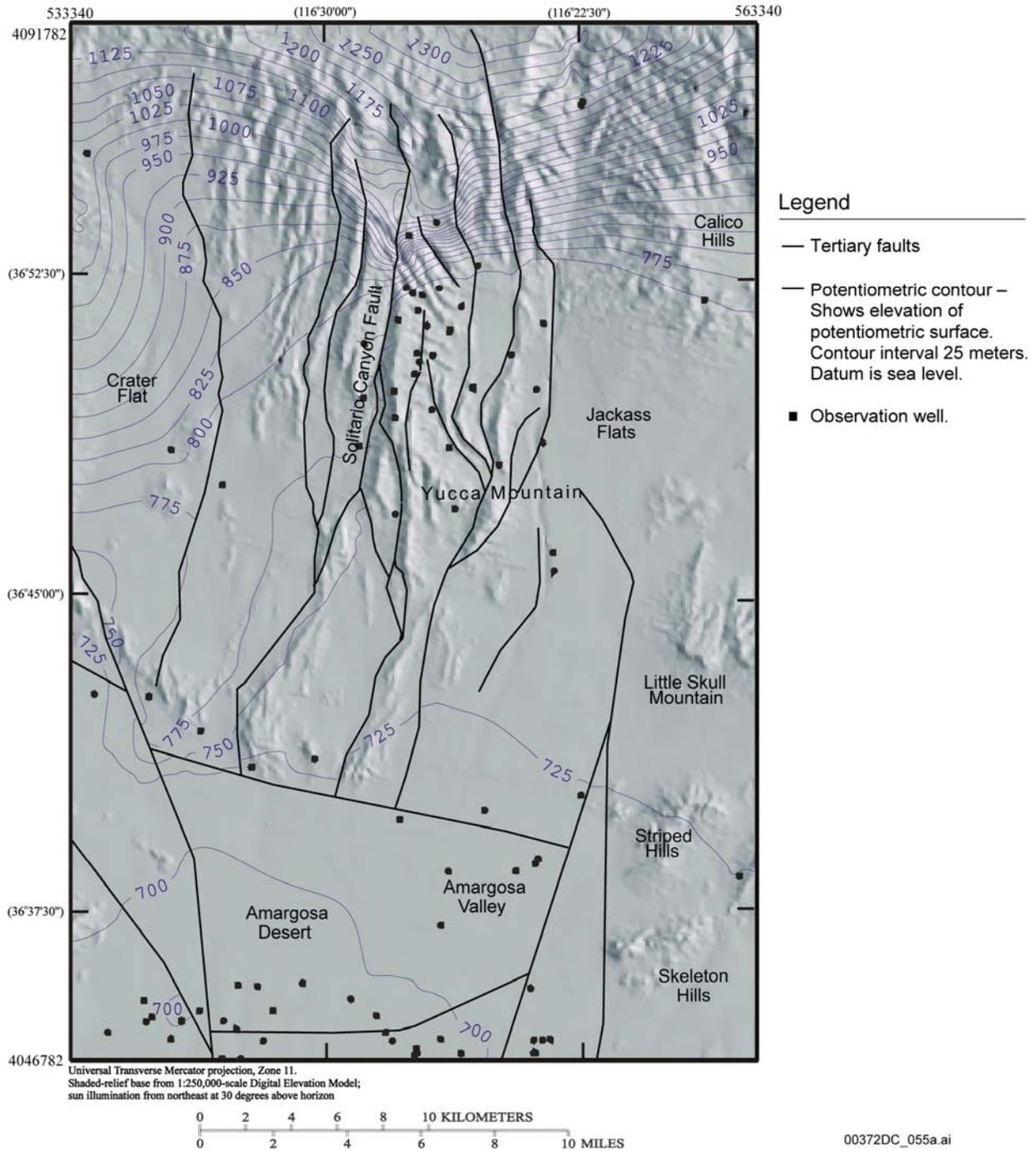
Source: USGS 2001 [DIRS 154625], Figure 1-2

Figure 8-15. Potentiometric-Surface Map of the Site-Scale Saturated-Zone Flow Model Area
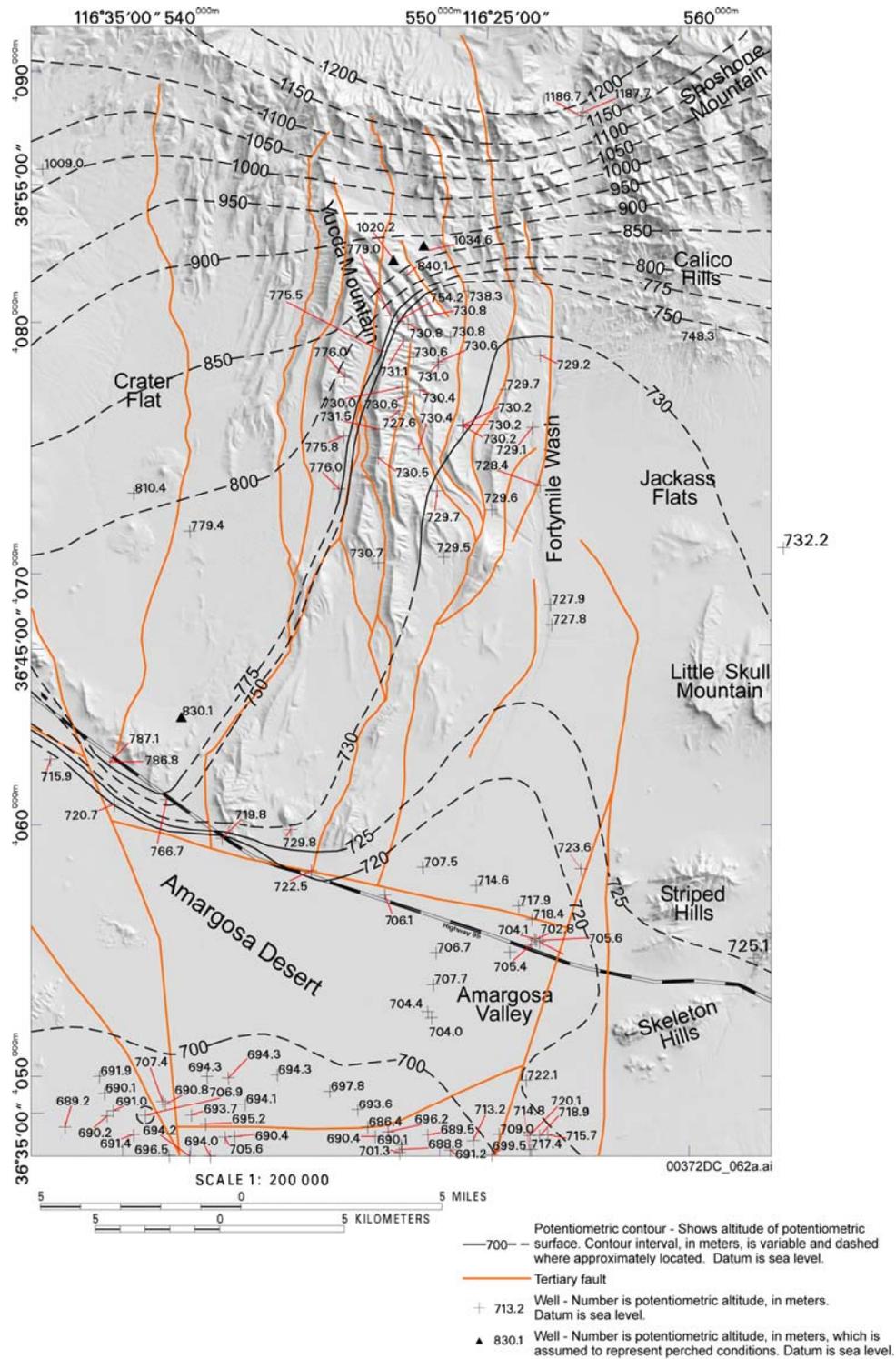
DTN: GS010608312332.001 [DIRS 155307]

Source: USGS 2002 [DIRS 165615], Figure 6-1

Figure 8-16. Potentiometric-Surface Map, Assuming Perched Conditions North of Yucca Mountain
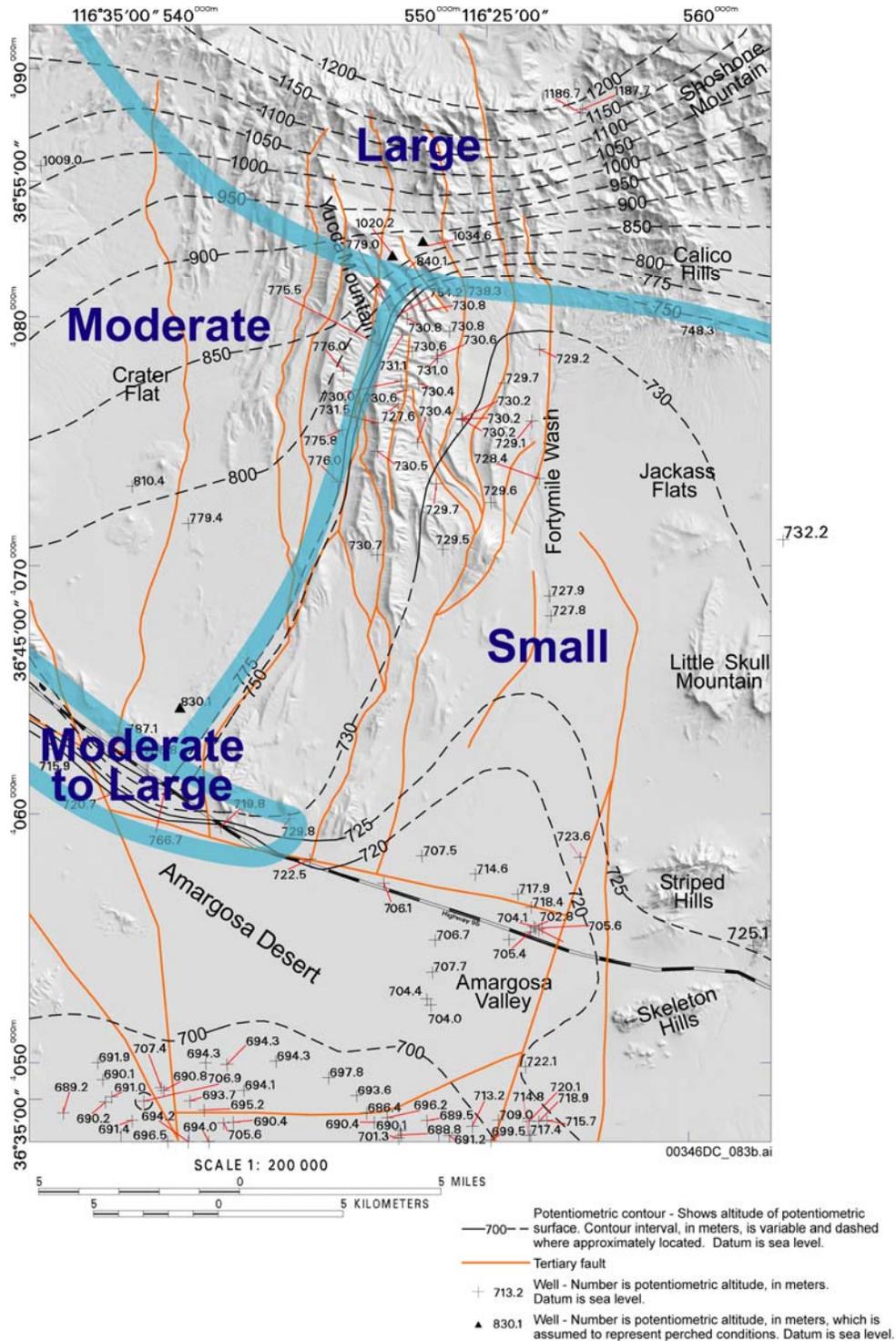
Source: Based on USGS 2002 [DIRS 165615], Figure 6-1

NOTE: Diagrammatically added general locations of hydraulic gradient areas to Figure 8-16 based on text in the source.

Figure 8-17. General Location of Four Hydraulic Gradient Areas
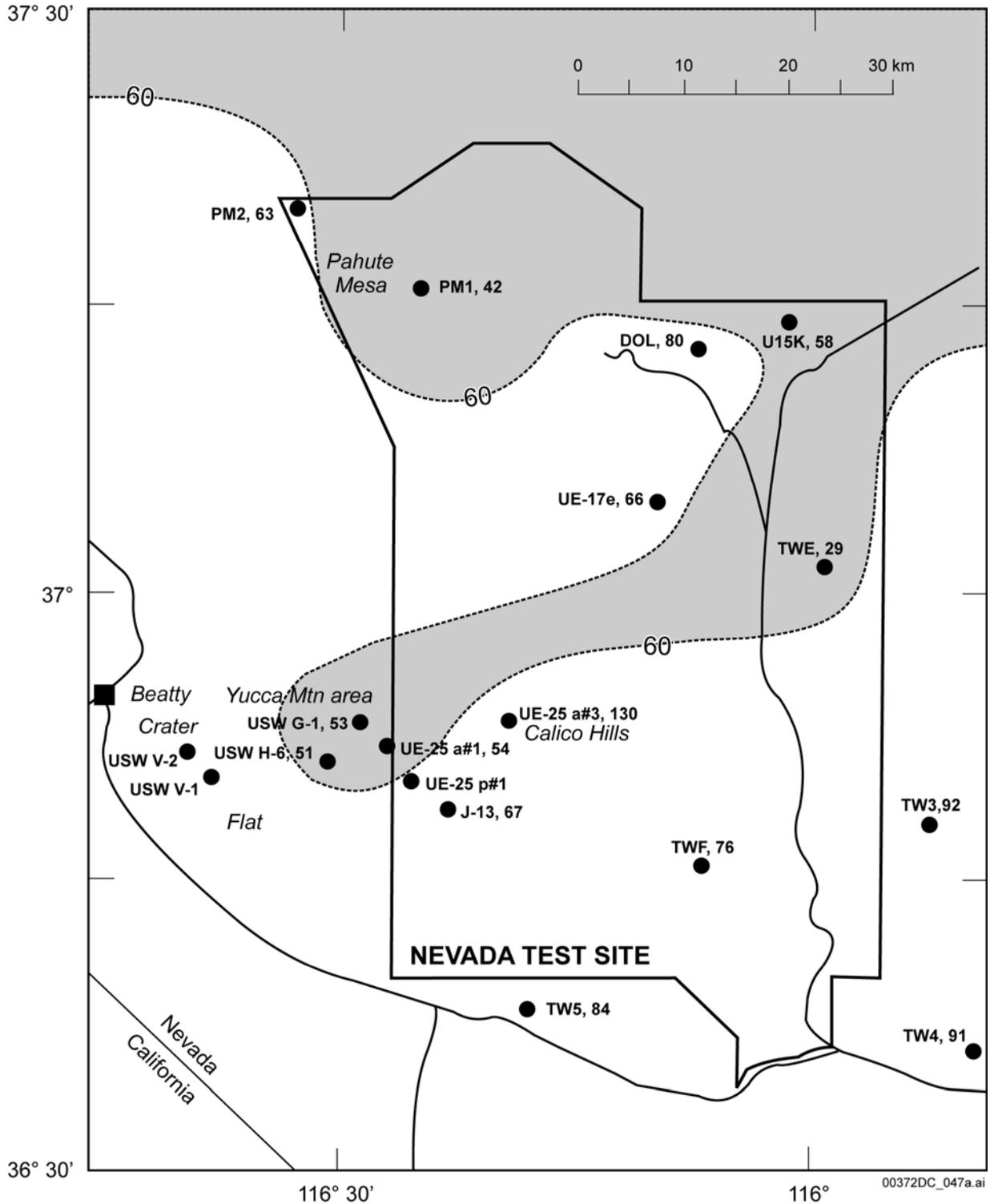
DTN: MO0312SEPSDHTF.000 [DIRS 166494]

Source: Based on Sass et al. 1988 [DIRS 100644], Figure 14

NOTE: Values following borehole identification numbers are heat flow (mW/m^2).

Figure 8-18. Heat Flows for Boreholes in the Nevada Test Site Area

DTN: MO0312SPESDTWT.000 [DIRS 166383]

Source: Sass et al. 1995 [DIRS 101288], Figure 8.4

NOTE: Values given at borehole locations (black dots) are degrees Celsius (°C).

Figure 8-19. Temperatures at the Water Table
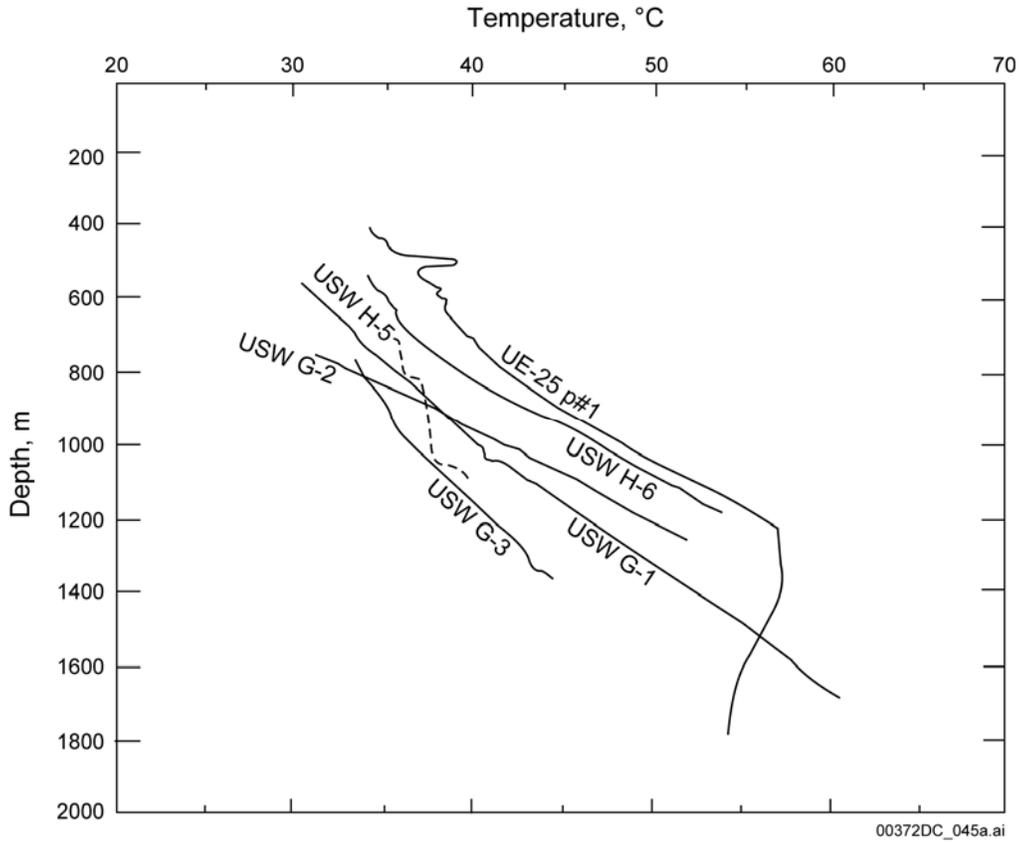
Temperature, °C

DTN: GS930208318523.001 [DIRS 145763]

Source: Sass et al. 1988 [DIRS 100644], Appendix 1

Figure 8-20. Saturated Zone Temperature Logs
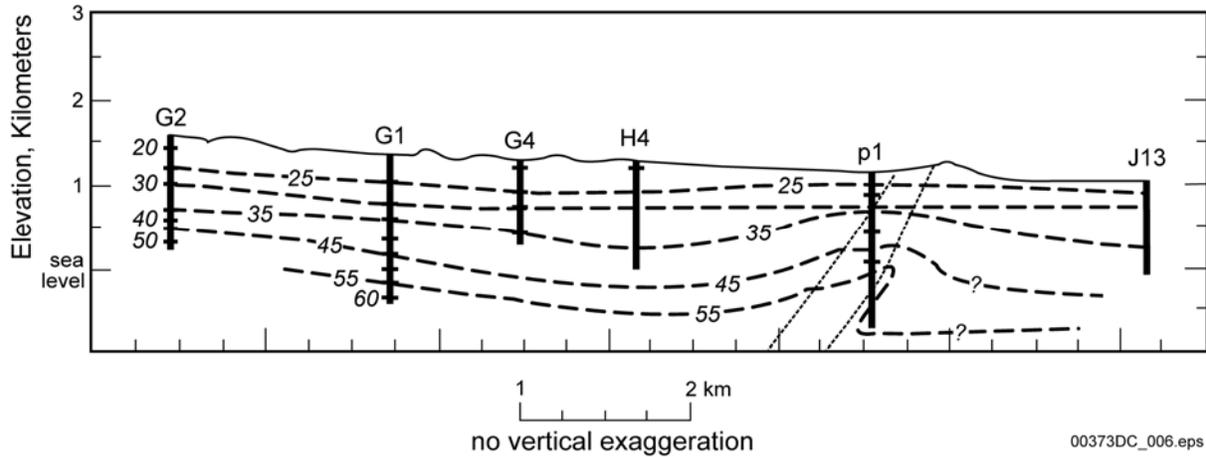
DTN: GS930208318523.001 [DIRS 145763]

Source: Based on Sass et al. 1988 [DIRS 100644]

NOTE: Figure shows upwelling of isotherms along faults intersected by Borehole UE-25 p#1.

Figure 8-21. Interpretive Thermal Cross-Section Between Boreholes USW G-2 and UE-25 J-13
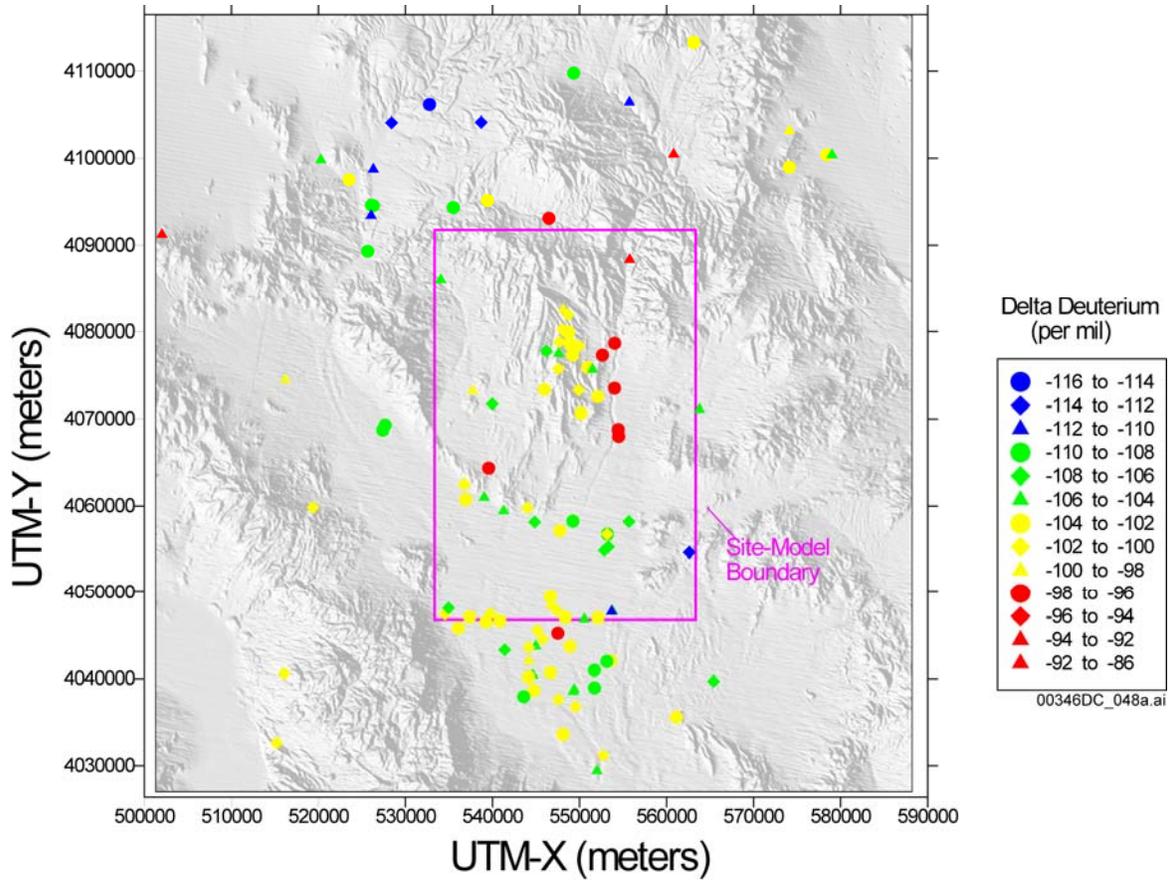
DTNs: LA0309RR831233.001 [DIRS 166546]; LA0309RR831233.002 [DIRS 166548]

Source: BSC 2003 [DIRS 167211], Figure 6.7-21

Figure 8-22. Deuterium (δ^2H) in Groundwaters near Yucca Mountain
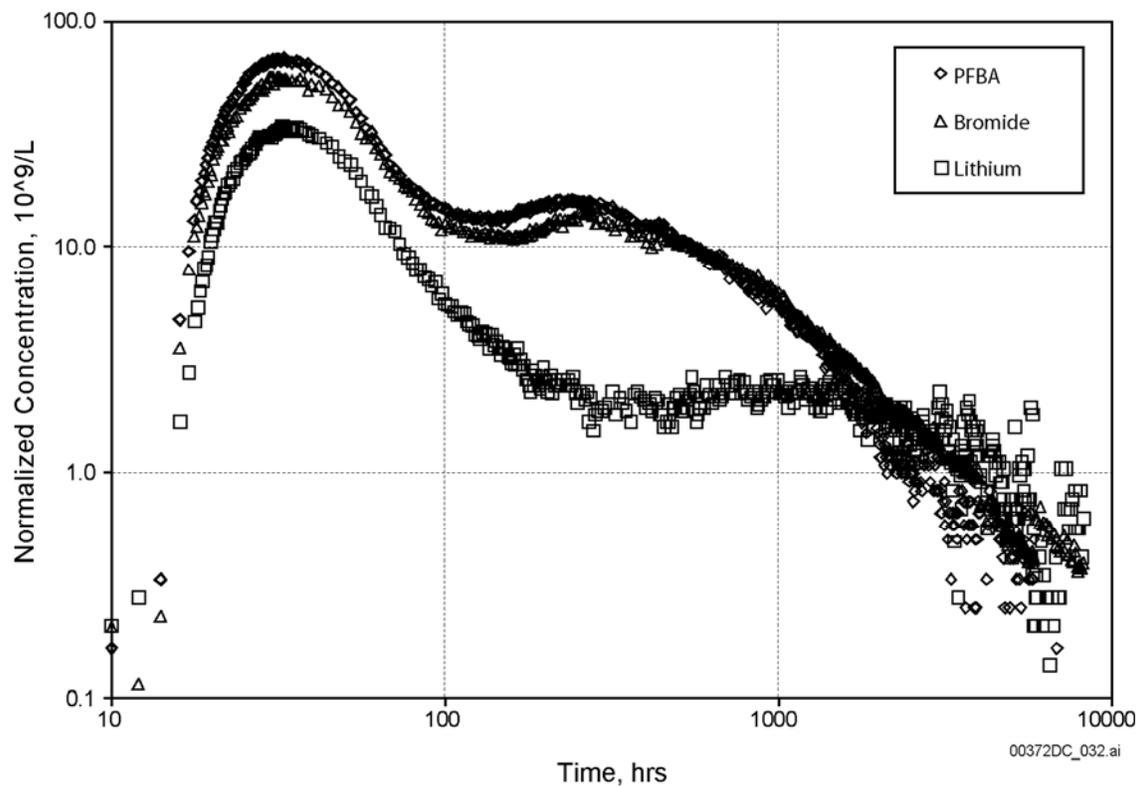
DTN: LA0007PR831231.001 [DIRS 156043]

Source: BSC 2003 [DIRS 167209], Figure 6.3-19

NOTES: PFBA = pentafluorobenzoic acid. Tracer breakthrough curves for these three soluble tracers are plotted as normalized concentration versus time (where normalization was performed by dividing by the tracer mass injected) at the production borehole. Tests conducted from October 1996 to September 1997.

Figure 8-23. Normalized Tracer Concentrations versus Time in the Bullfrog Tuff Tracer Test
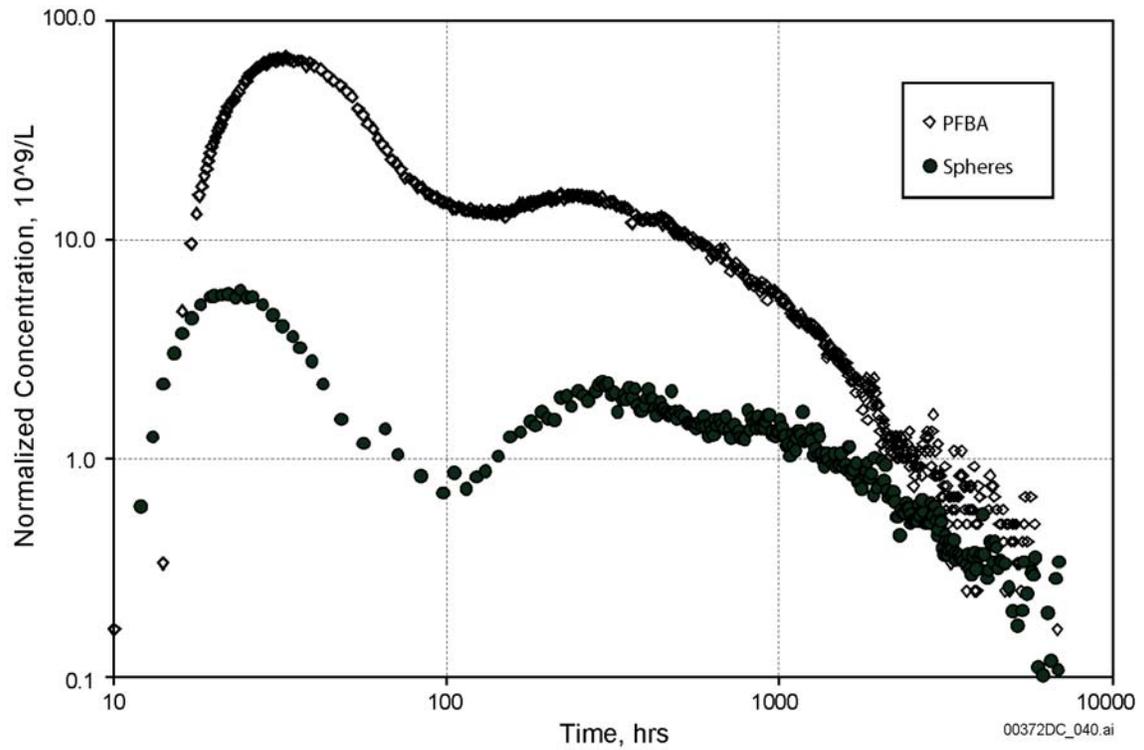
DTN: LA0007PR831231.001 [DIRS 156043]

Source: BSC 2003 [DIRS 167209], Figure 6.3-20

NOTE: Test used 360-nanometer diameter carboxylate-modified polystyrene microspheres.

Figure 8-24. Normalized Tracer Concentrations versus Time for Pentafluorobenzoic Acid Microspheres in the Bullfrog Tuff Tracer Test
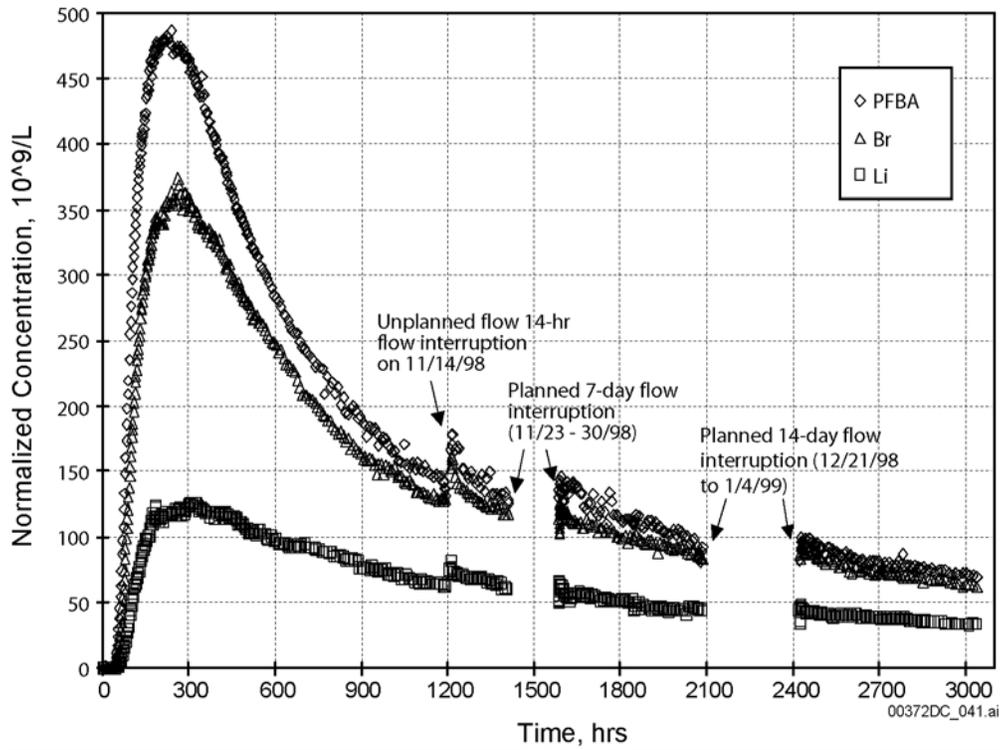
DTN: LA0007PR831231.001 [DIRS 156043]

Source: BSC 2003 [DIRS 167209], Figure 6.3-22

NOTE: Test conducted from September 1998 to January 1999.

Figure 8-25. Normalized Tracer Concentrations versus Time in the Prow Pass Tracer Test
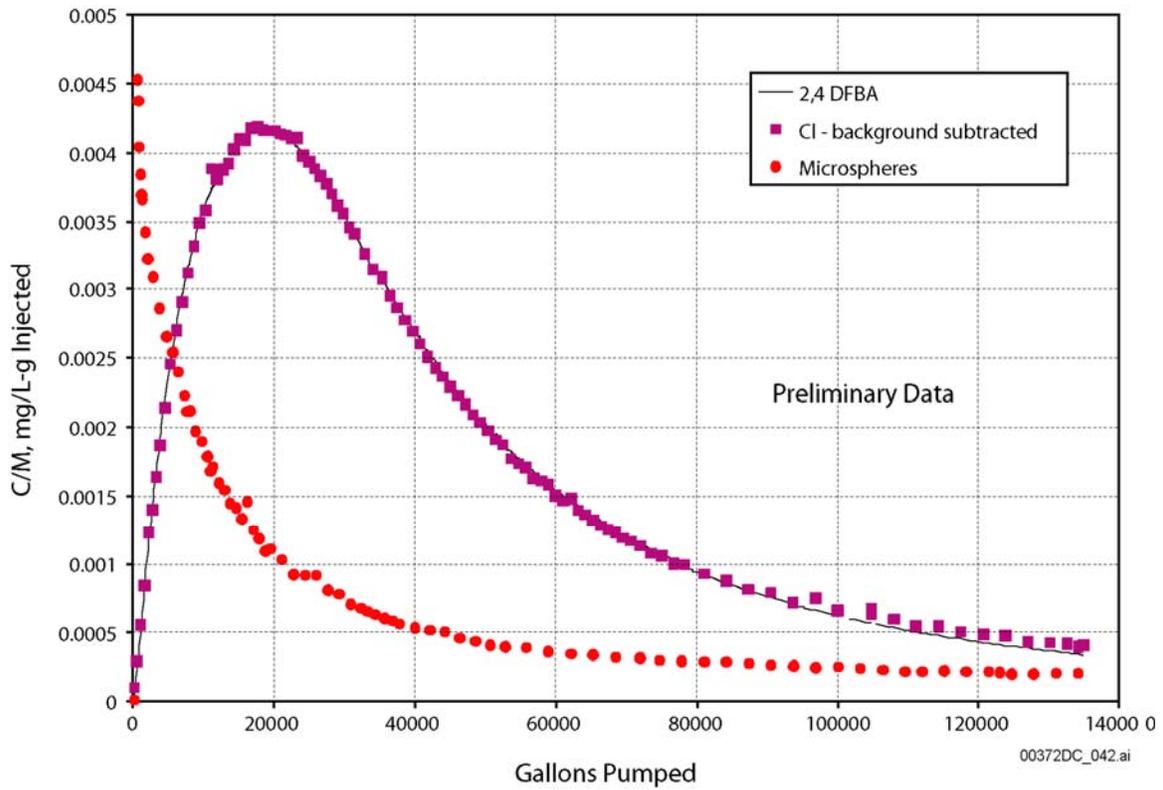
DTN: UN0109SPA008IF.006 Archived [DIRS 162442]; LA0207PR831352.001 [DIRS 162431]

Source: BSC 2003 [DIRS 167209], Figure 6.5-18

Figure 8-26. Normalized Tracer Concentrations in Water from NC-EWDP-19D1 as a Function of Volume Pumped after a Rest Period of about 0.5 Hours
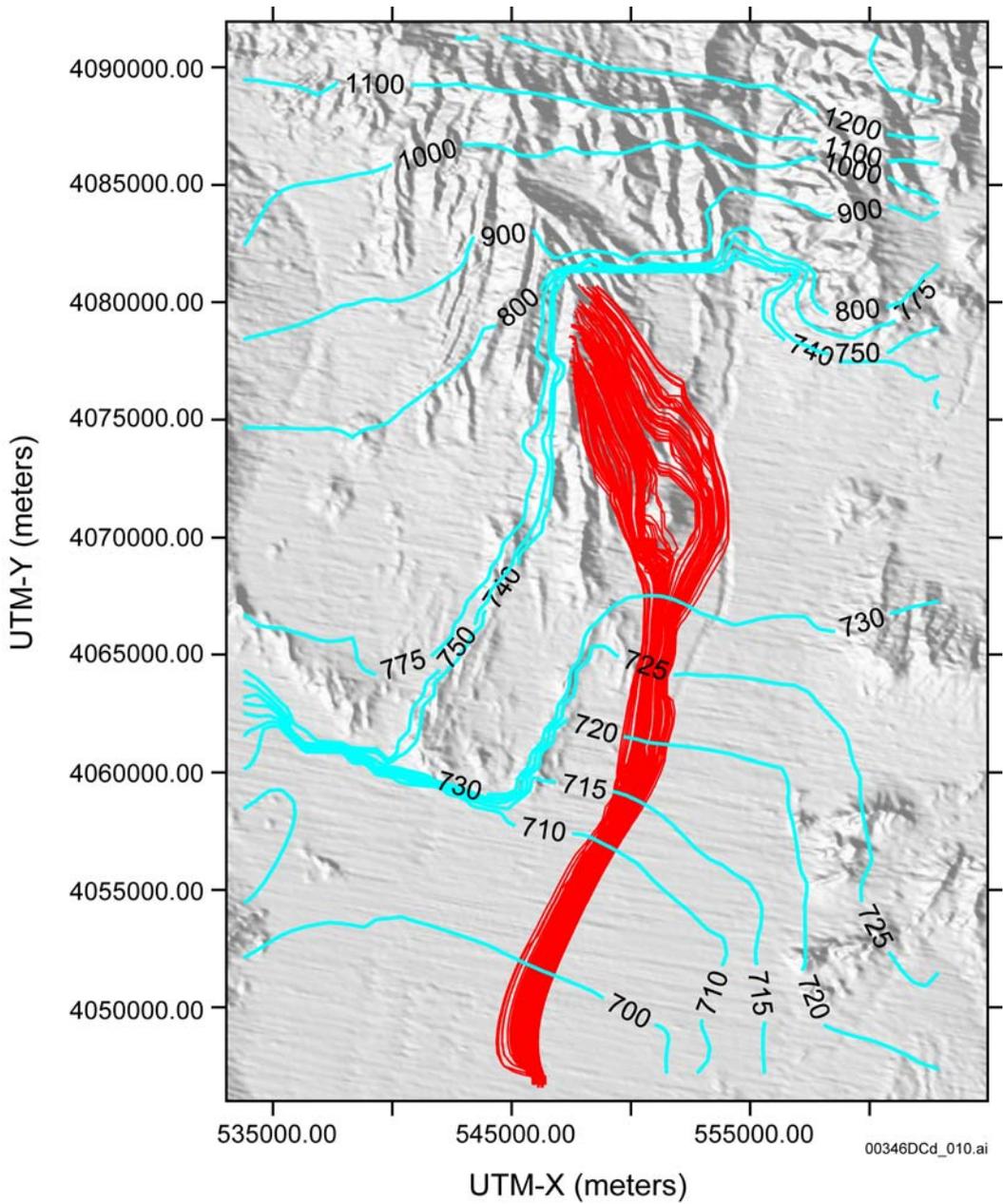
Source: BSC 2003 [DIRS 166262], Figure 3

Figure 8-27. Flow Paths Predicted by Site-Scale Saturated Zone Flow and Transport Model
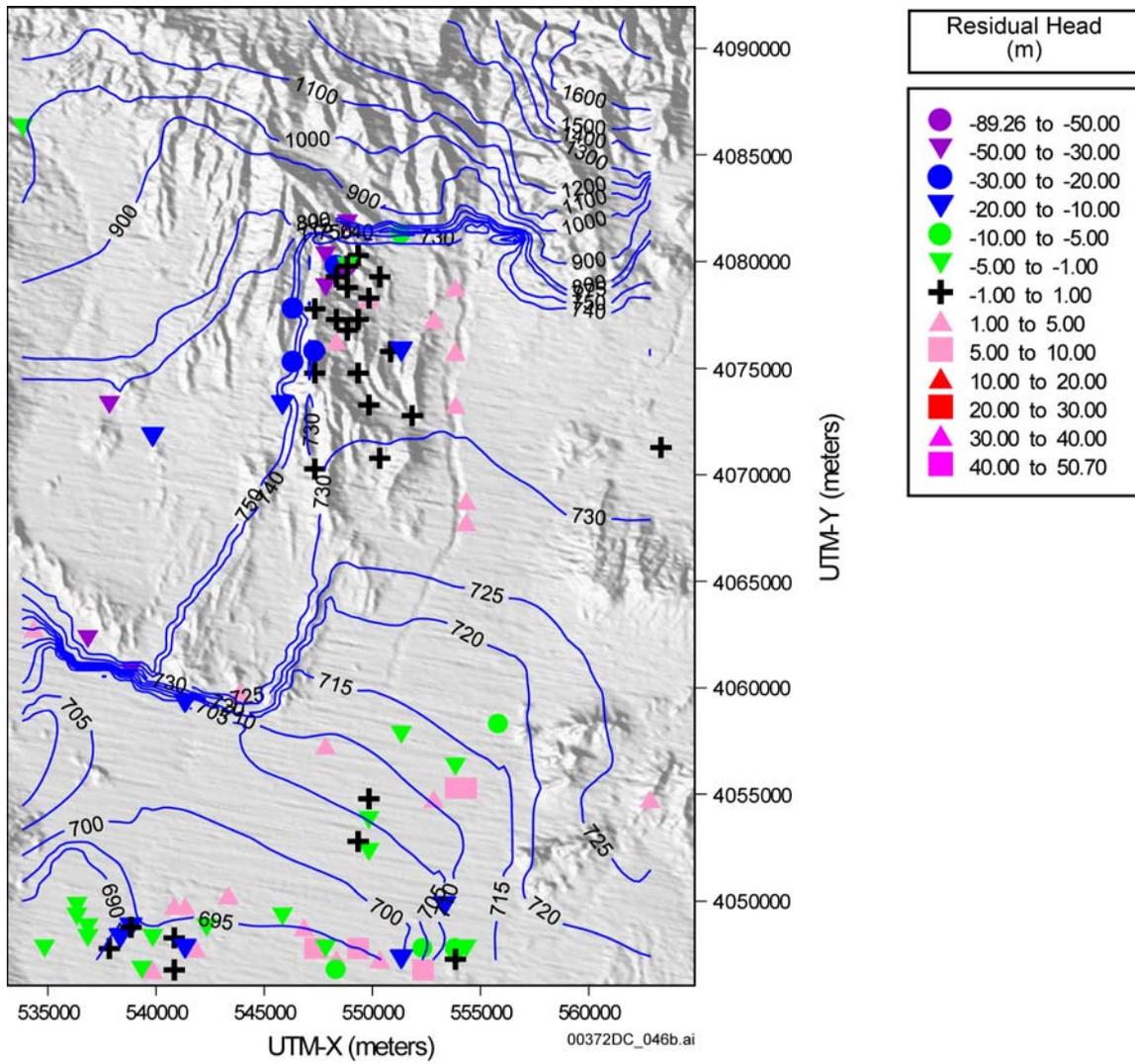
Source: BSC 2003 [DIRS 166262], Figure 9

NOTE: Symbols indicate borehole locations.

Figure 8-28. Simulated Potentiometric Surface
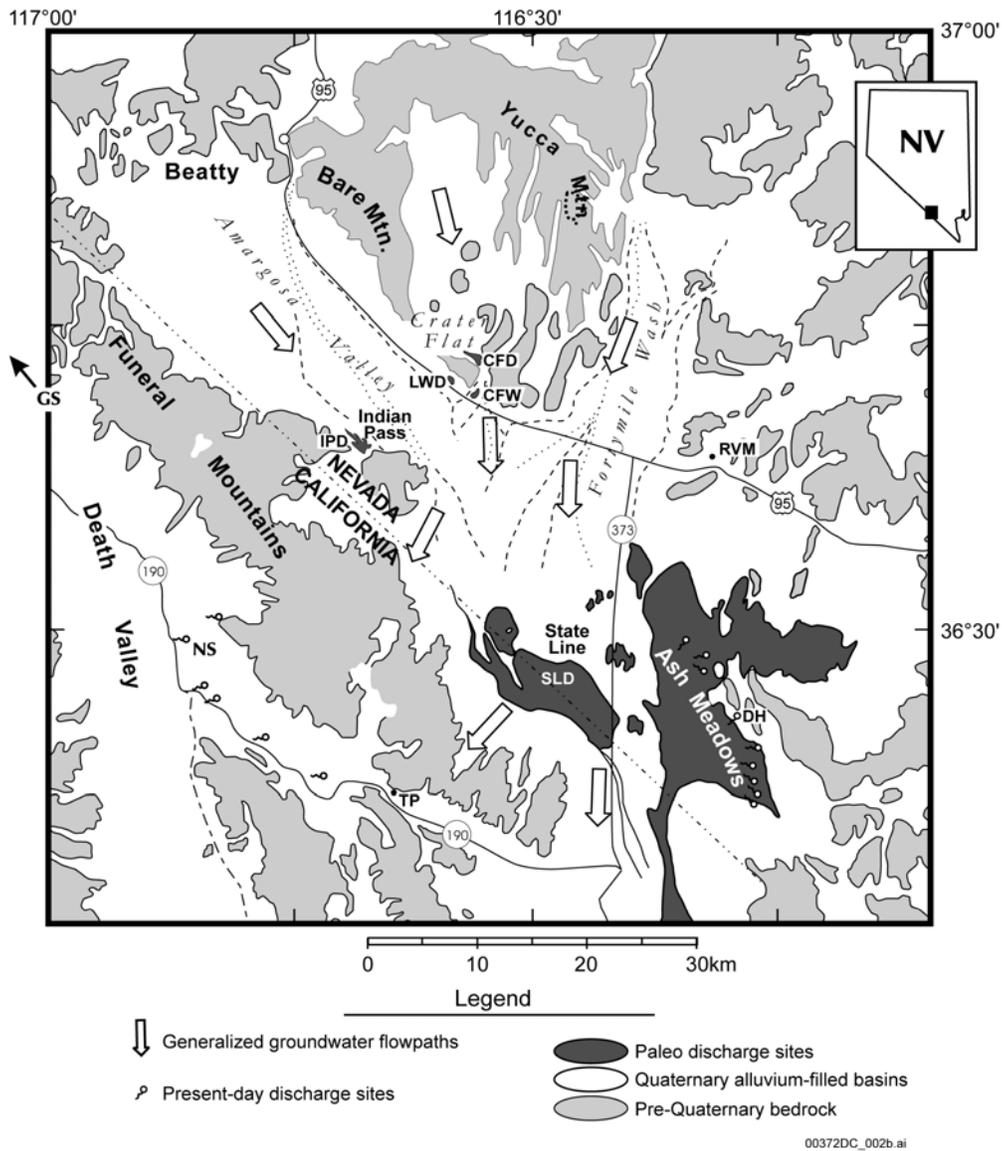
Source: Paces et al. 1997 [DIRS 109148], Figure 1

NOTE: CFD = Crater Flat Deposit; LWD = Lathrop Wells Diatomite; CFW = Crater Flat Wash; DH = Devils Hole; RVM = Rock Valley Mound; SLD = State Line Deposits; IPD = Indian Pass Deposit; TP = Travertine Point; NS=Nevares Spring; GS = Grapevine Spring.

Figure 8-29. Paleodischarge Deposits in the Yucca Mountain Region
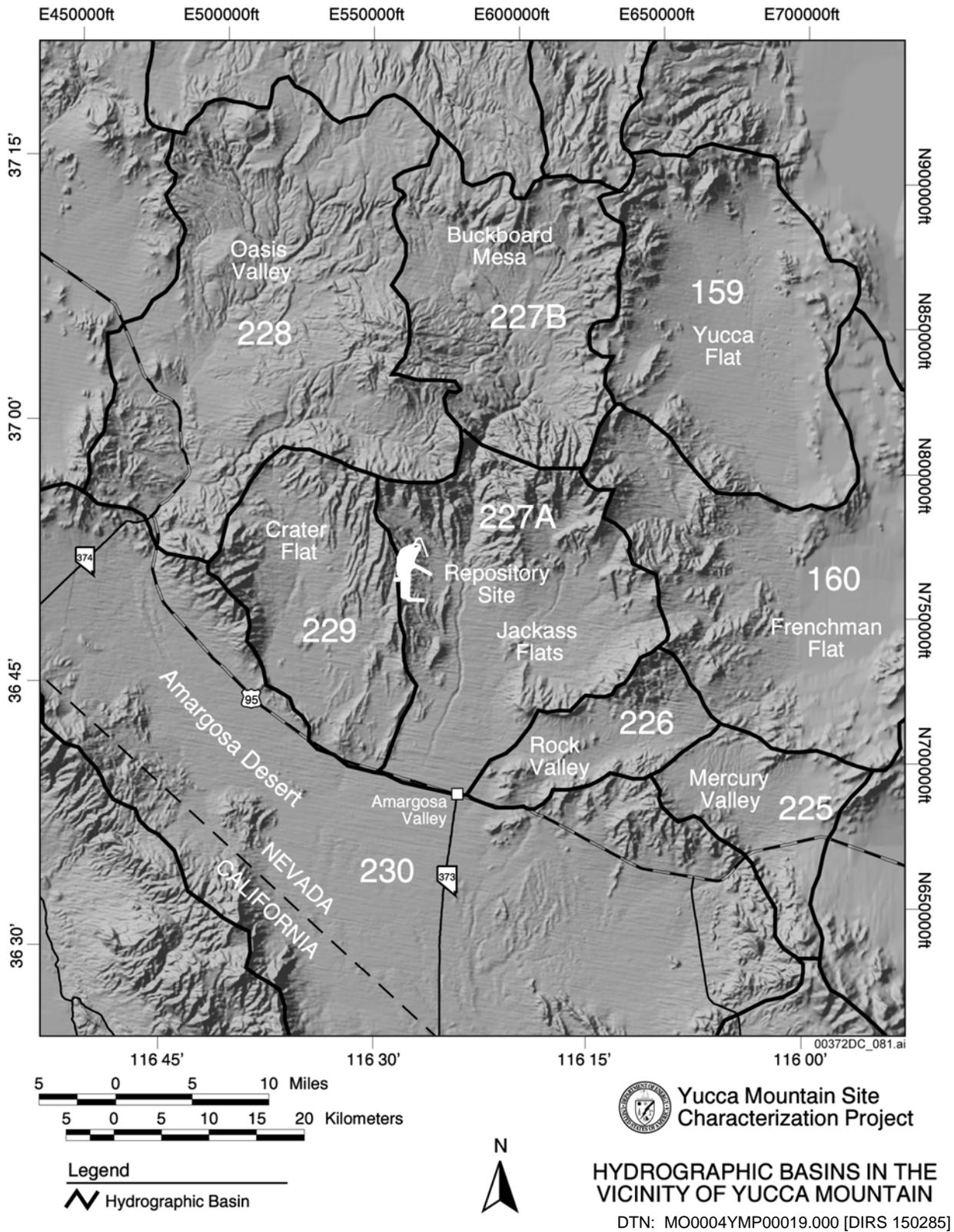
Figure 8-30. Hydrographic Basins in the Vicinity of Yucca Mountain

DTN: MO0004YMP00019.000 [DIRS 150285]

Table 8-1. Hydrogeologic Units for the Death Valley Region

Hydrogeologic Units	UGTA Units (DOE 1997 Table 4-3, p. 4-5 to 4-9 [DIRS 103021])	Yucca Mountain Units (D'Agnese et al. 1997 [DIRS 100131])	Description of Primary Components
Quaternary-Tertiary valley fill alluvium	AA	QTvf	Alluvium/valley fill
Quaternary-Tertiary valley-fill playa deposits	---	Qp	Playa deposits
Undifferentiated Volcanic Rocks	VU	QTv, Tv	Undifferentiated volcanic rocks
volcanic aquifer	VA	QTv, Tv	Volcanic aquifer – southern Nevada TestSite
volcanic confining unit	VCU	QTV, Tv	Volcanic confining unit – southern Nevada TestSite
Timber Mountain aquifer	TMA	QTv, Tv	Timber Mountain aquifer
Paintbrush/ Calico Hills tuff cone	TC	QTv, Tv	Paintbrush/Calico Hills tuff cone
Bullfrog confining unit	TCB	QTv, Tv	Bullfrog confining unit (nonwelded tuffs)
Belted Range aquifer	TBA	QTv, Tv	Belted Range aquifer (welded tuffs)
Basal confining unit	TBCU	QTv, Tv	Basal confining unit (nonwelded tuffs)
Basal aquifer	TBQ	QTv, Tv	Basal aquifer (welded tuffs)
Tertiary sediments/Death Valley section	TSDVS	Tvs	Tertiary sediments/Death Valley section
Rocks of Mesozoic Age	---	Mvs	Mesozoic volcaniclastic and sedimentary rocks
Mvs_LC	---	Mvs	Mesozoic volcaniclastic and sedimentary rocks – Lee Canyon thrust
Mvs_KS	---	Mvs	Mesozoic volcaniclastic and sedimentary rocks – Keystone thrust
upper carbonate aquifer	LCA3	---	Upper carbonate aquifer
upper clastic confining unit	UCCU	ECU	Upper clastic confining unit
lower carbonate aquifer	LCA	P2	Lower carbonate aquifer
lower clastic confining unit	LCCU	P1, pCgm	Lower clastic confining unit
lower carbonate aquifer, upper plate of thrust system	LCA_T1	---	Lower carbonate aquifer – Specter Range, and Wheeler Pass thrusts (upper plate)

Table 8-1. Hydrogeologic Units for the Death Valley Region (Continued)

Hydrogeologic Units	UGTA Units (DOE 1997 Table 4-3, p. 4-5 to 4-9 [DIRS 103021])	Yucca Mountain Units (D'Agnese et al. 1997 [DIRS 100131])	Description of Primary Components
lower clastic confining unit, lower plate of the Specter Range and Wheeler Pass thrust	LCCU_T1	---	Lower clastic confining unit – Schwaub Peak, Specter Range, and Wheeler Pass thrusts (upper plate)
Lee Canyon thrust	---	---	Lower carbonate aquifer - Lee Canyon thrust
Gass Peak thrust	---	---	Lower carbonate aquifer - Gass Peak thrust
lower carbonate aquifer, lower plate of thrust system	LCA_T2	---	Lower carbonate aquifer - Schwaub Peak, Specter Range, and Wheeler Pass thrusts (lower plate)
Gass Peak thrust	---	---	Lower clastic confining unit – Gass Peak thrust
lower clastic confining unit, upper plate of the Specter Range and Wheeler Pass thrust	LCCU_T2	---	Lower clastic confining unit – Schwaub Peak, Specter Range, and Wheeler Pass thrusts (lower plate)
Late Proterozoic sedimentary rocks	LCCU	pCgm	Precambrian granites and metamorphic rocks
Crystalline granitic rocks of Mesozoic and Tertiary age	I	TJg	Tertiary – Jurassic intrusives

Source: D'Agnese et al. 2002 [DIRS 158876], Table 1

NOTE: UGTA - Underground Test Area model.

Table 8-2. Statistical Distributions for the Hydraulic Conductivity of Generalized Hydrogeologic Units in the Death Valley Region

Generalized Hydrogeologic Unit or Subunit	Geometric Mean K (m/d)	Arithmetic Mean K (m/d)	Min. K (m/d)	Max. K (m/d)	95-% CI(GM) (m/d)	Number of Analyses
Younger alluvial aquifer and Older alluvial aquifer	2	11	0.001	130	0.6-4	43
Alluvial confining Unit	3	11	0.003	34	0.6-10	13
Lava flow unit	--	--	0.002	4	nd	2
Younger volcanic unit and Volcaniclastic and sedimentary rocks unit	0.06	1.5	0.00004	6	0.01-0.4	15
Tertiary volcanic rocks	0.1	4	0.000001	180	0.08-0.2	159
Rhyolitic to rhyodacitic lava flows	0.1	0.6	0.000007	4	0.04-0.4	25
Ash-flow tuff	0.1	5	0.000002	180	0.06-0.2	109
Nonwelded to partially welded	0.06	7	0.003	180	0.03-0.2	43
Partially to moderately welded	0.04	1	0.000002	19	0.03-0.1	35
Moderately to densely welded	2	13	0.02	55	0.18-15	7
Unaltered	0.4	8	0.00002	180	0.2-0.9	71
Zeolitized and argillized	0.04	1	0.000002	25	0.02-0.08	63
Tuff breccia and ash-flow tuff	0.3	4	0.0008	15	0.03-3	11
Bedded ash-fall and reworked tuff and ash-flow tuff	0.1	2	0.00009	15	0.03-7	14
Thirsty Canyon-Timber Mountain volcanic aquifer	0.01	2	0.0002	20	0.001-0.01	11
Paintbrush volcanic aquifer	0.02	4	0.000007	22	0.001-0.09	9
Calico Hills volcanic unit	0.2	0.6	0.008	2	0.08-0.5	14
Belted Range unit	0.3	1	0.01	4	0.06-2	6
Crater Flat volcanic unit	0.2	6	0.000002	180	0.09-0.3	91
Older volcanic unit	0.004	0.07	0.000001	1	0.001-0.01	46
Intrusive confining unit	0.01	0.3	0.0006	1	0.001-0.01	7
Sedimentary rocks confining unit	0.002	0.02	0.0002	0.3	0.0007-0.005	16
Upper carbonate aquifer and Lower carbonate aquifer	0.6	90	0.00001	820	0.2-2	51
Faulted and karstic	3	120	0.01	820	3-4	18
Unfaulted	0.1	2	0.0001	14	0.02-0.5	19
Upper clastic confining unit and Lower confining clastic unit	0.00003	0.2	0.000000003	5	0.000003-0.0003	30
Upper clastic confining unit (shales)	0.01	0.07	0.0003	0.4	0.002-0.06	9
Lower clastic confining unit (quartzites)	0.0000006	5	0.000000003	5	0.00000007-0.000005	19
Crystalline confining unit	nd	nd	0.00000002	<0.4	nd	nd

DTN: MO0312SEPSDHCU.000 [DIRS 166550]

Source: Based on Belcher et al. 2001 [DIRS 158458], Table 2

NOTE: Min. = minimum; Max. = maximum; CI(GM) = Confidence Interval of Geometric Mean; K = hydraulic conductivity; nd = no data.

Table 8-3. Correlation of Generalized Stratigraphy with Unsaturated and Saturated Hydrogeologic Units in the Vicinity of Yucca Mountain

Systems and Series	Stratigraphic Unit	Hydrogeologic Units		Saturated Hydrogeologic Units[a]	Comments
		Unsaturated	Saturated		
QUATERNARY and TERTIARY	Alluvium, colluvium, eolian, spring, lacustrine, and playa deposits; basalt lavas	QAL, Alluvium	Qta; Valley-fill aquifer QTc; Valley-fill confining unit		QAL restricted to stream channels on Yucca Mountain. Qta occurs in Amargosa Desert; major water-supply source.
TERTIARY Miocene	TIMBER MOUNTAIN GROUP Rainier Mesa Tuff	--	--		Minor erosional remnants at Yucca Mountain.
	PAINTBRUSH GROUP Tiva Canyon Tuff	TCw, Tiva Canyon welded unit	--		Mainly densely welded; caprock on Yucca Mountain. Not known in saturated zone at or near Yucca Mountain.
	(bedded Tuff). Yucca Mountain Tuff Pah Canyon Tuff	PTn, Paintbrush nonwelded unit	--		PTn includes bedded and nonwelded tuffs between basal part of Tiva Canyon and upper part of Topopah Spring Tuffs.
	Topopah Spring Tuff (Vitrophyre and nonwelded tuffs at base)	TSw, Topopah Spring welded unit	UVA; upper volcanic aquifer	upper volcanic aquifer	About 300 m of densely welded tuff in unsaturated zone. Host rock for repository. In saturated zone where downfaulted to east, south, and west of site.
	Calico Hills Formation	CHn, Calico Hills nonwelded unit	UVC; upper volcanic confining unit	upper volcanic confining unit	Mainly nonwelded tuff with thin rhyolite lavas in northern Yucca Mountain area, vitric in the southwest, and zeolite near or below water table.
	CRATER FLAT GROUP Prow Pass Tuff Bullfrog Tuff Tram Tuff	Cfu, Crater Flat undifferentiated unit	MVA[b]; middle volcanic aquifer	lower volcanic aquifer	Small amount in unsaturated zone; widespread in saturated zone. Variably welded ash-flow tuffs and rhyolite lavas. Commonly zeolitized. Most permeable zones are fracture-controlled.
	Unnamed flow breccia Lithic Ridge Tuff	--	MVD; middle volcanic confining unit	lower volcanic confining unit	Nonwelded tuff, pervasively zeolitized.
	Volcanics of Big Dome	--	LVA[b]; lower volcanic aquifer	?[c]	Lava flow and welded tuff not known at Yucca Mountain.

Table 8-3. Correlation of Generalized Stratigraphy with Unsaturated and Saturated Hydrogeologic Units in the Vicinity of Yucca Mountain (Continued)

Systems and Series	Stratigraphic Unit	Hydrogeologic Units		Saturated Hydrogeologic Units[a]	Comments
		Unsaturated	Saturated		
(Lower Tertiary?)	Older Volcanics	--	LVC; lower volcanic confining unit	?[c]	Nonwelded tuff, pervasively zeolitized. Tuffaceous sediments in lower part.
PERMIAN PENNSYLVANIAN MISSISSIPPIAN- DEVONIAN	Bird Spring Formation Tippipah Limestone	--	UCA; upper carbonate aquifer	?[c]	Limited distribution in saturated zone north and east of Yucca Mountain.
	Eleana Formation. (Chainman Shale)	--	ECU; eleana confining unit	upper clastic confining unit	Argillite (mudstone) and siltstone. Occurrence inferred beneath volcanics of northern Yucca Mountain.
DEVONIAN SILURIAN ORDOVICIAN CAMBRIAN	Devils Gate Limestone, Nevada Formation, Ely Springs Dolomite, Eureka Quartzite, Pogonip Group, Nopah Formation, Dunderberg Shale, Bonanza King Formation, Upper Carrara Formation Lower Carrara Formation	--	LCA; lower carbonate aquifer	Lower carbonate aquifer	Mainly limestone and dolomite with relatively thin shales and quartzites. Major regional aquifer, greater than 5 km thick.
PROTEROZOIC (Upper Precambrian)	Proterozoic Rocks	--	QCU; Precambrian confining unit	Proterozoic confining unit	Quartzite, slate, marble. Fractures commonly healed by mineralization.

Source: Based on Czarnecki et al. 1997 [DIRS 141643], Table 1; Luckey et al. 1996 [DIRS 100465], Figure 7; Montazer and Wilson 1984 [DIRS 100161], p. 9-19

NOTES: SZ = saturated zone; UZ = unsaturated zone.
[a] Luckey et al. 1996 [DIRS 100465], Figure 7.
[b] The middle volcanic aquifer in this table correlates to the lower aquifer of Luckey et al. 1996 [DIRS 100465]. The lower aquifer in this table correlates with volcanics of Big Dome, which is not addressed by Luckey et al. 1996 [DIRS 100465] because it is not recognized at Yucca Mountain.

[c] Shown on Figure 7 in Luckey et al. 1996 [DIRS 100465] as a "?" because the units have not been confirmed to be present or absent in the vicinity of Yucca Mountain.

Table 8-4. Estimated Apparent Mean Hydraulic Conductivity Values from Single-Borehole Tests

Borehole	Apparent Mean Hydraulic Conductivity (m/d)					Reference
	Upper Volcanic Aquifer	Upper Volcanic Confining Unit	Lower Volcanic Aquifer	Lower Volcanic Confining Unit	Carbonate Aquifer	
USW H-1			4.3×10^{-1}	5.5×10^{-6}		Rush et al. 1984 [DIRS 101054]
USW H-3			$<3.7 \times 10^{-3}$	$<3.2 \times 10^{-3}$		Thordarson et al. 1985 [DIRS 105670], Table 3
USW H-4			4.3×10^{-1}	1.1×10^{-1}		Whitfield et al. 1985 [DIRS 101067] , Table 7, p. 20 to 28
USW H-5			6.0×10^{-1}			Robison and Craig 1991 [DIRS 101286]
USW H-6			8.0×10^{-1}	1.8×10^{-4}		Craig and Reed 1991 [DIRS 101206] , Table 4
USW G-2		3.5×10^{-2} [a]				O'Brien 1998 [DIRS 101278] , Table 16
USW G-4			1.4			Lobmeyer 1986 [DIRS 101050] , Table 2
UE-25 b#1		2.6×10^{-1}	4.9×10^{-1}	$<1.0 \times 10^{-4}$		Lahoud et al. 1984 [DIRS 101049], p. 39; Moench 1984 [DIRS 148783]
C-Wells Complex		2.0×10^{-2}	7.0×10^{-2}			Geldon 1996 [DIRS 100396]; multiple well test
UE-25 p#1			3.3×10^{-2}	5.8×10^{-3}	1.9×10^{-1}	Craig and Robison 1984 [DIRS 101040]
USW WT-10	19 [c]					O'Brien 1997 [DIRS 101277] , Table 3, p. 9 to 12
UE-25 WT#12	1.3×10^{-1} [d]	1.3×10^{-1} [d]				O'Brien 1997 [DIRS 101277] , Table 8, p. 14 to 23
UE-25 J-13	1.0	1.2×10^{-1} [e]	7.6×10^{-3}	2.6×10^{-3} [f]		Thordarson 1983 [DIRS 101057], Table 12, p. 22 to 50

DTN: MO0312SEPSDAMH.000 [DIRS 166551]

Source: Adapted from Luckey et al. 1996 [DIRS 100465], Table 4

NOTES: Question marks imply not knowing how much of the reported transmissivity should be allocated to the UVA or UVCU.

= no data; < = less than.

[a] Although the top 3 m of the water column in Borehole USW G-2 were in the upper volcanic aquifer, the upper volcanic confining unit (saturated interval of 256 m) is considered to be the interval tested.

[c] Average of three tests.

[d] Of the saturated interval tested in Borehole UE-25 WT#12, 41 m were completed in the upper volcanic aquifer and 12 m were completed in the upper volcanic confining unit. See discussion in text.

[e] Average determined from three values from two tests. (Thordarson 1983, Table 12 [DIRS 101057]).

[f] Includes part of the lower volcanic aquifer.

Table 8-5. Results from Hydraulic Testing at the Alluvial Testing Complex

Parameter	Value	Units
Transmissivity from single-hole hydraulic testing	300	ft^2/d
Hydraulic Conductivity from single-hole hydraulic testing	0.67	ft/d
Transmissivity from cross-hole hydraulic testing	3,300	ft^2/d
Hydraulic conductivity from cross-hole hydraulic testing	7.5	ft/d
Storativity from cross-hole hydraulic testing	0.00045	
Specific Storage from cross-hole hydraulic testing	0.000001031	ft^{-1}
Approximate qualitative direction of max. principal horizontal hydraulic conducitivity	NE-SW	
Well efficiency of NC-EWDP-19D1	9.1	%
Upper limit of leakage from screens #5, #6, and #7 into screen #4 when pumping screen #4	23	%
Barometric Efficiency of alluvium at NC-EWDP-19D1	56.54	%
Total porosity from Specific Storage and Barometric Efficiency	40.7	%
Maximum total porosity from grain-size distributions	33	%

Source: GS031008312316.002 [DIRS 166523]

Table 8-6. Water Level Information for Boreholes and Borehole Intervals Monitored from 1985 to 1995

Borehole	Minimum (m)	Maximum (m)	Range (m)	Mean (m)	Median (m)	Standard Deviation (m)	Sample Size
USW WT-1	729.98	730.50	0.52	730.35	730.35	0.092	128
USW WT-2	730.14	730.81	0.67	730.65	730.70	0.128	106
UE-25 WT#3	729.41	729.85	0.44	729.64	729.70	0.126	119
UE-25 WT#4	730.28	731.17	0.89	730.78	730.81	0.118	131
UE-25 WT#6	1,033.29	1,036.09	2.80	1,034.60	1,034.52	0.553	117
USW WT-7	775.47	775.99	0.52	775.83	775.85	0.096	113
USW WT-10	775.56	776.21	0.65	776.00	776.00	0.114	132
USW WT-11	730.21	730.81	0.60	730.66	730.69	0.099	119
UE-25 WT#12	729.11	729.58	0.47	729.47	729.48	0.074	123
UE-25 WT#13	728.53	729.43	0.90	729.11	729.14	0.119	118
UE-25 WT#14	729.29	729.98	0.69	729.68	729.69	0.073	135
UE-25 WT#15	728.98	729.42	0.44	729.22	729.22	0.070	124
UE-25 WT#16	737.82	738.57	0.75	738.27	738.29	0.147	123
UE-25 WT#17	729.45	729.84	0.39	729.70	729.72	0.083	117
UE-25 WT#18	730.52	730.92	0.40	730.75	730.76	0.095	38
UE-25 b#1, upper interval	730.48	730.79	0.31	730.65	730.63	0.065	99
UE-25 b#1, lower interval	728.52	730.25	1.73	729.67	729.77	0.425	67
UE-25 p#1	751.92	752.69	0.77	752.44	752.49	0.161	120
USW VH-1	779.30	779.60	0.30	779.44	779.45	0.048	147
USW G-2	1,019.58	1,020.56$_a$	0.98	1,020.17	1,020.12	0.241	28
USW G-3	729.96	730.83	0.87	730.50	730.51	0.169	113
UE-25 J-11	732.09	732.40	0.31	732.21	732.20	0.055	71
UE-25 J-12	727.81	728.15	0.34	727.93	727.94	0.053	100
UE-25 J-13	728.30	728.69	0.39	728.44	728.44	0.065	121
USW H-1, tube 1	785.00	786.05	1.05	785.49	785.49	0.272	101
USW H-1, tube 2	735.67	736.28	0.61	735.97	735.95	0.161	75
USW H-1, tube 3	730.35	730.81	0.46	730.60	730.62	0.098	108
USW H-1, tube 4	730.51	731.04	0.53	730.85	730.90	0.126	124
USW H-3, upper interval	731.07	731.93	0.86	731.52	731.41	0.287	128
USW H-3, lower interval	747.39	759.61	12.22	755.91	756.80	3.098	59
USW H-4, upper interval	730.20	730.52	0.32	730.40	730.40	0.061	128
USW H-4, lower interval	730.18	730.83	0.65	730.51	730.52	0.108	101
USW H-5, upper interval	774.96	775.72	0.76	775.46	775.47	0.139	106
USW H-5, lower interval	774.95	775.86	0.91	775.62	775.64	0.186	54

Table 8-6. Water Level Information for Boreholes and Borehole Intervals Monitored from 1985 to 1995 (Continued)

Borehole	Minimum (m)	Maximum (m)	Range (m)	Mean (m)	Median (m)	Standard Deviation (m)	Sample Size
USW H-6, upper interval	775.83	776.20	0.37	776.02	776.03	0.087	118
USW H-6, lower interval	775.71	776.08	0.37	775.94	775.95	0.070	79

DTN: GS960908312312.010 [DIRS 105063]

Source: Adapted from Graves et al. 1997 [DIRS 101046], Table 2

NOTE: [a] The water level in Borehole USW G-2 has been declining since the borehole was completed on 10-24-81. On 11-10-81, the water level elevation was 1,031.82 m; on 09-17-82, it was 1,028.84 m (Robison et al. 1988 [DIRS 105536], p. 85 to 86). Range of water-level change since 11-01-81 is 12.24 m.

Table 8-7. Vertical Head Differences in Monitoring Boreholes in the Yucca Mountain Area

Borehole	Open Interval (m below land surface)	Potentiometric Level (m above sea level)	Head Difference deepest - shallowest intervals (m)	Source Data	Remarks
USW H-1 tube 4	573-673	730.94	54.7	GS930408312312.015 [DIRS 148665]	1991 mean level Luckey et al. 1996 [DIRS 100465], Table 3
USW H-1 tube 3	716-765	730.75		GS930408312312.015 [DIRS 148665]	1991 mean level Luckey et al. 1996 [DIRS 100465], Table 3
USW H-1 tube 2	1097-1123	736.06		GS930408312312.015 [DIRS 148665]	1991 mean level Luckey et al. 1996 [DIRS 100465], Table 3
USW H-1 tube 1	1783-1814	785.58		GS930408312312.015 [DIRS 148665]	1991 mean level Luckey et al. 1996 [DIRS 100465], Table 3
USW H-3 upper	762-1114	731.19	28.9	GS980308312312.004 [DIRS 155272]	1996 mean level Graves (1998 [DIRS 155411], p. 59)
USW H-3 lower	1114-1219	760.07		GS980308312312.004 [DIRS 155272]	1996 mean level Graves (1998 [DIRS 155411], p. 59)
USW H-4 upper	525-1188	730.49	0.1	GS930408312312.015 [DIRS 148665]	1991 mean level Luckey et al. 1996 [DIRS 100465], Table 3
USW H-4 lower	1188-1219	730.56		GS930408312312.015 [DIRS 148665]	1991 mean level Luckey et al. 1996 [DIRS 100465], Table 3
USW H-5 upper	708-1091	775.43	0.2	GS930408312312.015 [DIRS 148665]	1991 mean level Luckey et al. 1996 [DIRS 100465], Table 3
USW H-5 lower	1091-1219	775.65		GS930408312312.015 [DIRS 148665]	1991 mean level Luckey et al. 1996 [DIRS 100465], Table 3
USW H-6 upper	533-752	775.99	2.2	GS930408312312.015 [DIRS 148665]	1991 mean level Luckey et al. 1996 [DIRS 100465], Table 3
USW H-6 lower	752-1220	775.91		GS930408312312.015 [DIRS 148665]	1991 mean level Luckey et al. 1996 [DIRS 100465], Table 3
USW H-6	1193-1220	778.18		GS931008312312.025 [DIRS 148668]	1/84-5/84 mean level Luckey et al. 1996 [DIRS 100465], Table 3
UE-25 b #1 upper	488-1199	730.71	-1.0	GS930408312312.015 [DIRS 148665]	1991 mean level Luckey et al. 1996 [DIRS 100465], Table 3
UE-25 b #1 lower	1199-1220	729.69		GS930408312312.015 [DIRS 148665]	1990-91 mean level

Table 8-7. Vertical Head Differences in Monitoring Boreholes in the Yucca Mountain Area (Continued)

Borehole	Open Interval (m below land surface)	Potentiometric Level (m above sea level)	Head Difference deepest - shallowest intervals (m)	Source Data	Remarks
UE-25 p#1 (volcanic)	384-500	729.90	21.4	GS920408312314.009 [DIRS 148168]	Luckey et al. 1996 [DIRS 100465], Table 3
UE-25 p#1 (carbonate)	1297-1805	751.26		GS920408312314.009 [DIRS 148168]	Luckey et al. 1996 [DIRS 100465], Table 3
UE-25 c#3	692-753	730.22	0.4	GS930408312312.015 [DIRS 148665]	1990 mean level
UE-25 c#3	753-914	730.64		GS930408312312.015 [DIRS 148665]	Luckey et al. 1996 [DIRS 100465], Table 3 1990 mean level
USW G-4	615-747	730.3	-0.5	MO0008WTRALTG4.000 [DIRS 155456]	Luckey et al. 1996 [DIRS 100465], Table 3 Luckey et al. 1996 [DIRS 100465], Table 3
USW G-4	747-915	729.8		MO0008WTRALTG4.000 [DIRS 155456]	Luckey et al. 1996 [DIRS 100465], Table 3
UE-25 J -13 upper	282-451	728.8	-0.8	GS930408312132.007 [DIRS 129625]	Luckey et al. 1996 [DIRS 100465], Table 3
UE-25 J -13	471-502	728.9		GS930408312132.007 [DIRS 129625]	Luckey et al. 1996 [DIRS 100465], Table 3
UE-25 J -13	585-646	728.9		GS930408312132.007 [DIRS 129625]	Luckey et al. 1996 [DIRS 100465], Table 3
UE-25 J -13	820-1063	728.0		GS930408312132.007 [DIRS 129625]	Luckey et al. 1996 [DIRS 100465], Table 3
NC-EWDP-1DX (shallow)	WT-419	786.8	-38.0	MO0112DQRWLNYE.017 [DIRS 157186], MO0112DQRWLNYE.024 [DIRS 157192]	5/99-2/00
NC-EWDP-1DX (deep)	658-683	748.8		MO0112DQRWLNYE.024 [DIRS 157192], MO0112DQRWLNYE.017 [DIRS 157186]	8/99-2/00
NC-EWDP-2D (volcanic)	WT-493	706.1	7.2	MO0112DQRWLNYE.020 [DIRS 157199], MO0112DQRWLNYE.024 [DIRS 157192]	1/99
NC-EWDP-2DB (carbonate)	820-937	713.3		MO0112DQRWLNYE.020 [DIRS 157199], MO0112DQRWLNYE.025 [DIRS 157193]	11/15/00-11/22/00
NC-EWDP-3S probe 2	103-129	719.8	-1.5	MO0112DQRWLNYE.015 [DIRS 157200], MO0112DQRWLNYE.019 [DIRS 157188], MO0111DQRWLNYE.003 [DIRS 157173], MO0112DQRWLNYE.022 [DIRS 157190]	5/06/99-12/06/00
NC-EWDP-3S probe 3	145-168	719.4		MO0112DQRWLNYE.015 [DIRS 157200], MO0112DQRWLNYE.019 [DIRS 157188], MO0111DQRWLNYE.003 [DIRS 157173], MO0112DQRWLNYE.022 [DIRS 157190]	5/06/99-12/06/00
NC-EWDP-3D	WT-762	718.3		MO0112DQRWLNYE.024 [DIRS 157192], MO0112DQRWLNYE.016 [DIRS 157185]	3/99-8/99

Table 8-7.   Vertical Head Differences in Monitoring Boreholes in the Yucca Mountain Area (Continued)

Borehole	Open Interval (m below land surface)	Potentiometric Level (m above sea level)	Head Difference deepest - shallowest intervals (m)	Source Data	Remarks
NC-EWDP-4PA	124-148	717.9	5.7	MO0112DQRWLNYE.025 [DIRS 157193], MO0112DQRWLNYE.005 [DIRS 157175]	1/13/00-10/26/00
NC-EWDP-4PB	225-256	723.6		MO0112DQRWLNYE.025 [DIRS 157193], MO0112DQRWLNYE.006 [DIRS 157176]	1/21/00-10/26/00
NC-EWDP-9SX probe 1	27-37	766.7	0.1	MO0112DQRWLNYE.011 [DIRS 157181], MO0112DQRWLNYE.019 [DIRS 157188], MO0111DQRWLNYE.004 [DIRS 157174], MO0112DQRWLNYE.021 [DIRS 157189]	5/13/99-12/06/00
NC-EWDP-9SX probe 2	43-49	767.3		MO0112DQRWLNYE.011 [DIRS 157181], MO0112DQRWLNYE.019 [DIRS 157188], MO0111DQRWLNYE.004 [DIRS 157174], MO0112DQRWLNYE.021 [DIRS 157189]	5/13/99-12/06/00
NC-EWDP-9SX probe 4	101-104	766.8		MO0112DQRWLNYE.011 [DIRS 157181], MO0112DQRWLNYE.019 [DIRS 157188], MO0111DQRWLNYE.004 [DIRS 157174], MO0112DQRWLNYE.021 [DIRS 157189]	5/13/99-12/06/00
NC-EWDP-12PA	99-117	722.9	2.2	MO0112DQRWLNYE.025 [DIRS 157193], MO0112DQRWLNYE.010 [DIRS 157180]	4/18/00-11/15/00
NC-EWDP-12PB	99-117	723.0		MO0112DQRWLNYE.025 [DIRS 157193], MO0112DQRWLNYE.012 [DIRS 157182]	4/18/00-11/15/00
NC-EWDP-12PC	52-70	720.7		MO0112DQRWLNYE.025 [DIRS 157193], MO0112DQRWLNYE.013 [DIRS 157183]	4/27/00-11/15/00
NC-EWDP-19P	109-140	707.5	5.3	MO0112DQRWLNYE.025 [DIRS 157193], MO0112DQRWLNYE.014 [DIRS 157184]	3/13/00-6/17/00
NC-EWDP-19D	106-433	712.8		MO0112DQRWLNYE.025 [DIRS 157193], MO0112DQRWLNYE.018 [DIRS 157187]	6/14/00-6/22/00

Source: USGS 2001 [DIRS 157611], Table 6-1

NOTE: Negative value indicates downward gradient.

Table 8-8. Heat Flows Calculated for Deep Boreholes at Yucca Mountain

Borehole	Heat Flow (mW/m^2)	Linear segment Depth (m)	Remarks
UE-25 b#1	23-40 [a]	1000-1200	Convection Effects
UE-25 J#13	(UZ 66) [b]	--	SZ-ND, pumping effects
UE-25 p#1	(UZ 62)	--	SZ-ND, uphole flow
USW G-1	53 [a]	1067-1697	--
USW G-2	53-65	750-1250	Downhole flow
USW G-3	36	1050-1360	Uphole flow?
USW G-4	(UZ-34)	--	SZ-ND, uphole flow
USW H-1	54	1000-1830	--
USW H-3	32	975-1190	Uphole flow (slight)
USW H-4	24-45	900-1220	Convection effects
USW H-5	27-50	1100-1200	Large convection effects
USW H-6	50-65	825-1210	See discussion in text

DTN: MO0312SEPSDHFC.000 [DIRS 166381]

Source: Based on Sass et al. 1988 [DIRS 100644]

Notes: ND = Not determined.
[a] Where a range is given, the smaller value is apparent heat flow, based on least-squares gradient; the larger value of a range and single values are probably conductive, based on gradients of linear segments.
[b] UZ denotes heat-flow value for interval above water table.

Table 8-9. Annual Groundwater Discharges from Wells UE-25 J-12 and UE-25 J-13 (1983 to 1997)

Well	Year	Annual Discharge (m³)	Annual Discharge (acre-ft)
Well UE-25 J-12	1983	93,075	75.39
	1984	93,440	75.69
	1985	98,915	80.12
	1986	108,040	87.51
	1987	77,015	62.38
	1988	77,380	62.68
	1989	127,020	102.89
	1990	117,895	95.49
	1991	131,035	106.14
	1992	47,450	38.43
	1993	94,535	76.57
	1994	181,405	146.94
	1995	135,050	109.39
	1996	162,790	131.86
	1997	63,510	51.44
Well UE-25 J-13	1983	174,105	141.03
	1984	155,125	125.65
	1985	104,025	84.26
	1986	66,065	53.51
	1987	123,370	99.93
	1988	96,360	78.05
	1989	64,240	52.03
	1990	77,380	62.68
	1991	62,415	50.56
	1992	99,645	80.71
	1993	158,410	128.31
	1994	159,870	129.49
	1995	184,325	149.30
	1996	104,390	84.55
	1997	123,005	99.63

Source: Adapted from Tucci and Faunt 1999 [DIRS 145962], Table 1

Table 8-10. Annual Groundwater Withdrawals from Basin 227A (1961 to 1992)

Year	Annual Withdrawal (m^3)	Annual Withdrawal (acre-ft)
1961	113,580	92
1962	230,865	187
1963	691,359[a]	560[a]
1964	691,359[a]	560[a]
1965	691,359[a]	560[a]
1966	691,359[a]	560[a]
1967	691,359[a]	560[a]
1968	N/A	N/A
1969	N/A	N/A
1970	N/A	N/A
1971	N/A	N/A
1972	N/A	N/A
1973	N/A	N/A
1974	N/A	N/A
1975	N/A	N/A
1976	N/A	N/A
1977	N/A	N/A
1978	N/A	N/A
1979	N/A	N/A
1980	N/A	N/A
1981	140,741	114
1982	70,370	57
1983	267,902	217
1984	249,383	202
1985	202,469	164
1986	174,074	141
1987	200,000	162
1988	174,074	141
1989	191,358	155
1990	196,297	159
1991	193,827	157
1992	146,914	119

Source: Adapted from CRWMS M&O 2000 [DIRS 145966], Table 4.10

NOTES: [a] Data represent annual average values, as reported by Young 1972 [DIRS 103023].

N/A = not available

Table 8-11. Basin 227A (Including Jackass Flats) Pumping Summary (1993 to 1997)

Year	Wells (UE-25 J-12 + UE-25 J-13) m³/yr. (acre-ft/yr)	C-hole Wells m³/yr. (acre-ft/yr)	Total (UE-25 J-12 + UE-25 J-13 + C-hole Wells) m³/yr. (acre-ft/yr)	YMP Pumpage m³/yr. (acre-ft/yr)	Other Pumpage[a, b] m³/yr. (acre-ft/yr)
1993	253,087 (205)	0	253,087 (205)	98,766 (80)	154,321 (125)
1994	341,976 (277)	0	341,976 (277)	93,827 (76[c])	249,383 (202)
1995	319,754 (259)	23,457 (19)	343,210 (278)	139,506 (113)	203,704 (165)
1996[d]	306,173 (248)	227,161 (184)	533,334 (432)	309,877 (251)	223,457 (181)
1997	186,420 (151)	238,272 (193)	424,692 (344)	316,050 (256)	108,642 (88)
Average	281,482 (228)	97,450 (79)	379,013 (307)	191,358 (155)	187,655 (152)

Source: Adapted from CRWMS M&O 2000 [DIRS 145966], Table 4.11

NOTES: [a] Other pumpage = (Total pumpage of wells UE-25 J-12 + UE-25 J-13 + C-hole Wells) – (Yucca Mountain Project pumpage)

[b] Other pumpage is diverted for use on the Nevada Test Site.

[c] Value includes 0.63 acre-ft pumpage from well USW VH-1 in Crater Flat.

[d] The 1996 values in this table differ somewhat from the 1996 values presented in Table 8-9 because there are differences in values reported in their respective sources. However, this difference does not impact the conclusions presented in this section.